IIT Madras

CONSEC24

September 25 – 27, 2024 | Chennai, India | www.consec24.com

Concrete under Severe Conditions

– Environment & Loading

Proceedings of

10th International Conference (CONSEC 24)

Chennai, India

September 25-27, 2024

Centre of Excellence on Technologies for Low Carbon & Lean Construction

Edited by
Radhakrishna G. Pillai

Local Organizing Committee

Radhakrishna G. Pillai, IIT Madras — Chair
Ravindra Gettu, IIT Madras
Manu Santhanam, IIT Madras
Piyush Chaunsali, IIT Madras
Surender Singh, IIT Madras
Keerthana Kirupakaran, IIT Madras
Aslam Kunhi Mohamed, IIT Madras

Steering Board

International Advisory Committee

International Scientific Committee

Proceedings Editing Team

Anupama V A
Bipina T V
Jayasree C
Keerthy V T
Krishnan Unni
Menchaca Ballinas L. E.
Mansi Thakur
Nerswn Basumatary
Nidhi M
Nilakanmani M
Ramakrishna S
Resmi G
Saikat Das
Sai Sri K V C
Saranya P
Saranyadevi D
Shefali Aggarwal
Sreelakshmi S
Sriram Pradeep
Tamali Bhowmik
Umashankar Biswal

Conference Secretariat

Prof. Radhakrishna G Pillai
BTCM Office, BSB Room 205
Department of Civil Engineering
Indian Institute of Technology Madras
Chennai, Tamil Nadu, 600 036, India
Email: CONSEC24@civil.iitm.ac.in

Preface

The International Conference on CONcrete under SEvere Conditions -Environmental & Loading (CONSEC) covers the advancements in design, construction, testing, and preservation of various construction materials and systems exposed to severe environmental and loading conditions. Previous CONSECs were held in Japan (1995), Norway (1998), Canada (2001), South Corea (2004), France (2007), Mexico (2010), China (2013), Italy (2016) and Brazil (2019). The Centre of Excellence on Technology for Low-Carbon and Lean Construction (TLC2) at the Indian Institute of Technology Madras (IITM) feels proud and privileged in organizing the 10th CONSEC 2024 (CONSEC24) in Chennai, India. CONSEC24 provides a singular platform for exchanging ideas and presenting findings in designing, constructing, and conserving reinforced concrete structures, experiencing severe conditions.

CONSEC24 aims to present the state-of-the-art themes related to Advanced materials in severe conditions, Lab/field testing and characterization, Repair and strengthening materials and methods, Damage, deterioration and transport properties, Service life, reliability, sustainability and resilience, and Special concretes and construction techniques. These selected themes will pose a scenario for joint action among experts in Materials, Construction Management, Structures, Design, Preservation, and Testing. CONSEC24 will provide the grounds for a multidisciplinary dialogue and ideas interchange to cultivate innovation in construction under severe environmental and loading conditions.

The CONSEC24 proceedings assemble 10 plenary talks, 19 keynote talks, and over 200 national and international contributory papers from academia and industry, covering all the 6 themes. I am grateful to the Program committee and Reviewers for their valuable time and feedback, which has significantly contributed to the quality of this conference proceedings. I am also extending my gratitude to all authors for their contribution to the proceedings and thank all participants for attending the conference to make it a grant success.

CONSEC24 **Radhakrishna G Pillai**

Table of contents

Plenary

Keynotes

Contributory papers

Advanced materials for severe conditions

Lab/field testing and characterization

Repair and strengthening materials and methods

Damage, deterioration and transport properties

Service life, reliability, sustainability and resilience

Special concretes and construction techniques

Plenary

Alkali Activated Binders Based on Precursors of Limestone and Recycled Pulverized Concrete

J I. Escalante-Garcia*[1], J Rodríguez-Morales[2], J M Hernández-Bielma[3], P Perez-Cortes[4+]

[1] *Cinvestav Campus Saltillo, Ramos Arizpe, México*
Email: ivan.escalante@cinvestav.edu.mx
[2] *Cinvestav Campus Saltillo, Ramos Arizpe, México*
Email: Juliana.rodriguez@cinvestav.mx
[3] *Cinvestav Campus Saltillo, Ramos Arizpe, México*
Email: josue.hernandez@cinvestav.mx
[3] *Cinvestav Campus Saltillo, Ramos Arizpe, México*
Email: pedro.perez@molins.es

*Corresponding author, + currently at R&D Group Cementos Molins S.A, Spain

ABSTRACT

Limestone (LS) has been a cornerstone in construction and building materials for over 11,000 years, from ancient sites like Göbekli Tepe to Roman lime-based cements. Its ongoing significance is evident in modern Portland cement (PC), where LS is the primary role material, and in recent innovative applications in alternative cements like LC3 and alkali-activated cements (AAC).). This paper explores the role of LS and recycled pulverized hardened concrete (PHC) as promising precursors in AAC, examining their chemistry, strength, and environmental benefits. LS and PHC are highlighted as sustainable alternative cementitious precursors amidst the increasing demand for construction materials driven by population growth. This paper underscores LS versatility, extending from its historical roots to its current and future potential in creating environmentally friendly construction materials.

KEYWORDS*: Limestone; Sustainability; Construction materials, Concrete; Alkali Activated Cements*

1. Introduction

Limestone is a sedimentary rock primarily composed of calcium carbonate ($CaCO_3$). On a global scale, carbonate rocks cover 9.4% of ice-free land, as continuous carbonate rocks (Goldscheider, et. al., 2020), (Figure 1A). It is estimated that 20.3 million km^2, accounting for 15.2% of the Earth's land surface, contains carbonate rocks (Rakhimova, 2022). LS has played a crucial role as a fundamental constituent in building materials for millennia. The first uses have been traced to more than 11,600 years ago, as evidenced by discoveries at the archaeological site of Gobekli Tepe (Courland, 2011), where LS carvings and lime-based products were unearthed. The Romans, pioneers in the application of lime-based cements, mixed lime (calcined limestone) with volcanic ash in their constructions, creating enduring structures that have withstood the test of centuries.
Lime based cements remain useful and are durable owing to their "closed loop" nature, where the final reaction product and the starting raw material is $CaCO_3$ (in Fig 1B). However, these cements exhibit slower setting and strength gains and are mostly used in preservation and restoration of cultural heritage (Saba et.al., 2019).

2. Current uses of limestone

Limestone remains an indispensable and versatile mineral with enduring significance in the global contemporary cement and construction industry. A notable application involves its extensive use as aggregates in mortars and concretes. The annual global production of concrete, of about 30,000 million tons (Monteiro et.al., 2017), relies heavily on aggregates, which can constitute up to about 75% of the concrete volume. LS also makes up about 80% of the raw materials to produce clinker of PC, which is

produced in rotary kilns operated at 1450°C using fossil fuels, requiring about 3.5 GJ/t clinker (Juenger et.al., 2019). The cement industry, producing over 4.1 Gt/year, contributes with more than 8% of the anthropogenic CO_2 emissions (Ortega-Zavala et.al., 2019) and the production is expected to grow up to 4.68 Gt/year (Schneider, 2019).

Additional roles of LS are found in the following applications in cements:

- As a supplementary cementitious material, replacing up to 35% of Portland cement (European Comission for Standarization, 2020; Cembureau, 1991); nonetheless, some controversy exists regarding durability aspects when applied in concrete structures (Villagran-Zacardi et.al., 2022).
- As an ingredient (about 15%wt) in sustainable alternative LC3 cements (Scrivener et.al., 2018).
- Incorporated in recent commercialized innovative technologies in Europe, incorporating 50% LS, approximately 30% low-carbon supplementary cementitious materials (SCMs), and 20% clinker (ECOCEM, 2024). These engineer particle size distribution and incorporate dispersants.

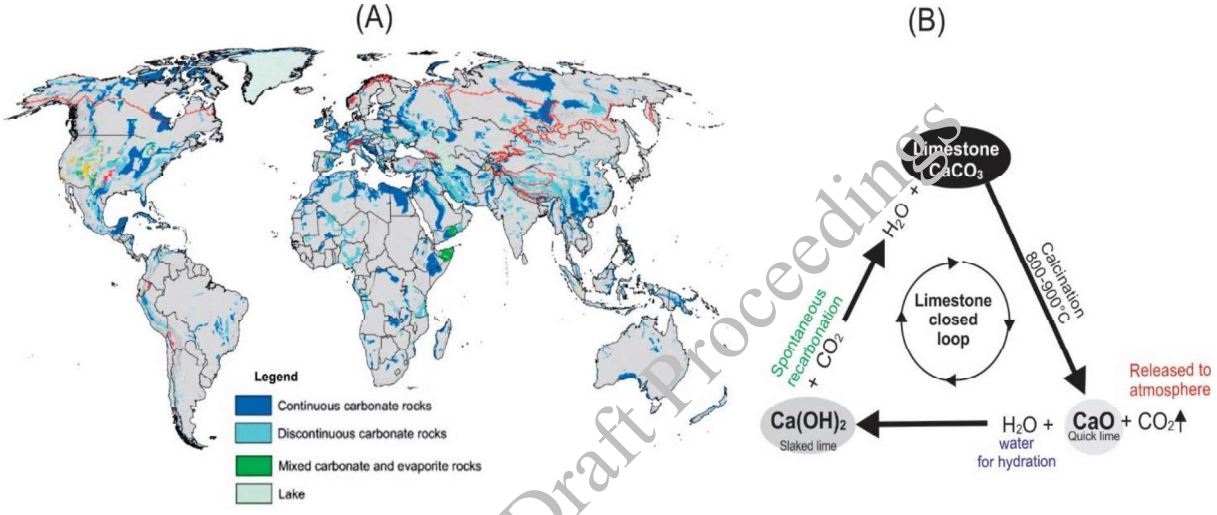

Figure 2. (A) Distribution of carbonate rocks. Modified from (Goldscheider, et. al., 2020 (B) Closed loop of lime (limestone) based cements

Recent developments have included LS into alkali activated cements (AAC). The ensuing exploration outlines the various roles and benefits of LS, with sustainability, performance, and environmental considerations.

3. Limestone in Alkali activated Cements

Alkali activated cements (AAC) rely on an alkaline activator to chemically act on a precursor, forming cementitious reaction products. The most common precursors are aluminosilicates of mineral, synthetic or byproduct origins. The use of precursors like blastfurnace slag dates from 1940 (Purdon, 1940) and gained popularity from the work of Glukhovsky in 1950 (Krivenko, 2017); however, the use of non-calcined LS is more recent.

Limestone has been recently used in AAC combined with several other common precursors in variable amounts. Neat LS based AAC (Ortega-Zavala et.al., 2019) exhibited its chemical reactivity in an alkaline environment; mechanical properties and structural aspects of the reaction products were also discussed. Substitutions of metakaolin (MK) with 20% LS (Yip et.al. 2008) showed limited advantages, while 50% LS rendered lower strengths (Cwirzen et.al., 2014). Combining LS with blast furnace slag showed interesting strength and low alkali consumptions (Sakulich et.al., 2009); nonetheless, the slag availability is limited as it is predominantly consumed by the Portland cement industry. The combination of LS with other waste streams like coal fly ash (Gao et.al., 2015) or waste glass (Menchaca-Ballinas and Escalante-Garcia, 2020) have also shown interesting results.

The ideal AAC should depend on globally abundant and easily accessible raw materials for precursors. LS and MK meet the requirements; LS is also cheap, while MK entails a straightforward calcination process less demanding than Portland cement (i.e. requiring only 0.35 GJ/t clay, Juenger et.al., 2019). The

confluence of these factors renders LS and MK as AAC precursors feasible and highly advantageous. Blends of LS-MK have been statistically studied to optimize strength and sustainability indicators (Perez-Cortes and Escalante-Garcia, 2020a; Perez-Cortes and Escalante-Garcia, 2020b). Numerous recent reviews further describe the use of LS in alkaline cements (Rakhimova, 2022; Ma et.al., 2022; Rashad, 2022, Chan and Zhang, 2023), indicating interest and active research worldwide on the subject.

3.1 Chemistry of CAA involving limestone

In CAA based on neat limestone, it reacts with the alkaline compounds/activators, forming cementitious calcium silicate hydrates ($CaO\text{-}SiO_2\text{-}H_2O$), similar to PC (Ortega-Zavala et.al., 2019). When combined with other precursors, 10% LS behaves as an inert filler (Aboulayt et.al., 2017; Quian and Song, 2015). A chemical interaction has been suggested, in which LS releases Ca^{2+}, influencing the assemblage of cementitious reaction products like calcium carboaluminate phases and possibly calcium (alumino)-silicate hydrates (Yip et.al., 2008; Rakhimova et.al., 2018; Cwirzen et. al., 2014). The molecular structure of MK-based cements showed that the LS introduction modifies the conventional sodium aluminosilicate hydrate ($Na_2O\text{-}Al_2O_3\text{-}SiO_2\text{-}H_2O$) towards ($Na_2O\text{-}(CaO)\text{-}Al_2O_3\text{-}SiO_2\text{-}H_2O$) (Perez-Cortes and Escalante-Garcia, 2020c), preserving its 3D structure and enhancing the strength. Evidently, the LS reactivity towards alkalis is lower compared to other common precursors used in AAC; further research is needed to increase the knowledge of these complex systems.

3.2 Strength and environmental indicators of alkali activated cements with limestone

Optimized AAC of MK-LS, indicated replacing a MK with 30%LS (Perez-Cortes and Escalante-Garcia, 2020a). However, other optimized blends with 60%LS (40%MK) also displayed noteworthy compressive strengths of 56 and 61 MPa after 1 and 28 days, chemical and thermal resistances, with residual strengths >50 MPa after exposures to 0.1 N HCl, 5% $MgSO_4$ (Perez-Cortes and Escalante-Garcia, 2023), or 300°C (Perez-Cortes et.al. 2021). These properties could expand the applications as part of the future toolkit of durable binders. Moreover, such MK-LS exhibited environmental and economic advantages, with 62.9% fewer CO_2 emissions, 14% lower energy consumption and 15.5% cost reduction compared to a PC reference, as shown in Fig 2 (Perez-Cortes and Escalante-Garcia, 2020a). Further increases in LS contents to 80% maintained competitive strengths of 50 MPa (Perez-Cortes and Escalante-Garcia, 2020b), accompanied by even more favorable sustainability indicators.

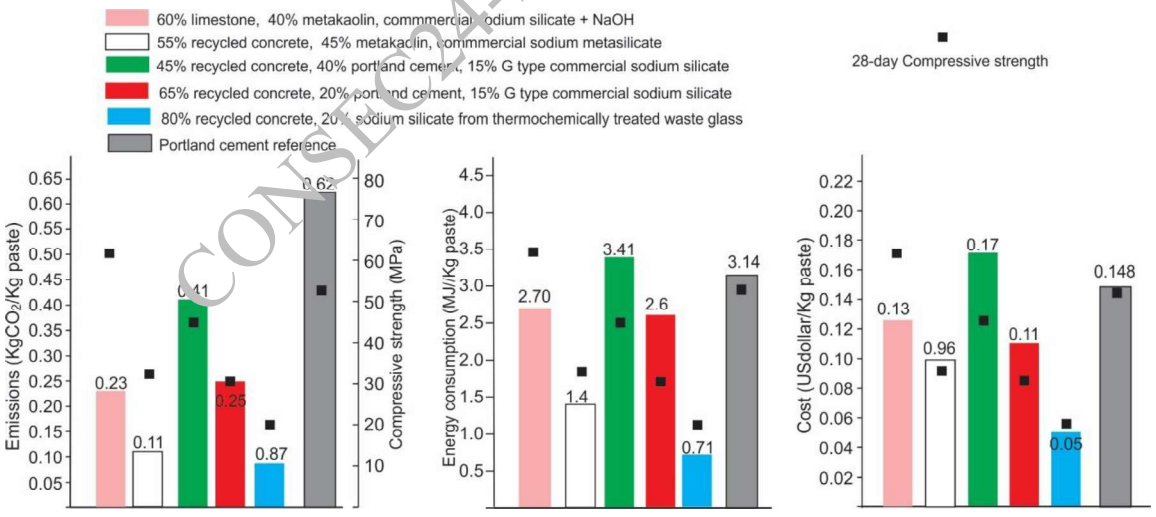

Figure 3. Comparative of various alkali activated cements with a portland cement reference in terms of CO_2 emissions, energy consumption and cost. Data adapted from (Perez-Cortes and Escalante-Garcia, 2020a), (Rodriguez-Morales and Escalante-Garcia, 2024), (Hernandez-Bielma, 2024).

The sustainability of these cements is also influenced by the alkaline activator demand, which increase costs and emissions. An AAC of 100% MK would require up to 25%Na_2O_{eq}; however, replacing MK with 80%LS reduced Na_2O demand to 4% (Perez-Cortes and Escalante-Garcia, 2020b). Similar advantages were reported on one-part type cements combining 49%LS, portland cement and sodium silicates, with lower emissions and similar strengths relative to a Portland cement reference (Santana-Carrillo et.al., 2022).

The environmental benefits associated to LS stem from its exemption of any thermal treatment, saving energy and CO_2 emissions that would otherwise arise from decarbonation and fossil fuels consumption. Additionally, grinding LS rock is less energy demanding than Portland cement.

Table 1. Composition and compressive strength of various concretes prepared with binders of limestone-metakaolin, cured under different thermal regimes. Sand and gravel used were of limestone

Component	Contents in the binder (wt.%)	kg/m^3 in the concrete	Curing Temperature	Compressive strength (Mpa)	
				7 day	28 day
Limestone	60	240	20°C	47	57
Metakaolin	40	160			
%Na_2O*	10.7	42.8			
Limestone	60	240	70°C for 24h, then at 20°C	33	40
Metakaolin	40	160			
%Na_2O*	8.5	34			
Limestone	30	120	20°C	50	68
Metakaolin	60	280			
%Na_2O*	16.9	67.6			

3.3 Limestone-metakaolin cements in concretes.

Table 1 shows properties of concretes based on AAC of MK replaced with 30% and 60% LS (Escalante-Garcia and Perez-Cortes, 2018). These formulations excluded special additives or aggregate granulometry special considerations. The three formulations used 400 kg_{binder}/m^3 with different %Na_2O. High 7 and 28 days compressive strengths were noted even when curing at 20°C; comparable strengths using Portland cement would require higher cement consumption and/or special design considerations. Moreover, concretes with 40%MK-60%LS have demonstrated effective passivation of steel reinforcement (Vazquez-Leal et.al., 2023), rendering these cements promising for structural applications.

4. Recycled concrete as cementitious material

The global concrete production is approximately 30,000 million tons (Monteiro, et al., 2017), its production accounts for ~46 % of all materials extracted from the Earth (Shah et al., 2022), and drives the need for cementitious materials. Construction activities generate construction and demolition wastes (C&DW), either during construction or at the end of the service life of structures, due to obsolescence or unforeseen circumstances. C&DW account for approximately 10,000 Mt/year of solid waste globally, constituting around ~30% of the total solid wastes generated worldwide, with about 35% being landfilled (Chen et al., 2020). C&DW is heterogeneous composition varies depending on infrastructure type, construction materials (e.g. concrete, mortars, bricks, wood, gypsum, etc.), demolition technologies, age of structures, raw materials, regional development, etc. C&DW recycling rates also vary, with more developed countries such as Holland, Denmark and Germany recycling more than 80% of C&DW (Özalp et al., 2016), while highly populated countries like China and India recycle less than 5% (Akhtar and Sarmah, 2018).

Beyond the current use of C&DW as recycled aggregates, to reduce the demand for natural aggregates, this environmental passive can have more added value, as a potential resource as a cementitious material, in line with circular economy trends. Various workers have reported on C&DW of different mineralogy, and in different mixtures with conventional precursors, as alkaline cement precursors (e.g. (Borrachero et al., 2022, (Ahmari et al., 2012, Villaquirán-Caicedo et al., 2021, Komnitsas et al., 2015) in two-part type cements with activators of NaOH or blends of NaOH with commercial sodium silicates.

Table 2 shows various cementitious alternative formulations of one-part type alkaline cements based on recycled pulverized hardened concrete (PHC) formulated with limestone aggregates. Some binders contain PC, are activated using commercial sodium silicates or alternative sodium silicates based on the

thermocheical treatment of waste glass (another global waste stream of about 130 million tons/year). Replacing MK with 55-75% PHC with MK (#1 and 2) resulted in about 30 MPa using commercial activators. For binders of 45%PHC with PC (e.g. #3 and 4) the alternative activator was more effective strengthwise than commercial ones. On the other hand, neat PHC also showed its pottential for activation, as its mixtures with 15-20% of commercial or alternative activators resulted in up to 20 MPa. The microstructures shown in Figure 3 of alkaline binders based on PHC, with MK and with PC, showed relatively dense matrices of reaction cementitious products of various types, in agreement with the strenngths reported.

Figure 2 also compares CO_2 emissions, energy demand and cost of some of PHC based concretes with PC and LS-MK cements. The alterantive waste glass based activator is effective and of low environmental impact and cost, and its combination with PHC is promising.

Table 2. Compressive strength of pastes using pulverized hardened concrete with different supplementary precursors and different alkaline activators

		Supplementary precursor					Curing regime**
	(%) Recycled concrete	Metakaolin	Portland cement	Commercial or synthetic activator	%Na_2O	28-day compressive strength, MPa	
1	55	45		Commercial sodium metasilicate, Ms=1	10	30	60-20°C
2	75	25		Commercial sodium metasilicate, Ms=1	12	28.5	60-20°C
3	45		40	15% of a commercial sodium silicate C type, Ms=3.2	2.9	45.2	20°C
4	45		50	Sodium silicate from waste glass, Ms=3.5	1.2	55.8	20°C
5	85			15% of a commercial sodium silicate Ms=3.2	3.39	16	20
						12	60-20°C
6	80			20% silicate from waste glass, Ms=4	5%	12*	20°C
						19.8	80-20°C

Ms= modulus of sodium silicate
**Increased to 19MPa after 90 days*
*** 60-20°C or 80-20°C indicates the first 24 h curing at 60 or 80°C, then continued at 20°C*

The amount of C&DW beyond the concrete fraction that could be incorporated into AAC is potentially larger, since several C&DW constituents have also been reported as viable precursors in AAC, i.e. ceramic clay bricks, tiles, and glass. Further research is needed to understand the role of such C&DW components.

5. Challenges and perspectives.

The growing global population continues to drive an increased demand of construction materials, and concrete is among the most sustainable alternative among other materials like steel, plastics, glass and aluminium. The global population in urban areas, particularly in less economically developed regions, is anticipated to increase by 52.5% (from 4,378 to 6,679 million from 2020 to 2050 (United Nations, 2018)), which will bring a critical demand for new infrastructure, mandating a strategic approach imbued attended with sustainable development criteria.

While the incorporation of LS and PHC in alkaline cements presents numerous advantages and aligns with contemporary sustainability objectives, challenges persist. The durability of these AAC is an ongoing subject of investigation. However, the reported formation of cementitious products similar to Portland cement and other alkaline cements, allows for an optimistic outlook.

Addressing these challenges requires further research across various domains. The control of rheology and setting times, which impact construction operations, also requires investigation, with promising

possibilities for 3D printing (Perales-Santillan et al, 2024). Additionally, understanding the compatibility of LS and PHC with different alkali activators and precursors for long-term performance remains an ongoing research priority.

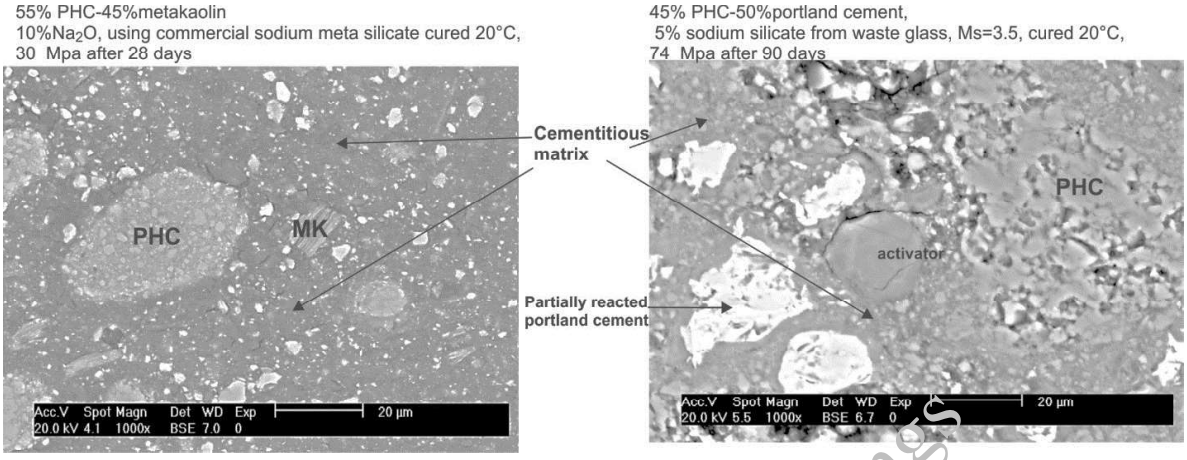

Figure 4. Microstructures of AAC prepared with pulverized hardened concrete, obtained by scanning electron microscopy, backscattered electron images.

6. Conclusions

Historically crucial, limestone remains indispensable in the production of Portland cement and concrete. The use of limestone and limestone based recycled concrete in alkaline cements signifies promising sustainable alternative cements. Further research will enhance the understanding and optimization of these alternative cements, supporting their broader application in sustainable construction.

Acknowledgements

Thanks are due to the grants: (1) 154 SEP-Cinvestav and (2) Conacyt Ciencia de Frontera 2023 CF-2023-G-405. The Conacyt scholarships of Rodríguez-Morales, Hernández-Bielma and Perez-Cortes are also acknowledged

References

Aboulayt, A., Riahi, M., Anis, S., et al. (2009). Mechanical and microstructural characterization of an alkali-activated slag/limestone fine aggregate concrete. Constr. Build. Mater., 23(8), 2951–2957. https://doi.org/10.1016/j.conbuildmat.2009.02.022

Aboulayt, A., Riahi, M., et al.. (2017). Properties of metakaolin-based geopolymer incorporating calcium carbonate. Adv. Powder Technol., 28, 2393–2401. https://doi.org/10.1016/j.apt.2017.06.022

Ahmari, S., Ren, X., Toufigh, V., & Zhang, L. (2012). Production of geopolymeric binder from blended waste concrete powder and fly ash. *Construction and Building Materials*, 35, 718-729.

Akhtar, A., & Sarmah, A. K. (2018). Construction and demolition waste generation and properties of recycled aggregate concrete: A global perspective. *Journal of Cleaner Production*, 186, 262-281.

Borrachero, M. V., Payá, J., Brito, S., Segura, Y. P., Soriano, L., Tashima, M. M., & Monzó, J. M. (2022). Reusing construction and demolition waste to prepare alkali-activated cement. *Materials*, 15(10), 3437

Cembureau, The European Cement Association. (1991). Cement Standards of the World, Brussels, Belgium. Retrieved from http://www.cembureau.eu (Accessed: 20 January 2024).

Chan, C.L., Zhang, M. (2023). Effect of limestone on engineering properties of alkali-activated concrete: A review. Const BuildMater, 362, 129709.

Chen, K., Wang, J., Yu, B., Wu, H., & Zhang, J. (2021). Critical evaluation of construction and demolition waste and associated environmental impacts: A scientometric analysis. *Journal of Cleaner Production*, 287, 125071.

Courland, R. (2011). Concrete Planet. Prometheus Books, New York.

Cwirzen, A., Provis, J.L., Penttala, V., Habermehl-Cwirzen, K. (2014). The effect of limestone on sodium hydroxide-activated metakaolin-based geopolymers. *Construction and Building Materials*., 66, 53–62.

ECOCEM Global, 2024. ACT The next generation of low carbon cement technology, https://www.ecocemglobal.com/act/ (accessed 10 February 2024).

Escalante-Garcia, J. I., Perez-Cortes, P., Hydraulic cement based on alkaline earth carbonates like limestone and calcined clay and process to make pastes, mortar and concretes of high performance (in Spanish), Patent application MX/a/2018/ 016140

European Committee for Standardization. (2000). Cement - part 1: composition, specifications and conformity criteria for common cements. EN 197-1, Brussels.

Gao, X., Yu, Q.L., Brouwers, H.J.H. (2015). Properties of alkali activated slag–fly ash blends with limestone addition. *Cement and Concrete Composites*., 59, 119–128.

Goldscheider, N., Chen, Z., Auler, A.S., Bakalowicz, M., Broda, S., Drew, D., Veni, G. (2020). Global distribution of carbonate rocks and karst water resources. *Hydrogeology Journal*

Hernandez-Bielma, J.M. (2024), Pulverized recycled concrete as a precursor in alkaline cements with metakaolin, Progress 1st progress report of Ph.D. thesis, Cinvestav Saltillo

Juenger, M.C.G., Snellings, R., Bernal, S.A. (2019). Supplementary cementitious materials: New sources, characterization, and performance insights. *Cement Concrete Research*, 122, 257-273.

Komnitsas, K., Zaharaki, D., Vlachou, A., Bartzas, G., & Galetakis, M. (2015). Effect of synthesis parameters on the quality of construction and demolition wastes (CDW) geopolymers. *Advanced Powder Technology*, 26(2), 368-376.

Krivenko, P. (2017). Why Alkaline Activation – 60 Years of the Theory and Practice of Alkali-Activated Materials.*Journal of Ceramic Science and Technology*, 08(3), 323-334. DOI: 10.4416/JCST2017-00042

Ma, J., Wang, T., et al. (2022). A state-of-the-art review on the utilization of calcareous fillers in alkali-activated cement. *Construction and Building Materials* .357, 129348.

Menchaca-Ballinas, L.E., Escalante-García, J.I. (2020). Limestone as aggregate and precursor in binders of waste glass activated by CaO and NaOH. *Construction and Building Materials*.262, 120013.

Monteiro, P. J.M., Miller S A, Horvath A. (2017). Towards Sustainable Concrete. Nature Materials, 16(7), 698–99.

Ortega-Zavala, D., Santana-Carrillo, J.L., Burciaga-Díaz, O., Escalante-Garcia, J.I. (2019). An Initial Study on Alkali Activated Limestone Binders. *Cement Concrete Research*, 120, 267–78.

Özalp, F., Yılmaz, H. D., Kara, M., Kaya, Ö., & Sahin, A. (2016). Effects of recycled aggregates from construction and demolition wastes on mechanical and permeability properties of paving stone, kerb and concrete pipes. Construction and Building Materials, 110, 17-23.

Perales-Santillan, M.E., Díaz-Aguilera, J.H., Mendoza-Rangel, J.M. (2024). Evaluation of the rheological behavior for alkaline-activated cements of metakaolin and limestone for its potential application in 3D printing. Iran J Sci Technol Trans Civ Eng.

Perez-Cortes, P., Escalante-Garcia, J.I. (2020a). Alkali activated metakaolin with high limestone contents – Statistical modeling of strength and environmental and cost analyses. *Cement Concrete Composites*, 106, 103450.

Perez-Cortes, P., Escalante-Garcia, J.I. (2020b). Design and optimization of alkaline binders of limestone-metakaolin: a comparison of strength, microstructure, and sustainability with Portland cement and geopolymers. *Journal of Cleaner Production* 273, 123118.

Perez-Cortes, P., Escalante-Garcia, J.I. (2020c). Gel composition and molecular structure of alkali-activated metakaolin-limestone cements. *Cement Concrete Research*., 137, 106211.

Perez-Cortes P., Cabrera-Luna K., Escalante-Garcia J.I., (2021). Alkali-activated limestone/metakaolin exposed to high temperatures: structural changes. *Cement Concrete Composites* 122, 104147.

Perez-Cortes, P., Escalante-Garcia, J.I. (2023). Effect of the Limestone Content on the Durability of Alkali-Activated Limestone-Metakaolin Subjected to Acidic and Sulfate Environments, in Proc 75th RILEM Annual Week. RILEM Bookseries, Vol 40, Escalante-Garcia J.I. et al. (eds)

Purdon, A. (1940). The action of alkalis on blastfurnace slag. Journal of the Society of Chemical Industry - Transactions and Communications, 59, 191-202.

Qian, J., Song, M. (2015). Study on influence of limestone powder on the fresh and hardened properties of early age metakaolin-based geopolymer. In: K. Scrivener, A. Favier (Eds.), Calcined Clays for Sustainable Concrete: Proc 1st Int Conf on Calcined Clays for Sustainable Concrete, Springer, Dordrecht, pp. 253–259.

Rakhimova, N.R., Rakhimov, R.Z., Morozov, V.P., Gaifullin, A.R., Potapova, L.I., Gubaidullina, A.M., Osin, Y.N. (2018). Marl-based geopolymers incorporated with limestone: a feasibility study. J. Non-Cryst. Solids, 492, 1–10.

Rakhimova, N. (2022). Calcium and/or magnesium carbonate and carbonate-bearing rocks in the development of alkali-activated cements – A review. *Construction and Building Materials*, 325, 126742.

Rashad, A.M. (2022). Effect of limestone powder on the properties of alkali-activated materials – A critical overview. *Construction and Building Materials*, 356, 129188.

Rodriguez-Morales, J., Burciaga-Diaz, O., Gómez-Zamorano, L.Y., & Escalante-Garcia, J. I. (2024). "Transforming construction and demolition waste concrete as a precursor in sustainable cementitious materials: An innovative recycling approach". *Resources, Conservation & Recycling*. 204 (2024) 107474.

Saba, M., Hernandez-Romero, L.N., Lizarazo-Marriaga, J., Quiñones-Bolaños, E.E. (2019). Petrographic of limestone cultural heritage as the basis of a methodology to rock replacement and masonry assessment: Cartagena de Indias case of study. *Case Studies in Construction Materials,* 11, e00281.

Sakulich, A.R., Anderson, E., Schauer, C., Barsoum, M.W. (2009). Mechanical and microstructural characterization of an alkali-activated slag/limestone fine aggregate concrete. *Construction and Building Materials*, 23, 2951–2957.

Santana-Carrillo, J.L., Burciaga-Díaz, O., Escalante-Garcia, J.I. (2022). Blended limestone-Portland cement binders enhanced by waste glass based and commercial sodium silicate - Effect on properties and CO2 emissions. *Cement and Concrete Composites*., 126, 104364.

Schneider, M. (2019). The cement industry on the way to a low-carbon future. Cem Concr Res, 124, 105792.

Scrivener, K., Martirena, F., Bishnoi, S., Maity, S. (2018). Calcined clay limestone cements (LC3). *Cement and Concrete Research*, 114, 49-56.

Shah, I. H., Miller, S. A., Jiang, D., & Myers, R. J. (2022). Cement substitution with secondary materials can reduce annual global CO2 emissions by up to 1.3 gigatons. *Nature communications,* 13(1), 5758.

United Nations. (2018). World Urbanization Prospects. Department of Economic and Social Affairs Population Dynamics. Retrieved from https://population.un.org/wup/dataquery/2018.

Vázquez Leal, F.R., Mendoza-Rangel, J.M., Andrade, C., Perez-Cortes, P., Escalante-García, J.I. (2023). Electrochemical Behaviour Of Steel Embedded In Alkali Activated Metakaolin/Limestone Based Mortar. In RILEM Bookseries Vol 40, Escalante-Garcia, J.I. et al. (Eds.), Proc 75th RILEM Annual Week Mérida México.

Villagrán-Zaccardi, Y., Pareja, R., et al. (2022). Overview of cement and concrete production in Latin America and the Caribbean with a focus on the goals of reaching carbon neutrality. *RILEM Technical Letters*, 7, 30-46.

Villaquirán-Caicedo, M. A., & de Gutiérrez, R. M. (2021). Comparison of different activators for alkaline activation of construction and demolition wastes. *Construction and Building Materials*, 281, 122599.

Yip, C.K., Provis, J.L., Lukey, G.C., van Deventer, J.S.J. (2008). Carbonate mineral addition to metakaolin-based geopolymers. *Cement and Concrete Composites*., 30, 979–985.

Material and Process Design in 3D Concrete Printing via AI Driven Experiments and Modelling

Francesco Soave[1]*, Andrea Marcucci[2], Giacomo Rizzieri[3] and Liberato Ferrara[4]

[1]Politecnico di Milano, Milano, Italy
Email: francesco.soave@polimi.it
[2]Politecnico di Milano, Milano, Italy
Email: andrea.marcucci@polimi.it
[3]Politecnico di Milano, Milano, Italy
Email: giacomo.rizzieri@polimi.it
[4]Politecnico di Milano, Milano, Italy
Email: liberato.ferrara@polimi.it

*Corresponding author (s)

ABSTRACT

The development of a printable concrete mix-design is a complex process that typically involves a trial-and-error phase for fine-tuning the exact proportions of each component. Predicting how rheological parameters will be affected by selected materials and dosages poses a significant challenge. In this paper, a methodology specifically tailored to regulate the printability of cementitious composites is introduced. The work starts with an experimental preliminary characterization of the rheological properties (via flow table test) of 3Dprintable mixes, taken from the literature. Then, leveraging a previously developed and validated numerical model (Rizzieri et al. (2023a)), the approach has been employed to evaluate whether the static yield strength and viscosity of the selected mixes align with key factors like printing speed, nozzle height, and the maximum number of admissible layers (all integral aspects of the printing process). Once the rheological characteristics have been defined, a meticulously designed Artificial Neural Network (ANN) has been employed, trained using a database containing data on various concrete mixtures from existing literature, in order to correlate the rheological parameters allowing printability as per previously performed numerical modelling, to potential mix-design constituents and dosages, ensuring they meet the specified requirements and the feasibility.

KEYWORDS: *3D Printing Concrete, Artificial Neural Networks, Numerical model, Printability and Rheology.*

1. Introduction

In the context of technological innovation in the construction sector, 3D concrete printing (3DCP) technology represents a significant advancement in streamlining production processes. This innovative method offers numerous advantages compared to traditional practices. One notable benefit is the elimination of the need for formwork, which facilitates the creation of intricate geometric shapes. This not only broadens architectural possibilities but also reduces material consumption, thereby promoting environmental sustainability in the construction sector. Furthermore, the adoption of highly automated construction processes results in a substantial reduction in manual labor, consequently decreasing overall time and costs and improving also the health and safety for workers. Additionally, it enhances precision and control over the final product geometry, achieved through advanced monitoring and control capabilities (De Schutter et al (2022)). However, it is essential to acknowledge that despite these promising features, numerous phases of experimentation and adjustment are required in practice to control the 3D printing process and achieve reliable results. This results in significant time and resource wastage, limiting the widespread adoption of 3DCP (Wangler et al (2016)). This challenge arises due to the presence of numerous variables that can influence and alter the expected outcome, such as material rheological properties, printing parameters (nozzle shape, printing speed, extrusion pressure, and tool path), the geometry and

characteristics of the desired artifact, as well as environmental conditions during the printing phase (temperature and humidity).
Therefore, it is crucial to develop a standardized methodology capable of controlling and systematizing the entire complex process. The approach proposed in this project aims to provide a reliable methodology to address the challenges related to the printability of the 3D concrete properties, supporting designers and 3DCP operators. Furthermore, there is an ambition to integrate this tool into a broader optimization framework for the printing process to determine the best combination of materials and process parameters required to print a specific object.

2. Methodological Procedure/Optimized Approach

The process involves integrating various techniques and methodologies into a unified system aimed at managing and enhancing the 3D concrete printing process. Illustrated in Figure 1, the workflow primarily incorporates three different technologies: a Finite Element Method (FEM) numerical model, an artificial neural network, and the implementation of a simplified experimental test, all described in detail in subsequent chapters.

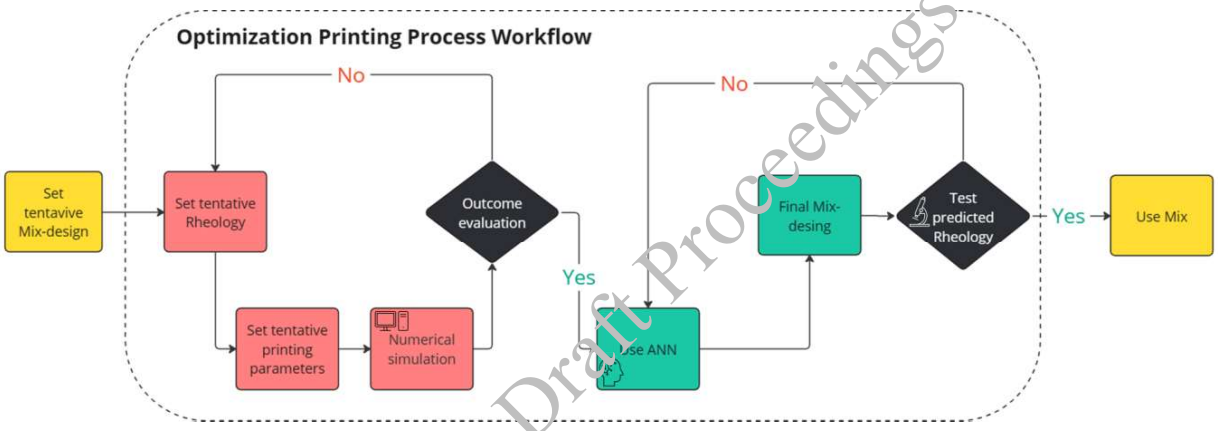

Figure 1. Methodological approach for controlling and optimizing the printing process

In the initial phase of the process, a "tentative" mix is formulated to preliminarily assess its rheological characteristics, aiming to examine and understand its printability. These parameters can be derived from previous experiments or collected from databases containing information on printable mixes. Subsequently, through a series of numerical simulations, the relationships between the concrete rheological parameters and the printing parameters are established, initiating an iterative process of adjustment and optimization of the parameters based on predefined objectives and specific application needs of the additive method. In the second step, a pre-trained Artificial Neural Network (ANN) is employed, utilizing data from various concrete mixtures found in the literature. This facilitates the establishment of correlations between rheological parameters, such as static strength and plastic viscosity, and the varied constituents and proportions within the mix design, enabling the prediction of mixes that satisfy the criteria and the results of the numerical modelling. Following this, the mix designs generated by the neural network undergo experimental validation using the flow table test, a method that swiftly and reliably evaluates the material's rheology, thereby validating the accuracy of the neural network's predictions. Should disparities arise between predictions and experimental outcomes, adjustments are made to the neural network, and the process is iterated until a blend with the desired rheological properties is achieved. If experimental tests confirm the printability of the mixture, it can be immediately employed for printing. It is crucial to emphasize that over time, the continuous use and enrichment of the database associated with the Artificial Neural Network (ANN) will lead to progressive learning. This will enable the network to partially replace traditional experimental tests, thereby contributing to optimizing and accelerating the overall process. This progress is fundamental to empower this methodology as an effective tool for designers aiming to expand the application of additive technology, facilitating rapid and efficient assimilation of new discoveries in the field.

2.1 Particle Finite Element Method (PFEM)

In this optimized approach, a numerical model developed at Politecnico di Milano (Rizzieri et al (2023a), Rizzieri et al (2023b), Rizzieri et al (2023c)) within the framework of the Particle Finite Element Method (PFEM) (Cremonesi et al (2020)) was utilized. This model facilitated the analysis of the interaction between printing parameters and the rheological properties of concrete, evaluating their influence on the composition and geometry of the extruded filament (**Error! Reference source not found.**-a). Through an extensive s eries of simulations, correlations among diverse parameters, including static yield stress, plastic viscosity, nozzle diameter, and height, were established. Utilizing these correlations, it became feasible to numerically delineate optimal conditions to ensure the accurate printability of the concrete layer, customized to the specific case study and selected application field. Nonetheless, it's crucial to emphasize that this methodology is not the exclusive option; various alternative numerical models, such as those employing different fluid solvers or the Discrete Element Method, could offer additional insights and enhanced control over numerical simulation.

2.2 Artificial Neural Network (ANN)

Within this framework, an Artificial Neural Network (ANN) is formulated to establish associations between mix design parameters and rheological characteristics. The ANN consists of nine input neurons (Marcucci et al (2023)), representing different components of the hypothetical mix design, and one output neuron responsible for predicting concrete rheological properties (**Error! Reference source not found.**-b). F ollowing this construction, the ANN undergoes training and subsequent validation, including experimental verification. Through this iterative process, utilizing a continuously enriched database, the accuracy of predictions will improve over time, potentially replacing or complementing traditional methods of experimental prediction.

2.3 Flow Table Test

This methodology, akin to the slump test, has previously been employed in scientific research, as documented in study conducted by Jayathilakage et al. (2022). This test is commonly used to assess the workability of concrete, involving the use of a vibrating table that facilitates the lateral spreading of concrete. By measuring the spread diameter (Figure-c) of the concrete on the table, detailed, immediate, and valuable information about the concrete's rheology can be obtained. Using analytical relationships widely cited in the literature, it was possible to directly determine the expected values of the concrete's static strength. This procedure was first validated using various mixes found within the literature as a reference (Soave et al (2024)) and subsequently used to further validate the mixes suggested by the neural network.

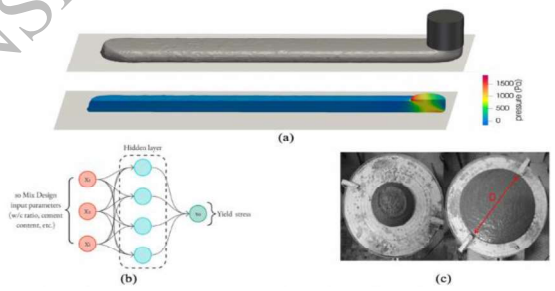

Figure 2. Various tools used within the optimized approach. Numerical analysis (a), Neural network (b), and Flow table test (c)

3. Conclusions

In conclusion, the proposed method represents an innovative integration of diverse disciplines aimed at optimizing the 3D printing process of concrete. Through the synergy between advanced numerical models, artificial neural networks, and experimental tests, a comprehensive understanding of the intricate interactions between printing parameters and the rheological properties of the material is achieved. This approach not only facilitates the rapid development of more efficient concrete mixes but also contributes

to enhancing the consistency and quality of production. The primary objective of this methodology is to promote broader and immediate adoption of 3D printing technology by designers and industry operators. However, it is essential to recognize that this method serves as a starting point. Further research is imperative to refine and further optimize this strategy to maximize its potential and make its practical applications more tangible.

Acknowledgements

The work described in this paper has been performed in the framework of the MUSA – Multilayered Urban Sustainability Action – project, funded by the European Union – NextGenerationEU, under the National Recovery and Resilience Plan (NRRP) Mission 4 Component 2 Investment Line 1.5: Strengthening of research structures and creation of R&D "innovation ecosystems", set up of "territorial leaders in R&D". The collaboration of MEng Simone Meni is also acknowledged, in partial fulfilment of the requisites to obtain the MSc in Civil Engineering.

References

Cremonesi, M. Franci, A. Idelsohn, S. and Oñate, E. (2020). "A State of the Art Review of the Particle Finite Element Method (PFEM)." *Archives of Computational Methods in Engineering,* 27:1709-1735

De Schutter, G. Lesage, K. Mechtcherine, V. Nerella, V.N. Habert, G. and Agusti-Juan. (2010). "Vision of 3D printing with concrete—technical, economic and environmental potentials". *Cement and Concrete Research.*

Jayathilakage R., Rajeev, P. and Sanjayan, J. (2022). "Rheometry for Concrete 3D Printing: A Review and an Experimental Comparison". *Buildings*, 12,1190.

Marcucci, A. Gaggiotti, C. and Ferrara, L. (2023). "A prediction of the printability of concrete through Artificial Neural Networks (ANN)" *Materials Today: Proceedings*

Ramyar, E. and Cusatis, G. (2022). "Discrete Fresh Concrete Model for Simulation of Ordinary, Self-Consolidating, and Printable Concrete Flow." Journal of Engineering Mechanics 148(2): 04021142.

Rizzieri, G., Ferrara, L. and Cremonesi, M. (2024). "Numerical simulation of the extrusion and layer deposition processes in 3D concrete printing with the Particle Finite Element Method". *Computational Mechanics*.

Rizzieri, G. Cremonesi, M. and Ferrara, L. (2023). "A 2D numerical model of 3D concrete printing including thixotropy", *Materials Today: Proceedings*. ISSN 2214-7853.

Rizzieri, G., Ferrara, L. and Cremonesi, M. (2024). "Simulation of viscoelastic free-surface flows with the Particle Finite Element Method", *Computational Particle Mechanics.*

Roussel N. (2018). "Rheological requirements for printable concretes". *Cement and Concrete Research*

Soave, F. Muciaccia, G. and Ferrara L. (2024). "A Simplified Metrology for On-Site Assessment of the effects of Corrosion Inhibitor on the rheology of 3D printed Concrete", *Italian Concrete Conference: Proceedings.*

Wangler, T. Lloret, E. Reiter, L. Hack, N. Gramazio, F. Kohler, M. et al. (2016). "Digital concrete: opportunities and challenges. *RILEM Technical Letters* 10(1):67–75.

Wolfs, Rob J. M. Bos, Freek P. and Salet, Theo A. M. (2008). "Early age mechanical behaviour of 3D printed concrete: Numerical modelling and experimental testing." *Cement and Concrete Research,* 106:103-116.

An Overview of Regional Risk (and Resilience) Analysis

P. Gardoni[1*]

[1] *Department of Civil and Environmental Engineering, University of Illinois Urbana-Champaign, Urban, USA*
Email: gardoni@illinois.edu

[*]Corresponding author (s)

ABSTRACT

Civil structures and infrastructure provide vital services that support and enable societal functions. Ensuring their reliability and prompt recovery is critical for the public's well-being and economic prosperity. Past disasters around the world have raised concerns about the vulnerability of civil structures and infrastructure and have highlighted the significance of risk mitigation and management. The maintenance, repair, or replacement of existing vulnerable, deficient, and deteriorating structures and infrastructure represents a significant investment. To wisely invest the limited funding, it is crucial to use advanced risk analysis tools in the decision-making process. This presentation discusses a general formulation for regional risk analysis, which includes resilience analysis. The presentation explains how to conduct a regional risk analysis considering multiple hazards and different infrastructure, as well as the effects of deterioration and interdependencies among infrastructure. The presentation also shows how the physical damage to structures and infrastructure can be cascaded to predict the likelihood and duration of business interruption. The presentation includes examples of regional risk and resilience analysis considering a hypothetical earthquake in the New Madrid seismic zone in the USA.

KEYWORDS*: Risk analysis, Resilience, Fragility functions, Infrastructure*

1. Introduction

Probability and risk are often used as measures for decision-making (Gardoni 2017). In particular, comparative risk analysis can be used to weigh the risks associated with different options or designs (Gardoni and Murphy 2014, 2017, Gardoni et al. 2016). However, in risk analysis for natural and anthropogenic hazards, the consequences typically considered are narrowly defined (Murphy and Gardoni 2006) and there is no consideration of the possible inequalities of the impacts across society. While inequalities are typically present before the occurrence of a hazard (e.g., in the state of well-being of individuals as well as in their vulnerability to hazards), the occurrence of an extreme event may affect people differently (Gardoni et al. 2016). Inequalities among individuals can be both spatial (across different areas) and temporal (across different generations). As noted in Murphy and Gardoni (2008), spatial and temporal variability of the impacts call for considerations toward inter- and intra-generational equity (both concepts tied to sustainability). Finally, for risk evaluation, it is critical to look at the time of recovery, which calls for consideration of resilience (Gardoni 2019).

The opportunities that individuals have are constitutive components of the level of societal well-being (Sen 1999). Such opportunities depend on what an individual has (e.g., personal resources, skills, and knowledge) and what he/she can do with local legal, economic, and social constraints as well as the characteristics of the physical infrastructure. For example, infrastructure play a critical role in the opportunities of being mobile, being nourished, having shelter, and being educated. The ability of infrastructure to recover from the impact of a hazardous event directly affects the ability of individuals to regain their opportunities and with them improve their well-being.

Considering the performance and safety of infrastructure, in the past decade significant attention has been devoted to infrastructure components (e.g., bridges, buildings, and electrical substations) (e.g., Gardoni et al. 2002, Ramamoorthy et al. 2008, Pillai et al. 2010, 2014) and, more recently, individual infrastructure considered in isolation (e.g., Kang et al. 2008, Guidotti et al. 2017a). However, each infrastructure typically depends on other (supporting) infrastructure, and loss of functionality of the supporting infrastructure can

have cascading effects on the dependent infrastructure (Ellingwood et al. 2016, Sharma et al. 2020a, 2022). More generally, there are dependencies/interdependencies among physical infrastructure and non-physical infrastructure (e.g., socio-economic systems) (Iannacone et al. 2022, Sharma et al. 2022, Tabandeh et al. 2022, 2023). So, to assess the functionality of infrastructure it is critical to consider the relevant dependencies/interdependencies.

Assessing and evaluating societal risks require the definition of relevant measures of societal impact as well as new multidisciplinary models that translate the impact of a hazard on the infrastructure into the measures of societal impact (Boakye et al. 2022a). Commonly used measures of impact include direct physical damage, dollar loss, and duration of downtime (Gardoni and LaFave 2016). However, Murphy and Gardoni (2006) pointed out that such measures are incomplete (both as measures of the immediate impact and to gauge the state of recovery). In addition, hazards often have larger impacts on vulnerable populations (e.g., Kajitani et al. 2005). Therefore, there is a need to define measures of impact that can describe the spatial and temporal variability of the impact. Since the opportunities that individuals have are manifestations of the level of societal well-being (as noted earlier), Murphy and Gardoni (2006, 2007, 2008, 2010, 2011), Gardoni and Murphy (2008, 2009, 2010, 2014, 2017), and Tabandeh (2017) proposed to use changes to such opportunities as measures of impact as well as a general formulation to quantify the spatial and temporal variability of the impact.

This work presents a formulation to quantify and predict the societal impact of hazards by bringing together multidisciplinary models and formulations. In the modeling of the impact of hazards on infrastructure, special considerations are given to the treatment of dependencies/interdependencies, the impact of aging and deterioration, the impact of climate change, and the conversion of physical damage into reduction or loss of functionality. In the assessment of the societal impact, genuine opportunities are used to gauge societal well-being, and changes to such opportunities are used to gauge the impact of hazards. The general formulation is probabilistic to account for and propagate the relevant uncertainties (Gardoni et al. 2002, Gardoni 2017, Tabandeh et al. 2022).

Section 2.1 discusses how to model the dependencies/interdependencies of infrastructure. The remaining of Section 2 discusses some of the factors that need to be considered when assessing the impact of hazards including the aging and deterioration of infrastructure components (discussed in Section 2.2), climate change (discussed in Section 2.3), and the process for going from the physical damage and reduction or loss of infrastructure functionality to the societal impact (discussed in Sections 2.3 and 2.4). Section 3 gives relevant considerations to resilience.

2. Regional Risk Analysis

There are three main steps in assessing the impact of hazards on infrastructure. First, intensity measures (IMs) of the hazard are propagated so that each point in the relevant footprint of the infrastructure has a corresponding value of the IMs (Gardoni et al. 2003). Then, the physical inventory needs to be defined providing information on the structures/infrastructure. For example, for the buildings in the region of interest information needs to be provided on their construction type and material, year of construction, and other classification parameters that are used in the next step. Spatially distributed networks (e.g., transportation, electric power, and water and wastewater networks) consist of nodal elements (e.g., bridges, distribution nodes, and pumping stations) and linear elements (e.g., roads, electric power distribution lines, and pipelines). An adjacency matrix can be used to describe the topology of the networks (Guidotti et al. 2016). The final step estimates the level of damage of the elements in the infrastructure for the given IMs at the site using fragility curves for the nodal elements (e.g., Gardoni et al. 2002), and repair rate curves for the linear elements (Iannacone and Gardoni 2022).

2.1 Modelling Dependencies/Interdependencies among Infrastructure

The failure of a network is typically defined as the loss of connectivity of one or more nodes from the remaining of the network (Kang et al. 2008). Different measures of connectivity like the diameter and efficiency of the network have been proposed to describe the state of a network (Crucitti et al. 2003, Guidotti et al. 2017a). However, these measures only consider individual networks and do not capture dependencies and interdependencies among networks. Expanding the adjacency matrix with sub-adjacency matrices can capture the dependencies and interdependencies among networks (Guidotti et al. 2016). Guidotti et al. (2017b) proposed a Multi-layer Heterogeneous Network modeling approach to model and assess the

reliability of dependent/interdependent physical and non-physical infrastructure. In this approach, the component types define the different elements in the system of infrastructure and the layers define the types of dependencies/interdependencies. In the Multi-layer Heterogeneous Network modeling approach connectivity metrics can be generalized to describe dependent/interdependent infrastructure. More recently, Sharma and Gardoni (2022) developed an object-oriented approach for the modeling of interdependent infrastructure that uses interface functions that modify the defining characteristics of infrastructure to include the effects of interdependencies. The formulation can be used for complex networks with different types of interdependencies.

2.2 The Impact of Aging and Deterioration of Infrastructure

Aging and deterioration due to multiple deterioration mechanisms can affect the state, service, and reliability of infrastructure (Choe et al. 2010, Gardoni and Rosowsky 2011, Kumar et al. 2015, Pillai et al. 2010, 2014). Specifically, aging and deterioration can lead to higher values of fragility, repair rates and failure probabilities resulting in reductions in the functionality and service life of infrastructure. Deterioration mechanisms are likely to interact with each other leading to a faster deterioration of the overall state of infrastructure than when simply superimposing the effects of single mechanisms. Jia et al. (2017) and Jia and Gardoni (2018) developed a state-dependent formulation to predict the impact of aging and deterioration on the state and reliability of infrastructure accounting for the possible interaction of deterioration mechanics. Using the state-dependent formulation, Iannacone et al. (2022) specifically modeled the time-varying reliability and resilience of deteriorating infrastructure. These models can be used, for example, in a Renewal Theory-based Life-cycle Analysis (Kumar and Gardoni 2014, Kumar et al. 2015, Jia et al. 2017) to model the entire service life of an infrastructure.

2.3 The Impact of Climate Change

Recent studies (Gardoni et al. 2016, Murphy et al. 2018) have shown that it is increasingly important to account for the effects of climate change when conducting regional risk analysis. First, climate change is affecting the likelihood of occurrence, magnitude, and consequences of specific natural hazards like heat waves and droughts, severe precipitations, and hurricanes. Second, climate change is affecting the aging and deterioration of infrastructure. Shock deteriorations might become more frequent due to the higher likelihood of occurrence of severe natural events, and gradual deteriorations might be accelerated by the changes in the environmental conditions they depend on. Finally, climate change is increasing the overall uncertainty in the prediction of the physical damage to infrastructure as well as of the societal impact.

2.4 Going from Physical Damage to Reduction or Loss of Functionality

To assess the societal impact of hazards, we need to assess the reduction or loss of functionality of the infrastructure that results from their direct physical damage and the damage to the supporting infrastructure (Ellingwood et al. 2016, Guidotti et al. 2019, Boakye et al. 2022b). For example, the functionality of a water network could be affected by the physical damage to the supporting electric power network. Guidotti et al. (2016) developed a probabilistic procedure to assess the reduction or loss of functionality resulting from the physical damage to a system of infrastructure accounting for their possible dependencies/ interdependencies as well as aging and deterioration.

2.5 Going from Physical Damage and Reduction or Loss of Functionality to Societal Impact

For natural events to turn into disasters, there must be social vulnerability (Ribot 1995, Wisner et al. 2003, Adger 2006, Gardoni et al. 2016, Boakye et al. 2022a). Here vulnerability is defined as the propensity of society to be impacted. Based on past disasters, some researchers (e.g., Kajitani et al 2005) identified socio-economic characteristics of individuals and households that make them more vulnerable. It is essential to account for social vulnerability when estimating the impact of changes in the infrastructure on the well-being of individuals. Understanding why individuals and households might be particularly vulnerable is important also in the development of effective mitigation strategies that promote social equity. However, social vulnerability studies are typically case-specific and lack the quantitative generalizability needed to couple vulnerability analysis with regional risk analysis. A Capability Approach (Murphy and Gardoni 2006, 2007, 2008, 2010, 2011, Gardoni and Murphy 2008, 2009, 2010, 2014, 2017, and Tabandeh et al. 2017) can be used to assess the societal impact of hazards on the well-being of individuals in a way that can be naturally coupled with regional risk analysis. This approach is discussed next.

Murphy and Gardoni (2006, 2007, 2008, 2010, 2011) and Gardoni and Murphy (2008, 2009, 2010, 2014, 2017) proposed a Capability Approach to assess and evaluate the societal impact of hazards. Capabilities are the opportunities an individual has to do or become things of value like the opportunities of being mobile, being nourished, having shelter, and being educated (Sen 1999). Capabilities (or opportunities) define the level of societal well-being of individuals.

The capabilities an individual has depend on his/her personal resources (including wealth, skills, and knowledge), what he/she can do with what he/she has given legal, economic, and social constraints, as well as the characteristics of the physical infrastructure. For example, infrastructure play a critical role in the opportunities of being mobile, being nourished, having a shelter, and being educated (Boakye et al. 2022b). The ability of infrastructure to recover from the impact of a hazardous event also affects directly the ability of individuals to regain their opportunities and with them their well-being. Based on this observation, Murphy and Gardoni (2006) proposed to gauge the impact of hazards in terms of the changes in individual capabilities.

3. Regional Resilience Analysis

Resilience is generally defined as the ability of a subject (e.g., individual, community, economic system) to return to normal functioning within a reasonable timeframe following a disruption (Doorn et al. 2019, Gardoni 2019,). Judgments on the tolerability of a risk take into account the time period during which an individual is below the acceptable threshold level of capability. So, resilience plays a crucial role in enabling an individual to recover quickly and therefore rendering a risk tolerable. Several elements influence resilience, including importantly infrastructure, which is the subject of this section.

3.1 Recovery and Resilience of Infrastructure

Current design approaches and mitigation strategies are increasingly promoting infrastructure and community resilience. The recovery process of infrastructure can be modeled mathematically using the stochastic formulation in Sharma et al. (2018) and Sharma et al. (2020b). This stochastic formulation models: 1) the completion time of the recovery steps (which are a group of recovery activities that improve the reliability or functionality of the system) and the occurrence time of disrupting shocks, as well as 2) the system state after the completion of each recovery step or the occurrence of a disrupting shock. In addition, Guidotti et al. (2016) Iannacone et al. (2022), and Tabandeh et al. (2023) studied the impact of network dependencies on the resilience of infrastructure and found that network dependencies can significantly slow down the recovery of dependent networks.

3.2 Recovery and Resilience of Society

Since the functionality of infrastructure affects the well-being of society, the recovery of the infrastructure after a disaster is essential for the recovery of society, and the resilience of infrastructure translates into the resilience of society. A Capability Approach can be used to translate the predicted infrastructure recovery into a prediction of societal recovery (Murphy and Gardoni 2010). Specifically, the estimates of the functionality of the relevant infrastructure derived from the modeling of the infrastructure recovery can be used as time-dependent values of the regressors in predictive models. Using such time-dependent values instead of the values of the regressors before or immediately after the occurrence of an extreme event gives time-dependent values of the indicators of well-being. Mathematically this can be done, for example, using a Dynamic Bayesian Network (DBN) (Tabandeh et al. 2019).

4. Conclusions

Natural and anthropogenic hazards can have significant impacts on the well-being of society. Infrastructure play a critical role in the well-being of society both before the occurrence of a hazard by providing the required services and after the occurrence of a hazard by making the recovery of well-being possible. Regional risk analysis, which includes resilience analysis, can help predict the impact of hazards and guide the development of mitigation and recovery strategies that promote well-being.

A question addressed in this work is how to convert the state of the infrastructure into a measure of well-being. Since the opportunities that individuals have are manifestations of the level of societal well-being, a Capability Approach (where capabilities are the genuine opportunities that individuals have) can be used

to bridge this gap. A Capability Approach can also capture social vulnerability factors that, along with the state of the infrastructure, shape the level of societal well-being and offers the means for evaluating risks as acceptable or tolerable with considerations toward resilience, sustainability, and social justice.

References

Adger, W.N. (2006). Vulnerability. *Global Environmental Change*, 16(3), 268-81.

Boakye, J., Gardoni, P., Murphy, C., and Kumar, R. (2022a). "Which consequences matter in risk analysis and disaster assessment?" *Journal of Disaster Risk Reduction*, 71, 102740.

Boakye, J., Guidotti, R., Gardoni, P., and Murphy, C. (2022b). "The role of transportation infrastructure on the impact of natural hazards on communities," *Reliability Engineering & System Safety*, 219, 108184.

Choe, D., Gardoni, P., and Rosowsky, D., (2010). "Fragility increment functions for deteriorating reinforced concrete bridge columns," *ASCE Journal of Engineering Mechanics*, 136 (8), 969-978.

Crucitti, P, Latora, V., Marchiori, M., and Rapisarda, A., (2003). Efficiency of scale-free networks: error and attack tolerance. *Physica A: Stat. Mech. and its Applications*, 320, 622–42.

Doorn, N., Gardoni, P., and Murphy, C., (2019). "A multidisciplinary definition and evaluation of resilience: the role of social justice in defining resilience," *Sustainable and Resilient Infrastructure*, 4(3), 112-123.

Ellingwood, B.R., Cutler, H., Gardoni, P., Peacock, W.G., van de Lindt, J.W., and Wang, N. (2016). The Centerville virtual community: A fully integrated decision model of interacting physical and social infrastructure systems. *Sustainable and Resilient Infrastr.*, *1*(3-4), 95-107.

Gardoni, P., (Ed.), (2017). *Risk and Reliability Analysis: Theory and Applications*. Springer.

Gardoni, P., (Ed.), (2019). Routledge Handbook of Sustainable and Resilient Infrastructure, Routledge.

Gardoni, P., Der Kiureghian A., Mosalam K.M., (2002). "Probabilistic capacity models and fragility estimates for RC columns based on experimental observations," *ASCE Journal of Engineering Mechanics*, 128 (10), 1024-1038.

Gardoni, P., and LaFave, J., (Eds.) (2016). *Multi-hazard Approaches to Civil Infrastructure Engineering*, Springer.

Gardoni, P., Mosalam K.M., and Der Kiureghian A., (2003). "Probabilistic seismic demand models and fragility estimates for RC bridges," *Journal of Earthquake Engineering*, *7* (Special Issue 1), 79-106.

Gardoni, P., and Murphy, C., (2008). "Recovery from natural and man-made disasters as capabilities restoration and enhancement," *International Journal of Sustainable Development and Planning*, 3 (4), 1-17.

Gardoni, P., and Murphy, C., (2009). "Capabilities-based Approach to measuring the societal impacts of natural and man-made hazards in risk analysis," *ASCE Natural Hazards Review*, 10 (2), 29-37.

Gardoni, P., and Murphy, C., (2010). "Gauging the societal impacts of natural disasters using a Capabilities-based Approach," *Disasters*, 34 (3), 619-636.

Gardoni, P., and Murphy, C., (2014). "A scale of risk," *Risk Analysis*, 34 (7), 1208-1227.

Gardoni, P., and Murphy, C., (2017). "Society-based Design: Promoting Societal Well-being by Designing Sustainable and Resilient Infrastructure," *Sustainable and Resilient Infrastr.* (under review).

Gardoni, P., Murphy, C., Rowell, A., (Eds.) (2016) *Societal Risk Management of Natural Hazards*, Springer.

Gardoni, P., and Rosowsky, D., (2011). "Seismic fragility increment functions for deteriorating reinforced concrete bridges," *Structure and Infrastructure Engineering*, 7 (11), 869-879.

Guidotti, R., Chmielewski, H., Unnikrishnan, V., Gardoni, P., McAllister, T., and van de Lindt, J. (2016). "Modeling the resilience of critical infrastructure: the role of network dependencies," *Sustainable and Resilient Infrastructure*, *1*(3-4), 153-168.

Guidotti, R., Gardoni, P., and Chen, Y. (2017a). Network reliability analysis with link and nodal weights and auxiliary nodes," *Structural Safety*. Vol. 65, pp 12–26.

Guidotti, R., Gardoni, P., and Chen, Y. (2017b). "Multi-layer heterogeneous network model for interdependent infrastructure systems," In *Proc. of the 12th International Conf. on Structural Safety & Reliability* (ICOSSAR 2017), August 6-10, 2017, Vienna, Austria.

Guidotti, R., Gardoni, P., and Rosenheim, N., (2019) "Integration of physical infrastructure and social systems in communities" reliability and resilience analysis," *Reliability Engineering & System Safety*, 185, 476-492.

Iannacone, L., and Gardoni, P. (2022). "Physics-based repair rate curves for segmented pipelines subject to seismic excitations," *Sustainable and Resilient Infrastructure*, 8(1), 121-141.

Iannacone, L., Sharma, N., Tabandeh, A., and Gardoni, P. (2022). "Modeling time-varying reliability and resilience of deteriorating infrastructure," *Reliability Engineering & System Safety*, 217, 108074.

Jia, G., and Gardoni, P. (2017). "State-dependent stochastic models: A general stochastic framework for modeling deteriorating engineering systems considering multiple deterioration processes and their interactions," *Structural Safety* (under review).

Jia, G., Tabandeh, A., and Gardoni, P., (2017). "Life-cycle Analysis of Engineering Systems: Modeling Deterioration, Instantaneous Reliability, and Resilience," in Paolo Gardoni (Ed.) *Risk and Reliability Analysis: Theory and Applications*, Springer.

Kajitani, Y., Okada, N., Tatano, H., (2005). "Measuring Quality of Human Community Life by Spatial-Temporal Age Group Distributions-Case Study of Recovery Process in a Disaster-Affected Region," *Natural Hazards Review*, 6 (1), 41-47.

Kang, W.H., Song, J., and Gardoni, P. (2008). "Matrix-based system reliability method and applications to bridge networks," *Reliability Engineering and System Safety*, 93, 1584–93.

Kumar, R., and Gardoni, P., (2014). "Renewal theory-based life-cycle analysis of deteriorating engineering systems," *Structural Safety*, 50, 94-102.

Kumar, R., Cline, D., and Gardoni, P., (2015). "A stochastic framework to model deterioration in engineering systems," *Structural Safety*, 53, 36-43.

Murphy, C., and Gardoni, P., (2006). "The role of society in engineering risk analysis: a Capabilities-based Approach," *Risk Analysis*, 26 (4), 1073-1083.

Murphy, C., and Gardoni, P., (2007). "Determining public policy and resource allocation priorities for mitigating natural hazards: a Capabilities-based Approach," *Science and Engineering Ethics*, 13 (4), 489-504.

Murphy, C., and Gardoni, P., (2008). "The acceptability and the tolerability of societal risks: a Capabilities-based Approach," *Science and Engineering Ethics*, 14 (1), 77-92.

Murphy, C., and Gardoni, P., (2010). "Assessing capability instead of achieved functionings in risk analysis," *Journal of Risk Research*, 13 (2), 137-147.

Murphy, C., and Gardoni, P., (2011). "Evaluating the source of the risks associated with natural events," *Res Publica*, 17 (2), 125-140.

Murphy, C., Gardoni, P., and McKim, R., (Eds.) (2018) *Climate Change and Its Impact: Risks and Inequalities*, Springer.

Pillai, R.G., Hueste, M.D., Gardoni, P., Trejo, D., and Reinschmidt, K.F., (2010). "Time-variant service reliability of post-tensioned, segmental, concrete bridges exposed to corrosive environments," *Engineering Structures*, 32 (9), 2596-2605.

Pillai, R.G., Trejo, D., Gardoni, P., Hueste, M.B., and Reinschmidt, K.F., (2014). "Time-variant flexural reliability of post-tensioned, segmental concrete bridges exposed to corrosive environments," *ASCE Journal of Structural Engineering*, 140(8), A4014018.

Ramamoorthy, K.S., Gardoni, P., and Bracci, M.J., (2008). "Seismic fragility and confidence bounds for gravity load designed reinforced concrete frames of varying height," *ASCE Journal of Structural Engineering*, 134 (4), 639-650.

Ribot, J. (1995). "The causal structure of vulnerability: Its application to climate impact analysis," *GeoJournal*, 35(2), 119-22.

Sen, A. (1999). *Development as Freedom*. New York: Anchor Books.

Sharma, N., Tabandeh, A., and Gardoni, P. (2018) "Resilience Analysis: A Mathematical Formulation to Model Resilience of Engineering Systems," *Sustainable and Resilient Infrastructure*, 3(2), 49-67.

Sharma, N., Nocera, F., and Gardoni, P. (2020a). "Classification and mathematical modeling of infrastructure interdependencies," *Sustainable and Resilient Infrastructure*, 6(1–2), 4–25.

Sharma, N., Tabandeh, A., and Gardoni, P. (2020b). "Regional Resilience Analysis: A Multi-Scale Approach to Optimize the Recovery of Interdependent Infrastructure," *Computer-Aided Civil and Infrastructure Engineering*, 35(12), 1315-1330.

Sharma, N., Gardoni, P. (2022). "Mathematical modeling of interdependent infrastructure: An object-oriented approach for generalized network-system analysis," *Reliability Engineering & System Safety*, 217, 108042.

Tabandeh, A., Gardoni, P., and Murphy, C. (2017). "Reliability-based capability approach: A system reliability formulation for the capability approach," *Risk Analysis*: DOI: 10.1111/risa.12843.

Tabandeh, A., Gardoni, P., Murphy, C., Myers, N. (2019). "Societal risk and resilience analysis: a dynamic Bayesian network approach," *ASCE Journal of Risk and Uncertainty Analysis*, 5(1), 04018046.

Tabandeh, A., Sharma, N., and Gardoni, P. (2022). "Uncertainty propagation in risk and resilience analysis of hierarchical systems," *Reliability Engineering & System Safety*, 219, 108208.

Tabandeh, A., Sharma, N., and Gardoni, P., (2023). "Seismic risk and resilience analysis of industrial facilities," *Bulletin of Earthquake Engineering*, 22, 255-276.

Wisner, B., Blaikie, P., Cannon, T., and Davis, I. (2003). *At risk: Natural hazards, people's vulnerability and disasters* (2nd edition). New York: Routledge.

Performance Evaluation of Concrete Under Specific Conditions for Nuclear Reactor Buildings

I. Maruyama[1*]

[1]*The University of Tokyo, Tokyo, Japan*
Email: i.maruyama@bme.arch.t.u-tokyo.ac.jp

[*]Corresponding author

ABSTRACT

This contribution delineates a cumulative overview of pivotal research initiatives conducted in Japan, aimed at assessing and enhancing the resilience of concrete utilized within nuclear facilities. Spanning over a decade, the projects on radiation-induced concrete degradation collectively underpin Japan's strategic approach to maintaining structural integrity amidst aging and radiation challenges.

KEYWORDS*: Aging management, Neutron irradiation, Rock-forming minerals, Amorphization, Physical property change*

1. Introduction

This contribution aims to review the technical studies on aged concrete in nuclear power plant facilities, especially on radiation-induced concrete degradation, over the past decade or so to share the discussion points in Japan.
Reinforced concrete components in nuclear power plant buildings are significant and necessary to support and protect various equipment and devices and ensure workers' safety in the buildings. The maintenance and management guidelines published by the Architectural Institute of Japan (AIJ) (Architectural Institute of Japan, 2015) define the following functions for reinforced concrete members: Supporting function, Pressure resistance function, Shielding function, Leak-proof function, Negative pressure holding function, Function for preventing secondary accidents, and Usage function. If these functions will not hold the required level due to aging and/or accidental deterioration, it is necessary to take various measures such as repair, reinforcement, replacement, etc. For this purpose, quantitative prediction of deterioration is necessary. The effects of radiation-induced deterioration and the long-term effects of general environmental factors such as heat and drying are of particular interest in long-term operation. These issues must be addressed in the technical assessments of facility aging or the special inspection for renewal licenses above 40 years of service life.

2. Summary of JAMPS project

The Nuclear Regulation Authority (NRA) conducted a project *JAMPSS*, Japan aging management program for system safety, from FY 2008 to FY 2016 to study radiation effects on concrete using neutron irradiation tests (Kojima et al., 2019; Ippei Maruyama et al., 2017), gamma irradiation tests (Ishikawa et al., 2019; Ippei Maruyama et al., 2018, 2017), and thermal and drying tests of concrete (Lin et al., 2015; Ippei Maruyama, Sasano, et al., 2014), aggregate (Igarashi et al., 2015), and paste (Ippei Maruyama et al., 2015; Ippei Maruyama, Nishioka, et al., 2014; Ippei Maruyama & Rymeš, 2019). A prediction by the numerical program DEVICE (Damage EValuation for Irradiated ConcretE) for the physical properties of concrete in large section members was developed (Ippei Maruyama et al., 2016; Ippei Maruyama & Igarashi, 2015). They demonstrated that under a neutron irradiation environment, the strength and Young's modulus of concrete decrease due to aggregate expansion, mainly caused by the amorphization-induced volume expansion of quartz (Ippei Maruyama et al., 2017).

It was experimentally confirmed that the effect of the irradiation became apparent at approximately 1.0×10^{19} (> 0.1MeV) n/cm^2 in the irradiation environment of the JEEP-II reactor in Norway Institute for energy technology (IFE) at approximately 75 ℃. The maximum irradiation doses were $8.2–9.6\times10^{19}$ (> 0.1MeV) n/cm^2. The changes in strength and Young's modulus were 55% and 28% of the original values at the highest neutron fluence, respectively, indicating substantial deterioration in physical properties. In addition, the degradation was differentiated by the coarse aggregate type. When we use the meta-chert, which has large quartz content (~90 mass%), the degradation was severer than the concrete containing sandstone in which the quartz content is about 50% by mass. In the neutron fluence range (6.2×10^{19} (> 0.1MeV) n/cm^2), which corresponds to the maximum expected value of Japanese pressured water reactors (PWRs), aggregate swelling was significantly greater for sandstones with a higher quartz content. In contrast, no swelling occurred in the case of limestone.

In the case of gamma irradiation, the concrete, aggregate, and hardened cement paste exhibited no changes beyond those caused by thermal and drying effects after irradiation to up to 200 MGy.

The Nuclear Regulation Authority of Japan (NRA) published a report on the concern of physical property changes caused by aggregate expansion above 1.0×10^{19} (>0.1MeV) n/cm^2, which is one order of magnitude less than the previously accepted reference value of 10.0×10^{19} (>0.1MeV) n/cm^2 (Kojima et al., 2019). A summary of the report was released to the public.

3. Summary of JCAMP project

In response, the Japanese Agency for Natural Resources and Energy and the Ministry of Economy, trade, and Industry (METI) launched a project in FY 2017 called *JCAMP* (Japanese Concrete Aging Management Project) to upgrade technologies for technical assessments of facility aging, particularly in terms of radiation effects on concrete and concrete members (I. Maruyama et al., 2017). In this project, the following three research items are conducted: 1) preparing a database of radiation-induced volume expansion of concrete aggregates covering rock types used in domestic nuclear reactors, 2) proposing integrity evaluation methods for levels of aggregate, concrete, and structural member, and 3) clarifying the amorphization mechanism of rock-forming minerals in concrete aggregates and evaluation of the effect of neutron flux.

Regarding item 1), we have completed the aggregate irradiation tests and are currently summaryzing the data of dimensional and density evaluation and X-ray diffraction tests. This project irradiated andesite, basalt, pyroxene, sandstone, artificial quartz, and quartz glass. Some of our efforts have been published (Ippei Maruyama et al., 2022, 2023).

Regarding item 2), it is necessary to establish a method for evaluating the performance of reinforced concrete members affected by changes in the physical properties of the concrete due to aggregate expansion. Here, from the viewpoint of the reinforced concrete members, the bond characteristics change between the reinforcing bars and the concrete is also important. Using the rigid-body spring network model (RBSM), a constitutive law that can reproduce the physical properties changes of concrete due to neutron irradiation was developed for this project. In this method, heat, drying, aggregate expansion, and changes in the physical properties of aggregate are explicitly considered (Sasano & Maruyama, 2021, 2024; Sasano et al., 2020).

This constitutive law was extended and applied to the tension-stiffening behavior of reinforced concrete (RC) by subjecting the RC to aggregate expansion. This evaluation was conducted after calibrating the tension-stiffening behavior of wet or dried RC specimens (Kambayashi et al., 2023b). It was discovered that circumferential cracking similar to delamination occurred in the concrete biological shield wall due to aggregate expansion distribution according to neutron attenuation (Kambayashi et al., 2020).

For the seismic performance of the concrete biological shield wall, the analysis of the miniature reinforced concrete hollow cylindrical specimens with the radiation-induced expansion of the aggregate elements was conducted after calibration of the reference specimens with/without temperature gradient simulating the accidental condition (Kambayashi et al., 2023a). The effect of cracking due to aggregate expansion on the ultimate bearing shear capacity and stiffness was clarified. Using these findings, we propose a simple structural performance evaluation method and develop a method to evaluate the performance using a commercial FEM.

Regarding item 3), this project irradiates the same aggregate and artificial quartz with three different neutron fluxes. Using ion irradiation tests and molecular dynamics calculations, we have elucidated the

mechanism of amorphization by neutron irradiation, identified the healing and/or annealing effect in the amorphization, and constructed a model to explain the experimental facts. Attempts were made to predict the expansion behavior of actual irradiated fluxes by incorporating the healing effects believed to exist due to amorphization. These are under preparation for publication.

4. Summary

Here, the author introduces recent research activities and their achievements in aging management for concrete structures in nuclear power plants. Some research topics may be very scientific and require international collaboration, while others are inherent to Japan's environment. By disclosing our research results, the author will continuously contribute to the aging management of concrete structures in nuclear power plants.

References

Architectural Institute of Japan. (2015). Guidelines for maintenance and management of structures in nuclear facilities (in Japanese). Maruzen.

Igarashi, G., Maruyama, I., Nishioka, Y., & Yoshida, H. (2015). Influence of mineral composition of siliceous rock on its volume change. *Construction and Building Materials*, 94, 701–709.

Ishikawa, S., Maruyama, I., Takizawa, M., Etoh, J., Kontani, O., & Sawada, S. (2019). Hydrogen production and the stability of hardened cement paste under gamma irradiation. *Journal of Advanced Concrete Technology*, 17(12),

Kambayashi, D., Maruyama, I., Kontani, O., Sawada, S., Ohkubo, T., Murakami, K., & Suzuki, K. (2023a). Impact of Radiation-induced Expansion of Aggregate on Structural Performance of Hollow Cylindrical RC Member. *Journal of Advanced Concrete Technology*, 21(7), 536–554.

Kambayashi, D., Maruyama, I., Kontani, O., Sawada, S., Ohkubo, T., Murakami, K., & Suzuki, K. (2023b). Tension stiffening affected by radiation-induced volume expansion of aggregate. *Journal of Advanced Concrete Technology*, 21(5), 351–366.

Kambayashi, D., Sasano, H., Sawada, S., Suzuki, K., & Maruyama, I. (2020). Numerical Analysis of a Concrete Biological Shielding Wall under Neutron Irradiation by 3D RBSM. *Journal of Advanced Concrete Technology*, 18(10), 618–632.

Kojima, M., Nakano, M., & Taguchi, K. (2019). NRA Technical Report Series, Effects of Neutron Irradiation on Concrete Strength, NTEC-2019-1001 (p. 59). Nuclear Regulatory Authority.

Lin, M., Itoh, M., & Maruyama, I. (2015). Mechanism of Change in Splitting Tensile Strength of Concrete during Heating or Drying up to 90°C. *Journal of Advanced Concrete Technology*, 13(2), 94–102.

Maruyama, I., Takizawa, M., Sato, O., Etoh, J., Kontani, O., Sawada, S., & Ishikawa, S. (2017). Post-Japanese NRA Research Project On Soundness Evaluation Criteria For Radiation-Induced Concrete Degradation. In Iaea (Ed.), IAEA Fourth International Conference on Nuclear Power Plant Life Management (pp. CN246-70). IAEA.

Maruyama, Ippei, Haba, K., Sato, O., Ishikawa, S., Kontani, O., & Takizawa, M. (2016). A numerical model for concrete strength change under neutron and gamma-ray irradiation. *Journal of Advanced Concrete Technology*, 14(4), 144–163.

Maruyama, Ippei, & Igarashi, G. (2015). Numerical approach towards aging management of concrete structures: Material strength evaluation in a massive concrete structure under one-sided heating. *Journal of Advanced Concrete Technology*, 13(11), 500–527.

Maruyama, Ippei, Igarashi, G., & Nishioka, Y. (2015). Bimodal behavior of C-S-H interpreted from short-term length change and water vapor sorption isotherms of hardened cement paste. *Cement and Concrete Research*, 73, 158–168. https://doi.org/10.1016/j.cemconres.2015.03.010

Maruyama, Ippei, Ishikawa, S., Yasukouchi, J., Sawada, S., Kurihara, R., Takizawa, M., & Kontani, O. (2018). Impact of gamma-ray irradiation on hardened white Portland cement pastes exposed to atmosphere. *Cement and Concrete Research*, 108(vember 2017), 59–71.

Maruyama, Ippei, Kondo, T., Sawada, S., Halodova, P., Fedorikova, A., Ohkubo, T., Murakami, K., Igari, T., Rodriguez, E. T., & Suzuki, K. (2022). Radiation-induced alteration of meta-chert. *Journal of Advanced Concrete Technology*, 20(12), 760–776.

Maruyama, Ippei, Kontani, O., Takizawa, M., Sawada, S., Ishikawa, S., Yasukouchi, J., Sato, O., Etoh, J., & Igari, T. (2017). Development of soundness assessment procedure for concrete members affected by neutron and gamma-ray irradiation. *Journal of Advanced Concrete Technology*, 15(9), 440–523.

Maruyama, Ippei, Meawad, A., Kondo, T., Sawada, S., Halodova, P., Fedorikova, A., Ohkubo, T., Murakami, K., Igari, T., Rodriguez, E. T., Maekawa, K., & Suzuki, K. (2023). Radiation-induced alteration of sandstone concrete aggregate. *Journal of Nuclear Materials*, 583, 154547.

Maruyama, Ippei, Nishioka, Y., Igarashi, G., & Matsui, K. (2014). Microstructural and bulk property changes in hardened cement paste during the first drying process. *Cement and Concrete Research*, 58, 20–34.

Maruyama, Ippei, & Rymeš, J. (2019). Temperature dependency of short-term length-change and desorption isotherms of matured hardened cement. *Journal of Advanced Concrete Technology*, 17(5), 188–194.

Maruyama, Ippei, Sasano, H., Nishioka, Y., & Igarashi, G. (2014). Strength and Young's modulus change in concrete due to long-term drying and heating up to 90 ℃. *Cement and Concrete Research*, 66, 48–63.

Sasano, H., & Maruyama, I. (2021). Mechanism of drying-induced change in the physical properties of concrete: A mesoscale simulation study. *Cement and Concrete Research*, 143, 106401.

Sasano, H., & Maruyama, I. (2024). Investigation into the changes in the splitting tensile strength of concrete subjected to long-term drying using a three-phase mesoscale RBSM. *Cement and Concrete Composites*, 148, 105462.

Sasano, H., Maruyama, I., Sawada, S., Ohkubo, T., Murakami, K., & Suzuki, K. (2020). Meso-Scale Modelling of the Mechanical Properties of Concrete Affected by Radiation-Induced Aggregate Expansion. *Journal of Advanced Concrete Technology*, 18(10), 648–677.

Resilience of Reinforced Concrete Structures in Corrosive Conditions

R.E. Melchers*

Centre for Infrastructure Performance and Reliability, The University of Newcastle, Callaghan, Australia
E-mail: rob.melchers@newcastle.edu.au

*Corresponding author

ABSTRACT

Reinforced concrete structures, properly made, can endure very aggressive conditions for very long periods of time without reinforcement corrosion or concrete deterioration. Evidence for this has been available for many years but largely ignored in the face of results from laboratory experiments, even though these do not properly represent the behaviour of actual concrete structures. For high quality well-compacted, low-permeability concretes it is not the inward diffusion of oxygen that controls the rate of long-term corrosion but the slow outward leaching of concrete alkalis, aided in the case of $Ca(OH)_2$ by the presence of chlorides. So-called 'carbonation' of concrete usually assumed to cause reinforcement corrosion, is contrary to basic thermodynamic principles. The critical mechanism is the slow loss by outward leaching of $Ca(OH)_2$. The calcium carbonate layer ("carbonation') on the external surface in fact acts as a diffusion barrier for such leaching. There is increasing evidence that reinforcement corrosion may be the result of the break-down of concrete protection through alkaline-silicate reactivity (ASR) or alkaline-aggregate reactivity (AAR) of the aggregates in the concrete. Comments are made also about the possible advantages of use of coarse calcareous aggregates instead of fine-ground limestone.

KEYWORDS*: Reinforcement, Corrosion, Marine, Carbonation, Long-term.*

1. Introduction

Reinforced concrete (RC) is a well-established and enduring material extensively used in infrastructure applications. Properly made RC structures can endure very aggressive conditions for very long periods of time without reinforcement corrosion or concrete deterioration. Despite relatively recent concerns about the durability and hence resilience of RC structures in aggressive environments (Gjorv 2009) multiple counter examples exist that demonstrate, for actual RC structures, long-term durability - in some cases over 100 years. This raises the question why some RC structures have shown poor durability and others very good durability. Herein the focus is on bare concrete exposed to natural environments (atmosphere, water immersion). Structures protected by a physical barrier (e.g. ceramic or other low permeability tiles), protective but not impermeable coatings such durable paints or bituminous materials, or enclosed within the weather-proof skin of a building, or subject to cathodic protection are all much less prone to deterioration. However, all these protective systems require adequate (and periodic) maintenance.
Despite the extended use of RC structures, understanding of their durability has remained unclear until recently mainly as a result of insufficient detailed examination and comparisons for actual RC structures (as distinct from laboratory samples) and poorly developed understanding of the mechanisms involved in the development of the natural process of corrosion of steel in wet environments (as distinct from the widely-used electrochemical experiments that attempt to accelerate the corrosion process).

2. Chloride-induced' reinforcement corrosion

Chlorides such as in seawater have long been held to be the main threat for reinforcement in concretes. Many laboratory tests have shown that as the chloride concentration increases the risk of corrosion also increases. But there is a problem with such observations - they were nearly always carried out in solutions

rather than actual concrete and the solutions were *stirred*, largely to accelerate the reactions. In actual concretes, however, any porewater solutions are stagnant. This makes an enormous difference to the outcomes. It has been known since at least 1908 that the addition of salts (including NaCl) to stagnant solutions has almost no effect on the rate of early corrosion, and this has been clearly demonstrated in carefully controlled experiments by Mercer and Lumbard (1995) showing that the rate of stirring is the primary driver, not the chloride concentration. Further, attempts to rationalize the many conflicting and widely varying estimates of the 'critical chloride concentration' to initiate reinforcement corrosion have been unsuccessful (Angst et al. 2009), with some efforts being made to try to find alternative scenarios, so far without success (Melchers 2021).

Both longer-term laboratory tests of model reinforced concretes and much closely examined actual concrete structures have led to the conclusion that the critical issue is not the presence of chlorides but the presence of air-voids and water at the interface between the reinforcement steel and the concrete (Melchers and Chaves 2019, 2020, Melchers 2021). Detailed observations of concretes over 80 years exposed to Pacific Ocean immersion tidal, splash and atmospheric zones have shown that concretes well-compacted, with no presence of voids next to the bars show no signs of any reinforcement corrosion (Melchers et al. 2017). This has been found also for other structures, including the Phoenix caissons used off the coast of France during WW2 (Melchers and Howlett 2020). For these the extensive damage that can be clearly seen in drone images is due to storm damage (Jellet 1948) rather than reinforcement corrosion. This example highlights the need to be very careful in damage assessment and in objective interpretation of information.

Reinforcement corrosion will initiate at the edges of the voids, through a process known in the corrosion literature as 'differential aeration'. It uses the water and oxygen in the void, both perhaps replenished, in poor quality, highly permeable concretes with poor quality inadequate thickness concrete cover, by inward diffusion. At the same time, and with the same parameters, outward diffusion of concrete alkalis can occur. Of these the most important is the alkali calcium hydroxide ($Ca(OH)_2$). It has a slow rate of dissolution in water, but this rate is accelerated by up to about 60% in the presence of chlorides (Johnson and Grove 1931). Once the residual pH from the $Ca(OH)_2$ reaches less than about 9 corrosion, if initiated, can continue.

It follows that about from chlorides being hygroscopic and therefore retaining water longer within the concrete, the main effect of chlorides is in the longer-term rate of corrosion. But it is clear that for design, the main effort should go into ensuring that initiation does not begin - and that requires low permeability concretes well-compacted around the bars. Unfortunately, this very practical issue has not been a matter of much interest for academic research and has so far received little attention from academic researchers.

3. Carbonation-induced' reinforcement corrosion

Carbon dioxide constitutes only some 400 ppm (0.04%) of the atmosphere but is held responsible for a phenomenon known as 'carbonation' of concrete that then is held responsible for reinforcement corrosion on the basis that carbonation lowers the pH of the concrete around the reinforcement bars sufficiently to initiate corrosion. Unfortunately, this runs counter to long-established research on real concrete structures (rather than laboratory tests) that showed a disconnect between the depth of carbonation (the depth to which carbon dioxide had penetrated into the concrete) and the initiation of reinforcement (Hamada 1968). The current thinking on carbonation is directly almost exclusively to estimating the depth of carbon dioxide penetration and then assuming that this 'carbonation front' represents the direct risk to corrosion initiation. This follows from the notion that the carbon dioxide CO_2 reacts with the alkali calcium hydroxide $Ca(OH)_2$ within the concrete to produce calcium carbonate and calcium bicarbonate.

The net result is that the local pH of the concrete is reduced to around 9.5-10 (Richardson 2002). This is not low enough for the thermodynamics to allow corrosion to initiate. Leaching of alkalis is required to achieve that through lowering the pH even further (Melchers and Richardson 2023). The mis-match has gradually become recognized, with a RILEM committee proposing that more research attention needs to be given to the conditions that permit reinforcement corrosion to occur rather than the depth of carbonation (RILEM 2020).

Finally, because the molecular size of CO_2 is relatively large, its diffusion through concrete usually is slow, much slower than that of oxygen (O_2) or water (H_2O). Thus, for most good quality, high density, low permeability concretes, carbonation usually is not of practical concern (Parrott, 1987). This is important because carbonation of concretes has been identified as beneficial in helping alleviate climate issues (IPCC 2023).

4. Concrete alkali-aggregate reactivity and reinforcement corrosion

Alkali-aggregate reactivity (AAR) is the chemical action of alkalis in the concrete on some types of aggregate, primarily causing slow, long-term expansion of the aggregate and hence the concrete matrix. Alkali-silicate reactivity (ASR) is the most common form, that may affect some dolomites and even limestones. Reactivity can be identified, with some degree of accuracy (Lindgård et al. 2012).
The realization that AAR may affect reinforced concrete structures has taken a long time (Broekmans 2012). Sometimes field observations show cracking somewhat aligned with that of the reinforcement bars closest to the surface (Godart and de Rooij 2017). This has meant that superficial examination might leas to the conclusion that the cracking was caused by reinforcement corrosion rather than that the cracking permitted reinforcement corrosion to occur. The latter is likely a much more severe problem than commonly acknowledged (Melchers and Humphrey 2023).

5. Limestone as aggregate

Finely ground limestone has been proposed as a part substitute or replacement for cement in an effort to reduce green-house gas emissions resulting from cement-making (Palm et al. 2016). However, the need for fine grinding of the limestone rock remains and this has environmental implications. Recently it has been shown that the use of coarse limestone aggregate can be beneficial in reducing concrete permeability and increasing strength through the improved bonding between cement reaction products and limestone surfaces. The improved bonding has been known for many years (Farran 1956) and would have been accepted as 'normal' in those locations where limestone or dolomite aggregates are the norm. However, in more modern tests the difference between these and other aggregate types became apparent for model concretes, over a variety of water-cement and aggregate-cement ratios with only the aggregates being different (Melchers et al. 2024). The full implications of these results remain for further study.

6. Discussions

Concern about the durability of RC structures is not new, but many lessons of the past appear to have been ignored or not absorbed into the scientific literature, perhaps because experiences differed. This has been illustrated by interpretations of reinforcement corrosion for highway bridges, for which physical damage caused by heavy-duty traffic loading and inadequate concrete cover and often the lack of a bitumen riding surface has been clearly identified (e.g. Volkswein and Dorner, 1986) even though de-icing salts (calcium and sodium chlorides) are still held as the primary causative agent. As noted also for AAR of concrete, the causative agent too often has been assumed *a priori* to be chlorides or carbonation, without proper consideration of other causes. Although not discussed herein, deep concrete cracking, deep enough to reach the reinforcement, also can have serious consequences for long-term corrosion of reinforcement, a matter hardly considered in the existing literature and ignored by codified requirements that focus only on crack width.

7. Conclusions

In this review it was shown that for good quality, well-compacted concretes:

1. Chlorides, long held to be the primary driver for reinforcement corrosion in marine conditions, can have an effect on the progression of corrosion once it as initiated but not in initiation,
2. Carbonation of concrete does not lower the concrete pH sufficiently to permit reinforcement corrosion. The latter also requires sufficient loss of concrete alkalis.
3. Concrete strength deterioration due to alkali-aggregate reactivity of the concrete can permit reinforcement corrosion to occur and appears in many cases to have been mis-diagnosed as reinforcement corrosion causing concrete cracking,
4. The use of limestone or dolomite as concrete aggregates may have beneficial environmental effects in regions where such aggregates have not been used.

References

Angst, U., Elsener, B., Larsen, C.K. and Vennesland, O. (2009) "Critical chloride content in reinforced concrete – A review", *Cement and Concrete Research,* 39: 1122-1138.

Broekmans, M.A.T.M. (2012) "Deleterious reactions of aggregate on concrete", *Re. Mineralogy & Geochem.*, 74: 281.

Farran, J. (1956). "Contribution minéralogique à l'étude de l'adhérence entre les constituants hydratés des ciments et les matériaux enrobés", *Revue des matériaux de construction*, Nos. 490-491, 491: 155-172, 191-209.

Gjorv, O.E. (2009) "Durability design of concrete structures in severe environments", London, Taylor & Francis.

Godart, B. and de Rooij, M.R. (2017) "Diagnosis, appraisal, repair and management", Ch 5. (in) Sims, I. & Poole, A. (Eds.) *Alkali-aggregate reaction in concrete: A world review*, CRC Press, Boca Raton.

Hamada, M. (1968) "Neutralization (carbonation) of concrete and corrosion of reinforcing steel", (in) Proc., 5th Int. Symp. on Chemistry of Concrete, Vol. 3 Part 3 Carbonation of Concrete, 343-369.

IPCC (2023) Intergovernmental Panel on Climate Change, 6th assessment report, https://www.ipcc.ch/report/ar6/wg1/downloads/report/IPCC_AR6_WGI_Full_Report.pdf (last accessed 3 March 2023).

Jellett J.H. (1948) "The lay-out, assembly, and behaviour of the breakwaters at Arromanches Harbour (Mulberry B)". In *The Civil Engineer in War*, Vol 2 – Docks and Harbours. Inst. of Civil Engineers, London, UK: 291–312.

Johnston, J. and Grove, C. (1931) "The solubility of calcium hydroxide in aqueous salt solutions". *Journal of the American Chemical Society*, 53 (11) 3976–3991.

Lindgård, J., Andiç-Çakır, Ö., Fernandes, I., Rønning, T. F. and Thomas, M. D. A. (2012) "Alkali–silica reactions (ASR): Literature review on parameters influencing laboratory performance testing". *Cement and Concrete Research*, 42(2), 223-243.

Melchers, R.E. (2021) "Experienced-based physico-chemical models for long-term reinforcement corrosion", *Corros. Materials Degradation*, *I*(1), 100-119.

Melchers R.E. and Chaves, I.A. (2019) "Reinforcement corrosion in marine concretes - 1: Initiation", *ACI Materials Journal*, 116(5) 57-66.

Melchers R.E. & Chaves, I.A. (2020) "Reinforcement Corrosion in Marine Concretes - 2. Long-Term Effects", *ACI Materials Journal*, 117(2) 217-228.

Melchers, R.E. and Howlett C.M. (2020) "Reinforcement corrosion of the Phoenix caissons after 75 years of marine exposure", *Proc. Inst. Civil Engrs, Maritime Engineering*, 174(1019-30.

Melchers, R.E. and Humphrey, H. (2023) "Concrete alkali-aggregate reactivity and initiation of steel reinforcement corrosion", *Corrosion and Materials Degradation*, 4: 428-444.

Melchers, R.E., Papé, T.M., Chaves, I.A. & Heywood, R. (2017) "Long-term durability of reinforced concrete piles from the Hornibrook Highway bridge", *Australian J. Structural Engineering*, 18(1): 41-57.

Melchers R.E. and Richardson, P.J. (2023) "Carbonation, neutralization and reinforcement corrosion for concrete in long-term atmospheric exposures", *Corrosion*, 79(4) 395-404.

Melchers R.E., Chaves I.A. and Simundic G. (2024) "Effect of coarse calcareous aggregates on corrosion of steel reinforcement in marine conditions", *Structure and Infrastruct. Eng*

Mercer, A.D. and Lumbard, E.A. (1995) "Corrosion of mild steel in water", *Brit. Corrosion J*., 30 (1) 43-55.

Palm S., Proske T., Rezvani M., Hainer S. and Müller C. (2016). "Cements with a high limestone content - Mechanical properties, durability and ecological characteristics of the concrete". *Constr. and Building Mat.,* 119, 308-318.

Parrott, L.J. (1987) "A review of carbonation in reinforced concrete", Building Res. Est., Dept. of the Env., UK.

Richardson, M.G. (2002). "Fundamentals of durable reinforced concrete". London: SponPress.

RILEM TC 281-CCC (2020) "Corrosion of steel in carbonated concrete: mechanisms, practical experience, and research priorities - a critical review", *RILEM Technical Letters*, 5: 85-100.

Stefanoni, M., Angst, U. and Elsener, B. (2018) "Corrosion rate of carbon steel in carbonated concrete - A critical review", *Cement and Concrete Research*, 103: 35-48.

Volkswein, A. and Dorner, H. (1986) "Untersuchungen zur Chloridkorrosion der Bewehrung von Autobahn-Brucken aus Stahl-oder Spannbeton, Forschung Strassenbau und Strassenverkehrstechnik", Heft 460, Bundesminister fur Verkehr, Abteilung Strassenbau, Bonn-Bad Godesberg, Germany.

Next Generation of Integrated Low-Damage Precast Building Systems to Enhance Community Resilience and Sustainability

S. Pampanin[1*]

[1] *Sapienza University of Rome, Italy*
Email: stefano.pampanin@uniroma1.it

[*]Corresponding author

ABSTRACT

The severe socio-economical impact of recent earthquake events have further highlighted the severe mismatch between societal expectations over the reality of seismic performance of modern buildings. A paradigm shift in performance-based design criteria and objective towards damage-control or low-damage design philosophy and technologies is urgently required.

This paper and associated plenary lecture presentation will provide an overview of recent advances and unique opportunities to enhance the community resilience and sustainability, based on the development and implementation of the next generation of precast concrete technologies for an integrated (skeleton + non-structural elements) low-damage building systems.

KEYWORDS*: Low-damage Building System, Resilient Community, Safety and Sustainability, Precast Concrete, Jointed Ductile Connections*

1. Need for a Paradigm Shift: from Life-Safety to Low- Damage and Minimum Losses

Targeting Life Safety is clearly not enough for the general public, who would rather expect an "earthquake-proof" building. The overall performance of the modern building stock, represented in a schematic in Figure 1 (left), where structural, non-structural and soil-structure interactions aspects are summarized, has come with a shocking surprise to the general population. The new challenge for the Earthquake Engineering community is to "raise the bar" and develop cost-effective design methodologies and technologies for the Next Generation of high performance Low-damage (Damage-Control) building systems (Figure 1 right)

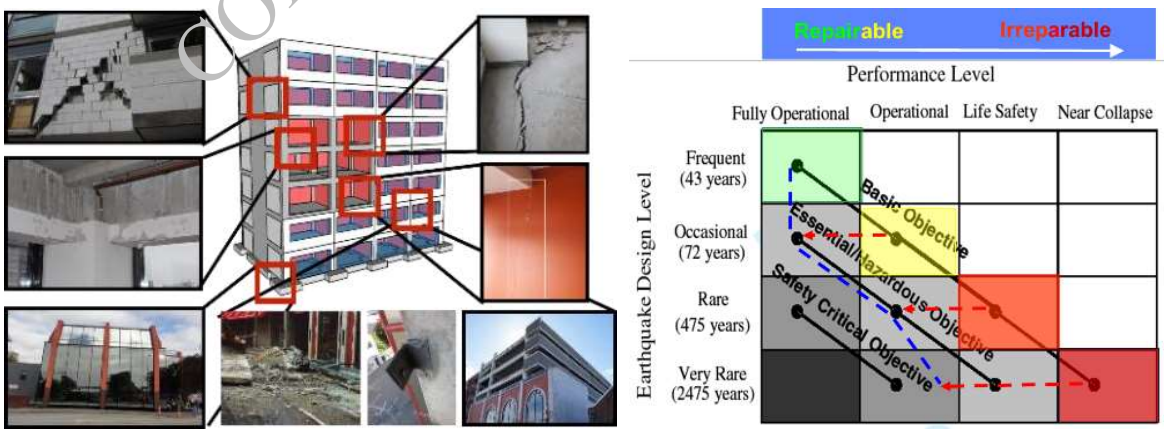

Figure 1. Left: schematics of damage/performance to a modern code-based building (modified after Johnston et al., 2014); Right: performance objective matrix modified from SEAOC Vision 2000 (1995) to emphasize a damage-control objective and design philosophy (modified after Pampanin, 2009, 2012, 2015)

2. The Next Generation of Integrated Low-Damage Building Systems: From Theory to Practice

In the past decades, particular interest and effort has been focusing on the development of so called "low-damage" systems, based on dry jointed ductile connections (PRESSS or PRES-LAM technologies in concrete and timber, respectively), through unbonded post-tensioning, with a peculiar controlled rocking & dissipative mechanisms, see Fig. 2 (Priestley, 1991, Stanton et al., 1997, Priestley et al., 1999, Pampanin, 2005, 2012; NZCS, 2010).
During the shaking, the inelastic demand is accommodated through a *controlled rocking* (dissipative and re-centering mechanism) within the connection itself The effects is similar to a fuse action, or "internal isolation mechanism" with negligible or no damage in the structural elements, when compared to a traditional monolithic systems relying upon plastic hinges (material damage). The rocking-dissipative system can also include special external and replaceable dissipaters, referred to as *Plug&Play*, acting as seismic fuses, easy to access, and, if needed, be replaced after an earthquake (Pampanin, 2005; Marriott et al., 2008, NZCS, 2010; Sarti et al., 2013).

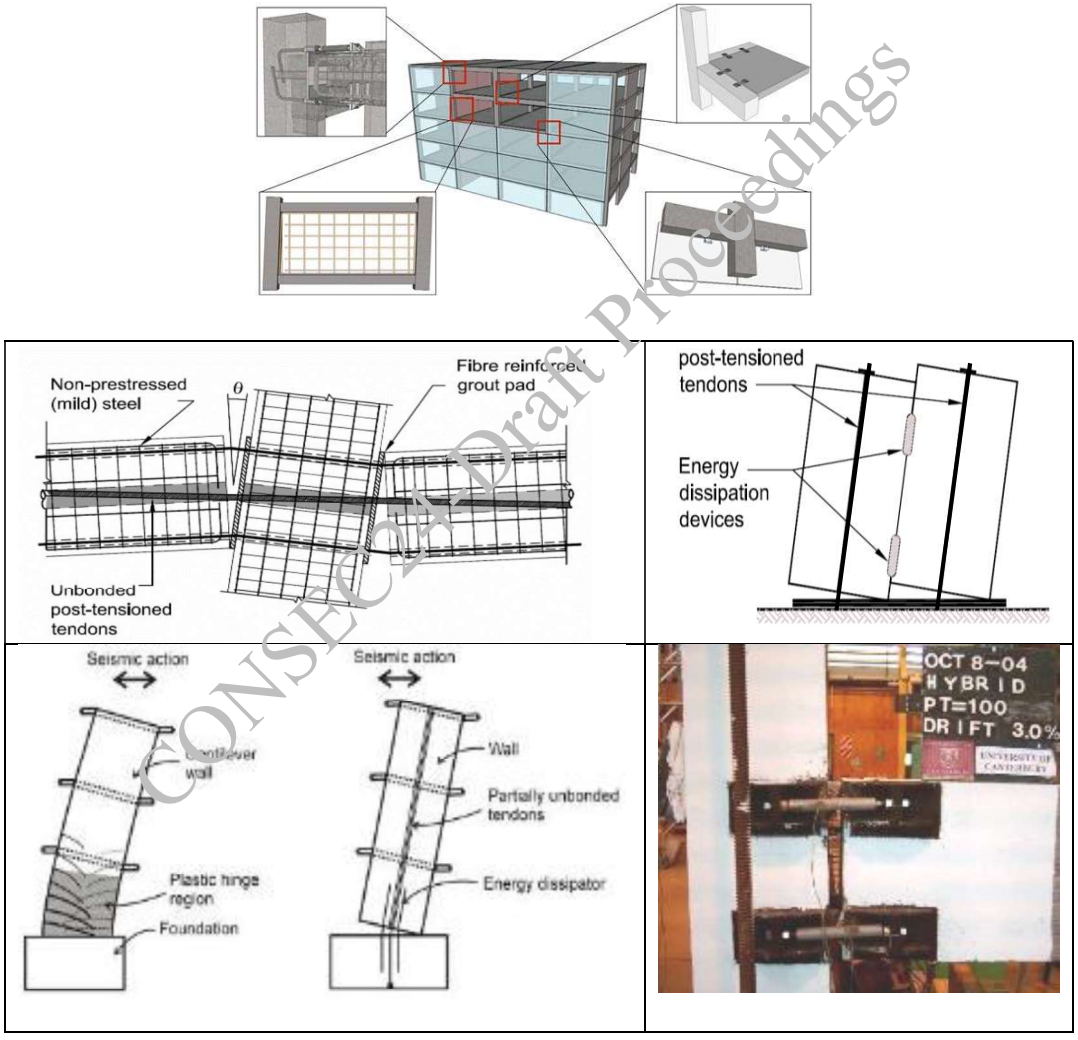

Figure 2. Concept of integrated (structure/skeleton including floor/diaphragms, and non-structural/envelope) low-damage building system (modified after Johnston et al., 2014, Pampanin et al. 2002-)

In order to achieve am integrated low-damage building system, a substantial effort has been dedicated at the University of Canterbury since 2009 to the development of equivalent low-damage non-structural components counterparts (Palermo, Pampanin et al., 2010), either in the form of vertical elements, e.g. infills/partitions (Tasligedik et al., 2012) and façades (Baird et al., 2011), as well as horizontal components, e.g. ceilings (Dhakal et al., 2014).

In the case of drift-sensitive non-structural components, the conceptual solution relies upon the development of an articulated internal rocking mechanism or jointed system to accommodate the overall drift demand within few discrete locations between adjacent panels and between panel and surrounding frame (Fig. 3). Alternatively, in the case of precast concrete facades/claddings, the target strategy could rely upon either a full disconnection between the facade and the bare structures or a controlled disconnection with supplemental damping. For example, horizontal sliding jointed articulated details can be employed, with alternative connection solutions and detailing, relying upon rods of different length, and/or slotted-bolted connections, and/or dissipative systems, such as the U-shape Flexural Plates (Skinner et al, 1972; Priestley et al., 1999, Baird et al., 2011). An overview on state of art of alternative solutions and fragility functions for most typical traditional and innovative low-damage solutions for architectural non structural vertical elements (facades, partitions) can be found in Bianchi and Pampanin, 2022.

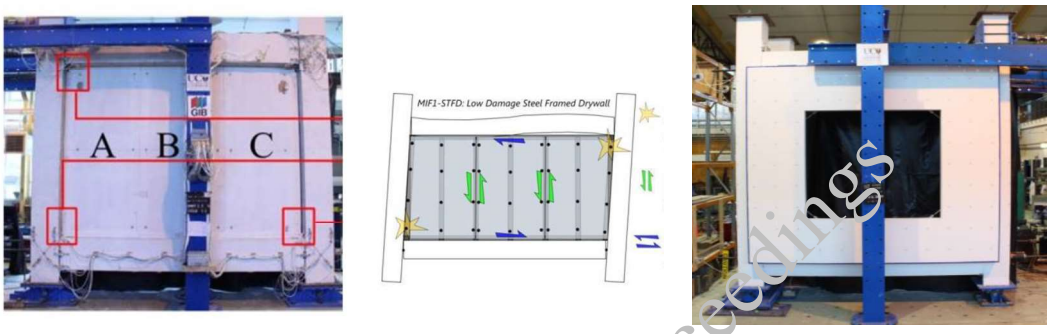

Figure 3. Low-damage solution for: Left – infilled walls/partitions (after Tasligedik et al., 2014. 2015); Right – precast concrete facades with UFP connectors (after Baird et al., 2014)

3. On Site Implementation of Low-Damage Building Systems

A wide range of alternative arrangements of jointed ductile connections using Low-Damage Precast Concrete (referred to as PRESSS) technology is currently available to designers and contractors for practical applications. On site implementations have occurred in different seismic-prone countries around the world, e.g. U.S., Central and South America, Europe and New Zealand (Fig 4). Overviews of research and developments, design criteria and examples of on-site implementations can be found for in Pampanin et al., (2005) and in the PRESSS Design Handbook (NZCS, 2010) for precast concrete structures.

Figure 4. Top: First multi-storey PRESSS buildings in NZ. Unbonded Post-Tensioned (PT) frames with external Plug&Play dissipaters and PT walls coupled with steel beams (Struct. Engineers: Dunning Thornton Consultants; Cattanach and Pampanin, 2008). Bottom: Southern Cross Hospital Endoscopy Building, Christchurch. PT frames with internal (top-only) mild steel and PT walls coupled with UFPs (Struct. Engin.: Structex Metro, Pampanin et al., 2011).

4. Seismic loss reduction of low-damage integrated building systems

Cost/performance-based evaluations of integrated building systems, implementing either traditional or low-damage technology for the structural skeleton and/or the building envelope (Bianchi et al., 2018, 2020, Ciurlanti et al., 2023) confirmed the significant benefits - in terms of expected annual losses (EAL) - of adopting an integrated structural/non-structural low-damage system (Fig. 5). Worth noting that the sole implementation of low-damage non-structural components in combination with traditional structural skeletons would lead to a considerable reduction of repair costs, especially for heavy infill walls.

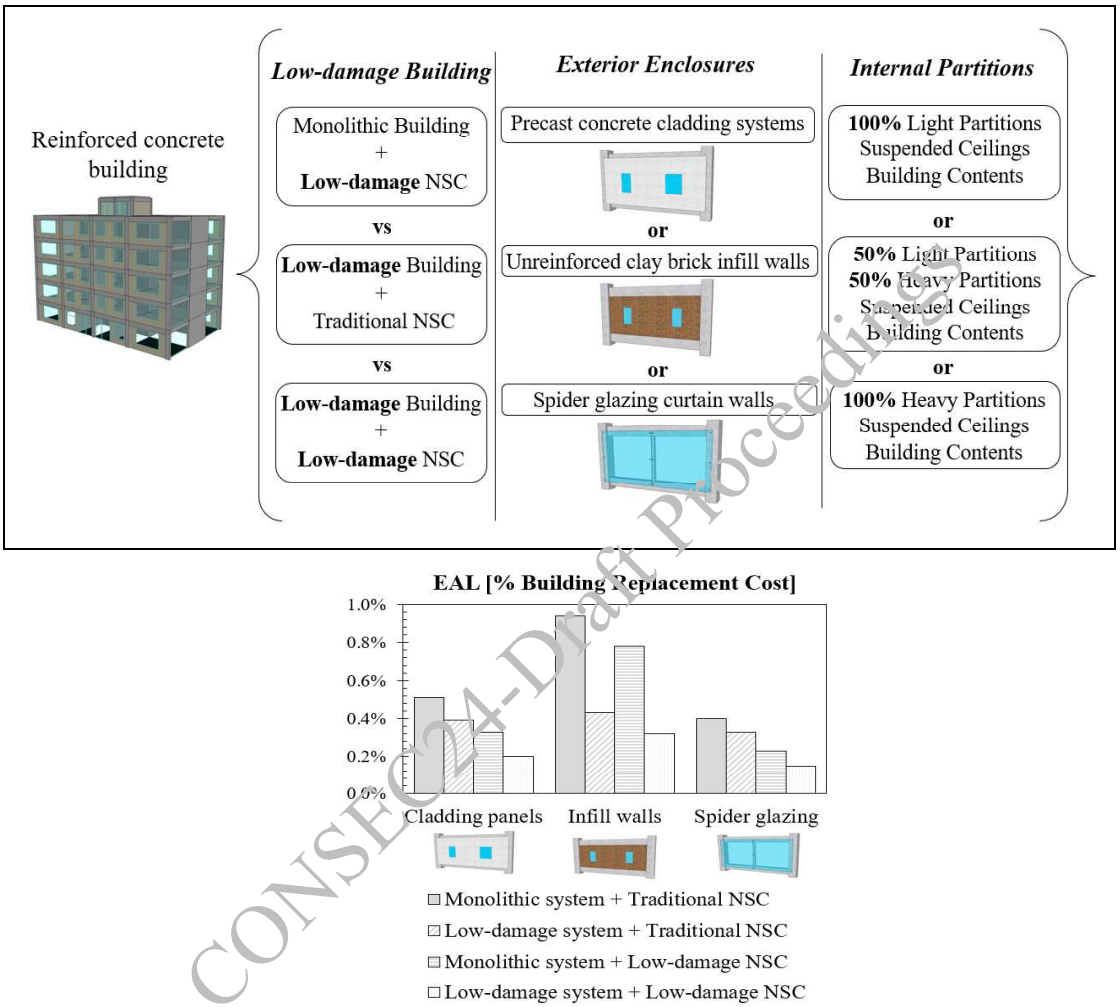

Figure 5. Top: Integrated Building System Configurations (modified after Bianchi et al., 2018, 2020): 1) a monolithic structure with low-damage non-structural components; 2) a low-damage structure with traditional non-structural component: 3) an integrated structural/non-structural low-damage system bottom: Comparison of Expected Annual Losses (EAL) values for the case of Light partitions (modified after Bianchi et al., 2018,2020)

References

Baird, A., Tasligedik, A., S., Palermo, A., Pampanin, S., 2014 Seismic Performance of Vertical Non-Structural Components in the 22nd February 2011 Christchurch Earthquake

Bianchi, S., Ciurlanti, J., Pampanin, S., 2020, Comparison of traditional vs low-damage structural and non-structural building systems through a cost/performance-based evaluation, *Earthquake Spectra*

Bianchi, S.,Ciurlanti, J.,Perrone, D.,Filiatrault, A., Costa, A. C., Candeias, P. X.,Correia, A.A., Pampanin, S. 2021. Shake-table tests of innovative drift sensitive nonstructural elements in a low-damage structural system. *Earthquake Engineering and Structural Dynamics*, 50(9), 2398–2420

Bianchi, S., Pampanin S., 2022 Fragility Functions for Architectural Nonstructural Components, *Journal of Structural Engineering (United States)*, Volume 148, Issue 101, Article number 03122005

Cattanach A., and Pampanin, S., 2008. 21st Century Precast: the Detailing and Manufacture of NZ's First Multi-Storey PRESSS-Building, *NZ Concrete Industry Conference*, Rotorua

Ciurlanti, J., Bianchi, S., & Pampanin, S. 2023. Raising the bar in seismic design: Cost–benefit analysis of alternative design methodologies and earthquake-resistant technologies. *Bulletin of Earthquake Engineering*

Devereux, C.P., Holden, T.J., Buchanan, A.H., Pampanin, S., 2011. NMIT Arts & Media Building - Damage Mitigation Using Post-tensioned Timber Walls, *Proceedings of the Ninth Pacific Conference on Earthquake Engineering, "Building an Earthquake-Resilient Society*", 14-16 April, Auckland, New Zealand, paper 90

Dhakal, R.P., Pampanin, S., Palermo, A., MacRae, G, Pourali, A., Tasligedik, S., Yeow, T., Baird, A.. 2014, Seismic Performance of Non-Structural Components and Contents in Buildings: *An Overview of NZ Research, Int. Workshop in Non-Structural Element*, China

fib, 2003, International Federation for Structural Concrete. Seismic Design of Precast Concrete Building Structures. Bulletin No. 27, Lausanne, 254

Johnston, H., Watson, C., Pampanin, S., Palermo, A., 2014. Shake Table Testing of an Integrated Low Damage Building System, 2nd ECEES, Istanbul 25-29 Aug

Kam W.Y., Pampanin S., Palermo A., Carr A. 2010. Self-centering structural systems with combination of hysteretic and viscous energy dissipations. *EESD*; 39:10, 1083-1108.

Kam, W.Y., Pampanin, S., Elwood, K., 2011. Seismic Performance of Reinforced Concrete Buildings in the 22 February Christchurch (Lyttleton) Earthquake, Special Issue, *Bulletin of the New Zealand Society of Earthquake Engineering*, Vol. 44(4), 239-279, ISSN 1174-9875

Marriott, D., Pampanin, S. , Palermo A., 2008 Quasi-static and Pseudo-Dynamic Testing of Unbonded Post-tensioned Rocking Bridge Piers with External Replaceable Dissipaters, *EESD*,38(3): 331-354, March

Marriott, D., Pampanin, S., Bull, D., Palermo A., 2008. Dynamic Testing of Precast, Post-Tensioned Rocking Wall Systems with Alternative Dissipating Solutions, *Bulletin of the NZ Society for Earthq. Engineering*, 41(2): 90-103

NZCS, Wellington

Pampanin, S., 2005. Emerging Solutions for High Seismic Performance of Precast -Prestressed Concrete Buildings, *ATC Journal*, invited paper, 3(2), 202-222.

Pampanin, S., 2012. Reality-check and Renewed challenges in Earthquake Engineering: Implementing low-damage structural Systems – from theory to practice, *Bulletin of the New Zealand Society for Earthquake Engineering*, 45(4), pp. 137-160, December, ISSN 1174-9875. Keynote Lecture, 12th WCEE, Lisbon 2012.

Pampanin, S., 2015 "Towards the "ultimate earthquake-proof" building: development of an integrated low-damage system Chapter in Perspectives on European Earthquake Engineering and Seismology, Ansal A. (ed.); *Series: Geotechnical, Geological and Earthquake Engineering.* 39 (13) 321-358

Pampanin, S., 2022. NextGen building systems - S4: Seismically safer, sustainable and smart - raising the bar to enhance community resilience and sustainability *Springer Proceedings in Earth and Environmental Sciences*, 343 – 3622022; doi:10.1007/978-3-031-15104-0_21

Pampanin, S., Ciurlanti, J., Bianchi, S., Perrone, D., Granello, G., Palmieri, M., Grant, D.N., Palermo, Al., Costa, A.C., Candeias, P.X., Correia, A.A., 2023. Triaxial shake table testing of an integrated low-damage building system, *Earthquake Engineering and Structural Dynamics* , 52(10), 2983–3007

Priestley, M. J. N., Sritharan, S., Conley, J. R. and Pampanin, S., 1999. Prelim. results and conclusions from the PRESSS five-story precast concrete test building. PCI J., 44(6), 42-67.

Sarti, F., Smith, T., Palermo, A., Pampanin, S. Bonardi, D., Carradine, D.M. 2013. Experimental and analytical study of replaceable Buckling-Restrained Fused-type (BRF) mild steel dissipaters, NZSEE Conf., Wellington, 26-28 April

Tasligedik, A.S., Pampanin, S., Palermo, A., 2014, Low-damage Seismic Solutions for non-structural drywall partitions, *Bulletin of Earthquake Engineering* 13(4): 1029-1050, 13 (4), 1029-1050, 2015

Design Considerations, Experimental Testing, and Field Applications of HPFRC Reinforcement in Bridge Piers

I. Beltracchi[1], I. Trabucchi[2], A. Reggia[3*], G.A. Plizzari[4]

[1] DICATAM, University of Brescia, Brescia, Italy
Email: ivan.beltracchi@unibs.it
2 DICATAM, University of Brescia, Brescia, Italy
Email: ivan.trabucchi@unibs.it
3 DICATAM, University of Brescia, Brescia, Italy
Email: adriano.reggia@unibs.it
4 DICATAM, University of Brescia, Brescia, Italy
Email: giovanni.plizzari@unibs.it

[*]Corresponding author

ABSTRACT

Recent collapses of reinforced concrete (RC) bridges in many Western countries have highlighted significant challenges associated with aging infrastructure. Many of these bridges, constructed over 50 years ago, have deteriorated, raising concerns about their safety and service life. As a consequence, governments and authorities are now focusing on the assessment of the structural safety of RC structures and their impact on the resilience of entire road networks. In this context, this paper deals with some design considerations, experimental testing, and field applications of High-Performance Fiber Reinforced Concrete (HPFRC) as an advanced solution for enhancing the durability and performance of existing bridges, often deteriorated by corrosion. In particular, the paper presents results from an EU-funded project involving the retrofitting of two road bridges in Italy using HPFRC. Within the project, bridge piers and cap beams were successfully retrofitted with a HPFRC jacketing, reducing the need for steel reinforcement and minimizing jacketing thickness to 60 mm. As a further support, an extensive experimental program was carried out at the University of Brescia on structural elements of the real bridges, focusing on the bending behavior of bridge piers through quasi-static tests on 1:2 scaled specimens. The results demonstrate a significant increase of the bearing capacity of the bridge pier under bending by approximately 100%, along with a 30% improvement in ductility, measured through displacement and curvature. The paper includes a discussion on the implications of these findings for design as well as on the implementation of this repair technique. Finally, the paper considers the environmental impacts of the retrofitting solution through a comparative Life Cycle Assessment (LCA), carried out from the cradle-to-gate stage.

KEYWORDS: *Bridge piers, Corrosion, HPFRC, Structural response, Sustainability*

1. Introduction

In many western countries, the extensive efforts to rehabilitate bridges reflect the growing collective awareness of the need to adapt aging structures to meet contemporary traffic demands. Bridges over 50 years old face increasing challenges due to the rising weight and volume of vehicles, the natural degradation of construction materials, and heightened seismic risk awareness. Structural problems are present in reinforced concrete (RC) bridges, often resulting from corrosion caused by concrete carbonation or by the de-icing salts and runoff water due to inadequate waterproofing of the deck (Andrade, 2020; Andrade and Izquierdo, 2020; Buttlar et al., 2018; Enright and Frangopol, 1998).
In Italy, considerations for seismic design in building codes were first introduced in the early 1900s but significantly developed during the 1970s and 1980s with increased awareness of seismic risk. Significant updates in 2003 included the extension of the seismic hazard map to the whole national territory. The 2008 earthquake (around L'Aquila) significantly enhanced the design guidelines, including the seismic safety provisions, and established new procedures for assessing and retrofitting existing constructions based on

vulnerability classifications. As a result of this regulatory evolution, many structures, including the majority of the bridges, were built without considering the seismic resistance.
In addition, the remarkable increase of traffic loads (both in term of weight and number of vehicles), as well as recent bridge failures (in Italy and around the world), underline the need to urgently address these issues through action plans to ensure the safety and efficiency of the entire road transport system (Zanini et al., 2017), which represents the principal transportation route for people and goods in many Countries. Modern repair techniques for retrofitting concrete bridges using new materials and technologies, often more effective than traditional methods, are now codified in current building codes.
High-Performance Fiber-Reinforced Concrete (HPFRC) is increasingly recognized as an effective solution for retrofitting bridge elements such as piers and decks. Based on a high-performance concrete matrix and fibers, HPFRC offers low permeability and high resistance to compression and tension, even after cracking, due to the bridging effect of the fibers. The application of HPFRC through an external jacketing enhances structural performance by increasing resistance to vertical loads and improving the lateral resistance and ductility of vertical elements. Moreover, it effectively protects existing reinforcements by significantly reducing the risk of corrosion of rebars, as they are protected by a durable new layer of concrete.
The present paper concerns the retrofitting of two bridges in Brescia (Italy), constructed in the 1970s, which suffered severe pier corrosion and were retrofitted by using HPFRC jacketing. The retrofitting process is detailed, and experimental tests (carried out at the laboratory for testing materials of the University of Brescia's) for evaluating column behavior before and after HPFRC jacketing are presented and discussed. This application of HPFRC for bridge retrofitting exemplifies the adoption of innovative materials and technologies aimed at enhancing the resilience and longevity of critical transportation infrastructure. The findings from this intervention provide valuable insights into the design of effective approaches to bridge maintenance and rehabilitation.

2. Field application

Two bridges were retrofitted as part of the EU funded Sustainable and Resilient Mobility project (Mo.So.Re) between 2020 and 2021 (Reggia et al., 2022). Each bridge has three spans of about 9 m with two piers as central supports. The latter consist of four-column frames where each column was 41 cm wide and 90 cm deep, and was reinforced with 14Ø16 longitudinal steel rebars and Ø10 stirrups spaced 20 cm. Average concrete strength of the existing piers was 31 MPa while yielding strength of steel reinforcement was about 440 MPa. Figure 1 clearly evidences the significant degradation of piers and cap beams, mainly due to poor water management and damage from de-icing salts. Water ingress through deck joints provoked concrete deterioration and reinforcement corrosion, particularly visible at the cap beam ends and columns. Retrofitting focused on the piers and was mainly based on the removal of degradated external concrete covers to expose internal bars. New longitudinal and transverse reinforcements were added, including eight Ø16 longitudinal bars and Ø12 stirrups every 20 cm in columns, and 4Ø20 top and bottom bars for beams. In the cap beam, additional Ø16 deformed bars spaced 20 cm. were added. A jacketing layer of HPFRC, having 40 to 60 mm thickness, strength class C70/85 and toughness class 6b (according to Model Code 2010), was placed around existing elements. B450C steel rebars (yielding tension of 450 MPa) were used.

(a) (b) (c)

Figure 1. Bridge before intervention (a), detail of corrosion (b), and bridge after repair (c).

3. Experimental program

3.1 Test specimens

The experimental research carried out at the University of Brescia investigated the structural response of the bridge columns to lateral loading (out of the frame plane) by means of four 1:2 scaled specimens: two samples (Reference #1 and #2) represented the original condition, while the other two (Reinforced #1 and #2) simulated the columns after repair. Strengthening consisted in replacing the concrete cover (partially removed to simulate deteriorated concrete removal) with a HPFRC jacketing 20-30 mm thick, increasing the section from 45 × 21 cm to 50 × 25 cm. Fourteen Ø8 bars were post-installed at the base as longitudinal reinforcements with chemical anchors to the foundation.

3.2 Test setup

The experimental test setup described in Figure (a) and (b) included a beam fixed to the base (1) subjected to a quasi-static horizontal load to simulate seismic actions with a cyclic drift-based protocol (ACI (2013)) applied with a horizontal mechanical jack (2). To reproduce the axial load on the column due to the bridge deck, a vertical load was applied to the top of the column using two hydraulic jacks connected to a steel beam above the column (3). The specimens were fixed to the base to prevent rotations and horizontal movements using two hold-down systems (4). The vertical load was kept constant throughout the whole test, with a total average value of 125 kN. Cyclic loading consisted in pushing and pulling phases, with three load repetitions for each target displacement. The maximum displacement at the load point was related to a prescribed drift history as the horizontal load applied at each step was measured by a load cell (5).

3.3 Structural responses

The experimental results, in terms of horizontal load vs. horizontal displacement are shown in Figure 2(c) with the average envelope curves of cyclic loading, demonstrate an increase in initial stiffness and a significant increase of the load-bearing capacity of the Reinforced specimen. The initial stiffness increased from 11 kN/mm for the Reference specimens to 15 kN/mm for the Reinforced specimens. The maximum lateral load doubled, with the Reinforced specimens reaching approximately 80 kN compared to the Reference specimens reaching 40 kN. All tests were carried out up to fracture of the longitudinal reinforcement bars, occurring at a maximum displacement of approximately 50 mm for the Reference specimens and of 70 mm for the Reinforced specimens. The experimental results confirm a ductile failure with energy dissipation and plastic hinge formation at the base of the columns.

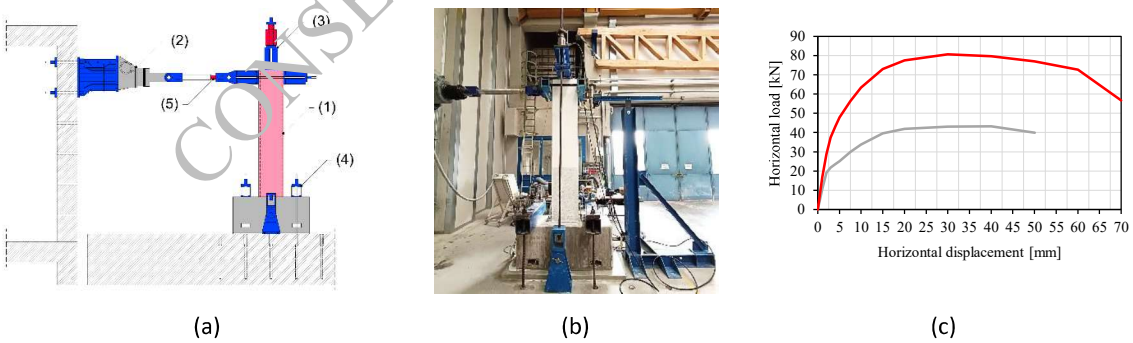

Figure 2. Experimental test setup for quasi-static cyclic lateral loading tests (a), picture of an experimental test (b), and structural responses of columns before (grey line) and after repair (red line) (c).

4. Design considerations

The primary purpose of HPFRC jacketing of bridge piers is to enhance their structural performance in terms of load-bearing and displacement capacity under seismic horizontal loads. Additionally, it aims to improve load-bearing capacity for gravitational loads, such as those related to traffic. It is worth noting that the reduction in the structure's natural period due to the increased flexural stiffness does not lead to increased

seismic actions in structures with inherently low natural periods, like the one studied. Consequently, the enhanced load-bearing capacity can be fully utilized.
Another key benefit is the enhanced crack control in the repaired structure. The tests confirmed that, after the initial phase where stresses are below the concrete's tensile strength, crack development in the Reinforced specimens is better controlled with respect to the Reference specimens. A dense network of fine cracks, with openings less than 0.05 mm, forms as the load increases to the Serviceability Limit State. This feature significantly enhances the structure's durability when exposed to low intensity earthquakes, which the bridge pier can experience during the Service Life, as the fibrous reinforcement in the high-performance matrix effectively limits crack propagation.
Finally, when managing the need for intervention on an existing bridge, the challenge of minimizing the environmental impact should be considered. Repair with HPFRC jacketing is a promising solution due to minimal material use and fewer on-site construction phases. A comparative life cycle assessment (LCA) shows significant advantages of repair over demolition and reconstruction. For the cradle-to-gate stage (A1+A2+A3), HPFRC repair offers an 89% reduction in carbon dioxide emissions, 86% reduction in freshwater use, and 95% reduction in non-harmful waste disposal. Additionally, HPFRC can be made by using materials with a high quantity of secondary raw materials (up to 23%), as compared to the limited amount used in ordinary concrete.

5. Concluding remarks

From the aforementioned analyses, we can draw the following conclusions:

- Repairing bridge piers with fiber-reinforced concrete (HPFRC) with a cubic compressive strength exceeding 100 MPa is a viable strategy that can be implemented under standard working conditions using conventional construction techniques and suitable concrete mixers. The field application herein described has provided practical experience confirming its effectiveness.
- The structural response of the Reinforced columns demonstrated a significant increase in load-bearing capacity and a slight improvement in displacement capacity, as compared to the reference columns. This enhanced performance correlates with a better response to seismic actions, thereby increasing the overall structural safety of the bridge itself.
- Structural design of the repair can employ simple design equations or numerical models to emphasize both enhanced structural performance and improved crack control, thereby increasing durability of the repair. Structural optimization, achieved by employing high-performance materials, aims to minimize concrete usage, thereby enhancing environmental sustainability.

Acknowledgements

The Authors would like to express their gratitude and sincere appreciation to Heidelberg Materials Cementi Italia for supporting this research work. Special recognition goes to Eng. Stefano Guerini, Augusto Botturi, Andrea Del Barba and Luca Martinelli for their support in the implementation of the experimental project.

References

ACI Committee 374. (2013). Guide for testing reinforced concrete structural elements under slowly applied simulated seismic loads. *American Concrete Institute*.

Andrade, C. (2020). Initial steps of corrosion and oxide characteristics. Structural Concrete, 21(5), 1710-1719.

Andrade, C., & Izquierdo, D. (2020). Propagation period modeling and limit state of degradation. *Structural Concrete*, 21(5), 1720-1731.

Buttlar, W. G., Chabot, A., Dave, E. V., Petit, C., & Tebaldi, G. (Eds.). (2018). Mechanisms of cracking and debonding in asphalt and composite pavements (Vol. 28, pp. XXI-237). Cham, Switzerland: Springer International Publishing.

Enright, M. P., & Frangopol, D. M. (1998). Probabilistic analysis of resistance degradation of reinforced concrete bridge beams under corrosion. *Engineering structures*, 20(11), 960-971.

Reggia, A., Trabucchi, I., Morbi, A., & Plizzari, G. A. (2022). Actual achievements and future challenges of HPFRC for structural rehabilitation of bridges. *In MATEC Web of Conferences* (Vol. 364, p. 04018). EDP Sciences.

Zanini, M. A., Faleschini, F., & Pellegrino, C. (2017). Bridge residual service-life prediction through Bayesian visual inspection and data updating. *Structure and Infrastructure Engineering*, 13(7), 906-917.

Sulphate Attack of Concrete – After 20 Years Of 'Whither'ing

Manu Santhanam[1*] and Piyush Chaunsali[2]

[1] Professor, Department of Civil Engineering, IIT Madras, Chennai, India
Email: manus@civil.iitm.ac.in
[2] Associate Professor, Department of Civil Engineering, IIT Madras, Chennai, India
Email: pchaunsali@iitm.ac.in

[*]Corresponding author (s)

ABSTRACT

This paper explores how the understanding about sulphate attack of concrete has improved in some respects and stayed the same in others over the last 20+ years. It builds on the ideas discussed by the first author in a 2001 paper titled: *Sulfate Attack Research: Whither Now*. The new knowledge of the chemistry and microstructure and the role of blended cementitious systems is explored. A special focus is also given to the development of test methods and the constant attempt to recreate field-like conditions for testing. The paper finally puts forward a wish list for what should be the approach in the future for this subject.

KEYWORDS*: Sulfate attack, Mechanism, Testing methods*

1. Introduction

The attack of cementitious systems by external solutions containing sulphates leads to the alteration of the hydration products and subsequent formation of specific attack products such as gypsum and ettringite, and in some cases, thaumasite. While a number of mechanisms operate in conjunction to lead to damage of the cementitious matrix, it is universally accepted that the phenomenon is a coupled diffusion/permeation – reaction one. In other words, sulphates from an external environment diffuse into the matrix because of concentration gradient or sometimes permeate due to pressure gradient and interaction with the hydration products in an aqueous medium. A good compendium of sulphate attack mechanisms is available in Skalny et al. (2001), while several more instances of reviews can be seen in current literature.

From the number of publications (since 2000) on sulphate attack, it is clearly seen from Figure 1 that there has been a large amount of interest in recent years. The number of papers on quantitative modelling of the phenomenon, coupled with the use of thermodynamic approaches made possible due to the development of software tools (such as GEM), have been a major cause of the revival in interest in this subject (Lothenbach et al. 2012). Further, the most recent interest has been from the perspective of sulphate resistance of low clinker cements, primarily ternary blended systems involving limestone (Lee et al. 2008; Irassar, 2009; Dhandapani et al. 2022) as well as alternative cementitious systems involving alkali-activated aluminosilicate composites or Magnesium based cements (Muthu et al. 2023), or special concretes such as Self Compacting Concrete (De Schutter et al. 2008; Nehdi and Bassuoni, 2008) or foam concrete (Ranjani and Ramamurthy 2012). In terms of the chemistry of the sulphate-damaged systems, a lot of attention was focused on the formation of thaumasite (Macphee and Barnett 2004; Collett et al. 2004), which also led to proposals of alternative test methods (which will be discussed in a later section). More recently, the papers on sulphate attack have been regarding the performance of concrete with recycled concrete aggregate or industrial waste as aggregate, which do not really significantly impact the literature.

This paper attempts to outline the progress in sulphate attack research since the publication of the review paper of the first author in 2001 (Santhanam et al. 2001), which was also followed by commentaries and reviews by well-known experts on the subject (Bensted, 2001; Neville, 2003). A critical look at the developments in sulphate research, particularly with respect to the understanding of the mechanisms, proposal of suitable test methods, and developing methodologies for prediction of field performance, is included in this paper. The final attempt in the paper is to propose a way forward for research on sulphate attack, with a view of incorporating strategies for design in concrete codes around the world.

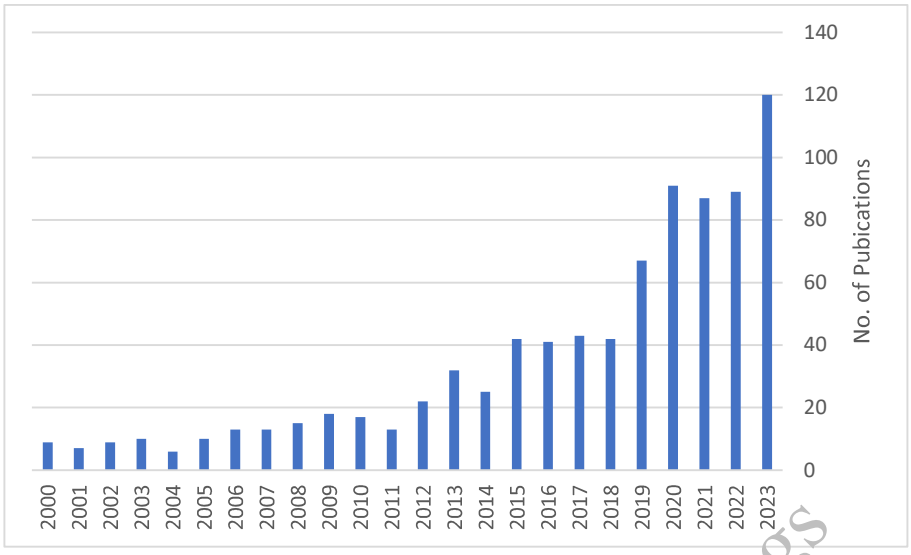

Figure 1. Number of publications (source: Scopus) on sulphate attack since 2000 (Note: The search string used was: "Articles/Reviews/Chapters having Sulphate/Sulfate/Attack in the title")

2. Developments in sulphate attack research since 2001

2.1 Understanding of the mechanism

Sulphate attack is associated with expansion, cracking and spalling of concrete. The extent and magnitude of the degradation depends on the cation (Na, K, Ca, Mg) present in sulphate solution along with its concentration. Sodium and magnesium sulphate are the most common soluble salts used in studying sulphate attack. It's important to differentiate the mechanism of attack between sodium sulphate and magnesium sulphate (Santhanam et al. 2003). Sulphate attack leads to zonation with the outermost layer containing ettringite and gypsum in case of sodium sulphate attack, as opposed to gypsum and brucite in case of magnesium sulphate attack. The presence of magnesium silicate hydrate (M-S-H) has been reported in magnesium sulphate attack due to extensive calcium leaching from C-S-H and its conversion to M-S-H. As discussed in the preceding paragraph, the expansion due to ettringite precipitation has been the precursor to the damage in sulphate attack. However, no strong correlation between the amount of ettringite formed and expansion has been observed (Kunther, 2012). Crystallisation of ettringite is governed by the degree of supersaturation in pore solution. High supersaturation promotes growth of ettringite in small pores, further indicating that the expansion is caused by the precipitation of ettringite in small pores. The relationships between crystallisation stress and degree of supersaturation (IAP/K) and crystal curvature are shown below (Eq. 1 and 2):

$$\sigma_c = \gamma_c \kappa_c \tag{1}$$

$$\gamma_c \kappa_c = \frac{RT}{\nu_c} \ln\left(\frac{IAP}{K}\right) \tag{2}$$

where σ_c is the crystallization stress, γ_c is crystal/liquid interfacial energy, κ_c is curvature of crystal, ν_c is the molar volume of the crystal, *IAP* is ion activity product, *K* is the solubility product, *R* is the gas constant and T is the temperature.

Crystallization stress originating due to high supersaturation levels in the pore solution results in the expansion of matrix. There seems to be a broader agreement on the role of crystallisation pressure in explaining the observed expansion due to ettringite precipitation in sulphate attack (Flatt 2002; Kunther et al. 2013; Müllauer et al. 2013). Factors affecting the crystallization stress are pH, humidity, pore size and existence of solid solutions (Scherer 1999 & 2004; Flatt and Scherer, 2008). However, the kinetics of

ettringite formation governs the expansion rate which has been reported to be slower at low sulphate concentration (Müllauer et al. 2013).

2.2 Modelling of the process

Attempts have been made to model the sulphate ingress in concrete. Lothenbach et al. (2010) performed thermodynamic modelling using GEMS which predicted formation of gypsum, ettringite in the layer next to sulphate rich solution. Moreover, the leaching of Ca from C-S-H could also be effectively predicted. GEMS also predicted the change in porosity because of sulphate attack. The deviation of thermodynamic predictions from experimental observations has been attributed to the slow kinetics of phase formations and difference in the rate of ionic diffusion (Kunther, 2012). Thermodynamic modelling has been shown to provide similar but fast results in comparison to chemical-transport modelling, which are typically based on the diffusion-reaction approach (Tixier and Mobasher, 2003). Attempts to model the deterioration process and its manifestation have also been made (Idiart et al. 2011). Furthermore, a model based on diffusion and thermodynamically-induced chemical reaction has been developed to understand the microstructure development during external sulphate attack (Feng et al., 2017).

2.3 Evaluation of the influence of mineral additives

The use of mineral additives is increasing because of the obvious importance of these additions in lowering the carbon impact of the concrete. Several studies conducted with fly ash, slag and silica fume as partial replacement of cement indicated distinctly improved performance in traditional methods of sulphate testing, such as complete immersion in highly concentrated sodium sulphate solutions (e.g. ASTM C1012, where mortar specimens are completely immersed in sodium sulphate solution with 33800 ppm SO_4 at 23 ºC). However, a common issue identified in these tests was the lesser extent of curing in blended cementitious systems in this test, as the sulphate exposure is expected to be started when the mortars have reached a strength of 20 MPa. Alternative methods with increased curing durations were also devised and clearly showed a suitable performance of the blended systems. Another issue with the ASTM test, which is widespread in its use, is the use of a constant flow value to design the mortars, instead of a constant w/c. This often leads to the blended systems having a higher w/c than the control, which affects the performance. Anyhow, since these tests were extensively used, a number of variants were prescribed for blended systems, to overcome the negatives of the standard method (which also include the influence of the solution pH, the frequency of changing the solution etc.).

While the method suggested by ASTM C1012 and its variants is extremely simple, the results of the test are only seen after a significant period of time. In most cases, the test can run upwards of 6 months for any discernible expansion. Thus, setting limiting values for the expansion when a new blend needs to be certified for use in a project involving concrete exposed to sulphates can be difficult.

One more common problem with understanding the role of cementitious blends is the performance in magnesium sulphate or ammonium sulphate (Skalny et al., 2003) . Several research studies (Bassuoni and Nehdi, 2012; Amin and Bassouni, 2017) have shown that when the attacking solution is of the type that can create acid like conditions, the blended systems show a poor performance – this is usually seen in laboratory studies with small scale specimens and highly concentrated solutions. This occurs because blended systems have lesser alkaline buffer, causing the attacking solution to attack the CSH directly, and eventually leading to a loss of the cementitious structure because of CSH disintegration. In the case of magnesium sulphate, the absence of the impermeable brucite layer that forms on the sulphate because of the interaction with $Ca(OH)_2$ – since much of the $Ca(OH)_2$ is consumed by the pozzolanic reaction – the penetration of the sulphates leads to a direct interaction with the CSH and subsequent decalcification.

Specifically, there has been a marked increase in the use of limestone powder as a partial replacement in binary and ternary blends (Dhandapani et al. 2021). Limestone is an obvious choice as a cement replacement because of its ready availability at the cement production units. Further, the possibility of using even the non-cement-grade limestone (approx. CaO < 40%) from the mines gives another major benefit of reducing wastage of materials. In the last two decades, most of the sulphate deterioration work seems to have been focused on limestone-based blends, and this has also prompted researchers and standardization agencies to come up with means of testing the performance of such blends in sulphate conditions.

In the early 2000s, the occurrence of thaumasite in concrete exposed to sulphate environments, specifically at low temperatures, was reported extensively. While in most cases, the concrete involved the use of limestone powder as an ingredient of the cement, there were a few cases reported where there was no

specific addition of limestone in the concrete – these cases arose presumably due to the combined action of carbonate ions (due to carbonation) and sulphate ions. The fact that thaumasite was found in concretes that had shown significant deterioration seemed to suggest that the formation of that phase was the cause of the deterioration. As a result, the test methods to evaluate sulphate resistance were extended to understanding the behaviour at low temperatures, and later standardized in some countries (such as in Canada as CSA A3004-C8 Procedure B). A 2016 PCA report by Hooton and Thomas [2016] described results of sulphate resistance tests conducted in lab and simulated field conditions, specifically focusing on blends with 5 – 15% limestone as replacement. SCMs in combination with limestone-based cements were seen to show good performance. 5 ºC testing seemed to not capture the effect of thaumasite until significant deterioration. The report recommends the use of standard ASTM C1012 protocol for limestone-based cements. Thaumasite formation was only reported as a late stage of attack; the deterioration process even at low temperatures was seen to be similar – with gypsum and ettringite formation dominating.

There is a need to move towards performance specifications that can capture the influence of mineral admixtures with respect to their impact in sulphate diffusion and permeability, rather than simply relying on laboratory methods, which sometimes put them at a disadvantage.

2.4 Standardization of sulphate attack testing

One of the common strands in research on sulphate attack is the development of test methods for sulphate exposure, and use of different types of parameters for defining the alteration induced by this phenomenon. The combination of aspects seen in standards and other procedures followed in sulphate attack research is shown in the graphic in Figure 2. The standard tests are already discussed in the previous section, and one of the common threads in such tests is the long time period for such tests. It is clear that many of the combinations are adopted in order to get a result within a reasonable time frame to suit the research period. However, in many cases, the mechanisms are very different from the operating conditions in actual field exposure. Field evaluation of sulphate attack often reveals a combination of mechanisms involving physical and chemical deterioration. In other words, salt crystallization also acts in conjunction with gypsum and/or ettringite formation to deteriorate the concrete. All these actions cannot be simulated in standardized laboratory tests. A good compendium of testing methods for sulphate attack is available in Tittelboom et al. (2012).

While a number of laboratory assessments have used sophisticated measurement techniques to assess sulphate deterioration, their contribution to the development of reliable and repeatable tests for sulphate attack has been minimal.

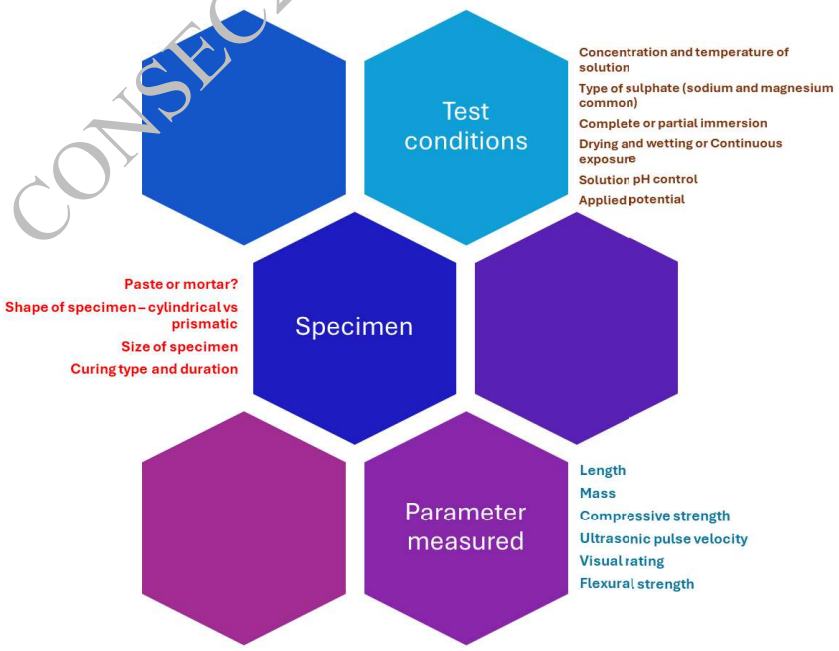

Figure 2. Variations seen in test methods

The following are some of the common issues with the adoption of varying conditions:

- The choice of concentration of the solution determines the dominating product of attack. At low to moderate concentrations, the attack is characterized by ettringite formation and resultant expansion, while for high to very high concentrations (> 10000 ppm sulphate) that are typically adopted in laboratory tests, gypsum formation seems to dominate.
- The use of high temperatures to accelerate attack may lead to destabilization of some phases and lead to secondary effects that are not reflective of the actual phenomenon.
- The type of cation present (sodium, magnesium, ammonium etc.) can lead to major differences in performance in the case of blended cementitious systems. In addition, the use of a mixture of solutions (i.e. sulphates with different cations) seems to reduce the scale of the damage, as reported in Kunther et al. (2013).
- The instances of partial immersion along with drying and wetting that are typically seen in the field are not easy to simulate in the standardized tests, although there have been some attempts in this regard (Hartell et al. 2011). Liu et al. (2019) found that the partial exposure to Na_2SO_4 showed more damage by physical effects such as salt crystallization, while the $MgSO_4$ exposed specimens showed damage in the submerged portions. The use of electrical migration as a means of accelerating the attack could lead to a two-way movement of ions, thus altering the overall mechanism. However, when such tests are done to simulate field conditions, such as the study by Fang et al. (2023), the presence of stray currents that result in electrical migration combined with diffusion seems to accelerate the damage.
- The control of pH during sulphate exposure in laboratory studies (to simulate the field conditions of continuous flow of the sulphate solution) can change the nature of the attack, because of the creation of acidic conditions. Laboratory studies should simulate the field pH environment. Furthermore, differentiating acid attack from sulphate attack is important.
- When mortar or concrete are used instead of paste, the influence of interfacial transition zone (ITZ) dominates – in other words, the role of permeability and pore structure becomes more crucial than simple diffusion of sulphate.
- The shape and size of specimen affect the extent of deteriorated volume in relation to the overall volume of the specimen (Suma et al. 2020). When smaller specimens are used, even minor deterioration can lead to a rapid loss of mechanical properties. This is one of the major reasons for poor performance of blended cementitious systems in magnesium sulphate attack (Ganjian and Pouya, 2005). Further, when square or rectangular specimens are used as opposed to cylindrical specimens, edge or corner effects also come into play (Massaad et al. 2017).
- The duration of curing can be crucial for studying the relative performance of blended cementitious systems, prepared using additives that are slow reacting, such as fly ash.
- The choice of the test parameter can be crucial with respect to addressing the nature of the damage. While expansion is commonly seen in laboratory specimens, loss of surface material and strength is seen in field studies. Further, the impact of the surface damage cannot possibly be as critical when compressive strength is used as the test parameter rather than the flexural strength.

From the above discussion, it is clear that it is almost impossible to clearly use an objective set of parameters for testing the resistance of cementitious systems to sulphate solutions. However, a suitable strategy for testing should employ the following measurements:

(a) A parameter linked to diffusion

(b) A parameter linked to permeability, and

(c) A parameter that indicates potential for sulphate deterioration, such as the formation of gypsum or ettringite.

The use of a multi-criteria approach has been attempted in the past (El-Hachem et al. 2012), but it is yet to find a way into the standard testing methods. Massaad et al. (2016) also proposed easily accessible monitoring parameters to study sulphate attack, using physical, chemical and microstructural approaches.

The provisions followed in building codes with respect to resistance against sulphate attack are primarily restricted to the choice of the cementitious system and the maximum permissible water to cement ratio to be used in the concrete. However, it is universally accepted that this does not entirely address the situations specific to any jobsite. For instance, sulphate resistant cements may not work well in a mixed exposure environment, with chlorides and sulphates. Another instance could be the use of the test procedures at 5 ºC

(like the Canadian procedure) – it is seen that ASTM Type V (i.e. Sulphate Resistant) cements do not pass this test (Hooton and Thomas, 2016).
The choice of the diffusion related parameter brings into focus the extent of sulphates available in the groundwater (which is further linked to the type of cation associated with the sulphate) – the more soluble sulphates lead to greater penetration into the concrete. The permeability aspect brings the attention on the mixture design. Further, the chemistry of the system is assessed by the last parameter (potential for sulphate deterioration). It is therefore imperative that future test protocols be developed with a combination of the above.

2.5 Preventive measures against sulphate attack

Common mitigation strategies that have been used in sulphate attack include:

- Use of low C_3A cements – While this helps to some extent in reducing the ettringite related deterioration, the performance is suspect when it comes to other mechanisms such as gypsum corrosion or CSH being attacked.
- Use of special cements including supersulphated and high alumina cements – Stability problems with such cements is the reason why such cements are not utilized.
- Use of supplementary cementitious materials – This is by far the best approach and research has shown that it works is most situations involving sulphates. While there is a lot of information about poor performance at small scale when silica fume or slag is used in magnesium sulphate, the large scale performance would be better dictated by the lowered permeability caused by the use of SCMs.
- Use of low w/b, consequently low porosity and permeability – Universally, sulphate attack mitigation involves one common strategy, which is to control the w/b or w/c in sulphate rich conditions. The impact of permeability (resulting from w/c) is shown to be much more critical than the impact of C_3A content in actual field performance (Kurtis and Monteiro, 2003).
- Use of additional protective measures – such as coatings and sealants that can reduce the rate of water penetration.

The above strategies have not changed over the years. This is because it is universally accepted that the role of porosity and pore structure is much more in sulphate attack than the actual chemistry. However, a clear strategy for sulphate resistance in a given environment is not universally available, with most building codes simply giving prescriptions for sulphate resistance in terms of the type of cement to be used, the maximum permissible water to cement ratio, and the use of additional protective measures. There is also a relatively new standard on performance specification for hydraulic cement (ASTM C1157-2010), which has options for Moderate (MS) and High (HS) Sulphate Resistance, based on the ASTM C1012 expansions being less than 0.1% at 6 months and 12 months, for MS and HS respectively. Perhaps the same limits could be used for alternative cementitious systems to define the required resistance in a project. However, the long-term nature of the test makes it difficult to adopt such strategies on real life construction projects.

3. Way Forward

The current paper attempts to showcase the improvement in understanding of the phenomenon of sulphate attack on cementitious composites in the last two decades. While the extent of research in the subject has grown exponentially, the actual growth in understanding is mostly restricted to the mechanisms of sulphate expansion, with insufficient contribution to the methodology of assessing the resistance to sulphate attack, and coming up with methods that can actually mimic the deterioration in the field within a reasonable amount of time in the lab.
The authors are of the opinion that the following actions are required from the research community in the future:

- Focus on developing a rapid and reliable test method that captures the effects of physical and chemical sulphate attack on cementitious systems.
- Adopt performance-based specifications for real projects, with a combination of tests indicating sulphate diffusion, permeation and chemistry in the chosen binder system.

References

Amin, M. and Bassuoni, M.T., (2018) "Performance of concrete with blended binders in ammonium-sulphate solution. *Journal of Sustainable Cement-Based Materials*, 7(1):15-37.

Bassuoni, M.T. and Nehdi, M.L., (2012) "Resistance of self-consolidating concrete to ammonium sulphate attack". *Materials and Structures*, 45:977-994.

Collett G.; Crammond N.J.; Swamy R.N.; Sharp J.H., (2004) "The role of carbon dioxide in the formation of thaumasite", *Cement and Concrete Research*, 34(9):1599 – 1612.

De Schutter G.; Ye G.; Audenaert K.; Bager D.; Baroghel-Bouny V.; Bellmann F.; Boel V.; Bonen D.; Boström L.; Corradi M.; Gartner E.; Hama Y.; Jacobsen S.; Jansson R.; Justnes H.; Khayat K.; Khrapko M.; Leemann A.; Luco L.F.; Magarotto R.; Nowak A.S.; Persson B.; Poppe A.-M.; Qian C.; Setzer M.J.; Sideris K.; Skarendahl A.; Sonebi M.; Stark J.; Tang L.; Trägardh J.; Wallevik O.; Zhu W.; Zverev I., (2008) "Final report of RILEM TC 205-DSC: Durability of self-compacting concrete", *Materials and Structures*, 41(2): 225 – 233.

Dhandapani, Y., Joseph, S., Bishnoi, S., Kunther, W., Kanavaris, F., Kim, T., Irassar, E., Castel, A., Zunino, F., Machner, A. and Talakokula, V., (2022) "Durability performance of binary and ternary blended cementitious systems with calcined clay: a RILEM TC 282-CCL, review". *Materials and Structures*, 55(5):145.

El-Hachem R.; Rozière E.; Grondin F.; Loukili A., (2012), "Multi-criteria analysis of the mechanism of degradation of Portland cement based mortars exposed to external sulphate attack", *Cement and Concrete Research* , 42(10): 1327 – 1335.

Fang Z.; Li Z.; Zhou Y.; Xie Q.; Peng H.; Zhou S.; Wang C., (2023), "Effect of stray current and sulfate attack on cementitious materials in soil", *Construction and Building Materials*, 408: 133723.

Ganjian, E. and Pouya, H.S., (2005). "Effect of magnesium and sulfate ions on durability of silica fume blended mixes exposed to the seawater tidal zone". *Cement and concrete research*, 35(7):1332-1343.

Hartell J.A.; Boyd A.J.; Ferraro C.C.,(2011) "Sulfate attack on concrete: Effect of partial immersion", *Journal of Materials in Civil Engineering* , 23(5): 572 – 579.

Hooton, R.D. and Thomas, M.D.A., (2016) "Sulfate Resistance of Mortar and Concrete Produced with Portland-Limestone Cement and Supplementary Cementing Materials: Recommendation for ASTM C595/AASHTO M 240". PCA R&D SN3285a, Portland Cement Association, Skokie, IL.

Idiart A.E.; López C.M.; Carol I.,(2011) Chemo-mechanical analysis of concrete cracking and degradation due to external sulfate attack: A meso-scale model, *Cement and Concrete Composites* , 33(3): 411 – 423.

Irassar, E.F., (2009). "Sulfate attack on cementitious materials containing limestone filler—A review". *Cement and Concrete Research*, 39(3):241-254.

Kunther W.; Lothenbach B.; Scrivener K.L.,(2013) "Deterioration of mortar bars immersed in magnesium containing sulfate solutions, *Materials and Structures*, 46(12):2003 – 2011.

Lee S.T.; Hooton R.Doug.; Jung H. S.; Park D.-H.; Choi C.S.,(2008) "Effect of limestone filler on the deterioration of mortars and pastes exposed to sulfate solutions at ambient temperature", 38(1):68 – 76.

Liu C.; Gao J.; Chen F.; Zhao Y.; Chen X.; He Z.,(2019) "Coupled effect of relative humidity and temperature on the degradation of cement mortars partially exposed to sulfate attack", *Construction and Building Materials*, 216: 93 – 100.

Lothenbach, B., Kunther, W., & Idiart, A. E. (2012). "Thermodynamic modeling of sulfate interaction". In M. G. Alexander, H. D. Beushausen, F. Dehn, & P. Moyo (Eds.), Concrete repair, rehabilitation and retrofitting III 1444-1449.

Macphee D.E.; Barnett S.J.,(2004), " Solution properties of solids in the ettringite - Thaumasite solid solution series", *Cement and Concrete Research*, 34(9):1591 – 1598.

Massaad G.; Rozière E.; Loukili A.; Izoret L.,(2017) "Advanced testing and performance specifications for the cementitious materials under external sulfate attacks", *Construction and Building Materials*, 127: 918 – 931.

Massaad G.; Rozière E.; Loukili A.; Izoret L.,(2017) "Do the geometry and aggregates size influence external sulfate attack mechanism?", *Construction and Building Materials*, 157:778 – 789.

Menéndez, E., García-Rovés, R., Aldea, B. and Salem, Y., (2020) " Review of the incidence of the sulphate attack in Spain. Evaluation of field concrete cases". In External Sulphate Attack–Field Aspects and Lab Tests: RILEM Final Workshop of TC 251-SRT (Madrid-SPAIN, 2018) (15-30). Springer International Publishing.

Murugan Muthu, Sanjeev Kumar and Lukasz Sadowski, (2023) "Performance of Pozzolan-Based Reactive Magnesia Cement Mixes Against Sulphate Attack", *Applied Sciences* 2023, 13(19), 11012.

Nehdi M.L.; Bassuoni M.T.,(2008) "Durability of self-consolidating concrete to combined effects of sulphate attack and frost action", *Materials and Structures*, 41(10), 1657 – 1679.

Ranjani, G.I.S. and Ramamurthy, K., (2012) "Behaviour of foam concrete under sulphate environments". *Cement and Concrete composites*, 34(7), pp.825-834.

Santhanam, M., Cohen, M. D., and Olek, J., (2001) "Sulfate Attack Research: Whither Now," *Cement and Concrete Research* Vol. 31, 845 – 851.

Suma, M.F., Santhanam, M. and Rahul, A.V., (2020) "The effect of specimen size on deterioration due to external sodium sulphate attack in full immersion studies". *Cement and Concrete Composites*, 114, 103806.

Tixier R.; Mobasher B.,(2003), "Modeling of damage in cement-based materials subjected to external sulfate attack. I: Formulation*", Journal of Materials in Civil Engineering*, 15(4), 305 – 313.

Van Tittelboom, K., De Belie, N. and Hooton, R.D., (2013) "Test methods for resistance of concrete to sulfate attack– a critical review". Performance of Cement-Based Materials in Aggressive Aqueous Environments: State-of-the-Art Report, RILEM TC 211-PAE, 251-288.

Holistic Advances for Corrosion Durability in Reinforced Concrete Systems

David Trejo*, PhD, PE, FACI

Professor and Hal Pritchett-Beavers Endowed Chair in Civil and Construction Engineering
Oregon State University, Corvallis, Oregon, USA

*Corresponding author (s)

1. Introduction

About 100 years ago, the First Transcontinental Motor Convoy (FTMC), was planned to assess the dependability of mobility in the United States. This convoy started in Washington DC and ended in San Francisco, California. Lieutenant Dwight D. Eisenhower participated in this 62-day convoy in which 11% of the vehicles were destroyed and 21 people were injured, mostly due to inferior infrastructure. The need for a national and standardized infrastructure system was clear.

In 1953, Dwight Eisenhower became the 34th US president. The need for a strategic highway system, both for improved military and economic growth, was evident. In 1956, President Eisenhower signed the Federal Aid Highway Act, guaranteeing full, dedicated funding for the National Highway Defense System (NHDS), also known as the Interstate Highway System. In 1992 the originally planned interstate systems was deemed complete. Much of this infrastructure was placed in aggressive coastal environments (~40% of the US population live near the coastal areas) and much of the infrastructure was exposed to de-icing salts. The infrastructure's exposure to these aggressive environments, especially salts, began to expose durability challenges. Understanding this challenge, in 1998, the National Institute of Standards and Technology (NIST) organized the first workshop on predicting the service life of infrastructure systems.

Although significant advances have been made to promote long-lasting infrastructure systems since 1996, several challenges still exist. A significant push was implemented early to model the transport and degradation of reinforced concrete systems. These advanced models are now representative of actual mechanisms. Although representative, the input data for these models have often been assumed and less effort has been put into generating representative and realistic data. More so, little effort has been invested in correlating service life and exposure environment. It is well known that reinforced concrete (RC) systems subjected to aggressive corrosive environments will require more durable, and often more expensive, materials and methods. The need to correlate exposure severity and infrastructure performance can reduce maintenance, repair, and improve safety and economy. This paper will address the following needs for infrastructure durability:

- Development of a systematic and science-based exposure environment classification system that relates environment with infrastructure performance;
- Development of a standardized test suite to quantify key variables that directly correlate with corrosion performance, and;
- Development of a risk-based approach to defining how much salts, specifically chlorides, can be allowed in new concrete.

Addressing and clarifying these needs will enhance infrastructure durability, can improve economy, and can eliminate confusion associated with durability of RC systems.

2. Classifying Corrosive Exposure Environments

The exposure environment in which a RC system exposed will influence the design, materials, craftmanship, and costs associated with these structures. Severe exposure conditions will generally require more of each. As such, the environment must be defined prior to design and construction. Corrosive exposure classes must be based on exposure conditions that directly contribute to corrosion initiation and/or propagation of steel reinforcement embedded in concrete. It is well known that the electrochemical process

includes anodic and cathodic reactions that include iron (Fe), oxygen (O_2), and water (H_2O). If any of these are not present and available, the corrosion process will not occur. Even if all are present and available, in uncarbonated 46ortland cement concrete (PCC) the high pH pore solution protects the steel reinforcement from significant corrosion due to the formation of a passive film. Unfortunately, the passive film can be destroyed when the salt concentration, commonly chlorides, at the steel surface reaches a critical value. When RC systems are exposed to chloride containing environments, the concentration of the chlorides in the exposure solution, the type of exposure (constantly wet [predominantly diffusion-based transport] or wetting and drying [predominantly advection-based transport near the exposure surface]), and the duration or frequency of exposures are all critical variables that can influence the time to corrosion. Other variables can also influence time to corrosion but because of space limitations will not be addressed here (e.g., temperature).

For exposure conditions where moisture, oxygen, and chlorides may be present, the severity of exposure conditions for steel reinforcement embedded in PCC will be considered here to be dependent on the following:

- the availability of oxygen;
- the moisture content of the RC;
- the presence or absence of chlorides, and;
- exposure temperature.

When chlorides are present in the exposure environment, the following conditions will also influence the time to corrosion of the embedded reinforcement:

- the concentration of chlorides in the exposure solution;
- the type of exposure (i.e., continuous exposure to solution or wetting and drying), and;
- if the exposure includes wetting and drying, the number of chloride solution applications.

The term “continuous exposure” herein refers to mainly diffusion-based transport at the concrete surface, typically RC elements that are continuously submerged or immersed. Wetting and drying of the concrete surface is generally associated with advection-based transport, such as RC elements exposed to tidal zones or atmospheric conditions. Wetting and drying with chloride-containing solutions will increase the surface chloride build-up rate and will increase the maximum surface chloride concentration when compared with continuous exposure conditions. Thus, the type of exposure will influence the transport rate of chlorides into the RC system.

Exposure environment will be based on potential aggressiveness and associated risk of the environment and will be classified as follows: very low (CS0), low (CS1), low to moderate (CS2), moderate (CS3), moderate to severe (CS4), and severe (CS5). Criteria for defining salt exposure classes should be based on identifying whether criteria necessary for corrosion initiation and propagation are present in sufficient quantities in the exposure environment. This would include assessing whether moisture, oxygen, and/or chlorides are present in sufficient quantities at the location of the RC. Table 1 shows a full factorial design for potential chloride-induced corrosion exposure conditions (i.e., whether moisture, oxygen, and/or chlorides are present in sufficient quantities). When only 1 of the 3 variables is present in sufficient quantities in the exposure solution, in general, there is a very small risk of corrosion, and the environments are classified as CS0. If 2 of the 3 variables (i.e., oxygen, moisture, and/or chlorides) are present in the exposure environment, some risk of corrosion does exist and the risk of corrosion depends on these exposure conditions. When all three conditions (moisture, oxygen, and chlorides) are present in the exposure environment, there is a potential for severe corrosion and more information on the environment is needed to define these classes.

For the exposure conditions when all three variables (oxygen, moisture, and chlorides) are present in sufficient quantities in the exposure environment, the rate at which the chlorides are transported into the concrete depends on the following:

- the dominant mechanism of transport (diffusion-based transport [e.g., continuous exposure] or advection-based transport [e.g., cyclic wetting and drying]);
- the concentration of the chlorides in the exposure solution, and;
- the frequency of chloride exposures or number of wetting and drying applications

Table 2 shows a full factorial design including the two exposure types, chloride concentrations, and frequency of chloride exposures. Diffusion-based mass transport (i.e., continuous exposure conditions) with lower chloride concentrations should exhibit lower chloride transport rates and thus a lower exposure

classification. Alternatively, advection-based transport (i.e., wetting and drying of the concrete surface) with exposure solutions containing high chloride concentrations and a high frequency of applications would be considered a severe exposure for corrosion for the conditions shown. The table also shows recommended exposure classes

3. Quantifying Exposure Conditions

Up to this point in this paper, only subjective descriptors have been used to identify limits for the exposure conditions (e.g., sufficient, insufficient, low, moderate, high). Objective and data-based thresholds are necessary. Table 3 presents threshold limits and test requirements for defining exposure environments. The table also refences papers that were used to justify these threshold values. Note that these thresholds are for exposure environments where the structure will be exposed to liquid water. Atmospheric and soil exposure conditions have been addressed elsewhere but due to space limitations are not address here. See Tepke and Isgor (2023).

Table 1. Partial list of exposure classes for variables that influence corrosion of steel.

Oxygen Present in Sufficient Concentration?	H_2O Present in Sufficient Quantity?	Are Chlorides Present?	Exposure Class
No	No	No	Not likely to occur
		Yes	Not likely to occur[1]
	Yes	No	CS0
		Yes	CS2
Yes	No	No	CS0
		Yes	CS2[2]
	Yes	No	CS1
		Yes	See Table 2

1. *Consult corrosion expert to define potential risk of corrosion due to hydrogen reduction reaction when exposu2re condition occurs.*
2. *Because salt is hygroscopic, moisture is often present under this condition. If it can be ensured that moisture will not be present, exposure classification CS1 can be used.*

Table 2. Partial list of exposure classes for conditions when H_2O, O_2, and chlorides are present.

Main Chloride Transport Mechanism	Chloride Concentration	Frequency of Chloride Exposures	Exposure Class
Continuously Submerged/Immersed (Diffusion-based)	Moderate	NA (continuous exposure)	CS3
	High	NA (continuous exposure)	CS3
Wetting and Drying (Predominantly Advection-based)	Moderate	Low	CS3
		High	CS4
	High	Low	CS4
		High	CS5

It is important to note that assessing an environment and then correlating this information with whether the concrete will contain sufficient moisture to promote corrosion is non-trivial. In general, any concrete exposed to direct moisture or the atmosphere should be considered to have sufficient moisture present for corrosion to initiate. RC protected from the environment and under conditioned environmental settings can be considered "dry" if the designer can ensure that the concrete will not exceed 60% pore saturation. Research is needed to correlate environmental conditions with pore saturation and pore saturation with corrosion activity.

4. Standardizing Testing for Critical Chloride Threshold

The concentration of chlorides necessary to initiate corrosion of reinforcement steel embedded in concrete is referred to as the critical chloride threshold content, C_T. Quantifying C_T is critical to estimate the time to corrosion initiation and service life of reinforced concrete structures. However, there is no standardized test method to determine the C_T of a reinforced concrete system. The published C_T data obtained using different test methods exhibits significant scatter and varies between approximately 0.1 and 3.1 % by weight of binder (Angst et al. 2009). One cause of this variability is the lack of a standard test to quantify C_T. A standard test, the OC_{crit} test, has been developed and now been tested and evaluated.

Table 3. Threshold values for classifying exposure conditions.

Exposure Variable	Exposure Level	Exposure Limit	Test Standard	Reference/Notes
Moisture	Not Present	Concrete pore saturation < 60%	None. Design engineer to quantify if environment will exceed threshold.	Lopez and Gonzalez (1993)
	Present	Concrete pore saturation ≥ 60%		
Oxygen	Not Present	Dissolved oxygen in solution < 5 ppm	ASTM D888	Walsh (2015)
	Present	Dissolved oxygen in solution ≥ 5 ppm		
Chlorides	None/very low	< 500 mg/L (500 ppm)	ASTM D512	Based on specifications for potable water, chloride thresholds for black steel, and concentration of sea water.
	Low	500 mg/L ≤ [Cl-] < 7000 mg/L	ASTM D512 or ASTM D4458	
	Moderate	7000 mg/L ≤ [Cl-] < 21,000 mg/L	ASTM D4458	
	High	≥ 21,000 mg/L	ASTM D4458	

This test setup consists of individual dog-bone shaped anodes connected to a cathode (see Halmen and Adil 2021). The anodes and the cathode are made using a mortar mixture with a water-cement ratio of 0.42 and sand-cement ratio of 1.375. The anode of the OC_{crit} test has a fully embedded 140 mm (5.5 in.) long, 16 mm (No. 5) reinforcing steel bar. The reinforcing steel bar located between the thicker ends of the specimen has a thin, uniform mortar cover with a radial cover thickness of 4.75 mm (0.1875 in.). The anodes are exposed to a saturated lime solution with 3.3% by weight NaCl. Threaded connectors are attached to the reinforcing bars in the anodes and cathodes and protrude from the samples to facilitate electrical connections. The cathode is a mortar prism with five completely embedded 280 mm (11 in.) long, 16 mm (No. 5) steel reinforcing bars with a mortar cover of 25.4 mm (1 in.). The cathode is exposed to a saturated lime solution and the anode and cathode solutions are connected using a salt bridge to complete the macro-cell circuit. Specimens have a minimum 2:1 cathode to anode surface ratio. The steel bars in the anode and cathode specimens are evaluated in as-received conditions to mimic field performance.

The open circuit potential values ”f th’ steel reinforcement embedded in the anodes are monitored daily and testing is terminated when an anode sample exhibits a steel potential less than -350 mV vs. $CuCuSO_4$ for two consecutive readings. After termination of testing, the uniform, thin mortar cover at the center of the anode is crushed and pulverized until mortar powder passes a 0.85 mm (#20) sieve. Either water- or acid-soluble chloride contents of the mortar powder can be determined following ASTM C1152 and ASTM C1218, respectively. Vaddey and Trejo (2021) reported that the acid-soluble chloride content measured from the center area of the anode, expressed as a percent of weight of cementitious materials, Cl_{test}, can be converted to a critical chloride value, C_T, at the reinforcing bar-mortar interface of the anode using:

$$C_T = (0.492 + 0.004 \times T_{act}) \times Cl_{test} \quad (1)$$

where T_{act} is the test duration in days and Cl_{test} is the chloride content of the thin mortar cover. This equation is used for individual samples containing 48ortland cement-binders and converts each chloride test result (mean chloride concentration of mortar cover) to a C_T value.

The C_T distributions obtained from two studies using ASTM A615 Grade 60 steel reinforcement samples embedded in mortar (Type I/II cements meeting ASTM C150 requirements) is shown in Figure 1. The data were deemed to be normally distributed. The mean value of the combined data is 0.396% by weight of cement with a standard deviation of 0.155, which translates into a 95% confidence interval between 0.373 and 0.418% by weight of cement. The median C_T value is 0.396% by weight of cement between a minimum value of 0.091 and a maximum value of 0.897. The test results show significantly lower scatter that published results.

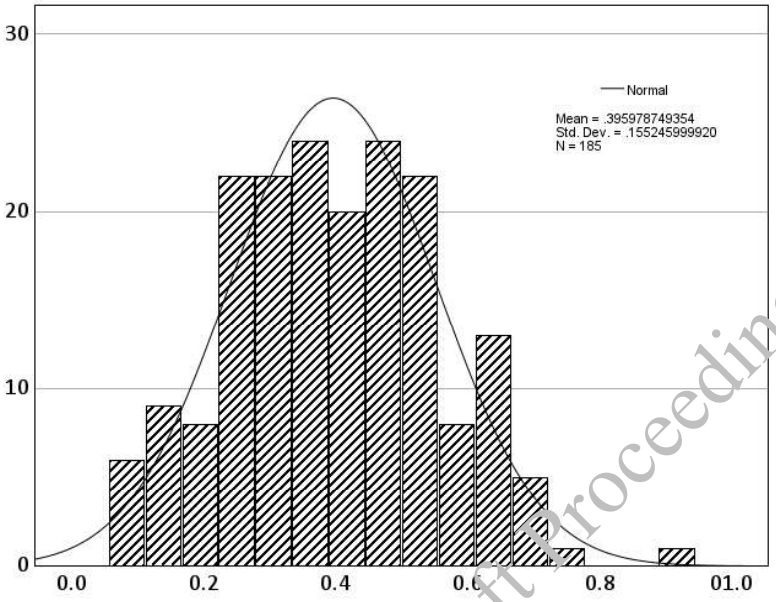

Figure 1. Distribution for C_T for ASTM A615 steel reinforcement embedded in Type I/II mortar; acid-soluble results.

5. Allowable Chloride Limits in New Concrete

Much or the constituents used to make concrete can contain chlorides. Because chlorides can result in corrosion of steel reinforcement embedded in concrete, limits must be placed on how much chlorides can be included in new concrete. To date, this topic has received little attention in the US, although allowable chloride limits, or C_{limit} values, for new concrete are published by many organizations. Here, C_{limit} refers to the concentration of chlorides that can be allowed in new concrete from all constituent materials. Chopperla et al. (2022) provided a comprehensive assessment of challenges and inconsistencies associated with requirements on C_{limit} values.

If chlorides in new concrete are sufficiently high, corrosion of steel reinforcement can initiate. If limits are too low, the economics of producing concrete can be excessive. Because of this, it is essential that C_{limit} values be quantified using a risk-based approach. The earlier section presented new research on defining C_T. Using these C_T data will allow for a limit state design (LSD) approach, which can be used to define justifiable C_{limit}. These C_{limit} values will be a function of some probability of failure, or initiation of active corrosion, caused by the admixed chlorides incorporated into new concrete. The C_T data will provide for more comprehensive, justifiable, and defendable C_{limit} values.

An LSD approach is presented here to quantify C_{limit} values for new concrete based on the distributions of admixed chlorides, C_{admix}, and C_T values, and some acceptable probability of failure (P_f). Note that C_{admix} is the total amount of chlorides in the new concrete. This approach quantifies the probability of corrosion caused by C_{admix} for conventional steel reinforcement embedded in concrete exposed to a wet environment containing no chlorides (i.e., $C_{limit+wet}$). C_{limit} values for exposure conditions containing chlorides, $C_{limit-wet+cl}$, can be deduced using the analysis from $C_{limit-wet}$. Further, the allowable chloride limit for dry conditions, $C_{limit-dry}$, can be deduced from these data, noting that $C_{limit-wet+cl} \leq C_{limit-wet} \leq C_{limit-dry}$.

The probability of failure, P_f, involving two normal distributions can be determined by first identifying the reliability index, β, as follows:

$$\beta = \frac{\mu_{admix} - \mu_T}{\sqrt{(\sigma_{admix})^2 + (\sigma_T)^2}} \quad (2)$$

where μ_{admix} and μ_T are the mean values of C_{admix} and C_T and σ_{admix} and σ_T are the standard deviations of C_{admix} and C_T, respectively. The standard deviations can be defined as a percentage of the respective mean values using the respective coefficient of variances (CoV) values, as follows:

$$\sigma_{admix} = CoV_{admix} \times \mu_{admix} \quad (3)$$

$$\sigma_{crit} = CoV_T \times \mu_T \quad (4)$$

As the CoV increases, the probability of corrosion (P_f) increases and the limit of admixed chlorides, C_{limit}, will likely decrease. After β is determined, P_f can be estimated as follows:

$$P_f = \Phi(-\beta) \quad (5)$$

where Φ is the inverse cumulative normal function. To implement the LSD principle, the CoV of both the C_{admix} and C_T distributions are required. Using the C_{admix} and C_T data and distributions, the mean value of the C_{admix} can be varied and representative P_f values can be determined. Using these P_f values, reasonable P_f values can be identified to define an allowable C_{limit} value for RC structures exposed to wet conditions. Values of C_T were determined using data from the critical chloride testing procedure developed by Trejo et al. (2021) and reported by Halmen and Adil (2022). Acid-soluble test data were converted to water-soluble data for analysis and the non-normal distribution for C_{admix} was transformed to a normal distribution Table 4 shows P_f values for select C_T and C_{admix} values. The table shows P_f values for a CoV_{admix} value of 51.7% and a CoV_T value of 31.3%. This table is applicable for these conditions only.

Table 4. Probability of Failure for various C_{admix} and C_T values. Note COV and mean values above.

Mean Water-soluble C_{admix} (% Mass of Cement)	Mean Water-soluble C_{crit} (% Mass of Cement)						
	0.30	0.32	0.34	0.36	0.38	0.40	
0.01	0.50%	0.50%	0.49%	0.48%	0.48%	0.47%	
0.02	0.65%	0.63%	0.62%	0.60%	0.59%	0.57%	
0.03	0.84%	0.81%	0.77%	0.74%	0.72%	0.70%	
0.04	1.09%	1.02%	0.97%	0.92%	0.88%	0.84%	
0.05	1.39%	1.29%	1.20%	1.13%	1.07%	1.02%	1% line
0.06	1.77%	1.62%	1.49%	1.39%	1.30%	1.23%	
0.07	2.23%	2.02%	1.84%	1.70%	1.58%	1.48%	
0.08	2.80%	2.50%	2.26%	2.07%	1.90%	1.77%	
0.09	3.48%	3.08%	2.76%	2.50%	2.29%	2.11%	2% line
0.10	4.29%	3.77%	3.35%	3.01%	2.73%	2.50%	
0.11	5.25%	4.58%	4.04%	3.61%	3.25%	2.96%	
0.12	6.37%	5.51%	4.84%	4.29%	3.85%	3.48%	
0.13	7.65%	6.59%	5.76%	5.08%	4.53%	4.08%	
0.14	9.11%	7.82%	6.80%	5.98%	5.31%	4.75%	
0.15	10.75%	9.21%	7.98%	6.99%	6.18%	5.51%	5% line
0.16	12.57%	10.75%	9.29%	8.12%	7.16%	6.37%	
0.17	14.57%	12.45%	10.75%	9.37%	8.24%	7.31%	

Table 4 can also be used to determine the probability of failure associated with different mean C_{admix} and mean C_T values. For example, for a C_T value of 0.36% and a C_{admix} value of 0.10%, the associated probability

of failure is 1.80%. It can be seen from the table that the probability of failure increases when the mean values of C_{admix} and C_T become closer in proximity to each other.

Recommendations provided by the authors for C_{limit} limits are shown in Table 5. In the first scenario (no oxygen present) and the second scenario (no moisture present), a C_{limit} value of 0.30% is recommended; this value is slightly lower than the C_T (0.32%) as determined by Halmen and Adil (2021). Although corrosion will mostly not occur under these dry scenarios, there is a likelihood that these conditions could change during the service life of the structure. Therefore, to minimize the risk of active corrosion, it is recommended to specify a C_{limit} that is slightly lower than the C_T. For the next two scenarios, where oxygen and moisture are present but no external chlorides are present, a C_{limit} of 0.10% is recommended. Note that this corresponds to an approximate P_f of 2.5%. Other P_f values could be selected. For other scenarios, where oxygen, moisture, and external chlorides are present, C_{limit} values are specified based on the logic that $C_{limit\text{-}wet+cl} \leq C_{limit\text{-}wet} \leq C_{limit\text{-}dry}$.

Table 5. Proposed exposure classifications and C_{limit} values for OPC-based systems containing conventional reinforcement.

Exposure Classification	Reason for Exposure Classification	Some typical conditions	Max. mean water-soluble chlorides[1,2], C_{limit}
CS0	No O_2	RC well below water surface	0.30%
	No H_2O	Interior RC that will never have sufficient moisture to result in corrosion	
CS1	No chlorides present, but O_2 and H_2O present.	RC that is below freshwater surface but close to surface such that water contains O_2; RC in a freshwater splash zone	0.10%
CS2	O_2, H_2O, and moderate Cl^- present, slow Cl transport	RC that is below brackish water surface but close to surface such that water contains O_2; coastal atmospheric conditions (i.e., airborne chlorides)	0.08%
CS3	O_2, H_2O, and moderate to high Cl^- present, slow to fast Cl^- transport	RC in a brackish water splash zone; RC that is below seawater surface but close to surface such that water contains O_2	0.08%
CS4	O_2, H_2O, and high Cl^- present, fast Cl transport	RC is seawater splash zone; RC structures exposed to less than 5 appls of anti- or deicers per annum	0.08%
CS5	O_2, H_2O, and high Cl^- present, fast Cl transport	RC structures exposed to more than 5 appls of anti-icers or deicers per annum	0.06%

3. *In percent by mass of cementitious materials; for calculations, mass of SCM cannot exceed mass of cement;*
4. *Testing to be performed on concrete of ages between 28 and 42 days as per ASTM C1218, min. of 3 samples is required.*

6. Conclusions

Infrastructure exposed to salts can prematurely deteriorate, resulting in high maintenance or repair costs and decreased safety. This paper presented systematic, science-based approaches for quantifying key parameters, specifically corrosive exposure classifications, critical chloride thresholds, and limits on allowable chlorides. By taking these science-based approaches, key design parameters are defined, thereby enhancing the economics, durability, and validation to ensure long-lasting and safe RC infrastructure.

References

Angst, U., Elsener, B., Larsen, C. K., Vennesland, Ø. "Critical Chloride Content in Reinforced Concrete — A Review," *Cement and Concrete Research*,39(12): 1122-1138.

Chopperla, K.S.T., Smith, S., Drimalas, T., Vaddey, N.P., Bentivegna, A., Kurtis, K.E., Thomas, M.D.A. and Ideker, J.H., 2022. "Unified Durability Guidance in ACI Committee Documents," *ACI Materials Journal*, 119(2): 29-41.

Halmen, C. and Adil P., 2022, "A Collaborative Study for the Development of a Standard Critical Chloride Threshold Test Method," Concrete Research Council, ACI Foundation, 183

Tepke, D. and Isgor, O. B., "Is the Inside of Your Structure Safe from Corrosion?," *ACI Concrete International*, Vol. 45, No. 8, August 2023.

Trejo, D., Vaddey, N. P., and Halmen, C., 2021, "Standardizing Test to Quantify Chloride Threshold of Steel in Concrete," *ACI Materials Journal*,118(1):177-187.

*Vaddey, N.G. and Trejo, D., "Optimizing Test Parameters For Quantifying Critical Chloride Threshold, *ACI Materials Journal,*" March 2021,118(No. 2) :53-66.

Digital Technologies for Accelerating and Improving Quality in Construction

Koshy Varghese[1*]

[1]*Professor, Department of Civil Engineering*
Indian Institute of Technology Madras
E-mail: koshy@iitm.ac.in

[*]Corresponding author (s)

EXTENDED ABSTRACT

Quality is an essential project requirement and has a significant impact on project success. Historically, the focus on construction quality was primarily reserved for landmark structures, where the cost of quality was expected to be high, reflecting the prestige and importance of these structures. In recent times, quality has become an expectation for all types of projects ranging from landmark structures to cost effective housing.

The science of ensuring quality has evolved over the years from both a management and a technology perspective. On the management aspect, the principles that were developed for the Toyota Production System (Ohno, 1988) has had a global impact on the quality management systems and has resulted in frameworks such as Total Quality Management (Martínez-Lorente, et. al, 1998), Lean Management (Womack & Jones, 2013) as well as standards such as ISO-9000 (International Organization for Standardization, 2021). These approaches have been used on construction projects to bring about significant improvement in quality assurance practices and thereby deliver the required quality while meeting challenging cost and schedule targets.

In addition to quality revolution through management systems, digital technologies have had a significant impact on field quality assurance and control processes. The objective of this article to present the technologies and its relevance to field-quality measurement and improvement within the context of a framework that is based on Industry 4.0 principles and the Internet of Things (IOT) architecture (Dey, Hassanien, et. al. 2018) and discuss how Digital Twin concepts are applicable to monitor quality from concept to demolition of built facilities.

Table -1 shows the different layers typically associate with an IOT architecture. The table also shows the function of each layer, some technology options and an example of application in the construction quality area.

Table 1. IOT Architecture Components

Layer	Function	Technology	Examples
Perception / Sensing	Data from site collected by sensors.	Sensors for: Phys/ Chem. Characteristics. Vision, RFID, Induction, etc.	Temperature Sensor: Probe or Infrared Sensor
Sensor Mounting	Mobility of sensor on site	Static, Human-based, AGV, Drones,	Temperature probe embedded in concrete, Infrared sensor mounted on a drone.
Data Transport/ Communication	One-Time, Periodic or Real-Time	LAN, Wi-Fi, Bluetooth, Zigbee,	LAN or Wi-Fi transmission of raw data to server.
Processing / Analysis	Applying algorithms and models to process the data and determine the output values	Algorithms, Statistics, Artificial Intelligence, Image Processing, Big-Data, Fuzzy Logic, Rule-Based Systems	Processing the raw data stream(s) and analysis to interpret and display results
Application Decisions	Inferencing systems to interpret the output data and decision models on the quality performance in the field situation	Dashboards, Digital Twin, BIM, Augmented/Mixed Virtual Reality	Decision if the temperature measurements are within the acceptable range for the quality requirements
Business Decisions	Strategic analysis and decisions on the long-term quality performance of the project or company	Business Process Management, Data Analysis, Rule Based Systems	Analyse impact of quality issues in the business outcome of the project - determine root causes if required and take corrective preventive actions.

It can be seen from the above table that there are several stages and technologies that enable digital technology-based monitoring of construction field-quality. The deployment of these technologies can be done in (i) procurement, (ii) construction and (iii) operational phase of a project.

In the procurement phase, the basic properties of raw materials such as moisture content can be rapidly assessed with digital technologies, in addition other properties such as morphology can be measured using vision-based sensing and image processing.

In the construction phase, the technologies can be used to assess the construction material properties dynamically as the construction progresses, as well as the assembly parameters such as dimensional deviations and equipment, environment and process characteristics that might result in a visibly poor-quality product or deviation from the standards.

In the operational phase, the behaviour and durability of the components as well as the system can be assessed. Embedded sensors can provide data on the structural health of the facility while arrays of sensors mounted on mobile platforms can detect issues such as cracks or corrosion and alter facility management for rapid corrective action.

In all the phases, the technology not only assesses the condition but also communicate the results to all stakeholders and automates the record keeping enabling business process analysis that is part of a robust quality management system.

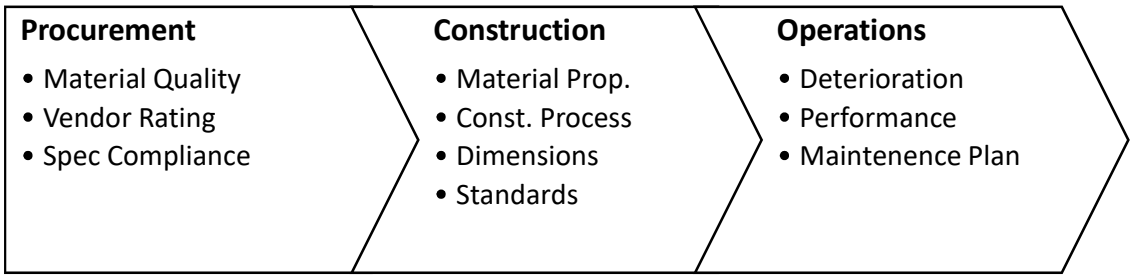

Figure 1. Digital Field-Quality Management System

An integrated platform to plan, monitor and control the quality over the construction entire project lifecycle including the pre-procurement phases can be based on the Digital Twin (DT) concepts.

A basic definition for DT is "as the virtual representation of a physical asset using DT-enabling technologies such as sensors, communication networks, and 3D models to obtain real-time updates and effect bi-directional coordination such that the virtual model represents a replica of the physical asset" (Madubuike, et. al. 2022)

DT concepts expand on the conventional IoT architecture by adding a "System Emulation" layer that models the behaviour of the project over its lifecycle. While conventional digital twins focus on modelling the operational phase of the facility or artifact, a lifecycle DT that dynamically evolves with the facility from concept to demolition phase of built facilities has been proposed (Sacks, et. al. 2020).

The terms Foetal Digital Twin, Child Digital Twin and Adult Digital Twin are proposed by (Sacks, et. al. 2020) to represent the Design, Construction and Operation phase of a built facility. While field-quality assessment is relevant to the Construction and Operation phases, the decisions taken during project conceptualization and design has significant impact on the quality control process.

The extension of IoT based architecture to digital twins and its applications for quality assurance and control is an emerging area of research that can have significant impact improving quality performance. In addition to the specific sensing and analysis technologies to predict, detect and control behaviour, platforms to improve the processes that assure quality is also a key area for continued research.

KEYWORDS: *Quality, Internet of Things, Digital Twin, Project Lifecycle*

References

Dey, N., Hassanien, A. E., Bhatt, C., Ashour, A. S., & Satapathy, S. C. (2018). *Internet of things and big data analytics toward next-generation intelligence*. Springer.

International Organization for Standardization (2021). ISO 9000 – Quality management.

Madubuike, O. C., Anumba, C. J., & Khallaf, R. (2022). A review of digital twin applications in construction. *Journal of Information Technology in Construction, 27*, 1-20.

Martínez-Lorente, A. R., Dewhurst, F., & Dale, B. G. (1998). Total quality management: Origins and evolution of the term. *The TQM Magazine, 10*(5), 378-386.

Ohno, T. (1988). Toyota production system: Beyond large-scale production (1st ed.). Productivity Press.

Sacks, R., Brilakis, I., Pikas, E., Xie, H. S., & Girolami, M. (2020). Construction with digital twin information systems. *Data-Centric Engineering, 1*, e3.

Womack, J. P., & Jones, D. T. (2013). Lean thinking: Banish waste and create wealth in your corporation. Simon & Schuster UK, Materials and Structures, 43(6): 857-874

Keynotes

Post-tensioned Concrete Members Under Severe/Heavy Loading Conditions

Asit N Baxi

Baxi Engineering Inc., Houston, USA
Email: asit@baxi-engineering.com

ABSTRACT

This paper presents an overview of design, detailing, and construction considerations for post-tensioned members subjected to severe/heavy loading conditions. A brief discussion of considerations for members subjected to severe environmental conditions is also presented. In most cases, post-tensioned members subjected to very large load magnitudes are transfer members. There could be instances where an individual member supports very heavy loads. Regardless, these members are critical load-bearing components of a structure and require a higher standard of care at all stages of a project. All project participants should be aware of the importance of these members and must treat it as such from the very beginning of a project. This paper pertains to post-tensioned members primarily for structures in the United States. However, the various considerations presented can apply to all post-tensioned structures, regardless of location. With significant advances in post-tensioning systems, the use of either unbonded or bonded tendons provides very efficient and economical solutions to support severe/heavy loads over long spans and for severe environmental conditions. This paper also provides examples of a few successfully completed projects.

KEYWORDS: *Post-tensioned transfer members, Transfer girders, Podium slabs, Unbonded tendons, Bonded tendons*

1. Introduction

Prestressed concrete members, whether pre-tensioned or post-tensioned, inherently offer the most efficient and economical method of supporting loads, especially of severe or extreme magnitudes. The prestressing steel —tendons for post-tensioning or strands for pre-tensioning can be stressed and profiled to efficiently balance the applied loads on the member even if their magnitudes are large. Post-tensioned members offer two salient advantages over pre-tensioned members especially for structures with severe/heavy loading and in severe environments. The first is that post-tensioned members allow for staged tensioning. Hence, for very heavy loads where the total applied load from superimposed dead and live loads is several times its self-weight (more than 100% to 125%), post-tensioning allows for the tendons to be stressed in stages as the structure is being built and loaded. The other advantage is that in severe environments such as exposure to corrosive elements or other scenarios, post-tensioned anchorages and ducts/sheathing provide better long-term protection in preserving the prestressing force in the member compared to pre-tensioned members where the prestressing force in the strands is held by bond.

This paper provides an overview of the design, detailing, and construction considerations for post-tensioned (PT) members subjected to severe/heavy loading conditions. Such severe/heavy loading conditions typically occur in structures with transfer members and will be the primary focus of this paper. However, there could be applications where individual members are subjected to excessively heavy loads as well. Although this paper focuses primarily on post-tensioned members for structures in the North American market, the various considerations presented can apply to any structure with post-tensioned members regardless of location. Two examples of projects with severe loading conditions have been presented: (i) transfer girders at the Bush International Airport in Houston, Texas with prestressing forces of 20,000 kips (89,000 kN) using unbonded tendons, and (ii) entire floor of transfer girders supporting 44 levels of a high-rise building in Philadelphia using bonded tendons.

Like any structural framing system, structures using post-tensioning as the primary floor system have continuously evolved with refinement in analysis and design tools, construction techniques, and significant

advances in post-tensioning systems. The current post-tensioning systems offer high-quality materials with enhanced corrosion protection characteristics. This has provided owners with well-designed, durable structures and overall superior performance.

The author wants to emphasize that post-tensioned concrete members supporting severe/heavy loading like the ones described in this paper require a higher standard of care at all stages of a project. All project participants should treat it as such from the very beginning of a project. While there are many finer points about the design and construction of post-tensioned members and are beyond the scope of this paper, this paper attempts to summarize the most significant considerations. Baxi (2024) provides an in-depth discussion of post-tensioned transfer members.

2. Structural Framing Options

Applications where post-tensioned members are the preferred option to support severe/heavy loads are as follows:

a) large clear spaces required between columns
b) bridging over existing structures or infrastructure
c) supporting another structure using an alternate material such as wood, light gauge steel, structural steel, cast-in-place, precast concrete, or where upper levels have an offset column arrangement

Examples of large spaces between columns (Figures 1 and 2) can be ballrooms in hotels, large amenity areas for conference rooms in hotels and mixed-used buildings, gymnasiums, spaces to let vehicular traffic pass through at a lower level or for a porte-cochère that is part of the main building envelope. Most members have the loads imparted at the top of the member, however, there are cases where the loads can be imparted at the soffit of the member. In this case, the columns below the member are hung and in tension. Figure 2 shows a building where loads occur both below and above the post-tensioned transfer frame (shaded floors on Levels 5 and 6). Another use for transfer members is to bridge across existing structures as shown in Figure 3, wherein two cases of massive transfer girders bridge over an existing rail tunnel structure.

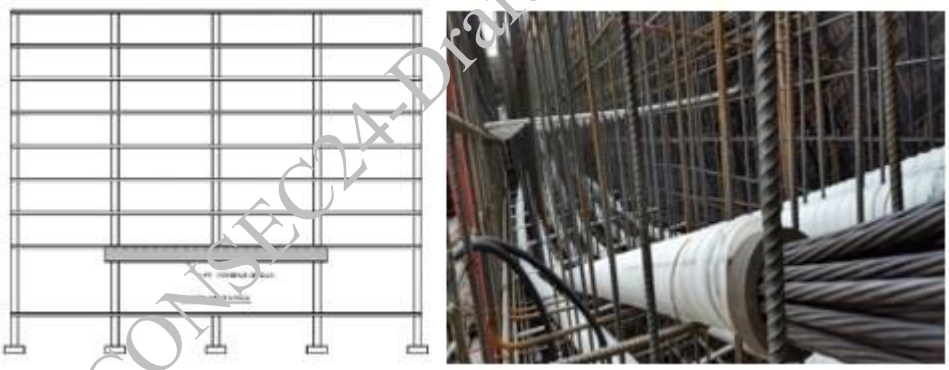

Figure 1. Use of Post-tensioned Transfer Girders to create large open spaces in a High-Rise Building

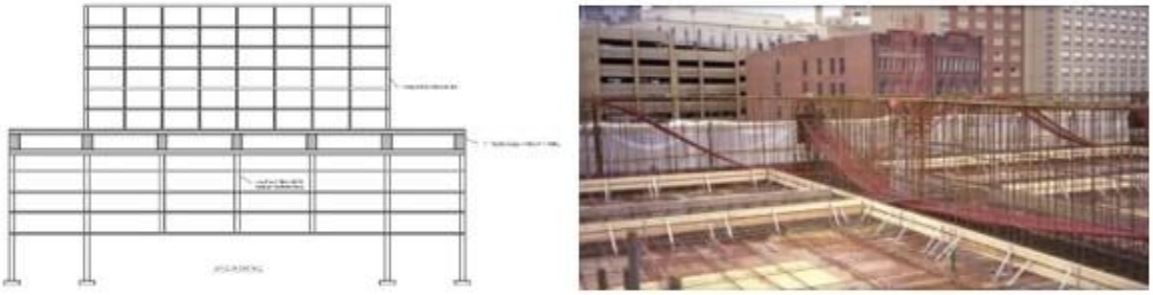

Figure 2. Use of Post-tensioned Vierendeel Moment Frames to create large open spaces in a High-Rise Building

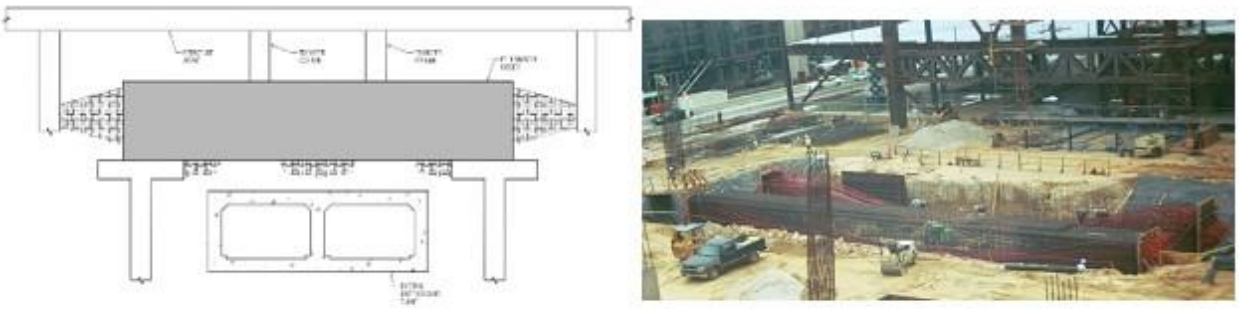

(a) Example of Unbonded Transfer Girders that bridge over ITT Tunnel at Bush IAH Airport, Houston, TX (Courtesy – Suncoast Post-tension Ltd)

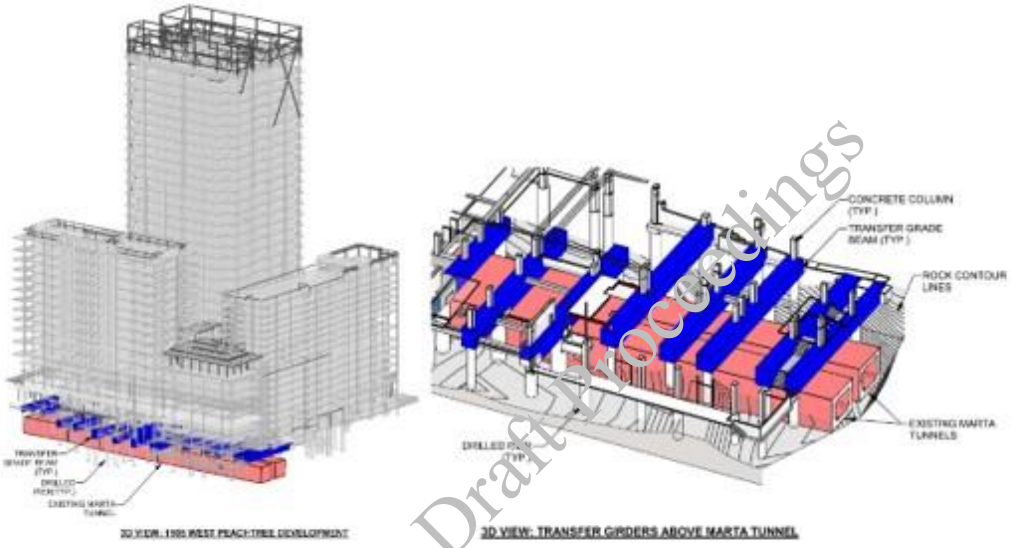

(b) Example of Bonded Transfer Girders that bridge over Marta Tunnel in Atlanta, GA (Courtesy – Uzun+Case)

Figure 3. Use of Extra-Large Post-tensioned Transfer Girders to bridge over existing Infrastructure

Another common use of post-tensioning to support very heavy loads is where the entire superstructure is of a different material or if the superstructure has an alternate column arrangement (offset columns). In this application, portions of a level or the entire level are post-tensioned and are commonly referred to as a Podium Slab. Podium transfer slabs can support 3 to 5-story wood-framed or 6 to 10-story steel light-gage structures or even a precast or cast-in-place superstructure (Figure 4). These slabs are typically popular in high-density areas in cities where space is a constraint.

Figure 4. Use of Podium slab to support superstructure made of different materials (wood, steel, precast, CIP concrete)

Depending on the type of structure, load magnitude, headroom, allowable long-term deflection, stressing access, and construction options, the following framing options can be considered for design:

- PT transfer girders or individual beams
- PT transfer frames (two or more levels) with or without moment connections at the joints
- PT transfer slabs (Podium Slabs)

PT Transfer girders or beams are typically the most effective and economical solution to support very severe/heavy loading. The member size is a function of the following factors:
Primary factors are the magnitude and position of the loads within the span, available headroom, maximum allowable deflection in the span, single or multiple spans, and available concrete strength
Secondary factors are anchorage placement/fitting of the anchors, stressing access, overall reinforcement congestion, stage stressing, etc.
The magnitude of the loads will always govern the overall size of the girders. The most common constraint to girder size is the headroom under the girder. It is always advisable to discuss this with the architect/owner at the very outset of a project rather than wait until the tail end of the design process. The magnitude of the loads will also affect the immediate and long-term deflection of the member. It is very critical for the design professional to determine in advance the acceptable absolute deflections and allowable deflection limits of the girders. In the case of tall high-rise buildings, it is critical that the transfer girder deflection is as small as possible because it has the potential to affect floor elevations, attachment of structural and non-structural elements, building façade elements, and drainage, to name a few. The distinct advantage of post-tensioning over other framing systems is the control of deflections by load balancing. In the example presented in this paper, the long-term deflection of transfer girders supporting 44 levels was less than 1/4 inch (6.35 mm).
It is advisable to use concrete with as high a strength as possible for all post-tensioned members. It is common in the US to use 28-day concrete strengths for transfer girders between 6,000 to 10,000 psi (41.4 to 69 MPa). Higher-strength concrete helps in many ways: it reduces member depth, flexural stresses, total prestressing forces, and the amount of nonprestressed reinforcement. It increases overall member stiffness, allows for early stressing, and helps reduce anchorage zone and initial stress issues.
PT Transfer Frames, while complex to build, offer very high overall member stiffness and can support severe and excessively heavy loads. The total depth of the transfer frame can vary from several feet to the height of an entire floor or even multiple floors (Figure 2). Most transfer frames have rigid joints/moment connections with a top and bottom chord; however, pinned struts could be used. The top and bottom chords are typically post-tensioned. Vierendeel moment frames provide very stiff and high load-carrying capacity with greatly reduced deflections. The space between the top and bottom chords can be used to run MEP lines and store mechanical and electrical equipment or for other uses.
PT Transfer slabs (Podiums) are the ideal framing option when loads from an entire or part of a building, either framed differently (offset columns) or framed using different materials, must be transferred below (Figure 4). The use of post-tensioning in these slabs will provide the most efficient, functional, and economical structural solution as opposed to using an alternate framing system. The podium slabs can be designed as one-way slabs with beams, two-way flat plates, two-way with drop caps, or using a wide shallow beam system. Post-tensioned two-way flat plates are popular because they keep the formwork cost to a minimum, allow for all MEP lines to run straight under the slab, and provide architects with flat exposed slab soffits and clean exterior lines, which are preferred. Punching shear is handled by using headed shear stud reinforcement (stud rails) at the columns.

3. Design Considerations

There are many considerations that should be made during the design of post-tensioned members supporting severe/heavy loads. All of them cannot be covered in this paper. However, some of the more important considerations are presented. Baxi (2024) provides a comprehensive discussion on this topic. To reiterate the statement made earlier: post-tensioned members supporting severe/heavy loads command a higher standard of care since they are critical load path-carrying elements of a structure. The best approach for design is to have a clear understanding of the structural behavior of these members and their interaction with the overall behavior of the structure. The general goal is to design members that perform adequately during service, possess the required strength and ductility (ACI 318-2022), and are durable for the service life of the building.

Gravity Loads: It is recommended that the gravity loads should be calculated based on an envelope solution from a frame analysis of the structure and tributary loads acting on any transfer columns from the levels above. The design professional should exercise judgment when making this decision. In general, the approach should be to determine the most realistic service loads anticipated on the member, considering the effects of span continuity (reactions due to unbalanced moments), secondary moments, and construction sequence that affect these reactions. Transfer loads on podium slabs are imparted differently than transfer beams. Most podium slabs have gravity loads transferred through a combination of bearing walls and columns. Depending on the bearing wall/column layout and the magnitude of the loads, either a "*smeared loading*" or "*true reaction*" approach should be used considering cases of concentrated loads. Since transfer members typically have loads coming down from multiple levels, the question of whether the full live load on all levels should be considered or not is relevant. The design professional should use their judgment when considering how much live load reduction should be used.

Lateral Loads: The effects of lateral loads, whether seismic or wind, must be considered in the design. These actions can be determined from a lateral load analysis of the structure for the different load combinations. The various actions (upward and downward reactions, in-plane reactions, and moments) must be applied on the member, whether beam or slab, with the appropriate load combination factors considering both directions (E-W and N-S) and an envelope solution determined. Podium slabs also serve as diaphragms and should be designed to resist the in-plane forces due to lateral loads. The diaphragm elements to be designed are the chords and collectors.

Unbonded vs. Bonded Post-tensioning: The choice of unbonded vs. bonded post-tensioning depends on various factors. Unbonded post-tensioning is the method of choice in the United States. More than 98% of all post-tensioned prestressed concrete buildings in the US use unbonded post-tensioning. The primary reason for this option is the lower material cost and ease of installation and handling of unbonded tendons. Bonded tendons have a slightly higher material cost; however, the biggest difference between the two systems is in the additional labor costs to install the ducts, placement of the tendons inside the ducts, and grouting of the ducts. Members with bonded tendons require a reduced amount of mild reinforcement by design, and hence, a reduction in rebar material and labor costs should be included in a cost comparison. However, considering all the costs; in general, bonded tendons will cost more than unbonded tendons.

Bonded tendons have traditionally been chosen in transfer members, especially in transfer girders, because of the inherent redundancy in being able to retain the prestressing force in case of tendon breakage (from corrosion or any other reason) and in providing enhanced crack control. However, due to advances in manufacturing, installation, and inspection of encapsulation unbonded systems, in the author's opinion and experience, members with unbonded tendons provide comparable or better corrosion protection than bonded tendons. Unbonded tendons can be easily replaced during service if the need arises.

Average Prestress: Typical prestress values in transfer girders, including the beam web and slab cross-section, will range from 200 psi to 400 psi (1.38 to 2.76 Mpa). Girder sizes proportioned to provide prestress values in this range provide efficient designs, prevent reinforcement (tendon + rebar) congestion, and reasonable fit of the anchorages at the member ends. Prestress values of 500 psi (3.45 Mpa) and higher may be used with appropriate measures to account for the effects of restraint to shortening and after ensuring that there is adequate fit of the anchorages considering the column and beam reinforcement at the member ends. Most post-tensioned podium slabs supporting 4 to 5 levels of wood-framed structure will require an average slab precompression between 150 to 200 psi (1.03 to 1.38 Mpa). These prestress values will vary depending on the slab thickness, spans, loading, and stage stressing requirements. Making the slabs too thin will result in high prestress values and may result in over-balancing, triggering initial stress requirements, higher punching shear stresses, and excessive shortening. An upper bound value of 300 psi (2.07 Mpa) in slabs is strongly recommended (ACI 423.3R-17, 2017).

Restraint to Shortening (RTS): All concrete members, whether non-prestressed or prestressed, undergo shortening due to slab shrinkage and creep, in addition to movement from temperature change and elastic shortening for post-tensioned members. This should be considered in the design. The effects of restraint and potential cracking can be mitigated by using several techniques (PTI DC20.2-22, 2022).

Stage Stressing: Most transfer members require stage stressing because the amount of prestressing force imparted at any stage should be in proportion to the superimposed loads acting on the member. Full prestressing with no superimposed loads will more than likely create high initial stresses, exceeding the tensile strength of concrete at transfer (f'_{ci}), and may cause premature cracking. This cracking is not desirable and should be avoided at all costs. Stage stressing should be carefully determined for each stage

so that the initial stresses, the service level stresses, and the deflection under the member at any given stage do not exceed project allowable/acceptable values. The number of tendons stressed at a given stage should enable the member to have the capacity for service and strength to support not only the transfer loads present at the time of stressing but also the transfer loads expected to occur just prior to the next stage of stressing.
Shoring: Stressing operations, whether initial or staged, must be coordinated carefully with the removal of shoring. For transfer girders with bonded tendons, the design professional should carefully evaluate the sequencing of the stage stressing, grouting of the ducts, and shoring requirements for each stage.

4. Detailing Considerations

Proper detailing of the post-tensioned transfer members – girders, slabs, and frames is critical for a successful project outcome. Proper detailing starts with an accurate and clear set of structural drawings, details, notes, and specifications. This enables other trades, such as the rebar supplier, PT supplier, general contractor, installer, and inspector, to ensure that the project has been built to specifications. In the author's opinion, transfer girders should be drawn in an elevation view showing the transfer girder supports, transfer columns, girder reinforcement, tendon forces & profiles, tendon bundling details, and end anchor views with anchorage zone details.
Post-tensioning: The post-tensioning tendons are the most critical reinforcement within a transfer member. The final effective prestressing force or the number of tendons with qualification of the minimum final effective force required per tendon should be called out accurately on the drawings along with their profile and any other relevant information. The PT supplier must detail the post-tensioning information in a manner so that the shop drawings provide the required tendon quantities, tendon bundling information, stage stressing information (if any), jacking information, tendon length, required tendon elongation, tendon profiles – (reverse parabolas, simple parabolas, or harped profile), offset low points, tendon curves including hairpins and end anchor details showing the anchorage zone reinforcement.
For bonded tendons, the anchor type, anchor components, jack and jacking information, duct type and profile, grout port information & locations, grouting details and installation, stage stressing information, end anchor details showing column vertical reinforcement, anchorage zone reinforcement, and stressing access blockouts if any must be provided. Stage stressing of tendons with sequencing (if applicable) must be shown on the structural and PT shop drawings for the benefit of the installer, inspector, and general contractor. The stage stressing should be typically shown and executed in the field in a manner such that the tendon stressing does not create undue horizontal or vertical eccentricity at the anchorages.
Anchorage Zone: Transfer members typically have large prestressing forces, which produce extremely large bearing and bursting forces in the anchorage zone. The anchorage zone regions - local and general zones of transfer girders and podium slabs with both unbonded and bonded tendons should be detailed, showing backup bars or spiral reinforcement in the local zone and bursting reinforcement in the general zone. The Post-tensioning Manual (PTI TAB.1-23, 2023) provides extensive information on the different methods to determine the anchorage zone reinforcement.

5. Construction Considerations

The construction of post-tensioned transfer members is equally important as its design and detailing. All parties involved in its construction, starting from the design professional, architect, owner, contractor, subcontractors, and inspecting agency, should realize the importance of this structural element and be clear on the responsibilities of their portion of the work. Communication and general coordination must be continuous throughout the construction process between all relevant parties. Typical issues that arise in the construction of transfer members are as follows:

a) Formwork under transfer girders, removal of formwork, and shoring/reshoring sequences
b) Access for stressing, especially on heavy transfer girders – bonded and unbonded tendons Being able to fit all the anchors – bonded and unbonded within the column vertical steel
c) Discussion with installers to ensure that any congestion issues are discussed at an early stage rather than later
d) Coordination with electrical, mechanical, and plumbing trades to ensure that slab and girder sleeving is acceptable to the licensed design professional

e) The design professional and the third-party inspector at a minimum must review and approve the installation prior to concrete placement
f) Special care must be taken to ensure proper concrete vibration in and around anchorage zone areas
g) Installation, stressing, and inspections should be performed by experienced personnel
h) Stage tensioned tendons should be protected from the elements to prevent water from entering the wedge-cavity area of the anchor. There are several methods to protect the tendon tails.
i) Grout material, grouting equipment, grouting procedures, grout sampling, and grout testing should be coordinated with the relevant trades. Proper grouting is essential for the performance of bonded tendons.
j) Tendon elongations should be sent to the licensed design professional as soon as possible; usually within 24 hours. Elongation discrepancies should be resolved to the satisfaction of the design professional
k) Tendon finishing is a key component of preserving the longevity and durability of a post-tensioning tendon and relevant local codes must be followed.

6. Structures in Severe Environments

Advances in post-tensioning systems and materials provide adequate protection for structures depending on the degree of exposure. PTI/ASBI M50.3-19 and PTI M55.1-19 (2019) specifications must be used for grouting.

7. Examples

Examples of post-tensioned members supporting very heavy loads are as under:
Example#1: This is an example of transfer girders using unbonded tendons. Transfer girders 96” (W) x 120” (D) (2438 mm x 3048 mm) shown in (Figure 5) span about 107 feet (32.6 m) over the ITT Tunnel supporting the Terminal E Parking Garage at the Bush Intercontinental Airport in Houston, TX. The girders support transfer columns of an 8-level long-span parking garage. The final effective force in each girder is 20,000 kips (88,964 kN) and is probably one of the few girders ever built for a building application with such high prestressing forces.

Figure 5. Transfer Girders that bridge over ITT Tunnel at Bush IAH Airport (Courtesy – Suncoast Post-tension Ltd)

Example#2: This is an example of transfer girders with bonded tendons in a 52-story building (Westin Hotel) in downtown Philadelphia. Level 8 of this building has 4 transfer girders spanning 44’-3” (13.5 m) (Figure 6) with sizes from 72”x144” to 96”x144” (1829x3658 mm to 2438x3658 mm) that support 44 levels. The transfer girders provided a large clear space at the ballroom/amenity levels. The girder prestressing forces varied from 4,650 to 6,020 kips (20,684 to 26,779 kN) with tendons stressed in 3 stages.

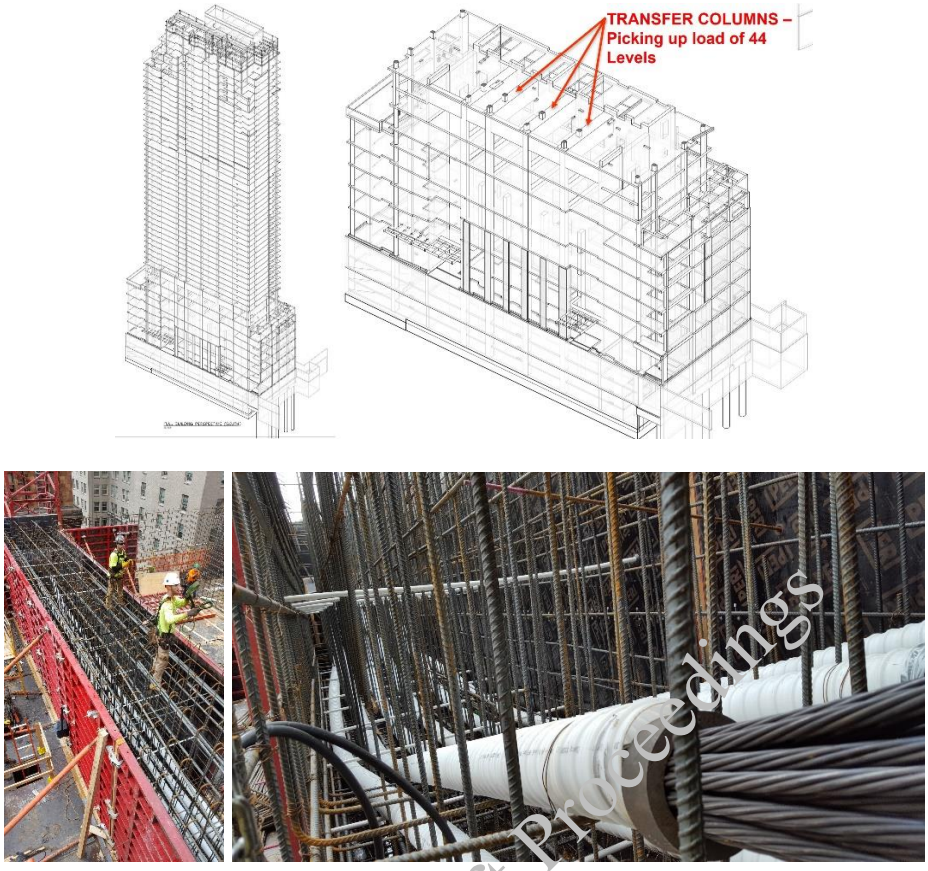

Figure 6. 52-story Westin Hotel in Philadelphia with Transfer Girders on Level 8 supporting 44 Levels

8. Summary

Post-tensioned members provide an efficient and economical solution for supporting structures subjected to severe/heavy loads. Advances in post-tensioning systems allow for enhanced corrosion protection of the members including at anchorage zones, thus providing superior durability. An overview of important design, detailing, and construction considerations for post-tensioned members subjected to severe/heavy loading conditions was presented. Examples of transfer applications with extra heavy loads that have been successfully implemented were presented. While the paper pertains to post-tensioned members primarily for structures in the United States, the various considerations presented can be applied to all structures with post-tensioned members regardless of location.

References

ACI Committee 318 (2022) "Building Code Requirements for Structural Concrete (ACI 318-19) and Commentary (ACI 318R-19) (Reapproved 2022)," *American Concrete Institute*, Farmington Hills, MI.

ACI 423.3R-17 (2017) "Recommendations for Concrete Members Prestressed with Single-Strand Unbonded Tendons", *American Concrete Institute*, Farmington Hills, MI.

Baxi, A.B. (2024) "Post-tensioned Transfer Members in High-Rise Buildings in the United States", *PTI Journal*, Issue 1, 19-36.

PTI Building Design Committee DC20.2-22 (2022) "Restraint Cracks and Their Mitigation in Unbonded PT Building Structures," *Post-tensioning Institute*, Farmington Hills, MI.

PTI/ASBI M50.3-19 (2019) "Specification for Multistrand and Grouted Post-tensioning", *Post-tensioning Institute*, *American Segmental Bridge Institute*, Farmington Hills, MI

PTI M55.1-19 (2019) "Specification for Grouting of PT Structures", *Post-tensioning Institute*, Farmington Hills, MI

PTI TAB.1-23 (2023) "Post-Tensioning Manual," Seventh Edition, *Post-tensioning Institute*, Farmington Hills, MI.

Carbonation of Low Clinker Concretes: When it is a Concern and When it is not

Shashank Bishnoi

Department of Civil Engineering, Indian Institute of Technology Delhi, Hauz Khas, New Delhi 110016, INDIA

1. Introduction

As the reduction of clinker content becomes an important strategy to reduce CO_2 emissions of cement production, carbonation is gaining significant attention. Since clinker is the main phase that contributes to the calcium content and reserve alkalinity of cement, blended cements are more prone to losing alkalinity due to carbonation. This makes it very important to understand the process of carbonation and the associated risk of corrosion of reinforcement in blended cements. Along with being more susceptible to carbonation, it has been shown that there is a coarsening of the pore-network in the case of blended cements, increasing the risk of corrosion (Shah et al., 2018). However, carbonation does not always lead to corrosion as the environmental conditions that are optimal for carbonation, may not necessarily be optimal for corrosion. This paper presents how carbonation is different in low clinker concretes and how it affects the risk of corrosion of concrete.

2. Process of Carbonation

Carbonation is the reduction of the pH of the pore-solution in concrete, due to a neutralisation reaction with dissolved atmospheric carbon dioxide. CO_2 enters the concrete through unsaturated pores and dissolves in the pore-water, converting into carbonic acid. This carbonic acid reacts with the alkalis in the pore-solution, neutralising them and forming carbonates. Since most cements contain excess calcium, this calcium buffers the more soluble sodium and potassium ions. The calcium precipitates in the form of calcium carbonate ($CaCO_3$). The depletion of calcium in the pore-solution leads to a further dissolution of calcium-rich phases in the cement, including unreacted clinker phases and hydration products. The process of carbonation continues until no further calcium can dissolve and the pH of the pore-solution drops to a value below 9.0 (Papadakis, 2000). The drop in concentration of calcium ions leads to an outward diffusion of calcium ions from the uncarbonated concrete inside.

As diffusion of CO_2 into the concrete is the slowest step in the process of carbonation, the carbonation of concrete prevents a deeper ingress of CO_2, creating a clear carbonation front. The carbonation front progresses only when the reserve alkalis in the outer part of concrete have been exhausted. Since blended cements contain lower reserve alkalis than ordinary Portland cement (OPC), the carbonation front advances faster into the concrete (Shah and Bishnoi, 2018).

Depending on the clinker or hydrate phases that dissolve, other phases such as silica gel, moisture, aluminium hydroxide, etc. are formed along with $CaCO_3$. For example, the dissolution and carbonation of tricalcium silicate (C_3S) leads to the formation of silica-gel along with $CaCO_3$. Similarly, the carbonation of CH leads to the formation of water and the carbonation of ettringite also leads to the formation water and aluminium hydroxide. Depending on the phases that are formed, the pore-volume may increase or reduce (Shah et al., 2018).

Carbonation, in itself, does not lead to a reduction in the engineering performance of concrete. It usually leads to an increase in compressive strength and reduction cracking risk due to shrinkage during service. Elastic modulus is also known to increase. It is, however, the reduction in pH due to carbonation that leads to ruptures in the passivating film that protects reinforcement and is stable at higher pH values. This, in suitable environments, may lead to the initiation of corrosion of reinforcement.

3. When does carbonation lead to corrosion

Although the reduction of pH that results from carbonation, increases the risk of corrosion of reinforcement, the corrosion does not always occur. The conditions required for the corrosion of reinforcement include the availability of moisture and oxygen, while carbonation occurs in a lower relative humidity range of 40% to 60%. For this reason, not all reinforcement in carbonated concrete corrodes. Carbonation-induced corrosion is usually limited to regions that either go through wetting and drying cycles, or where moisture is available on one surface of concrete, while another surface is dry. The rate of corrosion depends on the rate of moisture and oxygen transport to the corrosion site. Measurements on old structures have shown that toilets and kitchens are most susceptible to corrosion. Reinforcement at locations that remain relatively dry after carbonation does not usually corrode.

Most blended cements usually reduce the rates of moisture and ionic transport in concrete, so it is assumed that the rate of corrosion of reinforcement in carbonated blended concrete will be lower than in OPC. However, studies have shown a coarsening of the pore-structure after carbonation and this may increase the rate of corrosion. This coarsening reduces the resistivity of the cement matrix, increasing the rate of transport of moisture, gases and ions to the reinforcement and potentially the rate of corrosion.

When the carbonation of CH takes place, $CaCO_3$ and water are formed. Depending on the polymorph of $CaCO_3$ (calcite, vaterite or aragonite), the solid volume increases by 11% to 15%, reducing the porosity and pore-connectivity. This implies, that in systems that have a sufficiently high amount of CH and a sufficiently low porosity, the reduction in porosity due to carbonation can be sufficient to close all pores and prevent any further ingress of CO_2. Carbonation in some cements can, therefore, be a self-limiting process.

However, in the case of blended cements, where the quantity of CH can be low, the carbonation of C-S-H and other phases like ettringite may occur. The carbonation of these phases leads to a reduction in the solid volume, a release of free water and an increase in porosity and pore-connectivity. While the released water can reduce the ingress of CO_2 into the microstructure until it is lost through evaporation, in the long-term, the increase in porosity is likely to increase CO_2 ingress. However, at lower w/b, even in blended cements, since the carbonation of the unhydrated clinker phases is likely to occur before the carbonation of other hydration products, an increase in the solid volume and a reduction in the porosity would occur. The release of moisture from the carbonation of C-S-H or ettringite would also support further hydration of the unhydrated clinker phases, further reducing porosity. Therefore, at sufficiently low w/b, carbonation can be a self-limiting process even in blended cements.

4. Preventing carbonation-induced corrosion

Whenever carbonation is a self-limiting process, providing adequate clear cover should be sufficient to prevent the corrosion of reinforcement. It has been shown that it is difficult to prevent corrosion in reinforcement with clear cover values less than 10 mm to 15 mm even in the case of OPC. In the case of blended cements, a slightly higher value must be ensured and a low w/b must be used. However, the reduction of w/b can be counterproductive to sustainability as higher cement contents may be required in concrete and other measures to prevent carbonation induced corrosion may be required. There can be two approaches for this: first preventing carbonation or second preventing corrosion.

Various chemical treatments can be used to prevent carbonation of concrete using SCMs. Acrylic and polymer-based anti-carbonation coatings are currently available in the market. These coatings could be applied to concrete at locations where carbonation may lead to corrosion. Such coatings create an impermeable layer on the surface of concrete, preventing the ingress of CO_2 into the concrete. While these coatings are easy to apply, being exposed to the environment, they suffer from wear and tear and require regular replacement. Other chemicals may be impregnated into the concrete, creating a highly dense, low porosity cover concrete, preventing the ingress of CO_2. Calcium-rich injections that carbonate, leading to formation of $CaCO_3$ and closure of pores, can be imagined. Such treatments are likely to be more durable.

In the second approach, if the ingress of moisture in carbonation concrete is prevented, then corrosion would not occur. Several types of water-proofing chemicals are available in the market. A comparison of pore-blocking and hydrophobic types of chemicals has shown that hydrophobic impregnation can significantly reduce transport properties in carbonated blended mortars, to levels similar to those in carbonated OPC. However, the type of chemical varies from one cement to another. It was observed that

there is no significant additional advantage of mixing these chemicals at the time of production of the concrete, compared to application after construction. This implies that the chemicals need not necessarily be mixed in the concrete and can be applied afterwards, preferentially at locations where corrosion is likely to occur. Surprisingly, carbonation depth was also observed to be lower in blended cements treated with these chemicals.

5. Reduction of w/b to prevent corrosion

In most practical situations, it may not be required to make carbonation a completely self-limiting process. Reducing the rate of carbonation may be sufficient to achieve required service life. For example, the amendment no. 6 to IS456:2000 recommends the reduction of the w/c by 0.05 when LC^3 is used compared to the recommended maximum values for other cement types including PPC and PSC, in Table 5 of the standard. The same table also lists the minimum grade of concrete required to be produced under specific exposure conditions. The table below compares the water to binder ratios recommended for PPC and LC^3 subjected to various exposure class along with the usual water to binder ratio used for the production of concrete of the recommended grade for that exposure class. The values in the table show that the recommended reduction of w/b is unlikely to lead to a reduction in the cement content in concrete mixes. This shows that limiting the w/b can be an effective means to control the risk of carbonation induced corrosion when blended cements are used.

Table 1. W/b ratios for PPC and LC^3

Exposure class	Recommended w/b for PPC	Recommended w/b for LC3	Minimum grade	Usual w/b for grade
Mild	0.55	0.50	M20	0.50
Moderate	0.50	0.45	M25	0.45
Severe	0.45	0.40	M30	0.40
Very Severe	0.45	0.40	M35	0.37
Extreme	0.40	0.35	M40	0.34

6. Influence of carbonation on chloride ingress

Blended cements are known to have slower rates of chloride ingress and higher chloride binding than OPC. However, after carbonation, the rate of chloride ingress is significantly higher, increasing the risk of chloride-induced corrosion. Additionally, since the chloride threshold for corrosion is lower at lower pH values, as are present in blended cements, the rate of corrosion can be higher. It has been observed that the surface application of hydrophobic chemicals on carbonated blended cements can significantly reduce the rate of chloride ingress. Although situations where both carbonation and chloride ingress can occur are rare, the risk of corrosion can be reduced whenever they occur.

7. Conclusions

Although carbonation does not always lead to corrosion, the risk of corrosion increases when blended cements carbonate. Additionally, the rate of corrosion is also likely to be higher in case of carbonated blended cements. Similar to OPC, it should be possible to self-limit the process of carbonation, although this would require low w/b. Controlling w/b ratios can also help in reducing carbonation depths in the case of blended cements. Since corrosion only occurs at specific locations in structures, surface treatment of concrete at locations with a high risk of corrosion can be an effective means to improve service-life.

References

V. Shah, K. Scrivener, B. Bhattacharjee, and S. Bishnoi, ‘Changes in microstructure characteristics of cement paste on carbonation’, *Cement and Concrete Research*, vol. 109, pp. 184–197, Jul. 2018

V. G. Papadakis, ‘Effect of supplementary cementing materials on concrete resistance against carbonation and chloride ingress’, *Cement and Concrete Research*, vol. 30, no. 2, pp. 291–299, Feb. 2000

V. Shah and S. Bishnoi, 'Carbonation resistance of cements containing supplementary cementitious materials and its relation to various parameters of concrete', *Construction and Building Materials*, vol. 178, pp. 219–232, Jul. 2018,

Concrete Durability in Vulnerable Coastal Communities. The role of the Participatory Action Research (PAR) for Social Appropriation

J.A. Briceño-Mena[1,2], J.A. Puc-Vázquez[3], P. Castro-Borges[4]*, M.T. Castillo-Burguete[5]*

[1] Center for Research and Advanced Studies, Mérida, Yucatán, Mexico
Email: jorge.briceno@cinvestav.mx
[2] National Council of Humanities, Sciences and Technologies, México
Email: jorge.briceno@cinvestav.mx
[3] Center for Research and Advanced Studies, Mérida, Yucatán, Mexico
Email: jaset.p.vazquez@gmail.com
[4] Center for Research and Advanced Studies, Mérida, Yucatán, Mexico*
Email: pcastro@cinvestav.mx
[5] Center for Research and Advanced Studies, Mérida, Yucatán, Mexico*
Email: maria.castillo@cinvestav.mx

*Corresponding authors (s)

ABSTRACT

The aim of this paper is to discuss the mechanism of social appropriation of knowledge about concrete durability in vulnerable coastal communities through Participatory Action Research (PAR). The Community of Puerto de San Crisanto in Yucatan, Mexico, has suffered the effects of climate change for several decades, which involve the loss of beaches, hurricanes, storms and floods, which have as one of the main consequences the loss of their precarious homes. Through PAR exercises and for more than 25 years, the community has been able to propose stilt houses to contend with the effects of climate change. Over the years, six prototypes of stilt houses made of durable concrete have been built with the support of all the parties involved. The project partners (formal scientists) transmitted the technical knowledge to the facilitators (empirical researchers from the community) through the PAR with various teaching/learning techniques. In one of the recent stages, and because of the social appropriation of knowledge, communities can now instrument their homes to periodically measure the corrosion and carbonation potential of concrete with electrodes made by themselves and inexpensive and easily acquired instruments. The paper describes and discusses some of the techniques that allow the social appropriation of knowledge.

KEYWORDS: *Participatory action research, Concrete, Durability, Corrosion, Climate change.*

1. Introduction

To work with community or group problems, where participation is essential to solve problems, Paredes and Castillo (2018) point to a "family" of theoretical approaches to carry it out. Among them is participatory action research (PAR) that brings together participation and action, involving theory, practice, collaboration, education, emancipation, criticism and reflection. With this approach, professional researchers seek to strengthen interested parties to be autonomous and self-managed (Castro Borges, 2011). In these processes, participation is more than physical presence, Castillo Burguete (2001, 2015) points out that "community participation is structured as the action of participating or intervening in an event in the stages for its realization, either directly, through physical presence, the contribution of ideas, planning and carrying out actions, or indirectly, mediated through the contribution of resources, knowledge and skills, in groups whose activity goes beyond the benefit of the family, covering segments of the population or its totality that are expressed somewhere, in scenarios, environments and relationships". These approaches and ways of working are distant for disciplines such as civil engineering, which are more aligned with the hard sciences. However, the communities also handle concepts related to construction and durability from their

experience. This paper discusses the mechanism of social appropriation of knowledge about the durability and sustainability of concrete in the vulnerable community of San Crisanto, Yucatán through PAR.

2. Methodology

The research methodology involved participatory teaching-learning processes in action, from horizontality. Another return of the spiral began by reactivating the previous group, inviting previous members to participate and, those who agreed, responded to a diagnosis of concepts about PAR and durability. We gathered data on how they understood and appropriated the problem of interest and workshops were designed and adapted to the coastal community context, with recreational activities for community researchers to incorporate new concepts into their daily lives.

3. Results and discussion

3.1 Participants

The groups participating in PAR are usually open and formed organically, there was an initial invitation from the work team, but the participants themselves invited other people from the community. 28 people from San Crisanto were invited, of whom 21 responded to the knowledge diagnosis (Table 1). The participants named themselves the new group "Building a Sustainable Future". The group had 24 participants, 14 of whom were in the previous project of the Stilt house Group (SG) and 10 were new.

Table 1. General information of SG participants.

Gender	Participants of the SG	Average age (years)	Guests	Answered the diagnosis	Participation in the new group
Female	23	53	22	16	12
Male	8	58	6	5	2
Total	31		28	21	14

3.2 Interviews with community researchers

In visits to the community researchers, it was possible to recognize the community dynamics, learn about the rhythms of daily activities and rediscover the landscape of the place. Valuable information was obtained on the characteristics of daily life through individual interviews and meetings, which allowed us to know the community's willingness to participate in the study. The diagnosis on PAR and durability consisted of 36 open questions, the answers indicated that the participants empirically knew the concepts, even referring to examples to expand their answers. In the community there were previous PAR projects, through which prototypes of durable housing were built.

3.3 Workshops

13 weekly meetings were held, with central activities. Each session was planned to last 90' maximum, considering the time of the participants, but, although we took care of the duration, the participants stayed longer talking, making agreements or finishing a snack. Each session required designing and creating materials, finding equipment for experiments and activities (Table 2).

Table 2. Name of the activities carried out in the sessions.

Activities		
1. Name the group	5. The wear of metals	9. Evaluation
2. Let's put it to the test	6. Let's measure corrosion	10. Constructions well done
3 Concept memory	7. Salinity in concrete	11. Landing concepts
4. Let's cook concrete	8. Lottery	12. Concept crossword
		13. Activity clothesline

We recorded participant attendance, conducted icebreaker activities, and allocated more time to the core activity to address technical concepts. We tried to have spaces for dialogue during and after the activities.

Table 2 lists the central activities. We will take as an example activity 6 "Let´s measure corrosion", whose objective was for participants to identify and appropriate the concepts about corrosion.
During the workshop, participants built, as in a community laboratory, the electrode used to measure corrosion and diagnose the health status of the reinforced concrete. Most of the materials used are easily accessible and easy to use by participants: syringe, cork, multimeter, solutions, cables, etc. The diagnosis was made as an analogy between reinforced concrete and a human being, whereas in a laboratory, we carry out tests to know the "health" of the material (Martín Kú et al, 2010). Each team had to physically analyze their reinforced concrete specimen and write what they observed on the diagnosis sheet. Reinforced concrete specimens were different, some of them had cracks (bad condition) and some of them were in good condition, so differences in diagnosis could be observed. For this task, they were given instructions about wetting the element, assembling the equipment, and taking stable results (Fig. 1). The concepts addressed with this activity were: crack, fissure, reinforced concrete, steel, corrosion potential.

Figure 1. Community participants measure the corrosion potential.

Activity 8 "Lottery" is a traditional Mexican game. There, the typical figures characteristic of Mexican humor were replaced by 36 concepts about durability and PAR (Fig. 2). The objective was to reaffirm the concepts in a playful way.
Each booklet contained 9 of the 36 technical concepts addressed in the workshops. One participant was the responsible to read each concept with or without showing the figure. To reaffirm the knowledge of the concepts, the person who filled out the booklet and shared with the group the meaning of some concept in the booklet won. Another form of the activity was to read the definition of the concepts taken from the decks, and the participants must know the concepts to mark them on the booklet. In this way, all the concepts were addressed with this activity.

Figure 2. Photo illustrating the lottery game of durability and PAR concepts.

4. Final thoughts.

The environment generated with the integration of professional researchers with community researchers facilitated the social appropriation of knowledge about durability. However, working WITH the community represents a great challenge, attending and participating in the workshops is not immediately achieved. The progress in the appropriation of the concepts was observed in each workshop and not only in the final evaluation, which indicates gradual progress. Each session allowed participants to strengthen their

understanding and apply the knowledge acquired in a practical way. As the workshops progressed, greater confidence and skill in handling the key concepts of durability and sustainability could be noted. In addition, other significant achievements emerged in these processes. The community's trust in the research team was strengthened, creating an environment conducive to participants expressing their doubts, interests, and feelings. This level of openness made it easier to identify specific community needs and allowed project activities to be adjusted to be more relevant and effective. The community of San Crisanto participated in this work and teachers and educational psychologists from Chicxulub, another nearby port, interested in learning about the way of working with PAR, doctoral and postdoctoral students from Cinvestav and members of the National Council of Humanities, Science and Technology also joined. In the end, we observed that the participants of San Crisanto internalized the concepts with expressions that allow them to make them part of their daily lives and the care of their homes, such as cleaning the house, cooking, or watching television.

Acknowledgements

The authors thank the participation of the inhabitants of San Crisanto and Commissioner Martina Chuc for the facilities provided to carry out this study.

References

Castillo-Burguete, M.T. (2001). Gender relations in the areas of community participation of a town on the Yucatecan coast (in Spanish). *PhD Thesis in Social Anthropology*, Department of Political and Social Sciences, Mexico City: Universidad Iberoamericana.

Castillo-Burguette, M. T., García-Gómez, C., Castro-Borges, P., Dickinson, F. (2015) "I´m not afraid of him; That dog barks but he don´t bite. PAR processes, gender equity and emancipation with women in Yucatán, Mexico", *The SAGE Handbook of action research*, Chapter 28: 291-300.

Castro Borges, P., Dickinson, F., Castillo, T., Torres Acosta, A. A., García, C. (2011) "Participatory research to create durable housing" (in Spanish), in *Proceedings of the XI Latin American Congress of Construction Pathology and XII Congress of Quality Control in Construction*, Eds. R. Chang, O. Flores, La Antigua Guatemala, Guatemala, October, ISBN 978-9929-40-

Martín-Kú, J. R., Castro-Borges, P., Balancán-Zapata M., Torres-Acosta, A. A. (2010) "Construction and characterization of a concrete stilt house in the Gulf of Mexico" (in Spanish), paper 28, 4th National Congress of ALCONPAT-Mexico, Nov, Xalapa Veracruz, México, ISBN 978-607-95042-5-0: 220-233

Paredes-Chi, A. and Castillo-Burguete, M.T. (2018). "There is no [single] path walker, the path is made by walking": in Participatory Action Research and its repercussions in practice (in Spanish). *Rev. colomb*. Soc.,41(1)

Stress Corrosion Cracking in Prestressed Concrete Bridge –A Case Study

Gino Ebell[1*], Thoralf Müller[2], Andreas Burkert[3]

[1,2,3]Bundesanstalt für Materialforschung und -prüfung (BAM), Berlin, Germany
Email: gino.ebell@bam.de

[*]Corresponding author

ABSTRACT

Bridge structures built using the prestressing block method can exhibit hydrogen-induced stress cracks across the entire cross-section of a prestressing channel due to their design. Crack growth can progress over the service life as a result of dynamic loading and lead to prestressing wire fractures.

KEYWORDS: *Hydrogen-induced stress corrosion cracking, prestressing steel, sensitive prestressing steel*

1. Introduction

Hydrogen-induced stress corrosion cracking on high-strength steels, such as prestressing steels, is based on a damage mechanism that is downstream of a corrosion reaction. The presence of atomic hydrogen is essential for the damage mechanism. This can be formed by the cathodic partial reaction of a corrosion reaction (Fig. 1). [Kaplan (2021)]

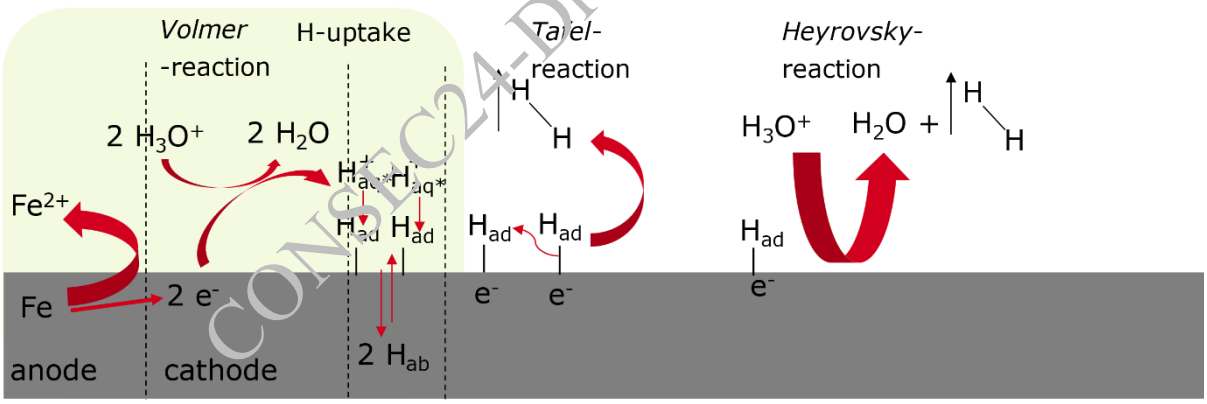

Figure 1. Schematic representation of the anodic and cathodic partial reaction of the corrosion process at pH <5 and hydrogen adsorption-absorption

If the microstructure of the prestressing steel is irreversibly influenced by the effect of the absorbed hydrogen, cracks can occur in the microstructure if the stress is sufficiently high. Cracks that have formed in the construction phase of the structure during active corrosion reactions can result in crack growth without further corrosion reactions in the regular operating state. In this case, a prestressing wire fracture can occur significantly later. In order to determine whether a highly sensitive prestressing steel is present, magnetic particle tests are generally carried out in advance to examine the prestressing steel for cracks, as well as optical emission spectrometry (OES) to determine the alloy composition. Subsequently, tensile tests are carried out on crack-free prestressing steels and metallographic examinations are performed to verify the microstructure. The susceptible prestressing steels are all oil-shot quenched and tempered, depending on the manufacturing process. A metallographically proven quenched and tempered structure validates the classification of prestressing steel, together with a corresponding alloy composition and an ultimate tensile

strength greater than 1500 N/mm², as highly sensitive prestressing steel. Cracks do not have to be present for classification as high-sensitivity prestressing steel.

2. Overview of the building

The bridge at the Altstädter Bahnhof in Brandenburg a.d. Havel was built in 1969 and opened as part of the celebrations for the 20th anniversary of the German Democratic Republic. The bridge structure consisted of two substructures, the main structure (TBW 1), which crosses Magdeburger Straße over the tracks/parking lot and Zanderstraße, and the feeder (TBW 2). The main structure contains two lanes with two traffic lanes each as well as a double-track streetcar line and was unusually wide with a length of 174 m and a superstructure width of ≈ 37 m, see Fig. 2. The resulting superstructure cross-section has nine box girders with a variable construction height between 1.46 m and 1.54 m. The box girders that were not accessible as planned had a clear height of ≈ 1.22 m and 1.06 m respectively, with a width of 2.68 m. Except for the shorter end bay, the box girders are braced in the middle of the bay by cross girders. Furthermore, cross girders are arranged in the support axes. In the connection area of the feeder (axis C), two secondary cross girders are arranged in addition to the main cross girder.

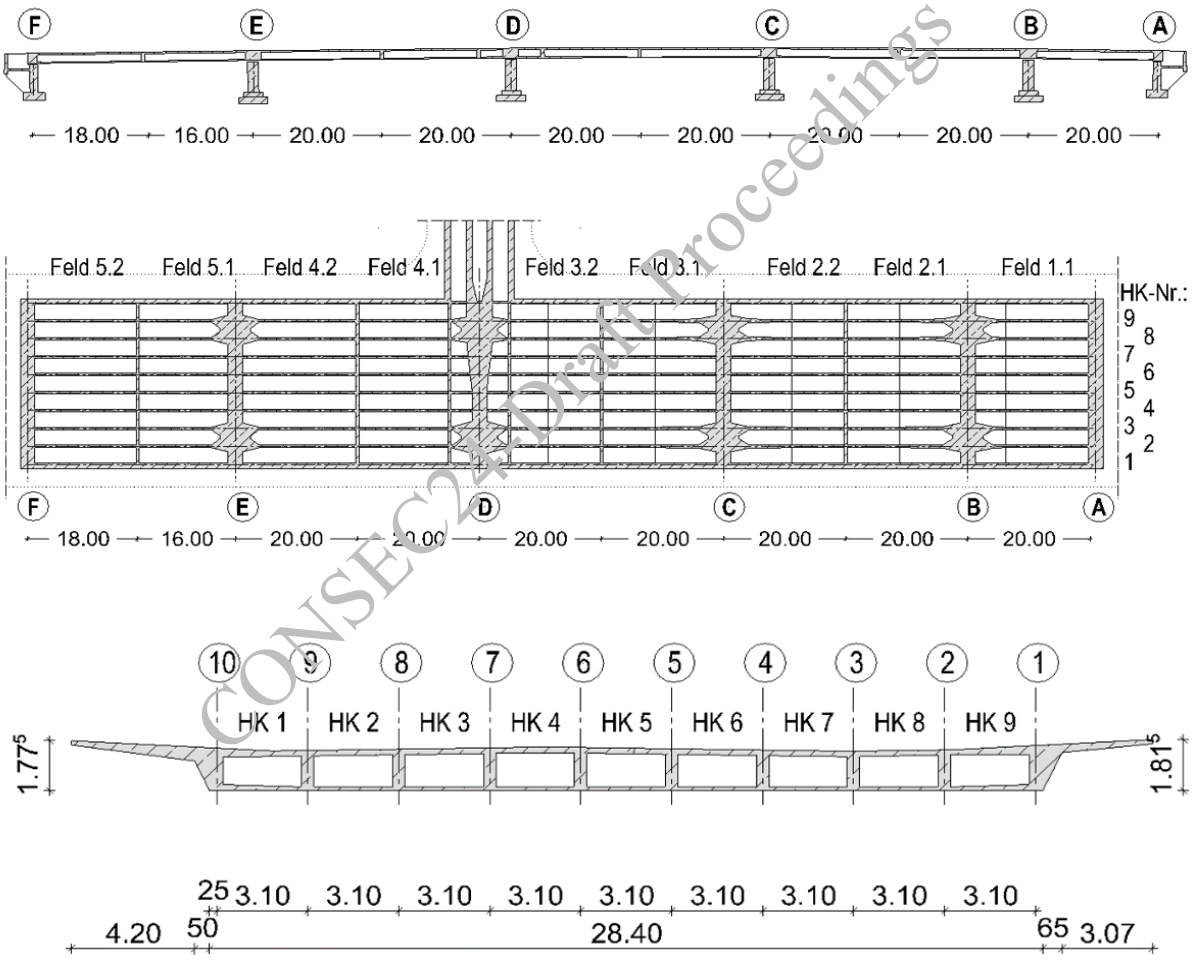

Figure 2. Main supporting structure, longitudinal section, cross-section [Kaplan (2021)]

At that time, the prestressing block method used for the construction of the bridge had been superseded by the introduction of TGL 173-33(TGL 173-33 (1967)). However, in contrast to the normative specifications, a special form was used. Instead of the usual prestressing wire with a cross-sectional area of 40 mm², prestressing wires with a cross-sectional area of 35 mm² were used. This is due to the fact that only the Hennigsdorf prestressing wires with a cross-sectional area of 35 mm² were available in the required delivery length of 175 m. In addition, a larger tensioning box (tendon box for SSG 1400 instead of SSG 1200) was required to accommodate the larger number of individual wires, 392 in total. This meant that a tensioning

force of 12 MN could be applied to each main girder. The 392 individual wires were installed in accordance with the specifications and secured in position using spacers, as can be seen in Fig. 3.

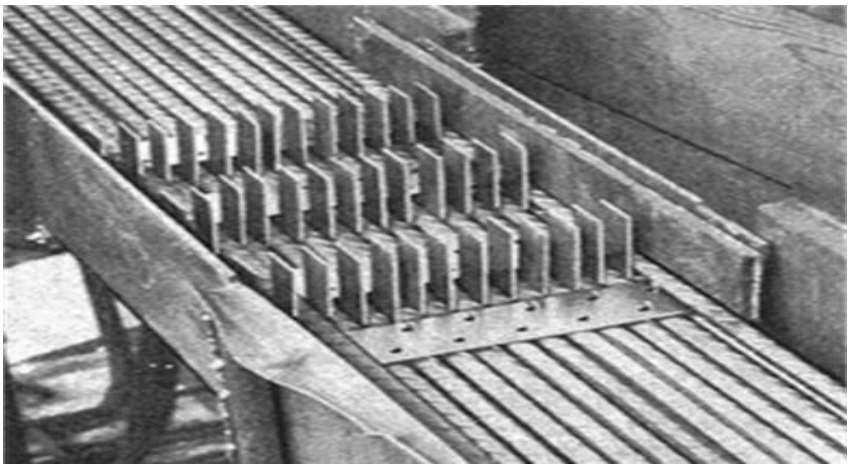

Figure 3. Envelope box with spacers at a deflection point [Lippold (1969)]

3. Structural investigation of the demolished structure

An assessment was carried out after the bridge structure was demolished. Support area C facing the B 102 federal highway (section 2.2) was accessible for the assessment of exposed prestressing steel. The fracture surfaces of the prestressing steels could be examined at the exposed prestressing channels. With the exception of a few prestressing steels, the majority of the prestressing steels were brittle.
Without exception, the brittle fractures show lenticular discoloration and are based on hydrogen-induced stress corrosion cracking. The discoloration is due to the ingress of H_2O in the form of water vapor. A further finding was that beam number 3 in bay 2.2 in the immediate vicinity of support axis C must have cracked over almost the entire cross-section of the prestressing wire bundle even before the blast. An indication of this is provided by the fracture pattern shown in Fig. 4 with already corroded residual fracture surfaces.

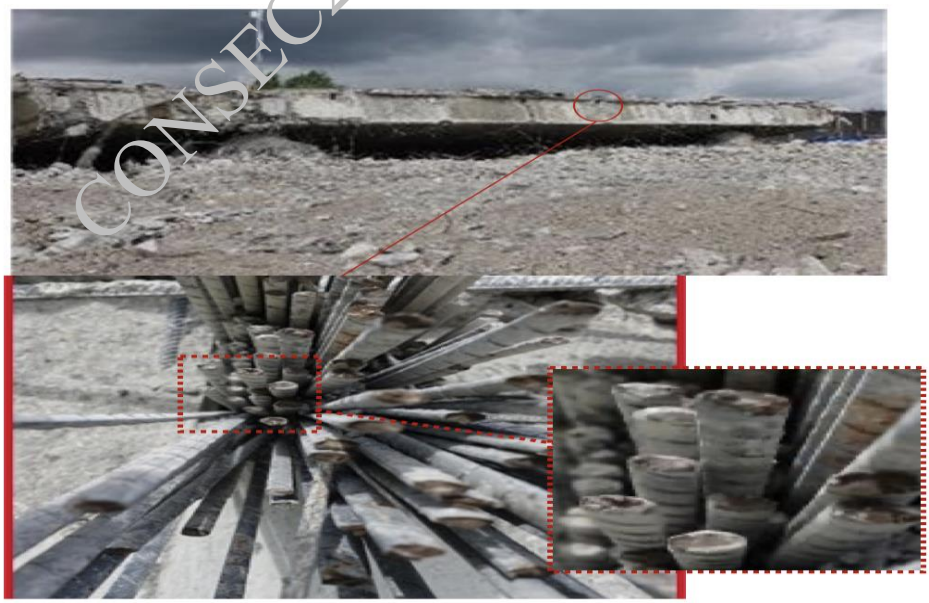

Figure 4. Tensioning wire bundle cracked due to hydrogen-induced stress corrosion cracking in beam 3 bay 2.2 near support C

During the dismantling of the bridge, it was also observed that fractures occurred on the side to the right of the axis C support when the prestressing wire bundles were twisted into the containers provided for disposal.

Prestressing steels removed from this area exhibited hydrogen-induced stress cracks distributed over the entire surface. An example of a prestressing steel with typical cracks is shown in Fig. 5, with and without UV light irradiation, after magnetic particle testing.

Figure 5. Tension wire with significant cracks, top: without UV light, bottom: with UV light

The prestressing steel removal to the left of the support in axis E, from panels 5.1 and 5.2, showed a completely different corrosion condition of the prestressing steels. The tendons were screwed in for disposal in the same way as on the right-hand side of axis C but for the most part without any fractures in the prestressing steels. In this area, significantly fewer cracks were detected on the removed prestressing wires. One exception, however, is the area of the horizontally arranged spacers, where many cracks were localized on both axis E and axis C. The combination of bending the prestressing steels by twisting and spacers in the bending radius led to fractures, see Fig. 6.

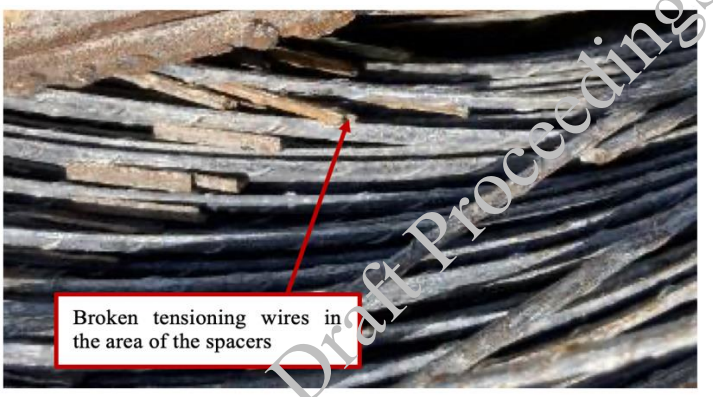

Figure 6. Tensioning wire bundle with wire breaks in the area of the spacers

A stressing box with clear corrosion damage could be localized, the grouting condition between the duct and prestressing steels was very good, and no signs of corrosion could be detected on the adjacent prestressing steels. Chloride-induced corrosion can be ruled out with a chloride content of the grout of 0.02 wt.% in the area of the corroded duct.

4. Characterization of the prestressing steels

The assignment of the extracted wires was carried out in accordance with the dimensions specified in TGL 101-036/02: 1966 (TGL101-036/2 (1966)). According to this, 131 pieces were identified as St 140/160 oval 35 mm² and 2 pieces as oval 30 mm². The FES analyses have shown that the chemical composition meets the specifications of TGL 101-36/01: 1966 (TGL 101-036/1 (1966)) corresponds. Some samples were found to be slightly below the carbon content and the silicon content. The metallographic examinations revealed a tempered structure. Fig. 7 shows a longitudinal section of prestressing steel with a typical quenched and tempered microstructure and stress cracking as well as slight edge decarburization. Of the 133 tension wires taken, 21 tension wires with a length of up to 1.90 m could be assessed as crack-free using magnetic particle testing. In total, 131 crack-free sample sections with a length of 50 cm could be worked out

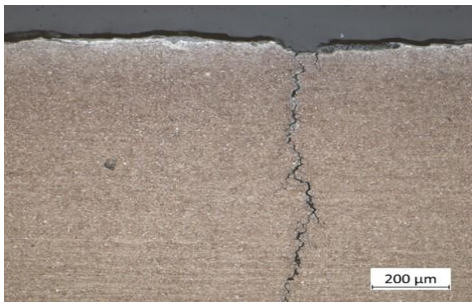

Figure 7. Metallographic longitudinal section etched with tempered structure and crack

. From the tensile tests on the undamaged 50 cm prestressing wire sections, an average $Rp_{0,2}$ of 1393 N/mm² and an R_m of 1524 N/mm² were determined. The fractures on the undamaged prestressing wires were all ductile. One of the 4 prestressing wires tested was damaged by a previously undetectable stress crack, similar to Fig. 7. The R_m of this sample was above the mean value, but the fracture only occurred with a slight necking strain and the fracture pattern is more similar to a brittle fracture. The target values according to TGL are 1373 N/mm² for $Rp_{0,2}$ and 1570 N/mm² for R_m, the latter may be undercut by 29 N/mm². The increased mass of the actual load-bearing cross-section due to the rib portion is not taken into account when determining the cross-sectional area, nor is the reduction in the cross-section of the prestressing wire at the base of the rib. Taking these factors into account, the deviation between the nominal and actual values is not considered significant.

Based on the available results, the prestressing steel taken can be classified as highly sensitive to hydrogen-induced stress corrosion cracking due to the manufacturing process, as:

- the alloy composition complies with the specifications of the TGL
- the metallographic examinations confirm a tempered structure
- the tensile strength is greater than 1500 N/mm².

5. Summary

The initiation phase of the hydrogen-induced stress corrosion cracking on this bridge structure is largely due to the ingress of moisture (rainwater or condensation) during the construction period. Such damage patterns are also known from other bridge structures. A special feature that has not been found to date is the initiation of damage across the entire cross-section of the prestressing duct in the grouted cladding tube condition. In this design, the position of the individual prestressing wires is secured by spacer plates (Fig. 8). In the free span length, the distance between the spacers should be between 1000 mm and 1500 mm in accordance with TGL 173-33 (1967). In the area of the deflection points, the spacers are arranged closer together depending on the project. The spacing in the deflection area is shown in Fig. 9 as an example of this bridge structure and is between 180 mm and 250 mm according to measurements on-site.

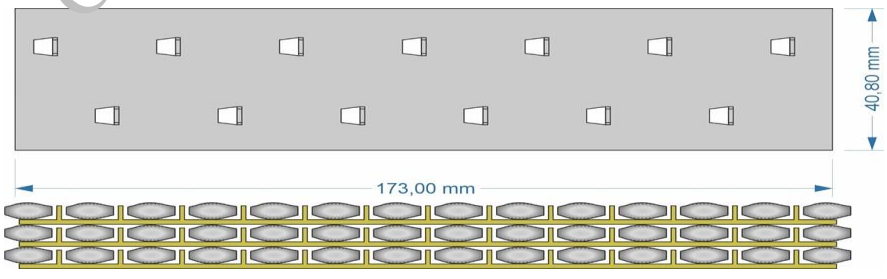

Figure 8. Schematic representation of a spacer plate as a punched part for securing the position (top); a section through three prestressing steel layers with spacer plates (bottom)

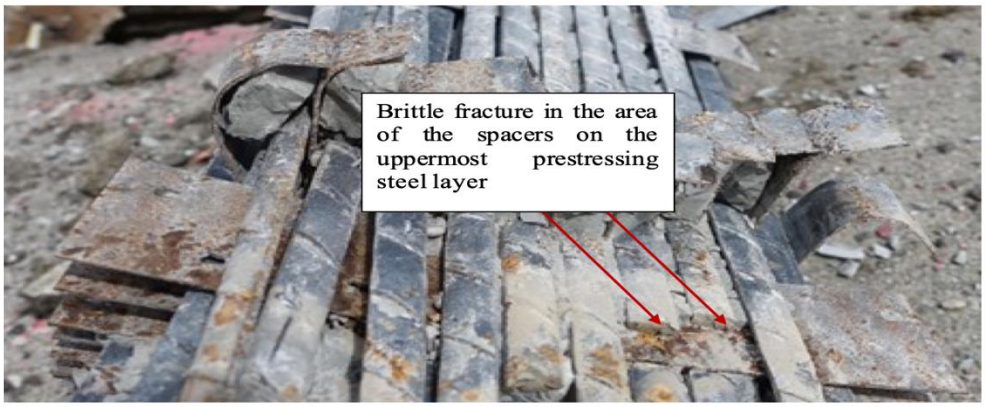

Figure 9. Tensioning wire package in the support or deflection area with horizontal and vertical spacers (spacing not regulated according to TGL)

Tensioning steels removed from this area show an increased number of cracks in the contact areas to the spacer. Figures 10.1 and 10.2 show the uncleaned contact point and subsequent magnetic particle inspection with clear cracks. Figures 10.3 and 10.4 show the cleaned contact area and the subsequent magnetic particle inspection, which produces an improved crack indication in terms of clarity and number of cracks.

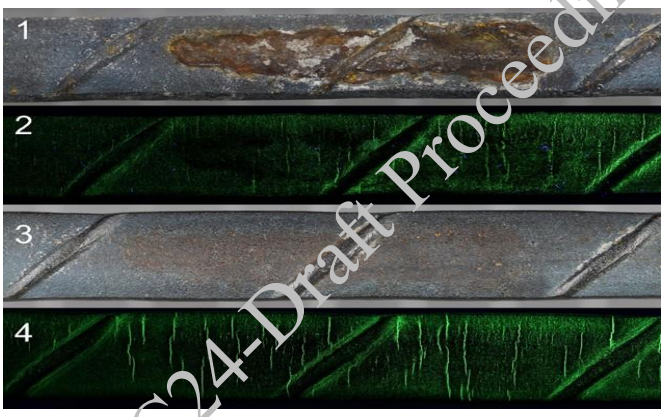

Figure 10. 1: Contact point with signs of corrosion, 2: Magnetic particle inspection with crack indication; 3, 4 as 1, 2 only with cleaned surface

The examination of the prestressing steels in the deflection areas above a support has shown that signs of crevice corrosion occur at the contact points of the prestressing steels with the horizontal spacer plates as a result of insufficient grouting. Due to the relatively wide spacer plates and the pressing of the prestressing steel in the deflection areas against these plates, it is not possible for the grout to enter and a critical crevice arrangement is achieved here. In these areas, the progression of the corrosion reaction and the lack of an alkaline buffer lead to acidification of the crevice electrolyte. At pH values below 5, the cathodic partial reaction takes place with the formation of hydrogen. A sufficient supply of moisture can be assumed over a long period after pressing. In the long term, this leads to hydrogen-induced embrittlement and cracking in the steel, resulting in crack growth and subsequent breakage of the prestressing wire due to dynamic loads. A change in traffic routing, which leads to greater dynamic loads, can result in stable crack growth.
The previous assumptions regarding the initiation of stress cracks due to hydrogen embrittlement on prestressing steels in the subsequent bond assume a corrosive load on the prestressing steels before grouting in the duct or a corrosive load during the service life, e.g. due to de-icing salt exposure and rusting through of the duct with subsequent corrosion of the prestressing steels. Corrosion can also occur in areas that are not grouted or are inadequately grouted. Crevice geometries in smooth cladding tubes can also cause crevice corrosion in deflection areas on the adjacent prestressing steels; in contrast to the present design, however, this would only affect a few prestressing steels of a prestressing steel bundle.
The damage patterns found show that with this type of construction, even after scheduled grouting, hydrogen can develop at the support areas of the spacers due to crevice corrosion, which can result in embrittlement of the adjacent prestressing steels. The splitting situation also occurs over the entire cross-

section of the prestressing channel and can therefore affect each individual prestressing wire.
In a standard assessment of prestressing steel by removal from bridge structures, the removal usually does not take place in the deflection areas due to static requirements or structural conditions. Detection of existing cracks is therefore not necessarily possible, particularly for opening lengths below the spacer installation distance of 1 to 1.5 m. At the same time, the formation of crevices may be less critical due to the lack of pressure in these areas.
Based on the available results, it can be assumed that hydrogen-induced stress cracks can occur in highly sensitive Hennigsdorfer prestressing steels St 140/160 despite the bridge structure being constructed using the prestressing block method (no pre-corrosion, proper grouting condition, no water ingress via cracks).
The examination of the crack surfaces with multiple crack lenses (see Fig. 11) at fresh fracture points shows that there is a reduction in the prestressing steel cross-section of up to 46 %. A residual cross-section of the prestressing wire of 54 % does not provide sufficient reserves for loads and stresses such as prestressing force, dead load, temperature, and traffic, which was confirmed by acoustic emission measurements.

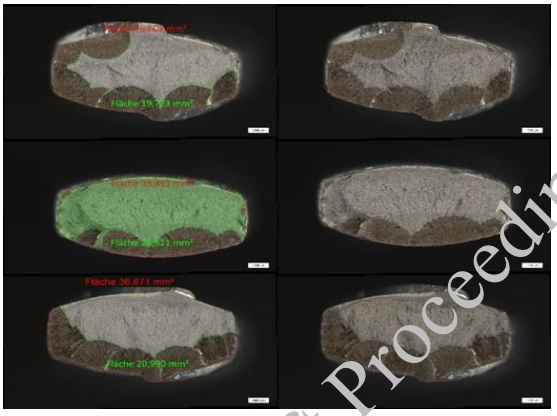

Figure 11. Multiple crack lenses at a fresh fracture site

The lasting damage to a structure caused by hydrogen-induced stress corrosion cracking is not only indicated by prestressing steel fractures but primarily by existing cracks.
The speed of crack growth due to dynamic stress depends on the stress and thus on the position of the crack in relation to the moment curve. The fractures in the area of the support on axis C confirm this.

6. Conclusions

The damage was initiated during the construction of the structure by hydrogen-induced stress corrosion cracking, and the damage progression by crack growth (fatigue) resulting from cyclic/dynamic loading of the structure (Kaplan 2022). Once the critical residual load-bearing area is undercut, a prestressing wire fracture occurs. The resulting load redistribution can lead to an exponential increase in wire fractures over time.

References

Lippold, P. (1969) *Concentrated tendons in road bridge construction*, In: Bauplanung - Bautechnik, 172ff.
Kaplan, F.; Steinbock, O.; Bösche, T.; Niederleithinger, E.; Ebell, G.; Saloga, K.; Kind, T.; Kilian, A. and Fiedler, G.; et al, (2021) *B1 - Brücke Altstädter Bahnhof in Brandenburg an der Havel,Bauwerksuntersuchungen vor dem Rückbau*, Landesbetrieb Straßenwesen.
Kaplan, Felix; Steinbock, Oliver; Saloga, Katrin; Ebell, Gino; Schmidt, Sebastian (2022) *Überwachung der Brücke am Altstädter Bahnhof*, In: Bautechnik 99, 222-230, (2022)
TGL 101-036 (1996) Sheet 1 *Prestressing steel St 140/160 oil-tempered, steel brands, technical delivery conditions*.
TGL 101-036 (1996) sheet 2 *Spannsthal St 140/160, oil tempered, oval ribbed, dimensions*.
TGL 173-33 (1967) *Tensioning block method, tendons with nominal tensioning force 600 to 1600 Mp*.

Dual Purpose Titanium Alloy Anodes for Near-surface Mounted Retrofit and Impressed Current Cathodic Protection

A.K. Slawinski[1], C. Higgins[2], O.B. Isgor[3*]

[1]Consor Engineers, Holualoa, Hawaii, USA
Email: akslawinski@gmail.com
[2]Oregon State University, Corvallis, OR, USA
Email: chris.higgins@oregonstate.edu
[3]Oregon State University, Corvallis, OR, USA
Email: burkan.isgor@oregonstate.edu

*Corresponding author

ABSTRACT

Near surface mounted retrofit (NSMR) using Titanium alloy bars (TiABs) is an established technique to strengthen structurally deficient reinforced concrete structures. This paper presents a new approach that allows structural TiABs to be used for a secondary purpose as Impressed Current Cathodic Protection (ICCP) anodes. Experiments on large-scale structural beams show that TiABs were able to maintain cathodic potentials in the expected linear region of the polarization curve of the steel rebars, and the 100-mV potential decay criterion was satisfied upon the interruption of the protection current. The applied current and potential to achieve the required cathodic potentials were stable and were satisfactorily maintained while achieving the structural retrofit requirements. This dual-purpose application has the potential to revolutionize how structurally deficient structures can simultaneously be strengthened and protected from further corrosion.

KEYWORDS: *Corrosion, retrofit; Strengthening; Cathodic protection; Titanium, Steel rebar*

1. Introduction

Strengthening reinforced concrete structures using the near-surface mounded retrofit (NSMR) technique is an established technique (Higgins and Barker 2015, Parvin and Shah 2016). In recent years, titanium alloy bars (TiABs) have been shown to effectively and economically increase shear and flexural strength of existing reinforced concrete structures in NSRM applications (Higgins and Barker 2015; Higgins *et al*. 2017). ASTM Grade 1 or 2 Titanium − mainly in the form of embedded wire mesh, strips, or discrete anodic bars − is also a widely used anode in impressed current cathodic protection (ICCP) systems to mitigate reinforcement corrosion issues in existing structures (Segan *et al*. 1982, TM0294 2016). These titanium anodes are often coated with mixed metal oxides (MMO) to increase their efficiency, stability, and durability (IOS 2018); however, they do not provide any structural benefits. The utilization of TiABs as a dual purpose NSMR/ICCP material creates the unique opportunity for a multi-functional solution that can provide immediate capacity restoration and long-term corrosion mitigation. The utilization of TiABs in NSRM applications is described in existing materials standards and design and construction guidelines (ASTM B1009 2018; AASHTO NSMT-1 2020). Typically, TiABs that are used as NSMR material are made up of the Ti-6Al-4V alloy, which corresponds to ASTM Grade 5 and ASTM B1009 Class 130 (Sun *et al*. 2011; ASTM B1009 2018). Since TiABs are not specifically developed for ICCP applications, they are not MMO coated. The lack of surface coating might have implications with respect to their ICCP performance and durability. The main objective of this paper is to address the major challenges associated with applying dual-purpose TiAB anodes in NSMR/ICCP applications. The NSRM and ICCP performance of TiAB anodes is presented when they are used for the structural retrofit of large-scale beams undergoing active corrosion.

2. NSRM/ICCP Application

2.1 Experimental Setup

Figure 1 shows an application of dual purpose TiAB anodes for retrofitting a structurally deficient flexural beam (a) and a shear beam (b) (Slawinski 2022). The concrete mix design closely matched the concrete properties that were widely used in bridges constructed during the mid-twentieth century and had a 28-day compressive strength of 23.4 MPa. Mixing water included 1.5% chlorides in the form of reagent grade NaCl to ensure active corrosion of the embedded rebars. Steel rebars in all beams were confirmed to be corroding at the time of ICCP application. Grade 60 #9 and Grade 40 #4 carbon steel rebars were used as internal longitudinal and shear reinforcement, respectively. The flexural beam was retrofitted with #5 longitudinal TiABs, while the shear beam was retrofitted with #2 transverse TiABs. An electrically conductive structural grout (ECSG) was used to bond the TiABs into saw cut grooves. The ECSG had a compressive strength of 69 MPa and electrical resistivity of 4.65 kΩ-cm. Note that in conventional NSRM applications, epoxy-based adhesives are used that would effectively isolate the TiABs; therefore, ECSG is needed for the NSRM/ICCP application to allow ions to flow between the surfaces of the reinforcing steel and TiAB anodes.

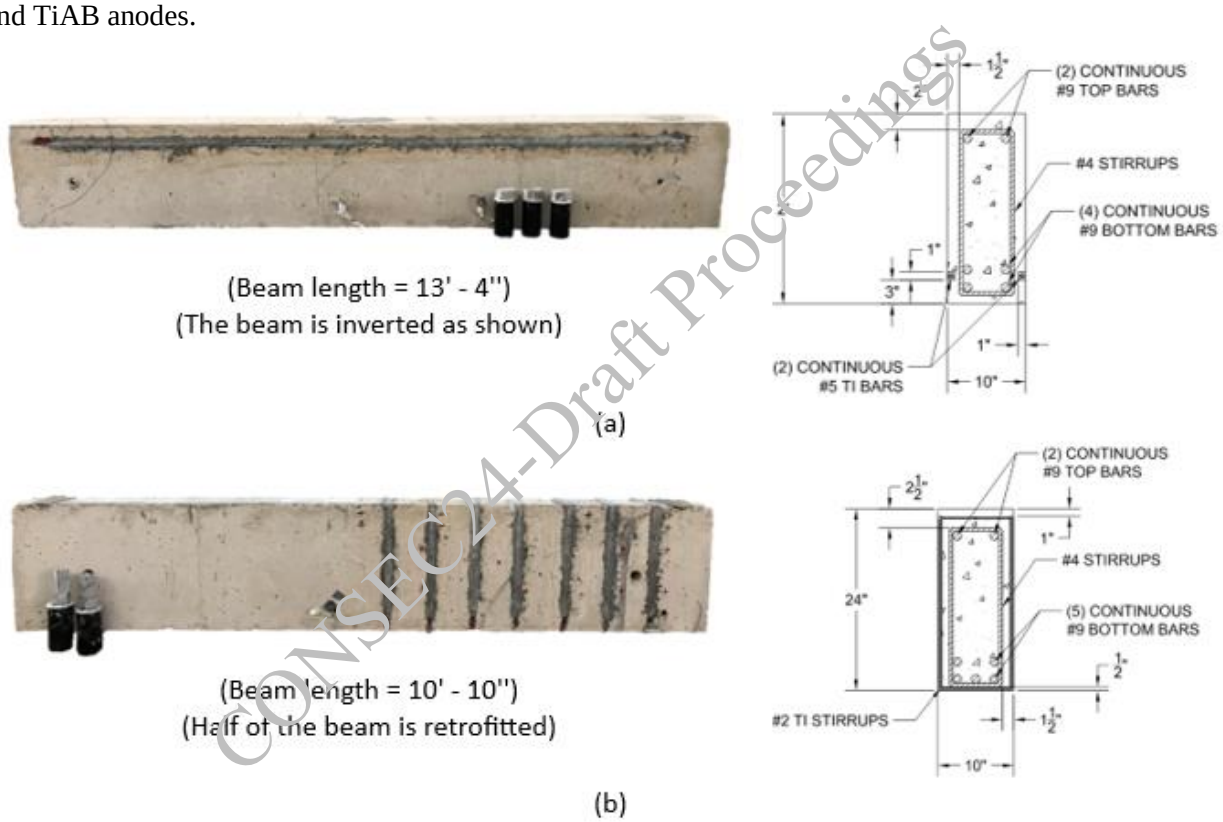

Figure 1. NSRM/ICCP application (a) flexural beam, (b) shear beam (1 in. = 25.4 mm; 1 ft = 0.305m)

Flexural tension steel and stirrups were electrically isolated from one another at their interfaces. The steel bars were drilled and tapped, allowing for external connection to copper wires that were used to apply ICCP. ICCP was applied using a potentiostat. Anodic polarization scans were performed to determine the linear portion of the cathodic polarization curve that decribes the operating cathodic potential in the ICCP application. The polarization test informed the cathodic potential to operate the ICCP setup, which was active for five (5) hours. During the ICCP application, half-cell potential (HCP) of the rebars were measured. After the five (5) hours of ICCP, the cathodic current was turned off and the HCPs were measured and recorded at five (5) locations along each #9 rebar at 10-minute intervals over the course of four (4) hours. This data was also used to assess the effectiveness of the ICCP using the 100-mV polarization shift criterion. Following the ICCP tests, the beam specimens were tested structurally until failure. The structural testing indicated that all beams exceeded their retrofit goals. Results of the structural tests are not shown here for brevity; however, they are reported in Slawinski (2022).

2.2 ICCP Results

ICCP was conducted with an applied current of 143.9 mA for the flexural beam (current density of 8.28×10^{-6} A/cm^2) and 102.5 mA for the shear beam (current density of 5.62×10^{-6} A/cm^2). The applied currents were stable throughout the ICCP operation and did not require major adjustments to the applied potential, establishing that even without an MMO coating the TiAB bars were able to sustain the required current, and the ECSG was able to serve as a conductive medium between the TiAB anodes and concrete substrate. Experiments performed on both the flexural and shear beam specimens demonstrated that the 100 mV criterion was met, thereby proving that ICCP can be achieved with ASTM B1009 Class 130 TiABs in NSMR applications. Both #5 longitudinal TiABs and #2 transverse TiABs were able to locally protect the steel rebars in the concrete beam specimens. Figure 2 shows the depolarization of the selected longitudinal and transverse steel rebars in the flexural and shear beams after the ICCP was shut off. Full details for other rebars can be found in Slawinski (2022).

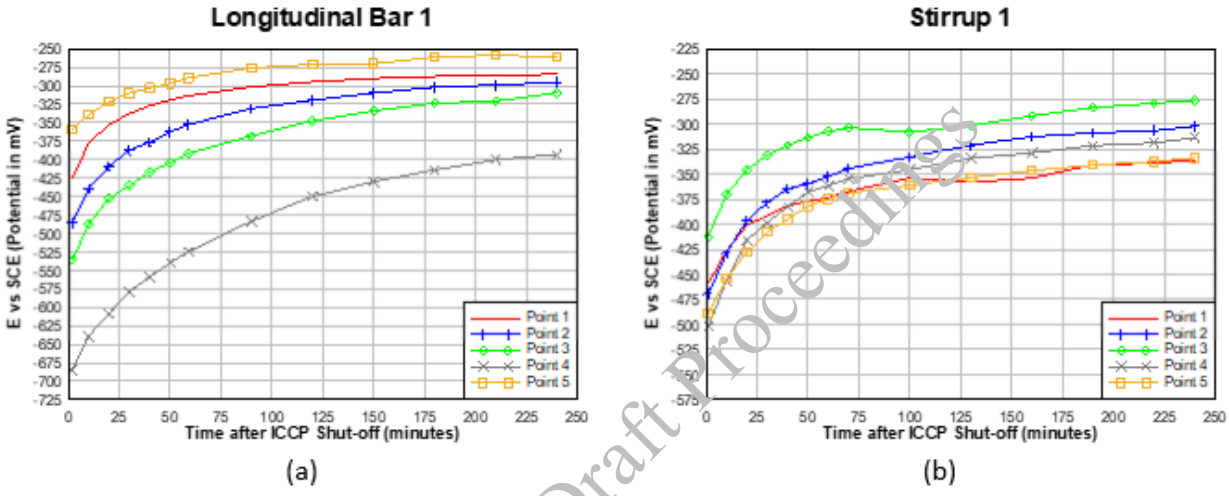

Figure 2. NSRM/ICCP application (a) flexural beam, (b) shear beam

Additional work is needed through future research to develop a more robust knowledge of this multifunctional application. While TiABs are impervious to corrosion in conventional applications, the long-term corrosive behavior of the TiABs in ICCP systems requires further study to ensure designs can achieve the expected service life. It is recommended that an understanding of TiAB corrosion products and their impact on the bond with the ECSG needs to be evaluated. Another area of interest is the exploration of MMO coatings for TiABs. Since TiABs are not specifically developed for ICCP applications, they are not presently MMO coated. MMO coatings for TiABs require development and could improve ICCP performance and delay consumption of the anode which would extend their service life.

3. Conclusions

This study developed new materials and approaches to deploy TiABs as a NSMR material that can be used to both strengthen and preserve existing reinforced concrete elements experiencing rebar corrosion. The experimental results reported here demonstrated that impressed current cathodic protection of steel reinforcement in reinforced concrete beams can be achieved using TiABs embedded in an ECSG. This dual-purpose application has the potential to revolutionize how structurally deficient structures can simultaneously be strengthened and protected further from corrosion. The long-term performance of TiAB bars in ECSG within ICCP systems as well as the need for MMO coatings will be investigated in the future.

Acknowledgements

The authors wish to express their gratitude and sincere appreciation to Mr. Jim Perryman, Sr., company leadership, technical staff, and Ms. Jill Adkins of The Perryman Company, Houston, PA for supporting this research work and for fabricating the TiABs used in the study. Material donations were provided by Asbury

Carbons, Five Star Products, and BASF Solutions. Additional funding for this work was provided by the US Department of Transportation through the Coastal Research and Education Actions for Transportation Equity (CREATE) Center, a BIL UTC under Grant No. 69A3552348330.

References

AASHTO NSMT-1 (2020), Guide for Design and Construction of Near-Surface Mounted Titanium Alloy Bars for Strengthening Concrete Structures, American Association of State Highway and Transportation Officials: Washington, D.C.

ASTM B1009 (2018), Standard Specification for Titanium Alloy Bars for Near Surface Mounts in Civil Structures, ASTM International: West Conshohocken, PA.

Higgins, C., and L. Barker (2015), Methods for strengthening reinforced concrete bridge girders containing poorly detailed flexural steel using near-surface mounted metallics, Oregon Department of Transportation: Salem, OR.

Higgins, C., Amneus, D., and L. Barker (2017), Shear and flexural strengthening of reinforced concrete beams with titanium alloy bar, in Proceedings of the 2nd World Congress on Civil, Structural, and Environmental Engineering (CSEE'17), Barcelona, Spain.

IOS (2018), Accelerated life test method of mixed metal oxide anodes for cathodic protection — Part 1: Application in concrete, International Organization for Standardization (IOS).

Parvin, A. and T.S. Shah (2016), Fiber reinforced polymer strengthening of structures by near-surface mounting method. Polymers, 8(8).

Segan, E.G., Bukowski, J., and A. Kuma (1982), Titanium anodes in cathodic protection, U. S. Army Construction Engineering Research Laboratory.

Slawinski, A.K. (2022), Dual purpose utilization of titanium alloy bars for impressed current cathodic protection and near surface mounted retrofit in reinforced concrete beams, M.S. Thesis, Oregon State University, Corvallis, OR.

Sun, M., et al. (2011), Deicing Concrete Pavement Containing Carbon Black/Carbon Fiber Conductive Lightweight Concrete Composites, ICTIS 2011, 662–668.

TM0294 (2016) Testing of embeddable impressed current anodes for use in cathodic protection of atmospherically exposed steel-reinforced concrete, NACE International: Houston, TX.

Modelling the Durability of Structures Under Multiphysical Loads

L. Lacarrière[1]*, L. Ibrahim[2], A. Sellier[3] and T. Vidal[4]

[1,2,3,4] *Université de Toulouse, UPS, INSA, LMDC (Laboratoire Matériaux et Durabilité des Constructions), 135 Avenue de Rangueil, 31077 Toulouse Cedex 04, France*
Email: laurie.lacarriere@insa-toulouse.fr

*Corresponding author

ABSTRACT

This paper proposes a multi-scale thermo-hydro-chemical (THC) modelling strategy, suitable for structure-scale calculations and couplable with a poro-mechanical concrete model. The model thus developed can be used to predict the mechanical behaviour of structures subjected to carbonation and leaching. The chemical model considers cement mineralogy, derived from a hydration model, and predicts its evolution during chemical degradation. The objective of the modelling strategy is to improve computational efficiency to enable coupling of the THC model with mechanics (M) at the structural scale. Improving the numerical efficiency of the THCM model is based on a "model reduction" methodology. The influence of temperature on chemical degradation is integrated via its effect on hydrate thermodynamic equilibrium and species diffusion. As an application example, the modelling strategy is applied to the study of the long-term behaviour of underground concrete structures, such as radioactive waste storage solutions.

KEYWORDS: *Finite element modelling, Durability, Concrete, Leaching, Carbonation*

1. Introduction

Large civil engineering structures such as bridges, tunnels and dams are designed to stand up to a variety of natural and man-made loads. The durability of these structures over long periods has become a central issue in civil engineering. In the long term, chemical degradation of these structures is not limited to a few centimetres, but can extend over a larger scale, affecting their structural performance.
However, experimental characterization of long-term residual mechanical behaviour under chemical degradation requires considerable time. To overcome this problem, modelling and numerical simulation approaches offer the possibility of projecting the chemical behaviour induced by degradation and its effect on structural mechanical behaviour over very long periods. Since the relevance of these models lies in their ability to adapt automatically to a certain diversity of materials, they must be able to consider the composition and mineralogy of different concretes to enable the prediction of mineralogical evolutions (and therefore of the different solid phases) over time. This then allows to deduce the changes in mechanical properties required to calculate the long-term stability of the structure.

2. Modelling principles

2.1 Chemical substitution model

The approach to designing a chemical substitution model is presented here in the case of coupled leaching-carbonation degradation in saturated and unsaturated conditions. In this case, the substitution model can be defined solely from 4 state variables: the calcium concentration in the interstitial solution ($\boldsymbol{Ca^{2+}}$), the carbon concentration in dissolved form in the interstitial solution ($\boldsymbol{CO_{2d}}$), the water content ($\boldsymbol{W_L}$). The model reduction is based on several hypothesis allowing to express some chemical variables according to the 2 ones selected hear as state variables. First an instantaneous equilibrium between gas and liquid phase is supposed for CO_2 content. The transport of this specie can thus be modelled only through the transport of dissolved carbon (CO_2 in the gas phase is expressed according to the dissolved one using Henry's law and K_H coefficient). Then, in this context of degradation by carbonation and leaching, the stability of the hydrated

phases present in the cement matrix is assumed to depend solely on the calcium concentration. The chemical kinetics of decalcification and dissolution of these phases are assumed to be very rapid compared with the diffusion phenomena and are therefore neglected. This means that this source term can be included as a capacity via the term $\partial Cas/\partial Ca^{2+}$. The 3 associated conservation laws can then be written in the following form (only the general form is shown here, for more details see (Ibrahim et al. 2024)).

$$\left(W_L + K_H(\emptyset - W_L)\right) \cdot \frac{\partial CO_{2d}}{\partial t} + \mathrm{div}\left[-D_{CO} . \overrightarrow{\mathrm{grad}}\, CO_{2d}\right] = -S_{CaCO3} - CO_{2d} \frac{\partial\left(W_L + K_H(\emptyset - W_L)\right)}{\partial t} \quad (1)$$

$$\left(W_L + \frac{\partial Cas}{\partial Ca^{2+}}\right) \cdot \frac{\partial Ca^{2+}}{\partial t} + \mathrm{div}\left[-D_{Ca^{2+}} . \overrightarrow{\mathrm{grad}}\, Ca^{2+}\right] = -S_{CaCO3} - Ca^{2+} \frac{\partial W_L}{\partial t} \quad (2)$$

$$\frac{\partial W_L}{\partial t} + \mathrm{div}\left[-D_{W_L} . \overrightarrow{\mathrm{grad}}\, W_L\right] = S_W \quad (3)$$

In this model, leaching-carbonation coupling is achieved by considering the rate of calcite precipitation S_{CaCO3}, which consumes both $\boldsymbol{Ca^{2+}}$ and $\boldsymbol{CO_{2d}}$. This precipitation rate is estimating using mass action law according to calcium and carbonates concentration. In our approach the relation between carbonates and total dissolved carbon is approached using an analytical function modelling pH variation and its effect on the proportion of dissolved carbon on carbonates form ($f_{pH}(\boldsymbol{Ca^{2+}}, \boldsymbol{CO_{2d}})$), this function depending of the chemical state variables (Ibrahim et al. 2024).

$$S_{CaCO3} = k_c \cdot W_L \cdot Ca^{2+} \cdot CO_3^{2-} \text{ and } CO_3^{2-} = CO_{2d} \cdot f_{pH}(Ca^{2+}, CO_{2d}) \quad (4)$$

Consideration of the material's initial mineralogy and its evolution during degradation is managed by internal variables associated with each solid phase of the cementitious matrix (CH, C-S-H, Afm, Aft, Hexahydrate) and one internal variable managing porosity ($\emptyset$). The model is then automatically adapted to different mineralogy by calculating the equilibrium curve governing the dissolution of calcium hydrates (and acting in the model via its partial derivative). The amount of calcium present in solid form (Cas) can be calculated as the sum of the calcium present in each hydrate, and for each hydrate this amount depends on the concentration $\boldsymbol{Ca^{2+}}$. This dependency can be reproduced for numerical implementation by the continuous and derivable function $f_i(\boldsymbol{Ca^{2+}})$ defined below.

$$Cas = \sum_i Cas_{0i} \cdot f_i(Ca^{2+}) \text{ and } f_i(Ca^{2+}) = 1 - \exp\left[-\ln(2)\left(\frac{Ca^{2+}}{Ca^{2+}_{eq\,i}}\right)^{m_i}\right] \quad (5)$$

Where $Ca^{2+}_{eq\,i}$ is determined for each hydrate using the thermodynamical equilibrium characteristics of the considered hydrate (using Cemdata database (Lothenbach et al. 2008)). By way of illustration, the equilibrium curves $Cas(\boldsymbol{Ca^{2+}})$ thus obtained for 2 cements with different initial mineralogy (a CEMI and a CEMV) are plotted below.

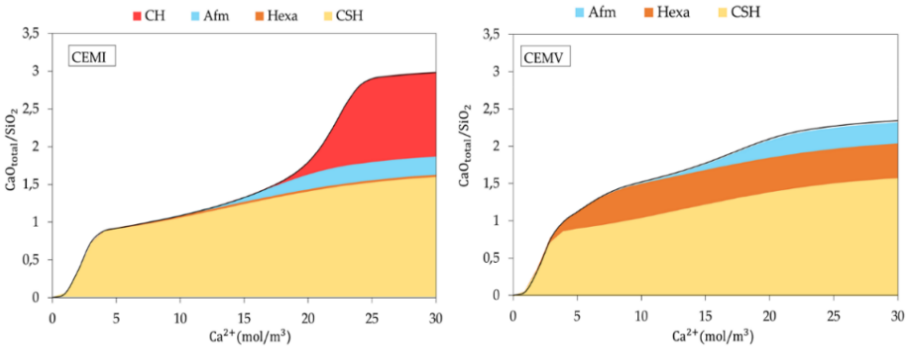

Figure 1. Predicted equilibrium curve for two different cement pastes

2.2 Chemo-mechanical coupling

Knowing the evolution of the phases within the cementitious matrix exposed to degradation, it is then possible to use the Mori-Tanaka scheme (Mori and Tanaka 1973) (with VER proposed in Figure 2a) to predict the compressibility and shear coefficients (and therefore the Young's modulus) of concrete.
In order to predict the evolution of fracture behaviour, a non-linear homogenization technique is required. In this work, the method used is that developed by (Ghorbanbeigi et al. 2016) and adapted to our case. In this approach, homogenization is performed in 3 stages (as shown in Figure 2b). The difference with the linear homogenization approach is that the solid phases are separated from the porosity. At the 1ezr level, crystallized and anhydrous phases (CH, aluminates, calcite, anhydrous) are considered as infinitely rigid inclusions in a matrix composed of the solid part of C-S-H (without voids). At the top scale, the pores are considered non-cohesive. This scheme allows the homogenized solid matrix to behave according to the Drucker-Prager criterion (whose cohesion and friction angle friction evolve with phase proportions).

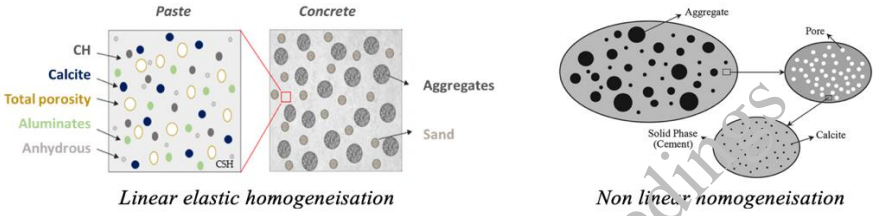

Figure 2. Illustration of the selected homogenization schemes

3. Application to a tunnel

The chemo-mechanical model was then applied to the study case that was part of the European project dealing with the study of chemo-mechanical behaviour of underground waste storage repositories (Ibrahim et al. 2024). This base case represents a 10,000 year study of the chemo-mechanical behaviour of a concrete tunnel subjected to mechanical pressure induced by the surrounding rock, as well as to chemical perturbations induced by the water contained in this rock (with low mineralisation) and the atmosphere inside the tunnel (with CO2) as specified in Figure 3.

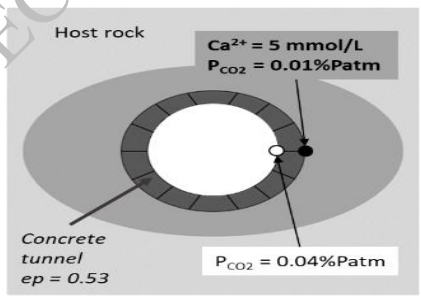

Figure 3. Geometry and chemical boundary conditions

The application of the substitution chemical model to this structure is made after implementing the conservation equations and associated evolution laws of internal variables in the finite element code Cast3M. It allows predicting the evolution of the paste composition along the width of the tunnel as illustrated at 2 ages on Figure 3.

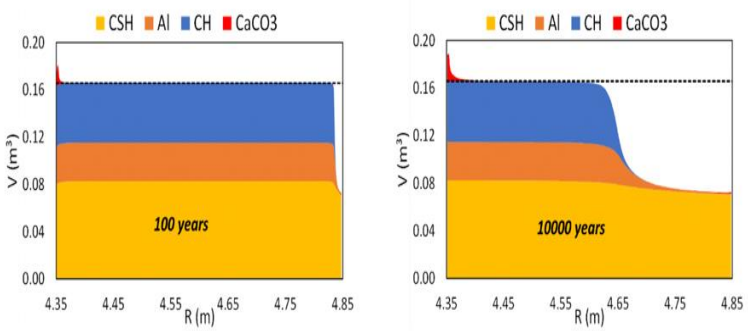

Figure 4. Predicted evolution of paste composition along the radius (dotted line represents the initial paste volume of paste)

The application of the selected and implemented homogenisation scheme at each node of the structure mesh and at each date allows to obtain the evolution of Young's modulus and compressive strength in the concrete tunnel induced by carbonation and leaching (Figure 4).

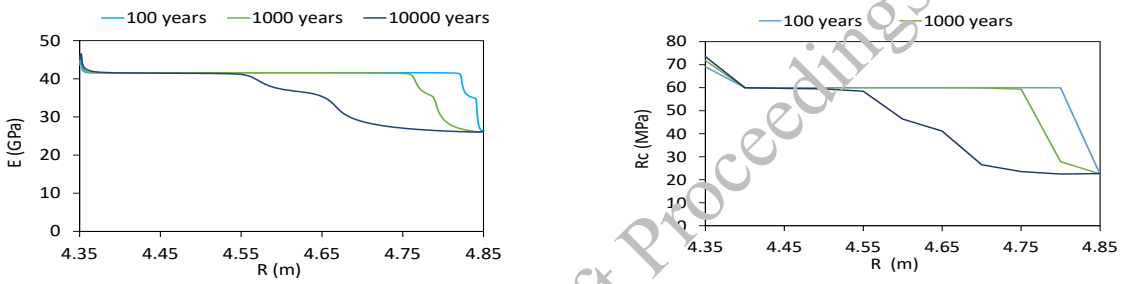

Figure 5. Predicted evolution of Young modulus and compressive strength along the radius at different ages

We observe a loss of performance (both elastic and strength) under the effect of leaching (predominant phenomenon on the extrados of the tunnel) and a slight increase on the intrados under the effect of carbonation. Knowledge of these properties at each mesh node and at each date is then coupled with a mechanical model of concrete behaviour implemented in the Cast3M code to assess the residual bearing capacity of the structure over time.

4. Conclusions

The thermo-hydro-chemo-mechanical (THCM) model presented in this article couples calcium leaching and carbonation. An evolution law has been developed to describe both the thermodynamic equilibrium of cement hydrates with the porous solution, considering the variety of cement mineralogy, the effect of temperature and the progressive dissolution of hydrates. The equations of this model have been implemented in the Cast3M finite element code. The model predicts variations in porosity, degree of saturation, quantity of residual hydrates, carbonation depth and calcium leaching. A mechanical homogenization scheme uses the phase volumes calculated by the chemical model to predict the elastic and strength properties of concrete at each stage of degradation. It allows the evaluation of structural strength capacity. The model's advantage is that it can be adapted to model different structures and different types of cement, and can be used to make predictions over long periods at a reasonable numerical cost compared with conventional geochemical codes coupled with mechanical finite element codes.

Acknowledgements

The financial support from the European Joint Programme on Radioactive Waste (EURAD), WP MAGIC, is acknowledged (HORIZON 2020 project EURAD. EC Grant agreement no: 847593).

References

Ghorbanbeigi, H., W. Shen, I. Yurtdas, and J.-F. Shao. (2016) "Num Anal Meth Geomechanics - 2015 - Ghorbanbeigi - A micromechanics-based model for concrete materials subjected to.pdf.", *International Journal for Numerical and Analytical Methods in Geomechanics*, 40: 1203–1218.

Ibrahim, L., S. Gonzales, L. Lacarriere, V. Vilarrasa, A. Narkuniene, P. Poskas, and A. Sellier. (2024) *Chemo-mechanical processes in safety structures*. Final version of deliverable D16.9 of the HORIZON 2020 project EURAD. EC Grant agreement no: 847593.

Lothenbach, B., T. Matschei, G. Möschner, and F. P. Glasser. (2008) "Thermodynamic modelling of the effect of temperature on the hydration and porosity of Portland cement", *Cement and Concrete Research*, 38 (1): 1–18.

Mori, T., and K. Tanaka. (1973) "Average stress in matrix and average elastic energy of materials with misfitting inclusion", *Acta Metallurgica*, 21 (5): 571–574.

Viability of Utilizing Supplementary Cementitious Materials for Subsurface Infrastructure

Lyn Zemberekci[1] and Sriramya Duddukuri Nair[2]*

[1]Cornell University, Ithaca, NY, USA
Email: lz549@conell.edu
[2]Cornell University, Ithaca, NY, USA
Email: sn599@cornell.edu

*Corresponding author

ABSTRACT

Subsurface infrastructure applications (e.g., cementing geothermal wells) require durable materials that do not fail under severe conditions of high pressure and high temperature (HPHT). Influenced by well-studied stable building materials, widely available supplementary cementitious materials (SCMs) such as fly ashes and slags could be a viable option to partially replace cement for such severe exposure conditions. The pozzolanic reaction of SCMs with calcium hydroxide at these conditions increases the yield of calcium silicate hydrate. Thus, further characterization to identify all possible phase morphologies that form as curing occurs at higher temperatures and pressures is necessary to qualify the stability of said phases and the overall cementing material. This extended abstract presents our findings for the case of employing a high content of ground granulated blast furnace slag (GGBFS) as an SCM-containing slurry. We observed that calcium hydroxide (CH) decreased in amount when GGBFS was used at HPHT after 48 h compared to only using cement. Additionally, unreacted GGBFS can contribute to later age hydration reactions leading to the formation of a denser calcium silicate hydrate. Identifying phases in cementitious systems curing at HPHT is a step toward assessing the durability of subsurface infrastructure elements subjected to severe conditions over their service life.

KEYWORDS: *Geothermal systems, Well cementing, Aluminosilicates, Cement chemistry*

1. Introduction

Cementing of subsurface infrastructure, such as geothermal wells, necessitates durable formulations to maintain the structural integrity of wells exposed to elevated high pressure and high temperature (HPHT) conditions. For instance, wells drilled to tap into renewable geothermal energy are subjected to the operational temperature of the geothermal system (80 – 120 ˚C for direct heat use and 150 – 300˚C for electricity production). At such temperature profiles, cement slurries are at risk of forming metastable phases. Calcium silicate hydrate (C-S-H) and calcium hydroxide (CH) are the main hydration products of cement that undergo phase transitions with elevated temperatures. C-S-H can transition into α-C_2-S-H above 110 ˚C – a phenomenon known as strength retrogression, where the metastability α-C_2-S-H of leads to a loss in compressive strength and increase in permeability (Bezerra et al., 2011). Figure 1 illustrates the adverse impact of strength retrogression on creating microcracks that can form pathways for the migration of unwanted fluids and greenhouse gases, e.g., methane and carbon dioxide, to the surface of the Earth.
Widely available supplementary cementitious materials (SCMs) such as fly ashes, slags, and other emerging waste materials could be a viable option to replace cement partially or completely for severe HPHT exposure conditions. However, the pozzolanic reaction of SCMs with CH is also temperature-dependent and yields new morphologies. Therefore, there is a need to identify the morphology of such phases forming at HPHT conditions to assess their stability and temperature tolerance with time. To address this gap, in this work, a high calcium SCM-containing slurry was cured at temperatures of 80 ˚C and 120 ˚C and a pressure of 24.1 MPa and compared to that of the frequently employed class H cement slurry. Both slurries were systematically developed based on a methodology described elsewhere (Zemberekci,

Genedy, and Nair, 2022). The major phases that formed with adequate early-age bulk-scale performance were identified using energy dispersive spectroscopy with the future goal of predicting the long-term durability of the cemented wells that are subjected to extreme HPHT conditions.

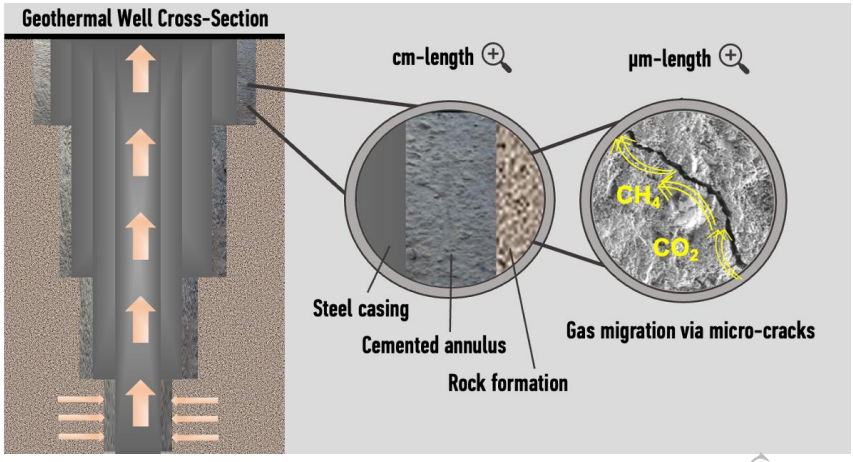

Figure 1. The appearance of micro-cracks due to weak phases in cemented annuli of HPHT geothermal wells may create pathways for unwanted migration of gases and oils to the Earth's surface.

2. Materials and Methods

2.1 HPHT Curing and Testing

Class H cement from Lafarge and grade 100 Ground Granulated Blast Furnace Slag (GGBFS) from Ash Grove were used to prepare cement slurries. The oxide composition of both materials is given in Table 1.

Table 1. Oxide analysis of materials.

Oxide (%)	Class H Cement	GGBFS
CaO	63.6	39
SiO2	21.5	37
Al2O3	3.2	9
Fe2O3	4.5	0.84
MgO	2.7	9.2
Other minor oxides (+LOI)	4.5	5.0

We outlined a detailed procedure in a previous study, in which the flowability of slurries was optimized with temperature (Zemberekci, Genedy, and Nair, 2022). Following the same procedure, two slurries were prepared with similar rheological profiles. The first is the Baseline slurry with a water-to-cement ratio of 0.38, containing class H cement without any additives or SCMs. The second is the Slag slurry containing 35% of GGBFS by weight of cement and < 1% chemical admixtures at a water-to-cementitious-materials ratio of 0.31. To conduct the compression tests, 8 cubes were crushed after 48 h of curing, and a universal testing machine with a ~266 kN capacity was used. Average values are reported.

2.2 Microstructural Characterization

Fractured samples were dehydrated using absolute ethanol for 3 days, which was exchanged every 24 h. The samples were embedded with low-viscosity epoxy, cut to expose a fresh surface that was ground and polished with diamond paste. After storing the polished samples in the desiccator for at least 2 days, they were carbon coated for Scanning Electron Microscopy (SEM) and Energy Dispersive Spectroscopy (EDS) characterization. Zeiss Gemini 500 SEM and an Oxford Instruments EDS detector were employed in backscattered mode to study the surface morphology of polished samples. The voltage was maintained at 20 kV and a working distance of 7.5–8 mm.

3. Results

3.1 Compressive Strength with Temperature

Figure 2 shows the compressive strength of Baseline and Slag cubes with temperature. Slag demonstrated a higher compressive strength than Baseline at both temperatures. However, the compressive strength of both slurries cured at 120 ˚C decreased compared to their counterparts that were cured at 80 ˚C. As presented in Table 1, both starting materials contained a high calcium oxide content and thus, could experience strength retrogression when cured above > 110 ˚C (Bezerra et al., 2011).

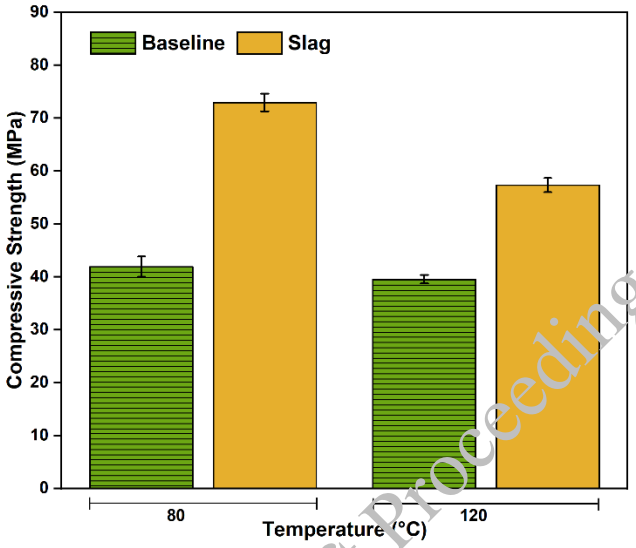

Figure 2. Compressive strength of 5×5×5 cm3 samples cured at HP (24.1 MPa) HT (80 ˚C, 120 ˚C)

3.2 Microstructural Characterization

Morphological information of the Baseline and Slag samples that were cured at 120 ˚C and 24.1 MPa are provided in Figure 3. The EDS maps demonstrate the similarity and variation of the elemental composition of both samples. Outer product (OP) and inner product (IP) C-S-H were detected in both samples, with a small substitution of Al in the Slag sample. Ca/(Si+Al) ratios of C-S-H were comparable in both samples (example points in Table 2). Anhydrous C_3S, Mg-substituted C_3S (C_3S M3) (Fernandes et al., 2020), and anhydrous GGBFS were detected after 48 h of curing at HPHT, which can be beneficial for hydration reactions that occur at later ages. Other phases, such as ferritic and precipitated MgO, were present in both samples. Al in Baseline preferred to uptake in the ferritic phase (Figure 3 a), as Class H cement does not contain C_3A in its anhydrous phase composition, but it contains ~10% C_4AF. In Slag, Al and Mg were also present in ferritic phases as well as hydrotalcite-like phases (Whittaker et al., 2014), which appeared frequently in the microstructure (Figure 3 b).

Comparing the backscattered micrographs of the samples, hollow shells and voids were present in both samples, however, the overall observed porosity of the Baseline was higher than that of the Slag. Fewer CH crystals were detected in the Slag sample, which is likely due to the formation of C-S-H via pozzolanic reaction. Thus, despite containing a high calcium oxide content, the increased starting content of silicon dioxide in GGBFS facilitated the production of more C-S-H at 120 ˚C by consuming available CH crystals.

Table 2. Select Ca/(Si+Al) ratios of IP and OP C-S-H in Figure 3 obtained via EDS

Sample	IP C-S-H	OP C-S-H
Baseline	1.64 (p1)	1.75 (p2)
Slag	1.61 (p3)	1.78 (p4)

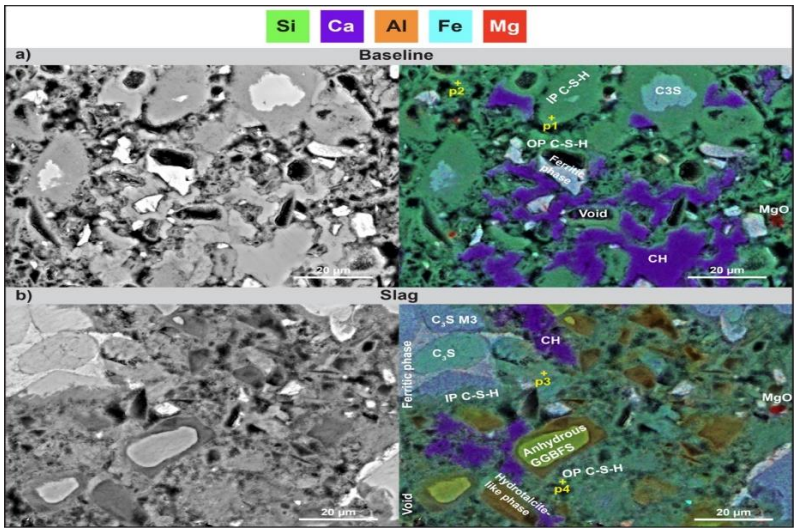

Figure 3. SEM micrographs and EDS maps of polished samples cured at HP (24.1 MPa) and HT (120 ˚C) of a) Baseline and b) Slag. Field width: 100 µm.

4. Conclusions

This extended abstract addressed the early-age behavior of high calcium-containing samples cured at HPHT. Above 110 ˚C, strength retrogression was experienced in both samples, Baseline and Slag, at an early age. Supplementing GGBFS at a high volume increased the compressive strength compared to the baseline despite the loss of strength with temperature. The starting silicon dioxide content may have contributed to forming C-S-H by reacting with available CH crystals. Additionally, microstructural characterization of Baseline and Slag showed that the latter was less porous, contained additional phases due to higher alumina and magnesia contents, with similar Ca/(Si+Al) ratios. In progress studies aim to assess the viability of using emerging SCMs and characterize the durability of such systems at HPHT.

Acknowledgments

The authors acknowledge financial support received from the Cornell Atkinson Center for Sustainability and the National Academy of Sciences, Engineering, and Medicines. This work made use of the Cornell Center for Materials Research Facilities supported by the National Science Foundation DMR-1719875.

References

Bezerra, U. T., Martinelli, A. E., Melo, D. M. A., Melo, M. A. F., & Oliveira, V. G. (2011) “The strength retrogression of special class Portland oilwell cement” *Ceramica*, *57*(342): 150–154.

Fernandes, W. V., Torres, S. M., Kirk, C. A., Leal, A. F., Lima Filho, M. R., & Diniz, D. (2020) “Incorporation of minor constituents into Portland cement tricalcium silicate: Bond valence assessment of the alite M1 polymorph crystal structure using synchrotron XRPD data” *Cement and Concrete Research*, *136*.

Whittaker, M., Zajac, M., Ben Haha, M., Bullerjahn, F., & Black, L. (2014) “The role of the alumina content of slag, plus the presence of additional sulfate on the hydration and microstructure of Portland cement-slag blends” *Cement and Concrete Research*, *66*: 91–101.

Zemberekci, L., Genedy, M., & Nair, S. D. (2022) “Rheology-Based Approach to Design Cement Slurries for Enhanced Geothermal Wells” *Transactions - Geothermal Resources Council*, *46*: 1579–1589.

Calcium Focused Design for Longevity of Concrete Structures in Silage Environment

Z. Gong[1], D. Thompson[2], and S. Nanukuttan[3]*

[1,2,3] Queen's University Belfast, Northern Ireland, United Kingdom
Email: s.nanukuttan@qub.ac.uk

*Corresponding author

ABSTRACT

Silage effluent contains organic acids such as lactic, acetic and volatile fatty acids and several salts including chlorides, sulfates and phosphates. In concrete exposed to silage effluent, decalcification and carbonation are the common deterioration mechanisms. To reduce the impact of silage led deterioration, several concrete mixes with low to ultra-low calcium content were studied in: (1) laboratory conditions for 3.5 years, and (2) in situ exposure in a gully of a silage storage with a constant flow of raw silage effluent for 3 years. The performance of the specimens studied through visual damage, mass loss, and compressive strength loss against reference specimens stored in water. Parallelly, evolution of microstructural properties was studied using XRD, TGA, SEM-EDS using paste specimen. The findings confirm that decalcification and carbonation are the significant changes occurring to PC-based ternary and alkali activated blast furnace slag concrete. However, the mass change for example is 3rd of that reported for PC based mortars. The geopolymer concretes, composed of fly ash or metakaolin, respectively, were not affected by exposure and gained strength. In these blends changes to aluminium and iron minerals were noted, but to depths 1/10th that of ternary blends. Study confirms that a calcium focused design of mixes will ensure performance against silage effluent exposure.

KEYWORDS: *Silage effluent, Low Ca binders, geopolymers, Alkali activated concrete, Durability, microstructural analysis, Strength/mass loss*

1. Introduction

Silage effluent contains numerous aggressive chemicals including organic acids (e.g., lactic acid, acetic acid, and other volatile fatty acids), chlorides, sulphates, phosphate, and other substances at high concentrations. These are detrimental to cement-based materials and the embedded reinforcement. For instance, the concentration of lactic acid in effluent is 4.9-29 g/L, and the pH of effluent ranges from 3.7 to 5.8. Previous studies show that these acids react with the hydrated and anhydrous phases of the cement paste to produce soluble salts or complexes and causes the size of pores within the cement matrix to increase and the mechanical strength to decrease. Further, a new surface is exposed to the effluent and the cycle continues until the structure is no longer serviceable. This process was less pronounced in alkali-activated binder samples than in PC due to the absence of free calcium hydroxide in their hydrates, lower Ca/Si ratio, and a high level of polymerisation of silicate chains. This study further explores the performance of mixes with low to ultra-low calcium content.

2. Materials and Methods

2.1 Materials

The PC used in this study was CEM I 42.5N, produced by Mannok Cement in Ireland. The blast furnace slag (GGBS) used in this study was produced by Heidelberg Materials, UK. Fly ash (FA) (Class F) was supplied by Power Minerals Ltd, Drax Power Station, North Yorkshire, UK. Densified silica fume (SF) with a typical bulk density of 500 to 700 kg/m^3 was supplied by Elkem, UK. The calcined clay binder used

in this study was provided by Banah UK Ltd and had two parts: Calcined clay(a), a powder component, and Calcined clay(b), a liquid component. Calcined clay(a) based on an aluminosilicate, namely altered basalt sourced from the Interbasaltic formation of the Antrim Lava Group (Northern Ireland), was manufactured by lithomarge calcination at circa 750 ℃, followed by grinding (Kwasny et al 2016). Calcined clay(b) contained alkali silicate with a water content of 41.2%. Oxide compositions of all cementitious materials used in this study are shown in Table 1.

Table 1. XRF results of cementitious materials.

Material	SiO_2	CaO	Al_2O_3	Fe_2O_3	MgO	TiO_2	MnO	Na_2O	K_2O	SO_3	LOI
FA	46.8	2.2	22.5	9.2	1.3	1.1	0.05	0.89	4.09	0.90	3.57
GGBS	29.4	43.7	11.2	0.4	6.9	0.7	0.51	1.05	0.93	1.76	2.40
PC	20.2	63.0	4.8	2.8	1.9	0.3	0.08	0.19	0.59	2.6	3.16
Calcined clay(a)	32.0	7.8	24.9	25.2	1.7	3.2	0.37	0.36	0.15	0.22	3.08

Alkali activators: for FA and GGBS binders was prepared by mixing sodium silicate solution and sodium hydroxide solids, followed by stirring for 24 hours. The sodium silicate solution produced by PQ Corporation consisted of 15% Na_2O, 30% SiO_2 and 55% water. The sodium hydroxide was solid particles with 99% purity. The coarse aggregates used in this study was 10mm crushed basalt from Northern Ireland, and 4 mm sand (silicate sand abundant in quartz).

2.2 Mix proportions

The focus was to determine the resistance of mixes as the available calcium compounds diminishes. Four blends chosen are as shown in Table 2. "Ternary" consisted of 20% PC, 70% GGBS and 10% SF. The water/binder (w/b) was 0.49. The blend named "GGBS" is an alkali activated GGBS based system with lower Ca/Si ratio which offers better resistance to silage (Aiken et al 2017). "GGBS-0", consisted of 100% GGBS, and w/b of 0.5. The alkali-activating solutions used in these blends are sodium silicate solutions combined with sodium hydroxide. The alkali modulus (AM), defined as the mass ratio of Na_2O/SiO_2 in the alkali solutions, was 2.22. The alkali dosage (M+), defined as the mass ratio of sodium oxide (Na_2O) in the activating solution to the binder dry mass, was 4%. The blend named "FA" was a fly ash based geopolymer system, with a w/b of 0.46, and the dosages of alkali activator was AM = 0.97, M+ = 11.6%. The blend named "Calcined clay" is a commercial calcined clay based geopolymer system of w/b 0.435.

Table 2. The proportion of each blend (kg/m^3).

Label	PC	GGBS	Silica Fume	Fly Ash	Calcined clay(a)	Calcined clay(b)	Na_2SiO_3 Solution	NaOH	Fine Agg	Coarse Agg	Added Water
Ternary-1	89.6	313.6	44.8	-	-	-	-	-	876.0	876.0	248.5
GGBS-0	-	434.2	-	-	-	-	26.1	17.4	876.0	876.0	241.2
FA	-	-	-	483.4	_	-	193.8	35.0	876.0	876.0	143.2
Calcined clay	-	-	-	-	384.7	224.0	-	-	876.0	876.0	132.2
Note: Calcined Clay binder was composed of (a) power form and (b) liquid form. Added water includes w/b plus water for surface saturation of aggregates minus water in the activators. The water absorption of the fine and coarse aggregate was 1.1% and 2.2%, respectively.											

2.3 Curing

Paste and concrete were prepared in a typical manner that adheres to relevant standards. Deviations are noted below. Once demoulded all but FA specimens were cured in water for 28 days at 20°C. Specimens from the "FA" blend were placed in an oven at 50°C for 7 days. Afterwards, they were demoulded and placed in a sealed container for 21 days at a constant temperature (20°C).

2.4 Exposure

These concrete specimens were exposed to raw silage effluent in two ways: laboratory exposure and in situ exposure. For laboratory exposure, 50 mm prepared cube specimens were submerged in 0.45L of raw silage effluent in 2 L plastic boxes. The boxes were placed in an outside (sheltered) natural environment. The initial pH of the effluent was 4.1. The concentration of metals in the raw effluent was tested by the Inductively Coupled Plasma Optical Emission Spectroscopy (ICP-OES). Results in ppm are Al = 0.49 ppm, Ca = 318.6, K = 5908, Mg = 80.4, Na = 33.8, P = 99.6 and Si = 43.6. The effluent was replaced every week during the first six months of exposure. After which effluent was not replenished for 3 years, due to Covid 19 lock down. Control concrete specimens from each blend were submerged in water and kept in the same environment. For *in situ* exposure, 100 mm diameter cylindrical specimens of 25mm thickness were submerged in a gulley of silage storage clamp for exposure to natural uncontrolled flowing silage effluent and weather, for a duration of 3 years. The location was Blakiston Houston Estate, Belfast, Northern Ireland. Similar size specimens were kept in water as control.

3. Results

3.1 Appearance after exposure:

Figure 1 shows cross-section of paste samples after 3.5 years of laboratory exposure. The exposure face is at the top, and the bottom is towards core of the specimens. For Ternary-1, the different layers to which silage effluent has introduced a change is clear. Darkness decreases from outside towards the core. These layers represent three zones of influence, inspired by Bertron et al (2007):

1) Zone 1 is the affected area where minerals and pore structure changed significantly.
2) Zone 2 is the partially affected area where slight decalcification occurred.
3) Zone 3 is the unaffected area that has not been attacked.

GGBS-0 also showed three distinct zones similar to the Ternary mix. Such zones are not evident in FA and Calcined clay mixes, i.e., low calcium geopolymers appear to have better resistance against silage effluent.

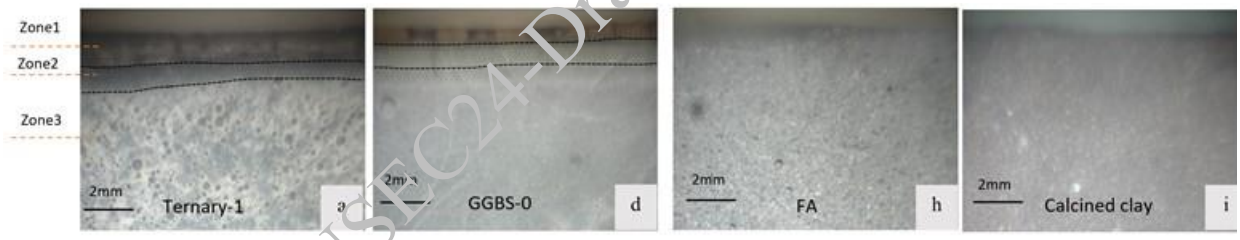

Figure 1. Optical microscope images of paste specimens after 3.5 years of laboratory exposure to silage

Figure 2 shows the concrete specimens after 3 years of field exposure Ternary-1 specimen was significantly cracked, some coarse aggregate had come off, and the overall shape was affected. The concrete specimens from GGBS-0 blends were more intact, but some parts were not recovered, and the colour was deeper. "FA" and "Calcined clay" were more or less intact, with the surface slightly stained, but the overall shape was unaffected. "FA" had some aggregates visible, and "Calcined clay" had minimal changes.

3.2 Mass loss & Strength:

Mass loss and strength gain (Figures 2 and 3) convey a similar story. Ternary-1 and GGBS-0 mixes lost mass, whereas FA and calcined clay, stabilised or gained mass over time. This was similar for both laboratory and field exposure, confirming that the observation is linked to the performance of the mixes. The gain in alkali activated mixes may be attributed to the products of aluminosilicate polymer depolymerisation precipitated as gel or zeolites when exposed to acid solutions or leachate entering the polycondensate tunnels and thus increasing the mass (Bakharev, 2005).

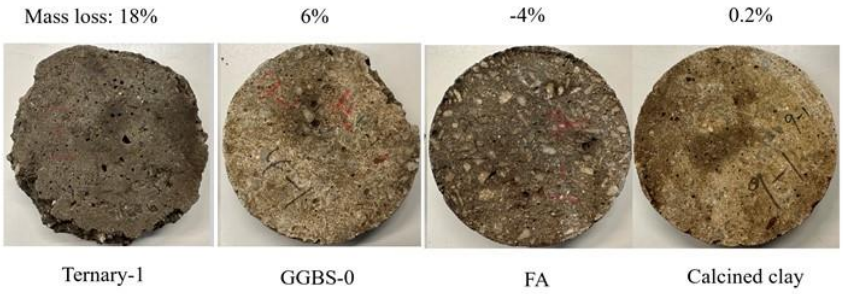

Figure 2. Images of concrete specimens recovered from silage gulley after 3 years of *in situ* exposure.

Both FA and Calcined clay concrete gained strength in laboratory exposed samples, after 6months as well as 3.5 years. It seems the hydrate structure in these blends are immune to silage effluent attack and it may well be the case that further reactions are supported by the elements in silage effluent, the exact nature of this will need studied further. Opposite is true for Ternary-1 and GGBS-0 mixes and is likely that Ca-based hydrates in these mixes are dissolved by the acidic components in silage effluent, resulting in a weaker structure and strength loss.

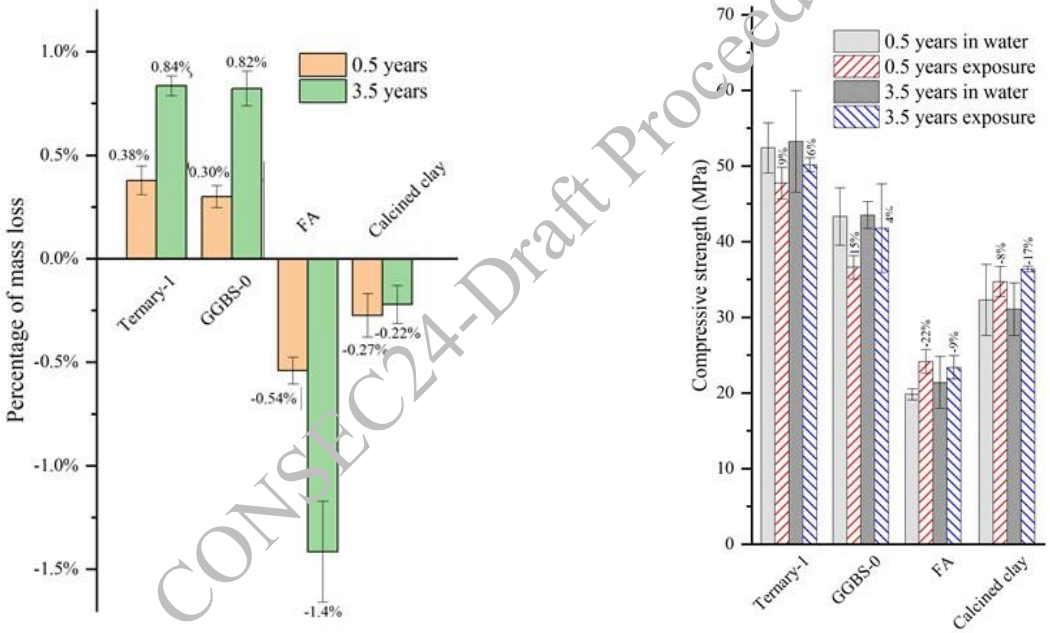

Figure 3. Changes in mass compared to specimens kept in water and strength loss/gain for concrete specimens, after 0.5 and 3.5 years of laboratory exposure to silage effluent

4. Conclusions

An array of analytical tests was performed to determine changes to minerals/pore structure. For Ternary-1 and GGBS-0, in Zone 1, the silage exposure led to the disappearance of CSH and ettringites, and were replaced by calcites. These confirm decalcification of strength giving minerals and thus weakening the microstructure. Extend of influence was determined using elemental analysis (Ca, C, Al, Mg, Fe) and it was 1.2mm, 0.75mm, 0.12mm and 0.11mm for Ternary, GGBS, FA and Calcined clay, respectively. The dominant alumino-silicate structure of FA and Calcined Clays were unaffected by silage effluent exposure and combined with low calcium contents, these mixes showed superior resistance against silage effluent.

Acknowledgements

The data presented here is extracted from an upcoming article titled “Resistance of ternary cement-based and alkali-activated concretes against silage effluent attack” in Construction and Building Materials.

References

Kwasny, J. Soutsos, M., McIntosh, J. A., & Cleland, D. J., banahCEM – comparison of properties of a laterite-based geopolymer with conventional concrete, *Proc. of 9th International Concrete Conference 2016: Environment, Efficiency and Economic Challenges for Concrete*, University of Dundee, 2016, pp. 383-394.

Aiken, T.A., Sha, W., Kwasny, J., Soutsos, M.N., (2017) Resistance of geopolymer and Portland cement based systems to silage effluent attack, *Cement and Concrete Research*, 92, 56-65.

Bertron, A., Duchesne, J., Escadeillas, G., (2007) Degradation of cement pastes by organic acids, *Materials and Structures*, 40(3), 341-354.

Bakharev, T., (2005) Resistance of geopolymer materials to acid attack, *Cement and Concrete Research*, 35(4), 658-670.

Effect of Climate Change on Building Materials: Predictions from Accelerated Testing and Machine Learning

Sze Dai Pang[1*], Felipe Basquiroto de Souza[2], Anthoni Giam[3], Yijie Chen[4], Sida Wu[5] and Daniel Blackwood[6]

[1]National University of Singapore, Singapore, Singapore
Email: ceepsd@nus.edu.sg
[2]National University of Singapore, Singapore, Singapore
Email: fbs@nus.edu.sg
[3]National University of Singapore, Singapore, Singapore
Email: giam.a@nus.edu.sg
[4]National University of Singapore, Singapore, Singapore
Email: ejaychen@nus.edu.sg
[5]National University of Singapore, Singapore, Singapore
Email: sida@nus.edu.sg
[6]National University of Singapore, Singapore, Singapore
Email: msedjb@nus.edu.sg

[*]Corresponding author

ABSTRACT

According to the projections of various global climate models, Singapore will face increased average temperatures (1.4–4.6 °C) within the coming decades, in addition to extreme rainfall and drought events. Such climate change is predicted to directly impact the durability of the building infrastructure, particularly façade materials, as they provide buildings with the first layer of protection against the weather. In this study, a comprehensive experimental and simulation framework is proposed to further understand and predict the impact of climate change on critical façade materials – including cementitious materials such as tile adhesive and plaster mortars, rubber materials such as sealants in curtaining walls, and metallic materials such as fixings. The outcome of this project is expected to assist governmental agencies to make informed decisions regarding the design of more resilient façade systems and routine inspection/maintenance regimes.

KEYWORDS: *Service life, Climate change, Durability; Machine learning*

1. Introduction

The deterioration of building façade materials poses a significant risk to public safety and property, particularly in densely populated urban environments. This degradation may lead to the loosening, detaching, and disengagement of façade elements from heights, which could result in potentially hazardous situations. In Singapore, the increasing frequency of such incidents has raised alarm bells. A considerable number of these incidents could have been prevented through routine inspections and proper maintenance. While preventive measures are crucial, a more comprehensive understanding of the rate of material deterioration can significantly enhance inspection and maintenance strategies. This would allow for more informed decisions regarding the frequency of inspections, thereby preventing potential hazards.

Currently, Singapore has instituted a new periodic façade inspection system. Under this system, buildings that are more than 20 years old and taller than 13 m are required to undergo façade inspections every seven years. This translates to an annual inspection of approximately 4,000 buildings. However, this inspection cycle may need to be re-evaluated in the future due to the effects of climate change. As climate conditions become increasingly extreme, the service life of building façade materials could be reduced, potentially undermining the integrity of these systems and requiring more frequent inspections. The 2nd National Climate Change Study for Impacts due to Climate Change suggests that building façade materials could

experience a reduction in their service life under local climate conditions, though no concrete study has been conducted to confirm or quantify these effects.
The primary objective of this study is to establish guidelines and standards for a material testing framework that can predict the service life of façade materials in Singapore. This will provide asset owners with the necessary information to make informed decisions about façade inspections and maintenance. The overarching goal is to determine the changes in the service life of critical and commonly used façade materials in Singapore due to the effects of climate change, and to formulate appropriate adaptation measures and strategies that ensure the safety and resilience of building façades.

2. Objectives

The objectives of this research are outlined as follows:
•**Identification of Common Façade Materials and Defects**: Identify critical common façade materials used in Singapore and the common defects that these materials are subjected to under local weathering conditions.
•**Development of a Testing Framework**: Develop a robust scientific testing and experimental framework to determine the material service life of these critical façade materials under current and future climate conditions.
•**Physical Testing and Service Life Evaluation**: Conduct physical tests using the validated testing framework to evaluate the service life of critical façade materials under current climate conditions and against the projected effects of climate change in Singapore through the year 2100.
•**Climate Projections and Material Impact**: Analyze the change in the service life of critical façade materials under prolonged exposure to extreme climate change conditions, including changes in temperature, rainfall intensity, and wind speed.
•**Validation with Meteorological Data**: Consult with the Meteorological Services Singapore to confirm the suitability of climate projection data used in the study for simulating extreme climate change conditions up to the year 2100.

3. Research Approach

To investigate the effect of climate change on the service life of materials that are critical in Singaporean building facades, a method involving accelerated weathering testing was adopted in this project (Figure 1). Accelerated weathering chambers were used to 1) replicate the weathering under specified standards and 2) isolate the effect of climate factors (e.g., temperature). The accelerated aging procedure for the service life prediction was designed based on the BS ISO 15686-2:2012, ASTM E632, and NBS Technical Note 1120 standards, which have been widely applied in the industry for estimating the degradation rate of materials.
One of the key steps in the above-mentioned standards is the validation of the degradation mechanisms of the samples subjected to accelerated tests with the long-term aging mechanisms of the materials in the natural environment. In this context, samples from accelerated short-term weathering exposures should be compared with similar components exposed to long-term weathering conditions. The purpose of the comparison is to assert whether the chosen accelerated methodology can induce a similar deterioration mechanism to that observed in actual building applications. Different long-term exposure conditions are recommended, including field exposure, inspection of buildings, experimental buildings, and in-use exposure. In this project, local field samples from buildings of varying types and ages were characterized/tested (i.e., inspection of buildings/in-use exposure method) for comparison with the laboratory samples exposed to accelerated short-term weathering.

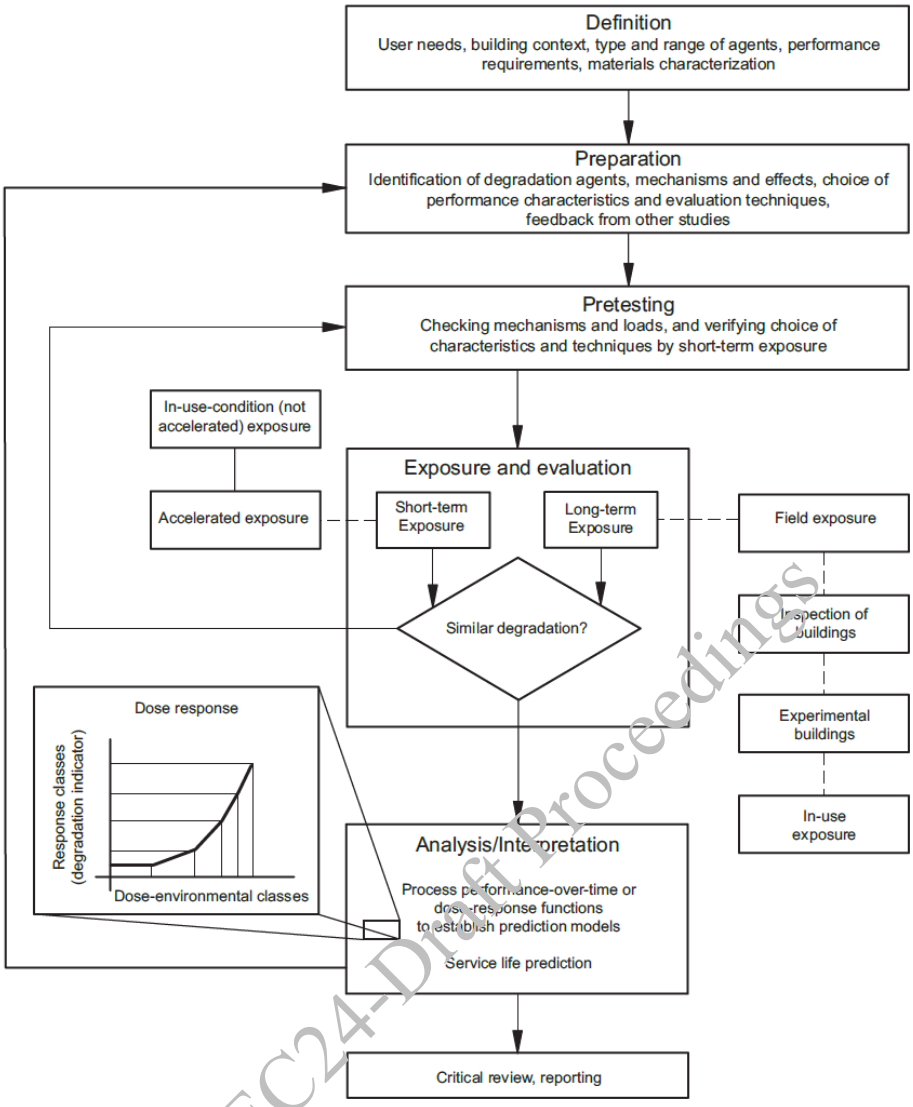

Figure 1. Systematic methodology for SLP of building components according to the BS ISO 15686-2:2012

A key component of the research framework is the incorporation of machine learning into the prediction model. Machine learning will be employed to enhance the prediction models as new data sets are collected both during and beyond the duration of this project. This approach will enable continuous updating of the prediction models, allowing for more accurate forecasting of the effects of climate change over time. To begin this process, a numerical model will be established to capture the mechanical and environmental factors that contribute to material degradation. This model will be validated using data points obtained from accelerated lab weathering tests. Once validated, the model will generate a wide range of data points across different material properties and weathering conditions. These numerical data, combined with sample experimental data from lab weathering tests, will serve as the foundation for the machine learning process. The goal is to build a robust prediction model that can adapt to new data as it becomes available.

4. Key Findings

The experimental program involved a combination of accelerated weathering tests, field testing, and extensive machine learning and mathematical modeling. The focus was on assessing the impact of future climate change scenarios on the service life of critical façade materials used in Singapore. The results of this study, along with findings from previous desk studies, provide valuable insights that can inform future regulatory measures for the inspection and maintenance of building façade systems in Singapore.
The findings of the study are summarized by material type:

•**Rubber-Based Materials**: This study revealed that previous predictions overestimated the impact of climate change on the service life of rubber-based façade materials. For example, the durability of silicone sealants was confirmed, with structural silicone and weather silicone sealants predicted to have service lives of approximately 50 years and 35 years, respectively. Climate change was found to have a negligible impact on these materials. For EPDM-based materials, the prediction models indicated a service life of 22–29 years. The study found that the impact of climate change on EPDM materials has reduction of approximately 13%.
•**Metallic Materials**: A reverse trend was observed for metallic materials, where previous estimates had underestimated the effects of climate change on their service life. The mathematical models predicted a longer service life for steel elements under current climate conditions compared to prior estimates. For instance, stainless steel brackets were estimated to have a service life of 125 years. However, under future climate scenarios, the service life of stainless steel and galvanized steel was predicted to be shortened by 11.2% and 6.5%, respectively.
•**Cement-Based Materials**: New insights were gained into the durability of cement-based façade materials under weathering conditions. For tile systems, a service life of approximately 50 years was estimated. It is anticipated that increased temperature and rainfall could accelerate the deterioration of tile adhesive mortar, potentially reducing the system's service life by up to 30%. Plaster and fibre-cement board materials were found to be highly resistant to weathering, with minimal impacts from climate change. Nevertheless, field observations highlighted potential durability issues, such as cracking in plaster that could lead to water seepage and premature failure in fibre cement boards at connections and edges.

5. Conclusions

This research has demonstrated the critical need to reassess the service life of building façade materials under the influence of climate change in Singapore. Through a combination of accelerated weathering tests, machine learning, and mathematical modeling, this study has provided new insights into how climate change will affect the durability of rubber-based, metallic, and cement-based façade materials. The results of this research will inform future regulatory measures, ensuring that Singapore's buildings remain safe and resilient in the face of evolving climate conditions. Ultimately, this study provides the tools and knowledge necessary for asset owners and policymakers to make informed decisions regarding the inspection, maintenance, and adaptation of building façade systems.

Acknowledgements

This research was supported by the National Research Foundation, Singapore, and Ministry of National Development, Singapore under its Cities of Tomorrow R&D Programme (CoT Award No. COT-V2-2020-3). Any opinions, findings and conclusions or recommendations expressed in this material are those of the author(s) and do not reflect the views of National Research Foundation, Singapore and Ministry of National Development, Singapore.

References

BSI Standards. BS ISO 15686-2:2012 Buildings and constructed assets — Service life. 2014.
ASTM Standards. ASTM E 632 – 82: Standard Practice for Developing Accelerated Tests to Aid Prediction of the Service Life of Building Components and Materiais. 1996.
National Bureau of Standards. NBS 1120: An approach to improved durability tests for building materials and components. 1980.

Long-term Performance of GFRP rebars in Civil Infrastructure Applications

Mohan Krishna Paleti[1], Debapriyo Ghosh[2], and S Suriya Prakash[3*]

[1]Department of Civil Engineering, Indian Institute of Technology, Hyderabad, India
Email: ce20resch13002@iith.ac.in
[2]Department of Civil Engineering, Indian Institute of Technology, Hyderabad, India
Email: ce23resch11005@iith.ac.in
[3]Department of Civil Engineering, Indian Institute of Technology, Hyderabad, India
Email: suriyap@ce.iith.ac.in

[*]Corresponding author

ABSTRACT

Glass fibre-reinforced polymer (GFRP) rebars are non-corrosive in nature. Due to their superior mechanical properties and noncorrosive properties, they are being used as a replacement for steel rebar in reinforced concrete (RC) structures. For effective utilization of those rebars in the construction of RC structures, it is essential to understand the mechanical properties and durability of these bars. The alkaline reaction of FRP composite in concrete is one of the major durability concerns in RC structures. The high alkalinity in concrete has the potential for severe degradation of the GFRP rebars, leading to a reduction in mechanical properties. In this study, the durability of GFRP rebars in an alkaline environment is measured by means of a reduction in mechanical properties such as tensile strength and horizontal and transverse shear strength. The key parameters considered in the experimental evaluation are immersion time (60 and 30 days), immersion medium (alkaline environment and tap water), and temperature (room temperature and 60℃). Test results show that the GFRP rebars are susceptible to higher degradation when exposed to alkaline environment at higher temperatures.

KEYWORDS: *GFRP, Durability, Alkaline environment, Corrosion*

1. Introduction

Corrosion of steel in reinforced concrete (RC) structures is a major concern in marine structures. The corrosion of steel reinforcement results in an increase in volume. The increase in the volume of steel exerts pressure on the surrounding concrete and leads to cracking and, eventually, it spalls. Glass fiber-reinforced polymer (GFRP) rebars are widely used as an alternative to steel reinforcement in concrete structures. GFRP rebars offer several advantages over traditional steel reinforcement, making them suitable for various structural applications. Due to the non-corrosion nature of GFRP bars the risk of concrete degradation can be minimized that can help in extending the service life of the structure. Even though GFRP bars do not corrode, they are susceptible to degradation when exposed to certain environmental conditions such as alkaline exposure, ultraviolet exposure, temperature change, de-icing chemical exposure, mechanical stress cycles, moisture, and water. Usually, in reinforced cement concrete, the rebars are embedded inside the concrete, and the concrete is highly alkaline in nature. Therefore, it is essential to understand the durability of GFRP bars exposed to an alkaline environment. Understanding the durability of GFRP bars is more complex than steel bars because they compose of matrix and fibers and due to their anisotropic nature. The degradation of GFRP bars initiates when water molecules and free and hydroxyl ions diffuse through the matrix (Chen et al. (2007)). Chen et al. (2007) investigated the durability performance of GFRP bars by accelerated aging tests. They noted that elevated temperatures accelerate the degradations, and the normal concrete environment is more aggressive than the high-performance concrete. Ceroni et al. (2006) discussed the effect of external and concrete environments on the durability issues of RC members with FRP bars and summarized the reduction factors applied in various international codes to account for durability

performance. The expansion of defects in GFRP bars may take place when subjected to sustained loads. Due to the expansion of defects, diffusion of alkalis and moisture takes place and accelerates the degradation (Hao and Zeng (2024)). Al-Khafaji et al. (2021) and Benzecry et al. (2021), conducted the durability assessment of GFRP bars extracted from 15-20 year old bridges in the US. A slight degradation near the outer radius of the bars is observed from the scanning electron microscopy, and a slight to moderate loss in shear and tensile strength is observed. Manalo et al. (2020), investigated the durability of GFRP bars in concrete and simulated concrete environments by conducting horizontal shear test. They noted that the diffusivity of GFRP bars depends on temperature and solution type. In addition, the degradation of the horizontal shear strength is higher for bare GFRP bars immersed in a simulated concrete environment than the bars embedded in concrete. Pan and Yan (2021), investigated the durability of GFRP and hybrid FRP bars under an alkaline environment. The carbon FRP layer on top of GFRP delays diffusion of OH^- and water and improves durability. In this study, a detailed review of existing literature on the durability of GFRP bars is conducted, and an experimental evaluation of the durability of GFRP exposed to an alkaline environment is carried out by measuring the residual strength of rebars under tension, horizontal, and transverse shear.

2. Experimental Study

The mechanical properties of GFRP bars degrade when exposed to adverse environmental conditions. Therefore, it is important to determine the mechanical properties after exposing the GFRP rebars to the alkaline solution. Both conditioned and unconditioned GFRP bars are tested to determine the tensile, horizontal, and transverse shear strength. The test program includes variables such as alkaline solution and accelerated exposure in an environmental chamber (humidity and temperature). Therefore, in the present work, the long term performance of the GFRP bars is evaluated by subjecting them to accelerated aging using an environmental chamber at 60°C and 95% humidity for 30 and 60 days for two different solutions (alkaline solution with pH = 12.6-13 and tap water of pH = 8.5) and also at room temperature (RT). This resulted in eight different types of accelerated specimens. Nomenclature of specimens are assigned as #&@ (#- corresponds to temperature i.e., room temperature-RT, 60℃-T60, &- represents the type of solution, A- alkaline solution and W- for tap water and @- corresponds to time 30 and 60 days). For example, T60A30 means bars immersed in alkaline solution for 30 days at 60℃. The alkaline solution was prepared as per the requirements given in ASTM D7705 (ASTM (2019)). The pH of the alkaline solution is maintained at 12.6 to 13.0 throughout the conditioning period.

3. Results and Discussion

3.1 Degradation of GFRP bars

After removing the specimens immersed in the alkaline solution from the humidity chamber, the degradation of resin on the surface of the GFRP bar and fibers is observed (Fig. 1). Firstly, the degradation of resin is initiated, and then the degradation of the exposed fibers is observed.

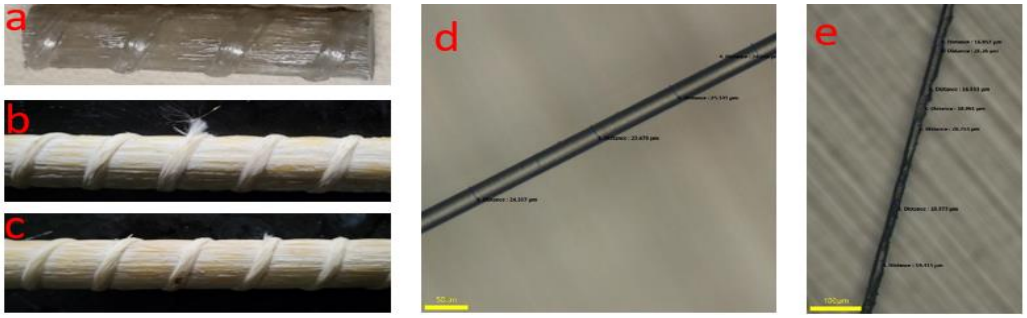

Figure 1. Degradation of GFRP bars and glass fibers on exposure to alkaline environment. (a), (d) without exposure, and (b), (c), and (e) on exposure to alkaline environment

The damaged ribs were also observed in the specimens immersed in an alkaline solution at 60℃, as shown in Fig. 1(b). Due to the degradation of resin, fibers, and the resin-fiber interface, the degradation in

mechanical properties is observed. The microscope images of glass fibers with and without exposure to an alkaline environment are shown in Fig. 1(d and e).

3.2 Tensile strength

The tensile strength test has been conducted as per recommendations given in ASTM D7205/D7205M-21 (ASTM (2021a)). The tensile test setup and stress-strain curves of GFRP bars immersed in alkaline solution and tap water are shown in Fig. 2. The tensile strength retention at the end of 60 days of immersion of the GFRP bars at room temperature and 60°C in tap water were 89% and 79%, respectively. The strength retention was 82% and 73% in alkaline solution for bars at room temperature and 60°C, respectively. A broom shape mode of failure is observed for GFRP bars subjected to tensile load, as shown in Fig. 3.

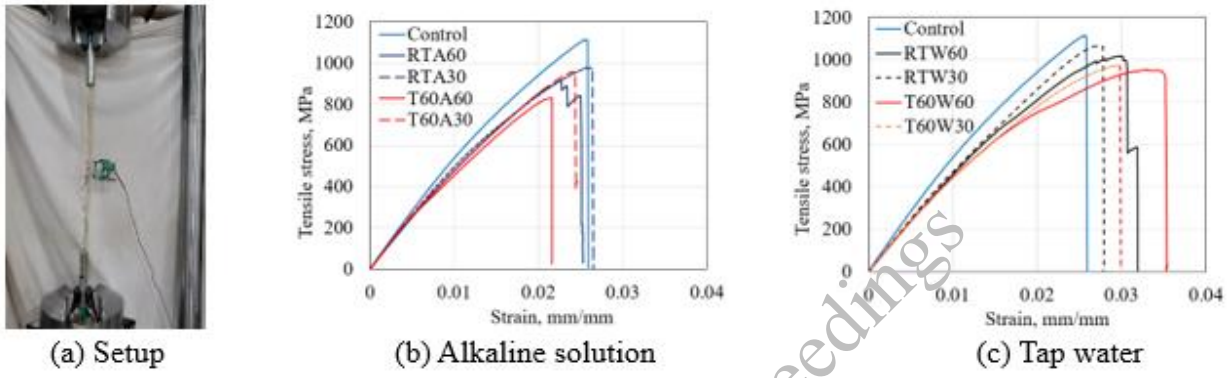

Figure 2. (a) Tension test setup and tensile stress-strain response of GFRP bars immersed in a) Alkaline solution and b) Tap water under different conditioning schemes

Figure 3. Splitting type of failure of GFRP bars under tension

3.3 Horizontal shear strength

The horizontal shear test was conducted as per recommendations given in (ASTM (2021b)). The horizontal shear test setup and load-deflection curves of GFRP bars immersed in alkaline solution and tap water are shown in Fig. 4. The horizontal shear strength can be expressed by Eq (1), as per ASTM D4475 (ASTM (2021b))

$$T_{max} = \frac{0.849P}{D^2} \quad (1)$$

Where T_{max} is the horizontal shear strength, D is the diameter of the GFRP bar (mm), and P is the peak load (kN). The horizontal shear strength retention at the end of 60 days of immersion of the bare GFRP bars at room temperature and 60°C were 88%, and 81% in tap water. They were 86%, and 75%, respectively in alkaline solution. The horizontal cracks along the mid-plane of the bar are noticed as the mode of failure under the horizontal shear test, as shown in the Fig. 5.

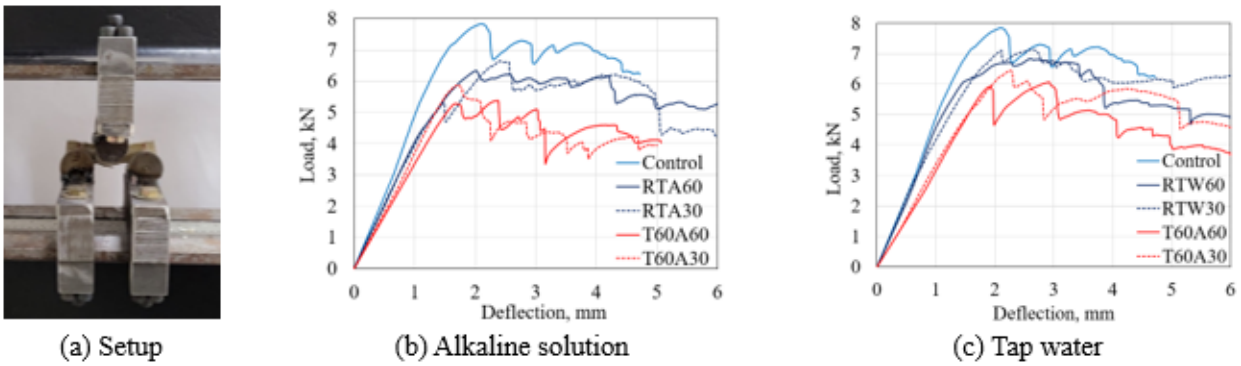

Figure 4. (a) Horizontal shear test setup and horizontal shear load-deflection response of GFRP bars immersed in b) Alkaline solution and c) Tap water under different conditioning schemes

Fig. 2. Failure mode of GFRP bars in horizontal shear

3.4 Transverse shear strength

The transverse shear test was conducted as per the recommendations given in ASTM D7617/D7617M (ASTM (2017)). The transverse shear test setup and stress-strain curves of GFRP bars immersed in alkaline solution and tap water are shown in Fig. 6(a and b). The reduction in transverse shear strength is shown in Fig. 6. It is reduced by 8% and 25%, respectively, for rebar exposed to an alkali atmosphere for 60 days and 90 days. That reduction is due to the degradation of the resin in the rebar. The failure mode of GFRP bars under transverse shear is the cleavage of the bar into three pieces, as shown in Fig. 6(c).

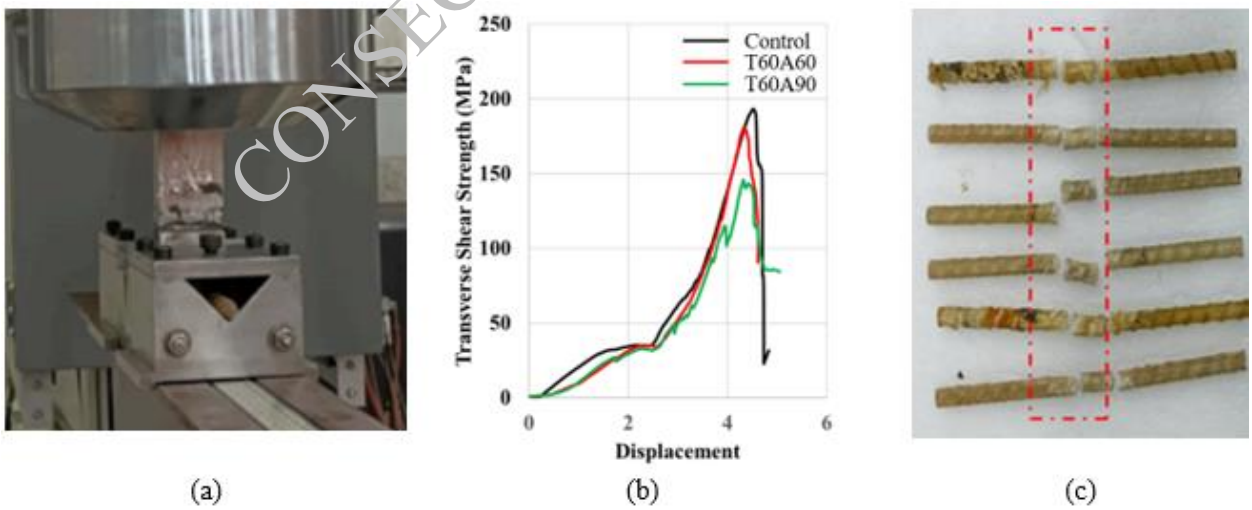

Figure 5.(a) Transverse shear test setup, (b) transverse shear strength-displacement response of GFRP bars immersed in alkaline solution, and c) failure mode

4. Conclusions

The durability of GFRP bars exposed to alkaline environment was assessed by studying the degradation in their mechanical properties. The key conclusions drawn from the present work are as follows
The degradation is severe for the GFRP bars subjected to elevated temperatures in the alkaline environment. The alkaline environment at elevated temperature is critical for GFRP bars, resulting in 27% and 25% degradation in tensile and horizontal shear strengths, respectively.

- The reduction of mechanical properties is due to the degradation of resin and fibers due to the diffusion of water molecules and hydroxyl ions. The chosen resin and fiber influence the performance of GFRP bars exposed to an alkaline environment.
- The degradation will be much higher if the bars are subjected to sustained loads under alkaline environmental conditions due to the expansion of the defects.
- The degradation of GFRP bars immersed in the simulated concrete environment depends on the temperature and exposure time.
- The GFRP bars immersed in a simulated concrete environment were subjected to more degradation than the GFRP bars embedded in concrete. Therefore, bare GFRP immersed in a simulated concrete environment is the most critical case, and they may not degrade to that extent in real situations.
- The durability of GFRP bars exposed to a high-performance concrete environment is better than that of the normal concrete environment.

References

Al-Khafaji, A. F., R. T. Haluza, V. Benzecry, J. J. Myers, C. E. Bakis, and A. Nanni. (2021) “Durability Assessment of 15- to 20-Year-Old GFRP Bars Extracted from Bridges in the US. II: GFRP Bar Assessment.” *J. Compos. Constr.*, 25 (2): 1–13.

ASTM. (2017) “Standard Test Method for Transverse Shear Strength of Fiber-reinforced Polymer Matrix Composite Bars. ASTM D7617/D7617M-11R17, *ASTM Int. WestConshohocken, PA.*, i (Reapproved): 1–12.

ASTM. (2019) "Standard Test Method for Alkali Resistance of Fiber Reinforced Polymer (FRP) Matrix Composite Bars used in Concrete Construction." ASTM D7705, *ASTM Int.* West Conshohocken, PA, United States.

ASTM. (2021a) "Standard Test Method for Tensile Properties of Fiber Reinforced Polymer Matrix Composite Bars." ASTM D7205/D7205M, *ASTM Int.* West Conshohocken, PA, United States.

ASTM. (2021b) “Standard Test Method for Apparent Horizontal Shear Strength of Pultruded Reinforced Plastic Rods By the Short-Beam Method". ASTM D4475, *ASTM Int.* West Conshohocken, PA, United States.

Benzecry, V., A. F. Al-Khafaji, R. T. Haluza, C. E. Bakis, J. J. Myers, and A. Nanni. (2021) “Durability Assessment of 15- to 20-Year-Old GFRP Bars Extracted from Bridges in the US. I: Selected Bridges, Bar Extraction, and Concrete Assessment.” *J. Compos. Constr.*, 25 (2): 1–9.

Ceroni, F., E. Cosenza, M. Gaetano, and M. Pecce. (2006) “Durability issues of FRP rebars in reinforced concrete members.” *Cem. Concr. Compos.*, 28 (10): 857–868.

Chen, Y., J. F. Davalos, I. Ray, and H. Y. Kim. (2007) “Accelerated aging tests for evaluations of durability performance of FRP reinforcing bars for concrete structures.” *Compos. Struct.*, 78 (1): 101–111.

Hao, Z. H., and J. J. Zeng. (2024) “Effect of sustained loads on the durability of GFRP bars with and without UHP-ECC cover.” *Eng. Struct.*, 309 (March): 118050. Elsevier Ltd.

Manalo, A., G. Maranan, B. Benmokrane, P. Cousin, O. Alajarmeh, W. Ferdous, R. Liang, and G. Hota. (2020) “Comparative durability of GFRP composite reinforcing bars in concrete and in simulated concrete environments.” *Cem. Concr. Compos.*, 109 (July 2019).

Pan, Y., and D. Yan. (2021) “Study on the durability of GFRP bars and carbon/glass hybrid fiber reinforced polymer (HFRP) bars aged in alkaline solution.” *Compos. Struct.*, 261 (May 2020): 113285. Elsevier Ltd..

Shrinkage and Bond Response of Ultra-High-Performance Concrete (UHPC)-based HFSTs for Roadway Applications

A.R. Biehl[1*], K.F. Maeger[2], and P.R. Rangaraju[3]

[1]Graduate Student, Clemson University, Clemson, United State of America
Email: arbiehl@clemson.edu
[2]Graduate Student, Clemson University, Clemson, United State of America
Email: kmaeger@clemson.edu
[3]Professor, Clemson University, Clemson, United State of America
Email: prangar@clemson.edu

[*]Corresponding author

ABSTRACT

High Friction Surface Treatment (HFST) is an effective roadway remediation technique to decrease the frequency of crashes due to insufficient pavement friction. To increase roadway coefficient of friction HFSTs typically utilize a thin layer of epoxy binder embedded with calcined bauxite as aggregate. These systems are effective but require specialty materials that are expensive. To decrease the material cost of HFSTs studies have been undertaken to identify alternative materials that meet the service requirements of typical HFSTs. Multiple studies investigated the use of regionally available alternative aggregates; however, these studies have generally shown that alternative aggregates are inferior to calcined bauxite in their performance. While a suitable alternative to calcined bauxite has not been discovered, alternative binders present another opportunity for cost reduction. A promising alternative binder is ultra-high performance concrete (UHPC). UHPC is a cementitious binder with high compressive strength (>120 MPa), high bond strength, and increased toughness. Previous research has indicated that UHPC can meet the necessary properties for HFST although UHPC-based HFSTs were not investigated. This study investigates the bond strength, compressive strength, and shrinkage of UHPCs with and without intermixed calcined bauxite as a preliminary step to determine suitability of UHPC based HFSTs. Findings from this study indicate that UHPC exhibits sufficient compressive strength and bond strength, but further optimization is needed to decrease the shrinkage to below the tensile strain capacity to minimize shrinkage-induced cracking.

KEYWORDS: *UHPC, HFST, Calcined Bauxite, Bond Strength, Shrinkage*

1. Introduction

High Friction Surface Treatments (HFSTs) are a roadway remediation technique used to improve the friction on pavement surfaces to reduce crashes (Wilson et al., 2016). Initially implemented along horizontal curves, HFST usage has increased based upon their cost effectiveness and low construction times compared to replacement (Merritt and Moravec, 2014). Typical pavement surfaces that benefit from HFST implementation are those that have polished (interchanges), were improperly designed (interchanges), or have poor drainage (highways) (Atkinson et al., 2016). The US Federal Highway Administration (FHWA) estimates an 83% reduction in weather-related crashes and a 57% reduction in total crashes where HFSTs are applied (Merritt et al., 2020; Coppinger et al., 2021). This improvement is supported by studies undertaken by other departments of transportation (DOTs), which monitored the implementation of HFSTs in their state and found a similar trend (Sprinkel et al., 2015; Cheung and Julian, 2015; Bledsoe, 2015). Based upon the savings in financial cost and human life associated with reducing the severity and frequency of crashes, increased use of HFST as a roadway treatment option is essential.

HFSTs are built by applying a thin layer of epoxy resin binder onto a pavement surface and embedding a high-quality aggregate under gravity. Before applying the binder, the roadway surface must be prepared to

ensure an adequate and consistent bond across the surface. Once prepared, the binder and aggregate are applied to the surface; depending on the size of the project, the application could be completed manually or with specialized machinery. After curing the loose aggregate is removed by a power broom or vacuum sweeper. This process is completed to remove loose debris from the roadway surface. The loose aggregate is often reclaimed and reused in future work (as a partial replacement of virgin aggregate) (Atkinson et al., 2016). Due to a limited funding for all their projects, DOTs have aimed to reduce the cost of implementation, which could increase the breadth of applications across pavement networks (Wilson et al., 2016).

The main requirements for an HFST binder are a strong bond between the HFST aggregate and the binder layer, a strong bond between the binder layer and the substrate, the avoidance of differential shrinkage between the binder and the substrate, the ability to handle repeated traffic loads, and the ability to cover large areas economically (Coppinger et al., 2021). UHPC is a class of cementitious composite characterized explicitly by its high compressive strength, workability, abrasion resistance, and bond strength, making it uniquely qualified to handle these stresses. Furthermore, all five of these HFST requirements are ones that ultra-high performance concrete (UHPC) typically exceed (Kusumawardaningsih et al., 2015; Farzad et al., 2019; Wu, P. et al., 2019; Teng et al., 2021; Li et al., 2021; Feng et al., 2022). Testing focused on the flow properties in the fresh state and bond strength, compressive strength, and shrinkage in the hardened state of UHPC. Additionally, the performance of the UHPC samples with intermixed calcined bauxite was tested to determine how calcined bauxite impacts the performance.

2. Materials and Methods

2.1 Materials

In this study an ASTM C150-22 Type III Portland Cement with a Blaine's Fineness of 485 m^2/kg and has a specific gravity of 3.15 was used. Additionally, three different silica fumes (SF1, SF2, and SF3) with varying particle sizes (Figure 1) and amorphous contents were used (SF1=92.6%, SF2=93.9%, and SF3=98.1% amorphous). In this study manufactured granite sand (SG=2.69, Abs.=0.38%) and pond fines from the same quarry (SG= 2.70, Abs.=0.44%) were used as fine aggregate. In addition, calcined bauxite (SG=3.19, Abs.=2.33%) as HFST aggregate was used in the intermixed calcined bauxite UHPC mixtures. The particle size distribution of the binder components and aggregates are shown in Figure 1. The mix water used for this study conformed to ASTM C1602-22. A poly-carboxylate based ether (PCE) liquid superplasticizer was used for this study, with a solids content of 50% and a specific gravity of 1.08.

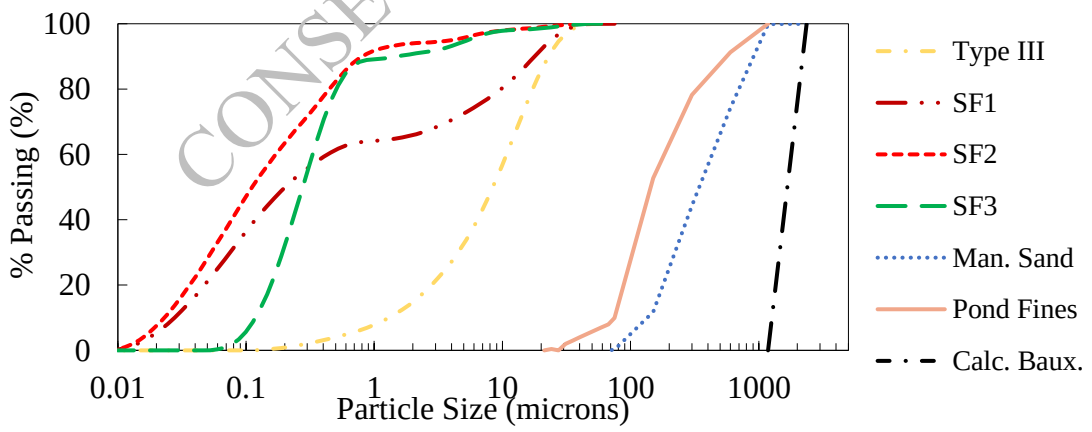

Figure 1. Particle Size Distribution of Constituent Solids

2.2 Mixture Proportions

The mixture proportions for the UHPC mixtures are shown in Table 1, where the sample ID (for ex: SF1-3.5) is the source of silica fume followed by the HRWR dosage as a percentage of the binder. The mixture proportions were optimized using the Modified Andreasen and Andersen (MA&A) method with a q-value of 0.19 based upon the maximum and minimum particle size (Liu et al., 2022). Generating the mixture proportions was an iterative process where the material dosage rates were modified to decrease the

difference between the theoretical and real particle size curve. Iterations of varying mixture proportions were completed to maximize R^2 value between the actual and theoretical q. The mixture proportions of samples with calcined bauxite included calcined bauxite at a ratio of 3.0 to the mass of the cementitious materials.

Table 1. Mixture Proportions for UHPC Mixtures Without Intermixed Calcined Bauxite

Sample ID	C/CM	SF/CM	S/CM	PF/CM	W/CM	HRWR/CM
SF1-3.5	0.80	0.20	0.7	0.4	0.2	0.035
SF1-4.5	0.80	0.20	0.7	0.4	0.2	0.045
SF2-3.5	0.80	0.20	0.6	0.4	0.2	0.035
SF2-4.5	0.80	0.20	0.6	0.4	0.2	0.045
SF3-3.5	0.85	0.15	0.6	0.5	0.2	0.035
SF3-4.5	0.85	0.15	0.6	0.5	0.2	0.045

2.3 Mixing Procedure

In this study a 20-quart Hobart Mixer with a 0.5 HP motor and three speeds of low (planetary motion 60 rpm and paddle 107 rpm), medium (planetary motion 113 rpm and paddle 198 rpm), and high (planetary motion 207 rpm and paddle 365 rpm) was used for mixing the UHPC mixtures. All mixing and batching was conducted in laboratory conditions (23±1℃ and 50±5% relative humidity), with batching completed directly before mixing. The mixing procedure used for this study is based on recommendations from literature and previous experimental work (Figure 2) (Hiremath and Yaragal, 2017; Wu et al., 2019). Additionally, for samples with intermixed calcined bauxite an additional step at low speed for one minute is included after the normal UHPC mixing process.

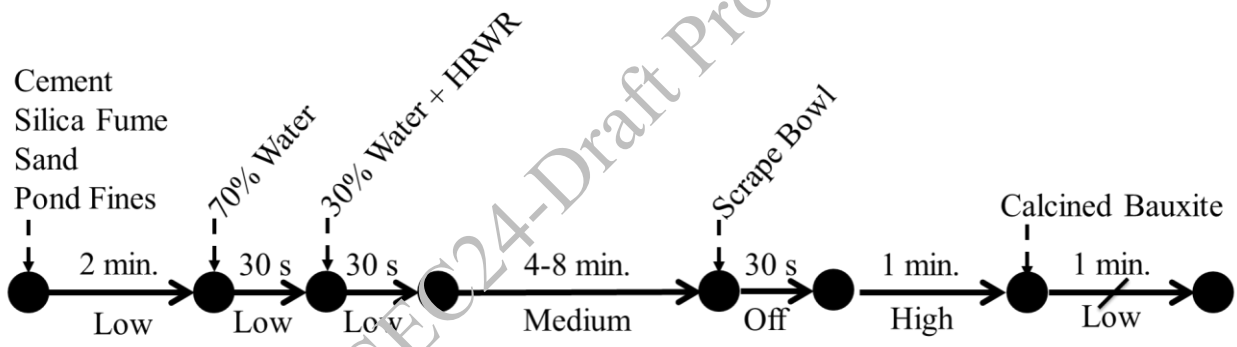

Figure 2. Mix Procedure for UHPC and Intermixed UHPC

2.4 Methods

2.4.1 Flowability

The flowability was measured for UHPC mixes using the modified flow table test per ASTM C1856-17. However, for intermixed calcined bauxite samples the flowability was measured using the standard flow table test per ASTM C1437-23 due to the lower flowability being outside the test range of ASTM C1856-17. The flowability was measured directly after mixing concluded. Each flowability reading was completed in triplicate, and the average and standard deviation are included in the results section.

2.4.2 Bond Strength

The bond strength was measured using the pull-off test in ASTM C1583-20. Testing was completed at 7 and 28-days on concrete substrates (3.37 MPa tensile strength) and at 28-days asphalt substrates (0.32 MPa tensile strength) prepped to match an International Concrete Repair Institute (ICRI) concrete surface profile chip six. Test criteria was based on FHWA recommendation for HFST binders, where a passing test either exceeds 1.72 MPa or fails in the substrate (Merritt et al., 2021).

2.4.3 Drying Shrinkage

Drying shrinkage was measured according to ASTM C596-23. An initial reading is taken 3 days after casting with subsequent measurements at 7, 14, 21, and 28-days after initial casting. The failure criteria for this test are based upon the tensile strain capacity of unreinforced cementitious (200 microstrain), which when converted to unrestrained shrinkage is -0.02% (Roziere et al., 2014; Frosch et al., 2017). This differs from UHPC, which typically contains fibers that provide post crack ductility, but also initially crack at 200 microstrain (Dai et al., 2021).

2.4.4 Compressive Strength

The compressive strength of UHPC was measured in accordance with ASTM C109-23 on 50mm cubes at 1,7, and 28-days. The ASTM C109-23 method was used in this study instead of ASTM C1856-17 for UHPC (cylinders) due to the ease of casting and consistency of test surfaces of cubes. The early age performance follows part of the compressive strength requirements set out in the AASHTO MP-41 specification, expecting to achieve the 35 MPa at 7-days as required for resin systems (AASHTO, 2013). The later ages strength requirements are based on ASTM C1856-17, the ASTM standard practice for testing UHPC, which requires a compressive strength of at least 120 MPa for classification as a UHPC (ASTM, 2023).

3. Results and Discussion

3.1 Flowability

The flowability of the six selected UHPC mixes using ASTM C1856-17 is shown in Figure 3. The designed mixes extend across the recommended workability from 100-150% flow, which provides a workable UHPC mixture that is easily consolidated without segregating. Segregation is a key concern for UHPC-based HFST, as proper aggregate embedment, fiber dispersion, and the strength would become less reliable (Wang et al., 2017). The mixes containing higher dosages of HRWR on average flowed 17% more than the lower dosage mixes. The flow differences between the SF1, SF2, and SF3 are due to the different sand dosages, SF dosages, SF PSD, and SF chemical composition.

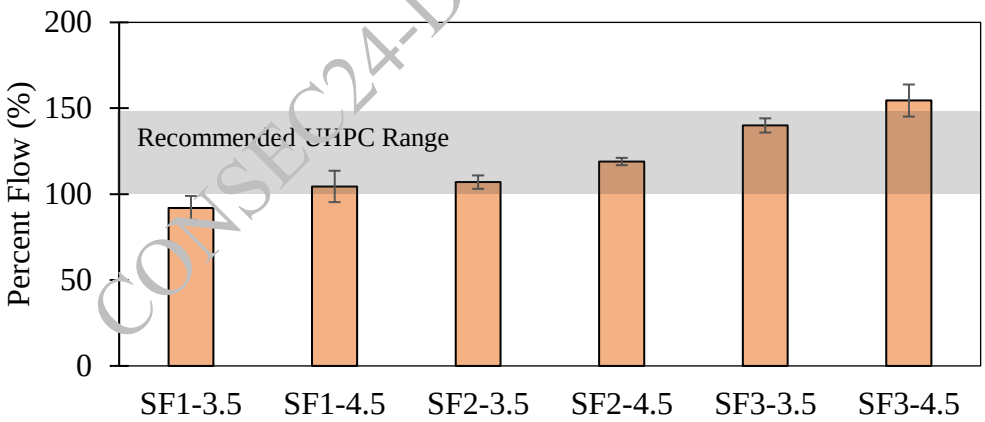

Figure 3. Flowability of Selected Mixes via Modified Flow Table Test

The flowability of the intermixed calcined bauxite samples tested using ASTM C1437-23 is shown in Figure 4. If these samples were tested according to ASTM C1856-17 procedure each would have received a flow value of 0%. However, testing using ASTM C1437-23 also showed flows at the lower end of the testing range. The intermixed calcined bauxite samples demonstrated flows between 5-20%, which indicates that mixes containing high dosages of calcined bauxite would require external compaction or vibration to achieve sufficient consolidation.

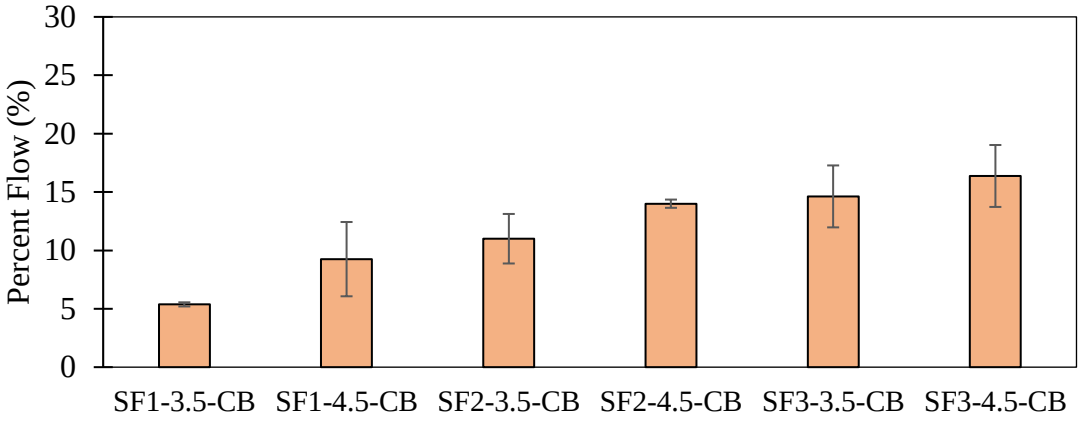

Figure 4. Flowability of Intermixed Calcined Bauxite via Flow Table Test

3.2 Bond Strength

The bond strength of the UHPC samples without calcined bauxite are shown in Table 2. Test results indicate that all samples exceeded the required 1.72 MPa or failed in the substrate. For overlays on the concrete substrates the 7-day performance for the UHPC samples either exceeded or was equal to that of epoxy samples, ranging between 96% and 134%. However, at 28-days the tensile strength of UHPC was less than the epoxy due to a lower strength gain rate (73%-113%). For the asphalt substrates all samples failed at relatively low strengths but failed in the substrate indicating a passing test. However, the epoxy samples were able to generate additional strength in the substrate by filling the voids present in the asphalt samples. This resulted in epoxy-resin sample failing at 1.36 MPa, whereas the UHPC samples failed between 0.44-0.60 MPa. This testing indicates that UHPC while having sufficient bond strength to meet criteria for asphalt surfaces is inferior to epoxy resins mechanically.

Table 2. Bond Strength Results of UHPC Samples

Sample ID	Concrete (psi)				Asphalt (psi)	
	7 Day	% of Epoxy	28 Day	% of Epoxy	28 Day	% of Epoxy
Epoxy	2.17	100%	2.62	100%	1.36†	100%
SF1-3.5	2.92	134%	2.60	99.2%	0.52†	38.6%
SF1-4.5	2.86	132%	1.92	73.1%	0.60†	44.1%
SF2-3.5	2.67	123%	1.92	73.1%	0.59†	43.1%
SF2-4.5	2.09	96.1%	2.96	113%	0.52†	38.1%
SF3-3.5	2.12	97.8%	1.93	73.7%	0.44†	32.5%
SF3-4.5	2.23	103%	2.35	90.0%	0.47†	34.5%

†: Failure in the Substrate

The bond strength of the intermixed calcined bauxite samples is listed in Table 3. For the asphalt samples the same trend was observed as the UHPC without calcined bauxite where the epoxy provided an elevated level of bond strength.

Table 3. Bond Strength Results of Intermixed Calcined Bauxite Samples

Sample ID	Concrete (MPa)				Asphalt (MPa)	
	7 Day	% of Epoxy	28 Day	% of Epoxy	28 Day	% of Epoxy
Epoxy*	2.17	100%	2.62	100%	1.36†	100%
SF1-3.5-CB	1.73	80.0%	2.83	108%	0.50†	37.1%
SF1-4.5-CB	1.96	90.1%	2.53	96.6%	0.53†	39.1%
SF2-3.5-CB	1.91	87.9%	2.47	94.2%	0.60†	44.1%
SF2-4.5-CB	1.74	80.2%	2.56	97.9%	0.50†	37.1%
SF3-3.5-CB	1.59	73.3%	2.90	111%	0.68†	50.2%
SF3-4.5-CB	1.33	61.2%	2.79	107%	0.45†	33.0%

*Does not contained intermixed calcined bauxite
†: Failure in the Substrate

However, the testing on concrete substrates differed from the UHPC samples. The 7-day tensile strengths were less than the epoxy, with 2 samples failing due to increased porosity. However, at 28-days the tensile strength equaled or exceeded the epoxy in part due to further hydration because of the available porosity allowing water intrusion to the interface.

3.3 Drying Shrinkage

Drying shrinkage testing was completed on the UHPC samples and on SF3-4.5-CB. It was assumed that the use of intermixed calcined bauxite will predominately act as a filler (reducing paste volume available for shrinkage). This is demonstrated by the lower shrinkage for the sample with CB included. The results from this testing are included in Figure 3. Results also show that all samples exceeded the maximum permissible shrinkage of 0.02%, with a shrinkage range of 0.06-0.08% at 25 days. Exceeding that value increases the likelihood of cracking and premature failure, necessitating shrinkage remediation techniques. While the intermixing of calcined bauxite demonstrated an ability to significantly reduce drying shrinkage with SF3-4.5-CB (0.038%) being 50% less than SF3-4.5 (0.074%) the mix still exceeded the 0.02% threshold and indicates that multiple techniques are necessary at once. Other mitigation measures include the inclusion of fibers to improve the tensile strain capacity by providing a ductile post peak behavior or the inclusion of a shrinkage reducing admixture to reduce the surface tension of the pore solution and thereby reduce the buildup of capillary stresses when drying.

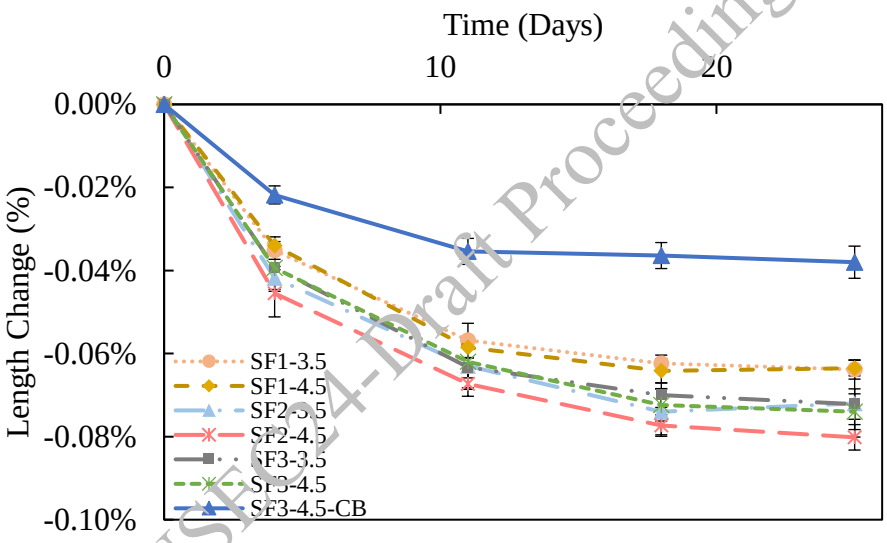

Figure 5. Drying Shrinkage of UHPC Samples Without Intermixed Calcined Bauxite

3.4 Compressive Strength

The compressive strength of UHPC was evaluated for both the UHPC samples and the intermixed calcined bauxite samples. Testing on the UHPC samples focused on 1, 7, and 28-day strengths (Figure 6). At 1-day samples ranged from 48-66 MPa and at 7-day 75-82 MPa, which both exceeded the 7-day requirement for typical HFSTs. The compressive strengths at 28-days ranged from 85-104 MPa, which fell below the specification for UHPCs. However, supplemental testing on the lowest strength sample (SF3-4.5) with 2% steel fibers by volume had a compressive strength of 120 MPa matching the ASTM requirement. While the inclusion of fibers will meet the strength threshold for UHPC classification, the benefits of fiber are not assumed to greatly influence the likely failure modes of an HFST binder (bond failure or aggregate loss), and the exclusion of fiber can nearly half the cost of the mixture.

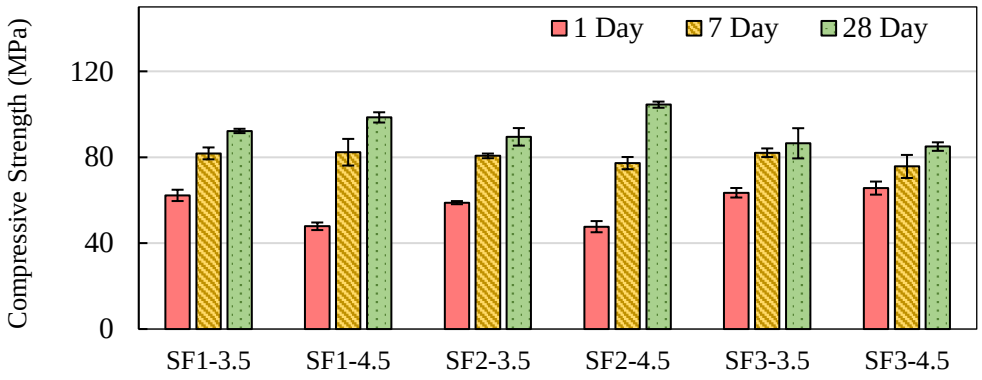

Figure 6. Compressive Strength of UHPC Samples Without Intermixed Calcined Bauxite

Figure 7 further supports the classification of these mixes as UHPC, as samples containing calcined bauxite intermixed at a replacement rate of 3.0 exceeded 120 MPa on two occasions with the 28-day compressive strength varying between 111-128 MPa. Furthermore, these mixes also exceeded the required 7-day compressive strength of 35 MPa at 1-day with strengths ranging from 50-58 MPa. While calcined bauxite is a specialty material that should not be included in typical UHPCs since it is being included primarily as a friction providing aggregate this boost in strength is a promising benefit. The strength of the calcined bauxite helps to overcome the weakness added to the mix in manufactured granite aggregate.

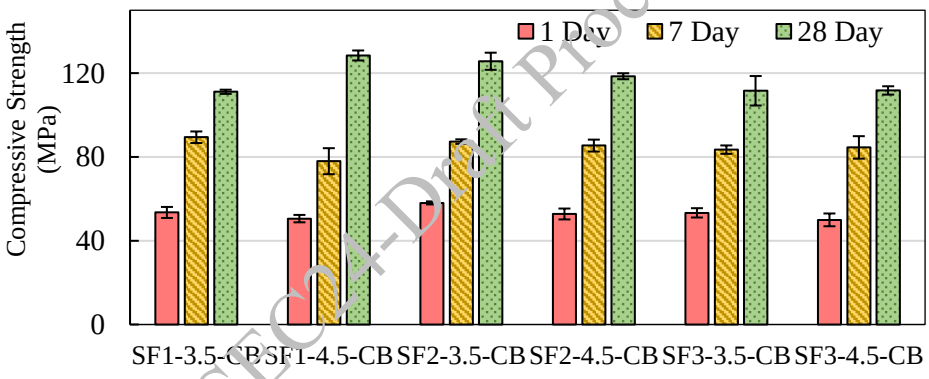

Figure 7. Compressive Strength of Intermixed Calcined Bauxite Samples

4. Conclusions

Based upon the results several conclusions can be drawn:

- The utilization of UHPC-based HFSTs is mechanically possible and provides a competitive binder on concrete substrates to the current epoxy resin systems. For asphalt substrates the UHPC-based HFSTs meets the bond strength requirement but did not provide equivalent performance to the epoxy resin.
- The use of intermixed calcined bauxite had some failures below the required bond strength and needs additional optimization to determine the ideal dosage for maximum density and mechanical performance.
- The shrinkage of UHPC-based HFSTs exceed the expected tensile strain capacity. Further testing is warranted to evaluate the effects of intermixed calcined bauxite, fibers, and shrinkage reducing admixtures to determine ideal strategies to mitigate cracking risk.
- The compressive strength of these mixes is sufficient to handle the traffic load at as early as 1-day and is classifiable as a UHPC at 28-day depending on the inclusion of steel fibers and/or intermixing calcined bauxite.

Acknowledgements

The author would like to thank the SCDOT for sponsoring this research (SPR-762). Additionally, the following companies supported this research by providing materials: ARGOS USA, SIKA USA, FX Minerals, and Vulcan Materials USA.

References

AASHTO.(2013) "AASHTO MP 41-13: Standard Practice for High Friction Surface Treatment for Asphalt and Concrete Pavements", AASHTO Standard Practice

ASTM C1856-23. (2023) "Fabricating and Testing Specimens of Ultra-High Performance Concrete", ASTM

Atkinson, J., J. Clark, and S. Ercisli.(2016), " High Friction Surface Treatment Curve Selection and Installation Guide"

Bledsoe, J. (2015) "Missouri Demonstration Project: The Use of High-Friction Surface Treatments on Missouri Highways"

Cheung, J. and Julian. F(2015) "Northern California US 199-Del Norte County High Friction Surface Treatment"

Coppinger, K., . Keen, M., Gissel,J. and . Rainville, L.(2021) "High Friction Surface Treatments Final Report"

Dai, J.G., Huang, B.T. and Shah, S.P. (2021) "Recent Advances in Strain-Hardening UHPC with Synthetic Fibers", *Journal of Composites Science*, 5(10):283

Farzad, S. and Azizinamini. (2019) "Experimental and numerical study on bond strength between conventional concrete and Ultra High-Performance Concrete (UHPC)", *Engineering Structures*. 186: 297

Feng, S., Xiao, H., Liu, M., Zhang, F. and Lu, M. (2022) "Shear behaviour of interface between normal-strength concrete and UHPC: Experiment and predictive model", *Construction and Building Materials*,342: 127919

Frosch, R., D. Fowler, E. Nawy, W. Hansen, M. Brander, H. Haynes, E. Schrader, D. Darwin, W. Suaris, and F. Fouad. (2017) "Control of Cracking in Concrete Structures"

Hiremath, P.N. and Yaragal, S.C. (2017) "Influence of mixing method, speed and duration on the fresh and hardened properties of Reactive Powder Concrete", *Construction and Building Materials*, 141: 271-288

Kusumawardaningsih, Y., Fehling, E., Ismail, M. and Aboubakr, A.A.M. (2015) "Tensile strength behavior of UHPC and UHPFRC", *Procedia Engineering*, 125:1081-1086

Li, J., Wang, X., Chen, D., Wu, D., Han, Z., Hou, D., Zhen, Z., Peng, C., Ding, Q. and Yin, B.(2021) "Design and application of UHPC with high abrasion resistance", *Construction and Building Materials*, 309:125141

Liu, K., Yin, T., Fan, D., Wang, J. and Yu, R. (2022) "Multiple effects of particle size distribution modulus (q) and maximum aggregate size (Dmax) on the characteristics of Ultra-High Performance concrete (UHPC): experiments and modeling", *Cement and Concrete Composites*, 133:104709

Merritt, D., Himes, S. and . Porter., R. J. (2021) "High Friction Surface Treatment Site Selection and Installation Guide"

Merritt, D., Lyon, C., Persaud, B. and Torres, H. (2020) "Developing Crash-Modification Factors for High-Friction Surface Treatments"

Merritt, D., and M. Moravec. 2014. An Update on HFST for Horizontal Curves.

Roziere, E., Cortas, R. and Loukili, A. (2015) "Tensile behaviour of early age concrete: New methods of investigation", *Cement and Concrete Composites*, 55:153-161

Sprinkel, M.M., McGhee, K.K. and de León Izeppi, E.D. (2015) "Virginia's experience with high-friction surface treatments", *Transportation research record*, 2481(1):100-106

Teng, L., Valipour, M. and Khayat, K.H., 2021. Design and performance of low shrinkage UHPC for thin bonded bridge deck overlay. *Cement and Concrete Composites*, 118:103953

Wang, R., Gao, X., Huang, H. and Han, G. (2017) "Influence of rheological properties of cement mortar on steel fiber distribution in UHPC", *Construction and Building Materials*, 144:65-73

Wilson, B.T., Brimley, B.K., Mills, J., Zhang, J., Mukhopadhyay, A. and Holzschuher, C. (2016) "Benefit–cost analysis of Florida high-friction surface treatments", *Transportation Research Record*, 2550(1):54-62

Wu, P., Wu, C., Liu, Z. and Hao, H., 2019. Investigation of shear performance of UHPC by direct shear tests. *Engineering Structures*, 183:780-790

Wu, Z., Khayat, K.H. and Shi, C. (2019) "Changes in rheology and mechanical properties of ultra-high performance concrete with silica fume content", *Cement and Concrete Research*, 123:105786

Phosphate Treatments to Enhance the Durability of Cementitious Substrates

E. Sassoni

University of Bologna, Bologna, Italy
Email: enrico.sassoni2@unibo.it

ABSTRACT

Phosphate treatments consist in the impregnation of a substrate with an aqueous phosphate solution, to form new calcium phosphate (CaP) as the reaction product between phosphate ions present in the solution and calcium ions coming from the substrate or externally added. In the present study, after a brief summary of the main results obtained on the use of phosphate treatments for the improvement of natural stones and lime-based mortars, their application to cementitious substrates is reviewed. First, different strategies to form new CaP are discussed, namely a "chemical route" and a "biogenic route". Then, studies reporting improvements in physical-mechanical properties (dynamic elastic modulus, compressive strength, abrasion resistance, indentation, stain resistance) and durability (resistance to freeze-thaw cycles) are summarized. The possibility to develop self-healing cementitious materials by exploiting in situ CaP formation is also presented. Finally, available data on the environmental sustainability of the phosphate treatment, in comparison with alternative commercial products, are reported and discussed.

KEYWORDS: *Cement, Ammonium phosphate, Calcium phosphates, Durability, Sustainability*

1. Introduction

Phosphate treatments were proposed in 2011 for the conservation of carbonate substrates, e.g. marble and limestone (Sassoni et al., 2011; Matteini et al., 2011; Yang et al., 2011). Phosphate treatments consist in the application of a phosphate solution (typically an aqueous solution of diammonium hydrogen phosphate, DAP, $(NH_4)_2HPO_4$)) onto the substrate, by spraying, poulticing or brushing. By reaction between the calcium-rich substrate and the phosphate solution, new calcium phosphates (CaP) are quickly formed, the treatment duration being typically set to 24 h (Sassoni et al., 2011; Sassoni, 2018). Ideally, hydroxyapatite (HAP, $Ca_{10}(PO_4)_6(OH)_2$), which is the least soluble CaP at pH>4, is formed, according to the reaction:

$$10CaCO_3 + 5(NH_4)_2HPO_4 \rightarrow Ca_{10}(PO_4,CO_3)_6(OH,CO_3)_2 + 5(NH_4)_2CO_3 + 3CO_2 + 2H_2O \quad (1)$$

where the possible substitution of PO_4^{3-} and OH^- ions by CO_3^{2-} ions is indicated (Sassoni et al., 2011). In case CO_3^{2-} ions, coming from the substrate and/or from the atmosphere, are incorporated into the crystal structure, carbonated apatite is formed, which reportedly has higher mechanical properties than stoichiometric HAP (Li et al., 2019). Alongside HAP, other CaP minerals can be formed, having different Ca/P ratio and different water solubility, such as octacalcium phosphate (OCP, $Ca_8H_2(PO_4)_6{\cdot}5H_2O$) and dicalcium phosphate dihydrate (or brushite, DCPD, $CaHPO_4{\cdot}2H_2O$). Besides being provided by dissolution of the substrate, Ca^{2+} ions needed for the formation of new CaP can also be present directly in the phosphate solution, by adding a suitable calcium source (Naidu and Scherer, 2014). Among the calcium salts that have been tested (Naidu and Scherer, 2014), $CaCl_2$ has provided the best results, in terms of ability to speed up CaP formation and formation of a continuous CaP coating over the substrate. To avoid direct precipitation of CaP directly in the phosphate solution, the ratio between the phosphate precursor and the calcium source needs to be accurately defined. Usually, a 1:1000 molar ratio between $CaCl_2$ and DAP is recommended (Naidu and Scherer, 2014). In addition to favouring CaP formation, external calcium addition can also inhibit dissolution of the substrate, so that new CaP can be formed *over* the substrate, rather than *by consuming* the substrate itself (Naidu and Scherer, 2014). The addition of a calcium source directly to the DAP solution makes it possible to form new CaP also on substrates where the availability of Ca^{2+} ions to

form CaP is low, such as silicate stones (Sassoni, 2018) and mortars based on natural hydraulic lime and cement (Sassoni and Franzoni, 2020). Given the versatility of this approach and the very promising results obtained on a multiplicity of substrates in the laboratory and on real monuments, phosphate treatments are receiving increasing attention, both in the field of cultural heritage conservation and new constructions, as described in the following.

2. Phosphate treatments for enhancement of natural stones and lime-based mortars

Considering the very low water solubility of HAP compared to calcite (Naidu et al., 2016), several studies investigated the feasibility of developing continuous, crack-free and pore-free coatings of HAP over calcitic substrates, especially marble (Naidu et al., 2016; Graziani et al., 2016; Graziani et al., 2017; Sassoni et al., 2018). By using low DAP concentrations (to prevent cracking during drying) and by adding little amounts of alcohol (to enhance the reactivity of phosphate ions), complete and dense films of HAP over marble have been obtained with a solution containing 0.1 M DAP+0.1 mM $CaCl_2$ in 10 vol% ethanol (Graziani et al., 2016; Sassoni et al., 2018). Thanks to formation of such a HAP layer, a significant reduction in marble dissolution in rain has been achieved (Sassoni et al., 2018).
In addition to formation of HAP on the surface of calcitic substrates, its formation inside the substrate (e.g. in intergranular fissures between grains and inside the pores) has proven to lead to substantial increases in mechanical properties, including dynamic elastic modulus, compressive strength, tensile strength and abrasion resistance (Sassoni, 2018). Such mechanical improvement is possible since the newly formed CaPs act as bridges among the grains, thus increasing the cohesion in the material and its mechanical properties. Thanks to the increase in tensile strength after treatment, significant increases in the resistance to weathering processes such as salt crystallization and freezing-thawing cycles have been registered on stones (Sassoni et al., 2016) and mortars (Gabrielli et al., 2024). The improvement in durability caused by phosphate treatments was shown to be greater than that provided by alternative treatments, such as nanolimes, ethyl silicate and acrylic resin (Sassoni et al., 2016; Masi and Sassoni, 2021; Masi et al., 2023).

3. Phosphate treatments for enhancement of cementitious substrates

Formation of new CaP on cementitious substrates has been achieved by "chemical" and "biogenic" routes. In the case of the chemical route, similar to the case of natural stones, CaP can be formed by treatment with phosphate solutions containing a phosphate precursor and possibly a calcium source, to increase the availability of Ca^{2+} ions that, otherwise, come from dissolution of portlandite, calcite and calcium silicate hydrates present in the substrate. Among phosphate precursors, DAP has been the most studied one, with concentrations ranging between 0.1 M and 2 M, often with the addition of $CaCl_2$ in 1:1000 molar ratio to DAP (Sassoni and Franzoni, 2020; Pasco et al., 2023; Zhao et al., 2023). As an alternative to DAP, in a recent study different phosphate precursors have been compared, namely DAP, dipotassium hydrogen phosphate (DPP, K_2HPO_4) and disodium hydrogen phosphate (DSP, Na_2HPO_4), always with $CaCl_2$ addition as a calcium source (Pasco et al., 2023). By combining thermodynamic modeling and experimental tests, it was shown that, independently of the precursor used, HAP is the new CaP phase formed after treatment.
Thanks to formation of HAP on the surface and in the cracks of cementitious substrates, significant increases in surface properties (abrasion resistance, indentation, stain resistance, Pasco et al., 2023), bulk properties (dynamic elastic modulus and compressive strength, Sassoni and Franzoni, 2020) and durability (resistance to freeze-thaw cycles, Zhao et al., 2023) have been obtained. DPP was shown to provide higher increases in physical-mechanical properties than DAP and DSP, hence the investigation of this phosphate salt was deepened. Using a solution of 1 M DPP+1 mM $CaCl_2$ was found to be the most promising condition, as higher concentrations led to formation of potassium calcium phosphate hydrate ($KCaPO_4 \cdot H_2O$), which is undesired as it is highly soluble. Notably, by using a 1 M DPP+1 mM $CaCl_2$ solution, no soluble K-containing salts were found and the treated samples retained the improvement in physical-mechanical properties also after exposure to water, which suggests that good can be expected (Pasco et al., 2023).
As an alternative to the "chemical route", also a "biogenic route" has been proposed for CaP formation on cementitious substrates (Turner et al., 2017; Turner et al., 2021). The substrate was treated with a solution containing a suitable bacterium (*Pseudomonas fluorescens*), a growth medium, KH_2PO_4 and K_2HPO_4 for 20 days. As a result of the bacteria metabolism, a local alkaline environment is formed, which is favourable

to HAP precipitation (Turner et al., 2017; Turner et al., 2021). Compared to the "chemical route", some advantages have been reported for the "biogenic route" (Turner et al., 2017; Turner et al., 2021), but a direct comparison between the optimized formulations of the two routes is still lacking.

4. Phosphate treatments to achieve self-healing ability

The ability of phosphate solutions to induce an increase in the mechanical properties of cementitious substrates by formation of new CaP has been exploited to achieve self-healing ability (Li et al., 2019). By impregnating hydrogel with DSP (Na_2HPO_4) and by incorporating the DSP-impregnated hydrogel into a cement paste, when cracks develop in the hardened cement paste the hydrogel is fractured and releases DSP. By reaction between Ca^{2+} ions present in the pore solution and DSP released from the hydrogel, calcium-deficient HAP was formed (Li et al., 2019). Importantly, no DSP release from the hydrogel was detected until the paste was artificially cracked. In terms of mechanical properties, thanks to the formation of calcium-deficient HAP, 28 days after cracking the compressive strength of the cracked paste was shown to reach the value of the non-cracked paste (Li et al., 2019). It is noteworthy that the hydrogel addition to the paste mix was responsible for a significant initial decrease in the paste compressive strength.

5. Environmental sustainability of phosphate treatments

A recent study has investigated the environmental sustainability of phosphate treatments when applied to natural stones and mortars, in comparison with commercial alternatives (namely ethyl silicate, nanolimes and acrylic resin) (Dal Pozzo et al., 2024; Masi et al., 2023). A life cycle assessment (LCA) was performed adopting a cradle to gate approach, considering that the final compounds formed by each product are expected to remain in the substrate for its entire life. The impact of each product was evaluated in terms of global warming potential (GWP, expressed as kg CO_2eq). Two scenarios were considered: (i) application of the different products until saturation of the substrate (however without information on the resulting strengthening efficacy) or (ii) application of different amounts so as to reach a certain level of improvement in mechanical properties (the higher the amount used, the higher the strengthening efficacy). In both scenarios, the phosphate treatment (3 M DAP followed by limewater) was shown to have a lower GWP than the alternative products, mostly because the DAP-treatment is water-based, while ethyl silicate, nanolimes and acrylic resin are dissolved or suspended in white spirit, ethanol and acetone, respectively (Dal Pozzo et al., 2024). Notwithstanding the low GWP, it should be noted that the DAP-treatment is still responsible for non-negligible impacts in terms of human toxicity (HT), acidification (ACD) and eutrophication (EUT), due to the release of ammonia into the atmosphere as the final outcome of the decomposition of ammonium carbonate formed according to the reaction (1) (Dal Pozzo et al., 2024). A possible strategy to reduce the above-mentioned impacts of the phosphate treatment could be using DPP as the phosphate precursor, instead of DAP. Indeed, the improvement in physical-mechanical properties caused by DPP is fully comparable (if not superior) to that caused by DAP, without apparent formation of K-containing efflorescence (Pasco et al., 2023), with the advantage that no ammonia is released into the atmosphere. Additional studies are in progress to ascertain this aspect.

6. Conclusions

Based on the results summarized above, phosphate treatments appear as highly promising not only for the conservation of heritage stones and mortars, but also of cementitious substrates. Thanks to CaP formation, significant increases in surface properties, bulk properties and durability have been reported, which can be exploited to extend the service life of existing concrete buildings (also belonging to cultural heritage) and new buildings and infrastructures. In the case of new cementitious materials, the development of self-healing ability has been achieved by incorporating hydrogel impregnated with a phosphate precursor into the mix. When the hardened cementitious matrix is cracked, the phosphate precursor is released and new calcium phosphates are formed, which can seal cracks and increase mechanical properties.
Phosphate solutions of diammonium hydrogen phosphate (DAP) have also been shown to have a lower global warming potential than alternative commercial treatments commonly used for monument conservation. This is mostly due to the aqueous solvent used for the phosphate treatments, in contrast to organic solvents used in most commercial products. The environmental impact of phosphate treatments is

mostly originated from the release of ammonia into the atmosphere, which is expected to be significantly reduced if phosphate precursors different from DAP (e.g. DPP and DSP) are used.

Acknowledgements

The author would like to thank all the colleagues and students that have worked on topics related to the present study, especially Prof. George W. Scherer, Prof. Elisa Franzoni, Dr. Sonia Naidu, Prof. Barbara Lothenbach, Dr. Hélène Pasco, Dr. Gabriela Graziani, Dr. Giulia Masi, Prof. Alessandro Dal Pozzo, Prof. Alessandro Tugnoli, M.Eng. Alessio Gabrielli, M.Eng. Chiara Valvano.

References

Dal Pozzo, A., Masi, G., Sassoni, E., Tugnoli, A. (2024) "Life cycle assessment of stone consolidants for conservation of cultural heritage", *Building and Environment* 249:111153

Gabrielli, A., Ugolotti, G., Masi, G., Sassoni, E. (2024) "Resistance of consolidated lime mortars to freeze–thaw and salt crystallization cycles by different accelerated durability tests", *Materials and Structures*, 57:70

Graziani, G., Sassoni, E., Franzoni, E., Scherer, G.W. (2016) "Hydroxyapatite coatings for marble protection: Optimization of calcite covering and acid resistance", *Applied Surface Science*, 368:241-257

Graziani, G., Sassoni, E., Scherer, G.W., Franzoni, E. (2017) "Resistance to simulated rain of hydroxyapatite- and calcium oxalate-based coatings for protection of marble against corrosion", *Corrosion Science* 127:168–174

Li, Q., Liu, Z., Chen, W., Yuan, B., Liu, X., Chen, W. (2019) "A novel bio-inspired bone-mimic self-healing cement paste based on hydroxyapatite formation", *Cement and Concrete Composites* 104:103357

Masi, G., et al. (2023) "Choosing the consolidant for carbonate substrates: Technical performance and environmental sustainability of selected inorganic and organic products", *Construction and Building Materials* 407:133599

Masi, G., Sassoni, E. (2021) "Air lime mortar consolidation by nanolimes and ammonium phosphate: Compatibility, effectiveness and durability", *Construction and Building Materials* 299:123999

Matteini, M., et al. (2011) "Ammonium phosphates as consolidating agents for carbonatic stone materials used in architecture and cultural heritage: Preliminary research", *Int. J. Archit. Herit.* 5:717–736

Naidu, S., Blair, J., Scherer, G.W. (2016) "Acid-resistant coatings on marble", *J. Am. Ceram. Soc.*, 99:3421–3428

Naidu, S., Scherer, G.W. (2014) "Nucleation, growth and evolution of calcium phosphate films on calcite", *J. Colloid Interface Sci*. 435:128–137

Pasco, H., Naidu, S., Lothenbach, B., Sassoni, E. (2023) "Enhancement of surface properties of cementitious materials by phosphate treatments", *Cement and Concrete Composites* 141:105124

Sassoni E. (2018) "Hydroxyapatite and Other Calcium Phosphates for the Conservation of Cultural Herit-age: A Review", *Materials* 11:557

Sassoni, E., Franzoni, E. (2020) Lime and cement mortar consolidation by ammonium phosphate. Con-struction and Building Materials 245:118409

Sassoni, E., Graziani, G., Franzoni, E. (2016) "An innovative phosphate-based consolidant for limestone. Part 2: Durability in comparison with ethyl silicate", *Construction and Building Materials*, 102:931-942

Sassoni, E., Graziani, G., Franzoni, E., Scherer, G.W. (2018) "Calcium phosphate coatings for marble conservation: influence of ethanol and isopropanol addition to the precipitation medium on the coating microstructure and performance", *Corrosion Science* 136:255–267

Sassoni, E., Naidu, S., Scherer, G.W. (2011) "The use of hydroxyapatite as a new inorganic consolidant for damaged carbonate stones", *Journal of Cultural Heritage*, 12:346-355

Turner, R. J.; Renshaw, J. C.; Hamilton, A. (2017) "Biogenic Hydroxyapatite: A New Material for the Preservation and Restoration of the Built Environment", *ACS Applied Materials and Interfaces*, 9:31401–31410

Turner, R. J. et al. (2021) "(Hydroxy)apatite on cement: insights into a new surface treatment", *Mater. Adv.*, 2:6356–6368

Yang, F., Zhang, B., Liu, Y., Wei, G., Zhang, H., Chen, W., Xu, Z. (2011) "Biomimic conservation of weathered calcareous stones by apatite". *New J. Chem*. 35:887–892

Zhao, H., et al. (2023) "A bio-inspired mineral precipitation method to improve the freeze-thaw resistance of cement concrete pavement", *Journal of Cleaner Production*, 419:138277

Does Carbon Footprint Reduction Impair Technical Performance of Concrete?

M. Serdar[1*], K. Ram[2], M. Flegar[3], A-D. Basic[4]

[1,2,3,4]Department of Materials, Faculty of Civil Engineering, University of Zagreb, Croatia
**marijana.serdar@grad.unizg.hr*

[*]Corresponding author

ABSTRACT

This paper considers how different interventions in concrete, aimed at reducing its environmental impact, affect the technical performance of concrete. Two case studies are briefly presented. In the first, two strategies to reduce the environmental impact were introduced into the concrete used for a newly built bridge on the Adriatic coast, and the impact of these strategies on the overall sustainability performance of the mix was assessed. The second case study presents the changes introduced by replacing part of the calcium aluminate cement with SCMs.

KEYWORDS: *CO_2, service life, Limestone calcined clay, Calcium aluminate cement*

1. Introduction

It is becoming increasingly clear that the (over)design of cement-based concrete elements to a certain compressive strength will be an undesirable practice in the future. There are various strategies to reduce the environmental impact of concrete, such as reducing the amount of concrete in an element, reducing the amount of cement in the concrete, reducing the amount of clinker in the cement, etc Schneider et al. (2023). While reducing the amount of clinker in cement is a very efficient strategy, any change in cement chemistry changes the technical performance of the material known and used by engineers. The question remains as to how far one can go in changing the concrete to still achieve the same or better technical performance required for construction. In addition, new durability challenges may arise when changing the cement chemistry.
In this paper, a brief overview is given of two case studies focusing on the development of different binders with lower environmental impact, using locally available materials as cement substitutes. Calcined clay cement, Ram et al. (2023), Flegar et al. (2023) and calcium aluminate cement, Skocibusic Pejic et al. (2024) are presented with their specific challenges in terms of performance.

2. Case study 1: Limestone-calcined clay (LC3) binder based on low kaolin clay

The aim of the study was to evaluate to what extent the changes in the concrete mix, which allow a reduction in the carbon footprint, affect the mechanical performance and durability of the concrete structure. The starting point of the benchmark was the concrete mix used in a recently constructed reinforced concrete Pelješac Bridge in the Adriatic Sea. The target strength and slump were 50 MPa and 80–120 mm respectively.

2.1 Material and methods

The bridge mix was designed using blended cement with slag addition, CEM II B–S, while the primary material for LC3 was Portland cement (CEM I 42.5R). Two clays from distinct sources were employed in the investigation, and both had a lower amount of kaolinite, 14% for CC1 and 18% for CC2. Fly ash was obtained from the Tuzla thermal power plant in Bosnia and Herzegovina. The fly ash and raw clay were dried for 24 h at 60 ± °C and ground for 30 s in a laboratory ball mill. Clays were calcined for an hour at 800 °C in a high-temperature laboratory furnace.

Two bridge mixes were prepared denoted BD435 and BD340. In BD435, the whole mix design was derived from the real mix (binder content, water/binder ratio, and aggregate amount), whereas in BD340, the binder content was reduced while maintaining the same water/binder ratio. In the first round of experiments the amount of cement in the initial bridge mix was significantly lowered, without jeopardising workability of the mix. In the second round, the main part of the cement was substituted with the combination of fly ash and limestone or calcined clay and limestone. Workability, compressive strength and chloride migration were used as performance indicators. Service life was calculated using measured chloride diffusion coefficient and environmental impact was calculated using inventory data of used materials. To allow comparison of the mixes, the overall performance of each mix was expressed using five-performance index (I5P) based on the study by Yu et al. (2021).

2.2 Results

The compressive strength of the mixes that satisfied the targeted compressive strength after 7 and 28 days is depicted in Figure 1 (a). Compressive strengths of BD435 and BD340 were comparable, and a 22% decrease in cement content had no discernible effect on compressive strength. It is visible that the fly ash-limestone mix (FALS40) is a promising alternative to the bridge mix (BD435), capable of achieving at least 80% strength when compared to BD435. Although the performance of the calcined clay mixtures were slightly lower than that of fly ash, compressive strength still exceeded 50 MPa at 28 days with a high level of cement replacement and despite the lower kaolinite content. In contrast to the compressive strength, the chloride penetration resistance of alternative binders was found to be dependent on the binder content and type of binder, Figure 1 (b). Among all the mixtures, BD435 demonstrated the highest resistance to chlorides. Clearly, the bridge mix exhibits the least penetration due to the presence of blast furnace slag in cement itself. When in both the system with 340 kg/m^3 and 300 kg/m^3 of cement, part of the cement was substituted with fly ash and limestone or calcined clay and limestone, a significant improvement in chloride resistance was achieved.

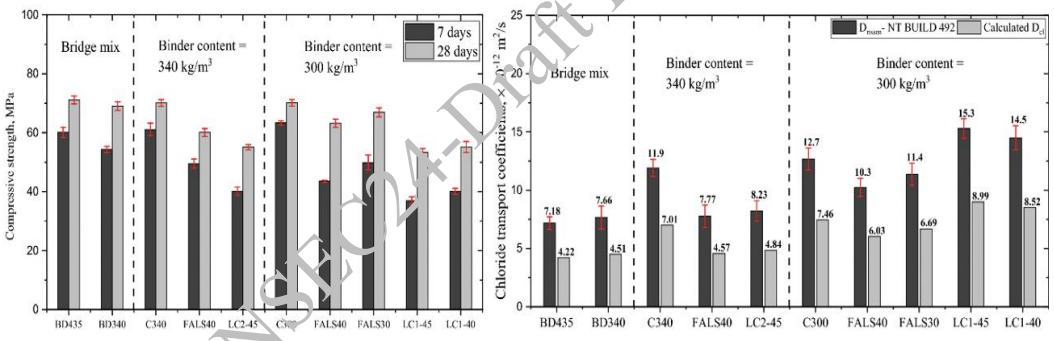

Figure 1. Compressive strength after 7 and 28 days (left) and chloride migration and diffusion coefficient (rigth) of all tested mixes

In the Figure 2, the individual indices of BD435 (the original bridge mix design), and mixes with lower cement content (BD340, C340, and C300) are shown. From this first image it is visible that by just lowering cement content, higher indices connected to environmental impact can be achieved. However, there is a tipping point, at which the mix is increasing the indices connected to environmental impact, but at the same time sacrificing service life. In the case of alternative binders with a total binder content of 340 kg/m^3, Figure 2 (b), the significant reduction in the cement content and at the same time better durability (service life) was possible, leading to similar mechanical and service life indices and higher environmental indices. Finally, when considering mixes with a total binder content of 300 kg/m^3, Figure 2 (c), compared to the original bridge mix design, it is evident that a limit in performance was reached. While alternative mixes do reach significantly higher environmental impact indices, the performance (mechanical and durability) are impaired.

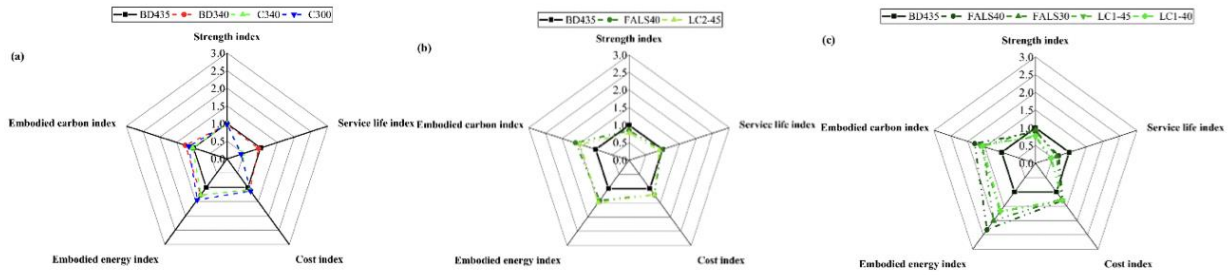

Figure 2. Comparison of individual indices of all mixes a BD435 versus control mixes with lowering cement content (a), BD435 versus alternative binder content = 340 kg/m^3 (b), and BD435 versus alternative binder content = 300 kg/m^3 (c)

3. Case study 2: Calcium-aluminate cement (CAC) with slag/calcined clay substitution

The focus of this case study was to evaluate whether calcined clay can be used instead of slag in combination with CAC, to lower ecological impact of CAC, while at the same time controlling the conversion process. Since conversion process can be accelerated by curing at elevated temperatures (Adams et al. (2018)), compressive strength development was evaluated over 56 days of curing at 20°C and 38°C.

3.1 Materials and methods

The studied samples were produced using calcium aluminate cement with 52.67% of Al_2O_3 produced by Calucem company from Pula, Croatia. Specific surface area of used cement was 4000 cm^2/g. Slag used in this study was received industrially milled with Blaine size 4580 cm^2/g, while clay was received as raw material without prior processing. Prior to mixing, clay was first dried for 24h at 60°C to remove the moisture, then ground (for 90 s) to Blaine size of 5930 cm^2/g, and at the end calcined at 850 °C for one hour. According to the mass loss (%) from 350 – 600 °C, calcined clay had 40% kaolinite/illite. To access conversion process of CAC cement, a reference mixture (labelled CAC100), one mixture with 30 % replacement of CAC by slag (labelled CAC70S30), and one mixture with 30 % replacement of CAC by calcined clay (labelled CAC70C30) were prepared. Compressive strength was monitored over a period of 56 days. To access conversion process one set of samples was cured in water bath at 20 °C, and one set in water bath at 38 °C.

3.2 Results

Development of compressive strength over 56 days for samples cured at 20°C and 38°C is shown in Figure 3 a) and b), respectively. During curing at 20°C, the mixture with slag exhibited a lower initial compressive strength. However, at the end of the measurements, after 56 days of curing, the compressive strength was higher than that of the reference mixture. When cured at 20°C, the mixture with calcined clay exhibited lower compressive strength than the reference mixture throughout the test period. Once cured at 38°C, the compressive strength of reference CAC mix started to decrease after five days of curing, indicating the occurrence of the conversion process. By prolonged curing, rate of conversion process started to increase, and compressive strength started to decrease rapidly. After 28 days of curing, compressive strength of CAC mixture reached the lowest value, implying that the conversion process was completed. On the contrary, once cured at 38°C, both mixes with slag and calcined clay during prolonged curing exhibited a continuous increase in compressive strength compared to the initial values.
From the results it is evident that the addition of calcined clay to CAC slightly reduced overall compressive strength, however a decrease in compressive strength was avoided when cured at higher curing temperature, making this mix the most stable.

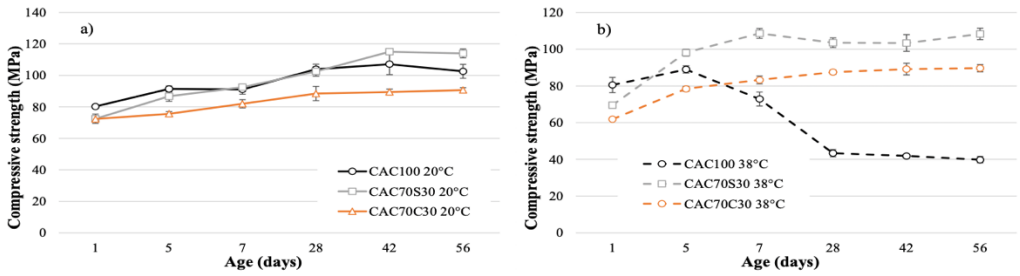

Figure 3. Development of compressive strength over 56 days for samples cured at: a) 20°C, b) 38°C

4. Conclusions

Two case studies presented show that significant environmental savings can be achieved through changes in the design of concrete without compromising the technical properties of concrete. The first case study showed how far we can reduce the cement and clinker content without compromising the required technical performance of the concrete. It was shown where the limit for lowering the cement content lies and that this limit can be extended even further by introducing SCMs. Furthermore, it was shown that even locally available SCMs with lower kaolin content can provide concrete with satisfactory technical properties. The second case study showed how the addition of SCMs to calcium aluminate cement results in lower initial compressive strength,but allows stable compressive strength during curing at higher temperatures, i.e. prevents the conversion process. Both studies clearly show that the optimization of the overall binder content and the use of alternative binders (especially those that are locally available) are crucial factors in ensuring the overall sustainability of concrete.

Acknowledgements

Correlation between the microstructure and properties of binders is part of a scientific project “Alternative binders for concrete: understanding the microstructure to predict durability, ABC" (UIP-05-2017-4767), funded by Croatian Science Foundation. The development of LC3 binders was part of a scientific project “Advanced low CO_2 cementitious materials”, ACT (grant no. IZHRZO 180590/1), financed within the Croatian–Swiss Research Program of the Croatian Science Foundation and the Swiss National Science Foundation with funds obtained from the Swiss-Croatian Cooperation Program. The development of CAC with the addition of SCMs was part of a scientific project “Development of a new innovative ECO2Flex product” (KK.01.2.1.02.0034)”, funded by European Union, European Regional Development Fund.

References

Adams, M.P., Lute, R.D., Moffatt, E.G., Ideker, J.H (2018) “Evaluation of a Procedure for Determining the Converted Strength of Calcium Aluminate Cement Concrete” *Journal of Testing and Evaluation* 46, 4, 1659-1672.

Flegar, M., Ram,K., Serdar, M., Bosnar, K., Scrivener, K (2023) “Durability Challenges of Low-Grade Calcined Clay Opposed to High-Volume Fly Ash in General Purpose Concrete”, *Advances in civil engineering materials*, 12, 1; 237-250.

Ram, K., Serdar, M., Londono-Zuluaga, D., Scrivener, K (2023) “Does carbon footprint reduction impair mechanical properties and service life of concrete?”, *Materials and structures*, 56, 6; 6, 16.

Schneider, M., Hoenig, V. Ruppert, J., Rickert, J (2023) “The cement plant of tomorrow”, *Cement and Concrete Research*, Volume 173, 2023, 107290, ISSN 0008-8846,

Skočibušić Pejić, J.; Bašić, A.-D.; Grubor, M.; Serdar, M (2024) “Link between the Reactivity of Slag and the Strength Development of Calcium Aluminate Cement”, *Materials*, 17, 3551.

Yu J, Mishra DK, Hu C, Leung CKY, Shah SP (2021) “Mechanical, environmental and economic performance of sustainable grade 45 concrete with ultrahigh-volume limestone-calcined clay (LCC)”, *Resour Conserv Recycl.* Volume 175, 105846.

Enhancing the Performance and Durability of Cementitious Materials through Nanotechnology

Aarti Solanki[1], U. Sharma[2], D. Ali[3], L.P. Singh[4*]

[1]Academy of Scientific and Innovative Research (AcSIR), Ghaziabad, India,
Email: solanki.cbri@gmail.com
[2]CSIR- Central Building Research Institute, Roorkee - 247667, India
Email: purohitusa41@gmail.com
[3]CSIR- Central Building Research Institute, Roorkee - 247667, India
Email: dilshadali1990@gmail.com
[4]National Council for Cement and Building Materials, Ballabgarh, India,
Email: dg@ncbindia.com

[*]Corresponding author

ABSTRACT

This paper presents a systematic hydration study on pure phases of Portland cement, i.e., tricalcium aluminate (C_3A) and tricalcium silicate (C_3S) with or without incorporation of nano-silica (n-SiO_2) to understand the effect of n-SiO_2 on hydration mechanism during early age of hydration. Further, compressive strength and durability studies were performed on concrete to understand the impact of micro level changes to macroscale properties. The results show that nSiO_2 initially accelerates the hydration kinetics of C_3A, however, after 10 min of hydration, it shows retarding effect due to the formation of hydrated gel like products. While with C_3S, a significant acceleration was observed, and it was also observed that nSiO_2 modified the calcium silicate hydrate packing density and enhanced the formation of HD C-S-H during early age of hydration. Due to the formation of HD C-S-H, the compressive strength of concrete samples was found to be higher during age of hydration and 28 days strength achieve within 3 to 14 days of curing. Further, durability studies on sulphate attack show that in nSiO_2 incorporated concrete samples show 40% reduction in sulphate attack as compared to concrete samples. Therefore, nSiO_2 incorporated nano-engineered concrete show higher early age strength and longer durability due to the formation of more compact C-S-H gel.

1. Introduction

The construction industry continuously seeks innovative methods to enhance the performance and durability of cementitious materials, which are foundational to modern infrastructure. As global demands for sustainable and resilient construction materials increase, the focus has shifted toward advanced technologies capable of improving the inherent properties of cement and concrete. Among these, nanotechnology has emerged as a promising approach to address the limitations of traditional cementitious systems (Sobolev K et al. (2005), Metaxa ZS et al.(2013), Singh L.P et al. (2012 a), Singh L.P et al. (2012 a)). Nanotechnology, characterized by the manipulation and application of materials at the nanoscale, has demonstrated significant potential in enhancing the mechanical properties, durability, and sustainability of cement-based materials. The incorporation of nanomaterials, such as nano-silica (n-SiO_2), nano-titanium dioxide (n-TiO_2), and nano-alumina (n-Al_2O_3), into cementitious systems has been shown to modify the hydration process, refine the microstructure, and improve the overall performance of concrete (Nicoleau L and Nonat (2016), Quennoz A et al. (2013), Singh L.P, Bhattacharyya SK et al. (2015), Joseph S et al. (2019), A. Quennoz and K. Scrivener (2012)).

Extensive research has highlighted the benefits of n-SiO_2 as a supplementary material in cement. Studies have demonstrated that n-SiO_2 accelerates the early hydration of silicate phases, such as tricalcium silicate (C_3S) and dicalcium silicate (C_2S), leading to a denser microstructure and enhanced mechanical strength. Additionally, the use of n-SiO_2 has been linked to improved durability by mitigating the effects of harmful chemical reactions, such as sulfate attack, which are critical concerns in the longevity of concrete structures

(Corstanje, W.A et al. (1973), J. Pommersheim (1986)). This paper aims to explore the role of nanotechnology in enhancing the performance and durability of cementitious materials. By reviewing current research and advancements, the study will provide insights into the mechanisms by which nanomaterials improve the properties of cement and concrete. Present study examines how the incorporation of n-SiO_2 affects the morphology of hydrated products during the hydration of C_3A, with a focus on its implications for the durability of the cementitious system.

2. Materials and methods

2.1 Materials

C_3A and C_3S were prepared in the laboratory using the high-temperature solid-state reaction method. Calcium carbonate ($CaCO_3$) and aluminum oxide (Al_2O_3) were mixed in a stoichiometric ratio of 3:1 for C_3A and calcium carbonate and quart (SiO_2) were mixed in same stoichiometric ratio for C_3S, and these mixes were blended for 1 h to ensure homogeneity (Mondal P. and Jeffery J.W.(1975)). The blends were first heated to 1000°C at a rate of 10°C/min for 5 h to decarbonate, then further heated to 1500°C at 5°C/min and cured for 12 h. The developed clinkers were ground in a ball mill with isopropanol as a dispersing agent and then dried at 40°C. Nano-silica was synthesized in the laboratory using the sol-gel method. Water glass was used as the silica precursor, and cetrimonium bromide (CTAB) served as a dispersing agent, with hydrochloric acid (HCl) as the catalyst (Singh, L.P, Agarwal et al. (2011)). Ordinary Portland cement (OPC-43 grade) with Blain fineness of 390m^2/kg confirm IS 8112:1989 (IS-8112:1989, 1989) and class F type with surface area 252 m^2/kg confirming IS 3812 (part 2): 2003 (IS-3812, 2013) was used in the concrete studies. For casting the concrete specimens, river sand with a fineness modulus of 2.72 and specific gravity 2.57 was used as fine aggregates. While angular crushed siliceous aggregates having maximum size ~12.5 mm were used as a coarse aggregate having specific gravity 2.62 and fineness modulus 7.34. The aggregates were found to be satisfying the specifications of IS: 383:1970 (IS-383, 1970). Fourth generation superplasticizer (SP) polycarboxylic ether (Glenium 51 of BASF, India) was used to achieve the desired workability of concrete confirming to IS 9130:1999 (IS-9130-1999).

2.2 Sample preparation

For hydration study with pure phases of Portland cement nano-silica were first mixed with C_3S or C_3A in dry form to make a homogenous blend and then water is added to the mixture using a w/b ratio 0.4. Hydration process was stopped at different time intervals using iso propanol. After treatment with isopropanol, the sample were dried at 50°C for 12 hours and stored in a vacuum desiccator to minimize carbonation until further analysis. Further, M20, M30 and M40 grade concrete mixes were made with the help of IS-10262:2009; these mixes were designed for normal strength concrete (M20, M30 and M40 grade). The details of the mixes are given in Table 1.

Table 1. Mix proportion for different grade concrete

Constituents	M20		M30				M40		M60	
	Control	C+nSiO_2	Control		C+nSiO_2		Control	C+nSiO_2	Control	C+nSiO_2
Cement (kg)	360	360	390		390		445	445	470	470
Fine aggregates (kg)	540	540	682.2		682.2		706	706	687.7	687.7
Coarse aggregates	(20mm)		20 mm	10 mm	20 mm	10 mm	>20mm		10mm	
	1080	1080	819	351	819	1160	1160	1160	1278	1278
SNPs (%)	-	3	-		3		-	3	-	3
Water (lt)	198	198	163.8		163.8		169.1	169.1	136.7	136.7

The Indian code only could make up to M40 grade concrete. Hence, for the design of M60 grade concrete, a method suggested by Sobolev et al. (2004) was used. According to IS 10086:1982, 100x100x100 mm size cubes were cast for the testing of compressive strength. The prism specimens of size 100x100x500 mm were cast for sulphate attack and carbonation test as per ASTM C1012, 2015 and RILEM CPC-18.

3. Experimental techniques

Powder X-ray Diffraction (XRD) with Cu-Kα radiation (λ = 1.54 Å) was used to analyse the hydrated phases, with scanning parameters set at 0.02° steps and a 2θ range of 5° to 80° at 0.5°/min. Fourier Transform Infrared Spectroscopy (FTIR) examined the chemical bonding in the hydrated phases. Thermogravimetric Analysis (TGA/DTG) was conducted from room temperature to 980°C at a heating rate of 10°C/min under a nitrogen atmosphere. Morphological changes were observed using Field Emission Scanning Electron Microscopy (FESEM) at 20–30 kV. Hydrated samples were gold-coated for improved conductivity, and elemental analysis was performed with an Energy Dispersive X-ray (EDX) detector. The compressive, tensile and flexural strength test was carried out using Universal Testing Machine (UTM) (make: Shimadzu, model: UH-1000knI) of capacity 1000 KN at loading rate 0.5mm/min was used with ±1% potential error. All experiments were conducted at room temperature, with precautions taken to prevent carbonation.

4. Results and discussion

4.1 Hydration studies on C_3A

X-Ray Diffraction is a well-known instrumentation technique for the analysis of cement-based materials. Diffraction pattern of hydrated tricalcium aluminate at different time intervals (10 min, 1 h, 6 h, 24 h, 2 days, and 10 days) with and without n-SiO_2 is presented in Fig. 1.

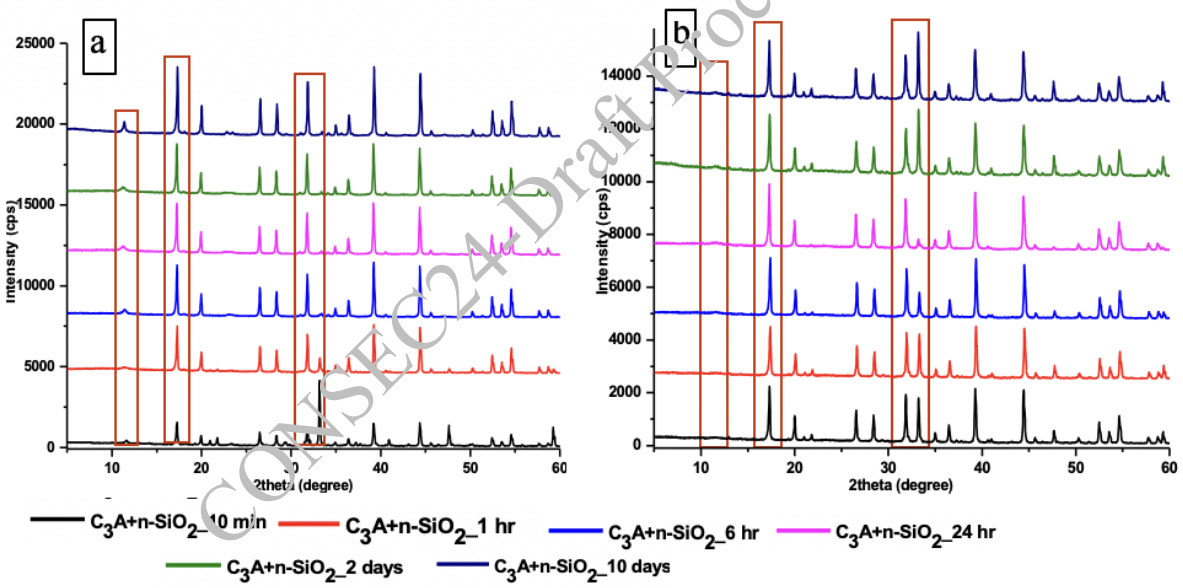

Figure 1. XRD pattern of hydrated tricalcium aluminate at different time intervals (a) in absence of silica nanoparticles, (b) and in presence of silica nanoparticles.

In hydrated C_3A samples, it was observed that the intensity of characteristic diffraction peak of unhydrated C_3A (2θ ~33°) decreased gradually as the hydration proceed and completely disappeared at 6 h of hydration showing continual C_3A hydration (Fig. 1a). As the hydration period increases, increment in diffraction peak intensity at 2θ ~17° and ~11° was observed showing the formation of katoite along with hydroxy-AFm phases, respectively [Zheng, D. Monasterio et al. (2021)]. While, in n-SiO_2 incorporated C_3A samples, an intense peak of unhydrated C_3A is observed at 6 h of hydration, which indicates retardation in C_3A hydration in presence of n-SiO_2. In addition to this, no diffraction peak was observed at 2θ ~11° showing hindrance in formation of hydroxy-AFm phases in the presence of n-SiO_2. Less intense diffraction peak of katoite was observed than without n-SiO_2 incorporated C_3A samples shows lesser katoite formation in presence of n-SiO_2. (Fig. 1b). In TGA analysis, it was observed that at 10 min of hydration, the endothermal peak of

katoite was more intense in n-SiO_2 incorporated C_3A samples compared to the control. However, after 1 h, the control samples exhibited a stronger katoite peak, a pattern that persisted up to 24 h. (Fig. 2).

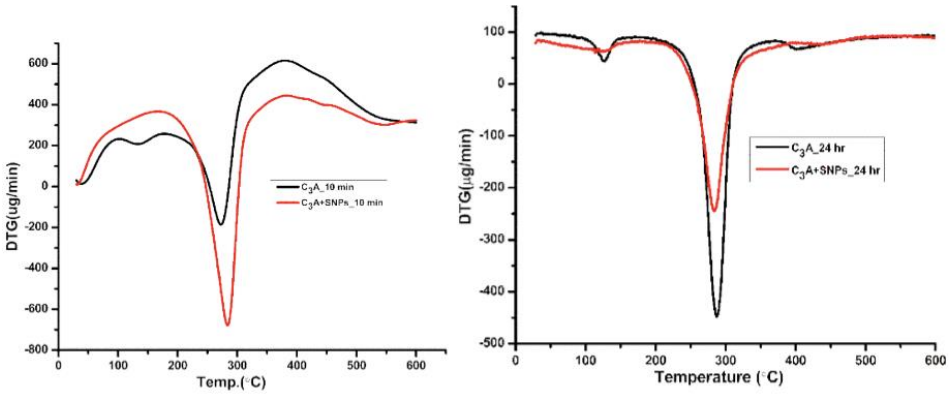

Figure 2. TGA pattern of hydrated tricalcium aluminate with and without incorporation of nano-silica.

FTIR results show that in hydrated C_3A, a strong peak at ~525 cm^{-1} and a broad peak at 790 cm^{-1}, indicating katoite was observed (Fig. 3). While, in n-SiO_2 incorporated C_3A samples, multiple peaks appear between 400-1250 cm^{-1}, showing the presence of C-S-H and C-A-S-H [Wells L.S. and Carlson E.T. (1956), H.F.W. Taylor (1997), Solanki A et al. (2021)]. Further, FESEM analysis reveals distinct microstructural changes in hydrated C_3A with and without n-SiO_2, impacting the durability of the cementitious system. Initially, C_3A without n-SiO_2 shows hexagonal-flake-like h-AFm phases, which gradually transform into stable polyhedral katoite crystals, indicating increased durability [Breval E. (1976)]. In contrast, C_3A with n-SiO_2 shows gel-like C-S-H/C-A-S-H products forming early, with fewer hexagonal phases and increased gel content over time (Fig. 4). This shift suggests that n-SiO_2 promotes the formation of durable C-S-H/C-A-S-H phases while reducing less stable katoite, enhancing the system's long-term durability [Solanki A et al, (2022)].

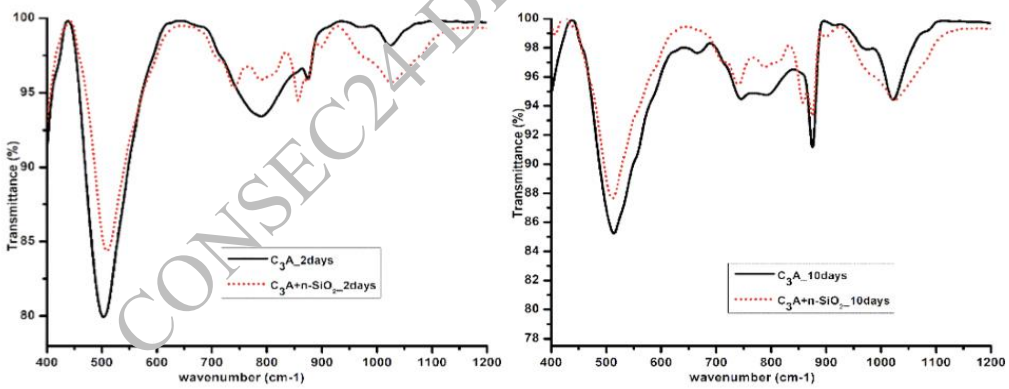

Figure 3. FTIR pattern of hydrated tricalcium aluminate with and without incorporation of Nano-silica

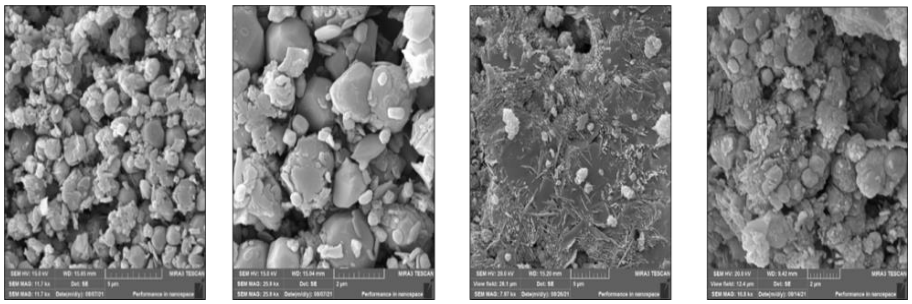

Figure 4. FESEM micrograph of hydrated C_3A (a & b) and n-SiO_2 incorporated C_3A samples (c & d) at 10 days of hydration

4.2 Hydration studies on C_3S

SNPs also show nucleation effect other than its well-known pozzolanic effect. Quantification of hydrated products from TGA curve show that the rate of products formation increases rapidly in presence of SNPs during acceleration period of hydration. Figure 4. shows that with SNPs, hydration reaction is accelerated maximum at 8 h, when the growth of CH and C-S-H is higher than the control. While at 24 h of hydration, ~43% additional C-S-H is formed and ~38% reduction is found in the content of CH showing its pozzolanic effect. Further, it was also found that the CH content formed in SNPs incorporated samples on complete hydration is 50% lower (0.57 moles) than the control, which is 1.5 times of SNPs content (Fig. 5).

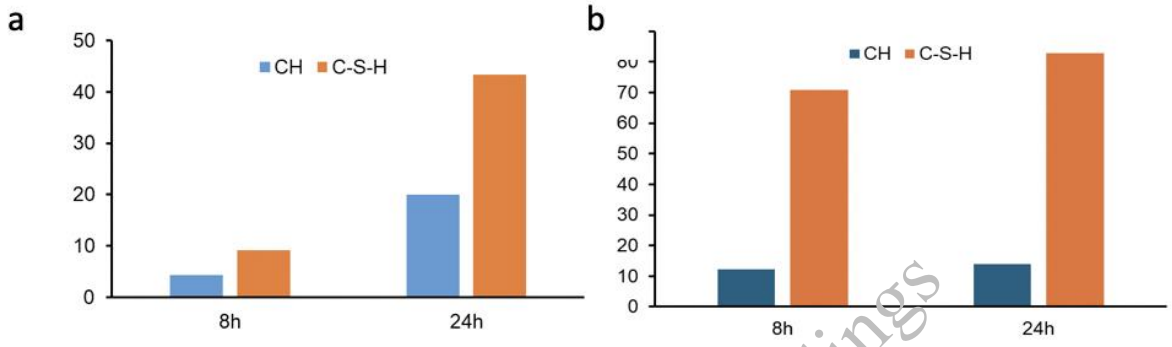

Figure 5. Percentage of C-S-H and CH formed during hydration of C_3S and SNPs incorporated C_3S samples at different time intervals

In Fig. 6, the statistical histogram plots of the Young's modulus results, fitted with 4 Gaussian distribution curves are presented for control and SNPs incorporated C_3S samples at 15 and 24 h, respectively.

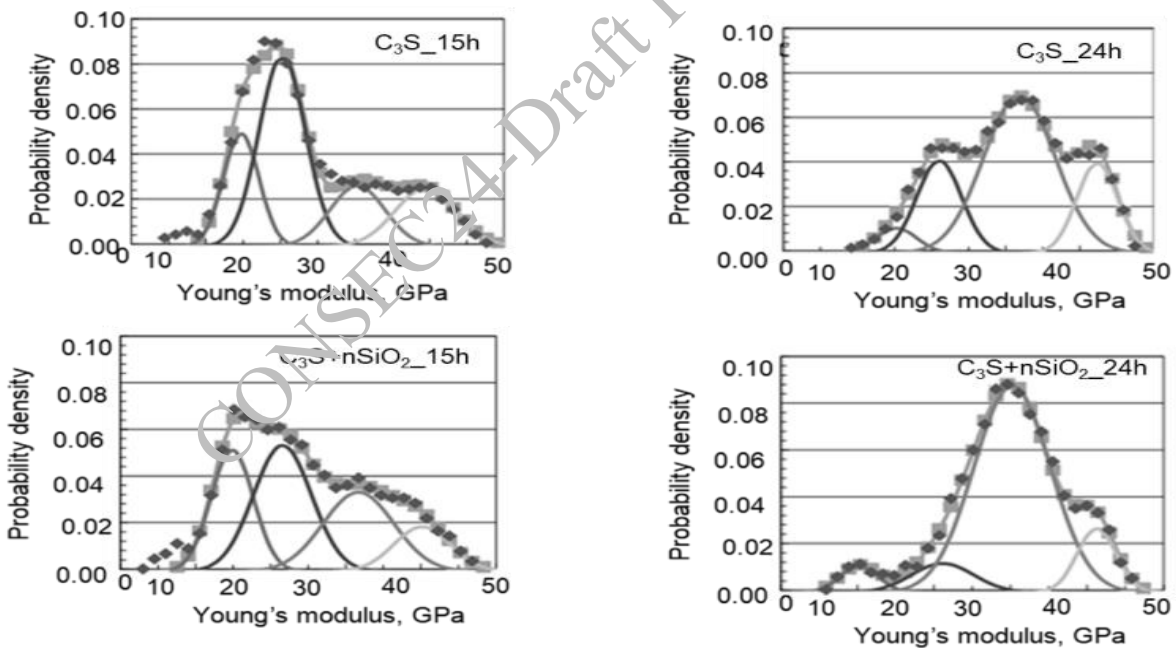

Figure 6. Young's modulus histogram plots (E< 50 GPa) with 4 Gaussian curves fitted, each representing one of the main hydrate phases.

For low density (2nd peak from the left) and high density C-S-H (3rd peak from the left), Young's modulus values of ELD C-S-H ~22 GPa and EHD C-S-H ~30 GPa, respectively were determined from the deconvolution of the statistical nanoindentation data. Early age cementitious paste for all phase distribution plots (Fig. 7) show large quantities of loose-packed (LP C-S-H) and low density C-S-H (LD C-S-H). In general, with progress of hydration a shift from the lower qualities of C-S-H to higher qualities of high density C-S-H (HD C-S-H) was noticeable. Regarding C_3S pastes with SNPs addition, the nanoindentation

results on such systems show in comparison to their reference materials higher quantities of HD C-S-H. At the same time the contents of loose-packed C-S-H and LD C-S-H were found to be significantly smaller.

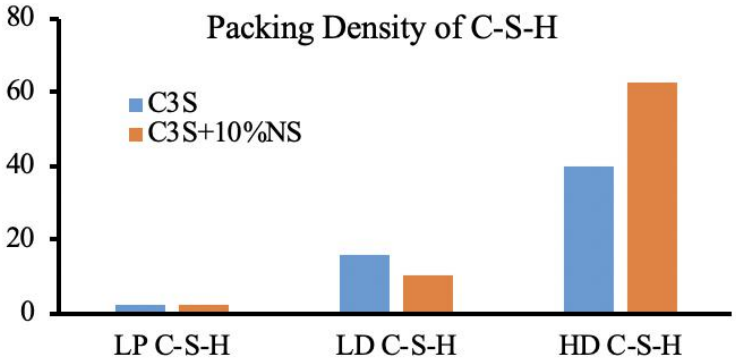

Figure 7. Phase contents plots for all pastes, relative phase content of the C-S-H

4.3 Studies on concrete

Compressive strength results show that incorporation of nano-silica enhance the early age mechanical properties significantly. The results show that with the incorporation of $nSiO_2$, 28 days strength can be achieved between 3 to 14 days of water curing and this phenomenon occur due the formation of additional C-S-H in the presence of $nSiO_2$ (Fig. 8). Sulphate attack in the prism specimens (100 × 100 × 500 mm) was investigated as per ASTM C1012. After 7 days of water curing, the prism specimens were placed in the sulphate solution, containing 5% magnesium sulphate at room temperature and at a pH range of 6.0-8.0 was maintained throughout the period of exposure. For determining sulphate ion concentration, split slice (50 x 100 x 100 mm) from the prism was used and tested at 28, 90 and 180 days of exposure. The chemical analysis determined the sulphate ion concentration as per IS 4032: 1985. Backscattered electron (BSE) images and elemental colour mapping of 30FA and 30FA3SNPs mixes are shown in Fig. 9 (a & b).

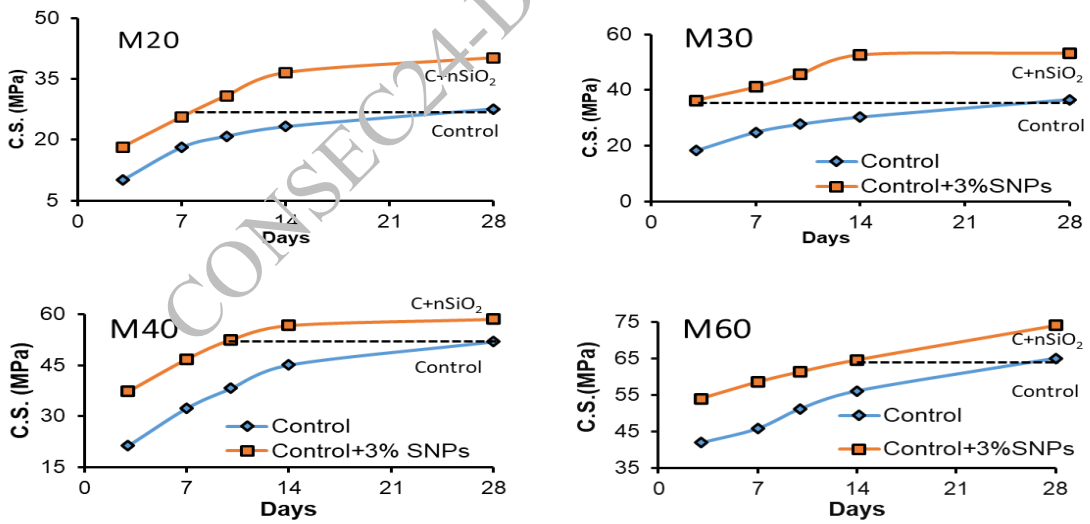

Figure 8. Compressive strength of different grade concrete with or without incorporation of nano-silica

It is a very useful technique to analyse the hydration products, and it gives the perfect information of the interfacial transition zone (ITZ) in the concrete microstructure. The hydration products can be recognized because of the descending brightness of hydrated and unhydrated cement particles in the concrete system. In BSE image, the dark black part considers as voids and damages, whereas the light grey part to dark grey part can be recognized as the hydration products, i.e. CH and C-S-H. The BSE image of 30FA mix after 365 days of exposure in sulphate solution clearly shows that the black pits near the ITZ in 30FA mix are demonstrating the destruction due to the sulphate attack which is destroying the ITZ and can clearly see the breaking of the hydration product near ITZ (Fig. 9a). The colour mapping is also supporting the BSE image,

in which it is cleared that the concentration of sulphate is more visible in the black pits, which shows that the pits are being formed due to sulphate attack, while the SNPs sample has a lot of dense microstructures as compared to the control sample (Fig. 9 b).

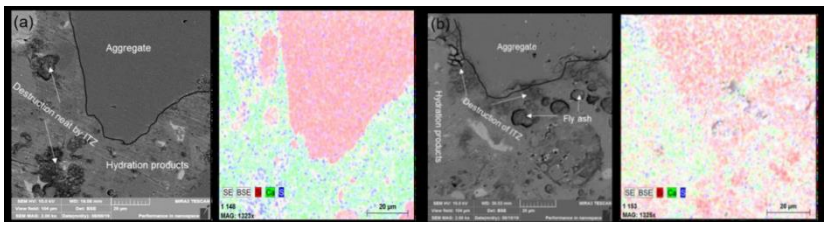

Figure 9. BSE images with colour mapping of fly ash concrete specimens (a) 30FA sample and (b) 30FA3SNPs sample

5. Conclusions

In the present study, the effect of n-SiO_2 on C_3A hydration was studied through XRD, FTIR, TGA and FESEM. The following conclusions can be drawn:

1. Nano-silica's Effect on Hydration Phases: Nano-silica retards the formation of hexagonal flakes and crystals (hydroxy-AFm) and cubical-katoite, promoting instead the formation of polyhedron-katoite and gel-like hydrated products (C-S-H/C-A-S-H).
2. Nano-silica accelerate the hydration kinetics of C_3S and modify the packing density of C-S-H gel during early age of hydration.
3. Nano-silica incorporated concrete show higher early age strength more resistance to sulphate attack as compare to control samples.

The incorporation of n-SiO_2 in cementitious systems promotes the formation of durable phases like Si-hydrogarnet, C-S-H, and C-A-S-H, enhancing resistance to sulphate and improving mechanical strength. This makes n-SiO_2 a valuable additive for enhancing the performance and durability of cementitious materials.

Acknowledgment

Authors, Aarti Solanki and Usha Sharma are thankful to UGC, New Delhi and CSIR, New Delhi, for financial support.

References

A. Quennoz, K. Scrivener (2012), "Hydration of C_3A–gypsum systems", *Cem. Concr. Res.* 42 1032–1041.

Breval, E., (1976) "C_3A hydration", *Cement and Concrete Research"*, 6(1), 129-137.

Corstanje, W.A., Stein, H.N. and Stevels, J.M., (1973) "Hydration reactions in pastes C_3S + C_3A+ $CaSO_4$.2aq + H_2O at 25° C", *Cement and Concrete Research*, 3(6), 791-806.

H.F.W. Taylor (1997), *Cement Chemistry*, 2nd Edition. Thomas Telford, London.

J. Pommersheim (1986) "Kinetics of hydration of tricalcium aluminate", Cem. Concr. Res., 16 440–450.

Joseph, S., Skibsted, J. and Cizer, Ö., (2019) "A quantitative study of the C_3A hydration", *Cement and Concrete Research*, 115, 145-159.

Metaxa ZS, Konsta-Gdoutos MS, Shah SP (2013) "Carbon nanofiber cementitious composites: effect of debulking procedure on dispersion and reinforcing efficiency", *Cem Concr Compos*, 36:25–32.

Mondal, P. and Jeffery, J.W., (1975) "The crystal structure of tricalcium aluminate, $Ca_3Al_2O_6$", *Acta Crystallographica Section B: Structural Crystallography and Crystal Chemistry*, 31(3), 689-697.

Nicoleau L, Nonat A (2016) "A new view on the kinetics of tricalcium silicate hydration", *Cem Concr Res*., 86:1–11

Quennoz A, Scrivener K., (2013) "Interactions between alite and C3A-gypsum hydrations in model cement", *Cem Concr Res.*, 44:46–54.

Singh L.P, Bhattacharyya SK, Ahalawat S (2012) "Preparation of size controlled silica nano particles and its functional role in cementitious system", *J Adv Concr Technol*, 10:345–52.

Singh L.P, Bhattacharyya SK, Mishra G, Ahalawat S (2012) "Reduction of calcium leaching in cement hydration process using nanomaterials", *Mater Technol*, 27:233–8.

Singh L.P, Bhattacharyya SK, Shah SP, Mishra G, Ahalawat S, Sharma U (2015) "Studies on early stage hydration of tricalcium silicate incorporating silica nanoparticles: part I", *Constr Build Mater*.;74:278–86.

Singh, L.P., Agarwal, S.K., Bhattacharyya, S.K., Sharma, U. and Ahalawat, S., (2011) "Preparation of silica nanoparticles and its beneficial role in cementitious materials", *Nanomaterials and Nanotechnology*, 1, 9.

Sobolev K, Gutierrez MF (2005) "How nanotechnology can change the concrete world: part 2", *Am Ceram Soc Bull*;84(11):16–9.

Sobolev, K., (2004) "The development of a new method for the proportioning of high-performance concrete mixtures", *Cem. Concr. Compos*., 26, 901–907.

Solanki, A., Singh, L.P., Karade, S.R. and Sharma, U., (2021) "Functionality of silica nanoparticles on hydration mechanism and microstructure of tricalcium aluminate", *Construction and Building Materials*, 299, 124238.

Solanki, A., Singh, L.P., Karade, S.R. and Sharma, U., (2022) "Mineralogy of tricalcium aluminate hydration with silica nanoparticles", *Construction and Building Materials*, 340, 127707.

Wells, L.S. and Carlson, E.T., (1956) "Hydration of Aluminous Cements and Its Relation to the Phase Equilibria in the System Lime-Alumina-Water", *Journal of Research of the National Bureau of Standards*, 57(6).

Zheng, D., Monasterio, M., Feng, W., Tang, W., Cui, H. and Dong, Z., (2021) "Hydration Characteristics of tricalcium aluminate in the presence of nano-silic", *Nanomaterials,* 11(1), 199.

Strategies to Induce Sustainability in Rigid Pavements Through Recycling of Concrete Waste — IITM Experience

S. Singh[1]* and R. Gettu[2]

[1]Assistant Professor, Department of Civil Engineering, Indian Institute of Technology Madras, Chennai, Tamil Nadu, India
Email: surender@civil.iitm.ac.in
[2]V.S. Raju Chair Professor, Department of Civil Engineering, Indian Institute of Technology Madras, Chennai, Tamil Nadu, India
Email: gettu@iitm.ac.in

*Corresponding author

ABSTRACT

Using recycled materials such as recycled concrete aggregates (RCA) extracted from waste concrete has always been regarded as a means of induced sustainability in concrete structures, especially rigid/concrete pavements. However, sustainability indicators such as embodied energy and carbon dioxide emissions could depend on numerous factors such as recycling plant location, comminution type, quality of RCA which again depends on various conditions, paving mixture type and its quality, and most importantly the dimensions of pavement stretch made with such materials for different traffic and loading conditions. Existing valorization techniques to address the negative effects of adhered mortar in RCA are either energy-intensive or not large-scale implementable and therefore, not sustainable. This paper highlights the work carried out at the Indian Institute of Technology Madras, Chennai with an aim to induce sustainability in the highway sector through the use of RCA.

KEYWORDS: *Recycled Aggregates, Concrete Pavements, Valorization, Crushing Method, Solar Energy*

1. Introduction

Recycled Concrete Aggregates (RCA) extracted from waste concrete debris have been identified as a suitable alternative to natural stones and sands for concrete manufacturing. However, RCA cannot be used to completely substitute the natural materials in structural elements owing to the inferior physical and mechanical characteristics imparted by the low-density porous adhered mortar (AM) present around its periphery. In addition to increasing the porosity of aggregates, AM could lower the surface roughness of aggregates by around 35% (Pal and Singh (2024)); rough textured aggregate forms better mechanical interlocking with the cement mortar phase resulting in higher strength. Since the AM content is inversely proportional to RCA size, the suitability of finer fractions for concrete production is lower compared to coarse RCA. The AM content in RCA could be a function of numerous other parameters such as parent concrete grade and its composition, crushing energy, parent rock mineralogy, and preprocessing/beneficiation methods, etc. (Pal and Singh (2024)). For example, multiple crushing of RCA leads to a lowering of the AM; similarly, heating the waste concrete at around 450°C followed by ball-milling could result in the complete removal of the AM (Prajapati et al. (2021)). The AM could also be completely removed by adopting chemical methods such as immersion in an acidic solution followed by abrasion. However, these valorization techniques are neither large-scale implementable nor sustainable. The latest approaches to enhance the RCA quality include strengthening the AM rather than its removal. These techniques aim to fill the micro-pores and cracks in the AM as well as bond enhancement with the parent rock. Strengthening approaches focus on three aspects viz. secondary hydration of the chemical constituents such as the conversion of Portlandite to calcium silicate hydrate or to calcium carbonate, hydration of unhydrated cement particles, and surface modifications (Yang et al. (2023)). Slurry

impregnation and artificial carbonation are the most popular AM strengthening methods. However, these methods are again not large-scale implementable and storing the liquid CO2 is energy intensive.
Field-scale inapplicability and high-energy demand are the two drawbacks associated with most of the beneficiation techniques resulting in lowering the suitability of RCA for structural applications. Structures especially rigid pavements made with untreated RCA are non-sustainable compared to paving slabs made with natural materials. This is due to the increase in the slab thickness owing to reduced mechanical properties on account of the incorporation of RCA; inclusions of RCA have been found to reduce the modulus of rupture by ~25% resulting in an increase of slab thickness by ~16% compared to slabs made with natural stones and sand (Pal (2024)). Even for low-volume roads, where the slab strength requirement is lesser, the use of 100% RCA could increase the cement demand by 16-34% leading to a significant increase in carbon emissions and embodied energy (Pal (2024)). Therefore, unless the RCA is treated, efforts to induce sustainability in rigid pavements through the use of recycled aggregates might not be beneficial. This paper highlights the technologies and strategies developed at the Indian Institute of Technology Madras (IITM) to induce sustainability in rigid pavements.

2. Strategies Developed at IITM

RCA enhancement techniques could be classified under three heads viz. recycling process optimization where the crushing operations are optimized (Pal and Singh (2024)), concrete mix optimization wherein the inferiority imparted by AM is addressed by adjusting the mixture proportion *(Selvam et al. (2023))*, and beneficiation technique which either deals with AM strengthening (Kosuri et al. (2023)) or its removal from the aggregate surface (Prajapati et al. (2021)).

2.1 Recycling Process Optimization

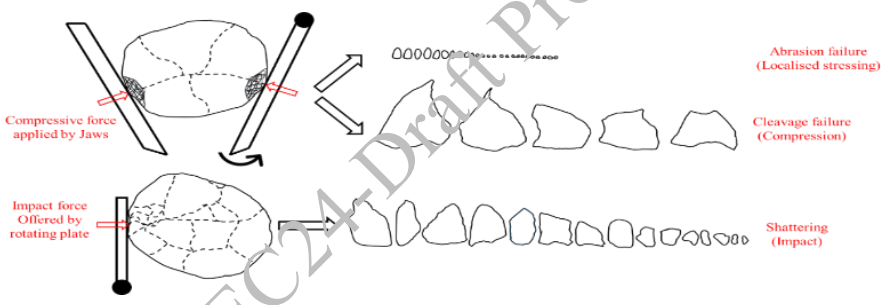

Figure 1. Crushing Mechanisms Associated with Compression and Impact Crushers (Pal and Singh (2024))

In most Indian recycling plants, waste concrete undergoes three stages of crushing viz. primary, secondary, and tertiary. Compression-based crushers are used as the primary and secondary crushers to produce coarse RCA. In contrast, impact-based crushers are used in the end to improve the morphological characteristics of fine RCA. The use of heavy-duty machinery in fragmenting the debris in three stages involves significant CO2 emissions and embodied energy. Shifting to impact-based crushing instead of compression (as primary stages) could have twin benefits viz. reducing numerous crushing stages and production of relatively better-quality RCA fractions. This is because the comminution mechanism associated with impact crushers is significantly different from that of compression crushers (Fig. 1). In jaw crushers, particle fragments along the loading axis as well as the weakest plane, leading to the production of big-sized irregularly shaped particles (cleavage failure) demanding further crushing for size reductions. Also, localised stressing at the interface of jaws and rock leads to the abrasion of stones resulting in lowering the reactivity of concrete fines (Pal and Singh (2024)). On the other hand, in impact-based crushers, under high energy, the concrete debris shatters i.e. simultaneous stressing of numerous points; due to shattering, regular-sized and shaped RCA are produced from horizontal shaft crushers. RCA produced through an impact-based crusher exhibited ~12% lower AM content than the RCA crushed through 2 stages of compression crushing (Pal and Singh (2024)). This reduction in the AM content helped in achieving 8-15% higher strength and subsequently demanded 20-30 mm lower slab thickness (for different traffic and loading conditions) than the concrete slab made with jaw-crusher-produced RCA (Pal (2024)). The detached AM was found to increase the pozzolanic reactivity of concrete fines by 29% compared to concrete fines generated through the jaw crusher (Pal and Singh (2024)).

2.2 Concrete Mix Optimization

In general, the presence of porous AM lowers the workability of paving concrete which could be addressed by increasing the moisture content (80-90% of the absorption capacity of RCA) of the mixture without increasing the effective water-binder ratio. However, during the mixing stage, RCA absorbs only 50-70% of the water and the remaining water facilitates enhanced workability; full moisture absorption may require 4-6 hours (Selvam et al. (2023)). This absorbed water in the long run helps in curing the concrete internally — paving concrete made with 100% RCA exhibited ~35% strength gain between 28 days and 90 days against ~10% in the conventional paving concrete (curing was stopped at 28 days and specimens were exposed to open environment) (Pal (2024)). However, the ultimate strength difference between conventional concrete and RCA concrete could be as high as 30% for medium-strength concrete and 55% for ultra-high-performance concrete. This difference in the strength may warrant either a 15-20% thicker pavement slab or 15-34% excess cement for the same traffic and loading conditions (Pal (2024). However, this difference could be lowered in special paving concrete such as roller compacted concrete pavements (RCCP) by synergetic improvement in the particle packing density following packing approaches coupled with increased lubrication offered by water-reducing admixtures. Interestingly, an RCCP mixture having 100% soaked RCA and optimum dosage of superplasticisers exhibited 20-47% higher tensile strength than conventional RCCP (Selvam et al. (2023)). This is because the load-carrying capacity of stiff mixes not only depends on the cement hydration but also on the aggregate-to-aggregate interlocking which could be enhanced by increasing the lubrication as well as particle packing density. These findings indicate higher suitability of untreated RCA for zero-slump concrete such as RCCP and dry lean concrete subbases.

2.3 Beneficiation Techniques

2.3.1 AM Strengthening through Slurry Impregnation Coupled with Natural Carbonation

AM strengthening techniques involve the introduction of external agents to enrich the RCA. These external agents (CO_2, pozzolanic mineral admixtures, bacteria, etc.) could fill the cracks and pores and in some cases, could even enhance the bonding of AM with the parent stone. But, as mentioned earlier, these methods cannot be carried out at large scale. However, stockpiling of the different fractions, post-crushing, in a loose state in an open environment for 12-14 months could lead to complete carbonation of the RCA (Kosuri et al. (2023)). Once the RCA is carbonated, the remaining cracks and pores can be filled using any mineral admixture slurry (6 hours of immersion and 40% concentration). Paving concrete made with treated RCA exhibited 15-25% higher strength, 10-12% higher abrasion resistance, and 10-26% lower porosity than the mixes made with untreated RCA (Kosuri et al. (2023)). In fact, most of the mixes made with 100% coarse RCA exhibited a modulus of rupture of more than 5 MPa recommended for paving high-volume roads in India. However, compared to natural materials, 10-15% strength reduction will always be associated with concrete mixes made with treated RCA indicating to completely remove the AM, if the desire is to achieve similar performance to conventional paving concrete.

2.3.2 AM Removal through Thermo-Mechanical Beneficiation Using Concentrated Solar Energy

A typical crushed RCA consists of 50-60% coarse fractions, 40-60% fine RCA, and 3-8% concrete fines; however, most of the AM beneficiation techniques deal only with the valorisation of coarse RCA. Subsequently, CO_2 emissions associated with the AM removal process are double if the fine RCA are not utilized (Quattrone et al. (2014)). The use of thermo-mechanical beneficiation technique does not only produce high-quality coarse RCA, but good-quality fine RCA having comparable properties to natural sand. In this method, waste concrete debris is heated at a temperature of 450-500°C followed by cooling in the ambient environment (Prajapati et al. 2021). Heating dehydrates the hydration products, and owing to sudden cooling, the mortar phase experiences thermal shock, both leading to weakening of the AM phase. Once the AM is weak, it could be detached from the aggregate surface following mechanical scrubbing. Concrete manufactured with treated coarse RCA and fine RCA exhibited similar performance to conventional concrete made with granite and river sand (Prajapati et al. 2021). The only drawback associated with the conventional thermo-mechanical technique is the utilization of electricity in heating the concrete chunks. This limitation can be overcome by shifting to solar energy which could save 250 kWh of electricity per tonne of concrete waste (Prajapati et al. 2022). The first demonstration of thermo-mechanical beneficiation using concentrated solar energy was conducted in India at Mount Abu, Rajasthan (Fig. 2). Concrete made with these RCA exhibited properties at par with conventional concrete made with natural

materials. In fact, concrete fines obtained through this process consisted of 55% hydrated or unhydrated cement particles indicating potential for high-value applications such as supplementary cementitious admixtures and raw meal for cement manufacturing.

Figure 2. Demonstration of RCA Beneficiation using Concentrated Solar Energy (Prajapati et al. 2022)

3. Conclusions and Way Forward

- It is possible to reduce the AM content slightly by changing the crushing energy from compression to impact. Impact-based crushers not only produce relatively better-quality coarse RCA but also good-quality concrete fines. This finding needs to be linked with the parent concrete grade and composition, as only 1 grade of concrete was considered in this study.
- Stockpiling of RCA in an open environment for 12-14 months leads to its complete carbonation. Treatment of these RCA following optimized slurry impregnation technique further enhances the RCA quality. However, the slurry impregnation technique needs to be optimized for beneficiating the finer fractions of RCA. Also, the stockpiling duration needs to be related to parent concrete characteristics.
- The use of concentrated solar energy instead of conventional hydraulic/coal-based electricity seems to be sustainable in valorizing the RCA. However, achieving a temperature of 450-500°C at all the geographical locations is not possible and therefore, alternate heating methods needs to be explored.

References

Kosuri, M., Singh, S. and Bhardwaj, B.B. (2023) "Optimization of slurry impregnation technique for upcycling carbonated recycled concrete aggregates for paving concrete applications", *Journal of Materials in Civil Engineering*, 35(5): 04023053

Prajapati, R., Gettu, R. and Singh, S. (2021) "Thermomechanical beneficiation of recycled concrete aggregates (RCA)", *Construction and Building Materials*, 310:125200

Pal, R. and Singh, S. (2024) "Role of Impact and Compression-Based Crushing on the Physical, Chemical, and Morphological Characteristics of Recycled Concrete Aggregates", *Journals of Materials in Civil Engineering*, 36(5):04024094

Pal, R. (2024) "Influence of Crushing Methods on the Characteristics of Recycled Concrete Aggregates for Rigid Pavement Applications", *Master's thesis, Indian Institute of Technology Madras, Chennai, India.*

Prajapati, R., Gettu, R., Singh, S. and Rathod, B.J. (2022) "A novel beneficiation process for producing high-quality recycled concrete aggregates using concentrated solar energy", *Materials and Structures*, 55:233

Quattrone, M., Angulo, S.C. and John, V.M. (2014). "Energy and CO2 from high performance recycled aggregate production". *Resources, Conservation and Recycling*, 90, pp.21-33.

Selvam, M., Singh, S. and Anjana, A.G. (2023) "Enhancing the Performance of Roller-Compacted Concrete Pavement by Synergetic Improvement of Packing Density, Lubrication, and Moisture State of Recycled Concrete Aggregate", *Transportation Research Record*, 2677(6): 594-608

Yang, X., Liu, Y., Liang, J., Meng, Y., Rong, H., Li, D., Chen, Y., Lv, J., Jiang, Y. and Liu, Y. (2023) "Straightening methods for RCA and RAC—A review." *Cement and Concrete Composites*, 141:105145.

Application of Service Life Modeling to Reinforced Concrete Structures

A. S. Sohanghpurwala

CONCORR, Inc., Sterling, Virginia, USA
Email: ali@concorr.com

ABSTRACT

Corrosion of reinforcement is the primary deterioration process which impacts the durability of and controls the service life of reinforced concrete structures which are in marine or deicing salt environments. To repair, rehabilitate, or update a structure to meet the latest codes or increase its functional capacity, it is essential to obtain information on the present corrosion condition and the likely future progression of corrosion. To determine whether it is cost effective to replace, repair and install a corrosion mitigation system, or to ascertain which section(s) or element(s) of the structure need a corrosion mitigation system, this information is essential. Many testing protocols have been used, including those which utilized measuring the level of chloride contamination at steel depth, measuring the carbonation depth, conducting half-cell potential survey, performing corrosion rate measurement, or measuring the resistivity of the concrete. These protocols often required significant field work and were cost intensive. In 1995 we introduced a methodology which, when compared to other methodologies, requires less intensive field work and utilizes mathematical modeling to provide the requisite information. Over the last three decades this methodology has been implemented on numerous structures all over the United States and has been proven to be a cost-effective method to obtain the critical information. The results of the modeling also provide information for performing life cycle cost analysis for repair and rehabilitation.

KEYWORDS*: Corrosion, Chloride Profile, Service Life Modeling, Carbonation, Concrete*

1. Introduction

Reinforced concrete structures are often located in aggressive environmental conditions which initiate, support, and accelerate several different deterioration processes which reduce the service life of the structure. Corrosion of the reinforcement is the most prominent amongst them, especially in marine or deicing salt environments, and results in significant damage at a much earlier age than when compared to less aggressive areas. Conventional reinforcement in concrete does not corrode due to the generation of a protective layer by high pH of the concrete. This protection is compromised by the presence of a threshold level of chloride ions or carbonation, i.e. the reduction of concrete pH to levels at or below 10 at the steel-concrete interface. Threshold levels of chloride ions are generally not present in fresh concrete at any depth, unless a chloride-based admixture is used. Generally, chlorides diffuse into the concrete from the environment and accumulate at the steel-concrete interface. When the concentration exceeds the threshold, corrosion initiates. Similarly, carbonation, a reduction in pH of the concrete due to a reaction with carbon dioxide or monoxide in the air, slowly progresses into the concrete starting from the exposed surface. When carbonation reaches the steel-concrete interface, corrosion initiates. The rate of diffusion of chloride ions and the progression of carbonation into the concrete can be accelerated by the development of cracking caused by other deterioration processes such as freeze-thaw (FT) damage, alkali-silica reactivity (ASR), and delayed ettringite formation (DEF). If more than one of these deterioration processes is present, the synergy between them can significantly accelerate the development of damage. The time required for chloride ions to diffuse into the concrete and accumulate at the steel-concrete interface to concentrations at the threshold level or for carbonation to progress to the steel-concrete interface, is termed time-to-initiation (t_i). The time required for damage to occur after corrosion has initiated is termed time-to-damage-development (t_d). Corrosion induced damage or damage developed by the synergy of more than one deterioration process can impact structural integrity if not addressed in a timely fashion. Many different

approaches have been developed for the repair and rehabilitation of these structures. The simplest amongst them is to regularly repair observable concrete damage and to maintain the dimensional stability. This does not extend service life and can result in the acceleration of damage development due to the "Halo or Ring effect" ACI 364.6T-02, (2011). To properly address the development of damage, the deterioration processes need to be mitigated. Deterioration processes such as FT, ASR, and DEF can be mitigated by reducing exposure to moisture, whereas a corrosion control system is required for mitigating corrosion. The primary focus of this discussion is on corrosion and other deterioration processes are discussed as necessary. In the past, repairing and rehabilitating existing structures was a norm but, with shrinking resources, preservation has become a priority. To cost-effectively preserve a structure, the optimal time to install a corrosion mitigation system needs to be identified and structures prioritized based on their present condition for repair and installation of corrosion control systems. In addition to preserving structures, they often need to be updated, widened, or expanded to meet present codes or increase their functional capacity. To cost effectively modernize a structure, certain sections or elements need to be replaced and the remaining rehabilitated and protected to match the service life of the replaced element(s). To accomplish this, it is essential to ascertain the present condition of the structure and to determine the future propensity for corrosion for each section or element and identify which can be retained and have its service life extended and which one needs to be replaced.

2. Proposed Approach

To ascertain the present condition of each section or element of the structure and to identify the optimal repair/rehabilitation strategy, various techniques have been employed. In 1995 we introduced a methodology to ascertain the present condition and obtain sufficient information to model the future progression of corrosion induced damage. This methodology utilizes minimal testing and only requires collection of concrete cores, clear concrete cover, and documentation of damage whether previously repaired or extant. Instead of measuring the physical parameters of the corrosion process occurring on the reinforcement, this methodology requires measurement of the concentration of chloride ions at various depths (chloride profile) and the average depth of carbonation. Mathematical modeling is then used to project future chloride profiles and the future average depth of carbonation. This protocol entails collecting core samples from each of the element types and/or variation in exposure condition. Sufficient core samples need to be collected from each of the element types such as the footings, columns, struts, caps, beams, and deck of a bridge. Modeling must be performed for each of the element types separately, and if one element has more than one exposure condition, then it needs to be modeled for each exposure condition. For bridge substructure elements in a marine environment, the aggressiveness of the environmental exposure varies for each element type. For example, the footings are in the splash zone and the caps, beams, and deck are only exposed to air borne chlorides. On a bridge deck in colder climes, the shoulder lanes have a very different exposure condition than the driving lanes, as salt laden snow accumulates there during snow removal and can also affect the substructure by runoff upon melting. Each core collected from the structure is utilized to develop a chloride profile and the average depth of carbonation. One half of the core is used for carbonation testing and the chloride ion concentration at various depths is measured from the other half of the core. To locate and avoid reinforcement at the coring sites, ground penetrating radar surveys are conducted. In addition to locating the rebars, these surveys also provide clear concrete cover information. A solution to Fick's Second Law of diffusion is fitted to the chloride profile from each core to obtain apparent surface chloride ion concentration (C_o) and the apparent diffusion coefficient (D). The results of all cores from a given element are then used to develop statistical distributions of C_o and D. These distributions are useful in modeling. An average chloride profile is developed for each element at each elevation (when necessary) from all the cores collected from it. The average chloride profile is then analyzed with the average cumulative clear cover. The analysis of the average chloride profile and the average cumulative clear concrete cover provides a clear picture of the propensity for corrosion in the element with elevation as shown in Figure 1. This analysis was based on using 500 parts per million (ppm) of chloride ion concentration as a threshold for corrosion initiation. This analysis clearly shows that all reinforcement at the five feet elevation is exposed to chloride ion concentration more than the threshold and can be expected to experience corrosion initiation. A projected chloride profile, 20 years in the future is also shown.

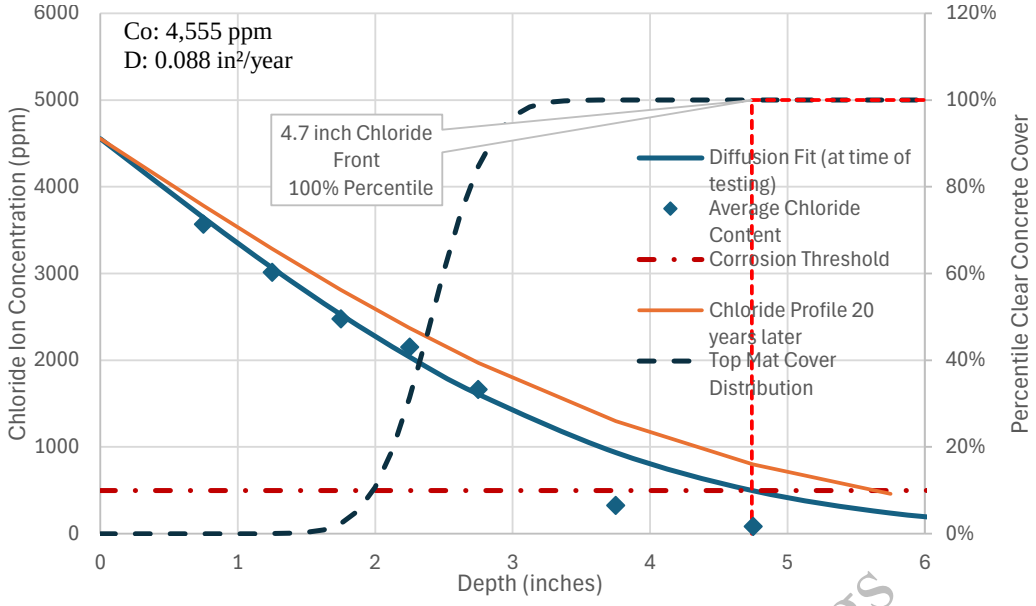

Figure 1. Average distribution of chloride ions and cumulative clear concrete cover for all piles at 5 ft elevation

A similar analysis for the 14 feet elevation, presented in Figure 2, exhibits that none of the reinforcement at this elevation is yet exposed to threshold levels of chloride ions. A projected chloride profile in the future is not presented as, 20 years hence, it is not very different from the present one.

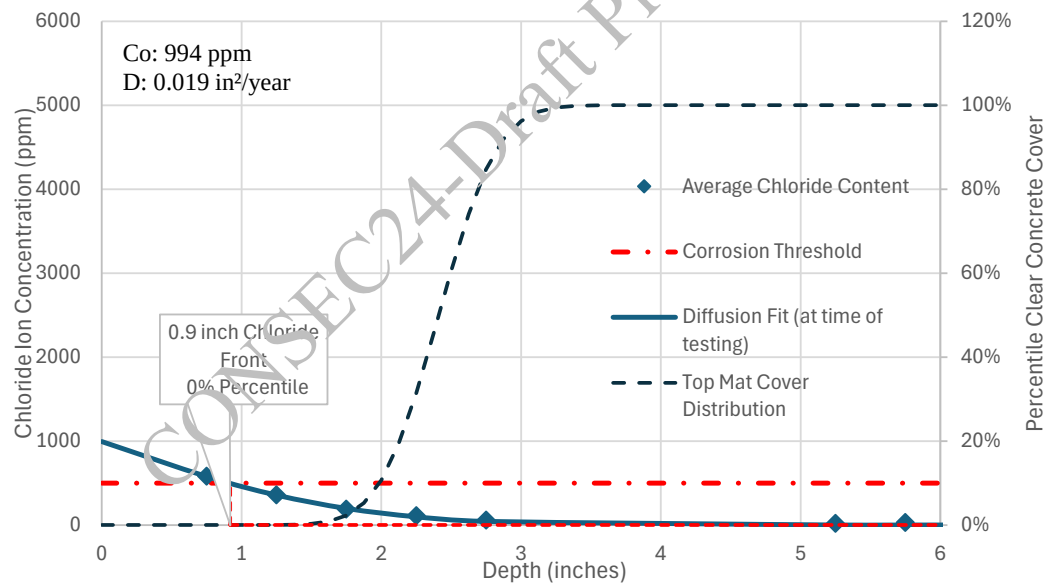

Figure 2. Average distribution of chloride ions & cumulative clear concrete cover for all piles at 14 feet elevation

With the existing chloride profile and modeling, the chloride profile at any time in the future can be projected. This information is critical in identifying areas that need corrosion mitigation to obtain the desired remaining service life. Similarly, the existing carbonation depth can be used to project the carbonation depth at any point of time in the future by modeling. Therefore, the knowledge of present chloride profile and carbonation depth can provide accurate information on the present corrosion condition and the likely future propensity for corrosion. In general, the rate of carbonation progression on bridge elements in the United States is quite slow and does not generally impact service life.

3. Service Life Modeling

The surface chloride ion concentrations, the diffusion coefficients, clear concrete cover, and damage data are then used to model the future development of damage on each element and the future chloride profile and carbonation depth. The algorithm developed for service life modeling in NCHRP Report 558 by Sohanghpurwala (2006) utilizes the Monte Carlo Simulation by randomly sampling the distributions of diffusion coefficient, surface chloride ion concentration, and clear concrete cover and then applies the solution of Fick's Second Law of Diffusion to each random set to obtain t_i for each set. The solution to Fick's Second Law of Diffusion requires a threshold chloride ion concentration at which corrosion is expected to initiate to obtain t_i. The chloride ion threshold at which corrosion initiates for various kinds of reinforcement is available in the literature. However, this model does not utilize a known chloride ion threshold, it loops through increasing levels of chloride ion concentrations until the damage predicted by the model at the age of collection of the cores is equal to damage existing at that age. The chloride ion concentration at which the model reaffirms existing damage is then used to project damage in the future. The algorithm starts modeling the diffusion process at the date of construction of the structure with surface chloride ion concentration starting from zero and increasing linearly to the present value, i.e. the value randomly selected from the surface chloride ion concentration distribution in each set. The increase of the surface chloride ion concentration is capped at a defined value based on the exposure condition. The algorithm models the process from age zero to 100 years. If carbonation and/or epoxy coated rebars are present, then the progression of carbonation and/or the progression of epoxy degradation with time is also modeled simultaneously with the chloride ion diffusion and carbonation. The modeling process results in a distribution of t_i. Similarly, a distribution of t_i due to carbonation is also developed. There are models available to calculate t_d, however, they require additional testing. Assuming t_d for an environment has been found to provide reasonably good results. The summation of t_i and t_d provides the distribution of total time required for damage to occur. The cumulative total time to damage is plotted to obtain progression of damage in the future as shown in Figure 3.

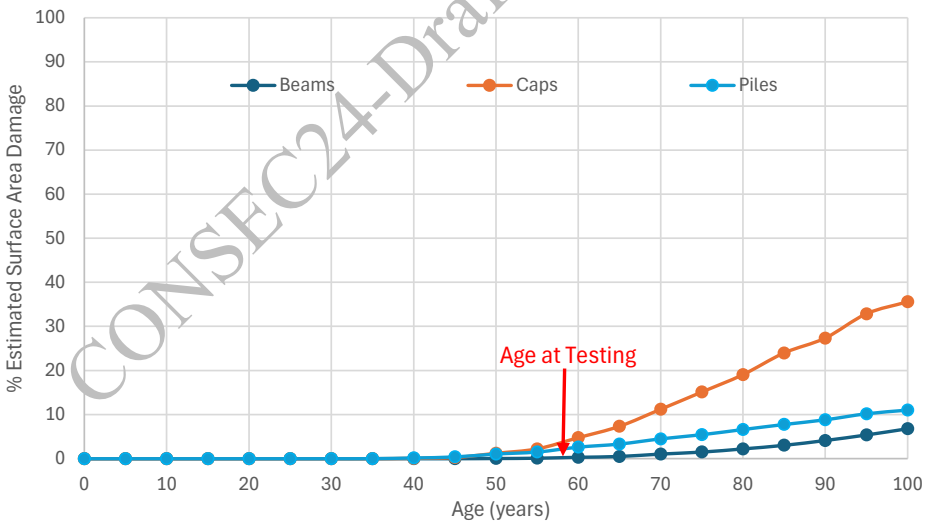

Figure 3. Projection of damage resulting from corrosion of reinforcement of piles, caps and beams

In addition to modeling the progression of damage, future chloride profiles are modeled to identify where the chloride concentrations will be exceeding the threshold. For the above piles, Figure 4 shows how the chloride concentrations will be distributed with elevation 20 years after the time of testing. The yellow color shows where the chloride concentration will be more than 500 ppm. This allows determination of the elevation of the piles that will need to be protected if the next repair project is slated to be performed 20 years from now.

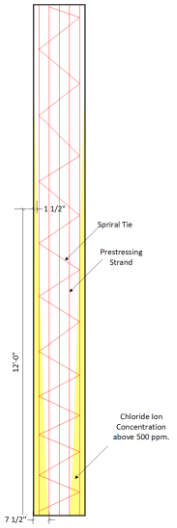

Figure 4. Distribution of chloride ions – 20 years hence

The result of the modeling along with the present condition are utilized to identify viable combinations of repair and corrosion mitigation strategies and to perform life cycle cost analysis for each strategy. The results of life cycle cost and initial cost, along with the resources available to monitor and maintain the corrosion mitigation system, are used to identify the optimal solution for the structure.

This strategy has been successfully utilized on numerous bridge structures and parking garages located all over the United States. This methodology has or is presently being considered for application on iconic bridges such as the Sunshine Skyway Bridge in Tampa, Florida, the Seven Mile Bridge in the Florida Keys, Florida, and the historic Torey Pines Bridge in California.

4. Conclusions

The proposed approach of only collecting core samples and documenting visually observable repaired and extant damage from reinforced concrete structures and supplementing the laboratory data obtained from the core samples with mathematical modeling results in an efficient and cost-effective protocol. The process of collection of the cores generates clear concrete data which is essential for mathematical modeling without any extra effort. The crew to be used for collecting the core samples does not have to be highly qualified and personnel from the construction area can be used to control the cost of field evaluation. The cost of processing the core samples in the laboratory is minimal. This allows more agencies to use this tool to obtain the necessary information to develop a cost-effective long-term repair and rehabilitation strategy. In addition to being an affordable protocol to implement, the result of this methodology provides information that allows targeting elements or sections of the structure for cathodic protection that are essential to realizing the desired extension in service life. This results in significant savings in construction costs for repair and rehabilitation.

References

ACI 364.6T-02. (2011) "Concrete Removal in Repairs Involving Corroded Reinforcing Steel", *ACI 364.6T-02(11)*. ACI.

Sohanghpurwala, A. S. (2006) "Manual on Service Life of Corrosion-Damaged Reinforced Concrete Bridge Superstructure Elements", Transportation Research Board.

Carbonation of Concretes with SCMs

A. Vollpracht[1*], G.J.G. Gluth[2], B. Rogiers[3], I.D. Uwanuakwa[4], Q.T. Phung[3], Y. Villagran Zaccardi[5], C. Thiel[6], H. Vanoutrive[7], J.M. Etcheverry[8], E. Gruyaert[7], S. Kamali-Bernard[9], A. Kanellopoulos[10], Z. Zhao[11], I.M. Martins[12], S. Rathnarajan[13], N. De Belie[8]

[1]Institute of Building Materials Research, RWTH Aachen University, Aachen, Germany
Email: vollpracht@ibac.rwth-aachen.de
[2]Division 7.4 Technology of Construction Materials, Bundesanstalt für Materialforschung und -prüfung (BAM), Berlin, Germany
Email: gregor.gluth@bam.de
[3]Sustainable Waste & Decommissioning, Belgian Nuclear Research Centre (SCK CEN), Mol, Belgium
Emails: bart.rogiers@sckcen.be, quoc.tri.phung@sckcen.be
[4]Department of Civil Engineering, Near East University, Mersin 10, Turkey
Email: ikeuwanuakwa@gmail.com
[5]Materials and Chemistry Unit, Flemish Institute for Technological Research (VITO), Mol, Belgium
Email: yury.villagranzaccardi@vito.be
[6]Construction Materials, Department of Civil Engineering, OTH Regensburg, Germany
Email: charlotte.thiel@oth-regensburg.de
[7]KU Leuven, Materials and Constructions, Department of Civil Engineering, Ghent, Belgium
Emails: hannevanoutrive@gmail.com, elke.gruyaert@kuleuven.be
[8]Magnel-Vandepitte Laboratory, Department of Structural Engineering and Building Materials, Ghent University, Ghent, Belgium
Email: JuanManuel.Etcheverry@ugent.be, Nele.DeBelie@ugent.be
[9]Institut National des Sciences Appliquées (INSA-Rennes), LGCGM, Université de Rennes, Rennes, France,
Email: Siham.Kamali-Bernard@insa-rennes.fr
[10]School of Physics, Engineering & Computer Science, Centre for Engineering Research, University of Hertfordshire, UK
Email: a.kanellopoulos@herts.ac.uk
[11]Department of Structural Engineering, College of Civil Engineering, Tongji University, Shanghai, China
Email: zengfengzhao@tongji.edu.cn
[12]Departamento de Materiais, Laboratório Nacional de Engenharia Civil, Lisbon, Portugal
Email: imartins@lnec.pt
[13]Department of Civil Engineering, Indian Institute of Technology Madras, Chennai, India
Email: sundarrathinaraj@gmail.com

[*]Corresponding author

ABSTRACT

Due to the urgent need to reduce CO_2 emissions, cement and concrete producers aim to substitute increasing proportions of Portland cement by supplementary cementitious materials (SCMs). However, lowering the clinker content can lead to an increasing risk of neutralisation of the concrete pore solution and reinforcement corrosion due to carbonation. Carbonation mechanisms and kinetics depend on hydrate phase assemblage, pore solution chemistry and porous structure as well as the exposure conditions. To study the effects of mix-design, curing, preconditioning and storage conditions on carbonation resistance, the RILEM TC 281–CCC established a comprehensive database, consisting of 1044 concrete and mortar mixes with their associated carbonation depth data over time. The dataset comprises mix designs with a large variety of binders and includes information on chemical composition and physical properties of the raw materials, compressive strengths, curing and carbonation testing conditions. Both natural and accelerated carbonation with CO_2 concentrations of up to10 vol.-% were considered. The analysis of the available data confirmed that the $w/CaO_{reactive}$ ratio is a decisive factor for carbonation resistance, but curing and exposure conditions also influence carbonation. Probabilistic inference suggests that both accelerated and natural carbonation processes follow a square-root-of-time behavior, but direct conversion between accelerated and natural carbonation by solely taking the CO_2 concentration into account is not possible. Accelerated carbonation

testing and application of the square-root-of-time law yield predicted natural carbonation depths that tend to be lower than the measured values. This effect was particularly noticeable for concretes with a higher SCM fraction ($w/CaO_{reactive}$ > ~1.1).

KEYWORDS: *Natural carbonation, Accelerated carbonation, SCMs, Database*

1. Introduction

1.1 Carbonation reactions in cementitious systems

The term carbonation describes the ingress of CO_2 into the porous structure of cementitious materials, its dissolution in the pore solution and the following reactions of the dissolved carbonates with hydration products. These reactions are taking place with calcium ions that are released from hydrate phases. According to thermodynamic calculations summarized by von Greve-Dierfeld et al (2020), initially any monosulfate- and hemicarbonate-AFm phases will destabilise to monocarbonate. Afterwards, portlandite is reacting to form calcium carbonate. During this phase, the pH remains above 12.5. After all accessible portlandite is consumed, C–S–H starts to decalcify by removing CaO from the interlayer space. The Ca/Si ratio is reduced to 1.3. The pH decreases slightly during this step. The released silicon and aluminium from the C–S–H react with monocarbonate to form strätlingite. In parallel, C–S–H continues to be consumed without change of its Ca/Si ratio. After monocarbonate is consumed, the decalcification and decomposition of the C–S–H continues down to Ca/Si of 0.75 and pH of 11. Upon further carbonation strätlingite decomposes, followed by ettringite at pH around 10. The released aluminium and sulfur are bound in aluminium hydroxide or zeolites and gypsum, respectively. In parallel, the C–S–H decalcifies to Ca/Si of around 0.67 while the pH is lowered to 10. During the decalcification process, the chain length of C–S–H increases until finally it decomposes into calcite and hydrated amorphous silica and the pH drops rapidly to 8.5. At the final stage, hydrotalcite decomposes at pH around 8.5. More detailed information can be found in Hargis et al (2017) and De Weerdt et al (2019).
For CEM I mixes, the maximum CO_2 bound is around 40 to 50 g CO_2/100 g Portland cement. For concrete and mortars with SCMs, the maximum CO_2 binding depends on the individual binder composition. Since calcium is the most prominent reactant for the CO_2, the amount of reactive CaO in the binder (see Equation 1) can be used as an indicator for the carbonation resistance.

$$CaO_{reactive} = CaO_{total} - CaO_{CaCO3\ init} - CaO_{CaSO4} \quad (1)$$

CaO_{total}: total amount of CaO in the binder (including CaO in the SCMs)
$CaO_{CaCO3\ init}$: CaO in limestone powder ($CaCO_3$) used as binder component
CaO_{CaSO4}: CaO in the sulfate carrier (gypsum, hemihydrate, anhydrite)
It is important to note that the ingress of CO_2 also plays a major role in the whole process and therefore the porosity and the pore structure of the material are crucial. The most relevant factors that influence the porosity of cementitious materials are the w/b ratio, the binder composition and degree of hydration. In order to combine the chemical resistance and the physical resistance to diffusion, Leemann et al (2015) and (2017) established the $w/CaO_{reactive}$ ratio. The water saturation of the pores is another influencing factor; on one hand water is needed to dissolve CO_2, on the other hand the gas transport is hindered by high saturation degrees. Therefore, the carbonation conditions need to be considered as well.
To quantify the effects of mix design, curing and carbonation conditions on carbonation kinetics, a database has been established by the RILEM TC 281-CCC ‘‘Carbonation of concrete with supplementary cementitious materials’’, which is described in the following paragraph.

1.2 Description of the carbonation database

The database is published by Vollpracht et al (2024) as an electronic supplement. It includes 1044 concrete and mortar mixes, which contain a large variety of binders / binder components (19 different cement types ranging from CEM I to CEM V/A, siliceous fly ash (sFA), ground granulated blast furnace slag (GGBS), calcined clays (CC) and a few others). These materials are used in different mixture compositions including binary and ternary combinations. The water/binder ratio varies between 0.26 and 0.75. The collected data includes chemical compositions and physical properties of the raw materials, mix-designs, compressive

strengths, curing and carbonation testing conditions. In many cases, natural carbonation was recorded for several years with both indoor and outdoor results being considered. Furthermore about 400 accelerated carbonation tests are included, in some cases in parallel to natural carbonation.

2. Main results

In the first step, the database was used to investigate the effect of specific parameters on carbonation rate. This analysis strongly supports the importance of $w/CaO_{reactive}$ as an efficient universal parameter to describe the combined effects of transport properties and buffer capacity of concrete with different types of binders as shown in Fig. However, the scatter of the data is quite high, even within the specific types of binders.

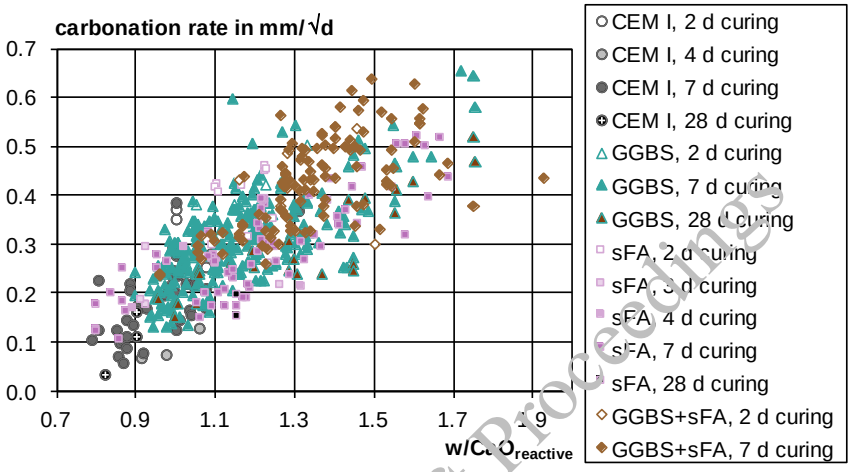

Figure 1. Carbonation rate versus $w/CaO_{reactive}$ for natural carbonation at 20 °C and 60-65 % RH for Portland cement-based mixes as well as binary and ternary blends with GGBS and / or sFA

Even though the $w/CaO_{reactive}$ ratio captures most of the effects related to porosity on carbonation resistance, it was observed that, for the same $w/CaO_{reactive}$, concrete with higher compressive strength tends to exhibit a higher carbonation resistance (see Fig). This might be related to effects of particle size distribution (of the aggregate and the binder) and the effects of the curing type and period. Thus, additional parameters that are related to compressive strength, and thus also the effective diffusivity of CO_2, may further refine and improve estimates of concrete carbonation resistance.

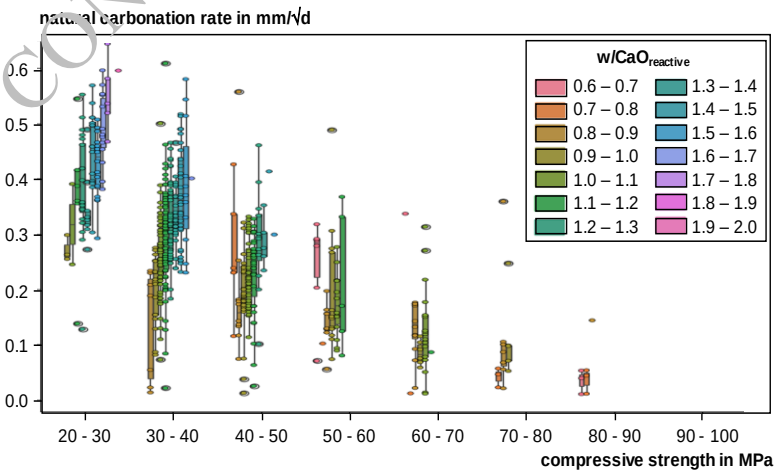

Figure 2. Natural carbonation rate versus range of compressive strength (28 d, 150 mm cubes), Vollpracht et al (2024)

The present analysis indicated that accelerated carbonation testing (i.e., testing at CO_2 concentrations higher than 0.04 %) and application of the square-root-of-time law yield predicted natural carbonation rates that

tend to be lower than the corresponding measured natural carbonation rates. This effect was particularly noticeable for carbonation rates above 0.2 mm/√d, which translates to w/$CaO_{reactive}$ ratios higher than ~1.1. The causes for this effect are not known in detail; thus, it is necessary to study the related phenomena in depth to be able to suggest reliable improvements in present testing standards and conversion instructions. In the second step, a collective analysis of all variables within the compiled dataset was performed using a machine learning approach. The predictive tool incorporates the most relevant factors identified for carbonation resistance: compressive strength, RH, CO_2 concentration, $CaO_{reactive}$ content, and temperature. Unexpectedly, the probabilistic inference suggested that in the equation to predict carbonation depth, $CaO_{reactive}$ needs an exponent, which is considerably less than one. The discrepancies between accelerated and natural carbonation tests have been quantified here, in the form of an exponent for the CO_2 concentration that is less than 0.5 (square-root behaviour), whereas only minimal deviation from progression with the square root of time was obtained. Finally, the machine learning exercise as well as the conventional analysis indicates that the curing time could be used as a parameter to further refine estimates of carbonation depth. The following equation has been derived to calculate the carbonation depth d_c at a specific carbonation time t.

$$d_c = 2630 \cdot 10^{-0.00821 f_c} \cdot \left(1 - \frac{RH}{100}\right)^{0.595} \cdot [CO_2]_0^{\,0.431} \cdot t^{0.511} \cdot CaO_{reactive}^{\,-0.722} \cdot 10^{-374/T} \qquad (2)$$

f_c: compressive strength at an age of 28 d in MPa,
RH: relative humidity during carbonation in %,
$[CO_2]_0$: CO_2 concentration at the surface in vol.-%,
T: temperature during carbonation in K

Acknowledgements

The authors gratefully acknowledge the support by the researchers who provided additional information or unpublished data for the database: Andreas Leemann (Empa, Switzerland), Alexander Haynack (TUM, Germany), Federica Lollini (POLIMI, Italy), Christoph Müller (VDZ, Germany), Gisela Cordoba (UNICEN, Argentina), Bettina Kraft (FIB, Germany)

References

De Weerdt, K., Plusquellec, G., Revert, A.B., Geiker, M.R., Lothenbach, B. (2019) "Effect of carbonation on the pore solution of mortar", *Cement Concr Res* 118:38–56.

Hargis, C.W., Lothenbach, B., Müller, C.J., Winnefeld F. (2017) "Carbonation of calcium sulfoaluminate mortars", *Cement Concr Compos* 80:123–134.

Leemann, A.; Nygaard, P.; Kaufmann, J.; Loser, R. (2015) "Relation between carbonation resistance, mix design and exposure of mortar and concrete", *Cement and Concrete Composites* 62: 33-43

Leemann, A.; Moro, F.: Carbonation of concrete (2017) "The role of CO_2 concentration, relative humidity and CO_2 buffer capacity", *Materials and Structures* 50: 30

Vollpracht, A., Gluth, G.J.G., Rogiers, B., Uwanuakwa, I.D., Phung, Q.T., Villagran Zaccardi, Y., Thiel, C., Vanoutrive, H., Etcheverry, J.M., Gruyaert, E., Kamali-Bernard, S., Kanellopoulos, A., Zhao, Z., Martins, I.M., Rathnarajan, S., De Belie, N. (2024) "Report of RILEM TC 281-CCC: Insights into factors affecting the carbonation rate of concrete with SCMs revealed from data mining and machine learning approaches, *Materials and Structures* - accepted

von Greve-Dierfeld, S., Lothenbach, B, Vollpracht, A., Wu, B., Huet, B., Andrade, C., Medina, C., Thiel, C., Gruyaert, E., Vanoutrive, H., Saéz del Bosque, I.F., Ignjatovic, I., Elsen, J., Provis, J.L., Scrivener, K., Thienel, K.-C., Sideris, K., Zajac, M., Alderete, N., Cizer, Ö., Van den Heede, P., Hooton, R.D., Kamali-Bernard, S., Bernal, S.A., Zhao, Z., Shi, Z., De Belie, N. (2020) "Understanding the Carbonation of Concrete with Supplementary Cementitious Materials – a critical review by RILEM TC 281-CCC", *Materials and Structures* 53:136

Advanced Materials for Severe Conditions

Accelerated Carbonation of Municipal Solid Waste Incineration Bottom Ash for Alternative Aggregate Production

I.E. Kanjo[1*], J. Hubert[1], J.T. Tchuindjang[1], S. Marquis[2], Ph. Descamps[2], L. Dupont[3], L. Courard[1]

[1] Université de Liège, Urban and Environmental Engineering, Liège, Belgium
[2] Centre Terre et Pierre, Tournai, Belgium
[3] IPALLE, Froyennes, Belgium
EMail: ImadEddine.Kanjo@uliege.be

[*]Corresponding author

ABSTRACT

Municipal solid waste incinerated bottom ash (MSWI-BA) is a byproduct from waste incineration process, which is used mainly as replacement of sand and natural aggregates in road foundations and concrete pavements. Usually, MSWI-BA undergoes a maturation treatment before being used by exposing it to the atmosphere for a period of minimum 18 weeks. This study investigates an accelerated carbonation process for MSWI-BA maturation, which aims to enhance both its engineering properties and its environmental sustainability. The results demonstrate significant improvements in shortening treatment duration without compromising physical properties such as density and water absorption while concurrently reducing greenhouse gas emissions through CO_2 sequestration. These findings have established that accelerated carbonation could be an effective maturation technique for MSWI-BA, thus offering new insights for its practical implementation in waste management and resource recovery strategies.

KEYWORDS*: Municipal solid waste incinerated bottom ash, Accelerated carbonation, Accelerated maturation, Aggregates, Concrete.*

1. Introduction

Municipal solid waste incinerated bottom ash (MSWI-BA), which makes up 80% of the residual waste after combustion, is the main by-product of municipal solid waste incineration. The European Union produces 19 million tonnes of MSWI-BA annually (CEWEP, 2017). Due to its similar density and particle size distribution, MSWI-BA is often used as a substitute for natural sand and aggregate (Dhir et al., 2018a; Courard et al., 2002). Before utilization, MSWI-BA typically undergoes natural aging, where it is stored in stockpiles for at least 18 weeks and sometimes up to 6 months. During this period, natural carbonation and leaching processes occur, leading to the formation of carbonates, mainly calcite, and reducing the content of heavy metals. This results in a significant decrease in pH from 12 to around 10 (Dhir et al., 2018b; Arm et al., 2011). Accelerated aging mimics these chemical reactions but at a faster rate by optimizing conditions such as temperature, relative humidity, and moisture content to stimulate the reactions. To potentiate the accelerated carbonation of MSWI-BA, the materials can be placed in a CO_2 enriched controlled environment chamber which can shorten the treatment duration from months to days (Lin et al (2015a). This study explores the potential of accelerated carbonation as a method for stabilizing MSWI-BA.

2. Materials and methods

2.1 Raw materials

The MSWI-BA used in this investigation was collected from the waste incineration plant of Thumaide (IPALLE) directly after the incineration process. Its granular fraction is between 0 and 20 mm (BA0-20) with a moisture content of around 20% (wt.%). A portion of the MSWI-BA was wet sieved to obtain a granular fraction between 0 and 2 mm (BA0-2) with a moisture content of around 45% (wt.%).

2.2 Accelerated carbonation experiment

The accelerated carbonation was carried out in CO_2 incubator maintaining a volume concentration of 12% CO_2 at atmospheric pressure. The temperature and relative humidity inside the incubator were kept at 30±1 °C and 60±3%, respectively.
The experiment was carried using two approaches:

- Approach A: the MSWI-BA was conditioned in a climate chamber at a temperature of 30±1 °C and relative humidity of 60±3% until its weight stabilised (4 days). The moisture content of the samples decreased from 20% to 2% for both BA0-20_A and BA0-2_A before starting the accelerated carbonation.
- Approach B: the carbonation was carried out directly without any type of pre-conditioning (BA0-20_B and BA0-2_B).

Samples were collected after being carbonated for 1, 2, 4, 8, 24, 48 and 168 h where $CaCO_3$ content, CO_2 uptake, pH value and moisture content were measured.

2.3 Method analysis

After accelerated carbonation, the MSWI-BA samples were crushed using grinding disc up to d <300 µm. The calcium carbonate content of the samples was calculated by means of thermogravimetric analysis (Netzsch STA Jupiter 449). A quantity of 30-40 mg milled was weighed in a sample pan heated from 40 to 1000 °C under a nitrogen atmosphere at a heating rate of 10 °C/min. The CO_2 uptake (in g/kg of MSWI-BA) was calculated from weight loss recorded by the microbalance between 500 and 800°C (Chang et al (2015)) during the decarbonation reaction (1). The calcium carbonate content is calculated from the stoichiometry equations (2).

$$CaCO_3 \rightarrow CaO + CO_2 \quad \text{..... (1)}$$

$$CaCO_3\ (\text{wt.}\%) = CO_2\ (\text{wt.}\%) \times \frac{MW_{CaO}(\text{g/mole})}{MW_{CO_2}(\text{g/mole})} \quad \text{..... ..(2)}$$

where MWCaO (g/mole) is the molecular weight of CaO and MWCO2 (g/mole) is the molecular weight of CO2.
pH was measured on a solution with a liquid-to-solid ratio (L/S) of 1, using crushed MSWI-BA (<300 µm) and deionized water was prepared. This solution is then homogenized using a magnetic stirrer for 30 minutes. The physical properties including density, water absorption and wear resistance (Micro-Deval) of fresh, carbonated and traditionally aged MSWI-BA were measured using the standards procedures NBN EN 1097-6 (2022) and NBN EN 1097-1 (2023).

3. Results and discussions

3.1 $CaCO_3$ content

Figure 1 illustrates the evolution of calcium carbonate content in fresh bottom BA0-20 and BA0-2 over carbonation duration. For the BA0-20, the $CaCO_3$ content rises proportionally with storage time, reaching a plateau at 4 hours for approach A and 8 hours for approach B. Beyond these points, $CaCO_3$ content stabilizes. Notably, approach B exhibits a more pronounced increase in $CaCO_3$ content compared to approach A.
For BA0-2, the $CaCO_3$ content increases with time up to 8 hours for approach B and remains constant afterwards. However, with approach A, there is no observed gain in $CaCO_3$ content even after 7 days of carbonation.

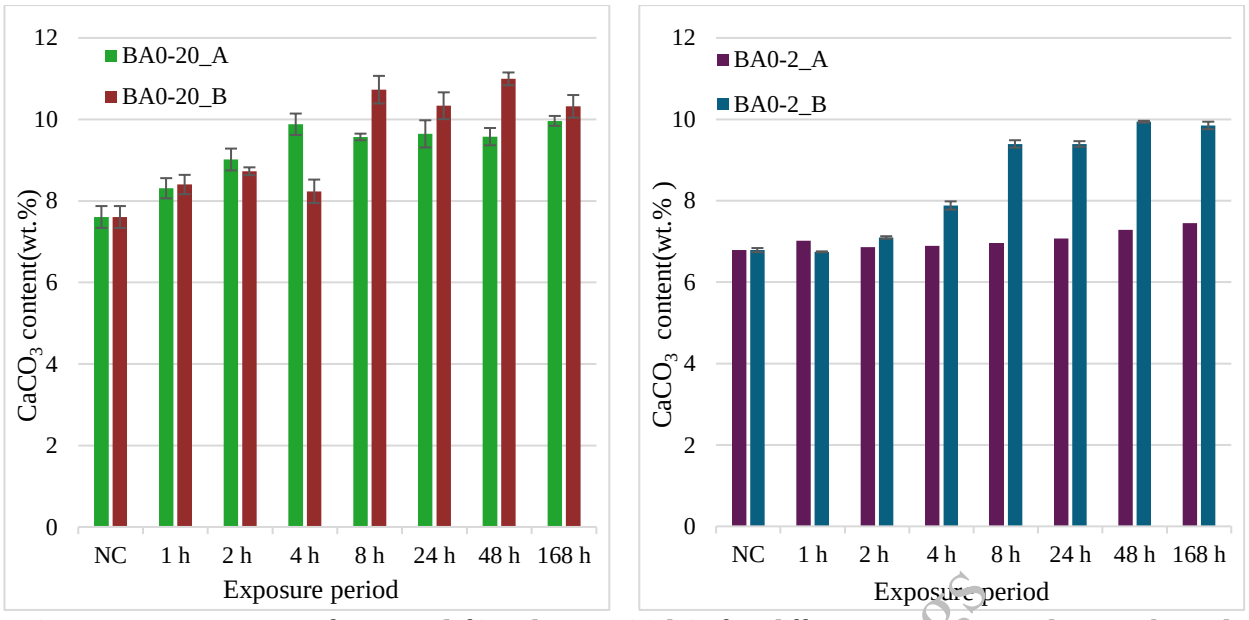

Figure 1. CaCO3 content of BA0-20 (left) and BA0-2 (right) after different exposure periods to accelerated carbonation.

3.2 CO_2 Uptake

The evolution of the CO_2 uptake was represented in a similar way to the evolution the $CaCO_3$ content. Figure 2 shows that the CO_2 uptake of BA0-20 rises proportionally with time, reaching its maximum value at 4 hours for approach A and 8 hours for approach B. Beyond these points, CO_2 uptake stabilizes. Notably, approach B exhibits a more pronounced increase in equivalent CO_2 uptake where it reached almost 14g/kg of MSWI-BA compared to approach A (only 10 g/kg). A similar behavior is observed for BA0-2, where the CO_2 uptake increases with time up to 8 hours for approach B, after which the results remain constant. However, with approach A, the gain in CO_2 uptake was negligible compared to approach B even after 7 days of carbonation. The results were similar to those obtained by Lin et al (2015a), Lin et al (2015b) and Yoa et al (2022).

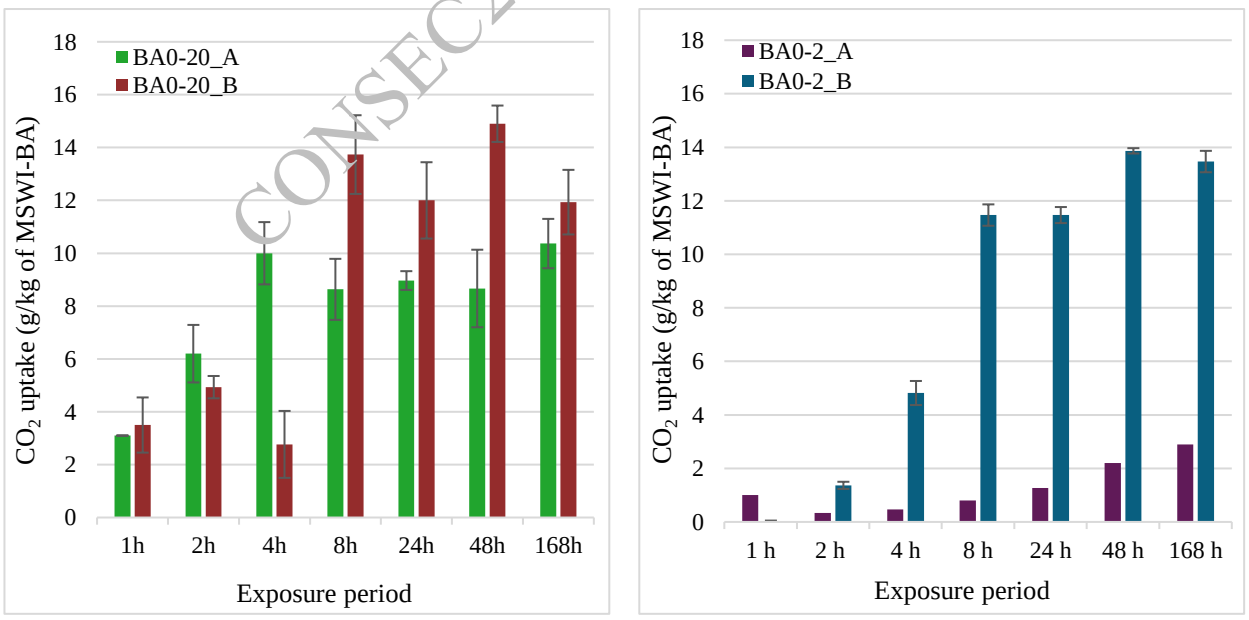

Figure 2. CO_2 uptake of BA0-20 (left) and BA0-2 (right) after different exposure periods to accelerated carbonation.

3.3 Influence of moisture content

In order to understand why approach B was more effective than approach A, the evolution of the degree of carbonation (DoC) and the actual moisture content (WC) as a function of the exposure period for both BA0-20 and BA0-2 were checked. Figures 3 show that the evolution of the degree of carbonation is greater when the water content is between 10 and 15% for the BA0-20_B and between 10 and 30% for BA0-2_B. This is in line with previous findings by Lin et al (2015b) on the effect of the initial moisture content on the efficiency of the accelerated carbonation process of BA. This means that a minimum but limited moisture content is needed for carbonation process.

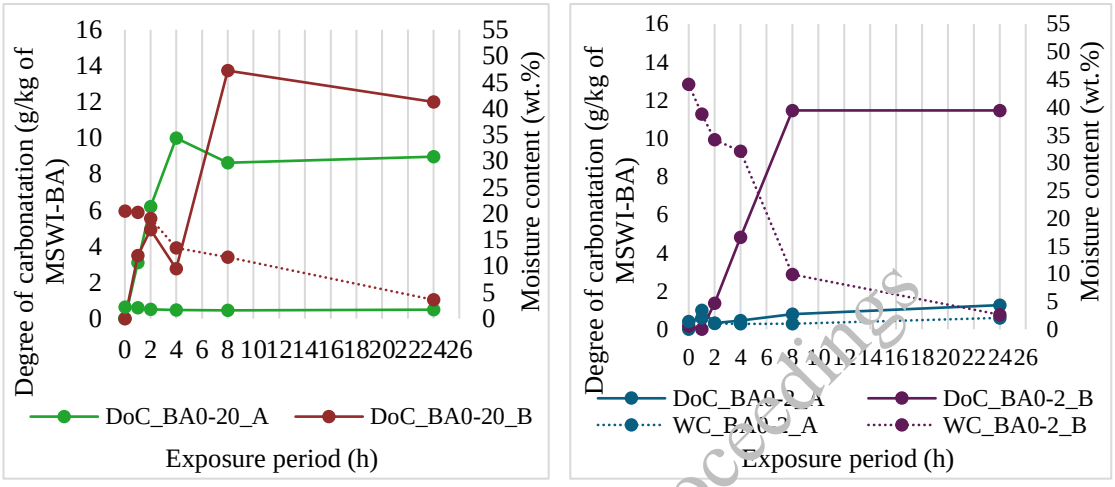

Figure 3. Evolution of the degree of carbonation and the moisture content of BA0-20 (left) and BA0-2 (right) during accelerated carbonation.

3.4 pH evolution

Equivalent results were obtained regarding the evolution of pH as figure 4 shows that the pH of the MSWI-BA decreased more significantly with carbonation using approach B over approach A, for BA0-20 and BA0-2 as well. In both cases, using approach B successfully descended the pH of MSWI-BA from 12 to 10 similar to the pH value of traditionally maturated MSWI-BA (Dhir et al (2018b), Arm et al (2011)) which aligns with previous studies done by Lin et al (2015a).

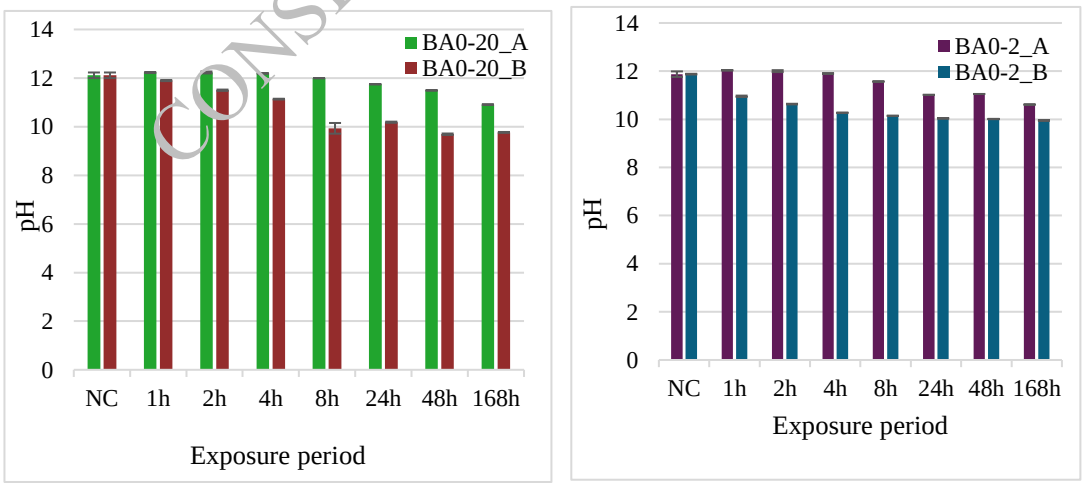

Figure 4. pH measurements of BA0-20 (left) and BA0-2 (right) after different exposure periods to accelerated carbonation.

3.5 Physical properties

Table 1 and 2 show the physical properties of fresh, traditionally maturated MSWI-BA and also MSWI-BA maturated by accelerated carbonation in controlled environment chamber using approach B for a duration of 24h. Results show improvement of the density of carbonated MSWI-BA fines aggregates compared to the fresh and the maturated samples: this is due to the transformation of most of the CaO into calcite although this didn't reflect in any decrease in water absorption capacity. For the coarse aggregates, neither the carbonation nor the maturation significantly affected the density or the water absorption capacity. This is mostly due to the fact that most of the carbonatable content is present in the fine fraction of the MSWI-BA aggregates (Lin et al (2015a)). This was reflected on the wear resistance test which was concluded on the coarse aggregates fraction as we can see that the carbonation nor the maturation process has any significant effect on the results.
Considering that the majority of the results mentioned in table 1 and 2 were in the same range as the ones obtained in the literature by Dhir et al (2018a), Becquart & Abriak (2013) and Descamps et al (2011) on the properties of traditionally maturated MSWI-BA, it's safe to say that neither the accelerated carbonation nor the traditional maturation treatment has any significant effect on the physical properties of MSWI-BA.

Table 1. Density and water absorption capacity of fines and coarse MSWI-BA aggregates under different treatment conditions compared to literature results (Dhir et al (2018a)).

		Fresh	Carbonated	Maturated	Literature
Fines MSWI-BA aggregates	**Density (kg/m^3)**	1840	2145	2239	2150-2850
	Water absorption (%)	6.9	7.3	8.24	2.2-17.3
Coarse MSWI-BA aggregates	**Density (kg/m^3)**	2280	2360	2239	1860-2680
	Water absorption (%)	2	2.4	4	7.2-15

Table 2. Wear resistance of MSWI-BA under different treatment conditions compared to literature results (Becquart & Abriak (2013); Descamps et al (2011)).

	Fresh	Carbonated	Maturated	Literature
Wear resistance (wt.%)	21	24	21	18-31

4. Conclusions

This study attempts to explore the carbon capture in MSWI-BA using accelerated carbonation and its effect on the maturation process and the physical properties of MSWI-BA. Fresh MSWI-BA was carbonated using different approaches to assess their effect on the carbonation process and pH variation. The following conclusions could be drawn according to the experimental results:

- For both fractions studied, moist carbonation (approach B) was more effective regarding carbon capture and pH stabilisation and more practical since no pre-conditioning was required.
- Regarding the type of treatment used (accelerated carbonation or traditional maturation) there was no significant improvement in the physical properties of MSWI-BA.

While this study covered the effect of accelerated carbonation on the physical properties of MSWI-BA, additional studies are required in order to investigate the effect of accelerated carbonation on chemical properties and the leaching of MSWI-BA which are the main obstacles limiting its use as secondary materials.

Acknowledgements

The authors extend their gratitude to the Walloon region and the European Union (NextGeneration EU) for providing funding for this research within the framework of the PNRR REMIND CARBOC project.

References

Arm, M., Suer, P., Arvidsson, H., Lindqvist, J.-E., (2011). "Technical and environmental long-term properties of industrial residues", *Waste Management*, 31(1): 101–107. https://doi.org/10.1016/j.wasman.2010.09.004

Becquart, F., Abriak, N.E., (2013). "Experimental investigation of the Rowe's dilatancy law on an atypical granular medium from a municipal solid waste incineration bottom ash", POWDERS AND GRAINS 2013: *Proceedings of the 7th International Conference on Micromechanics of Granular Media*, Sydney, Australia, 471–474. https://doi.org/10.1063/1.4811970

CEWEP (2017) "Bottom Ash Factsheet". FINAL-Bottom-Ash-factsheet.pdf (cewep.eu)

Chang, E.-E., Pan, S.-Y., Yang, L., Chen, Y.-H., Kim, H., Chiang, P.-C., (2015). "Accelerated carbonation using municipal solid waste incinerator bottom ash and cold-rolling wastewater: Performance evaluation and reaction kinetics", *Waste Management*, 43: 283–292. https://doi.org/10.1016/j.wasman.2015.05.001

Courard, L., Degeimbre, R., Darimont, A., Laval, A.-L., Dupont, L., Bertrand, L. (2002). "Utilisation des mâchefers d'incinérateur d'ordures ménagères dans la fabrication des pavés en béton", *Mater. Struct*, 35: 365-372.

Descamps, P., Janssens, B., Dupont, L., Lefevre, L. (2011). "Memorandum technique pour l'utilisation des mâchefers de l'unité de valorisation par incinération de Thumaide"

Dhir, R.K., Brito, J. de, Lynn, C.J., Silva, R.V., (2018a). "Municipal Incinerated Bottom Ash Characteristics", *Sustainable Construction Materials*: 91–138. https://doi.org/10.1016/B978-0-08-100997-0.00004-X

Dhir, R.K., Brito, J.D., Lynn, C.J., Silva, R.V., (2018b). "Municipal Solid Waste Composition, Incineration, Processing and Management of Bottom Ashes", *Sustainable Construction Materials*: 31–90. https://doi.org/10.1016/B978-0-08-100997-0.00003-8

Lin, W.Y., Heng, K.S., Sun, X., Wang, J.-Y., (2015a). "Accelerated carbonation of different size fractions of MSW IBA and the effect on leaching", *Waste Management*, 41: 75–84. https://doi.org/10.1016/j.wasman.2015.04.003

Lin, W.Y., Heng, K.S., Sun, X., Wang, J.-Y., (2015b). "Influence of moisture content and temperature on degree of carbonation and the effect on Cu and Cr leaching from incineration bottom ash", *Waste Management*, 43: 264–272. https://doi.org/10.1016/j.wasman.2015.05.029

NBN EN 1097-1 (2023). "Tests for mechanical and physical properties of aggregates - Part 1: Determination of the resistance to wear (micro-Deval)"

NBN EN 1097-6 (2022). "Tests for mechanical and physical properties of aggregates - Part 6: Determination of particle density and water absorption"

Yao, Z., Prabhakar, A.K., Cadiam Mohan, B., Wang, C.-H., (2022). "An innovative accelerated carbonation process for treatment of incineration bottom ash and biogas upgrading", *Waste Management*, 144: 203–209. https://doi.org/10.1016/j.wasman.2022.03.033

Investigating Sewer Environmental Conditions and Their Link to Biogenic Acid Corrosion in Sewer Concretes

Alice T Bakera,[1,2*] and Mark G Alexander[2]

[1] University of Dar es Salaam, Tanzania
Email bakera.alice@udsm.ac.tz
[2] University of Cape Town, South Africa
Email: mark.alexander@uct.ac.za

[*]Corresponding author

ABSTRACT

The degree of biogenic acid corrosion in sewers is profoundly influenced by the sewer headspace conditions, which create a conducive environment for microbial colonisation, which may result in significant concrete degradation. These environmental conditions encompass the concentration of gases, notably hydrogen sulfide (H_2S), carbon dioxide (CO_2), and oxygen (O_2), sewer headspace temperature, relative humidity, and hydraulic actions. While numerous studies have been conducted involving field and laboratory investigations to explore these conditions, a definitive connection between these factors and biogenic acid corrosion has yet to be established. This knowledge gap challenges engineers seeking to design durable sewer concrete infrastructure. The study assesses and describes the environmental conditions of three sewers in Cape Town, South Africa, adding to the sewer inventory data that can be employed to gauge sewer severities and, subsequently, design durable sewer concrete structures. This information can save substantial costs by reducing the frequency of sewer rehabilitation and repair operations.

KEYWORDS*: Biogenic acid corrosion, Sewer environmental conditions, Sewer concrete infrastructure, Repair and rehabilitation of sewer concrete.*

1. Introduction

Environmental conditions in the sewer headspace or atmosphere play a pivotal role in fostering conditions conducive to microbial colonisation and subsequent sulfuric acid production on sewer walls (Anwar et al., 2022; Kaushal et al., 2020, Wei et al., 2013). These factors include the concentration of gases such as hydrogen sulfide (H_2S), carbon dioxide (CO_2), and carbon monoxide (CO), as well as sewer headspace temperature and relative humidity (RH), influenced by climatic seasons, wastewater sources, and hydraulic flow.

According to Jiang et al. (2015), an H_2S concentration below 10 ppm is sufficient in initiating concrete corrosion; beyond this, the H_2S oxidation rate becomes the controlling factor. Sun et al. (2015) also suggest that prolonged concrete exposure to high H_2S concentrations might lead to a significant accumulation of elemental sulphur in the corrosion layer, resulting in a decrease in the H_2S adsorption rate and potentially inhibiting Sulphur Oxidizing Bacterial (SOB) activity. However, with a lack of specified thresholds in the literature, it is surmised that higher H_2S concentrations will affect the corrosion rates in long-term exposure. CO_2 and CO gases in sewers are due to the decomposition of organic matter in the wastewater, which are emitted with H_2S into the sewer headspace under sewer hydraulic actions. With unknown thresholds, CO_2 gas combines with the moisture on the sewer concrete surface to form carbonic acid, which can react with concrete, reducing surface pH from 12 to 9 and creating conditions more conducive for SOB colonisation (Hudon et al., 2011). CO gas, on the other hand, is rarely reported as a significant contributor to sewer concrete corrosion despite being widely known as a toxic gas, thus raising a concern as to whether it can affect SOB growth.

Sewer headspace temperature influences the emission of H_2S from the wastewater; higher temperatures increase the concentration in the sewer headspace (Yongsiri et al., 2004), simultaneously altering SOB proliferation and accelerating H_2S adsorption and oxidation rate on the sewer wall (Jiang et al., 2014; L. Wu et al., 2018). According to Pramanik et al. (2024), the H_2S oxidation rate slows down at temperatures below 15.6°C, while an increase from 20°C to 25°C results in a 15% oxidation rate increase.
The difference in temperature between sewer headspace and wastewater plays a role in determining RH, which subsequently affects the moisture in the sewer atmosphere (Noeiaghaei et al., 2017; M. Wu et al., 2020). When wastewater temperature exceeds that of the sewer headspace, RH increases, causing a condensate film on the concrete walls. The condensate film, with RH between 60% and 100%, promotes SOB proliferation and creates the environment for further oxidation, eventually producing sulfuric acid on the sewer wall (Li et al., 2017).
Despite extensive research, a comprehensive understanding and definitive correlation between these sewer environmental conditions and biogenic acid corrosion are still elusive. Besides, there is limited data on sewer environmental conditions to establish this correlation. Therefore, this study assesses the environmental conditions of live sewer sites, with the resulting data assisting in evaluating sewer severity and providing useful thresholds for sewer service life prediction. Consequently, engineers can design more robust sewer concrete structures capable of withstanding corrosion, reducing the frequency and cost of sewer rehabilitation and repair operations.

2. Methodology

2.1 Sewer site background

Three sewer manholes in the City of Cape Town, South Africa, two on the Northern Area Sewer (NAS), manhole 19 (NAS M19) and manhole 54 (NAS M54), and the Langa pump station manhole (LPS), were used to assess the environmental conditions of the sewers.
The 8.7 km long Northern Area Sewer (NAS) serves roughly 4000 hectares. It collects and delivers wastewater to the Langa pump station, which pumps to the Athlone Wastewater Treatment Works. Two specific manholes were singled out for study in this sewer line. See Figure ; NAS M54 is classified as low-severity and serves as the upstream manhole for the NAS line, capturing mainly domestic and public hospital wastewater. The cumulative flow rate at this manhole is estimated to be approximately 190 megalitres/day. NAS M19 is considered a medium to high severity downstream manhole, collecting wastewater from the NAS line and the sub-catchment area of a domestic and industrial area. The cumulative flow of this manhole is approximately 260 megalitre/day.

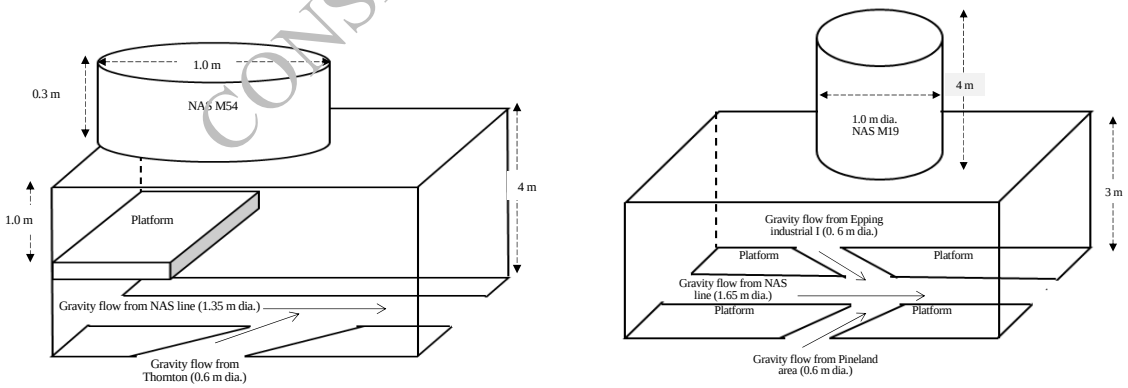

Figure 1. Schematic of the NAS M54 and M19 showing its interior and wastewater collecting channels

Langa Sewer Pump Station serves the catchment areas to deliver wastewater to the Athlone Wastewater Treatment plant. The station consists of a minor pump station that receives only domestic wastewater and the main pump station that receives primarily domestic and industrial wastewater from NAS. The manhole used for this study is between the two pump stations, as shown in Figure . It receives mainly domestic wastewater pumped periodically from the minor pump station and a continuous domestic wastewater flow. It is important to mention that this study was conducted during the COVID-19 pandemic national lockdown,

which led to a manhole breakdown due to some localised flooding followed by a lack of maintenance. It was then taken out of service for some time to allow its reconstruction.

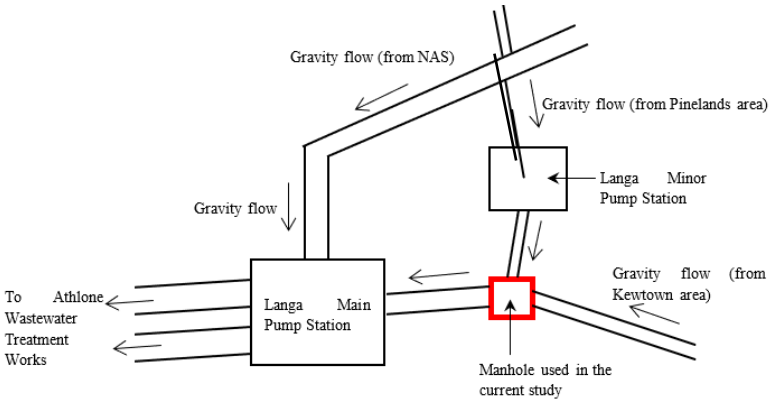

Figure 2. Schematic of the sewer network at Langa Pump Station showing two feeders into the manhole used in the current study (20 m downstream of the Minor Pump Station)(Moses Wapicho Kiliswa, 2016)

2.2 Sewer headspace condition assessment

Three sets of sewer headspace conditions, i.e., H_2S, CO_2 and O_2 gas concentrations, headspace temperature, and RH, were measured monthly for 12 hours on a selected day from March to November 2021. This covered four seasons of a year: summer (November to February), Autumn (March to April), Winter (May to August), and Spring (September to October).

The ambient temperature and RH were measured using a Hygrolog HL-20D data logger, while the gas concentrations were monitored with an Industria scientific MX6 Ibrid gas monitor. These devices were suspended in the manhole headspace to ensure reading correspondence with the locations experiencing sewer concrete corrosion.

3. Results and discussion

3.1 H_2S gas concentration

Figure 3 presents 12-hour H_2S gas fluctuation curves for a single selected day of a month from March to November 2021 at the three sites. Figure 4 displays a summary of each month in bar lines, showing the maximum, minimum, and average values at the centre of the bars.

H_2S concentrations at the LPS manhole show the highest concentration in March (365.5 ppm) and November (348.5 ppm) and the lowest in May (96.1 ppm) and June (78.2 ppm) of the year 2021. The remaining months had concentrations ranging between 200 ppm and 100 ppm. The average concentration of H_2S gas was 59.5 ± 4.9 ppm in autumn, 51.5 ± 9.0 ppm in winter, 37.5 ± 1.2 ppm in spring, and 51.1 ± 2.0 ppm in summer. The wastewater in this manhole is periodically pumped from a minor pump station every 30 minutes, leading to the periodic rising and falling of H_2S gas (see Figure 3). However, this behaviour was particularly evident from August to November after the repair work following an earlier breakdown on this manhole.

The highest H_2S concentrations in NAS M 19 were obtained in March (104.6 ppm) and April (101.1 ppm), and the lowest concentrations in September (11.5 ppm). Concentrations in other months in descending order were 41.0 ppm (May), 44.6 ppm (June), 22.7 ppm (July), 22.8 ppm (August), 25.1 ppm (October), and 40.4 ppm (November). Variations of the maximum H_2S concentrations in this manhole were primarily influenced by the peak periods of activity among the population served by the NAS line. Consequently, patterns of diurnal discharge regarding H_2S gas concentration were evident, characterised by the highest peaks during morning and evening and lower peaks during the day, down to virtually 0 ppm H_2S, see Figure 3. On average, the H_2S gas concentration was 23.6 ± 9.3 ppm in autumn, 6.4 ± 2.0 ppm in winter, 6.8 ± 3.2 ppm in spring and 13.6 ± 8.5 ppm in summer.

In NAS M54, data on H_2S concentrations for August and September were unavailable. However, for the remaining months, the maximum concentrations were 16.7 ppm in March, 16.6 ppm in April, 16.1 ppm in

May, 6.0 ppm in June, 5.3 ppm in July, 10.6 ppm in October, and 13.5 ppm in November. Since this manhole is upstream in the NAS line, primarily receiving domestic wastewater from a smaller population, the lowest gas concentrations were recorded. On average, H_2S gas concentration measured 8.6 ± 0.8 ppm in autumn, 4.3 ± 3.0 ppm in winter, 4.8 ± 1.8 ppm in spring, and 4.8 ± 2.0 ppm in summer.

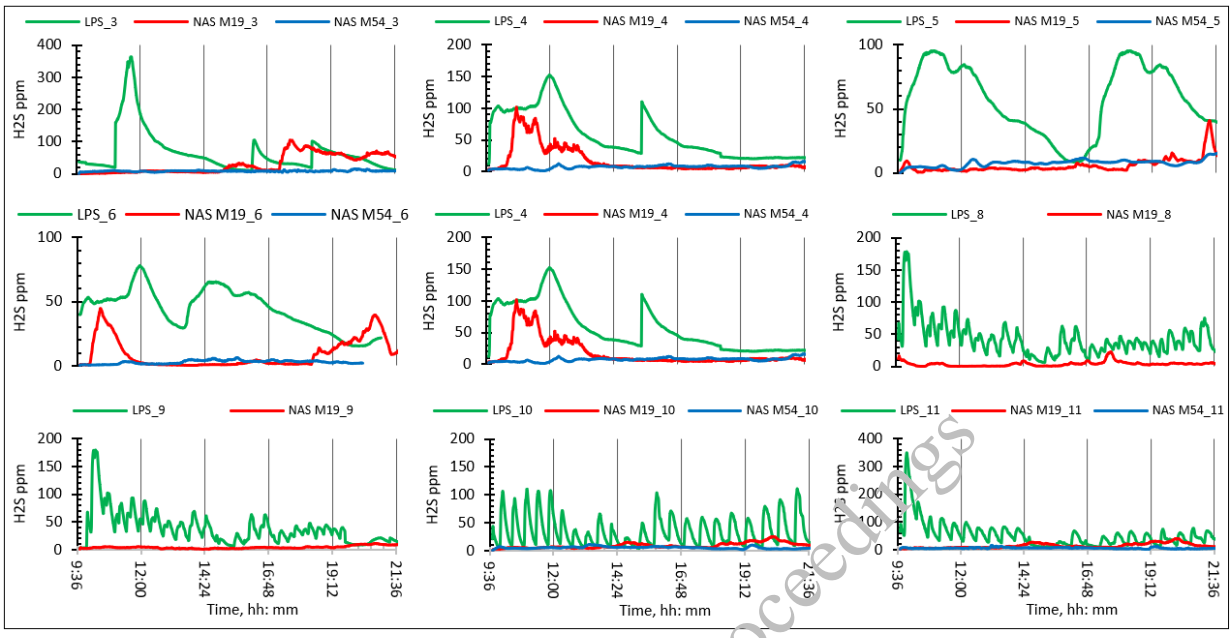

Figure 3. Diurnal and seasonal variation of H_2S gas in ppm at three sewer sites from March (3) to November (11) 2021

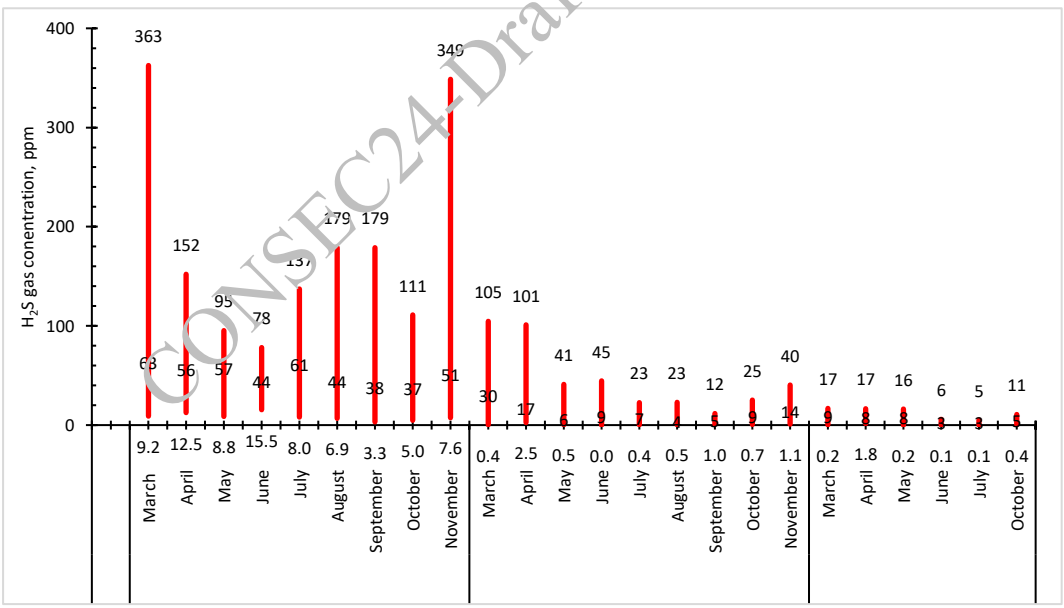

Figure 4. H_2S gas concentrations of three sewer sites from March to November 2021, with the bars showing the average, maximum and minimum concentrations.

Overall, the LPS showed the highest H_2S gas concentration, followed by the NAS M19 and then NAS. The maximum concentrations were in summer and autumn (November, March, and April), and the lowest was in winter (May, June, July and August), which concurs with Kiliswa (2016). The diurnal curves of H_2S concentration at the LPS were somewhat similar to those observed in Melbourne's Western Trunk Sewer in Australia (Sun et al., 2015). These diurnal, seasonal, and other periodic sewer events lead to significant H_2S gas fluctuation, which, in turn, varies the H_2S diffusion gradient into the sewer concrete surface, subsequently affecting the H_2S oxidation processes (Gutierrez et al., 2009; Sun et al., 2019), while

occasional high H_2S concentrations in the sewer headspace may inhibit H_2S adsorption (Sun et al., 2015). Since H_2S is crucial for service life prediction of sewer concrete (Sun et al., 2014, 2015, 2019), evaluating the H_2S adsorption solely on average concentrations might lead to over- or under-estimation of both H_2S adsorption and corrosion rate, particularly where significant fluctuations are often observed.

3.2 CO_2 gas concentration

In Figure 5 and Figure 6, CO_2 results from March to November 2021 at the three sites are presented, with a 1.0% CO_2 gas concentration equivalent to 10,000 ppm of CO_2 gas. Thus, the values indicate that the CO_2 gas concentration in these manholes is higher than H_2S gas.

The highest CO_2 concentration at LPS was 5.0%, observed in March, April, October, and November. In May, the concentration was 2.7%, 3.8% in June, 0.7% in July, 1.7% in August, and 2.7% in September. On average, the concentration was 3.9 ± 0.9 % in Autumn, 1.6 ± 0.3 % in winter, 3.3 ± 0.9 % in spring, and about 5.0 % in summer. In the NAS M19, the maximum concentrations were 1.2% in March, 1.8% in April, and 0.7% in May, while the other months had 5.0%. On average, the concentration was 0.9 ± 0.1 % in Autumn, 2.8 ± 0.5 % in winter, 4.8 ± 0.2 % in spring, and 4.3 ± 0.9 % in summer. In the NAS M 54, the maximum concentration was 0.5% in March, 0.9% in April, 1.2% in May, 0.7% in June, 0.7% in July, 2.2% in October, and 3.8% in November. On average, the concentration was 0.4 ± 0.1 % in Autumn, 0.6 ± 0.1 % in winter, 1.2 ± 0.5 % in spring, and 1.8 ± 0.9 % in summer.

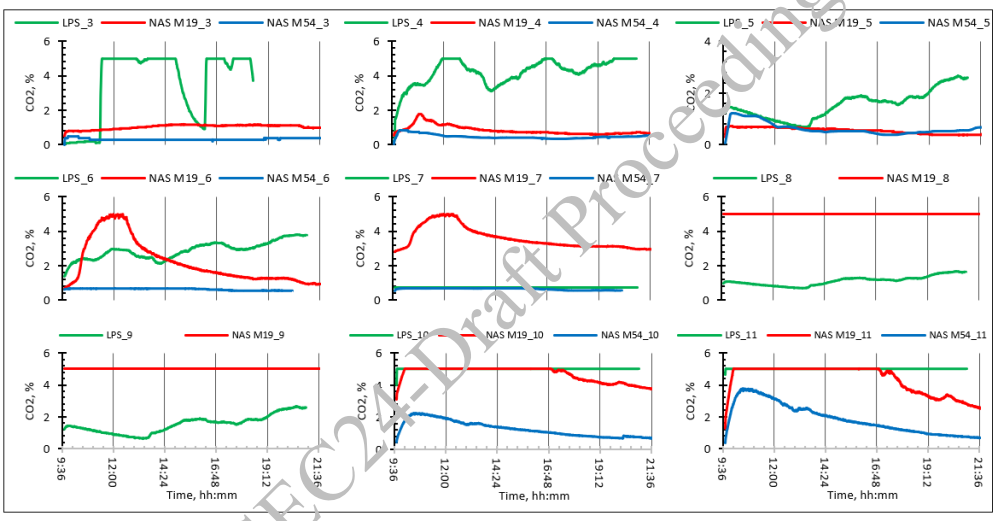

Figure 5. Diurnal and seasonal variation of CO_2 gas in % of three sewer sites from March (3) to November (11) 2021

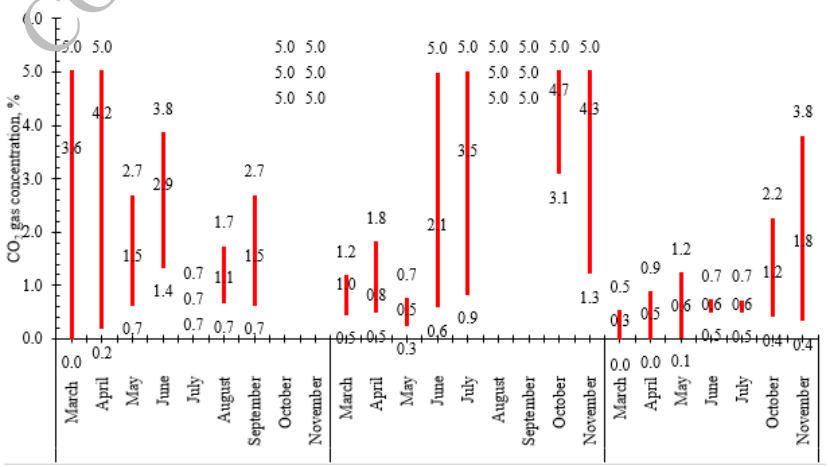

Figure 6. CO_2 gas in % of three sewer sites from March to November 2021, with the bars showing the average, maximum and minimum concentrations.

Despite NAS M54 showing lower CO_2 concentrations than LPS and NAS M19, such concentrations can cause significant carbonation if RH is between 50% and 80% (Steiner et al., 2020). The difference between LPS and NAS M19 was observed in the first three months (March to May), where the LPS showed a wide range of gas concentrations from 0.0 to 5.0 %, while NAS M19 showed about 0.5 to 1.8 %. In the subsequent months, the concentrations for the LPS decreased, while in the NAS M19, the concentrations increased. In August and September, a very high concentration approximating a constant value of 5% was observed in the NAS M19 and in October and November for the LPS.

With such high CO_2 concentrations, the concrete subjected to these sites will likely experience significant carbonation, especially when the exposed surface is continuously corroded, removed, and renewed by the influence of sewer hydraulics or gravity. This could also affect service life prediction modelling since carbonation is rarely considered. Besides, neither a significant relationship between CO_2 and H_2S concentrations nor a distinct diurnal or seasonal trend of CO2 gas was observed.

3.3 CO gas concentration

The CO gas results are presented in Figure 7 and Figure 8, similar to previous gas readings. LPS showed the highest concentration throughout the year, ranging from 0 ppm to about 1800 ppm, followed by NAS M19, about 0 to ≈ 400 ppm higher in November and March and lower in July, and then NAS M54, which had the lowest concentration of below 50 ppm.

The CO diurnal curves had similar trends as H_2S diurnal curves; see Figure 3 and Figure 7. The periods with high H_2S peaks also have high CO gas peaks. The rank of the sites from the highest to the lowest was also like that of the H_2S gas concentration. However, It was also observed that the CO concentration was higher than that of H2S gas. This, therefore, raises a discussion of whether CO gas plays any functional purpose in influencing the concentration of H_2S gas in sewers.

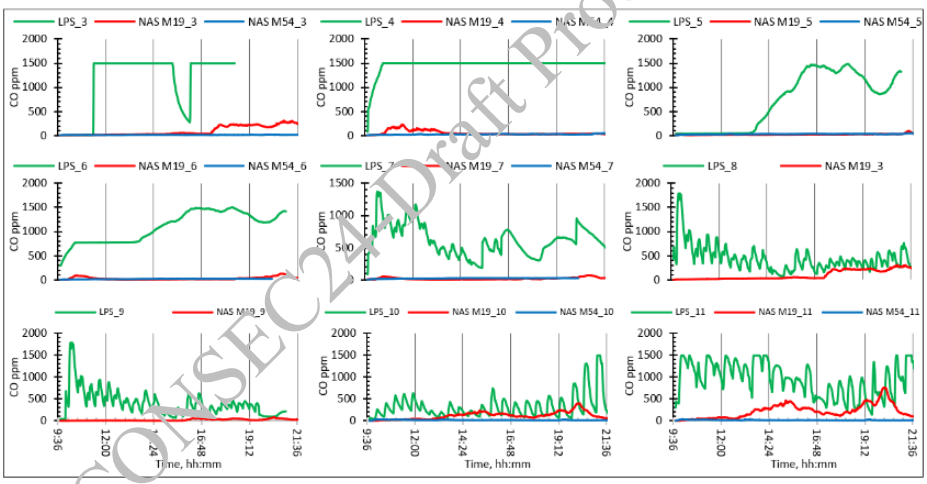

Figure 7. Diurnal and seasonal variation CO gas in ppm of three sewer sites from March (3) to November (11) 2021

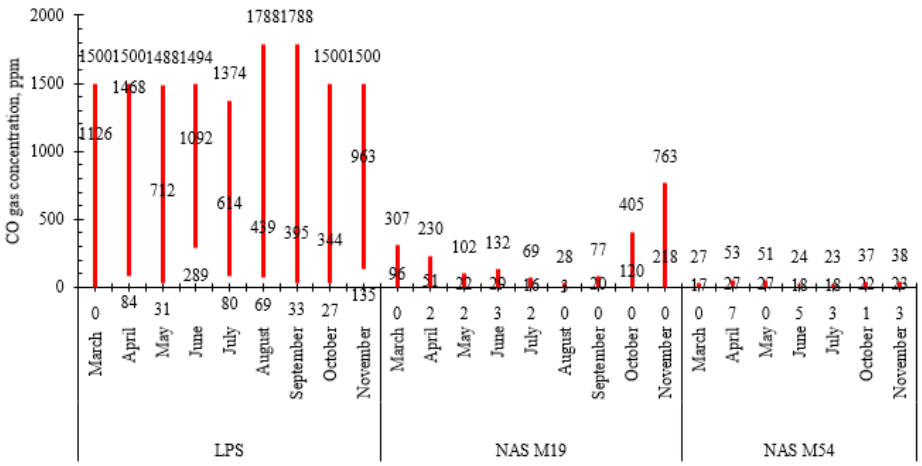

Figure 8. CO gas in ppm of three sewer sites from March to November 2021, with the bars showing the average, maximum and minimum concentrations

3.4 Temperature and RH of the sewer sites

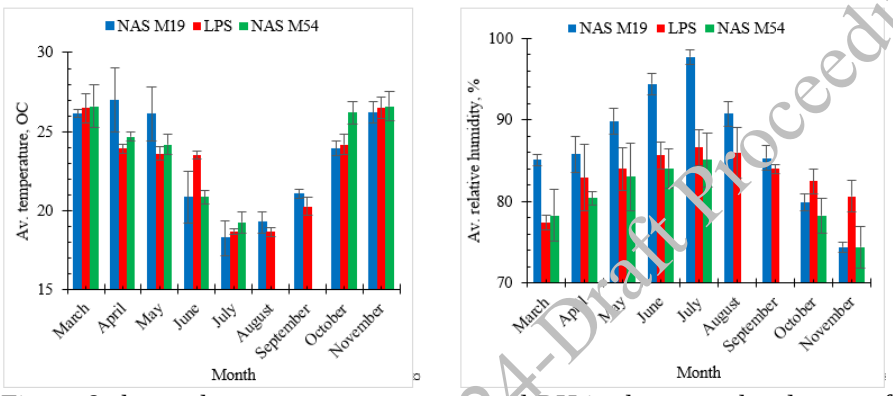

Figure 9 shows the average temperature and RH in the sewer headspace of the three sites from March to November 2021. Measurements in August and September for the NAS M54 were not captured.

The average temperatures of the sites range between 15ºC and 30ºC, with a decrease from March to July and then an increase towards November. This complies with the annual seasons, as winter occurs from May to August. Minor temperature variations among the sites were observed.

RH readings had the opposite trend to the temperature readings. RH increased from March to July and then decreased towards November, reflecting the year's seasons. The NAS M19 has the highest RH, followed by the LPS, and NAS M54 with the lowest. The average RH ranged between 70 % and 100 %, slightly higher than Li et al. (2017)observation, which reported that sulphuric acid on the sewer wall is formed when the RH in the sewer ranges between 60% and 100%.

The RH variation is influenced by the temperature differences between the wastewater and the sewer gaseous phase, the sewer wall temperature and the external environment (Joseph et al., 2012). Therefore, climate and geography influence H_2S corrosion (Saucier & Kaitano, 2018).

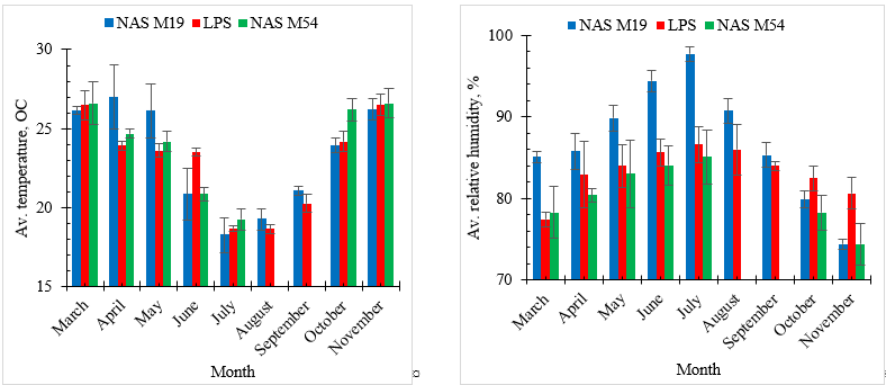

Figure 9. Temperature reading of three sites, NSM M19, NSA M54 and LPS

4. Observations and Conclusions

Based on the specific sewer environmental conditions presented in this paper, the following can be concluded:

- At the LPS, gas fluctuations are influenced by regular wastewater pumping, occasionally resulting in peak concentrations. At NAS M19, higher concentrations are observed during peak sewer hours, correlating with high sewer flow. Conversely, NAS M54 demonstrates minimal gas concentration, with peaks corresponding to minimum sewer flow. Therefore, sewer hydraulics significantly affect sewer headspace conditions and thus should be considered in service life prediction.
- H2S gas concentrations in sewer headspaces exhibit diurnal, seasonal, and periodic variations, with higher concentrations in colder and lower in warmer seasons. Therefore, average H2S concentrations may not accurately reflect sewer corrosion for service life prediction.
- Despite seasonal changes, CO2 gas remains consistently higher than H2S gas, indicating a significant potential for concrete carbonation. Therefore, it should be considered in service life prediction.
- Diurnal curves of CO gas mirror those of H2S, suggesting a potential functional relationship warranting further investigation.
- Sewer headspace temperatures typically range from 15°C to 30°C, with lower values in winter and higher in summer. Relative humidity (RH) levels are between 70% and 100%, with winter yielding the highest readings. These results concur with the literature.

Acknowledgements

The authors would like to thank LafargeHolcim (LH) Lyon in France, the Holcim Innovation Centre for their financial and material support; the Water and Sanitation Department of the City of Cape Town (CCT), South Africa, for providing access to the Northern Area Sewer line for conducting field experiments; and the University of Cape Town, South Africa, for providing facilities for conducting the study.

References

Anwar, A., Liu, X., & Zhang, L. (2022, September 1). Biogenic corrosion of cementitious composite in wastewater sewerage system–A review. *Process Safety and Environmental Protection*. Institution of Chemical Engineers.

Gutierrez, O., Sharma, K. R., & Poch, M. (2009). Advanced assessment of Sulfide and Methane emissions from sewers of Mediterranean cities, 2006–2009.

Hudon, E., Mirza, S., & Frigon, D. (2011). Biodeterioration of Concrete Sewer Pipes: State of the Art and Research Needs. *Journal of Pipeline Systems Engineering and Practice*, *2*(2), 42–52.

Jiang, G., Keller, J., & Bond, P. L. (2014). Determining the long-term effects of H2S concentration, relative humidity and air temperature on concrete sewer corrosion. *Water Research*, *65*, 157–169.

Jiang, G., Sun, X., Keller, J., & Bond, P. L. (2015). Identification of controlling factors for the initiation of corrosion of fresh concrete sewers. *Water Research*, *80*, 30–40.

Joseph, A. P., Keller, J., Bustamante, H., & Bond, P. L. (2012). Surface neutralization and H2S oxidation at early stages of sewer corrosion: Influence of temperature, relative humidity and H2S concentration. *Water Research*, *46*(13), 4235–4245.

Kaushal, V., Najafi, M., Love, J., & Qasim, S. R. (2020). Microbiologically Induced Deterioration and Protection of Concrete in Municipal Sewerage System: Technical Review. *Journal of Pipeline Systems Engineering and Practice*, *11*(1).

Kiliswa, M. W. (2016). *Composition and microstructure of concrete mixtures subjected to biogenic acid corrosion and their role in corrosion prediction of concrete outfall sewers* (PhD thesis). *PhD thesis, Department of Civil Engineering*. University of Cape Town, South Africa.

Li, X., Kappler, U., Jiang, G., & Bond, P. L. (2017). The ecology of acidophilic microorganisms in the corroding concrete sewer environment. *Frontiers in Microbiology*, *8*(April), 1–16.

Noeiaghaei, T., Mukherjee, A., Dhami, N., & Chae, S.-R. (2017). Biogenic deterioration of concrete and its mitigation technologies. *Construction and Building Materials*, *149*, 575–586.

Pramanik, S. K., Bhuiyan, M., Robert, D., Roychand, R., Gao, L., Cole, I., & Pramanik, B. K. (2024, April 15). Bio-corrosion in concrete sewer systems: Mechanisms and mitigation strategies. *Science of the Total Environment*.

Saucier, F., & Kaitano, T. (2018). H2S Biogenic Corrosion : Why Using Calcium Aluminate Concrete and Mortars to Rehabilitate Corroded Sewer Infrastructures. *IMESA Conference Port Elizabelt*, 143–148.

Steiner, S., Lothenbach, B., Proske, T., Borgschulte, A., & Winnefeld, F. (2020). Effect of relative humidity on the carbonation rate of portlandite, calcium silicate hydrates and ettringite. *Cement and Concrete Research*, *135*.

Sun, X., Jiang, G., Bond, P. L., Wells, T., & Keller, J. (2014). A rapid, non-destructive methodology to monitor activity of sulfide-induced corrosion of concrete based on H2S uptake rate. *Water Research*, *59*, 229–238.

Sun, X., Jiang, G., Bond, P. L., & Keller, J. (2015). Impact of fluctuations in gaseous H2S concentrations on sulfide uptake by sewer concrete: The effect of high H2S loads. *Water Research*, *81*, 84–91.

Sun, X., Jiang, G., Bond, P. L., & Keller, J. (2019). Periodic deprivation of gaseous hydrogen sulfide affects the activity of the concrete corrosion layer in sewers. *Water Research*, *157*, 463–471.

Wei, S., Jiang, Z., Liu, H., Zhou, D., & Sanchez-Silva, M. (2013). Microbiologically induced deterioration of concrete - A review. *Brazilian Journal of Microbiology*, *44*(4), 1001–1007.

Wu, L., Hu, C., & Liu, W. V. (2018). The sustainability of concrete in sewer tunnel-A narrative review of acid corrosion in the city of Edmonton, Canada. *Sustainability (Switzerland)*, *10*(2).

Wu, M., Wang, T., Wu, K., & Kan, L. (2020, April 10). Microbiologically induced corrosion of concrete in sewer structures: A review of the mechanisms and phenomena. *Construction and Building Materials*.

Yongsiri, C., Vollertsen, J., & Hvitved-Jacobsen, T. (2004). Effect of temperature on air-water transfer of hydrogen sulfide. *Journal of Environmental Engineering*, *130*(1), 104–109.

Influence of GFRP Minibars on the Mechanical Properties of Self-Compacting Concrete in Flexural and Shear

Moussa Coulibaly[1], Olivier Helson[2], Anne-Lise Beaucour[1], Javad Eslami[1], Xavier Bourbon[2], Albert Noumowé[1]

[1](L2MGC) Laboratoire de Mécanique et Matériaux du Génie Civil, CY Cergy Paris Université, 5 mail Gay-Lussac, Neuville sur Oise 95031 Cergy-Pontoise cedex, France
[2](ANDRA) Agence Nationale de Gestion des déchets Radioactifs 1/7, rue Jean Monnet Parc de la Croix-Blanche 92298 Châtenay-Malabry cedex, France

*Corresponding author

ABSTRACT

The aim of this experimental research work is to develop non-metallic fiber-reinforced concrete that could be used as an alternative material for the structures of Cigeo (Industrial Center for Geological Disposal). The use of non-metallic fiber could constitute a solution to reduce the amount of steel reinforcement in concrete structures and therefore limit the consequences of corrosion in the underground tunnel environment. This solution is an alternative way to increase the durability of the construction materials while maintaining the high mechanical performance, since these fibers are not subject to corrosion. The properties required by the test materials aim in the proposed application a concrete compressive strength class C60/75 in accordance to EN 1992-1-1 standard. For this purpose, the AR-glass fibers minibars are used. The fresh and hardened properties of fiber reinforced self-compacting concrete (FRSCC) are investigated with the variation of the volume fraction (vf) of fibers. The concretes mix design was developed in such a way as to quantify the influence of fibers on concretes mechanical behavior. The mechanical properties of the concretes are evaluated based on three points flexural test and four points shear test conducted on 14×14×56 cm specimens. The modes of failure of fibers are highlighted by SEM observations on samples after concrete failure in flexural. The results indicate that the addition of AR-glass fibers increases the residual strength of concretes in flexural and shear resistance. However, from 2% of fiber volume fraction, this trend reverses probably due to the breakage of fibers during mixing.

KEYWORDS*: Non-metallic fiber, Self-compacting concrete, Fiber volume fraction, Minibars AR-glass fibers, Mechanical properties*

1. Introduction

The reinforcement of construction materials, particularly concrete, with fibers is a technique used to solve the problem of brittleness, as well as improving their toughness. This incorporation of fibers is intended to enhance mechanical properties and durability [1]. The majority of fiber reinforced concrete (FRC) use steel fibers because of the high mechanical performance they provide to concrete, compared with that of non-metallic fibers. However, the incorporation of these fibers can be problematic in the long term. Steel fibers are not only vulnerable to corrosion, but also, at high incorporation rates, increase the structure's dead weight [2][3], reduce the workability of the concrete and, depending on the geometry, promote fibers balling [3], thus creating zones of weakness leading to losses in mechanical performance. The use of non-metallic fibers can be a solution for controlling concrete cracking and absorbing stresses in the area of cracks, while improving the durability of the structure, since these fibers are not subject to corrosion. Glass and basalt fibers are popular alternatives. Their popularity has grown in recent decades, and they have become a common and effective technique for reinforcing and repairing concrete structures. The drawback of glass and basalt fibers is their susceptibility to degradation in alkaline environment due to their chemical composition (mainly composed of SiO_2). For these reasons, the manufacturers of these fibers have come up with two solutions. The first is to add zirconium to their composition [4], and these fibers are known as

alkali-resistant (AR) fibers. The second solution is to reinforce them with a polymer matrix (FRP). The polymer matrix forms the first line of defense of the fibers against corrosive environments and offers a level of protection to fibers [5]. Recently a novel FRP, commercially named minibars, was developed by ReforceTech manufactory, which are essentially the scaled-down version of FRP bars [3].

The minibars fibers tensile strength is higher than that of steel fibers (1000 vs 400 MPa), but their elastic modulus is lower (44 vs 195 GPa). Their high tensile strength and lower stiffness lead to the activation of toughness mechanisms that can only be achieved by adding hybrid fibers only [6]. Minibars fibers have a density (1.9 to 2.1) almost similar to that of concrete, which contributes to the production of fiber reinforced concrete (FRC) with excellent workability as well as the possibility of exceeding the volume fraction considered critical for fibers with higher densities. Another advantage of this property is the resistance to static or dynamic segregation. Minibars do not sink or float in the mix[7], making their distribution favorable. It combines the advantages of stiff steel and non-stiff nonmetallic fibers [8]. Their helical profile provides excellent bond in the matrix, resulting in good pull-out resistance [7] and improved stress absorption at cracks, which in turn leads to better-performing concretes. Minibars act in much the same way as metal fibers, increasing the deformation capacity of concrete while limiting crack propagation [9]. They provide excellent ductility properties to concrete through pull-out and fiber rupture [3][10].

However, the impact of minibars on the mechanical performance of concretes in compression is the subject of divergence. J. Branston and al [3] observed a drastic loss of compressive strength after adding minibar basalt fiber to concretes and state that adding minibars fibers to concrete is not an effective method to improve the compressive strength of concretes. However, according to a study conducted by Coulibaly and al [10], glass-AR and basalt fiber minibars were found to improve the compressive performance of concrete by up to 17% compared with concrete without reinforcement. These two studies show that, despite the negative or negligible impact of minibars on the mechanical performance of concrete in compression, they improve the ductility of concrete in compression.

Numerous studies have highlighted the ability of steel fibers to replace part of the traditional steel reinforcement, thanks to their tensile, flexural and shear strength [3][11]. Being generally macrofibers with lengths between 18 mm and 56 mm, and acting in a quasi-similar way to steel fibers by providing a very high residual load capacity to concrete in tension, minibars fibers could constitute a potential alternative for the partial substitution of metal reinforcement in structures. Their use in concrete could therefore be an excellent solution for reducing or eliminating corrosion in the material [12]. However, very little data exists on their long-term durability in environments that could challenge their mechanical performance. The vinylester matrix, they are reinforced with, provides a protective layer against chemical attack that can give the reinforced material good durability. It should be noted that a study of the durability of minibars is currently being carried out in solutions simulating concrete interstitial solutions, but unfortunately the results will not be presented in this paper.

2. Experimental procedure

2.1 Materials

All concretes were made with CEM III/A 52.5 L CE PM-ES-CP cement. The crushed washed sand (0/4) and gravel (4/12) used for the mixing are of limestone origin. The minibars used in this study are composed of 18% polymer (vinylester) and 82% AR-filaments. The composites have a length of 33 mm, a diameter of 0.7 mm, a tensile strength of 1116±41 MPa and a density of 2.1. In order to achieve the rheological properties required for the study concretes in the fresh state, the master ease 3500 superplasticizer was used. In order to adjust the granular distribution, the limestone filler betoflow was used.

To study the influence of fibers on the rheological and mechanical properties of the concretes, all the blends were made with the same type of aggregates. The FRC studied are self-compacting concretes (SCC), with a target spread class of SF1 (which means that the spread at the Abrams cone must be between 550 and 650 m). The target value of the ratio (H2/H1) in L-Box (while H1and H2 represent the heights of concrete at the beginning and end of the horizontal section, respectively), was minimum 0.8. The different volumes fractions of fibers are 0%, 1%, 2% and 3% and these concretes are identified by PC, FRC33-1, FRC33-2 and FRC33-3. For all mixtures, the aggregates were substituted by fibers, while keeping constant the W/C ratio. These substitutions are aimed at compensating the loss of workability caused by the increase in fiber dosage. It is well known that the increase of fiber volume fraction has significant impact on the properties

of SCC in the fresh state. For this purpose, the quantity of limestone filler, the dosage of superplasticizer and the value of G/S ratio are adjusted by trial batches. The dosages selected are those that give the concrete sufficient workability to satisfy the desired slump flow diameter (SF1). To this end, the G/S ratio were kept constant (G/S = 0.66) for PC, FRC33-1 and FRC33-2 and decrease (G/S=0.49) for FRC33-3 (see table1). The Water/Paste $_{(\text{Cement} + \text{limestone filler})}$ ratios decrease with increasing fiber dosage and are: 0.32, 0.31 and 0.27 for FRC33-1, FRC33-2 and FRC33-3 respectively. The specimens were demolded 24 h after casting and kept in water for 28 days.

Table 1. Mixture composition and fresh properties of the concretes (SP stands for superplasticizer, G for gravel, S for sand, C for cement and w for water), $RC_{90\ days}$ for compressive strength at 90 days, W/P for water to paste (cement + limestone filler) ratio

	Unit content (kg/m^3)			
	PC	FRC33-1	FRC33-2	FRC33-3
Cement	475	475	475	475
Limestone filler	100	100	123	200
Sand 0/4	987.3	971.3	941.6	982.6
Gravel 4/12	655.7	645.1	625.4	482.1
Minibars	0	21	42	63
SP	7.1	9.3	10.5	13.5
Water	186.2	186.2	186.2	186.2
G/S	0.66	0.66	0.66	0.49
W/C	0.392	0.392	0.392	0.392
W/P	0.32	0.32	0.31	0.27
Slump flow (cm)	72.5	64.5	60.4	58
L-box (-)	1.04	0.91	0.84	0.88
$RC_{90\ days}$ (MPa)	63.7	79.7	73.1	90.7

2.2 Test methods

2.2.1 Three points flexural tensile strength

The flexural test was completed following the guidelines of the European standard NF EN 14651 +A1 [13]. The tests were carried out on three prismatic specimens at 28 days (for each mixture) with 140×140 mm in cross-section and 560 mm in length fig.1. A notch of 15 mm width was realized at mid-span of the specimens in order to obtain a distance of 125 mm between the notch tip and the top surface of the specimen (hsp). However, the depth of the notch varied between 17 and 23 mm due to inaccuracy during sawing. The span length is 500 mm and the tests series were displacement controlled at 1 mm/min and were carried out on a Zwick/Roell (Z400) machine with an estimated loading capacity of 250 kN. The DIC (digital image correlation) technique was used in this experimental program on one face of each beam, using DSLR 5D-camera with 6720 pixels (sensor width) and 4480 pixels (sensor height). The camera is positioned at a distance from the surface of the specimen and perpendicular to the center of the zone of interest, so as to record images continuously (each second). This method involves measuring the displacement field on the surface between the reference image and a series of deformed images recorded during the test [14]. The behavior of the prism samples was analyzed using GOM software. GOM software allowed for the placement of numerical extensometers in various directions [15]. Through the horizontal numerical extensometers placed at the base of the notch, the Crack Mouth Opening Displacement (CMOD), are measured.

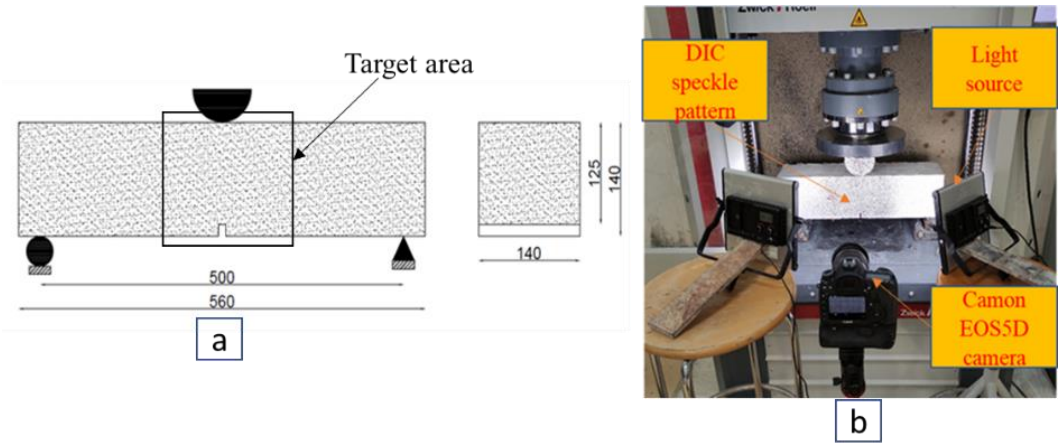

Figure. 1(a) Schematic of flexural tensile test, 1(b) flexural tensile test setup

2.2.2 Shear test

The shear tests were carried out based on the testing protocols used by Vu [16] and A Khanlou and al. [17]. The tests were conducted on three prismatic specimens at 28 days, with a 140 × 140 mm cross-section and a length of 560 mm. The shear configuration was designed such that the notched zone is subjected to the maximum shear stress fig.2. In order to avoid cracking outside the intended failure shear plane, a 30 mm deep and 5 mm width notch was realized at mid-span and all arounds of the specimens. However, the depth of the notch varied between 30 and 37 mm due to inaccuracy during sawing. The tests were carried out on a Zwick/Roell (Z400) machine. The loading speed was set equal to 1 mm/min. The DIC technic was used to extract the crack opening and the crack slip.

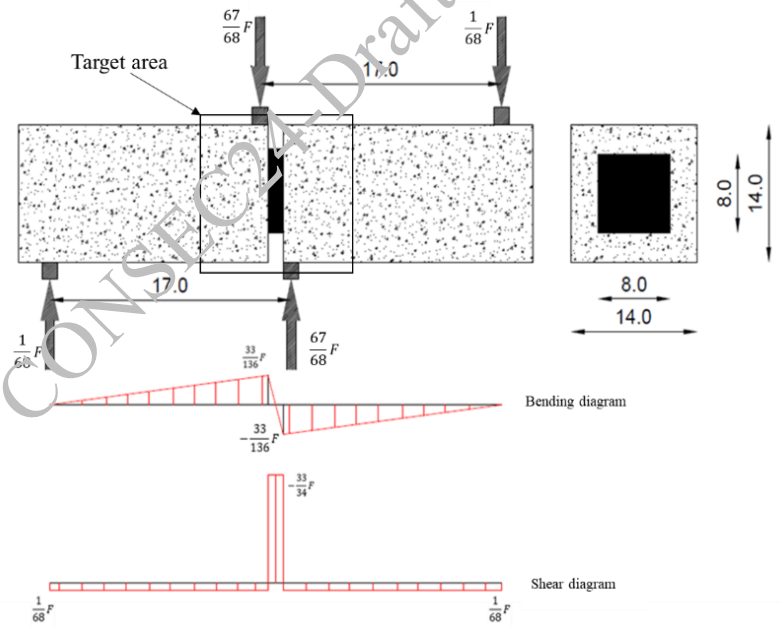

Figure 2: Shear test setup

3. Results and discussion

3.1 Flexural tensile strength

The stress vs CMOD curves for FRC are shown in Fig.3. This graph shows the mean values of the curves obtained after testing the three specimens for each batch. The tested concretes exhibit different types of behavior. These behaviors depend largely on the volume fraction of the fibers. As expected, the plain

concrete (PC) exhibits a brittle behavior. After the first cracks initiate (matrix failure), characterized by a fall of the peak stress, no stress recovery is observed. The load bearing capacity drastically decreases after the peak stress was reached, which is typical of concrete with 0% of fiber. The specimens containing 33 mm AR-glass minibar fibers show more noticeable displacement capacities, with significant stress recovery after the failure of the matrix. After a temporary drop after cracking, FRC33-2 and FRC33-3 present a subsequent upward trend toward the maximum stress in concrete strength up to a maximum stress value occurring between 0.31 and 0.28 mm of crack opening respectively. After reaching ultimate stress, two observations can be made for FRC33. For FRC33-3, a rapid softening of the curve is observed, resulting in a break in slope on the curve from a CMOD of 0.6 mm. This corresponds to the degradation of the reinforcing fibers [18]. For FRC33-2 and FRC33-1, a hardening of the behavior is observed, expressed by a concavity of the curves revealing the more ductile behavior of these concretes. Overall, the addition of AR-glass minibar fibers improves the pre-peak and post-peak behavior of concretes compared to plain concrete (PC) fig.3. However, from a design point of view, the residual strength corresponding to a CMOD of 0.5 mm (SLS) increases significantly between 1 and 2%, but less between 2 and 3%. At CMOD 2.5 mm (SLU), concretes reinforced with 2% exhibit the better behavior

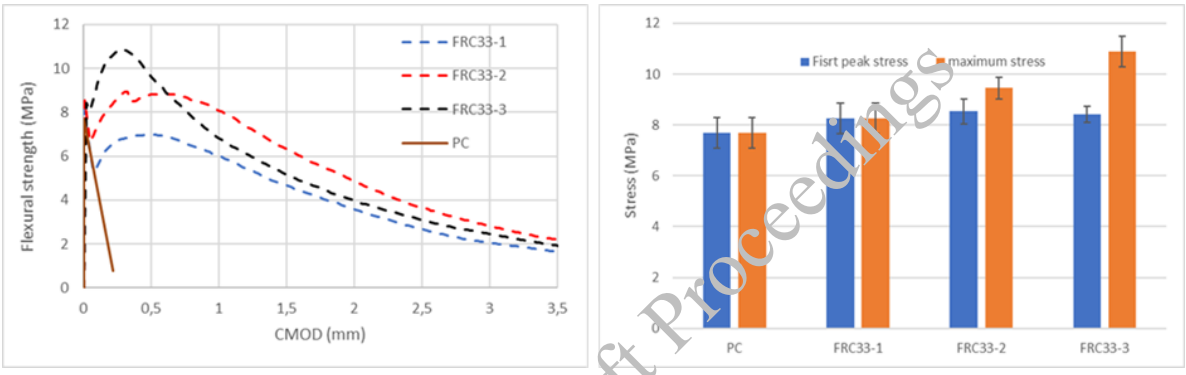

Figure 3. Flexural tensile strength of concrete - CMOD curves of concretes obtained from bending test (left); first peak and maximum stress vs fibers volume fraction (right)

3.1.1 Failure modes of fibers in flexural

In order to analyze the failure mode of fibers during the bending test, a 6×6 cm section of concrete was taken from the failure surface of the prisms after the flexural test fig.4. SEM microstructural observations were carried out to highlight the different failure modes of fibers. For all the concretes in the study, two failure modes can be observed

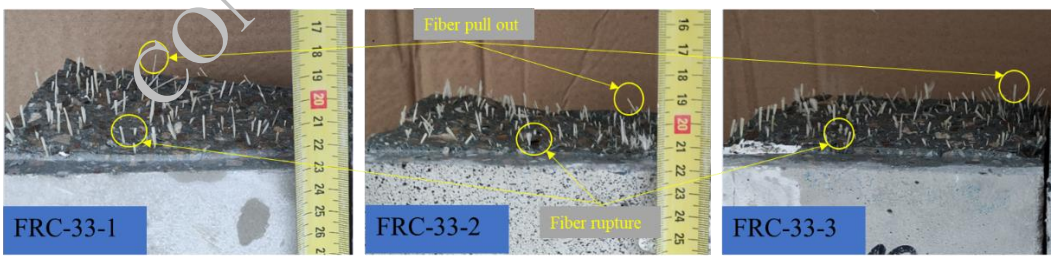

Figure 4. Failure surface of FRC33 after flexural tensile test

The first failure mode involves the pull-out of fibers fig.5(a)(b)(c). The absence of polymers on these fibers can be explained by an adhesion between the matrix and the polymer that is greater than the adhesion between the polymer and fibers filaments. As for the second failure mode, it involves fibers failure by rupture fig.5 (d)(e)(f). These two failure modes were observed by [3][10][19]. However, the fig.5(f) shows the presence of cement paste on and between some fiber filaments, which can be explained by the breakage of fibers during mixing, allowing the paste to penetrate easily. Indeed, during mixing, fiber breakage was observed, and this increased with increasing fiber content. To this end, it can be observed that, the second failure mode (fiber rupture) becomes more abundant above 1% volume fraction fig.4.

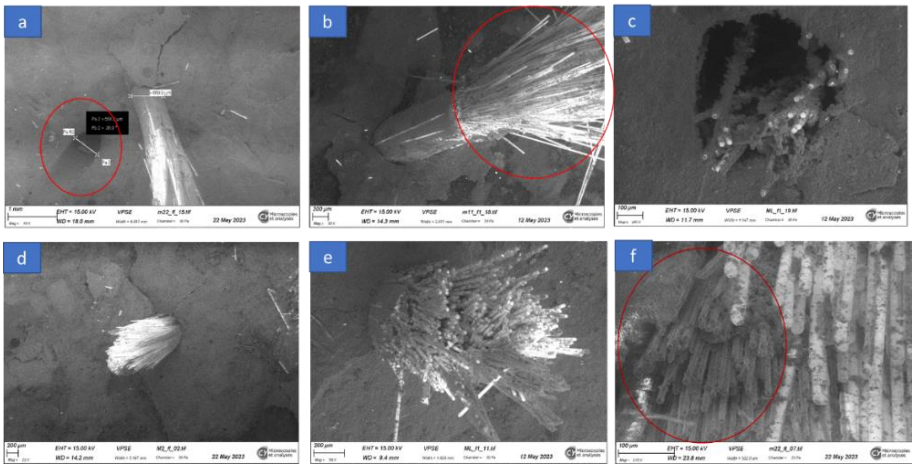

Figure 5. SEM images of fibers of minibars on failure surface

3.2 Shear strength

The overall behavior of 33 mm fiber-reinforced concrete in the shear test can be divided into four main phases fig.6. During the first loading phase, the prisms deform in a quasi-elastic manner, characterized by a quasi-linear rise in the stress vs crack opening /crack slip curves, with a total absence of opening or slip of the prism blocks. During this phase, prism behavior is governed by the strength of the cementitious matrix. At the end of this phase, the first microcracks appear in the notches, leading to the localization of the main macrocrack. At this stage, mode I crack propagation is observed due to the contribution of the bending moment in the notches fig.2. The end of this phase is observed once the maximum ultimate shear stress has been reached. The third phase is characterized by a softening of the curves on the graphs, and at this point, mode II crack propagation is observed in the notches. The fourth phase is characterized by a break in slope, showing the significant opening of the main macrocrack, highlighting the damage to the reinforcing fibers. The fig.6 shows shear stress vs crack opening and shear stress vs crack slip respectively. After the elastic phase, plain concrete (PC) exhibits brittle behavior and the FRC33 show a hardening behavior with pronounced stress recovery, followed by significant softening at crack openings of 0.5 mm, 1.25 mm and 1 mm for FRC33-3, FRC33-2 and FRC33-1 respectively. However, the stress vs crack slip curves decrease sharply for slip displacement of less than 1 mm. Indeed, all concretes exhibit hardening behavior; however, FRC33-2 shows a significantly higher degree of deformability compared to FRC33-1 and FRC33-3. Additionally, it is observed that, the softening phase of FRC33-3, which indeed has the highest maximum shear stress, occurs very quickly.

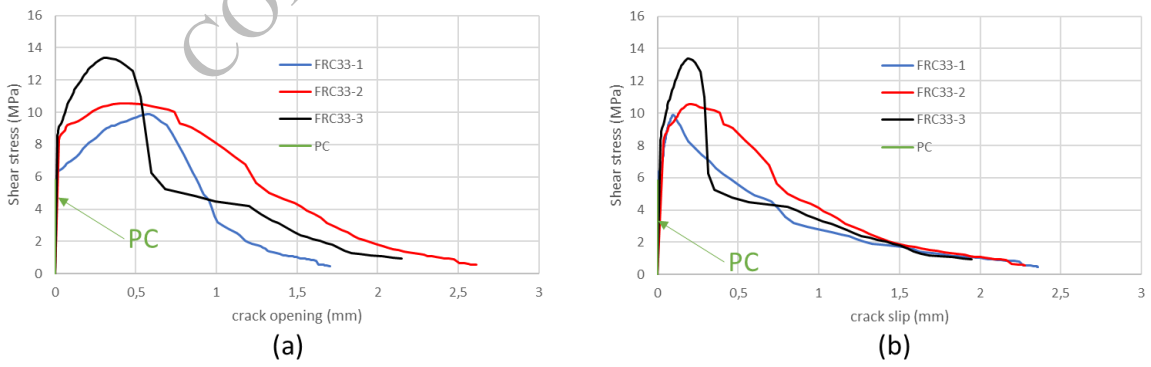

Figure 6. Shear stress vs crack opening (left); Shear strength vs crack slip (right)

The fig.7 summarizes the contribution of fibers to improving the pre-peak and post-peak behavior of concretes. It can be observed that the additions of 33 mm AR-glass minibars fibers enhance the first-peak and ultimate shear strength compared with the PC. The fibers improve concrete performance at first peak

by 3.9%, 36.9% and 33.6% and at post-peak by 63.4%, 78.1% and 122.7% for FRC33-1, FRC33-2 and FRC33-3 respectively.

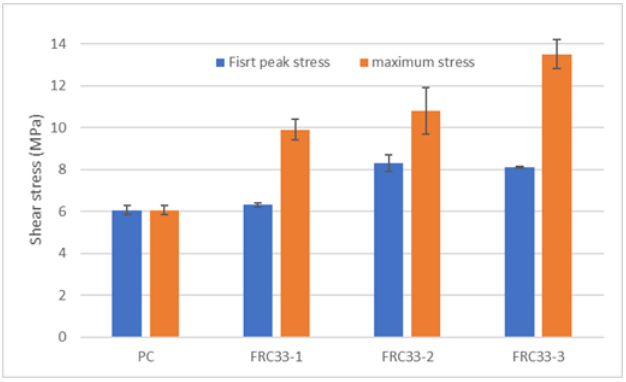

Figure 7. Shear first peak and maximum stress vs minibars volume fraction

The fig.8 shows the evolution of concretes crack slip vs crack opening. Before maximum shear stress of the tested concretes is reached, the crack opening increases faster than concretes blocks slip. In the softening phase, the trend is reversed, i.e., the crack slip becomes more significant, while the evolution of the crack opening is very slight. This shows the typical behavior of crack slip vs crack opening [16]. However, for FRC33-2 and FRC33-3, it is found that crack openings and crack slip evolve in a quasi-proportional manner in the softening phase.

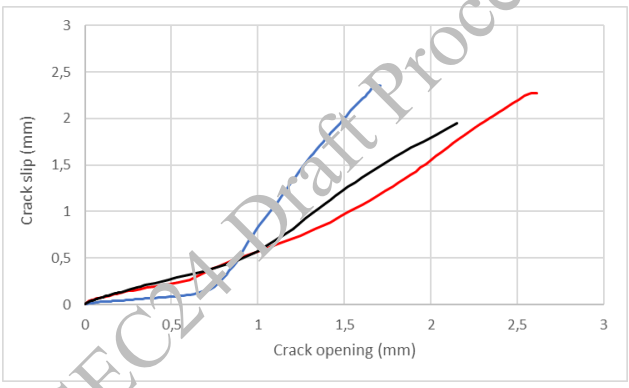

Figure 8. Crack slip vs crack opening curve

4. Conclusions

This paper focused of fibers volume fraction on the mechanical properties of concretes. The results of this study show that the addition of AR-glass minibars fibers modifies the fracture mechanism in flexural and shear, and results in a high deformation capacity of the concrete. The addition of glass fiber increases the residual strength of concrete with increasing fiber volume fraction. However, above 2% volume fraction, there is a loss of residual flexural and shear strength. This loss of strength is probably due to an accentuation of fiber breakage during concrete mixing, resulting in a reduction in fiber size and the creation of short fibers, which are less efficient than long fibers in the post-peak phase. Overall, the addition of glass fibers increases the flexural and shear strength of concrete as the fiber volume fraction increases. Based on their contribution in improving concretes flexural and shear performance, and their corrosion resistance, AR-glass minibars fibers constitute a viable alternative to steel fibers in aggressive environments. Future investigations will focus on their ability to replace part of metal reinforcement in Reinforced Cement concrete (RCC) elements.

References

P. Zhang, Y. Yang, J. Wang, S. Hu, M. Jiao, et Y. Ling, « Mechanical Properties and Durability of Polypropylene and Steel Fiber-Reinforced Recycled Aggregates Concrete (FRRAC): A Review », *Sustainability*, vol. 12, no 22, Art. no 22, janv. 2020, doi: 10.3390/su12229509.

Q. Wang, Y. Ding, et N. Randl, « Investigation on the alkali resistance of basalt fiber and its textile in different alkaline environments », *Construction and Building Materials*, vol. 272, p. 121670, févr. 2021, doi: 10.1016/j.conbuildmat.2020.121670.

J. Branston, S. Das, S. Kenno, et C. Taylor, « Mechanical behaviour of basalt fibre reinforced concrete », *Construction and Building Materials*, vol. 124, p. 878-886, oct. 2016, doi: 10.1016/j.conbuildmat.2016.08.009.

Ya. V. Lipatov, S. I. Gutnikov, M. S. Manylov, et B. I. Lazoryak, « Effect of ZrO2 on the alkali resistance and mechanical properties of basalt fibers », *Inorg Mater*, vol. 48, no 7, p. 751-756, juill. 2012, doi: 10.1134/S0020168512060106.

N. Ravindran et E. H. Cho, « Durability of glass-fiber-reinforced polymer nanocomposites in an alkaline environment », *Journal of Vinyl and Additive Technology*, vol. 12, no 1, p. 25-32, 2006, doi: 10.1002/vnl.20063.

S. Adhikari, « Mechanical and structural characterization of mini-bar reinforced concrete beams », 2013. Consulté le: 6 juin 2023.

M. Rengarajan, Laboratory testing of shotcrete with fibres of steel, basalt or synthetic materials. 2020. Consulté le: 5 juin 2023. [En ligne]. Disponible sur: https://urn.kb.se/resolve?urn=urn:nbn:se:kth:diva-287310

S. Sandbakk, « Fibre Reinforced Concrete: Evaluation of test methods and material development », Doctoral thesis, Norges teknisk-naturvitenskapelige universitet, Fakultet for ingeniørvitenskap og teknologi, Institutt for konstruksjonsteknikk, 2011. Consulté le: 5 juin 2023. [En ligne]. Disponible sur: https://ntnuopen.ntnu.no/ntnu-xmlui/handle/11250/236730

N. Nikolov et O. Sultani, « Effect of basalt minibars and steel fibers on the mechanical behavior of concrete. », Bachelor thesis, uis, 2021. Consulté le: 30 novembre 2023. [En ligne]. Disponible sur: https://uis.brage.unit.no/uis-xmlui/handle/11250/2774352

M. Coulibaly, « Evaluation des performances mécaniques des bétons autoplaçants renforcés de fibres non-métalliques », *Academic Journal of Civil Engineering*, vol. 41, no 1, Art. no 1, juin 2023, doi: 10.26168/ajce.41.1.34.

Y. Fritih, « Apport d'un renfort de fibres sur le comportement d'éléments en béton autoplaçant armé », These de doctorat, Toulouse, INSA, 2009. Consulté le: 6 juin 2023. [En ligne]. Disponible sur: https://www.theses.fr/2009ISAT0048

J.-S. Branston, « Properties and applications of basalt fibre reinforced concrete », M.A.Sc., Ann Arbor, United States, 2015. Consulté le: 6 juin 2023. [En ligne]. Disponible sur: https://www.proquest.com/docview/1728024951/abstract/3BFE42CF76D84225PQ/1

« NF EN 14651+A1 », Afnor EDITIONS. Consulté le: 12 mars 2024. [En ligne]. Disponible sur: https://www.boutique.afnor.org/fr-fr/norme/nf-en-14651-a1/methode-dessai-du-beton-de-fibres-metalliques-mesurage-de-la-resistance-a-l/fa155701/30255

A. Belbachir, S. Y. Alam, M. Matallah, et A. Loukili, « Effet d'échelle sur le comportement en cisaillement des poutres en béton armé : Analyse avec corrélation d'images », *Academic Journal of Civil Engineering*, vol. 34, no 1, Art. no 1, juin 2016, doi: 10.26168/ajce.34.1.12.

H. Ibrahim, G. Wardeh, et H. Fares, « Reliability of Digital Image Correlation Techniques for Cementitious Composite Fracture Characterization », *Passer Journal of Basic and Applied Sciences*, vol. 6, no Special Issue, p. 57-70, janv. 2024, doi: 10.24271/psr.2024.188477.

D.-T. Vu, « Modélisation numérique du comportement des bétons de fibres métalliques sous des sollicitations multiaxiales tenant compte l'effet de l'orientation des fibres : application aux voussoirs du tunnel », phdthesis, Université Gustave Eiffel, 2022. Consulté le: 31 octobre 2023. [En ligne]. Disponible sur: https://theses.hal.science/tel-04061842

A. Khanlou, G. A. MacRae, A. N. Scott, S. J. Hicks, et G. C. Clifton, « Shear performance of steel fibre-reinforced concrete », 2012, Consulté le: 30 avril 2024. [En ligne]. Disponible sur: http://ir.canterbury.ac.nz/handle/10092/10654

P. Casanova, « BETONS RENFORCES DE FIBRES METALLIQUES : DU MATERIAU A LA STRUCTURE - ETUDE EXPERIMENTALE ET ANALYSE DU COMPORTEMENT DE POUTRES SOUMISES A LA FLEXION ET A L'EFFORT TRANCHANT », juin 1995. Consulté le: 25 janvier 2023. [En ligne]. Disponible sur: https://www.semanticscholar.org/paper/BETONS-RENFORCES-DE-FIBRES-METALLIQUES-%3A-DU-A-LA-ET-Casanova/16196185c52254afb481c944b2f60faad741a86d

J. H. Muhammad et A. R. Yousif, « Effect of basalt minibars on the shear strength of BFRP-reinforced high-strength concrete beams », Case Studies in Construction Materials, vol. 18, p. e02020, juill. 2023, doi: 10.1016/j.cscm.2023.e02020.

Acid Resistance of 3D Printable Earth-Based Materials Stabilized by Alkali-Activated Binders: Effect of Excavated Soil and Sucrose

Pitabash Sahoo[1] and Souradeep Gupta[2*]

[1] PhD research scholar, Bengaluru, India
Email: pitabashs@iisc.ac.in
[2] Assistant professor, Bengaluru, India
Email: souradeep@iisc.ac.in

[*]Corresponding author

ABSTRACT

3D printable earth-based alkali activated mortar utilizes natural clay from the soil to improve the rheological properties. It provides adequate fresh and hardened properties for 3D printable materials. To develop a durable 3D printable material, it is essential to evaluate the mechanical performance in aggressive acids like H_2SO_4. Herein different 3D printed earth-based alkali activated mortar are employed to 28 days and 120 days of exposure to diluted sulfuric acid of pH 0.5 (3% of concentration by mass of water). The mechanical and microstructural performances are evaluated by visual observation, compressive strength, mass loss, water accessible porosity, and scanning electron microscopy (SEM). It is revealed that incorporation of lateritic clay-based soil increases the formation of gypsum in the 3D printable alkali activated mortar. Formation of gypsum adds expansion and cracking to the matrix resulting in increased cracks and enhanced mass loss. It results in a higher reduction in compressive strength of earth-based 3D printable mortar. Further addition of sucrose-based bio retarder to earth-based 3D printable mortar reduces the acid-based degradation.

KEYWORDS: *Laterite soil, Durability, Sulfuric acid, Porosity, Bio-retarder*

1. Introduction

The research and development in digitalization of construction sector by 3D printing have seen a rapid boom in recent times due to its geometrical freedom, lower cost, and faster construction (Chang et al., 2023; Hou et al., 2021; Zhang et al., 2021). However, 3D printed cement-based construction consumes 1.5-2 times cement than the conventional construction (Dilawar Riaz et al., 2023; Zhang et al., 2021). Production of cement is responsible for 8% of total carbon emission globally (Alghamdi et al., 2019). Developing 3D printable alkali activated materials by utilising industrial by-products (slag, fly ash, silica fume, red mud, waste glass, mine tailings, rice husk ash, metakaolin etc.) as precursors reduces the consumption of cement (Dai et al., 2023; Fernández-Jiménez & Palomo, 2005). Further, to develop a durable 3D printable alkali activated cementless mortar, the physical and mechanical properties of the materials, heterogeneity and weakness of the materials due to layered deposition, need to be further studied under extreme harsh conditions. It is important to develop durable 3D printable material which can resists different environmental conditions for a longer period without significant deterioration.

The durability of the 3D printable alkali activated materials primarily depends on types of binder, activator, and concentration of activator, pore structure along the filament and between the filament, curing condition, types of additives and pore development at the interlayer zone (Runzhuo Cao, 2022). It is known that alkali activated materials are more resistant to ordinary Portland cement (OPC) due to its high alkalinity. Acids can degrade the 3D printable concrete more severely by penetrating the interlayer zone of the 3D printed structural elements. Among the acids, sulfuric acid (H_2SO_4) is one of the most harmful acids pertaining to combined effect of acids and sulphate attack (Runzhuo Cao, 2022). The reaction kinetics are explained in Eq. 1 and 2.

$$2NaOH + H_2SO_4 \rightarrow Na_2SO_4 + 2H_2O \quad (1)$$

$$CaO.SiO_2.xH_2O + H_2SO_4 \rightarrow CaSO_4 + SiO_2 + xH_2O \quad (2)$$

In recent time, natural soil is utilized to develop low carbon 3D printable materials with adequate compressive strength (18-42 MPa based on mix compositions), improve the extrudability, and buildability of the material (Sahoo & Gupta, 2023). The earth-based 3D printable mixes need to be further studied to develop a durable material. This study evaluates the durability of 3D printable alkali activated materials under sulfuric acid (pH 0.5). It can contribute scientifically to develop 3D printed sewer structures, special industrial applications, construction site, foundation structures etc. vulnerable to sulphate ions penetration found in ground water. The objective of the study is to investigate the mechanical and microstructural properties due to ingress of sulfuric ions at low pH (pH 2.0 and 0.5) and further physio-chemical degradation of 3D printable mortar due to addition of excavated soil to the alkali activated system.

2. Materials and methods

2.1 Raw materials

The mix proportions are prepared by using ground granulated blast furnace slag (GGBS), class F fly ash (FA) as binder in a ratio 3:1 and 8 mol/liter (M) sodium hydroxide (NaOH) as activator. The GGBS mainly composed of calcium oxide (38.6 %), aluminum oxide (16.6 %), silicon dioxide (34.8 %), and magnesium oxide (5.4 %). The FA consists of calcium oxide (3.43 %), aluminum oxide (25.4 %), silicon dioxide (60.3 %), and ferric oxide (5.17 %) predominantly. Manufactured sand (M-sand) is used as fine aggregate. Naturally available lateritic clay-based soil (clay> 42%) is used as a supplementary material by replacing 25% of M-sand by mass. The detailed particle size distribution of M-sand and soil used is depicted in Fig. 1. The liquid limit and plastic limit of the soil is 32±1 and 18±1 respectively. Sucrose (98% purity) was added to the 3D printable mortar by 1% of binder (by mass) to develop the biopolymer-based 3D printable earth-based 3D printable material.

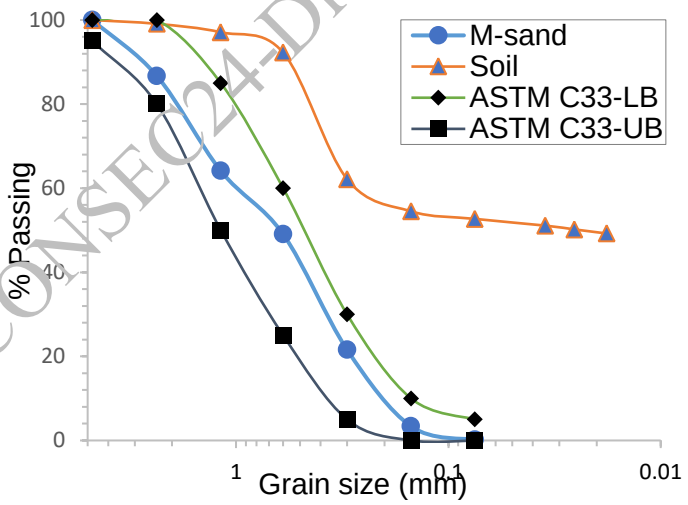

Figure 1. Grain size distribution of M-sand and soil. Upper bound (UB) and lower bound (LB) are depicted as per ASTM C33.

2.2 Mix compositions and sample preparation

Four mortar mixes that include excavated soil (E) and sucrose (S) are reported as in Table 1. The required 8M NaOH is prepared by adding 10 M NaOH activator solution by adding required doses of sucrose diluted with deionized (DI) water. The materials for different mix proportions are added to a planetary mortar mixture of 60-liter capacity and thoroughly dry mixed for 2 minutes. After the completion of dry mixing of mortar, the required amount of activator (NaOH solution added with sucrose doses) is added during the material mixing. The materials are mixed in the planetary mixture for 3 minutes. Then, the mortar is scrapped from the bottom of the planetary mixture and rotated for 2 minutes again to mix the materials

thoroughly. The 3D printing is carried out by a 40 mm nozzle and 4 layers of printing and layer height of 15 mm each. The materials after printing are spread between 51 mm to 58 mm, which are chopped from the sides and top to prepare 50±2 mm cubes. The specimens are exposed to sulfuric acid (pH 0.5) for 4 months after 28 days of curing (6 days of burlap curing after demolding at 1-day and 21 days dry curing). The same number of specimens are kept in DI water for the same time for an appropriate comparison.

Table 1. Mix composition of 3D printable mixes used for durability test under sulfuric acid attack (pH 0.5)

Mix code	GGBS (g)	FA (g)	M-sand (g)	Soil (g)	Sucrose (g)	8 mol/liter (M) NaOH (g)	Flow (mm)
0S-0E-AAM	75	25	200	0	0	68	190±5
1S-0E-AAM	75	25	200	0	1	62	168±3
0S-25E-AAM	75	25	150	50	0	75	136±1
1S-25E-AAM	75	25	150	50	1	68	125±1

2.3 Test methodology

The changes in visual appearance (pictures of specimens) and mass of each type are recorded in every 7 days of immersion for 4 months for both exposed to sulfuric acid (pH 0.5) and DI water. Before taking the mass and picture of specimens, the surface of specimens is washed and cleaned carefully to remove the loosely attached surface materials. The average compressive strength and water accessible porosity of specimens is examined by a universal testing machine (UTM) in compliance with at 28 days and 120 days. The exposed and unexposed mortar specimens are analyzed for SEM/EDS. The areas with severe decomposition are mainly considered for the analysis.

3. Results and discussion

3.1 Visual appearance

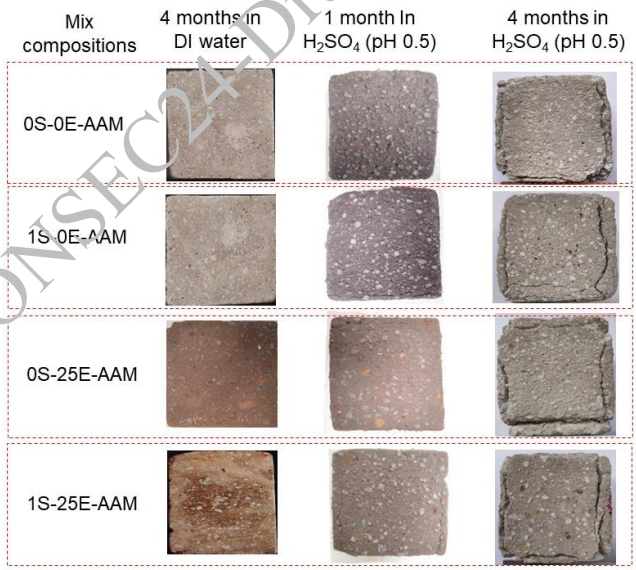

Figure 2. Physical appearance of mortars after 1 month and 4 months of H2SO4 (pH 0.5) acid exposure

Fig. 2 displays the photographs of 3D printed mortar specimen exposed to sulfuric acid (H_2SO_4, pH 0.5) solution for 1 month and 4 months. When the specimens (0S-0E-AAM and 1S-0E-AAM) are exposed to sulfuric acid solution, pH 0.5, the light brown colour of the non-earth-based 3D printed specimens are lost and converted to off-white/gray colour. Further, the reddish-brown colour of the earth-based 3D printed specimens (0S-25E-AAM and 1S-25E-AAM), are also turned to white-gray colour. The cracks were started generating in 28-days earth-based specimens. The surface deterioration is also significant in earth-based 3D printable specimens.

3.2 Mass change

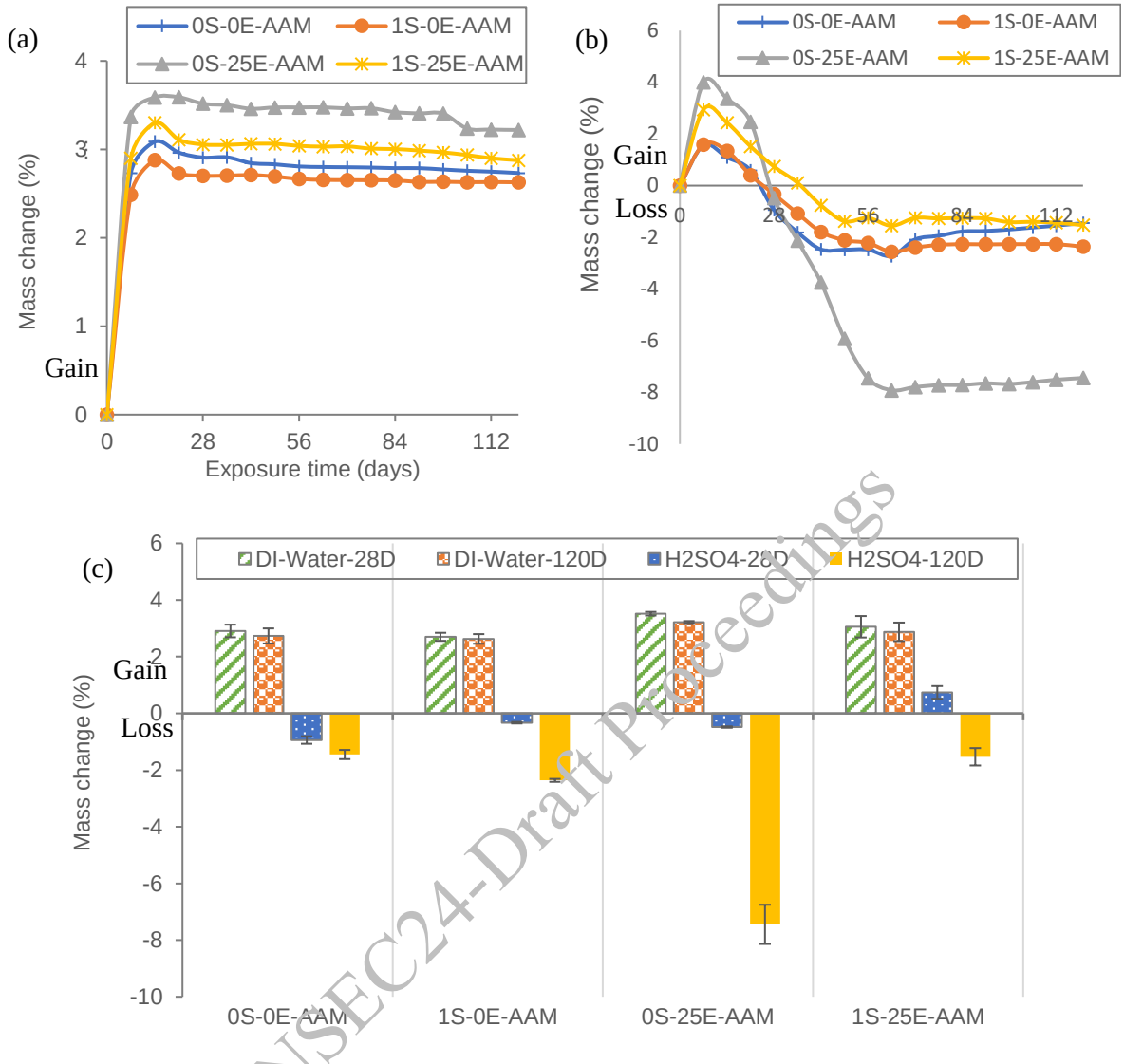

Figure 3. Mass change of 3D printable mortar specimens exposed to sulfuric acid for 4 months, a. specimens exposed to DI water, b. specimens exposed to sulfuric acid (pH 0.5), c. mass change at 1 month and 4 months.

Fig. 3 displays the mass variation of 3D printable earth-based alkali activated mortar during the 120 days, exposed DI water and sulfuric acid solution. The mass change (%) showing negative value indicates mass loss and positive value represents mass gain. The mass loss due to surface erosion of 3D printed earth-based specimens (0S-25E-AAM) is significantly higher than its counterpart (0S-0E-AAM). 3D printed earth-based specimens suffers >4 times higher mass loss than its counterpart at 120 days. The expansion cracks are also reported in earth-based specimens. The higher mass loss in earth-based 3D printable materials is due to increased decomposition calcium (alumino) silicate hydrate (C-(A)-S-H) gel (Fig. 4a and 4b). The higher decomposition of C-(A)-S-H gel is due to the higher porosity of earth-based specimens and accelerated gypsum formation in 0S-25E-AAM which is reported in the next section 3.3. When the specimens are exposed to sulfuric acid, the hydrogen ions from sulfuric acid decompose the (C-(A)-S-H) gel and reacts excess sodium hydroxide (NaOH) present in pore solution (Eq. 1 and Eq. 2). The NaOH increases the alkalinity of the pore solution in alkali activated mortar. It protects the decomposition of C-(A)-S-H binding gel. Sulfuric acid reacts with NaOH to form Na_2SO_4 and Na_2SO_4 is washed away due to its solubility in water. Further, C-(A)-S-H was decomposed into silica and gypsum. The SEM image in Fig. 4a shows the C-(A)-S-H gel which gets decomposed, and gypsum is formed (Fig. 4b). Gypsum is expansive in nature, which causes spalling in earth-based 3D printable materials.

Further addition 1% sucrose to earth-based 3D printable mix reduces the loss of mass due to lower water accessible porosity (WAP) (the WAP of 1S-25E-AAM is 4-5% lower than 0S-25E-AAM) which is discussed in the next section 3.3. The reduction in mass continues up to 56 days in every mix composition. However, after 56 days the mass of specimens increased. The increase in mass was due to the formation of insoluble gypsum.

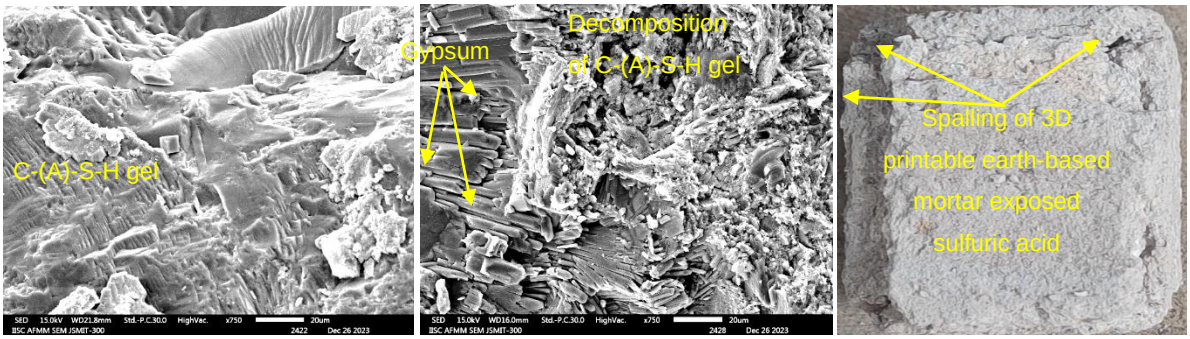

(a) (b) (c)

Figure 4 (a). SEM image of 3D printable earth based mortar exposed to DI water for 4 months, (b). sulfuric acid (pH 0.5) for 4 months, and c. spalling of mortar caused due t expansion of gypsum.

3.3 Mechanical performance

Fig 5 displays the engineering performance of 3D printable earth-based alkali activated mortar exposed to sulfuric acid (pH 0.5) after curing for 28 days. The compressive strength variation of the mortar is depicted in Fig. 5a. Addition of excavated soil to the alkali activated mortar increases the loss of compressive strength of the 3D printable mortar. The loss of compressive strength in earth-based alkali activated mortar (0S-25E-AAM) is 79±2.2% compared to 60±1.8% for its counterpart (0S-0E-AAM). The higher loss of compressive strength in earth-based mortar is due to the higher mass loss and spalling (reported in section 3.2, Fig. 4c). Further sucrose-based alkali activated mortar improves compressive strength of 3D printable mortar by 4-5% in sulfuric acid exposure condition, depicted in Fig. 5a. The improved compressive strength in sucrose-based alkali activated 3D printable mortar is due to reduced mass loss and crack in sucrose-based materials as reported in section 3.1. The water accessible porosity of 3D printable mortars is reported in Fig. 5b. The higher mass loss and spalling in earth-based alkali activated 3D printable mortar (0S-25E-AAM) causes increased porosity. The water accessible porosity in 0S-25E-AAM increased by 15.3% (36.3% to 51.6%) compared to 13.2% in 0S-0E-AAM. Further addition of sucrose further reduced the water accessible porosity (by 3-6%).

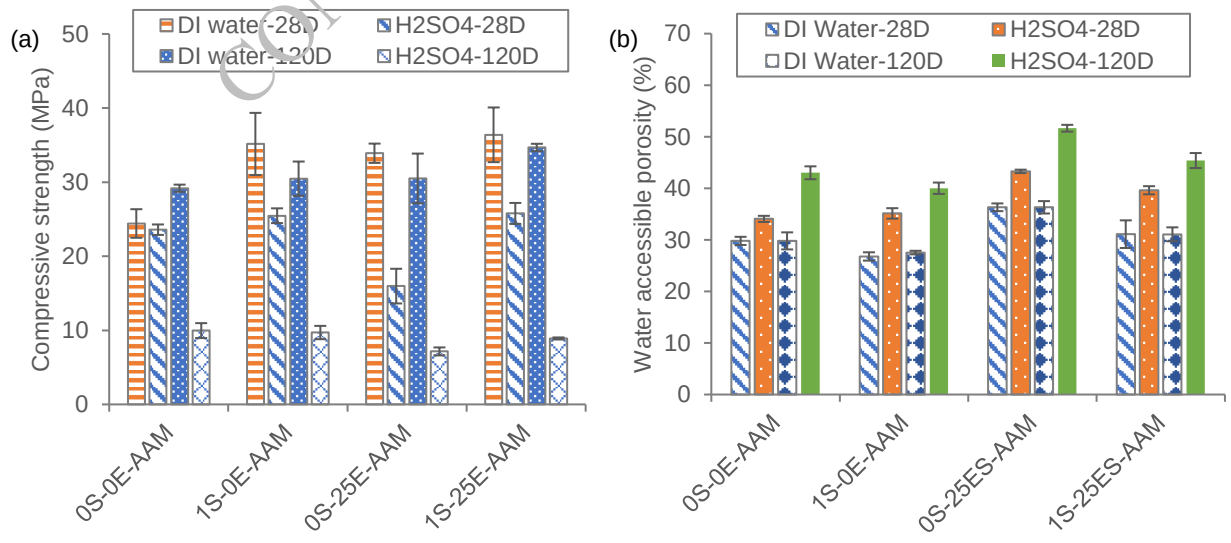

Figure 5. Mechanical performance of 3D printable alkali activated mortar exposed to sulfuric acid (pH 0.5) after 28 days of curing, a. Compressive strength, b. water accessible porosity.

4. Conclusions

Earth based alkali activated 3D printable mortar are more susceptible to sulfuric acid (pH 0.5) degradation. The mass loss in earth-based mortar is increased by 4-5 times compared to its counterpart (only M-sand based alkali activated mortar). It causes higher surface degradation in earth-based 3D printable materials. The increased mass loss and surface degradation is due to enhanced decomposition of C-(A)-S-H gel and gypsum formation. It causes lower compressive strength and water accessible porosity. The earth-based alkali activated 3D printable materials shows 25% higher loss of compressive strength and 15% increase in water accessible porosity than its counterpart. Addition of sucrose-based bio retarder reduces the degradation of 3D printable mortar due to reduction in water accessible porosity. The addition of sucrose reduces water accessible porosity by 4-5%. It causes lower reduction in compressive strength i.e. 3-5% in only M-sand based 3D printable alkali activated mortar and 6-8% in earth-based alkali activated 3D printable mortar.

Acknowledgements

Financial support from Department of Science and Technology, India and ACT-CCUS technologies (TPN: 85364) is acknowledged. Prime Minister Research Fellowship (PMRF) awarded to the first author is also appreciated

References

Alghamdi, H., Nair, S. A. O., & Neithalath, N. (2019). Insights into material design, extrusion rheology, and properties of 3D-printable alkali-activated fly ash-based binders. *Materials and Design*, 167. https://doi.org/10.1016/j.matdes.2019.107634

Chang, Z., Liang, M., Xu, Y., Wan, Z., Schlangen, E., & Šavija, B. (2023). Early-age creep of 3D printable mortar: Experiments and analytical modelling. *Cement and Concrete Composites*, 138. https://doi.org/10.1016/j.cemconcomp.2023.104973

Dai, X., Tao, Y., Van Tittelboom, K., & De Schutter, G. (2023). Rheological and mechanical properties of 3D printable alkali-activated slag mixtures with addition of nano clay. *Cement and Concrete Composites*, 139. https://doi.org/10.1016/j.cemconcomp.2023.104995

Dilawar Riaz, R., Usman, M., Ali, A., Majid, U., Faizan, M., & Jalil Malik, U. (2023). Inclusive characterization of 3D printed concrete (3DPC) in additive manufacturing: A detailed review. In *Construction and Building Materials* (Vol. 394). Elsevier Ltd. https://doi.org/10.1016/j.conbuildmat.2023.132229

Fernández-Jiménez, A., & Palomo, A. (2005). Composition and microstructure of alkali activated fly ash binder: Effect of the activator. *Cement and Concrete Research*, 35(10), 1984–1992. https://doi.org/10.1016/j.cemconres.2005.03.003

Hou, S., Duan, Z., Xiao, J., & Ye, J. (2021). A review of 3D printed concrete: Performance requirements, testing measurements and mix design. In *Construction and Building Materials* (Vol. 273). Elsevier Ltd. https://doi.org/10.1016/j.conbuildmat.2020.121745

Sahoo, P., & Gupta, S. (2023). 3D Printable Earth-Based Alkali-Activated Materials: Role of Mix Design and Clay-Rich Soil. RILEM Bookseries, 45, 333–352. https://doi.org/10.1007/978-3-031-33465-8_27

Zhang, C., Nerella, V. N., Krishna, A., Wang, S., Zhang, Y., Mechtcherine, V., & Banthia, N. (2021). Mix design concepts for 3D printable concrete: A review. In *Cement and Concrete Composites* (Vol. 122). Elsevier Ltd. https://doi.org/10.1016/j.cemconcomp.2021.104155

Carbon Curing as a Chloride Binding Strategy in Blended Concrete

Madhu Sudhan. Bolla[1], and Anjaneya. Dixit[2*]

[1] *Indian Institute of Technology Roorkee, Roorkee, India.*
Email: bm_sudhan@ce.iitr.ac.in
[2] *Indian Institute of Technology Roorkee, Roorkee, India.*
Email: anjaneya.dixit@ce.iitr.ac.in

[*]Corresponding author

ABSTRACT

Chlorides can enter concrete through its ingredients or natural weathering. Recently, water used for concrete production has become a major concern for the construction industry in India. The use of underground water containing high chlorides has started causing premature damage or corrosion of reinforcement in many urban infrastructures. Al-rich supplementary cementitious materials (SCMs) such as fly ash and blast furnace slag can bind the free chlorides in the concrete by forming Friedel's salt and lower the intensity of their ensuing damage. This study aims to explore an additional avenue of chloride binding by employing CO_2 curing in the early ages and utilizing the densification of pore structure to further trap free chlorides in the system. In this study, chlorides were added to the mixing water at 0, 500 mg/l, and 1000 mg/l, and this water was then used for mortar preparation. After 24 hours of pre-hydration in the molds, carbon curing was performed for 24 hours. The 'carbonated' specimens are kept for water curing for seven days. For mortar specimens, compressive strength at 2 and 7 days is determined. Free and total chlorides present in hydrated and carbonated specimens from the crushed mortar specimens are determined based on IS: 14959-(Part 2): 2001 guidelines. The compressive strength of the mortar increases due to the addition of chlorides and carbonation. The experimental results show that carbonation is more effective at binding the chlorides added to the mortar than the hydration.

KEYWORDS*: Chlorides, Carbon curing, Compressive strength, Free and total chlorides.*

1. Introduction

With the declining availability of potable water for concrete production, groundwater sources have become a significant supply for construction projects in urban areas. However, the quality of water is questionable due to the presence of contaminants, such as chlorides and sulphates. While contracts, codes, and government by-laws dictate the proper treatment of this water before use, the financial burden towards setting up of treatment plants, tight project schedules, and general leniency in implementation can lead to the use of untreated, chloride-rich water for concrete production. This causes a noticeable degradation in the mechanical and durability properties of the concrete and, consequently, the structure. The chlorides are present either in the bound state (such as Friedel's salt) or the free state in the pore solution. They cause corrosion of reinforcement due to a reduction in pH of the pore structure and breakage of passive film around the reinforcement. Free chlorides cause more significant damage to concrete compared to the chlorides that are bound in the hydration products. Hence, new materials or, curing approaches, or other procedures which can bind or absorb the chlorides coming into the concrete would be helpful for the construction industry. Stoichiometrically, chlorides react with aluminates to form Friedel's salt, as shown in equation (Suryavanshi et al. 1996).

$$C_3A + 2NaCl + Ca(OH)_2 + 10H_2O \rightarrow C_3A.CaCl_2.10H_2O + 2\,Na^+ + 2\,OH^- \quad (1)$$

Traditionally, Al-rich SCMs have been used to reduce free chlorides in concrete (Abd El-Fattah et al. 2024). Nowadays, carbon curing or carbonation has been used in the early ages of concrete curing to densify microstructure. Carbonation is an accelerated version of natural weathering due to CO_2 in which CO_2 reacts

with alkaline materials to precipitate stable carbonates. While it has shown positive changes in concrete's early strength and microstructure, the effect of carbon curing on chloride binding properties, if any, has not yet been studied. If done right, this strategy may provide a pathway for the utilization of water contaminated with chlorides, provided free chlorides decrease after the carbon curing. Accordingly, in this study, 50 mm mortar cubes are cast with added chlorides in the proportion of 0, 500, 1000 mg/l in the mixing water. Carbonation or carbon curing of mortar samples was done for 24 hours after a pre-hydration of 24 hours. The effect of carbonation and chlorides on compressive strength was measured at 2 and 7 days, and free and total chlorides at two days after the carbonation are determined by following the recommendations of IS: 14959-(Part 2): 2001 (IS :14959 (Part 2) 2001). Paste samples are used to study the hydration kinetic and mineralogical changes using Iso-thermal calorimetry (ITC) and X-ray Diffraction (XRD), respectively.

2. Raw materials and Specimen preparations

Portland cement (OPC) 43 grade was used to prepare mortar with a water-to-binder ratio (w/b) of 0.5. Ground granulated blast furnace slag (GGBS-G), and fly ash (FA-F) were used to replace the OPC in the proportion of 25 % by weight, and a sand-to-binder ratio (s/b) of 2.5 was adopted. Mortar cubes of 50 mm were prepared for compressive strength and chloride determination. Distilled water (DW) was used to prepare the samples, with an externally dosed proportion of chlorides at 0, 500, and 1000 mg/l to the weight of the water using lab-grade NaCl. The salt was added to the water prior to mixing in the mortar. In this paper, the nomenclature of the mix is represented based on mortar mix, chloride proportion, and curing type (H-hydrated/ C-carbonated). For example, G-25-500-C refers to the "carbonated mortar mix of G-25 having chloride proportion of 500 mg/l". For XRD and hydration kinetic studies, paste samples were prepared with the same proportion as mortars but without sand.

2.1 Experimental study

Mortar cubes were pre-hydrated in covered molds for 24 hours to prevent the evaporation of water. After demolding, half of the mortar cubes were kept in a carbonation chamber for 24 hours, and the remaining half was kept in water curing. Carbonation of mortar cubes was performed at atmospheric pressure with a CO_2 concentration of 20 %, temperature of 27 ± 2 °C, and relative humidity of 60-70 %. After carbonation, cube specimens are kept in water curing for seven days.

3. Results and Discussions

3.1 Hydration kinetics with chlorides

The addition of chlorides impacts the hydration kinetics of cement pastes (Sun et al. 2022). The hydration kinetics are not evaluated in CO_2-rich environments due to operational and equipment limitations. The hydration kinetics of mixes performed by ITC are represented in Figure 1, and the same mixes as without sand are adopted, and chlorides are added to DW and stirred well before adding them to the binder. From Figure 1 (a) of the OPC mixes, adding 500 mg/l increased the peak intensity but delayed its occurrence by approximately 2 hours as compared to no chloride mix. This is due to the collapse of the protective layer formed around the hydration products by adding chlorides. Conversely, for the higher concentration of 1000 mg/l, the hydration peak is decreased because the dissolution of chloride (Cl) ions prolongs the saturation time of the Ca^{2+} in the solution, interrupting the formation of hydration products (W. Liu et al. 2023). Furthermore, the induction period of the mixes with GGBS and FA decreases due to the addition of chlorides, and the peak of heat flow increases with the addition of chlorides, which is maximum at 1000 mg/l.

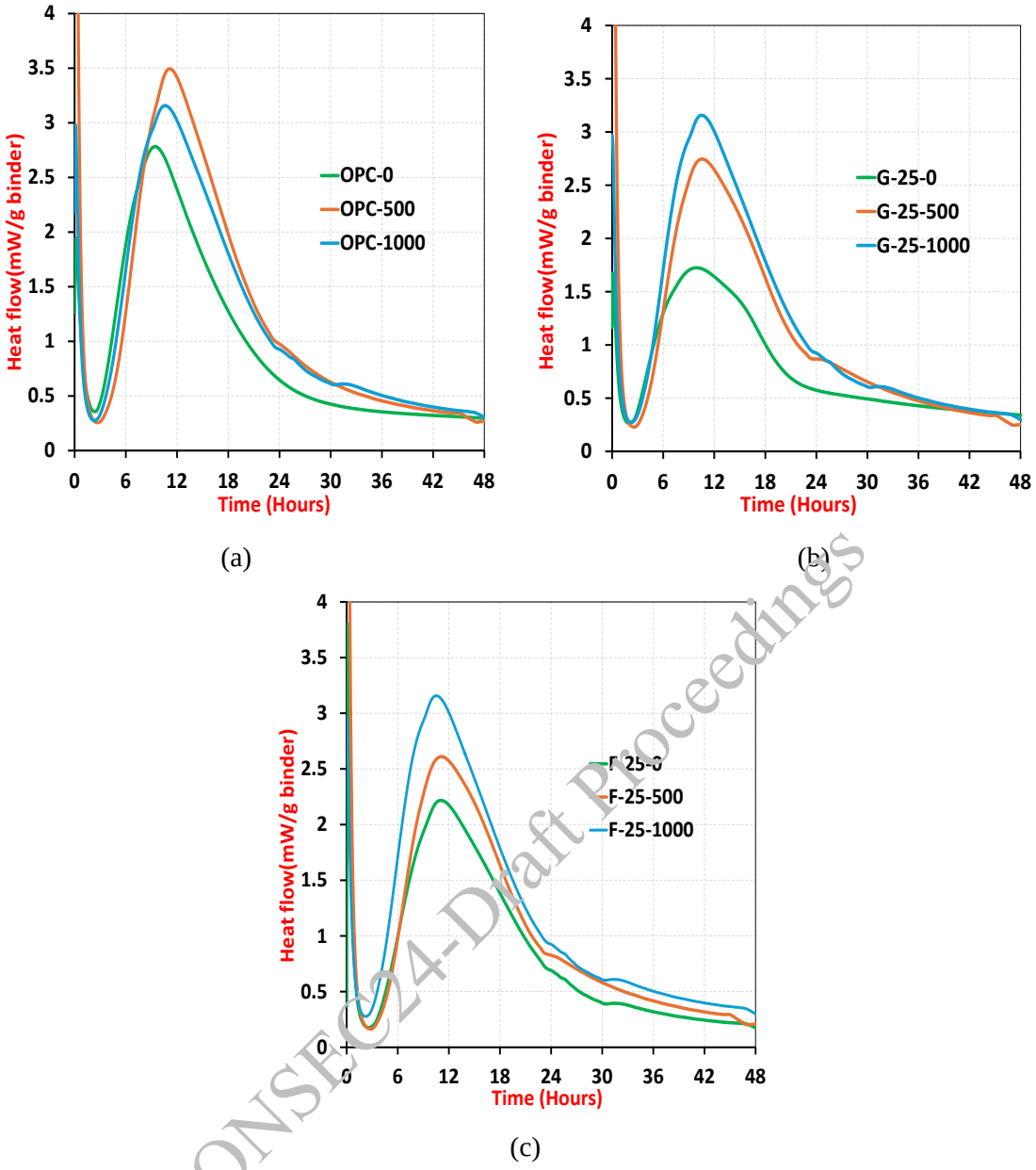

Figure 1. Heat flow rates of mixes with chlorides used in this study (a) OPC, (b) G-25, and (c) F-25.

3.2 Compressive strength

The effect of adding chlorides for carbonated and hydrated specimens on their compressive strength was determined using 50 mm mortar cubes. The strength tests were performed at 2 and 7 days and are shown in Figure 2. Here, the compressive strength test is performed at two days to evaluate the effect of carbonation. The early-age CS of the specimens with chlorides of 500 and 1000 mg/l have slightly higher strength than the distilled water specimens without chlorides. The results agree with the calorimetry results where intensified C_3S peaks were obtained. It has been reported that the presence of chlorides at an early age tends to accelerate alite hydration (Li et al. 2021). Furthermore, the strength of all the carbonated specimens is greater than that of hydrated specimens due to the densification of pore structure with the precipitation of carbonates during carbonation. For the mixes with FA and GGBS, adding chlorides has resulted in higher compressive strength of slag blended specimens compared to fly ash blended specimens due to the lower reactivity of FA.

3.3 Free and total chlorides

After the compressive strength test, the crushed mortars were grounded in a ball mill to a size less than 1 mm. Grounded mortar was used to determine the free and total chlorides in carbonated and hydrated specimens. Separate samples were prepared for the determination of free and total chlorides. Approximately 1000±5 g of grounded mortar powder of approximately gr was kept in 1000 ml of distilled water for 24 hours. The mixture was then stirred vigorously, warmed for 15 minutes, and kept for up to 24 hours. 200 ml of the top supernatant was extracted and filtered through the Whatman filter paper No. 1. 50 ml of the filtered solution was taken to determine the free chlorides (FC). 5 ml of 6N of HNO_3 and a known volume (X) - 25 ml of 0.2 N $AgNO_3$ were added. Thereafter, 1 ml of ferric alum and 5 ml of nitrobenzene were added, and the solution was shaken vigorously to coagulate the precipitate. The excess $AgNO_3$ was titrated with 0.2 N NH_4SCN until a permanent faint reddish-brown color appeared. The initial and final volumes of NH_4SCN were noted (Y). The free and total chlorides is determined according to equation (2) as follows,

$$\text{Chloride (\%)} = 0.00142\,(X-Y) \tag{2}$$

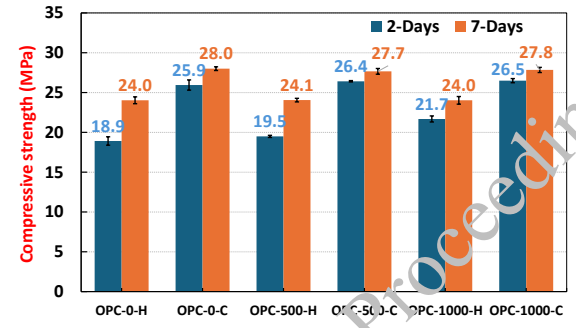

(a)

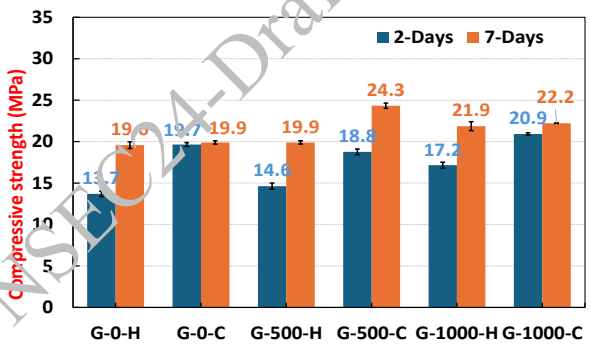

(b)

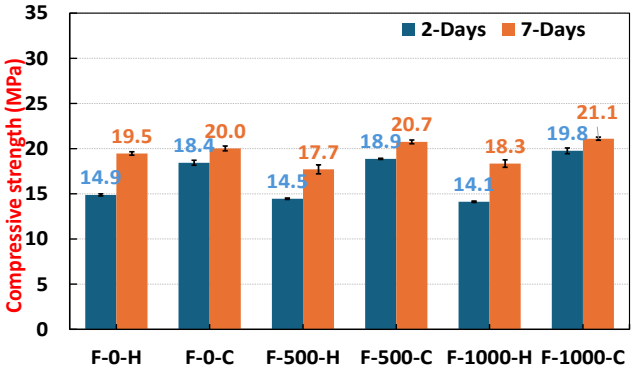

(c)

Figure 2. Compressive strength of mortar mixes with chlorides of 2 and 7 days (a) OPC (b) G-25 (C) F-25.

The experimental analysis shows that all the carbonated samples have fewer free chlorides than the hydrated samples, as presented in Table 3. Conversely, the bound chlorides of carbonated specimens are higher than those of hydrated specimens. Mixes with FA have fewer free chlorides than other mixes due to their high Al content and the consequent ability to bind the chlorides (Abd El-Fattah, Abd El-Zaher, and Kohail 2024). The synergistic effect of carbonated products like carbonates and silica gel with SCMs shows some potential to reduce the free chlorides in concrete.

Table 3. Free and Total chlorides (% mass of the mortar) at the age of 2 days.

Mix	Carbonated			Hydrated		
	Free	Total	Bound	Free	Total	Bound
OPC-0	0.027	0.071	0.044	0.0043	0.011	0.007
OPC-500	0.033	0.082	0.048	0.022	0.046	0.024
OPC-1000	0.039	0.095	0.055	0.029	0.055	0.026
G-0	0.009	0.043	0.034	0.023	0.028	0.005
G-500	0.027	0.064	0.037	0.031	0.031	0.0007
G-1000	0.033	0.085	0.053	0.034	0.034	0.004
F-0	0.007	0.037	0.03	0.003	0.008	0.005
F-500	0.02	0.054	0.034	0.001	0.024	0.023
F-1000	0.023	0.06	0.037	0.011	0.035	0.024

3.4 Mineralogical changes

Generally, adding chlorides into the mortar changes the mineralogy of the hydration products. In this study, mineralogical changes are studied with the help of the X-ray diffraction (XRD) characterization technique. For the early age (2 days), there is evidence of mineralogical changes due to adding chlorides for carbonated and hydrated samples. The Friedel salt formation due to adding chlorides n 'H' series samples (seen at 12°) does not appear in the carbonated samples. This suggests that the chlorides may be bounded as some other mineral(s) shown in Figure 3. Furthermore, the proportion of CH decreases in carbonated specimens due to precipitation of calcite and silica gel (Dixit, Du, and Pang 2021). In addition, the proportion of unhydrated C_3S/C_2S also decreases due to carbonation as compared to hydrated specimens (J. Liu et al. 2024).

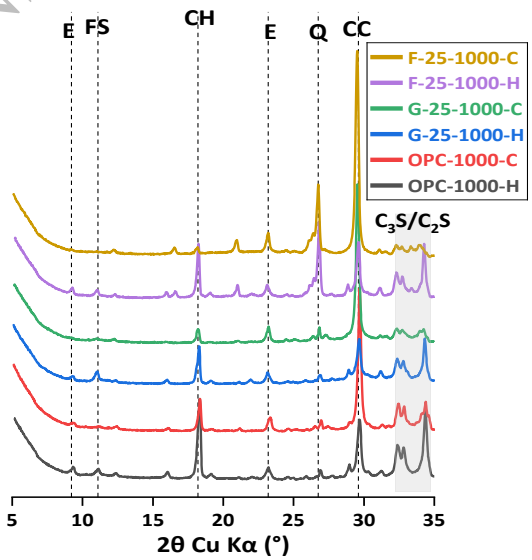

Figure 3. XRD of hydrated and carbonated samples of with 1000 mg/l of chlorides, here E-ettringite, FS-Friedel salt, CH-calcium hydroxide, Q- Quartz, CC-calcium carbonate.

4. Conclusions and Future Scope

In this study, blended cement mortars incorporating FA and GGBS were prepared with chloride-rich water. The efficacy of carbon curing in improving its early strength and binding the free chlorides was investigated. From the experimental study, the following conclusions can be drawn:

1. The addition of chlorides increases the hydration rate of both OPC and blended mixes of OPC with GGBS and FA.
2. Carbonation reduces the free chlorides present in the pore structure of the mortar, as observed in the titration results.
3. Carbonation also improves the compressive strength at an early age for all the samples, regardless of their chloride content.

Further studies are required to delve into the chloride binding capabilities of carbonated mortar or concrete. Topics such as the effect of adding chlorides on the carbon storage in OPC and OPC with SCMs, the chloride binding capabilities of carbonation, long-term mechanical and durability of carbonated mortar with internally added chlorides, etc. may present interesting results towards the dual advantage of chloride binding and carbon storage in concrete.

References

Abd El-Fattah, Heba, Yehia Abd El-Zaher, and Mohamed Kohail. (2024) "A Study of Chloride Binding Capacity of Concrete Containing Supplementary Cementitious Materials", *Scientific Reports*, 14(1): 1–20

Dixit, Anjaneya, Hongjian Du, and Sze Dai Pang (2021) "Carbon Capture in Ultra-High Performance Concrete Using Pressurized CO2 Curing",*Construction and Building Materials*, 288: 123076

IS :14959 (Part 2).(2001) "Method of Test Determination of Water Soluble and Acid Soluble Chlorides in Mortar and Concrete, Part 2: Hardened Mortar and Concrete [CED 2: Cement and Concrete]", *Bureau of Indian Standards, New Delhi*

Li, P., Li, W., Sun, Z., Shen, L. and Sheng, D.(2021) "Development of Sustainable Concrete Incorporating Seawater: A Critical Review on Cement Hydration, Microstructure and Mechanical Strength", *Cement and Concrete Composites*,121: 104100

Liu, J., Wu, Y., Qu, F., Zhao, H. and Su, Y. (2024)"Assessment of CO2 Capture in FA/GGBS-Blended Cement Systems: From Cement Paste to Commercial Products" ,*Buildings*, 14(1): 154

Liu, W., Du, H., Li, Y., Yi, P., Luo, Y., Tang, L. and Xing, F. (2023)"Effects of Chloride Content on Early Hydration Performance of Cement Pastes", *Materials Today Communications*, 35:106257

Sun, Y., Lu, J.X., Shen, P. and Poon, C.S.(2022)"Hydration Kinetics and Microstructure Evolution of NaCl-Mixed Tricalcium Silicate Pastes" ,*Cement and Concrete Research*, 161: 106934

Suryavanshi, A.K., Scantlebury, J.D. and Lyon, S.B.(1996) "Pi1 Sooos-8846(96)00052-X Mechanism of Friedel's Salt Formation in Cements Rich in Tri-Calcium Aluminate", *Cement and Concrete Research Research*, 26(5): 717–27

Influence of Seawater on Mechanical and Durability Performance of Concrete for Marine Environment

Mavoori Hitesh Kumar[1] and Prabha Mohandoss[2*]

[1] Ph.D. Candidate, National Institute of Technology, Tiruchirappalli, India
Email: 403120052@nitt.edu
[2] Assistant Professor, National Institute of Technology, Tiruchirappalli, India*
Email: prabham@nitt.edu

[*]Corresponding author

ABSTRACT

The overexploitation of fresh water for hydroelectric power, agriculture, nuclear power, and construction industry (which alone uses nearly 14% of available fresh water) could lead to global water scarcity. Therefore, utilizing seawater for concrete production would be beneficial for construction industry to counter water scarcity issue moderately. However, use of seawater for concrete mix could cause significant corrosion of steel reinforcement due to the presence of chloride ions. Apparently, GFRP bars being a non-corrosive material has gained higher attention and could be found suitable for seawater concrete. Based on the research, seawater concrete exhibits lower alkalinity than normal concrete due to high concentration of chloride, sodium and magnesium ions. This environment would be better for the durability performance of GFRP bars since GFRP bars are sensitive to alkaline environment. Therefore, combining the use of GFRP bars in seawater concrete could be the best sustainable approach for marine infrastructure since seawater is a readily available source for mixing and curing of concrete. Therefore, the current paper focuses on understanding the mechanical and durability properties of Seawater concrete in comparison to normal concrete. The mechanical behaviour of seawater concrete is studied for 3, 7 and 28 days of curing to understand the performance over normal concrete. The water absorption (%), sorptivity, RCPT and UPV tests were conducted to investigate the durability performance of seawater concrete and compared with that of normal concrete. It is observed that the mechanical and durability performance of seawater concrete is better at 7th day of curing over normal concrete which gradually exhibits similar behaviour to NC after 28 days of curing.

KEYWORDS*: Seawater concrete, Compressive strength, Sorptivity, Water absorption (%), RCPT.*

1. Introduction

Water is the most essential natural resource for sustaining life and microorganisms on Earth. However, the massive growth in the world's population led to the huge demand for infrastructure globally which creates a huge burden on the resources especially water. Subsequently, the construction sector uses some billion tons of fresh water for mixing, curing, and cleaning every year which might pose severe issue on availability of fresh water in coming years. The World meteorological organisation reported that the water scarcity issue will arise in almost half of the globe by 2025 (Parvizi et al., 2020). To conserve fresh water, the researchers suggest to use seawater in concrete should be seriously considered. Moreover, allowing seawater as one of the components in concrete would be convenient and cost-effective, particularly for coastal construction projects. The only major issue of using seawater in concrete mix is the corrosion of reinforcement due to presence of excessive chloride ions. However, structures near the coastal areas falls under the vulnerable category due to its location and prevailing marine environment. Various cases of cracking and spalling of concrete structures near the coastal line has been witnessed primarily due to corrosion of steel reinforcement. Therefore, Glass fiber reinforced polymer (GFRP) bars can be recommended as reinforcement in seawater concrete for coastal construction.

Significant research has been in progress since decade to study the mechanical and durability behaviour of seawater concrete. Apart from the corrosion problem, the outcomes of the research on use of seawater in concrete seemed to be favourable to be recommended for construction. Kaushik & Islam, 2005 noted an initial strength enhancement up to 7 days, followed by a subsequent 13% decrease at 28 days. However, after 18 months of exposure, seawater-based concrete exhibits a 5-10% strength reduction compared to its freshwater counterpart. This is due to the leaching of hydrated products when cured in normal water. The mechanical properties of seawater concrete are significantly influenced by the curing regime and duration. In the early stages at 7 and 14 days, concretes mixed and cured in seawater exhibit higher compressive, tensile, flexural, and bond strengths compared to those mixed and cured in freshwater due to the rapid acceleration in the cement hydration induced by seawater (Mohammed et al., 2004; Jenson & Pratt, 1987). Consequently, concrete mixed and cured in seawater after 28 and 90 days exhibits slightly lower mechanical performance over concrete mixed and cured in freshwater (Etxeberria et al., 2016). Limited research on the incorporation of Supplementary Cementitious Materials (SCMs) in seawater concrete has shown promising results. The combined effect of Metakaolin (MK) and seawater notably enhances compressive strength both in the early and later stages. The addition of 5% MK with seawater achieves the highest compressive strength with enhancement by 52% at 28 days (Li et al., 2015; Cheng et al.,2018). Notably, cement mixed with seawater exhibits a 25% reduction in both initial and final setting time compared to normal water, attributed to a higher rate of hydration reaction. However, this also contributes to increased drying shrinkage issues associated with seawater concrete (Khatibmasjedi 2018; Kaushik & Islam, 2005). Minimal effect on workability is noticed with the use of seawater provided the mix was slightly cohesive and viscous (Cruz et al., 2018). The differences in mechanical behaviour of seawater concrete are due to the lack of proper understanding of microstructural behaviour which has to be studied in depth.

2. Experimental design

2.1 Materials Used

The raw materials used for the M40 grade concrete mix are OPC 53 grade cement, sand conforming to Zone-II, 20 and 12.5 mm sized coarse aggregates, Superplasticizer (Conplast SP 430), normal water and seawater. The physical property of cement is shown in Table 1, whereas the properties for sand and coarse aggregates are shown in Table 2. The chemical composition of seawater and normal water is presented in Table 3. The mix proportions for M40 grade adopted in this study is shown in Table 4.

.

Table 1. Physical properties of cement

Material	Initial Setting Time (minutes)	Final Setting Time (minutes)	Specific gravity	Fineness (m^2/kg)
Cement (OPC 53S)	34	620	3.14	355

Table 2. Physical properties of sand and coarse aggregates

Material	Fineness modulus	Water absorption (%)	Specific gravity
M-sand	2.84	5	2.81
Coarse Aggregates (20 mm)	7.54	0.5	2.76
Coarse Aggregates (12.5 mm)	7.23	0.73	2.74

Table 3. Chemical composition of seawater and tap water

Ions (mg/l)	Chlorides	Sulphates	Calcium	Magnesium	Potassium	Sodium	pH
Seawater	19250	3012	411	1326	387	9956	8.8
Tap water	55	11	102	14	9	34	7.6

Table 4. Mix proportions of M40 grade concrete for 1 m^3 work

Concrete type	Cement (kg/m^3)	Normal Water (kg/m^3)	Seawater (kg/m^3)	FA (kg/m^3)	CA (kg/m^3)		SP (kg/m^3)
					20 mm	12.5 mm	
NC	378	191	----	688.5	760.3	508	2.269
SWC	378	----	191	688.5	760.3	508	2.269

NC – Normal concrete cured in lime water, SWC – Seawater concrete cured in seawater

2.2 Experimental program

The experimental program includes the casting of M40 grade mix to study the mechanical and durability of fresh and seawater concrete. Mechanical characterization includes investigation of compressive strength, split tensile strength and elastic modulus and durability performance is checked in terms of water absorption (%), sorptivity, RCPT and UPV. Each testing involved casting of three samples.

3. Results & Discussions

3.1 Mechanical properties of normal (NC) and seawater concrete (SWC)

The compressive strength for SWC at 3rd and 7th day curing is 29.6 MPa and 38.3 MPa respectively which is 6.4% and 8.4% higher than that of normal concrete as shown in Figure 1. However, the compressive strength at 28th curing is almost similar for both SWC and NC. Similar trend is seen for split tensile strength and elastic modulus which are higher at 3rd and 7th day curing for seawater concrete over normal concrete. This behaviour is very well in good agreement with the literature available on seawater concrete. The use of seawater in concrete accelerates the hydration process in the initial days due to the presence of excess chloride ions which gradually declines due to formation of salts and its salt crystallization (Khatibmasjedi 2018; Kaushik & Islam, 2005, Wegian 2010).

3.2 Durability properties of normal (NC) and seawater concrete (SWC)

The durability assessment was investigated by Sorptivity test, Water absorption, RCPT and UPV performed as per ASTM C1585, ASTM C570, ASTM C1202, ASTM C597 respectively. The durability performance of SWC after 7 days of curing is much better than NC which is obvious due to dense microstructure of SWC at the early stage. However, SWC and NC showed similar durability performance after 28 days of curing. This is due to the gradual reduction in hydration process due to which the SWC attains similar microstructure as that of NC. Because of this, the mechanical and durability performance of SWC and NC becomes almost similar after 28 days of curing. Similar trend is observed for the rest of the durability tests. The rate of water absorption for NC is higher than SWC at 7th day of curing but achieved similar absorption rate to SWC at 28 days as shown in Figure 2(a). A drop by 9.4% and 9.6% in water absorption (%) and voids (%) is seen in case of SWC over NC at 7th day of curing but both NC and SWC tends to exhibit similar behaviour after 28 days of curing as shown in Figure 2(b). Subsequently, both SWC and NC showed moderate chloride ion penetration ability at 7th day whereas the chloride penetration for both SWC and NC dropped significantly after 28 days of curing as seen in Figure 2(c). SWC showed higher chloride penetrability at 7th because of the presence of abundant amount of chloride ions within the system that accelerated the penetration and increased the value. The reduction of value after 28th day of curing is due to the presence of lesser voids at the end of 28th day than 7th curing. Similarly, UPV results reported that concrete quality for SWC is excellent for both 7th and 28th day whereas concrete quality for NC was good at 7th day followed by excellent at 28th day as shown in Figure 2(d). This also indicates the presence of lower porosity for SWC at 7th than NC and both attained even lower porosities after 28th day.

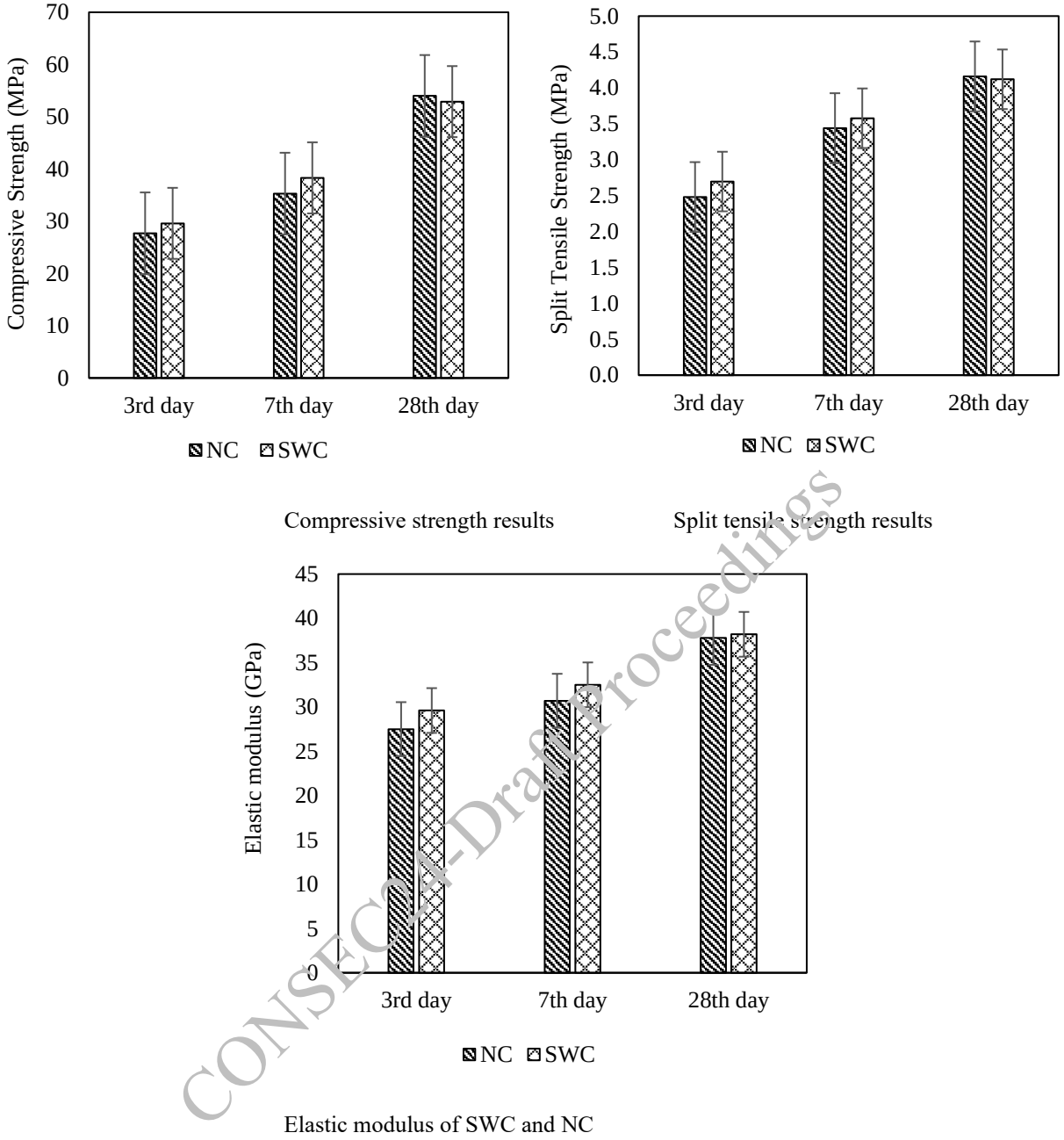

Figure 1. Mechanical properties of Normal and Seawater concrete

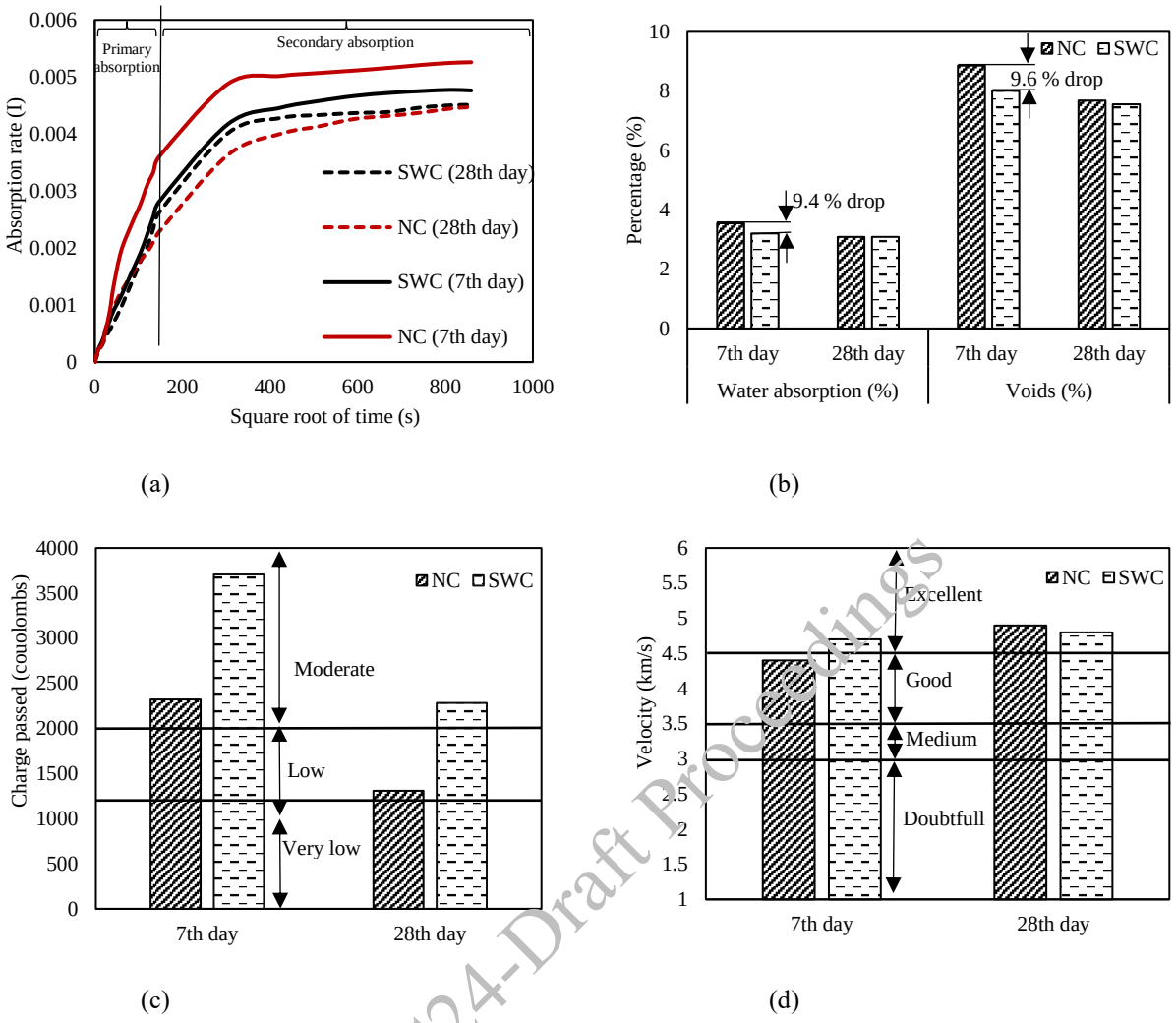

Figure 2. Durability results after 7 & 28 days of curing (a) Sorptivity (b) Water absorption(%) (c) RCPT (d) UPV

4. Conclusions

Mechanical and durability checks were performed for SWC and compared with NC to investigate its performance and understand its feasibility in the construction industry. Mechanical behaviour was assessed by compressive, split tensile strength and Elastic modulus tests whereas the durability check is performed through sorptivity, water absorption, RCPT and UPV tests. The significant findings from the experiments are summarised below.

- SWC showed similar mechanical performance to NC, exhibiting higher compressive, split tensile strength and Elastic modulus at 3rd and 7th day of curing followed by similar behaviour at 28th day of curing.
- The rate of water absorption and water absorption (%) is higher in case of NC than SWC after 7th day of curing. However, both SWC and NC showed similar absorption rate after 28 days of curing. After 28th day of curing, both SWC and NC attained similar microstructure with almost same porosity.
- RCPT test indicated moderate chloride ion penetrability for SWC whereas NC showed lower chloride ion penetration after 7th day. Whereas chloride penetration ability was dropped significantly after 28 days of curing for both SWC and NC because of attainment of denser microstructure.

- The quality of SWC is better than NC after 7th day but was excellent for both SWC and NC after 28 days of curing as per UPV results. This is an indication of reduction in number of voids due to the formation of hydrated products which fills up the void spaces after 28 days of curing.
- SWC is comparatively more durable than NC at 7th day of curing and exhibited similar durability performance to NC after 28 days of curing.
- SWC could be recommended as the performance of SWC is almost similar to NC but with GFRP bars reinforcement.

References

Cheng, S., Shui, Z., Sun, T., Huang, Y. and Liu, K., 2018. Effects of seawater and supplementary cementitious materials on the durability and microstructure of lightweight aggregate concrete. Construction and Building Materials, 190, pp.1081-1090

Etxeberria, M., Gonzalez-Corominas, A. and Pardo, P., 2016. Influence of seawater and blast furnace cement employment on recycled aggregate concretes' properties. Construction and Building Materials, 115, pp.496-505.

Jensen, H.U. and Pratt, P.L., 1987. The effect of fly ash on the hydration of cements at low temperature mixed and cured in sea-water. MRS Online Proceedings Library (OPL), 113.

Kaushik, S.K. and Islam, M.M., 2005. Physical and mechanical behavior of concrete in seawater under high hydrostatic pressure. J. Inst. Eng. Malaysia, 66, pp.46-52.

Khatibmasjedi, M., 2018. Sustainable concrete using seawater and glass fiber reinforced polymer bars (Doctoral dissertation, University of Miami).

Li, Q., Geng, H., Shui, Z. and Huang, Y., 2015. Effect of metakaolin addition and seawater mixing on the properties and hydration of concrete. Applied Clay Science, 115, pp.51-60.

Mohammed, T.U., Hamada, H. and Yamaji, T., 2004. Performance of seawater-mixed concrete in the tidal environment. Cement and concrete research, 34(4), pp.593-601.

Parvizi, M., Noël, M., Vasquez, J., Rios, A. and González, M., 2020. Assessing the bond strength of Glass Fiber Reinforced Polymer (GFRP) bars in Portland Cement Concrete fabricated with seawater through pullout tests. Construction and Building Materials, 263, p.120952.

Sena-Cruz, J., Pereira, E.N.B., Freitas, N., Pereira, E. and Soares, S.R.R., 2018. Bond behaviour between GFRP rods and concrete produced with seawater: experimental research. 9th International Conference on Fibre-Reinforced Polymer (FRP) Composites in Civil Engineering (CICE 2018), Paris, July 2018.

Wegian, F.M., 2010. Effect of seawater for mixing and curing on structural concrete. The IES Journal Part A: Civil & Structural Engineering, 3(4), pp.235-243.

The Effect of Grinding on the Properties of Pelletized Aggregates Made of AOD Slag

Manoj Kumar[1*], Kizhakkumodom Venkatanarayanan Harish[2]

[1]Department of Civil Engineering, IIT Kanpur, Kanpur, India
Email: manojkm@iitk.ac.in
[2]Department of Civil Engineering, IIT Kanpur, Kanpur, India
Email: kvharish@iitk.ac.in

[*]Corresponding author

ABSTRACT

The production of construction materials has seen a growing focus on sustainability and resource utilization. One such initiative involves converting industrial waste materials into useful products, thereby addressing both environmental concerns and fulfilling the demand for alternative construction materials. A promising approach in this context is the utilization of AOD (Argon Oxygen Decarburization) slag, a by-product of stainless-steel manufacturing, for the production of artificial aggregates. In this study, two types of aggregates were produced i.e., PRC8 (Raw slag-based pelletized aggregates) and PPC8 (processed slag-based pelletized aggregates) with 8 % cement as a binder and 18 % moisture content. Various tests, including particle size analysis, crushing strength tests, soundness tests, and water absorption tests, were conducted to assess the impact of grinding. Experimental results showed that the performance of processed slag-based aggregates was superior to that of raw slag-based pelletized aggregates. Furthermore, raw slag based pelletized aggregates type, PRC8 displayed cracks resulting from volume expansion, which may be due to due to the formation of calcium hydroxide and magnesium hydroxide from free lime and magnesia chunks respectively. Both aggregate groups met the required standards in the soundness test, as the weight loss was well below 12% when subjected to a sodium sulphate solution. This research provides valuable insights into the potential of AOD slag-based aggregates as a sustainable alternative and emphasizes the importance of processing methods in optimizing their performance, thus contributing to the development of eco-friendly construction materials.

KEYWORDS*: AOD slag, Pelletized aggregates, Soundness test, Crushing strength, Eco-friendly construction material*

1. Introduction

Concrete is the most widely used construction material across the globe next to the water (Gagg, 2014). Conventional concrete constitutes cement, fine and coarse aggregates other than water, and other cementitious materials. Out of which, aggregate constitutes approximately 60-80% volume in the concrete mix causing scarcity of natural crushed aggregate near construction sites (Manzi et al., 2013). Nowadays different industrial waste materials are being used in concrete production to fulfill the increasing demand for concrete for different applications. At the same time, they are also lessening the burden on virgin natural materials, which is economically sustainable from an environmental point of view because the carbon dioxide emission is also reduced. There are various supplementary cementitious materials i.e., fly ash, silica fume, ground granulated blast furnace slag (GGBS), etc. are being used in concrete to reduce the clinker quantity in the cement. Similarly, alternate aggregates are also being used as a partial or full replacement of conventional aggregates to reduce the burden on natural resources. Alternate aggregates comprise recycling aggregates, lightweight natural aggregates, and lightweight artificial aggregates i.e., pelletized aggregates, etc. The alternate aggregates are being produced using various types of industrial-based materials i.e. fly ash, GGBS, etc (Gesoğlu et al., 2012). However, concrete made of cold-bonded pelletized aggregates has limited applications due to its poor mechanical properties because of the poor performance

of cold-bonded aggregates. To counteract the poor performance of cold bonded aggregates sintered aggregates are also being used which have superior mechanical properties but at the same time, they are not suited well in lieu of sustainability due to high power consumption because the temperature during the sintering process is about 1000ºC-1200ºC (Nadesan & Dinakar, 2017). The AOD slag is not as popular as other supplementary cementitious materials due to its poor reactivity. Hence its use as a replacement for cement is very limited, alternate ways to utilize this unused slag are explored in this study by making artificial aggregates. AOD slag is a by-product of the stainless-steel manufacturing industry. During the refining process, a large quantity of AOD slag is produced; approximately one-third of the stainless steel produced (Gupta & Sachdeva, 2019). Cold-bonded aggregates produced from AOD slag have poor mechanical properties because during the formation of pellets only natural compaction takes place which leads to several voids in the produced pellets. Artificial aggregates using mechanical compaction were produced to enhance their mechanical performance.

Artificial aggregates are produced from various types of industrial waste materials through various techniques. Out of which pelletization of fine aggregates has a popularity in the last few decades. To address this issue, artificial aggregates produced through the pelletization process of industrial waste materials, such as AOD slag and fly ash, can meet the increasing demand for natural aggregates in certain concrete applications. This approach also provides an alternative and sustainable method for utilizing significant quantities of unutilized AOD slag in the country. The objective of this study is to utilize the underutilized AOD slag as a useful construction material for certain applications.

2. Materials properties

In this study, OPC43-grade cement and AOD slag were used to produce pelletized aggregates. The properties of materials are shown in Table 1 and Figures 1 and 2.

Table 1. Chemical composition and physical properties of materials

Materials	Oxide Composition (% by total mass)										LOI (%)	Sp. Gr.
	CaO	SiO_2	Al_2O_3	Fe_2O_3	MgO	SO_3	K_2O	Na_2O	MnO	Cr_2O_3		
OPC	58.42	20.54	4.50	4.26	3.62	2.46	0.26	0.84	-	-	4.80	3.15
AOD slag	57.54	13.03	0.95	0.80	16.43	0.81	0.03	0.08	5.30	1.36	2.20	3.10

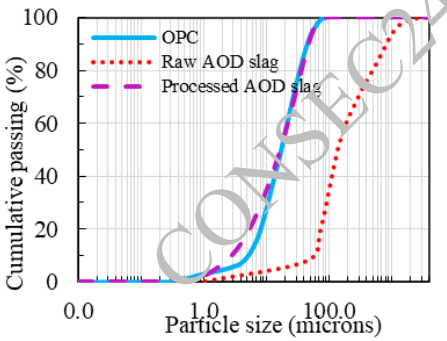

Materials	Mean size (D_{50} in µm)
Raw slag	125.71
Processed Slag	16.87
OPC	17.15

Figure 1. Particle size distribution of different materials and their respective mean size

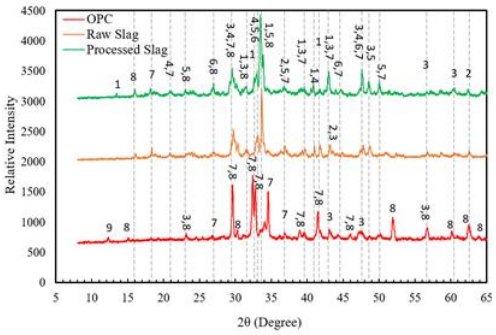

1. Merwinite (PDF# 00-035-0591), 2. Periclase (PDF# 00-004-0829), 3. Calcite (PDF# 00-005-0586), 4. Andradite (PDF# 00-010-0288), 5. Brownmillerite (PDF# 00-030-0226), 6. Calcium silicate (PDF# 00-043-1460), 7. Larnite (PDF# 00-031-0302), and 8. Alite (PDF# 00-042-0551)

Figure 2. XRD analysis of different materials used in this study and identified minerals

3. Mixture proportions and Production process of pelletized aggregate

AOD slag used in this study was provided form Rimjhim Ispat Ltd located in Hamirpur district of Uttar Pradesh part of India. Ordinary Portland cement of 43 grade was provided from Ultratech cement factory. Mixture proportion used in this study is given below:

- PLWA, AOD slag (92 % by weight), cement (8% by weight),
- 17% water of the total weight of AOD slag and cement was used

The production process from mixing to final testing of pelletized aggregates is explained in Figure1. Pelletized aggregates were produced from AOD (Argon Oxygen Decarburization) slag and cement. The raw and fine ground AOD slag was mixed with binder i.e., OPC cement, and fed into the rotating disc, the required quantity of water was sprayed with the water spraying device as shown in Figure 3(b) (Gesoğlu et al., 2012) The disc was rotated at a specified speed and angle and was so adjusted that the dominancy of centrifugal and gravity force was avoided for the higher efficiency of pelletization. After 10 to 12 minutes, the formation of pellets started, and the total time of pelletization for proper compaction of pellets was 20 to 25 minutes. The obtained pellets, also known as fresh pellets, were subjected to an initial impact test for stockpiling by dropping the fresh pellets from a height of 68 cm, as shown in Figure 3 (c). The fresh pellets were kept for 24 hours at room temperature and 80% RH and then subjected to normal water curing for 28 days. The hardened aggregates were then subjected to various physical and mechanical tests to check the suitability of construction materials for different purposes.

(a) Mixture proportioning (b) Spraying of water after dry mixing (c) Formation of pellets

(d) Aggregate obtained after pelletization (e) Aggregate sample in the curing chamber (f) Test setup for finding single aggregate crushing strength

Figure 3. Experimental procedure for making cubical aggregates

4. Test performed on alternate aggregates

Tests performed in this study are summarized in Table 2 as shown below:

Table 2. Experiment performed on pelletized aggregates

Experiment/test methods	Salient feature	Relevant standards/References
Unit weight/Bulk density	Test performed as per the standard mentioned except the aggregates were not tamped using the tamping rod	ASTM: C29/C29M-09 (2017)
Water absorption and specific gravity	Test performed as per the standard mentioned	ASTM C127 (2004)
Crushing strength test	Single aggregates were subjected to gradual compressive load as per the different standard literature $\sigma \approx \frac{2.8*P}{\pi*d^2}$, where P and d are the crushing load and dimensions of the aggregates	Baykal and Döven (2000); Gesoğlu et al. (2012); Gomathi & Sivakumar (2015); Tuncel & Pekmezci (2018)
Soundness test	Aggregates were subjected to alternate wetting and drying in sodium sulphate solution A total of five cycles were employed to determine the loss in weight	IS:2386 (Part V) (1963)
Visual observation analysis	Aggregates were kept under observation and images were taken at different ages	Palankar et al. (2016)

5. Results and Discussions

Aggregates passing through 10 mm size sieve and retained on 4.7 mm size sieve were taken into consideration for further test. Table 3 shows the water absorption, specific gravity, bulk density, crushing strength, and soundness results of different types of alternate aggregates. Processed slag-based pelletized aggregates type PPC8 showed higher bulk density, specific gravity, crushing strength, and lower water absorption. The crushing strength results of the individual aggregates were comparable to those reported in studies by Baykal and Doven (2000) and Gesoglu et al. (2012), which used cement and lime as binders. At an 8% binder replacement, the performance of PRC8 and PPC8 was superior to that observed in the previous research. Processed slag based peleltized aggregates also showed better durability performance compared to raw slag based pelletized aggregates as the loss in weight was lower after alternate wetting and drying in sodium sulphate solution. This may be attributed to the enhanced reactivity of processed AOD slag upon grinding as the particle size of processed slag was almost ~8 times lower compared to the raw slag which may further lead to the improvement in the various other properties of processed slag based pelletized aggregates. The rate of absorption was very high during the intial period of absorption as the aggregates were in dry condition and almost saturated after 24 hours period of absorption in water as the absorption was almost ~98% of 48 hours water absorption.

Table 3. Summary of the test results

Properties/types of aggregates	PRC8	PPC8
Bulk density (kg/m3)	1391	1410
Water absorption (%), at 24 hrs	11.91	10.89
Water absorption (%), at 48 hrs	12.15	11.43
Specific gravity	2.09	2.11
Singh aggregate crushing strength, (MPa)	6.40	6.89
Soundness (% loss in weight)	3.44	3.21

Both aggregate groups met the required standard in this test, as the weight loss was well below 12% in the case of sodium sulphate solution (IS:2386 (Part V), 1963). No signs of cracks were observed on the surface of the aggregates after five cycle of alternate wetting and drying in sodium sulphate solution, however a slight change in the color of the aggregates were observed. **Figure 4** shows the different types of alternate

aggregates after different ages. Raw slag-based aggregates experienced visible cracking after 90 day period of curing whereas processed slag-based pelletized aggregates did not experience any visible cracks even after 180 days of normal water curing. Raw slag-based aggregates contain chunks of free lime (*f*-CaO) and free magnesia (*f*-MgO), when these come in contact with water they react with water and produce expansive compounds like calcium and magnesium hydroxides etc. These compounds exert pressure on the surrounding paste matrix. When the tensile stresses exceed the surrounding paste tensile capacity, cracking occurs (Palankar et al., 2016; Palankar et al., 2016). These cracking were not observed in the case of processed slag-based pelletized aggregates because of the uniform distribution of free lime and magnesia chunks due to grinding which also stabilizes the slag.

(a) Cracks were observed after 90 days

(b) No cracks were observed after 90 days

Figure 4. (a) show the deterioration due to cracking and pop out of the surface of raw AOD slag-based aggregates, (b) show no sign of deterioration of processed AOD slag-based pelletized aggregates

6. Conclusions

- Processed slag-based aggregates showed improved performance compared to raw slag-based aggregates
- PPC8 types of aggregates show higher bulk density, specific gravity, crushing strength, and lower water absorption and loss in weight compared to PRC8.
- Processed slag-based aggregates lead to the uniform distribution of free lime and magnesia chunks, resulting in improved physical and mechanical properties of PPC8 types of aggregates.
- Both aggregate groups met the required standard in the soundness test, as the weight loss was well below 12% in the case of sodium sulphate solution.

References

Astm:C29/C29M-09. (2017). Standard Test Method for Bulk Density (“ Unit Weight ”) and Voids in Aggregate. *ASTM International*, i(c), 1–5. https://doi.org/10.1520/C0029

ASTM C127. (2004). Standard Test Method for Density, Relative Density (Specific Gravity), and Absorption of Coarse Aggregate. *Annual Book of ASTM Standards*, 1–5. https://doi.org/10.1520/C0127-15.2

Baykal, G., & Döven, A. G. (2000). Utilization of fly ash by pelletization process; theory, application areas and research results. Resources, *Conservation and Recycling*, 30(1), 59–77. https://doi.org/10.1016/S0921-3449(00)00042-2

Gagg, C. R. (2014). Cement and concrete as an engineering material: An historic appraisal and case study analysis. *Engineering Failure Analysis*, 40, 114–140. https://doi.org/10.1016/j.engfailanal.2014.02.004

Gesoğlu, M., Güneyisi, E., Mahmood, S. F., öz, H. öznur, & Mermerdaş, K. (2012). Recycling ground granulated blast furnace slag as cold bonded artificial aggregate partially used in self-compacting concrete. *Journal of Hazardous Materials*, 235–236, 352–358. https://doi.org/10.1016/j.jhazmat.2012.08.013

Gesoğlu, M., Güneyisi, E., & Öz, H. Ö. (2012). Properties of lightweight aggregates produced with cold-bonding pelletization of fly ash and ground granulated blast furnace slag. *Materials and Structures/Materiaux et Constructions*, 45(10), 1535–1546. https://doi.org/10.1617/s11527-012-9855-9

Gomathi, P., & Sivakumar, A. (2015). Accelerated curing effects on the mechanical performance of cold bonded and sintered fly ash aggregate concrete. *Construction and Building Materials*, 77, 276–287. https://doi.org/10.1016/j.conbuildmat.2014.12.108

Gupta, T., & Sachdeva, S. N. (2019). Laboratory investigation and modeling of concrete pavements containing AOD steel slag. Cement and Concrete Research, 124(May), 105808. https://doi.org/10.1016/j.cemconres.2019.105808

IS:2386 (Part V). (1963). Methods of Test for Aggregates for Concrete, Part V- Soundness. Bureau of Indian Standards (BIS), 1–14.

Manzi, S., Mazzotti, C., & Bignozzi, M. C. (2013). Short and long-term behavior of structural concrete with recycled concrete aggregate. *Cement and Concrete Composites*, 37(1), 312–318. https://doi.org/10.1016/j.cemconcomp.2013.01.003

Nadesan, M. S., & Dinakar, P. (2017). Structural concrete using sintered flyash lightweight aggregate: A review. Construction and Building Materials, 154, 928–944. https://doi.org/10.1016/j.conbuildmat.2017.08.005

Palankar, N., Ravi Shankar, A. U., & Mithun, B. M. (2016). Durability studies on eco-friendly concrete mixes incorporating steel slag as coarse aggregates. *Journal of Cleaner Production*, 129, 437–448. https://doi.org/10.1016/j.jclepro.2016.04.033

Tuncel, E. Y., & Pekmezci, B. Y. (2018). A sustainable cold bonded lightweight PCM aggregate production: Its effects on concrete properties. *Construction and Building Materials*, 181, 199–216. https://doi.org/10.1016/j.conbuildmat.2018.05.269

Performance of Portland Limestone Cements under Sulphate Environment

Puneet Kaura[1*], Brijesh Singh[1], P N Ojha[1] and Dr L P Singh[1]

[1]National Council for Cement and Building Materials, India,
Email: cdrncbb@gmail.compuneet.kaura@ncbindia.com

[*]Corresponding author

ABSTRACT

The present study aims to investigate the sulphate resistance of mortars, immersed up to one year at 6°C and 23°C in sodium sulphate solutions. In this study, samples of clinker and limestone were obtained from cement plants from different regions of India to cover quality variation of clinker and limestone. The blends prepared with 15% replacement of five different types of clinker by eight different sources of limestone has been used for conducting performance of Portland limestone cement (PLC) based concrete under sulphate environment. Standard mortar samples 25 × 25 × 285 mm prisms have been prepared for conducting the test. The study indicates that sulphate resistance expansion of PLC cement is at par with the control cement. However, the thaumasite expansion (which forms at low temperatures below 6°C) is mostly on higher side for PLC cement as compared to control cement. At a free water-cement ratio of 0.485 and one year of exposure, PLC mortar bars kept at 6°C were found be distorted in shape with heavy cracking. On the other hand, the bars kept at 23°C were in good shape and only linear expansion was found. In sulphate environments, the mortar bars show signs of deterioration during preliminary stages in the form of cracking and spalling, accompanied with expansion, which is similar to conventional sulfate attack. Thaumasite expansion in PLC concrete is found to be higher and damaging for concrete, therefore use of PLC concrete in cold regions is not advisable.

KEYWORDS: *PLC, Sulphate attack, Thaumasite*

1. Introduction

Studies available in the field of Portland limestone cement (PLC) for structural use, recommend limestone content up to 15% as a part substitution of Portland cement clinker (Puneet et al (2023), Dhandapani et (2021)). However, there is a class of researchers that are apprehensive about the performance of PLC when exposed to a sulphate environment. This issue is the most critical constraint in the application of the PLC in sulphate sulphate-laden environment. In concrete, sulphate attack mainly occurs in two forms that can be manifested in terms of expansion due to the formation of ettringite and gypsum or disintegration of the concrete along with mass loss due to the formation of thaumasite. Ettringite ($3CaO{\cdot}Al_2O_3{\cdot}3CaSO_4{\cdot}32H_2O$) or gypsum ($CaSO_4{\cdot}2H_2O$) formation is the result of a chemical reaction between C3A and $Ca(OH)_2$ with the sulphate ion respectively that generally occurs in moderate temperature condition. Thaumasite ($CaSiO_3{\cdot}CaCO_3{\cdot}CaSO_4{\cdot}15H_2O$) formation results from the reaction between CSH and sulphate ion taking place at low-temperature conditions (Gao et al (2021), Pipilikaki et al (2008)). Since it is quite evident that the formation of thaumasite needs a source of carbonates and low temperature, therefore the presence of limestone poses a potential threat to the cementitious system that contains limestone. In this regard, limited studies are available with the Indian materials exposed to sulphate attack. This study was carried out using Indian clinkers and limestones. In the study, PLC blends were prepared at 15% limestone content with 5 different varieties of clinker and 8 types of limestone to account of the quality variation in clinker and limestone. The cement mortar made with PLC blends was exposed to an accelerated sulphate environment at 6 ℃ and 23℃ temperatures.

2. Methodology and Materials

The samples of clinker and limestone were obtained from cement plants from different regions of India to cover quality variation of clinker and limestone. The blends were prepared with 15% replacement of five different types of clinker (C1 to C5) by eight different sources of limestone (L1 to L8). Some of the chemical properties of the clinkers and limestones are given in table 1a and table 1b.

Table1. a Chemical Composition of Clinker

Test Parameter	Clinker				
	C 1	C 2	C 3	C 4	C 5
Silica (SiO_2)%	20.63	20.82	21.42	21.49	21.01
Calcium oxide (CaO)%	62.70	63.87	63.96	65.20	63.90
Magnesium oxide (MgO)%	3.62	1.93	1.76	2.24	0.74
Sulphur Anhydride (SO_3)%	1.62	1.41	1.05	0.31	1.45
C_3A	7.29	7.95	7.44	8.28	9.16
C_4AF	13.21	11.05	11.20	10.50	13.33
C_3S	50.70	56.97	54.81	60.62	48.22
C_2S	21.18	17.02	20.37	16.21	24.14

Table1. b Chemical Composition of limestone

Test Parameter	Limestone							
	L1	L2	L3	L4	L5	L6	L7	L8
Loss on Ignition%	35.46	40.91	36.33	38.17	23.49	46.08	33.39	36.26
Silica (SiO2)%	16.22	6.72	11.96	8.53	31.88	12.40	21.95	12.75
Calcium oxide (CaO)%	39.30	44.83	43.20	46.37	28.74	37.79	42.30	45.10
Magnesium oxide (MgO)%	4.00	5.98	1.45	1.15	1.04	15.37	0.30	0.62

PLC blends were prepared using inter-grinding method. For preparation of PLC blends,OPC clinkers and 15 % crushed limestone along with gypsum were ground to fineness of 380±10 kg/m^3 in ball mill of 6 Kg capacity. The quantity of gypsum was kept such that SO_3 in the cement is limited to 3.00±0.20%. The PLC blends were characterized for some of the physical parameters as mentioned in table 2

Table 2. Physical characterization of PLC blends

PLC Blend	Blaine Fineness (m2/kg)	Compressive Strength (MPa)				Le Chatelier's Soundness mm	Autoclave Soundness %	Initial Setting time min	Final Setting Time min
		D	3D	7D	28D				
C1-CTL	380	20.50	43.00	55.00	70.00	1.00	NA	60	110
C1-L1	383	15.00	31.50	42.00	57.50	1.00	0.1	90	150
C1-L2	396	22.00	33.00	44.00	55.00	1.00	0.08	55	105
C2-L3	385	22.50	35.50	40.50	48.50	1.00	0.06	115	155
C2-L4	407	22.50	36.00	41.50	46.00	1.00	0.06	100	135
C3-L5	398	20.50	29.00	33.00	39.00	1.00	0.05	115	170
C3-L6	397	25.00	35.00	37.00	46.00	1.00	0.05	130	175
C4-L7	390	25.00	33.50	39.00	46.00	2.00	0.06	95	140
C5-L8	368	16.00	33.00	43.50	50.00	1.50	0.07	110	115

3. Experimental Setup and Test Procedure

Sulphate attack in a concrete is primarily comprises of a series of chemical reactions between sulphate ions and the components of hardened concrete. As these reactions may lead to cracking, spalling or strength loss in the concrete structures, appropriate test methods are needed to determine the resistance of concrete under sulphate exposure. Accelerated test methods are the most suitable since sulphate attack is typically a long-term process. In the present study , standard test procedure given in ASTM C1012:2018 was followed. The

test method gives a procedure to acclerate the attack of sulphate ions by using a solution with a high sulphate concentration in which mortar specimens cast at w/c 0.485 were immersed. A 50 g/L sodium sulphate (Na2SO4) solution within pH range of 6.0-8.0 was used as sulphate exposure environment. About12 mortar cubes of size 50 mm and 8 mortar bars of length 285 mm and cross section 25×25 mm were cast. The cubes of all the PLC blends as well as control mix were tested for at regularly compressive strength until strength of 20 MPa was achieved. After the cubes attained 20 MPa strength, 4 number of mortar bars were dipped in 5%Na2SO4 at temperature 23±2 °C for ettringite sulphate attack and rest 4 cubes in 5 % Na2SO4 at temperature 6 °C in cooling water bath for thaumasite sulphate attack. The change in length for both the sets of bars was determined at 1, 2, 3, 4, 8, 13, 15 weeks, 4 months, 6 months, 9 months and 12 months of age using length comparator.

4. Test results and discussions

The test results of the sulphate expansion conducted at moderate temperature (23°C) and low temperature (6 °C) are shown in Figure 1 and Figure 3. The pictorial representations of the mortar bar exposed to a high sulphate environment (5% Na_2SO_4) after one year are shown in Figure2 and Figure 4.On the perusal of the test results, it can be observed that linear expansion of the mortar bars immersed in the sulphate solution kept at 23 °C after an exposure period of 6 months was found to be 0.035% for the control cement (C1-CTL) whereas expansion value of PLC blends was found in the range of 0.036% to 0.052% which is higher than that of the control sample. However, this sulphate expansion value in the mortar bar made with PLC blends is at par with the limit of 0.05% prescribed in ASTM C595, for cement that is highly resistant to a sulphate environment. Similarly, the linear expansion value after an exposure period of 1 year was observed to be 0.045% in the control cement whereas in the case of PLC blends, it was observed in the range of 0.050 to 0.061%. The sulphate expansion value at the age of 1 year was found to be well within the permissible limit of 0.1 % of ASTM C595. The linear expansion of the mortar bars immersed in the sulphate solution kept at 6 °C after an exposure period of 6 months was found to be 0.021% for the control cement (C1-CTL) whereas the expansion value of PLC blends was found in the range of 0.018% to 0.044% which is higher than that of the control sample. The linear expansion value after an exposure period of 1 year was observed to be 0.026% in the control cement whereas in the case of PLC blends, it was observed in the range of 0.025 to 0.056%. The sulphate study conducted at low temperature (i.e. 6°C) indicates a rapid deterioration of the cement mortar bar samples made with PLC cement involving bending, cracking, and spalling along with severe loss of cohesion due to the formation of thaumasite. The test results of the sulphate expansion study conducted at 6°C indicate that most of the bars were damaged after 6 months of exposure as shown in Figure 4, indicating the formation of thaumasite. During the testing, the first sign of distress was observed at the corners of the bars, followed by the occurrence of hairline cracks along the length. As the exposure period increases, bars start bending leading to abnormal cracks and expansion. Similar observations were also reported by Skaropoulou et al (2007), Kakali et al (2003). Even the study conducted on the PLC blends containing 15 % limestone by Pipilikaki et al (2008) at various temperature regimes of 5°C, 10°C and 20°C shows significant deterioration in the appearance of the bars due to the formation of thaumasite at 5 °C within 1-year exposure period under accelerated testing. However, bars exposed at 20 °C temperature were observed to be intact.

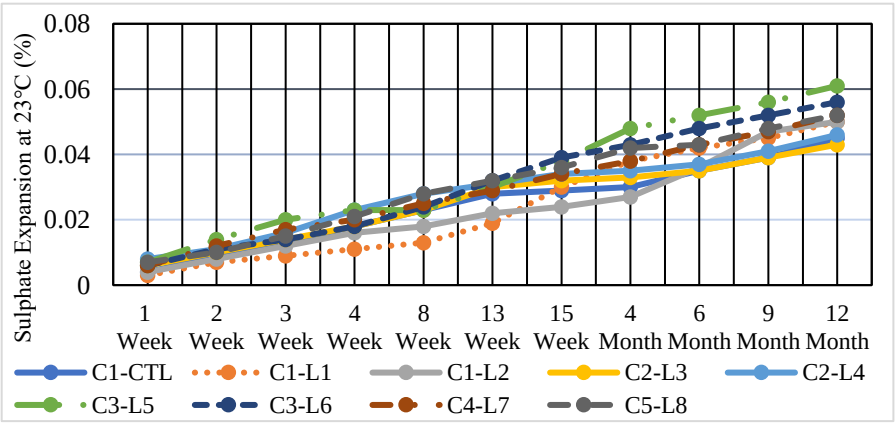

Figure 2. Mortar bars exposed to 5% sulphate for one year at 23°C

Figure 1. Sulphate Expansion of PLC (23°C)

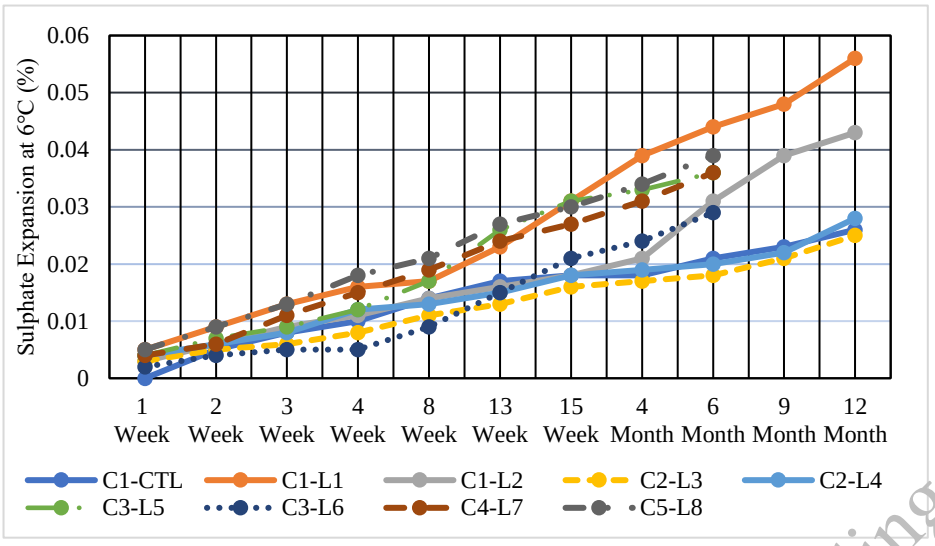

Figure 4. Mortar bars exposed to 5% sulphate for one year at 6°C

Figure 3. Sulphate Expansion of PLC (6°C)

Similar observations were noticed in our study also when bars were exposed to sulphate solution at 23℃. Even though the linear expansion value of the mortar bar exposed in a moderate temperature regime of 23 ℃ was higher than that of the low-temperature regime of 6 ℃, the rate of deterioration was found to be severe in the mortar bars tested under the low-temperature regime of 6 ℃ in comparison to the testing conducted at moderate temperature regime of 23 ℃. This is mainly due to the decalcification of CSH at 6℃ leading to disintegration of the bars. The study conducted by Tiburzi at al (2020) also shows similar results while classifying the cementitious system to be sulphate resistant or not. Under present circumstances, it is not advisable to use PLC in cold regions.

5. Conclusions

The sulphate resistance expansion of PLC cement tested at 23 ℃ is on par with the control cement. However, the thaumasite expansion (which forms at low temperatures below 6℃) is mostly on higher side for PLC cement as compared to control cement. After one year of exposure, mortar bars kept at 6℃ were found be distorted in shape with heavy cracking. On the other hand, the bars kept at 23°C were in good shape and only linear expansion was found. Thaumasite expansion in PLC concrete is found to be higher and damaging for concrete, therefore use of PLC concrete in cold regions is not advisable.

References

Dhandapani, Yuvaraj, Manu Santhanam, Gopakumar Kaladharan, and Sivakumar Ramanathan (2021) "Towards ternary binders involving limestone additions—A review", *Cement and concrete research*, 143: 106396.

Gao, Yuxin, Yaoling Luo, Lili Jia, Wen Yang, and Chong Wang (2021) "Effect of limestone powder on thaumasite form of sulfate attack (TSA) of cement-based materials" ,*Advances in Civil Engineering* 2021: 1-12.

Kakali, G., S. Tsivilis, A. Skaropoulou, J. H. Sharp, and R. N. Swamy (2003) "Parameters affecting thaumasite formation in limestone cement mortar", *Cement and Concrete Composites* 25, no. 8: 977-981.

Kaura, Puneet, Ojha, P., N. and Jain, Hardik (2022) "Mechanical and Durability performance of Portland limestone cement (PLC) made with intergrinding having high fineness limestone in concrete",*17th NCB International Conference on Cement, Concrete and Building materials*, New Delhi, India.

Pipilikaki, Penny, D. Papageorgiou, Ch Teas, E. Chaniotakis, and M. Katsioti (2008) "The effect of temperature on thaumasite formation." *Cement and Concrete Composites* 30, no. 10: 964-969.

Skaropoulou, A., K. Sotiriadis, G. Kakali, and S. Tsivilis (2007) "A long term study on thaumasite form of sulfate attack (TSA) in limestone cement pastes", *In Proc*, vol. 12.

Tiburzi, Nicolas B., Jose Garcia, Thano Drimalas, and Kevin J. Folliard (2020)"Sulfate resistance of portland-limestone cement concrete systems: Linking laboratory and field performances", *Construction and Building Materials* 250: 118750.

Carbonation and Corrosion Rate of Concrete Made with Composite Cement

P N Ojha[1] and Puneet Kaura[2*]

[1]National Council for Cement and Building Materials, India,
Email: cdrncbb@gmail.com
[2]National Council for Cement and Building Materials, India,
Email: puneet.kaura@ncbindia.com

[*]Corresponding author

ABSTRACT

Composite cement is a low-clinker cement that replaces a significant portion of clinker with a combination of fly ash and granulated blast furnace slag (GBFS). In India, composite cement typically consists of 35%-65% Portland cement clinker/ ordinary Portland cement (OPC) along with 15%-35% fly ash and 20%-50% GBFS. However, using composite cement with such a varied clinker content may not be suitable for RCC structures due to potential carbonation and carbonation-induced corrosion issues. To investigate this, a study was conducted using five possible specifications of composite cement. Ten concrete mixtures of composite cement were designed at a 0.60 water-cement ratio. The performance of these mixtures against carbonation and carbonation-induced corrosion was compared to concrete mixtures made with Portland Pozzolana Cement (fly ash based) and Portland Slag Cement (PSC). The carbonation resistance of the concrete mixtures was evaluated over an exposure period of 70 and 140 days in a CO2 environment, following ISO 1920 Part 12 guidelines. Additionally, a study on the carbonation-induced corrosion rate was conducted on reinforced concrete specimens, and the corrosion rate was determined using the linear polarization technique. Based on the study's findings, it is recommended that composite cement should contain at least 50% OPC, fly ash in the range of 10%-25%, and GGBS in the range of 25%-40 % to achieve performance against carbonation and carbonation-induced corrosion that is equivalent to or better than PPC and PSC.

KEYWORDS*: Carbonation, Corrosion, Composite cement*

1. Introduction

Developing low-Portland clinker cement is one of the best solutions the cement industry can offer to reduce CO2 emissions. Composite cement is a low-clinker cement in which a combination of fly ash and granulated slag replaces a significant proportion of the clinker. In India, composite cement typically consists of 35%-65% Portland cement clinker/ ordinary Portland cement (OPC) along with 15%-35% fly ash and 20%-50% GBFS. However, using composite cement with such a varied clinker content may not be suitable for RCC structures due to potential carbonation and carbonation-induced corrosion issues. The study conducted by researchers like Arora et al(2020), Cheah et al (2019), and Sengul et al (2009) shows insignificant improvement in the microstructure of the composite cement blends made by various combinations of fly ash and slag. This is mainly due to the formation of secondary C-S-H gels due to pozzolanic reaction at the later ages that creates a closely-packed geometry, contributing to further densification of the binder phase matrix. However, replacing the Portland cement clinker significantly with fly ash and slag will also influence the pore chemistry. The study by Vineet et al. also indicates significant changes in the pore chemistry of composite blends that influenced carbonation resistance. Although the carbonation process has been studied extensively, the behavior of rebar in carbonated concrete has not gained adequate attention. It is understood that pH reduction and consequent de-passivation of rebar in concrete made with blended/composite cement may occur earlier than OPC. However, early carbonation-induced de-passivation may not always cause a significant reduction in the service life of concrete elements demarcated

by cracking of cover concrete. To investigate this, a study was conducted using five possible specifications of composite cement. Ten concrete mixtures of composite cement were designed at a 0.60 water-cement ratio. The performance of these mixtures against carbonation and carbonation-induced corrosion was compared to concrete mixtures made with Portland Pozzolana Cement (fly ash based) and Portland Slag Cement (PSC).

2. Methodology and Materials

Formulating specifications for composite cement for general purpose use, considering the durability aspect, especially carbonation-induced corrosion, with due consideration to sustainability. The following probable proportions for the specifications and combinations were studied.

Table 1 Probable proportions for possible specifications

SI.No.	Possible specification	OPC ,%	Fly ash ,%	GGBS ,%
1.	SP1 (min. OPC= 35%, fly ash =15-25%, GGBS=40-50%)	35	15	50
2.		35	25	40
3.	SP2(min. OPC= 40%, fly ash =10-25%, GGBS=35-50%)	40	10	50
4.		40	25	35
5.	SP3(min. OPC= 45%, fly ash =10-25%, GGBS=30-45%)	45	10	45
6.		45	25	30
7.	SP4(min. OPC= 50%, fly ash =10-25%, GGBS=25-40%)	50	10	40
8.		50	25	25
9.	SP5(min. OPC= 55%, fly ash =10-25%, GGBS=20-35%)	55	10	35
10.		55	25	20

The materials used in manufacturing composite cement, i.e., fly ash, slag, and OPC 43, conform to the requirements of the relevant Indian standards. The coarse aggregate (20 mm and 10 mm) and fine aggregate (crushed), conforming to the appropriate Indian standards, were used in the production of the concrete. A total of 13 concrete mixes, including ten composite cement mixes and three no's of control mixes (made with OPC, PPC, and PSC), were designed at a w/c ratio of 0.60 at a cement content of 300 kg/m^3 for a workability range of 75-100 mm and dosage of superplasticizer was adjusted accordingly.

3. Experimental Setup and Test Procedure

A compressive strength test was conducted on concrete cubes (size 150mm x 150mm x 150mm) as per IS: 516 (Part 1/ Sec1) at 7 and 28 days. For the carbonation and carbonation-induced reinforcement corrosion test, reinforced concrete specimens with dimensions 300x250x100 mm (No's=2)) with cover thicknesses of 10 mm and 15 mm, as shown in Figures 1 and 2, were cast. After 28 days of water curing, the concrete specimens were conditioned in a controlled laboratory environment (temperature = 27+ 2 ℃ and Relative humidity = 65+5%) for 28 days. After laboratory conditioning, the side faces of the RCC slabs were sealed using epoxy, mainly Araldite, and carbonation was allowed on the cast and shutter face. After the sealing, the reinforced concrete slabs were shifted to the carbonation chamber with a CO2 level kept at 4+0.5 % (by volume), temperature of 27+ 2℃, and relative humidity of 65+5%. The average carbonation depth was measured by extracting a concrete core with a diameter of 25 mm and a length of 100 mm and exposing the cut surface to 1% phenolphthalein solution, a reliable method for measuring carbonation depth. The reinforced concrete specimens were exposed to carbon dioxide for 70 and 140 days. The corrosion rate reading was measured when the carbonation front had crossed the Clear cover + R/F diameter. Here Clear cover= 10 mm & R/F diameter= 12 mm. The linear polarization resistance (LPR) method, a reliable method, measures the corrosion rate.

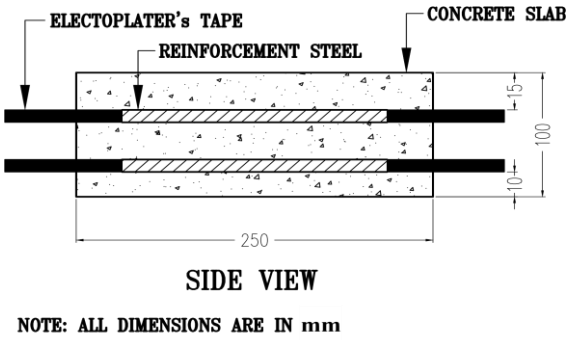

Figure 1. Schematic diagram of the test specimen

Figure 2. RCC specimen

4. Test results and discussions

The compressive strength study was carried out at two ages, i.e., 7 days and 28 days, and the results are mentioned in Table 1. From the study, it was observed that compressive strength values are influenced by parameters like percentage of OPC content and fly ash content. Further, it was also observed that when OPC content is > 50%, the composite cement mixes had compressive strength at par with concrete mixes designed with conventional Portland systems like OPC, PPC, and PSC.

Table 1. Compressive strength, carbonation depth and corrosion rate of concrete

S.No.	Composition (OPC:FA:GGBS)	water cement ratio = 0.60					
		Compressive Strength (MPa)		Carbonation Depth (mm) at exposure period of		carbonation front progress from 70 days to 140 days in mm (B-A)	Corrosion rate when carbonation front reaches beyond 22 mm
		7-day	28-day	70 days (A)	140 days (B)		(in mm/yr)
1	Control	22.6	26.0	9.97	16.40	6.43	0.0057
2	65:35:00	13.0	20.8	17.00	26.34	8.62	0.0063
3	40:0:60	19.7	27.9	15.25	23.87	9.34	0.0065
4	35:15:50	14.7	22.0	22.15	33.62	11.47	0.0109
5	35:25:40	11.0	21.8	24.93	37.56	12.63	0.0098
6	40:10:50	19.2	24.0	17.53	27.09	9.56	0.0087
7	40:25:35	17.9	23.1	19.92	30.47	10.55	0.0075
8	45:10:45	18.8	28.9	15.92	24.81	8.89	0.0064
9	45:25:35	15.6	25.2	17.39	26.89	9.50	0.0058
10	50:10:40	23.0	28.6	12.92	20.57	7.65	0.0055
11	50:25:25	19.0	27.7	14.93	23.41	8.48	0.0048
12	55:10:35	21.4	28.0	10.45	17.08	6.63	0.0041
13	55:25:20	16.6	26.5	12.50	19.98	7.48	0.0039

The test results of carbonation depth, the progress of the carbonation front (defined as the difference between the depth of carbonation between the two exposure periods), and the corrosion rate are mentioned in Table 1. The test results of the carbonation depth for a CO_2 exposure period of 70 days & 140 days and carbonation front progress from an exposure period of 70 days to 140 days for different fly ash slag composite cement were graphically represented in Figure 3 to Figure 5. The graphical representation of the test results indicates the relationship between OPC content and maximum fly ash content, as well as minimum fly ash content value. In this study, carbonation depth and progress of carbonation depth are compared with the conventional Portland system, i.e., PPC. Based on the accelerated carbonation depth study, it was observed that composite cement performs at par with PPC, provided that it has a minimum OPC content of less than 50 %. In the present study, a cementitious system that mainly comprises various combinations of fly ash and slag was designed with OPC content as low as 35 %; problems related to carbonation-induced corrosion were a significant concern. The addition of fly ash as a substitute to Portland

cement clinker not only reduces the initial alkalinity but also leads to the consumption of Ca(OH)2 produced from the hydration of Portland cement clinker, whereas slag also requires some amount of Ca(OH)2 for the reaction. However, products formed during the hydration process in the fly ash slag composite cement generate additional CSH and CASH, leading to pore refinement that may stifle the ingress of CO2. As evident, carbonation is not a simple process; instead, it involves a chain of chemical and physical reactions. The accelerated carbonation test covers the chemistry part of this process, whereas the corrosion test involves both phenomena. The test results of the carbonation-induced reinforcement corrosion study carried out at fly slag composite cement concrete mixes designed at w/c of 0.60 are shown in Figure 6, and values are mentioned in Table 4. From the study, it is evident that fly ash slag composite cement should have at least 50 % OPC content to achieve comparable performance with respect to conventional Portland cement systems in a carbonation-induced corrosion environment.

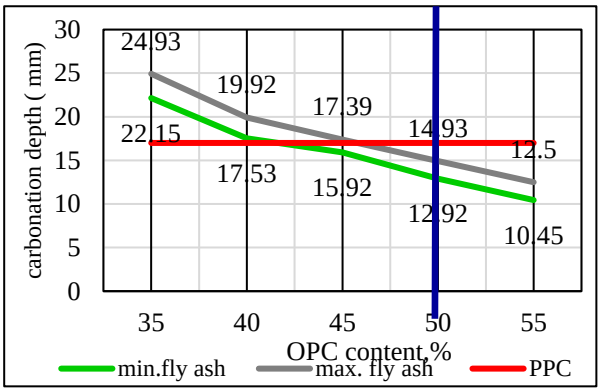

Figure 3. Carbonation Depth after 70 Days Exposure

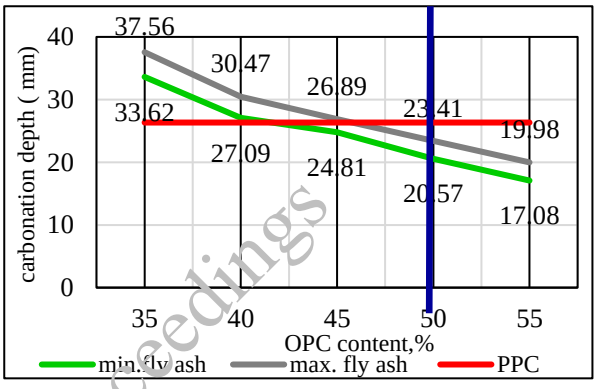

Figure 4. Carbonation Depth after 140 Days Exposure

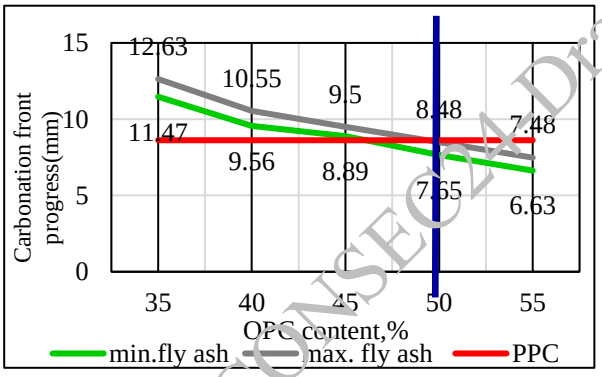

Figure 5. Progression of the Carbonation front from Exposure period of 70 days to 140 days

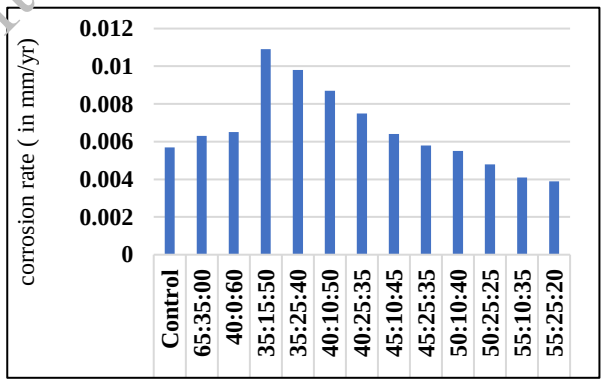

Figure 6. Corrosion rate when carbonation front reaches beyond 22 mm

5. Conclusions

Intrinsic parameters like fly ash content and OPC content greatly influence the Compressive strength of concrete made of fly ash slag composite cement. As the fly content increases or OPC content reduces, the compressive strength value reduces accordingly. Further, it was also observed that when OPC content is at least 50%, the composite cement mixes had compressive strength at par with concrete mixes designed with conventional Portland systems like OPC, PPC, and PSC.

The carbonation depth of concrete made with composite cement was found at par with conventional Portland systems when OPC content is not less than 50 %, whereas a corrosion rate study indicates that fly ash slag composite systems have better-resisting ability against the ingress of CO2 in comparison to conventional Portland system even at OPC content 45 %.

Overall, based on the mechanical as well as durability test results, especially carbonation as well as carbonation-induced reinforcement corrosion, it was recommended to keep OPC content at least 50%, fly

ash in the range of 10-25%, and GGBS in the range of 25-40 % to achieve performance equivalent or better than PPC or PSC.

References

Arora, V.V., Kaura, P., Mittal, P. and Mohapatra, B.N. (2020) "Performance assessment of concrete made with ternary cementitious blends against chloride ingress and CO2 attack",*Civil Engineering and Construction Review*, May 2020

Cheah, C.B., Tiong, L.L., Ng, E.P. and Oo, C.W. (2019) "The engineering performance of concrete containing high volume of ground granulated blast furnace slag and pulverized fly ash with polycarboxylate-based superplasticizer", *Construction and Building Materials*, 202: 909-921

Sengul, O. and Tasdemir, M.A. (2009) "Compressive strength and rapid chloride permeability of concretes with ground fly ash and slag. ", *Journal of materials in civil engineering*, 21(9): 494-501

Shah, V. and Bishnoi, S. (2018) "Carbonation resistance of cements containing supplementary cementitious materials and its relation to various parameters of concrete", *Construction and Building Materials*,178: 219-232

Investigation on Effect of Basalt Waste Fines as Replacement of River Sand in One-part Geopolymer Mortar

D. Jain[1*] and S. D. Adhikary[2]

[1]*Ph.D. Student, Department of Civil Engineering, Indian Institute of Technology (Indian School of Mines) - Dhanbad, 826004, India*
Email: 21DR0051@cve.iitism.ac.in
[2]*Associate Professor, Department of Civil Engineering, Indian Institute of Technology (Indian School of Mines) - Dhanbad, 826004, India*
Email: satadru@iitism.ac.in, 2020satadru@gmail.com

[*]Corresponding author

ABSTRACT

This study examines the potential use of basalt waste fines, a waste generated after the basalt rock crushing process, as an eco-friendly replacement of conventional river sand in one-part geopolymer mortar, aiming to optimize its mechanical and durability properties. The investigation was designed into three series to test different mix proportions to improve the mechanical and durability properties of mortar. In Series I, the study evaluates the incremental substitution of river sand with basalt waste fines, ranging from 0% to 100%, while keeping the activator-to-binder and aggregate-to-binder ratios fixed. In this phase, a 50% replacement percentage is selected as the optimal percentage for achieving the balance between mechanical strength and workability. Progressing to Series II, the study examines variations in the activator-to-binder ratio, identifying 0.15 as the ideal activator-to-binder ratio for significantly enhancing mortar performance. Below this ratio, a notable degradation in performance was observed. Series III further explores the mix design by modifying the aggregate-to-binder ratio, revealing that an increase in this ratio enhances strength, indicating the significant impact of mix proportion. The results, based on mechanical properties, durability assessments, and microstructural analyses, confirm the feasibility of using basalt waste fines as a viable alternative in one-part geopolymer mortar and underscore the importance of mix design in achieving enhanced material performance.

KEYWORDS: *One-part Geopolymer Mortar; Basalt Waste Fines; Mechanical Properties; Durability Properties; Microstructural Properties*

1. Introduction

The construction industry, a crucial component of the global economy, uses cement and aggregate as primary and secondary materials. However, this reliance on aggregate, particularly river sand (RS), has led to significant environmental and sustainability challenges. The over-extraction of RS has caused severe environmental degradation, including riverbank erosion, groundwater depletion, and biodiversity loss, as well as deterioration of water quality and disruption of aquatic ecosystems (Bhattacharya et al., 2019; Guo et al., 2020). As an alternative, basalt waste fines (BWF), a by-product of basalt rock crushing, offer a sustainable replacement for river sand. Basalt rocks exhibit high strength, specific gravity, and sound resistance, making BWF a viable substitute that also mitigates the environmental impact of sand extraction (Yılmaz, 2022). In the pursuit of eco-friendly construction materials, geopolymer concrete emerges as a promising low-carbon alternative to traditional Portland cement concrete. Geopolymers, synthesized through alkaline activation of aluminosilicate precursors, offer advantages such as improved workability and enhanced strength (Al Bakri et al., 2012; Davidovits, 1989). However, challenges in the preparation of caustic solutions hamper their production at large scale (Adesanya et al., 2020). Research in the geopolymer industry led to the development of one-part geopolymers (OPG), which simplify the mixing and curing processes, providing a more practical solution (Duxson & Provis, 2008).This study investigates the use of

BWF as a fine aggregate in OPG mortar, aiming to enhance mechanical and durability properties. Additionally, it explores the effects of variation of solid activators to binder ratio and aggregate to binder ratios to optimize the mix design of OPG mortar.

2. Methodology

Class F fly ash (FA) and ground granulated blast furnace slag (GGBS) were used as Al-Si precursor conforming to IS3812Part1 (2013) and IS16714 (2018). Sodium metasilicate pentahydrate (SMSP), used as a solid activator, has a modulus ratio (SiO_2/Na_2O) 0.99. BWF, collected from a rock-crushing plant in Dhanbad, conforms to Zone 2 as per IS383 (2016). The methodology for the OPG mortar is formulated in three series. Series 1 investigates the impact of varying proportions of BWF (25%, 50%, 75%, and 100%) as a replacement for RS. The activator-to-binder ratio and binder-to-aggregate ratio were set at 0.12 and 1, respectively. The water-to-binder ratio was determined to be 0.23, in accordance with IS4031Part4 (1988), and adjusted based on aggregate content. Series 2 examines the effect of activator to binder ratio after identifying the optimum mix from Series 1. The activator-to-binder ratio was adjusted to 0.15 and 0.18, while the aggregate-to-binder ratio remained unchanged. The water-to-binder ratio was maintained at 0.23. In Series 3 aggregate, the aggregate-to-binder ratio was adjusted to 2.2 to evaluate its effect on the mortar properties, using the optimum mix from Series 2. The water-to-binder ratio was adjusted to maintain consistent workability. The mix proportions for the samples are provided in Table 1. Mixes are represented as OGM-XXX-YY-ZZ. Where 'XXX' represents the replacement of RS with BWF. 'YY' and 'ZZ' represent the activator-to-binder ratio and aggregate-to-binder ratio. In the preparation process, aggregates at saturated surface-dry (SSD) condition and binder powder were dry mixed in a mixer for 3 minutes. Water was gradually added, and the mixture was further mixed for 10 minutes to achieve a homogeneous consistency. The mix was then poured into molds, which were set at ambient temperature. After demolding, the specimens were cured at an ambient temperature of 25 ± 2 °C with a relative humidity of 75%.

Table 1. Mix Proportion of One part Geopolymer Mortar

Series	Mix	Binder (kg/m^3)			Fine Aggregate (kg/m^3)		Water (kg/m^3)
		FA	GGBS	SMSP	RS	BWF	
I	OGM-000-0.12-1	415	415	113	943	0	216
	OGM-025-0.12-1	416	416	113	709	236	217
	OGM-050-0.12-1	416	416	113	473	473	217
	OGM-075-0.12-1	417	417	113	237	712	218
	OGM-100-0.12-1	418	418	114	0	951	218
II	OGM-050-0.15-1	402	402	141	473	473	217
	OGM-050-0.18-1	387	387	170	472	472	217
III	OGM-050-0.15-2.2	265	265	93	686	686	190

3. Results

Workability: Flow table tests were performed in accordance with IS5512 (1983) to measure the workability of fresh mortar. The workability of mortar mixes decreases as the replacement percentage of BWF increases. Flowability of series 1 of mix OGM-000-0.12-1, OGM-025-0.12-1, OGM-050-0.12-1, OGM-075-0.12-1 and OGM-100-0.12-1 are 45%, 35%, 33%, 25% and 25%, respectively. This reduction is attributed to the non-uniform particle size and rough surface texture of the BWF, which increases friction between particles, thereby decreasing workability (Westerholm et al., 2008). Compressive Strength Test: Compressive strength tests were done in accordance with IS4031Part6 (1988). In Series 1, the compressive strength increased with the replacement percentage of BWF, as shown in Figure 1, at 28 days. The variation in particle size enhanced the strength by filling voids, resulting in a more compact and dense matrix (Yücel et al., 2023). Mix OGM-050-0.12-1 demonstrated optimal results for both workability and compressive strength, making it the basis for further investigation in Series 2. In Series 2, mix OGM-050-0.15-1 yielded the best results due to increased geopolymerization and C(N)ASH gel formation. Higher activator content led to rapid hardening and void formation, reducing the strength (Wan-En et al., 2022). Series 3, mix OGM-050-0.15-2.2, achieved a strength of 39.1 MPa. This is due to higher BWF content, which improves aggregate

interlocking and elongates the path of crack propagation in the matrix, resulting in strength enhancement (Haruna et al., 2020).

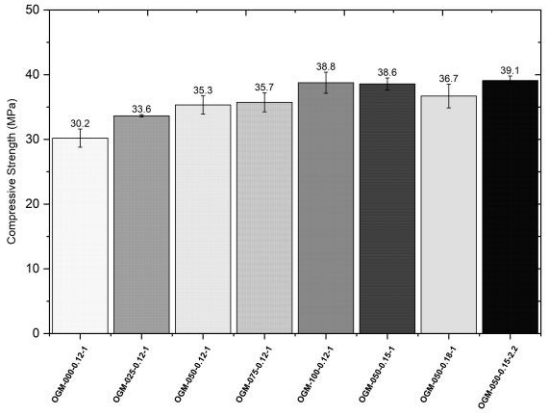

Figure 1. Compressive strength of One-part Geopolymer Mortar

Acid Resistance Test: Acid resistance tests were performed after 28 days of ambient curing, followed by 28 days of immersion in sulfuric acid at a pH of 1.3. In series 1, the replacement percentage of BWF increased, and mass loss decreased, as shown in Figure 2. This is attributed to the finer particles filling voids and preventing acid ingress. Further, these samples with high BWF percentages maintained high compressive strength due to their dense structure and minimal mass loss. Series 2 samples showed the least mass loss, likely due to higher activator content enhancing geopolymerization and acid resistance. However, compressive strength decreased due to rapid hardening and void formation from higher activator content. In Series 3, the higher aggregate-to-binder ratio of 2.2 resulted in increased mass loss, attributed to the lower geopolymer paste content leading to strength loss.

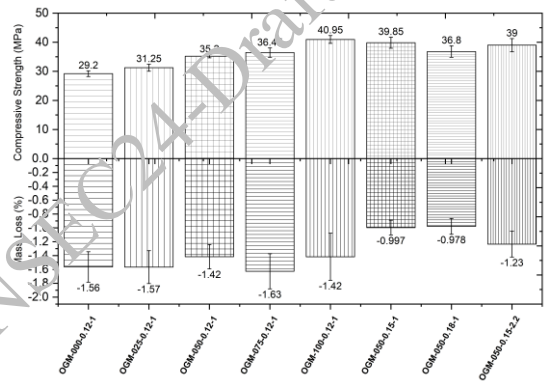

Figure 2. Compressive Strength and Mass Loss of Acid Immersed Sample

XRD Analysis: XRD analysis in Series 1 for mixes OGM-000-0.12-1 and OGM-100-0.12-1 revealed distinct peaks for quartz (SiO_2), CASH and NASH, as shown in Figure 3. The 0% basalt mix showed quartz peaks related to SiO_2 content, while intensified CASH peaks were observed at 29° 2θ (Luukkonen et al., 2018). Quartz peaks at 21° 2θ and 80° 2θ diminished, indicating the substitution effect of BWF. Additional C(N)ASH peaks at 31° 2θ, indicating enhanced polymerization activity due to BWF.

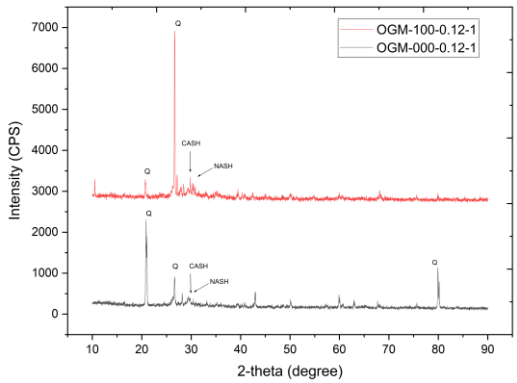

Figure 3. XRD Analysis of One-part Geopolymer Samples

4. Conclusion

This study investigates the effect of basalt waste fines as a replacement for natural sand in one-part geopolymer mortar. It also examines the impact of the activator-to-binder ratio and the aggregate-to-binder ratio on mix design optimization. The findings reveal that increasing basalt waste fines decreases workability but improves compressive strength due to the particle size variation and effective bonding. Finer basalt particles enhance polymerization, as evidenced by XRD analysis. Higher replacement ratios also improve acid resistance. An activator-to-binder ratio above 0.15 negatively impacts compressive strength, while an aggregate-to-binder ratio of 2.2 enhances strength. This study demonstrates that basalt waste fines can effectively replace river sand, improving mechanical, durability, and microstructural properties, and highlights the need for careful adjustment of mix proportions for modern construction practices using greener alternatives like geopolymer.

Acknowledgments

This research has been funded by the Institution of Engineers (India), 8 Gokhale Road, Kolkata 700020 under R&D Grant-in-Aid scheme (IEI/2023-2024/50/CE), which is gratefully acknowledged.

References

Adesanya, E., Ohenoja, K., Di Maria, A., Kinnunen, P., & Illikainen, M. (2020). Alternative alkali-activator from steel-making waste for one-part alkali-activated slag. *Journal of Cleaner Production*, *274*, 123020.

Al Bakri, A. M., Kamarudin, H., Bnhussain, M., Nizar, I. K., Rafiza, A., & Zarina, Y. (2012). The processing, characterization, and properties of fly ash based geopolymer concrete. *Rev. Adv. Mater. Sci*, *30*(1), 90-97.

Bhattacharya, R. K., Das Chatterjee, N., & Dolui, G. (2019). Consequences of sand mining on water quality and instream biota in alluvial stream: a case-specific study in South Bengal River, India. *Sustainable Water Resources Management*, *5*, 1815-1832.

Davidovits, J. (1989). Geopolymers and geopolymeric materials. *Journal of thermal analysis*, *35*(2), 429-441.

Duxson, P., & Provis, J. L. (2008). Designing precursors for geopolymer cements. *Journal of the American Ceramic Society*, *91*(12), 3864-3869.

Guo, M., Hu, B., Xing, F., Zhou, X., Sun, M., Sui, L., & Zhou, Y. (2020). Characterization of the mechanical properties of eco-friendly concrete made with untreated sea sand and seawater based on statistical analysis. *Construction and Building Materials*, *234*, 117339.

Haruna, S., Mohammed, B. S., Wahab, M., & Liew, M. (2020). Effect of paste aggregate ratio and curing methods on the performance of one-part alkali-activated concrete. *Construction and Building Materials*, *261*, 120024.

IS383. (2016). Coarse and Fine Aggregate for Concrete-Specification. In. New Delhi, India: *Bureau of Indian Standards*.

IS3812Part1. (2013). Pulverized Fuel Ash-Specification Part 1 for use as pozzolana in cement, cement mortar and concrete. In. New Delhi, India: *Bureau of Indian Standards.*

IS4031Part4. (1988). Method for physical test for hydraulic cement. In. New Delhi, India: *Bureau of Indian Standards*.

IS4031Part6. (1988). Methods of physical tests for hydraulic cement, Part 6: Determination of compressive strength of hydraulic cement other than masonry cement. In. New Delhi, India *Bureau of Indian Standards.*

IS5512. (1983). Specification of flow table for use in test of Hydraulic Cement and Pozzolanic Material. In. New Delhi, India: *Bureau of Indian Standards.*

IS16714. (2018). Ground Granulated Blast Furnace Slag for use in cement, cement mortar and concrete-Specification. In. New Delhi, India: *Bureau of Indian Standards.*

Luukkonen, T., Abdollahnejad, Z., Yliniemi, J., Kinnunen, P., & Illikainen, M. (2018). Comparison of alkali and silica sources in one-part alkali-activated blast furnace slag mortar. *Journal of Cleaner Production*, *187*, 171-179.

Wan-En, O., Yun-Ming, L., Cheng-Yong, H., Ngee, H. L., Abdullah, M. M. A. B., Khalid, M. S. B., Loong, F. K., Shee-Ween, O., Seng, T. P., & Jie, H. Y. (2022). Towards greener one-part geopolymers through solid sodium activators modification. *Journal of Cleaner Production*, *378*, 134370.

Westerholm, M., Lagerblad, B., Silfwerbrand, J., & Forssberg, E. (2008). Influence of fine aggregate characteristics on the rheological properties of mortars. *Cement and Concrete Composites*, *30*(4), 274-282.

Yılmaz, A. (2022). Engineering properties of basalt aggregates in terms of use in granular layers of flexible pavements. *Case Studies in Construction Materials*, *17*, e01182.

Yücel, H. E., Dutkiewicz, M., & Yıldızhan, F. (2023). The Effect of Waste Ballast Aggregates on Mechanical and Durability Properties of Standard Concrete. *Materials*, *16*(7), 2665.

Effects of Mixture Ingredients on the Workability and Compressive Strength of Magnesium-Silicate-Hydrate (Mgo-Sio$_2$) Binders

D. Kumar[1]*, N. N. Lwin[2], K. U.A. Sanalkumar[3], and E.H. Yang[4]*

[1] School of Civil and Environmental Engineering, Nanyang Technological University (NTU), Singapore
Email: dhanendra.kumar@ntu.edu.sg
[2] School of Civil and Environmental Engineering, Nanyang Technological University (NTU), Singapore
Email: NUNU0002@e.ntu.edu.sg
[3] Department of Civil Engineering, Indian Institute of Technology (IIT) Madras, Chennai, India
Email: askrishnanunni@yahoo.com
[4] School of Civil and Environmental Engineering, Nanyang Technological University (NTU), Singapore
Email: ehyang@ntu.edu.sg

*Corresponding author

ABSTRACT

The Magnesium-Silicate-Hydrate (MSH) binders are developed using the hydration reaction between magnesium oxide (MgO) cement and reactive silica (SiO_2) sources. The MSH binders possess lower pH values than Portland cement and are suitable for nuclear waste encapsulation. The fresh and hardened properties of MSH binder are primarily influenced by the ratio of the MgO cement and silica source, in addition to other mix design variables. The objective of this study was to systematically investigate the effects of mix design parameters on the workability and compressive strength of the MSH binders. The mix design parameters investigated in this research were – MgO cement/Silica ratio, water-to-binder (w/b), sand-to-binder, and superplasticizer. Two types of silica sources – silica fume and metakaolin were used. The study employed the Taguchi method of experimental design for a systematic understanding of the effects of these mixture ingredients on the performance of MSH binders. The workability was characterized using the flow table tests, and unconfined compression tests were conducted after 28 days of casting. The flow diameter of the MSH binders decreased with the increase in silica content. However, the compressive strength was not significantly influenced by the silica content within the investigated range, and the effects of other mix design parameters were more prominent. The results of this research are expected to aid in developing the mix design guidelines for MSH binders.

KEYWORDS: *Magnesium-Silicate-Hydrate (MSH), MgO cement, Silica source, Workability, Compressive strength*

1. Introduction

The production of Portland cement contributes to around 8% of global CO_2 emissions (Peng & Unluer (2024)). Continuous efforts have been made to decarbonize the cement industry by utilizing supplementary cementitious materials or developing alternative low-carbon binders. Magnesia cement or MgO cement is one such binder produced at a low calcination temperature (~700°C) and can be obtained from waste materials such as reject brine (Kumar et al. (2022); Peng & Unluer (2024)). The magnesium-silicate-hydrate (MSH) cementitious system is a low pH binder formed by the hydration reaction between MgO cement and amorphous silica (Zhang et al. (2011)). The hydration of MgO cement results in the formation of brucite [$Mg(OH)_2$], which combines with silica source (SiO_2) to form poorly crystalline MSH binding phases responsible for providing mechanical strength to the composites (Tran (2019); Tran & Scott (2017); Zhang et al. (2014)). The proportion of silica and MgO in the mixture constituents governs the content and stoichiometry of MSH phases in the binder (Brew & Glasser (2005); Tran & Scott (2017)). The MSH system mostly utilized silica fume as the source of reactive silica, with fly ash, rice husk ash, and metakaolin showing potential application for the development of MSH (Sonat & Unluer (2019); Tran (2019)). Further,

due to the very fine content of raw ingredients, a high amount of water-reducing admixture is required for the processing of MSH binders (Kumar et al (2022)). The mix ingredients and their respective proportions control the fresh and hardened properties of MSH binders. The MSH binders typically utilize phosphate-based additives such as sodium hexametaphosphate, sodium triphosphate, sodium orthophosphate, and dipotassium phosphates to modify the rheology (Kumar et al. (2022); Li et al. (2022); Zhang et al. (2014)). A few studies have utilized polycarboxylate ether (PCE) based superplasticizers in MSH binders (Dhakal et al (2021); Tran & Scott (2017)). The selection of water-reducing admixture affects the pH of the suspension and governs the workability and compressive strength of the composites (Kumar et al. (2022); Zhang et al. (2014)). However, there is a lack of understanding of the effects of mix design parameters, such as water/binder ratio and water-reducing admixture content, on workability and mechanical strength. To better understand the performance of MSH binders, it is necessary to study the effects of mixture constituents and their content on the fresh and hardened properties. The research aims to address this knowledge gap on the individual and interaction effects of basic mix design parameters– silica/binder ratio, water/binder ratio, sand/binder ratio, and superplasticizer content on the workability and compressive strength, and thus guide the performance-based design of MSH binders.

2. Experimental Methodology

The Taguchi method of design of experiments was employed to select the mixture ingredients parameters. The L9 orthogonal array for four parameters varying at three levels was adopted. A total of 18 mixtures (9 each with silica fume and metakaolin) were investigated. The mixture design parameters for each mixture are reported in Table 1. The MSH mixtures used MgO cement (with MgO content >90%), silica fume or metakaolin as silica source (referred to as silica in Table 1), PCE-based superplasticizer (SP), and microsilica sand with a mean particle size of 180 µm. The binder includes MgO + silica fume for silica fume-based and MgO + metakaolin for metakaolin-based MSH cementitious system. The mixtures were prepared in a Hobart mixer. The workability of the fresh mixtures was determined using the flow table test using a mini-slump brass cone (height 50 mm; top diameter 70 mm and base diameter 100 mm) following ASTM C1437 (2020) after 25 drops. The drop in vertical height is referred to as a mini-slump. The spread diameter of the fresh mixture was measured in two orthogonal directions, and the average was reported as the flow value. Three 50 mm cubes were cast for each mixture to characterize compressive strength. The cubes were demolded after 24 hours and submerged in water for 13 days of underwater curing, followed by 14 days of air exposure under lab conditions. The compression testing was done after 28 days of casting at a loading rate of 55 kN/min following ASTM C109/C109M (2024).

Table 1. Mixture design parameters

Mix No.	Silica/Binder	Water/Binder	Sand/Binder	SP (%)
1.	0.40	0.40	0.00	2.0
2.	0.40	0.45	0.40	2.5
3.	0.40	0.50	0.80	3.0
4.	0.50	0.40	0.40	3.0
5.	0.50	0.45	0.80	2.0
6.	0.50	0.50	0.00	2.5
7.	0.60	0.40	0.80	2.5
8.	0.60	0.45	0.00	3.0
9.	0.60	0.50	0.40	2.0

3. Results and Discussions

The influence of the four mixture design parameters on the workability (flow value and mini-slump) and compressive strength for both silica fume and metakaolin-based MSH cementitious systems is presented in Figure 1. The mean values are presented in Figure 1 to demonstrate the main effects of each mixture design parameter. The effects of each mixture design parameter on the investigated fresh and hardened properties are discussed below.

Silica/binder ratio: The flow and mini-slump values decreased with the silica/binder ratio increase. The mean particle size of silica source (both silica fume and metakaolin) is smaller than MgO cement, increasing

the water demand, thus reducing the flow value and slump values. The corresponding workability values were smaller for silica fume mixtures than metakaolin due to very fine particle size (thus very high specific surface area). The compressive strength of metakaolin-based MSH mixtures does not change with the silica/binder ratio. On the contrary, the compressive strength decreased with the silica/binder ratio for silica fume-based MSH mixtures, which was attributed to lower MgO content for the available reactive silica.

Water/binder (w/b) ratio: The w/b ratio showed an initial decrease and then increasing trend for the flow and mini-slump values for metakaolin MSH mixtures. It is expected that the initial increase in water content is absorbed by metakaolin (clayey mineral) interlayers, and the further increase in water content is available freely to lubricate the particles, increasing the flow and mini-slump values. In case of silica fume MSH mixtures, the increase in water content led to a monotonic increase in flow and mini-slump values. The increase in the w/b ratio led to a similar reduction in the compressive strength of both metakaolin and silica fume MSH mixtures. This reduction is similar to that observed in Portland cement composite, which is attributed to the increased porosity of the composite specimens.

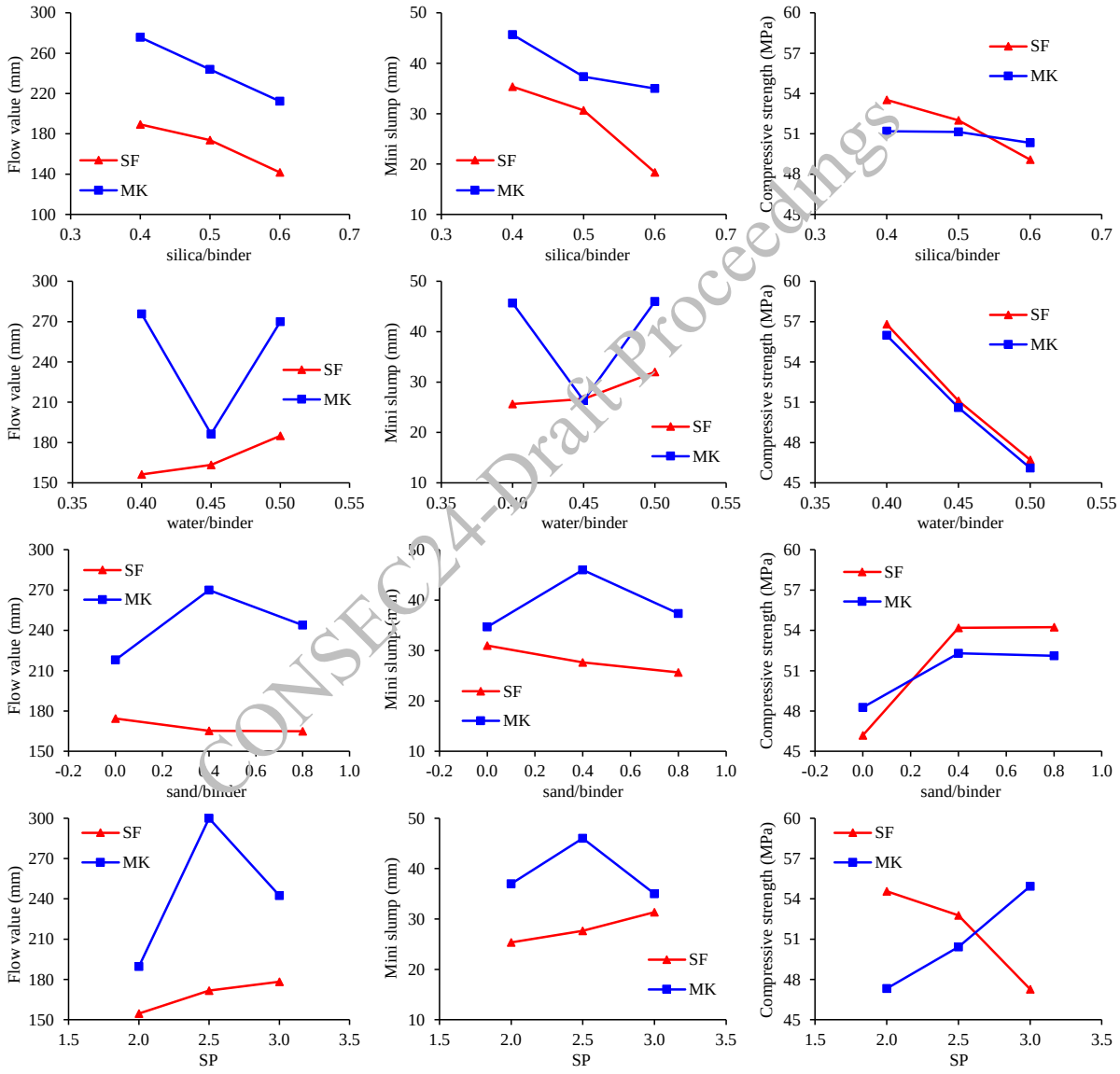

Figure 1. Influence of mixture design parameters on flow value, mini-slump, and compressive strength

Sand/binder ratio: The flow and mini-slump value slightly reduced with increase in sand/binder ratio in silica fume MSH mixtures, which could be due to increased inter-particle frictional resistance of sand particles offering resistance to mixture flow. In metakaolin-based MSH mixtures, the flow value and mini-slump initially increased with the sand/binder ratio and thereafter dropped slightly. The initial increase is due to the breaking of strong inter-particle attraction between metakaolin particles by sand, whereas a

further increase in sand content increases the frictional resistance and decreases the flow properties. The compressive strength of both metakaolin and silica fume MSH mixtures increased with initial increase in sand content and became constant after that. The increase in compressive strength with the addition of aggregates has been observed in conventional concrete and is due to the interlocking action of aggregates.
Superplasticizer (SP) content: The flow and mini-slump values increased with SP content for silica fume MSH mixtures due to the increase in available water within the mixture. The metakaolin MSH mixtures also showed an initial increase in flow and mini-slump values with increased SP content but decreased beyond 2.5%. This indicates a potential optimum SP value at 2.5%, and additional SP acts as water in metakaolin MSH mixtures. The SP content showed interesting effects on compressive strength. The contrasting effects were observed for metakaolin and silica fume MSH mixtures. The reduced compressive strength for silica fume MSH composites is attributed to the increased freely available water. In case of metakaolin MSH mixtures, the compressive strength increased with SP content.

4. Conclusions

The effects of mixture proportions – silica/binder ratio, water/binder ratio, sand/binder ratio, and superplasticizer content on the workability and compressive strength of the MSH cementitious system were investigated. The effect of silica/binder ratio on flow and mini-slump values was similar in silica fume and metakaolin MSH cementitious system. The effect of other mix design parameters (water/binder ratio, sand/binder ratio, and superplasticizer content) was different in silica fume and metakaolin MSH mixtures, showing the influence of silica source characteristics (mineralogical composition, particle size, and morphology) on MSH cementitious system performance. The influence of water/binder ratio (monotonic reduction) and sand/binder ratio (initial increase and constant thereafter) on compressive strength was similar in silica fume and metakaolin MSH mixtures. The compressive strength was reduced with increased silica/binder ratio in silica fume MSH mixtures and remains constant in metakaolin MSH cementitious system. The superplasticizer content showed contrasting effects on compressive strength with enhancement in metakaolin MSH system and reduction in silica fume MSH cementitious system. The results will help develop mix design guidelines for the MSH cementitious system.

References

ASTM C1437-20 (2020) "Standard test method for flow of hydraulic cement mortar", *ASTM International*, West Conshohocken, PA.

ASTM C109/C109M-21 (2024) "Standard Test Method for Compressive Strength of Hydraulic Cement Mortars", *ASTM International*, West Conshohocken, PA.

Brew, D., & Glasser, F. (2005) "Synthesis and characterisation of magnesium silicate hydrate gels", *Cement and Concrete Research*, 35(1): 85-98

Dhakal, M., Scott, A. N., Shah, V., Dhakal, R. P., & Clucas, D. (2021) "Development of a MgO-metakaolin binder system", *Construction and Building Materials*, 284

Kumar, S., Lei, J., Yang, E.-H., & Unluer, C. (2022) "Influence of different additives on the rheology and microstructural development of MgO–SiO_2 mixes", *Composites Part B: Engineering*, 235

Li, Z., Lin, L., Yu, J., Tang, H., Qin, J., & Qian, J. (2022) "Performance of magnesium silicate hydrate cement modified with dipotassium hydrogen phosphate", *Construction and Building Materials*, 323

Peng, Y., & Unluer, C. (2024) "Understanding the rheological behavior of reactive magnesia-metakaolin system in the context of digital construction", *Cement and Concrete Composites*, 149

Sonat, C., & Unluer, C. (2019) "Development of magnesium-silicate-hydrate (MSH) cement with rice husk ash", *Journal of Cleaner Production*, 211: 787-803

Tran, H. (2019) "Development of magnesium silicate hydrate binder systems", Ph.D. Thesis, University of Canterbury, New Zealand

Tran, H., & Scott, A. (2017) "Strength and workability of magnesium silicate hydrate binder systems", *Construction and Building Materials*, 131: 526-535

Zhang, T., Cheeseman, C. R., & Vandeperre, L. J. (2011) "Development of low pH cement systems forming magnesium silicate hydrate (MSH)", *Cement and Concrete Research*, 41(4): 439-442

Zhang, T., Vandeperre, L. J., & Cheeseman, C. R. (2014) "Formation of magnesium silicate hydrate (MSH) cement pastes using sodium hexametaphosphate", *Cement and Concrete Research*, 65: 8-14

Transforming a Conventional Tunnel into a Self-Cleaning and Air-Purifying Infrastructure: A Case Study

A. Maury-Ramirez[1*] and M. Rinke[1]

[1] Architecture Department, Faculty of Design Sciences, University of Antwerp, Antwerp, Belgium*
Email: anibal.maury-ramirez@uantwerpen.be; mario.rinke@uantwerpen.be

[*]Corresponding author

ABSTRACT

The Colombia Avenue Tunnel, located in Santiago de Cali (Colombia), is an urban transport infrastructure strategically located in the city, allowing fast connectivity between the north and south districts passing under the city center. However, due to its high-volume traffic, there is a significant air pollution and fast deterioration of the tunnel surfaces, which demand regular cleaning activities that cause negative traffic and environmental impacts. To prevent these effects, this research evaluates the potential implementation of a coating (i.e., mortar or paint) that, using titanium dioxide photocatalysis, could develop self-cleaning and air-purifying properties on the tunnel surfaces. Photocatalytic evaluation of the coating samples was performed at the laboratory scale, using methylene blue (MB) and rhodamine b (RhB) as dyes and UV-A as activation source. Using the software Image J for image processing, the sample area covered with the dye was monitored before and after the UV-A exposure. Results showed that the photocatalytic paint (two layers) removed approximately 50% of the RhB compared to the 30% obtained with the photocatalytic mortar with 5% TiO2. Moreover, it was observed that applying additional paint layers (i.e., four and six layers) did not improve the photocatalytic performance; on the contrary, the removal was reduced up to 35% using six layers.

KEYWORDS: *Self-cleaning properties, Air-purifying properties, Titanium dioxide photocatalysis, Photocatalytic mortar, Photocatalytic paint.*

1. Introduction

Materials selection, construction processes and architectural design of buildings and infrastructure are key elements to efficiently respond to the challenging environmental, social and economic demands of sustainable development (Maury-Ramirez and De Belie, 2023). An interesting way to satisfy simultaneously these demands is the use of photocatalytic materials for developing self-cleaning and air-purifying properties. With this aim, but with different results, already some pioneering projects with TiO_2 loaded materials have been erected worldwide (Castro-Hoyos et al., 2022). For example, regarding the application of TiO_2 photocatalysis for reducing urban air pollution in tunnels, two cases are interesting (Figure 1).

First, with a length of 348 m and 9000 m2, the Umberto I tunnel located in Rome (Italy) was covered with a commercially available TiO2 cementitious paint which is commercialized for air-purifying purposes. Additionally, a special lighting system using UV and visible light was installed inside the tunnel. During two monitoring campaigns at different seasons, NOx reductions between 20% (measured) and 50% (statistical estimation) were reported. Similarly, sampling particle matter (PM total) inside the tunnel during the two campaigns has also evidenced not release of TiO2 nanoparticles in the air. Second, a similar photocatalytic coating and UV lighting system were installed and evaluated by a three-step field campaign on the Tunnel Leopold II located in Brussels (Belgium). With a photocatalytic area of about 2700 m² and a tunnel section of about 160 m in length, no significant photocatalytic removal of NOx was evidenced (below 2%). This not very promising result was mainly associated to the environmental conditions (i.e. high humidity and low temperatures), high wind speed (up to 3 m/s) and UV light intensity inside the tunnel (below 4 W/m2). Therefore, considering the importance of determining the real potential of this technology

before implementation, the preliminary evaluation of a photocatalytic mortar (5% of the cement content) and a photocatalytic paint (two, four and six layers) for the tunnel located at the Colombia Avenue in the city of Santiago de Cali (Colombia) was developed (Figure 2).

Figure 1. Tunnels covered with photocatalytic coatings and UV lighting to reduce urban air pollution.(a) Umberto I in Rome (Italy); (b) Leopold II in Brussels (Belgium). (Boonen & Beeldens, 2014; Maury-Ramirez, 2011).

Figure 2. Location and geometry of the Tunnel of Colombia Avenue in Santiago de Cali (Colombia). (Castro-Hoyos et al, 2022).

2. Methodology and materials

2.1 Case study

This project is aimed to evaluate the use of photocatalytic materials based on TiO_2 to produce air-purifying and self-cleaning properties on the Colombia Avenue Tunnel located in Santiago de Cali at the southwest Colombia. This urban infrastructure project, which is 650 m long and 14 m wide, is located in a zone near to the city centre with high traffic volumes (i.e. 5000 vehicles per hour).

2.2 Photocatalytic removal of organic dyes

This research evaluates the implementation of a coating (i.e., mortar or paint) that, using titanium dioxide photocatalysis, could develop self-cleaning and air-purifying properties on the tunnel surfaces. To do this, two commercially available photocatalytic products (i.e. TiO_2 powder and TiO_2 paint) were assessed using disks of architectural mortar (Table 1). First, a set of 3 replicate samples were prepared with 5% TiO_2 related to the cement content by weight. Second, a set of 3 replicate samples were brush painted with 2, 4 and 6 photocatalytic layers, respectively. Also, a set of 3 replicate samples without any TiO_2 were used as references during the photocatalytic tests.

Table 1. Main properties of TiO_2 commercially available applied on architectural mortars samples.

Material	Appearance		Crystal Form	TiO_2 content	Surface area (dry)
CristalACTiV™ PC-S7	TiO2 Paint		Anatase	~ 10 wt%	~ 350 m2/g
CristalACTiV™ PC105	TiO2 powder		Anatase	~ 99 wt%	~ 90 m2/g

Finally, the evaluation consisted on the monitoring of photocatalytic removal of two organic dyes, methylene blue and rhodamine b, which having the same concentration (0.0015 g/ml) and a molecular structure closely resembling the pollutants of the environment, could indicate the potential self-cleaning and air-purifying properties under UV-A exposure. The simulation of UV-A rays was performed with 2 lamps blacklight F20T12BL General Electric with an irradiation of 510 mW/cm^2 and wavelength between 350 and 400 nm (Figure 3). Then, using the software Image J for images processing, the sample area covered with the dye was monitored before (0 h) and after the UV-A exposure (4, 8 and, 24 h). This monitoring process can be observed for samples coated with the photocatalytic paint (2 layers) in Figure 4.

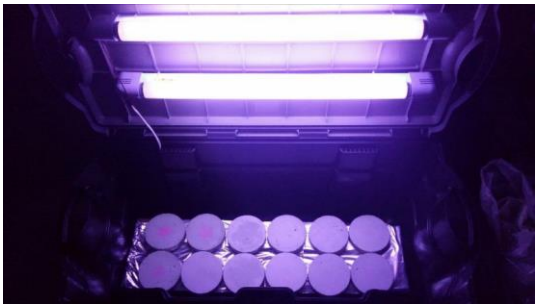

Figure 3. Photocatalytic test removal of rhodamine B on architectural mortar samples containing TiO_2.

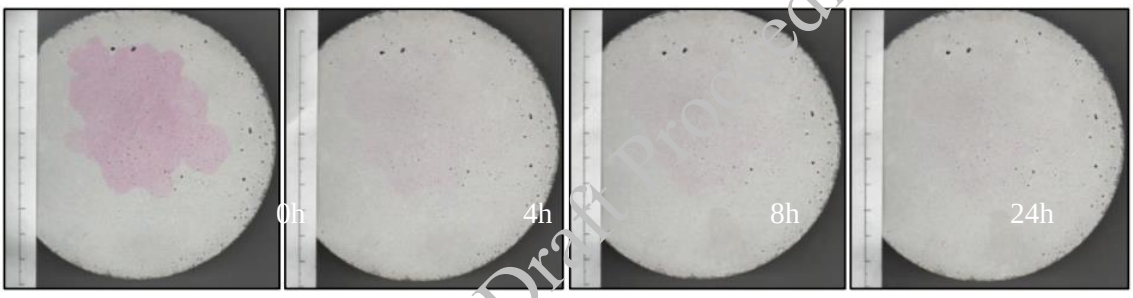

Figure 4. Photocatalytic removal of RhB on architectural mortar disks coated with TiO_2 paint (2 layers).

3. Results analysis

Test results after 24 h of UV-A exposure showed that the photocatalytic paint applied on the architectural mortars in two layers removed approximately 50% of the RhB compared to the 30% obtained with the photocatalytic mortar with 5% TiO_2 (Figure 5). This result might be explained by the differences in the location of nanoparticles and surface area. First, the encapsulation of TiO_2 particles by the hydration products in 5%TiO_2 samples adversely reduced their contact with RhB and UV-A light. Second, the significantly higher surface area of the photocatalytic paint (350 m^2/g) compared to the TiO_2 particles (90 m^2/g) played a major role in the photocatalytic removal of RhB. Compared to the best performance of RhB removal obtained (i.e. 50%), higher removal rates (63% approx.) are reported when using the same paint applied by means of 3 layers on top of self-compacting architectural mortars samples which were exposed to UV-A during 26 h at 3 W/m^2 approx. In this case, the architectural mortar samples used white cement and metakaoline as cement phase, as well as crushed recycled glass as fine aggregate. Similarly, the RhB concentration was set lower at 0.0005 g/ml (Guo et al., 2016).

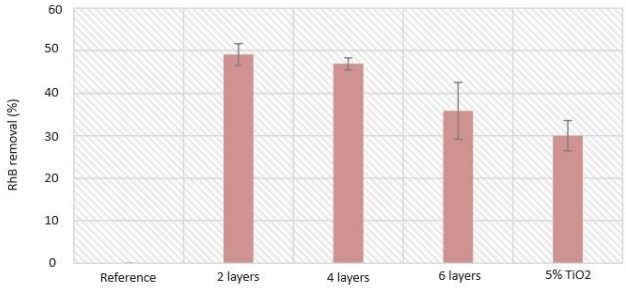

Figure 5. Photocatalytic test removal of rhodamine B on architectural mortar samples containing TiO_2 (Medina-Medina et al., 2016).

Additionally, it was observed that applying four and six layers of the paint did not improve the photocatalytic performance; on the contrary, the removal was reduced by up to 35% using six layers. This might be due to the longer paint drying process which could induce TiO_2 particles agglomeration. Moreover, the transparent colour from the paint transformed into a whitish appearance. On the other hand, although the photocatalytic removal of methylene blue and rhodamine b was evaluated at similar sample conditions and UV-A exposure, results were significantly different among these organic dyes. Photolysis, a chemical reaction in which molecules of a chemical compound are broken down by photons, was very pronounced in the photocatalytic removal of methylene blue, particularly during the first 4 hours of light exposure. This phenomenon is easily observed on the reference samples, without any TiO_2 (Figure 6). Even though this is not a desired result, it is in complete agreement with former results for water treatments reported by Wen et al. (2020).

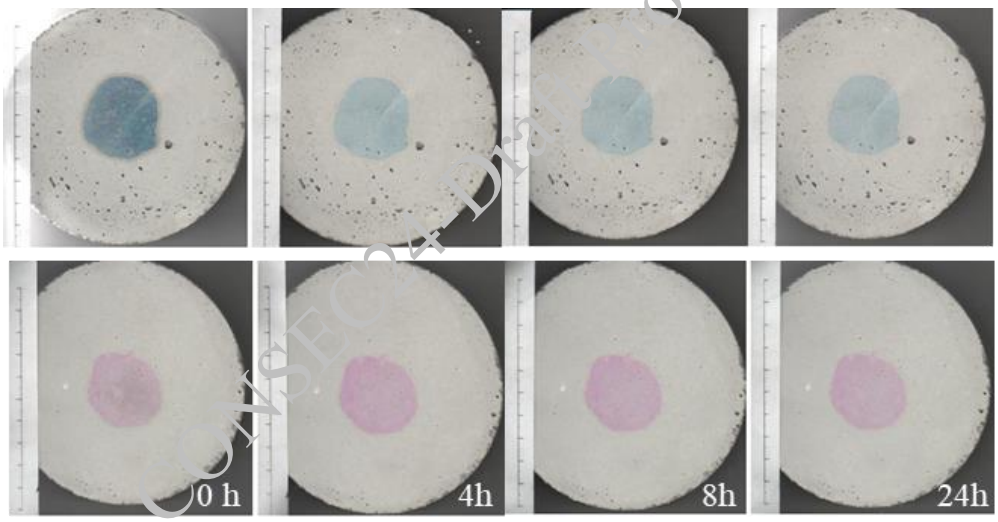

Figure 6. Photocatalytic removal of methylene blue and rhodamine B on architectural mortar disks without any photocatalytic material (reference samples) (Medina-Medina et al., 2016).

4. Conclusions

Considering the RhB photocatalytic removals of 50% and 30% obtained for the samples coated with the TiO_2 paint (2 layers) and mortar samples with 5% TiO_2 intermixed, respectively, the photocatalytic paint performed the best for transforming the Colombia Avenue Tunnel into a self-cleaning and air-purifying infrastructure. This result, which is in agreement with the estimated results for the Umberto I Tunnel, is mainly due to the relatively higher surface area and the outer positioning of the TiO_2 in the photocatalytic paint compared to the TiO_2 that is intermixed. Similarly, higher removal rates (63% approx.) were reported when using the same TiO_2 paint applied by means of 3 layers on top of self-compacting architectural mortars samples which were exposed longer time to UV-A and using a lower RhB concentration. Furthermore, it can be concluded that RhB is much more chemically stable than MB to assess the photocatalytic performance. Moreover, it was observed that applying additional TiO_2 paint layers (i.e., four

and six layers) did not improve the photocatalytic performance; on the contrary, the removal was reduced up to 35% using six layers. This might be due to the longer paint drying process which could induce TiO_2 particles agglomeration.

References

Boonen, E.; Beeldens, A. (2014) "Recent Photocatalytic Applications for Air Purification in Belgium", *Coatings 4.*

Castro-Hoyos, A.M.; Rojas Manzano, M.A.; Maury-Ramírez, A. (2022) "Challenges and Opportunities of Using Titanium Dioxide Photocatalysis on Cement-Based Materials", *Coatings, 12: 968.*

Guo, M-Z.; Maury-Ramirez, A.; Poon, CS. (2016) "Self-Cleaning Ability of Titanium Dioxide Clear Paint Coated Architectural Mortar and Its Potential in Field Application", *Journal of Cleaner Production, 112: 3583.*

Medina Medina, A.F.; Torres Rojas, D.F.; Meza Girón, G.; Villota Grisales, R.A. (2016) "Design of a System to Generate Air Purification and Self-Cleaning in the Surfaces of the Colombia Avenue Tunnel"; *Pontificia Universidad Javeriana Cali: Cali, Colombia.*

Maury-Ramírez, A. and De Belie, N. (2023) "Environmental and Economic Assessment of Eco-Concrete for Residential Buildings: A Case Study of Santiago de Cali (Colombia)", *Sustainability, 15: 12032.*

Maury-Ramirez, A. (2011) "Cementitious Materials with Air-Purifying and Self-Cleaning Properties
Using Titanium Dioxide Photocatalysis"; *Ghent University: Ghent, Belgium.*

Wen, D.; Li, W.; Lv, J.; Qiang, Z.; Li, M (2020) "Methylene blue degradation by the VUV/UV/persulfate process: Effect of pH on the roles of photolysis and oxidation", *Journal of Hazardous Materials, 391: 121855.*

Sustainable Nano-modified Seawater Concrete with Enhanced Service Life (NanoSeaCon)

Sundar Rathnarajan[1*], Pawel Sikora[1*], and Wojciech Stawowy[1]

[1] West Pomeranian University of Technology in Szczecin, Poland
Email: srathnarajan@zut.edu.pl, pawel.sikora@zut.edu.pl

[*]Corresponding authors

ABSTRACT

Countries facing extremely severe water-stress are looking for an alternative source of water for industrial purposes including concrete production. The United Nations General Assembly proposed measures to avert a global water crisis by proposing the Water Action Decade between 2018 and 2028. Aligning with this global cause, a significant increase in the research on concrete produced with seawater-mixing has been carried out in the past few years. Researchers focused on understanding the interaction of ions in seawater with hydrated cement phases in OPC and blended cementitious systems. However, a systematic assessment of the long-term strength and durability of seawater-mixed concrete (SWC) is unavailable. NanoSeaCon focuses on evaluating these long-term properties on ternary-blended concretes with nano-SiO_2 (nS) and nano-Al_2O_3 (nA). The presence of metakaolin and slag in concrete contributed to the active binding of chloride ions and thus reduced the availability of free chlorides in cementitious matrix, which could be detrimental for embedded steel in concrete. The early-age hydration behaviour and the role of seawater ions in reducing the setting time of the cementitious systems were evaluated with isothermal calorimetry studies. Also, the fresh properties and hardened properties of SWC were evaluated to elucidate the role of ions in seawater on reduction in flow and improvement in early-age strength development, respectively. Moreover, the long-term durability of SW-mixed concretes was assessed through resistivity, sulphate attack, and bulk diffusion tests. Based on the durability assessment, the service life of SWCs was calculated, and the feasibility of adapting SWCs for niche applications is discussed.

KEYWORDS*: Concrete, Seawater-mixing, Durability, and Service life*

1. Introduction

Seawater-mixed concrete (SWC) is a novel approach recommended to produce concrete for niche applications with alternative reinforcement for regions facing extremely severe water stress (Ebead et al., (2022)). Project NanoSeaCon aims to develop sustainable nano-modified concrete with enhanced service life by evaluating the performance of concrete mixes in recent literature. As a first step, a systematic analysis of the literature was carried out and the research gaps were identified to make a significant contribution to this fast-growing area of research (Rathnarajan and Sikora, (2023)). Figure 1 shows the increase in the research interest in SWC in recent years, and primarily more studies are focused on using seawater as a mixing agent and sea sand as an alternative to conventional aggregates. However, meta-analysis of the literature reveals that very limited works are available on understanding the seawater-mixed concretes made with supplementary cementitious materials, as indicated in Figure 1. The research articles considering the ternary blended cementitious materials in SWC are less than 10, and this work intends to contribute significantly to that gap in the literature. The role of supplementary cementitious materials (SCMs) in enhancing the chloride binding ability of cementitious matrix is key to achieve a durable SWC. Also, a preliminary investigation was conducted to evaluate the suitability of the seawater-mixing for producing lightweight aggregate concrete with nano-SiO_2, waste glass, dune sand, and quartz (Sikora et al., (2023)). A significant reduction in the water footprint was observed in the novel light-weight aggregate mixes. These contributions impacted the formulation of the research objectives of the NanoSeaCon project,

which focuses on the optimization of blended cementitious systems with mineral admixtures like fly ash, slag, and metakaolin.

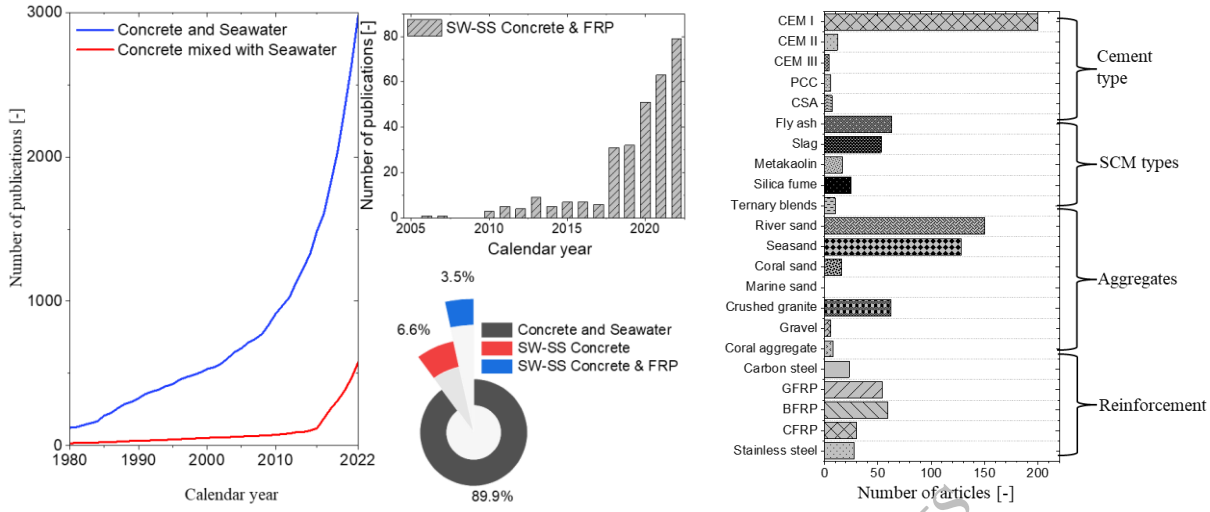

Figure 5. Current state of art: Increase in research interest on seawater-mixed concretes and type of materials used in SWC. [Rathnarajan and Sikora (2023)]

2. Optimization of blended cementitious systems suitable for seawater-mixing

A preliminary investigation was conducted on 35 binder combinations produced with fresh- (FW) and seawater (SW). Table 1 summarises the number of paste mixes produced at a similar water-to-binder ratio to evaluate the tasks mentioned in the project. From the analysis of this wider research task, it is evident that there has been a significant improvement in the early-age hydration and strength development of ternary blended cementitious systems compared to binary or CEM I-based combinations. Rathnarajan et al., (2024) presented the most suitable combinations of CEM I and SCMs for seawater-mixing with a reasonable acceleration in the early-age hydration and maximum strength improvement up to 28 days. Among these mixes, the most suitable 12 binder combinations were selected for producing concrete for evaluating the strength and durability characteristics of seawater-mixed concrete.

Table 2. Detailed experimental program to understand early age hydration of SW-mixed binder systems

All concrete mixes are cast with binder content = 550 kg/m3 and water-to-binder ratio: 0.4			
Binder composition (xx, yy: SCM content)	No. of mixes (FW & SW)	Replacement level % by weight	Remarks
CEM I (PC)	2	0	-
CEM I + Fly ash (PFxx)	8	10 - 40%	Binary
CEM I + Slag (PSxx)	6	30 – 70%	Binary
CEM I + Metakaolin (PMxx)	6	10 – 30%	Binary
CEM I + Limestone (PLxx)	6	10 – 30%	Binary
CEM I + Fly ash + Slag (PSxxFyy)	8	30 – 60%	Ternary
CEM I + Fly ash + Limestone (PFxxLyy)	4	30 – 45%	Ternary
CEM I + Slag + Limestone (PSxxLyy)	4	30 – 45%	Ternary
CEM I + Metakaolin + Limestone (PMxxLyy)	4	30 – 45%	Ternary
CEM I + Slag + Metakaolin (PSxxMyy)	6	30 – 60%	Ternary
CEM 1 + Fly ash + Metakaolin (PFxxMyy)	6	30 – 60%	Ternary

2.1 Mechanical performance of SW-mixed concretes

Based on the preliminary investigation, one CEM I, 4 binary, and 7 ternary binder compositions were selected for producing 24 concretes. The binder content and water-to-binder ratio of the produced concretes were kept constant at 360 kg/m^3, and 0.45, respectively. Compressive strength of cubes (size: 100 mm) was measured at 7, 28, and 90 days to understand the effects of seawater-mixing on strength development. Figure 2a summarizes the percentage change in compressive strength between FW-mixed and SW-mixed

concretes at the above-mentioned ages. A significant improvement in strength at 7 days was observed in specimens produced with SW-mixing due to acceleration in the hydration process. Despite the reduction in strength at a later age (say the 90th day), the mean value of the strength reduction is not less than 10% in the concretes except the CM30 mix. In general, ternary blended cementitious systems have a faster gain in strength at an early age and a lesser reduction in strength at a later age with seawater-mixing. Among the ternary blended systems, CS30M15 comprises 30% slag and 15% metakaolin replacing the CEM I fraction by weight in binder which demonstrates the maximum benefit with seawater mixing. Furthermore, 3% nano-SiO_2 (nS) and 1% nano-Al_2O_3 (nA) by weight of binder were used in the mix to further enhance the microstructure of the SW-mixed CS30M15. Figure 2b indicates this effect of rapid strength development in SW-mixed concrete at early ages (say 1 and 7) compared to the improvement in strength observed in CEM I concrete (CC).

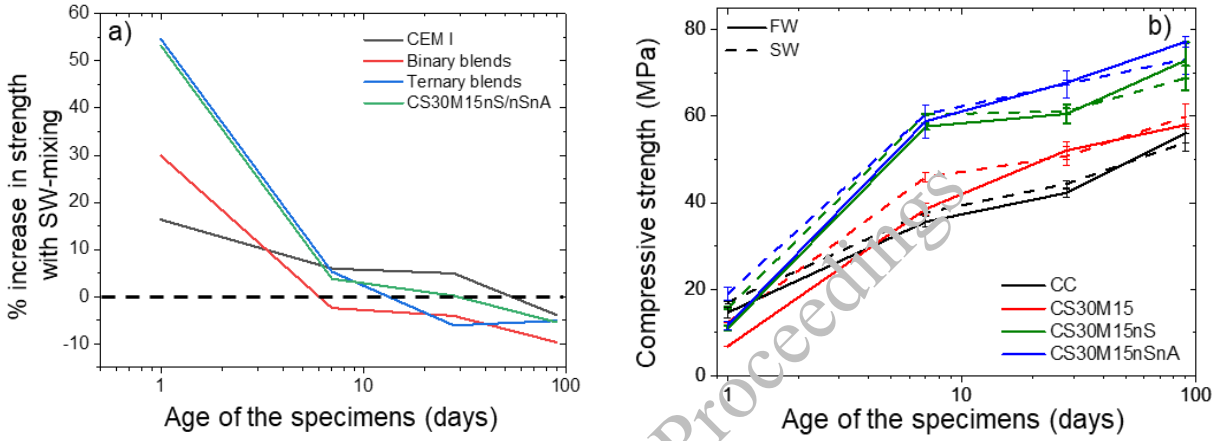

Figure 6. Compressive strength development in SW-mixed concretes: (a) % change in strength with time, (b) compressive strength of concretes with nano-additions

2.2 Durability of SW-mixed concretes

Beyond the assessment of mechanical properties, the durability potential of the SW-mixed concretes was assessed by monitoring the electrical resistivity of the concretes using the Wenner-4-probe method. Cylindrical specimens of diameter 100 mm and height 200 mm. Figure 3 presents the development of surface resistivity in the concretes CC and CS30M15 with and without nano-additives. Compared to the FW-mixed concretes, the ternary-blended cementitious systems mixed with seawater achieved higher resistivity within 7 days of hydration. The presence of nano-additives further accelerated this process with SW-mixing and a resistivity of 50 kΩ.cm which indicates a lower likelihood of corrosion within 7 days.

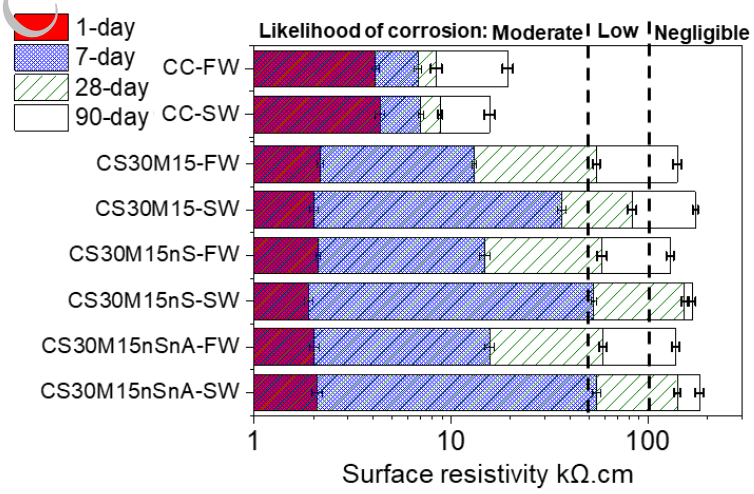

Figure 7. Surface resistivity measurements at 1, 7, 28, and 90 days

The chloride binding in early age hydration and its effect on structural evolution could be attributed to the denser microstructure of SW-mixed concretes (Ji et al., (2024)). A larger study on SW-mixed concretes is being conducted under the exposure of complete immersion in sodium sulphate solution, bulk diffusion, carbonation, and wet-dry cycles of 3.5% sodium chloride to understand their long-term durability in this project. Based on these results, the calculated service life of concretes made with SW-mixing will be presented.

3. Conclusions

NanoSeaCon is a first-of-its kind project that extensively explores the possibilities of using SW-mixing in ternary blended concretes. A significant breakthrough was achieved by identifying the ternary combination of slag and metakaolin at a replacement level of 30% and 15%, respectively being the most optimal for adapting SW-mixing through the assessment of mechanical properties. Furthermore, ongoing durability studies like long-term shrinkage, bulk diffusion, carbonation, sulphate attack, and corrosion studies do not show any rapid deterioration after a few weeks of exposure. These long-term studies are extended further to look at the prospects of adapting CS30M15 concrete with nano-silica and nano-alumina as a durable mix for producing SWC.

Acknowledgements

This research is part of the project No. 2021/43/P/ST8/00945 co-funded by the National Science Centre and the European Union Framework Program for Research and Innovation Horizon 2020 under the Marie Sklodowska-Curie grant agreement No. 945339.

References

Ebead U., Lau D., Lollini F., Nanni A., Suraneni P, Yu T. (2022) “A review of recent advances in the science and technology of seawater-mixed concrete”, Cement and Concrete Research, 152: 106666.

Ji Y., Zhang X., Pel L., Sun Z. (2024) “NMR investigations on Cl and Na ion binding during early hydration process of C_3S, C_3A, and cement paste: A combined modelling and experimental study”, Composites Part B, 283: 111624.

Rathnarajan S., Sikora P. (2023) “Seawater-mixed concretes containing natural and sea sand aggregates-A review”, Results in Engineering, 20: 101457.

Rathnarajan S, Cendrowski K., Sibera D., Sikora P. (2024) “Comprehensive evaluation of early-age hydration and compressive strength development in seawater-mixed binary and ternary cementitious systems”, Archives of Civil and Mechanical Engineering, 24(2):121.

Sikora P., Afsar L., Rathnarajan S., Nikravan M., Chung S-Y., Stephan D., Elrahman M. (2023) “Seawater-mixed lightweight aggregate concretes with dune sand, waste glass, and nanosilica: Experimental life cycle analysis”, International journal of concrete structures and materials, 17: 47

Production of Sustainable and Durable Ternary Cement Concrete Using Co-Firing of Coal and Sugarcane Bagasse

G. Jyothsna[1*], and A. Bahurudeen[2]

[1]Doctoral Research Scholar, Birla Institute of Technology and Science Pilani, Hyderabad Campus, India
Email: p20190417@hyderabad.bits-pilani.ac.in
[2]Associate Professor, Birla Institute of Technology and Science Pilani, Hyderabad Campus, India
Email: bahurudeen.civil@gmail.com

ABSTRACT

Use of agricultural by-products such as bagasse, rice husk as biomass becomes most preferred for sustainable electricity production. Nevertheless, limited availability of coal and substantial carbon-dioxide emissions from coal burning leads to utilisation of biomass along with coal to cut carbon footprint with notable green energy generation. Although, bagasse ash and fly ash are well-known pozzolans, the combined use of them in ternary cement production is exceedingly limited. Despite of abundant availability of bagasse near to the thermal plants, cofiring of coal with bagasse is hindered due to the lack of availability and accessibility data. Hence, the current study aims to utilise bagasse for co-firing with coal in thermal power plants to produce durable ternary cement and green power. Therefore, a significant amount of sustainable energy can be produced. The residual bagasse ash-fly ash from bagasse-coal cofiring can be used to generate durable ternary blended cement. In this study, Maharashtra state was considered. The possibility of cofiring of bagasse and coal and the production of ternary cement with residual ashes were analysed. From the results, it is observed that by utilising bagasse available in the nine districts of Maharashtra state where thermal plants are located led to production of about 4000 MW of sustainable power. Moreover, the residual co-fired ash can be used to produce notable sustainable and durable ternary cement. A reduction of 83.33% in carbon emissions was noted when bagasse was utilised instead of coal to produce the same amount of power.

KEYWORDS*: Blended cements; Sugarcane bagasse ash; Fly ash; Co-firing; Sustainability*

1. Introduction

The depletion of fossil fuels and the significant release of carbon dioxide emissions have prompted global research to prioritise the development of sustainable methods for generating electricity. Biomass-based energy generation is a viable alternative. It plays a crucial role in facilitating the shift towards a low-carbon energy system, improving energy security, and fostering sustainable development. In 2015, the United Nations introduced 17 Sustainable Development Goals (SDGs) as a means of promoting sustainability in all aspects. Among the 17 recommended goals, goal-7 represents the objective of achieving affordable and clean energy, which forms one of the major focuses of the current study (United Nations, 2015). Agriculture has a significant role in India's economy. It possesses promising biomasses such as rice husk and sugarcane bagasse, both of which have the potential to be utilised in the generation of clean energy. Consequently, the cofiring of biomass in conjunction with coal, which results in a reduction in carbon dioxide emissions, is of the utmost importance. The utilisation of bagasse for cofiring with coal is hampered due to a lack of availability and accessibility data, despite the fact that a significant amount of sugarcane bagasse is available in the proximity of thermal plants. The aim of this study is to investigate the possibility of using sugarcane bagasse in conjunction with coal for the purpose of cofiring. Fly ash and bagasse ash are two types of residual ash that are produced when coal and sugarcane bagasse are cofired together. In addition, these ashes are well-known pozzolans, and can be employed in the production of ternary blended cement. Therefore, the current research focuses on the utilisation of sugarcane bagasse for the purpose of cofiring with coal in existing thermal plants in order to provide sustainable and clean energy. Additionally, the manufacturing of ternary blended cements, which have a substantial impact on carbon emissions associated

to the production of conventional cement and coal based thermal energy, is also a focus of this research. The study focuses on Maharashtra state, which is one of the largest states in terms of sugarcane production.

2. Results and discussion

Each district is considered as a solitary zone. The data related to the thermal power plants are obtained from the Central Electrical Authority of India (Central Electrical Authority of India 2021). All the districts of Maharashtra state which have existing thermal plants, are pinned in ArcGIS. The zones that were considered for the study along with thermal power plants locations are depicted using ArcGIS, as shown in Figure 1. The availability of sugarcane is obtained from the Ministry of Agriculture, Government of India (Ministry of Agriculture and Farmers Welfare 2021). About 50% of the total bagasse generated are utilised by the sugar mills for cogeneration. Hence, the excess sugarcane bagasse is moved to existing thermal plants for cofiring along with coal for sustainable energy generation. A total of 11 thermal plants from nine zones were included in the study. The depiction of sugarcane production (million tons) in the zones considered for the study are shown in Figure 2.

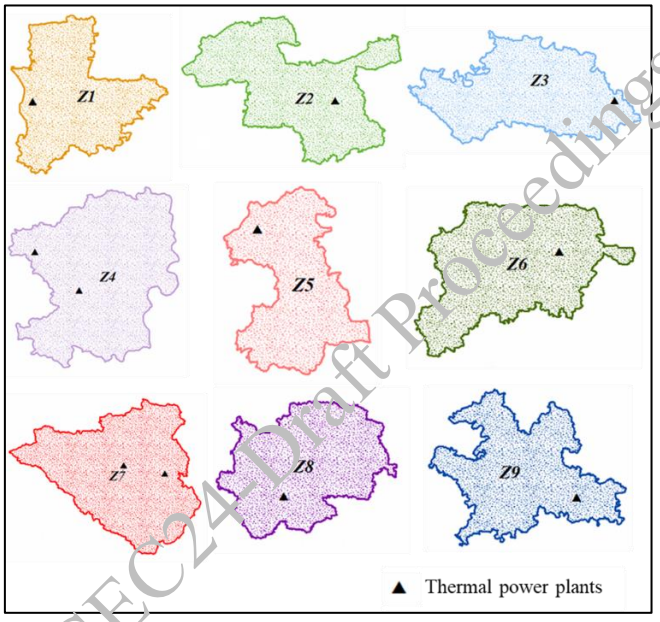

Figure 1. Depiction of zones and thermal power plants considered for the study

The residual ashes generated from the cofiring of coal and sugarcane bagasse acts as potential pozzolans and are used for the production of ternary blended cements. In this study, the available excess bagasse is considered to be cofired. The optimum replacement of sugarcane bagasse ash and fly ash for ternary blended cement are taken to be 10% and 20% respectively (Jittin et al., 2020). The amount of bagasse available for cofiring is about 12.62 million tons. To get the cofired ash in optimum combination of 10% bagasse ash and 20% fly ash, one part of coal should be burnt with about six parts of sugarcane bagasse. This is because of the fact that the volume reduction of bagasse is more than that of coal. Thus, to completely utilise the available bagasse for cogeneration, about 2.17 million tons of coal is required. The quantity of bagasse and coal utilised for cogeneration and the respective quantity of cofired ash that can be generated from the study zones are illustrated in Figure 3.

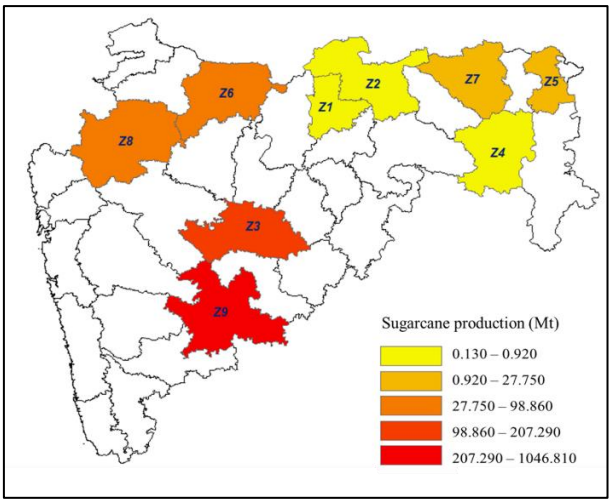

Figure 2. Depiction of sugarcane production in zones considered for the study

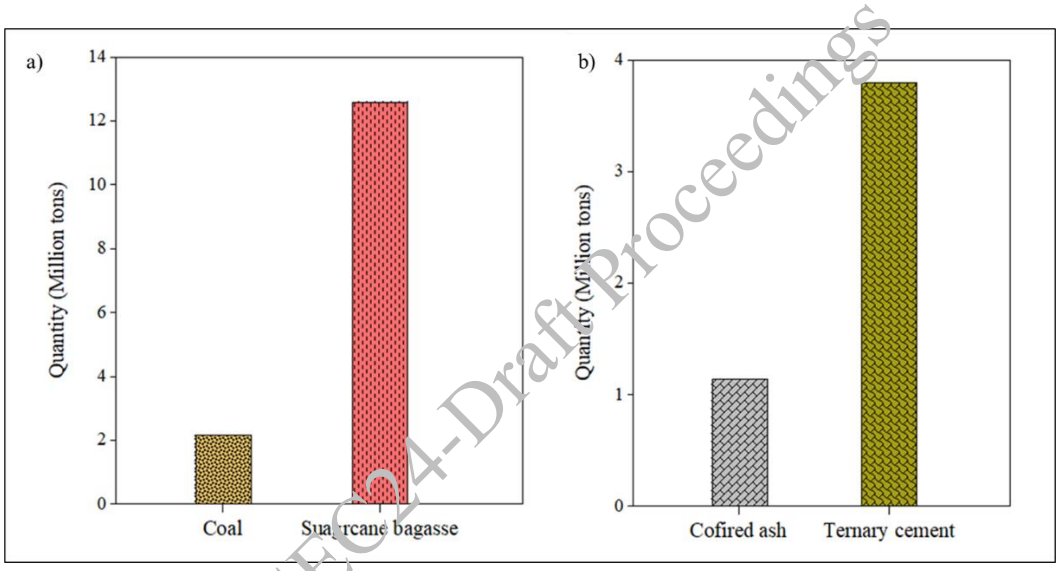

Figure 3a). Quantity of coal and sugarcane bagasse utilised in the study; 3b). Quantity of cofired ash and ternary blended cements generated

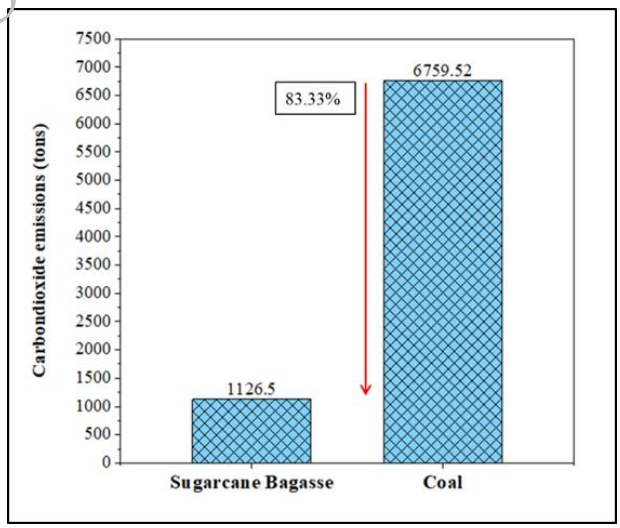

Figure 4. Impact of sugarcane bagasse and coal on carbon dioxide emissions for generating the equivalent amount of power

Hence, a combined cofired ash mixture of about 1.14 million tons generated produces around 3.8 million tons of ternary blended cements, which is very significant. Considering the dry bagasse, the calorific value is taken as 17640 KJ/kg (Kabeyi and Olanrewaju, 2023). The amount of power that can solely be generated by utilising the total amount of bagasse is
around 4000 MW. There can be a significant impact on clean and sustainable energy generation if such type of cofiring is incorporated into all the thermal plants that have biomass in their vicinity.
To generate the equivalent amount of power using coal, it requires approximately 2630 tons of coal, which generates around 6760 tons of carbon dioxide, whereas the bagasse produces 1126.5 tons of carbon dioxide. Figure 4 implies that a reduction of about 83.33% in carbon emissions is observed if coal is replaced by sugarcane bagasse for the equivalent amount of power generated. Furthermore, the above-discussed results are with respect to the study areas considered. A significant carbon mitigation can be achieved if this cofiring mechanism is incorporated into all the existing thermal power plants.

3. Conclusions

Sugarcane bagasse is abundantly available in Maharashtra state. Hence, utilising the sugarcane bagasse available in the proximity of the thermal plants for cofiring with coal results in sustainable energy generation. In addition, the residual ashes (sugarcane bagasse ash and fly ash) generated as by-products can be utilised in the production of ternary blended cements. Furthermore, the carbon emissions are greatly mitigated, having a significant impact on the environment.

Acknowledgements

This research was funded by the Birla Institute of Technology and Science - Pilani CDRF grant-C1/23/231 and the Ministry of Human Resources and Development, India's SPARC project Grant- P2360.

References

Central Electrical Authority of India. 2021. PDM Division: List of thermal power plants in India. http://cea.nic.in.
Ministry of Agriculture and Farmers Welfare. 2021. Area and Production Statistics. India
United Nations, 2015. Sustainable Development Goals. https://sdgs.un.org/goals
Kabeyi, M.J.B., Olanrewaju, O.A., 2023. Bagasse Electricity Potential of Conventional Sugarcane Factories. J. Energy 2023, 1–25. https://doi.org/10.1155/2023/5749122
V. Jittin, R. Rithuparna, A. Bahurudeen, and B. Pachiappan, "Synergistic use of typical agricultural and industrial by-products for ternary cement: A pathway for locally available resource utilisation," J. Clean. Prod., vol. 279, 2021p. 123448, 2021, doi: 10.1016/j.jclepro.2020.123448.

Behaviour of Slender Reinforced Concrete Columns with GFRP Bars and Discrete Fibres – An Analytical Study

Taraka Malleswara Rao Balla[1*], Sanket Saharkar[2*], and S. Suriya Prakash[3]

[1] Postdoctoral Fellow, Department of Civil Engineering, Indian Institute of Technology, Hyderabad, India
Email: ce18resch11004@iith.ac.in
[2] Graduate Student, Department of Civil Engineering, Indian Institute of Technology, Hyderabad, India
Email: sanket.saharkar@alumni.iith.ac.in. #Equivalent First Author
[3] Professor, Department of Civil Engineering, Indian Institute of Technology, Hyderabad, India
Email: suriyap@ce.iith.ac.in

[*]Corresponding author

ABSTRACT

Fibre-reinforced polymer (FRP) rebars are replacing steel in some reinforced concrete (RC) applications. The FRP RC slender columns can undergo larger deformations, which can lead to significant second-order effects. The performance of slender glass FRP (GFRP) RC columns can be improved with the addition of a macro-synthetic polyolefin (PO) and hybrid (HB) combination of PO and steel fibres. The addition of discrete fibres helps delay crack propagation and improves the post-cracking tensile strength of concrete. This study presents an analytical approach to predict the load and lateral displacement response of GFRP RC slender columns with and without fibres under eccentric compression. The geometrical and material nonlinearities are considered in the analytical approach. The analytical approach was validated using experimental data on steel and GFRP RC slender columns (with and without fibres) available in the existing literature. A parametric analysis is carried out using the validated approach to understand the effect of the volume fraction of fibres. Parametric studies show that hybrid fibres significantly improve the strength and ductility of slender GFRP RC columns compared to synthetic fibres.

KEYWORDS: *FRP; GFRP Bars; Fibre Reinforced Concrete; Slender Columns; Eccentric Compression.*

1. Introduction

Steel is widely used in concrete structures as an internal reinforcement because of its high strength, modulus, and ductility. When subjected to adverse environmental conditions, steel rebars corrode and lose their strength and bond with concrete. Fibre-reinforced polymer (FRP) bars as internal reinforcement are becoming popular because of their high strength and inertness to environmental effects (De Luca et al. 2010; Afifi et al. 2014). As an alternative to steel bars, FRP bars have been used in concrete structures where high corrosion resistance is needed, and electromagnetic transparency is a critical design criterion (Patil and Prakash 2021). The major problem with FRP bars is their brittle failure and low modulus of elasticity. Unlike steel, which undergoes large deformation before fracturing, FRP bars fail abruptly. Failure of FRP RC beams in tension is more brittle than their failure through crushing of concrete in compression (Gao et al. 2021). The codal guidelines of CAB/CSA S806-12 (2012) and ACI 440.1R-15 (2015) recommends designers avoid the tension failure of FRP bars.

Slender columns are more likely to experience second-order effects, such as lateral deflections and increased moments when subjected to axial loads due to their length being considerably longer than their cross-sectional dimensions. According to ACI 318-19 (2022), columns reinforced with steel are considered slender when their slenderness ratio (λ) exceeds 22. The existing studies (Mirmiran et al. 2001; Zadeh and Nanni 2013; Abdelazim et al. 2020) show that the second-order effects in the GFRP RC slender columns are high compared to the steel RC columns. For GFRP RC columns, a slenderness ratio of 17 is identified as the upper limit, according to a parametric study conducted by (Mirmiran et al. 2001). Mirmiran et al. (2001) developed an analytical approach to investigate the behaviour of slender GFRP RC columns.

Further, a detailed parametric study was conducted to understand the influence of various types of FRP bars, FRP reinforcement ratio, eccentricity and slenderness effect. The FRP RC columns are more vulnerable to the slenderness effect compared to the steel RC columns. Only limited studies are available to understand the effect of the discrete fibre on the behaviour of GFRP-reinforced slender columns. ACI 440.1R-15 (2015), AASHTO (2018) and CAB/CSA S806-12 (2012) provisions are conservatively recommended to ignore the contribution from the FRP bars in compression. The AASHTO (2018) and CAB/CSA S806-12 (2012) provisions for the design of FRP RC short columns were developed based on the wide range of test data from the existing studies. However, CAB/CSA S806-12 (2012) provides the classification of short and slender FRP columns based on the slenderness limit. Therefore, efficient analytical models need to be developed for understanding the behaviour of the slender FRP RC columns to delineate the effect of fibres as the current guidelines are based on very minimal experimental evidence.

2. Analytical Study

The aim of the analytical work is to create a computer program that can forecast moment-curvature and load-deflection curves. A layer-by-layer methodology was employed to construct the moment-curvature response. For predicting the load-deflection curve, Newmark's central difference scheme was utilized. The moment-curvature outcomes serve as input for determining the load-deflection curve using this method.

2.1 Section analysis

The stress-strain behaviour of the normal concrete (G-00) and fibre-reinforced concrete under compression are considered based on the theoretical model proposed by Sun et al. (2018). The macro-synthetic polyolefin (PO) and hybrid (HB) combination of PO and steel fibre dosages varying from 0.5% and 1% are considered. The compressive stress-strain response used in the approach is shown in Fig. 3. The concrete residual strength in tension is calculated using the model proposed by Bhosale et al. (2020). The concrete residual strength calculation is carried out for PO and HB fibre dosages varying from 0.5% to 1%. However, the stress value drops to zero for concrete without fibre dosage at a tensile strain of 0.0005. The ultimate strength and elastic modulus of GFRP bars in compression is considered are taken as 595 MPa and 49 GPa. For GFRP bars in tension, the ultimate strength and the elastic modulus are taken as 850 MPa and 49 GPa. The strain distribution is assumed to be linear across the cross-section of the column. A layered approach is followed to calculate the forces in the concrete subjected to bending moment and axial force. The cross-section is divided into 'n_l' number of layers. The value of 'n_l' in this study is set to 1500, which is adequate to achieve equilibrium of forces with a 10^{-4} N tolerance. The forces in each layer are calculated using the area of each layer and stress values corresponding to strain calculated in the concrete or rebar. For equilibrium, the externally applied eccentric force, P, should be equal to the summation of all the internal forces.

$$\sum F_{ci} + \sum P_i = P \tag{1}$$

Since the layer-by-layer approach is followed in the calculation of forces, the value on the left-hand side of the equation may not precisely match the right-hand side of the equation. Hence, some tolerance values must be chosen to achieve convergence. In calculating all the results, a tolerance of 10^{-4} N is assumed. The moment of forces due to concrete about the centroid of the section is given by

$$M = \sum \mathrm{F}_{ci} * \left(\frac{D}{2} - y_{ci}\right) + \sum P_i * \left(\frac{D}{2} - y_i\right) - P * e \tag{2}$$

And, the curvature for this moment is given by

$$\phi = \frac{\epsilon_{cu}}{y_{NA}} \tag{3}$$

2.2 Member level analysis

The results obtained from the section analysis are inputs for member-level analysis. The moment-curvature response at different axial compression loads is used to predict the column's load-lateral deformation curve. Newmark's central difference scheme is the method used to calculate the load vs lateral deflection curve.

The column under consideration must be divided into segments. The length of each segment is Δl. The eccentricity at the top and bottom of the column can be taken as 'e_1'and 'e_2' with pin-pin end conditions. The bottommost grid is numbered as '*1*' and the topmost as 'n'. Deflection at any grid point can be calculated by assuming the deflection at *2nd* grid point. The value assumed needs to be changed based on the value of deflection obtained at the last grid point. For the *1st* iteration, it can be assumed as zero. Eq. (4) is used to predict the deflection at the next grid point, where, ϕ_i is the curvature at the i^{th} grid point.

$$\delta_{i+1} = 2\delta_i - \delta_{i-1} - \phi_i(\Delta l)^2 \quad (4)$$

The methods used for the prediction of ascending and descending branches are different. The load-control technique is adopted for the ascending branch, and the descending branch, the deflection-control technique is adopted. The algorithm for ascending is shown in Figure 4.

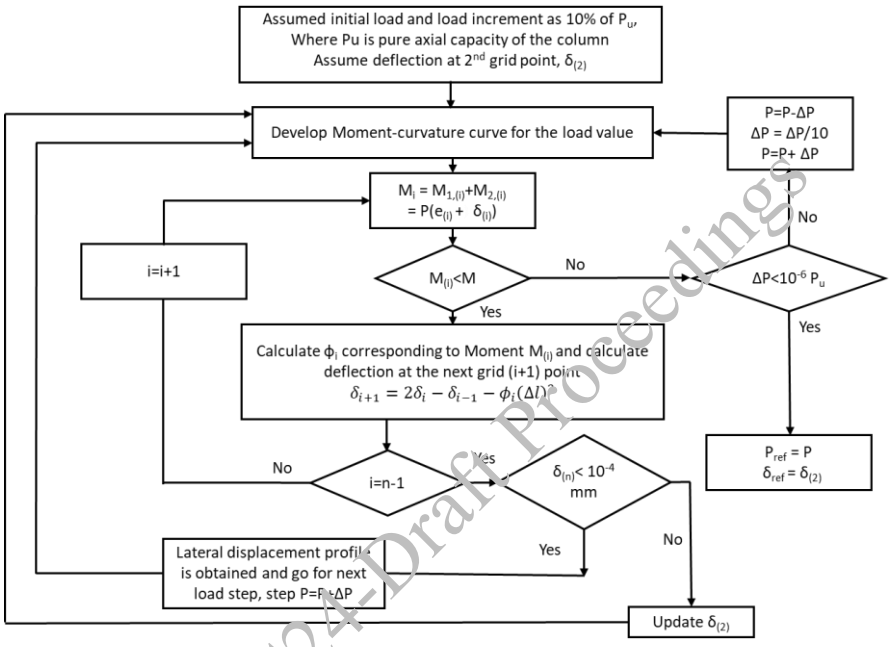

Figure 4. Ascending branch algorithm for calculation of load-mid displacement curve

3. Validation of Analytical Predictions

The comparison of load vs mid-lateral displacements of analytical predictions with experimental results is shown in Figure 5.

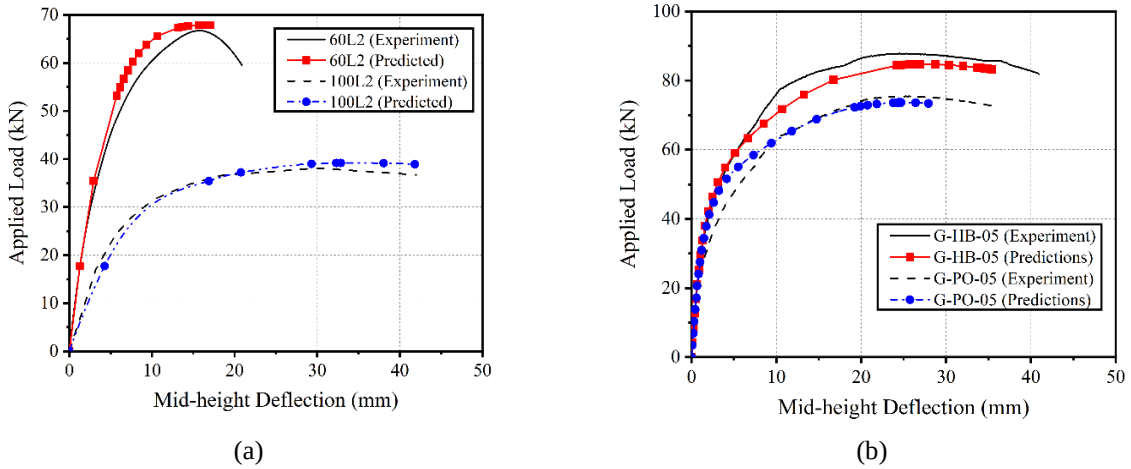

(a) (b)

Figure 5. Comparison of load vs mid-lateral displacements of analytical predictions with experimental results

The analytical approach is validated using various experimental test data on steel and FRP reinforced slender columns available in the literature (Kim and Yang 1995; Khorramian and Sadeghian 2020; Balla et al. 2024). The specimen IDs used are taken the same as those reported in the literature. The geometry and material properties of the specimens in the analysis have been chosen to match the details described in the literature. The predicted and experimental results are summarised in Table 3. Hybrid fibres are found to be more effective than PO fibres in improving strength and ductility.

Table 3. Comparison of analytical predictions with experimental results

Source	Specimen ID	Width (mm)	Height (mm)	e (mm)	λ	$P_{u,exp}$ (kN)	$P_{u,pred}$ (kN)	$\frac{P_{u,exp}}{P_{u,pred}}$
Validation for Steel RC Columns								
Kim et al. (1995)	60L2	80	80	24	60	66.6	67.9	0.98
	100L2	80	80	24	100	38.1	39.2	0.97
Validation for GFRP RC Slender Columns								
Khorramian and Sadeghian (2020)	G40-e23-r4	306	205	47.2	40	1109.2	1116.1	0.99
	G60-e23-r4	306	205	47.2	60	843.7	940.6	0.89
Validation for GFRP reinforced Slender Columns with FRC								
Balla et al. (2024)	G-PO-05	125	125	62.5	41	72.4	73.6	0.98
	G-HB-05	125	125	62.5	41	87.0	84.7	1.02

4. Parametric Study

The validated analytical model was used to perform parametric studies. A parametric study has been conducted to understand the behaviour of slender GFRP columns reinforced with hybrid fibres. The volume fraction of hybrid fibres is varied from 0 to 1%. Figure 6(a) and (b) show the load-deflection curves with varying volume fractions of fibres. The load-carrying capacity and ductility increased with the addition of fibre. This is because of the improved post-peak response of FRC under compression when compared to concrete without fibres.

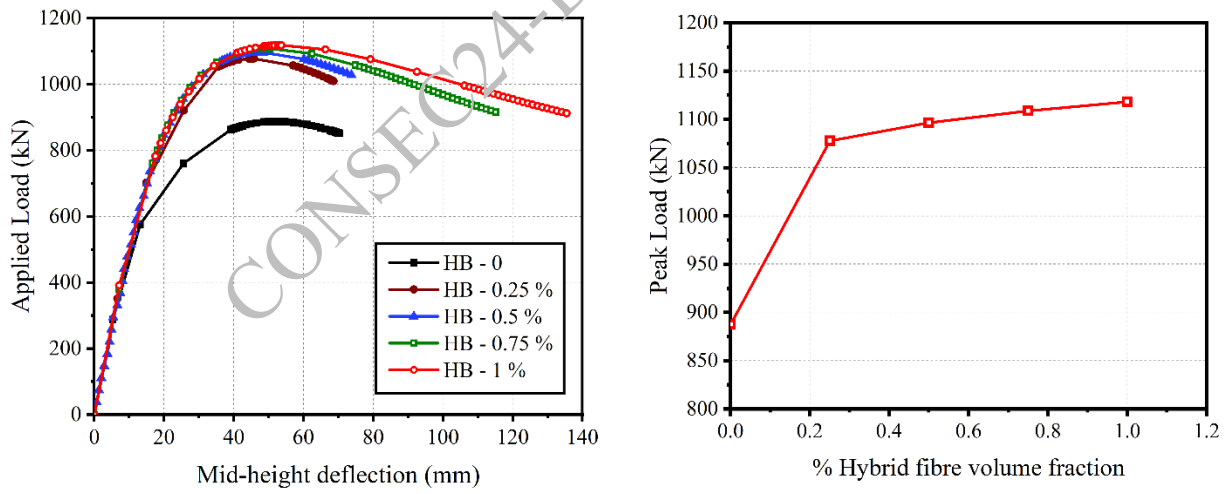

(a) (b)

Figure 6. Comparison of load-deflection curves (a) Effect of hybrid fibre volume fraction; (b) Peak load capacity vs % hybrid fibre volume fraction

5. Conclusions

An efficient analytical model was developed to capture the second-order effects in slender FRC columns reinforced with steel and FRP bars. The analytical approach presented was validated with test results carried

out by the authors and the ones available in the literature. Based on the results presented in this study, the following conclusions can be drawn:

- Analytical predictions matched closely with the experimental results for slender specimens reinforced with GFRP and steel bars with and without fibres.
- GFRP RC slender columns with hybrid fibres had improved strength and stiffness compared to the columns reinforced with PO fibres.
- The increase in strength and ductility is observed with an increase in the HB fibre dosage in the slender GFRP RC columns.

Acknowledgements

The authors thankfully acknowledge the Ministry of Education, India for providing the fellowship to first and second authors.

References

Abdelazim, W., Mohame, H. M., Benmokrane, B., and Afif, M. Z. (2020). "Effect of critical test parameters on behavior of glass fiber-reinforced polymer-reinforced concrete slender columns under eccentric load." *ACI Structural Journal*, 117(4), 127–141.

Afifi, M. Z., Mohamed, H. M., and Benmokrane, B. (2014). "Axial Capacity of Circular Concrete Columns Reinforced with GFRP Bars and Spirals." *Journal of Composites for Construction*, 18(1), 04013017.

Balla, T. M. R., Saharkar, S., and Prakash, S. S. (2024). "Role of Fibre Addition in GFRP Reinforced Slender RC Columns under Eccentric Compression – Experimental and Analytical Study." *Journal of Composites for Construction*.

Bhosale, A. B., Lakavath, C., and Suriya Prakash, S. (2020). "Multilinear tensile stress-crack width relationships for hybrid fibre reinforced concrete using inverse analysis and digital image correlation." *Engineering Structures*, Elsevier, 225(February), 111275.

Gao, K., Xie, H., Li, Z., Zhang, J., and Tu, J. (2021). "Study on eccentric behavior and serviceability performance of slender rectangular concrete columns reinforced with GFRP bars." *Composite Structures*, Elsevier Ltd, 263(September 2020), 113680.

Khorramian, K., and Sadeghian, P. (2020). "Experimental Investigation of Short and Slender Rectangular Concrete Columns Reinforced with GFRP Bars under Eccentric Axial Loads." *Journal of Composites for Construction*, 24(6), 04020072.

Kim, J. K., and Yang, J. K. (1995). "Buckling behaviour of slender high-strength concrete columns." *Engineering Structures*, 17(1), 39–51.

De Luca, A., Matta, F., and Nanni, A. (2010). "Behavior of full-scale glass fiber-reinforced polymer reinforced concrete columns under axial load." *ACI Structural Journal*, 107(5), 589–596.

Mirmiran, A., Yuan, W., and Chen, X. (2001). "Design for slenderness in concrete columns internally reinforced with fiber-reinforced polymer bars." *ACI Structural Journal*, 98(1), 116–125.

Patil, G. M., and Prakash, S. S. (2021). "Effect of Macrosynthetic and Hybrid Fibers on the Behavior of Square Concrete Columns Reinforced with GFRP Rebars under Axial Compression." *Journal of Composites for Construction*, 25(6), 1–12.

Sun, L., Hao, Q., Zhao, J., Wu, D., and Yang, F. (2018). "Stress strain behavior of hybrid steel-PVA fiber reinforced cementitious composites under uniaxial compression." *Construction and Building Materials*, Elsevier Ltd, 188, 349–360.

Zadeh, H. J., and Nanni, A. (2013). "Design of RC Columns Using Glass FRP Reinforcement." *Journal of Composites for Construction*, 17(3), 294–304.

Impact of Graphene Oxide on the Formation of Calcium Silicate Hydrate in Cementitious Materials

M. Nithurshan[1], Y. Elakneswaran[2*], Y. Yoda[3] and R. Kitagaki[4]

[1]Division of Sustainable Resources Engineering, Hokkaido University, Sapporo, Japan
Email: nithurshanm@gmail.com
[2]Division of Sustainable Resources Engineering, Hokkaido University, Sapporo, Japan
Email: elakneswaran@eng.hokudai.ac.jp
[3] Shimizu Corporation, Shimizu Institute of Technology, Center for Construction Engineering, Japan
Email: yoda.y@shimz.co.jp
[4]Shimizu Corporation, Shimizu Institute of Technology, Center for Construction Engineering, Japan
Email: ryoma@eng.hokudai.ac.jp

[*]Corresponding author

ABSTRACT

Graphene oxide (GO) has been demonstrated to enhance the mechanical properties of cementitious materials. However, the reinforcing mechanism remains unclear. Investigating the properties of calcium silicate hydrate (CSH), the primary stress-bearing hydrate in cementitious materials may offer insights into this mechanism. Therefore, this study synthesised calcium silicate hydrate (CSH) with and without GO. Experimental techniques, including thermogravimetric analysis (TGA), X-ray diffraction (XRD), silicon nuclear magnetic resonance spectroscopy (^{29}Si NMR), and scanning electron microscopy (SEM), were employed to investigate the microstructural properties of CSH. The experimental results reveal that GO acts as a nucleation site for the formation of CSH on its surface. This facilitates the formation of more ordered, highly crystalline CSH. Moreover, the GO-incorporated CSH exhibits finer pores and higher density than pure CSH. This study underscores the beneficial effects of GO incorporation on the properties of CSH, leading to enhanced mechanical properties and durability of cementitious materials.

KEYWORDS*: Graphene oxide, Calcium silicate hydrate, Reinforcing mechanism, Microstructure*

1. Introduction

High-strength and durable cement-based materials are increasingly sought to meet the demands of complex architectural structures, rapid urbanisation, and implementing carbon emission reduction strategies. In response to this demand, graphene oxide (GO) has emerged as a promising additive in cementitious materials, offering exceptional performance and enhanced properties (Li et al., 2018). Graphene oxide (GO) possesses a unique combination of properties, making it an ideal candidate for improving the strength and durability of cement-based materials. One of the key advantages of GO is its ability to serve as an effective nucleation site. GO contains multiple oxygen-containing groups, such as epoxide, hydroxyl, carboxylic, and carbonyl. These functional groups facilitate the adsorption of clinker minerals, promoting the nucleation and growth of hydration products within the cement matrix (Qureshi and Panesar, 2019). As a result, the addition of GO enhances the microstructure of the cementitious material, leading to improved mechanical properties and durability (Basquiroto de Souza et al., 2022). Furthermore, GO exhibits remarkable tensile strength due to its carbon bonds, which are significantly stronger than steel (Li et al., 2017). This high tensile strength not only reinforces the cement matrix but also helps to mitigate cracking and improve the overall structural integrity of the cement-based material. Several studies have reported the beneficial effects of graphene oxide (GO) on the strength of cement paste, mortar, and concrete, although the extent of improvement varies significantly. This variation may be attributed to factors such as the dosage of GO, dispersion techniques employed, and the purity of the GO used. Additionally, there are contrasting proposed mechanisms regarding the role of GO in cementitious materials. For example, (Lv et al., 2014) suggested that GO adsorbs clinker particles onto its surface, promoting the nucleation of calcium silicate

hydrate (CSH), which then grows outward in a flower-like structure due to spatial constraints. However, some studies proposed that these flower-like structures result from calcite polymers formed during prolonged environmental exposure during scanning electron microscope (SEM) sample preparation (Cui et al., 2017). Similarly, while some studies have indicated that GO significantly influences the hydration of clinker minerals, others have reported no significant change in the degree of hydration. Moreover, while a few studies have suggested that GO improves the strength of mortar by enhancing hydration without altering the CSH structure (Kang et al., 2019), many others have reported that the incorporation of GO significantly affects the morphology of CSH (Djenaoucine et al., 2024). Therefore, further research is required to elucidate its reinforcement mechanisms in cement-based materials. The most abundant calcium-bearing hydrate phase in cement-based materials is calcium silicate hydrate (CSH). CSH has a highly complex structure and serves as these materials' main stress-bearing hydrate phase. Therefore, investigating the effect of GO on the formation of CSH provides valuable insights into the overall impact of GO on cement-based materials. This study aims to investigate the microstructural properties of CSH with and without the incorporation of GO during the synthesis procedure. By examining the influence of GO on CSH formation, we can gain a better understanding of the effect of GO on cement-based materials. Additionally, these findings will contribute to optimising GO utilisation and designing novel cement-based materials with enhanced properties.

2. Materials and Methods

Graphene oxide (GO) was obtained from Ceylon Graphene Technologies (Pvt) Ltd (Sri Lanka) in dispersed form at a concentration of 10 g/L. The CSH was synthesised with and without the incorporation of GO. The synthesis process involved mixing $Ca(OH)_2$ and SiO_2 at a molar ratio 1:1 in deionised water at a water-to-powder ratio of 20 mL/g. For the CSH with the incorporation of GO, GO was included at 0.5 wt.% of the total weight of $Ca(OH)_2$ and SiO_2. The resulting mixture was sealed after N_2 purging and cured for ten days. After the curing process, the slurry was filtered using a suction filter, and the solid particles were washed three times with deionised water to remove ions adsorbed on the CSH surface. The washed solid particles were freeze-dried for 48 hours and stored in a desiccator to prevent carbonation before analysis. The synthesised CSH was characterised using X-ray diffraction (XRD) and X-ray fluorescence (XRF). Additionally, thermal gravimetric analysis (TGA), X-ray diffraction (XRD), silicon nuclear magnetic resonance spectroscopy (^{29}Si NMR), and scanning electron microscopy (SEM) were employed to study the microstructural changes of CSH with and without the incorporation of GO.

3. . Results and Discussion

X-ray diffraction (XRD) analysis showed that in the presence of GO, the primary diffraction peaks at 7.82°, 29.42°, 32.12°, 49.96°, and 55.24° became narrower, and their intensities increased, as depicted in Fig. 1a. This indicates that GO acts as a nucleation site during the formation of CSH and promotes the nucleation and growth of CSH crystals with a more ordered and crystalline structure (Basquiroto de Souza *et al.*, 2022), which leads to sharper and more intense XRD peaks with presence of GO. Furthermore, TGA analysis revealed a higher water loss in the temperature range of 50 °C to 250 °C due to the evaporation of absorbed water and the dehydration of CSH in samples incorporating graphene oxide (CSH-GO 0.5) compared to pure CSH (Fig. 1b). This observation suggests that incorporation of GO promotes CSH nucleation and enhances the formation of a more ordered crystalline structure. This increased crystallinity of CSH with GO leads to more tightly bound water molecules within the CSH structure (Zhao et al., 2018). As a result, more water is lost during the dehydration of CSH in samples containing GO than in pure CSH.

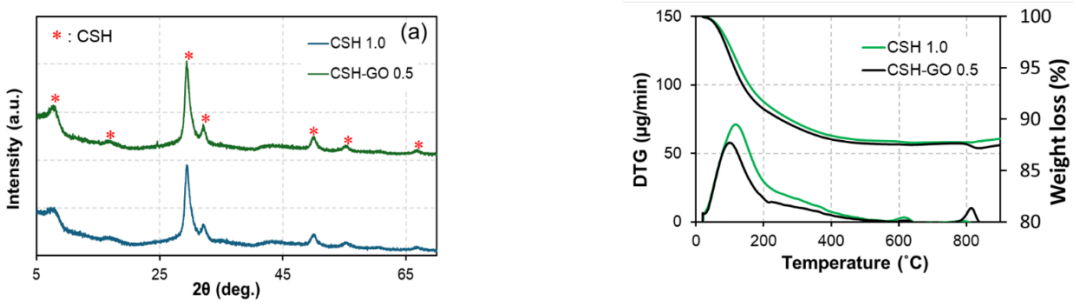

Figure. 1. XRD (a) and TGA (b) analysis of pure CSH and CSH with GO incorporation.

^{29}Si NMR analysis was conducted to investigate the silicon chain in CSH with and without the incorporation of GO. Fig. 2 illustrates the deconvolution of the ^{29}Si NMR spectra for CSH and CSH-GO 0.5. The results demonstrate a significant impact of GO incorporation on the state of the silicon atom. In the presence of GO, the percentage of paired oxygen in the SiO_4 tetrahedron (Q^{2p}) decreases from 32.88% to 6.60%, while the percentage of bridged oxygen in the SiO_4 tetrahedron (Q^{2b}) increases from 26.69% to 47.43%. The similar characteristic is consistent with Kai et al. (2022).

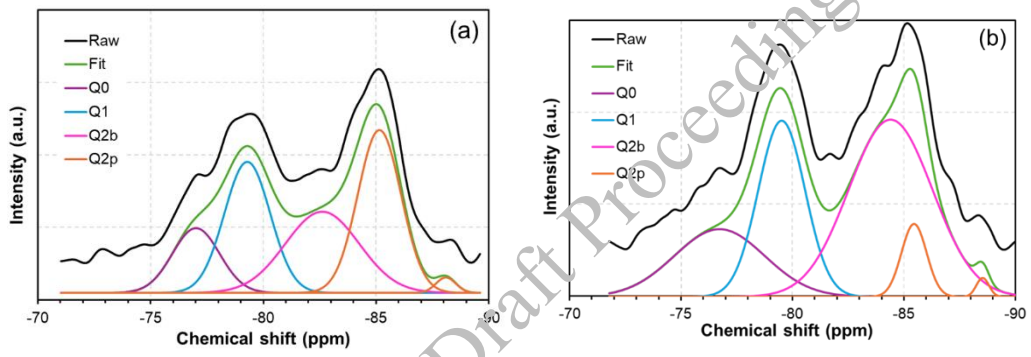

Figure. 2. Deconvoluted Si NMR Spectra of CSH (a) and CSH-GO 0.5 (b)

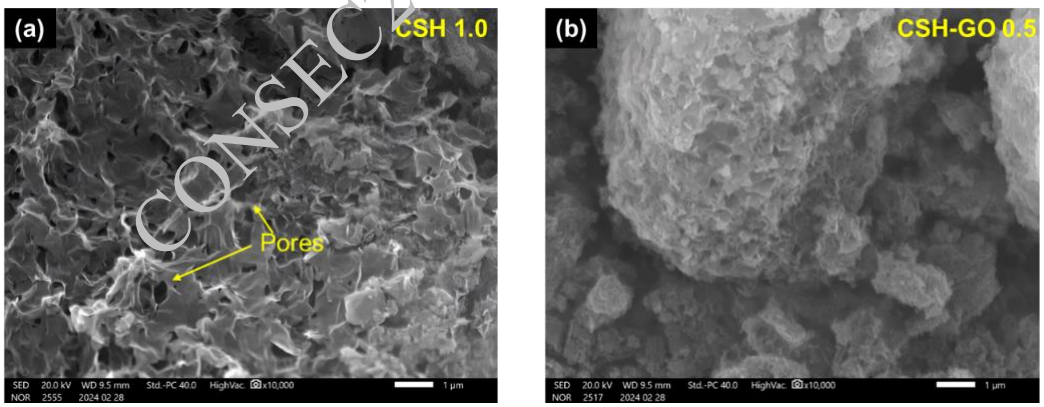

Figure. 3. SEM images of CSH 1.0 (a) and CSH-GO 0.5 (b).

Additionally, the mean chain length was calculated using Equation (1).

$$MCL = \frac{2(Q^1+Q^2)}{Q^1} \quad (1)$$

Where Q^1 and Q^2 represent the integral intensities of the signals of end-chain (Q^1) and middle-chain (Q^2) SiO_4 tetrahedron, respectively. The mean chain length of CSH was observed to decrease with the incorporation of GO from 6.44 to 6.09. This observation can be attributed to the fact that GO acts as a nucleation site due to its functional oxygen groups, thereby promoting the formation of CSH with shorter silicon chains on its surface. As a result, the formation of longer chains is restricted, leading to enhanced

crystallinity of CSH with GO and more ordered chains. SEM images further supported this effect, as shown in Fig. 3. In the absence of GO (CSH 1.0), more defective CSH with larger pores were formed. However, with the presence of GO, the crystallinity of CSH was significantly improved, leading to the healing of defects and the formation of more ordered crystallites (Basquiroto de Souza et al., 2021).

4. Conclusions

The incorporation of GO into CSH significantly influences its properties. TGA analysis showed that CSH samples incorporating GO (CSH-GO 0.5) exhibited higher water loss, which suggests that GO promotes CSH nucleation and enhances the formation of a more ordered crystalline structure. The XRD analysis further supported this, indicating that GO acts as a nucleation site during CSH formation, leading to larger and more ordered crystallites. ^{29}Si NMR analysis revealed that the presence of GO decreased the percentage of paired oxygen in the SiO_4 tetrahedron while the percentage of bridged oxygen increased. Additionally, the mean chain length of CSH decreased with the incorporation of GO, indicating the formation of more ordered chains. Furthermore, SEM images demonstrated that the presence of GO improved the crystallinity of CSH, resulting in the healing of defects and the formation of more ordered crystallites. Overall, these findings highlight the beneficial effects of GO incorporation on the properties of CSH, paving the way for the development of enhanced cementitious materials.

Acknowledgements

JST SPRING provided support for this research under Grant Number JPMJSP2119.

References

Basquiroto de Souza, F., Shamsaei, E., Chen, S., Sagoe-Crentsil, K. and Duan, W. (2021) "Controlled growth and ordering of poorly-crystalline calcium-silicate-hydrate nanosheets", *Communications Materials*, 2(1):84

Basquiroto de Souza, F. Shamsaei, E., Sagoe-Crentsil, K. and Duan, W. (2022)"Proposed mechanism for the enhanced microstructure of graphene oxide–Portland cement composites", *Journal of Building Engineering*, 54: 104604

Cui, H., Yan, X., Tang, L. and Xing, F. (2017) "Possible pitfall in sample preparation for SEM analysis - A discussion of the paper "Fabrication of polycarboxylate/graphene oxide nanosheet composites by copolymerisation for reinforcing and toughening cement composites" by Lv et al. *Cement and Concrete Composites*, 77:81–85

Djenaoucine, L., Picazo, A., de la Rubia, M.A., Gálvez, J.C. and Moragues, A. (2024) "Effect of graphene oxide on the hydration process and macro-mechanical properties of cement", *Boletín de la Sociedad Española de Cerámica y Vidrio*

Kai, G., Miaohong, H., Wenhao, P. and Jinguo, W. (2022)"Molecular dynamics of C-S-H production in graphene oxide environment", *Reviews on Advanced Materials Science*, 61(1):90–101

Kang, X., Zhu, X., Qian, L., Liu, J. and Huang, Y.(2019) "Effect of graphene oxide (GO) on hydration of tricalcium silicate (C_3S)", *Construction and Building Materials*, 203: 514–524

Li, X., Lu, Z., Chuah, S., Li, W., Liu, Y., Duan, W.H. and Li, Z. (2017) "Effects of graphene oxide aggregates on hydration degree, sorptivity, and tensile splitting strength of cement paste", *Composites Part A: Applied Science and Manufacturing*, 100:1–8

Li, X., Li, C., Liu, Y., Chen, S.J., Wang, C.M., Sanjayan, J.G. and Duan, W.H. (2018) 'Improvement of mechanical properties by incorporating graphene oxide into cement mortar', *Mechanics of Advanced Materials and Structures*, 25(15–16):1313–1322

Lv, S., Ting, S., Liu, J. and Zhou, Q.(2014) 'Use of graphene oxide nanosheets to regulate the microstructure of hardened cement paste to increase its strength and toughness', *CrystEngComm*, 16(36): 8508–8516

Qureshi, T.S. and Panesar, D.K. (2019) " Impact of graphene oxide and highly reduced graphene oxide on cement based composites", *Construction and Building Materials*, 206:71–83

Zhao, L., Guo, X., Liu, Y., Zhao, Y., Chen, Z., Zhang, Y., Guo, L., Shu, X. and Liu, J. (2018) "Hydration kinetics, pore structure, 3D network calcium silicate hydrate, and mechanical behavior of graphene oxide reinforced cement composites", *Construction and Building Materials*, 190:150–163

Hydration and Microstructure Development in Ternary Blends of Low-grade Limestone with Fly ash/Calcined Clay

B. Asha[1*], and M. Santhanam[2]

[1] Research scholar, Indian Institute of Technology Madras, Chennai, India
Email: bahulayanasha@gmail.com
[2] Professor, Indian Institute of Technology Madras, Chennai, India
Email: manusanthanam@gmail.com

[*]Corresponding author

ABSTRACT

Ternary blends of ordinary Portland cement with supplementary cementitious materials have interested researchers due to their low-carbon footprint. Synergistic effects are reported in ternary blends of ordinary Portland cement with limestone and fly ash/calcined clay. Most studies on ternary blends used pure limestone (cement-grade limestone) to produce the blends. Impure limestone (low-grade limestone) containing silica, clay, and dolomite beyond the levels specified for cement-grade limestone is used as an alternative to pure limestone in the present study. The hydration and microstructure of ternary blends of ordinary Portland cement with low-grade limestone and fly ash/calcined clay are studied. A replacement level of 45% of ordinary Portland cement and an SCM: limestone ratio of 2:1 was used in the study. Hydration kinetics was studied using isothermal calorimetry. Compressive strength measurements on mortar cubes were done to understand the variation in strength. The microstructure of the blends was studied using mercury intrusion porosimetry. Results indicate that the ternary blends containing fly ash and calcined clay give comparable strength at all ages. However, the acceleration in early hydration was more significant in the blends with calcined clay. Also, ternary blends with calcined clay gave a better microstructure than the fly ash blend. The refined microstructure in the ternary blends of ordinary Portland cement with low-grade limestone and fly ash/calcined clay will make it suitable for application in severe conditions.

KEYWORDS: *Ternary cement, Low-grade limestone, Microstructure, Calorimetry, Compressive strength*

1. Introduction

Concrete is the most consumed material in the world next to water. The demand for cement is increasing every year. Production of cement causes emission of greenhouse gases of the order of 6-8%(Oliver et al., 2014). Supplementary cementitious materials (SCMs) as a partial replacement for cement clinker is one of the methods adopted to mitigate the emission issues (Tam, 2009). SCMs like fly ash, slag, etc., have been used for decades. Limestone is a comparatively new addition to the category of SCMs. Binary blends of ordinary Portland cement (OPC) prepared by blending one SCM and ternary blends prepared by combining two SCMs exhibit excellent performance.

Ternary blends of OPC with limestone and an SCM have the benefits of limestone addition and the pozzolanic reaction of SCM. Limestone calcined clay cement (LC^3) is the most popular ternary cement with a clinker factor as low as 0.5. Ternary blends of OPC with fly ash and limestone have also been reported to perform excellently. Pure limestone or cement-grade limestone is usually used to prepare ternary blends. Limestone, which does not qualify for cement production (commonly known as low-grade), also has very high calcite content. The presence of silica, dolomite, clay, etc., beyond the levels specified makes the limestone unsuitable for cement production. The present study attempts to understand the hydration and microstructure in ternary blends of OPC with low-grade limestone and calcined clay/ fly ash. A replacement level of 45% of OPC is adopted. The reaction kinetics was studied using isothermal calorimetry, and the microstructure was studied using mercury intrusion porosimetry. Compressive strength measurements on cement mortar samples were done to examine how impurities affect the strength of the blends.

2. Materials and methods

A commercially available OPC 53-grade cement conforming to IS 269:2015 was used in the study. Three low-grade limestone samples were collected from various mines in India. The limestone samples containing silica, clay, and dolomite as the major impurities were designated as LGL-S, LGL-C and LGL-D, respectively. The calcite content of the samples was determined using thermogravimetry. It was found that except LGL-C, all the samples had calcite content sufficient for cement production. However, the samples were classified as low-grade due to the higher amount of silica or dolomite. A cement-grade limestone powder collected from a cement manufacturing company was used as a reference limestone (CGL-R).
Processed fly ash (Class F) was procured from a company in south India. Kaolinite clay, sourced from Gujrat, was calcined at 820 °C in a muffle furnace, with a soaking time of two hours. Blends were prepared by interblending 55% OPC, 30% calcined clay/fly ash and 15% limestone. No additional gypsum was used. A control mix of OPC was also prepared. Standard Ennore sand conforming to IS 650:1991 was used to prepare cement mortar cubes. The cement paste samples and mortar cubes were prepared using distilled water with a water/binder ratio 0.45. The properties of the materials used in the study are given in Table 1.

Table 1. Properties of materials used in the study

Property	Cement	LGL-S	LGL-C	LGL-D	CGL-R	Fly ash	Calcined clay
Specific gravity	3.19	2.82	2.67	2.90	2.76	2.09	2.64
D_{50} (µm)	18	5	6	8	10	24	14
$CaCO_3$ content (%)	0	85.22	55.76	81.8	89.77	-	-

The hydration kinetics of the blends were studied using isothermal calorimetry. The experiment was conducted at 23 °C using a Cal Metrix I-Cal HPC 4-channel calorimeter. 50 g of binder was mixed in a high-shear mixer at 1600 rpm for two minutes. Water was preconditioned at 23 ˚C for 24 hours before mixing. Data was collected for the first 72 hours. Pascal 140-440 Mercury intrusion porosimetry instrument was used to measure the porosity of the blends. Cement paste samples were prepared in small plastic bottles of 10ml capacity and sealed for 28 days. Then, they were cut into small slices of approximately 3 mm thickness. The cut slices were immersed in isopropyl alcohol for three days for hydration stoppage. Samples were kept in fresh IPA for one more day and in a desiccator until the testing date. The slices were broken into small pieces for the mercury intrusion porosimetry test. Cement mortar cubes of 50x50x50mm were prepared with a cement: sand ratio of 1:3. A front-mounted Hobart mixer was used to mix cement mortar. Cement mortar was filled in the mould in 3 layers, with 25 tamping for each layer. Cubes were kept at 25 °C and a relative humidity of 65% for the first 24 hours. Later, the cubes were demoulded and kept in a moist room until testing. Mortar cubes were tested at 1, 7, 28, and 90 days of curing. Mortar cubes were tested in compression using Controls 250 kN compression testing machine at a loading rate of 35 N/mm^2/min as per IS 4031 Part 6:2005.

3. Results and discussions

The heat flow curves of the ternary blends of OPC with fly ash and calcined clay (normalised by the weight of cement) are given in Fig. 1a and Fig. 1b, respectively. Blends with fly ash did not accelerate much in early hydration, whereas blends with calcined clay showed a significant acceleration. Reactive alumina in calcined clay contributes to the early acceleration (Krishnan et al., 2018). Fly ash is reported to accelerate early-age hydration slightly (De Weerdt et al., 2011). However, the nature of the impurity in limestone was not found to affect the behaviour in both blends. Fig. 2a and 2b show the cumulative heat generated (normalised by the weight of the binder) in the blends with fly ash and calcined clay, respectively. Blends with fly ash generated much less heat than the control mix of OPC. Meanwhile, the cumulative heat generated by the blends with calcined clay was more significant than that generated by the control mix of OPC. Calcined clay is a fast-reacting SCM, whereas fly ash reacts slowly.

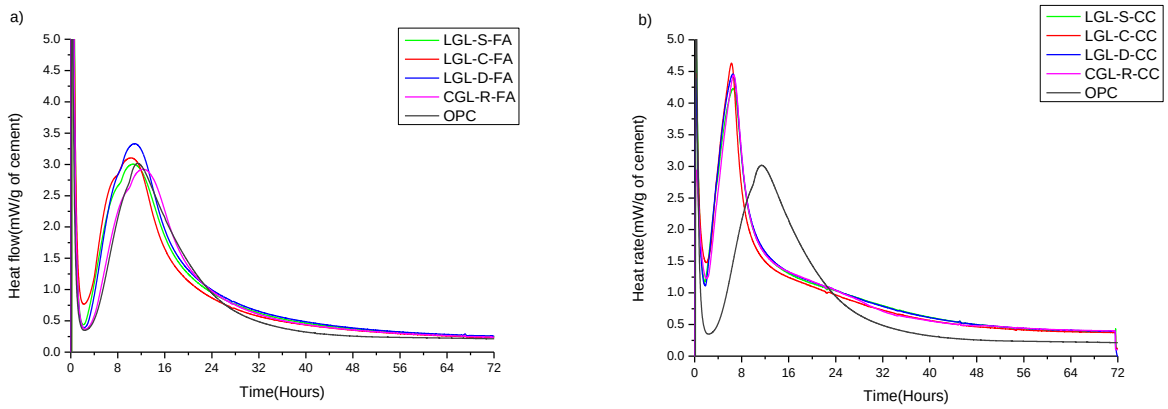

Figure 1. Heat flow curves of the blends with (a) fly ash and (b) calcined clay (normalised by the weight of cement)

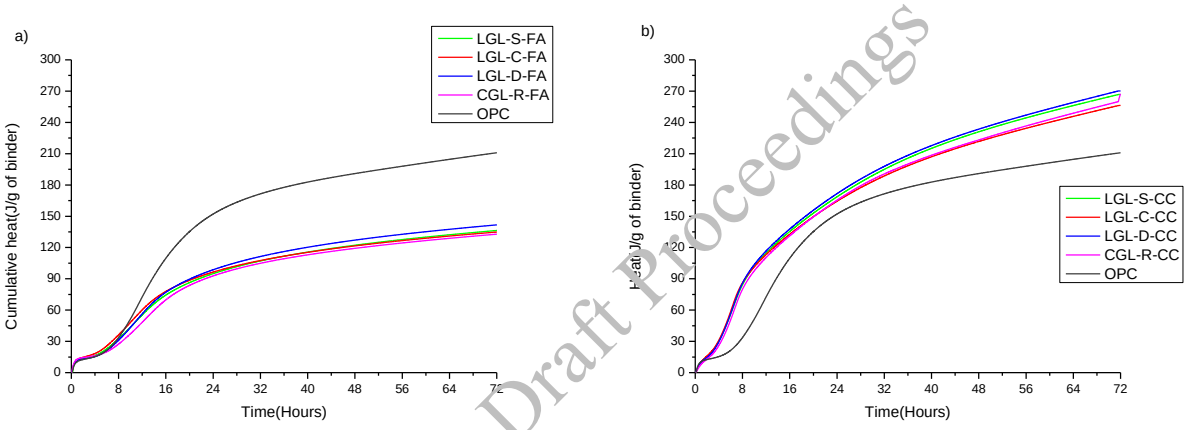

Figure 2. Cumulative heat curves of the blends with (a) fly ash and (b) calcined clay (normalised by the weight of the binder)

The compressive strength of the ternary blends of OPC with fly ash and calcined clay are shown in Fig.3a and Fig.3b, respectively. Almost similar strength was obtained for all the blends in one day. However, calcined clay blends showed a significantly higher strength in 7 days. Blends with calcined clay showed higher strength than fly ash blends at 28 days and 90 days. A considerably higher strength was found in the blend with dolomitic limestone and calcined clay at 28 and 90 days. LC^3 cement with dolomitic limestone is reported to show higher strength at later ages (Krishnan et al., 2018)

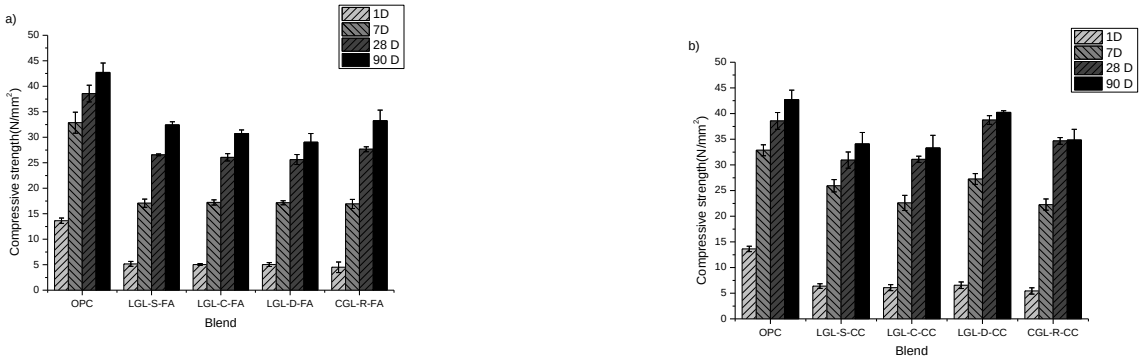

3.1.1.1.1

Figure 3. Compressive strength of the blends with (a) fly ash and (b) calcined clay

The pore size distribution of the ternary blends of OPC with fly ash and calcined clay are given in Fig. 4a and Fig. 4b, respectively. Intruded pore volume was lower in blends with calcined clay than fly ash blends, indicating a better microstructure in blends with calcined clay. The addition of calcined clay results in a well-refined pore structure in cementitious systems (Tironi et al., 2014).

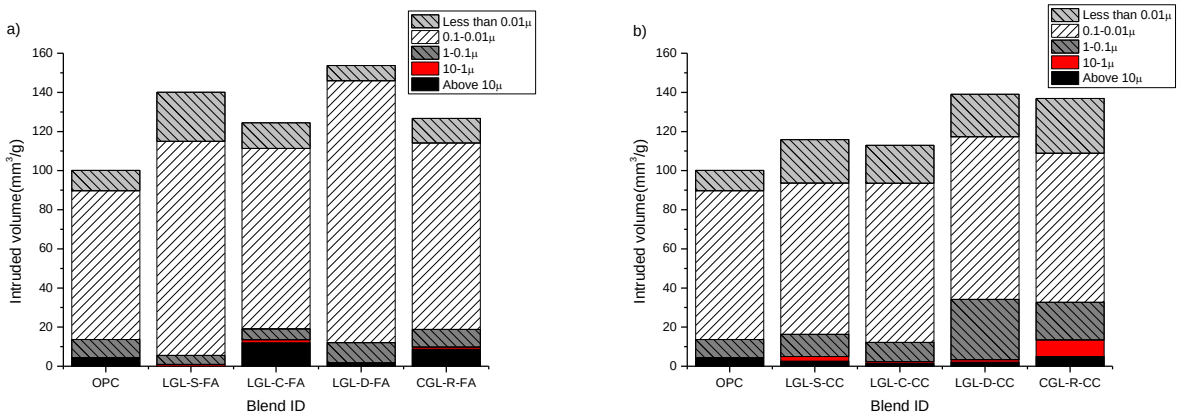

Figure 4. Pore size distribution of the blends with (a) fly ash and (b) calcined clay

4. Conclusions

The following conclusions were arrived at from the present study

Ternary blends of OPC with calcined clay showed significantly higher acceleration than blends with fly ash. Blends with calcined clay had a considerably higher cumulative heat than OPC, whereas blends with fly ash had substantially lower cumulative heat.

Blends with fly ash and blends with calcined clay gave almost similar compressive strength in one day. However, there was a significant increase in strength in the blends with calcined clay in 7 days. At 28 and 90 days, blends with calcined clay showed higher strength than blends with fly ash.

Intruded pore volume was less in the blends with calcined clay than in the blends with fly ash. This indicates a more refined microstructure in the calcined clay blends.

Acknowledgements

The authors would like to acknowledge the support of the Centre of Excellence for Technologies on Low Carbon and Lean Construction at IIT Madras for the study.

References

De Weerdt, K., Haha, M. B., Le Saout, G., Kjellsen, K. O., Justnes, H., & Lothenbach, B. (2011). Hydration mechanisms of ternary Portland cements containing limestone powder and fly ash. *Cement and Concrete Research*, *41*(3), 279–291.

Olivier, J.G.J.,Janssens-Maenhout,G., Peters,J.A.H.W. (2014). *Trends in global CO2 emissions 2014*.

Krishnan, S., Kanaujia, S. K., Mithia, S., & Bishnoi, S. (2018). Hydration kinetics and mechanisms of carbonates from stone wastes in ternary blends with calcined clay. *Construction and Building Materials*, *164*, 265–274.

Tam, C. (2009). *Cement Technology Roadmap 2009: Carbon Emissions Reductions up to 2050*. www.wbcsd.org

Tironi, A., Castellano, C., Bonavetti, V. L., Trezza, M. A., Scian, A. N., & Irassar, E. F. (2014). Kaolinitic calcined clays - Portland cement system: Hydration and properties. *Construction and Building Materials*, *64*, 215–221.

Corrosion Performance of Galvanized Rebar Reinforced Concrete – A Review

Reshma P.[1*], and Jayachandran K.[2]

[1]PhD Scholar, Civil Engineering Department, National Institute of Technology Calicut, Kerala, India
Email: reshma_p220257ce@nitc.ac.in
[2]Assistant Professor, Civil Engineering Department, National Institute of Technology Calicut, Kerala, Calicut, India
Email: jk@nitc.ac.in

*Corresponding author

ABSTRACT

The interaction of zinc in Galvanized Steel Rebars (GSRs) with cement paste, focusing on the corrosion behaviour of galvanized steel reinforcement in various concrete environments, is reviewed, and the results are discussed to enable future research. The reaction of zinc with cement forms protective layers such as, calcium hydroxide zincate (CHZ), which initially protects the core steel against corrosion. However, in the later stages, the sacrificial layer may be degraded under aggressive conditions, such as chlorides and carbonation, even in highly alkaline environments. The corrosion resistance of galvanized steel varies with environmental factors such as carbonation, chloride concentration, pH of the concrete, loss of coating thickness, and damage due to transportation and erection, etc. Some of the electrochemical tests, including Open Circuit Potential (OCP), Linear Polarization Resistance (LPR), Electrochemical Impedance Spectroscopy (EIS), reveals that galvanized steel performs better than black steel in many conditions, though its effectiveness can diminish in harsh environments like coastal areas. The chloride threshold for galvanized steel is notably higher than for black steel, indicating a greater resistance to chloride-induced corrosion. This review underscores the complexity of zinc's behaviour in concrete and highlights the need for further research to optimize its use in reinforcing concrete structures.

KEYWORDS: *Galvanized Steel Rebars, Corrosion, Electrochemical test, Impedance spectroscopy, Sacrificial zinc oxide layer*

1. Introduction

Galvanised Steel Rebars (GSRs) are commonly preferred in scenarios where the utilization of corrosion inhibitors, cathodic protection, and construction quality, among other factors, pose significant challenges Fontana (2005). Zinc can be applied to the surface of steel using different methods like Hot- Dip Galvanizing, Electro galvanizing, Sherardizing/ vapour phase galvanizing, applying Zinc rich paints, Thermal spraying etc. However, for structural steel with a thickness more than 5 mm, hot dipping is preferred, Porter (1991). Based on the studies, it is observed that the hot dip Zinc coating was more susceptible to corrosion, most likely due to the initial presence of contaminants in the galvanising bath (e.g., Al, Pb, and Sb) Porter (1988) and Gowripalan (1998). Thus, care should be taken while galvanising. Furthermore, the preferred crystal orientation of the coatings had no substantial impact on corrosion behaviour, unlike in pure zinc, Park (1998). Based on these learnings, the sacrificial layers is expected to damage due to many prevailing situations, which will be discussed next.

2. Interaction of Zinc with cement paste

According to Feitknecht et al., (1972), zinc oxides and hydroxides come in several forms in concrete, like ZnO, $Zn(OH)_2$, CHZ, ZnO_2, $ZnCO_3$. Identifying corrosion products of zinc is challenging. Lieber (2004) showed the nature of crystal form on the surface of Zn in contact with cement paste. The mechanism is given in the equation

$$Zn + 2H_2O \leftrightarrow Zn(OH)_2 + H_2 \uparrow \quad (1)$$

$$2Zn(OH)_2 + 2H_2O + Ca(OH)_2 \rightarrow Ca(Zn(OH)_3)_2.\ 2H_2O \quad (2)$$

The product obtained in Equation (2) was identified as Calcium Hydroxide Zincate (CHZ), Hong (2004). The pH value of water mixed with cement depends on the alkali content of the cement, however sulphates in the solution always keep the pH approximately below 13. The surface of steel is already covered by a protective layer of calcium hydroxizincate, ensuring the endurance of the galvanized coating. While theoretical behaviour may not always be replicated in concrete or mortar due to heterogeneity, additional factors such pore humidity may cause some variation in results.

3. Corrosion of Galvanized Steel in Alkaline Media

The behaviour of zinc in both weak and strong alkaline solutions has been widely studied and reported in the literature. Zinc exhibits stability within a broad pH range of roughly 6-12.5. However, it is worth noting that corrosion rates increase exponentially both below and beyond these pH values, Yeomans (1994). In aqueous pore solutions with alkaline pH values, the dissolution of zinc occurs at a faster rate due to the presence of hydrogen. This is because the initial corrosion potential is lower than the potential for hydrogen evolution, rendering the metal unstable in such a media. Liu Shuan (2013) found that galvanized layer passivation is not stable within the pH range of 12 to 12.7. The $Ca(OH)_2$ solution yielded ZnO, $Zn(OH)_2$ and $Zn_5(OH)_6(CO_3)_2$ as corrosion products. The stability of zinc coating passivation was seen when the pH exceeded 12.7. Since they generate sacrificial layers of zinc hydroxides on this surface and become passive, they are anticorrosive in neutral or mild alkali aqueous solutions; however, they may corrode in strong alkali and lead to hydrogen evolution, Murgami (2009). Bird (1992) found that below a specific OH- concentration, $Zn(OH)_2$ is the primary anodic product, but at pH greater than 2.9, the main anodic product is the soluble zincate ion (ZnO_2-). Grauer and Kaesche (2005) found a thin layer of zinc oxide (ZnO) in 0.1 M NaOH solutions, Andrade (2004). Tan (2008) found that alloyed coatings with Fe-Zn intermetallic phases take longer to passivate than pure zinc coatings. Lower zinc content delays passivation by limiting CHZ production. Further investigation on galvanized rebar on different curing condition by Tittarelli (2010) found that that oxygen, not water, is the primary oxidizing agent for the rapid production of a passivation layer as the product of CHZ on zinc coating. However, the reduction of pH due to carbonation breaks the passivating layer of CZH forming protective amorphous products $ZnCO_3$ and $Zn_5(CO_3)_2(OH)_6$ by Roventi (2002).

4. Corrosion behaviour of Galvanized Steel in Aggressive Environments

In aggressive environments, the zinc layer corrodes more rapidly due to its reactivity compared to steel. The rate of corrosion can be influenced by factors like the presence of chlorides, acidic or alkaline conditions, and high moisture levels. For instance, in coastal areas with high salinity, zinc corrodes quickly, leading to accelerated deterioration of the galvanized layer. However, in particularly harsh environments, it may require additional protective measures, such as coatings or regular maintenance, to extend its service life and ensure continued performance.

4.1 Corrosion of Galvanized steel in Carbonated concrete and chloride environments

The carbonation of the concrete cover is one of the principal reasons for reinforcement corrosion. The pH of the aqueous phase changes from highly alkaline to values around neutrality (pH 7). The passivity of the galvanized steel will change when the pH less than 6. Thus, in this case the carbonation does not substantially accelerate the corrosion rate of galvanized bars in concrete; in fact, it may even decrease it in some instances empirically, Bellezze (2011). The corrosion rates of galvanized and bare steel rebars have been studied over time, focusing on how they are affected by humidity, mortar carbonation, and the presence of chloride ions. Chloride ions (Cl^-) and carbonation initially led to very negative corrosion potentials, around -1000 mV (vs SCE). These potentials then became less negative, stabilizing around -400 mV (SCE). When chloride ions and carbonation occurred together, the corrosion potential stabilized more gradually. In cases where carbonated mortar contained chloride ions, the final corrosion potential was around -500 mV (SCE), Marcia Suzzanna (2024). Black steel exhibits high corrosion rates during wetting

periods after carbonation, whereas galvanized steel maintains a consistent, low corrosion rate, staying passive. The CaHZn layer on galvanized steel disappears when the concrete matrix carbonates. X-ray diffraction (XRD) cannot identify the passivating products that protect the zinc coating in carbonated concrete due to their poor crystallization. However, energy-dispersive X-ray (EDX) maps of zinc-coated steel embedded in carbonated concrete reveal the presence of zinc carbonates, Gonzalez (1982).
Galvanized steel is more resistant to chlorides and provides additional production as a sacrificial anode during corrosion. When black steel reaches the critical chloride threshold (0.4% to 0.6% by cementitious mass, active corrosion begins, Farnia (2007). $Zn_5(CO_3)_2(OH)_6$'s high content in later corrosion stages contributes to the galvanized layer's protection. However, its loose and porous nature limits its impact on hot-dip galvanized steel corrosion resistance, Reilly (2007). Experimental studies were conducted on galvanized steel on marine conditions where Neutral Salt Spray (NSS) and applied current accelerated corrosion tests demonstrated lower corrosion resistance and higher corrosion rate.

5. Thickness influences GSR corrosion

To measure zinc coating thickness on metal surfaces, laser vibration signals are evaluated, Liu (2024). The better corrosion resistance was achieved at an 80µm layer thickness, Yan (2022). Camurri et al. (2005) studied crack initiation and propagation in hot dip galvanized steel and found that reducing the formation of thinner brittle layers in the coating can enhance anti-cracking effectiveness. When zinc bars have corrosion potentials higher than -410 mV CSE, the likelihood of active corrosion is low. However, if the corrosion potentials are above -460 mV CSE, there is a high chance of corrosion, especially with a coating thickness of 135 µm, Ogunsanya (2018). There is uncertainty in the range between these values. Mixed active/passive potentials are recorded, with specific measurements depending on the polarized area of the rebar and the proportion of the area that is actively corroding.

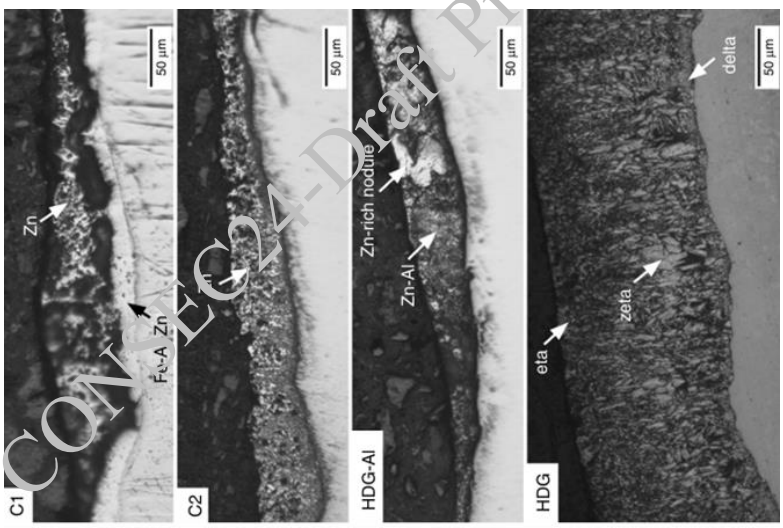

Figure 1. Micrograph of cross sections of the galvanized coatings.[34]

Figure 1 presents micrographs of the coatings on galvanized bars, highlighting significant non-uniformity, particularly in the C1 (~50 µm, 0.25% Al in Zn bath), C2 (~50 µm, in specification with ASTM A1094, HDG-Al bars (~30 µm, HDG with ~7% Al in Zn bath) and HDG bars (~75-135 µm in specification with ASTM A767. Contrary to the specifications provided by steel suppliers, these images indicate that the C1 bars more closely conform to ASTM Standard A1094, which mandates the presence of a Fe-Al-Zn inhibition layer. Despite this, the inhibition layer on the C1 bars is found to be uneven and discontinuous. Notably, in certain regions, the layer exceeds the approximately 100 µm thickness recommended by the International Zinc Association, reaching up to around 250 nm as suggested by Guttmann et al., (2006). Conversely, in other regions, the layer is too thin to be accurately measured. This variability in coating thickness and distribution underscores the need for a more consistent application to meet industry standards.

6. Acceptable level for coating damage and specifications of repair

Repairs to damaged coating cannot exceed 1% of the total surface area per 0.3-m bar length. Limits on damaged coating repair do not apply to sheared or cut ends fixed with zinc-rich formulation. Repair damaged coating by zinc-rich formulation in line with procedure given in ASTM A780, from manufacture and handling to job-site shipment. When coated bars are cut during fabrication, the cut ends must be coated with a zinc-rich formulation. According to **IS 12594**, minor coating damage like small scratches is acceptable if it doesn't expose the steel or affect the coating's protective role. For significant damage, the area must be cleaned, primed, and re-coated properly. The standard requires that repairs be checked to ensure they meet quality standards and restore the coating's effectiveness.

7. Electrochemical corrosion Tests on Galvanized Steel

Electrochemical corrosion tests on galvanized steel assess its resistance to corrosion in various environments. These tests typically involve exposing the galvanized steel to electrolytes, simulating real-world conditions. By measuring parameters such as corrosion rate and corrosion potential, researchers can evaluate the effectiveness of the galvanization process.

7.1 Linear Polarisation Resistance

Low polarization resistance (Rp) values obtained from linear polarization tests indicate high corrosion rates, which are associated with increased loss of metallic particles, and conversely, high Rp values suggest lower corrosion rates. According to literature, LPR tests can detect the level of corrosion activity on a metal surface when the resistance provided by the solution or electrolyte is below 37 kΩ.cm, Kessler and Gehlen (2016); Rengaraju et al. (2019); Tait (2012). LPR approach is crucial for tracking E_{corr} and i_{corr} over time, revealing the system's dynamics. Researchers have been doing investigation on galvanized steel in which, as the corrosion time expanded from 14 to 21 days. The solution was primarily decreased by H^+ or dissolved oxygen, causing hydrogen evolution corrosion on hot dip galvanized steel surfaces. Meanwhile, the low i_{corr} value indicates robust physical protection from the corrosion product layer, Farina (2007). The degrading process of industrially manufactured hot dip galvanized steel was reported. Galvanized steel samples were exposed in 3.5% NaCl for 15 days. The observed corrosion process only affected the galvanized coating, with no deterioration of the steel. Another galvanized steel sample was damaged, leaving an uncoated area in direct contact with the electrolyte. Meeusen et al. (2024) investigated a study employed odd random phase electrochemical impedance spectroscopy (ORP-EIS) to assess non-stationarities per frequency decade over time. This evaluation aimed to screen silica- and phosphate-based corrosion inhibitors for hot-dip galvanized steel and explore potential synergistic effects. Aperador (2015); done the polarization curves for different materials with Rp value of coated rebars as 121.2 kΩ-cm^2 and Un-coated rebar value showed 42.4 kΩ-cm^2.
Figure 2 illustrates that the polarization resistance (Rp) of steel embedded in concrete varies over time in LPR test results, with each point on the curve representing the average of three measurements.

7.2 Electrical Impedance Spectroscopy

The EIS technique has been widely employed in the investigation of the corrosion characteristics of surface coatings, employing a semi-quantitative approach. A lot of researchers also use EIS to describe how covered metals behave in different situations. Nishikata et al., (2022) used the AC impedance method to look into how different metals corrode in the atmosphere when covered in thin layers. They found that a dimensional distributed constant-type (TML) equivalent circuit can be used to show the impedance behaviour of metals that are covered with a thin electrolyte layer. They also used the EIS to show how the current spread across a working electrode. EIS was done on galvanized steel reinforcement in concrete exposed to sea and dead sea water over time by Sami et al., (2010). In both cases, galvanized steel showed corrosion resistance throughout the test. EIS was helpful in assessing galvanized steel corrosion in concrete. After 150 days in tap water, Nyquist graphs showed straight lines above 1 Hz instead of the expected semicircle. This shows that no corrosion products generated during the test. Bode graphs showed that bare steel has 170 ohms of resistance. Galvanized steel had no corrosion and had impedance values of 180 to 300 ohms above 10Hz. Dead sea water corroded after 25 days. Zinc corrodes in sea water due to its higher reactivity than steel, as shown by the galvanic series.

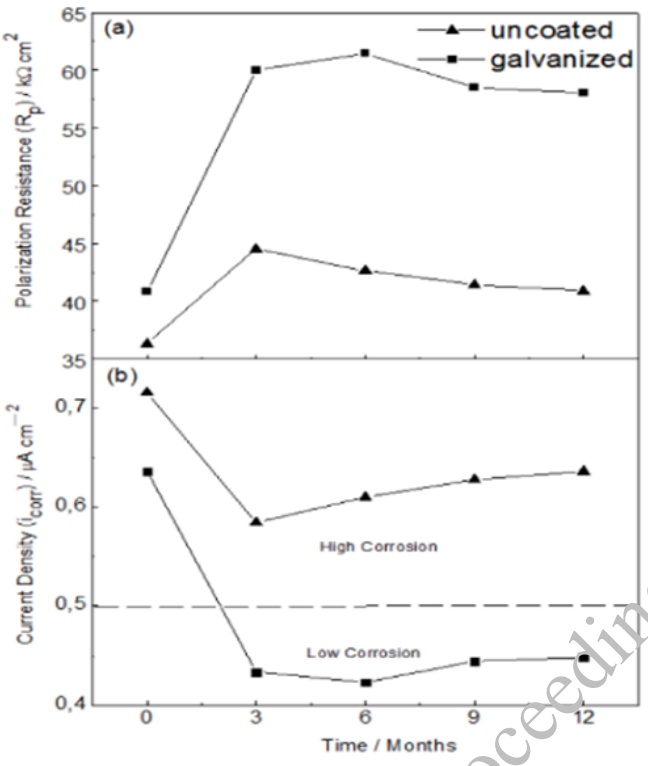

Figure 2. Rp variation for different systems by LPR technique [46].

The corrosion current density i_{corr} and corrosion potential E_{corr} of zinc-coated steel were studied in a range of wet to dry conditions. In the used cyclic wet±dry environments with chloride ions, the E_{corr} measured during the immersion period moves in the noble direction up to 0.85 to 0.80 mV vs SCE. Saravanan et al., (2001) utilized the EIS technique to compare galvanized rebars treated with and without chromate. The results indicated that chromated galvanized rebars exhibited superior performance to both galvanized rebar and bare steel. This phenomenon may be attributed to the development of a zinc oxide layer and zincate, as well as the formation of the zinc corrosion product Simonkolleite ($Zn_5(OH)_8Cl_2H_2O$). Chromate is superior to galvanization on account of chromate ion inhibition. The experimental findings indicate that the corrosion resistance of the rebars, which were coated with 10AZ (10% Al-90%Zn), 100 (100% Zn) and 90% Zn-10% Al and embedded in mortar, remained unaltered when subjected to simulated concrete pore solution and chloride ions. Nevertheless, the corrosion resistance of the rebar coated with 100Z and the level of protection provided by the 100Z coating experienced a decline after the chloride ions reached the interface where corrosion occurred, Ogunsanya (2018).

8. Chloride Threshold for Galvanized Steel

Galvanizing protects steel by acting as a sacrificial layer. Similar to black steel, chloride ion coatings exhibit the most damaging corrosion. Yeomans (1994) investigated that galvanized reinforcement to withstand chloride (Cl-) levels in concrete that are at least 2.5 times greater than those that cause corrosion in black steel under similar concrete and exposure conditions. David Darwin (2007) conducted the critical chloride threshold for galvanized rebars. The bars took between 6 to 36 weeks to start corroding, with an average corrosion rate of 1.37 µm/yr and an average corrosion potential of -0.619V vs CSE. After excluding outliers, the average chloride threshold for all 12 specimens was 1.52 kg/m³. Individual chloride contents varied from 0.131 to 4.64 kg/m³, with average values ranging from 0.593 to 2.92 kg/m³. The coefficient of variation (COV) for individual bars was between 0.31 and 0.97, and the COV for the average threshold values was 0.62. Galvanized reinforcement has a wider chloride concentration spectrum at corrosion onset than conventional reinforcement. Galvanized reinforcement has critical corrosion thresholds that range from standard steel to three to four times greater.

In the zinc coating, the maximum chloride level is 0.4% of the cement weight in concrete, exceeding black steel, Molina (2017). Laboratory and field research show galvanizing increases Chloride Threshold Level (CTL). Treadaway et al. (2002) found that galvanized steel in concrete structures exposed to corrosion slowed corrosion initiation and led in a 0.9% CTL by cement weight. Unfortunately, most published data focuses on black steel. Limited data exists on chloride threshold (CT) for galvanized steel in tropical marine environments. Recent research suggests galvanized steel can control infrastructure corrosion in Mexico, with its effectiveness being studied in Yucatan Peninsula concretes made with native resources.

9. Conclusions

This literature review underscores the significant benefits of galvanized steel rebars in concrete reinforcement, highlighting their superior corrosion resistance compared to conventional black steel due to their protective zinc coating. Despite their advantages, such as reduced corrosion rates in challenging environments and the formation of protective compounds like calcium hydroxyzincate, GSRs face challenges related to coating variability, pH levels, and carbonation. Electrochemical techniques, including polarization resistance (R_p) measurements, provide crucial insights into their performance. Overall, while GSRs enhance structural durability, ongoing research is necessary to refine coating methods, address environmental impacts, and ensure the long-term effectiveness of galvanized steel in diverse construction applications.

References

Mars G. Fontana,(2005),Corrosion Engineering, M C Graw Hill.

F. Porter , *Zinc hand Book*. New York.: Marcel Dekker, 1991.

S.R Yeomans (1994), "Performance of Black, Galvanized, and Epoxy–Coated Reinforcing Steels in Chloride-Contaminated Concrete", *Corrosion Engineering*, Vol 50, No 1, 72-81.

M. A. Baltazar-zamora, L. Landa-ruiz, Y. Rivera, and R. Crotte(2020), "Electrochemical Evaluation of Galvanized Steel and AISI 1018 as Reinforcement in a Soil Type MH," vol. 5, no. 3, pp. 259–263.

Effect of pH on the corrosion products and corrosion rate of zinc in oxygenated aqeous solutions," *Metals and Alloys*, vol. 3, pp. 73–76, 1932.

Andrade, M. C., & Macais(1988), "Galvanized reinforcements in concrete," *Surface Coating Technology*, vol. 2, no. Chapter 3.

S. W. Tonini, D.E., & Dean (1976), "Chloride corrosion of steel in concrete," American Society for Testing and Materials., vol. ASTM STP 6.

B. Elsener, C. Andrade, J. Gulikers, R. Polder, and M. Raupach(2003), "Half-cell potential measurements - Potential mapping on reinforced concrete structures," Materials and Structures/Materiaux et Constructions, vol. 36, no. 261, pp. 461–47.

F. C. Porter, A. M. Stoneman, and R. G. Thilthorpe(1988), "The range of zinc coatings," *Transactions of the IMF*, vol. 66, no. 1, pp. 28–33.

N Gowripalan., H M Mohamed(1988), "Chloride Ion Induced Corrosion of Galvanized and Ordinary Steel Reinforcement in High Performance Concrete," *Cement and Concrete Research* ,vol. 01, no. 8, pp. 1–23.

H. Park and J. A. Szpunar(1988), "The role of texture and morphology in optimizing the corrosion resistance of zinc-based electrogalvanized coatings," *Corrosion Science*, vol. 40, no. 4–5, pp. 525–545.

P. R. Seré, J. D. Culcasi, C. I. Elsner, and A. R. Di Sarli(1999), "Relationship between texture and corrosion resistance in hot-dip galvanized steel sheets," *Surf Coat Technol*, vol. 122, no. 2–3, pp. 143–149.

Geoffrey Newbold, *The Zinc Hydroxide- Zinc Oxide-Water System*. United Kingdom, 1972.

Zhong Lin Wang(2004), "Zinc oxide nanostructures growth, properties and applications," *Journal of Physics*, vol. 16, p. 2.

Andrade,M.C & Macais ,A.(1988), "Galvanized Reinforcements in Concrete", *Surface and Coating Technology*, Vol 2 , Chapter 3.

S. Liu, H. Y. Sun, and L. J. Sun(2013), "Effects of pH values and temperature on the electrochemical corrosion behavior of galvanized steel in simulated rust layer solution," *Gongneng Cailiao/Journal of Functional Materials*, vol. 44, no. 6, pp. 520–527.

K. Murakami, H. Kanematsu, and K. Nakata(2009), "Corrosion characteristics in concrete environment of hot dip galvanised steel and Zn alloy hot dip coated steel," *Transactions of the Institute of Metal Finishing*, vol. 87, no. 1, pp. 23–27.

C. Andrade and C. Alonso(2004), "Electrochemical Aspects of Galvanized Reinforcement Corrosion.

K. Saravanan, S. Muralidharan, M. Natesan, G. Venkatachari, and S. Srinivasan (2001), "Studies on corrosion resistance of galvanized reinforcement bars in simulated concrete environments," Transactions of the Institute of Metal Finishing, vol. 79, no. 4, pp. 146–150.

Z Q Tan and C M Hansson(2008), "Effect of surface condition on the initial corrosion of galvanized reinforcing steel embedded in concrete", *Corrosion Science, 2512-2522*

F. Tittarelli and T. Bellezze(2010), "Investigation of the major reduction reaction occurring during the passivation of galvanized steel rebars," *Corrosion Science* ,vol. 52, pp. 978–983.

G. Roventi, T. Bellezze, G. Giuliani, and C. Conti (2014), "Corrosion resistance of galvanized steel reinforcements in carbonated concrete: effect of wet – dry cycles in tap water and in chloride solution on the passivating layer", *Cement and Concrete Research*, vol. 65, pp. 76–84.

T. Bellezze, G Roventi, E. Barbaresi , N Ruffini and R. Fratesi(2011)," Effect of concrete carbonation process on the passivating products of galvanized steel reinforcements", *Materials and Corrosion,* 62, No. 2

G. R. M. Marcia Suzanna Dutra Abreu Borges da Fonseca (2024), "Accelerated Chloride corrosion of hot dipped galvanized reinforcements and its influence of bond strength to concrete," *Materials Science Forum,* 2024, vol. 426, no. 136123.

J. A. Gonzalez and C. Andrade (1982), "Effect of Carbonation, Chlorides and Relative Ambient Humidity on the Corrosion of Galvanized Rebars Embedded in Concrete", *Corrosion Science,* vol. 17, no. 12.

S. B. Farina and G. S. Duff (2007), "Corrosion of zinc in simulated carbonated concrete pore solutions," vol. 52, pp. 5131–5139.

M. O. Reilly, L. Xing, J. Browning, M. O. Reilly, and L. Xing(2007), "Critical chloride corrosion threshold for galvanized reinforcing", *Report on Research Sponsored by the International Lead Zinc Research Organization*.

Y. Liu, H. Gao, H. Wang, X. Tao, and W. Zhou(2024), "International Journal of Electrochemical Science Study on the corrosion behaviour of hot-dip galvanized steel in simulated industrial atmospheric environments," vol. 19, no. October 2023.

X. Yan, Y. Cong, G. Wang, and Z. Zhang(2022), "Effects of various accelerated corrosion conditions on corrosion behaviour of galvanized steel in marine atmospheric environment," *Proceedings - 2022 IEEE Sustainable Power and Energy Conference, iSPEC 2022*, pp. 1–5.

Y. Bergengren and A. Melander, "An experimental and theoretical study of the fatigue properties of hot- dip-galvanized high-strength sheet steel," *Int J Fatigue*, vol. 14, no. 3, pp. 154–162, 1992.

Crastiu, P. F. Druta, C. Zoituc, C. Gozman-Pop, C. Voica, and L. Bereteu, "Determination of the Galvanizing Layers Thickness by Vibration Measurement of Thin Plates," *SISY 2020 - IEEE 18th International Symposium on Intelligent Systems and Informatics, Proceedings*, pp. 67–70, 2020.

H. M. Yousif, N. J. A. Kader, W. M. Salih, and P. S. Ahmed, "Comparsion study between hot DIP galvanizing steel and coated steel used in oil storage tank and oil pipe transportation," *2017 International Conference on Environmental Impacts of the Oil and Gas Industries: Kurdistan Region of Iraq as a Case Study, EIOGI 2017*, vol. 2018-Janua, pp. 76–79, 2017.

P. Carlos Camurri, G. Raúl Bellavente, S. Isidoro Roa, and C. Claudia Carrasco, "Deformation and fatigue behavior of hot dip galvanized coatings," *Mater Charact*, vol. 55, no. 3, pp. 203–210, 2005.

G. Ogunsanya and C. M. Hansson, "The influence of coating thickness and composition on the corrosion propagation rates of galvanized rebar in cracked concrete," *Corrosion*, vol. 74, no. 1, pp. 134–143, 2018.

ASTM A 780, "Standard Practice for Repair of Damaged and Uncoated Areas of Hot-Dip Galvanized Coatings," *American Standard Testing Method*, 2019.

ASTM D 1654-08, "Standard Test Method for Evaluation of painted or coated specimens subjected to corrosive environments," pp. 5–6, 2005.

S. L. Esfahani, Z. Ranjbar, S. Rastegar, S. L. Esfahani, Z. Ranjbar, and S. Rastegar, "Comparison of corrosion protection of normal and galvanised steel coated by cathodic electrocoatings using EIS and salt spray tests Comparison of corrosion protection of normal and galvanised steel coated by cathodic electrocoatings using EIS and salt spr," vol. 2782, no. May, 2016.

F. J. L. Molina, M. C. A. Alonso, M. S. Moreno, and R. J. Centenero, "Corrosion protection of galvanized rebars in ternary binder concrete exposed to chloride penetration," vol. 156, pp. 468–475, 2017.

Y. Liu, "EIS Investigation and Structural Characterization of Different Hot-Dipped Zinc-Based Coatings in 3.5% NaCl Solution," vol. 3981, no. June 2013, 2016.

B. P. Baltazar-garcía, D. F. Baltazar-zamora, G. Santiago-hurtado, V. Moreno-landeros, and D. Lozano, "Behavior of Potential of Half-Cell AISI 1018 and GS in Concrete Buried in Sand in the Presence of MgSO 4," vol. 9, no. 1, pp. 32–36, 2024.

L. Fan, W. Meng, L. Teng, and K. H. Khayat, "Effect of steel fibers with galvanized coatings on corrosion of steel bars embedded in UHPC," *Compos B Eng*, vol. 177, no. September, 2019, doi: 10.1016/j.compositesb.2019.107445. M. Meeusen et al., "The effect of time evolution and timing of the

electrochemical data recording of corrosion inhibitor protection of hot-dip galvanized steel," vol. 173, no. June, 2020

Masadeh, S. (2015) 'Performance of Galvanized steel reinforcement in concrete in sea and dead sea water', *Journal of M aterial Science and Chemical Engineering, 2015, 3,46-53.*

ASTM A1094/A1094M – 20 Standard Specification for Continuous Hot Dip Galvanized Steel Bars for Concrete Reinforcement", *ACI Specifications, 2018*

ASTM A767/A767 M-09 Standard specification for Zinc Coated (Galvanized) steel rebars for concrete reinforcement", *ACI Specifications, 2009*

ASTM A 780-01 ," Standard Practice for Repair of Damaged and Uncoated areas of Hot Dip Galvanized Coatings", *ACI Specifications*

W. Aperador, M.Plaza, A. Delgado.,"Improved protection against corrosion of galvanized steel embedded in Alkali Aggregated Concrete", *International Journal of Electrochemical Science,* Vol 10, 4585-4595, 2015.

IS 12594," Hot-dip Zinc coating on Structural Steel Bars for concrete Reinforcement ", *Bureau of Indian Standards, 1988.*

Potential of Rice Husk Ash Waste in Production of Cold-Bonded Lightweight Aggregate

Venkata Naresh Kopuru[1], and Raghava Kumar Vanama [2*]

[1] Research scholar, Tiruchirappalli, India Email: 403121054@nitt.edu
[2] Assistant Professor, Tiruchirappalli, India Email: vanama@nitt.edu*

[*]Corresponding author

ABSTRACT
Rice production yields large quantities of rice husk as a byproduct, accounting for approximately 25% of the weight of rice grains. Most rice husk is discarded in landfills or burned, causing air pollution. Also, rice husk is used for energy generation in cogeneration plants but still produces ash waste. There is an immediate need for sustainable ways to recycle rice husk ash. In this study, a novel kind of artificial lightweight aggregates was created by pelletizing rice husk ash (RHA), ground granulated blast furnace slag (GGBFS), and ordinary Portland cement (OPC) using the cold-bonding method. Investigations were conducted into the effects of varying rotation angles (18°, 36°, and 54°) and speeds (20, 30, and 40 rpm) on the pelletization efficiency and particle size fraction (4 mm–10 mm, and 10 mm–20 mm) of rice husk ash aggregates (RHAA) with varying percentages of RHA (50, 60, 70, 80%), GGBFS (40, 30, 20, 10%), and OPC (10%). The pelletization efficiency, particle size fraction, and optimum water content required to manufacture different types of RHAA were also studied.

KEYWORDS*: Pelletization, Rice husk ash, Lightweight aggregate, Cold-bonded aggregate*

1. Introduction

Rice is a crucial crop, feeding billions worldwide, producing approximately 502 million metric tonnes in the 2022-23 crop year. India, the second-largest producer, contributes 29.6% of global rice production, following China at 34.1%. However, rice cultivation generates significant agricultural waste in the form of rice husks, comprising about 25% of the rice grain weight, as shown in Figure 1. Current disposal methods, such as landfilling and open burning, pose environmental challenges, including methane emissions and air pollution. Despite some use as fuel, rice husks leave behind ash waste, which contains valuable silica, suggesting potential for recycling into sustainable construction materials.

Cold-bonding pelletization is a well-researched method for creating artificial lightweight aggregates from waste materials, offering a sustainable alternative to natural aggregates in concrete production. Various industrial byproducts, including fly ash, bottom ash, sewage sludge ash, waste biomass ash, and incinerator bottom ash, have demonstrated potential as feasible raw materials for artificial aggregate production (Gesoğlu et al. (2006); Ghafari et al. (2018); Liu et al. (2022); Zhou et al. (2022); Li et al. (2023)). The quality of these aggregates and the resulting concrete is influenced by production variables like binder type and content, curing techniques, and mixture proportions (Yıldırım and Özturan (2013); Pei Tang et al. (2020); Chen et al. (2021); Fan et al. (2023); Kumar Behera et al. (2023); Lin et al. (2023a); Lin et al. (2023b); Ouyang et al. (2023); Wang et al. (2023); Zhang et al. (2023)). Prior studies highlight the importance of mixture design in achieving sufficient mechanical strength and durability (P. Tang et al. (2017); Narattha and Chaipanich (2018); Parthiban and Karthikeyan (2020); Yıldırım and Özturan (2021); Kumar et al. (2023)). Aggregate characteristics such as shape, texture, and porosity also significantly impact concrete workability, strength, and stability (Ferone et al. (2013); Güneyisi et al. (2013); Vasugi and

Ramamurthy (2014a); Gomathi and Sivakumar (2015); Terzić et al. (2015a); Tang and Brouwers (2018)). Optimized mixtures of artificial aggregates can produce high-quality lightweight concrete comparable to that made with natural aggregates (Kockal and Ozturan (2010); Vasugi and Ramamurthy (2014b);Güneyisi et al. (2015); Hwang and Tran (2015); Terzić et al. (2015b); Frankovič et al. (2017); Tajra et al. (2018)).

Traditionally, Ordinary Portland Cement (OPC) has been used as a binder in pelletization, but more sustainable alternatives like alkali-activated binders and LC3 cement systems are being explored (Gesoğlu et al. (2012); Colangelo and Cioffi (2013); Shivaprasad and Das (2018); Hasan et al. (2021)). There is limited research on using rice husk ash (RHA) for artificial aggregates and understanding its properties' impact on aggregate quality (Gesoğlu et al. (2007); Güneyisi et al. (2013); Güneyisi et al. (2015)). Standardized specifications are needed for widespread adoption in construction ((Geetha and Ramamurthy (2010); Gesoĝlu et al. (2012); Gesoğlu et al. (2014b); Gesoğlu et al. (2014a); F. Colangelo et al. (2017)).

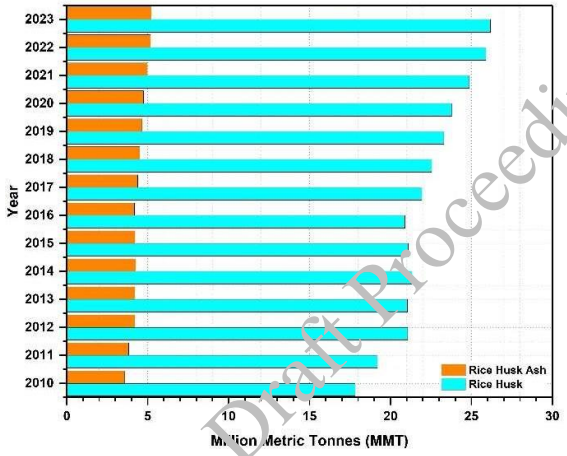

Figure 1. Rice husk ash waste generated in the past decade

This research aims to optimize the use of RHA by producing Rice Husk Ash Aggregates (RHAA) through cold-bonding, using a blend of RHA, ground granulated blast furnace slag (GGBFS), and OPC. The study focuses on determining the pelletization efficiency, particle size fraction, and optimum water content for RHAA production with varying RHA compositions.

2. Materials and methods

2.1 Raw materials

In the present study, RHAA was produced from rice husk ash (RHA) with binding agents as ordinary Portland cement of grade-53 (OPC 53) confirming to IS: 269 and ground granulated blast furnace slag (GGBFS), as depicted in Figure 2. The RHA underwent sieving through a 600-micron sieve to remove larger particles. The material properties of these components are detailed in Table 1.

Figure 2. Raw materials used for the production of RHAAable 1 Properties of raw materials

Table 1. Chemical and physicaproperties

Constituents %	CaO	SiO_2	Al_2O_3	Fe_2O_3	MgO	Na_2O	K_2O	LOI	
OPC 53	62.98	25.38	6.24	3.83	1.02	0.17	0.33	2	
GGBFS	40.66	34.32	14.97	1.07	7.39	-	-	1.4	
RHA	22	88.9	2.5	2.19	-	0.41	0.28	3.9	
Physical properties									
Properties	Color	Specific gravity	Specific surface (m^2/kg)	area	Initial setting time (min)	Final setting time (min)	Compressive strength (28 Days) MPa		
OPC 53	Grey	3.14	348		63	385	53.8		
GGBFS	White	2.85	390		-	-	-		
RHA	Grey	2.25	-		-	-			

2.2 Raw material composition for different types of RHAA production

In this study, through different trials, we aimed to generate aggregates with varying RHA and GGBFS compositions while maintaining OPC at a constant 10% by weight of the raw material. RHA content ranged from 50% to 80% in increments of 10%, while GGBFS content varied from 10% to 40% in increments of 10%. The resulting aggregate types were labeled as follows: RHAA-50, comprising 50% RHA, 40% GGBFS, and 10% OPC; RHAA-60, comprising 60% RHA, 30% GGBFS, and 10% OPC; RHAA-70,
comprising 70% RHA, 20% GGBFS, and 10% OPC; and RHAA-80, comprising 80% RHA, 10% GGBFS, and 10% OPC. The material compositions used for pelletization trials to produce different types of RHAA are presented inTable **2**.

Table 2. Material compositions for different types of RHAA

Total raw materials per trial = 2500 g

RHAA	RHA (g)	GGBFS (g)	OPC 53 (g)
RHAA-50	1250	1000	250
RHAA-60	1500	750	250
RHAA-70	1750	500	250
RHAA-80	2000	250	250

2.3 Optimization of water content, disc angle, and rotation speed for production of RHAA

The water content plays a crucial role in forming RHAA for the given specific composition of raw materials. Through trials, it was noted that failure to apply the correct amount of water hindered RHAA formation, even after a 30-minute pelletization period. Conversely, excessive water led to the formation of large mud balls, impeding the process. Thus, determining the optimal water quantity is essential for successful RHAA production.

A series of trials were conducted to identify the ideal water content for RHAA-50, RHAA-60, RHAA-70, and RHAA-80 production. Initial trials commenced with 30% water content (by weight of raw material), incrementally increasing by 5% until the optimum water content was determined for each RHAA type. It was observed that as the RHA content increased, so did the water demand. Ultimately, the optimal water content for RHAA-50, RHAA-60, RHAA-70, and RHAA-80 was found to be 40%, 45%, 50%, and 55%, respectively.

The disc angle and speed of the pelletizer disc are crucial factors influencing the formation of pellets, affecting both the compactness and particle size distribution of the resulting RHAA. This study examined disc angles of 18°, 36°, and 54°, with corresponding disc rotation speeds of 20, 30,

and 40 rpm trialed for each angle setting. The pelletization duration was constant at 20 minutes across all types of RHAA. The optimal angle and rotation speed were determined by evaluating pelletization efficiency. Pelletization efficiency is defined as the percentage of aggregates formed with sizes greater than 4.75 mm out of the total aggregates produced, serving as the criterion for assessing effectiveness. It was observed that effective pelletization of the raw materials was possible only at a disc angle of 54° and rotation speed of 30 rpm. The pelletization efficiency achieved for different rotation speeds (rpm) at a 54° disc angle is presented in Figure

Also, the particle size fractions of aggregates produced for different compositions of RHAA are presented in Figure 4.

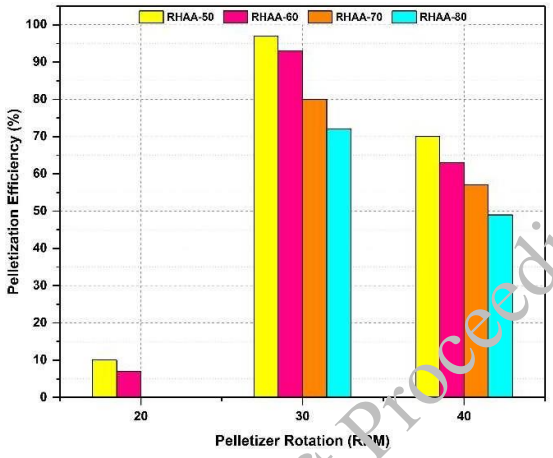

Figure 3. Pelletization efficiency of RHAA

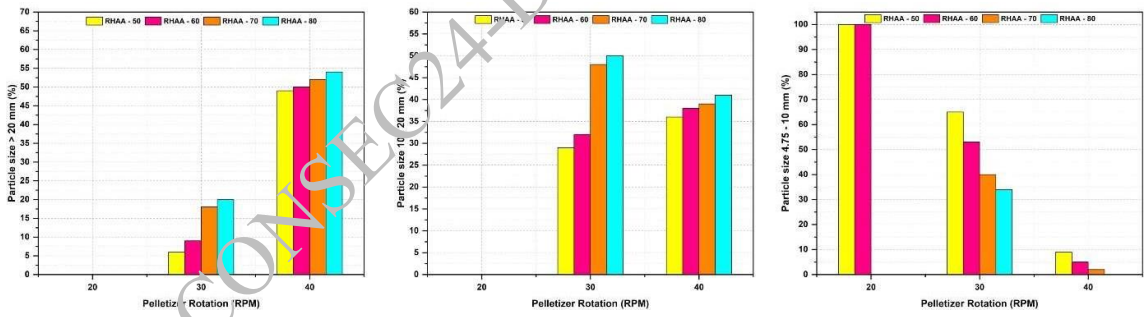

Figure 4. Particle size fractions of RHAA

3. Conclusions

This study successfully produced Rice Husk Ash Aggregates (RHAA) with varying compositions of rice husk ash (RHA) and ground granulated blast furnace slag (GGBFS) while maintaining a constant 10% ordinary Portland cement (OPC) by weight of the raw material. The compositions tested included RHAA- 50, RHAA-60, RHAA-70, and RHAA-80.

Optimal water content for RHAA production was critical, with optimal values identified as 40% for RHAA- 50, 45% for RHAA-60, 50% for RHAA-70, and 55% for RHAA-80. These values ensured successful pelletization, avoiding issues such as incomplete formation (due to less water content) or the creation of large lumps (due to excess water content)

Pelletization trials indicated that the disc angle and rotation speed significantly influenced pellet formation. The optimal settings were found to be a disc angle of 54° and a rotation speed of 30 rpm, maximizing pelletization efficiency, defined as the percentage of aggregates greater than 4.75 mm in size.

These findings highlight the feasibility of producing high-quality artificial aggregates from rice husk ash, presenting a sustainable solution for waste management and contributing to the development of green construction materials. Further research and standardization are recommended to facilitate the widespread adoption of these aggregates in the construction industry.

Acknowledgments

The authors thank the National Institute of Technology, Tiruchirappalli, India, for supporting the work.

References

Chen, Y. X., G. Liu, K. Schollbach, and H. J.H. Brouwers. 2021. Development of cement-free bio-based cold-bonded lightweight aggregates (BCBLWAs) using steel slag and miscanthus powder via CO2 curing. Journal of Cleaner Production 322. Elsevier Ltd. https://doi.org/10.1016/j.jclepro.2021.129105.

Colangelo, F., F. Messina, L. Di Palma, and R. Cioffi. 2017. Recycling of non-metallic automotive shredder residues and coal fly-ash in cold-bonded aggregates for sustainable concrete. *Composites Part B: Engineering* 116. Elsevier Ltd: 46–52. https://doi.org/10.1016/j.compositesb.2017.02.004.

Colangelo, Francesco, and Raffaele Cioffi. 2013. Use of cement kiln dust, blast furnace slag and marble sludge in the manufacture of sustainable artificial aggregates by means of cold bonding pelletization. *Materials* 6: 3139–3159. https://doi.org/10.3390/ma6083139.

Fan, Xu, Zhenlin Li, Weizhuo Zhang, Hesong Jin, Jun Liu, Feng Xing, and Luping Tang. 2023. New applications of municipal solid waste incineration bottom ash (MSWIBA) and calcined clay in construction: Preparation and use of an eco-friendly artificial aggregate. *Construction and Building Materials* 387. Elsevier Ltd. https://doi.org/10.1016/j.conbuildmat.2023.131629.

Ferone, Claudio, Francesco Colangelo, Francesco Messina, Fabio Iucolano, Barbara Liguori, and Raffaele Cioffi. 2013. Coal combustion wastes reuse in low energy artificial aggregates manufacturing. *Materials* 6: 5000–5015. https://doi.org/10.3390/ma6115000.

Frankovič, Ana, Violeta Bokan Bosiljkov, and Vilma Ducman. 2017. Lightweight aggregates made from fly ash using the cold-bond process and their use in lightweight concrete. *Materiali in Tehnologije* 51. Institute of Metals Technology: 267–274. https://doi.org/10.17222/mit.2015.337.

Geetha, S., and K. Ramamurthy. 2010. Environmental friendly technology of cold-bonded bottom ash aggregate manufacture through chemical activation. *Journal of Cleaner Production* 18. Elsevier Ltd: 1563–1569. https://doi.org/10.1016/j.jclepro.2010.06.006.

Gesoğlu, Mehmet, Erhan Güneyisi, Swara Fuad Mahmood, Hatice öznur öz, and Kasim Mermerdaş. 2012. Recycling ground granulated blast furnace slag as cold bonded artificial aggregate partially used in self-compacting concrete. *Journal of Hazardous Materials* 235–236: 352–358. https://doi.org/10.1016/j.jhazmat.2012.08.013.

Gesoğlu, Mehmet, Erhan Güneyisi, and Hatice Öznur Öz. 2012. Properties of lightweight aggregates produced with cold-bonding pelletization of fly ash and ground granulated blast furnace slag. *Materials and Structures/Materiaux et Constructions* 45. Kluwer Academic Publishers: 1535–1546. https://doi.org/10.1617/s11527-012-9855-9.

Gesoğlu, Mehmet, Erhan Güneyisi, Turan Özturan, Hatice Öznur Öz, and Diler Sabah Asaad. 2014a. Self-consolidating characteristics of concrete composites including rounded fine and coarse fly ash lightweight aggregates. *Composites Part B: Engineering* 60: 757–763. https://doi.org/10.1016/j.compositesb.2014.01.008.

Gesoğlu, Mehmet, Erhan Güneyisi, Turan Özturan, Hatice Öznur Öz, and Diler Sabah Asaad. 2014b. Permeation characteristics of self compacting concrete made with partially substitution of natural aggregates with rounded lightweight aggregates. *Construction and Building Materials* 59: 1–9. https://doi.org/10.1016/j.conbuildmat.2014.02.031.Gesoğlu, Mehmet, Turan Özturan, and Erhan Güneyisi. 2006. Effects of cold-bonded fly ash aggregate properties on the shrinkage cracking of lightweight

concretes. *Cement and Concrete Composites* 28: 598–605. https://doi.org/10.1016/j.cemconcomp.2006.04.002.

Gesoğlu, Mehmet, Turan Özturan, and Erhan Güneyisi. 2007. Effects of fly ash properties on characteristics of cold-bonded fly ash lightweight aggregates. *Construction and Building Materials* 21: 1869–1878. https://doi.org/10.1016/j.conbuildmat.2006.05.038.

Ghafari, Hafez, Hilmi Bin Mahmud, Payam Shafigh, and Salmaliza Salleh. 2018. Oil palm shell as an agricultural solid waste in artificial lightweight aggregate concrete. *European Journal of Environmental and Civil Engineering* 22. https://doi.org/10.1080/19648189.2016.1182084.

Gomathi, P., and A. Sivakumar. 2015. Accelerated curing effects on the mechanical performance of cold bonded and sintered fly ash aggregate concrete. *Construction and Building Materials* 77. Elsevier Ltd: 276–287. https://doi.org/10.1016/j.conbuildmat.2014.12.108.

Güneyisi, Erhan, Mehmet Gesoğlu, and Süleyman Ipek. 2013. Effect of steel fiber addition and aspect ratio on bond strength of cold-bonded fly ash lightweight aggregate concretes. *Construction and Building Materials* 47: 358–365. https://doi.org/10.1016/j.conbuildmat.2013.05.059.

Güneyisi, Erhan, Mehmet Gesoglu, Turan Özturan, and Süleyman Ipek. 2015. Fracture behavior and mechanical properties of concrete with artificial lightweight aggregate and steel fiber. *Construction and Building Materials* 84. Elsevier Ltd: 156–168. https://doi.org/10.1016/j.conbuildmat.2015.03.054.

Güneyisi, Erhan, Mehmet Gesoğlu, Özgür Pürsünlü, and Kasim Mermerdaş. 2012. Durability aspect of concretes composed of cold bonded and sintered fly ash lightweight aggregates. *Composites Part B: Engineering* 53: 258–266. https://doi.org/10.1016/j.compositesb.2013.04.070.

Güneyisi, Erhan, Mehmet Gesoğlu, Inan Altan, and Hatice Öznur Öz. 2015. Utilization of cold bonded fly ash lightweight fine aggregates as a partial substitution of natural fine aggregate in self-compacting mortars. *Construction and Building Materials* 74. Elsevier Ltd: 9–16. https://doi.org/10.1016/j.conbuildmat.2014.10.021.

Güneyisi, Erhan, Mehmet Gesoğlu, Emad Booya, and Kasim Mermerdaş. 2015. Strength and permeability properties of self-compacting concrete with cold bonded fly ash lightweight aggregate. *Construction and Building Materials* 74. Elsevier Ltd: 17–24. https://doi.org/10.1016/j.conbuildmat.2014.10.032.

Hasan, Muttaqin, Taufiq Saidi, and Mochammad Afifuddin. 2021. Mechanical properties and absorption of lightweight concrete using lightweight aggregate from diatomaceous earth. *Construction and Building Materials* 277. Elsevier Ltd. https://doi.org/10.1016/j.conbuildmat.2021.122324.

Hwang, Chao Lung, and Vu An Tran. 2015. A study of the properties of foamed lightweight aggregate for self-consolidating concrete. *Construction and Building Materials* 87. Elsevier Ltd: 78–85. https://doi.org/10.1016/j.conbuildmat.2015.03.108.

Kockal, Niyazi Ugur, and Turan Ozturan. 2010. Effects of lightweight fly ash aggregate properties on the behavior of lightweight concretes. *Journal of Hazardous Materials* 179: 954–965. https://doi.org/10.1016/j.jhazmat.2010.03.098.

Kumar Behera, Shantanu, Kirti Kanta Sahoo, Avadhoot Bhosale, and Arpan Pradhan. 2023. Structural properties and temperature effect of sintered fly ash pellets concrete. *Materials Today: Proceedings*. https://doi.org/10.1016/j.matpr.2023.05.229.

Kumar, Pawan, Dinakar Pasla, and T. Jothi Saravanan. 2023. Self-compacting lightweight aggregate concrete and its properties: A review. *Construction and Building Materials*. Elsevier Ltd. https://doi.org/10.1016/j.conbuildmat.2023.130861.

Li, Zhenlin, Weizhuo Zhang, Hesong Jin, Xu Fan, Jun Liu, Feng Xing, and Luping Tang. 2023. Research on the durability and Sustainability of an artificial lightweight aggregate concrete made from municipal solid waste incinerator bottom ash (MSWIBA). *Construction and Building Materials* 365. Elsevier Ltd. https://doi.org/10.1016/j.conbuildmat.2022.129993.

Lin, Jiayi, Kim Hung Mo, Yingxin Goh, and Chiu Chuen Onn. 2023. Potential of municipal woody biomass waste ash in the production of cold-bonded lightweight aggregates. *Journal of Building Engineering*
63. Elsevier Ltd. https://doi.org/10.1016/j.jobe.2022.105392.

Lin, Jiayi, Kim Hung Mo, Yingxin Goh, and Jerome Song Yeo. 2023. Identification of different parameters influencing manufacture and properties of municipal woody biomass waste ash based cold-bonded aggregate. *Materials Today: Proceedings*. Elsevier Ltd. https://doi.org/10.1016/j.matpr.2023.03.711.

Liu, Jun, Zhenlin Li, Weizhuo Zhang, Hesong Jin, Feng Xing, and Luping Tang. 2022. The impact of cold-bonded artificial lightweight aggregates produced by municipal solid waste incineration bottom ash (MSWIBA) replace natural aggregates on the mechanical, microscopic and environmental properties, durability of sustainable concrete. *Journal of Cleaner Production* 337. Elsevier Ltd. https://doi.org/10.1016/j.jclepro.2022.130479.

Narattha, Chalermphan, and Arnon Chaipanich. 2018. Phase characterizations, physical properties and strength of environment-friendly cold-bonded fly ash lightweight aggregates. *Journal of Cleaner Production* 171. Elsevier Ltd: 1094–1100. https://doi.org/10.1016/j.jclepro.2017.09.259.

Ouyang, Gaoshang, Tao Sun, Zechuan Yu, Fang Xu, Jiawei Bai, and Dong Xu. 2023. Investigation on macroscopic properties, leachability and microstructures of surface reinforced phosphogypsum-based cold-bonded aggregates. *Journal of Building Engineering* 69. Elsevier Ltd. https://doi.org/10.1016/j.jobe.2023.106305.

Parthiban, P., and Jayakumar Karthikeyan. 2020. Artificial neural network to predict the compressive strength of semilightweight concrete containing ultrafine GGBS. *Journal of Testing and Evaluation*
48. ASTM International. https://doi.org/10.1520/JTE20180597.

Shivaprasad, K. N., and B. B. Das. 2018. Determination of optimized geopolymerization factors on the properties of pelletized fly ash aggregates. *Construction and Building Materials* 163. Elsevier Ltd: 428–437. https://doi.org/10.1016/j.conbuildmat.2017.12.038.

Tajra, Feras, Mohamed Abd Elrahman, Sang Yeop Chung, and Dietmar Stephan. 2018. Performance assessment of core-shell structured lightweight aggregate produced by cold bonding pelletization process. *Construction and Building Materials* 179. Elsevier Ltd: 220–231. https://doi.org/10.1016/j.conbuildmat.2018.05.237.

Tang, P., and H. J.H. Brouwers. 2018. The durability and environmental properties of self-compacting concrete incorporating cold bonded lightweight aggregates produced from combined industrial solid wastes. *Construction and Building Materials* 167. Elsevier Ltd: 271–285. https://doi.org/10.1016/j.conbuildmat.2018.02.035.

Tang, P., M. V.A. Florea, and H. J.H. Brouwers. 2017. Employing cold bonded pelletization to produce lightweight aggregates from incineration fine bottom ash. *Journal of Cleaner Production* 165. Elsevier Ltd: 1371–1384. https://doi.org/10.1016/j.jclepro.2017.07.234.

Tang, Pei, Dongxing Xuan, Jiangshan Li, Hiu Wan Cheng, Chi Sun Poon, and Daniel C.W. Tsang. 2020. Investigation of cold bonded lightweight aggregates produced with incineration sewage sludge ash (ISSA) and cementitious waste. *Journal of Cleaner Production* 251. Elsevier Ltd. https://doi.org/10.1016/j.jclepro.2019.119709.

Terzić, Anja, Lato Pezo, Vojislav Mitić, and Zagorka Radojević. 2015a. Artificial fly ash based aggregates properties influence on lightweight concrete performances. *Ceramics International* 41. Elsevier Ltd: 2714–2726. https://doi.org/10.1016/j.ceramint.2014.10.086.

Terzić, Anja, Lato Pezo, Vojislav Mitić, and Zagorka Radojević. 2015b. Artificial fly ash based aggregates properties influence on lightweight concrete performances. *Ceramics International* 41. Elsevier Ltd: 2714–2726. https://doi.org/10.1016/j.ceramint.2014.10.086.

Vasugi, V., and K. Ramamurthy. 2014a. Identification of design parameters influencing manufacture and properties of cold-bonded pond ash aggregate. *Materials and Design* 54. Elsevier Ltd: 264–278. https://doi.org/10.1016/j.matdes.2013.08.019.

Vasugi, V., and K. Ramamurthy. 2014b. Identification of admixture for pelletization and strength enhancement of sintered coal pond ash aggregate through statistically designed experiments. *Materials and Design* 60. Elsevier Ltd: 563–575. https://doi.org/10.1016/j.matdes.2014.04.023.

Wang, Shunfeng, Long Yu, Zheng Qiao, Hao Deng, Linglin Xu, Kai Wu, Zhenghong Yang, and Luping Tang. 2023. The toxic leaching behavior of MSWI fly ash made green and non-sintered lightweight aggregates. *Construction and Building Materials* 373. Elsevier Ltd. https://doi.org/10.1016/j.conbuildmat.2023.130809.

Yıldırım, Hasan, and Turan Özturan. 2013. *Mechanical properties of lightweight concrete made with cold bonded fly ash pellets*.

Yıldırım, Hasan, and Turan Özturan. 2021. Impact resistance of concrete produced with plain and reinforced cold-bonded fly ash aggregates. *Journal of Building Engineering* 42. Elsevier Ltd. https://doi.org/10.1016/j.jobe.2021.102875.

Zhang, Chao, Zhijuan Hu, Guanyu Cheng, Changliang Wu, Jingwei Li, Wen Jiang, Xujiang Wang, Shizhao Yang, and Wenlong Wang. 2023. Collaborative recycling of red mud and FGD-gypsum into multi- shell cold bonded lightweight aggregates: Synergistic effect, structure design and application in sustainable concrete. *Construction and Building Materials* 379. Elsevier Ltd. https://doi.org/10.1016/j.conbuildmat.2023.131134.

Zhou, Xianliang, Yulin Chen, Changwu Liu, and Fan Wu. 2022. Preparation of artificial lightweight aggregate using alkali-activated incinerator bottom ash from urban sewage sludge. *Construction and Building Materials* 341. Elsevier Ltd. https://doi.org/10.1016/j.conbuildmat.2022.127844.

Performance Enhancement of Sustainable Lime-Based Concrete

Shashi Bhushan Kumar[1*], and Vishwajit Anand[2]

[1] *Doctoral Research Scholar, Department of Civil Engineering, Indian Institute of Technology (BHU) Varanasi, India*
Email: bhushanshashi383@gmail.com
[2] *Assistant Professor, Department of Civil Engineering, Indian Institute of Technology (BHU) Varanasi, India*
Email: anand.civ@iitbhu.ac.in

*Corresponding author

ABSTRACT

Lime concrete is a complex mixture of hydrated lime and aggregates which has been used in construction worldwide since ancient times. Lime concrete offers good workability, plasticity, and waterproofing to a certain level. A crucial advantageous property of lime concrete is its very high durability. However, after the invention of Portland cement, the use of lime in concrete was almost replaced by Portland cement because of its quick setting and high early strength properties. However, the production of Portland cement consumes high energy and emits large quantities of carbon dioxide (CO_2). In this regard, the need of the hour is to reduce the carbon footprint of the construction industry, by partially or fully replacing cement with eco-friendly binders. Presently, lime is a naturally available binding material that can achieve sustainability in construction. However, this would require overcoming noticeable drawbacks of lime concrete, viz. long setting time and low early strength. This study evaluates the possible use of accelerated carbonation curing to improve the early strength of lime concrete. Accelerated carbonation curing of lime concrete samples is performed at 10% CO_2 concentration, 65% relative humidity, and 27°C temperature. The early strength gain in carbonation-cured lime concrete is compared with damp-cured samples. The rate of strength gain in damp curing and carbonation curing is also compared. This study also reports the CO_2 uptake of lime concrete during accelerated carbonation curing.

KEYWORDS*: Lime Concrete, Sustainability, Carbon footprint, Durability, Compressive Strength.*

1. Introduction

Concrete is the second largest consumed material on our planet by mass. The global consumption of concrete has reached about 30 billion tons per year (Monteiro *et al.*, 2017) and is increasing every year due to esteemed demand driven by rapid urbanisation, population growth and rehabilitation of aged structures worldwide (Nehdi *et al.*, 2023). Actually, developing countries are constructing new infrastructure while developed countries are upgrading or replacing their existing infrastructure. Cement is the most frequently used key-binding ingredient in concrete. The International Federation for Structural Concrete (FIB) and World Cement Association reported the global production of cement as approximately 4 billion tons which is expected to increase to 8.2 billion tons by 2030 to meet the worldwide demand for cement-based materials (Planning and Khakimov, 2024; Tkachenko *et al.*, 2023). India is the third largest producer of cement after China and United States.

However, the production of Portland cement consumes extensive energy and emits very high quantity of carbon dioxide (CO_2). Approximately, the production of one ton of Portland cement emits the same amount of CO_2 (Adesina and Olutoge, 2019). The release of CO_2 from cement industry is about 5-8% of total atmospheric CO_2 emissions worldwide (Ahmad *et al.*, 2017; Grist *et al.*, 2015; Grünhäuser Soares and Castro-Gomes, 2021; Jakobsen *et al.*, 2017; Kim *et al.*, 2022; Malathy *et al.*, 2023; Shah *et al.*, 2022; Sharma and Goyal, 2018; Wang and Chang, 2019; Zhang, Liu, *et al.*, 2020; Zhang *et al.*,

2016). This is likely to increase to more than 10.0% of the total global CO_2 emissions in 2030–2050 (Li and Wu, 2022). Apart from CO_2 emissions, poor durability of cement concrete compared to lime concrete (Zhang, Zhao, *et al.*, 2020), increases the demand for cement through frequent reconstruction. CO_2 is the most dominating greenhouse gas for global warming and also causes various environmental degradation. Researchers are working extensively on developing efficient strategies to mitigate CO_2 emissions involved in cement production. To meet aggressive demand for cement worldwide, consequently placing the new cement plants becomes a barrier to CO_2 mitigation strategies (Grünhäuser Soares and Castro-Gomes, 2021). Global climate change results in an urgent need to reduce the carbon footprint by implementing sustainable practices and technologies.

Some strategies suggested by the researchers in mitigating CO_2 emissions, establishing sustainability and reducing carbon footprint in cement and concrete industry (Li and Wu, 2022) includes use of Supplementary Cementitious Materials (SCMs), Development of energy-efficient technologies, Reduce, Reuse and Recycle (3Rs) for Industrial Waste, Exploration of eco-friendly binders to establish cement-free constructions and Capture and Utilization of CO_2.

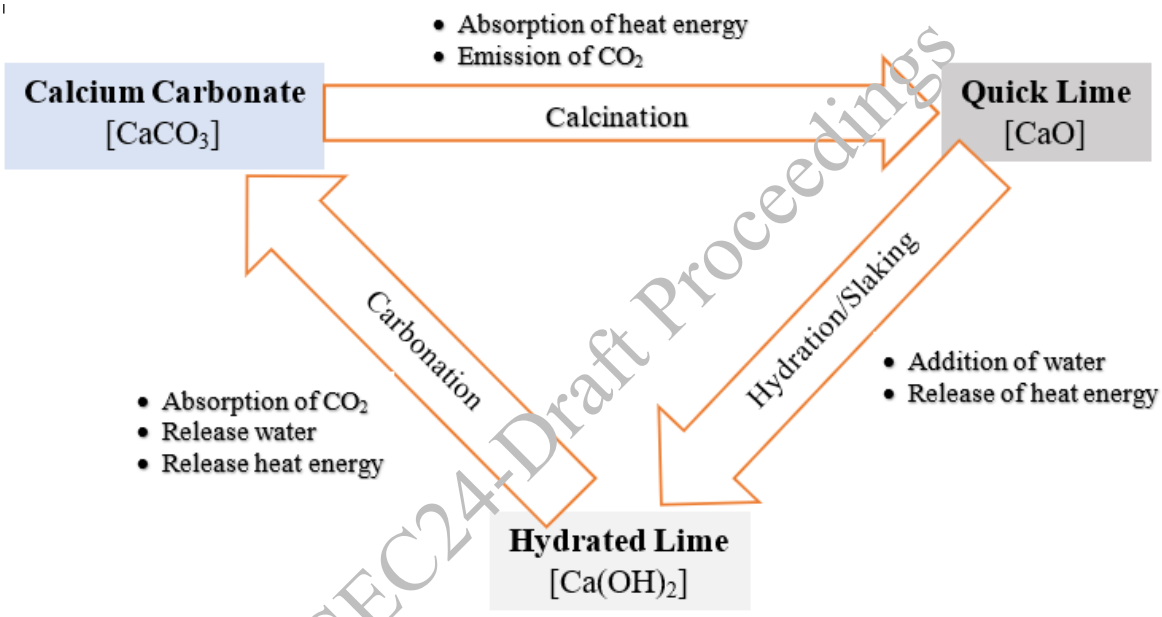

Figure 8. Life cycle assessment of hydrated lime.

Lime concrete, which has been used since historical times, can establish sustainability in construction. Production of lime requires less energy than that of Portland cement, making it a less energy-intensive and an eco-friendly binder compared to Portland cement (Ávila Cruces, 2023). Manufacturing process of lime requires less heat energy, so it produces a lesser amount of CO_2 compared to Portland cement. Production of each ton of lime emits approximately 0.7 tons of CO_2 (Campo *et al.*, 2021; Shan *et al.*, 2016). Yet, unlike cement, lime-based products reabsorb CO_2 from nearby environments and continue carbonation to sequester CO_2 as calcium carbonate over its in-used phase (Malathy *et al.*, 2023). The complete life cycle of lime creates a closed-loop process resulting in zero carbon emission (Campo *et al.*, 2021; Coia, 2020). Fig. 1 shows the closed life cycle of lime. Structures made of lime-based materials capture CO_2 from the atmosphere via direct air capture (DAC) and fix it permanently, which can be a potential approach to reducing the CO_2 concentration in the atmosphere (Campo *et al.*, 2021; Erans *et al.*, 2020). Though durability of lime-based construction is too high to predict (Velosa and Cachim, 2009; Zhang, Zhao, *et al.*, 2020), good condition of several existing historical structures is evidence of longevity of lime-based material (Pavlík and Užáková, 2016). High longevity of structures itself reduces construction materials consumption and construction and demolition waste (C&D waste) generation by avoiding frequent reconstructions. Higher durability also protects our environment directly by reducing burden on natural resources and pollution from C&D waste. So, investment in lime today is a step towards steady improvement in the health and well-being of our communities.

Along with zero carbon emission and enormous longevity, lime concrete also has good workability, plasticity and waterproofing properties. The drawbacks associated with lime concrete are its long setting time and low early strength (Cachim *et al.*, 2010; Grist *et al.*, 2015; Kalagri *et al.*, 2014). That's why today's rapid construction has shifted towards cement concrete. The reason behind long setting time and low early strength is slow carbonation process, which is responsible for setting and hardening of lime-based material (Alvarez *et al.*, 2021). In this process, hydraulic lime absorbs CO_2 from the atmosphere and converts it into calcium carbonate ($CaCO_3$) (Beltrame *et al.*, 2023). Equation 1 shows the chemical reaction involved in setting and hardening of lime. By accelerating the setting process, lime can be used as an alternative eco-friendly binder to established cement-free construction. Researchers also recognized the potential use of hydraulic lime as an alternative to Portland cement and acknowledged that underlying science has not been fully developed (Holmes and Wingate, 2002). Despite of long and ironic history, little research on hydraulic lime-based material has commenced (Grist *et al.*, 2015).

$$Ca(OH)_2 + CO_2 = CaCO_3 + H_2O + Heat \quad (1)$$

Accelerated Carbonation Curing (ACC) can improve the performance of lime-based material. In ACC, CO_2, at a concentration much higher than that in atmosphere, is intentionally introduced into the cementitious materials for a short time at an early age to react with calcium ions (Ca^{2+}). Carbonation is one of the prime factors that influences strength and durability of concrete (Zhang and Shao, 2016). While cement concrete primarily relies on hydration, lime concrete relies only on carbonation for its strength and durability. It is therefore intuitive that contribution of ACC in early strength gain of lime concrete is likely to be significant. This performance enhancement technique can be used in precast elements manufacturing and reducing carbon footprint of concrete industry.

This study attempts to improve early strength of lime concrete using ACC. Compressive strength of lime concrete subjected to ACC is determined, and compared with that of lime concrete under damp curing. The effect of ACC and damp curing on rate of strength gain is also studied. CO_2 uptake is also reported as percentage by weight of binder.

2. Experimental program

2.1 Materials and Mix Proportioning

Natural hydraulic lime (NHL) procured from a vendor in Varanasi region (Uttar Pradesh, India) is used as a binder in concrete preparation. The composition of NHL is determined by X-ray Fluorescence Spectroscopy (XRF) test, and reported in Table 1. The calcium oxide content in NHL sample is found to be 70.92%, while the loss on ignition (LOI) is 26.7%. River sand confirming to Zone-II (BIS, 2016) is used as fine aggregates. Locally available natural aggregates of maximum nominal size 20 mm (CA20) and 10 mm (CA10), are obtained for use. These aggregates, CA20 and CA10 are mixed in the proportion of 3:2 by weight to obtain coarse aggregate in sample preparation. The physical properties of coarse aggregates, fine aggregates and NHL are reported in Table 2 and are found to be in respective acceptable ranges (BIS, 2016, 2021c, 2021d).

Concrete mix proportion is determined based on BIS guidelines (BIS, 2019) for zero target slumps. Aggregates are used in saturated surface dry (SDD) conditions. The water content of fresh concrete is adjusted based on a number of mix trials. A motorized drum is used to produce concrete. A table vibrator is then used to compact concrete specimens in the moulds. Concrete specimens are cast in standard respective moulds. Table 3 shows the final mix proportion of eco-friendly lime concrete.

Table 1. Chemical composition of NHL.

Oxides	CaO	MgO	SiO_2	Al_2O_3	K_2O	Na_2O	Fe_2O_3	SO_3	LOI
Percentage in weight	70.92	0.76	0.61	0.08	0.01	0.06	0.05	0.76	26.7

Table 2. Physical properties of coarse aggregate, fine aggregate and binder.

Properties	Coarse Aggregates		Fine Aggregate	Binder
	CA20	CA10	(Sand)	(NHL)
Specific gravity (SSD)	2.74	2.7	2.5	2.18
Bulk density (kg/m^3)	1.58	1.53	1.77	0.67
Water absorption (%)	0.05	0.05	0.75	-
Fineness modulus	6.94	5.89	2.9	-
Fineness (%)	-	-	-	1.03
Gradation	-	-	Zone-II	-

Table 3. Mix proportion of concrete.

Constituent Materials	NHL	Water	CA20	CA10	Sand
Weight (kg/m^3)	311.90	272.91	591.90	394.60	554.94

3. Methodology

All test specimens for the study are prepared through a four-step process 1) casting 2) demoulding 3) ACC and 4) subsequent curing. Fig. 2 explains the time consumed at each step. In ACC, specimens are stored in a closed carbonation curing chamber for CO_2 exposure till the age of 7 days. The carbonation chamber was filled and supplied continuously with 99.8% pure CO_2 gas, to maintain 10% concentration at 24ºC room temperature and 65% humidity under atmospheric pressure. In damp curing, specimens are covered by moist jute bags under laboratory environmental conditions.

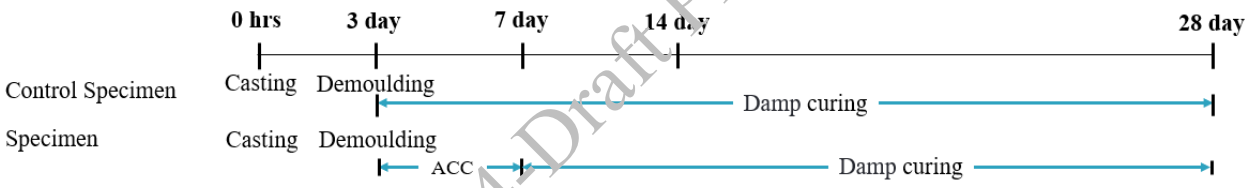

Figure 9 Details of steps involved in prepare specimens.

Experiments are conducted to assess extent of carbonation and compressive strength of lime concrete. Extant of carbonation is quantified by comparing the change in mass of the sample due to ACC. CO_2 uptake can be quantified by three methods; viz Mass gain method, Mass loss method, and Thermogravimetric analysis (TGA). Mass gain method is adopted for determining CO_2 uptake in this study. This method compares the mass of samples before and after the accelerated carbonation curing. The mass difference represents the carbon dioxide uptake by the samples. CO_2 uptake is expressed as a percentage of dry mass of lime using Eq. (2).

$$CO_2 \text{ uptake} = \text{Mass}_{CO_2} / \text{Mass}_{\text{Lime}} \quad (2)$$

Compressive strength of specimens is determined using a compression testing machine (BIS, 2021a), according to IS 516 (Part 1/Sec 1): 2021 (BIS, 2021b). The compressive strength of each group of specimens is tested at the age of 7 days, 14 days and 28 days. Three 150mm-cube specimens are tested for each group at each age, and the average value is reported as compressive strength.

4. Results and Discussion

4.1 Carbon uptake

Carbon uptake is determined by mass gain method. The CO_2 uptake due to ACC is calculated by finding the ratio of difference in weight of the specimens before and after ACC to the weight of dry lime in the specimen. It is found that the average CO_2 uptake in this study is 18.84% by the mass of binder (lime). Only 4 days ACC at low CO_2 concentration (10%) exhibits this CO_2 uptake confirming the high reactivity of lime concrete with CO_2. It is thereby expected that prolonged exposure to higher CO_2 concentration may exhibit even higher CO_2 uptake.

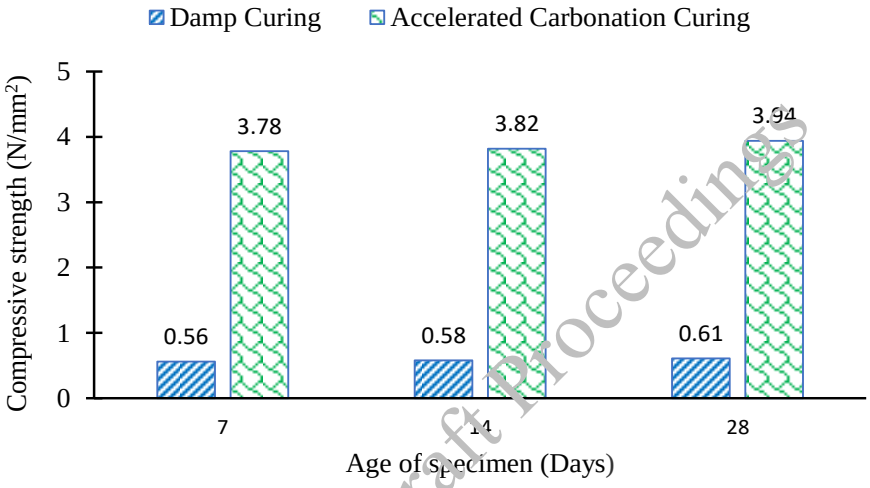

Figure 10. Compressive strength of damp and accelerated carbonation cured lime concrete specimens.

4.2 Compressive Strength

The compressive strength of damp cured (control specimen) and accelerated carbonation cured specimens measured at the age of 7 days, 14 days, and 28 days, are shown in Fig. 3. The compressive strength of damp cured lime concrete is very low. However, with few days of ACC, lime concrete improves its compressive strength by 6.75 times at an early age i.e. 7 days. Further damp curing after ACC curing causes little increase in compressive strength. Fig. 3 shows that the compressive strength increases very slowly with time in damp curing while carbonation curing improves compressive strength at a high rate. In damp-cured concrete 14th day and 28th day compressive strength is increased by only 3.57 % and 8.93 % respectively as compared to 7th day compressive strength. On the other hand, ACC till the age of 7 days increases the compressive strength of concrete by 575 % as compared to damp curing. This is because setting of lime concrete takes place by a very slow carbonation reaction in damp curing due to the low concentration of CO_2 present in the atmosphere. In ACC curing concrete is put in a high CO_2 concentrated environment, which accelerates the carbonation reaction and promotes rapid strength gain. High CO_2 uptake like 18.84% in low CO_2 concentration (10%) and small ACC duration (only 4 days) confirms the very rapid carbonation reaction leading to rapid strength gain.

5. Conclusions

Hydrated lime as a binder is less energy-intensive and eco-friendly. The life cycle of lime creates a closed-loop process resulting in zero carbon emission. However, lime concrete exhibits low early strength. Carbonation involves in setting of lime-based material. Hence accelerated carbonation curing is used to investigate the strength gain of lime concrete at an early age in this study. An effective

utilisation of CO_2 ensures the reduction in carbon footprint in the concrete industry. Based on experimental investigation, following conclusions can be drawn:

- It is possible to increase the early strength of lime concrete using ACC. High early strength may be achieved by optimizing the curing condition for ACC.
- The early age (i.e. 7 days) compressive strength of ACC cured lime concrete is observed to be 6.75 times that of damped cured lime concrete. The strength gain largely depends on CO_2 concentration during ACC.
- A very little increase in compressive strength has been seen with time during damp curing, for carbonated and non-carbonated lime concrete. The initial strength during damp curing largely depends on drying of lime concrete.
- Rapid consumption of CO_2 confirms high reactivity of lime concrete with CO_2. On an average upon 4 days of ACC, lime concrete sequesters 18.84% carbon dioxide by the dry mass of lime.
- The lime concrete studied has very low compressive strength. Ordinary or higher-grade strength may be achieved by adjusting the water-binder ratio and curing conditions of ACC.

It is worth noting that though the compressive strength of lime concrete increases manifold with ACC, it is still low compared to cement concrete. Therefore, lime concrete subjected to ACC can be used for non-structural applications. In order to achieve strength adequate for structural applications, pozzolanic materials, containing silica and alumina, may be added to lime concrete. This will result in lime concrete that relies on cementitious reaction in addition to carbonation, for strength gain.

References

Adesina, P. A., and Olutoge, F. A. (2019). Structural properties of sustainable concrete developed using rice husk ash and hydrated lime. *Journal of Building Engineering*, *25*(April), 100804. https://doi.org/10.1016/j.jobe.2019.100804

Ahmad, S., Assaggaf, R. A., Maslehuddin, M., Al-Amoudi, O. S. B., Adekunle, S. K., and Ali, S. I. (2017). Effects of carbonation pressure and duration on strength evolution of concrete subjected to accelerated carbonation curing. *Construction and Building Materials*, *136*, 565–573. https://doi.org/10.1016/j.conbuildmat.2017.01.069

Alvarez, J. I., Veiga, R., Martínez-Ramírez, S., Secco, M., Faria, P., Maravelaki, P. N., Ramesh, M., Papayianni, I., and Válek, J. (2021). RILEM TC 277-LHS report: a review on the mechanisms of setting and hardening of lime-based binding systems. *Materials and Structures/Materiaux et Constructions*, *54*(2). https://doi.org/10.1617/s11527-021-01648-3

Ávila Cruces, F. J. (2023). *Mechanical, structural and seismic behavior of rammed Earth constructions*. https://hdl.handle.net/10481/80013

Beltrame, N. A. M., Dias, R. L., Witzke, F. B., and Medeiros-Junior, R. A. (2023). Effect of carbonation curing on the physical, mechanical, and microstructural properties of metakaolin-based geopolymer concrete. *Construction and Building Materials*, *406*(September), 133403. https://doi.org/10.1016/j.conbuildmat.2023.133403

BIS. (2016). Coarse and Fine Aggregate for Concrete —- Specification. *IS : 383. Bureau of Indian Standards, New Delhi, India.*

BIS. (2019). Concrete mix Proportioning – Guidelines. *IS 10262. Bureau of Indian Standards, New Delhi, India.*

BIS. (2021a). Compression testing machine used for testing of concrete and mortar - requirements. *IS 14858* . *Bureau of Indian Standards, New Delhi, India.*

BIS. (2021b). Hardened concrete - Methods of test: Part 1 Testing of Strength of Hardened Concrete Section 1 Compressive, Flexural and Split Tensile Strength. *IS : 516. Bureau of Indian Standards, New Delhi, India.* www.standardsbis.in

BIS. (2021c). Methods of Test for Aggregates for Concrete: Part 1 Particle Size and Shape. *IS : 2386. Bureau of Indian Standards, New Delhi, India.* https://doi.org/10.4324/9780203967874-16

BIS. (2021d). Methods of Test for Aggregates for Concrete: Part 3 Specific Gravity, Density, Voids, Absorption and Bulking. *IS : 2386. Bureau of Indian Standards, New Delhi, India.*

Cachim, P., Velosa, A. L., and Rocha, F. (2010). Effect of Portuguese metakaolin on hydraulic lime concrete using different curing conditions. *Construction and Building Materials*, *24*(1), 71–78. https://doi.org/10.1016/j.conbuildmat.2009.08.010

Campo, F. Pietro, Tua, C., Biganzoli, L., Pantini, S., and Grosso, M. (2021). Natural and enhanced carbonation of lime in its different applications: a review. *Environmental Technology Reviews*, *10*(1), 224–237. https://doi.org/10.1080/21622515.2021.1982023

Coia, B. (2020). *Building lime materials yields negative carbon footprint*. Biolime Website. https://biolime.com/lime-vs-cement/#:~:text=Unlike cement%2C lime mortars and,(-2%25) carbon emissions.

Erans, M., Nabavi, S. A., and Manović, V. (2020). Carbonation of lime-based materials under ambient conditions for direct air capture. *Journal of Cleaner Production*, *242*. https://doi.org/10.1016/j.jclepro.2019.118330

Grist, E. R., Paine, K. A., Heath, A., Norman, J., and Pinder, H. (2015). Structural and durability properties of hydraulic lime-pozzolan concretes. *Cement and Concrete Composites*, *62*, 212–223. https://doi.org/10.1016/j.cemconcomp.2015.07.001

Grünhäuser Soares, E., and Castro-Gomes, J. (2021). Carbonation curing influencing factors of Carbonated Reactive Magnesia Cements (CRMC) – A review. *Journal of Cleaner Production*, *305*. https://doi.org/10.1016/j.jclepro.2021.127210

Holmes, S., and Wingate, M. (2002). *Building with Lime A practical introduction*. https://practicalactionpublishing.com/book/242/building-with-lime

Jakobsen, J., Roussanaly, S., and Anantharaman, R. (2017). A techno-economic case study of CO2 capture, transport and storage chain from a cement plant in Norway. *Journal of Cleaner Production*, *144*(2017), 523–539. https://doi.org/10.1016/j.jclepro.2016.12.120

Kalagri, A., Karatasios, I., and Kilikoglou, V. (2014). The effect of aggregate size and type of binder on microstructure and mechanical properties of NHL mortars. *Construction and Building Materials*, *53*, 467–474. https://doi.org/10.1016/j.conbuildmat.2013.11.111

Kim, H., Sharma, R., Pei, J., and Jang, J. G. (2022). Effect of carbonation curing on physicochemical properties of mineral admixture blended belite-rich cement. *Journal of Building Engineering*, *56*(May), 104771. https://doi.org/10.1016/j.jobe.2022.104771

Li, L., and Wu, M. (2022). An overview of utilizing CO2for accelerated carbonation treatment in the concrete industry. *Journal of CO2 Utilization*, *60*(April), 102000. https://doi.org/10.1016/j.jcou.2022.102000

Malathy, R., Shanmugam, R., Dhamotharan, D., Kamaraj, D., Prabakaran, M., and Kim, J. (2023). Lime based concrete and mortar enhanced with pozzolanic materials – State of art. *Construction and Building Materials*, *390*(November 2022). https://doi.org/10.1016/j.conbuildmat.2023.131415

Monteiro, P. J. M., Miller, S. A., and Horvath, A. (2017). Towards sustainable concrete. *Nature Materials*, *16*(7), 698–699. https://doi.org/10.1038/nmat4930

Nehdi, M. L., Marani, A., and Zhang, J. (2023). *Is net-zero feasible: Systematic review of cement and concrete decarbonization technologies*. https://doi.org/10.1016/j.rser.2023.114169

Pavlík, V., and Užáková, M. (2016). Effect of curing conditions on the properties of lime, lime-metakaolin and lime-zeolite mortars. *Construction and Building Materials*, *102*, 14–25. https://doi.org/10.1016/j.conbuildmat.2015.10.128

Planning, R., and Khakimov, S. (2024). *Study of the Properties of Concrete Based on Non- Fired Alkaline Binders*. *1*(1), 33–39.

Shah, I. H., Miller, S. A., Jiang, D., and Myers, R. J. (2022). Cement substitution with secondary materials can reduce annual global CO2 emissions by up to 1.3 gigatons. *Nature Communications*, *13*(1), 1–11. https://doi.org/10.1038/s41467-022-33289-7

Shan, Y., Liu, Z., and Guan, D. (2016). CO2 emissions from China's lime industry. *Applied Energy*, *166*, 245–252. https://doi.org/10.1016/j.apenergy.2015.04.091

Sharma, D., and Goyal, S. (2018). Accelerated carbonation curing of cement mortars containing cement kiln dust: An effective way of CO2 sequestration and carbon footprint reduction. *Journal of Cleaner Production*, *192*, 844–854. https://doi.org/10.1016/j.jclepro.2018.05.027

Tkachenko, N., Tang, K., McCarten, M., Reece, S., Kampmann, D., Hickey, C., Bayaraa, M., Foster, P., Layman, C., Rossi, C., Scott, K., Yoken, D., Christiaen, C., and Caldecott, B. (2023). Global database of cement production assets and upstream suppliers. *Scientific Data*, *10*(1), 1–9. https://doi.org/10.1038/s41597-023-02599-w

Velosa, A. L., and Cachim, P. B. (2009). Hydraulic-lime based concrete: Strength development using a pozzolanic addition and different curing conditions. *Construction and Building Materials*, *23*(5), 2107–2111. https://doi.org/10.1016/j.conbuildmat.2008.08.013

Wang, D., and Chang, J. (2019). Comparison on accelerated carbonation of β-C2S, Ca(OH)2, and C4AF: Reaction degree, multi-properties, and products. *Construction and Building Materials*, *224*, 336–347. https://doi.org/10.1016/j.conbuildmat.2019.07.056

Zhang, D., Cai, X., and Shao, Y. (2016). Carbonation Curing of Precast Fly Ash Concrete. *Journal of Materials in Civil Engineering*, *28*(11), 1–9. https://doi.org/10.1061/(asce)mt.1943-5533.0001649

Zhang, D., Liu, T., and Shao, Y. (2020). Weathering Carbonation Behavior of Concrete Subject to Early-Age Carbonation Curing. *Journal of Materials in Civil Engineering*, *32*(4), 1–10. https://doi.org/10.1061/(asce)mt.1943-5533.0003087

Zhang, D., and Shao, Y. (2016). Effect of early carbonation curing on chloride penetration and weathering carbonation in concrete. *Construction and Building Materials*, *123*, 516–526. https://doi.org/10.1016/j.conbuildmat.2016.07.041

Zhang, D., Zhao, J., Wang, D., Wang, Y., and Ma, X. (2020). Influence of pozzolanic materials on the properties of natural hydraulic lime based mortars. *Construction and Building Materials*, *244*, 118360. https://doi.org/10.1016/j.conbuildmat.2020.118360

Performance of Low-Carbon Concrete Prepared with Reactive Magnesium Oxide and Fly Ash in OPC Binder System

Lalit Singh[1*] and Anurag Misra[2]

[1] *Indian Institute of technology, Jammu, India*
Email: 2021rce2014@iitjammu.ac.in
[2] *Indian Institute of technology, Jammu, India*
Email: anurag.misra@iitjammu.ac.in

*Corresponding author

ABSTRACT

This research aimed to work on a binder system containing conventional Portland cement (OPC), Reactive Magnesium oxide (MgO) and fly ash (FA). Reactive MgO is produced by calcining magnesite at 600-700 °C. Calcination temperature of magnesite is lower than the calcite. In this study, the effect of using varying molarity (0.25M-0.75M) of hydration agent (Magnesium acetate) on hydration of reactive MgO and pH of concrete has been reported. Concrete prepared with Portland cement, Magnesium oxide and Fly ash (OPC-MgO-FA) was evaluated for compressive strength, flexural strength and initial surface absorption test (ISAT). This binder with incorporation of a hydration agent has a positive effect on compressive strength, flexural and initial surface absorption test (ISAT). The inclusion of reactive MgO and Fly ash in Concrete mix (OPC-MgO-FA) with 0.75M hydration agent produces comparable compressive strength, flexural strength development and ISAT values to concrete made with ordinary Portland cement (OPC). The results found to be comparable with OPC concrete. The reported compressive strength and flexural strength of Concrete mix (OPC-MgO-FA) with 0.75M hydration agent is 49.79MPa, 6.87 MPa respectively while the ISAT average value measured at 10,30 and 60 minutes were 0.461, 0.373 and 0.351 respectively. The outcomes emphasize to use Magnesium Oxide and Fly ash as partial replacement constituents of OPC.

KEYWORDS*: Hydration agent, Reactive MgO, ISAT*

1. Introduction

The quest for sustainable construction materials has led to increased interest in low-carbon concrete formulations that minimize environmental impact without compromising performance. One promising approach involves incorporating reactive magnesium oxide (MgO) and fly ash into ordinary Portland cement (OPC) binder systems. Reactive MgO offers potential as a binder due to its ability to sequester carbon dioxide (CO_2) during hydration, reducing overall carbon emissions(Jang et al., 2022). Fly ash, a by-product of coal combustion, not only enhances the durability and workability of concrete but also mitigates the environmental footprint by utilizing industrial waste(Nguyen et al., 2022).
Magnesite, derived from ultramafic rocks like serpentine, offers a rich source of magnesium carbonate. India's reserves stand at 395 million tonnes, while globally, reserves reach 7.6 billion tonnes(Bhavan, 2022). Magnesite's low calcination temperatures make it advantageous for MgO production compared to the energy-intensive OPC process(Ruan & Unluer, 2016). This underscores its potential as a sustainable alternative in construction materials. This study explores the performance of low-carbon concrete formulations utilizing reactive MgO and fly ash in OPC binder systems. When sufficient water is available, brucite reacts with a silica source to form M-S-H gel (Tran & Scott, 2017).Studies suggest that the compressive strength of Magnesium silicate hydrate-based cement is positively influenced by MgO and silica content, as well as age. Conversely, it exhibits a negative correlation with the water-to-

binder ratio (Zheng et al., 2023). The challenge with MgO as a binder stems from its slow reaction rate, due to the formation of a protective $Mg(OH)_2$ layer. Organic ligands act as potent chelating agents, influencing MgO binder reactions. Magnesium acetate, notably, enhances MgO hydration by promoting brucite precipitation in the solution (Kamala Ilango et al., 2024). Studies (Filippou & Katiforis, 1999; Matabola et al., 2010) highlight the efficacy of magnesium acetate in improving MgO hydration. This research aims to assess the viability and effectiveness of these sustainable materials in real-world applications. Understanding how these components interact within the concrete matrix and their impact on overall performance is essential for advancing the adoption of low-carbon concrete in the construction industry. Through comprehensive analysis and experimentation, this study seeks to contribute valuable insights into the development of environmentally friendly concrete solutions that meet the demands of modern construction while reducing environmental impact. By examining key properties such as compressive strength, flexural strength, and initial surface absorption test(ISAT).

2. Material and methods

Concrete was prepared with the binder consisting of three major materials during the experimental program. Mix design of 1:1.41:2.85 as per IS 10262 was used with different water-binder ratio. Binder comprises of OPC 53, MgO and Class-F fly ash. Superplasticizer AURAMIX procured from FOSROC chemical Ltd. and Magnesium acetate ($Mg(CH_3COO)_2$) as a hydrating agent was also used during the preparation of concrete mix. Chemical and Physical composition of OPC 53, MgO and Class-F fly ash as listed in table-1.

Table 1. Chemical composition of material

Percentage weight (%)								
Material	SiO_2	Al_2O_3	CaO	Fe_2O_3	MgO	Na_2O	K_2O	Specific gravity
OPC	19.45	5.78	61.92	2.86	2.45	0.36	1.12	3.13
MgO	0.38	0.45	2.64	0.38	90.23	0.23	0.08	3.28
FA	61.29	24.94	3.74	4.58	2.82	0.14	-	2.31

Table 2. Mix notation and description

Sl.no	Mix	Description (1:1.41:2.85)	PC (%)	MgO (%)	FA (%)	w/b	Molarity
1	Control Mix	OPC-0.4	100	..	..	0.4-SP	..
2		OPC-0.4-SP	100	..	..	0.4-SP	
3		OPC-0.45	100	..	..	0.45	
4		OPC-0.5	100	..	..	0.5	
5	OMF-1	OMF-0.75-0.4	50	30	20	0.4-SP	0.75M
6		OMF-0.75-0.4-SP	50	30	20	0.4-SP	
7		OMF-0.75-.45	50	30	20	0.45	
8		OMF-0.75-0.5	50	30	20	0.5	
9	OMF-2	OMF-0.5-0.4	50	30	20	0.4-SP	0.5M
10		OMF-0.5-0.4-SP	50	30	20	0.4-SP	
11		OMF-0.5-0.45	50	30	20	0.45	
12		OMF-0.5-0.5	50	30	20	0.5	
13	OMF-3	OMF-0.25-0.4	50	30	20	0.4-SP	0.25M
14		OMF-0.25-0.4-SP	50	30	20	0.4-SP	
15		OMF-0.25-0.45	50	30	20	0.45	
16		OMF-0.25-0.5	50	30	20	0.5	

Concrete mixes were prepared, cured and tested. The concrete mixes' series includes four different mixes. The series as per table-2 comprises of control mix having 100% OPC, OMF-1 with 0.75 molarity of Hydrating agent (Magnesium acetate), OMF-2 and OMF-3 is prepared with 0.5 and 0.25 molar hydrating agent respectively. Dosage of superplasticizer was kept 1% to provide workability to lower water to binder concrete mixes. OMF includes OPC, MgO and FA. Fine aggregates and coarse aggregates of saturated surface dry conditions were used.

Three different water to binder ratio were taken for mix preparation that includes 0.4-SP (w/b:0.4 with superplasticizer),0.45 and 0.5. During the trials, the binder composition was originally used to be 50%OPC, (20%, 25%, 30%) MgO and (20%, 25%, 30%) FA. The optimized proportion was found to be 50% OPC, 30% MgO and 20% FA. To avoid redundancy of mixes trials, 50% OPC, 30% MgO and 20% FA was found to be the working binder composition for concrete preparation and testing. The inclusion of 30% MgO and 20% FA will reduce the OPC content by 50% and resulting into low carbon cement and henceforth the concrete. The concrete mixes were casted into the cubes of 150mm x 150mm x 150mm and beams of 100mm x 100mm x 500mm. The notation description comprises of mix name-molarity-w/b e.g. OMF-0.75-0.45 depicts OMF is the mix name, 0.75 is the molarity and 0.45 is the water to binder ratio.

3. Results and discussions

3.1 Compressive strength

The mechanical property of concrete prepared with binder containing OPC (50%), MgO (30%) and FA (20%) has been evaluated in this section. The compressive strength of various concrete mixes has been reported after 7,14 and 28 days. For the mixes having 0.4 water to binder ratio with dosage of superplasticizer (0.4-SP) found to have highest compressive strength in their respective series. The control mix OPC-0.4-SP showed 35.50, 44.67 and 49.91 MPa for 7, 14 and 28 days respectively as illustrated in figure-1.

For OMF-0.75-0.4-SP, the reported 7, 14 and 28-day compressive strength were 33.75, 44.87 and 49.79 MPa respectively. The compressive strength of prior mix was significantly equal to that of the control mix OPC-0.4-SP. Compressive strength of mix is also affected by water to binder ratio (Mehta & Monteiro, 1987). It has been presented via a decrement of 16.64% and 22.07%, with 0.45 and 0.5 water to binder ratio respectively, when compared with OMF-0.75-0.4-SP (Dong et al., 2023; Luo et al., 2023; Wang et al., 2013). Similar trend was observed in control, OMF-2 and OMF-3 as depicted in figure-1.

Molar concentration of hydrating agent (Magnesium acetate) also plays a vital role in compressive strength (Dung & Unluer, 2016). The compressive strength enhanced as mixes subjected to higher concentration of hydrating agent(Arora et al., 2019). The strength increased by 34.2 % when the molarity is increased from 0.25 (OMF-3) to 0.75 (OMF-1). Whereas, 21% improvement is observed in case of 0.5 (OMF-2) molar concentration (Gonçalves et al., 2019; Zhang et al., 2014). With 0.75 molarity, the mixes (OMF-1) achieved the highest strength i.e., 49.79 MPa which is significantly closer to that of corresponding control mix. The control mix was strengthened by the formation of CSH while Combination of MSH and CSH were the governing hydration products for strength gain in case OMF mixes.

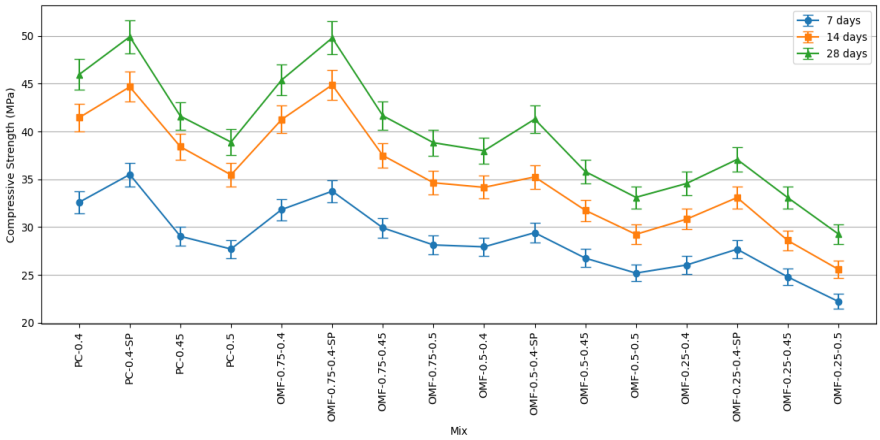

Figure 1. Compressive strength of mixes

3.2 Flexural strength

The flexural strength results of control, OMF-1, OMF-2 and OMF-3 mixes at 7,14 and 28-days curing are depicted in figure-2. The results revealed OMF-1 mixes were reported with significantly higher flexural strength than OMF-2 and OMF-3 mixes. Unlikely OMF-2 and OMF-3 mixes, the control mixes showed relatively comparable flexural strength. The 28-days flexural strength of control mix (OPC-0.4-SP) was 6.93 MPa which was comparatively same as 6.97 MPa of OMF-1 (OMF-0.75-0.4-SP).
The flexural strength showed a declining trend as the molarity of hydrating agent decreased.OMF-3 (OMF-0.25-0.4-SP) achieved 22.43% and 6.89% lesser flexural strength than corresponding OMF-1 and OMF-2 mix. However, the changes in w/b ratio showed relatively higher decrement of flexural strength in all mixes. For control mix, the value reduced by 22.62% as w/b changed from 0.4-SP to 0.5. On contrary, there was an average decrement of 18.25% in case of all OMF mixes when w/b ranged from lower to higher. The findings aligned with those of compressive strength results.

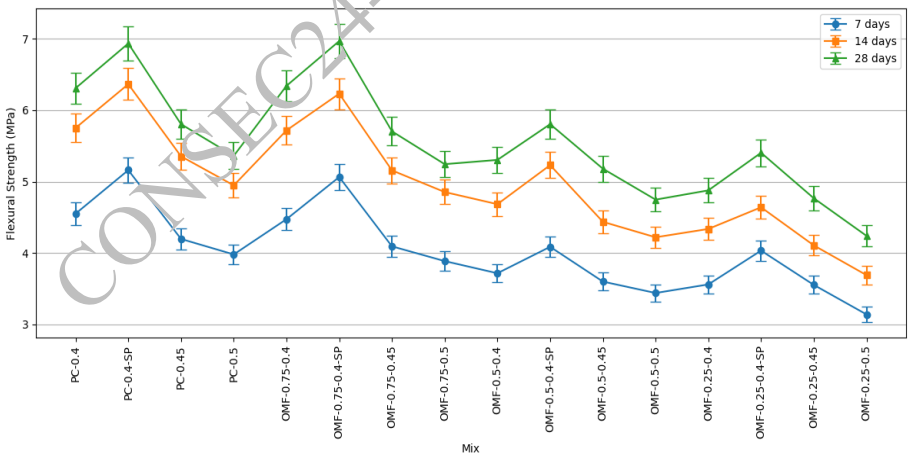

Figure 2. Flexural strength of mixes

3.3 Initial surface absorption test (ISAT)

The test results of water absorption of concrete after 28-days are presented in figure-3. The reported lowest ISAT values for control, OMF-1, OMF-2 and OMF-3 mixes at 60 minutes were 0.359,0.350 0.475 and 0.580 ml/(m^2.sec) respectively. Unlikely OPC based concrete, the OMF mixes consisted of half part of OPC and rest comprised of MgO and FA causing formation of C-S-H, $Ca(OH)_2$, M-S-H and $Mg(OH)_2$ as the main hydration products. The intensity of hydration product varied depending upon the

concentration of hydrating agent as evaluated for OMF-1 (OMF-0.75-0.4-SP). The absorption of water decreased as time of testing increased.

The recorded ISAT values at 0.5 w/b ratio for control, OMF-1, OMF-2 and OMF-3 mixes at 60 minutes were 0.498,0.492,0.595 and 0.649 respectively.

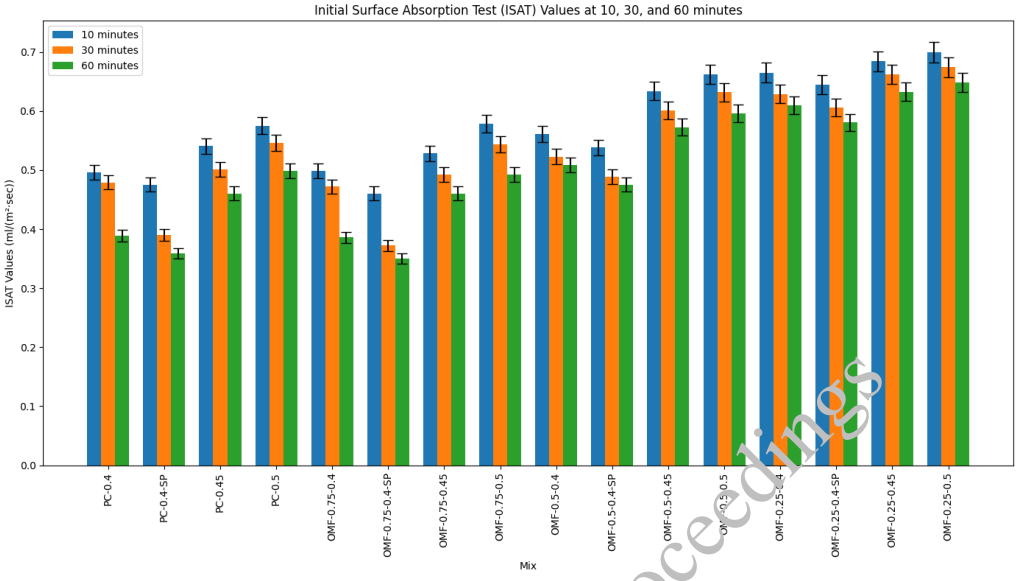

Figure 3. ISAT values of mixes

3.4 Significance of pH in severe environment

The concentration of the hydrating agent profoundly impacts the pH of the solution as depicted in figure-4. Higher molar solution like 0.75 exhibits lower pH due to the higher concentration of acetate ions, resulting in a more acidic environment, whereas a 0.25 molar solution causes a slight deviation in pH, leading to pH levels above 11.5. This variation in pH is attributed to the abundance of acetate ions, which contribute to acidity. Additionally, the water-to-binder ratio influences the solution's nature, with higher ratios diluting ion concentration and increasing pH towards basicity. The control mix, enriched with Ca^{2+} ions, yields a more basic solution. Concrete with lower pH and high compressive strength finds utility in applications like nuclear waste immobilization and heavy metal stabilization due to its ability to withstand harsh environmental conditions while maintaining structural integrity(Marsiske et al., 2021; Saadaoui et al., 2017).

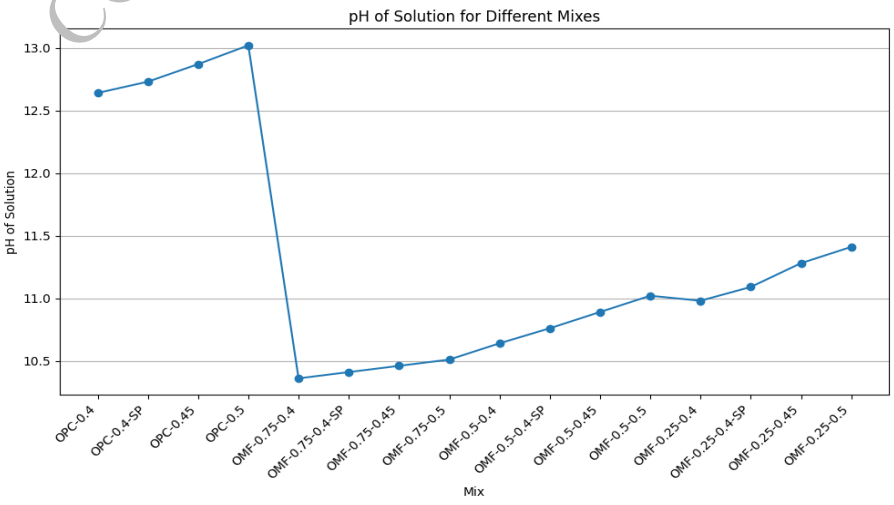

Figure 4. pH of all mixes

4. Conclusions

- Concrete mixes (OPC: 50%, MgO: 30%, FA: 20%) were tested for compressive strength after 7, 14, and 28 days. The 0.4 water-to-binder ratio with superplasticizer (0.4-SP) yielded the highest strengths, with OPC-0.4-SP reaching 35.50 MPa, 44.67 MPa, and 49.91 MPa, respectively.
- OMF-0.75-0.4-SP matched OPC-0.4-SP's strength. However, 0.45 and 0.5 ratios saw reductions of 16.64% and 22.07%, respectively, versus OMF-0.75-0.4-SP.
- Higher molar concentrations of magnesium acetate boosted compressive strength significantly. OMF-1 hit 49.79 MPa with a 0.75 molarity, highlighting the agent's vital role in strengthening concrete.
- OMF-1 showed notably higher flexural strength than OMF-2 and OMF-3. Flexural strength declined as hydrating agent molarity decreased, consistent with compressive strength findings.
- Mixes with higher water-to-binder ratios displayed higher ISAT values after 28 days. Control and OMF-1 mixes exhibited lower absorption due to denser matrices, while hydration product intensity varied with hydrating agent concentration.
- The concentration of the hydrating agent significantly affects solution pH, with higher concentrations leading to lower pH levels, while the water-to-binder ratio influences pH towards basicity, impacting concrete properties and applications.

Acknowledgements

The authors declare that they have no known competing financial interests or personal relationships that could have appeared to influence the work reported in this paper.

References

Arora, A., Singh, B., & Kaur, P. (2019). Novel material i.e. Magnesium phosphate cement (MPC) as repairing material in roads and buildings. *Materials Today: Proceedings*, *17*, 70–76. https://doi.org/10.1016/j.matpr.2019.06.402

Bhavan, I. (2022). *Indian Minerals Yearbook 2020 59th Edition Manganese Ore*. *2020*(0712).

Dong, S., Yu, S., Chen, L., Zhuo, Q., Wu, F., Xie, L., & Liu, L. (2023). Comparative Study on the Effects of Five Nano-Metallic Oxide Particles on the Long-Term Mechanical Property and Durability of Cement Mortar. *Buildings*, *13*(3). https://doi.org/10.3390/buildings13030619

Dung, N. T., & Unluer, C. (2016). Improving the performance of reactive MgO cement-based concrete mixes. *Construction and Building Materials*, *126*, 747–758. https://doi.org/10.1016/j.conbuildmat.2016.09.090

Filippou, D., & Katiforis, N. (1999). *On the kinetics of magnesia hydration in magnesium acetate solutions*. *328*(December 1998), 322–328.

Gonçalves, T., Silva, R. V., De Brito, J., Fernández, J. M., & Esquinas, A. R. (2019). Hydration of reactive MgO as partial cement replacement and its influence on the macroperformance of cementitious mortars. *Advances in Materials Science and Engineering*, *2019*. https://doi.org/10.1155/2019/9271507

Jang, H., So, S., & Lim, Y. (2022). Carbonation, CO2 sequestration, and physical properties based on the mineral size of light burned MgO using carbonation accelerator. *Journal of Cleaner Production*, *379*(P1), 134648. https://doi.org/10.1016/j.jclepro.2022.134648

Kamala Ilango, N., Nguyen, H., German, A., Winnefeld, F., & Kinnunen, P. (2024). Role of magnesium acetate in hydration and carbonation of magnesium oxide-based cements. *Cement and Concrete Research*, *175*(October 2023), 107357. https://doi.org/10.1016/j.cemconres.2023.107357

Luo, X., Li, Y., Lin, H., Li, H., Shen, J., Pan, B., Bi, W., & Zhang, W. (2023). Research on predicting compressive strength of magnesium silicate hydrate cement based on machine learning. *Construction and Building Materials*, *406*(September), 133412. https://doi.org/10.1016/j.conbuildmat.2023.133412

Marsiske, M. R., Debus, C., Di Lorenzo, F., Bernard, E., Churakov, S. V., & Ruiz-Agudo, C. (2021). Immobilization of (aqueous) cations in low pH M-S-H cement. *Applied Sciences (Switzerland)*, *11*(7). https://doi.org/10.3390/app11072968

Matabola, K. P., Van Der Merwe, E. M., Strydom, C. A., & Labuschagne, F. J. W. (2010). The influence of hydrating agents on the hydration of industrial magnesium oxide. *Journal of Chemical Technology and Biotechnology*, *85*(12), 1569–1574. https://doi.org/10.1002/jctb.2467

Mehta, P. K., & Monteiro, P. J. M. (1987). Effect of Aggregate, Cement, and Mineral Admixtures on the Microstructure of the Transition Zone. *MRS Proceedings*, *114*, 65–75. https://doi.org/10.1557/proc-114-65

Nguyen, H., Santos, H., Sreenivasan, H., Kunther, W., Carvelli, V., Illikainen, M., & Kinnunen, P. (2022). On the carbonation of brucite: Effects of Mg-acetate on the precipitation of hydrated magnesium carbonates in aqueous environment. *Cement and Concrete Research*, *153*, 106696.

Ruan, S., & Unluer, C. (2016). Comparative life cycle assessment of reactive MgO and Portland cement production. *Journal of Cleaner Production*, *137*(x), 258–273. https://doi.org/10.1016/j.jclepro.2016.07.071

Saadaoui, E., Ghazel, N., Ben Romdhane, C., & Massoudi, N. (2017). Phosphogypsum: potential uses and problems–a review. *International Journal of Environmental Studies*, *74*(4), 558–567. https://doi.org/10.1080/00207233.2017.1330582

Tran, H. M., & Scott, A. (2017). Strength and workability of magnesium silicate hydrate binder systems. *Construction and Building Materials*, *131*, 526–535. https://doi.org/10.1016/j.conbuildmat.2016.11.109

Wang, A., Yuan, Z., Zhang, J., Liu, L., Li, J., & Liu, Z. (2013). Effect of raw material ratios on the compressive strength of magnesium potassium phosphate chemically bonded ceramics. *Materials Science & Engineering C*, *33*(8), 5058–5063. https://doi.org/10.1016/j.msec.2013.08.031

Zhang, T., Vandeperre, L. J., & Cheeseman, C. R. (2014). Formation of magnesium silicate hydrate (M-S-H) cement pastes using sodium hexametaphosphate. *Cement and Concrete Research*, *65*, 8–14. https://doi.org/10.1016/j.cemconres.2014.07.001

Zheng, K., Xie, X., Gou, G., Chen, X., Huang, Y., & Gao, J. (2023). Comparative study on characteristics and microstructure of magnesium silicate hydrate utilizing quartz and silica fume as siliceous raw materials. *Case Studies in Construction Materials*, *19*(February), e02313. https://doi.org/10.1016/j.cscm.2023.e02313

Effect of Different Cooling Regimes on the Reactivity of Industrial Sludge Derived Supplementary Cementitious Material

Revathy Sunil [1], A. V. Rahul [2*], and Shihabudheen M. Maliyekkal [3]

[1] Department of Civil and Environmental Engineering, Indian Institute of Technology Tirupati, Tirupati, India, Email: ce22m305@iittp.ac.in

[2] Department of Civil and Environmental Engineering, Indian Institute of Technology Tirupati, Tirupati, India, Email: rahulav@iittp.ac.in

[3] Department of Civil and Environmental Engineering, Indian Institute of Technology Tirupati, Tirupati, India, Email: shihab@iittp.ac.in

[*]Corresponding author

ABSTRACT

Industrial sludges lead to significant environmental issues owing to their composition and currently practiced landfilling disposal method. Transforming them into supplementary cementitious materials (SCMs) presents a promising alternative that reduces ecological risks and serves as an economical and performance booster for the construction industry. This study examines the possibility of processing an industry effluent sludge obtained from the battery industry as an SCM. The sludge samples were calcined at a temperature of 850°C in a muffle furnace and then cooled. The samples were characterized by using inductively coupled plasma mass spectrometry (ICPMS) and X-ray diffraction (XRD). The ICPMS results indicate that oxides like SiO_2, Al_2O_3, and Fe_2O_3 are present in high quantities, thus potentially making it a suitable candidate for a pozzolanic material. The influence of three different cooling regimes, namely, water quenching, air cooling by spreading on a plate, and slow furnace cooling, on the reactivity of the calcined sludge was investigated. The R^3 bound water and calorimetry test were done to analyze the reactivity of sludges. The results indicate that only water-quenched samples are suitable for producing reactive SCMs as water quenching resulted in a sample with high amorphous content compared to the other cooling methods. In the future, more studies will be performed to assess the effect of other calcination parameters, such as temperature and the duration of calcination, on the reactivity of industry sludge derived SCMs.

KEYWORDS*: Industrial sludges, Supplementary cementitious materials (SCMs), Cooling regimes, Water quenching, Reactivity testing.*

1. Introduction

Concrete is the most widely used construction material. However, cement usage in concrete is associated with environmental pollution and greenhouse gas emissions (Adesina, 2020). Producing 1 kilogram of cement generates an equivalent amount of CO2, which constitutes almost 5% of the world's CO2 emissions (Benhelal et al., 2021). The construction industry has been actively pursuing ways to reduce its carbon footprint for the last decades. One of the most common and effective methods has been the partial replacement of Portland clinker with supplementary cementitious materials (SCMs) (Pisciotta et al., 2023; Scrivener et al., 2018). Interestingly, the primary challenge in implementing this solution has been the availability of suitable SCMs, rather than any performance issues arising from the reduction of clinker content (Juenger et al., 2019; Skibsted & Snellings, 2019). For example, in many developed countries like the United States, Japan, and Canada, around 40% of coal-fired power plants have shut down in the past five years, with plans to retire all remaining coal-fired plants by 2025,

limiting the availability of fly ash. Also, in many developed countries, there is more use of recycled steel instead of producing new steel, which leads to the reduction of steel slag, which is one of the most commonly used SCMs (Snellings et al., 2023). This urges the need to explore new sources of SCMs.
Industrial processes in various sectors generate considerable amounts of sludge, leading to significant environmental and management challenges. Battery manufacturing industries are particularly notable for producing large volumes of sludge containing heavy metals like lead, cadmium, and cobalt (Melchor-Martínez et al., 2021). Improper disposal of these sludges can result in severe environmental contamination, impacting soil, water bodies, and air quality. However, many industrial sludges also contain compounds like calcium, alumina, and silica that may give them pozzolanic or latent hydraulic properties (Das et al., 2007; Xia et al., 2023). Developing sludge-based SCMs not only reduces the environmental impact associated with the disposal of sludge but also provides a new source of SCM for the construction industry (Mohammadi & Ramezanianpour, 2023).
The transformation of industrial waste into SCMs may involve several critical steps, including proper pretreatment, calcination, and subsequent cooling (Snellings et al., 2023). There have been very limited studies on the effect of different cooling regimes on the reactivity of industrial sludge-based supplementary cementitious materials. The cooling method can greatly influence the phases formed and, as a result, the SCM's reactivity (Ono, 1981; Bullard 2015; Hong et al., 2001; Sazonova & Skripnikova, 2015). The current study aims to investigate the effects of three different cooling methods (fast cooling by water-quenching, air cooling by spreading on a plate, and slow cooling in the furnace) on the reactivity of battery industry sludge-based SCM.

2. Materials and methods

2.1 Materials used

The effluent treatment plant (ETP) sludge used in this study was collected from a battery industry (Amara Raja Batteries Limited, Tirupati, India). The collected sample is shown in Figure 1. Sludge was oven-dried at 105 ± 5 °C for 24 hours and ground before use.

Figure 1. ETP sludge

2.2 Calcination studies

The oven-dried sample was ground and sieved through a 90 μm mesh. Then, the raw mixture was homogenized and grounded for one hour in a ball mill (Scinomat Solutions India, 2Sx-V04). The calcination of the sludge was done in a muffle furnace. About 15 g of the sludge was placed in the muffle furnace, and the temperature was increased at a constant rate of 4°C until 850°C was reached. Thereafter, the temperature was maintained constant at 850°C for 1 hour. After calcination, the sample

was subjected to cooling. Three types of cooling methods were evaluated in the study - slow cooling in the muffle furnace, air cooling by spreading on a plate, and water quenching, as shown in Figure 2.

(a) (b) (c)

Figure 2. (a) Slow furnace cooling, (b) Air cooling by spreading on plate, (c) Water quenching

2.3 Chemical composition and particle size analysis

The oxide composition of the dried sludge was determined by inductively coupled plasma mass spectrometry (ICPMS). Digestion of 1-2 grams of powdered material was performed according to a specified digestion protocol. Initially, the samples were digested using 5 mL of nitric acid followed by an additional step with 300 µL of hydrofluoric acid. Then, the samples were treated with 2.4 mL of boric acid and diluted to a final volume of 50 mL using doubly deionized water. The measurements were conducted using PerkinElmer's NexION® 2000 ICPMS.

The crystalline phases in the sludge were identified by X-ray diffraction (XRD). The XRD analysis was performed on the dried sludge and also on the sludge sample after calcination and cooling using different methods. This was done to understand the effect of various cooling methods on the crystalline phases present in the sample. PANalytical Empyrean X-ray diffractometer equipped with CuKα radiation at λ = 1.54 A was used for performing the measurement. The data were collected at 45 kV and a current of 40 mA, over the 2θ range from 10 to 70, at a scan rate of 0.026 2θ/min. The obtained data were analyzed using X'Pert High Score Plus diffraction software.

The particle size distribution of the dried sludge and the sludge sample after calcination and cooling using different methods were determined by the laser diffraction method (Anton Paar PSA 1190). About 0.5–1 g of sample was analyzed using the wet method with isopropanol solvent.

2.4 Reactivity test by isothermal and bound water method

R^3 test (Li et al., 2018) is a newly developed test procedure for checking SCM reactivity. Table 1 presents the mix design details of the R^3 model paste used in this study (Avet et al., 2016). The reactivity of sludges was studied with a calorimetry test where samples of R^3 pastes were kept in an isothermal calorimeter at a temperature of 60°C for seven days, which resulted in obtaining the total heat release. Additionally, R^3 bound water test was performed for which the paste was kept for curing in sealed containers for seven days at 40°C. The cured samples were subjected to crushing and drying in an oven set at 105°C until a constant weight was achieved. Subsequently, the dried samples were heated at 350°C for 2 hours, and the amount of bound water was determined based on the weight change.

Table 1. R^3 model mix design

Components	SCM	Portlandite		Deionized water	KOH	K_2SO_4	Calcite
Mass (g)	11.11	33.33		60.00	0.24	1.2	5.56

3. Results and discussions

3.1 Oxide and phase composition

Table 2 shows the chemical composition of the oven-dried ETP sludge obtained from the ICPMS analysis. It contains predominantly CaO, Fe_2O_3, Al_2O_3, and SiO_2, which, upon processing like calcination, can exhibit cementitious properties (Flegar et al., 2020). European standard for assessing fly ash (EN 450-1, 2012) suggests the sum of SiO_2, Fe_2O_3, and Al_2O_3 to be greater than or equal to 70 % for ensuring adequate pozzolanic reaction when used in concrete. In the sludge sample studied in the current work, the sum of these oxides was equal to 74%. The sludge samples can be a potential SCM if the phases present are reactive, i.e., in an amorphous form. Other oxides, including heavy metal oxide like lead oxide, are also present in the sludge sample but only in very small quantities.

Table 2. ICPMS analysis of dried sludge

Chemical composition (%)										
CaO	SiO_2	Fe_2O_3	Al_2O_3	Mn_2O_3	PbO	MgO	Na_2O	P_2O_5	CuO	ZnO
19.59	9.32	39.25	25.63	0.28	2.46	2.15	0.86	1.26	0.08	0.12

Figure 3 shows the XRD pattern of oven-dried and also calcined sludges under different cooling conditions. The main crystalline phases of oven-dried sludge were hematite, fayalite, calcite, gibbsite, and quartz. Hematite and gibbsite are highly visible in furnace-cooled samples, which also contain some amount of calcite. The XRD pattern of the raw sludge indicates it contains mostly non-reactive minerals (crystalline phases). However, some of the crystalline peaks observed in the raw sample disappear, or their peaks decrease in intensity in the case of calcined samples. In the case of samples cooled by spreading on a plate, the intensity of peaks corresponding to hematite and gibbsite decreased, whereas quartz peaks have completely disappeared. This may indicate the potential amorphization of quartz, thereby giving rise to small amorphous humps in the pattern. However, a more significant reduction in the intensity of the crystalline peaks can be seen in the water-quenched samples. New phases, such as talc, appeared through water quenching. Phases like fayalite and gibbsite have completely disappeared. The existing peaks are broader, indicating a higher degree of amorphous content. This means the water-quenched samples may show higher reactivity than other samples as the amorphous content has been proven to show greater reliability in predicting the activity of supplementary cementitious materials (Walker & Pavía, 2011).

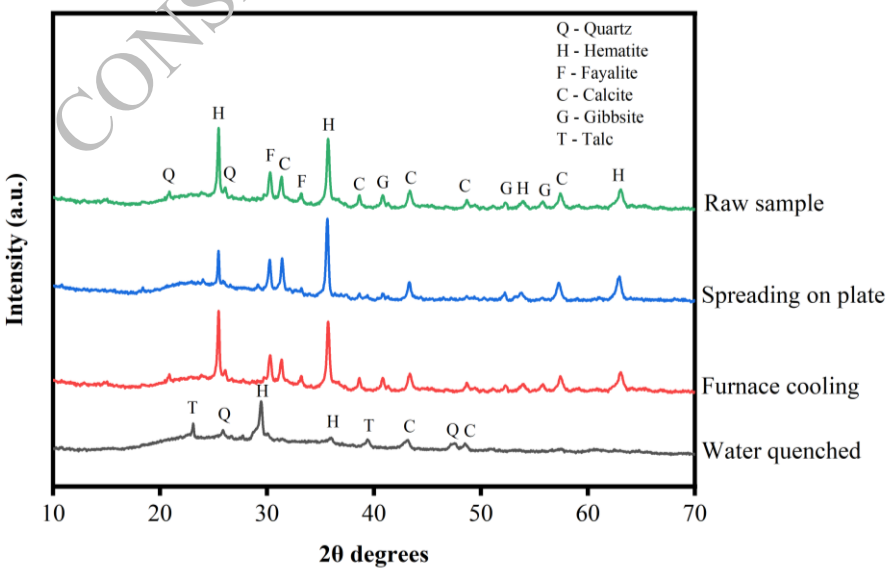

Figure 3. X-ray diffraction patterns of samples subjected to different cooling regimes

3.2 Particle size distribution under different cooling conditions

The reactivity of the SCM is found to be significantly affected by its grain size distribution (Bentz et al., 1999; Frigione & Marra, 1976; Wang et al., 1997). As shown in Figure 4, the raw ETP sample has a mean particle size of *45.7*µm, which was reduced to 30.1µm when samples were cooled by spreading on a plate. On the other hand, water-quenched samples had a much smaller mean particle diameter of only 22.3µm. Hence, water quenching is more beneficial as it results in a finer particle size distribution of the sludge, leading to better reactivity (Simonsen et al., 2020). The slow cooling in the furnace method resulted in bigger lumps; hence, its particle size distribution could not be measured. It was ground to a particle size similar to the water-quenched samples before performing the reactivity test.

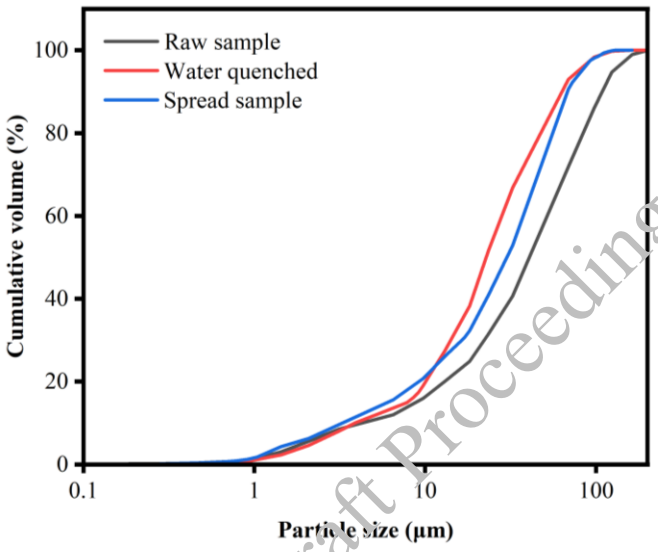

Figure 4. Variation of particle size distribution

3.3 Reactivity of sludges subjected to different methods of cooling

Figure 5 shows the results of the R3-calorimetry test. The water-quenched samples showed the best reactivity amongst others, with a higher amount of heat released after seven days. After seven days, the cumulative heat from hydration was smallest in the furnace-cooled sample (4 J/g) and highest in the sample that was water-quenched (120 J/g). This can be attributed to the higher content of reactive amorphous phases in water-quenched samples (Sivakumar et al., 2021), as seen in the XRD results. As seen in Figure 3, compared to other cooling methods, many crystalline peaks have disappeared, while some of the crystalline peaks have been significantly reduced (calcite and quartz), indicating that the water-quenched samples may have more amorphous content. It is been observed that the slope of the cumulative curve is sharpest for the water-quenched sample, indicating that the reaction is fastest in the water-quenched sample.

Figure 6 shows the bound water content of different systems which is in line with the calorimeter results. It was found that the bound water content (4.01%) was higher for the water-quenched system as it possessed a high amount of hydrated compounds, which decomposed between 105 and 350°C. Compared to water-quenched samples, the bound water content value obtained for the sample cooled by spreading on the plate and by furnace cooling was only 1.89% and 0.23%, respectively. This, again, demonstrates the higher reaction rates of water quenching compared with the other samples.

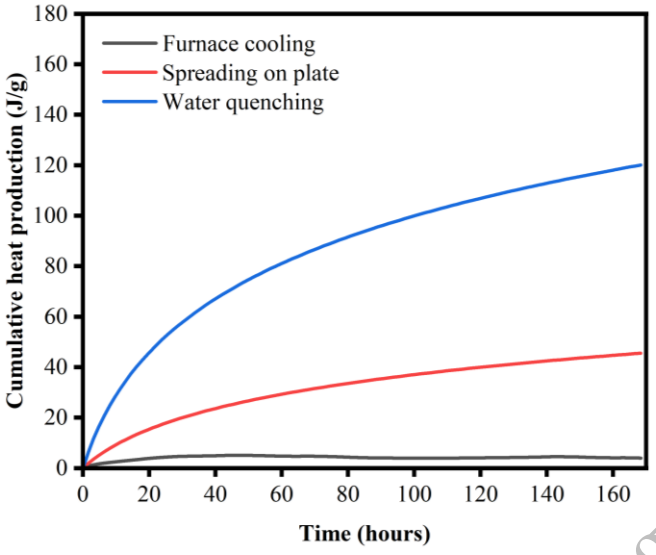

Figure 5. Heat of hydration obtained by R³ test using calorimetry

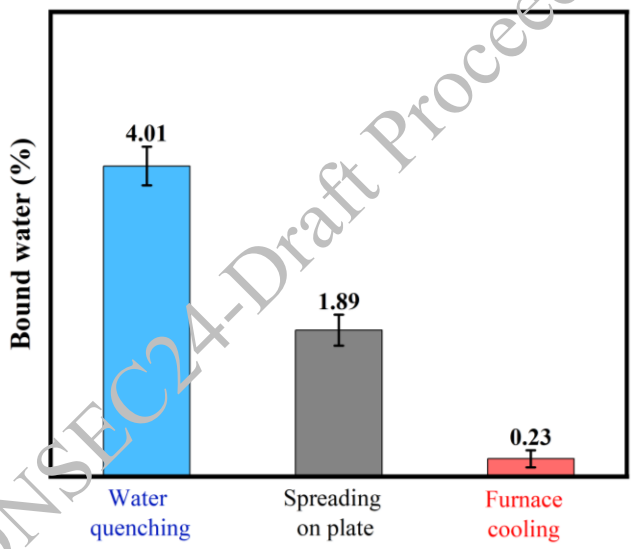

Figure 6. Bound water content obtained by the R³ test for reactivity

4. Conclusions

Due to the shortage of high-quality supplementary cementitious materials (SCMs) such as fly ash and blast furnace slag, there has been growing attention to a variety of moderately to low-reactive materials, including industrial sludges and incineration ashes. The current study evaluated the suitability of an effluent treatment plant (ETP) sludge obtained from a battery industry for producing SCMs. The oxide composition of the sludge confirms the presence of silica, alumina, and iron oxide in high quantities, thus suggesting that it can be used as a potential SCM. Heavy metals like lead are also present, but only in small amounts. The effect of different cooling regimes, namely, water quenching, spreading on a plate, and furnace cooling, on the reactivity of the ETP sludge was evaluated. The inspection of the X-ray diffraction pattern reveals that most of the crystalline peaks are reduced or entirely removed when calcined and cooled by water quenching. A higher amorphous hump is also visible after water quenching compared to other cooling methods. Also, water quenching resulted in a finer particle size distribution, while other cooling methods resulted in a coarser particle size distribution. This indicates that additional

processing, such as grinding, may be required for the slow-cooled samples. The reactivity of the sludge was assessed using R^3 calorimetry and the bound water method. Calorimetric analysis indicated that water quenching produced a higher cumulative heat release than other cooling methods. Bound water analysis showed that water quenching possessed a high amount of binder hydrates, again indicating the importance of water quenching while cooling the calcined sludge samples for producing reactive SCMs.

References

Adesina, A. (2020). Recent advances in the concrete industry to reduce its carbon dioxide emissions. *Environmental Challenges*, *1*, 100004. https://doi.org/10.1016/j.envc.2020.100004

Avet, F., Snellings, R., Alujas Diaz, A., Ben Haha, M., & Scrivener, K. (2016). Development of a new rapid, relevant and reliable (R3) test method to evaluate the pozzolanic reactivity of calcined kaolinitic clays. *Cement and Concrete Research*, *85*, 1–11. https://doi.org/10.1016/j.cemconres.2016.02.015

Benhelal, E., Shamsaei, E., & Rashid, M. I. (2021). Challenges against CO2 abatement strategies in cement industry: A review. *Journal of Environmental Sciences*, *104*, 84–101. https://doi.org/10.1016/j.jes.2020.11.020

Bentz, D. P., Garboczi, E. J., Haecker, C. J., & Jensen, O. M. (1999). Effects of cement particle size distribution on performance properties of Portland cement-based materials. *Cement and Concrete Research*, *29*(10), 1663–1671. https://doi.org/10.1016/S0008-8846(99)00163-5

Bullard, R. A. (2015). Effect of cooling rates on mineralization in Portland cement clinker. University of Missouri-Kansas City.

Das, B., Prakash, S., Reddy, P. S. R., & Misra, V. N. (2007). An overview of utilization of slag and sludge from steel industries. *Resources, Conservation and Recycling*, *50*(1), 40–57. https://doi.org/10.1016/j.resconrec.2006.05.008

Dolenec, S., Šter, K., Borštnar, M., Nagode, K., Ipavec, A., & Žibret, L. (2020). Effect of the Cooling Regime on the Mineralogy and Reactivity of Belite-Sulfoaluminate Clinkers. *Minerals*, *10*(10), 910. https://doi.org/10.3390/min10100910

European Standard. EN 450-1:2012 Fly Ash for concrete –Part 1: Definition, Specifications and Conformity Criteria; European Committee for Standardization: Brussels, Belgium, 2012

Flegar, M., Serdar, M., Londono-Zuluaga, D., & Scrivener, K. (2020). Regional Waste Streams as Potential Raw Materials for Immediate Implementation in Cement Production. *Materials*, *13*(23), 5456. https://doi.org/10.3390/ma13235456

Frigione, G., & Marra, S. (1976). Relationship between particle size distribution and compressive strength in portland cement. *Cement and Concrete Research*, *6*(1), 113–127. https://doi.org/10.1016/0008-8846(76)90056-9

Hong, H., Fu, Z., & Min, X. (2001). Effect of cooling performance on the mineralogical character of Portland cement clinker. *Cement and Concrete Research*, *31*(2), 287–290. https://doi.org/10.1016/S0008-8846(00)00445-2

Juenger, M. C. G., Snellings, R., & Bernal, S. A. (2019). Supplementary cementitious materials: New sources, characterization, and performance insights. *Cement and Concrete Research*, *122*, 257–273. https://doi.org/10.1016/j.cemconres.2019.05.008

Li, X., Snellings, R., Antoni, M., Alderete, N. M., Ben Haha, M., Bishnoi, S., Cizer, Ö., Cyr, M., De Weerdt, K., Dhandapani, Y., Duchesne, J., Haufe, J., Hooton, D., Juenger, M., Kamali-Bernard, S., Kramar, S., Marroccoli, M., Joseph, A. M., Parashar, A., … Scrivener, K. L. (2018). Reactivity tests for supplementary cementitious materials: RILEM TC 267-TRM phase 1. *Materials and Structures*, *51*(6), 151. https://doi.org/10.1617/s11527-018-1269-x

Melchor-Martínez, E. M., Macias-Garbett, R., Malacara-Becerra, A., Iqbal, H. M. N., Sosa-Hernández, J. E., & Parra-Saldívar, R. (2021). Environmental impact of emerging contaminants from battery waste: A mini review. *Case Studies in Chemical and Environmental Engineering*, *3*, 100104. https://doi.org/10.1016/j.cscee.2021.100104

Mohammadi, A., & Ramezanianpour, A. M. (2023). Investigating the environmental and economic impacts of using supplementary cementitious materials (SCMs) using the life cycle approach. *Journal of Building Engineering*, *79*, 107934. https://doi.org/10.1016/j.jobe.2023.107934

Ono, Y. (1981). Microscopical observation of clinker for the estimation of burning condition, grindability and hydraulic activity. In Proceedings of the Third International Conference on Cement Microscopy (pp. 198-210). Houston, Texas: International Cement Microscopy Association.

Pisciotta, M., Pilorgé, H., Davids, J., & Psarras, P. (2023). Opportunities for cement decarbonization. *Cleaner Engineering and Technology*, *15*, 100667. https://doi.org/10.1016/j.clet.2023.100667

Sazonova, N. A., & Skripnikova, N. K. (2015). Using the low-temperature plasma in cement production. *Journal of Physics: Conference Series*, *652*, 012063. https://doi.org/10.1088/1742-6596/652/1/012063

Scrivener, K. L., John, V. M., & Gartner, E. M. (2018). Eco-efficient cements: Potential economically viable solutions for a low-CO2 cement-based materials industry. *Cement and Concrete Research*, *114*, 2–26. https://doi.org/10.1016/j.cemconres.2018.03.015

Simonsen, A. M. T., Solismaa, S., Hansen, H. K., & Jensen, P. E. (2020). Evaluation of mine tailings' potential as supplementary cementitious materials based on chemical, mineralogical and physical characteristics. *Waste Management*, *102*, 710–721. https://doi.org/10.1016/j.wasman.2019.11.037

Sivakumar, P. P., Matthys, S., De Belie, N., & Gruyaert, E. (2021). Reactivity Assessment of Modified Ferro Silicate Slag by R3 Method. *Applied Sciences*, *11*(1), 366. https://doi.org/10.3390/app11010366

Skibsted, J., & Snellings, R. (2019). Reactivity of supplementary cementitious materials (SCMs) in cement blends. *Cement and Concrete Research*, *124*, 105799. https://doi.org/10.1016/j.cemconres.2019.105799

Snellings, R., Suraneni, P., & Skibsted, J. (2023). Future and emerging supplementary cementitious materials. *Cement and Concrete Research*, *171*, 107199. https://doi.org/10.1016/j.cemconres.2023.107199

Walker, R., & Pavía, S. (2011). Physical properties and reactivity of pozzolans, and their influence on the properties of lime–pozzolan pastes. *Materials and Structures*, *44*(6), 1139–1150. https://doi.org/10.1617/s11527-010-9689-2

Wang, A., Zhang, C., & Zhang, N. (1997). Study of the influence of the particle size distribution on the properties of cement. *Cement and Concrete Research*, *27*(5), 685–695. https://doi.org/10.1016/S0008-8846(97)00060-4

Xia, Y., Liu, Y., Wang, L., Song, Z., Sun, C., Zhao, Y., Lu, S., & Yan, J. (2023). Value-added recycling of sludge and sludge ash into low-carbon construction materials: Current status and perspectives. *Low-Carbon Materials and Green Construction*, *1*(1), 23. https://doi.org/10.1007/s44242-023-00023-5

Microstructural Performance of Lightweight Volcanic Aggregates as an Internal Curing Material for High-Performance Concrete

D. Dashti[1], A. Joseph[2], J. Chakkamalayath[3*] and Z. Awadh[4]

[1]Kuwait Institute for Scientific Research, Kuwait
Email: ddashti@kisr.edu.kw
[2]Kuwait Institute for Scientific Research, Kuwait
Email: ajoseph@kisr.edu.kw
[3]Kuwait Institute for Scientific Research, Kuwait*
**CoE on Technologies for Low-Carbon and Lean Construction (TLC2), IIT Madras, India (Present)*
Email: jchakkolath@gmail.com
[4]Kuwait Institute for Scientific Research, Kuwait
Email: zawadh@kisr.edu.kw

[*]Corresponding author

ABSTRACT

Internal curing for high-performance concrete with a low w/c ratio will help the rational use of water without wastage along with reducing autogenous shrinkage associated with the cement hydration and early age micro cracking, especially in countries where large quantities of "costly" desalinated water were engaged for external curing of concrete structures. Lightweight volcanic aggregates (LWVA), one of the prospective internal curing materials available in the Gulf Regions have not been explored completely. The comparative performance in the modifications of the microstructure of concrete samples with LWVA as a source for internal curing and conventional external water curing is highlighted in this paper. The microstructural analysis of high-performance concrete mixes prepared with pre-wetted lightweight volcanic aggregates (LWVA) of average size 10 mm and absorption capacity of 12% were studied through gas adsorption, X-ray diffraction (XRD), and FT-IR spectroscopy after 28 days of curing in air and water. The N_2 adsorption analysis confirmed that the incorporation of internal curing materials produced more mesoporous cement hydration products by effectively releasing water during cement hydration. XRD and FT-IR analysis showed the use of LWVA as an internal curing material caused a noticeable decrease in the formation of carbonation products as it restricts the formation of calcite by competing with pozzolanic reactions. The higher amount of chemically bounded water in LWVA incorporated samples was observed in FT-IR analysis due to the formation of more hydration products.

KEYWORDS*: FT-IR analysis, Gas adsorption analysis, Gulf region, mesoporous, X-Ray diffraction.*

1. Introduction

The strength and durability of concrete are affected by the effectiveness of the curing process of concrete. Curing keeps the concrete saturated and replenishes the moisture content to enhance the cement hydration process. However, low water to cement ratio in special purpose concretes, such as high-performance concrete (HPC) and ultra-HPC with supplementary cementitious materials like metakaolin (MK) and silica fume (SF), lack enough water molecules for the curing process to complete, hence resulting in chemical and drying shrinkage and early age micro cracking (Ignon et al (2017), (RILEM TC 196-ICC, (2007), ACI 308R (2016), Askar et al (2017). Conventional curing procedures are insufficient to solve these limitations, and therefore several methods of internal curing have been used to facilitate the hydration process (De Sensale and Goncalves (2014)). Internal curing materials

(ICMs) are promising solutions, especially for mitigating the early-age cracking and to provide effective concrete curing to maintain the performance of concrete structures, especially in countries like Kuwait, experiencing high ambient temperature and low relative humidity. Studies have shown that lightweight aggregates have high porosity with more water absorption capacity and has a density less than normal aggregates (Hamzah et al (2022)). The high absorption capacity of lightweight volcanic aggregates (LWVA) can significantly facilitate the release of moisture to concrete for internal curing. Even though several studies have reported about the advantage of using LWA in providing internal water, the studies on using LWVA as an ICM are limited. The void system of pre-saturated LWVA is filled with water, which can promote more hydration by desorbing the internal water and effectively maintaining the internal humidity (Cavalline et al (2019)). Therefore, regionally available pre-wetted lightweight volcanic aggregate (LWVA) obtained from Saudi Arabia was used as an internal curing material in this study, as it helps reduce the water evaporation from concrete surfaces and helps in water retention (Mousa et al., (2015)). A comparative evaluation of the concrete mixes containing LWVA and control mixes was conducted to study their effect on the microstructural development under air and water curing conditions.

2. Materials

The materials required for the preparation of high-performance concrete, including ordinary Portland cement (OPC), washed sand, normal coarse aggregates (NCA), and superplasticizer (SP) were collected from the local market**.** The complete characterization of the raw materials were conducted. The lightweight volcanic aggregate (LWVA) with a maximum size of 10 mm, selected as an internal curing material was imported from Super Burkhani Factory, Saudi Arabia. The mineralogical analysis of normal coarse aggregate (NCA) showed reasonable amounts of calcite ($CaCO_3$), along with Forsterite ($(Mg_{0.902}Fe_{0.098})\ (SiO_4)$), and Chrysotile ($Mg_3\ (Si_{2-x}O_5)\ (OH)_{4-4x}$). Washed sand contains only quartz (SiO_2). Anorthite ($(Ca_{0.86}Na_{0.14})\ (Al_{1.84}Si_{2.16}O_8)$), Forsterite ($(Mg_{1.635}Fe_{0.365})\ (SiO_4)$) and Albite ($(Na_{0.499}Ca_{0.491})\ (Al_{1.488}Si_{2.506})\ O_8$) were identified as major mineralogical phases in LWVA. The absorption and desorption properties of LWVA were determined according to ASTM C1761-17 as it is considered as the preliminary and vital step in the design of concrete mixes with ICMs.

3. Mix Design

The mix design of high-performance concrete with ICMs are based on the principle that the volume of chemical shrinkage is compensated with retained water from internal curing. Therefore, the mix proportioning with LWVA was carried out based on the following formula (1) suggested by earlier researchers (Bentz et al (2005), Montenari et al (2007)).
Accordingly, the mass of LWVA required is calculated using the formula,

$$M_{LWVA} = (C_f \times Cs \times \alpha_{max}) / (S \times \Phi_{LWVA}) \quad (1)$$

Where, M_{LWVA} = mass of LWVA in kg/m^3 in a dry state; C_f = cement content in kg/m^3; Cs = chemical shrinkage of cement (ml of water / g of cement), and varies from 0.06-0.08; α_{max} = expected maximum degree of hydration which is equal to 1 for a w/c of more than 0.36. For a w/c of less than 0.36, as in our case, it is equal to (w/c)/(0.36); S = degree of saturation expressed as a function of absorption; Φ_{LWVA} = absorption capacity of LWVA (kg of water/kg of dry LWVA). In proportioning of concrete with LWVA for internal curing, a volume of normal weight aggregate was replaced with an equal volume of LWVA, according to ASTM C1761-17. Accordingly, about 200 kg/m^3 of NCA was replaced with LWVA.
High performance concrete mix was designed for a strength of 45 MPa. The influence of LWVA on the concrete properties was evaluated by preparing the mix design for the control mix and test mixes. Accordingly, the mixes were designated as follows: Mix 1- C35 - Control mix with 0.35 w/c ratio; Mix 2 - C35LWVA - mix with LWVA at 0.35 w/c. A two-stage mixing procedure was adopted during the preparation of mixes with LWVA (Babu et al (2014), Awadh et al (2021)). In the case of mix with

LWVA, pre-soaking was done for 24 hours so that a maximum degree of saturation was achieved. Two different curing methods, water curing and air curing were adopted in the present investigations.

4. Experimental Methods

Samples for microstructural analysis were collected after 28 days of curing. The microstructural features of different HPC mixes were investigated through X-ray diffraction analysis, FT-IR analysis and Gas (N_2) adsorption analysis. The samples for FTIR analysis and XRD were prepared by taking special care to reduce the effects of aggregates by carefully removing the aggregates by sieving the crushed samples before grinding them to fine powder.

5. Results and Discussion

5.1 Characterization of Internal Curing Materials

The physical properties of normal coarse aggregate (NCA) and LWVA were determined and the test results are given in Table 1. The sieve analysis of LWVA samples was carried out according to ASTM C136 and ASTM C330 and the results (Figure 1) were compared with the grading requirements given in ASTM C1761. The grading curve shown in Figure 1 confirms that the sample lies in between the lines of the lower and upper grading limits indicating that the sample was well graded. The desorption property of LWVA showed that it can be used as an ICM as the desorption was 94.03%, which exceeds the limiting value of 85%.

Table 1. Physical Properties of NCA and LWVA

Property	NCA (10 mm)	LWVA (10 mm)
Percentage of Clay lumps (%) (ASTM C142)	0.12	0.23
Fineness Modulus (ASTM C136)	5.94	5.82
Materials Finer than 75-µn (No. 200) sieve in Mineral Aggregate by Washing % (ASTM C117)	-	0.8
Bulk Density (kg/m^3) ASTM C29	1548	731.4
Specific Gravity (OD) (ASTM C127)	2.669	1.512
Specific Gravity (SSD) (ASTM C127)	2.689	1.7
Water Absorption (%) (ASTM C127)	0.77	12.47
Los Angele's Abrasion test (% loss) ASTM C131	19.7	33.76

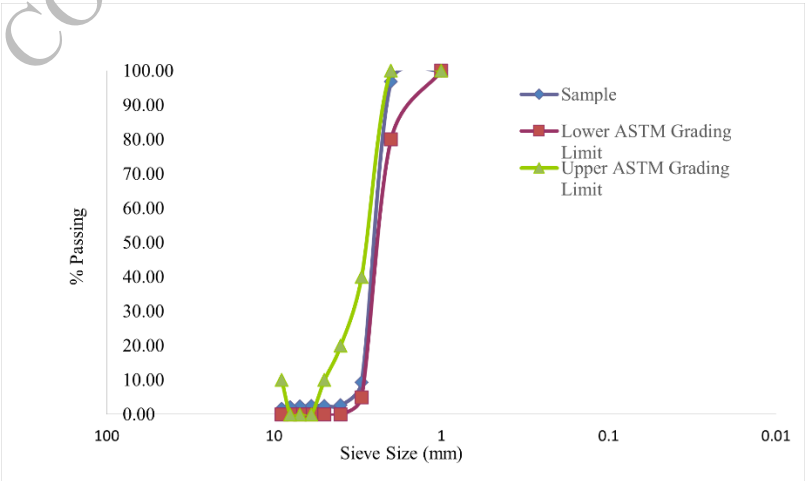

Figure 1. Sieve analysis of LWVA samples.

5.2 FT-IR Analysis

FT-IR transmission spectra were studied by Shimadzu-IR Tracer-100 spectrometer by Attenuated Total Reflection (ATR) technique in the scan range of 400–4000 cm^{-1} for the concrete mixes after 28 days of curing. The samples absorb IR radiation of definite wavelength depending on the chemical nature of the molecular bonds present. FT-IR can be used to study the vibrational nature of bonds present in amorphous as well as crystalline samples. Figure 2 shows the ATR spectra of concrete specimens recorded after 28 days of curing under water and air conditions.

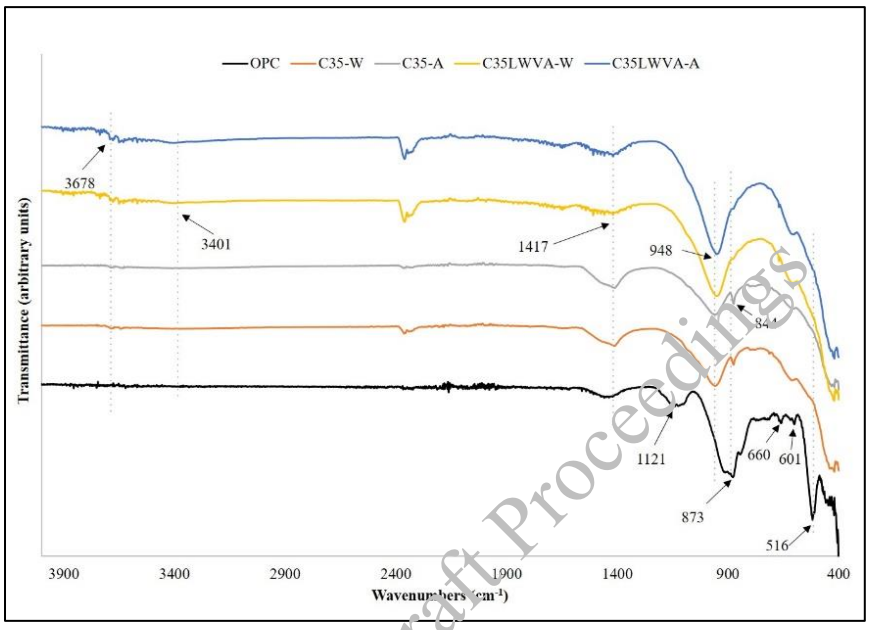

Figure 2. FT-IR spectra of OPC, Mix-1 and Mix-2 samples after 28 days of curing in water and air.

The strong bands observed approximately at 900 cm^{-1} (Si-O asymmetric stretching vibration, υ3), 516cm^{-1} (Si-O out-of-plane bending vibration, υ4), and 446 cm^{-1} (Si-O in-plane bending vibration, υ2) are the major vibrational bands observed in dry cement in the present experiments. The bands that appeared at 1121 cm^{-1} are due to S-O stretching vibrations (υ3) of SO_4^{2-} and the weak bands at 660 and 601 cm^{-1} are due to bending vibrations (υ2) of SO_4^{2-} present in the gypsum. Two distinct peaks at 1417 cm^{-1} (asymmetric Stretching, υ3 of -CO_3^{2-}) and a weak shoulder at approximately 844 cm^{-1}, corresponding to bending-out of plane vibrations of the $CaCO_3$ present both in dry cement and hydrated cement, arise from the reaction of atmospheric CO_2 with calcium hydroxide. The band at 3678 cm^{-1} is attributed to the OH from the $Ca(OH)_2$. The small broad bands appeared at 3402 cm^{-1} (overlapping stretching vibrations) and 1647 cm^{-1} (bending in-plane vibrations) of the –OH groups of free water molecules present in the cement (Askar et al (2017), ACI 308R (2016)). The changes in these vibrational bands during cement hydration will give valuable information about the extent of cement hydration.

A broader peak centred at 3401 cm^{-1} was more visible in the case of samples with LWVA (mix-2) indicating the presence of more water content in these samples. The asymmetric stretching vibrations (υ3) of CO_3^{2-} observed at 1417 cm^{-1} due to the formation of $CaCO_3$ by the reaction of $Ca(OH)_2$ with CO_2 present in the atmosphere. The intensity of this band is closely related to the ratio and extent of carbonation and this is important information in assessing the durability and longevity of concrete as carbonation can reduce the alkalinity and passivation of steel reinforcement leading to corrosion (Suzuki et al (1985), Chang and Chen (2006) and Fernandez-Carrasco and Vazques (2009)). The highest peak intensity of this band observed for C35-A shows these samples undergone more carbonation than other mixes. The weak shoulder band at 844 cm^{-1}, due to the out-of-plane bending vibrations of CO_3^{2-} shows the lowest degree of carbonation for the mixes with LWVA. The sulphate absorption bands (S-O stretching vibrations) observed at 1121 cm^{-1} due to the presence of gypsum in the OPC disappeared during the reaction with aluminate and ferrite phases in the course of cement hydration (Biricika and

Sarierb (2014)). The asymmetric stretching (υ3) vibration band of Si-O at 920 cm^{-1} in dry cement shifted towards a higher wavenumber (954 cm^{-1}) after cement hydration. Also, the relative intensities of Si-O out-of-plane bending vibrations (υ4, 517 cm^{-1}) and in-plane bending vibrations (υ1, 446 cm^{-1}) decreased drastically after 28 days of hydration indicate the polymerization of the crystalline silicate (SiO_4^{4-}) units to amorphous Si-O polymeric gel (Mollaha et al (2000)).

5.3 XRD Analysis

Figure 3 shows the X-ray diffraction analysis of concrete samples (C35 and C35LWVA) after 28 days of curing in water and air. No new phases were detected in both mixes other than quartz (SiO_2) from the aggregates, portlandite ($Ca(OH)_2$), calcite ($Ca(CO_3)$), a broad hump of C-S-H between 26 and 30 degrees two theta along with other crystalline peaks of dolomite ($CaMg(CO_3)_2$), negligible amount of ettringite ($Ca_6Al_2(SO_4)_3(OH)_{12}$ $26H_2O$), C_3S and C_2S depending on the curing conditions (Jumate and Manea (2011)).

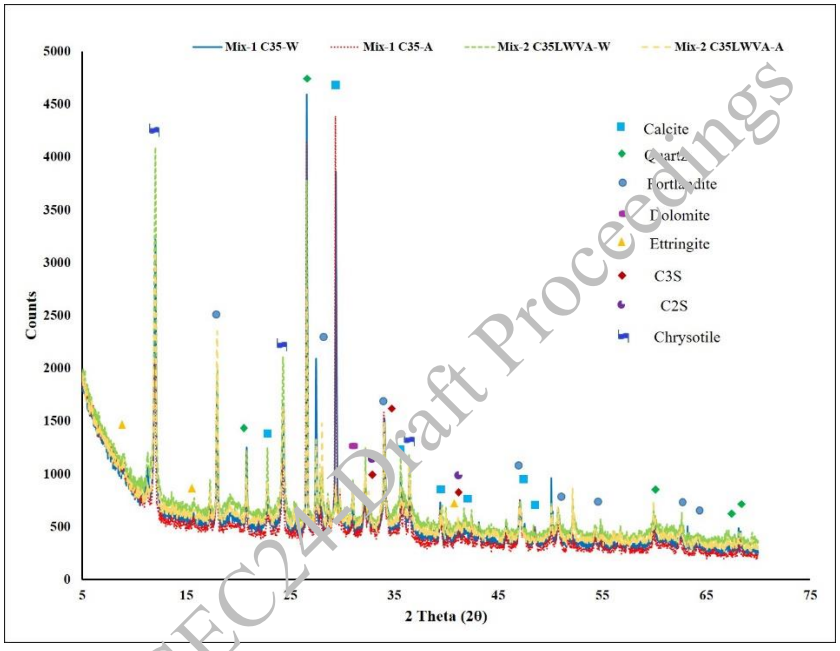

Figure 3. XRD analysis of Mix-1 and Mix-2 concrete samples after 28 days of curing in water and air.

After 28 days of curing, surprisingly the samples with LWVA show more calcium hydroxide (CH) than the control mix. Among the two LWVA mixes, the sample cured under air has more calcium hydroxide (CH) than that cured under water. This indicates that the LWVA added acts as a water releasing agent and effectively promotes the cement hydration process (Al Saffar et al (2019)). In Mix-2, LWVAs act both as a pozzolanic material in the early stages of cement hydration by reacting with CH forming CSH and in the later stages the remaining LWVAs behave like an effective water releasing material. Also, the highest amount of calcite was detected in the control sample cured under air conditions due to the reaction of CH with atmospheric CO2. Also, the presence of LWVA restricts the formation of calcite by competing with pozzolanic reactions in Mix-2.

5.4 Microstructural Analysis by Nitrogen Adsorption

The pore structure analysis of concrete mixes containing ICMs was evaluated using ASAP 2020 Plus. The samples were subjected to degassing/outgassing at 60 ºC for 2 hours under a high vacuum to remove all physically bound materials from the adsorbent surface before analysis, and they were weighed before and after degassing/outgassing (Snoeck et al (2015), Rouquerol et al (1994)). The multilayer surface adsorption model developed by Brunauer, Emmett and Teller (BET) (Gregg and Sing (1982)), Brunauer et al (1938)), an extension of Langmuir theory (Langmuir, (1916)) for monolayer to multilayer adsorption was used to compare the surface area of different samples as shown in Table 2.

Table 2. BET surface area (m^2/g) of concrete specimens cured under water and air for 28 days.

Curing Conditions (28 Days)	Control (C35)	Sample with LWVA (C35 LWVA)
Water	5.5598	8.295
Air	2.8889	6.7815

Table 2 shows the BET surface area of concrete samples after 28 days of curing in both water and air. Incorporating internal curing materials, increases the BET surface area compared to control samples for both water and air cured mixes, due to the formation of more hydration products. Also, in the case of mix-2 with LWVA, a reduction in the difference between the BET surface areas of air cured and water cured samples was observed compared to the control mix. This indicates the internal curing effects of LWVA for the formation of more cement hydration products.

The adsorption-desorption isotherms of concrete specimens (C35 and C35LWVA) after 28 days of curing under water and air are shown in Figure 4. The shape of the nitrogen adsorption isotherms of all the samples represent type II isotherms with H4 hysteresis loop according to IUPAC classification (Brunauer et al., (1940)), characteristics of mesoporous and macroporous materials with limited uptakes through narrow slit pores. It can be observed from Figure 4 that there is a gradual increase in N_2 adsorption isotherm after point 'A' due to the formation of a multilayer where the thickness of the adsorbed layer increased. However, a sudden rise in the adsorption isotherm was observed after point 'B', as a result of the well-known capillary pore condensation phenomenon (Kupwade-Patil et al (2016)). The N_2 adsorption isotherms for the sample containing LWVA (C35LWVA) have higher adsorption capacity compared to the control sample (C35) which indicates that the use of LWVA increased the porosity by the formation of large mesopores in those concrete samples.

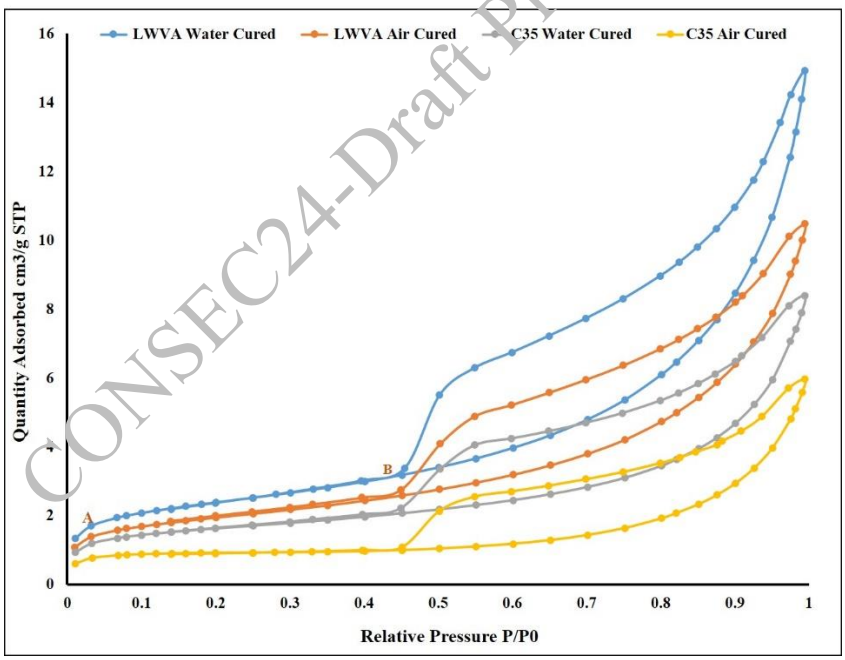

Figure 4. Adsorption-desorption isotherms of concrete samples after 28 days of curing in air and water.

A well-hydrated cement sample with a refined pore structure is typically more resistant to the ingress of harmful substances like chlorides and sulphates, which generally can enhance deterioration. The curing conditions significantly affect the hydration process and hence the formation of the resulting microstructure. This technique can be used to study the effects of different curing methods on the pore structure and surface area providing valuable information about the efficiency of the curing process.

6. Conclusions

The effects of Lightweight volcanic aggregates as an internal curing material on the microstructural properties of hardened concrete after 28 days of curing under water and air were investigated using Nitrogen adsorption, X-ray diffraction, and FT-IR analysis. Samples with LWVA have higher gas adsorption capacity than control samples indicating that the use of LWVA as an internal curing material increased the porosity by forming large mesopores in these concrete samples. The internal curing effect of the added LWVAs in Mix-2 caused a major reduction in the difference between the BET surface areas of the samples cured under water and air compared to the control mix. The X-ray diffraction analysis showed more calcium hydroxide (CH) in samples with LWVAs than in the control mix, which indicates that the LWVAs act as a water releasing agent and effectively improve the cement hydration process. The formation of high amounts of calcite ($CaCO_3$) was noticed in the case of the control mix cured under air due to the reaction of atmospheric CO_2 with the CH formed during cement hydration. The presence of LWVAs in mix-2 restricts the formation of calcite by competing with pozzolanic reaction, and by actively keeping the concrete mixture always moist and promotes the cement hydration rather than calcite formation. The FT-IR spectra showed a prominent broader peak centred at 3401 cm^{-1} for samples with LWVA indicating the presence of more chemically bounded water in these mixes. Also, the highest peak intensity of the asymmetric stretching vibrations ($\upsilon 3$) at 1417 cm^{-1} was observed for the control mix cured under air indicating the formation of more carbonated products in these mixes which was in line with the XRD results. Further, the polymerisation of crystalline silicate units to amorphous Si-O polymeric gel was confirmed by the shift in the Si-O stretching and bending vibrations towards a higher wavenumber compared to unhydrated cement. Thus the added LWVAs in HPC mixes effectively promote cement hydration by acting as a water releasing agent (ICM) at the expense of total porosity.

Acknowledgements

This study, EU130K, was financially supported by Kuwait Institute for Scientific Research (KISR). The authors are grateful to the Program Manager, Eng. Suad Al-Bahar, for the support extended during the study with lightweight volcanic aggregates. The authors also wish to thank the supporting staff at the Concrete and Material Testing Laboratory for the assistance provided while conducting experiments.

References

ACI 308R. (2016). "Guide to External Curing Concrete". ACI Manual of Concrete Practice, American Concrete Institute, Farmington Hills, MI.

Al Saffar, D. M. Al Saad, A. J. K. and Tayeh, B. A. (2019) "Effect of internal curing on behaviour of high performance concrete: An overview", Case Stud. Constr. Mat., 10, e00229.

Askar, L. K. et al. (2017). "Properties of ultra-high performance fiber concrete (UHPFC) under different curing regimes", Int. J. Civil Eng. Technol. 8 (4), 965 – 974.

ASTM C136. (2019). Standard Test Method for Sieve Analysis of Fine and Coarse Aggregates, ASTM International: Pennsylvania, USA.

ASTM C330/C330M. (2017). Standard Specification for Lightweight Aggregates for Structural Concrete, ASTM International: Pennsylvania, USA.

ASTM C1761-17 (2017) Standard Specification for Lightweight Aggregate for Internal Curing of Concrete, ASTM International: Pennsylvania, USA.

Awadh, Z. Dashti, D. Al-Bahar, S. J. Chakkamalayath. (2021). "Using the moisture retention property of recycled coarse aggregates for self-curing of high performance concrete", ICCEN conference, Singapore, Nov 19–21.

Babu, V.S. Mullick, A.K. Jain, K.K. Singh, P.K. (2014) Strength and Durability Characteristics of High Strength Concrete with Recycled Aggregate– Influence of Mixing Techniques. J. of Sustain. Cem.-Based Mater, 3(2), 88–110.

Bentz, D.P. Lura, P. and Roberts, J. W. (2005). "Mixture proportioning for internal curing", Concrete International, 35–40.

Biricika, H. and Sarierb, N. (2014). "Comparative Study of the Characteristics of Nano Silica–, Silica Fume– and Fly Ash–Incorporated Cement Mortars", Materials Research, 17(3), 570-582, DOI:http://dx.doi.org/10.1590/S1516-14392014005000054.

Brunauer, S. Deming, L. S. Deming, W. E. and Teller, E. (1940). "On a Theory of the van der Waals Adsorption of Gases", J. Am. Chem. Soc., 62, 1723-1732.

Brunauer, S. Emmett, P. H. and Teller, E. (1938). "Adsorption of Gases in Multimolecular Layers", J. Am. Chem. Soc., 60, 309-319.

Cavalline, T.L. Tempest, B.Q. Leach, J.W. Newsome, R.A. Loflin, G.D. and Fitzner, M.J. (2019). Internal Curing of Concrete Using Lightweight Aggregate, Technical Report, North Carolina University, United states.

Chang C-F and Chen J-W. (2006). "The experimental investigation of concrete carbonation depth". Cement and Concrete Research, 36, 1760-1767, http://dx.doi.org/10.1016/j. cemconres.2004.07.025.

De Sensale, G.R. and Goncalves, A.F. (2014). "Effects of Fine LWA and SAP as Internal Water Curing Agents", International Journal of Concrete Structures and Materials, 8(3), pp.229–238.

Fernández-Carrasco L and Vázquez E. (2009). "Reactions of fly ash with calcium aluminate cement and calcium sulphate. Fuel", 88, 1533-1538. http://dx.doi.org/10.1016/j. fuel.2009.02.018.

Gregg, S. J. and Sing, K.S.W. (1982). Adsorption, surface area and porosity, Academic Press Inc.: London – New-York.

Hamzah N. Mohd Saman H. Baghban MH. Mohd Sam AR. Faridmehr I. Muhd Sidek MN. Benjeddou O. and Huseien GF. (2022). "A Review on the Use of Self-Curing Agents and Its Mechanism in High-Performance Cementitious Materials. Buildings", 12(2):152. https://doi.org/10.3390/buildings12020152.

Ignon, A. Snoeck, D. Dubruel, P. Vlierberghe, S. V. and Belie, N. De. (2017). "Crack Mitigation in Concrete: Superabsorbent Polymers as Key to Success?" (Review). Materials. 10, 237; doi:10.3390/ma10030237.

Jumate, E. and Manea, D. L. (2011). "X-ray diffraction (XRD) study of hydration processes in the portland cement", J. Appl. Eng. Sci., 1(1), 79–86.

Kupwade-Patil, K. Al-Aibani, A. Abdulsalam, M. F. Mao, C. Rumajdad, A. Palkovic, S. D. and Büyüköztürk, O. (2016). "Microstructure of cement paste with natural pozzolanic volcanic ash and Portland cement at different stages of curing", Constr. Build. Mater, 113, 423-441.

Langmuir, I. (1916). "The Constitution and Fundamental Properties of Solids and Liquids", Part I. Solids. J. Am. Chem. Soc., 38, 2221-2295.

Mollaha, M. Y. A. Yub, W. Schennachb, R. and Cockeb, D. L. (2000). "A Fourier transform infrared spectroscopic investigation of the early hydration of Portland cement and the influence of sodium lignosulfonate", Cem Concrete Research, 30, 267–273.

Montenari, L. Suraneni, P. and Weiss, J. (2017). "Accounting for water stored in superabsorbent polymers in increasing the degree of hydration and reducing the shrinkage", Advan. in Civil Eng. Mater, 6(1): 20170098, DOI:10.1520/ACEM20170098.

Mousa, M. I. Mahdy, M. G. Abdel-Reheem, A. H. and Yehia, A. Z. (2015). "Mechanical properties of self-curing concrete (SCUC)", HBRC Journal, 11, 311–320.

RILEM TC 196-ICC: State of the Art Report 41, June 2007.

Rouquerol, J. Fairbridge, C. Everett, D. Haynes, J. Pernicone, N. Ramsay, J. Sing, K. and Unger, K. (1994). "Recommendations for the Characterization of Porous Solids", Pure and Applied Chemistry, 66, 1739.

Snoeck, D. Velasco, L. F. Mignon, A. Van Vlierberghe, S. Dubruel, P. Lodewyckx, P. and De Belie, N. (2015). "The effects of superabsorbent polymers on the microstructure of cementitious materials studied by means of sorption experiments", Cem. Concr. Res., 7, 26-35.

Suzuki, K. Nishikawa, T. and Ito, S. (1985). "Formation and carbonation of C-S-H in water", Cem Concr Res 15, 213–224.

High Temperature Impact on Sustainable Fly-Ash-Based Geopolymer Mortar

Manali Rathee[1*] and Anurag Misra[2]

[1] *Indian Institute of Technology, Jammu, India*
Email: manali.rathee@iitjammu.ac.in
[2] *Indian Institute of Technology, Jammu, India*
Email: Anurag.misra@iitjammu.ac.in

[*]Corresponding author

ABSTRACT

Geopolymer is an environment-friendly material and can potentially reduce the construction industry's carbon footprint due to the bulk use of fly ash instead of Portland cement. However, heat curing of fly ash-based binder systems limits its use in field applications. Therefore, attempts are being made to add suitable additives to achieve hardening of the binder system at room temperature. Several combinations of materials have been tried to produce geopolymer mortars and geopolymer concretes which could be cured at room temperature. In the present study, the geopolymer mortars have been prepared with fly ash, Ground Granulated Blast-furnace Slag (GGBS), natural sand and different concentrations of alkaline activators. The mortar cubes of 50 mm size were prepared using the above combinations and they were cured in air at room temperature for 28 days. The control mortar specimen was prepared using OPC and they were cured in water for 28 days.

After 28 days, the specimens were exposed to high temperatures varying from 200°C to 1000°C for one hour. The compressive strength and the weight loss of the specimens were evaluated after exposure to high temperatures (200°C to 1000°C) and compared with OPC mortars. The results show that the resistance of geopolymer mortar (GPM) against exposure to high temperature is better than the conventional OPC-based mortar. The compressive strength gets reduced by 44% in the case of GPM and 67% in the case of OPC-based mortar. X-ray diffraction (XRD) and Fourier Transform Infrared Spectroscopy (FTIR) have been used to study the changes in the bonding behaviour of C-A-S-H and N-A-S-H when exposed to high temperatures. These results indicated that the zeolite-like by-product of the N-A-S-H binder gel system in geopolymer mortar samples demonstrated superior stability at high temperatures as compared to OPC mortar.

KEYWORDS*: C**ompressive strength; Fly ash; Geopolymer; High temperature; Microstructure*

1. Introduction

Global cement production, projected at 4.4 billion cubic meters in 2021, is a major contributor to CO_2 emissions, with cement production responsible for 5-8% of global anthropogenic CO_2 emissions (Garside, 2022). The rising demand for construction materials due to urbanization is expected to increase these emissions further (Sarker, Haque and Ramgolam, 2013; Omer, Demirboga and Khushefati, 2015; Sattary and Thorpe, 2016; Singh, Sharma and Rathee, 2022). To address this, researchers are exploring low-carbon alternatives like geopolymers (Zhuang *et al.*, 2016; Scrivener, John and Gartner, 2018).
Geopolymers, derived from natural and industrial by-products such as metakaolinite, fly ash, and slag, are silicon-based inorganic binders formed through the reaction of silicates and aluminosilicates with alkaline activators (AbdulAleem and Arumairaj, 2011; Sharma *et al.*, 2022). The geopolymerization

process produces a polymeric structure with Si-O-Al and Si-O-Si bonds, making geopolymers a promising, environmentally friendly alternative to Portland cement (Dimas et al. 2009). They offer potential benefits in terms of durability and resistance to high temperatures (Karthik, Sudalaimani and Vijayakumar, 2017; Hassan, Arif and Shariq, 2019).

However, research on their performance, particularly under high temperatures, is limited. This study examines the impact of temperatures ranging from 200°C to 1000°C on geopolymer and OPC mortar samples, analyzing weight loss, compressive strength, and chemical changes using XRD and FTIR techniques to better understand their behavior.

2. Materials and methodology

2.1 Specification of materials

Class-F fly ash (FA) and Ground Granulated Blast-furnace Slag (GGBS) were used to prepare geopolymer mortars, with OPC serving as the control mix. The XRD patterns of FA, GGBS, and OPC are shown in Figures 1(a), 1(b), and 1(c), respectively. FA exhibited crystalline peaks corresponding to quartz (SiO_2) and mullite ($Al_6Si_2O_{13}$), with major quartz peaks at 2Θ = 27.093° and minor peaks at various angles. Mullite peaks appeared at 19.835°, 33.85°, 35.296°, and 58.877°. GGBS showed low-intensity peaks for calcite ($CaCO_3$) and a broad amorphous hump between 30° and 40°, indicating an absence of a crystalline phase. OPC displayed peaks for alite, belite, calcium sulfate, silicon oxide, and calcium silicon oxide. The FA and GGBS-based mortars were activated using a combination of sodium hydroxide (SH) and sodium silicate (SS) solutions, sourced from a local supplier in Jammu.

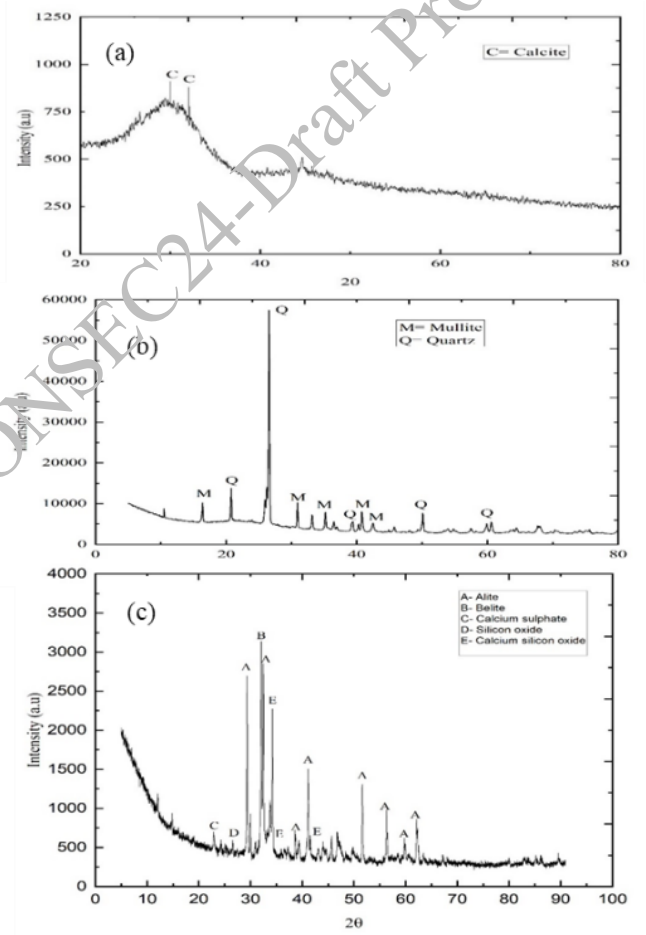

Figure 1. XRD of (a) Fly ash, (b) GGBS, (c) OPC


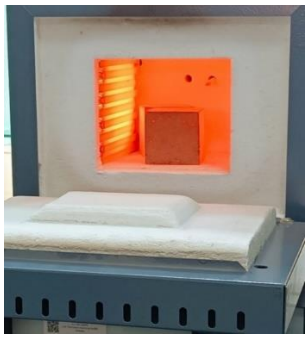

Figure 2. Muffle furnace

2.2 Preparation of OPC mortar and geopolymer mortar

Group Name and no	Mix designation	Mix description	Activator category	Silicate modulus (Si2O/ Na2O)	Alkali content (M)	Sand / Binder ration	Water or; Alkaline activators/ Binder ratio
Traditional mortar	OPC (Control)	100% OPC				1:3	0.4
Geopolymer mortar	GPM-10	80%FA+ 20%GGBS	SH+SS	2.5	10M	1:3	0.4
	GPM-8	80%FA+ 20%GGBS	SH+SS	2.5	8M	1:3	0.4
	GPM-6	80%FA+ 20%GGBS	SH+SS	2.5	6M	1:3	0.4

2.3 Exposure of the samples to high temperature

OPC mortar and GPM cubes (50mm³) were heated to 200°C, 400°C, 600°C, 800°C, and 1000°C after 28 days of curing, with subsequent cooling to room temperature. Mechanical and physical parameters of the heated samples were compared to those of unheated samples (27°C) and assessed against OPC at different temperatures.

3. Results and discussions

3.1 Weight loss of concrete specimens after high temperature exposure

When exposed to high temperatures, mortar samples lose moisture, leading to weight loss. GPM samples show less weight loss compared to OPC at 200°C due to their denser microstructure from geopolymerization. Between 25°C and 200°C, GPM loses less water, with peak water release occurring between 80-110°C.As temperatures rise to 1000°C, OPC samples exhibit a weight loss ranging from 4.5% to 14.3%, while GPM-10M samples show a range of 2.2% to 10.2%. This indicates that GPM is less affected by high temperatures than OPC, especially above 400°C. Additionally, lower molarity in GPM increases weight loss, with GPM-10M, 8M, and 6M showing losses of 10.17%, 12.63%, and 13.72% at 1000°C, respectively, due to reduced microstructural density. (Pan et al., 2009 ; Lee et al., 2014).

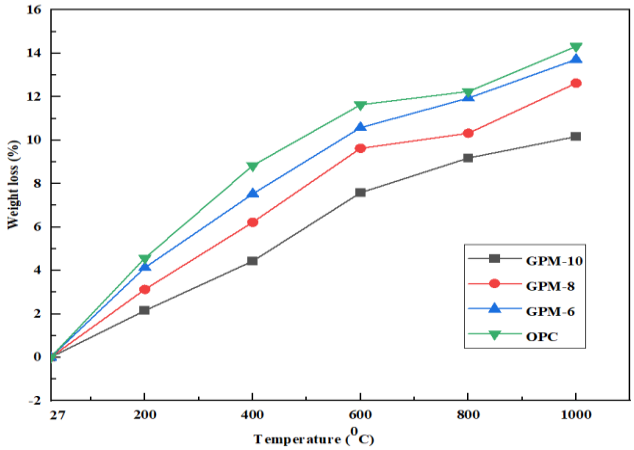

Figure 3. Weight loss in (%) of GPM and OPC mortar samples at different temperature

3.2 Compressive strength of mortar cubes at high temperature

The compressive strength of OPC and GPM samples exposed to temperatures from 200°C to 1000°C is shown in Figure 4. At room temperature (27°C), OPC mortar has a compressive strength of 34.72 MPa, which decreases to 11.19 MPa at 1000°C, representing a 67.77% reduction. For GPM samples, compressive strength increased by 7.61% for GPM-10 at 200°C due to ongoing polymerization. GPM-8 and GPM-6 showed similar trends with increases of 6.10% and 5.62%, respectively. However, at temperatures from 400°C to 1000°C, the compressive strength of GPM samples decreased. The reductions for GPM-10 were 12.3% at 400°C, 18.1% at 600°C, 36.5% at 800°C, and 44.9% at 1000°C (Figure-5). Despite these decreases, GPM samples retained better compressive strength compared to OPC mortar at higher temperatures due to their stable crystalline hydration products and high SiO_2 content (Qu *et al.*, 2020).

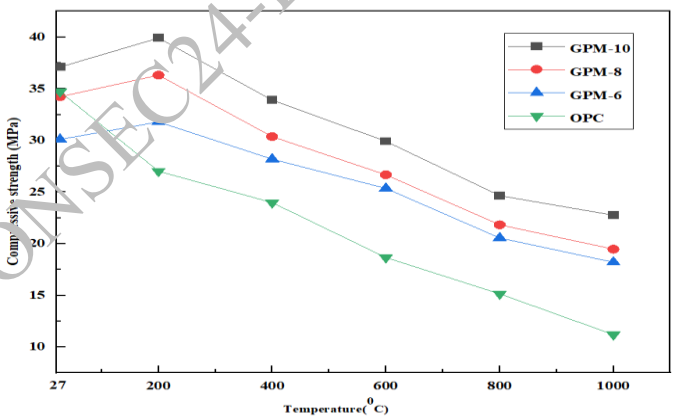

Figure 4. Compressive strength of GPM and OPC mortar samples at different temperature

4. XRD analysis at different temperature

4.1 Transformation of crystalline phase of geopolymer mortar

The XRD pattern of GPM samples at room temperature shows a diffuse band at 28º (2θ) indicating aluminosilicate gel and a diffuse peak at 32º (2θ) signifying C-A-S-H. Crystalline phases like quartz and mullite are also present (Figure 6). When heated to 200°C, the intensity of C-A-S-H (32º) and N-A-S-H (26º) peaks increased, reflecting the growth of these gels and a corresponding increase in compressive strength due to accelerated polymerization. At 400°C, the N-A-S-H gel's intensity

remained stable, but C-A-S-H gel intensity reduced slightly, leading to a decrease in compressive strength. At 600°C, the C-A-S-H gel intensity significantly decreased, and crystalline phases of akermanite ($Ca_2MgSi_2O_7$) and nepheline ($NaAlSiO_4$) appeared due to polymeric chain decomposition. At 800°C and 1000°C, the C-A-S-H gel peak disappeared, with akermanite, nepheline, and Clinohumite ($(MgFe)_9(SiO_4)_4(FOH)_2$) peaks becoming prominent, as also reported by Lee et al., 2017.

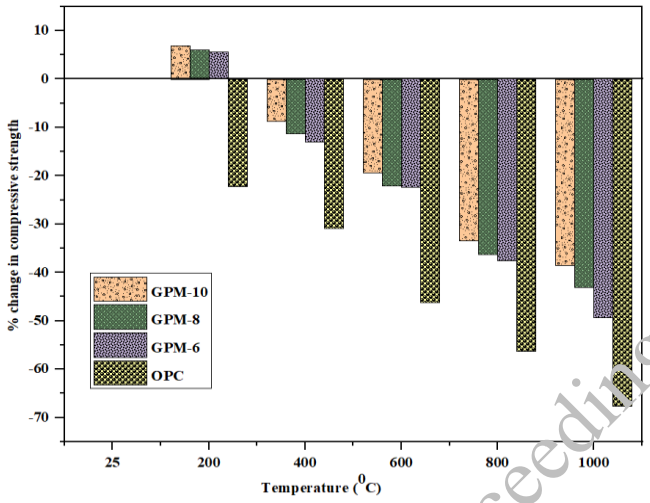

Figure 5. Increment and decrement percentage of compressive strength of GPM and OPC mortar samples at different temperature

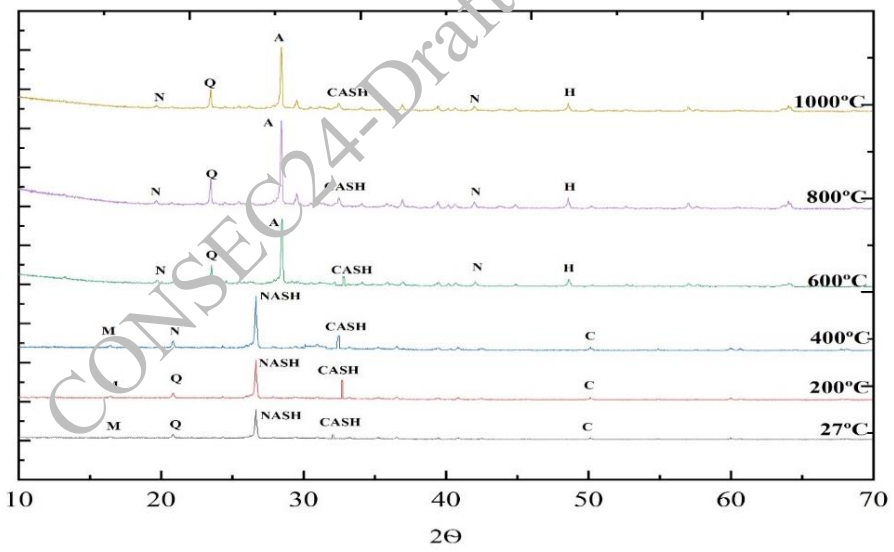

Figure 6. XRD of geopolymer mortar GPM-10 at different temperature

4.2 Transformation of crystalline phase of OPC mortar

At room temperature, the predominant phases in OPC mortar samples were portlandite ($Ca(OH)_2$), C-S-H, and β-C_2S, as shown in Figure 7. When exposed to 200°C, the XRD pattern of OPC mortar showed only marginal changes, indicating slight deterioration. The intensity of the C-S-H peak at $2\theta = 29.4^o$ and the $Ca(OH)_2$ peak at $2\theta = 26.6^o$ decreased, leading to reduced compressive strength. At 600°C, the intensity of the β-C_2S peak increased, while the peaks for $Ca(OH)_2$ and C-S-H vanished at 800°C due to chemical deterioration and loss of bound water. This decomposition led to the formation of lime (CaO), which was observed after exposure to 800°C. Calcite ($CaCO_3$) was also detected, likely formed

by the reaction of CaO with CO_2 in the furnace. These findings suggest that GPM has better heat stability than OPC mortar, as indicated by the XRD data (Alonso and Fernandez, 2004; Castellote *et al.*, 2004).

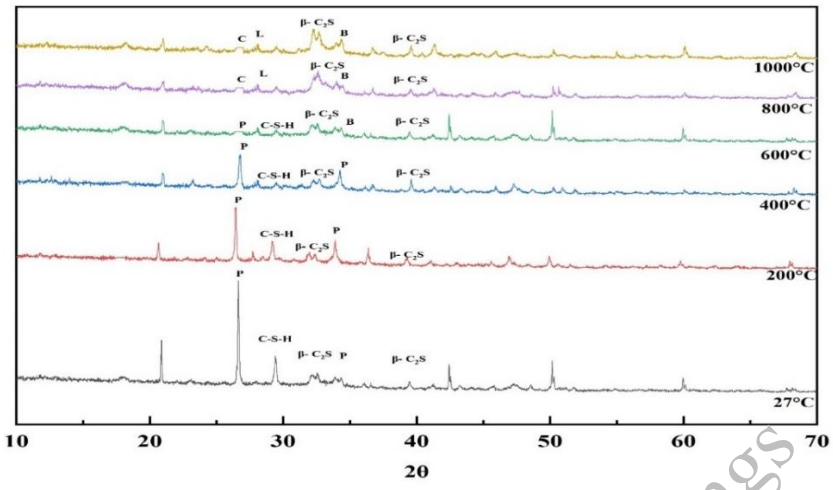

Figure 7. XRD of conventional OPC mortar at different temperature

5. Functional group analysis

5.1 Chemical transformation of geopolymer mortar

The FTIR spectra of GPM samples before and after exposure to high temperatures (200°C to 1000°C) are shown in Figure 8. Notable changes in peaks occurred at 3600 and 1690 cm^{-1}, corresponding to the removal of free and structural water from the GPM matrix, related to OH- stretching vibrations. As the temperature increased to 1000°C, the peak shifted from 1400 to 1450 cm^{-1}, indicating a drop in composite strength due to the asymmetric O-C-O stretching mode.

The peaks at 970 cm^{-1} and 790 cm^{-1} continuously decreased with rising temperatures, reflecting the breakdown of geopolymer bonds (C-A-S-H, N-A-S-H), which explains the loss in compressive strength. The reduction in the 970 cm^{-1} band, linked to the decomposition of C-A-S-H with N-A-S-H gel, and the increase in the Si-O-Al band at 790 cm^{-1}, indicate the formation of Si-O and Al-O bonds. This bond breakdown weakens the microstructure, leading to strength reduction at high temperatures.

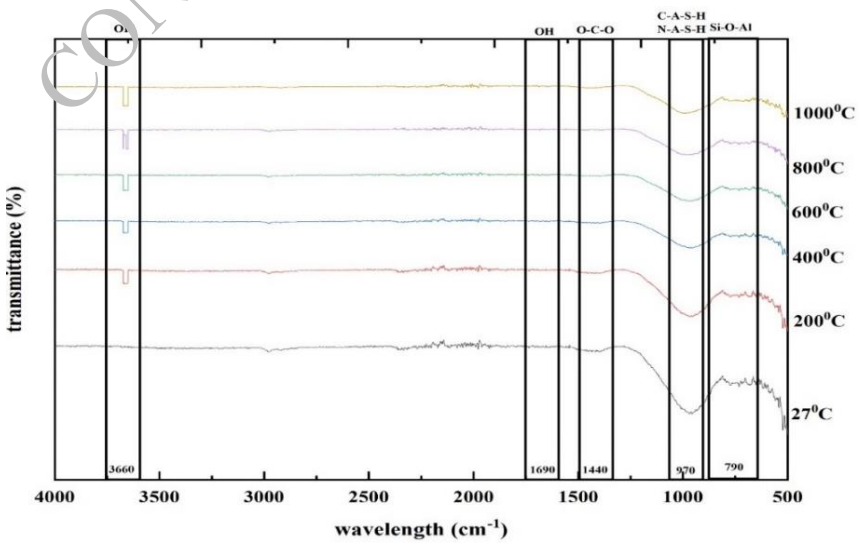

Figure 8. TIR of geopolymer mortar GPM-10 at different temperatures

5.2 Chemical transformation of OPC mortar

The FTIR spectra of OPC mortar (Figure 9) show major bands at 3445, 1645, 1420, and 980 cm^{-1}. The 980 cm^{-1} peak, linked to Si-O stretching in C-S-H, shifts and reduces with increasing temperature, indicating the reduction in compressive strength. The asymmetric vibration of the C-O bond in carbonates is reflected in peaks at 875 cm^{-1} and 1420 cm^{-1}. The broad band at 3000-3200 cm^{-1} is due to O-H vibration in free water, and the sharp peak at 3000 cm^{-1} is from OH stretching in crystal water. As temperature increases from 27°C to 400°C, the intensity of water and carbonate peaks diminishes, and the 980 cm^{-1} peak reduces, indicating water evaporation and C-S-H bond degradation, correlating to compressive strength loss. At temperatures of 600°C and above, new carbonate peaks appear at 1400 cm^{-1} and 1520 cm^{-1}, with increased intensity at 875 cm^{-1}, due to the carbonization of decomposed reaction products during thermal treatment.

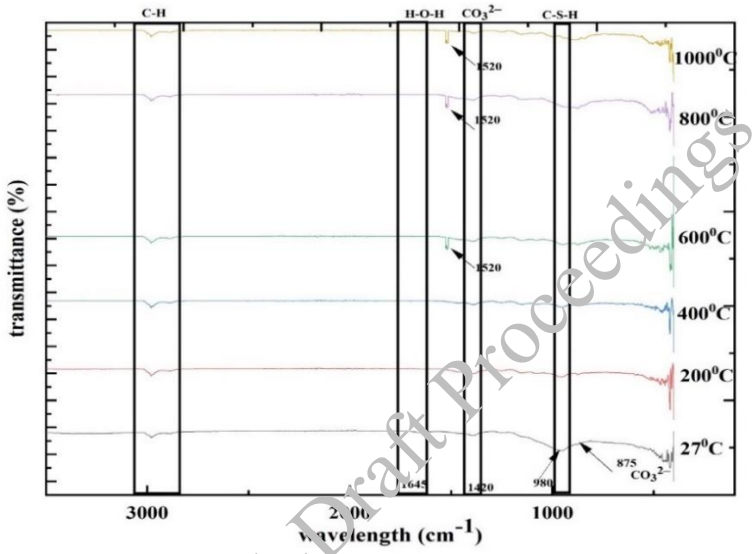

Figure 9. FTIR of OPC mortar at different temperatures

6. Conclusions

Based on the results and discussion following conclusions are formed-

- The compressive strength of GPM increased by 7.6% (as compared to control mix), when the specimen was exposed to 200^{0}C. Beyond 200^{0}C there was a gradual reduction in compressive strength (12.5% to 44.9% of the control mix) as the temperature increased from 400^{0}C to 1000^{0}C.
- The compressive strength of OPC mortar was found to decrease from 22.1% to 67.7% when the samples were exposed to 200^{0}C to 1000^{0}C. Hence, the reduction in compressive strength due to high temperature exposure of specimens for OPC mortar was higher than the GPM. This indicates better performance of GPM.
- The transformation of crystalline phase of GPM and OPC mortar when exposed to high temperature also validates that GPM had better heat resistance as the zeolite-like by-product of the N-A-S-H binder gel system in GPM samples showed better stability at high temperatures as compared to OPC mortar. This is also substantiated by FTIR technique.
- This study suggests that GPM are have potential to be used as a construction structural material especially where exposure of high temperature is expected.

References

AbdulAleem, M.I. and Arumairaj, P.D. (2011) 'A R eview of S eismic A ssessment of R einforced C oncrete S tructure using P ushover A nalysis', *International Journal of Engineering Sciences & Emerging Technologies*, 1(2), pp. 118–122.

Alonso, C. and Fernandez, L. (2004) 'Dehydration and rehydration processes of cement paste exposed to high temperature environments', *Journal of Materials Science*, 39(9), pp. 3015–3024. Available at: https://doi.org/10.1023/B:JMSC.0000025827.65956.18.

Castellote, M. *et al.* (2004) 'Composition and microstructural changes of cement pastes upon heating, as studied by neutron diffraction', *Cement and Concrete Research*, 34(9), pp. 1633–1644. Available at: https://doi.org/10.1016/S0008-8846(03)00229-1.

Dimas, D., Giannopoulou, I. and Panias, D. (2009) 'Polymerization in sodium silicate solutions: A fundamental process in geopolymerization technology', *Journal of Materials Science*, 44(14), pp. 3719–3730. Available at: https://doi.org/10.1007/s10853-009-3497-5.

Garside, M. (2022) *Cement production worldwide from 1995 to 2021*.

Hassan, A., Arif, M. and Shariq, M. (2019) 'Use of geopolymer concrete for a cleaner and sustainable environment – A review of mechanical properties and microstructure', *Journal of Cleaner Production*, 223, pp. 704–728. Available at: https://doi.org/10.1016/j.jclepro.2019.03.051.

Karthik, A., Sudalaimani, K. and Vijayakumar, C.T. (2017) 'Durability study on coal fly ash-blast furnace slag geopolymer concretes with bio-additives', *Ceramics International*, 43(15), pp. 11935–11943. Available at: https://doi.org/10.1016/j.ceramint.2017.06.042.

Lee, N.K. *et al.* (2017) 'Influence of binder composition on the gel structure in alkali activated fly ash/slag pastes exposed to elevated temperatures', *Ceramics International*, 43(2), pp. 2471–2480. Available at: https://doi.org/10.1016/j.ceramint.2016.11.042.

Lee, N.K., Jang, J.G. and Lee, H.K. (2014) 'Shrinkage characteristics of alkali-activated fly ash/slag paste and mortar at early ages', *Cement and Concrete Composites*, 53, pp. 239–248. Available at: https://doi.org/10.1016/j.cemconcomp.2014.07.007.

Omer, S.A., Demirboga, R. and Khushefati, W.H. (2015) 'Relationship between compressive strength and UPV of GGBFS based geopolymer mortars exposed to elevated temperatures', *Construction and Building Materials*, 94, pp. 189–195. Available at: https://doi.org/10.1016/j.conbuildmat.2015.07.006.

Pan, Z., Sanjayan, J.G. and Rangan, B. V. (2009) 'An investigation of the mechanisms for strength gain or loss of geopolymer mortar after exposure to elevated temperature', *Journal of Materials Science*, 44(7), pp. 1873–1880. Available at: https://doi.org/10.1007/s10853-009-3243-z.

Qu, F. *et al.* (2020) 'High temperature resistance of fly ash/GGBFS-based geopolymer mortar with load-induced damage', *Materials and Structures/Materiaux et Constructions*, 53(4), pp. 1–21. Available at: https://doi.org/10.1617/s11527-020-01544-2.

Sarker, P.K., Haque, R. and Ramgolam, K. V. (2013) 'Fracture behaviour of heat cured fly ash based geopolymer concrete', *Materials and Design*, 44, pp. 580–586. Available at: https://doi.org/10.1016/j.matdes.2012.08.005.

Sattary, S. and Thorpe, D. (2016) 'Potential carbon emission reductions in australian construction systems through bioclimatic principles', *Sustainable Cities and Society*, 23, pp. 105–113. Available at: https://doi.org/10.1016/j.scs.2016.03.006.

Scrivener, K.L., John, V.M. and Gartner, E.M. (2018) 'Eco-efficient cements: Potential economically viable solutions for a low-CO2 cement-based materials industry', *Cement and Concrete Research*, 114(June), pp. 2–26. Available at: https://doi.org/10.1016/j.cemconres.2018.03.015.

Sharma, A. *et al.* (2022) 'Potential of geopolymer concrete as substitution for conventional concrete: A review', *Materials Today: Proceedings*, 57, pp. 1539–1545. Available at: https://doi.org/10.1016/j.matpr.2021.12.159.

Singh, N., Sharma, B. and Rathee, M. (2022) 'Carbonation resistance of blended mortars and industrial by-products: A brief review', *Cleaner Materials*. Available at: https://doi.org/10.1016/j.clema.2022.100058.

Zhuang, X.Y. *et al.* (2016) 'Fly ash-based geopolymer: Clean production, properties and applications', *Journal of Cleaner Production*, 125, pp. 253–267. Available at: https://doi.org/10.1016/j.jclepro.2016.03.019.

Examination of Acid Resistance in Lightweight Conventional and Geopolymer Concrete Utilizing 100% SFA as Coarse Aggregate

Rohit Rawat[1] and Dinakar Pasla[2*]

[1]Research Scholar, School of Infrastructure, Indian Institute of Technology Bhubaneswar, Odisha – 752050
Email: a21ce09007@iitbbs.ac.in
[2]Professor, School of Infrastructure, Indian Institute of Technology Bhubaneswar, Odisha – 752050
Email: pdinakar@iitbbs.ac.in

[*]Corresponding author

ABSTRACT

The utilisation of sintered fly ash aggregate (SFA) manufactured from thermal power plant by-products to produce lightweight concrete (LWC) shows various environmental benefits. However, the durability performance of SFA in an acid attack environment has been relatively understudied. Acid exposure can result in the degradation of binder and strength in concrete, eventually leading to section loss. This research focuses on the effects of acid attack on lightweight conventional concrete (LCC) and geopolymer concrete (LWGC) incorporating SFA as coarse aggregate. The specimens were exposed to 3% sulfuric acid solution up to the age of 150 days, and the deterioration was measured in terms of mass loss and compressive strength loss. Subsequently, there was a noticeable increase in the percentage loss of both compressive strength and weight for LCC after 150 days. The results indicated that LWGC shows good resistance against acid attack compared to LCC.

KEYWORDS*: Acid attack, Compressive strength, Lightweight concrete, Sintered fly ash aggregate.*

1. Introduction

According to Joseph Davidovits (1993), the use of aluminosilicate-rich inorganic polymers, like geopolymers (GP), is an appropriate substitute for ordinary Portland cement (OPC) concrete. GP is an inorganic polymer produced through activating aluminosilicate-rich base materials using alkaline compounds. The GP paste exhibits significantly higher compactness and denser compared to the OPC paste. Additionally, the mechanical and durability attributes are enhanced as a result of the significantly denser hydration product of the GP binder. Moreover, replacing OPC with GP binder in concrete may greatly improve the binding capabilities of the aggregates. This results in a significantly denser interfacial transition zone (ITZ) and superior microstructures. Conversely, lightweight concrete (LWC) offers a cost-effective alternative to traditional concrete. LWC has superior fire resistance, cheaper initial costs, and a higher strength to mass ratio, making it advantageous for structural applications. The incorporation of lightweight aggregate (LWA) has the potential to enhance seismic performance, decrease density, and enhance thermal insulation as a result of its hollow or porous morphological features. Utilizing FA as a raw material for manufacturing LWA is highly encouraged as it is abundantly accessible and helps decrease reliance on natural resources. FA can be utilized to create artificial aggregates through hydrothermal treatment, sintering, and cold bonding. The FA utilisation percentages for the given techniques are as follows: 60-75%, 47%, and 90-100%. Furthermore, the mechanical and physical attributes of sintered fly ash aggregate (SFA) surpass those of cold bonded aggregates. Research has shown that SFA concrete is a viable option for constructing structural concrete due to its diverse range of structural properties as mentioned in Nadesan and Dinakar (2017). The durability of concrete is the fundamental characteristic that determines the lifespan of the material. The interactions

between concrete and the external environment are crucial in determining the durability of concrete. Among the several environmental conditions such as thaw, abrasion, corrosion, and acid attack, acid attack poses the greatest hazard. The degree of degradation after an acid attack on concrete is contingent upon the chemical composition of anions that are present. The type of aggregate and concrete also have an impact on the degree and severity of acid attack. While OPC is often used as a binder in the construction industry, its ability to withstand chemical attacks from substances like acids, chlorides, and sulfates is a significant issue. In recent years, GP binders have become a potential alternative to OPC binders due to their high early strength and resilience to acid attack as described in Rawat and Pasla (2024), in addition to their environmentally friendly nature. Song and Brungs (2005) conducted an accelerated test to assess the longevity of geopolymer concrete (GPC) in a 10% sulfuric acid solution over a period of 56 days. They reported that the GPC exhibited excellent durability. The lack of research assessing the efficacy of lightweight geopolymer concrete (LWGC) with 100% SFA in acidic conditions has prompted the need for this investigation. The purpose of this investigation is to evaluate the impact on FA-Ground granulated blast furnace slag (GGBS) based LWGC when exposed to sulfuric acid. The investigation involved measuring changes in weight and compressive strength as indicators of resistance to sulfuric acid. The results of the current study will be valuable in determining the suitability of geopolymer materials for usage in acidic environments and comparing them with lightweight conventional concrete (LCC).

2. Raw ingredients and methodology

2.1 Materials

The binder materials employed in this study are GGBS and Class-F FA for GPC, which are by-products from steel industries and thermal power plants, respectively. The specific gravity of GGBS is 2.83, while the specific gravity FA is 2.43. The experiment utilized for OPC 53 grade cement for conventional concrete as the primary binding material. **Table** 1 provides the precise specifications of the physical attributes of binders.

Table 1. Physical characteristics of binders

Properties	Units	OPC	FA	GGBS
Bulk density	kg/m^3.	1441	990	1205
Colour	-	Bluish grey	Greyish white	Off white
Moisture	%	<0.1	<0.1	<0.1
Specific gravity	-	3.15	2.43	2.83

SFA is a type of coarse aggregate that is produced from FA, a by-product resulting from the burning of coal in power plants. IMFA, located in Bhubaneswar, India, provided two distinct sizes of coarse SFA (4-8 mm and 8-12 mm) which were utilized as LWA, as depicted in **Figure 1**.

Figure 1. The proportion of SFA utilized in the inquiry

The physical characteristics of both SFA and sand utilised in this experiment are illustrated in Table 2. The results suggest that the properties of the SFAs meet the defined criteria set out in IS 9142 Part 2 (2018) for the manufacturing of LWA for utilising in structural concrete. Furthermore, **Table** 2 presents the characteristics of the SFAs according to the specifications stated in ASTM C330 (2023).

Table 2. Properties of aggregates.

Properties	Fine aggregate	SFA		IS Recommendation
		8-12 mm	4-8 mm	
Aggregate impact value (%)	-	23.40	-	< 40 (IS 9142 Part 2 (2018))
Absorption for 24 hours (%)	0.33	16.3.	17.6	<18 ((IS 9142 Part 2 (2018))
Abrasion value (%)	-	33.54	-	< 40(IS 9142 Part 2 (2018))
Crushing strength (%)	-	22.36	-	< 45(IS 9142 Part 2 (2018))
Loose dry density (kg/m3)	1352	785	800	< 800 (ASTM C330-04)
Specific gravity	2.65	1.44	1.42	-

3. Results and discussion

Figure 2 depicts the images of LCC and LWGC with an AC/B ratio of 0.5 after being submerged in sulphuric acid for a duration of six months. Evidently, there is a noticeable increase in surface deterioration in LCC. The use of LWGC typically leads to the production of a more compact and robust concrete that exhibits enhanced resistance against acid. This is due to a reduced amount of accessible solution to undergo a chemical reaction with the acid, as well as a limited amount of space for the formation of cracks. Earlier studies also reported that when conventional concrete is subjected to sulphuric acid, the acid causes the formation of a white layer of gypsum crystals on the surface of the specimens. However, there is no observable evidence to demonstrate the breakdown of gypsum on the exterior of the GPC, as clearly observed in **Figure** 2.

Figure 2. Acid attack consequences observed visually after a period of 150 days.

The changes in CS and weight of LCC and LWGC samples after 150 days in acid were compared to the samples' original CS and weight. After 150 days of exposure, the loss in mass for LCC is on higher side compared to LWGC; it is 3.31% and 1.89% for LCC and LWGC, respectively. And the CS losses for LCC and LWGC are 41.5% and 28.1%, respectively, compared to their initial CS values. Using finer particles, such as FA and GGBS compared to OPC to produce LWGC. The integration of smaller particles in the porous SFA has led to an improvement in the quality of LWGC. The degradation of LCC and LWGC is caused by the chemical and phase composition of the binder. The primary reason for the lesser susceptibility of LWGC to acid attack, as opposed to OPC, is the lower calcium concentration. More damage has been seen in LCC because of the formation of calcium sulphate. This happens when sulphuric acid ions interact with the C-(A)-S-H after they break through the matrix showed in Niş and Al-Antaki (2022).

4. Conclusions

When calcium hydroxide is present in an OPC-type binder, it breaks down the matrix network, which makes it less strong. When the other hydration product breaks down, it will make a gel-like layer made up of hydrogels made of silica, alumina, and ferric oxide. The deterioration of the network binder, visual appearance, and mechanical strength of LCC and LWGC, as well as the degradation of the binder with acid solution, are completely dependent on the rate of the hydration product reaction. Based on this review, both LCC and LWGC are susceptible to acid attack. LWGC has demonstrated superior resistance to acid attack in comparison to LCC.

References

ASTM. 2023. "Standard Specification for Lightweight Aggregates for Structural Concrete. C330/C330M-23." *West Conshohocken, PA: ASTM International*, 552 (18).

IS 9142 (Part 2). 2018. "Artificial Lightweight Aggregate for Concrete — Specification."

Joseph Davidovits. 1993. "Geopolymer Cements To Minimize Carbon-Dioxide Greenhouse-Warming." *Ceramic Transactions*, 37 (1): 165–182.

Nadesan, M. S., and P. Dinakar. 2017. "Structural concrete using sintered flyash lightweight aggregate: A review." *Constr Build Mater*, 154: 928–944. Elsevier Ltd.

Niş, A., and T. S. W. Al-Antaki. 2022. "Pumice Aggregate Based Lightweight Concretes Under Sulfuric Acid Environment." *Revista Romana de Materiale/ Romanian Journal of Materials*, 52 (2): 194–202.

Rawat, R., and D. Pasla. 2024. "Assessment of mechanical and durability properties of FA-GGBS based lightweight geopolymer concrete." *Constr Build Mater*, 426 (March): 135984.

Song X.J, Marosszeky M, Brungs M, M. R. 2005. "Durability of fly ash based geopolymer concrete against acid attack." *10 DBMC International Conference on Durability of Building Materials and Components. Lyon, France.*, 17–20.

Hierarchy Star Rating on Durability (HSRD) using Ferrochrome slag Concrete - Methodology and Justification by Microstructure

N. Manigandan[1*] and V. Ponmalar[2]

1Division of Structural Engineering, Department of Civil Engineering, College of Engineering Guindy, Anna University, Chennai, Tamil Nadu, India. Email: authormanigandan@gmail.com
2Division of Structural Engineering, Department of Civil Engineering, College of Engineering Guindy, Anna University, Chennai, Tamil Nadu, India.
Email:, ponmalar_v@annauniv.edu

*Corresponding author

ABSTRACT

A country's infrastructure is a major factor in development. Infrastructure development without cement and natural resources (aggregates) is impossible. Generally, cement combustion and production processes expel 860 kg $C0_2$/t. To diminish this, net-zero carbon, low carbon, decarbonation, sustainable cement, and green concrete are focused research areas. Focusing on concrete durability enhances the structure's longevity and reduces the need for repair and reconstruction work. This research showcases a methodology that focuses on evaluating the durability of Supplementary Cementitious Materials (SCMs) in conjunction with ferrochrome slag sand (FSS). Furthermore, the methodology is drafted using 10 mixes from both standard grade (M40) and high strength grade (M100). After 28 days of curing, a few tests are performed on the concrete to measure its transport longevity properties. These inspections encompass water permeability (WPT), water absorption (WA), surface resistivity (SR), ultrasonic pulse velocity (UPV), and rapid chloride ion penetration test (RCPT). The assimilation of five different durability data sets assigns the star rating based on ASTM, IS, and AASHTO limits. The 5 star rating indicates excellent quality; the 3 star rating means acceptable limit; and the 1 star rating indicates that the concrete is high risk. The purpose of the Hierarchy Star Rating on Durability (HSRD) is to assess the overall quality of concrete from multiple angles. Morphology intellectually justifies the HSRD of the optimum mix FSS40 and XFSS40 (40% slags with SCMs) with 4 and 5 stars, respectively. This simplified HSRD strategy guides society towards ensuring concrete's tangible quality.

KEYWORDS*: Durability, HSRD, Morphology, Ferrochrome slag sand, and Star rating*

1. Introduction

As stated by Scrivener (2016), the cement industry gives off almost 7–8% of the entire world's CO_2. The kiln and clinker processes to produce cement contribute nearly 861 kg CO2/t. Therefore, the entire cement chemistry community is actively working towards zero CO_2 emissions through a variety of techniques. The usage of supplementary Cementitious Materials (SCMs), reducing combustion emissions by co-processing fuel and carbon capture utilise and storage, are the most feasible techniques to reduce this effect on Scrivener et al (2023). SCMs such as metakaolin and nanosilica will boost performance in terms of longevity and hydration chemistry. The addition of Al-Si minerals (metakaolin) occupies the interstitial spot of Calcium Silicate Hydrate (CSH) to form Calcium Alumino Silicate Hydrate (C(A)SH), according to Lothenbach et al (2011). This fine mineral also destabilizes Calcium Hydroxide (CH) by pozzolanicity, forming secondary CSH. The kinetic pozzolanicity makes the concrete denser and more durable. Noteworthy, the nanosilica minerals contain a predominant SiO_2 in the amorphous phase, as per Le et al (2011). The nanosilica incorporation will accelerate the early hydration and pozzolanicity on or above the 3rd day. This combination of micro and nano minerals will

also block the transport action in concrete by the filler effect, as reported by Jennings and Tennis (2000). The use of virgin river sand for concrete production has a negative impact on the environment. As previously pointed out by Manigandan and Ponmalar (2020, 2022)., the state of Tamil Nadu consumes 14–16 million cubic feet of fine aggregate per day. This impact can be reduced by using industrial waste, such as air-cooled ferrochrome slag sand (FSS). The ferroalloy industry expels 16 metric tons of FSS every year, as per the International Chromium Development Activity (ICDA) report. In terms of durability, the proper granulometric of FSS and Crushed sand (Csand) performs better in 28, 91, and 365 days cured concrete. The interlocking effect of Csand (60%) and FSS (40%) performs better in RCPT, WPT, WA, and UPV, according to Dash and Prato (2018), Manigandan and Ponmalar (2023), and Santhanam (2019). The methodology is framed and compared with microstructural images of the 28-day result driven by these result data.

2. Materials and Test Procedure

2.1 Materials and Mix Design

The 53-grade Portland clinker with a specific gravity of 3.14 is used as a predominant binder. The physical and chemical properties of clinker are consistent with IS 12269 (1987) R2013. Referral M100 concrete incorporates fly ash (class F) and silica fume (SF) at 18% and 10%, respectively. 63% SiO_2 and 25% Al_2O_3 are the chemical compositions of fly ash. With a specific gravity of 2.63, the SF contains 99% SiO_2. At the micro scale, both fly ash and SF have spherical morphologies. Clinker replaces the micro mineral metakaolin by 8, 10, and 12%. Metakaolin is hexagonal and flaky, according to morphological investigation. Metakaolin's specific surface area and specific gravity are 19 (m^2/g) and 2.6, respectively. The sticky nature of the off-white is the appearance of metakaolin.

Table 1. Mix proportion of M40 and M100 concrete

Mix Id	Replacements	Binders					Fine aggregate		Coarse	w/b	SP
		Clinker	Fly ash 18%	SF 10%	MK	NS	Csand	FSS			
M40											
RC	-	400	-	-	0	0	812	0	1067	0.4	0.75
M10	MK10%	360	-	-	40	0	812	0	1067	0.4	0.75
N1	MK10%+NS1%	356	-	-	40	4	812	0	1067	0.4	0.75
FSS40	MK10%+NS1%-FSS40%	356	-	-	40	4	487	325	1067	0.4	0.75
FSS100	MK10%+NS1%-FSS100%	356	-	-	40	4	0	812	1067	0.4	0.75
M100											
XRC	-	658	164	91	0	0	734	0	594	0.21	1
XM10	MK10%	567	164	91	91		734	0	594	0.21	1
XN1	MK10%+NS1%	559	164	91	91	8	734	0	594	0.21	1
XFSS40	MK10%+NS1%-FSS40%	559	164	91	91	8	294	441	594	0.21	1
XFSS100	MK10%+NS1%-FSS100%	559	164	91	91	8	0	734	594	0.21	1

The nano-sized minerals undergo the second stage of SCM replacement. The nanosilica from the sol-gel process is used instead of clinker particles. The SEM image of nanosilica depicts clusters of spherical balls, yet precise evaluation of particle size and shape remains unattainable. The transmission electron microscope image demonstrates that nanosilica has no fringes on its surface, as per Manigandan and Ponmalar (2024). The spherical particles are positioned above each other, forming high-angle grain boundaries. Nanosilica's surface area and specific gravity are 202 (m^2/g) and 2.2, respectively.

Powdered nanosilica, in amounts of 0.5, 1, and 1.5%, replaces the clinker particles. Aggregates are the major filler material, which occupies 70% of concrete. Based on their size, the aggregates are differentiated into fine and coarse aggregates. The gravel from the crusher plant at the sizes of 18 mm (for M40) and 12 mm (for M100) is used as coarse aggregate. The fine aggregate is the second part of the replacement carried out by incorporating industrial waste FSS in place of Csand. The naphthalene base water reducer for M40 and the ether base high-range water reducer are used to prepare M100 concrete. Table 1 represents the mix proportion and mix notation of each replacement percentage of binders and fine aggregate as per Manigandan and Ponmalar (2022, 2023, and 2024).

2.2 Test Procedure

The multiple durability tests are conducted using a 150 mm cube. The UPV, WPT, WA, SR, and RCPT are conducted as per the IS, ASTM, and AASHTO test procedures. The UPV and SR are the simplest tests that can result directly from cured specimens. The pulse velocity's frequency is 150 kHz. The direct test method is followed to predict the UPV value as per IS 13311:2013. The UPV measures the density and packing action of the matrix. According to IS 3085:2021, experiments with the WPT begin after the specimen has cured for 28 days. The 150-mm cube is subjected to a water pressure of 10 kg/m^2 for 3 days. The pressured cubes are split into two, and the depth of water penetrated is measured manually. The WPT ensures the concrete's pore connectivity. ASTM C 642:2013 predicts the water-absorbing capacity of concrete blocks. The WA depicts concrete's ability to absorb water. AASHTO-TP95:2014 uses the Wenner four probes to find the SR. The outer two probes represent the concrete's current flow. Inner probes are used to relate the equipotential lines to the current flow line. The electrical resistivity is the easiest way to predict the Cl ion effect in concrete. The 50*100 mm sized concrete discs are allowed to pass Cl ions from the NaCl solution by inducing 60 volts. The eight intervals of 6 hours of data are noted as per ASTM C 1202:2019. Figure 1 represents the HSRD's various influencing parameters.

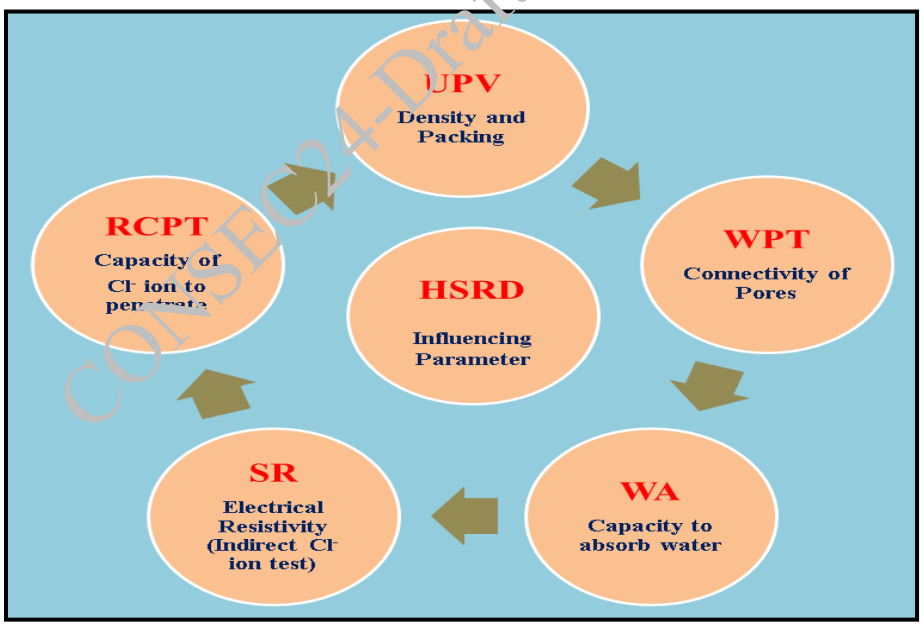

Figure 1. Influencing parameter of HSRD

3. Methodology Framing to Predict HSRD

Figure 2 illustrates the HSRD methodology through the use of durability test results. Initial test results are categorised based on star rating. Moreover, the star-rated value of each test result is formulated to predict the quality of concrete as per equation 1.

3.1 Star Rating

The 28 days durability reports are collected and split in to five categories. The acceptable limit (3 star) is initially assigned based on the allowable limits of the respective codes. The low star represents the durable quality of concrete: low-risk (2 star) and high-risk (1 star). The good and excellent quality of durable concrete are represented as 4 star and 5 star respectively. Figure 3 shows the limits and star ratings for durable concrete. The acceptable star rating of durable concrete should have a UPV of above 3.5 km/sec, a WPT of 30 to 20 mm depth, a WA of below 10%, an SR of above 50 kΩcm, and RCPT data below 2000 Coulomb.

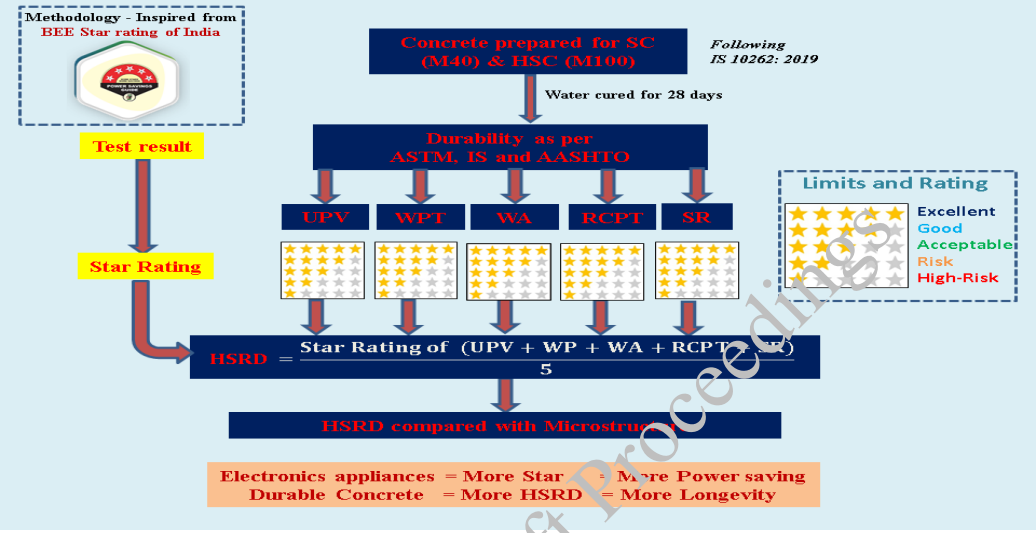

Figure 2. Methodology framing to predict HSRD

S.No.	UPV (km/sec)	WPT (mm)	WA (%)	SR (kΩcm)	RCPT (Coulombs)	Remarks	Star Rating
Codal Limits	IS 13311 :2013	IS 3085: 2021	ASTM C 642: 2013	AASHTO -TP95: 2014	ASTM C 1202: 2019	-	-
1	< 3	> 40	20 -15	< 10	> 4000	High Risk	★
2	3 - 3.5	40 – 30	15 - 10	10 - 50	4000 - 2000	Risk	★★
3	3.5 - 4	30 – 20	10 - 5	50 - 100	2000 - 1000	Acceptable	★★★
4	4 – 4.5	20 -10	5 – 2	100 - 150	1000 - 100	Good	★★★★
5	> 4.5	< 10	< 2	> 150	< 100	Excellent	★★★★★

Figure 3. Star rating based on codal limits

3.2 HSRD

The star ratings of separate data are hierarchic and cumulated using equation 1. This cumulated result represents the durable nature of concrete, similar to a star rating. On the other hand, a 5 star rating

indicates that the quality of concrete is excellent, while a 1 star rating indicates that the quality is high risk.

Hierarchy Star Rating on Durability, HSRD = [Star Rating (UPV+WPT+SR+RCPT)] / 5 (1)

3.3 Result and Discussion

Table 2 illustrates the star and HSRD results based on the figure 3 limits. The RC blend's star rating and HSRD are within an acceptable range (3 star). The M10 mix has increased the star rating to 3.4, while the HSRD of the round-off value is still in an acceptable range. The 10% of micro-metakaolin and nanosilica of 1% (N1 blend) accelerates the mean chain length of CSH to turn C(A)SH (equation 2) and also leads to a secondary hydration reaction (equation 3) as per Lothenbach et al (2011) and Manigandan and Ponmalar (2024). The optimum mix of M40 FSS40 blend falls under the good range (4 star) of HSRD. The improved interlocking action of Csand with FSS, combined with the powerful binder action of SCMs, refines the interconnectivity of pores and enhances the durability factor. The complete incorporation of FSS (FSS100 blend) shows a decrease in RCPT and SR star ratings and reflects in HSRD to 3 star (acceptable range). The bridging action between paste and coarse aggregate in 40% FSS and 60% Csand is the main cause of the escalated HSRD in the FSS40 mix.

$$CSH + Al_2O_3\,(\text{amorphous}) = C(A)SH \quad (2)$$

$$\text{Portlandite (CH)} + SiO_2\,(\text{amorphous}) = CSH \quad (3)$$

In HSRD, the M100 concrete referral mix (XRC) achieves a 3 star rating. The micro-mineral and nano-mineral mix (XM10 and XN1) forms a congruent and tightly bonded CSH, which reflects in the durability rating. Thus, the XM10 and XN1 mixes have a good rating (4 star). As a result, the FSS40 mix has a higher star rating and a 5-star HSRD (excellent rating). The precise granulometrics of both fine aggregates in 60:40 combinations refine the concrete system's bleed channel and improve its flow-resisting properties. The complete replacement blend FSS100 reduces the HSRD to 3 stars due to increased pore connectivity.

Table 2. HSRD results

Grade	Mix id	Star rating					HSRD value	Round off	HSRD Remarks
		UPV	WPT	WA	SR	RCPT			
M40	RC	4	2	4	2	2	2.8	3	Acceptable
	M10	4	3	4	3	3	3.4	3	Acceptable
	N1	5	4	5	3	4	4.2	4	Good
	FSS40	5	4	4	4	4	4.2	4	Good
	FSS100	3	2	4	2	2	2.6	3	Acceptable
M100	XRC	4	2	4	2	2	2.8	3	Acceptable
	XM10	5	3	4	3	3	3.6	4	Good
	XN1	5	4	5	4	4	4.4	4	Good
	XFSS40	5	4	5	5	4	4.6	5	Excellent
	XFSS100	5	2	4	3	2	3.2	3	Acceptable

3.4 HSRD Compared with Microstructure

Figure 4 demonstrates the respective HSRD with secondary electron SEM images on a 28-day-cured specimen. The RC mix shows 3 star and the SEM image shows the cluster of the hydration matrix with the ITZ gap. Furthermore, the phantasy needle and flower petals in the RC mix represent the AFt and AFm. Substituting metakaolin and nanosilica leads to an increase in the HSRD values due to secondary hydration. The SEM image from Manigandan and Ponmalar (2022) shows that the pozzolanicity of

these minerals (a mix of M10 and N1) makes the synergic durability action. The optimum blend of M40 (FSS40) has a higher amount of CSH (H) and rigidified ITZ. The proper packing and precise hydration product are besides the synergic durability factor (HSRD, 4 star). The SEM image of the FSS100 blend reflects why the HSRD value decreases. The spider nest-shaped Hadley grains stand out for their low-density CSH (L). The packing action affects durability and has a 3-star HSRD value. This contributes to the loss of strength and intensifies the transport action, which further negatively impacts durability. Although the FSS100 mix has flaws in microstructural packing, the HSRD is in an acceptable range.

Figure 4. Microstructure compared with HSRD

The M100 concrete control mix (XRC) features a 3 star rating for HSRD and a low-density CSH (L) with interconnected ITZ. The Portlandite and CSH are noted in the XRC mix. By replacing the eco-friendly metakaolin and nanosilica with cement, the mix (XM10 and XN1) refines the capillary pores like meso and micro. Whereas, the XN1 mix has a dense CSH cluster with a 4 star HSRD due to the meso-gel pore filler effect of nanosilica, as per Manigandan and Ponmalar (2024). Because of the better chemical binding action of SCMs in the 60:40 mix of C sand and FSS, the best M100 mix (XFSS40) has a uniform microstructure. Manigandan and Ponmalar (2024) schematic packing action illustrates how the XFSS40 mix refines the bleed channel and ITZ to inches in the HSRD, earning it a 5-star rating. The transport action related to diffusion, conductivity, migration, bulk water intake, resistivity, permeation, and path of passing ability of the XFSS40 mix performs superiorly with a 5-star durability rating. In the concrete system, the XFSS100 mix has flaws. According to Hadley (1972), the orientation of the hydrated phase against the smooth surface will affect the system's integrity. The wrap texture of Hadley grains against the smooth grains will reduce the durability factor to a 3 star HSRD.

4. Conclusions

A concise description of this probing portrays the simple and easiest way to state the combined transport durability of concrete in terms of HSRD. To frame and predict the combined effect of durability, the methodology employs a star rating. The codal provisions of IS, ASTM, and AASTHO frame the limits of each star. The acceptable range for concrete quality is 3 stars, while 1 star represents poor quality, and 5 stars indicate superior quality. The HSRD from the star rating states the durability quality of M40 and M100 concrete grades. The FSS40 and XFSS40 mixes have a higher HSRD (4 and 5 star) value, which was witnessed by the dense microstructure of the SEM images of the respective mixes. The

FSS100 and XFSS100 mixes have a lower HSRD value (3 stars), which is comparable to the optimum mix. This mix has flaws in the structural arrangement similarly to Hadley grains (spider nest shape and warp texture shape) that affect the integrity of concrete. Notably, the HSRD method can assist concrete producers in marketing concrete that excels in durability, making it easier for customers who lack prior technical knowledge of concrete. This recommends that concrete society move from a strength perspective towards a performance perspective.

Acknowledgements

Authors are clearly acknowledged to "Anna Centenary Research Fellowships Scheme Grant No: CFR/ACRF/19131191121/AR1" of Centre for Research, Anna University, Chennai, Tamil Nadu, India. For supported financially to research during 2019 to 2021.

References

AASHTO: TP 95: (2014) Method Of Test For Surface Resistivity Indication Of Concrete's Ability to Resist Chloride Ion Penetration, SAI Global Standards, Chicago

ASTM C642: (2013). Standard Test Method for Density, Absorption, and Voids in Hardened Concrete, ASTM International, West Conshohocken, PA

ASTM C1202: (2019) Standard Test Method for Electrical Indication of Concrete's Ability to Resist Chloride Ion Penetration, ASTM International, West Conshohocken, PA

Scrivener, K., Snellings, R. and Lothenbach, B. (2016). "A practical guide to microstructural analysis of cementitious materials*", Crc Press*,540.

Tennis, P.D. and Jennings, H.M. (2000) "A model for two types of calcium silicate hydrate in the microstructure of Portland cement pastes", *Cement and Concrete Research*, 30: 855-863

Lothenbach, B. Scrivener, K. and Hooton H,D. (2011) "Supplementary cementitious materials*", Cement and Concrete Research* 41(12):1244-1256

Santhanam M. (2019) "Durability issues in concrete – Part 1 to 6"*NPTEL-NOC IITM*

Hadley, W.H. (1972) "The nature of the paste - aggregate interface",*Ph.D.thesis, Purdue University of United States*

Manigandan, N. and Ponmalar, V. (2022) "M5 investigation on ternary binder incorporated with ferrochromeslag aggregate in concrete". *Applied Nanoscience*,12: 3925–3944

Manigandan, N. and Ponmalar, V. (2023) "Some investigation on ternary powder (binder) technology incorporated with ferrochrome slag as fine aggregate in concrete", *Journal of Material Cycles and Waste Management*,25: 2822–2834

Manigandan, N. and Ponmalar, V. (2024) "M100 concrete probing on quinary cementitious matrix incorporate with industrial ferrochrome slag sand". *Construction and Building Materials*, 420: 135478

Manigandan, N. and Ponmalar, V. (2020) "Ferrochrome slag and manufactured sand as fine aggregate replacement in concrete and mortar - A Brief Review". *Indian Journal of Science and Technology*, 13: 2657-2667

Li, Z. Zhou, X. Ma, H. and Hou, D. (2011) "Advanced Concrete Technology", *John Wiley & Sons*

Dash, M.K. and Patro, S.K. (2018) "Performance assessment of ferrochrome slag as partial replacement of fine aggregate in concrete". *European journal of Environmental and Civil Engineering*, 25: 1-20

Scrivener, K. Matschei, T. Georget, F. Juilland, P. Aslam K.M. (2023), Advances in hydration and thermodynamics of cementitious systems. *Cement and Concrete Research* 174: 107332

IS 12269 (1987) R2013, Ordinary Portland Cement 53 Grade – Specification. Bureau of Indian Standards, New Delhi, India

IS 383 (1970) R2016 Specification for Coarse and Fine aggregate from Natural Sources for Concrete. Bureau of Indian Standards, New Delhi, India

IS 10262 (2009) R2019 Concrete Mix Proportioning – Guidelines. Bureau of Indian Standards, New Delhi, India

IS 13311-1: (1992) Method of Non-destructive testing of concret, Part 1: Ultrasonic pulse velocity. Bureau of Indian Standards, New Delhi, India

IS 3805: (1965) Method of Test for Permeability of Cement Mortar and Concrete. Bureau of Indian Standards, New Delhi, India

Carbonated Geopolymer Aggregates for Sustainable Construction

Mohd Hanifa[1], Supriya[2], Srinivasa Rao Naik B[3], P.C. Thapliyal[4] and L.P. Singh*[5]

[1]Academy of Scientific and Innovative Research (AcSIR), Ghaziabad, India Email: hanifa.cbri20a@acsir.res.in
[1]CSIR- Central Building Research Institute, Roorkee, India, Email: hanifa.cbri20a@acsir.res.in
[2]CSIR- Central Building Research Institute, Roorkee, India, Email: supriya21a@acsir.res.in
[3]CSIR- Central Building Research Institute, Roorkee, India, Email: srinivas@cbri.res.in
[4]CSIR- Central Building Research Institute, Roorkee, India, Email: pcthapliyal@cbri.res.in
[5]National Council for Cement and Building Materials, Ballabgarh, India, Email: dg@ncbindia.com

*Corresponding author

ABSTRACT

Global concerns over the escalating CO_2 emissions and depletion of natural aggregates have underscored the urgency of sustainable solutions. In response to these environmental concerns, the utilization of industrial waste (class F fly ash and calcium carbide sludge) to produce carbonated geopolymer aggregates emerges as a highly promising alternative. The carbonated geopolymer aggregates were investigated through analytical techniques such XRD, FT-IR, TGA and ^{29}Si NMR. The FT-IR results show that C-A-S-H gel formed before carbonation, and after carbonation, C-A-S-H gel converted to N-A-S-H gel (polymerization). ^{29}Si NMR showed that Q_2(1Al) peak observed in non-carbonated aggregates was diminished and an intense Q_4(3Al) and Q_4(1Al) peak were observed after carbonation. Furthermore, the carbonated aggregates sequestered 13.33% CO_2 and the conversion of C-A-S-H to N-A-S-H gel through accelerated carbonation improved the single aggregate strength by 78.6% compared to non-carbonated aggregates. This approach can be the most effective method of producing carbonated geopolymer aggregates from industrial waste.

KEYWORDS*: Artificial aggregates, C-A-S-H, N-A-S-H and CO_2 uptake*

1. Introduction

In the construction industry concrete is the major part and aggregates contributes approximately 60% of its volume (Research, 2021). The use of CO_2 sequestered aggregates in the concrete contributes to a major reduction of CO2 emissions. Extensive research has been conducted on producing carbonated aggreges with the utilization of calcium-rich waste such as steel slag, paper waste, municipal solid waste, cement waste, construction and demolition waste reported in the previous literature (Colangelo et al., 2015; Qian et al., 2020; Tajra et al., 2019; Tang & Brouwers, 2018; Wei et al., 2017). Despite these advancements, challenges remain, particularly in the utilization of non-calcium waste materials like Class F fly ash (FA), which contains less than 10 % calcium content necessary for effective carbonation. FA is utilized in the production of geopolymer aggregates, which are also non-carbonated due to the formation of N-A-S-H gel in the geopolymer system. Therefore, limited literature has been reported on the production carbonated geopolymer aggregates using FA.

To fill the gap of knowledge, this study aimed to produce carbonated geopolymer aggregates by using FA and calcium carbide sludge (CCS) through accelerated carbonation. CCS is mainly composed of calcium hydroxide ($Ca(OH)_2$) possesses the advantageous ability to undergo accelerated carbonation (Guo et al., 2017; Wang et al., 2019). The detailed assessment of the effect of accelerated carbonation on the chemistry and structure of C-A-S-H/N-A-S-H gel and the carbonated products formed in the

artificial aggregates were investigated using advanced characterization techniques including TGA, XRD, FT-IR and ^{29}Si MAS NMR spectroscopy.

2. Materials and methods

2.1 Raw Materials

FA, CCS, and NaOH pellets were employed to prepare artificial aggregates. FA and CCS were obtained from Netra NTPC Limited in Udyog Vihar, India, and Axcel Gases in Rewari, Haryana, India. The average particle size of the FA, as indicated by the d_{10} and d_{90} values, was 4.9 µm and 149.0 µm, respectively (Fig. 1 a). Conversely, the average particle size of the CCS was 8.5 µm (d_{10}) and 333.6 µm (d_{90}) (Fig. 1 a). The chemical compositions FA and CCS are presented in Table 1. Additionally, the XRD of the FA and CCS are shown in Fig. 1 b.

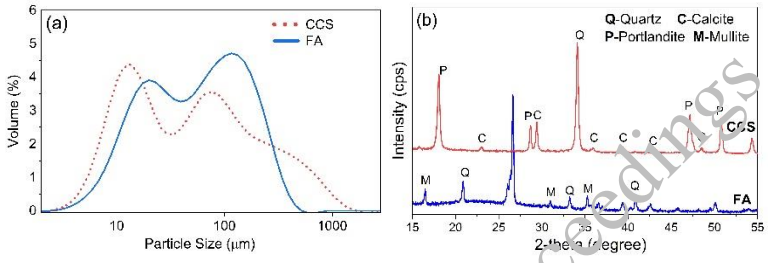

Figure 1. (a) Particle sizes distribution and (b) comparative XRD pattern of FA and CCS.

Table. 1. Chemical compositions of CCS and FA (wt. %)

Materials	CaO	SiO_2	Al_2O_3	Fe_2O_3	K_2O	Na_2O	SO_3	MgO	LOI
CCS	74.0	3.1	0.46	0.26	–	–	0.54	0.72	–
FA	1.61	55.2	26.69	8.14	1.76	0.13	0.25	0.39	1.33

2.2 Methods

2.2.1 Artificial aggregate production

Three mixes of different proportions of FA and CCS for artificial aggregates are prepared. In Mix-1, Mix-2 and Mix-3, FA is replaced with CCS by 20 wt.%, 30 wt.%, and 40 wt.% by weight, respectively. The experiment was performed using 3M, 5M and 7M NaOH concentrations.

The artificial aggregates were prepared through the granulation method using a disk pelletizer. The process parameters were optimized in a previous study, and the tilting angle and revolution speed were set at 45° and 40 rpm, respectively (Ren et al., 2021). A NaOH activator solution was continuously sprayed onto the mixture during agglomeration using a watering can. The aggregates formed were removed after 10 minutes of rotation and dried in an oven for 24 h at 80°C.

Following the initial curing period, the artificial aggregates underwent accelerated carbonation in a pressurized chamber. The carbonation process was conducted at room temperature (25-30°C), 99% CO_2 concentration, and 65-70% relative humidity (RH) for various durations of carbonation (4 h, 8 h, 12 h, and 24 h) at different pressure (4 and 6 bar). After the accelerated carbonation, the artificial aggregates were cured in water for 14 days at room temperature and stored for further testing and analysis.

3. Results and discussions

3.1 Optimization of mix proportion

Fig. 2 a represents the TGA of Mix-1, Mix-2 and Mix-3. The estimated CO_2 uptake and $CaCO_3$ formed during the accelerated carbonation of artificial aggregates were calculated by Eqs. (1) (Mehdizadeh et al., 2022; Mo et al., 2016; Pade & Guimaraes, 2007; Wu et al., 2022).

$$CO_2\ (Wt.\%) = \frac{\Delta M_{550\,°C-800\,°C}}{M_{950\,°C}} \times 100 \quad (1)$$

ΔM is the mass loss due to the $CaCO_3$ decomposition (550-810 °C). $CO_{2\ initial}$ and $CO_{2carbonated}$ are the weights of CO_2 in artificial aggregates before and after carbonation, respectively. The CO_2 uptake by Mix-1, Mix-2 and Mix-3 were 9.63%, 14.11% and 17.02% respectively (Table 2). The maximum single aggregate strength achieved by Mix-1, Mix-2 and Mix-3 was 4.2, 5.2 and 2.8 MPa, respectively, with 5M NaOH after 14 days of water curing (Fig. 2 b). The single aggregate strength achieved by Mix-2 was 5.2 MPa with 5M NaOH and 5 MPa with 7M NaOH after 14 days of water curing. Increasing the concentration of NaOH above 5M did not enhance the single aggregate strength. Furthermore, CO_2 uptake by artificial aggregate prepared by Mix-2 at different molar concentrations of NaOH (3M, 5M and 7M) were almost similar (approximately 14 %) after 12 h of carbonation (Fig. 2 c). An increase in the molar concentration of sodium hydroxide did not enhance the CO_2 uptake.

From the above result, we concluded that the single aggregate strength of artificial aggregates not only depends on the extent of carbonation but also the percentage of fly ash i.e activation of fly ash. Therefore, Mix-2 was the optimized composition to prepare carbonated aggregates at 5M NaOH concentration, which gives a maximum single aggregate strength of 5.2 MPa and total CO_2 uptake of 14.11%.

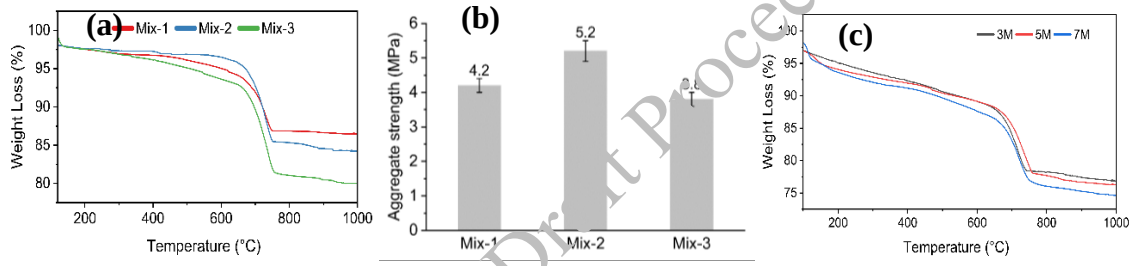

Figure 2. (a) TGA of artificial aggregates of three different Mix, (b) single aggregate strength of carbonated aggregates of three Mix at 5M concentration and (c) TGA of carbonated aggregates of Mix-2 at different molar concentration of NaOH

Table 2. Estimate total CO_2 uptake (%) (both natural and accelerated carbonation) by carbonated aggregates prepared from by three different mixes compositions.

Mix	$\Delta M_{550\text{-}800\,°C}$	$M_{950°C}$	CO_2 Uptake
Mix-1	95.21-86.85=8.36	86.75	9.63
Mix-2	96.97-85.03=11.94	84.63	14.11
Mix-3	94.75-81.05=13.70	80.48	17.02

3.2 X-ray diffraction

Fig. 3 shows the XRD pattern of the noncarbonated artificial aggregates, where calcite peaks are observed due to the natural carbonation of the CCS. The intensity of calcite peak increased as the duration of carbonation increases from 4 h to 24 h. There was no significant change in the intensity of the calcite peak when the accelerated carbonation duration was extended to 24 h, which indicated the maximum carbonation after 12 h of accelerated carbonation. However, the characterization of C-A-S-H and N-A-S-H gel using XRD is challenging due to their amorphous nature (Duxson et al., 2007; Garg et al., 2019; Li et al., 2010; Provis & Van Deventer, 2009). Therefore, additional techniques such as FT-IR, ^{29}Si and FE-SEM/EADX provide valuable information about the composition and structure of the amorphous gels formed in the artificial aggregates (Li et al., 2010; Provis & Van Deventer, 2009).

3.3 Fourier transform infrared spectroscopy analysis

Fig. 4 represents the FT-IR spectra of noncarbonated and carbonated aggregates prepared from optimized Mix-2. The asymmetrical stretching vibration band observed in noncarbonated aggregates in

the range of 949-956 cm^{-1} may be attributed to C-A-S-H gel and shifted to 1031 cm^{-1} after carbonation may be convert to N-A-S-H gel (García-Lodeiro et al., 2011). The absorption bands in the wavenumber 3400–3700 cm^{-1} region is caused by stretching vibrations of O-H and the sharp absorption band at 3642 cm^{-1} is assigned to the O-H in portlandite observed in non-carbonated aggregates (Baharom & Mamat, 2015; Yi et al., 2020; Yi et al., 2019). The absence of a stretching band of O-H bond of $Ca(OH)_2$ group in carbonated aggregates at 3642 cm^{-1} revealed the complete carbonation and the result is consistent with the XRD analysis. Further, the absorption band at 874 cm^{-1} attributed to the asymmetric bending vibration of the O-C-O bond of the CO_3^{2-} group and the absorption is more intense in carbonated aggregates due to the calcite formation.

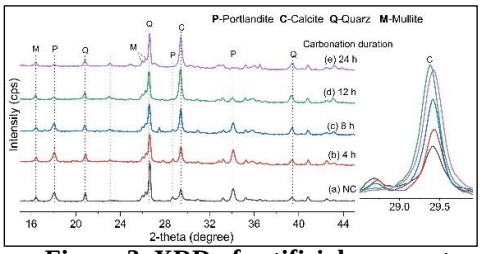

Figure 3. XRD of artificial aggregates at different duration of carbonation

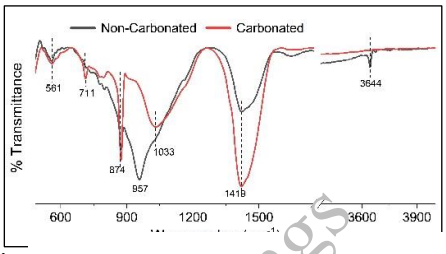

Figure 4. FT-IR spectra of non-carbonated and carbonated aggregates.

3.4 Solid State ^{29}Si MAS NMR Spectroscopy

The deconvoluted ^{29}Si NMR of noncarbonated and carbonated aggregates are shown in Fig 5. The obtained spectra were deconvoluted using Origin software employing the Gaussian line model.
A significant difference is observed before and after the acceleration of artificial aggregates. The content of the Q^2(1Al) site is 42.59 % in noncarbonated aggregates (Fig. 5 a), and after accelerated carbonation, Q^2(1Al) is completely diminished (Fig. 5 b). Conversely, the content of Q^4(3Al) and Q^4(1Al) sites significantly increased from 17 % to 29% and 34% to 59%, respectively, due to the conversion of C-A-S-H gel to N-A-S-H gel through accelerated carbonation. The content of Q^0 at -74 ppm and -65 ppm is 0.6 % and 3.2 % in noncarbonated aggregates, which is completely absent in the carbonated aggregates. The content of Q^4(0Al) at -115 ppm is present in noncarbonated aggregates, not observed in the carbonated aggregates, which may be due to the enhanced alkali activation reaction by carbonation reaction (Chancey et al., 2010; Gao et al., 2017; Ismail et al., 2014). These findings are consistent with the FT-IR analysis indicating the conversion of C-A-S-H gel to N-A-S-H gel via accelerated carbonation.

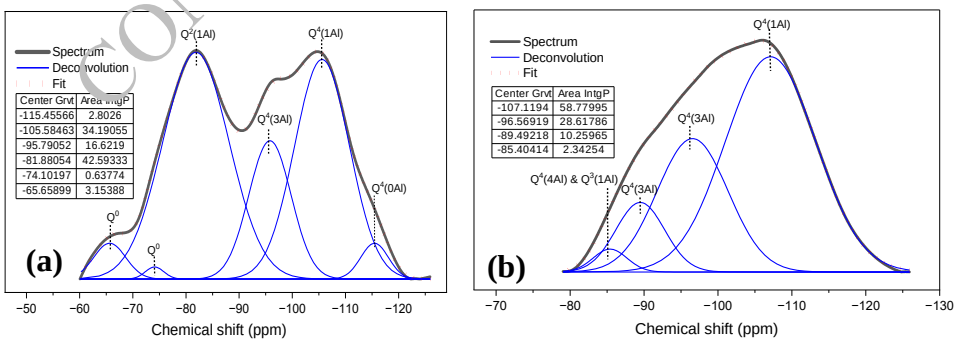

Figure 5. Deconvoluted ^{29}Si NMR spectra of (a) non-carbonated and (b) carbonated aggregate

4. Conclusions

- The conversion of the C-A-S-H gel into N-A-S-H gel through accelerated carbonation is confirmed by FT-IR and ^{29}Si NMR analysis i.e The alkali activated aggregates (non-carbonated aggregates)

converted into carbonated geopolymer aggregates (carbonated aggregates) through accelerated carbonation.

- Compared with noncarbonated aggregates, carbonated aggregates significantly enhanced their strength by 78.6 % due to the formation of a more complex N-A-S-H gel along with the calcite within the matrix.
- CO_2 uptake and quantity of $CaCO_3$ formed in optimised carbonated aggregates was 12.9% and 28.9%, respectively.

This study provides an efficient and environmentally friendly way to prepare carbonated geopolymer aggregates using industrial solid waste without any binder through accelerated carbonation. The results demonstrated the feasibility of producing CO_2-sequestered aggregates on a large scale to meet the increasing demand for aggregates in the concrete industry.

Acknowledgements

Authors, Mohd Hanifa and Supriya are thankful to UGC, New Delhi and DST, New Delhi for financial support.

References

Baharom, M. I. N. H., & Mamat, C. R. B. (2015). *Hydration and Properties of Blended Cement System Incorporatiing Aerogel* Universiti Teknologi Malaysia].

Chancey, R. T., Stutzman, P., Juenger, M. C., & Fowler, D. W. (2010). Comprehensive phase characterization of crystalline and amorphous phases of a Class F fly ash. *Cement and Concrete Research*, *40*(1), 146-156.

Colangelo, F., Messina, F., & Cioffi, R. (2015). Recycling of MSWI fly ash by means of cementitious double step cold bonding pelletization: Technological assessment for the production of lightweight artificial aggregates. *Journal of Hazardous Materials*, *299*, 181-191.

Duxson, P., Fernández-Jiménez, A., Provis, J. L., Lukey, G. C., Palomo, A., & van Deventer, J. S. (2007). Geopolymer technology: the current state of the art. *Journal of materials science*, *42*, 2917-2933.

Gao, X., Yu, Q., & Brouwers, H. (2017). Apply 29Si, 27Al MAS NMR and selective dissolution in identifying the reaction degree of alkali activated slag-fly ash composites. *Ceramics international*, *43*(15), 12408-12419.

García-Lodeiro, I., Palomo, A., Fernández-Jiménez, A., & Macphee, D. E. (2011). Compatibility studies between NASH and CASH gels. Study in the ternary diagram Na2O–CaO–Al2O3–SiO2–H2O. *Cement and Concrete Research*, *41*(9), 923-931.

Garg, N., Özçelik, V. O., Skibsted, J., & White, C. E. (2019). Nanoscale ordering and depolymerization of calcium silicate hydrates in the presence of alkalis. *The Journal of Physical Chemistry C*, *123*(40), 24873-24883.

Guo, B., Zhao, T., Sha, F., Zhang, F., Li, Q., Zhao, J., & Zhang, J. (2017). Synthesis of vaterite CaCO3 micro-spheres by carbide slag and a novel CO2-storage material. *Journal of CO2 Utilization*, *18*, 23-29.

Ismail, I., Bernal, S. A., Provis, J. L., San Nicolas, R., Hamdan, S., & van Deventer, J. S. (2014). Modification of phase evolution in alkali-activated blast furnace slag by the incorporation of fly ash. *Cement and Concrete Composites*, *45*, 125-135.

Li, C., Sun, H., & Li, L. (2010). A review: The comparison between alkali-activated slag (Si+ Ca) and metakaolin (Si+ Al) cements. *Cement and Concrete Research*, *40*(9), 1341-1349.

Mehdizadeh, H., Shao, X., Mo, K. H., & Ling, T.-C. (2022). Enhancement of early age cementitious properties of yellow phosphorus slag via CO2 aqueous carbonation. *Cement and Concrete Composites*, *133*, 104702.

Mo, L., Zhang, F., & Deng, M. (2016). Mechanical performance and microstructure of the calcium carbonate binders produced by carbonating steel slag paste under CO2 curing. *Cement and Concrete Research*, *88*, 217-226.

Pade, C., & Guimaraes, M. (2007). The CO2 uptake of concrete in a 100 year perspective. *Cement and Concrete Research*, *37*(9), 1348-1356.

Provis, J. L., & Van Deventer, J. S. J. (2009). *Geopolymers: structures, processing, properties and industrial applications*. Elsevier.

Qian, L.-P., Wang, Y.-S., Alrefaei, Y., & Dai, J.-G. (2020). Experimental study on full-volume fly ash geopolymer mortars: Sintered fly ash versus sand as fine aggregates. *Journal of Cleaner Production*, *263*, 121445.

Ren, P., Ling, T.-C., & Mo, K. H. (2021). Recent advances in artificial aggregate production. *Journal of Cleaner Production*, *291*, 125215.

Tajra, F., Abd Elrahman, M., & Stephan, D. (2019). The production and properties of cold-bonded aggregate and its applications in concrete: A review. *Construction and Building Materials*, *225*, 29-43.

Tang, P., & Brouwers, H. (2018). The durability and environmental properties of self-compacting concrete incorporating cold bonded lightweight aggregates produced from combined industrial solid wastes. *Construction and Building Materials*, *167*, 271-285.

Wang, J., Yang, Y., Jia, Q., Shi, Y., Guan, Q., Yang, N., Ning, P., & Wang, Q. (2019). Solid-waste-derived carbon dioxide-capturing materials. *ChemSusChem*, *12*(10), 2055-2082.

Wei, Y.-L., Cheng, S.-H., Ou, K.-T., Kuo, P.-J., Chung, T.-H., & Xie, X.-Q. (2017). Effect of calcium compounds on lightweight aggregates prepared by firing a mixture of coal fly ash and waste glass. *Ceramics International*, *43*(17), 15573-15579.

Wu, Y., Mehdizadeh, H., Mo, K. H., & Ling, T.-C. (2022). High-temperature CO2 for accelerating the carbonation of recycled concrete fines. *Journal of Building Engineering*, *52*, 104526.

Yi, H., Ai, Z., Zhao, Y., Zhang, X., & Song, S. (2020). Design of 3D-network montmorillonite nanosheet/stearic acid shape-stabilized phase change materials for solar energy storage. *Solar Energy Materials and Solar Cells*, *204*, 110233.

Yi, H., Zhan, W., Zhao, Y., Qu, S., Wang, W., Chen, P., & Song, S. (2019). A novel core-shell structural montmorillonite nanosheets/stearic acid composite PCM for great promotion of thermal energy storage properties. *Solar Energy Materials and Solar Cells*, *192*, 57-64.

Analyzing the Behaviour of Graphene Oxide on the Durability Characteristics of Rubberized Concrete

Ipshita Pandey[1*], Gyanendra Kr Chaturvedy[2], U K Pandey[3], Shweta Goyal[4]

[1]Under Graduate Student, Department of Civil Engineering, TIET Patiala (Punjab)- 147004
Email:- ipandey_be21@thapar.edu
[2]Research Scholar, Department of Civil Engineering, NIT Hamirpur (H.P.)-177005,
Email:- gyanendra_phd@nith.ac.in
[3]Associate Professor, Department of Civil Engineering, NIT Hamirpur (H.P).-177005,
Email:- ukp@nith.ac.in
[4]Professor, Department of Civil Engineering, TIET Patiala (Punjab)- 147004,
Email:- shweta@thapar.edu

*Corresponding author

ABSTRACT

Utilizing waste tire rubber as rubber aggregate (RA) in concrete offers environmental sustainability benefits, aligning with eco-friendly practices and resource conservation in construction applications. Durability in rubberized concrete (RC) is crucial for long-lasting infrastructure, as it enhances resistance to weathering and chemical attacks. This promotes sustainability, cost-effectiveness, and overall structural resilience. This research investigates the impact of graphene oxide (GO) on the durability characteristics of high-strength RC, exploring its influence on the RC's lasting structural properties. Concrete durability was evaluated by subjecting hardened specimens to acid resistance test, water sorptivity, and rapid chloride penetration test (RCPT) over test durations of 28 and 90 days. For acid resistance test, acidic environment was prepared by separately mixing hydrochloric acid and sulphuric acid in water. The losses in RC's mass were evaluated for the acid resistance test. GO proved its usefulness by reducing the mass loss, and chloride penetration in the RC. GO reduces the water absorption in the RC samples. The findings of this study affirm that GO effectively enhances the long-term durability characteristics of RC.

KEYWORDS: *Rubber aggregate, Durability properties, Acid resistance, Chloride resistance*

1. Introduction

Concrete, a construction material more recent in development compared to steel and stone, has undergone significant research over the past century aimed at improving its properties. This increase in research activity is directly linked to the expanding utilization of concrete in the field of construction. With the rapid pace of urbanization, there exists a substantial demand for natural aggregates (NA), encompassing both fine and coarse varieties, to meet the requirements of construction. Although Portland cement continues to serve as a crucial construction binder, its existing production process consumes a significant amount of energy and results in carbon emissions. The imperative for alternative construction materials characterized by lower energy consumption and reduced carbon footprints has spurred extensive research (Chaturvedy et al. (2023)). In 2015, the global production of NA amounted to 48.3 billion metric tons, as reported (Sharma and Khan, 2017). Subsequently, there was an increase in production to 51.7 billion metric tons by 2019, with expectations of a continued upward trend in the future (Freedonia (2016)). Exploring alternative sources of building aggregates is imperative to safeguard natural resources and maintain ecological balance. This necessity arises from the challenge of fulfilling the construction industry's aggregate demand solely from natural sources.

The exponential growth in population and the concurrent rise in the demand for automobiles have resulted in a significant build-up of discarded tires, triggering a pressing environmental concern. Landfills and storage sites across the globe are inundated with vast amounts of these unused tires, posing an imminent threat to the ecosystem due to their sheer volume. A noteworthy utilization involves incorporating waste rubber into concrete, yielding a product known as rubberized concrete (RC). Studies have demonstrated that the use of rubber aggregate (RA) in RC presents numerous benefits compared to fine and coarse aggregates, such as decreased density, resistance to freezing and thawing, sound absorption, enhanced ductility, resilience against acid and chloride permeability, heightened deflection capacity, improved deformation ability, and thermal insulation [Chaturvedy and Pandey (2022)].
Graphene oxide (GO) is a nanomaterial characterized by sp2 hybridized carbon atoms within its lattice. When incorporated into concrete, it exhibits remarkable performance due to its expansive specific surface area, high dispersibility in water, substantial aspect ratio, exceptional mechanical properties, and cost-effective production. The structure comprises multiple layers of folded 2-dimensional carbon sheets, featuring oxygen-containing functional groups like carbonyl (-COO), hydroxyl (-OH), epoxy (-O-), and carboxyl (-COOH) groups present on its surface or within the inter-sheet layers [Chaturvedy and Pandey (2023)].
In this current investigation, the focus is on evaluating the durability characteristics of high-strength RC and assessing the impact GO on its behavior. The examination of GO-induced RC's durability involves studying its response to acid exposure (including mass and compressive strength losses), sorptivity, and Rapid Chloride Permeability Test (RCPT). The primary aim of this research is to draw a comparative analysis between the durability attributes of the innovative RC and CC.

2. Materials and methods

2.1 Materials

High-strength RC was produced using essential materials such as OPC 53 grade cement, sand, RA, natural coarse aggregate (CA), GO, fly ash (FA), silica fume (SF), superplasticizer (SP) and water. The concrete, cast with OPC 53 grade cement, utilized SF and FA as cementitious materials with a sp. gr. of 2.2. Locally sourced sand, replaced by RA at 5% and 10% ratios by weight, belonged to Zone II per IS:383-2016 [BIS 383-2016]. The average RA size was 2.1 mm. Physical properties of RA, sand, and CA are in Table 1; while properties of GO are presented in Table 2.

Table 1. Physical properties of RA, sand, and CA

Aggregates	Crushing index	Rel. density	Water absorption	Fineness modulus	Grading zone (IS:383-1986)
Sand	26.2	2.32	0.55	2.43	Zone II
RA	-	0.79	0.5	2.55	Zone II
CA	20.1	2.71	0.72	6.66	-

Table 2. Properties of GO

Properties	Av. carbon content	Av. oxygen content	Av. hydrogen content	Av. sulfur content	Odor	Colour	Texture
Result	70%	20%	1.50%	< 1%	Odorless	Black	Soft

2.2 Mix details

To achieve high-strength RC, five distinct concrete samples were prepared in accordance with IS:10262-2019 [BIS 10262-2019]. Sand was substituted by RA at 5%, 10%, and 15% weight ratios, while GO replaced cement at 0%, 0.01%, and 0.1% weight proportions. FA and SF constituted 15% and 10% of the total cementitious materials, respectively. CA consisted of 20mm and 10mm aggregates in a 60:40 ratio. All other materials for concrete production (excluding RA, GO, cement, and sand) remained consistent across the concrete mixes. Concrete mix details are presented in Table 3.

Table 3. Concrete mix details

Mix no.	Cement	FA	SF	Sand	RA		SP	GO		Water	Total CA
	kg/m^3	kg/m^3	kg/m^3	kg/m^3	%	kg/m^3	kg/m^3	%	kg/m^3	kg/m^3	kg/m^3
R0G0	410.55	82.11	54.74	610.83	0	0	2.74	0	0	138	1081.64
R5G0	410.55	82.11	54.74	580.29	5	30.54	2.74	0	0	138	1081.64
R5G0.05	410.35	82.11	54.74	580.29	5	30.54	2.74	0.05	0.2	138	1081.64
R5G0.1	410.14	82.11	54.74	580.03	5	30.54	2.74	0.1	0.4	138	1081.64
R10G0	410.55	82.11	54.74	549.75	10	61.08	2.74	0	0	138	1081.64
R10G0.05	410.35	82.11	54.74	549.75	10	61.08	2.74	0.05	0.2	138	1081.64
R10G0.1	410.14	82.11	54.74	549.75	10	61.08	2.74	0.1	0.4	138	1081.64
R15G0	410.55	82.11	54.74	519.21	15	91.62	2.74	0	0	138	1081.64
R15G0.05	410.35	82.11	54.74	519.21	15	91.62	2.74	0.05	0.2	138	1081.64
R15G0.1	410.14	82.11	54.74	519.21	15	91.62	2.74	0.1	0.4	138	1081.64

2.3 Test procedures

The analysis of the durability characteristics of RC was conducted through assessments involving mass loss, compressive strength loss, sorptivity, and RCPT. Each of these tests spanned durations of 28 and 90 days. For acid attack test, 5% acidic solution was prepared using hydrochloric acid (HCl) and sulphuric acid (H_2SO_4) separately. Acid attack test, sorptivity test, and RCPT were performed following the ASTM C267 [ASTM C267], ASTM C1585-04 [ASTM C1585-04], and ASTM C1202 [ASTM C1202], respectively.

3. Results and discussions

3.1 Mass loss of concrete under HCl and H_2SO_4

Mass losses for RC, by the action of acids, are presented in Fig.1. The control concrete specimen exhibited reduced mass loss in comparison to the other concrete samples at each stage of both acid exposures (H_2SO_4 and HCl). It was also clearly observed that mass losses for HCl acid at 90 days exposure is near about to those of H_2SO_4 at 28 days. Following the incorporation of RA in the concrete mix, the mass loss escalated to 21.3% and 9.6% after exposure to H_2SO_4 and HCl acid at 90 days, respectively, relative to its initial mass without exposure to acid. The increased mass loss after adding RA is attributed to the loosening of concrete caused by RA-induced micro-crack formation, making the materials prone to corrosion and easy erosion by sulphuric acid (Sabapathy et al.(2020)).

GO was found effective to mitigate the strength reduction by RA. GO fills RA-induced gaps, creating a denser microstructure and reducing loose materials in the concrete matrix. Its widespread presence forms a protective shield, effectively preventing acid penetration (Chaturvedy et al.(2023), Chaturvedy and Pandey (2023)).

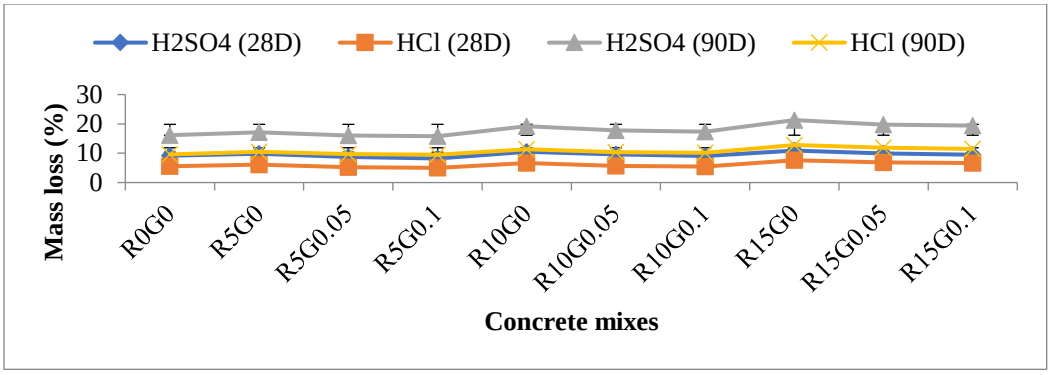

Figure 1. Mass losses for RC under acid attack at different exposure period

3.2 Sorptivity

Fig. 2 displays the sorptivity values of the concrete samples. For the control concrete specimen, the sorptivity was 0.175 and 0.155 mm/√s at 28 and 90 days, respectively. The inclusion of RA as a sand substitute resulted in increased sorptivity values. The highest sorptivity value occurred with 15% RA content during each sorptivity test period.

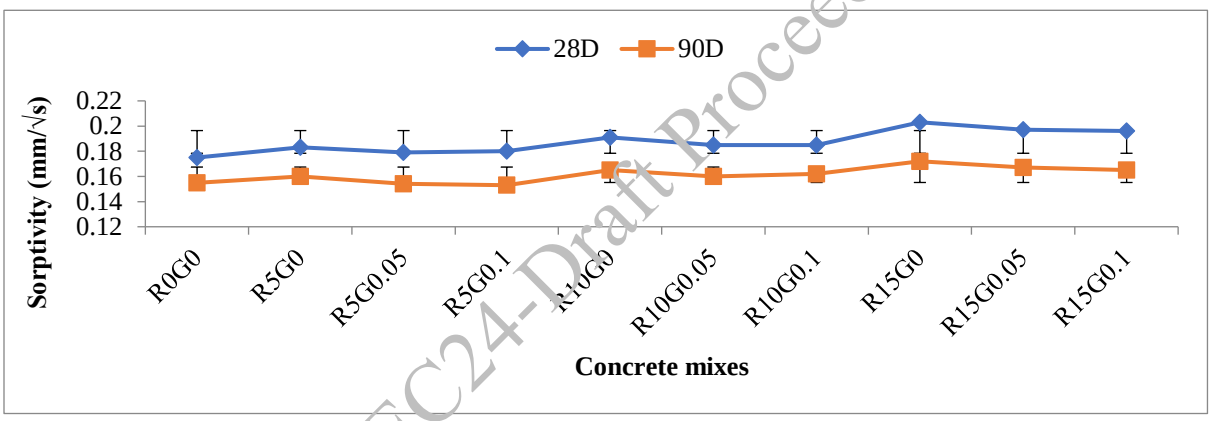

Figure 2. Sorptivity values at different testing period

The experimental findings also revealed that incorporating GO led to a reduction in water absorption in the RC mixes. For concrete samples having 15% RA, the water absorption reduced up to 3.45% and 4.07%, respectively after 28 and 90 days. The potential cause for the decline in sorptivity values following the introduction of GO into the RC mix is attributed to its nano-filler properties, effectively filling the pores within the concrete matrix. The dispersed and extensive structure of GO facilitates the filling of pores in the concrete matrix (Chaturvedy et al.(2023), Chaturvedy and Pandey (2023)).

3.3 RCPT

Fig.3 illustrates the experimental results of RCPT for the concrete specimens. The control concrete specimen demonstrated the highest electric current charges at both 28 and 90 days of the testing period. The introduction of RA in the concrete led to a reduction in the trend of charge passing. The charge passing through the concrete specimen decreased by 31.88% and 49.67% compared to the control concrete specimen at the 28 and 90-day testing periods, respectively. The decrease in charges passed with RA inclusion is attributed to void formation hindering charge transmission, and RA's hydrophobic and impervious nature resisting chloride passage in concrete specimens (Thomas et al. (2016), Yasser et al. (2023)).

The introduction of GO in the RC resulted in a reduction in the charge passed through the concrete specimen. GO significantly decreased the charge passed by 39.21% and 57.21% during the 28 and 90-day testing periods, respectively. The probable cause for the reduced charges with GO inclusion is the

refinement of the concrete matrix's microstructure, as GO fills voids and diminishes the quantity of transported chloride ions in the concrete mix [Chu et.al. (2022), Guo et.al. (2019), Yu and Wu , (2020)].

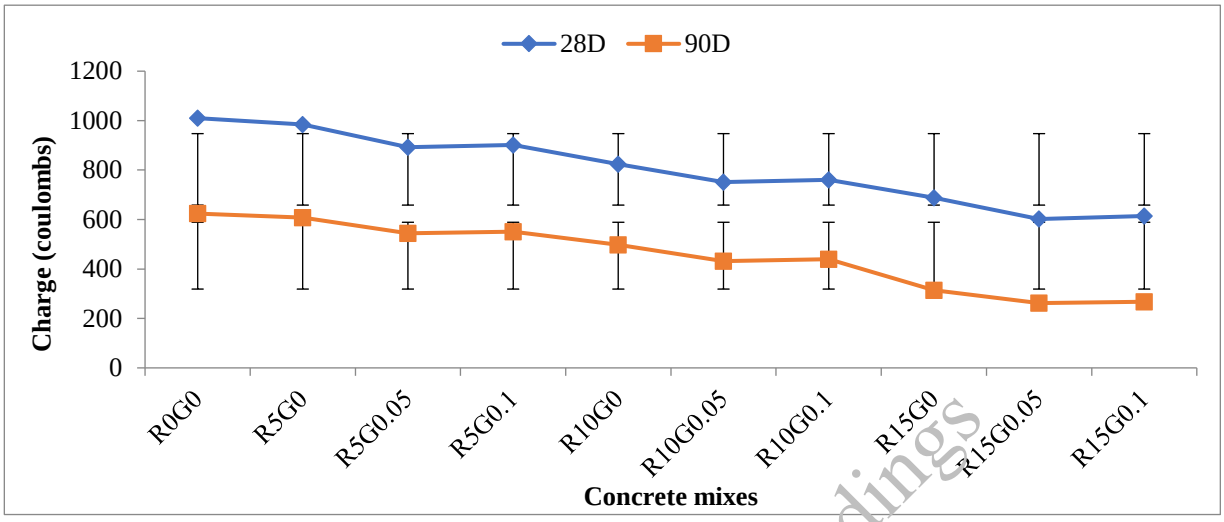

Figure 3. Effect of GO on RCPT values of RC

4. Conclusions

The mass loss in concrete specimens due to acid attack escalated with higher RA content and prolonged exposure periods. Additionally, the severity of mass loss was more pronounced under sulphuric acid exposure compared to hydrochloric acid. Concrete samples with 15% RA and a 90-day exposure period exhibited an increased mass loss of up to 21.3% and 12.8% for sulphuric acid and hydrochloric acid, respectively. The incorporation of GO proved effective in mitigating mass loss during both acid attacks, attributed to its nano-filler action and its role as a protective shield. The sorptivity of concrete samples rose with higher RA content and decreased with the curing period. A marginal decline in sorptivity values was noted for 15% RA content over curing periods from 28 to 90 days. The inclusion of GO significantly lowered the sorptivity values in the RC samples, with the maximum reduction observed at 0.05% GO content for each RA content level at every curing period. The quantity of charge transmitted through the concrete specimen diminished with both RA and GO content. The incorporation of RA and GO resulted in a reduction of the transmitted charge.

Utilizing durability assessment, it becomes evident that GO-induced RC exhibits similarity to CC. In simpler terms, it can be asserted that RA can be a reliable substitute for NA. Consequently, incorporating RA stands out as a preferable alternative to NA, representing a sustainable approach to alleviate the environmental impact of waste rubber tire disposal and lessen dependence on natural aggregates for concrete production.

References

ASTM C267 Standard Test Methods for Chemical Resistance of Mortars, Grouts, and Monolithic Surfacings and Polymer Concretes

ASTM. ASTM C1585-04 (2004) "Standard test method for measurement of rate of Absorption of water by hydraulic cement concretes."

ASTM. ASTM C1202 "Standard test method for electrical indication of concrete's ability to resist chloride ion penetration"

Chaturvedy, G. K.; Pandey, U. K.; Kumar, H.(2023) " Effect of graphene oxide on the microscopic, physical and mechanical characteristics of rubberized concrete." Innov. Infrastruct. Solut. 8, 163.

Chaturvedy, G. K.; Pandey, U. K. (2022) "Performance characteristics of rubberized

concrete: a multipoint review." Innov. Infrastruct. Solut., 7, 43.
Chaturvedy, G. K.; Pandey, U. K. (2023) " Investigating the effect of graphene oxide on the physical and mechanical properties of high-strength rubberized concrete using RStudio." Multiscale Multidiscip. Model. Exp. Des.
Chu, H.; Zhang, Y.; Wang, F. (2020)"Effect of Graphene Oxide on Mechanical Properties and Durability of Ultra-High-Performance Concrete Prepared from Recycled Sand." Nanomater.
Freedonia(2016) World construction aggregate. Industry study 3389 Accessed March.
Guo, K.; Miao, H.; Liu, L.; Zhou, J.; Liu, M. (2019) "Effect of graphene oxide on chloride penetration resistance of recycled concrete." Nanotechnol. Rev., 8, 681–689.
Indian Standard. IS:383-2016 Specification for coarse and fine aggregates from natural sources for concrete.
Indian Standard. IS:10262-2019 Concrete mix proportioning – guidelines.
Sabapathy, L.; Mohammed, B. S.; Al-Fakih, A.; Wahab, M. M. A.; Liew, M. S.; Amran, Y.
H. M.(2020) "Acid and sulphate attacks on a rubberized engineered cementitious composite containing graphene oxide." Mater., 13, 14, 3125.
Sharma, R.; Khan, R. A. (2019) "Sustainable use of copper slag in self compacting concrete containing supplementary cementitious materials." J. Clean. Prod.
Thomas, B. S.; Gupta, R. C.; Panicker, V. J.(2016) " Recycling of waste tire rubber as aggregate in concrete: durability-related performance." J. Clean. Prod. , 112, 504-513..
Yasser, N.; Abdelrahman, A.; Kohail, M.; Moustafa, A. (2023) "Experimental investigation of durability properties of rubberized Concrete." Ain Shams Eng. J., 14, 102111.
Yu, L.; Wu, R.(2020) " Using graphene oxide to improve the properties of ultra-high-performance concrete with fine recycled aggregate." Construct. Build. Mater., 259, 120657.

Performance of Concrete with Ground Glass Pozzolan as Partial Cement Replacement

Srishti Banerji[1*], Sushant Poudel[2], and Robert J. Thomas[3]

[1] *Assistant Professor, Department of Civil and Environmental Engineering, Utah State University, Logan, USA*
Email: srishti.banerji@usu.edu
[2] *Ph.D. Student, Department of Civil and Environmental Engineering, Utah State University, Logan, USA*
Email: sushant.poudel@usu.edu
[3] *Assistant Professor, Department of Civil and Environmental Engineering, Clarkson University, Potsdam, USA*
Email: rthomas@clarkson.edu

[*]Corresponding author

ABSTRACT

Cement is a primary binder in concrete, but its production is a significant source of carbon dioxide emissions. Pozzolans are frequently employed instead of cement in concrete to lessen the negative environmental impacts. Meanwhile, post-consumer glass (soda-lime) is of mixed color and is usually disposed of in landfills due to its unsuitability for recycling into new glass. Prior research has demonstrated that glass can exhibit pozzolanic reactions and produce strength-imbibing calcium silicate hydrate (C-S-H) gel when it is ground into a fine micro-size powder. Currently, there are limited studies on the properties of post-consumer recycled glass, which has a high alkalinity of 10-15% and can influence the strength and durability properties of concrete. Thus, the present study evaluates the performance of landfill-bound ground glass from a local recycling facility in Utah as a pozzolan in concrete. The glass was milled to a mean particle size of 10 μm and used to replace 10%, 20%, and 30% of the cement in conventional concrete mixtures. In this study, material characteristics including compressive strength, strength activity index, surface resistivity, and the alkali-silica reaction of the resulting concrete mixes were evaluated. The results show that local post-consumer waste glass can be a viable cement replacement to reduce the carbon footprint associated with concrete production.

KEYWORDS: *Concrete, Cement replacement, Waste glass, Ground glass pozzolan, Recycling.*

1. Introduction

Cement, a binding material in concrete, consumes about 10-15% of industrial energy and emits approximately 5-9% of the global anthropogenic CO_2 during its production (Bueno et al., 2020; Kalakada et al., 2020). Approximately 1 ton of CO_2 is produced during the production of 1 ton of cement which is environmentally taxing (Bueno et al., 2020; Krstic & Davalos, 2019). On the other hand, approximately 7% of the global solid waste consists of waste glass (WG) (Li et al., 2022). In 2018, 12.25 million tons of municipal WG were produced in the United States where only 25% of them were recycled and the remaining were either combusted (13.4%) or landfilled (61.6%) (EPA, 2020). The use of cement and its contribution to global warming can be reduced by incorporating waste glass as a supplementary cementitious material (SCM) to partially replace cement in concrete (Krstic & Davalos, 2019). Glass primarily comprises silicon dioxide (SiO_2) which reacts with the calcium hydroxide ($Ca(OH)_2$), a by-product of the hydration reaction between cement and water, to form additional calcium silicate hydrate (C-S-H) gel in concrete. Previous studies have demonstrated that waste glass when crushed and milled to a very fine powder of less than 300 μm particle size shows pozzolanic behavior, enhancing the mechanical and durability properties of concrete (Bueno et al., 2020). However, several factors, including the waste glass's particle size, ratio of cement replacement, and chemical composition

affect the performance of the resulting ground glass pozzolan (GGP) concrete (Ahmad, Zhou, et al., 2022). Each year, the United States produces approximately 11.5 tons of post-consumer glass, wherein 90% of glasses are soda-lime. Processing soda-lime glass as pozzolan can potentially lead to enhancement in the mechanical properties of concrete. However, soda lime glass has high alkalinity which can result in alkali-silica reaction (ASR) expansion in concrete. The addition of alkalis from glass in the concrete mix would exacerbate the formation of expansive ASR gel that will negatively affect the properties of concrete. Numerous studies have reported the use of industrially manufactured GGP as an SCM, while outlining the improvements in the mechanical and durability properties of the concrete. However, limited studies have been conducted on the performance of concrete containing locally available post-consumer soda-lime waste glass as a potential SCM. To overcome the current knowledge gaps, in this study, post-consumer waste glass from a local glass recycling facility in Utah was used to replace 10%, 20%, and 30% cement in conventional concrete mixtures, and its effect on the different properties of the concrete mixtures are evaluated.

2. Experimental Program

In this study, Type I/II (ASTM C150) ordinary Portland cement (PC) with a specific gravity of 3.15 and a mean particle size of 17μm is utilized. Coarse aggregate of a maximum size of 19 mm with a specific gravity of 2.65 and non-reactive siliceous river sand with a fineness modulus of 2.60 and oven-dry specific gravity of 2.67, obtained from Rocky Mountain Landscape Products, Richmond, Utah were used. For the alkali-silica reaction (ASR) test, the reactive aggregate was sourced from Rupert Pit in Idaho having the composition of approximately 25% quartzite, 20% basalt, 20% rhyolite, 15% siltstone, 15% obsidian. Recycled waste glass with an initial particle size of 210 μm was collected from Momentum Recycling in Salt Lake City, Utah. The glass was subjected to a grinding process in a laboratory ball mill with the help of steel balls for 2 hours to produce GGP with a mean particle size of 10 μm. Four concrete mixes as shown in Table 1 were fabricated with 0%, 10%, 20%, and 30% (by weight) cement replacement levels by GGP. Each batch mix (B) is named B-X-Y, wherein the variable X denotes the water-to-cement (W/C) ratio, while Y signifies the percentage of cement replacement for that mix. A constant water-to-cement (W/C) ratio of 0.45 was used in order to concentrate on understanding the effect of GGP on the partial replacement of cement. Concrete cylinders with 100 mm diameter and 200 mm height for the compressive test and 50 mm * 50 mm mortar cubes for the strength activity index (SAI) test according to ASTM C311 were prepared for all batches. ASTM C311 requires only a 20% cement replacement level to assess the pozzolanic reactivity of GGP, however in this study, 10% and 30% replacement levels were also studied to better understand the optimum cement replacement level by GGP. The same cylinders were used for surface resistivity tests before subjecting them to compressive strength tests. All the mixes were sufficiently workable, and the fabricated specimens were cured in lime-saturated water until the day of testing. In addition, 25 mm * 25 mm * 285 mm mortar prisms for each batch were prepared and immersed in 1N NaOH solution at 80°C for 14 days for the alkali-silica reaction (ASR) test.

Table 1. Concrete batch mix proportions.

Ingredient	B-0.45-0	B-0.45-10	B-0.45-20	B-0.45-30
Coarse aggregate (kg/m^3)	950	950	950	950
Fine aggregate (kg/m^3)	653	653	653	653
Cement (kg/m^3)	482	434	386	337
Ground Glass Pozzolan (kg/m^3)	0	48	96	145
Water (kg/m^3)	217	217	217	217

3. Results and discussion

The measured compressive strength values of the concrete cylinders with various replacement ratios of cement with GGP at 28 and 56 days are shown in Figure 1. Overall, the compressive strength of all batches increases with curing time due to the ongoing hydration of the cementitious materials within

the concrete. The increase in strength in later days is more pronounced in GGP-incorporated concrete than in the control mix. The highest compressive strength of 53 MPa and 61 MPa was obtained at 10% replacement at 28 days and 56 days, respectively. This is attributed to the optimal balance between the formation of Ca(OH)2 and its reaction with silica from glass to form additional C-S-H gel. The compressive strength for the 20% and 30% replacement levels are 9% and 17% lower than that of the control mix at 28 days. However, at 56 days, the compressive strength of 20% and 30% replacement levels are 3% and 2% higher than that of the control mix respectively. This increase in strength in later days is contributed by the pozzolanic activity of glass powder that produces more denser and stronger microstructure within the concrete matrix, as compared to the control batch. Strength Activity Index (SAI) is a measure to evaluate the pozzolanic reactivity of SCMs when used as a partial replacement for cement. SAI is calculated by comparing the compressive strength of the mortar cubes with SCM to that of the control mix (with cement as the only binder) at given days of curing. For this, ASTM C1866 requires the SAI to be 85% at 28 days after casting. Figure 2 shows the SAI for GGP is more than 100% for all mixes at both 28 and 56 days of curing, which is much higher than the required limit of 85%, indicating pozzolanic reactivity of GGP. This is attributed to secondary hydration between Ca(OH)2 and silica from the glass powder that produces additional strength imbibing C-S-H gel in the concrete matrix. The highest SAI at 28 days is achieved with 10% replacement whereas at 56 days, 20% replacement gives the highest SAI. This is due to the availability of a higher amount of silica at a 20% replacement level to react with Ca(OH)2. However, at a 30% replacement level, lower cement is present for hydration and this leads to the production of lower amounts of Ca(OH)2 reducing the formation of primary C-S-H gel and the overall strength.

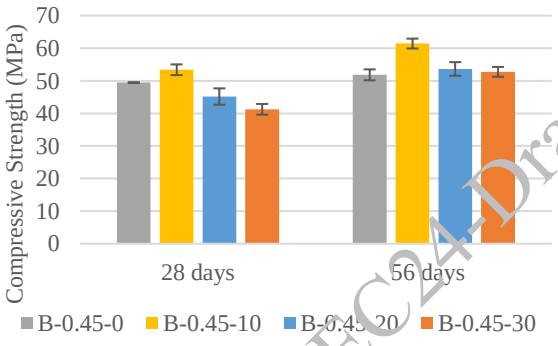

Figure 1. Compressive strength of mixes.

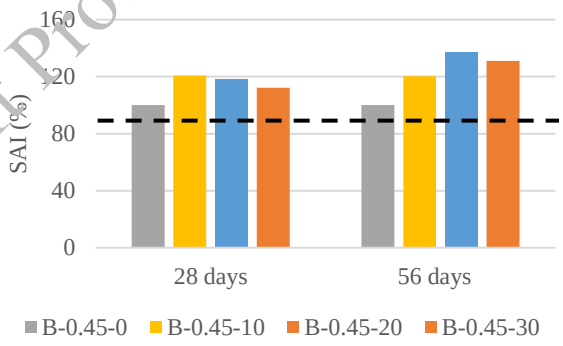

Figure 2. Strength activity index of mixes.

The surface resistivity is an indication of the ability of concrete to resist harmful chloride ion penetration through its surface. The measured surface resistivity for the tested specimens from different batches is shown below in Figure 3. The surface resistivity values of 10% cement replacement were similar to those of the control mix. Overall, the surface resistivity of the concrete specimens increases with replacement levels for all the batches at later days of curing (56 days). At 28 days, the 30% replacement level exhibits the highest surface resistivity of 25.5, followed by 20% replacement with 17.8, and 10% replacement with 15.9 respectively. However, 28-day resistivity values are surpassed in the 20% mix by 71% and in the 30% mix by 91% at 56 days indicating low chloride ion penetration. The higher surface resistivity values are an indication of pore refinement and decreasing permeability with increasing glass pozzolans. Although the hydration is not complete, its effect on pore structure alteration might have been captured in the surface resistivity tests.

The potential ASR expansion is evaluated according to ASTM 1567 for GGP-incorporated mixes by immersing the prismatic specimens in 1N NaOH solution at 80°C for 14 days. The measured expansions are shown in Figure 4. Overall, the ASR expansion decreases with an increase in the GGP content in the mortar bars. This is due to alkali dilution and consumption of alkali hydroxides in the pore solution of concrete with increasing GGP. An acceptable innocuous expansion of 0.092% is exhibited by only 30% GGP incorporated mortar bars at 14 days. Both the control batch and the 10% replacement batch

show detrimental expansions of 0.45% and 0.29% respectively due to ASR effects, although the expansion was reduced with the incorporation of GGP.

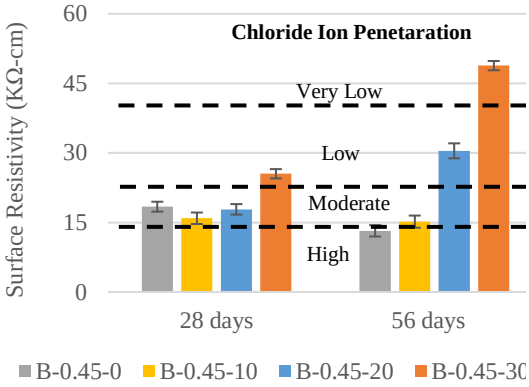

Figure 3. Surface Resistivity of Mixes.

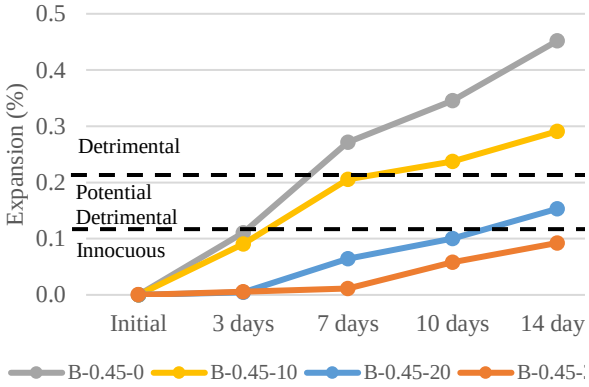

Figure 4. ASR Expansion of Mixes.

4. Conclusions

The results presented in this paper show that ground glass pozzolan (GGP) can serve as a promising SCM for use in concrete. Based on the findings from this study, the following conclusions can be deduced:

- The 10% cement replacement level by GGP demonstrated the highest compressive strength of concrete at 28 and 56 days. When compared to the control mix, cement replacement at 20% and 30% showed slightly lower strengths at 28 days but similar strengths at 56 days.
- The SAI at all substitution level is higher than 100% at 28 and 56 days, indicating pozzolanic reactivity of GGP. The 20% replacement reached the maximum SAI at 56 days. In contrast to the 10% cement replacement level, the 20% and 30% cement replacement levels displayed a lower SAI at 28 days but a greater SAI at 56 days.
- The 20% and 30% cement replacement levels by GGP showed higher surface resistivity, especially at 56 days, indicating superior resistance to corrosion caused by the ingress of chloride ions. The 10% cement replacement and control batches had comparable surface resistivity.
- The alkali-silica reaction expansion decreases consistently with the increase in the cement replacement levels by GGP with innocuous expansion at 30% cement replacement by GGP.
- Overall, the current results show that 10% cement replacement is optimum from strength perspective, whereas 30% cement replacement is optimum from the durability viewpoint.

Acknowledgments

The authors acknowledge the support of the Utah Department of Transportation (UDOT) for funding this research. Additionally, the authors would like to thank Momentum Recycling for providing recycled waste glass, Jeremy Wilcox from Jack B. Parson Ready Mix Concrete for providing the reactive aggregates, and Dr. James Bay for providing support with the use of the ball mill equipment for grinding waste glass into pozzolan.

References

Ahmad, J., Zhou, Z., Usanova, K. I., Vatin, N. I., & El-Shorbagy, M. A. (2022). A Step towards Concrete with Partial Substitution of Waste Glass (WG) in Concrete: A Review. *Materials (Basel, Switzerland)*, *15*(7), 2525. https://doi.org/10.3390/ma15072525

Bueno, E. T., Paris, J. M., Clavier, K. A., Spreadbury, C., Ferraro, C. C., & Townsend, T. G. (2020). A review of ground waste glass as a supplementary cementitious material: A focus on alkali-silica reaction. *Journal of Cleaner Production*, *257*, 120180. https://doi.org/10.1016/j.jclepro.2020.120180

EPA. (2020). *Advancing Sustainable Materials Management: 2018 Fact Sheet*. https://www.epa.gov/sites/default/files/2021-01/documents/2018_ff_fact_sheet_dec_2020_fnl_508.pdf

Kalakada, Z., Doh, J. H., & Zi, G. (2020). Utilisation of coarse glass powder as pozzolanic cement—A mix design investigation. *Construction and Building Materials*, *240*, 117916. https://doi.org/10.1016/j.conbuildmat.2019.117916

Krstic, M., & Davalos, J. F. (2019). Field Application of Recycled Glass Pozzolan for Concrete. *ACI Materials Journal*, *116*(4). https://doi.org/10.14359/51716716

Li, Q., Qiao, H., Li, A., & Li, G. (2022). Performance of waste glass powder as a pozzolanic material in blended cement mortar. *Construction and Building Materials*, *324*, 126531. https://doi.org/10.1016/j.conbuildmat.2022.126531

Investigations on the Effectiveness of Zeolite and Coconut Shell Powder as SCMs on the Mechanical Characteristics of Concrete

N. Bharath[1*], Dr S. Kavitha[2], and Dr S. Vijaya[3]

[1] Dept of Civil Engineering, Dr. Ambedkar Institute of Technology, Bengaluru, India, Email: bharathn5419@gmail.com
[2] Faculty in Civil Engineering, Dr. Ambedkar Institute of Technology, Bengaluru, India, Email: sajjalakavitha@gmail.com
[3] Faculty in Civil Engineering, Dr. Ambedkar Institute of Technology, Bengaluru, India, Email: vijaya_s.cv@drait.edu.in

*Corresponding author

ABSTRACT

This study investigates the use of Zeolite 13X and coconut shell powder (CSP) as supplementary cementitious materials (SCMs) to enhance concrete's mechanical properties. Zeolite (10%, 20%, 30%) and CSP (1%, 3%, 5%) were incorporated into concrete mixes. Coconut shell powder demonstrated a positive correlation with strength, with 1% matching control concrete at 7 and 28 days, and higher Coconut shell powder contents maintaining strength in flexural and split tensile tests. Zeolite showed mixed results: 10% increased strength, while higher dosages reduced it. The findings suggest CSP improves concrete's mechanical performance and sustainability, while Zeolite's optimal dosage requires further research. Zeolite requires further research to optimize dosage for strength benefits. Future studies on combined effects of these SCMs could lead to improved concrete.

KEYWORDS*: Zeolites, Coconut Shell Powder, SCMs, Mechanical properties*

1. Introduction

The construction industry is a major contributor to global environmental concerns, accounting for a significant portion of resource consumption and greenhouse gas emissions. As a result, there is a growing emphasis on sustainable construction practices that minimize environmental impact (Rajnivas, 2020). In contemporary construction practices, the quest for sustainable and efficient materials has led to the exploration of Supplementary Cementitious Materials (SCMs) to enhance the mechanical characteristics of concrete.

Zeolite 13X is a synthetic material. It is produced through a carefully controlled chemical process known as hydrothermal synthesis. Zeolite contains reactive silica and alumina, which react with calcium hydroxide to form additional calcium-silicate-hydrate (C-S-H) gel. This enhances concrete strength, durability, and reduces porosity. Coconut shells, a waste product, can be ground into CSP, which also exhibits similar beneficial pozzolanic properties (Anviti, and Manish, 2018). Utilizing these byproducts reduces reliance on virgin materials and promotes waste valorization.

The utilization of zeolite as an SCM in concrete is grounded in its chemical composition and structural properties. Zeolites are characterized by a three-dimensional framework of tetrahedral units, creating channels and cages within their structure (Nagrockiene, 2016). These voids enable zeolites to effectively trap and exchange ions, making them valuable in various industrial applications, including concrete production (Rajnivas, 2020).

Similarly, Coconut Shell Powder (CSP) presents unique advantages as an SCM in concrete formulations. CSP is a byproduct of coconut processing industries, offering an eco-friendly alternative to traditional filler materials (Nadzri, 2019). The addition of CSP not only reduces the demand for

conventional cement but also enhances the packing density of concrete particles, thereby improving its mechanical strength and resistance to cracking (Leman et al., 2016). This research involves the systematic analysis of concrete mixtures with varying proportions of zeolite 13X and CSP, along with control mixes without these additives, to assess their performance under different curing conditions and environmental exposures.

2. Experimental Investigation

2.1 Materials

Coconut shell powder is a natural byproduct derived from the processing of coconut shells. This fine, white powder is obtained by grinding dried coconut shells uniformly. CSP was procured from Renumata Agro, Latur, India, and Zeolite 13X was procured from Shreenath Marketing_Mehsana, North Gujarat, India. Similarly, other materials such as cement, Fine aggregates and Coarse aggregates were from various sources.

The specific gravity of Coconut Shell Powder (CSP) was 1.93, indicating a lighter material compared to the Zeolite with a specific gravity of 2.3, which is denser. CSP's 12% fineness and Zeolite's 6% fineness reflect their different impacts on concrete.

Figure 1(a) shows the SEM images of Zeolite 13X and 1(b) represents CSP. The morphology of Zeolite sample was distinguished by homogeneous dispersion of crystals with a spherical shape which contributes to its ability to fill voids within the concrete matrix, leading to denser and stronger concrete. The porous nature of Zeolite 13X helps in reducing the permeability of concrete by filling microvoids and reducing the connectivity of pores. Additionally, morphology of CSP sample described the surfaces were quite irregular and the surface textures are irregular and a rough surface texture led to better adhesion and improved strength of the concrete.

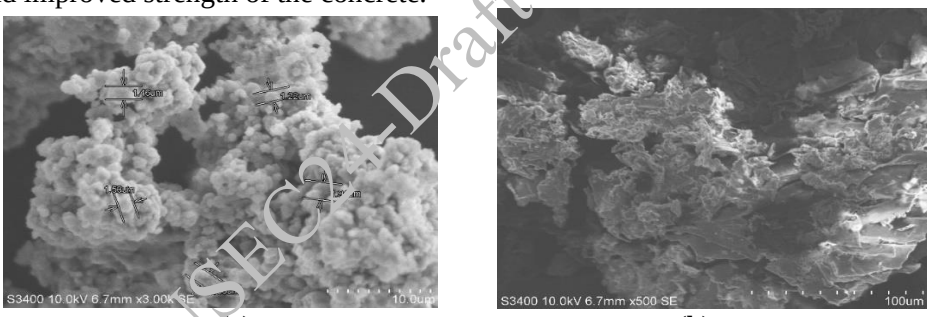

(a) **(b)**

Figure 1. (a) SEM image of Zeolite 13X and (b) CSP respectively

2.2 Mix Proportions

The mix proportions in concrete design are crucial to achieve the desired strength, durability, and workability. For M25 concrete, designed with a water-cement ratio of 0.5 and obtained with a mix proportion of 1:1.44:2.75 as per IS 10262 (2009), ensures the appropriate balance of materials for optimal performance. The specimens' names are given below Conventional concrete CC, additives for CC of Zeolite were added in 10%, 20% and 30% and Coconut shell powder in 1 %, 3%, and 5%, were named as Z10, Z20, Z30, CSP1, CSP3, CSP5, respectively.

2.3 Results and Discussions

2.3.1 Workability test

The conventional concrete had a slump value of 65 mm. With the addition of 10% Zeolite 13X and 1% CSP, the slump increased to 75 mm, indicating improved workability. This improvement is attributed to Zeolite and CSP's smooth surface and fine particles, which reduce internal friction and fill voids, resulting in a denser, more workable concrete mix. However, with 20% and 30% Zeolite 13X, the

concrete showed a zero slump, and adding 3% and 5% CSP resulted in slump values of 50 mm and 40 mm, respectively. This decrease in workability is due to the zeolite and CSP binding too much water, reducing the fluidity of the concrete.

2.3.2 Compressive Strength (CS)

Compressive strength tests were conducted following IS 516-1959. Results are presented in Tables 1 and 2 and Figures 2(a) and 2(b). At 7 days, Zeolite 13X at 10% (Z10) and 1% Coconut Shell Powder (CSP1) showed 16.083% and 14.25% higher strength, respectively, compared to conventional concrete. In contrast, Zeolite 13X at 20% (Z20) and 30% (Z30) exhibited 28.01% and 36.903% lower strength, while CSP at 3% and 5% showed 7.72% and 16.97% lower strength. At 28 days, CSP1 maintained a 9.76% increase in strength due to improved particle packing and microstructure, whereas all other mixes demonstrated reduced strength due to increased porosity and water absorption. Zeolite 13X at 10%, 20%, and 30% led to lower strength by absorbing excess water, disrupting particle distribution, decreasing cement content, and delaying hydration.

Table 1. Avg CS value of CC and Zeolite

SI.NO	Mix Proportion	Avg CS N/mm2	
		7 days	28 days
1	CC	21.588	37.253
2	Z-10	25.06	26.93
3	Z-20	15.54	16.77
4	Z-30	13.62	16.44

Table 2. Avg CS value of CC and CSP

SI.NO	Mix Proportion	Avg CS N/mm2	
		7 days	28 days
1	CC	21.588	37.253
2	Z-10	24.88	40.89
3	Z-20	19.92	30.03
4	Z-30	17.92	28.59

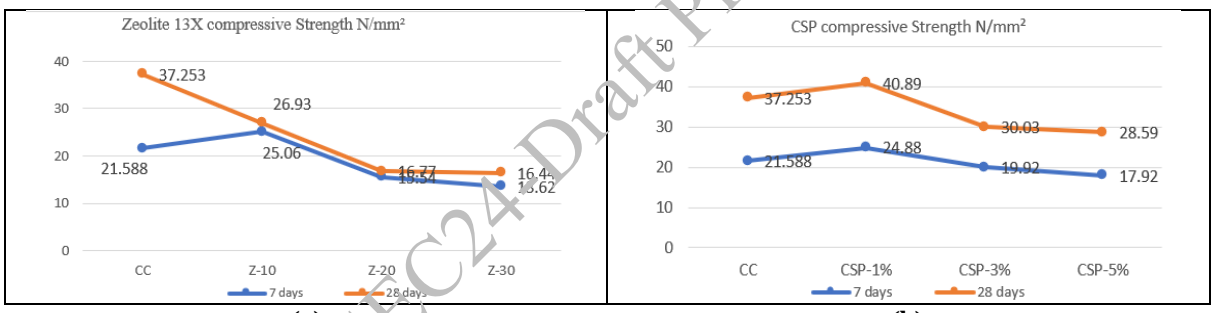

(a) **(b)**

Figure 2. (a) Compressive Strength of Zeolite 13X (b) CSP

2.3.3 Flexure Strength Test (FS)

Flexure Strength results obtained for different specimens cast are discussed as below. The Flexure Strength achieved are shown in Table 3 and Table 4 and represented in figure 3(a) and 3(b) respectively.

Table 3. Avg FS value of CC and Zeolite

SI.No	Mix Proportion	Average FS N/mm²	
		7 days	28 days
1	CC	4.75	4.625
2	Z-10	3.875	4.375
3	Z-20	2.875	2.875
4	2.825	2.825	2.375

Table 4. Avg FS value of CC and CSP

SI.No	Mix Proportion	Average FS N/mm²	
		7 days	28 days
1	CC	4.75	4.625
2	CSP-1%	4.125	4.375
3	CSP-3%	3.625	5.125
4	CSP-5%	3.875	5

At 28 days, CSP concretes (CS3 with 5.125 N/mm²) achieved the highest performance, surpassing conventional concrete (CC) by up to 8.1%. This improvement is due to CSP enhancing the concrete's microstructure, which results in better stress distribution and increased flexural strength. In contrast, the

Z series concretes exhibited lower flexural strength compared to CC, as high levels of Zeolite 13X increase porosity and weaken the concrete's resistance to bending stresses.

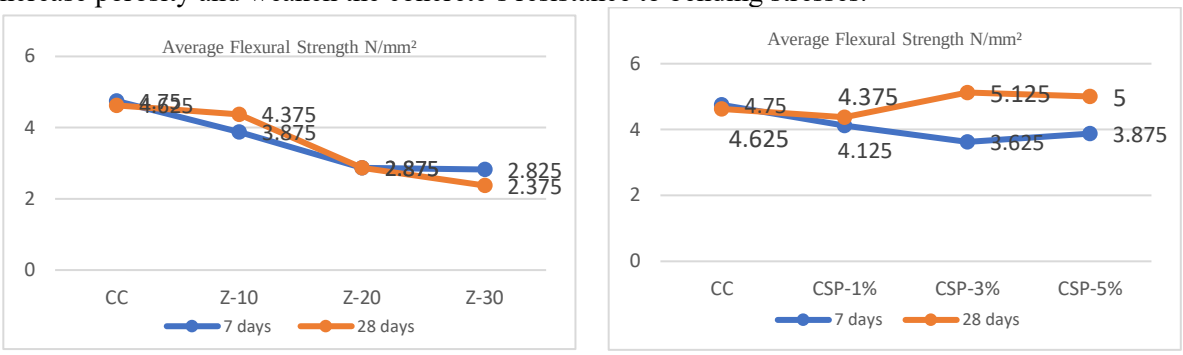

(a) **(b)**

Figure 3. (a) Average Flexural Strength of Zeolite 13X (b) CSP

2.3.4 Split Tensile Strength (STS)

Split Tensile Strength results obtained for different specimens cast are discussed as below. The Split Tensile Strength are shown in Table 5 and Table 6 respectively. At 7 days, CSP concrete (specifically CSP5) excelled in split tensile strength, surpassing conventional concrete (CC) by 27.86%. Other mixtures showed lower values compared to CC. By 28 days, the trend continued with CSP5 again showing the best results (6.78% higher than CC), while Z series concretes remained lower than CC in split tensile strength.

Table 5. Avg CS value of CC and Zeolite

SI.No.	Mix Proportion	Average STS N/mm2	
		7 days	28 days
1	CC	1.830	2.594
2	Z-10	1.747	1.997
3	Z-20	1.439	1.39
4	Z-30	1.3	1.34

Table 6. Avg CS value of CC and CSP

SI.No.	Mix Proportion	Average STS N/mm2	
		7 days	28 days
1	CC	1.830	2.594
2	CSP-1%	2.115	2.195
3	CSP-3%	1.455	2.235
4	CSP-5%	2.34	2.77

3. Conclusions

The investigation into the effectiveness of Zeolite and Coconut Shell Powder (CSP) as supplementary cementitious materials (SCMs) on the mechanical characteristics of concrete reveals distinct impacts on performance. The test results indicate that Coconut Shell Powder (CSP) concrete can be a promising alternative to conventional concrete. CSP category 1 (CSP1) showed the most improvement in compressive strength at 28 days, exceeding conventional concrete by 9.76%. While other CSP mixes and Zeolite 13X (Z) mixes generally fell short of conventional concrete in compressive strength, they likely achieved sufficient strength for certain applications Overall, CSP shows promise for improving concrete properties, while the use of Zeolite requires careful management to optimize its benefits without compromising performance.

Acknowledgements

The Authors are thankful to professor and head, dean, Dept of civil engineering, Dr. Ambedkar Institute of technology, Bengaluru.

References

Bhartiya, A., & Dubey, M. (2018). "Replacement of cement with coconut shell ash and eggshell powder for preparation of fresh concrete", *Int Res J Eng Technol*, *5*(6):1272-1275.

Leman, A. S., Shahidan, S., Senin, M. S., & Hannan, N. I. R. R. (2016), "A preliminary study on chemical and physical properties of coconut shell powder as a filler in concrete", In IOP Conference Series: *Materials Science and Engineering* (Vol. 160, No. 1, p. 012059). IOP Publishing.

Najimi, M., Sobhani, J., Ahmadi, B., & Shekarchi, M. (2012). An experimental study on durability properties of concrete containing zeolite as a highly reactive natural pozzolan. *Construction and building materials*, 35, 1023-1033.

Nadzri, S. N. I. H. A., Sultan, M. T. H., Shah, A. U. M., & Safri, S. N. A. (2019, November). A short review on the use of coconut shell powder as filler in cement concrete. In IOP Conference Series: *Materials Science and Engineering* (Vol. 670, No. 1, p. 012027). IOP Publishing.

Rajnivas, P., Freeda Christy, C., Selva Mugunthan, A., & Saravana Perumal, M. (2020). Effect of Zeolite in the Mechanical Properties of Concrete and its CO.

Investigation on Fresh Properties, Compressive Strength, and Microstructure of Self-Compacting Geopolymer Concrete

Akhil Charak[1*] and Bulu Pradhan[2]

[1] *Research scholar, Department of Civil Engineering, Indian Institute of Technology Guwahati, Guwahati, India*
Email: a.charak@iitg.ac.in
[2] *Professor, Department of Civil Engineering, Indian Institute of Technology Guwahati, Guwahati, India*
Email: bulu@iitg.ac.in

[*]Corresponding author

ABSTRACT

This study investigates the development of self-compacting geopolymer concrete (SC-GPC) using fly ash and ground granulated blast furnace slag (GGBFS) as precursor materials, activated by an alkaline activator solution comprising of sodium hydroxide (NaOH) and sodium silicate (Na_2SiO_3) solutions. Three different proportions of fly ash to GGBFS were examined: 100/0, 80/20, and 60/40 while maintaining a constant NaOH solution concentration of 12 M. The fresh properties were assessed by performing tests for slump flow spread, $T_{500\,mm}$ flow time, V-funnel flow time, passing ratio, and sieve segregation resistance. The compressive strength at 7-day and 28-day was evaluated and microstructure study was conducted through X-ray diffraction (XRD) and Fourier-transform infrared spectroscopy (FTIR) analyses. The test results revealed that slump flow spread, $T_{500\,mm}$ flow time, and V-funnel flow time increased with increase in GGBFS content while sieve segregation ratio decreased with increase in GGBFS content indicating an increase in the viscosity of mix. The 7-day compressive strength was lower in SC-GPC made with 20% GGBFS when compared with fly ash-based mix while 28-day compressive strength showed an increasing trend with increase in GGBFS content. In XRD patterns, nepheline, anorthoclase, and albite were identified, indicating the formation of geopolymer gels. Additionally, C-S-H gel peak was also identified in the XRD patterns of fly ash-GGBFS-based SC-GPC. The FTIR spectra showed the shifting of Si-O-T (T = Si or Al) bond towards lower wavenumber on the addition of GGBFS in self-compacting geopolymer concrete.

KEYWORDS: *Self-compacting geopolymer concrete, Fly ash, GGBFS, XRD, FTIR spectra.*

1. Introduction

The release of carbon dioxide (CO_2) emissions into the atmosphere due to the production of cement is well known. The two approaches were suggested to reduce the CO_2 emissions released through the production of cement: (1) partial or full replacement of cement with binders obtained from waste products, (2) alternate energy resources for the production of cement clinkers (Farooq et al (2021)). This study focused on the first approach, i.e., cement replacement with industrial by-products. The utilization of industrial by-products as an alternative to cement in the construction sector led to the development of geopolymer concrete (GPC). GPC is produced from the alkali activation of materials rich in aluminosilicates (John et al (2021)). However, the alkaline activator solution used in the production of GPC has a viscous nature which can affect the rheological properties of GPC. This may even adversely affect the compaction process causing more voids in GPC (Thunuguntla and Rao (2018)). The performance of concrete is greatly influenced by the compaction process irrespective of the quality of the mix design (Bheel et al (2021)). Thus, this study is an attempt to prepare the self-compacting geopolymer concrete (SC-GPC). SC-GPC is a special type of concrete that holds the properties of both GPC and self-compacting concrete. SC-GPC must be placed and compacted without any external effort

and cohesive enough to eliminate segregation and bleeding problems. SC-GPC has the ability to flow under its own weight even through confined spaces and eliminates the compaction process, resulting in a faster rate of construction.

2. Materials and mix proportions

The different materials used in the preparation of SC-GPC were precursor materials (fly ash and GGBFS), a combination of sodium hydroxide (NaOH, SH) solution of 12 M and sodium silicate (Na_2SiO_3, SS) solution as an alkaline activator solution, coarse aggregates (20 mm and 10 mm), fine aggregates, poly-carboxylic ether (PCE) based superplasticizer, and water. The fly ash and GGBFS were used in three different proportions (fly ash/GGBFS: 100%/0%, 80%/20%, and 60%/40%). The density of SC-GPC was kept constant at 2250 kg/m^3 for all SC-GPC mixes which included the fixed proportion of binder content, alkaline activator solution content, aggregate content, and water content at the values of 500 kg/m^3, 270 kg/m^3, 1460 kg/m^3, and 20 kg/m^3, respectively. In addition, superplasticizer was added at a dosage of 2% by weight of binder content.

3. Test methodology

The preparation of SC-GPC was carried out in a laboratory concrete drum mixer. After homogeneous mixing of ingredients, the concrete was discharged from the mixer and subjected to different tests to evaluate the fresh state properties of SC-GPC which include: a) slump flow spread test, b) $T_{500\ mm}$ flow time test, c) V-funnel flow time test, d) L-box test with three vertical bars, and e) sieve segregation resistance test. After evaluating the fresh state properties, SC-GPC mixture was paced in the cube moulds of size 150 mm without any vibration and compaction. The SC-GPC mixture comprised of 100% fly ash was left under laboratory conditions in moulds for 48 hours followed by oven curing at 80 °C for 48 hours. After that, SC-GPC specimens were demolded and left under laboratory conditions till compressive strength testing. On the other hand, fly ash-GGBFS blended SC-GPC mixes were demolded after 24 hours without oven curing and left under laboratory conditions till compressive strength testing. The compressive strength test was performed on 150 mm cube specimens at the testing age of 7 days and 28 days using a compression testing machine. The average compressive strength of three replicates for each mix was recorded as the compressive strength of the mix. Further, the microstructure of SC-GPC mixes was studied through X-ray diffraction (XRD) and Fourier Transform Infrared (FTIR) spectroscopy techniques.

4. Results and discussions

4.1 Fresh state properties of SC-GPC mixes

The test results of fresh state properties of SC-GPC mixes are given in Table 1. From this table, the slump flow spread of SC-GPC mixes decreased with the increase in fly ash proportion. This may be attributed to the finer particle size of fly ash, which increased the water requirement to wet the fly ash particles (Awoyera et al (2020) and Huseien et al (2021)). Further, higher water absorption of fly ash may also cause a detrimental effect on the slump flow spread with the increase in the proportion of fly ash. The increase in slump flow spread with the increase in GGBFS content may also be attributed to the increase in viscosity of SC-GPC mixes, as EFNARC (2005) guidelines suggested that concrete with a low viscosity will have a very quick initial flow and then stop while concrete with a high viscosity may continue to creep forward over an extended time. The $T_{500\ mm}$ flow time and V-funnel flow time increased with the increase in GGBFS content, indicating an increase in the viscosity of SC-GPC mixes. The passing ratio assessed through L-box test did not show any variation with the incorporation of GGBFS (Table 1). The segregation index (sieve segregation ratio) decreased with the increase in GGBFS content, indicating an improvement in the stability of SC-GPC mixes (Table 1). The results of sieve segregation resistance test are well corroborated with the results of $T_{500\ mm}$ flow time and V-funnel

flow time tests i.e., more the viscosity less the chances of segregation. Also, the faster polymerization reaction at higher GGBFS content resulted in higher resistance against segregation.

4.2 Compressive strength

The compressive strength of SC-GPC mixes are given in Table 1. From this table, the compressive strength of SC-GPC mixes increased with the increase in testing age due to the greater extent of the polymerization reaction, causing the formation of more geopolymer gel and resulting in a denser microstructure. The difference in 7-day and 28-day compressive strength of fly ash-based mixes was much lower than fly ash-GGBFS blended mixes. It may be due to the differences in the extent of the polymerization reaction at early ages, as fly ash-based mixes were oven-cured while fly ash-GGBFS blended mixes were cured under laboratory conditions. The 28-day compressive strength increased with the increase in GGBFS content. The higher amount of CaO in GGBFS resulted in an exothermic reaction, accelerating the polymerization reaction and promoting the formation of geopolymer gel and C-S-H gel, thus improving the compressive strength of SC-GPC mixes. However, the 7-day compressive strength of a mix with 100% fly ash was higher than the mix with 20% GGBFS while lower than the mix with 40% GGBFS. This may be attributed to the slower polymerization reaction at a lower dosage of GGBFS which would have caused the polymerization reaction to a lower extent at early ages when cured under laboratory conditions while oven-curing would have caused a higher degree of polymerization in fly ash-based SC-GPC mix, which is also evident from the difference in 7-day and 28-day compressive strength of SC-GPC mixes.

Table 1. Test results of fresh state properties and compressive strength of SC-GPC mixes

Description	12 M-100/0	12 M-80/20	12 M-60/40
Slump flow spread (mm)	715	730	745
$T_{500\ mm}$ flow time (s)	2.7	2.72	3.85
V-funnel flow time (s)	6.13	6.31	12.97
Passing ratio	0.91	0.91	0.91
Segregation index (%)	17.86	14.55	5.96
7-day compressive strength (N/mm^2)	45.48	27.85	47.41
28-day compressive strength (N/mm^2)	45.93	54.22	65.48

4.3 Microstructure investigations

The XRD spectra of SC-GPC mixes at 7 days and 28 days are shown in Figure 1 (a and b).

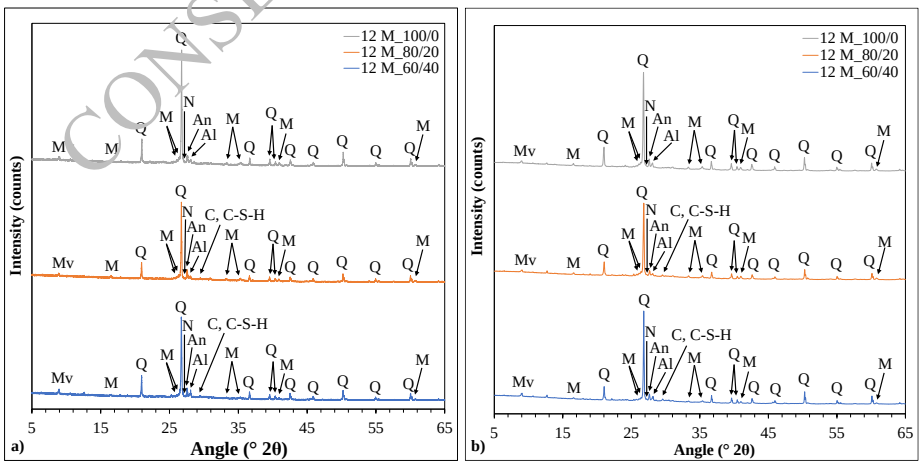

Figure 1. XRD spectra of SC-GPC mixes at different ages: a) 7 days; and b) 28 days

From Figure 1, the crystalline peaks associated with the quartz and mullite were observed in all SC-GPC mixes irrespective of testing age, suggesting the presence of unreacted/partly reacted fly ash. In addition to crystalline peaks, the semi-crystalline to amorphous peaks associated with nepheline, anorthoclase, albite, and calcite along with calcium-silicate-hydrate (C-S-H) gel were also identified.

However, the peak of C-S-H gel was not identified in fly ash-based SC-GPC mixes. The peak intensity of albite and C-S-H gel increased with the increase in GGBFS content irrespective of testing age, indicating the increase in the formation of calcium-based products, which can be attributed to the higher compressive strength at higher GGBFS dosage. The peak intensity of nepheline, anorthoclase, albite, and C-S-H gel increased with the increase in testing age indicating the formation of more geopolymer gel and C-S-H gel, and led to higher compressive strength at later ages (Figure 1). Despite the similarity in XRD patterns among different SC-GPC mixes, variations may exist in the chemical bonding which can potentially change the chemical network, consequently influencing the properties of the SC-GPC mixes. Hence, FTIR analysis was carried out for a better understanding of chemical bonding in SC-GPC mixes.

The FTIR spectra of SC-GPC mixes at 7 days and 28 days are shown in Figure 2 a and b.

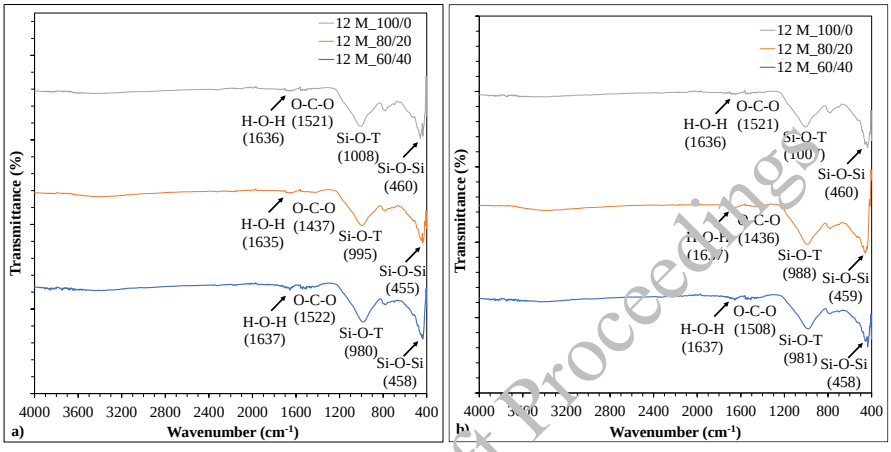

Figure 2. FTIR spectra of SC-GPC mixes at different ages: a) 7 days; and b) 28 days

From Figure 2, it was observed that the Si-O-T bond shifted towards the lower wavenumber with the increase in GGBFS content, indicating the differences in the degree of polymerization (Luo et al (2022)). The shift in Si-O-T bond towards lower wavenumber indicates the formation of geopolymer gel and integration of aluminium in the geopolymer gel (Luo et al (2022)). The position of C-A-S-H and N-A-S-H gel was reported centered at 950 cm^{-1} and 1020 cm^{-1}, respectively (Tu et al (2023)). In this study, the Si-O-T bond associated with reaction products exhibited a range from 980 cm^{-1} to 1008 cm^{-1}, suggesting the co-existence of C-A-S-H and N-A-S-H gel. The slight appearance of a peak around wavenumber 1600 cm^{-1} is associated with O-C-O bonds representing the presence of calcite in the geopolymer gel matrix (Tu et al (2023)). A small hump around 3400 cm^{-1} is associated with the vibration from free water while the bending vibration band of H-O-H around wavenumber 1650 cm^{-1} indicates the presence of physically and chemically bound water within the reaction products (Luo et al (2022)).

5. Conclusions

- The slump flow spread, viscosity, and resistance against segregation of SC-GPC mixes increased with the increase in the proportion of GGBFS content.
- The formation of calcium-based reaction products increased with the addition of GGBFS which increased the compressive strength.
- Higher peak intensity of geopolymer gel and C-S-H gel in XRD spectra of SC-GPC were observed with increase in age.
- FTIR analysis revealed the coexistence of N-A-S-H and C-A-S-H gel in SC-GPC.

References

Awoyera, P.O., Kirgiz, M.S., Viloria, A. and Ovallos-Gazabon, D. (2020). "Estimating Strength Properties of Geopolymer Self-compacting Concrete Using Machine Learning Techniques", Journal of Materials Research and Technology, 9 (4): 9016–9028.

EFNARC. (2005). "The European Guidelines for Self-compacting Concrete", Brussels, Belgium.

Farooq, F., Xin, J., Javed, M.F., Akbar, A., Shah, M.I., Aslam, F. and Alyousef, R. (2021). "Geopolymer Concrete as Sustainable Material: A State of the Art Review", Construction and Building Materials, 306: 124762.

Huseien, G.F., Sam, A.R.M. and Alyousef, R. (2021). "Texture, Morphology and Strength Performance of Self-compacting Alkali-activated Concrete: Role of Fly Ash as GBFS replacement", Construction and Building Materials, 270: 121368.

John, S.K., Nadir, Y. and Girija, K. (2021). "Effect of Source Materials, Additives on the Mechanical Properties and Durability of Fly Ash and Fly Ash-slag Geopolymer Mortar: A Review", *Construction and Building Materials*, 280: 122443.

Luo, Y., Li, S.H., Klima, K.M., Brouwers, H.J.H. and Yu, Q. (2022). "Degradation Mechanism of Hybrid Fly Ash/Slag Based Geopolymers Exposed to Elevated Temperatures", *Cement and Concrete Research*, 151:106649.

Thunuguntla, C.S. and Rao, T.D.G. (2018). "Mix Design Procedure for Alkali-activated Slag Concrete Using Particle Packing Theory", *Journal of Materials in Civil Engineering*, 30 (6): 04018113.

Tu, W., Fang, G., Dong, B. and Zhang, M. (2023). "Multiscale Study of Microstructural Evolution in Alkali-activated Fly Ash-slag Paste at Elevated Temperatures", *Cement and Concrete Composites*, 143: 105258.

Design Strategies for Optimising UHPC Bridge Girders

Leela Aparna Devi Kondapalli[1], Radhika V[2] and Bijily Balakrishnan[3*]

[1]Indian Institute of Technology Tirupati, India
ce22d504@iittp.ac.in
[2]Indian Institute of Technology Tirupati, India
radhikav@iittp.ac.in
[3] Indian Institute of Technology Tirupati, India
bijily@iittp.ac.in

[*]Corresponding author

ABSTRACT

Ultra High-Performance Concrete (UHPC) is an advanced construction material characterised by its exceptional compressive strength, which exceeds 120 MPa, along with significantly improved tensile and flexural properties. Even though there are various guidelines for the constitutive relationships of this material, the most widely used standard providing comprehensive design guidelines for UHPC is NF P18-710. The present study aims to explore two design strategies for UHPC, considering plain, rebar-reinforced, and prestressed UHPC sections to determine the optimal approach for each. The goal is to identify the optimal strategy for the design of bridge girders by adjusting the sectional properties and reinforcements to ensure economical and safe designs.

KEYWORDS*: UHPC, Sectional efficiency, Constitutive relationship, Design strategies*

1. Introduction

UHPC, a specialised concrete with enhanced compressive strength and superior mechanical properties, is increasingly being used in bridge applications worldwide. The limited availability of design standards for UHPC has encouraged further research in this field. While many countries are actively working on developing their own design standards, these are still under development. The French standards NF P 18-710 (Afnor and Droll, 2016) and NF P 18-470 (Standard F, 2016) are the most widely used for UHPC designs globally. Consequently, the design requirements for this study have been adopted from NF P 18-710 (Afnor and Droll, 2016).

The present study aims to evaluate two different design strategies for UHPC to determine the most suitable approach for plain, reinforced, and prestressed members. A 27-meter span bridge girder with a rectangular cross section is analysed to compare the two design strategies and their respective design capacities. The first strategy limits the maximum tensile strain in the bottom fibre, while the second strategy restricts the maximum compressive strain in the top fibre of the specimen. The primary aim here is to ensure that the members are efficiently designed, utilising the enhanced properties of the material to the maximum possible extent.

2. Methodology

Two design strategies are compared in this study. The first strategy involves limiting the maximum tensile strain in the cross-section, utilising both the tensile and compressive parts of the UHPC constitutive relationship as defined by NF P 18-710 (Afnor and Droll, 2016), shown in Figure 1. The second strategy focuses on limiting the maximum compressive strain in the section. It may be noted that this approach ignores the limited contribution of UHPC in tension. Plain UHPC sections are designed according to the first strategy, while the other two rebar-reinforced (R-UHPC) and prestressed (P-

UHPC) sections are designed using both strategies. Figure 2 summarises the five different cases (labelled I to V) examined in this study. The discussed strategies are applied to a 27-meter span bridge girder with a rectangular cross-section of 1m in width (Figure 3). The analysis is conducted using STAAD Pro, with limited deflections according to Eurocode 2 (Code P, 2005).

According to NF P 18-710 (Afnor and Droll, 2016), UHPC members can be designed without minimum reinforcement, as the steel fibers enhance the ductile behavior of concrete and contribute to its tensile strength. With no external reinforcement present, the only feasible design strategy for designing a plain UHPC section is to limit the maximum tensile strain (Case I in Figure 2). The section cracks and fails once the maximum tensile stress is reached.

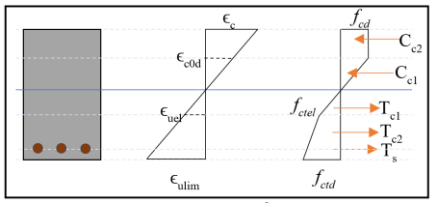

Figure 1. Constitutive relationship for UHPC

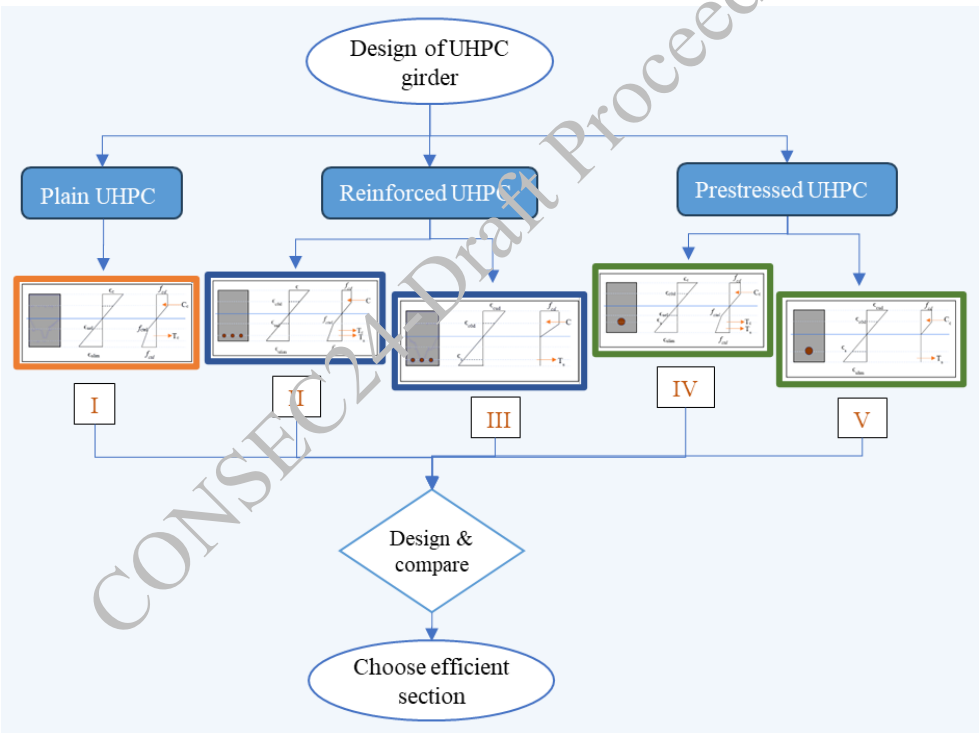

Figure 2. Schematic representation of methodology

When the maximum tensile strain is limited in R-UHPC and P-UHPC, the corresponding maximum compressive strain in the section can vary depending on the amount of reinforcement provided. Here, the top fibre may or may not reach the maximum strain limit. However, in the second approach, when the compressive strain is limited in the section, the strains in the bottom fibres would exceed the tensile limit, and the rebars will take up the tensile stress. The limiting values for prestressing forces are taken from IS 1343-2012 (IS 1343, 2012) since there are no provisions for the same in the French codes. The optimization technique followed in this study is shown in the Figure 4. Optimised cross-sections are identified for plain UHPC, R-UHPC and P-UHPC and the results are presented in the next section.

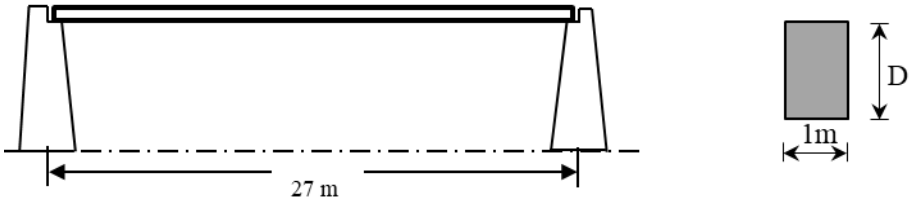

Figure. 3. Schematic representation of specimen used in the study

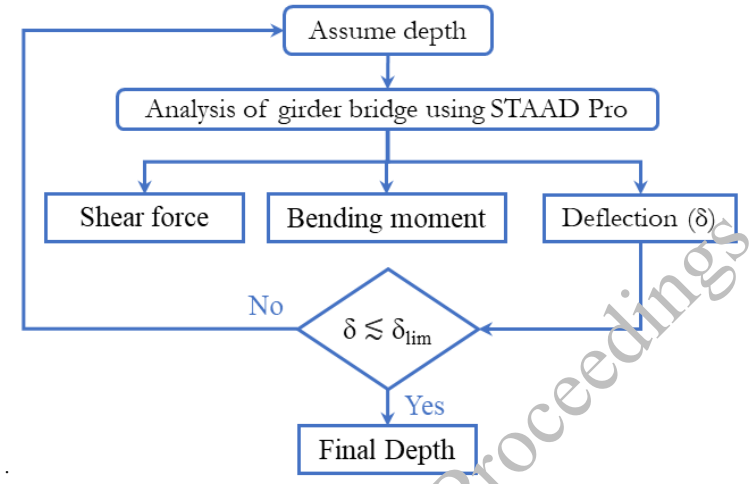

Figure. 4. Algorithm for optimization of cross-section

3. Results and discussions

Table 1 presents the moment demand along with the optimised cross sections for each case specified in Figure 2.

Table 1. Optimised sections for 27m bridge girder

	Plain UHPC (Case I)	Reinforced UHPC		Prestressed UHPC	
		Case II	Case III	Case IV	Case V
Moment Demand (kNm)	15343	14082	14082	13464.5	13464.5
Moment Capacity (kNm)	7701	14186	14104	13567	13581
p_t (%)	0	1.277	1.926	1.68	1.26
Strain in concrete at top fibre (ϵ_c)	$\epsilon_c = \epsilon_{c0d}$	$\epsilon_{c0d}<\epsilon_c<\epsilon_{cud}$	ϵ_{cud}	ϵ_{cud}	ϵ_{cud}
Depth of beam (mm)	1700	1400	1400	1250	1250
Strain in steel reinforcement (ϵ_s)	-	$\epsilon_s > \epsilon_y$ (Yielded)	$\epsilon_s > \epsilon_y$ (Yielded)	$\epsilon_s < \epsilon_y$ (Not yielded)	$\epsilon_s > \epsilon_y$ (Yielded)
d'/D	-	0.025	0.025	0.08	0.08

ϵ_{c0d} Elastic compressive strain in UHPC
ϵ_{cud} Ultimate compressive strain in UHPC
ϵ_y Yield strain for steel reinforcement

As discussed in Section 2, plain UHPC sections are designed by limiting the maximum tensile strain (Prisco et al., 2009). However, due to the limited tensile capacity of the material, these sections can fail rather suddenly once this limit is reached. This approach also results in significant underutilisation of

UHPC in compression, as the compressive strains remain well below their limiting values when the tensile strain limit is reached. Figure 5(a) presents the variation of moment capacity and maximum compressive strain in the section with varying depth-to-width ratios. Very large cross sections are required to meet moment demands, increasing the self-weight and cost of the structure. Therefore, designing such a member with plain UHPC is not practical. R-UHPC, when designed by limiting the maximum tension (Case II), has higher moment capacity when compared to the design by limiting the maximum compressive strain (Case III) (Figure 5(b)) for varying percentages of steel reinforcement. However, the optimal section identified in Case III fully utilises the compressive capacity of the member, whereas in Case II, UHPC in compression is not fully utilised. Figures 5(c) and 5(d) show the variation of moment capacity along with the maximum compressive strain in UHPC and tensile strain in rebar for Cases II and III, respectively. It is noteworthy that the limiting percentage of steel, which marks the boundary between under-reinforced and over-reinforced sections, is relatively lower in Case III. When P-UHPC is designed by limiting the tensile strain (Case IV), the prestressing reinforcement does not yield, rendering the section inefficient. Therefore, for P-UHPC, designing the section by limiting the compressive strain (Case V) results in greater sectional efficiency.

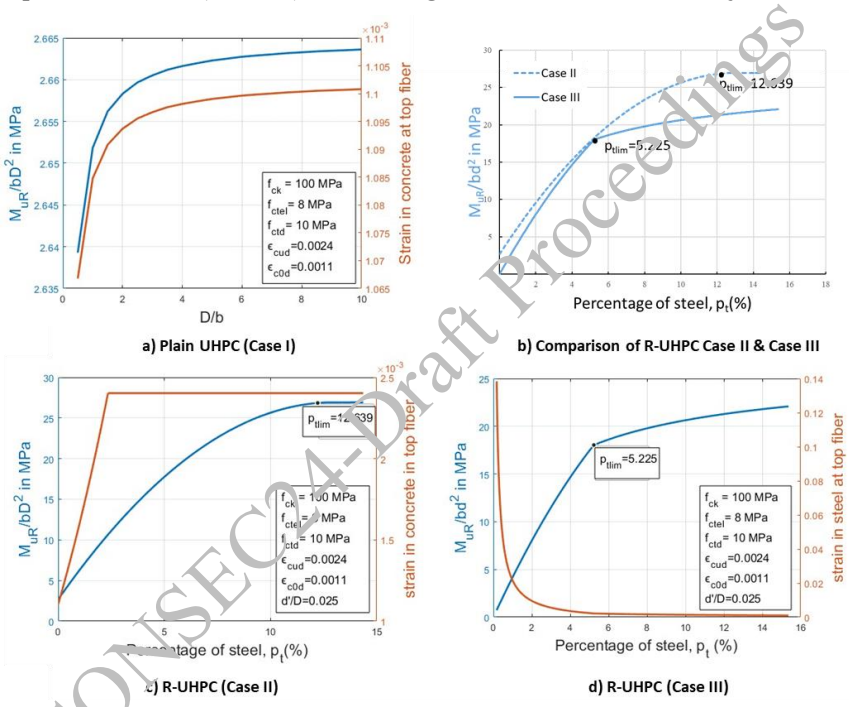

Figure 5. Variation of moment capacity and strains for plain UHPC and R-UHPC sections

4. Conclusions

The major conclusions drawn from the study are:

- Plain UHPC sections cannot be designed economically for bridge girders.
- For R-UHPC, the design strategy that limits tensile strain is found to give higher moment capacity, even though the compression capacity of the section is not completely utilised.
- The recommended design strategy for P-UHPC is to limit the maximum compressive strain.
- Among plain, reinforced, and prestressed UHPC members, P-UHPC is found to be the most efficient and economical.

It may be noted that all the aforementioned studies are conducted using a rectangular section, which is considered uneconomical for a bridge girder. The study may be repeated with I- and U-girders to achieve the maximum optimisation of the girder design.

References

Afnor, N., and Droll, K. (2016). *P18-710:* "National addition to Eurocode 2–Design of concrete structures: Specific rules for ultra-high performance fiber-reinforced concrete (UHPFRC) ", Association Française de Normalisation.

Code, P. (2005). "Eurocode 2: design of concrete structures-part 1–1: general rules and rules for buildings",*British Standard Institution*, London, 668: 659-668.

Di Prisco, M., Plizzari, G. and Vandewalle, L. (2009) "Fibre reinforced concrete: new design perspectives", *Materials and structures*, 42:1261-1281.

IS 1343. (2012) " Indian Standard Prestressed Concrete - Code of Practice", *Bureau of Indian Standards*, Manak Bhavan, New Delhi

Standard, F. (2016) "NF P18-470-concrete-ultra-high performance fibre-reinforced concrrte-specifications, performance, production and conformity", *La Plaine Saint-Denis: Association Française de Normalisation*, 94.

Development of Binary Blended Green Concrete with Enhanced Properties for Marine Applications

Jerus Anna Kurian [1], M V Varkey [2] and Manu Harilal [3, *]

[1] *Department of Civil Engineering, Amal Jyothi College of Engineering, Kanjirappally India, jerusannakurian@gmail.com*
[2] *Department of Civil Engineering, Amal Jyothi College of Engineering, Kanjirappally India, mvvarkey@amaljyothi.ac.in*
[3] [*]*Department of Metallurgical and Materials Engineering, Amal Jyothi College of Engineering, Kanjirappally India, manuharilal@amaljyothi.ac.in*

[*]Corresponding author

ABSTRACT

Corrosion presents a substantial risk to the strength and durability of concrete structures exposed to marine conditions. Utilizing fly ash, a byproduct from coal-based power plants, as a supplementary cementitious material in concrete is a common practice for enhancing its durability. However, studies indicate early-age performance issues in fly ash concrete, such as low initial strength, delayed setting time, and increased calcium leaching. To address these challenges, this research endeavors to overcome the drawbacks of fly ash concrete by incorporating a $NaNO_2$ based corrosion inhibiting admixture into concrete. Six mix proportions of M45 grade concrete were formulated, including conventional concrete (OPC) with 100% OPC, 60% OPC and 40% fly ash concrete (CF), and fly ash concrete with the addition of 1%, 2%, 3%, and 4% $NaNO_2$ (CFI1%, CFI2%, CFI3%, CFI4%, respectively). Specimens were cured for 28 days in freshwater, and various mechanical properties such as compressive strength, split tensile strength, and flexural strength were assessed. Ultrasonic Pulse Velocity (UPV) of the mix proportions were also measured to determine the quality of the concrete. The outcomes indicated that the inclusion of the inhibitor effectively addressed the deficiencies of fly ash concrete, enhancing its early-age properties. These findings offer valuable insights for developing sustainable solutions in marine infrastructure with improved performance.

Keywords: *Binary blended concrete, Mechanical properties, Corrosion inhibitor, Marine environment*

1. Introduction

Concrete is the most widely used construction material globally due to its high strength and cost-effectiveness. However, cement production contributes to approximately 8% of global CO_2 emissions, posing a significant environmental threat and challenging the sustainability of conventional concrete [1]. Green concrete, which incorporates eco-friendly waste materials, plays a crucial role in reducing CO2 emissions and minimizing environmental impact. It not only lowers carbon footprints by approximately 40-50% during production but also offers excellent thermal insulation and high fire resistance, enhancing the sustainability and durability of construction materials. Additionally, green concrete contributes significantly to resource conservation and waste reduction. By using recycled materials such as fly ash, blast furnace slag, and recycled aggregates, green concrete helps in the efficient utilization of industrial by-products, thereby promoting a circular economy in the construction industry [2, 3]. Fly ash, a by-product of coal-based power plants, mainly consists of SiO_2, Al_2O_3, Fe_2O_3, and CaO, along with minor impurities. Utilizing high volumes (>40%) of fly ash in concrete mixes is cost-effective and enhances desirable properties such as durability and workability [4]. However, there are certain drawbacks that needs to be addressed for improved performance. Fly ash concrete (FA

concrete) often shows high levels of calcium leaching, but the degree of weight reduction and deterioration is generally minimal. Additionally, a notable problem with concrete containing high levels of fly ash is the slower setting time and reduced early strength gain [5]. The corrosion of reinforcing steel in concrete has become a major global concern, especially in structures like buildings, bridges, and tunnels that are exposed to seawater or corrosive chemicals. This deterioration has resulted in high repair expenses, which have become a significant component of infrastructure budgets [6]. Employing corrosion-inhibiting admixtures is regarded as a highly cost-effective approach to addressing this widespread issue. These admixtures can be readily and affordably applied to both new and existing structures [7]. Corrosion inhibitors in concrete, such as sodium nitrite, are used to extend the lifespan of steel reinforcements by mitigating the corrosive effects of chloride ions and other aggressive agents. Sodium nitrite, in particular, acts as an anodic inhibitor, forming a protective oxide layer on steel surfaces, which significantly reduces the rate of corrosion [8]. However, inhibitors and fly ash alone do not provide adequate protection against corrosion. Their combination, however, offers substantial benefits in HPC by significantly increasing resistance to chloride diffusion [9]. This study seeks to create a sustainable binary blended green concrete by blending fly ash and improving its properties with the addition of a corrosion inhibitor, tailored specifically for marine environments. Furthermore, it will evaluate the mechanical properties of this enhanced concrete.

2. Materials and Methods

2.1 Materials used

Ordinary Portland Cement (OPC 43 grade) with a specific gravity of 3.15 and a fineness modulus of 8.2, conforming to IS 8112-2013 [10], was used for casting the concrete specimens. Class F Fly ash (Siliceous type) was used as a partial (40%) cement replacement material according to IS 3812 [11]. Crushed river sand belonging to Zone II with a specific gravity 2.56 was utilized as fine aggregates. Crushed black granite within 12 to 20mm size range, each having a specific gravity of 2.675, were used in equal proportions as coarse aggregates. The selection of aggregates complied with IS 383 standards [12]. Ceraplast 300 was used as the superplasticizer, conforming to BIS 9103:1999/ASTM C494 [13] type F for imparting workability for design mixes. The corrosion inhibitor used in this study is a commercially available sodium nitrite-based compound which is brown in colour.

2.2 Mix design and proportioning

The mix design for the binary blended green concrete was developed according to IS 10262:2009 [14] guidelines. Six distinct M45 grade concrete mixtures were produced: Control Concrete (OPC), Fly Ash Concrete (CF), Fly Ash Concrete with 1% $NaNO_2$ (CFI1%), 2% $NaNO_2$ (CFI2%), 3% $NaNO_2$ (CFI3%), and 4% $NaNO_2$ (CFI4%). Details of the mix design are outlined in **Table 1**. The CFI mixes were formulated with a reduced water-to-cement (w/c) ratio of 0.35, while the OPC and CF mixes had a w/c ratio of 0.36.

Table 1. Mix proportion of the six various compositions used in the study

NOMENCLATURE	Cement (Kg/m^3)	Fly ash (Kg/m^3)	FA (Kg/m^3)	CA (Kg/m^3)	Nitrite (Kg/m^3)	W/C
OPC	450	-	614.56	1180	-	0.364
CF	270	180	614.56	1180	-	0.364
CF11%	267.3	180	614.43	1178.51	2.7	0.359
CFI2%	264.6	180	614.22	1176.7	5.4	0.358
CFI3%	261.9	180	613.89	1175.23	8.1	0.358
CFI4%	259.2	180	613.54	1175.11	10.8	0.357

2.3 Test Specimens and Testing Methods

To design binary blended concrete, careful material selection, precise dosages, thorough mixing, proper compaction, and adequate curing are essential for achieving uniformity. Initially, cement and fly ash were combined with water in a concrete mixer, followed by the addition of fine and coarse aggregates, which were mixed for 3-5 minutes. A superplasticizer was then incorporated with the total water content using a handheld mixer for one minute, after which the corrosion inhibitor was added. The workability of the fresh mix was evaluated immediately using the slump test. The concrete was mixed thoroughly, placed into standard molds, and cast. Finally, the specimens were cured in a laboratory tank with water at room temperature for 28 days. Compressive strength tests were carried out in accordance with ASTM C39/C39M-18 [15] on 150 mm concrete cubes at 3, 7, and 28 days, using a digital compressive testing machine, with a total of 72 cubes evaluated. For split tensile strength, cylindrical specimens with a diameter of 150 mm and a height of 300 mm were tested after 28 days following ASTM C496/C496M-17 [16], involving a total of 18 cylinders tested using a compression testing machine. Flexural strength tests were performed according to ASTM C293/C293M-16 [17] on standard 100 x 100 x 500 mm beams using a Universal Testing Machine under two-point loading conditions, with 18 beams tested. The ultrasonic pulse velocity test on concrete is conducted according to ASTM C597 [18], which involves measuring the time it takes for an ultrasonic pulse to travel through the concrete specimen. Concrete cube specimens of 150 mm size were used for the test and 18 specimens were tested.

3. Results and Discussions

3.1 Compressive strength

The compressive strength results of the concrete specimens after 3, 7 and 28 days of curing in fresh water are presented in **Fig. 1**. It was observed that the OPC concrete specimens showed a significant increase in strength compared to all other mixes and achieved 65% of target strength at 3 days. This could be due to the high levels of hydration and early age strength gain in OPC concrete. CF specimen achieved 20.5% of target strength and among the inhibitor admixed specimens, CFI2% achieved approximately 34% of the target strength after 3 days of curing in water. After 7 days of curing, OPC specimens attained 69% of their target strength, whereas CF specimens attained 35.3% at the same stage. Among the inhibitor admixed mixes, CFI2% exhibited the maximum strength gain (48.4%).

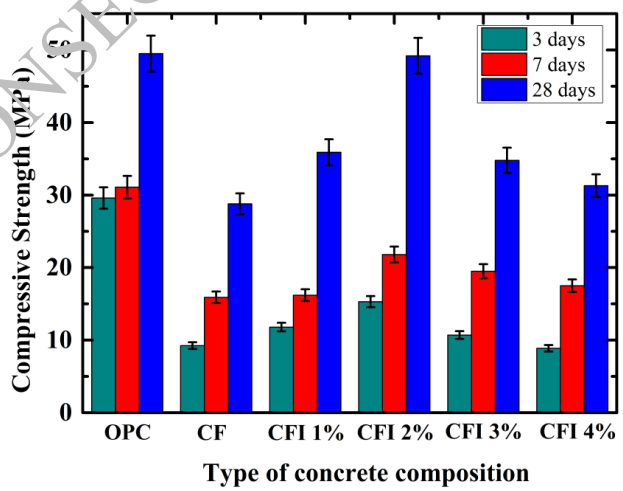

Figure 1. Compressive strength of the concrete specimens after 3, 7 and 28 days

At the end of the 28-day curing period, the OPC specimens achieved a higher compressive strength (49.5 MPa) than the expected target mean strength. The CF specimens showed a slight reduction in target mean compressive strength compared to the OPC specimens (only 64%). Notably, the CFI2% concrete specimens attained a similar compressive strength (49.2 MPa) as compared to the OPC

specimens. However, with increased $NaNO_2$ incorporation, the compressive strength decreased as evident from the values for CFI3% and CFI4% compositions. Thus, 2% may be the optimum quantity of $NaNO_2$ inhibitor that could be added to fly ash concrete to overcome its early age limitations.

3.2 Split tensile strength

The 28-day curing results for the split tensile strength of concrete, shown in **Fig. 2**, reveal that the ordinary Portland cement (OPC) specimens attained an ultimate tensile strength of 3.96 MPa. In contrast, the CF specimens exhibited a lower tensile strength of 2.4 MPa, which is attributed to the incorporation of fly ash and its associated reduction in early-age strength. Notably, the CFI2% specimens recorded the highest tensile strength among all mixes, reaching 4.1 MPa. These findings demonstrate a significant increase in the tensile strength of fly ash-admixed concrete compared to the OPC mix, highlighting the synergistic effect of fly ash and the added inhibitor. However, with 3% and 4% additions of the inhibitor, the split tensile strength again decreased as indicated by the values of 2.47 MPa and 2.12 MPa, respectively in CFI3% and CFI4% specimens. Thus, 2% nitrite addition to fly ash significantly improves the properties of fly ash concrete.

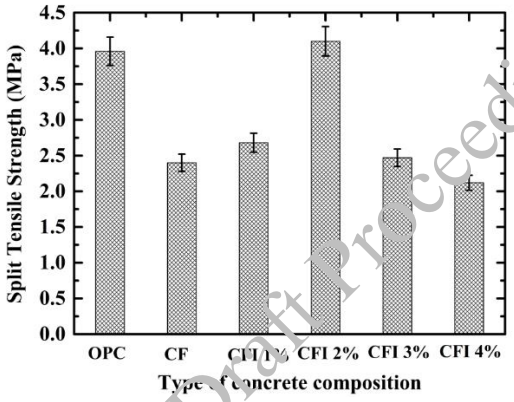

Figure 2. Split tensile strength of the concrete specimens after 28 days

3.3 Flexural strength

Beam specimens measuring 500 x 100 x 100 mm were tested under two-point loading using a Universal Testing Machine until failure. The flexural strength values of all the concrete mixes are shown in **Fig. 3**. The OPC concrete specimens demonstrated a flexural strength of 5.08 MPa, whereas the CF specimens showed a lower flexural strength of 4.35 MPa, reflecting the reduced early-age strength due to fly ash. Among all mixes, the CFI2% mix achieved the highest flexural strength at 5.91 MPa. In comparison, the CFI3% and CFI4% specimens had flexural strength values of 3.94 MPa and 3.73 MPa, respectively. These results are consistent with the split tensile strength findings, indicating that the addition of 2% inhibitor to fly ash concrete yields the maximum strength.

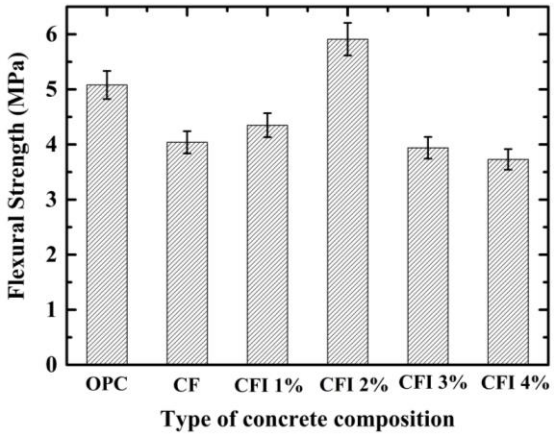

Figure 3. Flexural strength of the concrete specimens after 28 days

3.4 Ultrasonic pulse velocity (UPV)

The ultrasonic pulse velocity (UPV) test is a widely used non-destructive method for evaluating the uniformity and relative quality of concrete, as well as for detecting the presence of cracks, cavities, and defects, and estimating the depth of cracks. According to ASTM C597 [18], UPV values between 3.66 and 4.58 km/s classify concrete as being in good condition, implying the absence of significant voids or cracks that could compromise structural integrity. UPV values exceeding 4.5 km/s indicate superior concrete quality in terms of density, uniformity, and homogeneity. Low UPV values suggest the presence of internal voids or porous aggregates in the concrete [18, 19]. The UPV measurement results, presented in **Fig. 4**, clearly show that all concrete compositions had UPV values above 4.5, indicating their superior quality. The CFI2% mix exhibited the highest UPV value of 4.97 km/s, confirming that the addition of 2% inhibitor to fly ash significantly enhances the quality and properties of fly ash concrete.

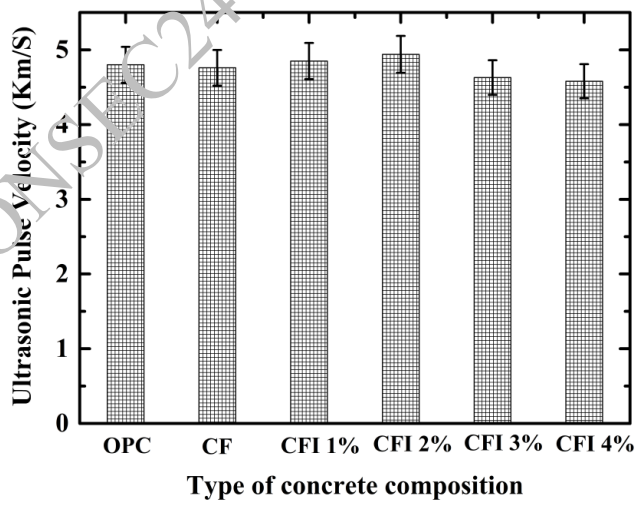

Figure 4. UPV values of the concrete specimens after 28 days

4. Conclusion

This study reports the development of a novel binary blended green concrete (CFI) incorporating 40% fly ash and $NaNO_2$ inhibitor (1%, 2%, 3% and 4%) into conventional concrete made with 100% OPC. The improvement in the properties of the developed concrete composition was assessed based on the compressive strength, split tensile strength and flexural strength results. The quality of the concrete

specimens was measured through UPV test. It was observed that among different compositions, CFI2% exhibited compressive strength values similar to OPC concrete after 28 days of curing, which indicates that inhibitor addition can improve the early age strength of fly ash concrete. Further, the CFI2% specimens exhibited the highest split tensile strength and flexural strength among all the mixes. The highest UPV value was also shown by CFI2%, confirming its superior quality. Thus, 2% inhibitor addition to fly ash concrete can significantly improve the properties of fly ash concrete due to the synergistic effect of the two additives.

References

Andrew, Robbie M. Global CO_2 emissions from cement production. *Earth System Science Data* 10, no. 1 (2018): 195-217.

Liew, K. M., A. O. Sojobi, and L. W. Zhang. Green concrete: Prospects and challenges. *Construction and building materials* 156 (2017): 1063-1095.

Sivakrishna, A., Adeyemi Adesina, P. O. Awoyera, and K. Rajesh Kumar. Green concrete: A review of recent developments. *Materials Today: Proceedings 27 (2020*): 54-58.

Sun, Jinfeng, Xiaodong Shen, Gang Tan, and Jennifer E. Tanner. Compressive strength and hydration characteristics of high-volume fly ash concrete prepared from fly ash. *Journal of Thermal Analysis and Calorimetry* 136 (2019): 565-580.

Hemalatha, T., and Ananth Ramaswamy. A review on fly ash characteristics–Towards promoting high volume utilization in developing sustainable concrete. *Journal of cleaner production* 147 (2017): 546-559.

Broomfield, John P. Corrosion of steel in concrete: understanding, investigation and repair. Crc Press, 2023.

Angst, Ueli M. Challenges and opportunities in corrosion of steel in concrete. *Materials and Structures* 51, 1 (2018): 4.

Hayyan, Maan, Shatha A. Sameh, Adeeb Hayyan, and Inas M. AlNashef. Utilizing of sodium nitrite as inhibitor for protection of carbon steel in salt solution. *International Journal of Electrochemical Science* 7, 8 (2012): 6941-6950.

Harilal, M., Rathish, V. R., Anandkumar, B., George, R. P., Mohammed, M. H. S., Philip, J., & Amarendra, G. (2019). High performance green concrete (HPGC) with improved strength and chloride ion penetration resistance by synergistic action of fly ash, nanoparticles and corrosion inhibitor. *Construction and Building Materials*, 198, 299-312.

] BIS: 8112, Specification for 43 grade ordinary Portland cement by Bureau of Indian Standards, 2013.

Indian Standard (IS-3812 -Part 1), Pulverised fuel ash-Specification, Part-1, for use as pozzolana in cement, cement mortar and concrete. *Bureau of Indian Standards*, (1981) New Delhi, India.

IS: 383-1970, Specifications for coarse and fine aggregates from natural sources for concrete, *Bureau of Indian Standards*, New Delhi, India.

ASTMC 94. Standard specification for ready-mixed concrete. Philadelphia: *American Society for Testing and Materials*; 2002.

IS 10262: 2009 Guidelines for concrete mix design proportioning - Indian standard method., *Bureau of Indian Standards* (BIS)., New Delhi.

ASTM C39/C39M-18, Standard Test Method for Compressive Strength of Cylindrical Concrete Specimens, *ASTM International*, West Conshohocken, PA (2017)

ASTM C496/C496M-17, Standard Test Method for Splitting Tensile Strength of Cylindrical Concrete Specimens, *ASTM International*, West Conshohocken, PA (2017)

ASTM C293/C293M-16, Standard Test Method for Flexural Strength of Concrete (Using Simple Beam with Center-Point Loading), *ASTM International*, West Conshohocken, PA (2016)

ASTM C 597. Standard Test Method for Pulse Velocity through Concrete; *American Society for Testing and Materials*: West Conshohocken, PA, USA, 2016.

Prusty, J.K. and Patro, S.K., 2015. Properties of fresh and hardened concrete using agro-waste as partial replacement of coarse aggregate–A review. *Construction and Building Materials*, 82, pp.101-113.

Synergistic Application of Optimized Quality Recycled Concrete Aggregate with Marble dust: An Alternative Concrete for Severe Conditions

Amit Kumar [1,2*], Babu Lal Chauhan [3], and Gyani Jail Singh [4]

[1] *Department of Civil Engineering, National Institute of Technology Patna-800005, India, Email: amitk.phd19.ce@nitp.ac.in*
[2] *Department of Civil Engineering School of Engineering and technology Sandip University Nashik India, Email: amit.kumar1@sandipuniversity.edu.in*
[3] *Department of Civil Engineering, National Institute of Technology Patna-800005, India, Email: babuc.phd20.ce@nitp.ac.in*
[4] *Assistant Professor, Department of Civil Engineering, National Institute of Technology Patna-800005, India, Email: gyani@nitp.ac.in*

*Corresponding author

ABSTRACT

This study illustrates the synergistic application of recycled concrete aggregates (RCA) and marble waste powder (MWP) to concrete. High quality RCA is produced using an optimized mechanical treatment in a Los Angeles abrasion machine. The Puntke method is used to evaluate an optimized cement replacement by MWP (14%) based on packing density. MWP has a strength activity index (SAI) of approximately 0.66. The compressive strength and tensile strength of recycled aggregate concrete (RAC) are reduced by only 8.11% and 2.24%, respectively, when 14% MWP is substituted for cement. Compressive strength and tensile strength of RAC with MWP (14%) are similar to those of natural aggregate concrete (NAC) with deviations below 5%. RAC with MWP (RAC-MWP) exhibits a RCPT value less than 1000 Coulombs and an electrical resistivity greater than 208 ohm-m, making it a very low permeability material and more resistant to chemicals dissolved in water. Because RAC-MWP has lower RCPT values, as well as a higher surface resistivity, it may demonstrate better durability under severe environmental conditions.

KEYWORDS*: Durability, Marble dust, Puntke methods, Recycled aggregate concrete, Strength.*

1. Introduction

Global aggregate consumption of 9 to 10 billion tonnes is estimated, of which 7.2 billion tonnes are used in concrete each year (Bhasya and Bharatkumar 2018). According to the Central Pollution Control Board, India generates approximately 43.5 million tons of solid waste each year, of which 25% comes from the construction industry. There is a need to find an alternative material to natural aggregate (NA) due to the increase in aggregate demand and the generation of construction and demolition waste (C&DW). Moreover, recycled concrete aggregate (RCA) produced from C&DW is of low quality. RCA exhibits low relative density and high-water absorption compared to its parent natural aggregate (NA). RCA also has a high abrasion value, impact value, and crushing value. As a result of the degraded material properties of RCA, recycled aggregate concrete (RAC) possesses poor mechanical and durability characteristics. In the meantime, Kumar et al. (2023) developed a novel mechanically treated green RCA. Researchers proposed a mechanical treatment accompanied by optimization in order to identify high-quality RCA. With 100% replacement for NA, these aggregates produce concrete with similar physical, mechanical, and durability properties to natural aggregate concrete (NAC).

Marble cutting and sawing operations produce marble waste powder (MWP) as a by-product. In general, 20–25% of the total excavated marble generates MWP (Rana et al. 2015, Aruntas et al. 2010, Aliabdo et al. 2014). India produces approximately 3 million tons of MWP each year (Indian mining industry, 2013). It was reported in 2011 by the Department of Mines and Geology, Rajasthan, that about 15.7 metric tons (Mt) of marble were excavated, resulting in the generation of approximately 5-6 metric tons of MWP (Misra et al. 2010). Thus, the application of MWP to concrete may be a crucial step towards achieving sustainable development (Vuk et al. 2001). In their Corinaldesi et al. (2010) and Vardhan et al. (2015) examined the impact of MWP on mortar, and they found that it exhibits a filler effect in concrete and does not actively participate in the hydration process.

In accordance with Choudhary et al. (2021), inclusion of MWP did not result in major changes in phase composition of CSH, CASH, Portlandite, and quartz, which confirms its inert nature. The majority of the authors concluded that a substitution of 5% to 10% cement with MWP significantly improves the mechanical properties of concrete (Arel Hasan Sahan 2016). As a result of replacing 10% of cement with MWP, Rodrigues et al. (2015) observed satisfactory mechanical properties of concrete. The filler property of MWP enhances the compressive and bending strength of a concrete by 12% and 5%, respectively, when 5% cement is replaced with MWP (Ergün Ali 2011). 10% MWP can reduce CO_2 emissions by approximately 12% and concrete production costs by 17%, without affecting the mechanical specifications of concrete (Ergün Ali 2011; Rodrigues et al. 2015; Uysal and Yilmaz 2011). In accordance with Khodabakhshian et al. (2018), cement replacement with 5% MWP increases compressive strength and modulus of elasticity. The concrete produced by 10% and 20% replacement of cement with MWP, however, shows a lower strength compared to the control concrete.

Incorporating fine grains of MWP in concrete improves its mechanical properties and durability due to its microfiller properties (Ghalehnovi et al. 2023) According to Rana et al. (2015), 10% marble slurry reduces porosity, resulting in improved chloride and water penetration. Choudhary et al. (2021) found that 10% MWP enhanced the compressive strength, resistance to water and chloride permeability, carbonation and drying shrinkage of the material. In contrast, higher concentrations of MWP (20% and 30%) resulted in a reduction in resistance to these properties. A number of works have been reported regarding the application of MWP in NACs and RACs. However, the synergistic effects of MWP with high quality RCA are rarely reported. Accordingly, the present study examines the synergistic effects of 100% RCA and MWP for producing a novel and sustainable concrete. Based on the concept of particle packing density, the present study optimizes the MWP dose. Therefore, the objective of the present study is to evaluate the performance of novel green concrete that is composed of high-quality RCA and MWP by exploring their physical, mechanical, durability, and microstructural properties.

2. Materials and methodology

2.1 Recycled concrete aggregate

RCAs of high quality are developed closely in accordance with Kumar et al. (2023). Therefore, in this study, the highest performing aggregate is obtained from the same source and is subjected to the same treatment. RCA conforms to the physical and mechanical properties of high-quality RCA, and it is closer to NA in terms of physical and mechanical properties (Table 1).

Table 1. Physical and mechanical properties of coarse aggregate, and physical properties of fine aggregate

Physical properties	NA	RCA	Fine aggregate (River sand) Zone-III
Water absorption (%)	0.70	1.02	0.4
Specific gravity	2.82	2.75	2.65
Impact value (%)	9.44	11.42	
Crushing value (%)	17.21	17.44	
Abrasion value (%)	15.40	18.54	
Rodded bulk density, kg/m^3	1536.00	1583.33	
Void content (%)	44.53	42.43	
Flakiness (%)	27.20	12.89	
Elongation (%)	41.19	19.62	

Fineness modulus			2

2.1.1 Marble waste powder (MWP)

MWP consists primarily of calcite and dolomite, with a noticeable amount of quartz (Choudhary et al. 2020, Vardhan et al. 2015). An XRF test was conducted to determine the elemental chemical composition of MWP. Elemental chemical composition of MWP is shown in Table 2. In accordance with XRF analysis, MWP contains a high level of calcium oxide (52.20%) and a notable level of silica (19.35%). Similar findings have been reported in the literature (Bilir et al. 2022). The strength activity index (SAI) test is used to measure the reactivity of MWP in accordance with IS 4031-VI 2000 (BIS 2000), and ASTM C-618 (ASTM 2012). When evaluating SAI, cubes (70.6 mm) are used for the strength test of the mortar. After 7 and 28 days of hydration, MWP has SAIs of 0.61 and 0.66, respectively. The SAI of MWP at 7- and 28-days is lower than the minimum requirement (0.75) for pozzolanic materials under ASTM C618 (ASTM 2012). Thus, MWP has a primarily filler effect. The present study optimized the MWP replacement by 14% using particle packing density methodology (Kumar et al. 2024) (Figure 1). MWP has a specific gravity of 2.85 and a specific surface area (m^2/kg) of 690.

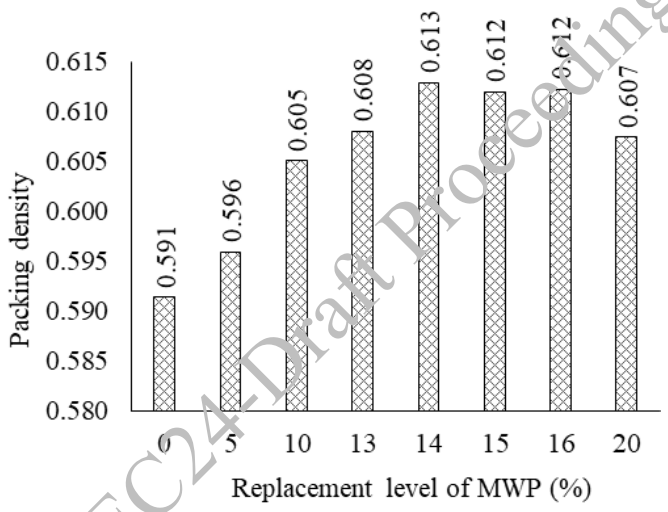

Figure 1. Packing density of MWP.

2.2 Mixture proportioning

RCA and NA serve as coarse aggregates, while river sand serves as a fine aggregate. RAC and NAC mixture proportioning is carried out using potable water, Auramix-400 (superplasticizer), and OPC (43-Grade). River sand confirms IS 383 (IS 2016) with a water absorption of 0.4%, a specific gravity of 2.65, and a fineness modulus of 2. The chemical composition of OPC and MWP is shown in Table 2. Concrete mixtures consisting of 100% RCA, 100% NA, and 100% RCA with MWP (14%) will be abbreviated as RAC, NAC, and RAC-MWP, respectively. As described in Table 3, the mix proportions are calculated using IS 10262 (BIS 2019) for a water-cement ratio of 0.35 and a slump of 75 mm. A specimen is compacted in a standard mold using a table vibrator. The samples are immersed in water for 28 days and cured immediately after opening the mold after 24 hours. Based on the average of three specimens, the reported values have been calculated.

Table 2. Chemical composition of OPC and MWP

Chemical composition	CaO	SiO_2	Al_2O_3	Fe_2O_3	K_2O	Na_2O	SO_3	MgO
OPC	63.73	23.64	4.25	2.80	0.86	0.61	1.75	1.49
MWP	52.20	19.35	0.69	0.72	0.04	0.25	0.05	16.20

Table 3. Mixture proportion of concrete.

Ingredients	Weight (Kg/m^3)		
	NAC	RAC	RAC-MWP
Cement	432.42	432.42	371.88
MWP			60.54
Water	151.35	151.35	151.35
Coarse aggregate	1154.51	1172.20	1154.86
Fine aggregate	712.58	712.97	712.80
superplasticizer	3.89	4.32	3.46

3. Results and discussion

The bulk density of all mixtures is determined according to ASTM C642 (ASTM 1997). NAC, RAC, and RAC-MWP have bulk densities of 2410.94, 2366.56, and 2362.55 kg/m^3, respectively. Bulk density of RAC-MWP is comparable to that of NAC and RAC. The UPV values of NAC, RAC, and RAC-MWP are 5.3, 5.2, and 5.1 km/sec, respectively. Since all concrete mix has a UPV value greater than 4.4km/sec IS 516-V (BIS 2018), it belongs to a high-quality class in terms of structural integrity. Therefore, the filler properties of MWP may be confirmed. The following paragraph discusses the mechanical and durability properties of NAC, RAC, and RAC-MWP.

3.1 Compressive strength

Specimens are tested for compressive strength on 150 mm concrete cubes in accordance with IS 516-I (IS 2021). Figure 2 shows the compressive strength of each mix after 7 days, 28 days, and 91 days. The RAC has a compressive strength of 8.43% greater than the NAC after 28 days. The compressive strength of RAC-MWP is, however, 11% lower than that of RAC. Furthermore, there are no significant differences in compressive strength between NAC and RAC-MWP. In comparison with RAC, the early age strength of RAC-MWP is reduced by 11.57%. In conjunction with MWP, the lower SAI may indicate a slower hydration rate for the cement. A low hydration rate may lead to a reduced amount of CSH gels, which are responsible for low strength gains at an early stage. RAC compressive strength cannot be improved by improving new interfacial zone (NITZ) strength alone without improving old interfacial zone (OITZ) strength as well. Since OITZ is the primary factor determining the strength of high-strength RAC. Thus, it can be concluded that removing adhered mortar to an optimal level improves the surface characteristics of the RCA. In addition to increasing its self-cementing properties, this may also facilitate the penetration of the binder particles, thereby strengthening the OITZ. This study suggests that OITZ in RAC-MWP is as strong as ITZ in RAC and NAC (Kumar et al. 2024).
Due to the decrease in hydration products, cement replacement with a higher MWP may reduce the compressive strength of concrete. According to literature, replacing cement with MWP up to 15% increases compressive strength due to the filler effect (Aliabdo et al. 2014, Belouadah et al. 2019, Khodabakhshian et al. 2018, Bilir et al. 2022). Contrary to these studies, Rana et al. (2015), Vardhan et al. (2015), and Deepankar (2018) reported that 10% MWP substitution did not reduces the compressive strength. As the percentage of MWP replacement increases, the compressive strength of the concrete may reduce due to a decrease in cementing materials as tricalcium silicate (C_3S) and dicalcium silicate (C_2S). The reaction between tricalcium aluminate (C_3A) and calcium carbonate ($CaCO_3$) produces calcium carbo-aluminate if the cement contains sufficient amounts of C_3A. Thus, this reaction accelerates the hydration process, resulting in an increase in compressive strength. As a result, MWP increases concrete performance at an early age. Moreover, MWP is not a pozzolanic material, but neither is it a fully inert material, according to Uysal and Yilmaz (2011). Finaly, 14% cement replacement with MWP results in a compressive strength of RAC-MWP which is lower than RAC but comparable to NAC.

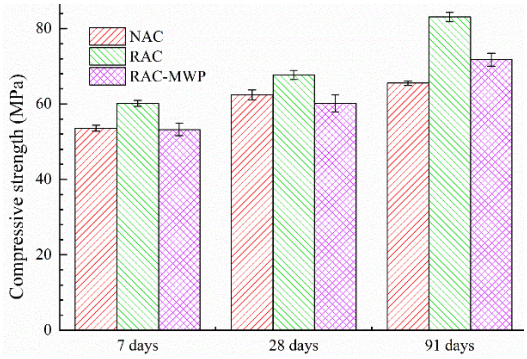

Figure 2. Compressive strength of concrete mix.

3.2 Tensile strength

According to ASTM C496 (ASTM 2004), concrete cylinders of 150 mm in diameter and 300 mm in height are tested for split tensile strength. Figure 3 illustrates the average split tensile for NAC, RAC, and RAC-MWP. A statistical analysis (error bar) indicates that there is no significant difference in the tensile strength of the concrete mix. Increased mortar matrix strength and coarse aggregate surface texture play a significant role in improving concrete tensile strength (Kumar et al. 2024). Therefore, the results of the present study indicate that blending of MWP improves mortar strength. As a result of better interlocking between the aggregate and mortar matrix, quality optimized RCA with MWP increases tensile strength. A satisfactory tensile strength can be achieved by using MWP up to 15% cement replacement (Bilir et al. 2022, Deepankar 2018). Moreover, the present study found that when cement replacement is optimized with MWP (14%), there is no reduction in concrete tensile strength as a result.

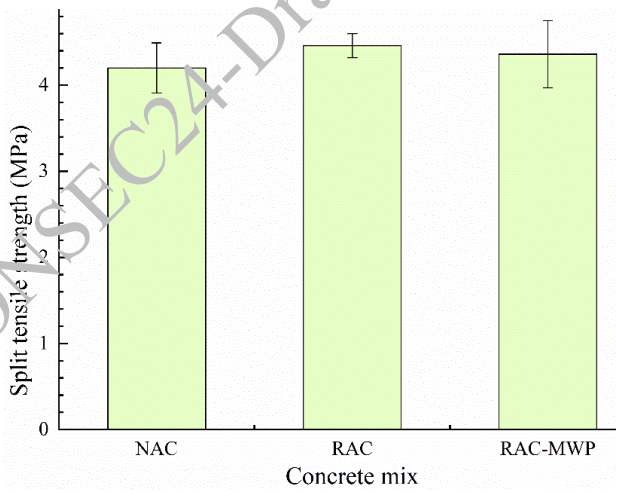

Figure 3. Split tensile strength of concrete mix.

3.3 Rapid chloride penetration test (RCPT) and resistivity

A RCPT is conducted in accordance with ASTM C1202 (ASTM 2019). Figure 4 shows the RCPT values for NAC, RAC, and RAC-MWP. The penetrability of chloride ions through these concrete mixes is very low (< 1000 Coulombs). A high confidence interval is also indicated by the error bar for RCPT data. Despite having higher ion penetration than RAC, RAC-MWP still falls within a very low class. Rashwan et al. (2020) reports a similar observation. By refining the adhered mortar pores and preventing the interconnectivity of capillary pores, the filling effect of MWP reduces the volume of pores. As a result, increased impermeability of RAC-WMP reduces ion penetration. For very low permeability classes, electrical resistivity should range from 208 Ωm to 2,000 Ωm (AASHTO 2017). The RAC-MWP

resistivity of more than 208 Ωm ensures that concrete has minimized interconnected capillary pores, providing a high level of chemical ion protection. The results of UPV and bulk density clearly indicate that the addition of MWP improves the structure of the concrete pores as a result of the microaggregate filling effect of MWP. According to the literature (Bilir et al. 2022, Rana et al. 2015), 15% cement replacement with MWP may be considered as a limiting replacement for achieving satisfactory chloride penetration in RAC-MWP.

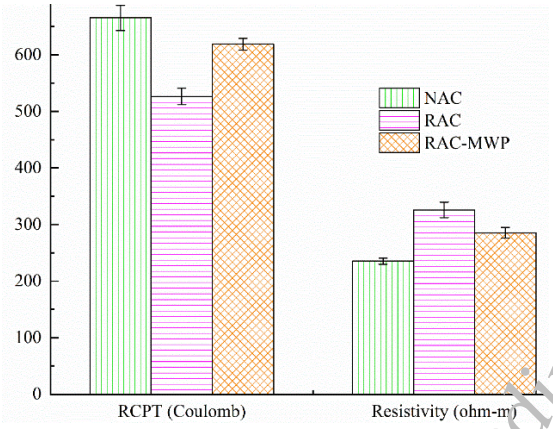

Figure 3. Chloride ion penetration and resistivity of concrete mix

4. Conclusions

In light of the meticulous experimental findings, the following key conclusions can be drawn:

- By using the particle packing density method, the percentage replacement of cement by MWP has been estimated at 14%. As with the cement substitutions made by WMP for NAC, it is justified for RAC as well. WMP has an SAI of 0.66 and shows primarily filler effects in RAC.
- NAC, RAC, and RAC-MWP are similar in terms of bulk density and UPV. After seven and 28 days of curing, RAC-MWP compressive strength is 11% lower than RAC. The compressive strength of RAC-MWP is still comparable to that of concrete composed of its parent natural aggregate (NAC).
- RAC-MWP, NAC and RAC show no significant deviation in tensile strengths, indicating the same level of mortar strengthening in all concrete mixes. High quality RCA with MWP provides improved interlocking and strengthening of the old interfacial transition zone, resulting in satisfactory mechanical properties.
- MWP has a filling effect due to its high fineness, resulting in refinement of interconnected capillary pores. Thus, RAC-MWP has a very low chloride ion penetration class, a high resistivity, and ensures an excellent level of resistance to chemical ions.

References

AASHTO. 2017. Standard practice for developing performance engineered concrete pavement mixtures. AASHTO PP 84-17. Washington, DC: AASHTO.

ASTM. 2012., Standard specifications for coal fly ash and raw or calcined natural pozzolan for use in concrete. ASTM C618-12. West Conshohocken, PA: ASTM.

ASTM. 1997. Standard test method for density, absorption, and voids in hardened concrete. ASTM C642-97. West Conshohocken, PA: ASTM.

ASTM. 2004. Standard test method for splitting tensile strength of cylindrical concrete specimens. ASTM C 496M-04. West Conshohocken, PA: ASTM.

ASTM. 2019. Standard test method for electrical indication of concrete's ability to resist chloride ion penetration. ASTM C1202-19. West Conshohocken, PA: ASTM.

Aliabdo, A.A., Abd Elmoaty, M. and Auda, E.M., 2014. Re-use of waste marble dust in the production of cement and concrete. Construction and building materials, 50, pp.28-41.

Arel, H.Ş., 2016. Recyclability of waste marble in concrete production. Journal of Cleaner Production, 131, pp.179-188.

Aruntaş, H.Y., Gürü, M., Dayı, M. and Tekin, İ., 2010. Utilization of waste marble dust as an additive in cement production. Materials & Design, 31(8), pp.4039-4042.

Belouadah, M., Rahmouni, Z.E.A. and Tebbal, N., 2019. Influence of the addition of glass powder and marble powder on the physical and mechanical behavior of composite cement. Procedia Computer Science, 158, pp.366-375.

Bilir, T., Karadağ, Ö. and Aygün, B.F., 2022. Waste marble powder. In Sustainable Concrete Made with Ashes and Dust from Different Sources (pp. 479-506). Woodhead Publishing.

BIS (Bureau of Indian Standards)., 2000. Determination of compressive strength of hydraulic cement other than masonry cement. IS 4031-6. New Delhi, India: BIS.

BIS (Bureau of Indian Standards)., 2016. Coarse and fine aggregate for concrete—Specification. IS 383. New Delhi, India: BIS.

BIS (Bureau of Indian Standards). 2018. Hardened concrete-methods of test: Part 5—Non-destructive testing of concrete. IS 516. New Delhi, India: BIS.

BIS (Bureau of Indian Standards). 2019. Concrete mix proportioning Guidelines. IS 10262. New Delhi, India: BIS.

BIS (Bureau of Indian Standards). 2021. Hardened concrete-methods of test: Part 1—Compressive, flexural, and split tensile strength. IS 516. New Delhi, India: BIS.

Bhasya, V. and Bharatkumar, B.H., 2018. Mechanical and durability properties of concrete produced with treated recycled concrete aggregate. ACI Materials Journal, 115(2), pp.209-217.

Choudhary, R., Gupta, R., Alomayri, T., Jain, A. and Nagar, R., 2021. Permeation, corrosion, and drying shrinkage assessment of self-compacting high strength concrete comprising waste marble slurry and fly ash, with silica fume. In Structures (Vol. 33, pp. 971-985).

Corinaldesi, V., Moriconi, G. and Naik, T.R., 2010. Characterization of marble powder for its use in mortar and concrete. Construction and building materials, 24(1), pp.113-117.

Deepankar .K. A., 2018. Feasibility of waste marble powder in concrete as partial substitution of cement and sand amalgam for sustainable growth. Journal of Building Engineering, 15, pp.236-242.

Development of Indian Mining Industry – The Way Forward; FICCI Mines and Metals Division, October 2013 <www.ficci.com>.

Ergün, A., 2011. Effects of the usage of diatomite and waste marble powder as partial replacement of cement on the mechanical properties of concrete. Construction and building materials, 25(2), pp.806-812.

Ghalehnovi, M., Rahdar, H., Ghorbanzadeh, M., Roshan, N. and Ghalehnovi, S., 2023. Effect of marble waste powder and silica fume on the bond behavior of corroded reinforcing bar embedded in concrete. Journal of Materials in Civil Engineering, 35(3), p.04022460.

Khodabakhshian, A., De Brito, J., Ghalehnovi, M. and Shamsabadi, E.A., 2018. Mechanical, environmental and economic performance of structural concrete containing silica fume and marble industry waste powder. Construction and Building Materials, 169, pp.237-251.

Kumar, A., Singh, G.J., Kumar, S.B. and Kumar, R., 2023. Performance-based quality optimization approach for mechanically treated recycled concrete aggregates. Journal of Materials in Civil Engineering, 35(9), p.04023315.

Kumar, A., Jail Singh, G., Chauhan, B.L. and Kumar, R., 2024. Strength and durability performance of recycled aggregate structural concrete with silica fume, furnace slag, and M-fine. Journal of Materials in Civil Engineering, 36(7), p.04024165.

Misra, A.K., Mathur, R., Rao, Y.V., Singh, A.P. and Goel, P., 2010. A new technology of marble slurry waste utilisation in roads.

Rana, A., Kalla, P. and Csetenyi, L.J., 2015. Sustainable use of marble slurry in concrete. Journal of cleaner production, 94, pp.304-311.

Rashwan, M.A., Al-Basiony, T.M., Mashaly, A.O. and Khalil, M.M., 2020. Behaviour of fresh and hardened concrete incorporating marble and granite sludge as cement replacement. Journal of Building Engineering, 32, p.101697.

Rodrigues, R., De Brito, J. and Sardinha, M., 2015. Mechanical properties of structural concrete containing very fine aggregates from marble cutting sludge. Construction and Building Materials, 77, pp.349-356.

Uysal, M. and Yilmaz, K., 2011. Effect of mineral admixtures on properties of self-compacting concrete. Cement and Concrete composites, 33(7), pp.771-776.

Vardhan, K., Goyal, S., Siddique, R. and Singh, M., 2015. Mechanical properties and microstructural analysis of cement mortar incorporating marble powder as partial replacement of cement. Construction and Building Materials, 96, pp.615-621.

Vuk, T., Tinta, V., Gabrovšek, R. and Kaučič, V., 2001. The effects of limestone addition, clinker type and fineness on properties of Portland cement. Cement and concrete Research, 31(1), pp.135-139.

Compatibility Assessment of Binary and Ternary Blends Incorporating Agro-Industrial Byproducts in Cementitious Systems

K.Gayathiri[1], and S.Praveenkumar[2*]

[1] Research Scholar, Department of Civil Engineering, PSG College of Technology, Coimbatore, India
Email: gayathirikcivil.com
[2] Associate Professor, Department of Civil Engineering, PSG College of Technology, Coimbatore, India
Email:spk.civil@psgtech.ac.in

*Corresponding author

ABSTRACT

The admixture of pozzolans derived from both agricultural and industrial wastes is emerging to achieve better performance at its optimal dosage. Rice Husk Ash (RHA) and Bagasse ash (BA) falls under the category of tremendously available biomass pozzolans from the agricultural sector, whereas Nano Silica (NS) and Ground Granulated Blast Furnace Slag (GGBS) is an industrial pozzolan. The process of proportioning the agro-industrial pozzolans depends on both their physical and chemical composition. Theoretically, mixing pozzolans of various fineness enhances the Particle Packing Density (PPD) by filling the voids present between the cement grains. This, in turn, governs the microstructure of the proposed mix through augmented reactivity of the binders. Hence, this study involves decoupling the understanding of fineness and reactivity of the binary (0.5NS, 1NS and 1.5NS) and ternary blends (NG, NB and NR) of the cementitious system in terms of physical parameters and chemical constituents. Experimental investigations are conducted to evaluate the characteristics of various blends involving SSA, Lime Reactivity Test, Dry packing density, Compressive Strength, followed by microstructural characterization through SEM. The optimum PPD mix exhibits better performance in reactivity and hydration at all ages. In binary and ternary blends, the nano-sized pozzolan acts as the nucleation seeds, thereby increasing reactivity and promoting the hydration process of alite (C_3S) and belite (C_2S), resulting in a densified microstructure through the increased formation of Calcium Silicate Hydrates (CSH) in the mix. The reactivity of the coarser micro-particles is also enhanced due to the incorporation of nano-sized particles with a higher specific surface area.

KEYWORDS*: Specific Surface Area, Packing Density, Reactivity, Hydration Process, Densified Microstructure*

1. Introduction

As reported by Directorate of Economics and Statistics, India produces 361Million tons of sugarcane and 105 million tons of Rice in the year 2012-2013. This production resulted in increasing the crop residue up to 500 million tons per year, which is highlighted by Indian Ministry of New and Renewable Energy (MNRE) Bhuvaneshwari et al (2019). Bagasse Ash (BA) produced by utilizing the residues from the sugarcane cultivated farm for boiler cogeneration of electricity and steam generation at the controlled temperature of 600˚C to 700˚C is disposed as waste in cultivation farms that possess the pozzolanic properties due to the presence of silica which is due to the polymerization of the orthosilicic acid Bahurudeen et al (2015) Kamalakar et al (2021). The Rice Husk Ash (RHA), produced by incinerating the rice hulls at the temperature ranging between 550˚C to 700˚C possess the amorphous silica which is highly reactive. The pozzolanic performance i.e., the reactivity of the silica in amorphous phase is directly proportional to the Specific Surface Area (SSA) of the ashes Chindaprasirt et al (2009).

Whereas incorporation of Industrial pozzolans like Nano Silica (NS) and Ground Granulated Blast Furnace Slag (GGBS) to the cementitious system are alreadystreamlined in the research and some of them met the practical applications. But, admixing both agricultural and Industrial pozzolans are started emerging in research field at recent times.

2. Lime Reactivity Test

The lime reactivity test was performed to evaluate the reactivity of the secondary binders (BA, RHA, GGBS and NS) as per IS1727-1967. Two different types of BA (I & II) and RHA (I &II) were collected from different sources were assessed to determine its reactivity in cementitious system. Totally four agricultural pozzolans and two industrial pozzolans were tested. Out of that two agricultural pozzolans i.e., BA-II and RHA – I produce more than 15% variation from the average value in strength attainment, which is classified as "faulty". Hence these samples are not considered for the further characterization.

3. Materials and Methods

3.1 Materials

Ordinary Portland Cement (OPC – 53 grade) confirming to IS 12269–2013 was utilised as a primary binder in the current research. NS and GGBS were sourced commercially. BA- I was sourced from sugar production unit near Coimbatore, India. Whereas RHA-II was commercially sourced. The physio chemical properties of the binders were assessed through Laser Particle diffraction and X-ray Fluorescence Spectroscopy (XRF). Specific Surface Area (SSA) of each binder was determined by BET Surface Analyzer. Physio Chemical properties of binders were presented in Table 1.

Table 1. Physio Chemical properties of binders

Oxide Composition	OPC	NS	RHA	BA	GGBS
CaO	66.56	-	0.82	15.3	42.19
SiO_2	21.49	99.4	94.66	70.74	33.12
Al_2O_3	5.19	-	0.01	2.06	18.96
Fe_2O_3	2.78	-	0.47	2.51	0.589
SO_3	4.14	-	0.21	0.515	1.42
K_2O	1.01	-	1.58	3.98	0.52
SrO	575.2*	-	66.7	739.4*	569*
MnO	0.107	-	662.9*	997.2*	1.89
P_2O_5	0.385	0.348	1.94	3.93	-
TiO_2	0.295	-	106.7*	0.223	1.15
Physical Properties					
Mean Size (µm)	80.16	0.014	38.66	66.43	15.92
D10 (µm)	5.15	-	9.65	9.56	2.83
D50 (µm)	18.66	0.12	34.13	66.43	12.73
D90 (µm)	354.29	-	72.99	154.08	32.12
Appearance	Grey	white	Dark Grey	Grey	White
Specific gravity	3.14	2.2	2.1	2.35	2.79
Fineness (m^2/kg)	337	3,47,000	342	322	464.9

The fine and coarse aggregates confirming to IS 383-2016 was used with the constant water-to-binder ratio of 0.43 was adopted to constitute M40 grade of concrete. The ratio of the binders was varied with the corresponding replacement of primary binder in the mix. Mix designations were presented in Table

2. To maintain the workability of the mix, the polycarboxylic based super plasticizer was incorporated into the secondary binder admixed mix.

Table 2. Mix Designations

3.2 Experimental Investigation

The gap graded cementitious system in the designated mixes were densified through packing density.

Blends	Combinations	Mix Designation	OPC (%)	Replacement Percentage (By weight of OPC)			
				NS (%)	RHA (%)	BA (%)	GGBS (%)
Nullary	OPC Brand - A	C	100	-	-	-	-
Binary Blends	OPC-A + NS	NS1	99.5	0.5	-	-	-
		NS2	99	1	-	-	-
		NS3	98.5	1.5	-	-	-
Ternary blends	OPC-A +NS+ RHA	NR10	89	1	10	-	-
		NR15	84	1	15	-	-
		NR20	79	1	20	-	-
	OPC-A +NS + BA	NB5	94	1	-	5	-
		NB10	89	1	-	10	-
		NB15	84	1	-	15	-
	OPC-A+ NS+ GGBS	NG30	69	1	-	-	30
		NG40	59	1	-	-	40
		NG50	49	1	-	-	50

Initially all the mixes from binary to ternary were modelled through Modified Andreasen and Andreassen (MAA) model considering the Particle Size Distribution (PSD) of the binders. Whereas the wet packing method developed by Puntke, were attempted in this study to establish the packing density of the powders in wet condition (real situations of binders as paste). The compressive strength of each mix at 28 days of curing ages were determined as per IS516-1959. To characterize the surface morphology of each blend, SEM image analysis was done.

4. Results and Discussions

4.1 Packing Density

The gradation curve of nullary mix modelled (using EMMA) by considering the distribution factor fixed as '0.3' (Medium Workability) exhibits the divergences with target curve indicates the possibilities of presence of voids. Whereas the gradation curves of binary and the ternary blends fits the target curve. This is due to the admixing of the secondary binders in the cementitious system with high SSA. Further these curve fitting was further subjected to statistical analysis based on "Marquardt algorithm" to confirm the exponential relation with the target curve (Fig 1). The statistical analysis revealed, increase in binder replacement with high fines enhanced the packing density of the mix (NG > NR > NB > NS > C).

4.2 Compressive Strength

The compressive strength of all the mixes at 28 days were presented in Fig.2. Nullary blend possess the strength of 52.58MPa. Whereas binary blends NS1, NS2 and NS3 possess the enhanced strength attainment of 7.5%, 13.27% and 5.45% greater than nullary mix. In ternary blended mixes, NG30, NG40 and NG50 possessed increased in strength of about 23.31%, 33.26% and 28.22% respectively when compared to nullary mix. The strength of the ternary mixes admixed with BA and RHA also increased

up to 16.66% (NB10) and 22.32% (NR15) due to the presence of the NS which acts as nucleating seeds and in turn increased the formation of the secondary CSH which densified the microstructure of the entire mix. The declined trend in the strength attainment of NS3, NR20, NB15 and NG50 is due to the wall effect where the non-reacted secondary binders may act as fillers.

Figure 1. Gradation curve for optimized blend

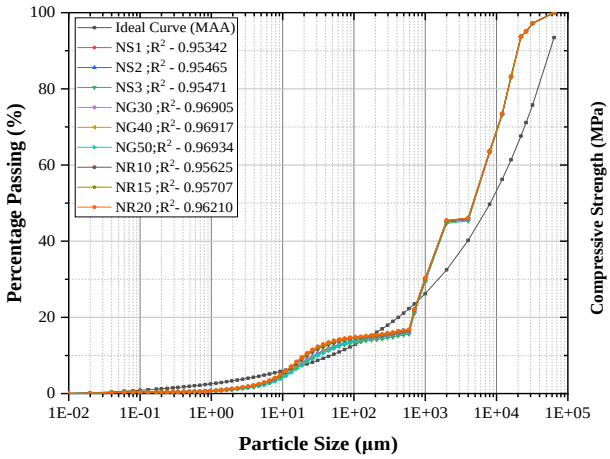

Figure 2. Compressive strength of all mixes

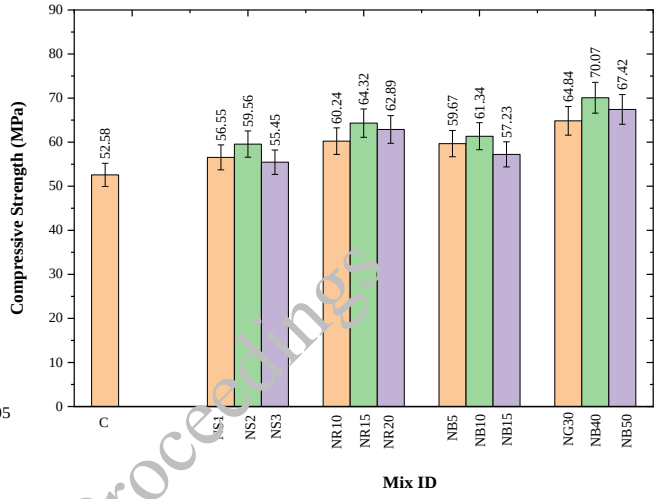

4.3 SEM Analysis

SEM image of Nullary (C), Binary (NS2), Ternary (NG40) was shown in Fig 3. From morphology study, it is inferred that the addition of high fines/SSA increases the secondary hydration (C_3S & C_2S) of cementious system by acting as nucleation sites. This helps in altering the microstructure of the designated mixes.

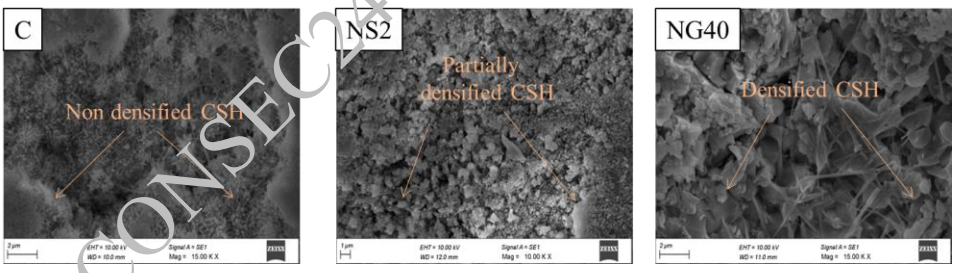

Figure 3. SEM image of Nullary (C), Binary (NS2), Ternary (NG40)

5. Conclusions

Admixing the secondary binders in the gap graded cementitious system increases the packing density of the mix (ternary > nullary) which in turn elevates the interaction between the particle-to-particle. Moreover, this will help in formation of the denser microstructure through secondary hydration.

References

Bahurudeen, A., Kanraj, D., Gokul Dev, V., and Santhanam, M., (2015) "Performance evaluation of sugarcane bagasse ash blended cement in concrete", *Cement Concrete Composites,* 59:77–88

Bhuvaneshwari, S., Hettiarachchi, H. and Meegoda, J. N. (2019) "Crop residue burning in India: Policy challenges and potential solutions," *International Journal Environmental Research Public Health,*16(5)

Chindaprasirt, P., and Rukzon, S., (2009) "Pore Structure Changes of Blended Cement Pastes Containing Fly Ash, Rice Husk Ash, and Palm Oil Fuel Ash Caused by Carbonation," *Journal of Materials in Civil Engineering*, 21(11): 666–671

Kamalakar Mali, A., and Nanthagopalan, P., (2021) "Development of a framework for the selection of best sugarcane bagasse ash from different sources for use in the cement-based system: A rapid and reliable path," *Construction and Building Materials*, 293:123386

Evaluation of Chemical Admixture Effects on Laterised Geopolymer Mortar

David Clement [1*], and Rajasekaran C [2]

[1] Research Scholar, National Institute of Technology Karnataka, Surathkal, India, Email: davidtvpm@gmail.com
[2] Associate Professor, National Institute of Technology Karnataka, Surathkal, India, Email: bcrajasekaran@nitk.edu.in

*Corresponding author

ABSTRACT

In the quest for refining geopolymer mortar (GM) properties, chemical admixtures emerge as crucial elements. This research focuses on assessing the impact of accelerator, retarder, and superplasticiser on the fresh and hardened states of fly ash-based lateritic GM. This research integrates various chemical admixtures, including calcium chloride, sodium sulphate, sodium hexametaphosphate, and MasterGlenium SKY 8233, a super plasticiser based on polycarboxylic ether (PCE). Evaluations were carried out on the properties of GM formulations, encompassing flowability, initial and final setting times, and compressive strength. Concurrently, microstructural analyses were performed on GM samples following 56 days of ambient curing. This study shows that calcium chloride and sodium sulphate effectively decrease both the initial and final setting times of the geopolymer paste, demonstrating its effectiveness as an accelerator, with calcium chloride exhibiting better efficacy than sodium sulphate. Conversely, sodium hexametaphosphate acts as a retardant, significantly extending the initial setting time of the geopolymer paste. The addition of modified polycarboxylic ether (PCE) based superplasticiser MasterGlenium Sky 8233 into the mortar matrix resulted in a prolonged initial setting time while causing a marginal decrease in compressive strength compared to the other mixes. These findings strongly support the idea of customising geopolymer blends to achieve desired properties under ambient curing conditions, particularly when integrating chemical admixtures.

KEYWORDS*: Ambient Curing, Chemical Admixtures, Setting Time, Flowability, Compressive Strength*

1. Introduction

Conventional cement production, a cornerstone in construction materials, presents significant environmental challenges. The global cement industry is a significant contributor to greenhouse gas emissions, with nearly 1 ton of cement produced annually per person, and each ton of cement produced yields approximately 810 kg of carbon dioxide (CO_2), 1 kg of sulphur dioxide (SO_2), 2 kg of nitrogen oxides (NO_x), and 10 kg of dust (Zhang et al. 2018). Approximately 4 billion tons of cement is produced annually worldwide, contributing 7% of global CO_2 emissions which necessitates a urgent action to develop alternative binding materials to mitigate environmental harm by minimising CO_2 emissions and reducing other polluting gases and waste dust in the construction sector (Onuaguluchi et al. 2022; Zhang et al. (2018). Researchers have unearthed promising substitutes in the quest for alternatives to traditional cement, with geopolymeric materials emerging as the frontrunners. Drawing inspiration from ancient construction techniques, the utilisation of geopolymer materials dates back to the construction of the Egyptian pyramids around 2630BC–2611BC. This ancient practice lay dormant until French material scientist Joseph Davidovits reintroduced the concept, coining the term "geopolymer"(J Davidovits. 1994). Geopolymeric materials are distinguished by their inorganic molecular chains or networks,

offering a novel approach to binding agents in concrete and other construction applications. Using geopolymeric materials, researchers aim to mitigate the environmental impact of traditional cement while harnessing the benefits of a proven historical practice(J Davidovits. 1994). Geopolymer materials rely on raw materials abundant in silicon (Si), aluminium (Al), and alkaline activator solutions (Duxson et al. 2007). Unlike conventional cement-based binders, geopolymeric materials derive their binding properties through polymerisation, which sets them apart. One of the primary benefits of geopolymers is their ability to mitigate industrial waste disposal problems by utilising by-products such as rice husk ash, ground granulated blast furnace slag (GGBFS), fly ash, and silica fume (Singh et al. 2015)).

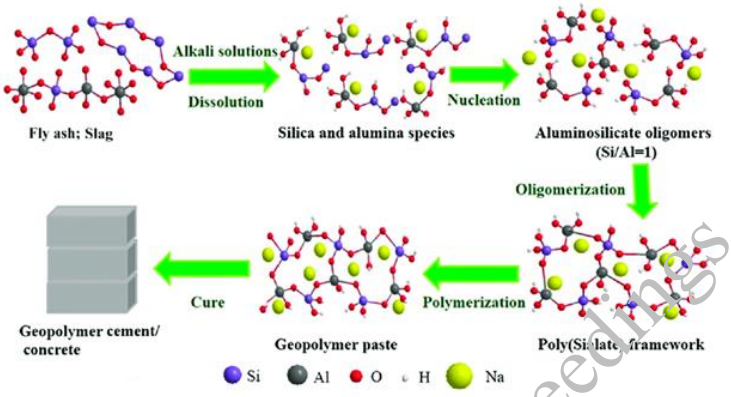

Figure 1. Geopolymerisation process (Shamsaei et al. (2021))

The growing demand for sustainable infrastructure development is increasing the need for natural resources, mainly river sand. However, the excessive removal of sand from riverbeds or quarries is causing significant and irreversible environmental problems. So, it is imperative and crucial to identify alternative materials to replace river sand and ensure the longevity of the non-replenishable resources. In light of these challenges, this present research explores the use of fly ash as a binder material with sodium hydroxide and sodium silicate as the activator solution and incorporates laterite soil (LS) and river sand (RS) in various proportions as fine aggregates to create GM paste (Mathew and Paul. 2013); Santha Kumar et al. 2022)). The primary objective of this study is to analyse the effect of chemical admixtures in GM with different proportions of LS and RS.

2. Materials and Method

2.1 Materials

The various materials used for the present research are:

2.1.1 Fly ash

Fly ash, a residual product derived from pulverised coal combustion in thermal power plants is globally abundant. With its high silica and alumina content, FA is activated through alkaline solutions to create aluminosilicate gel, serving as a binder in GM. The FA utilised in this study was sourced from a thermal power plant in Karnataka. Classified as Class F FA, it exhibits a specific gravity of 2.09, as tested with Le Chatelier's flask.

Table 1. Constituents of Fly Ash

Content	Al_2O_3	SO_3	Fe_2O_3	SiO_3	CaO	MgO	K_2O	Na_2O	LOI
% Present	32.34	0. 52	2.82	58.76	0.71	0.86	1.14	0.33	0.03

(a) (b) (c)

Figure 2. (a) Fly ash (b) NaOH pellets (c) Sodium Silicate solution

2.1.2 Alkaline Activator solution

An alkaline activator solution comprising sodium hydroxide (NaOH) and sodium silicate (Na_2SiO_3) was chosen for the present study. Sodium hydroxide, available in pellet form with a purity of 97%, is utilised to prepare a 12M NaOH solution. The molarity of NaOH solution was fixed based on the literature study Memon et al. 2013; Tabassum and Khadwal. 2015). After the preparation of NaOH solution, the solution is allowed to cool down for at least 24h before mixing with sodium silicate solution, usually referred to as water glass or liquid glass.

2.1.3 Fine Aggregates

Two types of fine aggregates were employed in this study: RS and LS. Both aggregates, complying with the Indian Standard (IS) and passing through a 4.75 mm IS sieve, were used in the mortar preparation. The grading of aggregates was performed according to IS 383-1970 guidelines, which define construction aggregate standards (Figure 3). Furthermore, tests were conducted to ascertain the specific gravity and fineness modulus of the fine aggregates. The various properties of LS and RS are detailed in Table 2.

Table 2. Properties of LA and RS

Characteristics	Obtained Value	
Type	LS	NFA
Specific Gravity	2.72	2.62
Fineness	2.73	2.63
Grading Zone	II	II

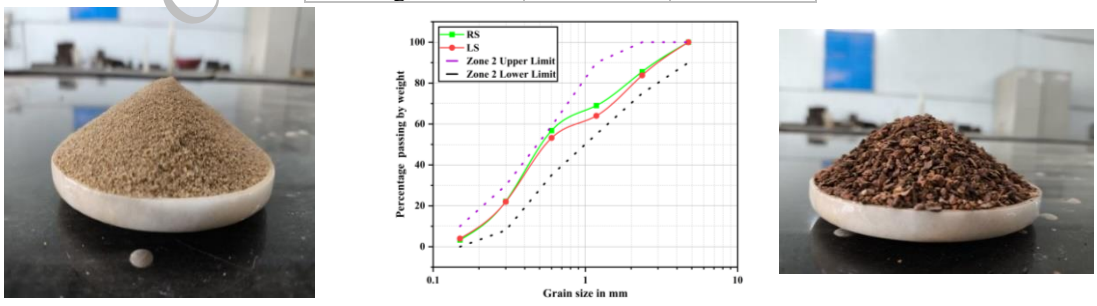

(a) (b) (c)

Figure 3. (a) River sand (b) Particle size distribution of LS and RS (c) Laterite soil

2.2 Processing of laterite soil

The crushed LS is initially passed through a 4.75 mm sieve. Following this, it undergoes a washing process on a wooden frame sieve with a mesh size of 150 µm. Washing is crucial in LS processing as it removes fine clay particles within the material. Previous research has emphasised the formation of clay ball-like structures when unprocessed LS is employed to replace RS in fine aggregate. This phenomenon reduces compressive strength due to the clay fraction of the LS absorbing substantial quantities of water (Yaragal et al. 2019). Washing is implemented to mitigate this problem. A considerable portion of the problematic clay fraction is removed by washing the LS. The soil is then sun-dried and stored in containers for future testing purposes.

(a) (b) (c) (d)

Figure 4. (a) Unprocessed LS (b) Wet Sieving of LS (c) Drying of LS (d) Dried LS

2.2.1 Chemical Admixtures

Four chemical admixtures were utilized in this study, each belonging to the superplasticizer, accelerator, or retarder categories. These included MasterGlenium SKY 8233, a state-of-the-art superplasticizer based on modified polycarboxylic ether (PCE); calcium chloride ($CaCl_2$), an accelerator that reduces setting time; sodium sulphate (Na_2SO_4), an alternative slag activator; and sodium phosphate (Na_2PO_4), a retarder that extends workability by controlling setting times.

2.2.2 Mix design procedure

The mix design methodology for GM was developed through a series of trials that led to the formulation of an exact procedure. The fixed parameters for designing the mixes are provided in Table 3.

Table 3. Fixed Parameters for the present study

Parameter	Value
Binder content	600 kg/m^3
Na_2O dosage required	8 %
Ms (Activation Modulus)	1
Water/Binder ratio	0.4
Molarity of NaOH	12M
Binder to aggregate ratio	1:2
Curing condition	Ambient curing
Dosage of SKY 8233	1% by weight of binder
Dosage of $CaCl_2$	1% by weight of binder
Dosage of Na_2SO_4	1% by weight of binder
Dosage of Na_2PO_4	1% by weight of binder

The experiments were mainly carried out in two phases. In the first phase, GM mixes were designed with different proportions of LS and RS. These designed mixes were labelled as LxRy for ease of understanding where x and y stand for the proportion of material in the mix and L and R are used as initials for depicting LS and RS used. In the second phase, four different admixtures were incorporated

into the five mix designs from the first phase, each at a fixed dosage of 1% by weight of fly ash, resulting in a total of 20 distinct mix designs. The detailed quantities of materials required for casting nine 5cm size cubes are listed in Table 4.

Table 4. Quantity of materials required for casting 9 GM cubes

Sl.No.	Mix ID	LS %	RS%	LS	RS	FA	NaOH (12M)	Na_2SiO_3	Extra Water
				(kg)	(kg)	(kg)	(liters)	(liters)	(liters)
1	L100	100	0	1.908	0.000	0.898	0.118	0.177	0.086
2	L75 R25	75	25	1.431	0.459	0.898	0.118	0.177	0.086
3	L50 R50	50	50	0.954	0.919	0.898	0.118	0.177	0.086
4	L25 R75	25	75	0.477	1.378	0.898	0.118	0.177	0.086
5	R100	0	100	0.000	1.838	0.898	0.118	0.177	0.086

The preparation of the GM mix involved mixing fly ash (FA) as a binder with fine aggregates for 3 minutes to create a homogeneous dry mix. The alkaline activator solution was then incorporated into the dry mix and mixed thoroughly for an additional 3 minutes, ensuring uniformity and homogeneity in the final mixture. The fresh properties of GM were determined immediately after the mix preparation, following the guidelines of ASTM C1437-20. For each mix design, nine cubes of 50x50x50 mm were cast, with three cubes each designated for compressive strength evaluation at 28, 56, and 90 days, according to IS 4031-6 (1988). In total, 180 cubes were cast for this study (Ng et al. 2018)). The initial and final setting times of the mixes were also determined using IS 4031-5 (1988) guidelines for this present study (Thampi et al. 2014).

3. Results and Discussions

3.1 Flow Table Test

The flow table test results of GM with various admixtures are illustrated in Figure 5. The plotted graph indicates a clear trend of decrease in flow value as the LS content increases, which can be attributed to the rough surface and high water absorption properties of LS. While examining the impact of different admixtures, it is clear that MasterGlenium SKY 8233 and Na_2PO_4 consistently improve workability and increase flow values in all mixes. In contrast, the inclusion of $CaCl_2$ and Na_2SO_4 causes a reduction in flow values. Among the admixtures, Na_2PO_4 has the most significant positive impact, while $CaCl_2$ exhibits the most pronounced negative impact on the flow value of GM.

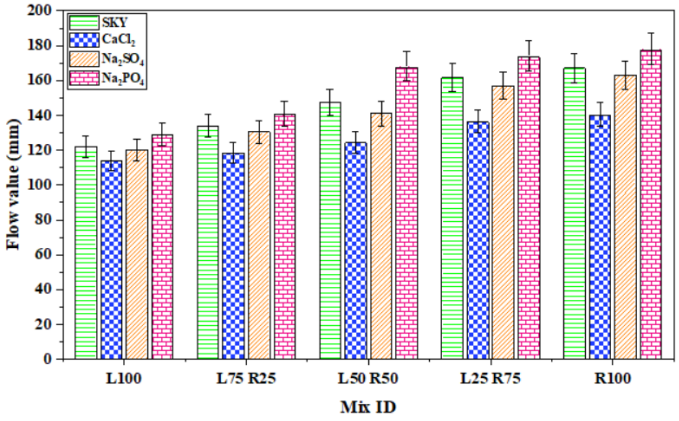

Figure 5. Flow Table values of geopolymer mix designs after incorporating various admixtures

3.2 Setting Time Test

The setting time values of various design mixes incorporating different admixtures are presented in Figure 6. The trend indicates that both initial and final setting times decrease as the LS content in the mix increases, due to the high water absorption and rough texture of LS. The addition of admixtures such as MasterGlenium SKY 8233 and Na_2PO_4 has a minimal impact on setting times, although they tend to increase the values slightly. On the other hand, $CaCl_2$ and Na_2SO_4 addition show a notable decrease in setting times, with $CaCl_2$ having a more pronounced effect than Na_2SO_4. This clearly indicates that $CaCl_2$ enhances the geopolymerization process more effectively than the other admixtures.

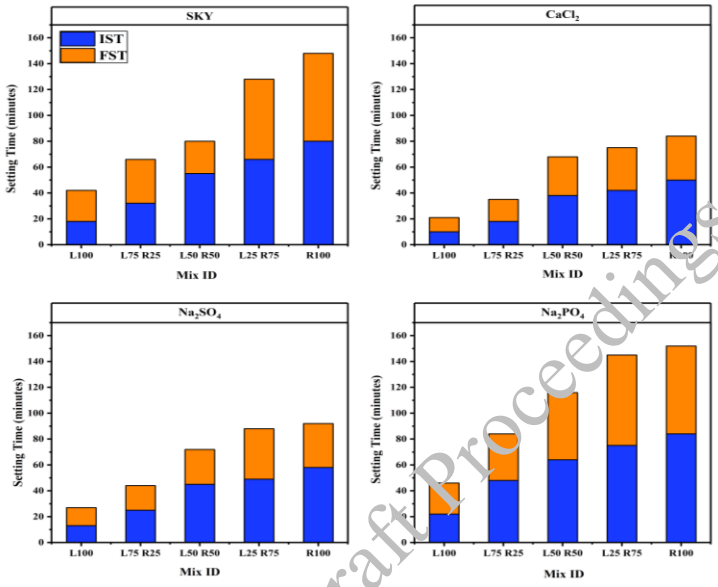

Figure 6. Setting Time values of geopolymer mix designs after incorporating various admixtures

3.3 Compressive Strength Test

The compressive strength test results for geopolymer mixes with various admixtures, shown in Figure 7, reveal a non-linear trend.

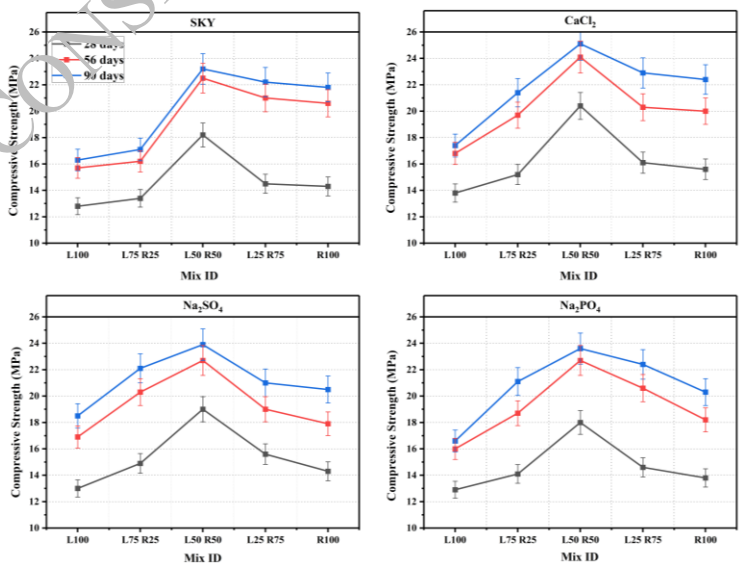

Figure 7. Compressive Strength values of geopolymer mix designs after incorporating various admixtures

Compressive strength values increase gradually as the LS content rises from 0% to 50%, reaching a maximum at the L50R50 mix, which contains 50% LS and 50% RS. Beyond 50% LS, there is a sharp decline in compressive strength, indicating that the optimal LS content for maximum strength is 50%. The addition of superplasticizers does not significantly impact the compressive strength at 56 and 90 days, although CaCl2 slightly enhances the 28-day strength compared to other admixtures. Additionally, the minimal gain in compressive strength from 56 days to 90 days indicates that the majority of the geopolymerization process is completed by 56 days, with only minor changes thereafter. complete geopolymerisation process.

3.4 Microstructural Analysis

For SEM analysis, crushed samples from the 56-day compressive strength test were collected from selected mix designs, specifically L50R50 and L100. Figures 8 and 9 show the SEM images of the L50R50 and L100 mix design with CaCl2 as added as an admixture. The SEM images indicate that the L50R50 mix has a dense structure with minimal voids and a few unreacted fly ash particles. In contrast, the L100 mix is porous and contains numerous unreacted fly ash particles. The L50R50 mix also features many needle-shaped mullite structures, signifying extensive geopolymerization. This extensive geopolymerization resulted in the dense structure formation in L50R50 mix design, contributing to its superior compressive strength compared to other mix designs. Conversely, the L100 mix shows more unreacted fly ash particles and fewer mullite crystals, suggesting minimal geopolymerization, which correlates with its lower compressive strength.

Figure 8. SEM images of L50R50 mix design

Figure 9. SEM images of L100 mix design

4. Conclusions

The primary objective of this study was to assess the fresh and hardened properties of GM by incorporating various chemical admixtures, namely MasterGlenium SKY, $CaCl_2$, Na_2SO_4, and Na_2PO_4, in binary mixes with different proportions of RS and LS. Through a comprehensive examination of these mix designs, the following conclusions were obtained:

- Increase in LS content results in longer setting times and lower flow values, caused by the higher water absorption and rough surface of LS. Additionally, when the LS content in the mix is

increased up to 50%, there is a gradual improvement in compressive strength. However, beyond 50% LS content, up to 100%, a significant drop in compressive strength is observed.

- Incorporating $CaCl_2$ results in higher compressive strength at 28 days relative to other admixtures. It also decreases the setting time and flow value of the mortar.
- In terms of flow value, setting times, and compressive strength, $CaCl_2$ demonstrates a more significant effect than Na_2SO_4.
- Adding MasterGlenium SKY 8233 consistently boosts workability properties in all mixes and delays setting times, without affecting compressive strength enhancement.
- Adding Na_2PO_4 enhances the flow value by retarding the geopolymerization process, which in turn leads to an increased setting time.
- The compressive strength values at 90 days are similar across all mixes, suggesting that the admixtures exert minimal influence on the long-term compressive strength values.

References

Duxson, P., Provis, J. L., Lukey, G. C. and Deventer, J. S. J. van. (2007)"The role of inorganic polymer technology in the development of 'green concrete', *Cement and Concrete Research*, 37(12):1590–1597

J Davidovits. (1994). "Properties of geopolymer cements" *First international conference on alkaline cements*, 131–149

Mathew, G. and Paul, M. M. (2013). "Influence of Fly Ash and GGBFS in Laterized Concrete Exposed to Elevated Temperatures" *Journal of Materials in Civil Engineering*, 26(3):411–419

Memon, F.A., Nuruddin, M.F., Khan, S., Shafiq, N.A.S.I.R. and Ayub, T. (2013) "Effect of sodium hydroxide concentration on fresh properties and compressive strength of self-compacting geopolymer concrete", *Journal of Engineering Science and Technology*, 8(1):44–56

Ng, C., Alengaram, U. J., Wong, L. S., Mo, K. H., Jumaat, M. Z., and Ramesh, S. (2018)"A review on microstructural study and compressive strength of geopolymer mortar, paste and concrete", *Construction and Building Materials*, 186:550–576

Onuaguluchi, O., Ratu, R., and Banthia, N. (2022)"Effect of sodium sulfate activation on the early-age matrix strength and steel fiber bond in high volume fly ash (HVFA) cement mortar", *Construction and Building Materials*, 341:127808

Santha Kumar, G., Saini, P. K., Deoliya, R., Mishra, A. K., and Negi, S. K. (2022)"Characterization of laterite soil and its use in construction applications: A review", *Resources, Conservation & Recycling Advances*, 16: 200120

Shamsaei, E., Bolt, O., Basquiroto de Souza, F., and Benhelal, E. (2021)"Pathways to commercialisation for brown coal fly ash-based geopolymer concrete in Australia", *Sustainability*, 13(8): 4350

Singh, B., Ishwarya, G., Gupta, M. and Bhattacharyya, S.K.(2015)"Geopolymer concrete: A review of some recent developments", *Construction and building materials*, 85:78–90

Tabassum, R. and Khadwal, A. (2015)"Effect of sodium hydroxide concentration on various properties of geopolymer concrete", *International Journal of Engineering and Technical Research*, 3(10):2454–4698

Thampi, T., Sreevidya, V and R Venkatasubramani. (2014)"Strength studies on geopolymer mortar for ferro geopolymer water tank" *International Journal of Advanced Structures and Geotechnical Engineering*, 03(02): 2319–5347

Yaragal, S. C., Basavana Gowda, S. N., and Rajasekaran, C. (2019) "Characterization and performance of processed lateritic fine aggregates in cement mortars and concretes" *Construction and Building Materials*, 200: 10–25

Zhang, P., Zheng, Y., Wang, K., and Zhang, J. (2018) "A review on properties of fresh and hardened geopolymer mortar" *Composites Part B: Engineering*, 152:79–95

Valorization of Low-grade Limestone for Producing Calcium Sulfoaluminate-Belite Cement

Bipina Thaivalappil* and Piyush Chaunsali

Department of Civil Engineering, IIT Madras, Chennai, India
Email:ce20d700@smail.iitm.ac.in, pchaunsali@iitm.ac.in

*Corresponding author

ABSTRACT

Over the past few decades, calcium sulfoaluminate-belite cement has gained interest in the research community due to its technical and environmental benefits as an alternative binder to Portland cement for various applications. This cement is conventionally produced using raw materials such as limestone, clay, bauxite, and gypsum and has a significantly reduced CO2 footprint attributed to its production compared to PC. The lower CO2 emissions are achieved due to lower clinkering temperature (~200 °C less than that of Portland cement), reduced energy requirements for clinker grinding, and lower clinker content due to higher calcium sulfate/gypsum content in cement. Calcium sulfoaluminate-belite -based binders provide high early-age strength, shrinkage compensation, improved resistance against sulfate attack, acid attack, etc. Unlike Portland cement, where the presence of alite is crucial for early-age strength development, calcium sulfoaluminate-belite cement has ye'elimite as its primary strength-contributing phase. Consequently, its cement production can utilize low-grade limestone, which is typically unsuitable for Portland cement production due to the lack of sufficient lime content and the presence of impurities. This presents an opportunity to utilize vast quantities of rejected limestone from existing cement plants, thereby reducing the strain on limestone reserves. This study explores the feasibility of employing two types of low-grade limestone, with siliceous and clayey impurities, for producing calcium sulfoaluminate-belite cement. Laboratory-scale synthesis of the cements using these low-grade limestones was conducted, and the impact of raw meal composition and sintering and formation of clinker phases was examined. The resulting clinkers were characterized using X-ray diffraction and thermogravimetry analysis techniques. Calcium sulfoaluminate-belite cements produced with low-grade limestone were compared with the cement synthesized using cement-grade limestone, providing insights into the potential of utilizing alternative raw materials for sustainable cement production.

KEYWORDS*: Calcium sulfoaluminate-belite cement; Clinkering; Low-grade limestone*

1. Introduction

The origin of calcium sulfoaluminate-belite (CSAB) cement can be traced back to the development of ye'elimite, or calcium sulfoaluminate ($C_4A_3\hat{S}$) by Alexander Klein in the 1960s (Alexander and Calif (1966)). Initially, ye'elimite was used as an expansive agent in ordinary Portland cement (OPC) to create shrinkage-compensating binders due to its rapid hydration reaction in the presence of calcium sulfate forming ettringite (expansive reaction). This innovation led to the production of CSAB cements in China in the early 1970s (Zhang, Su, and Wang (1999)). CSAB cement comprises phases such as ye'elimite, belite (C_2S), ferrite (C_4AF), and calcium sulfate ($C\hat{S}$). Clinkering for this type of cement can be carried out in a rotary kiln typically used for Portland cement production, with clinkering reactions occurring between 1250 °C and 1300 °C (Zhang (2000)). Due to its lower requirements for limestone, reduced kiln temperatures, and decreased clinker content and grinding energy, CSAB cement significantly reduces carbon dioxide emissions compared to conventional Portland cement production (Gartner (2004)).

Ye'elimite, the primary phase in CSAB cement, requires less CaO for its formation compared to alite, the main phase in PC. Hence, the overall lime requirement in the raw mix is reduced which allows the

possibility of using low-grade limestone, which is unsuitable for PC production due to its lower calcium oxide content and higher impurity content, for CSAB clinker production.
Given the excess of limestone rejected from cement plants due to impurities, using it in CSAB cement manufacturing could help reduce the pressure on limestone reserves for cement production. Researchers have successfully produced CSAB cement from alternative raw materials, including industrial waste, without compromising the mechanical performance compared to CSAB cement made from traditional sources (Canbek, Shakouri, and Erdoğan (2020); Chen and Juenger (2012); Huang et al. (2020)). However, most studies focus on finding alternative and cheaper alumina sources to partially replace bauxite, potentially lowering the manufacturing costs of CSAB cement. There is limited literature on using low-grade limestone in CSAB manufacturing. This study aims to synthesize CSAB phase assemblages by incorporating low-grade limestone in the raw mix and to understand the effect of raw mix proportions on the clinker phase composition. The challenges associated with the formation of the gehlenite phase and the impact of the lime saturation factor are also investigated.

2. Materials and Methodology

Limestone, bauxite, and calcium sulfate were used as raw materials for synthesizing the CSAB cement phase assemblages in a laboratory scale. Two compositions of low-grade limestones collected from the Ariyalur district of Tamil Nadu, India, were used to substitute the conventional raw materials partially. These limestones were rejected from PC plants due to the presence of clayey and silicious impurities. The oxide composition obtained from X-ray fluorescence spectroscopy (XRF) and loss on ignition values of the raw materials are shown in Table 1.
The raw materials proportioning was carried out using adapted Bogue equations for the phase assemblage $C_4A_3\hat{S}$-C_2S-C_4AF- $C\hat{S}$ (Chen and Juenger (2012)), aiming to achieve ~40% $C_4A_3\hat{S}$, ~40% C_2S, ~20% C_4AF, and <5% $C\hat{S}$ in the clinker. The raw mix proportions are shown in Table 2. To compensate for the potential SO_3 volatilization during clinkering beyond 1200 °C (Huang et al. (2020); Shen et al. (2014)), an extra 5% of $C\hat{S}$ was added to the raw mix.

Table 1. Major oxide composition of raw materials

(wt%)	CaO	Al_2O_3	SiO_2	SO_3	Fe_2O_3	TiO_2	MgO	LOI
Limestone – cement grade (C)	46.0	1.9	13.9	0.1	4.8	< 0.1	0.4	37.3
Limestone – low grade (L_1)	36.3	7.2	23.8	< 0.1	3.6	0.4	1.9	25.3
Limestone – low grade (L_2)	23.6	12.6	31.2	0.3	6.3	-	1.3	22.1
Bauxite (B)	0.7	88.4	2.6	0.1	2.7	3.2	0.4	-
Calcium sulfate ($C\hat{S}$)[1]	41.2	-	-	58.8	-	-	-	-

[1] *Laboratory-grade*

Table 2. Raw mix proportions used for CSAB cement synthesis

(wt%)	B	C	L1	L2.2	$C\hat{S}$	Extra $C\hat{S}$
CSAB_0L	15	79	0	0	6	5
CSAB_20L1	17	54	20	0	9	5
CSAB_20L2	19	53	0	20	8	5

The clinkering was carried out in a high-temperature muffle furnace. The raw mixes were heated to a peak temperature of 1300 °C, with a heating rate of 5 °C/min and a retention time of one hour. The resulting clinkers were then air-cooled to room temperature and ground to the required fineness in a planetary ball mill. X-ray diffraction (XRD) was used to determine the clinker phase composition. The XRD

quantification was performed using the Rietveld refinement method with PANalytical X'pert High Score Plus Software V.3. Thermogravimetric analysis (TGA) was conducted on hydrated cement pastes prepared from the selected clinkers.

3. Results and Discussion

Figure 3 shows the XRD of the synthesized CSAB clinkers. The obtained proportion of ye'elimite and belite is observed to be closely similar to the target composition in the case of CSAB_0L and CSAB_20L$_1$. In both cases, the amount of brownmillerite formed is lower than expected, possibly because of the potential incorporation of iron into the main clinker phases (Abir et al. (2022); Bullerjahn, Haha, and Scrivener (2015); Chen, Feng, and Long (1993)). However, in CSAB_20L$_1$, a small fraction of gehlenite is also formed as a minor phase. These clinkers were ground to similar fineness and assessed for early hydration. 15% gypsum was added to the clinkers, and paste mixes were prepared using a water-to-binder ratio of 0.5. The TGA curves for the 3-day hydrated pastes are shown in Figure 5. The major hydration products in both the pastes were ettringite, along with some amorphous aluminium hydroxide. It can be seen that both mixes yielded similar mass loss peaks after 3-day hydration, indicating that the early age hydration progress was not affected by the use of 20% low-grade limestone (L$_1$) in the CSAB raw mix.

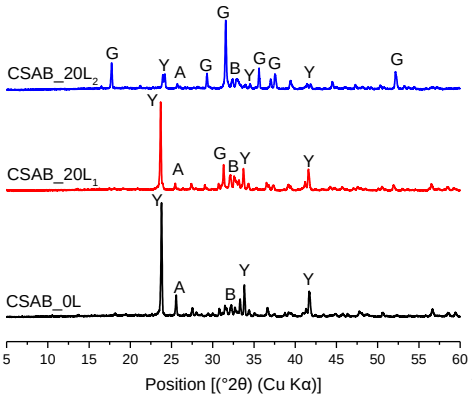

Figure 3. XRD of synthesized CSAB clinkers (Y: Ye'elimite, Anhydrite, G: Gehlenite, B: Belite)

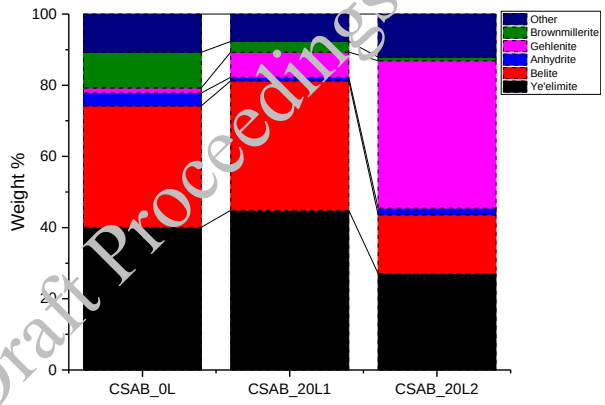

Figure 4. Phase composition of synthesized CSAB clinkers obtained from QXRD

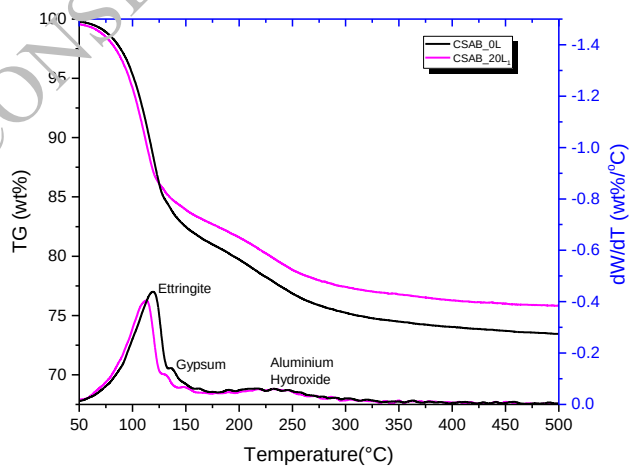

Figure 5. Thermogravimetry of 3-day hydrated CSAB cements prepared in laboratory

In the CSAB_20L$_2$ clinker, ye'elimite and belite formation was suppressed due to stabilization of gehlenite as a major phase (>40%) Figure 4. Gehlenite is hydraulically less reactive and hence it is not preferred in the cement clinker(Sabbah and Zhutovsky 2022). Gehlenite is formed as a intermediate phase below 1000 °C, and it further reacts with CaO and $CaSO_4$ to form ye'elimite and belite (Eq. 1–3). When CaO or SO_3

contents are not sufficient in a clinker, gehlenite may be left over in the clinker. To understand the effect of CaO on the formation of gehlenite, additional CaO was added to the raw meal of CSAB_20L₂. The XRD of resulting clinkers at different percentages of extra CaO are shown in Figure 6.

$$2\mathrm{C} + A + S \rightarrow C_2AS \qquad (900 - 950\ °\mathrm{C}) \ \ldots\ldots\ldots\ldots\ldots\ldots\ldots\ldots\ldots\ldots\ldots\ldots .. \ 1$$

$$3\mathrm{C} + 3A + \mathrm{C}\hat{\mathrm{S}} \rightarrow C_4A_3\hat{\mathrm{S}} \qquad (950 - 1000\ °\mathrm{C}) \ \ldots\ldots\ldots\ldots\ldots\ldots\ldots\ldots\ldots\ldots\ldots ......2$$

$$3\mathrm{C} + 3C_2AS + \mathrm{C}\hat{\mathrm{S}} \rightarrow C_4A_3\hat{\mathrm{S}} + 3C_2S \quad (1000 - 1050\ °\mathrm{C}) \ \ldots\ldots\ldots\ldots\ldots\ldots\ldots\ldots\ldots\ldots\ldots ...3$$

The presence of extra CaO in the raw mix could bring a drastic difference in the resulting clinker composition. With just 5% additional CaO, the gehlenite peak is considerably reduced, and more ye'elimite and belite formation can be observed from XRD. An additional 10% CaO could convert almost all the gehlenite to ye'elimite and belite. With the observed results, the authors attempted to correlate the formation of gehlenite to the CaO available in the raw meal. A formula for lime saturation factor (LSF) was devised for CSAB phase assemblage (Eq. 4), which is the ratio between CaO available in the raw meal and CaO required for forming the clinker phases.

$$\mathrm{LSF} = (\%C - 0.7 * \%T)/(1.867 * \%S + 0.54 * \%A + 1.05 * \% \ \ldots\ldots\ldots\ldots\ldots\ldots\ldots .4$$

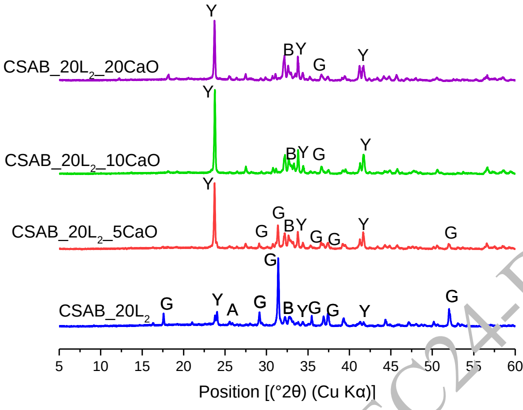

Figure 6. XRD of synthesized CSAB clinkers using limestone L₂ with varying amounts of extra CaO

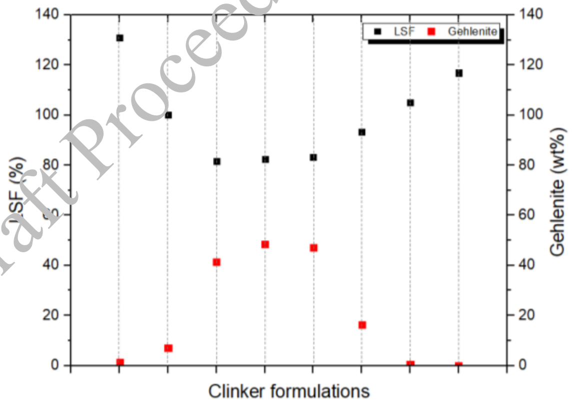

Figure 7. Amount of Gehlenite in clinker vs LSF calculated for CSAB raw mix

Figure 7 illustrates the relationship between the calculated LSF and the amount of gehlenite in the synthesized clinkers from this study. It can be inferred that a deficiency of lime in the system promotes the formation and stabilization of gehlenite, thereby hindering the formation of ye'elimite and belite. Raw mixes having LSF greater than 95% could limit the gehlenite content to less than 10% in the clinkers.

4. Conclusions

This study investigated the use of low-grade limestone with varying siliceous and clayey impurities to partially replace cement-grade limestone in CSAB clinker raw mixes. The chemical compatibility of these limestones was analyzed using XRF, and clinkers were produced in the laboratory by incorporating 20% low-grade limestone to match the target clinker composition. Successful clinkering was achieved with limestone L₁, showing that early-age hydration reactivity was comparable to CSAB cement made from conventional raw materials. However, limestone L₂, with less than 25% CaO and more than 40% (SiO_2 + Al_2O_3), resulted in a significantly higher formation of gehlenite in the clinker for the desired proportion. The study also explored the effects of additional CaO on the gehlenite formation, finding that the Lime Saturation Factor (LSF) was crucial in controlling gehlenite formation. An LSF greater than 95% limited gehlenite content to <10% in clinkers.

Acknowledgements

The experimental facilities provided by the Department of Civil Engineering of IIT Madras and the support from the Centre of Excellence on Technologies for Low-Carbon and Lean Construction are gratefully acknowledged. The first author would also like to thank the Ministry of Education, India, for the Prime Minister's Research Fellowship.

References

Abir, F. Z., M. Mesnaoui, Y. Abouliatim, L. Nibou, Tariq Labbilta, Y. El Hafiane, and A. Smith. 2022. "Effect of the Addition of Iron Oxide on the Microstructure of Ye'elimite." *Cement and Concrete Research* 151(October 2021):106625. doi: 10.1016/j.cemconres.2021.106625.

Alexander, Klein, and Danville Calif. 1966. "Expansive and Shrinkage Compensated Cement." *United States Patent Office*.

Bullerjahn, Frank, Mohsen Ben Haha, and Karen L. Scrivener. 2015. "Iron Solid Solutions of Ye ' Elimite -Effect on Reactivity Iron Solid Solutions of Ye ' Elimite - Effect on Reactivity." (October).

Canbek, Oğulcan, Sahra Shakouri, and Sinan T. Erdoğan. 2020. "Laboratory Production of Calcium Sulfoaluminate Cements with High Industrial Waste Content." *Cement and Concrete Composites* 106.

Chen, Dun, Xiuji Feng, and Shizhong Long. 1993. "The Influence of Ferric Oxide on the Properties of 3CaO · 3Al2O3 · CaSO4." *Thermochimica Acta* 215(C):157–69. doi: 10.1016/0040-6031(93)80088-R.

Chen, Irvin A., and Maria C. G. Juenger. 2012. "Incorporation of Coal Combustion Residuals into Calcium Sulfoaluminate-Belite Cement Clinkers." *Cement and Concrete Composites* 34(8):893–902. doi: 10.1016/j.cemconcomp.2012.04.006.

Gartner, Ellis. 2004. "Industrially Interesting Approaches to ' 'low-CO2 ' ' Cements." *Cement and Concrete Research* 34:1489–1498 Industrially. doi: 10.1016/j.cemconres.2004.01.021.

Huang, Yongbo, Yan Pei, Jueshi Qian, Xin Gao, Jiao Liang, Guangbin Duan, Piqi Zhao, Lingchao Lu, and Xin Cheng. 2020. "Bauxite Free Iron Rich Calcium Sulfoaluminate Cement: Preparation, Hydration and Properties." *Construction and Building Materials* 249:118774. doi: 10.1016/j.conbuildmat.2020.118774.

Sabbah, Adam, and Semion Zhutovsky. 2022. "Effect of Sulfate Content and Synthesis Conditions on Phase Composition of Belite-Ye ' Elimite-Ferrite (BYF) Clinker." *Cement and Concrete Research* 155(November 2021):106745. doi: 10.1016/j.cemconres.2022.106745.

Shen, Yan, Jueshi Qian, Junqing Chai, and Yanyan Fan. 2014. "Calcium Sulphoaluminate Cements Made with Phosphogypsum: Production Issues and Material Properties." *Cement and Concrete Composites* 48:67–74. doi: 10.1016/j.cemconcomp.2014.01.009.

Zhang, Liang. 2000. "Microstructure and Performance of Calcium Sulfoaluminate Cements (Doctoral Dissertation)." (June):388.

Zhang, Liang, Muzhen Su, and Yanmou Wang. 1999. "Development of the Use of Sulfo- and Ferroaluminate Cements in China." *Advances in Cement Research* 11(1):15–21. doi: 10.1680/adcr.1999.11.1.15

Epoxy Coated Rebars in Concrete: Integration of Nano-Clays and Self-Healing Microcapsules for Sustainable Construction

N. Sharma[1*], S. Sharma[2], S. K. Sharma[3], and R. Mehta[4]

[1] Research Scholar, Civil Engineering Department, TIET, Patiala, India
Email: nsharma60_phd19@thapar.edu
[2] Professor, Civil Engineering Department, TIET, Patiala, Indi,
Email: shrutisharma.ced@thapar.edu
[3] Associate Professor, Mechanical Engineering Department, TIET, Patiala, India
Email: sksharma@thapar.edu
[4] Professor, Chemical Engineering Department, TIET, Patiala, India
Email: rmehta@thapar.edu

[*] Corresponding author

ABSTRACT

Among the broad spectrum of approaches aimed at mitigating steel corrosion in concrete, the application of epoxy coatings to reinforcing bars in concrete has exhibited significant effectiveness. Our investigation centres on advancing the corrosion resistance attributes of epoxy coated rebars through the integration of different nano-clay based fillers and self-healing microcapsules in epoxy. This encompasses different nano-clays like montmorillonite (MMT) and halloysite (HNT), tung-oil based self-healing microcapsules (ME) and a combination of montmorillonite nano-clay with self-healing microcapsules (MMT_ME). Concrete cylinders with epoxy coated bars were subjected to accelerated impressed current corrosion and their performance was evaluated by visual inspection, impressed corrosion current and ultrasonic guided wave measurements. The addition of nano-clays and self-healing microcapsules within epoxy coatings has demonstrated remarkable effectiveness in contrast to uncoated and pure epoxy coatings for corrosion inhibition in aggressive environments. The nano dispersion of clay in epoxy enhances toughness, tensile, and flexural properties while creating tortuous paths for moisture diffusion as evidenced by minimal corrosion current rise and drop in ultrasonic guided wave signal indicative of deterioration due to pitting corrosion. The ultrasonic signals exhibit a decrease to 100% for MMT coatings and 80% for HNT-based coatings following a 90-day period of accelerated corrosion testing. On the other hand, self-healing tung-oil microcapsules-based coatings inhibit the corrosion progression after initiation. A combination of nano-clay and microcapsules (MMT_ME) delivers promising results as it is capable of delivering dual-protection mechanism for corrosion inhibition. This marks a significant step towards construction practices aimed at reducing the need for frequent repairs and rehabilitation, thus aligning with the overarching objective of sustainable construction.

KEYWORDS: *Epoxy coated rebars, Nano-clays, Tung-oil, Accelerated corrosion, Ultrasonic guided wave measurement*

1. Introduction

Corrosion in concrete infrastructure presents a significant global challenge. The degradation of structures due to corrosion results in billions of dollars for repair, rehabilitation, and sometimes complete reconstruction. Approximately USD 100 billion is allocated annually worldwide to maintain structures impacted by corrosion Sharma et al (2022). Infrastructure reconstruction also has indirect environmental implications, as construction processes and cement production contribute to CO_2 emissions Chen et al (2017). Therefore, efforts focused on mitigating corrosion and extending the lifespan of concrete infrastructure are crucial not only as an economic measure but also for fostering sustainable environmental development. Epoxy coating is highly effective in combating corrosion by creating a physical barrier. However, its application is constrained by the presence of inherent micro-pores or its brittle nature Wang et al (2018).

Therefore, nano-modification of epoxy coatings has been suggested, utilizing nano-fillers such as nano-clays, graphene derivatives, etc., or employing self-healing methods like micro-encapsulated coatings, to overcome these limitations Sharma et al (2023). Incorporating nano-clay particles into epoxy coatings enhances their ability to offer cathodic protection, attributed to the hydrophobic nature of clay, which markedly decreases water ingress into the coating Shirehjini et al. (2017). Beryl et al. (2021) investigated the impact of functionalized HNT nano-clay in epoxy resin and found that even a small quantity of nano-clay significantly bolstered the adhesion strength of the coating, owing to the extensive surface area of the nanoparticles. Similarly, Graphene Oxide (GO) filler demonstrates exceptional bonding characteristics with an epoxy matrix when utilized at the optimal concentration. A study determined that incorporating 0.3 wt.% GO in epoxy lead to improvised performance, suggesting an improved overall performance of the composite material Zheng et al (2020). The use of self-healing agents in epoxy-based coatings shows great promise, as these smart materials can protect the coating from mechanical damage during transportation or handling. Research on Epoxy Coated Rebars (ECRs) has explored various self-healing agents, including tung oil, linseed oil, and epoxy esters, which can repair cracks or damage caused by mechanical impact or corrosion Chen et al (2017) and Sharma et al (2020). Generally, tung oil is a conjugated oil, reacts with oxygen in the air to quickly form a solid, waterproof layer, which serves as a barrier protecting the substrate from external environmental factors. The microencapsulation-based self-healing coating approach offers the best long-term protection, as the self-healing agent is safely enclosed and only activated by damage. In studies by Samadzadeh et al (2011) and Boura et al (2012), it is reported that tung oil and linseed oil microcapsules effectively conferred self-healing properties to epoxy without needing an additional catalyst, reducing water penetration through the healed coating. This study evaluates the corrosion inhibition capabilities of epoxy-based coatings modified with nano-clays (Montmorillonite-MMT, and Halloysite-HNT), tung-oil microcapsules (ME), and a combination of MMT with tung-oil microcapsules (MMT_ME). These were compared to uncoated (control) and plain epoxy-coated rebars. The coated rebars underwent accelerated corrosion testing by embedding them in concrete cylinders. The coatings' performance assessed through non-destructive monitoring of corrosion current, ultrasonic guided waves, and visual inspection over 90 days or until the ultrasonic guided wave signals disappeared. The research focused on comparing and reporting the results obtained from these non-destructive monitoring methods for nano-modified coated bars embedded in concrete.

2. Methodology

Araldite CY 230-1 and Aradur HY 951 epoxy used in this study. Nano-clays (MMT and HNT) and tung-oil (a China wood oil) are used as a fillers. Ordinary Portland Cement (OPC) of grade 43, coarse and fine aggregates, were used for concrete samples. Mild steel bar of grade Fe 250 is used in this study. Tung-oil microcapsules were prepared as reported in Sharma et al (2020). For synthesis of nano-modified epoxy coatings, a consistent basic three-step mixing procedure was employed. This procedure involved high shear homogenization, probe ultrasonication, and mechanical stirring. For MMT_ME coatings, first nano-clay was dispered in epoxy resin using three step mixing procedure then at last tung-oil microcapsules were added into the matrix and coating applied to rebars. Before applying the coating, the rebar surfaces are cleaned with emery paper and acetone to remove any residual dust, ensuring a uniform coating application. The coated bars were then cured in an oven at 80°C for a duration of three days. All coated bars (as described in Table 1) embedded in concrete specimens through a casting process. Reinforced concrete samples were cast using M20 grade concrete with a design mix proportion of 1:1.45:2.91 (cement, sand, and coarse aggregates) and a water-to-cement ratio of 0.45. Standard cubes measuring 150mm in size were prepared to assess the characteristic compressive strength. The average compressive strength after 7 days was 17.8 N/mm^2, and after 28 days, it was 28.3 N/mm^2. Concrete cylinders with dimensions of 100mm×200mm were cast, featuring a 12mm rebar positioned in the centre of the cross-section with a 300mm length. The casted concrete sections were cured for 28 days before undergoing accelerated corrosion testing. For accelerated corrosion testing, concrete specimens were wrapped with stainless steel wire mesh serve as cathode and the mild steel bar, serving as the anode in the corrosion circuit. Specimen then submerged in a 3.5wt% NaCl solution, which served as the electrolyte. It was then connected to a constant voltage source, specifically an Aplab Make device with a rating of 0-5 A and 0-64V. At 15V constant voltage supply, samples were corroded. The performance of samples experiencing corrosion was monitored periodically by non-destructive testing of corrosion current, ultrasonic guided waves and visual assessment. Corresponding

current increment was observed continuously during the testing period through power supply and for visual assessment samples condition were monitored by taking digital images, without disturbing them. The corroded rebar underwent Ultrasonic Guided Wave (UGW) testing at 1MHz using a specific longitudinal L (0, 7) mode. This mode was chosen as it was capable of effectively detecting the pitting effect caused by corrosion using a conventional Ultrasonic Testing (UT) arrangement Sharma et al (2020). As corrosion progresses or pitting occurs in rebar as a consequence of corrosion, the ultrasonic signal strength decreases. All samples were periodically monitored throughout testing period and the variation in their signal was quantified by comparing the ratio of peak-to-peak voltage with escalating corrosion exposure days to their initial healthy signal on day 1.

Table 1. Details of coating prepared and testing matrix

Nomenclature	Description/Details	Sapmles Tested
		Coated Bars in Concrete Cylinders
Control	Uncoated Sample	3
PE	Plain epoxy coated rebar	3
MMT	Montmorrilonite nano-clay modified coating (2wt% of epoxy resin)	3
HNT	Halloysite nano-clay modified coating (2wt% of epoxy resin)	3
ME	Tung-oil Micro-encapsulated coating (10wt% of epoxy resin)	3
MMT_ME	Montmorrilonite nano-clay with Tung-oil micro-encapsulated coating (2wt% & 10wt% of epoxy resin, respectively)	3

3. Results and discussions

An increase in corrosion current under constant voltage conditions indicates rebar corrosion and the degradation of the passive layer. Figure 1-a shows the variation in corrosion current over the duration of corrosion exposure for concrete samples. Simultaneously, ultrasonic signatures were recorded at regular intervals during testing, and their peak-to-peak voltage was calculated. Each signature's voltage was divided by its initial (day 1) voltage, and this variation is depicted as peak-to-peak voltage versus corrosion exposure duration in Figure 1-b. The deterioration of rebars due to corrosion is indicated by a loss in transmitted signal strength or a decrease in the peak-to-peak ratio (demonstrated in Figure 1-b).

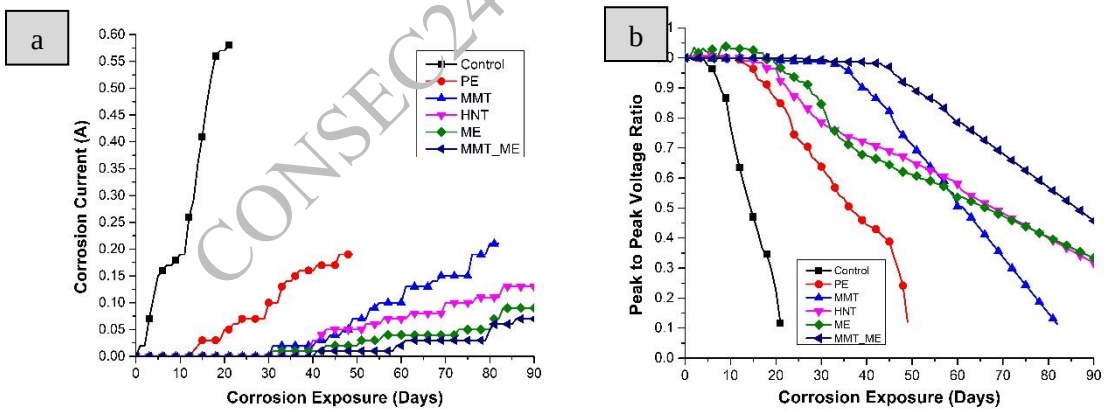

Figure 1. Accelerated corrosion testing results, (a) Corrosion current, and (b) Ultrasonic guided waves

Figure 1a shows that the corrosion current for uncoated samples reaches approximately 0.58A, while for plain epoxy (PE) samples, it reduces to 0.19A at the end of the corrosion period. Testing of corroded rebars was halted either when the amplitude of their ultrasonic guided wave signals dropped to nearly zero or when the corrosion exposure duration reached 90 days. For MMT_ME samples, the corrosion current was the lowest, reaching only 0.07A after 90 days. Figure 1b shows that the voltage ratio of MMT_ME coated rebars remains stable for the initial 40-45 days, indicating no corrosion initiation, which aligns with the corrosion current data and visual inspections. In contrast, signals for nano-clay coatings (MMT and HNT) begin to drop after 20-30 days, while those for micro-encapsulated coatings (ME) start declining before 20 days. Peak to peak voltage ratio for control, PE and MMT coated rebars were completely vanished after 21, 49 and 82 days respectively and they removed from corrosion testing. However, rest of three samples

(HNT, ME and MMT_ME) continued for 90 days. MMT_ME coatings, signals only start decreasing after 45 days and reches to a ratio of 0.45 after 90 days, demonstrating their superior effectiveness.
Upon visual inspection of the control sample at the conclusion of the testing, a significant longitudinal crack was noted, originating from the cross-sectional ends and causing the concrete section to fracture into multiple pieces. This longitudinal crack was parallel to the embedded rebar. In contrast, narrower cracks were observed in the PE and nano-clay rebar samples, with most corrosion products accumulating at the cross-sectional ends. The MMT_ME and ME samples exhibited the least cracks after 90 days of testing.

4. Conclusions

Nano-clay's bridge the micro-pores present in the coating resulting in the complete elimination of defects and improve the performance of coatings (MMT and HNT) in comparison to plain epoxy (PE) coatings. However, in self-healing coating (ME) corrosion initiation was similar to PE coatings but progression was delayed by self-healing mechanism. In MMT_ME coating, dual inhibition mechanism is provided by the combination of nano-clay with tung-oil microencapsulated coatings. Initiation is delayed by slow diffusion of aggressive chloride ions provided by nano-clay modification. However, once the corrosion initiates progression was further arrested by self-healing mechanism provide by tung-oil microcapsules. Overall, nano-modification and self-healing ability of epoxy coatings can significantly extend the lifespan of the infrastructure and reduces maintenance, thereby contributing to sustainable approach.

Acknowledgements

The research funds received from the Department of Science and Technology, SERB-POWER, Govt, of India vide ECR Grant No: SPG/2021/003533 and by CEEMS (Centre for Excellence in Emerging Materials), TIET, Patiala, is gratefully acknowledged.

References

Boura, S. H., Peikari, M., Ashrafi, A. and Samadzadeh, M. (2012) "Self-healing ability and adhesion strength of capsule embedded coatings—Micro and nano sized capsules containing linseed oil", *Progress in organic coatings*, 75(4):292-300

Chen, Y., Xia, C., Shepard, Z., Smith, N., Rice, N., Peterson, A. M. and Sakulich, A. (2017) "Self-healing coatings for steel-reinforced concrete", *ACS Sustainable Chemistry & Engineering*, 5(5):3955-3962

Samadzadeh, M., Boura, S. H., Peikari, M., Ashrafi, A. and Kasiriha, M. (2011) "Tung-oil: An autonomous repairing agent for self-healing epoxy coatings", *Progress in Organic Coatings*, 70(4):383-387

Sharma, N., Sharma, S., Sharma, S. K. and Mehta, R. (2020) "Evaluation of corrosion inhibition and self healing capabilities of nanoclay and tung-oil microencapsulated epoxy coatings on rebars in concrete", *Construction and Building Materials*, 259:120278

Sharma, N., Sharma, S., Sharma, S. K., Mahajan, R. L. and Mehta, R. (2022) "Evaluation of corrosion inhibition capability of graphene modified epoxy coatings on reinforcing bars in concrete", *Construction and Building Materials*, 322:126495

Sharma, N., Sharma, S., Sharma, S. K., Mahajan, R. L. and Mehta, R. (2023) "Investigations on corrosion inhibition performance of self-healing nano-clay modified epoxy coatings", *Journal of Building Engineering*, 70:106368

Shirehjini, F. T., Danaee, I., Eskandari, H. and Zarei, D. (2016) "Effect of nano clay on corrosion protection of zinc-rich epoxy coatings on steel 37", *Journal of Materials Science & Technology*, 32(11):1152-1160

Wang, X. H., Chen, B., & Tang, P. (2018) "Experimental and analytical study on bond strength of normal uncoated and epoxy-coated reinforcing bars", *Construction and Building Materials*, 189:612-628

Zheng, W., Chen, W. G., Feng, T., Li, W. Q., Liu, X. T., Dong, L. L. and Fu, Y. Q. (2020) "Enhancing chloride ion penetration resistance into concrete by using graphene oxide reinforced waterborne epoxy coating", *Progress in Organic Coatings*, 138:105389

Mechanical and Durability Performance of Mortar Incorporating Malawi Clay in Limestone Calcined Clay Cement

Uma Shankar Biswal[1], and Manu Santhanam[2*]

[1] Postdoctoral fellow, Department of Civil Engineering, IIT Madras, Chennai, India
Email: usb10@iitbbs.ac.in
[2] Professor, Department of Civil Engineering, IIT Madras, Chennai, India
Email: manus@iitm.ac.in

[*]Corresponding author

ABSTRACT

This article provides a comprehensive analysis of the viability of Malawi clay as a potential source material for limestone calcined clay cement (LC3). The research was conducted on mortars manufactured by substituting cement (OPC) with a 1:2 ratio of limestone and calcined clay at 30% and 45% proportions. Two different water-to-binder ratios (w/b) were utilized: 0.35 and 0.5. This study examined six mortar mixes, two of which were reference blends with each w/b. The concrete equivalent mortar method was used for the mortar mix design. The compressive strength test assessed the mechanical property, and durability performance was evaluated through the bulk resistivity test. The findings suggest that incorporating limestone calcined clay (LC2) into mortar led to comparable compressive strength and up to a threefold increase in bulk resistivity compared to the reference mix. Therefore, it is feasible to deduce that the incorporation of Malawi clay into mortar mixes increases the durability performance and is appropriate for the production of LC3.

KEYWORDS*: Limestone calcined clay, Bulk resistivity, Sustainability*

1. Introduction

To promote a sustainable environment, it is crucial to increase the use of waste or other materials with lower energy intensity as partial substitutes for cement in concrete and mortar. Flyash and GGBS, which are industrial by-products, have proven to be effective as supplementary cementitious materials (SCM). They can replace up to 30-50% of cement in order to create concrete that is both sustainable and durable. (Panesar 2019). However, their limitation lies in suboptimal early age strength and limited availability in the local area. This necessitates the development of limestone calcined clay cement (LC3), addressing the imperative for sustainable concrete without compromising early age strength (Dhandapani et al. 2021). LC3 binder, produced on a large scale, has demonstrated promising compressive strength compared to Ordinary Portland Cement (OPC) and superior strength to Portland Pozzolan Cement (PPC) when utilizing the same clinker. This underscores its potential application in commercial building materials (Krishnan and Bishnoi 2015). In the presence of limestone, the active component of calcined clay gives rise to an augmented quantity of AFm phases (specifically monocarboaluminate and hemi-carboaluminate), resulting in a synergistic reactivity between calcined clay and limestone (Bonavetti et al. 2001). However, the ability to use this technology to create durable and environmentally-friendly concrete depends on the availability of nearby sources of calcined clay and limestone. This emphasizes the necessity of conducting thorough investigations into substantial clay deposits on a worldwide scale. This report is dedicated to examining the suitability of clay sourced from the Linthepe region in Malawi, Southern Africa, for integration into the LC3 system. The assessment encompasses both mechanical and durability performance. Mechanical characteristics were evaluated through the compressive strength, while durability performance was gauged through bulk resistivity test.

2. Experimental Procedures

2.1 Materials

Ordinary Portland cement (OPC) (43 grade), conforming to IS 269 (2015), was used as the primary binding material. Raw clay, sourced from the Linthepe region in Malawi in Southern Africa having a kaolinite content of 66.25%, was calcined at 800 ºC for a duration of 2 hours. Subsequently, the material was allowed to cool gradually within the furnace, avoiding sudden exposure to the atmosphere. High-grade limestone from Gujurat was sourced and used along with the calcined clay in 1:2 (limestone: calcined clay) mass proportion for the LC3 mix used in the study. Locally available river sand with a maximum nominal size of 4.75 mm was utilized as the fine aggregate.

2.2 Mixture proportions

In the present investigation, 6 mortar mixes were prepared. Series I consists of three mixes that are made with w/b of 0.35 and a replacement level of 0, 30, and 45% of LC2. Series II consists of three mixes with w/b of 0.5 and replacement levels of 0, 30, and 45% of LC2. To simulate the behavior of concrete and mortar in the fresh state, concrete equivalent mortar (CEM) method is adopted. In this method coarse aggregate fraction is replaced by sand to ensure a constant wettable surface (Schwartzentruber and Catherine 2000). The final mix design for mortar mixes is provided in Table 1.

Table 1. Details of mortar mixes used in the investigation

Series	Mix ID	w/b	Replacement (%)	Cement (kg/m^3)	Calcined clay (kg/m^3)	Limestone (kg/m^3)	Sand (kg/m^3)
1	35L00	0.35	0	549	0	0	818
	35L30	0.35	30	384	110	55	807
	35L45	0.35	45	302	164	82	802
2	50L00	0.50	0	384	0	0	888
	50L30	0.50	30	269	77	38	880
	50L45	0.50	45	211	115	57	876

2.3 Test methods

To assess the influence of Malawi clay based LC2 on compressive strength mortar cubes of 50 mm size were cast in various mortar mixtures. The specimens obtained from the mist room, was evaluated at 7, 14, 28, and 56 days in accordance with IS 516 (Part 1/Sec 1- 2021). Whereas bulk resistivity was determined as per ASTM C1876 (2019). 50 mm cubes were cured in the curing room till the testing age. Then saturated sponges were placed between the plate electrodes and end surface of the specimen (Fig. 1). The test was performed at a frequency range of 1×10^6 Hz to 1 Hz using Solarton si1287 frequency response analyzer and the value of bulk resistance in ohms was recorded from Nyquist plot (Fig. 2) and used in equation 1 to get the bulk resistivity (ρ):

$$r = \frac{RA}{L} \quad \ldots 1$$

R = electrical resistance of specimen in kohms; A = specimen cross-sectional area in cm^2, and L= average specimen length in cm.

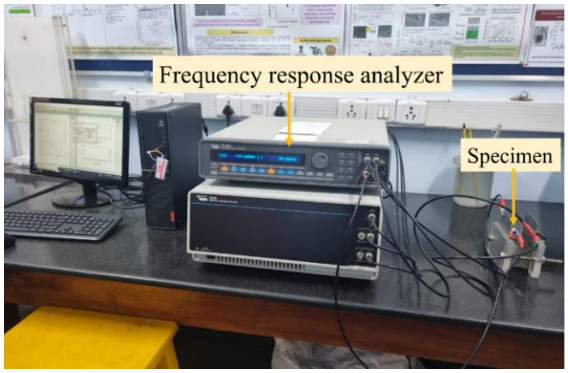

Figure 1. Setup for bulk resistivity test

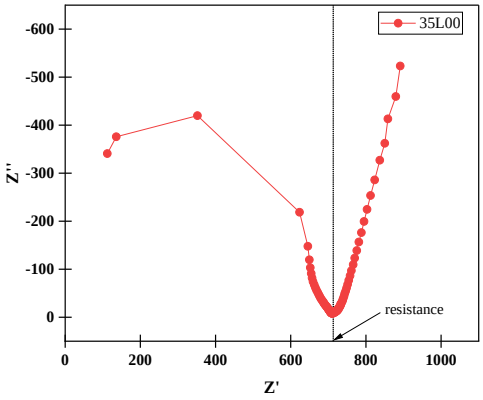

Figure 2. Typical Nyquist plot

3. Test results and discussions

3.1 Compressive strength

Compressive strength test was conducted for all mortar mixes. It can be observed from Fig. 3 that 30% binder replacement has resulted in strength similar to the reference mixes, whereas a reduction in the compressive strength value was obtained for 45% replacement. It can also be understood that increase in the percentage replacement of OPC with LC2 decreases the compressive strength in the earlier days. The impact is more for high w/b. This could be attributed due to the low reactivity of the LC3 based system. However, increase in the curing time enhances the reactivity of LC2 based systems due to its pozzolanic activity (Berodier and Scrivener 2015). This resulted in enhanced load carrying capacity presumably due to the pore refinement that is effective after 28 days of curing. Similar trend is observed for both the w/b ratios used in this study as shown in Fig. 3.

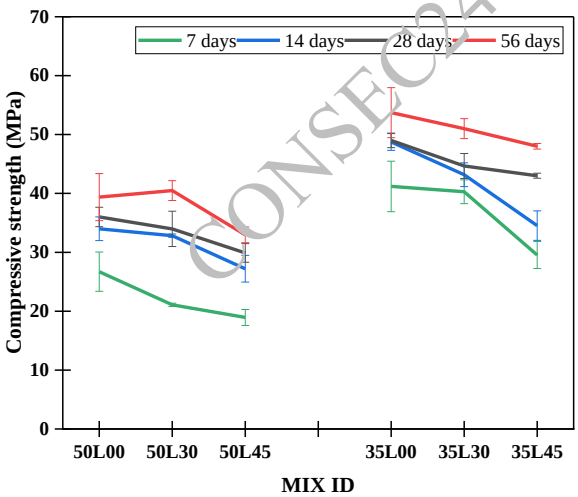

Figure 3. Compressive strength results

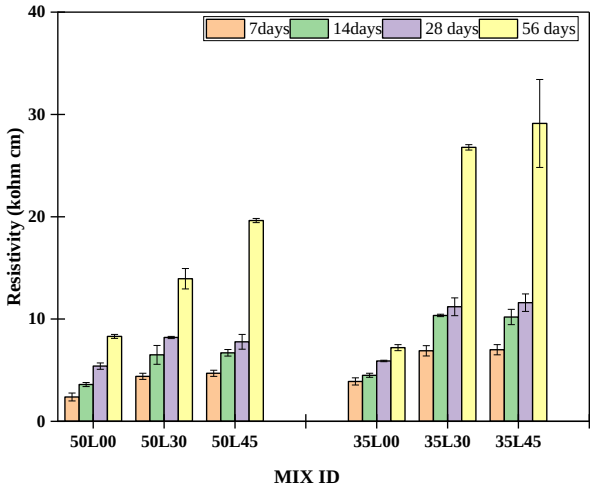

Figure 4. Bulk resistivity results

3.2 Bulk Resistivity

The bulk resistivity data for all the mixtures is depicted in Fig. 4. It is discernible that an augmentation in the replacement of LC2 correlates with an increase in the resistivity value across all ages. Furthermore, this trend persists consistently for mixtures with both water-to-binder (w/b) ratios. Notably, the increase is

particularly significant at the 56-day. This may be due to not enough available portlandite in the mix in earlier days to carry out pozzolanic reaction. The increase in resistivity is significantly higher compared to the improvement in mechanical properties, suggesting the formation of softer phases that do not contribute to strength. Specifically, for a w/b ratio of 0.35, the bulk resistivity for the system with 45% LC2 is nearly three times compared to the reference mix. This substantial difference is likely attributed to the enhanced pore refinement in the former compared to the reference mix (Dhandapani and Santhanam 2017). However, considering the porosity of LC3 system with 45% replacement at 0.35 w/b ratio, the obtained bulk resistivity values are counter-intuitive in nature, on comparison with LC3 system with 30%. This may be due to entrapped air porosity and a segment of the saturated porosity within the cement paste matrix of the mortar (Bu et al. 2014).

4. Conclusions

The following inferences can be made based on the replacement of Portland cement with LC2 in mortars:

- A comparable compressive strength can be achieved with a 30% LC2 binder replacement, while a 45% LC2 replacement only marginally reduces compressive strength.
- The bulk resistivity value of the mortar system increases two-fold with a 0.5 w/b ratio and three-fold with a 0.35 w/b ratio when 45% LC3 is used, compared to mortars containing only Portland cement.
- The impact of LC3 is more pronounced at lower w/b ratios.

Acknowledgements

The authors would like to acknowledge Technology & Action for Rural Advancement (TARA) for resourcing essential materials and financial support for smooth conduct of research.

References

ASTM C1876. (2019) "Standard Test Method for Electrical Resistivity or Conductivity of Concrete." *ASTM International*, i(Reapproved): 98–100

Berodier, E., and Scrivener, K. (2015) "Evolution of pore structure in blended systems." *Cement and Concrete Research*, 73: 25–35

Bonavetti, V., Rahhal, V. and Irassar, E. (2001) "Studies on the carboaluminate formation in limestone filler-blended cements." *Cement and Concrete Research*, 31(6): 853–859

Bu, Y., Spragg, R. and Weiss, W. J. (2014) "Comparison of the Pore Volume in Concrete as Determined Using ASTM C642 and Vacuum Saturation." *Advances in Civil Engineering Materials*, 3(1): 20130090

Dhandapani, Y. and Santhanam, M. (2017) "Assessment of pore structure evolution in the limestone calcined clay cementitious system and its implications for performance." *Cement and Concrete Composites*, 84: 36–47

Dhandapani, Y., Santhanam, M., Kaladharan, G. and Ramanathan, S. (2021) "Towards ternary binders involving limestone additions — A review." *Cement and Concrete Research*, 143: 106396

IS:269. (2015) "Ordinary Portland Cement - Specification." *Bureau of Indian Standards*, New Delhi, India

IS 516 (Part 1/Sec 1). (2021). "Hardened concrete - Method of Test Part 1 Testing of strength of Hardened Concrete Section 1 Compressive, Flexural and Split Tensile strength." *Bureau of Indian Standards*, New Delhi, India

Krishnan, S. and Bishnoi, S. (2015) "High Level Clinker Replacement in Ternary Limestone-Calcined Clay-Clinker Cement." *Advances in Structural Engineering*, Springer India, New Delhi: 1725–1731

Panesar, D. K. (2019) "Supplementary cementing materials." *Developments in the Formulation and Reinforcement of Concrete*, Elsevier: 55–85

Schwartzentruber, A. and Catherine, C. (2000) "La méthode du mortier de béton équivalent (MBE)—Un nouvel outil d'aide à la formulation des bétons adjuvantés." *Materials and Structures*, 33(8): 475–482

Review on the Light Weight Angular Aggregate Concrete for Structural Applications

Mohanapriyan Muralidharan[1], Mashudha Sulthana U.[2]

[1] *Department of Civil Engineering, National Institute of Technology, Tiruchirappalli, India*
mohanapriyan172@gmail.com
[2] *Department of Civil Engineering, National Institute of Technology, Tiruchirappalli, Indiasmash@nitt.edu*

*Corresponding author

ABSTRACT

The increasing emphasis on sustainable infrastructure fuels interest in structural lightweight aggregate concrete, which diminishes dead load and seismic weight, allowing for smaller, lighter components. Economic benefits include reduced design, transportation, and handling costs due to decreased density. The review examines gaps that optimizes material ratios, evaluates strength properties, and assesses sustainability benefits in structural lightweight aggregate concrete, guiding future research and promoting sustainable construction practices. Angular aggregates are produced by crushing sintered briquettes containing fly ash, binder, and water, eliminating the need for pelletization. Although widely used commercially, pelletized fly ash aggregates encounter drawbacks due to their round shape, such as diminished interlocking effect, necessitating energy-intensive processes and lacking reproducibility. This study conducted a comprehensive review of existing literature and explored various combinations of binders and fly ash proportions, ultimately recommending an optimal binder range of 15-20% and a water-to-fly ash ratio of 0.25. The study also evaluated the strength characteristics of structural lightweight concrete incorporating angular fly ash aggregate. While lightweight aggregate concrete typically has lower compressive strength than normal weight concrete, factors like water-cement ratio, shape index and aggregate type can enhance it. Concrete utilizing angular aggregates meets ASTM C330 standards, demonstrating compressive strength between 22.23 MPa and 35.12 MPa, split tensile strength ranging from 2.42 MPa to 3.93 MPa and flexural strength of 3.51 MPa to 4.5 MPa. This confirms the efficacy of lightweight fly ash aggregate concrete for sustainable structural applications, aiding in resource conservation and pollution reduction.

KEYWORDS: *Angular aggregate, Binder, Fly Ash, Sintering, Lightweight concrete, Sustainability.*

1. Introduction

Around the word, 80% of the yearly production of by-products from coal combustion occurs in fly ash, a by-product of burning coal in power plant boilers; bottom ash makes up the remaining 20%. Fly ash is divided into Class F and Class C according to ASTM C618. Class F fly ash, sourced from anthracite or bituminous coal, contains at least 70% combined silicon dioxide (SiO_2), aluminium oxide (Al_2O_3) and iron oxide (Fe_2O_3), and exhibits pozzolanic properties. In contrast, Class C fly ash, derived from lignite or sub-bituminous coal, contains at least 50% of these oxides and has both cementitious and pozzolanic properties. According to Kamal and Mishra (2020), the properties of fly ash vary among thermal power plants due to differences in production methods and coal quality, as noted by Bhattacharjee and Kandpal (2002) and Manikandan and Ramamurthy (2007). Even fly ash from the same source can exhibit variations in physical and chemical properties due to differences in coal quarry sources, grinding extent, boiler burning temperature, gas cleaning apparatus, and boiler configuration. Managing fly ash waste is a significant environmental concern due to its adverse effects on landfill space, soil quality, and air and water pollution. Despite these issues, fly ash is widely used in various engineering applications. There is a continuous demand for improved utilization methods. Concrete, the most common construction material, is a key focus for incorporating recycled industrial waste like fly ash. Integrating fly ash into concrete can address

environmental concerns while enhancing concrete performance. Therefore, research and development efforts are ongoing to discover effective ways to utilize fly ash in concrete construction.

Terzic et al (2014) recognizes extensive research to develop high-performance artificial lightweight aggregates for concrete, which have a substantially lower bulk density(<1900kg/m^3) compared to standard concrete while maintaining a strength range of 30-80MPa. Lightweight concretes offer a host of benefits, including the ability to construct lighter and thinner upper structures and footings, reduce the dimensions of columns and beams, thereby maximizing space utilization, and produce smaller and more cost-effective pre-cast elements that are easier to handle and transport. Additionally, they provide superior thermal and acoustic insulation and enhance fire resistance, Wegen and Bijen (1985). Given that aggregates typically occupy 65-75% of the total concrete volume, using waste in the production of angular aggregates presents an exceptionally sustainable recycling solution. This not only helps conserve depleted natural resources but also significantly reduces environmental impact.

The concept of using fly ash in manufacturing aggregates for concrete has gained traction among researchers. Synthetic lightweight aggregates (LWA) such as expanded clay or shale, vermiculite, slate, blast furnace slag aggregate, and fly ash aggregate (FAA) are commonly used for structural applications. Among these, fly ash aggregate is considered the most suitable for structural use.

Various methods, including cold bonding, autoclaving and sintering are employed to harden artificially prepared FAA. Cheeseman et al. (2005) suggest that sintered aggregates have a dense structure with fewer non-interconnected pores, while cold-bonded aggregates have open and interconnected pores that allow for high water absorption. The properties and strength of the FAA are significantly influenced by the physical and chemical properties of fly ash and binders. The sintering behaviour of ash, and consequently the interior structure of FAA is greatly influenced by the chemical components present in fly ash during sintering. Binders are added during the preparation of fly ash aggregate to coalesce fly ash particles, enhancing productivity and mechanical properties.

Sintered aggregate has low density, reducing the dead load and material handling costs during large-scale constructions. As aggregate is a major constituent of concrete, there is an urgent need for techniques to produce aggregate from fly ash, Adell et al (2007). Kamal and Mishra (2020) states that the lightweight concrete (LWC) is gaining importance due to its advantages such as enhanced seismic and earthquake resistance, reduced self-weight, and improved sound thermal properties. Utilizing lightweight aggregates in concrete is one of the best ways to achieve lightweight concrete with lower density and sufficient strength.

Fly ash aggregates have lower density than natural aggregates and play a significant role in the production of lightweight concrete. The behaviour of lightweight aggregates used in concrete production affects the performance of Light Weight Concrete. Concrete made using lightweight aggregates is lighter than normal-weight concrete, and the structural advantages of LWC are well-known and accepted. However, there is still much work needed to explore and improve the performance of sintered aggregates as the maximum utilization of FAA is currently limited to non-structural applications.

2. Materials and Methodical Methodologies

2.1 Properties of Raw materials and Curing methods

Singh and Patel (2023) recognize that fly ash obtained from thermal power stations are ready to manufacture fly ash aggregates with hydrated lime and OPC-53 as binders. The specific gravity was measured, and the experiments are conducted according to IS 2720: Part 3, and wet sieve analysis was conducted using IS sieves of 0.425, 0.075 and 0.045-mm sieves. As per ASTM C618 standards, the classification of fly ash is being identified and if it is found to be Class F, then the obtained fly ash seems to be unfit for cement, mortar and concrete composition as it retains 37% of grain over the 0.045mm sieve, exceeding the 34% limit. The aggregate is suitable for fly ash due to its combination of silicon dioxide, alumina and iron oxide content of 95.1%. According to IS 3812 (Part 1) hydrated lime must contain approximately 71% CaO for manufacturing this aggregate. Table 1 presents the types of fly ash and binders used, along with their properties for aggregate production, alongside relevant parameters sourced from Nadesan and Dinakar(2017).

Table 1. Production of Aggregate: Characteristics and Limitations (Nadesan and Dinakar (2017))

Categories of Fly ash	Fineness (cm^2/gm)	Binder classifications	Dosage (%)	Moisture Content (%)	Sintering Temp (°C)	Duration (min)	Citations for references
Class F	4280	Bentonite, Cement, Lime	8-30	-	1100	60	Ramamurthy and Harikrishnan (2006 a)
Class C	3928	Cement, Lime	8	-	-	-	Baykal and Doven (2000)
Class F	4000	Bentonite	20	25	950	-	Gomathi and Sivakumar (2015)
Class F	4280	-	-	15-35	1100	60	Ramamurthy and Harikrishnan (2006 b)
Bituminous pond ash	2520	Clay, Bentonite	5-25	24-33	900-1100	45-120	Vasugi and Ramamurthy (2014)
Lignite pond ash	2810	Kaolinite, Bentonite					
Class F	2880	Bentonite, Glass powder	-	22-25	1100-1200	165-180	Kockal and Ozturan (2011)
Bottom ash	2120	Kaolinite,Metakaolin, Clay, Bentonite	5-20	26-33	800-1100	30-120	Geetha and Ramamurthy (2011)
Class F	-	Shale	30-50	18	950-1100	120	Mu et al (2011)
Class F	2570	Bentonite Kaolinite	4-30	23-35	-	-	Manikandan and Ramamurthy (2007)
Class C	4140						

The study utilized various curing methods as illustrated by Shahane and Patel (2021) were described below:

- Sealed curing: After compaction, the samples were sealed in airtight polythene bags and kept at ambient temperature for one to three days.
- Open curing: After compaction, the samples were left in an open atmosphere at ambient temperature for one to three days.
- Steam curing: After compaction, the samples were placed in a steam chamber at atmospheric pressure with a temperature of 90±2°C for 24 hours.
- Humidity curing: After compaction, the samples were stored in a humidity chamber at varying temperatures between 50°C and 80°C, maintaining with a constant humidity of 70% for 24 hours.
- Hot water bath curing: Singh and Patel (2023) explain about this curing procedure stating that after preparation, achieve initial setting by placing specimens in hot air at 50°C for 6 hours. Following initial setting, place the specimens in a hot water bath at 65 °C-95 °C for 1 to 3 days. After curing, let the hardened specimens rest at ambient conditions (32 ± 2°C, 70 ± 2% relative humidity) for 24 hours.
- Auto clave curing: After preparing the freshly moulded specimens, they were initially set at ambient temperature for 3-15 hours to ensure proper strength. Subsequently, autoclaving can be done at 0.2-1.2 MPa steam pressure for 3-24 hours, with 1.2 MPa achieved within 2 hours. Finally, the hardened specimens were kept at ambient temperature for 24 hours.

2.2 Manufacturing procedure for fly ash aggregate

The following procedures are involved in the production of angular shaped fly ash coarse aggregate, as stated by Singh and Patel (2023):

- Mixing: Binders and fly ash should be mixed evenly and dry. For the manufacturing of high-quality aggregate, add the necessary amount of water (Moulding moisture < Optimal moisture content) and thoroughly mix to make a homogenous mixture.
- Compaction-Extrusion Technique: To attain the highest dry unit weight, compact the mixture as soon as it is homogeneous in three layers using a hydraulic static press in a cylindrical mould with a 50mm diameter and 100mm height. The compressed specimen should be extruded using a hydraulic extruder.
- Curing Techniques: Use an autoclave or a hot water bath to cure the cylindrical specimens.

- Crushing: To produce aggregates with right size, manually crush the failed Unconfined Compressive strength concrete specimens with a hammer and screen through IS sieves of 4.75mm -40mm respectively.

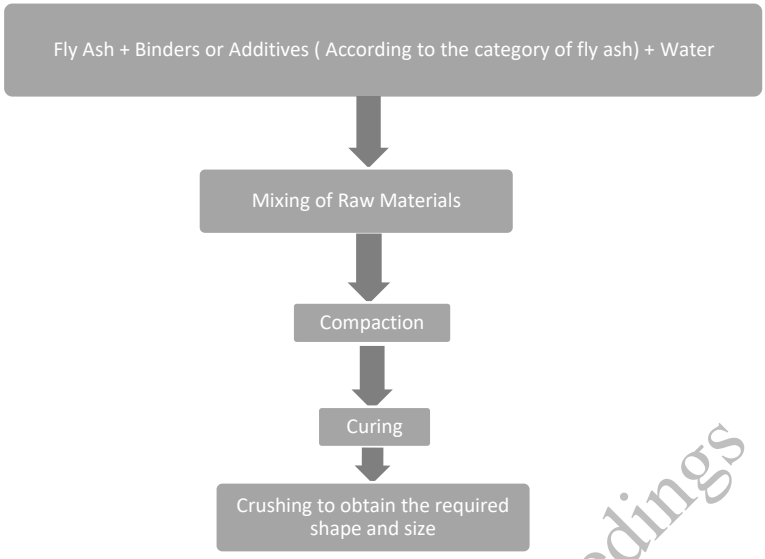

Figure 1. Process step for the production of angular fly ash aggregates (Shahane and Patel (2021))

2.3 Mix proportions

The mix proportions are done and curing were done as described from the article Singh and Patel (2023). Initial trials involved adding 4% lime to fly ash and curing at 75°C in a water bath, as per Shahane and Patel (2021). The binder content is based on dry weight. According to IS 2720: Part 8, the fly ash-binder mixtures had maximum dry unit weight and OMC values of 13.8-14.0 kN/m^3 and 17.5-18.2% respectively. Cylindrical specimens were prepared with varying moulding moisture levels to achieve maximum dry unit weight and investigate the effect on aggregate strength to determine the optimum moulding moisture.

3. Mechanical properties of fly ash aggregate concrete

3.1 Effects on Compressive strength

Nadesan and Dinakar (2017) recognizes that the compressive strength is crucial for structural concrete which must have densities between 1600-2000kg/m^3 and compressive strength over 15MPa as per RILEM (1978). Wasserman and Bentur (1997) illustrates that concrete strength depends on both aggregate and paste matrix strength, with the interfacial transition zone (ITZ) playing a significant role. Studies show that lightweight aggregate concrete (LWAC) can achieve higher compressive strength than normal aggregate concrete, despite lower aggregate strength. Factors like test specimen size and loading rate have less influence on LWAC. Adding supplementary materials like silica fume improves strength, with sintered fly ash aggregates outperforming cold-bonded ones. Aggregate volume, crushing strength and shape index also significantly affect LWAC strength.

3.2 Effects on Split tensile strength

The tensile properties of Lightweight Aggregate concrete are typically inferior to those of normal concrete due to the lower strength and stiffness of porous aggregates as described by Nadesan and Dinakar (2017). However, Kayali (2008) have shown that the split tensile strength of LWAC can be comparable or even superior to that of normal aggregate concrete. ASTM C 330 requires a minimum split tensile strength of 2 MPa for structural grade LWAC. Research highlights strong bonding in the interfacial zone and minimal impact from lack of curing. The ratios of split tensile and flexural strength to compressive strength are lower in LWAC compared to normal concrete. Adding fibers can enhance toughness and ductility. Among

predictive models, EN 1992 is the most accurate for estimating split tensile strength, although a more precise model is still needed.

3.3 Effects on Elastic Modulus

As stated by Nadesan and Dinakar (2017), the elastic modulus of fly ash aggregate concrete is typically lower than that of normal aggregate concrete with similar strength, due to higher paste content and lower aggregate stiffness. Increasing the LWA volume in the mix further reduces peak stress and elastic modulus Walveren et al (1995). Aggregate shape also significantly affects elastic modulus with hard rock materials displaying a linear stress-strain relationship, unlike porous aggregates. Fibers do not notably enhance LWAC stiffness, and curing conditions have minimal impact. The elastic modulus correlates with compressive strength, unit weight and aggregate source correction factors. As per ACI Committee (ACI 213R-03) NS 3473 is the most accurate predictive model for fly ash aggregates concretes, but a more precise model is still needed.

3.4 Effects of Bond Strength on LWAC

Lightweight aggregate concrete (LWAC) tends to be more brittle than standard concrete, raising the risk of splitting cracks and delamination. It is found that LWAC has lower bond strength in direct pullout tests compared to normal aggregate concrete, likely due to weaker aggregates as per Organgun (1967). However, sintered fly ash aggregate concretes can achieve bond strength comparable to normal aggregates. However, LWAC exhibits lower bond stress in beam tests, possibly due to air entrapment beneath steel bars during vibration which can be mitigated by using fully saturated aggregates. Fiskeli et al (1995) show that the type of lightweight aggregate minimally impacts bond parameters in self-compacting LWAC under lateral pressure.

3.5 Fractural Effects on Lightweight Aggregate Concrete

Nadesan and Dinakar (2017) recognize that due to the excellent bond within the LWAC matrix, fractures pass through the aggregate instead of bypassing it, unlike in conventional concretes where fractures form around the aggregates. Aggregate properties significantly influence concrete performance as aggregates occupy most of the volume, Clarke (2005). According to Walveren (1995), the fracture behaviour of concrete with sintered lightweight aggregate aligns with linear elastic fracture mechanics. The type of lightweight aggregate does not affect fracture energy. LWAC has lower toughness, indicated by its low ‘characteristic length’, requiring special attention under concentrated loads. In shear stress failure, normal aggregates act as shear arresters, whereas lightweight aggregates lead to smoother crack faces. Adding crumb rubber enhances impact energy but reduces compressive and flexural strength.

3.6 Creep and Shrinkage Effects on Lightweight Aggregate Concrete

Studies on LWAC shrinkage properties present mixed conclusions as illustrated by Nadesan and Dinakar (2017). Some research indicates that lightweight aggregate mortar shrinks twice as much as normal aggregate mortar, with shrinkage ranging from 600 to 1000 micro strains. Shrinkage above 850 micro strains is generally unsuitable for reinforced concrete and LWAC can continue to shrink even after one year, Yamamoto et al (1991). However, other studies show that LWAC’s shrinkage behaviour is similar to normal aggregate concretes with some lightweight aggregates can halve drying shrinkage. As per AS 3600 (1994), Australian standard for concrete structures, pre-wetted sintered fly ash lightweight fine aggregates (36-39%) can mitigate autogenous shrinkage and early-age cracks, enhancing durability due to a delayed drop in relative humidity. Autoclaved aggregates exhibit higher shrinkage than sintered aggregates, likely due to lower restraining capability. Although lower stiffness in LWAs suggests higher creep, research shows comparable creep in sintered and natural aggregates concrete, with sintered fly ash aggregates having a faster initial creep rate but similar final values.

3.7 Structural Efficiency of LWAC

Nadesan and Dinakar (2017) acknowledged that the primary reason for using lightweight concrete is to reduce self-weight, providing more utility space, architectural freedom and easier constructability. The word ‘Structural efficiency’ refers to the strength-to-density ratio of the material, which is more significant in lightweight aggregates concretes than in normal concretes. The density used is the air-dry density, reflecting actual field conditions. Self-weight for structural design should be based on equilibrium density,

typically achieved after 90 days of air-drying. In the present study, the structural efficiency of lightweight concrete was compared to normal aggregate concrete, with normal weight concrete (NWC) assumed to have a density of 2400 kg/m^3. The results showed that 95% of the lightweight concretes studied were superior to 40 MPa normal aggregate concrete, and 63% had a higher strength-to-density ratio than 60MPa normal aggregate concrete. Therefore, SLWACs have significantly higher structural efficiency than normal aggregate concrete, positively impacting sustainable development.

Table 2. Typical fly ash aggregate engineering characteristics produced by autoclave curing method (Singh and Patel, 2023)

Properties	Fly ash angular aggregate	Regular Stone Aggregates	IS 9142: Part 2 (2018) specifications for sintering aggregate	IS 383(2016) specifications for stone aggregate for the usage in concrete		MORTH (2013) requirements of stone aggregate for use in road
				Wearing surfaces	Non-wearing surfaces	
Loose Bulk Density	850 kg/m^3	1534 kg/m^3	≤950 kg/m^3	-	-	-
Rodded Bulk Density	944 kg/m^3	-	-	-	-	-
Specific gravity	1.50	2.65	-	-	-	-
Water absorption	21%	0.7%	≤18%	≤2%	≤2%	≤2%
Impact Value	25%	16%	≤40%	≤30%	≤45%	≤30%
Crushing Value	35.5%	22%	≤45%	≤30%	-	-
Abrasion Value	35%	23%	≤40%	≤30%	≤50%	≤40%
Soundness (Na_2SO_4)	7.2%	-	≤12%	≤125	<12%	≤12%

4. Engineered characteristics of fly ash angular aggregate

Singh and Patel (2023) emphasize that the developed fly ash aggregate features a rough surface and angular shape, enhancing mechanical interlocking compared to pelletized aggregate. The pelletization-sintering process produces smooth, spherical aggregates by fusing fly ash particles at around 1200^{o}c. In contrast, the proposed fly ash aggregate is made by crushing cured fly ash blocks, resulting in surfaces resembling natural stone aggregates. The rodded bulk density of the developed fly ash aggregate improved by approximately 10% compared to its loose bulk density, demonstrating superior interlocking capacity over sintered fly ash aggregates, which showed only a 5.39% improvement (Gomathi and Sivakumar, 2015). The angularity number of 7-9 for the proposed aggregate falls within the typical range of 5-9 observed in various natural aggregates, indicating its suitability for construction. With a specific gravity of 1.50, the fly ash aggregate is significantly lighter than natural aggregates, typically ranging between 2.6 and 2.7. Its high-water absorption rate of 21% reflects its porous structure, aiding in initial water retention during construction and facilitating internal curing, which reduces susceptibility to inadequate curing compared to conventional concrete (Nadesan and Dinakar, 2017). Table 2 confirms that the developed aggregate meets IS 9142: Part 2 criteria for lightweight artificial aggregate for concrete. Its impact, crushing, abrasion, and soundness values meet MORTH standards for road aggregate and IS 383 for coarse aggregate in non-wearing structural concrete surfaces. The production process for this aggregate consumes less energy than the pelletization-sintering process, which requires temperatures around 1200^{o}C. In contrast, the current method operates at approximately 195^{o}C. Moreover, utilizing waste steam from thermal power plants for autoclave steam curing further reduces energy consumption, making this method more efficient than producing sintered aggregates.

5. Summary and Conclusions

A review of literature assessed the feasibility of integrating fly ash lightweight angular aggregate into structural concrete. Detailed discussions covered production processes and critical parameters influencing aggregate properties.

- Physical, mechanical and durability characteristics of sintered fly ash LWAC were thoroughly examined which includes the key findings such as various combinations of binders and fly ash proportions, ultimately recommending an optimal binder range of 15-20% and a water-to-fly ash ratio of 0.25.
- The strength characteristics of structural lightweight concrete incorporating angular fly ash aggregates as the traditional method of producing lightweight concrete possess lower strength compared to normal weight concrete.
- Based on various trials, autoclave curing yielded significantly superior results compared to other curing methods, especially for low calcium fly ash as there is a need for higher temperature to achieve strength. Specifically, steam temperature in the autoclave at 1.2MPa pressure reached 190ºC, whereas the water bath temperature was 95ºC.
- Factors such as water-binder ratio, shape index and aggregate type require careful consideration in producing angular fly ash aggregates. Concrete using these aggregates meets ASTM C330 standards, demonstrating compressive strengths from 22.23 to 35.12MPa, split tensile strengths from 2.42 to 3.93MPa, water absorption of 10-25% and E-modulus from 16.7 to 30.65 GPa, highlighting their superior suitability for structural applications compared to conventional concrete.

References

ACI Committee 213, Guide for Structural Lightweight Aggregate Concrete, American Concrete Institute (ACI 213R-03), Farmington Hills, 2003.

Adell, V., Cheeseman, C.R., Ferraris, M., Salvo, M., Smeacetto, F., and Boccaccini, A.R. (2007) "Characterising the sintering behaviour of pulverised fuel ash using heating stage microscopy", *Materials Characterization*, 58(10): 980-988.

AS 3600-1994, Australian Standard for Concrete Structures, Standards Australia, Sydney, 1994.

ASTM,Standard Specification for Coal Fly Ash and Raw or Calcined Natural Pozzolan for Use in Concrete, C 618-22, ASTM International, West Conshohocken, PA, 2022.

ASTM, Standard Specification for Lightweight Aggregates for Structural Concrete, C 330, Annual Book of ASTM Standard, 2006.

Baykal, G. and Doven, A.G. (2000) "Utilization of fly ash by pelletization process; theory application areas and research results", Resource Conservation and Recycling,: 59-77

Bhattacharjee, U. and Kandpal, T.C. (2002) "Potential of fly ash utilisation in India", *Energy*, 27(2): 151-166.

Bjerkeli, L., Hansen, E.A. and Thorenfeldt, E. (1995) " Tension lap splices in high strength LWA concrete" *International Symposium on Structural Lightweight Aggregate Concrete, Sandelfiord, Norway*, 131-142.

CEB, Functional classification of lightweight concrete, Recommendations LC2, Second edition, RILEM, 1978.

Cheeseman, C. R., Makinde, A. and Bethanis, S. (2005) "Properties of lightweight aggregate produced by rapid sintering of incinerator bottom ash", *Resources Conservation and Recycling*, 43(2):147-162.

Gomathi, P. and Sivakumar, A. (2015) "Accelerated curing effects on the mechanical performance of cold bonded and sintered fly ash aggregate concrete", *Construction Building Materials*, : 276-287.

IS, Artificial Lightweight Aggregate for Concrete-Specification-Sintered Fly Ash Coarse Aggregate, 9142 (Part 2), Bur. Indian Stand., New Delhi, 2018.

IS, Coarse and Fine Aggregate for Concrete-Specification, 383, Bur. Indian Stand., New Delhi, 2016.

IS, Determination of Specific Gravity- Fine, Medium and Coarse Grained Soils, 2720 (Part 3/Sec 2), Bur. Indian Stand., New Delhi, India, 1980 Reaffirmed, 2002.

IS, Determination of Water Content- Dry Density Relation Using Heavy Compaction, 2720 (Part 8), Bureau of Indian Standards, New Delhi, 1983 Reaffrmed 2006.

IS, Method of Test for Aggregate for Concrete-Particle Size and Shape, 2386 (Part 1), Bur. Indian Stand., New Delhi, 1963 Reaffirmed 2002.

IS, Methods of Test for Aggregates for Concrete -Mechanical Properties, 2386 (Part 4), Bur. Indian Stand., New Delhi, 1963 Reaffirmed 2002.

IS, Methods of Test for Aggregates for Concrete-Soundness, 2386 (Part 5), Bur. Indian Stand., New Delhi, 1963 Reaffirmed 2002.

IS, Methods of Test for Aggregates for Concrete-Specific Gravity, Density, Voids, Absorption and Bulking, 2386 (Part 3), Bur. Indian Stand., New Delhi, 1963 Reaffirmed 2002.

IS, Methods of Test for Pozzolanic Materials, 1727, Bur. Indian Stand., New Delhi, India, 1968 Reaffirmed, 2004.

IS, Pulverized Fuel Ash- Specification-For Use Pozzolona in Cement, Cement Mortar and Concrete, 3812 (Part 1), Bureau of Indian Standards, New Delhi, India, 2013.

Kamal, J. And Mishra, U.K. (2020) "Influence of Fly ash Properties on Characteristics of Manufactured Angular fly ash aggregates", *Journal of the Institution of Engineers (India).*

Kayali, O. (2008) "Fly ash lightweight aggregates in high performance concrete", *Construction and Building Materials,*22:2393-2399.

Kockal, N.U. and Ozturan, T. (2011) "Optimization of properties of fly ash aggregates for high-strength lightweight concrete production", *Material and Design,* 32: 3586-3593.

MORTH, Specifications for Road and Bridge Works, Ministry of Road Transport and Highways, Indian Road Congress, New Delhi, India, 2013.

Mu, S., Ma, B., Schutter, D., Li, X., Wang, Y. and Jian, S.(2011) " Effect of shale addition on properties of sintered coal fly ash", *Construction Building Materials,* 25: 617-622.

Nadesan, M.S. and Dinakar, P. (2017) "Structural Concrete using sintered flyash lightweight aggregate: a review", *Construction and Building Materials,* 154:928-944.

Orangun, C.O. (1967) "The bond resistance between steel and lightweight-aggregate (Lytag) concrete", *Building Science,* :21-28.

Ramamurthy, K. and Geetha, S. (2011) "Properties of sintered low calcium bottom ash aggregate with clay binders", *Construction Building Materials,* 25: 2002-2013.

Ramamurthy, K. and Harikrishnan, K.I. (2006a) "Influence of binders on properties of sintered fly ash aggregate", *Cement and Concrete Composite*: 33-38.

Ramamurthy, K. and Harikrishnan, K.I. (2006b) " Influence of pelletization process on the properties of fly ash aggregates", *Waste Management,* 26:846-852.

Ramamurthy, K. and Manikandan, R. (2007) "Influence of fineness of fly ash on the aggregate pelletization process", *Cement Concrete and Composite,* 29: 456-464.

Ramamurthy, K. and Vasugi, V. (2014) "Identification of admixture for pelletization and strength enhancement of sintered coal pond ash aggregate through statiscally designed experiments", *Material and Design,* 60:563-575.

Shahane, H.A. and Patel, S. (2021) "Influence of curing method on characteristics of environment-friendly angular shaped cold bonded fly ash aggregates, *Journal of Building Engineering,* 35.

Shergold, F.A. (1953) "The percentage voids in compacted gravel as a measure of its angularity", *Mag. Concrete Res.,*5:3-10.

Singh, S. and Patel, S. (2023) "Development of angular-shaped lightweight coarse aggregate with low calcium fly ash using autoclave curing- Experimental and microstructural study", *Journal of Building Engineering,* 79.

Terzic,A., Pezo,L., Mitic,V. and Radojevic, Z. (2014) "Artificial fly ash based aggregates properties influence on lightweight concrete performances", *Ceramics International,* 41: 2714-2726.

Walraven, J., Ujil Den, J., Al-Zubj, N. (1995) "Structural Lightweight concrete: recent research", *Heron,* 40(1):5-30.

Wasserman, R. and Bentur, A. (1997) "Effect of lightweight fly ash aggregate microstructure on the strength of concretes", *Cement and Concrete Research,* 27(4):525-537.

Wegen, G.J.L. and Bijen, J.M.J.M. (1985) "Properties of concrete made with three types of artificial PFA coarse aggregate", *International Journal of Cement Composites and Lightweight concrete,* 7(3): 159-167.

Yamamoto, T., Mihashi, H. and Hirai, K. (1991) "Advanced utilization of fly-ash as artificial aggregates", *Waste Material,* 48: 621-622.

Comprehensive Investigation of Properties and Performance in Geopolymer Mortar Utilizing Fly Ash, GGBS, and Metakaolin

Banoth Gopalakrishna[1*], Dinakar Pasla[2]

[1] Indian Institute of Technology Bhubaneswar, India
Email: bg13@iitbbs.ac.in
[2] Indian Institute of Technology Bhubaneswar, India
Email: pdinakar@iitbbs.ac.in

[*]Corresponding author

ABSTRACT

The use of industrial by-products, such as Fly Ash (FA), Ground Granulated Blast Furnace Slag (GGBS), and Metakaolin (MK), in geopolymer mortar has garnered significant attention for their potential as sustainable construction materials. This study aims to assess the properties and performance of geopolymer mortar formulations incorporating varying proportions of FA, GGBS, and MK as binding agents. The research entails a thorough analysis of the physical, mechanical, and durability characteristics of these geopolymer mortars. Different combinations of FA, GGBS, and MK are employed to examine their impact on compressive strength, and water absorption. Notably, compressive strength tests conducted over varying curing durations indicate the mechanical strength of the developed mortars, achieving 50MPa at the age of 56 days. Preliminary findings indicate encouraging outcomes concerning the influence of FA, GGBS, and MK on the properties of geopolymer mortar. This investigation exhibits the potential of these industrial by-products as efficient supplementary materials, enhancing mechanical strength, reducing porosity, and enhancing durability in geopolymer mortar formulations. Ultimately, this research contributes to the expanding knowledge base on sustainable construction materials, providing valuable insights into optimizing FA, GGBS, and MK-based geopolymer mortars for structural applications. This offers environmentally-friendly and economically viable alternatives within the construction industry.

KEYWORDS: *Fly ash; GGBS; Metakaolin; Compressive strength; Geopolymer mortar.*

1. Introduction

The construction industry is increasingly adopting geopolymer concrete (GPC) as an eco-friendly alternative to traditional cement. This shift is driven by the need to reduce the consumption of natural resources in ordinary Portland cement (OPC) production. GPC utilizes industrial waste and by-products as binders, including materials such as ground granulated blast furnace slag (GGBS), rice husk ash, fly ash (FA), and metakaolin (MK) (Bashar et al. 2014). Despite the growing interest in GPC, the massive demand for concrete in construction makes it challenging to completely phase out OPC. The continued extraction of raw materials for cement and concrete production is causing significant environmental damage and depleting natural resources. Projections suggest that global cement consumption could surpass 4 billion tons annually in the near future. Studies indicate that GPC offers substantial environmental benefits compared to OPC, particularly in terms of reduced energy requirements and lower carbon dioxide (CO_2) emissions during production (Chana 2011). The carbon footprint of geopolymer mortar could be further decreased by optimizing its manufacturing process. However, the construction sector faces obstacles in fully transitioning to alternative cementitious materials due to the sheer scale of concrete demand and its associated CO_2 emissions. Nonetheless, the integration of waste materials as geopolymer binders represents a promising step towards more sustainable construction practices.
Among alkaline activators, a combination of sodium hydroxide (SH) and sodium silicate (SS) solutions, mixed in various ratios, is frequently employed in geopolymer production (Djwantoro Hardjito, Steenie E.

Wallah, Dody M. J. Sumajouw 2004; Gopalakrishna and Dinakar 2024b; Gopalakrishna and Dinakar 2024c; Gopalakrishna and Dinakar 2024a). The formation of geopolymers involves multiple reaction stages, beginning with initial pozzolanic polymerization and culminating in the development of the final microstructure, a process reminiscent of zeolite formation. The strength development and chemical reactions in geopolymer concrete are influenced by numerous factors, including the composition of the alkaline activator content (AAC), the types of industrial by-products used, and the curing conditions applied. For instance, fly ash-based geopolymer mortars typically require oven curing to facilitate polymerization. After the curing period, samples are usually cooled to room temperature before undergoing compressive strength testing. To enhance the properties of FA-based GP, GGBS is often incorporated into the binder. This modification allows for curing at ambient temperatures and generally results in improved compressive strength (CS) compared to geopolymer mortars made solely from FA (Temuujin et al. 2010). This approach represents an ongoing effort to optimize geopolymer formulations for practical applications in construction (Rao et al. 2020; Gopalakrishna and Dinakar 2023a; Gopalakrishna and Pasla 2023).

Metakaolin (MK), a key component in early geopolymer development, is prized for its pure aluminosilicate content. This pozzolanic material is produced by calcining kaolinitic clay at temperatures between 500°C and 800°C. MK offers environmental advantages over ordinary Portland cement (OPC), requiring lower calcination temperatures and emitting 80-90% less CO_2 during production (Davidovits 2008; Gopalakrishna and Dinakar 2023b; Gopalakrishna and Pasla 2024a; Gopalakrishna and Pasla 2024b; Gopalakrishna and Dinakar 2024d). The high reactivity of MK with AAC is attributed to its rich aluminum and silicon oxide composition, which promotes enhanced geopolymerization. Research has shown that incorporating GGBS into FA based GPC can improve CS (Islam et al. 2014; Kumar et al. 2023; Tejas and Pasla 2023; Rawat and Pasla 2024a; Rawat and Pasla 2024b; Kumar et al. 2024). Similarly, adding calcium from various sources to MK-based GPC has been found to enhance its mechanical properties. The concept of geopolymers as alternative cementitious materials was introduced by Davidovits in 1978. Since then, geopolymer concrete utilizing industrial by-products like FA, GGBS, and MK has emerged as a promising substitute for traditional concrete (Davidovits 1994).

A recent study aimed to investigate the CS of GP mortar using locally available waste materials - GGBS, FA, and MK - as binders. The research explored how varying the proportions of these binders' affected CS while maintaining consistent ratios of sand and AAC. The goal was to determine the optimal binder composition for maximum CS. These GP cement pastes, rich in silica and alumina, offer an environmentally friendly alternative to traditional cement, as they don't release greenhouse gases during the polymerization process. The AAC provides the binding characteristic necessary for the reaction between the materials. This innovative GP cement paste shows potential for application in heritage structure restoration, combining modern technology with preservation needs.

2. Examination of raw materials and mixing methodology

2.1 Materials

This research utilized FA as the primary aluminosilicate source for creating the geopolymeric binder. The study specifically employed low-calcium FA obtained from the NALCO facility located in Odisha, India. To determine the chemical composition of the FA, X-Ray Fluorescence (XRF) analysis was conducted. The results of this analysis are presented in Table 1. GGBS is a valuable industrial by-product used in the production of cement-free binders. Unlike typical supplementary cementitious materials, GGBS possesses both pozzolanic and cementitious characteristics. When GGBS interacts with water, it exhibits hydraulic activity. The material's composition, predominantly calcium, alumina, and silicates (comprising about 90% of its content), aligns with the criteria for pozzolanic substances. The chemical makeup of GGBS is detailed in Table 1, while Table 2 outlines its physical attributes. For this study, metakaolin (MK) was produced by calcining kaolin at 650°C for a duration of 3 hours. The resulting material exhibited a faint cream hue, attributed to the mild acidity developed during the dihydroxylation process of calcination. MK is known for its high reactivity as a pozzolanic mineral additive, offering significant potential in the creation of geopolymer mortar composites. The physical characteristics of the MK are presented in Table 2, while its chemical composition is detailed in Table 1.

Table 4. XRF analysis of GP binder.

Sl.No	Oxide	Dry weight (%)		
		MK	GGBS	FA
1	SiO_2	53.3	35.32	50.13
2	Al_2O_3	40	15.63	27.28
3	Fe_2O_3	4.21	1.56	9.28
4	CaO	0.43	40.15	3.25
5	Na_2O	0.13	0.21	1.12
6	K_2O	0.51	0.52	2.82
7	MgO	0.09	6.54	1.52
8	Other oxides	0.64	1.02	1.76
9	LOI	0.69	0.41	2.9

Table 5. Physical properties of GP binder

Material properties	Units	FA	GGBS	MK
Color		Greyish white	Off white	Cream
Specific surface area	m^2/kg	390	430	15,000
Moisture	%	<0.1	<0.1	<0.212
Specific gravity		2.1	2.83	2.59
Bulk density	kg/m^3	995	1200	357

Fine aggregate in the form of river sand is frequently employed in construction due to its consistent grading and inherent cleanliness. In GP binder paste, it serves to enhance the homogeneity of the mixture. For this experiment, locally sourced river sand was used. This natural sand, obtained from a nearby river, has a specific gravity of 2.63.

GP are synthesized from materials rich in silicates and aluminates. When activated with an AAC solution, these raw materials form a complex aluminosilicate gel through polymerization. The alkaline solution's composition significantly impacts the geopolymerization process. Research has explored the effects of Na_2SiO_3 to NaOH ratio and NaOH molarity on FA, GGBS and MK -based GP mortars. Optimal CS was achieved with a Na_2SiO_3 to NaOH ratio of 1.5 and a 16M NaOH solution. AAC typically contain soluble alkalis, predominantly Na or Ka -based compounds. For GPC production, a combination of NaOH and Na_2SiO_3 is commonly used as the alkaline activator. The specific properties of the sodium-based AAC used in this study, including their chemical composition and specific gravity, are presented in Table 3.

Table 6. Chemical composition of AAC solution.

Properties	pH	Specific gravity	Molecular weight (g/ mol)	Color	Density (g/cm^3)	SiO_2 (%)	Na_2O (%)	H_2O (%)
NaOH	13–14	2.2	40	White	2.14	–	45.71	54.29
Na_2SiO_3	11.42	1.36	122.06	Clear colorless	1.39	29.9	10	60.8

This study involved the development of five distinct mix designs. The composition of each GP mortar is detailed in Table 4. These mixtures incorporated varying percentages of FA, MK, and GGBS. To isolate the effect of the binders, the AAC and natural sand quantities remained constant across all mixes. A binder to fine aggregate ratio of 1:3 was maintained throughout. The mixing process began with combining the ternary binders (MK, FA, and GGBS) with sand in a bowl mixer at low speed for approximately 5 minutes. Subsequently, the AAC was introduced gradually over the next 5 minutes while maintaining the same mixing speed. The resulting mortar was then poured into 70.6 mm cubic moulds in three layers, with appropriate compaction applied at each stage. Twelve specimens were prepared for each mix proportion. To eliminate entrapped air and bubbles, the samples underwent vibration using a rod and vibrating table, ensuring standard compaction. Post-casting, the 100% FA specimens were covered with plastic film to prevent moisture loss during the 24-hour oven curing process at 60°C. The remaining mix specimens were left to cure at ambient temperature until testing.

Table 7. Percentages of binder in mixtures

Mix ID	Binders (%)		
	Fly ash	GGBS	MK
M1	100	0	0
M2	80	20	0
M3	70	20	10
M4	65	20	15
M5	60	20	20

The porosity characteristics of the mortar matrix were evaluated through evaporation studies. This method involves comparing the mass of samples in dry and water-saturated states at various temperatures. Research suggests that capillary porosity can be determined by measuring weight loss at temperatures between 40-50°C, while gel porosity is reflected in moisture loss between 40-105°C (Romer 2005; Yang et al. 2014). In this study, capillary and gel porosities were assessed by measuring the moisture loss of saturated specimens dried at 40°C and 105°C, respectively, until their mass stabilized. The following equations were used to calculate capillary and gel porosities:

$$\text{Capillary porosity} = \frac{M_0 - M_{40}}{\rho_w a^3} \times 100 \quad (1)$$

$$\text{Gel porosity} = \frac{M_{40} - M_{105}}{\rho_w a^3} \times 100 \quad (2)$$

In these equations, M_0 represents the saturated sample mass, ρ_w is water density, M_{40} and M_{105} are sample masses after drying at 40°C and 105°C, and 'a' denotes the cube specimen dimension.
Absorption tests were conducted on 100 mm cube specimens following established standards. The process involved weighing specimens before and after oven-drying at 105°C until the mass difference between two consecutive 24-hour interval measurements was less than 0.5% of the lower weight accordance with the ASTM C 642 (1997) standard (American Society for Testing and Materials 1997). Once fully dried and cooled to room temperature, samples were submerged in water, with weights recorded at regular intervals until stabilization (denoted as B1, B2, etc.). The absorption percentage and permeable voids volume were calculated using the following formulas:

$$\text{Absorption after immersion (\%)} = \frac{(B-A)}{A} \times 100 \quad (3)$$

$$\text{Permeable voids volume (\%)} = \frac{(C-A)}{(C-D)} \times 100 \quad (4)$$

Where, A is the weight of dried sample after complete drying; B is the weight of surface dry sample after immersion in normal water; C is the weight of surface dry sample after immersion and boiling in water; and D is the apparent mass of the sample after immersion and boiling in water.

3. Results and Discussions

3.1 Compressive strength

CS serves as a key indicator of performance for alternative source materials in GP mortar, offering insight into the quality of the geopolymerization product. The development of CS over time (at 7, 28 and 56, days) is illustrated in Figure 1. As per the methodology, specimens composed entirely of FA underwent oven curing at 60°C for 24 hours. This elevated temperature curing accelerates strength development. However, Figure 1 reveals that using 100% FA in GP mortar results in lower CS. Partial replacement of FA with GGBS leads to improved CS, though increasing FA beyond 65% negatively impacts strength. This suggests that calcium and aluminum oxide content significantly influence mortar strength. Figure 1 demonstrates that mix M4, containing 15% MK, 20% GGBS, and 65% FA, cured at room temperature, achieved the highest CS of approximately 50 MPa. Reducing MK from 15% to 20% while appropriately same FA led to

lower CS. This trend persisted as MK content was further reduced to 0%. The inclusion of MK generally enhances CS, possibly due to changes in the Si/Al ratio during geopolymerization. Comparing 7-day test results with 56-day CS reveals that most specimens achieved between 40-49% of their 56-day strength within the first week. This data provides valuable insights into the strength development patterns of these GP mortars over time.

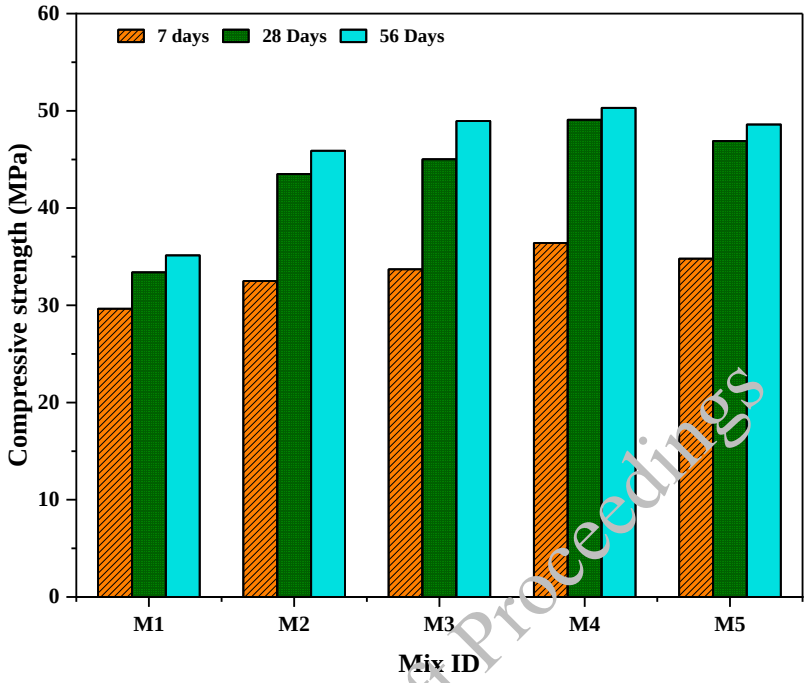

Figure 1. CS of GP mortar at various % of GGBS and MK.

3.2 Evaporation studies

Figure 2 presents the gel and capillary porosity test results for various GP binder mortar mixtures. The data reveals that most mortar compositions exhibit similar gel porosity volumes, ranging from 6.4% to 16.5%. The MK content emerges as a crucial factor influencing gel porosity, which in turn significantly affects overall mortar porosity. A notable trend is the inverse relationship between MK percentage and capillary porosity. As MK content decreases, so does the capillary porosity, possibly due to a reduction in porous material and an increase in binder content within the mortar mix. This phenomenon aligns with previous observations in concrete research (He 2011; Nandanam et al. 2021). Figure 2 illustrates that Mix M4 exhibits lower capillary porosity compared to Mix M1. The incorporation of GGBS and MK notably reduces the system's gel porosity. This reduction may be attributed to their microfilling effect and their capacity to generate additional calcium aluminate silicate hydrate (CASH) and calcium silicate hydrate (CSH) gel, contributing to higher compressive strength. While GGBS and MK effectively decrease gel porosity, their impact on capillary pores appears minimal. To accurately determine porosity in GP mortar, a more comprehensive understanding of the evaporation process is necessary. This highlights the need for further research in this area to fully elucidate the porosity characteristics of GP mortars.

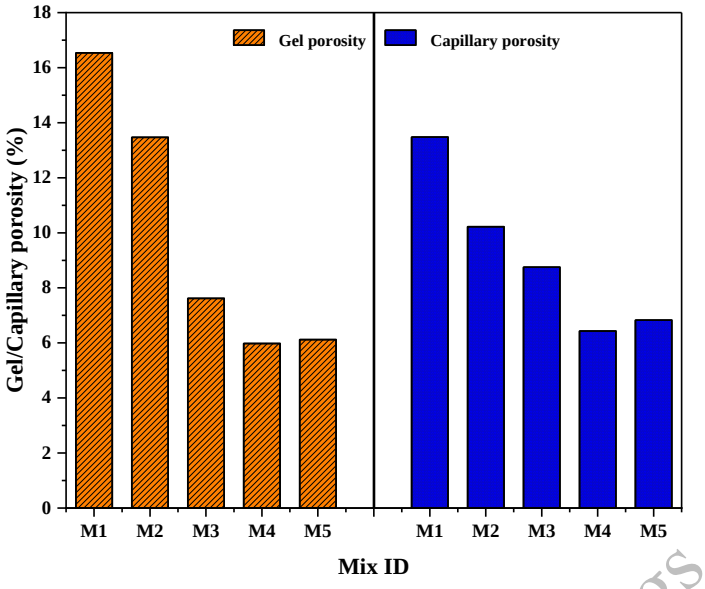

Figure 2. Gel/Capillary porosity of GP mortar

To assess the results, this study employed the evaluation criteria established by the Concrete Society (CEB, 1989) (CEB-FIP 1989). Figure 3 presents the absorption test results for all GP mortar mixtures. The graph illustrates how absorption characteristics vary across GP mortars with different proportions of GGBS and MK replacements. The data indicates that the M4 mix has a minimal impact on the absorption properties of the GP mortar. Interestingly, despite variations in strength and AAC to binder ratios among the different mixes, their absorption characteristics fall within a relatively narrow range. This suggests that the absorption properties of these GP mortars remain fairly consistent across the different mix designs tested.

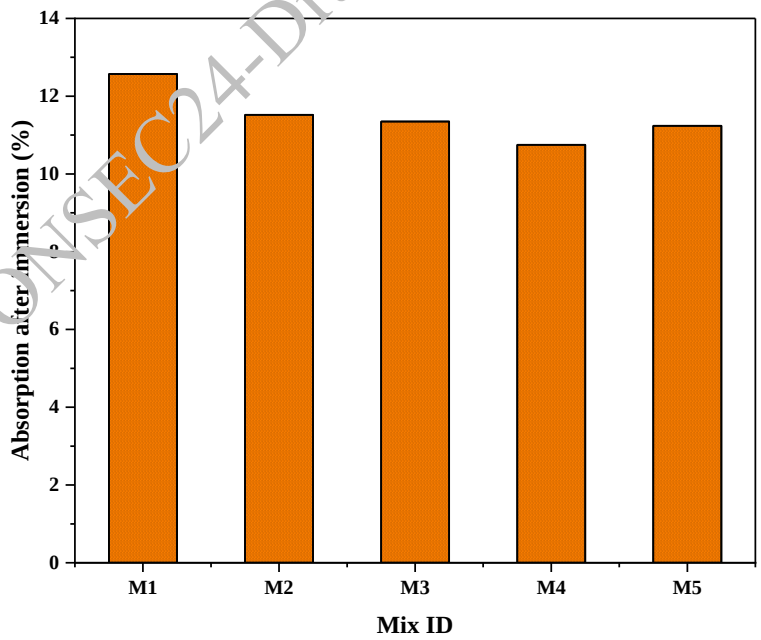

Figure 3. Water absorption of GP mortar

4. Conclusions

The study reveals significant insights into the development of GP mortar using various binder combinations. When using 100% FA as a binder, the GP mortar achieved a CS of 35 MPa at 56 days, but only after undergoing oven curing at 60°C for 24 hours. This highlights the necessity of heat treatment for

FA-based GP to achieve adequate strength. However, the research demonstrates that by combining FA with GGBS, it's possible to develop GP cement paste that reaches the desired CS of 45 MPa without the need for heat curing. This finding is particularly significant as it offers a more energy-efficient and practical approach to GP mortar production. Among the various mix designs tested, the optimal composition was found to contain 15% MK, 20% GGBS, and 65% FA. This combination not only exhibited the highest CS but also demonstrated superior durability characteristics. The synergistic effect of these materials likely stems from their complementary chemical compositions and reactivity rates. The inclusion of MK, even in relatively small amounts, appears to play a crucial role in enhancing the GP's properties. MK is known for its high pozzolanic activity and its ability to improve the microstructure of GP matrices. The GGBS component contributes calcium to the system, which can accelerate the geopolymerization process and improve early strength development.

Further research could focus on long-term performance, scaling up production, and exploring additional supplementary cementitious materials to further optimize these eco-friendly GP mortars. The development of such sustainable alternatives to OPC represents a significant step towards reducing the environmental impact of the construction industry.

Acknowledgements

The authors appreciate the support provided by IIT Bhubaneswar, India, for providing lab facility for smooth completion of the research project.

References

American Society for Testing and Materials (1997) Standard Test Method for Density, Absorption, and Voids in Hardened Concrete C642-97. ASTM Int (March):1–3.

Bashar II, Alengaram UJ, Jumaat MZ, Islam A (2014) The effect of variation of molarity of alkali activator and fine aggregate content on the compressive strength of the fly ash: Palm oil fuel ash based geopolymer mortar. Adv Mater Sci Eng 2014.

CEB-FIP (1989) Diagnosis and assessment of concrete structures - State of art report

Chana P (2011) Low Carbon Cements: The Challenges and Opportunities. In: First Global Future Cement Conference 2011

Davidovits J (2008) Geopolymer chemistry and applications. Geopolymer Institute

Davidovits J (1994) Properties of Geopolymer Cements. First Int Conf Alkaline Cem Concr :131–149

Djwantoro Hardjito, Steenie E. Wallah, Dody M. J. Sumajouw and BVR (2004) On the Development of Fly Ash-Based Geopolymer Concrete. Mater J 101(6):467–472

Gopalakrishna B, Dinakar P (2024a) An innovative approach to fly ash-based geopolymer concrete mix design: Utilizing 100 % recycled aggregates. Structures 66:106819. https://doi.org/10.1016/j.istruc.2024.106819

Gopalakrishna B, Dinakar P (2024b) Mechanical Performance of 100% Recycled Aggregate Based Geopolymer Concrete at Various Concentrations of NaOH. pp 37–48

Gopalakrishna B, Dinakar P (2024c) Life cycle assessment (LCA) and the influence of alkaline activator content on mechanical and microstructural properties of geopolymer mortar. J Eng Res. https://doi.org/10.1016/j.jer.2024.01.010

Gopalakrishna B, Dinakar P (2023a) Mix design development of fly ash-GGBS based recycled aggregate geopolymer concrete. J Build Eng 63:105551. https://doi.org/10.1016/j.jobe.2022.105551

Gopalakrishna B, Dinakar P (2023b) The study on various temperature condition of fly ash based geopolymer mortar. Mater Today Proc 93:234–238. https://doi.org/10.1016/j.matpr.2023.07.176

Gopalakrishna B, Dinakar P (2024d) The evaluation of the life cycle and corrosion properties of recycled aggregate geopolymer concrete incorporating fly ash and GGBS. J Build Eng 94:109977.

Gopalakrishna B, Pasla D (2023) Development of metakaolin based high strength recycled aggregate geopolymer concrete. Constr Build Mater 391:131810.

Gopalakrishna B, Pasla D (2024a) Study of Ambient Cured Fly Ash-GGBS-Metakaolin-Based Geopolymers Mortar. pp 27–35

Gopalakrishna B, Pasla D (2024b) Durability Performance of Recycled Aggregate Geopolymer Concrete Incorporating Fly Ash and Ground Granulated Blast Furnace Slag. J Mater Civ Eng 36(4).

He YX (2011) Experimental Research on Pore Structure of RCA and its Impact on Drying Shrinkage. Adv Mater Res 335–336:1141–1144. https://doi.org/10.4028/www.scientific.net/AMR.335-336.1141

Islam A, Alengaram UJ, Jumaat MZ, Bashar II (2014) The development of compressive strength of ground granulated blast furnace slag-palm oil fuel ash-fly ash based geopolymer mortar. Mater Des 56:833–841.

Kumar P, Dinakar P, Saravanan TJ (2024) Development and Mechanical Performance of Self-Compacting Lightweight Aggregate Concrete Using Sintered Fly Ash Aggregates. J Mater Civ Eng 36(7).

Kumar P, Pasla D, Jothi Saravanan T (2023) Self-compacting lightweight aggregate concrete and its properties: A review. Constr Build Mater 375:130861.

Nandanam K, Biswal US, Dinakar P (2021) Effect of Fly Ash, GGBS, and Metakaolin on Mechanical and Durability Properties of Self-Compacting Concrete Made with 100% Coarse Recycled Aggregate. J Hazardous, Toxic, Radioact Waste 25(2):04021002.

Rao MG, Jagadish V, Venu M, Rao GM, Kumar YA, Vengala J, Venu M (2020) Performance of Fly Ash and Ggbs Based Geopolymer Concrete Using Single Alkaline Activator Solution and Its Cost Analysis. IOP Conf Ser Mater Sci Eng 998(1).

Rawat R, Pasla D (2024a) Assessment of mechanical and durability properties of FA-GGBS based lightweight geopolymer concrete. Constr Build Mater 426:135984.

Rawat R, Pasla D (2024b) Mix design of FA-GGBS based lightweight geopolymer concrete incorporating sintered fly ash aggregate as coarse aggregate. J Sustain Cem Mater :1–16.

Romer M (2005) Effect of moisture and concrete composition on the Torrent permeability measurement. Mater Struct Constr 38(279):541–547.

Tejas S, Pasla D (2023) Assessment of mechanical and durability properties of composite cement-based recycled aggregate concrete. Constr Build Mater 387:131620.

Temuujin J, Van Riessen A, MacKenzie KJD (2010) Preparation and characterisation of fly ash based geopolymer mortars. Constr Build Mater 24(10):1906–1910.

Yang K, Basheer PAM, Bai Y, Magee BJ, Long AE (2014) Development of a new in situ test method to measure the air permeability of high performance concretes. NDT E Int 64:30–40.

Evaluating the Strength and Durability of Concrete Using Industrial Wastes as Potential Supplementary Cementing Materials

Samidha Pathak[1*], Hemant Aiyer[2]

[1] *Manager R&D, Nuvoco Vistas Corp. Ltd, India,*
Email: samidha.pathak@nuvoco.com
[2] *Vice President R&D, Nuvoco Vistas Corp. Ltd, India,*
Email: hemat.aiyer@nuvoco.com

[*]Corresponding author

ABSTRACT

In recent years, with infrastructural boom, the consumption of raw materials has led to a fast decline in available natural resources. The high scale industrial production generates a considerable amount of waste materials which may cause adverse impacts on the environment. The marble industries, glass industries, agricultural industries generate a huge amount of waste which is likely to increase in the future. Marble waste is highly alkaline in nature, glass being non biodegradable in nature and agricultural waste accumulation causing dusting and disposal issues are all of serious environmental concerns. In this study, effects of marble dust, glass powder and agricultural waste on strength and some durability properties such as water absorption and permeability, chloride penetration and drying shrinkage of concrete. It is observed that 3-7% OPC can be replaced in ordinary grade concrete with marble dust and agricultural ash with better durability and unaffected strength. Utilization of industrial by products in concrete production is a sustainable solution reducing CO_2 footprint.

KEYWORDS*: Durability, Industrial by products, Strength, Sustainable*

1. Introduction

Currently, concrete is considered to be the most used construction material globally (F. Aslani et al., 2018). Cement production has significant environmental impact being energy intensive and generating CO_2 emissions in the process. To mitigate these environmental impacts, recycling and reusing of industrial wastes is being implemented (Balegamire et al, 2022). Glass is one of the most essential and commonly used materials globally. Glass wastes (GW) creates an environmental hazard by consuming landfill spaces and it is also non biodegaradble in nature (Adesina et al., 2022). Globally, among the 200 million tons of solid waste, 7% of the waste comprises of the glass waste (Chindaprasirt et al., 2022). Marble finds application an important building material, especially in decorative constructions. Processing of marble such as dimensional shaping and polishing for specified applications creates by products like marble dust and aggregates (O. Gencel et al., 2012). While cutting, shaping and polishing processes of marble, almost 20-25% of marble dust is being generated and India is the third exporter of marble globally (Kumar et al., 2015). Agricultural wastes are burned and it contributes to significant pozzolanic value. The concrete industry can be a major consumer for valorization of industrial by products (S. Raffoul et al., 2016). Considering these environmental impacts, the literature suggests that the industrial and agricultural waste can be used in the concrete industry as partial percent substitutes for aggregate, binder and additives in concrete. The major objectives of this study are to reduce the landfill space which will enable to utilze these spaces for costruction than dumping and to reduce the environmental footprint by developing alternative supplementary cementing materials. In this study, the effect of utilization of the marble waste, glass powder and agricultural waste on fresh, durability and strength properties of concrete was investigated understanding the gaps from previous studies. The goal is to evaluate the % replacement of Ordinary Portland Cement with these alternate industrial wastes, over and above the fly ash replacement.

2. Materials and Methodology

2.1 Materials

Ordinary Portland cement (OPC 53) was used in this study conforming to IS 269. Crushed manufactured sand and basalt rock were utilized as fine aggregates and coarse aggregates respectively, maximum size of fine aggregate adopted was 4.75 mm and coarse aggregate was 20 mm. Fly ash was confirming with requirements as per IS 1489. Aggregates specified as per IS 383. Waste glass was collected from glass industry scrap and was crushed using jaw crusher to achieve a size of fine aggregate and was further ground in ball mill to obtain the desired fineness. The glass powder was ground to fineness such that maximum retention on 90 micron sieve is 2-3%. The marble dust was obtained in a powdered form with 0-2% retention on 90 micron sieve. The agricultural ash was also in a powdered form 100% passing through 90 micron and the retention on 45 micron sieve was 30%. Mid range plasticizers confirming to IS 9103 were used as water reducers. Consumable water was usd for mixig and curing of concrete. The chemical composition of Ordinary Portland Cement, fly ash, marble dust, glass waste and agricultural ash are described in the following table.

Table 1. Chemical composition of various binders

Parameter	OPC 53	Fly ash	Marble dust	Glass waste	Agricultural ash
SiO_2	18.91	59.04	0.82	76.73	68.45
Fe_2O_3	4.94	2.1	0.48	0.72	1.78
Al_2O_3	4.51	34.08	0.66	1.84	1.34
CaO	66.67	0.22	47.19	11.48	9.23
MgO	0.87	0.43	4.26	5.17	3.12
SO_3	2.50	0.05	0.35	0.36	2.11
Na_2O	0.12	0.5	0.17	2.96	0.35
K_2O	0.43	0.76	0.054	0.24	7.45

The physical properties were evaluated for these different binders along with chemical composition. Table 2 highlights the physical properties which find significance for utilization in concrete mix.

Table 2. Physical properties of various binders

Parameter	OPC 53	Fly ash	Marble dust	Glass waste	Agricultural ash
Specific gravity	3.15	2.21	2.68	1.93	1.22
Glass content				85.16%	
90 micron retention (%)	1.5%	-	8%	2-3%	-
45 micron retention (%)	-	30%	-	-	30%

2.2 Methodology

In this study, the fresh properties, strength and durability of concrete produced from marble dust, waste glass and agricultural ash were evalauted. Fresh concrete was casted in mixer and it was assessed for various properties like homogeneity of mix, initial slump and retention of concrete. The concrete was mixed in a lab mixer.The initial and later age compressive strength were evaluated at different repalcement % of these binders. Initial strength was determined at 1 day which is not recommended by the testing standards, howver it was tested to get an idea regarding the setting of concrete. Water permeability, water absorption and chloride penetartion was evaluated for assessing the durability of concrete. 75% OPC + 25% fly ash was considered as the reference mix design. Ordinary grade conceret mix of M25 and M30 were evaluated as these are majorly consumed.

2.3 Results

2.3.1 Fresh Properties

The freshly prepared concrete was monitored for workability and retention of concrete. The impact of w/b ratio and the amount of plasticizer was measured on the concrete. It was observed that from 3-7% replacement of OPC 53 with marble dust and at a constant w/b ratio and equal amount of plasticizer was maintained for both reference mix and mixes with OPC 53 replaced by marble dust. Glass powder was used to replace OPC by 5-10% and agricultural ash was used to replace OPC 53 by 3-5%. The w/b ratio was maintained constant in all the cases and amount of plasticizer was determined based on the requirement to obtain initial collapse slump which would retain in fresh stage for 180 min. Replacing 3-7% OPC 53 with marble dust had no negative impact on the fresh properties as can be seen from the initial slump and slump after 180 min. Using glass powder as 5-10% replacement to OPC 53, Replacing OPC 53 with agricultural ash required slightly higher plasticizer amount initially in order to maintain the similar fresh properties and workability like reference concrete mix. The reference mix was labelled as TM 001, mix with marble dust was labelled as TM 002, mix with glass powder was labelled as TM 003 and mix with agricultural ash was labelled as TM 004.

Table 3. Effect on fresh properties of concrete using various binders as partial replacement to OPC 53

Parameter	Reference mix	Mix with marble dust	Mix with glass powder	Mix with agricultural ash
% OPC replaced	0%	3–7%	5-10%	3-5%
w/b ratio	0.40-0.42	0.40-0.42	0.40-0.42	0.40-0.42
Plasticizer %	0.8-1%	0.8-1%	1.2-1.4%	1-1.1%
Initial slump (mm)	200-220	200-220	200-220	200-220
180 min slump (mm)	120-140	120-140	110-120	120-140

2.3.2 Compressive strength

The compressive strength of all the concrete mixes was measured for 1 day, 7 days and 28 days. The 1D compressive strength was measured additional to the compliance requirements to check the impact of delayed early strength gain on concrete if any.

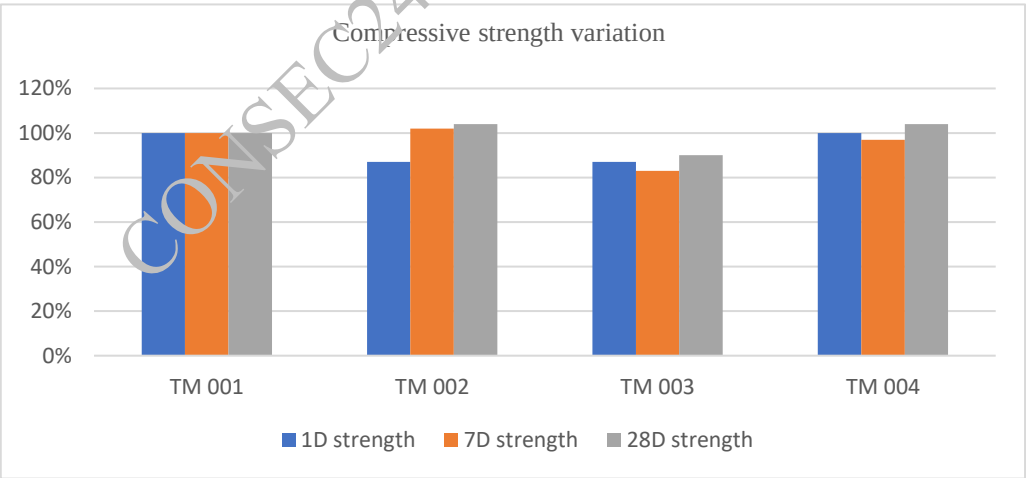

Figure 1. Effect on compressive strength using various binders as partial replacement to OPC 53

Concrete made with utilization of marble dust and agricultural ash as a replacement to OPC 53 has offered equivalent strength at 28 days. It can be observed that utilization of marble dust has contributed to the strength gain by formation of additional hydrated calcium silicate phases in concrete. The strength increase is highly attributed to the filler effect and pozzolanic activity in case of glass powder and agricultural ash utilization, however it has not been able to match the 28D equivalence in strength due to the amount of calcium hydroxide being converted to calcium silicate hydrates can be lower in volume and further needs to be examined.

2.3.3 Durability of concrete

The durability of the reference mix was measured and compared with the durability of concrete mixes produced with alternate binders. The durability parameters of concrete measured were water permeability at 5 bars pressure as per BS standards, water absorption of concrete as per BS 1881 standards and chloride penetration (RCPT) as per ASTM C1202 standards.

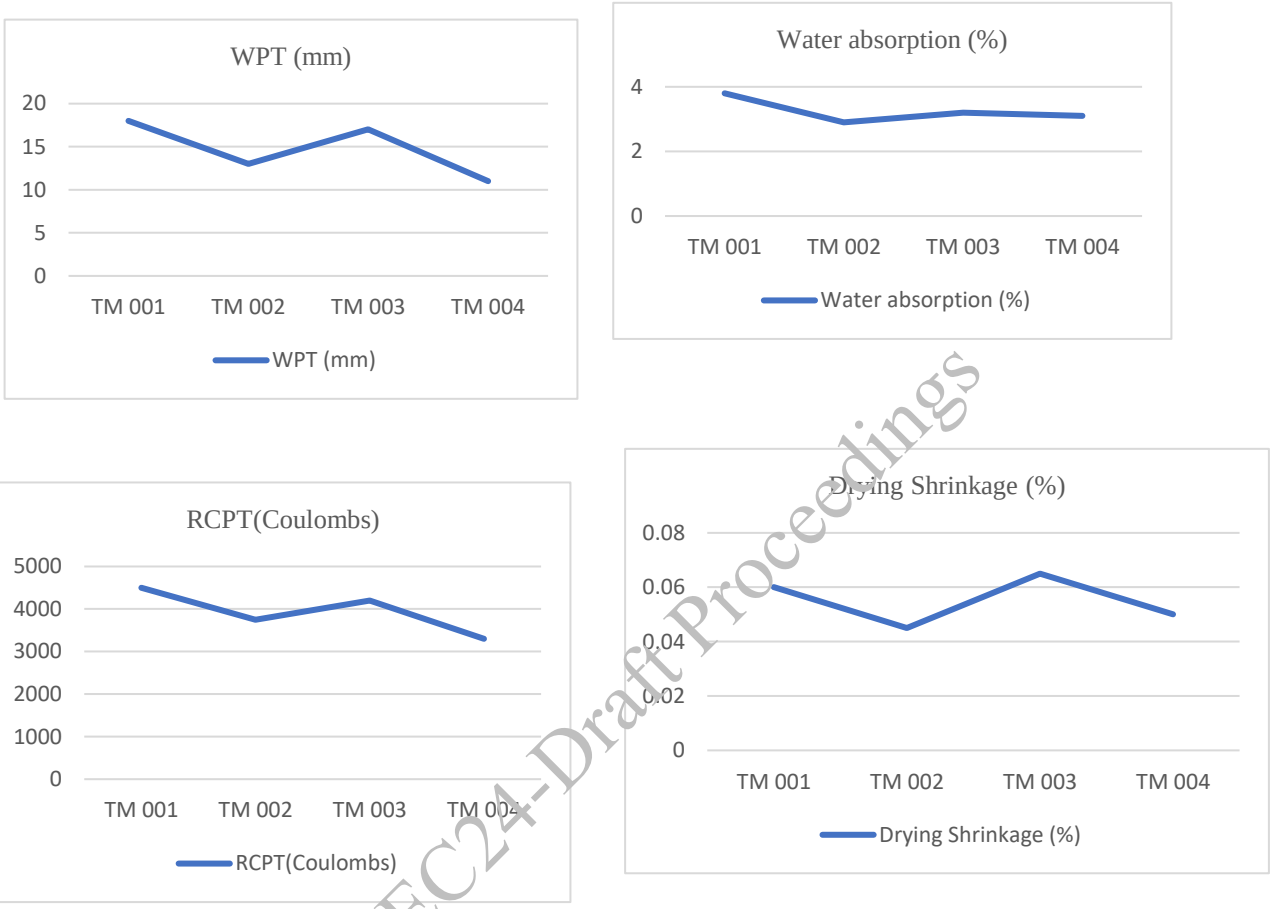

Figure 2. Effect on durability of concrete using binders as partial replacement to OPC 53 respectively

3. Conclusions

- 3-7% OPC 53 can be replaced using marble dust without any effect on fresh properties. The concrete mix with marble dust has similar fresh properties compared to conventional concrete. The compressive strength is slightly better compared to control concrete and durability parameters are equal or better.
- Glass powder has a good glass content of 85%, however on replacing 5-10% OPC 53 with glass powder as a binder it has been observed that the compressive strength reduces by 5-13% at 28 days with reference to control concrete. Drying shrinkage is slightly higher compared to control concrete.
- Replacing OPC 53 by 3-5% agricultural ash has no negative effect on fresh properties of concrete. The compressive strength is slightly better at all ages and durability parameters are also better than control concrete.
- The replacement in the above alternate raw materials is over and above the 25% OPC replacement by fly ash. These industrial wastes can replace OPC in the range of 3-5% which can better offset carbon emissions and reduce the embodied energy of the concrete mix.
- It is recommended to utilize these alternate binders as a replacement to OPC 53 in the said limits which will be better in terms of sustainability by reducing a part of carbon footprint generated during OPC 53 production. Further studies are scoped to evaluate the utilization by using some activators for better

strength and durability of concrete. Industrial scalability of these initiatives should be prioritized to promote sustainable initiatives.

References

Adesina, A., de Azevedo, A.R., Amin, M., Hadzima-Nyarko, M., Agwa, I.S., Zeyad, A.M. and Tayeh, B.A.(2022) "Fresh and mechanical properties overview of alkali-activated materials made with glass powder as precursor", *Clean. Materials*, 3: 100036

Aslani, F., Ma, G., Wan, D.L.Y. and Muselin, G.(2018) "Development of high performance self compacting concrete using waste recycled concrete aggregates and rubber granules", *Journal of Cleaner Production*., 182: 553-566

Balegamire, C., Nkuba, B. and Dable, P. (2022) "Production of gold mine tailings based concrete pavers by substitution of natural river sand in Misisi, Eastern Congo*", Cleaner Engineering and Technology*,7:100427

Chindaprasirt, P., Lao-un, J., Zaetang, Y., Wongkvanklom, A., Phoo-ngernkham, T., Wongsa, A. and Sata, V. (2022) "Thermal insulating and fire resistant performances of geoploymer mortar containing auto glass waste as fine aggregates", *Journal of Building Engineering*, 60:105178

Gencel, O., Ozel, C., Koksal, F., Erdogmus, E., Martínez-Barrera, G. and Brostow, W.(2012) "Properties of concrete paving blocks made with waste marble", *Journal of Cleaner Production*, 21:62-70

Kumar, R. and Kumar, S.K. (2015) "Partial replacement of cement with marble dust powder", *International Journal of Engineering Research and Applications*, 5(8):106-114

Raffoul, S., Garcia, R., Pilakoutas, K., Guadagnini, M. and Medina, N.F.(2016) "Optimisation of rubberised concrete with high rubber content: an experimental investigation", *Construction and Building Materials*, 124:391-404

Sadek, D.M., El-Attar, M.M. and Ali, H.A. (2016) "Reusing of marble and granite powders in self-compacting concrete for sustainable development", *Journal of Cleaner Production*, 121:19-32

Preliminary Investigation on Use of Raw Marl as Partial Replacement of Cement

Amitkumar R. Chauhan[1*], Manu Santhanam[1]

[1, 1] Department of Civil Engineering, Indian Institute of Technology Madras, Chennai, India*
ce21d008@smail.iitm.ac.in, manus@civil.iitm.ac.in

[*] Corresponding author

ABSTRACT

In the last few decades, there has been a rise in the use of new supplementary cementitious materials (SCM). The use of different types of SCMs as a partial replacement of cement reduces the overall carbon footprint, thus improving sustainability. Depending on the kind of processing required for a SCM, its use reduces the overall cost of the binder. However, the availability of conventional SCMs in the long term is uncertain. Therefore, there is a need to look at the feasibility of using unexploited materials, like limestone mining waste, as a partial replacement of cement. This study explores the feasibility of using raw marl, that is a waste excavated from limestone mines. In this work, we have used 20% and 30% of raw marl as a partial replacement of cement. The feasibility of raw marl as a supplementary cementitious material is determined with the help of isothermal calorimetry, thermogravimetric analysis (TGA), and compressive strength results. The reactivity test results show that marl is a latent hydraulic but less reactive material. The 7-day mortar compressive strength of marl is less as compared to the OPC mortar. So, the replacement level of marl with cement needs to be further optimised.

KEYWORDS*: Pozzolan, Raw Marl, Reactivity test, Sustainability, Supplementary cementitious material*

1. Introduction

There has been huge interest in reducing the carbon dioxide (CO_2) emissions coming from the cement industry. These CO_2 emissions can be reduced by using low-carbon fuels or by reducing the clinker factor by partially replacing clinker with a substitute material (Ramanathan et al., 2020; Suraneni & Weiss, 2017). But there is an upper limit to enhance this process, as the clinker quality cannot be compromised. One of the widely used solutions to make cement sustainable is the partial substitution of cement with supplementary cementitious material (SCM) (Wang et al., 2022). All the supplementary materials don't have the same reactivity as cement. So, they can be categorised as inert fillers with no reactivity or SCMs with pozzolanic or latent hydraulic reactivity. (Suraneni & Weiss, 2017) showed that in recent years, different materials have been explored to find their suitability with cement substitution. However, the availability of these SCMs vary geographically, and their future availability is also uncertain. Therefore, there is a huge need to explore the unexploited pozzolans. On the other hand, inert materials don't have any pozzolanic reactions. Fine inert material can help in better particle packing of system or enhance clinker hydration by forming nucleation sites. Earlier, limestone was considered an inert material. But its reaction in alumina rich cementitious system shows the formation of carboaluminate phases. This shows that it has some reactivity (Antoni et al., 2012). The study on the use of limestone in binary and ternary cementitious systems has gained a lot of interest. The addition of limestone is limited in the cementitious system because of its lower dissolution. That leads to a reduction in compressive strength with higher limestone replacement. However, the availability of cement-grade limestone is reducing with an increase in cement demand. Therefore, there needs to be a shift in utilisation of waste generated from the limestone mines. Marl is the excavated waste of overburden layer from the limestone mines. It is mainly clay contaminated with 3-15% calcium carbonate. As per the IBM minerals report, the use of marl is not clearly defined. Utilisation of marl in burnt clay products has a popping-out problem under moisture exposure. (Danner & Justnes) used calcined marl as SCM in cementitious system. The calcination of marl was done at 800 °C.

They reported that in the reactivity test the calcium hydroxide consumption of calcined marl was half that of calcined clay. The mix with calcined marl showed less compressive strength at 7 days, while the 28 days strength was comparable to reference mix (Danner & Justnes) (Bahhou et al., 2021).
In this work, we have studied the feasibility of using raw marl in a binary cementitious system. Raw marl is used here to check its feasibility as SCM, in order to avoid the energy consumption for calcining it. To evaluate the pozzolanic reactivity of raw marl, the R3 test method was used as proposed by (Avet et al., 2016). As per this test, the reactivity of the material can be assessed by measuring the total heat release using isothermal calorimetry and bound water by thermogravimetric analysis. These results are further compared with the 7 days mortar compressive strength to find out the pozzolanic reactivity of marl.

2. Materials

Raw marl obtained from the limestone mines and Ordinary Portland cement of 53 grade were used. Their chemical composition obtained by X-ray fluorescence and loss on ignition values and specific gravity are mentioned in Table 1. Also, the mean particle size (d50, μm) as obtained by the laser diffraction method is listed.

Table 1. Chemical Composition of the materials used in the study.

Oxides	OPC	Marl
CaO	65.3	10.5
SiO_2	16.4	51.2
Al_2O_3	4.1	13.1
Fe_2O_3	6.3	3.3
MgO	0.4	1.6
SO_3	3.3	-
K_2O	0.7	3.5
Na_2O	0.2	0.2
LOI	3.1	15.5
Specific gravity	3.1	2.7
d50, μm	18	10*

*The raw marl was ground with a ball mill to obtain this fineness level

3. Experimental Methods

3.1 Heat flow measurement using Isothermal Calorimetry

The cumulative heat release was measured using an isothermal calorimeter over 7 days at 40 °C. The mixing ingredients were conditioned overnight at 40 °C before testing. The total weight of the paste was 110 g; this was mixed for 2 minutes at 1600 rpm and kept in the calorimeter using containers. As per (Avet et al., 2016) the mix design is followed for the R3 test as shown in Table 2.

Table 2. Mix design for R3 test

Marl (g)	Portlandite (g)	K_2SO_4 (g)	KOH (g)	H_2O (g)
12.50	37.50	1.47	0.32	60

3.2 Compressive strength

50 mm mortar cubes were used for assessing the evolution of the compressive strength of mortar mixes. The mortar cubes were tested at 3 and 7 days for OPC and Marl systems.

3.3 Bound water content

Around 20 mg of sample was taken from the paste used for isothermal calorimetry to determine the bound water content using thermogravimetric analysis (TGA). The paste sample was heated from 23 °C to 1000

°C at a rate of 10 °C/min in nitrogen purge gas conditions. The bound water content was found using the tangent method by finding the weight loss between 110 °C and 400 °C. The bound water content was further normalised to grams of bound water per 100 grams of SCM.

4. Results and discussions

4.1 Heat release

The cumulative heat release obtained from isothermal calorimetry in (J/100g of SCM) at 1 day and 7 days for the system consisting raw marl is shown in Table 3. The heat release at 7 days is 365 (J/g of SCM).

Table 3. Total heat release from isothermal calorimetry at 1 and 7 days

	Heat release (J/g of SCM)	
SCM	1 day	7 days
Marl	301	365

4.2 Compressive strength

The compressive strength results for OPC and raw marl mortar are shown in Table 4. We can see that as the replacement of marl in cement increases the mortar strength is decreasing. So the replacement of marl in the OPC system needs to be further optimised to get the equivalent strength.

Table 4. Compressive strength of OPC and Marl mortars at 3 and 7 days

	Compressive strength (MPa)	
Mix ID	3 days	7 days
OPC	13.28	26.5
Marl_20	11.35	18.94
Marl_30	7.79	15.23

4.3 Bound water content

The bound water content measured using the thermogravimetric analysis is shown in the Table 5 as (g/100g of SCM). The bound water content for the marl system is 23.95 g/100 g of SCM.

Table 5. Bound water content at 7 days using TGA.

Bound water (g/100g of SCM)	
SCM	7 days
Marl	23.95

As shown in the Table 6, the total heat release at 7 days and bound water content measured using thermogravimetric analysis shows that raw marl is a latent hydraulic and less reactive material (Ramanathan et al., 2020).

Table 6. Summary from reactivity test

	Heat release (J/g of SCM)	Bound water (g/100g of SCM)
SCM	7 days	7 days
Marl	365	23.95

5. Conclusions

Different types of tests, like isothermal calorimetry, TGA analysis, and compressive strength results, are used to study the reactivity of raw marl as SCM. The conclusion of this study is:

- Heat release and bound water content from the R3 test show that marl is a latent hydraulic but less reactive material.

- The heat release at 1 day and 7 days in the Marl system is not very different. So, the test can be reduced to one day.
- There is a decrease in the compressive strength of Marl mortars with 20% as well as 30% replacement at 7 days as compared to the OPC system.
- Thus, the optimisation of marl in cementitious system needs to be further evaluated.

Acknowledgements

Authors would like to acknowledge the Department of Civil Engineering and Technologies for Low Carbon and Lean Construction (TLC2) at Indian Institute of Technology Madras, India for providing all the technical and financial support.

References

Antoni, M., Rossen, J., Martirena, F., & Scrivener, K. (2012). Cement substitution by a combination of metakaolin and limestone. *Cement and Concrete Research*, 42(12), 1579–1589. https://doi.org/10.1016/j.cemconres.2012.09.006

Avet, F., Snellings, R., Alujas Diaz, A., Ben Haha, M., & Scrivener, K. (2016). Development of a new rapid, relevant and reliable (R3) test method to evaluate the pozzolanic reactivity of calcined kaolinitic clays. *Cement and Concrete Research*, 85, 1–11. https://doi.org/10.1016/j.cemconres.2016.02.015

Bahhou, A., Taha, Y., Khessaimi, Y. El, Hakkou, R., Tagnit-Hamou, A., & Benzaazoua, M. (2021). Using calcined marls as non-common supplementary cementitious materials—a critical review. *Minerals*, 11(5). https://doi.org/10.3390/min11050517

Danner, T., & Justnes, H. (n.d.). Calcined Marl as Pozzolana for Sustainable Development of the Cement and Concrete Industry Lignosulfonate for Future Concrete View project Durable Aluminum Reinforced Environmentally-friendly Concrete Construction-DARE2C View project. https://www.researchgate.net/publication/259005747

Ramanathan, S., Kasaniya, M., Tuen, M., Thomas, M. D. A., & Suraneni, P. (2020). Linking reactivity test outputs to properties of cementitious pastes made with supplementary cementitious materials. *Cement and Concrete Composites*, 114. https://doi.org/10.1016/j.cemconcomp.2020.103742

Suraneni, P., & Weiss, J. (2017). Examining the pozzolanicity of supplementary cementitious materials using isothermal calorimetry and thermogravimetric analysis. *Cement and Concrete Composites*, 83, 273–278. https://doi.org/10.1016/j.cemconcomp.2017.07.009

Wang, Y., Ramanathan, S., Burris, L., Shearer, C. R., Douglas Hooton, R., & Suraneni, P. (2022). A rapid furnace-based gravimetry test for assessing reactivity of supplementary cementitious materials. *Materials and Structures/Materiaux et Constructions*, 55(7). https://doi.org/10.1617/s11527-022-02029-0

Development of Lime and GGBFS Based Mortar: A Sustainable Approach to Construction Technology

Banoth Gopalakrishna[1]*, Kandagaddala Revanth Kumar[2], Prakash Nanthagopalan[3]

[1]*Civil Engineering Department, Indian Institute of Technology Bombay, Mumbai, Maharashtra – 400076, gopalakrishna@iitb.ac.in*
[2]*Civil Engineering Department, Indian Institute of Technology Bombay, Mumbai, Maharashtra – 400076, revanthkumar@iitb.ac.in*
[3]*Civil Engineering Department, Indian Institute of Technology Bombay, Mumbai, Maharashtra – 400076, prakashn@civil.iitb.ac.in*

*Corresponding author

ABSTRACT

Conventional construction primarily utilizes cement-based mortars, with the cement manufacturing process being a significant source of global CO_2 emissions, comprising up to 10% of the total. Consequently, there are significant environmental concerns associated with cement mortar usage. Lime mortars emerge as a sustainable alternative, boasting a 30% reduction in embodied CO_2. Moreover, lime mortars offer advantages over cement-based counterparts, including greater flexibility to accommodate wall movement and improved resistance to dampness. However, lime mortars exhibit drawbacks such as prolonged setting times, up to 91 days, and lower strength. Incorporating Ground Granulated Blast Furnace Slag (GGBS) offers a promising solution to overcome these limitations. With this background, the present study investigates the properties of hydraulic and non-hydraulic lime mortar with varying proportions of GGBFS to improve its performance against the drawbacks. Through comprehensive testing, encompassing setting time, and compressive strength, the performance of lime and GGBS based mortar is assessed. The results underscore the feasibility of this mortar for construction applications, including load bearing structures and architectural elements.

KEYWORDS: *Lime, GGBS, Compressive strength, Setting time.*

1. Introduction

Mortar plays a crucial role in civil engineering by bonding bricks and blocks in construction. Traditionally, mortars have been either lime-based or cement-based. Lime mortar, which has been in use for centuries, was the preferred choice until the advent of cement mortars. There are three primary types of lime: hydrated, non-hydraulic, and hydraulic (https://www.lime-mortars.co.uk/lime-mortar/guides/the-lime-mortar-guide). The lime cycle (Figure 1) illustrates that lime is produced by burning chalk or limestone to produce quicklime (calcium oxide, CaO), which is then slaked with water to form calcium hydroxide ($Ca(OH)_2$). If the original limestone or chalk lacks clay, the resulting lime is classified as 'non-hydraulic'. Lime putty, which typically contains about 90% calcium hydroxide and 10% calcium oxide, hardens by reacting with carbon dioxide in the air to form calcium carbonate through a process called carbonation.

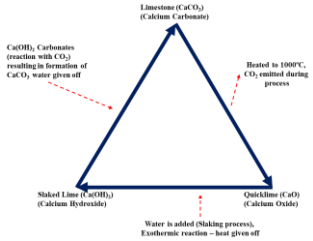

Figure 1. The lime cycle process.

Non-hydraulic lime is commonly used in its saturated form as lime putty, produced by slaking quicklime with excess water over several weeks to achieve a creamy texture or by stirring hydrated lime into water and conditioning for at least 24 hours. Lime putty, often combined with sand, is used directly as pure lime mortar, particularly in restoration and conservation work. It sets solely through carbonation, making it non-hydraulic. The carbonation process is slow, leaving the mortar weak and susceptible to damage for an extended period. In contrast, hydraulic lime or natural hydraulic lime (NHL) sets by hydration, allowing it to set underwater. NHL mortars are derived from limestone naturally containing silicates and/or aluminates in addition to calcium hydroxide (BS EN 459-1:2015). The production process involves burning argillaceous or siliceous limestones, followed by slaking and sometimes grinding. NHL is classified into three European grades: NHL 2, NHL 3.5, and NHL 5, which correspond to minimum compressive strengths at 28 days as specified in (BS 5628-1:1978, BS 5628-1:1992). These grades are also known as feebly hydraulic, moderately hydraulic, and eminently hydraulic, respectively. Both hydraulic and non-hydraulic lime mortars are breathable, but hydraulic mortars set more quickly, while non-hydraulic mortars better accommodate wall movement. However, lime mortars generally have longer setting times, which can delay construction and lead to economic drawbacks. Cement-based mortars, in contrast, achieve maximum strength within 28 days and are classified into four different designations as shown in Table 1**.**

Table 1. Various designations of cement-based mortars and their corresponding mean and minimum compressive strengths at 28 days, according to BS 5628 [3].

Mortar Designation Typical	Cement: Lime Ratio	Sand Ratio	Known as	Mortar Class	Compressive Strength Range (MPa)
A	1:0 to 0.25[1/4]	3	1:3	M12	9 – 12
B	1:0.5	4	1:0.5:4	M6	6 – 8.9
C	1:1	6	1:1:6	M4	3 – 5.9
D	1:2	8/9	1:2:9	M2	1.5 – 2.9

As strength decreases, flexibility increases, with designation (iv) being the most flexible. Designations (iii) and (iv) are typically used with bricks and low-density blockwork in construction. However, cement has a significantly high carbon footprint, contributing extensively to global anthropogenic CO2 emissions (L.G. Briendl et. al, 2005). Climate change, driven by excessive atmospheric carbon dioxide (CO2), leads to rising global temperatures and is both cumulative and irreversible over centuries). The production of cement, which involves burning fossil fuels, contributes to the greenhouse gas effect, a major driver of climate change. Consequently, the cement industry accounts for up to 10% of total global CO2 emissions, a stark contrast to the 3% attributed to the aviation industry (B. Gopalakrishna et. al, 2023). Energy efficiency in cement production can be improved by reducing the amount of clinker and using supplementary cementitious materials (SCMs) or partial cement replacements, which require less process heating and produce lower CO2 emissions (P. de Groot, 2021). Established SCMs include pulverized fuel ash (PFA or fly ash), ground granulated blast furnace slag (GGBS), metakaolin (MK), and silica fume (SF). Novel SCMs, such as rice husk ash (RHA) from agricultural waste, are also being explored. Pozzolans like PFA, MK, SF, and RHA need to react with calcium hydroxide to gain cementitious properties, while GGBS can directly replace cement due to its chemical similarity (A.K. Mali et. al, 2021).

When cement interacts with water, it forms calcium silicate hydrates (CSH), which are the primary contributors to the strength of mortars and concrete. Most pozzolans are rich in silica (SiO2), which reacts with calcium hydroxide to produce CSH, enhancing strength. Consequently, adding a pozzolan or a direct cement replacement like GGBS can increase the setting time and strength of lime mortars. It is essential to distinguish between a direct cement replacement and a pozzolan. A direct cement replacement can substitute Portland cement without requiring pozzolanic activity. GGBS, a by-product of the iron and steel industry and a fine white powder, is the most common direct cement replacement. Due to its chemical similarity to cement, GGBS can replace up to 90% of cement in some structural concrete, although the typical replacement range is between 30% and 70% (A.K. Mali et. al, 2021). In concrete, the interactions between Portland cement, GGBS, and water is intricate. Initially, Portland cement reacts with water to form insoluble hydration products, such as calcium silicate hydrate, while also producing a more soluble byproduct, calcium hydroxide, which migrates through the pore solution. GGBS then reacts with the excess free calcium hydroxide, acting as a catalyst to form calcium silicate hydrates (CSH), which reduces the size

of capillary pores [5]. Given that most types of lime contain significant amounts of calcium hydroxide, a similar reaction is anticipated when GGBS is added to lime mortar, potentially enhancing strength and reducing setting times through the formation of CSH. This paper presents the findings of a study conducted to evaluate the mechanical properties of non-hydraulic lime mortar containing GGBS, which could reduce curing time and mitigate one of the drawbacks of lime mortars. Additionally, lime production emits less CO2 than cement production, as it involves burning at lower temperatures, thereby conserving fuel and reducing pollution and greenhouse gas emissions. The embodied CO2 is approximately 30% lower than that of cement, making lime more sustainable and eco-friendlier. Therefore, incorporating GGBS into lime-based mortar could address the slow strength development and offer a more robust and sustainable alternative to cement-based mortars.

2. Materials and Methodology

Experimental work was conducted to determine the mechanical properties of non-hydraulic lime mortar with specified GGBS content. A series of tests were performed to assess the compressive strength of cubes (40x40x40 mm) and the flexural strength of prisms (40x40x160 mm). Sample preparation and testing adhered to relevant standards as outlined in this paper. High calcium lime and standard sand were utilized in the research. Mortar samples were produced to evaluate both fresh and mechanical properties, with water added to adjust workability according to the increase in GGBS content. Table 2 lists the prepared mixes. The mix ratio followed the standard 1:3 of binder (lime + GGBS) to sand by weight, with slag (GGBS) added as a percentage of the total binder weight.

Table 2. Mix proportion of the present study

Mix ID	Lime	GGBS
M1	100	0
M2	90	10
M3	80	20
M4	70	30

3. Results and Discussions

Different proportions of GGBS and lime were used as binders. Water was utilized as the liquid phase to measure the Initial Setting Time (IST) and Final Setting Time (FST) of the various composites studied, as shown in Figure 2. It can be observed from Figure that the IST of the mixes decreased when a portion of the mix was replaced with lime. Due to its finer particles and higher reactivity with water, lime reacted and set more quickly than other mixes, resulting in shorter IST. The GGBS content in the mixes ranged from 10% to 30%. Mixes M1 to M4, which included GGBS, exhibited ISTs of 335 and 593 minutes, respectively. A similar trend was observed in the Final Setting Times, with mixes containing lime showing lower FSTs, ranging from 895 to 1054 minutes.

Mortar cubes of size 40 mm × 40 mm × 40 mm were cast using a binder-to-fine aggregate ratio of 1:3, with a water-to-binder ratio of 1. These cubes were tested for compressive strength after 3, 7, and 28 days of air curing. The test results are illustrated in Figure 3**.** The compressive strength of mortar cubes at various ages of ambient curing showed that GGBS-based mixes (M2-M4) had higher compressive strength compared to the 100% lime mix (M1). Even after 3 days of curing, all cubes exhibited compressive strengths ranging from 31% to 53% of their 28-day strength. This suggests that lime and GGBS mixes are well-suited for repair or precast works. Mixes containing only lime demonstrated lower compressive strength compared to the GGBS blends (M2-M4). These findings suggest that adding lime to GGBS-based mortar does not enhance strength. However, further research is necessary to thoroughly investigate the proportioning and durability of concrete prepared with this new binder composite activated by an alkaline medium.

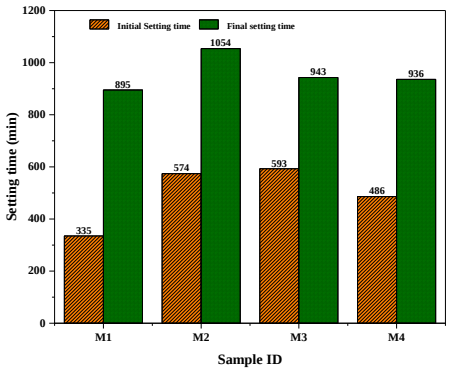

Figure 2. Setting time of Lime and Lime +GGBS mix

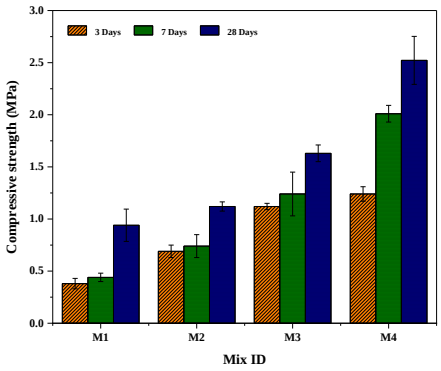

Figure 3. Compressive strength of Lime and Lime +GGBS mix

4. Conclusions

Based on the experimental results of various composite binder proportions used in this study, the following conclusions can be drawn: GGBS-based mortar systems perform better than 100% lime-based mixes. Replacing lime with GGBS in the mortar system increases the setting times and requires liquid activators for improved lubrication.

References

A.K. Mali, P. Nanthagopalan, Comminution: A Supplementation for Pozzolanic Adaptation of Sugarcane Bagasse Ash, J. Mater. Civ. Eng. 33 (2021) 1–15. https://doi.org/10.1061/(asce)mt.1943-5533.0003985.

A.K. Mali, P. Nanthagopalan, Framework for Investigations on Variability in Characteristics and Pozzolanic Reactivity of Sugarcane Bagasse Ash during the Crushing Period, J. Mater. Civ. Eng. 33 (2021) 1–14. https://doi.org/10.1061/(asce)mt.1943-5533.0003978.

BS EN 459-1:2015 - TC, Building lime - Definitions, specifications and conformity criteria, 2015. https://knowledge.bsigroup.com/products/building-lime-definitions-specifications-and-conformity-criteria?version=tracked.

BS 5628-1:1978, BS 5628-1:1992 Code of practice for use of masonry. Structural use of unreinforced masonry (AMD7745)(AMD13680)(Withdrawn),2005.

B. Gopalakrishna, D. Pasla, Development of metakaolin based high strength recycled aggregate geopolymer concrete, Constr. Build. Mater. 391 (2023) 131810. https://doi.org/10.1016/j.conbuildmat.2023.131810.

Conserv Lime Products, THE LIME MORTAR GUIDE, Conserv Lime Prod. (n.d.). https://www.lime-mortars.co.uk/lime-mortar/guides/the-lime-mortar-guide.

https://www.thenbs.com/PublicationIndex/documents/details?Pub=BSI&DocId=260482.

L.G. Briendl, F. Mittermayr, A. Baldermann, F.R. Steindl, M. Sakoparnig, I. Letofsky-Papst, I. Galan, Early hydration of cementitious systems accelerated by aluminium sulphate: Effect of fine limestone, Cem. Concr. Res. 134 (2020) 106069. https://doi.org/10.1016/j.cemconres.2020.106069.

P. de Groot, The economics of global warming, Int. Aff. 69 (1993) 371–372. https://doi.org/10.2307/2621656.

Durability of Geogrid-Based Textile Reinforced Concrete

Mohan Lal[1, 2*], and R Siva Chidambaram[2]

[1] Academy of Scientific and Innovative Research (AcSIR), Ghaziabad, UP, India
Email: mp917444@gmail.com
[2] CSIR-Central Building Research Institute, Roorkee, UK, India
Email: krsinelastic@gmail.com

*Corresponding author

ABSTRACT

Geogrids are type of geosynthetic materials made of polymer materials and have a wide range of applications in civil engineering mostly used for soil stabilization. Geogrids have been used for reinforcing the soil, embankment retaining walls, etc. for a few decades. Due to the rapid development of the geosynthetic industry and geogrids as reinforcement has a wide range of applications due to its non-corrosiveness, high strength and ductility, durability, and cost-effectiveness. But very limited number of studies have been done to investigate the potential of Geogrid as a reinforcement in concrete and mortar. This study aims to investigate the potential of geogrid as a reinforcement in Textile Reinforced Concrete (TRC). Parameters such as tensile behavior and long-term durability have been investigated. The study includes the application of polyester-based bi-axial geogrid coated with SBR as reinforcement in textile reinforced concrete and Tensile behavior and effect on SBR coating have been studied by keeping the specimen in different pH solutions, the specimens were also kept for natural aging for 5 years to investigate both tensile and durability behavior of geogrid under concrete. The study reveals that geogrid has tensile capacity after natural aging can reduce up to 30%.

KEYWORDS: *Textile reinforced concrete, Geo-grid, Tensile behaviour, Durability, Accelerated aging, Natural aging*

1. Introduction

Geogrids are polymeric geosynthetics mostly used to provide soil reinforcement [3]. But some of studies shows that the geogrid can also be used for reinforcing concrete elements such as beams, columns, and slabs [1, 2]. The mostly used geogrid are made of polypropylene (PP), polyester terephthalate (PET), and polyethylene (PE) [3]. The geogrids can be effectively used as confinement and reinforcement in concrete and mortar, their two dimensional and three-dimensional open structure interlocks the surrounding concrete or mortar. This bonding between concrete or mortar and geo-grid reinforcement creates more efficient and cost-effective structure.

There is still uncertainty regarding the durability of these polymeric materials, specifically with regard to their ability to maintain their design properties even after undergoing construction stresses and being exposed to harsh environments for an extended period of time, given the relatively limited experience with them. The deterioration of polymer geogrid reinforcement, with time will depend on the properties of a particular polymer, its configuration, and the environment it is exposed. Thus, further study in this field is required.

Durability of geogrids inside concrete is the main concern. When these geogrids are poured in concrete the pH of concrete is about 13.5 (alkaline), but with the change in environment the pH changes and becomes acidic (pH<8.5). Which can affect the coating at the surface of geogrids and polyester fibers comes in direct contact with concrete\e and degrade with the time.

To access the durability generally two types of methods are adopted namely accelerated aging and natural aging. In accelerated aging geogrids are kept inside the chemical solutions and kept it for some time durations. And post acceleration aging affects are found out in terms of mechanical performance bond and durability.

The objective of this study is to evaluate the long-term durability of polymeric geogrid inside concrete under natural aging for five years. And experimentally evaluate the mechanical performance of geogrid using uniaxial tensile testing.

2. Material and methods

To assess the durability of polymeric geogrid, polyester geogrid named as SGU 200 chosen for the study and it is embedded inside concrete and subjected to natural aging in Roorkee Uttarakhand. The climate condition in the location generally vary from 10° to 46° in temperature and 23 to 80 % in relative humidity over the year. SGU 200 is taken out carefully from the concrete specimen and close view of the same can be seen in fig.1b shows degradation on the texture of geogrid and coating. Further microscopic images show that the SBR coating was damaged inside concrete (fig.2b).

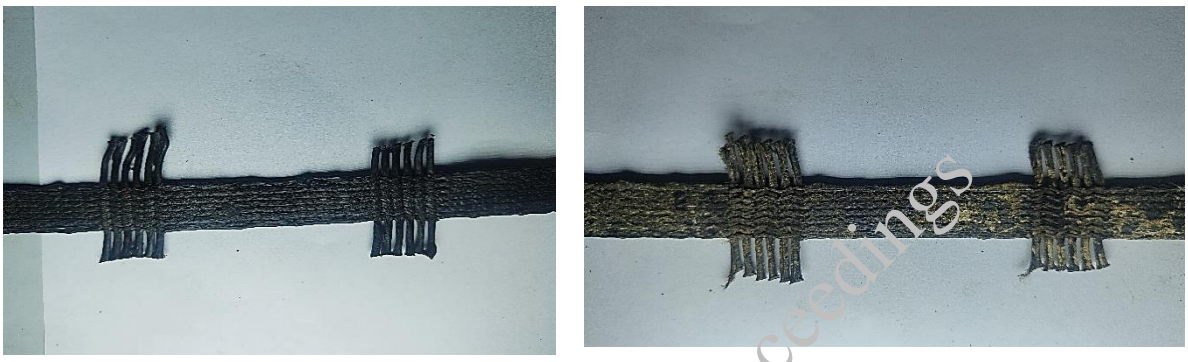

(a) Undegraded SGU 200 **(b) SGU 200 taken out form concrete specimen after 5 years of degradation**

Figure 1. Close view of SGU 200

3. Microscopic view

As the geogrids are protected against harsh environment by applying protective coatings on them such as SBR coatings. The long term effect on these coatings needs to be study for its durability point of view.

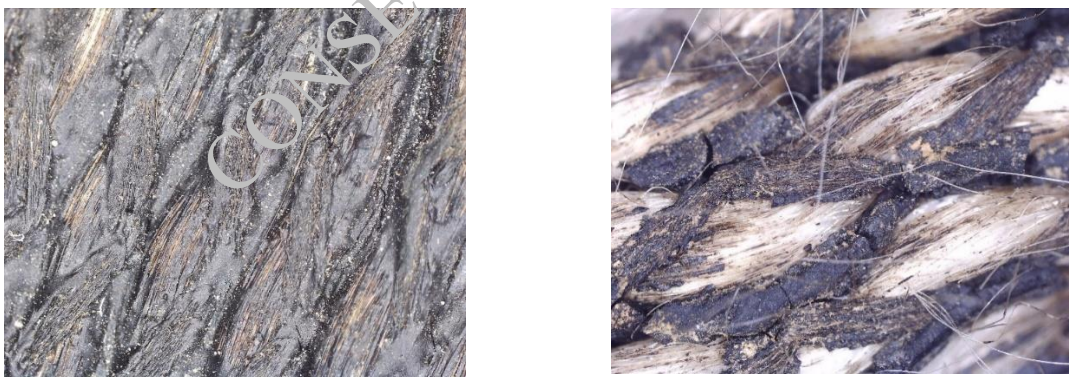

(a) Undegraded GG **(b) GG taken out form concrete specimen after 5 years of degradation**

Figure 2. Micro structure at 200X magnification

To study the defect or damage in coating of geogrid due to natural aging after five years, digital microscope is used having magnification of 20X and it was found the almost 50-60% coatings were damaged and polyester fibers were visible as shown in figure 2.

4. Uniaxial Tensile test

All the geogrid specimens were tested under uniaxial tensile testing. Tensile tests were performed on tensile testing machine as shown in Fig. 3. The machine has a load capacity of 100 kN. The geogrid specimen was prepared and the ends were hydraulically gripped and uniform loading were applied at the loading rate of 20.0 mm/min as per ASTM D-6637.

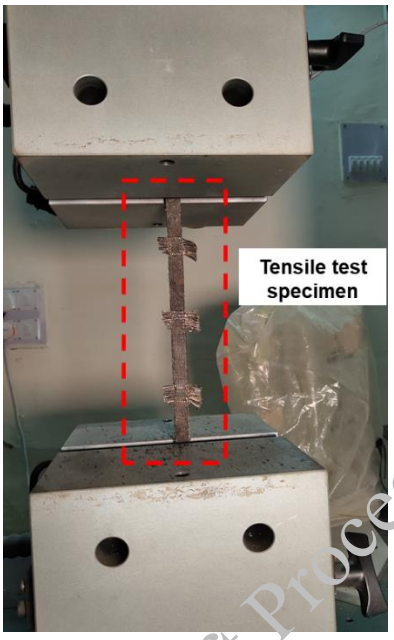

Figure 3. Tensile test set-up

Total four number of geogrid specimens were tested under uniaxial tensile testing among which one is control specimen and other three were exposed to natural aging for five years. Here in the terms GG_5YR_N, GG represents for geogrid 5YR represents for 5 Year natural aging and N represents for specimen number.

5. Results and Discussions

This section discusses about the results obtained from the uniaxial tensile test.

5.1 Load vs deformation curve

Figure 4 represents tensile stress vs deformation curve obtained from uniaxial tensile testing as mentioned in fig.3. The graph represents that for all the cases the initial curve up to 2 mm, there is variation in the stiffness, GG_Control has less stiffness due to is ductile nature whereas the degraded specimens (GG_5YR_1-3) embedded in the concrete has some more stiffness due to absorption of inorganic materials, buts once the loading increased there is almost similar stiffness in all the specimens up to 10 mm displacement and for GG_Control specimen it is reaching the peak load of 10.2 kN but GG_5YR_1-3 failed nearly 10-10.5 mm displacement with peak loads of 6.67-7.36 kN. The test results show that maximum load for undegraded specimen is 10.2 kN while the degraded specimens show 27.8 to 34.4 % decrease in tensile strength.

5.2 Failure Patterns

The below table 1. shows the peak load and failure patters of tested tensile specimens under uniaxial tensile loading. The control specimen shows sudden rupture at the middle of the gauge length while the degraded specimen shows sudden localized rupture (As shown in fig. 5).

Table 1. Peak load and failure patterns

Specimen ID	Peak Load (kN)	Failure patterns
GG_Control	10.2	Sudden rupture of GG
GG_5YR_1	6.69	Yielding of GG followed by localized rupture
GG_5YR_2	7.36	Yielding of GG followed by localized rupture
GG_5YR_3	7.03	Yielding of GG followed by localized rupture

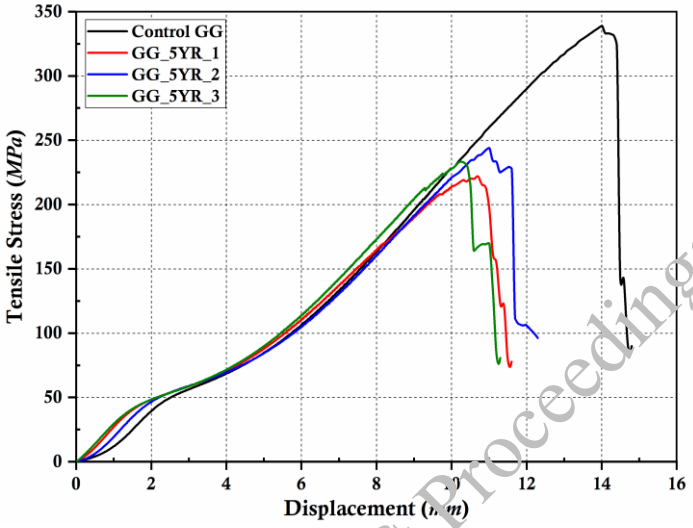

Figure 4. Load vs deformation curve

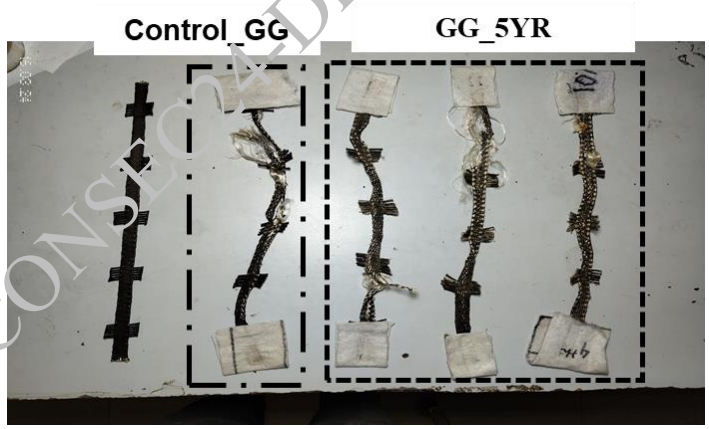

Figure 5. Failure patterns after tensile testing

6. Conclusions

- Tensile capacity of Geogrid with natural aging decreases which affect the long-term performance the material. The experimental results also show that the decrease I tensile capacity is about 27-35 % when the geogrid is exposed to five years of natural aging.
- Long-term durability study of geogrid for its application as a reinforcement in concrete structures is essential for the development of sustainable building material.
- Most of the study have focused on accelerated aging technique which may not provide better results to check the long-term durability
- Natural aging technique can give satisfactory results for long-term durability study.

- The present study opens up the possibility of using GG textiles for TRC, with suitable coating and matrix modification, as an alternative to the more expensive AR-glass fiber textiles.

Acknowledgements

The author is thankful to the director of CSIR-CBRI, Roorkee, for research support and strata India for supplying Geogrids for various research purposes in the area of civil engineering.

References

Chidambaram, R.S. and Agarwal, P., 2015. Flexural and shear behavior of geo-grid confined RC beams with steel fiber reinforced concrete. *Construction and Building materials*, 78, pp.271-280.

Sivakamasundari, S., Daniel, A.J. and Kumar, A., 2017. Study on flexural behavior of steel fiber RC beams confined with biaxial geo-grid. *Procedia engineering*, 173, pp.1431-1438.

Reddy, D.V., 2000. Strength and durability of backfill geogrids for retaining walls (No. WPI 0510738,).

Mechanical Properties of Concrete Made using Recycled Aggregate from C&D Waste

V.Bhashya[1*], and S. Bhaskar[2]

[1] Principal Scientist, CSIR-Structural Engineering Research Centre, Chennai, India
Email: bhashya@serc.res.in
[2] Chief Scientist, CSIR-Structural Engineering Research Centre, Chennai, India
Email: bhaskar@serc.res.in

[*]Corresponding author

ABSTRACT

The use of construction and demolition (C&D) waste as alternative aggregates for new concrete production gaining importance to preserve natural resources; reduce the impact on environmental pollution; and the need for disposal. It is reported that the average annual C&D waste generation is about 150 million tonnes. Many studies are reported on the use of recycled concrete aggregate (RCA) prepared in the laboratory, however, in the present study, the recycled aggregate (RA) obtained from a C&D waste processing plant located in Chennai is used in the concrete preparation. Physical and mechanical properties of RA have been evaluated experimentally and mechanical properties of concrete made by using RA are also evaluated. Three different w/c ratios viz., 0.55, 0.45 and 0.35 are used in the concrete mix preparation with 100% replacement of natural aggregate with RA. For relative comparison, conventional concrete mix is also developed and the results are compared. It is observed from the results that the recycled aggregates have lower specific gravity and higher water absorption when compared to natural aggregates. Also, concrete made using recycled aggregate showed lower compressive strength, split tensile strength and flexural strength when compared with natural aggregate concrete. This could be due to the presence of adhered mortar, brick waste, tiles waste, etc in the recycled aggregates. Nevertheless, concretes up to 40MPa compressive strength can be made by using RA with 100% replacement of natural aggregate.

KEYWORDS: *Recycled aggregate, Brick waste, Tiles waste, Recycled aggregate concrete, Compressive strength.*

1. Introduction

The construction industry is one, to a great extent depends on natural resources. There is a large-scale depletion of natural resources due to extraction of natural aggregates. Simultaneously, huge amount of construction and demolition (C&D) waste is being produced during construction (construction waste) and due to demolition of aged/unused concrete structures (demolition waste). India generates about 150-500 million tonnes of C&D waste every year (PIB Delhi,2024). Municipal corporations facing a big challenge in managing and handling of C&D waste in Indian cities. Due to insufficient number of landfills for dumping such waste led to search for a viable option for effective utilization of C&D Waste. Ram et al (2020) reported a case of Chennai, where the existing dumpsites had been overflowing with C&D wastes necessitating the need for newer dumpsites to meet the city's disposal requirements. Kumar and Deoliya (2022) focused on the application of recycled concrete fine aggregate. Prajapati et al (2021) made an effort to optimize the thermo-mechanical beneficiation for the treatment of RCA. Bhashya and Bharatkumar (2018) carried out experimental studies on the applicability of recycled concrete coarse aggregate (RCA). Meng et al (2023) reported that the recycled aggregate had waste brick content of around 13%. Zeng and Xiao (2023) studied the physical properties of RA. The values for the apparent density reported was 2270 kg/m3 and water absorption was 14.97%. Xu et al (2023) reported that the apparent density of RA was 2430 kg/m3 and water absorption was 10.4%. In the present study, attempts are made to use the recycled aggregate (RA) generated from a C&D waste processing plant located in Perungudi, Chennai. RA is

produced from C&D waste that has undergone industrial treatment processes involving sorting, crushing, and screening, washing etc. The RA was a mixture of waste concrete, brick waste, tiles, glass, and a small amount of metals and the proportion of these materials in 10mm RA is approximately 90.3%:5.5%:3.2%:0.7%: 0.3%, respectively, whereas for 20mm RA these proportions are 82.1%:8.3%:9.2%:0.3%:0.1%, respectively.

2. Experimental Investigations

2.1 Materials

Experimental investigations have been carried out on concrete by replacing the natural aggregates 100% with recycled aggregates. Ordinary 53-grade Portland cement confirming to IS 269-2015 was used. Locally available river sand passing through a 4.75-mm sieve was used as fine aggregate. Blue granite crushed stone aggregate of size 20mm and 10 mm was used as natural aggregate for control concrete mix. The water absorption of 10mm and 20mm NA is 0.53% and 0.55 %, respectively. The water absorption of recycled concrete aggregate of size 10mm and 20mm are 6.42 times and 7.96 times more when compared with natural aggregate, respectively. Recycled aggregates have lower specific gravity when compared to natural aggregates. This was due to the presence of adhered mortar, brick waste, etc in the recycled aggregates. Specific gravity of recycled aggregates of nominal size 10mm and 20mm are 11.26% and 17.72% less when compared to natural aggregates (2.71 and 2.74), respectively.

2.2 Casting of concrete test specimens

The concrete mix proportions were designed in accordance with IS 10262-2019, with a common target slump of 70 ± 10 mm. Sulphonated naphthalene formaldehyde (SNF) based superplasticizer is used and its dosage is 0.5 to 1 % by weight of the binder. To adjust the higher water absorption of recycled aggregate, additional amount of water was added to the concrete mix to prepare recycled aggregate concrete (RAC). Three different w/c ratios of 0.55,0.45 and 0.35 are used for both conventional concrete and recycled aggregate concrete.

2.3 Testing of the specimens

Cubes of size 100mm were tested for compressive strength and the cylinders of size 100mm diameter and 200mm length were tested for splitting tensile strength. Compression test was carried out at the age of 7 and 28 days, split tensile strength and flexural tests were carried out at the age of 28 days using compression testing machine of 1000kN capacity. Flexural test was carried out on a beam specimen with dimension 500x100x100mm. The compression test, splitting tensile test and flexural tests have been carried out as per IS 516-2021. The tests were carried out at a uniform stress rate, after the specimen was centered in the testing machine. The loading was continued till the specimen reaches its ultimate load.

2.4 Results and discussions

2.4.1 Compressive strength of RAC

The results of the compressive strength of recycled aggregate concrete at the age of 28 days are shown in Figure 1**.** For recycled aggregate concrete, the results show that the replacement of NA with RA resulted in reduction of concrete compressive strength when compared with that of the control concrete. It is seen from the results that the reduction in compressive strength of RAC based mix were 21.93%, 18.45% and 26.61% for w/c ratios 0.55,0.45 and 0.35, respectively, at the age of 28 days. This reduction could be attributed due to the lower crushing value (resulted from brick aggregates, tiles, etc) of recycled aggregates compared to that of conventional aggregates. It could also be contributed by the porous structure of the attached mortar of the recycled aggregates, leading to a weak interfacial transition zone in RAC when compared to that of NAC based mixes. Nevertheless, concretes up to 40MPa compressive strength can be made by using RA with 100% replacement of natural aggregate. Durability parameters evaluation is being studied to ensure long term durability of concrete structures made by RAC.

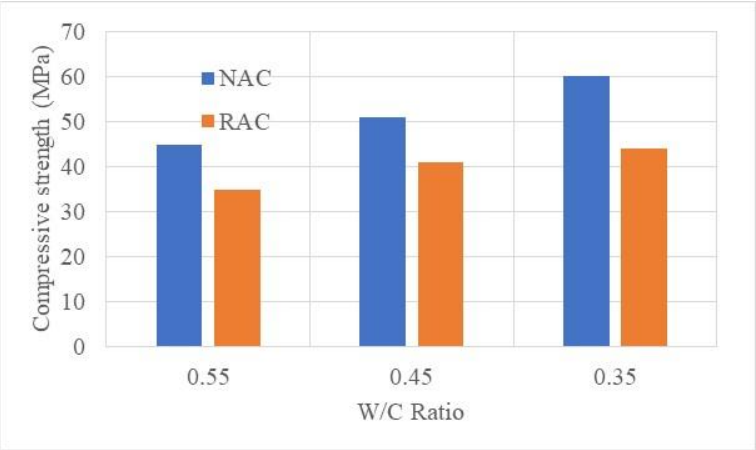

Figure 1. Compressive strength of RAC at the age of 28 days

2.4.2 Splitting tensile strength of RAC

For recycled aggregate concrete, the results show that the splitting tensile strength of recycled aggregate concrete were lower when compared with conventional concrete in a similar manner to that observed in the compressive strength tests. The split tensile strength of conventional concrete are 3.01 MPa,3.15MPa and 3.78 MPa for w/c ratio 0.55, 0.45 and 0.35, respectively. The reduction in splitting tensile strength for RAC were 18.85%, 21.97% and 28.85% for w/c ratio 0.55, 0.45 and 0.35, respectively. As expected, reduction in splitting tensile strength of RAC when compared with NAC were due to the adhered old cement mortar, brick waste, tiles waste, etc. in the recycled aggregate and the weaker interfacial zone between new cement mortar and recycled aggregate.

2.4.3 Flexural strength of RAC

Figure 2 shows the results of flexural strength of recycled aggregate concrete with different water cement ratios. The results show that the concrete specimens with recycled aggregate have the lower flexural strength when compared to the concrete specimens with conventional aggregate. The reduction in flexural strength of RAC were 8.37%, 8.84% and 7.72% for w/c ratio 0.55, 0.45 and 0.35, respectively. The reason explained for the reduction in compressive strength of RAC due to the incorporation of RA can also apply to the flexural behaviour of concrete.

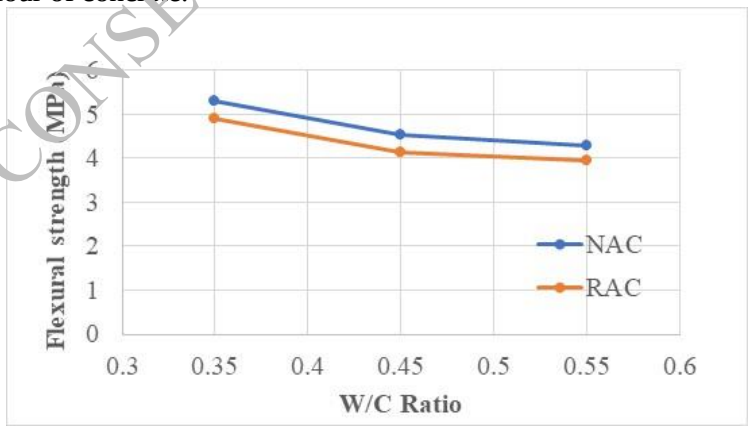

Figure 2. Flexural strength of recycled aggregate concrete

3. Conclusions

In the present study, experimental investigations were carried out on concrete made by using recycled coarse aggregate (RA) which are obtained from a C&D waste processing plant located in Chennai. Physical and mechanical properties of RA and also mechanical properties of concrete made by using RA are evaluated. Effect of three different w/c ratios (0.55,0.45 and 0.35) of concrete made using 100%

replacement of natural aggregate are studied in detail. The water absorption of recycled aggregate are 6 to 8 times more when compared to that of natural aggregate. Specific gravity of recycled aggregates are 11 to 17 times less when compared to natural aggregates. The replacement of NA with 100% recycled aggregates resulted in a reduction of concrete compressive strength 21 to 27% when compared with the control concrete. The splitting tensile strength of recycled aggregate concrete were lower when compared with conventional concrete in a similar manner to that observed in the compressive strength tests. Also, the use of RA resulted in 7 to 9% reduction in flexural strength when compared with control concrete. This could be due to the presence of adhered mortar, brick waste, tiles waste, glass waste, etc in the recycled aggregates. Nevertheless, concretes up to 40MPa compressive strength can be made by using RA with 100% replacement of natural aggregate.

Acknowledgements

This paper is being published with kind permission of the Director, CSIR-Structural Engineering Research Centre (SERC) Chennai. Authors gratefully acknowledge the support of project team and technical staff at Advanced Materials Laboratory (AML), SERC, Chennai during the experimental work. This paper has been assigned the registration number CSIR-SERC-1129/2024 and the research is funded by generous grant from CSIR, New Delhi.

References

Bhashya, V. and Bharatkumar, B.H. (2018) "Mechanical and durability properties of concrete produced with treated recycled concrete aggregate'' ACI Materials Journal, 115 (2):209-217.

Bureau of Indian Standards (BIS) "Ordinary Portland cement-specification", IS 269-2015, BIS, New Delhi, India

Bureau of Indian Standards (BIS), "Concrete mix proportioning- Guidelines", IS: 10262-2019, BIS, New Delhi, India.

Bureau of Indian Standards (BIS), "Hardened concrete- Methods of test", IS: 516 (Part 1/Sec 1)-2021, BIS, New Delhi, India.

https://pib.gov.in/PressReleaseIframePage.aspx?PRID=2007086, PIB Delhi, February 19, 2024

Kumar, G.S. and Deoliya, R. (2022) "Recycled cement and recycled fine aggregates as alternative resources of raw materials for sustainable cellular light weight flowable material", Construction and Building Materials, 326:126878.

Meng, T., Yang, X., Wei, H., Meng, R. and Zhou, W. (2023) "Study of the relationship between the water binder ratio and strength of mixed recycled aggregate concrete based on brick content", Construction and Building Materials, 394:132148.

Prajapati, R., Gettu, R. and Singh, S. (2021) "Thermomechanical beneficiation of recycled concrete aggregates (RCA)", Construction and building materials, 310:125200.

Ram, V.G., Kishore, K.C. and Kandindi, S.N. (2020) "Environmental benefits of construction and demolition debris recycling: Evidence from an Indian case study using life cycle assessment", Journal of Cleaner Production, 255:120258.

Xu, K., Deng, P., Huang, P., Xiao, A. and Guo, S. (2023) "Experimental investigation on the mechanical properties of concrete utilizing pre-coated Brick-Concrete recycled coarse aggregates", Construction and Building Materials, 403:133113.

Zheng, Y. and Xiao, Y. (2023) "A comparative study on strength, bond-slip performance and microstructure of geopolymer/ordinary recycled brick aggregate concrete", Construction and Building Materials, 366:130257.

NaoH-Pretreated Recovered Solid Fuel and Biomass Ash for Alkali-Activated Materials: The Effect of Content of Fly Ash and Bottom Ash on Mechanical Performance and Metal Leaching

Suman Kumar Adhikary [1*], Tero Luukkonen [2], Priyadharshini Perumal [3]

[1] *Faculty of Technology, Fiber, and Particle Engineering Research Unit, PO Box 4300, 90014, University of Oulu, Finland, suman.adhikary@oulu.fi*
[2] *Faculty of Technology, Fiber, and Particle Engineering Research Unit, PO Box 4300, 90014, University of Oulu, Finland, tero.luukkonen@oulu.fi*
[3] *Fiber, and Particle Engineering Research Unit, PO Box 4300, 90014, University of Oulu, Finland, priyadharshini.perumal@oulu.fi*

[*]Corresponding author

ABSTRACT

The growing global population drives the production of millions of tons of incineration ashes containing metallic aluminum, hindering their application in cementitious or alkali-activated materials due to volume expansion. Moreover, incinerated ash poses environmental hazards due to its toxic components, necessitating stringent management strategies to mitigate risks to both the environment and human health. To address this issue, fly ash from solid recovered fuel and biomass incineration was pretreated with NaOH to oxidize the metallic aluminum (Al0) before its utilization in alkali-activated materials. The formed slurry after the treatment was subsequently used to prepare alkali-activated material by mixing it with bottom ash and sodium silicate. In this study, several mixes were prepared with different contents of fly ash to study the impact on mechanical performance and heavy metal leaching. The proposed method offers a highly efficient and rapid solution for eliminating the drawbacks caused by the presence of metallic aluminum, and it can be conveniently implemented on construction sites as a "one-part" process. The content of fly ash in alkali-activated materials shows a significant impact on compressive strength and shows elevated levels of heavy metal leaching. However, alkali-activated technology also shows evidence of notable reductions in the leaching of Ba, Cr, Cu, Mo, and Pb, highlighting the environmental remediation potential of alkali-activation methods.

KEYWORDS: *Alkali-activated materials; Bottom ash; Fly ash; Metallic aluminum; Recovered solid fuel*

1. Introduction

The practice of incinerating solid waste plays a crucial role in waste management by facilitating volume reduction and enabling energy recovery from municipal solid waste (MSW). In Finland alone, a total of 1,515,000 tonnes of municipal waste was used for energy recovery in 2016. During incineration, three types of ash are produced as by-products: bottom ash, fly ash, and air pollution control residues. In many countries, due to the large-scale production of ash, most of it ends up in landfills. Additionally, many countries have restricted the use of untreated ash in various applications due to the presence of heavy metals (Blasenbauer et al., 2020). In recent years, researchers have developed innovative methods to stabilize the heavy metals in incinerated ash, facilitating its reuse in construction while meeting regulatory requirements for heavy metal leaching (Luo et al., 2018). Concrete, the world's second most used material, has the potential to incorporate such ash as a partial replacement for cement or aggregates. However, incinerated ash might contain metallic aluminium, which reacts with alkalis to form hydrogen gas, resulting in the expansion of cementitious or alkali-activated materials (Tian et al., 2020). This expansion can negatively impact the mechanical and durability performance of building materials (Huang et al., 2020). Therefore, it is necessary to treat the ash before its utilization in concrete or alkali-activated materials. A recent study by (Bertolini et al., 2004) and (Pera et al., 1997) reported that treating incineration ash with alkalis can

effectively convert metallic aluminium into oxidized aluminium. Literature also indicates that under highly alkaline conditions, the aluminium, silicon, and calcium in the ash might dissolve and promote the formation of aluminosilicate gel, leading to the formation of C-S-H and C-(N)-A-S-H, and resulting in a 3D network of aluminium and silica tetrahedra (Van Jaarsveld et al., 1997). During alkali activation, many heavy metals are encapsulated within this network structure (Zhang et al., 2008). Extensive literature studies indicate that incineration ash might have potential applications in producing building materials. Therefore, it is necessary to study the performance of incinerated ash in alkali-activated materials. The chemical composition of incinerated ash is largely impacted by geographical location and the fuel used during incineration, making it important to study the performance of Finnish incinerated ash for future references. In recent years, researchers have explored the performance of alkali-activated materials with various types of ash, including coal fly ash, municipal solid waste incinerated ash, and biomass ash. However, very limited studies have been conducted on recovered solid fuel and biomass ash. To fill this gap, this study investigates the performance of alkali-activated materials made with Finnish recovered solid fuel and biomass ash. This study also examines the impact of fly ash content on the mechanical properties and heavy metal leaching of alkali-activated materials. In this study, incinerated fly ash was pre-treated with NaOH to minimize the volume expansion of the alkali-activated materials.

2. Materials and methods

Fly ash and bottom ash derived from the co-combustion of solid recovered fuel and biomass (comprising wood and peat) were sourced from the Oulun Energia power plant in Oulu, Finland. The fly blast furnace slag was utilized as precursors in the production of alkali-activated mortars, while the fly ash bottom ash served as a fine aggregate. The bulk densities of the bottom ash and fly ash were measured at 1408 kg/m³ and 574 kg/m³, respectively, with surface areas of 0.28 m²/g and 3.65 m²/g. The particle size of the bottom ash ranged from 0 to 2 mm, whereas the fly ash particles were smaller than 250 µm. The silicon dioxide (SiO2) content in the bottom ash and fly ash was approximately 64% and 32%, respectively. In this study, sodium silicate solution (Na_2O 14.7 wt%, SiO_2 30.3 wt%, H_2O 55%; manufacturer: Woellner) was used as an activator. Before activation, a NaOH solution was prepared by mixing with water, and subsequently, the fly ash was treated with the NaOH solution. To study the impact of varying fly ash levels, three distinct samples were prepared, each maintaining to identical liquid-to-solid ratios and SiO_2/Na_2O ratios as outlined in Table 1. Throughout the process, the liquid-to-solid ratio (L/S) remained constant at 0.29 for all samples, with the liquid being a combination of NaOH solution and sodium silicate. Initially, NaOH and water were blended for 2 minutes. Then, the solution was mixed with fly ash in a plastic container and stirred at 200 rpm for 60 minutes to pre-treat and convert metallic aluminium into oxidized aluminium. Systematic view of pre-treatment of fly ash and subsequent alkali-activated mortar preparation is presented in Figure 1.

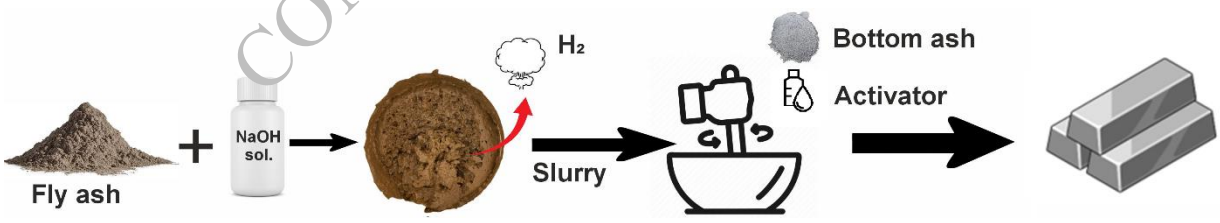

Figure 1. Systematic view of pre-treatment of fly ash and subsequent alkali-activated mortar preparation

Table 1. Mixing composition of alkali-activated materials (materials in grams).

Sample ID	Fly ash	Bottom ash	Slag	NaOH	Sodium silicate	Water	L/S	SiO_2/Na_2O
A	0	100	40	3.79	8.40	32.2	0.29	1.4
B	10	90	40	3.79	8.40	32.2	0.29	1.4
C	30	70	40	3.79	8.40	32.2	0.29	1.4

After the pre-treatment step, the resulting slurry was manually mixed with bottom ash, slag and activators. Following a manual stirring period of 2 minutes, the mixture was poured into prisms of size 20 x 20 x 80 mm. Plastic wrap was used to prevent water loss, and the samples were left at room temperature for 48

hours for hardening process. Subsequently, the hardened samples were removed from the molds and kept at room temperature for an additional 14 days before assessing their compressive strength and other characteristics. The compressive strength of the samples was assessed following 14 days of exposure to open air. Compressive strength was conducted using Zwick testing apparatus set to a maximum load of 50 kN and a loading force of 2.4 kN/s. The leaching of heavy metals from the specimens was conducted following the EN 12457-2:2004 standard, with samples being crushed to ensure a size smaller than 4 mm.

3. Results and discussions

Study results presented in Figure 2 show that the fly ash content has a significant impact on the strength of the alkali-activated mortar. It can be clearly observed that as the fly ash content increases, the strength of the alkali-activated material also increases. A compressive strength of around 16.6 MPa was measured for the alkali-activated material without fly ash, which increased to 20 MPa when the fly ash was completely replaced with bottom ash. The increase in strength development might be attributed to an increased silica source. In this study, only blast furnace slag and sodium silicate were considered as silica sources for calculating the SiO2/Na2O ratio. Probably due to the fact that when the fly ash content increases, the silica source also increases, resulting in improved compressive strength. The silica source from the fly ash likely increases the formation of high-strength calcium and sodium silicate and aluminosilicate gels (C-S-H and C-(N)-A-S-H), resulting in increased compressive strength(Manjunath et al., 2019; Nodehi and Taghvaee, 2021).

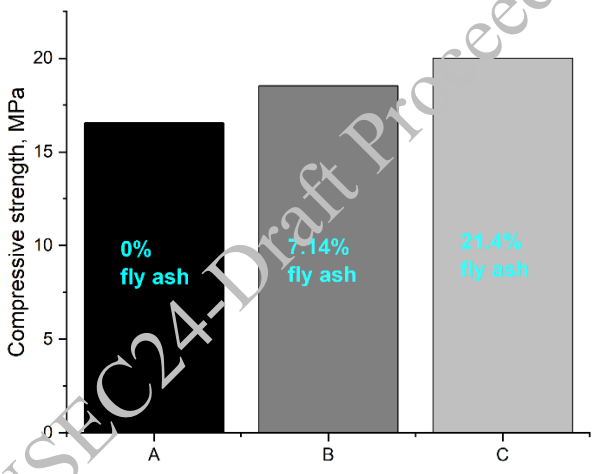

Figure 2. Compressive strength of alkali-activated materials.

To evaluate the environmental leaching risk, leaching tests were performed on both the raw ashes and the alkali-activated material samples. The results were then compared with the standards outlined in the Finnish decree 843/2017 for earth construction materials. The study results presented in Table 2 show that except for V, all of the heavy metal leaching was within the legislative limits recommended by the Finnish government.

Table 2. heavy metal leaching of raw fly ash, bottom ash and alkali-activated materials, mg

Elements, [mg/kg]	Raw fly ash	Raw bottom ash	A (fly ash 21.4%)	B (fly ash 7.14%)	C (fly ash 0%)	Legislation limit
Leaching L/S=10 As	0.022	0.14	0.66	0.22	0.14	2
Leaching L/S=10 Ba	2	3.1	<0,06	0.2	0.58	100
Leaching L/S=10 Cr	36	0.45	0.043	0.082	0.2	10
Leaching L/S=10 Cu	0.08	<0,01	0.09	0.12	0.054	10
Leaching L/S=10 Mo	13	0.3	0.28	1	2.4	6
Leaching L/S=10 Pb	15	0.015	<0,004	0.0089	0.019	2
Leaching L/S=10 Se	0.27	<0,04	0.14	0.14	0.15	0.7
Leaching L/S=10 V	0.032	0.26	30	19	9.2	3

It was observed that V leached even more than the raw fly ash and bottom ash. The study results also indicate that the leaching of V increased with higher fly ash content. Interestingly, the leaching of As, Cu, Se, and V from alkali-activated materials was higher than that from the raw fly ash and bottom ash. Several researchers have reported similar high leaching of As, Se, and V from alkali-activated materials compared to the starting materials (Ahmari and Zhang, 2013; Yliniemi et al., 2015). This phenomenon can be attributed to the high solubility of As, Se, and V metals in the high pH of the alkali-activation process.

4. Conclusions

The study results lead to the conclusion that assessing heavy metal leaching in both raw ashes and alkali-activated materials is crucial for evaluating environmental risks in construction applications. The increase in fly ash content in alkali-activated mortar significantly enhances compressive strength, likely due to the formation of calcium and sodium silicate gels, thus offering improved mechanical performance. Leaching tests conducted on both raw ashes and alkali-activated materials, compared against Finnish regulatory standards, generally revealed acceptable levels of heavy metal leaching, with the exception of V exceeding permissible limits. Alkali-activated materials exhibited higher leaching of certain heavy metals (such as As, Cu, Se, and V) compared to raw ashes, probably attributed to their elevated solubility in the alkaline conditions of the activation process.

Acknowledgements

This research received support from the European Union's Horizon Europe research and innovation program under grant agreement No 101058162 (AshCycle), as well as from the Research Council of Finland under grant No 347678 (SUSRES).

References

Ahmari, S., Zhang, L., 2013. Durability and leaching behavior of mine tailings-based geopolymer bricks. *Constr. Build. Mater*. 44, 743–750.

Bertolini, L., Carsana, M., Cassago, D., Curzio, A.Q., Collepardi, M., 2004. MSWI ashes as mineral additions in concrete. *Cem. Concr. Res*. 34, 1899–1906.

Blasenbauer, D., Huber, F., Lederer, J., Quina, M.J., Blanc-Biscarat, D., Bogush, A., Bontempi, E., Blondeau, J., Chimenos, J.M., Dahlbo, H., Fagerqvist, J., Giro-Paloma, J., Hjelmar, O., Hyks, J., Keaney, J., Lupsea-Toader, M., O'Caollai, C.J., Orupõld, K., Pajak, T., Simon, F.G., Svecova, L., Šyc, M., Ulvang, R., Vaajasaari, K., Van Caneghem, J., van Zomeren, A., Vasarevičius, S., Wégner, K., Fellner, J., 2020. *Legal situation and current practice of waste incineration bottom ash utilisation in Europe*. Waste Manag. 102, 868–883.

Huang, G., Yang, K., Chen, X., Lu, Z., Sun, Y., Zhang, X., Feng, Y., Ji, Y., Xu, Z., 2020. Use of pretreatment to prevent expansion and foaming in high-performance MSWI bottom ash alkali-activated mortars. *Constr. Build. Mater*. 245, 118471.

Luo, Y., Zheng, S., Ma, S., Liu, C., Wang, X., 2018. Preparation of sintered foamed ceramics derived entirely from coal fly ash. *Constr. Build. Mater*. 163, 529–538.

Manjunath, R., Narasimhan, M.C., Umesh, K.M., Shivam Kumar, Bala Bharathi, U.K., 2019. Studies on development of high performance, self-compacting alkali activated slag concrete mixes using industrial wastes. *Constr. Build. Mater*. 198, 133–147.

Nodehi, M., Taghvaee, V.M., 2021. Alkali-Activated Materials and Geopolymer: a Review of Common Precursors and Activators Addressing Circular Economy. *Circ. Econ. Sustain*. 2021 21 2, 165–196.

Pera, J., Coutaz, L., Ambroise, J., Chababbet, M., 1997. Use of incinerator bottom ash in concrete. *Cem. Concr. Res*. 27, 1–5. https://doi.org/10.1016/S0008-8846(96)00193-7

Tian, X., Rao, F., León-Patiño, C.A., Song, S., 2020. Effects of aluminum on the expansion and microstructure of alkali-activated MSWI fly ash-based pastes. *Chemosphere* 240, 124986.

Van Jaarsveld, J.G.S., Van Deventer, J.S.J., Lorenzen, L., 1997. The potential use of geopolymeric materials to immobilise toxic metals: Part I. Theory and applications. *Miner. Eng.* 10, 659–669.

Yliniemi, J., Pesonen, J., Tiainen, M., Illikainen, M., 2015. Alkali activation of recovered fuel–biofuel fly ash from fluidised-bed combustion: Stabilisation/solidification of heavy metals. *Waste Manag*. 43, 273–282.

Zhang, J., Provis, J.L., Feng, D., van Deventer, J.S.J., 2008. Geopolymers for immobilization of Cr6+, Cd2+, and Pb2+. J. *Hazard. Mater*. 157, 587–598.

Lab/Field Testing and Characterisation

A Multiscale Approach for Adhered Mortar Quantification Using Chemical Treatment of RCA

P. Saraswat[1*], M. S. Parihar[2], K. Sandeep[3], and B. Singh[4]

[1]Research Scholar, IIT Jodhpur, India
Email: saraswat.3@iitj.ac.in
[2]Research Scholar, IIT Jodhpur, India
Email: parihar.4@iitj.ac.in
[3]Research Scholar, IIT Jodhpur, India
Email: sandeep.2@iitj.ac.in
[4]Assistant Professor, IIT Jodhpur, India
Email: bhupendra@iitj.ac.in

[*]Corresponding author

ABSTRACT

Recycled concrete aggregates (RCA) have gained prominence in the construction industry due to their environmentally friendly and cost-effective nature. However, the presence of adhered mortar on RCA surfaces poses a significant challenge, potentially impacting the mechanical and durability properties of concrete when used as an aggregate. Traditional methods such as hammering, mechanical abrasion, and thermal treatment often lack precision and yield inconsistent results. While these methods are relatively easy to employ, they are concurrently associated with substantial time requirements. This requires a quick, onsite approach to treat RCA for efficient utilization. The present study focuses on the impact of a 24-hour chemical treatment for the removal of adhered mortar. It utilizes a comprehensive, multiscale approach for quantifying the percentage of removal. RCA samples of sizes 31.5-26.5 mm and 26.5-19 mm were utilized. These samples underwent treatment with three different acids: sulfuric acid (H_2SO_4), hydrochloric acid (HCl), and phosphoric acid (H_3PO_4) at different concentrations (0.1 M, 0.25 M, and 0.5 M). An image analysis method (IAM), percentage weight reduction method, and measurements of the thickness and specific gravity of RCA after treatment are all part of the multiscale approach for quantifying adhered mortar. Additionally, scanning electron microscopy (SEM) will provide microscopic insights into the effects of the chemical treatment on RCA. The anticipated results from this study will facilitate the identification of an effective acid concentration for the chemical treatment of RCA. The multiscale evaluation will allow for a clear comparison of the effectiveness of various methods used in this study.

KEYWORDS: *RCA, IAM, SEM, Mortar, Treatment.*

1. Introduction

Recycled concrete aggregates (RCA) have emerged as a promising solution in the construction sector, offering both environmental benefits and cost-effectiveness (Saraswat & Singh, 2024). However, the presence of adhered mortar on RCA surfaces presents a significant challenge, potentially compromising the mechanical and durability properties of concrete when RCA is used as an aggregate. Traditional methods to remove adhered mortar, such as hammering, mechanical abrasion, and thermal treatment, often yield inconsistent results and require significant time investment. Recent studies have explored acid soaking as a method to corrode and remove adhered mortar from RCA surfaces (Pacheco-Torgal et al., 2013; Tahmoorian et al., 2017; Tsujino et al., 2007). Tam et al. (2007) proposed a 24-hour acid soaking treatment using a 0.1 M solution of sulfuric acid (H_2SO_4), hydrochloric acid (HCl), and phosphoric acid (H_3PO_4), finding that H_2SO_4 offers better mechanical properties with low water absorption. Akbarnezhad et al. (2013) suggested that higher concentrations of H_2SO_4 (>2 M) and extended soaking periods (>5 days) effectively remove adhered mortar, but these methods increase costs and pose environmental and safety risks due to hazardous chemical disposal (Katkhuda & Shatarat, 2017; Omrane et al., 2014). Moreover, prolonged acid

soaking can weaken the aggregate, increasing porosity and reducing mechanical strength. The study aims to evaluate the effectiveness of a 24-hour chemical treatment using a multiscale approach for adhered mortar quantification (MAAMQ). Specifically, it investigates the use of H_2SO_4, HCl, and H_3PO_4 at various concentrations (0.1 M, 0.25 M, and 0.5 M) for different sizes of RCA (31.5-26.5 mm and 26.5-19 mm). By employing an image analysis method (IAM), this research addresses the inconsistencies and inefficiencies of traditional mortar removal methods, which affect the mechanical and durability properties of RCA. The multiscale approach provides a novel and comprehensive method for evaluating the effectiveness of chemical treatments by quantifying the % weight reduction, thickness index (T_i) and specific gravity of the treated RCA. Additionally, a statistical analysis will validate the relationship of fixed variables (size of RCA, acid type, and acid concentration) on the dependent relational parameters (% mortar removal (IAM), % weight reduction, thickness index (T_i), and specific gravity). This research strengthens RCA's usability and performance in construction, contributing to theoretical knowledge and practical applications.

2. Methodology

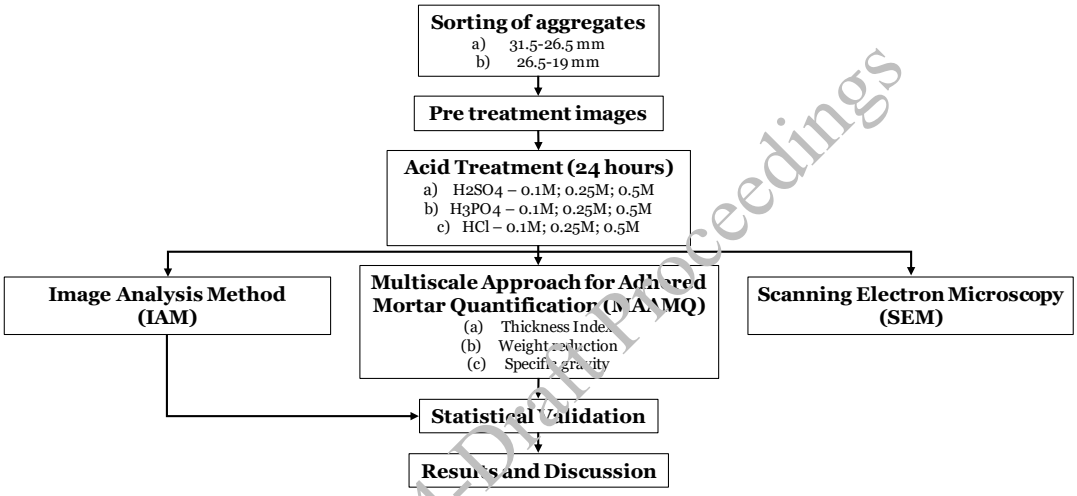

Figure 1. Methodology chart

A total of 54 kg of RCA was separated and weighed, resulting in 27 kg for each range of size: 31.5-26.5 mm and 26.5-19 mm (see Fig. 1). This 27 kg sorted RCA sample was further divided into a batch of 9 kg samples for each type of acid (H_2SO_4, HCl, and H_3PO_4) and a 3-kg sample for each concentration (0.1 M, 0.25 M, and 0.5 M). Following the sorting of the aggregates into batches based on size, acid type, and concentration, the 54 kg RCA was divided into 18 batches with two size ranges, three acid types, and three concentration levels. The face and orientation of the RCA were fixed while capturing images of the batches before and after the treatment. Using IAM, these images were processed to quantify the amount of adhered mortar that was adhered (Wang et al., 2021). The weight reduction, thickness index, and specific gravity of RCA after 24-hour treatment were measured to introduce relational parameters as MAAMQ. These relational parameters were assessed in batches. Weights of untreated (W_u) and treated (W_t) RCA were recorded to ascertain the percentage of weight reduction as given in equation (1). The thickness index (T_i) of these treated aggregate samples was determined by passing them through a flakiness gauge in accordance with IS 2386-1: (1963). Under the assumption that acid attack resulted in a reduction in the thickness of all aggregates in the sample batches, the treated RCA in the size ranges of 31.5-26.5 mm and 26.5-19 mm was sieved and passed through the flakiness gauge with aperture sizes of 31.5 to 25 mm and 25 to 20 mm, respectively. The flakiness index of the untreated RCA (FI_1) and of the treated RCA sample (FI_2) was subsequently measured to determine T_i as given in equation (2). Additionally, the specific gravity of both untreated and treated aggregates was ascertained in accordance with IS 2386-1: (1963).

Moreover, ANOVA with post hoc analysis (Bonferroni adjustment) was performed following the IAM and MAAMQ analyses to determine the impact of RCA size, acid type, and concentration on both relational parameters and IAM results. This rigorous methodology guarantees a thorough assessment and comprehension of the consequences of acid treatment on recycled concrete aggregates. The microstructural alterations in the aggregates before and after acid treatment were analyzed using scanning electron

microscopy (SEM). The macroscopic observations provided by IAM and relational parameters measurement were supplemented by the inclusion of SEM analysis, which was necessary to obtain insight into the morphological alterations occurring at a microscopic level.

$$\%\ weight\ reduction = \frac{W_u - W_t}{W_u} \times 100 \quad (1)$$

$$Thickness\ Index\ (T_i) = \frac{FI_1}{FI_2} \quad (2)$$

3. Results and Discussion

The IAM analysis of 24-hour acid treatment shows variable trends. For HCl-treated RCA, reductions in adhered mortar are 39.97%, 19.11%, and 42.60% for RCA in the 31.5–26.5 mm size range at concentrations of 0.5 M, 0.25 M, and 0.1 M, respectively. Similarly, for RCA sized 26.5–19 mm, reductions are 40.56%, 34.95%, and 57.35% at the same concentrations. For H_3PO_4-treated RCA in the 31.5–26.5 mm size range, reductions are 22.26%, 6.99%, and 14.3% at concentrations of 0.5 M, 0.25 M, and 0.1 M, respectively. Likewise, for RCA sized 26.5–19 mm, reductions are 25.5%, 6.41%, and 32.88% at the same concentrations. Lastly, for H_2SO_4-treated RCA, reductions of 11.33%, 9.39%, and 7.2% are observed at concentrations of 0.5 M, 0.25 M, and 0.1 M, respectively, for the 31.5–26.5 mm size range. For RCA sized 26.5–19 mm, reductions are 21.99%, 25.46%, and 23.31% at similar concentrations.

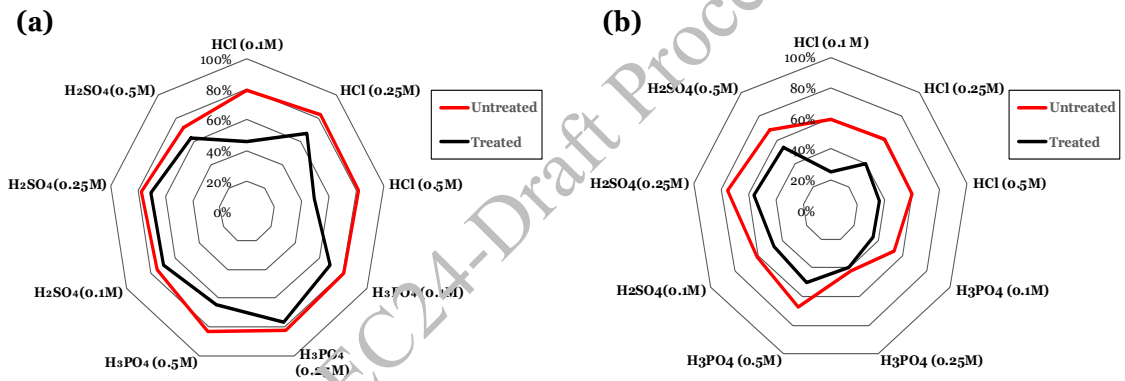

Figure 2. Influence of Acid types and concentrations on adhered mortar removal (IAM) in RCA across size ranges: (a) 31.5–26.5 mm, and (b) 26.5–19 mm.

Fig. 2 illustrates that acid treatment has a more pronounced effect on RCA in the 26.5–19 mm size range compared to the 31.5–26.5 mm range. Additionally, HCl treatment generally shows better mortar removal efficiency than H_3PO_4 and H_2SO_4, regardless of concentration or RCA size. Specifically, for RCA in the 31.5–26.5 mm range, either 0.1 M or 0.5 M HCl, or 0.5 M H_3PO_4, are effective. For RCA in the 26.5–19 mm range, 0.1 M, 0.25 M, or 0.5 M HCl, as well as 0.1 M H_3PO_4, are effective for removing adhered mortar after 24 hours of acid treatment.

The % weight reduction for larger RCA diameters (31.5–26.5 mm) in HCl decreases and subsequently increases as the acid concentration increases from 0.1 M to 0.5 M. The initial decrease may be attributed to the development of protective layers or the surface saturation effect (SSE), while the subsequent increase may be associated with altered reaction pathways or enhanced acid penetration. The % weight reduction of smaller RCA sizes (26.5–19 mm) increases linearly with the acid concentration. This linear relationship suggests that mortar removal is restricted by factors other than acid availability at lower concentrations, such as surface area or reactivity. However, this limitation becomes less significant at higher concentrations, enabling more efficient mortar degradation. The % of weight reduction for H_3PO_4 and H_2SO_4 is comparable. Both acids immediately reduce weight; however, they reach a plateau as the acid concentration increases. These patterns may be dominated by SSE at higher acid concentrations. Mortar removal may be restricted by surface area or reactivity at lower concentrations. Because these limiting variables become less significant, more mortar is removed as concentration increases. Table 1 contains the

values of specific gravity and Ti as reported for treatment with different acids and at different sizes of RCA. Optimum acid concentration and its type will effectively increase the value of FI_2 which ultimately reduces Ti. Henceforth, it can be stated that as the value of Ti decreases, efficiency of the treatment process increases.

Table 1. Specific gravity and thickness index (Ti) from experimental procedure.

Sl. No.	Property	Size of RCA (mm)	H_3PO_4			H_2SO_4			HCl		
			0.1	0.25	0.5	0.1	0.25	0.5	0.1	0.25	0.5
1.	Specific Gravity	26.5-19	2.47	2.52	2.48	2.25	2.18	2.69	2.42	2.55	2.60
		31.5-26.5	2.16	2.41	2.35	2.32	2.3	2.35	2.37	2.43	2.49
2.	Thickness Index (T_i)	26.5-19	0.45	0.39	0.34	0.55	0.54	0.41	0.22	0.28	0.29
		31.5-26.5	0.39	0.31	0.29	0.49	0.47	0.36	0.2	0.25	0.27

SEM imaging before and after acid treatment aids in understanding the mechanisms underlying the removal of adhered mortar and the overall effectiveness of the treatment process. Pre-treated images reveal the presence of gypsum crystal, which, on exposure to acids, dissociates, leading to the formation of insoluble salts ($CaSO_4$, $Ca(H_2PO_4)_2$, and $CaCl_2$). The salts are responsible for the surface saturation effect.

The ANOVA analysis establishes statistical significance within the context of a 24-hour acid treatment of RCA. It validates a significant relationship between the fixed variables (size of RCA, acid type, and acid concentration) and the dependent relational parameters (% mortar removal (IAM), % weight reduction, thickness index (T_i), and specific gravity). The results indicate that the size of the RCA does not significantly affect % mortar removal (IAM), acid type does not influence specific gravity, and acid concentration does not impact either % mortar removal (IAM) or % weight reduction. The Bonferroni post hoc analysis (except for size of RCA, where variables were <3) suggests that statistically, HCl offers more % adhered mortar reduction (IAM), % weight reduction, and T_i at 0.1 M concentration for a suggested 24-hour acid treatment with an insignificant effect on specific gravity as compared to H_3PO_4 and H_2SO_4.

4. Conclusions

The study demonstrates the effectiveness of a 24-hour chemical treatment using H_2SO_4, HCl, and H_3PO_4 at various concentrations for removing adhered mortar from RCA. Employing a multiscale approach, the research reveals that HCl at a concentration of 0.1 M is particularly effective for mortar removal. The study finds that acid treatments vary in efficiency depending on the RCA size and acid concentration, with smaller RCA sizes (26.5–19 mm) showing more substantial mortar removal. Overall, the research highlights that optimal acid concentration and type can enhance the efficiency of RCA treatment, improving its usability in construction. The statistical analysis confirms that IAM is significantly more effective than MAAMQ and represents a superior approach for acid treatment over a 24-hour duration.

References

Akbarnezhad, A., Ong, K. C. G., Zhang, M. H., & Tam, C. T. (2013). Acid Treatment Technique for Determining the Mortar Content of Recycled Concrete Aggregates. *Journal of Testing and Evaluation*, *41*(3), 20120026.

Katkhuda, H., & Shatarat, N. (2017). Improving the mechanical properties of recycled concrete aggregate using chopped basalt fibers and acid treatment. *Construction and Building Materials*, *140*, 328–335.

Omrane, M., Mouli, M., Benosman, A. S., & Senhadji, Y. (2014). Deterioration of Mortar Composites in Acidic Environment. *Advanced Materials Research*, *1064*, 3–8.

Pacheco-Torgal, F., Tam, V. W. Y., Labrincha, J. A., Ding, Y., & de Brito, J. (2013). *Handbook of recycled concrete and demolition waste*. Woodhead Publishing Limited.

Saraswat, P., & Singh, B. (2024). Utilization of recycled concrete aggregates in LDPE-bonded cementless paver blocks. *Construction and Building Materials*, *419*, 135467.

Tahmoorian, F., Samali, B., Tam, V., & Yeaman, J. (2017). Evaluation of Mechanical Properties of Recycled Material for Utilization in Asphalt Mixtures. *Applied Sciences*, *7*(8), 763.

Tam, V. W. Y., Tam, C. M., & Le, K. N. (2007). Removal of cement mortar remains from recycled aggregate using pre-soaking approaches. *Resources, Conservation and Recycling*, *50*(1), 82–101.

Tsujino, M., Noguchi, T., Tamura, M., Kanematsu, M., & Maruyama, I. (2007). Application of Conventionally Recycled Coarse Aggregate to Concrete Structure by Surface Modification Treatment. *Journal of Advanced Concrete Technology*, *5*(1), 13–25.

Wang, Y., Liu, J., Zhu, P., Liu, H., Wu, C., & Zhao, J. (2021). Investigation of Adhered Mortar Content on Recycled Aggregate Using Image Analysis Method. *Journal of Materials in Civil Engineering*, *33*(9).

Developing and Characterizing Self-Crack-Healing Roman Concrete for Bridge Decks Applications

Mehrnoosh Nazari[1], Srishti Banerji[2*], and Robert J. Thomas[3]

[1] Ph.D. Student, Civil and Environmental Engineering, Utah State University, Logan, Utah, USA
Email: mehrnoosh.nazari@usu.edu
[2] Assistant Professor, Civil and Environmental Engineering, Utah State University, Logan, Utah, USA
Email: srishti.banerji@usu.edu
[3] Assistant Professor, Civil and Environmental Engineering, Clarkson University, Potsdam, New York, USA
Email: rthomas@clarkson.edu

[*]Corresponding author

ABSTRACT

Roman concrete has endured for centuries owing to its ability to self-heal cracks through the reaction of its constituent ingredient, quicklime with water (H_2O) and carbon dioxide (CO_2). This reaction produces calcium carbonate ($CaCO_3$), which recrystallizes to fill pores and cracks. The present study uses quicklime aggregates to develop self-crack-healing concrete and characterizes its performance for use in bridge decks under water and deicing salt solution exposures. Three mixtures were designed, including a control mix and two mixes with quicklime as 2% and 4% partial aggregate replacement. The specimens were tested to evaluate compressive strength, splitting tensile strength, surface resistivity, and drying shrinkage. The crack-healing ability of pre-cracked specimens with varying crack widths in the range of 100-500μm was monitored using optical microscopy after being exposed to 60 days of wet/dry cycles. The results show that incorporating 2% and 4% quicklime into pre-cracked specimens with 100-200 μm crack widths results in partial healing, while no healing occurred in 300-500 μm cracks, regardless of exposure conditions and quicklime content.

KEYWORDS: *Quicklime, Calcium carbonate, Crack, Roman concrete, Self-healing.*

1. Introduction

Early-age cracking, a frequent phenomenon in concrete bridge decks, has intensified over the years in the United States, resulting in a significant economic impact, including the annual direct cost of $8.3 billion in corrosion-related losses (Koch et al., 2002). To address concrete cracks post-formation, diverse self-healing strategies have been investigated, including autogenous, chemical, biological, polymeric, crystalline admixtures, mineral additives, and fiber-reinforcement agents. However, each mechanism faces challenges that hinder their widespread adoption. Autogenous healing is less effective for larger cracks and is highly dependent on specific environmental conditions. Chemical healing mechanisms may suffer from non-uniform agent distribution and could lead to incomplete healing, which affects long-term durability. Biological techniques are promising but struggle with bacterial survival in concrete's high pH environment and carry high costs. Issues with the long-term durability of polymeric capsules within the alkaline concrete matrix also present significant concerns. To combat these gaps, this study proposes to investigate a new self-healing concrete incorporating quicklime to extend the service life of concrete bridge decks.
Seymour et al. (2023) detailed the exploration of healing mechanisms in quicklime-based self-healing concrete in their recent study, however, the potential of this technology for crack repair in concrete remains inconclusive due to insufficient test data, underscoring the importance of further research to support its practical application. The presented study aims to expand on the limited research by developing self-crack-healing quicklime-based concrete, particularly for use in bridge decks subjected to wet/dry cycles of two exposure conditions: water and a deicing salt solution to represent different exposures.

2. Experimental program

The purpose of the presented study is to fabricate quicklime-based self-healing concrete, specifically designed for Utah bridge decks, utilizing locally sourced materials. Portland cement Type I/II was used as the main binder, with 20% replaced by Class F fly ash. Granitic aggregates ranging in size from 4.75- 19 mm and siliceous river sand below 4.75 mm were employed, meeting ASTM C33, with specific gravities of 2.68 and 2.65 for the coarse and fine aggregates, respectively. Additionally, quicklime aggregates, with particle sizes below 4.75 mm, having a high calcium oxide (CaO) purity of 95.5%, with a specific gravity of 3.31, were used as a partial replacement for aggregates. Moreover, Sika ViscoCrete-2110 based super-plasticizer was used to adjust workability. Deicing salt consisting of 0.4, 0.09, 0.19, and 98.8% wt. sulfate (SO_4), calcium (Ca), magnesium (Mg), and sodium chloride (NaCl), respectively, was used in this study.
The mix proportions for the control and the quicklime-based self-healing concrete used in this experiment are shown in Table 1. These proportions follow the guidelines set by Seymour et al. (2023) and Utah Department of Transportation's (UDOT) mix design for bridge decks, resulting in three mixtures: a control mix without quicklime (LBSH-Q 0%), and two mixes with quicklime constituting 2% (LBSH-Q 2%) and 4% (LBSH-Q 4%) replacements for both coarse and fine aggregates, while maintaining a constant fine to coarse aggregate ratio across all mixes. During the preparation, the aggregates and half of the cementitious materials, including Portland cement and fly ash, were initially mixed with half of the water and super-plasticizer in the mixer for 2 min. The remaining cementitious materials, water, and super-plasticizer were then added into the mixing drum and mixed for 3 min. Quicklime was then added directly to the mixture and mixed for 60-90 seconds. The specimens were molded by rodding 25 times in three layers and then cured in conditioned air at 23±2 ℃ for 28 and 90 days for measuring strength, durability, and crack-healing characteristics.

Table 1. Mix proportion of concrete mixtures in this study.

Mix ID.	Cement (Kg/m^3)	Fly ash (Kg/m^3)	Water (Kg/m^3)	Coarse Aggregate (Kg/m^3)	Fine Aggregate (Kg/m^3)	Quicklime Aggregate (Kg/m^3)	Super-Plasticizer (Kg/m^3)
LBSH-Q 0%	397.419	99.35	220	930.467	666.244	-	-
LBSH-Q 2%	397.419	99.35	220	900.93	642.45	66.3	2.813
LBSH-Q 4%	397.419	99.35	220	863.37	626.58	132.6	5.626

3. Experimental Methods, Results and Discussion

3.1 Mechanical properties

Compressive strength was tested at 28- and 90-days following ASTM C39, using Universal testing machine with a capacity of 1300 kN. At 28 days, strength values were 32.7 MPa for LBSH-Q 0%, 42.6 MPa for LBSH-Q 2%, and 53.4 MPa for LBSH-Q 4%. By 90 days, they increased to 36.6 MPa, 48.2 MPa, and 58.2 MPa respectively, as illustrated in Figure 1.a.
Cylindrical specimens were tested for splitting tensile strength at 28 and 90 days using ASTM C496. As presented in Figure 1.b, the splitting tensile strength of concretes showed the same trend as the compressive strength displaying consistent increases in strength with increasing amount of quicklime (Ahmida et al., 2023). For instance, a 28-day tensile strength of 3.3 MPa for LBSH-Q 0% increased to 4.5 MPa with 2% and 5.1 MPa with 4% quicklime. The enhancements observed can be attributed to the formation of additional calcium silicate hydrate (C-S-H) gel resulting from the reaction of quicklime with the silica (SiO_2) and alumina ($Al2O_3$) present in the cementitious environment, as well as the development of calcium carboaluminate ($Ca_4Al_2O_6(CO_3).11H_2O$) from quicklime's interaction with the alumina phase in cement. Additionally, the quicklime's filler effect creates a denser interfacial transition zone with the aggregates (Acharya et al. (2016)).

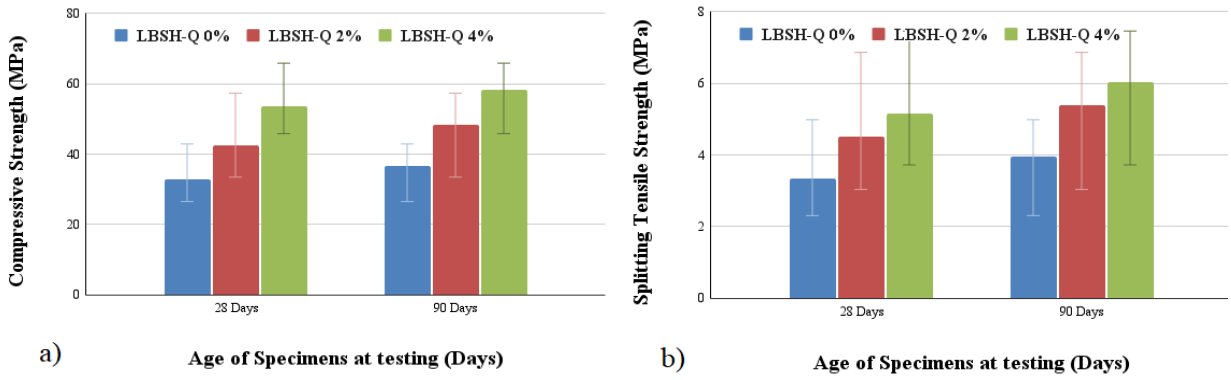

Figure 1. a) Compressive, b) Splitting tensile strength of quicklime-based self-healing concrete at 28 and 90 days.

3.2 Durability properties

In accordance with ASTM C157, drying shrinkage tests on prism specimens were carried out by immersing them in lime-saturated water at 23°C for 30 minutes before initial length measurements are taken using a comparator. After a 28-day period of lime-water curing, specimens were transferred to a drying room, with length changes recorded at 7, 14, and 28 days of air curing. Figure 2.a indicates that the mix containing 4% quicklime exhibited more drying shrinkage compared to the LBSH-Q 0% and LBSH-Q 2% mixes. Moreover, the LBSH-Q 0% mix displayed the least amount of shrinkage, measuring 7.5% less than LBSH-Q 2% and 14.7% less than LBSH-Q 4%. The higher shrinkage with quicklime can be attributed to additional water demand and heat production during hydration, as well as its contribution to the formation of C-S-H gel, leading to volumetric changes during setting and drying.

The surface electrical resistivity of concrete, relevant for estimating chloride penetration potential as per AASHTO T358, was measured for the all specimens. According to Figure 2.b, 28-day resistivity values were 18.5, 20.8, and 19.0 kΩ•cm for LBSH-Q 0%, LBSH-Q 2%, and LBSH-Q 4% respectively, suggesting low to moderate potential for chloride ingress. An increasing trend in resistivity over time was noted, with values at 90 days rising to 25.3, 31.1, and 30.9 kΩ•cm, respectively. As time progresses, the concrete's microstructure continues to densify due to ongoing hydration processes and reactions with supplementary cementitious materials (SCMs), such as fly ash, leading to an enhanced microstructure and reduced permeability. Moreover, the presence of quicklime contributes to increased formation of C-S-H gel, more effectively refining the pore structure compared to specimens without quicklime.

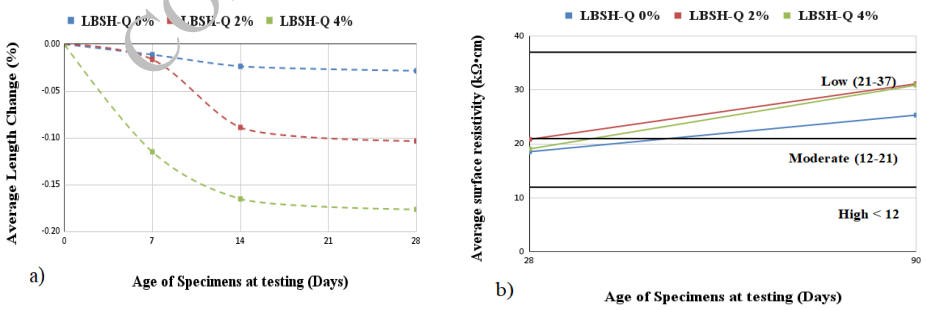

Figure 2. a) Average Length Change (%), b) Average surface resistivity of specimens.

3.3 Extent of crack

The crack-healing ability of concrete specimens was evaluated following 28 days of air curing. Two sets of cylindrical specimens were prepared for each of the three mixes and each set included specimens with induced crack widths of 100-200 µm, 200-300 µm, and 300-500 µm. These cracks were created by cutting 100 mm by 200 mm cylindrical specimens into 50 mm height discs, with 5 mm notch at the center, and

then performing splitting tensile loading to create two hemi-spherical sections. Silicone sheets and a steel band were used to rejoin these two sections with controlled crack widths. Following the initial curing period, one set of specimens from each mix was subjected to cycles of exposure alternating between 3.5 days of water immersion and 3.5 days of air-drying, repeated over 60 days, while the other set experienced similar cycles using a 20% NaCl deicing salt solution during the wetting phase. Crack healing was monitored using optical microscopy. Figure 3.a shows that the LBSH-Q 2% specimen, with a crack width of 100-200 µm, exhibited partial self-healing in cyclic water/air conditions. Similar crack closure was replicated in the mix with 4% quicklime under both types of cycles. Conversely, specimens with 0% quicklime and 100-200 µm crack widths showed negligible healing in both exposure conditions. However, as shown in Figure 3.b, LBSH-Q 2% specimen with a crack width of 300-500 µm did not exhibit significant healing after 60 days. A similar lack of healing was noted in 300-500 µm cracks for specimens with 0% and 4% quicklime. The monitoring of crack healing will be continued for the next two months.

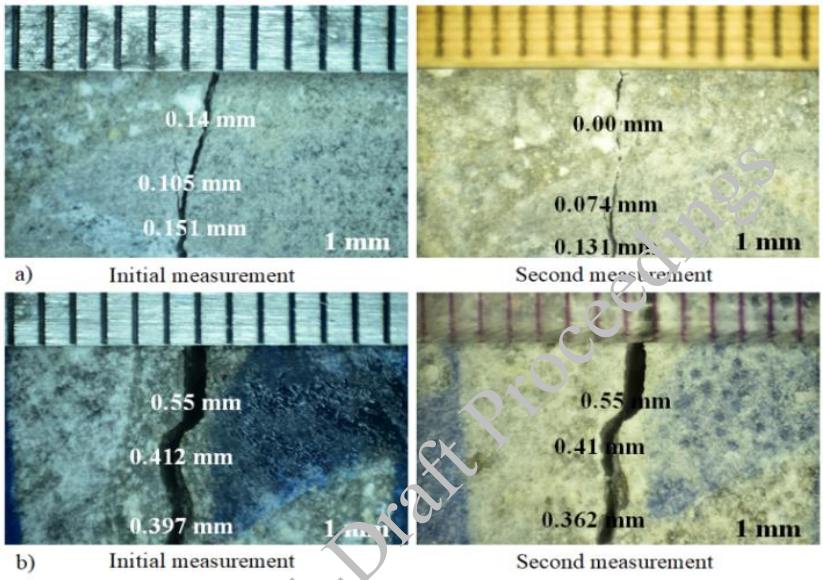

Figure 3. LBSH-Q 2% a) with 100 to 200 µm and, b) 300 to 500 µm crack width before and after being subjected to 60 days of cyclic water/air-dry exposure.

4. Conclusions

Based on the results obtained in this ongoing study, the following conclusions can be drawn:

- The addition of quicklime resulted in higher compressive and splitting tensile strength, with the highest values of 58.2 and 6 MPa for LBSH-Q 4% after 90 days.
- The incorporation of 2% and 4% quicklime in concrete mixes improved the resistivity to chloride ingress, however, higher quicklime contents leads to greater drying shrinkage.
- Incorporation of both 2% and 4% quicklime into pre-cracked specimens with 100-200 µm crack widths results in partial healing after 60 days, while no healing occurred in 300-500 µm cracks, regardless of exposure conditions and quicklime content.

Acknowledgements

The authors would like to thank the Utah Department of Transportation (UDOT) for funding this research. We also extend our gratitude to Graymont for supplying the quicklime aggregates and Sika for providing the ViscoCrete-2110 based super-plasticizer used in this study.

References

Koch, G. H., Brongers, M. P., Thompson, N. G., Virmani, Y. P., & Payer, J. H. (2002) "Corrosion cost and preventive strategies in the United States", *United States. Federal Highway Administration.*

Seymour, L. M., Maragh, J., Sabatini, P., Di Tommaso, M., Weaver, J. C., and Masic, A. (2023) "Hot mixing: Mechanistic insights into the durability of ancient Roman concrete", *Science Advances*, *9*(1),

Ahmida, F., Sayah, G. M., Zineb, D., and Quéneudec-t'Kint, M. (2023) "Experimental study on the effect of lime and aluminium content on porosity, introduced porosity, compressive strength and thermal conductivity of a lightweight cellular concrete based on limestone sand", *Construction and Building Materials*, 392, 131552

Acharya, P. K., Patro, S. K., and Moharana, N. C. (2016) "Effect of lime on mechanical and durability properties of blended cement based concrete", *Journal of The Institution of Engineers (India): Series A*, *97*, 71-79

Investigation of Corrosion-Induced Deteriorations in Existing Reinforced Concrete Structures

E.P.T.Pathirana[1]*, R.Savitha[2]

1 Civil Engineer, National Building Research Organisation, Sri Lanka
Email: thushari8814@gmail.com
2 Senior Engineer, National Building Research Organisation, Sri Lanka
Email: savitha_nbro@yahoo.com

*Corresponding author

ABSTRACT

Concrete, globally acclaimed for its exceptional compressive strength and durability, stands as the most extensively used building material. Reinforced Concrete (RC) undergoes multifaceted degradation mechanisms, including rebar corrosion, chemical attack, Alkali-Aggregate Reaction (AAR), freeze-thaw degradation, and Delayed Ettringite Formation (DEF). These deteriorative mechanisms compromise the safety and serviceability of RC structures, corrosion of embedded rebar is the dominant concrete deterioration mechanism experienced in both coastal and inland regions. The defective civil infrastructures incur substantial financial burdens, prompting the implementation of various techniques to detect the onset of corrosion.

An accurate interpretation of corrosion kinetics needs an understanding of the electrochemical and physical properties of the cover zone and Steel Concrete Interface (SCI). Half-cell potential measurements offer the probability of corrosion, their efficacy is influenced by numerous factors, and monitoring individual parameters, particularly electrical current, is inadequate for assessing corrosion status across diverse exposure settings. This study seeks to address this gap by comprehensively examining parameters related to rebar corrosion and proposing integrated test requirements for the effective detection of corrosion conditions. The findings denote that for Chloride-induced corrosion, considerations for corrosion potentials, Cl concentration profiles, threshold limits, Chloride binding capacity for particular concrete, and electrical conductivity are essential factors. In carbonation-induced corrosion, important parameters include pore structure refinement, pH value and moisture content. By focusing on these aspects, the research aims to contribute valuable insights for the diagnosis of corrosion-induced deterioration in existing structures.

KEYWORDS: *Reinforced Concrete, Deterioration, Corrosion*

1. Introduction

At present, the most prominent building material in civil infrastructure is concrete because of its exceptional mechanical and durability properties. However, many reasons specially poor construction practices caused concrete deterioration namely rebar corrosion, chemical attack, Alkali-Aggregate Reaction (AAR), freeze-thaw degradation and Delayed Ettringite Formation (DEF). The corrosion of reinforcement is the most common degradation mechanism which incurs large sums of money for repair and diminishes the designed service life of Reinforced Concrete (RC) structures.
The cracks and rust stains appeared in the RC structure after the corrosion reached an advanced status. Early detection and reliable understanding of the corrosion kinetics of particular concrete is crucial. Many advanced techniques are introduced to detect the onset of corrosion such as electrochemical and physical sensor systems. The installation of sensors for aged existing RC structures is challenging and
The most promising and simple method of corrosion detection is the open circuit potential method called half-cell potential testing. According to Elsener et al(2003), Poursaee and Hansson (2009), Pour-Ghaz et al (2009), Reichling et al (2013) and Yodsudjai and Pattarakittam(2017) there are more influencing factors

for Half-cell potential testing such as exposure conditions, pH, chloride or sulphide content of concrete, concrete cover depth, resistivity, presence of cracks, condition of steel rebar and oxygen availability. In addition, interpretations of Half-cell potential test results are standardized in the ASTM C876 and cannot be used straightforwardly. To interpret test results, the ASTM C876 standard provides three main threshold potential values, 200mV to 350 mV denotes that corrosion is uncertain, difficult to acknowledge actual scenario and may lead to results misinterpretations. However, monitoring individual parameter corrosion current is inadequate and subsequent to the corrosion kinetics, electro-chemical and physical properties of the concrete are transformed and facilitate valuable data for on-site corrosion detection. Apart from the laboratory-controlled conditions, testing on real RC structures presents reliable test results and correlates with corrosion activity. Poursaee and Hansson(2009) stated that laboratory experiments in a controlled environment accelerate the onset of corrosion in young, immature concrete and at relatively constant ambient conditions maintain is not similar to the field environment. This paper demonstrates the interim test results of a research project to examine corrosion-related test parameters of existing RC structures in the coastal and inland regions.

2. Methodology

After the visual inspections carried out in school buildings, 22nos of 225mm×225mm sized typical RC columns located in different exposure settings were selected for the research study. Considering the age of construction, the strength of the concrete was assumed as Grade 25 constituted with Ordinary Portland Cement (OPC) binder. Firstly, cover measurements were taken and rebar arrangements were located in selected concrete areas where existing plaster or skimcoat finishes were completely removed. Then, drilling was initiated using 12mm Dia. drill hammer, concrete powdered samples from the surface and near rebar were collected to determine Cl content as per the ASTM C1218/C1218M standard. When sampling minimizing human errors is a crucial factor for accurate interpretations of test results. Accordingly, careful monitoring and repetitive sampling measures were taken to avoid mixing plaster dust, other impurities in surface concrete and corrosion products or steel particles in the SCI. The percentage of Cl content by cement mass was computed assuming a minimum cement content of 300kg/m^3 and a concrete density of 2400kg/m^3, the data given in the project specification of the Education Ministry. If these assumptions are incorrect computed Cl content by cement mass could be deviated from the actual values. However, laboratory test results of Cl content by concrete mass represented the Cl concentrations of all column concrete comparatively.The phenolphthalein solution was sprayed in drilled holes to determine pH differences and carbonations. The moisture meters were used to measure concrete moisture conditions. After that,pre-wetted the particular area and Half-cell potential & surface resistivity readings were taken using Proceq profometer 600 and resipod respectively. Cu/Cuso4 electrode was used as a reference electrode for corrosion probability measurements. Obtained test results were tabulated and grouped the data in accordance with the result similarities. Finally, examined the compatibility of corrosion-related test parameters with half-cell results and the importance of those parameters for interpreting half-cell potential readings accurately.

3. Test Results

Performing Half-cell potential testing and measuring surface resistivity in column concrete are shown in Figure 1 & Figure 2 respectively. The obtained cover meter readings, carbonation depth measurements, surface conditions, resistivity, Cl content and value range of Half-cell potential readings are tabulated in Table 1.

Figure 1. Measurement of surface resistivity

Figure 2. Half-cell potential testing on column location

Table 1 Summary of test results

ID	Avg.Cover (mm)	Carbonated Depth(mm)	Moist/Dry	Avg.Resistivity (kΩ cm)	Cl^- Content (wt% by concrete)		H/Cell Potential value range(mV)
					External 0-10mm	SCI	
C1	25	40	Moist	212	<0.01	<0.01	250-300
C2	20	10	Moist	12	0.15	0.15	350-450
C3	20	30	Dry	45	0.05	0.05	225-300
C4	15	30	Moist	285	<0.01	<0.01	250-350
C5	20	35	Moist	242	0.01	0.01	225-275
C6	15	25	Dry	32	0.09	0.08	200-250
C7	20	15	Moist	11	0.08	0.08	325-400
C8	24	30	Moist	270	0.01	0.01	225-300
C9	20	5	Moist	104	0.02	0.02	200-250
C10	20	35	Moist	255	0.01	0.01	250-300
C11	25	15	Moist	86	0.03	0.03	200-275
C12	20	35	Dry	24	0.06	0.06	250-300
C13	20	15	Dry	132	0.01	<0.01	150-200
C14	20	35	Moist	245	0.01	0.01	250-325
C15	15	5	Moist	15	0.07	0.07	300-400
C16	25	15	Moist	146	0.01	0.01	100-200
C17	20	45	Dry	46	0.10	0.08	250-300
C18	15	10	Moist	14	0.10	0.09	325-450
C19	20	10	Moist	9	0.08	0.08	375-450
C20	20	10	Moist	123	<0.01	<0.01	150-225
C21	25	10	Moist	8	0.10	0.10	350-425
C22	20	30	Dry	35	0.07	0.07	225-325

4. Analysis of the results

After analysing the obtained results four types of cases were mainly identified and relevant column IDs are given in Table 2.

Table 2 Classification of column IDs as per results similarities

Case 1	Case 2	Case 3	Case 4
C2,C7,C15,C18,C19,C21	C9,C11,C13,C16,C20	C1,C4,C5,C8,C10,C14	C3,C6,C12,C17,C22

In the first case, more negative half-cell readings were recorded in high Cl-concentrated, moist column concrete where the average cover concrete was 20mm. The readings indicated a 90% probability of rebar corrosion as per the ASTM C876 standard. In the second case, half-cell readings were below 250mV, moist

status was similar with a lower level of Cl content. In general, critical Cl content varied with the type of binder, in this study the Cl threshold level was considered for OPC concrete. Pillai et al. (2020) illustrated that Chloride threshold reduction is evident from OPC to fly ash (PFA) to LC3 systems about 0.4 to 0.1 % by weight of the binder, which can be attributed to the lower pH in the PFA and LC3 systems. In both cases, carbonation was insignificant at the time of testing. The resistivity values denoted that the likelihood of corrosion risk was high and negligible in the first and second scenarios respectively. Drilled points where rebar was exposed and the condition of particular concrete revealed that corrosion was already initiated in Case 1 and no signs of rebar corrosion in Case 2.

In the third and fourth cases half-cell potential values ranged between 200-350mV, as per the ASTM C876 threshold values, readings fell in an uncertain range. In both cases, carbonation experienced was beyond the embedded rebar, average 20mm cover and concrete underwent moist and seasonal wetting and drying conditions. In high-resistive media such as carbonated concrete, locating small corroded points will become a challenge. Elsener et al. (2003) stated that Half-cell potential measurements taken on concrete structures with high resistive surface layers due to carbonation show more positive potentials of both, passive and corroding rebars.

In the third case, Cl concentration was lower and resistivity indicated negligible risk of corrosion kinetics, in the fourth case higher Cl concentrations were recorded in the SCI and resistivity exhibited a likelihood of corrosion was at moderate risk. However, in both scenarios, the alkalinity of SCI was decreased to 9 or below which intimated lower pH and susceptibility of embedded rebar corrosion. In further analysis, exposed the specified rebar locations in the drilled points and observed signs of corrosion initiation in the tested column concrete. To detect the embedded rebar corrosion activity in the third and fourth types of cases pore structure refinement due to carbonation is essential to consider. Castellote et al. (2002) explained that electrical conduction through concrete is dominated by ionic conduction effects using the continuous pore network between the electrodes. Therefore, in addition to the open circuit potential measurements or electrical current, it is required to examine other corrosion-related parameters of particular concrete.

5. Conclusions

Early detection of defective concrete is very important to perform timely repair measures. The half-cell potential test is a well-known electrochemical technique to find the probability of corrosion kinetics of rebar. However, measurements of a single parameter, electrical current is inadequate for reliable corrosion measures. If corrosion is susceptible to Cl attack, the Cl content of SCI and surface resistivity results demonstrate the real interpretations of corrosion status. Half-cell results of the carbonated concrete shall be misinterpreted in real scenarios and higher resistivities records due to the pore structure refinement. Accordingly, to provide a precise understanding of corrosion kinetics it is required to conduct an integrated test program consisting of half-cell potential testing associated with the corrosion-related other parameters.

Acknowledgements

The financial support received from the National Building Research Organisation (NBRO) under the project titled Developing System for Building Assessments and Condition Reporting is greatly appreciated.

References

ASTM.(2015) “Standard Test Method for Half-Cell Potentials of Uncoated Reinforcing Steel in Concrete”, *ASTM C 876-15*, West Conshohocken, PA

ASTM.(2017) “Standard Test Method for Water-Soluble Chloride in Mortar and Concrete”,*ASTM C1218/C1218M-17*, West Conshohocken, PA

Castellote, M., Andrade, C. and Alonso, M.C. (2002) “Standardization, to a Reference of 25 °C, of Electrical Resistivity for Mortars and Concretes in Saturated or Isolated Conditions”,*ACI Materials Journal*, 99(2):119-127

Elsener, B., Andrade, C., Gulikers, J., Polder, R., and Raupach, M.(2003) “Half-cell potential measurements-Potential mapping on reinforced concrete structures”, *Materials and Structures*,36(7): 461–471

Reichling,K.,Raupach,M.,Broomfield,J.,Gulikers,J.,’Hostis,V.L.,Kessler,S.,Osterminski,K.,Pepenar,I., Schneck,U.,Sergi,G. and Taché,G. (2013) “Full surface inspection methods regarding reinforcement corrosion of concrete structures”,*Materials and Corrosion*, 64:116–127

Pillai, R.G., Gettu, R. and Santhanam, M. (2020) "Use of supplementary cementitious materials (SCMs) in reinforced concrete systems -Benefits and limitations", *Revista ALCONPAT*, 10(2): 147–164.

Pour-Ghaz,M., Isgor,O.B. and Ghods, P.(2009) "Quantitative interpretation of half-cell potential measurements in concrete structures", *Materials in Civil Engineering*, 21(9): 467-475

Poursaee,A and Hansson,C.M.(2009)"Potential pitfalls in assessing chloride-induced corrosion of steel in concrete", *Cement and Concrete Research*, 39 (5):391–400

Finite Mixture Models for Improving Resolution of Rebar Spacing Estimation in Reinforced Concrete using Pulsed Eddy Current

Vishnu R [1], Ankur Agarwal [2*], and Siddharth Tallur[3]

[1]*Indian Institute of Technology (IIT) Bombay, Mumbai, India*
Email: 22m1189@iitb.ac.in
[2]*Indian Institute of Technology (IIT) Bombay, Mumbai, India*
Email: ankur_ee@iitb.ac.in
[3]*Indian Institute of Technology (IIT) Bombay, Mumbai, India*
Email: stallur@ee.iitb.ac.in

*Corresponding author

ABSTRACT

Pulsed eddy current (PEC) inspection offers a non-invasive solution for assessing steel rebars in reinforced cement concrete structures. A PEC system typically uses a pair of excitation and detection coils to estimate rebar depth and diameter through extraction of suitable features. Grid scan profiles are created by moving the PEC sensor along the surface of the structure, repeatedly acquiring signal from the detection coil. However, challenges arise with closely spaced rebars leading to errors in cover thickness estimates and rebar localization. This interference stems from the interaction of eddy currents induced in each rebar contributing simultaneously to the detection coil response. Commercially available equipment such as Profometer 650AI use multiple coil arrangements in the sensor probe to solve this issue. However, this adds to the cost of the solution and therefore PEC non-destructive testing solutions are typically not affordable for large-scale use. In this work, we introduce finite mixture models (FMMs) for analyzing the detection coil response to a surface scan as a combination of multiple underlying distributions, each representing signal contribution from a single rebar. By carefully analyzing the parameters of these individual distributions, the model effectively separates overlapping signals, enabling reliable rebar localization and separation. Using this method, we have enhanced rebar localization performance of iPEC, a low-cost handheld PEC instrument developed at IIT Bombay. We demonstrate the ability to resolve 12mm and 16mm diameter rebars spaced as close as 60mm for cover depth of 60mm using a single pair of coils, offering performance comparable to Profometer 650AI.

KEYWORDS: *Pulsed eddy current, Non-destructive testing, Finite mixture models, Rebar localization*

1. Introduction

Rebar size estimation and localization are crucial for structural audits, ensuring the structural integrity and longevity of reinforced concrete structures. Accurate localization aids in effective repairs, preventing structural failures and errors by ensuring no damage to rebars during concrete core cutting. Most popular technologies for rebar localization include Ground Penetrating Radar (GPR) and PEC sensors. While ultrasound has been explored for rebar localization, its applications are mostly limited to damage localization in other structures, e.g. pipes (Wu, et al., 2023).

GPR operates by transmitting high-frequency electromagnetic waves into the ground and analysing the reflected signals to create subsurface images. The data obtained from GPR can be challenging to analyse due to the complexity of the reflected signals, which often contain noise and overlapping reflections from various subsurface features. Additionally, interpreting these images requires specialized knowledge and experience to accurately distinguish between different materials and structures. To automate rebar detection from GPR imagery, template matching of hyperbolic signatures in B-scans has been employed (Dinh Gucunski and Duong, 2018, Ma et al., 2018, Xiang Ou and Rashidi, 2021). These methods rely on predefined thresholds and are not generalisable. The computational demand of the approach also renders it

impractical for extensive case studies. Recent advancements in Machine Learning (ML) and Deep Learning (DL) techniques have shown promise in enhancing rebar detection from B-scan images (Asadi et al., 2020, Park et al. 2021). However, these algorithms require substantial volume of labelled datasets, a time-intensive endeavour that may not adequately cover all conceivable scenarios.

Unlike GPR, PEC sensors offer a low-cost alternative to rebar assessment. The PEC sensor operates by inducing eddy currents in conductive materials through one or more exciter coils, generating a secondary magnetic field. Detectors then measure the secondary magnetic field variations, allowing for the detection and localization of rebar within concrete structures. Resolving closely spaced rebars poses a significant challenge in PEC detection, as the signatures from secondary magnetic fields from adjacent rebars can overlap, leading to errors in cover measurements. To tackle this issue, commercially available rebar locators often utilize multiple exciter and detector configurations, which in turn increase device complexity and cost, thus limiting their scale of adoption, particularly in low- and middle-income countries (LMICs) and developing economies. In this work, we propose a finite mixture model (FMM) method to effectively address this challenge. By employing FMMs, we can accurately separate out individual rebar contributions from the combined magnetic field signals. We have implemented this approach using our in-house developed PEC sensor, known as iPEC (Agarwal, et al., 2024). Applying the finite mixture model to the cover profile generated by the iPEC during scans along the rebar surface allows for precise localization of each rebar without the need for multiple exciters and detectors. This innovative solution holds promise for significantly improving the accuracy of rebar detection while simultaneously reducing device complexity and cost, thereby enhancing its practicality and suitability for widespread adoption in the industry.

2. Localisation using Finite Mixture Models (FMMs)

FMMs, fundamental in statistical analysis, analyse complex distributions as a blend of simpler component distributions, termed as mixture components. Gaussian or Lorentzian mixture models are plausible choices for modelling the underlying distributions within the composite response. These models assume that the overall response is a blend of Gaussian or Lorentzian distributions, with each distribution representing the signal contribution from a single rebar. The Gaussian mixture model (GMM) is expressed as:

$$f(x; \boldsymbol{\mu}, \boldsymbol{\sigma}, \boldsymbol{\pi}) = \sum_{i=1}^{k} \pi_i \cdot \frac{1}{\sqrt{2\pi\sigma_i^2}} \cdot \exp\left(-\frac{(x-\mu_i)^2}{2\sigma_i^2}\right) \quad (1)$$

where x represents the input variable, $\boldsymbol{\mu}$ denotes the vector of means, $\boldsymbol{\sigma}$ represents the vector of standard deviations, $\boldsymbol{\pi}$ signifies the vector of mixing coefficients, and k denotes the number of mixture components. Similarly, the Lorentzian mixture model (LMM) is defined as:

$$f(x; \boldsymbol{\mu}, \boldsymbol{\gamma}, \boldsymbol{\pi}) = \sum_{i=1}^{k} \pi_i \cdot \frac{\gamma_i^2}{\pi[\gamma_i^2 + (x-\mu_i)^2]} \quad (2)$$

where $\boldsymbol{\gamma}$ represents the vector of scale parameters in LMM. In the context of embedded rebars in an RCC structure, the cover profile measured using the PEC probe will be continuous. This cover profile was obtained by moving the PEC probe over the RCC surface along a straight line. The measured cover thickness reaches a minimum when the PEC probe is directly atop a rebar. When the rebars are tightly spaced together, these signatures overlap, with multiple minima merging together. To analyse this, we inverted the cover estimation time-series by subtracting it from the highest error-free measurement possible with iPEC (100mm). A mixture model is then applied to this modified time-series. The mean of each individual distribution in the mixture model (μ_i) corresponds to the estimated position of each rebar in the profile. The width of each individual distribution is a function of the cover and the diameter of the rebar.

3. Experimental Work

3.1 iPEC

The iPEC prototype depicted in the Figure 1(a), used for creating the line scan signals for rebar localisation, has been developed in-house at IIT Bombay (Agarwal et al., 2024). This probe features a single pair of

coils for the excitor and detector. The area under the curve (AUC) for various portions of the time-series detector response were used as features for estimation of rebar diameter and cover (Tamhane et al., 2021).

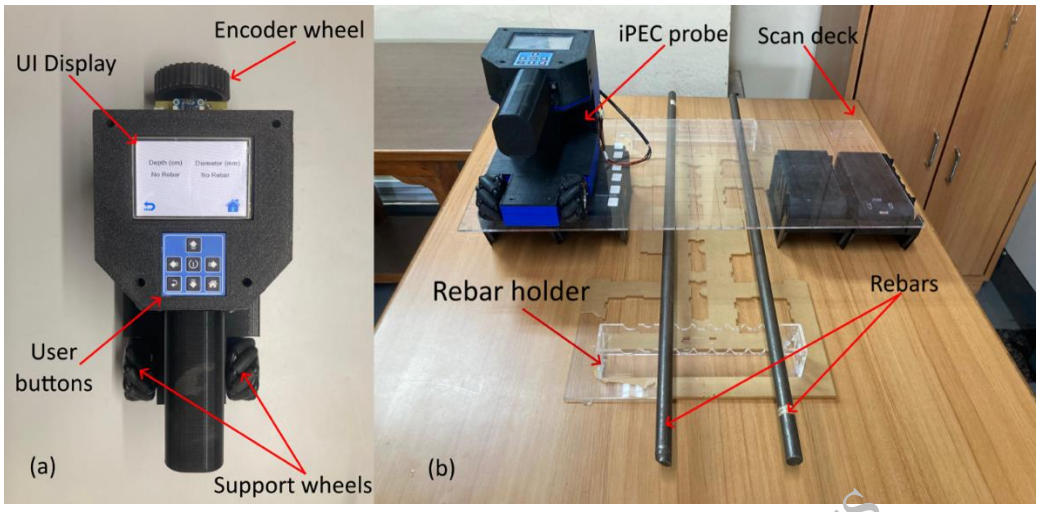

Figure 1 a). iPEC unit with encoder wheel attachment, b) Scanning setup for data collection

Cover and diameter are estimated independently by computing a polynomial fit on the computed AUCs. The rotary encoder, affixed to the wheel, tracks the probe's position as it moves across the concrete surface. The measurement resolution of the rotary encoder was set at 1mm. The encoder unit was externally fixed on the unit since the mechanical design did not have provision for housing the encoder inside the unit. Future designs will include provision for fitting the encoder mechanism inside the iPEC unit.

3.2 Data collection

The scanning setup is shown in Figure 1(b). The rebars were positioned in slots within a pair of holders located beneath the stage. Each pair of holders was custom-made to accommodate rebars of known diameter and cover. The cover profile was generated by scanning along the surface of the stage in a straight line with iPEC configured in continuous acquisition mode. Measurements were conducted with two identical rebars placed at pre-determined separation. The diameters of the rebars used in the experiment were 12mm and 16mm. For each rebar pair, measurements were carried out at cover depths of 40mm and 60mm. We have introduced binning (moving average) of the data collected along the scan to reduce variations in cover estimate. We have carried out evaluation of mixture model performance for different bin sizes, and determined 3mm to be the optimum bin size.

4. Results

Estimation error in separation between the rebars was studied with different mixture models. The separation estimates between two rebars were computed for a combination of rebar cover, diameter, and separation parameters using both GMM and LMM. Distribution of residuals in the linear fits between the actual and estimated separation from both mixture models were evaluated. Figure 2 displays the errors in the estimated separations compared to the actual separations for both methods. The standard deviation of the error for GMM is 25.38 mm. For LMM, the standard deviation of the error is significantly lower at 3.5 mm. Additionally, the mean error for GMM is 5.67 mm, while for LMM, it is only 0.78 mm.

5. Conclusions

In conclusion, we showcase the potential of FMMs in rebar localization. The utilization of LMM proves to be notably superior to GMM, especially in minimizing separation estimation errors. Future work includes refining the resolution for detecting rebars at distances closer than 60mm, exploring alternative models for improved accuracy, and integrating the FMM analysis into iPEC for real-time analysis.

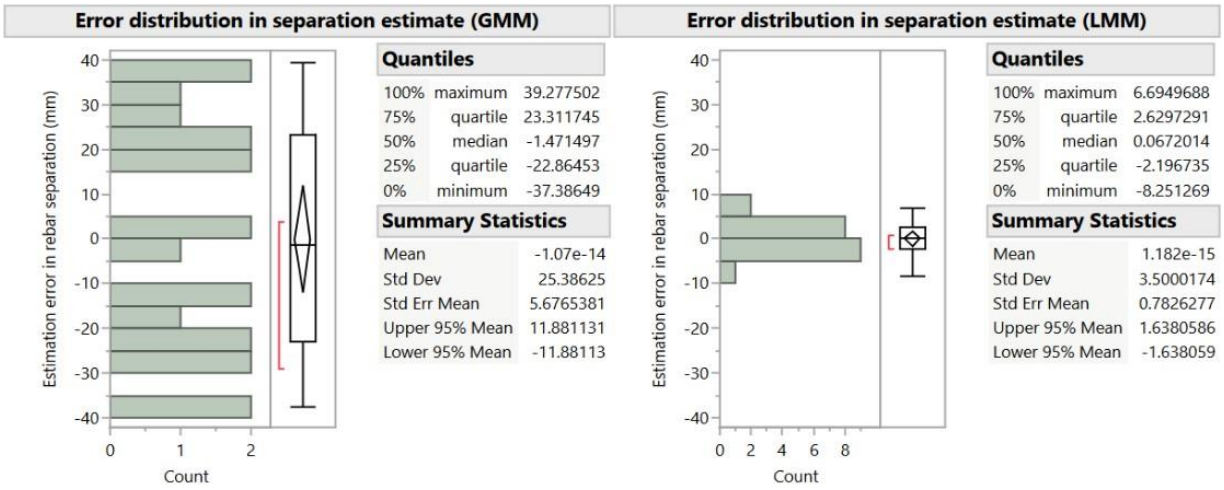

Figure 2. Distributions of error in estimated rebar separation from actal separation for both GMM and LMM

Acknowledgements

The authors thank staff at the Wadhwani Electronics Lab (WEL) at the Department of Electrical Engineering, IIT Bombay for technical expertise extended towards establishment of experimental facilities.

References

A. Ankur; Kajal, S; Supriya, I. and Siddharth, T. (2024) "A non-invasive and handheld detector for characterizing steel rebars in concrete." *2024 IEEE Applied Sensing Conference* IEEE, 2024.

Asadi, P.; Gindy, M.; Alvarez, M. and Asadi, A. (2020) "A computer vision based rebar detection chain for automatic processing of concrete bridge deck GPR data." *Automation in Construction* 112:103106.

Dinh, K.; Gucunski, N. and Duong, T. H. (2018) "Migration-based automated rebar picking for condition assessment of concrete bridge decks with ground penetrating radar." *NDT & E International* 98: 45–54.

Ma, X., Liu, H., Wang, M. L., and Birken, R. (2018) "Automatic detection of steel rebar in bridge decks from ground penetrating radar data." *Journal of Applied Geophysics* 158: 93–102.

Park, S., Kim, J., Jeon, K., Kim, J., and Park, S. (2021) "Improvement of GPR-Based Rebar Diameter Estimation Using YOLO-v3." *Remote Sensing* 13: 2011.

Tamhane, D., Patil, J., Banerjee, S. and Tallur, S. (2021) "Feature engineering of time-domain signals based on principal component analysis for rebar corrosion assessment using pulse eddy current." *IEEE Sensors Journal* 21.19: 22086-22093.

Wu, Y., Yongping W., Dan L., and Jian Z. (2023) "Two-step detection of concrete internal condition using array ultrasound and deep learning." *NDT & E International* 139:102945.

Xiang, Z., Ge O., and Abbas R. (2021) "Robust cascaded frequency filters to recognize rebar in GPR data with complex signal interference." *Automation in Construction* 124:103593.

A Comparative study of Unloaded Stress States for Structural Reuse using Digital Image Correlation

Sushree Sunayana[1,2], Subha Ghosh [2], and Lisbeth M. Ottosen [3]

[1] MNIT Jaipur, Rajasthan, India,
Email: sushree.ce@mnit.ac.in
[2] DTU Sustain, Technical University of Denmark, Kongens Lyngby, Denmark.
Email: subgo@dtu.dk
[3] Professor, DTU Sustain, Technical University of Denmark, Kongens Lyngby, Denmark.
Email: limo@dtu.dk

*Corresponding author

ABSTRACT

The exponential growth of concrete infrastructures is alarming in the context of sustainability. There is an urgent need to establish a balance between optimizing resources, minimizing CO2 emissions from raw materials production, and at the same time meeting the demand for new infrastructures. In this regard, reusing structural concrete elements obtained from selective demolition of old structures presents a compelling solution. This paper focusses on analysing the surface microcracking behavior in concrete during unloading using the non-destructive digital image correlation (DIC) method. Concrete prism specimens were subjected to compression loading in two scenarios: (i) up to 90% and (ii) up to 60% of peak stress followed by complete unloading. The evolution of full-field strain was compared between the two cases during unloading. On comparison, higher localized strain area was observed even after complete unloading when the specimens are unloaded from 90% of peak stress. A novel technique was developed to check the accuracy of DIC analysis. For this purpose, the strain field obtained from numerically generated speckle data was assessed for a prescribed displacement function. This comparative analysis of full-field strain pattern can be useful to evaluate the surface microcracking phenomenon during unloading of structural elements and its future reuse potential.

KEYWORDS: *Digital image correlation, Full-field displacement, Strain, Reuse, Unloading*

1. Introduction

The increasing rise in the demand of new concrete infrastructures poses sustainability concerns in terms of resource management and limiting waste generation. Construction and demolition wastes produced globally account for 30% of the total waste generated (Purchase et al, 2021). Total demolition and recycling process for the wastes is more energy intensive with heavier equipment and less focus on quality materials for reuse (Gálvez-Martos et al., 2018). On the other hand, the selective demolition process focuses more on the extraction of materials or components with a greater potential for reuse and avoids the large quantity of waste generation, sorting, and treatment process (Andersen et al., 2022). Besides environmental benefits in terms of waste reduction, the selective demolition process also allows to utilize the full capacity of the load-bearing structural components. Reusing of old structural components in a new construction can be an effective way provided the performance requirements are satisfied. This highlights a need to reassess the structural health of concrete load-bearing elements after unloading from the existing part of any building. Surface microcracking constitute an important parameter for structural health assessment and evaluating structural integrity. The surface microcracks generated in concrete during loaded state might get altered during unloading when the applied stress is released. This needs to be investigated.
In the context of reuse, non-destructive methods are crucial for microcracks assessment. Various methods like ultrasonic testing (Hellier, 2003), radiographic methods (Dabous et al., 2017) and tomographic testing method (du Plessis and Boshoff, 2019) are available for detecting internal cracks initiation and propagation.

These methods are effective in various applications but are restrictive when it comes to surface crack assessment, resolution limitation for finer cracks, requirement of small sample size and skilled operator for the complicated test set up etc. For surface microcracking, the digital image correlation (DIC) technique provides a better alternative due to its versatility and adaptability to different materials and scales, high resolution, and accuracy to provide full-field displacement and strains, non-contact method, rapid assessment for real-time monitoring (Pan et al., 2009; Gheitasi et al., 2018). The DIC method has been previously applied to study fracture behaviour of reinforced concrete beam in flexure (Kuntz et al., 2006; Lecompte et al., 2006), reinforced concrete slabs (Helm, 2008), masonry walls (Tung et al., 2008), fatigue loading (Jia et al., 2022). To the best of Authors knowledge, besides the extensive uses of DIC in different materials and loading, its capability in assessing surface microcracks during unloading of concrete to get insights about its reuse potential has not been explored previously.
This study investigates the capability of DIC in assessing surface microcracks in concrete when it is unloaded from compression stress states. A sensitivity study was performed to choose an appropriate subset size used as input for the DIC analysis. Concrete prism specimens were tested under compression loading and unloading and full-field strains were observed using two-dimensional DIC analysis.

2. Experimental Method: Test Set up

Digital image correlation method is a non-contact digital imaging method where full-field displacement and strains are obtained by correlating the reference and deformed images. Concrete prism specimens of cross-section 100 mm x 100 mm and height 300 mm were cast and cured for 28 days for a design compressive strength of 30 MPa. The test set up is shown in Fig. 1. Prior to the testing, the prism specimens' surface was painted white. Black-coloured chalk-based spray paint was used to form speckle patterns to achieve sufficient contrast between the background and speckles. Specimens were loaded in a force-controlled way at a loading rate of 0.5 kN/s and then unloaded at a displacement-controlled rate of 0.001 mm/s till the load dropped to zero. This loading and unloading process was recorded with a 16-megapixel E M5-II Camera, 80 mm f/5.6, ISO: 200 and Shutter Speed of 1/125. The digital images were imported to GOM correlate professional software version 2019 (denoted as GOM,2019) to perform the 2D DIC analysis.

Figure 1. (a) Experimental set up and specimen with speckle paint (b) schematic representation of DIC subset

3. Selection of subset size based on minimum error

During the experimental testing, speckle patterns are formed on the concrete prism specimens using spray paint. However, in the post processing of DIC results, synthetic speckle data sets are numerically generated to check the accuracy of the analysis method and to choose an appropriate subset size based on minimum standard deviation error for a prescribed displacement field. Speckle patterns applied on the specimens in the experiment were statistically characterized to get the speckle size distribution and area fraction. These parameters were used to numerically generate synthetic speckled images. Rigid body displacement was then prescribed to the synthetic images. Different trials of DIC analysis with varying the subset sizes were

carried out to compute displacement field. Mean and standard deviation of errors in displacement were calculated for the DIC inspection points spanning throughout the entire domain and plotted in Fig 2. The standard deviation of errors was used as a basis to find out a suitable subset size. It was observed that, 27 pixel subset size gives minimum standard deviation of error for a domain of 1000 pixel x 3000 pixel.

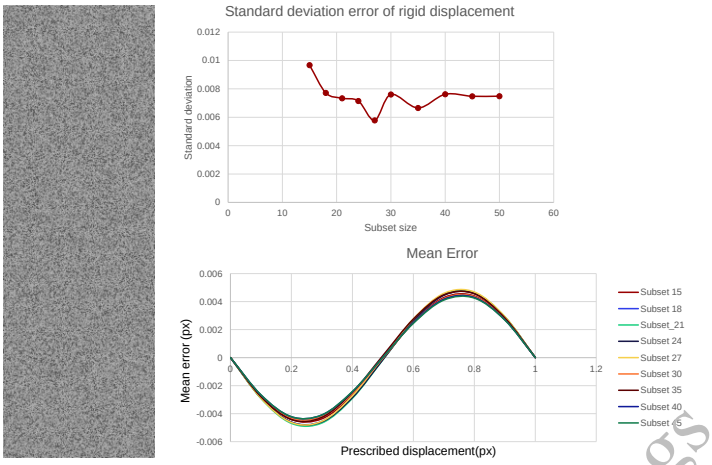

Figure 2. Mean and standard deviation error using Synthetic speckle image

4. Computation of Full-field strain

DIC analysis was performed during the compression loading and unloading from two different load levels (90% and 60% of the peak load). Full-field strain development was observed in this process. Tensile strain increased with increasing load and strain localization occurred which were more prominent in the specimens unloaded from 90% of the peak load. Though the strain localized region had decreased in unloaded state compared to the state at maximum compression load, a significant part of the region could be identified even in the relaxed state as shown in Fig. 3.

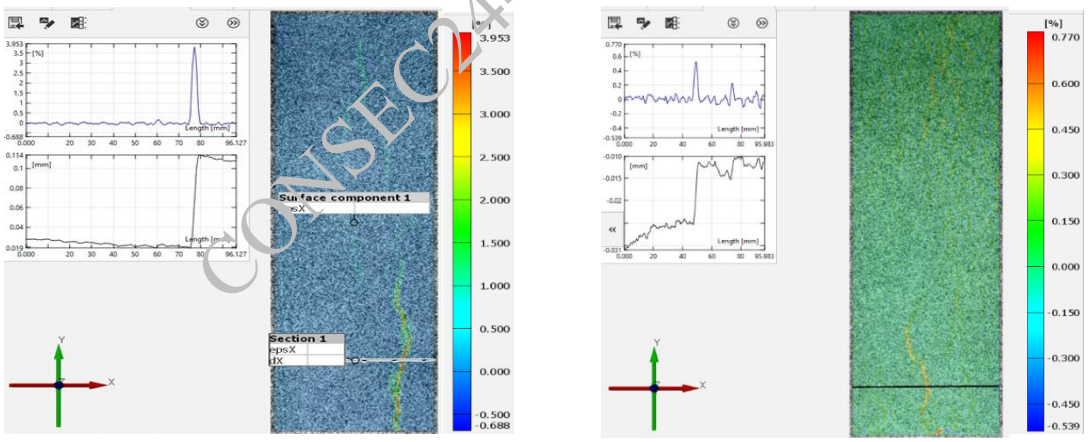

(a) (b)

Figure 3. Full-field strain in the complete unloaded state obtained in DIC analysis (a) specimen unloaded from 90% of peak load (b) unloading from 60% of peak load

Permanent deformation of the specimen is therefore linked to that region and may further contribute to the reuse potential of the element. A significant residual strain fields were observed in the specimens' surface when unloaded from 90% peak load level as compared to that strain developed in concrete unloaded from 60% of peak load.

5. Conclusions

This paper investigates the loading and unloading behaviour of concrete during compression using a digital image correlation analysis. The accuracy of the analysis was validated using numerically generated speckles data. The sensitivity study performed on different subset sizes indicates that a subset size of 27 pixel gives minimum error for a domain size of 1000 pixel x 3000 pixel. Full-field strains were obtained through out the loading and unloading stages for compression concrete elements unloaded from different stress states. Localization of strain after complete unloading underlines a significant permanent strain in concrete when unloaded from 90% of peak load. Further investigation of the strain localization process is needed to assess the reuse potential of concrete structural elements.
The performance of concrete structural components extracted from existing old buildings can be reassessed using the crack patterns and their propagation during the process of unloading from old structures and reloading when reused in any new structure. DIC results can give an idea about the crack patterns which will be used to predict the reuse potential of elements. This is ongoing research being done by our group and constitute future scope of work.

Acknowledgements

The presented work is part of a project funded by COWI Fonden. This research is an ongoing effort to study surface microcracks using digital imaging as the primary tool for the purpose of structural reuse. The authors would like to acknowledge the experimental facilities provided at the Technical University of Denmark (DTU).

References

Andersen, R., Ravn, A. S., & Ryberg, M. W. (2022). Environmental benefits of applying selective demolition to buildings: A case study of the reuse of façade steel cladding. *Resources, Conservation and Recycling*, 184, 106430.
best management practice in Europe." *Resources, conservation and recycling*, 136, 166-178.
Dabous, S. A., Yaghi, S., Alkass, S., & Moselhi, O. (2017). "Concrete bridge deck condition assessment using IR Thermography and Ground Penetrating Radar technologies." *Automation in Construction*, 81, 340-354.
du Plessis, A., & Boshoff, W. P. (2019). "A review of X-ray computed tomography of concrete and asphalt construction materials." *Construction and Building Materials*, 199, 637-651.
Gálvez-Martos, J. L., Styles, D., Schoenberger, H., & Zeschmar-Lahl, B. (2018). "Construction and demolition waste
Gheitasi, A., Harris, D. K., & Hansen, M. (2018). "An experimental-computational correlated study for describing the failure characteristics of concrete across two scale levels: mixture and structural component." *Experimental Mechanics*, 58, 11-32.
Hellier, C. (2003). Handbook of nondestructive evaluation (No. 19496). Mcgraw-Hill Professional.
Helm, J. D. (2008). Digital image correlation for specimens with multiple growing cracks. Experimental mechanics, 48, 753-762.
Jia, M., Wu, Z., Rena, C. Y., & Zhang, X. (2022). "Experimental investigation of mixed mode I–II fatigue crack propagation in concrete using a digital image correlation method." *Engine*
Küntz, M., Jolin, M., Bastien, J., Perez, F., & Hild, F. (2006). Digital image correlation analysis of crack behavior in a reinforced concrete beam during a load test. *Canadian Journal of Civil Engineering*, 33(11), 1418-1425.
Lecompte, D., Vantomme, J., & Sol, H. (2006). "Crack detection in a concrete beam using two different camera techniques." *Structural Health Monitoring*, 5(1), 59-68.
Pan, B., Qian, K., Xie, H., & Asundi, A. (2009). "Two-dimensional digital image correlation for in-plane displacement and strain measurement: a review." *Measurement science and technology*, 20(6), 062001.
Purchase, C. K., Al Zulayq, D. M., O'Brien, B. T., Kowalewski, M. J., Berenjian, A., Tarighaleslami, A. H., & Seifan,M. (2021). "Circular economy of construction and demolition waste: A literature review on lessons, challenges, and benefits." *Materials*, 15(1), 76.
Tung, S. H., Shih, M. H., & Sung, W. P. (2008). Development of digital image correlation method to analyse crack variations of masonry wall. Sadhana, 33, 767-779.

Porosity & Microstructure of Multi-decade Aged Blended Cement Samples

S.W.A Latimer[1], E.J. Butcher[2] and J.L. Provis[1,3]

[1] Department of Material Science and Engineering, University of Sheffield, Sheffield, UK
Email: swalatimer1@sheffield.ac.uk
[2] National Nuclear Laboratory (NNL), Sellafield, Cumbria, UK
[3] (current address) Paul Scherrer Institut, Laboratory for Waste Management, Forschungsstrasse 111, 5232 Villigen PSI, Switzerland

*Corresponding author

ABSTRACT

Analysis of multi-decade aged cementitious materials is typically based on forensic study of field-exposed samples of (at best) partially-documented provenance. This research builds on the unique opportunity to provide chemical and microstructural characterisation of long term aged waste specimens produced from a range of mature hydrated blended cements of UK nuclear sector specifications. The cements investigated are blends of Portland cement (PC), ground granulated blast furnace slag (GGBFS) and pulverised fuel ash (PFA), and are between 38 - 40 years old. The data presented here show the porosity and the uptake of water vapour determined by mercury intrusion porosimetry (MIP) and dynamic vapour sorption (DVS). The influence of blend and W/C ratio on cement paste pore structure is well documented at early ages. However, the early-age differences in pore structure related to blend and W/C ratio reduce significantly at late stages of hydration, suggesting that when given sufficient time for latent hydraulic or pozzolanic reaction, the quantity of SCMs has a diminishing effect on the overall pore network. Additional information that increases the understanding of the long-term properties of hydrated cements used in wasteforms is important to further underpin the UK nuclear industry's long-term safety assessments, and also in improving our knowledge of mature cement durability in broader civil engineering contexts.

KEYWORDS: *Supplementary cementitious material, PC, PFA, GGBFS, Aged Cement*

1. Introduction

A definitive model of the pore structure of cement pastes has proved to be elusive, largely due to the time-dependent and multi-scale nature of the pore structure development process. Porosity investigations have involved the use of combinations of conventional and other supplementary analytical techniques such as mercury intrusion porosimetry, micro-computed tomography, gas adsorption, 1H NMR, SEM image analysis, and others.

Mercury intrusion porosimetry has for many years been one of the most widely applied technique for investigating the pore structure of cement pastes (Muller et al., 2017). However, MIP has some important disadvantages. It is regularly cited that MIP cannot intrude inaccessible pore networks, and is limited by the throat thickness at the entrance to the pore network and the careful consideration of ‘ink bottle pores’ and drying technique (Muller et al., 2017, Zhang et al., 2022), and these have led to strident criticisms of its use to study cements (Diamond, S., 2000 and 2001). However, MIP can be utilised as an effective tool to provide comparative data, provided that the user understands the limitations of the assumptions made (Scrivener K., 2015).

Dynamic vapour sorption (DVS) is by comparison a relatively new analytical technique within the field of cement science. DVS has for many years been applied in fields such as pharmaceutical science, assessing moisture uptake of porous materials under stepped relative humidity profiles (Shah B., 2006). DVS works by measuring the amount of adsorbate, in this case water, that is retained as the humidity is increased, typically between 0% up to 100% relative humidity. Similar to N_2 adsorption, the BJH (Barret, E.P. 1951)

and BET (Brunauer S. et al, 1938) equations can be used to estimate surface area and pore network characteristic parameters from DVS adsorption and desorption isotherms (Bardestani, R. et al. 2019, De Belie, N. et al., 2010). However, similar to MIP, DVS has some important limitations to note. DVS can only intrude accessible pores and cannot penetrate blocked or collapsed pore networks, it is also highly sensitive to experimental parameters. The pore range accessible by DVS lies between 0.3 nm and 11 nm which provides an overlap between the accessible pore size range of MIP.

2. Methods

Table 1 outlines the mix composition and SCM type of each of the samples investigated in this study by DVS and MIP.

Table 1. Sample specifications. W/C is the mass ratio of water to the total cementitious materials (PC + SCM).

Sample ID	SCM type	SCM/PC (mass ratio)	W/C	Age (yrs)
SLC	GGBFS	3:1	0.35	40
FAC	PFA	3:1	0.42	38

2.1 Mercury Intrusion Porosimetry (MIP)

MIP tests were performed on samples of approximately 1.7 g, with each sample split into three smaller segments with sharp angular edges removed. Due to the slow ongoing rate of reaction, hydration stoppage was not carried out. A Micromeritics MicroActive AutoPore V 9600 1.02 instrument was used. The mercury surface tension and contact angle between the mercury and the solid surface were 482 mN/m and 140º, respectively. The pore diameter was related to the applied pressure a using the Washburn equation (Washburn, E.W., 1921).

2.2 Dynamic Vapour Sorption (DVS)

DVS tests were performed using a Surface Measurements Systems DVS Adventure instrument. Samples of 100 mg of ground cement powder passing a 63 µm sieve, were analysed. The test measured samples at relative humidities set in increasing steps from 0% RH to 100% RH, and then decreasing back to 0% RH, at 10% RH intervals. The chamber temperature was held at 25ºC, and each step was held until reaching a mass change rate < 0.0015 %/min with a stabilisation period of 15 minutes.

3. Results/Discussion

The results from MIP and DVS analysis are presented in Figure 1a and Figure 1b. DVS data are presented as percentage mass change (%) per log radius increment, whereas the MIP data is presented as differential pore volume per log radius increment; the intention of overlaying the two data types is to show a comparison between the information provided by these two very different techniques, rather than to show that one or the other provides "more correct" results. The profiles of the data curves follow similar distributions between 2 – 10 nm for both GGBFS and PFA blends. The data obtained from DVS suggests that the majority of the pore radii for GGBFS blend is below 2nm and can therefore be classified as micropores De (Belie, N. et al., 2010). This is likely due to the age and density of the GGBFS samples, as it is expected that the pore network reduces in both pore volume and pore radius as hydration progresses (Kondraivendhan, B. and Bhattacharjee, B., 2010).

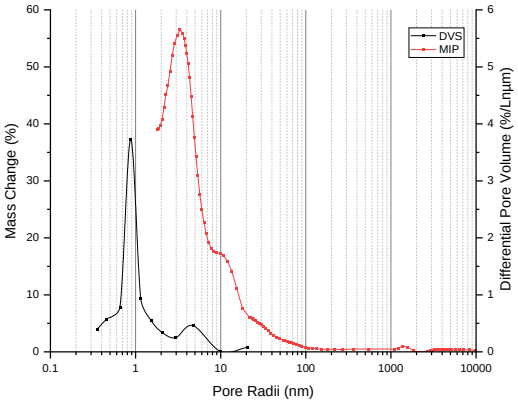

Figure 1a. SLC DVS & MIP Combined Data

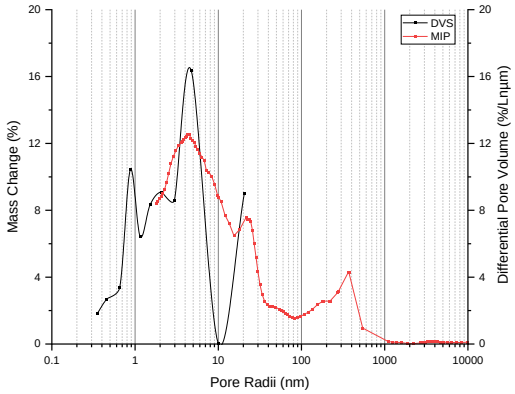

Figure 1b. FAC DVS & MIP Combined Data

Figure 1a and Figure 1b indicate that MIP alone is not sufficient to probe the full pore structure. The majority of the pores are observed to fall below the 2 nm range, which is beyond the limit of the MIP instrument; applying higher pressures than the usual maximum (around 400 MPa) would be expected to cause severe damage to the samples in any case.

Figure 1a and Figure 1b suggest there is good compatibility between the data obtained from MIP and DVS. Figure 1a in particular shows good agreement between the two data sets. The porosity of PFA blended cements is notoriously difficult to assess due to the contribution of Hadley grains (Hadley, 1972) and the inherent PFA grain porosity contributing to the pore network. Figure 1b indicates that the pore network for PFA cements is far more convoluted as the samples display pores throughout the meso and macropore range. Importantly there is again good agreement between the two data sets.

4. Conclusions

There is good agreement, at least in a qualitative sense, between the data obtained from the MIP and DVS analysis approaches, particularly considering that the majority of the porosity for the GGBFS blended cement is within the micropore range and subsequently is outside of the range of MIP equipment. However, PFA has a more complex and less defined pore network with pores within the micro, meso and macro ranges

Acknowledgements

This project was funded through the Nuclear Decommissioning Authority (NDA) PhD Bursary scheme, with support from NNL, Nuclear Waste Services (NWS), and Sellafield Ltd. The authors thank, Helen Farris, and all other colleagues involved in making and maintaining samples over an extended period. We are grateful to Oday Hussein, Ian Ross, Hajime Kinoshita, and Brant Walkley for support with experiments, and the Royce Institute / EconoMiser grant for funding the purchase of the DVS instrument.

References

A.C.A. Muller and K.L. Scrivener. (2017). “A reassessment of mercury intrusion porosimetry by comparison with 1H NMR relaxometry”, *Cement and Concrete Research*. 100: p. 350-360.

B. Kondraivendhan and B. Bhattacharjee (2010), “Effect of Age and Water-Cement Ratio on Size and Dispersion of Pores in Ordinary Portland Cement Paste”, *ACI Materials Journal* **107**(2): p. 147-154.

B. Shah, V. K. Kakumanu, and A. K. Bansal. (2006). “Analytical techniques for quantification of amorphous/crystalline phases in pharmaceutical solids”, *Journal of Pharmaceutical Sciences* **95**(8): p. 1641-1665.

D.W. Hadley, *The nature of the paste-aggregate interface*. 1972: Purdue University.

E.P. Barrett, L.G. Joyner, and P.P. Halenda. (1951) “The Determination of Pore Volume and Area Distributions in Porous Substances. I. Computations from Nitrogen Isotherms”, *Journal of the American Chemical Society* **73**(1): p. 373-380.

E.W. Washburn, (1921) The dynamics of capillary flow. *Physical Review*, 1921. **17**(3): p. 273-283.

K. Scrivener, R. Snellings, and B. Lothenbach. (2015). A Practical Guide to Microstructural Analysis of Cementitious Materials. 2015.

N. De Belie, J. Kratky, and S. Van Vlierberghe. (2010). "Influence of pozzolans and slag on the microstructure of partially carbonated cement paste by means of water vapour and nitrogen sorption experiments and BET calculations", *Cement and Concrete Research*. **40**(12): p. 1723-1733.

R. Bardestani, G.S. Patience, and S. Kaliaguine. (2019) Experimental methods in chemical engineering: specific surface area and pore size distribution measurements—BET, BJH, and DFT. *The Canadian Journal of Chemical Engineering*. **97**(11): p. 2781-2791.

S. Brunauer, P.H. Emmett, and E. Teller. (1938). Adsorption of gases in multimolecular layers. *Journal of the American chemical society*. **60**(2): p. 309-319.

S. Diamond. (2001) A discussion of the paper "Mercury porosimetry—an inappropriate method for the measurement of pore size distributions in cement-based materials", *Cement and Concrete Research* 31(11): p. 1657-1658.

S. Diamond. (2000). Mercury porosimetry: An inappropriate method for the measurement of pore size distributions in cement-based materials. *Cement and Concrete Research*. 30(10): p. 1517-1525.

Y. Zhang, et al. (2022) "A reappraisal of the ink-bottle effect and pore structure of cementitious materials using intrusion-extrusion cyclic mercury porosimetry", *Cement and Concrete Research*, 2022. 161: p. 106942.

Identification of fatigue damage mechanisms in plain concrete through cluster analysis of AE data

Radhika V[1*] and J M Chandra Kishen[2]

[1] *Indian Institute of Science Bangalore*
Email: radhikav@iisc.ac.in
[2] *Indian Institute of Science Bangalore*
Email: chandrak@iisc.ac.in

[*]Corresponding author

ABSTRACT

Acoustic emission (AE) is one of the most effective techniques for studying internal microcracking in concrete. This study investigates the damage mechanisms in plain concrete specimens under monotonic and fatigue loading through a parametric study of the AE data collected from twelve beam specimens under three-point bending. By applying k-means clustering to the AE data, four distinct damage mechanisms in plain concrete are identified.

KEYWORDS*: Acoustic emission, Fatigue loading, Cluster analysis, Damage mechanisms*

1. Introduction

Concrete structures such as bridges, offshore platforms, wind towers, and pavements are routinely subjected to repeated loading and unloading cycles leading to degradation of their strength, stiffness, and durability. The fatigue behaviour of concrete structures is influenced by several factors such as age and quality of concrete, type of loading, frequency and amplitude of loading and environmental conditions. In order to understand how a quasi-brittle material such as concrete behaves under different types of loading, it is essential to comprehend the internal processes taking place within the material. One of the most widely used techniques for assessing and understanding damage in concrete structures is acoustic emission.

AE is defined as the class of phenomena whereby elastic waves are generated by the rapid release of energy from the localised source or sources within a material. Different parametric features extracted from the recorded AE signal can be used to characterise and diagnose the extent of damage in different materials. Clustering of AE data has been widely used to identify and characterise different damage mechanisms in a variety of materials such as metals, composites and concrete (Han et al., 2019, Hou et al., 2021,). Clustering can be done directly on AE parameters or on principal components computed from these parameters.

This study presents the analysis of AE data obtained from notched plain concrete specimens subjected to monotonic and fatigue loading. The AE data is processed using principal component analysis followed by cluster analysis, leading to the identification of four distinct damage mechanisms in plain concrete

2. Principal Component Analysis

Principal Component Analysis (PCA) is a statistical technique used for reducing the dimensionality of a large dataset by identifying the underlying patterns and relationships among the variables. This is achieved by transforming the original dataset into a new set of variables called principal components, which are linear combinations of the original variables that capture the maximum amount of variation in the data. Acoustic emission data is comprised of various features, including amplitude, duration, rise time, count, and absolute energy. The visualisation of data that involves so many parameters can be challenging. However, the application of PCA to acoustic emission data can help extract the most important features and facilitate better visualisation through principal components.

3. Cluster Analysis

The comprehension of the physical processes and microstructural phenomena that govern the fracture and fatigue behaviour of concrete on a macroscopic scale is still lacking. A multi-variable cluster analysis of recorded acoustic signals is performed to differentiate damage mechanisms in the material based on the typical AE signals and their timing of occurrence. In this study, the widely used k-means clustering algorithm is applied to identify the significant damage mechanisms in concrete.

K-means clustering is a popular unsupervised machine-learning technique that groups data points into a predefined number of clusters. This algorithm aims to divide a given dataset into k clusters, with each cluster being represented by its centroid, which is the average value of all data points assigned to that cluster. In order to determine the optimal number of clusters for the AE data set, two cluster validation indices, namely Silhouette index and the Davies-Bouldin index, are computed. The optimal number of clusters can be chosen as the one that gives a high Silhouette index and a low Davies-Bouldin index (Han et al., 2019).

4. Experimental Program

An experimental investigation designed to study the fatigue crack growth behaviour in plain concrete beams is considered here (Keerthana and Kishen, 2020). Notched beam specimens of dimension 680 x 150 x 50 mm with a span-to-depth ratio of 4 are tested. The specimens are subjected to three-point loading in a computer-controlled servo-hydraulic machine. Before conducting fatigue tests, beams are subjected to monotonic loading up to failure and the average static strength is found to be 3.35 kN. Subsequently, the specimens are tested under constant amplitude fatigue loading with load control mode. The minimum load amplitude is maintained at 0.25 kN to ensure sufficient contact between the loading device and the specimen while the maximum load amplitude is kept as 80% of the static peak load. The specimens are tested under three different loading frequencies: 0.5, 2.0, and 4.0 Hz. For each loading condition, three identical specimens are tested.

The micro and macro cracking behaviour occurring within the test specimen is monitored by Physical Acoustic Corporation system. R6D type piezoelectric AE sensors are glued to the surface using high vacuum silicon grease as a couplant. By conducting a noise test on a dummy specimen, the threshold value for noise reduction is set at 35 dB. The signals captured by AE sensors are amplified with a preamplifier with a gain of 40 dB and recorded by the data acquisition system. The location of AE sensors along with the geometry of the beam specimen is shown schematically in Figure 1.

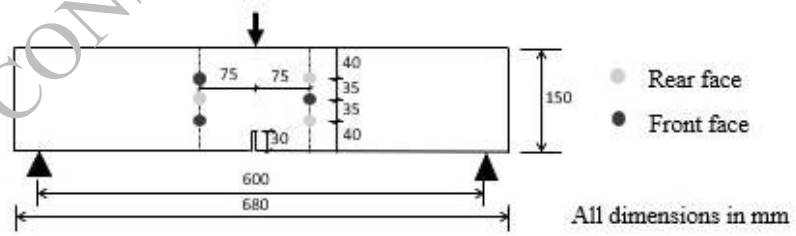

Figure 1. Geometry of beam specimen and arrangement of AE sensors

5. Results and Discussions

Concrete is a highly heterogeneous material that exhibits different behaviours even within identical samples. To mitigate the effects of this heterogeneity in the outcomes, the AE events recorded for all three identical specimens are analysed collectively.

PCA is conducted on five AE features, namely amplitude, rise time, duration, count, and absolute energy, resulting in five principal components - PC1 to PC5. The percentage of variance explained by each principal component, along with the cumulative values of explained variance, is presented in the form of scree plots

in Figure 2. PC1 and PC2 together explain a substantial portion of the variation in the data, ranging from 78.3% to 84.3% depending on the loading case. Furthermore, the first three principal components collectively account for over 90% of the variation in all loading cases. Consequently, PC1, PC2 and PC3 are used for clustering the AE data.

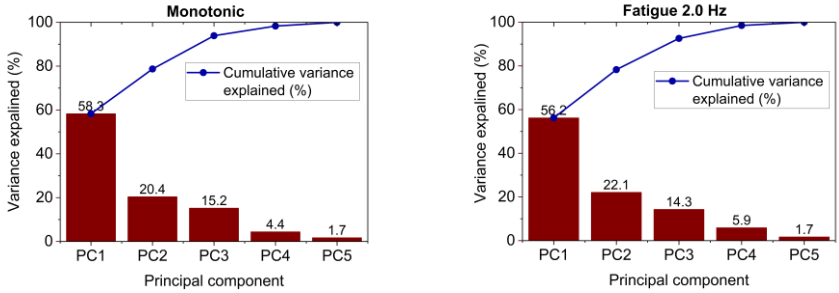

Figure 2. Scree plots presenting percentage variance explained by principal components

To determine the optimal number of clusters, both the Silhouette index and Davies-Bouldin indices are assessed, with the number of clusters ranging from 2 to 8. The computed values for the indices are presented in Figure 3 for monotonic and fatigue loading. Considering a high Silhouette index and a low Davies-Bouldin index, the optimal number of clusters is chosen as four for monotonic as well as fatigue loading.

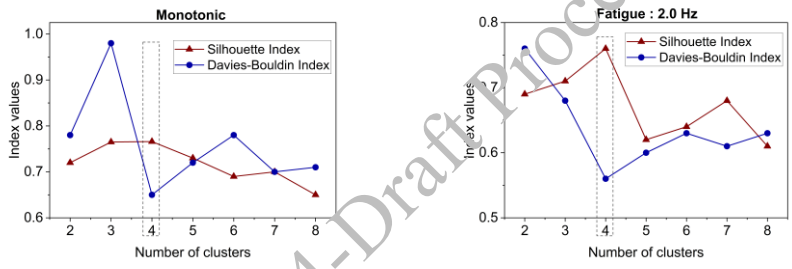

Figure 3. Evaluation of the optimal number of clusters

The AE data from monotonic and fatigue tests are subjected to the k-means algorithm, which partitions the acoustic data into four distinct clusters that share similar acoustic signal properties. In order to link each cluster with a specific damage mechanism of plain concrete, the distributions of amplitude, rise time and absolute energy are analysed. Distributions of these three AE parameters in each cluster with normalised time for monotonic and fatigue loadings are shown in Figures 4 and 5. The following observations are noted:

- Cluster 1, which encompasses 72% - 79.1% AE events, is distinguished by low values of amplitude, and absolute energy, as well as low to intermediate values of rise time. These observations, along with the lowest mean amplitude value, suggest that cluster 1 may be linked to cement mortar cracking in concrete.
- Cluster 2 comprises data points exhibiting low amplitude, intermediate absolute energy values, and significantly high-rise time values. The high value of rise time in turn suggests a high value of rise angle and hence a shear-dominated damage mechanism. The mean amplitude value of this cluster is quite close to that of cluster 1. However, this cluster only represents a very small percentage of events (0.12% - 2.3%) and may be associated with aggregate slip in concrete.
- Cluster 3 is marked by intermediate values of amplitude and energy, as well as low to intermediate values for rise time. This cluster has the second highest percentages of events, ranging from 20.6% - 25.6%, under all loading conditions. It may be attributed to interfacial transition zone (ITZ) cracking. ITZ refers to the region of the cement paste surrounding the aggregate particles, which is perturbed by the presence of the aggregate. This zone is characterised by microstructural

differences leading to higher porosity and lower strength and is generally considered as a weak link in the concrete matrix.

- Cluster 4 includes data points with the highest values of amplitude and energy, but low values of rise time. The percentage of events in this cluster varies in the range 0.2% - 1.5%. This cluster has the highest mean amplitude and can probably be attributed to aggregate cracking in the specimen. Among the three main components of concrete, namely, the cement mortar, ITZ, and aggregates, the aggregates typically exhibit the highest value of elastic modulus. They are less prone to cracking, and often necessitating a significant amount of energy.

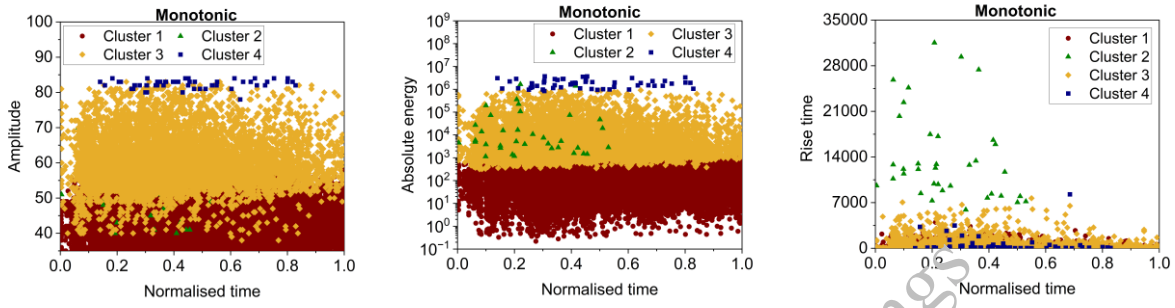

Figure 4. Distribution of AE parameters versus normalized time for monotonic loading

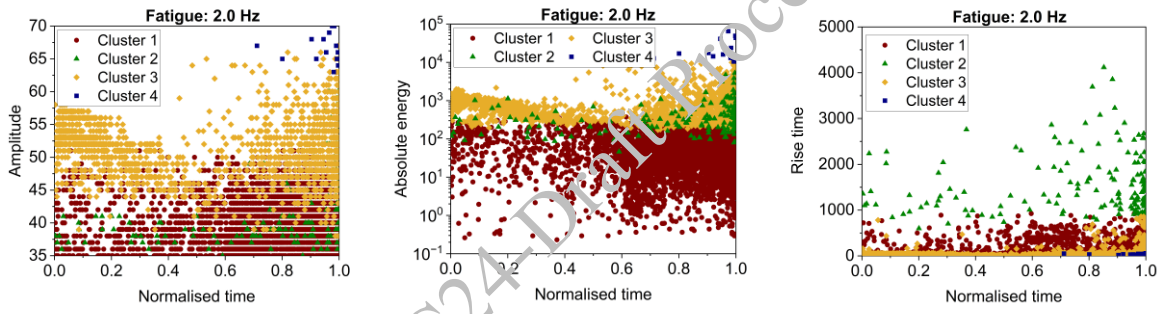

6. Conclusions

In the present study, parametric analysis of acoustic data is conducted to study the damage mechanisms in plain concrete beams. AE data from twelve specimens - three for monotonic and nine for fatigue (three for each loading frequency) - are analysed. Features such as amplitude, duration, rise time, count and absolute energy are extracted from the AE signals. The first three principal components derived from these AE features account for over 90% of the explained variance and are thus utilised in the cluster analysis. Four damage mechanisms in plain concrete, namely cement mortar cracking, aggregate slip, ITZ cracking, and aggregate fracture, are identified using the k-means algorithm for clustering.

References

Han, Q., Yang, G., Xu, J., Fu, Z., Lacidogna, G. and Carpinteri, A (2019) "Acoustic emission data analyses based on crumb rubber concrete beam bending tests." *Engineering Fracture Mechanics*, 210: 189-202.

Hou, G., Shang, D.G., Zuo, L.X., Qu, L.F., Guo, Y.E., Xia, M., Wu, S.D. and Yin, X. (2021) "Fatigue damage identification of SiC coated needled C/SiC composite by acoustic emission." *Ceramics International*, 47.11: 15129-15138.

Keerthana, K., and JM Chandra Kishen. (2021) "Micromechanical effects of loading frequency on fatigue fracture in concrete." *Journal of Engineering Mechanics* 147.12: 04021111.

Insights from Durability Inspection of Half a Century old RC Building in Composite Climatic Zone

L. Dudi[1*], and S. Bishnoi[2]

[1] Department of Civil Engineering, Indian Institute of Technology Delhi, New Delhi, India
Email: lupeshdudi@gmail.com
[2] Department of Civil Engineering, Indian Institute of Technology Delhi, New Delhi, India
Email: bishnoi@iitd.ac.in

ABSTRACT

Global warming and sustainable construction practices drive the adoption of cement with a low-carbon footprint, typically characterized by a low-clinker composition. However, concerns arise regarding the performance of these systems under carbonation and carbonation-induced corrosion. This study investigates a structure susceptible to carbonation and carbonation-induced corrosion, focusing on identifying critical locations within a residential building. Critical areas are pinpointed by applying semi-destructive and non-destructive testing techniques. Firstly, the study uses carbonation depth data to evaluate the average carbonation rate over time, providing insights into the time required for rebar de-passivation in different structural members. Secondly, corrosion rate values are utilized to assess the cumulative damage experienced by the structure over the years. Contrary to common belief, the study reveals that a highly carbonation-susceptible region does not always correspond to a high corrosion rate. Additionally, the corrosion rate within the structure is significantly influenced by moisture levels. Consequently, despite rebar de-passivation occurring decades ago, corrosion-induced damage remains minimal in many locations. In conclusion, this study identifies zones within the structure where protective measures should be implemented when utilizing low-clinker cement to mitigate the risk of corrosion and corrosion-induced structural deterioration.

KEYWORDS*: Carbonation, Corrosion, Semi-destructive technique, Service life.*

1. Introduction

In the last few decades, owing to sustainability needs, there has been an increase in scientific studies on the development and performance assessment of environment-friendly binder compositions. These innovative cementitious binders are low-clinker compositions blended with supplementary cementitious materials (SCMs), i.e., fly ash, slag, calcined clay, limestone, etc. Studies have shown that these new binder compositions have a lower carbonation resistance due to the low buffering capacity of these systems arising from the dilution effect and reaction of SCMs with portlandite to produce secondary calcium silicate hydrate (C-S-H) (Sisomphon and Franke, 2007). A primary concern related to the carbonation of structures is the loss of passivating film due to a fall in pH, which leaves the rebar susceptible to active corrosion (Tuutti, 1982).

Current design and durability standards and practices are based on preventing the carbonation front from reaching the rebar level rather than the structure's corrosion rate or deterioration rate. However, the question arises: Does carbonation depth reaching the reinforcement mean active corrosion has begun? Moreover, what is the expected corrosion or deterioration rate if the corrosion rate has begun? The present study is undertaken to shed light on these questions and collect data to serve as a benchmark for similar studies in the future. A 50-year-old RC residential building has been investigated, prone to carbonation and carbonation-induced corrosion. The data on carbonation depth and corrosion rate has been collected throughout the structure, covering different structural members and regions in the residential building to understand the factors influencing the processes and rate of deterioration.

2. Experimental Framework

2.1 Structure Examined - Background

The structure under investigation was constructed during the mid-1970s, having G + 3 floors, and is located in New Delhi. The structure was designed as a residential apartment complex with a frame-type structure comprising beams, columns, and slabs, with brickwork for walls. A nominal mix-design of 1:2:4 of cement: sand: aggregate was adopted to achieve the M15 grade of concrete for constructing an RC structure. The primary reinforcement in columns consisted of 32 mm high-yield strength deformed (tor) bars, while in beams, reinforcement in tension had a diameter of 16 mm and, in compression, 12 mm. A cover of 25 mm was adopted for beams and columns. As per the National Building Code of India (2016), Delhi comes in a composite climatic zone, which experiences very low (10°C) to high temperatures (45°C) and relative humidity varying from 20 to 95% during a year. Fig. 1 shows the monthly mean temperature and precipitation fluctuations from 1982 to 2023 recorded at the nearest meteorological station from the building location. Such environments are deemed to be most susceptible to carbonation and carbonation-induced corrosion.

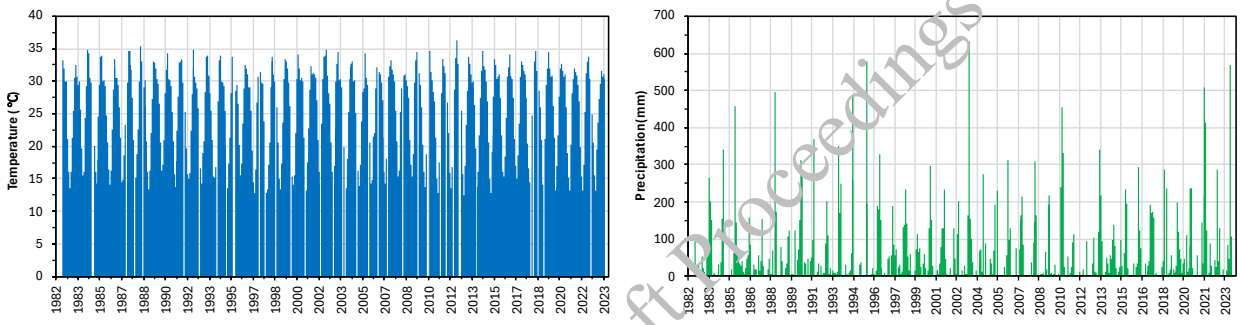

Figure 1. Monthly mean temperature (left) and precipitation (right) recorded at Safdarganj, New Delhi, from June 1982 to June 2023.

2.2 Testing Conducted on Site

On preliminary inspection, based on distress signs like cracking due to rust, rust stains, spalling and delamination, moisture accumulation, and saturation zones, locations for the semi-destructive testing were identified. Since the secondary inspection focused on checking strength degradation and deterioration in primary structural members, most test locations were selected on the beams and the columns. However, these locations were distributed evenly among external and internal members. The following experiments were performed on site:

Carbonation Depth: Carbonation depth was measured by spraying phenolphthalein indicator onto the freshly extracted core samples. Overall, 8 measurements were taken around the circumferences of the core, and the average value has been reported.

Corrosion rate: The RapiCor instrument had been employed to determine the corrosion rate directly on site. The instrument works by tracking potential fluctuations after providing a galvanostatic current via a counter electrode. The instrument also provided complimentary resistivity, and half-cell potential values, along with corrosion rate values. Half-cell potential values were based on silver and silver chloride as reference electrode.

3. Results

Fig. 2 shows the carbonation depth obtained from the core extracted from the column and beams. A few samples were taken from the façade and slabs; however, they were observed to be fully carbonated; hence, the results are not presented here. Interestingly, the carbonation depth observed for all the structural

members was much higher than the cover provided, indicating that de-passivation had occurred throughout the structure. Members adjacent to the kitchen area observed higher carbonation depth, probably due to the local microclimate effect of high carbon dioxide concentration and moderate relative humidity (50-70%). Members adjacent to the washroom and prone to wetting and drying effects due to rain observed lower carbonation depths.

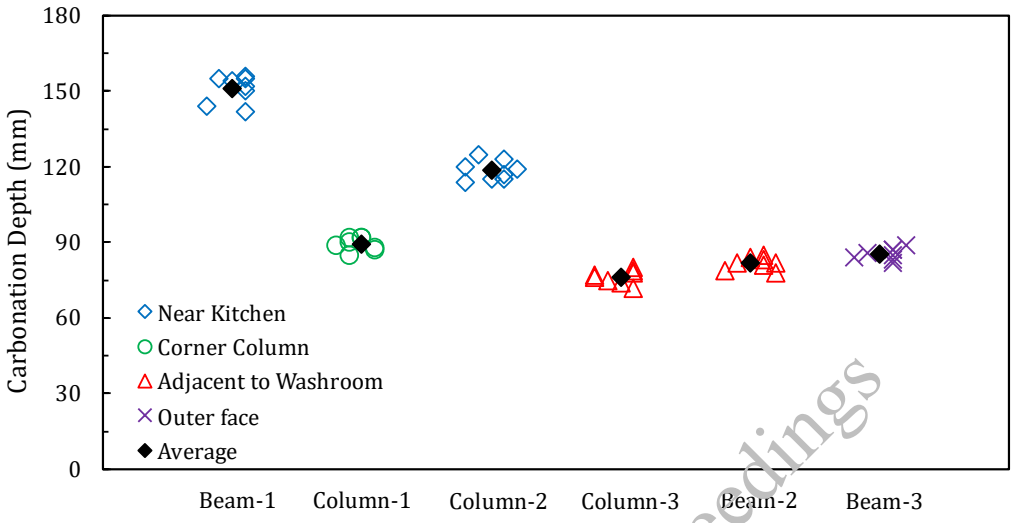

Figure 2. Carbonation depth determined from the extracted cores.

The corrosion rate, resistivity, and half-cell potential values obtained from the testing of columns in different locations are presented in Fig. 3. It can be observed that 3 out of 6 columns had corrosion rate lower than 20 µm/year, 2 columns had corrosion rate between 20 – 40 µm/year, and one column showed exceptionally high corrosion rate of 98.87 µm/year. Column 6 was adjacent to the washroom and had cracks, which probably led to a direct supply of moisture and oxygen at the rebar level, leading to high corrosion rate values. Column 3 and Column 4 were adjacent to the washroom and kitchen, respectively, and both had moisture-dampness signs. The remaining columns were either corner or outside face columns, which were observed to have seasonal wetting and drying. As a general observation, when resistivity was low (< 30 kohm-cm) and half-cell potential values were lower than -260 mV (silver and silver chloride electrode), the corrosion rate was high.

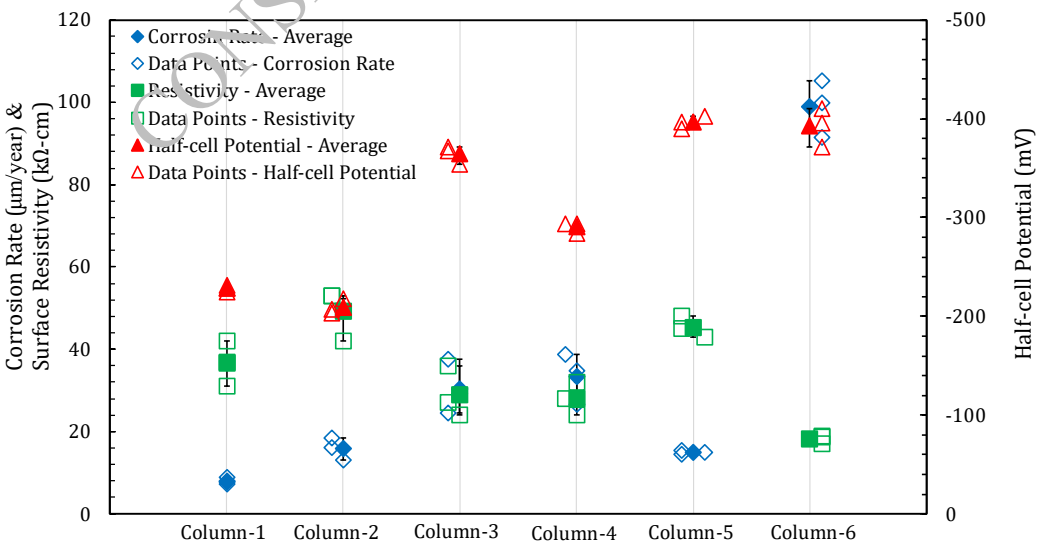

Figure 3. Corrosion rate, resistivity, and half-cell potential values obtained from RapiCor.

4. Discussions

The average carbonation coefficient and corrosion rate grouped as per the location characterized in the structure are given in Table 1. It can be observed that a higher carbonation rate does not necessarily mean that the corrosion rate will be higher at those locations because the role of moisture in the two processes is opposite. Furthermore, considering the lowest carbonation coefficient of 11.18 mm/year$^{0.5}$, the carbonation depth would have crossed the reinforcement level (25 mm clear cover + 32 mm rebar diameter) in around 25 years. They indicate that rebar throughout the structure would have lost its passivating film over two decades ago. However, no widespread corrosion signs existed throughout the structure; corrosion activities were limited to specific regions.

Table 1. Carbonation and corrosion rate values for characterized locations in the structure.

Location	*Carbonation coefficient (mm/year$^{0.5}$)*	*Corrosion rate (μm/year)*
Moist region – near the washrooms, or where regular splash of water happen	11.18	64.67
Kitchen – columns and beams adjacent to kitchen area	19.05	33.4
Outdoors – corner columns, middle columns, and beams under the slab on edge	12.35	12.99

Considering the extreme corrosion rate for members in moist regions, the effective diameter loss would be 1.62 mm after an additional 25 years. The visual examination of these members revealed the presence of flakes of rust chipping off the rebar and the critical condition of the rebar. Even in moist regions, the corrosion rate is initially moderate and jumps to high values after the appearance of cracks (see Fig. 3). For indoor members. However, carbonation depth was highest, but due to low relative humidity, signs of corrosion were missing. Most of the members in the kitchen area did not show any corrosion signs; however, the one investigated for corrosion in the present study had a low cover depth of 15 mm, highlighting that low cover depths can be critical as they result in fast transport of moisture and oxygen to rebar leading to high corrosion rates. Outdoor members who observed wetting and drying due to rain showed one-fifth of the corrosion rate compared to members in moist regions, as these members were relatively dry at the time of the investigation. During rainy weather, high corrosion rates can be expected in these members.

5. Conclusion

The carbonation rate within the structure can vary considerably depending on the microclimatic conditions, such as carbon dioxide concentration and relative humidity in different regions. The results from the present study showed that carbonation of the structure does not lead to widespread corrosion throughout the structural members in the building, as often believed. Corrosion is localized to specific regions characterized by moisture, i.e., frequent wetting and drying due to rain, continuous moisture near the washroom or kitchen plumbing, and damp regions. Members or regions with inadequate cover depth can also lead to aggressive corrosion conditions. For future low-clinker blend compositions, protection measures can be focused on highlighted regions to limit the corrosion activity in the structure.

References

Bureau of Indian Standards, National Building Code of India (2016), New Delhi: *Bureau of Indian Standards*.

Sisomphon, K., & Franke, L. (2007). "Carbonation rates of concretes containing high volume of pozzolanic materials", *Cement and Concrete Research*, 37(12), 1647-1653.

Tuutti, K. (1982). Corrosion of steel in concrete.

Early Age Linear and Nonlinear Creep of 3D Printable OPC Mortar

D. Mohanraj[1*], A. S. Dwivedi[2], M. N. Shariff[3]

[1]Indian Institute of Technology Bombay, India
Email: 30005268@iitb.ac.in
[2]Indian Institute of Technology Bombay, India
[3]Indian Institute of Technology Bombay, India

*Corresponding author

ABSTRACT

Cement mortar exhibits a viscoelastic-plastic behaviour due to the creep and consolidation effects. The effects of creep are pronounced in the fresh state affecting the dimensional stability of the 3D printed element, in addition to increasing the distance from the nozzle to the deposition layer. In this study, the early age creep and consolidation behaviour of 3D printable OPC mortar is experimentally evaluated by varying the age of loading using a 180-second holding pattern. The fresh-state mechanical properties, such as compressive strength and the variation of elastic and creep compliance with time, are experimentally evaluated, and a fitting model is presented. The sustained stress on the concrete is varied such that it ranges from the linear domain to the nonlinear domain. The creep compliance function for the concrete is evaluated theoretically using the parallel creep law, using the step-by-step method. The method is capable of handling both constant stress and varying stress patterns. This theoretical method can be used to estimate the time-dependent deformation in 3D printable concrete during the printing process.

KEYWORD: *Time dependent strength evolution, Early age strength, 3D printing, Creep compliance, Creep coefficient, Loading-unloading cycles*

1. Introduction

3D printing has recently gained significant attention in the housing and large-scale construction sectors. This advanced technology paves the way for development of intricate structures effortlessly, a task that would be impossible with traditional construction techniques. 3D printing is a form of additive manufacturing which assembles the entire structures by layering individual concrete filament without the necessity of formwork. The maximum height of the structure that can be printed without notable deformation is called buildability which is basically a material property. 3D printing demands specific rheological properties at different stages of printing. A typical 3D printing process involves four key stages: mixing, pumping, extraction, and printing. Mixing and pumping demands a low static yield strength and low dynamic viscosity. For smooth extrusion, the filament must exhibit higher dynamic viscosity. The term extrusion is defined as the ability of the fresh concrete to pass through the hopper and nozzle and extruded as a continuous filament. Finally, the printed layer should rapidly gain static yielding to withstand the self-weight of subsequent layers without undergoing plastic deformation.

The rheological and mechanical properties of 3D printable concrete can be evaluated through various experimental methods including stress growth test, vane shear test, rotational rheometer, direct shear test, and uniaxial unconfined compression test. These tests provide insights into the load and instantaneous deformation behaviour of the concrete under static loading conditions. In 3D printing as the layer are printed with very high precision and it is essential to consider the deformation undergone by the printed layers. Deformation of the printed layers is attributed by both instantaneous deformation and time dependant deformation by the applied loading. The accumulation of successive layers on the printed filament may further lead to delayed deformations that could escalate over time, posing challenges to the precision and stability of the printed structure. This time dependant deformation is contributed by various factors such as

basic creep, autogenous shrinkage, plastic shrinkage, and consolidation which are collectively known as early age creep (Esposito et al., 2021).
This research investigates the time-dependent deformation of 3D printable Ordinary Portland Cement (OPC) based concrete mixtures under different stress levels such as 0.2 fu, 0.3 fu, and 0.4 fu. Ultimately, to establish an experimentally validated analytical model for various stress levels and the deformation responses of the concrete.

2. Experimental investigation

2.1 Mix design

A self-developed 3D printable OPC based mortar was used in the study. The raw material used are 53 grade ordinary Portland cement with natural fine aggregate of maximum size 2.36 mm. The smooth finish of the 3D printed filament is ensured by maintaining higher binder and powder content. Along with cement, flyash is also used to increase the binder content and the powder content is increased by adding quartz powder and silica fume. Low water to binder ratio is adopted to achieve good early age strength and stiffness. The pumpability is ensured by lowering the static yield strength by adding PCE based superplasticizer with 30 % of solid content and 70% of water. The mix proportion of the concrete is elaborated in another study of the research team in Reddy et al. As the early age creep is highly sensitive to environmental conditions and geometry of the sample, a uniform cylindrical sample is considered with 80 mm diameter and 100 mm length.

2.2 Testing setup and protocol

While printing, the printed filaments remain stationary to facilitate the setting process followed by the deposition of additional filaments on to it. Usually, the deposition could happen any time before the material sets and even after that. Layering of subsequent filament before the preceding layer sets would be much crucial for deformations. Hence understanding the development of strength and stiffness of the printed filament is important. In this study, the elastic material deformation under external loading is evaluated through uniaxial unconfined compression testing, while the time-dependent deformation is assessed using early age creep testing as shown in Figure 1 and 3 respectively.

2.3 Early age strength

The development of strength and stiffness of 3D printed concrete from the initial setting time to the final setting time is referred to as early age strength. Analysis of strength in the early stages includes assessment of instantaneous deformation at various concrete age. This assessment is carried out in a similar way to the uniaxial unconfined compression test (UUC) typically performed on soil specimens. Nonetheless, the modifications are implemented to the sample dimensions in order to reduce the risk structural instability. The specimens are of cylindrical in shape with a height-to-diameter ratio (h/d) of 1.25. The adopted dimensions are 80 mm in diameter and 100 mm in height as shown in Figure 1.
These specimens are cast not printed. While casting, the concrete is poured into moulds as three layers with compaction being carried after each layer. Subsequently, the UCC test is executed using a displacement-controlled hydraulic apparatus with a loading rate set at 0.1 mm/sec(Chang et al., 2023). The vertical alignment and uniform load distribution of the loading is ensured with a swirl joint and parallel plate configuration as illustrated in Figure 1, are implemented. The axial displacement and applied load on the sample are continuously monitored using a LVDT and load cell coupled to an HBM data acquisition system, which records data at a frequency of 5 Hz. The evaluations are conducted at five distinct aging intervals, specifically at t = 30 min, 45 min, 60 min, 75 min, 90 min, and 105 min. Here, t = 0 min is when water has been added to the dry mixture signifying the start of hydration. For each aging time, a total of five samples are tested. As a result, the load-displacement curves derived from experiments, along with the evolution of concrete strength and stress-strain relationships, are depicted in Figure 4 and 5. Analysis of the experimental findings reveals a notable enhancement in both the strength and stiffness of the material at the chosen

intervals. From Figure 2 it is evident that, all samples exhibit a characteristic compressive failure pattern, indicating that the verticality of the load is maintained until failure.

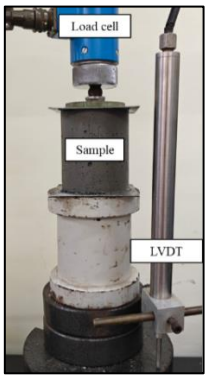

Figure 1. Early age strength test setup

Figure 2. Failure modes of early age strength test

Figure 3. Early age creep test setup

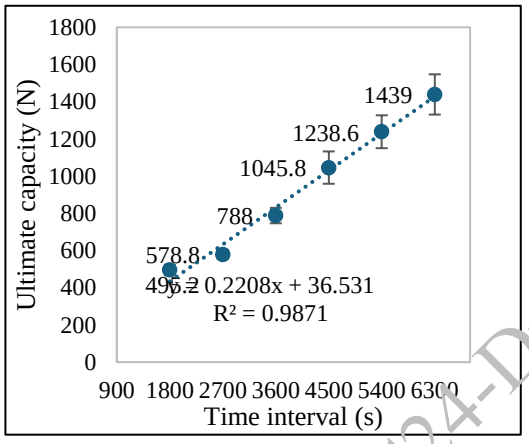

Figure 4. Strength evolution of fresh concrete

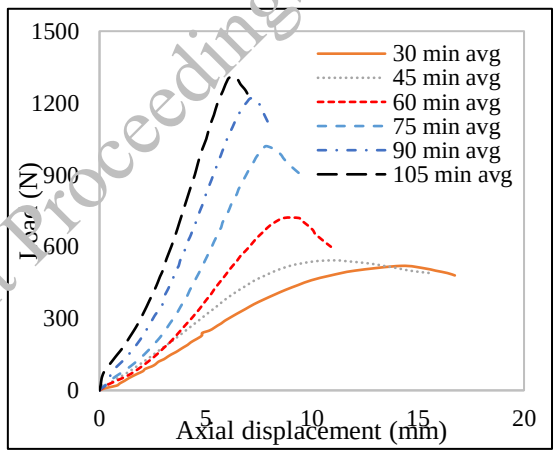

Figure 5. Load-displacement curve

2.4 Creep test

The early age creep test is a quasi-static compressive loading-unloading cycle test. This test has been carried out at five distinct aging durations, specifically t = 30 min, 45 min, 60 min, 75 min, 90 min, and 105 min, under various sustained loading. Throughout the testing procedure, a constant temperature and humidity are maintained to prevent plastic shrinkage. The primary objective of this investigation is to establish the connection between creep deformation and level of hardening. This involves assessing creep deformation across different microstructures at various hydration levels, as well as consolidation deformation under continuous compressive loading.

Ideally, the load should be applied to the same microstructures for determining the creep deformation. Nonetheless, the evolution of microstructures is an ongoing process. Therefore, in theory, the load should be applied for an infinitely short duration to estimate the creep deformation of a specific microstructure. However, creep deformation is a time-dependent, long-term phenomenon, necessitating the adoption of multiple loading cycles. This research illustrates the creep behaviour under four loading and unloading cycles. Based on the research of Irfan-ul-hassan et al.(2016), the loading duration is adopted as 180 s, assuming minimal changes in microstructure.

The UCC test enables the determination of the strength evolution of fresh concrete. Three loading levels corresponding to 0.2 fu, 0.3 fu, and 0.4 fu have been chosen. These levels are selected to examine both linear and non-linear creep regimes of the 3D printable concrete. The early age creep test is carried out in the consolidation setup which can apply the quasi-static loading and unloading cycles at sustained stress

levels. Deformation measurements are taken with the linear measuring devices of accuracy one micron. The total loading and unloading duration are exceptional quick, at approximately 2 seconds, with precautions taken to prevent impact loading. Figure 6 illustrates the loading path of the quasi-static loading-unloading creep test, while Figure 7 displays the creep deformation three samples of age 1800s subjected to 0.2 of the ultimate capacity (f_u).

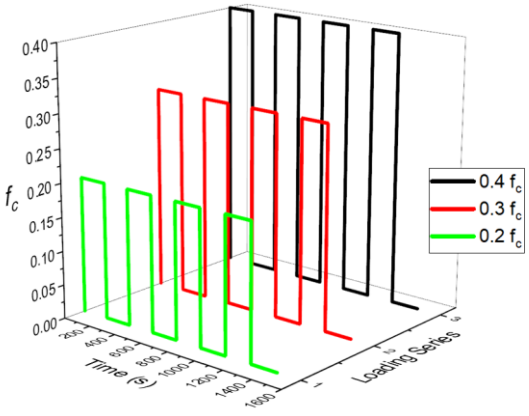

Figure 6. Loading path of early age creep test

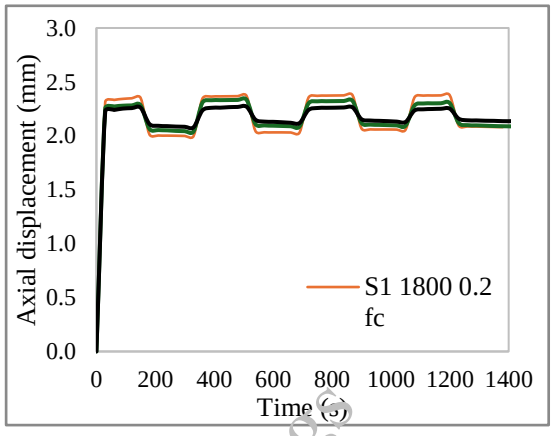

Figure 7. Creep deformation

3. Quantification of creep behaviour

Based on the experimentally derived creep deformation, an analytical model was developed using the power-law and linear function to fit the early age creep behaviour and elastic compliance for the time range of 20 min to 105 min. when calibrating the analytical model, the function is determined by the highest R-square value.

From the Figure 8 it can be clearly seen that power law function can the fit the creep behaviour of the printable mortar and the compliance function is given below.

$$Creep\ compliance = \frac{1}{\alpha + \beta t_0} \cdot (t - t_0)^c \quad (1)$$

On considering the three loading cycles of 0.2 f_c, 30 min, the constant in the mentioned function is determined as $\alpha = -296$, $\beta = 0.5$ and $c = 0.32$. Similarly for 0.3 f_c and 0.4 f_c at varies hardening time was analysed and a combined compliance function was developed incorporating loading time and aging time.

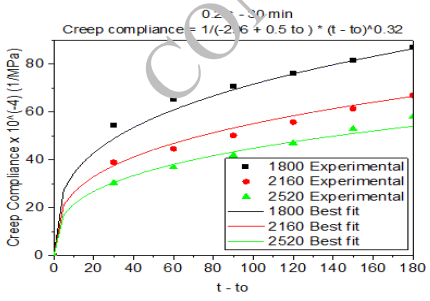

Figure 8(a). 0.2 fc – 30 min

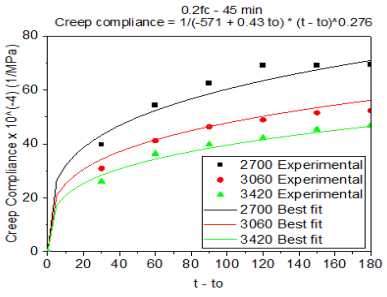

Figure 8 (b). 0.2 fc – 45 min

4. Conclusions

In this study a quasi-static loading and unloading cycles were performed to experimentally analyse the early age creep behaviour of 3D printable mortar. Based on the experimental results an analytical model is developed to predict the elastic and creep compliance of the fresh 3D printable mortar.

References

Chang, Z., Liang, M., Xu, Y., Wan, Z., Schlangen, E., & Šavija, B. (2023). Early-age creep of 3D printable mortar: Experiments and analytical modelling. *Cement and Concrete Composites*, *138*. https://doi.org/10.1016/j.cemconcomp.2023.104973

Esposito, L., Casagrande, L., Menna, C., Asprone, D., & Auricchio, F. (2021). Early-age creep behaviour of 3D printable mortars: Experimental characterisation and analytical modelling. *Materials and Structures/Materiaux et Constructions*, *54*(6), 1–16. https://doi.org/10.1617/s11527-021-01800-z

Irfan-ul-Hassan, M., Pichler, B., Reihsner, R., & Hellmich, C. (2016). Elastic and creep properties of young cement paste, as determined from hourly repeated minute-long quasi-static tests. *Cement and Concrete Research*, *82*, 36–49. https://doi.org/https://doi.org/10.1016/j.cemconres.2015.11.007

Effect of different activation methods on the microstructure of alkali-activated silica fume

L.E. Menchaca-Ballinas[1*], P. Chaunsali[2], and M. Santhanam[3]

[1] *Centre of Excellence on Technologies for Low-Carbon and Lean Construction, IIT Madras, Chennai, India*
Email: Menchaca.ballinas@gmail.com
[2] *Centre of Excellence on Technologies for Low-Carbon and Lean Construction, IIT Madras, Chennai, India*
Email: pchaunsali@iitm.ac.in
[3] *Centre of Excellence on Technologies for Low-Carbon and Lean Construction, IIT Madras, Chennai, India*
Email: manus@civil.iitm.ac.in

[*]Corresponding author

ABSTRACT

Siliceous materials are not extensively used as main precursors to produce alkali-activated binders because they can form an unstable silica gel. In this study, silica fume was activated with various alkaline activation systems to improve the stability of silica gel: NaOH solution (as a reference), NaOH solution + CaO power, Na_2CO_3 powder and CaO powder and Na_2CO_3 powder and $Ca(OH)_2$ powder.
The mechanical properties, chemical composition, and microstructure of paste and mortars changed significantly among the activation systems. System 1 produced silica gel which composed mortars with a 28-day compressive strength of 15 MPa but showed poor underwater performance. While adding calcium activators, systems 2, 3, and 4 formed an intermixture of silica gel and CSH which improved the underwater performance of mortars. Moreover, such calcium-bearing systems showed a more heterogeneous microstructure and chemical composition than the silica gel formed from the activation of silica fume with NaOH.

KEYWORDS*: Silica gel, Ca-modified silica gel, Alkali-activated materials, Microstructure, $CaCO_3$*

1. Introduction

Alkali-activated materials can be classified according to the chemical composition of the precursor as Ca-rich precursors such as ground-granulated blast furnace slag and Fly ash class C which after activation produce calcium silicate hydrates (CSH) or calcium aluminosilicate hydrates (CASH) as main reaction products. A second group include Al and Si-rich precursors such as metakaolin and fly ash class F which can form CASH or sodium aluminosilicate hydrates (NASH) (Provis & Deventer, 2014). However, silica-rich precursors such as waste glass and rice husk ash with low calcium and alumina content do not fit in any of the above groups. Also, these Si-rich precursors cannot form significant amounts of CSH, CASH or NASH alone and require adding Ca or Al sources to be stable. Otherwise, a soluble silica gel will form instead which can contribute to high strength (up to 140 MPa) but lose strength underwater (Marchand et al., 2018; Menchaca-Ballinas et al., 2022; Redden & Neithalath, 2014).
Studies on the activation of waste glass with CaO and NaOH solutions showed the coexistence of silica gel and CSH in the paste microstructure while those activated only with NaOH solutions were composed by silica gel with a low Ca/Si ratio ~0.14. Moreover, one-part activation method consisting of a dry mix of CaO + Na_2CO_3 and ground waste glass resulted in better underwater performance than using CaO powder and NaOH solutions (Menchaca-Ballinas & Escalante-Garcia, 2019; Menchaca-Ballinas & Escalante-García, 2020; Menchaca-Ballinas & Escalante-Garcia, 2023). Nonetheless, the inherited content of CaO (10-15 wt. %), Na_2O (10-15 wt. %), MgO (3-5 wt.%), and Al_2O_3 (< 2 wt.%) in the waste glass left some questions about the true nature of silica gel in alkali-activated cementitious systems.
Considering the above, this study used silica fume which is >95 wt.% amorphous silica to better compare the effect of four activation methods on the microstructure and chemical composition of the reaction products by Field Emission Scanning Electron Microscopy (FESEM).

2. Materials and methodology

2.1 Materials

The powder alkaline activators were laboratory-grade CaO (95% Purity), Na_2CO_3 (98% purity), and NaOH pellets (98% purity)

2.2 Compressive strength

The compressive strength of mortar was determined in dry and underwater curing regimes at 1 day and 28 days. Underwater cured specimens were dried at 50 °C for 2 h before testing. The hydration products were characterized in selected pastes at 28 days of curing. The paste samples were cut into small monoliths and then submerged in isopropanol for 48 hours, followed by drying in a vacuum chamber at 25 ± 3 °C for 24 h to stop the hydration reactions.

2.3 Field-emission scanning electron microscopy (FESEM)

Pieces of selected pastes were characterized by FESEM. Two different sample preparation methods were used to study the microstructure, morphology, and chemical composition of the alkali-activated silica fume paste, which are described below:

- Polished sample: Paste pieces were impregnated with epoxy resin, then ground and polished using SiC paper and diamond paste of 9, 3, and 1 µm. These samples were used to perform EDS spot analyses.
- Fractured sample: Paste pieces were fractured attaining the flattest fracture possible. These samples were used to observe the morphological features of the reaction products.

Each sample was then sputter coated with gold to make them conductive. An *Inspect F scanning electron microscope* was used with secondary electrons (SE) or backscattered electrons (BSE) as required. The SEM was operated at 20 kV with a working distance of 8-10 mm to obtain micrographs of the matrix and points of interest (POI). The energy dispersive spectrometer (EDS) was operated at 20 keV with a working distance of 6-8 mm to acquire spot chemical analyses of the matrix and POI. Six to seven zones were selected for each formulation, with a separation of 200-1000 µm to ensure a representative sampling of the microstructure and chemical composition. The normalized ternary Ca-Si-Na atomic compositional diagrams included 70 elemental spot analyses of the matrix and 30 spot analyses per POI using BSE mode on a polished sample.

2.4 Methodology

The water/binder ratios of paste and mortars were 0.55 and 0.6 respectively. The NaOH solutions were prepared by adding NaOH pellets equivalent to 8% Na_2O relative to the mass of silica fume to the water of the paste or mortar. While utilizing NaOH solutions, silica fume and CaO were premixed first, and then the NaOH solution was added. In the case of powder activators, these were dry mixed with silica fume in a blender with planetary movement and then water was added. Pastes were cast in cubic molds of 2.3 × 2.3 × 2.3 cm and the mortars were prepared using river sand (particle size < 6 mm) with an aggregate/binder ratio of 3:1 (by wt.). Subsequently, they were cast in 5 × 5 × 5 cm acrylic cubic molds. The paste and mortars were cured at 50° C for 24 h and then cured at ambient temperature. Some mortar cubes were submerged in drinkable water to test their underwater performance. The amount of activators was relative to the mass of silica fume.

Four activation methods were selected: Formulation 1 (F1) used only 8% Na_2O:NaOH solution, Formulation 2 (F2) used 8% Na_2O:NaOH solution and 15% CaO powder, Formulation 3 (F3) used 8% Na_2O:Na_2CO_3 powder and 15% CaO powder and Formulation 4 (F4) used 8% Na_2O:Na_2CO_3 powder and 15% CaO:$Ca(OH)_2$ powder.

3. Results and discussion

The activation of silica fume with NaOH promoted the formation of sodium silica gel with a very homogeneous chemical composition as indicated by the clustering of the 70 spot analyses towards the Si apex in the Ca-Si-Na ternary diagrams shown in Figure 1. The compressive strength drastically reduced underwater, corroborating the poor underwater stability of silica gel (Menchaca-Ballinas et al., 2022; Redden & Neithalath, 2014). Also, since there is no calcium in F1, is clear that silica gel alone can contribute to the strength development of mortars. The morphology of silica gel showed to be dense with a rounded morphology (see Figure 2); some semi-reacted silica fume particles were also observed.

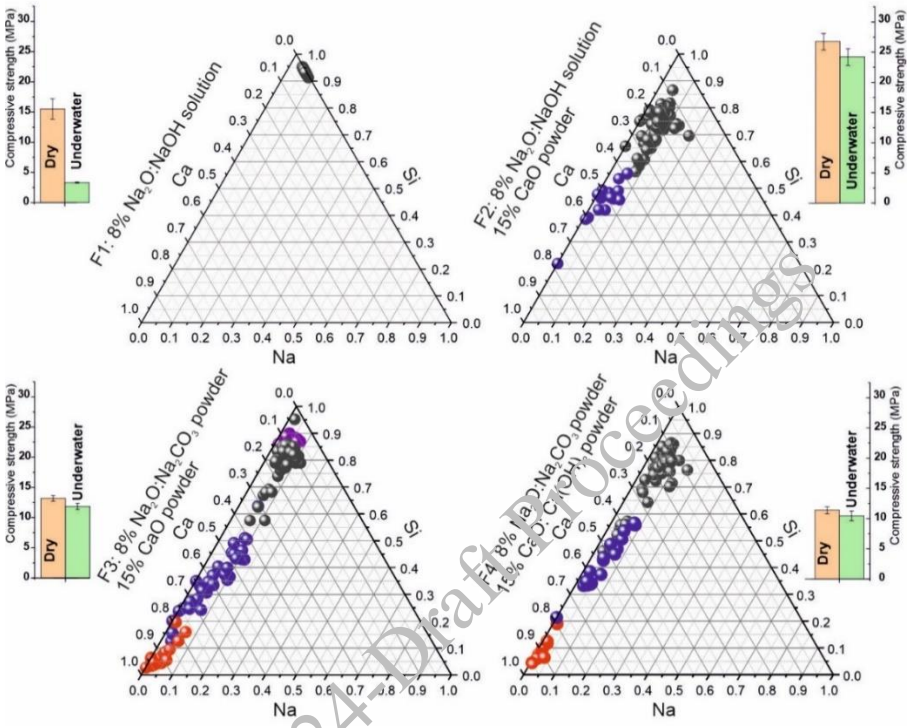

Figure 1. Ternay chemical composition diagram of alkali-activated silica fume pastes. The black, blue, and red spheres correspond to the matrix, Ca-Si-rich, and Ca-rich phases, respectively. Mortar 28-day compressive strength in dry and underwater curing conditions is also shown.

All the pastes activated with CaO or $Ca(OH)_2$ powder showed a heterogeneous chemical composition which scattered towards the Ca apex. Also, some clusters of calcium silicate-rich phases were observed, and their chemical compositions were located between the Ca and Si apex. Their morphology is shown in Fig. 2 and included more voids than the silica gel while the cloudy morphology resembled the morphology of low Ca/Si ratio C-S-H (Ba et al., 2023).

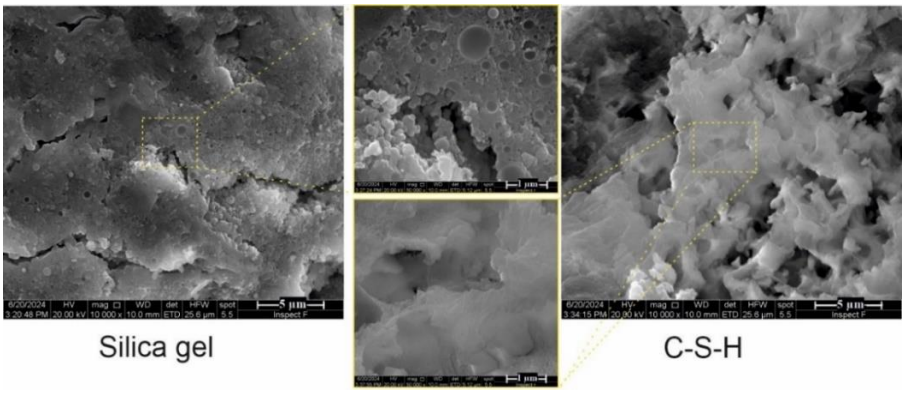

Figure 2. Morphology of silica gel and C-S-H formed during the alkaline activation of silica fume.

The use of CaO or $Ca(OH)_2$ and Na_2CO_3 in F3 and F4 produced a caustification reaction as shown in Equation 1. Therefore, such systems showed a different chemical composition distribution and new morphological features.

$$Ca(OH)_2 + Na_2CO_3 = CaCO_3 + 2NaOH \quad (1)$$

Paste F3 and F4 showed a similar chemical composition displacement as F2 but presented an agglomeration of Ca-rich phases (see Figure 3). Such phases showed a crystal-like dense morphology and may be related to the formation of semi-crystalline $CaCO_3$ which formed after the interaction of $Ca(OH)_2$ with Na_2CO_3.
It is noteworthy that after adding a Ca-based activator, the underwater stability of mortars at 28 days of curing significantly improved, despite of the coexistence of silica gel and C-S-H-like compounds. However, long-term studies will provide better insights into which activation system is better for long-term durability and underwater stability.

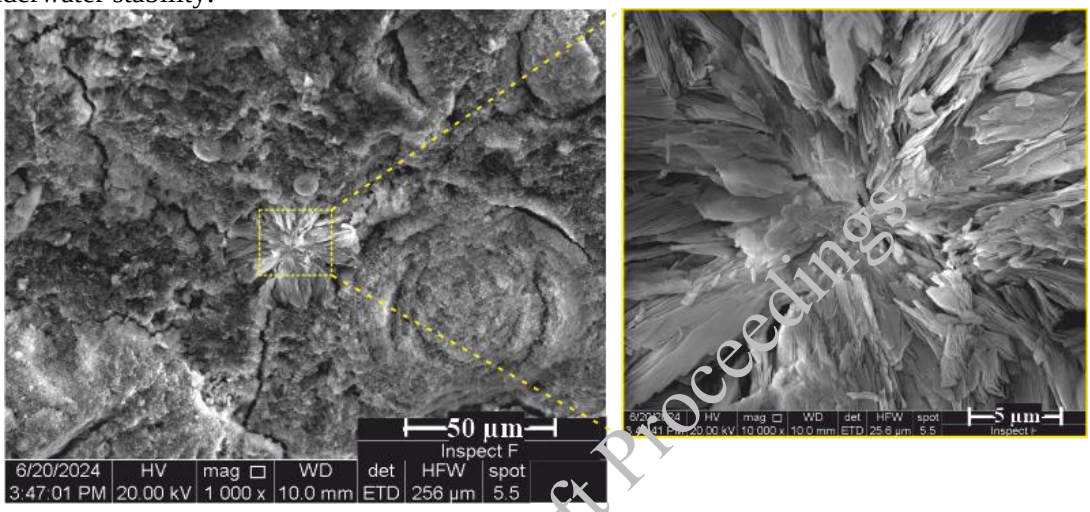

Figure 3. Morphology of Ca-rich agglomeration.

4. Conclusions

Utilizing solution activators or powder activators has a significant effect on the chemical composition and morphology of the reaction products in alternative construction materials.

References

Ba, H., Li, J., Ni, W., Li, Y., Ju, Y., Zhao, B., Wen, G., & Hitch, M. (2023). Effect of calcium to silicon ratio on the microstructure of hydrated calcium silicate gels prepared under medium alkalinity. Construction and Building Materials, 379. https://doi.org/10.1016/j.conbuildmat.2023.131240

Marchand, B., Lanier, S., Davy, C. A., Albert-Mercier, C., & Tricot, G. (2018). Are calcium silicate hydrates (C-S-H) present in alkali-activated glass cullet cement? Materials Letters, 219, 104–108. https://doi.org/10.1016/j.matlet.2018.02.046

Menchaca-Ballinas, L. E., & Escalante-Garcia, J. I. (2019). Low CO2 emission cements of waste glass activated by CaO and NaOH. Journal of Cleaner Production, 239, 117992. https://doi.org/10.1016/j.jclepro.2019.117992

Menchaca-Ballinas, L. E., & Escalante-García, J. I. (2020). Limestone as aggregate and precursor in binders of waste glass activated by CaO and NaOH. Construction and Building Materials, 262(120013). https://doi.org/10.1016/j.conbuildmat.2020.120013

Menchaca-Ballinas, L. E., & Escalante-Garcia, J. I. (2023). Hydraulic Pastes of Alkali-Activated Waste Glass and Limestone Cement Using in Situ Caustification. In Proceedings of the 75th RILEM Annual Week 2021 656–666.

Menchaca-Ballinas, L. E., Martinez-Lopez, R., & Escalante-Garcia, J. I. (2022). Compressive strength and microstructure of alkali-activated waste glass-slag cements. Journal of Sustainable Cement-Based Materials. https://doi.org/10.1080/21650373.2022.2066029

Provis, J., & Deventer, J. (2014). Alkali Activated Materials (J. L. Provis & J. S. J. van Deventer, Eds.; RILEM TC 2). Springer. https://doi.org/10.1007/978-94-007-7672-2

Redden, R., & Neithalath, N. (2014). Microstructure, strength, and moisture stability of alkali-activated glass powder-based binders. Cement and Concrete Composites, 45, 46–56. https://doi.org/10.1016/j.cemconcomp.2013.09.011.

Development of a New Test Method for Assessing the Susceptibility of Prestressing Steels to Hydrogen-induced Stress Corrosion Cracking

L. Seifert[1*], T. Müller[2], and G. Ebell[3]

[1]Bundesanstalt für Materialforschung und -prüfung (BAM), Berlin, Germany
Email: lando.seifert@bam.de
[2]Bundesanstalt für Materialforschung und -prüfung (BAM), Berlin, Germany
[3]Bundesanstalt für Materialforschung und -prüfung (BAM), Berlin, Germany

[*]Corresponding author

ABSTRACT

For prestressing steel's factory production control, approvals, and continuous surveillance in Germany, a susceptibility test against hydrogen-induced stress corrosion cracking is performed. The measured time to fracture results (in hours) must be reproducible and reliable in the test. ISO 15630-3 gives currently unpersuasive and diverging results using a free corrosion approach for hydrogen charging. A newly developed test method uses cathodic polarization for defined hydrogen charging instead of an uncontrolled and variable electron supply by metal dissolution during free corrosion. With this new test method, a reliable differentiation is possible between highly susceptible-known "old-type" quenched and tempered prestressing steel, i.e., Neptun, Hennigsdorfer, Sigma, and currently approved cold-drawn wires St 1470/1670 (CDS-1670) and St 1570/1770 (CDS-1770). The reproducibility of the new test method was evaluated in a round-robin test with eight attended testing institutes on a St 1470/1670 (CDS-1670) batch.

KEYWORDS: *Hydrogen charging; ISO 15630-3; Prestressing steels, Round-robin; Stress corrosion cracking*

1. Introduction

In ISO 15630-3, the normative stress corrosion test to evaluate the susceptibility of prestressing steels against hydrogen-induced stress corrosion cracking (HiSCC) is specified as a constant load test (CL) in different electrolytes for prestressing steel products wires, bars, and strands. CL specifications aim to simulate practical conditions in a prestressed concrete building. The whole failure mechanism from corrosion onset to hydrogen charging and the fracture of the specimen is covered by the test. Unfortunately, the time to onset of corrosion, thus the intensity of hydrogen charging varies from test to test. The test standard is used in approvals and surveillance procedures, such as product type testing or third-party continuous surveillance. However, the history of test practice showed that the test is unpersuasive and provides limited information on susceptibility due to its high scattering.

Therefore, Seifert et al. (2023) developed a new test method in the WIPANO research project. The objective was to deliver a practicable and reproducible test method to allow a distinction between susceptible and robust prestressing steels. The first step investigated the influence of surface condition and test solution composition on hydrogen charging during free corrosion, see Seifert et al. (2024a).

In the second part, the test method was developed to allow as well to be applied in prestressing steel factory production control. In the meantime, the new test method, "Stress corrosion cracking test in thiocyanate solution with galvanostatic current," has been published in EN ISO 15630-3 (2024) in informative Annex B, where a new test cell and setup for cathodic polarization is presented, see also Figure 1.

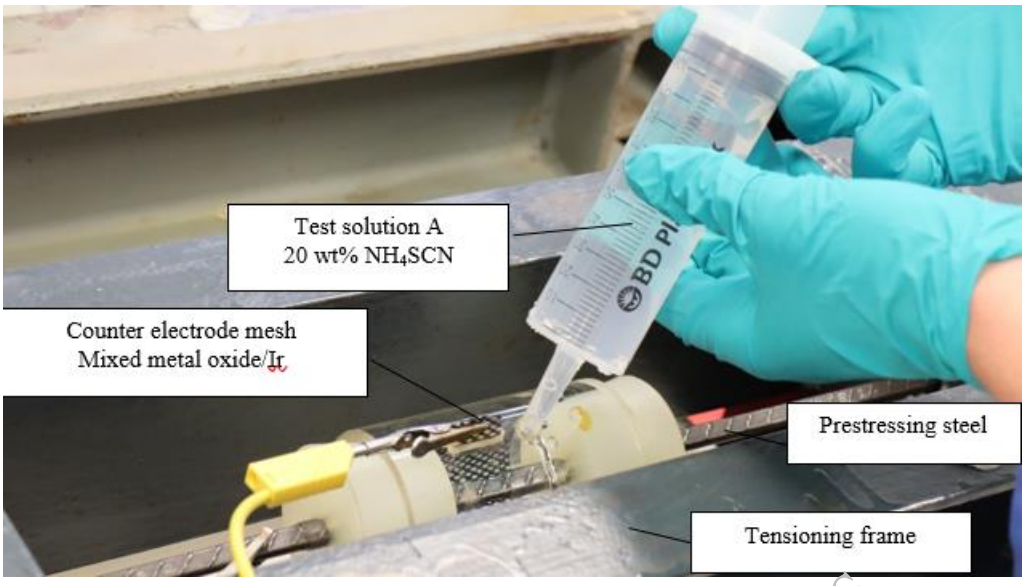

Figure 1. The newly designed test cell for stress corrosion tests with cathodic polarization.

A cathodic polarization immediately creates uniform hydrogen charging conditions from the test's start by locating the partial cathodic area at the steel surface. Thus, the anodic partial reaction is vice versa located at a counter electrode. The intensity of hydrogen adsorption can be adjusted in dependence on the galvanostatic cathodic current density to the steel surface (supply of electrons), forcing the so-called Volmer-Reaction (Equation 1).

$$H^+ + e^- \rightarrow H_{adsorbed} \quad (1)$$

As a result of a more intense Volmer-Reaction, the equilibrium, according to Equation 2, will balance due to hydrogen absorption/uptake (hydrogen charging) into the microstructure of the prestressing steel.

$$H_{adsorbed} \rightleftharpoons H_{absorbed} \quad (2)$$

The absorbed hydrogen $H_{absorbed}$ can induce stress corrosion cracking and thus the brittle fracture of the prestressing steel specimen. However, cathodic polarization oxidizes the solution's anion. This oxidation might influence the test solution's ability to act as a recombination poison. This work will focus on this and the limitations of this new test method. Finally, the gradation-ability of HiSCC-susceptibility between different prestressing steels with the new test method is described.

2. Experimental

According to EN ISO 15630-3 (2024), Annex B, test solution A consists of distilled/demineralized water and ammonium thiocyanate NH_4SCN with a mass fraction of 20 wt% NH_4SCN. Solution A was tempered at 50°C±1 K for 24 hours before testing and then cooled to a laboratory temperature of 22°C±3 K. During the stress corrosion test a temperature of 22°C±1 K was adjusted at the BAM laboratory. At the start of the test, the prestressing steels were preloaded to a constant load level of 80% tensile strength R_m. The test cell consists of an acrylic glas tube in which a mixed metal oxide coated (MMO) Ir-mesh was assembled along the inner circumference of the tube. The test cell was filled with solution A, see Figure 1. The prestressing steel was covered entirely with the solution at the start of the test. One minute later, the prestressing steel was cathodically polarized in galvanostatic mode using a Bank Wenking MP-87 potentiostat/galvanostat. For this, the prestressing steel was contacted as the working electrode, and MMO/Ir-mesh was approached as the counter electrode. Experiments were performed at a cathodic current density of 0.125 mA cm-2. The required DC was determined by multiplying the current density by the surface area in contact with the solution. The DC could be adjusted with an accuracy of ±2 µA. The time measurement started with galvanostatic operation, and the DC value was reached immediately. The load level and temperature were kept constant during the test. The time to brittle fracture was rounded to an accuracy of 0.01 h. The tested prestressing steel wires for evaluating the new test method are listed in Table 1.

Table 1. Used prestressing steels.

Designation	Rm [MPa]	Heat treatment, surface, geometry	Nominal cross-section [mm^2]	Currently, approved in Germany
Neptun	1663[a]	quenched and tempered, ribbed, edged	40.0	no
Hennigsdorfer	1524[a]	oil-quenched and tempered, ribbed, oval	35.0	no
Sigma	1569[a]	quenched and tempered, ribbed, oval	20.0	no
CDS-1670[c]	1670[b]	cold drawn, smooth, round	38.5	yes
CDS-1770	1770[b]	cold drawn, smooth, round	38.5	yes

[a] actual strength value; [b] nominal strength value; [c] round-robin batch

The chemical composition was determined by spark emission spectrometry (OES), see Table 2.

Table 2. Chemical composition of the prestressing steels used in percent by mass [wt.%].

Designation	C	Si	Mn	P+S	Cr	Ni	Mo	V	Cu
Neptun	0.641	1.322	1.028	0.033	0.070	0.071	0.010	0.002	0.178
Hennigsdorfer	0.591	0.918	1.076	0.040	0.133	0.064	0.012	0.002	0.195
Sigma	0.706	0.751	1.220	0.052	0.027	0.035	0.004	0.002	0.071
CDS-1670	0.833	0.285	0.749	0.022	0.158	0.059	0.013	0.002	0.090
CDS-1770	0.813	0.253	0.895	0.018	0.271	0.030	0.008	0.032	0.009

Where references were available, no differences were found between the measured chemical compositions and the tolerance specifications in the approval documents.

3. The influence of cathodic current density on time to fracture

This chapter is adapted from Seifert et al. (2023):

Stress corrosion tests at the 80% load level R_m with test solution A at 22°C were performed on polished surface conditions with different cathodic current densities $i_{cat.}$ on the *Hennigsdorfer* and CDS-1670. The results of these stress corrosion tests are shown in Figure 2.

The times to fracture decrease with increasing cathodic current density compared to free corrosion. Thus, cathodic polarization tests also shorten the test times compared to free corrosion tests, which is beneficial for factory production control, approvals, and continuous surveillance. The scatter of the results also decreases with increasing cathodic current density. Testing CDS-1670, the times to fracture at 0.250 mA cm^{-2} are similar to those at 0.375 mA cm^{-2}. However, compared to the *Hennigsdorfer*, the CDS-1670 shows a higher scatter at all cathodic current densities considered. This absolute scatter is material-dependent, which is oriented towards the susceptibility to HiSCC. In contrast, the relative scatter is similar for all tests. *Hennigsdorfer* seems to break before the CDS-1670 for each hydrogen charging situation considered, but the temporal differentiation between these high- and low-susceptible conditions is small at 1.000 mA cm^{-2}, 0.500 mA cm^{-2}, 0.375 mA cm^{-2}, and 0.250 mA cm^{-2}. A clear and reliable differentiation between high- and low-susceptible conditions is available at a cathodic current density of 0.125 mA cm^{-2}.

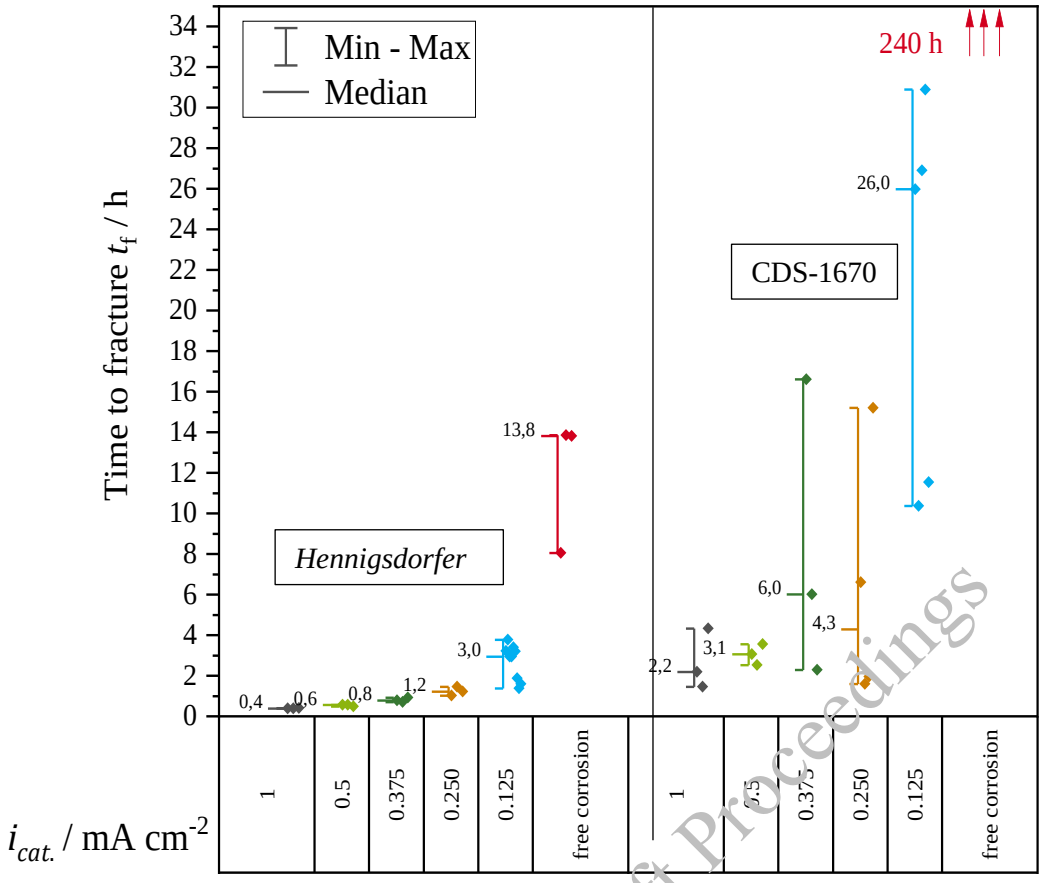

Figure 2. Times to fracture of the *Hennigsdorfer* (left side) and CDS-1670 (right side) at 80% in test solution A at 22°C. *Rm* in test solution A at 22°C with different cathodic current densities compared to the time to fracture results with free corrosion. Reproduced with permission, Seifert et al. (2023) Copyright 2023, Bundesanstalt für Materialforschung und -prüfung (BAM).

4. Importance of surface polishing

This chapter is adapted from Seifert et al. (2024b):
One goal for the new test method was to study the influence of the microstructure in combination with the stress level applied upon the susceptibility of the prestressing steel. The influence of the surface condition as a result of the manufacturing process is studied according to ISO 15630-3 in product type testing. The question was, which surface condition delivers the best results? Studies on the surface's influence on the steel's electrochemical polarization behavior concluded that testing on delivery condition surfaces is not recommended. The test surfaces should be homogenized using polishing as a sample preparation, see also Seifert et al. (2024a). Figure 3 directly compares specimens with delivery surfaces vs. samples with polished surface conditions in stress corrosion tests with cathodic polarization at 0.125 mA cm-2 cathodic current density.

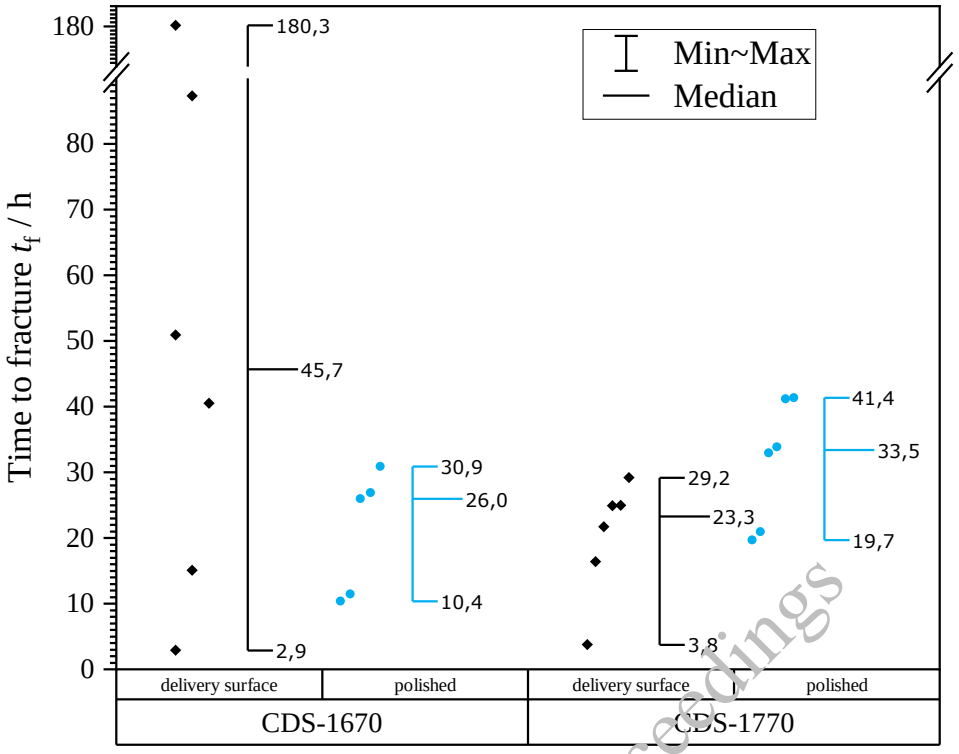

Figure 3. Stress corrosion tests on the CDS-1670 and CDS-1770 at 80% R_m in solution A at 22°C with cathodic polarization of 0.125 mA cm^{-2}. The scattering of results for delivery surface vs. polished surface was compared. Only fractures were considered. Reproduced with permission. [Seifert et al. (2023)] Copyright 2023, Bundesanstalt für Materialforschung und -prüfung (BAM).

No early fractures far below the median were measured with the polished surfaces. From a testing point of view, surface polishing offers the advantages of less extended scattering. The problem with delivery surfaces is the localized surface artifacts caused by the manufacturing or transportation process before testing. Artifacts (scratches) in the drawing layer cannot be excluded on prestressing steels. Polished surfaces without a drawing layer have a lower electrochemical polarization resistance with less extended scattering than delivered surfaces.

In cathodic polarization tests, hydrogen charging is controlled by applying a cathodic current density and begins immediately. Using the delivery surfaces with their artifacts (scratches) in the drawing layer influences polarization. Since the current seeks the path of least electrical resistance, and in the case of delivery surfaces, lower polarization resistances act in the area of the scratches than in the rest of the surrounding drawing layer. According to a parallel connection of resistors, the areas of the scratches have lower polarization resistivities, thus higher polarization currents. Consequently, the current density changes depending on the number, distribution, and area size of the artifacts on the drawing layer.

5. Recommended evaluation

This chapter is adapted from Seifert et al. (2024b). The desired safety level (conformity criterion of low susceptibility) of prestressing steels is orientated on the WIPANO project results. Some test procedures for assessing conformity were considered: Six experiments are required. Individual experiments can be stopped after 100 h and scored as a pass. The test is passed if all six individual time-to-fracture values are $\geqslant$ 16.6 h (criterion 1). If at least one particular result is less than 16.6 hours, a statistical evaluation with an outlier (Grubbs) test at the 95% confidence level is mandatory. If outliers are identified, they must be eliminated for further statistics. The passes (if any) are counted as individual values of 100 h in the statistical evaluation as if they were fractures. A test termination before 100 h is not a pass and must not be statistically evaluated. Determining the mean of the time to fracture, the sample standard deviation s, and the sample size n of the data without outliers is mandatory. Further, the $\mu_{lower,est}$ in hours is determined according to Equation 3.

$\mu_{lower,est}$ = mean + (t_p (s/sqrt(n))) $\mu_{lower,\,est} = \bar{x} + \left(t_p \frac{s}{\sqrt{n}}\right)$ (3)

The $\mu_{lower,est}$ is the lower interval estimate of the mean when the population standard deviation σ is unknown, also compare section 6.2 in ISO 12491. In other words, in 5 out of 100 cases, at a 95% confidence level, the sample times-to-fracture mean is below $\mu_{lower,est}$. The corresponding t-distribution fractile t_p can be taken from ISO 12491. If$\mu_{lower,\,est} \geq \mu_{lower,est} \geq$ 16.6 h, the criterion 2 is fulfilled. The t-distribution allows, especially for small sample sizes, to estimate the mean of the population. A normal distribution was tested and confirmed in Seifert et al. (2023). Considering passes with 100 h values in the statistics is controversial because the samples are supposedly "worse" evaluated, and the sample standard deviation *s* is reduced. However, this is accepted for evaluating the sample to be able to make a statistic with six experiments at all. An upper estimate is practically negligible for evaluation. Nevertheless, the maximum test duration of 100 h allows a wide range to differentiate between high and low-susceptible prestressing steel wires. If the sample size is six, lower estimate $\mu_{lower,est}$ of the mean is recommended for evaluating the desired safety level of prestressing steel wires. If criterion 1 is fulfilled, the test is passed; if not, fulfilling criteria 2 can lead to passing the test; otherwise, six experiments must be repeated.

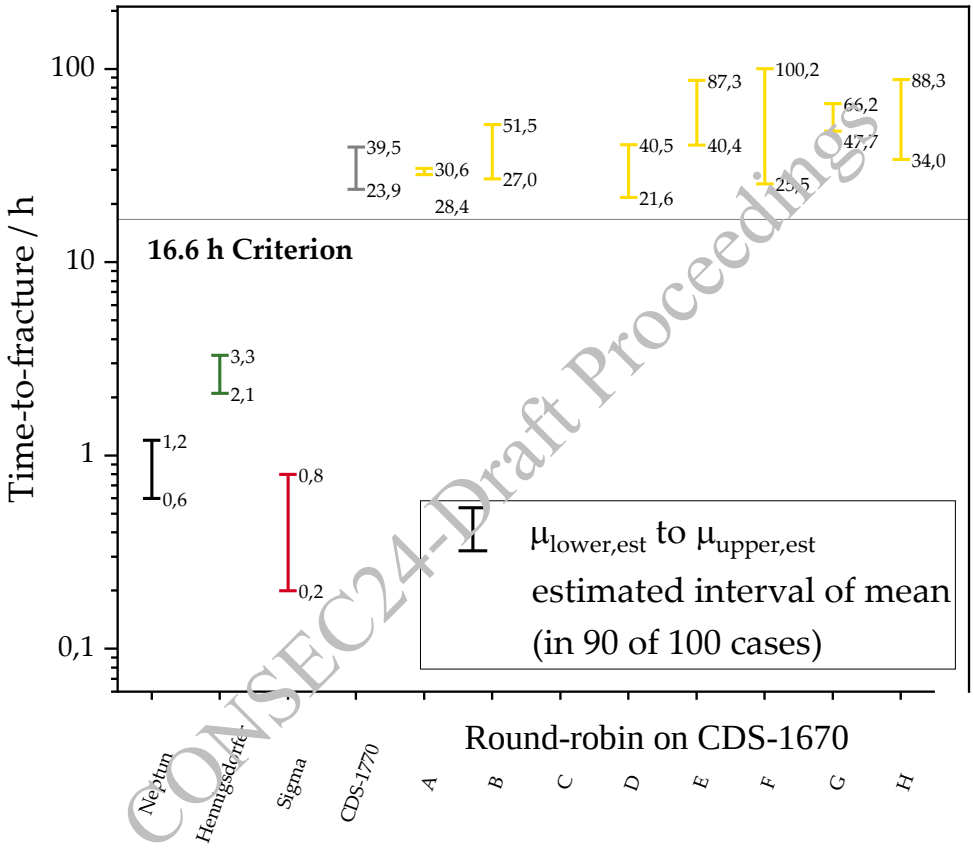

Figure 4. Comparison of stress corrosion test results at 80% R_m load level in solution A at 22°C±3 K with cathodic polarization of 0.125 mA cm^{-2} on polished prestressing steel wires. [adapted from Seifert et al. (2024b)]

6. Results with new test method according to EN ISO 15630-3:2024 (Annex B)

This chapter is adapted from Seifert et al. (2024b):
The test results of all investigated prestressing wires and samples with important estimates, determined according to Equation 3, are graphically summarized in Figure 4. Raw data and statistics can be read in Seifert et al. (2024b). There is a differentiation between highly susceptible-known quenched and tempered "old-type" wires Neptun, Hennigsdorfer, and Sigma (i.e., without Cr-alloying and manufactured until 1965) and the currently approved cold-drawn wires CDS-1670 and CDS-1770 (with Cr alloying), which are tested to have a lower susceptibility to hydrogen-induced stress corrosion cracking. The differentiation is significant and robust against the statistical scattering.

During the cathodic polarization of the prestressing steels in solution A, the anodic partial reaction is the electrochemical oxidation of the thiocyanate anion SCN^- located at the counter electrode. Less information is published about the electrochemical oxidation of SCN^-. Using platinum electrodes, cyclic voltammetry data from Liu et al. (2009) reported the products of total oxidation, i.e., the sulfate anion SO_4^{2-} and the cyanate anion OCN^-. Therefore, special care is demanded regarding protective clothing and disposal considerations. However, the formation of the sulfate anion SO_4^{2-} and the cyanate anion OCN^- can probably be avoided by applying an anodic current density lower than 1.0 mA cm^{-2}. As reported by Krishnan (2007), at these anodic current densities, the oxidative polymerization of thiocyanate forms brick-red polythiocyanogen $(SCN)_x$, according to Equation 4.

$$x\ SCN^- \rightarrow (SCN)_x + x\ e^- \text{ (Polymerization)} \quad (4)$$

This color of the solution was also observed in the course of the stress corrosion tests. In contrast to the monomers and total oxidation products, no information regarding the hazardous nature of polythiocyanogen has been found. To avoid total oxidation at the counter electrode in the shown test setup, the anodic current density is lower than 0.01 mA cm^{-2}. However, the counter-reaction according to Equation 4, changing the concentration of thiocyanate, which acts as a recombination poison for hydrogen evolution, is not studied in this paper but is estimated to have a minor influence on the stress corrosion test since the concentration of SCN^- is very high in solution A. Related work from Ichiba et al. (2016) has studied the effect of NH_4SCN concentration on time-to-fracture results at 50°C indicating that the consumption of SCN^- during stress corrosion tests is negligible since times to fracture of the tested prestressing steel are similar using 15, 18, and 20 wt% NH_4SCN.

7. Conclusions

This chapter is adapted from Seifert et al. (2024b). The key factors for the development of a new test method for assessing the susceptibility of prestressing steels to HiSCC were studied. The cathodic current density of 0.125 mA cm^{-2} at the test surface of the prestressing steel specimen guarantees a proper time-to-fracture differentiation. The importance of pre-polishing to minimize the spread of results was emphasized.
Knowing this, the BAM laboratory found a significant differentiation in time to fracture between highly susceptible "old-type" quenched and tempered prestressing steel wires and those currently approved and made by cold drawing. The reproducibility of the new test method with cathodic polarization was proved in the reported interlaboratory round-robin test. The importance of the found differentiation between highly susceptible "old-type" wires and currently approved wires CDS-1670 and CDS-1770 needs to be underlined as well because a misinterpreting of the susceptibility of wires is unlikely with this test method.
The new test method is ready for standardization in ISO 15630-3. For wires, the test method created a finer gradation of susceptibility from which users can benefit. Thus, prestressing steel producers can use it as a tool for evaluation in product development.
Regarding limitations, the test method can be applied in principle to wires and bars, although the conformity criterion of 16.6 h is only recommended based on prestressed steel wires results. More data on prestressing steel bars is needed to recommend a robust criterion for conformity; standards committees must consider this. For strands (twisted 2-, 3-, or 7-wires), the experimental problem is determining the effective surface area to polarize. Thus, in cathodic polarization, the needed galvanostatic current density of 0.125 mA per cm^2 cannot be ensured, leading to an undefined hydrogen charging intensity. Experimental solutions to test strands with the cathodic polarization method should also be developed.

Acknowledgments

The authors thank the German Federal Ministry for Economic Affairs and Climate Action (BMWK) for funding through the WIPANO initiative, Knowledge and Technology Transfer via Patents and Standards, FKZ: 03TNH019/A.

References

Ichiba, M., Takai, K., Sakai, J. (2016) "Effects of Test Conditions on Corrosion Reactions and Hydrogen Absorption in Hydrogen Embrittlement Tests Using an Ammonium Thiocyanate Solution" *ISIJ International*, 56, 397, https://doi.org/10.2355/isijinternational.ISIJINT-2015-288

ISO 12491:1997: Statistical methods for quality control of building materials and components.

Krishnan, P. (2007) "The effect of concentration in electrochemical oxidation of thiocyanate on platinum electrode" *Journal of Solid State Electrochemistry*, 11, 1327, https://doi.org/10.1007/s10008-007-0295-3

Liu, L., Feng, J., Wu, G., Lü, X., Gao, Q. (2009) "Dynamical Complexity in Electrochemical Oxidations of Thiocyanate" *Chinese Journal of Chemistry*, 27, 649. https://doi.org/10.1002/cjoc.200990106

EN ISO 15630-3:2024: Steel for the reinforcement and prestressing of concrete – Test Methods – Part 3: Prestressing Steel.

Seifert, L., Grunewald, A., Müller, T., Ebell, G. (2024) "Stress corrosion tests for prestressing steels—Part 1: The influence of surface condition and test solution composition on hydrogen charging", *Materials and Corrosion*, 1–13, https://doi.org/10.1002/maco.202313948

Seifert, L., Müller, T., Moersch, J., Ebell, G. (2024) "Stress corrosion tests for prestressing steels—Part 2: Round-Robin Test Proves Reproducibility of New Test Method with Cathodic Polarization and Surface Polishing", *Materials and Corrosion*,1–13., *submitted*

Seifert, L., Philipp, M., Ebell, G., Moersch, J., Müller, T. (2023) "A New Test Method for Evaluating Prestressing Steels' Susceptibility to Stress Corrosion Cracking", Final Report on WIPANO Research Project (FKZ: 03TNH019A/B/D); *Bundesanstalt für Materialforschung und -prüfung (BAM*) *Berlin*, https://doi.org/10.26272/opus4-58126

Strategic Approaches to Mitigate Execution Challenges in Condition Assessment and Restoration of Old RCC Structures: A Case Study of an Industrial Building

Rushabh Surendra Karnavat[1*] and Pallavi Prashant Nehete[2*]

[1]Founder and Head of M/s. Rushabh Surendra Karnavat, Mumbai 400 092, India
Email: rushabhkarnavat@gmail.com
[2]Assistant Professor, Department of Civil Engineering, A.P.Shah Institute of Technology, Thane 400 615, India
Email: papatil@apsit.edu.in

[*]Corresponding author

ABSTRACT

The sustainability and resilience of existing structures necessitate restoration as an imperative means. As societies increasingly prioritise the renovation of ageing infrastructure, understanding the diversified problems arising during the execution of condition assessment and restoration projects becomes crucial for successful implementation. Before execution, the study of the condition assessment of existing structure is important to identify and implement the right materials for the restoration. This research paper scrutinises the myriad challenges encountered during the execution phase of condition assessment and restoration of an existing 60 to 70-year-old industrial building. The structure was critically surveyed and diagnosed. Due to some practical difficulties, the categorisation of the building was done after non-destructive testing (NDT), and hence, a systematic operating procedure (SOP) has been finalised for condition assessment. The challenges involved were selection of test point and their location, interpretation of test results, camouflaged members, unavailability of detailed structural and architectural drawings, moving the meter room beneath, moving the high-tension cable wires, running industrial units, selecting materials for restoration works, etc. Restoration measures suggested are ready-mix polymer-modified mortar, ready-mix self-flowing non-shrinkable micro concrete, shear connectors and injection grouting.

KEYWORDS: *Condition assessment, Execution challenges, Non-destructive testing*

1. Introduction

Reinforced Concrete Cement (RCC) structures stand as enduring symbols of human innovation and engineering prowess, forming the backbone of modern infrastructure across the globe. Yet, as these structures age, they inevitably face a myriad of challenges, ranging from environmental degradation to material deterioration, threatening their structural integrity and functionality (Allen & Lano, 2019). Among the diverse array of RCC structures, industrial buildings occupy a pivotal role, serving as vital hubs for economic activity and industrial operations. However, the preservation and restoration of old industrial RCC structures present unique and formidable challenges, necessitating strategic approaches to navigate the complexities of condition assessment and restoration execution.

1.1 Contextualising the Challenge

The preservation of old RCC structures transcends mere historical preservation; it is imperative rooted in economic viability, environmental sustainability, and societal well-being (Lv et al., 2023). Industrial buildings serve as critical infrastructure supporting a wide range of industrial activities, from manufacturing and production to warehousing and distribution. However, the relentless march of time inevitably takes its toll on these structures, manifesting in various forms of deterioration, such as corrosion, cracking, and structural fatigue.

The challenge of preserving and restoring old industrial RCC structures is multifaceted, influenced by a confluence of factors unique to this context. Unlike residential or commercial buildings, industrial structures are subjected to heightened operational demands, exposing them to increased stressors and vulnerabilities. Furthermore, the structural configurations and materials used in industrial buildings may differ from conventional RCC structures, necessitating tailored approaches to assessment and restoration. Consequently, the execution of restoration projects for old industrial RCC structures requires meticulous planning, innovative methodologies, and strategic foresight to ensure both structural integrity and operational continuity (Shroff & Rout, 2021).

1.2 Significance of Strategic Approaches

Strategic approaches to mitigating execution challenges in the condition assessment and restoration of old RCC structures offer a departure from reactive, piecemeal interventions to proactive, systematic solutions. By adopting a strategic mindset, engineers and stakeholders can anticipate potential hurdles, optimise resource allocation, and prioritise interventions based on criticality and feasibility. Moreover, strategic approaches facilitate collaboration among multidisciplinary teams, fostering a holistic understanding of project objectives and constraints.

The significance of strategic approaches is underscored by their potential to enhance the efficacy and efficiency of restoration projects while minimising disruptions to industrial operations. By leveraging innovative technologies such as non-destructive testing (NDT), structural health monitoring (SHM), and Building Information Modeling (BIM), engineers can gather comprehensive data on the structural condition of old RCC structures, enabling informed decision-making and targeted interventions (Malekloo et al., 2022). Furthermore, strategic approaches emphasise stakeholder engagement and communication, ensuring that project goals align with organisational objectives and regulatory requirements.

1.3 Objectives of the Research

In light of the challenges mentioned above and opportunities, the primary objective of this research article is to elucidate strategic approaches for mitigating execution challenges in the condition assessment and restoration of old RCC structures, with a specific focus on industrial buildings. To achieve this objective, the research aims to:

Identify the key execution challenges encountered in the assessment and restoration of old industrial RCC structures, drawing insights from empirical data and case studies.

In essence, this research article seeks to advance knowledge and practice in the preservation and restoration of old RCC structures by providing actionable insights and guidance for navigating the complexities of execution challenges. Through theoretical synthesis, it endeavours to inform decision-makers, practitioners, and researchers about the strategic imperatives driving the sustainable preservation of our built structures.

2. Case study

2.1 Study area

Mumbai's small-scale industrial estate premise was taken as the study area. Coastal regions host a multitude of ageing structures, subject to accelerated deterioration due to their exposure to harsh environmental conditions. Saltwater corrosion, high humidity, and extreme weather events pose significant challenges to the maintenance and retrofitting of these structures. Traditional condition assessment methods often fall short in accurately characterising deterioration, necessitating innovative approaches to ensure structural integrity and resilience.

Understanding the complex degradation mechanisms specific to coastal environments is crucial for effective retrofitting strategies. Corrosion of steel reinforcements, erosion of concrete surfaces, and biological growth exacerbate structural deterioration, compromising safety and functionality. Moreover, the historical and cultural significance of many old coastal structures adds complexity, requiring a balanced approach that integrates structural engineering principles with heritage preservation objectives (Xio et al., 2021).

2.2 Standard operating process (SoP) for condition assessment

Preparation

Necessary permissions and access from building owners or relevant authorities were obtained for the execution of the case study. However, historical documents and previous assessments were not available to understand the structural history and any past issues. Historical documents provide valuable context regarding the construction, materials used, and previous maintenance activities. Without this information, it becomes challenging to understand the building's original design intent and the evolution of its condition over time. The absence of previous assessments makes it difficult to establish the structural reliability of the building. Structural weaknesses or deficiencies may go undetected, increasing the risk of structural failure or collapse. To mitigate these difficulties, alternative methods such as non-destructive testing, advanced imaging techniques, and forensic analysis can be employed to gather as much information as possible about the building's condition and history.

Visual inspections

Certain areas of a building, such as concealed spaces, high ceilings, or areas obstructed by furniture or equipment, were difficult to access visually. This limited accessibility can hinder the inspector's ability to evaluate these areas for potential issues thoroughly. Some areas of the building were obscured by machinery or other structures. This can make it hard for inspectors to examine all areas for signs of deterioration or damage thoroughly.

In poor lighting conditions, especially in areas that are not frequently accessed, it's a struggle to properly assess the condition of structural components, leading to potential oversights or inaccuracies in their evaluations (Figure 1). The building featured large, open floor areas without internal support columns, allowing for uninterrupted manufacturing processes. While aesthetically pleasing and functional, these expansive spaces posed challenges in assessing structural integrity, especially for hidden defects or deterioration in the roof or ceiling structures.

The typical utilisation of steel or reinforced concrete columns and beams to support the roof and transfer loads to the foundation exhibited signs of corrosion, fatigue, or deformation over time, especially pertaining to atmospheres with high humidity or exposure to chemicals used in manufacturing processes. Inspecting these elements requires access to all sides of the columns and beams, which can be challenging in densely packed production areas.

Restoring a structure with unknown original concrete specifications presents a complex engineering challenge. While the suggested M40 grade concrete may offer potential benefits in terms of strength and durability, it also poses risks related to compatibility, structural integrity, and adherence to preservation guidelines. Careful assessment, testing, and consideration of alternative approaches are crucial in addressing these challenges and ensuring the successful restoration of the structure.

The meter room consisted of heavy machinery and totally decapitated high-tension cables. This resembled the accessibility problem in identifying and executing the issues. The heavy wiring carrying current twisted the worker's mind, which made it difficult to execute the task. Shifting the high-tension lines installed approximately 60 years ago for slab casting unveiled the greatest challenge for engineers.As the industries are running 24 hours a day power supply shutdown could not be possible. Condition assessment and implementation of mitigation strategy without hurdling the industrial working posed remarkable mission for engineers.

Figure 1. Structural deteriorations observed in the structure

The foundation of an industrial building must be capable of supporting heavy machinery and equipment loads while resisting settlement and soil movement. Common foundation problems in old buildings include differential settlement, cracks, and soil erosion, which can compromise the stability of the entire structure. Assessing the condition of the foundation may require geotechnical investigations and soil testing to identify potential risks.

Non-destructive testing (NDT)

Each material has its unique properties and response to NDT methods, requiring inspectors to select appropriate techniques for different areas of the building. Surface conditions can significantly impact the effectiveness of NDT techniques. Rust, paint, coatings, and surface irregularities may interfere with signals or readings, leading to false positives or negatives. Surface preparation may be necessary to ensure accurate results, adding time and cost to the inspection process. Environmental conditions within industrial buildings, such as temperature, humidity, and airborne contaminants, can influence the performance of NDT techniques. Extreme temperatures may affect equipment calibration, while high humidity levels can lead to condensation or corrosion on inspection tools. Conducting NDT inspections in industrial

environments poses safety risks to inspectors and other personnel. Hazards such as moving machinery, elevated work areas and exposure to hazardous materials must be efficiently managed to safeguard everyone involved in the inspection process.
Interpreting NDT results obtained during condition assessment involves assessing a building's structural health and integrity based on various parameters such as material properties, cracks, voids, corrosion, and other defects. The goal was to identify potential issues or areas of concern that may require further investigation or remediation. When transitioning between old and new NDT codes, differences in testing methodologies, acceptance criteria, and reporting standards could influence the interpretation of results. However, the presence of variations does not automatically indicate structural failure. Instead, it underscores the need for a nuanced approach to interpretation. The interpretation of NDT results relies on the expertise and judgment of qualified engineers or inspectors who can critically evaluate the data in light of relevant factors such as building usage, occupancy levels, environmental conditions, and regulatory requirements.

Structural analysis

Structural analysis of old industrial buildings for condition assessment was complex due to factors such as diverse and unknown construction methods, material deterioration, dynamic loads, foundation considerations, nonlinear behaviour, seismic vulnerability, and limited inspection access. Engineers faced challenges in accurately modelling structural systems, accounting for material degradation, and assessing seismic risk, requiring a multidisciplinary approach and advanced analysis techniques to ensure comprehensive evaluation and effective maintenance strategies.

2.3 Standard operating process (SoP)

Based on the observations in section 2.2, the SoP for condition assessment shall be as follows, Carry out a series of detailed external visual inspections and broad condition assessments of the building mentioned above, with special emphasis on the accessible and possible external structural members Identify locations of possible spalling of concrete distressed spots and highlight them in the report. Collect photographic evidence of distressed damages and prepare NDT and SDT layouts. Tapping by Light Fiber Hammer (On RCC Members) for inspection of internal units Inspection of terrace areas, staircase and passage areas.
The condition of concrete, compressive strength, condition of steel reinforcement and corrosion effect shall be tested by rebound hammer test (RH), ultrasonic pulse velocity test (UPV), carbonation test, half cell potentiometer test (HCP), sulphate contents test, chloride contents test, pH, core cutting compressive strength measurement test (semi destructive test), cover meter, rebar mapping test.
Preparation and submission of a detailed Structural Audit and Assessment report based on visual inspections, NDT, and SDT with Photographic evidence covering the detailed extent of distresses and suggesting techno-commercially the most suitable methodology for repair, retrofitting, and strengthening measures if required.

3. Summary

Preserving and restoring aging reinforced concrete structures (RCC) presents significant challenges, particularly in execution. This paper delves into strategic methodologies aimed at mitigating these challenges in the condition assessment and restoration of old RCC structures, illustrated through a detailed case study of an industrial building. The paper begins by emphasizing the importance of preserving historic RCC structures, recognizing their architectural and cultural significance. It underscores the necessity of addressing execution challenges while balancing preservation goals with structural integrity.
Navigating through the complexities of execution challenges, the paper identifies key obstacles including structural deficiencies, material degradation, logistical constraints, and regulatory compliance. Each challenge is analyzed to uncover its underlying causes and potential impacts on restoration efforts. To tackle these challenges, the paper advocates for a strategic framework tailored to RCC structure restoration. Central to this framework is the integration of advanced assessment techniques such as non-destructive testing (NDT) and structural health monitoring (SHM). These methodologies provide vital insights into structural condition, facilitating informed decision-making and targeted interventions.

Furthermore, the paper highlights the importance of interdisciplinary collaboration in successful restoration endeavors. By fostering partnerships between various stakeholders including engineers, materials scientists, preservationists, and regulatory authorities, a comprehensive approach is fostered, leveraging diverse expertise to address restoration challenges holistically.

Innovative methodologies and materials are also explored, offering sustainable and cost-effective alternatives to traditional restoration techniques. These solutions, ranging from advanced ready mix repair mortars to self-flowing non shrinkable micro concrete, enhance the longevity and resilience of restored RCC structures.

Through a detailed case study of an industrial building undergoing restoration, the paper illustrates the practical application of strategic approaches. Key insights and lessons learned from the project lifecycle—from initial assessment to implementation and monitoring—are presented, providing valuable guidance for future RCC structure restoration initiatives.

Addressing the structural complexities in the condition assessment of old industrial buildings requires a comprehensive approach that combines visual inspection, structural analysis, material testing, and specialised engineering expertise. Utilising proficient specialists possessing expertise in industrial infrastructure evaluations can facilitate the identification of potential hazards and the formulation of proficient maintenance and restoration methodologies, thereby extending the operational longevity of these invaluable facilities. The NDT inspections of old industrial textile buildings should be conducted by qualified personnel with experience in industrial building assessments and NDT techniques. A comprehensive inspection plan should be developed to address specific challenges and ensure the accurate detection of hidden defects, ultimately facilitating informed decision-making regarding maintenance and repair strategies.

4. Conclusions

This research paper has explored strategic approaches to address the significant execution challenges inherent in the condition assessment and restoration of old RCC structures, with a specific focus on an industrial building as a case study. Through an in-depth analysis, it has been demonstrated that a proactive and comprehensive strategy is essential for effectively mitigating these challenges.

The findings highlight the importance of thorough condition assessments, utilising advanced technologies such as non-destructive testing and structural health monitoring, to accurately identify deterioration and structural deficiencies. Additionally, strategic planning and resource allocation are crucial for developing tailored restoration solutions that address the unique complexities of each structure while ensuring cost-effectiveness and long-term sustainability.

Moreover, fostering collaboration among multidisciplinary teams, including structural engineers, architects, contractors, and stakeholders, is essential for leveraging diverse expertise and perspectives throughout the assessment and restoration process. This collaborative approach facilitates innovative problem-solving and ensures the successful implementation of restoration strategies.

Furthermore, the paper emphasises the significance of adhering to international standards and best practices in structural engineering and construction and complying with local regulations and codes. By prioritising safety, quality, and durability, organisations can enhance the resilience of old RCC structures and safeguard against future deterioration.

Overall, this research underscores the importance of adopting a holistic and proactive approach to mitigate execution challenges in the assessment and restoration of old RCC structures. By integrating advanced technologies, strategic planning, interdisciplinary collaboration, and adherence to standards, organisations can effectively preserve the integrity and functionality of these vital infrastructures for future generations.

Acknowledgements

We would like to express our sincere gratitude to all those who contributed to the completion of this paper. We are also thankful to the Managing committee of Small-Scale Industrial Estate, Mumbai, for providing the necessary resources and support throughout this study. Their encouragement and assistance have been invaluable in advancing our research endeavours. Additionally, we extend our appreciation to our office staff and personnel involved in the case study of the industrial building, whose cooperation and assistance facilitated the collection of essential data and information vital to this research. Furthermore, we

acknowledge the contributions of our colleagues, peers, and mentors who provided valuable feedback, guidance, and encouragement during this project. Lastly, we express our gratitude to our families for their unwavering support, understanding, and encouragement during the various stages of this endeavour. Their collective contributions have been indispensable in the completion of this paper, and we are sincerely grateful for their support and encouragement.

References

Allen, E., & Iano, J. (2019). Fundamentals of building construction: materials and methods. John Wiley & Sons. Lv, W., Dai, D., Wei, R., & Bai, L. (2023). Restoration of the Nanjing Circumvallation in Sustainable Urban Planning: Application of Environmental Ethical Decision-Making Model. *Sustainability*, 16(1), 5.

Malekloo, A., Ozer, E., AlHamaydeh, M., & Girolami, M. (2022). Machine learning and structural health monitoring overview with emerging technology and high-dimensional data source highlights. *Structural Health Monitoring*, 21(4), 1906-1955.

Shroff, T. S. K., & Rout, K. (2021). Remaining Life Assessment (RLA) Study and Retrofitting Old and Dilapidated Buildings. *Recent Developments in Sustainable Infrastructure: Select Proceedings of ICRDSI 2019* (pp. 377-394). Springer Singapore.

Xiao, X., Seekamp, E., Lu, J., Eaton, M., & van der Burg, M. P. (2021). Optimizing preservation for multiple types of historic structures under climate change. *Landscape and Urban Planning*, 214, 104165.

Probable Issues with using Sulfur Characteristic X-ray Peak Position to Quantify Iron Sulfides in Aggregates: Peak Shifts Due to Beam Exposure Time and Beam Current

D. Banik[1], A. S. Brand[2*]

[1]Virginia Polytechnic Institute and State University, Blacksburg, Virginia, USA
Email: dipbanik@vt.edu
[2]Virginia Polytechnic Institute and State University, Blacksburg, Virginia, USA
Email: asbrand@vt.edu

[*]Corresponding author

ABSTRACT

Concrete deterioration due to the presence of oxidizable iron sulfides in coarse aggregates is a major durability issue in certain regions of the world. It is important to identify and quantify sulfides with oxidation potential to screen deleterious coarse aggregates before use in concrete. Based on oxidation states, sulfur shows a distinctive peak at the Kα X-ray peak position that can be leveraged to differentiate sulfur with oxidation potential for this screening process. Previously, researchers have used sulfur (S) Kα shifts to quantify sulfur oxidation potential in silicate glass formed due to volcanic processes using an electron probe microanalyzer (EPMA). However, the SKα shifts during microanalysis can be influenced by other factors, such as physical properties of the mineral, surface conditions, beam current, and acquisition time, leading to the generation of significant thermal energy. This study was undertaken to observe the shifts in SKα peak energy due to two different beam currents and three different acquisition times using an EPMA to develop a proper sulfide quantification method that leverages peak shifts. It was observed that the experimental conditions affected the SKα peak shifts differently based on the minerals. Moreover, both beam current and acquisition times affected the peak positions of the minerals; however, there was no clear relationship between the shifts.

KEYWORDS: *EPMA, Sulfur Speciation, Sulfur Kα Peak Shifts, Beam Damage*

1. Introduction

Sulfur is one of the most abundant earth materials, and sulfur ranges from –2 to +6 in oxidation states at the conditions relevant to the rock formation in our solar system (Chowdhury et al., 2023). Because of that, different sulfur-bearing minerals of sulfide (pyrites, marcasite, pyrrhotite) and sulfate (gypsum, anhydrite) are found in coarse aggregates sourced from different quarries for concrete production (Cruz-Hernandez et al., 2020). Among these minerals, pyrrhotite ($Fe_{1-x}S$) and pyrite (FeS_2), in the presence of suitable conditions (oxygen and moisture), can oxidize to sulfates (Chinchón-Payá et al., 2015). When aggregates that contain pyrite and pyrrhotite are used in concrete, the released sulfate can react with hydration products and generate conditions for an internal sulfate attack (Jana, 2022a). Compared to pyrite, pyrrhotite has almost four times higher solubility, and it oxidizes faster in the presence of oxygen than pyrite (Jana (2022b)). Volume expansion due to primary expansions from the oxidation of pyrite and pyrrhotite can be up to 209.96 cm^3/mol of sulfide, whereas the internal sulfate attack-related secondary volume expansions can be up to 182.89 cm^3/mol of sulfide (Jana, 2022a). As concrete has poor tensile resistance, such expansion force has the potential to degrade and generate cracks in structures. Deteriorations in concrete structures due to the oxidation of iron sulfides in aggregates have been observed in parts of Europe (Norway, Ireland, Spain, Wales), Canada (Quebec, Montreal), and the USA (Connecticut, Kentucky, Massachusetts) (Jana, 2022b). Over 35,000 homes in Connecticut and 10,000 homes in Massachusetts were reported facing widespread cracking and crumbling of foundations due to pyrrhotite oxidation in the coarse

aggregates (Jana, 2022b). Considering the severity of iron sulfide attacks, several researchers (*e.g.*, Castillo Araiza et al., 2024, Cruz-Hernandez et al., 2020, Marcelino et al., 2020, Rodrigues et al, 2016a, Santos et al., 2024) are working on qualitative and quantitative identifications of the presence of iron sulfide minerals in concrete aggregates.

Techniques including X-ray fluorescence spectroscopy (XRF), combustion total sulfur analyzer, ion-exchange chromatography, gravimetry methods, *etc*., are popular methods to analyze total sulfur in samples regardless of oxidation states. Rodrigues et al. (2016b) proposed a screening methodology of identifying coarse aggregates with oxidation potential considering total sulfur content as the primary check. However, quantifying the presence of sulfides is the most important criterion for screening coarse aggregates to prevent concrete damage due to oxidation. There are some techniques, such as mineral decomposition based on temperature, X-ray photoelectron spectroscopy (XPS), electron probe microanalysis (EPMA), wavelength-based X-ray fluorescence spectroscopy (WXRF), and X-ray absorption near edge structure (XANES), that can identify different sulfur oxidation states (Chubarov et al., 2016. Based on the ratios of sulfur to other elements present in minerals, sulfur oxidation states can be identified. However, to properly quantify elemental concentration, matrix-matched standards are always required, which makes the analysis process difficult and time-consuming. Moreover, sulfur makes it difficult to assign oxidation state just based on composition alone as multiple states of sulfur can coexist within the mineral structure (Golla-Schindler et al. (2006)). However, sulfur oxidation states influence the position of $SK_{\alpha 1,2}$, $SK_{\beta 1,3}$ peaks and these microanalysis techniques can leverage this phenomenon and differentiate between different sulfur species (Chubarov et al., 2016, Rowe et al., 2007). Using EMPA, it is possible to control beam size to analyze specific minerals ranging from 1 µm to 50 µm and the higher resolution allows for monitoring the different elemental peak positions with significant ease (Rowe et al., 2007). However, it is sometimes important to analyze a particular area of a sample multiple times to collect ranges of information. Based on analysis conditions and technique, multiple beam interactions can affect the composition and structure of the mineral (Hughes et al., 2020).

To leverage this technique of differentiating sulfides from sulfates, it is important to study the changes in the peak shifts due to other factors rather than pure oxidation states. A small proportion of the energy carried by the incident electron beam during microanalysis manifests as X-rays, photons, and other forms of electromagnetic radiation, with the majority being transformed into thermal energy within the target material (Reed, 2005). The temperature change due to beam interaction can change the composition of the analytes in the forms of oxidation and element migration, generally referred to as "beam damage" (Hughes et al., 2020, Rowe et al., 2007). Reed (2005) reported that this temperature change depends on the incident electron energy, current, beam diameter, and thermal conductivity of the analyte without having a concern about the acquisition time. The assumption behind the exclusion of acquisition time during temperature prediction was that the surface will immediately reach equilibrium temperature conditions when the electrons are incident. However, defects can be present in the surface coating during the experiments, which can trap electrons and create an inhomogeneous temperature profile. Therefore, different analytical conditions and surface defects can influence the peak position of elements. It is imperative to note that the presence of different metals and changes in the metals-to-sulfur ratios can affect the bond geometry and further influence the sulfur peak position (Buckley & Woods, 1984). Moreover, trace metal inclusions can alter the thermal conductivity of a mineral and change the level of temperature rise due to beam interactions (Diment & Pratt, 1988).

In light of this literature review, it is imperative to state that quantifying the available sulfides in aggregates based on the sulfur oxidation state is a powerful microanalysis technique. However, to leverage that effectively and confidently, it is critical to learn, alongside the oxidation state, which other factors influence the SKα X-ray peak shifts. Thus, this study was undertaken to observe the potential SKα X-ray peak shift due to conditions related to analysis techniques (*i.e.*, beam current, data acquisition time), as comprehensive studies related to this topic are absent in the current literature.

2. Experimental Program

A JEOL JXA-iHP200F field emission electron microprobe was used to analyze the SKα X-ray peak shift of different sulfur mineral standards under a 15 kV accelerating voltage and 20-micron beam diameter. The EPMA is equipped with five different wavelength dispersive spectrometers (WDS detectors), which sort X-rays based on wavelength. Each spectrometer is equipped with analyzing crystals and a detector. Based

on the orientation of the crystals, the spectrometers allow the detection of only one element at a time. Table 1 presents the available crystals in these different spectrometers and which elements are properly detectable using those crystals. As the pentaerythritol crystal was mostly optimized to detect the SKα line, spectrometers 1, 2, 3, and 4 were used in this study.

Table 1. Available crystals in the different spectrometers and detectable elements using these crystals.

Crystal	Name	Available in Spectrometer	Detectable Elements (Characteristic X-ray)
LDE1	Synthetic W-Si Layered Dispersive Element	1	C-F (Kα) Optimized for O analysis
LDE2	Synthetic Ni-C Layered Dispersive Element	1, 5	B-O (Kα) Optimized for C analysis
TAP	Thallium Acid Phthalate	1, 2, 5	O-Si (Kα) Cr-Y (Lα) La-Os (Mα)
PETJ	Pentaerythritol	1, 2, 3, 4	Si-Cr (Kα) Kr-Pm (Lα) Hf-U (Mα)
LiF	Lithium Fluoride	3, 4	K-Rb (Kα) Sn-U (Lα) Pu (Mα)

The information about the sulfate and sulfide minerals in this study is presented in Table 2. Six spots were analyzed in every mineral under two different beam currents (50 nA and 100 nA) and three different exposure times (100 ms, 300 ms, and 1000 ms). The captured signals were then analyzed using OriginPro (v.2024, OriginLab Corporation, Northampton, MA, USA) to identify the peak locations. A predefined "Gauss" peak search function was to deconvolute the signals and locate the peaks.

Table 2. Standard minerals used in the study.

S Oxidation State	Mineral	Formula	S Weight (%) (Measured using EDX)
Sulfide (S^{2-})	Marcasite	FeS_2	53.19
	Arsenopyrite	FeAsS	17.89
	Cinnabar	HgS	15.00
Sulfate (S^{6+})	Anhydrite	$CaSO_4$	23.68
	Celestine	$SrSO_4$	17.66
	Baryte	$BaSO_4$	13.58

3. Results and Discussions

This section presents the SKα peak shift due to the different beam currents and spectra acquisition times. However, it is important to note that due to the differences in the spectrometer configuration, the acquired spectra can show differences in peak position and intensity. Figure 1 presents the S spectra acquired for anhydrite under 50 nA current and 100 ms acquisition time. Even though every experimental condition was identical, due to differences in the spectrometer configurations, the acquired spectra showed some differences in terms of peak intensity and peak position. Therefore, it is important to be consistent with the spectrometers while comparing the different mineral peak positions. For this report, sulfur spectra captured using only spectrometer 2 was considered to compare different minerals and the effects of beam damage.

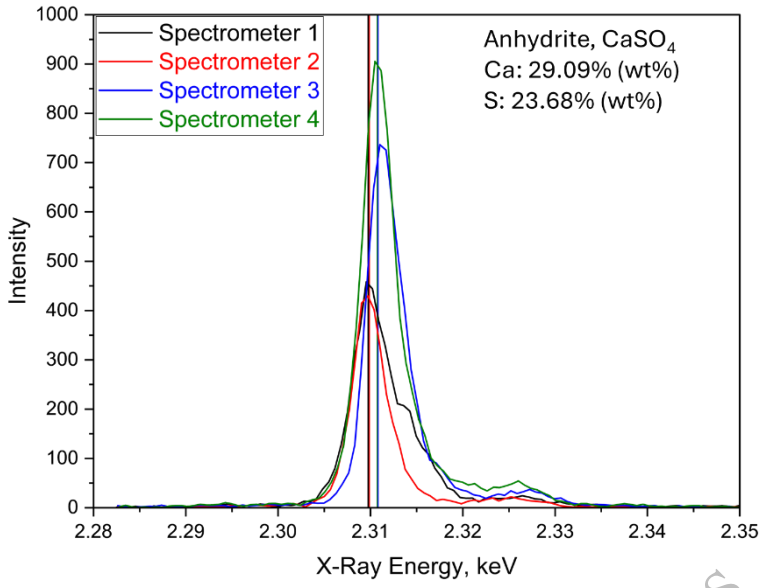

Figure 1. SKα peak position shift for anhydrite due to spectrometer configurations.

Figure 2 presents the sulfur X-ray peak positions of different oxidation states using EPMA spectrometer 2. This graph indicates ~1.16 eV peak shifts (Anhydrite ~ Marcasite) due to the oxidation states of S. Previous researchers (Chubarov et al., 2016, Rowe et al., 2007) showed that it is possible to approximate the relative proportions of sulfides and sulfate based on the SKα peak position. This makes analyzing sulfur peak position in a sample a useful tool to study the presence of sulfate to screen the aggregates with pyrrhotite.

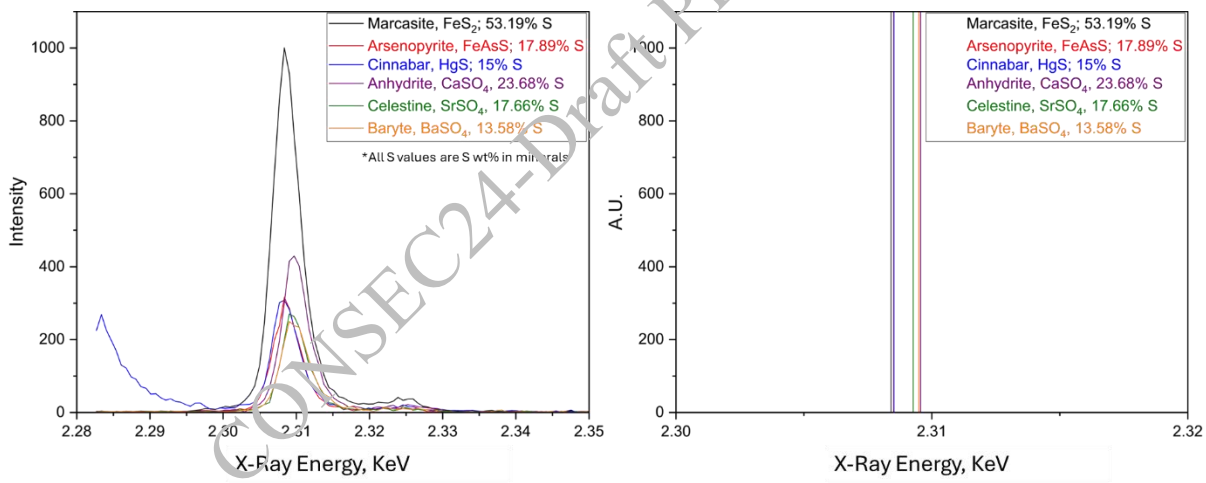

Figure 2. Sulfur X-ray peak position shifting due to different oxidation states under EPMA. The peak positions were measured under 50nA beam current and 100ms acquisition time. All the sulfide peaks were clustered around 2.3085 keV position, and the sulfates were clustered around 2.3095 keV position.

3.1 Observable beam damage

Figure 3 and Figure 4 present the observable beam damage in anhydrite and arsenopyrite minerals under different conditions. It can be observed that the anhydrite showed more visible vulnerabilities to beam conditions compared to the arsenopyrite. This is due to the differences in thermal and electric conductivity that can properly channel the electrons to resist higher temperature rise and damage to the specimens. This damage is responsible for peak shifts in the SKα X-rays. Also, another way to increase the conductivity of the sample and decrease the temperature rise is to properly coat the sample with a conductive layer. However, if the sample contains bubbles underneath the surface, then, due to the poor resistivity, the bubbles can rupture and strip the coating off. This in return can damage the coating, trap electrons, and increase the heat of the surface leading to significant beam damage.

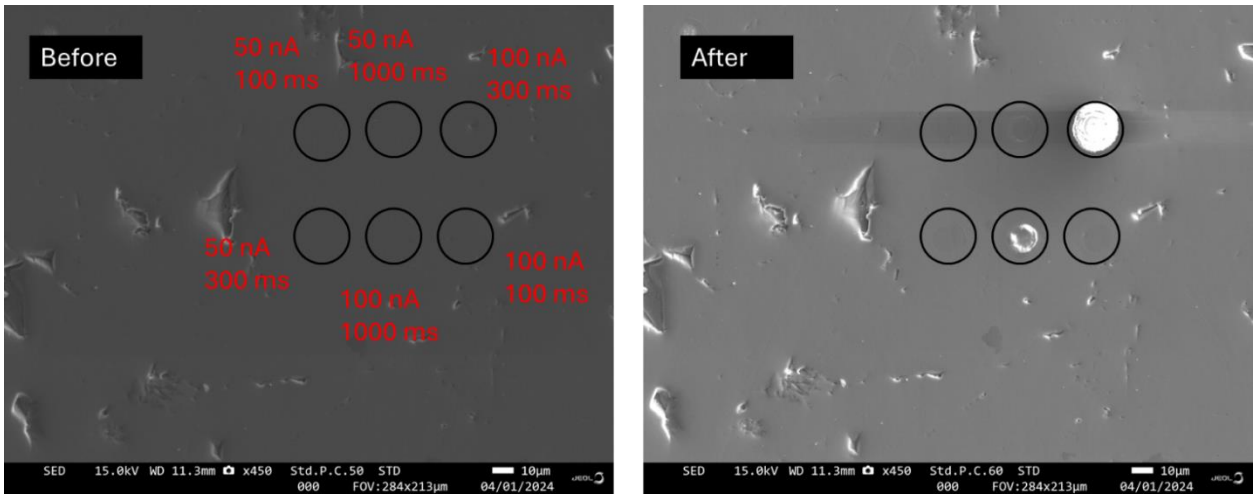

Figure 3. Observable beam damage after the analysis of the anhydrite mineral under different experimental conditions.

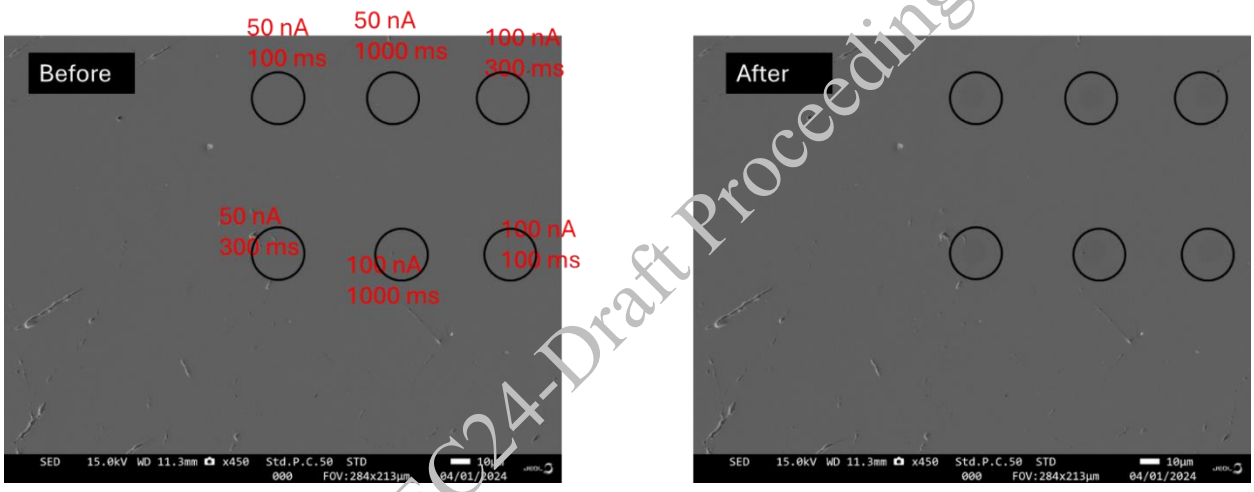

Figure 4. Observable beam damage after the analysis of the arsenopyrite mineral under different experimental conditions.

3.2 SKα peak shifts due to experimental conditions

Figure 5 presents the sulfur spectra of anhydrite under different experimental conditions. Higher beam energy and acquisition time showed significant changes in the peak intensity as those influenced the X-ray generation. Moreover, these variable experimental conditions influenced the SKα peak positions too. Figure 6 presents the peak positions of the anhydrite mineral under different experimental conditions calculated using peak decomposition. It shows that both beam current and acquisition time influenced the peak position. However, 100 nA and 300 ms showed deviation from the peak shifts compared to other observations for anhydrite; this was due to the significant beam damage in the specimen observed in the Figure 3.

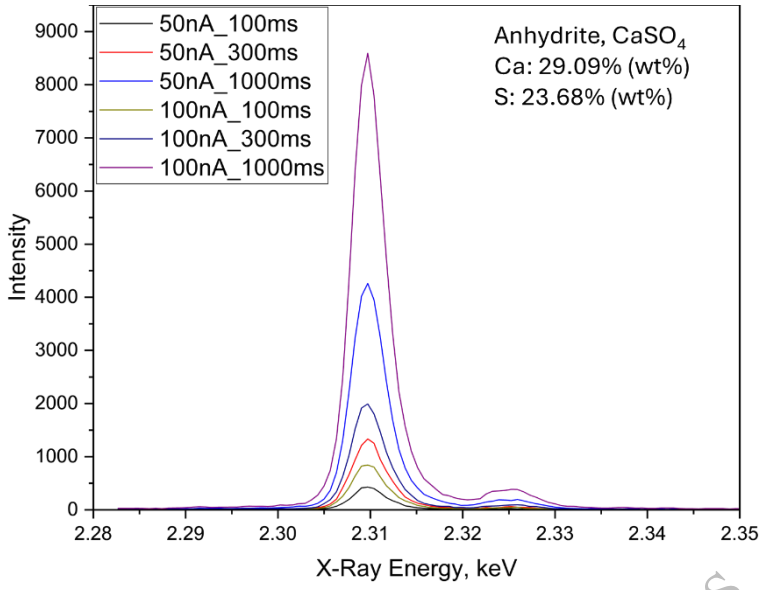

Figure 5. Acquired S spectra of anhydrite under different experimental conditions using spectrometer 2.

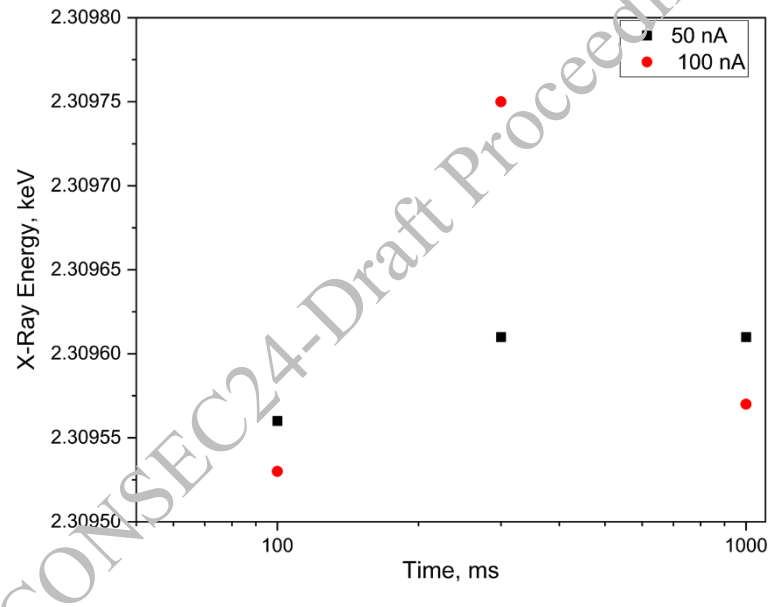

Figure 6. Changes in the S X-ray peak position of anhydrite mineral due to experimental conditions.

Figure 7 presents the changes in peak shifts in all the minerals due to the variable experimental conditions. There are observable peak shifts among sulfates and sulfides due to the specific mineralogical compositions. Moreover, changes in the peak positions were observed due to the beam damage. The amounts of damage varied based on the minerals, as the physical characteristics and sample homogeneity (presence of bubble, conductive coating) during the analysis are the major influences in the analysis. For 50 nA only celestine and cinnabar and for 100 nA all the sulfates showed deviations in the peak positions due to variable acquisition times. For 50 nA, changing of acquisition time from 100 ms to 300 ms brought the highest of 0.29 keV and changes of 100 ms to 1000 ms brought the highest of 0.36 keV in peak shifts for celestine. Whereas, for 100 nA, changing of acquisition time from 100 ms to 300 ms brought the highest of 0.29 keV and changes of 100 ms to 1000 ms brought 0.36 keV in peak shifts for baryte.

Moreover, changing beam current from 50 nA to 100 nA showed peak shifts of 0.51 keV for celestine for 100 ms acquisition time, 0.16 keV for baryte for 300 ms acquisition time, and 0.27 keV for cinnabar for 1000 ms acquisition time. It is imperative to note that marcasite had the highest sulfur content among all the minerals and showed the highest stability in terms of peak energy positions under all these experimental conditions.

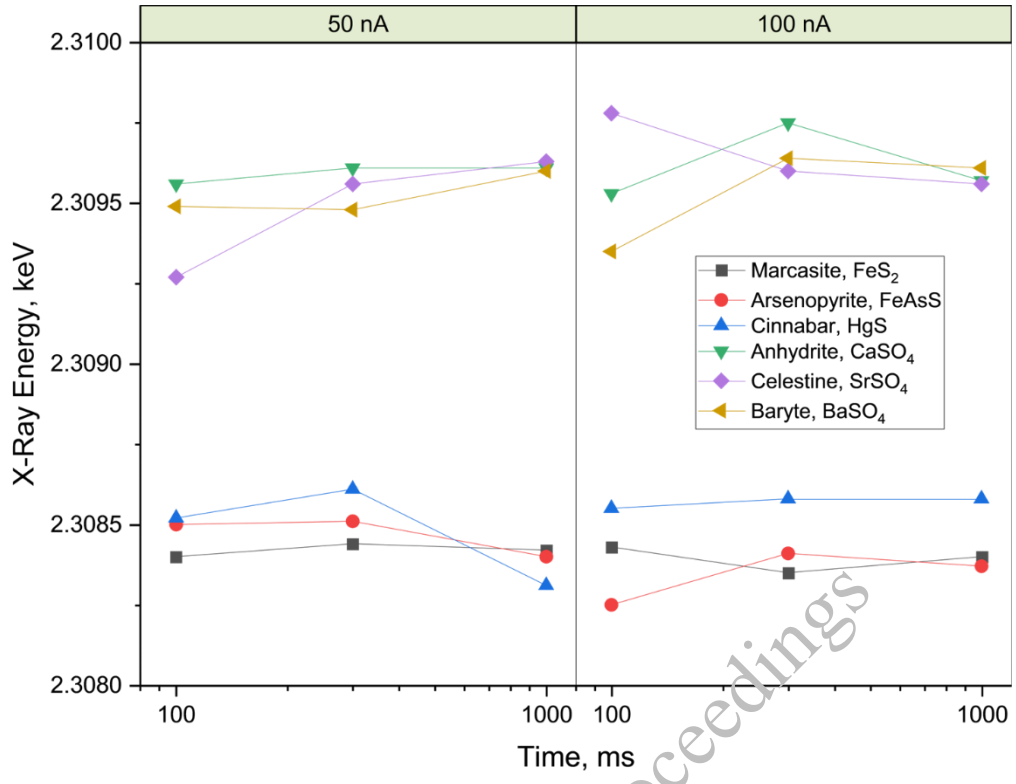

Figure 7. S X-ray peak shifts for all the minerals due to different beam experimental conditions.

4. Conclusions

Considering the results in the scope of this experiment, the following conclusions were drawn:

- Based on oxidation states identifiable peak shifts are observed for the SKα X-rays. Moreover, there are differences in the peak positions within classes of sulfides and sulfates due to the mineralogical compositions.
- SKα X-ray peaks were affected differently due to the changes in the experimental conditions based on the physical properties of the minerals and surface conditions (*e.g.*, presence of bubbles, conductive coatings).
- The maximum peak shift between sulfate and sulfide was 1.16 keV for 50 nA and 100 ms conditions. Whereas, changing the acquisition time from 100 ms to 1000 ms for 50 nA showed peak shifts of 0.29 keV for celestine, which is significant considering the shifts between sulfate and sulfide. These indicate that proper and consistent beam conditions and acquisition time need to be decided before approximating sulfate-to-sulfide ratios considering the present minerals.
- The results also suggest that there might be a relationship between the peak shift and the actual sulfur concentration in the mineral, which needs to be explored in future work.

Acknowledgements

This work was performed under the following financial assistance award 70NANB23H272 from U.S. Department of Commerce, National Institute of Standards and Technology. Additional financial assistance was provided by the ACI Foundation and the National Stone, Sand and Gravel Association. The EPMA analyses were performed at Virginia Tech using a JEOL JXA-iHP200F field emission electron microprobe. The authors would like to thank Dr. Lowell Moore for his assistance.

References

Buckley, A., & Woods, R. (1984). An X-ray photoelectron spectroscopic study of the oxidation of chalcopyrite. *Australian Journal of Chemistry*, *37*(12), 2403. https://doi.org/10.1071/CH9842403

Castillo Araiza, R., Rodrigues, A., Fournier, B., & Duchesne, J. (2024). A new accelerated testing scheme to evaluate the potential oxidation reaction of sulfide-bearing aggregates in concrete specimens. *Cement and Concrete Research*, *180*, 107507. https://doi.org/10.1016/j.cemconres.2024.107507

Chinchón-Payá, S., Aguado, A., Coloma, F., & Chinchón, S. (2015). Study of aggregate samples with iron sulfides through micro X-ray fluorescence (μXRF) and X-ray photoelectron spectroscopy (XPS). *Materials and Structures*, *48*(5), 1285–1290. https://doi.org/10.1617/s11527-013-0233-z

Chowdhury, P., Brounce, M., Boyce, J. W., & McCubbin, F. M. (2023). The oxidation state of sulfur in apatite of Martian Meteorite—Shergotty. *Journal of Geophysical Research: Planets*, *128*(6), 1–17. https://doi.org/10.1029/2022JE007634

Chubarov, V., Amosova, A., & Finkelshtein, A. (2016). X-ray fluorescence determination of sulfur chemical state in sulfide ores. *X-Ray Spectrometry*, *45*(6), 352–356. https://doi.org/10.1002/xrs.2712

Cruz-Hernandez, Y., Chrysochoou, M., & Wille, K. (2020). Wavelength dispersive X-ray fluorescence method to estimate the oxidation reaction progress of sulfide minerals in concrete. *Spectrochimica Acta - Part B Atomic Spectroscopy*, *172*, 105949. https://doi.org/10.1016/j.sab.2020.105949

Diment, W. H., & Pratt, H. R. (1988). *Thermal Conductivity of Some Rock-forming Minerals: A Tabulation*. Open-File Report 88-690. U.S Geological Survey. https://doi.org/10.3133/ofr88690

Golla-Schindler, U., Hinrichs, R., Bomati-Miguel, O., & Putnis, A. (2006). Determination of the oxidation state for iron oxide minerals by energy-filtering TEM. *Micron*, *37*(5), 473–477. https://doi.org/10.1016/j.micron.2005.11.002

Hughes, E. C., Buse, B., Kearns, S. L., Brooker, R. A., Di Genova, D., Kilgour, G., Moser, H. M., & Blundy, J. D. (2020). The microanalysis of iron and sulphur oxidation states in silicate glass - Understanding the effects of beam damage. *IOP Conference Series: Materials Science and Engineering*, *891*(1). https://doi.org/10.1088/1757-899X/891/1/012014

Jana, D. (2022a). Concrete deterioration from the oxidation of pyrrhotite – A state-of-the-art review. In *Pyrite and Pyrrhotite: Managing the Risks in Construction Materials and New Applications* (pp. 137–222). Nova Science Publishers. https://doi.org/10.52305/XFJA6706

Jana, D. (2022b). Cracking of residential concrete foundations in eastern Connecticut, USA from oxidation of pyrrhotite. *Case Studies in Construction Materials*, *16*, e00909. https://doi.org/10.1016/j.cscm.2022.e00909

Marcelino, A. P., Calixto, J. M., Gumieri, A. G., Caldeira, C. L., Delbem, I. D., & Ferreira, M. C. (2020). A feasible evaluation protocol to determine the most reactive sulfide-bearing aggregate for use in concrete. *Construction and Building Materials*, *242*, 118031. https://doi.org/10.1016/j.conbuildmat.2020.118031

Reed, S. J. B. (2005). Electron microprobe analysis and scanning electron microscopy in geology. In *Encyclopedia of Materials: Science and Technology*. Cambridge University Press. https://doi.org/10.1017/CBO9780511610561

Rodrigues, A., Duchesne, J., & Fournier, B. (2016a). Quantitative assessment of the oxidation potential of sulfide-bearing aggregates in concrete using an oxygen consumption test. *Cement and Concrete Composites*, *67*, 93–100. https://doi.org/10.1016/j.cemconcomp.2016.01.003

Rodrigues, A., Duchesne, J., Fournier, B., Durand, B., Shehata, M. H., & Rivard, P. (2016b). Evaluation protocol for concrete aggregates containing iron sulfide minerals. *ACI Materials Journal*, *113*(3), 349–359. https://doi.org/10.14359/51688828

Rowe, M. C., Kent, A. J. R., & Nielsen, R. L. (2007). Determination of sulfur speciation and oxidation state of olivine hosted melt inclusions. *Chemical Geology*, *236*(3–4), 303–322. https://doi.org/10.1016/j.chemgeo.2006.10.007

Santos, L., Wille, K., & Chrysochoou, M. (2024). Application of X-ray principles to quantify sulfur oxidation states in concrete. *Spectroscopy Letters*, 1–11. https://doi.org/10.1080/00387010.2024.2361709

Application of Electrical Impedance Spectroscopy to Assess the Condition of the Blended System Exposed to Different Curing Conditions

M, Shrivastava[1], and H.K. Venkatanarayanan[2*]

[1] *Graduate Student, Department of Civil Engineering, Indian Institute of Technology, Kanpur, India*
Email: mahimash@iitk.ac.in
[2] *Assistant Professor, Department of Civil Engineering, Indian Institute of Technology, Kanpur, India*
Email: kvharish@iitk.ac.in
[*]*Corresponding author (s)*

ABSTRACT

The aim of this study is to evaluate the competency of the EIS technique in analyzing the hydration behaviour of CBMs subjected to different long-term curing conditions. In this investigation, plain and silica fume blended mortars specimens were exposed to air, burlap, and moist curing conditions for a period of one year. The condition assessment was carried out using Electrochemical Impedance Spectroscopy (EIS), compressive strength, and Scanning Electron Microscopy (SEM). EIS provides Nyquist plots, which were further analyzed using an electrical circuit to acquire better understanding of the microstructure of specimens. It was found that the electric circuit parameters, R_1 and R_b increase with age for all mixtures, suggesting the formation of more hydration products and refinement of pore structure. Nevertheless, the R_1 and R_b values of the air-cured specimen were significantly higher than those of the burlap and moist-cured specimens. This is due to the high humidity in the burlap and the moist curing process, which adds additional moisture to the specimen, thereby enabling the movement of ions within the specimen, and, hence, decreased values were observed. Additionally, it was observed that the capacitance C_1 value decreased until 28 days. The decrease was a result of the formation of hydration products, which create a tortuous pore structure that restricts the movement of ions and reduces ionic polarization. At a later age, specifically at 6 months and 1 year, the C_1 value increased, suggesting that the specimen developed cracks as a result of the low relative humidity of the air and burlap curing conditions.

KEYWORDS: *Electrical Impedance Spectroscopy (EIS), Scanning Electron Microscopy (SEM), Curing conditions, Nyquist Plot, Equivalent Electric Circuit*

1. Introduction

Electrical Impedance Spectroscopy (EIS) is a non-destructive technique that was initially introduced in 1988 by McCarter to understand the hydration behaviour of the Cement-Based Materials CBMs (McCarter et al , 1998). Subsequently, numerous researchers have being using EIS to assess the impedance behaviour of the CBMs and to observe the microstructural development and hydration behaviour dielectric behaviour, and corrosion of reinforced concrete with the help of electrical properties of the CBMs (Gu et al., 1992, Gu et al., 1993, McCarter,1994, McCarter, 1996, Andrade et al., 1999, Sanish et al., 2013, Sánchez et a, 2013, Deus et al., 2014). To get these information EIS uses alternating current (A.C.) signals to assess the electrical properties of CBMs in both fresh and hardened state. It measures the impedance over a broad spectrum of frequencies (Hz to MHz) at a low level of applied A.C. voltage (millivolt). The electrical response was measured in terms of real and imaginary impedance and graphically displayed as a Nyquist plot, as depicted in Figure 1. Nevertheless, the Nyquist plot does not provide a significant amount of information about the specimen and requires additional interpretation (Gu et al, 1992). Thus, the Nyquist plot is fitted and evaluated using an Equivalent Electric Circuit (EEC), which offers a more comprehensive understanding of the specimen depicted in Figure 2. Table 1 provides information on the Nyquist plot parameters and electrical elements of the EEC.

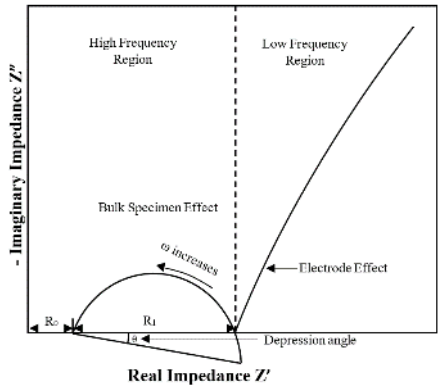

Figure 1. Nyquist plot

Despite its usage in numerous studies, this approach found to extremely sensitive to the presence of water, which becomes an important limitation. The presence of water during testing may result in an erroneous outcome. Therefore, it is essential to examine the impact of various curing conditions on the findings of the EIS test. The primary aim of the study is to investigate the impact of the curing condition of the specimen on the measurements obtained by EIS procedures. Furthermore, the EIS test methods used to evaluate changes in the microstructural characteristics of the specimen exposed to various curing conditions.

Figure 2. Equivalent Electric Circuit (EEC)

Table 1. Circuit elements and associated parameters for CBMs (Shrivastava et al., 2022)

Elements	Description of elements	Parameters associated with hydration behaviour of CBMs	Used/Not Used in the study
R_b	Overall bulk resistivity of the sample	Representation of pore structure	Used
R_1	Resistance at the solid-liquid interface	Representation of interspatial area between solids (cement & silica fume) & liquid (water) present in the system	Used
CPE_1 *	Double-layer capacitance at the solid-liquid interface	Representation of physically & chemically absorbed ions in the interfacial area along the capillary pores	Used
R_0	Meaning less parameters or Resistance offered by liquid phase	Representation of solution resistance in micro-pores & capillaries	Not Used
R_2	Charge transfer resistance between specimen electrode interface	Represents an energy required to transfer a charge through an energy barrier develops across specimen electrode interface	Not Used
CPE_2	Double-layer capacitance at the specimen electrode interface	Represents alignment of the ionic charges at the boundary between specimen & electrode	Not Used

*CPE provide C_0 and n value after fitting which were used to calculate effective capacitance (C_1) was calculated using the below formula: $C_1 = C_0^{1/n} \times (R_0^{-1} + R_1^{-1})^{\left(\frac{n-1}{n}\right)}$

2. Materials, Mixture Proportion and Test Methods

2.1 Materials

The materials used in this study include Ordinary Portland cement (OPC) having 276 m^2/kg fineness, sand, and silica fume having a D50 value of ~0.20 µm, and the surface area of the SF was ~21 m^2/g. Table 2 display the oxide composition of OPC and silica fume, respectively. The river sand used in this study belongs to the Type III sand category of IS 383 specifications, having water absorption and a fineness modulus value of 2.1% and 2.47, respectively. In this study, mortars were prepared using a water-to-cement (w/c) ratio of 0.45 (by weight) and a sand-to-cement ratio of 2.5 (by weight). No superplasticizer was used in any of the mixtures.

Table 2. Oxide composition of OPC and silica fume

Material	Oxide composition (% by total mass)							
	CaO	SiO_2	Al_2O_3	Fe_2O_3	MgO	SO_3	K_2O	Na_2O
Cement	63.91	17.69	4.12	5.47	3.31	3.7	0.99	0
Silica fume	0.95	92.07	0.19	-	0.94	1.36	2.04	0.22

2.2 Test methods

Electrical Impedance Spectroscopy (EIS)

Prism specimens of 50 x 50 x 150 mm size were cast using a specially designed acrylic mould. The specimens were then cured using three curing methods in a temperature-controlled room with a temperature range of 23°C–27°C.

- Moist Curing (MC) involves curing specimens in a sealed container, where the relative humidity is maintained at 100%.
- Wet Burlap Curing (BC) involves covering the top of the specimen with damp burlap for a period of 28 days. After this, the specimens are stored at room temperature without any further curing.
- Air Curing (AC) involves simply placing the specimen in a temperature-controlled room with a temperature range of 23°C–27°C.

The specimens underwent a curing process for a duration of over one year. Measurements were conducted at an interval of 1, 3, 7, 28 days, 6 months, and 1 year, in accordance with the prescribed curing parameters. Figure 3 depicts the experimental test setup of EIS used in the research.

(a) Testing mould *(b) Testing of specimen* *(c) Moist curing* *(d) Air curing* *(e) Burlap curing*

Figure 3. Experimental test setup for EIS

Scanning Electron Microscopy (SEM)

SEM was used to examine the microstructure of the mortar specimens at 28 days and 1 year. The specimens were prepared in accordance with Vishavkarma and Harish (2024).

3. Results and Discussion

3.1 Electrical Impedance Spectroscopy (EIS)

Recorded Nyquist plot of all mortar mixtures fitted using EEC shown in Figure 2. After fitting derived electrical parameters were listed in Table 3. In this study, only important parameters such as R_b, R_1 and C_1 from Table 3 are discussed in the form of graph in further sections.

Table 3. Electrical circuit parameters extracted from Nyquist plot

Curing Period (days)	Mortar ID	Electric circuit parameters				
		R_b (Ohms.m)	R_1 (Ohms)	$Q_1 \times 10^{-10}$ ($S.s^{n1}$)	n_1	C_{eff1} (pF)
After 3 days	SF-0%-AC	27	1389	0.97	0.99	85
	SF-0%-BC	14	530	4.47	0.93	141
	SF-0%-MC	21	1011	1.60	0.97	96
	SF-10%-AC	29	1519	1.41	0.97	82
	SF-10%-BC	21	1035	1.59	0.97	103
	SF-10%-MC	22	1034	1.76	0.97	104
After 7 days	SF-0%-AC	49	2712	0.72	0.99	64
	SF-0%-BC	19	883	1.36	0.99	109
	SF-0%-MC	33	1781	0.92	0.99	76
	SF-10%-AC	74	4065	1.41	0.95	61
	SF-10%-BC	54	2893	1.30	0.96	68
	SF-10%-MC	46	2557	1.36	0.96	73
After 14 days	SF-0%-AC	82	4626	0.74	0.98	55
	SF-0%-BC	26	1189	0.50	1.04	88
	SF-0%-MC	42	2285	0.70	1.00	65
	SF-10%-AC	116	6712	0.95	0.96	57
	SF-10%-BC	76	4359	1.42	0.94	59
	SF-10%-MC	64	3627	1.72	0.93	62
After 28 days	SF-0%-AC	128	7478	2.89	0.90	53
	SF-0%-BC	44	2425	0.67	1.00	65
	SF-0%-MC	45	2488	0.86	0.98	64
	SF-10%-AC	195	11531	1.11	0.95	56
	SF-10%-BC	99	5766	1.26	0.95	59
	SF-10%-MC	82	4769	1.93	0.92	61
After 180 days	SF-0%-AC	18136	890990	2.17	0.93	116
	SF-0%-BC	16374	814045	13.22	0.95	948
	SF-0%-MC	39	2138	1.33	0.96	69
	SF-10%-AC	188565	10195200	3.38	0.95	257
	SF-10%-BC	15201	776455	2.80	0.92	135
	SF-10%-MC	95	5489	2.22	0.91	55
After 365 days	SF-0%-AC	100163	4894900	2.15	0.95	154
	SF-0%-BC	28985	1264900	11.26	0.95	797
	SF-0%-MC	38	2093	1.10	0.97	68
	SF-10%-AC	335489	17137500	3.96	0.94	279
	SF-10%-BC	46855	2318900	4.33	0.96	328
	SF-10%-MC	172	9541	1.91	0.92	63

3.1.1 Bulk Resistivity (R_b)

Figure 4 shows the R_b values for all mixtures. The R_b of the specimen was found to be substantially affected by the different curing conditions, curing time, and silica fume replacement. With the curing period and silica fume replacement, it was observed that the R_b values of the specimen increased. At day 28, MC, BC and AC increased the R_b value of SF-0% by 53%, 69%, and 79%, respectively. Whereas at day 28, for SF-10%, the R_b value increased by 73%, 78%, and 85% when exposed to MC, BC, and AC, respectively. The increase in R_b value for the MC specimen was seen due to the formation of the microstructure during cement hydration and the pozzolanic reaction. This development leads to a reduction in pore connectivity over time (Andrade et al., 1999). Nevertheless, the primary cause of the increase in R_b value under AC conditions was the evaporation of water (Andrade et al., 1999). However, for BC, it is probable that both factors contributed to an increase in R_b value. In addition, at 28 days, the R_b value of SF-0%-AC and SF-10%-AC specimens was higher than SF-0%-MC and SF-10%-MC specimens by 183% and 139%, respectively. The increase was due to specimen drying and low relative humidity, indicating the dominance of pore fluid volume over microstructure development (Gu et al., 1995, Sánchez et al., 2013, Deus et al., 2014). Moreover, until 28 days for the BC specimen, no significant difference was observed in R_b values when compared with the MC specimen. However, at a later age, higher R_b values were observed as compared to the MC specimen due to the low relative humidity condition.

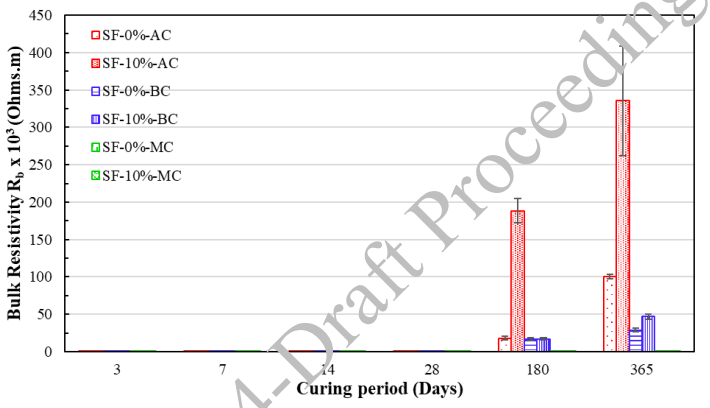

Figure 4. Bulk resistivity of the mortar

3.1.2 High-frequency resistance (R_1)

Figure 5 illustrates the impact of the curing condition on R_1 for all specimens. Based on the data shown in Figure 5, it was found that the R_1 value after 28 days showed a significant rise of 59%–81% for the SF-0% specimen. Similarly, the SF-10% specimen exhibited a substantial increase of 78%–87% under various curing conditions.

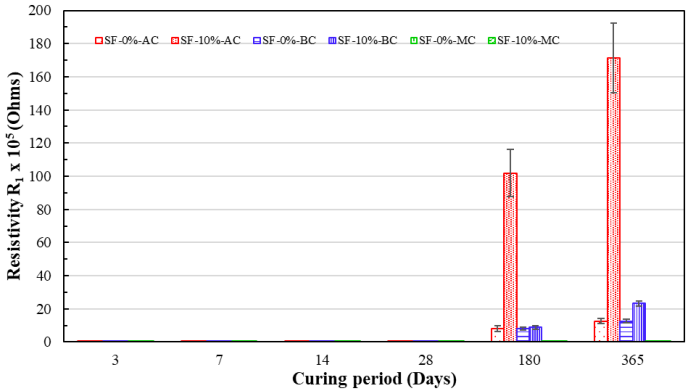

Figure 5. High-frequency resistance of the mortar

The increase in R_1 value can be attributed to multiple factors: (i) the formation of hydration products, which increases the interfacial area between solids and liquid; (ii) obstructions in the capillary pores; (iii) the presence of open pores; and (iv) the evaporation of water present in the open pores of the specimen due to their easier drying (Andrade et al (1999), Scrivener (2018)). Furthermore, at 28 days, the substitution of silica fume leads to a 35%–48% increase in the R_1 value compared to SF-0% under various curing conditions. The increase in the interfacial area was seen because of the densification of the cement matrix and the pore-blocking effect of the silica fume (Berg et al 1992). Furthermore, it was discovered that the AC specimen had the highest R_1 value for SF-0%, followed by MC and BC for all curing ages. The BC showed decreased R_1 values over the entire curing duration, potentially attributable to the periodic wetting of the burlap. The wetting of the specimen resulted in the infiltration of moisture into its open pores, leading to an increase in ions concentration and generating an excessive movement of ions when voltage was applied. However, after a period of 6 months and 1 year of curing, the BC specimen exhibited higher R_1 values compared to the MC specimens. This difference can be attributed to the fact that the BC specimens underwent air-curing after 28 days, resulting in lower relative humidity. The SF-10% specimen subjected to BC exhibited contrasting behaviour due to the compaction of the matrix, leading to the formation of secondary C-S-H gel because of wet burlap. Consequently, the pore size and pore volume on the top surface of the specimen decrease, preventing the absorption of excess moisture. Therefore, the amount of moisture that enters the specimen is restricted, and it does not have any impact on the R_1 value.

3.1.2 Capacitance (C_1)

Figure 6 illustrates the impact of the curing condition on C_1 for all the specimens. The C_1 value for both SF-0% and SF-10% specimens decreased with the increase in curing period under all curing conditions. At 28 days, the SF-0% specimen showed a decrease of 34%–54%, whereas the SF-10% specimen showed a decrease of 32%–43% under different curing conditions. The advancement in cement hydration and the pozzolanic reaction led to a transformation in the water state within the specimen, changing from a free state to a bound state (Berg et al, 1992, Ding et al, 1996, Shen et al, 2016, Jamil et al, 2013). This change limits the capacity of charged ions to polarize under an applied electric field, resulting in a decrease in C_1. Furthermore, the substitution of silica fume also decreases the C_1 values in comparison to the SF-0% specimens across all curing ages. Furthermore, it was observed that the AC specimen had the lowest C_1 value at 28 days, compared to the BC and MC specimens. This phenomenon may be caused by the evaporation of unbound water, resulting in a decrease in ionic polarization (Sánchez et al, 2013). However, in the case of the SF-0%-BC specimen, the C_1 value was consistently higher than that of the MC specimen across all curing times. The higher C_1 was attributed to the moisture present due to the periodic soaking of the burlap. This moisture enhances the ionic polarization, leading to an increase in C_1. In contrast, the SF-10%-BC specimen showed a lower C_1 value as compared to the SF-10%-MC specimens, potentially due to the compaction of the cement matrix. This compaction reduces water infiltration and confines ions within the pores, limiting their migration when an electric field is applied. After a period of 6 months and 1 year, it was noted that the C_1 value exhibited an increase in both the BC and AC specimens. The increase in the C_1 value could be attributed to the development of a crack within the specimen, possibly due to exposure to a low relative humidity environment. This can lead to the formation of drying and shrinkage cracks in the specimen, which allows for the unrestricted movement of the ions that were initially non-rotational (Sánchez et al, 2013, Gu et al, 1995, Barsoukov and Macdonald, 2005). The presence of these cracks allows the non-rotating ions to move freely and become polarized when voltage is applied, increasing the capacitance value.

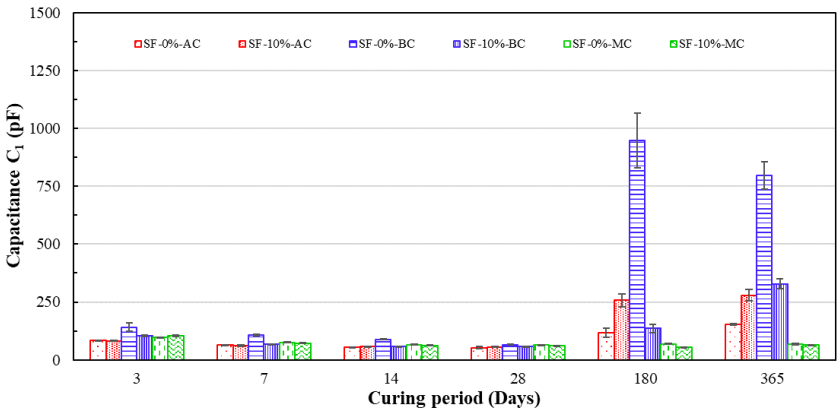

Figure 6. Capacitance of the mortar

3.2 Scanning Electron Microscopy (SEM)

This study examined the effect of various curing conditions on the microstructural characteristics of the SF-0% and SF-10% specimens after 1 year of curing, using scanning electron microscopy (SEM). Figure 7 illustrates a comparison of backscattered SEM images for all the mixtures. The unhydrated cement particles were identified as a white region, the fine aggregates as a dark grey region, the matrix as a greyish region, the pores as black spots, the interfacial transition zone (ITZ) as a thin line between the fine aggregate and matrix, and the cracks as continuous thin lines in the matrix. According to Figure 7(a), the SF-0%-AC specimen showed a high presence of unhydrated cement particles, porosity, and cracks. Furthermore, a significant crack was detected, originating from ITZ, and extending into the matrix. Similarly, the SF-10%-AC specimen shows a higher number of unhydrated cement particles shown in Figure 7(b). Furthermore, pores were detected along the ITZ, and the matrix exhibited numerous cracks and voids. The presence of a greater quantity of unhydrated cement particles and pores at the ITZ in both air-cured mixtures suggests an incomplete hydration process (Xie et al (1993)). The cement particles remain unhydrated due to the lack of moisture in the air-cured specimen. The moisture in the specimen evaporates due to the decreased relative humidity during air curing, leading to the formation of multiple cracks in the matrix. Nevertheless, the number of pores and voids detected in ITZ of the SF-10%-AC composite was lower in comparison to the SF-0%-AC composite. The reduction in the size of the pores and empty spaces was a result of the silica fume filling the pores and the chemical reaction between reactive silica and calcium hydroxide in the presence of moisture (Zain et al (2000), Bhattacharya and Harish (2018)). When AC is used, there is less moisture in the system, which means that the pore-filling action is more prominent.

Figures 7(c) and 7(d) illustrate the microstructure of the SF-0%-BC and SF-10%-BC, respectively. It was noted that periodically watering the burlap during the BC process helps maintain a specific level of humidity in the system. This promotes the hydration process, resulting in a lower amount of unhydrated cement grains compared to AC. While BC does help maintain a specific amount of humidity, it also leads to the formation multiple cracks in the matrix for both the SF-0%-BC and SF-10%-BC samples. Furthermore, the SF-0%-BC specimen exhibits a larger number of voids and pores along the ITZ in comparison to the SF-10%-BC specimen. Evidently, the inclusion of silica fume resulted in the enhancement of the microstructure by the reduction in void size and the decrease in pores along the ITZ. The microstructure refinement resulted from the pozzolanic reaction and pore-filling effect (Zain et al (2000)).

In addition, the SF-0%-MC and SF-10%-MC specimens exhibit the lowest quantity of unhydrated cement particles, as depicted in Fig. 7(e) and 7(f) correspondingly. Furthermore, moist curing resulted in a significant reduction in the pores along the ITZ, pore size, and matrix cracks. Moist curing maintains a higher level of relative humidity compared to AC and BC, which enhances the hydration process and leads to a more favourable microstructure. Furthermore, the inclusion of silica fume in the SF-10%-MC mixture improves the microstructure by decreasing pore size and creating a more compact matrix.

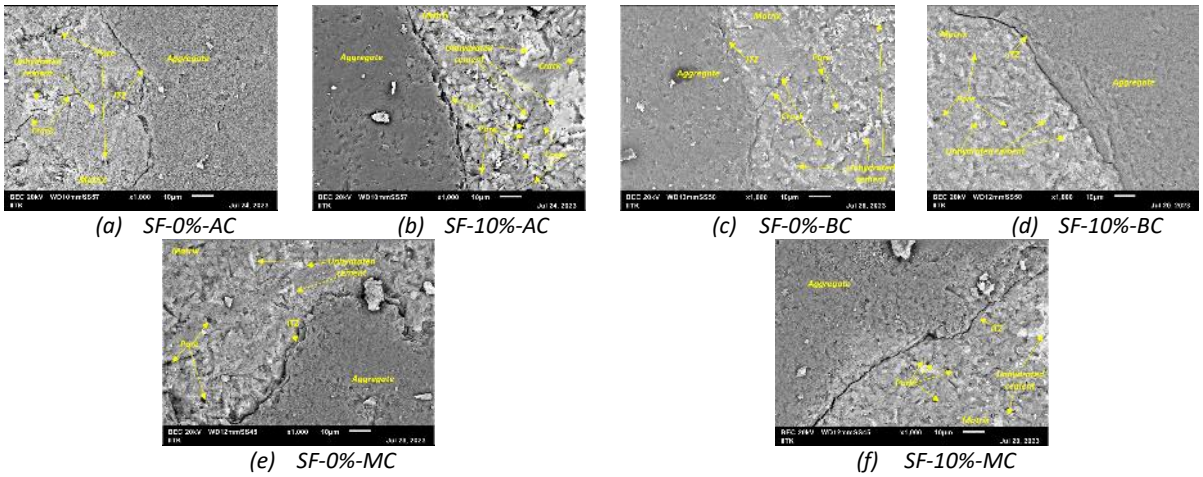

(a) SF-0%-AC *(b) SF-10%-AC* *(c) SF-0%-BC* *(d) SF-10%-BC*

(e) SF-0%-MC *(f) SF-10%-MC*

Figure 7. SEM images of SF-0% and SF-10% at different curing conditions (AC, BC, and MC) after 1 Year

4. Conclusions

- The Electrical Impedance Spectroscopy (EIS) technique measures the electrical parameters R_b, R_1, and C_1 that are associated with the resistivity, resistance, and capacitance at the interface between the solid and liquid phases of the specimens. These parameters are shown to be significantly influenced by the presence of moisture throughout the curing process.
- The R_b values and R_1 values were lower for the moist cured specimens compared to the burlap and air cured specimens. This could be due to the increased relative humidity present throughout the curing process, which leads to lower R_b and R_1 values.
- The C_1 value was found to be higher for the burlap-cured specimens until 28 days, indicating an increase in the ionic polarisation within the specimen due to the increased moisture from the wet burlap. However, the subsequent rise may be attributed to the presence of fissures in the material, which allow for the mobility of free ions at the surface of the cracks.
- Scanning electron microscopy (SEM) photographs revealed a higher abundance of unhydrated cement grains, voids, and cracks in the specimens that were air cured or treated with burlap in comparison to the specimens that were moist cured.
- The inclusion of silica fume enhanced the microstructure, particularly in the specimens that underwent moist curing. This created an ideal environment for continuous hydration and growth of the microstructure.

References

A. Berg, G.A. Niklasson, K. Brantervik, B. Hedberg, L.O. Nilsson, (1992) "Dielectric properties of cement mortar as a function of water content", *J Appl Phys*, 71:5897–5903.

Arvind Vishavkarma, Harish Kizhakkumodom Venkatanarayanan, (2024) "Assessment of pore structure of foam concrete containing slag for improved durability performance in reinforced concrete applications", *Journal of Building Engineering*, 86:108939.

C. Andrade, V.M. Blanco, A. Collazo, M. Keddam, X.R. Nóvoa, H. Takenouti, (1999) "Cement Paste Hardening Process Studied by Impedance Spectroscopy", *Electrochim Acta* 44:4313–4318.

E. Barsoukov, J.R. Macdonald, (2005) "Impedance Spectroscopy Theory, Experiment, and Applications".

I. Sánchez, C. Antón, G. De Vera, J.M. Ortega, M.A. Climent, (2013) "Moisture distribution in partially saturated concrete studied by impedance spectroscopy", *J Nondestr Eval*, 32: 362–371.

J.M. Deus, B. Díaz, L. Freire, X.R. Nóvoa, (2014) "The electrochemical behaviour of steel rebars in concrete: An Electrochemical Impedance Spectroscopy study of the effect of temperature", *Electrochim Acta*, 131:106–115.

K. Scrivener, R. Snellings, B. Lothenbach, (2018) "A Practical Guide to Microstructural Analysis of Cementitious Materials"

K.B. Sanish, N. Neithalath, M. Santhanam, (2013) "Monitoring the evolution of material structure in cement pastes and concretes using electrical property measurements", *Constr Build Mater*, 49:288–297.

M. Bhattacharya, K.V. Harish, (2018) "An integrated approach for studying the hydration of portland cement systems containing silica fume", *Constr Build Mater*, 188:1179–1192.

M. Jamil, M.K. Hassan, H.M.A. Al-Mattarneh, M.F.M. Zain, (2013) "Concrete dielectric properties investigation using microwave nondestructive techniques", *Materials and Structures/Materiaux et Constructions*, 46:77–87.

M.F.M. Zain, M. Safiuddin, H. Mahmud, (2000) "Development of high performance concrete using silica fume at relatively high water-binder ratios", *Cem Concr Res*, 30:1501–1505.

Mahima Shrivastava, Hiwot Tsegaye, Suneel Kumar, Kizhakkumodom Venkatanarayanan Harish, (2022) "Assessment of hydration behaviour of Portland Cement-Based materials containing brick powders as partial replacement for fine aggregates", *Materials Today: Proceedings*, 65-Part 2:1095-1104.

P. Gu, P. Xie, J.J. Beaudoin, (1995) "Some applications of AC impedance spectroscopy in cement research, Cement, Concrete and Aggregates" 17 113–118.

P. Gu, P. Xie, J.J. Beaudoin, R. Brousseau, (1992) "A.C. IMPEDANCE SPECTROSCOPY (I): A New Equivalent Circuit Model for Hydrated Portland Cement Paste", *Cem Concr Res*, 22:833–840.

P. Gu, P. Xie, J.J. Beaudoin, R. Brousseau, (1993) "AC Impedance Spectroscopy (II): Microstructural Characterization of Hydrating Cement-Silica Fume Systems", *Cem Concr Res*, 23:157–168.

P. Shen, L. Lu, Y. He, F. Wang, S. Hu, (2016) "Hydration monitoring and strength prediction of cement-based materials based on the dielectric properties", *Constr Build Mater*, 126:179–189.

P. Xie, P. Gu, Z. Xu, J.J. Beaudoin, (1993) "A Rationalized A.C. Impedance Model For Microstructural Characteization of Hydrating Cement systems", *Cem Concr Res*, 23:359–367.

W.J. Mccarter, (1994) "A Parametric Study of The Impedance Characteristics of Cement/Aggregate Systems During Early Hydration", *Cem Concr Res*, 24:1097–1110.

W.J. McCarter, (1996) "The A.C. Impedance Response of Concrete During Early Hydration", *J Mater Sci*, 31:6285–

W.J. McCarter, S. Garvin, N. Bouzid (1988) "Impedance Measurements on Cement Paste", *Journal of Material Science*,7:1056–1057.

X.Z. Ding, X. Zhang, C.K. Ong, B.T.G. Tan, J. Yang, (1996) "Study of dielectric and electrical properties of mortar in the early hydration period at microwave frequencies", *J Mater Sci*, 31:5339–5345.

Experimental Investigation of Impact of Alkali Silica Reaction and Sulphate Attack in Durability of Hydraulic Structures

A. Srivastav [1] R. Yadav[2], M. K. Pal [3*]

[1] PG Student, Indian Institute of Technology (BHU) Varanasi, India, and Email: adarshsrivastav.rs.civ22@itbhu.ac.in
[2]PG Student, Indian Institute of Technology (BHU) Varanasi, Varanasi, India, and Email: riteshyadav.rs.civ23@itbhu.ac.in
[2] Faculty, Indian Institute of Technology (BHU), Varanasi, India, Email: mahendra.civ@iitbhu.ac.in

*Corresponding author

ABSTRACT

On contrary to popular belief that concrete is durable against weathering condition, failure of Rihand Dam and Konar Dam have triggered the discussion of weathering affects, chemical attacks and thermal induced failure in massive concrete structures. In the lieu of these, Alkali Silica Reaction (ASR), Internal sulphate attack and thermal induced stresses have become matter of major concern as these phenomena are deleterious in durability and serviceability of hydraulic structures. To devise a repair and maintenance strategy against these phenomena, it is essential to have comprehensive understanding of impact of each factor, individually and in combinations.In this study, we aim to study the impact of ASR and internal sulphate attack in hydraulic structure due to alkalinity of water stored in its reservoir. At first, susceptibility towards ASR and internal sulphate attack have been investigated on locally available material from three different sources using mortar bar test (ASTM C1260). Preliminary results show that there is expansion in length and concrete has cracked suggesting weathering action. Further presence of ettringite, and thenardite compound in specimen confirms the occurrence of ASR or ISA.

KEYWORDS: *Alkali silica Reaction (ASR), Internal sulphate attack (ISA), Mortar Bar Test,XRD, Dam Safety.*

1. Introduction

Dams are an important infrastructure and serve the community through irrigation, water supply, and other associated economical activities. Any significant damage in these dams has a potential to bring catastrophic scenario. Therefore, concrete has been a popular choice of construction material due to its durability properties particularly against weathering action. However, failure of concrete gravity dam namely Rihand dam and Konar dam raises the concern over safety of dam. ASR induced distress was first observed in 1940s by Stanton when most of concrete structure in United States affected by ASR leading to severe cracks and become deficient over time (TE Stanton, 2008). Following the pioneering work by Stanton, extensive research efforts have been made to understand the mechanism of ASR. But there has been limited success (Sims & Poole, 2016). ASR initiate when reactive phase in aggregate (mineralogical constituents) generally Quartz with undulatory extinction in its composition interact with alkali content of cement paste i.e. sodium (Na^+), Potassium(K^+) and their accompanying hydroxyl ions (OH^-). The high pH level in concrete allows hydroxyl ions to intrude on the reactive silica (SiO_2) leading to formation of alkali silica gel which is hygroscopic leading to expansion and finally crack and ASR-induced distress (Çavdar & Yetgin, 2010; Fanijo *et al*., 2021; Mary & College, 2016.; Sanchez *et al*.,2016.; Soares *et al*., 2016.; Werner*et al.*, 2016.). Conductive Scenario for ASR to trigger are Pore solution with high pH, Reactive Aggregateand Sufficient moisture (Hasdemir *et al.*, 2012; Piersanti *et al*., 2016). Symptoms of ASR are strains and gel exudation on the cement surface, disordered cracks in map configuration (Pereira *et al*., 2023). In recentyears Several researchers worked towards the understanding of combined effect of ASR induced distress and internal

sulfate attack (ISA). ISA occurs due to sulfide minerals originating from various sources suchas aggregate, groundwater or cementitious materials which reacts with oxygen, water and cement hydratedcompounds (including gypsum ,portlandite) forming expansive compounds which leads to internal pressureultimately result in cracking, deterioration, and structural damage within the concrete(Casanova *et al*., 2016; Chinchón-Payá *et al*., 2012).Both ASR and ISA are multistage and slow process and are difficult todiagnose at the initial stages as their macroscopic manifestation as the exudations from generated phases and cracks in structure ,may take years to be observed(Pereira *et al.*, 2023).It is observed that ISA dependson oxygen and moisture concentration on external faces ISA intensifies due to presence of atmospheric oxygen and have a tendency of differential expansions concerning the internal portion of concrete. ISA occurs soon after oxidation of sulfides, so a more accurate analyzes of initial period is essential.

Various methods are developed to evaluate detrimental effect of ASR in short period of time such as the ASTM C 295: Petrographic examination of aggregates(Standard Guide for Petrographic Examination of Aggregates for Concrete 1), ASTM C 1260: Accelerated mortar bar test (AMBT) (Standard Test Method for Potential Alkali Reactivity of Aggregates (Mortar-Bar Method) 1, and ASTM C 1293: Concrete prism test (CPT) (International & indexed by mero.)and AASHTO T 380 in 2019 - Miniature concrete prism test (MCPT)(Standard Method of Test for Potential Alkali Reactivity of Aggregates and Effectiveness of ASR Mitigation Measures (Miniature Concrete Prism Test, MCPT), 2020).

SAR and ISA are slow yet continuous reaction requiring round the clock monitoring to assess the detrimental effects at microscopic scale. However, most of the methods presen macroscopic response. Hence, there is a need of systematic investigation using above-mentioned test and advanced material characterization so that formation of triggering component with its evolution can be traced.

In this study, authors aim to comprehend the mechanism of ASR and ISA by monitoring the changes in physical properties and chemical composition using accelerated mortar bar test and XRD, respectively. The notion here is to identify the influencing chemical compound which is responsible for or product of these reactions. Accelerated mortar bar test confirms the occurrence of ASR and/or ISA and XRD result confirm the presence of ettringite, and thenardite compound, which is a product of ASR. Thus, the eventuality of ASR and its underlined effects are presented.

This article is organized in four sections. The first section presents introduction and a brief literature survey on the topic. Section two briefly outlines the description on materials used and methods of experimental investigation. Results are discussed into the Section three and article is summarized in the section four.

2. Materials and Method

2.1 Materials

In this paper aggregate from three different source were selected which differ in terms of their minerology and more in texture. These aggregates are codified as A, B, C. The physical properties are mentioned in Table.1.

Table.1 Physical Properties of Aggregate

Aggregate Type	Fineness Modulus	Bulk Density(Kg/L)	Specific Gravity	Water Absorption(%)
A	6.515	1.64	2.875	0.175
B	6.47	1.47	2.54	2.62
C	6.56	1.72	2.89	0.25

For understanding the chemical composition handheld XRF from Brucker type S1 TITAN is employed. It is evident from test that chemical composition of aggregate of type A contains 59.58% of silicon dioxide (SiO_2) and B, C aggregate contains 68.23%, 44.94% SiO_2, respectively. Aggregate sample used are shown in Figure.1. Grading of aggregate has been done as per ASTM C1260.

(a) A Aggregate (b) B Aggregate (c) C Aggregate

Figure 1. Graded aggregates

The Ordinary Portland cement (OPC) cement of Grade-43 is used; whose chemical properties are mentioned in Table.2.

Table. 2 Cement: chemical characterization

Chemical tests									
Loss on ignition (%)	Al_2O_3 %	SiO_2 %	Fe_2O_3 %	Cao %	MgO %	SO_3 %	Free CaO %	Equiv.Alkal. %	Insoluble residue %
4.89	4.78	18.49	2.62	61	3.52	2.72	0.61	0.70	1.42

2.2 Mix Design and Accelerated mortar bar test (AMBT)

Six samples of micro-mortar bars (25×25×285 mm) were prepared using three different types of aggregates (A, B, C), with mix design and aggregate grading adhering to ASTM C1260 guidelines. The water-to-cement ratio (w/c) was maintained at 0.47, and the cement-to-aggregate ratio was 0.45.

After casting, the specimens were allowed to set for 24±2 hours at room temperature. Subsequently, they were removed from the molds and placed in tap water for an additional 24 hours at 80±2.0°C in an oven. The initial reading, referred to as the zero reading, was recorded at this point.

Following this, the specimens were fully immersed in a container filled with 1N NaOH solution at 80±2.0°C. The container was sealed, and the specimens were returned to the oven. Comparator readings were taken periodically, with at least three intermediate readings within the first 14 days after the zero reading.

Beyond the initial 14-day period, one reading per week was taken until the conclusion of the 91-day experiment. This comprehensive monitoring allowed for the assessment of the specimens' behavior over time under the specified conditions.

Expansion of length was calculated according to the equation where L is length after thermal treatment and L_0 is its initial length (right after demolding).

$$c = (L - L_0) / L \quad (1)$$

As per ASTM C1260, expansions measuring under 0.10% at the 16-day mark post-casting generally signify innocuous behavior. Expansions falling between 0.10% and 0.20% at this same point encompass aggregates that may exhibit either innocuous or deleterious performance in field conditions. Expansions exceeding 0.20% at the 16-day stage post-casting suggest a potential for deleterious expansion. According to many researchers' threshold of 0.10% and testing days of 16 days is inadequate to characterize an aggregate as susceptible to ASR expansion (Author *et al.*, 2005; Ideker *et al.*, 2010). Hooton (Hooton, 1991) suggested extending the testing period to 28 and 56 days, with expansion thresholds set at 0.28% and 0.48%, respectively, to ensure accurate classification of slow-reacting aggregates.

3. Results and Discussion

Accelerated mortar bar test on each aggregate type has been performed and expansion in length was recorded for three types of aggregate. An average of six samples was taken for each aggregate type. The test readings were recorded up to the 13th week for all samples. Change in total length and relative increments are presented in the Fig 2 and 3, respectively. The initial increment in specimen A, B, and C are 10.68, 12.42 and 11.49 mm respectively. A, B and C aggregate mortar bar expansions are 0.43%, 0.21%, and 0.29%, respectively, which are above 0.20% suggesting the deleterious behavior. In the experiment duration of 91 days, aggregate B shows the lowest rate of expansion despite the maximum initial expansion. On contrary to that, aggregate A exhibits lowest initial increment but have higher rate of expansion in experiment duration. The relative increment in aggregate A is higher than 0.2% with highest value in the fourth week amounting to 0.79%, except for 10th week, where relative increment is 0.05%. It is because specimen of aggregate A started cracking (Fig 4). In the case of A aggregate mortar bar, significant expansion is noticeable between the 4th and 6th weeks of the test including visible cracks on the surface. These cracks were observed in four out of six specimens, prompting an investigation into the potential causes of expansion.

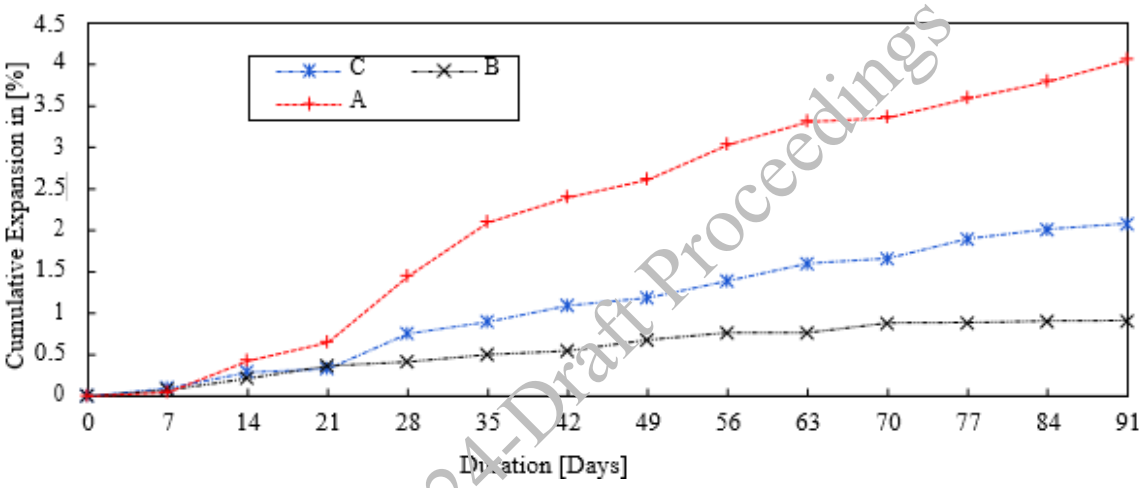

Figure 2. Cumulative elongation of bar specimen

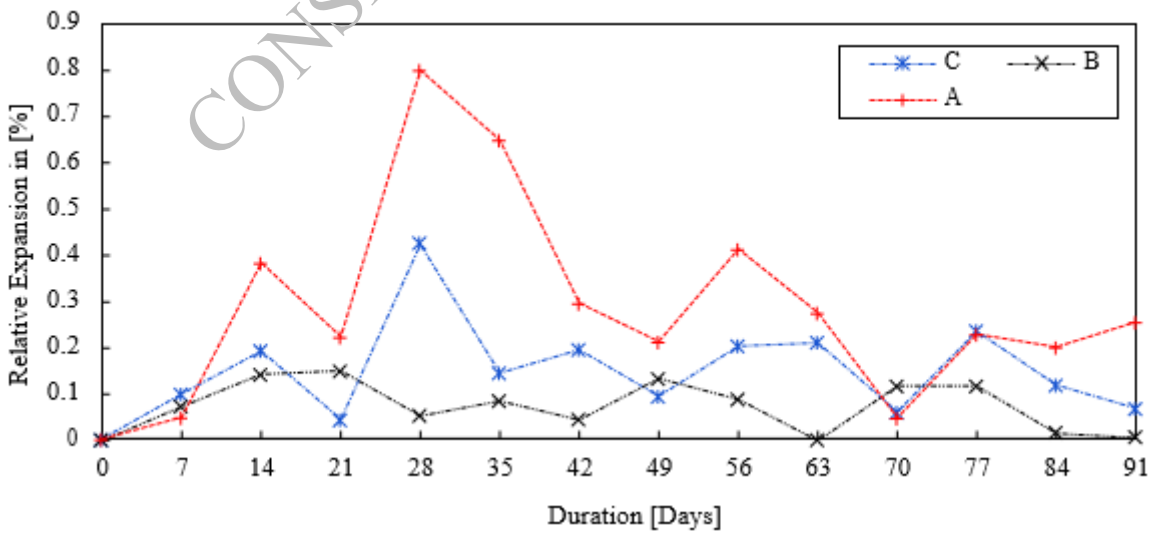

Figure 3. Dimensional variation of mortar bar, with different aggregate

(a) Specimen #1 (b)Specimen #2

Figure 4. Crack Pattern observed on surface of Mortar Specimens of D type aggregate.

Further, white efflorescence with a brownish tint appeared on the surface of mortar bar of each aggregate (Fig 5). Presence of white efflorescence signals the formation of harmful phases. Gypsum can contribute to efflorescence, which is the migration of soluble salts to the surface of concrete. When water evaporatesfrom the concrete surface, it can leave behind gypsum crystals, resulting in unsightly white deposits on thesurface of the concrete. Significant leaching of calcium carbonate is also observable, suggesting the presence of calcite. This process can contribute to the degradation and weakening of the mortar over time.Importantly, these changes become apparent starting from the fourth week onward.

(a) Aggregate A (b) Aggregate B (c) Aggregate C

Figure 5. White efflorescence observed on surface of specimens

To analyze the evolution of phases over time and determine the causes of deterioration, micro-analysis using the Rigaku Smart Lab 9kW Powder X-ray Diffractometer (without χcradle) was conducted. A reference mortar was cast using the same aggregates and following the procedure outlined in ASTM C1260, except that the mortar bars were submerged in tap water instead of NaOH solution to obtain reference sample. XRD analysis of both specimen at the age of 91 days were performed and the results were compared (Fig 6).

The XRD analysis of aggregate A, as depicted in Fig 6, exhibits the presence of ettringite and gypsum which are not observed in reference sample indicating the presence of detrimental phases. It is a potential explanation for the observed cracks in the mortar when immersed in NaOH solution. Notably, surface cracks became visible starting from the fourth week of testing and persisted throughout the duration of the experiment. Cracks are highlighted in for clear visualization in Figure.4.

Further, exposed specimen also has gypsum in higher amount than that in reference material. It explains the observed white efflorescence as gypsum is known as contributing chemical in efflorescence, facilitates the migration of soluble salts to the concrete surface. As water evaporates from the concrete surface, gypsum crystals may remain, leaving unsightly white deposits. Additionally, noticeable leaching of calcium carbonate suggests the presence of calcite. This process can lead to the degradation and weakening of the mortar over time. Importantly, these alterations become noticeable starting from the fourth week onward.

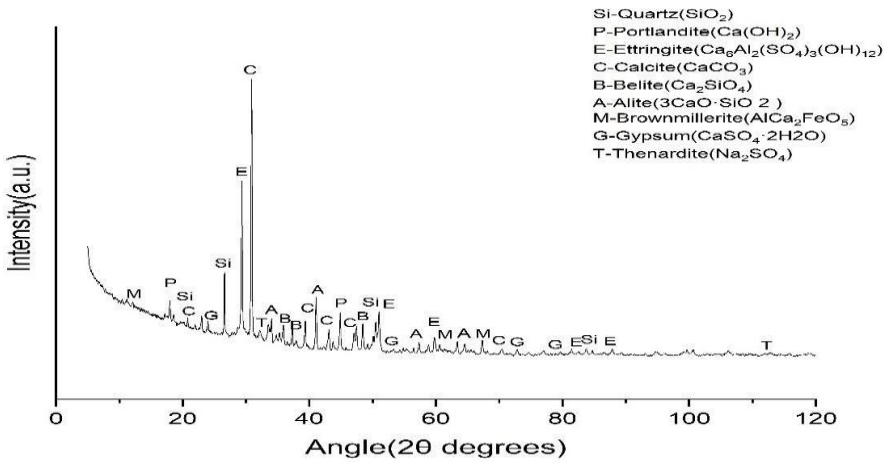

(a) Specimen in NaOH solution

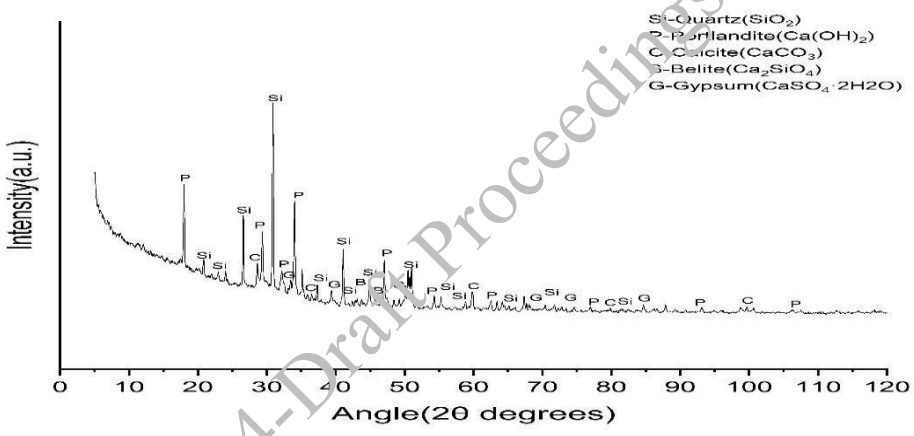

(b) Reference specimen

Figure 6. XRD of specimen of aggregate A

4. Conclusions

In accordance with ASTM C1260 standards, tests were conducted on mortar bars, revealing expansions exceeding 0.20% for all three aggregate sources: A, B, and C, with expansions measuring 0.43%, 0.22% and 0.29% respectively. These findings indicate potential deleterious behavior. Further investigation was prompted by observations of white efflorescence with a brown tint on the surface for B and C aggregate mortars, and crack formation for A aggregate mortar. XRD analysis was performed to understand these changes, comparing mortar bars exposed to tap water versus NaOH for a test duration up to the 13th week. The analysis revealed the presence of gypsum, ettringite, and thenardite in mortar bars with B and A aggregates, suggesting unfavorable conditions. Conversely, only gypsum phase was observed in C aggregate mortar. The formation of expansive products generates internal stresses in mortars, indicating both ASR and ISA, which become evident when observing the expansion in mortar bars during accelerated tests. In these tests, all mix proportions containing deleterious agents showed expansions greater than those observed in reference mortars. The investigation suggests that noticeable changes or abrupt shifts occurred after the 4th week of testing, underscoring the inadequacy of a 28-day duration.

References

Casanova, I., Agulló, L., & Aguado, A. (2016). *Aggregate Expansivity Due to Sulfide Oxidation-I. Reaction System andRate Model*.

Çavdar, A., & Yetgin, Ş. (2010). Investigation Of Mechanical and Mineralogical Properties of Mortars Subjected to Sulfate. *Construction And Building Materials*, *24*(11), 2231–2242. Https://Doi.Org/10.1016/J.CONBUILDMAT.2010.04.033

Chinchón-Payá, S., Aguado, A., & Chinchón, S. (2012). A Comparative Investigation of The Degradation Of Pyrite And Pyrrhotite Under Simulated Laboratory Conditions. *Engineering Geology*, *127*, 75–80. Https://Doi.Org/10.1016/J.Enggeo.2011.12.003

Fanijo, E. O., Kolawole, J. T., & Almakrab, A. (2021). Alkali-Silica Reaction (ASR) In Concrete Structures: Mechanisms,Effects and Evaluation Test Methods Adopted in The United States. *Case Studies in Construction Materials*, *15*. Https://Doi.Org/10.1016/J.Cscm.2021.E00563

Folliard, K. J., Barborak, R., Drimalas, T., Du, L., Garber, S., Ideker, J., Ley, T., Williams, S., Juenger, M.,Fournier, B., & Thomas, M. D. A. (2005). *Preventing ASR/DEF In New Concrete: Final Report (0-4085-5)*. Www.Ntis.Gov.

Hasdemir, S., Turul, A., & Yilmaz, M. (2012). Evaluation Of Alkali Reactivity of Natural Sands. *Construction And Building Materials*, *29*, 378–385. Https://Doi.Org/10.1016/J.CONBUILDMAT.2011.10.029

Hooton, R. D. (1991). *New Aggregate Alkali-Reactivity Test Methods*.

Ideker, J. H., East, B. L., Folliard, K. J., Thomas, M. D. A., & Fournier, B. (2010). The Current State of The Accelerated Concrete Prism Test. *Cement and Concrete Research*, *40*(4), 550–555. Https://Doi.Org/10.1016/J.Cemconres.2009.08.030

International, A., & Indexed by Mero, Files. (N.D.). *Standard Test Method for Concrete Aggregates by Determination ofLength Change of Concrete Due to Alkali-Silica Reaction 1*. Www.Astm. Org

Mary, Q., & College, W. (2016). *The 9th International Conference on Alkali-Aggregate Reaction in Concrete 1992 AlkaliSilica Reactivity Mechanisms of Gel Formation and Expansion A Bpooie*.

Pereira, E., Pereira, E., Pianaro, S. A., Farias, M. M., Bragança, M. D. O. G. P., & Oliveira, I. C. (2023). Combined Effect of Alkali-Aggregate Reaction (AAR) And Internal Sulfate Attack (ISA): Microstructural and Porous Structure Modifications of Portland Cement Mortars. *Construction And Building Materials*, *362*. Https://Doi.Org/10.1016/J.Conbuildmat.2022.129676

Piersanti, M., Shehata, M., Macdonald, C.-A., & Senior, S. (2016). *Expansion Of Concrete Containing Reactive Reclaimed Concrete Aggregates of Different Reactivity and Composition*.

Sanchez, L., Fournier, B., Jolin, M., Bastien, J., Mitchell, D., & Noel, M. (2016). *Thorough Characterization of ConcreteDamage Caused by Aar Through the Use of a Multi-Level Approach*.

Sims, I., & Poole, A. (2016). *A Worldwide View of Aar: Updating Swamy*.

Soares, D., Santos Silva, A., Mirão, J., Fernandes, I., & Menéndez, E. (2016). *STUDY ON THE FACTORS AFFECTINGALKALIS RELEASE FROM AGGREGATES INTO ASR*.

Standard Guide for Petrographic Examination of Aggregates for Concrete 1. (N.D.). Https://Doi.Org/10.1520/C0295-08

Standard Method of Test for Potential Alkali Reactivity of Aggregates and Effectiveness of ASR Mitigation Measures (Miniature Concrete Prism Test, MCPT). (2020). Https://Www.Osha.Gov/Dsg/Annotated-Pels/

Standard Test Method for Potential Alkali Reactivity of Aggregates (Mortar-Bar Method) 1. (N.D.). Https://Doi.Org/10.1520/C1260-23

TE Stanton. (2008). *Expansion Of Concrete Through Reaction Between Cement and Aggregate*. Https://Trid.Trb.Org/View/868520

Werner, D., Meng, B., & Weise, F. (2016). *Influence Of Aggregate Size on The Damage Potential of Alkali-Silica Reaction*.

Concrete Mixed with Non-potable water: Probability of Compliance to Codes of a Few Countries

P. Agrahari[1], R. Sharma[1], J. Kumari[1], N. Jain[1], S. Dauji[2,3*], V. S. Kumar Delhi[4]

[1] Indian Institute of Technology Bombay, Mumbai, India
Email: emprakhar@gmail.com
[2] Bhabha Atomic Research Centre, Mumbai, India
Email: acad.dauji@gmail.com; dauji_saha@yahoo.com
[3] Homi Bhabha National Institute, Mumbai, India
[4] Indian Institute of Technology Bombay, Mumbai, India
Email: venkatad@iitb.ac.in

*Corresponding author

ABSTRACT

Recent findings by the Intergovernmental Panel on Climate Change (IPCC) highlight increasing water stress worldwide, posing significant challenges to achieving Sustainable Development Goal (SDG) No. 6: clean water and sanitation. Concrete production, a substantial consumer of potable water, stands as a pivotal area for sustainability improvements. This study advocates the use of non-potable water for concrete mixing to preserve potable reserves for essential uses. Given the diverse global standards for non-potable water in concrete, this research collates international data, employing a bootstrap resampling methodology to probabilistically assess code compliance in four regions: the USA, Europe, Australia, and India. Results indicate varying probabilities of compliance, underscoring the need for broader acceptance of non-potable water use to achieve SDG No. 6 globally. This approach not only aids in conserving water resources but also supports regulatory confidence in non-potable water's efficacy, encouraging its adoption in concrete production worldwide.

KEYWORDS: Non-potable water, Concrete strength, Code compliance, Probabilistic evaluation, Sustainable concrete

1. Introduction

The alarming projections by the Intergovernmental Panel on Climate Change (IPCC) indicate that many regions worldwide will face medium to severe water stress in the upcoming decades, presenting significant challenges in achieving Sustainable Development Goal (SDG) No. 6: clean water and sanitation (IPCC, 2022). One of the predominant consumers of potable water is the concrete production industry (Nikookar et al., 2023). This research advocates for the utilization of non-potable water in concrete manufacturing as a sustainable alternative. Existing global codes and standards offer varied guidelines for the use of non-potable water in concrete, primarily assessed through deterministic methods due to the limited number of tests for a probabilistic evaluation (Dauji, 2023). Our study collates international data from previous studies to create a comprehensive database, employing bootstrap re-sampling techniques to assess the probability of code compliance for concrete mixed with non-potable water in four regions such namely the USA, Europe, Australia, and India. Our findings indicate a promising potential for using non-potable water without compromising concrete strength, thereby supporting water conservation and advancing SDG No. 6 globally.

2. Literature Review

In the realm of sustainable concrete production, the utilization of non-potable water has been explored across various studies. A literature review indicates that while potable water is traditionally recommended for concrete due to its predictable effects on properties like compressive strength and durability, several

forms of non-potable water present viable alternatives (Alqam et al., 2014). Notably, magnetized seawater has been shown to enhance compressive strength and reduce detrimental chloride contents, potentially increasing the longevity of reinforced concrete (Naveen et al, 2023). Conversely, non-magnetized seawater and certain industrial wastewaters, like de-inking wastewater, have demonstrated varying impacts on concrete strength, underscoring the necessity for detailed parameter checks such as sulphate, chloride, organic content, and pH levels. Interestingly, alternative sources like grey-water and highly alkaline water samples have shown promising compatibility with concrete standards, achieving near-comparable compressive strengths and workabilities to those made with potable water (Tsimas et al., 2010). These findings support the potential for broader code compliance assessments using probabilistic methods, which could bolster regulatory confidence in non-potable water usage for concrete production.

3. Data and Methodology

This study focuses on evaluating the use of non-potable water in concrete production through a probabilistic analysis of water quality parameters and their impact on concrete strength. We have compiled a comprehensive dataset from 41 research papers selected from reputed scientific portals namely Scopus, ScienceDirect, and reputed publishers such as Elsevier, Springer, and Wiley. These papers were chosen based on their analysis of pH, sulphates, and chlorides, alongside tests for compressive strength, accumulating 192 data points across various parameters, including pH, and content levels of sulphates and chlorides. The detailed methodology followed is shown in Figure 1.

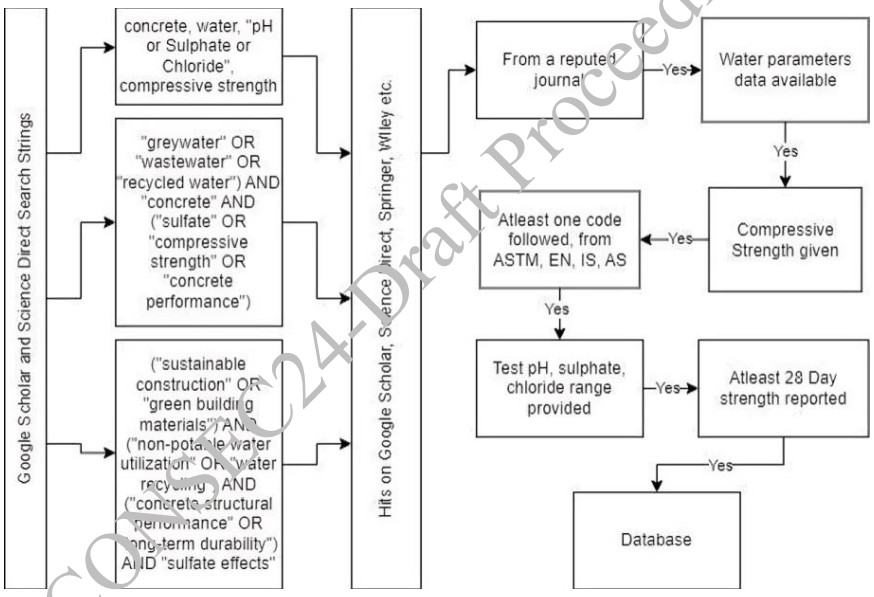

Figure 1. Process Flowchart for Database creation

We employed a bootstrap re-sampling method to estimate the probability of code compliance concerning standards like ASTM (American Society for Testing and Materials), EN (European Standard CEN), IS (Indian Standard, BIS), and AS (Australian Standard, SA) for the parameters studied. This methodology used Python and statistical libraries namely Matplotlib and Pandas. Notably, the non-parametric bootstrap approach allowed for estimation under the assumption of non-normal distributions, providing a probabilistic evaluation of the compliance of non-potable water used in concrete production.

4. Code Compliance

We delve into the Compliance Code Analysis, focusing on the water quality parameters and mechanical properties according to various global standards: American (ASTM C1602M, ACI 318M-08), European (EN 1008), Indian (IS 456), and Australian (AS 1379). These standards dictate specific limits for sulphates, chlorides, pH, and compressive strength, which we rigorously assessed through a broad database of global

studies. Water quality parameter compliance shows a relatively balanced distribution among the codes (Figure 2), with the EN standard slightly leading with 130 data points and the Indian standard showing the lowest at 122. In terms of mechanical properties, the 7-day strength compliance rates are fairly close among all standards, hovering around 52% for ASTM, EN, and IS, with AS just slightly lower at 50.69% (Figure 3). The compliance rates improve significantly for the 28-day strength, where all codes exhibit compliance rates exceeding 70%, with EN showing a slight advantage at 73.61% (Figure 4).

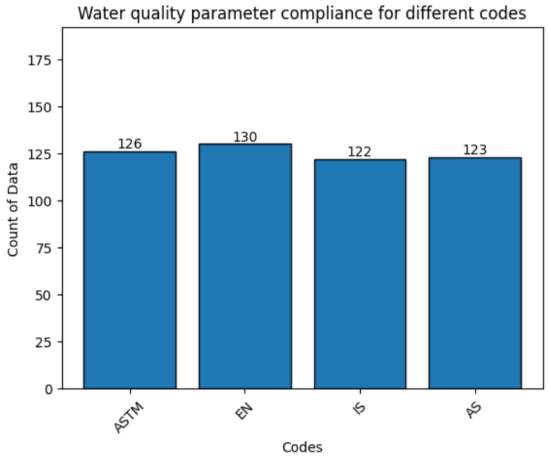

Figure 2. Data complying w.r.t different codes for water parameters.

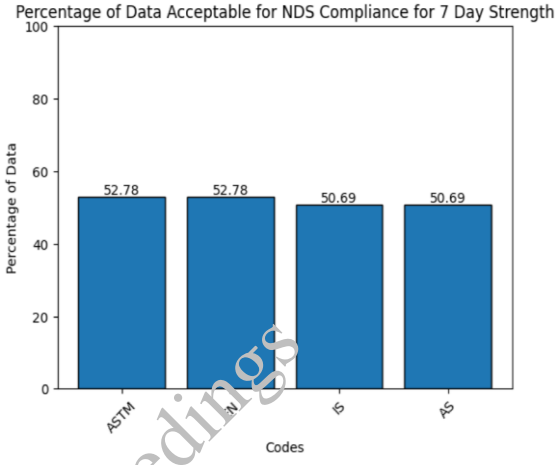

Figure 3. Percentage of data complying to different standards w.r.t. 7-days strength

Probabilistic analysis of non-compliance for 7-day and 28-day strengths (Figure 5 and Figure 6) reveals increasing probabilities of non-compliance as the confidence levels rise, with the EN standard showing the highest probabilities of non-compliance. This suggests a more stringent standard for European countries.

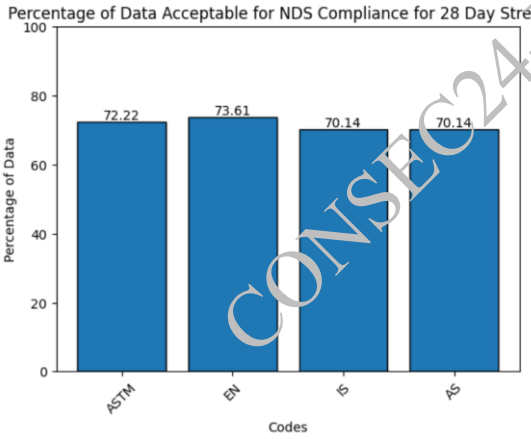

Figure 4. Percentage of data complying to different standards w.r.t. 28-days strength

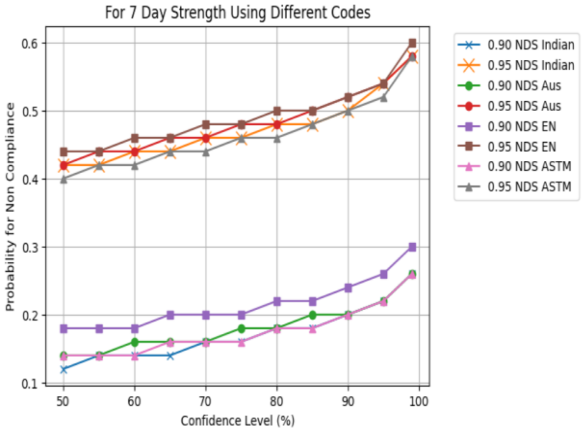

Figure 5. Probability of Non-Compliance on different confidence levels for 7-days NDS w.r.t different code

Additionally, the initial setting time (IST) compliance is strong across all codes except for IS, which shows slightly lower compliance at 66% compared to 79% for others (Figure 7). Final setting time (FST) compliance is reported only for ASTM and EN, showing moderate compliance rates of 53% and 55%, respectively which is suboptimal, indicating potential areas for further research. Due to limited data availability in our study, we were unable to conduct a more comprehensive analysis. Future scholars are encouraged to investigate this matter in greater detail.

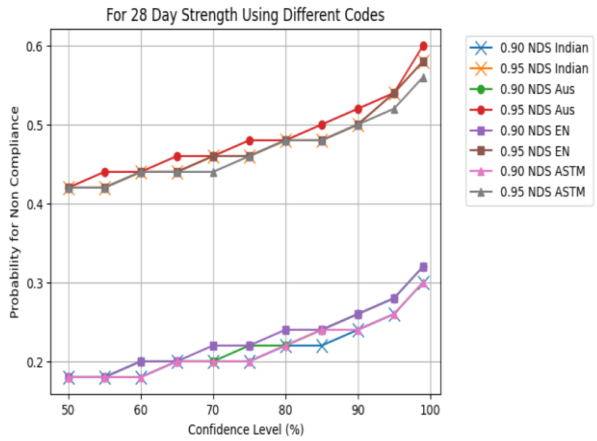

Figure 6. Probability of Non-Compliance on different confidence levels for 28-days NDS w.r.t different country codes

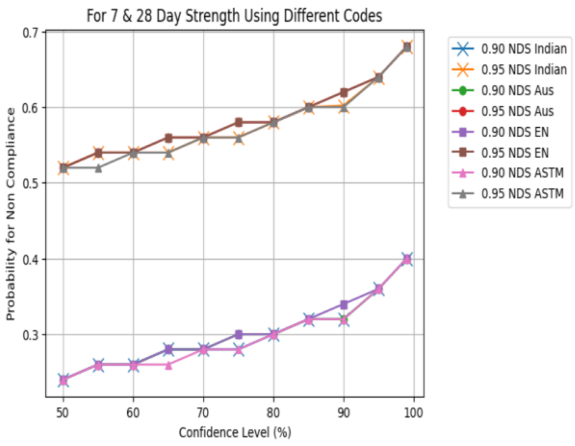

Figure 7. Probability of Non-Compliance on different confidence levels for 7-days and 28-days NDS w.r.t different country codes

Overall, these figures provide robust evidence that non-potable water can be utilized effectively in concrete production under varying international standards, though some variability and challenges in compliance remain, particularly under the EN standard.

6. Conclusions

- Water quality parameter compliance is relatively balanced among ASTM, EN, IS, and AS standards, with EN slightly leading in compliance data points.
- Compliance rates for 28-day compressive strength are significantly higher across all standards compared to 7-day strength, indicating better long-term performance of non-potable water in concrete production.
- Initial Setting Time (IST) compliance is strong for all codes except IS, which is lower at 66%. Final Setting Time (FST) compliance is moderate, with ASTM and EN showing rates of 53% and 55%, respectively.

References

Alqam, M., Jamrah, A., Abd Al-Hafith, B., Al-Zubi, R., & Al-Shamari, N. (2014). "Fresh and Hardened Properties of Sustainable Concrete Using Recycled Household Greywater", *Arabian Journal for Science and Engineering*, 39(3), 1701–1708. https://doi.org/10.1007/s13369-013-0733-8

American Concrete Institute. (2008). Building Code Requirements for Structural Concrete (ACI 318M-08) and Commentary. *American Concrete Institute*.

ASTM C1602/C1602M-18. Standard specification for mixing water used in the production of hydraulic cement concrete. West Conshohocken, PA: *ASTM International*; 2018

Dauji, S. (2023) "Non-Potable Water for Sustainable Concrete: Strength Compliance in India for Varying pH of Mixing Water and Future Scope." *Sādhanā*, 48(4). https://doi.org/10.1007/s12046-023-02280-3

European Committee for Standardization. (2002). Mixing Water for Concrete - Specification for Sampling, Testing, and Assessing the Suitability of Water, including Water Recovered from Processes in the Concrete Industry, as Mixing Water for Concrete (EN 1008). *European Committee for Standardization*.

Naveen, V., Bommisetty, J., & Sumith Kumar, E. (2023). "Effect of magnetized saltwater on long-term strength of concrete: An experimental study." *Materials Today: Proceedings.* https://doi.org/10.1016/j.matpr.2023.02.078

IPCC. (2022) Climate Change 2022: Impacts, Adaptation, and Vulnerability, *Intergovernmental Panel on Climate Change*. https://www.ipcc.ch/report/ar6/wg2/

IS: 456:2000, Indian Standard Code for Plain and reinforced concrete-code of practice, 4th Revision, *BIS*, New Delhi, 2000.

Nikookar, M., Brake, N. A., Adesina, M., Rahman, A., & Selvaratnam, T. (2023) "Past, current, and future re-use of recycled non-potable water sources in concrete applications to reduce freshwater consumption- a review." *Cleaner Materials*, 9, 100203. https://doi.org/10.1016/j.clema.2023.100203

Standards Australia. (2007). Specification and Supply of Concrete (AS 1379). Standards Australia.
Tsimas, S., & Zervaki, M. (2011, January 4). "Reuse of waste water from ready-mixed concrete plants", *Management of Environmental Quality*. http://dx.doi.org/10.1108/14777831111098444

Uncertainty in estimated concrete strength from core test using Indian Standards

S. Dauji[1, 2*], R. Sharma[3], P. Agrahari[4] and S. Manohar[5]

[1] Bhabha Atomic Research Centre, Mumbai, India;
Email: acad.dauji@gmail.com; dauji_saha@yahoo.com
[2] Homi Bhabha National Institute, Mumbai, India
[3] Department of Civil Engineering, Indian Institute of Technology Bombay, Mumbai, India
Email: 210040122@iitb.ac.in
[4] Department of Civil Engineering, Indian Institute of Technology Bombay, Mumbai, India
Email: 23v0033@iitb.ac.in
[5] Department of Civil Engineering, Indian Institute of Technology Bombay, Mumbai, India
Email: swathym@iitb.ac.in

[*]Corresponding author

ABSTRACT

Many concrete structures across the world are reaching the end of their design lives. Health assessment needs to be conducted for extending the service life through which these concrete buildings may continue to perform the intended functions. Health assessment also becomes a necessity when the concrete structure displays visible signs of distress. This would become mandatory in case the concrete building has undergone an accident such as impact, fire, or blast. Therefore, assessment of in-situ concrete strength is an important topic of research. This might be conducted by performing non-destructive and partially destructive tests on the structure and interpretation of the results. Core test performed on an existing structure is the most direct and reliable method to estimate the in-situ concrete strength. However, the number of cores that can be taken from an existing old building is limited, primarily due to the cost and the consequent weakening of the structure. Hence, for estimation of the in-situ concrete strength from core test data, the data often becomes insufficient for employing a statistical approach. The alternate is to adopt the strength estimate using the prevalent national code / standard. However, this would involve uncertainty of the estimated strength, because of the small number of core tests, as well as the approximate formulations of the code adopted. Quantification of this uncertainty has not been performed for in-situ concrete strength estimated from core tests using Indian standard. The present paper would examine this aspect in detail with sample problems.

KEYWORDS*: Concrete, Health Assessment, In-situ Strength of Concrete, Core Test, Uncertainty*

1. Introduction

Concrete structures of the last century, and most of those constructed even in the present day, are generally designed for a service life of 50 years. Even near the end of their design life, many existing in-service buildings are apparently healthy. To extend the service life, health assessment therefore becomes as essential confirmatory exercise. The compressive strength of concrete is a basic parameter that is required for assessment of the overall health of an existing structure, which may be obtained from non-destructive tests (NDT) and partially destructive tests (PDT). Rebound hammer test and ultrasonic pulse velocity test are popular NDTs; core test, half-cell potential test, and pull-out test are popular PDTs. Statistical approaches can provide some estimate of strength from NDTs, with associated uncertainties, but only PDTs (core test) alone can provide a direct estimation of the in-situ concrete strength.
Because of their partially destructive nature, the number of PDTs on existing structures is generally low, which renders the employment of regular statistical approaches infeasible. Indian codes BIS 456 (BIS, 2000), and BIS 516 (BIS, 2018) provide stipulations for the estimation of the concrete strength from limited

core test results. Because of the low number of core tests and the prescriptive nature of the stipulations, uncertainties would be associated with such estimates. In literature, to the best of the knowledge of this author, presently there is no study on the uncertainty associated with concrete strength estimated from core results using the code stipulations, specifically for India. Therefore, the present study was undertaken to examine this aspect of concrete strength estimated from core results, according to the applicable Indian standards BIS 456 (BIS, 2000), and BIS 516 (BIS, 2018). This would be addressed by use of statistical simulations, and resampling approaches.

2. Stipulations in Indian codes for estimation of concrete strength from core tests

The Indian codes BIS 456 (BIS, 2000), and BIS 516 (BIS, 2018) stipulate conditions for acceptance of concrete in the new structures (contractual acceptance for conformance to specification); and the existing structures (acceptance for structural adequacy). The second condition would be equivalent to estimation of the in-situ strength of concrete from limited core tests. It may be noted that the confidence level and the probability considerations stipulated in BIS (2018) are similar to those stipulated for estimating the characteristic strength of concrete from cube tests BIS (2000). These observations provide sufficient justification to adopt the acceptance criteria for in-situ concrete BIS 456 (BIS, 2000), and BIS 516 (BIS, 2018) as equivalent to the estimation of in-situ strength of concrete in existing structures – in the absence of sufficient data for the application of regular statistical approaches.

According to the Indian code (BIS (2000)), the strength of concrete can be estimated as lower of:

- Average core strength divided by 0.85; and
- Minimum core strength divided by 0.75.

Another Indian code (BIS (2018)) provides a slightly different formulation for the estimation of the strength of concrete as the lower of:

- Deduct 3 MPa from average core strength and divide by 0.85 to obtain the estimated concrete strength.
- Minimum core strength divided by 0.75.

Therefore, the estimation of concrete strength from core results by the two codes BIS 456 (BIS, 2000), and BIS 516 (BIS, 2018) would yield the same result when the minimum strength criterion is governing, and the code BIS (2018) would yield lower strength when the average strength criterion is governing.

3. Data and methods

3.1 Data

The data used in the simulation study is taken from the Indian code BIS (2000), pertaining to the concrete characteristic strength (20 MPa to 50 MPa) and corresponding standard deviation (4 MPa to 5 MPa). Indian codes BIS 456 (BIS, 2000), and BIS 516 (BIS, 2018) stipulate a minimum of three cores for the estimation of concrete strength, and further, ten cores are indicated as a minimum when large number of cube sets have failed BIS (2018). Studies reported analysis of 3-core and 9-core data for investigating the inherent variability (Masi *et al.* 2019). Considering these, simulations are based on 3-core and 9-core data, synthetically generated as described below.

3.2 Methods

Concrete strength is generally represented by Normal or Gaussian distribution (Neville and Brooks, 2010). Therefore, using the characteristic strength and standard deviation, the mean strength is first estimated according to the Indian code BIS (2000). Subsequently, 100 random concrete strength values are simulated from Normal distribution having the mean and corresponding standard deviation. These strength values would represent the possible 100 core test results. Readers may refer to textbooks (Ayyub and McCuen, 1997) for details regarding generating random Normal variables from mean and standard deviation sets.

Bootstrap resampling is an elegant tool for uncertainty analysis (Efron and Tibshirani, 1994) and this has been successfully applied for concrete (Dauji and Bhargava, 2016, Dauji and Bhargava, 2018 and Dauji and Karmakar, 2022). In the present study, therefore, bootstrap resampling is employed for estimation of

the uncertainty in concrete strength from 3-core and 9-core sets. These sets are selected randomly from the 100 (synthetic) core strength values generated earlier. The number of bootstrap samples adopted for the study is 100, and the 90 percent confidence interval will be discussed. Readers can refer the aforementioned textbook, and research papers for further details of the bootstrap resampling procedure. This process is repeated for all the seven characteristic strength sets of concrete mentioned earlier and the results are reported.

4. Results and discussions

4.1 Validation of simulation strategy

The characteristic strength (5 percentile value) was estimated from the 100 simulated data using parametric and non-parametric methods. In parametric method, the underlying distribution is assumed for obtaining the five-percentile value (BIS, 2000), whereas in the non-parametric approach, the five-percentile value is directly estimated from the data. Both the characteristic strength values, as well as the corresponding standard deviations obtained (parametric and non-parametric) from simulations matched well with the target characteristic strength, and this synthetic data was now employed for the simulation study.

4.2 Results of 3-core sets

Using bootstrap resampling technique, 100 values of in-place concrete strength was estimated from 100 random 3-core sets, according to the Indian codes BIS 456 (BIS, 2000), and BIS 516 (BIS, 2018). The estimated in-place strength (from 3-core sets) was much higher than the characteristic strength estimated from the whole synthetic data (100 nos.) in both cases. Further, as was expected, the estimation according to BIS (2018) yielded lower values of in-place strength when compared to BIS (2000). The 90 percent confidence interval was estimated from the bootstrap samples of in-place strength and the results are presented in Table 1 for 3-core sets from all grades of concrete. A further observation from the table is that there is a large uncertainty in the estimated in-place concrete strength, for all grades of concrete. The 90% confidence interval ranged between 9 MPa to 11 MPa – and this value appeared to increase slightly for higher grades of concrete. The uncertainty is higher for lower grades, the 90% confidence interval being almost 50% of the characteristic strength for M20, and this confidence interval is reduced to around 20%-25% of characteristic strength for M50.

Table 1. Ninety percent confidence interval for in-place concrete strength (3-core sets)

Target characteristic strength (MPa)	90% confidence interval of estimated in-place concrete strength (MPa)	
	BIS (2000)	BIS (2018)
20	26.42 – 36.85	24.87 – 34.18
25	31.74 – 40.12	28.99 – 37.72
30	37.90 – 50.42	36.49 – 47.42
35	44.60 – 55.09	41.67 – 52.16
40	50.88 – 61.74	48.00 – 58.74
45	57.12 – 68.48	54.12 – 65.58
50	63.58 – 73.79	60.78 – 70.79

4.3 Results of 9-core sets

Table 2. Ninety percent confidence interval for in-place concrete strength (9-core sets)

Target characteristic strength (MPa)	90% confidence interval of estimated in-place concrete strength (MPa)	
	BIS (2000)	BIS (2018)
20	23.41 – 31.97	23.41 – 31.21
25	26.13 – 38.98	26.13 – 35.98
30	34.57 – 47.62	34.57 – 45.22
35	43.21 – 51.82	43.21 – 49.84

40	51.69 – 58.30	50.13 – 57.06
45	57.72 – 66.26	57.11 – 63.47
50	62.51 – 71.14	60.49 – 68.18

Similarly, as was performed for the 3-core sets, the in-place concrete strength was estimated using 9-core sets from the same sets of synthetic data and the observations were similar. The 90% confidence intervals are estimated for the 9-core sets and are reported in Table 2. With the increase in number of cores, the range of interval has become wider: from 9–11 MPa for 3-core sets to around 7–13 MPa for 9-core sets. The range of uncertainty is around 42% of the characteristic strength for M20, and reduced to 17% of characteristic strength for M50. Apparently, the absolute values of these variations do not seem to be related to the strength of concrete, but appear to be random in nature. However, the uncertainty as a percentage of characteristic strength decreased with increasing concrete grade.

4.4 Discussions

The point of concern is that for all 14 cases (seven grades and two different numbers of cores) investigated in this study, the in-place strength was substantially lower than those estimated from the core tests (Table 1 for 3-core sets; Table 2 for 9-core sets). For M20 grade of concrete, the median value of the mean concrete strength (26.77 MPa) corresponded well with the target mean strength (26.6 MPa, BIS, 2000). Also, the median value of the minimum strength (20.51 MPa) matched well with the characteristic strength of concrete (20.00 MPa). However, in estimating the in-place concrete strength, these values were divided by values less than unity: by 0.85 or by 0.75 (refer to Section 2) – thereby increasing the estimated in-place concrete strength values. This was observed for all grades of concrete, similar to the conclusions of Klinger et al. (2022), though their approach was different. The findings of this small simulation exercise open up a possible concern over the concrete strength estimated from limited data (3-core set or 9-core set) according to Indian BIS 456 (BIS, 2000), and BIS 516 (BIS, 2018). More research with experimental data and broader simulations would be necessary before some definite conclusion may be arrived at regarding this issue.

5. Conclusions

- There is large uncertainty associated with the estimation of in-place concrete strength from core results by the Indian codes: BIS 456 and BIS 516.
- Between 3-core sets and 9-core sets, there is little to choose – considering the associated uncertainty.
- The actual in-place strength would be much less than those estimated from cores according to the Indian codes BIS 456 (BIS, 2000), and BIS 516 (BIS, 2018) irrespective of the grade of concrete (M20 to M50) and several cores (3 or 9).

The uncertainty discussed in this paper corresponds to that arising out of the method of estimating in-place strength from core results. There are other large variability issues associated with the core test, such as, within-structure variability; there are huge uncertainties associated with the method and workmanship during extraction and testing of cores, and these may be investigated in future studies.

References

Ayyub, B. M., and McCuen, R. H. (1997) "Probability, Statistics, & Reliability for Engineers", *CRC Press*, Boca Raton, Florida

Bureau of Indian Standards (2000) "Plain and Reinforced Concrete – Code of Practice", *IS 456: 2000, Bureau of Indian Standards*, New Delhi, India

Bureau of Indian Standards (2018) "Hardened Concrete – Methods of Test, Part 4 Sampling, Preparing, and Testing of Concrete Cores, IS 516 (Part 4): 2018", *Bureau of Indian Standards*, New Delhi, India

Dauji, S., and Bhargava, K. (2016) "Estimation of concrete characteristic strength from limited data by bootstrap", *Journal of Asian Concrete Federation*, 2(1): 81–94, http://dx.doi.org/10.18702/acf.2016.06.2.1.81

Dauji, S., and Bhargava, K. (2018) "Comparison of concrete strength from cube and core records by bootstrap", *Journal of Asian Concrete Federation*, 4(1): 35–46 https://doi.org/10.18702/acf.2018.07.3.1.35

Dauji, S., and Karmakar, S. (2022) "Estimating concrete strength from non-destructive testing with few core tests considering uncertainties", *ASME-ASCE Journal of Risk and Uncertainty in Engineering Systems Part B: Mechanical Engineering*, 8(4): 041102, https://doi.org/10.1115/1.4053639

Efron, B., and Tibshirani, R. J. (1994) *An Introduction to the Bootstrap*, Chapman and Hall/CRC, Boca Raton, USA
Klinger, J., Lobo, C. L., Connolly, E. F., and Suprenant, B. A. (2022) "Expect compressive strength test results less than specified strength on every project", *Concrete International*, February 37–43,
Masi, A., Digrisolo, A., and Santarsiero, G. (2019) "Analysis of a Large Database of Concrete Core Tests with Emphasis on Within-Structure Variability", *Materials,* 12:1985. https://doi.org/10.3390/ma12121985,
Neville, A. M., and Brooks, J. J. (2010) *Concrete Technology*, Pearson Education Limited, Essex, England.

Evaluation of Protective Coatings on Steel Rebar: Performance Under Diverse Environmental Conditions

Goldi Gupta[1*], Naveet Kaur[2], and Shweta Goyal[3]

[1] *CSIR-Central Road Research Institute, New Delhi, India*
Email: goldi.crri23a@acsir.res.in
[2] *CSIR- Central Road Research Institute, New Delhi, India*
Email: nkaur.crri@nic.in
[3] *Thapar Institute of Engineering and Technology, Patiala, India*
Email: shweta@thapar.edu

[*]Corresponding author

ABSTRACT

This paper evaluates the performance of three types of protective coatings—Zinc-Aluminium (Zn-Al), Hot Dipped Galvanized (HDG), and Fusion Bonded Epoxy Coated (FBEC)—on steel rebar, comparing them with uncoated rebar Thermo Mechanically Treated (TMT) bar. The study assesses the ability of these coatings to protect the underlying steel from corrosion and deterioration under various conditions. The evaluation includes exposure to marine environments, acidic conditions, alkaline conditions, and applied electric currents. Key tests conducted include salt spray corrosion testing to simulate marine conditions, where the coated and uncoated rebar specimens are exposed to sodium chloride solutions. This test assesses visual signs of corrosion, pin-hole detection, and weight loss. The impressed current test is performed to evaluate the performance of the epoxy coating under an applied electrical current, simulating the electrochemical stresses encountered in real-world environments. The bend test measures the resistance of the coatings to mechanical deformation, ensuring that the coating integrity remains intact under physical stress. The alkali dipping test examines the coatings' resistance to highly alkaline conditions, which are common in concrete environments. Additionally, specimens are exposed to sulphuric acid to evaluate the durability of the coatings in polluted, acidic environments. Throughout the study, the coated rebar's performance is meticulously compared with uncoated rebar to determine the effectiveness of each protective coating. The results provide insights into the coatings' ability to maintain structural integrity and prevent corrosion, thereby extending the service life of steel rebar in various challenging environments. This comprehensive evaluation contributes to the understanding of how different protective coatings perform under diverse environmental conditions, informing better material selection for construction and industrial applications.

1. Introduction

Corrosion is an electrochemical degradation of a metal resulting from its reaction with environmental elements, leading to the formation of oxides, hydroxides, or other compounds. This discussion focuses on both coated and uncoated rebar Thermo -Mechanically Treated (TMT) bars. Coated rebar is designed to mitigate the corrosion process by providing a protective barrier between the steel and the corrosive environment. Zinc-Aluminium (Zn-Al) coatings offer sacrificial protection, where zinc corrodes preferentially to steel, thereby protecting the rebar, while the aluminium component enhances the coating's resistance and extends its protective life. Similarly, Hot Dipped Galvanized (HDG) coatings involve a layer of zinc applied through galvanization, which acts as a sacrificial anode to protect the steel from corrosion. The galvanization process also creates a robust metallurgical bond that improves adhesion and durability. Fusion Bonded Epoxy Coating (FBEC) provides a physical barrier that isolates the steel from corrosive elements. The epoxy coating adheres strongly to the steel surface, preventing moisture and chlorides from reaching the steel (Rajbanul et al., 2024). However, the performance of FBEC can be compromised if the coating is damaged, leading to localized corrosion. Understanding the mechanisms and benefits of these coatings is crucial for effectively protecting steel rebar in various environments.

1.Salt Spray Test -Methodology describes a clear and organized process for conducting salt spray corrosion tests on coated steel samples, following the guidelines of IS: 9844-1981 (2024). These tests are designed to assess how well different coatings protect steel from corrosion in conditions that simulate real-world use. To ensure that the results are reliable and accurate, several important factors are carefully controlled. These include thorough cleaning of the steel samples, making sure the samples are positioned uniformly in the spray cabinet, controlling the rate at which condensation forms, maintaining the spray cabinet regularly, and keeping the temperature steady throughout the test.

The preparation of the salt spray solution is also carefully managed, with strict attention. The tests are conducted on different types of steel, including Thermo Mechanically Treated (TMT) bars, Fusion Bonded Epoxy Coated (FBEC) bars, Hot Dipped Galvanized (HDG) bars, and Zinc-Aluminium (Zn-Al) coated bars. Each sample has specific dimensions of 12 mm in diameter and 500 mm in length. The samples are placed in the spray cabinet in a way that ensures they are all exposed to the same conditions, as shown in the figures provided. Additionally, a Handheld XRF device is used to check for any changes in the chemical composition of the samples after the test.

The salt spray test itself is a widely used method to simulate and accelerate the corrosion process of steel bars might experience in real environments. By exposing the steel samples to a controlled salty mist, the test can quickly show how well the coatings protect the steel from rust and degradation. This information is crucial for understanding the long-term durability of different coatings and helps in selecting the right materials for use in construction and other industries where corrosion resistance is important.

The salt spray test is not valid method for assessing the corrosion resistance of steel bar that will be embedded in concrete. Because steel reinforcement in concrete is exposed to various conditions, including different moisture levels, the presence of chlorides (if any), and the protective alkalinity of the concrete. The salt spray test does not account for these variables and is therefore not a comprehensive test for evaluating steel bars to be embedded in concrete.

2.Exposure in acidic environment- The tendency of steel reinforcement to corrode in environments such as concrete can be understood through the electrical potential of the steel relative to its surroundings. In the highly alkaline conditions typical of cement mortars and concrete, steel remains in a passive state with a positive potential, protecting it from corrosion. However, in solutions containing sodium chloride or sodium sulfate, the potential becomes negative, leading to free corrosion. Introducing these salts into the alkaline solution disrupts the steel's passivity, causing corrosion. According to IS: 9077-1979, sodium chloride or sodium sulfate solutions are used to accelerate corrosion in steel embedded in concrete. (Ahmad, 2003). This study aims to assess the effect of protective coatings (FBEC, Zn-Al, and HDG) on steel bars compared to uncoated bars (TMT). Specimens, 500 mm in length and 12 mm in diameter, are immersed in 3% NaCl and 7% H_2SO_4 solutions for one month as shown in figure2. Changes in weight loss, tensile strength, and elongation are measured after exposure periods of 7, 20, and 30 days.

While direct immersion testing may not perfectly simulate real-world conditions, it is still useful for comparing the relative performance of different coatings (FBEC, Zn-Al, HDG) and uncoated steel bars (TMT). By subjecting all specimens to the same accelerated conditions, the test provides comparative data that can inform decisions about which coatings offer better protection under harsh conditions. The test is particularly valid for understanding how steel reinforcement might behave in extremely aggressive environments, such as those exposed to industrial pollutants, acid rain, or areas with high chloride content (e.g., marine environments). In such scenarios, the test provides valuable data on the potential performance of the steel and its coatings under severe conditions.

3.Rebar under Impressed current - The Impressed Current Test is a crucial method used to evaluate the effectiveness of epoxy coatings, particularly those with organic compositions like Fusion Bonded Epoxy Coatings (FBEC). In this test, the FBEC-coated steel bar serves as the anode, while a reference bar acts as the cathode. A direct current (DC) power source connects to the cathode, initiating ion flow from the FBEC-coated bar to the reference bar over a 30-day period, illustrated in Figure3. This specific test is tailored to FBEC due to its susceptibility to detachment from the metal surface during electron movement in corrosion processes. Accelerated corrosion is induced by designating the FBEC-coated bar as the anode, compelling electrons to pass through its coating. The electrolyte used is a 7% sodium chloride solution. During the 30 days, the development of the first holiday in the coating is closely monitored. If no undercutting is observed, deliberate 6 mm diameter holes are made in both the cathode and anode, followed by an additional 25-hour period to confirm coating integrity. Impressed current testing operates on cathodic protection principles, aimed at reducing the potential energy difference between anodic and cathodic areas on metal surfaces

submerged in conductive electrolytes such as water, concrete, or soil (Singh and Ghosh, 2005). Conducted in accordance with IS 13620-1993, this method evaluates the electrical and electrochemical stresses impacting the bond and film integrity of the coating. Typically involving anodes connected to a DC power source, often through an AC-linked rectifier, this setup ensures controlled conditions for assessing coating durability and performance in simulated operational environments.

The debonding observed during this test is a result of the extreme and controlled stresses applied to the coating, which are not representative of the typical conditions in the field. In the field, debonding of epoxy coatings is more commonly due to mechanical damage, poor surface preparation, or gradual chemical degradation, rather than the electrical stresses simulated in the impressed current test. Thus, while impressed current testing might cause debonding in a laboratory setting, it does not necessarily indicate that similar debonding will occur in the field under normal service conditions. This lab test is also predicting the long-term performance & reliability of coating under condition where corrosion risk is high.

4.Bend test of Rebar- The bending test for reinforcement steel bars evaluates ductility without compromising strength, following the IS: 1599-1985 standard. This method ensures that steel can bend without fracturing, using a mandrel in a Universal Testing Machine (UTM) to achieve specified angles of 90°, 120°, or 180°, depending on requirements. The test specimen, typically 600 mm in length and 12 mm in diameter, undergoes bending either manually with a bending fixture or in a UTM, as illustrated in Figure4. During testing, the direction of grain flow influences how the steel bar bends, impacting test outcomes. According to IS: 1786-2018, the steel bar must double over the mandrel under continuous pressure until the sides are parallel. Success is determined by the absence of visible ruptures or cracks on the bent section, detectable to the naked eye under standard vision conditions (IS 1786, 2008). Calculation of the distance between lower supports follows a specified formula to ensure consistent testing conditions. This method provides crucial insights into the bending properties of both coated and uncoated steel bars, supporting quality assessment and performance evaluation in construction and infrastructure applications.

5.Alkali dipping test- The alkali dipping or chemical resistance test, conducted per IS 13620-1993, offers a structured approach to evaluate how coatings perform under exposure to various alkaline solutions. This method immerses coated steel bars in distilled water, calcium chloride, sodium hydroxide, and calcium hydroxide solutions as shown in figure5 to assess their resistance against common environmental and industrial substances. Specimens are intentionally prepared with 6 mm diameter holes in the coating to scrutinize potential vulnerabilities, then submerged for 45 days at a controlled temperature of 30±5 °C. Success criteria are clearly defined: the coating should resist blistering, maintain bond integrity without softening, and exhibit no development of voids or gaps. Additionally, the absence of undercutting around intentionally made holes demonstrates the coating's ability to protect vulnerable areas effectively. The methodology's clarity and logical structure, complemented by visual aids, enhance understanding of the experimental setup, and ensure reliable assessment of coating durability under harsh chemical conditions.

Figure 1. Salt Spray Chamber

Figure 2. Sample kept in acidic solution

Figure 3. Impressed current

Figure 4. Bend test

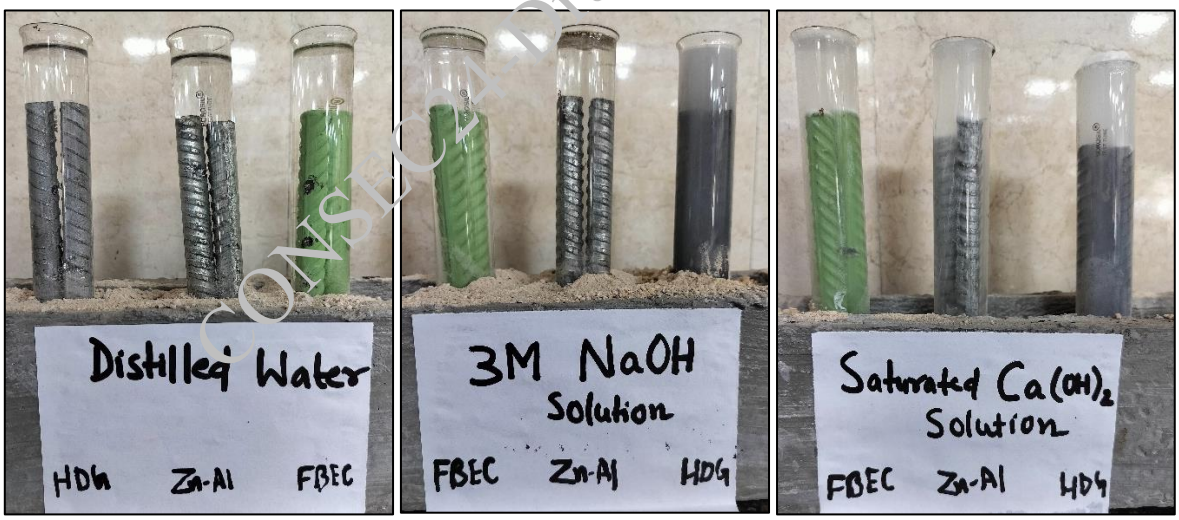

Figure 5. Samples of different coated bars are kept in various solutions for 45 days

3. Conclusions

The conclusion on various steel bars and coatings underscores significant differences in their performance under simulated environmental conditions. Thermo Mechanically Treated (TMT) bars displayed higher susceptibility to corrosion and greater weight loss under salt spray exposure, indicating their vulnerability in corrosive environments. Assessment of tensile strength loss revealed varying degrees of resistance among bars. TMT bars exhibited significant strength reduction in acidic conditions, highlighting their corrosion sensitivity. Coated bars, including HDG and Zn-Al, experienced reduced tensile strength, emphasizing the importance of evaluating long-term durability despite coatings.

During bending tests, uncoated rebars demonstrated good ductility and fracture resistance typical of mild steel, while coated bars, notably HDG and Zn-Al, displayed cracks, indicating potential mechanical limitations. FBEC-coated bars exhibited superior resistance to cracking as compared to HDG & Zn-Al suggesting enhanced performance in construction settings.

Chemical resistance tests indicated robustness of HDG and Zn-Al coatings against corrosive solutions, whereas FBEC showed vulnerability in distilled water. This highlights areas for improving FBEC formulations to bolster protection in mild environmental conditions.

This article gives a detailed evaluation of different protective coatings on steel rebar, looking at how they perform under various environmental conditions. It also aims to help in developing coatings that provide better protection and are environmentally friendly.

References

Ahmad S. Reinforcement corrosion in concrete structures, its monitoring and service life prediction—a review. Cem. Concr. Compos. 2003 May 1;25(4–5):459–71.

Bureau of India Standard. IS 1786 (2008): High strength deformed steel bars and wires for concrete reinforcement.

Rajbanul Akhond Md, Irfan A, Sharif A. An overview of corrosion behavior and contemporary management techniques of thermomechanically treated rebars in concrete structures. Journal of Structural Integrity and Maintenance. 2024 ;9(1). https://www.tandfonline.com/doi/full/10.1080/24705314.2023.2259721

Singh DDN, Ghosh R. Unexpected Deterioration of Fusion-Bonded Epoxy-Coated Rebars Embedded in Chloride-Contaminated Concrete Environments. Corrosion. 2005;61(8):815–29.

Standard Practice for Operating Salt Spray (Fog) Apparatus 1. [cited 2024 Sep 11]; Available from: www.astm.org

Seismic Performance Assessment of heritage structures through Field Testing and Numerical Simulations

A. Chaturvedi[1] and P. Sengupta[2*]

[1 1] M.Tech Student, Indian Institute of Technology (ISM) Dhanbad, India,
Email: 23MT0088@iitism.ac.in
[2] Assistant Professor, Indian Institute of Technology (ISM) Dhanbad, India,
Email: piyali@iitism.ac.in

[*]Corresponding author

ABSTRACT

Presence of heritage structures in the regions of tectonic or induced seismicity necessitates the seismic performance assessment so as to ensure their resilience in impending earthquakes. The heritage building inside the IIT (ISM) Dhanbad campus considered in this study is a two-storey multiple bay British Colonial Style Architecture. An extensive visual structural in-situ survey is conducted on the heritage building under consideration using a historical as well as engineering approach. Subsequently, experimental investigations involving sample collections, field tests, non-destructive tests and material characterizations are conducted extensively in order to deduce a realistic structural characterization of the heritage building under consideration. Thereafter, a numerical simulation approach is employed to develop realistic structural models of the heritage building utilising the field survey and experimental results. Since the heritage building under consideration is a complex structure, numerical models of different building units are developed incorporating the presence of adjacent building units. Then, seismic performance of the heritage building is assessed under different ground motion records for structural response characterization and damage classifications. At the end, incremental dynamic analysis methodology is adopted to develop seismic fragility functions of the heritage building for different damage states. Seismic fragility functions derived from this study can be utilized to select as well as prioritize the seismic repair and retrofit measures of different structural components of the heritage building. This research will bring forth an optimized solution to strengthen the weaker structural components of the heritage building where immediate interventions may be required.

KEYWORDS: *Heritage Structure, Visual Structural In-Situ Survey, Field Test, Non-destructive Test, Seismic Fragility*

1. Introduction

Heritage structures are cultural treasures that serve as a testament to craftmanship and architectural styles of our ancestors preserving the glorious history. Heritage structures are the special structures, premises or artifacts that are important for its history, architecture, art, beauty, culture or the environment. Heritage structures needs to be taken care of and preserved to retain its value. Earthquakes represent one of the most devastating natural calamities having the potential of causing severe destructions across the world. Consequently, presence of heritage structures in seismically active regions necessitates important measures for their safety in impending earthquakes. There is abundance of heritage structures in seismically active regions of the Indian sub-continent which do not meet the latest seismic design criteria due to increased seismicity of the heritage site, ageing-induced material degradation and insufficient maintenance over centuries. Consequently, seismic fragility assessment of heritage structures is of high significance to the engineering community.

Corigliano *et al.* (2012) compiled an earthquake catalogue for northern Tamil Nadu for performing probabilistic seismic hazard analysis (PSHA). Patil *et al.* (2018) conducted PSHA of the archaeological sites of Gol Gumbaz in Vijaypura based on Cornell-McGuire approach, applying uniformly distributed

seismicity in seismogenic zones. Aranha *et al.* (2019) assessed the complex structural geometry, building morphology, foundation details, material properties, reinforcement details and interaction between different structural elements of Rashtrapati Bhavan, the presidential palace of India by undertaking historical and geometrical survey, non-destructive and semi-destructive tests. A smeared crack approach was utilized using DIANA software to capture the strength degradation resulting from tensile cracking and decohesion in shear. Arede *et al.* (2019) conducted semi-intrusive/destructive tests on interface joints and infill material of the stone masonry historical structures to provide input data to numerical simulations. Manohar *et al.* (2020) assessed deterioration of Ramanathaswamy Temple, built before 16th century, using in-situ visual inspections, non-destructive test and different laboratory tests on coral stone samples (e.g compressive strength test, mineralogical tests, etc.). Erosion due to rain and wind was deduced as a primary reason behind the deterioration of the temple.

In this research, the heritage building inside the IIT (ISM) Dhanbad campus is considered as a case study for seismic performance assessment. The heritage building under consideration is a two-storey multiple bay British Colonial Style Architecture. An extensive structural in-situ survey of the heritage building is conducted, combining both historical and engineering perspectives. Then, an experimental investigation encompassing sample collection, field testing, non-destructive evaluation and material characterization is performed to characterize the structural geometry and material properties of the heritage building. Then, a realistic numerical model of the heritage building is built, integrating the field survey and experimental results. Thereafter, seismic performance of the heritage building is assessed under diverse ground motion records for structural response characterization, damage classification and seismic fragility assessment. Incremental dynamic analysis approach is adopted to derive seismic fragility functions for the heritage building for different damage states so as to select and prioritize the seismic repair and retrofit measures of different structural components.

2. Field Survey

An extensive visual structural in-situ survey is conducted for the two-storey multiple bay heritage building inside the IIT (ISM) Dhanbad campus, as seen in Figure 1. Construction of the heritage masonry building, built in the form of british colonial style architecture, was completed in 1926. A thorough field survey is conducted to identify the structural geometry as well as to assess the existing damages in the building. Rebound Hammer is utilized to perform non-destructive testing at different locations of the heritage building to identify the material characteristics. Additionally, samples are accumulated from the damaged portion of the heritage building for material characterization in the concrete laboratory of the institute.

Figure 1. Front View of Heritage Building of IIT (ISM) Dhanbad

3. Numerical Model Development

Numerical models of the heritage building are built based on the visual structural in-situ survey and non-destructive test results. The isometric view of the heritage building model is presented Figure 2 while the front view and side view of the heritage building model are shown in Figure 3 and Figure 4 respectively. In the numerical model, the material characteristics of every component of the heritage building are applied as per the field test results. Since the masonry panels are having very small thickness, shell elements are used to model them in the heritage building.

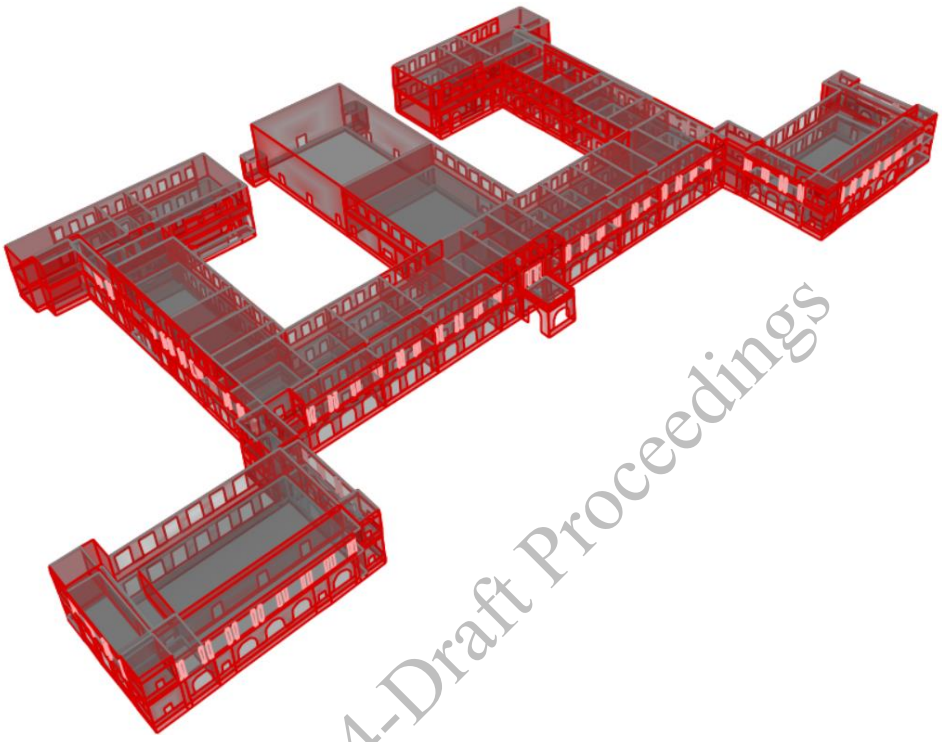

Figure 2. Isometric View of Numerical Model of Heritage Building of IIT (ISM) Dhanbad

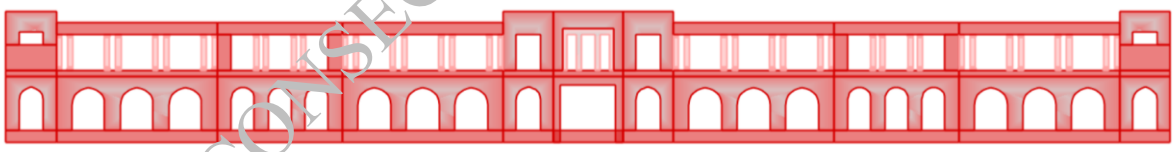

Figure 3. Front View of Numerical Model of Heritage Building of IIT (ISM) Dhanbad

Figure 4. Side View of Numerical Model of Heritage Building of IIT (ISM) Dhanbad

4. Derivation of Fragility Curves

Seismic Fragility functions represent the conditional probability of a particular structure surpassing a certain damage state when subjected to seismic excitations. Seismic fragility function can be mathematically expressed in terms of conditional probability as follows:

$$F(DS/IM = im) = \int_{EDP} F(DS/EDP).dF(EDP/IM = im) \quad (1)$$

$F(DS/IM = im)$ represents the seismic fragility of a structure i.e., the conditional probability of exceeding a Damage State (DS) for a structure for a given seismic Intensity Measure (IM). i.e. IM = im. Damage States (DS) represent the threshold levels of damages experienced by the structural components under a given loading environment. $F(DS/EDP)$ represents the conditional probability of exceeding a particular Damage State (DS) for a specific Engineering Demand Parameter (EDP). An engineering demand parameter (EDP) is a scalar or a functional quantity that can define the seismic demand of a structural element at any point of the loading history. It is assumed that for a given EDP, DS is statistically independent of IM. $F(EDP/IM)$ represents the conditional probability of exceeding EDP for a given Seismic Intensity Measure (IM). Eventually, F (EDP/IM) requires structural response analysis while F (DS/EDP) requires structural damage analysis. In this study, incremental dynamic analysis approach is adopted so as to derive seismic fragility functions of the heritage building for low, moderate and severe damage states, as shown in Figure 5.

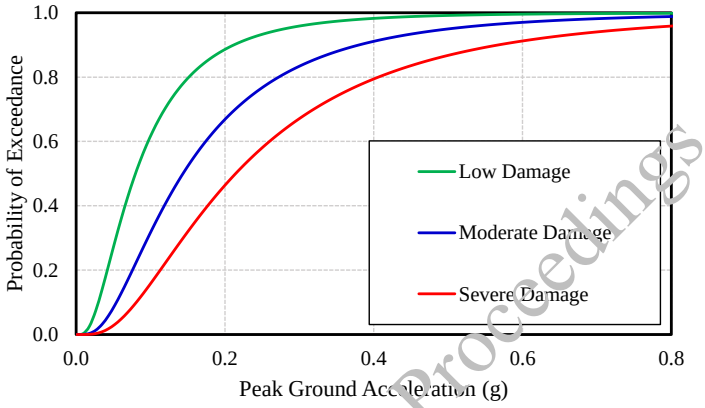

Figure 5. Seismic Fragility Curves of Heritage Building of IIT (ISM) Dhanbad

5. Conclusions

This study presents seismic fragility assessment of the two-storey multiple bay heritage building inside the IIT (ISM) Dhanbad campus. An extensive visual structural in-situ survey, non-destructive testing, sample collection and material characterization are conducted to build a realistic numerical model of the heritage building conforming to british colonial style architecture. Subsequently, incremental dynamic analysis methodology are adopted to derive the seismic fragility functions of the heritage building for low, moderate and severe damage states. Seismic fragility functions derived from this study can serve as a tool to select as well as prioritize the seismic strengthening of different structural components of the heritage building.

References

Aranha, C.A., Menon, A. and Sengupta, A.K. (2019) "Determination of the causative mechanism of structural distress inthe presidential palace of India", Engineering Failure Analysis, 95:312-331. https://doi.org/10.1016/j.engfailanal.2018.09.023

Arede, A., Almeida, C., Costa, C. and Costa, A. (2019) "In-situ and lab tests for mechanical characterization of stone masonry historical structures", Construction and Building Materials, 220:503-515. https://doi.org/10.1016/j.conbuildmat.2019.06.039

Corigliano, M., Lai, C.G., Menon, A. and Ornthammarath, T. (2012) "Seismic input at the archaeological site of Kancheepuramin Southern India", Natural Hazards, 63:845-866. https://doi.org/10.1007/s11069-012-0195-4

Patil, S.G., Menon, A. and Dodagoudar, G.R. (2018) "Probabilistic seismic hazard at the archaeological siteof Gol Gumbaz in Vijayapura, south India", Journal of Earth System Science, 127:16,1-24. https://doi.org/10.1007/s12040-018-0917-4

Manohar, S., Bala, K., Santhanam, M. and Menon, A. (2020) "Characteristics and deterioration mechanisms in coral stones used in a historical monument in a saline environment", Construction and Building Materials, 241: 118102. https://doi.org/10.1016/j.conbuildmat.2020.118102

Field Mock-Up Studies on Heavy Density Concrete Structures for Nuclear Fuel Cycle Facilities

R.Mano [1], H.Vaidyanathan[2] , G.Padmanabhan[3 &4 *] and K.S.Rahaman

[1] Scientific Officer E, Fast Reactor Fuel Cycle Facility, Nuclear Recycle Board, Bhabha Atomic Research Center Email: rmano@igcar.gov.in

[2] Technical Officer E, Fast Reactor Fuel Cycle Facility, Nuclear Recycle Board, Bhabha Atomic Research Center Email: vaithih@igcar.gov.in

[3,4] Scientific Officer G, Fast Reactor Fuel Cycle Facility, Nuclear Recycle Board, Bhabha Atomic Research Center & Faculty, Homi Bhabha National Institute, Mumbai Email: padman@igcar.gov.in*

[5] Project Director, Fast Reactor Fuel Cycle Facility, Nuclear Recycle Board, Bhabha Atomic Research Center Email: sarif@igcar.gov.in*

[*]Corresponding author (s)

ABSTRACT

Concrete with density higher than 2500 kg/m^3 is often used in the construction of nuclear fuel cycle facilities for limiting the radiation exposures. Generally heavy density aggregates in the form of iron ores were utilized for production of heavy density concrete. However, the issues like segregation were reported while placement of heavy density concrete which compromises the functional requirement of the structures. Hence a careful selection of material, proper mix design and placement methodologies plays an important role in the construction using heavy density concrete. With an aim to identify the pits during the actual construction, field simulation studies need to be carried out in the planning stage and the results needs to be incorporated in the actual construction to achieve defect free concrete. In this paper, the field mock-up studies carried out on heavy density structures were presented. Uniformity studies indicated that the wet density of heavy concrete before and after pumping during the initial stage is relatively lower and increased after stabilization of pumping. The results of non-destructive evaluation conducted on core samples also suggested uniformity in placement methods. Utilizing these qualified work procedure and methods, major heavy density cell walls, and slabs were successfully completed in nuclear fuel cycle facilities located at nuclear power plant site located at Kalpakkam.

KEYWORDS: *Heavy density concrete, Segregation, Uniformity, Field mock up studies*

1. Introduction

Concrete is often used as a shielding material in the construction of nuclear power plants and fuel cycle facilities. While light weight materials are required for neutron shielding , heavy density materials are required for gamma ray shielding. Concrete, being by its virtue of density and availability of free and chemically bound water, is considered as a best shielding material. However, the thickness required for shielding is governed by source term of the nuclear material. For the higher source terms, larger thickness of normal density concrete is required which may not be feasible considering the layout of the facility and economic aspects. This necessitate the usage of heavy density concrete in construction of nuclear facilities. Concrete with density lower than 2500 kg/m^3 is often defined as normal density concrete and concrete with density higher than 2500 kg/m^3 are defined as heavy density concrete. The aggregates for producing heavy density concrete shall meet the requirements for specific gravity and grading specified in ASTM C 637. The density of heavy density concrete mainly depends on specific gravity of aggregate & other constituent materials of the concrete and the gradation of aggregates. The selection of aggregates is a primary aspects in development of heavy density concrete and generally heavy density concrete is made of haematite, magnetite, illmonite, steel punching and iron shots. Even though specific gravity of aggregate is the essential requirement of development of heavy density concrete, strength, durability and workbaility concrete also to be considered while developing high density concretes.

Gencel et al (2010, 2011, 2012) and Ouda (2015) studied characteristics of heavy density concrete with magnetite, limonite-steel and serpantine. Basyigit et al (2011) studied heavy density concrete made of different mineral origins and investigated the shielding efficiency. However, there is no specific literature is available on the filed performance of developed concrete in terms of uniformity in density while placing, strength development with age at field and durability aspects. Considering these identified gap area in prediction of field performance of heavy density concrete, the work carried out for construction of nuclear facility underground storage vault was systematically analyzed and reported in this paper. Subsequently larger pours were taken up as the part of construction of under ground storage vault. Stringent field quality control measures enhanced the performance of heavy density concrete in terms of uniformity in density of placement, strength and durability. The main objective of the current study is to investigate the field performance of heavy density concrete developed using hematite aggregate sourced form different origin in terms of uniform distribution of density, strength and durability aspects.

2. Materials & mix proportions

OPC cement confirming to IS 269, Fly ash confirming to IS 3812 and heavy density Hematitite Fe_2O_3aggregate meeting ASTM C 637sourced from South African mines (Fig 1), potable water in the form of ice and polycarboxylate type super plasticizing chemical admixture confirming IS 9103 were used for proportioning Heavy density mix used in this work. The salient physical properties of OPC cement and fly ash is shown in Table 1. The physical properties of heavy density aggregate is indicated in Table 2.

Table 1. Properties of Cement and Fly ash

Material	Chemical Composition							Specific Gravity	Specific Surface m^2/kg
	CaO	SiO_2	Al_2O_3	Fe_2O_3	MgO	SO_3	LOI		
Cement	60.5	18.8	5.2	4.1	2.8	2.8	4.4	3.15	254
Fly ash	0.7	62.4	29.42	1.27	0.6	0.4	0.2	2.11	357

Table 2. Physical properties of heavy density aggregate

Property	Sand	20 mm aggregate	12.5 mm aggregate
Specific Gravity	4.5	4.78	4.73
Iron Content	60.59	-	-
Material passing75 microns	8.57	-	-
Water absorption	2.21%	0.47%	0.83%
Flakiness+ Elongation	-	16.21%	14.95%

The work-ability, strength and durability limits of heavy density concrete required for the project at field is specified in Table 3.

Table 3. Desired properties of heavy density concrete

Properties	Desired values
Slump at the end of 60 min	130 -180 mm
Unit Weight/density	≥3600 kg/m^3
Compressive Strength at 28 days	38.25 N/mm^2
Flexural Strength at 28 days ($0.7\sqrt{fck}$)	3.83 N/mm^2
Water permeability	25 mm of peneteration

With an objective of achieving the desired parameters, heavy density concrete mix were proportioned using American Concrete Institute (ACI) method of absolute volume method incorporating 1% of entrapped air in the volume proportion as used by various researchers Bunsell &Renard (2005), Kaplan (1989). After a series of trials, sand to total aggregate ratiowas kept around 45% for all the mixes and water to cement ratio was maintained as 0.355. The entire water demand was met by adding ice flakes to maintain the placement temperature of heavy density concrete at 23°C. The mix proportions for 1 m^3 concrete is listed in Table 4 whcih was meeting the properties as specified in Table 3.

Table 4. Mix proportions

Mix designation	Ingredients in kg for 1 m^3 of Heavy density concrete							Sand to Aggregate ratio
	OPC	Fly ash	H sand	H aggregate 20 mm	H aggregate 12.5 mm	Super plasticizer	Ice	
HDTM 6	390	70	1409	844	835	2.30	161	45.63%

3. Field Mock up studies

Subsequent to the laboratory trials and after establishing the physical and mechanical properties for various aggregates, a field mock up study was performed with an objective to evaluate the segregation resistance, pumpability, uniformity in placement and construction feasibility of the developed heavy density concrete. A portion of the 1.3 m thick underground storage vault slab was constructed along with associated duct penetrations of 1.1 m x 0.6 x 0.6 m size and compensatory shielding blocks weighing 5 MT. The salient features of the mock up structure are indicated in Fig 1 and the completed mock up structure is shown in Fig 2.

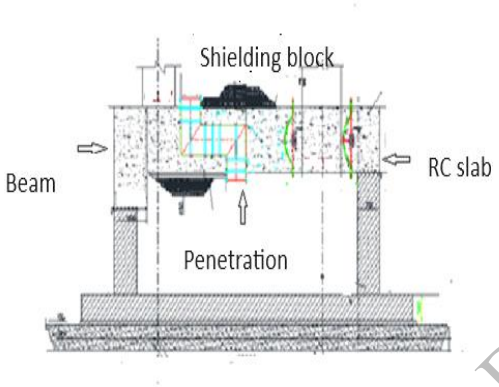

Figure 1. Details of the mock up

Figure 2. Completed heavy density slab

The 2 m deep beam and 1.3 m thick slab was casted in single pour (65 m^3) maintaining 250 mm layer thickness and by restricting free fall of concrete to 1.5 m preventing segregation and to ensure uniform distribution of heavy density concrete over the entire structural portion. The entire heavy density concrete was placed by pumping decreasing using boom placer and concrete pumps maintaining a rate of pour of 10 cum/hr. Saturated surface dry density was also evaluated for 90 samples during the mock up studies. The minimum reported value is 3694 kg/cum (Sample 19) and the maximum reported value is 3814 kg/cum (Sample 21). The average wet density value is 3730 kg/cum which is higher than the specified value 3600 kg/cum. The standard deviation is observed as 20.58 kg/m^3. The variation of average wet density observed is shown in Fig 3.

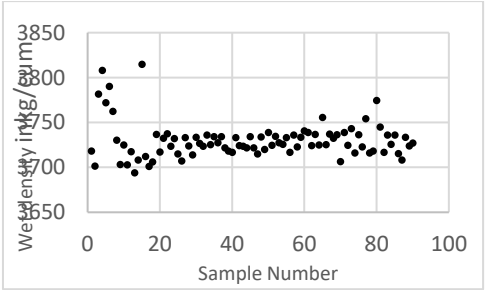

Figure 3. Variation of wet density during field mock up

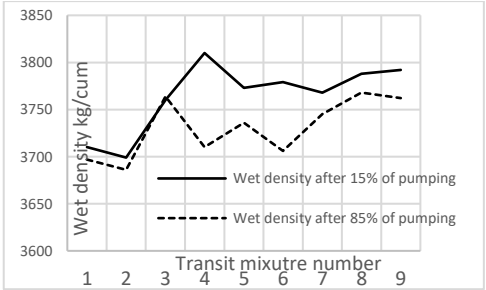

Figure 4. Variation of wet density

Uniformity of concrete during placement were tested by measuring the wet density of heavy density concrete before and after pumping by measuring concrete wet density after 15% and 85% of placement from 9 transit mixture.The variation of field wet density is plotted results obtained are shown in Fig 4. The wet density observed after 15% of pumping is higher than that after 85% of pumping in most of the observations except for the third observation where the wet density after 15% is slightly lower than that after 85% of pumping. However, all the density data are found to be more than the required wet density of 3600 kg/cum. The NDE performed on the cube and core samples were also meeting the required parameteres for the HDC.

4. Performance of Heavy density concrete in construction

Underground storage vault is being constructed at the project site located near South Cost India, Kalpakkam to receive and store high level liquid waste. This underground storage vault consists of RCC walls which is to be covered with heavy density concrete slab of size 108 m x 54 m. The total heavy density concrete required for the work is around 8000 m^3. The heavy density slab consists of provisions for ventilation ducts and sampling tubes. Adequate compensatory shielding plates are also to be embedded in the heavy density concrete to compensate the shielding loosed due to penetrations. As per the shielding calculation the slab thickness is 1.3 m and this is supported by columns and beam arrangement. Highly congested reinforcement, openings for ducts and its associated erection of CSB, in confined space were challenging tasks, and the same was taken up with a systematic approach involving field mock up studies involving development of high performance HDC explained in the previous sections with stringent quality control & safety during execution. The entire roof slab was taken up in 10 pours with suitable construction joints.

5. Conclusions

The, field mock up studies on high performance heavy density developed for the project, provided following major conclusions.

- Addition of fly ash as mineral admixture increased the pumpability of heavy density concrete and maximum pumping rate of 28 Cum/hr could be achieved in the project.
- The high-performance heavy density concrete developed for the project consistently exceeded the required density, strength and permeability values.
- The field mock up studies involving NDE examination proved that the pumping doesn't affect the uniformity in placement of heavy density concrete.
- There is a variation in strength and density properties during the initial period of pumping and later part of pumping the variation is reduced. This suggest need of stringent field quality control during the initial stages of pumping.

References

ASTM C 637. Standard specification for Aggregates for radiation Shielding Concrete

Ouda, Ahmed S. "Development of high-performance heavy density concrete using different aggregates for gamma-ray shielding." Progress in Nuclear Energy 79 (2015): 48-55.

Gencel, Osman, et al. "Determination and calculation of gamma and neutron shielding characteristics of concretes containing different hematite proportions." Annals of Nuclear Energy 38.12 (2011): 2719-2723.

Gencel, Osman, et al. "Combined effects of fly ash and waste ferrochromium on properties of concrete." Construction and Building Materials 29 (2012): 633-640.

Gencel, Osman, et al. "Concretes containing hematite for use as shielding barriers." Mater. Sci 16.3 (2010): 249-256.

Indian Standard 269, Specification for Ordinary Portland cement

Indian Standard 456:2000, Code for Plain Cement Concrete and Reinforcement Cement Concrete.

Indian Standard 3812, Pulverized fuel ash Specification

Indian Standard 9103, Concrete admixture Specification

Indian Standard 383, Coarse and fine aggregate for concrete Specification

American Concrete Institute, ACI 318, Building Code Requirements for Structural Concrete

Bunsell, A. R., & Renard, J. (2005). Fundamentals of fiber reinforced composite materials. CRC Press.

Kaplan, M. F. (1989). Concrete radiation shielding.

Indian Standard, 456: Code of practice for plain and reinforced concrete

ASTM c 143 , Standard test method for slump of hydraulic cement concrete

Conservation of Heritage Stones: Assessing Salt Weathering and Acid Resistance with Consolidative Treatments

Shipin Prakash[1]*, Anavadya Anilkumar[2], and Swathy Manohar[3]

1 IIT Bombay, Mumbai, India
Email: shipinprakash94@gmail.com
2 IIT Bombay, Mumbai, India
Email: anavadyaanilkumar98@gmail.com
3 IIT Bombay, Mumbai, India
Email: swathym@iitb.ac.in

ABSTRACT

Preserving the integrity of heritage structures remains a paramount concern in the face of environmental degradation and pollution. The current study investigates the susceptibility of stones such as marble and basalt, to salt weathering and acid corrosion. Our investigative approach revolves around a series of controlled laboratory experiments carefully designed to simulate real-world conditions of salt weathering and acid corrosion to understand the degradation process. These findings underscore the need for stone-specific conservation strategies. To address these vulnerabilities, consolidative treatments centred on diammonium hydrogen phosphate (DAP), ammonium oxalate (AmOx), and tetraethyl orthosilicate (TEOS) treatments are evaluated for their efficiency to mitigate degradation in these stones. The consolidants are applied by brushing until the refusal. These techniques aim to bolster stone resilience against salt weathering and acid attacks, facilitating the long-term conservation of heritage structures. Furthermore, our scrutiny extends to microstructural analyses, encompassing scanning electron microscopy and mineralogical examination, shedding light on the structural transformations engendered by the application of these conservational interventions. The research contributes critical insights into the preservation challenges posed by basalt and marble in heritage contexts. Ongoing investigations and further analysis will refine and tailor conservation strategies for each of these stone types.

KEYWORDS: *Heritage stones, Salt weathering, Acid corrosion, Preservation, Conservation*

1. Introduction

The conservation and preservation of heritage structures are vital for maintaining our cultural heritage. These structures, often recognized by local, national, or international authorities, include buildings and monuments of historical or cultural significance. Unfortunately, many of these structures are at risk of damage or are currently undergoing repair. Commonly used stones in the construction of these heritage buildings include limestone, marble, basalt, and sandstone (Doherty et al., 2007). Architectural heritage is subjected to various decay processes due to harsh environmental conditions, posing significant challenges to its longevity and conservation (Charola, 2000). Moisture, originating from rain, condensation, or capillary action, plays a crucial role in the deterioration of porous materials (Lourenço et al., 2006) (Rirsch & Zhang, 2010). Moisture is a key factor in many decay processes, such as freeze-thaw cycles, crystallization of soluble salts, biological growth, chemical deterioration from acid rain, and wind erosion (Sandrolini & Franzoni, 2006). Soluble salts contribute to the degradation process at varying rates, influenced by crystallization conditions that occur when the environment's relative humidity falls below the salt's equilibrium level (Angeli et al., 2007). This study examines the impact of sodium sulfate crystallization on marble, alongside investigating artificial acid weathering caused by H_2SO_4. These factors are known to cause substantial damage to heritage stones. Throughout these processes, porosity emerges as a pivotal factor influencing the degradation of these historical materials.

To safeguard against stone dissolution due to rain, protective coatings are often employed. These coatings aim to render the stone surface hydrophobic or create a layer with decreased solubility. Additionally, consolidants are frequently utilized to enhance grain cohesion and reinforce mechanical properties. However, assessing the effectiveness of consolidation presents challenges, primarily due to the intricate relationship between the stone substrate and the applied treatment (Pinto & Rodrigues, 2008). In this study, consolidants such as Diammonium hydrogen phosphate ($(NH_4)_2HPO_4$, DAP), Tetra ethoxy silane (TEOS), and Ammonium oxalate ($(NH_4)_2C_2O_4$, AmOx) were utilized. This paper places special emphasis on scanning electron microscopy (SEM), thin section studies, and other microstructural characteristics to comprehend the changes in porosity following consolidation.

2. Materials and Methods

For the artificial salt weathering test, samples were soaked in a 10% sodium sulphate solution for 2 hours, followed by 19 hours of oven drying at 60°C and 3 hours of air drying, repeated cyclically over 15 days. Microstructural changes were examined using imaging techniques. In the prolonged artificial acid weathering test, specimens were immersed in a diluted H_2SO_4 solution with a controlled pH of 4 for 14 days, mimicking acid rain conditions. Continuous pH monitoring ensured accurate replication of real-world scenarios. Microstructural properties were assessed using a range of imaging methods, such as Scanning Electron Microscopy (SEM), petrographical analysis with thin sections etc.

3. Results and Discussions

3.1 Petrographical Analysis

The petrographical images of marble samples upon the action of different consolidants are shown in Figure 1.

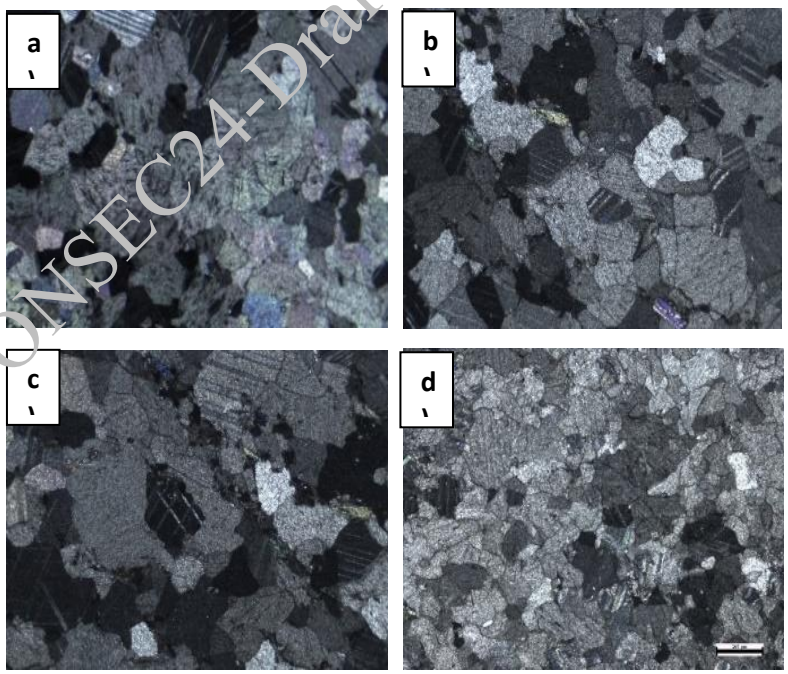

Figure 1. Petrographical images of thin sections of marble specimens before consolidative treatment,with (b) DAP, (c) AmOx and (d) TEOS consolidants which were subjected to accelerated salt weathering

The petrographical images show distinct mineral features under cross-polarized light. In Figure 1(a), irregularities make it hard to identify some minerals. Treatments with DAP and AmOx improved optical properties, while TEOS showed minor changes. These results highlight the effectiveness of DAP and AmOx in improving mineral clarity and the need for further optimization.

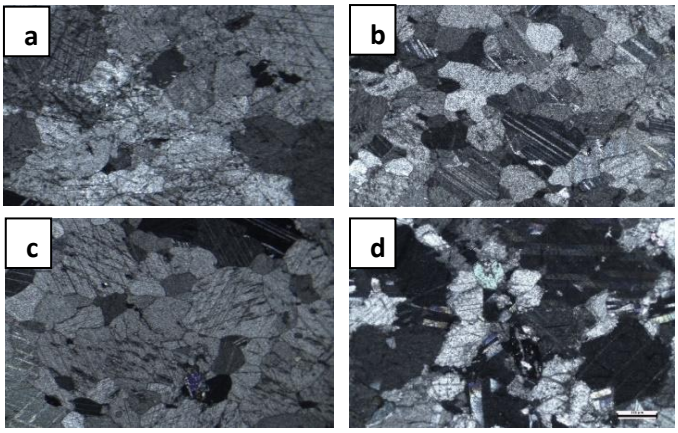

Figure 2. Petrographical images of thin sections of marble specimens (a) before consolidative treatment,with (b) DAP, (c) AmOx and (d) TEOS consolidants which were subjected to accelerated acid weathering

Figure 2(a) shows images after artificial acid weathering, with treatments in 2(b) (DAP), 2(c) (AmOx), and 2(d) (TEOS). Acid weathering degraded the specimens, obscuring minerals. DAP treatment improved clarity the most, revealing features like cleavage planes. AmOx also improved clarity but left some pores. TEOS improved appearance but did not show clear calcite cleavage planes. DAP was the most effective, followed by AmOx, with TEOS having limitations.

3.2 Scanning Electron Microscope (SEM) Analysis

Scanning Electron Microscope (SEM) was used to observe the morphology and surface topography of stone samples before and after consolidative treatments. Marble and basalt specimens subjected to accelerated salt weathering, with and without treatments, showed significant variations in their pore networks. Consolidants reduced porosity and improved surface uniformity. Before treatment, the porosity under accelerated salt weathering was 6.52%, while after treatment with DAP, TEOS, and AmOx, the porosity values were 4.79%, 6.22%, and 5.47%, respectively, indicating DAP as the most effective. For accelerated acid weathering, the initial porosity was 7.20%, and after treatment with DAP, TEOS, and AmOx, the values were 4.53%, 6.84%, and 5.78%, respectively, again highlighting DAP's superior performance in reducing porosity and mitigating damage.

In the case of accelerated acid weathering, the results indicate that treatment with DAP led to the most significant reduction in porosity compared to TEOS and AmOx consolidants, suggesting its potential as an effective solution for mitigating acid weathering-induced damage. However, further investigation into the long-term durability and performance of these consolidants in real-world acid weathering conditions is required to validate their efficacy.

In the case of Ultrasonic Pulse Velocity (UPV) test method, the increase in UPV value for DAP- treated marble sample under accelerated salt weathering was 6.34% compared to that of AmOx and 11.11% compared to that of TEOS. For accelerated acid weathering, the increase in UPV value for DAP- treated marble sample under accelerated salt weathering was 24.63% compared to that of AmOx and 33.33% compared to that of TEOS. From the results it was evident that, though all the three consolidants show improvement in UPV over time, DAP consistently provides the most significant improvement in UPV over time, indicating an enhanced consolidation effect compared to the other treatments in the case of marble specimens. The UPV values for DAP-treated samples show a steady increase, reflecting improved material integrity and reduced porosity due to effective consolidation.

AmOx also demonstrates a positive effect, but to a lesser extent than DAP. The increase in UPV for AmOx-treated samples suggests that it contributes to the consolidation process, though it does not achieve the same level of efficacy as DAP.

4. Conclusions

Our study assessed the effects of artificial acid weathering and artificial salt weathering on marble and basalt stones to simulate environmental conditions and understand degradation mechanisms. Although these tests may not fully replicate real-world complexities, they are crucial for evaluating protective treatments. Using SEM and petrographical analysis, we found that DAP and ammonium oxalate were more effective in reducing porosity compared to TEOS in the case of marble specimens. In the case of basalt samples, TEOS proved to be more effective as it is a siliceous rock. These findings highlight the need for further research on optimization and additives to enhance consolidant efficiency, with significant implications for heritage preservation practices.

Acknowledgements

The authors are grateful to SAIF (Sophisticated Analytical Instrument Facility) at IIT Bombay for generously providing access to their ESEM facility.

References

Angeli, M., Bigas, J.-P., Benavente, D., Menéndez, B., Hébert, R., & David, C. (2007). Salt crystallization in pores: quantification and estimation of damage. Environmental Geology, 52(2), 205–213.

Charola, A. E. (2000). Salts in the deterioration of porous materials: An overview. Journal of the American Institute for Conservation, 39(3), 327–343.

Doherty, B., Pamplona, M., Selvaggi, R., Miliani, C., Matteini, M., Sgamellotti, A., & Brunetti, B. (2007). Efficiency and resistance of the artificial oxalate protection treatment on marble against chemical weathering. Applied Surface Science, 253(10), 4477–4484.

Lourenço, P. B., Luso, E., & Almeida, M. G. (2006). Defects and moisture problems in buildings from historical city centres: A case study in Portugal. Building and Environment, 41(2), 223–234.

Pinto, A. P. F., & Rodrigues, J. D. (2008). Stone consolidation: The role of treatment procedures. Journal of Cultural Heritage, 9(1), 38–53.

Rirsch, E., & Zhang, Z. (2010). Rising damp in masonry walls and the importance of mortar properties. Construction and Building Materials, 24(10), 1815–1820.

Sandrolini, F., & Franzoni, E. (2006). An operative protocol for reliable measurements of moisture in porous materials of ancient buildings. Building and Environment, 41(10), 1372–1380.

Condition of Concrete with Calcium Nitrate and Nitrite after 20 Years Exposure to Marine Environment

H. Justnes[1*] and M. Torabzadegan[2]

[1] SINTEF Community. Trondheim, Norway
Email: harald.justnes@sintef.no
[2] Yara International, Porsgrunn, Norway
Email: Mehrdad.torabzadegan@yara.com

*Corresponding author

ABSTRACT

Three wall elements of self-compacting concrete with w/c ≈ 0.45 have been standing 12 years in the tidal zone in the Trondheim fjord and laying additional 8 years in the tidal zone of the sea outside Porsgrunn, Norway. One was without corrosion inhibitor and the two others with 4% calcium nitrate and 2.8% calcium nitrite of cement mass, respectively. Cores were drilled with the objective of seeing effect on the corrosion state of the steel with nominal cover of 20 and 50 mm and inspect the condition of the concrete in general. The concrete condition was characterized in terms of strength, porosity by capillary suction, element distribution of cross-section by µXRF scanner, analytical chloride profiles as well as microstructure by SEM. Despite having total chloride levels up to 5x higher than what is considered the limit (0.07% total Cl^- of concrete weight) for initiation of steel corrosion, all wall elements had reinforcement in pristine condition, so no conclusion could be drawn regarding effect of corrosion inhibitor. However, Friedel salt crystals were found throughout the binder, so the fraction of chloride in the pore water is not known. All concretes were rated watertight based on resistance number from capillary suction experiments but concrete with nitrate and nitrite was rated lower than the reference. Especially the concrete with nitrite had a strength drop over time due to massive ettringite formation, and the increased hydration of C_4AF by nitrite bringing more CAH to the system is discussed as potential reason.

KEYWORDS: *Chloride, ettringite, Marine exposure, Microstructure, Porosity.*

1. Introduction

The phase changes in concrete exposed to sea water are complex due to the presence of a variety of ions in the sea water such as sodium, chloride, magnesium, sulphate, calcium and carbonate ions. These ions can affect the phase assemblage of the concrete in different ways (Mather, 1964; Duval and Hornain, 1992; Mehta, 2003; De Weerdt et al., 2014a; De Weerdt and Justnes, 2015). Most studies on the effect of sea water on concrete focus on the ingress of chloride ions in concrete as chlorides pose a threat to the reinforcement by causing pitting corrosion. The chloride ingress from sea water can, however, be influenced by the other ions present in the sea water either by changing the chemistry and/or porosity or even by causing scaling.

The concrete wall elements in question were cast in 2002 and are described in detail by Justnes (2006). In previous studies by De Weerdt et al (2013, 2014b) the phase changes in a concrete wall element exposed in the tidal zone of the Trondheim fjord for 10 years were investigated and it was shown that the chloride level near the exposed surface is low (higher further in) as the chloride peak is preceded by a magnesium enriched zone followed by a sulphate enriched zone. In addition, these zones showed signs of carbonation. Justnes et al. (2012) discussed the role of magnesium in more detail. Such zoned attack has also been observed by Marchand et al. (2003), Chabrelie et al. (2008) and Jakobsen (2013) on marine exposed concrete.

2. Experimental

Table 1 shows the concrete recipe of the wall elements. The amount of limestone filler is 12% of cement mass for all mixes. However, the water-to-cement ratio (w/c) ranges from 0.467, 0.459 to 0.444 for the reference, nitrate mix and nitrite mix, respectively. The calcium nitrate content is 4.0 % dry material of cement mass, while the calcium nitrite content is 2.8% dry material of cement mass corresponding to 3.5% calcium nitrate molar equivalent. The calcium nitrite dosage is within the recommended dosage as corrosion inhibitor (10-30 litre/m^3). Calcium nitrate was added as 50% solution and calcium nitrite as 33% solution and the water in the admixture was subtracted from water to be added. The aggregate-to-cement ratio (a/c) is 4.874, 5.031 and 5.015 for the reference, nitrate mix and nitrite mix, respectively, including limestone filler. The lower w/c and lower air content (5% strength decrease per vol% air increase) may partly explain the higher strength for the nitrite mix relative to the nitrate mix. The mix with calcium nitrate was added sodium gluconate as retarder while the commercial calcium nitrite as corrosion inhibitor contained a retarder already to delay setting.

Table 1. The concrete recipes (kg/m^3) for the 3 wall elements.

Concrete mix	Reference	Nitrate	Nitrite
OPC	366.1	355.0	357.2
Limestone filler	43.9	42.6	42.9
Calcium nitrate (50% solids)	-	28.4	-
Calcium nitrite (33% solids)	-	-	30.3
Total added water	171.1	148.7	138.4
Årdal sand, 0-8 mm	842.9	844.6	851.2
Bjørkmyr sand, 0-2 mm	210.3	211.3	210.1
Årdal gravel, 8-11 mm	343.7	343.7	343.7
Årdal gravel, 11-16 mm	343.7	343.7	343.7
Scanflux CP30 super-plasticizer	2.2	2.1	2.1
Sodium gluconate retarder	-	0.18	-

The concrete wall elements were placed standing in the tidal zone of the Trondheim fjord after 3 days in mould and left there for 12 years. The tide here is high so the elements were submersed and on dry land two times every 24 h. After 12 years the wall elements were moved to Porsgrunn, Norway, and placed laying down in the tidal zone since the tidal difference is much lower there (30 cm versus 2.5 m).
Compressive strength was measured on 10 cm cast cubes the first year and thereafter drilled cores with 100 mm diameter.
For some cores, powder was ground off every 10 mm in a lath and collected. This powder was digested in nitric acid, filtered and the liquid analysed for chlorides to calculate the total chloride of concrete mass.
Discs were cut from some cylinders, dried to constant mass at 50°C and subjected to a capillary suction test as described in Justnes et al. (2001) allowing for calculation of densities, porosities, and resistance to water penetration.
Other cylinders were cut along their axes and element mapping over the cross-section was performed by a µXRF scanner.
From some of the cores 40mm · 25 mm thin sections without glass cover were made so they could be studied by SEM after being sputtered with carbon for electrical conductivity.

3. Results and discussion

The initial properties up to 1 year reported by Justnes (2006) are reproduced in Table 2 illustrating the accelerating effect of calcium nitrite relative to calcium nitrate, from 7 days onwards. There is calcium in both admixtures, so it is likely that it is the nitrite that makes a difference even though there is more calcium due to higher dosage in the element with calcium nitrate. This could be explained by nitrite accelerating C_4AF hydration. C_4AF constitutes about 10% of the cement. The lower air content in the nitrite mix will be in favour of higher strength (σ_c) but can only explain 10% as strength is increased by ≈5% for each vol% of lesser air content. The higher strength at 1 year as a result as higher degree of hydration is also reflected in a lower apparent chloride diffusion coefficient, which also would be affected by more chloride binding

if C_4AF is activated by nitrite. In addition to the compressive strength, σ_c (MPa), Table 2 also list the density, ρ (kg/m^3), apparent surface concentration of chlorides, $C_{0,\,Cl}$ (%), and apparent diffusion coefficient, D_{Cl} (10^{-12}m^2/s), when the chloride profile is fitted to the solution of Fick's second law of diffusion, in addition to the electrical conductivity, ρ_r (Ω·m).

The compressive strengths for the 3 parallel cores drilled from the wall elements after 20 years in the tidal zone were 63.1±5.3 MPa (one high value), 56.7±1.9 MPa and 53.5±1.3 MPa for the reference, nitrate mix and nitrite mix, respectively. The densities for the same cores were 2422±50 kg/m^3(one high value), 2382±5 kg/m^3 and 2368±10 kg/m^3 for the reference, nitrate mix and nitrite mix, respectively. If the unusual high value of on sample for the reference is dropped, the values for the two remaining cylinders of the reference will be 60.2±2.3 MPa and 2394±3 kg/m^3 for strength and density, respectively. If this latter value is used, there is a good correlation between compressive cylinder strength and cylinder density.

Table 2. Properties of concrete for the 3 wall elements

Properties	Ref.	Nitrate	Nitrite
Fresh mix Density (kg/m^3) Air (vol%)	 2,384 5.2	 2,344 4.8	 2,380 3.0
1 day σ_c (MPa)	 22.1±0.2	 19.0±0.3	 24.4±0.3
7 days σ_c (MPa)	 45.3±0.1	 47.8±0.6	 61.9±0.4
≥28-Days (d) σ_c (MPa)	35 d 56.9±0.7	34 d 58.3±0.5	28 d 73.5±0.6
1 year σ_c (MPa) ρ (kg/m^3) $C_{0,\,Cl}$ (%) D_{Cl} (10^{-12}m^2/s) ρ_r (Ω·m)	 65.2±0.3 2412±5 0.89±0.07 7.8±1.0 73±1	 65.5±1.0 2397±2 0.96±0.01 9.9±1.3 70±2	 85.4±2.4 2457±2 0.99±0.07 6.4±0.5 69±2

The chloride profiles of the concretes are shown in Figure 1. There are sufficient chloride contents to initiate corrosion of steel both with 20- and 50-mm nominal concrete cover since the anticipated level for corrosion initiation is 0.07% Cl$^-$ of concrete mass (the value used both by the Norwegian Road directorate and Equinor for initiation of rebar corrosion in their condition surveys of structures).

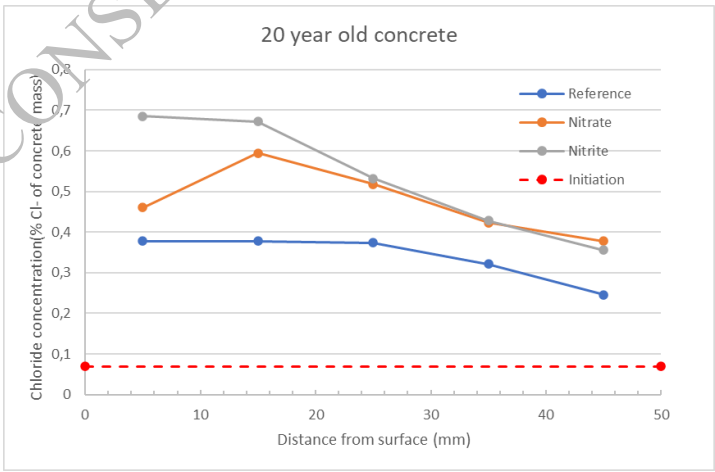

Figure 1. Chloride profiles for the three different concrete wall elements. The anticipated chloride concentration for corrosion initiation of rebars (0.07% Cl$^-$ of concrete mass) is indicated as a dashed red line.

The reinforcement steels for all three concrete mixes with nominal cover of 20 and 50 mm was split out, and the photo of the steels and their imprint are shown in Figure 2 for the reference and the inhibitor mixes. Firstly, the real concrete cover turned out to be 25-32 and 62 mm rather than the nominal 20 and 50 mm for all three wall elements. Secondly, even the reinforcement steel for the reference at 25 mm was in pristine

condition with no sign of corrosion and no rust in the concrete imprint despite the chloride level at 25 mm being >5x the limit for initiation of corrosion, providing that the chloride ingress is uniform all over the wall element. There was no sign of corrosion for the rebars in the nitrate mix or the nitrite mix either, except for a small rust stain near the drilled surface for both (likely appeared after drilling). No conclusion can be drawn on the effect of nitrate or nitrite as corrosion inhibitors since reference rebar was not corroded, but they do not promote corrosion. Images of the rebars with their concrete imprints are shown in Figure 3.

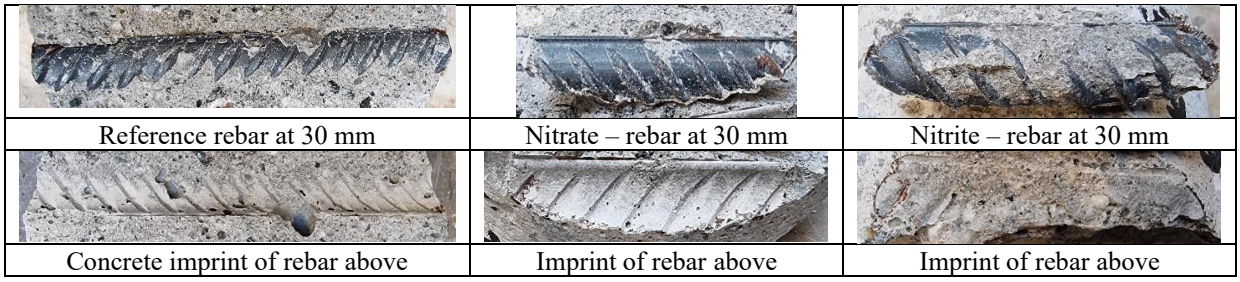

Figure 3. Images of rebars with their concrete imprints drilled from the 3 wall elements.

Parameters obtained by the capillary suction technique are listed in Table 3, while the water absorption profiles are plotted in Figure 4.

Table 3. Results from the capillary suction test of the concrete in the 3 wall elements

Concrete	Reference	Nitrate	Nitrite
Number of discs	6	6	6
Total porosity, ε_{tot} (vol%)	13.7±0.3	15.5±0.4	15.5±0.2
Capillary porosity, ε_{cap} (vol%)	11.1±0.3	12.1±0.3	12.2±0.1
Air volume, ε_{air} (vol%)	2.6±0.4	3.4±0.4	3.23±0.04
Dry concrete density, ρ_{dry} (kg/m^3)	2291±9	2237±16	2232±4
Density of solids, ρ_{solid} (kg/m^3)	2654±14	2648±8	2641±7
Capillary coefficient, k (10^{-3}·kg/m^2·√s)	13.2±0.6	17.4±1.2	17.9±0.8
Water resistance number, m (10^7·s/m^2)	6.6±0.7	4.6±0.6	4.2±0.3

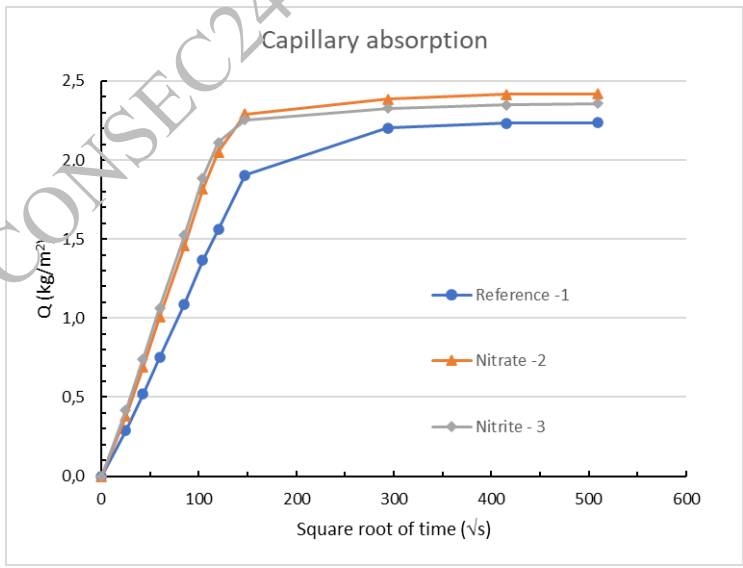

Figure 4. Average capillary suction profiles for the 6 discs from reference concrete, concrete with nitrate and concrete with nitrite, respectively.

Comparing the resistance numbers of the concretes in Table 3 with the data from experience, all concretes are rated as watertight (m > $3.2 \cdot 10^7$ s/m^2). The reference is rated as a very good concrete in terms of watertightness, while the concrete with nitrate and nitrite is rated as medium good concretes. The concrete with nitrate is slightly better than the concrete with nitrite.

The SEM investigation of the reference concrete show that several sand grains are exposed on the surface, indicating that the original cement paste layer has been eroded away. There is a long crack from the surface, through an air void progressing further in with precipitated magnesium hydroxide. There are magnesium ions in the seawater and when they penetrate cracks they will precipitate as brucite when meeting the high pH of sound concrete. This is quite common for concrete exposed to sea water. Further into the crack even a cluster of ettringite and possibly thaumasite is formed. The binder itself seems to be affected the first 0.5 mm by carbonate precipitation or leaching. In another section, the microstructure starts with a 0.8 mm dense zone due to precipitations or carbonation, followed by a more open structure which again turns into a denser zone again at 3.8 mm. Friedel's salt; $Ca_3Al_2O_3{\cdot}CaCl_2{\cdot}12H_2O$, as identified by EDS is found at both 6.7 mm and even at 19.1 mm from the surface.

An overview of the surface for the concrete with nitrate revealed that the binder is full of microcracks. There is also visual evidence of a border between a more porous zone and a denser zone at 8 mm from the surface. The cracked zone contains some clusters of ettringite; $Ca_3Al_2O_6{\cdot}3CaSO_4{\cdot}32H_2O$, in the binder as exemplified in Figure 5 (left) at 1.3 mm from the surface. Friedel's salt is also found.

An overview near the surface of the concrete with nitrite show aggregates poking out of the surface indicating that original cement paste skin (and maybe more) has been eroded away. There is a lot of microcracks in the binder below the surface. There seems also to be a border between a more porous zone and a denser zone at about 7 mm from the surface. The right image of Figure 5 show examples of massive ettringite clusters (possible mixed with isostructural thaumasite) at 0.9 mm from the surface in the cracked zone.

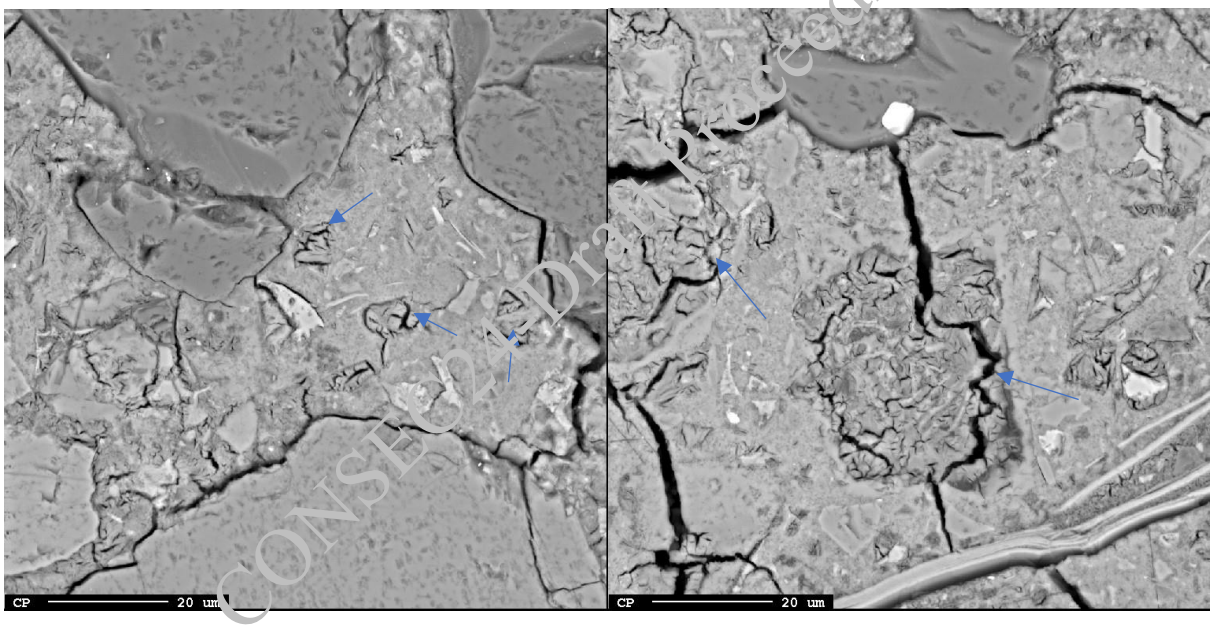

Figure 5. Examples of ettringite crystal embedded in the binder of concrete with nitrate to the left at 1.3 mm from the surface, more massive clusters of ettringite (possibly including isostructural thaumasite) in the concrete with nitrite at 0.9 mm from the surface. In both cases, ettringite examples are marked with arrows.

A comparison of a sulphur (e.g. sulphate) mapping by µXRF over cross-sections of concrete cores until 80 mm from the surface is shown in Figure 6 and reveal that there are much more hot-spots of sulphate further in for concrete with nitrite.

The calcium aluminate hydrates in the binder are the key to many of the observations. The OPC used 20 years ago contained 7.5% C_3A which will immediately react with interground gypsum prior to setting to ettringite (AF_t):

$$C_3Al_2O_6 + 3\ CaSO_4{\cdot}2H_2O + 26\ H_2O = Ca_3Al_2O_6{\cdot}3CaSO_4{\cdot}32H_2O \quad (1)$$

A while after setting when more C_3A has reacted and there is insufficient gypsum, the ettringite will be converted to calcium monosulphoaluminate (AF_m):

$$Ca_3Al_2O_6{\cdot}3CaSO_4{\cdot}32H_2O + 2\ C_3Al_2O_6 + 4\ H_2O = 3\ Ca_3Al_2O_6{\cdot}CaSO_4{\cdot}12H_2O \quad (2)$$

But not when there is ample calcium carbonate around as filler as in these concretes, which will instead stabilize ettringite (De Weerdt and Justnes, 2009):

$$C_3Al_2O_6 + CaCO_3 + H_2O = Ca_3Al_2O_6{\cdot}CaCO_3{\cdot}11H_2O \text{ preventing conversion of ettringite} \quad (3)$$

or

$$3\ Ca_3Al_2O_6{\cdot}CaSO_4{\cdot}12H_2O + 2\ CaCO_3 + H_2O = Ca_3Al_2O_6{\cdot}3CaSO_4{\cdot}32H_2O + 2\ Ca_3Al_2O_6{\cdot}CaCO_3{\cdot}11H_2O \quad (4)$$

The analogue of Eq. 3 (or 4) can also happen with calcium nitrate and nitrite in the beginning being more soluble and available than calcium carbonate:

$$C_3Al_2O_6 + Ca(NO_3)_2 + H_2O = Ca_3Al_2O_6{\cdot}Ca(NO_3)_2{\cdot}12H_2O \text{ preventing conversion of ettringite} \quad (5)$$

$$C_3Al_2O_6 + Ca(NO_2)_2 + H_2O = Ca_3Al_2O_6{\cdot}Ca(NO_2)_2{\cdot}12H_2O \text{ preventing conversion of ettringite} \quad (6)$$

The reaction in equation 5 is partly explaining why calcium nitrate increases strength in the longer run in cement without calcium carbonate. Preventing conversion of ettringite and binding more water.
If calcium nitrite (and to a lesser extent calcium nitrate?) is accelerating hydration of C_4AF (about 10% of the OPC), one can imagine the following reaction where a lot more water can be bound leading to increased strength (as in Table 2):

$$Ca_4Al_2Fe_2O_{10} + Ca(NO_2)_2 + 16\ H_2O = Ca_3Al_2O_6{\cdot}Ca(NO_2)_2{\cdot}12H_2O + Ca(OH)_2 + 2\ Fe(OH)_3 \quad (7)$$

Apart from ettringite, all the other calcium aluminate compounds called AF_m-phases are actually layered structures where anions between positively charged layers can be interchanged depending on availability and which version that is most stable. According to Balonis (2010) the stability order is $Cl^- > NO_3^- > NO_2^- > CO_3^{2-} > SO_4^{2-} > OH^-$.
Exposing concrete to seawater means exposing it to chloride and sulphates. Due to smaller mass, chlorides diffuse faster and will have the opportunity to form Friedel's salt on the way with AFm-phases. For instance:

$$Ca_3Al_2O_6{\cdot}Ca(NO_2)_2{\cdot}12H_2O + 2\ Cl^- \rightarrow Ca_3Al_2O_6{\cdot}CaCl_2{\cdot}12H_2O + 2\ NO_2^- \quad (8)$$

An analogue reaction as in Eq. 8 happens with nitrate as well. When sulphate comes in later it can form ettringite as observed and lead to expansion and cracking eating its way inwards:

$$SO_4^{2-} + Ca(OH)_2 + H_2O \rightarrow CaSO_4{\cdot}2H_2O + 2\ OH^- \quad (9)$$

$$Ca_3Al_2O_6{\cdot}CaCl_2{\cdot}12H_2O + 2\ CaSO_4{\cdot}2H_2O + SO_4^{2-} + 16\ H_2O = Ca_3Al_2O_6{\cdot}3CaSO_4{\cdot}32H_2O + 2\ Cl \quad (10)$$

The more calcium aluminate hydrates you have in the binder, the more ettringite you can form and more expansion and cracking and strength loss one sees in particular for the concrete with nitrite where the strength was reduced from 85 MPa at 1 year (correspond to 72 MPa cylinder strength) to 71 MPa cylinder strength after 12 years (Østnor et al., 2014) and 54 MPa cylinder strength after 20 years. Reference changed from 65 MPa cube strength (≈ 55 MPa cylinder strength) at 1 year to 50 MPa compressive strength at 12 years and 60 MPa at 20 years, while concrete with nitrate changed with 65 MPa cube strength (≈ 55 MPa cylinder strength) at 1 year to 65 MPa compressive strength at 12 years and 57 MPa at 20 years. Considering the uncertainties with only one cylinder at 12 years, evidently the concrete with nitrite had the largest drop in strength. This is probably caused by extensive ettringite formation as observed by SEM until 38 mm from the surface. The µXRF scanner indicates ettringite formation deeper in to 80 mm from surface (deepest observed limited by sample size) or the concrete with nitrite in Figure 6.
The microcracking caused by ettringite formation may be the reason why the resistance number to water penetration is rated considerably lower for the concrete with nitrate and nitrite compared to reference.

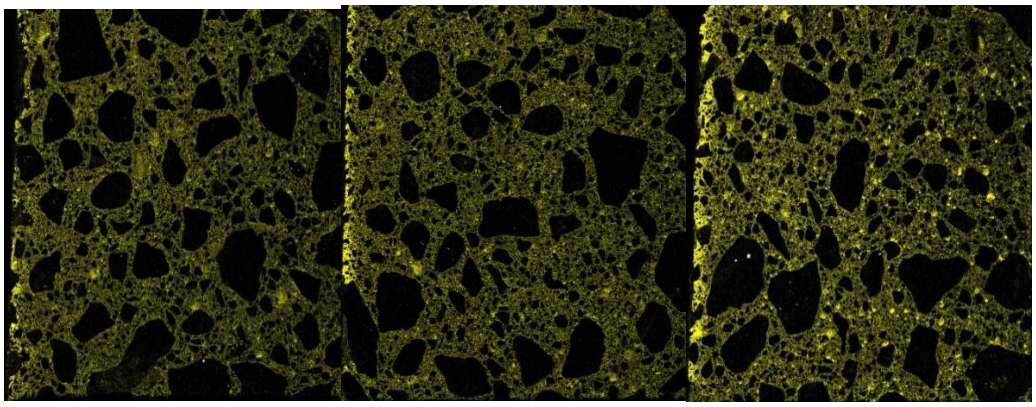

Figure 6. Distribution of the element sulphur (i.e. sulphate) over the cross-section of concrete without calcium salts (left image), with calcium nitrate (middle image) and with calcium nitrite (right image). The brighter the yellow color, the higher is the sulphur concentration. Ignoring the artificial edge-effect to the left of each image at the concrete surface, the concrete with calcium nitrite has more sulphate intruded with many "hot-spots" (e.g. ettringite clusters) all the way to the maximum depth of 80 mm (size of sample). Aggregate appears black.

4. Conclusions

Three wall elements of self-compacting concrete have been standing 12 years in the tidal zone in the Trondheim fjord and laying 8 years in the tidal zone of the sea outside Porsgrunn, Norway. One element was without corrosion inhibitor and the two others with 4.0% calcium nitrate and 2.8% calcium nitrite of cement mass, respectively. Cores were drilled with the objective of seeing the effect on the corrosion state of the steel with nominal cover of 20 and 50 mm and inspect the condition of the concrete in general.
Despite having chloride levels up to 5x higher than what is considered the limit (0.07% Cl^- of concrete weight) for initiation of steel corrosion, all wall elements had reinforcement in pristine condition, so no conclusion could be drawn regarding the effect of corrosion inhibitor.
Especially the concrete with nitrite had a strength drop over time due to massive ettringite formation. Activation of the ferrite cement mineral by nitrite (and nitrate?) could bring more calcium aluminate hydrates to the binder which in turn forms expansive ettringite with sulphate supplied by seawater leading to microcracking.
All concretes were rated watertight based on resistance number from capillary suction experiments but concrete with nitrate and nitrite was rated lower than the reference. The reference concrete had 1 vol% fewer capillary pores than the other two concretes despite having somewhat higher w/c (0.467) compared to concrete with nitrate (0.459) and concrete with nitrite (0.444). Hence, it is likely that microcracks have been counted as capillary pores in the capillary suction test. The discs for the test were cut far from the surface to avoid such effects, indicating that the effect goes deep.

Acknowledgements

Funding from Yara International is gratefully appreciated.

References

Balonis, M. (2010) "The Influence of Inorganic Chemical Accelerators and Corrosion Inhibitors on the Mineralogy of Hydrated Portland Cement Systems", *PhD Dissertation*, University of Aberdeen, 294 pp.

Chabrelie A., Gallucci E., Scrivener K. and Müller U. (2008) "Durability of field concretes made of Portland and silica fume cements under sea water exposure for 25 years". In: Bager DH, editor. *Nordic exposure sites – input to revision of EN206-1*. Hirtshals – Denmark: workshop proceeding from a Nordic mini-seminar.

De Weerdt, K. and Justnes, H. (2009) "Synergic Reactions in Triple Blended Cements", *Proceedings of the 11th NCB International Seminar on Cement and Building Materials*, 257-261, 17-20 November, New Delhi, India.

De Weerdt, K. and Justnes, H. (2015) "The effect of sea water on the phase assemblage of hydrated cement paste", *Cement and Concrete Composites*, 55: 215-222.

De Weerdt K., Geiker M.R. and Justnes H. (2013) "10 year old concrete wall in tidal zone examined by SEM-EDS". In: Hjorth Jakobsen U, editor. *14th Euroseminar on microscopy applied to building materials*. Helsingør, Denmark.

De Weerdt, K., Justnes, H. and Geiker, M. (2014a) "Changes in the phase assemblage of concrete exposed to sea water", *Cement and Concrete Composites*, 47: 53-63.

De Weerdt K., Justnes H. and Geiker M.R. (2014b) "Changes in the phase assemblage of concrete exposed to sea water". *Cement and Concrete Composites*, 47: 53–63.

Duval R. and Hornain H. (1992) "Chaptre 9: La durabilité des bétons vis-à-vis des eaux aggressives". In: Baron J, Ollivier JP, editors. Presses de l'École Nationale des Ponts et Chaussées.

Jakobsen U.H. (2013) "Microstructural surface deterioration of concrete exposed to seawater: results after 2 years exposure. In: Jakobsen U.H., editor. *Proceedings of the 14th Euroseminar on microscopy applied to building materials*: 62-66, Helsingør, Denmark.

Justnes, H. (2006) "Corrosion Inhibitors for Reinforced Concrete", *Proceedings of the Seventh CANMET/ACI International Conference on Durability of Concrete*, Montreal, Canada, May 28 – June 3, ACI SP234-4, pp. 53-70.

Justnes, H., Thys, A. and Vanparijs, F. (2001) "Reasons for Increase in Long Term Compressive Strength of Concrete by the Set Accelerator Calcium Nitrate", *Proceedings of the Kurdowski Symposium "Science of Cement and Concrete"*, 265-278, Kraków, June 20-21.

Justnes, H., De Weerdt, K. and Geiker, M.R. (2012): "Chloride Binding in Concrete by Sea Water – The Role of Magnesium", *Proceedings of the mini-symposium "Degradation and durability of structural materials: contribution of transfer properties" at the First International Conference on Performance-based and Life-cycle Structural Engineering (PLSE 2012)*, 875-884. Hong-Kong, 5-7 December.

Marchand J., Samson E., Burke D., Tourney P., Thaulow N. and Sahu S. (2003) "Predicting the microstructural degradation of concrete in marine environment". *ACI Special Publication SP-212-69*:1127-53.

Mather B. (1964) "Effects of sea water on concrete". Highway research record. Highway Research Board; pp. 33–42.

Mehta PK. (2003) "Causes of deterioration of concrete in seawater. Concrete in the marine environment". Routledge: Taylor & Francis Books, Inc.; 2003 [Chapter 5].

Østnor, T.A., Justnes, H. and Franke, W. (2014): "A Condition Survey of Concrete Elements with Corrosion Inhibitors Exposed 12 Years for Sea Water in Tidal Zone", *Proceedings of the 2nd International Congress on Durability of Concrete (2nd ICDC)*, Paper 64, 13 pp, 4-6 December, New Delhi, India.

Performance of Calcium Sulfoaluminate Based Binders in Sewer Environment

Tom Damion[1] and Piyush Chaunsali[2*]

[1] Institute of Eminence - Postdoctoral Fellow, Centre for Sustainable Technologies, IISc, Bangalore, India
Former PhD Scholar, Dept of Civil Engineering, IIT Madras, Chennai, India
Email: tomdamion@gmail.com
2 Associate Professor, Department of Civil Engineering, IIT Madras, Chennai, India
Email: pchaunsali@civil.iitm.ac.in

[*]Corresponding author

ABSTRACT

Sewer structures are subjected to severe and rapid deterioration, mainly due to the biogenic acid attack. The bacteria such as *Thiobacillus thiooxidans* thrives in the pH range of 0.5 – 3 and converts H_2S gas into sulfuric acid, causing the corrosion of sewer crown, leading to catastrophic failure of sewer and overlying structures. In addition to the structural failure, any resultant cracks due to the acid attack in sewers can lead to leakage of wastewater into groundwater and soil, causing environmental hazards and disease outbreaks. Hence, durable sewers are required and acid-resistant binders (being the reactive component in concrete) are needed for their construction. To that end, calcium sulfoaluminate (CSA) cement offers a promising alternative for acid resistant binder. This study was performed in the field conditions at two sewer locations at IIT Madras campus. The neutralisation offered by aluminium hydroxide and bacteriostatic effect made CSA cement to perform relatively better in sewer environment. The findings show superior performance of CSA cement than Portland cement in highly acidic environments.

KEYWORDS: *Sulfuric acid, Calcium Sulfoaluminate, Portland cement, Sewer, Thiobacilli*

1. Introduction

Severe deterioration of masonry mortar and lining material was observed near the roof and walls of an outfall sewer in Los Angeles two years after its construction in 1895, as reported by Olmstead and Hamlin (1900). This damage was attributed to hydrogen sulfide (H_2S) oxidizing into sulfuric acid (H_2SO_4). The damaged cement paste was identified by the formation of silica and gypsum. Such a deterioration was observed in different parts of the world in the beginning of the twentieth century itself and the reason was viewed as a pure chemical H_2S-to-H_2SO_4 conversion. Parker (1945a; b) highlighted the role of bacteria similar to Thiobacillus thiooxidans in the damage process. Further, sulfate-reducing bacteria were identified as the source of H_2S formation as explained by Allen (1949). Hence, this bacteria-driven acid corrosion has been termed as "biogenic acid attack".

The biogenic acid attack of cement-based composites occurs in three stages according to House and Weiss (2014) and Kaushal et al. (2020), characterised by pH reduction. In stage 1 carbonation happens to reduce pH to less than 9, beyond which Stage 2 occurs characterised with biofilm attachment, and when the pH reaches less than 4, it is said to be in Stage 3 and severe sulfuric acid attack happens because of bacteria belonging to *Thiobacilli ASTM C1894 (2019); Islander et al. (1992); O'Connell et al. (2010)*.

Calcium aluminate cement (CAC) was found to have superior performance in sewer environment and one reason for this is the bacteriostatic effect of CAC as per Ding et al. (2017) as the aluminium ions released could stiffle the metabolism of bacteria. However, high cost and undesirable conversion reaction are the main drawbacks of CAC Scrivener et al. (1999); Zawrah et al. (2011). Among alternative binders for application in sewer environment, calcium sulfoaluminate (CSA) cement, a low CO_2 binder, has useful characteristics such as rapid hardening and shrinkage-compensation. Similar to hydrated CAC, hydrated

CSA cement contains aluminum hydroxide and can be a potential candidate for sewer structures. In an in-situ sewer exposure experiment reported by Bakera and Alexander (2022, 2024), it was found that CSA cement outperformed sulfate-resisting Portland cement. Hence, by using CSA cement both durability and sustainability can be achieved. For that use in sewer structures, durability of hydrated CSA cement in acidic environment needs to be evaluated. In this study, the suitability of CSA cement in sewer structures is evaluated by monitoring its biogenic acid resistance in a real sewer environment exposure for one year.

2.2 Materials and Methods

Portland Cement (PC) of grade 53 as per IS 12269: 2013 and commercially available CSA cement (CSA(HY)) were used in this research.

Table 1. Oxide composition

Binders	**SiO_2**	**CaO**	**Al_2O_3**	**SO_3**	**Fe_2O_3**	**MgO**	**K_2O**	**TiO_2**	**SrO**	**Na_2O**	**LOI***
CSA(HY)	14.0	39.8	20.9	14.5	3.6	2.8	0.5	1.1	0.1	0.2	1.8
PC	18.9	63.3	5.2	2.7	5.7	0.9	0.6	0.5	0.0	0.0	2.2

LOI*: Loss on ignition

Paste specimens were prepared with water cement ratio 0.4 using floor-mounted planetary Hobart mixer according to ASTM C305: 2020. Prismatic specimens of size 40 × 40 × 160 mm were prepared, cured for 28 days in fog room, and suspended in triplicate inside a basket at a manhole location *(12.9873 N, 80.2356 E)* at IIT Madras campus.

The flexural strength was determined at 28 days of curing and after one year of exposure according to ASTM C348 (2021) using a span of 120 mm and at a loading rate of 43 N/s. The neutralised depth was measured using the phenolphthalein test. Freshly cut exposed specimens were sprayed with phenolphthalein, causing the altered areas to remain colourless and the unattacked areas to turn pink. Images of these specimens were then analysed using ImageJ software to calculate various depths. Detailed characterisation was performed using X-Ray Diffraction (XRD) using MiniFlex Rigaku powder X-ray diffraction instrument using Cu Kα (wavelength 1.5405 Å), Thermogravimetric Analysis (TGA) carried out in the range of 30 °C – 900 °C with heating rate of 15 °C/min in a nitrogen-purged environment using alumina crucibles with 5 – 10 mg of the sample, and Scanning Electron Microscopy (SEM) using FEI-Quanta FEG 200F equipment, dwell time was 30 µs, accelerating voltage 20 kV, beam current 1 nA, and spot size 2.5 nm. The samples for XRD and TGA were ground and sieved through 75 µm.

2.3 Results

In Stage 1 acid attack, as Damion and Chaunsali (2024) reported, CSA(HY) binder showed a rapid pH drop compared to PC-dominated binders due to its lower pore solution pH. After observing the specimens retrieved after one year of field exposure in this study, it is evident that the acid attack environment was extremely severe, resulting in PC-dominated binders reaching Stage 3 of the acid attack. The flexural strength of the specimens before and after exposure are plotted in **Figure 1**(a). There was a severe strength loss in PC compared to CSA(HY). This could be attributed to weak regions created by the biogenic acid attack. According to the literature, this is due to the precipitation of acid attack products such as gypsum and expansive ettringite, which induce cracks according to Khan et al. (2019)and Santhanam et al. (2002). Additionally, portlandite is converted to calcium sulfate, and C-S-H to calcium sulfate and silica gel, through biogenic acid attack. The silica gel significantly shrinks upon drying, causing further cracking as in Dyer (2017).

The neutralisation depths of the specimens determined by phenolphthalein spraying and image analysis are plotted in **Figure 1**(b). The measured neutralisation depth resulted from carbonation and acid attack. The lower neutralisation depth in CSA(HY) is attributed to the less alteration by the environment. Though PC had higher strength than CSA(HY) at 28 days, it had relatively poor performance. This underscores the inadequacy of strength alone in predicting durability performance in sewer environments. The observed

material loss in PC specimens, their vulnerability to biogenic acid, and the superior performance of CSA(HY) suggest that some intrinsic mechanisms in CSA(HY) provide better resistance to biogenic acid attack. The phenolphthalein was sprayed over the specimens subjected to the flexural strength test. PC-dominated binders had random pink regions, with non-pink areas indicating weak zones. CSA(HY) cement showed a failure zone with a uniformly pink core.

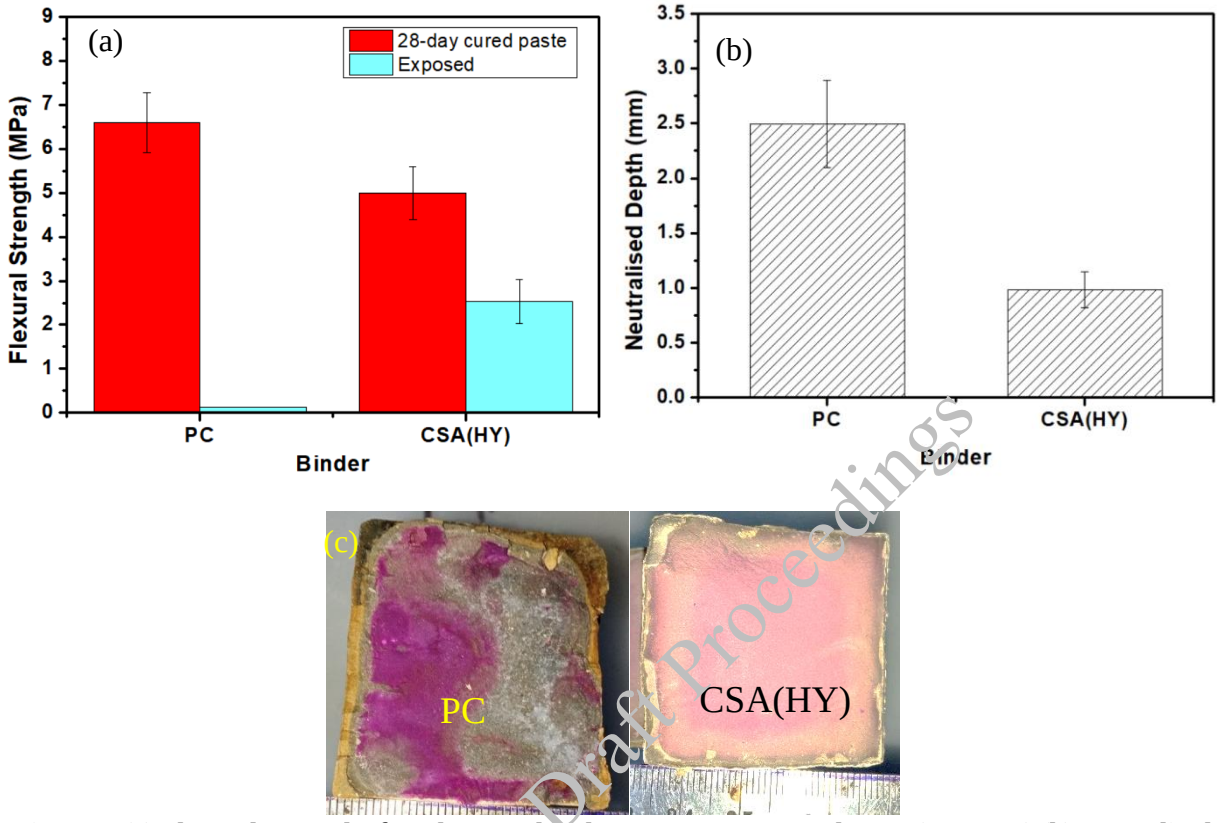

Figure 1. (a) Flexural strength of 28-day cured and 1-year sewer-exposed paste (w/c = 0.4) (b) Neutralised depth (mm) observed in specimens (c) Phenolphthalein sprayed PC and CSA specimen Damion and Chaunsali (2024)

It was observed in Damion et al. (2022) and Damion and Chaunsali (2022) that the presence of the aluminium hydroxide phase in CSA(HY) provided increased acid resistance at low pH. *Thiobacilli* require an extremely acidic environment for survival, creating severe acidic conditions that lead to rapid corrosion of PC binders, as observed in low pH (pH 0.5) attack in Damion (2023). However, this phenomenon was explored by examining the exposed surfaces. Two reasons for the overall better performance of CSA(HY) are explained further.

Specimens taken out from the field had slime layer over the surface. This was characterised by TGA and confirmed it as biofilm. There was a small mass loss at 150ºC corresponding to gypsum. Then a broad DTG peak was observed at 200 – 500 ºC, which matched to be biofilm in Shen et al. (2018). The sewer biofilm, approximately 1 mm thick, consists of inorganic salts and organic substances including microbial cells, extracellular polymeric substances (EPS), and components like proteins, polysaccharides, and humic materials Li et al. (2019). Some amount of gypsum and an amorphous hump corresponding to biofilm were confirmed through XRD. Thus in biogenic acid attack, the weathered gypsum layer becomes incorporated into the biofilm, providing a habitat for bacteria and thus exacerbating acid attack. The specimen surface below the biofilm was explored using XRD. The surface or the white region was characterised to be mainly gypsum. This was followed by an yellow region containing quartz and other phases. Then innermost core region was unaffected and characterised to have portlandite, CSH, and other hydrated phases. While the biogenic acid attacked CSA(HY) surface had lower gypsum formation than PC. Immediately below this layer the unaffected core region with ettringite and other unhydrated phases were identified in Damion and Chaunsali (2024).

The exposed specimen surfaces were further characterised by SEM as explained in Damion and Chaunsali (2024). The PC-dominated binders had a large bacterial population on their surfaces. While the CSA(HY) binder also had bacterial cells, but these cells were found to be in a collapsed (dead) state. The bacterial

cells were rod-shaped structures, typical of acidophilic *Thiobacilli*, with lengths of 1-3 µm. The collapse of bacterial cells in CSA(HY) could be due to the bactericidal effect of CSA(HY), potentially caused by aluminum ions affecting osmotic stability and causing leakage of cell organelles. This bactericidal effect prevents bacterial reproduction and colonisation within the biofilm, effectively terminating the acid source. The combination of this bactericidal effect and the gypsum-based biofilm causing a constant low pH sulfuric acid attack explains the superior performance of CSA(HY) binder.

3. Conclusions

The study presents findings from a field investigation on biogenic acid attack on various cementitious binders. The biogenic acid-induced gypsum did not act as a barrier but exacerbated the attack by becoming part of the biofilm, which produced highly acidic conditions. CSA(HY) demonstrated a bacteriostatic effect similar to CAC, reducing the source of acid. The neutralisation capacity offered by aluminium hydroxide phase of CSA offered its enhanced acid resistance. All these factors explain the better performance of CSA cements in sewer environment.

Acknowledgements

The first author would like to acknowledge the doctoral scholarship received from the Ministry of Education, Gov. of India, and the Post Doctoral Equivalent Fellowship from IIT Madras. All authors would like to acknowledge the resources provided by the Department of Civil Engineering at the Indian Institute of Technology (IIT) Madras towards the usage of experimental facilities in this study. The last author is also grateful for the financial support from the New Faculty Seed Grant (CE1920426NFSC008926) by Industrial Consultancy and Sponsored Research (ICSR) centre at IIT Madras. The Centre of Excellence on Technologies for Low Carbon and Lean Construction at IIT Madras is also gratefully acknowledged.

References

Allen, L. A. (1949). "The Effect of Nitro-Compounds and Some Other Substances on Production of Hydrogen Sulphide By Sulphate-Reducing Bacteria in Sewage." *Proceedings of the Society for Applied Bacteriology*, 12(2), 26–38.

ASTM C1894. (2019). "Standard Guide for Microbially Induced Corrosion of Concrete Products." 1–8.

ASTM C348. (2021). "Standard Test Method for Flexural Strength of Hydraulic-Cement Mortars." *Annual Book of ASTM Standards*.

Bakera, A. T., and Alexander, M. G. (2022). "Sewer concrete subjected to biogenic acid corrosion: analysis of concrete deterioration phases using QEMSCAN." *MATEC Web of Conferences, International Conference on Concrete Repair, Rehabilitation and Retrofitting (ICCRRR 2022)*, 03012.

Bakera, A. T., and Alexander, M. G. (2024). "In situ concrete sewer performance: comparison of Portland cement, calciumsulfoaluminate cement, and calcium aluminate cement." *Materials and Structures*, Springer Netherlands.

Damion, T. (2023). "Performance of Calcium Sulfoaluminate- Based Binders in Acidic Environments." *Ph.D. Thesis (IIT Madras)*.

Damion, T., Cepuritis, R., and Chaunsali, P. (2022). "Sulfuric acid and citric acid attack of calcium sulfoaluminate-based binders." *Cement and Concrete Composites*, Elsevier Ltd, 130(April), 104524.

Damion, T., and Chaunsali, P. (2022). "Evaluating Acid Resistance of Portland Cement, Calcium Aluminate Cement, and Calcium Sulfoaluminate Based Cement Using Acid Neutralisation." *Cement and Concrete Research*, Elsevier Ltd, 162(December), 1–17.

Damion, T., and Chaunsali, P. (2024). "Biogenic acid resistance of calcium sulfoaluminate cement : Revelations from a field study." *Cement and Concrete Composites*, Elsevier Ltd, 145(May 2023), 105324.

Ding, L., Weiss, W. J., and Blatchley, E. R. (2017). "Effects of Concrete Composition on Resistance to Microbially Induced Corrosion." *Journal of Environmental Engineering (United States)*, 143(6), 1–9.

Dyer, T. (2017). "Influence of cement type on resistance to attack from two carboxylic acids." *Cement and Concrete Composites*, Elsevier Ltd, 83, 20–35.

House, M. W., and Weiss, W. J. (2014). "Review of microbially induced corrosion and comments on needs related to testing procedures." *Proceedings of the 4th International Conference on the Durability of Concrete Structures, ICDCS 2014*, (July), 94–103.

Islander, B. R. L., Devinny, J. S., Member, A., Mansfeld, F., Postyn, A., and Shih, H. (1992). "Microbial e c o l o g y o f c r o w n corrosion in sewers." 117(6), 751–770.

Kaushal, V., Najafi, M., Love, J., and Qasim, S. R. (2020). "Microbiologically Induced Deterioration and Protection of Concrete in Municipal Sewerage System : Technical Review." *Journal of Pipeline Systems Engineering and Practice*, 11(1), 1–10.

Khan, H. A., Castel, A., Khan, M. S. H., and Mahmood, A. H. (2019). "Durability of calcium aluminate and sulphate resistant Portland cement based mortars in aggressive sewer environment and sulphuric acid." *Cement and Concrete Research*, Elsevier, 124(July), 105852.

Li, W., Zheng, T., Ma, Y., and Liu, J. (2019). "Current status and future prospects of sewer biofilms: Their structure, influencing factors, and substance transformations." *Science of the Total Environment*, Elsevier B.V., 695, 133815.

O'Connell, M., McNally, C., and Richardson, M. G. (2010). "Biochemical attack on concrete in wastewater applications: A state of the art review." *Cement and Concrete Composites*, Elsevier Ltd, 32(7), 479–485.

Olmstead, W. H., and Hamlin, H. (1900). "Converting Portions of the Los Angeles Outfall Sewer into a Septic Tank." *Engineering News and American Railway Journal*, XLIV(19), 317–318.

Parker, C. (1945a). "The Corrosion of Concrete: 1. The Isolation of a Species of Bacterium Associated With the Corrosion of Concrete Exposed To Atmospheres Containing Hydrogen Sulphide." *The Australian Journal of Experimental Biology and Medical Science*, 23(2), 81–90.

Parker, C. (1945b). "The Corrosion of Concrete: 2. The Function of Thiobacillus Concretivorus (Nov. Spec.) in the Corrosion of Concrete Exposed To Atmospheres Containing Hydrogen Sulphide." *Australian Journal of Experimental Biology and Medical Science*, 23(2), 91–98.

Santhanam, M., Cohen, M. D., and Olek, J. (2002). "Mechanism of sulfate attack: A fresh look - Part 1; Summary of experimental results." *Cement and Concrete Research*, 32(6), 915–921.

Scrivener, K. L., Cabiron, J. L., and Letourneux, R. (1999). "High-performance concretes from calcium aluminate cements." *Cement and Concrete Research*, 29(8), 1215–1223.

Shen, Y., Huang, P. C., Huang, C., Sun, P., Monroy, G. L., Wu, W., Liu, J., Espinosa-Marzal, R. M., Boppart, S. A., Liu, W. T., and Nguyen, T. H. (2018). "Effect of divalent ions and a polyphosphate on composition, structure, and stiffness of simulated drinking water biofilms." *npj Biofilms and Microbiomes*, Springer US, 4(1), 1–9.

Zawrah, M. F., Shehata, A. B., Kishar, E. A., and Yamani, R. N. (2011). "Synthesis, hydration and sintering of calcium aluminate nanopowder for advanced applications." *Comptes Rendus Chimie*, Academie des sciences, 14(6), 611–618.

Comparative Study on Properties of Normal and Recycled Aggregate Concrete Experimental and Numerical Analysis

Manjunath Patil[1*], Pranjal Vishnukumar[2], and Ananth Ramaswamy[3]

[1] *Indian Institute of Science, Bengaluru, India*
Email: manjunathpm@iisc.ac.in
[2] *Indian Institute of Science, Bengaluru, India*
Email: pranjalv@iisc.ac.in
[3] *Indian Institute of Science, Bengaluru, India*
Email: ananth@iisc.ac.in

[*]Corresponding author

ABSTRACT

Reinforced concrete structures are the backbone of modern infrastructure, but their life and maintenance costs are unpredictable due to varying environmental and loading conditions. The construction industry is concerned about the disposal of construction and demolition waste in an environmentally and eco-friendly manner at the end of their service life. The limited availability of natural aggregate has created a need for an alternate sustainable solution to produce concrete. Recycling construction and demolition(C&D) waste is the only way to overcome these difficulties. Recent studies on using C&D waste have shown promising results as a replacement for natural aggregates. However, a comprehensive study is required to quantify the engineering and physical properties of recycled coarse aggregate (RCA) and recycled fine aggregate (RFA) and their influence on the strength of the concrete so produced. The current study attempts to address this challenge. The study incorporates testing of the engineering and physical properties of RCA and RFA procured during the demolition of a concrete column of a metro project in Bangalore. The RCA and RFA are used in manufacturing concrete of grade M40. Its comparison with M40 grade concrete made of conventional natural aggregates (NA) in terms of compressive strength, split tensile strength, and flexure strength has been studied. The results showed an increase in the 28-day compressive strength and split tensile strength, whereas a decrease in the flexure strength of recycled aggregate concrete (RAC) compared to natural aggregate concrete (NAC). However, more variation in the strength parameters was observed amongst the RAC specimens than in the NAC specimens. In parallel, a detailed numerical modelling approach using the Abaqus Finite Element Method software will be developed to predict the mechanical response of the concrete specimens under compressive and flexural loading conditions. This research employs a combined experimental and numerical approach to investigate the performance of M40-grade concrete incorporating recycled aggregates.

KEYWORDS: *RAC,NAC, Recycled aggregates, Beams*

1. Introduction

Concrete is a widely used construction material, but its production has significant environmental impacts(Alsaif & Alshannag, 2022). To address these concerns, sustainable concrete design and construction methods are crucial. One promising approach is using recycled aggregates in reinforced concrete structures(Gislason et al., 2022)(Damme, 2018), which reduces the demand for virgin aggregates and minimises construction and demolition waste. Through experimental and numerical analysis, this study investigates the performance and feasibility of reinforced concrete structures incorporating recycled aggregates. The use of recycled aggregates in concrete has been explored, highlighting their potential benefits, such as internal curing and reduced shrinkage, potentially enhancing durability. However, the mechanical properties and long-term performance of these materials require further investigation.

2. Methodology

This study investigates the use of recycled aggregates in M40-grade concrete, employing a combined experimental and numerical approach. The research aims to understand how recycled coarse aggregate and recycled fine aggregate affect the concrete's engineering properties. The experimental phase involves rigorous testing of recycled and natural aggregates and creating and evaluating M40-grade concrete specimens. These specimens are then tested for compressive, split tensile, and flexural strength to quantify the impact of using recycled aggregates. Parallel to the experiments, numerical models are developed using Abaqus software to simulate the concrete's behaviour under various loading conditions. These models are validated against experimental data to ensure their accuracy and reliability. By integrating experimental findings with numerical simulations, the study provides a comprehensive understanding of the structural implications of using recycled aggregates in concrete, ultimately supporting the development of sustainable construction materials and practices.

3. Materials and Testing

This study investigates the use of locally sourced recycled concrete aggregates (RFA and RCA), processed to meet IS 10262:2009 standards, in M40-grade concrete. Locally sourced crushed stone and natural sand, conforming to relevant IS 10262-2009 standards, will serve as control materials. Ordinary Portland cement (IS 12269-2013) of properties given in Table 1 was used, and potable water (IS 456:2000) and a Fosroc Conplast SP430 superplasticizer admixture were used.

Table 1: Properties of opc-53 grade cement.

Property	Value
Compressive Strength (MPa)	53 (minimum) at 28 days)
Initial Setting Time (minutes)	30 (minimum)
Final Setting Time (minutes)	150-160 (maximum)
Fineness (m^2/kg)	300-350 (minimum)
Le Chatelier Expansion (mm)	10 (maximum)
Auto Clave Expansion (%)	0.8 (maximum)

The recycled and natural aggregates' physical and mechanical properties in accordance with IS 2386-1963. Compressive Strength: 150mm cubes tested at 7 days,14 days, and 28 days according to IS 516:1959. The specimen was tested on a UTM (Universal Testing Machine). Split Tensile Strength: 150mm diameter x 300mm height cylinders tested at 28 days according to IS 5816:1999. Flexural Strength: 150mm x 150mm x 550mm prisms tested at 7 days, 14 days and 28 days under three-point bending according to IS 516:1959.

3.2 Concrete Mix Design and Specimen Preparation

An M40 concrete mix design, targeting a compressive strength of 40 MPa at 28 days, was used for both natural aggregate concrete and recycled aggregate concrete. The mix proportion was 1:1:2 (cement: sand: coarse aggregate), with a water-cement ratio of 0.35 and 2.5% superplasticiser. The only difference between the mixes was the use of 100% recycled aggregates in the RAC. Standard 150mm cube, 150mm diameter x 300mm cylinder, and 150mm x 150mm x 550mm prism specimens were cast for compressive, split tensile, and flexural strength testing, respectively. Specimens were cured in moulds for 24 hours, then demoulded and submerged in water for 28 days. 18 cubes, 18 cylinders and 18 beams were used for testing.

3.3 Experimental Program

This study will investigate the engineering properties of recycled coarse and fine aggregates sourced from a demolished concrete column and their influence on the compressive strength, tensile strength, flexural strength and modulus of elasticity of concrete. The experimental setup includes a universal testing machine with a 6000KN load capacity, as shown in figure 1, a material testing system with a load capacity of 1200KN capacity, as shown in figure 2 and a darted loading system of 400KN capacity, as shown in figure 3.

Figure 1: experimental setup for cube compression test

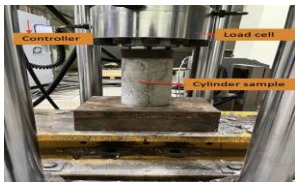

Figure 2: experimental setup for cylinder compression test

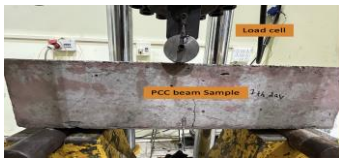

Figure 3: experimental setup for three point bending test of plain cement concrete beams

3.4 Numerical Modelling

3.4.1 Model Development

This study employed numerical modelling, utilising Abaqus finite element software, to complement experimental investigations into the behaviour of concrete specimens under compression and flexural loading. A Concrete Damaged Plasticity model was implemented to simulate concrete's nonlinear response. Three-dimensional models of a 150mm concrete cube, a 150mm diameter x 300mm cylinder, and a 150mm x 150mm x 550mm beam were developed, incorporating rigid components to replicate experimental setups for uniaxial compression and three-point bending tests. Material properties were assigned based on Table 2. Interactions and boundary conditions were carefully defined to reflect experimental constraints. A displacement-controlled load was applied for compression tests. Mesh sizes of 5mm, 6mm, and 8mm were used for the cube, cylinder, and beam, respectively.

3.4.2 Concrete Constitutive Model: The CDP model in Abaqus was used to represent the concrete behaviour, considering its compressive and tensile strengths, damage behaviour, and plasticity.

Table 2: CDP parameters used in the Abaqus Finite element model

Parameter	Value	Description
Dilation Angle (ψ)	38 degrees	Governs the flow rule of the plastic potential
Biaxial/Uniaxial Ratio $\frac{\sigma b_o}{\sigma c_o}$	1.16	Reflects the ratio of strength in biaxial to uniaxial compression
Eccentricity (ϵ)	0.1	Defines the rate at which the flow potential approaches the asymptote
Viscosity Parameter	0	Introduces rate-dependence in the material model
k Parameter	0.667	Ratio of the second stress invariant on the tensile meridian to that on the compressive meridian
Young's Modulus (E),N/mm²	For RAC = 37727.651 For NAC = 35258.130	Initial stiffness of the concrete

3.4.3 Meshing and Refinement

In this study, C3D8R elements were used for concrete and T3D2 for reinforcement. Mesh refinement was performed by identifying high-stress areas using partitioning and seeding to ensure smooth transitions. A convergence study confirmed the stability of the results with finer meshes. For compression tests, displacement-controlled loading was applied to the top, with the bottom restrained. Flexural tests involved a midspan load on a supported beam. Static general analysis in Abaqus was used, extracting key parameters such as compressive strength, stress-strain curves, crack patterns, and load-deflection curves to analyse the concrete's behaviour.

4. Results and Discussion

This study presents a detailed analysis and discussion of its experimental and numerical results. The findings are evaluated to draw meaningful conclusions about the influence of recycled concrete aggregates (RCA) and recycled fine aggregates (RFA) on the structural performance of M40-grade concrete. This study comprehensively analyses the mechanical performance of Normal Aggregate Concrete (NAC) and Recycled Aggregate Concrete (RAC). The study evaluates the material properties, mortar compressive

strength, and the compressive, flexural, and split tensile strengths of NAC and RAC to determine their suitability for structural applications.

4.1 Aggregate Characterization

Table 3: Material properties of RFA as per the tests governed by IS:2386-1963(Part1-Part5)

SL.No.	Name of the Test	Trial 1	Trial 2	Results
1	Specific Gravity	1.435	1.435	1.435
2	Water Absorption	2.34%	2.34%	2.34%
3	Material finer than 75 microns	12.40%	12.40%	12.40%
4	Bulk Density	1.426 kg/I (compacted)	1.342 kg/I (loose)	-
5	Soundness Test	8.40%	-	8.40%
6	Silt Content	10%	-	10%

Table 4: Material properties of RCA as per the tests governed by IS:2386-1963(Part1-Part5)

SI.No.	Name of the Test	Trial 1	Trial 2	Results
1	Crushing Strength	33.98%	32.49%	33.23%
2	Specific Gravity	2.29	2.27	2.28
3	Water Absorption	3.58%	3.57%	3.58%
4	Bulk Density	1.448 kg/I (compacted)	1.353 kg/I (loose)	-
5	Impact value	26.207%	23.94%	25.07%
6	Abrasion Test	34.88%	-	34.88%
7	10% fines value	5.89T	-	-
8	Soundness Test	4.16%	-	4.16%

4.2 Mortar strength

A mortar mix of 1:2 ratio and water cement ratio of 0.5 was taken to prepare a sample for mortar strength testing. The variation of strength over 7 days,14 days and 28 days has been depicted in the figure 4.A total of 9 samples of RA mortar cube and NA mortar cube were tested. The RA mortar exhibited a comparable and slightly higher compressive strength at 28 days compared to the NA mortar, indicating that recycled aggregates can produce mortar with sufficient compressive strength for construction purposes.

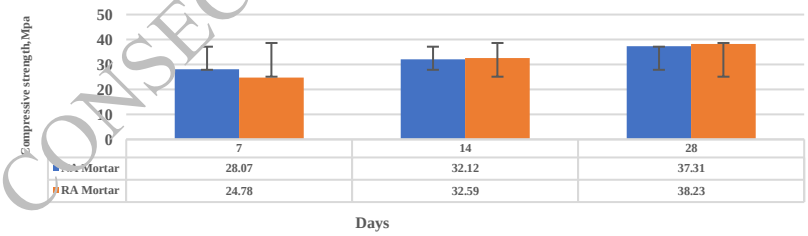

Figure 4. Represents the cube compressive strength of recycled aggregate cement mortar and normal aggregate cement mortar.

4.3 Concrete compressive strength

The compressive strength development of natural aggregate concrete (NAC) and recycled aggregate concrete (RAC) over 7, 14, and 28 days. RAC achieves a higher 28-day compressive strength compared to NAC in both cube and cylinder tests, with RAC showing 61.72 MPa for cubes and 43.24 MPa for cylinders, indicating that recycled aggregates can effectively enhance the mechanical properties of concrete as shown in the figure 5,figure 6.And in the figure 7 the stress-strain curve of RAC and NAC concrete samples obtained from experiments conducted on cylinder in compression tests.

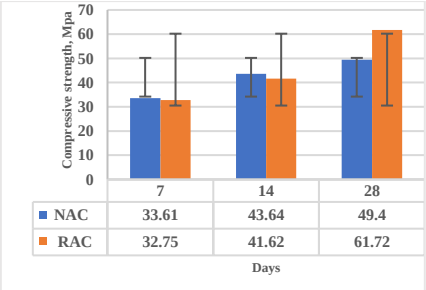

Figure 5:Cube compressive strength of NAC and RAC samples

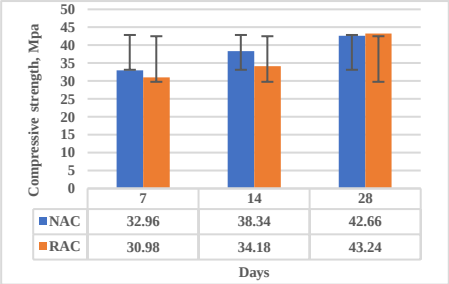

Figure 6:Cylinder compressive Strength RAC and NAC samples

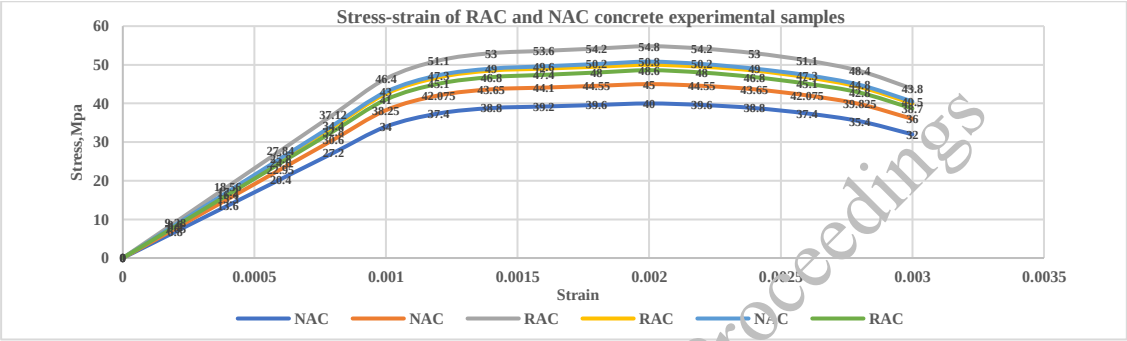

Figure 7: Stress-strain curve of NAC and RAC samples

4.3.1 Cube compression test

Figures 8 and 9 illustrate the tested and finite element models for both natural aggregate and recycled aggregate concrete cubes. The models were validated using force-time analysis in Abaqus, as shown in Figure 10. Peak loads from the models (1060.6 KN for NAC, 1309.61 KN for RAC) closely matched experimental values (1063 KN for NAC, 1312 KN for RAC). Figure 11 shows the close agreement between simulated and experimental force-displacement curves.

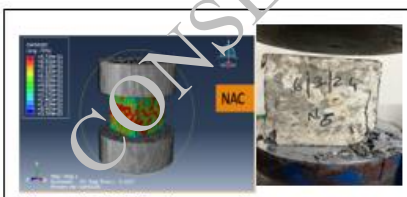

Figure 8: NAC cube sample

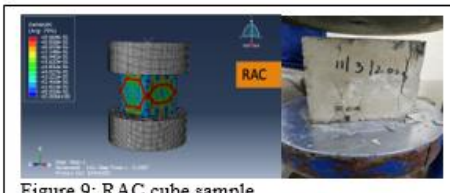

Figure 9: RAC cube sample

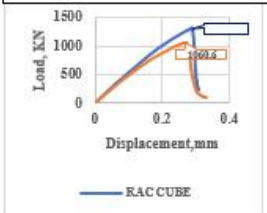

Figure 10:Cube compression test load-deflection curve in Abaqus.

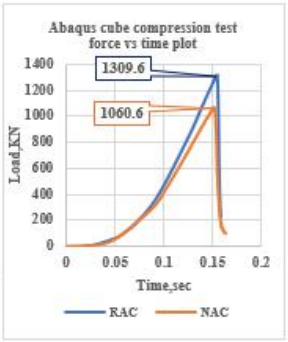

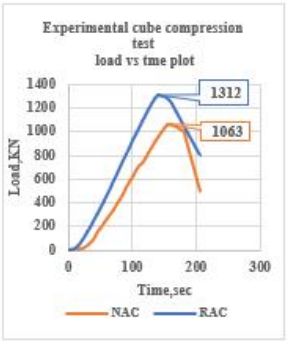

Figure 11: load vs time curve of cube compression test in Abaqus and experiments.

4.3.2 Cylinder compression test

The FEM model of the concrete cylinder and the experimental sample are shown in Figure 12 for the RAC sample and in Figure 13 for the NAC sample. The force-displacement curve of the experiments and the FEM model generated a force-displacement curve that showed a similar trend. The peak load recorded in the experiments were 875.92 KN for the NAC sample and 695.9 KN for the RAC sample. Whereas the peak load in the FEM analysis was 879.37 KN for the RAC sample and 691.46 KN for the NAC sample. The FEM models were validated concerning the force-displacement study, as shown in the figure 14.

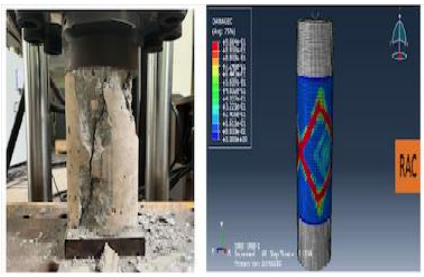

Figure 12: RAC cylinder sample

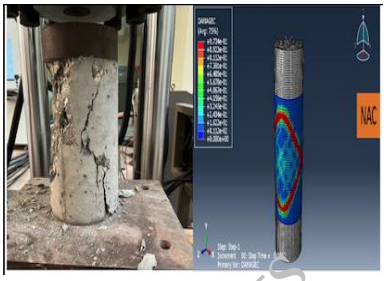

Figure 13: NAC cylinder sample

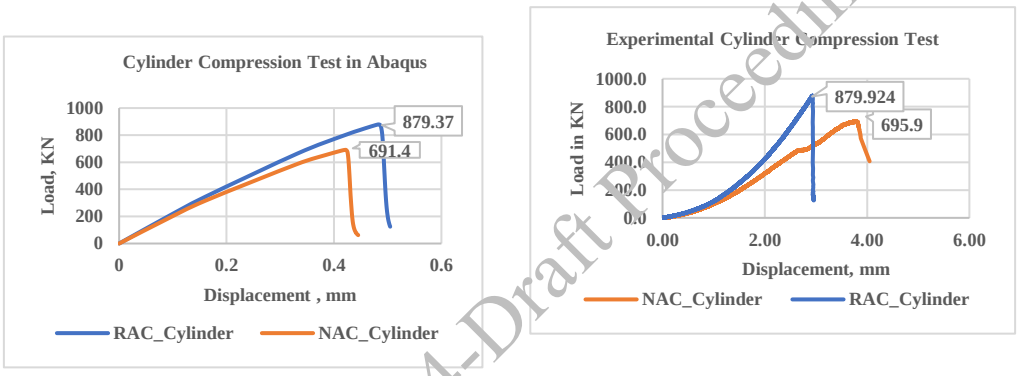

Figure 14: Force displacement curve of FEM model and experimental test

4.4 Flexure strength

The experimental results were analysed to quantify the differences in strength properties between concrete made with natural aggregates (NAC) and recycled aggregate concrete (RAC). The findings show that the NAC beams exhibited higher flexural strength compared to RAC beams, the RAC beams still provided adequate strength for many structural applications. **NAC Beams** flexural strength increased from 3.51 MPa at 7 days to 4.94 MPa at 28 days. Whereas **RAC Beams** flexural strength increased from 2.91 MPa at 7 days to 3.92 MPa at 28 days. The lower flexural strength of RAC may be due to the quality of the recycled

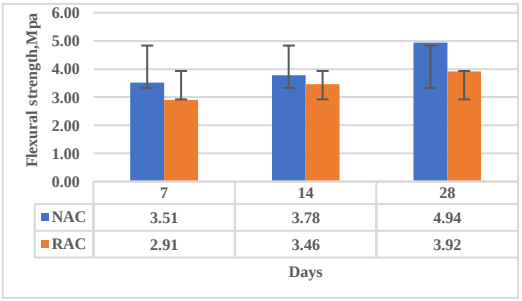

Figure 15: Flexural Strength of NAC and RAC Beam Samples.

aggregates and the bond between the aggregates and the cement matrix. The flexure strength variation between NAC and RAC beams in figure 15.

Finite element models of plain cement concrete beams containing recycled aggregates and natural aggregates were created using C3D8R elements, as depicted in Figures 16 and 17, respectively. The models were validated against experimental data, with force-displacement plots showing good agreement. Peak failure loads in the models (34.84 KN for RAC, 27.35 KN for NAC) were similar to experimental values (36.16 KN for RAC, 28.20 KN for NAC) according to Figure 18.

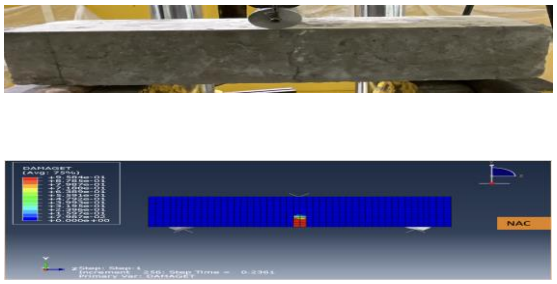

Figure 16: NAC FEM model and Experiment sample

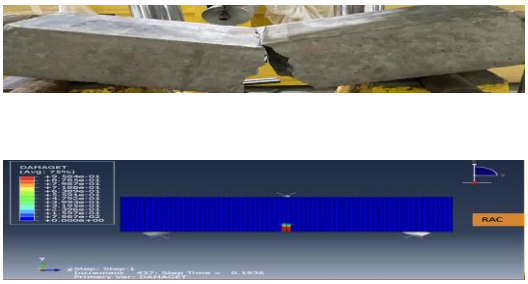

Figure 17: RAC FEM model and Experiment sample

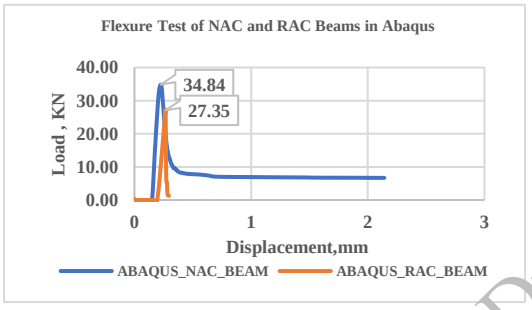

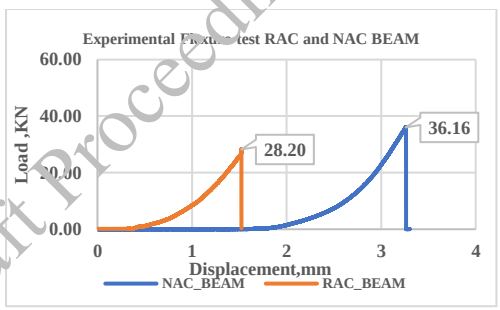

Figure 18: Force displacement plot of FEM model and experimental flexure test.

4.5 Tensile strength

The NAC Cylinders split tensile strength ranged from 4.06 MPa at 7 days to 4.92 MPa at 28 days. And **RAC Cylinders** split tensile strength ranged from 4.01 MPa at 7 days to 5.50 MPa at 28 days. The split tensile strength results indicate that RAC cylinders can achieve similar or higher strengths compared to NAC cylinders over time. This suggests that recycled aggregates can provide adequate tensile capacity for concrete structures. The strength variation between RAC and NAC samples can be seen in Figure 19.

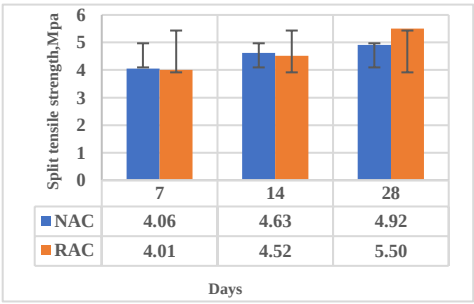

Figure 19: Split Tensile Strength of NAC and RAC samples.

5. Conclusion

For a similar mix design, NAC is more workable than RAC. It was also observed that NAC's initial setting time is longer than RAC's during casting operations. RAC's mean cube compressive strength is 24.9% more

with respect to NAC. RAC samples' mean cylinder compressive strength is 1.35% more than the NAC samples. The mean flexure strength of RAC beam samples is 20.6% less than the mean flexure strength of NAC beam samples, and also, the flexure failure plane of the RAC beam is rough compared to the flexure failure plane of NAC beams. RAC samples' mean split tensile strength is 11.7% more than that of NAC samples. The results from the material properties, mortar compressive strength, and the compressive, flexural, and split tensile strength tests demonstrate that RAC can perform comparably to NAC in various structural applications. The significant increase in compressive strength of RAC at 28 days highlights the potential of recycled aggregates to serve as a viable alternative to natural aggregates in concrete production. While RAC beams exhibited slightly lower flexural strength, their overall performance in tensile and compressive tests supports the use of RAC in sustainable construction practices. Further research is recommended to optimise RAC's mix design and processing techniques to enhance its performance, particularly in flexural applications. This study contributes to the growing knowledge on using recycled materials in concrete. It reinforces the potential of RAC to meet the mechanical requirements of concrete structures, promoting sustainability in the construction industry.

References:

Milad Hafezolghorani, Farzad Hejazi Ramin Vaghei, Mohd Saleh Bin Jaafar (Prof.) & Keyhan Karimzade (Msc) (2017) Simplified Damage Plasticity Model for Concrete, Structural Engineering International, 27:1,68-78, DOI: 10.2749/101686616X1081

Tomasz Jankowiak, Tomasz Lodygowski, Identification of parameters of concrete damage plasticity constitutive model, Found. Civil Environ. Eng. 6 (1) (2005) 53–69.

Mohamadreza Shafieifar, Mahsa Farzad, Atorod Azizinamini, Experimental and numerical study on mechanical properties of Ultra High-Performance Concrete (UHPC), Construction and Building Materials, Volume 156,2017, Pages 402-411, ISSN 0950-0618,

D.K. Shin, H.C. Kim, and J.J. Lee Numerical analysis of the damage behavior of an aluminum/CFRP hybrid beam under three-point bending, Composites Part B, Engineering Volume 56, January 2014, Pages 397-407. https://doi.org/10.1016/j.compositesb.2013.08.030

Bui, N K., Satomi, T., & Takahashi, H. (2019, March 1). Influence of industrial by-products and waste paper sludge ash on properties of recycled aggregate concrete. Elsevier BV, 214, 403-418. https://doi.org/10.1016/j.jclepro.2018.12.325

Caner, F C., & Bažant, Z P. (2013, December 1). Microplane Model M7 for Plain Concrete. II: Calibration and Verification. American Society of Civil Engineers, 139(12), 1724-1735. https://doi.org/10.1061/(asce)em.1943-7889.0000571

Corinaldesi, V., & Moriconi, G. (2010, April 1). Recycling of rubble from building demolition for low-shrinkage concretes. Elsevier BV, 30(4), 655-659. https://doi.org/10.1016/j.wasman.2009.11.026

Nana, W., Bui, T., Limam, A., & Abouri, S. (2017, May 1). Experimental and Numerical Modelling of Shear Behaviour of Full-scale RC Slabs Under Concentrated Loads. Elsevier BV, 10, 96-116. https://doi.org/10.1016/j.istruc.2017.02.004

Prasad, D., & Kishore, R. (2021, October 1). Studies on Cent Percent Utilization of Recycled Coarse and Fine Aggregates in the Construction Industry. , 9(6), 1812-1836. https://doi.org/10.13189/cea.2021.090615

Takahashi, Y., Masuda, Y., & Takeuchi, H. (2011, January 1). THE STUDY ON INFLUENCE OF MIXED MORTAR ON THE PROPERTIES OF RECYCLED AGGREGATE CONCRETE. , 76(668), 1755-1761. https://doi.org/10.3130/aijs.76.1755

Wang, J., Zheng, K., Cui, N., Cheng, X., Ren, K., Hou, P., Li, F., Zhou, Z., & Xie, N. (2020, July 7). Green and Durable Lightweight Aggregate Concrete: The Role of Waste and Recycled Materials. Multidisciplinary Digital Publishing Institute, 13(13), 3041-3041. https://doi.org/10.3390/ma13133041

Yang, B., Wang, C., Chen, S., Qiu, K., & Jiang, J. (2023, August 24). Optimisation of the Mechanical Properties and Mix Proportion of Multiscale-Fibre-Reinforced Engineered Cementitious Composites. Multidisciplinary Digital Publishing Institute, 15(17), 3531-3531. https://doi.org/10.3390/polym15173531

Zhou, G., Li, A., Li, J., Duan, M., Spencer, B F., & Zhu, L. (2018, November 1). Beam Finite Element Including Shear Lag Effect of Extra-Wide Concrete Box Girders. American Society of Civil Engineers, 23(11). https://doi.org/10.1061/(asce)be.1943-5592.0001297

Alsaif, A., & Alshannag, M J. (2022, October 19). Flexural Behavior of Portland Cement Mortars Reinforced with Hybrid Blends of Recycled Waste Fibers. Multidisciplinary Digital Publishing Institute, 14(20),13494-13494.https://doi.org/10.3390/su142013494.

Gislason, S., Bruhn, S., Breseghello, L., Sen, B., Liu, G., & Naboni, R. (2022, January 21). Lightweight 3D Printed Concrete Beams Show an Environmental Promise: A Cradle-to-Grave Comparative Life Cycle Assessment. Research Square (United States). https://doi.org/10.21203/rs.3.rs-1253072/v1

Damme, H V. (2018, October 1). Concrete material science: Past, present, and future innovations. Elsevier BV, 112, 5-24. https://doi.org/10.1016/j.cemconres.2018.05.002

Investigation of the Impact of Accelerated Carbonation in Lime-Based Mortar Mixes

V.A. Anupama[1*], Divyasri K.S.[2], and Manu Santhanam[3]

[1] *Doctoral research scholar, Indian Institute of Technology, Madras, Chennai, India*
Email: vaanupama9@gmail.com
[2] *Project associate, Indian Institute of Technology, Madras, Chennai, India*
Email: divyakathir2212@gmail.com
[3] *Professor, Indian Institute of Technology, Madras, Chennai, India*
Email: manus@civil.iitm.ac.in

[*]Corresponding author

ABSTRACT

Lime mortar is a major constituent of heritage masonry structures in India. Considering the low strength gain, higher shrinkage and low strength potential of lime mortars, cement addition is widely practised in architectural conservation works. However, scientific studies on the evolution of material properties of lime-based mortar mixes are limited and demand further research. As lime-based mortars develop strength through extended carbonation, accelerated tests are adopted to investigate their long-term properties. This study focuses on the impact of accelerated carbonation on pure lime mortar and lime-based mortar containing 50% Ordinary Portland Cement subjected to accelerated carbonation at 3% CO2 concentration. The investigation examines the extent of carbonation in 50 mm cubes at different exposure durations using the phenolphthalein indicator test. The test indicates the reduced carbonation rate in mortars containing cement due to a densified microstructure. The matrix integrity can also be determined qualitatively using the non-destructive Ultrasonic Pulse Velocity (UPV) test. The denseness of the matrix is correlated to the mortar's compressive strength and corresponding porosity using Mercury Intrusion Porosimeter (MIP) at each stage of exposure. Calcium carbonate can be found in four distinct polymorphic forms - amorphous calcium carbonate, calcite, vaterite and aragonite. The influence of exposure duration in the morphology of calcium carbonate crystals is investigated using Scanning Electron Microscopy (SEM). This study contributes to extending the understanding of the influence of carbonation on lime-based mortars and offers insights into their strength and microstructural properties.

KEYWORDS: *Carbonation, accelerated carbonation, lime, OPC, mortar*

1. Introduction

Pure air lime-based mortar systems develop strength through carbonation, whereas the strength of cement-based compositions develops through hydration. The exothermic reaction of carbonation in the lime-based mortars takes place after the setting phase of the mortar and can be summarised as below:

$$Ca(OH)_2\ (s) + CO_2\ (g) \rightarrow CaCO_3\ (s) + H_2O\ (aq) + 74\ kJ/mol \quad (1)$$

Temperature, humidity, pore systems and porosity, mineralogical and geochemical composition, water-to-binder ratio and concentration of CO_2 influence carbonation (Cultrone et al., 2005; Ergenç et al., 2018; Ergenç & Fort, 2018; Silva et al., 2021). During accelerated carbonation at a higher concentration of CO_2, the excess CO_2 molecules, which have not already reacted with the CH, can penetrate deeper into the mortar, producing a thicker carbonated area, leading to faster carbonation. In the case of natural carbonation, the CO_2 molecules immediately react with CH available near the surface; hence, the front will not move more inwards to the core. Accelerating the carbonation results in early calcium carbonate formation, which can mask the surface pores. Hence, the mortar surface becomes unresponsive to more CO_2, and 100% carbonation cannot be achieved (Cizer et al., 2008; Ergenç & Fort, 2018). The properties of mortar mixes exposed to natural carbonation are expected to differ from those exposed to accelerated carbonation. The

study investigates the properties of air lime mortar and cement-containing lime mortar under accelerated and long-term natural carbonation.

2. Materials and Methods

The study used dry hydrated lime powder, Ordinary Portland Cement, equal proportions of standard sand (grades I, II, and III) and distilled water to make cubic specimens of size 50 mm. A binder-to-aggregate ratio of 1:3 was followed, and a water-to-binder ratio, which gave a flow of 165 ± 5 mm in the flow table test as per IS5512 and water retention of 70% as per IS 2250, was chosen. Pure lime mixes (L) were cast with a water-to-binder ratio of 0.85, and mixes containing 50% OPC and 50% dry hydrated lime (OL) were cast with a water-to-binder ratio of 0.626. A higher water-to -binder ratio is required for lime-based mixes than cement-based mixes and the former have higher water retentivity than the latter due to the abundance of plate-like portlandite crystals. The specimens for accelerated carbonation were stored in the accelerated carbonation chamber at 3% CO_2 concentration, 27 °C and 55-65% RH after demoulding, till the age of testing. The specimens were sheltered in the natural exposure site at IITM for natural carbonation. The compressive strength of the specimens was tested at regular intervals in a Servo Hydraulic Compression Testing machine with a capacity of 250 kN at a loading rate of 167 N/s. The strength development was also observed through the ultrasonic pulse velocity test with transducers of frequency 54 kHz as per ASTM C597-2016. The extent of carbonation was monitored periodically to investigate the rate of carbonation. XRD, MIP and TGA were used to characterize the specimens. Secondary Electron Images of the specimens were obtained to investigate the morphological variations caused by ageing and carbonation. The particle size distribution data of the dry hydrated lime and OPC are presented in Figure 2.

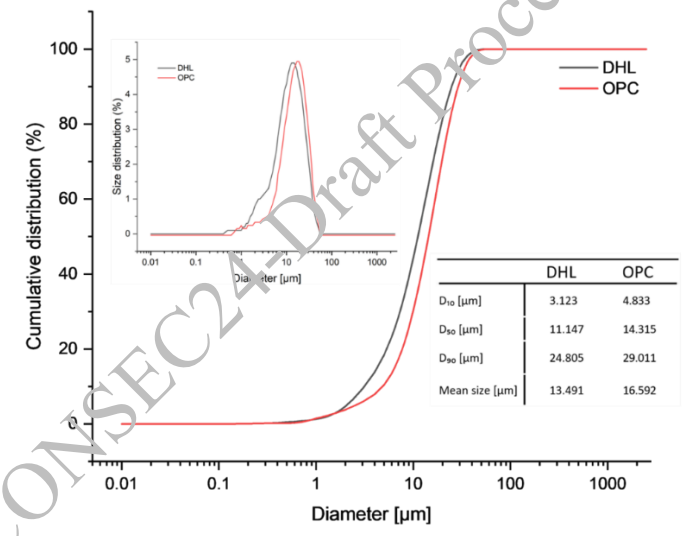

Figure 2 Particle size distribution of raw materials

3. Laboratory experiments

3.1 Carbonation

Carbonation depth was measured using the phenolphthalein indicator. The rate at which carbonation proceeds is faster in a 3% CO_2 atmosphere in an accelerated carbonation chamber in L and OL specimens (Figure 3). Although OL mortar specimens also show increased carbonation when exposed to the chamber compared to their naturally carbonated counterparts, the rate is slower than the carbonation rate of the L specimens. The slower progression of carbonation could be attributed to the reduced accessible porosity and permeability of the OL specimens compared to that of the L specimens, which is confirmed through porosity characterization. The rate of natural carbonation of OL mixes is also lower than that of L mixes due to the compact microstructure of OL mortar. L mix attained full carbonation under accelerated carbonation within four days of exposure, and OL mixes required 22 days to achieve complete carbonation. L mixes needed four months of natural carbonation to achieve the extent of carbonation observed within

2.5 days of accelerated carbonation. Also, for OL mixes, four days of accelerated carbonation attained a depth of carbonation similar to those exposed to four months of natural carbonation. However, Liesegang patterns, as mentioned in several literature sources (Rodriguez-navarro et al., 2002), were missing from the specimens.

3.2 Compressive strength

The compressive strength of the pure air lime-based binders is due to carbonation, whereas that of OPC is due to hydration. Hence, carbonation and hydration contribute to the strength of the OL mortar mix. The strength data shows that the strength attainment reached almost constant after five days of accelerated carbonation in lime mortar. Morphological changes in calcium carbonate crystals are expected even after the complete carbonation of the mortar. However, the strength data indicates that the morphology of calcium carbonate does not significantly influence the strength of lime-based mortar mixes. The strength attained by OL mixes is much higher than that of L mixes due to the combined effect of carbonation and hydration under accelerated and natural carbonation conditions.

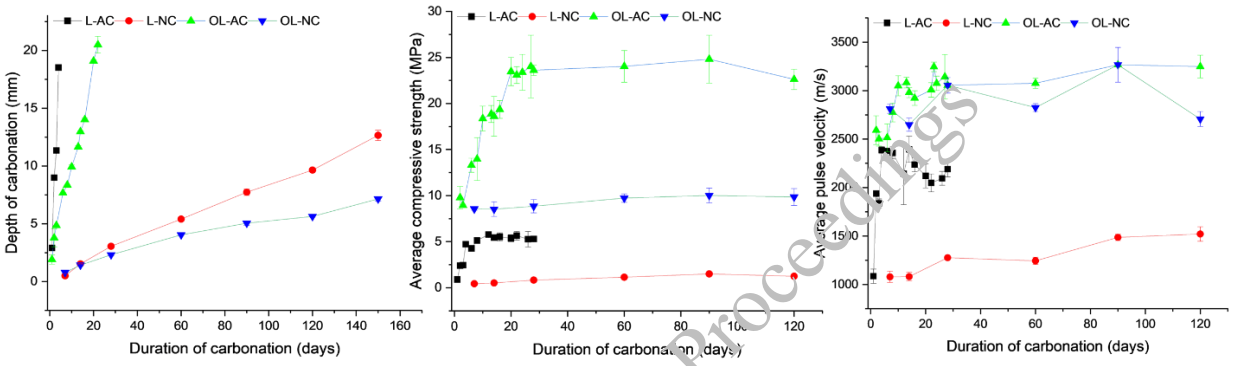

Figure 3 Carbonation depth, compressive strength and ultrasonic pulse velocity of specimens

3.3 Ultrasonic pulse velocity

The ultrasonic pulse velocity results complement the observations on the strength development of L and OL mixes. A higher ultrasonic pulse velocity indicates the presence of a denser microstructure with lesser pores. OL specimens show significantly higher pulse velocity than lime-based mix, indicating a more compact microstructure than pure lime based mixes. Naturally carbonated pure air lime mortar cubes had the lowest UPV values due to their higher porosity. Observations suggest that no significant increase in the pulse velocity occurs after the complete carbonation of the system. It could be, therefore, inferred that the evolution in calcium carbonate crystal morphology does not significantly alter the compactness of the microstructure.

3.4 Porosity characterization

A larger critical pore diameter (1000 nm -2000 nm) indicates the coarser pore structure of the lime mortars, whereas the OL mixes have a refined pore structure (300 nm – 400 nm). Accelerated carbonation densifies the matrix faster, resulting in a lesser critical pore diameter than natural carbonation for the same duration. Lime mortar majorly consists of pores above 1 μm. More than 40% of the total pore volume in lime mortar constitutes inter-micropores (between 1 μm and 10 μm). OL mortar majorly consists of pores less than 1 μm, most of which are sub-micropores of size between 0.1 μm and 1 μm. Nanopores are about 30% - 40% of the total pore volume. Inter-micropores are comparatively lesser in percentage (<10%).

3.4 Mineralogical and Morphological Characterization

Samples were collected from the carbonated area of the mortar specimens to observe the morphological evolution of calcium carbonate crystals over time.

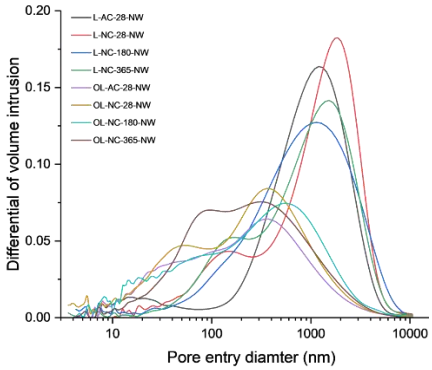

Figure 4 Differential volume intrusion curve of lime and OL mortar mixes

The morphology of the calcium carbonate crystals evolves over time even after complete carbonation of the system. The reduction in porosity can also be observed from the secondary electron images of the mortars. Samples were collected from the surface near the specimen exterior for powder XRD analysis. The XRD result also indicates the presence of various polymorphs of calcium carbonate crystals as the mortar microstructure evolves. Porosity characterization conducted using MIP showed the difference in the critical pore size and pore size distribution between L and OL specimens under natural accelerated carbonation. MIP captured the change in the porosity characteristics. It is observed that the pore size distribution does not change significantly after complete carbonation, for lime-based mixes whereas porosity decreases, critical pore size shifts to a lower value in OL mixes due to continuous hydration. However, the difference in OL mixes after complete carbonation was not significant enough to alter the compressive strength and ultrasonic pulse velocity.

4. Conclusions

The study focussed on investigating the carbonation rate when pure air lime-based mortar and the lime-cement mortar composition were exposed to natural and accelerated carbonation. The morphological evolution of calcium carbonate crystals after complete carbonation does not significantly influence the compressive strength and UPV values of the mortar mixes. The porosity characteristics governed the rate of carbonation and the strength development. OL mixes with lesser porosity than L carbonates at a much slower rate. However, the combined contribution of hydration and carbonation to the strength resulted in its higher strength than L specimens.

Acknowledgements

The authors would like to gratefully acknowledge the funding from the Ministry of Education, Government of India, towards the Fellowship of the first author. The authors are grateful to the Building Technology and Construction Management (BTCM) Division, Department of Civil Engineering at Indian Institute of Technology Madras, India, for providing the laboratory facilities.

References

Cizer, O., Van Balen, K., Elsen, J., & Gemert, D. Van. (2008). Crystal Morphology of Precipitated Calcite Crystals From Accelerated Carbonation of Lime Binders. *2nd International Conference on Accelerated Carbonation for Environmental and Materials Engineering, Rome, Italy,1-3 October 2008*, *November 2014*, 1–3.

Cultrone, G., Sebastián, E., & Huertas, M. O. (2005). Forced and natural carbonation of lime-based mortars with and without additives: Mineralogical and textural changes. *Cement and Concrete Research*, *35*(12), 2278–2289.

Ergenç, D., & Fort, R. (2018). Accelerating carbonation in lime-based mortar in high CO2 environments. *Construction and Building Materials*, *188*, 314–325.

Ergenç, D., Gómez-Villalba, L. S., & Fort, R. (2018). Crystal development during carbonation of lime-based mortars in different environmental conditions. *Materials Characterization*, *142*(May), 276–288.

Rodriguez-navarro, C., Cazalla, O., Elert, K., Sebastian, E., & A, P. R. S. L. (2002). *Liesegang pattern development in carbonating traditional lime mortars Liesegang pattern development in carbonating*. 2261–2273.

Silva, B. A., Ferreira Pinto, A. P., Gomes, A., & Candeias, A. (2021). Effects of natural and accelerated carbonation on the properties of lime-based materials. *Journal of CO2 Utilization*, *49*(May), 101552.

Repair and Strengthening Materials and Methods

Proactive Assessment of RC Structures with Half-Cell Potential Mapping and Gradient Analysis for Predicting Corrosion

Zameel D.V.[1*], Dhruvesh Shah[2]

[1] *Project Manager, Radhe Structorepair Pvt. Ltd., Ahmedabad, India*
Email: zameeldv@gmail.com
[2] *India Business Head, Vector Corrosion Technologies, Vadodara, India*
Email: dhruveshs@vector-corrosion.com

[*]Corresponding author

ABSTRACT

Distress in reinforced concrete (RC) structures can arise from various factors, necessitating comprehensive evaluations to determine effective remedial measures. This study discusses the method for iassessing corrosion in RC structures using Half-Cell Potential (HCP) mapping and a newly developed Potential Gradient Analysis. The latter, a 2D representation of potential differences, identifies areas at risk of developing macrocell corrosion. A case study of a distressed RC structure demonstrates the methodology, highlighting the effectiveness of HCP mapping and Potential Gradient Analysis in distinguishing corrosion hotspots. These techniques enable proactive intervention strategies, offering a comprehensive approach to enhancing the durability and service life of RC structures.

KEYWORDS*: HCP map, Delta plot, Potential gradient, Condition assessment, Reinforced concrete.*

1. Introduction

Corrosion of steel in reinforced concrete (RC) structures is a pervasive issue worldwide, significantly compromising the integrity and longevity of such structures. Reinforced concrete structures often exhibit premature damage due to environmental actions. Unlike mechanical actions, the environmental actions are not reversible and accumulate hazardous components such as chloride ions in concrete (RILEM TC 154 EMC 2003).

Reinforced concrete, despite its robustness and durability, is susceptible to deterioration primarily due to the ingress of chlorides and carbon dioxide, which disrupt the protective passive layer around the steel (Chess and Broomfield 2014). This accelerates corrosion initiation and propagation, leading to expansive forces that cause cracking, spalling, and eventual structural failure (Liu, Su and Xu 2021). India faces aggressive environmental challenges due to its diverse climatic conditions, ranging from coastal to arid and semi-arid zones, exposing RC structures to varying degrees of deterioration. Consequently, maintaining the durable life or adopting a holistic approach to repairing corroded structures is crucial for maintaining safety and extending their service life. In order to have the right repair strategy, the root cause has to be addressed which demands a holistic condition assessment.

Quantifying the extent of the distresses or the potential threat is crucial to develop a holistic approach. A detailed assessment shall include the cause of damage or loss of protection, degree and amount of damage, expected progress of damage with time, and its effect on structural behaviour and serviceability (RILEM TC 124-SRC 1994). A high percentage of damage results from insufficient planning, underestimation of environmental severity, and poor workmanship, necessitating repairs after a short service life (RILEM TC 154 EMC 2003). Awareness regarding the need for comprehensive health assessments is limited in India, with many focusing only on mechanical parameters and limited number of durability parameters tested on limited structural elements rather than conducting widespread assessments across various elements of the entire structure.

Detail durability assessment includes various non-destructive tests (NDT) like half-cell potential (HCP) test, chemical analysis of concrete, cover meter survey, and measurement of corrosion rate of bars and concrete resistivity. HCP result at a point or individual elements will give probability of ongoing corrosion

of the embedded bar at the point, whereas to identify the hotspots of corrosion HCP mapping is required. Typical portable reference electrodes (such as saturated copper/copper-sulphate reference electrode) are used at field for the mapping of the half-cell potential at suitable grid spacing. The Rilem TC 154-EMC (2003) recommends using a grid size of 0.5 to 2 m, if the potentials are measured at discrete points, which are then used to plot the equipotential contour map. HCP does not provide the quantitative information on the actual rate of corrosion but is a qualitative assessment which must be used as a complementary data with other NDT results.

HCP mapping can help in understanding the high and low corrosion risk areas. A rapid change in potential is seen as steeper gradient, which indicates a greater risk of corrosion (Broomfield 2023). A study on the metallic pipelines shows that the differences in the natural corrosion potentials of adjacent areas can result in corrosion current flow, and thus increased corrosion rate (Liu and Liu 2020). Thus, the potential difference between various equipotential contours in a HCP map is important, as there is a possibility of conventional current flow from the cathodic region to the anodic region, provided there is a conductive path for the electron flow between the sources of potential, and the ionic movement is possible within these sources.

This paper discusses the use of HCP mapping and introduces the derivation of the Delta plot, a 2D representation of the difference of half-cell potentials. The following sections present a case study of a distressed RC structure, detailing the assessment methods and insights gained from the investigation.

2. Methodology

2.1 Structure and the repair history

The corrosion assessment of the two basements of a multistory building by HCP and Delta mapping is discussed in this section. The basements are used to facilitate parking in the building. The multistory reinforced concrete framed structure, which was about 10 years old, were observed to have severe distresses in the form of corrosion of bars and delamination of concrete on various structural elements such as slabs, beams, columns, and ramps. The structure was partly repaired previously. As part of the previous repair, several NDT and partial destructive tests such as compression test on extracted cores, rebound hammer test, and ultrasonic pulse velocity test etc. were carried out on the structure. Though the structure was facing durability related distresses, there were minimal NDT related to durability of RC structure involved in the decision making of the repair strategy.

As a previously attempted but unsuccessful remedial measure to a few elements, patch repair and jacketing using flowable cementitious micro-concrete were carried out. The repair procedure involved removing the loose concrete, cleaning the exposed bars and coating with field applied epoxy coating, restoration with micro-concrete, and strengthening using glass fibre reinforced polymer (GFRP) wraps with a philosophy of retarding corrosion by reducing exposure to oxygen & moisture. Once the anodic reactions are stopped at the patched regions, it naturally stops the production of hydroxyl ions at the cathodic region. Thus, the regions which were previously protected from corrosion will now rise above the critical chloride/hydroxyl ratio and corrosion will be initiated as in Figure 1(a). This is known as incipient anode formation (Broomfield 2023). It is worth noting that there was neither an electrochemical treatment involved, nor a treatment for the protection of the bars adjacent to the repair areas. These patch areas and elements strengthened using GFRP system showed further distresses within 2 years, as they failed due to the unchecked corrosion by the formation of incipient anode effect (Figure 1(b)).

(a) (b)

Figure 1. Incipient anode formation (a) failed concrete adjacent to repair, (b) cracks developed due to incipient anode effect within a previously repaired and strengthened column.

2.2 Condition assessment of the structure

A better evaluation of the structure is necessary to achieve the better results. As part of a holistic repair strategy, the two levels of the basements were tested for various durability parameters using several NDTs such as the HCP mapping, chloride content test and profiling, carbonation test, corrosion rate measurement using galvanostatic pulse method, concrete resistivity test, plotting of deflection contour, cover meter survey to assess the concrete cover, and borescope analysis of post-tensioned tendons. Only the assessment using HCP mapping, and the Delta plot are included in this paper. The detailed assessment of the structure and the remedial measures incorporated may be published elsewhere.

The floor area of each basement is around 5000 m^2, which were divided into various segments for the ease of identification. Each segment was further divided into orthogonal grids of size 1.5 m × 1.5 m. At least one access to rebars was made at every 30 m × 30 m area. A portable copper/copper sulphate (saturated) reference electrode (CSE) was used for the half-cell potential measurements with the help of a high impedance multimeter. Electrical continuity of the bars was checked using either measuring the DC potential between the two accesses to verify a potential difference less than 1 mV: or by measuring the HCP of a common point between the two access points by taking connections from these access points, to result in a value not variable than ±5 mV.

Once the connections were established, the potential was measured sequentially. All the readings were measured at almost uniform ambient temperature as well as after pre-wetting the surface and maintaining surface dry condition. The location of delamination has been identified & recorded, and any point where delamination of concrete has happened is considered as -350 mV for the continuity of the contour. The potentials were then plotted in a 2D plot using digital contour plotter as shown in Figure 2. The yellow dashed line shows the position of the expansion joint.

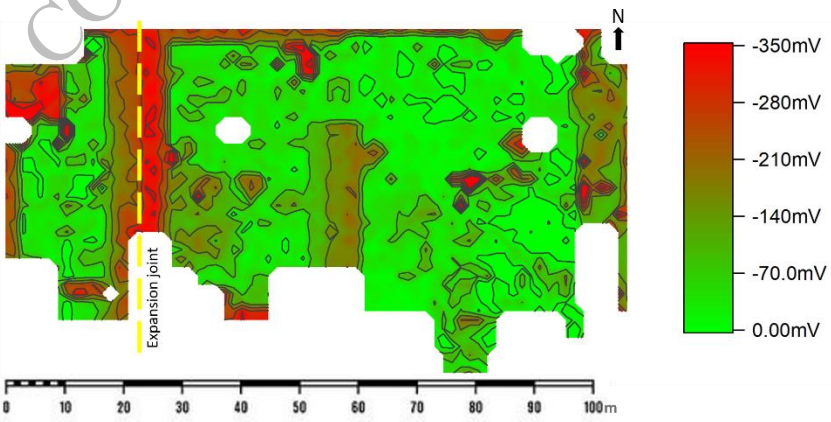

Figure 2. HCP mapping on the soffit of the ground level slab.

To generate the Delta plot, the potential differences at individual points are considered. The difference of the potential of a point and each of the adjacent points (up to 8 points in this case) is calculated. The

maximum magnitude of these values is considered as the Delta value at that particular point. Delta for each point has been generated and plotted as Delta plot (Figure 3).

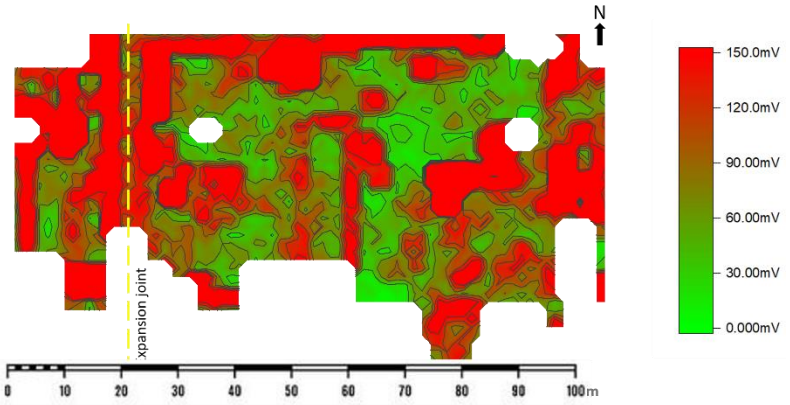

Figure 3. Delta plot of the HCP map for the soffit of the slab at ground level.

3. Discussions

3.1 HCP mapping

HCP mapping can help to target the hotspots of active corrosion as part of the repair strategy. The half-cell potentials are categorized to various probability of active corrosion as per ASTM C876 (1999). In Figure 2, bright red colour indicates area with high probability of active corrosion of the embedded bars, while the green colour indicates the presence of relatively passive steel.

The expansion joint, with severe leakage, shows significant corrosion in adjacent members, decreasing with distance from the joint. Plot boundaries, more exposed to external water, exhibit higher corrosion potential. The HCP map highlights these areas as critical repair hotspots. Corrosion potential shifts to the passive range as distance from water sources increases.

3.2 Delta plot

The Delta plot identifies probable corrosion hotspots within the structure. Areas with a potential difference of 100 mV or more between adjacent points are flagged as high-risk due to the likelihood of macrocell current flow initiating corrosion. This threshold is taken conservatively, based on references indicating that a protection current capable of polarizing the steel by 100 mV can significantly alter the corrosion kinetics of the bars (Barlo and Thomas 2001). In Figure 3, bright red areas indicate regions most susceptible to near-future corrosion. These areas often coincide with the boundaries of the target region defined by the HCP map. The interior of the slab generally exhibits lower potential gradients, suggesting a reduced risk of macrocell corrosion in those areas.

The Delta plot offers a valuable tool for proactive corrosion management. By targeting the identified high-risk regions, preventative measures can be implemented to mitigate corrosion and prolong the lifespan of the structure.

3.3 How to make use of HCP and Delta maps

HCP maps effectively pinpoint areas susceptible to active corrosion, making them ideal for guiding targeted corrosion protection strategies. Electrochemical treatments, such as cathodic protection, are well-suited for these regions. Such areas with a high probability of corrosion often require substantial protective currents (Whitmore, et al. 2019).

Delta plots, on the other hand, identify potential hotspots for macrocell corrosion development. To prevent macrocell corrosion, a more modest protective current is typically significant (Sergi, Seneviratne and Simpson 2022). By strategically employing both HCP and Delta maps, infrastructure managers can proactively address corrosion risks, ensuring structural integrity and extending the lifespan of critical assets.

3.4 Limitations and further study

While HCP mapping is a valuable tool, it has certain limitations, such as the need for continuity of reinforcing bars and effects of temperature variations, concrete resistivity, moisture content, and oxygen availability in concrete. In the present study, a grid size of 1.5 m × 1.5 m was used. A finer grid or wheel-type reference electrodes could provide detailed distribution of corrosion potentials.
Furthermore, the Delta plot analysis in this study focused solely on potential differences between adjacent points. Future research should incorporate distance-based calculations of potential gradients, considering the impact of concrete resistivity on ionic conduction. Restrictions in ionic movement can hinder corrosion current flow, even in the presence of a potential difference. As suggested by Reichling and Raupach (2014), visualizing corrosion potentials as a vector field could offer insights into potential gradients. Further study is needed to determine the actual potential gradient per unit distance that may initiate corrosion.

4. Conclusions

A comprehensive approach is essential to effectively combat both ongoing and potential steel corrosion in reinforced concrete (RC) structures. Traditional patch repairs often fall short due to the formation of incipient anodes. For long-lasting and reliable repairs, addressing the root cause of corrosion is crucial. Half-cell potential mapping enables the identification of active corrosion hotspots, allowing for targeted interventions. The Delta plot, which visualizes potential gradients, helps visualize areas prone to macrocell corrosion. By combining these techniques, proactive repair strategies can be developed to ensure the durability and longevity of RC structures. This paper presents a methodology for generating Delta plots and a case study demonstrating its application.

References

ASTM C876-99. 1999. Standard Test Method for Corrosion Potentials of Uncoated Reinforcing Steel in Concrete. ASTM International.

Barlo, and J. Thomas. 2001. "Origin and Validation of the 100 mV Polarization Criterion." *Corrosion.* NACE-01581.

Broomfield, John P. 2023. Corrosoin of Steel in Concrete Understanding, Investigation, and Repair. CRC Press.

Chess, P. M., and J. P. Broomfield. 2014. Cathodic Protection of Steel in Concrete and Masonry. CRC Press.

Liu, Bin, and Yingwei Liu. 2020. "Study on mechanism of differential concentration corrosion." Scientific Reports.

Liu, Qi-Fang, Ray Kai Leung Su, and Fei Xu. 2021. "Quantification of the actual expansion and deposition of rust in reinforced concrete." *Construction and Building Materials* 297.

Reichling, Kenji, and Michael Raupach. 2014. "Method to determine electrochemical potential gradients without reinforcement connection in concrete structures." *Cement & Concrete Composites* 47: 3-8.

RILEM TC 124-SRC. 1994. Draft recommendation for repair strategies for concrete structures damaged by reinforcement corrosion. *Materials and Structures*, 415-436.

RILEM TC 154 EMC. 2003. Half-cell potential measurements - Potential mapping on reinforced concrete structures. *Materials and Structures.*

Sergi, George, Gamini Seneviratne, and David Simpson. 2022. "Long term control of corrosion of steel reinforcement by a two stage cathodic protection method." Matec Web of Conferences. 02004.

Whitmore, David, Liao Haixue, David Simpson, and George Sergi. 2019. "Two-Stage, Self-Powered, Corrosion Protection System Extends the Life of Reinforced Concrete Structures." *Corrosion.* AMPP/NACE International. NACE 13011.

Retrofitting Measures of Distressed Structural Members of a RCC Building-A case study on the SOPC Building at Kolkata

A. Bagchi [1*], M. K. Sinha [2], B. Roy [3], D. Kar [4] and S. Dutta [4]

[1] Senior Engineer, AECOM, Kolkata, India
Email: aritra.bagchi@aecom.
[2] M.E. Student in Jadavpur University, Kolkata, India
Email: manabjgec@gmail.com
[3] Associate, AECOM, Kolkata, India
Email: Bodhisatwa.Roy@aecom.com
[4] Research Scholar in IIEST Shibpur, Kolkata, India
Email: debjyoti.kar82@gmail.com
[4] Research Scholar in IIEST Shibpur, Kolkata, India
Email: sumandutta@gmail.com

[*]Corresponding author

ABSTRACT

Buildings of urban cites in India are generally affected by chlorination and carbonation respectively along with deterioration due to lack of proper maintenance. Further, in some cases, distress may get aggravated due to overloading, faulty design, substandard material, or poor construction of buildings. Also, there have been instances where structural members of buildings start showing signs of distress at early stages of design life leading to retrofitting. This paper deals with a case study of condition survey and retrofitting measures of a distressed newly constructed SOPC building at Subodh Mullick Square, Kolkata. The objective of this paper is the assessment of the building condition which includes detailed distress mapping of structural members, analyzing the cause of distress and subsequent proposal for suitable retrofitting measures.

The retrofitting of the newly constructed building became necessary due to constructional defects that caused early distresses in the structure. The structural members of the buildings were properly assessed in terms of crack mapping, measurement of crack width, chipping of the structural members for assessment of clear cover along with as-built condition of provided reinforcement. Finally, suitable strengthening measures were worked out based on the residual capacity in order to match with the required strength ensuring design life.

KEYWORDS: *Distress Mapping, Crack Mapping, Condition Survey, Residual Stress, Retrofitting Scheme.*

1. Introduction

The SOPC building is a two-story reinforced concrete frame building, situated at Raja Subodh Mullick Square, Kolkata. The newly constructed building was proposed to have a boxing ring on the ground floor and a multipurpose gym on the first floor. It has two numbers of staircases namely ST-01 & ST-02. Based on the structural drawings, the construction activity was started at the site. Eventually, the RCC framework had been completed. During the construction activity regarding the block work, several distresses were observed at various locations of the structure. Visual inspection has been carried out at the site and the distresses have been identified and mapped on the structural drawings. At a few locations, the distresses have been measured with local chipping to identify the nature of the crack and the extent of the crack progression. At some locations, Non-Destructive tests have been carried out. Based on the collected data, the distressed structure has been modelled in FEM analysis software and the adequacy is checked. Finally, based on the investigation results, the structural strengthening methodology is finalized and executed at the site to ensure structural integrity and safety.

Basic structural arrangement
The following are the salient structural features of the building:

Table 1. Building Dimensions

Subject	Dimension
Plan dimensions	25200 mm x 15850 mm
Overall height of the building	11.2 m
Staircase height	14.0 m

Table 2. Building Levels

Subject	Level
Ground Level / Top of Tie beam	+0.00 m
Bottom level of footing	-1.5 m
Top of First floor slab / Top of Canteen Roof slab	+4.00 m
Top of Second-floor slab	+7.6 m
Top of Roof Level	+11.2 m
Top of stair (ST-02) roof slab	+14.00 m

Different level plans and cross sections are shown for better understanding .

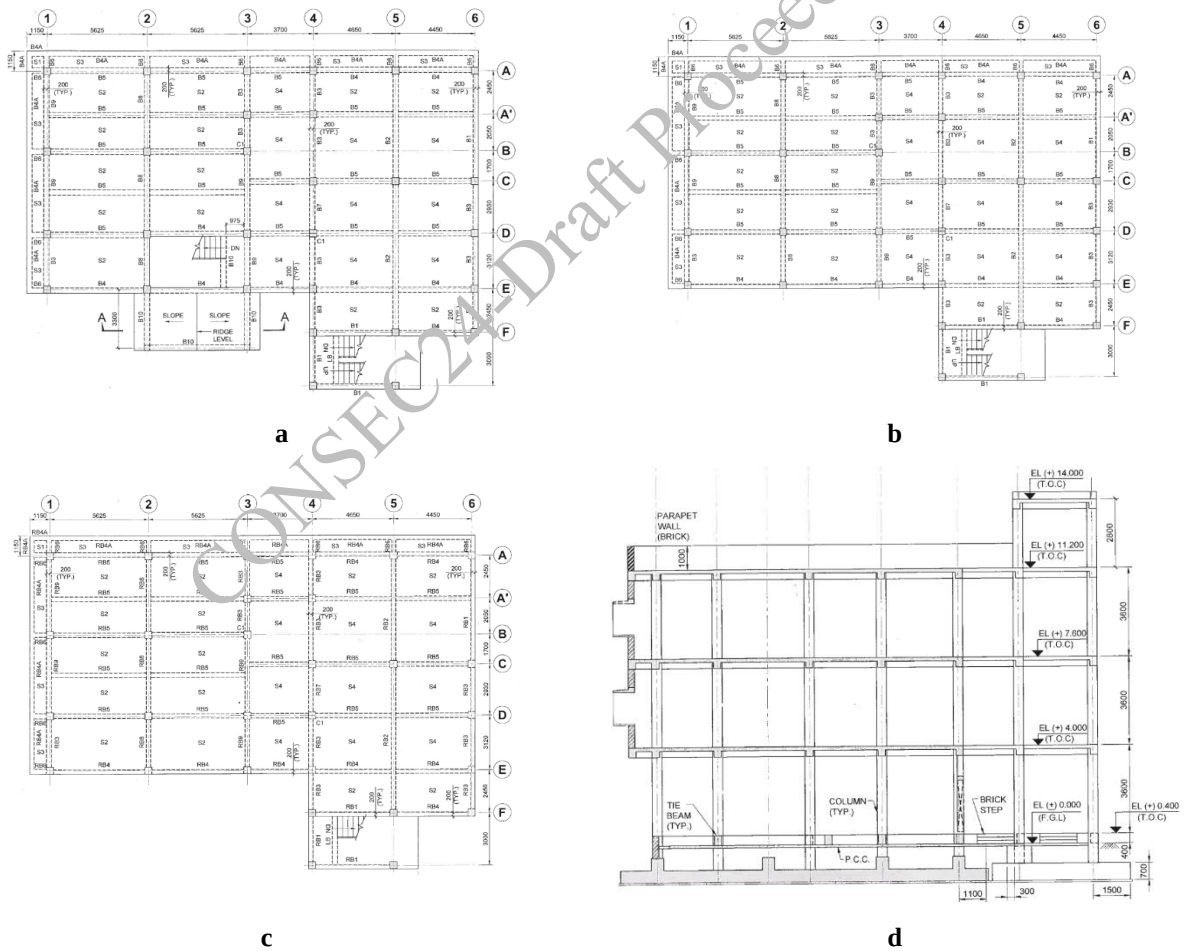

Figure 1. (a) Plan at First Floor Level (b) Plan at Second Floor Level (c) Plan at Roof Level (d) Cross Section of the building

2. Visual inspection

Visual Inspection has been done and several distresses have been observed. The observations were mapped on the first and second-floor level beam drawings. A few distresses have been highlighted below:

- Plenty of honeycombing in beams and columns were found with reinforcements exposed.

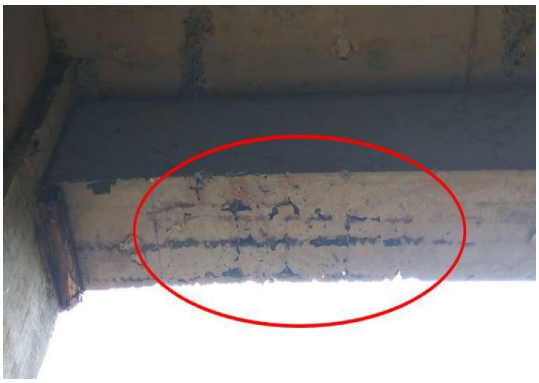

Figure 2. Reinforcements exposed in beam

Figure 3. Reinforcements exposed in beam

- Sagging was noticed in first & second floor-level beams (based on approximate visual estimation) and at some locations of second floor beams cracks were observed.
- Beams are eccentric at almost all the beam-column junctions. Especially, at one location the
- beam is partially supported on the other direction beam.

Figure 4. Beams are eccentric at the beam-column junction

- In most of the beams and slabs the exposure of bottom face reinforcements has not been properly maintained. Hence the impression of main rebars and shear links are visible to the naked eye. Also, the main rebar is eccentrically placed.

Figure 5. Reinforcements exposed in beam

Figure 6. Reinforcements exposed in beam

- Verticality of columns is not maintained. Column size suddenly changed from plinth beam level at some locations.

Figure 7. Non-verticality of column

Figure 8. Non-verticality of column

- Slab bottom reinforcements visible.

Figure 9. Slab bottom reinforcements visible

From the overall visual inspection, it is found that workmanship is very poor. The distress of the superstructure portion can be observed, but the same in the foundation is difficult to investigate.
Overall distresses have been mapped in the plan drawing, as shown below.

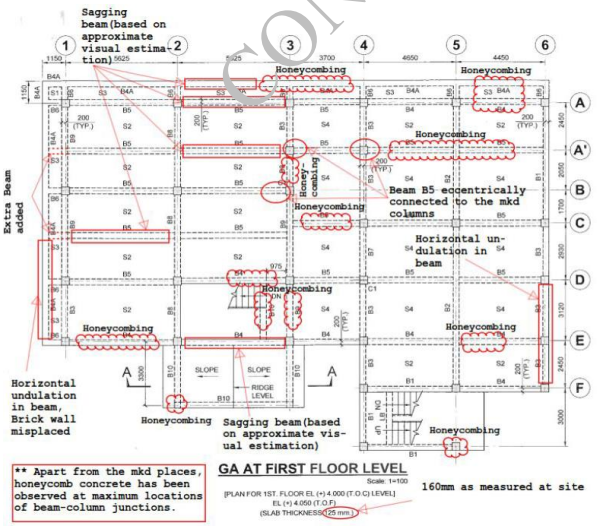

Figure 10. Distress Mapped at First Floor Level Plan

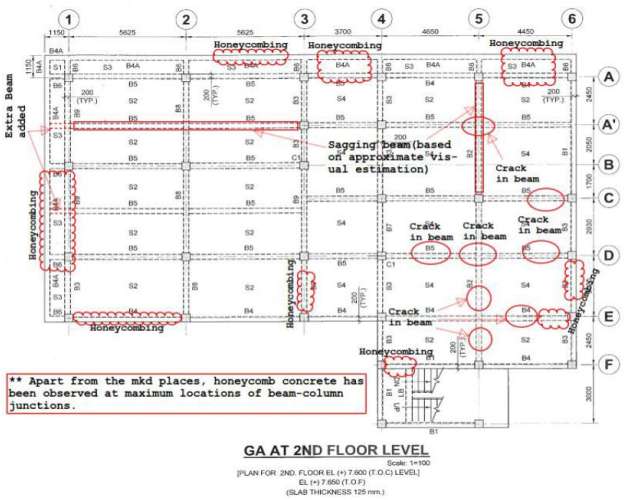

Figure 11. Distress Mapped at First Second Level Plan

3. Determination of Crack Propagation of Beam Marked B2

Initially, a cracked location in beam [second-floor beam B2 (250X700) between grid 5/D & 5/E] has been identified, and chipping of concrete was executed to determine the crack propagation. The outcome is given below:

- As per the RC drawings of second-floor beam B2, the first layer of bottom reinforcement should consist of three nos of T20 rebar throughout the span of the beam. Out of three, two rebars were revealed through chipping.
- At the chipped location, the lap between the main bars is only 30mm to 50mm (approximately), which is not in line with the structural drawing as well as, does not satisfy the codal [1] provisions.
- Chipping revealed that the rebars are placed with 180 mm cover which is also not in line with the structural drawing and the codal provisions as well.

Figure 12. Chipping of Concrete at Beam Marked B2

Figure 13. Improper Lapping and Cover

Figure 14. Chipping of Concrete at Beam Marked B2

Figure 15. Crack in Beam B2

4. Non-Destructive Test (NDT)

Different Non-destructive tests have been performed to assess the strength and load-carrying capacity of different structural members. The summary of NDT work, carried out at the site has been presented below:

- **Rebound Hammer Test –** Rebound Hammer Data has been collected for each element and based on the results the existing strength of the concrete have been evaluated. For the rebound hammer test the average rebound number has been calculated based on IS:8900-1978 [2]. From this, the existing compressive strength of concrete has been determined using the graph which is provided with the hammer itself. For different positions, different graphs have been used.
- **Cover-meter Test –** Cover Meter Test results indicate the existing clear cover of the reinforcement. However, the data may be erroneous if any further plastering work is done at the surface of the concrete. Based on the judgement the assessment of quality of the concrete and depth of the concrete cover has been evaluated.

- **Manual Hammering –** By manual hammering the portion of the concrete surface has been marked where live sound is generated. This portion has been presented as a sketch and the quantification of concrete patchwork has been evaluated.

5. Design Adequacy Check

To check the design adequacy of the structure, a model has been prepared in FEM analysis software and the design of all the beams has been rechecked considering reduced stiffness. The building has been modelled as a space frame structure. It has two staircases (ST-01 & ST-02) among which the combined foundation beneath the external staircase (ST-02) has been modelled separately with plate elements to avoid the complexity of analysis. The data collected from the Non-Destructive Test has been the guiding input for this analysis.

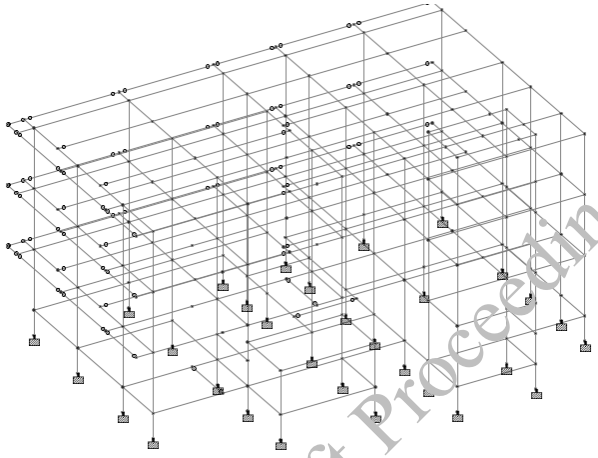

Figure 16. Staad Model of the structure

As per the analysis model, the span bending moment at the crack location (approximately 700mm from the face of beam B2) has been checked with respect to the capacity of the beam. Similarly, other distressed beams have been checked with respect to the size and reinforcement as shown in the drawings and found to be adequate.

6. Conclusions And Recommendation

Based on the investigations carried out at this structure, Cracks noticed on the beam marked B2 suggest that failure of the beam occurred due to improper detailing of reinforcement bars. To overcome this problem, structural strengthening of the beam marked B2 at second-floor level is to be done. Structural strengthening [3] in the form of RCC jacketing is proposed.

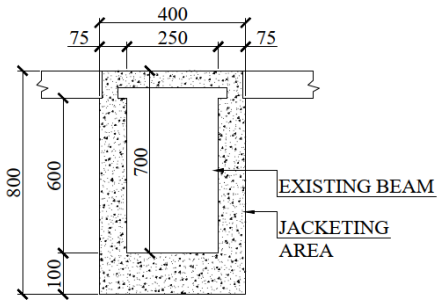

Figure 17. Typical Cross Section Showing Dimensional Detail of Beam

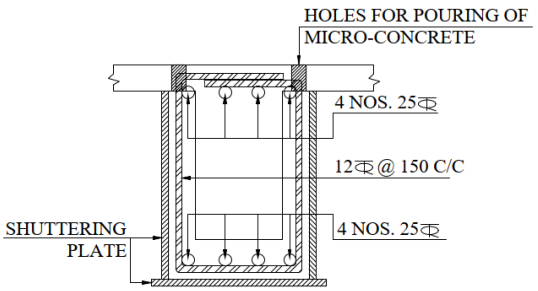

Figure 18. Typical Cross Section Showing Shuttering Details for Pouring Micro-Concreting from Top

Jacketing of the beam needs to be done as per the following steps [4] –

- At first supporting arrangement is to be done at the slab adjacent to the beam.
- All surfaces of the beam are to be chipped manually to create a proper bond between old and new concrete.
- Hole at the existing slab is to be created by drilling operation. U-shaped bar for shear strengthening is to be provided through the existing slab.
- Chipping and taking out of cover concrete at the top of the beam is to be done by manual chipping.
- Top and bottom longitudinal reinforcement is to be provided.
- Acrylic-based bonding agent is to be applied over exposed concrete area.
- Finally concreting is to be done with the free-flowing prepacked micro concrete system from the hole of the roof slab.

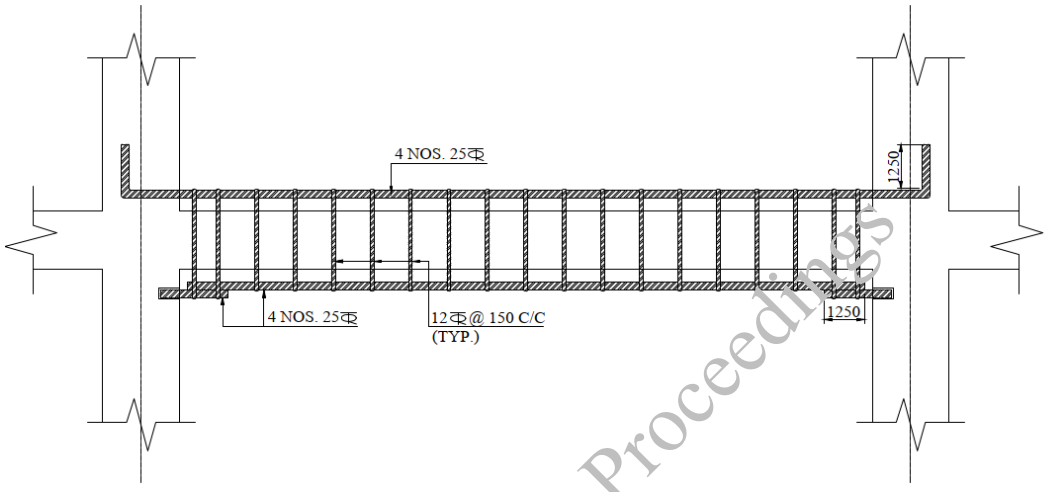

Figure 19. Typical Long Section of Beam Marked B2 at Second Floor Level

References

IS:456-2000: Plain and Reinforced Concrete – Code of Practice.
IS:8900-1978: Criteria for the rejection of outlying observations.
IS 15988-2013: Seismic Evaluation and Strengthening of Existing Reinforced Concrete Buildings – Guidelines.
Raval S.S and Dave U. V. (2013) "Effectiveness of Various Methods of Jacketing for RC Beams", Procedia Engineering, volume 51.

Structural Assessment and Rehabilitation of an Institutional Building

Rhythm Garg, Dr Shweta Goyal, and Er Aman Deep

Student, Patiala, India
Email: rgarg3_be21@thapar.edu
Professor, Patiala, India
Email: shweta@thapar.edu
Consultant, Delhi NCR, India
Email: aman.str@gmail.com

*Corresponding author

ABSTRACT

Numerous historic buildings in India are either in danger of collapsing, need repair, or have reached the end of their safe service life. Ageing has caused many structures to lose strength, and external environmental factors have also caused concrete structural components to deteriorate or to break. Many load-bearing elements make up the structure, and when those members are harmed or distressed, the structural elements begin to disintegrate, and the area becomes dangerous for occupants. The state of the structures is evaluated using Non-Destructive Testing (NDT) and Health Monitoring techniques (using instruments strategically positioned) so that preventive measures can be taken before undue harm is done to the failing structures. A range of tests depending on the project needs, are carried out to assess the strength and stability of a building.

A structural audit was carried out for the project under consideration (an institutional building in Surat, Gujarat) and a case study being presented covering the evaluation of the building's state, identification of distresses level using basic non-destructive testing, and mapping of the condition of the structural elements. The objective of evaluation process was to determine in- situ condition of the structure and to establish adequacy for the current use. Additionally, methods and guidelines for the structural repairs and reinforcement of the troubled buildings were worked out for the rehabilitation purpose. The entire assessment and strengthening/repair work for the structural renovation and upgradation is covered in depth in this paper as a case study.

KEYWORDS: *Repair, Strengthening, Rehabilitation, Corrosion, Service life.*

1. Introduction

The institutional building in Surat, Gujarat is a stilt +7 storey RCC framed structure (figure 1). It has shown symptoms of severe distress such as cracks, spalling of concrete, corrosion of reinforcement steel and deflection of the slab panels etc. at some locations in the recent past. Visual inspections and Non-destructive tests as well as detailed structural analysis have been carried out for the condition assessment of the building. This technical paper suggests technical solutions/ recommendations to resolve the issues related to deterioration of RCC elements due to corrosion of reinforcement steel, which have been identified as a major cause of concern for the safety of the building structure. It discusses the way forward for the structural rehabilitation and retrofitting works considering the strength and durability aspects of the structure. This paper includes the methodologies/ steps to be followed for the rehabilitation works of the corrosion affected structural elements of the building.

Figure 1. Front Elevation

2. Points of Concern

- The main reason for distress in the building is found to be high chloride content in the concrete of the RCC elements which has caused corrosion of reinforcement of steel bars and thereafter deterioration of concrete resulting spalling and cracks on RCC surface (figure 2). This continued cyclic process has resulted in severe deterioration of RCC elements at some locations of RCC members exposed to environment moisture/ water (figure 3).
- Concrete strength got affected and found to be lower at some locations probably caused by the reinforcement corrosion induced stresses and internal cracks of the concrete.
- Due to deterioration of the structural elements, the earthquake safety of the building has been reduced and does not meet the current safety requirements in current condition.
- The durability of the building is also a concern if not taken up for repair with adequate precautions and technical consideration.

Figure 2. Corroded Reinforcement

Figure 3. Cracks induced by reinforcement corrosion

3. Analysis of Distress Remediation Feasibility

Considering the analysis, it was found out that the building could be made habitable with extensive repair and strengthening using state of the art technologies. The repair and rehabilitation/ retrofitting strategy should comply the safety requirement of latest Indian standards as well as durability concerns need to be addressed. Following are the highlighted points which are the mojor concerns and have been considered for addressing the rehabilitation/ retrofitting works (intervention) as a way forward to resolve the technical issues:

- Rust treatment of the existing reinforcement steel bars

- Containment of free chloride in the existing concrete core to prevent further corrosion of the reinforcement steel after the intervention.
- Improve the pH value of existing concrete wherever required to improve passivation of reinforcement corrosion.
- Prevention of the corrosion for new supplementary reinforcement bars in case of requirement of reinforced concrete jacketing.
- Earthquake safety of building as per the updated Indian Standards
- Methodologies to cover above critical aspects for Safe, Durable and Economical rehabilitation/ retrofitting works.

4. Existing Structural System

The structural system of the building has Column-Beam frame arrangement with RCC walls at some locations and slab supported over beams. Floor slabs act as rigid diaphragms in horizontal direction. The existing design of building was performed considering Indian Standards IS 456:2000/ IS: 1893(Part1)-2002. This existing Structural frame is a Special Moment Resisting Frame and the Ductile Detailing is confirmed from the available structural drawings and site data. The system was designed as per the Limit State Method of design to meet the required safety level/ performance. The structure lies in seismic Zone III as per applicable Indian Standard IS 1893-2016.

5. Basis of Evaluation

- Due to visible cracks and rusting on the existing reinforcement steel in the structural elements, the structural capacity of load carrying members have been found to be reduced and requires adequate repair work/ intervention.
- In columns and beams, to achieve the required durability, there is a requirement of protection coatings/ jacketing etc. even after the required structural capacity enhancement by any means. Considering the above, it has been found to be recommendable to upgrade the structural capacities to meet the latest standards especially the earthquake safety standard IS 1893 -2016 by providing chiefly RCC jacketing besides other special strengthening techniques as per site condition.
- Therefore, the structural analysis has been considered for the modified structural members sizes considering the revised stiffnesses into account for evaluating the structural capacities for the intervention requirements.

6. Details of Structural Evaluation

Structural Evaluation is a process of determining the structural adequacy of the entire structure or any element therefore for its current intended use or performance objectives. The evaluation determines the level of structural adequacy in terms of strength, serviceability and durability.
The objective of the evaluation process was to determine the in-situ condition of the structure and to establish adequacy for the current use. Evaluation process includes:

- Tests to confirm reinforcement locations, type of reinforcement, bar diameters and their mechanical properties, strength of existing concrete and other properties.
- Presence of any contaminants.
- Analysis of test results to establish statistical equivalent material properties.
- Estimation of structural capacity on the basis of above findings and tests.
- Analysis of observation and tests for assessment of mechanisms and causes of damage, distress and deterioration.
- Compiling demand loading, serviceability limits on lateral displacement and durability requirements.
- Analysis of the structure to evaluate the existing capacity of the structure to withstand current or future loads and comply with serviceability criteria.
- Determine demand-capacity ratio of the existing structure to evaluate structural adequacy; and to ascertain and judge the need for repair and rehabilitation.
- Determine the maintenance requirements necessary for the service life of the structure.

7. Details of Structural Findings for Strength

The existing building was analyzed with the updated member sizes with RCC jacket for strengthening. The dynamic behavior of the structure has been analyzed. It is observed that the building structure is having Transnational Mode of vibration as the Fundamental Mode and meets the requirement of the Indian Standards with the revised structural menber sizes/ stiffness. Capacity Requirements of the RCC Frame members have been computed in order to meet Demand requirements.

7.1 Main outcomes of the Assessment and the structural analysis are as below:

- The structural capacities of columns with RCC jacket (considered for repair/ strengthening) satisfy all the safety and serviceability requirements according to relevant Codes of practice.
- Structural capacities of beams and slabs with repair/RCC jacketing are adequate.
- Story Drifts are under limit as per IS 1893:2016 requirements.
- Story Stiffness is under limit as per IS 1893:2016 requirements. No Soft Storey found.

7.2 Root Cause Analysis of Causes of Distress/accelerated deterioration of the RCC elements

- The distresses in the building have been found to be due to high chloride contents causing corrosion of reinforcement bars and thereafter deterioration of concrete resulting in spalling and cracks on RCC surface. This continued cyclic process has resulted in severe deterioration of RCC elements at some locations exposed to moisture/ water.
- The concrete strength has been affected and found to be lower at some locations probably caused by the reinforcement corrosion induced stresses on the concrete.
- Due to improper maintenance of the building, the drainage system was choked at many locations, especially terrace and the water was stagnant and overflowed into the building from terrace causing favorable conditions for the reinforcement corrosion. Due to deterioration of the structural elements, the earthquake safety of the building has been reduced and does not meet the current safety requirements in current condition.
- The durability of the building would be a serious concern if it is not taken up for repair with adequate precautions and technical consideration on an urgent basis.

In light of the above, analysis is concluded that the building requires immediate intervention covering all required maintenance repairs and strengthening works.

8. Details of Provisions Considered for Durability

Following provisions have been considered for durability aspects while working out the strctural interventions:

- Separation of existing core concrete and new jacketing concrete using Epoxy Coating such that migration of Chloride ions from existing concrete is eliminated/minimized.
- Jacket the existing Columns-Beams-Slabs using:
- High Performance concrete/ Ultra High-Performance concrete.
- Use of high-grade corrosion resistant stainless steel.
- Use Duplex Stainless Steel / FRP rod connectors between existing RCC and new RCC in the concrete jacket.
- Use of corrosion inhibitors to minimize the current flow causing corrosion of reinforcement.
- Application of Sacrificial Anodes (cathodic protection) for better durability and long-term protection of structural RCC members
- Cement grout to improve the alkalinity of the existing core concrete for natural corrosion passivation of reinforcement steel.
- Use of Pre-stressed carbon fibre laminates to control the deflections and to strengthen the structural elements.
- Application of Rust passivation coatings to the existing reinforcement bars.

- Waterproofing/ watertightness of all exposed surfaces to be upgraded and two lines of defense proposed because water is an essential component to cause reinforcement steel corrosion and by preventing water penetration into the RCC elements would safeguard the reinforcement steel from corrosion.
- Use Anti Carbonation/ Hydrophobic Coatings on exposed surfaces to prevent water ingress into RCC concrete.

9. Further possible actions to be taken up in future for service life enhancement

- Monitoring of the health of the building by regular testing for half-cell potentials and i-CORR.
- Application of self-healing concrete compound for the cracks filling in the external face of the RCC elements of the building to prevent ingress of water or harmful environmental elements into the concrete.

10. Recommendaed Repair and Strengthening Methodologies for RCC elements

10.1 For Beam/ Column/ Slab

To strengthen the RCC elements by special reinforced concrete jacketing, following needs to be done:
Step-1: Supporting of the Structural Elements: Provide relief in stress and strains of structural members, which have severe level of deterioration or overstressing, and there by required be repaired or strengthened. This load relief would be planned by transferring dead and live loads safely through an alternate system to the Suitable Base through jack supports.
Step-2: Surface Preparation by Chipping of Unsound Concrete: Chip-off and remove all the plaster and weak, loose concrete (till behind the rebar by at least 20mm) from deteriorated/ unsound concrete portions of RCC elements by chiselling, chipping, etc using low impact-high frequency chipper to avoid any damage to the existing structural members. Expose the sound concrete and if rusting signs are found on reinforcement steel, de-rust the same with a wire brush or sandpaper. Use portable air blowers to make the surface free from loose material, dirt, etc.
Step-3: Rust Treatment of the Reinforcement needs to be followed:

1. **Alkaline rust converting primer application/ Rust Cleaning of Reinforcement:** Apply water blast of high pressure (150 bar) to remove the surface rust/chlorides. After the removal of weak concrete, wherever reinforcement is found to be corroded, apply a coat of alkaline rust converting primer by brush (using small brush of size 1") to reinforcement surface along the full length of rusted surface.
2. **Anti-corrosive Coating (Rust-Passivation) application on Reinforcement:** Apply the Anti-corrosive protective coating (cementitious) for the exposed and cleaned reinforcement bars. The application of coating shall be done by brush or spray and to be left for air-curing as prescribed by manufacturer.
3. **Application of Concrete Penetrating Corrosion Inhibitor:** Insert corrosion inhibitors in the concrete core.

Step-4: Cement Injection Grouting: Non-shrink cement slurry admixed with corrosion inhibitor grouting shall be done. For grouting 12mm dia NRV nozzles shall fixed at 500mm staggered spacing at larger face of the column.
Step-5: Cathodic Protection: Sacrificial Anodes shall be put up at the locations of the old concrete near jacket treatment areas where the electrical resistivity of concrete changes.
Step-6: Application of impermeable surface layer: Apply two coats of Acrylic based multipurpose polymer for waterproofing and bonding adhesion slurry over the complete exposed chipped concrete surface as per the manufacturer recommendation followed by sprinkling of quartz sand.
Step-7: Supplementary Reinforcement: Additional reinforcement steel (Stainless steel of Grade SS 550) as per the structural design requirements would be supplemented at required spacing and alignment. The supplementary reinforcement (main reinforcement/ ties) shall be inserted/ anchored into the structural member using appropriate post-installation anchorage chemical.
Step-8: Reinforced Cement Concrete Jacket: The concrete jacket of thickness as per structural requirements shall be provided after the application of the bond coat and as per the structural requirement/ guided by the structural engineer. The jacket concrete shall be shrinkage compensating high flow

consistency, high performance concrete with specified mix and strength as per the structural requirements. The concrete shall be poured immediately after the application of the bonding coat when the coat is tacky.
Step-9: After de-shuttering, finish the surface of the concrete members and apply the curing compound. Concrete surface shall be finally finished with plaster and anti-carbonation painting on external (environmentally exposed) members, wherever required hydrophobic coating shall also be applied on surfaces exposed to water.

11. Conclusions

The main reason for distress in the building is higher chloride concentration than the acceptable threshold value of 0.6 Kg/ Cum for RCC concrete which has caused the accelerated corrosion of steel reinforcement bars and thereafter deterioration of concrete which experience tension in concrete cover zone, resulting cracks and spalling on RCC concrete surface. This continued cyclic process has resulted in severe deterioration of RCC elements at some locations exposed to moisture/ water. The way forward for the intervention is a three-step process.

- Repairs and strengthening of the structural elements using ultra high-performance concrete and stainless-steel reinforcement bars after the rust treatment, application of corrosion inhibitors to the existing reinforcement to minimize the corrosion current.
- Long term safety from corrosion using Cathodic Protection and by improving the alkalinity of the core concrete using cement slurry pressure grouting.
- Preventive measures by providing barrier to free chlorides of concrete under the existing reinforcement by providing an acrylic based impervious layer and also a coating of anti-carbonation protection on the final RCC element surface exposed to environment so that ingress of air and water into the RCC elements can be protected for high durability preventing the reinforcement corrosion.

With the three-stage protection of RCC elements by the interventions proposed throughout the building, the RCC members would be safe to perform well during its design life, however, continuous monitoring of the same using appropriate instrumentation is also suggestible. The building need to be maintained with appropriate technical system throughout its service life, mainly to address the prevention of water ingress into the RCC elements and to protect the building structural elements from cracks/ exposure to corrosive environment.

Acknowledgments

I would like to express my sincere gratitude to my mentor Dr Shweta Goyal for her invaluable support and valuable guidance, monitoring, encouragement, and constructive feedback.
I express my gratitude to Er Aman Deep for providing all the necessary information & resources throughout the project. His expertise and support have been instrumental in the successful completion of this study.
Finally, I would like to acknowledge the support and encouragement of my institution faculty, family and friends, who have supported me throughout the project.

References

IS:456-2000 Plain And Reinforced Concrete - Code of Practice
IS:1893(Part1)-2002, 2016 Criteria For Earthquake Resistant Design Of Structures
IS:15988-2013 Seismic Evaluation and Strengthening of Existing Reinforced Concrete Building - Guidelines
IS:13920-2016 Ductile Design and Detailing of Reinforced Concrete Structures Subjected to Seismic Forces - Code of Practice

Tensile Behaviour of Leno Weave Carbon Textile-Reinforced Mortar

Premkumar N[1], and Anil Agarwal [2 *]

[1] Research Scholar, Department of Civil Engineering, Indian Institute of Technology, Hyderabad, India.
Email: ce23resch01007@iith.ac.in
[2] Associate Professor, Department of Civil Engineering, Indian Institute of Technology, Hyderabad, India.
Email: anil@ce.iith.ac.in

*Corresponding author

ABSTRACT

Textile-reinforced mortar (TRM) is a composite material with fabric reinforcement embedded in cement mortar. This research aims to assess textile–reinforced mortar's efficiency under different – orientations through a uniaxial tensile test. The proposed technique entails the use of novel leno weave carbon textiles as a composite material for strengthening purposes in conjunction with the cement mortar. Leno weaves with yarns of 12k filament are extremely stable weaves that provide holes between two threads of 7 mm size. The lateral (warp) yarn is firmly twisted around the longitudinal (weft) yarn in this weave. Two options were explored for structural applications: epoxy-coated and uncoated (dry) textile. The textile mesh used in the TRM was placed in two different orientations, 0^o and 90^o to study the bond effect in the weft and warp directions. A dumbbell-shaped specimens made of such TRM were tested for tensile strength following respective directions of mesh placement. In addition, Digital Image Correlation (DIC) technique was used to monitor the crack initiation, propagation, and overall displacement/ strain limits. Apart from experimental works a theoretical component-based model is proposed to estimate the bilinear curve response of the TRM composites in pure tension.

KEYWORDS*: Textile Reinforced Mortar (TRM), Leno weaves mesh, Textile coating, Orientation mesh, and Tensile behaviour.*

1. Introduction

Fiber Reinforced Polymer (FRP) is commonly used as a strengthening material in recent times for the enhancement of deficient structural systems (J. Maheswaran et al., (2022)). Two primary methods, namely Externally Bonded (EB) FRP laminates and Near Surface Mounted (NSM) strips, are commonly employed FRP strengthening techniques (Saumitra Jain et al., (2017)). These methods have been utilized to strengthen structural systems under various loads, including flexural, shear, and compression (M. Chellapandian et al., (2018)). In these conventional strengthening practices, an epoxy-based polymer matrix is typically used to hold the fibers together and bond the fiber laminate to the original structural element (Hemanth Kumar Chinthapalli et al., (2020)). However, these polymer resins undergo significant degradation and can lose their strength when exposed to elevated temperatures (Yousef A. Al-Salloum et al., (2016)).
A matrix made of cementitious materials may offer a viable alternative by providing better resistance to elevated temperatures. Consequently, composite materials made of fabric and cementitious mortar, known as Fabric-Reinforced Cementitious Mortar (FRCM) or Textile-Reinforced Mortar (TRM), are increasingly used as alternatives to FRP. FRCM consists of fabric meshes and cementitious mortar. The fabric meshes are created using long-woven, knitted, or unwoven fiber roving arranged in two perpendicular directions (bi-directional) and are affixed to concrete surfaces using cementitious mortar. Various types of textiles, including steel, polyphenylene benzobisoxazole (PBO), glass, carbon, and basalt, are used as reinforcement in the FRCM system. However, due to the smooth texture of the fibers typically used in such applications, most cement-based materials do not develop mechanical bonds with them. This challenge can be addressed

by creating a macroscopic mechanical bond between the fiber and the matrix (Brameshuber et al., 2006; ACI 549 (2013)).

In a leno weave, there are two sets of threads: weft threads and leno threads, which cross each other at right angles. (a) In uniaxial reinforced leno weaves, the reinforcing threads are woven as weft threads. These weft threads are intertwined with leno threads using additional yarns for extra strength. (b) In biaxial reinforced leno weaves, the reinforcing threads and extra yarns are used as leno threads, reinforcing the weave in two directions (A. Schnabel et al., (2011)). A leno weave with 7 mm openings provides a very stable structure with a macroscopically rough texture. Textile-reinforced cementitious composites with a strong bond between the fabrics and the mortar matrix exhibit a trilinear tensile stress-strain response characterized by three stages: linear elastic, crack development, and cracked stages. In contrast, TRM (Textile Reinforced Mortar) with a sufficient bond between the fabrics and the mortar matrix shows a bilinear behavior, representing the linear elastic stage and the pseudo-ductility post-failure stage (Van Doan Truong and Dong Joo Kim, (2021)). Textile-reinforced specimens failed due to slippage of carbon textiles, but short synthetic fibers can significantly improve the failure mode and crack patterns due to the bridging effect of the short fibers. Similarly, CFRP textiles can also enhance the failure mode and crack pattern (Ruizhe Li et al., (2024)).

A carbon textile-reinforced mortar (TRM) comprising leno-weaved carbon textile and cement mortar is proposed for study. It is essential to understand how a carbon fiber weave with macroscopic openings bonds with cement mortar without a polymer matrix. Substituting the polymer matrix with a cementitious matrix could offer significant advantages for the construction industry, as it allows fibers and carbon textiles to be used directly instead of impregnating them with epoxy resin. Most research relies on epoxy coating to stabilize the textile mesh, facilitating interlocking between the textile and mortar. However, this study aims to replace the polymer coating with a stable weave of the textile.

2. Experimental Preparation

2.1 Details of specimens

The uniaxial tension test was carried out the difference orientations leno- weave samples for comparing the overall behaviour Dog-bone shaped specimens of approximately 600mm length, 60mm width, and 10- and 15-mm thickness were fabricated. The textile reinforcement was placed at every 5-mm thickness of mortar. The width of the coupons at ends were increased as 100mm (as shown in Figure 1) to accommodate them with the testing grips and avoid edge failure. In addition, the ends of the coupons were wrapped with carbon fiber mesh to avoid failure at the grip location. Figure 1 shows a schematic of the test coupon. The specimens were tested under pure tension. Detailed information on the specimens is provided in Table 1.

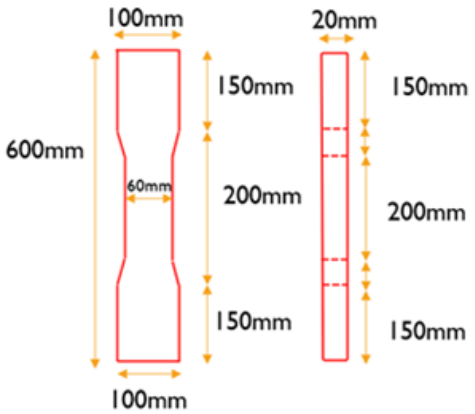

Figure 1. Dog-bone shape specimen

Table 1. Details of the Test matrix

Specimens	CFRP grid		Fiber content (%)
	Orientation	Layers	
T-0-1L	0	1	0.5
T-90-1L	90	1	
T-0-2L	0	2	
T-90-2L	90	2	

2.2 Proportioning of Design Mix for Specimens

The mix design for the development of Fiber-Reinforced Mortar (FRM) specimens are as follows: cement -638 kg/m3, Fine aggregate -1276.8 kg/m3, water- 319.2 kg/m3, and HRWRA- 1180 kg/m^3. To confirm the standard definition, mortar with fibers, such as polypropylene, was used to mix the (FRM) with a 0.5% volume fraction. Pozzolanic Portland cement of grade 43 was used as the mix's significant binder. The fine aggregate utilized in this project was ultra-fine river sand, which passes through a 1.18 mm IS sieve to achieve better particle packing. Furthermore, a poly-carboxylate ether-based water reducer was added at a minimum dose of 1% of the total binder component to lower the water content and enhance the workability of the FRM mix. A desired compressive strength of 40MPa was attained by casing and testing multiple trials before choosing the necessary material proportions.

2.3 Fabric Tensile Test

In this study, carbon fiber leno weave, as shown in Figure 2, was used. For the 7 × 7 mm CFRP grid, the longitudinal and transverse fiber bundles are woven in a leno weave, and two warp threads twist around the weft threads, holding them tightly. The tensile strength of textiles, a methodology along the lines of wide strips test for geo grids, was calculated by ASTM standards (ASTM D6637-01 (2007) to better understand their general behavior under tension. Here, the specimen dimension is 350mm long and width 50mm, and the textile strip is gripped across its entire width in the tensile machine, leaving a free length of 200mm. The fibers were tested in a loading condition mode at a moderate speed of 0.4 mm/min to capture the entire behavior accurately. During the tensile test, an extensometer of 50mm length was attached to the samples to record displacement, which could be used to calculate strain. The elongation and failure strain percentages were determined from the values of the corresponding maxima of the recorded stress-strain graph. Table 2 shows the tensile strength and elastic modulus characteristics of textile fabric. The average data combined with the calculated standard deviation values are shown for each metric, such as tensile strength, modulus, and strain. In Table 2, “C” represents coated, and “UC” represents uncoated.

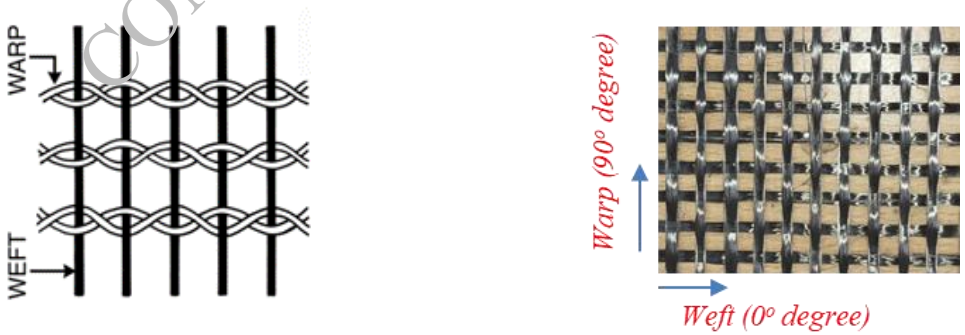

(a) (b)

Figure 2. (a) schematic figure leno wave fabric (b) Carbon fiber leno weave fabric

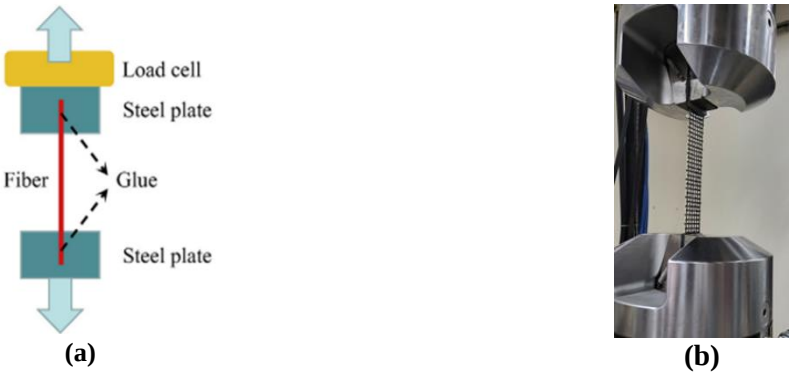

Figure 3. Fabric test setup

Table 2. Details of the test results

Type	Size (mm)	Tensile strength (MPa)	Rupture strain (%)	Youngs modulus of elasticity (GPa)	Cross-sectional area ($mm^{2)}$
CFRP (C_0)	7x7	1755.2	3.12	76.40	2.75
CFRP (C_90)		1572.8	2.94	53.53	
CFRP (UC_0)		1015.8	2.54	50.03	
CFRP (UC_90)		903.8	2.83	31.93	

2.4 Preparation of specimen

Dumbbell-shaped samples were made to test tensile strength under uniaxial tension. Each sample was 600 mm long, with a gauge length (the part of the specimen where measurements are taken) of 200 mm. The cross-section of the samples had a thickness of either 10 mm or 15 mm, and the width in the middle of the gauge length was 60 mm, as illustrated in Figure 1. All the test samples were created using wooden molds. The matrix material was poured in layers, with each layer including a CFRP (Carbon Fiber Reinforced Polymer) grid textile, as shown in Figure 4. The matrix layers between the carbon grids were about 5 mm thick. The outermost layers on the top and bottom were also set to be 5 mm thick to protect the inner textiles. The carbon fiber grid was positioned in the center and arranged symmetrically along the depth direction. When only one layer of textile was used, it was placed in the middle of the sample. When two layers of carbon fiber grids were used, there was a 5 mm space between the textile layers, and the thickness of the outer layers was also 5 mm. The thickness of the matrix layers and the position of the textiles were controlled using scale marks on the inside of the mold. All samples were left to cure for 28 days.

(a). Wooden molds

(b). First layer of matrix

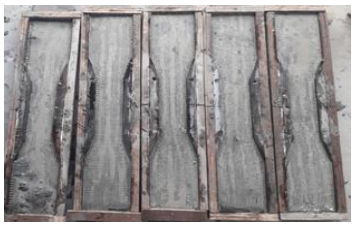

(c). Carbon fiber grid was placed on top of the matrix

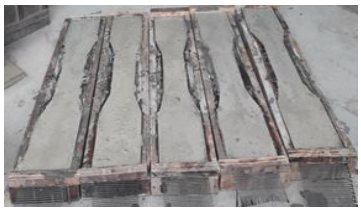

(d). The outer matrix covered and finished trowel

Figure 4. The construction processes of textile-reinforced specimens.

2.5 Test setup and instruments

A uni-axial tension test was performed to determine the overall behavior of TRM specimens with various leno weave fabrics. The dumbbell-shaped TRM samples were tested, and care was taken to avoid crushing failure at the ends. Hence, Carbon fiber was wrapped with epoxy in the specimen. It is suitable for preventing the formation of cracks since the stress is concentrated due to narrowing the centre area. The specimens were tested at a slow speed of 0.4 mm/min, in a controlled displacement control mode. The displacement is obtained using the data recorded by LVDTs placed at the centre line specimen at the back side, covering a gauge length of 150mm. Crack propagation and force-displacement behaviour were measured using the DIC technique and LVDTs respectively.

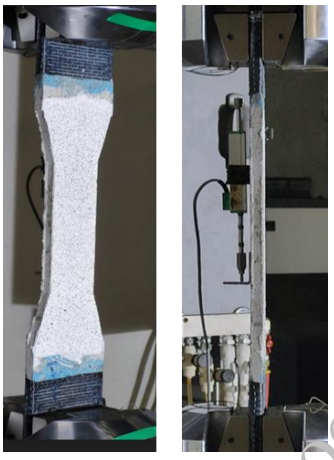

Figure 5. Tensile test setup

3. Results and discussion:

Figure 6 depicts the simplified stress-strain curves, categorized into three stages: (1) the elastic stage, where stress rises linearly with strain, and there is no slippage between the mortar and fabric; (2) the FRM matrix develops cracks, with polypropylene fiber bridges preventing further cracking; and (3) the embedded fabric resists crack propagation, marking the strain-hardening stage. As crack width increases, the fabric remains under tension until it eventually fractures.

Figure 7 illustrates the three primary failure modes observed in TRM specimens after the tensile test: (a) Failure Mode A: This mode denotes premature failure due to localized concentrated stress near the gripping region. This type of failure typically occurs close to the clamping area. (b) Failure Mode B: This mode involves the delamination of the textile fabric within the cementitious composite, where the layers of the matrix separate from the textile. (c) Failure Mode C: This mode is characterized by the complete fracture of the textile fabric within the gauge length, indicating a full breakage within the tested section of the specimen

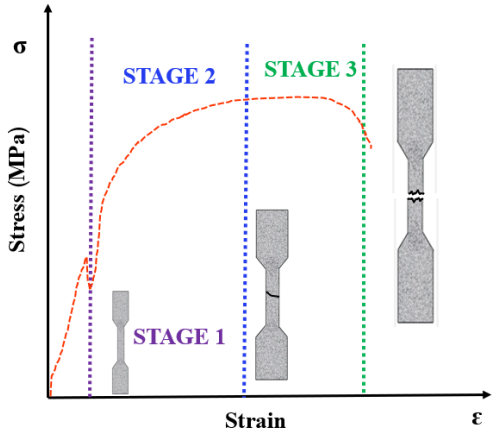

Figure 6. Stress-Strain Relationship of Textile fabric with FRM specimens

For TRM specimens reinforced with uncoated carbon fiber fabric, Figure 6 illustrates typical stress-strain relationships. Increasing the number of fabric layers from 1 to 2 enhances both peak load and corresponding displacement. Initially, the slope of all specimens is identical, as seen in the zoom-in view of Figure 8. The peak load increases by 50% when transitioning from 1 layer to 2 layers. For fabric orientations at 0° and 90°, the peak load increases by approximately 8.99%. Displacement at peak load remains similar between 0° and 90° orientations, with a slight 2.3% increase in displacement for 2-layer specimens compared to 1-layer ones.

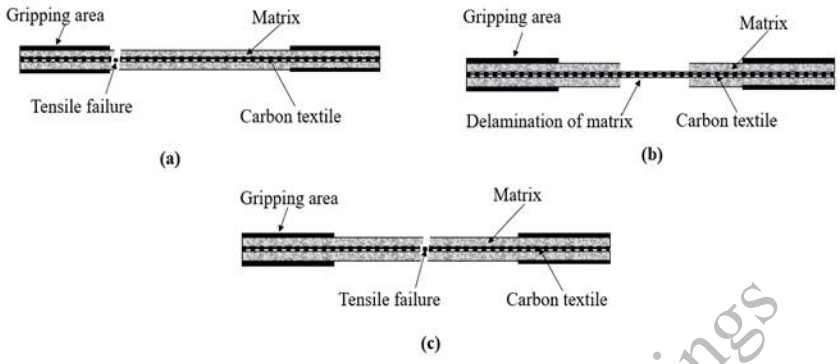

Figure 7. Typical failure modes

The DIC method was utilized to analyze the crack development and damage process in the tensile test. Commercial software Vic-2D 7 (Correlated Solutions Inc.) was used to perform the image analysis. Initially, cracks start to form at the edges (Figure 9a) and move toward the center of the specimen. By the end of stage II (Figure 9b), a primary set of cracks has fully developed at locations corresponding to the position of the transverse reinforcement roving. Figure 9 illustrates that stress transfer between the fabric and binding matrix after cracking is more efficient in 2-layer specimens, facilitating multiple cracking and strain hardening. This stage terminates at the point of the first crack, followed by pronounced strain hardening with reduced stiffness. It is found that crack strength and post-cracking stiffness increase with the rising volume of fraction fiber, which proves the role of fibers in controlling cracks.

Table 3 presents the results of the CFRP grid–FRM tensile test. Ductility increased by 43% in 2-layer specimens, compared to 35% in 1-layer specimens at 0° orientation and 24% at 90° orientation (Figure 10 depicts the failure mode of the specimens). In these FRM fabrics, dry conditions initially hindered load sharing among fiber filaments in the bundles, resulting in fractured external filaments and core filament slippage. In CFRP fabric with FRM specimens, when CFRP fabric was a dry grid, the fiber filaments in the fiber bundle did not collaborate in uniform load, resulting in the fracture of external fiber filaments and slippage of core fiber filaments. From observation, Figure 10 (T-90-1L) shows slippage of textile fabric inside cementitious composites accompanied by partial fractures in the textile fabric.

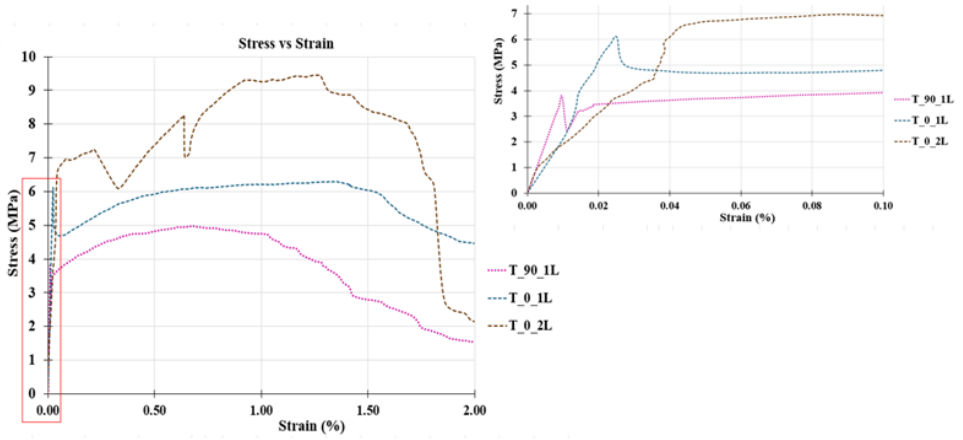

Figure 8. Tensile stress-strain curve

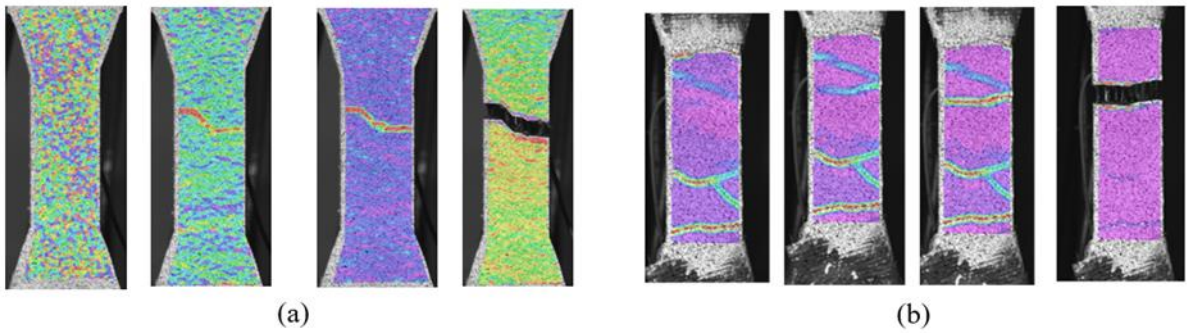

Figure 9. Crack initiation and propagation from the DIC system

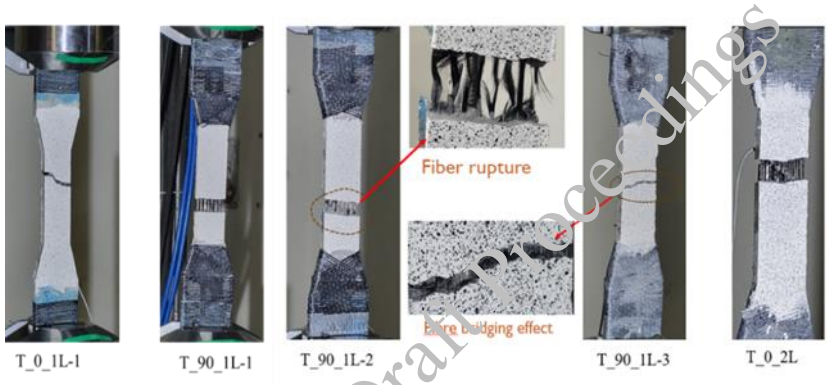

Figure 10. Failure modes of specimens

Table 3. Results CFRP grid- FRM tensile test

Specimens	ε_{cr} (%)	σ_{cr} (MPa)	ε_t (%)	σ_t (MPa)
T-0-1L	0.03	6.09	1.35	6.29
T-90-1L	0.01	3.78	0.67	4.97
T-0-2L	0.22	7.23	1.28	9.45

4. Conclusions

- The results from the material characterization test indicate that coating enhances fabric tensile performance by 73% compared to uncoated fabric in both directions.
- The stress-strain relationship clearly shows a bilinear curve pattern. Increasing the number of fabric layers results in higher ultimate stress, ultimate strain, multiple cracking behavior, and increased ductility. The direct tension tests demonstrated TRM's significant ductile capability, with all specimens sustaining tension loads with a minimum ultimate strain of 1.5%. Coating the fabric embedded in a cementitious matrix enhanced tensile strength significantly, promoted the formation of multiple cracks, and facilitated strain-hardening behavior even with a single layer of fabric.
- Textile-reinforced mortar offers a practical method for enhancing the tensile properties of cement-based materials while providing sustainability benefits and improved crack control. These composites have the potential to support stronger, more environmentally friendly, and economically advantageous construction techniques.

Acknowledgements

The experimental work performed was funded by the Science and Engineering Research Board (SERB), under the project "**Development of textile reinforced mortar based strengthening technique for elevated temperature conditions**" with the sanction ID: CRG/2021/007533. The authors would like to acknowledge the support for carrying out the research work.

References

J. Maheswaran, M. Chellapandian, and N. Arunachelam (2022) "Retrofitting of severely damaged reinforced concrete members using fiber reinforced polymers: A comprehensive review," *Structures,* 38:1257-127

Saumitra Jain, M. Chellapandian, and S. Suriya Prakash (2017) "Emergency repair of severely damaged reinforced concrete column elements under axial compression: An experimental study," *Construction and Building Materials,* 155:751-761

M. Chellapandian, and S. Suriya Prakash (2018) "Rapid repair of severely damaged reinforced concrete columns under combined axial compression and flexure: An experimental study," *Construction and Building Materials,* 173:361-380

Hemanth Kumar Chinthapalli, M. Chellapandian, Anil Agarwal, and S. Suriya Prakash(2020) "Rapid repair of severely damaged reinforced concrete columns under combined axial compression and flexure: An experimental study," *Engineering Structures,* 211:1145058

Yousef A. Al-Salloum, Tarek H. Almusallam, Hussein M. Elsanadedy, and Rizwan A. Iqba (2016) "Effect of elevated temperature environments on the residual axial capacity of RC columns strengthened with different techniques," *Construction and Building Materials,* 115:345-361

Brameshuber, W. Ed. (2006) "Textile reinforced concrete State-of-the-art Report of RILEM Technical Committee TC 201-TRC", Report 36, *RILEM Publications*.

ACI 549 (2013) "Design and construction guide of externally bonded FRCM systems for concrete and masonry repair and strengthening,". *ACI Publication, USA*.

A. Schnabel, T.Gries (2011) "Non-crimp fabric composites Manufacturing, properties and applications", *Woodhead Publishing limited,* 10.1016/B978-1-84569-762.

Van Doan Truong, Dong Joo Kim (2021) "A review paper on direct tensile behavior and test methods of textile reinforced cementitious composites", *Composite Structures,* 263:113661.

Ruizhe Li, Mingke Deng, Liying Guo, Ding Wei, Yangxi Zhang, Tong Li (2024) "Tensile behavior of high-strength highly ductile fiber-reinforced concrete with embedded carbon textile grids", *Construction and Building Materials,*414: 134957.

ASTM D6637-01 (2007) "Standard Test Method for Determining Tensile Properties of Geogrids by the Single or Multi-Rib Tensile Method," *ASTM Publication, USA.*

Investigation of the efficiency of Concrete Conductive Anode Paint (CAP) as an ICCP Anode for Reinforced Concrete Structures

Arpit Goyal[1*], Homayoon Sadeghi Pouya[2], and Eshmaiel Ganjian[3]

[1] *Assistant Professor, Thapar Institute of Engineering and Technology, Patiala, Punjab, India, 147004, Email: arpit.goyal@thapar.edu*
[2] *Senior Materials Engineer, Structural Rehabilitation, Transportation UK and Europe, Atkins, Birmingham, United Kingdom, Email: Homayoon.Sadeghipouya@atkinsglobal.com*
[3] *Concrete Corrosion Tech Ltd., Birmingham, United Kingdom, Email: eganjian@yahoo.co.uk*

[*]Corresponding author

ABSTRACT

The increasing risk of chloride contamination on reinforced concrete structures necessitates innovative repair solutions. Impressed Current Cathodic Protection (ICCP) has been proven to effectively mitigate corrosion regardless of chloride content. The major part of the system is the anode material. This paper introduces a novel conductive paint anode, Concrete CAP (Patent No-533126), suitable as an ICCP anode for protecting chloride-contaminated reinforced concrete. The polarization performance of Concrete CAP on a beam specimen exposed to atmospheric conditions has been evaluated. The result showed that the anode performed satisfactorily, satisfying the BS EN 12696:2022 polarisation criterion. Finally, the paper presents a field application of Concrete CAP on a crossbeam in a car park supporting the Coventry Ring Road in the United Kingdom.

KEYWORDS*: ICCP Anode, Corrosion, Cathodic Protection, Conductive Paint, Reinforced Concrete*

1. Introduction

Reinforced concrete (RC) structures are susceptible to corrosion when exposed to chloride ingress. Impressed Current Cathodic Protection (ICCP) offers a well-established technique to mitigate corrosion by applying a low-level direct current (DC). The current is passed from a permanent anode (which can be fixed at the surface or into the concrete) through the concrete electrolyte to the steel bars. The current passed should be sufficient to drastically reduce the anodic reactions and cathodic reactions can occur at the steel, Consequently, the steel potential is shifted to a more negative value, effectively halting corrosion. However, the long-term performance and durability of ICCP systems rely heavily on the selection and functionality of the anode material (Goyal et al., 2023). An ideal ICCP anode should not only deliver the required current efficiently but also maintain a stable interface with the concrete over the design life to avoid compromising system effectiveness (Bertolini et al., 1998). Over the past few decades, research efforts have explored various anode materials for ICCP systems, including activated titanium mesh, metalized zinc, conductive mortars, and conductive carbon-based paints (Orlikowski et al, 2004; Byrne et al., 2016). While commercially available coating anodes offer advantages like ease of application and good initial performance, their durability and long-term service life can be limited (Goyal et al., 2018).
The paper discusses the performance of new patented Concrete Conductive Anode Paint (CAP) for atmospherically exposed reinforced concrete structures. Laboratory investigations and field application of the three-year performance of the developed anode applied on a crossbeam in a car park supporting the ring road in Coventry, United Kingdom, are discussed.

2. Experimental Investigations

2.1 Materials and Mix Design

To replicate the conditions of existing aged reinforced concrete (RC) structures potentially susceptible to chloride contamination, all concrete specimens in this study were cast with an M30 concrete strength grade and a water-cement ratio of 0.5. The concrete mix composition mirrored typical field practices, utilizing 360 kg/m³ OPC 43 cement, 640 kg/m³ fine aggregate, and 1190 kg/m³ coarse aggregate. River sand was used as fine aggregate and 20mm down aggregates were used as coarse aggregates. To accelerate the chloride-induced corrosion process within the concrete specimens, 3% by weight of the cement of sodium chloride (NaCl) was deliberately incorporated into the mixing water during casting. Concrete Conductive Anode Paint (Patent No- 5233126) was used as an anode and Anomet wire with a diameter of 0.8mm was used as a primary anode conductor.

2.2 Specimen Preparation and Test Setup

A beam of 3x0.12x0.33m was cast with a steel: anode ratio of 1:1 and steel: concrete ratio of 0.28:1. Each beam contained four ribbed steel bars, 10 mm in diameter, with a concrete cover of 25 mm. To monitor stee/concrete/reference electrode potentials, thirteen MMO/Ti decay probes and two Ag/AgCl/0.5M KCl reference electrodes were strategically positioned along the reinforcing bars. The specific placement details of these probes are illustrated in Figure 1. The MMO/Ti decay probes were installed at 0.5 m intervals near the top and bottom steel bars throughout the beam length. The beams were exposed to atmospheric conditions and impressed current densities of 10 mA/m² and 20 mA/m² per steel surface area were applied. Additionally, separate tests were conducted to evaluate current throwability and determine the optimal number of connections required for complete polarization where the primary anode conductor was connected to the power supply at one end and at both ends (in a ring form).

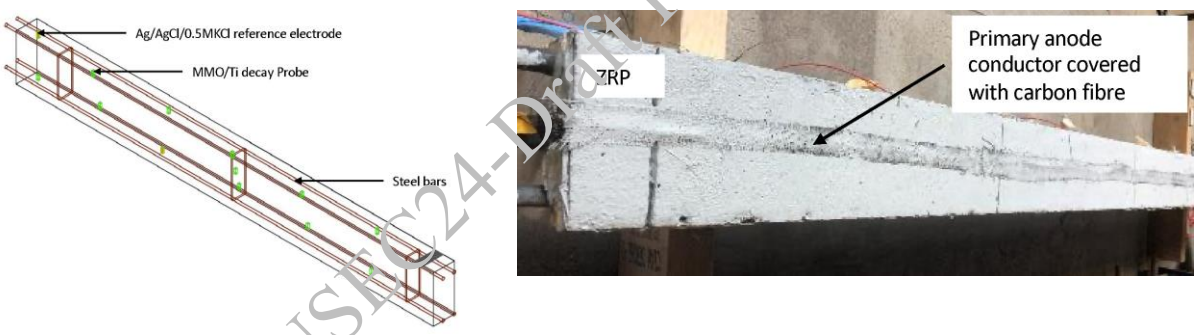

Figure 1. Specimen preparation and reference electrode installation

After casting and curing the specimen, Concrete CAP was applied in two layers. After the first layer, the primary anode conductor was installed and covered with a carbon fibre strip to protect it from mechanical damage. It is ensured that Anomet wire is fully embedded between two layers of Concrete CAP. To initiate cathodic protection, the positive terminal is attached to the Anomet wire and the negative terminal to the steel bar. Constant current density is supplied until the polarization potentials become constant. Using a data logger system, the steel/concrete anode potentials were recorded every minute. The performance is monitored and analyzed as per BS EN ISO 12696:2016 (BSI 2016). In addition, service life test was performed in accordance with NACE TM0294.

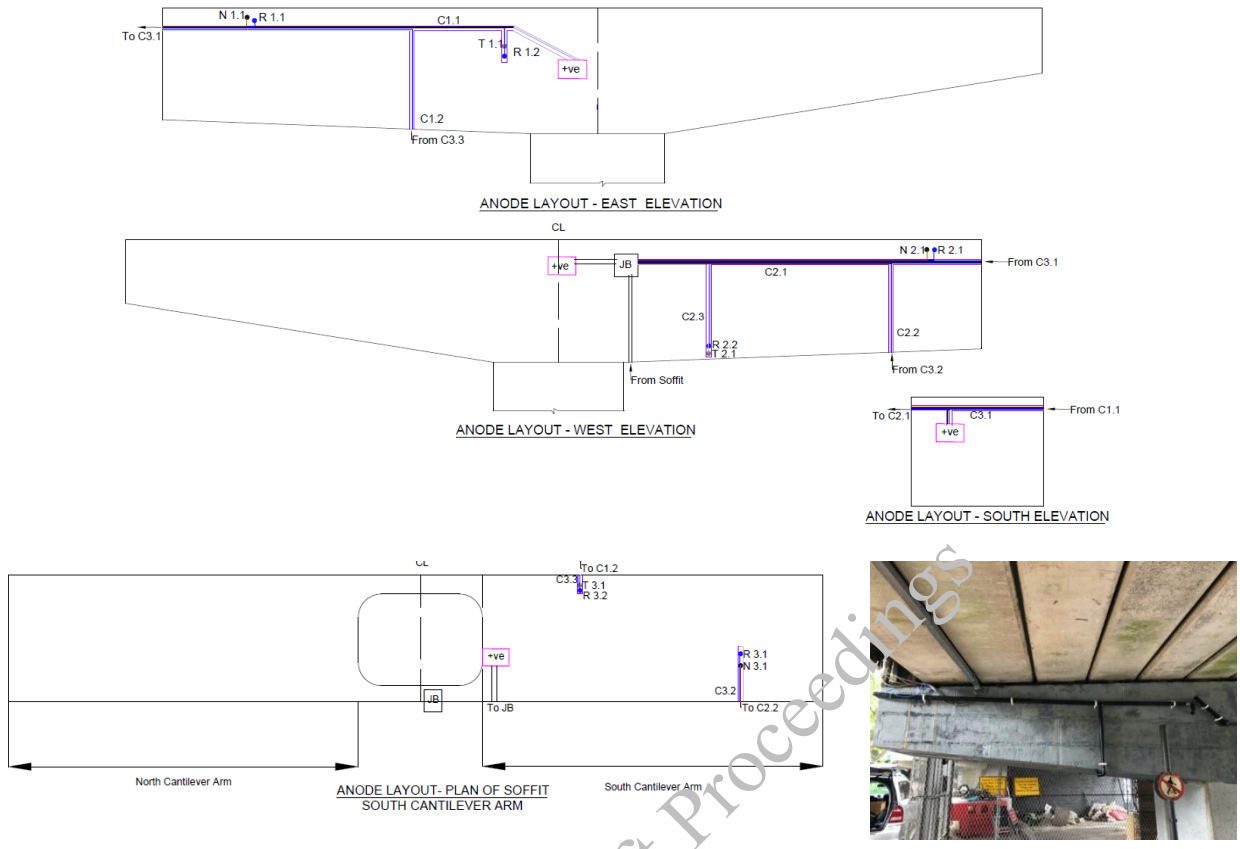

Figure 2. Application of Concrete CAP on a crossbeam at Coventry, UK

3. Field Application

For field application, a cross beam of the Ringway Whitefriars section of the ring road in Coventry, England, was selected, which was severly corroded due to poor carriageway drainage. The crossbeam was divided into three zones (Figure 2a). After surface preparation, negative connection to the steel, installation of reference electrodes and first coat of anode, Anomet wire was installed in a ring form, followed by final coat of paint anode. The wire connections were routed through plastic conduits and secured to the Junction box (Figure 2b). The wires were at last connected to the electrical cabinet via multicore cable. The system was initially energized at 20% of the design current density for each zone and then maintained according to the conditions.

4. Results and Discussions

4.1 Polarization Performance of Beam Specimens exposed to Atmospherically exposed conditions

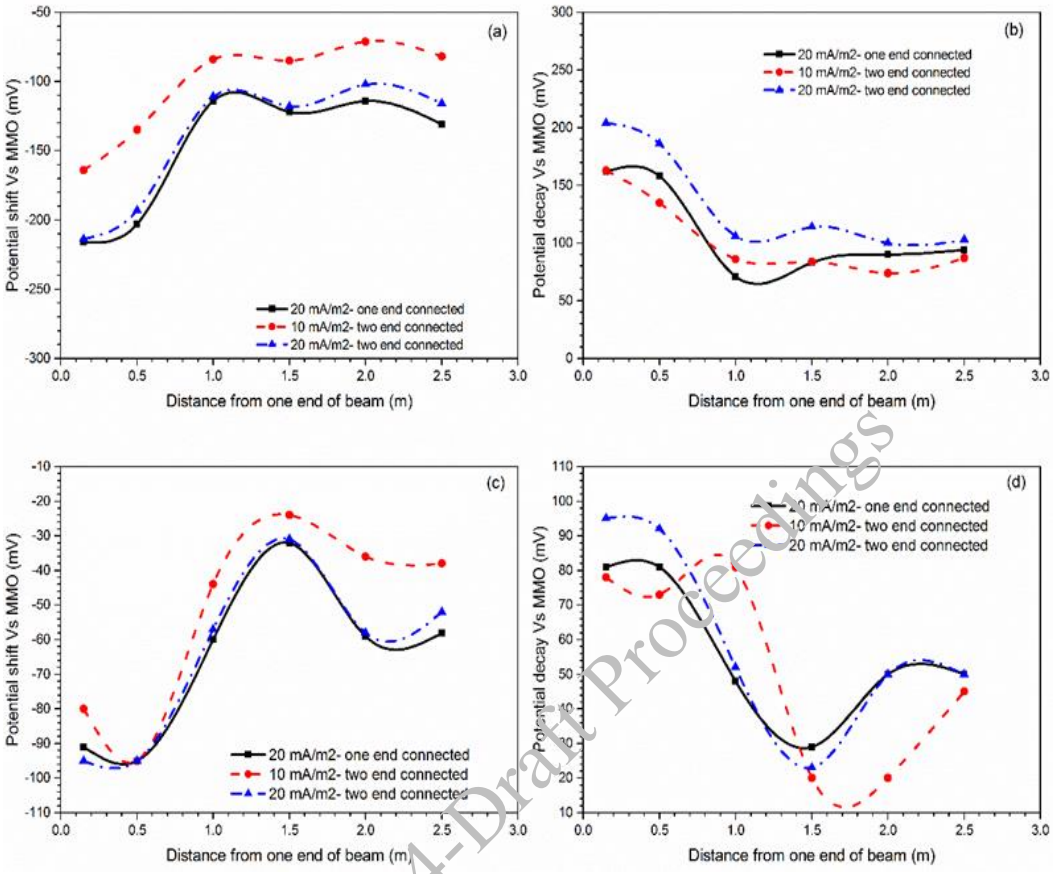

Figure 3. (a) Potential shift-top bar (b) Potential decay-top bar (c) Potential shift-bottom bar and (d) Potential decay-bottom bar of 3m CAP coated beam specimens at different current densities w.r.t MMO reference electrode

As observed in Figure 3, for the top bars to satisfy the BS EN ISO 12696:2016 (BSI 2016) protection criterion, both ends of the primary anode conductor must be connected to the power supply. Moreover, 20 mA/m^2 of current density per steel surface area was required to protect the steel bars. When the specimens were polarised for 20 mA/m^2 current density with just one end of the primary anode conductor connected to the power supply, the steel/concrete potential decays varied from 80-150 mV along with the top reinforcement at different points. The bottom bars did not meet the decay criterion. However, when the primary anode conductor was connected at two extreme ends for the same applied current density, all points on the top reinforcement met the decay criterion. No change was observed for the bottom reinforcement potentials. The as-found voltage dropped from 15V to 10V. Due to the higher depth of the beam specimen, the bottom bars did not satisfy the polarisation criterion as expected and required the anode to be applied on more than one face of the beam.

4.2 Field Performance of Concrete CAP applied on a Crossbeam

The results of the test are shown in Table 1. The initial existing potentials were determined after 24 hours of system installation. As observed from the data, all the reference electrodes installed near the cantilever side of the cross beam (potentials more negative than -350mV Vs Ag/AgCl/0.5M KCl) were severely corroded compared to sensors installed in the center of the crossbeam (potentials less negative than -150mV Vs Ag/AgCl/0.5M KCl). All the reference electrodes installed near the cantilever side of the crossbeam showed a high potential shift (300-400mV), whereas the other reference electrodes showed a 100-200mV shift. This indicated that most of the protection current was flowing towards the cantilever side of the

crossbeam. This may be due to high corrosion and lower resistivity in the area due to water seepage. In addition, the Z1.1 electrode showed the highest potential shift. The electrode was the one that was most exposed to the water drainage area. The shift in the potentials showed that the cathodic polarization was reached. After three years of commissioning, no drastic change in current was observed. The depolarization results (Table 1) showed that all the reference electrodes achieved more than 100 mV decay in 24 hours at each depolarization conducted, satisfying the BS EN ISO 12696:2016 criterion. In addition, reference electrode Z1.1 also achieved more than -720mV instantaneous OFF potential at the end of each polarization. The service life result showed that when anode is operated at 20 mA/m2 current density, it can perform satisfactorily for up to approximately 30-45 years

Table 1. Results of polarization and depolarization for different anode zones

Zones	Reference Electrode	Initial Potential (mV)	Instant OFF Potential-initial (mV)	24 hour decay (mV): 1 month	24 hour decay (mV): 1 Year	24 hour decay (mV): 2 Year	24 hour decay (mV): 3 year
1	Z1.1	-352.3	-964.6	123.8	101 (satisfied criterion 1)	190	92 (satisfied criterion 1)
	Z1.2	-99.8	-310.1	143	117	165	171
2	Z2.1	-482.7	-802.9	237.9	201	112	269
	Z2.2	-165.9	-274.4	119.8	173	112	271
3	Z3.1	-369.2	-490.1	163.2	147	149	115
	Z3.2	-86.9	-334.5	250	153	276	277

5. Conclusions

It can be observed that the new anode system is successfully protecting the chloride-contaminated RC structures as per the relevant standard. Laboratory investigation showed that the primary anode conductor needs to be placed in a ring form to work the anode system successfully. The anode successfully reduces the corrosion state of beam specimens with large steel: anode ratio, maintaining the as-found voltage within limits. In addition, field investigation showed that the system has been satisfying the depolarization requirements for the three reported years. The anode can maintain the design current, shifting the potential of steel to a more negative direction even in the worst exposed water damage condition.

References

Bertolini, L., Bolzoni, F., Pedeferri, P., Lazzari, L., & Pastore, T. (1998). "Cathodic protection and cathodic prevention in concrete: principles and applications". *Journal of applied Electrochemistry*, 28, 1321-1331.

BSI, BS EN ISO 12696: Cathodic protection of steel in concrete, London, 2016.

Goyal, A., Pouya, H. S., & Ganjian, E. (2023). "Electrochemical Performance of Concrete Conductive Anode Paint Used as an Impressed Current Anode Material". *Journal of Materials in Civil Engineering*, 35(7), 04023199.

Goyal, A., Pouya, H. S., Ganjian, E., & Claisse, P. (2018). "A review of corrosion and protection of steel in concrete". *Arabian Journal for Science and Engineering*, 43, 5035-5055.

Orlikowski, J., Cebulski, S., & Darowicki, K. (2004). "Electrochemical investigations of conductive coatings applied as anodes in cathodic protection of reinforced concrete". *Cement and Concrete Composites*, 26(6), 721-728.

Byrne, A., Holmes, N., & Norton, B. (2016). "State-of-the-art review of cathodic protection for reinforced concrete structures". *Magazine of Concrete Research*, 68(13), 664-677.

Health Assessment, Strengthening and Rehabilitation of a Fire-Damaged Structure in a Refinery Complex: A Case Study

Ankit Verma[1*]

[1] *Engineers India Limited*

*Corresponding author

ABSTRACT

This paper is about the Structural Health Assessment, Strengthening, and Rehabilitation of a fire-damaged reinforced concrete structure located somewhere in the coastal region of Southern India. The existing structure was under retrofitting due to its deteriorated condition while the fire took place. RCC structures located in coastal areas which are rich in chloride ions frequently suffer from corrosion phenomena. Corrosion in reinforcement causes degradation in the strength of reinforced concrete structures and decreases its design life. Also, fire is one of the most severe hazards that structures may experience during their lifetime. The Industrial Structure is primarily made of Reinforced Cement Concrete (RCC), consisting of floor slabs, beams, and columns. An unexpected fire incident took place inside the refinery complex during the Covid-19 pandemic period resulting in the shutdown of the process plant. To re-commission / start up the plant in normal operating condition, damaged structure, piping, and equipment need to be retrofitted and re-erected in the minimum possible time. A structural health assessment study has been carried out to finalize the rehabilitation scheme with the help of non-destructive tests and visual inspection. Finally, all repairs and retrofitting have been carried out to reinstate the structure in operating condition.

KEYWORDS*: Rehabilitation, Retrofitting, Non-destructive tests, Structural health assessment*

1. Introduction

The reinforced concrete Structure located in the coastal region was under retrofitting at the time of fire incident took place. The Structure was in distress condition and the main reason for the concrete's spalling, cracks, and rebar exposure at many places was the corrosion in the rebars. Corrosion in rebar is the process that results in an expansion in the steel rebar and due to an increase in the volume of rebar, an internal stress is generated that causes a force to push concrete apart and results delamination of the concrete. Metal insert plates which were placed at the face of concrete (embedded through lugs inside concrete) were the core initiator and propagator of corrosion in the Structure. Here in this paper, the methodology for the restoration of the deteriorated structure along with the rehabilitation activity performed after the fire incident has been presented.

Figure 1. Images after the fire Incident

Figure 2. Image after rehabilitation & retrofitting

The fire lasted for one hour. The extent of damage and subsequent repair are presented in Fig. 1 & 2. A fire incident happened in May 2021 and the steel beam connected to the main RCC frame got severely damaged, buckled, twisted, and came out along with their fixing lugs due to thermal expansion. Also, the carbon fiber wrapping of retrofitted columns burned completely. Refer to Fig. 3 to 6 for the various kinds of damages that took place due to the fire incident.

Figure 3: Steel beam came out along with inserts

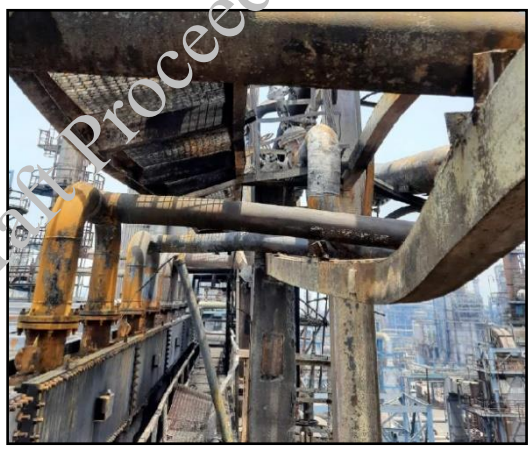

Figure 4. Steel beam deflected and bucked

Figure 5. Carbon fiber wrapping burned

Figure 6. Steel bracket twisted and lost its connection

The process plant inside the refinery was in a shutdown state. Structure, piping, and equipment were under damaged condition due to the fire incident and the same has to be retrofitted, replaced, and re-erected in the minimum possible time. Therefore, a structural health assessment was carried out to finalize the rehabilitation scheme with the help of non-destructive tests and visual inspection.

2. The Structure Under Consideration

- The industrial structure is primarily of RCC construction consisting of RCC floor slabs. RCC frames and air fin coolers at EL. 123.000 (23 meters from the ground). The ground floor is with stacked exchangers which were directly resting on soil through pedestals and foundation.
- 1st floor (EL. 108.500) & 2nd floor (117.500) support drums, exchangers, and other misc. equipment.
- 3rd floor is supporting Air fin coolers. Air fin coolers are of steel Structures and without fireproofing.
- Major piping is resting on steel beams at many locations which are further resting on RCC framed structure through insert plates. Steel beams have been part of the main structure since the initial stage. In industrial structures, steel beams are generally used for various pipe supports.
- Monorails for holding exchanger bundles or the equipment at different elevations are primarily supported on RCC frames through insert plates

3. Methodology for restoration of the deteriorated RCC structure before the fire incident

The structure was under repair to counter and prevent exiting cracks, concrete spalling, and corrosion in reinforcement (refer Fig. 7) and was under retrofitting to take the enhanced loads for some new equipment. The retrofitting process was performed for columns, beams, slabs, and inserts for brackets in line with BS EN 1504. Also, carbon fiber wrapping/laminate was done for some of the columns.

Figure 7. Deteriorated Structural Column, beam & slab before repair

The Slab was propped/ supported till the repaired portion gained adequate strength. Edges, where concrete was removed, should be cut at a minimum angle of 90° to avoid undercutting and a maximum angle of 135° to reduce the possibility of de-bonding with the top surface of the adjacent sound concrete as shown in Fig. 8.

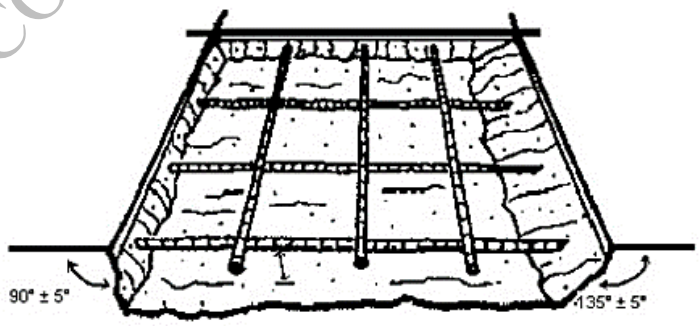

Figure 8. A view of the slab after cutting the edges to provide a mechanical key

To prevent the flow of water on the bottom face of the slab through the opening provided for the pipes access, a kerb wall of 100 mmx100 mm shall be made all around the opening on the slab as shown in Fig. 9.

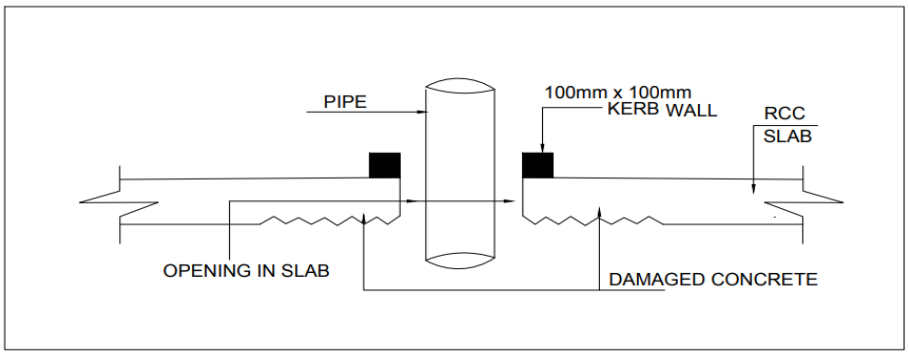

Figure 9. Sectional view of slab opening with kerb wall of 100 mm x 100 mm all around

4. Structural health assessment after Fire incident

The age of the structure was approximately 25 years when the fire incident took place. To quantify the damage and implement repair methodology for rehabilitation in the minimum possible time it was suggested to group the Structural columns, beams, slabs, inserts, etc. which require a similar repair methodology based on visual inspection and NDT testing reports. Mainly all three floors of bays 3, 4 & 5 were affected by fire. Fig. 10 shows the bay and grid layout of the structure.

Hydrocarbon fire is severe in nature and it causes a sudden rise in the temperature of the fire zone, therefore to assess the damage in RCC due to fire NDT tests of fire zone concrete compared with the concrete i.e. away from the fire zone.

The following tests have been proposed to assess the damage in the RCC Structure.

- Visual and Delam Survey
- Rebound Hammer Test (RHT)
- Core test
- Ultrasonic Pulse Velocity Test (UPV)
- Carbonation depth Test (CD)
- Half Cell Potential Meter (CP)
- Pull out test for RCC slabs

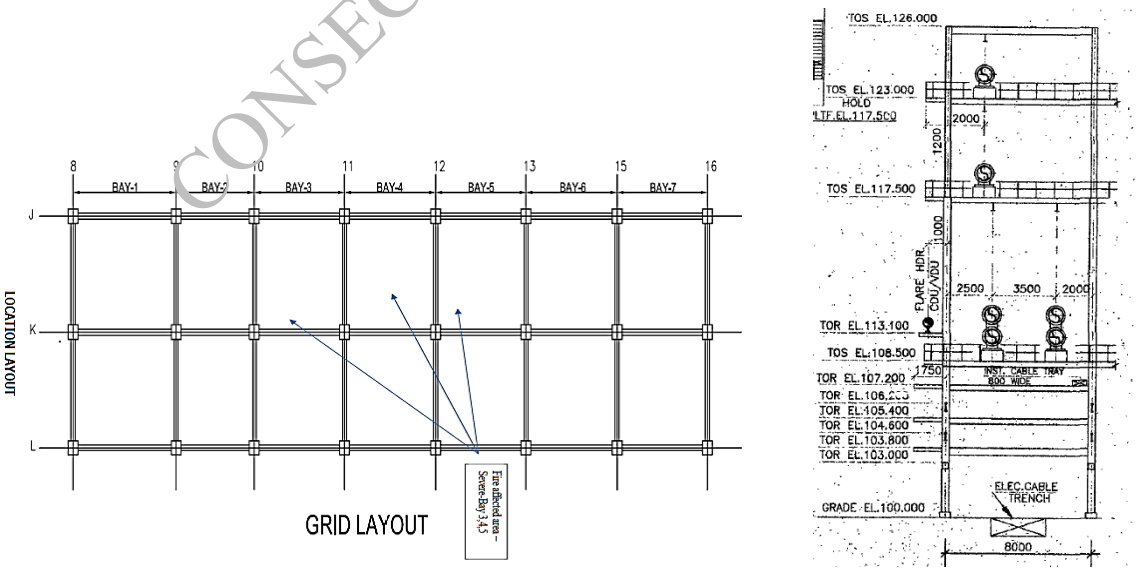

Figure 10. Grid layout and elevation of structure

Structural Steel members that are twisted, wrapped, and deflected from their original position are proposed to replace and re-erect in their original position in line with as-built drawings. However, Pipe-supporting steel beams which are apparently without any visible deformation wrapping or buckling have been tested

for strength/elongation indirectly through specimens taken from the web of beams to enquire about the change in material properties due to thermal stress of fire.
The test reports suggest suggestive of losing its strength for certain beams where UPV reading is ≤3 KM /Sec and the core test results of concrete were giving the values much below M20. RCC slab ceilings were exposed to fire and the floor's top is unlikely to be exposed to fire. The primary reason is that the frame behavior does not get compromised due to local loss of strength in the beam or column due to fire. Wherever insert plates are highly damaged due to fire and corrosion at the Site, it is proposed to adopt a collar system (refer to Fig. 11) by encasing columns to support steel beams for pipe supports.
The average carbonation depth of the industrial structure was measured as 30-40 mm and the potential level for percentage susceptibility of corrosion activity was found uncertain as per ASTM C876 therefore to prevent further corrosion activity in the existing structure, cathodic protection (CP) system and vapor corrosion inhibitor proposed.

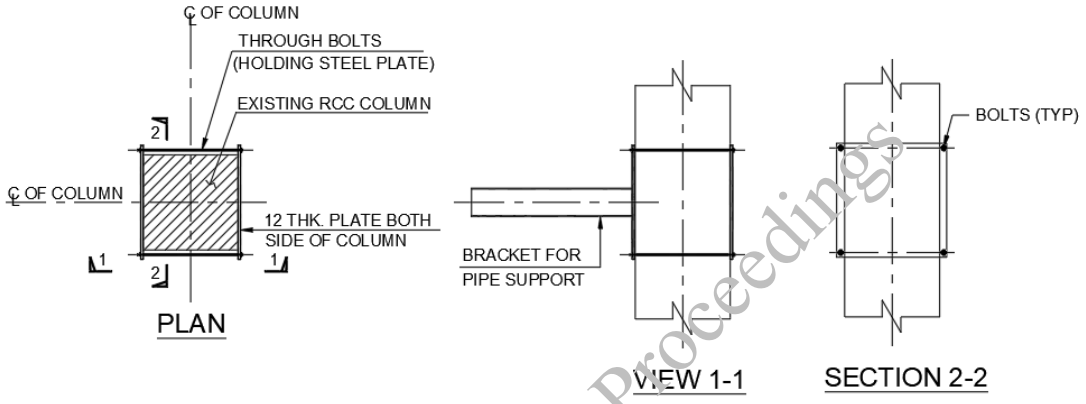

Figure 11. Collar System to provide bracket on RCC column

Additional support in the form of a hanger or stub taken from top or bottom RCC beams through steel plate collars, refer to Fig. 15. Wherever slab bottom rebar is already exposed due to corrosion and subsequent exposure to fire. It is advised to provide Structural steel beams below slabs with collars at ends in addition to retrofitting by restoring the damaged concrete in line with Fig. 14.

5. Structural retrofitting performed before Plant Start-up / Commissioning

As the results do not support desired concrete strength in primary frame members, it is suggested an enhanced Structural resisting system of columns with corner angles and laced/battened beams with additional plates with top and bottom. The other reason is that Structural steel being a highly elastic member will exhibit stresses through deformation, which will be visible and will give a warning before sudden shear or flexural failure of concrete.
Based on the findings and as per the codal provision and standard practices, the following were recommended for the rehabilitation of the industrial structure. The proposed retrofitting is in addition to the repair works pertaining to the restoration of the damaged concrete and corroded reinforcement bars in columns, beams, and slabs. Immediate measures are as follows which are required before the start-up of the plant. Refer to Fig. 10 for columns and beams locatio

5.1 Columns

Table 1. Grid location

Sl. no.	Grid location	Height (Elevation)	Retrofitting scheme
1	L 10’	100.000 (grade) to 117.500	4 corner angles to be provided along with batten plates
2	J 12’ & J 13’	100.000 (grade) to 108.500	
3	K 12’ & K 13’	100.000 (grade) to 108.500	
4	L 12’ & L 13’	100.000 (grade) to 108.500	
5	K 12’ & K 13’	108.500 to 117.500	

Refer Fig. 12 for the retrofitting scheme

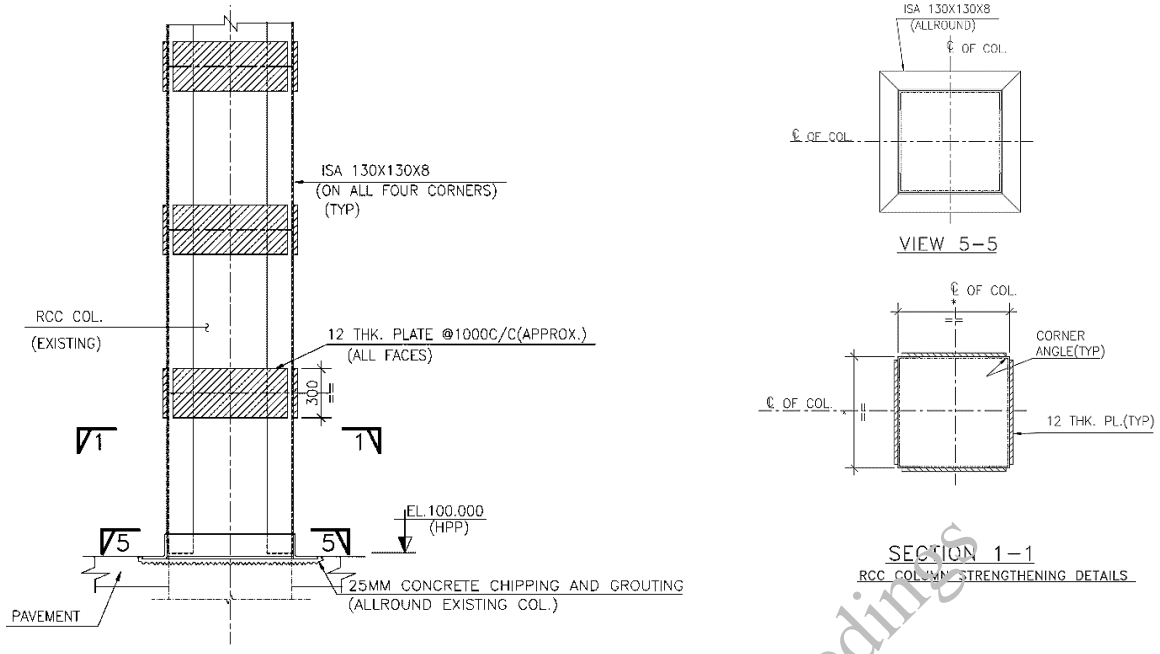

Figure 12. Retrofitting scheme for columns

5.2 Beams

- J to K & K to L – On grid 12’ at elevation 108.500
- J to K & K to L – On grid 13’ at elevation 108.500

25 Thk. Plate at beam soffit (B1) and 25 Thk. Plates at intervals at the top of the beam (T1) are to be provided, the plates B1 and T1 shall be connected through bolts/collars of flats, refer to Fig. 13.

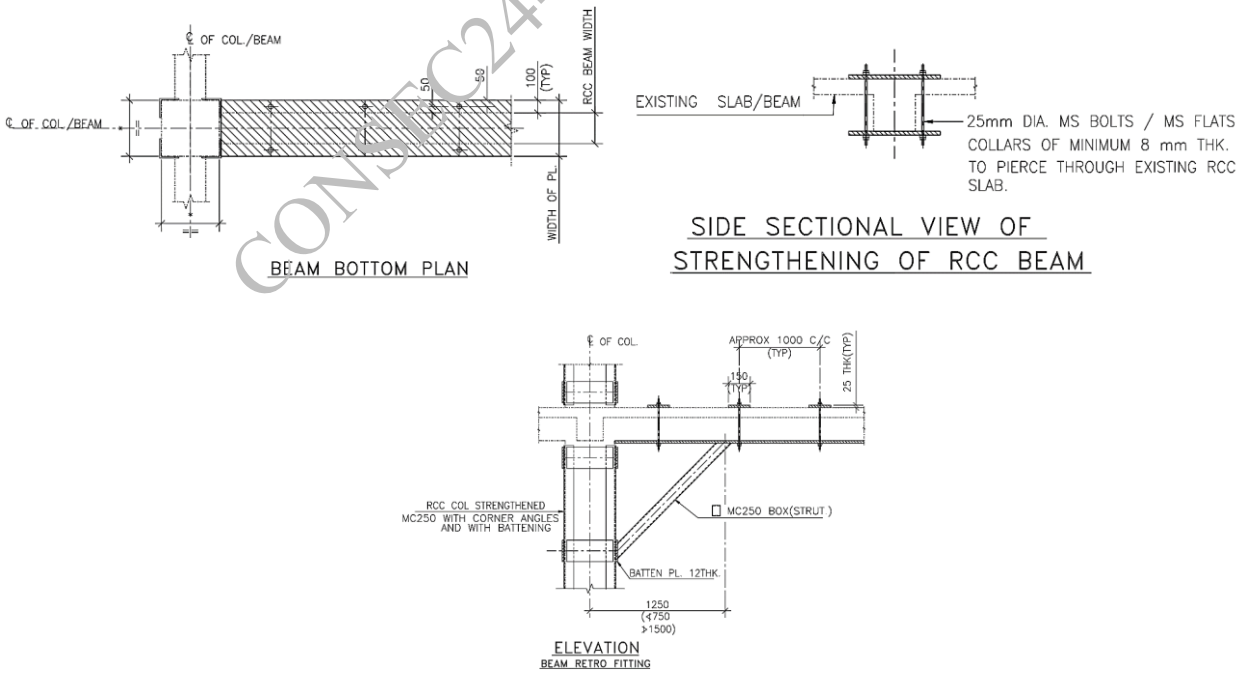

Figure 13. Retrofitting scheme for beam

5.3 Intermediate prop supports as an immediate measure

Provide prop supports at the following locations between elevations 100.000 & 108.500:

- On grid 11' between grid K& L
- On grid 12' between J & K AND K & L
- On grid 13' between J & K AND K & L

Prop support of 2 ISMC 400 (400 mm apart), connected with batten plates (350x350x8 thk.) @ 750 c/c is to be provided, or 16" CS pipe of thickness minimum 10 mm to be introduced.
However, it may be noted that the strengthening of beams with additional plates at the beam top and bottom as per Fig. 13 shall be taken up.

5.4 Slabs

Since the outcome of the pull-out test was not satisfactory therefore additional Structural steel beams at the slab bottom are to be provided as per Fig. 14.
However, for start-up retrofitting between grids 10' to 13' shall be taken up at EL. 108.500, 117.500 & for grids 12'& 13' at EL. 123.000. Refer to Fig. 14 for implementation of the retrofitting scheme.

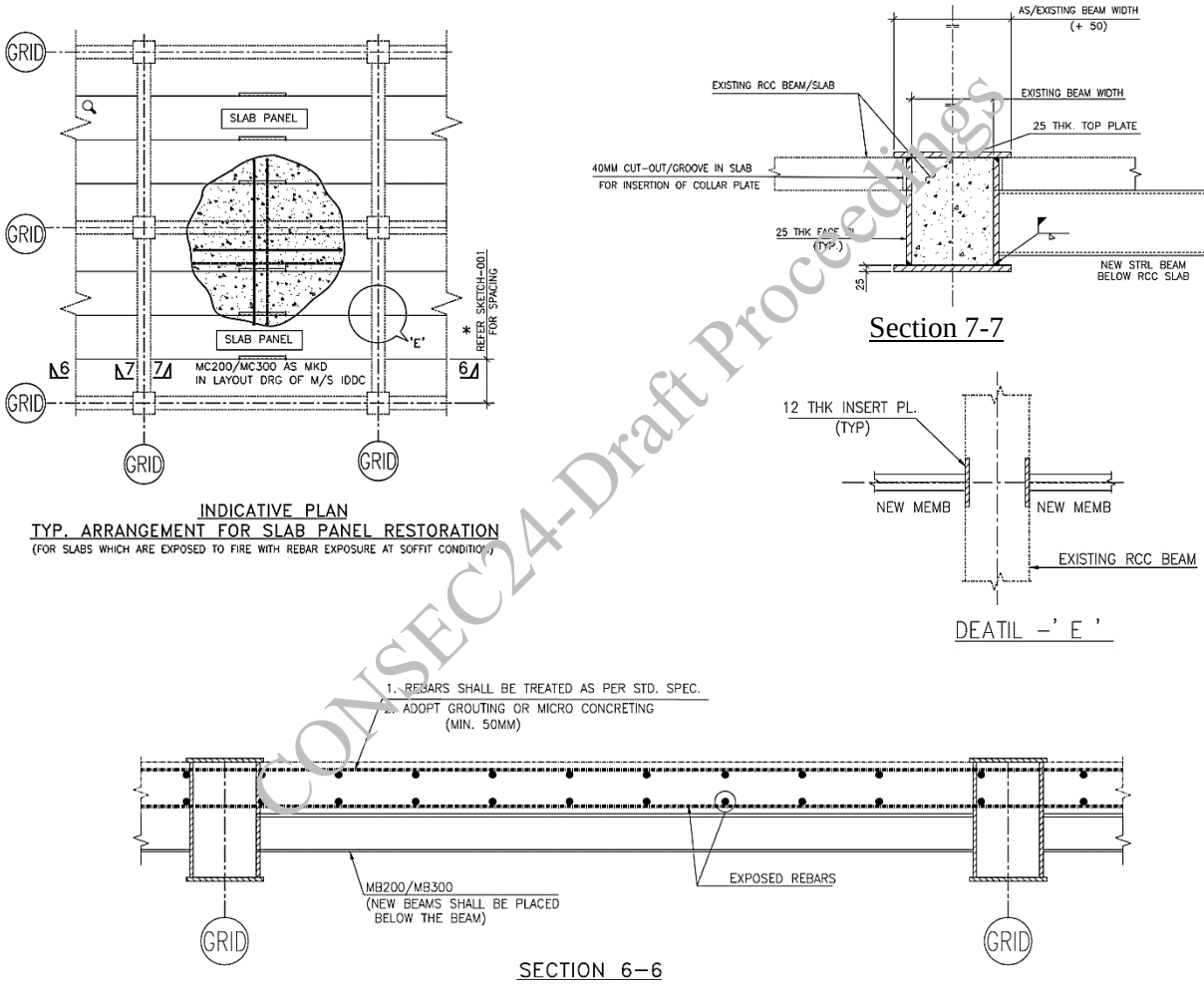

Figure 14: Retrofitting scheme for slabs

5.5 Pipe Supports

Restoration of pipe supports is to be carried out by using a collar system. Additional Stubs or hangers are to be provided for redundancy in the supporting system as per Fig. 15.
Also, it is advised that all the pipe support beams and their connections shall be taken before start-up.

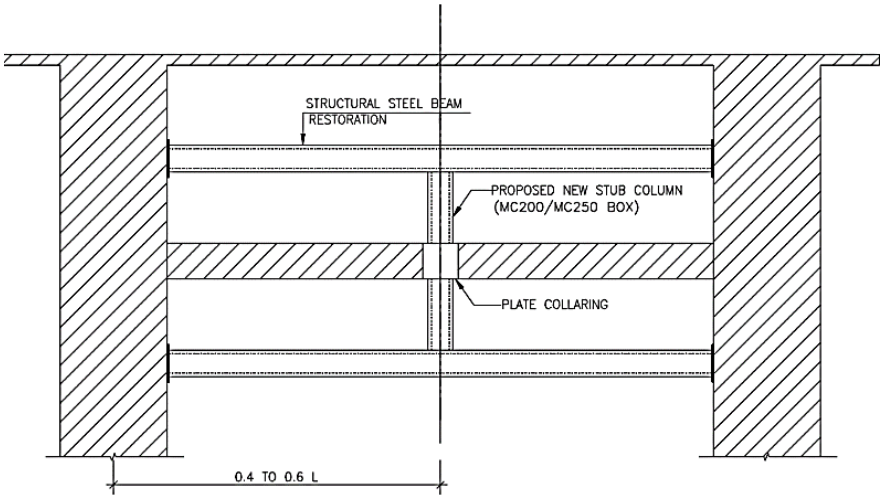

Figure 15. Beams retrofitting for pipe supports

6. Conclusions

Structural repair, retrofitting, and rehabilitation activities as mentioned above were successfully implemented at the project site. At present the industrial structure is in operational condition.
Also, it is advised that the Structure needs to undergo visual inspection every six months and compulsory NDT tests after 3 years to examine the Structural fitness.

Acknowledgments

I sincerely thank my head of the department Mr. Anurag Sinha for his continuous support, guidance, and valuable suggestions in the preparation of this paper. I also thank CONSEC24 for providing this great opportunity.

References

BS EN 1504,
IS 516,
IS 13311

Post Fire Performance of Concrete-Filled Steel Tubular Stub Column Under Axial Compression

Preeti[1,2] and Prasanta Kar[2*]

[1] AcSIR, CSIR-CBRI, Roorkee, India
Email: preeti.cbri21a@acsir.res.in
[2] CSIR-CBRI, Roorkee, India
Email: prasantakar@cbri.res.in

[*]Corresponding author

ABSTRACT

Concrete Filled Steel Tubes (CFSTs) are one of the popular composite structural systems used in civil engineering applications in various countries due to their excellent load-carrying capacity, high strength, ductility and durability. It has been used in various structural engineering applications like high-rise buildings, towers, bridges, etc. In this paper, a study has been presented on square Concrete-Filled Steel Tube (CFST) stub column under axial compression after exposure to high temperature. The Specimens were tested, under ambient temperature condition and also for post fire exposure condition. The stub column was exposed to a maximum temperature of 800˚C. The load deformation and stress- strain curves have been recorded. A significant drop in the peak load values of the specimen was observed after exposure to fire. The residual strength of the stub column specimen and the failure patterns also presented in the study. Also, the test results were compared with different codal provisions.

KEYWORDS: *CFST, Fire performance, axial compression, Residual strength.*

1. Introduction

Concrete-Filled Steel tube (CFST) columns, having outer steel encasing and filled with core concrete are widely used in the construction of high-rise buildings, bridges, etc. It has a higher load-carrying capacity (Liew et al., 2016), energy absorption (Ekmekyapar, 2016), ductility (L. H. Han et al., 2014), fire resistance and stiffness(Zhou et al., 2005) over steel tubes. Due to their improved performance in construction practices, CFST is becoming popular in construction. Large numbers of research have been carried out in the past regarding the behavior of the CFST columns (Ekmekyapar, 2016; Evirgen et al., 2014; Thai et al., 2019 , etc) under axial compression.

Research has also been done in the past on behaviour of CFST under post fire loading condition ((L.-H. Han et al., 2003; L. Han et al., 2013; L. H. Han et al., 2003; Rodrigues & Laím, 2017; Xiong & Liew, 2021; Yin et al., 2006). However, limited research has been reported on the systematic study of post–fire behavior of CFST columns under axial compression verified from the codal provision.

In the current study, the CFST column has been studied after exposure to temperature and compared with the codal values EN-1994-1-1(*Eurocode 4, BS EN 1994-1-1:2004*), ANSI/AISC 360-16 (AISC, Chicago. IL, 2005), AIJ (Architectural Institute of Japan; 1997) and AS/NZS 5100 (AS 5100.6-2004, Bridge design Part 6) available for the calculation of residual capacity.

2. Experimental work

2.1 Materials

2.1.1 Concrete

The Portland pozzolana cement was used for the casting of the specimens. The cement was free from lumps and any moisture content. The fine aggregate used in the concrete mix was zone II. The size of the fine aggregate was taken in the range of 4.75 mm to 150 microns. The coarse aggregate used in the concrete mix was taken in two proportions. First, the coarse aggregate of the size ranged from 20 mm to 10 mm and the other was taken in the range of 10 mm to 4.75 mm. Both the range of the sizes was taken in 1:1 proportion. The water-cement ratio of the mix was kept as 0.45. The cement, fine aggregate, coarse aggregate and water was mixed in the proportions of 1:1.67:2.94 to achieve the desired mix. In single batch of concrete, both specimens of CFST column and three concrete cubes were cast of standard size of (150×150×150) mm. The cast cubes were removed from the mold after 24 hours.Then the cubes were kept for curing for next 28 days. After the curing period was over the cubes were tested under the universal testing machine to get the compressive strength of the concrete. The properties of the constituent materials are listed below in Table 1. The average compressive strength of the cubes were 33.05 MPa.

Table 1. Concrete mix design details

Ingredients	Mix (kg/m$^{3)}$
Cement (PPC)	400
Sand (4.75 mm to 150 micron)	668.701
Coarse aggregate (MSA 10 and 20 in 1:1)	1177.268
Water (0.45 w/c ratio)	180

2.1.2 Steel

The thickness of the specimen was taken as 2.8 mm. To determine the material properties of the steel, a tensile coupon test was conducted. Three coupons were prepared from the hollow steel section, obtained from random location (except the welding region). The dimensions and the loading protocol were followed according to the ASTM standards(*ASTM, E8/E8M-15a)*. The dimension and coupon specimen are shown in Figure 1. The average modulus of elasticity, yield strength and the ultimate yield strength obtained from the tensile test are 2×10^5 MPa, 273.66 MPa, and 353.0 MPa respectively. The detailed results of the coupon specimen are given in Table 2. The stress strain graph obtained from the coupon test is shown in Figure 2.

Table 2. Mechanical Properties of steel

Coupon	E_a (GPa)	f_y (MPa)	f_u (MPa)
1	193.50	280.49	352.10
2	202.52	268.48	354.46
3	202.11	272.01	353.93
Mean	199.37	273.66	353.50
SD	5.09	6.17	1.24
COV	0.0255	0.0225	0.0035

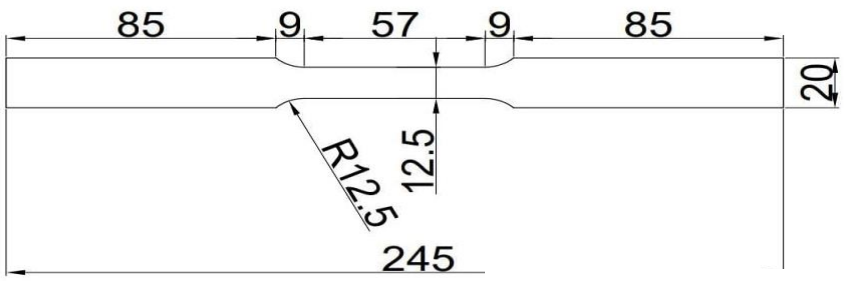

All dimensions are in mm

(a)

(b)

(c)

Figure 1. (a) Dimensions of coupon specimen, (b) Coupon specimen before tensile test, (c) Coupon specimen after tensile test

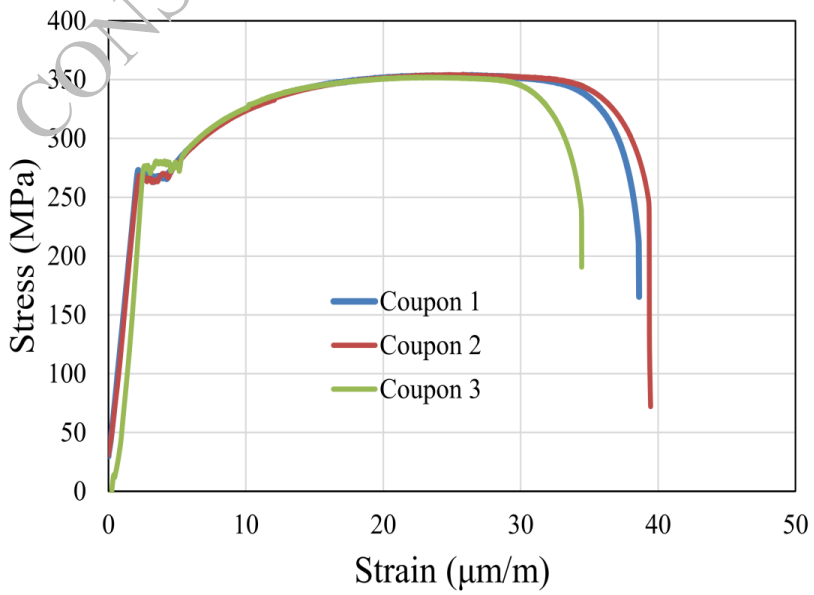

Figure 2. Stress- strain graph obtained from tensile test

2.2 Instrumentation, Test setup and Procedure

The experimental work was carried out to study the influence of post-fire behavior on the CFST stub columns. The main objective was to find the axial load-carrying capacity of the stub column under post-fire conditions after an exposure from 20℃ to 800˚C. Two specimens were cast. The specimens were of 150×150 mm cross-section and 450 mm height. Using the material properties obtained from the tests. One was tested for ambient temperature conditions and the other was kept in the electric furnace for the temperature starting from 20˚C to 800˚C following the fire curve shown in Figure 3. The specimen was tested under a 5000 kN capacity Compression Testing Machine. The specimen labelled C-1 and CF-2 were the CFST stub columns tested under ambient temperature and post-fire condition, respectively. Prior to the testing, the top surface of the CFST columns were ground smooth and flat to ensure that the load is applied uniformly to steel and concrete (L. H. Han et al., 2002). Strain gauges were used at the center to measure the axial strain, and Linear Variable Displacement Transducer (LVDT) to measure the axial displacement. The load was applied and maintained at a constant rate throughout the experiment.

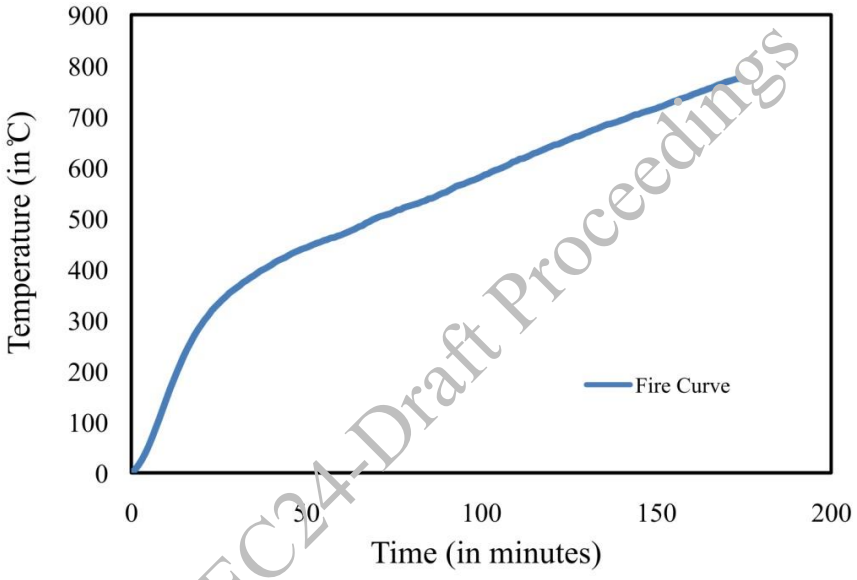

Figure 3. Fire Curve

3. Results

The results obtained from the stub columns test are provided in Tables 2 and 3. The test results were compared with different codal provisions. For the stub column under ambient conditions, the applicability was compared with AS5100 (AS 5100.6-2004, Bridge design Part 6), BS5400 (*BS5400-5, British Standards Institution; 2005*), DBJ13-5(*DBJ/T13-51-2010*), and EC4 (*Eurocode 4, BS EN 1994-1-1:2004*), and is tabulated in Table 2. The test results obtained from the post-fire specimen were compared with formulae given in the codes AS5100 (AS 5100.6-2004, Bridge design Part 6), AISC 360-16 (AISC, Chicago. IL, 2005), AIJ (Architectural Institute of Japan; 1997) and EC4 (*Eurocode 4, BS EN 1994-1-1:2004*), and the test results are provided in Table 3. The residual strength capacity of CFST columns may be utilized to assess the potential damage caused by fire. The formula used to caluculate the residual strength index of the experimental test conducted is given in equation (1).

Table 2. Stub Column Test under ambient temperature condition

Specimen	N_{ue} (kN)	AS5100		BS5400		DBJ13-51		EC4	
		N_{uc} (kN)	N_{uc}/N_{ue}	N_{uc} (kN)	N_{uc}/N_{ue}	N_{uc} (kN)	N_{uc}/N_{ue}	N_{uc} (kN)	N_{uc}/N_{ue}
C-1	1319	894.60	0.678	795.02	0.603	1110.03	0.8415	994.00	0.754

Table 3. Stub Column Test under post fire condition

Specimen	$N_{u(T)}$ (kN)	AS/NZS 5100		ANSI/AISC 360-16		AIJ		EN-1994-1-1	
		$N_{uc(T)}$ (kN)	$N_{uc(T)}/N_{u(T)}$	$N_{uc(T)}$ (kN)	$N_{uc(T)}/N_u$	$N_{uc(T)}$ (kN)	$N_{uc(T)}/N_{u(T)}$	N_{uc} (kN)	N_{uc}/N_{ue}
CF-2	964	543.276	0.563	677.58	0.703	505.78	0.524	410.77	0.426

After exposure to fire, the specimen $N_{ue}(t)$= 964 kN

$$\text{Residual strength (RSI)} = N_{ue}(t)/ N_{ue} \quad (1)$$

$$N_{ue}(t)/ N_{ue} = 0.731 \quad (2)$$

where, N_{ue} (t) is the residual strength corresponding to fire duration time (t) of the CFST column and N_u is the ultimate strength of the CFST under ambient temperature condition.

3.1 Load Vs Deflection Curve

The effect of post fire behaviour of the column is shown in Figure 4. The axial deformation of the specimen was observed by the linear transducers. For 2.8 mm thickness, the ultimate load carrying capacity of the column is 1319 kN and that of the column under ambient condition is 964 kN respectively. The strength of the square CFST column under fire is reduced by 26.91% compared to the CFST column under ambient condition.

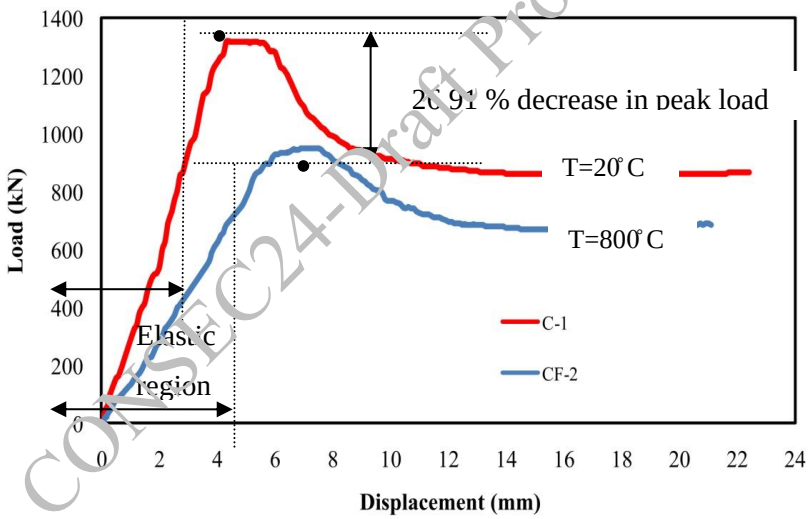

Figure 4. Load vs Deflection curve

3.2 Load Vs Strain curve

The test continued to fail in a ductile manner. The strain reading was measured using the strain gauge placed at the mid length of the column. The plot between the axial load vs strain is shown in Figure 5. The load increases linearly with elastic strain. Both the specimens shows linearly increasing values until they reach the peak load. On reaching peak load, the load- strain curve showed that it entered the yield stage and the slope began to decrease. The C-1 specimen shows a sharper drop in the decending part of the graph and CF-1 specimen shows a gradual decrease. The gradual decrease of curve of the load-strain curve shows the ductile behaviour of the CFST column (Zhang et al., 2023). It is observed that the CF-2 specimen shows more ductile nature than the C-1 specimen.

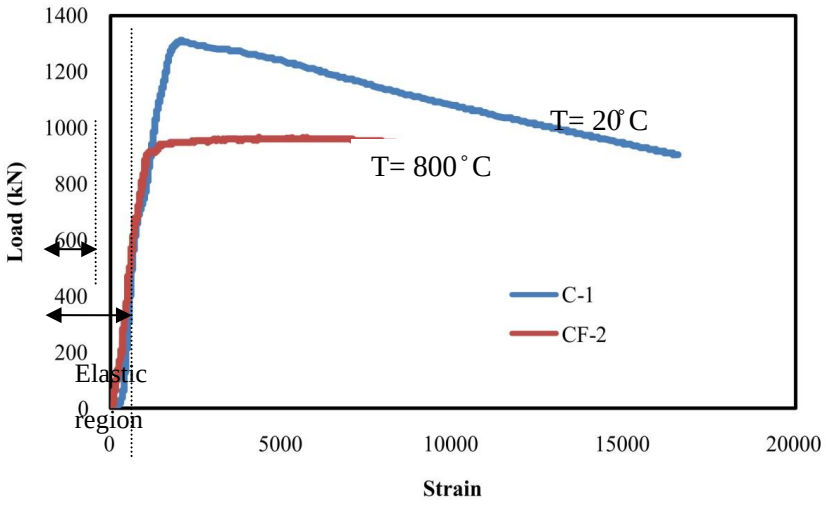

Figure 5. Load vs Stain curve

3.3 Failure modes

Figure 6 (a) shows the specimen under ambient temperature conditions before testing. Figures 6 (b) and (c) show the specimen after failure under ambient temperature and post fire respectively. Similar failure pattern were observed in both the specimen. The initaiation of the buckling at the middle part of CFST followed by the other part in the specimen was observed in both the specimen. It was observed that the failure pattern of the specimen remain unchanged even after exposure to fire but have a significant loss in the ultimate load carrying capacity of the column.

(a) CFST Stub Column Specimen **(b) Failure under ambient condition** **(c) Failure under post fire loading condition**

Figure 6. Specimen before and after failure

Conclusions

Based on the experimental results obtained in the current study, the following conclusions can be drawn –

- A significant decrease of 26.91 % was observed in the strength of the stub column after exposure to fire upto 800˚C.

- The stiffness of the curve of the fire specimen was also reduced compared to the specimen under ambient temperature.
- Similar failure pattern (i.e., local buckling) was observed at the same location for both the tested stub columns. It shows that the failure pattern is not affected by the temperature of the exposure.
- The test results were compared to the codes. It was seen that Eurocode 4 and Australian code (AS5100) predicted conservative results for the CFST columns under ambient temperature conditions. And also Eurocode 4, Australian code(AS5100) and Japenese codes (AIJ) provide conservative results for calculating the residual strength of concrete. An accurate prediction model needs to be developed in order to provide accurate results in case of post fire perforamance.

References

AIJ (1997). "Recommendations for design and construction of concrete filled steel tubular structures", Architectural Institute of Japan

AISC (2005), Resistance Factor Design Specification for Structural Steel Buildings, AISC, Chicago. IL,

ASTM (2005), E8/E8M-15a, Standard Test Methods for Tension Testing of Metallic Materials,ASTM International, West Conshohocken, PA

BS5400-5 (2005), Steel, concrete and composite bridges, Part 5, Code of practice for design of composite bridges, London: British Standards Institution

DBJ/T13-51-2010 (2010),Technical Specifications for Concrete-Filled Steel Tubular Struc- tures (Revised Version. Fuzhou, China: The Housing and Urban–Rural Development Department of Fujian Province [in Chinese]

Ekmekyapar, T. (2016). "Experimental performance of concrete fi lled welded steel tube columns". *Journal of Constructional Steel Research*, 117, 175–184.

Eurocode 4, BS EN 1994-1-1:2004: Eurocode 4. Design of composite steel and concrete structures. Part 1.1, General rules and Rules for Buildings

Evirgen, B., Tuncan, A., & Taskin, K. (2014). Structural behavior of concrete filled steel tubular sections (CFT/CFSt) under axial compression. *Thin-Walled Structures*, 80(July), 46–56.

Han, L.-H., Zhao, X.-L., Yang, Y.-F., & Feng, J.-B. (2003). Experimental Study and Calculation of Fire Resistance of Concrete-Filled Hollow Steel Columns. *Journal of Structural Engineering*, 129(3), 346–356.

Han, L., Chen, F., Liao, F., Tao, Z., & Uy, B. (2013). Fire performance of concrete filled stainless steel tubular columns. *ENGINEERING STRUCTURES*, 56, 165–181.

Han, L. H., Li, W., & Bjorhovde, R. (2014). Developments and advanced applications of concrete-filled steel tubular (CFST) structures: Members. *Journal of Constructional Steel Research*, 100, 211–228.

Han, L. H., Yang, Y. F., & Xu, L. (2003). An experimental study and calculation on the fire resistance of concrete-filled SHS and RHS columns. *Journal of Constructional Steel Research*, 59(4), 427–452.

Han, L. H., Yang, Y. F., Yang, H., & Huo, J. S. (2002). Residual strength of concrete-filled RHS columns after exposure to the ISO-834 standard fire. Thin-Walled Structures, 40(12), 991–1012.

Liew, J. Y. R., Xiong, M., & Xiong, D. (2016). Design of Concrete Filled Tubular Beam-columns with High Strength Steel and Concrete. Structures, 8, 213–226.

Rodrigues, J. P. C., & Laím, L. (2017). Fire resistance of restrained composite columns made of concrete filled hollow sections. *Journal of Constructional Steel Research*, 133, 65–76.

Thai, S., Thai, H. T., Uy, B., & Ngo, T. (2019). Concrete-filled steel tubular columns: Test database, design and calibration. *Journal of Constructional Steel Research*, 157, 161–181.

Xiong, M. X., & Liew, J. Y. R. (2021). Fire resistance of high-strength steel tubes infilled with ultra-high-strength concrete under compression. *Journal of Constructional Steel Research*, 176, 106410.

Yin, J., Zha, X. X., & Li, L. Y. (2006). Fire resistance of axially loaded concrete filled steel tube columns. *Journal of Constructional Steel Research*, 62(7), 723–729.

Zhang, S., Miao, K., Wei, Y., Xu, X., Luo, B., & Shi, W. (2023). Experimental and Theoretical Study of Concrete-Filled Steel Tube Columns Strengthened by FRP/Steel Strips Under Axial Compression. *International Journal of Concrete Structures and Materials*, 17(1), 1–22.

Zhou, X. L., Han, L. H., & Lu, H. (2005). Concrete Filled Tubular Members and Connections.

Mechanical Behavior and Strengthening of Reinforced Concrete with 3D Geosynthetic Cementitious Composite Mats

Sakthivel T.[1*] and Vishnu Rooban M[2].

[1] *PSG Institute of Technology and Applied Research, Coimbatore, India*
Email: thanga.sakthivel@gmail.com
[2 1] *PSG Institute of Technology and Applied Research, Coimbatore, India*
Email: 22s08@psgitech.ac.in

[*]Corresponding author

ABSTRACT

Geosynthetic Cementitious Composite Mats (GCCMs) have emerged as a promising alternative to conventional repairing technique in building construction. Past research indicates that GCCMs offers substantial load-bearing capacity, corrosion resistance, and durability. Unlike traditional method of repairing the concrete structure, GCCMs involve pre-filling cement-based powder into the 3D fabric, allowing easy shaping and immediate solidification upon water application, making it suitable for a wide range of applications. The 3D fabric orientation enhances mechanical properties, and GCCMs can be deployed with minimal material loss even in active watercourses. The present study shows that GCCMs offering superior tensile strength, especially in the weft direction, and achieving compressive strength of 40 MPa in two days. The material's mechanical properties are directionally dependent, with enhanced flexural strength observed when oriented perpendicularly. Overall, GCCMs present a sustainable and efficient solution to traditional construction challenges, with ongoing research aimed at further enhancing their capabilities and expanding their applications.

KEYWORDS*: Geosynthetic Cementitious Composite Mats, Strength, Strengthening Technique*

1. Introduction

In recent years, there has been a significant increase in research on Textile Reinforced Cementitious Composites (TRCC) as a alternative building materials, offering a replacement to conventional reinforced concrete systems. TRCC has exhibited remarkable characteristics, such as substantial load-bearing capability, resistance to corrosion, and greater durability (Daskiran et al., 2020; Rawat et. al., 2022). The textile reinforcements is be classified into two main categories: two-dimensional (2D) fabric and three-dimensional (3D) fabric. 3D fabric is particularly notable for its high energy absorption efficiency and its ability to resist delamination. The use of spacer yarns in the thickness direction enhances the overall structural stability (Haik et al., 2017).Geosynthetic Cementitious Composite Mats (GCCMs) or Concrete Canvas is a 3D fabric reinforced cementitious material is especially notable due to its high potential as an alternative product in infrastructural projects. Unlike conventional TRCC which uses slurry-filling technology, GCCM involves the pre-filling of a cement mortar into the spacer layer of the 3D fabric as shown in Figure 1 (a). Moreover, GCCM may be easily shaped and distorted to fit a variety of working surfaces, such as canvas, and it can be immediately sprayed with water to solidify and mould. As a building or component is being built, it may tightly cover any surface without the need of mixing tools, similar to soft fabric. The applications of this material vary from inflatable tents, slope protection, strengthening of existing elements. The characteristics such as the cement matrix, type of fibre, and geometric pattern of the fabric, directly influenced the mechanical strength and volume stability of GCCMs (Liu et al., 2023; Eller et al., 2023; Xiang et al., 2023). According to (Haik et al., 2017) tensile and flexural parameters, were increased significantly in reinforced CC samples. According to Concrete Canvas Ltd.'s CO_2 footprint study (2022), one square metre of GCCM used for channel lining contains 45% of the embodied carbon of an equal square metre of traditional poured concrete and two 17 ton ready-mix concrete trucks may be simply

replaced by one pallet of GCCM. It is furthermore offered as man-portable, pre-cut batched rolls. This significantly minimise the number of vehicle transfers while making it much easier to carry and use. The 3D matrix traps the speciality cementitious material, preventing material loss during installation. As a solution, GCCM may be laid and hydrated within active watercourses with a low loss of fines of roughly 3% as opposed to the typical of 10–15% seen when utilising specialized underwater concretes.

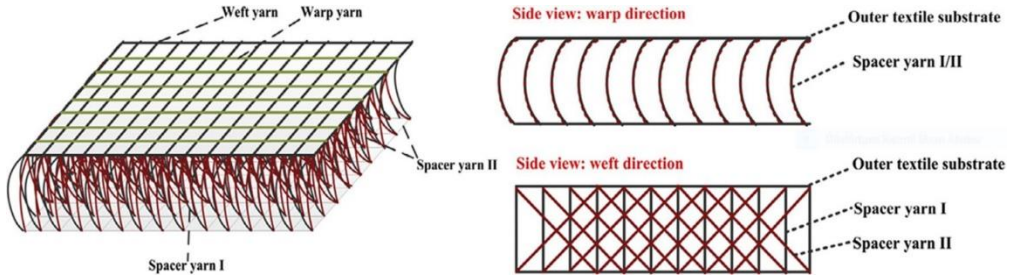

Figure 1. (a) A typical 3D spacer fabric (Han et al., 2014)

2. Experimental Work and Test Methodology

Tensile strength tests were conducted on concrete fabric with and without a cement matrix, in both parallel and perpendicular directions, following ASTM D-5035. The uni-axial tensile strength was evaluated in different alignments (X and Y) with 30 x 120 mm size as shown in figure in Fig. 2.Three-point tests was adopted to determine the flexural behaviour of GCCM and the test was performed in accordance to ASTM D8058-19 with dimensions of 50 ×125 mm (X and Y directions).The displacement rate is fixed as 0.5 mm/min, and the bending load is kept within the load capacity range. To test the compressive strength, 300 x 300 mm square specimens were used in accordance with the ASTM D8329 standards. The specimens were loaded for ultimate load. The basic materials properties has been provided in Table 1.

Table 1. Properties of Geosynthetic Cementitious Composite Mats.

Thickness (mm)	Width of the roll (m)	Density (kg/m^3)	Density (kg/m^2)
8	1.10	1500±50	10

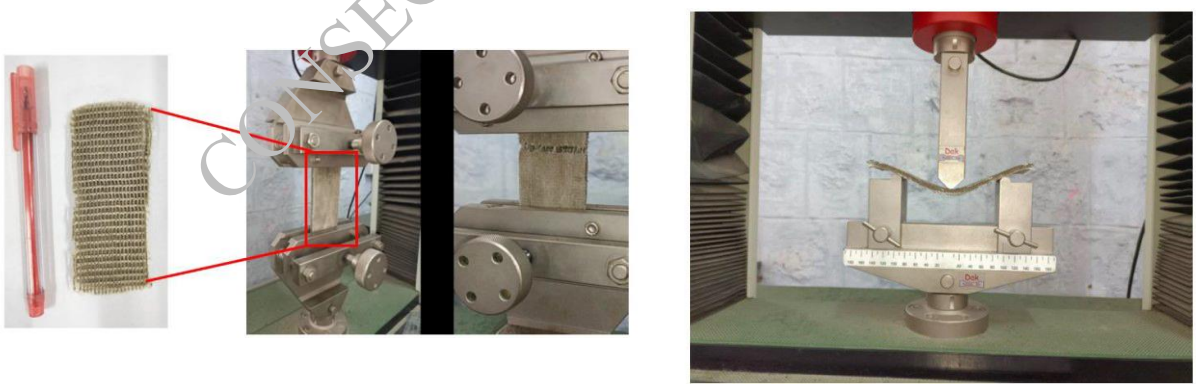

Figure 2 Geosynthetic Cementitious Composite Mats for tensile and flexural strength

Figure 3 depicts the tensile properties of 3D textiles in terms of warp and weft orientations. The fabric stress-strain curves show a significant strain under the preload at the start of the tensile test due to deformation in the GCCM fibre and elongation. The width of sample in the transverse (perpendicular) direction to the tensile axis decreased as the expanding process progressed and withstood tensile tension, and the force. The findings confirmed that the tensile strength is differed due to the materials' different structures. It illustrates the tensile performance of the composites with cement matrix. The parts were stretched at the start of the test, and afterward, the top layer of 3D fabric was not torn, but the bottom layer,

along with the layer impregnated with the adhesive and the 3D fabric spacer yarns, was torn; this behaviour was observed for all specimens irrespective of the orientation of the fabric

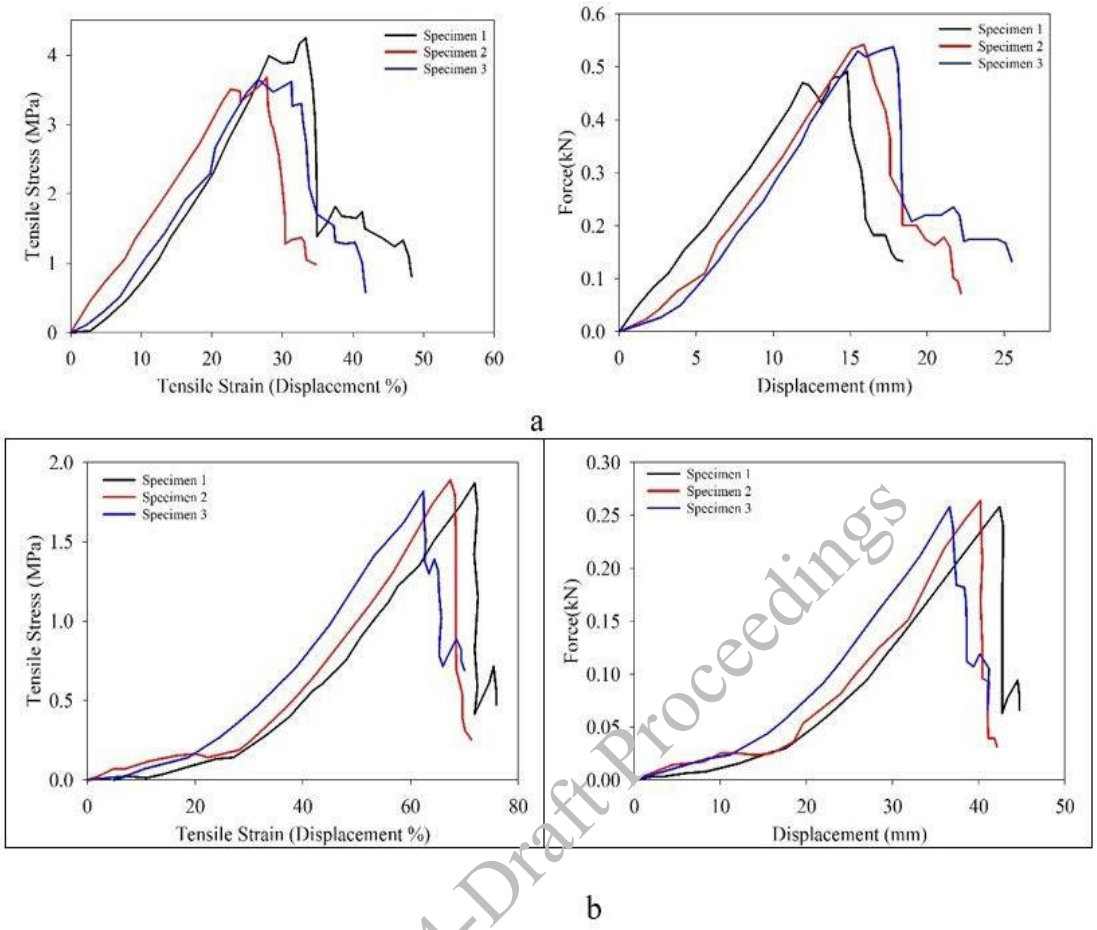

Figure 3 (a). Stress Vs Strain and Force Vs Displacement of GCCM without cement matrix in parallel to the direction of weaving. (b). Stress Vs Strain and Force Vs Displacement of GCCM without cement matrix in perpendicular to the direction of weaving.

3. Conclusions

Based on the tested conducted on the Geosynthetic Cementitious Composite Mats, the following conclusion has been derived.

- The study finding highlight that the Geosynthetic Cementitious Composite Mats are exceptionally well-suited for providing support under static stresses, effectively protecting the slope of any structural member. The material demonstrates the ability to be loaded to achieve optimal form, and subsequent application of Geosynthetic Cementitious Composite Mats, helps drive the material down to the supportive protection layer.
- In terms of mechanical properties, it was found that GCCMs exhibit superior tensile strength and lower strain in the weft direction compared to the warp direction. This observation held true both with and without the presence of a cement matrix, indicating a consistent pattern of performance.
- The Young's modulus in the parallel direction was found to be approximately 10% higher than that in the perpendicular direction during testing. This distinction in modulus values was consistently observed in both patterns, emphasizing the directional dependence of the material's mechanical behaviour.
- Notably, when the Geosynthetic Cementitious Composite Mats was oriented perpendicularly, it enhanced flexural strength. The study showed a 25% increase in strength compared to the parallel direction, highlighting the influence of orientation on the flexural performance.

- The compressive strength of GCCMs was found to be around 40 MPa, and notably, this strength was achieved at the early age of 2 days. This promising result suggests that it holds considerable potential for use in slope protection, providing early and robust support for various infrastructure engineering applications.

References

Daskiran, M.M., Daskiran, E.G., M. Gencoglu, M., (2020) "Mechanical and durability performance of textile reinforced cementitious composite panels", *Construction and Building Materials*. 264, 120224, https://doi.org/10.1016/j.conbuildmat.2020.120224.

Rawat, P., Liu, S., Guo, S., Rahman, M.Z., Yang, T., Bai, X., Yao, Y., Mobasher, B., Zhu, D., (2022) "A state-of-the-art review on mechanical performance characterization and modelling of high-performance textile reinforced concretes", *Construction and Building Materials* 347, 128521, https://doi.org/10.1016/j.conbuildmat.2022.128521.

Haik, R., Sasi, E.A., Peled, A., (2017) Influence of three-dimensional (3D) fabric orientation on flexural properties of cement-based composites. *Cement and Concrete Composites*, 2017, 80, 1–9.

Liu, S., Ma, X., Ma, Y., Chen, Z., Dong, Z., Ma, P., (2023). "Review on the design and application of concrete canvas reinforced with spacer fabric", *Journal of Engineered Fibers and Fabrics*. 18, 15589250231152591, https://doi.org/10.1177/15589250231152591.

Xiang, Z., Wang, J., Niu, J., Zhou, J., Wang, J., (2023). "Experimental study on the mechanical properties of Concrete Canvas and CFRP jointly confined circular concrete columns under axial compression", *Construction and Building Materials*. 385, 130800, https://doi. org/10.1016/j.conbuildmat.2023.130800

Eller, B., Rad, M.M., Fekete, I., Szalai, S., Harrach, D., Baranyai, G., Kuhlen, D.,Sysyn, M., Fischer, S.,(2023). :Examination of Concrete Canvas under quasi-realistic loading by computed tomography:, *Infrastructures*. 8 (2) 23, https://doi.org/ 10.3390/infrastructures8020023.

ASTM D5035-11(2019) Standard Test Method for Breaking Force and Elongation of Textile Fabrics (Strip Method)

ASTM D8058-19 Standard Test Method for Determining the Flexural Strength of a Geosynthetic Cementitious Composite Mat (GCCM) Using the Three-Point Bending Test

ASTM D8329-21 'Standard Test Method for Determination of Water/Cementitious Materials Ratio for GCCMs and Measurement of the Compressive Strength of the Cementitious Material Contained Within

Axial Buckling Resistance of Concrete-Filled Cold-Formed Steel Columns– A New Strengthening Approach

Chanchal Sonkar[1*], Mickey Mecon Dalbehera[2], Ajay Chourasia[3] and Ashish Kapoor[4]

[1] Senior Scientist, CSIR-Central Building Research Institute, India
Email: chanchalsonkar@cbri.res.in
[2] Principal Scientist, CSIR-Central Building Research Institute, India
Email: mickey@cbri.res.in
[3] Chief Scientist, CSIR-Central Building Research Institute, India
Email: ajayc@cbri.res.in
[4] Scientist, CSIR-Central Building Research Institute, India
Email: ashishkapoor@cbri.res.in

[*]Corresponding author

ABSTRACT

This paper discusses about the structural behavior of concrete-filled cold-formed steel columns (CFSTC) subjected to axial loading. These members perform better in terms of ultimate strength, stiffness, energy absorption capacity and earthquake-resistance. Better structural performances are due to the mutual interaction of the cold-formed steel built-up (CFSBU) tube and concrete section; the CFSTU tube provides confinement to the circumferential enlargement of concrete section while behaving as formwork whereas the concrete section prevents the CFSBU tube from buckling inward, relieving the local buckling effect. Nine specimens have been tested and the ultimate axial load-bearing capacity, load–deformation behavior, buckling interactions and failure pattern of CFSTC columns are discussed investigated in detail. Square built-up sections by joining four U-sections with dimensions of 140 mm (web), 50 mm (flange) using self-drilling screws have been conceptualized for making CFSTC specimens using 1.2 mm thick cold-formed steel galvanized sheet. Effect of parameters such as concrete grade and rate of loading are discussed in detail. Tests for mechanical properties of CFS and compressive strength of concrete cubes have also been conducted. A comparison will be carried out between experimentally obtained results and predicted values using EN 1994-1-1 formulations to assess its efficacy. CFSBU tube can be effectively utilized as novel techniques for strengthening deteriorated structures as it imparts confinement to the circumferential expansion of concrete section and increases its capacity and service life.

KEYWORDS*: Concrete-filled cold-formed steel columns (CFSTC), Ultimate strength, Buckling, Load–deformation, Concrete.*

1. Introduction

The composite concrete-filled cold-formed steel columns (CFSTC) are utilized in many different types of structures because of their superior axial capacity. Over the past few decades, extensive studies have been carried out on CFSTC's (Shanmugam and Lakshmi (2001), Uy et al. (2011), Wang et al. (2020), Tao et al., (2013), Rahnavard et al. (2022a)). The utilization of CFSTC in construction has a number of advantages such as higher speed of construction, lesser use of formwork (for casting of concrete), less wastage, higher strength-to-weight ratio etc. (Shanmugam and Lakshmi (2001), Uy et al. (2011)). The concrete section mitigates the premature local buckling of the cold-formed steel built-up (CFSBU) tubular section and the confinement imparted by the CFSBU tubes to the concrete augments the growth of the strength of the concrete section.

Consequently, these CFSTC columns offer better fire resistance together with enhanced strength and rigidity cost-effectively in an environmentally responsible way. Also, design methodologies described by various international codal provision (AS 5100.6 (2004), AS/NZS 2327 (2004), ANSI/AISC 360-05 (2005), DBJ/T 13-51 (2010), JGJ 138 (2016), EN 1994-1-1 (2004)) needs to be assessed for their accuracy in

predicting the axial load bearing capacity of CFSTC columns. Few of the previous studies on CFSTC sections are discussed:

Rahnavard et al. (2022a, 2022b) assessed the compressive performance of closed built-up CFS columns filled with concrete experimentally and numerically. Results were utilized to check the relevance of EN 1994-1-1 codal provision for the estimation of the CFSTC columns buckling resistance. Recommendations were given by the authors for evaluating the effective cross-sectional areas of Class 4 sections, by considering various parameters.

Chen et al. (2023) investigated 42 short CFSTC columns with fixed-end boundary conditions. The experimentally obtained axial strengths were utilized to verify the accuracy of ACI 318 (2014). The comparison showed that the ACI 318 provides inaccurate estimtions.

Teoh et al. (2023a) performed experimental investigation on 24 CFSTC columns filled with lightweight concrete subjected to compression. Cross-section and grade of concrete were the different parameters considered in the study. Obtained test results were adopted to verify the accuracy of design formulae's in various codal provisions (AS/NZS 2327 (2017), ANSI/AISC 360-16 (2016), EN 1994-1-1 (2004)). Teoh et al. (2023b) performed studies of the buckling performance of self-compacting lightweight concrete (LWSCC)-filled CFSTC columns. Sixteen filled columns and four hollow columns were tested considering different parameters such as member relative slenderness's ratios, concrete strengths and cross-section sizes.

In view of the above discussed research gaps and problems, detailed experimental investigations have been carried out on the axial behaviour of CFSTC section filled with different grades of concrete and varied screw spacing. The details of the performed study are discussed in detail in the section below.

2. Experimental Campaign

Nine full-scale experiments have been performed in the present study to investigate the buckling behaviour, load-deformation curve and ultimate strength of CFSTC sections. Subsequent section discusses about the taken up experimental investigation in this study.

2.1 Specimen details

Table 1 discusses about the tested specimen's details. Seven specimens have been tested to assess their performance under compression. The specimens were fabricated using four CFS U-sections assembled together using self-drilling screws to form closed square box sections. The thickness of the CFS U-sections was 1.2 mm. Fig. 1 shows the cross section and elevation of the typical CFSTC specimen, where a is the screw spacing (100 and 150mm).

2.2 Infilled-concrete details

Three standard concrete cubic (of 150 mm × 150 mm ×150 mm dimensions) tests were tested to obtain the material properties of concrete. The test on the concrete cubes was conducted as per IS 456 (2000) for concrete compression testing. Table 2 summarizes, mean concrete compressive strength.

2.3 Imperfection measurements

Geometric imperfection was also measured using the laser displacement-based test up shown in Fig. 2 (a and b) of the CFS C-sections used for fabricating the built-up box sections with different screw spacing which is later filled with concrete of various grades for specimen preparation.

Measured imperfections of the 5 typical CFS sections normalized to the base metal thickness has been reported in Table 3 which may be further adopted by researchers for numerical modelling of CFSTC sections.

Table 1. Specimen Configuration details

Test Number	Specimen	Sheathing details
1	CFSTC_1	CFS unfilled hollow section with 100mm screw spacing
2	CFSTC_2	CFS unfilled hollow section with 150mm screw spacing
3	CFSTC_3	CFSTC section with M40 concrete and 100 mm screw spacing
4	CFSTC_4	CFSTC section with M40 concrete and 150 mm screw spacing
5	CFSTC_5	CFSTC section with M30 concrete and 100 mm screw spacing
6	CFSTC_6	CFSTC section with M30 concrete and 150 mm screw spacing
7	CFSTC_7	CFSTC section with M20 concrete and 100 mm screw spacing
8	CFSTC_8	CFSTC section with M20 concrete and 150 mm screw spacing
9	CFSTC_9	CFSTC section with M20 concrete and 150 mm screw spacing without clamps

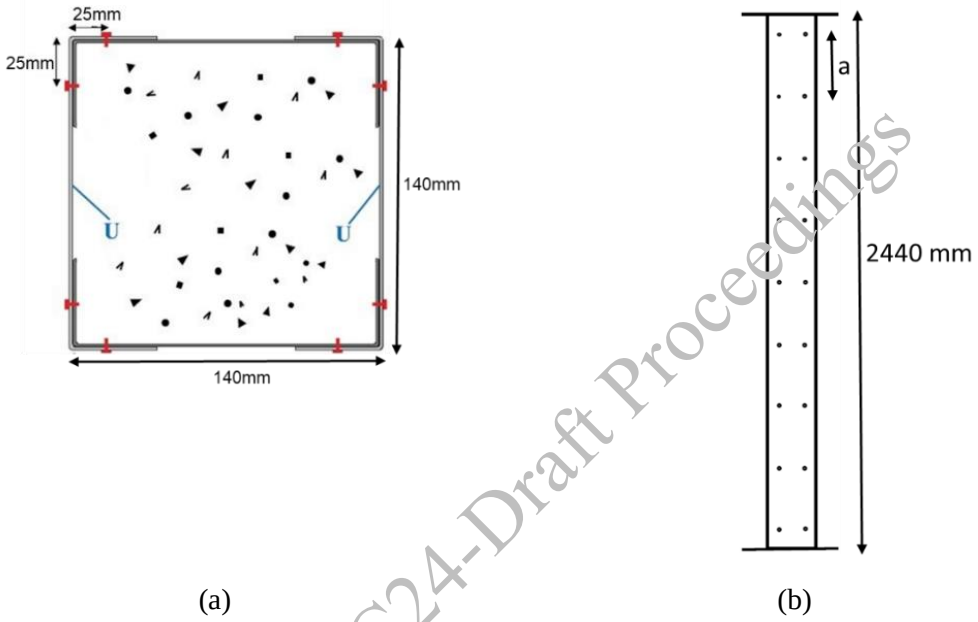

(a) (b)

Figure 1. Specimens considered for testing (a) cross-section; and (b) elevation of the CFSTC specimen.

Table 2. Test results of the concrete cube samples.

Sl.No.	Test Specimen Name	$f_{ck,cube}$			
		Sample 1	Sample 2	Sample 3	Average
1	M20	28.59	29.65	30.25	29.49
2	M30	39.92	42.10	41.19	41.07
3	M40	51.23	52.56	52.8	52.19

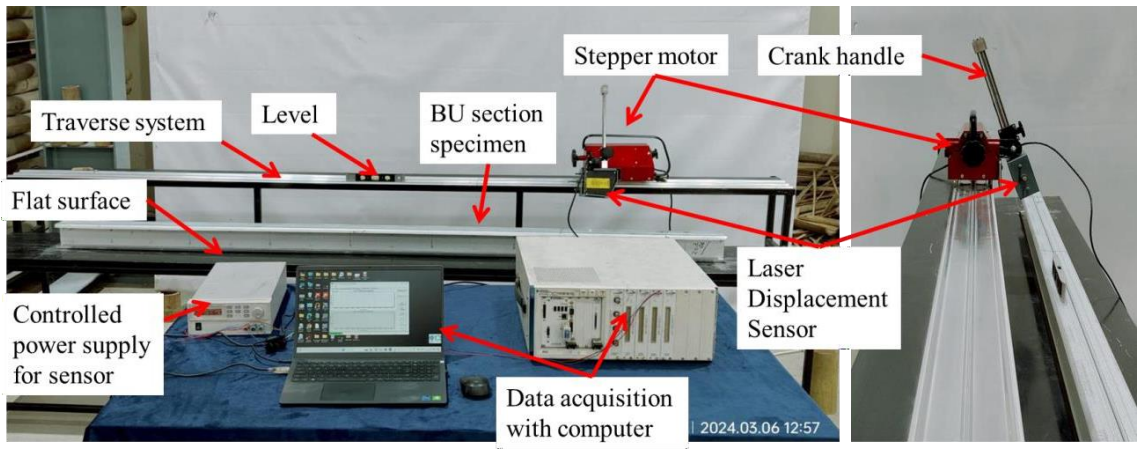

(a)

(b)

Figure 2. Details of imperfection measurement: (a) imperfection measuring set-up; (b) laser displacement sensor used for measuring imperfection;

Table 3. Normalized Maximum Measured Geometric Imperfection

S. No.	Specimens	Maximum Measured Geometric Imperfection
1	CFS U-section-1	1.63
2	CFS U-section-2	1.36
3	CFS U-section-3	1.98
4	CFS U-section-4	2.19
5	CFS U-section-5	1.78

2.4 CFS coupon test details

CFS coupon was tested as per IS 1608 (2005) for obtaining mechanical properties of the CFS used for fabricating the CFSTC sections.

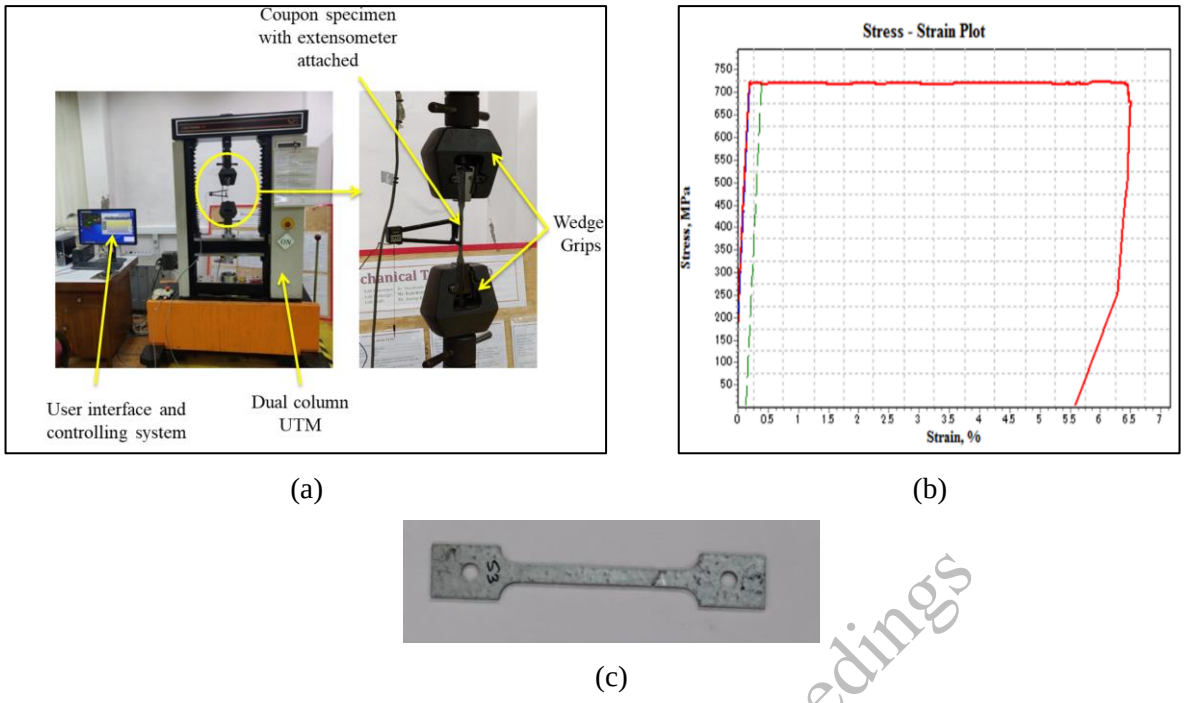

Figure 3. CFS coupon test (a) 10 ton UTM used for the test; (b) stress–strain curve; and (c) tested CFS coupon.

2.5 Experimental test set-up for compression

300-ton UTM in the Structural Laboratory, CBRI, Roorkee, India is utilized for performing the test. As shown in Fig. 4(a). MS clamps were used for fixing the CFSTC sections at both the ends to fix the specimen at the top and bottom of the specimen [Fig. 4(b)]. Axial displacement was applied at a rate of 0.5 mm/min.

Figure 4. (a) Experimental test set-up for axial load testing of CFSTC sections; and (b) boundary end conditions for CFSTC sections at the top and bottom respectively.

3. Experimental results and discussion

Table 4 shows the ultimate axial strength of the CFSTC specimens considered for testing in the present study.

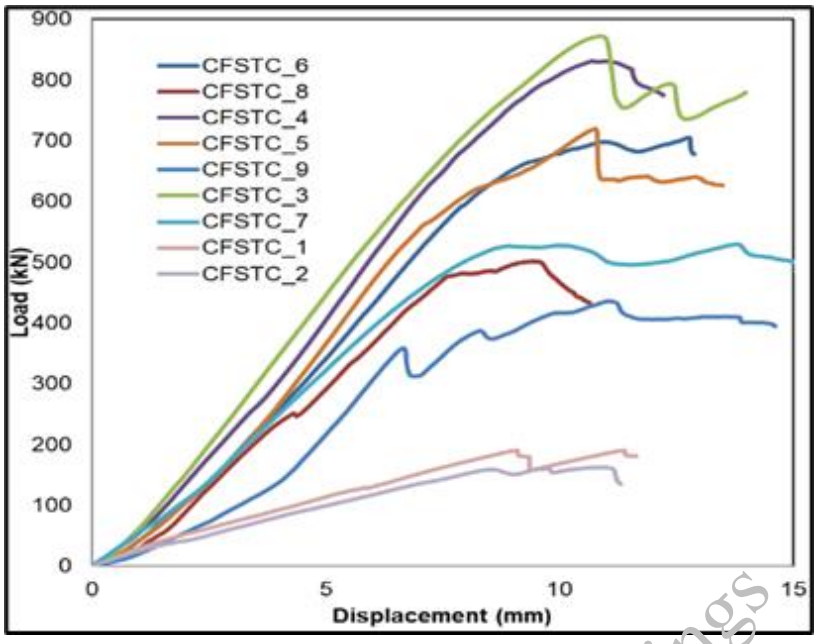

Figure 5. Load vs. displacement curve of the tested CFSTC specimens

Table 4. Ultimate strength of the tested CFSTC specimens

Sr. No.	Specimens	Ultimate axial strength (in kN)
1	CFSTC_1	190.45
2	CFSTC_2	162.40
3	CFSTC_3	872.02
4	CFSTC_4	831.40
5	CFSTC_5	719.99
6	CFSTC_6	705.22
7	CFSTC_7	529.59
8	CFSTC_8	502.06

Fig. 5 shows the experimentally obtained load vs. axial displacement curves. One of the samples CFSTC_9 filed prematurely as shown in Fig. 5. This particular test did not include clamping devices, which led to the premature collapse. Further comparisons did not take this test result into account.

The highest axial load-bearing capacity of 872.02kN was obtained for the CFSTC-3 specimens because of the highest concrete strength and lesser screw spacing of 100m. For the CFSTC-4, CFSTC-5, CFSTC-6, CFSTC-7, and CFSTC-8 specimens, the axial load-bearing capability was 831.40kN, 719.99kN, 705.22kN, 529.59kN and 502.06kN respectively.

Fig. 6 shows the failure patterns of the various specimens considered for testing in the present study. The results for all specimens show that the deformation of the columns was representing local buckling (global buckling was not observed). Fig. 6 (a) shows the tearing of the CFS U-section in CFSTC_3 specimen at corner. Fig. 6 (b) shows local buckling waves observed near peak load in CFSTC_3 specimen. Fig. 6 (c) shows local buckling observed in CFSTC_4 specimen near the bottom.

Fig. 6 (d and e) local observed near the bottom and top clamps in CFSTC_6 specimen respectively. Fig. 6(f) shows the screw breakage observed in CFSTC_8 specimen and Fig. 6 (g and h) local buckling and web bulging observed in CFSTC_8 specimens. Local buckling was observed in CFSTC 1 near top clamp as shown in Fig, 6 (g).

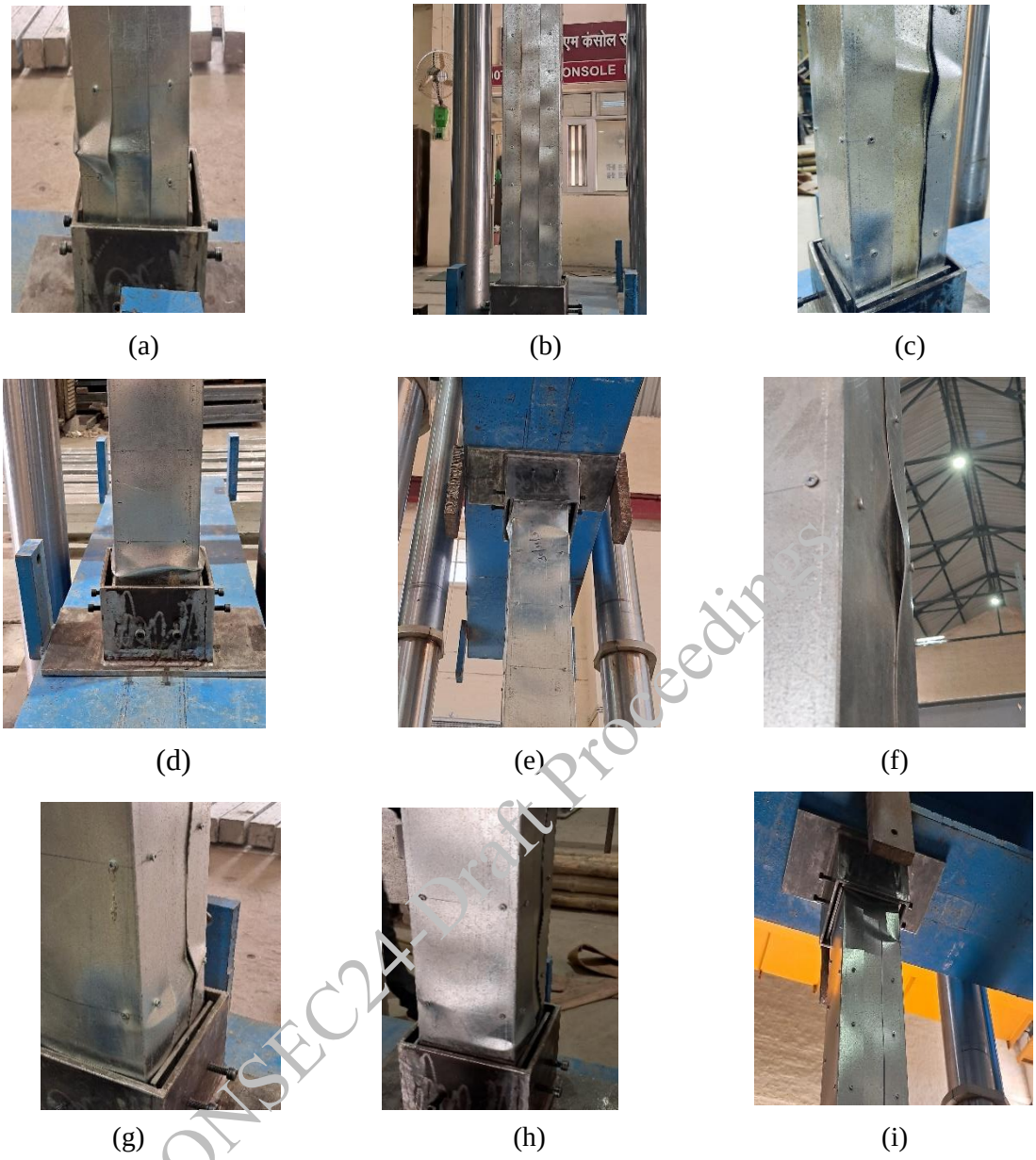

Figure 6. Failure patterns observed in various specimens (a and b) CFSTC_3; (c) CFSTC_4; (d and e) CFSTC_6; (f to h) CFSTC_8; and (i) CFSTC_1.

4. Analytical Studies

According to EN 1994-1-1 (2004), the plastic resistance ($P_{pl,Rd}$) of the CFSTC specimens may be calculated using Eqs. (1-12), which takes into account the plastic resistance of the steel tube section, concrete infill, and steel reinforcement. Various researchers have adopted the EN 1994-1-1 (2004) for predicting the axial load carrying capacity of concrete-filled steel tubular columns (Rahnavard et al. (2022a, 2022b)). Efficacy of the EN 1994-1-1 (2004) in preditcng the strength of concrete-filled steel tubular columns may be observed by the results reported in Table 5 by Rahnavard et al. (2022a).

$$N_{\text{pl,Rd}} = A_a f_{yd} + 0.85 A_c f_{cd} + A_s f_{sd} \quad (1)$$

$$N_{\text{pl,Rd,1}} = A_a f_{yd} + 0.85 A_c f_{cd} \quad (2)$$

$$N_{\text{pl,Rd,2}} = A_a f_{yd} + A_c f_{cd} \quad (3)$$

$$\delta = \frac{A_a f_{yd}}{N_{Pl,Rd}} \quad (4)$$

$$N_{\text{b,Rd,n}} = \chi N_{\text{pl,Rd,n}} \quad (5)$$

$$\chi = \frac{1}{\Phi + \sqrt{\Phi^2 - \lambda^2}} \quad (6)$$

$$\Phi = 0.5[1 + \alpha\,(\lambda - 0.2) + \lambda^2] \quad (7)$$

$$\lambda = \sqrt{\frac{N_{pl,Rd}}{N_{cr}}} \quad (8)$$

$$\text{N}_{\text{cr}} = \frac{\pi^2 (EI)_{eff}}{L_e^2} \quad (9)$$

$$EI_{eff} = E_a I_a + k_e E_{cm} I_c \quad (10)$$

$$EI_{eff} = E_a I_a + keE_{c,eff}\, I_c \quad (11)$$

$$EI_{c,eff} = Ecm \frac{1}{1 + (\frac{N_{G,Ed}}{N_{Ed}})\varphi_t} \quad (12)$$

where, $N_{pl,Rd}$ - composite columns' plastic resistance, δ - steel contribution, $N_{b,Rd}$ - design buckling resistance of a composite, χ - the column reduction factor, α - imperfection factor determined following EN 1993-1-1, λ -relative slenderness., L_e - effective length of the column, I_a and I_c -second moments (structural steel section / uncracked concrete section), k_e -correction factor and φ_t - creep coefficient.

Table 5. Normalized Maximum Measured Geometric Imperfection

S. No.	Specimens	$P_{u,test}$ (kN)	$P_{u,test}/N_{b,Rd,1}$	$P_{u,test}/N_{b,Rd,2}$	$P_{u,test}/N_{b,Rd,3}$	$P_{u,test}/N_{b,Rd,4}$
1	$R-2C+2U-1$	498.59	0.81	0.77	1.08	1.00
2	$R-2C+2U-2$	486.53	0.79	0.75	1.05	0.98
3	$R-2C+2U-3$	462.66	0.76	0.72	1.00	0.93
Mean Value			0.78	0.75	1.04	0.97
Standard Deviation			0.03	0.02	0.04	0.037
Coefficient of Variation (%)			3.79	3.79	3.79	3.79

5. Conclusions

The axial behaviour of concrete-filled cold-formed steel columns (CFSTC) columns was investigated in the present study. An experimental program consisting of 9 CFSTC column specimens of three different concrete grades and two different screw spacing's used for connecting the CFS U-section to form the CFSTC sections. The experimental program encompassed material tests, fresh concrete properties tests, initial global geometric imperfection measurements and pin-ended column tests. The mechanical behaviours including failure modes, lateral deflections, flexural buckling resistances, load-end shortening relationship were reported and discussed. The following summarizes the findings:

- The experimental results showed the following axial load capacities of 831.40kN, 719.99kN, 705.22kN, 529.59kN and 502.06kN for the CFSTC-4, CFSTC-5, CFSTC-6, CFSTC-7, and CFSTC-8 specimens, the respectively.
- Local buckling was major failure mode observed in all the specimens, screw breakage only occurred in CFSTC_8 specimen having screw spacing of 150mm, therefore 100mm screw spacing is recommended.
- Clamping device restricted the premature failure of the CFSTC specimens and lead to proper distribution of the load at the top of the specimens.
- The obtained experimental axial capacities will be compared with the predicted axial capacity values derived from EN 1994-1-1 for assessing its efficacy.

References

ACI318, Building Code Requirements for Structural Concrete and Commentary. ACI 318-14, American Concrete Institute, Farmington Hills, Michigan, USA, 2014.

ANSI/AISC 360-05, Specification for Structural Steel Buildings, American Institute of Steel Construction; Chicago (IL, USA), 2005.

BD-032. AS/NZS 2327: Composite structures—composite steel-concrete construction in buildings. Standards Australia; 2017.

Chen, M. T., Zhang, T., & Young, B. (2023). Behaviour of concrete-filled cold-formed steel built-up section stub columns. *Thin-Walled Structures*, *187*, 110692.

Committee on Specifications. ANSI/AISC 360-16: Specification for structural steel buildings. Chicago, Illinois: American Institute of Steel Construction; 2016.

DBJ/T 13-51-2010, Technical Specification for Concrete-Filled Steel Tubular Structures, The Department of Housing and Urban–Rural Development of Fujian Province, Fuzhou (China), 2010.

Eurocode 4. Design of Composite Steel and Concrete Structures, Part 1.1: General Rules and Rules for Building. BS EN 1994-1-1: 2004, British Standards Institution; London (UK), 2004.

IS (Indian Standard), Metallic Materials—Tensile Testing at Ambient Temperature. IS 1608, IS, New Delhi, India, 2005.

IS 456-2000, Plain and Reinforced Concrete - Code of Practice (Fourth Revision).

JGJ 138-2016, Code for Design of Composite Structures, Ministry of Housing and Urban-Rural Development of the People's Republic of China, China, 2016, (in Chinese).

Rahnavard, R., Craveiro, H. D., Lopes, M., Simões, R. A., Laím, L., & Rebelo, C. (2022a). Concrete-filled cold-formed steel (CF-CFS) built-up columns under compression: Test and design. *Thin-Walled Structures*, *179*, 109603.

Rahnavard, R., Craveiro, H. D., Simões, R. A., Laím, L., & Santiago, A. (2022b). Buckling resistance of concrete-filled cold-formed steel (CF-CFS) built-up short columns under compression. *Thin-Walled Structures*, *170*, 108638.

Shanmugam, N. E., & Lakshmi, B. (2001). State of the art report on steel–concrete composite columns. *Journal of constructional steel research*, *57*(10), 1041-1080.

Standards Australia, Bridge Design, Part 6: Steel and Composite Construction. AS 5100.6-2004, Sydney (Australia), 2004.

Tao, Z., Wang, Z. B., & Yu, Q. (2013). Finite element modelling of concrete-filled steel stub columns under axial compression. *Journal of constructional steel research*, *89*, 121-131.

Teoh, K. B., Chua, Y. S., Dai Pang, S., & Kong, S. Y. (2023a). Experimental investigation of lightweight aggregate concrete-filled cold-formed built-up box section (CFBBS) stub columns under axial compression. *Engineering Structures*, *279*, 115630

Teoh, K.B., Chua, Y.S., Dai Pang, S. and Kong, S.Y(2023b). Experimental investigation of flexural buckling behaviour of self-compacting lightweight concrete-filled cold-formed built-up box section (CFBBS) columns. *Thin-Walled Structures*, *187*, p.110751.

Uy, B., Tao, Z., & Han, L. H. (2011). Behaviour of short and slender concrete-filled stainless steel tubular columns. *Journal of Constructional Steel Research*, *67*(3), 360-378.

Wang, F., Young, B., & Gardner, L. (2020). Compressive behaviour and design of CFDST cross-sections with stainless steel outer tubes. *Journal of Constructional Steel Research*, *170*, 105942.

In-Plane Behaviour of Brick Masonry Walls Strengthened with High-Strain Materials: An Experimental Study

M.K. Deekshitha[*1], Mohan Lal[*2], and R. Siva Chidambaram[*3]

[1]Ph.D Scholar, Academy of Scientific and Innovative Research (AcSIR), Ghaziabad 201002, India
ACSC Group, CSIR-Central Building Research Institute, Roorkee – 247667, India
Email: deeksh2901@gmail.com
[2]Ph.D Scholar, Academy of Scientific and Innovative Research (AcSIR), Ghaziabad 201002, India
ACSC Group, CSIR-Central Building Research Institute, Roorkee – 247667, India
Email:mp917444@gmail.com
[3] Senior Scientist, ACSC Group, CSIR-Central Building Research Institute, Roorkee – 247667, India and
Assistant Professor, CSIR-CBRI, Academy of Scientific and Innovative Research (AcSIR), Roorkee, India
Email:dr.krsiitr@gmail.com

[*]Corresponding author

ABSTRACT

Brick masonry structures are prone to collapse during earthquakes, highlighting the need for effective strengthening techniques. Recent research concentrates on modern strengthening techniques such as textiles due to their lightweight nature, affordability, and time-saving benefits. This study aims to assess the efficacy of integrating high-strain materials such as geogrids and Glass Fiber Textile Reinforced Mortar (GFTRM), in enhancing the in-plane behavior of masonry wallets through methodical experimentation. The specimens were externally reinforced with Glass Fiber Textile Reinforced Mortar (GFTRM) and internally reinforced with polypropylene geogrids, and these were compared against control specimens that were not internally reinforced. This research compares the failure modes, crack patterns, load-displacement behavior, and energy dissipation of the strengthened specimens with those of the control specimens. The brick wallet specimens were subjected to a diagonal shear test to assess their shear behavior. It was found that the specimens integrated with geogrids exhibited higher stiffness until reaching the peak load and showed approximately a better post-peak performance in the higher displacements, which offered adequate ductility to the specimen. Experimental findings indicated that GFTRM notably improved the inelastic behavior concerning energy dissipation, stiffness degradation, and failure pattern. Moreover, they demonstrated superior ductility to the control specimens, rendering them an economical and practical solution for seismically active zones.

KEYWORDS: *Brick Masonry, Strengthening, GFTRM, Polypropylene Geogrid, In-plane behavior*

1. Introduction

Brick masonry has been employed for centuries and remains a popular choice [1-2] due to its durability, aesthetic appeal, and ease of construction. Despite being strong enough to resist the compressive action of loads, brick masonry walls possess zero or negligible resistance to tensile forces acting on the structure. Unreinforced masonry structures built in the ancient days are a combination of brick-and-mortar units that are vulnerable along their bed joints, especially during severe earthquakes [3,4]. In order to improve the structural performance against seismic forces, confined masonry is being practiced on a larger scale in the masonry structures. However, the confined masonry technique could be applied in new constructions [5] or on large-scale repair and rehabilitation works to serve as an effective and economical option to withstand seismic activities. For the existing brick masonry buildings, strengthening of walls poses as a better choice to improve the ductility. Hence, strengthening the brick masonry structures by traditional strengthening methods like repointing and RC jacketing has been practiced in the earlier days. Since the traditional techniques occupied excessive floor space, consumed more time, and required additional labour, modern research on strengthening focusses on affordable and quicker solutions that could be adapted in the future.

One such modern strengthening measure is the utilization of textiles like Fiber Reinforced Polymers (FRP), Welded Wire Meshes (WWM) in the masonry walls. FRPs are made of glass, carbon, and aramids, are light in weight, and are easy to use in various forms, including meshes, laminates, rods, etc. Previous studies have proposed external textile strengthening of the masonry walls subjected to Diagonal Shear or Cyclic loads according to different seismic standards available [6,7]. This experimental research utilized geogrids, mostly used in slope stabilization [8] due to their high strain property, as an internal reinforcement along all the bed joints in the clay brick masonry walls. The other specimen category included internal reinforcement with polypropylene geogrids and external reinforcement with the Glass Fiber Textile Mesh (GFTM) to analyze the behavior under Diagonal Shear according to ASTM E519/519-M15. The study compared the failure modes, crack patterns, load vs. deflection behaviour, and energy dissipation characteristics of the conventional brick walls to that of the strengthened ones. Burnt clay bricks of dimensions 220mm x 110mm x 70mm, Portland Pozzolana Cement (PPC), and the locally available sand were used to erect the Unreinforced Masonry (URM) walls used in the study. Uniaxial geogrids of 25mm x 25mm apertures (SGU 60 – Strata Grid Uniaxial 60) and Glass Fiber Textile Mesh were utilized in the internal and external strengthening of the URM walls. The compressive strength of bricks and mortar was determined based on the ASTM C67/C67M-20 by filling the brick frogs with 1:3 grade cement mortar and cubes of sizes 50mm x 50mm x 50mm as 23.8MPa and 17.9MPa (28 days) respectively. The tensile strength of the single rib and multiple rib tests of geogrids and glass fiber textiles along the machine directions were analyzed as per ASTM D6637/D6637 M – 15 and were found to be 63kN/m and 110kN/m.

2. Specimen configuration and Strengthening Details

Diagonal Shear Tests were conducted on three categories of two URM wall specimens under each (total six), classified as DS1, DS2, and DS3 of dimensions 480mm x 480mm x 110 mm adopted according to ASTM E519/519-M. The walls were cast for single wythe thickness in Stretcher bond and cured for seven days before strengthening them. Among the six walls, the first two exactly replicated the conventional brick masonry wall without any strengthening and are classified under the category DS1. The following two URM walls under the category DS2 were internally strengthened with single layers of SGU 60 geogrids along all the mortar bed joints. In the internal strengthening process, the geogrid layers cut for the dimensions 480mm in the direction of length and 110mm in the direction of thickness were embedded between 5mm mortar above and below geogrids in every brick course. Finally, the remaining two walls under DS3 were internally reinforced with SGU 60 and externally reinforced with a single layer of GFTM on both wall surfaces.

The strengthening process is initiated with the surface preparation of the walls, followed by drilling the holes for anchorage. GFTM used in external strengthening was anchored with the flat-head masonry screws to resist bending in the central regions of the walls. The surfaces were prewetted with the cement slurry, and then GFTM was fixed on the first mortar layer. The anchorage setup was tightened, covered with another layer of mortar, and finally plastered to finish the external strengthening. The in-plane shear response of every specimen considered in this study was determined by the Diagonal Shear Test according to ASTM E519/519-M15 Standards. The experimental setup included a 30T load cell attached to an actuator in the 75T loading frame. The specimen was placed on the steel shoes on the top and bottom. The displacements were measured using three Linear Variable Differential Transducers (LVDT) placed on the actuator to measure the stroke and two on the specimens in the horizontal and vertical directions to measure the tension and compression, respectively. These instruments were connected to the Data Acquisition System to collect the data at the time of testing.

3. Results and Discussions

3.1 Crack Pattern and Failure Modes

The unreinforced and unstrengthened control specimen DS1 experienced a sudden brittle shear step failure, resulting in a complete collapse without prior warning. The cracks formed in the mortar joints due to the applied loads, ultimately leading to debonding of the mortar joints at the time of failure. The major crack initiated from the bottom of the specimen along the vertical diagonal, further forming multiple new cracks under increased deflections. As another common observation in both the strengthened specimens, the SGU

60 geogrids placed in every brick course yielded, to impart ductility, especially when the cracks multiplied eccentric to the vertical diagonal. Under the increased compression, specimen DS2 experienced a spalling of plaster with an onset of shear sliding failure in the first brick course from the top of the specimen. In specimen DS3, the provision of GFTM deviated the initiated crack paths by shifting its original vertical direction to the anchorage positions in the border regions, significantly improving the shear resistance against bending in the central regions, which is evident from the rupture of GFTM in higher displacements. The crack patterns observed in DS1, DS2, and DS3 after the Diagonal Shear Test are depicted in Figure 1.

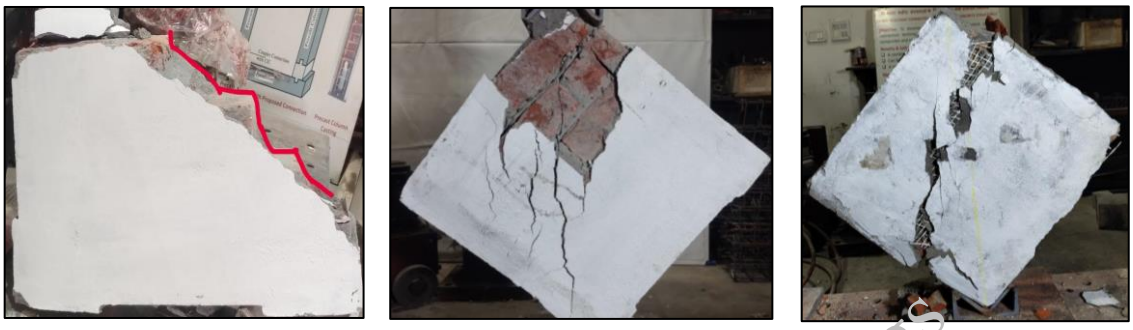

Figure 1. Failure modes and crack patterns

3.2 Load-Deflection Behaviour

The load-deflection behaviour of the specimens DS1 to DS3 tested for shear resistance are illustrated in Figure 2. All the specimens showed linear progress in the load-bearing capacity, followed by strength degradation when the cracks originated along the bed joints. The peak load of the control specimen was recorded as 35kN. The sudden collapse in DS1 after attaining the peak is clear from the drop in the load-deflection curve.

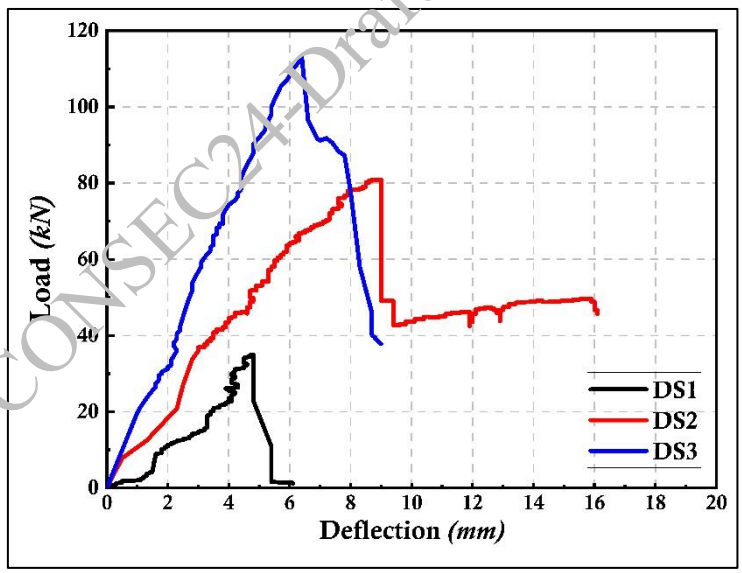

Figure 2. Load-Deflection behaviour

Every strengthened specimen had an increased load-bearing capacity compared with the control specimen. The maximum load attained by the strengthened specimens DS2 and DS3 increased by nearly 130% and 225% than DS1. The major cracks formed in the strengthened specimens at 70% of the peak load attained by DS2 and DS3. The stiffness of all the specimens, including DS1, followed a similar path with an increasing pattern. The strengthened specimens showed a higher initial stiffness than DS1 in the elastic region. The highest maximum strength of 113.4kN was attained by the specimen that was both externally and internally reinforced with textiles. In the post-peak, the provision of geogrids and external strengthening offered a linear degradation in the curve instead of an unexpected collapse as in the control specimen.

3.3 Energy Dissipation

Energy dissipation behavior depicts the ability of the structure to absorb and dissipate energy during seismic events. Energy dissipation is quantified as the area under the load-deflection curve, with higher energy dissipation indicating the ductile performance of the specimens. It is calculated by the cumulative addition of the energy dissipated at each deflection point obtained during the test. Every specimen in the study followed the increasing trend till 6mm deflection in the energy dissipation graph shown in Figure 2. However, under increased loads, the unreinforced and unstrengthened specimen DS1 failed with the least energy absorption in comparison with the rest of the specimens. The specimen DS2 experienced a dip in energy dissipation which might be due to the minimal ability of the wall to absorb energy in the earlier stages. However, after the occurrence of the major crack, the energy trend of DS2 followed a linear pattern like DS3 till the failure. The specimens DS2 and DS3 exhibited a remarkable increase of 961.454% increase and 1143.08% increase in energy than the DS1 respectively.

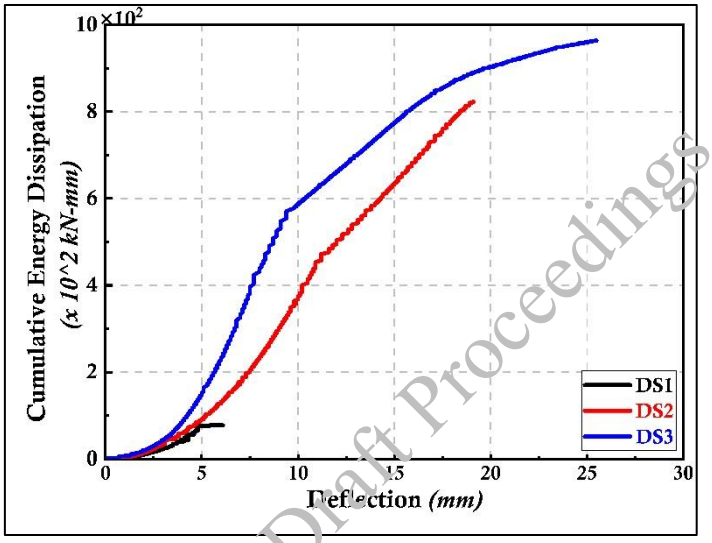

Figure 3. Energy Dissipation behaviour

4. Conclusions

Three categories of specimen-unreinforced, internally strengthened, both internally and externally strengthened with Glass Fiber Textiles (GFT) and Geogrids were subjected to Diagonal Shear Tests. The walls devoid of reinforcement were assumed to be the control DS1, and the results of the strengthened specimens were compared to those of the DS1. The inferences drawn from the experimental study are discussed here.

- The unreinforced and unstrengthened wall underwent a brittle failure whereas the strengthening offered in the specimens extended the time of failure, especially after the occurrence of the major crack.
- The strengthened specimens showed an increase of 130% to 225% in the maximum load attained, based on the number of layers strengthened, along with a higher stiffness than the control specimen.
- The improved energy dissipation capacity by approximately 1140% proves the effectiveness of textiles in enhancing the performance of brick masonry buildings, especially during the earthquakes.

References

Almssad, Asaad, Amjad Almusaed, and Raad Z. Homod. (2022) 'Masonry in the Context of Sustainable Buildings: A Review of the Brick Role in Architecture.' *Sustainability* 14, no. 22: 14734.

Borah, Bonisha, Hemant B. Kaushik, and Vaibhav Singhal. (2023) 'Analysis and Design of Confined Masonry Structures: Review and Future Research Directions.' *Buildings* 13, no. 5: 1282.

Shabdin, M., M. Zargaran, and Nader K. A. Attari. (2018) 'Experimental Diagonal Tension (Shear) Test of Un-Reinforced Masonry (URM) Walls Strengthened with Textile Reinforced Mortar (TRM)'. *Construction and Building Materials* 164 :704–15.

Kaptan, Kubilay. (2016). 'Shear Failure of Historic Masonry Walls'. Bitlis Eren University Journal of Science and Technology 6.

Caggegi, Carmelo, Giulia Carozzi, Stefano De Santis, F. Fabbrocino, Francesco Focacci, Łukasz Hojdys, Emma Lanoye, and Luigia Zuccarino. (2017). 'Experimental Analysis on Tensile and Bond Properties of PBO and Aramid Fabric Reinforced Cementitious Matrix for Strengthening Masonry Structures'. *Composites Part B: Engineering* 127: 175–95.

Boem, Ingrid. 'Masonry Elements Strengthened with TRM: A Review of Experimental, Design and Numerical Methods'. *Buildings* 12, no. 9 (September 2022): 1307.

Siva Chidambaram, R., and Pankaj Agarwal. (2014) 'The Confining Effect of Geo-Grid on the Mechanical Properties of Concrete Specimens with Steel Fiber under Compression and Flexure'. *Construction and Building Materials* 71 (2014): 628–37.

The Influence of CO_2 Curing Period and Pressure on the Uptake of CO_2 And Compressive Strength of Concrete

Divya Rachel Rooby[1] and Jayachandran K[2]

[1] *Department of Civil Engineering, National Institute of Technology Calicut, Kozhikode, Kerala, India, Email: Email: divya_p210036ce@nitc.ac.in*

[2] *Department of Civil Engineering, National Institute of Technology Calicut, Kozhikode, Kerala, India, Email: Email: jk@nitc.ac.in*

*Corresponding author

ABSTRACT

Carbon dioxide (CO_2) sequestration in cementitious material has been gaining importance in recent years due to its ability for permanent storage of CO_2 as calcium carbonates. Early-age CO_2 curing is one of the sequestration techniques, which also shows improvement in mechanical and durability properties of concrete apart from CO_2 storage. This paper presents a review of the literature showcasing the influence of the duration of CO_2 curing and carbonation pressure on the percentage of CO_2 uptake and the compressive strength of concrete. Various parameters impact the sequestration of CO_2 in cementitious material, among which a few most important ones repeatedly reported in most literature are chosen and studied for their effect on the CO_2 uptake and compressive strength of concrete. Carbonation curing is done in 3-stages including pre-conditioning, CO_2 curing process, and subsequent water curing. Duration of CO_2 curing and CO_2 gas pressure are the major parameters under study in addition to w/b ratio and duration of pre-conditioning that may affect the percentage CO_2 uptake in concrete and compressive strength. Sufficient water content in the interconnected pores of concrete is required for the effective dissolution of CO_2 molecules, however, saturated pores hinder the carbonation process. Therefore, an optimum w/b ratio is to be determined. Similarly, an optimal duration of pre-conditioning would reduce the free water from pores and make room for CO_2 diffusion. Although injecting CO_2 at higher pressure can diffuse more CO_2 into concrete, excess pressure can cause sudden release of free water leading to microcracking in concrete. Furthermore, a longer duration of CO_2 curing can be beneficial to improve CO_2 uptake and compressive strength, however, it would not be feasible and economical. Also, after a certain amount of time of curing, the CO_2 uptake and compressive strength saturate due to the formation of a layer of carbonation products and lesser free water which hinders further carbonation process. Hence, the optimum value of these influencing parameters is essential to achieve maximum CO_2 uptake without compromising the compressive strength of concrete.

KEYWORDS*: CO_2 sequestration, CO_2 curing, Carbonation pressure, CO_2 uptake, Compressive strength*

1. Introduction

Cement production is one of the significant contributors to CO_2 emissions, accounting for 5-7 % of total anthropogenic CO_2 emissions in several countries, including India [Andrew (2019)]. Therefore, sequestration of CO_2 in concrete structures could be an effective technique to reduce the cement content and significantly reduce the concrete's carbon footprint. Fabrication of concrete by capturing and utilizing carbon dioxide has been gaining much interest in recent years as a method to reduce its impact on the environment. CO_2 curing is one of the techniques to sequester carbon dioxide and store it in concrete in its stable form.

Weathering carbonation of mature concrete, which occurs naturally over time, is a major durability threat to concrete structures. Carbonation can lead to a drop in the pH of the pore solution, which can be ruinous to reinforced concrete structures due to the occurrence of rebar corrosion [Hussain et al. (2017)]. In addition, the natural process is too slow, and it can take hundreds of years to reabsorb all the emitted CO_2.

Early-age carbonation of fresh concrete has several advantages. Carbonation reaction involves the formation of calcium carbonate, and it leads to certain changes in the properties of concrete such as decreased permeability, modification of pore structure, increase in compressive strength, etc [Kazemian and Shafei (2023)]. In carbon curing, concrete samples are exposed to a closed environment filled with CO_2 gas. This alters and accelerates the conventional hydration reaction of calcium silicates and forms decalcified C-S-H and solid calcium carbonate precipitate. However, in the practice of carbonation curing, the CO_2 exposure time is delayed after mixing of calcium silicate and water which allows a pre-hydration of cement to occur ahead of carbonation. The pre-hydration products and calcium silicates simultaneously get carbonated. The calcium carbonates produced make the concrete dense, improving its mechanical and durability properties [Z. Liu and Meng (2021)]. This paper discusses the potential of employing carbon dioxide gas for curing cementitious material to improve its properties apart from acting as a carbon storage facility. It also summarizes the influence of various factors and their impact on CO_2 uptake and compressive strength of concrete.

2. CO_2 curing

Carbonation curing involves subjecting concrete to an environment of high CO_2 concentration a few hours after being molded. The rate of carbonation is dependent mainly on the diffusion of CO_2 into the concrete matrix. Therefore, the connectivity of the pores is an important parameter to achieve maximum carbon uptake through CO_2 curing. Several studies have thus formulated typically a three-stage approach to carry out carbonation curing, which includes (1) in-mould curing or pre-conditioning, (2) carbon curing and (3) post-curing or post-hydration. The most commonly adopted experimental curing conditions are tabulated in Table 1 [(Alimi et al. 2022; He et al. 2016; Qin, Gao, and Chen 2019; Song et al. 2022; Zhang et al., 2016)].

Table 1. Stages of CO_2 curing

Stages	In-mould curing or pre-conditioning	CO2 curing	Post-hydration
Conditions	20-25˚C, 40-60% RH, 2-24h, 1 m/s (wind speed)	20-25˚C, 60-75% RH, 2-24h, 1-5 atm	Curing in water or saturated Ca(OH)2 solution till testing

Pre-conditioning of concrete is done by keeping concrete specimens in the moulds at ambient conditions for a few hours until the initial setting, depending on the mix proportions, and then demoulded and cured in similar conditions until exposed to CO_2 environment. In some studies, air is blown at an average speed of 1 m/s over concrete specimens after demoulding to ensure uniform water dispersion loss and make more paths for CO_2 to penetrate [Li et al. (2019)]. The second stage of the curing regime is to expose the concrete specimens to a high concentration CO_2 filled environment by placing them in a carbonation chamber set to an optimum set of conditions. The final step in the curing process, which is post-hydration, is essential because it is important to replenish the lost water to continue the hydration process in the cementitious system [Alimi et al. (2022a)]. Studies suggest that ample water curing after carbonation produces more hydration products and increases compressive strength. It is also seen that over the subsequent standard curing for 27 days, the pH value at the surface of the carbonated concrete sample rises to above 12 [He et al. (2016)].

3. Factors influencing CO_2 uptake and compressive strength of concrete

3.1 W/b ratio

Optimum water content is required for the effective diffusion of CO_2 molecules through concrete specimens because pore water serves as a medium for CO_2 gas dissolution. However, saturation of pores would hinder the process as well [Wang et al. 2017; Mehdizadeh et al. 2021]. Although there is no obvious relationship established between w/b and CO_2 uptake, it is commonly inferred that samples with a higher w/b ratio have more porous microstructure which helps in better ingress of CO_2 molecules [Zhang et al. 2020)]. **Figure 1**

summarises the influence of w/b ratio on CO_2 uptake [Guo et al. 2023; Mehdizadeh et al. 2021; Zhang et al.2020; Wang et al. 2017)]. Higher w/b mixes require less water loss to provide enough space for CO_2 diffusion, whereas lower w/b mixtures require more water loss to produce the same amount of channel space [Liu and Meng (2021)]. A study by Wang et al. (2017) shows that the amount of cement is not enough for carbonation reaction in concrete with w/b ratio beyond 0.55, and the carbonation degree is no longer improved. Hence, an optimal water content in concrete would achieve a high carbonation degree and hydration reactivity.

3.2 Duration of pre-conditioning

Pre-conditioning of samples by placing them in an environmental chamber with 50-60 %RH at 20-25˚C is found to have been beneficial in increasing the CO_2 uptake. The duration of this initial curing is not directly influential to carbonation reaction efficiency; however, it decreases the free water and makes room for CO_2 molecules to diffuse through micropores in concrete [(El-Hassan and Shao 2014)]. **Figure 1** depicts the impact of pre-conditioning duration on CO_2 uptake. An accelerating process of CO_2 uptake is observed by Chen and Gao (2019)as pre-conditioning duration increases during the initial hours of carbonation. Furthermore, a significant increase in CO_2 uptake from 8.4% to 21.4% is reported by El-hassan, Shao, and Ghouleh (2013) between samples that are not pre-conditioned and the ones that are CO_2 cured after 4 hours of pre-conditioning, respectively. On the other hand, at a later hydration age, the carbonation reaction appears to be less rigorous (lesser CO_2 uptake %) due to reduced free water for the reaction to progress [(Zhang, Cai, and Jaworska 2020)]. An optimum water loss of 40% has been reported that could result in higher CO_2 uptake without compromising the workability and compressive strength of concrete [Zhang, Ghouleh, and Shao 2017; K. Chen et al. 2022].

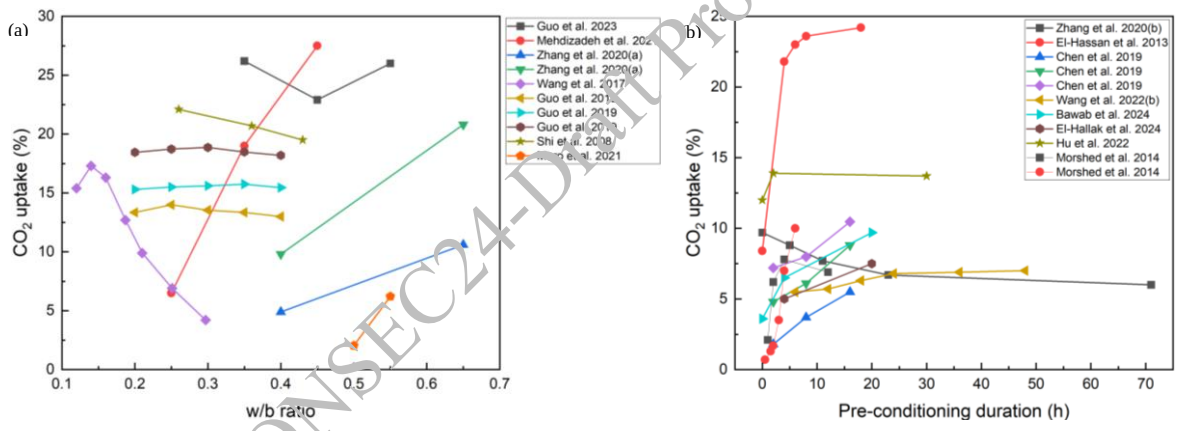

Figure 1. Influence of (a) w/b ratio and (b) preconditioning duration on CO_2 uptake

3.3 CO_2 gas pressure

Curing at higher pressure helps the amount of CO2 dissolution into pore water, however, the enhancement in CO_2 uptake is marginal. A slight increase of around 10-20% was only observed at 10 bar pressure as compared to 1.3 bar [(Librandi et al. 2019)]. The degree of carbonation is not proportional to the partial pressure, and as pressure increases, the rate of growth decreases [(Zhan, Poon, and Shi 2016; Liu and Meng 2021)] as seen in **Figure 2**. Xian et al. (2022) have shown that concrete cured under 0.014 bar pressure for 12 hours could achieve 12% CO_2 uptake. Additionally, the study by Zhan et.al. shows the highest rate of increase in CO_2 uptake when pressurized from 0.1 bar to 0.5 bar. There is hardly any improvement in CO_2 uptake when increasing pressure beyond 2 bar. Although it is obvious that CO_2 uptake is greater when injected in pressurized form than curing at atmospheric pressure, the enhancement with increasing gas pressure is minimal. Furthermore, the impact of CO_2 pressure on the compressive strength of concrete is difficult to comprehend by comparing different research studies. However, an enhancement in the compressive strengths has been noticed with increasing CO_2 pressure to a certain value. Zhan et al. (2016) observed a rise in the compressive strength of mortar specimens from 18.9 MPa to 20.9 MPa when increasing gas pressure from 0.1 bar to 0.5 bar. However, beyond 0.5 bar the compressive strength value remained at 25.5 MPa even after raising the pressure to up to 4 bar. Additionally, very high pressure is

considered undesirable for carbonation reaction to occur as a large amount of heat may be generated which tends to increase the risk of microcracking [(Z. Liu and Meng 2021)].

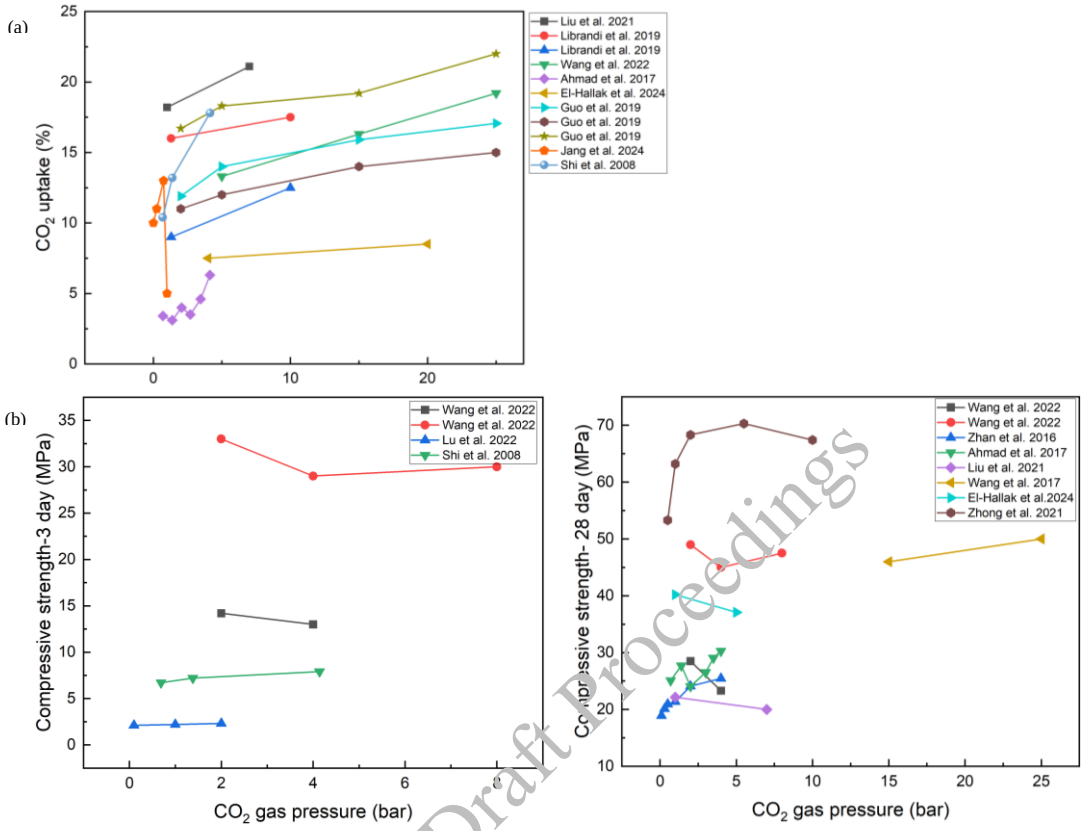

Figure 2. Influence of CO2 gas pressure on (a) CO2 uptake (b) compressive strength

3.4 CO_2 curing duration

CO_2 uptake shows significant enhancement with increasing curing time as reported in the literature and the carbonation reaction rate appears to be time-dependent. **Figure 3** shows that CO_2 uptake and compressive strength increase with time however the rate of gain considerably reduces with time. This may be due to the precipitation of carbonation products in the pores and it further hinders the diffusion of CO_2 molecules. Additionally, the carbonation reactants, calcium hydroxide, and C-S-H also deplete and free water evaporates as the duration extends [(Zhang, Liu, and Shao 2020)]. About 50% of CO_2 uptake was obtained in 2h when compared to 12h. An accelerating rate of reaction is observed in the first few hours (1-2 hours) due to the high amount of water content in the interconnected pores of pre-conditioned concrete which enables faster diffusion of CO_2 molecules [(L. Liu et al. 2022; T. Chen and Gao 2019; Zhang and Shao 2016)]. Furthermore, prolonged CO_2 curing seems to enhance the compressive strength of concrete and helps in gaining early-age strength because of the densification of microstructure. The $CaCO_3$ precipitates fill the pores and make it more dense [(Qin, Gao, and Chen 2019)]. It has been found that concrete samples subjected to accelerated carbonation curing at only 60 psi (4.13 bar) pressure attained a strength of 30 MPa after 10h, similar to the strength of moist-cured samples at 3 days [(Ahmad et al. 2017)]. In addition, it's commonly observed that the rate of strength gain reduces with time. Rapid carbonation reaction in the first 2 hours of the curing period was observed to be hindered due to a large amount of free water loss and a layer of carbonation products formed preventing further reaction [(Zhan et al. 2016)]. As reported in [(T. Chen and Gao 2019)], the 3-day and 7-day compressive strength significantly increased when cured in CO_2 from 2 hours to 16 hours and then decreased when extended to 24 hours. Although early-age strength is found to be enhanced upon CO_2 curing, the 28-day compressive strength had no notable impact upon increasing the CO_2 curing duration. It is also been reported that early-age compressive strength is only proportional to CO_2 uptake and not to reaction time [(Z. Liu and Meng 2021)].

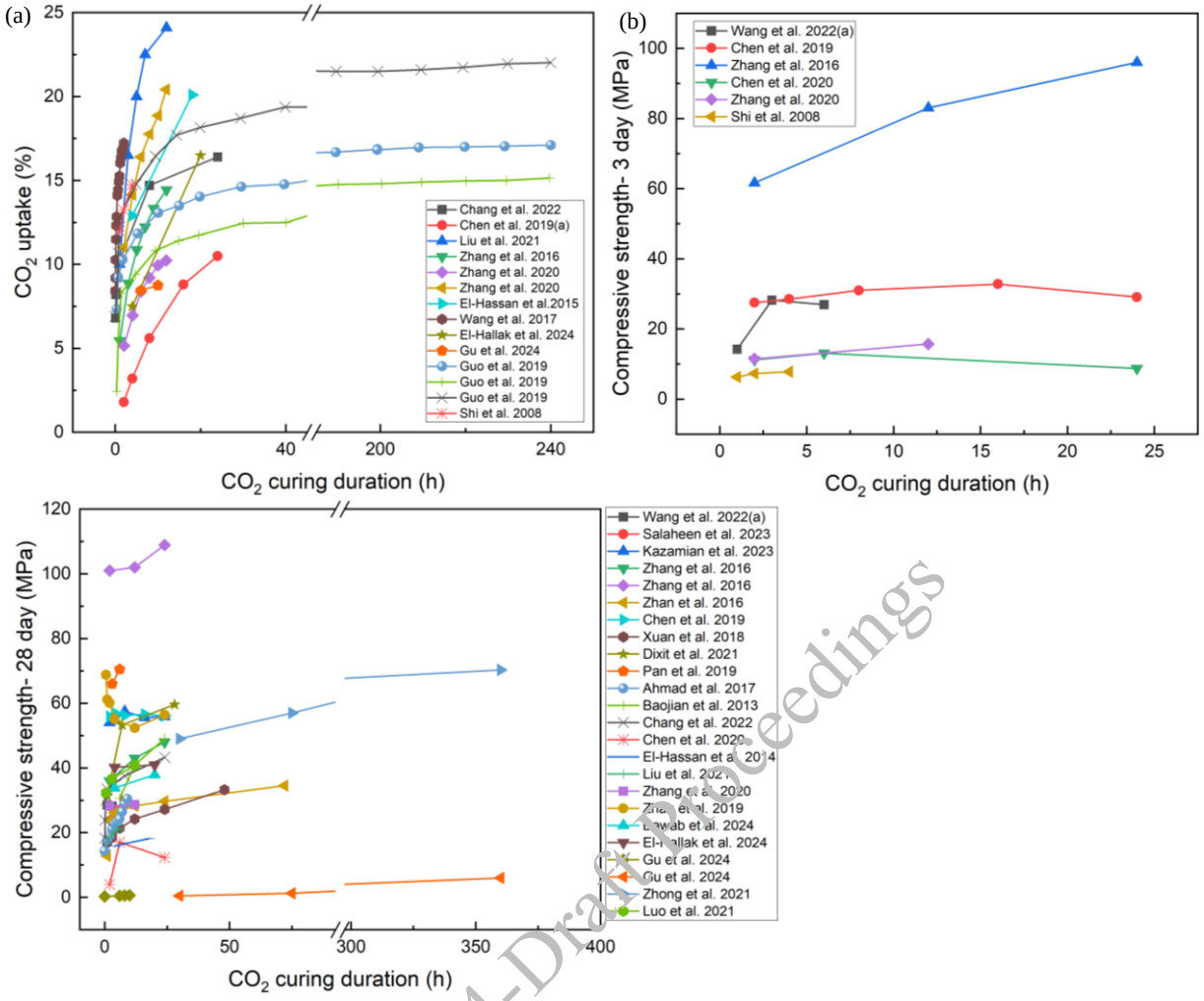

Figure 3. Influence of CO_2 curing duration on (a) CO_2 uptake (b) compressive strength

4. Conclusions

CO_2 curing is carried out in three stages which include pre-conditioning, carbonation curing, and post-hydration process. CO_2 curing can lead to compressive strength gain by 15–550% and achieve nearly 0.3–30% CO_2 uptake during the early period for various mixtures. The reaction efficiencies are significantly influenced majorly by curing parameters such as CO_2 gas pressure and CO_2 curing duration. The most impacting parameter is the curing period. CO_2 uptake and compressive strength increase with a prolonged curing period, however, the rate of increase diminishes with time. Although it is obvious that CO_2 uptake is greater when injected in pressurized form than curing at atmospheric pressure, the enhancement with increasing gas pressure is minimal. The w/b ratio and the duration of pre-conditioning are also influential towards achieving greater CO_2 uptake. An adequate amount of free water is desirable for better CO_2 diffusion, however, if in excess amount, will hinder the diffusion of CO_2 into the concrete. Therefore, it is essential to remove the excess free water. At the same time, an adequate w/b ratio needs to be maintained for the proper workability of concrete. Hence, these parameters are required to be optimized based on the desired compressive strength and to obtain maximum CO_2 uptake for various mixtures.

References

Ahmad, Shamsad, Rida Alwi Assaggaf, Mohammed Maslehuddin, Omar S.Baghabra Al-Amoudi, Saheed Kolawole Adekunle, and Syed Imran Ali. 2017. “Effects of Carbonation Pressure and Duration on Strength Evolution of Concrete Subjected to Accelerated Carbonation Curing.” *Construction and Building Materials* 136:565–73. https://doi.org/10.1016/j.conbuildmat.2017.01.069.

Alimi, Wasiu O., Saheed K. Adekunle, Shamsad Ahmad, and Abduljamiu O. Amao. 2022a. "Carbon Dioxide Sequestration Characteristics of Concrete Mixtures Incorporating High-Volume Cement Kiln Dust." *Case Studies in Construction Materials* 17 (June): e01414. https://doi.org/10.1016/j.cscm.2022.e01414.

Alimi, Wasiu O, Saheed K Adekunle, Shamsad Ahmad, and Abduljamiu O Amao. 2022b. "Case Studies in Construction Materials Carbon Dioxide Sequestration Characteristics of Concrete Mixtures Incorporating High-Volume Cement Kiln Dust." *Case Studies in Construction Materials* 17 (August): e01414. https://doi.org/10.1016/j.cscm.2022.e01414.

Chen, Ke yu, Jin Xia, Ren jie Wu, Xin yuan Shen, Jie jing Chen, Yu xi Zhao, and Wei liang Jin. 2022. "An Overview on the Influence of Various Parameters on the Fabrication and Engineering Properties of CO2-Cured Cement-Based Composites." *Journal of Cleaner Production* 366 (March). https://doi.org/10.1016/j.jclepro.2022.132968.

Chen, Tiefeng, and Xiaojian Gao. 2019. "Effect of Carbonation Curing Regime on Strength and Microstructure of Portland Cement Paste." *Journal of CO2 Utilization* 34 (April): 74–86. https://doi.org/10.1016/j.jcou.2019.05.034.

El-Hassan, Hilal, and Yixin Shao. 2014. "Carbon Storage through Concrete Block Carbonation." *Journal of Clean Energy Technologies* 2 (3): 287–91. https://doi.org/10.7763/jocet.2014.v2.141.

El-hassan, Hilal, Yixin Shao, and Zaid Ghouleh. 2013. "Reaction Products in Carbonation-Cured Lightweight Concrete," no. June, 799–809. https://doi.org/10.1061/(ASCE)MT.1943-5533.0000638.

Guo, Bingbing, Guixing Chu, Ruichang Yu, Yan Wang, Qi Yu, and Ditao Niu. 2023. "Effects of Sufficient Carbonation on the Strength and Microstructure of CO 2 -Cured Concrete" 76 (April).

He, Pingping, Caijun Shi, Zhenjun Tu, Chi Sun, and Jiake Zhang. 2016. "Effect of Further Water Curing on Compressive Strength and Microstructure of CO 2 -Cured Concrete." *Cement and Concrete Composites* 72:80–88. https://doi.org/10.1016/j.cemconcomp.2016.05.026.

Hussain, Shaik, Dipendu Bhunia, and S. B. Singh. 2017. "Comparative Study of Accelerated Carbonation of Plain Cement and Fly-Ash Concrete." *Journal of Building Engineering* 10 (December 2016): 26–31. https://doi.org/10.1016/j.jobe.2017.02.001.

Kazemian, Maziar, and Behrouz Shafei. 2023. "Carbon Sequestration and Storage in Concrete: A State-of-the-Art Review of Compositions, Methods, and Developments." *Journal of CO2 Utilization* 70 (February): 102443. https://doi.org/10.1016/j.jcou.2023.102443.

Li, Zhen, Zhen He, and Xiaorun Chen. 2019. "The Performance of Carbonation-Cured Concrete," 1–14.

Librandi, P., P. Nielsen, G. Costa, R. Snellings, M. Quaghebeur, and R. Baciocchi. 2019. "Mechanical and Environmental Properties of Carbonated Steel Slag Compacts as a Function of Mineralogy and CO2 Uptake." *Journal of CO2 Utilization* 33 (February): 201–14. https://doi.org/10.1016/j.jcou.2019.05.028.

Liu, Lixi, Yilun Liu, Xiaogeng Tian, and Xi Chen. 2022. "Superior CO2 Uptake and Enhanced Compressive Strength for Carbonation Curing of Cement-Based Materials via Flue Gas." *Construction and Building Materials* 346 (June): 128364. https://doi.org/10.1016/j.conbuildmat.2022.128364.

Liu, Zhuo, and Weina Meng. 2021. "Fundamental Understanding of Carbonation Curing and Durability of Carbonation-Cured Cement-Based Composites: A Review." *Journal of CO2 Utilization* 44 (December 2020): 101428. https://doi.org/10.1016/j.jcou.2020.101428.

Mehdizadeh, Hamideh, Xiaoxiao Jia, Kim Hung, and Tung-chai Ling. 2021. "Effect of Water-to-Cement Ratio Induced Hydration on the Accelerated Carbonation of Cement Pastes *." *Environmental Pollution* 280:116914. https://doi.org/10.1016/j.envpol.2021.116914.

Qin, Ling, Xiaojian Gao, and Tiefeng Chen. 2019. "Influence of Mineral Admixtures on Carbonation Curing of Cement Paste." *Construction and Building Materials* 212:653–62. https://doi.org/10.1016/j.conbuildmat.2019.04.033.

Song, Baixing, Songhui Liu, Xiang Hu, Kai Ouyang, Gensheng Li, and Caijun Shi. 2022. "Compressive Strength , Water and Chloride Transport Properties of Early CO 2 -Cured Portland Cement-Fly Ash-Slag Ternary Mortars." *Cement and Concrete Composites* 134 (April): 104786. https://doi.org/10.1016/j.cemconcomp.2022.104786.

Wang, Tao, Hao Huang, Xutao Hu, Mengxiang Fang, Zhongyang Luo, H Huang, X Hu, M Fang, Z Luo, and R Guo. 2017. "Key Words."

Xian, Xiangping, Duo Zhang, Han Lin, and Yixin Shao. 2022. "Ambient Pressure Carbonation Curing of Reinforced Concrete for CO2 Utilization and Corrosion Resistance." *Journal of CO2 Utilization* 56 (November 2021): 101861. https://doi.org/10.1016/j.jcou.2021.101861.

Zhan, Bao Jian, Dong Xing Xuan, Chi Sun Poon, and Cai Jun Shi. 2016. "Effect of Curing Parameters on CO2 Curing of Concrete Blocks Containing Recycled Aggregates." *Cement and Concrete Composites* 71:122–30. https://doi.org/10.1016/j.cemconcomp.2016.05.002.

Zhang, Duo, S M Asce, Xinhua Cai, and Yixin Shao. n.d. "Carbonation Curing of Precast Fly Ash Concrete," 1–9. https://doi.org/10.1061/(ASCE)MT.1943-5533.0001649.

Zhang, Duo, Xinhua Cai, and Beata Jaworska. 2020. "Effect of Pre-Carbonation Hydration on Long-Term Hydration of Carbonation-Cured Cement-Based Materials." *Construction and Building Materials* 231:117122. https://doi.org/10.1016/j.conbuildmat.2019.117122.

Zhang, Duo, Zaid Ghouleh, and Yixin Shao. 2017. "Review on Carbonation Curing of Cement-Based Materials." *Journal of CO2 Utilization* 21 (July): 119–31. https://doi.org/10.1016/j.jcou.2017.07.003.

Zhang, Duo, Tianlu Liu, and Yixin Shao. 2020. "Weathering Carbonation Behavior of Concrete Subject to Early-Age Carbonation Curing" 32 (4): 1–10. https://doi.org/10.1061/(ASCE)MT.1943-5533.0003087.

Zhang, Duo, and Yixin Shao. 2016. "Early Age Carbonation Curing for Precast Reinforced Concretes." *Construction and Building Materials* 113:134–43.

An Effective Blast Retrofit Strategy for Reinforced Concrete Highway Bridge Decks

S. Biswas[1*] and P. Sengupta[2]

[1] Indian Institute of Technology (ISM), Dhanbad, India
Email: souvikbiswas.20dr0144@cve.iitism.ac.in, 20dr0144@iitism.ac.in
[2] Indian Institute of Technology (ISM), Dhanbad, India
Email: piyali@iitism.ac.in

[*]Corresponding author

ABSTRACT

Highway bridges play a crucial role in the infrastructural and economic development of a country by providing fast and smooth transportation networks across different regions. Bridges may become susceptible to accidental or deliberate explosions due to their public access and utilization, economic significance and strategic importance. Blast loading differs from conventional loadings because of the very high magnitudes of peak blast pressure and extremely short loading duration. A high blast load resulting from an explosive charge may cause extensive damage to bridge components, leading to local failures culminating in global failure of the bridge. In order to preserve the existing older bridges that are not equipped with a blast-resistant design philosophy, a suitable retrofit strategy can be employed depending on its efficiency, ease of application, and cost benefits. This study highlights the efficiency of fibre-reinforced polymer jacketing, steel jacketing, concrete jacketing and engineered cementitious composite jacketing in RC bridge decks subjected to blast loads using a three-dimensional numerical simulation approach. Numerical simulation results of retrofitted bridge decks under explosion are validated with respect to experimental results from the literature. An extensive parametric study is conducted to identify the most efficient blast retrofit scheme for RC bridge decks incorporating diverse structural and loading parameters. Subsequently, an incremental dynamic analysis approach is adopted to derive the fragility functions of bridge decks before and after retrofit under explosion for different damage states. Excerpts from this study will enlighten the engineering community about an effective blast retrofit strategy for highway bridges.

KEYWORDS: *Retrofit, Highway Bridges, Reinforced Concrete, Blast, Fragility*

1. Introduction

Highway bridges serve as pivotal elements in the infrastructural framework of any nation, underpinning economic growth and facilitating seamless transportation networks across diverse regions. These critical structures, however, are increasingly vulnerable to the risks posed by accidental or deliberate explosions. Due to their public accessibility, economic significance, and strategic importance, highway bridges are prime targets that can suffer severe damage from blast events (Williamson and Winget (2005)). Unlike conventional loadings, blast loading is characterized by extremely high peak pressures and very short durations, imposing unique challenges on structural integrity. The catastrophic effects of high-magnitude blast loads can lead to significant damage to bridge components, often initiating localized failures that can escalate into the global failure of the entire bridge structure (Biswas et al. (2022)). Given the prevalence of older bridges that were not originally designed with blast-resistant techniques, there is an urgent need for effective retrofit strategies to enhance their resilience against such explosive threats. The selection of an appropriate retrofit method must balance efficiency, ease of application, and cost-effectiveness to ensure practical implementation.

This study investigates the efficacy of various retrofit strategies for reinforced concrete (RC) highway bridge decks subjected to blast loads. Specifically, the study evaluates fibre-reinforced polymer (FRP)

jacketing, steel jacketing, concrete jacketing, and engineered cementitious composite (ECC) jacketing through a three-dimensional numerical simulation approach. The simulation results of these retrofitted bridge decks under explosive conditions are validated against experimental findings from existing literature, ensuring robustness and reliability. Furthermore, an extensive parametric study is conducted to determine the most effective blast retrofit scheme, considering a range of structural and loading parameters. Following this, an incremental dynamic analysis approach is employed to derive fragility functions for bridge decks before and after retrofitting across various damage states.

2. Experimental Data from Literature

The present study considered two reinforced concrete slab specimens from the experimental study by Wu et al. (2009). One specimen was a normally reinforced slab of 2000 mm in length, 1000 mm in width, and 100 mm thick, and it was reinforced on both the tension and compression sides. The bulk modulus of the concrete used was 28.3 MPa, and the compressive strength was 39.5 MPa. The reinforcing steel used was 12 mm in diameter, with spacings of 100 mm and 200 mm in the major and minor bending planes, respectively, having a rebar ratio of 1.34%. The bulk modulus of the steel was 200 GPa, and the ultimate yield strength was 600 MPa. The other specimen was identical to the first specimen retrofitted with two plates of carbon fibre-reinforced polymer (CFRP) strips running longitudinally through the length of the slab. Wu et al. (2009) subjected both the specimens to a charge weight of 1 kg TNT equivalent, with four different specimens of the normally reinforced slab placed at various stand-off distances of 1.4, 1.5 and 3 m, and the CFRP-retrofitted slab placed at a stand-off distance of 1.4 m.

3. Numerical Modelling and Validation

Numerical models of the two specimens from the literature were developed in the finite element package ABAQUS. The concrete slab and the reinforcing steel were modelled as solid C3D8R elements, and the CFRP strips were modelled as continuum shell SC8R elements. The nonlinear behaviour of concrete material was modelled using the concrete damage plasticity model (CDPM), the reinforcing steel was modelled using the Johnson-Cook damage model and the CFRP material was modelled using the Hashin damage parameters. The reinforcing steel, as well as the CFRP strips, were assumed to be perfectly bonded to the concrete deck slab.

The blast loading was defined using the CONWEP algorithm built into the ABAQUS software. Figure 4 shows the numerical (finite element) model of the CFRP retrofitted slab.

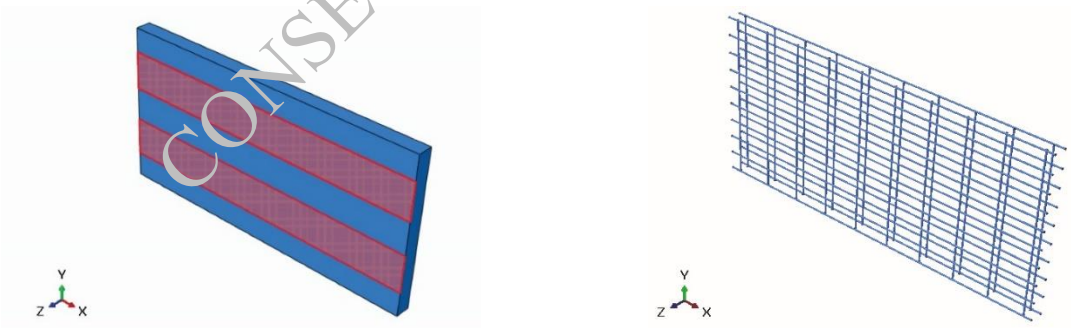

(a) (b)

Figure 4. Numerical model of CFRP retrofitted slab – (a) highlight showing the CFRP strips and (b) reinforcement bars

The finite element analysis results obtained from ABAQUS were validated using the experimental data from the study by Wu et al. (2009). The maximum deflection of the slabs under CONWEP blast loading was compared with the corresponding results from the literature. The normally reinforced concrete slab was subjected to four cases of blast loading with different charge weights and stand-off distances, and the CFRP retrofitted slab was subjected to one case of blast loading. Table 2 shows a comparison of the numerical results and the experimental results. The numerical results are found to be in good agreement with the experimental results.

Table 2. Validation of Numerical Results

SL. No.	Specimen	Charge Weight (kg)	Stand-off Distance (m)	Maximum deflection (mm)		Error (%)
				Experimental	Numerical	
1	NRC*	1	3	1.5	1.697	13.13
2	NRC*	8	3	10.5	10.86	3.43
3	NRC*	3.4	1.4	13.9	13.47	3.09
4	NRC*	8	1.5	38.9	39.78	2.26
5	CFRP retrofitted	1	1.4	3.77	3.3	14.24

*Normally retrofitted concrete slab

4. Parametric Study

A parametric study was performed by modifying the geometrical aspects of the numerically validated models. A slab thickness of 200 mm was considered, with the length and width remaining at 2000 mm and 1000 mm, respectively. The rebar ratio was kept at 1.34%. With the retrofit scheme being identical to the literature considered, four cases were considered - CFRP strips, steel plates, engineered cementitious composite (ECC) layers and high-performance concrete (HPC) layers. Commercially available 4-layer CFRP sheets with a thickness of 5.6 mm were considered in the parametric study. Steel plates of 5.6 mm thickness were considered in steel retrofitting, and the material data was obtained from Ebead and Marzouk (2022). ECC and HPC were applied in a layer of 20 mm thickness in the respective case studies. ECC and HPC material data were obtained from laboratory experiments. The ECC had a bulk modulus of 21 MPa and an ultimate compressive strength of 72 MPa, whereas the HPC had a bulk modulus of 35 MPa and an ultimate compressive strength of 60 MPa. The retrofitting strips, viz., CFRP, steel, ECC and HPC, were assumed to be perfectly bonded with the concrete slab. Three different scaled stand-off distances (z) were considered for this study for each charge weight – 0.25, 0.50 and 1.00. Figure 5 shows comparisons in the results of the parametric study.

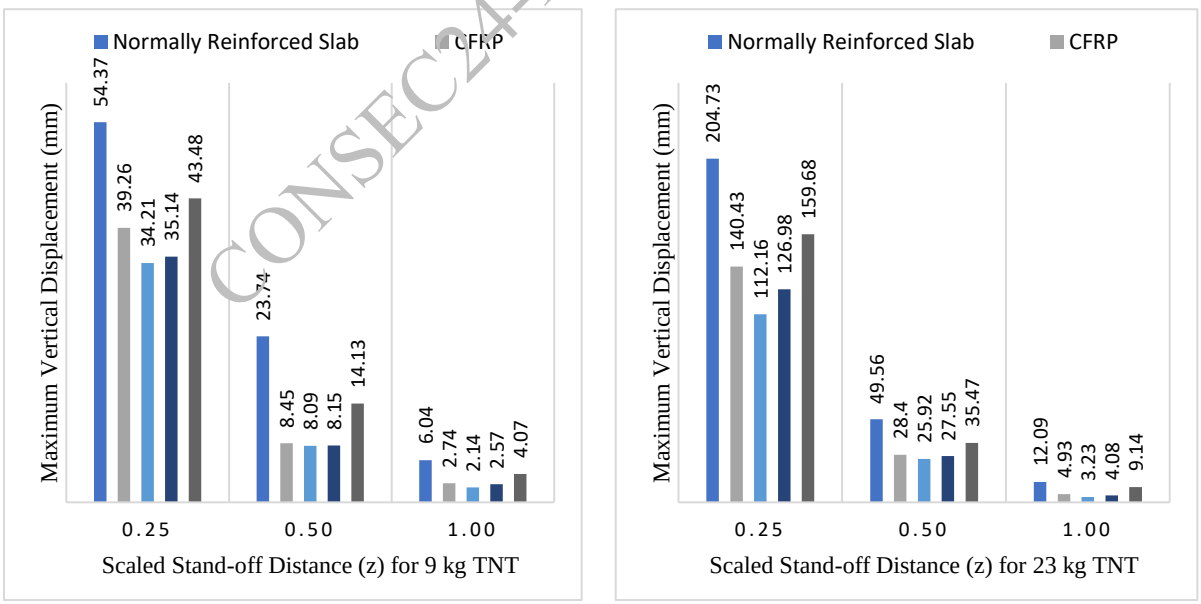

(a) (b)

Figure 5. Finite element analysis results of the parametric study with (a) 9 kg and (b) 23 kg TNT charges

5. Results and Development of Fragility Curves

The results from the parametric study indicate that the steel plates offer the most resistance to the blast loads with a 70% reduction in maximum displacement compared to a normally reinforced concrete slab, followed by ECC, then CFRP, and lastly, HPC. However, steel is not suitable for lightweight applications. Since the retrofitting materials were on the compressive side of the slab under the blast load, the high ductile material properties could not be employed to mitigate the blast response. Notably, the thickness of the ECC layer (20 mm) played the most important role in preventing damage to the slab. The CFRP layer of 5.6 mm thickness performed better than the HPC layer of 20 mm thickness, indicating that CFRP retrofitting is a superior choice when the slab thickness is constrained due to the lower mass and superior stiffness of the material. The fragility functions were derived for un-retrofilled and retrofitted bridge deck slabs, with different retrofit options, against explosions, as shown in Figure 3. In this study, a dimensionless parameter, maximum deflection (Δ) by span length (L), was taken as the engineering demand parameter (EDP). The inverse of the scaled stand-off distance was adopted as an intensity measure. The damage states were categorized as Low, Moderate and Severe, with Δ/L less than 0.025 accounting for Low Damage, Δ/L between 0.025 and 0.05 accounting for Moderate Damage and Δ/L greater than 0.05 accounting for Severe Damage. By providing a thorough evaluation of different retrofit techniques, the research equips engineers with the knowledge to enhance the resilience and safety of highway bridges against explosive threats.

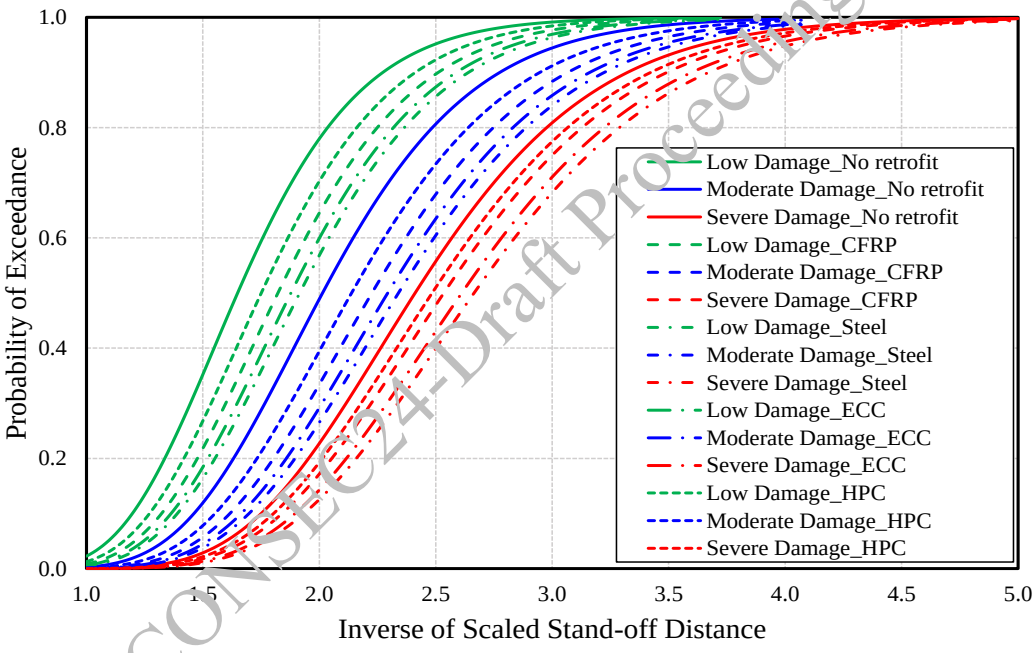

Figure 3. Fragility Curves of Un-retrofitted and Retrofitted Bridge Decks under Blast Loading

6. Conclusions

The research presented in this study highlights the critical need for effective blast retrofit strategies for reinforced concrete (RC) highway bridge decks. Given the increasing vulnerability of these essential infrastructural components to both accidental and deliberate explosions, the findings offer valuable insights into the optimization of retrofitting techniques. By utilizing a three-dimensional numerical simulation approach, the study rigorously evaluated various retrofit strategies, including fibre-reinforced polymer (FRP) jacketing, steel jacketing, concrete jacketing, and engineered cementitious composite (ECC) jacketing. The CONWEP algorithm was used to run blast simulations using ABAQUS software. The charge weights and stand-off distances were varied to conduct a parametric study to assess the structural response of the retrofitted RC slabs. The results point out that CFRP is the superior choice when there are space and weight constraints.

References

C. Wu, et al. “Blast testing of ultra-high performance fibre and FRP-retrofitted concrete slabs.” *Engineering structures* 31.9 (2009). 2060-2069.

E. B. Williamson and D. G. Winget, “Risk management and design of critical bridges for terrorist attacks,” *Journal of Bridge Engineering*, vol. 10, no. 1, pp. 96–106, 2005, doi: 10.1061/(ASCE)1084-0702(2005)10:1(96).

S. Biswas, S. Kulshreshtha, and P. Sengupta. “Blast performance of retrofitted reinforced concrete highway bridges.” Current Perspectives and New Directions in Mechanics, Modelling and Design of Structural Systems. CRC Press, 2022. 583-588.

U. Ebead and H. Marzouk, “Strengthening of two-way slabs using steel plates,” *ACI Structural Journal*, vol. 99, Jan. 2002.

Shear Behaviour of RC Beams Strengthened with a Hybrid Combination Using FRP And UHPC

Rahul Reddy Morthala [1*], Balla Taraka Malleswara Rao [2], and S. Suriya Prakash [3]

[1] *Research Scholar, Department of Civil Engineering, Indian Institute of Technology, Hyderabad, India*
Email: ce22resch01007@iith.ac.in
[2] *Post-Doctoral Fellow, Department of Civil Engineering, Indian Institute of Technology, Hyderabad, India*
Email: ce18resch11004@iith.ac.in
[3] *Professor, Department of Civil Engineering, Indian Institute of Technology, Hyderabad, India*
Email: suriyap@ce.iith.ac.in

[*]Corresponding author

ABSTRACT

Reinforced concrete (RC) beams in buildings and bridges often require shear strengthening. Strengthening is usually carried out to address factors like increased loads, defects during construction and deterioration due to environmental factors. This research focuses on understanding the shear behaviour of the RC beams strengthened with different hybrid configurations, including strengthening with only ultra-high-performance concrete (UHPC) and a combination of UHPC and fibre-reinforced polymer (FRP). UHPC has superior mechanical characteristics such as high strength, stiffness, ductility, durability, chemical resistance and impermeability. Three RC beams of 300 x 300 x1500 mm are cast, strengthened and tested. The test specimens consist of (i) the control RC beam (CB), (ii) three sides of the RC beam strengthened with UHPC (UB), and (iii) the RC beam strengthened with a hybrid combination (HB) of CFRP laminates and fabric attached on soffit of the RC beam and UHPC on three sides of the beam. Test results demonstrate that CFRP laminates in the hybrid configurations act as additional shear reinforcement, resulting in higher stiffness and shear strength than control and the specimens with UB strengthening. Therefore, observation from the experimental results indicates that the hybrid combination of UHPC and FRP can be effectively used in field applications.

KEYWORDS*: RC Beam, CFRP Laminate, UHPC strengthening, Hybrid and Shear Loading.*

1. Introduction

The shear strengthening of reinforced concrete beams and bridge decks in buildings and bridges is often required to improve performance in terms of strength and ductility. Various reasons for degradation of RC bridge decks and beams are corrosion and deterioration due to extreme environmental conditions, spalling of concrete cover, ageing of infrastructure, vehicular loading, damage due to accidental loading such as impact and blast, upgradations due to changes in use and additional loading requirements, defects in design and construction, and change in design codes (Aaleti and Sritharan 2019; Gardena't and Hollaway 1998; Huang et al. 2019; Malleswara Rao and Prakash 2021). Several conventional strengthening techniques are used to repair and rehabilitate concrete structures, such as concrete jacketing, external prestressing, steel plate bonding, and steel jacketing. However, these methods are ineffective since they might increase the member's dead weight and are less durable due to extreme environmental conditions. UHPC is a novel and widely adopted material because of its primary qualities: high compressive, tensile strength, high durability and lower permeability. Using steel fibres in UHPC helps improve the ductility in compression and tension high ductility((Aaleti and Sritharan 2019; Lakavath and Prakash 2024)).
The use of the FRP composites in the sheer strengthening in combination with UHPC strengthening can help improve the shear performance and ductility of the beam compared to the UHPC strengthening. The FRP strengthening has numerous advantages: (i) less weight/strength ratio, (ii) corrosive resistance, (iii) easy installation, (iv) requiring less space and time, and (v) higher durability (Balla and Prakash 2024; Rao

et al. 2023)). Overall, the synergy between the FRP and UHPC overlay enhances the shear performance of the hybrid configuration.

2. Research Significance

Most of the existing studies on the shear strengthening of the beams focus on the EB with FRP fabric or with FRP laminates ((R Balla et al. 2023; Rizzo and De Lorenzis 2009) or the strengthening of the beams with UHPC overlay(Huang et al. 2022; Martinola et al. 2010) However, to the author's knowledge, there is a lack of studies investigating the impact of a hybrid combination of FRP and UHPC overlays on the shear strengthening of beams. The present experimental investigation focused on understanding the shear behaviour of RC beams strengthened with UHPC and a hybrid strengthening, combining the UHPC overlay and FRP strengthening.

3. Experimental Program

Three RC beams of size 300×300×1500 are tested, cast, and cured for 28 days. After 28 days for two beams, the three surfaces, the left, right, and soffit of the beam, are roughened with the grooving technique. The surface roughness index (SRI) is measured for the grooved technique, which is 6.3mm. The sand-filling method is used for measuring SRI(Feng et al. 2022; Yazdi et al. 2020). After surface treatment, shear links are provided on the side surface of the beam with the 150 mm centre-to-centre spacing. After providing the shear links, UHPC is cast and cured for 28 days. All the beams are tested under three-point bending using a 1000kN MTS activator with a shear span length of 522 mm. The concrete mix is designed for 25MPa per IS 10262, and the average compressive strength of the three-cylinder samples is 28 MPa. UHPC cubes of 100×100×100 are tested with a loading rate of 1MPa/sec. The compressive strength of the UHPC is 124 MPa. Table 3 the tensile properties of the CFRP fabric, laminate and steel reinforcement.

Table 3. Material properties of the reinforced materials

Material	Steel Reinforcement	CFRP Fabric	CFRP laminate
Tensile Strength (MPa)	500	985	2800
Elastic Modulus (GPa)	200	99.8	165

Table 4. Test matrix and details of the strengthening configurations

Specimen Name	Control Beam (CB)	UHPC overlay (UB)	Hybrid(HB)
Size of the beam	300×300×1500	400×320×1500	400×320×1500
Longitudinal Reinforcement	8 Nos of 12 mm bars		
Transverse Reinforcement	8 mm dia. @ 300 mm c/c in the test zone and 150mm c/c in the remaining span		
Strengthening Details	Control with no strengthening	50 mm UHPC overlay on two side of the beam and 20mm overlay on the soffit of the beam	Four 50*1.75 mm laminate and two 440GSM fabric is bonded on the soffit of the beam, 50 mm UHPC overlay on two side of the beam and 20mm overlay on the soffit of the beam

The cross-sectional details and strengthening details are presented in Table 4. Figure 1 shows the cross-section details of the beam. UB is the beam strengthened with UHPC on two sides of the RC beam, with a thickness of 50 mm and 20 mm on the bottom side. HB is the hybrid combination of FRP and UHPC. Initially, the four 50×1.75 mm CFRP laminate and two 440 GSM CFRP fabric are bonded to the soffit of the beam. After the FRP strengthening, the UHPC of 50 mm thick on the sides of the beam and 20mm thick on the soffit of the beam over the FRP is cast.

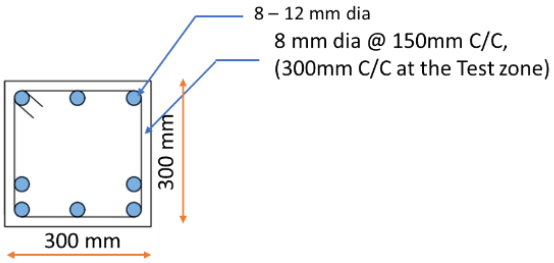

Figure 1. Cross-section details of the RC beams

4. Results and discussions

Figure 2 shows the load-displacement behaviour of all the tested beams. Displacement plotted in the graph is the vertical displacement measured using the LVDT at the loading point. All the strengthened beams are much higher in flexural strength and stiffness than the CB. Table 5 compares the test control and all the results of the strengthened beam. The shear capacity of the HB and UB is 169 and 88% higher than CB's. The sear capacity of the HB is 43% higher than the UB. Fig. 2 shows that the stiffness of the UB and HB is higher than CB. All the beams tested failed in diagonal shear. Moreover, the flexure crack is initiated and propagated in UB near the ultimate load; then flexure crack is converted to the diagonal shear crack. Therefore, the post-peak response of the UB is a ductile behaviour. In CB and HB specimens, shear crack is initiated at pre-peak load and the dowel action from the longitudinal rebar and the steel fibres in UHPC results in the softening response of the beams post-peak.

Table 5. Summary of the tested beams

Specimen ID	Peak Load (kN)	% increase	Displacement at Peak Load (mm)
CB	190.9		3.5
UB	359.1	88	4.0
HB	514.2	169	5.5

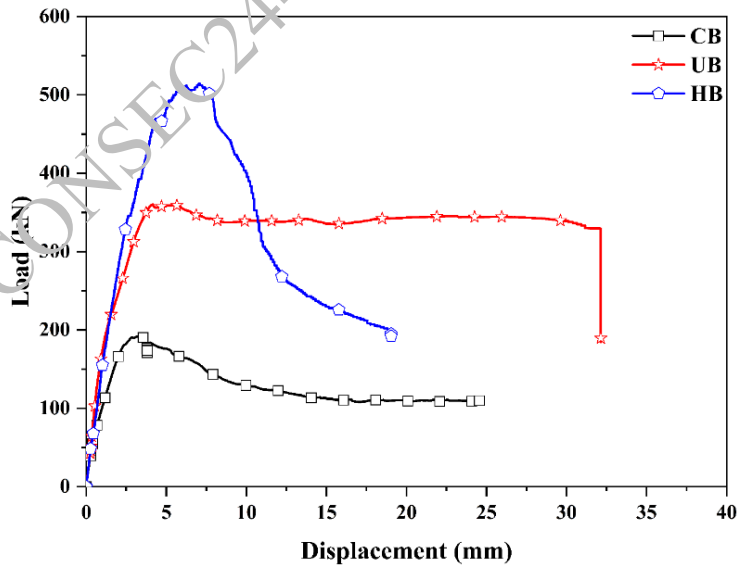

Figure 2. Load vs Displacement curves of the tested beams

5. Conclusions

The control, UHPC overlay and a hybrid combination of UHPC and FRP-strengthened RC beams were tested under shear loading to understand the effect of various strengthening configurations on improving

the shear capacity. The following observations are drawn based on the experimental results of the current study:

- All the strengthening configurations are an effective solution for improving the shear strength, stiffness, and ductility of the RC beams.
- The shear capacity of UB, and HB is 88% and 169% higher compared to CB, respectively,
- All the specimens failed in a diagonal shear failure

Acknowledgments

The authors would like to thank Castcon lab members for their help in testing and review and HEXACURE, a division of the BHOR chemicals and plastics Pvt. Ltd. for sponsoring the FRP materials used in the research work.

References

Aaleti, S., and S. Sritharan. 2019. "Quantifying Bonding Characteristics between UHPC and Normal-Strength Concrete for Bridge Deck Application." *Journal of Bridge Engineering*, 24 (6). American Society of Civil Engineers (ASCE). https://doi.org/10.1061/(asce)be.1943-5592.0001404.

Balla, T. M. R., and S. S. Prakash. 2024. "Cracking and failure mode behaviour of hybrid <scp>FRP</scp> strengthened <scp>RC</scp> column members under flexural loading." *Structural Concrete*. https://doi.org/10.1002/suco.202300789.

Feng, S., H. Xiao, M. Liu, F. Zhang, and M. Lu. 2022. "Shear behaviour of interface between normal-strength concrete and UHPC: Experiment and predictive model." *Constr Build Mater*, 342. Elsevier Ltd. https://doi.org/10.1016/j.conbuildmat.2022.127919.

Gardena't, H. N., and L. C. Hollaway. 1998. *An experimental study of the failure modes of reinforced concrete beams strengthened with prestressed carbon composite plates*. *Composites Part B*.

Huang, X., L. Sui, F. Xing, Y. Zhou, and Y. Wu. 2019. "Reliability assessment for flexural FRP-Strengthened reinforced concrete beams based on Importance Sampling." *Compos B Eng*, 156: 378–398. Elsevier Ltd. https://doi.org/10.1016/j.compositesb.2018.09.002.

Huang, Y., S. Grünewald, E. Schlangen, and M. Luković. 2022. "Strengthening of concrete structures with ultra high performance fiber reinforced concrete (UHPFRC): A critical review." *Constr Build Mater*. Elsevier Ltd.

Lakavath, C., and S. S. Prakash. 2024. "Interface Shear Behavior of Ultrahigh-Performance Fiber-Reinforced Concrete Using Digital Image Correlation Technique." *Journal of Materials in Civil Engineering*, 36 (3). American Society of Civil Engineers (ASCE). https://doi.org/10.1061/jmcee7.mteng-16817.

Malleswara Rao, B. T., and S. S. Prakash. 2021. "Shape Effects on the Behavior of Hybrid FRP–Strengthened Rectangular RC Columns under Axial Compression." *Journal of Composites for Construction*, 25 (5). American Society of Civil Engineers (ASCE). https://doi.org/10.1061/(asce)cc.1943-5614.0001152.

Martinola, G., A. Meda, G. A. Plizzari, and Z. Rinaldi. 2010. "Strengthening and repair of RC beams with fiber reinforced concrete." *Cem Concr Compos*, 32 (9): 731–739. https://doi.org/10.1016/j.cemconcomp.2010.07.001.

R Balla, T. M., R. Reddy Morthala, and S. Prakash Shanmugam. 2023. "EFFECTIVENESS OF HYBRID FRP STRENGTHENING ON THE SHEAR BEHAVIOUR OF REINFORCED CONCRETE BEAMS SEE PROFILE." https://doi.org/10.5281/zenodo.8155764.

Rao, B. T. M., R. R. Morthala, and S. Suriya Prakash. 2023. "Experimental Investigation on Flexural Behaviour of RC Beams Strengthened with Various FRP Composite Configurations." 121–128.

Rizzo, A., and L. De Lorenzis. 2009. "Behavior and capacity of RC beams strengthened in shear with NSM FRP reinforcement." *Constr Build Mater*, 23 (4): 1555–1567. https://doi.org/10.1016/j.conbuildmat.2007.08.014.

Yazdi, M. A., E. Dejager, M. Debraekeleer, E. Gruyaert, K. Van Tittelboom, and N. De Belie. 2020. "Bond strength between concrete and repair mortar and its relation with concrete removal techniques and substrate composition." *Constr Build Mater*, 230. Elsevier Ltd. https://doi.org/10.1016/j.conbuildmat.2019.116900.

Cathodic Protection of Marine Prestressed Concrete Bridges – Review of Case Studies

Suraksha Sharma[1*], Karla Hornbostel [1,2], and Mette Rica Geiker [1]

[1] Norwegian University of Science and Technology, Trondheim, Norway.
Email: suraksha.sharma@ntnu.no
[2] NPRA The Norwegian Public Roads Administration, Oslo, Norway

[*]Corresponding author

ABSTRACT

Reinforcement corrosion is the main deterioration mechanism in marine exposed reinforced concrete structures. Recent investigations show that not only the ordinary reinforcement but also possible prestressed tendons might be affected. The present paper discusses considerations in connection with the potential application of cathodic protection (CP) systems on marine prestressed concrete bridges. It mainly addresses the challenges encountered by reviewing several case studies.

KEYWORDS: *Corrosion, Marine environment, Prestressed concrete bridges, Cathodic protection*

1. Introduction

In a study conducted by Angst (2018), the direct cost of corrosion in the U.S. is estimated to be 3.1% of the total GDP, amounting to approx. US$575 billion annually. Nearly half of these direct costs are attributed to infrastructure, with approx. 8% of these are associated with reinforced concrete bridges. Also, a substantial portion of Europe's modern infrastructure was developed shortly after World War II. Many prestressed bridges were built during that period, and some of them now require repair to meet the structural demand and ensure their continued safety and functionality Bridge Masters (2021).

Deterioration in the prestressed bridges depends on the construction methodology of the structure, hence it is important to understand the fundamental difference between the two primary systems: post-tensioned and pretensioned. In a pretensioned system, the strands are tensioned before the concrete is placed and hardened, whereas for the post-tensioned system, initially the concrete surrounding the duct is hardened, then the strands are placed inside the duct and tensioned. Finally, a filler material is pumped inside the duct making it a bonded or un-bonded (dependent on the material) post-tensioned system. The prestressed systems, especially the post-tensioned system, provide superior corrosion protection compared to ordinary reinforced structures. To prevent corrosion, the prestressed tendons have multiple layers of protection; the concrete cover, the duct (metallic or plastic), and the filler material (grout or flexible fillers). Despite high protection levels, case studies have shown that post-tensioned structures can be prone to corrosion Menga et al. (2023) due to the infiltration of harmful substances such as moisture, chloride, and carbon dioxide Sousa et al. (2020). In addition to their vulnerability to chloride-induced corrosion, the prestressed reinforcement exhibits an inherent susceptibility to brittle fracture due to stress corrosion cracking (SCC), e.g. induced by hydrogen embrittlement (HE) Bertolini et al. (2013) and ACI Committee 222 (2001).

According to COST 534 (2009), there are several potential methods to control corrosion of prestressed structures including cathodic prevention, cathodic protection (CP), and chloride removal. CP was initially pioneered by Humphry Davy in 1824 to protect metal in seawater. Since then, it has been extensively applied to metallic and buried metallic structures. The application of CP on reinforced concrete was introduced decades later, in the year 1957 in the US Poursaee (2016) and in Europe in 1985 Ducasse-Lapeyrusse et al. (2023). Today it is accepted that CP is a highly effective way to control corrosion in chloride-contaminated ordinary reinforced concrete structures Callon et al. (2004), COST 534 (2009). However, the applicability and effectiveness of CP on prestressed structures are yet to be confirmed. The

theoretical aspects of using CP on prestressed concrete structures, especially the risk of HE, have been discussed in detail in the COST534 report COST 534 (2009).
The theory of CP involves using direct current to prevent or reduce the corrosion of a metal surface. Corrosion occurs when metal oxidization occurs (i.e., it releases electrons). When the electrons are intentionally supplied to the metal surface, the cathodic reaction is accelerated (consuming the electrons), while simultaneously inhibiting the anodic reaction (i.e., dissolution of the metal). The two principal methods through which CP can be achieved are: (i) using inert anodes V. Ashworth (1994) in combination with applying an external direct current (impressed current CP, ICCP) Polder et al. (2009) and Bromfield and Wyatt (2018) and ii) employing less noble anodes (e.g., magnesium, zinc, or aluminium Wilson et al. (2013) (sacrificial anode CP, SACP) to generate a driving current. There are so-called hybrid systems combining the principles, where initially ICCP is implemented for a short time to re-alkalize the corrosion sites using an anode which later works as a sacrificial anode in an SACP system to prevent corrosion in the long run Christodoulou and Kilgour (2013).
In a prestressed bridge structure, CP is implemented with three primary objectives i) to protect the ordinary reinforcement ii) to protect the prestressed reinforcement or iii) to protect both prestressed and ordinary reinforcement. In this paper, the first objective is regarded as Strategy I whereas, the second and third objectives are considered as Strategy II. The application of CP can pose several challenges depending on the intended use (Strategy I and II) or the methods employed (ICCP, SACP or hybrid system).
This paper reviews case studies of prestressed bridges employing CP systems. In Section 2, challenges potentially associated with the use of CP on prestressed structures are summarized. These challenges are classified based on relation to prestressing steel (2.1) and those concerning the general application of CP (2.2). Section 3 brings an overview of case studies summarizing the challenges observed. Both applications of Strategy I and II are addressed. Section 4 discussed the applicability of CP using either ICCP, SAPC or a combination (hybrid) considering the impact on both the ordinary reinforcement and the prestressed reinforcement. Section 5 provides the conclusions.

2. Challenges associated with the application of CP

2.1 Challenges related to prestressed reinforcement

Various material aspects of prestressed reinforcement set it apart from ordinary reinforcement, making it more vulnerable to deterioration: a) metallurgical variables ACI Committee 222 (2001) and Poursaee (2016) b) heat and mechanical treatment ACI Committee 222 (2001), Perrin et al. (2010) and Atienza et al. (2012) c) chemical composition Lv et al. (2020) d) surface texture Li et al. (2011) and e) forms of prestressed reinforcement Li et al. (2011) and Poursaee (2016). These aspects complicate the application of CP on prestressed reinforcement, compared to ordinary reinforcement, resulting in several challenges as discussed below.

2.1.1 Hydrogen embrittlement

One of the main challenges of the applicability of ICCP on prestressed bridges is the risk of HE. It can occur in both Strategy I and II as mentioned above. For Strategy I it can occur due to the overprotection of ordinary reinforcement in the vicinity of prestressed tendons. For Strategy II it can take place due to the direct application of CP on prestressed reinforcement leading to hydrogen evolution as a cathodic reaction below a threshold potential.
Various experimental laboratory studies showed that the potential at which hydrogen evolution occurs depends on the type of environment of the prestressed reinforcement. The investigation led by Price et al. (1992) indicated that hydrogen can enter the prestressed reinforcement as a result of CP. Several groups Parkins et al. (1982), Hartt et al. (1993), Isecke and Mietz (1993), and Funahashi et al. (1994) investigated the so-called threshold potential for HE in aggressive environments (see Figure 1). Isecke and Mietz (1993) discovered that in a chloride-exposed environment (simulated by a solution of $Ca(OH)_2$ + 3% Cl, pH=12.6), the occurrence of cathodic overprotection during the CP of prestressed strands elevated the risk of HE at potentials lower than -1141 $mV_{SCE,}$ and increased hydrogen activity was observed below this potential. It could be mentioned that Hartt et al. (1993) observed that the increase in chloride content did not affect the normalized fracture load of the prestressed reinforcement. According to Funahashi et al. (1994), for steel

embedded in mortar with pH 12.4 and pH 9, hydrogen was developed at potentials -974 and -750 mV_{SCE}, respectively. This aligns with the values mentioned by Bertolini et al. (2013).

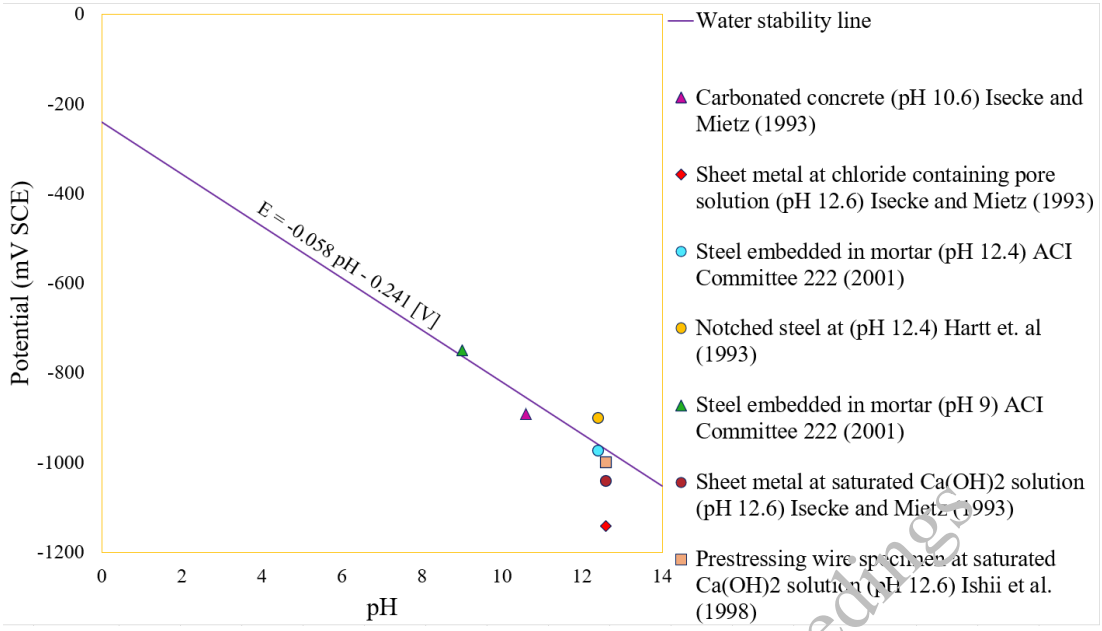

Figure 1. Threshold potentials below which risk of hydrogen embrittlement (HE) exists as a function of pH.

Full-scale testing was also conducted for the application of CP, based on the threshold potential of HE, on both post-tensioned and pre-tensioned bridges by Funahashi and Young (1996). It was observed that at -700 mV_{SCE}, hydrogen was not generated on the wires and rods of pretensioned and post-tensioned beams. However, hydrogen evolution could occur where the concrete was contaminated (lower pH). Observations were made on the potential difference between the metallic duct and the rod, which was determined to be insufficient to cause HE. Similarly, Smeltzer et al. (1992) applied CP on concrete beams containing tendons providing protection levels of -524 mV_{SCE} to -1224 mV_{SCE} for up to 3 months to investigate HE. However, no loss of capacity or signs of brittle fracture were found. Li et al. (2022) studied the effect of CP on corroded prestressed cable stay high-strength steel wires in the atmospheric marine environment. The results from the experiment showed that the application of ICCP effectively reduced the corrosion of the steel wires and the specimens showcased no to slight corrosion; however, aspects of HE were not discussed. A recent study Elomari (2019) conducted on CP of corroded pre-tensioned tendons also concluded that no signs of HE were observed between the potential of -694 to -794 mV_{SCE} for both galvanized and ungalvanized tendons. The test was conducted for 553 days for ungalvanized and 137 days for galvanized tendons. However, at -1044 to -1244 mV_{SCE}, loss of ductility was observed in galvanized corroded pre-tensioned bars, but it was solely not due to HE. The study concluded that strength, degree of corrosion, and the level of pre-stress appear to have more influence on the bars than the application of CP.

The disparities between the results are quite noteworthy. Full-scale tests, being closer to real-world conditions, exhibit reduced susceptibility to HE Smeltzer et al. (1992) and Elomari (2019) owing to a less aggressive environment. This might not be true in marine-exposed environments (where chloride-induced pitting corrosion is observed) as mentioned by Bertolini et al. (2013), who pointed out the risk for hydrogen evolution in corrosion pits (with localized acidification). This real-world condition has been overlooked in the presented studies. Consequently, the applied potential at which HE occurs in the presence of damaged prestressed tendons (active pitting corrosion) is still uncertain.

2.1.2 Stress corrosion cracking

Stress corrosion cracking (SCC) refers to the initiation and propagation of sharp cracks in metal leading to failure without warning from the combined action of corrosion under a specific mechanical and environmental load (externally applied or residual) Bertolini et al. (2013). As the prestressed reinforcement in prestressed bridges are in a tensioned state, they are prone to SCC. An example of SCC occurring in a floating bridge structure in a marine environment was mentioned by Hong (1982). However, the

observations of the possible occurrence of SCC in prestressed reinforcement in chloride containing environment are quite contradictory Manning (1988), Moore et al. (1970), Hong (1982), and Li et al. (2008). In both Strategy I and II, SCC can be promoted by HE if overprotection of CP is present, thereby accelerating crack growth and potentially leading to premature failure of the prestressed reinforcement.

2.1.3 Shielding effect

The uneven distribution of current within the prestressed reinforcement, arising from the presence of layers of reinforcement in the pretensioned system and due to the presence of ducts in the post-tensioned system, is referred to as the shielding effect.
For Strategy I: instead of acting as a challenge, the shielding effect of other layers of reinforcement and/or ducts effectively prevents the polarization of prestressed reinforcement. Also, it reduces the risks of HE in prestressed reinforcement. Whereas for Strategy II: it presents a challenge for both metallic and plastic ducts and/or a dense layer of reinforcement in front of pre-stressed wires in pre-tensioned structures. It significantly reduces the efficiency of CP on the strands. From study conducted by Funahashi and Young (1996) and Hope and Ip (1993), it was found that the shielding effect was prominent when the metallic duct was electrically connected to the post-tensioned rods as the impressed current followed the path of the ducts. Similarly, the use of plastic ducts acted as an insulator. Shielding can also be a concern for pretensioned bridges if the anodes are not distributed uniformly in the structure. In the experiment conducted by Funahashi and Young (1996) on pretensioned beams, the pretensioned wires on the opposite side of the impressed anode did not receive significant CP.

2.2 General challenges related to the application of CP

There are various general challenges related to the design, installation, and operation of CP. The challenges mentioned below were observed in the case studies described in Section 3.

2.2.1 Inadequacy in polarizing steel by the anodes

In a CP system, poor design (specifically relating to the location, and quantity) and maintenance of anodes can result in inadequately polarized steel due to uneven current distribution. In SACP, there might be cases where the prestressed reinforcement might not be polarized due to the inadequacy of the sacrificial anodes to generate the required current Bennett and Schue (1995).

2.2.2 Inhomogeneous moisture condition

Inhomogeneous moisture content of the concrete may lead to varying and potentially uncontrollable protection levels. Insufficient moisture in concrete leads to conductivity issues leading to difficulties in maintaining the CP system. The presence of moisture in the concrete can be beneficial for CP as it provides conductivity in a CP system, maintaining its ability to protect the reinforcement. However, this might not be the case in the presence of high moisture loads, e.g., running water. In this case, the current chooses the low resistance path to complete the circuit leading to a short circuit in the system.

2.2.3 Debonding of anode

Debonding refers to the separation of the overlay or anode from the concrete to be protected. This generally happens due to incorrect installations, inadequate surface preparations, poor adhesion of coatings, or exposure to harsh environmental conditions Bennett and Schue (1995), COST 534 (2009), and Van den Hondel et al. (2018). A study conducted in 2009 COST 534 (2009), highlighted that the production of acid in the anode region can also lead to cement paste softening, ultimately causing loss of bond.

2.3 Field experiences of CP

CP has been used in prestressed bridges to protect both the ordinary and the prestressed reinforcement (Strategy I and II). As per European standards NS-EN ISO 12696:2022 (2022), by maintaining the overpotential threshold of - 900mV_{SCE}, CP appears to be feasible to protect ordinary reinforcement in the same structure without harming the tendons at normal operating conditions. There are also cases where CP has been used directly to protect the prestressed reinforcement.
Table 1 provides an overview of CP systems employed in the prestressed bridges for Strategy I and II. It also includes the challenges observed in the bridges as detailed in Section 2. As mentioned in Section 2, SCC is recognized as a potential issue in prestressed bridges due to the high tensile stresses in the tendons,

but this issue was not observed in any of the case studies presented. Neither was shielding mentioned in the case studies. In addition to the observed challenges, the table indicates whether or not the CP system was found to be effective in the respective case studies. But it is important to note that this assessment only covers a short duration.

Table 1. Overview of observed challenges (HE: hydrogen embrittlement, IM: inhomogeneous moisture, De: debonding, IPS: inadequate steel polarization), and effectiveness (E) of CP system applied on prestressed bridges Strategy I & II (see text). Pre: pretensioned, Post: post-tensioned, NA: data not available.

	Bridge	Damaged component	Type of CP & anode	Time of eval.(yrs)	Challenges observed				E
					HE	IM	De	IPS	
Strategy I	Overpass of I-74, IL[1]	Abutment & pier cap (Pre)	SACP & Zn hydrogel	1, 2, 3	NA	Yes	Yes	No	No
	I-55 over Sugar Creek, IL[1]	Abutment (Pre)	SACP & Zn hydrogel	1, 2, 3	NA	Yes	Yes	No	No
	Neerbossche Bridge, NL[2]	Segment 1 & 2 (Post)	SACP & Zn	3, 4	No	Yes	Yes	No	Yes
	Saint-Cloud Viaduct, FR[3]	Abutments & junction (Post)	ICCP & Ti	3	No	No	No	Yes	Yes
Strategy II	Twin structure over I-474, IL[1]	Abutment (Pre)	SACP & sprayed Zn	1	No	No	No	Yes	No
	Willoughby Bay Bridge on I-64, VA[4]	Piles (Pre)	SACP & Zn grout jacket	1.2	No	Yes	No	No	Yes
			SACP & Al-Zn-In		No	Yes	No	No	Yes
	Howard Frankland Bridge, FL[5]	Beam Piles (Pre)	SACP & Zn	3.2	No	No	No	No	Yes
			ICCP & Ti mesh	3.2	No	No	No	No	Yes
			Cond. rubber	0.1, 2.7	No	Yes	No	Yes	Yes
	Abbey Road Bridge, OH [6]	Soffit of box beams (Pre)	SACP/ ICCP & metalized Zn	0.6, 3.1	No	Yes	No	Yes	No
	West 130th St. Bridge, OH [6]	Soffit of box beams (Pre)	ICCP & conductive coating	2.4	No	Yes	Yes	No	No
	Route 37 Bridge, NY [7]	Box Beam (Pre)	SACP & embedded galvanic anodes	2	NA	No	No	No	Yes
	Kyle of Tongue Bridge, UK [8]	Beam (Pre)	Hybrid, hybrid	1.6	No	No	No	No	Yes
	North-South Viaduct, BE [9]	Column head and deck (Pre)	ICCP & Ti strips	0.1	No	No	No	No	Yes

1: Gawedzinski (2002) 2: Van den Hondel et al. (2018) 3: Ducasse-Lapeyrusse et al. (2023) 4: Clemeña and Jackson (1999) 5: Bennett and Schue (1995, Virmani and Clemena (1998, Vinik and Duncan (2021) 6: Bennett and Schue (1995, Virmani and Clemena (1998) 7: Whitmore and Ball (2007) 8: Christodoulou and Kilgour (2013) 9: COST 534 (2009)

2.3.1 Hydrogen embrittlement (HE)

From the case studies for both Strategy I and II, HE was not detected in the reported cases (no data for 4 of 15 case studies). In most of the case studies, the possibility of HE was discarded based on the measured electrochemical potential. For bridges in Florida and Ohio, it was found that even at zones where the potentials were more negative than the threshold potentials, HE was not observed Bennett and Schue (1995). In the first year, West 130th Bridge was overprotected in many areas but after 2.4 years the potentials were maintained Bennett and Schue (1995). Also, the bridge piles in Florida containing conductive rubber showed potentials below the threshold due to inhomogeneous moisture conditions Bennett and Schue (1995). In addition to the mentioned case studies in the table, 30 bridges with beam heads undergoing corrosion in ordinary reinforcement, prestressed tendons, and anchorage were protected by employing ICCP in the Netherlands Hondel et al. (2015). After 2 years of installation, it was found that all components of the beam heads were well protected and as the potential was monitored throughout, issues of HE were not observed Hondel et al. (2015). It is generally accepted that above -900 mV_{SCE} HE does not occur. However, COST 534 (2009), and Bertolini et al. (2013) noted that in areas with pitting, hydrogen development can occur above -900 mV_{SCE} as well. HE cases may be underreported as they often coincide with other corrosion mechanisms like pitting ACI Committee 222 (2001), reducing the focus on further tests for HE.

2.3.2 Inhomogeneous moisture distribution

A SACP system was installed on prestressed concrete I beams in Illinois using sprayed-on metalizing anodes Gawedzinski (2002). After a year of installation, the effectiveness of the sacrificial anodes was evaluated and no reduction in corrosion potentials was observed. The areas with more water had high corrosion potential leading to the ineffectiveness of anode to drive potential. Similarly, for both bridges in Ohio, due to inhomogeneous moisture content, it was difficult to maintain the polarization decay criteria Bennett and Schue (1995). In the Neerbossche Bridge, Netherlands Van den Hondel et al. (2018), both current output and potential decay decreased after 3-4 years of application, due to drying of concrete.

2.3.3 Debonding

Early (0.2 years) signs of debonding of conductive paint anodes in form of blistering, were observed in 5% of the total area of the West 130th Street bridge Bennett and Schue (1995). Initially, debonding was also observed in Neerbossche Bridge Van den Hondel et al. (2018).

2.3.4 Inadequacy in polarizing steel

The SACP on the Abbey Road bridge was unable to generate enough current, and the system was shifted to ICCP after few months Bennett and Schue (1995). Similarly, for the bridge over I-474, the sprayed-on zinc anode was not able to develop enough current to arrest corrosion and the installation was terminated. In the case of the viaduct in France, ICCP was used to protect the ordinary reinforcement by creating subzones Ducasse-Lapeyrusse et al. (2023). The anodes were omitted in the zones where post-tensioned tendons were present. The results after 3 years showed that the top inside, central, and bottom zones were successfully protected. However, at the top outside zone (near tendon) high current demand was observed and the potential decay criteria was not met. This discrepancy was explained by the presence of ducts and high chloride content in the region.

2.4 Applicability of CP on prestressed bridges

Challenges anticipated from Sections 2 and 3 are provided in Table 2. These challenges necessitate careful consideration in the design, construction, and maintenance of CP systems on prestressed bridges to ensure their safety and longevity.

Table 2. Summary of challenges anticipated on prestressed bridges applying Strategy I or II.

	HE	SCC	Shielding	CP challenges
Strategy I	X			X
Strategy II	X	X	X	X

Considering the observed challenges and effectiveness (Table 1, Section 3), CP is found to be applicable for pre-tensioned bridges. However, the direct application of CP on corroded post-tensioned tendons

appears inadvisable COST 534 (2009). A study by Liao et al. (2022) mentioned the use of sacrificial anodes in tendon repair projects for post-tensioned bridges in 2012 in the US after the issues of grout dissimilarity causing failure in the repair of corroded tendons; unfortunately, documentation related to it was not found. According to Manickam and Pillai (2023), an experimental study indicates that protecting strands in anchorage regions using sacrificial anodes in combination with regrouting seems to be a viable option. The study showed that the galvanic anode connected to the strand end of the anchorage was sufficient to protect the strands inside the anchorage region. Preliminary numerical analyses were performed to check the effectiveness of ICCP on an initially passive strand in a post-tensioned tendon where an anode was employed as a middle strand in a helically twisted seven-wired strand. The preliminary results are promising, however, more research is required and also corroded wires should be taken into account to consider the risks of HE. Few case studies on the application of hybrid systems on prestressed bridges indicated effective application Christodoulou and Kilgour (2013). However, more studies and documentation on the practical application of hybrid systems are required to measure their long-term effectiveness.

As a summary, Table 3 provides an overview of today's experience with the application of CP on prestressed bridges exposed to the marine environment.

Table 3. Applicability of CP (impressed current (ICCP), sacrificial anodes (SACP), or a combination (hybrid)) on prestressed bridges considering both the ordinary reinforcement (OR) and prestressed reinforcement (PR).

Type of prestressing	Reinforcement type and state		
	OR (corroded)	PR	PR (corroded)
Pretensioned	Well-established: ICCP, SACP Limited experience: Hybrid	Well-established: ICCP, SACP Limited experience: Hybrid	Well-established: ICCP, SACP Limited experience: Hybrid
Post-tensioned	Well-established: ICCP, SACP Limited experience: Hybrid	Limited experience and research required: all	Research required: all

3. Conclusions

Case studies revealed that CP presents different challenges when intended for ordinary reinforcement (Strategy I) and for prestressed reinforcement and ordinary reinforcement (Strategy II). General challenges encountered for both Strategy I and II include inhomogeneous moisture conditions, debonding, and inadequacy in polarizing the reinforcement.

The main conclusions drawn are:

- For Strategy I: Hydrogen embrittlement can be a challenge if the potential is low. However, shielding limits the polarization of the prestressed reinforcement.
- For Strategy II: Both hydrogen embrittlement and shielding are challenges.
- For Strategy I, the application of CP (ICCP and SACP) appears feasible for all prestressed structures on the condition that potential limits are not exceeded.
- For Strategy II, the application of CP (ICCP and SACP) appears feasible for prestressed reinforcement in pretensioned bridges. For post-tensioned bridges, more research is needed and especially ICCP as per today is not advisable.

Acknowledgment

The authors acknowledge Green Management of Structures for Infrastructure, known as EXCON (Research Council Norway project number 340843) for their funding support.

References

ACI Committee 222, (2001). "Corrosion of Prestressing Steels", *ACI 222.2R-01*, Farmington Hills, MI. 43.

Angst, U. M. (2018). "Challenges and Opportunities in Corrosion of Steel in Concrete", *Materials and Structures* 51(1): 4.

Atienza, J. M., et al. (2012). "The Role of Residual Stresses in the Performance and Durability of Prestressing Steel Wires", *Experimental Mechanics*, 52(7): 881-893.

Bennett, J. E. and T. J. Schue, (1995). "Cathodic Protection Field Trials on Prestressed Concrete Components", FHWA-RD-95-032, ELTECH Research Corporation, Virginia.

Bertolini, L., et al. (2013). Corrosion of Steel in Concrete: Prevention, Diagnosis, Repair.

Bridge Masters. (2021). "Think U.S. Bridge Infrastructure Is in Rough Condition? Check out Europe's.", 2023, from https://bridgemastersinc.com/europes-infrastructure/.

Bromfield, J. and B. Wyatt (2018) "Cathodic Protection of Steel in Concrete - the International Perspective", AZoM, Corrosion Protection Association.

Callon, R., et al. (2004). "Selection Guidelines for Using Cathodic Protection Systems for Reinforced and Prestressed Concrete Structures", *CorrproTechnical Library*, CP-118.

Christodoulou, C. and R. Kilgour (2013). "The World's First Hybrid Corrosion Protection Systems for Prestressed Concrete Bridges", Corrosion and Prevention, Australasian Corrosion Association Inc.

Clemeña, G. G. and D. R. Jackson, (1999). "Evaluation of Anodes for Galvanic Cathodic Prevention of Steel Corrosion in Prestressed Concrete Piles in Marine Environments in Virginia", VTRC-00-R3, VDOT, VTRC & FHA, Virginia.

COST 534, (2009). "New Materials System, Methods and Concepts for Prestressed Concrete Structures", Electrochemical Maintenance and Repair Methods-Part 4, COST Office. 32.

Ducasse-Lapeyrusse, J., et al. (2023). "Assessment of the Impressed Current Cathodic Protection System after 4 Years Operation: Case Study of the Saint-Cloud Viaduct (France)", *Case Studies in Construction Materials*, 18: e02023.

Elomari, I. R. (2019). "Cathodic Protection of Corroded Pre-Stressed Tendons", Doctoral, Sheffield Hallam University.

Funahashi, M. and W. T. Young (1996). "Cathodic Protection of Prestressed Bridge Members-Full-Scale Testing", *Transportation Research Record*, 1561(1): 13-25.

Funahashi, M., et al., (1994). "Cathodic Protection Developments for Prestressed Concrete Components", FWHA-RD-94-001, Federal Highway Administration, United States.

Gawedzinski, M., (2002). "Evaluation of Sprayed-on Metallizing for Precast Prestressed Concrete I-Beams", FHWA/IL/PRR-141, Illinois DoT & Bureau of Materials and Physical Research, United States.

Hartt, W. H., et al. (1993). "Influence of Potential, Chlorides, Ph, and Precharging Time on Embrittlement of Cathodically Polarized Prestressing Steel", *Corrosion*, 49(05).

Hondel, A. J., et al. (2015). "Application of Cathodic Protection on 30 Concrete Bridges with Pre-Stressing Steel: Remaining Service Life Extended with More Than 20 Years", *ICCRRR - International Conference on Concrete Repair, Rehabilitation and Retrofitting – Leipzig*, Germany.

Hong, A. S. Y. (1982). "The Stress-Corrosion Cracking of Prestressing Steel Tendons", Masters, The University of New South Wales School of Metallurgy.

Hope, B. B. and A. K. C. Ip (1993). "Problems Associated with Cathodic Protection of Prestressed Concrete Structures", *Corrosion Science*, 35(5): 1641-1647.

Isecke, B. and J. Mietz (1993). "The Risk of Hydrogen Embrittlement in High-Strength Prestressing Steels under Cathodic Protection", *Steel Research*, 64(1): 97-101.

Li, F. M., et al. (2008). "Stress Corrosion Cracking Susceptibility of Steel Strands in Concrete Contaminating Salt", *Proceeding of the first international conference of microstructure related durability of cementitious composites*, Nanjing, China.

Li, F., et al. (2011). "Corrosion Propagation of Prestressing Steel Strands in Concrete Subject to Chloride Attack", *Construction and Building Materials*, 25(10): 3878-3885.

Li, S., et al. (2022). "Corrosion Evaluation of Prestressed High-Strength Steel Wires with Impressed Current Cathodic Protection Based on Acoustic Emission Technique", *Structural Control and Health Monitoring*, 29(5): e2934.

Liao, H., et al. (2022). "Post-Tensioning Investigation and Corrosion Mitigation in Voided Slab Bridges", *11th International Conference on Short and Medium Span Bridges*, Toronto, Canada.

Lv, S., et al. (2020). "Corrosion of High-Strength Steel Wires under Tensile Stress", *Materials (Basel)*, 13(21).

Manning, D. G., (1988). "Durability of Prestressed Concrete Highway Structures", NCHRP Synthesis of Highway Practice 140, Washington, D.C. 75.

Menga, A., et al. (2023). "Corrosion-Induced Damages and Failures of Post-Tensioned Bridges: A Literature Review", *Structural Concrete*, 24(1): 84-99.

Moore, D. G., et al., (1970). "Protection of Steel in Prestressed Concrete Bridges ", National Cooperative Highway Research Program, Washington.

NS-EN ISO 12696:2022, (2022). "Cathodic Protection of Steel in Concrete ", Standard Norge.

Parkins, R. N., et al. (1982). "Environment Sensitive Cracking of Pre-Stressing Steels" *Corrosion Science*, 22(5): 379-405.

Perrin, M., et al. (2010). "Hydrogen Embrittlement of Prestressing Cables", *Corrosion Science*, 52(6): 1915-1926.
Polder, R., et al. (2009). Guideline for Smart Cathodic Protection of Steel in Concrete, FEHRL.
Poursaee, A. (2016). 12 - Corrosion Protection Methods of Steel in Concrete. "Corrosion of Steel in Concrete Structures". Oxford, Woodhead Publishing: 241-248.
Price, S., et al. (1992). "The Role of Notches in the Hydrogen-Assisted Cracking of Steel Prestressing Tendons", *Materials forum*, Rushcutters Bay.
Smeltzer, W. W., et al., (1992). "Hydrogen Evolution Laboratory Investigation: Research Report Mat-92-08", Ontario Ministry of Transportation, Ontario.
Sousa, M. L., et al., (2020). "Expected Implications of Climate Change on the Corrosion of Structures", European Union, Luxembourg.
V. Ashworth (1994). Principles of Cathodic Protection. "Corrosion Control". R. A. J. L.L. Shreir, and G.T. Burstein, Butterworth-Heinemann, Third Edition.
Van den Hondel, A. J., et al. (2018). "A 5 Year Track Record on a Galvanic Cp System Applied on a Light Weight Concrete Bridge with Prestressed Steel – Developments in Time of the Effectiveness as Determined by Depolarisation Values and Current Densities", *MATEC Web Conf*, 199: 05004.
Vinik, P. and M. Duncan, (2021). "Utilization of Cathodic Protection to Extend the Service Life of Reinforced Concrete Bridges – an Overview of the Installation and Maintenance of the Cathodic Protection Systems Protecting the Howard Frankland and Crescent Beach Bridges ", FHWA-HIF-22-004, Florida Department of Transportation and Greenman Pedersen, Inc., Florida.
Virmani, Y. P. and G. G. Clemena, (1998). "Corrosion Protection-Concrete Bridges", US Department of Transportation, Virginia.
Whitmore, D. and C. Ball (2007). "Galvanic Corrosion Protection of Prestressed Post-Tensioned Structures", *Stucture Congress: New Horizons and Better Practices*.
Wilson, K., et al. (2013). "The Selection and Use of Cathodic Protection Systems for the Repair of Reinforced Concrete Structures", *Construction and Building Materials*, 39: 19-25.

A Pull-Out Test to Evaluate the Adhesive Bonding of Concrete Strengthening with CFRP Under Accelerated Carbonation

Dania Kabalan[1], Amandine Célino[2], Frédéric Grondin[1], and Emmanuel Rozière[1*]

[1] Nantes Université, Ecole Centrale Nantes, CNRS, GeM, UMR 6183, F-44000 Nantes, France
Email: dania.kabalan@ec-nantes.fr
Email: frederic.grondin@ec-nantes.fr
Email: emmanuel.roziere@ec-nantes.fr
[2] Nantes Université, Ecole Centrale Nantes, CNRS, GeM, UMR 6183, F-44600 Saint-Nazaire, France
Email: amandine.celino@univ-nantes.fr

*Corresponding author

ABSTRACT

The reinforcement and repair techniques of infrastructures weakened by environmental actions have been the subject of numerous research works, particularly to assess their durability. A promising approach in civil engineering is the use of bonded composite reinforcements, offering versatile applications. This article focuses on the durability of the adhesive bond between concrete and carbon fiber-reinforced polymer (CFRP) systems, with a study under accelerated carbonation at 3% of CO_2 concentration. Mechanical characterization was performed on both control and carbonated samples to assess the evolution of adhesive properties. Pull-out test revealed various behaviors influenced by multiple factors, such as concrete surface preparation methods like sandblasting and grinding, the presence of carbonated layer, and the test configuration used to evaluate the bond strength. Notably, the bond strength increased significantly with carbonation duration. Carbonation is known to enhance the compressive strength of the concrete through the production of calcium carbonates. This research demonstrates its favorable impacts on the durability of composite-reinforced structures. These findings can be valuable to engineers and stakeholders involved in the reinforcement and the extension of the service life of structures.

KEYWORDS: *Accelerated carbonation, FRP, Adhesive, Durability, Cementitious materials.*

1. Introduction

Concrete is the most widely used construction material. Its utilization poses significant challenges due to various environmental factors. Across the globe, a considerable number of reinforced or pre-stressed concrete structures require attention and structural monitoring. Many of these structures undergo aging and deterioration, while others have been damaged by natural disasters or other events. In Europe, the cost of repairing reinforced concrete structures due to reinforcement corrosion is estimated to be over 600 million euros per year (Rizkalla et al., 2003). Given the magnitude and urgency of this issue, it is increasingly necessary to find innovative and cost-effective solutions to repair and reinforce concrete structures. The use of Fiber Reinforced Polymer (FRP) materials is one of the approaches that has garnered the most interest in recent years (Pantazopoulou et al., 2001). By providing additional strength, FRP materials can contribute to extending the lifespan of aging structures and making them more resilient to future events. Among the various techniques for reinforcing concrete structures using FRP, externally bonded FRP (EB-FRP) is the most recommended (Li et al., 2022). The system manufacturer typically develops the installation procedure of the EB-FRP system. It varies from one system to another and even within the same system depending on the condition of the structure. The most widely used reinforcement technique is the manual application of the wet lay-up or prefabricated systems using a cold-curing adhesive bond. The main characteristic, or even the most important one, of this technique is that in EB-FRP systems, the fibers are arranged as much as possible parallel to the direction of the main tensile stresses (Setunge et al., 2002). This technique is quick and relatively easy to install, making it an attractive option for professionals in the field. Furthermore,

EB-FRP can provide additional strength while enhancing resistance to corrosion and other forms of damage by bonding FRP materials to the surface of a concrete structure. It is worth noting that EB-FRP systems come in various forms, including sheets, strips, grids, and fabrics, which can be tailored to meet the specific needs of a given project. The relative ease of EB-FRP installation also means it can be a cost-effective option for repairing and reinforcing concrete structures compared to other techniques that may require extensive demolition and reconstruction work. Therefore, it is not surprising that EB-FRP has become the widely adopted technical element for concrete structure reinforcement, with an increasing number of publications highlighting its effectiveness (Green et al., 2006) (Maria et al., 2006) (Xie and Hu, 2013).
Understanding the impact of carbonation on structure durability and developing strategies to mitigate its effects is crucial. While extensive research has been conducted on the effects of carbonation on traditional concrete structures, its impact on composite materials, particularly on the bonding performance of externally bonded FRP composites to cementitious materials, has received less attention in the literature. Carbon dioxide absorbed by cement paste or concrete when exposed to the atmosphere alters the microstructure of the cement paste, potentially influencing various properties such as strength, shrinkage, creep, and corrosion in concrete and reinforced concrete structures. The extent of these effects depends on the degree of carbonation reached by the structure (Pihlajavaara, 1968). In the case of FRP composites, increasingly used in structural applications and rehabilitation, understanding the effect of carbonation on the bonding performance between cementitious materials and composite materials is essential. Therefore, this study aims to investigate comprehensively the effects of carbonation on the mechanical properties and bonding performance of externally bonded FRP composites to cement-based materials. By acquiring knowledge about these interactions, effective mitigation strategies can be developed to enhance the performance and service life of FRP-reinforced structures exposed to carbonation.

2. Experimental program

2.1 Materials and samples preparations

In this study, the materials used include Type CEM I 52.5N Portland cement and natural silica sand with a particle size of 0-4 mm. This sand was chosen to ensure that the observed calcium carbonate comes solely from the carbonation of the cement paste. The water-to-cement ratio was 0.60, as recommended for exposure classes XC (carbonation-induced corrosion). A superplasticizer was incorporated at a dosage of 0.3% by mass of cement to enhance the workability and fluidity of the fresh mortar. Additionally, a stabilizer, xanthan gum, was introduced at a concentration of 0.6% by mass of water. The choice of xanthan gum was motivated by its effectiveness as a stabilizing agent. The selection of these dosages underwent an iterative process to achieve the desired homogeneity properties.
Four mortar slabs measuring 20 x 30 x 5.5 cm³ were manufactured. The samples were kept in their molds for 24 hours, then demolded and immersed in tap water for curing for a period of 28 days at a temperature of 23 ± 1°C. Since the study focuses on evaluating the impact of the carbonated layer on the adhesion behavior of FRP composites, the exposed surfaces have dimensions of 30 x 30 cm², perpendicular to the direction of casting of the slabs. To ensure that carbonation occurs exclusively on these two surfaces in a unidirectional manner, aluminum sheets were applied to the other faces after the 28-day curing period in water. After the application of aluminum, a pre-conditioning (Figure 1) step was applied before the carbonation tests. The samples were dried at 40°C for 28 days until their mass stabilized, then stored in a climate-controlled room (T = 20°C, relative humidity RH = 55%) for an additional 7 days to homogenize internal moisture and achieve an optimal water saturation level for carbonation (Thiery, 2005). The temperature of 40°C was specifically chosen to facilitate the drying of materials without altering the structure of the cement hydration products. The aim of this pre-conditioning step is to promote the diffusion of CO_2 during the subsequent carbonation step.
The program includes the fabrication of mortar cylinders to monitor the evolution of mechanical properties throughout the process. 15 cylinders with a height of 14 cm and a diameter of 7 cm were used. Adhesive aluminum was used to cover the top and bottom faces of the cylinders. The same pre-conditioning process as that of the slabs was applied to the cylindrical samples.

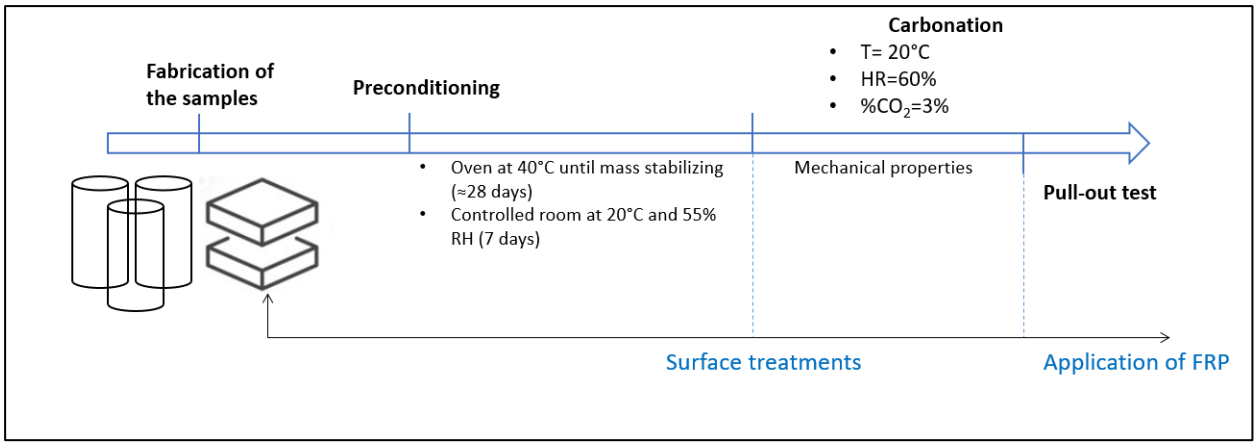

Figure 2. Experimental procedure.

For the composite materials, the commercial product Sika CarboDur M was selected (Table 1). It is a pultruded composite strip with a thickness of 1.4 mm and a width of 50 mm, consisting of carbon fibers encapsulated in an epoxy matrix. For bonding the strips to the surface of the substrate, the structural adhesive used was Sikadur-30. It is worth noting that these materials are currently used in practical applications of structural reinforcement, which aligns perfectly with the objectives of this study (Benzarti et al., 2011)

Table 6. Physical and mechanical properties of FRP (extracted from the datasheet provided by the supplier).

	Density (g/cm^3)	Volumetric percentage of fibers (%)	Rupture elongation (%)	Tensile strength (MPa)
CFRP	1.6	68	1.35	3200

2.2 Exposure conditions

One of the most common mechanisms of structural degradation is carbonation-induced corrosion. When CO_2 permeates cementitious materials, it reacts with hydration products, leading to the precipitation of calcium carbonates $CaCO_3$ and a decrease in the pH of the interstitial solution. This change in pH can damage the protective oxide layer on the surface of the steel and lead to subsequent corrosion (Chi et al., 2002). Due to the inherent slowness of this process, accelerated carbonation protocol is used in laboratory studies. This approach allows for precise control over the concentration of CO_2, relative humidity, and temperature. In our study, and for the sake of representing the evolution of the microstructure compared to natural carbonation, the applied CO_2 rate is 3%, with a relative humidity of 60% ± 5%, and a temperature of 20°C. It is worth noting that the application of fiber-reinforced polymer composite materials onto the mortar required specific surface treatment. The most commonly used techniques by the scientific community include sandblasting, grinding, brushing, scarifying, steel shot blasting, and brush hammering, each with different associated advantages and disadvantages in terms of the level of roughness provided, cost, processing time, and application difficulties (Soares et al., 2019). In this study, we selected two specific techniques, namely sandblasting and grinding with sandpaper, to assess their effects and differences. The surface treatment was conducted immediately before the carbonation tests, after the preconditioning process, to mitigate any potential influence of preconditioning on this stage. This ensured that the observed effects were solely attributed to the carbonation tests.

2.3 Experimental procedure

2.3.1 Mechanical properties of the mortar

To assess the evolution of compressive strength during exposure, three samples were tested at specific carbonation durations - 0, 28, and 60 days - and the average values were calculated. The initial tests were conducted before the preconditioning process (immediately after the initial 28-day curing). This initial measurement helps evaluate the influence of preconditioning on compressive strength. During the

compression test, the load was applied at a loading rate of 0.5 MPa/s until failure. The evolution of the Young's modulus was determined simultaneously with the compressive strength using a dynamic testing method (*Grindosonic*). By applying a slight impact to the sample, the device allows for the determination of two natural frequencies. Subsequently, the modulus of elasticity was calculated from these frequencies and the sample's volumetric mass using the Spinner and Teft model (El-Khoury et al., 2022).

2.3.2 Pull-out test

For this assessment, a pull-out device was used with a digital acquisition system (Figure 2), and the tensile load at failure (kN) was calculated at specific stages - after curing (before preconditioning) and after 0, 28, and 60 days of carbonation. At each interval, when a slab was removed from the carbonation chamber, the surfaces of the FRP plates (5x5 cm^2) and the steel piece from the pull-out test were meticulously prepared using sandpaper before bonding them together and affixing them to the surface of the slab (Figure 2).

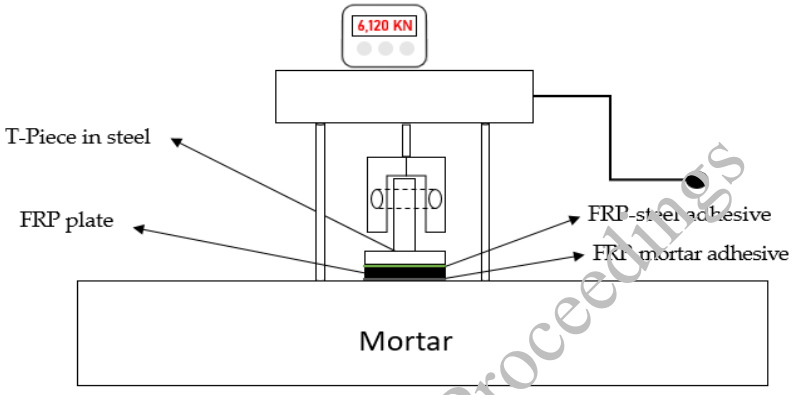

Figure 3. Digital pull-out tester set-up.

Initially, a commercial two-component epoxy adhesive, known as ISOBOND 735, was applied between the FRP plates and the steel piece, with a waiting period of approximately 30 ± 15 minutes. The choice of this adhesive was made to ensure that the failure of the mortar-composite interface precedes any steel-composite rupture. Then, a separate adhesive was applied between the FRP plates and the surface of the slab, and a waiting period of 24 hours was observed. The choice of this adhesive (Sikadur-30) was guided by the supplier company of the FRP plates to ensure compatibility with cementitious materials. This process guarantees optimal adhesion between the FRP plates and the surfaces of the steel and mortar slab, strictly adhering to the recommended time intervals for each adhesive application (Figure 3).
For each surface treatment, three measurements were recorded for the upper and lower surfaces of the slab, and the average value was calculated from these datasets.

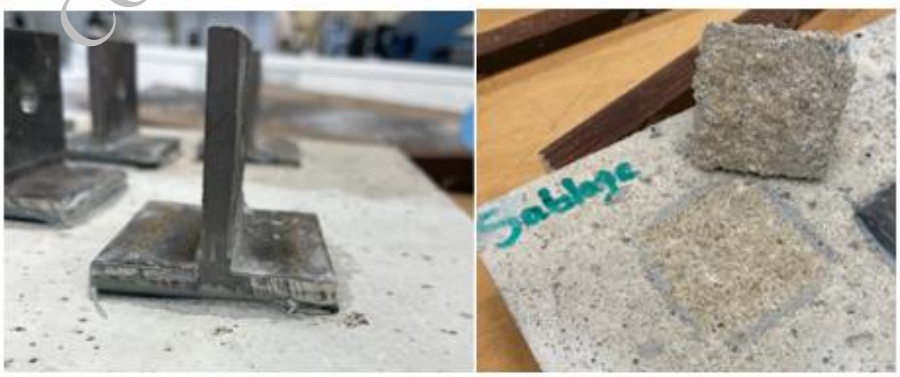

Figure 4. Pull-out test before and after failure.

3. Results and discussions

3.1 Carbonation depth

Figure 4 shows the depths of carbonation in the slabs as a function of accelerated carbonation time. The calculation of carbonation depth is based on the use of the phenolphthalein pH indicator, which produces a colorless reaction in the presence of carbonated material and a purple color in non-carbonated areas. This method allows for an accurate determination of the extent of carbonation penetration into the mortar slabs over time. The natural carbonation depth over the same period, assessed on a control slab, is 2 mm.
The depth of carbonation increases proportionally to the square root of the carbonation time, following a typical diffusion model (Wang et al., 2024).

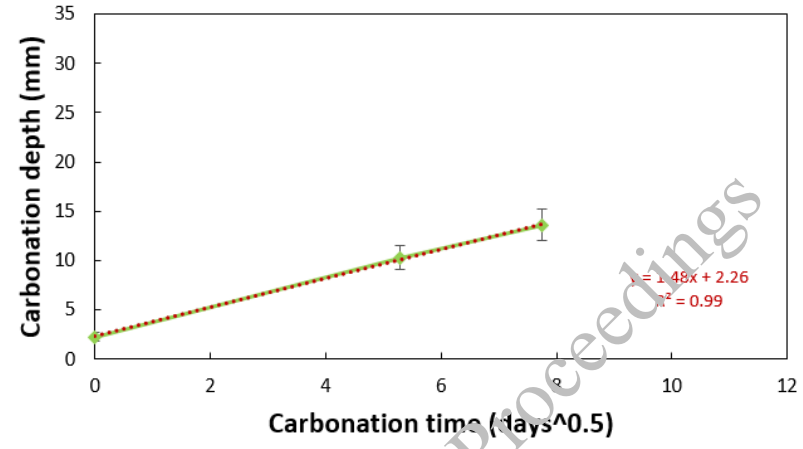

Figure 5. Depth of carbonation as a function of carbonation time for the mortar slabs.

3.2 Compressive Strength and Young's Modulus

Figure 5 illustrates the evolution of compressive strength as a function of carbonation time for the mortar cylinders. Compressive strengthincreased with carbonation time. This result is corroborated by various authors, such as (Kim et al., 2009) (Lu et al., 2022), who have also observed the positive correlation between carbonation time and compressive strength of Portland cement-based cementitious materials.

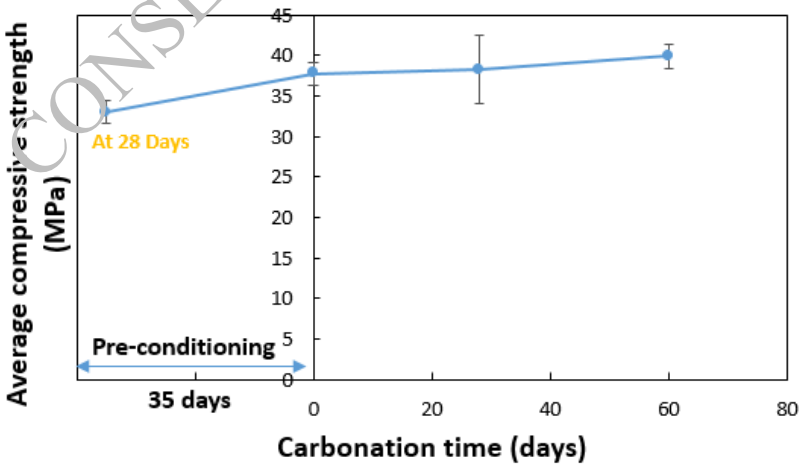

Figure 6. Average compressive strength as a function of carbonation time for cylindrical samples.

This result can be attributed to the formation of calcium carbonates within the porosity of cementitious materials, following the carbonation reaction (1):

$$Ca(OH)_2(s) + CO_2\ (g) \rightarrow CaCO_3\ (s) + H_2O\ (l) \quad (1)$$

Figure 6 illustrates the evolution of the average dynamic Young's modulus as a function of carbonation time for the mortar cylinders. Particularly, an increase in the dynamic modulus of elasticity with carbonation time is observed. The initial decrease observed during preconditioning may be attributed to drying shrinkage micro cracking that could have developed during the drying phase.

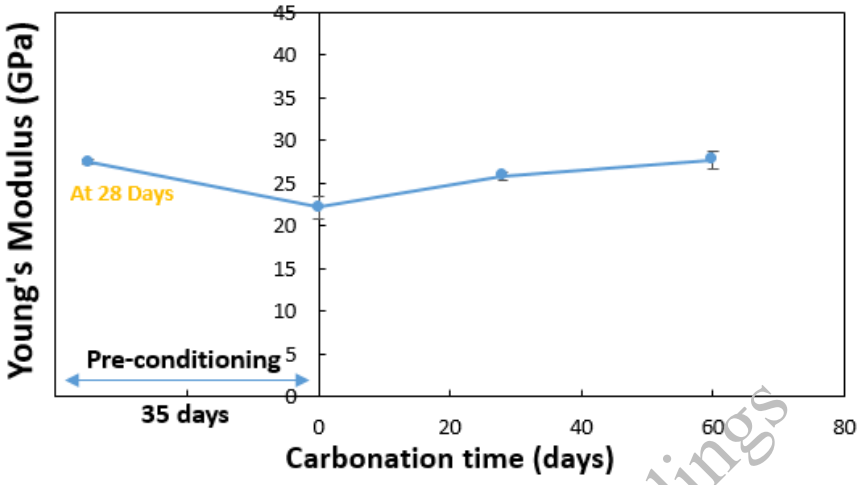

Figure 7. Average dynamic Young's modulus as a function of carbonation time for cylindrical samples.

3.2.1 Pull-out strength

Figure 7 illustrates the evolution of the average tensile strength as a function of carbonation time for sandblasted and grinded mortar slabs. The increase in carbonation time, indicating the modification of cement hydration products and the propagation of the carbonated zone inward into the slab, is accompanied by a notable increase in the tensile strength required to detach the composite from the slab. For example, in the case of sandblasting, the tensile strength increased from 2.8 MPa before carbonation to 3.7 MPa after 60 days of carbonation, indicating an increase of 31%. For grinding, the tensile strength increased from 2.6 MPa before carbonation to 3.4 MPa after 60 days of carbonation, indicating an increase of 30%. The results confirm the positive impact of carbonation on the bonding strength between FRP composite plates and cementitious materials. This trend was observed for both surface treatment methods, namely sandblasting and grinding.

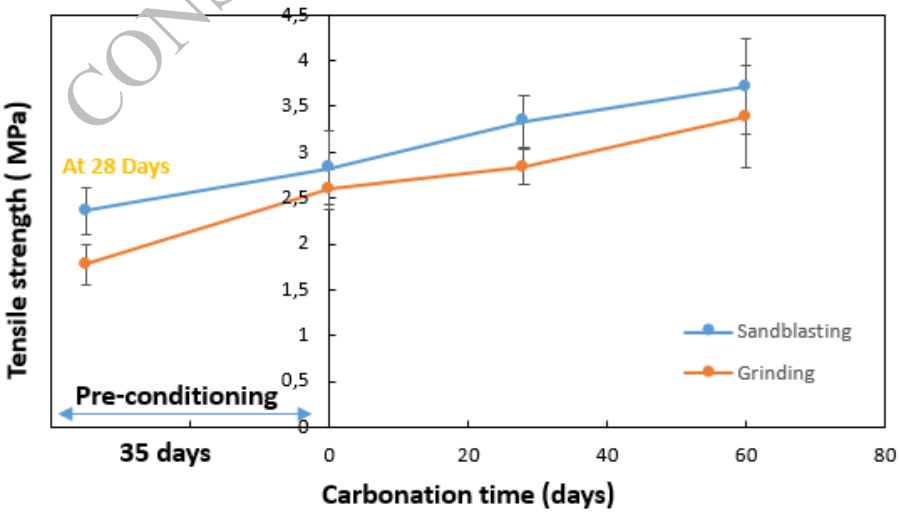

Figure 8. Average Tensile Strength as a function of Carbonation Time for Two Different Surface Treatments.

One can also observe that the preconditioning period also influences the tensile strength. Before preconditioning, the tensile strength was 2.4 MPa, and it increased to 2.8 MPa at the beginning of

carbonation, representing an increase of approximately 20%. The overall evolution of compressive strength for the entire specimen appears relatively modest. However, examining the modification of average tensile strength reveals a more substantial increase. This suggests that the bonding strength primarily originates from the carbonated layer, as it is responsible for this notable change, rather than a significant change in the material's strength as a whole.

4. Conclusions

In summary, the study highlights essential aspects of the interaction between carbonation and the adhesion behavior of fiber-reinforced polymers (FRP) and cementitious materials. Conclusions can be drawn from the experimental results of the study:

- Carbonation influence: The study reveals a substantial influence of carbonation on behavior with a notable improvement in bonding strength between FRP and the cementitious material substrate.
- Evolution of the carbonated material layer: Although the overall change in compressive strength was relatively low, a notable increase in average tensile strength suggests that the carbonated layer mainly influences bonding strength. For sandblasting, the increase in tensile strength was 31%, and 30%for grinding
- Surface treatment impact: Surface treatments, including sandblasting and grinding, play a secondary but significant role in increasing pull-out strength, emphasizing the importance of these substrate preparation methods.

Acknowledgements

The financial support from Ecole Centrale de Nantes through the PhD thesis grant of Mrs Dania KABALAN is gratefully acknowledged.

References

Benzarti, K., Chataigner, S., Quiertant, M., Marty, C., Aubagnac, C., 2011. Accelerated ageing behaviour of the adhesive bond between concrete specimens and CFRP overlays. Constr. Build. Mater. 25, 523–538. https://doi.org/10.1016/j.conbuildmat.2010.08.003

Chi, J.M., Huang, R., Yang, C.C., 2002. Effects of Carbonation on Mechanical Properties and Durability of Concrete Using Accelerated Testing Method. J. Mar. Sci. Technol. 10. https://doi.org/10.51400/2709-6998.2296

El-Khoury, M., Roziere, E., Grondin, F., Cortas, R., Chehade, F.H., 2022. Experimental evaluation of the effect of cement type and seawater salinity on concrete offshore structures. Constr. Build. Mater. 322, 126471. https://doi.org/10.1016/j.conbuildmat.2022.126471

Green, M.F., Bisby, L.A., Fam, A.Z., Kodur, V.K.R., 2006. FRP confined concrete columns: Behaviour under extreme conditions. Cem. Concr. Compos. 28, 928–937. https://doi.org/10.1016/j.cemconcomp.2006.07.008

Kim, J.-K., Kim, C.-Y., Yi, S.-T., Lee, Y., 2009. Effect of carbonation on the rebound number and compressive strength of concrete. Cem. Concr. Compos. 31, 139–144. https://doi.org/10.1016/j.cemconcomp.2008.10.001

Li, M., Shen, D., Yang, Q., Cao, X., Liu, C., Kang, J., 2022. Rehabilitation of seismic-damaged reinforced concrete beam-column joints with different corrosion rates using basalt fiber-reinforced polymer sheets. Compos. Struct. 289, 115397. https://doi.org/10.1016/j.compstruct.2022.115397

Lu, B., Drissi, S., Liu, J., Hu, X., Song, B., Shi, C., 2022. Effect of temperature on CO2 curing, compressive strength and microstructure of cement paste. Cem. Concr. Res. 157, 106827. https://doi.org/10.1016/j.cemconres.2022.106827

Maria, H.S., Alcaino, P., Luders, C., 2006. Santa Maria, H., Alcaino, P. and Luders, C., 2006, April. Experimental response of masonry walls externally reinforced with carbon fiber fabrics. In Proc., 8th US National Conf. on Earthquake Engineering.

Pantazopoulou, S.J., Bonacci, J.F., Sheikh, S., Thomas, M.D.A., Hearn, N., 2001. Repair of Corrosion-Damaged Columns with FRP Wraps. J. Compos. Constr. 5, 3–11. https://doi.org/10.1061/(ASCE)1090-0268(2001)5:1(3)

Pihlajavaara, S.E., 1968. Some results of the effect of carbonation on the porosity and pore size distribution of cement paste. Matér. Constr. 1, 521–527. https://doi.org/10.1007/BF02473640

Rizkalla, S., Hassan, T., Hassan, N., 2003. Design recommendations for the use of FRP for reinforcement and strengthening of concrete structures. Prog. Struct. Eng. Mater. 5, 16–28. https://doi.org/10.1002/pse.139

Setunge, S., Kumar, A., Nezamian, A., 2002. Decision support tools for concrete infrastructure rehabilitation (using FRP composites).

Soares, S., Sena-Cruz, J., Cruz, J.R., Fernandes, P., 2019. Influence of Surface Preparation Method on the Bond Behavior of Externally Bonded CFRP Reinforcements in Concrete. Materials 12, 414. https://doi.org/10.3390/ma12030414

Thiery, M., 2005. Modélisation de la carbonatation atmosphérique des matériaux cimentaires : Prise en compte des effets cinétiques et des modifications microstructurales et hydriques.

Wang, X., Yang, Q., Peng, X., Qin, F., 2024. A Review of Concrete Carbonation Depth Evaluation Models. Coatings 14, 386. https://doi.org/10.3390/coatings14040386

Xie, J., Hu, R., 2013. Experimental study on rehabilitation of corrosion-damaged reinforced concrete beams with carbon fiber reinforced polymer. Constr. Build. Mater. 38, 708–716. https://doi.org/10.1016/j.conbuildmat.2012.09.023

Impermeability Restoration Method for Cut Residual Asphalt Layer On Bridge Deck Concrete

M.H. Masayuki Hashimoto [1*], O.T. Osamu Takahashi [2], and S.O. Shuichi Ono [3]

[1] Doctoral Program of Nagaoka University of Technology, Nagaoka City, Japan
Email: hashimoto@cmi.or.jp
[2] Nagaoka University of Technology, Nagaoka City, Japan
Email: roadman@vos.nagaokaut.ac.jp
[3] Japan Construction Method and Machinery Research Institute, Fuji City, Japan
Email: ono@cmi.or.jp

*Corresponding author

ABSTRACT

Concrete of bridge decks is not only constantly damaged by traffic loads, but also suffers significant damage when the pavement is replaced. In a replacement work of bridge deck pavements, cutting the asphalt layer and removing its thin residue layer considerable damage to the existing waterproof membrane and slab concrete. The present study investigated a method for repairing and reusing the residual layer as an interlayer between the new pavement and the waterproof membrane. The residual layer always has damage such as cracking and chipping, but it can be used as an interlayer by restoring the water impermeability when the existing waterproofing and slab concrete are sound. Based on this idea, a method of asphalt emulsion penetration was assessed for the damaged residual layer. A sample with the reproducing damage as the residual layer of the actual bridge deck was prepared, and visualization of the inside and pressurized permeability tests were carried out. As a result, the present study confirmed that the asphalt emulsion penetration method can close the cracks in the residual layer and restore the impermeability. In addition, it was shown that the asphalt emulsion penetration method not only restored the water impermeability but also increased the bending stress at a low temperature for the residual layer.

KEYWORDS: *Protection of concrete, Bridge deck pavement, Residual layer, Water impermeability, Asphalt emulsion penetration method*

1. Introduction

Reinforced concrete slabs on road bridges have susceptibility of fatigue damage, because they directly support live loads. The fatigue deterioration is accelerated, when moisture infiltrates slab concrete. To prevent the moisture ingress, a waterproof membrane is standardly installed between slab and bridge deck pavement in Japan. Progress has been made to improve the performance and extend the lifespan of waterproof membranes. Therefore, the slab, waterproof membrane, and pavement are considered to be closely related to each other. In a replacement work of bridge deck pavements, pavement cutting is a factor that causes damage to the existing waterproof membrane and slab concrete. Even if the existing waterproof membrane is sound condition, the membrane is usually reconstructed at the same time as the replacement of the pavement.

This study investigated possibility of restoring and reusing water impermeability of the residual layer which is likely to have cracks and other damage after cutting. It means that the restored residual layer is reused as an asphalt interlayer, and the existing waterproof membrane and slub caoncrete remain intact. In addition to the longer-term use of the waterproof membrane, the maintenance cost and the construction period required to replace the bridge deck pavement can be reduced.

Based on the research objective, this study quantified the damage to the residual layer on an actual bridge deck, and investigated a method to restore the impermeability of the damaged residual layer. The

mechanical properties of the restored layer were also confirmed. The effectiveness of the restolation method was considered based on the results of evaluation tests.

2. Actual state of residual layer after cutting

The residual layer after cutting is likely to be damaged by repeated impacts and fatigue from traffic loads, environmental loads such as rainwater invasion and temperature changes, and impacts during cutting, resulting in cracking and aggregate scattering. In order to investigate the reuse of this residual layer, we first confirmed the actual damage to the residual layer on the actual bridge. Therefore, the residual layer was sampled from the bridge deck pavement of a 30-year-old simple steel non-composite box girder bridge. The cutting condition of the base layer is shown in Figure 1, and the collected samples are shown in Figure 2. The damage to the residual layer was visually some of the samples were visible and some were not. The air voids obtained from the collected samples was 6.5 %. Therefore, it was decided to quantify the damage to the residual layers by air voids. The air voids of the specimens used in this study was set to 6.5 %.

Figure 1. Cutting of base layer asphalt concrete

Figure 2. Base layer asphalt concrete collected

3. Method and materials for asphalt emulsion panetration

In this study, a method to close cracks and restore near impermeable conditions by applying a permeable material to the residual layer was investigated. Figure 3 schematically illustrates the concept of performance restoration using the asphalt emulsion penetration method, and Table 1 shows the properties of the selected high-concentration modified asphalt emulsions. Emulsion A is a type that is used in combination with a decomposing agent (fast curing type), and the standard application volume is 1.2 ℓ /m^2 . Emulsion B is a type that does not use a decomposing agent (slow curing type), and the standard application volume is 1.1 ℓ/m^2 .

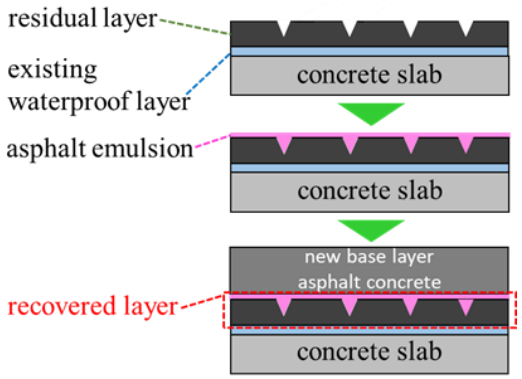

Figure 3. Concept of performance restoration by asphalt emulsion penetration method

Emulsion A, which uses a degrading agent, decomposes immediately to form a film. Emulsion B is gradually decomposed to form a film, as is the case with ordinary asphalt emulsions. The Engler degree, which is an index of viscosity, is smaller for emulsion B than for emulsion A, suggesting that emulsion B

has higher penetration into cracks. The evaporation residue, which is considered to affect the filling ability to close cracks, was similar for emulsion A and B.

Table 1. Property values of high-concentration modified asphalt emulsion

test type	emulsion A	emulsion B
engler penetration (25°C)	10	6
evaporation residue (%)	67	67
hardness (25°C, 1/10mm)	68	88
softness (°C)	51.5	62
grasping power (25°C, N・m)	7.7	11
clinging power (25°C, N・m)	4.1	6.1

4. Evaluation of restoration effects

The asphalt emulsion penetration method is expected to close cracks in the residual layer and restore impermeability. It also has the potential to restore mechanical properties. In this section, we describe the results of a confirmatory test on the restoration of performance by the asphalt emulsion penetration method.

4.1 Clack closing effect

4.1.1 Outline

The asphalt emulsion penetration method is expected to close cracks in the residual layer after cutting and to restore impermeability. In this section, we attempted to visualize the gaps in the compacted asphalt mixture and confirmed the crack-closing effect of the asphalt emulsion penetration method.

4.1.2 Visualization of gaps inside the asphalt mixture

To visualize the gaps in the asphalt mixture, Maruyama et al. evaluated the gaps using the fluorescent epoxy resin impregnation method, and this evaluation was referred to in this study.
The specimens used in the evaluation were prepared using a Superpave Gyratory Compactor (SGC), which is possible of compaction closer to that of actual pavement than a marshall rammer, which compresses from the vertical direction. The SGC is a device that can perform compaction while providing kneading action by rotating the specimen while fixing it at a constant pressure. The mixture was a dense-graded asphalt mixture (maximum aggregate particle size 13 mm) with a binder of 60/80 straight asphalt and a air voids of 6.5 %, with a diameter of 150 mm and a height of 100 mm.
As a test procedure of the fluorescent epoxy resin impregnation method, as shown in Figure 4, the sides and bottom of a specimen molded to a diameter of 100 mm were coated with epoxy resin, and the specimen was placed in a PVC pipe placed vertically. Epoxy resin with high permeability mixed with fluorescent pigment was poured into the pipe, and the mixture was depressurized at about 100 kPa for one hour to impregnation the gaps inside the mixture. The asphalt binder is a thermoplastic material, and there was concern that the reaction heat of the resin would melt the asphalt binder and close the gaps in the mixture. Therefore, during depressurization, the area was surrounded with ice water to prevent the resin from reacting too rapidly. The specimens were then removed from the PVC pipe and controlled in a thermostatic bath at 10 °C for 2 to 3 days while the reaction heat of the resin was installed. The specimens were then cut, and the penetration of the resin was observed by irradiating the cut surface with ultraviolet light.
The cut surface observed by the fluorescent epoxy resin impregnation method is shown in Figure 5. Both sides of the cut surface are shown because of the possibility of localized aggregate removal during cutting. As a result, resin penetration into the gaps was confirmed, and it was judged that it was possible to visualize the gaps inside the mixture. Resin penetration tended to be more remarkable near the surface than in the inside.

4.1.3 Effects of pavement cutting

To confirm the effect of pavement cutting on the asphalt mixture layer, specimens with a air voids of 6.5 % fixed at the sides and bottom with gypsum, and the surface of the specimens was cut with a small cutting

machine. The cutting situation and the specimen after cutting are shown in Figure 5, and the cut surface observed by the fluorescent epoxy resin impregnation method is shown in Figure 6.
Observations confirmed the penetration of resin into the gaps. Although there were individual differences, there was relatively little penetration compared to the specimens without cutting. Possible reasons for this include the removal of the layer with many pores near the surface by cutting, the closing by impact of the gaps that should normally have been consolidated by setting the air voids of the specimens at 6.5%, and the penetration of a small amount of dust and mud into the gaps during cutting.
Based on the above, we considered that it would be difficult to determine the effects of cracking caused by cutting on specimens that showed significant resin penetration prior to cutting. Therefore, we performed the same check on a dense-grained asphalt mixture with a air voids of 3 %, in which no resin penetration was observed prior to cutting. The ultraviolet irradiated image of the cut surface observed by the fluorescent epoxy resin impregnation method is shown in Figure 8. Although no crack propagation into the inside of the mixture was observed, resin penetration under the surface-exposed aggregate particles was observed. From the above, it is considered that the coarse aggregate near the surface is likely to loosen at the interface due to the cutting process.

a) specimen coating b) after pouring resin

Figure 4. Test situation (before decompression)

a) cutting situation b) specimen

Figure 5. Cutting conditions and spesimen after cutting

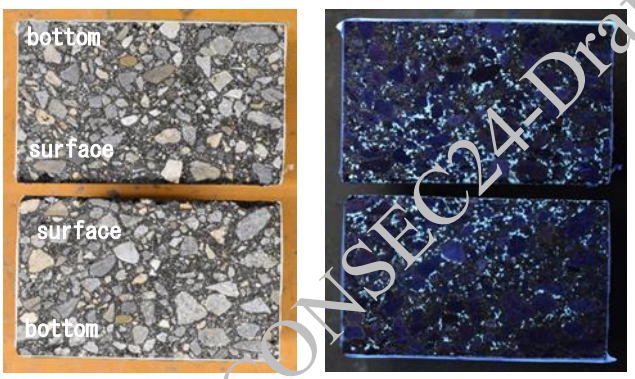

a) visible image b) ultraviolet irradiation image

c) d)

Figure 6. Cutting surface observation results (uncut)

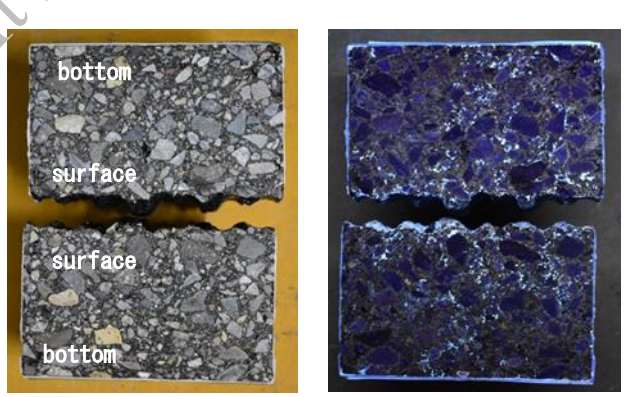

a) visible image b) ultraviolet irradiation image

c) d)

Figure 7. Cutting surface observation results (cut)

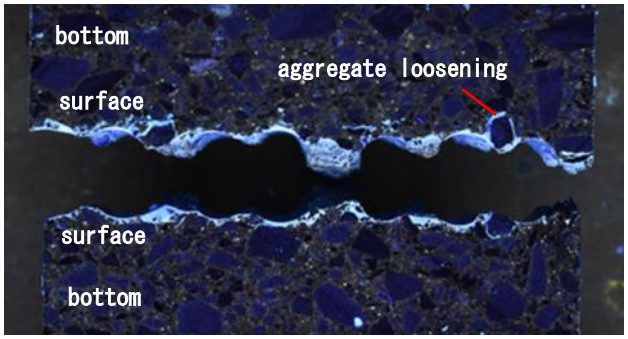

Figure 8. Ultraviolet irradiation image of cut surface (dense-grained asphalt mixture with 3% air voids)

4.1.4 Confirmation of crack closure effect

In order to confirm the crack-closing effect of applying the asphalt emulsion penetration method, specimens with a air voids of 6.5 % were cut in the same as previously described, and emulsion A and B were applied in standard amounts. Figure 9 shows the appearance of the emulsion-coated specimen after cutting, and Figure 10 shows a ultraviolet illuminated image of the cut surface observed by the fluorescent epoxy resin impregnation method.
Observations showed that no resin penetration into the inside of the mixture was observed for both Emulsion A and Emulsion B, confirming the effectiveness of the asphalt emulsion penetration method in closing the cracks.

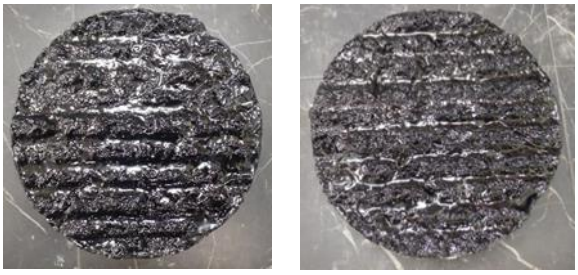

emulsion A emulsion B

Figure 9. Appearance of specimen with emulsion applied after cutting

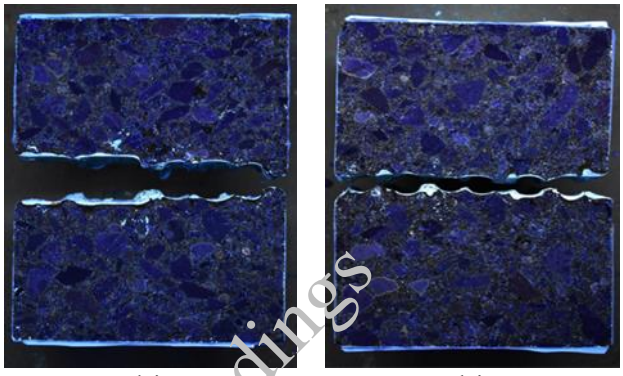

emulsion A emulsion B

Figure 10. Ultraviolet irradiation image of cut surface (after application of asphalt emulsion penetration method)

4.2 Water impermeability

4.2.1 Outline

The residual layer after cutting is expected to restore impermeability by applying the asphalt emulsion infiltration method. In this section, the effect of restoring impermeability was quantitatively evaluated, and the specifications of the construction method were also considerd. The number of specimens for each test value was two.

4.2.2 Evaluation of impermeability recovery effect

To evaluate the effect of restoring impermeability, a pressurized permeability test was conducted in accordance with the pressurized permeability test method described in the Hosochosa & Shikenhobinran, assuming that the bridge is in service.
However, the water pressure is about 1 kPa when the surface of the residual layer is filled with water as high as the road surface, and the pressure applied by the wheel load is dispersed horizontally. Therefore, 150 kPa is considered to be considerably larger than the water pressure that actually acts on the surface. In this test, the water pressure was set to 50 kPa.
The specimens used in the evaluation were dense-graded asphalt mixtures compacted to a diameter of 100 mm. Air voids was set at a standard value of 6.5 % to reproduce the degree of damage in real bridges, and at 0.5 % intervals from 6.5 % to 8.0 % to evaluate the safe side (when the damage is more progressed). Comparisons were then made between no emulsion application, emulsion A applied at a standard volume of 1.2 ℓ/m^2 , and emulsion B applied at a standard volume of 1.1 ℓ/m^2 .
In order to eliminate errors due to crack propagation by cutting and unevenness of the construction surface, and to evaluate the effect of air voids as an indicator of the degree of damage, specimens without cutting were used in the study.
The results of the pressure permeability test are shown in Figure 11. It was confirmed that the application of Emulsion A and Emulsion B decreased the coefficient of permeability of the residual layer and restored impermeability. The emulsion A tended to reduce the coefficient of permeability, and the test values were close to the approximate value of 10^{-4} cm/s or less, which is the approximate value for coarse-grained asphalt mixtures as shown in the Hosochosa & Shikenhobinran.

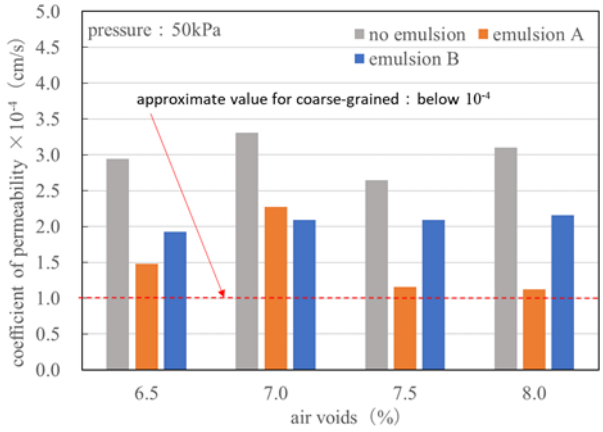

Figure 11. Results of pressure permeability test (single application)

4.2.3 Effect of increased number of applications

Figure 12 shows the results of a pressurized permeability test using two applications to confirm the critical performance of the method. As a result, it was confirmed that the method was more effective in restoring impermeability than a single application. The emulsion A tended to have a lower coefficient of permeability than the emulsion B, as was the case with the single application. At a air voids of 6.5%, both Emulsion A and Emulsion B satisfied the test values below 10^{-4} cm/s, which is the approximate value for coarse-grained asphalt mixtures. In addition, the surface roughness tended to be smaller when two coats were applied than when one coat was applied.

Figure 13 shows the results of a pressurized permeability test (pressure: 50 kPa) with three applications (three applications of the standard coating amount, three times the coating volume). Emulsion A showed zero permeability at all air voids values, and emulsion B showed zero permeability at 6.5 % air voids. The permeability of emulsion A tended to be lower than that of emulsion B, as was the case for the one and two application times. The appearance of the emulsion after three coats tended to be less uneven than that of the emulsion after two coats.

As an overall trend, emulsion A tended to be more effective in restoring impermeability than emulsion B. This is thought to be because emulsion A has a lower permeability than emulsion B, drying time is shorter, and a film is easily formed on the coated surface due to the combination of decomposition agents.

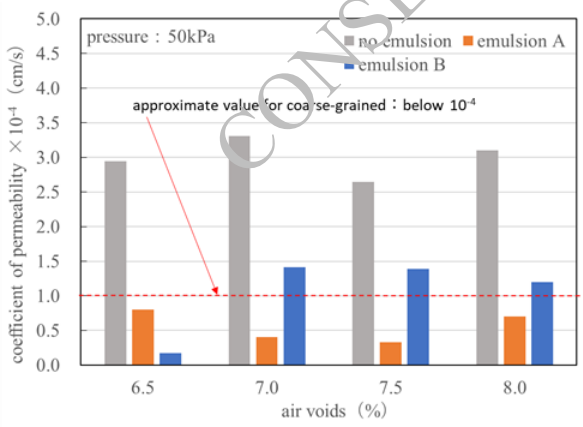

Figure 12: Results of pressure permeability test (two applications)

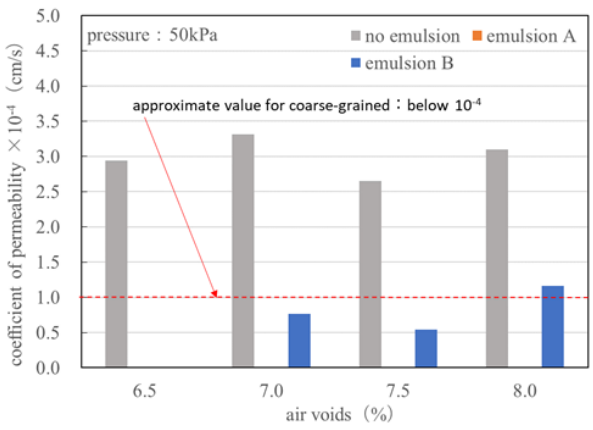

Figure 13: Results of pressure permeability test (three applications)

4.2.4 Mechanism of impermeability restoration effect

Based on the previous findings, the effect of restoring impermeability is discussed. There are three possible recovery mechanisms using the asphalt emulsion penetration method: (a) recovery by filling voids in the mixture, (b) recovery by filling cracks, and (c) recovery by surface coating. In this study, damage due to

in-service wheel loading and cutting was quantified by air voids, so it was assumed that (a) and (b) were generally the same in the evaluation. In addition, the recovery effect of (c) is also considered to have occurred. Although it is difficult to evaluate these effects separately, the restoration of impermeability by the asphalt emulsion penetration method is considered to be a synergistic effect of these effects.

4.3 Mechanical property

4.3.1 Outline

When the asphalt emulsion penetration method is applied to the residual layer, there is a possibility that the mechanical properties of the residual layer can be restored because the cracks are filled with a high concentration of modified asphalt emulsion. Therefore, we focused on the bending properties at low temperatures and quantitatively evaluated the effect of the emulsion on the mechanical properties.

4.3.2 Evaluation of bending properties at low temperatures

The bending properties at low temperatures were evaluated by referring to the static bending test using a small specimen proposed by Nitta et al. because the residual layer with a thickness of 20 mm was evaluated in this study.

The specimen used for evaluation was a dense-graded asphalt mixture prepared with a roller compactor and compacted from the center to a width of 20 mm x thickness of 20 mm x length of 120 mm.

As in the previous section, a void ratio of 6.5 %, which reproduced the degree of damage in the actual bridge, was used as the standard, and comparisons were made between no emulsion, emulsion A applied at a standard volume of 1.2 ℓ/m^2 , and emulsion B applied at a standard volume of 1.1 ℓ/m^2 . In order to eliminate errors due to crack propagation by cutting and unevenness of the construction surface, and to evaluate the effect of air voids as an indicator of the degree of damage, specimens without cutting were used in the study.

The test conditions were as follows: the compaction surface and the emulsion-applied surface were set on the top surface, the test specimen was placed 80 mm between supports, the loading speed was 0.2 mm/min, and the test temperature was -10°C. The bending strength and bending strain were measured from the static bending test. The static bending test is shown in Figure 14.

The results of bending strength and bending strain at failure are shown in Figure 15 and Figure 16. The results show that the application of the asphalt emulsion penetration method to a mixture with a air voids of 6.5%, which reproduced the degree of damage in an actual bridge, tends to increase the bending strength and bending strain.

As for the difference in emulsion type, the bending strength tended to be higher with emulsion B, and the bending strain tended to be higher with emulsion A. The emulsion B had a higher grasping power, was considered to be less prone to brittle fracture at low temperatures, but the bending strain showed a different trend. The reason for this may be that the emulsion A has a lower hardness, which indicates softness, than emulsion B. Because the emulsion construction surface is in a compression zone higher than the neutral axis, which may advantageous emulsion A, which has relatively hard properties. However, due to the small test size, additional evaluation tests are necessary.

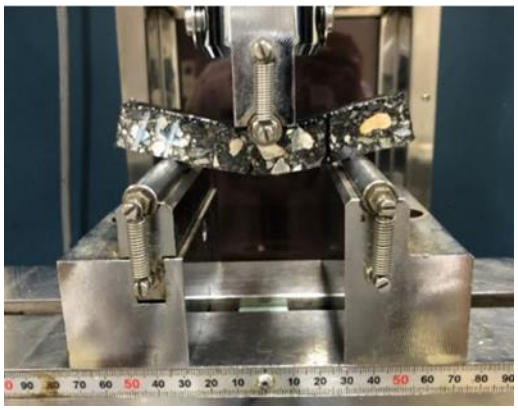

Figure 14. Static bending test situation

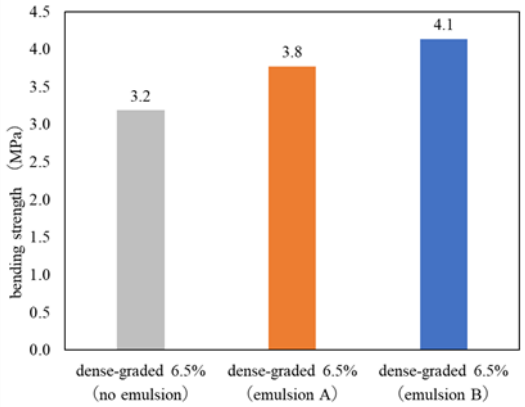

Figure 15. Results of bending strength

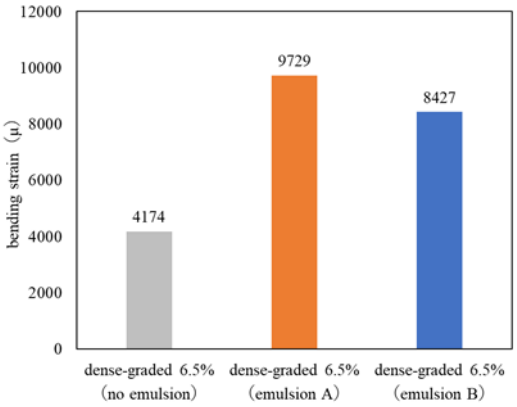

Figure 16. Results of bending strain at failure

5. Conclusions

This study investigated the actual state of the residual layer of he bridge deck pavement after cutting and quantified the degree of damage. The asphalt emulsion penetration method was applyed to the residual laye and effects on crack closing, restoration of impermeability, and recovery of mechanical properties were evaluated. The findings of this study are summarized as follows.

- The rsult of the air voids in the cut residual layer was about 6.5 %. It was much higher than that in an normal dense-graded HMA mixture due to damage not only during service period but also during cutting operations. Therefore, the degree of damage of residual layers can be quantified by the air voids.
- The fluorescent epoxy resin impregnation method can be applied to visualize the voids inside the residual layer and to observe the loosening of coarse aggregate particles by the cutting operations. It was also confirmed that the voids inside the residual layer were closed with the asphalt emulsion.
- A single application of asphalt emulsion penetration to the residual layer reduces coefficient of permeability to less than 10^{-4} cm/s, which is approximately the same as that of a coarse-graded HMA mixture. The effect of restoring impermeability is improved as increasing the number of applications.
- The application of the asphalt emulsion penetration method to the residual layer after cutting recovers the bending properties at low temperatures.

The above results confirmed that the application of the asphalt emulsion penetration method to the cut residual layer can close the cracks in the residual layer and restore not only impermeability but also bending properties at low temperatures. As a reseult, this study indicates that the asphalt emulsion penetration is an effective method for restoring dameged residual layer on bridge deck pavemants.

Acknowledgements

This study also utilizes data from experiments conducted by Takahiro Yanai and Junta Onishi, who completed their master's theses at the Nagaoka University of Technology. The authors would like to express their gratitude to all parties involved.

References

Sigeyui,M. Kouji,O. and Kazuhiro,N. (1998),"Reinforced concrete slab and damage (Part2)", *Bridge and foundation* Japan Road Association (2002), *Dorokyoshihosyo & Doukaisetsu I Kyotsu-hen*

Kimio,M. and Takashi,K. (2017),"Evaluation by fluorescent epoxy resin impregnation method for pavement mixture subjected to freeze-thaw action", *72th Society of Civil Engineers academic lecture*

Japan Road Association (2019), *Hosochosa & Shikenhobinran*

Hiroyuki,N. Atushi,K. and Itaru,N. (2012),"Evaluation of bending test characteristics and medium-temperature mixture with small specimen", *67th Society of Civil Engineers academic lecture*

Performance of Inhibitor Admixed Self-Flowing Concrete for Use in RC Jacketing Technique

M.S. Anuman Surya[1], M.S. Haji Sheik Mohammed[1*], Md Muheeb Ahmed[1], and Mohd Umar[1]

[1]B.S. Abdur Rahman Crescent Institute of Science and Technology, Chennai, INDIA
Email: hajisheik@crescent.education

*Corresponding author

ABSTRACT

This investigation analyses the performance of the inhibitor admixed self-flowing concrete (ISFM) for use in repair and rehabilitation work involving reinforced concrete (RC) jacketing. Three self-flowing trial mixes (ISFM1, ISFM2, ISFM3) were developed in line with EFNARC standards using materials viz. Portland pozzolana cement, manufactured sand, 10 mm downgraded coarse aggregate, PCE based super plasticizer, sodium nitrite based corrosion inhibitor and potable water. Compressive strength and flexural strength test results exhibit marginally improved performance for ISFM3 mix as compared to commercially available micro concrete (CMC). There is a significant reduction in water absorption, and similar sorptivity behaviour for ISFM3 mix when compared with CMC. Eight beams of size 0.1 m x 0.15 m x 1 m were cast using M25 grade concrete without cover concrete, and exposing steel reinforcement bars. To simulate real-time repair conditions, these beam specimens were subjected to chloride exposure for a desired period, to accelerate corrosion in exposed steel reinforcement rods. The standard procedure was followed to repair the beams with RC jacketing by using CMC, and ISFM1, ISFM2, and ISFM3. The repaired beams were subjected to flexural strength test as per Indian standards. The load deflection behaviour exhibit an appreciably improved first crack load, ultimate load, moment carrying capacity and energy absorption capacity for beams jacketed with ISFM3 mix as compared to CMC. It can be concluded that ISFM3 mix can be used for RC jacketing considering its performance on par with CMC.

KEYWORDS: *Self-flowing concrete; Sodium nitrite-based corrosion inhibitor; Repair and rehabilitation; RC jacketing; Flexure strength*

1. Introduction

Micro concrete, a flowable mortar, finds application in the rehabilitation of reinforced concrete elements, particularly in situations with limited space or where vibration of the repair material is impractical. While micro concrete exhibits excellent homogeneity and minimal voids, it lacks sufficient protection against corrosive agents when employed as a repair material. Furthermore, the cost of micro concrete has witnessed a substantial rise in the recent years due to increased demand and the absence of readily available substitutes within the RC jacketing technique (Habib et al., 2020; Rahim Karim, 2020; Sakr et al., 2020). This cost inflation translates to a rise in overall construction expenditure for projects involving RC jacketing technique. Consequently, identifying an alternative to micro concrete presents a promising avenue for reducing repair costs without compromising the desired performance characteristics. The objective of this study is to develop inhibitor admixed self-flowing micro-concrete (ISFM) and conduct performance evaluation studies for use in RC jacketing technique.

2. Experimental program

Three types of ISFM mixes was developed viz. ISFM1, ISFM2 and ISFM3 and subjected to mechanical and durability test to evaluate its performance. A total of eight beams were cast without top and side covers and were subjected to corrosion to mimic real time distress condition at site. The distressed beams were repaired using RC jacketing technique with three types of inhibitor admixed self-flowing micro concrete

and a commercially available micro concrete (CMC). Flexural strength test was carried out on the repaired RC beams to evaluate their performance. Figure 1 shows the methodology flow chart of the study.

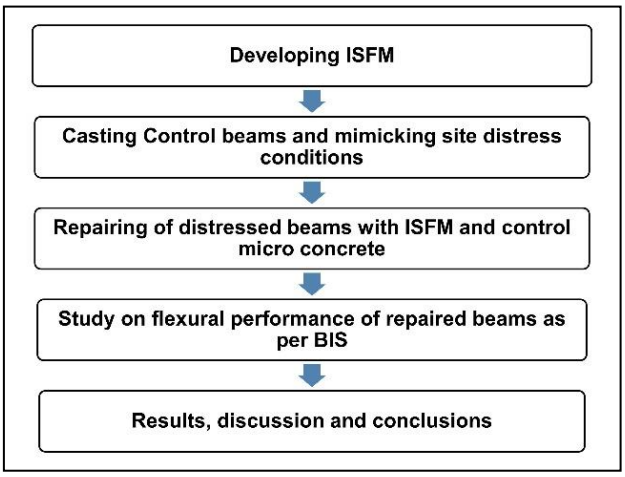

Figure 1. Methodology Flowchart

2.1 Materials

Portland pozzolana cement (PPC) confirming to IS 1489 (IS 1489 Part-1, 1991) was used having specific gravity of 3.14 and standard consistency of 32% tested as per IS 4031 (IS: 4031 (Part 11), 2019) and IS 4031 (IS: 4031 (Part 4), 2019) respectively. Manufactured sand (M-sand) with a specific gravity of 2.75 (IS: 2386 (Part 3), 2018), water absorption of 0.8% (IS: 2386 (Part 3), 2018) and corresponds to a grading Zone II (IS 2386 Part - 1, 1963) was used as fine aggregate. Fe 550D grade quenched and self-tempered steel rebars of sizes 6 mm (stirrups), 8 mm (compression reinforcement) and 10 mm (tension reinforcement) was used as reinforcement in the beam. A high performance poly-carboxylic ether based super plasticizer and sodium nitrite based corrosion inhibiting admixture was used as chemical admixture. Commercially available micro concrete was procured locally and used in control beams for comparison purpose. The potable water was used for casting and curing of beam specimens.

2.2 Development of inhibitor admixed self-flowing concrete

The development of inhibitor admixed self-flowing concrete (ISFM) was done as per the specifications of EFNARC standards (EN-206: EFNARC, 2005). The details of trial mixes and flow properties of developed mixes in comparison with EFNARC are given in Table 1 and Table 2 respectively. Slump flow test, V-funnel test and L-box test were carried out to confirm the flow properties of ISFM. Test results of all the trail mixes of ISFM are within the permissible limits of EFNARC (EN-206: EFNARC, 2005). Figure 2 shows the slump flow test in progress.

A total of 8 beams were cast without cover using M25 grade concrete in a steel mould of dimension 100 mm x 150 mm x 1000 mm. A 20 mm thick XPS foam boards were placed on both sides of the mould (in the longitudinal direction) before the rebar is placed to avoid concrete in the cover region. The specimen was demoulded after 24 hours and had a decreased dimension of 80 mm x 110 mm x 1000 mm. The beams were subjected to a 7-day conventional water cure, a 14-day 3% sodium chloride cure, and a 7-day alternate wet and dry curing, completing a 28-day curing time before repairing the beams using RC jacketing technique. Figure 3 shows the casting of control beams without cover.

The two control beams have been repaired using CMC. A wire brush was used to remove loose rust and dust from the exposed reinforcement. In the case of repair with CMC, the rebars were coated with a thin layer of zinc-rich primer, whereas in case of repair with developed ISFM, cement polymer anticorrosive (CPA) coating (Ahmed et al., 2021) was applied. An epoxy-based bond coat was applied over the entire repair surface area and micro concrete was poured within six hours of application of bond coat. Demoulding was carried out after 24 hours of repair and the repaired beams were cured for 14 days before testing. Figure 4 illustrates the steps involved in the repair of the beams using micro concrete.

Table 1. Details of trial mixes

Constituent	ISFM1	ISFM2	ISFM3
Cement (Kg/m^3)	440	440	440
Water (Kg/m^3)	194(0.44 w/c)	185(0.42 w/c)	180(0.4 w/c)
Coarse aggregate (Kg/m^3)	780	733	733
Fine aggregate (Kg/m^3)	860 (52%)	827 (53%)	827 (53%)
Superplasticizer (% bwoc)	0.6	0.7	0.8
Corrosion inhibitor (% bwoc)	0.6	0.6	0.6

*bwoc – by weight of cement

Table 2. Flow properties of trial mixes

Details of Mix	Slump Flow spread (mm)	V-Funnel flow time (sec)	Passing Ratio (H2/H1)
ISFM1	725	8	0.92
ISFM2	700	10	0.87
ISFM3	670	12	0.83
Specification as per EFNARC	600 – 800 mm	Less than or equal to 12	H2/H1 should not be less than 0.80

Figure 2. Slump flow test in progress

2.3 Flexural test

The flexural strength test was conducted on RC beams under 4-point loading method using 40 Ton capacity Universal Testing Machine (UTM) as per IS 516 (IS: 516, 1991). The sophisticated 8-channel Data Acquisition System (DAS) was employed to acquire the data from the specimen during testing. The spreader beam of length 400 mm was used to transfer the load (through the load cell) to the middle one-third portion of the beam. LVDT was provided at the bottom of the beam, centrally, for evaluating the central deflection. The LVDT was connected to the beam using an acrylic sheet to avoid friction at the contact surface. All the sensors were connected to DAS to acquire the results from LVDTs and a load cell as shown in Figure 5 (a and b). The loading was applied at a rate of 1.5 kN/min.

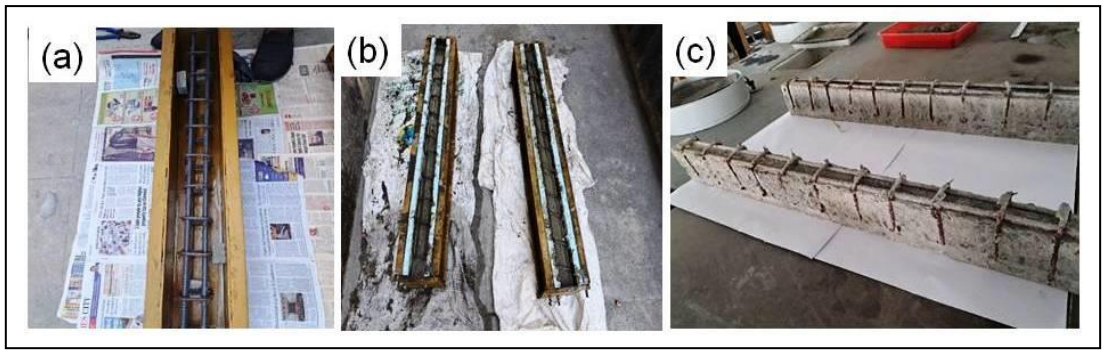

Figure 3. Casting of Control Beams without cover (a) View of mould with rebar cage (b) View of mould with XPS foams and poured concrete (c) View of beams without cover after de-moulding

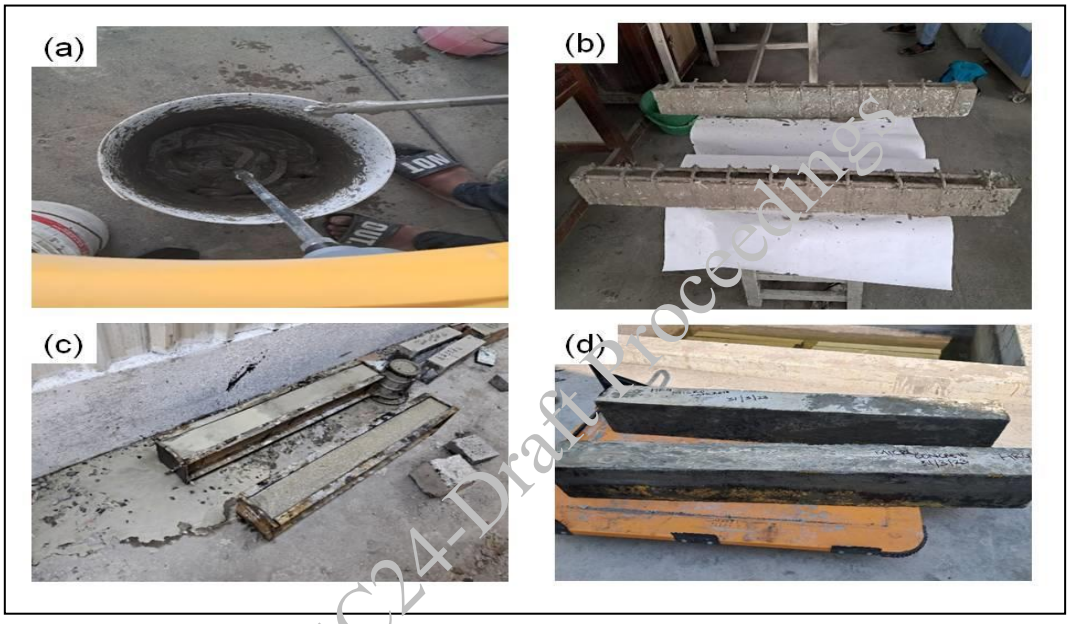

Figure 4. Repairing of beams (a) Mixing of micro concrete (b) View of beams without cover after demoulding (c) Repairing of beams with micro concrete (d) View of beams after repair

a) Test arrangement

b) b. Close view of load cell and LVDT

Figure 5. Flexure test set-up

3. Results and discussions

Figure 6 shows the comparison of compressive strength tests of three distinct trial mixes and CMC at different ages. It can be observed that the initial strength gain was higher in CMC as compared to other trial mixes whereas ISFM3 has attained marginally improved strength as compared to CMC after 28 days. Whereas ISFM1 and ISFM2 has attained marginally decreased compressive strength as compared to CMC after 28 days. Figure 7 shows the comparison of the 28day flexural strength of ISFM and CMC. There was a progressive increase in flexural strength from ISFM1 to ISFM3. The flexural strength increased up to 11.3%, 22.6%, and 38.5% for ISFM1, ISFM2, and ISFM3 respectively as compared to CMC.

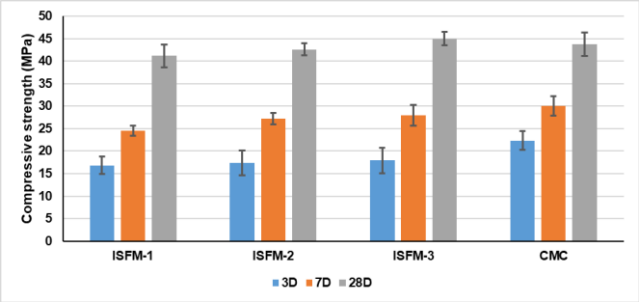

Figure 6. Compressive strength of trial mixes

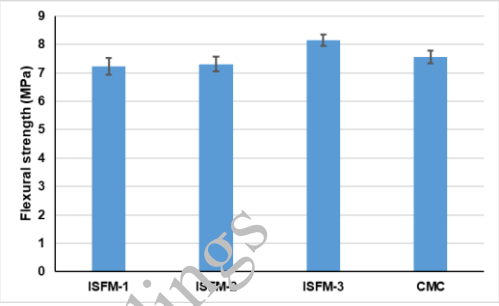

Figure 7. Comparison of flexural strength of concrete prisms

Figure 8 shows the comparison between water absorption for CMC and developed ISFM. It can be said that ISFM1 has slightly higher water absorption where as ISFM2 has marginally reduced water absorption and ISFM3 has significantly reduced water absorption as compared to CMC. Figure 9 shows the time vs rate of water absorption for three different trials mixes of ISFM and CMC. The data suggests that ISFM3 initially exhibited a higher rate of water absorption compared to the other mixtures. However, as the observation period progressed, the rate of water absorption for ISFM3 became the lowest amongst all the tested mixes.

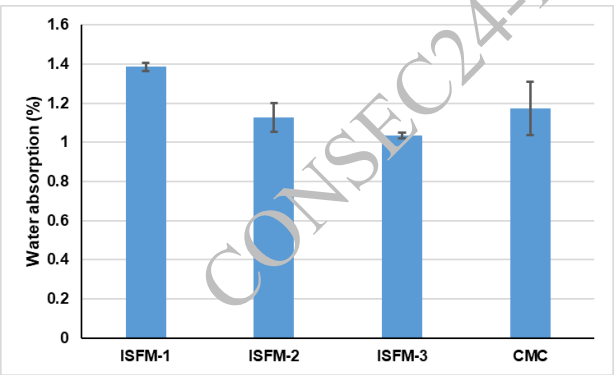

Figure 8. Comparison of water absorption

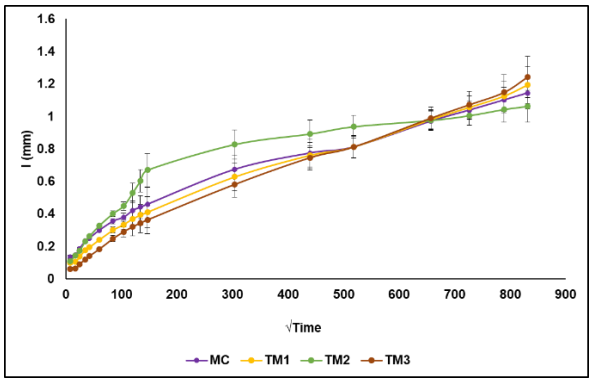

Figure 9. Time vs rate of water absorption behaviour

Figure 10 shows the comparison of the first crack loads of the three trial mixes of ISFM and CMC. It can be observed that the load at which the first crack appears is significantly higher in ISFM3 compared to CMC. ISFM2 and ISFM1 are similar in range at first crack loads but slightly lower than CMC. The load at which the first crack appears is 12% higher in ISFM3 as compared to CMC. Figure 11 shows the comparison of the ultimate loads of the trial mixes of ISFM and CMC. It can be noted that the ultimate load at which the specimen fails is greater for ISFM3 when compared to CMC. The ultimate load of ISFM3 is 15% higher compared to CMC. However, the ultimate load of ISFM1 and ISFM2 are 9% and 6% respectively lower than CMC. It can be inferred that ISFM3 offer a greater moment-carrying capacity compared to CMC which proves that ISFM3 repaired beams can handle higher safe allowable moment.

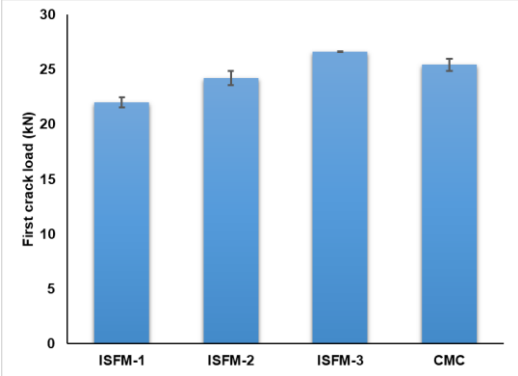

Figure 10. Comparison of first crack load of repaired beams

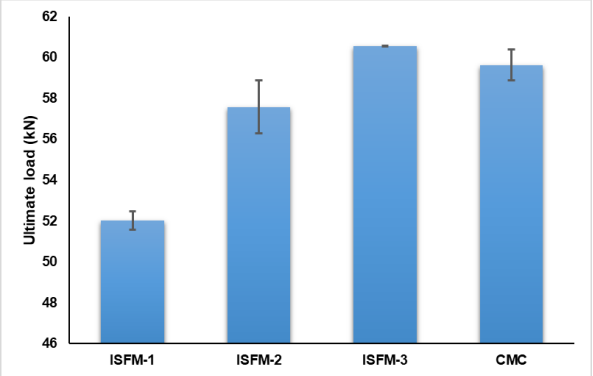

Figure 11. Comparison of ultimate load of repaired beams

Figure 12 illustrates the load-deflection response of beams repaired with ISFM and CMC mixes. The results reveal that CMC and ISFM2 exhibited comparable load-deflection behaviour. While ISFM2 offered a marginally superior energy absorption capacity (11% greater) compared to CMC, it fell short of ISFM3 by 6%. ISFM1 displayed the lowest energy absorption capacity amongst the tested repair mixes. The yield loads recorded for the beams repaired with CMC, ISFM1, ISFM2, and ISFM3 were 49 kN, 41 kN, 51 kN, and 53 kN, respectively. These values indicate a clear trend, with ISFM3 demonstrating the highest load carrying capacity (53 kN) – a significant improvement of 8% compared to the control (CMC). ISFM1 exhibited the lowest yield load (41 kN) among the repair mixes.

Furthermore, the deflection measurements at yield followed a similar pattern. The deflection observed for CMC (6 mm) was substantially greater than that of ISFM3 (4 mm), representing a remarkable reduction of 33% for the ISFM3 repaired beam. This finding suggests that ISFM3 enhanced not only the load carrying capacity but also the stiffness of the repaired beam compared to the control (CMC). ISFM3 exhibited a well-defined elasto-plastic region, characterized by a linear increase in load followed by a gradual yield plateau. This behavior indicates a more ductile response compared to the other mixes, which may be attributed to the improved material properties of the ISFM3 mix. Conversely, ISFM1 displayed significant variations within the linear and post-peak regions compared to CMC. This suggests a less predictable load-deflection response, possibly due to inconsistencies in the material properties or bond between the repair material and the steel. The ultimate load for all groups was reached at a deflection of 10 mm, indicating similar failure criteria. The ultimate loads themselves, however, varied amongst the groups. CMC achieved an ultimate load of 58 kN, followed by ISFM1 (52 kN), ISFM2 (57 kN), and ISFM3 (60 kN). Notably, ISFM1, ISFM2, and ISFM3 exhibited comparable maximum deflections, all exceeding that of CMC. This suggests that while these repair mixes offered enhanced load carrying capacity compared to CMC, their ultimate deformability was similar.

Based on the observed trends, it can be concluded that mix ISFM3 exhibited significantly superior mechanical and durability properties compared to CMC, ISFM1, and ISFM2 mixes. This enhanced performance can be attributed, in part, to the lower water-cement ratio employed in ISFM3. A lower water-cement ratio is well-established to promote a denser microstructure with reduced porosity within the composite material (Zajac et al., 2018). This densification not only improves the strength and stiffness of the repair material but also enhances its resistance to factors that can deteriorate its durability over time, such as chloride ingress and freeze-thaw cycles (Bajaj et al., 2020; Gu et al., 2024). These improvements in the microstructure likely contributed to the superior flexural performance of ISFM3 repaired beams.

Furthermore, the incorporation of a CPA coating on corroded rebars along with a bond coat might have further enhanced the engagement between the steel reinforcement and the repair concrete. This improved interfacial bond is critical for achieving superior flexural performance in repaired RC beams. A strong bond between the steel rebar and surrounding repair material ensures effective stress transfer between the two materials, enabling the composite section to behave more cohesively under load (Bajaj et al., 2020). Conversely, a weak interfacial bond can lead to debonding and premature failure of the repaired beam. The CPA coating likely plays a dual role in enhancing bond. First, by filling surface irregularities on the corroded rebar, the coating can create a more intimate contact between the steel and the repair concrete. Second, the cementitious nature of the CPA coating promotes good chemical compatibility with the

surrounding concrete, facilitating the formation of a strong mechanical bond (Ahmed et al., 2021). Additionally, the bond coat applied between the substrate concrete and the repair material serves a similar purpose of improving interfacial shear transfer and reducing the risk of debonding at the interface (Daneshvar et al., 2022).

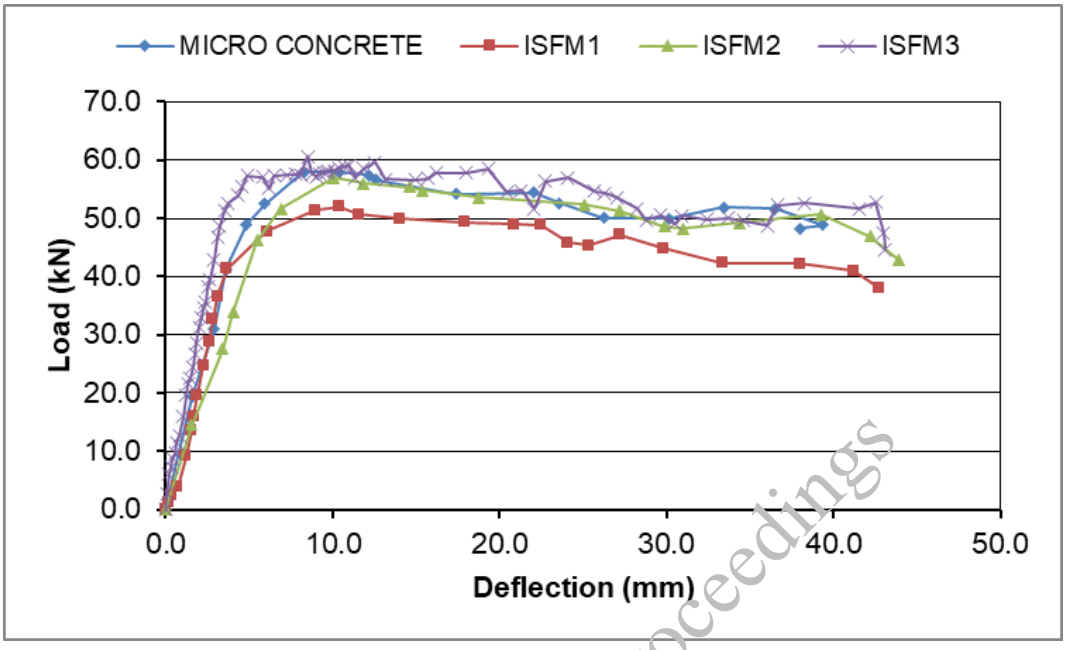

Figure 12. Load vs Deflection behaviour of repaired beams

4. Conclusions

Based on the results and further analysis, the following conclusions were drawn

- There is a significant increase in flexural strength of 38% for ISFM3 mix as compared to CMC. The water absorption and sorptivity results also exhibit the better performance of ISFM3 mix as compared to CMC and other tested mixes.
- The load at first crack of ISFM3 beams is 12% higher than that of the beams repaired with CMC. ISFM2 and ISFM1 beams exhibited similar first crack loads but slightly lower than the beams repaired with CMC.
- ISFM3 beams exhibited a higher energy absorption capacity compared to CMC beams.
- The better performance of the ISFM3 beams may be due to the reduced water cement ratio, improved microstructure and reduced porosity of ISFM3 mix.

References

Ahmed, M. M., Umar, M., Abdul Ahad, A., & Haji Sheik Mohammed, M. S. (2021). Optimisation of mix proportion for repair mortar modified with mineral and chemical admixtures. *Journal of Structural Engineering*, *48*(2), 89–103.

Bajaj, R., Wang, B., & Gupta, R. (2020). Characterization of enhanced itz in engineered polypropylene fibers for bond improvement. *Journal of Composites Science*, *4*(2). https://doi.org/10.3390/JCS4020053

Daneshvar, D., Behnood, A., & Robisson, A. (2022). Interfacial bond in concrete-to-concrete composites: A review. *Construction and Building Materials*, *359*, 129195. https://doi.org/10.1016/J.CONBUILDMAT.2022.129195

EN-206: EFNARC. (2005). *Specification & guidelines for self-compacting concrete, English Ed.*

Gu, Y., Mohseni, E., Farzadnia, N., & Khayat, K. H. (2024). An overview of the effect of SAP and LWS as internal curing agents on microstructure and durability of cement-based materials. *Journal of Building Engineering*, 109972. https://doi.org/10.1016/J.JOBE.2024.109972

Habib, A., Yildirim, U., & Eren, O. (2020). Column repair and strengthening using RC jacketing: a brief state-of-the-art review. *Innovative Infrastructure Solutions*, *5*(3), 1–11. https://doi.org/10.1007/S41062-020-00329-4/METRICS

IS: 2386 (Part 3). (2018). *Methods of test for aggregates for concrete: Specific gravity, Density, Voids, Absorption and Bulking*.

IS: 4031 (Part 11). (2019). *Methods of physical tests for hydraulic cement. Determination of density*.

IS: 4031 (Part 4). (2019). *Methods of physical tests for hydraulic cement. Determination of consistency of standadrd cement*.

IS: 516. (1991). *Methods of test for strength of concrete*.

IS 1489 Part-1. (1991). Portland pozzolana cement - specification. In *Bureau of Indian Standards*.

IS 2386 Part - 1. (1963). Particle Size and Shape, Indian Standard Methods of Test for Aggregates for Concrete. In *Bureau of Indian Standards*.

Rahim Karim, F. (2020). *Review on the Strengthening of Reinforced Concrete Columns by Reinforced Concrete Jacketing*. https://doi.org/10.36348/sjce.2020.v04i01.002

Sakr, M. A., El Korany, T. M., & Osama, B. (2020). Analysis of RC columns strengthened with ultra-high performance fiber reinforced concrete jackets under eccentric loading. *Engineering Structures*, *220*, 111016. https://doi.org/10.1016/J.ENGSTRUCT.2020.111016

Zajac, M., Skocek, J., Adu-Amankwah, S., Black, L., & Ben Haha, M. (2018). Impact of microstructure on the performance of composite cements: Why higher total porosity can result in higher strength. *Cement and Concrete Composites*, *90*, 178–192. https://doi.org/10.1016/J.CEMCONCOMP.2018.03.023

Enhancing Shear Friction Capacity in Concrete Structures with CFRP Composite Strips: A Numerical Investigation

Tanveer Habib[1*], S.A. Waseem[2], and F.A. Sofi[3]

[1] *National Institute of Technology, Srinagar, India*
tanveerhabib_2019phaciv014@nitsri.net
[2] *National Institute of Technology, Srinagar, India*
shakeelahmad@nitsri.net
[3] *National Institute of Technology, Srinagar, India*
sofifayaz@nitsri.ac.in

*Corresponding author

ABSTRACT

This numerical study delves into the shear friction capacity of reinforced concrete, focusing on external strengthening with Carbon Fiber Reinforced Polymer (CFRP) composite strips at specific failure planes. Utilizing uncracked push-off specimens with CFRP reinforcement, the research demonstrates a notable increase in shear friction capacity for reinforced concrete, correlating with the shear-to-normal stress ratio and investigating parametric studies of various CFRP wrapping schemes (two-sided, four-sided), CFRP laminate orientation, and different concrete strengths (M20, M40, and M60). In the current ABAQUS modeling of push-off samples, the lamina option is used to define CFRP material properties in ABAQUS, 2D shell elements are employed to model the CFRP strips, and cohesive contact is utilized to simulate the interaction between concrete and CFRP. The material model for concrete is concrete-damaged plasticity (CDP), and the bilinear material model is used for reinforcing steel. The study provides insights into enhancing shear friction strength for initially uncracked connections. The validation of experimental outcomes enables the determination of shear friction strength, offering valuable perspectives on the potential improvement of concrete structures through the external application of CFRP composite strips.

KEYWORDS*: Interface shear, Push-off test, Retrofitting, CFRP, ABAQUS modeling*

1. Introduction

Retrofitting concrete structures is essential for addressing various issues, including material degradation, design deficiencies, inadequate maintenance, evolving load specifications, and unexpected incidents like seismic events (Obaidat et al., 2010) In recent years, the advent of strong adhesives for concrete-CFRP interface joints and the excellent mechanical properties of CFRP have significantly increased the use of CFRP as external reinforcement (Frhaan et al., 2021; Obaidat et al., 2010). Carbon Fiber Reinforced Polymer (CFRP) composite strips have emerged as a viable solution for enhancing the shear friction capacity of concrete structures. The superior strength-to-weight ratio, corrosion resistance, and ease of application of CFRP composites make them an attractive choice for structural retrofitting projects (Khalifa, A., L. De Lorenzis, 2000; Shamass, Zhou, and Wu 2017; Teng et al., 2009). These materials extend the service life of existing structures and offer an efficient and cost-effective alternative to traditional reinforcement methods (ACI Committee 440, 2008).

Despite the growing interest and application of CFRP strips in concrete structures, understanding the detailed mechanics of their interaction with concrete under shear stress remains a critical area of study. The behavior of CFRP-reinforced interfaces under various loading conditions, particularly shear forces, is complex and influenced by numerous factors, including the properties of the concrete, the quality of the adhesive bond, and the configuration of the CFRP strips (Pham, Al-Mahaidi, and Saouma 2006) (Pham et al., 2006; Buyukozturk & Hearing, 1998; De Lorenzis & Tepfers, 2001).

This paper presents a numerical investigation to enhance the shear friction capacity of concrete structures using CFRP composite strips. Advanced computational models are employed to provide a deeper understanding of the shear transfer mechanisms and to identify optimal configurations for CFRP reinforcement. The findings of this research will contribute to developing more effective retrofitting strategies and guidelines for using CFRP composites in structural engineering. Using CFRP composite strips to enhance shear friction capacity in concrete structures offers significant potential for improving their durability and performance. Advanced numerical models can aid in understanding the complex interactions at play and develop optimized retrofitting strategies. This research underscores the importance of continued exploration of innovative materials and methods for structural enhancement (Buyukozturk et al., 2004; Deifalla & Ghobarah, 2010).

2. Shear friction

Several parameters influence the ultimate shear transfer strength across an interface in addition to the contact condition. Aggregate interlock, the use of shear reinforcement and any resulting dowel action, the surface preparation of the interface, the kind of aggregate chosen, and any restraints placed transverse to the shear plane are among these factors. According to Mattock (Mattock, Chen, and Soongswang 1976), Raths (Harding 2018), and Walraven (Walraven and Reinhardt 1981), the cohesiveness of the interface is significant to the shear friction mechanism. Several studies have been conducted in the last decades to study shear transfer in reinforced concrete (RC) members at an un-cracked plane (Mattock and Hawkins 1972; Mattock, Johal, Shejwadkar, Singh, and Waseem 2017; Sneed et al. 2016; Waseem and Singh 2016, 2018) and thus, to overcome the direct shear failure problem, push-off specimens under direct shear testing have been used to significantly improve understanding of the fundamental behavior of the interface shear capacities through experimental observations. Concrete strength, dowel steel across the interface, and constraints in a direction normal to the shear plane were found to be significant determinants of shear transfer behavior (Xu et al. 2015).

3. Methodology

The experimental setup illustrated in Figure 1 is designed for the direct shear testing of concrete push-off specimens. This setup involves a carefully arranged configuration where the push-off sample is placed between a loading actuator and a reaction frame. The sample features a predetermined shear plane, marked by two rectangular notches. These notches are strategically casted to ensure that the sample undergoes shear failure along the specified plane, thereby preventing other failure modes such as flexural compression or crushing. During the test, the loading actuator applies load to the sample, inducing shear stress along the plane. The reaction frame provides the necessary support to maintain the sample in place and resist the applied load. The notches ensure that the focus remains on the shear plane, providing clear and precise data on the material's shear performance. This methodology, aimed at accurately assessing the shear strength of concrete, has been widely adopted in various studies to ensure consistency and reliability in testing results (Shakeel Ahmad and Bhupinder 2018; Subhan Ahmad et al. 2020; Mattock, Li, and Wang 1976; Shejwadkar, Singh, and Waseem 2017; Waseem et al. 2016).

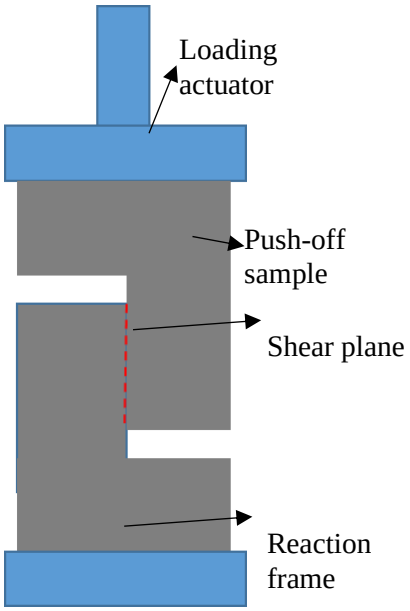

Figure 1. Test setup for testing concrete pushoff specimens

The methodology for this study on the shear friction capacity of concrete with external Carbon Fiber Reinforced Polymer (CFRP) strips involves numerical modeling shown in Figure 1 labeled (a), (b), (c), and (d), each configured with different CFRP reinforcement ratios and validation with experiments from literature (Saenz and Pantelides 2005). Numerically, 3D push-off specimens were modeled in ABAQUS, as shown in Figure 3, defining concrete and CFRP properties, simulating interactions, and bonding through cohesive zone modeling. Boundary conditions and shear loadings are applied to replicate experimental setups utilized by (Saenz and Pantelides 2005) in their experimental work. The modeling process involves creating a solid mesh for both the bottom and top concrete sections using C3D8R elements and a truss mesh for the reinforcement cage using T3D2 elements. The assembly of these components was designed to accurately replicate the experimental samples' physical configuration and loading conditions. A parametric study was then carried out in ABAQUS, wrapping configurations (2, 3, and 4 sides), composite layup orientations (0°, 45°, and 90°), and laminate orientations (0°, 30°, 45°, 60°, and 90°), to analyze their effects on shear friction capacity. The numerical results are compiled to identify the most influential factors.

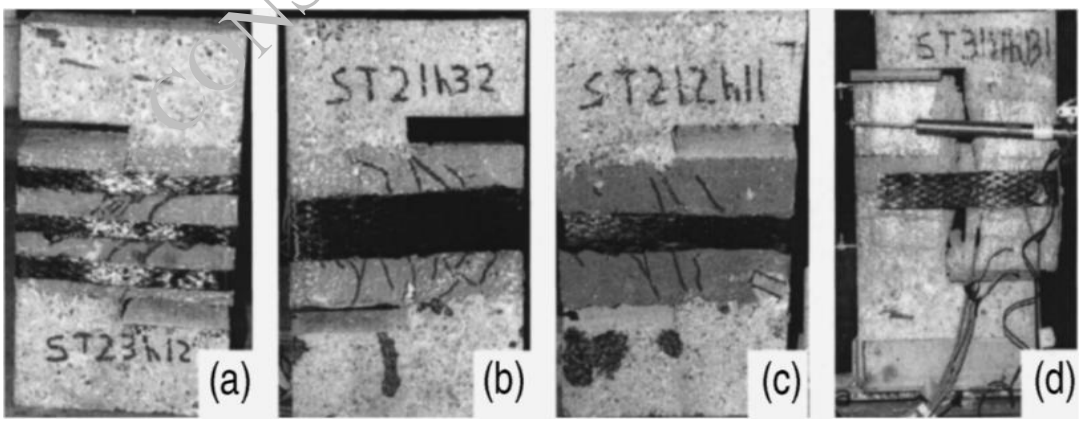

Figure 2. Push off specimens with CFRP strips from experiments (Saenz and Pantelides 2005).

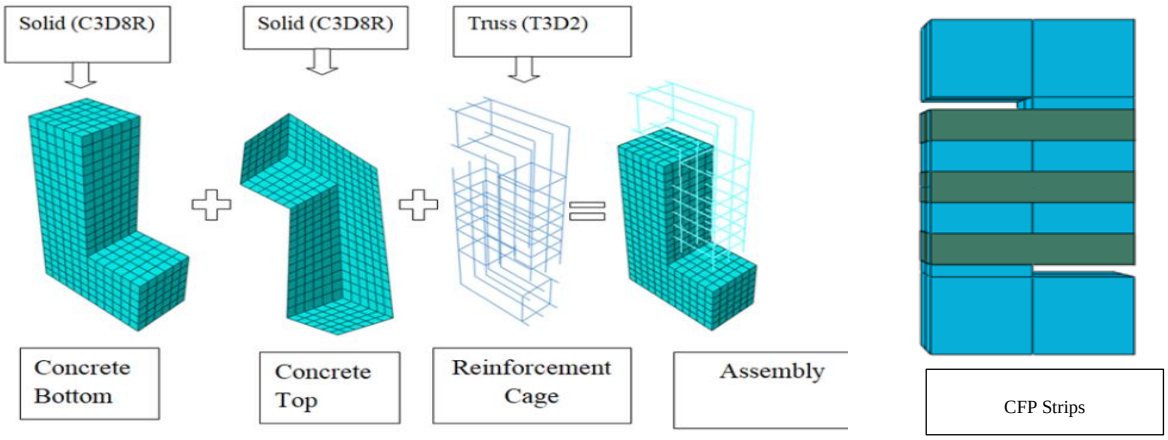

Figure 3. ABAQUS modelling of Push off specimens with CFRP strips

4. Finite element modelling

Uncracked push-off specimens were meticulously designed to investigate the shear friction capacity of concrete reinforced with CFRP strips. The specimens had a shear plane of width of 127 mm and length of 305 mm. The height of the specimens varied to achieve different shear-to-normal stress ratios (k) of 1.26, 1.50, and 1.85. This variation in height allowed for the analysis of the influence of stress ratios on the shear friction capacity. The specimens were externally reinforced with CFRP strips using a wet-layup process.
The damage plasticity model is a valuable tool for simulating the compression and tension of concrete(Ren et al. 2015). To visualize the behavior of nonlinear materials at higher strains, the uniaxial behavior of steel and concrete well outside the elastic range must be defined. The concrete smeared cracking model (CSCM), brittle cracking concrete (BCC) model, and concrete damaged plasticity (CDP) model are three constitutive models in ABAQUS (Dassault Systèmes Simulia 2012) for defining the inelastic behavior of concrete. The CDP approach requires the concrete compressive and tensile constitutive relationship, cracking and crushing damage parameters, and other material parameters such as dilation angles, eccentricity, biaxial compressive strength to uniaxial compressive strength ratio, coefficient K, and viscosity parameters (Dassault Systèmes Simulia 2012). The CDP model deals with plastic behavior, compressive behavior, tensile behavior, and the damage mechanism of concrete. Concrete, unlike steel, exhibits nonlinearity from the beginning when exposed to tension or compression testing. The present study uses a simplified version of the CDP theory suggested by (Hafezolghorani et al. 2017). Concrete damage plasticity assumes that cracking begins at sites where the tensile equivalent plastic strain is greater than zero to visualize cracking. In addition, the direction of the fracture, as shown in ABAQUS/visualization CAE's mode, is parallel to the direction of plastic strain.

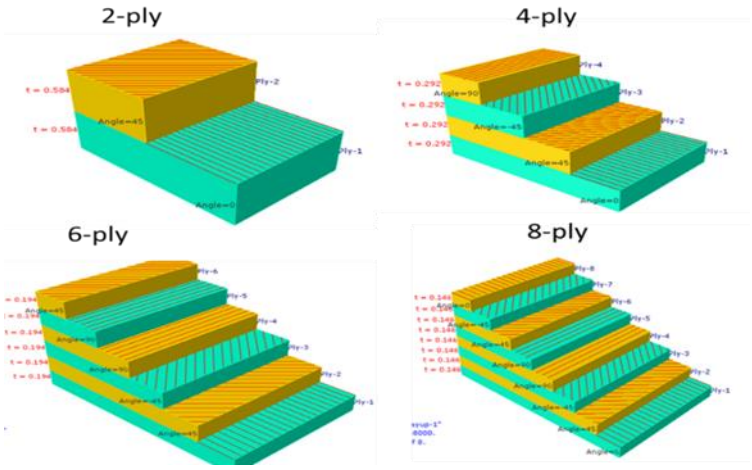

Figure 4. CFRP composite layup orientation and number of plys in CFRP laminate

Figure 4 illustrates the parametric study on the shear friction capacity of concrete with external Carbon Fiber Reinforced Polymer (CFRP) strips. The study examines different ply configurations and orientations, specifically 2-ply, 4-ply, 6-ply, and 8-ply setups. Each configuration displays the layers of CFRP strips applied at various angles (0°, 45°, and 90°) and thicknesses. In the 2-ply configuration, two layers of CFRP strips are oriented at 0° and 45°, respectively, with a thickness of 0.584 mm. The 4-ply configuration shows layers oriented at 0°, 45°, 45°, and 90°, each with a thickness of 0.292 mm. The 6-ply configuration involves layers oriented at 0°, 45°, 45°, 90°, 90°, and 45°, with a thickness of 0.194 mm per layer. Finally, the 8-ply configuration includes layers oriented at 0°, 45°, 45°, 90°, 90°, 45°, 45°, and 90°, each with a thickness of 0.146 mm. This visual representation helps understand the impact of different CFRP wrapping configurations and orientations on the shear friction capacity of concrete specimens.

5. Results and Discussions

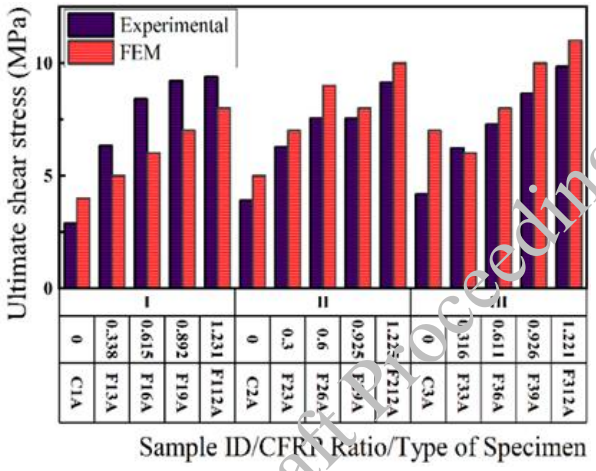

Figure 5. Comparison of experimental and FEM results

6. Conclusions

Figure 5 presents a comparative analysis of the ultimate shear stress (MPa) between experimental results and finite element method (FEM) simulations for different specimens of concrete with varying Carbon Fiber Reinforced Polymer (CFRP) ratios. The specimens are categorized into three groups, I, II, and III, based on shear-to-normal stress ratios (k) of 1.26, 1.50, and 1.85, each with different CFRP ratios. In all categories, the FEM simulations generally show higher ultimate shear stress compared to the experimental results. This trend is consistent across all sample IDs, indicating a potential overestimation of shear capacity by the FEM model. For category I with k=1.26 and CFRP ratio zero, the ultimate shear stress values are the lowest among all groups, both experimentally and numerically, highlighting the significant enhancement in shear capacity provided by the CFRP strips. In category II k=1.5 and CFRP ratio around 1.0, an increase in shear stress is observed, reflecting the positive impact of the CFRP reinforcement. Category III with k=1.86 (highest CFRP ratio) demonstrates the highest ultimate shear stress values, reinforcing the conclusion that higher CFRP ratios lead to increased shear capacity. The comparison between experimental and FEM results shows good agreement overall, though discrepancies are evident, particularly in categories II and III. These differences underscore the importance of refining numerical models to predict the shear behavior of CFRP-reinforced concrete more accurately. The results validate the effectiveness of CFRP strips in enhancing shear friction capacity, with numerical simulations providing a valuable tool for predicting structural performance while highlighting the necessity for ongoing calibration and validation against experimental data.

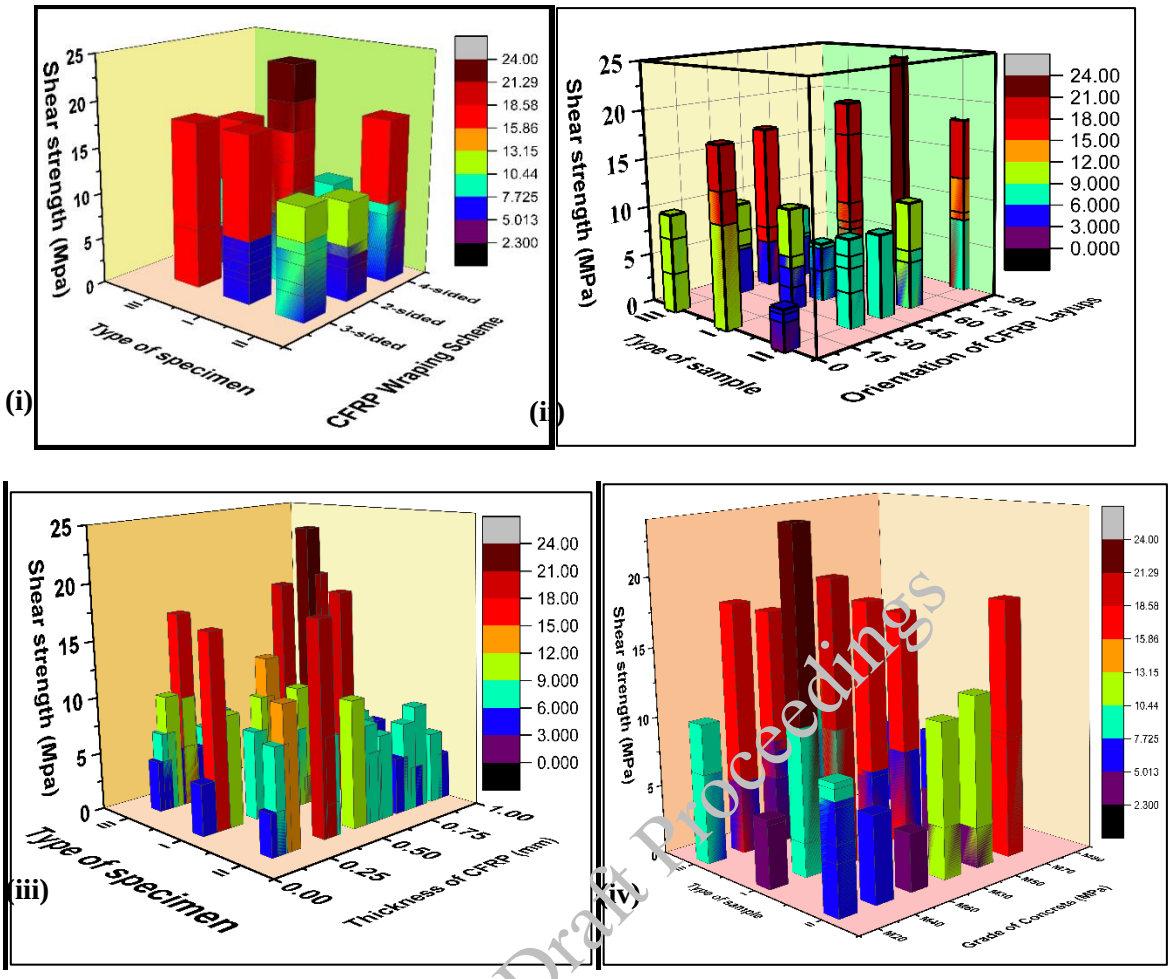

Figure 6. FEM shear stress results for (i) Wrapping scheme (ii) orientation of CFRP layups (iii) CFRP laminate thickness, (iv) Concrete grade

Figure 6 (i) illustrates the effect of different CFRP wrapping schemes (2-sided, 3-sided, and 4-sided) on the shear strength across the three categories. The trends indicate that the 4-sided wrapping scheme consistently provides the highest shear strength across all categories, with category III showing the most significant enhancement. This suggests that a more comprehensive wrapping scheme significantly improves the shear capacity of the concrete specimens. The FEM results from Figure 6 (ii) show the influence of CFRP layer orientation (0°, 45°, 90°, and a combination) on shear strength. The orientation at 45° also demonstrates substantial shear strength, highlighting its effectiveness in resisting shear forces. Both charts show that increasing the shear-to-normal stress ratio (from category I to III) results in higher shear strengths, regardless of the CFRP wrapping scheme or orientation. Figure 6 (iii) illustrates the shear strength (MPa) of various specimen types as a function of CFRP reinforcement thickness (mm). The shear strength values are represented by the height and color intensity of the bars, with the color scale ranging from 0 MPa (blue) to 24 MPa (red). It is observed that increasing the thickness of CFRP reinforcement generally leads to higher shear strength across different specimen types. Specimens with higher CFRP thicknesses (0.75 mm and 1.00 mm) exhibit significantly higher shear strength than those with lower thicknesses (0.25 mm and 0.50 mm). This indicates that the reinforcement configuration and thickness are critical in enhancing shear capacity. Figure 6 (iv) presents the shear strength (MPa) of various specimen types as a function of the concrete grade (MPa). Similar to the previous figure, the shear strength values are depicted by the height and color intensity of the bars, with the color scale ranging from 2.3 MPa (blue) to 24 MPa (red). Higher concrete grades, such as M40 and M50, generally result in higher shear strength across different specimen types. Conversely, specimens with lower concrete grades, such as M20 and M30, exhibit relatively lower shear strength, indicating that the concrete grade significantly influences the overall shear capacity. The combination of higher concrete grades and appropriate CFRP reinforcement configurations results in the highest shear strength values observed in the study. Overall, these figures highlight the importance of

optimizing both the CFRP reinforcement thickness and concrete grade to achieve maximum shear strength in concrete specimens. The parametric study provides valuable insights into identifying the most effective combinations of these factors to enhance the structural performance of reinforced concrete elements. This observation confirms that the effectiveness of CFRP reinforcement is more pronounced at higher stress ratios, thus emphasizing the importance of optimal CFRP wrapping schemes and orientations to maximize the shear friction capacity of concrete. Such insights are crucial for the practical application of CFRP in enhancing the structural integrity of concrete elements.

7. Conclusions

The study on the shear friction capacity of concrete with external Carbon Fiber Reinforced Polymer (CFRP) strips, by numerical (FEM) analyses, yielded several key insights:

- Effectiveness of CFRP Reinforcement: Both the experimental and FEM results consistently demonstrated that CFRP reinforcement significantly enhances the shear capacity of concrete. This enhancement was particularly noticeable with higher CFRP ratios, aligning with the general trend observed in categories with higher shear-to-normal stress ratios (k values).
- Overestimation by FEM Models: The FEM simulations generally showed higher ultimate shear stress compared to experimental results across all categories. This suggests a potential overestimation of shear capacity by the FEM models, highlighting the need for refinement and calibration of numerical models to match experimental observations better.
- Impact of CFRP Wrapping Schemes: The analysis revealed that the 4-sided CFRP wrapping scheme consistently provided the highest shear strength across all categories. This indicates that more comprehensive wrapping schemes are more effective in enhancing shear capacity. However, it is essential to note that the increased tensile strain efficiency observed in the 4-sided scheme does not directly translate to higher shear friction capacity due to the limiting factors of concrete cohesive failure and bond failure of the CFRP composite.
- CFRP Orientation Influence: The orientation of CFRP layers significantly affects shear strength. The combination of orientations and the 45° orientation were particularly effective in resisting shear forces, suggesting that optimizing the orientation of CFRP layers is crucial for maximizing shear friction capacity.
- Shear-to-Normal Stress Ratio: The shear strength increased with higher shear-to-normal stress ratios, indicating that the effectiveness of CFRP reinforcement is more pronounced under higher stress conditions. This trend was evident across all wrapping schemes and orientations, reinforcing the importance of considering stress ratios in the design and application of CFRP reinforcement.

Overall, this study validates the effectiveness of CFRP strips in enhancing the shear friction capacity of concrete while highlighting the necessity for ongoing refinement of numerical models to ensure accurate predictions of structural performance. These insights are crucial for the practical application of CFRP in improving the durability and strength of concrete structures.

References

Ahmad, Shakeel, and Waseem Bhupinder. 2018. "An Experimental Study on Shear Capacity of Interfaces in Recycled Aggregate Concrete." (December 2017): 230–45.

Ahmad, Subhan, Pradeep Bhargava, Ajay Chourasia, and Umesh Kumar Sharma. 2020. "Shear Transfer Strength of Uncracked Concrete after Elevated Temperatures." *Journal of Structural Engineering* 146(7): 04020133. https://ascelibrary.org/doi/10.1061/%28ASCE%29ST.1943-541X.0002681.

Dassault Systèmes Simulia. 2012. "Abaqus CAE User's Manual (6.12)." *Manuals*: 1174.

Frhaan, Waseem Khairi Mosleh, B. H. Abu Bakar, Nahla Hilal, and Abdulkader Ismail Al-Hadithi. 2021. "CFRP for Strengthening and Repairing Reinforced Concrete: A Review." *Innovative Infrastructure Solutions* 6(2): 49. https://doi.org/10.1007/s41062-020-00417-5.

Hafezolghorani, Milad et al. 2017. "Simplified Damage Plasticity Model for Concrete." *Structural Engineering International* 27(1): 68–78.

Harding, Karen. 2018. "Causality Then and Now: Al Ghazâlî and Quantum Theory." *Kader* 16(2): 525–36.

Khalifa, A., L. De Lorenzis, and A. Nanni. 2000. "FRP Composites for Shear Strengtheneing of RC Beams." *Advanced Composite Materials in Bridges and Structures*: 137–44.

Mattock, Alan H., K. C. Chen, and K. Soongswang. 1976. "Behavior of Reinforced Concrete Corbels." *J Prestressed Concr Inst* 21(2): 52–77.

Mattock, Alan H., and Neil M. Hawkins. 1972. "Mattock and Hawkins 1972;" *PCI Journal* 17(2): 55–75.

Mattock, Alan H., L. Johal, and H. C. Chow. 1975. "Shear Transfer in Reinforced Concrete with Moment or Tension Acting across the Shear Plane." *PCI Journal* 20(4): 76–93. https://www.pci.org/PCI/Publications/PCI_Journal/Issues/1975/July-August/Shear_transfer_in_reinforced_concrete_with_moment_or_tension_acting_across_the_shear_plane.aspx.

Mattock, Alan H, W K Li, and T C Wang. 1976. "Shear Transfer in Lightweight Reinforced Concrete." *PCI journal* 21(1): 20–39.

Obaidat, Yasmeen Taleb, Susanne Heyden, and Ola Dahlblom. 2010. "The Effect of CFRP and CFRP/Concrete Interface Models When Modelling Retrofitted RC Beams with FEM." *Composite Structures* 92(6): 1391–98. http://dx.doi.org/10.1016/j.compstruct.2009.11.008.

Pham, H. B., R. Al-Mahaidi, and V. Saouma. 2006. "Modelling of CFRP-Concrete Bond Using Smeared and Discrete Cracks." *Composite Structures* 75(1–4): 145–50.

Ren, Wei, Lesley H. Sneed, Yang Yang, and Ruili He. 2015. "Numerical Simulation of Prestressed Precast Concrete Bridge Deck Panels Using Damage Plasticity Model." *International Journal of Concrete Structures and Materials* 9(1): 45–54.

Saenz, Nicolas, and Chris P. Pantelides. 2005. "Shear Friction Capacity of Concrete with External Carbon FRP Strips." *Journal of Structural Engineering* 131(12): 1911–19.

Shamass, Rabee, Xiangming Zhou, and Zongyi Wu. 2017. "Numerical Analysis of Shear-Off Failure of Keyed Epoxied Joints in Precast Concrete Segmental Bridges." *Journal of Bridge Engineering* 22(1): 1–13.

Shejwadkar, Nikhil, Bhupinder Singh, and Shakeel Ahmad Waseem. 2017. "Shear Friction in Recycled Aggregate Concrete."*Journal of Sustainable Cement-Based Materials* 6(1): 17–36. https://www.tandfonline.com/doi/full/10.1080/21650373.2016.1212424.

Sneed, Lesley H., Kristian Krc, Samantha Wermager, and Donald Meinheit. 2016. "Interface Shear Transfer of Lightweight-Aggregate Concretes with Different Lightweight Aggregates." *PCI Journal* 61(2): 38–55. https://www.pci.org/PCI/Publications/PCI_Journal/Issues/2016/March-April/Interface_shear_transfer_of_lightweight-aggregate_concretes_with_different_lightweight_aggregates.aspx.

Teng, J. G. et al. 2009. "FRP Composites in Structures: Some Recent Research." *APFIS 2009 - Asia-Pacific Conference on FRP in Structures*: 179–86.

Walraven, J C, and H W Reinhardt. 1981. *Concrete Mechanics: Theory and Experiments on the Mechanical Behaviour of Cracks in Plain and Reinforced Concrete Subjected to Shear Loading*. Stevin-Laboratory of the Department of Civil Engineering.

Waseem, Shakeel Ahmad et al. 2016. "Shear Transfer Strength of Normal and High-Strength Recycled Aggregate Concrete – An Experimental Investigation." *Construction and Building Materials*. https://doi.org/10.1016/j.conbuildmat.2016.08.022.

Waseem, Shakeel Ahmad, and Bhupinder Singh. 2016. "Shear Transfer Strength of Normal and High-Strength Recycled Aggregate Concrete – An Experimental Investigation." *Construction and Building Materials* 125: 29–40.2018. "Strut-and-Tie Model for Shear Strength of Reinforced Concrete 'push-off' Specimens." *Proceedings of the Institution of Civil Engineers: Structures and Buildings* 171(4): 295–305.

Xu, Juechun, Chengqing Wu, Zhong-xian Li, and Ching-tai Ng. 2015. "Numerical Analysis of Shear Transfer across an Initially Uncrack Reinforced Concrete Member." *Engineering Structures* 102: 296–309. http://dx.doi.org/10.1016/j.engstruct.2015.08.022.

Evaluation of Input Parameters for the Electrochemical Modelling of Cathodic Protection Systems in Reinforced Concrete

Keerthi Vadakke Thalakkal [1*] and Radhakrishna G Pillai [2]

[1] Indian Institute of Technology Madras, Chennai, India
Email: keerthigopinath95@gmail.com
[2] Indian Institute of Technology Madras, Chennai, India
Email: pillai@civil.iitm.ac.in

[*]Corresponding author

ABSTRACT

Cathodic Protection using embedded galvanic anodes can be used to arrest ongoing corrosion and extend the service life of concrete structures. Usually, the long-term performance of anodes is assessed using the "100 mV polarization shift criterion" given in EN ISO 12696 (2016). This was developed based on corrosion studies on metals in low resistive systems and is not suitable for highly resistive concretes and repair mortars). Hence, a more rational criterion based on the resistivity of the system is required. To develop this criterion, the first step would be the electrical/electrochemical modelling of the concrete-steel-anode (C-S-A) system using finite element analysis in COMSOL Multiphysics. Potentiodynamic polarization (PDP) test was conducted to obtain the input parameters for the development of this model. In this study, the PDP test was performed on steel and zinc in a simulated pore solution. However, the polarization properties obtained did not represent the actual environmental condition where the concrete bulk resistivity, relative humidity, and oxygen concentration would have a significant effect on the steel corrosion rate. Hence, two sets of specimens were cast, where the first set consisted of a steel bar embedded in the cementitious mortar and the second set consisted of galvanic anodes (pristine) embedded in cementitious mortar and was the working electrode in the three-electrode setup. The anodic and cathodic Tafel slopes and the exchange current densities were found to be significantly different from common corrosion systems. Further steps towards the development of electrochemical modelling of the C S A system were discussed.

KEYWORDS*: Reinforced Concrete, Cathodic Protection, 100-mV potential shift criterion, Numerical modelling, Potentiodynamic polarization test*

1. Introduction

The corrosion of embedded steel rebars is one of the major deterioration mechanisms in reinforced concrete (RC) structures. Mitigating corrosion and extending the service of the RC structures are the key challenges in the infrastructure sector. Generally, patch repair is the conventional repair strategy adopted, which replaces contaminated concrete without addressing the root cause of corrosion – resulting in repeated repairs leading to the huge cost of corrosion (Krishnan et al., 2021). Although corrosion is an electrochemical problem, the repairs have been done without giving importance to the electrochemistry of the system. Cathodic protection (CP) system using galvanic anodes is one of the effective electrochemical repair techniques, that can stop ongoing corrosion and extend the service life of the structures. The efficiency of the CP system is assessed by using a monitoring box which involves measurement of polarized potential and output current density of galvanic anodes. The periodic depolarisation tests are carried out to obtain the E_{on} (the half-cell potential (HCP) of the rebars when it is connected to the anodes), $E_{off\text{-}inst}$ (HCP of rebars immediately when the anodes are disconnected), and $E_{off\text{-}24h}$ (HCP of rebars after 24 hours of depolarisation). The potential shift is the difference between $E_{off\text{-}inst}$ and $E_{off\text{-}24h}$ depolarised. Obtaining the 100 mV potential shift from this measurement is considered the acceptance criterion as per EN ISO 12696 (2022). However, this inspection method/acceptance criterion uses empirical assumptions for seawater/soil

electrolyte (low resistivity). These are being used, but unsuitable for GCP systems with steel bars, and zinc anodes in highly resistive concrete (Goyal et al., 2019). Also, there is a practical difficulty in setting up the monitoring boxes at all locations of installed anodes, so the anodes installed at predefined locations can only be tested. Hence, using the existing method, stakeholders are not able to routinely inspect and assess the quality/performance of numerous anodes installed. Presently, very few studies have been done on the field assessment of CP systems in concrete structures without using monitoring boxes. Hence, there is a need for a non-destructive test method for routine inspection of the CP system. Attempts were already made to model the CP system using the finite element method. This finite element modelling approach gives the potential and current distribution in a concrete-steel-anode (C-S-A) system considering the galvanic polarisation of steel by the anode and the concentration polarization of steel due to the transport of chloride and oxygen (Isgor and Razaqpur, 2004). Since the concrete domain is assumed to be homogenous and isotropic, the potential distribution inside the concrete can be obtained by solving the Laplace equation (Eq. (1)).

$$\frac{\partial^2 V}{\partial x^2} + \frac{\partial^2 V}{\partial y^2} + \frac{\partial^2 V}{\partial z^2} = 0 \quad (1)$$

where V is the potential inside the concrete in Volts. If the potential throughout the concrete domain is known, current at that point is calculated using Ohm's law considering the resistivity of the concrete. The kinetics of electrochemical reactions at the steel-concrete interface are represented using the Butler Volmer equation (Eq. (2)).

$$i_{corr} = \frac{i_{app}}{\left\{\exp\left(\frac{2.3\Delta E}{\beta_a}\right) - \exp\left(-\frac{2.3\Delta E}{\beta_c}\right)\right\}} \quad (2)$$

where i_{corr} is the apparent corrosion rate of steel, i_{app} is applied current, ΔE is potential shift, βa, and βc is the anodic and cathodic Tafel slope constants. All this requires information on the polarization properties of steel and anode, which cannot be obtained from the installed CP system. Hence, these input parameters are determined by a potentiodynamic polarization (PDP) test on the C-S-A system with a scan rate of 10 mV per minute using a simulated pore solution as the electrolyte. However, in most of the literature, the C-S-A system is modelled for corrosion by considering βa between 60 and 120 mV/dec and βc between 120 mV/dec and infinity. Hence, further studies on the polarization behaviour of steel in concrete with different exposure conditions need to be carried out. The corrosion parameters obtained while testing in an aqueous solution will not represent the polarization behaviour of steel embedded in concrete. Hence providing input parameters by testing in an aqueous solution will lead to inaccurate prediction of current and potential distribution on the steel rebar. Hence, choosing the correct polarization properties will give an accurate prediction of corrosion and potential distribution (Chang et al., 2008).

This study focuses on evaluating the polarization properties of steel and anode in a cementitious system. First, a brief background on the test method is provided. Then the PDP curve is analysed. Finally, the conclusion drawn from the analysis of the results is presented.

2. Polarization properties of steel and galvanic anode

The experimental study consists of casting two sets of mortar specimens, where the first set consists of steel rebar embedded in the cementitious mortar (CS system), and a second set of specimens, galvanic anodes-pristine (Zinc metal embedded in encapsulation mortar) was embedded and was used as the working electrode (CA system) (see Figure 1). Five different galvanic anodes available in the market were used for the study. However, the results for one of the galvanic anodes (A) are shown in this paper. The rebar samples were cut into desired lengths (150 mm) and a hole was drilled to make an electrical connection.

Polarization properties of the steel and the galvanic anode were obtained by conducting suitable PDP tests on the steel and anode in simulated pore solution (SPS) and also on the CS and CA systems separately using a three-electrode setup. Steel specimens tested in SPS were denoted as SS and galvanic anodes tested in SPS were denoted as SA. The CA and SA specimens were tested in saturated and submerged conditions (say, 95% relative humidity). In the three-electrode setup, the working electrode was steel/anode embedded in the cementitious mortar, nichrome wire mesh was the counter electrode, and saturated calomel electrode

(SCE) was the reference electrode. The test was carried out at an over-potential in the range of ± 300 mV versus OCP at a scan rate of 0.167 mV/S. The Tafel parameters were obtained by fitting the PDP curves. Bulk resistivity was measured using a two-electrode method using AC current at a frequency of 1000 Hz.

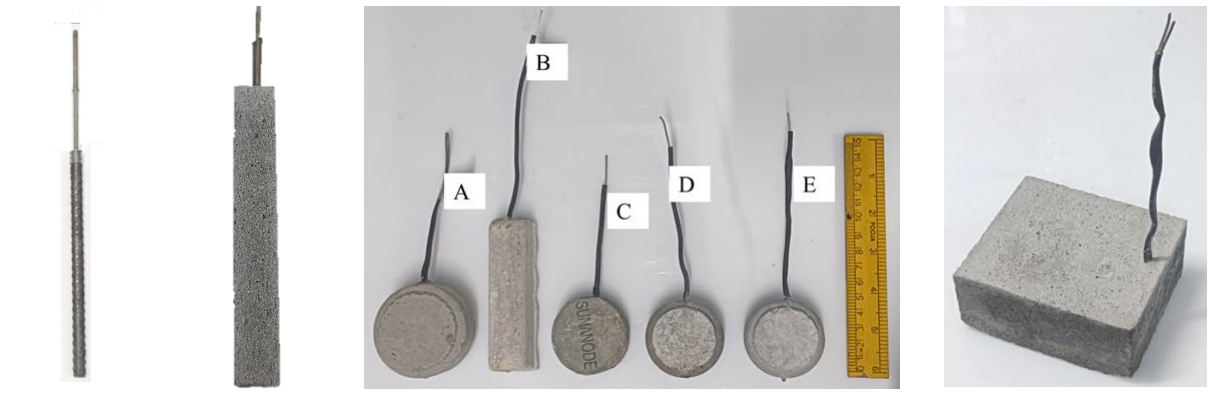

Steel specimens | CS system | Different types of galvanic anodes available | CA system

Figure 1. Specimens prepared for potentiodynamic polarization testing

2.1 Results and Discussions

Figure 2 shows the PDP curves for SS, CS, SA, and CA systems, which show a noticeable change in the potential, current density, and the slopes of cathodic, and anodic reactions. Both SPS and the cementitious mortar have a pH of 13.35, but the resistivity of the mortar is about five times that of the SPS.

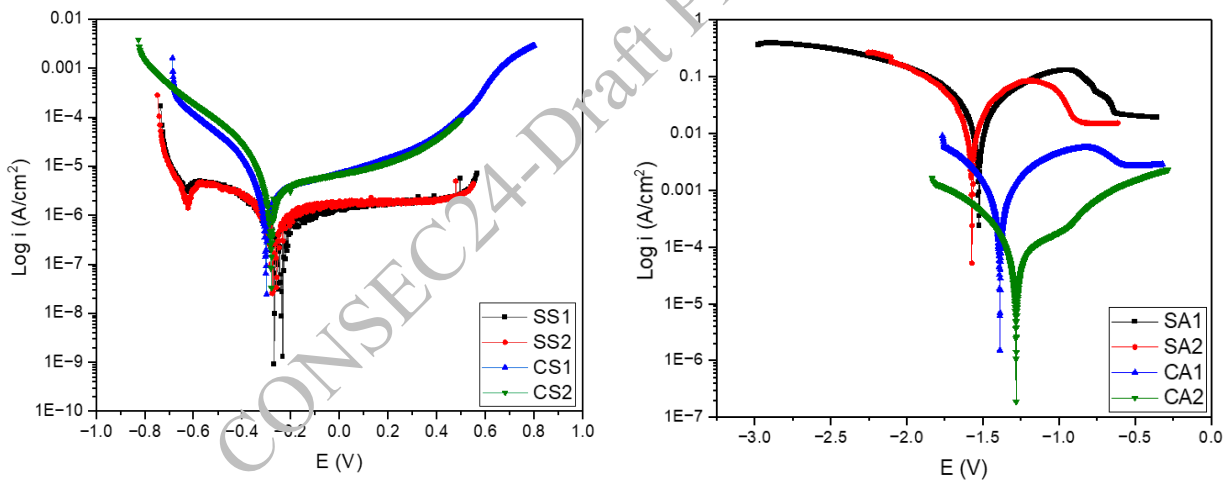

a) PDP curves of steel-solution and steel-cementitious system

b) PDP curves of Anode-solution and Anode-cementitious system

Figure 2. Variation in PDP curves when metal embedded in the cementitious system

The difference in PDP curves is evident when the electrolyte around the system changes, as illustrated in Figure 2. Table 1 provides the polarization properties derived from the fitting of PDP curves. In the CS system, the current density is lower than in the SS system. For the metal in the cementitious system, the passive film on the metal surface plays a significant role in the corrosion rate, which could result in different polarization behaviour. Additionally, the anodic slope increases, and the cathodic slope decreases negatively when metals are embedded in cementitious mortar. In the case of the galvanic anode, the current density decreases when embedded in mortar. However, testing the anode in SPS shows a much higher current density, which would not be observed when the anode operates in the actual CP system. It indicates that in severe exposure conditions, where the relative humidity is 95%, the corrosion current density was higher. This elevated value is due to the higher activity of the zinc with encapsulating mortar in submerged

conditions. Therefore, humidity should be carefully controlled when testing the anode for PDP. The anodic slopes and cathodic slopes for the CA system differ from those in the SPS.

Table 1. Polarization properties of metal in solution and cementitious systems

Electrode	Sample ID	E_{corr} (V_{SCE})	i_{corr} ($\mu A/cm^2$)	β_a (mV/dec)	β_c (mV/dec)	Resistivity (kohm.cm)
Active rebar	SS1	−0.235	0.42	209	−165	1
	SS2	−0.256	0.43	203	−169	
	CS1	−0.278	0.07	326	−105	5
	CS2	−0.299	0.06	387	−115	
Galvanic anode	SA1	−1.528	397	322	−305	1
	SA2	−1.573	322	246	−226	
	CA1	−1.389	14.5	235	−225	5
	CA2	−1.277	1	258	−185	

3. Conclusions

- The polarization properties of steel and galvanic anode when embedded in cementitious mortar exhibit a decrease in current density as compared to the metal-solution system
- As compared to steel in SPS, the anodic slope increased by 42% and the cathodic slope decreased by 34% for the CS system
- The relative humidity significantly affects the current density of the anodes, hence for the laboratory experiments, humidity conditions should be controlled.
- Using these polarization properties of the metals, an electrochemical model can estimate the accurate potential and current distribution in a C-S-A system.

Acknowledgements

The authors acknowledge the Prime Minister's Fellowship for Doctoral Research (PMFDR) from SERB-FICCI and industrial partner, Structural Specialities & Projects (India) Pvt. Ltd. The author also acknowledges the grant from Science and Engineering Research Board (SERB) under the core research grant (CRG) for the project titled "Electrical and electrochemical modelling for routine, non-destructive testing of cathodic protection systems in reinforced concrete structures". The authors also acknowledge the testing facility in the Construction Materials Research Laboratory at the Department of Civil Engineering, Indian Institute of Technology Madras, Chennai, India.

References

Chang, Z. T., Cherry, B., and Marosszeky, M. (2008a) "Polarisation behaviour of steel bar samples in concrete in seawater. Part 1: Experimental measurement of polarisation curves of steel in concrete', *Corrosion Science*, 50(2):357–364

Goyal, A., Pouya, H. S., Ganjian, E., Olubanwo, A. O., and Khorami, M. (2019) "Predicting the corrosion rate of steel in cathodically protected concrete using potential shift", *Construction and Building Materials*, 194:344–349

Ge, J., and Isgor, O. B. (2007a) "Effects of Tafel slope, exchange current density and electrode potential on the corrosion of steel in concrete", *Materials and Corrosion*, 58(8):573–582

Helm, C. and Raupach,M.(2020) "Numerical evaluation of the capacity of galvanic anode systems for patch repair of reinforced concrete structures," *Materials and Corrosion*, 71(5):726–737

ISO 12696. (2016). "EN ISO 12696 Standard - Cathodic protection of steel in concrete", 47.

Krishnan, N., Kamde, D.K., Veedu, Z.D., Pillai, R.G., Shah, D. and Velayudham, R. (2021)"Long-term performance and life-cycle-cost benefits of cathodic protection of concrete structures using galvanic anodes," *Journal of Building Engineering*, 42:102467

From Research to Guidelines – Results from Field Testing of Mortars for Cathodic Protection

K. Hornbostel[1,2*], E. Rodum[1], R.E. Antonsen[1,3], and S.H. Helgestad[1]

[1] NPRA The Norwegian Public Roads Administration, Oslo, Norway
[2] NTNU Norwegian University of Science and Technology, Trondheim, Norway
Email: Karla.Hornbostel@ntnu.no
[3] SINTEF The Foundation for Industrial and Technical Research, Narvik, Norway

[*]Corresponding author

ABSTRACT

This paper presents the findings from a three-year long field-testing program on mortars suitable for cathodic protection (CP) of steel in concrete. The study was conducted on an anchoring pillar of a suspension bridge in Northern Norway and includes both mortars used for pre-CP installation repairs and mortars recommended for embedding anode systems. The primary focus was on measuring the electrical resistivity of the mortars and studying its impact on the degree of cathodic protection. Different field and laboratory methods were used to measure the electrical resistivity of the mortars, and the suitability of the methods were evaluated. In accordance with today's standard recommendations, it was found that the electrical resistivity of repair mortars should be close to that of the original concrete, further that the resistivity of CP mortars should not exceed that of the repair mortars or concrete. Based on the laboratory experiments it is suggested that the electrical resistivity of mortars should be documented at an age of minimum 90 days, using water-saturated samples prepared from sprayed slabs. The findings of this research provide a methodology for documenting the properties of mortar products in the laboratory. This ensures the selection of suitable products for field application, thereby contributing to an effective operation of CP systems.

KEYWORDS*: Cathodic protection, Mortar, Laboratories testing*

1. Introduction and background

Reinforcement corrosion is the most frequently observed damage on Norwegian coastal concrete bridges. Cathodic protection (CP) is regarded as a possible maintenance measure where reinforcement corrosion is detected, in particular on bridges where reinforcement corrosion occurs over large areas without yet having caused extensive cracking and/or spalling of concrete. The correct choice of materials is crucial to achieve a good and long-lasting effect of the CP systems. In the process of installing cathodic protection, two types of mortars are typically applied, in Norway generally by dry spraying. These are repair mortars (here named Rep-mortars) and mortars designed for embedding anodes like titanium meshes (here referred to as CP-mortars). It is worth noting that while dry sprayed mortars is the focus of this investigation, other application methods may also be suitable. The two types of mortars included in the project, Rep- and CP-mortars, have many similarities. In product data sheets, it is indicated whether the mortar is intended for use in mechanical repair (Rep-mortars) or whether the mortar is intended for embedding anodes (CP-mortars). The mortar used in cathodic protection installations must adhere well to the original concrete and protect the anode from external exposure. It is crucial that the mortars ensure good electrolytic contact between the anode and the reinforcement. A key property of the mortar is therefore its electrical resistivity, which indicates its ability to resist current flow. However, there are few specific requirements for both measurement methods and threshold values for the electrical resistivity of these mortars. Several standards and guidelines are available (NS-EN 1504-10:2017+NA:2019, NS-EN 12696:2022, NPRA guideline R762 – Process code 2 (2018)), however current requirements are insufficient in defining threshold values or not applicable for dry-sprayed mortars. A central part of the field test program is measurements of electrical resistivity in

combination with monitoring the efficiency of the installed cathodic protection systems. Resistivity development in field is studied over several years to observe the effects of aging and natural variations in humidity and temperature. In addition, the effect of cement-based, elastic coatings on the sprayed CP mortars s studied. Resistivity, compressive strength, capillary absorption, and frost resistance for the various mortars were also tested in parallel in the laboratory. The study is in detailed described and reported in a series of NPRA reports: Hornbostel et al (2020), Helgestad et al (2023) and Hornbostel et al (2024).

2. Technical description of the test site

The technical setup for the cathodic protection testing site was designed to evaluate two types of CP installations. Variant 1 focused on areas with damaged concrete that was removed and repaired with repair mortars before CP installation. Variant 2 focused on areas where corrosion had started but not yet led to cracking or spalling, making preliminary repairs unnecessary. The location, an anchoring pillar of a suspension bridge (Figure 1 (a)), was chosen due to visible corrosion damage on the north side and minimal signs of corrosion on the south side.

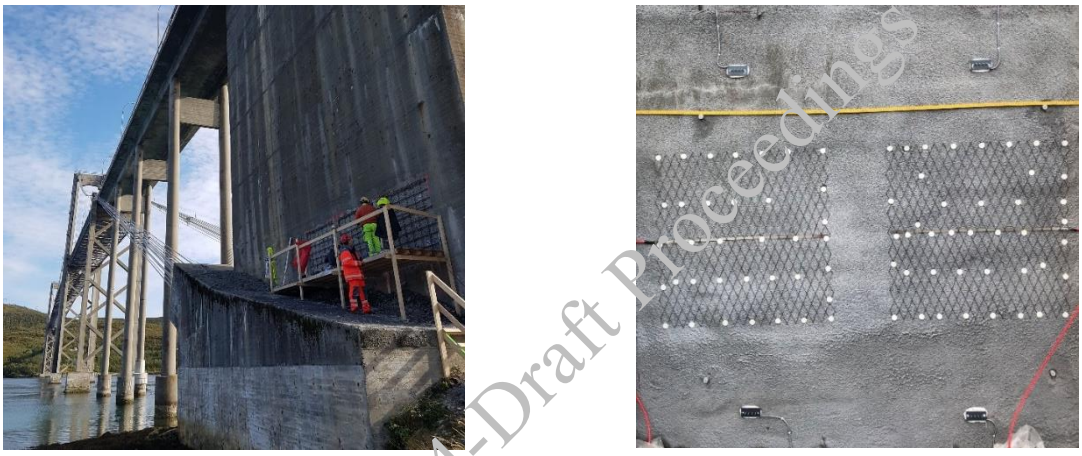

a) *Establishing test fields on the northern side of the bridge.*

b) *One test field with titanium mesh and sensors for measuring resistivity, prior to spraying CP-mortar.*

Figure 1. Overview and detail of the test fields.

Three separate test fields were established on each of the north and the south side of the pillar. On the north side, concrete was removed by hand chiselling to 20-40 mm behind the outer reinforcement layer (Variant 1). On the south side, the concrete surface was sandblasted to ensure good adhesion between the CP mortars and the original concrete, no other repairs were performed (Variant 2). Products from three Norwegian suppliers were used, each providing both repair and CP mortars, as well as a surface coating. Each test field was divided in two separate areas, only different by the final surface treatment (left part coated, right part not). Each test field was instrumented with sensors to measure electrical resistivity (Figure 1(b)). The sensors used, were both commercial multiring electrodes for measuring concrete resistivity at varying depths and custom-made sensors designed for bulk resistivity measurements using the Wenner-type method. None of these sensors had been previously used in sprayed mortars. Despite their limited performance, sufficient measurements were obtained to yield representative data. Two titanium meshes were installed on each of the six test fields, each CP area equipped with two reference electrodes and three reinforcement contacts.

3. Results and Discussions

This study examines the measuring techniques and suitable threshold values for the electrical resistivity of mortars in cathodic protection systems. It further investigates the correlation between electrical resistivity measured in the field and the resistivity measured in the laboratory. The effectiveness of cathodic protection, given the variable resistivity of the mortars, is also assessed. The study assess the impact of exposure conditions and surface treatments and evaluates the consequences of simplified mechanical repair

(without cleaning of reinforcement to Sa 2) on the corrosion process of the reinforcement. The results are shortly summarized in this section, more information can be found in Hornbostel et al (2024).
All methods for measuring electrical resistivity, both those used in the field (the two above mentioned sensors and a handheld 4-probe Wenner instrument) and in the laboratory (2-electrode system on either sealed or water cured samples), roughly rank the different mortars equally when comparing results obtained at the same temperature and maturity. The absolute values are, however, somewhat different, but this is to be expected as the measurement principles are different (measurement on small versus large mortar volumes) and as the moisture content in the mortars varies. The resistivity of the mortars increases with increasing age. In the field, there is a development in the electrical resistance over about one year. In the laboratory, during curing in water at 20ºC, the resistance somewhat flattens out after about 90 days. The studied mortars can be grouped according to their resistivity in three groups (see Table 1).

Table 1. Grouping of the mortars after resistivity determined in the lab at an age of 90 days (water cured at 20 ºC), and associated MRE (multiring electrode) values measured in the field at an age of 1-3 years and a temperature of 20 ºC and 0 ºC, respectively.

Product	Resistivity [Ωm]		
	Lab at 20ºC 90 days	Field (MRE) at 20±2ºC 1-3 years	Field (MRE) at 0±1ºC 1-3 years
CP1, CP2, Rep 1	< 200	<500	< 1250
CP3, Rep 3	1500-2000	1500-2300	5000-7500
Rep 2	>5000	>7000	>10000

In the field, the relationship between resistivity and temperature follows the Arrhenius equation. The relationship between temperature and resistivity is relatively similar for all mortars regardless of whether the resistivity is high or low. It is to be expected that the moisture content in the mortars in the field will develop differently: 1) On the south versus north side, due to different exposure to rain, wind and sun and 2) on the left versus right part of each test field (with or without surface treatment), depending on the water and water vapor permeability of the surface products. So far, after about three years of operation, it is not possible to see a clear effect either of exposure conditions or surface treatment on the mortars' resistivity. This will be followed up further. Operating data from the cathodic test fields show that the need for applied voltage between anode and reinforcement, in order to achieve the protection criterion of 24 hours depolarization of 100 mV (Figure 2), increases with increasing resistivity of the repair mortars (from Rep 1 to Rep 3 to Rep 2). Similarly, the voltage requirement increases when the resistivity of the CP mortar is much higher than in the underlying concrete/repair mortar (CP3).

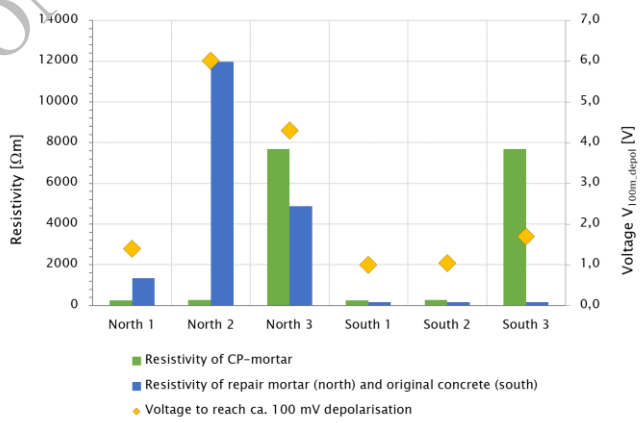

Figure 2. Electrical resistivity for all materials (solid bars, measured at 0°C with MRE sensors during a period of 1-3 years) and applied voltage for the different test fields (yellow markers) to achieve ca. 100 mV depolarisation after 24 hours.

Results from potential measurements suggests that the simplified mechanical repairs performed prior to the CP installation on the northern side of the pillars, has not significantly affected the corrosion activity of the

reinforcement. This implies, as expected, that the implementation of cathodic protection remains essential even for the repaired areas. The results underlines that it is important to have reference electrodes placed both in repaired and non-repaired areas to ensure that one has a good overview of the degree of protection. Within one anode zone in a CP system, there are often both repaired and non-repaired areas (simplified mechanical repair). The results from our experiments show that repaired areas should have a resistivity as close to the original concrete as possible, to ensure an even current supply to the reinforcement and reduce the risk of over- or under-protection. The often-used limit values of 50 – 200% of the bridge concrete's resistivity are found reasonable but must be used with care. The results further show that it would be advisable that the electrical resistivity of the CP mortar should be equal to or less than that of the repair mortar or concrete. This is to prevent acid formation around the anode. To be able to set requirements for the repair/CP mortars' resistivity, the original concrete's resistivity must be determined. This can be done by a combination of mapping with handheld equipment (NDT) in the field and drilling of cores for laboratory testing. The requirements for the mortars' resistivity, determined at 90 days of age, should be related to the concrete's resistivity determined by laboratory testing, i.e. after water storage at 20 ºC.

4. Conclusions

The study provides valuable insights into the application of cathodic protection (CP) for the maintenance of Norwegian concrete bridges affected by reinforcement corrosion. The research highlights the importance of selecting appropriate materials, including repair and CP mortars, to ensure the effectiveness and longevity of a CP system. Field and laboratory tests were conducted to measure the resistivity of various mortars over time and at different temperatures. The results highlight the influence of mortar resistivity on the performance of the CP system. The research concludes that areas pre-repaired should have a resistivity close to the original concrete, to ensure an even current supply to the reinforcement and reduce the risk of over- or under-protection. It also emphasizes the importance of having reference electrodes placed both in repaired and non-repaired areas to ensure a good overview of the degree of protection.

Acknowledgements

This work was conducted as part of the NPRA research and development program “Improved Bridge Maintenance (2017-2021)”. The authors acknowledge Green Management of Structures for Infrastructure, known as EXCON (Research Council Norway project number 340843) for their funding support for attending CONSEC.

References

NS-EN 12696:2022. “Cathodic protection of steel in concrete” *European standard*

NS-EN 1504-10:2017+NA:2019. “Products and Systems for the Protection and Repair of Concrete Structures-Definitions, Requirements, Quality Control and Evaluation of Conformity” *British Standards Institution*

NPRA guideline R762 (2018) “Process code 2, Standard description for bridges and quays, Main process 8” (in Norwegian)

Hornbostel, K., Antonsen R. E., Helgestad, S. H. and Rognan O.M. (2020) “Field trial - mortar suitable for cathodic protection: Description of the field trial”, *NPRA Report No. 671*. Oslo, Norway (in Norwegian)

Helgestad, S. H., Hornbostel, K., Bjøntegaard, Ø. and Antonsen R. E. (2023) “Field tests - mortar suitable for cathodic protection, Description of laboratory tests”, NPRA Report *No. 851*. Oslo, Norway (in Norwegian)

Hornbostel, K., Rodum, E., Antonsen R. E. and Helgestad, S. H. (2024) “Field trial - mortar suitable for cathodic protection: Results after 3 years field testing”, *NPRA Report No. 850*. Oslo, Norway (in Norwegian)

Damage, Deterioration and Transport Properties

Acid Resistance of Slag-based Concrete Activated with Industrial-Grade Soda Ash and Hydrated Lime

Jayashree Sengupta[1*], Nirjhar Dhang[2], and Arghya Deb[3]

[1] Research Scholar, Indian Institute of Technology, Kharagpur, India
Email: jaish.sengupta@iitkgp.ac.in
[2] Professor, Indian Institute of Technology, Kharagpur, India
Email: nirjhar@civil.iitkgp.ac.in
[3] Professor, Indian Institute of Technology, Kharagpur, India
Email: arghya@civil.iitkgp.ac.in

[*]Corresponding author

ABSTRACT

An experimental investigation evaluated the acid resistance of a one-part alkali-activated slag-based mixture. Instead of using expensive alkali solutions for activation, this study employed cost-effective industrial-grade powdered soda ash (SA) and hydrated lime (HL) as activators. Two distinct mixing procedures were adopted to test their susceptibility to 4% sulphuric acid exposure. The first method directly introduced powdered SA and HL, while the second pre-mixed SA with water before adding it to a dry powder mixture of ground granulated blast furnace slag (GGBFS), silica fume (SF), and HL. These were compared with a stoichiometrically similar two-part sample activated with sodium hydroxide (SH) solution and a conventional OPC-based sample. All samples were cured at room temperature, and acid resistance was evaluated by monitoring changes in dimension and mass over time. Additionally, any loss in compressive strength was examined. Microstructural compositions of the reaction products were observed through Field Emission Scanning Electron Microscopy (FESEM) and X-ray Diffraction (XRD) and compared across all samples. Overall, the one-part alkali-activated slag-based concrete exhibited superior performance compared to the OPC-based mix and was comparable to the corresponding two-part mix.

KEYWORDS: *Sulphuric acid resistance, Microstructure, Alkali-activated slag concrete, Soda Ash, Hydrated Lime*

1. Introduction

Sulphuric acid, commonly found in industrial effluents, accelerates the degradation of concrete through biogenic processes. This deterioration is exacerbated in humid conditions where sulfur dioxide combines with water to form acids. Upon contact with concrete, this process disrupts the chemical balance of Ca^{2+} and OH^- ions, leading to the dissolution of calcium silicate hydrate and subsequent structural damage (Mehta, 1983). Concrete's alkaline nature makes it particularly vulnerable to acidic environments, especially when pH levels drop below 6.5. Laboratory simulations using 4% sulphuric acid replicate these conditions for accelerated testing. This concentration is sufficiently severe to speed up the natural degradation mechanisms, allowing researchers to observe and analyse the effects of acid attack within a reasonable experimental timeframe.

Traditional cement concrete is highly susceptible to acid exposure, prompting research into alternatives such as two-part alkali-activated concretes (AACs). Previous studies (Mehta & Siddique, 2017; Sturm et al., 2018; Wan-En et al., 2023) have demonstrated AAC's potential to resist acid attack effectively. AACs employ aluminosilicate precursors activated by alkaline solutions, typically a combination of sodium hydroxide and sodium silicate. This activation process forms sodium-aluminate-silicate-hydrate gels, enhancing structural strength and durability (Bakharev, 2005; Bernal et al., 2012; Rajamane et al., 2012). When using calcium-rich precursors, these gels form calcium aluminate-silicate-hydrates, which can increase susceptibility to acid penetration due to higher concentrations of Ca^{2+} ions in the system. However,

unlike conventional cement, the degradation of alkali-activated paste involves a broader transition zone (Gu et al., 2020), leading to gradual property changes that contribute to improved resistance against acid attacks. Despite their advantages, two-part alkali-activated concretes (AACs) face challenges in in-situ applications such as the construction of sewage pipes or chimneys due to handling hazardous alkalis. To address this, one-part AACs are cast- the precursors and solid activators are dry-mixed, followed by the addition of water, similar to conventional concreting practices. Previously, the authors proposed a one-part AAC formulation incorporating GGBFS and SF activated with solid industrial-grade SA and HL (Sengupta et al., 2024b, 2024a). This study aims to comprehensively evaluate the acid resistance performance of the aforementioned mix under acidic conditions, addressing current research gaps concerning the durability of one-part alkali-activated concretes (AACs) against acid attack.

2. Materials

This study utilised GGBFS sourced from Jhargram, India, and SF from Waltar Enterprises as the aluminosilicate precursor and additive, respectively. The activators were prepared using an industrial-grade blend of SA and HL, chosen for its lower purity, as outlined by (Sengupta et al., 2024a). The OPC 53 grade was sourced directly from Ramco Cements in Kolaghat. Sodium hydroxide (SH) pellets, 98% purity, were obtained locally. Fine and coarse aggregates that were obtained locally were used in the research.

3. Methodologies

The particle packing density method was used to prepare these mixes (Sengupta et al., 2024b). These mixes consisted of hydrated lime (9.26%) and soda ash (13.25%), stoichiometrically equal to a 10% SH equivalent, with a 5% SF replacement of GGBFS content, a water-to-solid ratio (w/s) of 0.50, and an excess paste content of 32%. They were labelled as VM mixes, where activators were added to the mix in powdered form, followed by water. Another set of mix, PM, involved pre-mixing soda ash in water and adding this solution to a dry mix of GGBFS, SF, and HL. The CM mixes, or the control mixes, activated GGBFS and SF blends with a stoichiometrically equivalent SH solution, precisely a 4.5M solution. Additionally, the CEM mixes represented conventional OPC-based mixes. To improve mobility, sulphonated naphthalene formaldehyde was used at concentrations of 0.75% for VM, 0.5% for PM, 0.25% for CM, and 0.2% for CEM mixes, respectively. Table 1 illustrates the mix proportions of the concrete mixes.

Table 1. Weights (kg/m^3) of the materials required to produce one cubic meter of concrete.

Mix	Coarse Aggregates			Sand	GGBFS	SF	Cement	HL	SA	SH	Water
	20-16 mm	16-10 mm	10-4.75 mm								
VM, PM	154.72	361.02	515.74	687.65	367.24	21.48	---	35.96	51.50	---	238.09
CM	154.72	361.02	515.74	687.65	367.24	21.48	---	---	---	38.87	213.79
CEM	154.72	361.02	515.74	515.74	---	---	343.83	---	---	---	171.92

All mixes were cast in 100 mm × 200 mm cylindrical moulds and cured for 28 days. The specimen edges were protected with anti-corrosion paints and immersed in molten paraffin. Concrete samples were immersed in a 4% sulphuric acid solution for 28 days to assess acid resistance and simulate real-world acidic conditions. The acid solution was contained in a plastic tub, maintaining a consistent pH of approximately 0.23 ± 0.05.

Various methods were employed before and after immersion: initial and weekly weight measurements of coated samples to monitor weight loss, weekly pH measurements of the acid solution to ensure consistency, and compressive strength testing after 28 days compared to samples cured in water for 56 days to assess strength deterioration. To examine elemental composition and phases formed, test samples for SEM-EDS and XRD analysis were prepared by crushing and sieving mortar pieces from fractured concrete specimens after the compression test, followed by gold coating.

4. Results and Discussions

Visual analysis indicated minimal surface degradation in alkali-activated mixes, whereas conventional cement concrete showed significant degradation, exposing the matrix-aggregate interior (Figure 1.d). Cement concrete also exhibited the most substantial loss in compressive strength, consistent with trends observed in mass loss. Among the alkali-activated mixes, the control mix (CM) experienced minimal strength loss. PM mixes within the one-part mixes showed greater strength loss compared to VM mixes (Figure 2.a). VM mixes demonstrated the lowest mass loss, while PM mixes exhibited a mass gain at 28 days, suggesting the formation of additional phases.

Acid consumption was monitored weekly, with cement mixes (CEM) showing the highest consumption. Initially, acid consumption rates were similar across all mixes. VM and PM mixes exhibited comparable acid intake up to 21 days, with VM mixes showing slightly higher intake at 28 days. CM mixes consistently demonstrated lower acid intake throughout the testing period, correlating with their lower strength loss.

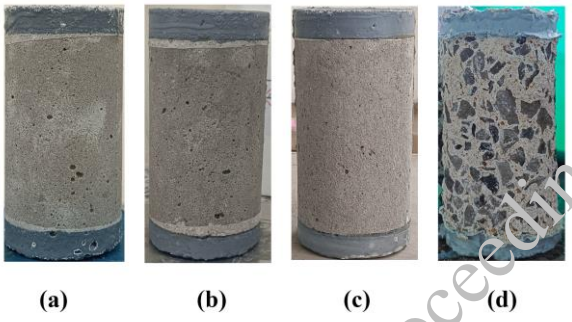

Figure 1. Alterations in surfaces following 28 days of immersion in a 4% H_2SO_4 solution in the order- (a) VM, (b) PM, (c) CM and (d) CEM

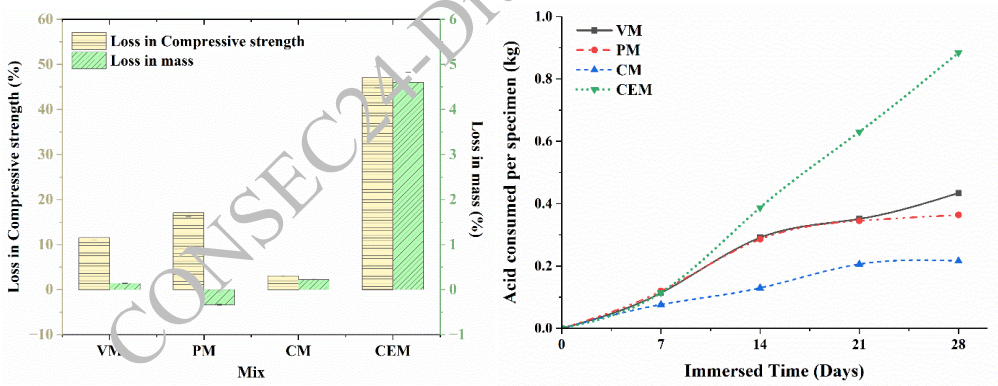

(a) (b)

Figure 2. (a) The loss in compressive strength and mass and (b) acid consumption per specimen of all mixes after 28 days of immersion in a 4% H_2SO_4 solution

SEM images revealed crystal formations in the microstructure. CEM mixes exhibited prismatic morphologies typical of gypsum, as depicted in Figure 3.d, whereas other mixes displayed fibrous morphologies. PM mixes also showed gypsum structures, albeit to a lesser extent than the cement mixes. EDS analysis indicated the highest sulfur content in the CEM mixes (Figure 4.a), followed by the PM mixes.

Further XRD analysis identified the phases present, as shown in Figure 4.b. Significant peaks of gypsum ($CaSO_4 \cdot 5H_2O$) were prominent at 11.6° (2θ), 20.735° (2θ), 29.123° (2θ), 31.120° (2θ), and 31.123° (2θ), confirming the disintegration of the cementitious structure, evident on the surface. Figure 4.b illustrates major gypsum peaks in the diffractograms of all mixes. Notably, CEM and PM mixes exhibited notable gypsum formations, consistent with higher sulfur content (Figure 4.a), indicating more pronounced degradation in these mixes. This finding aligns with the observed mass gain in the PM mix. In contrast,

VM and CM mixes showed more stable microstructures with less intense gypsum peaks. Thus, the susceptibility to sulphate attacks can be ranked as CEM > PM > VM > CM, highlighting the enhanced resilience of the latter two in acidic environments. Additionally, calcite peaks at 28.9° (2θ) and quartz peaks at 26.52° (2θ) were observed, alongside significant peaks of calcium magnesium carbonate at 30.954° (2θ) and 60.041° (2θ), as reported for unaffected samples (Sengupta et al., 2024a). VM, PM, and CM mixes also exhibited calcium aluminium silicate hydrate (CASH) and sodium aluminium silicate hydrate (NASH) phases.

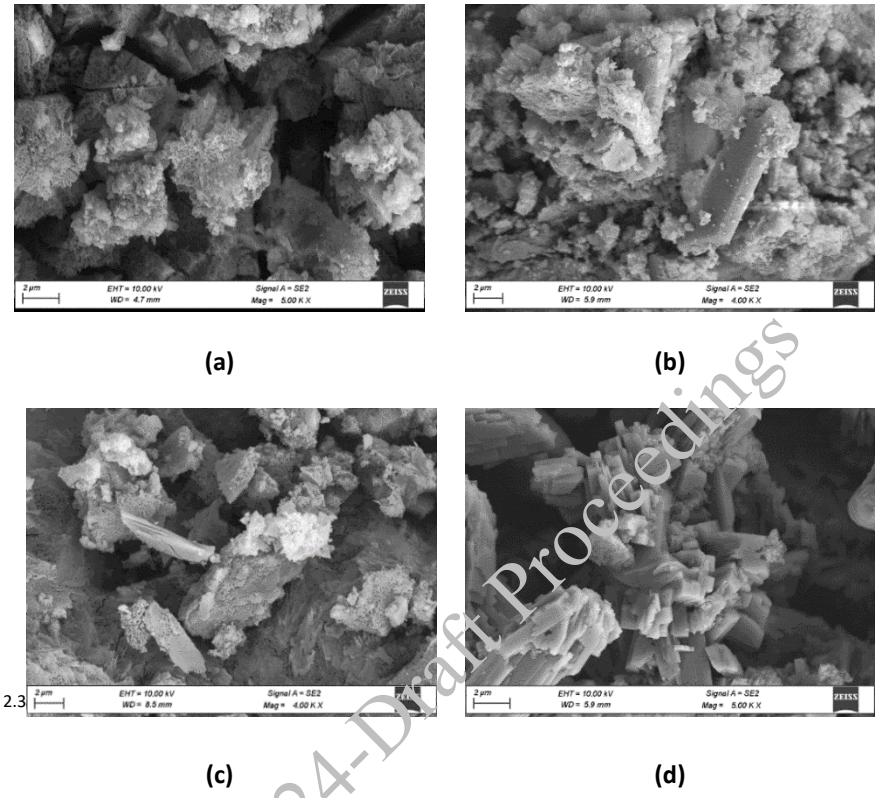

Figure 3. SEM images of (a) VM, (b) PM, (c) CM, and (d) CEM mixes after 28 days of immersion in a 4% H_2SO_4 solution

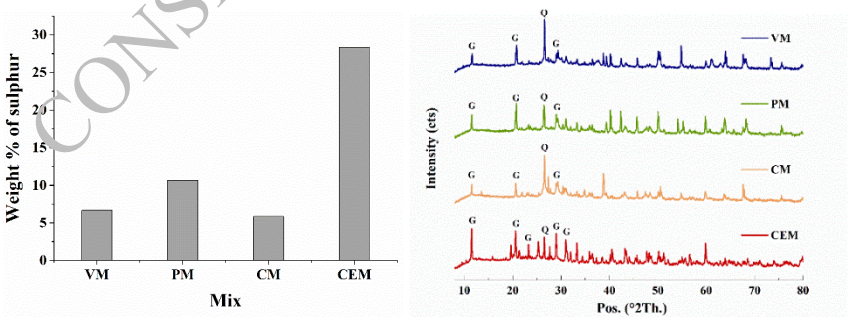

Figure 4. (a) Percentage of sulphur as weight % in the samples observed through EDS; (b) the phase analysis of different mixes after 28 days of immersion in a 4% H_2SO_4 solution obtained through XRD analysis. Q: Quartz and G: Gypsum.

5. Conclusions

This experimental study assessed the acid resistance of a one-part alkali-activated slag-based concrete using cost-effective industrial-grade soda ash (SA) and hydrated lime (HL) as activators. The following conclusions were drawn regarding the performance and characteristics of the different mixes:

- Conventional cement (CEM) mixes exhibited significant surface degradation and experienced the most substantial loss in compressive strength over time. This degradation exposed the matrix-aggregate interior and was accompanied by high acid consumption, indicating lower resistance to acid attack.
- The control mix (CM) demonstrated the lowest strength loss and acid intake among the alkali-activated mixes, suggesting superior durability. The VM mixes performed better than the PM mixes in terms of strength retention and lower mass loss. PM mixes even showed a mass gain at 28 days due to additional phase formation.
- SEM and EDS analyses revealed the presence of prismatic gypsum crystals predominantly in the CEM and PM mixes, with the highest sulfur content observed in the CEM mixes. This indicated significant gypsum formation, contributing to the degradation of the cementitious structure. XRD analysis confirmed substantial gypsum peaks in all mixes, particularly in CEM mixes, consistent with visual and microstructural degradation. Furthermore, VM, PM, and CM mixes showed the presence of calcium aluminium silicate hydrate (CASH) and sodium aluminium silicate hydrate (NASH), indicating the formation of stable phases that enhance overall durability.

Thus, alkali-activated concrete mixes, especially VM and CM mixes, demonstrated superior overall durability compared to conventional cement mixes. They exhibited lower acid consumption, reduced surface degradation, and the formation of stable phases, highlighting their potential for enhanced performance in acidic environments.

References

Bakharev, T. (2005). Durability of geopolymer materials in sodium and magnesium sulfate solutions. *Cement and Concrete Research*, *35*(6).

Bernal, S. A., Mejía De Gutiérrez, R., & Provis, J. L. (2012). Engineering and durability properties of concretes based on alkali-activated granulated blast furnace slag/metakaolin blends. *Construction and Building Materials*, *33*.

Gu, L., Visintin, P., & Bennett, T. (2020). Sulphuric Acid Resistance of Cementitious Materials: Multiscale Approach to Assessing the Degradation. *Journal of Materials in Civil Engineering*, *32*(7).

Mehta, A., & Siddique, R. (2017). Sulfuric acid resistance of fly ash based geopolymer concrete. *Construction and Building Materials*, *146*.

Mehta, P. K. (1983). Mechanism of sulfate attack on portland cement concrete - Another look. *Cement and Concrete Research*, *13*(3).

Rajamane, N. P., Nataraja, M. C., Dattatreya, J. K., Lakshmanan, N., & Sabitha, D. (2012). Sulphate resistance and eco-friendliness of geopolymer concretes. *Indian Concrete Journal*, *86*(1).

Sengupta, J., Dhang, N., & Deb, A. (2024a). A Cost-Effective Slag-Based Mix Activated with Soda Ash and Hydrated Lime: A Pilot Study. *Practice Periodical on Structural Design and Construction*, *29*(2).

Sengupta, J., Dhang, N., & Deb, A. (2024b). Efficient mix design of one-part alkali-activated concrete using packing density method and its optimisation through Taguchi-GRA. *Construction and Building Materials*, *438*, 136869.

Sturm, P., Gluth, G. J. G., Jäger, C., Brouwers, H. J. H., & Kühne, H. C. (2018). Sulfuric acid resistance of one-part alkali-activated mortars. *Cement and Concrete Research*, *109*.

Wan-En, O., Yun-Ming, L., Cheng-Yong, H., Abdullah, M. M. A. B., Li Ngee, H., Pakawanit, P., Wei Ken, P., Khalid, M. S., Md Razi, H., Lee, W. H., Soo Jin, T., Shee-Ween, O., & Yong-Jie, H. (2023). Acid-resistance of one-part geopolymers: Sodium aluminate and carbonate as alternative activators to conventional sodium metasilicate and hydroxide. *Construction and Building Materials*, *404*.

Static Loading Test of RC Slabs with Internal Horizontal Cracks Due to Frost Damage

Hiroshi Hayashida [1]

[1] Civil Engineering Research Institute for Cold Region, Sapporo, Japan
Email: hayashida@ceri.go.jp

*Corresponding author

ABSTRACT

In road bridge decks that are subject to frost damage, the deterioration progresses in the depth direction. Therefore, it is feared that the strength of the deck decreases as the deterioration progresses. However, the relationship between the depth of deterioration and the decrease in strength is not clear. In this study, a static loading test was conducted after subjecting a large slab specimen to frost damage from the top surface to half of its thickness. As a result, compared to the sound slab, stiffness and strength decreased in the frost-damaged slab. In addition, a punching shear cone occurred in the sound slab, but no punching shear cone occurred in the frost-damaged slab. Instead, horizontal cracks occurred near the upper distribution rebars in the frost-damaged slab. It was thought that horizontal cracks occurred in the frost-damaged slab because 1) narrow horizontal cracks occurred due to frost damage, and 2) diagonal cracks extending from the loading point progressed along the horizontal cracks due to load action, widening the crack width. It was thought that the stiffness and strength decreased in the frost-damaged slab because this horizontal crack reduced the thickness of the slab supporting the load.

KEYWORDS: *Bridge Deck, Frost Damage, Deterioration Depth, Strength, Horizontal Crack*

1. Introduction

In road bridge decks (RC Slabs) that are subject to frost damage, the deterioration progresses in the depth direction with the formation of horizontal cracks. Therefore, it is feared that the strength of the deck decreases as the deterioration progresses. However, the relationship between the depth of deterioration and the decrease in strength is not clear. In this study, a static loading test was conducted after subjecting a large slab specimen to frost damage from the top surface to half of its thickness.

2. Experiment outline

2.1 Slab specimen

Fig. 1 shows the dimensions and reinforcement arrangement of the slab specimen. For the concrete, no air-entraining agent was used and the water cement ratio was set at 65%, which is rather high, because it was necessary to generate frost damage at an early stage. The cement was ordinary portland cement, and the aggregates were crushed stone with a maximum size of coarse aggregate of 20mm.
The mix proportion is shown in Table-1.Data on the material properties of the concrete and the reinforcing bars are shown in Table-2. The experiment variables are whether or not freeze-thaw cycles were implemented. Table-3 shows the names of the specimens and the number of freeze-thaw cycles.

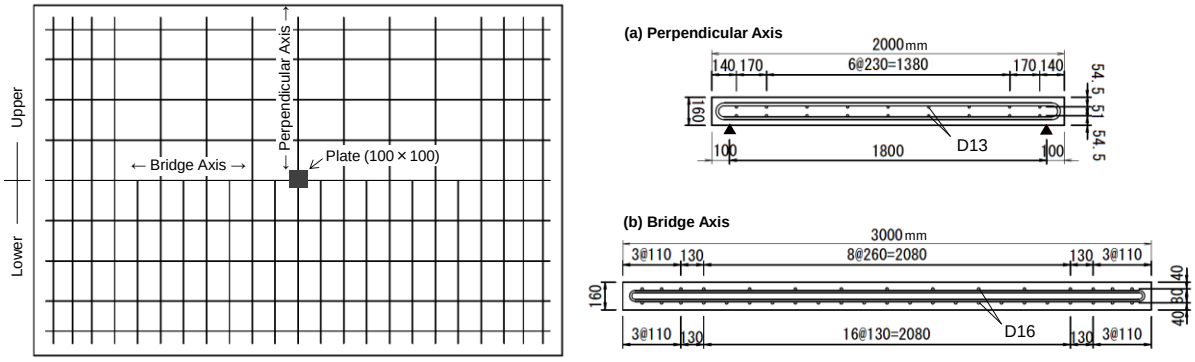

Figure 1. Specimen

Table 1. Mix proportion

W/C (%)	Air (%)	s/a (%)	mix ratio (kg/m^3)			
			W	C	S	G
65	2.0	48.6	171	263	904	947

Table 2. Material properties

Concrete Comp strength (N/mm^2)	Rebar Yield strength (N/mm^2)
21	384

Table 3. Experiment variables

Name	Freeze-thaw (cycles)
N	–
F	447

2.2 Freeze-thaw test

After placing the concrete, the concrete was cured in water until the 4th week, and then the freeze-thaw test was started. To reproduce the temperature conditions of a bridge deck, the following freeze-thaw experiment was performed. As shown in Fig. 2, only the upper surface of the specimen was subjected to cooling and heating. This was done by installing insulation to block heat supply on sides other than the upper surface. As shown in Fig. 2, freeze-thaw action was generated only in the range from the upper surface to the depth of 8 cm. The frozen condition was maintained at depths greater than 8 cm. Specifically, the temperature was controlled so that the temperature at the 8 cm point was -18 to 0°C. Under this temperature condition, the specimen was subjected to freezing in air and thawing in water 447 times.

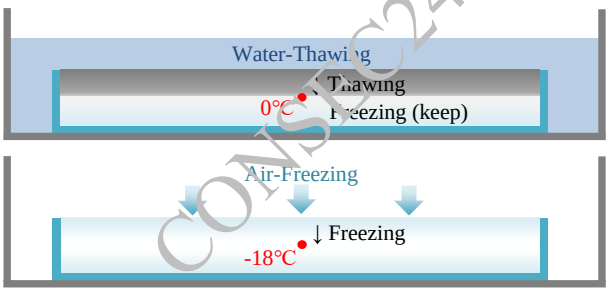

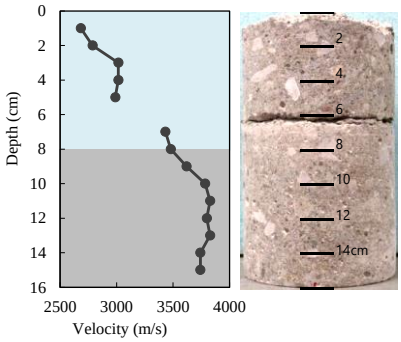

Figure 2. Freeze-thaw test

Figure 3. Ultrasonic velocity and horizontal crack

2.3 Static loading test

The specimen was simply supported at two sides, and the span was 1800 mm. A 100mm × 100mm steel plate was used as the loading plate. Concentrated loading was done at one point at the center of the specimen.

3. Condition of deterioration

To confirm the condition of deterioration, a core was taken from the specimen after the freeze-thaw test. As a result, as shown in Fig. 3, a horizontal crack occurred near the depth of 6cm.

Also, as a result of the ultrasonic velocity measurement conducted at the same time, the velocity was reduced in the freeze-thaw layer at a depth of 1-8cm. On the other hand, in the freeze-continuation layer at a depth of 9-15cm, the velocity did not decrease much.

4. Static Loading Test Results

Fig. 4 shows the load-displacement curve of each specimen. Fig. 5 show the cracks on the bottom surface of each specimen. Furthermore, Photo-1 show the cut surface of each specimen after loading.

4.1 Specimen N

As shown by the black line in Fig. 4, for specimen N, after the main reinforcing bars yielded at a displacement of 8.4 mm, the maximum load of 279kN was reached at a displacement of 12 mm. Immediately after reaching the maximum load, the load suddenly dropped, leading to failure. At that time, a punching shear cone was generated on the bottom surface of the specimen, as shown by the black line in Fig. 5. Additionally, as shown in Photo-1, on the cut surface, shear cracks that were continuous to the cracks in the punched shear cone were observed.

4.2 Specimen F

As shown by the red line in Fig. 4, for specimen F, the stiffness decreased from the early stage of loading. Thereafter, the main reinforcing bars yielded at a displacement of 10 mm, and then reached a maximum load of 255kN (91% of N's strength) at a displacement of 14 mm. Immediately after reaching the maximum load, the load decreased once, but it did not decrease significantly like in specimen N. After that, even if the displacement was increased, the load did not decrease much. When the displacement reached approximately 20 mm, cracks appeared on the bottom surface, as shown by the black lines in Fig. 5, but no punching shear cone occurred. In addition, on cut surface perpendicular to the bridge axis shown in Photo-1 , shear cracks that were continuous to the cracks on the bottom surface had occurred on the N side. On the other hand, no shear cracks were observed on bridge axis direction shown in Photo-1. Instead, horizontal cracks had developed near the upper distribution rebars.

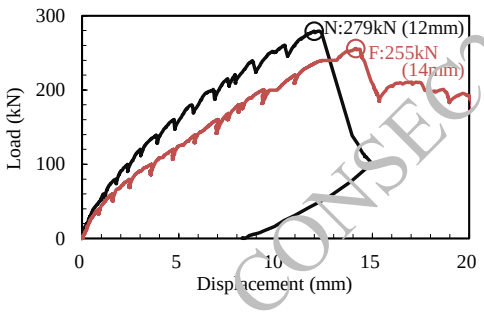

Figure 4. Load-displacement curves

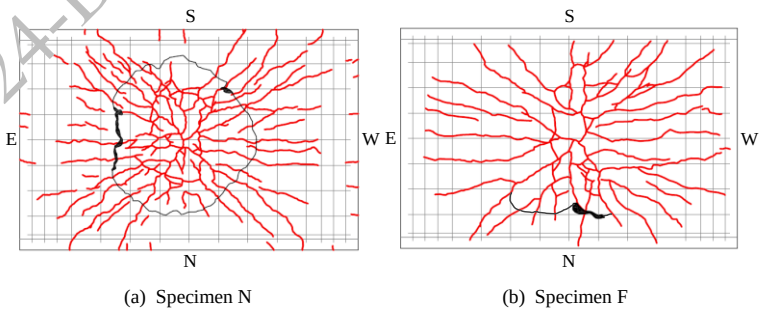

Figure 5. Loading cracks on the bottom surface

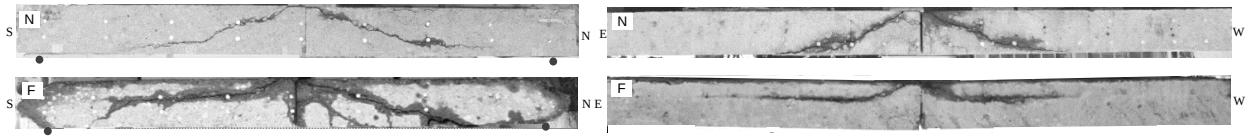

Figure 6. Cut Surface (Left: perpendicular axis direction Right: bridge axis direction)

5. Cause of difference in behavior of specimens

As mentioned in the previous chapter, the frost-damaged slab had a lower strength and its behavior at failure was different from that of the sound slab. A possible cause of this is "horizontal cracks" that occur in the frost-damaged slab. The basis for thinking this way is explained below.

5.1 Horizontal crack growth process

In this section, I will first consider how horizontal cracks developed. Fig. 7 is a conceptual diagram of the growth process of horizontal cracks. From now on, I would like to explain this diagram in order.

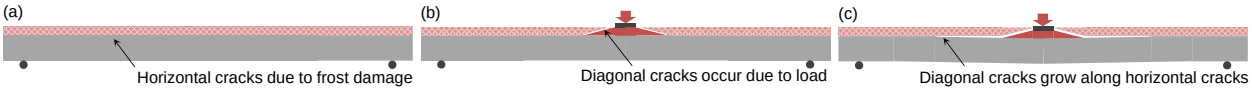

Figure 7. Growth process of horizontal cracks

5.1.1 Occurrence of horizontal cracks due to frost damage

As mentioned in Chapter 3, horizontal cracks had occurred in the frost-damaged slab due to freeze-thaw action. However, at this stage, the width of the crack was extremely narrow, and it is thought that it was so narrow that it could not be seen visually. This is because there are areas in the frost-damaged slab where horizontal cracks are not visible. For example, in the cut surface shown in Photo-1, horizontal cracks are visible near the loading point, but no horizontal cracks are visible away from the loading point or directly below the loading point. This is thought to be because the width of horizontal cracks caused by freeze-thaw action is so narrow that they cannot be visually confirmed.

5.1.2 Diagonal cracks occur in the deteriorated area due to load action

When the load started to act, diagonal cracks are thought to have occurred as follows:

1) Tensile stress acts on concrete due to shear deformation caused by load action.
2) However, as shown in Fig. 7, many micro-cracks have occurred in the deteriorated area due to frost damage.
3) Since these micro-cracks are "cracks" with "gaps", they easily widen when tensile stress is applied, resulting in wide cracks.
4) Because of such occurrence, diagonal cracks are thought to have occurred in the deteriorated area near the loading point.

5.1.3 Diagonal cracks grow along horizontal cracks

As the load increases further, the diagonal cracks tend to develop further. At this time, if there are no horizontal cracks, such as in the sound slab, the diagonal cracks will develop further downward. However, since the frost-damaged slab has horizontal cracks, the diagonal cracks are prevented from growing downward, and the cracks grow along the horizontal cracks. As a result, the width of horizontal cracks that had occurred due to frost damage is thought to have widened.

5.2 Reasons for the decrease in stiffness and strength

As mentioned in the previous section, as a result of the widening of the horizontal crack, the slab separates into a part above and a part below the horizontal crack, as shown in Fig. 8. Therefore, the load is supported only by the thinner lower part via the shear cone. The reason why the stiffness and strength of the frost-damaged slab decreased is thought to be because the thickness of the load-bearing slab became thinner, as described above.

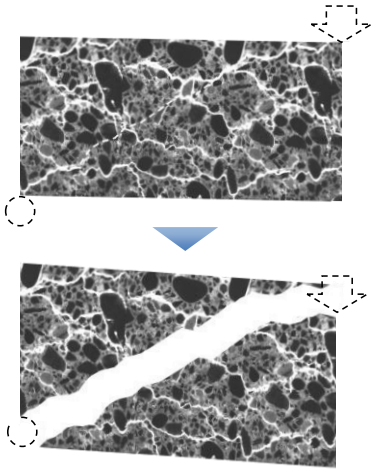

Figure 8. Diagonal cracks in the deteriorated area due to load action

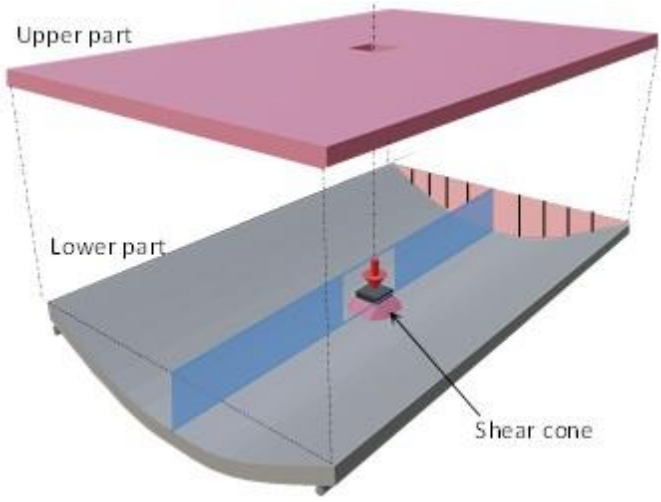

Figure 9. Slab separates into a part above and a part below the horizontal crack

6. Conclusions

A static loading test was conducted after subjecting a large slab specimen to frost damage from the top surface to half of its thickness. As a result, the following findings were obtained.

- Compared to the sound slab, the stiffness and maximum load decreased in the frost-damaged slab.
- Also, a punching shear cone occurred in the sound slab, but no punching shear cone occurred in the frost-damaged slab. Instead, horizontal cracks occurred near the upper distribution rebars in the frost-damaged slab.
- The following was thought to be the mechanism by which horizontal cracks occurred in the frost-damaged slab. 1) Narrow horizontal cracks occur due to freeze-thaw action, 2) Diagonal cracks occur in the deteriorated area near the loading point due to loading action, and 3) The width of the horizontal crack increases as this diagonal crack propagates along the horizontal crack.
- The decrease in stiffness and strength of the frost-damaged slab was thought to be due to the thinning of the load-bearing slab due to the occurrence of horizontal cracks.

Thaumasite Formation in Metakaolin and Limestone Cement Formulations in Cold Climates: A Thermodynamic Investigation

K. K. Schlage[1,2*], L.M. Ottosen[2], and W. Kunther[2]

[1] Sund & Bælt Holding A/S, Copenhagen V, Denmark,
Email: kaks@sbf.dk
[2] Technical University of Denmark, Kgs. Lyngby, Denmark
Email: limo@dtu.dk, wolku@dtu.dk

*Corresponding author

ABSTRACT

Marine exposure conditions present a challenge to the long-term integrity of concrete structures. With the increasing attention on using calcined clay and limestone as supplementary cementitious materials (SCMs) to reduce the CO_2 footprint of cement, uncertainties regarding thaumasite formation have risen. In cold climates, these uncertainties are related to seawater exposure. This study investigates the thaumasite formation in metakaolin and limestone cement formulations when exposed to seawater in cold climates. The thaumasite formation is investigated by thermodynamic modeling, using simplified chemical compositions of calcined clay, limestone, and seawater. The investigation is carried out based on different cement compositions, exploring the influence of limestone content on the thaumasite formation. The results based on the modeling indicate that thaumasite formation occurs at the expense of ettringite when C-S-H is consumed in all cases investigated. The volume of thaumasite is however dependent on the limestone content.

KEYWORDS: *Sulfate attack, thaumasite, calcined clay-limestone cement, durability, thermodynamic modeling.*

1. Introduction

Marine exposure conditions present a challenge to the long-term integrity of concrete structures. In addition to sodium chloride, seawater contains ions such as magnesium, sulfate, and carbonate which potentially can affect the concrete negatively (Jakobsen et al. (2016)). The service life of concrete structures in the marine environment is the result of the deterioration of reinforced concrete, including damages caused by the ingress of sulfate ions, also known as sulfate attack. Sulfate attack in cementitious materials can lead to a formation of phases such as ettringite ($3CaO{\cdot}Al_2O_3{\cdot}3CaSO_4{\cdot}32H_2O$), gypsum ($CaSO_4{\cdot}2H_2O$), and thaumasite ($CaSiO_3{\cdot}CaSO_4{\cdot}CaCO_3{\cdot}15H_2O$), as the sulfate reacts with hydration phases in the concrete. The consequences of these phase changes due to sulfate attack are expansion, cracking, softening, scaling, and thereby strength loss.

In recent years, calcined clay and limestone gained increasing attention as SCMs in cement to reduce the CO_2 emissions from cement production. Investigating the durability of these unexplored SCM mixtures can expand their applicability and thus contribute to limiting CO_2 emissions and material use when creating concrete structures. Limestone is commonly used as a filler in cement, however, higher carbonate content in cement through increased limestone filler has been identified to promote the formation of thaumasite in sulfate-containing environments (Justnes (2003)). Meanwhile, the addition of SCMs, such as calcined clay, often provides a higher sulfate resistance in many instances (Skaropoulou et al. (2009)). It is therefore essential to understand the synergy of the two SCMs when assessing the formation of thaumasite, as other studies often focus on the thaumasite formation caused by increased limestone content when exposed to Na_2SO_4 or $MgSO_4$ solutions. It is currently unclear if the use of calcined clay-limestone cement poses a durability challenge in large infrastructure projects when exposed to seawater.

Thaumasite formation occurs due to the reaction between C-S-H and sulfates in the presence of carbonate, e.g. from limestone. Thaumasite is stable at low temperatures, particularly between 0 and 5 °C, and does generally not form in temperatures above 20 °C (Skaropoulou et al. (2009)). Therefore, thaumasite poses a challenge for marine constructions in cold regions and can ultimately result in compromised structural integrity by the softening, and scaling of concrete.
The present work explores how thermodynamic modeling can be used to predict thaumasite formation in selected ternary cements with varying content of calcined clay and limestone, thereby contributing to a better understanding of the thaumasite formation in cement with a 35% blend of calcined clay (metakaolin) and limestone. In addition, the study aims to investigate how the seawater concentration contributes to the thaumasite formation and determine if thermodynamic modeling can be used for the prediction of thaumasite in cold regions.

2. Materials & methods

2.1 Cement and exposure solutions

The investigation is based on a blend of 65% Portland cement, CEM I 52,5 N (MS) (LA) (Oxide composition: 65.82% CaO, 19.93% SiO_2, 5.4% Al_2O_3, 3.81% Fe_2O_3, 5.03% others), and 35% mix of limestone (LS), and metakaolin (MK). The 35% substitution of the cement is investigated with various amounts of LS and MK. Both LS and MK are considered with simplified chemical compositions. LS is modeled as 100% $CaCO_3$, whereas MK is modeled as 54% SiO_2 and 46% Al_2O_3.
The exposure solution is based on the concentrations of the main elements in the Atlantic Ocean, provided by (Jakobsen et al. (2016)). The exposure solution is, therefore, a simplified seawater solution that contains a combination of NaCl, $MgSO_4$, and $NaHCO_3$, with a concentration of 460 mmol/L, 56 mmol/L, and 1.7 mmol/L, respectively.

2.2 Thermodynamic modeling

The phase assemblage of the different cement blends was studied with thermodynamic modeling. The thermodynamic modeling was carried out using the Gibbs free energy minimization software GEMS3 (https://gems.web.psi.ch) ((Kulik et al. (2013), Wagner et al. (2012)). The database was extended with the CEMDATA18, which contains data relevant to cementitious systems, including solubility products for the cement hydrate phases: Ettringite, AFm phases, hydrogarnet, hydrotalcite, and C-S-H (Lothenbach et al. (2019)). Data for zeolite phases was taken from zeolite21 for GEMS (Ma & Lothenbach (2020)). First, the initial phase assemblage was calculated for systems consisting of cement, metakaolin, and limestone. Afterward, the results were used as input to determine the phase assemblage after exposure to the seawater solution.
Thermodynamic modeling is used to calculate the composition of the stable hydrate assemblage assuming thermodynamic equilibrium. In general, it is assumed in these calculations that half of the MK reacts, which reflects the phase assemblage from (Kunther et al. (2016)). In addition, a full reaction of the cement is assumed as this study focuses on hydration over long periods. The initial conditions are calculated at 20 °C, as the model should represent concrete cast for large infrastructures. Such concrete elements are often cast and allowed to harden at temperatures close to room temperature before adding seawater in increasing quantities. The formation of thaumasite is investigated at a temperature of 5 °C, as thaumasite is expected to be stable at this temperature. It is the long-term effect of seawater exposure at low temperatures that is of interest in this study.

3. Results and discussion

3.1 Initial hydrate phases

To investigate the formation of thaumasite in different blends of cement, metakaolin, and limestone, thermodynamic modeling was used to first explore the hydration of such cements. The hydrate phase assemblage for cement with 35 % substitution of varying amounts of LS and MK was calculated with GEMS at a temperature of 20 °C, as displayed in figure 1. Thaumasite is not stable at 20 °C for kinetic reasons but may form in modeling and the phase was therefore excluded from the calculations at this stage.

For further investigations, three compositions were chosen for simplicity and to cover multiple aspects of the mix design. This included a blend with (i) 5% LS and 30% MK, (ii) 17% LS and 18% MK, and (iii) 30% LS and 5% MK. The mixtures are marked with vertical orange, blue, and green lines in figure 1 for mixes (i), (ii), and (iii), respectively.

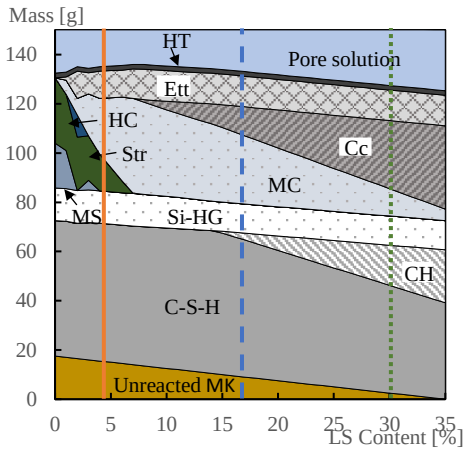

Figure 1. 35% substitution of cement with metakaolin (MK) and Limestone (LS) at 20 °C. Abbreviations: Calcite (Cc), Calcium hydroxide (CH), Ettringite (Ett), Hemicarbonate (HC), Monocarbonate (MC), Monosulfate (MS), OH-hydrotalcite (HT), Si-Hydrogarnet (Si-HG), Straetlingite (Str).

The hydrate phase assemblage varies based on the ratio between LS and MK. The phase assemblage in systems with a low content of LS and high content of MK, represented by the case (i), was found to be: Unreacted metakaolin (MK), C-S-H, Si-hydrogarnet (Si-HG), monosulfate (MS), straetlingite (Str), hemicarbonate (HC), monocarbonate (MC), ettringite (Ett) and OH-hydrotalcite (HT). With a low content of LS, the phase assemblage does not include portlandite (CH) and has a low calcite content. The amount of both CH and calcite increases as the LS content increase. In addition, the phases Str, MS, and HC are not a part of the phase assemblage for cement with a high content of LS, as represented by cases (ii) and (iii). The hydrate phase assemblage found in this study was also previously documented by laboratory experiments and analysis by ((Schmidt et al., 2008)), and the phase assemblage is comparable to the phase assemblage found by (Kunther et al. (2016)), who considered the hydration kinetics.

3.2 Effect of limestone content

If sulfate is added to the initial system, thermodynamic modeling indicates the formation of ettringite at the expense of AFm-phases such as monocarbonate. Seawater contains sulfate and is complex and difficult to model in detail. Therefore, a simplified solution containing only NaCl, $MgSO_4$, and $NaHCO_3$ is added to the system for the three chosen cement blends shown in figure 1. The thermodynamic modeling predicts the formation of thaumasite as shown in figure 2.

In figure 2, it can be seen that thaumasite forms at the expense of ettringite when C-S-H is consumed. The predicted ettringite amounts vary for the three blends due to differences in cement composition. This variation influences the formation of thaumasite, as thaumasite stabilizes when ettringite is destabilized. This is reported as thaumasite following after ettringite formation due to their similar crystal structures. The limestone and calcined clay content, therefore, influences the formation of thaumasite. The AFm-phase monocarbonate reacts and forms ettringite when exposed to sulfate, and this ettringite favors the formation of thaumasite.

The thermodynamic modeling indicated that the formation of thaumasite increases when other phases are decomposing. In addition, the modeling indicated that the formation of thaumasite in cement with a high LS content (iii) requires a higher sulfate concentration to form thaumasite, even though the total volume of thaumasite at 100 L added solution pr 100 g cement is comparable between cases (ii) and (iii). This was not expected based on previous studies and should be investigated experimentally. In general, the total volume of thaumasite is lower for the case with low LS content (i) compared to the case with high LS content (iii) when comparing thaumasite at 100 L added solution pr 100 g cement. The exact amount of thaumasite is more uncertain and needs to be confirmed by experimental investigations.

The thermodynamic model does not use reactive transport and, hence, a direct comparison with experimental data is not possible, as this approach has constant relationships between the ions in the exposure solution for all depths. However, the phase formation zones agree with the experimental results in other studies (Schmidt et al. (2008) and Skaropoulou et al. (2009)).

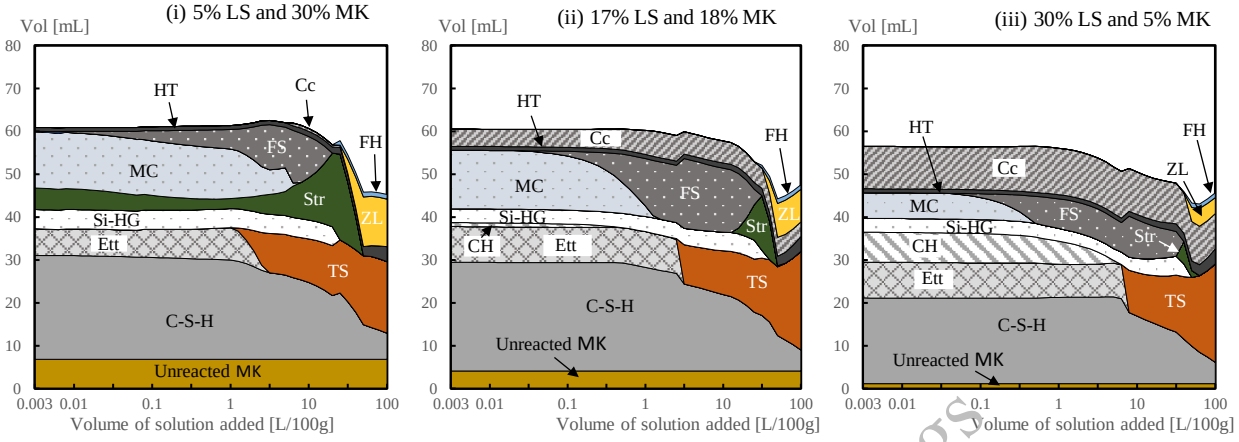

Figure 2. Interactions between cement with different contents of calcined clay and limestone, and simplified seawater solution at 5 °C. Abbreviations: Calcite (Cc), Calcium hydroxide (CH), Ettringite (Ett), Ferrihydrite-mc (FH), Friedel's salt (FS), Monocarbonate (MC), OH-hydrotalcite (HT), Si-Hydrogarnet (Si-HG), Straetlingite (Str), Thaumasite (TS), Zeolite (ZL).

4. Conclusions

The formation of thaumasite was investigated by thermodynamic modeling for cement containing both limestone and calcined clay where:

- The formation of thaumasite occurs at the expense of ettringite when C-S-H is consumed.
- Thermodynamic modeling shows the formation of thaumasite in calcined clay-limestone cement when exposed to a simplified seawater solution. The model needs to be confirmed by experimental data, to determine the amount of thaumasite formed.

Acknowledgments

The work presented is part of an industrial PhD project financed by Sund & Bælt Holding A/S and a grant from Innovation Fund Denmark (Innovationsfonden). This financial support is gratefully acknowledged.

References

Jakobsen, U. H., De Weerdt, K., & Geiker, M. R. (2016). Elemental zonation in marine concrete. *Cement and Concrete Research*, *85*, 12–27.

Justnes, H. (2003). Thaumasite formed by sulfate attack on mortar with limestone filler. *Cement and Concrete Composites*, *25*(8), 955–959.

Kulik, D. A., Wagner, T., Dmytrieva, S. V., Kosakowski, G., Hingerl, F. F., Chudnenko, K. V., & Berner, U. R. (2013). GEM-Selektor geochemical modeling package: Revised algorithm and GEMS3K numerical kernel for coupled simulation codes. *Computational Geosciences*, *17*(1), 1–24.

Kunther, W., Dai, Z., & Skibsted, J. (2016). Thermodynamic modeling of hydrated white Portland cement-metakaolin-limestone blends utilizing hydration kinetics from 29Si MAS NMR spectroscopy. *Cement and Concrete Research*, *86*, 29–41.

Lothenbach, B., Kulik, D. A., Matschei, T., Balonis, M., Baquerizo, L., Dilnesa, B., Miron, G. D., & Myers, R. J. (2019). Cemdata18: A chemical thermodynamic database for hydrated Portland cements and alkali-activated materials. *Cement and Concrete Research*, *115*, 472–506.

Ma, B., & Lothenbach, B. (2020). Synthesis, characterization, and thermodynamic study of selected Na-based zeolites. *Cement and Concrete Research*, *135*.

Schmidt, T., Lothenbach, B., Romer, M., Scrivener, K., Rentsch, D., & Figi, R. (2008). A thermodynamic and experimental study of the conditions of thaumasite formation. *Cement and Concrete Research*, *38*(3), 337–349.

Skaropoulou, A., Tsivilis, S., Kakali, G., Sharp, J. H., & Swamy, R. N. (2009). Thaumasite form of sulfate attack in limestone cement mortars: A study on long term efficiency of mineral admixtures. *Construction and Building Materials*, *23*(6), 2338–2345.

Wagner, T., Kulik, D. A., Hingerl, F. F., & Dmytrieva, S. V. (2012). GEM-Selektor geochemical modeling package: TSolMod library and data interface for multicomponent phase models. *The Canadian Mineralogist*, *50*, 1173–1195.

Phase-Field Coupled Cohesive Zone Model Predictions for Fracture in Fibre-Matrix Interface of Geopolymer Concrete

Sudakshina Dutta[1*], Reshmi Maria Jose[2]

[1]Indian Institute of Technology Roorkee, Roorkee, India
Email: sudakshina@ce.iitr.ac.in
[2]Indian Institute of Technology Roorkee, Roorkee, India
Email: reshmi.ce@sric.iitr.ac.in

[*]Corresponding author

ABSTRACT

A coupled phase field-cohesive zone scheme is used to comprehend the fracture occurring in matrix and the subsequent fibre-matrix interface cracking in geopolymer composites. The computational framework of phase field theory coupled with cohesive zone model in a finite element context has been popular in investigating the damage initiating and propagating in fibre-reinforced composites. In the current study, this model is adopted as the prototype model to investigate the fracture that nucleates and grows in the fibre-matrix interface. The key to this study is to consider geopolymer concrete as a composite consisting of a matrix with inclusions such as fibres present in it. A mesostructure containing geopolymer matrix and fibres is generated to investigate the various fracture processes taking place in the composite at the mesoscale level. Representative volume elements (RVE) are generated to accommodate various fibre volume fractions in the composite matrix which is then modelled as single-edge notched specimens under uniaxial tension. A concise parametric study is conducted to explore the effect of varying fibre content on the cracking process.

KEYWORDS: *Geopolymer composites, Phase-field modeling, Cohesive Zone Model, Fracture toughness, Crack trajectory*

1. Introduction

Fracture is one of the most frequently encountered modes of failure in composites, in general. It is a major concern to prevent micro-cracking and the cracking-induced damage in concrete structures. The tracking of complex crack trajectories largely helps the prediction of failure due to cracking. The numerical simulation of the damage in fibre-matrix interface is another arduous task. The phase field model, built upon Griffith's crack theory, is a promising approach to simulate crack nucleation, onset of crack propagation, complex crack paths arising due to crack branching and interaction among multiple cracks. This method coupled with the cohesive zone modeling is used in the current study to describe the evolution of damage from fibre-matrix interface in fibre-reinforced geopolymer concrete (FRGC). In the phase-field model, a continuous scalar variable is introduced to describe the smeared cracks in the solid materials. According to the variational approach to fracture mechanics (Francfort and Marigo (1998)), the evolution equation of the PF variable explicitly incorporates the criterion of crack propagation, which involves crack initiation, growth, branching and coalescence. These non-linear evolution equations of PF can be solved mathematically which makes it possible to track the complex crack paths.

The current work is intended to study the damage occuring in GPC using the phase-field regularised cohesive zone model. The key to this study is to consider GPC as a composite consisting of a matrix with inclusions such as fibres present in it. In this study, a mesostructure containing geopolymer matrix and fibres is generated to investigate the fracture processes taking place in the composite at the mesoscale level. The phase-field method helps in simulating the crack initiating, propagating, branching and coalescing in the matrix while a cohesive zone model is used to simulate the fibre-matrix interface damage.

2. Numerical Model

2.1 Phase field model

It is supposed that an arbitrary body $\Omega \subset R^d$ ($d \in \{1,2,3\}$) containing a crack represented by an internal discontinuity boundary Γ. $\partial\Omega \subset R^{ndim-1}$ is the external boundary, having an outward unit normal vector n, maybe split into two disjoint parts $\partial\Omega_u$ and $\partial\Omega_t$ such that $\partial\Omega_u \cap \partial\Omega_t = \emptyset$ and $\partial\Omega_u \cap \partial\Omega_t = \partial\Omega$. Let $\mathbf{u}(x)$ be the applied displacements for $x \in \partial\Omega_u$ and $\mathbf{t}(x)$ be the tractions applied for $x \in \partial\Omega_t$ as shown in Figure 1.

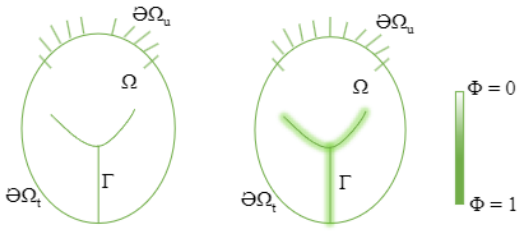

Figure 1. A solid body *Ω* having crack set with sharp cracks and then approximated with diffuse crack bands

The crack is represented using a diffusive crack topology in the PF model by the introduction of a scalar viz., the phase field variable $\varphi(x, t)$ whose value varies from 0 to 1, 0 for the intact domain and 1 for the fully cracked domain in Ω. As per Griffith's theory, brittle fracture is an energy minimization problem (Francfort and Marigo (1998), Miehe et al. (2010)) where the total potential energy is the sum of the strain energy density ψ and the critical energy release rate G_c as:

$$\Pi(u) = \int_\Omega \psi(\boldsymbol{\varepsilon}(\mathbf{u}))dV + \int_\Gamma G_c dS \quad (1)$$

where $\mathbf{u}$ and $\boldsymbol{\varepsilon} = (\nabla u^T + \nabla u)/2$ denote the displacement and strain fields respectively. $P(\mathbf{u})$ is the external potential energy functional given by:

$$P(u) = \int_\Omega \mathbf{b}.\mathbf{u}dV + \int_{\partial\Omega t} \mathbf{t}.\mathbf{u}dA \quad (2)$$

where $\mathbf{b}$ is the distributed body force so that the total energy functional becomes

$$\Pi(u) = \int_\Omega \psi(\boldsymbol{\varepsilon}(\mathbf{u}))dV + \int_\Gamma G_c dS - P(\mathbf{u}) \quad (3)$$

The minimization of the above functional gets restricted by the complexities related to tracking the fracture propagation surface Γ. A crack surface density function is introduced as:

$$\gamma(\varphi, \nabla\varphi) = \frac{1}{c_0}\left[\frac{1}{l_0}\alpha(\varphi) + l_0|\nabla\varphi|^2\right] \quad (4)$$

such that the phase field length scale $l_0 \rightarrow 0$, Γ converges to a sharp crack. $\alpha(\varphi)$ is the geometric crack function which determines the distribution of the crack phase-field, c_0 is the scaling parameter given by $c = 4\int_0^1 \sqrt{\alpha(\beta)}d\beta$. Incorporating Equation 4 in Equation 3 and introducing $\omega(\varphi)$, a degradation function, to simulate the reduction of stiffness with damage evolution, the total energy functional is obtained as:

$$\Pi(u, \varphi) = \int_\Omega \omega(\varphi)\psi(\boldsymbol{\varepsilon}(\mathbf{u}))dV + \int_\Omega G_c \frac{1}{2}\left[\frac{1}{l_0} + l_0(\nabla\varphi.\nabla\varphi)\right]dV - P(\mathbf{u}) \quad (5)$$

The strong form of the energy functional is obtained by taking the first derivative of $\Pi(u, \varphi)$ in Equation 5 with respect to the primal kinematic variables by making use of the Gauss divergence theorem as :

$$\begin{cases} \nabla.\boldsymbol{\sigma} + \mathbf{b} = 0 \quad \text{in } \Omega \\ \boldsymbol{\sigma}.\mathbf{n} = \mathbf{t} \quad \text{on } \partial\Omega t \\ \omega'(\varphi)\boldsymbol{H} + \frac{Gc}{c0}\left(\frac{\alpha'(\varphi)}{l0} - 2l0\nabla.\nabla\varphi\right) = 0 \quad \text{in } \Gamma \\ 2\frac{Gc}{c0}\, l0\nabla\varphi.\mathbf{n}\boldsymbol{\Gamma} = 0 \quad \text{on } \partial\Gamma \end{cases} \tag{6}$$

where **n** and $\mathbf{n}_\Gamma$ are the outward unit normal vector of external boundary of **Ω** and Γ. **σ** is the stress given by:

$$\sigma = \omega(\varphi)\sigma' = \omega(\varphi)E0 : \varepsilon \tag{7}$$

where $\omega(\varphi) \in [0, 1]$ is the monotonically decreasing energetic degradation function, $\mathbb{E}_0$ and ε are the elasticity and strain tensors respectively. To impose the irreversibility condition $\dot{\varphi} \geq 0$ on the crack phase field, Miehe et al. (2010) introduced the history strain variable $\boldsymbol{H}$ as

$$\boldsymbol{H} = \max\left(\frac{ft.ft}{2E0}, \max_{n\in[0,T]} Y_t\right) \tag{8}$$

where $Y_t = \frac{<\sigma'1>2}{2E0}$, $<\sigma'_1>$ is the major principal value, $E_0 = \lambda_0 + 2\mu_0$ is the elongation modulus with λ_0 and μ_0 being the Lame's constants of isotropic elasticity.

2.2 Cohesive Zone Model

A cohesive zone model (CZM) is required to model the fracture process zone ahead of the crack tip as well as to remove the bi-material singularity. Here, a bi-linear traction-separation law is used to describe the constitutive behavior of the CZM. The area under the traction-separation curve denotes the fracture toughness of the material in the corresponding fracture mode. The initiation of damage in the cohesive interface follows a quadratic nominal stress criterion as

$$\left(\frac{<tn>}{\sigma nI}\right)^2 + \left(\frac{<ts>}{\sigma sI}\right)^2 = 1 \tag{9}$$

where t_n and t_s are the normal and shear tractions and σ^n_I and σ^s_I are the interfacial tensile and shear strengths respectively. A displacement-based damage governed by the Benzeggagh-Kenane fracture criterion is used for the damage evolution.

$$G^n_I + (G^s_I - G^n_I)\left(\frac{Gs}{Gn + Gs}\right)^\eta = G_c \tag{10}$$

Equation 10 is followed to attain the critical energy release rate G_c where η is a material parameter and G^s_I and G^n_I denote fracture energy required to cause failure in shear and normal directions respectively.

2.3 Implementation of the model

The numerical implementation is done in the finite element software COMSOL Multiphysics using the staggered algorithm. A decohesion node is used to execute the fibre-matrix debonding according to the bilinear traction-separation law for the CZM in the interfaces. Contact pairs are initially created between the interfaces which later debond under the tensile displacement applied. The strong form equations in Equation 6 are used for solving the phase field problem. The history strain variable in Equation 8 is utilized in the computation of the effective crack-driving force which gets updated at the end of each increment. The non-linear governing equations in residual form, discussed in 2.1, are solved in an alternating manner which is repeated until the final solution converges.

3. Results and discussions

An RVE having dimensions height H = 50mm, width W = 50mm, an initial crack of length a_0 = 20mm on the left edge and an elliptical fibre inclusion of diameter 0.2mm and length=13mm at the center of the plate is simulated. The plate represents the solid geopolymer matrix which has an inclined fibre embedded in the center with an interface between the two phases as shown in Figure 1. The homogenized geopolymer matrix properties are: Young's modulus E = 15.5 GPa, Poisson's ratio ν = 0.153, tensile strength f_t = 1.58 MPa

and critical energy release rate G_m = 25N/m. The steel fibre has the following properties: Young's modulus E = 200 GPa and Poisson's ratio ν = 0.3. Plane strain quadrilateral elements are used for meshing. A mesh size of 0.1mm is adopted which is much smaller than the phase field length scale.

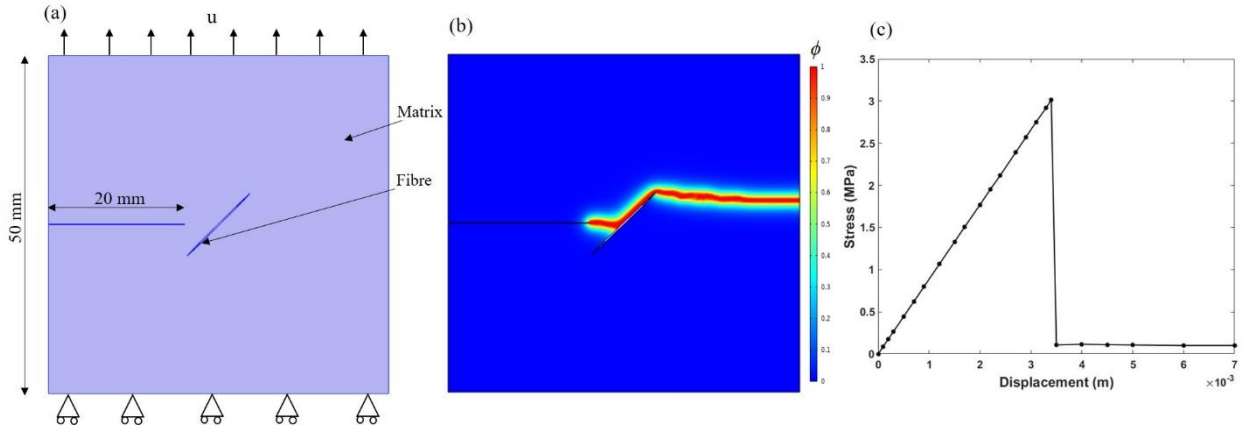

Figure 2. (a) The model of the RVE with inclined fibre subjected to uniaxial tension, (b) Phase-field value under the phase-field cohesive zone scheme, (c) the stress-displacement response of the RVE

The crack initiated from the initial notch and propagated towards the fibre where it takes deviation in its path suggesting a shear crack at the encounter of the inclined fibre. After which the cracks grows along the fiber-matrix interface and proceeds towards the opposite edge where the full damage potential is achieved. The stress-displacement response is also showing an interesting pattern where the initial elastic part is followed by a stress-peak at displacement of around 3mm which is the point at which damage is initiated. Phase field value takes a higher value than zero implying that the matrix is no longer intact. Damage proceeds further in the matrix material as the stress takes a sudden drop, however, there isn't entire collapse of the matrix due to the presence of the fibre. The higher displacement values indicate the toughening mechanism offered by the fibre in the matrix.

4. Conclusions

An interesting observation has been obtained in the damage modelling of the fibre-matrix interface. The shearing of the crack while encountering an inclined fibre is intriguing and requires further investigation on the damage occurring in the fibre-matrix interface. The coupled phase-field cohesive zone model is a powerful tool for the same. The study on the damage behaviour of geopolymer mortar reinforced with steel fibres is under progress. The effect of the varying parameters related to the fibre and matrix on the cracking patterns and damage response of the current material is also studied.

Acknowledgements

The authors would like to acknowledge the funding support from Department of Science and Technology (DST) - Science and Engineering Research Board (SERB), India via Start-up Research Grant (SRG/2020/000885).

References

Christian Miehe, Fabian Welschinger, and Martina Hofacker. (2010) "Thermodynamically consistent phase-field models of fracture: Variational principles and multi-field FE implementations", *International Journal for Numerical Methods in Engineering*, 83(10):1273–1311

Gilles A Francfort and J-J Marigo. (1998) "Revisiting brittle fracture as an energy minimization problem", *Journal of the Mechanics and Physics of Solids*, 46(8):1319–1342

Comparative Corrosion Behaviour of Plastically-Deformed Mild, TMT, and Stainless Steel Bars in Chloride-Contaminated Simulated Concrete Pore Solution

Bhanu Prakash Malladi [1], Prasanna Kumar Behera [2*]

[1]PhD student, Department of Civil and Environmental Engineering, Indian Institute of Technology, Tirupati, India
[2]Assistant Professor, Department of Civil and Environmental Engineering, Indian Institute of Technology, Tirupati, India

*Corresponding author

ABSTRACT

Rebar corrosion is one of the common deterioration phenomena in reinforced concrete structures, which affects their intended service life. Normally, rebar is subjected to elastic and plastic strains in reinforced concrete. While the elastic strains are typically induced on account of external loading, plastic deformation is inevitable near the bends of stirrups and cranked bars. In principle, the plastically deformed region of bent rebar is close to the exposed surface and could be critical, and hence, needs special attention while understanding the corrosion behavior. This work presents the corrosion behavior of different strained steel bars in a simulated concrete pore solution with chloride addition. As part of the experimental program, the corrosion behavior of three different types of steels, such as mild steel, Thermo-Mechanically Treated (TMT) bars, and stainless-steel bars, was analyzed using polarization studies to specifically understand the relative effectiveness of the commonly used steels in handling surface deterioration in strained conditions. Electrochemical tests, such as open circuit potential (OCP), linear polarization (LP), Electrochemical Impedance Spectroscopy (EIS), and Cyclic Polarization (CP) tests, were conducted on the bars in both unstrained and plastically-deformed conditions of the bars. In principle, strained steel has more corrosion tendency in all types of steel when compared to unstrained conditions, thus highlighting the criticality of bent zones in steel bars. Stainless steel bar has shown nobler potentials and less corrosion rate than TMT and mild steel in both strained and unstrained conditions. To better understand the underlying phenomenon, the changes in the microstructure of the bars induced on account of plastic deformation were examined, and efforts were made to correlate the same with the microstructural changes in the bars.

1. Introduction

Reinforcing steel bar (rebar) corrosion is a serious durability issue in concrete structures. Conversion of steel into its oxides and hydroxides in the presence of moisture and oxygen is a spontaneous reaction, and results in more voluminous products. In general, rebar in highly alkaline environments, like in good quality concrete, will be stable due to the tendency to form a protective passive film on its surface (Yonezawa et al., 1988). The composition and stability of passive film are the decisive factors governing the rate and extent of corrosion. These factors are influenced by the chemical composition and microstructure of the rebar, highlighting their significant impact on corrosion behavior. The varying corrosion behaviour observed among different steels can be mainly attributed to the differences in the surface conditions, microstructural characteristics, and elemental composition, resulting in varying passivation kinetics (Cai et al., 2021). Generally, two different steel rebars, like plain reinforcing bars and ribbed rebars, are commonly used in building construction. In recent years, extensive research has been dedicated to increase the passivation stability and rebar's anti-corrosive properties. On the other hand, superior corrosion resistance of stainless steel has led to its extensive use in numerous reinforcement projects in recent times, especially in aggressive marine environments (Yang et al., 2021). Interestingly, the rebars are plastically deformed even before placing in concrete. Prestraining the rebar at bent portions will experience macro and microstructural deformations, which can be considered as weakest zones, vulnerable to corrosion. Interestingly, the effect of inherent plastic deformation of rebar on its corrosion behaviour received scant

attention. This work aims to identify the relative effectiveness of commonly used steel rebars in resisting rebar corrosion in chloride-contaminated concrete environments in both undeformed and plastically deformed conditions using electrochemical testing.

2. Materials and Methods

Low carbon TMT, mild steel, and SS 304L rebar were used in this study. All three rebars were subjected to uniaxial tension up to a strain level of 5% using a Universal Testing Machine (UTM) as per IS 1608: 2005 standards. After inducing the desired strain level using the UTM, the rebars were unloaded, resulting in the presence of residual strain. To minimize the impact of gripping on the rebars during the tensioning, 150 mm test specimens were cut from the central section of the strained rebars. The cross-sections of the metallographic samples were initially ground with a belt grinder, and then polished up to 1500 grit size using SiC emery papers.

2.1 Electrochemical corrosion testing

Electrochemical corrosion testing was carried out at room temperature using an electrochemical workstation (Versa stat 3- 2.65). A flat corrosion cell with an exposed test area of 1 cm2 was employed to evaluate the rebar cross-sections. Within the flat cell configuration, a reference electrode of Ag/AgCl was used, which has a potential of +0.197 V relative to the standard hydrogen electrode. The working electrode consisted of specimens taken from the rebar, while a platinum wire mesh served as the counter electrode.
Electrochemical measurements were conducted in chloride-contaminated simulated concrete pore solution (SCPS + Cl-). To prepare the chloride-contaminated solution, 3.5% NaCl (by weight) was mixed with 0.1 M NaOH, 0.3 M KOH, 0.03 M Ca(OH)2, and 0.002 M gypsum (Behera et al., 2020). The first step involved stabilizing the open circuit potential (OCP) for all specimens. After stabilizing, the electrochemical impedance spectroscopy (EIS) analysis was conducted by sweeping the frequency range from 100 KHz to 10 mHz.
The obtained EIS data was analyzed using the ZsimpWin application. For evaluating the Linear Polarization Resistance (LPR), the stabilized potentials were polarized within a non-destructive range of -20 mV to +20 mV. The resistance exhibited by the metal against polarization was evaluated by Equation-1.

$$R_P = \left(\frac{\Delta E}{\Delta i}\right)_{\eta' \to 0} \quad (1)$$

Where ΔE is the change in the potential, Δi is the change in current and η' is the overpotential. The specimens were exposed to over-potentials ranging from -250 mV to +250 mV relative to their respective OCPs to examine the dynamic polarization behavior. The negative potentials with respect to OCP allowed for recording the cathodic polarization curves, while the positive potentials enabled the recording of the anodic polarization curves. In all the tests, a consistent scan rate of 0.5 mV/s was applied.

3. Results and Discussions

Figure 1 (a) shows the stabilized potential trend with respect to time for all the specimens. The stabilized potential values are given in Table 1. In all the three types of steel specimens, the OCP becomes more negative with an increase in strain level, suggesting that the metal's corrosion susceptibility and thermodynamic instability are higher in the plastically deformed condition than in the unstrained condition. The Nyquist plots of the specimens obtained in the EIS tests are given in Figure 1(b). The data was fitted using a two-time constant circuit, considering the tendency of a metal to form a passive film on its surface in the passivating electrolytic environment like simulated concrete pore solution. EIS results provide the charge transfer resistance (R_{ct}) values for different steel specimens under unstrained (0%) and strained (5%) conditions. The obtained EIS parameters for all the specimens are listed in Table 1. For TMT steel, R_{ct} decreased significantly from 19,630 Ω cm^2 to 5,170 Ω cm^2 under strain, indicating a substantial increase in the corrosion susceptibility. SS also shows a noticeable reduction in R_{ct} from 241,000 Ω cm^2 to 175,000 Ω cm^2 when strained, though it has more corrosion resistance among the tested steels. MS steel exhibits the greatest decrease in R_{ct} from 8,648 Ω cm^2 to 3,282 Ω cm^2, reflecting a pronounced decrease in its corrosion resistance under strain. These results confirm that pre-induced plastic strain, in general, adversely affects the corrosion resistance of steel, and the extent of this effect varies with the type of steel, and the effect is more significant in MS steel than SS rebar.

Table 1. Corrosion parameters obtained from electrochemical corrosion testing

Sl.No	Description	OCP, V_{SCE}	R_{ct}, Ω cm^2	R_p kΩ cm^2	i_{corr} μA/cm^2	E_{corr}, V_{SCE}
1.	0 TMT	-0.55	19630	22.20	0.36	-0.58
2.	5 TMT	-0.56	5170	9.57	0.68	-0.60
3.	0 SS	-0.31	241000	244.71	0.05	-0.30
4.	5 SS	-0.26	175000	165.58	0.08	-0.22
5.	0 MS	-0.39	8648	26.96	0.46	-0.45
6.	5 MS	-0.47	3282	4.49	2.44	-0.47

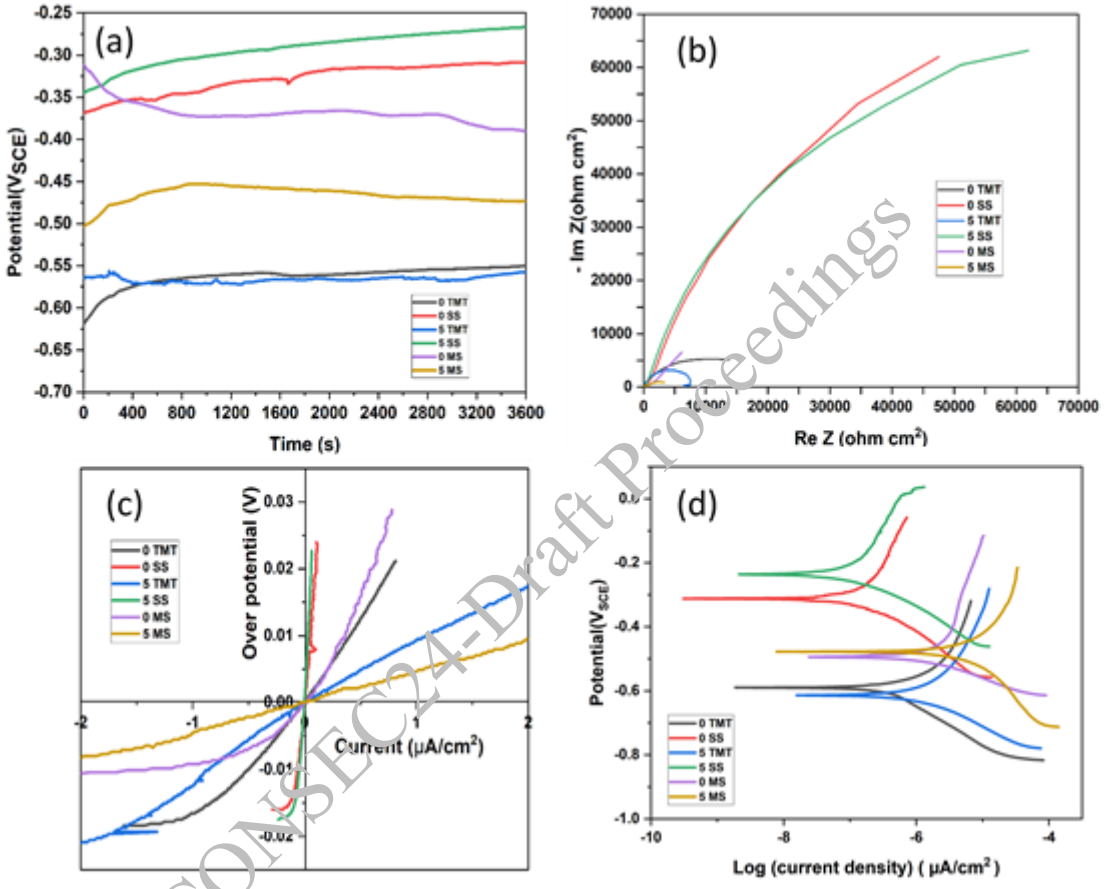

Figure 1. (a) OCP, (b) Nyquist plot, (c) LPR, (d) Tafel plots in SCPS + Cl^- electrolyte

The linear polarization response of all the specimens is shown in Figure 1(c), and the R_p values obtained from Equation-1 are summarized in Table-1. The LPR results show a decrease in polarization resistance (R_p) for all steel specimens when subjected to plastic deformation. As far as the polarization resistance of mild steel is concerned, the R_p dropped from 26.96 kΩ cm^2 to 4.49 kΩ cm^2 due to strain, indicating a significant reduction in the corrosion resistance. The R_p of SS has decreased from 244.20 kΩ cm^2 to 165.58 kΩ cm^2. However, SS has been observed to possess superior corrosion resistance as compared to other steels, and the TMT steel's R_p has reduced from 22.207 kΩ cm^2 to 9.577 kΩ cm^2 under the effect of pre-induced plastic strain.

Tafel plots of the specimens are shown in Figure 1(d), and the corresponding corrosion current densities obtained from Tafel extrapolation are listed in Table 1. The current densities obtained from Tafel plots in chloride-contaminated concrete pore solution revealed the effect of plastic deformation on the corrosion rates of different steel rebars. In strained conditions, TMT steel's current density increased from 0.36 μA/cm^2 to 0.685 μA/cm^2, indicating a higher corrosion rate. SS showed a smaller increase in current density from 0.05 μA/cm^2 to 0.08 μA/cm^2, however, maintaining the lowest corrosion rates among all the tested steels, even under strained conditions. MS exhibited a significant rise in current density from 0.46 μA/cm^2

to 2.44 μA/cm² under strain, indicating a significant tendency of MS steel to corrosion susceptibility when it undergoes plastic deformation. These results highlight that pre-induced plastic deformation in steel rebar generally increases the corrosion rates, with SS steel being the most resistant and MS steel the most affected by strain-induced corrosion.

4. Conclusions

Based on the electrochemical corrosion parameters extracted from the OCP, EIS, LPR, and Tafel analyses, it is evident that pre-induced plastic strain, in general, adversely affects the corrosion rate of steel rebar and the extent of the effect varies among different types of steel. While the effect is predominant in mild steel, it is relatively less significant in stainless steel.

References

Behera, P. K., Misra, S., & Mondal, K. (2020). Corrosion Behavior of Strained Rebar in Simulated Concrete Pore Solution. *Journal of Materials Engineering and Performance*, *29*(3), 1939–1954.

Cai, Y., Zheng, H., Hu, X., Lu, J., Poon, C. S., & Li, W. (2021). Comparative studies on passivation and corrosion behaviors of two types of steel bars in simulated concrete pore solution. *Construction and Building Materials*, *266*, 120971.

Yang, G., Du, Y., Chen, S., Ren, Y., & Ma, Y. (2021). Effect of secondary passivation on corrosion behavior and semiconducting properties of passive film of 2205 duplex stainless steel. *Journal of Materials Research and Technology*, *15*, 6828–6840.

Yonezawa, T., Ashworth, V., & Procter, R. P. M. (1988). Pore solution composition and chloride effects on the corrosion of steel in concrete. *Corrosion*, *44*(7), 489–499. https://doi.org/10.5006/1.3583967

Bowing Effect: Mechanism and Laboratory Simulation in the Marble Stone

Anupama Ghimire[1*], Maharshi Divekar[2], Swathy Manohar[3]

[1]M. Tech, Department of Civil Engineering, Indian Institute of Technology Bombay, Mumbai, Maharashtra, India
Email: 22M0622@iitb.ac.in
[2]B. Tech, Department of Civil Engineering, Indian Institute of Technology Bombay, Mumbai, Maharashtra, India
[3]Assistant Professor, Department of Civil Engineering, Indian Institute of Technology Bombay, Mumbai, Maharashtra, India.

*Corresponding author

ABSTRACT

Many well-known heritage structures of brick masonry are usually marble-clad for aesthetic purposes. Such marbles are deteriorating at an accelerated rate in the current days. Bowing is one of the major phenomena causing the deterioration. Bowing in marble stone cladding of the structure's facades can cause permanent deflection and weaken flexural strength and anchoring. This may lead to the detachment of cladding. Combined with wind pressure, it increases the risk of stone slab fracture and collapse. Bowing is caused by temperature variations, humidity, climatic conditions, and many more where temperature variation supersedes the other causes. This paper studies the bowing phenomenon of marble and its impact on heritage conservation methods. Also, the study discusses simulating the thermal variations in the laboratory on marble samples which gives suggestions on the probable effects of marble deterioration after bowing effects.

KEYWORDS: *Bowing effect, Marbles, Heritage structure, Stone heritage, Marble degradation*

1. Introduction

Stone heritage structures worldwide are experiencing accelerated deterioration, manifesting in various forms of physical weathering such as cracking, spalling, and bowing. This deterioration compromises the structural integrity and aesthetic appeal of these architectural marvels. Environmental factors, including temperature fluctuations, moisture ingress, and pollution, are primary contributors to these degradation processes as per Vázquez et al (2010). According to Sousa and Sousa (2018a), India boasts a rich cultural heritage, with numerous stone-built structures dating back centuries, such as temples, forts, and palaces. These architectural wonders are essential links to India's illustrious history, reflecting the craftsmanship and cultural sentiments of their time. Consequently, preserving these heritage structures is vital for maintaining cultural identity and fostering tourism, significantly contributing to the nation's socio-economic status. Marble has been a favored building material in India's architectural heritage, extensively used in facades, floors, and interior spaces of historic monuments. Known for its elegance and durability, marble symbolizes luxury and exemplifies Indian craftsmanship. Iconic structures like the Taj Mahal and the Dilwara Temples feature intricate marble carvings and decorations, showcasing the native art forms of Indian architecture (Sousa and Sousa, 2018b).

As per the report by Marini and Bellopede (2018), among the various deterioration phenomena observed in marble, bowing is particularly significant. Bowing refers to the gradual deformation of marble slabs, resulting in concave or convex curvatures along their surfaces. This slow, progressive process is influenced by several external factors, leading to compromised structural integrity and aesthetic disfigurement. Understanding the mechanisms driving bowing is crucial for implementing effective preservation strategies. Previous research indicates that the bowing phenomenon in marble is significantly influenced by its inherent porosity. Porosity refers to microscopic voids or pores within the stone matrix, which facilitate moisture absorption and migration. As moisture content fluctuates due to environmental factors,

differential expansion and contraction within the marble matrix may occur, leading to internal stress buildup and subsequent bowing deformation (Marini and Bellopede, 2009). Bowing in marble arises from complex interactions between environmental factors, material properties, and structural configurations. Elevated temperatures and humidity fluctuations induce thermal and hygral stresses within the marble slabs. These stresses are further aggravated by pre-existing microcracks and textural anisotropy, contributing to the progressive deformation observed in bowing.

Thus, bowing on marbles caused by thermal variations in the environment can cause alterations in the material properties and could be detrimental to various extents. This study examines the effects on the material properties in marbles by simulating the thermal variations similar to bowing conditions and evaluates the corresponding changes in porosity in the samples.

2. Materials and methodology

Makrana marble comes from northwest India and is widely used in historical structures worldwide. The white Makrana marble has tightly interlocking calcite grains that results in a glossy finish and impressive strength. Garg et.al. (2019) reveals its composition consists mainly of crystalline calcite. Due to its low silica content, Makrana marble stands out for its hardness, resistance to wear, and ease of crafting. Additionally, because of its lower porosity compared to other marbles, it has a longer lifespan, while its minimal impurities result in durability. As per the Geographical Indications Registry (2014), the chemical makeup of Makrana marble is 50-56% CaO, 0.8-1.8% MgO, 0.33-1.2% SiO_2, 0.1-0.28% Fe_2O_3, and 34.8-43.2% LOI.

Following the methodology outlined by El Boudani et al. (2015), an experimental setup for accelerated thermal weathering was established at the laboratory. Three marble samples of compressive strength 50MPa were shaped into 5cm × 5cm × 2.5cm each. The laboratory environment was maintained at a temperature of 25°C. The samples were then heated on a ceramic hot plate for 1 hour and cooled for 30 minutes by placing them on ice. This cyclic process was repeated for 24 thaw-freeze cycles, with temperatures ranging from 100°C to 400°C. At intervals of 8, 12, 16, and 24 cycles, a water absorption test was performed after 24 cycles to confirm any increase in porosity. Ultrasonic Pulse Velocity and Karsten tube tests were carried out to determine the water absorption rate. This comprehensive approach allowed for a thorough understanding of the effects of accelerated thermal weathering on the marble samples.

3. Results

3.1 Ultrasonic Pulse Velocity Test

The Ultrasonic Pulse Velocity test was used to observe the change in pulse velocity after the completion of each thermal weathering cycle. Figure 1 depicts that the pulse velocity was initially high, however, a drastic decline in velocity was observed with an increase in the number of cycles. This trend indicates that marble exhibits higher homogeneity and lower porosity initially which decreases as thermal weathering progresses.

3.2 Water absorption by Karsten Tube Test

The Karsten Tube test was used to measure water absorption rates and assess pore connectivity in marble samples. Initially, undeteriorated samples showed no water absorption over four hours, indicating minimal pore connectivity. After artificial deterioration, the test revealed increased water absorption, suggesting larger and more connected pores. This change highlights how thermal weathering affects the marble's microstructure, enhancing pore size and connectivity, which in turn increases water absorption. Figure 2 clearly illustrates a change in the water absorption rate, indicating a significant alteration in pore characteristics.

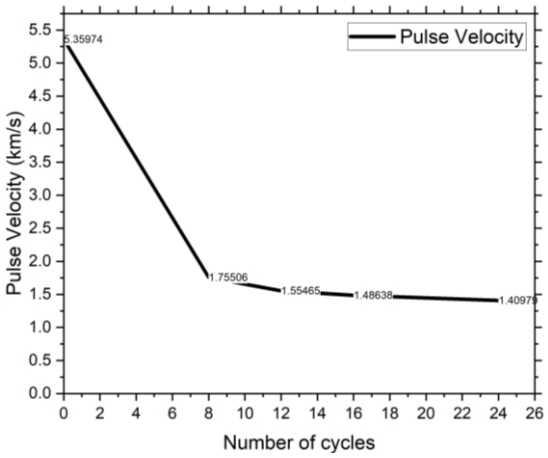

Figure 1. UPV test results for thermally weathered samples

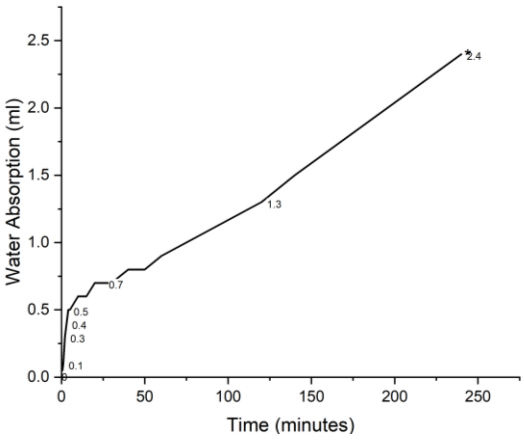

Figure 2. Karsten tube results for thermally weathered samples

3.3 Visual Observation:

The study conducted under a stereomicroscope revealed the presence of cracks (Figure 3) on the surface of all three samples, both before and after artificial deterioration. Initially, no cracks were observed on the surface of the samples. However, after subjecting the samples to artificial deterioration, hairline cracks emerged without any discernible patterns. This observation suggests that marbles are susceptible to cracking due to cyclic thermal changes. Moreover, the emergence of hairline cracks in the laboratory setting indicates a phenomenon that could be linked to on-site cracking. The study underscores the significance of understanding the effects of thermal weathering on the structural integrity of marble, particularly in heritage structures exposed to varying environmental conditions.

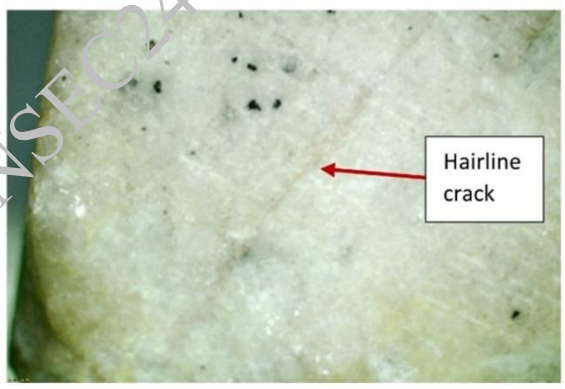

Figure 3. Hairline crack as observed in marble during the experiment

4. Discussions

As a result of repeated thermal cycles, marble expansion and porosity increase were observed through various tests. The Ultrasonic Pulse Velocity (UPV) test was conducted to assess the increase in porosity of the samples. Additionally, the water absorption rate was analyzed using the Karsten tube test. Furthermore, cracks with minimal depth were detected on the marble surface, indicating differential crystal expansion on the top and bottom surfaces. Bowing, a phenomenon resulting from the variable expansion on the two sides of the marble, was also observed. The marble sample bows until it reaches its tensile capacity, and once this limit is exceeded, cracks form. Therefore, crack formation can be considered the final stage of the bowing phenomenon which was observed in this test. Therefore, by reducing the depth of the sample and

by frequent interventions to note the observations after each cycle, one can witness a bowing phenomenon in the laboratory.

5. Conclusions

Bowing is identified as the most significant damage mechanism in marble stones, especially in countries exposed to tropical climates. The cause for this degradation mechanism is cyclic thermal variations. The current paper simulated cyclic thermal variations in samples of marble, and investigated the change in material properties such as porosity, water permeability, and tendency for cracking. The results indicated a significant decline in ultrasonic pulse velocity, reflecting increased porosity and decreased homogeneity due to thermal weathering. Water absorption tests further revealed enhanced pore connectivity, supporting the idea that thermal cycles worsen marble degradation. The study validates the damages in marbles due to thermal cycles and needs further elucidation on quantifying the extent of damage and correlating that to the changes in material properties. To prevent bowing and debonding in marble panels, it is essential to manage environmental factors such as temperature fluctuations and moisture content through protective barriers or coatings. Choosing marble with lower porosity and tighter grain structures, like Makrana marble, enhances durability and minimizes bowing risk. Timely maintenance, such as sealing cracks or replacing damaged panels, is crucial for addressing early signs of bowing and debonding.

References

El Boudani, M., Wilkie-Chancellier, N., Martinez, L., Hébert, R., Rolland, O., Forst, S., Vergès-Belmin, V. & Serfaty, S. (2015). Marble characterization by ultrasonic methods. *Procedia Earth and Planetary Science*, *15*, 249-256.

Garg, S., Kaur, P., Pandit, M., Fareeduddin, Kaur, G., Kamboj, A., & Thakur, S. N. (2019). Makrana marble: a popular heritage stone resource from NW India. *Geoheritage*, *11*, 909-925.

Geographical Indications Registry. (2014). G.I. Application Number – 405. *Government Of India Geographical Indications Journal No.64, 8.*

Marini, P., & Bellopede, R. (2009). Bowing of marble slabs: Evolution and correlation with mechanical decay. *Construction and Building Materials, 23, 2599–2605*

Siegesmund, S., Ruedrich, J., & Koch, A. (2008). Marble bowing: comparative studies of three different public building facades. *Environmental Geology, 56(3), 473–494.*

Sousa, H., & Sousa, R. (2018a). Durability of Stone Cladding in Buildings: A Case Study of Marble Slabs Affected by Bowing. *In J. F. Silva Gomes & S. A. Meguid (Eds.), Proceedings IRF2018: 6th International Conference Integrity-Reliability-Failure (pp. 831-841).*

Sousa, R., & Sousa, H. (2018b). Stability evaluation of marble stone cladding affected by bowing and wind pressure-A case study. In J. F. Silva Gomes & S. A. Meguid (Eds.), *Proceedings IRF2018: 6th International Conference Integrity-Reliability-Failure (pp. 7286-7295).*

Vázquez, P., Siegesmund, S., & Alonso, F. J. (2010). Bowing of dimensional granitic stones. *Construction and Building Materials, 23, 2599–2605.*

Assessment of Creep Behavior and Tensile Strength Retention in GFRP Rebars Exposed to Alkaline Condition

D. Ghosh [1*#], G. S. Hiremath [2#], S. Rai [3#] and S. S. Prakash [4]

[1] Department of Civil Engineering, Indian Institute of Technology, Hyderabad, India, Email: ce23resch11005@iith.ac.in*

[2] Department of Civil Engineering, Indian Institute of Technology, Hyderabad, India, Email: ce22resch15001@iith.ac.in*

[3] Department of Civil Engineering, Indian Institute of Technology, Hyderabad, India, Email: raisiddarth@alumni.iith.ac.in*

[4] Department of Civil Engineering, Indian Institute of Technology, Hyderabad, India, Email: suriyap@ce.iith.ac.in

Equivalent Authorship

*Corresponding author (s)

ABSTRACT

Glass Fibre Reinforced Polymer (GFRP) rebars are now used in many corrosions prone structures like marine, tunnels, bridge decks etc. It overcomes the disadvantage of steel reinforcement corrosion due to alkali attacks. The less carbon footprint during production of GFRP rebar makes it more environmentally sustainable than steel. There are few challenges associated with GFRP rebars such as low elastic modulus, inferior creep performance, no yielding before failure. This study focuses on the short term and long-term behavior of GFRP rebar which includes tensile strength, moisture absorption and creep performance. This study also shows the degradation of elastic modulus when exposed to alkaline atmosphere for 45, 60 and 90 days. The creep of GFRP rebars was assessed (strain behavior under sustained load of 30% and 36% of ultimate strength for 1000 hours. For the present study, for each test at least 5 specimens, except creep, were tested as per ASTM standards and results are presented. It was found that the performance in each test was found satisfactory as per the ASTM requirements. The experimental results reveal that there is no loss in tensile strength of the rebar after 60 days of exposure. However, after 90 days of exposure, a significant decrease in tensile strength was observed.

KEYWORDS: *GFRP rebar, Creep behavior, Alkaline environment, Tensile strength.*

1. Introduction

GFRP rebars are now emerging as the better choice for construction of reinforced concrete structures especially where the structure may be prone to corrosion. Due to its non-corrosive nature and cost effectiveness among the family of FRP rebars it is getting popular in construction of Pavements, Tunnels, Marine and many other structures, where water/chemicals may corrode the rebar. This rebar has the property of non-magneticity and non-conductivity which makes it suitable for uses where electromagnetic neutrality is required such as MRI rooms, power line structures etc. High strength to weight ratio of this material makes it effective for reinforced concrete structures. Considering its growing requirements, it is essential to measure the mechanical properties of GFRP rebars. The short-term mechanical properties are measured by many researchers but comparatively there is a gap in measuring the long-term mechanical properties. The retention of bar's strength after exposed to the alkali environment for a certain time also needs to be measured properly.The high strength-to-weight ratio of GFRP makes them advantageous for reducing the weight of structural components, improving transportation efficiency, and minimizing the need for maintenance and repairs. GFRP rebars are recyclable, contributing to resource conservation and reducing waste. (Ceroni et al., 2006) investigated durability issues of FRP rebars in reinforced concrete member. From the study, it was found that moisture and thermal exposure can have adverse effect on FRP

material as it leads to swelling, delamination and degradation of the material. Therefore, it can reduce the bond resulting in sudden failure of the element. (Won et al., 2008) examined the impact of alkaline environment on GFRP rebar to assess the mechanical properties and durability of the GFRP rebars. They found that the reduction in residual tensile strength of GFRP is more significant at higher temperature.

2. Test Specimens and Test Methodologies

2.1 GFRP specimen for Tensile Test

Tensile test is done as per the specifications of ASTM D 7205. The ribbed GFRP rebars is cut into pieces of 1000 mm[Figure 1]. For anchorages steel pipes of internal diameter 20 mm are used. For anchorage, epoxy resin and hardener in proportion of 1:1 is used along with sand as 25% of Epoxy resin amount. Gauge length of 400 mm and anchorage length of 300 mm was considered for specimen preparation.

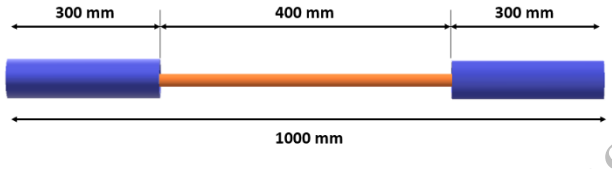

Figure 1. GFRP specimen for Tensile test

2.2 Moisture Absorption Test

Moisture Absorption tests were performed as per ASTM D 570. Length of the specimen was precisely cut to 25.4 mm. The specimen is kept in oven for conditioning at 50±3°C for 24 hours, after which it is transferred to desiccator in vacuum and cooled. Weights are taken after cooling the samples followed by transferring to humidity chamber in a tray filled with water for the absorption to start at 50±3°C and 95% RH. Then weights for repeated immersion after 2 hours of immersion is recorded. After completion of one day, weights are recorded for short term gain and then the specimens are transferred back to the humidity chamber.

2.3 Alkali Exposure

The specimens for mechanical properties were placed in a wooden box with epoxy coating inside, to localize the exposure conditions. The dimension of the box was so maintained that the depth of immersion for each specimen remained 10 mm, as shown in [Figure 2 (a)]. The alkaline solution composed of 8 grams of Potassium Hydroxide and 22 grams of Sodium Hydroxide making a pH of 13.6 in 1 liter of deionized water. All the specimens were kept in humidity chamber at 60ºC and 95% RH as shown in [Figure 2 (b)]. The specimens were exposed to high alkalinity and temperature in humidity chamber for 45, 60 and 90 days. After the exposure, it was evident that specimens had some staining on the surface due to the solution as seen in [Figure 2]. For residual tensile strength those specimens are cut in a similar fashion to the specimens for tensile strength [Figure 3].

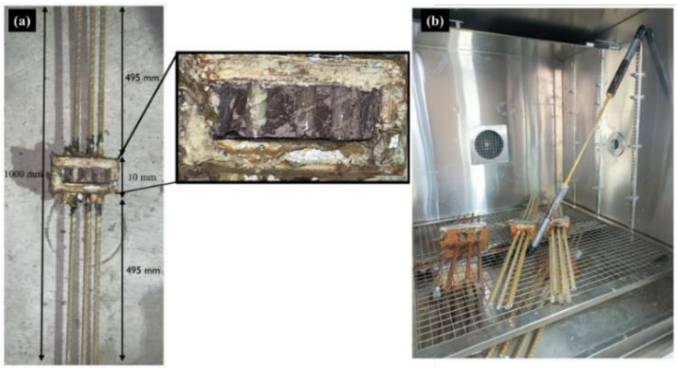

Figure 2. View of (a)setup and (b)GFRP exposed specimens in the humidity chamber

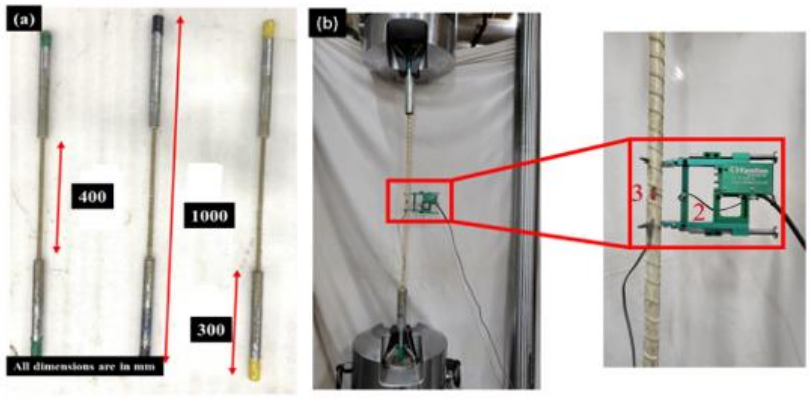

Figure 3. View (a) GFRP test specimens and (b) Tensile strength setup of GFRP

2.4 Creep Test

Creep is the long-term deformation under sustained load in a material over time. This deformation depends upon load level, material, cross-sectional geometry, duration of the applied load. The test was performed as per ASTM D 7337[16]. The test setup had 2 beams, upper beam holds the lower beam and lower beam is balanced for loading. These two beams with turn buckle carry 36 kN weight which increase the applied load by 100 times. The setup is connected by pin at each joint except the base and column which have fixed connection. Section 300mm×150mm with a plate thickness of 10 mm is chosen for the upper beam. Whereas the column and the base section have dimension of 250mm×250mm×10mm. Loading plate dimension is 200mm×200mm×10mm. When the turn buckle at the rear is utilized to balance the weights on the lower beam, these loads are magnified 100 times and this load acts on the specimen.

3. Results and Discussions

3.1 Residual Tensile Strength of GFRP

After the alkali exposure the resin of GFRP rebar deteriorated. It causes loosening of fibre in micro level which causes reduction in tensile strength and modulus of elasticity. The results of the tests are shown in [Figure 4]. The tensile strength decreases by 4%, 5% and 17% when it is exposed to alkali environment respectively for 45, 60 and 90 days. Elastic modulus for those specimens are decreased by 6%, 9%, 15% respectively for 45, 60 and 90 days.

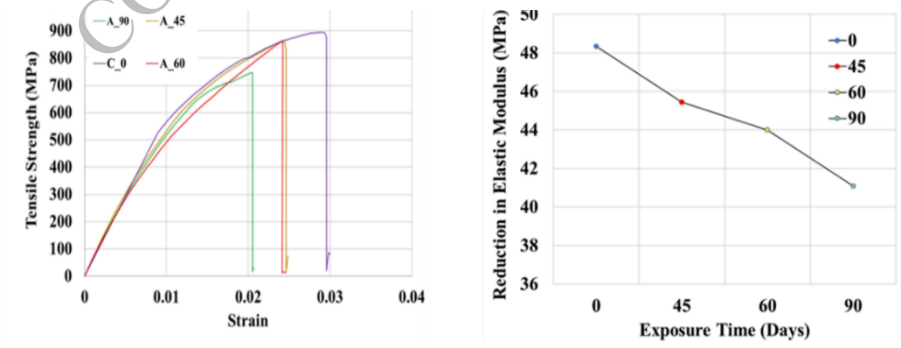

Figure 4. Tensile strength results (a)reduction in tensile strength and (b) reduction in elastic modulus.

3.2 Moisture Absorption Test of GFRP

For moisture absorption both short term absorption and long-term absorption are determined. For the short-term absorption, the increase in weight is measured after 24 hours followed by keeping the same sample in

the humidity chamber. For long term moisture absorption, the increase in weight is measured after 2nd week and 4th week. It shows 0.19% mass increase in short term and 0.75% in long term which is much lesser than 1%. It prooves that the rebar has good moisture absorption resistance at 50°C temperature.

3.3 Creep Strain Behaviour of GFRP

When tested for 1000 hours and 430 hours it was found that the increase in strain was 20% and 8% for load levels of 30% and 36% of ultimate strength respectively. No bars were ruptured at 1000 hours at 0.3 load factor. The results of both the load cases are shown in [Figure 5].

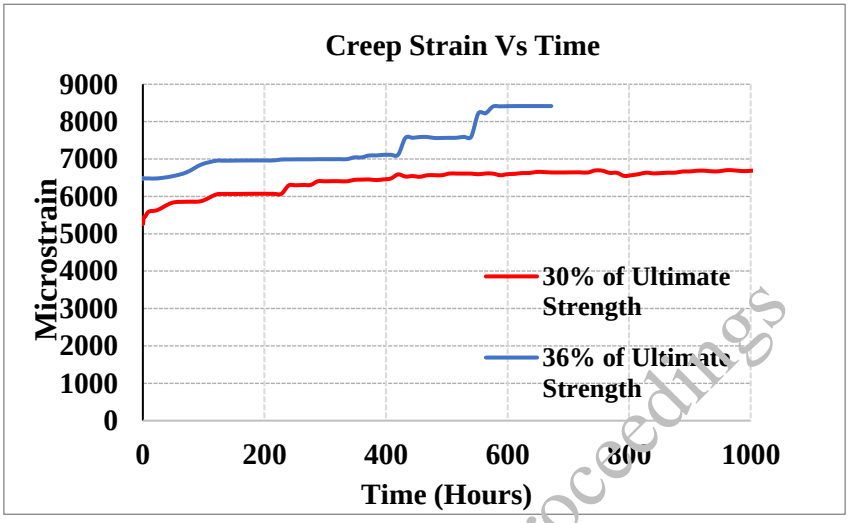

Figure 5. Creep strain response of GFRP

4. Conclusions

1. The degradation of tensile strength and other properties of rebar is due to the deterioration of resin matrix. The fibre is not affected by the alkali immersion after 90 days also. The deterioration of resin by alkali causes changes in interface properties but not in mechanical properties of fibres.
2. As the resin matrix is deteriorated with the increased time of alkali exposure, the stress transfer capacity of the GFRP rebar is reduced resulting in reduced strength.

References

Ahmad Sawpan, M. (2019). "Shear properties and durability of GFRP reinforcement bar aged in seawater".Polymer Testing, 75, 312–320.

Banibayat, P., & Patnaik, A. (2015). "Creep Rupture Performance of Basalt Fiber-Reinforced Polymer Bars" *Journal of Aerospace Engineering*, 28(3).

Ceroni, F., Cosenza, E., Gaetano, M., & Pecce, M. (2006). Durability issues of FRP rebars in reinforced concrete members. *Cement and Concrete Composites*, 28(10), 857–868.

Fergani, H., Di Benedetti, M., Miàs Oller, C., Lynsdale, C., & Guadagnini, M. (2018). Durability and degradation mechanisms of GFRP reinforcement subjected to severe environments and sustained stress. *Construction and Building Materials*, 170, 637–648.

Rossini, M., Saqan, E., & Nanni, A. (2019). Prediction of the creep rupture strength of GFRP bars. *Construction and Building Materials*, 227.

Shuaib, N. A., & Mativenga, P. T. (2017). Carbon Footprint Analysis of Fibre Reinforced Composite Recycling Processes. *Procedia Manufacturing*, 7, 183–190. https://doi.org/10.1016/j.promfg.2016.12.046

Won, J. P., Lee, S. J., Kim, Y. J., Jang, C. Il, & Lee, S. W. (2008). The effect of exposure to alkaline solution and water on the strength-porosity relationship of GFRP rebar. *Composites Part B: Engineering*, 39(5), 764–772.

Seismic Damage Characterization of Aged Concrete Gravity Dams

K. Pranava Gayathri[1*], Piyali Sengupta [2]

[1] IIT(ISM) Dhanbad, Dhanbad, India
Email: 22dr0102@iitism.ac.in
[2] IIT(ISM) Dhanbad, Dhanbad, India
Email: piyali@iitism.ac.in

*Corresponding author

ABSTRACT

Studying the seismic response of aged concrete gravity dams is crucial because they lose strength as the structures age. This decline introduces a potential risk of catastrophic consequences, encompassing dam failures that may result in casualties, significant economic losses, and environmental damage. The increasing frequency of earthquakes worldwide and few of the earthquakes accord near the dam site undergoes the consensus on the importance of assessing the seismic vulnerability of dams. In various regions, escalating seismic activity reveals that numerous existing dams do not meet the latest seismic design criteria. This discrepancy arises from newly defined seismic hazard levels specific to each dam site. Additionally, concerns about dam safety are amplified by factors like aging-induced material degradation, inadequate maintenance, and sediment deposition. To address these issues, the research's primary objective is to develop a numerical model that considers the aging process, material degradation, and sedimentation deposits within the dam-reservoir-sedimentation-foundation system. Subsequently, an extensive parametric study will investigate the impact of various factors, including geometric configurations and material grades, on the seismic vulnerability of aged concrete gravity dams. The numerical simulation results will then be utilized to explore various aspects of concrete aged gravity dams under earthquake loading, such as damage mechanisms, crack initiation, crack propagation, and potential failure modes. Moreover, determine the time-dependent seismic fragility functions of the aged dams in different damage states. Through the analysis of simulation results, the research aims to gain insights into how aged concrete gravity dams may experience damage and failure during earthquakes.

KEYWORDS: *Concrete Gravity Dams, Damage. Sedimentation, Aging-induced Degradation, Time-Dependent Seismic Fragility.*

1. Introduction

Concrete gravity dams are essential for electricity generation, water supply and flood control. Seismic incidents as experienced by Koyna Dam in India in 1967, Hsingfengkiang Dam in China in 1962 and Sefid-Rud Dam in Iran in 1990 have emphasized the critical need for assessing the seismic vulnerability of dams. The aging-induced degradations, lack of routine maintenance, sediment deposition, crack formation, followed by opening and closing of cracks, as well as sliding along crack planes, aggravate the seismic vulnerability of concrete gravity dams further. Chopra and Chakrabarti (1972, 1973) performed seismic analysis of an elastic model of Koyna Dam to deduce stresses in the dam-reservoir system. Tekie and Ellingwood (2003) conducted seismic fragility assessment of the Blue Stone Dam in West Virginia, incorporating dam-foundation-reservoir interaction. Gogoi and Maity (2005) assessed the effect of aging on seismic performance of an elastic Koyna Dam model through numerical simulations. Gogoi and Maity (2007) investigated the effects of varying sediment layer thicknesses on the seismic response of concrete gravity dams. Gorai and Maity (2021) determined the seismic performance of aging concrete gravity dams under near-field and far-field ground motions. The primary objective of this study is to formulate a numerical model that accounts for the aging process, material degradation and sedimentation deposits within the dam-reservoir-sedimentation-foundation system to determine the time-dependent seismic fragility functions of the aged concrete gravity dams.

2. Numerical model development

The dam-foundation-reservoir interaction model is created in ABAQUS Finite Element Software using the Concrete Damage Plasticity Model (CDPM). Each finite element (FE) model represents the foundation as a rock block with dimensions five times wider and thicker than the dam's base, and a depth nearly equal to the dam's. The dam base and foundation blocks are connected to prevent sliding at their interfaces in the FE models. Material properties for both dam and foundation are listed in Table 1.

Table 1. Material Properties for Dam and Foundation

Sl. No	Material property	Value
2	Concrete Density [kg/m^3]	2400
3	Concrete Poisson's Ratio	0.2
4	Rock Young's Modulus [GPa]	31.72
5	Rock Density [kg/m^3]	2400
6	Rock Poisson's Ratio	0.2

Hydrostatic pressure, pore pressure, hydrodynamic pressure is applied at the upstream face of the dam. Hydrodynamic pressure simulation employed Westergaard's added mass technique, as given by

$$\frac{7}{8}(\rho_w\sqrt{h_w(h_w-y)} \tag{1}$$

Here $h_w > y$, ρ_w is the density of the water and h_w is the height of the water in meters.

2.1 Evaluating the degradation of aging concrete dams

Concrete degradation, characterized by a reduction in the area capable of supporting loads, is influenced by a multitude of factors. Among these, degradation of compressive strength can be attributed to prolonged exposure to hydro-chemo-mechanical effects of reservoir water. In this study, degradation is observed in terms of porosity P, integrating initial porosity P_O, mechanical porosity P_M, and chemical porosity P_C. Therefore, total porosity is defined as:

$$P = P_O+P_C+P_M \tag{2}$$

Mechanical porosity, caused by the formation and extension of micro-cracks or micropores due to external mechanical forces, influencing the material's macroscopic properties, is defined as,

$$P_M = (1-P_O+P_C)d_m \tag{3}$$

d_M is a scalar degradation parameter. Exponential degradation function d_m is defined as

$$d_m = 1 - \frac{k_m^0}{k_m}\left[1-\alpha_m+\alpha_m e^{\beta_m(k_m^0-k_m)}\right] \tag{4}$$

Where, k_m^0 is initial damage threshold, k_m is current damage threshold, α_m and β_m are material parameters.

Chemical porosity arises from Alkali-Silica Reaction, where alkaline substances in aggregates react with silica in concrete, weakening their bond. Water in reservoir exacerbates this process. Chemical porosity is solely due to this reaction, and its isotropic degradation index is detailed by Gogoi and Maity (2007).

$$Pc = d_{ASR} = 1- (E_O/E_M) \tag{5}$$

Here, d_{ASR} represents Alkali-Silica damage factor, E_0 is initial elastic modulus of $5000\sqrt{f_{(t)}}$, t is age of concrete in years, $f_{(t)}$ is compression strength at a particular age and E_m is present elastic modulus. Concrete age can be correlated with both compressive strength in undegraded concrete and elastic modulus in degraded concrete, where E_i is an initial elastic modulus.

$$f(t) = 1.51 \ln(t) + 31.79 \quad (6)$$

$$E_{m(t)} = 0.175t^3 - 3.405t^2 + 28.807t - E_i \quad (7)$$

2.2 Evaluation of reflection coefficient due to sedimentation deposits

Sediments get accumulated at the reservoir bed due to stillness of water, altering its behavior by absorbing compression waves. α representing the wave reflection coefficient at the interface, is defined as the ratio of the reflected pressure wave's amplitude to the incident compression wave's amplitude. This coefficient is related to the acoustic impedance of the media. Here, c_f represents compression wave velocity in water (1438.7 m/s), c_s denotes compression wave velocity in sediment (1500 m/s), ρ_f stands for water density (1000 kg/m³) and ρ_s represents the sediment material's mass density (2000 kg/m³).

$$\alpha = \frac{1 - \frac{c_f \rho_f}{c_s \rho_s}}{1 + \frac{c_f \rho_f}{c_s \rho_s}} \quad (8)$$

The equivalent reflection coefficient resulting from the sediment layer and underlying foundation strata can be calculated as,

$$\alpha_{eq} = \frac{\alpha_1 h_1 + \alpha_2 h_2}{h_1 + h_2} \quad (9)$$

Where α_1 and α_2 represent reflection coefficients of the sediment layer and underlying foundation strata, while h_1 and h_2 stand for thickness of the sediment layer and foundation strata, respectively. In this study, it is considered that the change in sedimentation rate is 0.15 m/year.

3. Parametric study

A parametric study analyzes the dam-foundation-reservoir interaction, comparing two geometric configurations (GMC1 and GMC2) of equal volume. The study includes exploring seismic performance of dams of concrete grades M30, M40 and M50, empty and water-filled reservoirs, with and without sedimentation, age of dam 28-days, 25-years, 50-years, 75-years and 100-years under diverse ground motion histories. Hydrostatic, hydrodynamic, and pore pressures were applied at the upstream dam face. Figure 1 gives illustrations for structural configurations of GMC1 and GMC2.

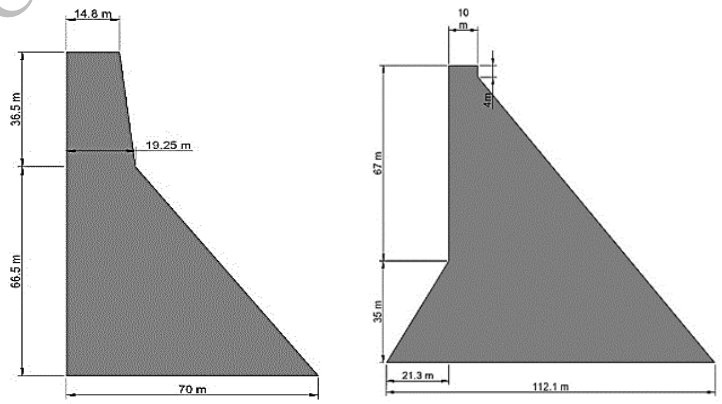

Figure 1. Geometric Configurations: GMC1 (left) and GMC2 (right)

Both dam configurations are modeled for different grades of concrete, different water contents in reservoir, with and without sedimentation, age 28-days, 25-years, 50-years, 75-years and 100-years. The dam models

are then subjected to a wide range of ground motions for evaluation of their seismic response. The resulting crack patterns for dams made of M30 concrete when subjected to Koyna ground excitation, with water-filled reservoir condition, with and without sedimentation deposits at 100-year intervals are shown in Figures 2-3 for GMC1 and GMC2 respectively.

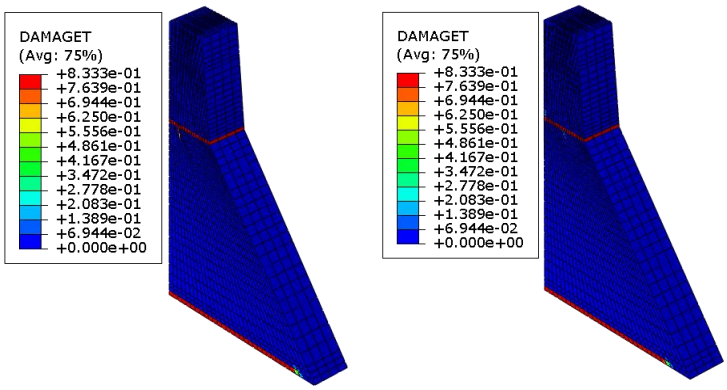

Figure 2. Crack Patterns of 100 year old GMC1 Dam made of M30 Concrete with Water-filled Reservoir with Sedimentation (left) and without Sedimentation (right)

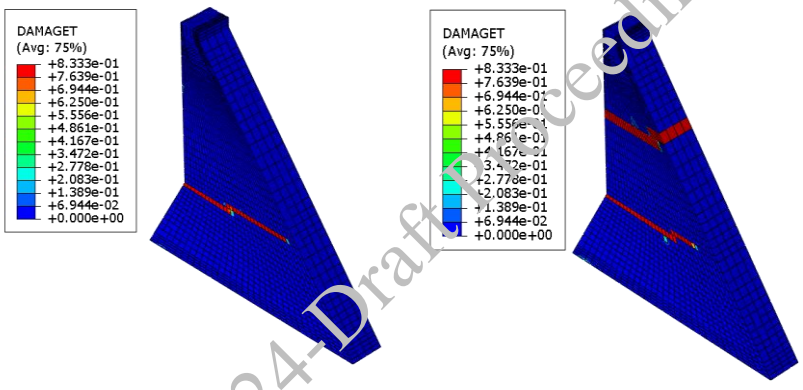

Figure 3. Crack Patterns of 100 year old GMC2 Dam made of M30 Concrete with Water-filled Reservoir with Sedimentation (left) and without Sedimentation (right)

Incremental dynamic analysis method is adopted to derive time-dependent seismic fragility functions of aged concrete gravity dams, as observed in Figure 4 for GMC1 (left) and GMC2 (right) for M30 Concrete for full reservoir condition for slight, moderate and severe damage states.

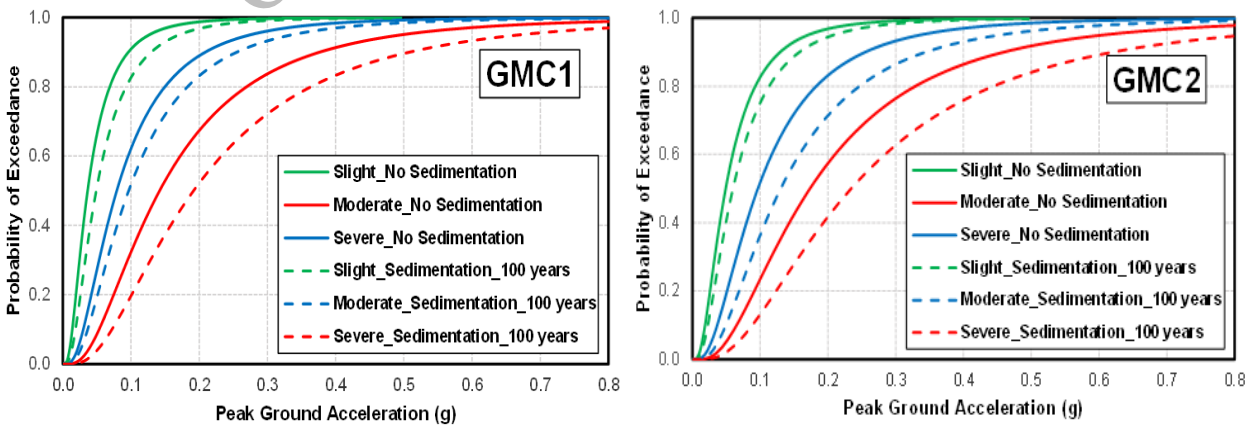

Figure 4. Seismic Fragility Curves of GMC1 (left) and GMC2 (right): M30 Concrete: Full reservoir: Without Sedimentation and With Sedimentation deposits: 100 years

4. Conclusions

This study examines seismic damage in aged concrete gravity dams across various geometries and reservoir conditions, with and without sedimentation. Empty reservoirs exacerbate vertical displacement compared to full ones, while sedimentation at the base reduces vertical displacement. Vertical displacement is more prevalent at 28 days and 100 years than at 25 years.

References

Bangert, F., Grasberger, S., Kuhl, D. and Meschke, G. (2003) Environmentally induced deterioration of concrete: physical motivation and numerical modeling", *Eng Fract Mech,* 70:891–910.

Chopra, A.K. and Chakrabarti, P. (1972) "The Earthquake Experience at Koyna Dam and Stresses in Concrete Gravity Dams", *Earthquake Engineering and Structural Dynamics*, 1: 151- 164.

Chopra, A.K. and Chakrabarti, P. (1973) "The Koyna Earthquake and the Damage to Koyna Dam", *Bulletin of the Seismological Society of America*, 63 (2): 381-397.

Gogoi, I. and Maity, D. (2005) "Seismic Safety of Aged Concrete Gravity Dams Considering Fluid Structure Interaction", *Journal of Earthquake Engineering*, 9(5): 637-656.

Gogoi, I. and Maity, D. (2007) "Influence of Sediment Layers on Dynamic Behavior of Aged Concrete Dams", *ASCE Journal of Engineering Mechanics*, 133 (4): 400-413.

Gorai, S. and Maity, D. (2021) "Numerical Investigation on Seismic Behavior of Aged Concrete Gravity Dams to Near Source and Far Source Ground Motions", *Natural Hazards*, 105: 943–966.

Tekie, P.B. and Ellingwood, B.R. (2003) "Seismic Fragility Assessment of Concrete Gravity Dams", *Earthquake Engineering and Structural Dynamics*, 32: 2221-2240.

Temperature-Dependent Chloride Binding Ability of Fly Ash and Silica Fume Modified Ordinary Portland Cement

Chandra Sekhar Das[1*], Xiao-Ling Zhao[2*], and Jian-Guo Dai[3*]

[1] PhD Student, The Hong Kong Polytechnic University, Hong Kong
Email: chandrasekhar.das@connect.polyu.hk
[2] Chair Professor, The Hong Kong Polytechnic University, Hong Kong
Email: xiao-lin.zhao@polyu.edu.hk
[3] Chair Professor, City University of Hong Kong, City, Hong Kong
Email: jiangdai@cityu.edu.hk

[*]Corresponding author

ABSTRACT

The affinity of chlorides for various cement hydration products is influenced by the type of binder used and the conditions of exposure. This research aimed to explore how temperature affects the chemical and physical binding of chlorides in four distinct mixes of ordinary Portland cement (OPC) that contain different amounts of fly ash and silica fume. The findings indicate that an increase in the alumina content of the binder does not linearly enhance the total capacity for chloride absorption at higher temperatures. At a chloride concentration of 0.5M, which is typical for seawater, the capacity for chloride binding remains unchanged in OPC and increases with a small addition of fly ash. However, this capacity significantly diminishes in binders with a high content of fly ash and silica fume. This decrease is linked to an increased uptake of aluminium by C-S-H, which negatively impacts its ability to physically adsorb chlorides. The effect is exacerbated by an increase in temperature, as well as higher levels of fly ash and silica fume. Therefore, at low chloride concentrations, the total absorption is predominantly due to physically adsorbed chlorides. At higher chloride levels (3M), aluminium tends to form additional AFm rather than being incorporated into C-S-H. Exposure to elevated temperatures further promotes the transformation of the AFt phase into AFm, thereby improving the binder's chloride binding capacity at high chloride concentrations (3M), with the binding being directly related to the amount of AFm formed.

KEYWORDS: *Concrete, Chlorides, Fly ash, Durability, Temperature*

1. Introduction

Chloride-induced corrosion is the primary cause of deterioration in coastal reinforced concrete (RC) structures. As chloride ions get transported through the pores of concrete, they engage in interactions with the products of cement hydration, resulting in the binding of some chloride portions. These interactions are both physical and chemical. The incoming chlorides mainly undergo chemical reactions with AFm phases, leading to the formation of either Friedel salt or Kuzel salt (Babaahmadi et al (2022)). Additionally, a fraction of the chlorides is physically adsorbed onto the surface of calcium silicate hydrate (CSH). Due to these binding processes, the concentration of chlorides within the concrete pores is diminished. This decrease in chloride concentration subsequently lowers the structure's corrosion risk, thereby markedly influencing its durability and service life (Martın-Pérez et al (2000)).

RC structures are subjected to varying temperature cycles throughout their lifespan, depending on their geographic location and environmental conditions, which influence the transport properties of chlorides (Guo et al (2020)). This variability casts doubt on the reliability of service life predictions based on chloride binding data obtained at standard laboratory temperatures (20-25°C). Research on how different temperatures impact chloride binding is limited, and the results that do exist are often inconsistent. A study by Zibara (2001) indicated that the effect of temperature on chloride binding depends on the concentration of chloride. At a lower chloride level (0.1 M), an increase in temperature led to a reduction in chloride

binding, whereas at a higher concentration (3M), the binding was enhanced by higher temperatures. Conversely, Dousti and Shekarchi (2015) reported a decline in chloride binding when the exposure temperature rose from 22℃ to 70℃ across various mixtures, regardless of the chloride concentration. Moreover, none of the existing literature sheds light on how exposure temperature affects the chlorides bound to different hydration products, such as hydrated calcium aluminate phases (AFm) and C-S-H. Thus, this study primarily aimed to clarify the ability of different cement hydration phases to bind chlorides at different temperature exposures and the mechanism behind this.

2. Experimental Program

Four different paste samples were prepared with a fixed water to binder of 0.38. The detailed mix designs are OPC (100% cement), 15FA (85% cement, 15% Fly ash), 35FA (65% cement and 35% fly ash) and 35SFA (57% cement, 35% fly ash and 8% silica fume). The weight replacements were by mass of cement. For the chloride exposure study, 30 grams of crushed powder sample water cured for 90 days and 15 grams of NaCl solutions (0.5M, 1M, 3M) were mixed in 50 ml centrifuge tubes. The main idea for a longer curing period was to eliminate the effect of further hydration during chloride exposure. These samples were stored in sealed plastic boxes and kept inside water baths maintained at 25℃ and 45℃ for eight weeks to ensure that binding had been completed and an equilibrium between free and bound chloride was achieved. Two sets of identical samples were used for each mix, and the reported results are an average of both samples. After exposure, the samples were tested for the total free chlorides by titration, and the chemically bound chlorides were determined using thermogravimetric analysis (TGA). The chloride adsorbed on the surface of C-S-H was obtained by subtracting the free chlorides and chemically bound chlorides from the external chloride added.

3. Results

Temperature significantly impacts the ability of cement mixtures to bind chlorides, as shown in Figures 1(a) and 1(b). The OPC mix exhibited similar chloride binding across different temperatures for chloride levels of 0.5 and 1M. Conversely, the 15FA formulation, with its lower fly ash content, demonstrated superior binding capabilities at 45℃ when compared to 25℃. However, the introduction of greater amounts of fly ash and silica fume (as seen in the 35FA and 35SFA mixes) led to diminished chloride binding at the elevated temperature of 45℃. When the exposure chloride concentration was increased to 3M, an increase in temperature improved the binding capacity in all the mixes. Among these, the 35SFA composition showed the lowest binding, whereas the 15FA and 35FA compositions exhibited comparably higher levels of chloride binding. Interestingly, at 45℃, aside from the 3M concentration scenario, the 15FA mix surpassed the 35FA in terms of chloride binding ability, questioning the prevailing belief that a higher fly ash content naturally leads to better binding due to the addition of alumina species.

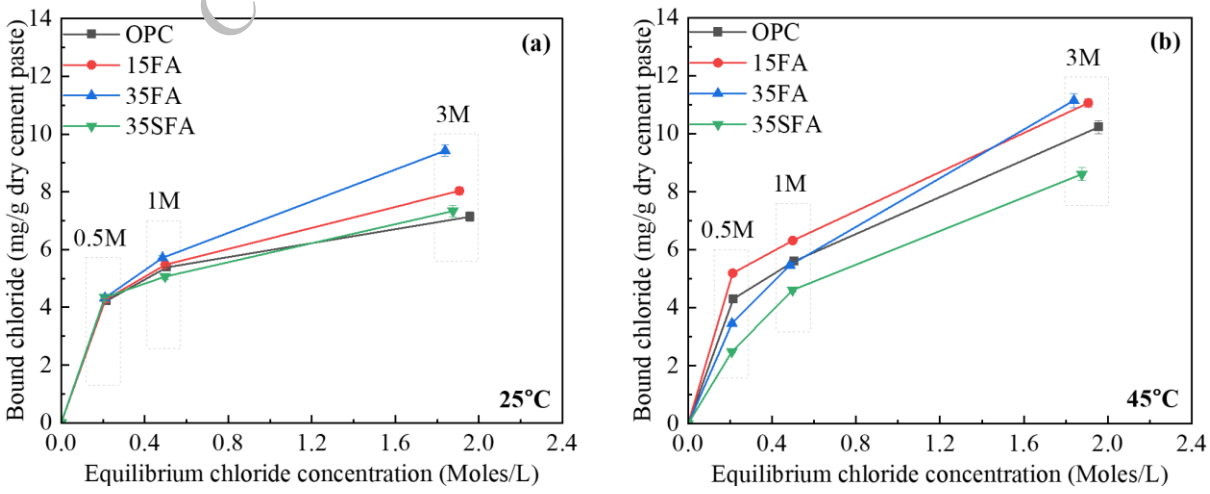

Figure 1. Chloride binding isotherms for the four mixes at (a) 25℃ and (b) 45℃

The chemically bound chloride content was determined from analysis of TGA curves by assuming that each mole of Friedel salt binds two moles of chloride based on previous research (Shi et al (2017)). The variations in chloride bound in different mixes based on exposure temperature are provided in Figure 2. It can be observed that the chemically bound chloride content increased when the temperature was raised from 25 to 45°C for the OPC, 15FA, and 35FA mixes. This could be attributed to two main factors: the potential formation of additional AFm from the reaction between any remaining unhydrated C_3A and calcium hydroxide, aiding in Friedel's salt formation (Chang et al. (2023)), and the temperature-induced acceleration of the ettringite to Friedel's salt transformation which was observed through XRD analysis. In contrast, the 35SFA mix experienced a decrease in chemically bound chlorides with a temperature increase. While this reduction was slight at a 0.5M chloride level, at a higher concentration of 3M, the chemically bound chlorides at 45°C were significantly lower, approximately 60% of those at 25°C. The analysis of the pH of the samples suggested that in the 35SFA mix, the pH dropped below 12 at elevated temperatures due to the dilution effect of adding SCMs and full consumption of calcium hydroxide in the mix. It has been known that Friedel salt becomes unstable at lower pH, and thus, the reversing trend for 35SFA is likely linked to the pH of the pore solution.

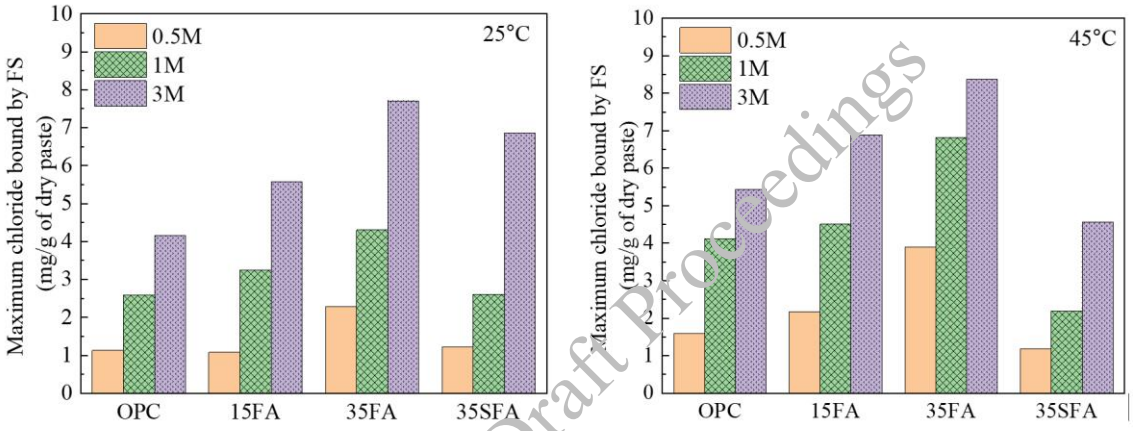

Figure 2. Maximum chemically bound chlorides in Friedel salt at (a) 25°C and (b) 45°C

The quantity of chlorides that are physically attached to the C-A-S-H is shown in Figure 3. This value was determined by deducting the sum of free and chemically attached chlorides from the total initial chloride levels. At a chloride concentration of 0.5M, the extent of physical adsorption is reduced as the temperature increases. This reduction was slight for OPC and 15FA samples but was more pronounced for samples containing a higher percentage of fly ash and silica fume (35FA and 35SFA). This resulted in a decrease in the total amount of chlorides bound, as depicted in Figure 1.

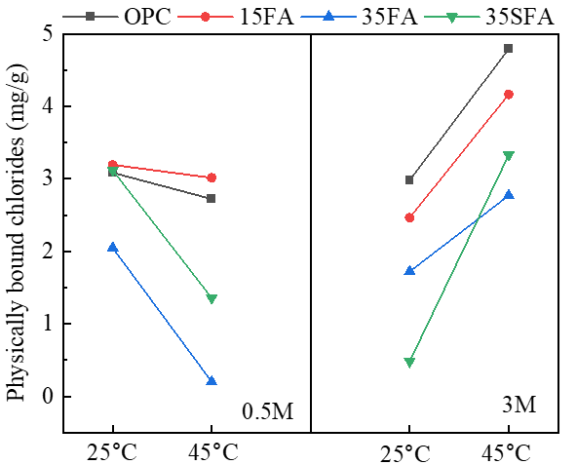

Figure 3. Variations in physically bound chlorides in C-A-S-H gels at different scenarios

This suggests that the commonly held belief that increased alumina content in raw materials enhances the chloride binding capacity of a binder may not hold true at lower chloride concentrations under higher

temperatures (e.g., the decrease in physical chloride attachment from 25℃ to 45℃ at 0.5M). Physical adsorption of chlorides plays a crucial role in such scenarios. At higher chloride concentrations of 3M, there is a noticeable trend of increased physical chloride binding across all mixtures. FTIR analysis was conducted to analyse the properties of C-S-H in different samples. It was observed that the uptake of aluminium in C-S-H was increased for elevated temperatures and in the presence of low chloride concentration (0.5M). It has been previously known that greater aluminium content in C-S-H reduces its ability to bind chlorides physically (Yoshida et al (2021)). This explains the decrease in physically adsorbed chlorides with increasing temperature for 0.5M chloride exposure. At higher chloride contents of 3M, all the aluminium in raw materials reacted to form Friedel salt. Thus, the physical binding ability due to its endothermic nature increased with increasing temperature from 25℃ to 45℃. It is essential to highlight that, regardless of the chloride levels, physical binding is significantly greater for 15FA and OPC samples at higher temperatures. This could be due to a higher Ca/Si ratio in low SCM substituted mixes, which have a greater ability to bind chlorides physically. This is despite expectations that more supplementary cementitious materials (SCMs) would lead to increased pozzolanic activity and, consequently, more C-S-H in the binders. Therefore, the Ca/Si ratio plays a more significant role than the quantity of C-S-H produced, corroborating findings from a prior study (Zibara et al (2008)).

4. Conclusions

The research indicates that the mechanisms of chloride binding observed at ambient temperatures might not hold at higher temperatures. The deviations in chloride binding with increased temperature imply that utilising chloride binding isotherms derived from standard temperature conditions to forecast the durability of structures against chloride exposure could lead to an overestimation of their lifespan. This is particularly evident in cement mixes with higher replacement by supplementary cementitious materials (SCMs) like fly ash and silica fume. In fact, fly ash replacement beyond 15% seems to have no net positive effect in binding the ingressing chlorides for elevated exposure conditions. The lower-than-expected binding at low chloride concentrations is attributed to the reduced physical adsorption in C-S-H, which plays a dominant role. This is due to the preferable uptake of aluminium by C-S-H. At higher chloride concentrations, the ability of matrices to chemically bind chlorides takes a prominent role, with higher chloride concentrations likely linked to alumina present in raw materials.

References

Babaahmadi, Arezou, Alisa Machner, Wolfgang Kunther, Joao Figueira, Petter Hemstad, and Klaartje De Weerdt. "Chloride binding in Portland composite cements containing metakaolin and silica fume." *Cement and Concrete Research* 161 (2022): 106924.

Chang, Honglei, Xiaolong Wang, Yunfei Wang, Chencong Li, Zhengkun Guo, Shuyuan Fan, Hongzhi Zhang, and Pan Feng. "Chloride binding behavior of cement paste influenced by metakaolin dosage and chloride concentration." *Cement and Concrete Composites* 135 (2023): 104821.

Dousti, Ali, and Mohammad Shekarchi. "Effect of exposure temperature on chloride-binding capacity of cementing materials." *Magazine of Concrete Research* 67, no. 15 (2015): 821-832.

Guo, Hongyuan, You Dong, and Xianglin Gu. "Durability assessment of reinforced concrete structures considering global warming: A performance-based engineering and experimental approach." *Construction and Building Materials* 233 (2020): 117251.

Martın-Pérez, B., H. Zibara, R. D. Hooton, and M. D. A. Thomas. "A study of the effect of chloride binding on service life predictions." *Cement and concrete research* 30, no. 8 (2000): 1215-1223.

Shi, Zhenguo, Mette Rica Geiker, Klaartje De Weerdt, Tone Anita Østnor, Barbara Lothenbach, Frank Winnefeld, and Jørgen Skibsted. "Role of calcium on chloride binding in hydrated Portland cement–metakaolin–limestone blends." *Cement and Concrete Research* 95 (2017): 205-216.

Yoshida, Satoshi, Yogarajah Elakneswaran, and Toyoharu Nawa. "Electrostatic properties of C–S–H and CASH for predicting calcium and chloride adsorption." *Cement and Concrete Composites* 121 (2021): 104109.

Zibara, H., R. D. Hooton, M. D. A. Thomas, and K. Stanish. "Influence of the C/S and C/A ratios of hydration products on the chloride ion binding capacity of lime-SF and lime-MK mixtures." *Cement and concrete research* 38, no. 3 (2008): 422-426.

Zibara, Hassan. "Binding of external chlorides by cement pastes." PhD diss., 2001.

Coupled Action of Loading and Carbonation on Transport Properties of Portland Cement-Slag-Limestone Concrete

Moro Sabtiwu[1*], Yuvaraj Dhandapani[1], Michal Drewniok[1], Samuel Adu-Amankwah[1, 2], and Susan A. Bernal[1*]

[1] School of Civil Engineering at the University of Leeds, Leeds, UK
**Email:S.A.BernalLopez@leeds.ac.uk*
[2] School of Engineering and Applied Science at Aston University, UK, Birmingham, UK

[*]Corresponding author

ABSTRACT

The carbonation performance of concrete made with ternary cements containing high volumes of supplementary cementitious materials (SCMs) and limestone is largely unknown, when the concrete is in a stressed state. In this study, seven days cured concrete made with neat cement (CEM I), blended Portland cement-slag (50% slag) and ternary Portland cement-slag-limestone cement (up to 20% limestone) were subjected to compressive loading and simultaneous accelerated carbonation (3% CO_2) or natural carbonation exposure for up to 28 days. Experiments were also conducted in corresponding specimens in unstressed states. After the carbonation exposure loading cycle, carbonation depths and water ingress were measured. It was identified that ~30% stress levels resulted in limited progression of the carbonation front relative to corresponding concretes in unstressed states. While CEM I exhibited better carbonation resistance in all scenarios compared to binary or ternary mixes, there is no indication of detrimental impact on transport properties particularly water absorption in slag-containing concretes with or without limestone. The ternary cement concrete containing 20% limestone demonstrate similar carbonation performance to binary slag cement in compressive stress or unstress states.

KEYWORDS: *Portland cement-slag-limestone, Creep, durability, Coupled loading and Carbonation*

1. Introduction

Limited studies have considered the coupled effect of loading and durability exposure condition on the performance of concrete, particularly when concrete is exposed to carbonation and/or chlorides/moisture ingress (Yao et al., 2013; Yao et al., 2023). This knowledge gap is more noticeable for concrete made from high volume of SCMs, which are expected to carbonate at a faster rate compared with CEM I (Von Greve-Dierfeld et al., 2020). Even though it has been identified that blast furnace slag addition refines porosity in hydrated samples relative to CEM I (Berodier and Scrivener, 2015; Vigor et al., 2024), the improved refinement may be compromised when subjected to carbonation due to volume changes arising from phase transformation and shrinkage due to decalcification (Borges et al., 2010; Wu and Ye, 2017). The increased carbonation rates in SCM containing concretes, may be detrimental to their transport properties. Carbonation-induced microstructural alteration can accelerate ingress of external deleterious species in moisture and/or ionic forms. This can exacerbate the deterioration of concrete structures that are typically load bearing. It is thus critical to develop an understanding of the long-term performance of novel cement systems with high volume SCM replacement levels, including composite ternary cements specified in the BS EN 197-5 (BSI, 2021). This is the main objective of the present study.

2. Materials and methods

2.1 Concrete mix design

The cement used for producing concrete were CEM 52.5N, and ~ 50% granulated blast furnace slag (GGBS) and/or powdered limestone. Anhydrite was added to cement towards maintaining total sulphate at

3%. The cements were formulated (wt. %) as follows; CEM I + slag (~50%); CEM I (~50%) + slag (~40%) + limestone (~10%); CEM I (~50%) + slag (~30%) + limestone (~20%). The aggregates and cement were mixed in a planetary mixer at a constant water binder ratio of 0.5 for 10 min. Table 1 shows the concrete mix design used in this study. The specifications of raw materials used (e.g. CEM I, blast furnace slag, limestone), characterisation of cement, aggregates and fresh properties are reported elsewhere (Sabtiwu, 2023).

Table 1. Concrete mix design. Quantities are reported in kg/m^3 of fresh concrete

Mix ID	CEM I 52.5N	Slag	Lime-stone	Anhydrite		Water	Sand	10mm Aggregates	20mm Aggregates
N	320.3	-	-	-		160.2	651.8	237.7	950.82
NS	164.0	155.4	-	0.8		160.2	648.8	236.6	946.5
NSL	165.6	125.6	28.3	0.8		160.2	648.2	236.4	945.5
NS2L	167.2	93.2	59.0	0.8		160.2	647.5	236.1	944.5

Concrete specimens were cast in plastic moulds according to BS EN 12390-2:2019 (BSI, 2019a) and demoulded after 24hrs, and then transferred to a curing room (maintained at 95% relative humidity (RH) and 20 ± 3^{o}C) until testing.

2.2 Test methods

The compressive strength evolution of all concrete mixes was determined at different curing ages up to 180 days on 100 mm cubes in triplicates, as per BS EN 12390-3 (BSI, 2019b) using a MATEST crusher at a loading rate of 6 kN/s.

Coupled effect of compressive stress and carbonation: 7 days cured 75×75×200 mm, surface dried concrete specimens were instrumented with 60 mm, 120-Ohm strain gauges and set up using load cell and data logger configuration as reported elsewhere (Sabtiwu, 2024). Two prisms per mix were loaded per creep set and exposed to accelerated carbonation [3% (CO_2), 60% RH, and 20^{o}C] according to EN 12390 - 12:2020 (BSI, 2020), and natural carbonation exposure at 60 % RH for 28 days. The applied stress was set at 1/3 of their compressive strength at age of loading in accordance with BS EN 12390-17 (BSI, 2019c), and computed as 63.4, 38.6. 37.1 and 37.1 kN for N, NS, NSL and NS2L, respectively. Correspondingly, two prisms per mix were carbonated per exposure type without load.

Impact of compressive stress and carbonation on water absorption properties: Two 50×50×75mm slices per mix were derived from one of the pre-loaded and non-loaded 75×75×200 mm concretes for water absorption testing. Preconditioning and testing was carried out according to BS 1881-208 (BSI, 1996) and BS EN 13057 (BSI, 2002) respectively. Mass changes were recorded at predetermined times up to 15 days.

3. Results and discussions

Figure 1 (a) shows that the slag containing concretes, with or without limestone, exhibited significantly lower compressive strength (a 40% reduction) after 2 days of curing compared to CEM I, but developed a comparable compressive strength to that of CEM I after 90 – 180 days of curing.

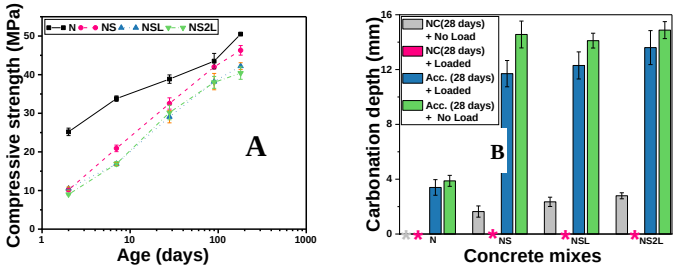

Figure 1. (a) Compressive strength evolution; (b) Carbonation depths after 28 days of exposure to ambient/natural (NC) or accelerated (Acc) carbonation for stressed (loaded) and non-stressed (unloaded) concretes. * denote no depth recorded for the concrete mix corresponding to the clolour code of exposure type

The carbonation depths of exposed concrete mixes, with and without load, as determined by phenolphthalein testing are shown in Figure 1(b). Independently of the exposure condition (natural vs.

accelerated, loaded vs. non-loaded) the binary and ternary mixes exhibited greater carbonation depth in comparison to CEM I. Under natural carbonation exposure, changes in pH were only recorded for concrete mixes made with the binary or ternary cement but not the reference CEM I. The extent of carbonation increased at higher limestone contents. However, differences where within the error of the measurements. Irrespective of the cement type, natural carbonation was hindered in the specimens loaded for 28 days, but it is worth mentioning a slight increase in depth was recorded at prolonged natural carbonation exposure with loading. The initial hindering of carbonation could be explained by partial closure of early-age micro-cracks under compressive loading, potentially impeding the ingress of CO_2 (Liu et al., 2022). Meanwhile, increased carbonation depths were recorded in the same time frame and compressive stress state when samples were exposed to elevated CO_2 concentration. This observation agrees with findings of the RILEM TC 281-CCC (Yao et al., 2023). The differences between natural and accelerated carbonation are expected given the extent of microstructural changes expected in the samples when exposed to high CO_2 concentrations, including an increase in the overall porosity. An effect that cannot be fully compensated for by the potential closure of microcracks/ small pores under compressive loading.

Figure 2 (a–d) shows the sorptivity profiles of stressed and unstressed concretes under natural exposure, and their associated quantified initial water absorption/sorption coefficient (linear slope) in Table 1. The sorption coefficient after 28 days of ambient carbonation reduces in concretes subjected to combined action of carbonation and loading, relative to the unstressed concretes. Meanwhile the coefficients for all mixes are comparable for each of the carbonation exposure conditions, with or without loading. While partial closure of microcracks can be attributed to reduction in water admissibility at the early ages of stressed concretes relative to the unstressed concretes, densification and secondary hydration related self-healing action in slag-containing system can also play a role (Liu et al., 2022, Maddalena et al., 2021). Comparing the impact of stress under accelerated or natural carbonation exposure, independent of the concrete mix type an increase in sorption coefficient can be observed in samples exposed to accelerated carbonation under loading.

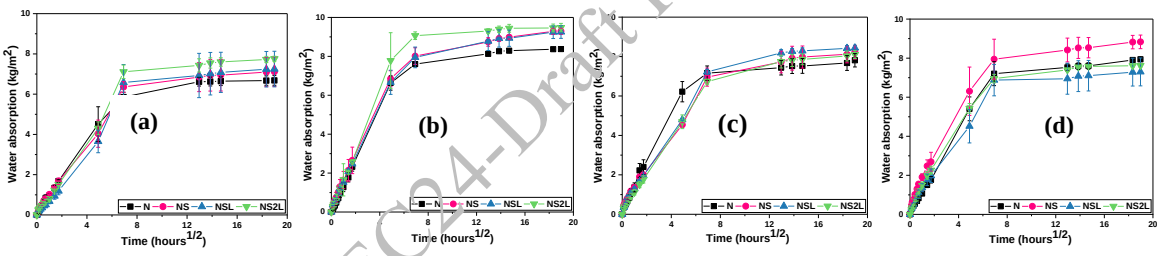

Figure 2. Sorptivity curves of tested concretes after (a) 28 days loading + natural carbonation; (b) 28 days unloaded + natural carbonation (c) 28 days loading + accelerated carbonation (d) 28 days unloaded + accelerated carbonation.

Table 2. Sorption coefficients ($kg*m^{-2}*h^{-0.5}$) of 28 days carbonated concretes with or without load

MixID	Natural carbonation		Accelerated carbonation	
	Stressed	Non-stressed	Stressed	Non-stressed
N	0.94 ± 0.05	1.32 ± 0.17	1.38 ± 0.31	0.96 ± 0.15
NS	0.91 ± 0.08	1.46 ± 0.5	1.38 ± 0.06	1.5 ± 0.41
NSL	0.63 ± 0.15	1.37±0.06	1.05 ± 0.01	1.11 ± 0.29
NS2L	0.8 ± 0.01	1.37±0.02	0.96 ± 0.13	1.32 ± 0.18

4. Conclusions

In loaded concrete, a reduced progression of carbonation front during early ages was observed independently of the cement composition, under natural carbonation exposure conditions. Conversely, carbonation depths increased significantly under accelerated exposure, with comparable values being recorded for stressed and unstressed CEM I concrete, but slight reductions were observed for NS, NSL and NS2L concrete, when exposed to carbonation under a stressed state.

Early age loading (such as 7days cured) of concretes made with composite cements has no detrimental impact on carbonation, when compared to unloaded concretes. However further investigation is required to

understand the causes of this phenomenon. The concrete mixes investigated under compressive stress exhibited a reduction in water admissibility, which seem to be significantly dependent on the type of carbonation exposure and stress state.

Acknowledgements

This study was sponsored by the Engineering and Physical Sciences Research Council (EPSRC) via ECF EP/R001642/M. Sabtiwu is grateful to EPSRC for his PhD CASE award co-sponsored by National Highways.

References

Berodier, E. and Scrivener, K. (2015. Evolution of pore structure in blended systems. *Cement and Concrete Research.* **73**:25-35.

Borges, P.H., Costa, J.O., Milestone, N.B., Lynsdale, C.J. and Streatfield, R.E. (2010. Carbonation of CH and C–S–H in composite cement pastes containing high amounts of BFS. *Cement and concrete research.* **40**(2), :.284-292.

BSI. (1996. BS 1881-208. Recommendations for the determination of the initial surface absorption of concrete.

BSI. (2002. BS EN 13057. Products and systems for the protection and repair of concrete structures. Test methods. Determination of resistance of capillary absorption.

BSI. (2019a. BS EN 12390-2. Testing hardened concrete. Making and curing specimens for strength tests.

BSI. (2019b. BS EN 12390-3. Testing Hardened Concrete: Compressive Strength of Test Specimens.

BSI. (2019c. BS EN 12390-17. Testing Hardened Concrete - Determination of creep of concrete in compression.

BSI. (2020. BS EN 12390-12: Determination of the carbonation resistance of concrete — Accelerated carbonation method.

BSI. (2021. BS EN 197-5. Portland-composite cement CEM II/C-M and Composite cement CEM VI.

Liu, Z., Van den Heede, P., Zhang, C., Shi, X., Wang, L., Li, J., Yao, Y. and De Belie, N. (2022) Influence of sustained compressive load on the carbonation of concrete containing blast furnace slag. *Construction and Building Materials.* **335**:127457.

Maddalena, R., Taha, H. and Gardner, D. (2021) Self-healing potential of supplementary cementitious materials in cement mortars: Sorptivity and pore structure. *Developments in the Built Environment.* **6**:100044.

Sabtiwu, M., Dhandapani, Y., Drewniok, M., Adu-Amankwah, S., and Bernal, Susan A. (2023) Engineering and durability performance of composite Portland cement- blast furnace slag-limestone concretes. In: *The 77th RILEM Annual Week & the 1st Interdisciplinary Symposium on Smart & Sustainable Infrastructures, Vancouver, BC, Canada*.

Sabtiwu, M., Dhandapani, Y., Drewniok, M., Adu-Amankwah, S., and Bernal, Susan A. (2024) Uniaxial compressive creep performance of concrete based on composite Portland -blast furnace slag-limestone cements. In: *fib ICCS – International Conference on Concrete Sustainability, Guimarães, Portugal*.

Vigor, J.E., Prentice, D.P., Xiao, X., Bernal, S.A. and Provis, J.L. (2024) The pore structure and water absorption in Portland/slag blended hardened cement paste determined by synchrotron X-ray microtomography and neutron radiography. *RSC advances.* **14**(7):.4389-4405.

Von Greve-Dierfeld, S., Lothenbach, B., Vollpracht, A., Wu, B., Huet, B., Andrade, C., Medina, C., Thiel, C., Gruyaert, E. and Vanoutrive, H. (2020) Understanding the carbonation of concrete with supplementary cementitious materials: a critical review by RILEM TC 281-CCC. *Materials and Structures.* **53**(6):1-34.

Wu, B. and Ye, G. (2017) Development of porosity of cement paste blended with supplementary cementitious materials after carbonation. *Construction and Building Materials.* **145**:.52-61.

Yao, Y., Wang, L., Li, J., De Belie, N., Shi, X., Van den Heede, P., Zhang, C., Liu, Z., Talakokula, V., Jin, Z., Xiong, C., Lu, J., Kamali-Bernard, S., Bansal, T., Li, B., Wang, Z. and Huang, Y. (2023) Report of RILEM TC 281-CCC: effect of loading on the carbonation performance of concrete with supplementary cementitious materials — an interlaboratory comparison of different test methods and related observations. *Materials and Structures.* **56**(6):110.

Yao, Y., Wang, L. and Wittmann, F.H. (2013) *Publications on durability of reinforced concrete structures under combined mechanical loads and environmental actions: an annotated bibliography.* Aedificatio Publishers.

Chloride Resistance of Concrete with Recycled Aggregates and Clay Brick Waste Powder as Supplementary Cementitious Material

S.A. Kahr[1*], W. Kunther[2] and L.M. Ottosen[3]

[1] *Department of Environmental and Resource Engineering, Technical University of Denmark, Kongens Lyngby, Denmark*
Email: salka@dtu.dk,
[2] *Department of Environmental and Resource Engineering, Technical University of Denmark, Kongens Lyngby, Denmark*
Email: wolku@dtu.dk, ,
[3] *Department of Environmental and Resource Engineering, Technical University of Denmark, Kongens Lyngby, Denmark*
Email: limo@dtu.dk

[*]Corresponding author

ABSTRACT

The high environmental impact of concrete production is well known in the construction industry, thus the motivation for this study is to lower the amount of virgin material used in new concrete. The study examines the chloride resistance and porosity of concrete with recycled clay brick waste powder (CBP) as partial cement replacement and partial replacement of aggregates with recycled concrete aggregates (RCA) at replacement levels of 20% regarding both aggregates and cement.

The study compares different mixtures of concrete in compressive strength, capillary suction and forced chloride migration. Capillary suction indicated lower porosity constituted by pores in the capillary size for the mixtures containing CBP than for the mixtures without, which is often associated with a higher resistance to chloride penetration. However, results from the chloride migration showed similar chloride penetration for samples with and without CBP. Low reactivity of the CBP results in lower adsorption of chloride ions in the hydration products, which might explain the opposite results on the relation between the capillary sized pores and chloride migration.

KEYWORDS: *Chloride resistance, Recycled concrete aggregates, Recycled clay brick waste*

1. Introduction

The environmental challenges in the concrete industry are well known, both regarding their CO_2 emissions from the cement production and the massive use of virgin gravel and sand as aggregates, Lehne and Preston (2018) and Greene, (2022). One way to limit the environmental impacts of new concrete is to partially replace these components.

Multiple studies have been conducted on this topic in recent years and have shown that partial replacement of cement by SCM leads to improved concrete properties. This occurs due to the filler effect, and the improvement is even more pronounced when the material exhibits pozzolanic properties, as is the case with CBP according to Lam et al. (2021). When partly replacing cement with CBP, studies have shown enhancement in properties with replacement levels up to 20%, Shao et al. (2019), and satisfying performance has been observed with replacement levels up to 40%, Elinwa (2005) and Lam et al. (2021).

When concrete is crushed for reuse purposes, most of the hydrated cement ends up in the finest aggregate size fractions, compromising the performance of the concrete in comparison to the fine sand fraction of virgin aggregates. Depending on the properties and treatment of the RCA, the coarse fractions can replace up to 30% of the aggregates in concrete with a minimum of strength reduction, Verian et al. (2018), while the fine fractions can be replaced with up to 20%, Carro-López et al. (2015).

This study investigates the properties of concrete with 20% cement replacement by CBP and 20% replacement of aggregates with RCA in terms of compressive strength, capillary sized porosity and chloride migration. The fixed replacement level was set to 20% to compare with DS/EN 197-6:2023 - CEM II/A F and Q; replacement with natural calcined and recycled concrete fines. Since the addition of CBP as cement replacement in this quantity has been shown to have a positive impact on the durability of concrete, Shao et al. (2019), Pitarch et al. (2020), Rani and Jenifer (2016), Baronio and Binda (1996) and Wu et al. (2024), it is being investigated whether the deterioration of properties caused using RCA as partial aggregate replacement can be balanced out. This has previously been shown to be the case in studies using fly ash as partial cement replacement in recycled aggregate concrete, Kou et al. (2007) and using CBP as partial cement replacement, Lam et al. (2021). Chloride resistance is an important factor influencing the durability of this new type of concrete, and since little is known on this subject from the literature, it is a performance criterion of this paper.

2. Materials and mixtures

For this project, marine aggregates from Denmark and RAPID (CEM I, 52.5 N) cement from Aalborg Portland A/S, Denmark, were used as virgin materials. Both RCA and CBP were provided by Norrecco A/S, Denmark. Before casting, the RCA were separated into 3 size factions: 0-4 mm, 4-8 mm and 8-16 mm, water saturated for a day and dripped off using a sieve until no more water droplets appeared. Hereafter the RCA was used for sample casting. The CBP were dried at 105°C in an oven for a day and crushed in a disc mill for 120 s to achieve a similar particle size distribution like the RAPID cement.
Table 1 shows the mixture proportions for the 4 different mixtures cast for this study. All mixing were performed according to the standards DS/EN 12390-2, 2019 and DS/EN 12390-1, 2021 for casting cylindric concrete samples, measuring d = 100mm and h = 200 mm. All samples were stored in the mould for a day in a climate chamber at 20°C, whereafter the samples were wet cured in limewater at 20°C until testing. The w/c ratios in table 1 accounts for the pendant water on the RCA after sieving and the partial replacement of cement. The water absorbed by the RCA was not accounted for in the w/c ratio.

Table 1. Mixture proportions and w/c ratios

				Marine aggregates [mm]			RCA [mm]			w/c ratio
	Water (g)	Cement (g)	CBP (g)	0-4 (g)	4-8 (g)	8-16 (g)	0-4 (g)	4-8 (g)	8-16 (g)	
MixRCA	1710	2870	-	6100	4430	4430	1520	1110	1110	0.77
MixCBP	1720	2300	570	7620	5540	5540	-	-	-	0.75
MixACB	1710	2300	570	6100	4430	4430	1520	1110	1110	0.96
MixREF	1720	2460	-	7620	5540	5540	-	-	-	0.70

3. Experimental details

Following the standard DS/EN 12390-3, the compressive strength at the ages 7, 28, 60 and 91 days were tested using the Servo Hydraulic test machine, model 300-Ton, Toni Technik, Germany, with the loading rate of 4.7 kN/s. The flat ends of the samples were ground before testing to ensure a plane surface.
Prior to testing the capillary suction, all samples were oven-dried at 105°C until constant weight were obtained. The samples were placed on a support grid and water was poured till 5 mm above the grid to ensure contact between the sample and water reservoir. The capillary suction was determined by the weight gain of each sample over a period of 6 h. All samples were cured 60 days before drying in the oven.
The chloride resistance was measured using electromigration. The ends of the cylindrical samples were ground to ensure a plane surface, and a chamber with a capacity of 250 ml was attached to each end. A constant current of 15 mA was applied axially to the samples. A 500 ml solution containing 0.01 M NaNO3 was pumped into the cathode chamber and a 500 ml solution containing 0.34 M NaCl was pumped into the anode chamber to provoke chloride migration. After 7 days in this setup, the samples were split axial and sprayed with 0.1 M AgNO3 to reveal the penetration depth of chloride.

4. Results and discussion

The compressive strength of the different mixtures is compared and illustrated in figure 1. Generally, the strength increases over time except for mixRCA, which decreases between 60 and 91. Excluding this, the mixRCA performs well in comparison to mixREF when considering the 20% replacement of the fine fractions and the slightly higher w/c ratio, which strongly influences the strength of concrete. The strength development of the mixCBP is delayed, which is common for concretes containing pozzolanic materials at this replacement level, Pitarch et al. (2020). The cement reacts with water and produces calcium silicate hydrates and calcium hydroxide, which the pozzolans convert into more calcium silicate hydrates, enhancing the strength of the concrete. These reactions may occur simultaneously, but many SCMs show less reactivity than e.g. pure Portland cement. The strength of mixCBP exceeds those of mixRCA and mixREF after 28 days, revealing low reactivity of the clay brick waste used in this study. XRD performed on cement paste with and without CBP by Bertelsen et al. (2023) on the same clay brick waste powder revealed a high degree of crystallinity, thus led to the same conclusion. The reactive silicates and aluminates in CBP are less reactive when originating from crystalline phases, than from amorphous phases, resulting in a slower dissolution of the reactants into the pore solution, Li et al. (2023). However, the addition of CBP as partial replacement of cement seems to improve the durability of the concrete over time aligning with the findings of Shao et al. (2019), Pitarch et al. (2020), Rani and Jenifer (2016), and Baronio and Binda (1996).

The compressive strength of mixACB is noticeably lower than the strength of the other mixtures, approximately 10 MPa throughout the test duration. Lam et al. (2021) conclude that the addition of CBP to concrete enhances the microstructure and that the rough surface of RCA strengthens the transition zone between the RCA and the new cement paste. However, this is not reflected in the results illustrated in figure 1. A likely reason for the lack of performance on the compressive strength might be the high w/c ratio in comparison to the other mixtures.

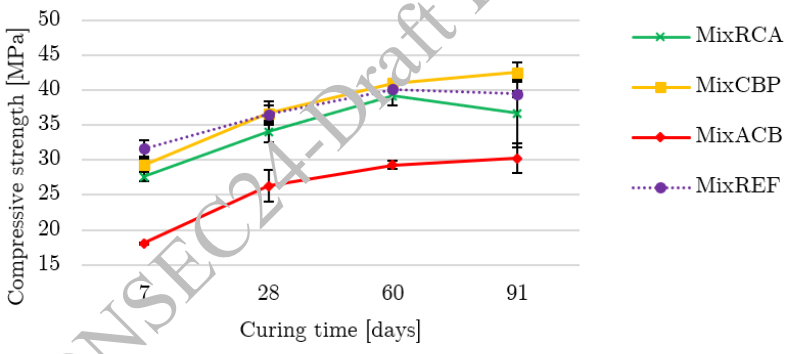

Figure 1. Compressive strength of concrete samples over time, ranging from 7 to 91 days.

Rukzon and Chindaprasirt (2012), Poon et al. (2005) and Wu et al. (2024) conclude that incorporating pozzolanic material in a concrete mixture lowers the porosity and enhances the chloride resistance. A method to examine the capillary sized porosity of a material is to test the capillary suction. The results of this testing are shown in figure 2a. The concrete mixtures containing CBP have a lower Q capacity, which translates to less water contained in the pores of the samples. The pore size greatly influences the capillary suction inside the pores, and if the pores are too large, the under pressure inside the pores will not be effective enough to suck water, Claisse (2021). To eliminate the explanation that the low capillary suction of CBP-containing samples is due to large pores, mixRCA, mixCBP and mixACB were impregnated with low viscosity, luminescent epoxy and photographed in UV-lighting. Based on the images in figure 2b, it was concluded that the mixtures containing CBP have a lower porosity of capillary sized pores than the mixtures without.

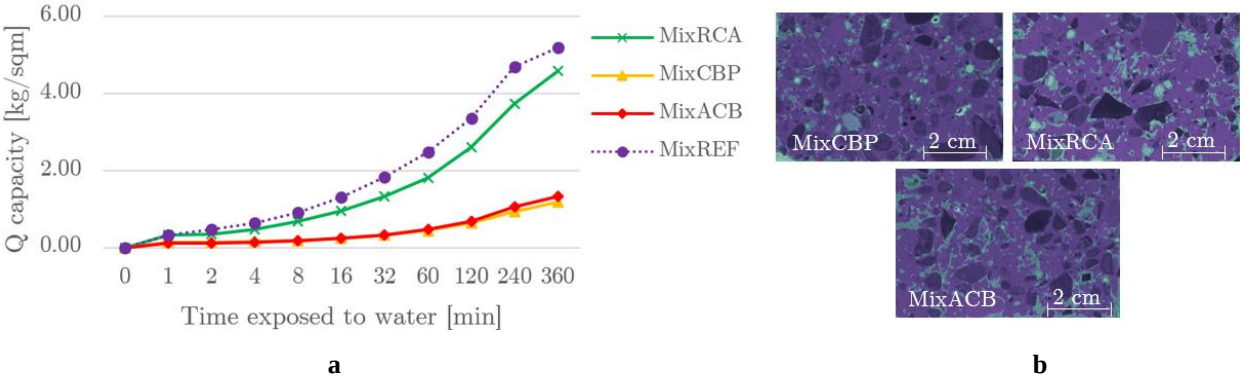

a **b**

Figure 2. a) Capillary suction of concrete samples for a period of 6 h. b) Images of samples impregnated with luminescent epoxy in UV lighting.

Figure 3 illustrates the penetration depth for the different concrete mixtures after 28 and 60 days of curing prior to the testing. All samples increase the chloride resistance with increasing curing time, indicating development in the microstructure lowering the porosity and increasing the tortuosity. The mixtures showed same level of resistance to chloride, taking the uncertainties of the test method into account. This opposite relation between porosity in capillay sized pores and chloride resistance contradicts findings on the total porosity and both forced and natural chloride resistance, by Wanga et al. (2017) and Hou et al. (2024). The findings in compressive strength and capillary suction does not indicate any issues with the samples containing CBP, compared to mixRCA and mixREF.

Chloride migration in concrete depends on the migration of chloride ions in the pore solution and the binding capacity of chloride in the cement hydrates through the concrete. MixRCA and mixREF performed slightly better than mixCBP and mixACB in hindering the chloride migration, which might be explained by a higher binding capacity in these samples. Guan et al. (2024) conclude that addition of CBP resulted in higher production of hydration productes, causing a more porous material and weakening the chloride ion binding capacity. This is due to a low reactivity of the CBP used in that study.

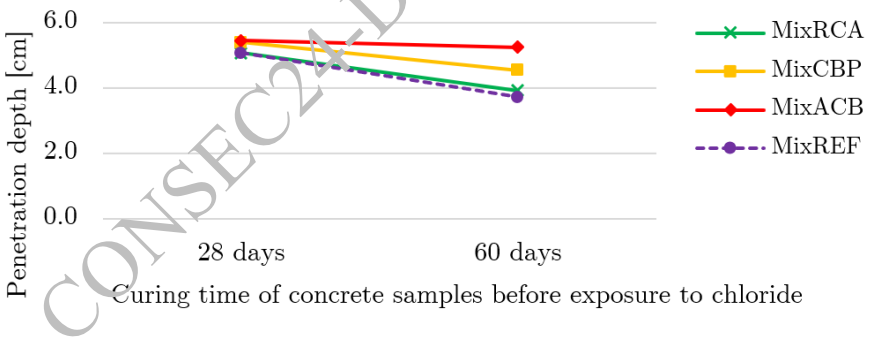

Figure 3. Chloride migration through concrete samples. Comparison of penetrability after curing for 28 and 60 days prior to testing chloride migration for 7 days.

The findings of Guan et al. (2024) fits well with the results in figure 3. The development in compressive strength in figure 1 and the findings of Bertelsen et al. (2023) all revealed a low reactivity of the CBP used in this study. A lower binding capacity of the mixtures containing CBP results in higher concentration of free chloride ions in the pore solution, leading to faster diffusion through the pores, Claisse (2021), and enhancing the penetration depth of the samples. Further testing is necessary to determine the reason for the low resistance to chloride.

5. Conclusions

The study concludes the following points:

- Replacing 20% of both fine and coarse aggregates with RCA in concrete did not result in noteworthy strength reduction.
- Replacing 20% of cement in concrete with RCB, the compressive strength exceeded the samples without CBP after 28 days of curing.

- The concrete samples containing 20% replacement of aggregates and 20% replacement of cement with RCA and CBP performed inferior compared to the other samples regarding compressive strength and resistance to chloride migration. However, the w/c ratio was considerably higher than for the rest of the samples.
- The capillary suction of mixtures containing CBP suggested lower porosity of capillary sized pores compared to samples without CBP.
- Mixtures containing CBP showed a slightly lower resistance to chloride than the mixtures without, which might be explained by the low reactivity of the CBP resulting in a lower binding capacity of chloride ions.

About the study

This paper is based on the findings of the master thesis written by the main author at DTU Sustain.

References

Baronio, G., Binda, L. (1996) "Study of the pozzolanicity of some bricks and clays", *Construction and Building Materials,* 11,(1): Pages 41-46

Bertelsen, I.M.G., Kahr, S.A., Kunther, W., Ottosen, L.M. (2023) "Clay Brick Powder as Partial Cement Replacement", *RILEM Bookseries 44* :142-152

Carro-López, D., González-Fonteboa, B., Brito, J., Martínez-Abella, F., González-Taboada, I., Silva, P. (2015) "Study of the rheology of self-compacting concrete with fine recycled concrete aggregates", *Construction and Building Materials,* 96 : 491–501

Claisse, P.A. (2021) "The transport properties of concrete and the equations that describe them", *Woodhead Publishing Series in Civil and Structural Engineering* : 1-16

Elinwa, A.U. (2005) "Experimental characterization of Portland cement-calcined soldier-ant mound clay cement mortar and concrete", *Construction and Building Materials,* 20 754–760

Greene, T. (2022), "50bn tonnes of sand and gravel extracted each year, finds UN study", *The Gardian,* Tue 26 Apr 2022 10.00 CEST

Guan, X., Ji, H., Qiu, J., Zhang, Y., Yu, J., Li, L. (2024) "Chloride ion permeability of concrete containing recycled composite powder from building demolition waste", *Construction and Building Materials,* 424: 135934

Hou, S., Hu, R., Xu, L., Zhang, Y., Ma, Z. (2024) "Understanding the chloride migration in recycled powder concrete: Effects of recycled powder type, replacement rate and substitution pattern", *Construction and Building Materials,* 436 136825

Kou, S.C., Poon, C.S., Chan, D. (2007) "Influence of fly ash as a cement addition on the hardened properties of recycled aggregate concrete", *Materials and Structures,* 41:1191–1201

Lam, M.N.T., Nguyen, D.T., Nguyen, D.L. (2021) "Potential use of clay brick waste powder and ceramic waste aggregate in mortar", *Construction and Building Materials,* 313: 125516

Lehne, J., Preston, F. (2018) "Making concrete change; innovation in low-carbon cement and concrete", *Chatham House*

Li, S., Chen, G., Zhao, Y., Xu, Z., Luo, X., Liu, C., Gao, J. (2023) "Investigation on the reactivity of recycled brick powder", *Cement and Concrete Composites,* 139 :105042

Pitarch, A.M., Reig, L., Tomás, A.E., Forcada, G., Soriano, L., Borrachero, M.V., Payá, J. Monzó M. (2021) "Pozzolanic activity of tiles, bricks and ceramic sanitary-ware in eco-friendly Portland blended cements", *Journal of Cleaner Production,* 279 123713

Poon, C.S., Kou, S.C., Lam, L. (2006) "Compressive strength, chloride diffusivity and pore structure of high performance metakaolin and silica fume concrete", *Construction and Building Materials,* 20: 858–865

Rani, M.U., Jenifer, M. (2016) "Mechanical Properties of Concrete with Partial Replacement of Portland Cement by Clay Brick Powder", *International Journal of Engineering Research & Technology,* (IJERT), 5 (02)

Rukzon, S., Chindaprasirt, P. (2012) "Strength, porosity, and chloride resistance of mortar using the combination of two kinds of pozzolanic materials", *International Journal of Minerals, Metallurgy and Materials,* 20,(8): 808

Shao, J., Gao, J., Zhao, Y., Chen, X. (2019) "Study on the pozzolanic reaction of clay brick powder in blended cement", *Construction and Building Materials,* 213: 209–215

Verian, K.P., Ashraf W., Cao, Y. (2018) "Properties of recycled concrete aggregate and their influence in new concrete production", *Resources, Conservation and Recycling,* 133:30-49

Wanga, D., Zhou, X., Fu, B., Zhang, L. (2017) "Chloride ion penetration resistance of concrete containing fly ash and silica fume against combined freezing-thawing and chloride attack", *Construction and Building Materials*, 169 740–747

Wu, H., Gao, J., Liu, C., Guo, Z., Luo, X. (2024) "Reusing waste clay brick powder for low-carbon cement concrete and alkali-activated concrete: A critical review", *Journal of Cleaner Production*, 449 141755

Beyond Changes in Alkalinity Measurements: Characterisation of The Natural Carbonation Front of Blended Cementitious Systems

Yuvaraj Dhandapani[1*], Leon Black[2], and Susan A. Bernal[3]

[1] School of Civil Engineering, University of Leeds, UK,
Email: y.dhandapani@leeds.ac.uk
[2] School of Civil Engineering, University of Leeds, UK,
Email: l.black@leeds.ac.uk
[3] School of Civil Engineering, University of Leeds, UK,
Email: s.a.bernallopez@leeds.ac.uk

[*]Corresponding author

ABSTRACT

There is a growing interest in evaluating concrete carbonation, particularly in low-clinker cement formulations, with a focus on determining their durability and estimating the CO_2 offset potential during an in-service period. Conventionally, carbonation assessments rely on measuring changes in alkalinity by applying pH indicators (e.g., phenolphthalein solutions). This approach provides limited insights into the intricate physicochemical changes occurring in the microstructure as the carbonation front progresses. Carbonation depths were determined using conventional phenolphthalein-based pH indicators, thermogravimetric analysis coupled with mass spectrometry (TGA-MS), and scanning electron microscopy coupled with energy-dispersive X-ray spectroscopy (EDX) in four cement types. The carbonation exposure was conducted under controlled conditions (atmospheric CO_2 at 20°C and 57% relative humidity) to simulate natural carbonation. While the conventional pH indicator did not show any signs of carbonation in reference Portland cement paste, the microstructural characterization offers a more rational method for assessing ongoing carbonation before complete consumption of Portlandite and benchmarking the carbonation performance, specifically in low-clinker cement. The analysis of the carbonation front using a combination of analytical techniques provided unique insights into the carbonation performance of new sustainable cements, demonstrating that chemical alterations identified through these methods contribute to a deeper understanding of the carbonation impact beyond changes in the material's alkalinity.

KEYWORDS: *Carbonation, Reaction front, Sulfate front, Alkalis, Microstructure*

1. Introduction

The construction industry faces a critical challenge in mitigating the embodied carbon footprint associated with building materials, which are considered hard-to-abate industrial processes. As the demand for sustainable building materials increases, low-clinker cement containing supplementary cementitious materials (SCMs) has emerged as a promising solution to reduce these emissions. Calcined clays, in particular, have been shown to improve various performance characteristics of cement and are seen to be an attractive option for sustainable cement production. The adoption of low-clinker cements in concrete construction is impeded by concerns about their long-term durability, especially when exposed to CO_2 in a process known as carbonation.

Carbonation is one of the major durability issues in reinforced concrete structures, as it can lead to the corrosion of steel reinforcement, thereby compromising structural integrity (Angst, 2023). This concern is prominent in cements with high volumes of clinker replacements, where the long-term carbonation resistance is not yet fully understood and is often considered relatively low based on accelerated test methods (Von Greve-Dierfeld et al., 2020). The current understanding is primarily based on accelerated test methods, as several of these low-clinker cements have limited track records in practical construction. Although commonly used, accelerated carbonation tests often fail to provide comprehensive insights due

to the non-representative nature of the testing conditions like constant RH and difference in phase assemblage, thus raising questions about their reliability in predicting real-world performance for a service life of 50-100 years.

This study aims to bridge this knowledge gap by characterising the carbonation process in cement paste exposed to atmospheric CO_2 conditions for composite cements containing calcined clays. The study utilizes conventional and analytical techniques to assess the carbonation performance of different cement blends. Through this comprehensive approach, the study aims to provide valuable insights into the long-term durability performance of low-clinker cements under carbonation conditions.

2. Materials and Methods

This study used commercial ordinary Portland cement (CEM I 52.5R) from Heidelberg Cement. Flash calcined clay (CCF), with an approximate kaolinite content of 50 wt.%, was supplied by Argeco Ltd. from France. The chemical compositions of the materials used are provided in Table 1. Limestone was also sourced from Heidelberg Cement. Four cement blends were prepared for the study: Ordinary Portland cement (OPC), binary blends containing 30% limestone or 30% calcined clay denoted as L30 or CCF30, respectively, and a ternary blend containing 30% calcined clay and 15% limestone, denoted as CCF30L15.

Table 1. Oxide composition in wt.% of the materials used determined by X-ray fluorescence

	CaO	Al_2O_3	SiO_2	MgO	SO_3	K_2O	MnO	Fe_2O_3	Na_2O	LOI*	Traces
OPC	64.80	3.90	21.80	0.76	3.57	0.67	0.05	2.33	0.30	2.20	0.73
Calcined clay	0.81	22.60	69.30	0.27	0.08	0.28	0.06	2.89	0.37	1.90	1.50
Limestone	52.70	0.98	3.51	0.53	0.11	0.13	0.05	0.43	-	41.50	0.12

*LOI stands for loss on ignition, determined at 900°C using a muffle furnace

Cement paste with a water-to-binder ratio (w/b) of 0.5 was cast into cylindrical specimens approximately 35 mm in diameter and 55 mm in height, then cured for 28 days in sealed conditions. These specimens were exposed to natural carbonation with their ends sealed to ensure unidirectional, circumferential carbonation in a standard conditioning chamber at a controlled temperature of 20±0.5°C and 57±3% relative humidity (RH), simulating sheltered carbonation conditions. Carbonation depths were monitored by spraying fresh mists of 1% phenolphthalein and 1% thymolphthalein indicator solutions (each prepared in 100 ml isopropyl alcohol) on freshly broken surfaces of mortar specimens. A small portion of the cement paste discs from the carbonated edge was dried and impregnated with low-viscosity epoxy resin for observation using a scanning electron microscope (SEM) in backscattered electron (BSE) mode. Line scans were conducted from the exposed surface to a depth of approximately 2 mm. Thermogravimetric (TG) measurements were performed between 30 and 1000 °C using a heating rate of 10°C/minute under a nitrogen atmosphere using a Netzsch STA 449. For TG analysis, 20 ± 1 mg of sample was used for each measurement sample from three regions: Carbonation region observed using phenolphthalein indicator (L1), immediately depth after carbonated region (L2) and uncarbonated region >10 mm depths (L3). L1 and L2 vary with the carbonation exposure, and a small amount (about 20 mg) was carefully removed and crushed using a mortar pestle.

3. Results and Discussion

3.1 Carbonation depth determined using a pH indicator

Figure 1 presents the carbonation depth after 240 days of exposure to atmospheric CO_2 at a relative humidity (RH) of 57%. The evaluation was conducted using two different pH indicators: 1% phenolphthalein and 1% thymolphthalein, commonly employed to determine carbonation depths in cementitious systems due to their ability to indicate pH changes visually. OPC paste exhibited limited signs of carbonation after 240 days of exposure when tested with either phenolphthalein or thymolphthalein indicators, whereas L30, CCF30 and CCF30L15 showed a clear and visible carbonation depth, i.e., a change to colourless, indicating carbonation in these paste samples.

About 8 points along the disc were measured using a digital calliper, and carbonation depth after 240, 400 and 750 days is presented in Figure 1b. While L30 and CCF30 had similar clinker content, the carbonation depth of L30 was about 1.8 mm by 750 days, while CCF30 had only 1.15 mm carbonation depth. This is indicative of the beneficial impact of pore refinement with calcined clay in comparison with relatively insert filler used at similar replacement levels. However, for CCF30L15, with a replacement level of 45%, carbonation depth was significantly higher than CCF30 and quite identical to L30 by 400 days and significantly higher (about 3.0 mm) by 750 days. The reduced clinker content lowers the reserve alkalis content despite beneficial pore refinement from calcined clay additions.

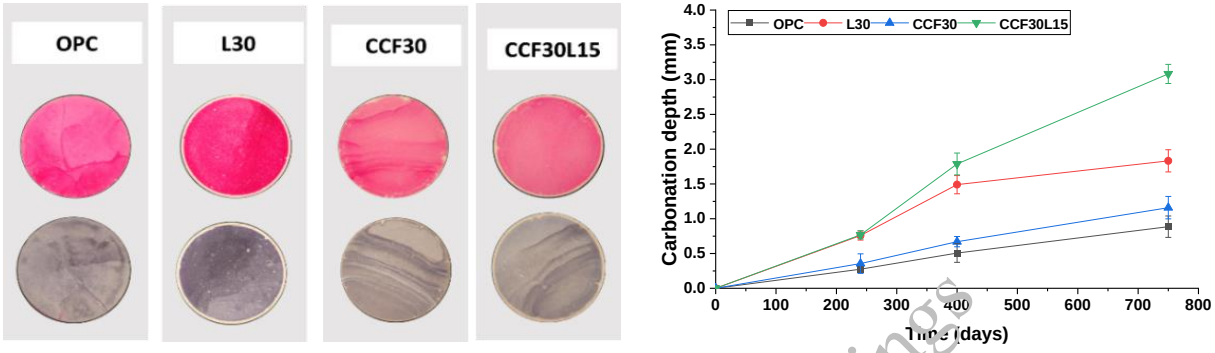

(a) (b)

Figure 1. (a) Carbonation measurement on cement after 240 days of carbonation exposure (Atmospheric CO_2 and RH 57%) using 1% phenolphthalein (purple) and 1% thymolphthalein (blue) indicator (and (b) carbonation depth up to 750 days of CO_2 exposure

3.2 SEM analysis of the carbonated regions

Figure 2 presents line scans (avg. of 5 line scans) using EDX for approximately 2 mm depth from the exposure surface, showing the distribution of sulphates and alkalis along the carbonation front. Alkalis enrichment in the carbonated surface shows the accumulation of alkalis, and sulphate depletion shows reduced amounts of ettringite (AFt) that tends to carbonate upon reaction with CO2. Beyond the carbonated affected depth, there is a homogeneous distribution of S, i.e., from AFt and alkalis within the microstructure.

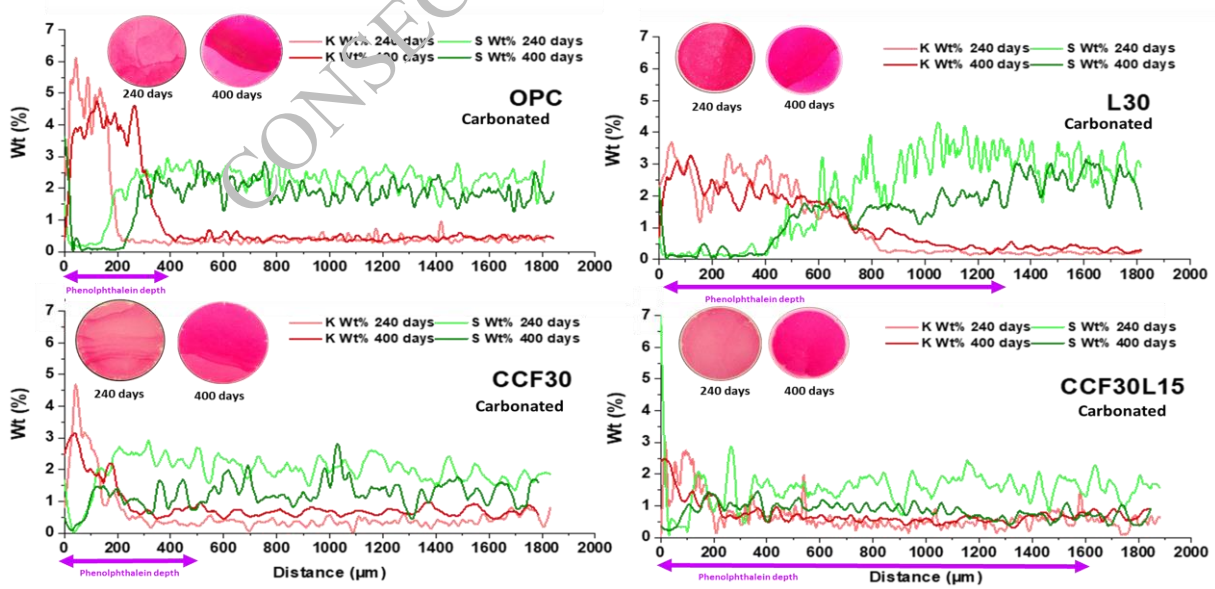

Figure 2. Line scan using EDX to show the difference in the distribution of sulphates (S, Green) and alkalis (K, Red) along the carbonation front

As per EDX line scans, OPC had a carbonation depth of about 200 μm and 400 μm by 240 and 400 days of CO_2 exposure. L30 showed the highest carbonation-affected depth, of about 800 μm (0.8 mm) and 1200 μm (1.2mm) by 240 and 400 days of CO_2 exposure, respectively. The carbonation depth of L30 matches the depth obtained using the pH indicator in Fig.1. The carbonation depth determined using a phenolphthalein indicator by 400 days is marked with a pink line in Figure 2, highlighting the difference from the EDX reaction front. Unlike the carbonation depth from the pH indicator, the EDX line scan shows that L30 had a higher carbonation depth than both calcined clay mixes due to a difference in the carbonation reaction mechanism in high clinker replacement systems i.e., higher carbonation depth due to higher porosity despite higher CH content in L30 and, reduced carbonation due to lower porosity despite lower CH in CCF30. L30 had a gradual change in line scan reflecting the partially carbonated region within the matrix. This transition zone was much sharper for OPC and CCF30, likely due to the pore-blocking effect along the carbonation front from calcite formation from the remnant CH reserves present in the partially carbonated zone in OPC (as shown in Figure 3) or dense pore structure initial in CCF30 reducing diffusivity of CO_2 (Dhandapani et al., 2024).

3.3 CH and Calcite content from TGA

Figure 3 illustrates the calcium hydroxide (CH) and calcite content in four binders across three regions. In OPC, the uncarbonated core (L3) had about 20 g of CH, which remained almost unchanged in L2 but dropped to 11 g in the partially carbonated surface region (L1). For L30, CH content in L3 was 15 g, decreasing to 10 g in L2 and 5.8 g in L1. CCF30 showed 8 g of CH in the L3 region due to CH consumption from pozzolanic reaction, with a similar decrease in L1 (5.7 g), while CCF30L15 showed no significant CH variation across regions due to high clinker replacement limit CH content and resulting in direct carbonation of C-A-S-H phase. Calcite content in OPC and L30 was nearly 30 g in L1, with a systematic decrease in L2 and L3, indicating ongoing carbonation (initial calcite in L30 should be subtracted for comparison). CCF30 had about 16 g of calcite in L1, i.e., 50% lower than OPC, but calcite content in L2 and L3 was higher due to partial carbonation. CCF30L15 also had about 16 g of calcite in L1, while the L2 and L3 regions have similar calcite content due to a sharp drop in carbonation affecting regions beyond L1. L30 showed more CH and calcite variation, indicating a gradual carbonation front, whereas OPC, CCF30, and CCF30L15 showed no difference between L2 and L3 due to denser microstructure in these systems.

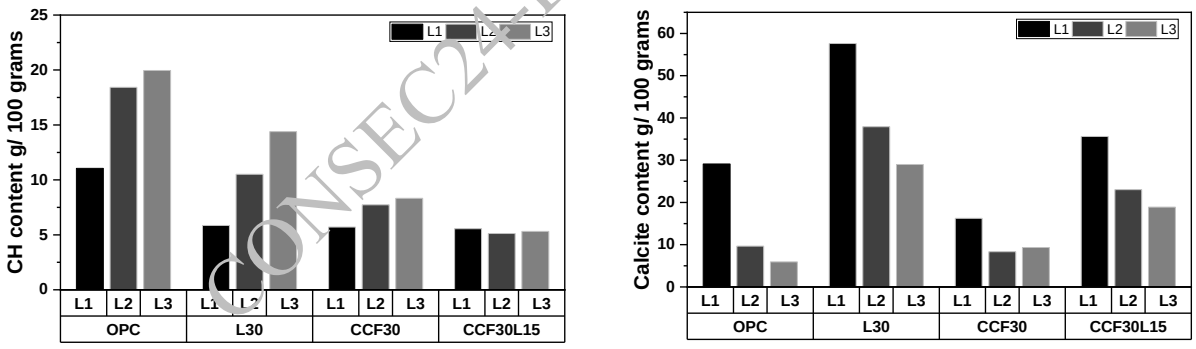

(a) (b)

Figure 3. Calcium hydroxide (CH) content and Calcite content (in g/ 100 g of paste) after 240 days using TGA.

4. Conclusions

Analysis of the carbonation-affected zones through EDX mapping and TGA analysis has revealed significant chemical alterations along the carbonated regions, reflecting the carbonation of various hydration products and the movement of free alkalis. These changes are useful for understanding their role in the carbonation mechanism in low-clinker cement beyond the conventional carbonation depth measurement using a pH indicator solution.

Acknowledgements

This study was sponsored by the NSF through award 1903457 and EPSRC through grant EP/T008407/1 and EP/W021811/1.

References

Angst, U. M. (2023). Steel corrosion in concrete – Achilles' heel for sustainable concrete? *Cement and Concrete Research*, *172*, 107239.

Dhandapani, Y., Black, L., Junger, M. C. G., & Bernal, S. A. (2024). Understanding the Carbonation Performance of Cements Containing Calcined Clay. In *In: Banthia, N., Soleimani-Dashtaki, S., Mindess, S. (eds) Smart & Sustainable Infrastructure: Building a Greener Tomorrow* (pp. 723–729).

Von Greve-Dierfeld, S. et al. (2020). Understanding the carbonation of concrete with supplementary cementitious materials: a critical review by RILEM TC 281-CCC. *Materials and Structures/Materiaux et Constructions*, *53*(6).

Effects of Temperature on the Delayed Behavior of Biaxially Prestressed Concrete

A. Nehme [1*], R. Tabchoury [2], T. Vidal [3], S. Multon [4], and G. Nahas [5]

[1] *Institute of radioprotection and nuclear safety, IRSN/PSN-EXP/SES/LMAPS, 92260 Fontenay aux Roses, France*
Email: alexandre.nehme@irsn.fr
[2] *Institute of radioprotection and nuclear safety, IRSN/PSN-EXP/SES/LMAPS, 92260 Fontenay aux Roses, France*
Email: rita.tabchoury@irsn.fr
[3] *Laboratoire Matériaux et Durabilité des Constructions, LMDC INSA/UPS Génie Civil, 31077 Toulouse, France*
Email: thierry.vidal@univ-tlse3.fr
[4] *Laboratoire Matériaux et Durabilité des Constructions, LMDC INSA/UPS Génie Civil, 31077 Toulouse, France*
Email: multon@insa-toulouse.fr
[5] *Institute of radioprotection and nuclear safety, IRSN/PSN-EXP/SES/LMAPS, 92260 Fontenay aux Roses, France*
Email: georges.nahas@irsn.fr

[*]Corresponding author

ABSTRACT

The delayed deformations of prestressed concrete structures under sustained loading exhibit a non-linear progression over time, impacting tension in the prestressed tendons and causing a subsequent decline in compression within containment vessel walls of nuclear power plants. Maintaining compression within these walls is critical for ensuring tightness under various operational conditions. Design codes provide analytical formulas for assessing these deformations, primarily based on tests involving prestressed concrete in a single direction, such as bridge decks. However, discrepancies between on-site measurements and analytical formulas arise in the case of biaxially prestressed structures such as containment vessels. Moreover, the impact of temperature on the kinetics of measured delayed deformations is overlooked in Eurocode 2 formulas. This study is a part of the European project ACES (Assessment of safety performance of Civil Engineering Structures), aiming to assess the analytical formulas of *fib* model code 2020 to address effects like biaxial prestressing, temperature, loading history on the evolution of concrete strains over time. The planned experimental program includes various Thermo-Hydro-Mechanical configurations, enriched by a few additional ones from other ACES project studies. It comprises two types of creep tests, uniaxial and biaxial loading, on small concrete slabs. These samples are instrumented with optical fiber sensors to measure strains in the three directions throughout the test period. The presented results pertain to temperatures of 20°C and 38°C in water conditions and are compared with those from databases of other studies from literature. Comparing experimental measurements with *fib* model code formulas will guide modifications to account for temperature effects, particularly in bi-axially prestressed structures.

KEYWORDS: *Delayed deformations, Biaxially prestressed concrete, Temperature effects.*

1. Introduction

Concrete structures exhibit ongoing deformation long after their construction, presenting a significant aspect for the safety assessment and lifespan evaluation of large-scale civil engineering projects. This delayed behavior holds relevance in scenarios such as the aging of French nuclear power plants (NPPs), where containment buildings are constructed with biaxially prestressed concrete. The incorporation of prestressing in these structures is essential for safety considerations during potential accidents (Charpin et al., 2018).
Understanding the evolution of delayed deformations in concrete, which leads to the relaxation of prestressing over time, is crucial for accurately evaluating the safety and lifespan of these critical containment buildings.

Beyond applied loads, additional factors, such as temperature and relative humidity, contribute to the manifestation of delayed deformations in concrete. Previous studies based on compressive creep tests have shown an increase in creep strains and their evolution kinetics with heating, which can be amplified by the combined effects of desiccation or thermal damage (Ladaoui et al., 2013).
Numerous design codes (EN, 2004; fib, 2023) offer time-evolution laws for the concrete delayed deformations under isothermal conditions and are largely based on creep tests conducted under uniaxial load. However, these models may not accurately represent the complexities observed in biaxially prestressed structures, such as containment vessels. The low accuracy is often attributed to intrinsic parameters of concrete mixes, which are increasingly variable, or to environmental conditions involving Thermo-Hydro-Mechanical (THM) coupling. To address this limitation and improve the study and prediction of delayed strains and prestress loss in the case of containment vessels under realistic loading conditions, an innovative creep frame has been specially designed for the experimental application of biaxial compressive stress in the laboratory.
An extensive research program is conducted as part of WP4 in the ACES project, aiming to assess and improve the effect of temperature on the evolution of concrete strains over time in the analytical formulas of the fib Model Code 2020, particularly in the case of biaxial prestressed structures. The study includes a variety of THM configurations tested on two different concrete mixes: B11 and VeRCoRs. These tests were conducted under different temperatures (20°C, 38°C, and 50°C), two relative humidity conditions (50% and water immersion), and various mechanical load configurations, including symmetrical and asymmetrical biaxial loads, uniaxial loads, and stress free samples.
This paper focuses on the evolution of uniaxial and biaxial compressive basic creep at two different temperatures, 20°C and 38°C, theses temperatures are representative of the intrados and extrados containment vessel in normal working conditions. Creep tests are conducted under steady and water immersion conditions to complete another study on internal swelling reactions and to avoid any combination between shrinkage and basic creep. In these tests, the concrete is subjected to a constant sustained stress while absorbing water. The results are analyzed and compared with findings from other study in the literature for the same concrete used in our study which will be presented in the next section. Additionally, the results are compared with the fib Model Code 2020 (fib, 2023).

2. Experimental programme

2.1 Materials

The concrete mix studied in this work is known as the B11 mix, which is representative of the concrete used in the French nuclear power plants. This formulation has been the subject of several works, such as Charpin et al. (2018). The B11 mix is characterized by a CEM II A-LL 42,5 R CE PM-CP2 NF cement, limestone aggregates (sand 0/4, gravel 4/11.2, gravel 11.2/20) and superplasticizer. Table 1 details the concrete mix.

Table 1. B11 concrete mix

Components	Proportion (kg/m^3)
CEM II A-LL 42,5 R CE PM-CP2 NF (Calcia, Airvault)	350
Limestone sand 0/4 mm, (Saint Maurice La Clouère quarry)	772
Limestone aggregate 4/11.2 mm, (Saint Maurice La Clouère quarry)	316
Limestone aggregate 11.2/20 mm, (Saint Maurice La Clouère quarry)	784
Efficient water	195
Superplasticizer CHRYSO®Plast Delta CER	1.225

To carry out the basic creep test campaign at various temperatures, samples have been poured during five concrete castings. After demoulding at one day, cylindrical specimens (diameter = 110 mm, height = 220 mm) were sealed and placed in a conditioned room at 20°C and 50% RH. Compressive strength fcm and Young modulus Ecm have been measured at 28 days according to NF EN 12390-3 and RILEM CPC8. The mechanical properties are presented in Table 2.

Table 2. Mechanical properties at 28 days of the different B11 castings

Characteristic	C1	C2	C3	C4	C5
f_{cm} (MPa)	39.7 ± 0.3	37.6 ± 0.3	40.5 ± 0.6	42.6 ± 0.6	43.9 ± 0.5
E_{cm} (GPa)	28.8 ± 1	29.5 ± 1.1	30.9 ± 0.8	30.2 ± 1.0	33.7 ± 2.7

The mean compressive strength and Young modulus for all castings are 40.7 ± 2 MPa and 30.4 ± 1.4 GPa, respectively. This indicates a dispersion of 4.9% and 4.7% for compressive strength and Young modulus, respectively, which is less than the acceptable threshold of 10%.

2.2 Strain measurement system and sample instrumentation

In this study, the samples are immersed in basic water (due to concrete leaching) at 38°C for periods of approximately six months. Sensors must be chosen with particular care to ensure great durability despite these severe conditions. Thus, concrete strains are measured using a network of distributed Optical Fiber sensors (OF). The advantage of this technique compared to the usual methods of strain measurement, such as LVDT sensors and gauges, is its high measurement precision and great resistance to storage conditions. The OF selected for the study is the NEUBREX FN-SILL3, which allows for distributed measurements with a spatial resolution of 650 µm. The measurable strain range extends to ±5000 µm/m, with a measurement uncertainty of ±25 µm/m. Figure 1 depicts the instrumentation setup of the OF sensors in the three directions of the prismatic mould prior to concrete casting.

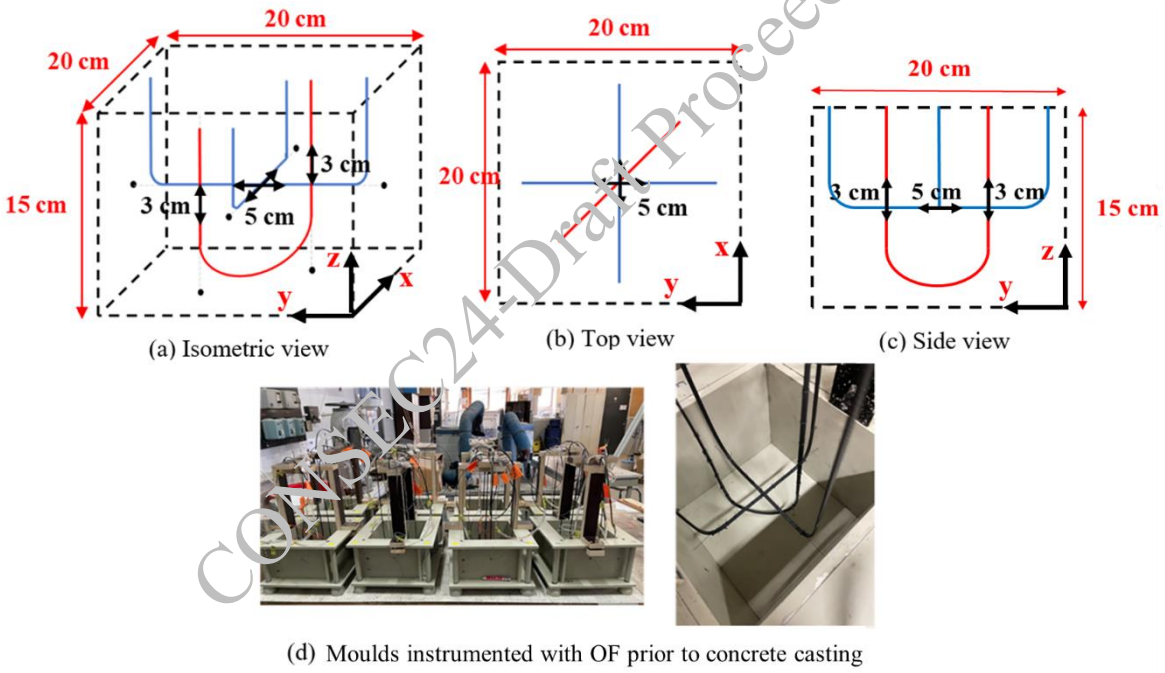

Figure 1. Instrumentation of the OF sensors in the three directions of the mould

Two OF sensing cables are embedded within the 20 cm x 20 cm x 15 cm concrete prisms. The first cable (shown in blue in Figure 1) is positioned to measure strain along the two longitudinal axes, x, and y, of the specimen. The longitudinal measurement is conducted on the central 5 cm of the cable in each direction. The second cable (shown in red in Figure 1) is placed to measure strain along the transverse axis, z. The transverse measurement is conducted across the 3 cm span of the central vertical section of the cable. This specific length of 3 cm is selected to obtain a correct evaluation of the concrete strain considering the strain transfer of the optical fiber while embedded in the concrete. Each cable is affixed to a pigtail at both ends. The pigtail serves as the component facilitating the connection of the cable to the OF interrogator for recording strain measurements within the concrete sample.

2.3 Description of biaxial compressive creep tests

A set of eight unique bi-axial compressive creep frames was designed specifically to carry out creep tests under all THM configurations planned for the ACES project. These frames, showed in Figure 2, are equipped with two hydraulic jacks (one in each direction) capable of applying at least the load corresponding to a stress of 12 MPa on the 20 cm x 15 cm surface of the concrete sample. These jacks are fixed to a highly rigid metal frame to avoid any bending deformation. The frame and the jack assembly can maintain stresses for long periods (approximately 6 months) and withstanding the thermo-hydric conditions of the test configurations, particularly immersion in basic water. A metal plate measuring 20 cm x 15 cm is used to assure a correct stress distribution between the jack and the concrete sample. Pressure is applied via a hydraulic pump and is controlled using a manometer for each load direction. Creep deformation of concrete, especially during the first days of loading, results in a loss of pressure in the jacks. Each jack is paired with a nitrogen accumulator (Figure 2) to compensate any pressure decrease along all the test period (Ladaoui et al., 2013). The frame is placed in a plastic tank to ensure water immersion of the concrete sample. A heater and pump are placed in the tank to maintain a homogenized water temperature. The plastic tank is kept closed during the creep test to avoid water evaporation, and the water level is adjusted as needed.

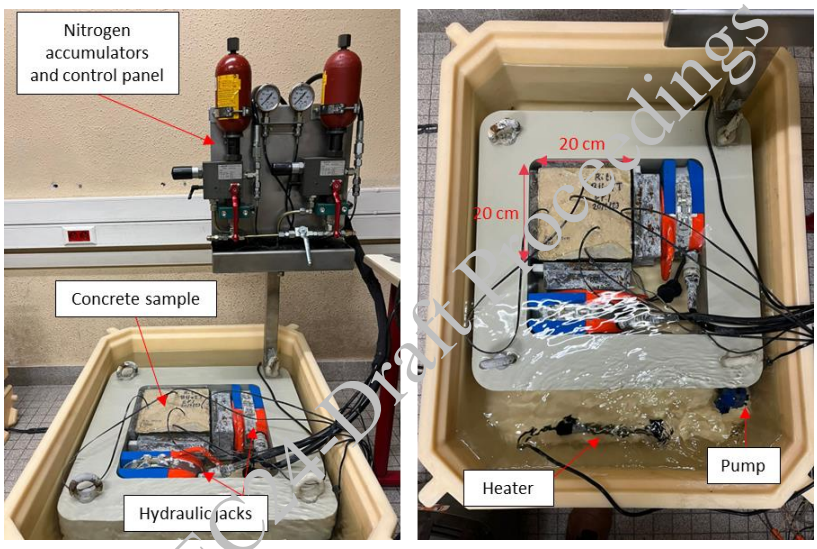

Figure 2. Experimental set-up for biaxial creep frame

Two mechanical loading cases were tested: a symmetrical 8.5 MPa loading and an asymmetrical 12 MPa / 8.5 MPa loading. The second type of loading represents the case of containment vessel prestressing. Each configuration was tested at 20°C and 38°C, resulting in a total of four tests of biaxial loading.

2.4 Description of uniaxial compressive creep tests

The uniaxial compressive tests were carried out on two slabs (20 cm x 20 cm x 15 cm) loaded at 8.5 MPa, immerged in water at 20°C and 38°C respectively (Figure 3). Compressive creep devices are equipped by a hydraulic jack and a nitrogen accumulator to maintain the pressure in spite of concrete creep (Ladaoui et al., 2013). The load is applied using a hydraulic pump and the pressure is controlled using a manometer. The creep frame allows two concrete specimens to be tested simultaneously at the same stress level by superimposing them one on top of the other. To guarantee a uniform distribution of the compressive stress in the sample, metal shims measuring 20 cm x 15 cm x 4.5 cm were added between the cylindrical 20 cm diameter jack, and the rectangular specimens faces of 20 cm x 15 cm.

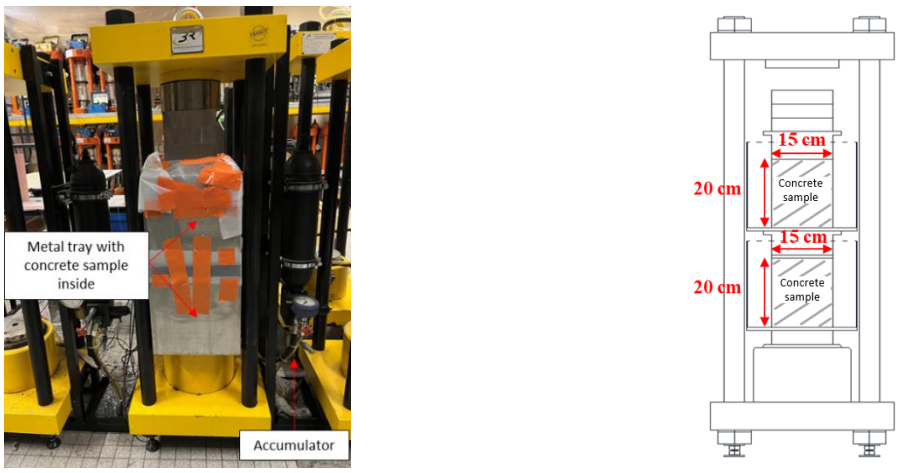

Figure 3. Experimental set-up for uniaxial creep frame

2.5 Thermo-Hydro-Mechanical conditions for creep tests

The chronology of the various THM (Thermo-Hydro-Mechanical) conditions of all the concrete specimens are detailed in Figure 4 from the day of casting until the day of unloading. To avoid complex combinations of physical mechanisms during the first days, each loading is applied separately with at least 3 days apart.

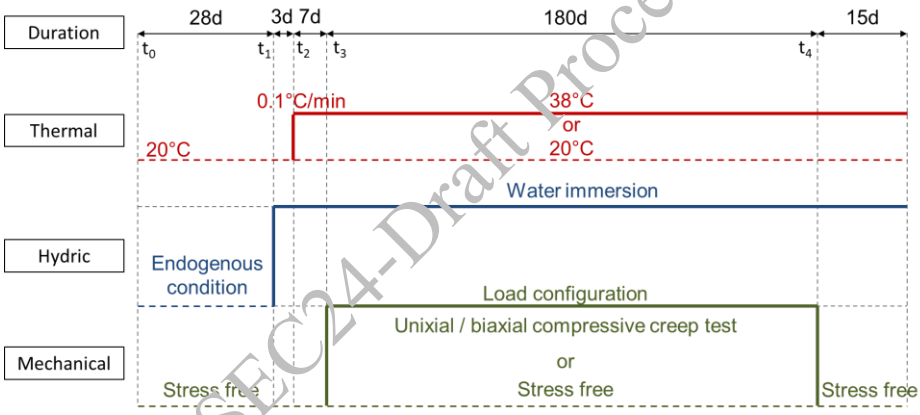

Figure 4. Chronology of THM conditions for all the specimens (stress free, uniaxial, and biaxial creep tests)

The day of casting is noted as t_0. After casting, concrete slabs were kept in their moulds, covered by plastic sheeting, and stored in a curing room at 50% ±5% RH and 20°C ±1°C. After one day, they were demoulded and covered by plastic sheeting to keep them in an endogenous condition and avoid moisture exchange. They were stored in closed plastic bags at 20°C for 28 days to stabilize hydration and be representative of the hygrometry conditions of concrete located in the mass of real structures.

At 28 days, concrete slabs were covered by aluminium foil on the four 20 cm x 15 cm lateral faces and immersed in water at room temperature (20°C). Only the two opposite faces of 20 cm x 20 cm are exposed directly to water to ensure unidirectional water diffusion in all the specimens whatever their loading conditions. The specimens not subjected to any load are immersed in plastic tanks. The specimens subjected to bi-axial loading are also immersed in water, along with the corresponding bi-axial devices, in individual plastic tanks (one tank per device). For specimens subjected to uniaxial loading, specimens are immersed in water in separate metal tanks. The date of immersion of specimens is noted as t_1.

After three days, water heating to 38°C was activated for samples subjected to creep tests at 38°C, with the water temperature controlled by a sensor with ±1°C precision. The heating rate was 0.1°C/min, as proposed by Ladaoui et al. (2013) to avoid thermal damage. The date of the temperature modification is noted as t_2.

Ten days after water immersion (seven days after heating activation), the corresponding mechanical load was applied. It is the beginning of concrete creep in the concrete samples. This date is noted as t_3.

After 180 days of creep test, concrete samples are unloaded, and the recovery strain of the sample are measured for 15 days. The date of mechanical unloading is noted as t_4.
Two stress free specimens are immersed in water at 20°C or 38°C, after three days of immersion at 20°C to measure the water absorption deformation in concrete samples without loading.

3. Fib Model Code 2020

The *fib* Model Code 2020 (*fib*, 2023) proposes assessing the basic creep strain $\varepsilon_{cc}(t,t_0)$, in the range of service stresses, using Eq.1:

$$\varepsilon_{cc}(t,t_0) = \varphi_{bc}(t,t_0)\frac{\sigma_c(t_0)}{E_{ci}} \quad (1)$$

Where $\sigma_c(t_0)$ is the creep-inducing stress applied at time t_0 and E_{ci} the modulus of elasticity at a concrete age of 28 days or at the time of loading.
The basic creep coefficient is calculated through:

$$\varphi_{bc}(t,t_0) = \beta_{bc1}.\beta_{bc}(f_{cm}).\beta_{bc}(t,t_0) \quad (2)$$

With $\beta_{bc}(f_{cm}) = \frac{1,8}{(f_{cm})^{0,7}}$ depending on the mean compressive strength at 28 days f_{cm} and $\beta_{bc1} = 1$ or can be fitted from experimental results.
The kinetic function is expressed by:

$$\beta_{bc}(t,t_0) = ln\left[\left(\frac{30}{t_{0,adj}} + 0.035\right)^2.(t-t_0)+1\right] \quad (3)$$

Where $t_{0,adj}$ is the adjusted time to consider the concrete maturity, which can be modified by curing temperature and the type of cement.

$$t_{0,adj} = t_0.\left[\frac{9}{2+{t_0}^{1.2}}+1\right]^{\alpha} \quad (4)$$

With α equal to -1, 0, or 1, depending on the type of cement. In this study α = 1 because the cement strength class is 42.5 R.
The effects of temperature on creep are considered through a multiplier factor applied to creep coefficient:

$$\varphi_{bc,T} = \varphi_{bc}.\varphi_T \quad (5)$$

With

$$\varphi_T = exp[0.015(T-20)] \quad (6)$$

T the temperature in °C.

4. Results and discussions

In this section, the results of basic creep strains in the loaded directions during the six-month loading period are presented from the date of loading t_3 until the end of loading t_4. Since all the creep test specimens are water-immersed, the water absorption strain measured on the stress-free concrete samples at 20°C and 38°C have been subtracted from the total creep strains to determine the basic creep of the concrete. This strains separation assumption is quite rough but commonly applied to analyse the creep strain in a first empirical approach. Figures 5, 6 and 7 present respectively the evolution of basic creep under a uniaxial load of 8.5 MPa, a symmetrical biaxial load of 8.5 MPa, and an asymmetrical biaxial load of 12 MPa / 8.5 MPa at 20°C and 38°C. The present study results are compared with other basic creep results obtained on the same concrete B11 by Charpin et al. (2018) and with the fitted *fib* Model. Compressive strains are presented as positive. In Figure 5, the evolution of basic creep is expressed in terms of specific creep: the creep strain is divided by the stress level to normalize the data per unit stress and to be able to compare with Charpin's results (performed at 12 MPa versus 8.5 MPa for the present study). In Figure 7(b), the experimental basic creep at 20°C from our study is not presented due to measurement problems in the 12 MPa loading direction.

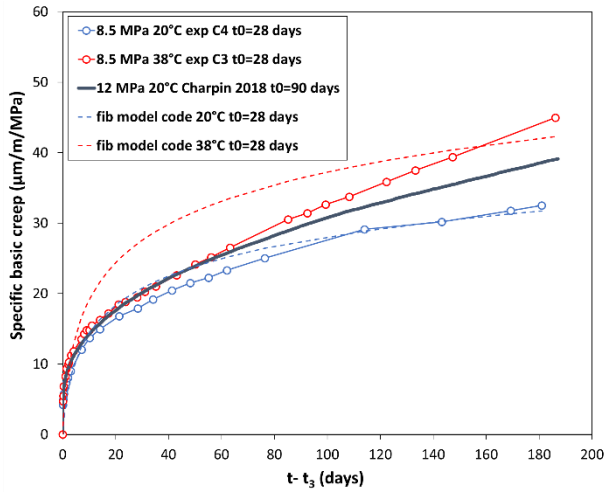

Figure 5. Specific basic creep under uniaxial load

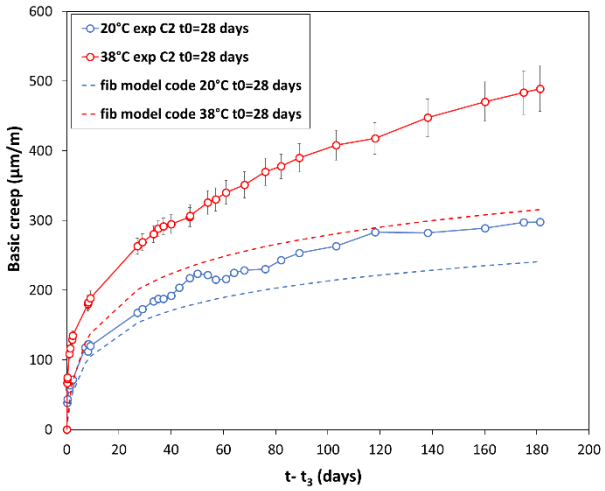

Figure 6. Basic creep under symmetrical biaxial load of 8.5 MPa

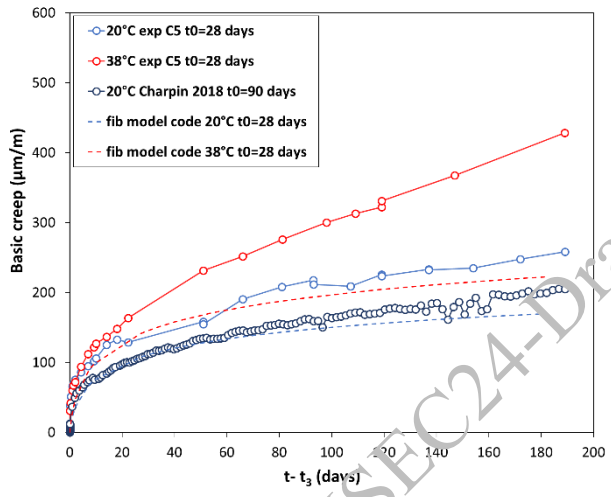

(a)

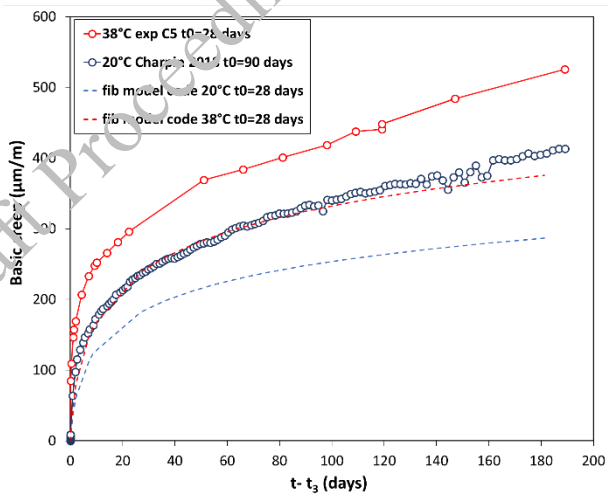

(b)

Figure 7. Basic creep under asymmetrical biaxial load of 12 MPa / 8.5 MPa; (a) direction loaded with 8.5 MPa; (b) direction loaded with 12 MPa

First, the results of the uniaxial creep test and the biaxial asymmetrical creep in the 8.5 MPa direction conducted at 20°C obtained in this study are similar to those reported by Charpin et al. (2018) for the same loading configuration. The small differences could be attributed to various factors, such as the water-to-cement ratio, which is 0.49 in Charpin's study compared to 0.46 in the present study. Additionally, the ten-year gap between Charpin's tests and our study may lead to differences in material quality. Other factors include the measurement technique, the age of loading and the sample conditioning during the creep test may explain these differences. The analysis of the creep results between 38°C and 20°C reveals significant effects of temperature on creep kinetics and amplitudes. For all configurations, the ratio of basic creep at 180 days between the tests conducted at 38°C and 20°C is approximately 1.41 to 1.67. This result aligns with a previous study by Vidal et al. (2016) on a high-performance concrete at 40°C. The increase in creep at 38°C is attributed to the decrease in water viscosity with temperature, which accelerates the sliding of C-S-H sheets. This can be verified by calculating the Arrhenius-type thermal activation law with an activation energy equivalent to that reducing the viscosity of water (2100 K) (Ladaoui et al., 2013). This law leads to a basic creep multiplier coefficient of 1.51 at 38°C, which is close to the ratio obtained from our experimental results.

Using equations 1 to 4, the basic creep according to the *fib* model code is modeled based on the experimental parameters such as σ_c, E_{ci} and f_{cm}. The single parameter β_{bc1} = 1.435 has been fitted to the uniaxial creep result at 20°C. For the 38°C tests, φ_T = 1.31 is determined based on equation 6, as it does not use another fitting parameter to account for temperature effects. The logarithmic form proposed by the *fib* model for uniaxial compressive creep appears relevant for reporting long-term delayed strain for concrete at 20 °C. For the 38°C uniaxial creep test, as shown in Figure 1, the predicted basic creep amplitude at 180 days matches well with the experimental results despite differences in the kinetics.
In the case of biaxial creep tests, the strain in each loaded direction is calculated using the generalized Hooke's Law and a Poisson's coefficient assumed to be equal to ν = 0.2. In the x direction the basic creep strain $\varepsilon_{cc_x}(t, t_0)$ will be: (For $\varepsilon_{cc_y}(t, t_0)$ swap x and y in the indices)

$$\varepsilon_{cc_x}(t, t_0) = \varphi_{bc}(t, t_0)\left(\frac{\sigma_{c_x}(t_0)}{E_{ci}} - \nu.\frac{\sigma_{c_y}(t_0)}{E_{ci}}\right) \quad (7)$$

As shown in Figures 6 and 7, despite the fitting, the *fib* model code underestimates the basic creep at 20°C and the effects of temperature for the biaxial loading cases.

5. Conclusions

This study focuses on the effects of temperature on the basic creep of concrete, particularly in the case of biaxially prestressing. An innovative biaxial creep frame was presented and different load configurations were tested on water-immersed concrete samples, which constitutes an originality of the study. Optical fiber technology was used to measure the creep strain. The 20°C creep test results were compared with a study presented in the literature to validate the frame and the measurement technique results. A comparison between the tests conducted at 20°C and 38°C shows an increase in the basic creep kinetics and magnitude over six months of creep testing. The origin of the creep increase lies in the decrease of water viscosity at this range of temperatures. A comparison with *fib* Model Code 2020 predictions is also proposed. It seems that the *fib* Model Code fitting, using a single parameter, is not sufficient to predict these strain evolutions particularly for creep under temperature and in the direction of the largest stress in asymmetrical biaxial loading. These limitations can be explained by the underestimation of temperature and biaxial loading effects. More THM configurations will be carried on another concrete mix and effect of temperature will be investigated at 50°C. The analysis of all the experimental data and the comparison with the *fib* Model will guide us in proposing possible improvements to the model.

Acknowledgements

This work was carried out at LMDC Toulouse in collaboration with, and with support from, IRSN. The authors thank P. Nicot and F. Réau from the Technology Transfer Division at LMDC for participating in the design of the biaxial creep frames and the experimental program. The authors want also to thank the ACES project members for funding this work (Grant Agreement No. 900012). ACES (aces-h2020.eu)

References

Charpin, L., Le Pape, Y., Coustabeau, É., Toppani, É., Heinfling, G., Le Bellego, C., Masson, B., Montalvo, J., Courtois, A., Sanahuja, J., Reviron, N., (2018) "A 12 year EDF study of concrete creep under uniaxial and biaxial loading", *Cement and Concrete Research* 103, 140–159.

EN, (2004) "Eurocode 2: Design of concrete structures, part 1-1: General rules and rules for buildings" Brussels, Belgium: *European Committee for Standardization*.

FIB (2023) "*fib Model Code for Concrete Structures (2020)*" Lausanne, Switzerland: *Fédération Internationale du Béton.*

Ladaoui, W., Vidal, T., Sellier, A., Bourbon, X., (2013) "Analysis of interactions between damage and basic creep of HPC and HPFRC heated between 20 and 80°C". *Materials and structures* 46, 13.

Vidal, T., Sellier, A., Cagnon, H., Ladaoui, W., Bourbon, X., (2016) "Experimental investigation and modelling of temperature effects on basic creep of concrete". *fib symposium*.

Gravimetric and Electrochemical Interpretation of Plant Extract as Corrosion Inhibitor for Embedded-Steel in Concrete Pore Solution

M. Gautam[1], N.P. Bhattarai[2*], and J. Bhattarai[3*]

[1]Central Department of Chemistry, Tribhuvan University, Kirtipur, Nepal,
Email: madhab.gautam@tmc.tu.edu.np
[2]Central Department of Chemistry, Tribhuvan University, Kirtipur, Nepal,
Email: neutan08@gmail.com
[3]Central Department of Chemistry, Tribhuvan University, Kirtipur, Nepal,
Email: bhattarai_05@yahoo.com

[*]Corresponding author

ABSTRACT

Nowadays, reinforced concrete infrastructures face a significant challenge of early corrosion of reinforced metal (RM). Understanding the corrosion mechanisms and developing effective mitigation strategies is crucial to ensure the durability and safety of the RM in concrete structures. The study aimed to investigate the effectiveness of leaf extracts from *Ziziphus budhensis* (LEZB) and *Tagetes erecta* (LETE) as eco-friendly corrosion inhibitors in a strongly alkaline solution with a pH of around 11.5 (SCP-simulated concrete pore solution). The weight loss experiment lasted over four months to assess the ability of these leaf-based extracts to inhibit corrosion of RM in SCP solution (SCPs) at various concentrations (500 ppm, 1000 ppm, 2000 ppm, and 4000 ppm). The LEZB outperforms LETE at all concentrations. The highest corrosion inhibition effectiveness is at 4000 ppm, with 91.22% and 81.48% efficacy through gravimetric (weight loss) and electrochemical methods, respectively. The corrosion current densities decrease with increasing concentrations of both plant-based extracts in the SCPs, as revealed by the polarization study. Both extracts contain phyto-molecules (polyphenols, alkaloids, and flavonoids), which adhere to the surface of steel rebars, thus impeding both cathodic and anodic reactions. These suggest that plant-based extract in SCPs enhances the efficacy of corrosion prevention.

KEYWORDS: *Gravimetric, Plant based inhibitor, Concrete corrosion, Polarization*

1. Introduction

Reinforced concrete infrastructures, abbreviated as RCIs, are widely utilized in modern engineering and construction sectors due to their exceptional ability to withstand heavy loads and harsh environmental conditions. Their durable nature ensures that these structures have a long lifespan, making them a choice for various construction projects. (Hemkemeier *et al.*, 2022). However, RCIs, despite their strength and durability, are prone to a significant drawback: the rapid corrosion of the reinforcing materials when they come into contact with corrosive atmospheres, such as those containing high amounts of salt or pollutants. This corrosion can weaken the structure and necessitate costly maintenance and repairs (Song *et al.*, 2024). The surrounding corrosive atmospheres of marine environments, with high levels of chloride ions, as well as of the polluted atmospheres with overburdened CO_2, sulfate, and sulfide gases in industrial and even urban areas (Sun *et al.*, 2022), can lead to a decrease in the pH of concrete aggregates from 12.5-13.5 to less than 10 (Broomfield, 2019). When the pH level of the concrete pore solution decreases below 10, it can lead to the corrosion of RM in concrete (Herb *et al.*, 2020). These are the main reasons for the rapid degradation of reinforced concrete structures through rust formation on the surface of RM instead of the formation of protective diffusion barrier passive films (Bhattarai, 2010).
Therefore, one of the inherent limitations of structural infrastructures constructed from reinforced concrete is the gradual deterioration of the metallic reinforcement in urban cities of Nepal (Laudari *et al.*, 2023; Phulara & Bhattarai, 2019). Over time, the interaction between the reinforced metal (RM) and the

surrounding corrosive environment results in corrosion damage, which weakens the reinforcement and ultimately threatens the structural integrity of the RCIs (Wang *et al.*, 2024). Failure to address this issue can lead to costly repairs, pose safety risks, and shorten the lifespan of the structural infrastructures (Andrade, 2019). Therefore, it is essential to implement appropriate measures to prevent, mitigate, or repair corrosion of RCIs (Bhattarai *et al.*, 2021). Various strategies have been employed, including electrochemical removal of chlorine (Bouteiller *et al.*, 2022), re-alkalization of concrete (Karmegam *et al.*, 2022), cathodic protection methods (Ha *et al.*, 2023; Arya & Dhanya, 2021), and use of inhibitors, for examples, inorganic compounds (Pradhan *et al.*, 2021; Reddy *et al.*, 2020), synthesized organic compounds (Roka *et al.*, 2023; Shen & Zhang, 2022), or phyto-molecules (Somai *et al.*, 2023) as concrete additives to mitigate reinforcement concrete corrosion.

Corrosion inhibitors stand out among these methods due to their high effectiveness, eco-friendliness, and cost-efficiency (Wang *et al.*, 2021; Amgain *et al.*, 2022). It is noticed in previous studies that synthetic organic compounds have gained popularity as corrosion inhibitors over inorganic ones due to their less toxic and environmentally benign nature (Alvarez *et al.*, 2023). However, more efficient, non-toxic, and environmentally friendly phyto-molecules can be extracted from different parts of plants (e.g., leaves, barks, stems, roots) and utilized to create plant extracts for corrosion inhibition of metals in corrosive electrolytes (Eddy *et al.*, 2023; Umoren *et al.*, 2019). Phyto-molecules having aromatic rings, unsaturated π-systems, and heteroatoms in plant-based extract play a crucial role in preventing the deterioration of steel rebar embedded in a concrete composite (Giri *et al.*, 2023; Angst, 2018).

The present study intends to investigate the efficacy of leaf extracts derived from *Ziziphus budhensis* (LEZB) and *Tagetes erecta* (LETE) plants as environmentally benign corrosion inhibitors in a saturated calcium hydroxide solution which presumes as simulated concrete pore (SCP) solution having pH around 11.5. The primary objective is to assess the feasibility of using LEZB and LETE as eco-friendly corrosion inhibitors in SCP. In this regard, the study aims to evaluate the effectiveness of both the plant-based inhibitors in protecting steel rebar in the SCP solution through gravimetric and electrochemical tests. The findings can offer valuable insights for implementing such inhibitors in concrete.

2. Experimental Methods

The leaves of the *Ziziphus budhensis* [Fig. 1(a)] and *Tagetes erecta* plants [Fig. 1(b)] were collected and authenticated at the National Herbarium and Plant Laboratory of the Plant Department in Godavari, Lalitpur. Subsequently, the leaves were separately dried, pulverized to make powder form, and soaked in methanol at a 1:2 ratio for two weeks with regular stirring, as illustrated in Fig. 1(c). Then, the supernatant was filtered and evaporated using a rotary evaporator [Fig. 1(d)], as described elsewhere (Subedi *et al.*, 2019), to obtain a semi-solid form of both plant extracts separately. The semi-solid extracts of *Ziziphus budhensis* and *Tagetes erecta*, abbreviated as LEZB and LETE, respectively, were stored at 4° C until used for the research. The SCP solution was prepared using a saturated solution of slaked lime in distilled water, with a pH of around 11.5.

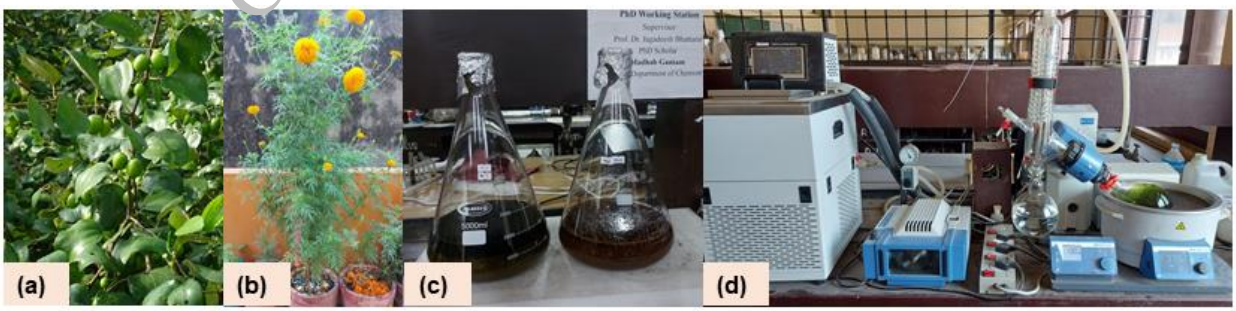

Figure 1. Photographs showing leaves of (a) *Ziziphus budhensis* and (b) *Tagetes erecta* plant, (c) soaking of pulverized leaf powder, and (d) rotary evaporator for removal of solvent

Twenty-seven rust-free mild steel rods, each with an average diameter of 113 mm, were prepared for gravimetric analysis, as discussed elsewhere (Bhattarai *et al.*, 2016). The initial weights of these specimens were recorded meticulously using a 5-digit micro-balance having an accuracy of 0.00001 grams. Among 27 samples, three were submerged individually in three 100 mL beakers, each containing 50 mL of

SCP solution without LEZB or LETE, which served as the control SCP solution. The remaining 24 samples were dipped individually in three 100 mL beakers, each containing 50 mL of SCP solution with 500, 1000, 2000, and 4000 ppm LEZB and LETE for four months or more. The steel rod pieces were subjected to regular weight measurements using a digital micro-balance at 7, 14, 28, 43, 60, 90, and 118 days while exposed to each SCP solution. Subsequently, the corrosion rate (CoR) of rod specimens in control SCP solution ($CoR_{control}$) or in SCP solution with LEZB or LETE ($CoR_{inhibit}$) and the corrosion inhibition efficiency (CoIE) were calculated (Magrati *et al.*, 2020), using the formula given in equations (1) and (2), respectively.

$$CoR_{Control\ /\ Inhibitor}\ (mm/y) = \frac{\Delta w\ (g) \times 87600}{A\ (cm^2) \times \rho\ (g/cm^2) \times t\ (hr)} \quad (1)$$

$$CoIE\ (\%) = \frac{CoR_{control} - CoR_{inhibitor}}{CoR_{control}} \times 100 \quad (2)$$

Where, Δw is the weight lost after immersion for t hour, A is the area of the steel rod specimen that was calculated using the 2πr (r+l) formula, and ρ is the density of the steel rod (7.86 g/cm³).

Similarly, the electrochemical analysis was carried out through a potentiodynamic polarization study using a potentiostat/Galvanostat (Iquant 64) connected to a cell with a three-electrodes system comprising a saturated calomel electrode (as a reference electrode), platinum electrode (auxiliary electrode), and steel rod (working electrode), as explained elsewhere (Bhattarai, 2023). The corrosion potential (ϕ_{corr}), corrosion current density (i_{corr}), CoR based on the i_{corr} (CoR_{icorr}), and CoIE based on the i_{corr} ($CoIE_{icorr}$) were obtained from potentiodynamic polarization measurements. The Tafel plots were extrapolated to calculate CoR_{icorr} and $CoIE_{icorr}$, following formulas (3) and (4), respectively (Reedy *et al.*, 1998; Fouda *et al.*, 2013). Furthermore, thermodynamic parameters were determined from the linear fit plots of the Langmuir adsorption model (Langmuir, 1916) as presented in equation (5).

$$CoR_{icorr} = 0.13 \times i_{corr} \times \frac{E}{\rho} \quad (3)$$

$$CoIE_{icorr}\ (\%) = \frac{i_{corr\ (control)} - i_{corr\ (inhibitor)}}{i_{corr\ (control)}} \times 100 \quad (4)$$

$$\frac{C_{LEZB\ /\ LETE}}{\theta} = \frac{1}{K_{ads}} + C_{LEZB\ /\ LETE} \quad (5)$$

Where E is the equivalent weight of rebar (55.85), $C_{LEZB\ /\ LETE}$ is the concentration of LEZB or LETE extract, θ is surface coverage, and K_{ads} is the equilibrium adsorption constant. The free energy change ($\Delta G°_{ads}$) can calculated using $K_{ads} = -2.303RT \times \log (55.55 \times K_{ads})$.

The functional groups in LEZB and LETE were characterized using FT-IR spectra (IR Affinity-1S, Shimadzu Corp., Japan). Primary screening tests were conducted on the extracts to identify their secondary metabolites. The surface analysis of the ReMS rod before and after exposure to the SCP solution was also studied using optical images taken by Olympus SZ 61 microscope.

3. Results and Discussions

The secondary metabolites of LEZB and LETE, confirmed by qualitative chemical screening tests, were found to be heteroatoms, unsaturated π-electrons, or aromatic rings containing secondary phyto-molecules (alkaloids, flavonoids, glycosides, phenols, tannins, and terpenoids). The results obtained from the chemical screening tests for LRZB (El Maaiden *et al.*, 2020; Elaloui *et al.*, 2016) and LETE (Chaudhari *et al.*, 2024; Chaudhary, 2023) are consistent with the findings documented in the existing literature. These phyto-molecules of LETE and leaf extract of *Ziziphus sps* can form a diffusion barrier passive layer on the surface of reinforcing steel through adsorption and prevent the corrosion of the rebar metal, which is consistent with previous literature (Mourya *et al.*, 2014; Sirajunnisa *et al.*, 2014).

The FTIR spectra shown in Fig. 2(a) and 2(b) indicate the identification of functional groups in LEZB and LETE, respectively. These are characterized by the FTIR peak values, at approximately 3363-3340 cm^{-1}

for O–H stretching vibration in aromatic compounds (Sulistiawan *et al.*, 2022), 1730-1715 for C–H or C=O stretching vibration (Saifitri *et al.*, 2021), 1605 cm^{-1} for aromatic C=C stretching (Yue *et al.*, 2018), 1457-1450 cm^{-1} for C–H stretching (Barcelo *et al.*, 2015), 1256 cm^{-1} for C-O stretching and C–H stretching at 1038-1026 cm^{-1} for O–H or C–H bending of aromatics (Veedu *et al.*, 2019).

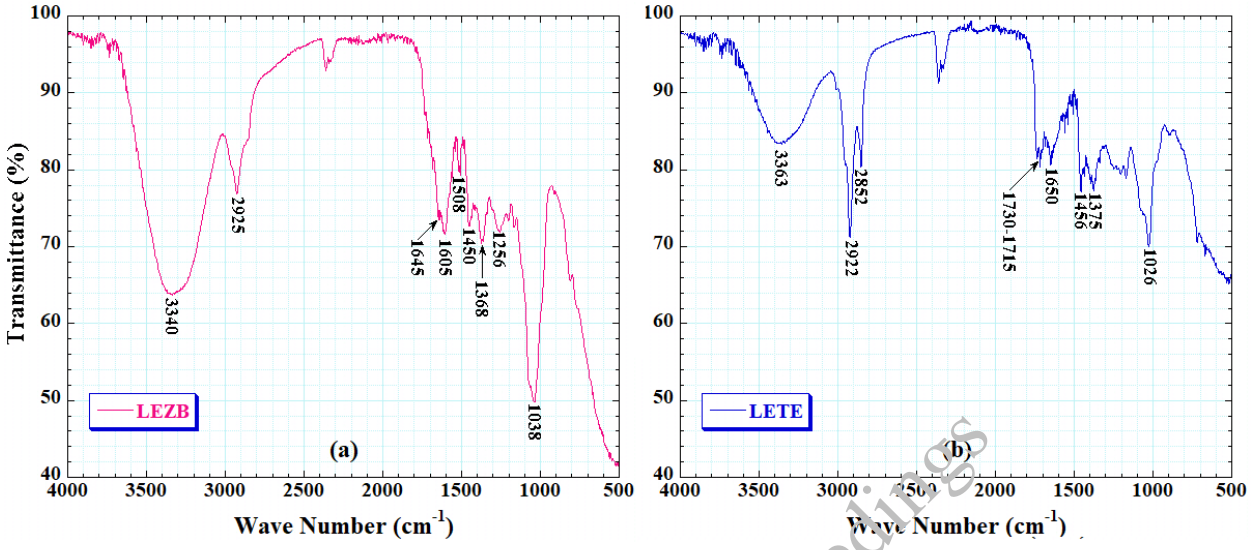

Figure 2. FTIR spectra of (a) LEZB and (b) LRTE.

The corrosion rates obtained from gravimetric analysis for the steel rebar immersed in SCPs at different immersion intervals are in Figs. 3(a) and 4(a). These figures demonstrate that the corrosion rate of mild steel decreases with the addition of LEZB or LETE concentrations in SCP solution, compared to SCP without inhibitors (i.e., control specimen). Explicitly, the corrosion inhibition effect of the LEZB in the SCP solution is remarkably higher than the LETE, indicating more effective corrosion prevention for the steel rebar, with increasing concentrations of LEZB in the SCP, as illustrated in Fig. 3(a).

Furthermore, Figs. 3(b) and 4(b) show the changes in the corrosion inhibition efficiencies (CoIE) of both LEZB and LETE extracts on the mild steel in SCP solution. In the addition of 500-1000 ppm of both the plant extracts in SCP, the CoIE increased at a steep angle, and it increases moderately with further increase in the extract concentrations, showing maximum CoIE at 4000 ppm LEZB or LETE in SCP solution for mild steel. The highest corrosion inhibition efficiency (CoIE), reaching 91.2%, was observed after immersing the mild steel rod for 2802 hours in a solution containing 4000 ppm of LEZB. A similar trend was observed in the corrosion resistance performance of SCP solution with 4000 ppm of LETE, reaching a maximum of 67.81% CoIE. A previous study reported that the adsorption of $Ca(OH)_2$ increases donor density and vacancy flux, reduces the defects diffusion coefficient, and accelerates the oxidation of Fe(II) to Fe(III) (Long *et al.*, 2022). It aids in forming a new passive film with improved resistance to corrosion. We anticipate that the presence of plant-based extracts significantly influences the nucleation and growth of the passive film when $Ca(OH)_2$ is involved.

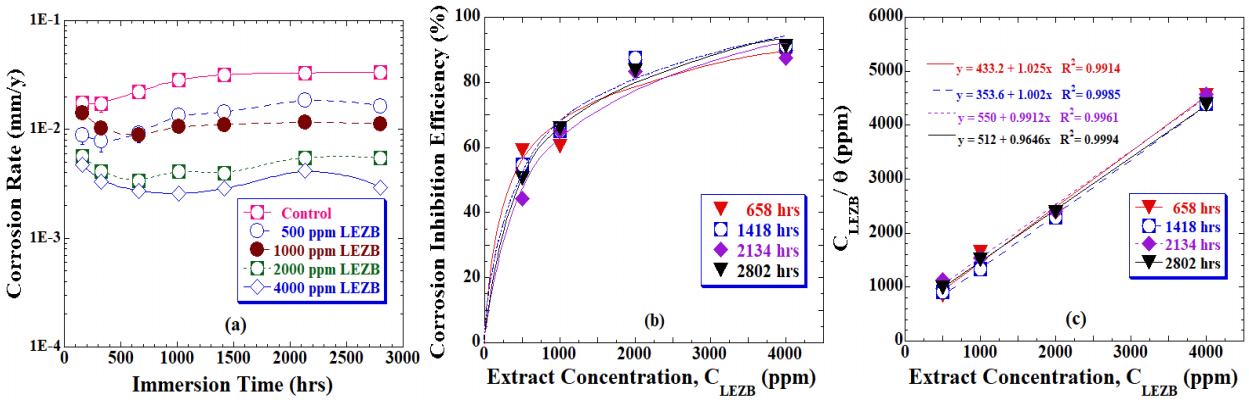

Figure 3. Variation of corrosion rate (a), corrosion inhibition efficiency (b) and Langmuir plots (c) of steel rod in SCP solution with different concentrations of LEZB.

The leaf-derived extracts of LEZB and LETE, as reported from the chemical screening tests above, consist of a diverse array of secondary phyto-molecules, including alkaloids, flavonoids, glycosides, phenols, and terpenoids. These secondary phyto-molecules, comprised of heteroatoms and π-electrons ring compounds, are postulated to act as focal points for interaction with the corroded surfaces of mild steel in a SCP solution with a strongly alkaline $Ca(OH)_2$ electrolyte (Umoren *et al.*, 2019). Another study indicated an 89% inhibition efficiency when a 3.5% NaCl-saturated $Ca(OH)_2$ solution was blended with a 4% organic inhibitor (Wang *et al.*, 2020). The study confirmed the protective effects for steel by detecting an organic film comprising aromatic groups of the blended-organic inhibitor on the surface of the carbon steel. Therefore, the corrosion-controlling process of the mild steel in SCP solution with plant-based inhibitors involved the development of a protective passive film on the steel surface (Rana *et al.*, 2017). This corrosion-protecting passive film formation is also due to the adsorptive interaction of phyto-molecules of the plant extract with the steel surface (Lgaz & Lee, 2024). The Langmuir isotherms describe the corrosion inhibition mechanism due to their ease of application and provision of sufficient information (Ahanotu *et al.*, 2020), as illustrated in Figs. 3(c) and 4(c). These maximum CoIE values in both plant extracts containing SCP solutions, estimated using the gravimetric (weight loss) method, are nearly in agreement with the CoIE estimated from the electrochemical analysis.

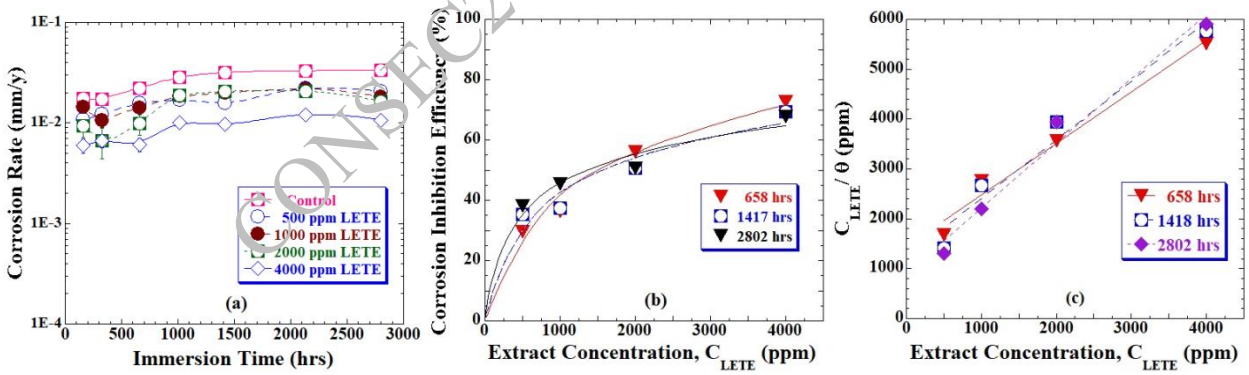

Figure 4. Variation of corrosion rate (a), corrosion inhibition efficiency (b) and Langmuir plots (c) of steel rod in SCP solution with different concentrations of LETE.

Furthermore, Figs. 5(a) and 5(b) depict the potentiodynamic polarization outcomes in the form of Tafel plots for steel in SCP solution without (control) and with different concentrations of LEZB and LETE, respectively. Following the extrapolation of Tafel plots using the LPR method, electrochemical parameters are estimated and presented in Table 1. The additions of either LEZB or LETE extract in the SCP solution enhance a decrease in the icorr value, suggesting the formation of a passive layer on the surface of the steel rebar.

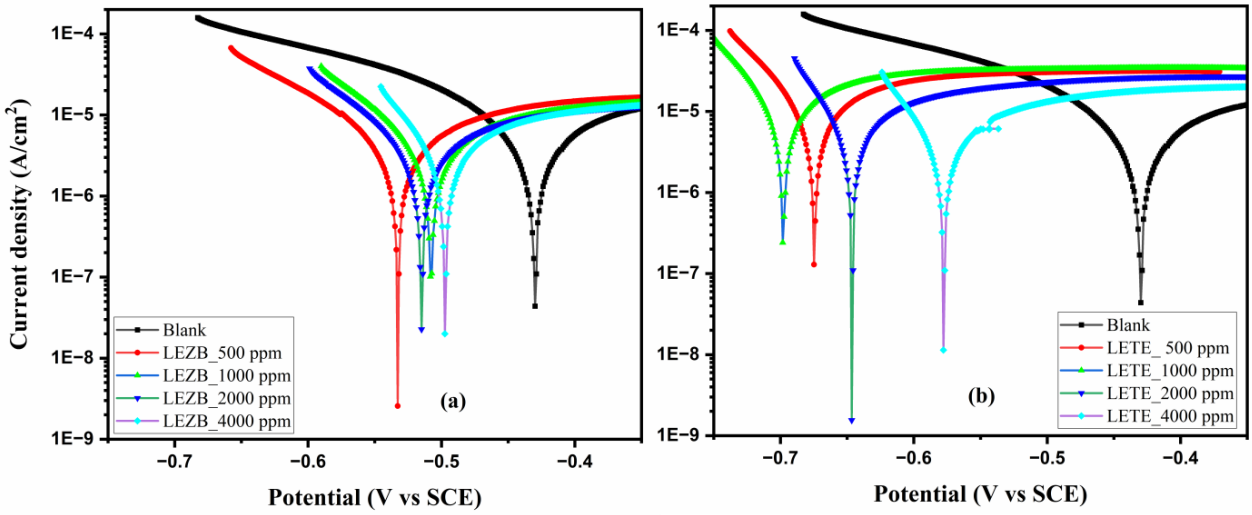

Figure 5. Potentiodynamic polarization curves for steel rebar immersed in SCPs without and with different concentrations of (a) LEZB and (b) LETE.

The addition of plant extracts enhances the potential for protecting steel rebar in SPC solution, as evidenced by the decreased corrosion rate (CR) and increased inhibition efficiency (IE%) values (Table 1). The highest inhibition efficiency (i.e., 81.4%) attains in SCP solution with 4000 ppm LEZB, compared with other concentrations of both extracts. These findings from electrochemical tests align closely with those obtained from gravimetric tests, indicating that the 4000 ppm of LEZB extract could be an effective corrosion inhibitor for concrete additives.

Table 1. Gravimetric and electrochemical parameters obtained from weight loss and LPR methods.

	Inhibitor (ppm)	ϕcorr (mV)	icorr (µA/cm2)	icorr – based CoR (mm/y)	icorr - based CoIE (%)	Wt.-based CoR (mm/y)	Wt.-based CoIE (%)
Control	–	-428.4	7.301	6.75	–	0.03324	–
LEZB	500	-529.5	3.111	2.87	56.74	0.01642	50.61
	1000	-508.4	3.027	2.79	58.67	0.01131	65.98
	2000	-514.3	1.925	1.78	73.63	0.00546	83.57
	4000	-495.8	1.357	1.25	81.48	0.00292	91.22
LETE	500	-673.6	3.606	3.33	50.67	0.02052	38.27
	1000	-698.7	3.105	2.87	57.48	0.01816	45.37
	2000	-646.9	3.039	2.81	58.37	0.01641	50.63
	4000	-576.2	1.918	1.77	73.78	0.01070	67.81

4. Conclusions

Based on both gravimetric weight loss and electrochemical tests, as the knowledge of the authors, for the first time, this study shows that plant extracts (LEZB and LETE) effectively inhibit corrosion in mild steel exposed to simulated concrete pore solution. The extracts create protective surface layers, reducing the corrosion rate of the steel. The optimal inhibition efficiency was 91.22% and 81.48% with 4000 ppm of LEZB in the concrete pore solution from the gravimetric and electrochemical tests. Both methods

confirmed the decrease in the corrosion rate of the steel. This finding motivates researchers to investigate the anti-corrosive characteristics of novel plant-based extracts as additives in concrete.

Acknowledgements

The University Grants Commission (UGC-Nepal) for providing Ph.D. Research Award: PhD-78/79 S&T-03 (MG).

References

Ahanotu, C.C., Onyeachu, I.B., Solomon, M.M., Chikwe, I.S., Chikwe, O.B. and Eziukwu, C.A. (2020) "*Pterocarpus santalinoides* Leaves Extract as a Sustainable and Potent Inhibitor for Low Carbon Steel in a Simulated Pickling Medium", *Sustainable Chemistry and Pharmacy*, 15: 100196.

Alvarez, L., de Rincón, O.T., Escribano, J. and Troconis, B.R. (2023) "Organic Compounds as Corrosion Inhibitors for Reinforced Concrete: A Review", *Corrosion Reviews*, 41(6): 617-634.

Amgain, K., Subedi, B.N., Joshi, S. and Bhattarai, J. (2022) "A Comparative Study of of the Anticorrosive Response of *Tinospora cordifolia* Stem Extract for Al and Cu in Biodiesel-based Fuels", *E3S Web of Conferences*, 355: 01005.

Andrade, C. (2019) "Propagation of Reinforcement Corrosion: Principles, Testing and Modelling", *Materials and Structructure*, 52: 2.

Angst, U.M. (2018) "Challenges and Opportunities in Corrosion of Steel in Concrete", *Materials and Structures*, 51: 4.

Arya, E.K. and Dhanya, B.S. (2021) "Corrosion Control of Reinforced Concrete Structures in Construction Industry: A Review", *IOP Conference Series: Materials Science and Engineering*, 1114: 012006.

Barcelo, J.M., Gatchallan, A.M., Aquino, I.J.B., Ollero, D.R.E., Cortez, F.L.D., Costales, T.M. and Marzo, L.A.Q. (2015) "FTIR Spectrum and Antimutagenicity of *coffea arabica* Pulp and *Arachis hypogaea* Test in Relation to Their *In vitro* Antioxidant Properties", *Asia Pacific Journal of Multidisciplinary Research*, 3(4): 99-108.

Bhattarai, J. (2010) "*Frontiers of Corrosion Science* (1st ed.)", Kshitiz Publication, Kirtipur, Nepal, pp. 304 (ISBN: 978-99946-47-30).

Bhattarai, J. (2023) "Development of Mn-Mo-X-Y-Z-O Based Electrocatalytic Materials for Making Hydrogen Fuel from Saline Water", *Materials Today: Proceedings*, 80: 918-924. https://doi.org/10.1016/j.matpr.2022.11.328

Bhattarai, J., Rana, M., Bhattarai, M.R. and Joshi, S. (2016) "Effect of Green Corrosion Inhibitor of Callistemon Plant Extract on the Corrosion Behavior of Mild Steel in NaCl and HCl Solutions", *CORCON 2016 Proceedings*, Publication of NIGIS/NACE, Paper No. MI-17 1-8.

Bhattarai, J., Somai, M., Acharya, N., Giri, A., Roka, A. and Phulara, N.P. (2021) "Study on the Effects of Green-Based Plant Extracts and Water-Proofers as Anti-Corrosion Agents for Steel-Reinforced Concrete Slabs", *E3S Web of Conferences*, 302: 02018.

Bouteiller, V., Tissier, Y., Marie-Victoire, E., Chaussadent, T. and Joiret, S. (2022) "The Application of Electrochemical Chloride Extraction to Reinforced Concrete- A Review", *Construction and Building Materials*, 351: 128931.

Broomfield, J.P. (2019) "*Corrosion of Steel in Concrete: Understanding, Investigation, and Repair* (2nd ed.)", London, UK: CRC Press, Taylor & Francis Group, pp. 296.

Chaudhari, D., Muthal, A., Mali, A., Salunke, M. and Shinde, V. (2024) "Phytochemical and Pharmacological Activities of *Tagetes erecta* L: An Updated Review", *International Journal of Herbal Medicine*, 12(1): 10-15.

Chaudhary, P.H. (2023) "Pharmacognostical and Phytochemical Studies on Leaves of *Tagetes erecta* Linn", *Journal of Ayurveda and Integrated Medical Sciences*, 8(7): 29-36.

Eddy, N.O., Odiongenyi, A.O., Ebenso, E.E., Garg, R. and Garg, R. (2023) "Plant Wastes as Alternative Sources of Sustainable and Green Corrosion Inhibitors in Different Environments", *Corrosion Engineering, Science and Technology*, 58(5): 521-533.

El Maaiden, E., El Kharrassi, Y., Qarah, N.A.S., Essamadi, A.K., Moustaid, K. and Nasser, B. (2020) "Genus *Ziziphus*: A Comprehensive Review on Ethnopharmacological, Phytochemical and Pharmacological Properties", *Journal of Ethnopharmacology*, 259: 112950.

Elaloui, M., Laamouri, A., Ennajah, A., Cerny, M., Mathieu, C., Vilarem, G., Chaar, G., Hasnaoui, B. (2016) "Phytoconstituents of Leaf Extracts of *Ziziphus jujuba* Mill. Plants Harvested in Tunisia", *Industrial Crops and Products*, 83: 133-139.

Fouda, A.S., El-desoky, A.M. and Ead, D.M. (2013) "Anhydride Derivatives as Corrosion Inhibitors for Carbon Steelin Hydrochloric Acid Solutions", *International Journal of Electrochemical Science*, 8: 8823-8847.

Giri, A., Gautam, M., Roka, A., Bhattarai, N.P. and Bhattarai, J. (2023) "Performance of anticorrosive measures of steel in concrete infrastructure by plant-based extracts", *Macromolecular Symposia*, 410(1): 2200115.

Ha, J., Jeong, J. and Jin, C. (2023) "Development of Conductive Mortar for Efficient Sacrificial Anode Cathodic Protection of Reinforced Concrete Structures-part 2: Four-year Performance Evaluation in Bridges", *Applied Sciences*, 14(5): 1797.

Harb, M.B., Abubshait, S., Etteyeb, N., Kamoun, M. and Dhouib, A. (2020) "Olive Leaf Extract as a Green Corrosion Inhibitor of Reinforced Concrete Contaminated with Seawater", *Arabian Journal of Chemistry*, 13(3): 4846-4856.

Hemkemeier, T.A., Almeida, F.C., Sales, A. and Klemm, A.J. (2022) "Corrosion Monitoring by Open Circuit Potential in Steel Reinforcements Embedded in Cementitious Composites with Industrial Wastes", *Case Studies in Construction Materials*, 16: e01042.

Karmegam, A., Avudaiappan, S., Amran, M., Guindos, P., Vatin, N.I. and Fediuk, R. (2022) "Retrofitting RC Beams Using High-early Strength Alkali-activated Concrete", *Case Studies in Construction Materials*, 17: e01194.

Langmuir, I. (1916), "The Constitution and Fundamentalproperties of Solids and Liquids: part I-Solid", *Journal of the American Chemical Society*, 38(11): 2221-2295.

Laudari, I., Phulara, N.R., Gautam, M. and Bhattarai, J. (2021) "Evaluation of Corrosion Condition of Some Steel-Reinforced Concrete Infrastructures Available in Pokhara Valley of Nepal", *Tribhuvan University Journal*, 36(1): 1-17.

Lgaz, H. and Lee, H.S. (2024) "Interfacial Adsorption Mechanism of Hydroxycinnamic Acids on Iron Surfaces: A Computational Perspective Toward Eco-friendly Corrosion Mitigation Strategies", *Applied Surface Science*, 644: 158763.

Long, H., Chen, L., Dong, B., Sun, Y., Yan, Y. and Chen, C. (2022) "The Electronic Properties and Surface Chemistry of Passive Film on Reinforcement: Effect of Composition of Simulated Concrete Pore Solution", *Construction and Building Materials*, 360: 129567.

Magrati, P., Subedi, D.B., Pokharel, D.B. and J. Bhattarai, J. (2020) "Appraisal of Different Inorganic Inhibitors Action on the Corrosion Control Mechanism of Mild Steel in HNO_3 Solution", *Journal of Nepal Chemical Society*, 41(1): 64-73.

Mourya, P., Banerjee, S. and Singh, M.M. (2014) Corrosion Inhibition of Mild Steel in Acidic Solution by *Tagetes erecta* (Marigold Flower) Extract as a Green Inhibitor", *Corrosion Science*, 85, 352-363.

Phulara, N.R. and Bhattarai, J. (2019) "Assessment on Corrosion Damage of Steel Reinforced Concrete Structures of Kathmandu Valley Using Corrosion Potential Mapping Method", *Journal of the Institute of Engineering*, 15(2): 45-54.

Pradhan, B. (2021) "A Study on Effectiveness of Inorganic and Organic Corrosion Inhibitors on Rebar Corrosion in Concrete: A Review", *Materials Today: Proceedings*, 65: 1360-1366.

Rana, M, Joshi, S. and Bhattarai, J. (2017) "Extract of Different Plants of Nepalese Origin as Green Corrosion Inhibitor for Mild Steel in 0.5 M NaCl Solution", *Asian Journal of Chemistry*, 29(5): 1130-1134.

Reddy, V.S., Prashanth, T., Raju, V.S.P. and Prashanth, P. (2020) "Effect of Organic and Inorganic Corrosion Inhibitors on Strength Properties of Concrete", *E3S Web of Conferences*, 184: 01112.

Reedy, C.L., Corbett, R.A. and Burke, M. (1998) "Electrochemical Tests as Alternatives to Current Methods for Assessing Effects of Exhibition Materials on Metal Artifacts", *Studies in Conservation* 43: 183-196.

Roka, A., Gautam, M. Giri, A., Bhattarai, N.P. and Bhattarai, J. (2023) "The Anti-degradation Consequences of Water Repellent-based Inhibitors for Controlling Mild Steel Corrosion in Concrete Composite", *E3S Web of Conferences*, 455: 01002.

Saifitri, E., Humaira, H., Nazaruddin, N., Susilawati, S., Murniana, M. and Md Sani, N.D. (2021) "*Dioscorea alata* L. Anthocyanin Extract as Methanol as a Sensitive pH Active Compound", *Journal of Physics Conference Series*, 1869(1): 012508.

Shan, H., Xu, J., Wang, Z., Jiang, L. and Xu, N. (2016) "Electrochemical Chloride Removal in Reinforced Concrete Structures: Improvement of Effectiveness by Simultaneous Migration of Silicate Ion", *Construction and Building Materials*, 127: 344-352.

Shen, L. and Zhang, H. (2022) "Corrosion inhibition and adsorption behavior of (3-aminopropyl)-triethoxysilane on steel surface in the simulated concrete pore solution contaminated with chloride", *Journal of Molecular Liquids*, 363: 119896.

Somai, M., Giri, A., Roka, A. and Bhattarai, J. (2023) "Comparative Studies on the Anti-corrosive Action of Waterproofing Agent and Plant Extract to Steel Rebar, Macromolecular Symposia", 410(1): 2100276.

Song, Z., Liu, L., Guo, M., Cai, H., Liu, Q., Donkor, S. and Zhao, H. (2024) "Inhibition Performance of Extract Reinforcement Corrosion Inhibitor from Waste Platanus acerifolia Leaves in Simulated Concrete Pore Solution", *Case Studies in Construction Materials*, 20: e02992.

Subedi, B.N., Amgain, A., Joshi, S. and Bhattarai, J. (2019) "Green Approach to Corrosion Inhibition Effect of Vitex negundo Leaf Extract on Aluminum and Copper Metals in Biodiesel and Its Blend", *International Journal of Corrosion and Scale Inhibition*, 8(3): 744-759.

Subramania, A. and Venkatraman, B.R. (2014) "The Inhibitive Effect of Ziziphus jujuba Leaves Extract on the Alkaline Corrosion of Aluminium", *European Journal of Applied Sciences and Technology*, 1, 23-31.

Sulistiawan, A., Setyaningsih, W. and Rohman, A. (2022) "A New FTIR Method Combined with Multivariate Data Analysis for Determining Aflatoxins in Peanuts (Arachis hypogaea)", *Journal of Applied Pharmaceutical Science*, 12(7): 199-206.

Sun, D., Cao, Z., Huang, C., Wu, K., De Schutter, G. and Zhang, L. (2022) "Degradation of Concrete in Marine Environment Under Coupled Chloride and Sulfate Attack: A Numerical and Experimental Study", *Case Studies in Construction Materials*, 17: e01218.

Umoren, S.A., Solomon, M.M., Obot, I.B. and Suleiman, R.K. (2019) "A Critical Review on the Recent Studies on Plant Biomaterials as Corrosion Inhibitors for Industrial Metals", *Journal of Industrial and Engineering Chemistry*, 76: 91-115.

Veedu, K.K., Kalarikkal, T.P., Jayakumar, N., Gopalan, N.K. (2019) "Anticorrosive Performance of *Mangifera indica* L. leaf Extract-based Hybrid Coating on Steel", *ACS Omega*, 4(6): 10176-10184.

Wang, J., Zhang, Z., Liu, X., Shao, Y., Liu, X. and Wang, H. (2024) "Prediction and Interpretation of Concrete Corrosion Induced by Carbon Dioxide Using Machine Learning", *Corrosion Science*, 233: 112100.

Wang, P., Wang, Y., Zhao, T. Xiong, C., Xu, P., Juan Zhou, P. and Fan, Z. (2020) "Effectiveness Protection Performance of an Internal Blending Organic Corrosion Inhibitor for Carbon Steel in Chloride Contaminated Simulated Concrete Pore Solution", *Journal of Advanced Concrete Technology*, 18(3): 116-128.

Yue, P.P., Hu, Y.J., Fu, G.Q., Sun, C.X., Li, M.F., Peng, F. and Sun, R.C. (2018) "Structural Differences Between the Lignin-Carbohydrate Complexes (LCCs) from 2- and 24-Month-Old Bamboo (*Neosinocalamus affinis*)", *International Journal of Molecular Sciences*, 19(1): 1.

Distribution of Corrosion Attack in Chloride Exposed Concrete, Summary of Field Observations

K. Baral[1*], M.R. Geiker[2], and J.A. Øverli[3]

[1] *Norwegian University of Science and Technology, Trondheim, Norway*
Email: kedar.baral@ntnu.no
[2] *Norwegian University of Science and Technology, Trondheim, Norway*
Email: mette.geiker@ntnu.no
[3] *Norwegian University of Science and Technology, Trondheim, Norway*
Email: jan.overli@ntnu.no

[*]Corresponding author

ABSTRACT

Reinforcement corrosion is the main deterioration mechanism in chloride-exposed reinforced concrete structures. Depending on the moisture level, corrosion might initiate when aggressive agents like chloride ions reach the reinforcement surface. Similarly, the propagation of active corrosion depends on both the moisture level and oxygen availability. Corrosion reduces the cross-sectional area and ductility of reinforcement. Depending on the severity of the attack and the corrosion products at the interface, it can lead to cracking and spalling of the concrete, thereby modifying bond-slip behavior. Knowledge of the distribution of corrosion attack is required for the structural assessment of existing marine-exposed concrete structures to extend their service life. This paper summarizes observations of corrosion distribution on rebars excavated from concrete elements after long-term exposure.

KEYWORDS: *Concrete, reinforcement corrosion, Chloride-induced corrosion, Distribution of attack, Field observations*

1. Introduction

Reinforcement corrosion is the primary cause of degradation of concrete structures exposed to a chloride environment. Chloride-induced corrosion is typically localized and results in so-called pits. Depending on the conditions, it might change to more general corrosion. The amount of chloride leading to sustained corrosion is, among others, affected by the metallurgy and surface characteristics of the reinforcement Angst and Elsener (2015), and the moisture conditions at the reinforcement Angst et al. (2019).
The material behavior of reinforcement is affected by the spatial distribution of corrosion pits (e.g., distribution of local strain Chen et al. (2020)), their geometry Hingorani et al. (2013), and their possible interference Kioumarsi et al. (2016), leading to changes in the stress-strain behavior of rebars Ou et al. (2016) and a shift in their failure mode (from ductile to brittle) Zhu and François (2014).
The present work aims to summarize observations of reinforcement corrosion attacked in long-term field-exposed concrete elements focusing on the main longitudinal reinforcement. Section 2 provides definitions used. Section 3 presents the cases and compares some observed features such as the development of corrosion pattern with time, pitting factor, pit size, and pit proximity. Section 4 briefly discusses possible explanations for the observed corrosion patterns. Section 5 provides the conclusions.

2. Definitions

The following definitions are used:

- **Corrosion-induced damage:** cracking and spalling due to the accumulation of voluminous corrosion products at the steel-concrete interface (SCI). Cracks induced by corrosion are also referred to as **corrosion-induced cracks**.

- **Corrosion initiation:** formation of a stable anode on the reinforcement surface.
- **Corrosion pattern**: localized corrosion, general corrosion (almost uniform corrosion), or a combination of both (mixed- non-uniform type of corrosion).
- **Defects:** refer to the inconsistencies that arise during construction.
- **Distribution of corrosion attack:** the spatial distribution and the extent of corrosion.
- **Initial cracks:** cracks developed in concrete due to loads and other actions before exposure to a corrosive environment.
- **Pitting factor (P_f)**: the ratio of the largest corrosion attack to the average corrosion attack. Note that the characteristics of the corrosion attack vary, see Table 1.
- **Pit proximity:** distance between two adjacent (nearest) corrosion pits on a rebar.
- **Simulated natural corrosion**: corrosion in an artificial environment that replicates natural conditions. (It neither involves mixing chlorides into the concrete nor employs other electrochemical procedures to accelerate corrosion).
- **Steel-concrete interface (SCI):** the complex, multi-phase, and multi-scale system comprising the reinforcement surface and the nearby part of the embedding concrete.
- **Top-bar effect:** effect of void formation in a downward direction under horizontal rebars in the upper part of a structure due to settlement, segregation, and bleeding of fresh concrete. The downward direction refers to the downward-facing surface (depends on the casting direction).

Table 1. Methods used for determination of pitting factor

Reference	Calculation method					Characterization method
	Parameter	Deepest pit		Average attack		
		Local	Global	Local	Global	
Zhao et al. (2020)	Diameter	x		x		Image analysis
Zhu et al. (2017)	Area		x		x	Gravimetric analysis
González et al. (1995)	Diameter	x			x	Micrometer, microscope, and gravimetric analysis
Tuutti (1982)	Diameter	x		x		Sliding calipers and gravimetric analysis

3. Observations

Observations from the literature on corrosion distribution in marine-exposed field elements are summarized in Table 2. As only three marine cases were identified where the reinforcement was fully excavated, the marine cases were supplemented with data from de-iced fields as well as salt (NaCl) exposed laboratory elements. Except for the 25-year-old marine-exposed beams studied by Geiker et al. (2021) and the 9-year-old marine-exposed panel by Geiker et al. (2023), all investigated elements exhibited some level of corrosion-induced damage at the time of the investigation.

3.1 Cases

Geiker et al. (2021) observed only localized corrosion (no general corrosion) in pre-cracked 25-year-old marine-exposed concrete beams (w/b=0.40) with plastic spacers. The beams were held vertically and exposed simultaneously to submerged, tidal, and atmospheric environments (variable tidal heights). Corrosion was primarily observed at a few spacers. The author hypothesized that the very local nature of corrosion was due to the cathodic protection of large parts of the rebars due to the early corrosion initiation at plastic spacers, classified as the ‘‘weakest link’’.

Geiker et al. (2023) examined the reinforcement from a pre-cracked concrete panel (w/b=0.40, crack width 0.2-0.3 mm) with a large concrete cover (>75 mm) exposed to marine submerged and tidal environments for 9 years. The cracks were maintained using shims and it was observed that it facilitated chloride ingress. Although chlorides were detected at the steel-concrete interface, any significant corrosion was not observed on the reinforcement. According to Geiker et al. (2023), the absence of corrosion was possibly due to the combination of the crack type and location, the large cover, and the binder composition, providing a sustained high hydroxyl ion concentration.

Table 2. Summary of literature observations of corrosion attack in chloride-exposed concrete

Exposure	Work by	Age (years)	Element, size (m)	Rebar diameter (mm)	Sustained load	Cover depth (mm)	w/b	Exposure			Initial «defects» (width (mm))	Corrosion induced damage	Corrosion pattern
								Marine1	De-iced	Wet/dry NaCl			
Field - Marine	Geiker et al. (2021)	25	Beams 3x0.3x0.15	16	x	25	0.40	S+T+A	-	-	Cracks (0.1-0.2) & spacers	-	Localized corrosion
	Geiker et al. (2023)	9	Panel 2x1x0.2	12	x(shims)	>75	0.40	S+T	-	-	Cracks (0.2-0.3)	-	-
	Dasar et al. (2017)	40	Beams 2.4x0.15x0.3	13	-	30	0.68	Spl+T (20y)2	-	-	Cracks & top-bar Top-bar	Cracking (10y)	Mixed
Field – De-iced	Lundgren et al. (2015)	30	Edge beams	16	Service load	35-85	?	-	x	-	Cracks	Local cracking & spalling	Primarily localized corrosion
	Fernandez and Berrocal (2019)	35	Edge beams	16	Service load	35-85	?	-	x	-	Cracks	Local cracking & spalling	Primarily localized corrosion
NaCl – Wet-dry	Zhang et al. (2009)	14/19/23	Beams 3x0.28x0.15	12	x	10	0.50	-	-	x3	Cracks & top-bar	Cracking (5y5)	Mixed
	Zhu and François (2014)	26	Beams 3x0.28x0.15	12	x	10	0.50	-	-	x3	Cracks (top-bar)	Cracking (5y5)	Mixed

	Zhu et al. (2017)	14/19/23/28	Beams 3x0.28x0.15	12	x	10	0.50	-	-	x3	Cracks (top-bar?)	Cracking (5y5)	Mixed	
	Chen et al. (2020)	4-5	Beams 1.1x0.18x0.1	10	-	30	0.47	-	-	x4	Cracks (0.1/0.4)	Cracking	Localized corrosion (“long pits”)	
											-			

1) S – Submerged, Spl – Splash, T – Tidal, A – Atmospheric
2) 0 to 20 years: marine environment at the Sakata Port, 20 to 35 years: sheltered from the rain at the laboratory, and 35 to 40 years: stored at Kyushu University
3) 0-6 years- continuous spraying, loaded; 6-9 years, loaded @20℃- a wetting-drying cycle of 35 g/l NaCl solution; 9-19 years- the wetting-drying cycle with 35 g/l NaCl solution @outside environment, loaded; 19-26 years- stop spraying, unloaded, outside environment; 26-28 years- the wetting-drying cycle with a NaCl solution, outside environment, unloaded
4) The wetting-drying cycle with 16.5% NaCl solution for three years (corresponding to the XS3 or XD3 exposure class in EN 206) and stored in the laboratory for an additional one or two years
5) Zhu and François (2015)

Dasar et al. (2017) investigated reinforcement bars in both pre-cracked (with loads removed after cracks formed) and uncracked beams that were placed horizontally and exposed to a marine splash and tidal environment for 20 years, stored at a laboratory, and sheltered from the rain for the next 15 years, and finally stored at Kyushu University for 5 years (no information on exposure for 5 years). According to Dasar et al. (2017), corrosion-induced cracks were observed after 10 years of exposure to a marine environment. After 40 years, the destructive investigation suggested that the reinforcement experienced both general and localized corrosion (mixed corrosion). Tensile bars in pre-cracked beams showed more severe localized corrosion on the reinforcements' downward-facing surfaces than in uncracked beams. The extent of corrosion on the upward-facing surfaces was similar for both pre-cracked and uncracked beams, noting only minor localized corrosion. In contrast, compressive bars in uncracked beams exhibited localized corrosion on the downward-facing reinforcement surfaces compared to those in pre-cracked beams. Additionally, the reinforcement in the uncracked beams had a larger corroded area on the upward-facing reinforcement surfaces than the pre-cracked beams. Notably, the corrosion was consistently more severe on the downward-facing reinforcement surfaces than on the upward-facing reinforcement surfaces. According to Dasar et al. (2017), this was due to the top-bar effect.

Lundgren et al. (2015) reported localized corrosion as a primary form of corrosion on reinforcement bars from the edge beam of a de-iced road bridge in service for 30 years. The edge beam had initial cracks due to inadequate design. They observed varying degrees of corrosion-induced damage, ranging from no signs to extensive cracking and spalling. Even though the corrosion-induced damages were severe, the authors reported localized corrosion as a primary corrosion pattern. According to their observation, localized corrosion typically affected one-half of the bar, sometimes almost eliminating the ribs, while the other half remained almost undamaged.

Continuing the investigations by Lundgren et al. (2015), Fernandez and Berrocal (2019) studied 52 m of reinforcement from edge beams exposed to de-icing salts for a minimum of 30 years. The bridge was in service for 30 years, whereas the exposure during the remaining 5 years is unclear. The condition of the rebars ranged from pristine to severely corroded, with the most severe cases exhibiting what the authors referred to as "uniform pitting". The authors highlighted that in specific regions the attack was highly localized with significant loss of cross-sectional area at pit locations in combination with a minimal overall average corrosion level.

Zhang et al. (2009) examined beams under sustained load exposed to a wetting-drying cycle with a NaCl solution for 14, 19, and 23 years. It was observed that, during the initial stage, the corrosion attack was localized in nature, at later stages it shifted to general-type corrosion (i.e. mixed corrosion). According to Zhang et al. (2009), during the initial stage of corrosion, macrocell corrosion was pronounced, with the steel at the crack tip acting as an anode. They also noted that the effect of bending cracks is suppressed over time due to crack healing. Further, the reinforcements in the compressive zone were affected by the top-bar effect (see Section 2).

From the same research group, Zhu and François (2014) investigated a beam exposed to the wetting-drying cycle with a NaCl solution for 26 years. The corroded beam had reached a stage where they observed both general and localized corrosion (i.e. mixed corrosion), with some zones exhibiting significant localized corrosion. The reinforcement exhibited a dominant localized form of corrosion on the downward-facing surface, extending almost the entire length. In contrast, on the upward-facing reinforcement surface corrosion appeared only in some discrete locations. Compared to the front tensile reinforcement, the back tensile reinforcement experienced less corrosion, both in terms of general and localized corrosion. Further, the corroded regions were observed to coincide with corrosion-induced cracking and spalling of the concrete cover. Similarly, they noted that the compressive reinforcement had more corrosion attacks on the downward-facing surfaces than the upward-facing surfaces, which they attributed to the top-bar effect.

Continuing the study by Zhang et al. (2009), Zhu and François (2014), and Zhu et al. (2017) further studied the corrosion propagation and corrosion patterns in beams exposed to the wetting-drying cycle with a NaCl solution after 14, 23, 26, and 28 years. They observed a clear progression of corrosion of the reinforcement with time (see Fig. 1 and further description in Section 3.2).

Chen et al. (2020) carried out a relatively short-term study (4-5 years) on the corrosion of pre-cracked (crack width 0.1 mm or 0.4 mm) and uncracked beams exposed to the wetting-drying cycle with a NaCl solution. The corrosion of the bars in this study was localized in nature. In the case of pre-cracked beams, they observed pits near the initial cracks, while in the case of uncracked beams, they observed numerous tiny pits on the surface of the bars. Most of the observed pits were elliptical-shaped, with some elongating

beyond the elliptical cavity. According to Chen et al. (2020), the long pits observed in the pre-cracked beams are likely a result of corrosion-induced cracks (no details given). However, these cracks were not extensive, possibly due to the relatively short age of the beams.

3.2 Development of corrosion pattern with time

This section reviews observations of the development of corrosion attack/pattern in chloride-exposed reinforced concrete. As described in Section 3.1, observations vary greatly: from localized corrosion in 25-year-old marine-exposed concrete beams (w/c = 0.40) with plastic spacers, to primarily localized corrosion along with corrosion-induced cracking and spalling in 30 to 35-year-old field-exposed de-iced edge beams, to mixed corrosion and corrosion-induced cracking in beams exposed to wetting-drying cycles with a NaCl solution (see Table 2).

The studies by the French group of researchers provide a unique data set of the distribution of corrosion attack in chloride-exposed concrete, all using similar beams and exposure conditions. Visual observations by Zhu and François (2015) and destructive investigations of corroded beams conducted by Zhang et al. (2009) and Zhu et al. (2017) illustrate the progression of corrosion with time under sustained loading and controlled wetting-drying cycles with a NaCl solution. Zhu and François (2015) reported the appearance of corrosion-induced cracks at the surface after 5 years, predominantly near initial cracks. Fig. 1 illustrates further corrosion pattern development with time. The corroded area extended from approximately 30% located at mid-span to cover almost the entire beam after 26-28 years.

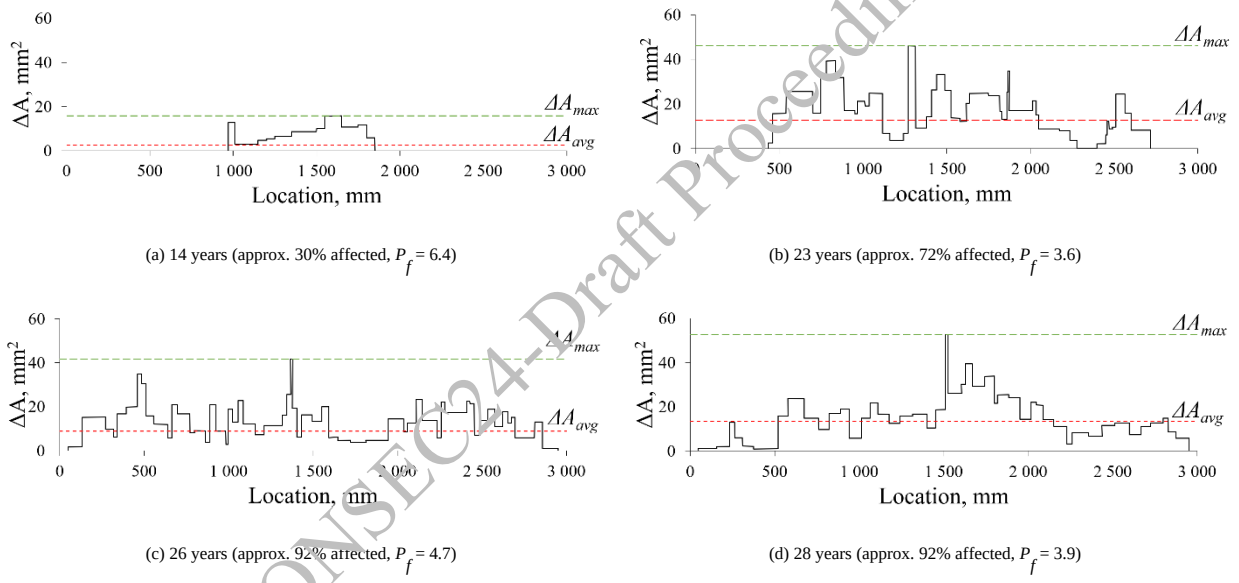

(a) 14 years (approx. 30% affected, P_f = 6.4)

(b) 23 years (approx. 72% affected, P_f = 3.6)

(c) 26 years (approx. 92% affected, P_f = 4.7)

(d) 28 years (approx. 92% affected, P_f = 3.9)

Figure 1. Development of corrosion pattern over time in beams with corrosion-induced cracks. Cross-sectional loss (ΔA) of tensile reinforcement (dia. 12 mm) in beams under service load exposed to the wetting-drying cycle with a NaCl solution ΔA was determined by gravimetry. (Data from Zhu et al. (2017)). Pitting factor, $P_f = \Delta A_{max} / \Delta A_{avg}$, ΔA_{max} is the maximum cross-section loss, where ΔA_{avg} is the average cross-section loss over the length.

Zhang et al. (2009) suggested that in the later stages of the corrosion propagation phase, during which corrosion-induced cracks propagate longitudinally, interconnect, and widen, the corrosion pattern is primarily influenced by the corrosion-induced cracks: at the initial stage of crack propagation when the cracks are small, localized (macrocell) corrosion remains the dominant type. However, once the cracks exceed a critical width, microcell corrosion becomes predominant, resulting in mixed corrosion. In summary, the beams exposed to the wetting-drying cycles with a NaCl solution exhibited a shift from localized to mixed corrosion. This transition was significantly affected by the corrosion-induced cracks. The transition is further demonstrated by a change in the pitting factor from over 6 after 14 years of exposure to around 4 after 28 years. Based on the observations, Zhu et al. (2017) suggested that the corrosion development of the investigated beams could be divided into three stages: an initiation stage, a development stage where the percentage of the bar affected (corroded area) increases (here approx. 5–29 years), and a stable mature stage after the entire bar is affected by corrosion (here 29 years).

A similar development of corrosion pattern was observed for the beams exposed to wetting-drying cycles investigated by Dasar et al. (2017). In their study of initially marine-exposed beams (w/b=0.68), Dasar et al. (2017) referred to an earlier study from their group by Hamada et al. (1988) where they reported that after 10 years the corroded surface area of steel bars was around 45% for pre-cracked beams and 6% for uncracked beams and that after 20 years, visual observations showed a significant increase in corroded area in both pre-cracked and uncracked beams; the reinforcement was highly corroded, exhibiting extensive corrosion cracking. After 40 years of combined marine and sheltered exposure, the corrosion pattern was mixed type and corrosion had spread throughout the reinforcement for both pre-cracked and uncracked beams and in both the tensile and the compressive reinforcements Dasar et al. (2017).

3.3 Pitting factor

Several authors have utilized pitting factors, i.e. the ratio of the largest corrosion attack to the average corrosion attack, to describe the intensity of corrosion attacks in chloride-rich environments. Note that pitting factors in the literature might not be directly comparable as the used characteristics of the corrosion attack vary (see Table 1). For the case of beams with corrosion-induced cracks at the time of investigation illustrated in Fig. 1, the maximum and the average cross-section reductions were determined from the graphs. The pitting factor ($P_f = \Delta A_{max}/\Delta A_{avg}$) was calculated as 6.4, 3.6, 4.7, and 3.9 for beams exposed for 14, 23, 26, and 28 years, respectively.

3.4 Pit size

Pit size includes depth, length, and width. Fig. 2 illustrates the correlation between pit depth and pit length.

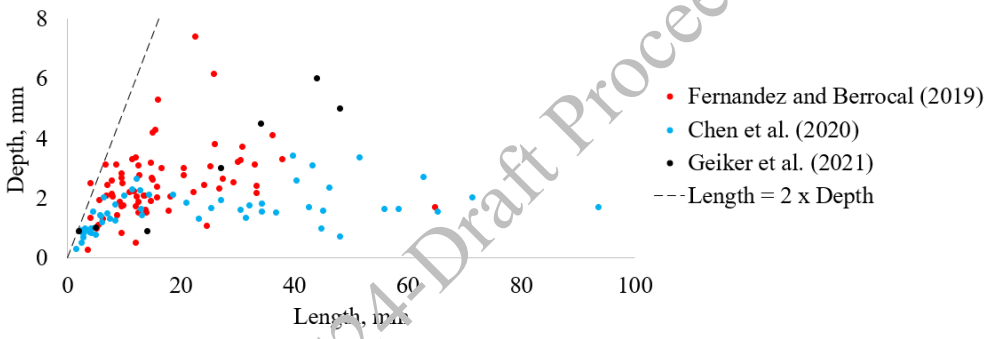

Figure 2. Pit depth vs pit length of localized corrosion in different exposure conditions (see Table 2 for exposure type and period)

Except for one pit, all pits had a length nearly equal to or larger than twice the pit depth (see line), indicating a half-sphere or more shallow shape of the pits. The general trend suggests that some pits exhibited symmetrical growth in both directions, while others grew more in length direction, resulting in a higher aspect ratio (the ratio of pit length to pit depth). The studies by Geiker et al. (2021) and Fernandez and Berrocal (2019), focusing on 25 years of marine-exposed beams and 30 years of de-iced concrete edge beams, respectively, highlighted substantial variation in pit depth, ranging from a fraction of mm to more than 0.5 cm. Similarly, the variation in pit length was larger, extending from a few mm to several cm. Moreover, the laboratory-exposed beams investigated by Chen et al. (2020) showed an even larger variation in pit length, with shallower pits after 4-5 years of the wetting-drying cycle with a NaCl solution.

3.5 Pit proximity

In the case of localized corrosion, the information on pit proximity (i.e. distance between nearest pits) could provide a basis for the representation of the spatial distribution of corrosion attack. In the study by Geiker et al. (2021) on pre-cracked 25-year-old marine-exposed beams, where only localized corrosion was observed, it was found that the proximity of corrosion pits depends on the concrete resistivity. For the concrete and exposure conditions investigated, a minimum resistivity of 5000 kΩ-cm² to the nearest major pit was observed.

4. Discussions

The summary of observations on corrosion attack and distribution in chloride-exposed structures highlights the complexity of reinforcement corrosion in concrete.
The initiation of chloride-induced corrosion is affected by the condition of the steel-concrete interface Angst et al. (2019), especially the metallurgy and surface characteristics of the reinforcement Angst and Elsener (2015) and the presence of inhomogeneities and the moisture conditions of the concrete part of the steel-concrete interface Angst et al. (2019). Moisture also greatly affects the rate of corrosion, among others as reduced electrical resistivity supports larger macro-cells Bertolini et al. (2013), Geiker et al. (2021).
The initiation and propagation of corrosion appear to be affected by possible design and construction errors causing defects. Examples reported in Table 2 include the use of plastic spacers (Geiker et al., 2021) and the top-bar effect Zhang et al. (2009), Dasar et al. (2017) caused by settlement, segregation, and/or bleeding, which is prominent in concrete with a high w/b ratio Dasar et al. (2017).
Robuschi et al. (2023) recently tested the hypothesis for the impact of transverse cracks on reinforcement corrosion reported based on literature data and found, among others, that corrosion pits are likely to form and grow in the proximity of transverse cracks and that corrosion pits seem to grow slower with time, whereas the number of corrosion pits per area was observed to increase. The impact of initial cracks was also observed in Zhang et al. (2009), Zhu and François (2014), Zhu et al. (2017), Dasar et al. (2017), and Chen et al. (2020). However, no such effects were reported by Geiker et al. (2021) and Geiker et al. (2023).
According to Boschmann Käthler et al. (2021), corrosion propagation at cracks highly depends on local moisture conditions and possible inhibition of corrosion. Inhibition could result from repassivation Boschmann Käthler et al. (2021), occupation of cracks by rust products Zhang et al. (2009), and possible self-healing Zhang et al. (2009), potentially limiting long-term corrosion propagation. Danner et al. (2020) found that cracks of widths smaller than 0.2 mm appeared closed after 25 years of marine exposure, which is in line with a recent review paper by Kanavaris et al. (2023).
Bertolini et al. (2013) mentioned that longitudinal and transverse cracks significantly affect reinforcement corrosion differently. This was observed by Zhu et al. (2017) who reported a change in the corrosion pattern from localized to more general corrosion after the formation of corrosion-induced cracks.
According to Bertolini et al. (2013), contact with chloride and subsequent drying, as in marine splash zones and de-iced structures, is a very aggressive exposure condition. The observations cover different exposure conditions (marine, de-iced, and cycling wetting-drying cycles with a NaCl solution). This might be supported by the reported observation (marine submerged vs marine splash and wetting-drying cycles with a NaCl solution). However, the present data are limited and do not allow for a clear description of the impact of exposure due to other factors affecting the initiation and propagation of corrosion.

5. Conclusions

Based on observations from the literature of corrosion distribution in marine-exposed or de-iced field elements and the wetting-drying cycle with a NaCl solution, the following conclusions are made:

- The number of destructive studies on long-term exposed concrete elements is limited.
- The observed corrosion patterns significantly vary between cases.
- Most of the published cases show a change in corrosion pattern from localized corrosion to a combination of pitting and general corrosion (mixed) in connection with corrosion-induced damage.
- The corrosion initiation and propagation appear greatly affected by possible design and construction errors causing defects and heterogeneities at the concrete-steel interface.

Acknowledgments

The authors gratefully acknowledge Extend - Functional Service Life Extension of Offshore Concrete Structures (financed by Equinor) and Excon – Green Management of Structures for Infrastructure (Research Council of Norway project number 340843) for their funding support.

References

Angst, U.M. and Elsener, B. (2015) "Forecasting Chloride-Induced Reinforcement Corrosion in Concrete—Effect of Realistic Reinforcement Steel Surface Conditions", *Proceedings of 4th international conference on concrete repair, rehabilitation and retrofitting (ICCRRR)*, Leipzig.

Angst, U.M., Geiker, M.R., Alonso, M.C., et al. (2019) "The Effect of the Steel–Concrete Interface on Chloride-Induced Corrosion Initiation in Concrete: A Critical Review by Rilem Tc 262-Sci", *Materials and Structures*, 52(4).

Bertolini, L., Elsener, B., Pedeferri, P., et al. (2013) "Corrosion of Steel in Concrete - Prevention, Diagnosis, Repair (2nd Edition)". *Newark, Newark: John Wiley & Sons*.

Boschmann Käthler, C., Angst, U.M., Ebell, G., et al. (2021) "Chloride-Induced Reinforcement Corrosion in Cracked Concrete: The Influence of Time of Wetness on Corrosion Propagation", *Corrosion Engineering, Science and Technology*, 56(1): 1-10.

Chen, E., Berrocal, C.G., Fernandez, I., et al. (2020) "Assessment of the Mechanical Behaviour of Reinforcement Bars with Localised Pitting Corrosion by Digital Image Correlation", *Engineering Structures*, 219: 110936.

Danner, T., Hornbostel, K. and Geiker, M.R. (2020) "Self-Healing and Chloride Ingress in Cracked Cathodically Protected Concrete Exposed to Marine Environment for 33 Years". *Microdurability Conference*, The Hague. The Netherlands.

Dasar, A., Hamada, H., Sagawa, Y., et al. (2017) "Deterioration Progress and Performance Reduction of 40-Year-Old Reinforced Concrete Beams in Natural Corrosion Environments", *Construction & Building Materials*, 149: 690-704.

Fernandez, I. and Berrocal, C.G. (2019) "Mechanical Properties of 30-year-old Naturally Corroded Steel Reinforcing Bars", *International Journal of Concrete Structures and Materials*, 13(1): 1-19.

Geiker, M., Danner, T., Michel, A., et al. (2021) "25 years of Field Exposure of Pre-Cracked Concrete Beams; Combined Impact of Spacers and Cracks on Reinforcement Corrosion", *Construction & Building Materials*, 286: 122801.

Geiker, M., Robuschi, S., Lundgren, K., et al. (2023) "Concluding Destructive Investigation of a Nine-Year-Old Marine-Exposed Cracked Concrete Panel", *Cement and Concrete Research*, 165: 107070.

González, J.A., Andrade, C., Alonso, C., et al. (1995) "Comparison of Rates of General Corrosion and Maximum Pitting Penetration on Concrete Embedded Steel Reinforcement", *Cement and Concrete Research*, 25(2): 257-264.

Hamada, H., Otsuki, N. and Haramo, M. (1988) "Durabilities of Concrete Beams under Marine Environments Exposed in Port of Sakata and Kagoshima (after 10 Years Exposed)", *Technical Note of the Port and Airport Research Institute*, 614: 3-43.

Hingorani, R., Pérez, F., Sánchez-Montero, J., et al. (2013) "Loss of Ductility and Strength of Reinforcing Steel Due to Pitting Corrosion", *Proceedings of the VIII International Conference on Fracture Mechanics of Concrete and Concrete Structures*. FraMCoS-8. Spain.

Kanavaris, F., Coelho, M., Ferreira, N., et al. (2023) "A review on the effects of cracking and crack width on corrosion of reinforcement in concrete", *Structural Concrete: Journal of the FIB*, 24(6): 7272-7294.

Kioumarsi, M.M., Hendriks, M.a.N., Kohler, J., et al. (2016) "The Effect of Interference of Corrosion Pits on the Failure Probability of a Reinforced Concrete Beam", *Engineering Structures*, 114: 113-121.

Lundgren, K., Tahershamsi, M., Zandi, K., et al. (2015) "Tests on Anchorage of Naturally Corroded Reinforcement in Concrete", *Materials and Structures*, 48(7): 2009-2022.

Ou, Y.-C., Susanto, Y.T.T. and Roh, H. (2016) "Tensile Behavior of Naturally and Artificially Corroded Steel Bars", *Construction & Building Materials*, 103: 93-104.

Robuschi, S., Ivanov, O.L., Geiker, M., et al. (2023) "Impact of cracks on distribution of chloride-induced reinforcement corrosion", *Materials and Structures*, 56(1).

Tuutti, K. (1982) "Corrosion of Steel in Concrete". Doctoral Thesis, Lund University.

Zhang, R., Castel, A. and François, R. (2009) "The Corrosion Pattern of Reinforcement and Its Influence on Serviceability of Reinforced Concrete Members in Chloride Environment", *Cement and Concrete Research*, 39(11): 1077-1086.

Zhao, Y., Xu, X., Wang, Y., et al. (2020) "Characteristics of Pitting Corrosion in an Existing Reinforced Concrete Beam Exposed to Marine Environment", *Construction & Building Materials*, 234: 117392.

Zhu, W. and François, R. (2014) "Corrosion of the Reinforcement and Its Influence on the Residual Structural Performance of a 26-Year-Old Corroded RC Beam", *Construction & Building Materials*, 51: 461-472.

Zhu, W. and François, R. (2015) "Structural Performance of RC Beams in Relation with the Corroded Period in Chloride Environment", *Materials and Structures*, 48(6): 1757-1769.

Zhu, W., François, R. and Liu, Y. (2017) "Propagation of Corrosion and Corrosion Patterns of Bars Embedded in RC Beams Stored in Chloride Environment for Various Periods", *Construction & Building Materials*, 145: 147-156.

Fatigue Life Prediction of Corroded Reinforced Concrete Beams Using EIFS and Fracture Toughness Degradation

Muneem Ahmad Dar[1] and K. M. Pervaiz Fathima [2*]

Indian Institute of Technology Jammu (IIT Jammu)
NH-44, PO Nagrota, Jagti, Jammu and Kashmir 181221
[1]e-mail: muneem.dar@iitjammu.ac.in
[2]e-mail: pervaiz.khatoon@iitjammu.ac.in

[*] Corresponding Author

ABSTRACT

Reinforced concrete (RC) structures, known for their strength and durability, face challenges in corrosive environments where degradation occurs due to a reduction in the cross-sectional area of the reinforcement steel. This degradation is accelerated in structures like bridges that endure repetitive loading, leading to fatigue damage. The reduction in the cross-sectional area of the corroded reinforcement paves way for fatigue crack initiation and subsequent crack growth. It is, therefore, important to understand and model fatigue crack propagation in the context of corrosion to enhance the durability and safety of reinforced concrete structures, especially when subjected to cyclic loading in corrosive environments. In this study, a model has been developed for predicting the fatigue life of reinforcement bars in aging RC beams exposed to corrosive environments. The proposed model is based on the Paris' law, which integrates principles of fracture mechanics and considers corrosion growth kinetics. The evaluation of the critical crack size considers the combined effect of mechanical loading and exposure to a corrosive environment. The crack growth in corrosive medium also depends on the rate of corrosion which is determined using Faraday's law of electrochemical corrosion. Fatigue life prediction results are validated with experimental results of corroded RC beams that are available in the literature.

KEYWORDS: *Corrosion fatigue, Reinforced concrete, Fatigue crack growth, Corrosion rate.*

1. Introduction

Due to its robustness, reinforced concrete (RC) is commonly used for constructing bridges and other structures subjected to cyclic loading, such as offshore buildings, wind turbine foundations, and dams. However, RC structures face the inevitable challenge of steel reinforcement corrosion, primarily caused by chloride ion infiltration from the surrounding environment (Rodrigues et al., 2021). RC bridges, in particular, are subject to repeated vehicle loads, causing damage to the steel reinforcement and the concrete due to high-cycle fatigue (Herwig, 2008). Previous studies have shown that the combination of corrosion and fatigue significantly accelerates structural degradation, shortens fatigue life, and often results in sudden, catastrophic failures (Devendiran and Banerjee, 2023). The fatigue behaviour of RC structures affected by corrosion is a complex phenomenon involving corrosion kinetics and fracture mechanics (Ma et al., 2014). Studies have shown that the fatigue strength of RC beams decreases with increased loading cycles and stress magnitudes (Gheorghiu et al., 2006). The combined effects of corrosion and cyclic loading further aggravate this phenomenon, leading to early fatigue crack initiation and accelerated crack propagation. Given the critical nature of this problem, predicting the corrosion fatigue life of RC structures has become a focal point of research. Various methodologies have been developed, including the use of S-N curves and fracture mechanics (FM) approaches. However, while simple, traditional S-N curve methods do not capture the complete fatigue failure process. In contrast, FM methods, which analyse fatigue crack propagation, offer a more comprehensive understanding but still face challenges, such as accurately accounting for initial crack sizes. The concept of Equivalent Initial Flaw Size (EIFS) has emerged as a useful approach, simplifying the complex fatigue failure process by using virtual initial flaw sizes to better predict fatigue

life (Liu and Mahadevan, 2009). Despite advancements, the relationship between corrosion and EIFS remains underexplored, highlighting the need for further research to improve the accuracy and reliability of corrosion fatigue life predictions for RC structures. Further, it has been observed experimentally that the critical crack size is a function of the degree of corrosion. However, the existing fatigue life prediction models available in the literature do not consider the critical crack size as a function of the corrosion mass loss.

This study aims to address the gap by investigating the effects of corrosion on the fatigue behaviour of RC beams. EIFS-based crack prediction methodology is used to account for short crack growth and, therefore, to enhance the accuracy of corrosion fatigue life prediction. The back extrapolation concept is used to obtain the correlation between EIFS and mass loss due to corrosion. In this work, a relation between corrosion degree and critical crack size is obtained by using experimental fracture toughness values for different degrees of corrosion. Based on the critical crack size and EIFS, the fatigue life of corroded reinforced concrete beams is predicted and validated using existing experimental results from the literature.

2. Fatigue crack growth rate in a corrosive environment

In order to evaluate the propagation of large cracks, the theory of fracture mechanics is generally adopted. Normally, the rate of fatigue crack growth (da/dN) is shown in relation to the stress intensity factor range $(\Delta K = K_{max} - K_{min})$. Crack propagation up to the threshold stress intensity factor range (ΔK_{th}) represents short crack growth, which is fast, haphazard and irregular. The Paris law becomes applicable only after (ΔK_{th}).

The relationship between (da/dN) and ΔK in a corrosive environment illustrates that environmental factors have a significant impact on fatigue crack propagation (Madia et al., 2021). Coupled effects of corrosion and fatigue come into place when cyclic loading occurs in corrosive reinforced concrete structures. The fatigue load may cause steel bars to accumulate damage and lead to concrete cover cracking, initiating corrosion of reinforcement bars in a chloride-laden environment (Yang et al., 2017). Chloride penetration resulting in reinforcement corrosion may reduce the cross-sectional area of steel bars and redistribute internal stresses. This loss of cross-sectional area increases the stress range on reinforcement bars and causes the degradation of concrete, reducing the fatigue strength of the RC members (Ma et al., 2014). Coupled corrosion-fatigue effects are essential when RC elements are simultaneously subjected to chloride attack and fatigue loading. Studies reveal a 20-30% reduction in fatigue strength due to coupled corrosion-fatigue phenomenon (Coca et al., 2011).

2.1 Fatigue life prediction based on EIFS

According to fracture mechanics theory, structural parts contain pre-existing flaws, and crack propagation begins due to localised stress concentration. This method relates the incremental crack growth rate per cycle to material parameters such as the geometry, loading conditions, and the stress intensity field surrounding the crack. An issue in predicting life, based on fracture mechanics is determining the initial crack size for analyzing crack growth.

The initial crack size can be used in the relationship between long crack growth rate and stress intensity factor range ($/dN$ versus ΔK) to predict fatigue life for materials with significant pre-existing flaws. Most metallic materials contain defects smaller than the microstructural features, such as the typical grain size. The behaviour of small fatigue cracks at the microstructural level differs significantly from that of large cracks. The concept of EIFS eliminates the need to model small-crack growth by using an estimated initial flaw size in extended crack growth analysis to match the observed fatigue life (Liu and Mahadevan, 2009). It is important to note that EIFS is an inferred quantity obtained by extrapolating experimental data rather than a directly measured physical parameter to simplify fatigue life prediction by using large crack growth analysis and avoiding the complexities of short crack growth modelling (Xiang and Liu, 2010). The deterioration of reinforcement bars in RC beams due to corrosion fatigue exhibits a clear relationship and distinct stages. These stages are (1) the initiation of small cracks at the base of corrosion pits, (2) the accumulation of damage and the steady propagation of cracks, and (3) the growth of the crack to a critical crack size (a_c), culminating in a sudden failure known as fatigue fracture. The fracture mechanics method is used to simulate this entire phenomenon, enabling the determination of corrosion fatigue life by integrating the fatigue crack growth rate from EIFS to a_c. Therefore, EIFS is given as (Liu and Mahadevan, 2009).

$$a_i = \frac{1}{\pi}\left(\frac{\Delta K_{th}}{\Delta\sigma_f\, Y}\right)^2 \quad (1)$$

where a_i is taken as the EIFS, ΔK_{th} is the threshold stress intensity factor range, $\Delta\sigma_f$ is the fatigue limit, and $Y$is a geometry correction factor dependent on the crack configuration. According to the Paris' law (Ma et al., 2014), the crack growth rate of reinforcing steel bars under fatigue loading can be expressed as.

$$da/dN = C[\Delta K]^m \quad (2)$$

where C and m are material constants known as fitting parameters, da represents the increase in fatigue crack propagation for an increment of dN in stress cycles, and ΔK is the stress intensity factor range. The applied stress, crack size, and crack geometry are related to the stress intensity factor range ΔK and are given as

$$\Delta K = \Delta\sigma Y\sqrt{\pi a} \quad (3)$$

Where Y is the geometry correction factor and can be given as (Forman and Shivakumar,1986).

$$Y = G(0.752 + 1.286\beta + 0.37L^3) \quad (4)$$

Where,

$$G = 0.92\left(\frac{2}{\pi}\right) sec\beta \left(\frac{tan\beta}{\beta}\right)^{\frac{1}{2}};\ \text{L=1-sin}\beta;\ \beta = \frac{\pi}{2}*\frac{d}{D} \quad (5)$$

D is the diameter of the bar, and d is the depth of the corrosion pit.

The geometric function Y, as is evident from Eq. (4), depends on corrosion pit depth, which makes ΔK also a function of the corrosion pit depth. Fatigue crack propagation occurs when the stress intensity factor ΔK reaches a threshold value, known as the threshold stress intensity factor range ΔK_{th}. Thus, for the crack to advance, the stress intensity factor must satisfy the following condition.

$$\Delta K > \Delta K_{th} \quad (6)$$

After substituting in Eq. (3), then Eq. (2) can be replaced as

$$dN = \frac{1}{C\Delta K^m}da = \frac{1}{C(\Delta\sigma Y\sqrt{\pi a})^m}da \quad (7)$$

The total number of fatigue cycles can be obtained by integrating Eq. (7)

$$N=\int dN = \int_{a_0}^{a_c}\frac{1}{C\Delta K^m}da = \frac{1}{C(\Delta\sigma Y\sqrt{\pi})^m}\int_{a_o}^{a_c} a^{\frac{-m}{2}}da \quad (8)$$

Where a_0 is the EIFS, a_c is the critical crack size contained in a material. Eq. (8) simplifies to

$$N = \frac{1}{C(\Delta\sigma Y\sqrt{\pi})^m}\,\frac{{a_0}^{1-\frac{m}{2}} - {a_c}^{1-\frac{m}{2}}}{\frac{m}{2}-1} \quad (9)$$

According to Eq. (9), the material parameters (C and m), geometry function (Y), initial crack size (a_0) critical crack size (a_c) and stress range ($\Delta\sigma$) all influence corrosion fatigue life. However, calculating the initial crack size (a_0) is crucial for evaluating the number of fatigue life cycles in a corrosive environment. By utilizing the concept of EIFS, a_0 can be replaced by a_{EIFS}.

3. Measurement of fracture toughness of reinforcement bars

Standardized ASTM E399 (ASTM E399, 1990) and ASTM E1304 (ASTM E1304, 2001) testing procedures should be followed to accurately measure the fracture toughness of steel bars. For these tests,

the samples are under tensile loading, and the crack position on the specimen must be perpendicular to the axis of the bar. The key dimensions for each specimen configuration are the thickness (B), crack length (a) and width (W). As per given ASTM standards, the calculated value of fracture toughness (K_{IC}) is valid only if the following condition up-holds.

$$B \; or \; a \; \geq \; 2.5 \frac{K_{IC}}{\sigma_y} \tag{10}$$

Where a is the crack length, B is the thickness of the sample, σ_y is the yield stress of the material, and K_{IC} is the measured fracture toughness. These limits guarantee a valid fracture toughness under a linear elastic behaviour regime. From Eq. 10, the maximum value of K_{IC} which is consistent with small-scale yielding, can be given as follows.

$$K_{IC} = \; 0.632\sigma_y \sqrt{B} \tag{11}$$

For a reinforcement bar with diameter D, the K_{IC} is given as (Elices et al., 2017).

$$K_{IC} = \; Q\sigma_y \sqrt{D} \tag{12}$$

The constant Q has a value of 0.385 for the Compact Tension (CT) specimen and 0.432 for the Single Edge Notched Bending (SENB) specimen.

3.1 Effect of corrosion on fracture toughness

Fracture toughness degradation is caused by corrosion, which is a critical factor in the structural integrity of RC structures. The residual fracture toughness, which measures a material's ability to resist crack propagation, decreases significantly with increased corrosion damage (Elices et al., 2017). This reduction in fracture toughness results in a lower load-bearing capacity and premature failure under tensile and fatigue loads. Consequently, accurate prediction of fracture toughness degradation is essential for assessing corroded steel's remaining fatigue life. Table 1 shows the residual fracture toughness in steel plates with corresponding degrees of corrosion. To quantify this decline in fracture toughness, an empirical relationship is fitted between the decrease in fracture toughness and the degree of corrosion, as given by Eq.13 and illustrated in Fig 1.

Table 1. Fracture toughness degradation factor with corresponding degree of corrosion

K_{IC} Degradation Parameter (γ)	Degree of Corrosion (R)
1	0
0.446280038	0.801
0.242769609	0.941
0.268322828	0.928
0.262803685	0.931
0.230119959	0.947
0.162938928	0.973
0.150230201	0.977
0.139879425	0.98

$$K_{IC}^{R} = K_{IC}(99.87R^4 \; - \; 118.7R^3 + \; 52.48R^2 - \; 10R \; + \; 1) \tag{13}$$

R is the degree of corrosion, K_{IC} fracture toughness of the uncorroded bar, and K_{IC}^{R} is the residual fracture toughness of a corroded bar after R degree of corrosion.

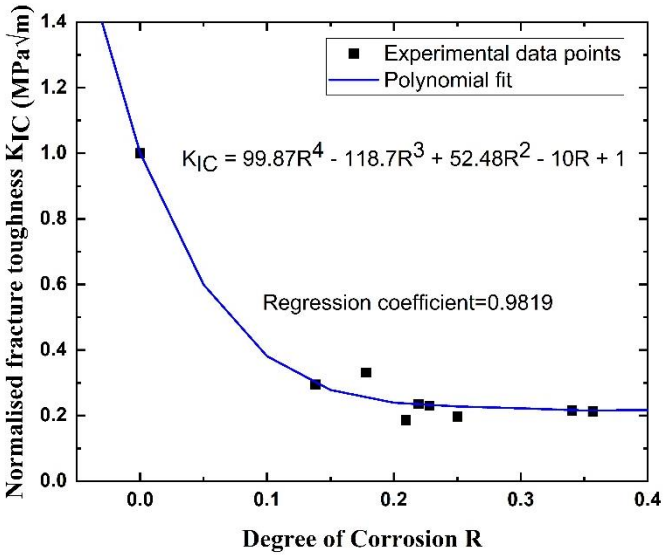

Figure 1. Fracture toughness and degree of corrosion

4. Calculation of critical crack size

There is a direct correlation between the critical crack size and fracture toughness, and is given as follows.

$$a_C = \frac{1}{\pi}\left(\frac{K_{IC}}{Y\sigma_y}\right)^2 \tag{14}$$

For corroded steel bars under cyclic loading, the critical crack size (a_c) is significantly influenced by the degree of corrosion, as a critical value of K_c decreases with increasing degree of corrosion. Detailed analysis of fracture toughness degradation is given in section 3.1. Fig. 2 clearly shows that higher corrosion degrees result in reduced values of a_c, indicating that corrosion significantly decreases the critical crack size. This relationship shows that as corrosion accelerates fatigue crack propagation, it substantially reduces the critical crack size, leading to an earlier onset of unstable crack propagation and fatigue fracture. Eqn. 15 shows an empirical fit between the degree of corrosion and critical crack size.

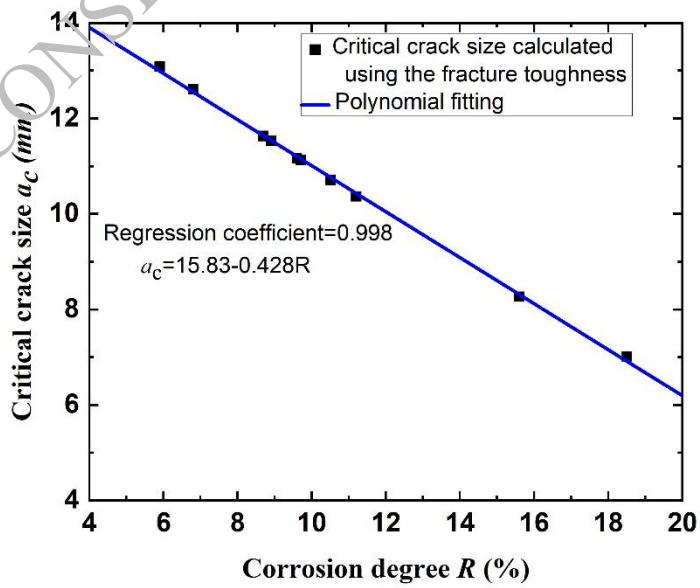

Figure 2. Relationship between critical crack size and degree of corrosion

$$a_C = 15.83 - 0.428R \quad (15)$$

5. Relationship between EIFS and corrosion degree

The need to obtain an estimate of the initial flaw size (EIFS) arises so that the Paris law, which describes the long crack growth behaviour, can be used to accurately calculate fatigue life prediction results by including the short crack regime as well. However, current EIFS estimation methods do not consider the effect of corrosion and are primarily based on the material's endurance derived from S-N curve data ($\Delta\sigma_f$ and ΔK_{th}). To accurately determine the quantitative relationship between the EIFS and the degree of corrosion, the available fatigue life test results of corroded RC beams under similar loading conditions and failure modes were analyzed. This includes collecting and calibrating data from existing studies (Sun et al., 2015), resulting in a comprehensive dataset of 11 experimental results. By using the analytical correlation for fatigue life prediction given by Eqn. (9) and eliminating outlier data to enhance the precision of data fitting, EIFS values at varying levels of corrosion mass loss were derived. The resulting scatter plot and fitted expression, as depicted in Fig.3 and Eqn.16 respectively, illustrate the correlation between EIFS and corrosion degree. This analysis shows that EIFS increases with higher degrees of corrosion, providing a clear and quantifiable link between the extent of corrosion damage and the initial flaw size impacting fatigue life.

$$a_{EIFS} = 0.328R - 1.25 \quad (16)$$

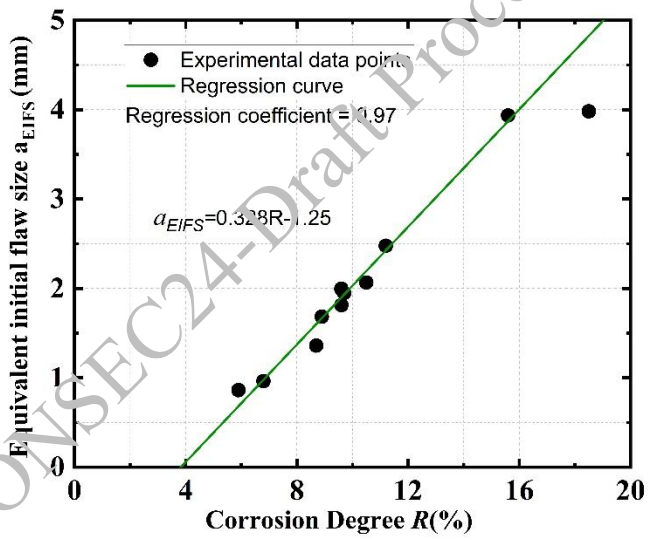

Figure 3. Correlation between EIFS and degree of corrosion

6. Validation of the proposed model

The results from accelerated and natural corrosion tests show only minor differences in the overall performance of corroded RC structures or their components. Therefore, data from accelerated corrosion tests can be effectively used to analyze and estimate the fatigue performance and lifespan of corroded RC beams. Using the above-proposed model, the fatigue life of corroded steel bars under various degrees of corrosion is predicted and verified by comparison of results with existing experimental data of corroded RC beams, as shown in Table 2.

Table 2. Corrosion fatigue test results collected that are used for the validation of the proposed model.

Author	No. of beam specimens	Dimensions of the beam L×B×H (mm)	Reinforcement Detailing	Fatigue loading (kN)	Stress ratio (S.R)
Sun et al., 2015	12 beams	1800×150×250	D=16mm F_y=478 MPa F_u=608 MPa	Min. =30 Max. =70	0.42
Fernandez et al., 2015	140 corroded bars	310-320	D=12mm F_y=548 MPa F_u=637 MPa	Min. =11.3 Max. =33.7	0.33
Yi et al., 2010	8 beams	3600×150×300	D=20mm F_y=390 MPa F_u=578 MPa	Min. =7 Max. =33	0.21
Wang et al., 2004	2 beams	1700×120×200	D=12mm F_y=400 MPa F_u=595MPa	Min. =7 Max. =36.5	0.19

The experimental data shows a significant decrease in the fatigue life of RC beams as the degree of corrosion increases. The proposed and available model (Sun et al., 2015) in the literature are compared to the experimental fatigue life of corroded RC beams, as illustrated in Figs. 4(a) and 4(b) respectively. A 45° line signifies that the predicted values are exactly equal to the experimental values, and data points close to this line indicate the precision of the predictions. From Figures 4 (a) and 4 (b), it is clear that the proposed model outperforms the existing model. The predicted outcomes of the proposed model align more closely with the 45-degree line, showing an average percentage error of 1.39%, compared to the 4.97% error of the existing model. This indicates that the proposed model has a better agreement with the test results. This validation highlights the effectiveness of the proposed model in predicting the fatigue life of corroded RC beams, making it a reliable tool for future research and practical applications.

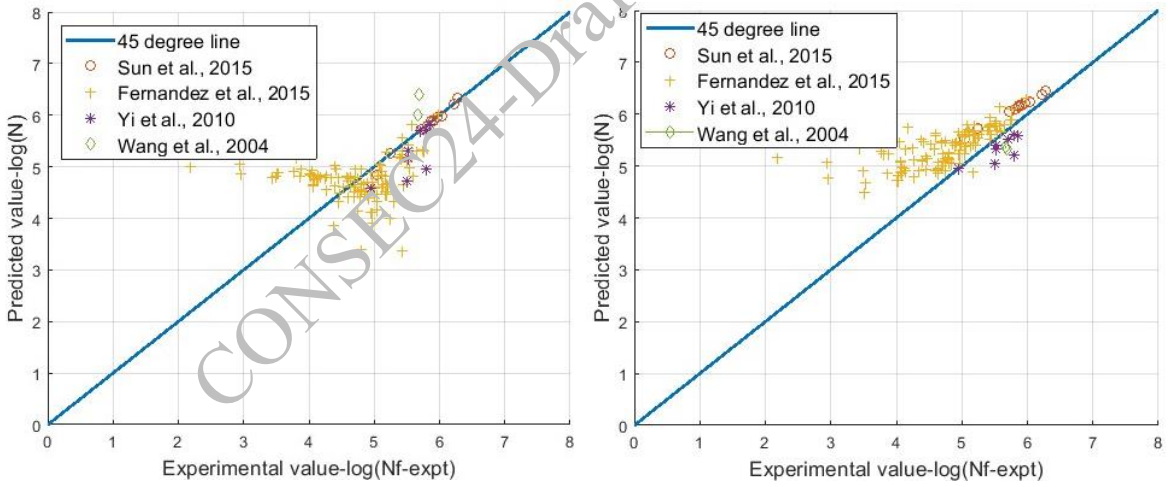

(a) (b)

Figure 4. Comparison of the predicted (N) and experimental (Nf-expt) results for the fatigue life of corroded RC beams (a) Using the proposed model given in this study (b) Existing model in the study.

7. Conclusions

- This study highlights the effect of corrosion on fatigue crack growth parameters and the prediction of corrosion fatigue life. A new empirical relationship between fracture toughness and the degree of corrosion is proposed. The critical crack size for corroded reinforcement is determined based on the reduction in fracture toughness. Accelerated corrosion test data from the literature is utilized to establish a quantitative relationship between the degree of corrosion and residual fracture toughness, demonstrating that fracture toughness decreases as the degree of corrosion increases.

- In this study, the coupled effects of corrosion and crack growth due to fatigue loading are studied by incorporating EIFS as an alternative to the initial flaw size for an embedded reinforcement in a concrete beam. The EIFS approach avoids the need to analyze small crack growth separately and thereby incorporates the large crack growth model to predict fatigue life.
- The proposed model for predicting the corrosion fatigue life of RC beams has been validated through comparison with experimental data from the literature. The findings show a good correlation between the predicted and experimental values, indicating the model's ability to estimate the remaining fatigue life of corroded RC beams. Additionally, the proposed model highlights the crucial importance of considering corrosion effects in fatigue life predictions, with significant implications for the safety and durability of materials in various engineering applications.

References

ASTM E1304. Standard test method for plane-strain (Chevron-Notch) fracture toughness of metallic materials; 2001.

ASTM E399. Standard test method for fracture toughness of metallic materials; 1990.

Coca, F. O., Tello, M. L., Gaona-Tiburcio, C., Romero, J. A., Martínez-Villafañe, A. B. E. M., & Almeraya-Calderón, F. (2011). Corrosion fatigue of road bridges: A review. *International Journal of Electrochemical Science*, *6*(8), 3438-3451.

Devendiran, D. K., & Banerjee, S. (2023). Influence of Combined Corrosion–Fatigue Deterioration on Life-Cycle Resilience of RC Bridges. *Journal of Bridge Engineering*, *28*(5), 04023014.

Elices, M., Perez-Guerrero, M., Iordachescu, M., & Valiente, A. (2017). Fracture toughness of high-strength steel bars. *Engineering Fracture Mechanics*, *170*, 119-129.

Fernandez, I., Bairán, J. M., & Marí, A. R. (2015). Corrosion effects on the mechanical properties of reinforcing steel bars. Fatigue and σ–ε behavior. *Construction and Building Materials*, *101*, 772-783.

Forman, R. G., & Shivakumar, V. (1986). Growth behavior of surface cracks in the circumferential plane of solid and hollow cylinders. In *Fracture mechanics: Seventeenth volume*. ASTM International.

Gheorghiu, C., Labossiere, P., & Proulx, J. (2006). Fatigue and monotonic strength of RC beams strengthened with CFRPs. *Composites Part A: Applied Science and Manufacturing*, *37*(8), 1111-1118.

Herwig, A. (2008). *Reinforced concrete bridges under increased railway traffic loads: Fatigue behaviour and safety measures* (No. 4010). EPFL.

Liu, Y., & Mahadevan, S. (2009). Probabilistic fatigue life prediction using an equivalent initial flaw size distribution. *International Journal of Fatigue*, *31*(3), 476-487.

Ma, Y., Xiang, Y., Wang, L., Zhang, J., & Liu, Y. (2014). Fatigue life prediction for aging RC beams considering corrosive environments. *Engineering Structures*, *79*, 211-221.

Madia, M., Vojtek, T., Duarte, L., Zerbst, U., Pokorný, P., Jambor, M., & Hutař, P. (2021). Determination of fatigue crack propagation thresholds for steel in presence of environmental effects. *International Journal of Fatigue*, *153*, 106449.

Rodrigues, R., Gaboreau, S., Gance, J., Ignatiadis, I., & Betelu, S. (2021). Reinforced concrete structures: A review of corrosion mechanisms and advances in electrical methods for corrosion monitoring. *Construction and Building Materials*, *269*, 121240.

Sun, J., Ding, Z., & Huang, Q. (2019). Corrosion fatigue life prediction for steel bar in concrete based on fatigue crack propagation and equivalent initial flaw size. *Construction and Building Materials*, *195*, 208-217.

Wang, H., Gong, J., & Song, Y. (2004). Experimental study on corrosion fatigue of RC beams. *Journal of Building Structures*, *25*(5), 105-110.

Xiang, Y., & Liu, Y. (2010). EIFS-based crack growth fatigue life prediction of pitting-corroded test specimens. *Engineering Fracture Mechanics*, *77*(8), 1314-1324.

Yang, D. H., Yi, T. H., & Li, H. N. (2017). Coupled fatigue-corrosion failure analysis and performance assessment of RC bridge deck slabs. *Journal of Bridge Engineering*, *22*(10), 04017077.

Yi, W. J., Kunnath, S. K., Sun, X. D., Shi, C. J., & Tang, F. J. (2010). Fatigue Behavior of Reinforced Concrete Beams with Corroded Steel Reinforcement. *ACI Structural Journal*, *107*(5).

Enhancing Geopolymer Concrete Performance Using Copper Slag as a Sustainable Fine Aggregate

Aman Deep [1], Pradip Sarkar *[2]

[1] Department of Civil Engineering, National Institute of Technology Rourkela, Odisha, 769008, India
Email: amandeep13507@gmail.com
[2] Department of Civil Engineering, National Institute of Technology Rourkela, Odisha, 769008, India
Email: sarkarp@nitrkl.ac.in

*Corresponding author

ABSTRACT

Geopolymer concrete (GPC), utilizing aluminosilicate precursor materials as binders, stands as an eco-friendly alternative to ordinary Portland cement concrete (OPCC). These precursors commonly include natural resources like metakaolin, volcanic ash, and industrial solid waste such as fly ash (FA) and ground granulated blast furnace slag (GGBFS). However, despite not utilizing cement, GPC still faces environmental challenges due to the use of natural aggregates, leading to resource depletion. To mitigate this issue, researchers have explored replacing natural aggregates with waste materials, aiding both resource conservation and waste management. Copper slag (CS) is one such waste material with potential as fine aggregate in GPC. This study conducts a comprehensive evaluation of FA-GGBFS-based GPC incorporating CS as fine aggregate. It was found that, GPC exhibited superior performance compared to OPCC in various aspects, including strength properties (such as compressive, split tensile and flexural strength)**,** transport properties (includes water absorption, permeable void and rapid chloride penetration test) and durability properties (like abrasion resistance and slake durability).

KEYWORDS*: Geopolymer concrete, Copper slag, Water absorption, Rapid chloride penetration test, Slake durability*

1. Introduction

Construction activity has increased dramatically in recent years in order to fulfil the ever-increasing need for infrastructure. It is clear that ordinary Portland cement-based concrete (OPCC) has become an essential and commonly used material in the majority of construction projects. The cement manufacturing process releases a significant amount of CO_2 into the environment through fuel consumption and raw material transformation. According to studies, producing one tonne of cement emits roughly the same amount of carbon dioxide into the environment (Neville (2012)). On the other hand, industrial waste generation has increased significantly, including fly ash (FA) from thermal power plants, ground granulated blast furnace slag (GGBFS) from the iron industry, red mud from the alumina industry, mine tailings from the mineral sector, Copper slag (CS) from the refining and smelting of copper ore, and so on. Environmentalists and researchers are facing significant challenges in disposing of and managing these wastes, as well as developing alternatives to cement. It is therefore extremely important to concentrate on better and more realistic methods to utilize industrial waste in the building construction. Geopolymer concrete (GPC) could be an excellent alternative to OPCC that reduces or eliminates the use of cement while also promoting the effective use of industrial waste (Turner et al (2013); McLellan et al (2011)).

Geopolymers are a class of inorganic polymers created through the alkali activation of materials rich in aluminosilicates. The process of geopolymerization involves three key stages: dissolution, condensation, and polycondensation, as described by Davidovits (2008). Typically, this reaction occurs at room temperature or higher, facilitated by alkaline activators, as noted by Verdolotti et al (2008). Common alkaline activators include alkali hydroxides (such as NaOH and KOH) and alkali silicates (like Na_2SiO_3, K_2SiO_3). However, FA-based GPC) presents two main challenges: it often requires elevated temperature

curing to enhance and accelerate the geopolymerization process, and it generally yields moderate compressive strengths Fernandez et al (2008). These issues can be mitigated by incorporating GGBFS alongside FA as a binder. Remarkably, FA-GGBFS-based GPC requires ambient temperature curing and results in reasonably high compressive strengths. The N-A-S-H (sodium-aluminium-silicate hydrate) gel structure forms in FA-based GPC, which accounts for its moderate compressive strength. In contrast, the inclusion of GGBFS leads to the development of C-A-S-H (calcium-aluminium-silicate-hydrate) and C-S-H (calcium-silicate-hydrate) gel structures, which enhance the compressive strength of the GPC (Nath et al (2014); Al-Majidi et al (2016)). However, using too much GGBFS can shorten the setting time of the GPC. Therefore, the GGBFS content in the mix should be kept 30% to maintain optimal performance (Deb et al (2014); Reddy et al (2018); Prusty et al (2020)).

CS, a waste material generated during the refining and smelting process of copper ore, could emerge as a viable competitor to natural sand (NS) in the manufacturing of GPC. India alone contributes approximately 22 million tons of the 400 million tonnes of CS produced globally annually Sharma (2022). A significant amount of CS is disposed of in landfills, occupying considerable land space and leading to the destruction of fertile topsoil. CS shares certain similarities with NS in terms of physical and chemical properties, and it also exhibits pozzolanic activity (Thomas et al (2018)). CS is reported to be used in OPCC as fine aggregate as well as binder materials as a sustainable alternative by many researchers. Also, some recent literature has attempted to use CS as a sustainable alternative to natural fine aggregate in GPC. The waste CS shows tremendous promise as an environmentally sustainable substitute in the construction sector, addressing waste management issues and conserving natural resources. While previous studies have investigated the effect of CS on certain strength and microstructural properties of GPC, many important aspects remain unaddressed. To bring this construction material into practical usage, it is crucial to thoroughly study all important aspects of this material. The associated research output will be useful in instilling confidence among stakeholders about the practical usage of this building material. The present study is a step forward in this direction which primarily focusses on three important aspects: strength, transport, and durability properties of hardened OPCC and FA-GGBFS-based GPC with varying percentages of CS in combination with NS as fine aggregates.

2. Methodology

The methodology adopted in the present study are- (i) collection of ingredients, (ii) material characterization, (iii) mix design for OPCC and GPC, (iv) specimen preparation, (v) conducting experiments, (vi) analysis of results, (vii) arrive at conclusion.

3. Experimental Program

3.1 Materials Characterization

The waste materials utilized in this study were sourced from the near vicinity of the state of Odisha, India. FA was obtained from the Rourkela Steel Plant in Rourkela, Odisha, while GGBFS was procured from Toshali Cement Private Limited in Cuttack, Odisha. CS was collected from Hindustan Copper Limited in Jharkhand. In this investigation, 20 mm nominal size graded natural coarse aggregates (NCA), conforming to IS 383 (2016), along with locally sourced river sand as fine aggregate, were used. The physical properties of the binders and aggregates are detailed in Tables 1 and 2, respectively. For the alkaline activation of the source materials, commercially available sodium hydroxide and sodium silicate with 98% purity (containing SiO_2 = 27.46%, Na_2O = 9.56%, and H_2O = 62.98%) were used, having specific gravities of 1.43 and 1.40, respectively. Additionally, 53-grade Portland cement, as per IS 12269 (1987) and ASTM C150 (2019) standards, with a specific gravity of 3.1 and normal consistency of 31%, was employed in this study. The physical appearance of FA, GGBFS, NS and CS used in this study is shown in Fig. 1.

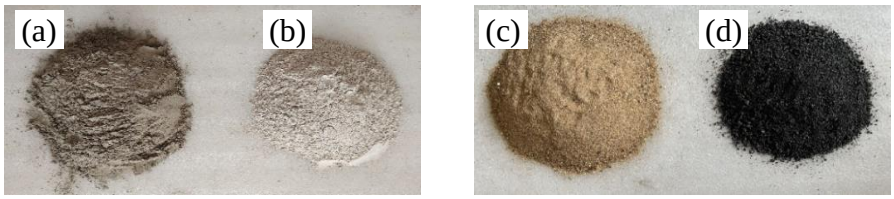

Figure 1. Physical appearance of (a) FA, (b) GGBFS, (c) NS and (d) CS

Table 1. Physical properties of binders used

Materials	Colour	Shape	Class *	Specific gravity	Specific surface (m^2/kg)	Fineness (%)	Moisture content (%)
Cement	Light greenish	Irregular	-	3.10	351	10	0.25
FA	Grey	Spherical	F	2.22	326	20	0.65
GGBFS	Off-white	Irregular	-	2.86	357	9	0.33
Max. limit	-	-	-	-	Min 320*, #	< 34*	< 2*

*IS 3812-1 (2013); *ASTM C618 (2019), #IS 16714 (2018)

Table 2. Physical properties of fine and coarse aggregates

Materials	Specific gravity	Water absorption (%)	Compacted bulk density (kg/m^3)	Fineness modulus	Material finer than 75 µm (%)
NS	2.62	0.80	1691	2.52	0.7
CS	3.90	0.40	2195	3.39	0.4
NCA	2.76	0.69	1581	7.54	-
Max. limit	-	< 2#	-	-	-

#IS 2386-3 (1963); ASTM C128 (2022)

3.2 OPCC and GPC Mix-Proportion

In the absence of established guidelines for GPC mix design, this study utilizes various references, including previous literature and current conventional cement concrete standards Pavithra et al (2016); Reddy et al (2018); ACI 211.1 (2002); IS 10262, (2019), for the design of FA-GGBFS based GPC. The ratio of the alkaline activator solution to binder solids (AAS/BS) was consistently maintained at 0.5 across all trial mixtures. A 12M NaOH solution was created by dissolving sodium hydroxide flakes in potable water, with a fixed Na_2SiO_3 to NaOH ratio of 1.5. To ensure the complete dissolution of the flakes and to manage the heat produced during the exothermic reaction, the NaOH solution was prepared 24 hours prior to casting. The combined alkaline activator solution (NaOH and Na_2SiO_3) was then mixed 3 to 4 hours before casting. The ratio of FA to GGBFS was consistently maintained at 70% to 30% in all trial mixes to achieve dense and workable GPC (Deb et al (2014); Reddy et al (2018); Prusty et al (2020)). Six distinct GPC mixes were developed by substituting NS with varying amounts of CS, labelled as GPC0, GPC20, GPC40, GPC60, GPC80, and GPC100, where the numbers represent the percentage of NS replaced with CS. Additionally, a control specimen (OPCC) composed of 100% cement, NS, and NCA was prepared using conventional cement concrete standards IS 10262 (2019) and designed to achieve a compressive strength of 40 MPa after 28 days. The mix design process was thorough and involved trial and error, considering the specific gravity of the raw materials. Table 3 outlines the detailed concrete mix proportions for the seven different combinations.

Table 3. Details of OPCC and GPC mixes (kg/m^3)

Constituents	Mix ID						
	OPCC	GPC0	GPC20	GPC40	GPC60	GPC80	GPC100
Cement	450	0	0	0	0	0	0
FA	0	315	315	315	315	315	315
GGBFS	0	135	135	135	135	135	135
NaOH	0	90	90	90	90	90	90
Na_2SiO_3	0	135	135	135	135	135	135
NS	605	643	514.4	385.8	257.2	128.6	0
CS	0	0	191.6	383.2	574.8	766.4	958
NCA	1210	1060	1060	1060	1060	1060	1060
Extra water	0	18	18	18	18	18	18
Water	180	0	0	0	0	0	0
SP	3.6	5.4	5.4	5.4	5.4	5.4	5.4

3.3 Specimen Preparation

As discussed earlier, this paper focuses on thoroughly evaluating the effect of CS on the properties of hardened FA-GGBFS-based GPC and OPCC. Laboratory experiments were carried out to examine its impact on strength characteristics (including compressive, split tensile, and flexural strengths), transport properties (such as water absorption, permeable void content, and rapid chloride penetration), and durability features (abrasion resistance and slake durability). Strength characteristics were determined through break tests. A detailed summary of the tests conducted in this research, along with the specifications of the test specimens, is provided in Table 4.

Table 4. Details of tests conducted

Sl. No.	Properties measured	Specimen details	Standard followed
1	Compressive strength	100 mm cube	IS 516 (1959)
2	Splitting tensile strength	100 mm dia. × 200 mm long cylinder	IS 5816 (1999)
3	Flexural strength	500 ×100 ×100 mm prism	IS 516 (1959)
4	Water absorption	100 mm cube	ASTM C642 (2013)
5	Permeable void	100 mm cube	ASTM C642 (2013)
6	Rapid chloride penetration test	Disc - 100 mm dia. × 50 mm thick	ASTM C1202 (2017)
7	Abrasion resistance test	70.6 × 70.6 × 30 mm block	IS 1237 (2012)
8	Slake durability test	40–60 g lumps	IS 10050 (1981)

4. Result and Discussion

4.1 Workability

The results, illustrated in Fig. 2, indicated a notable decline in the workability of fresh concrete as the level of CS replacement increased. This decrease was primarily due to factors such as the irregular, angular shape of CS particles and the higher specific gravity of CS compared to NS. The slump values observed for GPC with CS incorporation were in line with findings reported in Arunachelam et al (2022). However, the use of superplasticizer successfully counteracted these effects, enabling the attainment of the desired slump in GPC.

4.2 Strength Properties

The mean compressive strength of hardened OPCC and FA-GGBFS-based GPC at different curing ages was experimentally evaluated, and the results are presented in Fig. 3 for various mixes. Fig. 3 clearly indicates that substituting NS with CS significantly improves the strength characteristics of hardened concrete across all levels of CS replacement. Although both NS and CS fall within the Zone II grading limits for fine aggregates, CS is generally slightly coarser, while NS is somewhat finer. The combination of CS and NS results in a well-graded fine aggregate mix, leading to enhanced particle packing compared to using NS alone. This improved grading, along with the possible presence of natural pozzolanic properties

in CS, contributes to the superior strength observed in GPC containing CS. As the proportion of CS increases, so does the strength of the GPC. However, this positive trend starts to reverse when the CS replacement exceeds 60%. At higher levels of replacement, the introduction of coarser particles from CS may disrupt the optimal grading of the fine aggregate mix. Additionally, the lower water absorption capacity of CS results in excess water surrounding the fine aggregate particles in fresh GPC mixes. This surplus water increases void content and weakens the interfacial transition zone in the hardened GPC, potentially reducing its strength. Despite these challenges, it's important to note that GPC specimens with any percentage of CS replacement consistently show better strength than the control specimens using NS alone. Notably, a substantial increase of 26-29% in compressive strength, 24-28% in tensile strength, and 19-27% in flexural strength was observed in GPC60 compared to the control specimen (OPCC).

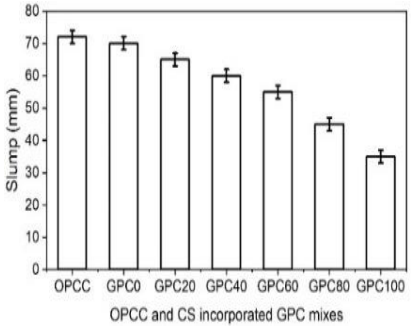

Figure 2. Workability of fresh OPCC and GPC

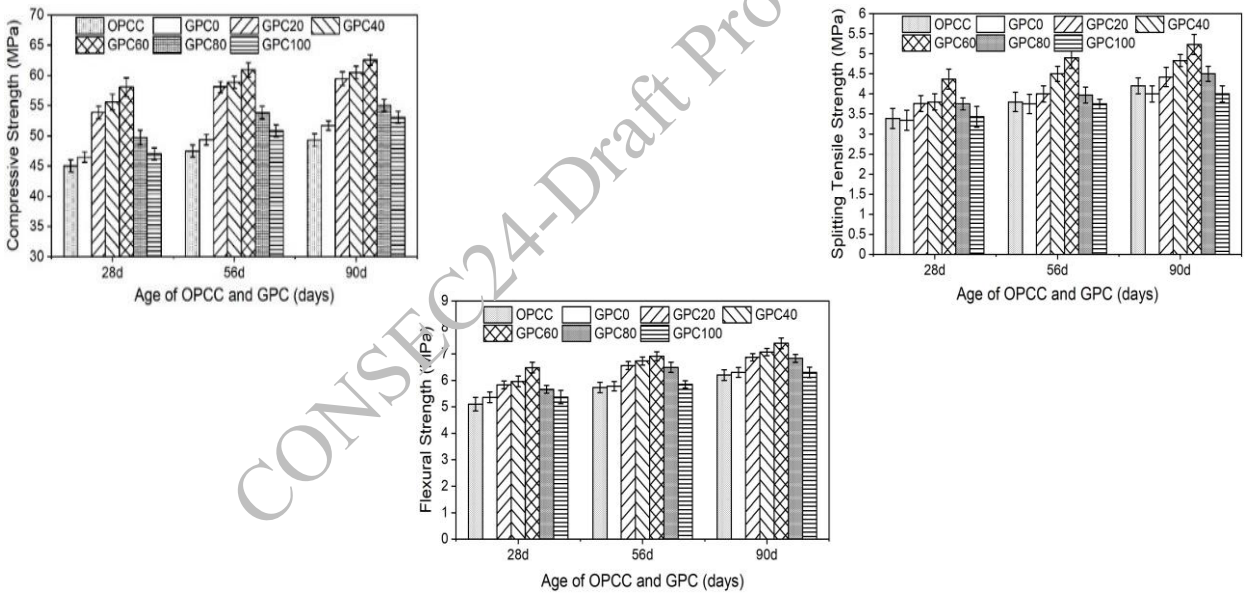

Figure 3. Strength properties of hardened OPCC and GPC

4.3 Transport Properties

Figure 4 illustrates the water absorption, permeable void content, and rapid chloride penetration test (RCPT) results for various hardened GPC and OPCC specimens at 28, 56, and 90 days. As the content of CS increases, there is a noticeable reduction in both water absorption and permeable voids in GPC, indicating an enhancement in concrete quality. Among the different mixes, GPC60 exhibits the most favourable performance. However, further increases in CS content beyond 60% begin to negatively impact concrete quality, aligning with the observations from the strength tests. GPC60 samples show a reduction in water absorption by 23-48% and in permeable voids by 20-35% compared to the control OPCC samples. Also, as CS replacement increases, the charge passed or chloride penetrability, decreases, indicating an improvement in the GPC quality. However, this trend is only observed up to a CS replacement of 60%. Beyond this level, an increase in CS content leads to higher chloride penetrability, although it remains lower

than that of the control OPCC samples. The results also highlight that extending the curing period from 28 to 90 days significantly enhances the concrete quality, emphasizing the importance of longer curing durations for improved durability. It was observed that chloride penetrability decreased by 58-72% for GPC60 samples compared to the control OPCC samples.

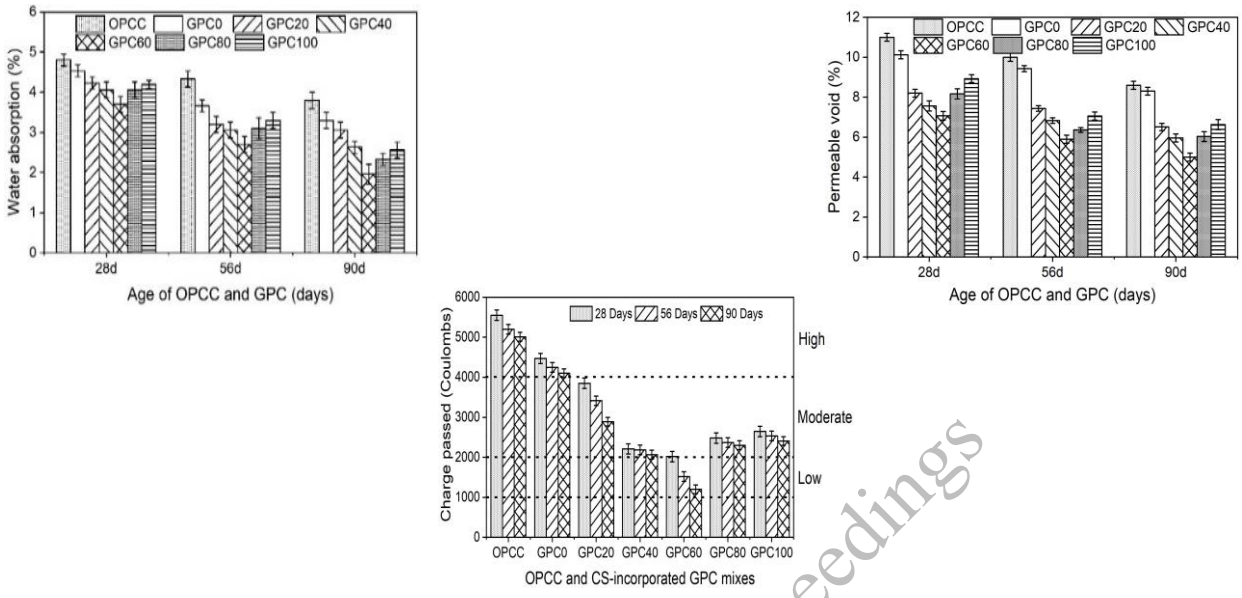

Figure 4. Water absorption, permeable void, RCPT of hardened OPCC and GPC

4.4 Abrasion Resistance

As mentioned earlier, the abrasion resistance of hardened GPC and OPCC specimens is quantified by measuring wear depth, with lower wear depth indicating better abrasion resistance. The average wear depth of all GPC specimens and OPCC after 28, 56, and 90 days of ambient curing is displayed in Fig. 5. The results show a decrease in wear depth as both the CS replacement percentage and the curing age of the GPC specimens increase. This improvement is likely due to the strong inter-particle bonding resulting from the well-graded fine aggregate mix created by combining CS and NS. Additionally, the potential pozzolanic properties of CS might contribute to the increased strength of GPC, leading to reduced wear depth. However, when the CS replacement exceeds 60%, an increase in wear depth was observed, potentially indicating weak inter-particle bonding in hardened GPC (Li et al (2006)). It was noted that the wear depth decreased by 35-53% for GPC60 samples compared to the control OPCC samples.

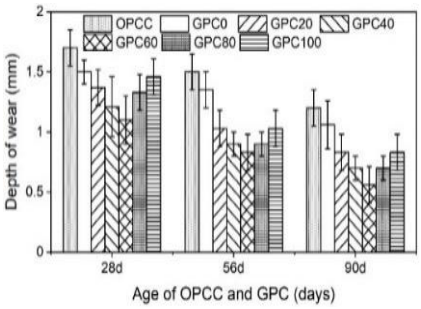

Figure 5. Depth of wear of hardened OPCC and GPC

4.5 Slake Durability

The slake durability test was carried out in the laboratory following the IS10050 (1981) standard, involving two cycles of wetting and drying. The slake durability indices for GPC and OPCC specimens were calculated after the completion of the second cycle. Fig. 6 displays the slake durability indices for all GPC and OPCC specimens at various curing ages. The data consistently reveal that GPC specimens incorporating CS exhibit higher slake durability indices compared to the control OPCC specimens, which

contain only NS, across different curing periods. This increased slake durability reflects greater resistance to disintegration, highlighting the beneficial effect of substituting natural fine aggregate with CS in enhancing the slake durability of concrete. Moreover, the slake durability index of GPC continues to rise as the CS replacement percentage increases up to 60%. This improvement can be attributed to the strong bond formed between the aggregate and the surrounding hydrated geopolymer paste in the GPC. An enhancement of 11-17% in slake durability index was observed in GPC60 compared to the control OPCC specimen.

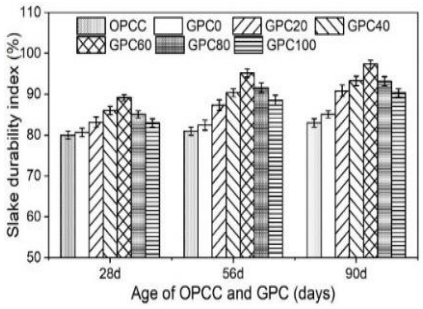

Figure 6. Slake durability of hardened OPCC and GPC

5. Conclusions

The disposal of waste materials such as FA, GGBFS, and CS poses significant environmental and industrial challenges. However, incorporating these materials into building construction presents a promising avenue for promoting sustainable development in the built environment. Extensive research is crucial to increase awareness among stakeholders and facilitate the practical application of these waste materials in the concrete construction industry. The results demonstrate that the inclusion of CS in GPC significantly enhances strength, transport, and durability properties. The following are the key conclusions drawn from the present study:

- Material characterization results indicate that CS can effectively replace NS in GPC production.
- The workability of fresh concrete decreases with higher CS replacement due to the irregular, angular shape and higher specific gravity of CS particles compared to NS.
- The strength of hardened GPC significantly improves with all levels of CS replacement, attributed to superior particle packing and natural pozzolans in CS.
- The water absorption and permeable voids in GPC decrease with higher CS content, indicating improved concrete quality and aligning with strength test results.
- RCPT indicates improved chloride resistance at 60% CS replacement, attributed to better particle packing, and natural pozzolanas in CS.
- Wear depth decreases with higher CS replacement and increased curing age of GPC specimens, due to strong inter-particle bonding from the well-graded combination of CS and NS.
- The slake durability of hardened GPC increases with higher CS replacement, due to the strong bond between the aggregate and the surrounding hydrated geopolymer paste.
- GPC with 60% optimum CS replacement (GPC60) demonstrates superior mechanical strength, minimal water absorption, permeable voids, chloride penetrability, high abrasion resistance, and enhanced slake durability compared to OPCC and other GPC mixes.

References

ACI 211.1 (2002) "Standard practice for selecting proportions for normal, heavyweight and mass concrete, ACI Committee Report".

A.M. Neville (2012) *Concrete Technology*, 4th Edn. Pearson Education Ltd. Publications, England.

A. Fernandez-Jimenez, M. Monzo, M. Vicent, A. Barba and A. Palomo (2008) "Alkaline activation of metakaolin–fly ash mixtures: Obtain of Zeoceramics and Zeocements", *Microporous Mesoporous Mater.* 108, 41-49.

ASTM C150/C150M (2019) "Standard specification for Portland cement", *ASTM International*, West Conshohocken, PA.

ASTM C618 (2019) "Standard specification for coal fly ash and raw or calcined natural pozzolanas for use in concrete", *ASTM International*, West Conshohocken, PA.
ASTM C642 (2013) "Standard test method for density, absorption and voids in hardened concrete", *ASTM International*, West Conshohocken, PA.
ASTM C1202 (2017) "Standard test method for electrical indication of concrete's ability to resist chloride penetration", *ASTM International*, West Conshohocken, PA.
ASTM C128 (2022) "Standard test method for relative density (specific gravity) and absorption of fine aggregate", *ASTM International*, West Conshohocken, PA.
B. C. McLellan, R. P. Williams, J. Lay, A. Van Riessen and G. D. Corder (2011) "Costs and carbon emissions for geopolymer pastes in comparison to ordinary Portland cement", *J. Clean. Prod.* 19(9-10), 1080-1090.
H. Li, M. H. Zhang and J. P. Ou (2006) "Abrasion resistance of concrete containing nano-particles for pavement", *Wear*, 260(11-12), 1262-1266.
IS 1237 (2012) "Cement concrete flooring tiles – Specification", *Bureau of Indian Standards*, New Delhi, India.
IS 10050 (1981) "Method for determination of slake durability index of rocks", *Bureau of Indian Standards*, New Delhi, India.
IS 10262 (2019) "Guidelines for concrete mix design proportioning", *Bureau of Indian Standards*, New Delhi, India.
IS 12269 (1987) "Ordinary Portland Cement, 53 Grade: Specification", *Bureau of Indian Standards*, New Delhi, India.
IS 2386 (Part III) (1963) "Methods of test for aggregates for specific gravity, density, voids, absorption and bulking", *Bureau of Indian Standards*, New Delhi, India.
IS 383 (2016), "Coarse and fine aggregates for concrete - Specification", *Bureau of Indian Standards*, New Delhi, India.
IS 516 (1959) "Method of tests for strength of concrete", *Bureau of Indian Standards*, New Delhi, India.
IS 5816 (1999) "Method of tests for splitting tensile strength of concrete", *Bureau of Indian Standards*, New Delhi, India.
IS 16714 (2018), "Ground granulated blast furnace slag for use in cement, mortar and concrete – Specification", *Bureau of Indian Standards*, New Delhi, India.
J. G. Davidovits (2008) *Geopolymer Chemistry and Applications*, 5th Edn., Institut Geopolymere, Saint-Quentin, France.
J. K. Prusty and B. Pradhan (2020) "Effect of GGBS and chloride on compressive strength and corrosion performance of steel in fly ash-GGBS based geopolymer concrete", *Mater. Today Proc.* 32, 850-855.
J. Thomas, N. N. Thaickavil and M. P. Abraham (2018) "Copper or ferrous slag as substitutes for fine aggregates in concrete", *Adv. Concr. Constr.* 6(5), 545-560.
L. K. Turner and F. G. Collins (2013) "Carbon dioxide equivalent (CO2-e) emissions: A comparison between geopolymer and OPC cement concrete", *Constr. Build. Mater.* 43, 125-130.
L. Verdolotti, S. Iannace, M. Lavorgna and R. Lamanna (2008) "Geopolymerization reaction to consolidate incoherent pozzolanic soil", *J. Mater. Sci.* 43, 865-873.
M. G. Sharma (2024) https://timesofindia.indiatimes.com/blogs/voices/copper-slag-converting-waste-into-sustainable-wealth/.
M. H. Al-Majidi, A. Lampropoulos, A. Cundy and S. Meikle (2016) "Development of geopolymer mortar under ambient temperature for in situ applications", *Constr. Build. Mater.* 120, 198-211.
M. S. Reddy, P. Dinakar and B. H. Rao (2018) "Mix design development of fly ash and ground granulated blast furnace slag based geopolymer concrete", *J. Build. Eng.* 20, 712-722.
N. Arunachelam, J. Maheswaran, M. Chellapandian, G. Murali, G. and N. I. Vatin (2022) "Development of high-strength geopolymer concrete incorporating high-volume copper slag and micro silica", *Sustain.* 14(13), 7601.
P. Nath and P. K. Sarker (2014) "Effect of GGBFS on setting, workability and early strength properties of fly ash geopolymer concrete cured in ambient condition", *Constr. Build. Mater.* 66, 163-171.
P. Pavithra, M. S. Reddy, P. Dinakar, B. H. Rao, B. K. Satpathy and A. N. Mohanty (2016) "A mix design procedure for geopolymer concrete with fly ash", *J. Clean. Prod.* 133, 117-125.
P. S. Deb, P. Nath and P. K. Sarker (2014) "The effects of ground granulated blast-furnace slag blending with fly ash and activator content on the workability and strength properties of geopolymer concrete cured at ambient temperature", *Mater. Des.* 62, 32-39.

Plastic Shrinkage Cracking Behaviour of Alkali Activated 3D Printable Mixtures

Abhay Dhasmana[1*], Prakash Nanthagopalan[2]

[1] Indian Institute of Technology Bombay, Mumbai, India
Email: 23d0276@iitb.ac.in
[2] Indian Institute of Technology Bombay, Mumbai, India
Email: prakashn@iitb.ac.in

[*]Corresponding author

ABSTRACT

Plastic shrinkage cracking is a critical issue in concrete construction, affecting the durability and structural integrity of concrete elements. The present study investigates the plastic shrinkage cracking behavior of alkali-activated 3D concrete printable mixtures, considering the effect of restrained conditions. The research employs a comprehensive experimental approach, encompassing fresh properties, strength (workability and compressive strength), and plastic shrinkage cracking assessment tests. Various alkali-activated mixes were formulated using different combinations of fly ash and slag as binders, with sodium hydroxide (NaOH) serving as the activator at a concentration of 14 M. Each mixture was prepared consistently, maintaining a constant water-to-binder ratio of 0.35. These tests are conducted under controlled environmental conditions to evaluate crack formation and crack width. Additionally, crack analysis was performed using numerical computing techniques to provide detailed insights into crack characteristics. To determine the workability for a printable mixture, a flow table test was conducted, selecting the mixture with an initial slump flow of 176 mm and a slump of 45 mm. This mixture remained within the printable range after remixing, which redistributed moisture and reduced viscosity, enabling additional workability. The selected mixture achieved a compressive strength of 58.70 MPa at 28 days and exhibited delayed cracking compared to OPC mortar. Crack analysis using MATLAB provided detailed measurements of crack dimensions.

Keywords: *3DCP, Alkali activation, Plastic Shrinkage cracking, Durability*

1. Introduction

Plastic shrinkage cracking in concrete arises from rapid surface moisture evaporation during early placement and finishing, exacerbated by environmental factors like high temperatures, low humidity, and wind. Various factors, including evaporation rate, settlement differentials, and surface restraint, contribute to cracking, influenced by mix properties like water-to-binder ratio and cement content (Boshoff & Combrinck (2013)). Mitigation strategies involve proper curing, controlled placement techniques, and adherence to ASTM guidelines. Alkali-activated cements, derived from aluminosilicate precursors, offer an eco-friendly alternative to Portland cement, exhibiting resistance to acids, sulphates, fire, and corrosion (Awoyera & Adesina (2019)). Despite their benefits, the plastic shrinkage behavior of alkali-activated 3D printable mortar remains understudied. This research investigates the plastic shrinkage cracking behavior of alkali-activated 3D printable concrete mixtures under restrained conditions, crucial for informing their successful application in construction projects.

2. Materials and methods

The alkali-activated mortar (AAM) mixture, comprising GGBFS, fly ash (15% by wt. of GGBFS)), and silica fume (10% by wt. of GGBFS)), as binders, was prepared with a 14 M sodium hydroxide solution and sodium silicate as the activator. The mass ratio of sodium silicate to NaOH solution was set to 0.6, with a

silica modulus of 2. A water-binder ratio of 0.35 ensured optimal printability for 3D concrete printing. The best-performing mix underwent evaluation for plastic shrinkage cracking behavior, alongside tests for compressive strength and flow. Shrinkage cracking was analysed using ASTM C1579 (2021) standards in controlled conditions, with numerical computing techniques aiding crack analysis under restraint. The methodology adopted for analysis is shown in Fig.1.

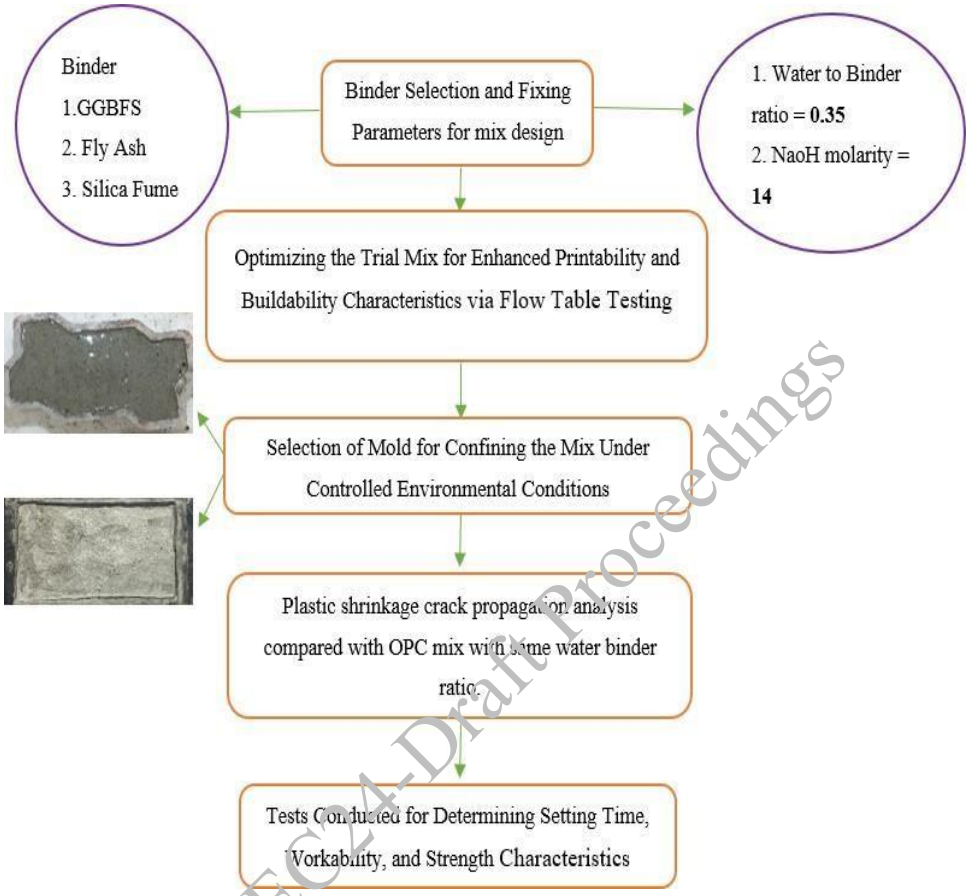

Figure 1. Methodology adopted for analysis of plastic shrinkage cracking of alkali activated mixture.

3. Results and Discussions

To determine the workability required for selecting a printable mixture, flow table test was conducted, measuring slump flow and slump. According to previous literature, a slump flow range of 150-190 mm is suitable for printability. From all tested mixtures, the one with an initial slump flow of 176 mm and a slump of 45 mm was chosen as show in in Fig.2(a). Slump loss was monitored every 10 minutes, revealing that after 30 minutes, the mixture fell out of the printable range. However, upon remixing, the mixture regained a printable slump range for an additional 40 minutes. Remixing reintroduced shear forces, redistributing the moisture and breaking up the early formation of the stable aluminosilicate gel. This restored the mix to a printable state by temporarily reducing the viscosity and reactivating the workability. Also, compressive strength tests were performed on the selected mix at 3, 7, and 28 days as shown in Fig.2(b). The alkali-activated mix achieved a strength of 58.70 MPa which is attributed to the stable, low-permeability gel that forms during the chemical reactions.

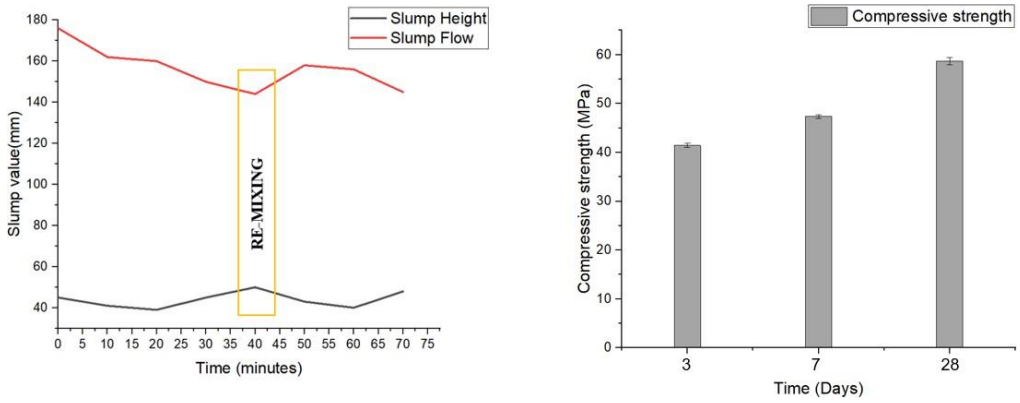

Figure 2. (a) Slump characteristics of AAM mixture (b) Compressive strength of AAM mixture.

In addition, the cracking behavior of alkali-activated mortar was investigated using two different mould shapes under restraint effect. When compared to OPC mortar, the cracks in the alkali system emerged after the completion of a 10 h plastic shrinkage crack test in both mould types. This delayed cracking phenomenon was observed, indicating a notable shrinkage difference compared to OPC mortar as shown in Fig.3 (a,b).

As stated in previous literature ((Matalkah et al (2019); Yang et al (2022); Ye & Radlińska (2017)), alkali-activated mortar exhibits less plastic shrinkage strain and delayed cracking compared to ordinary Portland cement (OPC) concrete due to several factors. AAM has a lower bleeding tendency, which minimizes surface water loss and shrinkage. It also has higher viscosity and yield stress, providing greater resistance to deformation. The chemical reactions in AAM create a stable, low-permeability aluminosilicate gel that retains moisture better. These factors, along with favourable rheological properties, reduce early-age deformations and delay cracking in alkali activated mortar.

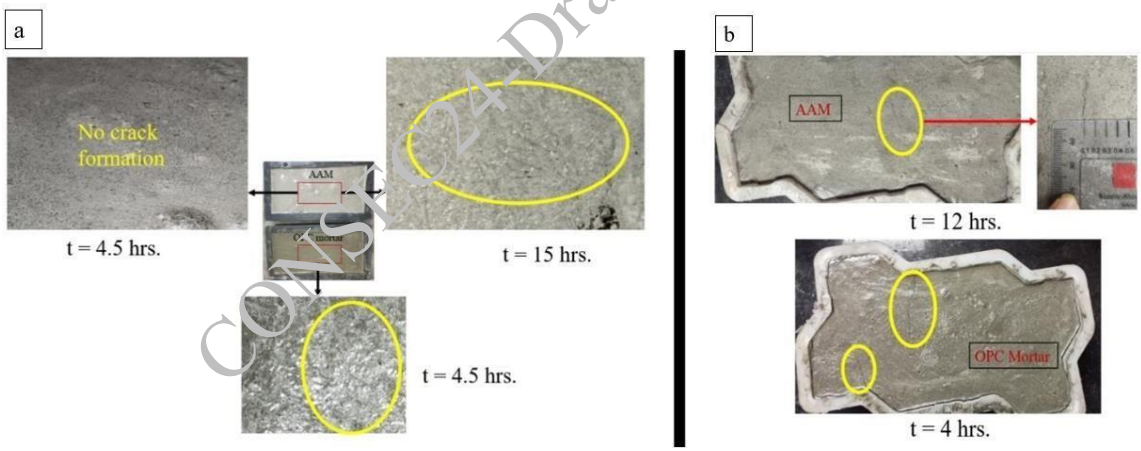

Figure 3. Comparative Analysis of cracking behaviour of AAM and OPC mortar under (a) normal (b) mould shape restraint condition.

The crack analysis of alkali-activated mortar was conducted using MATLAB. This MATLAB script, written to analyse crack width, crack length, and crack area, detects and measures cracks in an image through various image processing techniques. The process begins by reading and converting the image to grayscale, followed by enhancing the image and creating a binary representation to highlight the cracks. Noise reduction is achieved using median filtering, and morphological operations are employed to refine the edges. Precise crack boundaries are identified through Canny edge detection. Subsequently, the script identifies the largest crack, traces its boundary, and calculates its length, width, and area. To ensure accurate measurements, a reference image with a known scale is utilized to convert pixel measurements to millimeters. The dimensions of the crack are then displayed as shown in fig.4, providing detailed information essential for crack assessment. When compared to an OPC mix, which exhibited a crack area of 1.81 mm², a width of 0.21 mm, and a length of 38.1 mm, the alkali-activated mix demonstrated

significantly smaller crack dimensions, with a length of 15.50 mm, a width of 0.18 mm, and an area of 0.62 mm². This comparison indicates that the alkali-activated mix experiences considerably less plastic shrinkage cracking than OPC. The reduced crack dimensions in the alkali-activated mix suggest better performance in mitigating early-age deformations and lower susceptibility to plastic shrinkage compared to the traditional OPC mortar.

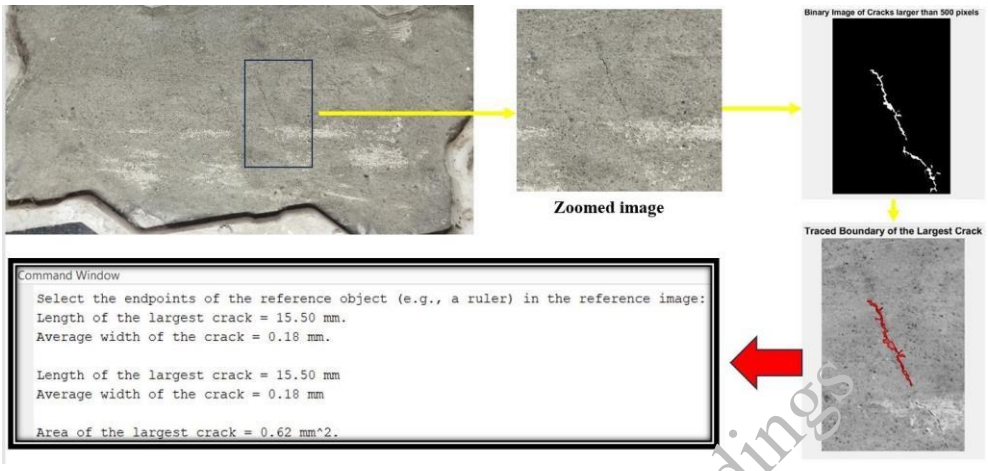

Figure 4. Crack analysis using MATLAB

4. Conclusions

The study on alkali-activated 3D printable mixtures revealed significant findings regarding their plastic shrinkage cracking behavior. Monitoring slump loss showed that remixing restored printability by reintroducing shear forces, redistributing moisture, and disrupting the early formation of stable aluminosilicate gel. Compressive strength tests demonstrated the mix's strength attributed to the low-permeability gel formed during chemical reactions. Compared to OPC mortar, alkali-activated mortar exhibited less plastic shrinkage and delayed cracking due to factors like lower bleeding tendency, higher viscosity, and the formation of a stable gel. Crack analysis using MATLAB provided precise measurements essential for assessing cracks. Overall, these results highlight the benefits of alkali-activated mixtures in mitigating early-age deformations and delaying cracking compared to traditional OPC mortar.

References

1579-21, A. C. (2021) Standard Test Method for Evaluating Plastic Shrinkage Cracking of Restrained Fiber Reinforced Concrete (Using a Steel Form Insert). *ASTM International*, *nurol llc*, 1–7.

Awoyera, P., & Adesina, A. (2019) A critical review on application of alkali activated slag as a sustainable composite binder. *Case Studies in Construction Materials*, *11*, e00268.

Boshoff, W. P., & Combrinck, R. (2013) Modelling the severity of plastic shrinkage cracking in concrete. *Cement and Concrete Research*, *48*, 34–39.

Matalkah, F., Jaradat, Y., & Soroushian, P. (2019) Plastic shrinkage cracking and bleeding of concrete prepared with alkali activated cement. *Heliyon*, *5*(4), e01514.

Yang, J., Sun, Z., Belie, N. De, & Snoeck, D. (2022) Mitigating plastic shrinkage cracking in alkali-activated slag systems by internal curing with superabsorbent polymers. *Cement and Concrete Composites*, *134*(September), 104784.

Ye, H., & Radlińska, A. (2017) Shrinkage mitigation strategies in alkali-activated slag. *Cement and Concrete Research*, *101* :131–143.

Corrosion Behaviour of Fly-Ash BlendedConcrete under Cyclic Chloride and Carbonation Exposure

Ashish Kumar Tiwari [1*], Purnima[2], and Shweta Goyal[3]

[1] *Research Associate, Indian Institute of Technology Roorkee, IndiaEmail: tiwariashish841@gmail.com*
[2] *Post-doctoral Researcher, Indian Institute of Technology Madras, IndiaEmail: dograpurnima07@gmail.com*
[3] *Professor, Civil Engineering Department, Thapar Institute of Engineering and Technology, IndiaEmail: shweta@thapar.edu*

[*]Corresponding author

ABSTRACT

The current study evaluates the corrosion behaviour of fly-ash based portland pozzolanic cement (PPC) concrete in comparison with OPC concrete exposed to cyclic chloride and carbonation ingress. The corrosion monitoring was done by the means of half-cell potential (HCP) and linear polarization resistance (LPR) on RC prisms. The outcomes revealed that although the chloride ions diffuse at a faster rate, carbonation plays a vital role in pushing the chlorides towards deeper depth increasing the risk of pitting corrosion. The corrosion got initiated after 10 cyclic exposures in both the concrete types. PPC concrete was observed to be more vulnerable as higher corrosion rates were obtained in PPC as compared to OPC.

KEYWORDS: *Corrosion, Chloride, Carbonation, Fly-ash, Electrochemical test*

1. Introduction

Sustainable development of construction industry can be achieved only by fully utilizing the cementitious and pozzolanic by-products (fly-ash, silica fume, slags). The use of SCM's (supplementary cementitious materials) has grown from the past three decades which contributes to the energy conservation practices. The total CO2 emissions from the cement industries which is nearly 8% can be therefore reduced to a much lower value by the replacement of cement with SCMs (Pacewska and Wilińska 2020). Besides this, the inclusion of SCMs cause microstructural changes in concrete matrix by secondary pozzolanic reactions, which in turn influence its durability properties (Juenger and Siddique 2015). As most of the concrete deterioration is caused due to corrosion of rebar, the effect of SCM's on the corrosion deterioration mechanism is vital to be studied.

There are two main corrosion catalysts, chlorides and carbonation. Chloride ions cause localized attack on rebar and cause pitting corrosion; while carbon-dioxide cause uniform corrosion of reinforced steel. It is worth mentioning that, incorporation of adequate amount of SCM have a significant impact on the permeability characteristics of concrete against diffusion of external agents. The individual impact of these two catalyst has been studied extensively in the past, but now a days the threat on steel is due to their combined action.

The severity level of corrosion can reach its highest when both chloride and carbonation occur conjointly than occurring individually as chloride-induced corrosion and carbonation of concrete are strongly influenced by each other (Batis et al. 2003). It has been found that weathering carbonation reduces the critical threshold level (CTL) of concrete required in corrosion initiation (Zhang and Shao 2016); alongside, carbonation of concrete leads to accelerated movement of free chloride ions, increasing the total chloride content available for attack on the rebar surface (Geng et al. 2016; Wang et al. 2017; Ye et al. 2016). Surprisingly, corrosion studies with SCM concrete subjected to cyclic chloride and carbonation environment is scanty. Hence, it is vital to study the combined effect of chloride and carbonation in a cyclic manner on the SCM incorporated concrete so as to develop a thorough understanding of the deterioration mechanism.

2. Material and Experimental methodology

Two types of cement, Ordinary Portland Cement (OPC) and Pozzolana Portland Cement (PPC) conforming to IS: 8112-2013 (BIS: 8112 2013) and IS 1489 (part 1)-1991 (BIS:1489 2008) were used. River sand was used as fine aggregates and crushed gravel of size 20mm and 10mm was used as coarse aggregates as per IS: 383-2016 (BIS: 383 2016) .Both the sizes were mixed in the ratio of 1:1 to get a well-graded mix. The concrete mix was designed as per IS 10262 (BIS: 10262 2019) [11] and the final mix proportion adopted was 1:1.39:2.91 (cement: fine aggregates: coarse aggregates) with w/c ratio of 0.43. The concrete mix prepared by using OPC was designated as OC; while the mix prepared by using PPC was designated as PC. Steel bars used as reinforcement for concrete were Quenched and Self-Tempered (QST) bars conforming to BIS: 1786-2008 (BIS: 1786 2008). The bars were 12 mm in diameter and were cut in the length of 360 mm. Threaded hole was made at one end of the bar in order to assure electrical connectivity. Before embedding the bars in concrete, they were prepared according to ASTM G109 guidelines (ASTM G109 2022).

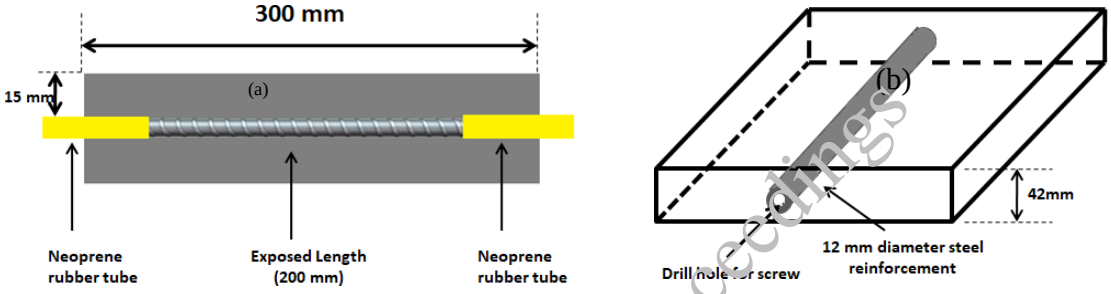

Figure 1. Cross-sectional details of (a) rebar; (b) prism specimen

Concrete prisms of size 300 × 300 × 42 mm were prepared with one bar embedded at a clear cover of 15 mm as shown in Fig.1b. Special type of mold was procured in order to maintain the rebar cover.

A typical 7-day exposure cycle (shown in Fig. 2a) used in this study consisted of 2 days of chloride ponding (3.5% NaCl solution), followed by 2 days of air drying, 2 days of CO2 exposure in a closed chamber (maintained at a concentration of 5% by volume at 30 ± 2˚ C temperature and 60-70% relative humidity) and 1 day of air drying. The cycle was chosen so as to ensure that while the chloride ions can penetrate into the concrete rapidly during the wetting period, adequate drying period is also maintained so that oxygen can ingress through concrete cover to sustain the cathodic reaction and consequent development of corrosion products can take place (Otieno et al. 2019). Fig. 2b and c shows the RC specimens subjected to chloride ponding and exposed to CO2 in carbonation chamber, respectively.

The effect of combined chloride and carbonation ingress on rebar corrosion was examined by using electrochemical methods as they are by far considered most suitable for corrosion monitoring in in RC structures. The tests carried out were half-cell potential (HCP), and linear polarization resistance (LPR) HCP and LPR measurements were carried out after every 2nd exposure cycle. For electrochemical measurement, corrosion monitoring equipment, ACM model: Gill AC (Serial no 1924) with guard ring was used. Before initiating the electrochemical test, pre-wetting of the testing surface was done by using methods explained in ASTM C876 (ASTM C876 2009). All the measurements were made with respect to the reference electrode - Standard Calomel Electrode (SCE).

For HCP, conducting sponge wetted with soap solution was placed on the surface of the prism to ensure proper electrical contact of embedded rebar with reference electrode (test setup shown in Fig. 2a). The measurements were made by placing the SCE along the length of bar at five different positions. LPR technique was employed to obtain the corrosion current density (icorr) of the embedded rebar by extrapolating Tafel slopes of anodic and cathodic branches of the recorded polarization curves. Before performing the test, wetted conducting sponge was placed on the surface of prism specimen for proper electrical contact with guard ring (test setup shown in Fig. 2b). Assembly of guard ring electrode, auxiliary electrode and reference electrode was then placed over the conducting sponge and electrical connection

were made to the WE. For the measurements, working electrode (WE i.e. steel reinforcement) was polarized to ±25 mV from the equilibrium potential at a scan rate of 0.167 mV/sec.

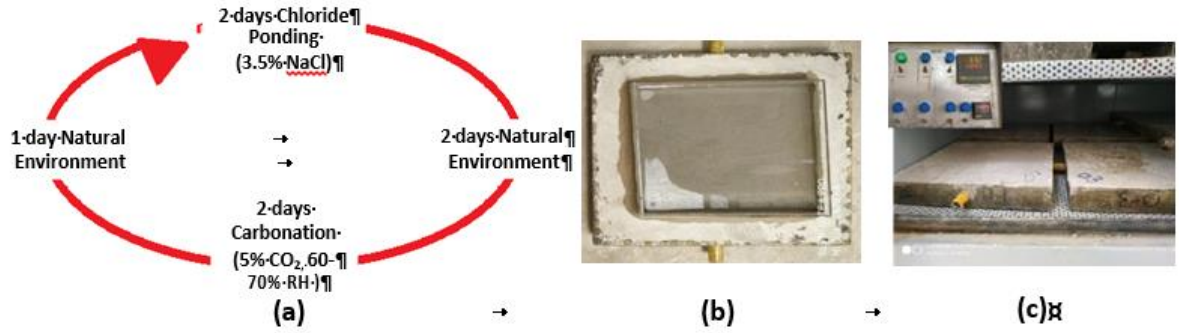

Figure 2. (a) Schematic representation of seven-day exposure cycle used in the study; (b) chloride ponding;

3. Results and Discussion

The HCP values and the determined corrosion current density values (icorr) for OC and PC specimens up to 50 exposure cycles were recorded and shown in Fig. 7a and b, respectively. The HCP readings can be correlated to the probability of corrosion as per the guidelines provided by ASTM C876 (ASTM C876 2009).

From Fig. 3a, it is observed that the HCP values of OC and PC remain at low corrosion risk zone initially i.e. before being exposed to the aggressive environment, which clearly demonstrates that a passive layer is present over the steel surface before exposure. A sudden drop in potential was seen after 2nd exposure cycle in OC; whereas in PC, the drop was observed after 4th cycle. Although the drop in PC is 2 cycles later than OC but PC specimens fell directly in the severe corrosive zone; whereas in OC the shift of zone from high risk to severe is steady and that too after a much longer time. The results thus, indicate that in combined aggressive environment, concrete made with pozzolanic cement is more susceptible to corrosion than OPC.

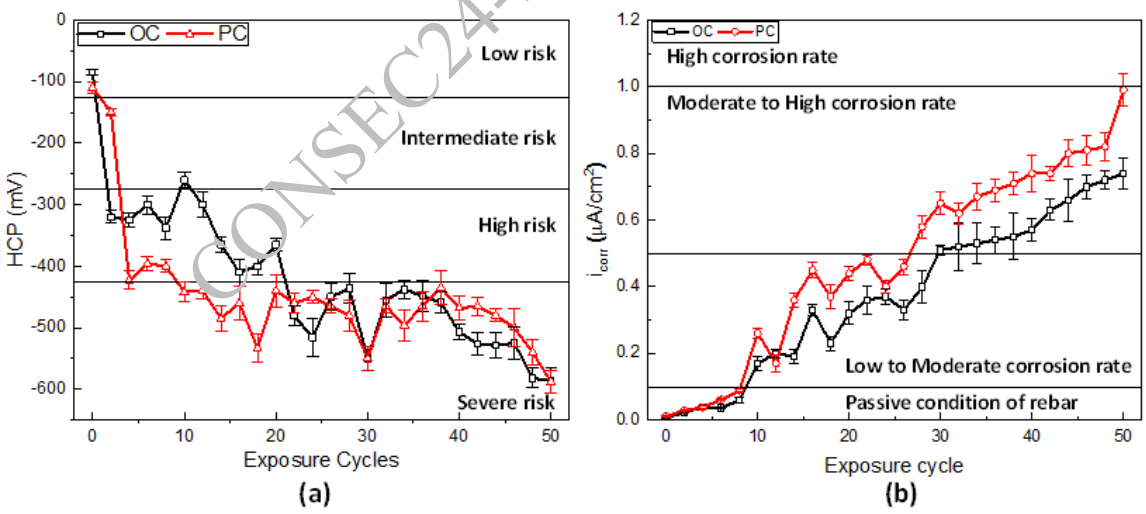

Figure 3. Variation in (a) HCP and (b) i_{corr} for OC and PC specimens with exposure duration

From Fig. 3b, it can be seen that i_{corr} values remained in passive zone upto the 8th exposure cycle for both OC and PC specimens. After 10th cycle, both OC and PC enter the 'low to moderate' corrosion region. From the graph, it can be seen that OC specimens took 32 exposure cycles to shift from moderate to high corrosion rate, while PC recorded the same shift after 28th exposure cycle. Also, at all exposure durations, PC specimens registered higher corrosion rate than OC specimen; clearly indicating more severe corrosion in pozzolanic cement concrete under combined exposure to chlorides and carbonation. The results are also in agreement with HCP values.

4. Conclusions

The current study was aimed to study the performance of fly-ash based concrete in comparison with OPC concrete under the cyclic exposure of chloride and carbonation. The shift in potential values and trend of corrosion current density values clearly concluded that PPC concrete is more vulnerable to corrosion during cyclic exposure of chloride and carbonation than the OPC concrete

References

A. Zaki, H.K. Chai, D.G. Aggelis, N. Alver, Non-destructive evaluation for corrosion monitoring in concrete: A review and capability of acoustic emission technique, *Sensors (Switzerland)*. 15 (2015) 19069–19101.

AMERICAN SOCIETY FOR TESTING AND MATERIALS, ASTM C 876/09 - Standard Test Method ASTM, Standard Test Methods for Determining Effects of Chemical Admixtures on Corrosion of Embedded Steel Reinforcement in Concrete Exposed to Chloride Environments, (2022).

ASTM C876 Half-Cell Potentials of Uncoated Reinforcing Steel in concrete. Annu. B. ASTM Stand. *Am. Soc. Test. Mater*. 91 (2009) 1–6.

B. Pacewska, I. Wilińska, Usage of supplementary cementitious materials: advantages and limitations: Part

BIS:10262, Indian Standard Guidelines for concrete mix design proportioning, Bur. Indian Stand. New Delhi. (2009) New Delhi,India.

BIS:1489 (Part 1), Portland-pozzolana cement-specification, Bur. Indian Stand. (1991) New Delhi,India.

D. Zhang, Y. Shao, Effect of early carbonation curing on chloride penetration and weathering carbonation in concrete, *Constr. Build. Mater*. 123 (2016) 516–526.

G. Batis, A. Routoulas, E. Rakanta, Effects of migrating inhibitors on corrosion of reinforcing steel covered with repair mortar, *Cem. Concr. Compos*. 25 (2003) 109–115.

H. Ye, X. Jin, C. Fu, N. Jin, Y. Xu, T. Huang, Chloride penetration in concrete exposed to cyclic drying- wetting and carbonation, *Constr. Build. Mater*. 112 (2016) 457–463.

I. C–S–H, C–A–S–H and other products formed in different binding mixtures, *J. Therm. Anal. Calorim*. 142 (2020) 371–393.

IS: 8112 – 1989, Specification for 43 grade Ordinary Portland Cement, BIS. (2013) 17.

IS:1786-2008, High Strength Deformed Steel Bars and Wires for Concrete reinforcement— Specification, Bur. Indian Stand. New Delhi. (2008) 1–12.

IS383, Coarse and fine aggregate for concrete, Indian Stand. Code. Third edit (2016) 1–17.

J. Geng, D. Easterbrook, Q.F. Liu, L.Y. Li, Effect of carbonation on release of bound chlorides in chloride-contaminated concrete, *Mag. Concr. Res*. 68 (2016) 353–363.

M. Otieno, G. Golden, M.G. Alexander, H. Beushausen, Acceleration of steel corrosion in concrete by cyclic wetting and drying: effect of drying duration and concrete quality, *Mater. Struct. Constr*. 52 (2019). https://doi.org/10.1617/s11527-019-1349-6.

M.C.G. Juenger, R. Siddique, Recent advances in understanding the role of supplementary cementitious materials in concrete, *Cem. Concr. Res*. 78 (2015) 71–80.

Y. Wang, S. Nanukuttan, Y. Bai, P.A.M. Basheer, Influence of combined carbonation and chloride ingress regimes on rate of ingress and redistribution of chlorides in concretes, *Constr. Build. Mater*. 140 (2017) 173–183.

Resistance of Concrete Made With the Effective Replacement of Fly- Ash Against Carbonation

Md Marghoobul Haque [1,*] and Supratic Gupta [2]

[1] *Indian Institute of Technology Delhi, New Delhi, India,*
Email: cez228417@iitd.ac.in
[2] *Indian Institute of Technology Delhi, New Delhi, India,*
Email: supratic@civil.iitd.ac.in

*Corresponding author

ABSTRACT

Cement production is a significant contributor to world CO_2 emissions, accounting for around 8% of the total. In order to address this issue, numerous novel and inventive approaches have been employed for a long period, such as utilising waste materials as an alternative binding agent or as a substitute for aggregate in concrete. This study employs Class F fly ash (FA) as a viable substitute for binder, and the mix designs are formulated according to the k-factor theory. This hypothesis is grounded in the notion of equal strength over a period of 28 days. Prior research has demonstrated favourable outcomes in both the mechanical and durability domains. Carbonation is one of the major durability issues that the construction industry is currently dealing with. Carbonation is a reaction between CO_2 and the cement hydration products resulting in the decrement of concrete's alkalinity. This reduction in alkalinity will result in the depassivation of oxide layer and the concrete will ultimately be subjected to the risk of corrosion. The present study highlights the use of fly ash as an effective binder replacement and studies about the mechanical (compressive strength) properties along with the carbonation resistance of concrete.

KEYWORDS: *Carbonation, Effective w/c, Fly ash, K-factor*

1. Introduction

Since the start of the industrial revolution, there has been an increase in the amount of CO_2 in the atmosphere. Global CO_2 emissions are estimated to be more than 36 billion tonnes annually, and they are still rising (Hannah Ritchie and Max Roser, 2020). The emissions of greenhouse gases by humans between 1860 and 2000 caused an approximate 1°C increase in global temperatures (McMichael & Haines, 1997). The cement industry itself accounts for around 8% of global CO_2 concentration (Haque et al., 2023; Singh, Gupta, et al., 2022; Singh, Haque, et al., 2022). Many methods have been proposed to deal with the emission of greenhouse gases. Since the cement industry is one big contributor to greenhouse gas emissions, utilization of alternate binding materials is anticipated. Approximately 700 million tonnes of byproducts are generated annually on a global scale, with FA accounting for 70% of this total. Using FA concrete is the most effective method for reducing cement usage because it allows for the acquisition of huge amounts of FA at a low cost (Filho et al., 2013). The inclusion of FA in concrete has proved to be beneficial in aspects of mechanical and many durability properties. However, previous research shows mixed results in the case of resistance of FA concrete against carbonation. This study focuses on the utilization of FA in normal strength concrete (w/b= 0.5) at varying (0%, 15%, and 30%) inclusion.

2. Experimental

2.1 Materials

OPC 43 grade conforming to (BIS:8112-1989) (Bureau of Indian Standard(BIS), 2013) was used having specific gravity of 3.14. Fly ash (FA) was obtained from Badarpur Thermal Power Station (BTPS) near

Delhi and was found to conform to IS 3812 (Part-1), 2013 (IS 3812: Part 1 (2013) specification, 2013). The specific gravity of fly ash was found to be 2.10. River sand was used as natural fine aggregate satisfying the requirements of IS 383-2016 (IS:383-2016, 2016) (zone II) with a specific gravity of 2.61. Natural coarse aggregate (NCA) was used satisfying the requirements of IS 383-2016 (IS:383-2016, 2016) with the maximum nominal size of 20mm. Polycarboxylic ether-based superplasticizer fulfilling the requirements of IS 9103 (IS 9103, 1999) is used.

2.2 Mix Design

Three concrete mixes have been designed at a fixed w/c of 0.5 with a varying fly ash percentage of 0% (control mix), 15% and 30%. The design of the concrete has taken into account the cementing efficiency factor (k-value) for FA. The cementing efficiency factor of fly ash was determined to be 1, 0.81, and 0.41 for concrete with 0%, 15%, and 30% FA, respectively, based on previous data and many concrete mix trials. The cementing efficiency factor is employed in the context of FA concrete, yielding the effective water-to-cement ratio (w/c) expressed as: **w/c = w/(c1 + k f)**. In this equation, w represents the water content, c represents the cement content, c1 represents the cement content of concrete containing FA, k represents the cementing efficiency factor, and f represents the FA content. Effective w/c and w/c for control mix will be same. The superplasticizer was added to exhibit a slump range of 125 to 160 mm. Table 1 represents the proposed mix design for present study.

Table 1. Concrete constituents in kg/m^3 based on mix design

Mix	Cement	FA	FA (%)	Water	k-value	w/c	Sand	NCA (10mm)	NCA (20mm)
CM	340	0	0	170	1.00	0.5	763	458	687
F15	298	53	15	170	0.81	0.5	751	450	676
F30	289	124	30	170	0.41	0.5	717	430	646

2.3 Experimental Programme

2.3.1 Compressive Strength Test

100 mm*100 mm *100 mm cubes were casted for all the mixes and tested after 7 and 28 days of curing following Indian standard IS 516 (1959).

2.3.2 Accelerated Carbonation Test

100 mm*100 mm *500 mm prism samples were casted for carbonation test. After 28 days of curing, the samples were preconditioned for 14 days in a humid chamber (RH= 65±5%, T= 27±2°c) (IS, 2021). Post preconditioning, the samples were sealed with epoxy paint on all the faces except one. The samples are then placed in carbonation chamber with CO_2 concentration of 4±0.5%, RH=65±5% and T= 27±2°c until the testing period. After every exposure period, 50mm slice is broken from prism and tested for carbonation depth. In the current study, carbonation depth is tested after 7 and 28 days of exposure period.

3. Results and Discussion

3.1 Compressive Strength

The compressive strength results of the control and FA concrete and comparison with expected strength are demonstrated in Fig 1 (a) and Fig (b) respectively. The strength remained nearly equal with fly ash % variation at a fixed w/b. A similar study was conducted by Babu and Rao, 1996 in which strength was equated for control and FA concrete by using “general efficiency factor” (Babu & Rao, 1996). The factor decreased as the FA percentage increased due to the dependence of the pozzolanic reaction of FA on the presence of $Ca(OH)_2$, alkalis, etc (Hwang et al., 2004).

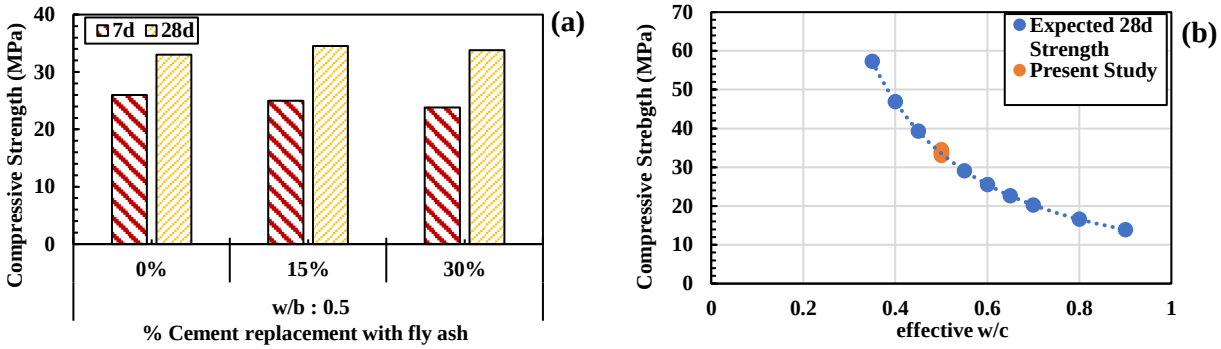

Figure 1. (a) Compressive strength of concrete at fixed w/b of 0.5 with varying FA% (b) comparison of present study results and expected results from theory

To compare the strength of control concrete and concrete with a high percentage of FA, it was observed that the cementing factor decreased gradually as the FA % increased. A decrease in cementing efficiency will lead to an increase in the amount of FA in the concrete. This will result in a lower ability to remove cement, with some of the FA reacting chemically with available calcium hydroxide. The remaining FA will serve as filler in the concrete's microstructure, thereby improving its strength (Shelote et al., 2023). The findings indicate that fly ash may be utilised in concrete with efficacy, without reducing its strength in comparison to the control concrete.

3.2 Accelerated Carbonation

Concrete carbonation after 28 days of curing and 7d and 28d of exposure are demonstrated in Fig 2 and Fig 3 presents phenolphthalein sprayed sample images. Carbonation increased with increase in exposure period for all the mixes. About 25% increase in concrete carbonation is observed with 15% inclusion of FA in concrete compared to normal concrete, however slight increment is observed in carbonation depth of 30% FA concrete with respect to 15% FA concrete. FA expedites the carbonation process and enhances the depth of carbonation because of the restricted presence of calcium hydroxide for subsequent hydration reactions (Wang et al., 2017).

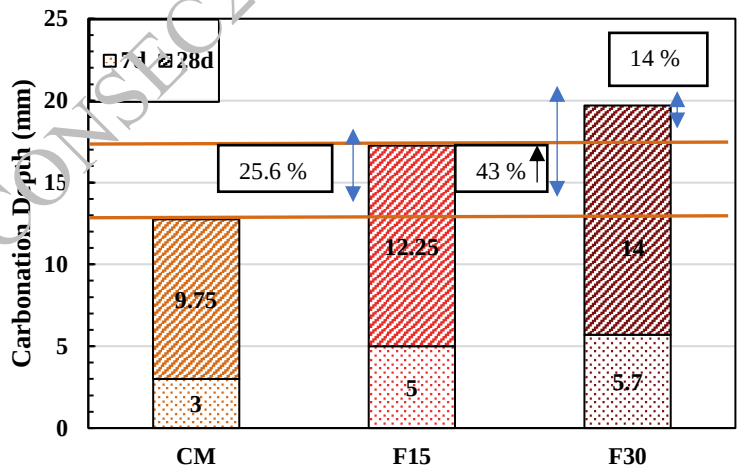

Figure 2. Carbonation of concrete after 7d and 28d exposure

Figure 3. Carbonation depth of concrete after 28d exposure visible in Phenolphthalein sprayed samples

4. Conclusions

The findings demonstrate that FA may be utilised in concrete with effectiveness, without affecting its strength when compared to control concrete with slower pozzolanic reaction and moderate rise in compressive strength. Effective utilisation of FA can significantly enhance both early and later age strength, while also benefiting the environment as an industrial waste came into utilization. A slight increase in carbonation depth was observed with increase in FA inclusion in concrete.

Acknowledgements

Authors acknowledge the support of Department of Civil Engineering, Indian Institute of Technology, Delhi, India for their help in performing the experimental programme.

References

Babu, K. ., & Rao, G. S. N. (1996). Efficiency Of Fly Ash In Concrete With Age. *Cem. Concr. Res*, *26*(3), 465–474.

Bureau of Indian Standard(BIS). (2013). IS: 8112 - 1989, Specification for 43 grade Ordinary Portland Cement. *Bureau of Indian Standards,New Delhi*, 17.

Filho, J. H., Medeiros, M. H. F., Pereira, E., Helene, P., & Isaia, G. C. (2013). High-Volume Fly Ash Concrete with and without Hydrated Lime: Chloride Diffusion Coefficient from Accelerated Test. *Journal of Materials in Civil Engineering*, *25*(3), 411–418.

Hannah Ritchie and Max Roser. (2020). *CO_2 emissions*. Our World in Data. https://ourworldindata.org/co2-emissions

Haque, M. M., Ankur, N., Meena, A. & Singh, N. (2023). Carbonation and permeation behaviour of geopolymer concrete containing copper slag and coal ashes. *Developments in the Built Environment*, *16*(August), 100276.

Hwang, K., Noguchi, T., & Tomosawa, F. (2004). Prediction model of compressive strength development of fly-ash concrete. *Cement and Concrete Research*, *34*(12), 2269–2276. https://doi.org/10.1016/j.cemconres.2004.04.009

IS:383-2016. (2016). Indian Standard Coarse and Fine aggregate for Concrete- Specification. *Bureau of Indian Standards, New Delhi, India*, *January*, 1–21. www.bis.org.inwww.standardsbis.in

IS. (2021). Hardened Concrete — Methods of Test Part 2 Properties of Hardened Concrete other than Strength Section 4 Determination of the Carbonation Resistance by Accelerated Carbonation Method (. *IS 516 (Part 2/Sec 4) : 2021*,.

IS 3812: Part 1 (2013) specification. (2013). Pulverized Fuel Ash - Specification: Part 1 For Use as Pozzolana in Cement, Cement Mortar and Concrete. *Bureau of Indian Standards, New Delhi, India*, 1–12.

IS 516. (1959). Method of Tests for Strength of Concrete. *Bureau of Indian Standards*, 1–30.

IS 9103. (1999). Specification for Concrete Admixtures. *Bureau of Indian Standards,New Dehli*, 1–22.

McMichael, A. J., & Haines, A. (1997). Global climate change: The potential effects on health. *British Medical Journal*, *315*(7111), 805–809.

Shelote, K. M., Meera, M., Supravin, K., & Gupta, S. (2023). Study on Modified Water Permeability Method for Fly Ash Concrete in Comparison with DIN 1048 (Part 5). *Arabian Journal for Science and Engineering*, *1048*(Part 5).

Singh, N., Gupta, A., & Haque, M. M. (2022). A review on the influence of copper slag as a natural fine aggregate replacement on the mechanical properties of concrete. *Materials Today: Proceedings*, *62*(6), 3624–3637.

Singh, N., Haque, M. M., & Gupta, A. (2022). Reviewing mechanical performance of geopolymer concrete containing coal bottom ash. *Materials Today: Proceedings*, *65*(2), 1449–1458.

Wang, W., Lu, C., Li, Y., Yuan, G., & Li, Q. (2017). Effects of stress and high temperature on the carbonation resistance of fly ash concrete. *Construction and Building Materials*, *138*, 486–495.

Effect of Corrosion Inhibiting Admixtures on Corrosion Characteristics of Steel in Carbonating Nanoparticles Based Fly Ash Concrete

Umesh Hule[1], Chandru Pichaimuthu[2], and Radhakrishna G. Pillai[3]*

[1] *Research Scholar, Indian Institute of Technology Madras, India*
Email: huleumesh@gmail.com
[2] *Assistant Professor, National Institute of Technology Calicut, India*
Email: pchandru.7@gmail.com
[3] *Professor, Indian Institute of Technology Madras, India*
Email: pillai@iitm.ac.in

*Corresponding author

ABSTRACT

The most effective method of lowering a rising carbon footprint is to design low-carbon systems. To accomplish sustainability, researchers worldwide are attempting to design low-carbon concrete with high-volume fly ash. On the other hand, it has been reported that increasing the fly ash replacements reduces the carbonation resistance of concrete. However, carbonation is not the major issue for the concrete, but the associated reduction in pH could initiate the corrosion of embedded steel and create durability issues. Adding corrosion-inhibiting admixtures (CIAs) in such concrete could increase the corrosion resistance of embedded steel. Therefore, there is a need to find the corrosion characteristics of steel in fly ash concrete with CIAs, to ensure the longer service life of structures exposed to carbonation. In this study, concrete prism specimens were cast with/without CIA containing OPC, OPC+40% fly ash, and OPC+40% fly ash with nanoparticles. Six reinforced concrete specimens were exposed to an accelerated CO_2 environment. Carbonation depth was periodically measured, and it was found that the carbonation rate of OPC concrete was lower than that of fly ash concrete, and the addition of CIA influenced on the carbonation depths of concrete. The corrosion resistance was monitored using linear polarization resistance (LPR) techniques. The measured inverse resistance to polarization (1/Rp) of steel in fly ash-based concrete was lower than the OPC system. However, the specimens with CIA showed even lower 1/Rp values than the ones without CIA.

KEYWORDS: *Carbonation, Corrosion inhibiting admixture, Fly ash concrete, Nanoparticles*

1. Introduction

Corrosion-inhibiting admixtures (CIAs) can obstruct or slow down the electrochemical corrosion process by providing a physical barrier, inhibiting anodic or cathodic reactions, or both at the S-C interface. The CIAs can affect the steel corrosion characteristics by strengthening the passive film or reducing the corrosion rate after the depassivation of steel. For better inhibiting efficiency, inhibitors should be adsorbed into the oxide layer to fill the defect of the passive film (Zulj et al. 2015). Calcium nitrite/nitrate-based inhibitors are commonly used as mixed inhibitors during reinforced concrete construction. However, most inhibitors have secondary effects on the fresh properties of concrete, like accelerating/retarding the setting of fresh concrete (Myrdal 2010), which could affect the carbonation resistance of concrete due to pore structure alteration. In chloride exposure conditions, CIA in steel-cementitious (S-C) systems can delay the corrosion initiation by 1.5 to 2 times more than in S- C systems without CIA (Karuppanasamy and Pillai 2017). A study by Guo et al. (2022) on carbonated solution found that composite inhibitors performed better than single inhibitors, which could be due to suppressing both anodic and cathodic reactions. Most studies with CIAs have quantified the corrosion resistance of steel exposed to chloride exposure. However, the long-term performance of CIAs in carbonating S-C systems is not well understood. Hence, there is a

need to quantify the long-term performance of CIAs in reducing the corrosion rate in carbonating systems, which could help design low-carbon binder systems to achieve high service life. This study focuses on determining carbonation depths in OPC, OPC+40% fly ash, and OPC+40% fly ash with nanoparticles and assesses the carbonation and corrosion resistance of these systems with/without inhibitors exposed to accelerated carbonation.

2. Materials and methods

The Ordinary Portland Cement (OPC) (53 grade), conforming to IS 269 (2015), was used as the primary binder. Class F fly ash (FaF) was used as the supplementary cementitious material (SCM) to replace the OPC by 40% by weight. Crushed stone sand conforming to IS:383-2016 with a maximum particle size of 4.75 mm was used. As per the particle size distribution, the sand conformed to Zone II of -IS 383 (2016) gradation limits. Two sizes of coarse aggregates, viz. 10 mm and 20 mm, conforming to IS:383-2016 were used. Commercially available nano-TiO_2 and nano-$CaCO_3$ in powder form were used to improve the mechanical and durability performance of the concrete. A bipolar inhibitor, having modified amino alcohol as the chemical base, was used in this study as a corrosion-inhibiting admixture (CIA) to delay the onset of corrosion by reducing the rate of anodic and cathodic reactions in the electrochemical process. A commercially available polycarboxylate ether (PCE) based superplasticizer was used to improve the workability of the concrete.

2.1 Concrete mix proportion

The different concrete mixes (MC1 to MC6) were designed as per IS 10262 (2019) for a target grade of M35 using different materials. The total binder content, and thus the water-to-binder ratio, was varied between 370 - 400 kg/m^3 and 0.38 - 0.43, respectively, in these mixes. The blending of the coarse and fine aggregates was done as per IS:383-2016. In all these mixes, the fine-to-coarse aggregate ratio of 40:60 and the 10 mm to 20 mm coarse aggregate ratio of 40:60 is constant. Based on the laboratory trials, the dosage of both admixtures was varied. Table 1 summarizes the mix proportion of all these mixes.

Table 1. Concrete mix composition

Ingredients / Mix ID	Cement (kg/m3)	FaF (kg/m3)	w/b	FA (kg/m3)	CA (10+20) mm	Nano (TiO2 + CaCO3) (%bwob)	CIA (%bwob)	SP (%sbwob)
OPC-370-0.43-0-0 (MC1)	370	-	0.43	732	694+463	-	-	-
40F-400-0.38-0-0 (MC2)	240	160	0.38	716	689+459	-	-	0.20
40F-380-0.40-2-0 (MC3)	220	152	0.40	791	708+460	1+1	-	0.28
40F-380-0.40-2-1 (MC4)	220	152	0.40	791	708+460	1+1	1	0.30
OPC-370-0.43-0-2 (MC5)	370	-	0.43	732	694+463	-	2	-
40F-400-0.38-0-2 (MC6)	240	160	0.38	716	689+459	-	2	0.20

Notes: Nomenclature for Mix ID: Binder type-binder content-w/b-total nanomaterial (%bwob)-corrosion inhibitor (%bwob); %bwob – % by the weight of binder; %sbwob - % solids by the weight of binder; FaF – Flyash (Class F); w/b – Water to binder ratio; FA – Fine aggregate; CA – Coarse aggregate; CIA – Corrosion inhibiting admixture; SP – Superplasticizer.

3. Result and discussion

3.1 Carbonation characteristics of concrete

The results show that concrete mixes containing 40% fly ash show higher carbonation depths than OPC concrete. However, the concretes with the addition of nanoparticles show lower carbonation depths than those without nanoparticle concretes. The 40% flash-based concrete with nanoparticles is comparable to OPC concrete in carbonation resistance by adding 2% nanoparticles (see Figure 1, MC3). The reduction in

carbonation depths can be attributed to the densification of the microstructure due to the addition of nanoparticles. The addition of CIA in fly ash-based concrete showed adverse effects on carbonation depths. The carbonation of specimens containing CIA is higher than specimens without CIA, even in nanoparticle concrete mix (MC6 and MC4). However, CIA in OPC concrete has not affected the carbonation resistance.

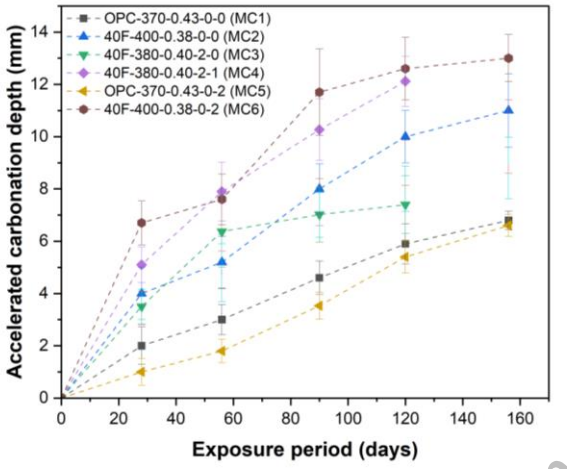

Figure 1. Accelerated carbonation depths of concrete mixes

3.2 Corrosion characteristics of steel in carbonating systems

The polarization resistance (Rp) is computed using the LPR method. Figure 2. The LPR results show that the S-C system with fly ash has lower 1/Rp values than OPC systems, even after the carbonation. However, S-C systems with CIA show even lower 1/Rp than specimens without CIA, possibly due to enhanced polarization resistance due to inhibiting action.

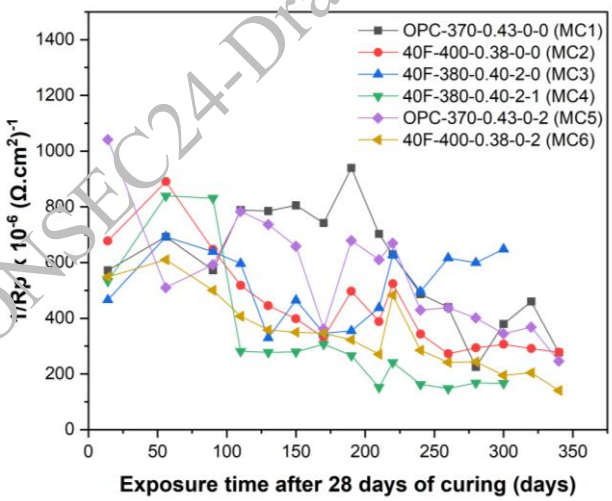

Figure 2. Measured 1/Rp of steel-concrete mixes

4. Conclusions

- The CIA had an adverse effect on carbonation performance, which could be due to changes in pore structure.
- The S-C specimens with CIA showed higher corrosion resistance than those without CIA, even with lower carbonation resistance.
- No clear sign of corrosion initiation is observed from 1/Rp data, even after carbonation.

References

Guo, Q., Li, X., Song, Y., and Liu, J. (2022). "Case Studies in Construction Materials Effect of rust inhibitor on the composition of steel passive film in carbonized concrete." *Case Studies in Construction Materials*, Elsevier Ltd, 16(October 2021), e00892.

Karuppanasamy, J., and Pillai, R. G. (2017). "A short-term test method to determine the chloride threshold of steel–cementitious systems with corrosion inhibiting admixtures." *Materials and Structures/Materiaux et Constructions*, Springer Netherlands, 50(4).

Myrdal, R. (2010). *Corrosion Inhibitors – State of the art COIN Project report, SINTEF Building and Infrastructure*.

Zulj, L. V., Serdar, M., and Martinez, S. (2015). "Effect of tartrate on the electrochemical behaviour and semiconductive properties of passive film on steel in saturated calcium hydroxide." *Materials and corrosion,* 66(11), 1344–1353.

Effect of Notch Length on the Fracture Behaviour of Geopolymer Concrete Beams

Sumit S Thakur [1], Dharmjeet Kumar[2], Sagar Kumar [3] and K. M. Pervaiz Fathima[4*]

Indian Institute of Technology Jammu, Jammu, India
Emails: [1] sumit.thakur@iitjammu.ac.in
[2] 2019uce0060@iitjammu.ac.in
[3]2019uce0061@iitjammu.ac.in
[4]pervaiz.khatoon@iitjammu.ac.in

[*]Corresponding author

ABSTRACT

Geopolymer concrete (GPC) utilises fly ash and is a sustainable alternative to ordinary Portland cement concrete (PPC). Variation of notch length of beams plays a crucial role to predict fracture behaviour of the structures since notch helps localise the fracture planes. Hence, notched beam specimens are used to evaluate the post cracking behaviour of concrete beams. In this work, M25 grade heat cured GPC beams of size 100mm (b) ×100mm (d) ×500mm (L) were tested in three-point bending to study the effects of three different notch lengths *viz.* 0.1d, 0.2d, and 0.3d at a constant loading rate. The load- (crack mouth opening displacement) CMOD curves and corresponding fracture energies were obtained and compared for the three notch lengths. The comparison was made for the same experiments performed on M25 grade PCC. It was found that the fracture energy of heat cured GPC was almost similar to that of PPC. But the percentage reduction in fracture energy with increasing notch lengths is more in PCC as compared to GPC. In addition, a predictive boundary effect model (BEM) is applied to the experimentally obtained data to study the size effect in PCC and GPC.

KEYWORDS: *Geopolymer concrete, Fracture mechanics, Notch-to-depth ratio, Size effect.*

1. Introduction

The global demand for cement for the construction of infrastructures is continuously rising to maintain ongoing growth and accommodate the needs of the increasing population. Ordinary Portland cement (OPC) has been traditionally used as a binder in concrete. About 1 tonne of carbon dioxide is emitted into the atmosphere in the production process of 1 tonne of cement [Singh et al (2015)]. This makes a significant contribution to the global greenhouse gas emissions. Therefore, the development of alternative binders utilizing industrial by-products is necessary to reduce the carbon footprint of the construction industry. Geopolymer is an emerging alternative binder for concrete that uses by-product material that is rich in silicon (Si) and aluminum (Al) and is reacted by an alkaline solution to produce the geopolymer binder. Source materials such as fly ash metakaolin and blast furnace slag can be used to make geopolymer. The product of the reaction is an inorganic polymer that binds the aggregates together to make geopolymer concrete. The ongoing research on fly ash-based geopolymer concrete studied several short-term and long-term properties. It was shown that heat-cured geopolymer concrete possesses the properties of high compressive strength, low drying shrinkage and creep, and good resistance to sulphate and acid [Dave & Bhogayata (2020)]. Geopolymer concrete was found to have higher bond strength with reinforcing steel and relatively higher splitting tensile strength than PCC concrete [Ganesan et al (2014)]. In another study geopolymer concrete beams and columns were tested for failure, and they showed similar or better performance as compared to PCC concrete members [Patankar et al (2015)]. Development of the constitutive model for a material requires its fracture parameters. The fracture characteristics of a material are used to describe the formation and propagation of cracks in the material. The crack path through a composite material such as concrete is dependent on the mechanical interaction between the aggregates and

the binder matrix [Carloni et al (2019)]. It is necessary to study the fracture parameters of geopolymer concrete to understand its failure behavior. In this study, the fracture properties of heat-cured fly ash-based geopolymer concrete specimens were determined using three-point bending test of notched beams. Fracture energy was also determined for PCC concrete specimens to compare with those of geopolymer concrete specimens of similar compressive strengths and containing the same aggregates. The fracture behavior of both types of concrete were compared using the test result.
In this work, fracture properties of PCC and GPC are compared for the similar compressive strength. They are compared for the flexural strength and overall fracture energy. Also size effect analysis based on boundary effect method is perfomed on both the types of concrete.

2. Experimental Work

In the experiment on the mechanical properties of PCC and GPC, the compressive strength of both was compared. The mix design for PCC was prepared according to IS code 10262:2016. Its strength was tested using a compressive strength testing machine, confirming that the mix design provided the desired strength. The mix design for PCC concrete was done for M25 grade as per IS 10262:2016, as shown in Table 1.

Table 1. Mix design for M25 PCC

Ingredients	w/c ratio	Water content	Cement content	Coarse aggregate	Fine aggregate
Mass per m^3	0.4	197.16 kg	450 kg	1153.1 kg	584.5 kg

The mix design for GPC does not have any pre-defined code or provision, so extensive research was conducted through various research papers to obtain a suitable mix design [Pavithra et al (2016)]. Thereafter, the mix design was tested for its strength to evaluate its performance. The GPC was tested for heat curing at 60^0C to assess the effects of these conditions on its strength.
For the GPC concrete, the mix design for M25 was obtained from the literature, as shown in Table 2.

Table 2. Mix design for M25 GPC

Ingredients	Fly ash	NaOH (12 M)	Na_2SiO_3	Coarse aggregate	Fine aggregate	Extra water
Mass per m^3	375 kg	58.92 kg	147.31 kg	1210 kg	519 kg	32.2 kg

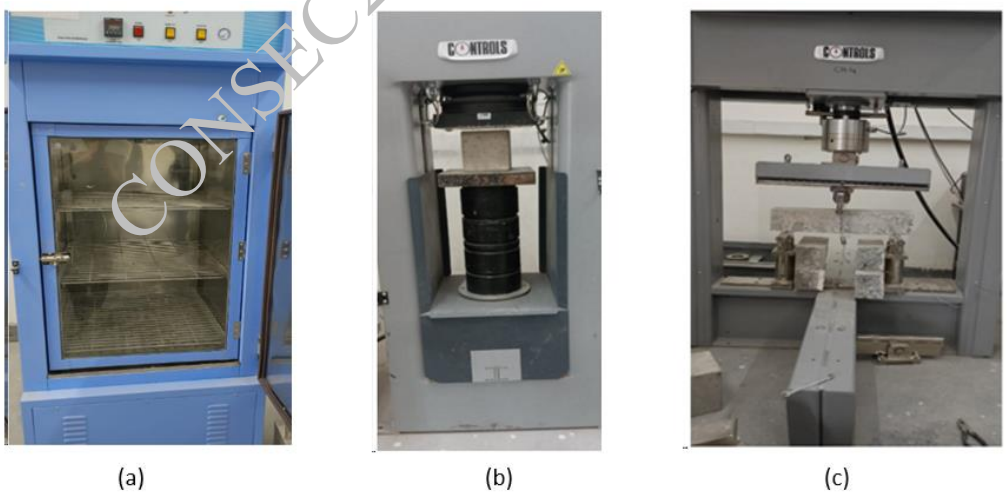

Figure 1. (a) Oven for heat curing of GPC (b) compression testing machine setup (c) flexure testing machine setup

Sixteen beams (500 mm x100mm x100mm) and twelve cubes (150mm x150mm x150mm) each for PCC and GPC were casted for the experiments. Both PCC and GPC mixtures were prepared with their respective ingredients in a mixer for 3 minutes. Workability was checked using a slump test. After mixing, cubes were compacted in molds on a vibrating table. PCC specimens were cured in a tank for 7 or 28 days, while GPC specimens were cured in an oven (Fig. 1 (a)) at 60°C for 7 or 28 days as required.

The concrete cube specimen, precisely positioned between the loading plates of the calibrated compression testing machine (Fig. 1(b)), faced a gradually increasing load until it reached failure. This load was applied according to testing standards, typically at a rate of 0.6 MPa/second. The machine then captured the maximum load and the corresponding compressive strength was calculated.
To assess the flexural strength and fracture energy of both notched and unnotched PCC and GPC beams, a three-point bending test was conducted (Fig. 1 (c)). Notches were precisely machined in the beam centers using a marble cutter. The testing machine was then configured for the experiment, including precise clip gauge attachment to measure crack mouth opening displacement (CMOD). After calibration for accurate readings, beams were placed horizontally on support rollers spaced 400 mm apart. A centered and leveled loading head applied a gradually increasing load to the beam center until failure, following standard loading rate specifications. Throughout the test, load, deflection, and CMOD data were meticulously recorded.

3. Results and discussions

3.1 Mechanical Behavior

Table 3 displays the compressive strength of PCC and GPC cubes after 7 and 28 days. The average strength for PCC after 7 days is 30.55 MPa while that of GPC is 32.06 MPa. The average strengths obtained after 28 days for PCC and GPC are 34.6 MPa and 35.01 MPa, respectively, indicating comparable strength between the two materials. However, the variation in strength is more pronounced in PCC compared to GPC. The maximum strength observed for the PCC cube is 36.5 MPa, while the minimum is 32.9 MPa, resulting in a difference of approximately 3.6 MPa. In contrast, for GPC samples, the maximum and minimum strengths are 35.7 MPa and 34.1 MPa, respectively, resulting in a difference of 1.6 MPa. Consequently, the difference in strength at 7 days and 28 days is notably lower in GPC compared to PCC. This means GPC attains early strength as compared to PCC.

Table 3. Compressive strengths PCC and GPC at 7 days and 28 days

Type of concrete	PCC (7 days)	GPC (7 days)	PCC (28 days)	GPC (28 days)
Avg. Compressive strength	30.55 MPa	32.06 MPa	34.40 MPa	35.01 MPa

The comparison of sample strength after seven days reveals that GPC samples gain strength far more rapidly than PCC samples. Specifically, the average strength for PCC after 28 days is 34.40 MPa, whereas the average strength for GPC after 28 days is 35.01 MPa.

3.2 Fracture behavior

For the comparison of fracture behavior, the fracture energy and flexural strength of the samples were calculated based on data obtained from the three-point bending test. In this test, specimens of the same size but with different notch depths were utilized. The flexural strength of a concrete beam quantifies the beam's ability to resist bending forces before failure. This property is determined through a standardized procedure called the flexural strength test, typically conducted on prismatic beam specimens.
The flexural strength of a concrete beam is commonly reported as the maximum bending moment or stress that the beam can withstand before fracturing. The test involves applying a load to the midpoint of a simply supported beam until it fails in bending. The flexural strength (f_t), or bending tensile strength, is calculated using the following formula:

$$f_t = \frac{3P_{max}\,L}{2b(d-a)^2} \tag{1}$$

where, P_{max} is the maximum load applied to the beam, L is the span of the beam, d is the depth of the beam and a is the initial notch length. The fracture energy of a material signifies the energy required to initiate and propagate a crack to fracture the material. It serves as a measure of the material's toughness and its ability to resist crack propagation. In this work, experimental testing is employed to determine the fracture energy.
In the context of concrete beams, fracture energy is often quantified using the area under the load versus the CMOD curve. It quantifies the energy absorbed by the concrete as cracks develop and propagate.

For the calculation of fracture energy, the area under the load vs CMOD curve was calculated. It is denoted as U_0. This calculation provides a quantitative measure of the energy absorbed by the concrete during the process of crack initiation and propagation.

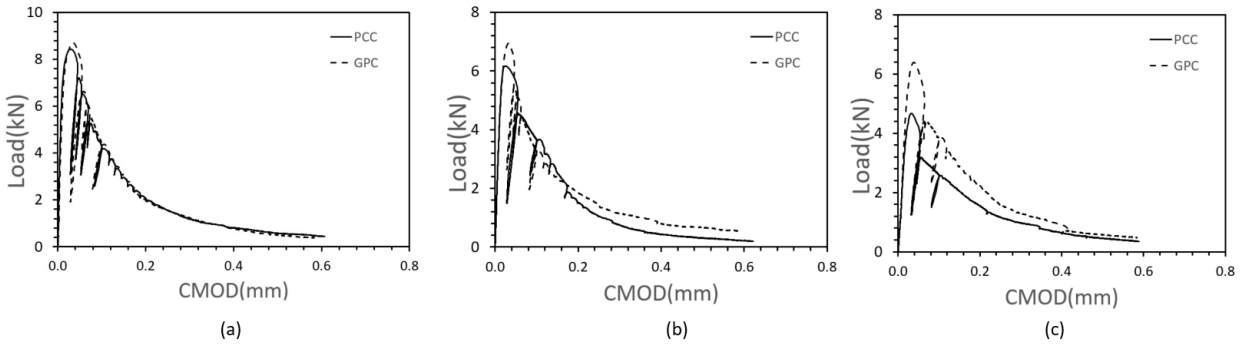

Figure 2. Load vs CMOD curve for PCC and GPC specimens for different initial notch lengths (a) 10 mm (b) 20mm (c) 30 mm

The fracture energy G_f is calculated by the equation:

$$G_f = \frac{U_0}{b(d - a_0)} \tag{2}$$

where U_0 is the area under load vs CMOD curve, b is the width of the beam, d represents the depth of the beam and a_0 is the initial notch length. Using this formula, the flexural strength and fracture energy of all available specimens were computed.

Table 4. Average fracture energy for PCC and GPC beams for the three notch sizes

Specimen	Initial notch length (mm)	Avereage Peak Load (kN)	Average Flexural strength (MPa)	Average Fracture energy (N/m)
PCC	0	10.48	6.29	-
	10	8.56	6.35	278.53
	20	6.63	6.23	187.72
	30	5.45	6.68	158.84
GPC	0	12.50	7.50	-
	10	9.10	6.74	245.30
	20	7.18	6.73	180.17
	30	6.60	7.16	160.02

Table 4 shows the average fracture enrgy for PCC and GPC beams for the three notch sizes. The fracture energy decreases for both types of concrete with increasing initial notch lengths. It is interesting to note that the average flexural strength was higher for GPC while the average fracture energy was almost the same for the respective initial notch size. This can be observed in load-CMOD curve as shown in Fig. 2. GPC generally exhibits comparable fracture energy and flexural strength to PCC. The geopolymer matrix in GPC provides enhanced toughness and crack resistance, resulting in similar fracture energy values. The peak at failure was observed to be sharper for GPC than that of PCC. This indicated more brittle failure in GPC as compared to PCC. However, the specific performance of PCC and GPC may vary depending on factors such as geopolymer composition, curing conditions, and specimen sizes.

The fractured surfaces of the beams of PCC and GPC is shown in Fig. 3. The fracture surface of geopolymer concrete exhibits less tortuosity compared to plain cement concrete. This difference might have arised from the more homogeneous nature of the geopolymer matrix compared to the Portland cement matrix. Consequently, cracks in geopolymer concrete are more prone to propagate in a straight line, whereas cracks in plain cement concrete tend to follow a more tortuous path. Tortuosity of a fracture surface refers to the roughness or irregularity of the surface. A higher level of tortuosity indicates a more complex propagation path for the crack, potentially resulting in decreased strength and toughness of the material.

Figure 3. Fractured surface of (a) PCC beam (b) GPC beam

3.3 Size effect

Cement-based materials fail gradually due to internal micro-cracks or defects. Fracture mechanics studies how these micro-cracks affect the material's overall performance. Understanding the material's fracture behavior relies on specific fracture parameters. However, it's challenging to measure these parameters accurately in a regular lab because they change with the specimen's size. This change is known as the "size effect" and happens because lab-sized specimens have uneven aggregates, which don't fit the assumptions of standard fracture mechanics for uniform materials. Classical fracture theories work when concrete specimens are over 2000 mm in dimension [Bazant and Xu (1991)]. Therefore, measuring accurate fracture properties for such large specimens in a regular lab is tough. Using lab fracture parameters directly for designing structures isn't practical unless the size effect is carefully considered, especially when using new materials. The boundary effect method is a size effect method in which the size effect of concrete beams is studied where beams of the same size have different notch lengths as shown in Fig. 4. In this work, BEM is applied using the flexural strength data of PCC and GPC beams.

Figure 4. Boundary effect tests with the same depth of the beam and increasing initial notch size

The maximum load P_{max} is given by:

$$P_{max} = f_t . A_e \tag{3}$$

In BEM, A_e the effective area is determined by the pure size and geometry measurement but with the composite microstructure d_{av} modification. a_e denotes equivalent crack, which is specially designed to deal with the boundary influences [Duan & Hu (2004)].

$$A_e = \frac{(d - a_0)(b - a_0 + 3d_{av})}{1.5\left(\frac{L}{b}\right)\sqrt{1 + \frac{a_e}{3d_{av}}}} \tag{4}$$

$$a_e = \left[\frac{(1-\alpha)^2 . Y(\alpha)}{1.12}\right]^2 . a_0 \tag{5}$$

$$Y(\alpha) = \frac{1.99 - \alpha(1-\alpha)(2.15 - 3.93\alpha + 2.7\alpha^2)}{\sqrt{\pi}(1+2\alpha)(1-\alpha)^{3/2}} \quad \left(for \frac{L}{d} = 4\right) \tag{6}$$

Where $Y(\alpha)$ is the geometric shape factor. α is notch length (a_0) to depth (d) ratio. L is the span of the beam. In this work, $L = 400$ and $d = 100$ making $L/d = 4$. Also, $d_{av} = 5mm$ is taken based on the mix of the concrete [Hoover et al (2013)].

As seen above, Eq. (3) takes the simple form of $Fracture\ Load\ (P_{max}) =$ flexural strength $(f_t) \times Equivalent\ area\ (A_e)$, where the equivalent area (A_e) is determined by the specimen dimensions and the average aggregate size d_{av}. This effectively isolates the flexural strength f_t as the only material property to be determined. In other words, Eq. (xx) establishes a direct relationship between P_{max} measurements and f_t estimates.

Furthermore, f_t results are assumed to follow a normal distribution with mean μ_{f_t} and standard deviation σ_{f_t}. By substituting $(\mu_{f_t} \pm 2\sigma_{f_t})$ in Eq. (3), a predictive model is obtained which indicates the mean quasi-brittle fracture curve with upper and lower bounds covering 95 % reliability.

$$P_{max} = (\mu_{f_t} \pm 2\sigma_{f_t}) . A_e \tag{7}$$

The lower and upper bounds of f_t are plotted for PCC and GPC in Fig 5. To facilitate a comparison of strength based on slope, P_{max}/A_e ratios are maintained consistently across both figures. Steeper slopes indicate higher f_t values. f_t estimates for both concrete types remain almost entirely within the 95% confidence interval, and the curves for PCC and GPC are similar. This suggests that GPC beams exhibit a similar size effect as that of PCC, confirming the possibility of size-dependent behavior in geopolymer concrete.

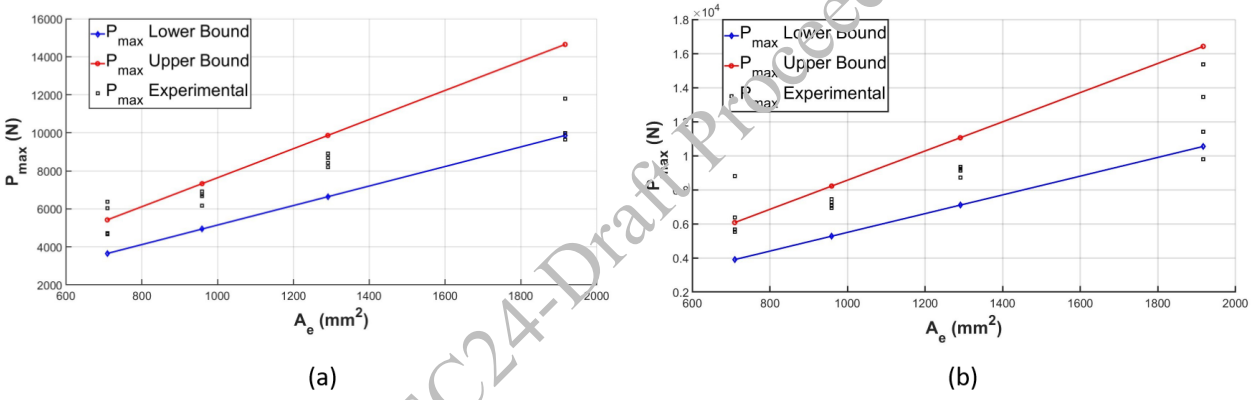

Figure 5. Boundary effect method applied for 95% confidence interval (a) PCC (b) GPC

4. Conclusions

In this work, fracture properties of PCC and GPC are compared for similar compressive strengths. They are compared for the flexural tensile strength and overall fracture energy. Also, size effect analysis based on the boundary effect method is performed on both the concrete. The following conclusions are made:

- The failure modes of the heat-cured GPC specimens were generally more brittle than those of the PPC concrete specimens. The fracture planes of the GPC specimens were less tortuous than those of the PCC concrete specimens.
- The fracture energy of geopolymer concrete was almost similar to that of PCC concrete. However, the variation of fracture energy is greater in PCC as compared to GPC.
- The heat-cured GPC gained early strength than that of PCC. The 7 day strength of GPC was higher than that of PCC.
- The flexure strength of GPC beams is higher than PCC beams having the same compressive strength.
- Predictive boundary effect model (BEM) is applied to the experimentally obtained data to study the size effect in PCC and GPC and it was found that the model fits well for the 95 % confidence interval. GPC beams exhibit a similar size effect as that of PCC, confirming the possibility of size-dependent behavior in geopolymer concrete.

References

Bazant, Z. P., & Xu, K. (1991). Size effect in fatigue fracture of concrete. *ACI Materials Journal*, *88*(4), 390-399.

Carloni, C., Cusatis, G., Salviato, M., Le, J. L., Hoover, C. G., & Bažant, Z. P. (2019). Critical comparison of the boundary effect model with cohesive crack model and size effect law. *Engineering Fracture Mechanics*, *215*, 193-210.

Dave, S. V., & Bhogayata, A. (2020). The strength oriented mix design for geopolymer concrete using Taguchi method and Indian concrete mix design code. *Construction and Building Materials*, *262*, 120853.

Duan, K., & Hu, X. (2004). Specimen boundary induced size effect on quasi-brittle fracture. *Strength, Fracture and complexity*, 2(2), 47-68.

Ganesan, N., Abraham, R., Raj, S. D., & Sasi, D. (2014). Stress–strain behaviour of confined Geopolymer concrete. *Construction and building materials*, *73*, 326-331.

Hoover, C. G., Bažant, Z. P., Vorel, J., Wendner, R., & Hubler, M. H. (2013). Comprehensive concrete fracture tests: Description and results. *Engineering fracture mechanics*, 114, 92-103.

Patankar, S. V., Ghugal, Y. M., & Jamkar, S. S. (2015). Mix design of fly ash based geopolymer concrete. In *Advances in structural engineering: Materials, volume three* (pp. 1619-1634). Springer India.

Pavithra, P., Reddy, M. S., Dinakar, P., Rao, B. H., Satpathy, B. K., & Mohanty, A. N. (2016). A mix design procedure for geopolymer concrete with fly ash. *Journal of cleaner production*, 133, 117-125.

Singh, B., Ishwarya, G., Gupta, M., & Bhattacharyya, S. K. (2015). Geopolymer concrete: A review of some recent developments. *Construction and building materials*, *85*, 78-90.

Investigation of Cathodic Protection of Reinforced Concrete in Marine Environment for the Application of Floating Offshore Wind Turbine

Deeksha Margapuram[1,2*], Marie Salgues[2], Raphaël Lami[3], Benjamin Erable[4], Océane Thibault[3], Michel Groc[5], Renaud Vuillemin[5], Bruno Hesse[5], Jean-Claude Souche[2], Florian Stratta[2], Marine Bayle[6], Jean-Bernard Memet[6], Laurent Zudaire[5], Fabrice Deby[1], Stéphane Laurens[7], Chantal Chalhoub[7], Elie Sassine[7], Fabien Nougarolles[1], Deepak Kamde[1], Alexandra Bertron[1*]

[1]LMDC, Université de Toulouse, UPS, INSA, Toulouse, France
margapuram@insa-toulouse.fr, bertron@insa-toulouse.fr, f_deby@insa-toulouse.fr, nougarol@insa-toulouse.fr, kamde@insa-toulouse.fr
[2]LMGC, IMT Mines Alès, University of Montpellier, CNRS, Alès, France
marie.salgues@mines-ales.fr, florian.stratta@mines-ales.fr, jean-claude.souche@mines-ales.fr
[3]Sorbonne Université, CNRS, LBBM, Observatoire Océanologique, Banyuls-sur-Mer, France
lami@obs-banyuls.fr, oceane.thibault@obs-banyuls.fr
[4]Laboratoire de Génie Chimique, Université de Toulouse, CNRS, INPT, UPS, Toulouse, France
benjamin.erable@ensiacet.fr
[5]Sorbonne Université, CNRS, - REMIMED FR3724, Observatoire Océanologique de Banyuls, Banyuls-sur-Mer, France.
laurent.zudaire@cnrs.fr, michel.groc@obs-banyuls.fr, renaud.vuillemin@obs-banyuls.fr, bruno.hesse@obs-banyuls.fr
[6]A-Corros Expertise, Arles, France
mbayle@a-corros.fr, jbmemet@a-corros.fr
[7]Corrohm, Labège, Toulouse, France
chantal.chalhoub@corrohm.com, elie.sassine@corrohm.com, stephane.laurens@corrohm.com

*Corresponding author

ABSTRACT

Reinforced concrete (RC) floaters to support floating offshore wind turbine (FOWT) can exhibit premature corrosion due to high chloride content in the marine environment. To address the concerns about their deterioration in harsh marine environment, such as corrosion of reinforcements, eventually influenced by biofouling on the material's surface, this study has been designed to understand the interrelations between natural seawater, biofouling, and cathodic protection for RC structures. The objective of the research study is to quantify the effectiveness of cathodic protection using sacrificial aluminium galvanic anode in conjugation with biofilm development. However, this paper presents a part of the long-term research study investigating the comparative effects of galvanic anodes on passive steel in concrete, using CEM I and CEM V cement types, in seawater. Experimental tests were conducted on RC blocks installed in the tidal zone of Banyuls-sur-mer harbour and connected to a data logger for continuous monitoring of the electrochemical state of steel. After three months of immersion, the exposed surface of RC blocks exhibited biofouling, while its influence on the cathodic protection should be probed in detail. Monitoring the mixed potential under temporal variations require careful consideration of tidal influences to ensure continued protection of reinforced concrete. Each binder was tested with three replicate RC blocks, in which the rebars exhibited similar trends in mixed potential and protection current density over time. The aluminium anode delivered slightly higher currents, resulting in greater consumption in the rebars of CEM I reinforced concrete blocks compared to those in CEM V.

KEYWORDS: *Cathodic protection, Submerged aluminium galvanic anode, Tidal zone, Low-CO_2-based cement*

1. Introduction

The conference of parties at the Paris Climate Agreement in 2015 aimed to limit global warming to less than 2 ºC. To achieve this, there is a dire need and interest to generate renewable energy, especially using solar and wind. In the past decade global investment in this sector has significantly increased by ≈100% to present investment of USD 77 billion (Metcalfe, 2024). The foundations of these floating offshore wind turbine structures, floaters, play a pivotal role in providing stability and contribute substantially to the overall cost of the FOWT. The floaters are generally made of steel, but considering their low service life, high maintenance requirement, and environmental concerns, this material is gradually being replaced by Reinforced Concrete (RC) due to their low maintenance (Mathern, 2021). However, corrosion of steel in concrete is one of the major deterioration mechanisms, and if not designed adequately, premature corrosion of steel could be a challenge for these structures. As a result, installing galvanic anodes before corrosion initiates could be a viable solution for extending the service life of these structures. Most of the field studies reported so far include RC without any protection. The long-term investigation by *Kwon et al.* reported that the blends incorporating supplementary cementitious materials (SCMs) demonstrate effective corrosion resistance and durability in marine environments (Kwon, 2017). They also indicate that the formation of calcareous deposits on the exposed concrete surface – leading to reduction in the porosity of concrete and the corrosion rate of embedded steel. However, the authors could not find any literature focusing on the effect of variable exposure conditions such as the alternating wet-dry cycles, high oxygen availability, temperature variations, high relative humidity, salinity, and the presence of microfouling followed by macrofouling on corrosion and protection of steel in concrete. Consequently, this article and the ongoing research aims to investigate the effect of these factors on corrosion and the efficiency of the performance of galvanic anodes in protecting the RC.

To protect embedded steel in concrete in the tidal zone, corrosion can be controlled using cathodic protection (CP). CP is a process that forces cathodic reactions on the surface of embedded rebars by continuously providing electrons to sustain metallic bonding. CP can be implemented by either applying a cathodic potential via impressed direct current and/or by attaching a sacrificial anode to the steel rebars. The use of CP facilitates shifting the electrochemical potential of steel in concrete to control the corrosion. For CP with sacrificial galvanic anodes, the more electronegative metals such as zinc, aluminum, magnesium can be connected to embedded steel to protect embedded reinforcement in concrete in marine environments. In lake water, *Rincon et al.* reported that the aluminium-alloy (Al-Zn-In) based anodes embedded in mortar containing 0.1% chloride ion concentration by cement mass when connected to steel in the concrete of piles in tidal and splash zones could polarize the steel in cathodic direction with the mixed potential of embedded steel and anode was reported to be −900 mV vs $Cu/CuSO_4$ (de Rincón, 1997). Another study on the aluminum alloy-based anode by *Bertolini et al.* submerged it in a 3.5% NaCl solution and found that it could protect passive steel rebars, while minimal protection was offered to corroding rebars (Bertolini, 2002). There is currently little field information on the use of aluminium anodes to protect steel reinforcement in highly resistive concrete, which is attempted to be investigated in this article. Although CP of RC structures has been extensively researched, their performance under field conditions is limited to fully comprehend their effectiveness and for efficient design and maintenance of CP systems in RC structures exposed to marine environments. Regular monitoring and adjustments are necessary to ensure consistent protection across varying environmental and structural conditions.

Therefore, the focus of this paper is to investigate the short-term performance of Al anode for cathodically protecting the steel embedded in concrete with CEM I (ordinary Portland cement) and low-carbon-based CEM V (composite cement) cements. Furthermore, the ongoing research will investigate the formation of biofilm on the exposed surfaces of concrete over time to assess its potential impact on the effectiveness of CP.

2. Materials and methods

Tests were conducted on six cubic reinforced concrete blocks with dimensions (20 × 20 ×11) cm shown in Figure 1A and C depicting the surface exposed to seawater. Each rebar measured 16 cm in length and was 2 cm in diameter. Four rebars were assembled in the form of a grid (see FigureD). An embeddable manganese dioxide-based reference electrode (Type ERE20 from Force Technology) was positioned next to the steel rebar (see FigureD) to measure the electrochemical potential of steel reinforcement and the

concrete cover was designed to be 5 cm. The electrical connections between steel rebar and submerged Al anode included a monitoring system. The anodes were positioned at a depth of one meter from the RC block in seawater. The steel reinforcement was connected to anodes in a parallel electrical circuit to assess the distribution of CP current in each RC block.

This study used two types of cement: CEM I and CEM V. The two commercial cements, namely, CEM I 52,5 N - SR 5 CE PM-CP2 NF and CEM V/A (S-V) were provided by *Lafarge* and *Ciments Calcia Heidelberg*, respectively. A water-to-binder ratio of 0.5 was used. The aggregates and sand were both siliceous alluvial in nature. The concrete mix design is summarized in Table 1. Three RC blocks were prepared for each cement type.

Table 1. Concrete mix design used in this study for 1 m^3 of concrete.

Type of cement	Binder/kg	Sand/kg	Aggregates/kg	Effective water/kg
CEM I	384.75	822.94	1024.56	158.28
CEM V	384.75	798.68	1000.59	169.65

After the curing period, electrical resistivities of CEM I and CEM V were measured according to the French standard, XP P 18-481 and found to be 151 Ωm and 304 Ωm , respectively. The water porosity (NF P 18-459) measurements for CEM I and CEM V concrete were 16 % and 17 %, respectively. The total charge pass rapid chloride permeability test, conducted following the XP P 18-462 standard, demonstrate that CEM V concrete (582 coulomb) exhibits chloride ion penetrability six times less than that of CEM I concrete (3479 coulomb).

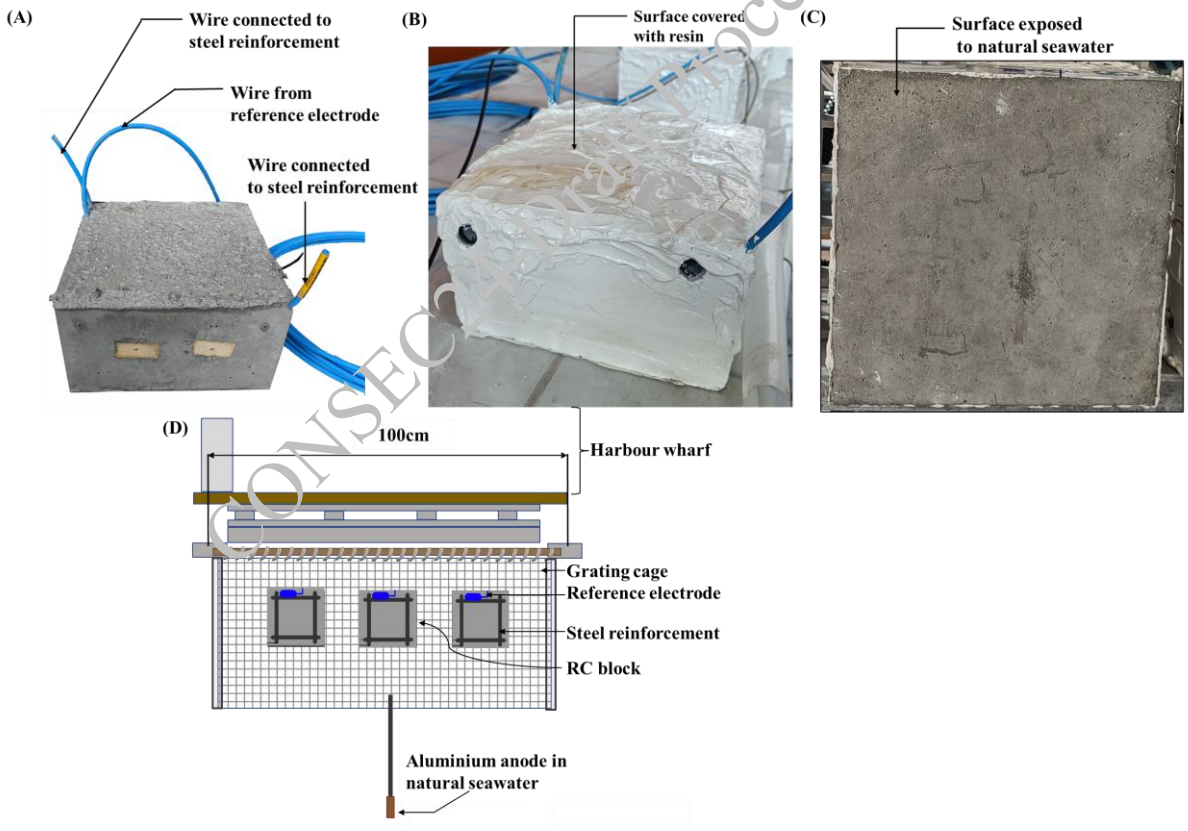

Figure 1. (A) Photograph of reinforced concrete block without resin; (B) and covered with resin on five sides; (C) Surface exposed to natural seawater; (D) Representative sketch illustrating the top view with three specimens fixed in a row in the grating cage fixed to the harbour wharf at the exposure site.

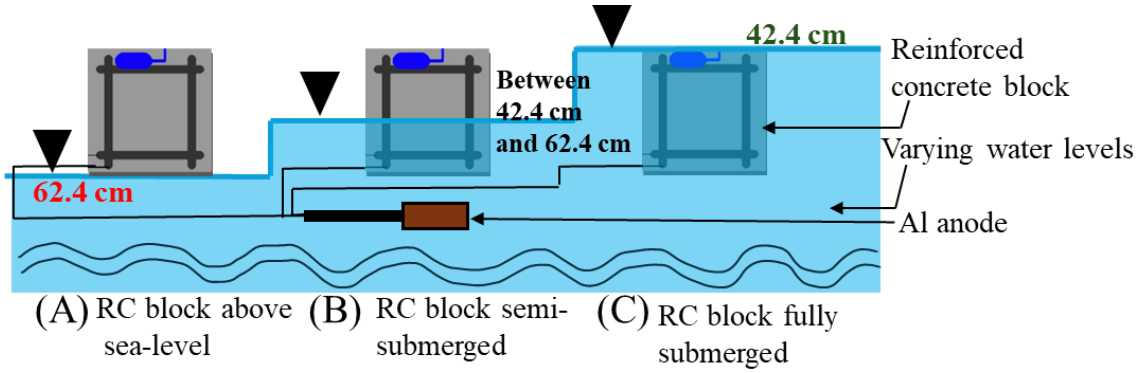

Figure 2. Schematic representation of RC blocks in natural seawater under three conditions: (A) above water level (≥ 62.4 cm), (B) semi-submerged condition with water levels between 42.4 cm and 62.4 cm, and (C) below sea level with water level below 42.4 cm (fully submerged condition).

3. Exposure of specimens and exposure conditions

The study site is in Mediterranean Sea at Banyuls-sur-Mer, France. The reinforced concrete blocks were fixed to a grating cage (see Figure 1D), with three CEM I concrete blocks in the first row, followed by CEM V placed in the next row. This grating cage was installed beneath the harbor wharf of the tidal region at Banyuls-sur-mer, France. Because of tidal fluctuations, the concrete blocks were subjected to both high and low tides. One face of RC specimen was exposed to the marine environment and the remaining faces were covered with epoxy resin (as shown in Figure 1C) to ensure the unidirectional ingress of chlorides. Note that anodes were placed about one meter below the specimen and are externally connected to the steel rebars using an electric board to facilitate the measurements during this research. The temperature, atmospheric pressure, relative humidity, and salinity at this location was monitored daily. An ultrasonic water-level measurement sensor was installed to monitor and record the water level every minute. Figure 2 illustrates the RC blocks experiencing three conditions based on water level. Specifically, a measurement between 42.4 cm and 62.4 cm indicates that the RC specimen is semi-submerged in seawater (see Figure 3A). Distances at or less than 42.4 cm indicate that the concrete is fully submerged in seawater, while measurements above 62.4 cm indicate the concrete is above sea level. The water level data provides information on the periods when the concrete is either fully submerged or partially submerged in seawater.

4. Results and discussions

The potential of passive rebars in the RC blocks before and after connection to a sacrificial anode is shown in Figure. The corrosion potential of the rebars in CEM I and CEM V-based concrete ranged from −390 mV to −500 mV vs MnO_2 (−470 mV to −580 mV vs $Cu/CuSO_4$/SHE) and −150 mV to −250 mV vs MnO_2 (−230 mV to −330 mV vs $Cu/CuSO_4$/SHE) before connection to the anode. The variation in the corrosion potential range of the rebar could possibly be attributed to the microclimate due to the different physical and chemical composition of the two types of cement. Upon connection to Al anode, the polarization caused a shift towards a more negative potential (between −500 mV (−580 mV vs $Cu/CuSO_4$/SHE) and −700 mV vs MnO_2 (−780 mV vs $Cu/CuSO_4$/SHE) – see Figure 3).

Figure 3(A), (B), (C), and (D) show the variations in water level, mixed potential, and protection current density over an exposure period of 120 days for CEM I and CEM V concrete. FigureB and C shows that the measured mixed potential and protection currents were found to be increasing with an increase in the water level (water levels < 42.4 cm). This increase could possibly be attributed to the saturation of the steel-concrete interface with seawater and that the corrosion process is controlled by oxygen diffusion. It is observed that the peaks for the water level, mixed potential, and protection currents (see Figure 3) are observed at the same time – indicating that the electrochemical activities are corelated with water level leading to changes in microclimate at the steel-concrete interface. Consequently, the mixed potential, representing the overall potential where anodic and cathodic reactions occur, may exhibit a slight trend towards more negative values due to increased cathodic protection current – indicating increased anodic activity and possible anodic dissolution of Al anode. These observations are made with limited data with

fluctuations in both mixed potential and current density flow. Therefore, to be certain, further investigations into the underlying causes of these are warranted.

The findings for CEM V- based binder system is shown in Figure 3B and D. The chemical composition of the CEM V binder includes 25% slag and 25% fly ash. The incorporation of SCMs in this binder significantly influences the corrosion process, primarily because blended cements exhibit lower permeability, enhanced chloride binding capacity, high resistivity of concretes, etc, due to the denser matrix of cementitious systems (Lothenbach, 2011). When galvanic anodes are connected to steel reinforcement embedded in CEM V-binder, the shift in mixed potential is between −500 mV to −650 mV versus MnO_2, (−580 mV to −730 mV vs $Cu/CuSO_4$/SHE) which is less negative than that observed by CP-protected steel embedded in CEM I-based concrete, which can be attributed to high resistivity of CEM V-based concrete. Note that the shift is greater than 100 mV (as per ISO 12696) – indicating that the steel rebar is cathodically protected by sacrificial anodes. The inclusion of SCMs could improve concrete durability by limiting the penetration of chlorides. Consequently, the protection current supplied by the anode were observed to be more consistent and effective over the exposure time of 120 days. Additionally, SCMs have the potential to modify the pH in the vicinity of the rebar (Angst, 2017). CEM V concrete may possibly provide greater resistance to ingress of aggressive ions and oxygen compared to CEM I, resulting in less current being available at the rebar in the former. According to the NF EN 12696 standard, the IR compensation method for measuring the instant OFF potential involves switching off the current and recording the potential between 0.1 s and 1 s. By measuring both the instant OFF and ON potentials, the ohmic drop and subsequently the resistance between the reinforcement steel and the reference electrode can be determined. In our study, the ohmic drop is considered negligible because the reference electrode and the reinforcement steel (working electrode) are positioned very close to each other. Consequently, the instant OFF potentials are nearly identical to the ON potentials.

The measurements collected during 120-day exposure period shows that the embedded steels in both types of concrete are protected by submerged aluminum anodes. Visual observations revealed the formation of biofilm, predominantly macroalgae, on the exposed concrete surfaces. Further investigations, including chlorophyll a analysis, will be conducted to quantify the biofilm and understand its role in the overall corrosion process.

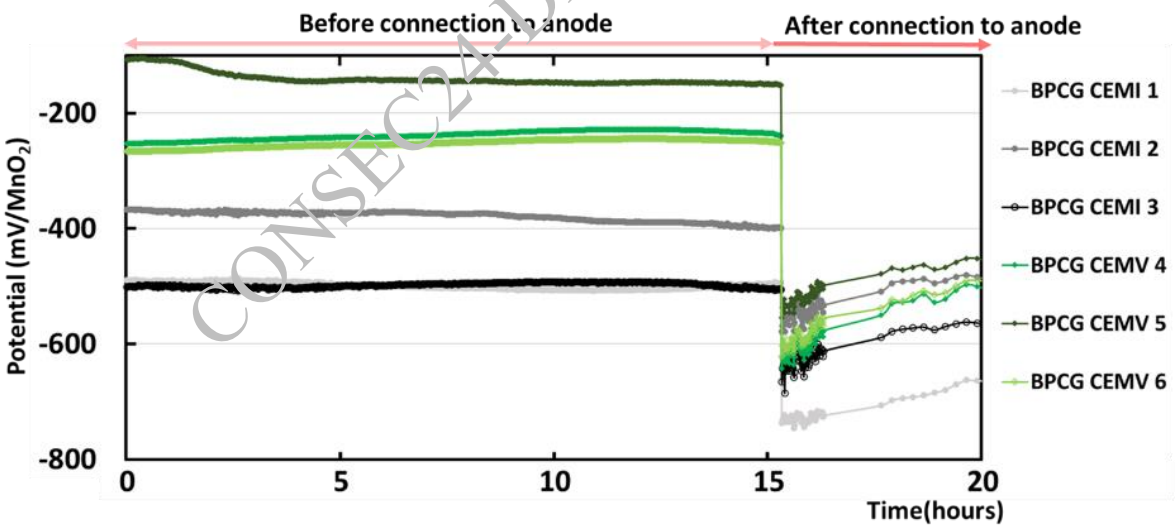

Figure 3. Potential of steel reinforcement before and after connection to aluminium anode. A conversion factor of - 0.080 V_{SHE} can be applied to obtain measured potentials in terms of $Cu/CuSO_4$ electrode

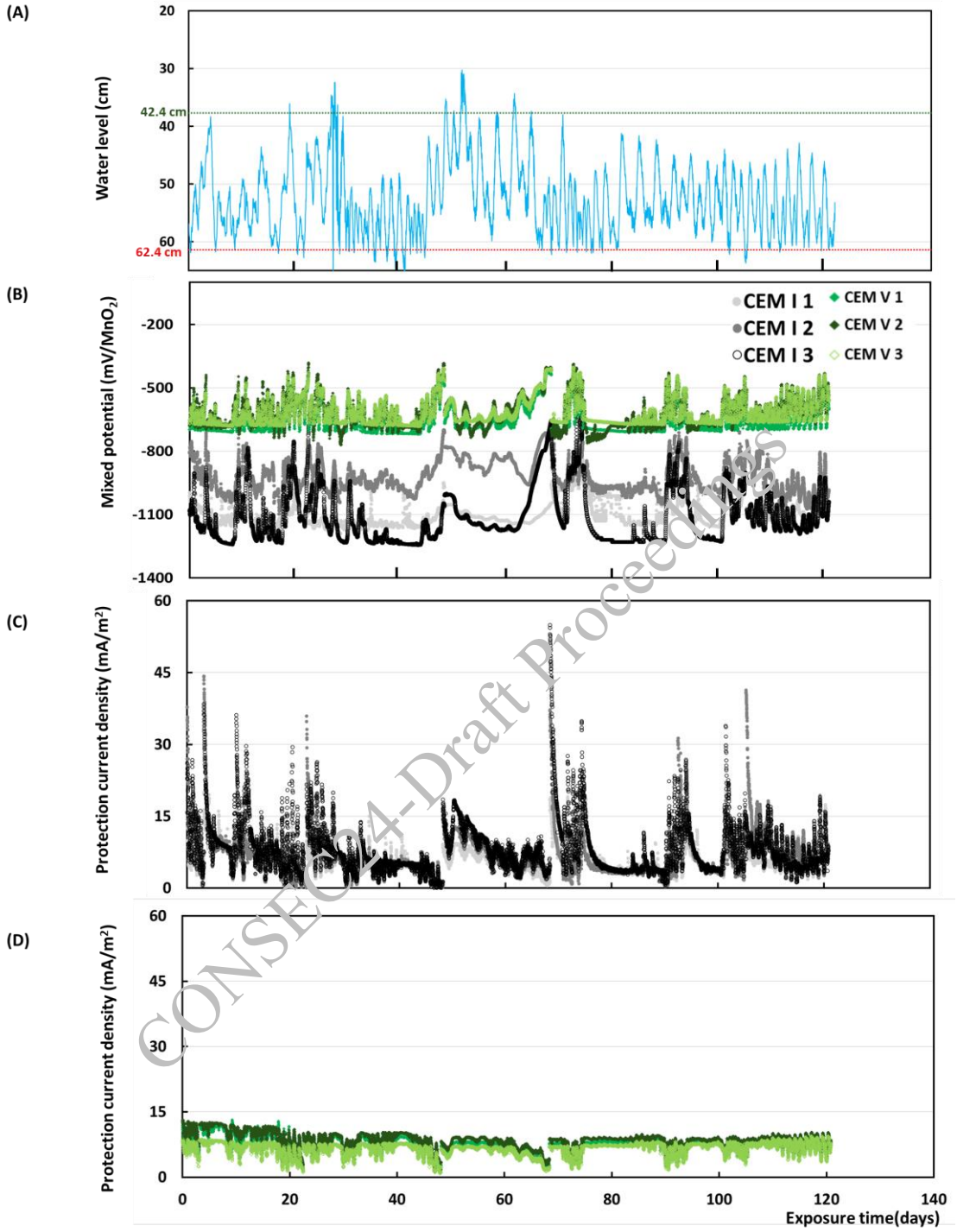

Figure 4. (A) Processed water level data recorded with an ultrasonic water sensor, (B) Mixed potential of steel reinforcement in CEM I and CEM V concrete; and (C) Protection current density delivered by galvanic anode to steel reinforcement in CEM I and (D) CEM V concrete.

5. Conclusions

This research was carried out over a 120-day of marine exposure, involving reinforced concrete specimens with CEM I and CEM V binders protected with cathodic protection (CP) using submerged sacrificial aluminium anodes. The findings presented here are preliminary and highlight that steel reinforcement in

CEM I concrete exhibited a higher probability of corrosion, and protection current supplied by Al anodes is higher for steel embedded in CEM I concrete than that of steel embedded in CEM V concrete. In summary, the steel in both types of concrete is adequately protected. So far, temporal variations in water levels do not appear to affect the performance of submerged aluminum anodes, indicating good performance. Nevertheless, certain limitations identified within the initial 120 days of this study will be addressed through more detailed investigations in future research. Subsequent studies will specifically examine the role of biofilm formation in influencing corrosion processes.

Acknowledgements

The authors are grateful to the Region Occitanie for its financial support (DuMaCoBio project), to the Wind'Occ agency for its federation and connection support during the construction and operation of the project, as well as Bio2Mar (K. Escoubeyrou) and Remimed technical platforms.

References

Angst UM, G. M. (2017) The steel–concrete interface. *Materials and Structures*, 1-24.

Bertolini L, G. M. (2002) Prevention of steel corrosion in concrete exposed to seawater with submerged sacrificial anodes. *Corrosion Science*, 44(7): 1497-1513.

BS EN ISO 12696, Cathodic Protection of Steel in Concrete, 2016.

de Rincón, O. d. (1997) Performance of sacrificial anodes to protect the splash zone of concrete piles, *Materials and Structures*, 30: 556-560.

Kwon, S. L. (2017) Long-term corrosion performance of blended cement concrete in the marine environment – A real-time study. *Construction and building materials*, 154: 349-360.

Lothenbach, B. K. (2011) Supplementary cementitious materials. *Cement and concrete research*, 1244-1256.

Mathern, A. C. (2021) Concrete support structures for offshore wind turbines: Current status, challenges, and future trends. *Energies*, 14(7): 3678.

Metcalfe, O. (2024, February 4) Bloomberg NEF. Retrieved from Bloomberg: https://about.bnef.com/blog/offshore-wind-investment-hit-all-time-high-in-2023/

AI-Based Prediction of Damage Severity in Blended Concrete Under Extreme Environmental Exposure Conditions

Ramesh Gomasa[1], Visalakshi Talakokula[2*], Sri Kalyana Rama Jyosyula[3], Tushar Bansal[4] and Nidhi Goyal[5]

[1] Research Scholar, Department of Civil Engineering, Mahindra University, Hyderabad, India
Email: ramesh.gomasa21pcie002@mahindrauniversity.edu.in
[2]Professor, Department of Civil Engineering, Mahindra University, Hyderabad, India
Email: visalakshi.talakokula@mahindrauniversity.edu.in
[3]Associate Professor, Department of Civil Engineering, Mahindra University, Hyderabad, India
Email: srikalyanarama.j@mahindrauniversity.edu.in
[4]Assistant Professor, Department of Civil Engineering, Sharda University, Greater Noida, India
Email: tushar.bansal@sharda.ac.in
[5]Assistant Professor, Department of Computer Science Engineering, Mahindra University, Hyderabad, India
Email: nidhi.goyal@mahindrauniversity.edu.in

[*]Corresponding author

ABSTRACT

Concrete structures such as buildings, bridges and dams are constructed in various locations worldwide. These structures are exposed to a wide range of environmental conditions that can impact their durability and performance over time, leading to strength loss, damage and compromised integrity. Non-destructive testing (NDT) methods mostly rely on the surface condition and not always provide information about the internal health of these structures. In such cases, embedded sensor-based structural health monitoring (SHM) techniques are required for a more comprehensive assessment. The embedded piezo sensor (EPS) based electro-mechanical impedance (EMI) technique is currently a central focus of research in the field of SHM. This study utilizes EPS for non-destructive damage monitoring of blended concrete exposed to a 5% concentration of sulfuric acid using the EMI technique. The acquired EMI data from the EPS are used for deterioration damage prediction of concrete using artificial neural networks (ANN), achieving a high predictive accuracy with an accuracy of 0.92. Additionally, a semi-parametric statistical analysis is performed using the Cox proportional hazard model. The relationship between the survival time of concrete and predictor variables is predicted with an accuracy of 0.53. The integration of EMI data with ANN can identify complex patterns and relationships within the data that are not easily detectable through conventional analysis methods and is capable of predicting potential deterioration and damage at an early stage, thereby facilitating timely maintenance.

KEYWORDS: *Blended concrete, Sulphuric acid exposure, EMI technique, Embedded piezo sensor, Artificial neural networks.*

1. Introduction

Concrete is widely used in civil engineering structures due to its strength, versatility, cost-effectiveness, and ease of availability of raw materials (Mehta & Monteiro, 2014). However, concrete structures are prone to deterioration when exposed to harsh environmental conditions, such as sulfuric acid, which is commonly found in sewer systems, industrial effluents and seawater. Sulfuric acid exposure leads to rapid deterioration of concrete, causing significant structural damage over time (Adediran et al., 2022; Hill et al., 2003). In recent years, the use of supplementary cementitious materials (SCMs) has gained significant importance, enhancing the mechanical and durability properties of concrete. SCMs undergo pozzolanic reactions during hydration, contributing to a denser microstructure and reduced permeability. Despite these advancements, predicting the damage severity of concrete under chemical exposure remains challenging due to the complex nature of these interactions (Bereda & Asteray, 2021; Lv et al., 2022). Traditional methods

primarily rely on destructive testing (DT) and non-destructive testing (NDT) methods provide limited insights into the internal health of concrete structures (Girardi & Maggio, 2011; Gomasa et al., 2023; Morwal et al., 2023; Parida & Moharana, 2023). Therefore, there is a growing need for innovative solutions that offer continuous and accurate monitoring of concrete integrity. Embedded piezo sensors (EPS) and the electro-mechanical impedance (EMI) technique have shown promise in this regard, offering high sensitivity to changes in mechanical stress and early detection of structural deterioration (Bansal & Talakokula, 2020; Girardi et al., 2010; Li et al., 2009; Ouyang et al., 2021; Wani, Vemuri, & Chenna, 2023; Wani, Vemuri, Chenna, et al., 2023; Yang et al., 2021). Recent studies have explored the application of artificial intelligence (AI) techniques, particularly artificial neural networks (ANN), for predicting concrete damage (Altabey & Noori, 2022; Amiri & Hatami, 2022; Bichri et al., 2020; Flah et al., 2021; Hewayde et al., 2007; Majlesi et al., 2023; Parida et al., 2022). These methods can effectively capture complex patterns and relationships within data, providing more accurate predictions compared to traditional modelling approaches. Furthermore, survival analysis particularly using the Cox proportional hazard model provides insights into the factors influencing the degradation process of concrete. This statistical method allows for the analysis of the survival time of concrete under various environmental stressors, offering a deeper understanding of the deterioration mechanisms. However, there is a limited work on the integration of EPS with ANN and survival analysis for non-destructive monitoring of blended concrete under sulfuric acid exposure. Several researchers (Na & Lee, 2013, Yan et al., 2022, Kim et al., 2017, Oh et al., 2017) explored the application of piezo sensors for health monitoring of concrete but did not explore the potential of integrating ANN for predictive analysis and survival analysis to understand long-term degradation trends. These gaps highlight the need for a holistic approach that leverages the strengths of EPS, EMI, ANN and survival analysis. This study aims to address these gaps by integrating EPS and EMI techniques with ANN and survival analysis for comprehensive monitoring of blended concrete under sulfuric acid exposure.

2. Materials

This section details the specific processes involved in the fabrication of the EPS to ensure proper functioning and durability within the concrete matrix, as well as the various raw materials used for the preparation of blended concrete.

2.1 Fabrication of EPS

Lead zirconate titanate (PZT) patch of 10 x 10 x 0.3 mm is cleaned with isopropyl alcohol to remove any contaminants on the surface. The positive and negative electrode lead wires are connected to the PZT patch using a soldering machine. The electrical continuity of the connections is verified using a multimeter and oscilloscope. Subsequently, epoxy adhesive is mixed according to the manufacturer's instructions and small amount of epoxy adhesive is applied to the soldered connections to enhance electrical conductivity and mechanical stability. A brush is used to ensure an even application of the protective coating, covering all exposed parts of the piezo sensor. The protective coating is then allowed to cure completely using pressure curing. After the curing process, the PZT patch is sandwiched between two mortar layers to protect the PZT sensor from environmental factors and mechanical damage. Finally, the prepared embedded sensor is embedded into the concrete mould, ensuring it is positioned correctly for accurate EMI measurements. The fabricated EPS is shown in Figure 1.

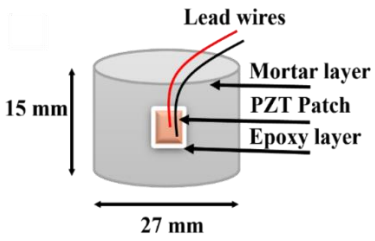

Figure 1. Fabricated embedded piezo sensor

2.2 Preparation of blended concrete

Figure 2 shows the various raw materials used in the study, Portland Pozzolana Cement [PPC] (IS 1489:2020), ground granulated blast furnace slag [GGBS] (IS 12089:2018) and concrete enhancer [CE] (SPARTEK, 2024) used as cementitious materials. Manufactured sand is used as the fine aggregate [FA], while 10 mm and 20 mm crushed gravels used as the coarse aggregate [CA] (IS 383:2016). A polycarboxylate ether-based superplasticizer [SP] is used as a chemical admixture (IS 9103:2018).

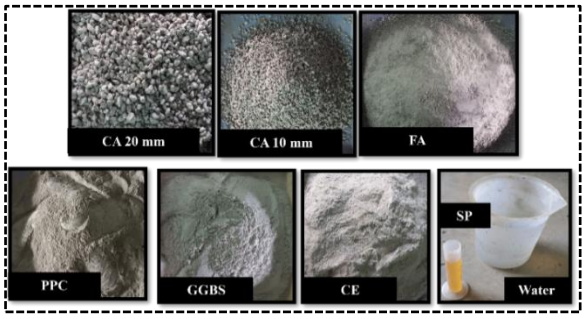

Figure 2. Raw materials used for the preparation of blended concrete

Table 1. Mix proportioning of blended concrete (kg/m^3)

PPC	GGBS	CE (%)	FA	CA	w/c	SP (%)
283	70.61	0.5	652	1200	0.4	0.6

Table 1 shows the mix proportioning of PPC, GGBS, CE, FA, CA, water-cement ratio (w/c) and SP for preparation of the blended concrete specimens. All materials are weighed according to the mix proportions. The concrete is mixed using a drum mixer for five minutes to ensure a homogeneous mixture to prevent bleeding and segregation. The mixed concrete is then poured into lubricated 150 mm x 150 mm x 150 mm cube moulds. An EPS is placed at the centre of each mould during casting. The moulds are gently compacted using a table vibrator to avoid damage to the EPS. A total of 15 concrete specimens are prepared and cured for 28 days at standard room temperature to achieve sufficient strength.

3. Experimental program

After curing, the concrete specimens are dried to remove any residual moisture. Figure 3 shows the experimental setup used to acquire EMI data from the EPS in the concrete specimen. The positive and negative terminals of the EPS are connected to a Keysight high-precision LCR meter using crocodile cables and a 1 V voltage is applied to the EPS. The baseline EMI data is acquired within a frequency range of 30 to 400 kHz. The concrete specimens are then immersed in a 5% sulfuric acid solution. EMI data are acquired at regular intervals over 35 days to monitor deterioration process in the concrete. After EMI data acquisition, the concrete specimens are removed from the sulfuric acid solution and the mass loss of the specimens is measured every week during the exposure period using a high-precision weighing balance.

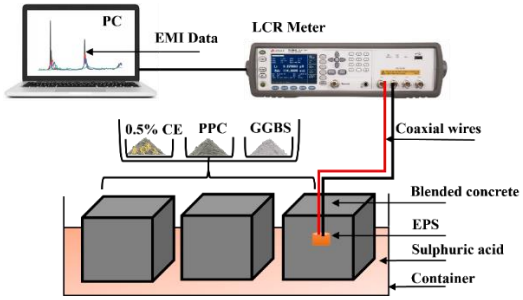

Figure 3. Experimental set-up for data acquisition from EPS

4. Results and discussions

This section presents the comprehensive findings of the study, highlighting the analysis based on conductance signatures, the prediction of deterioration damage using ANN and the survival probability of blended concrete.

4.1 Analysis based on conductance signature

The shifts in the conductance signatures over 35 days of sulfuric acid exposure from their baseline position are shown in Fig. These shifts are indicating that the ongoing chemical reactions and deterioration process within the concrete. The baseline conductance signature showed two resonant peaks at approximately 140 kHz and 160 kHz. With increased exposure to sulfuric acid, the conductance signatures shifted upward and to the left from their baseline position. These shifts indicate changes in the mechanical impedance of the concrete, attributed to the formation of ettringite and gypsum. Sulfuric acid reacts with calcium hydroxide to form calcium sulphate and water, leading to the leaching of calcium content and weakening of the concrete matrix (Hill et al., 2003). Further exposure leads to the formation of ettringite, causing expansion and deterioration in the concrete. These changes in the mechanical impedance of the concrete are reflected in the shifting conductance signatures (Bhalla, S., Moharana, S., Talakokula, V., & Kaur, 2017).

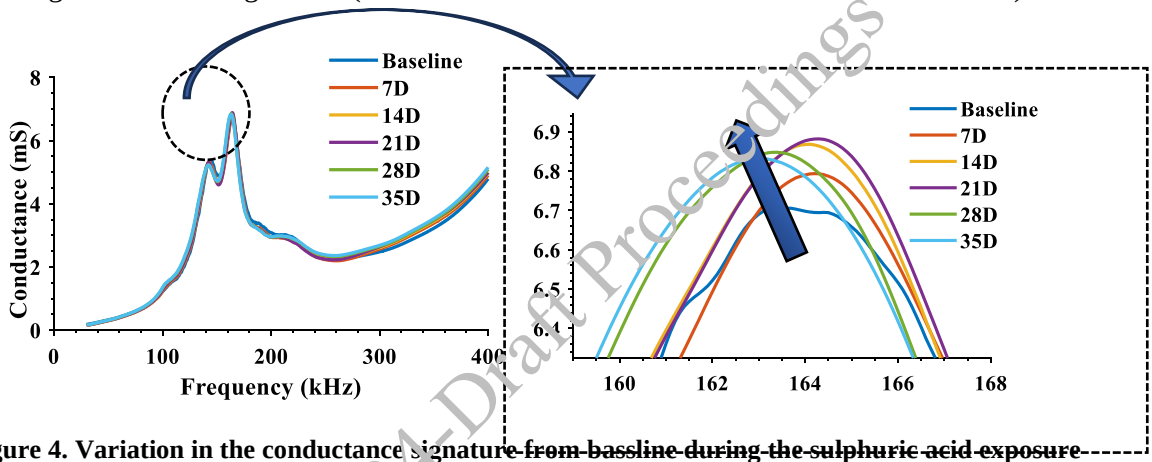

Figure 4. Variation in the conductance signature from bassline during the sulphuric acid exposure

4.2 Damage identification using artificial neural networks

Firstly, relevant libraries are imported into the Google Colab Python workspace, including TensorFlow for building the neural network, pandas for data manipulation, and Matplotlib for visualization. The total dataset, comprising 22,206 rows and 5 columns, the data is imported into the Python environment using the Colab import function. Next, the input features (X) and target variables are defined for training and testing the ANN model using the train test split function. Subsequently, exploratory data analysis (EDA) is performed to visualize the relationships between the input features and the target variable. This analysis also included visualizing the distribution of the target variables, as shown in Figure 5.

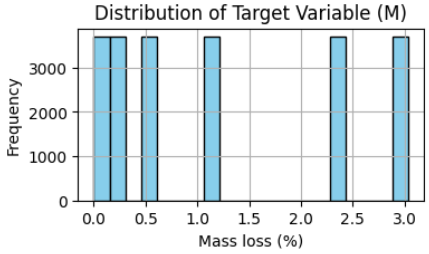

Figure 5. Distribution of target variable using EDA

The dataset is divided into training, validation, and testing sets in a 70:15:15 ratio using the train test split function from scikit-learn. The features are scaled using Min-Max normalization to ensure that each feature contributed proportionally to the model. A Sequential model is then constructed using TensorFlow's Keras API, comprising an input layer, one hidden layer with 5000 neurons, and an output layer with a single

neuron for predicting mass loss. The hidden layer contained densely connected neurons with a tanh activation function to introduce non-linearity into the model. A stochastic gradient descent (SGD) optimizer with a learning rate of 0.01 is employed. The flow chart of the ANN framework, detailing the steps from data acquisition and preprocessing to model training, testing, validation and prediction is shown in Figure 6.

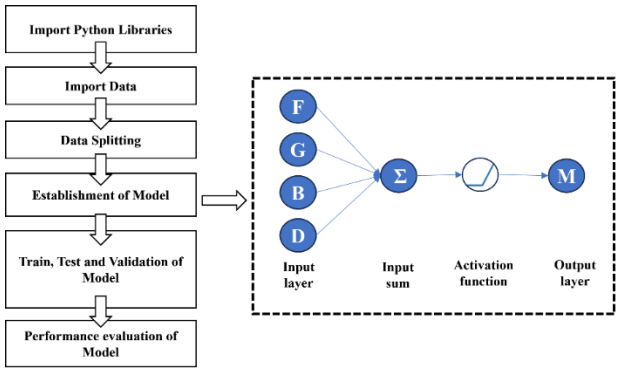

Figure 6. Flowchart of ANN framework

Figure 6 shows the schematic representation of ANN model, which consists of an input layer, a hidden layer with 5000 neurons and an output layer. The input features included Conductance (G), Susceptance (B), Frequency (F), Duration of exposure (D) and Mass loss as the target feature. The model is trained over 40 epochs with a batch size of 128, and its performance is evaluated on the training, validation and testing sets. Evaluation metrics such as mean squared error (MSE), root mean squared error (RMSE) and R-squared (R^2) score are computed to assess the model's predictive accuracy.

The ANN model demonstrated high predictive accuracy, achieving an R-squared score of 0.92 across training, validation and testing datasets. This high accuracy indicates that the ANN model effectively captures the complex interactions between the input features and the extent of deterioration damage of concrete. The ability of the ANN to predict mass loss with such precision suggests that this approach can be a valuable tool in the broader context of SHM.

Table 2. Hyperparameter tuning for prediction task

Learning Rate	Training RMSE	Validation RMSE	Testing RMSE	Training MSE	Validation MSE	Testing MSE	Training R^2 Score	Validation R^2 Score	Testing R^2 Score
0.01	0.3	0.29	0.3	0.09	0.08	0.09	0.92	0.92	0.92
0.02	0.3	0.3	0.3	0.09	0.09	0.09	0.92	0.92	0.92
0.03	0.3	0.3	0.3	0.09	0.09	0.09	0.92	0.92	0.92
0.06	0.31	0.3	0.31	0.09	0.09	0.09	0.92	0.92	0.92
0.08	0.31	0.31	0.31	0.1	0.09	0.1	0.92	0.92	0.92
0.1	0.31	0.31	0.31	0.09	0.09	0.09	0.92	0.92	0.92

The selection of the learning rate is crucial for training the neural network to overcome overfitting problems and perform better prediction tasks. For this reason, the hyperparameters are tuned with different learning rates, batch sizes and epochs. It is found that at a learning rate of 0.01, the highest accuracy and lowest error metrics are observed, as shown in Table 2. The tuning of hyperparameters at different learning rates for the ANN model is shown in Table 3.

Figure 7 shows the predicted versus actual mass loss values for the training, testing, and validation datasets. The high accuracy across all datasets indicates the reliability of the ANN model in predicting concrete deterioration. The performance of the prediction model against actual values for the training, testing and validation states offers a qualitative assessment of the model's predictive capabilities. It is observed that the model achieves an accuracy of 0.92 across all states. This high accuracy indicates that the ANN model's predictions closely match the actual values, suggesting that the model is highly effective and reliable in prediction tasks.

Table 3. Hyper parameters used in the study

Parameter	Value
Optimizer	Stochastic gradient descent (SGD)
Data scaling	Min-Max scaler
Input layer size	128
No. of neurons in the hidden layer	5000
Dropout layer value	0.5
No. of neurons in the output layer	1
Activation function	Tanh
Batch size	128
Epochs	40
Learning rate	0.01

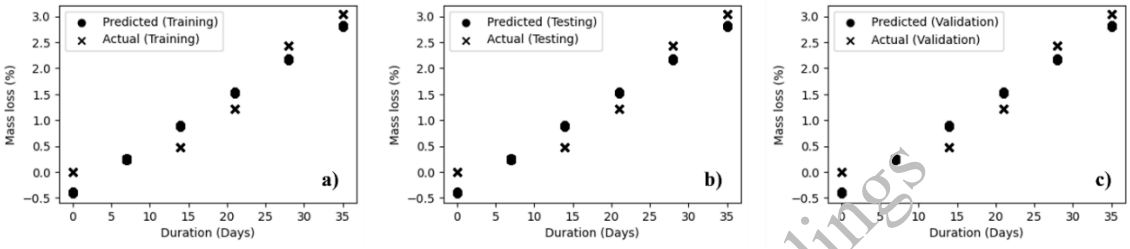

Figure 7. Prediction of deterioration damage in blended concrete; (a) training, (b) testing and (c) validation

Figure 8 shows the mean squared error (MSE), root mean squared error (RMSE) and loss function over epochs for the ANN model. These performance metrics are crucial for evaluating the effectiveness of the ANN model in predicting mass loss. The plots demonstrate the model's convergence and accuracy, indicating how well the model learns from the training data and generalizes to new data. It is observed that with an increase in the number of epochs, the MSE and RMSE values decrease. The best performance is identified at epoch 33, with the lowest training, testing and validation loss as highlighted and shown in Figure 8(c).

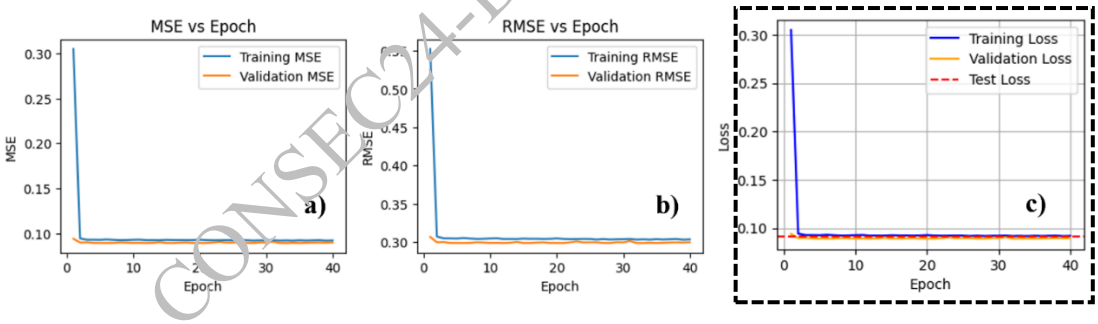

Figure 8. Performance evaluation metrics; a) MSE, b) RMSE and c) overall loss function

4.3 Survival probability of concrete

A semi-parametric statistical method of survival analysis is performed using the Cox Proportional Hazard model, as shown in Figure 9. The Cox Proportional Hazard model is a statistical technique used for analyzing the relationship between the survival time of individuals and predictor variables. It is commonly used in survival analysis to understand the factors that influence the timing of events, such as the failure of a particular system. The Cox model specifically focuses on modelling the hazard function, which represents the probability that an event (such as failure) will occur at a particular time, given that the individual has survived up to that time. Initially, the lifelines package and CoxPHFitter library are installed in the Python environment to perform survival analysis. The features and target variables are then defined, and the dataset is split into 70% training, 15% testing, and 15% validation sets. The total number of events observed is 18,505 out of 22,206. Survival analysis using the Cox proportional hazard model provided insights into the factors influencing the degradation process of blended concrete. The analysis showed that the survival

probability of concrete samples decreased with the duration of sulfuric acid exposure. The concordance index for the model is 0.53, indicating a moderate predictive ability.

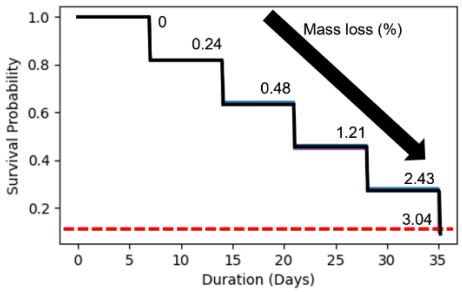

Figure 9. Survival probability of blended concrete

This study highlights the potential of combining SHM with AI techniques to improve the durability and safety of concrete structures. The high accuracy of ANN models in predicting damage, coupled with the insights gained from survival analysis, provides a powerful tool for proactive maintenance strategies. This integrated approach not only enhances the understanding of concrete degradation mechanisms but also supports the development of more resilient infrastructure.

5. Conclusions

This study introduces novel contributions to the field of SHM and concrete deterioration monitoring using EPS combined with ANN and survival analysis. The integration of EPS and EMI techniques with ANN and survival analysis represents a significant advancement in non-destructive testing and monitoring methods. This comprehensive approach not only enhances the ability to detect and predict concrete deterioration but also provides valuable insights into the underlying mechanisms of degradation. The use of survival analysis to understand the long-term performance of concrete under sulfuric acid exposure is particularly innovative, offering a new perspective on the factors influencing concrete durability. These contributions highlight the potential for combining advanced sensing technologies and deep learning algorithms to improve the maintenance and management of concrete structures, ultimately leading to more resilient and long-lasting infrastructure.

References

Adediran, A., Yliniemi, J., Carvelli, V., Adesanya, E., & Illikainen, M. (2022). Durability of alkali-activated Fe-rich fayalite slag-based mortars subjected to different environmental conditions. *Cement and Concrete Research*, *162*(September), 106984.

Altabey, W. A., & Noori, M. (2022). Artificial-Intelligence-Based Methods for Structural Health Monitoring. *Applied Sciences (Switzerland)*, *12*(24), 12–15.

Amiri, M., & Hatami, F. (2022). Prediction of mechanical and durability characteristics of concrete including slag and recycled aggregate concrete with artificial neural networks (ANNs). *Construction and Building Materials*, *325*(October 2021), 126839.

Bansal, T., & Talakokula, V. (2020). Study of Durability Aspects of Limestone Calcined Clay Cement Using Different Piezo Configurations. *RILEM Bookseries*, *25*, 723–730.

Bereda, A., & Asteray, B. (2021). Strength and Microstructural Investigation of Quaternary Blended High-Strength Concrete. *Advances in Civil Engineering*, *2021*.

Bhalla, S., Moharana, S., Talakokula, V., & Kaur, N. (2017). Piezoelectric materials: applications in SHM, energy harvesting and biomechanics.

Bichri, A., Kamzon, M. A., & Abderafi, S. (2020). Artificial neural network to predict the performance of the phosphoric acid production. Procedia Computer Science, 177, 444–449.

Flah, M., Nunez, I., Ben Chaabene, W., & Nehdi, M. L. (2021). Machine Learning Algorithms in Civil Structural Health Monitoring: A Systematic Review. Archives of Computational Methods in Engineering, 28(4), 2621–2643.

Girardi, F., & Maggio, R. Di. (2011). Resistance of concrete mixtures to cyclic sulfuric acid exposure and mixed sulfates: Effect of the type of aggregate. Cement and Concrete Compo*sites*, *33*(2), 276–285.

Girardi, F., Vaona, W., & Di Maggio, R. (2010). Resistance of different types of concretes to cyclic sulfuric acid and sodium sulfate attack. *Cement and Concrete Composites*, *32*(8), 595–602.

Gomasa, R., Talakokula, V., Kalyana, S., Jyosyula, R., & Bansal, T. (2023). A review on health monitoring of concrete structures using embedded piezoelectric sensor. *Construction and Building Materials*, *405*(August), 133179.

Hewayde, E., Nehdi, M., Allouche, E., & Nakhla, G. (2007). Neural network prediction of concrete degradation by sulphuric acid attack. *Structure and Infrastructure Engineering*, *3*(1), 17–27.

Hill, J., Byars, E. A., Sharp, J. H., Lynsdale, C. J., Cripps, J. C., & Zhou, Q. (2003). An experimental study of combined acid and sulfate attack of concrete. *Cement and Concrete Composites*, *25*(8), 997–1003.

Kim, J., Lee, C., & Park, S. (2017). Artificial neural network-based early-age concrete strength monitoring using dynamic response signals. *Sensors (Switzerland)*, *17*(6).

Li, G., Xiong, G., lü, Y., & Yin, Y. (2009). The physical and chemical effects of long-term sulphuric acid exposure on hybrid modified cement mortar. *Cement and Concrete Composites*, *31*(5), 325–330.

Lv, X., Yang, L., Li, J., & Wang, F. (2022). Roles of fly ash, granulated blast-furnace slag, and silica fume in long-term resistance to external sulfate attacks at atmospheric temperature. *Cement and Concrete Composites*, *133*(July), 104696.

Majlesi, A., Khodadadi Koodiani, H., Troconis de Rincon, O., Montoya, A., Millano, V., Torres-Acosta, A. A., & Rincon Troconis, B. C. (2023). Artificial neural network model to estimate the long-term carbonation depth of concrete exposed to natural environments. *Journal of Building Engineering*, *74*(November 2022), 106545.

Mehta, P. K., & Monteiro, P. J. (2014). Concrete: microstructure, properties, and materials. In *McGraw-Hill Education*.

Morwal, T., Bansal, T., Azam, A., & Talakokula, V. (2023). Monitoring chloride induced corrosion in metallic and reinforced/prestressed concrete structures using piezo sensors-based electro mechanical impedance technique: A review. *Measurement: Journal of the International Measurement Confederation*, *218*(February), 113102.

Na, S., & Lee, H. K. (2013). Neural network approach for damaged area location prediction of a composite plate using electromechanical impedance technique. *Composites Science and Technology*, *88*, 62–68.

Oh, T. K., Kim, J., Lee, C., & Park, S. (2017). Nondestructive concrete strength estimation based on electro-mechanical impedance with artificial neural network. *Journal of Advanced Concrete Technology*, *15*(3), 94–102.

Ouyang, B., Song, Y., Li, Y., Wu, F., Yu, H., Wang, Y., Yin, Z., Luo, X., Sant, G., & Bauchy, M. (2021). Using machine learning to predict concrete's strength: Learning from small datasets. *Engineering Research Express*, *3*(1).

Parida, L., & Moharana, S. (2023). A comprehensive review on piezo impedance based multi sensing technique. *Results in Engineering*, *18*(Febr, 101093.

Parida, L., Moharana, S., Ferreira, V. M., Giri, S. K., & Ascensão, G. (2022). A Novel CNN-LSTM Hybrid Model for Prediction of Electro-Mechanical Impedance Signal Based Bond Strength Monitoring. *Sensors*, *22*(24).

Spartek private limited (2024), Concrete Enhnacer., Accessed Jul, 2024., https://www.spartek.in/concrete-enhancer.php.

Wani, F. M., Vemuri, J., & Chenna, R. (2023). Prediction of storey drift for reinforced concrete structures subjected to pulse-like ground motions using machine learning classification models. *International Journal of Structural Integrity*, *August*.

Wani, F. M., Vemuri, J., Chenna, R., & Reddy, K. (2023). Investigating the efficiency of machine learning algorithms in classifying pulse-like ground motions. *Journal of Seismology*, *27*(5).

Yan, Q., Liao, X., Zhang, C., Zhang, Y., Luo, S., & Zhang, D. (2022). Intelligent monitoring and assessment on early-age hydration and setting of cement mortar through an EMI-integrated neural network. *Measurement: Journal of the International Measurement Confederation*, *203*(September), 111984.

Yang, Y., Zhang, Y., & Tan, X. (2021). Review on vibration-based structural health monitoring techniques and technical codes. *Symmetry*, *13*(11), 1–18.

Behavior of Reinforced Concrete Deep Beams under Simultaneous Corrosion and Fatigue Loading

Aamna Sarfaraz[1*],Kizhakkumodom Venkatanarayanan Harish [2]

[1] Ph.D. Student, Kanpur, India
Email: aamna@iitk.ac.in.com
[2] Associate Professor, Kanpur, India
Email: kvharish@iitk.ac.in

[*]Corresponding author

ABSTRACT

The corrosion of reinforcement in reinforced concrete structures has a significant impact on their performance and serviceability. This is particularly evident in coastal areas, where structures such as bridges are exposed to two critical factors throughout their service life: cyclic loads and chloride-induced corrosion. Cyclic loading, induced by repetitive stress, leads to damage accumulation in both concrete and steel components and bond loss between them. While corrosion of rebars results in loss of cross-sectional area, cracking in the cover, and a reduction in bond at the concrete/steel interface. The present study investigates the performance of reinforced concrete beams under the simultaneous influence of cyclic load and chloride corrosion. To simulate realistic conditions, beam specimens were subjected to cyclic loading, and the tensile rebars were artificially corroded using the impressed current technique. The research aimed to evaluate the structural behavior of the RC beams, examining cracking patterns, strain development in concrete and steel components, and deflection response. The synergy of corrosion and cyclic loading resulted in a noteworthy reduction in the fatigue life of the RC beams. This finding underscores the critical interplay between corrosion-induced degradation and the structural implications of fatigue loading in reinforced concrete structures. The study emphasizes the importance of addressing both factors for ensuring the long-term durability and performance of such constructions.

KEYWORDS: *Corrosion, RC deep beam, Fatigue, fracture, Simultaneous effect*

1. Introduction

Reinforced concrete (RC) structures such as highways experiences fluctuating loads throughout their operational lifespan. These structures often exhibit premature failure before completing their designed service life. Extensive literature has explored the detrimental impact of fatigue-induced degradation in structures, including the accumulation of damage in materials and the progressive bond loss at the concrete/rebar interface (Carpinteri et al. (2005), Coca et al. (2011), Dekoster et al. (2003)).Throughout service life of these structures, they are also susceptible to corrosion due to presence of chloride ions from seawater which causes bond degradation between the concrete and reinforcement (Fang et al. (2004); Zhao and Lin (2018)), deterioration in mechanical strength of rebars (Val and Chernin (2009)) and cracking in cover (Li et al. (2006)) ultimately led to overall deterioration of the structural performance. Researchers commonly induce corrosion in beams prior to subjecting them to fatigue loading however, real-world conditions often involve concurrent degradation due to both fatigue and corrosion. Studies by (Yi et al. (2010) and Oyado et al. (2003)) investigated the fatigue performance of corroded reinforced concrete beams and observed that corrosion of rebars decreased the fatigue life of beams which may lead to brittle failure mode at higher corrosion levels. The corrosion reduced the yield strength and elongation of steel rebar. Ma et al. (2014) formulated a model to predict the fatigue life of an aging reinforced concrete beam, considering both general and pitting corrosion of rebars. This simultaneous impact has the potential to intensify deterioration in structures compared to the individual effects of corrosion and fatigue load. Although some theoretical models have been proposed to evaluate this coupled effect (Bastidas-Arteaga et al. (2009), Yang

et al. (2017)) Notably, these studies have been confined to slender beams, and the impact of simultaneous action on deep beams (a/d<2 according to ACI 318-08 and AASHTO LRFD 2008) has been seldom investigated. Deep beams are extensively employed as structural members in various applications, including bridge girders, foundations, and offshore structures, due to their ability to support substantial loads over short spans. The separate investigation of deep beam's behavior under aforementioned effects is essential. Deep beams, are characterized by non-linear stress distribution, shear dominance over flexure, and the dowel action of tensile flexural reinforcement, exhibit distinct failure modes. These failure modes include 1) inclined crushing in the compression zone around the loading point, 2) Fatigue fracture of Stirrups, or 3) Fatigue fracture of tensile reinforcement (Fathalla and Mihaylov (2023), Ismail et al. (2017), Mohamed et al. (2020); Okamura and Ueda (1982)). The presence of rebar corrosion can alter these failure mechanisms, as demonstrated by Zhu et al. (2015), where the failure mode shifted from shear-dominated (arch effect) to flexure under static loading conditions.

This experimental study investigates the behaviour of RC deep beams subjected to the combined effects of corrosion and fatigue loading. Tensile reinforcements were artificially corroded using an impressed current technique, with current levels ranging from 0.5 to 4.5 A, corresponding to corrosion current densities of 400–4000 µA/cm². The beams were subjected to sinusoidal fatigue loading, varying between 10% and 60% of the ultimate load capacity at a frequency of 3 Hz. The performance assessment focused on failure modes, the progression of deflections, and strain degradation under simultaneous corrosion and fatigue damage. The results demonstrated that simultaneous corrosion significantly impacts the failure behaviour and reduces the fatigue life of deep beams.

2. Experimental program

2.1 Materials and Design of RC beam

In present study, Concrete mix-proportions was taken as 1.00:1.35:1.62 (by weight), i.e., ratio of cement: sand: stone. The w/c was considered as 0.31 and 53 grade Ordinary Portland cement (OPC) as per IS 269 specification was used. The 28-day compressive strength of 150 mm cube concrete was determined according to the IS 516 specification and found to be 55.5 MPa. A Fe 500 grade steel was used in the beam as reinforcement. The average yield and tensile strength of the rebars was found to be 524 and 597 MPa, respectively.

The beam specimens were designed for flexure having a span of 1500 mm and a cross section of 150 mm (b) × 250 mm (d) with two rebars of diameter 12 mm and 8 mm used for tension and compression reinforcement, respectively. For shear reinforcement, 6-mm double legged rebars with a spacing of 140 mm were provided along the length, ensuring adequate shear strength in accordance with the IS 456:2000 specification. The shear span-to-depth ratio was 1.6. The tensile bars were bent at one end of the beam to create a standard hook, while at the opposite end, they were extruded by 150 mm and connected with wires to facilitate corroding them externally for applying electric current.

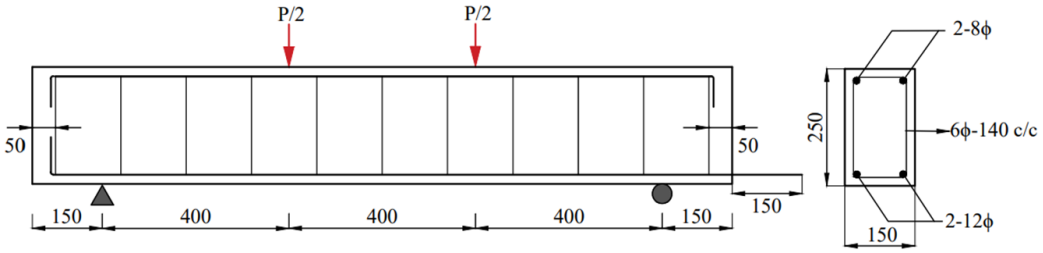

Figure 1. Geometrical and reinforcement details of RC beam specimen

Note: All dimensions are in mm

The instrumentation of the specimen included the measurements of strain and mid-span deflection. Prior to the concrete pouring, precautions were taken to electrically insulate the shear stirrups from tensile reinforcement by applying epoxy at the contact locations. Extruded bars were sealed with pipes to avoid any possibility of corrosion from contact with water. Rebar's surface was ground to ensure optimal bonding with the attached strain gauge. Electrical resistance strain gauges (gauge length of 5 mm and Resistance

350 ±1.0 Ω and 60 mm manufactured by Tokyo Sokki Kenkyujo Co., Japan were used. Two 5 mm strain gauges were attached to each tensile bar at the mid-point location and one strain gauge (Gauge length 60 mm and Resistance 120±0.3 Ω) was attached at the top surface of specimen. Linear variable differential transducers (LVDTs), with accuracy of ±0.01 mm, were used for deflection measurement. For simultaneous specimens, the LVDT was fixed at the top surface to account for corrosion pond located at the bottom. Data from strain gauges, LVDTs and the load cell were recorded at a sampling rate of 200 readings per second using the data acquisition system.

2.2 Test set up

The test setup for simultaneous corrosion and fatigue load is illustrated in Fig. 2. A reservoir filled with a 5% NaCl solution, was constructed for this purpose. A submersible motor pump, equipped with motor capable of lifting water, was employed to circulate the electrolyte from reservoir during the testing. A rectangular frame made of steel rod is fixed around the beam and an irrigation pipe is installed along the beam around the beam specimen, featuring spray nozzles on both sides. These nozzles were placed in proximity to the rebar surface to ensure electrolyte presence. A stainless-steel plate was utilized as cathode. A sponge was sandwiched between the bottom surface of specimen and the cathode plate for establishing a proper electric circuit between the anode (tensile rebars) and the cathode plate. To cover the lower part and half of the sides of the beam, a highly absorbent microfiber towel was used. Cotton tapes were sewn across the width of the towel at close intervals to ensure a secure grip between the beam and the towel. Subsequenlty, the tape ends were tightly fastened to the beam.Tensile rebars were corroded by applying varying magnitude of current ranging from 0.5 A to 4.5 by utilizing a DC power supply.

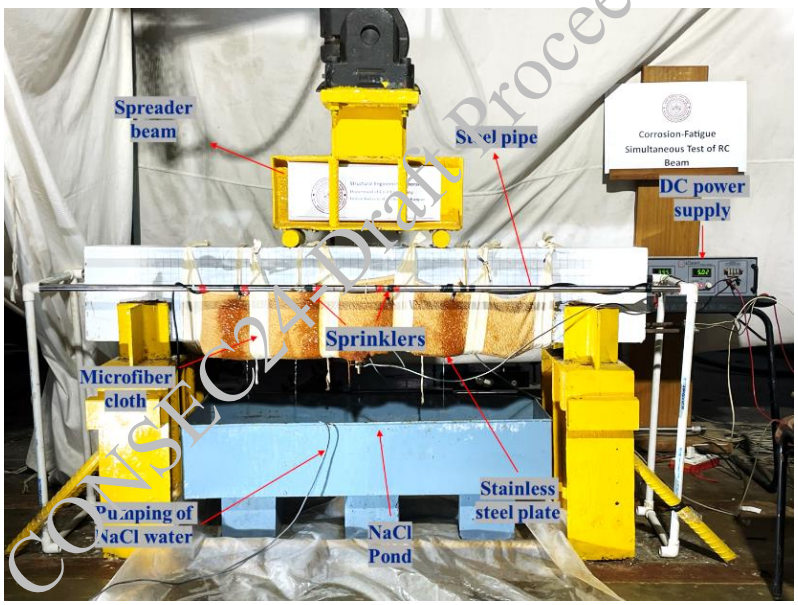

Figure 2. Set-up for simultaneous fatigue and corrosion test

3. Results and discussions

The static flexure behavior of beam was assessed through 4-point loading of specimens at a displacement rate of 0.5 mm/minute. Based on the ultimate load capacity (P_u) obtained from test, a sinusoidal cyclic load was applied at frequency of 3Hz using an MTS -servo hydraulic actuator under load control. Initially, specimens were gradually loaded to the mean, followed by fluctuation of a constant to achieve the desired stress range of $0.1P_u$-$0.6P_u$ The load was applied on a steel transfer beam, which conveyed it onto the RC beam specimen in two points spaced 400 mm apart. The beam specimen was simply supported with a span length of 1200 mm and the distance between support and point load as 400 mm. In total, 7 beam specimens were tested under different loading conditions: 2 beams under static,2 beams under fatigue loading and 3 beams under simultaneous fatigue and corrosion (CCF series). Two control beam specimens were tested till failure under four-point bending load and the average of the ultimate load capacity was obtained as 137

kN. Load values corresponding to stress range of 10% and 60% were calculated as 13.7 kN and 82.1 kN, respectively.

3.1 Failure Mode

Usually, the initiation of fatigue crack in reinforcement governs the ultimate failure of RC beam. Fig. 3(a) shows the crack observed in the surface of rebar extracted from corroded specimens after the failure of specimen. It can be seen that fatigue cracks initiated from the root of the transverse ribs which is primarily attributed to the presence of higher stress intensity at that location. It was observed that all the specimens exhibited failure due to the fatigue fracture of tensile reinforcing bars Fig 3(b). Furthermore, the critical section for control specimen going through the location of rebar fracture, was situated in the shear zone at the line of load, as shown in Fig. 4(a). It was observed that the critical section in corroded specimens was situated in the flexure zone (Specimen CC1 is shown as an illustration purpose).

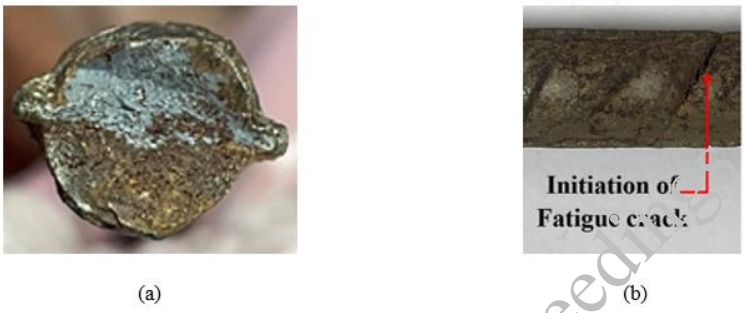

Figure 3. Photograph showing (a) Fracture surface (b) Crack initiation in rebar under fatigue loading in corroded specimens

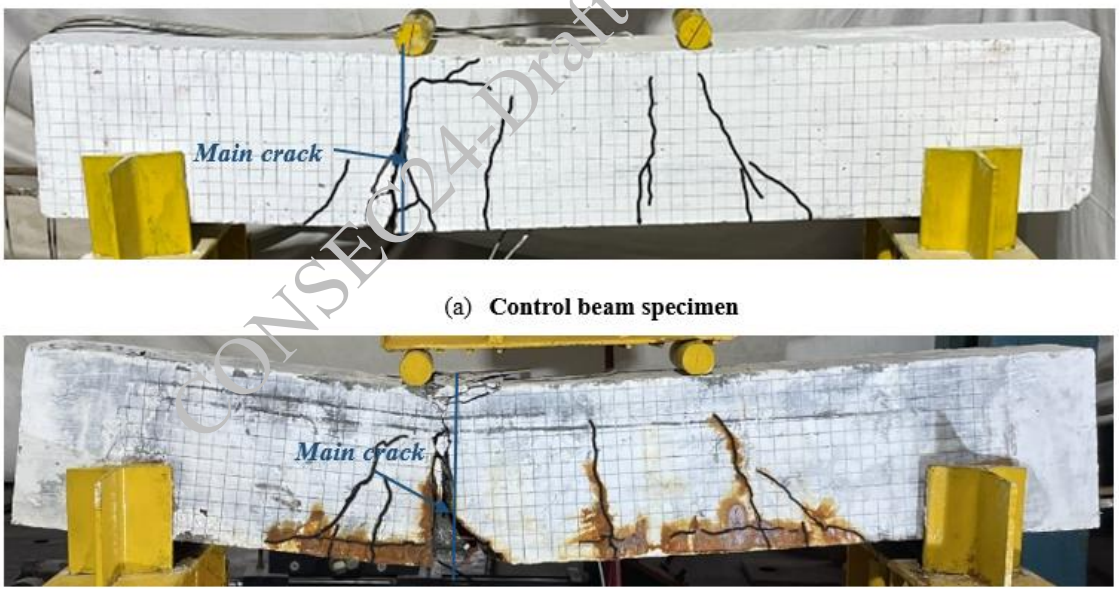

Figure 4. Crack patterns at fatigue failure of specimens

3.2 Structural behaviour under simultaneous corrosion and fatigue loading

3.2.1 Deflection

The evolution in the deflection response with increasing the load cycles is shown in Fig. 5. In the initial cycles, there is a significant rise in deflection across all specimens, attributed to a reduction in stiffness due to cracking in tension zone. Once the cracks reached a stabilized state, deflections exhibited a slower growth

rate on increasing cycles, indicating a gradual fatigue-induced degradation of materials. Subsequently, as the loading cycles reached the failure, the cracks widened, leading to an upward shift of the neutral axis, and resulting in the sudden jump in deflection. This three-stage development is commonly referred to as 'S curve' response in fatigue which indicates the continuous degradation in beam's stiffness.CCF series specimens exhibited a faster decrement in the deflection indicating higher degradation under simultaneous action. On increasing the corrosion current, the rate of deflection also increased which signifies a substantial degradation in the beam's performance resulting from the combined impact of corrosion and cyclic load.

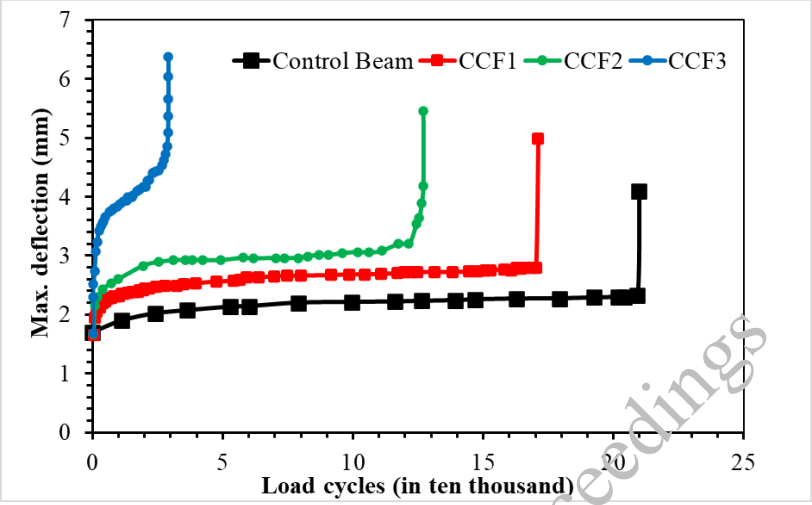

Figure 5. Evolution of deflection maximum load level with increasing load cycles

3.2.2 Fatigue life

Table 1 presents the fatigue life of the beam specimens obtained from cyclic test. The fatigue life of control specimens was recorded as 209868. It can be observed that increasing the corrosion current resulted in reduced fatigue life.

Table 1. Results of fatigue test specimens

Specimen ID.	Fatigue life (n)	Time (hrs.)	Current (amp)	Current density (µamp/cm^2)
Control Beam	209868	19.4	--	--
CCF1	171137	15.8	0.5	402
CCF2	126881	11.7	2.5	2011
CCF3	29110	2.7	4.5	3619

3.2.3 Strain

Fig. 6 presents the concrete strain recorded at the top compression zone in the mid-span. Strain gauges affixed to the tensile rebars were ineffective for CCF series specimens due to dissolution of steel during corrosion. The concrete strain increased with increasing the number of load cycles, attributed to accumulated fatigue damage of material and bond between concrete and rebars. In CCF series specimens, the strain exhibited a more rapid increase compared to Control Beam specimens.

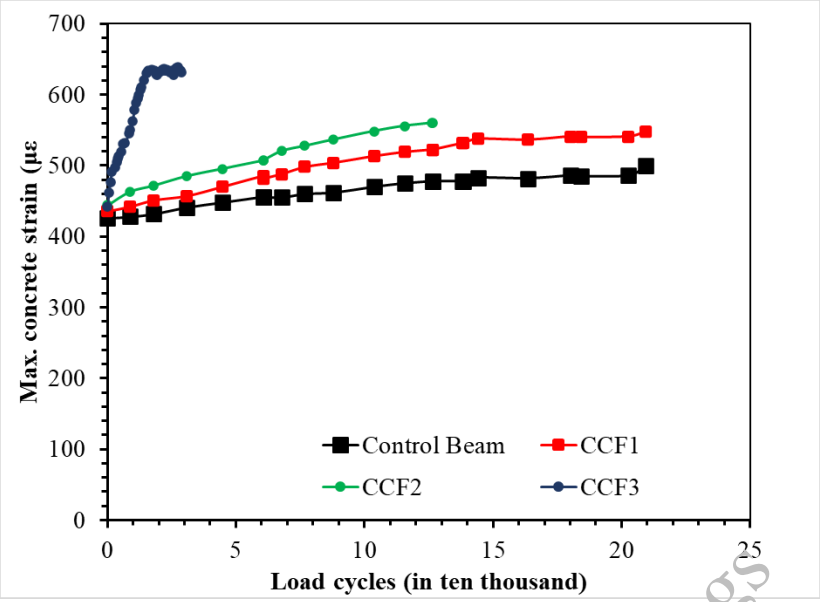

Figure 6. Evolution of strain at max. load load level with increasing load cycles

3.3 Corrosion characteristics of rebars

Fig. 7 illustrates the variation in the diameter of the in one of the tensile rebar along the length, extracted from the specimen after fatigue failure. It was observed that there is an increased rusting evident near the cracks in the beam specimen developed during fatigue loading. Furthermore, a significant reduction in the rebar's cross-sectional area is observed at the fracture location.

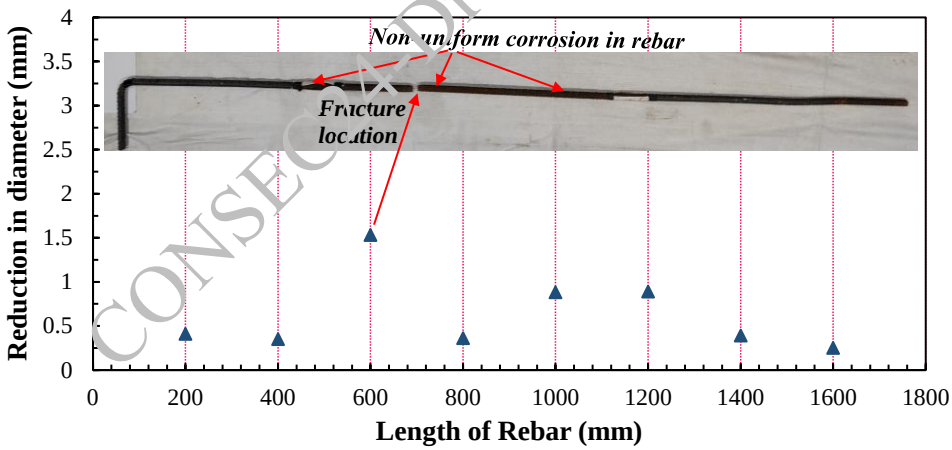

Figure 7. Typical rust distribution in CCF1 series specimen

4. Conclusions

The present investigation focused on understanding the performance of deep beams exposed to the synergetic influence of corrosion and fatigue loads. The impact of simultaneous degradation was examined in terms of failure mode, evolution in structural responses (deflections and concrete strain), stiffness degradation. Based on the obtained results, the following conclusions have been drawn:

- The failure mechanism of deep beams under fatigue loads is complex as indicated by comparing the failure behavior with beam loaded gradually till failure (static). Although beam exhibited ductile behavior under static loads, its behavior becomes rather more complex during fatigue, with rebar fracture occurring at section lying at the boundary of shear and flexure zone.

- The complexities in behavior of deep beams were intensified when corrosion occurred simultaneously, as observed by change in the cracking pattern of corroded specimen. In most of the specimens, the location of the critical section shifted towards the flexure zone. Furthermore, the interaction of corrosion-induced cracks has played a significant role in influencing the failure behavior of the deep beams
- The simultaneous occurrence of rebar corrosion led to substantial reduction in the mechanical response of deep beams including their fatigue life.

References

Bastidas-Arteaga, E., Bressolette, P., Chateauneuf, A., & Sánchez-Silva, M. (2009) "Probabilistic lifetime assessment of RC structures under coupled corrosion–fatigue deterioration processes". *Structural safety*,31(1), 84-96.

Carpinteri, A., Spagnoli, A., & Vantadori, S. (2005) "Mechanical damage of ordinary or prestressed reinforced concrete beams under cyclic bending", *Engineering fracture mechanics*,72(9), 1313-1328.

Chun-Qing, L., Melchers, R. E., & Jian-Jun, Z. (2006). "Analytical model for corrosion-induced crack width in reinforced concrete structures",*ACI structural journal*,103(4), 479.

Coca, F. O., Tello, M. L., Gaona-Tiburcio, C., Romero, J. A., Martínez-Villafañe, A. B. E. M., & Almeraya-Calderón, F. (2011) "Corrosion fatigue of road bridges: A review", *International Journal of Electrochemical Science*,6(8), 3438-3451.

Dekoster, M., Buyle-Bodin, F., Maurel, O., & Delmas, Y. (2003). "Modelling of the flexural behaviour of RC beams subjected to localised and uniform corrosion",*Engineering Structures*,25(10), 1333-1341

Fang, C., Lundgren, K., Chen, L., & Zhu, C. (2004) "Corrosion influence on bond in reinforced concrete", *Cement and concrete research*, 34(11), 2159-2167.

Fathalla, E., & Mihaylov, B. (2023). Fatigue behavior of deep concrete beams with critical shear cracks", *Structural Concrete*, 24(6), 7314-7333

Ismail, K. S. (2016) Shear behaviour of reinforced concrete deep beams(Doctoral dissertation, University of Sheffield).

Ma, Y., Xiang, Y., Wang, L., Zhang, J., & Liu, Y. (2014). Fatigue life prediction for aging RC beams considering corrosive environments",.*Engineering Structures*,79, 211-221.

Mohamed, A. M., Mahmoud, K., & El-Salakawy, E. F. (2020). Behavior of simply supported and continuous concrete deep beams reinforced with GFRP bars", *Journal of Composites for Construction*, 24(4), 04020032.

OYADO, M., HASEGAWA, M., & SATO, T. (2003). "Characteristics of fatigue and evaluation of RC beam damaged by accelerated corrosion".*Quarterly Report of RTRI*, 44(2), 72-77.

Val, D. V., & Chernin, L. (2009) "Serviceability reliability of reinforced concrete beams with corroded reinforcement", *Journal of structural engineering*,135(8), 896-905.

Yang, D. H., Yi, T. H., & Li, H. N. (2017). "Coupled fatigue-corrosion failure analysis and performance assessment of RC bridge deck slabs", *Journal of Bridge Engineering*,22(10), 04017077.

Yi, Weijian & Kunnath, Sashi & Sun, Xiaodong & Shi, Caijun & Tang, Fujian. (2010). Fatigue Behavior of Reinforced Concrete Beams with Corroded Steel Reinforcement", *ACI Structural Journal*. 107.

Zhao, Y., & Lin, H. (2019). The bond behaviour between concrete and corroded reinforcement: state of the art.

Zhu, W., François, R., Cleland, D., & Coronelli, D. (2015). Failure mode transitions of corroded deep beams exposed to marine environment for long period", *Engineering Structures*, 96, 66-77.

Enhancing Durability and Corrosion Resistance of Cementitious Composites with CA/Al-LDH Coated Biochar

Claudiane M. Ouellet-Plamondon[1], Saee Dharmadhikari[2], Balasubramanya Manjunath[3], Vellanki Lakshmi[2] and Chandrasekhar Bhojaraju[3*]

[1] Department of Construction Engineering, University of Quebec, École de technologie supérieure (ÉTS), 1100 Notre-Dame West, Montréal, QC, H3C 1K3, Canada
[2] Department of Chemistry, National Institute of Technology Karnataka, Surathkal, India.
[3] Department of Civil Engineering, St. Joseph Engineering College, Vamanjoor, Mangaluru, Karnataka, India.
Email:chandrasekhar.b@sjec.ac.in

*Corresponding author

ABSTRACT

This study investigates the effects of biochar and Ca-Al layered double hydroxide (LDH) modified biochar on cementitious composites. Characterization techniques, including FT-IR, BET, and SEM, revealed significant changes in surface functionalities, surface area, and morphology of the modified materials. The incorporation of biochar and LDH-biochar into cement mortars resulted in improved mechanical properties, with 2% LDH-biochar showing optimal performance in both compressive and tensile strengths. Water absorption tests indicated that 2% biochar and LDH-biochar mortars exhibited the lowest absorption rates. While biochar increased chloride ion penetration, LDH-biochar significantly improved chloride resistance, with 2% LDH-biochar showing a 36.4% reduction in rapid chloride permeability test values. Half-cell potential measurements demonstrated that 2% LDH-biochar composites had the most favorable and stable electrochemical properties over time. These findings suggest that LDH-modified biochar, particularly at 2% dosage, has potential applications in enhancing the performance and durability of cementitious materials, as well as in environmental remediation and electrochemical devices

KEYWORDS: *Ca-Al layered double hydroxide, biochar, Half-cell potential, Durability, Corrosion*

1. Introduction

On a global scale, the construction industry confronts a significant challenge in balancing the increasing demand for infrastructure with a pressing need to reduce its environmental impact (Rees 1999). Cement production, a cornerstone of modern construction, is a key contributor to global carbon dioxide (CO_2). According to a recent finding from the International Energy Agency, worldwide CO_2 emissions reached a record high level of 33 billion metric tons in 2019. The product of cement contributed approximately 8% of the anthropogenic emissions (Benhelal, Shamsaei et al. 2021). The alarming statistics highlight the urgent need for innovative solutions to reduce the carbon footprint of cementitious materials while maintaining and enhancing their performance.

In recent years, incorporating biochar in cementitious composites has gained significant attention as a potential strategy for carbon sequestration within the construction industry (Danish, Mosaberpanah et al. 2021). Biochar is a unique bio-renewable resource produced through the pyrolysis of biomass. Studies showed that adding biochar could greatly cut down on greenhouse gases. One ton of biochar could reduce around 900 kg of CO_2 (Roberts, Gloy et al. 2010). Wang et.al (Wang, Chen et al. 2020) demonstrated that incorporating even a small amount of biochar (1%) into cement composites resulted in a 10% increase in compressive strength. Moreover, it represents one of the most cost-effective methods of carbon capture storage and utilization. However, incorporating biochar in cementitious composites presents its own set of challenges. The high carbon content of biochar imparts conductive properties to cementitious composites. The amount of biochar can adversely affect the concrete's durability and corrosion resistance, which are crucial for the long-term performance of concrete structures. To address this limitation, this study

introduces a novel approach i.e., the use of Calcium/Aluminium Layered Double Hydroxide (CA/Al-LDH) Coated Biochar as an additive in cementitious composites (Chi, Huang et al. 2024). The CA/Al-LDH coating is designed to modify the surface properties of biochar, potentially enhancing its compatibility with the cementitious composite and improving its overall performance as an additive. This CA/Al-LDH modified biochar aims to provide the carbon sequestration benefits of biochar while addressing its adverse effects on concrete durability and corrosion resistance.

The primary objective of the study is to systematically assess the impact of incorporating various percentages (1%, 2%, and 3%) of both neat and CA/Al-LDH coated biochar on the mechanical, durability, and corrosion properties of cementitious composites. Absorption tests and resistivity measurements were used to assess the durability of the composites. Corrosion resistance was examined through the Rapid Chloride Permeability Test (RCPT) and half-cell potential measurements. In addition to this, mechanical characteristics, including compressive and tensile strength, were also thoroughly investigated.

By exploring this novel approach, we aim to develop more sustainable and durable construction materials. As the world faces the dual challenges of climate change and urbanization, innovations in sustainable construction materials become increasingly crucial. This research offers practical solutions for reducing the construction industry's carbon footprint and enhancing the durability of infrastructure, leading to high-performance cementitious composites.

2. Materials and methods

Ordinary Portland cement (OPC) confirming to IS standard was used as a primary binder. Fine aggregate (natural river sand) with a fineness modulus of 2.8 and a specific gravity of 2.65 was considered for the present investigation. All reagents and solvents used in the synthesis procedures were of >99% purity and used as received without further purification.

2.1 KOH Activation on Arecanut Husk

Ten grams of husk underwent acid treatment by refluxing in 200 mL of 1M HCl solution at 120°C for 3 hours. Following this, the husk was subjected to alkaline treatment, first with 200 mL of 15% Na2CO3 solution under reflux conditions for 4 hours, then with 200 mL of 1M KOH solution under stirring for 24 hours. The final step involved pyrolysis of the treated husk at 550°C for 2 hours, yielding 2.517 g of KOH-activated biochar. It's worth noting that after each chemical treatment step (HCl, Na_2CO_3, and KOH), the obtained mixture was filtered, washed with distilled water to neutralize the pH, and then dried at 120°C for 15-24 hours before proceeding to the next stage.

2.2 Synthesis of Ca-Al Layered Double Hydroxides on Biochar and KOH activated biochar

The synthesis of Ca-Al Layered Double Hydroxides (LDH) was performed on both KOH-activated (Taer, Febriyanti et al. 2021) and neat biochar using a similar procedure. In a 250mL beaker, 1.81g of $AlCl_3 \cdot 6H_2O$ was dissolved in 5 mL of distilled water. To this solution, 500mg of biochar (either KOH-activated or neat) was added and sonicated for 30 minutes to ensure thorough mixing of particles. Subsequently, 3.3g of $Ca(OH)_2$ was introduced and stirred, maintaining an Al: Ca molar ratio of 1:3.

The resulting mixture underwent an aging process, which involved oven-drying at 60°C for 2 hours. The dried mixture was carefully scraped from the beaker and washed with distilled water to remove clogged pores. The obtained precipitate was then covered with a watch glass and oven-dried at 60°C for 24 hours.

For the neat biochar composite, an additional washing step with distilled water was performed, followed by another 24-hour drying period at 60°C. Both composites were then ground using a mortar and pestle. The final products were grey-white coloured composites. The KOH-activated biochar composite yielded 3.80g (Shen and Fu 2018), while the neat biochar composite yielded 4.10g of material.

2.3 Preparation of Biochar-Modified Cementitious Composites

Biochar-modified cementitious composites were prepared using ordinary Portland cement (OPC), sand, and synthesized biochar materials. The mixes used are presented in Table 1. For each mix, a water-to-binder ratio of 0.5 was maintained. The dry ingredients (cement, sand, and biochar) were mixed thoroughly in a laboratory mixer for 2 minutes. Water was then added gradually while mixing continued for an additional 3 minutes to ensure homogeneity (Manjunath, Ouellet-Plamondon et al. 2023). The fresh mortar was cast into 50 mm cube moulds for compressive strength testing and a 50x100mm cylinder for tensile testing.

70mm cubes are used for resistivity and water absorption. For RCPT studies, mortar discs of 100 mm diameter and 50 mm thickness were cast for each mix. The fresh mortar was poured into cylindrical moulds and compacted using a vibrating table to ensure uniform density and remove entrapped air. To assess the corrosion resistance of the biochar-modified cementitious composites, samples were prepared for half-cell potential measurements (Bhojaraju, Mousavi et al. 2023). Cylindrical moulds with internal dimensions of 100 mm diameter and 200 mm height were used. A 10 mm diameter steel reinforcing bar was positioned centrally in each mould. The steel bar was cleaned thoroughly to remove any rust or scale, then degreased with acetone. The bar was positioned to extend 25 mm from the bottom of the mould and 25 mm from the top, leaving 150 mm embedded in the mortar.

Figure 1. Process to prepare Ca/Al-layered double hydroxide biochar

Table 1. Details of the mixes

Mix	Cement	Biochar	Water	Sand
Ref	1	0	0.5	2
1-B	1	1%	0.5	2
2-B	1	2%	0.5	2
3-B	1	3%	0.5	2
1-LDH-B	1	1% - M	0.5	2
2-LDH-B	1	2% - M	0.5	2
3-LDH-B	1	3% - M	0.5	2

3. Results and discussions

3.1 FT-IR Spectroscopy of biochar and modified biochar

FT-IR analysis was employed to determine the functional groups on the surfaces of biochar (BC), KOH-activated biochar (ABC), Ca-Al layered double hydroxides on biochar (LDH), and Ca-Al layered double hydroxides on activated biochar (ALDH). As illustrated in Fig. 2(A), the spectra reveal distinct characteristics for each material. Biochar exhibited relatively weak peaks at 1597 cm^{-1} and 1030 cm^{-1}, corresponding to -C=C- vibrations and -Si-O- bonds from ash content, respectively. In contrast, KOH-activated biochar showed more pronounced and well-defined peaks. Notable features include intense signals at 1059 cm^{-1} and 850 cm^{-1} (attributed to -Si-O- bonds in ash), 1030 cm^{-1} (-C-O bond), 1622 cm^{-1} (carbon-to-carbon triple bonds), and 686 cm^{-1} (aliphatic -C-H). The spectrum of Ca-Al LDH BC revealed a small peak at 3522 cm^{-1}, indicative of -OH stretching vibrations. For Ca-Al LDH on activated KOH

biochar (ALDH), several characteristic peaks were observed: 1422 cm^{-1} (-CH_2 vibrations), 520 cm^{-1} (symmetrical stretching and -Al-O bending), and 773 cm^{-1} (Ca-O lattice vibrations). Additionally, a minor peak at 3637 cm^{-1} was attributed to -OH stretching vibrations. These spectral features provide insights into the surface functionalities and structural changes resulting from the various treatments applied to biochar materials.

3.2 BET - Brunauer, Emmet and Teller

The pore size and surface area of the prepared composites were analyzed using BET N_2 adsorption-desorption tests. The results revealed significant changes in surface characteristics across the different materials. A notable threefold increase in surface area was observed from pristine biochar (10.586 m^2/g) to Ca-Al layered double hydroxide on biochar (LDH) (30.337 m^2/g). This substantial increase can be attributed to the intercalation of layered double hydroxides between biochar particles, which introduces additional adsorption sites and enhances the overall active surface area. KOH-activated biochar exhibited a twofold increase in surface area (18.334 m^2/g) compared to pristine biochar, likely because of the KOH treatment process. This activation method is known to develop porosity and increase surface area in carbonaceous materials. Pore size analysis revealed a significant increase in average pore radius from pristine biochar (23.7 Å) to LDH (64.86 Å). This dramatic enlargement in pore size can be attributed to the water-washing treatment employed during the synthesis process. This step effectively removes clogged materials from the pores, resulting in larger, more accessible pore structures and enhancing the material's adsorption capacity. These findings highlight the effectiveness of both LDH incorporation and KOH activation in modifying the surface characteristics of biochar, potentially improving its performance in various applications. Table 2 shows the surface area of the different samples of biochar.

3.3 Scanning electron microscopy of modified and unmodified biochar

Scanning electron microscopy (SEM) analysis revealed distinct morphological characteristics of biochar and LDH-modified biochar. Fig. 2(B) displays the unmodified biochar, characterized by a layered arrangement of thin sheets typical of biomass-derived biochar. This structure indicates the material's inherent porosity and contributes to its high surface area, properties that make it valuable for various applications, including as an additive in cementitious composites. In contrast, Fig. 2(C) presents the LDH-modified biochar, exhibiting a markedly different surface morphology. The most prominent feature is the presence of numerous needle-like structures uniformly distributed across the biochar particles' surface. These needle-shaped formations are characteristic of layered double hydroxide (LDH) crystals grown on the biochar substrate, indicating a successful modification process.

The LDH needle-like structures are expected to enhance the surface area and reactivity of the modified biochar compared to its unmodified counterpart. This morphological change may significantly impact the material's interactions with the cement matrix when used as an additive in cementitious composites, potentially affecting strength, durability, and ion exchange capacity. These SEM images provide clear visual evidence of the structural differences between biochar and LDH-modified biochar, demonstrating the efficacy of the modification process and suggesting potential performance enhancements in various applications.

Table 2. Surface area of the different samples of biochar

Sample/Tests	Biochar	LDH	KOH-activated Biochar	CA-LDH on KOH Biochar
Average pore radius (Å)	23.75	38.00	63.45	64.86
Total pore volume (cc/g)	1.25×10^{-2}	5.76×10^{-2}	5.81×10^{-2}	3.67×10^{-2}
Surface area (m^2/g)	10.58	30.33	18.33	11.31

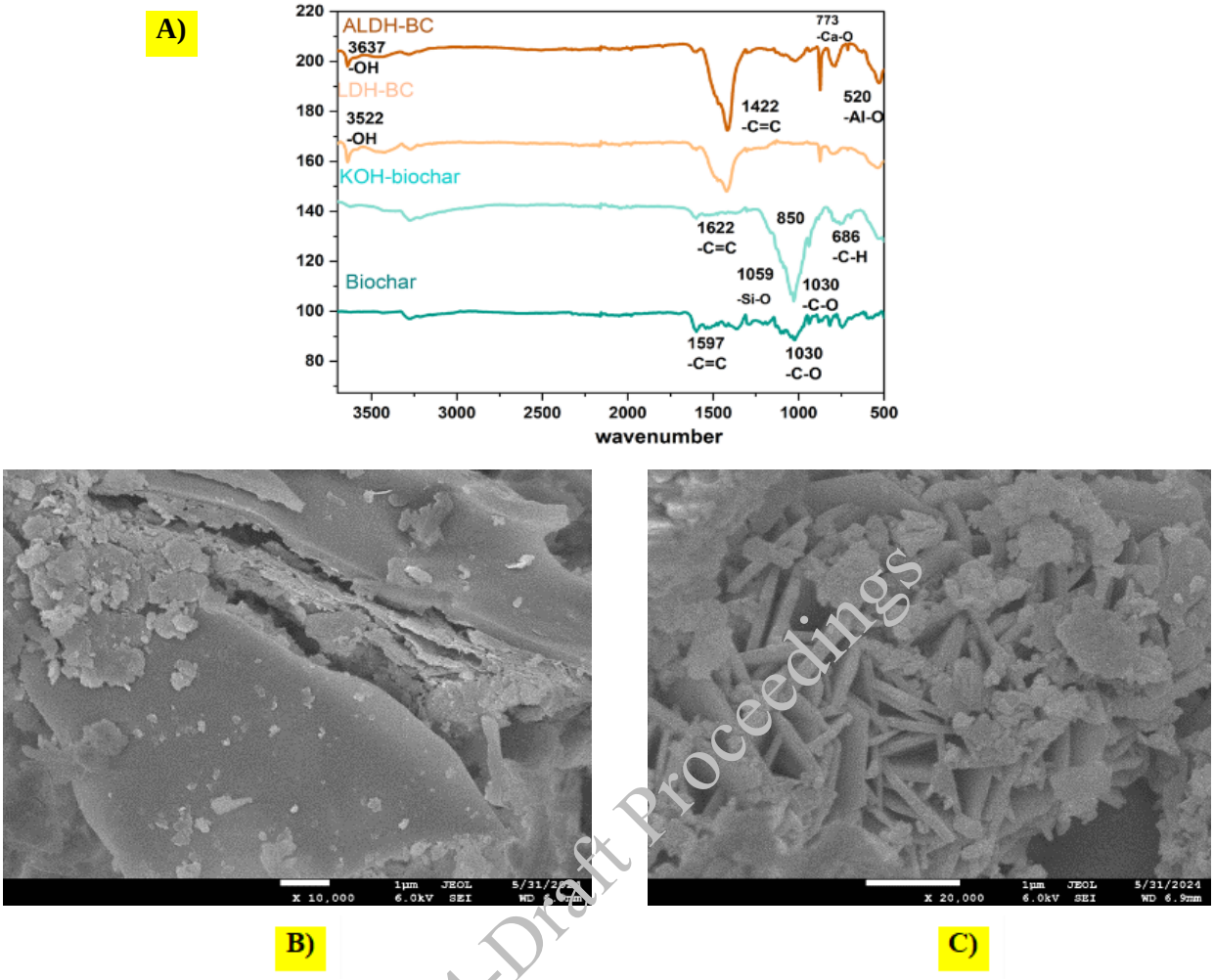

Figure 2. A) FT-IR Spectra of different adsorbents, B) SEM image of biochar, C) SEM image of LDH biochar

3.4 Mechanical characteristics of modified and unmodified biochar

The mechanical characteristics of biochar and LDH-biochar-modified cementitious composites are presented in Fig 3(A) and 3(B). These results present increasing trends in both compression and tension. For compression strength, the 7-day strength was 25MPa, increasing to 35 MPa for 28 days. 1 and 2% biochar additions improved compressive strength (28 MPa and 33 MPa at seven days; 39 MPa and 42 MPa at 28 days). However, a 3% addition of biochar decreased the early strength by 16%. For 28 days, there was an improvement compared to 7 days results. However, LDH biochar modifications significantly improved for 7 and 28 days. A similar tendency was also observed for tensile strength. The 7-day reference tensile strength was 3.6 MPa, increasing to 4.0 MPa at 28 days. Biochar-modified cement showed improvements across all percentages at 7 days (4.0 MPa, 4.4 MPa, and 3.8 MPa for 1%, 2%, and 3%, respectively) and further increases at 28 days (4.3 MPa, 4.8 MPa, and 4.4 MPa). These enhancements are attributed to biochar's filler effect and water retention properties. For LDH-modified biochar, the enhanced reactivity is because of additional nucleation sites and improved dispersion. The optimal dosage is around 2% for both types, balancing the benefits of biochar addition with potential adverse effects at higher percentages. The LDH modification proves particularly effective in improving both early-age and 28-day strengths for compressive and tensile properties.

3.5 Water absorption of biochar and LDH biochar-modified concrete

The water absorption characteristics of biochar and LDH biochar-modified cementitious composites are presented in Fig. 3(C), 3(D), and 3(E). Mortars with 1% and 3% biochar showed higher water absorption than the reference. In comparison, those with 2% demonstrated lower absorption. For 1% biochar-modified mortars, the increased water absorption is due to the hydrophilic nature of biochar particles, which can act

as water reservoirs within the matrix (Gupta, Kua et al. 2018). At 3% biochar content, the higher absorption is due to increased porosity resulting from the agglomeration of biochar particles. Interestingly, the 2% biochar-modified mortars show lower water absorption. This is mainly because of the optimal distribution of biochar particles, which lowers the porosity of the paste, reducing permeability and water absorptivity (Senadheera, Gupta et al. 2023).

LDH-Biochar modified displays a different trend. For 1% and 2%, LDH biochar mortars exhibit lower water absorption than the reference sample. It is attributed to the synergistic effect of LDH and biochar. LDH might enhance the dispersion of biochar particles and contribute to pore refinement, resulting in a denser microstructure that decreases the porosity of mortars. However, at 3% LDH-modified biochar content, the water absorption nearly equals that of the reference sample. It may be because of particle agglomeration or excessive void creation.

3.6 Electrical resistivity of biochar and LDH-modified biochar cement mortars

Fig. 3(F) presents the electrical resistivity of biochar and LDH-modified biochar cement mortars. The biochar-modified mortars consistently exhibit lower resistivity compared to a reference, with 3% biochar demonstrating lower resistivity values (42.6% to 61.3% reduction at 28 days). This may be attributed to the formation of the conductive network in mortar samples. However, LDH biochar-modified mortars exhibit an increasing resistivity trend with the addition of biochar, peaking at 2% before slightly decreasing at 3%. The intercalation of ions within the LDH layers may create barriers to electron flow, effectively increasing the overall electrical resistivity of the mortar matrix. Additionally, LDH's ability to refine the pore structure of the cement paste could lead to a more discontinuous network of conductive pathways.

3.7 Rapid chloride penetration of biochar and LDH-modified biochar cement mortars

Fig. 3(G) presents the RCPT (Rapid Chloride Permeability Test) values of biochar and LDH-modified biochar cement mortars. The results show significant variations in chloride ion penetration resistance among the different cement mortar compositions. Compared to the reference sample (3375 coulombs), all biochar-modified mortars (1-B, 2-B, 3-B) exhibited higher RCPT values, indicating increased chloride ion penetration. The increases were 13.8% for 1-B (3840 coulombs), 34.2% for 2-B (4530 coulombs), and a substantial 63.6% for 3-B (5520 coulombs). This trend depicts that increasing biochar content may lead to an increase in interconnected pore networks, facilitating easier chloride ion movement. Meanwhile, the LDH-modified mortars showed improved chloride ion resistance, with RCPT values lower than the reference. The reductions were 20.9% for 1-LDH-B (2670 coulombs), 36.4% for 2-LDH-B (2145 coulombs), and a slight improvement of 4.0% for 3-LDH-B (3510 coulombs). The enhanced performance of LDH-modified mortars, particularly 1-LDH-B and 2-LDH-B, can be attributed to the ion-exchange capacity of Calcium/Aluminium Layered Double Hydroxide, which may trap chloride ions and reduce their overall penetration.

3.8 Half-cell potential of biochar and LDH-modified biochar cement mortars

Fig. 3(H) presents Half-cell potential of biochar and LDH-modified biochar cement mortars. The results show that half-cell potentials of biochar and LDH-biochar composites become more negative over time, with plain biochar samples exhibiting more pronounced changes than LDH-biochar composites. Increasing biochar content from 1% to 2% generally leads to more negative potentials in plain samples, while the 2% LDH-biochar composite consistently demonstrates the least negative potentials among all samples. This suggests an optimal ratio of LDH to biochar for favorable electrochemical properties. The addition of LDH appears to moderate the electrochemical behavior and enhance stability over time. These findings have potential implications for various applications, including soil amendment, electrochemical devices, and contaminant remediation. Further research is needed to fully understand the mechanisms behind these observations and their practical significance.

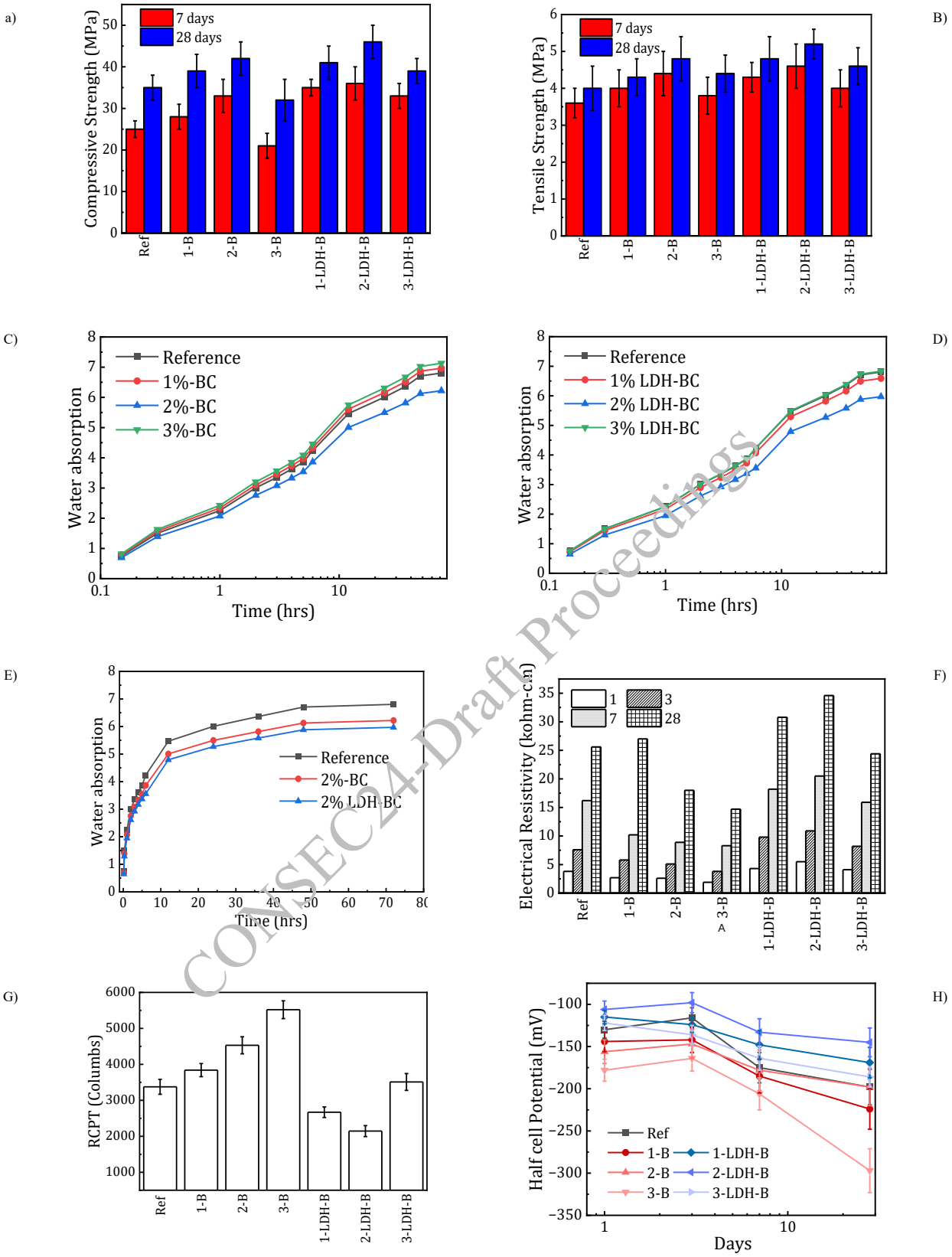

Figure 3. (A) (B) Mechanical characteristics, (C) (D) (E) Water absorption characteristics. (F) Electrical resistivity, (G) Rapid Chloride Penetration, (H) Half-cell potential

4. Conclusions

- 1. Adding biochar, especially LDH-modified biochar at an optimal dosage of 2%, significantly improves the compressive and tensile strengths of cement composites at both early (7-day) and later (28-day) stages. LDH biochar modifications demonstrate superior performance due to enhanced reactivity, dispersion, and hydration processes, indicating its potential as an effective strength-enhancing additive in cement-based materials.
- 2. The optimum percentage for water absorption is observed at 2% for neat and LDH-modified biochar.
- 3. The incorporation of biochar and LDH-biochar in cementitious mortars significantly alters their electrical resistivity, with biochar decreasing resistivity due to its conductive nature, while LDH-biochar increases resistivity, likely due to LDH's ion intercalation and pore refinement effects.
- 4. While biochar incorporation led to increased chloride ion penetration, with higher biochar content resulting in greater permeability, LDH modification demonstrated improved chloride resistance. The LDH-modified mortars, particularly 2-LDH-B with a 36.4% reduction in RCPT values, showed the most promising results
- 5. The study reveals that 2% LDH-biochar composite exhibits the most favorable and stable electrochemical properties over time, suggesting an optimal composition for potential applications in soil amendment, electrochemical devices, or environmental remediation.

Acknowledgments

The authors thank St Joseph Engineering College, Mangaluru, Karnataka, for their support throughout the research. The authors are grateful to the National Institute of Technology, Surathkal, Karnataka, for providing help with the SEM and FTIR facilities.

References

Benhelal, E., et al. (2021). "Challenges against CO2 abatement strategies in cement industry: A review." *Journal of Environmental Sciences* **104**: 84-101.

Bhojaraju, C., et al. (2023). "Influence of GGBFS on corrosion resistance of cementitious composites containing graphene and graphene oxide." *Cement and Concrete Composites* **135**: 104836.

Chi, L., et al. (2024). "Heavy metal immobilization of LDH@ biochar-containing cementitious materials: Effectiveness and mechanisms." *Cement and Concrete Composites* **152**: 105667.

Danish, A., et al. (2021). "Reusing biochar as a filler or cement replacement material in cementitious composites: A review." *Construction and Building Materials* **300**: 124295.

Gupta, S., et al. (2018). "Use of biochar as carbon sequestering additive in cement mortar." *Cement and Concrete Composites* **87**: 110-121.

Manjunath, B., et al. (2023). "Potential utilization of regional cashew nutshell ash wastes as a cementitious replacement on the performance and environmental impact of eco-friendly mortar." *Journal of Building Engineering* **66**: 105941.

Rees, W. E. (1999). "The built environment and the ecosphere: a global perspective." *Building Research & Information* **27**(4-5): 206-220.

Roberts, K. G., et al. (2010). "Life cycle assessment of biochar systems: estimating the energetic, economic, and climate change potential." *Environmental science & technology* **44**(2): 827-833.

Senadheera, S. S., et al. (2023). "Application of biochar in concrete–A review." *Cement and Concrete Composites*: 105204.

Shen, Y. and Y. Fu (2018). "Advances in in situ and ex situ tar reforming with biochar catalysts for clean energy production." *Sustainable Energy & Fuels* **2**(2): 326-344.

Taer, E., et al. (2021). "Enhancing the performance of supercapacitor electrode from chemical activation of carbon nanofibers derived Areca catechu husk via one-stage integrated pyrolysis." *Carbon Letters* **31**: 601-612.

Wang, L., et al. (2020). "Biochar as green additives in cement-based composites with carbon dioxide curing." *Journal of cleaner production* **258**: 120678.

Monte Carlo Simulation of the Hydraulic Diffusivity Function for Water Absorption in Fieldcrete

Mahesh Kumar[1], Kaustav Sarkar[2*]

[1] Research Scholar, School of Civil and Environmental Engineering, IIT Mandi, India, Email: d22042@students.iitmandi.ac.in
[2] Associate Professor, School of Civil and Environmental Engineering, IIT Mandi, India, Email: srkr@iitmandi.ac.in

*Corresponding author

ABSTRACT

Water absorption plays a crucial role in affecting the durability performance of concrete. The phenomenon is widely represented using Richard's equation with an exponential hydraulic diffusivity function as the transport parameter. Deterministic evaluation of this parameter based on laboratory experiments provides only a single value outcome and fails to account for the sources of variability inherent to the onfield concrete-making practice. In this paper, a basic Monte Carlo Simulation (MCS) is performed to assess the uncertainty associated with the hydraulic diffusivity function based on the tolerance limits of curing age, cement, water, and aggregate contents as permitted by the relevant standards of practice for fieldcrete. The mean values of sorptivity, cement, water, and aggregate contents adopted to implement the analysis correspond to a typical ordinary Portland cement concrete of 0.4 *w/c* and 100±5 mm slump. The MCS analysis reveals that the degree of hydration of cement and the capillary porosity of concrete, which serve as intermediate variables for the calculation of hydraulic diffusivity follow Weibull and generalized extreme value distributions, respectively. The results show that hydraulic diffusivity computed using the approximate analytical model of Lockington et al. (1999), follows a lognormal distribution at every saturation level and exhibits a decreasing COV as the latter increases. The COV values vary from 43.00% in the capillary saturated state to 69.80% in the completely dry state. The results indicate the need to consider hydraulic diffusivity function as an uncertain quantity while estimating water absorption profiles in concrete.

KEYWORDS: *Concrete, Hydraulic diffusivity, Monte Carlo Simulation, Sorptivity, Uncertainty.*

1. Introduction

Water intrusion in concrete significantly influences its long-term durability by directly affecting the microstructure or by facilitating the migration of detrimental species that cause subsequent deterioration (Sarkar and Bhattacharjee (2016)). Under service conditions, water absorption in unsaturated concrete acts as the dominant mode of transport and is widely represented using Richard's equation (Eq. 1) (Cerny and Rovnanikova (2002), Hall and Hoff (2021)).

$$\frac{\partial \theta_n}{\partial t} = \frac{\partial}{\partial x}\left(D(\theta_n)\frac{\partial \theta_n}{\partial x}\right) \quad (1)$$

where θ_n is the degree of saturation defined as $\theta_n=\theta/\theta_s$, θ (m^3/m^3) is the volumetric moisture content in unsaturated conditions, θ_s (m^3/m^3) is the volumetric moisture content at saturation, $D(\theta_n)$ (m^2/s) is the hydraulic diffusivity of concrete, and x (m) and t (s) are the space and time coordinates, respectively. $D(\theta_n)$, a measure of water transport through capillarity, is typically described by a highly non-linear function of θ_n. It governs the shape of the moisture intrusion profile and the depth of water penetration, making it an essential factor in determining the water transport behavior of concrete. An estimate of $D(\theta_n)$, needed at the stage of design, is typically obtained based on the deterministic value of sorptivity determined using laboratory samples which do not account for the variabilities associated with the onfield concrete making

(fieldcrete) process. Zhao et al. (2015) have highlighted that even the natural and measurement variabilities associated with the transport and storage properties of porous building materials can be significant and this may sometimes lead to unexpected performance results. The deviations may be even more pronounced when the variabilities associated with fieldcrete are also considered (Poyet et al., (2019)). This aspect has not been adequately researched as most of the previous studies have focused on the assessment of inherent variabilities and their influence on the performance parameters. For instance, Li et al. (2018) used the probabilistic Monte Carlo Simulation (MCS) method to estimate the hydraulic conductivity of concrete considering inherent variabilities in mortar matrix and interfacial transition zone (ITZ) properties, reporting a COV of around 36%. Similarly, Yang et al. (2021) employed MCS to analyze the uncertainty associated with the sorptivity of concrete and found that it has a COV value of 22%. In another study, Holm and Kuenzel (2002) investigated the impact of variations in transport properties, such as heat conductivity, vapor diffusion resistance, porosity, etc. on the drying process of autoclaved aerated concrete revealing a maximum deviation of 12-14% in the simulated water content. In this paper, a probabilistic Monte Carlo method is employed to quantify the uncertainties associated with the $D(\theta_n)$ of concrete, considering variations in the weight batching of concrete ingredients, curing age, and the reproducibility of sorptivity value based on pertinent standards and research literature.

2. Methodology

2.1 Mathematical Models

The application of the probabilistic MCS method for the uncertainty estimation of $D(\theta_n)$, which is commonly expressed as an exponential function of θ_n as given by Eq. (2a), requires a function relating the parameters D_0 and n with factors, such as water content (w, kg/m^3), cement content (c, kg/m^3), coarse and fine aggregate contents ($M_{fa,}$ and $M_{ca,}$ kg/m^3), and curing age (t_{cure}, days), which usually vary within the specified tolerance limits for fieldcrete. Lockington's approximate analytical method for the solution of Eqs. (1) and (2a) lead to Eq. (2b), relating D_0 and n, with sorptivity ($S_{c,}$ $m/s^{0.5}$ at θ_i), saturation, and initial (θ_s and $\theta_{i,}$ m^3/m^3) moisture contents. This method of assessing the diffusivity is widely accepted and accurate, having less than 1% absolute relative error (Lockington et al. (1999)). If the moisture content at saturation is assumed to be equal to the capillary porosity of concrete ($\theta_s \approx \Phi_c$), then, θ_s in Eq. (2b) can be calculated using Eqs. (3a) and (3b) after Neville and Brooks (2010) and Kondraivendhan and Bhattacharjee (2010) which incorporate the factors of w/c, M_{fa}/c, M_{ca}/c, a/c, and t_{cure}. Here it is to be noted that Eq. (3b) does not account for the effect of temperature and is valid until attaining a maximum degree of hydration of unity or (w/c)/0.36.

$$D(\theta_n) = D_0\, e^{(n\theta_n)} \quad (2a)$$

$$D_0 = \frac{n^2 S_c^2}{(\theta_s-\theta_i)^2.[e^{n}(2n-1)-n+1]} \quad (2b)$$

$$\Phi_c = \frac{\frac{w}{c}-0.36h+\frac{a}{c}}{0.32+\frac{1}{G_{fa}}\frac{M_{fa}}{c}+\frac{1}{G_{ca}}\frac{M_{ca}}{c}+\frac{w}{c}+\frac{a}{c}} \quad (3a)$$

$$h = 0.217\, ln\left(\frac{w}{c}\right) + 0.06\, ln(t_{cure}) + 0.618 \quad (3b)$$

where, the exponent n varies from 6 to 8 for porous building materials (Hall and Hoff (2021)), D_0 (m^2/s) is the diffusivity coefficient, a/c is air content per unit mass of cement, G_{fa} and G_{ca} are the specific gravity of fine and coarse aggregates, respectively, and h is the degree of hydration of ordinary Portland cement.

2.2 Experimental Data

In this study, a concrete mix of 0.4 w/c has been adopted for the analysis because commonly used structural grade concretes have a w/c close to this value. The mix design data and sorptivity value have been obtained from Korakuti (2022). The specific gravity of ingredients and mixture composition are presented in the

second and third columns of Table 1. A coarse-to-fine aggregate ratio of 1.22 was adopted by Korakuti (2022) to obtain an optimum packing density of 0.68, which along with a superplasticizer dosage of 0.06% of cement mass resulted in a slump value of 100±5 mm and a 28-day compressive strength of 40.79 MPa. Three cylinders of 100 mm diameter and 100 mm height were cast and specimens of 50 mm height were extracted from the middle portion of each cylinder for the measurement of sorptivity. The preconditioning of specimens was carried out in a step drying manner, involving oven-drying for 7 days at 60°C, followed by an increase in temperature of 5°C each day until reaching a maximum of 105°C which was subsequently maintained until specimen mass became constant. The capillary absorption test was performed in accordance with ASTM C1585 at 20°C, and the mean of three replicates was reported to be 1.22×10^{-5} m/s$^{0.5}$.

Table 1. Proportions, tolerances, and deviations of mix ingredients

Ingredient	Specific Gravity	Proportion (kg/m^3)	Tolerances (%) [lower limit, upper limit]	Standard Deviation = (upper limit – lower limit)/6
Water	1.00	201.93	±1 [199.91, 203.95]	0.67
Cement	3.13	504.83	±1 [499.78, 509.88]	1.68
Coarse aggregate	2.64	914.55	±2 [896.26, 932.84]	6.10
Fine aggregate	2.58	748.27	±2 [733.30, 763.24]	4.99

2.3 MCS Method

The MCS method is a probabilistic technique used to model and analyze complex processes characterized by inherent randomness and uncertainty. It utilizes probability distribution functions (PDF) of the input parameters to generate random realizations, which ultimately provide the PDF and associated statistics of the desired output (Ang and Tang (2007)). In this study, the mass of concrete ingredients (w, c, M_{fa}, M_{ca}) have been described using normal PDFs fitted between their lower and upper thresholds corresponding to the tolerance limits specified in IS 4925 (2023) and ACI 117-10 for fieldcrete. The tolerance limits and the calculated values of deviation are given in the last two columns of Table 1. S_c has been assumed to follow a lognormal distribution with a COV of 20%, translating to a deviation of 2.44×10^{-6} m/s$^{0.5}$ (Holm and Kuenzel (2002); Zhao et al (2015); Yang et al (2021)). The parameter n has been assumed to follow a uniform distribution with lower and upper limits of 6 and 8, respectively after Yang et al (2021) leading to a standard deviation value of 0.5773 calculated as (upper limit-lower limit)/√12. t_{cure} has been assumed to follow a normal distribution with a lower limit of 7 days, as specified for OPC by IS 456 (2000), and a mean of 28 days leading to a standard deviation of 7 calculated as (mean – lower limit)/3. In the present study, the variables S_c, n and θ_s ($\approx S_c$) are assumed to be independent.

One thousand random realizations of w, c, M_{fa}, $M_{ca,}$ and t_{cure} were generated using their respective mean, deviation, and PDFs and subsequently used for the estimation of the intermediate parameters w/c, M_{fa}/c, M_{ca}/c, h, and Φ_c. The corresponding $D(\theta_n)$ values were obtained by first calculating D_0 using Eq. (2b) and then using Eq. (2a) with inputs of D_0 and n at different θ_n values ranging from 0 to 1 in steps of 0.1. The PDFs for w/c, M_{fa}/c, M_{ca}/c, h, Φ_c, and $D(\theta_n)$ were determined empirically based on the generated data and verified using the statistical Kolmogrov-Smirnov (K-S) goodness of fit test applied at 5% significance level. The data were fitted against the most commonly used PDFs available in the MATLAB R2023a statistical toolbox, including normal (Gaussian), lognormal, exponential, gamma, beta, uniform, Weibull, extreme value, generalized extreme value, logistic, log-logistic, t-location, Nakagami, Rayleigh, Rician, inverse Gaussian, and Birnbaum-Saunders distributions.

3. Results and Discussion

The minimum, maximum, mean, and deviation of data generated for w/c, M_{fa}/c, M_{ca}/c, h, Φ_c, and $D(\theta_n)$ are presented in Table 2 along with the corresponding deterministic values which follow from the data presented in Section 2.1. A better insight into the variability of the intermediate parameters can be obtained by evaluating their distributions. Although w, c $M_{fa,}$ and M_{ca} have been assumed as normal variates, the analytical determination of the PDFs for w/c, M_{fa}/c, M_{ca}/c, h, $\Phi_{c,}$ and $D(\theta_n)$ is a formidable task. However, with MCS random realizations can be utilized to address the problem empirically. The obtained histograms and PDFs along with the fitted parameter values for the intermediate parameters are presented in Fig. 1. It can be seen that the normal PDF (Eq. 4) with a mean (μ) and standard deviation (σ) describes w/c, M_{fa}/c,

and M_{ca}/c satisfactorily at 5% significance level. Besides the normal PDF, lognormal, Birnbaum-Saunders, gamma, Rician, t-location, Nakagami, and inverse Gaussian distributions were also found to be suitable to describe these parameters. However, a normal PDF is relatively more intuitive to comprehend and shows that the possible range of values that these parameters can assume are symmetrically distributed about their deterministic values. Fig. 1 also reveals that h and Φ_c follow two special cases of extreme value distribution (Eq. 5) involving location (α), scale (β), and shape (γ) parameters. Depending upon the value of γ, GEV can lead to type I ($\gamma = 0$), type II ($\gamma>0$), or type III ($\gamma<0$) families of distributions (Kotz and Nadarajah (1999)). Here, h follows the Weibull distribution (Eq. 6), which with somewhat modified forms of the parameters belongs to the family of type III distributions, whereas Φ_c follows a type III distribution. This finding is in contrast to the previously reported normal (Zhao et al. (2015)) and beta (Yang et al (2021)) distributions for porosity. h and Φ_c have negatively and positively skewed distributions respectively with lower and upper end points typical of a type III distribution. Thus, it can be interpreted that onsite variations considered in this analysis result in h and Φ_c having a higher probability of assuming values that are respectively on the lower and higher sides of their deterministic estimates. This finding indicates a deterioration in the quality of concrete.

Table 2. Results of MCS and Deterministic analyses

Factors	MCS				Deterministic
	Min	Mean	Max	Deviation	
w/c	0.3943	0.4000	0.4058	0.0019	0.4
M_{fa}/c	1.4437	1.4818	1.5206	0.0113	1.4822
M_{ca}/c	1.7629	1.8119	1.8520	0.0134	1.8115
h	0.4541	0.6176	0.6541	0.0165	0.6191
Φ_c	0.0834	0.0897	0.1191	0.0030	0.0894
D_0 (m^2/s)	1.03×10^{-11}	7.27×10^{-11}	4.36×10^{-10}	5.07×10^{-11}	6.4×10^{-11}
$D(\theta_n = 1)$ (m^2/s)	1.28×10^{-08}	7.13×10^{-08}	2.46×10^{-07}	3.06×10^{-08}	7.09×10^{-08}

$$f(x) = \frac{1}{\sigma\sqrt{2\pi}} e^{\frac{-(x-\mu)^2}{2\sigma^2}} \tag{4}$$

$$f(x) = \left(\frac{1}{\beta}\right) e^{\left(-\left(1+\gamma\left(\frac{x-\alpha}{\beta}\right)\right)^{-\frac{1}{\gamma}}\right)} \left(1+\gamma\left(\frac{x-\alpha}{\beta}\right)\right)^{-1-\frac{1}{\gamma}} \quad \text{for } 1+\gamma\left(\frac{x-\alpha}{\beta}\right) > 0 \tag{5}$$

$$f(x) = \begin{cases} \frac{\gamma}{\beta}\left(\frac{x}{\beta}\right)^{\gamma-1} e^{-\left(\frac{x}{\beta}\right)^{\gamma}} & \text{if } x \geq 0 \\ 0 & \text{if } x < 0 \end{cases} \tag{6}$$

$$f(x) = \frac{1}{\sqrt{2\pi}(\zeta x)} e^{\left[-\frac{1}{2}\left(\frac{\ln x-\lambda}{\zeta}\right)^2\right]} \quad \text{for } x \geq 0 \tag{7}$$

The random realizations of $D(\theta_n)$ obtained using Eq. (2) at different saturation levels were found to follow a lognormal distribution (Eq. 7) with parameters λ and ζ. Figs. 2 (a) and 2 (b) show the histograms and fitted distributions of $D(\theta_n)$ for θ_n values of 0 and 1, respectively. The COV and skewness of $D(\theta_n)$ were found to decrease as θ_n increased from 0 to 0.9 with the lowest and the highest values of 0.427 and 1.28, and 0.698 and 1.92, respectively as shown in Fig. 2(c). Thus, $D(\theta_n)$ becomes more predictable and less uncertain at higher saturation level compared to drier conditions. This may be attributed to the greater influence of the complex microstructure of capillary pores on the flow phenomenon at low saturation levels when the moisture transport takes place primarily through pores of smaller sizes which exert higher resistance to the movement of water molecules due to surface forces. With an increasing degree of saturation, the flow paths through larger capillary pores become well established and the water transport mechanism shifts from surface creep to a fully developed capillary flow. A comparison of the maximum (D_{max}) and the minimum (D_{min}) values of $D(\theta_n)$ at each θ_n level from 0 to 1 in steps of 0.1 with their deterministic (D_d) counterparts is shown in Fig. 2(d). It can be observed that the ratio D_{max}/D_d decreases

with a decreasing rate from 7.24 at $\theta_n = 0$, to 3.50 at $\theta_n = 1$. On the other hand, the ratio of D_{min}/D_d increases from 0.161 at $\theta_n = 0$ to 0.200 at $\theta_n = 0.4$ and then gradually decreases to 0.183 at $\theta_n = 1$. This behavior emphasizes the complex relationship between saturation level and the predictability of diffusivity values in concrete, revealing the deterministic approach's limitations.

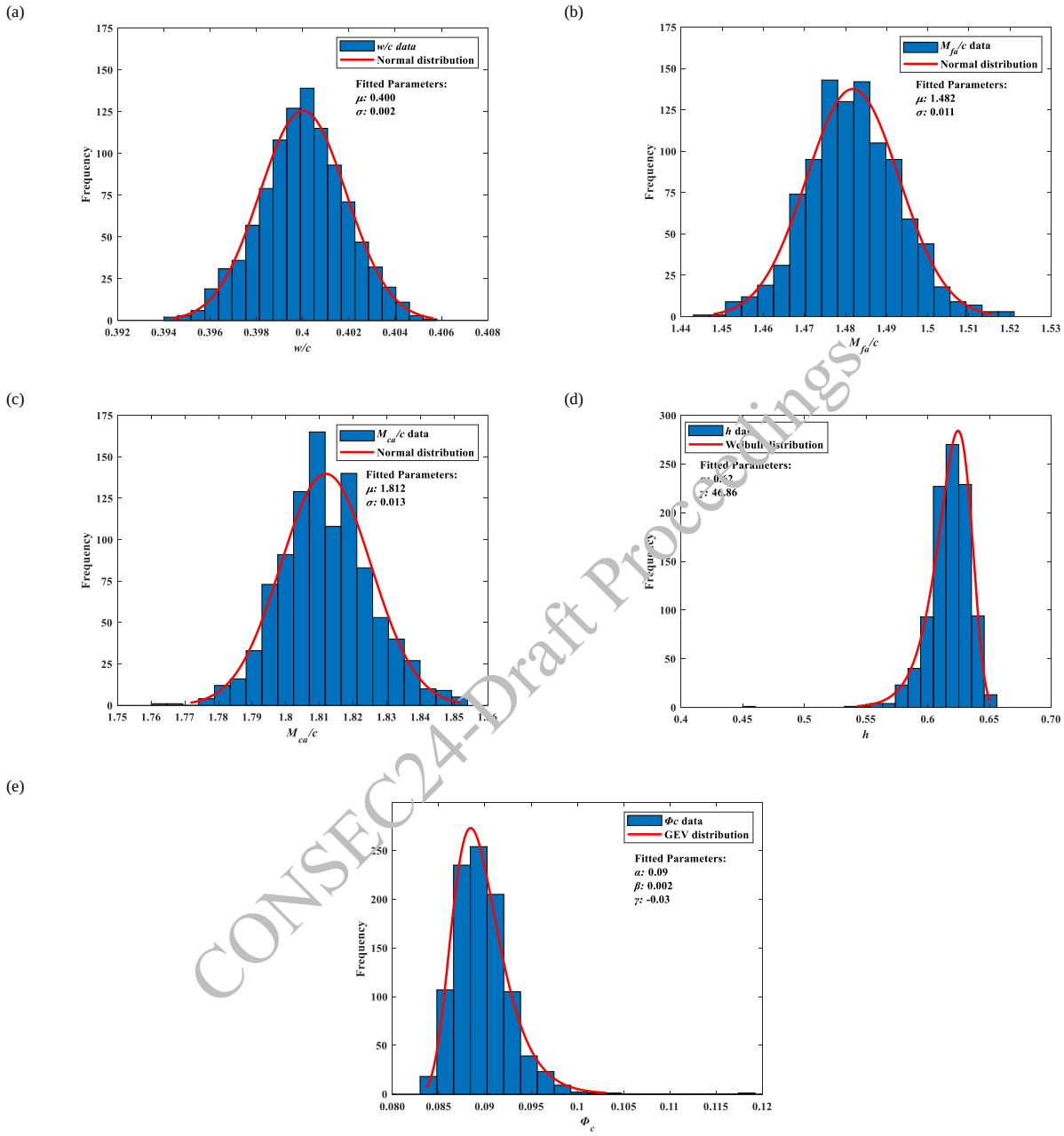

Figure 1. Histogram and PDF for (a) *w/c* ratio (b) M_{fa}/c (c) M_{ca}/c (d) *h* (e) Φ_c

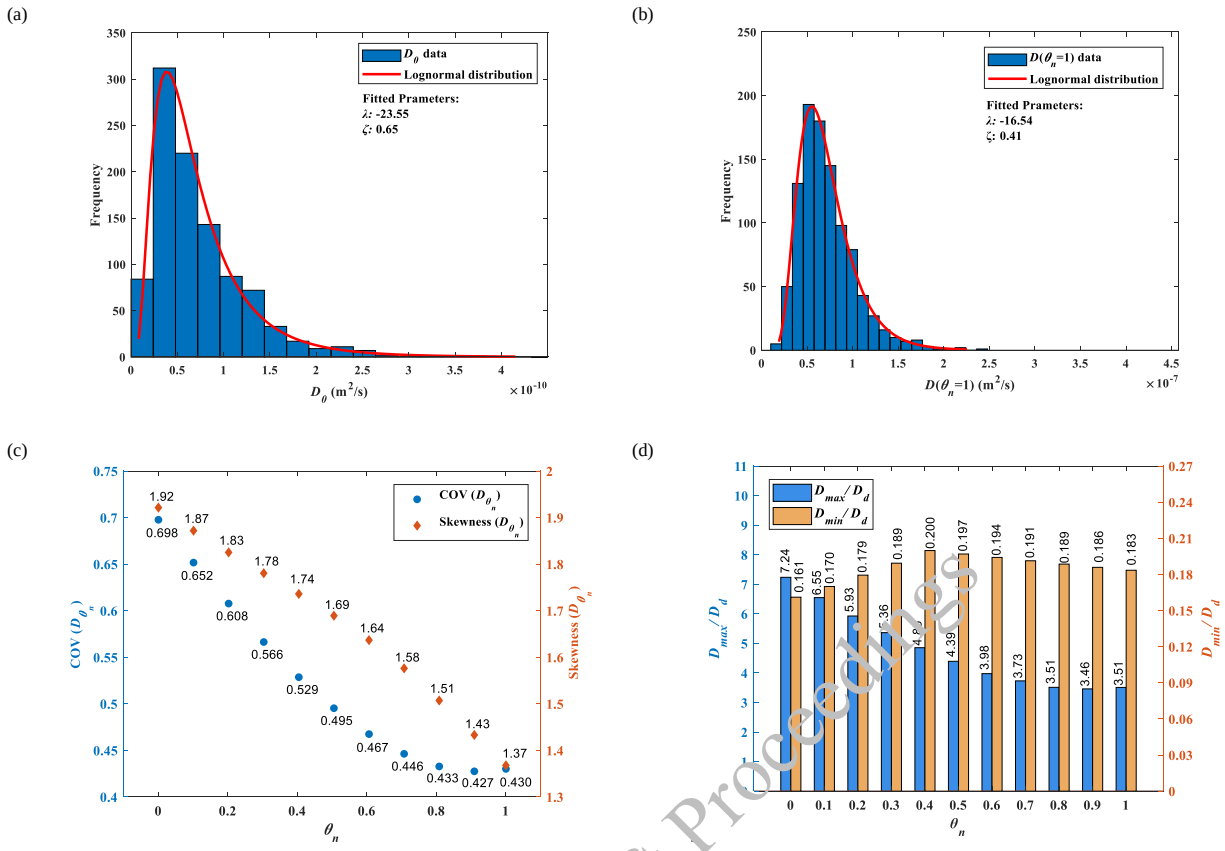

Figure 2. Histogram and PDF for (a) $D(\theta_n=0)$ (b) $D(\theta_n=1)$; (c) COV and skewness of $D(\theta_n)$ at different θ_n (d) D_{max}/D_d and D_{min}/D_d

4. Conclusions

A basic MCS was deployed to quantify the uncertainty associated with the hydraulic diffusivity of fieldcrete considering the variations in the weight batching of concrete ingredients, curing age, and the reproducibility of sorptivity value based on pertinent standards and research literature. Random realizations of the input factors were generated to capture their onfield variability assuming the distribution for mass of concrete ingredients and curing age to be normal and that for the sorptivity to be lognormal. The results of the MCS analysis lead to the following conclusions.

- Normal PDFs can be used to describe w/c, M_{fa}/c, and M_{ca}/c. Other PDFs can also empirically fit these parameters but are less intuitive and more complex.
- The degree of hydration of cement was found to follow a negatively skewed Weibull distribution with a COV of 2.67%. This finding was unreported in previous literature and is expected to be useful for future probabilistic studies.
- The porosity of concrete, which incorporates the combined effect of w/c, M_{fa}/c, M_{ca}/c, and t_{cure} was found to follow a positively skewed generalized extreme value distribution with COV of 3.34%. This is in contrast to the previously reported normal and beta distributions for porosity.
- The quality of concrete deteriorates as a consequence of onsite variations considered in this study. This is reflected in h and Φ_c having a higher probability of assuming values that are respectively on the lower and higher sides of their deterministic estimates.
- The diffusivity at all saturation levels exhibits a lognormally distributed variation with COV decreasing from 69.80% at $\theta_n = 0$ to 43.00% at $\theta_n = 1$. Thus, $D(\theta_n)$ becomes less uncertain at higher degree of saturation.
- The comparison of deterministic diffusivity values with probabilistically obtained maximum and minimum diffusivity values across the range of $\theta_n = 0$ to 1 reveals that the maximum value (at $\theta_n = 0$) is 7.34 times and the minimum (at $\theta_n = 0.4$) is 0.199 times of the deterministic value. This discrepancy

highlights the limitations of the deterministic approach in capturing the variability of concrete properties, emphasizing the need for probabilistic methods in concrete durability assessments.

In the absence of a reliable model relating S_c with *w/c*, t_{cure} and cement type, the MCS implemented in this study assumes S_c to be independent of these variables. Thus, the reported variations of $D(\theta_n)$ are on the conservative side. Furthermore, the study can be extended to incorporate the variations that may be induced due to on-site factors such as compaction quality, curing conditions and other time-dependent changes in the concrete microstructure for a wider range of concrete mixes. Advanced MCS methods with modified sampling techniques can also be adopted to reduce computational expenses.

Acknowledgments

The authors acknowledge the grant (CRG/2023/001443) provided by SERB, DST for the project "Study of Meso-climatic influences on the hygrothermal state of concrete exposed to natural environment & their modelling for pragmatic durability design".

References

ACI 117-10 (2015) "Specification for Tolerances for Concrete Construction and Materials and Commentary", *American Concrete Institute, Farmington Hills, MI, USA.*

Ang A.H.S. and Tang W.H. (2007) "Probability Concepts in Engineering: Emphasis on Applications in Civil & Environmental Engineering", *John Wiley & Sons, INC.* River Street, Hoboken.

ASTM C1585 (2020) "Standard Test Method for Measurement of Rate of Absorption of Water by Hydraulic Cement Concretes", *ASTM International, United States*.

Cerny R. and Rovnanikova P. (2002) "Transport Processes in Concrete", *Spon Pressan imprint of the Taylor & Francis Group. 711 Third Avenue, New York, NY 10017, USA.*

Hall C. and Hoff W.D. (2021) "Water Transport in Brick, Stone and Concrete*", CRC Press 2 Park Square, Milton Park, Abingdon, UK*.

Holm A.H. and Kuenzel H.M. (2002) "Practical application of an uncertainty approach for hygrothermal building simulations-drying of an AAC flat roof", *Building and Environment* 37: 883–889.

IS 456 (2000) "Plain and Reinforced Concrete-Code of Practice", *Bureau of Indian Standards*, New Delhi, India.

IS 4925 (2023) "Concrete Batching and Mixing Plant — Specification", *Bureau of Indian Standards*, New Delhi, India.

Kondraivendhan B. and Bhattacharjee B. (2010) "Effect of Age and Water-Cement Ratio on Size and Dispersion of Pores in Ordinary Portland Cement Paste", *ACI Materials Journal* 107(19): 147-154.

Korakuti H. (2022) "Improved Modelling of Sorptivity and Hydraylic Diffusivity based on Efficient Phenomenological Considerations", *PhD Thesis, Indian Institute of Technology Mandi,* Himachal Pradesh, India.

Kotz S. and Nadarajah S. (1999) "Extreme Value Distributions: Theory and Applications", *Imperial College Press, 57 Shelton Street, Covent Garden, London.*

Li C., Baji H. and Yang S. (2018) "Probabilistic study on hydraulic conductivity of concrete at mesoscale", *ACI Materials Journal* 115(5): 717-725.

Lockington D., Parlange J. and Dux P. (1999) "Sorptivity and the estimation of water penetration into unsaturated concrete", *Materials and Structures* 32 (6): 342–347.

Neville, A.M. and Brooks J. J. (2010) "Concrete Technology", *Pearson Education Limited Edinburgh Gate England (2): 94-120.*

Poyet S., Bary B. and Coppens E. (2019) "Analysis of water transport in unsaturated conditions: Comparison between labcrete and fieldcrete", *Construction and Building Materials* 205(2): 443-455.

Sarkar K. and Bhattacharjee B. (2016) "The Role of Moisture in Degrading Concrete" *National conference on emerging trends in civil engineering, Bhilai Institute of Technology, Chhattisgarh, India*: 134-142

Yang, W., Baji, H., Li, C.Q., and Shi, W. (2021) "A Probabilistic Study on Effective Hydraulic Sorptivity of Concrete", *ACI Materials Journal* 118(6): 55-66.

Zhao J., Plagge R., Ramos N.M.M., Simoes M.L. and Grunewald J. (2015) "Concept for development of stochastic databases for building performance simulation - A material database pilot project", *Building and Environment*, 84: 189–203.

Enhancing Geopolymer Concrete Performance Using Copper Slag as a Sustainable Fine Aggregate

Aman Deep [1], Pradip Sarkar *[2]

[1] *Department of Civil Engineering, National Institute of Technology Rourkela, Odisha, 769008, India*
Email: amandeep13507@gmail.com
[2] *Department of Civil Engineering, National Institute of Technology Rourkela, Odisha, 769008, India*
Email: sarkarp@nitrkl.ac.in

*Corresponding author

ABSTRACT

Geopolymer concrete (GPC), utilizing aluminosilicate precursor materials as binders, stands as an eco-friendly alternative to ordinary Portland cement concrete (OPCC). These precursors commonly include natural resources like metakaolin, volcanic ash, and industrial solid waste such as fly ash (FA) and ground granulated blast furnace slag (GGBFS). However, despite not utilizing cement, GPC still faces environmental challenges due to the use of natural aggregates, leading to resource depletion. To mitigate this issue, researchers have explored replacing natural aggregates with waste materials, aiding both resource conservation and waste management. Copper slag (CS) is one such waste material with potential as fine aggregate in GPC. This study conducts a comprehensive evaluation of FA-GGBFS-based GPC incorporating CS as fine aggregate. It was found that, GPC exhibited superior performance compared to OPCC in various aspects, including strength properties (such as compressive, split tensile and flexural strength)**,** transport properties (includes water absorption, permeable void and rapid chloride penetration test) and durability properties (like abrasion resistance and slake durability).

KEYWORDS: *Geopolymer concrete, Copper slag, Water absorption, Rapid chloride penetration test, Slake durability*

1. Introduction

Construction activity has increased dramatically in recent years in order to fulfil the ever-increasing need for infrastructure. It is clear that ordinary Portland cement-based concrete (OPCC) has become an essential and commonly used material in the majority of construction projects. The cement manufacturing process releases a significant amount of CO_2 into the environment through fuel consumption and raw material transformation. According to studies, producing one tonne of cement emits roughly the same amount of carbon dioxide into the environment (Neville (2012)). On the other hand, industrial waste generation has increased significantly, including fly ash (FA) from thermal power plants, ground granulated blast furnace slag (GGBFS) from the iron industry, red mud from the alumina industry, mine tailings from the mineral sector, Copper slag (CS) from the refining and smelting of copper ore, and so on. Environmentalists and researchers are facing significant challenges in disposing of and managing these wastes, as well as developing alternatives to cement. It is therefore extremely important to concentrate on better and more realistic methods to utilize industrial waste in the building construction. Geopolymer concrete (GPC) could be an excellent alternative to OPCC that reduces or eliminates the use of cement while also promoting the effective use of industrial waste (Turner et al (2013); McLellan et al (2011)).

Geopolymers are a class of inorganic polymers created through the alkali activation of materials rich in aluminosilicates. The process of geopolymerization involves three key stages: dissolution, condensation, and polycondensation, as described by Davidovits (2008). Typically, this reaction occurs at room temperature or higher, facilitated by alkaline activators, as noted by Verdolotti et al (2008). Common alkaline activators include alkali hydroxides (such as NaOH and KOH) and alkali silicates (like Na_2SiO_3, K_2SiO_3). However, FA-based GPC) presents two main challenges: it often requires elevated temperature curing to enhance and accelerate the geopolymerization process, and it generally yields moderate compressive strengths Fernandez et al (2008). These issues can be mitigated by incorporating GGBFS alongside FA as a binder. Remarkably, FA-GGBFS-based GPC requires ambient temperature curing and

results in reasonably high compressive strengths. The N-A-S-H (sodium-aluminium-silicate hydrate) gel structure forms in FA-based GPC, which accounts for its moderate compressive strength. In contrast, the inclusion of GGBFS leads to the development of C-A-S-H (calcium-aluminium-silicate-hydrate) and C-S-H (calcium-silicate-hydrate) gel structures, which enhance the compressive strength of the GPC (Nath et al (2014); Al-Majidi et al (2016)). However, using too much GGBFS can shorten the setting time of the GPC. Therefore, the GGBFS content in the mix should be kept 30% to maintain optimal performance (Deb et al (2014); Reddy et al (2018); Prusty et al (2020)).

CS, a waste material generated during the refining and smelting process of copper ore, could emerge as a viable competitor to natural sand (NS) in the manufacturing of GPC. India alone contributes approximately 22 million tons of the 400 million tonnes of CS produced globally annually Sharma (2022). A significant amount of CS is disposed of in landfills, occupying considerable land space and leading to the destruction of fertile topsoil. CS shares certain similarities with NS in terms of physical and chemical properties, and it also exhibits pozzolanic activity (Thomas et al (2018)). CS is reported to be used in OPCC as fine aggregate as well as binder materials as a sustainable alternative by many researchers. Also, some recent literature has attempted to use CS as a sustainable alternative to natural fine aggregate in GPC. The waste CS shows tremendous promise as an environmentally sustainable substitute in the construction sector, addressing waste management issues and conserving natural resources. While previous studies have investigated the effect of CS on certain strength and microstructural properties of GPC, many important aspects remain unaddressed. To bring this construction material into practical usage, it is crucial to thoroughly study all important aspects of this material. The associated research output will be useful in instilling confidence among stakeholders about the practical usage of this building material. The present study is a step forward in this direction which primarily focusses on three important aspects: strength, transport, and durability properties of hardened OPCC and FA-GGBFS-based GPC with varying percentages of CS in combination with NS as fine aggregates.

2. Methodology

The methodology adopted in the present study are- (i) collection of ingredients, (ii) material characterization, (iii) mix design for OPCC and GPC, (iv) specimen preparation, (v) conducting experiments, (vi) analysis of results, (vii) arrive at conclusion.

3. Experimental Program

3.1 Materials Characterization

The waste materials utilized in this study were sourced from the near vicinity of the state of Odisha, India. FA was obtained from the Rourkela Steel Plant in Rourkela, Odisha, while GGBFS was procured from Toshali Cement Private Limited in Cuttack, Odisha. CS was collected from Hindustan Copper Limited in Jharkhand. In this investigation, 20 mm nominal size graded natural coarse aggregates (NCA), conforming to IS 383 (2016), along with locally sourced river sand as fine aggregate, were used. The physical properties of the binders and aggregates are detailed in Tables 1 and 2, respectively. For the alkaline activation of the source materials, commercially available sodium hydroxide and sodium silicate with 98% purity (containing SiO_2 = 27.46%, Na_2O = 9.56%, and H_2O = 62.98%) were used, having specific gravities of 1.43 and 1.40, respectively. Additionally, 53-grade Portland cement, as per IS 12269 (1987) and ASTM C150 (2019) standards, with a specific gravity of 3.1 and normal consistency of 31%, was employed in this study. The physical appearance of FA, GGBFS, NS and CS used in this study is shown in Fig. 1.

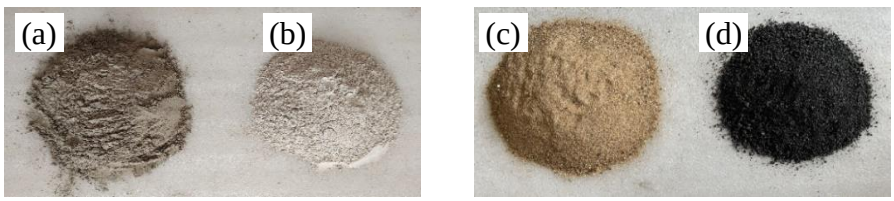

Figure 1. Physical appearance of (a) FA, (b) GGBFS, (c) NS and (d) CS

Table 1. Physical properties of binders used

Materials	Colour	Shape	Class *	Specific gravity	Specific surface (m^2/kg)	Fineness (%)	Moisture content (%)
Cement	Light greenish	Irregular	-	3.10	351	10	0.25
FA	Grey	Spherical	F	2.22	326	20	0.65
GGBFS	Off-white	Irregular	-	2.86	357	9	0.33
Max. limit	-	-	-	-	Min 320*, #	< 34*	< 2*

*IS 3812-1 (2013); *ASTM C618 (2019), #IS 16714 (2018)

Table 2. Physical properties of fine and coarse aggregates

Materials	Specific gravity	Water absorption (%)	Compacted bulk density (kg/m^3)	Fineness modulus	Material finer than 75 µm (%)
NS	2.62	0.80	1697	2.52	0.7
CS	3.90	0.40	2195	3.39	0.4
NCA	2.76	0.69	1581	7.54	-
Max. limit	-	< 2#	-	-	-

#IS 2386-3 (1963); ASTM C128 (2022)

3.2 OPCC and GPC Mix-Proportion

In the absence of established guidelines for GPC mix design, this study utilizes various references, including previous literature and current conventional cement concrete standards Pavithra et al (2016); Reddy et al (2018); ACI 211.1 (2002); IS 10262, (2019), for the design of FA-GGBFS based GPC. The ratio of the alkaline activator solution to binder solids (AAS/BS) was consistently maintained at 0.5 across all trial mixtures. A 12M NaOH solution was created by dissolving sodium hydroxide flakes in potable water, with a fixed Na_2SiO_3 to NaOH ratio of 1.5. To ensure the complete dissolution of the flakes and to manage the heat produced during the exothermic reaction, the NaOH solution was prepared 24 hours prior to casting. The combined alkaline activator solution (NaOH and Na_2SiO_3) was then mixed 3 to 4 hours before casting. The ratio of FA to GGBFS was consistently maintained at 70% to 30% in all trial mixes to achieve dense and workable GPC (Deb et al (2014); Reddy et al (2018); Prusty et al (2020)). Six distinct GPC mixes were developed by substituting NS with varying amounts of CS, labelled as GPC0, GPC20, GPC40, GPC60, GPC80, and GPC100, where the numbers represent the percentage of NS replaced with CS. Additionally, a control specimen (OPCC) composed of 100% cement, NS, and NCA was prepared using conventional cement concrete standards IS 10262 (2019) and designed to achieve a compressive strength of 40 MPa after 28 days. The mix design process was thorough and involved trial and error, considering the specific gravity of the raw materials. Table 3 outlines the detailed concrete mix proportions for the seven different combinations.

Table 3. Details of OPCC and GPC mixes (kg/m^3)

Constituents	Mix ID						
	OPCC	GPC0	GPC20	GPC40	GPC60	GPC80	GPC100
Cement	450	0	0	0	0	0	0
FA	0	315	315	315	315	315	315
GGBFS	0	135	135	135	135	135	135
NaOH	0	90	90	90	90	90	90
Na_2SiO_3	0	135	135	135	135	135	135
NS	605	643	514.4	385.8	257.2	128.6	0
CS	0	0	191.6	383.2	574.8	766.4	958
NCA	1210	1060	1060	1060	1060	1060	1060

Extra water	0	18	18	18	18	18	18
Water	180	0	0	0	0	0	0
SP	3.6	5.4	5.4	5.4	5.4	5.4	5.4

3.3 Specimen Preparation

As discussed earlier, this paper focuses on thoroughly evaluating the effect of CS on the properties of hardened FA-GGBFS-based GPC and OPCC. Laboratory experiments were carried out to examine its impact on strength characteristics (including compressive, split tensile, and flexural strengths), transport properties (such as water absorption, permeable void content, and rapid chloride penetration), and durability features (abrasion resistance and slake durability). Strength characteristics were determined through break tests. A detailed summary of the tests conducted in this research, along with the specifications of the test specimens, is provided in Table 4.

Table 4. Details of tests conducted

Sl.	Properties measured	Specimen details	Standard followed
1	Compressive strength	100 mm cube	IS 516 (1959)
2	Splitting tensile strength	100 mm dia. × 200 mm long cylinder	IS 5816 (1999)
3	Flexural strength	500 ×100 ×100 mm prism	IS 516 (1959)
4	Water absorption	100 mm cube	ASTM C642 (2013)
5	Permeable void	100 mm cube	ASTM C642 (2013)
6	Rapid chloride penetration test	Disc - 100 mm dia. × 50 mm thick	ASTM C1202 (2017)
7	Abrasion resistance test	70.6 × 70.6 × 30 mm block	IS 1237 (2012)
8	Slake durability test	40–60 g lumps	IS 10050 (1981)

4. Results and Discussions

4.1 Workability

The results, illustrated in Fig. 2, indicated a notable decline in the workability of fresh concrete as the level of CS replacement increased. This decrease was primarily due to factors such as the irregular, angular shape of CS particles and the higher specific gravity of CS compared to NS. The slump values observed for GPC with CS incorporation were in line with findings reported in Arunachelam et al (2022). However, the use of superplasticizer successfully counteracted these effects, enabling the attainment of the desired slump in GPC.

4.2 Strength Properties

The mean compressive strength of hardened OPCC and FA-GGBFS-based GPC at different curing ages was experimentally evaluated, and the results are presented in Fig. 3 for various mixes. Fig. 3 clearly indicates that substituting NS with CS significantly improves the strength characteristics of hardened concrete across all levels of CS replacement. Although both NS and CS fall within the Zone II grading limits for fine aggregates, CS is generally slightly coarser, while NS is somewhat finer. The combination of CS and NS results in a well-graded fine aggregate mix, leading to enhanced particle packing compared to using NS alone. This improved grading, along with the possible presence of natural pozzolanic properties in CS, contributes to the superior strength observed in GPC containing CS. As the proportion of CS increases, so does the strength of the GPC. However, this positive trend starts to reverse when the CS replacement exceeds 60%. At higher levels of replacement, the introduction of coarser particles from CS may disrupt the optimal grading of the fine aggregate mix. Additionally, the lower water absorption capacity of CS results in excess water surrounding the fine aggregate particles in fresh GPC mixes. This surplus water increases void content and weakens the interfacial transition zone in the hardened GPC, potentially reducing its strength. Despite these challenges, it's important to note that GPC specimens with any percentage of CS replacement consistently show better strength than the control specimens using NS alone. Notably, a substantial increase of 26-29% in compressive strength, 24-28% in tensile strength, and 19-27% in flexural strength was observed in GPC60 compared to the control specimen (OPCC).

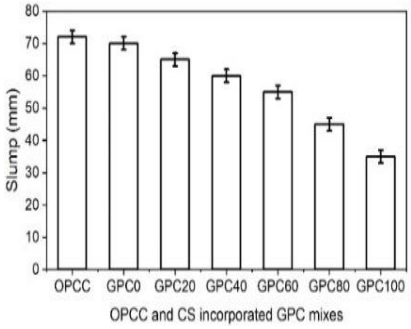

Figure 2. Workability of fresh OPCC and GPC

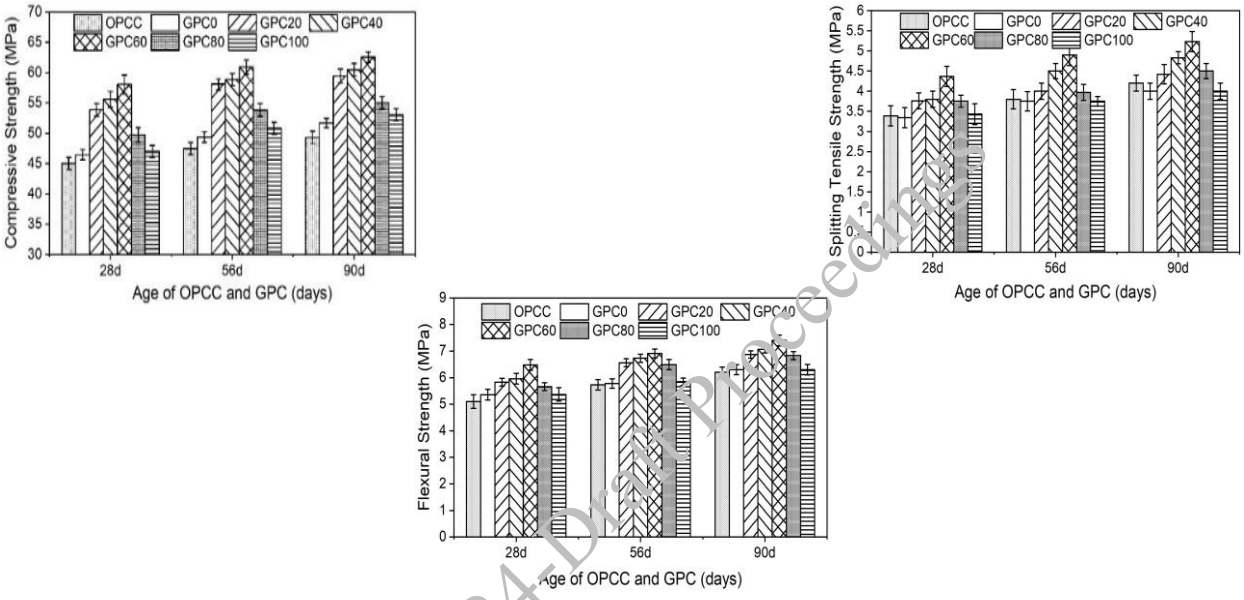

Figure 3. Strength properties of hardened OPCC and GPC

4.3 Transport Properties

Figure 4 illustrates the water absorption, permeable void content, and rapid chloride penetration test (RCPT) results for various hardened GPC and OPCC specimens at 28, 56, and 90 days. As the content of CS increases, there is a noticeable reduction in both water absorption and permeable voids in GPC, indicating an enhancement in concrete quality. Among the different mixes, GPC60 exhibits the most favourable performance. However, further increases in CS content beyond 60% begin to negatively impact concrete quality, aligning with the observations from the strength tests. GPC60 samples show a reduction in water absorption by 23-48% and in permeable voids by 20-35% compared to the control OPCC samples. Also, as CS replacement increases, the charge passed or chloride penetrability, decreases, indicating an improvement in the GPC quality. However, this trend is only observed up to a CS replacement of 60%. Beyond this level, an increase in CS content leads to higher chloride penetrability, although it remains lower than that of the control OPCC samples. The results also highlight that extending the curing period from 28 to 90 days significantly enhances the concrete quality, emphasizing the importance of longer curing durations for improved durability. It was observed that chloride penetrability decreased by 58-72% for GPC60 samples compared to the control OPCC samples.

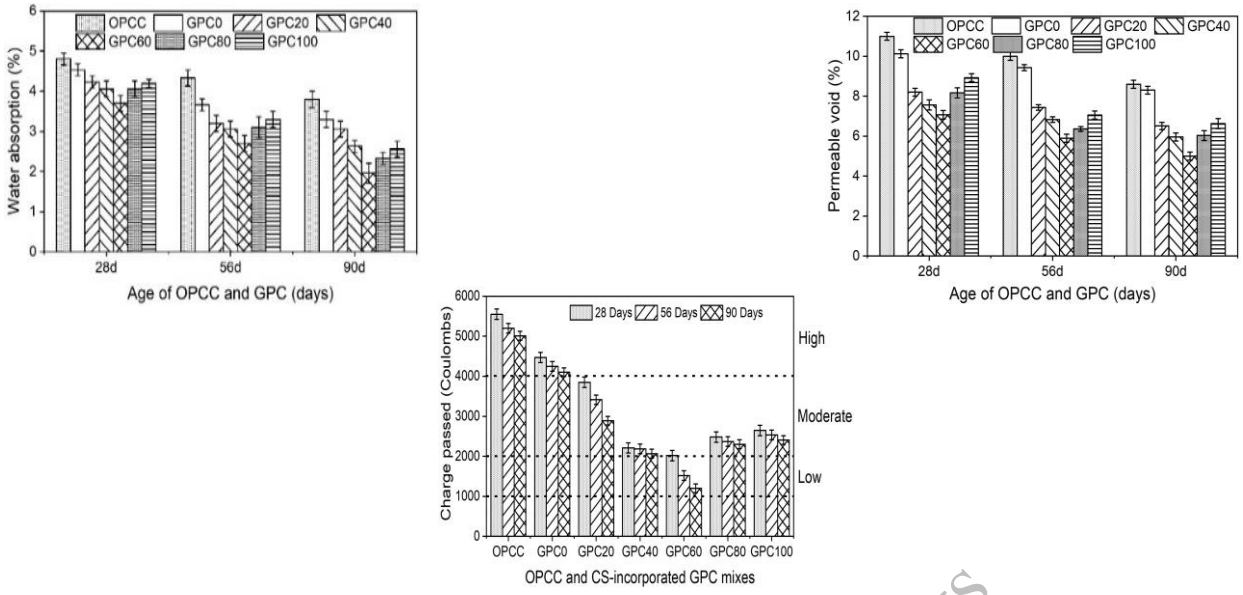

Figure 4. Water absorption, permeable void, RCPT of hardened OPCC and GPC

4.4 Abrasion Resistance

As mentioned earlier, the abrasion resistance of hardened GPC and OPCC specimens is quantified by measuring wear depth, with lower wear depth indicating better abrasion resistance. The average wear depth of all GPC specimens and OPCC after 28, 56, and 90 days of ambient curing is displayed in Fig. 5. The results show a decrease in wear depth as both the CS replacement percentage and the curing age of the GPC specimens increase. This improvement is likely due to the strong inter-particle bonding resulting from the well-graded fine aggregate mix created by combining CS and NS. Additionally, the potential pozzolanic properties of CS might contribute to the increased strength of GPC, leading to reduced wear depth. However, when the CS replacement exceeds 60%, an increase in wear depth was observed, potentially indicating weak inter-particle bonding in hardened GPC (Li et al (2006)). It was noted that the wear depth decreased by 35-53% for GPC60 samples compared to the control OPCC samples.

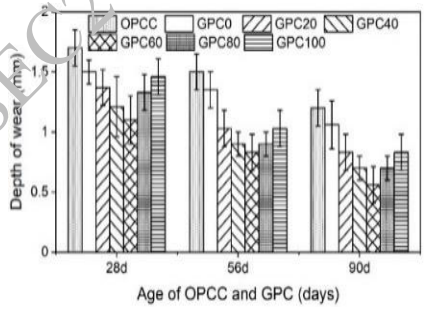

Figure 5. Depth of wear of hardened OPCC and GPC

4.5 Slake Durability

The slake durability test was carried out in the laboratory following the IS10050 (1981) standard, involving two cycles of wetting and drying. The slake durability indices for GPC and OPCC specimens were calculated after the completion of the second cycle. Fig. 6 displays the slake durability indices for all GPC and OPCC specimens at various curing ages. The data consistently reveal that GPC specimens incorporating CS exhibit higher slake durability indices compared to the control OPCC specimens, which contain only NS, across different curing periods. This increased slake durability reflects greater resistance to disintegration, highlighting the beneficial effect of substituting natural fine aggregate with CS in enhancing the slake durability of concrete. Moreover, the slake durability index of GPC continues to rise as the CS replacement percentage increases up to 60%. This improvement can be attributed to the strong bond formed between the aggregate and the surrounding hydrated geopolymer paste in the GPC. An

enhancement of 11-17% in slake durability index was observed in GPC60 compared to the control OPCC specimen.

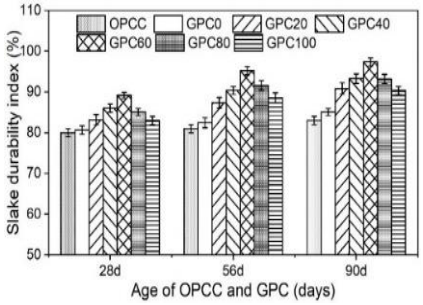

Figure 6. Slake durability of hardened OPCC and GPC

5. Conclusions

The disposal of waste materials such as FA, GGBFS, and CS poses significant environmental and industrial challenges. However, incorporating these materials into building construction presents a promising avenue for promoting sustainable development in the built environment. Extensive research is crucial to increase awareness among stakeholders and facilitate the practical application of these waste materials in the concrete construction industry. The results demonstrate that the inclusion of CS in GPC significantly enhances strength, transport, and durability properties. The following are the key conclusions drawn from the present study:

- Material characterization results indicate that CS can effectively replace NS in GPC production.
- The workability of fresh concrete decreases with higher CS replacement due to the irregular, angular shape and higher specific gravity of CS particles compared to NS.
- The strength of hardened GPC significantly improves with all levels of CS replacement, attributed to superior particle packing and natural pozzolans in CS.
- The water absorption and permeable voids in GPC decrease with higher CS content, indicating improved concrete quality and aligning with strength test results.
- RCPT indicates improved chloride resistance at 60% CS replacement, attributed to better particle packing, and natural pozzolanas in CS.
- Wear depth decreases with higher CS replacement and increased curing age of GPC specimens, due to strong inter-particle bonding from the well-graded combination of CS and NS.
- The slake durability of hardened GPC increases with higher CS replacement, due to the strong bond between the aggregate and the surrounding hydrated geopolymer paste.
- GPC with 60% optimum CS replacement (GPC60) demonstrates superior mechanical strength, minimal water absorption, permeable voids, chloride penetrability, high abrasion resistance, and enhanced slake durability compared to OPCC and other GPC mixes.

References

A.M. Neville (2012) *Concrete Technology*, 4th Edn. Pearson Education Ltd. Publications, England..

L. K. Turner and F. G. Collins (2013) Carbon dioxide equivalent (CO_2-e) emissions: A comparison between geopolymer and OPC cement concrete, *Constr. Build. Mater.* 43, 125-130.

B. C. McLellan, R. P. Williams, J. Lay, A. Van Riessen and G. D. Corder, Costs and carbon emissions for geopolymer pastes in comparison to ordinary Portland cement, *J. Clean. Prod.* 19(9-10), (2011) 1080-1090.

J.G. Davidovits (2008) *Geopolymer Chemistry and Applications*, 5th Edn. (Institut Geopolymere, Saint-Quentin, France,.

L. Verdolotti, S. Iannace, M. Lavorgna and R. Lamanna (2008) "Geopolymerization reaction to consolidate incoherent pozzolanic soil", *J. Mater. Sci.* 43, 865-873.

A. Fernandez-Jimenez, M. Monzo, M. Vicent, A. Barba and A. Palomo (2008), Alkaline activation of metakaolin–fly ash mixtures: Obtain of Zeoceramics and Zeocements, *Microporous Mesoporous Mater.* 108, 41-49.

P. Nath and P. K. Sarker (2014) "Effect of GGBFS on setting, workability and early strength properties of fly ash geopolymer concrete cured in ambient condition", *Constr. Build. Mater.* 66, 163-171.

M. H. Al-Majidi, A. Lampropoulos, A. Cundy and S. Meikle (2016) "Development of geopolymer mortar under ambient temperature for in situ applications", *Constr. Build. Mater.* 120, 198-211.
P.S. Deb, P. Nath and P. K. Sarker (2014), "The effects of ground granulated blast-furnace slag blending with fly ash and activator content on the workability and strength properties of geopolymer concrete cured at ambient temperature" *Materials and design.* 62,32-39.
M. S. Reddy, P. Dinakar and B. H. Rao (2018) "Mix design development of fly ash and ground granulated blast furnace slag based geopolymer concrete", *J. Build. Eng.* 20, 712-722.
J. K. Prusty and B. Pradhan (2020) "Effect of GGBS and chloride on compressive strength and corrosion performance of steel in fly ash-GGBS based geopolymer concrete", *Mater. Today Proc.* 32, 850-855.
M. G. Sharma (2024) https://timesofindia.indiatimes.com/blogs/voices/copper-slag-converting-waste-into-sustainable-wealth/.
J. Thomas, N. N. Thaickavil and M. P. Abraham (2018) "Copper or ferrous slag as substitutes for fine aggregates in concrete", *Adv. Concr. Constr.* 6(5), 545-560.
IS 383 (2016), Coarse and fine aggregates for concrete- Specification, *Bureau of Indian Standards*, New Delhi, India,
IS 12269 (1987) "Ordinary Portland Cement, 53 Grade: Specification", *Bureau of Indian Standards*, New Delhi, India,.
ASTM C150/C150M (2019), "Standard specification for Portland cement", *ASTM International*, West Conshohocken, PA,.
IS 3812 (Part I) (2013) "Specification for pulverized fuel ash", *Bureau of Indian Standards*, New Delhi, India.
ASTM C618 (2019) "Standard specification for coal fly ash and raw or calcined natural pozzolanas for use in concrete", *ASTM International*, West Conshohocken, PA.
IS 16714 (2018), "Ground granulated blast furnace slag for use in cement, mortar and concrete – Specification", *Bureau of Indian Standards*, New Delhi, India,.
IS 2386 (Part III), "Methods of test for aggregates for specific gravity, density, voids, absorption and bulking", *Bureau of Indian Standards*, New Delhi, India, (1963).
ASTM C128 (2022) "Standard test method for relative density (specific gravity) and absorption of fine aggregate", *ASTM International*, West Conshohocken, PA.
P. Pavithra, M. S. Reddy, P. Dinakar, B. H. Rao, B. K. Satpathy and A. N. Mohanty (2016) "A mix design procedure for geopolymer concrete with fly ash", *J. Clean. Prod.* 133, 117-125.
M. S. Reddy, P. Dinakar and B. H. Rao (2018) "Mix design development of fly ash and ground granulated blast furnace slag based geopolymer concrete", *J. Build. Eng.* 20, 712-722.
ACI 211.1(2002) "Standard practice for selecting proportions for normal, heavyweight and mass concrete, *ACI Committee Report*,.
IS 10262, "Guidelines for concrete mix design proportioning", *Bureau of Indian Standards*, New Delhi, India, (2019).
IS 516 (1959) "Method of tests for strength of concrete", *Bureau of Indian Standards*, New Delhi, India.
IS 5816 (1999) "Method of tests for splitting tensile strength of concrete", *Bureau of Indian Standards*, New Delhi, India,.
ASTM C642 (2013) "Standard test method for density, absorption and voids in hardened concrete", *ASTM International*, West Conshohocken, PA,.
ASTM C1202 (2017) "Standard test method for electrical indication of concrete's ability to resist chloride penetration", ASTM International, West Conshohocken, PA.
IS 1237 (2012) "Cement concrete flooring tiles – Specification", *Bureau of Indian Standards*, New Delhi, India.
IS 10050 (1981) "Method for determination of slake durability index of rocks", *Bureau of Indian Standards*, New Delhi, India,.
N. Arunachelam, J. Maheswaran, M. Chellapandian, G. Murali, G. and N. I. Vatin (2022) "Development of high-strength geopolymer concrete incorporating high-volume copper slag and micro silica", *Sustain.* 14(13), 7601.
H. Li, M. H. Zhang and J. P. Ou (2006) "Abrasion resistance of concrete containing nano-particles for pavement", *Wear*, 260 (11-12), 1262-1266.

Interpretation of Electrochemical Responses to Understand the Corrosion Initiation of Prestressing Steel in Slag-Based Binders

S. Srinivasan[1*], R.G. Pillai[2], and C. Andrade[3]

[1] PhD Student, Department of Civil Engineering, Indian Institute of Technology Madras, India
Email: ssreelakshmi24@gmail.com
[2] Professor, Department of Civil Engineering, Indian Institute of Technology Madras, India
Email: pillai@civil.iitm.ac.in
[3] Visiting Professor, CIMNE, Polytechnic University of Catalonia, Spain and Adjunct Faculty, Department of Civil Engineering, Indian Institute of Technology Madras, India,
Email: candrade@cimne.upc.edu

[*]Corresponding author

ABSTRACT

In recent years, the deterioration of prestressed concrete structures due to corrosion of the strands is becoming a serious issue; and has been described as the scourge of the century. Unlike structural deterioration, steel corrosion is not that vulnerable immediately after construction or loading. Instead, the corrosion is initiated, and the deterioration is active only when the concentration of deteriorating agents reaches a certain threshold. So, delaying the onset of corrosion is essential for ensuring durable and safe structures. Using SCMs like slag helps in delaying the initiation and reducing the carbon footprint of the structure. However, the effect of slag on the corrosion initiation of PSd steel is not reported. This paper presents a study on the passivation performance and corrosion initiation of PSd steel in cementitious systems with slag. For this, in-house developed PSd-ACT test method is used to determine the chloride threshold. Five lollipop test specimens in OPC+50 % slag binder, each at two stress levels (0 and 0.76fpu where, fpu = ultimate tensile strength) were made. Initially, the stressed specimens were cured for 28 days and then exposed to cyclic wet-dry exposure using simulated concrete pore solution with 2 % NaCl. At the end of every wet cycle the electrochemical impedance spectroscopy (EIS) measurements were made. Whereas the unstressed specimens were cured until the formation of intact passive film, which is ensured by continuous EIS measurement. From the continuous electrochemical measurements, the challenges in detecting the corrosion initiation, interpreting the electrochemical responses, choosing appropriate equivalent electric circuit are discussed.

KEYWORDS*: Corrosion, Prestressed concrete, Strand, Slag, Sulphide, Passivation, Impedance*

1. Introduction

Ever since the advent of prestressed concrete technology, its application in the construction industry has been increasing drastically. These PSC structures are perceived to be durable with a service life of 100+ years, as they are crack-resistant due to the pre-compression induced in the concrete. However, in recent years, the deterioration of such structures due to premature corrosion of the strands (within 10 to 20 years of construction) is becoming a serious issue; and has been described as the scourge of the century (Podolny, 1992). Corrosion in PSC structures is more crucial than that in conventionally reinforced concrete structures, as the corrosion is insidious and leads to the catastrophic failure of PSC structures (Rengaraju et al., 2020). Also, it should be noted that most of the seemingly good PSC bridges are very young (less than 20 to 40 years old), and the perception that they will remain corrosion-free for 100+ years might be wrong. ACI 222.2R (2001) states that corrosion in PSC structures has potentially more severe consequences than in non-PSC, emphasizing the vital efforts to be taken by engineers, designers, contractors, and owners to prevent such calamitous failure in the future.

However, there is significant difficulty in estimating the service life as the increased usage of supplementary cementitious materials (SCMs) and a considerable variation in the concentration of elements in PS steel

resulted in increased diversity of the PSC systems. Most of the current laboratory-based engineering models are suitable for conventional reinforced concrete systems with low resistive binders. This results in the requirement of a knowledge-based approach to durability of high resistive binder systems like slag, which would make the service life predictions at the engineering level more reliable. This necessitates the understanding of the Steel- Binder interface and their electrochemical behaviour to develop the framework for detecting initiation of corrosion, which is the befitting solution to ensure a durable service life of 100+ years.

The effect of the use of slag on the corrosion resistance of prestressing steel is not reported; and needs better understanding. The previous studies on the specimens with slag-based binders at different ages provided contradictory results. MacPhee, based on the theoretical interpretation of reducing properties of slag postulated that during hydration, slag consumes oxygen and other oxidized species, which inhibits formation of passive film. Based on the laboratory tests, it was reported that immediately after curing, the corrosion rate in slag mortars is about 10 times higher than that for ordinary Portland cement mortars and over time this difference decreases (Valentini et al., 1990). The presence of sulphides in slag affects the oxygen availability and decreases the chloride threshold and the initiation phase of corrosion.

Andrade (1985) reported that, when exposed to NaCl, steel in slag system repassivated more easily than that in the OPC systems. Also, the slag systems show long-term corrosion rates that are lower than that of PC systems. It has also been reported that despite the poor performance of slag-based binders based on the passivation and aqueous phase studies, slag concrete exhibits significantly reduced corrosion rates compared to plain concretes at later stages(Scott & Alexander, 2016).

To ensure durable PSC structures, it is important to understand the performance of prestressing steel in small-scale experiments using same binder as the realistic exposure conditions will prolong the similar responses from the controlled conditions. Nevertheless, most of the studies on slag are only based on aqueous systems and/or conventional reinforcement. This emphasizes the need for assessing the corrosion resistance of PSd steel on slag-based binders. Hence in this study, the effect of slag on the initial passivation of PSd steel is studied with specimens where the prestressing steel is embedded in slag-based binders under stressed and unstressed condition.

2. Experimental Program

In this study, king wires of 5.28 mm diameter extracted from 15.2 mm diameter prestressing strands (conforming to IS 14268) were used. These king wires were embedded in mortar made with the binder combination of Ordinary Portland Cement (OPC) (conforming to IS 12269:2013) blended with 50% slag. The fine aggregate component consists of a 50-50 mix of standard sands of Grade II (of particle size 1 mm to 0.5 mm) and Grade III (of particle size 0.5 mm to 0.09 mm) respectively, conforming to IS 650.

To assess the effect of stress on corrosion resistance, five lollipop specimens with pre-tensioned steel embedded in OPC blended with 50% slag were prepared. The stressing, casting and testing of the specimens were done with the in-house developed PSd- ACT method using the self-reacting frames (Joseline et al., 2021). The PS king wires were stressed to 76% of their ultimate tensile strength, followed by the casting of the OPC and OPC+50% slag matrix. The hardened specimens are cured for 28 days with the corrosion cell as shown in Figure 1. After curing, the specimens were exposed to cyclic 2d-wet and 5d-dry cycles in Simulated Pore Solution (SPS) + 2% NaCl solution. The SPS is prepared for every cycle with distilled water and reagent chemicals (10.4 g of NaOH, 23.2 g of KOH, 0.3 g of Ca(OH)2, in 966 g of distilled water. The pH of the prepared SPS is 12.8, so the alkalinity of the test specimens is maintained. Throughout testing, the stress level is maintained the same by the wedge and barrel arrangement at the ends of the frame. At the end of every wet cycle, the electrochemical impedance spectroscopy (EIS) measurements and linear polarisation resistance measurements were made.

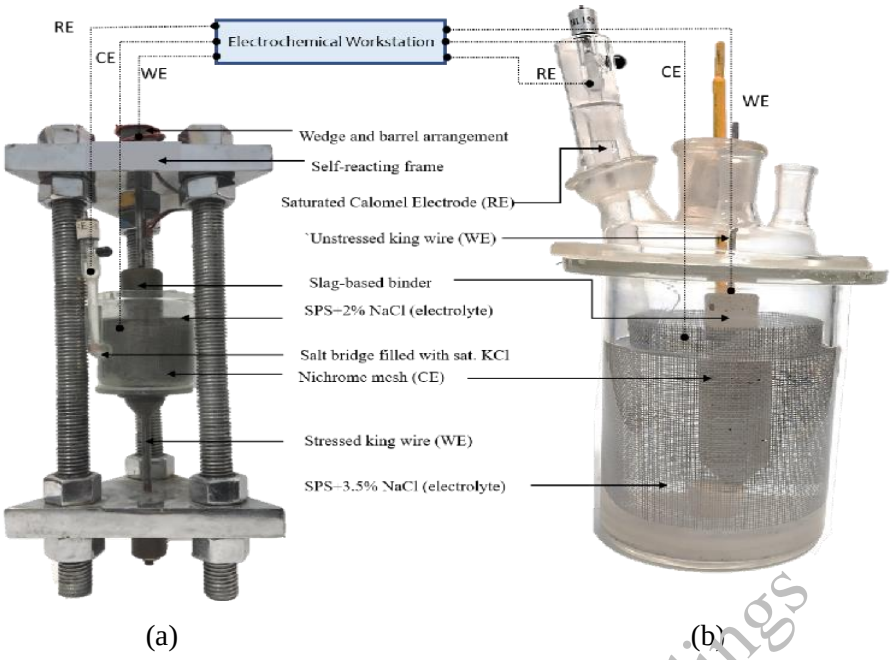

(a) (b)

Figure 1. Test Setup for testing (a) stressed and (b) unstressed lollipop specimens

To understand the passivation properties another set of five lollipop specimens were cast and they were neither stressed nor exposed to chlorides. It has been cured continuously and every week EIS measurements were made. The test setup for testing these unstressed specimens is shown in Figure 1.

3. Results and Discussions

The typical impedance responses from the unstressed PS steel in OPC + 50% slag mortar, is shown in **Figure 2**. In this case, to ensure the passivation of prestressing and to check if free sulphides can initiate corrosion without chlorides, the specimens were cured for six months.

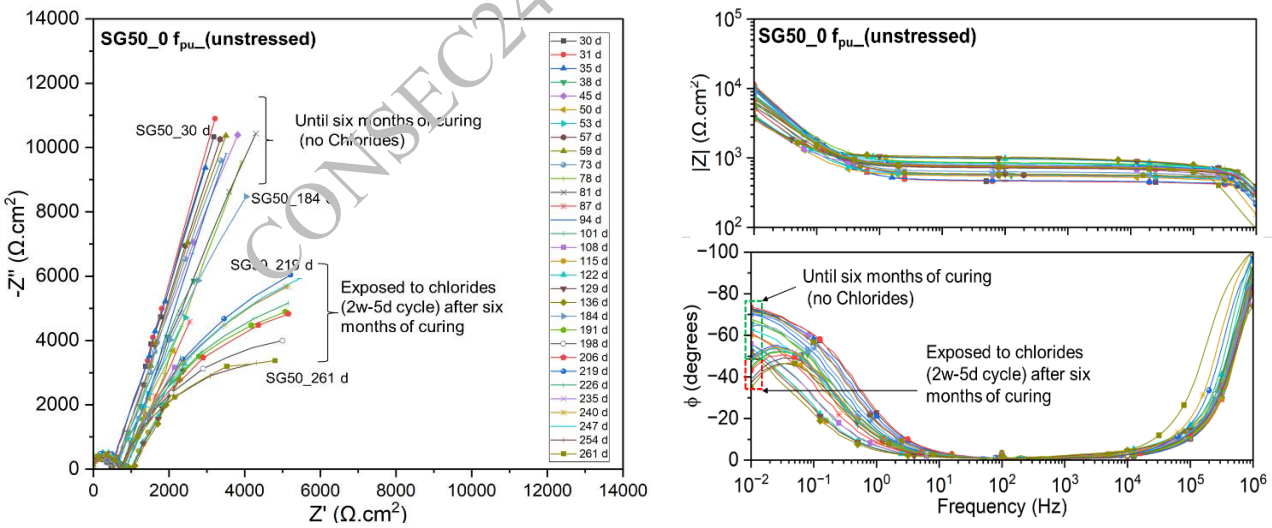

Figure 2. Typical evolution of the impedance responses at Ecorr (AC amplitude: ±10 mV[peak-to-peak]) obtained for prestressing steel in slag-based binders

As shown in Figure 2, the higher arc and higher resistance offered by the passive film indicates the formation of compact passive layer. Exposing the specimens after this stage only will give clear indication of corrosion initiation and hence appropriate service life. So, after 176 d of curing the specimens are exposed to chlorides. It can be observed from Figure 3, that unlike OPC systems which has sharp P- to-A transition, there is gradual decrease in Rox. Also, no initiation of corrosion was observed even after 12 weeks of exposure to chlorides, which indicates increased resistance to corrosion.

However, to understand the real-time behaviour, the test was conducted with stressed prestressing steel and exposed to chlorides right after 28 days of curing. The typical impedance response from the stressed prestressing steel (PSd) in OPC + 50% slag mortar, subjected to cyclic wet and dry exposure to SPS+2% NaCl, is shown in Figure 3

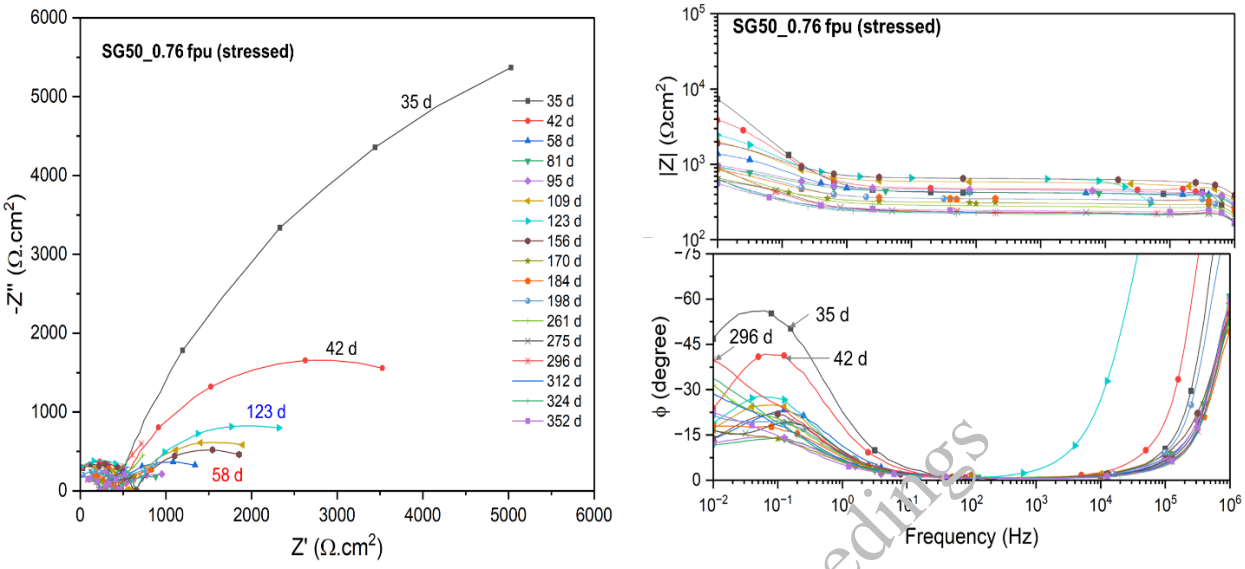

Figure 3. Typical evolution of the impedance responses at Ecorr (AC amplitude: ±10 mV[peak-to-peak]) obtained for prestressed steel in slag-based binders

During the early stages (35d and 42d) of exposure, the low frequency region (10 −1 Hz to 10 −2 Hz) of the Nyquist plot had a larger angle of arc, indicating passivation. The Rox (resistance offered by the oxide layer) of EIS responses drastically decreases after 58 d, which indicates the depassivation by the action of chlorides. This is the characteristic response for the "active" state. However, the specimens were cured again to observe the re-passivation capacity of slag. It can be seen from Figure 3a that from the Rox gradually increases till 123d, which indicates the re-passivation. However, after 123 d there is no change. This indicates that the presence of free sulphides in slag-based binders results in the formation of a compromised passive layer, which is not intact and susceptible to chloride attack. Further curing will not help in complete re-passivation. The specimens are thus exposed to chlorides after the repassivation to estimate the service life of the slag based binders. The specimens are being exposed to wet and dry cycle of SPS+2% NaCl for more than 14 weeks, still there is no corrosion initiation. This indicates that the slag systems have better tendency to re-passivate, if sufficient oxygen is available and that should be considered while estimating the service life. Otherwise, it may lead to the underestimation of the potential capacity of slag.

Hence, it is important to understand the passivation performance to understand the long-term behaviour of slag systems. However, choosing appropriate electrochemical method is crucial for estimating the resistance offered by the passive film. The three incomplete depressed semicircles indicate impedance offered by mortar (Rm and Qm), double layer (Rct and Qdl), and the passive film (Rox and Qox). Hence, a 3-RC circuit is used to model the response from steel-cementitious mortar systems (Rengaraju et al., 2019)(Rengaraju et al., 2019).This is suitable for the cases where the chlorides have already diffused. For example, in this study, in the stressed samples, the 3 RC circuit is used. However, for the passivation studies, where there is diffusion through the oxide layer, the Warburg element is also introduced. A comparison is made for the determination of passivation resistance with EIS and LPR techniques.

It can be observed from Figure 4 that for the passivation studies (in unstressed conditions), where Rox values are high, LPR results are not reliable. But EIS responses are consistent throughout the curing period. However, when exposed to chlorides and active corrosion takes place, the 1/Rp values from both EIS and LPR techniques are almost equal. The de-passivation and repassivation phases are also evident from both EIS and LPR responses. It is suggested that when the passivation resistance of the system is high EIS is the better tool for the estimation of corrosion initiation.

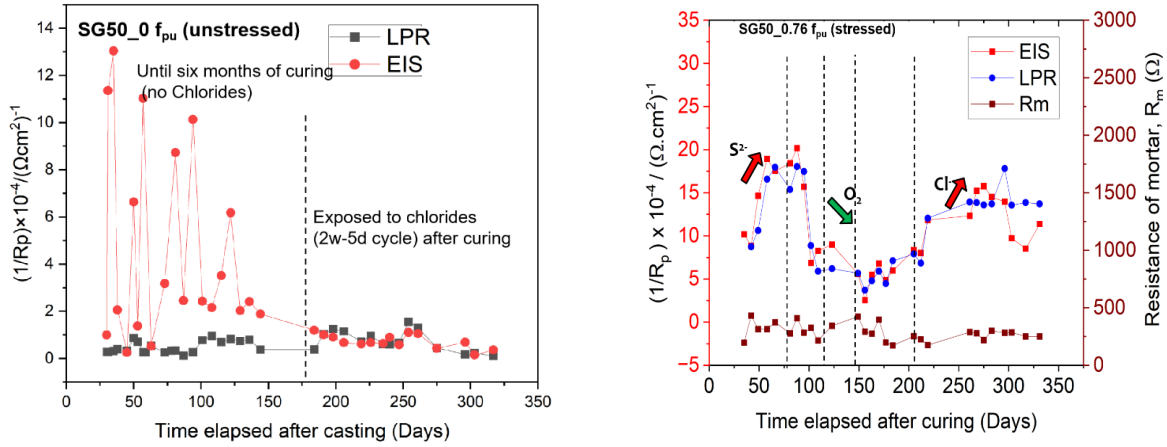

Figure 4. Comparison of 1/Rp values from EIS and LPR

.4. Conclusions

- In this work, EIS tests were performed on prestressed steel embedded in slag-based binders exposed to chlorides. From the EIS response, the passivation, depassivation and re-passivation of the prestressed steel in slag system was studied.
- Slag systems have better tendency to repassivated in the presence of sufficient oxygen
- From this it is evident that the test procedure to detect corrosion initiation must ensure the passivation of steel before the exposure to chlorides.
- For systems with high passivation resistance EIS is a better tool to determine corrosion initiation.

Acknowledgements

The authors acknowledge the grant from the Institute of Eminence Centre of Excellence on Technologies for Low Carbon and Lean Construction (TLC2) from the Ministry of Education via the Indian Institute of Technology Madras, Chennai, India. The authors also acknowledge the testing facility in the Construction Materials Research Laboratory at the Department of Civil Engineering, Indian Institute of Technology Madras, Chennai, India.

References

Podolny, W. (1992). Corrosion of Prestressing Steels and Its Mitigation Long-time PCI Professional Member.

Rengaraju, S., Godara, A., Alapati, P., & Pillai, R. G. (2020). Macrocell corrosion mechanisms of prestressing strands in various concretes. *Magazine of Concrete Research*, 72(4), 194–206. https://doi.org/10.1680/jmacr.18.00284

Valentini, C., Berardo, L., & Alanis, I. (1990). Influence of blast furnace slags on the corrosion rate of steel in concrete. ASTM Special Technical Publication, 1065, 17–28. https://doi.org/10.1520/stp25012s

Scott, A., & Alexander, M. G. (2016). Effect of supplementary cementitious materials (binder type) on the pore solution chemistry and the corrosion of steel in alkaline environments. *Cement and Concrete Research*, 89, 45–55. https://doi.org/10.1016/j.cemconres.2016.08.007s

Scott, A., & Alexander, M. G. (2007). `The influence of binder type, cracking, and cover on corrosion rates of steel in chloride-contaminated concrete. In *Magazine of Concrete Research* (Vol. 59, Issue 7). https://doi.org/10.1680/macr.2007.59.7.495

C. Andrade (1986). Pore solution chemistry and corrosion in hydrated cement systems containing chloride salts: a study of cation specific effects. *British Corrosion Journal*.

Joseline, D., Pillai, R. G., & Neelakantan, L. (2021). Initiation of Stress Corrosion Cracking in Cold-Drawn Prestressing Steel in Hardened Cement Mortar Exposed to Chlorides. *Corrosion*, 77(8), 906–922. https://doi.org/10.5006/3730

Rengaraju, S., & Pillai, R. G. (2021). An accelerated chloride threshold test for uncoated steel in highly resistive cementitious systems (hr-ACT test). *Construction and Building Materials*, 305(August). https://doi.org/10.1016/j.conbuildmat.2021.124797

Chloride Profile of Calcined Bauxite Incorporated Alkali-Activated Concrete Using Micro X-ray Fluorescence

Zuobang Yao[1], Ram Pal[2], Haemin Song[3], Ali Kashiani[4], and Taehwan Kim[5*]

[1] *Centre for Infrastructure Engineering and Safety, University of New South Wales, Sydney, Australia*
Email: zuobang.yao@student.unsw.edu.at
[2] *Centre for Infrastructure Engineering and Safety, University of New South Wales, Sydney, Australia*
Email: ram.pal@unsw.edu.au
[3] *Centre for Infrastructure Engineering and Safety, University of New South Wales, Sydney, Australia*
Email: haemin.song@unsw.edu.au
[4] *Centre for Infrastructure Engineering and Safety, University of New South Wales, Sydney, Australia*
Email: ali.kashani@unsw.edu.au
[5] *Centre for Infrastructure Engineering and Safety, University of New South Wales, Sydney, Australia*
Email: taehwan.kim@unsw.edu.au

[*]Corresponding author (s)

ABSTRACT

Various waste-derived cementitious materials have been studied and their mechanical and durability performance has been evaluated. Mining is the primary sector industry in Australia and the utilisation of mine wastes as cement replacement is also one of the promising ways to reduce both the consumption of clinker and mine wastes destined for landfills. This study presented the experimental results of chloride profile characterization using micro X-ray fluorescence (XRF) on the alkali-activated concrete incorporated with calcined bauxite tailings, which is a part of the project of exploring the beneficiation of mine tailings in construction materials. Chloride ingress in concrete plays a pivotal role in determining the onset of corrosion initiation of steel reinforcement. The test to determine the chloride profile in concrete requires a series of steps including, coring, grinding, and titration. This study used the micro XRF technique to determine the chloride profile and chloride apparent diffusion coefficient on alkali-activated concrete and compared the results with the conventional method (ASTM C1556). The results obtained from micro XRF techniques were comparable to those from the conventional tests while the formal technique significantly reduced human involvement.

KEYWORDS: *Alkali-activated concrete, Chloride profile, micro XRF, Diffusion*

1. Introduction

Different approaches to cutting the carbon footprint have been examined to achieve sustainable development in the construction sector. In particular, replacing clinker-based cement with waste-derived binders is one of the promising measures considering the large consumption of ordinary Portland cement and its contribution to global CO_2 emission, Scrivener et al (2018). A variety of alternative binders have been introduced and their mechanical and durability performance have been also evaluated. One of the alternative binders is alkali-activated materials (AAM) and, as expected, various types of waste-derived precursors have been introduced to reduce the carbon footprint of the material. However, the reliability of durability tests for AAM has been questioned because many of them is simply adapted from the empirical tests in OPC-based systems. This issue is also a concern for the chloride resistivity tests for concrete. It is well known that the setting of the rapid chloride penetration test (RCPT) described in ASTM C1202 has often failed in many alkali-activated systems, Alnahhal, et al (2024), Noushini and Castel (2018). Noushni and Castel (2018) proposed a modified ASTM C1202. However, the modified method requires further refinement and validation with extensive data. Therefore, until a new reliable accelerated test of chloride resistance for alkali-activated concrete, ASTM C1556 seems to be the most reliable method for alkali-activated concrete.

Though ASTM C1556 is a well-established test, the test involves profile grinding, acid dissolution of collected powder, and titration for Cl concentration. Also, the data is the average value of the pre-designated

depth of grinding. More fast and reliable tests by reducing human involvement would benefit the Cl profile in various binders. Moradllo et al (2017) used the micro XRF to determine the Cl profile in blended OPC-based concrete. To the best of the authors' knowledge, Dehghan et al (2017) first applied this technique to alkali-activated materials This study modified the data processing to obtain more reliable data using the alkali-activated concrete incorporated with the calcined bauxite tailings. The Cl profile obtained from micro XRF are compared with the Cl profile from the traditional ASTM C1556 method.

2. Material and experiment methods

Bauxite tailing (BT) was supplied by the AILLIQ ARC Linkage project. Rice husk ash (RHA) was purchased from NK Enterprises, India. Fly ash (FA) and ground granulated blast furnace slag (GGBFS) were supplied from Boral. Initially, BT was chunks of rock caused by the consolidation inside a storage facility, while other materials were fine powder. Therefore, the ring milling pulverizer was used to mill BT rock for 5 minutes to reach a preferred particle size distribution. Then, milled BT was calcined under 600 °C for 2 hours. The final product was denoted as calcined bauxite tailings (CBT). The chemical oxide composition is shown in the following ***Table 1***. NaOH pellets (98%, Chem-Supply Pty Ltd., Australia) were used to prepare 10 M NaOH solution. The commercial sodium silicate (SS) solution was purchased from PQ, Australia, and it was composed of 14.7% Na_2O, 29.4% SiO_2, and 55.9% H_2O. Both solutions were used as an alkaline activator of the geopolymer. Sydney sand and basalt aggregate (10 mm nominal size) were used as a fine aggregate and a coarse aggregate for fabricating geopolymer concrete.

Table 1. Chemical composition of binders.

	Al_2O_3	SiO_2	Fe_2O_3	TiO_2	Na_2O	MgO	P_2O_5	SO_3	K_2O	CaO	L.O.I.	Total
CBT	65.04	14.47	10.87	4.05	0.27	0.16	0.07	0.03	0.03	0.01	5.05	100.31
FA	23.52	66.37	3.93	1.03	0.90	0.86	0.18	0.10	1.54	1.73	N.D.	100.39
RHA	0.61	91.86	0.58	0.01	0.14	0.67	1.00	0.06	1.91	1.03	1.99	100.03
GGBFS	12.45	34.19	0.93	0.58	0.17	5.49	0.01	1.35	0.31	44.40	0.44	100.80

The detailed concrete mixture is shown in **Table 2**. First of all, concrete samples were cast into a cylindrical mold (100 mm Ø ×200 mm height). Then, they were wrapped with plastic wrap and cured at 23 °C for 28 days for their strength and pore structure development. Then, 100-mm Ø × 50-mm thick specimens were sawn from the middle of the concrete, and the top surface of the specimens (other sides all sealed with aluminum foil) was exposed to sodium chloride solution with 165g/L concentration after the vacuum saturation process with no compromise. The specimen exposed to NaCl solution will be removed after 35 days, and a profile grinding was processed to obtain powder from different layers (first 1mm is eliminated, then the next five layers with 2 mm depth and the following 4 layers with 3mm depth) for titration. It is noted that initial chloride content is determined from the remainder of the crushed and ground specimens. The μXRF analysis was conducted using Bruker M4 TORNADO. After being exposed to NaCl solution, the specimen was dry cut in half, and the selected area of cross section with 1.5cm width × 2.5 cm depth (with 60 um × 60 um pixel) was scanned through μXRF. Rather than selecting the points manually as done by Dehghan et al (2017), this study used more large data of points by scanning the area. To determine Cl concentration, a set of standards with known concentration was used to develop a calibration curve to convert the count data to Cl concentration. Finally, Matlab code was used to determine the concentrations of Cl per each depth.

Table 2. Concrete mixture design.

Labels	Material (kg)						Alkaline activator		
	GGBFS	FA	CBT	RHA	Sand	Coarse Agg.	w/s	Na2O/Binder ratio (%)	M.S
S50-BR25-F25	197.4	98.7	34.5	64.1	667.8	1020.6	0.5	6.9	1
S50-BR0-F50	194.0	194.0	0.0	0.0	667.8	1020.6	0.5	6.9	1

3. Results

3.1 µXRF raw data.

Figure 1 (a) shows the Si elemental mapping result. Notably, coarse and fine aggregate edges are easily detected through this Si map. By combining the Si and Cl maps (see Figure 1 (b)), it is easy to conclude the track of chloride ions transported through the mortar of the concrete. Most Cl passed through the pores in the mortar fraction of the concrete and was hindered by coarse aggregate. Also, no obvious high concentration of Cl is detected surrounding the coarse aggregate at the top, which is a good evidence that the dense interfacial transition zone was well established. In Figure 1 (c), a palette mode of Cl mapping is shown, and the concentration and distribution of Cl were calculated through the defaulted µXRF method that existed in the software. The Cl content presented through the defaulted method is not reliable because the high concentration of about 3.5% cannot be analyses. Therefore, a calibration curve is required to produce a reliable Cl concentration.

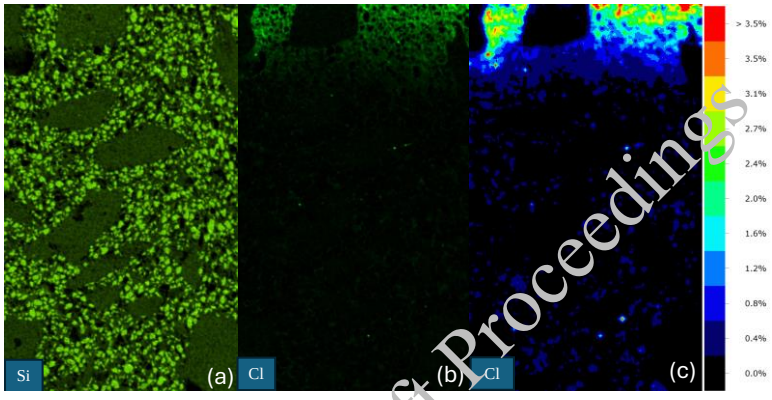

Figure 1. (a)(b) Example of Si and Cl elemental images of S50-BR25-F25 provided by µXRF. (c)Qmap result of Cl through the default method.

3.2 Calibration curve

A calibration curve is established from reference samples from the mortar part of S50-BR0-F50 concrete (with varied known Cl wt.%) to convert counts to concentration values. Because the chemical oxide composition of the two concrete mixtures is similar, the matrix effect is not considered. As shown in ***Figure 2***, a quadratic calibration curve is well established (with high R^2 = 0.9993), indicating the calibration is reliable.

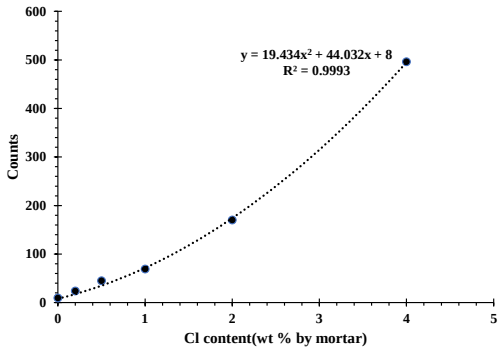

Figure 2. Cl calibration curve used to change from counts to weight percentage in the µXRF analysis.

3.3 µXRF converted profile through calibration curve vs Chloride grinding profile

As shown in Figure 3, the chloride grinding profile and µXRF exhibited very high similarity regardless of concrete mixtures. However, at 2 mm depth, the Cl content of µXRF presented a much higher content, especially in S50-BR0-F50. The apparent chloride diffusion coefficient (D_a) was calculated using a fitting

equation according to the ASTM C1556. For S50-BR25-F25, the D_a coefficient of μXRF converted and grinding profiles are 1.87E-12 m^2/s and 2.97E-12 m^2/s, respectively. Similarly, for S50-BR25-F25, the D_a coefficient of μXRF converted and grinding profiles are 1.47E-12 m^2/sec and 1.87-12 m^2/s, respectively. The diffusion coefficients from μXRF are slightly lower than those from the profile grinding test. The further research is going on to find the reason behind this.

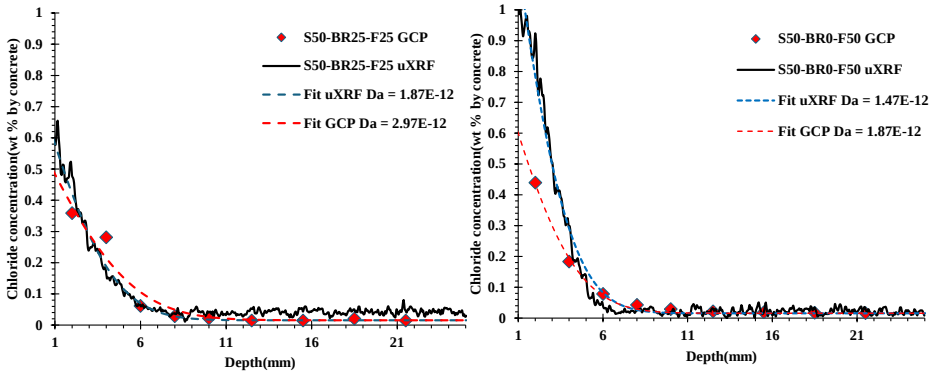

Figure 3. Chloride grinding profile vs μXRF converted chloride profile of concrete mixtures.

4. Conclusions

This study presented the experimental results of chloride profile characterization by comparing two different methods. μXRF chloride profile and grinding chloride profile reached consistent findings on the similar chloride ingress depth. However, the grinding profile exhibited a higher diffusion coefficient than the μXRF chloride profile, about 30% higher. Also, it is detected that the incorporation of calcined bauxite tailings and rice husk ash might lead to an ingress depth increase compared to fly ash which is also confirmed through a higher chloride diffusion coefficient when BR is incorporated.

References

Alnnahal, F.A., Hamdan, A., Hajimohammadi, A., Castel, A., and Kim, T., (2024) "Hydrothermal synthesis of sodium silicate from rice husk ash: Effect of synthesis on silicate structure and transport properties of alkali-activated concrete", *Cement and Concrete Research*, 178(107461).

Dehghan, A., Peterson, K., Riehm, G., Bromerchenkel, L.H., (2017) "Application of X-ray microfluorescenece for the determination of chloride diffusion coefficients in concrete chloride penetration experiments", *Construction and Building Materials*, 148, 85-95.

Leung, C.K.Y. and Cao, Q. (2010) "Development of Pseudo-ductile Permanent Formwork for Durable Concrete Structures", *RILEM Materials and Structures*, 43(7): 993-1007

Li, Z., Leung, C..K.Y. and Xi, Y. (2009) *Structural Renovation in Concrete*, Taylor and Francis, Oxon.

Moradllo, M.K., Sudbrink, B., Hu, Q., Aboustait, M., Tabb, B., Ley, M.T., and Davis, M.D. (2017) "Using micro-X-ray fluorescence to image chloride profile in concrete", *Cement and Concrete Research*, 92, 128-141.

Noushini, Amin and Castel, Arnaud, (2018) "Performance-based criteria to assess the suitability of geopolymer concrete in marine environments using modified ASTM C1202 and ASTM C1556 methods" *RILEM Materials and Structures*, 51(146).

UN Environment, Scrivener, K.L., John, V.M., and Gartner, E.M. (2018) "Eco-efficient cements: potential economically viable solutions for a low-CO2 cement-based materials industry", Cement and Concrete Research, 114: 2-26.

Wan, K.T. and Leung, C.K.Y. (2007a) "Fiber Optic Sensor for the Monitoring of Mixed-Mode Cracks in Structures", *Sensors and Actuators*, 135(2): 370-380

Wan, K.T. and Leung, C.K.Y. (2007b) "Applications of a Novel Distributed Crack Sensor for Concrete Structures", *Sensors and Actuators*, 135(2): 458-464

Zhang, J., Leung, C.K.Y. and Xu, S. (2010) "Evaluation of Fracture Parameters of Concrete from Bending Test using Inverse Analysis Approach", *RILEM Materials and Structures*, 43(6): 857-874

Comparison of Fracture Behavior of Geopolymer and Hydraulic Cement (OPC) Based Concrete

Brijesh Singh*[1], P N Ojha[2] and Amit Trivedi

[1]National Council for Cement and Building Materials, India,
Email: brijesh.singh@ncbindia.com
[2]National Council for Cement and Building Materials, India,
Email: cdrncbb@gmail.com

*Corresponding author

ABSTRACT

The study presents an experimental investigation of the fracture behavior of high calcium geopolymer concrete compared with Ordinary Portland Cement (OPC) based concrete with steel and hybrid fibers. The fracture parameters investigated includes fracture energy, stress intensity factor, energy release rate and characteristic length using RILEM recommendations. The mixes have been prepared in three different category–(i) control mix (ii) mix with 1% steel fiber by volume and (iii) mix with 1% of hybrid fiber by volume containing (75% steel fiber and 25% Polypropylene). Total twelve concrete mixes have been studied for both concrete systems. The addition of steel and hybrid fibers indicates that the fracture performance of both concrete systems improves significantly. In conventional concrete, steel fibers performed much better than hybrid fiber. Whereas, for geopolymer concrete, the hybrid fiber resulted in superior behavior than the steel fiber alone. The observation is in line with past studies which suggest the presence of finer pores in geopolymer concrete than in OPC concrete.

KEYWORDS: *Concrete, Geopolymer, OPC, Fracture behaviour and Fibers, Fracture energy*

1. Introduction

Concrete shows many desirable properties like good compressive strength, high durability, ability to be cast in any shape, and comparatively lower cost than other construction materials (Singh et al (2018), Patel et al (2020), Ojha et al (2021)). But one of the major limitations of concrete is its brittle nature and low crack resistance. This limits its ability to take the flexural load and makes it extremely dangerous under extreme events like earthquakes Arora et al (2017), Arora et al (2021a), Arora et al (2021b), Due to this weakness, concrete structures under flexural loads are susceptible to getting cracked and fail spontaneously without warning. One of the quantitative estimations of brittleness and ductility of concrete is its fracture properties. RILEM TC-50 proposes a three-point bending test on a notched beam to find the fracture parameters for concrete. Fracture energy is one of the most important fracture parameters and it can be defined as a parameter to analyze and compare the toughness and cracking resistance of the concrete. As per RILEM TC-50, Fracture energy is the amount of energy necessary to create a unit area of crack (RILEM (1985)). Other fracture parameters are fracture toughness, Energy release rate, and characteristic length. Fracture toughness refers to the resistance of brittle materials to the spread of cracks [Shah (1990)]. The energy release rate is the rate at which the energy is transformed with the fracture propagation in the material. Characteristic length is one of the measures of the brittleness of the concrete, a concrete can be considered more brittle if it shows a lower characteristic length. The present study evaluates these parameters using Load-deflection and load-CMOD (Crack Mouth Opening Displacement) curves obtained from the experimental investigation on beams of 100 x 100 x 500 mm size under a three-point bend test. The fracture parameters for the geopolymer concrete have been compared with the fracture performance of similar strength conventional concrete. The possible explanation for the observed trend has been established based on the microstructural investigations presented in past.

2. Materials and Mix proportions

As cementitious material in the OPC-based conventional concrete Ordinary Portland Cement of 53 grade as per IS 269:2015, Fly-ash and silica fume are used. The geopolymer concrete mix is prepared using granulated blast furnace slag (GGBS) and fly ash as a source of reactive alumino-silicates in a proportion of 70:30 by weight. A combination of Sodium hydroxide and sodium silicate and potable water is used as a chemical activator in the mix. For conventional and geopolymer concrete, crushed coarse aggregates with a maximum nominal size of 20 mm and crushed fine aggregates confirming Zone II specifications of IS 383:216 are used. Sodium hydroxide (NaOH), used as the activator in the geopolymer mix, was 97.16 percent pure. Sodium Silicate Gel (Na_2SiO_3) was also utilized as an activator in addition to sodium hydroxide. The study presents two mixes for the conventional OPC-based concrete and two for alkali-activated concrete. Table 1 gives the ratio of the materials used in the mixes of geopolymer and conventional concrete. The mentioned mixes were prepared in three different variations –(i) Control or Plain mix – P, (ii) With 1% Steel fiber by volume – S, and (iii) With 1% of hybrid fiber by volume containing 75% steel fiber and 25% Polypropylene fiber by volume -H. The Steel fibers used are 0.55 mm in diameter and 35 mm in length and have an aspect ratio of 63. The tensile strength of the fibers as per the manufacturer is 1486.99 N/mm^2. The polypropylene triangular fiber of 6 mm length has been used in the hybrid fiber mix. The density of SF is 7860 Kg/m^3, and the density of PPF is 910 Kg/m^3. Figure-1 shows the steel and Polypropylene fiber used in the study. The dose of admixture in conventional concrete was 0.45 and 0.70 respectively for mix CC1 and CC2 respectively.

Table 1. Mix details of geopolymer concrete

Mix Parameter	GC1 (w/c=0.50)	GC2 (w/c=0.40)	CC1 (w/c=0.36)	CC2 (w/c=0.27)
Total cementitious Binder (Kg/m3)	350	380	417	525
Na2O (% by weight of total binder)	7	8	-	-
Activator Modulus (SiO2/Na2O)	1	1	-	-
OPC (Kg/m3)	-	-	334	400
GGBS + Fly ash + Silica fume (Kg/m3)	245 +105 +0	266 +114+0	0+83+0	0+75+50
NaOH + Na2SiO3 gel (Kg/m3)	17.24 +74.20	21.39+92.12	-	-
Fine Aggregate (Kg/m3)	690	660.80	726	692
Coarse Aggregate (mm)–10 + 20 (Kg/m3)	515 + 631	540+662	730+487	754+406
Water (after correction) (Kg/m3)	132.48	107.58	-	-

3. Experimental Setup and Test Procedure

The test procedure of the 3-Point bending test described by RILEM and literature was used to assess various fracture parameters for a notched beam specimen. Figure 1(a) depicts a schematic design of the 3-Point bend test and the laboratory equipment setup for the test performed. The test specimen is a notched beam with a 35 mm notch at the mid-span. The dimensions of the beam are 100mm x 100mm x 500 mm. It is simply supported on two smooth rollers and bears a clear span of 400 mm, as illustrated in figure 2 (b).

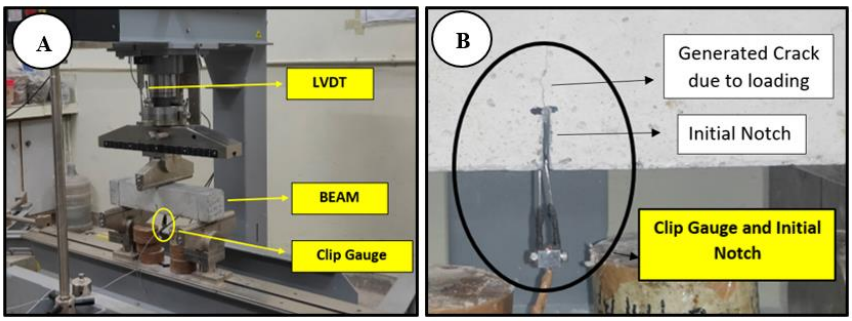

Figure 1. (a) Setup for three-point bend test, (b) Initial Notch, generated crack due to loading and clip gauge measuring CMOD during test

4. Test results and discussions

One of the basic properties of the material which is useful in analysing and determining crack resistance, brittleness and toughness is termed as Fracture energy (G_f) which can be defined as the energy required to create a unit crack in a given specimen. Figure 3, 4 and 5 shows the Load-CMOD and Load-deflection curves for different mix designs considered in the study. As seen in the plots the peak of the curves depends primarily on the grade of the concrete samples. Also, the curve peaks does not change significantly after the addition of fibers, however the post peak behaviour of the curves improved massively and will be reflected in the fracture parameters. The high strength conventional concrete with fibers shows an exceptional behavior and has the highest peaks. Also the peak in these samples were seen at higher CMOD level suggesting comparatively better ductility. The reason can be attributed to the action of the silica fume present in these mixes. Figure-6, 7, 8 and 9 provides fracture energy, stress intensity factor, characteritic length and energy release rate for different concrete mixes.

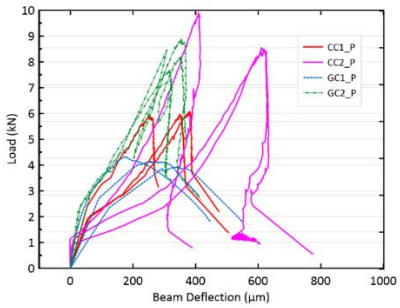

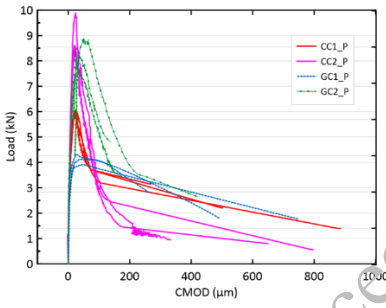

Figure-4. Load-deflection & Load-CMOD of Mixes without fiber

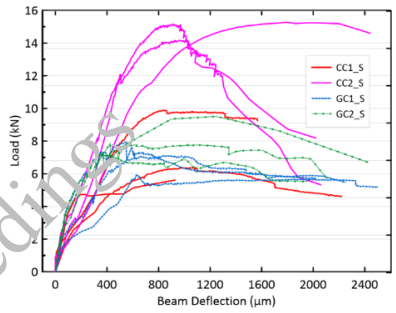

Figure-4.a Load-deflection and Load-CMOD with 1% steel fiber

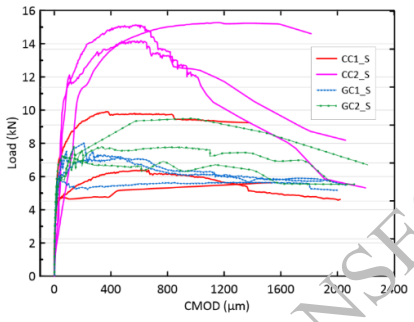

Figure-4.b Load-deflection and Load-CMOD with 1% steel fiber

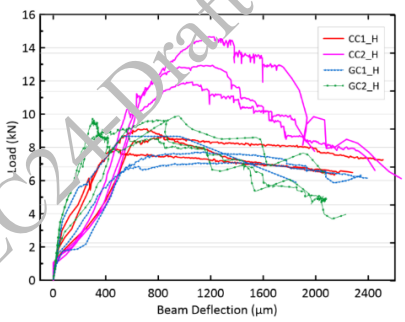

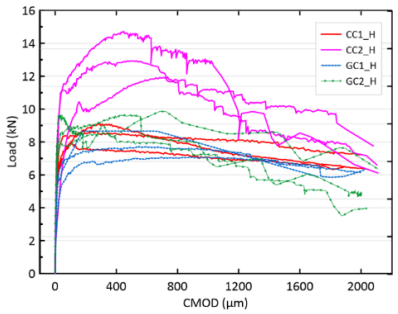

Figure 5. Load-deflection & Load-CMOD behaviour of Mixes with 1% Hybrid fiber (0.75% SF + 0.25% PP)

The highest fracture energy is shown by high strength conventional concrete with steel fibre followed by high strength conventional concrete with hybrid fibers. As explained earlier, the high strength concrete shows exceptional flexural properties due to the presence of silica fume in the mix. Along with this the improvement in the fracture performance of the concrete after the addition of fibers is related to the interlocking provided by the fibers by in the concrete. With addition of steel fibers, the stress intensity factor increases further when compared to the plain concrete. Also, similar to the fracture energy the high strength conventional concrete with steel and hybrid fibers shows exceptional behaviour due to the presence of silica fume. The stress intensity factor for the hybrid fiber reinforced geopolymer concrete is greater than that of the steel fiber reinforced geopolymer concrete, depicting an opposite trend to the conventional concrete. The characteristic length of concrete depends mathematically on the modulus of elasticity, fracture energy and the split tensile strength of the concrete. Since, plain geopolymer concrete has smaller modulus of elasticity than the conventional concrete the same has been reflected in the characteristic length.

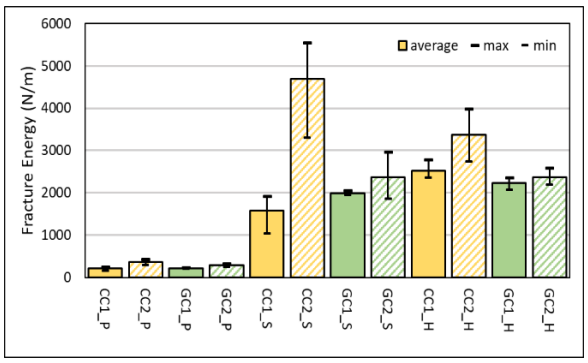

Figure-6. Fracture Energy

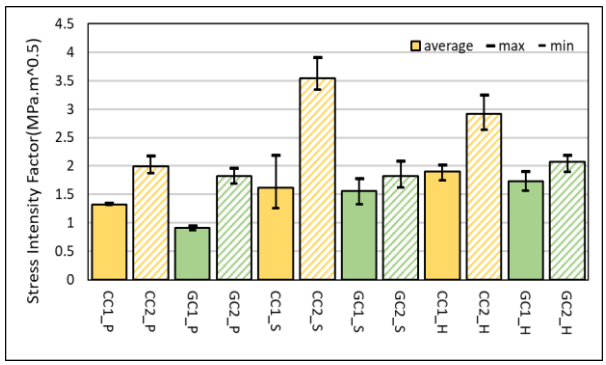

Figure-7. Stress intensity factor

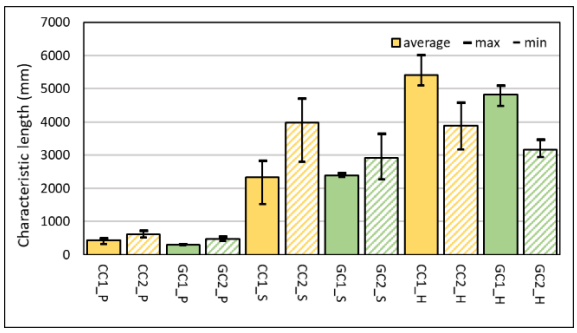

Figure-8. Characteristic length

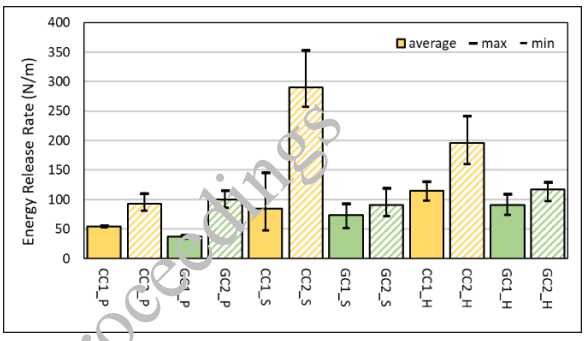

Figure-9. Energy release rate

Due to presence of more pores, bigger in size than the pores in geopolymer concrete, the fiber reinforced conventional concrete shows better characteristic length than the geopolymer concrete of comparable strength. In the case of hybrid fiber reinforcement, the polypropylene fibers gives a better interlocking of the concrete in the smaller pores of the geopolymer concrete than the steel fibers. the trend of variation of the energy release rate is opposite between the conventional and geopolymer concrete when steel and hybrid fiber reinforcement are compared. Due to dominant presence of meso-scale pores in geopolymer concrete the hybrid reinforcement is more effective in geopolymer concrete which is opposite to the conventional concrete where the steel fiber reinforcement shows the superior performance.

5. Conclusions

The fracture performance of geopolymer concrete is marginally lower than the conventional OPC concrete with comparable compressive strength. But the comparison considering the ratio of binder content suggests that with lower binder content the geopolymer concrete shows fracture performance at par with conventional concrete. With increase in grade of the concrete an improvement in the fracture parameters is observed in both conventional and geopolymer concrete. The conventional concrete mix with silica fume presented the best fracture performance among the considered mixes. With the addition of steel and hybrid fibers, the fracture performance of both concrete types improved significantly. However, adding fibers presented opposite improvement trends in conventional and geopolymer concrete. In conventional concrete, steel fibers performed much better than the hybrid fiber reinforcement. Whereas, for geopolymer concrete the hybrid fiber resulted in superior behaviour than the steel fiber alone. Due to the finer pore in geopolymer concrete, the Polypropylene fibers in hybrid fiber mix provided a better interlocking than steel fiber alone.

References

Arora VV, Singh B, Jain S. (2017). Effect of indigenous aggregate type on mechanical properties of high strength concrete. *Indian Concrete Journal*, 91:1 34-44

Arora V.V., Singh Brijesh, Patel Vikas, Trivedi Amit (2021a). Evaluation of modulus of elasticity for normal and high strength concrete with granite and calc-granulite aggregate. *Structural Concrete*, 22: S1. https://doi.org/10.1002/suco.202000023

Arora V.V., Singh Brijesh, Patel Vikas, Trivedi Amit (2021b). Evaluation of modulus of elasticity for normal and high strength concrete with granite and calc-granulite aggregate. *Structural Concrete*, 22: S1. https://doi.org/10.1002/suco.202000023

Ojha P, Singh B, Singh A, Patel V, Arora VV (2021). Experimental study on creep and shrinkage behaviour of high strength concrete for application in high rise buildings. *Indian Concrete Journal*, 95:2 30-42

Patel V., Singh B., Arora V.V. (2020). Study on fracture behaviour of high strength concrete including effect of steel fiber. *Indian Concrete Journal*, 2020; 94:4 1-9

RILEM TC-50 FMC (Draft Recommendation) (1985). Determination of the fracture energy of mortar and concrete by means of three-point bend tests on notched beams. *Material and Structures*, 18:106 285-290.

Shah SP (1990). Determination of fracture parameters (KIc s and CTODc) of plain concrete using three-point bend tests. *Materials and Structures*, 23:6 457-460. https://doi.org/10.1007/BF02472029

Singh B, Arora VV, Patel V. (2018). Study on stress strain characteristics of high strength concrete. *Indian Concrete Journal;* 92:6 37-43.

Experimental Study on Creep Coefficient of Normal, High and Ultra-High Strength Concrete

P N Ojha[1] and Brijesh Singh[2]*

[1]National Council for Cement and Building Materials, India,
Email: cdrncbb@gmail.com
[2]National Council for Cement and Building Materials, India,
Email: brijesh.singh@ncbindia.com

*Corresponding author

ABSTRACT

There are many creep models available internationally and study compares experimentally obtained creep coefficient for normal, high and ultra-high strength concrete with Bazant's B-3 & B-4 Model and Fib Model Code 2010. In this study, three different mixes with water to binder ratio of 0.47, 0.20 and 0.17 having compressive strength of 45 MPa, 100 MPa and 150 MPa respectively has been adopted. The creep test has been done on cylinder of 100 mm diameter and 200 mm height for ultra-high strength concrete and 150 mm diameter and 300 mm height for normal and high strength concrete. An experimental study has been done to determine the time induced creep strain using creep rig of capacity 2000 kN. The experimentally obtained creep coefficients for loading age of 28 days has been compared with B-3 model, B-4 Model and FIB model code 2010 for the test done upto 180 days. The creep coefficients determined using B3 and B4 model are over estimating the values in case of high and ultra-high strength concrete. Based on the comparison of experimental data of creep coefficient with models considered, it can be inferred that B3 and B4 model will not hold good for high and ultra-high strength concrete. FIB model code 2010 seems to be reasonable for prediction of creep coefficients of normal, high and ultra-high strength concrete.

KEYWORDS: *Creep, High strength, Ultra-high strength, Creep Models, Creep Coefficient*

1. Introduction

Creep performance is a key index in long-term properties of concrete, and the linear compressive creep deformation can reach one to four times of short term elastic compressive deformation (Wenzhong Z (2015)). Therefore, the creep behaviour must be considered in the design of concrete structures in order to provide desired safety and serviceability (Guo Z (2011), Huang G (2012)). There are various creep models available internationally, such as CEB-FIB series models (2010), ACI 209 series models, Gardener and Lockman (2000) model, B3 model of Bazant et al (1995), B4 model of Bazant et al (2001), Gong L (1988) etc. However, there are lot of differences in the influence factors, formula forms, applicable scope and prediction accuracy of various models due to limitation of specific experimental condition and the assumption considered by different researchers (Hanson (1953)). B3 model is only applicable for the concrete mixes prepared using OPC. B4 model is an extension and improvement over B3 model as it incorporates the effect of different dosages of mineral admixtures, chemical admixtures and aggregate type into concrete mix and introduces correction factors and scaling parameters for the same. The magnitude and the rate of development of creep depends upon many factors such as mix constituents, environmental conditions and stress level. As per Indian standard IS 456:2000, as long as the stress in concrete does not exceed one-third of its characteristic compressive strength, creep may be assumed to be proportional to the stress. In the absence of experimental data and detailed information on the effect of the variables, the ultimate creep strain may be estimated from the following values of creep coefficient; for long span structure, it is advisable to determine actual creep strain, likely to take place:

Age at loading	7 Days	28 Days	1 Year
Creep Coefficient	2.2	1.6	1.1
NOTE−The ultimate creep strain, estimated as described above does not include the elastic strain.			

The paper presents determination of creep coefficient on concrete cylinder of 100 mm diameter and 200 mm height for ultra-high strength concrete and 150 mm diameter and 300 mm height for normal & high strength concrete.

2. Materials and Mix proportions

2.1.1 Materials for Normal and High Strength Concrete:

Granite type crushed aggregate with a maximum nominal size of 20 mm was used as coarse aggregate and natural riverbed sand (quartz type) confirming to Zone II as per IS 383:2016 was used as fine aggregate. One brand of Ordinary Portland cement (OPC 53 Grade) with fly ash and silica fume were used in this study. Polycarboxylic group based superplasticizer for w/c ratio 0.20 and Naphthalene based for w/c ratio 0.47 complying with requirements of Indian Standard: 9103 was used throughout the investigation. For mixes having lower water cement ratio, PC based superplasticizer facilitate production of concrete with required workability when binary or ternary blends were used, which is not possible with Naphthalene based superplasticizer.

2.1.2 Materials for Ultra High Performance Concrete:

In this study, OPC- 53 Grade, flyash, GGBS, silica fume and nano-silica as cementitious materials were used. For better packing density of aggregates, different types of aggregate like Fine Quartz sand and Ground Quartz were used. Ordinary Portland Cement (OPC) 53 grade complying with IS 269:2015 and GGBS complying with IS 16714:2015 was used. GGBS particles were in the range of 1.15 to 250 microns. Flyash complying with IS 3812 and Silica fume complying with IS 15388 was used. The maximum particles of silica fume were in the range of 0 to 10 microns. The Brunauer-Emmett-Teller (BET) fineness and solid content of used nano silica are 24 m^2/g and 20 (% w/w) respectively. The specific density of nano silica was found to be 2.21 g/cm^3. In this study Ground Quartz particle size is on the coarser side of the particle size of cement particles. Ground Quartz was used as a micro filler to optimize the packing density of concrete mix. Its particle size range varies from 0.5 to 140 microns. It was also used to optimize the packing density of concrete mix having the particle size ranges from 150 to 996 microns. Polycarboxylate ether (PCE) based chemical admixture complying with requirement of IS: 9103 and Viscosity Modifying Admixture (VMA) has been used during mix preparation to achieve workability.

3. Mix design details

In this study, the two different mixes with w/c ratio 0.47 and 0.20 using granite aggregate were selected for determining creep coefficients for normal and high strength concrete. The slump of the fresh concrete was kept in the range of 75-100 mm. The laboratory conditions of temperature and relative humidity were monitored at 27±2°C and relative humidity 65% or more for maintain ambient curing condition. The mix proportion for ultra high strength concrete of individual cementitious material was decided using the Modified Andreasen and Andersen equation. The details of the mix composition (Table-2) of the optimized mix has been given below. The total cementitious content used has been kept as 1000 kg/m^3. To attain better particle packing density, a combination of fine aggregates was used i.e. Ground quartz and Fine quartz sand. The nano-silica was used as 3% replacement for OPC content.

Table 1. Concrete Mix Design Details Normal and High Strength Concrete

w/b	Total Cementitious Content [Cement (C) + Fly ash (FA) + Silica Fume (SF)] (kg/m^3)	Water Content (kg/m^3)	Chemical Admixture % by weight of cement	Fine Aggregate as % of Total aggregate by weight	28-Days cube compressive strength (N/mm^2)
0.47	362 (290+72+0)	170	1.00	35	48.93
0.20	750 (548+112+90)	150	1.75	35	106.25

Table-2. Concrete Mix Design Details Ultra High Strength Concrete

Mix ID	Mix Details A (Optimised Mix)
w/binder	0.17
Cementitious Content [Cement + Fly ash + GGBS + Silica fume + Nano Silica] kg/m^3	1000 (635 + 95 + 110 + 140 + 20)
Sand (FQS + GQ) kg/m^3	922 + 256
Admixture (%)	2 % SP and 1 % VMA
Water kg/m^3	170

4. Creep Test in Compression

The paper presents determination of creep coefficient on concrete cylinder of 100 mm diameter and 200 mm height for UHPC and 150 mm diameter and 300 mm height for normal and high strength concrete. The compressive strength of each mix was used for calculation of the load to be applied to the creep specimens, which was taken as 40% of the average compressive strength. The testing was carried out in creep test rig of 2000 KN capacity. The accuracy of load gauge of creep testing rig was ± 1% from 10% to 90% of full scale loading. The least count of the load indicator was 10 KN. The vibrating wire strain gauges were inserted in cylindrical specimens before casting. The specimens were cured by wrapping in Butyl Rubber Sheet upto 28 days**.** Relative humidity was maintained at 60% and temperature was maintained at 27^{0}C. The creep as per ASTM C-512 was measured using data readout units. In creep test, samples were kept in controlled and loaded condition for the time period of 180 days (Figure-1). Control specimen as well as specimen used for estimation for strength were kept under the same curing and storage treatment as the loaded specimen.

5. Test results and discussions

The creep coefficient from the experimental results and B3 model, FIB model code 2010 and B4 model has been worked out up to 180 days of loading and are given in Figure-2, 3 and 4. The results indicate that experimentally obtained creep coefficients for water cementitious ratio of 0.47 (normal strength concrete) are closer to corresponding creep coefficients obtained using all three models i.e. B3 model, FIB model code 2010 and B4 model. Among the three models, model B4 underestimates the creep coefficient values, though it is closest to the experimental values for mixes having higher water-cementitious ratio (i.e. normal strength concrete). The experimentally obtained creep coefficients for water cementitious ratio of 0.20 (high strength concrete) and 0.17 (Ultra High Performance concrete) are very less in comparison to creep coefficients obtained using B3 and B4 model. However, in between B3 and B4, the creep coefficients predicted by B4 is closer to experimentally obtained creep coefficient.

Figure 1 Creep Testing Arrangement

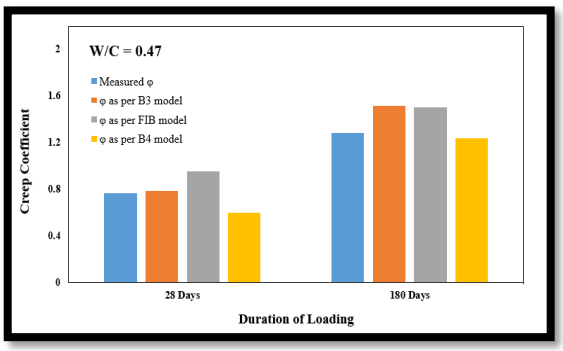

Figure-2 Experimental creep coefficient of concrete mix having w/c = 0.47 with Bazant's B3 model, FIB code 2010 & Bazant's B4 model

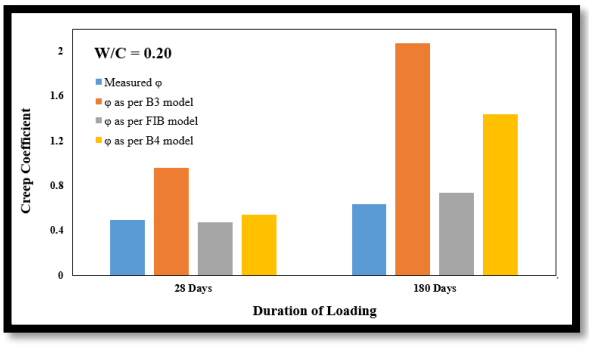

Figure-3 Experimental creep coefficient of concrete mix having w/c = 0.20 with Bazant's B3 model, FIB code 2010 & Bazant's B4 model

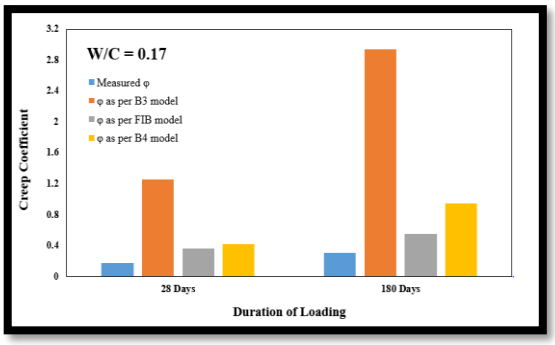

Figure-4 Experimental creep coefficient of concrete mix having w/c = 0.17 with Bazant's B3 model, FIB code 2010 & Bazant's B4 model

The results indicate that FIB model code 2010 seems to work well for all the three water-cementitious ratios as experimentally obtained creep coefficients for all the three water cementitious ratios are closer to corresponding creep coefficients obtained using FIB model code 2010. Therefore, based on the comparison of experimental data of creep coefficient with all the three models, it can be inferred that B3 and B4 model will not hold good for high strength concrete and ultra-high performance concrete. FIB model code 2010 seems to be reasonable for prediction of creep coefficients of both normal, high strength concrete and ultra-high performance concrete. The primary reason for over estimation of creep in high strength concrete using B3 and B4 model can be attributed to chemical volume reduction and self-desiccation along with decrease in pore humidity. The complications arise in creep prediction while using B3 and B4 model due to attenuating effects of diverse admixtures and reactive additives present in high strength concrete. Keeping in view that current provisions of IS 456:2000 are only valid up to M55 grade of concrete and not applicable for higher grades, it is recommended that FIB model code 2010 may be adopted in revision of IS 456:2000 for reasonable estimation of creep coefficients for higher grades of concrete. The advantage of adopting FIB model code 2010 is that it enables a more accurate analysis and better assessment of the creep deformation of concrete structures along with significantly reducing the complexities and excluding a range of influencing parameters from the model for simplicity and easy adaptation at the design stage

6. Conclusions

Based on the experimentally obtained creep and comparison of creep coefficients using B3 model, B-4 Model and FIB model code 2010, it is seen that all the three models seem to work well for normal strength concrete as the creep coefficients obtained using B3 model, FIB model code 2010 and B4 model are very close to experimentally obtained creep coefficients for normal strength concrete. However, the results indicate that experimentally obtained creep coefficients for high strength concrete and ultra-high performance concrete are lower in comparison to creep coefficients obtained using B3 and B4 model. Based on the comparison of experimental data of creep coefficient with all the models, it can be inferred that B3 and B4 model will not hold good for high strength concrete and ultra-high performance concrete. FIB model code 2010 seems to be reasonable for prediction of creep coefficients of normal, high strength concrete and ultra-high performance concrete. The creep coefficients in IS 456:2000 needs to be linked with grade of concrete and type of cement and cementitious materials, so that the creep coefficient of high strength concrete is addressed in a reasonable way for application in pre-stressed concrete and high rise buildings. In the case of high strength concrete, IS 456:2000 creep coefficients will not hold good and needs to be revised. The FIB model code 2010 empirical equations can be adopted for the revision of IS 456:2000 which gives reasonably closer values of creep coefficient to the experimental creep coefficient compared up to 180 days of loading for both normal and high strength concrete with sufficient margin of safety

References

Wenzhong Z. and Can T. (2015). "Study on the effect of the strength grade on the creep behaviour of concrete". *The open Civil Engineering Journal, Vol. 9, pp. 881-887.*

Guo Z. and Shi X. (2011). "Reinforced Concrete Theory and Analysis". *Tsinghua University Press, Beijing, pp. 58-64*

Huang G., Hui R. and Wang X. (2012). "Creep and Shrinkage of Concrete". *China Electric Power Press, Beijing, pp. 95-104.*

"FIB model code 2010". *International Federation for Structural Concrete (fib). ISBN 978-2-88394-095-6*

Bazant Z. P. (2001). "Prediction of concrete creep and shrinkage: past, present and future". *Nuclear Engineering and Design, vol. 203, pp.27-38.*

Bazant Z. P. and Baweja S. (1995). "Creep and shrinkage Prediction Model for Analysis and Design of Concrete Structures-Model B3". *RIIEM Recommendation. Materials and Structures, vol. 28, pp. 357-365.*

Gong L., Hui M., and Yang B. (1988). "Practical mathematical expressions for creep and shrinkage of concrete". *Journal of Building Structures, vol. no. 5, pp. 37-42.*

Hanson J. A. (1953) "A Ten-year Study of Creep Properties of Concrete. Concrete Laboratory". *US Department of the Interior, Bureau of Reclamation, Denver, Report no. SP-38.*

IS 456:2000. "Plain and reinforced concrete-code of practice". *BIS New Delhi*

TC-242-MDC (2014). "TC-242-MDC multi-decade creep and shrinkage of concrete: material model and structural analysis". *RILEM Technical Committee.*

Drying Shrinkage of low-calcium fly ash Geopolymer: The roles of External conditions and Binder Composition

[1] Mude Hanumananaik[1] and Kolluru V L Subramaniam [2*]

[1] Research scholar, Indian Institute of Technology, Hyderabad, India. ce15m17p000001@iith.ac.in
2 Professor, Indian Institute of Technology, Hyderabad, India. kvls@ce.iith.ac.in

*Correspondence author

ABSTRACT
Alkali activated fly ash (AAF) is an attractive binder to replace the conventional cement. Shrinkage of the low calcium fly ash based geopolymer under different curing conditions were evaluated in this study. The curing adopted was relevant to precast production where a high temperature is prescribed for a short duration. This process suits geopolymers and leads to accelerated geopolymer production. Curing conditions are varied in terms of the process variables such as, curing temperature and relative humidity (RH). The influence of humidity and temperature on the drying shrinkage measured in AAF pastes was evaluated. The mass loss is determined by the RH and curing temperature of the geopolymer. The measured drying shrinkage and mass loss is related with the porosity and sodium-alumino-silicate (N-A-S-H) gel content of the low calcium fly ash geopolymer. The drying shrinkage depends on the water and sodium contents in the activated paste. AAF mixture made with smaller water content has a refined pore structure, which results in increased shrinkage strain on drying while the mass loss is lower. Excess sodium in AAF produces a larger shrinkage strain on drying due to the pore refinement. Optimizing the mixture composition requires consideration of sodium content in the mixture to mitigate shrinkage.

KEYWORDS: *Geopolymer, Drying, N-A-S-H, Porosity, Shrinkage*

1. Introduction

Geopolymer binders, which are created by activating fly ash with alkali, are becoming more popular as environmentally-friendly substitutes for Portland cement. By incorporating fly ash into geopolymers, both environmental concerns and the increasing need for cement can be effectively addressed [Komljenovic (2015)]. The characteristics and attributes of geopolymers are greatly influenced by the composition of the source material and the substances utilized as activators. Low-calcium fly ash is very desirable since it is cost-effective and readily available. It also requires less energy for processing compared to Portland cement. Geopolymers derived from low-calcium fly ash provide similar or enhanced ability to withstand compression, increased resistance to damage from sulfate, minimum deformation over time, resistance to acid, and reduced shrinkage [Habert et al. (2011), Mclellan et al (2011), Pacheco-torgal et al. (2012), Duxson et al. (2007), Davidovits (2020)].
Extensive research has been conducted on the optimization of geopolymers derived from low-calcium fly ash [Duxson et al. (2005), Bhagath Singh & Subramaniam (2017)]. This research has specifically examined the relationship between the composition of the reaction products and the compressive strength of the geopolymers. It is essential to adjust the composition of the activating solution to correspond with the reactive properties of fly ash in order to attain geopolymers with high strength [Bhagath Singh & Subramaniam (2020)]. High-temperature curing is frequently required for effective geopolymerization, which makes low-calcium fly ash geopolymers well-suited for precast applications. Comprehending the shrinkage that occurs when materials are exposed to higher temperatures for a short amount of time is crucial for the advancement of these specific uses.
The majority of past research has been on alkali activated slag binders, with only a limited number of papers documenting geopolymer systems created using activated fly ash [Kumarappa et al (2018), Lizcano et al. (2012), Ye & Radlinska (2016), Ye et al. (2017), Zhang et al. (2022)]. According to the available data, the geopolymer has a decreased drying shrinkage compared to regular cement paste [Sagoe-Crentsil et al.

(2013)]. The range of values is between 12 and 14. The mass loss during drying in geopolymers formed by alkali activation of fly ash is not directly equivalent to the shrinkage observed in cement paste. This discrepancy might be attributed to variations in porosity and pore structure, as supported by previous studies [Hojati et al. (2019), Ma&Ye (2015), Ling et al. (2019)]. Upon the commencement of the drying process, the rate of shrinkage decreases significantly, and a state of equilibrium is reached within a span of seven days. The drying shrinkage is significantly affected by the activator composition, including the concentration of sodium hydroxide, the ratio of sodium silicate to sodium hydroxide, and the ratio of activating solution to binder. According to research, the drying shrinkage of the geopolymer paste is directly proportional to the levels of sodium and silica in the activating solution [Ma & Ye (2015)]. Mixtures containing a higher concentration of activator and a lower modulus (SiO2/Na2O) demonstrate increased drying shrinkage [Ling et al. (2019)]. The quoted shrinkage measurements have been shown to be dependent on the specific processing conditions. An intensified desiccating environment resulting from a reduction in relative humidity (RH) led to an augmentation in shrinkage [Hojati et al. (2019)]. Heat curing results in a higher rate of initial drying shrinkage compared to room-temperature curing, but it leads to reduced ultimate shrinkage [Hojati et al. (2019), Thomas et al. (2017)]. The fly ash that had the lowest calcium and medium amorphous concentrations showed the largest drying shrinkage [Gunesekera et al. (2019)].

The moisture content in the paste is essential in determining the extent of drying shrinkage. Simultaneously, the observed alteration in volume of the geopolymers is not linearly related to the amount of mass lost during the drying process [Hojati et al. (2019)]. Nevertheless, previous shrinkage studies have not specifically assessed the impact of the water concentration in the mixtures. The relationship between compositional factors and water content in the activated paste is frequently overlooked in research. Thorough investigation is required to examine the impact of the initial presence of water in the system. Previous studies have revealed the influence of the activating solution, but it is now understood that the composition of the activating solution can vary in mixes designed for strength. This is because the content of the fly ash can vary significantly. The activated mixes utilized in the study must be proportioned according to the reactive content present in the fly ash, and the measured shrinkage should be correlated to the content of the reaction product created in the activated mixtures. This correlation is necessary to establish a reliable basis for evaluating shrinkage. Prior research has made general conclusions about the impact of compositional or process variables on shrinkage, but has not connected these findings to the content of the reaction product in the AAF [Chen et al. (2021)].

This study examines the connections between shrinkage, the amount of reaction products, and the pore structure in low calcium fly ash based geopolymers. The composition of the activating solution is assessed by considering the quantity of reactive components present in fly ash. The presence of reactive silica and alumina in fly ash is utilized to calculate the amount of extra silica needed in the activating solution. The alumino-silicate content that is generated in the active system is directly linked to the pore structure and the behavior of shrinkage.

2. Materials and methods

The fly ash utilized in this investigation was obtained from a thermal power plant located in Ramagundam, Telangana, India, which has a power generation capacity of 2600 MW. The chemical composition of the fly ash was analyzed using X-ray fluorescence (XRF) spectroscopy and reported in Hanumanaik et al. (2022), following the guidelines for siliceous and class F fly ash as outlined in IS 3812 and ASTM C 618. The CaO content of the fly ash is 4.06%, considering the very low level of CaO, the fly ash further classified as low-calcium fly ash which consists of reactive silica and alumina as the amorphous glassy phase. The discovered crystalline phases consist of quartz and mullite, along with small amounts of magnetite, hematite, and rutile. The identification of these phases was accomplished using X-ray diffraction (XRD) investigation, and their characteristics were further improved using the Rietveld method.

The activating solution was prepared by mixing solutions of sodium hydroxide (NaOH) and sodium silicate ($Na_2O_xSiO_2$). An 8M NaOH solution was prepared by dissolving sodium hydroxide pellets with a purity of 98% in deionized water 24 hours before casting. The activating solution was formed by mixing sodium silicate solution, which had a silica modulus (SiO_2/Na_2O) of 2.32 and a pH of 12.98, with the 8M NaOH solution and extra water.

Three different alkali-activated fly ash (AAF) paste mixtures were prepared with varying water and sodium contents while maintaining consistent reactive oxide ratios. The mix proportions are detailed in Table 1. The mixture labeled "A" was formulated using a reactive (SiO_2/Al_2O_3) ratio of 2.0 and a reactive SiO_2/Na_2O ratio of 5.0, which is known to result in a high compressive strength. The solution-to-binder ratio, which is the ratio of activating solution to fly ash, was established at 0.41. The "B" mixture contained a decreased amount of water, resulting in a solution-to-binder ratio of 0.37. The "C" mix had a higher NaOH concentration while maintaining a constant amount of additional water.

Table 1: Paste composition of AAF for 100 grams of fly ash

Mix ID	Activating solution mass (g)			Reactive oxide ratios in AAF paste		
	$Na_2O.xSiO_2$ solution	NaOH	Added H_2O	SiO_2/Al_2O_3	SiO_2/Na_2O	NaOH Molarity
A	17.9	5.0	17.9	2	5	4.22
B	17.9	5.0	14.5	2	5	4.79
C	17.9	7.1	17.9	2	4	5.85

The AAF paste mixes were produced utilizing a pan mixer. The activating solution, comprised of a mixture of sodium silicate solution and 8M NaOH, was introduced to the fly ash. The paste was thoroughly blended until it reached a uniform and consistent texture. Subsequently, the paste was poured into molds and transferred to an environmental room set at a temperature of 60°C and a relative humidity of 95% for a duration of 24 hours. Following the initial curing process, the samples were removed from the molds and placed in a chamber maintained at a temperature of 60°C and a relative humidity of 50% for the whole duration of the testing period. The compressive strength of the material was determined at 1, and 28 days using 70 mm cubes, in accordance with the IS 4031-Part 6 standard. Following the compressive strength testing, a sample was obtained from the center of the cube. The samples were then subjected to solvent exchange and vacuum dried for a duration of 24 hours at a temperature of 40 degrees Celsius. The samples were dried and then stored in zip lock covers before being placed in a vacuum desiccator for further analysis.

2.1 Shrinkage measurements:

The measurement of drying shrinkage was conducted in accordance with the requirements set by ASTM C596. Prisms measuring 25 mm x 25 mm x 285 mm were fabricated, sealed, and subjected to a curing process at a temperature of 60°C. After a period of 24 hours, the prisms were removed from their molds, and first measurements were obtained using a length comparator with a precision of 0.0025 mm. Measurements of length change and mass loss were taken at regular intervals throughout the testing period. The samples were kept at a constant relative humidity of 50% and a temperature of 60°C.

Autogenous shrinkage was quantified in accordance with ASTM C1698 guidelines using a flexible corrugated pipe. The AAF paste was poured into pipes measuring 420 mm in length and 29 mm in diameter. The pipes were sealed at both ends and kept in storage at a temperature of 60°C and a relative humidity of 95%. Length measurements were initially taken every 50 seconds for a duration of three days using linear variable differential transformers (LVDT) with a precision of 0.001 mm. Subsequently, measurements were conducted using a length comparator.

3.0 Results and discussion

The compressive strength of the AAF paste cured at different curing conditions are depicted in figure 1. Figure 1(a) depicts the compressive strength of the AAF cured at 60°C and continuous moist curing for 28 days and figure 1(b) depicts the compressive strength of the AAF paste cured at 60°C and 50% RH after 1 day of moist curing at 60°C. The resuts indicate that the AAF paste with identical water cintent and increase in Na content (mix A and C) achieved similar strength. Decrease in water content resulted in increase in compressive strength of the AAF paste. Drying of AAF paste samples by decreasing the RH to 50% resulted in decrease in compressive strength irrespective of the AAF mix.

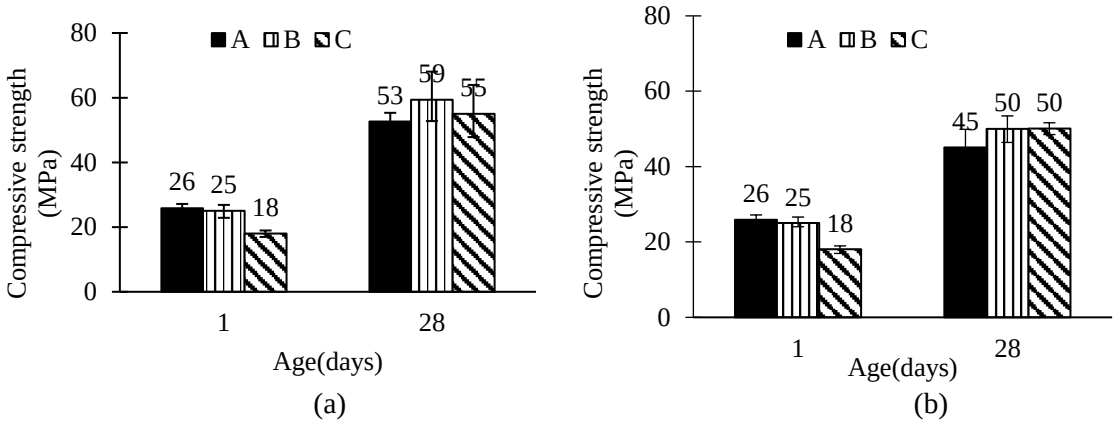

Figure 1: Compressive strength of AAF paste cured at (a) Continuous moist curing at 60ºC (b) After 1 day, curing at 60ºC and 50% RH

3.1 Reaction product content

XRD measurements were conducted using a Brucker D2 Phaser™ with a Cu-Kα radiation source and a LYNXEYE detector. The samples were scanned over 2θ angles from 10° to 70° with a step size of 0.02°. Crystalline phases were quantified using the Rietveld refinement procedure, and amorphous content was determined using intensity-based direct decomposition. An external standard, NIST SRM 676a α-Al_2O_3, was used for calibration.

The typical XRD signature of the 28-day AAF mixture "A" is shown in Figure 2. The Rietveld refining process is used to fit the intensity patterns of the distinct crystalline phases found in the activated paste. The primary crystalline phases are recognized as Quartz, Mullite, Hematite, and Rutile. Additionally, a small amount of newly formed crystalline substances was found in the AAF. A phase with hkl was designated for a cubic structure with Fm3m space group (Space group No. 225) in order to match the intensity pattern of the entire amorphous phase utilizing the Pawley refining process. The figure displays the intensity signature of the entire amorphous phase found in the AAF, as acquired via the Pawley refinement. Both the N-A-S-H and unreacted fly ash glassy phase collectively contribute to the overall intensity signature of the amorphous phase in the AAF. The pronounced peak in the intensity pattern between 20 - 40 degrees 2θ is a result of the presence of the completely disordered phase in the AAF.

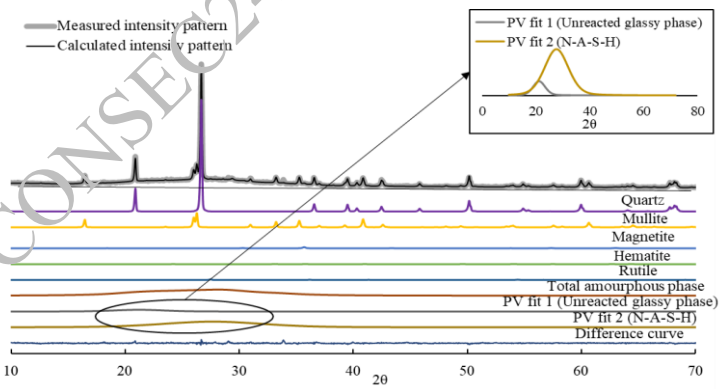

Figure 2: Total intensity signature and the intensity signatures of the crystalline and amorphous phases present in the 28-day Ms5-0.25W/S AAF.

Figure 5 displays the N-A-S-H content in the AAF paste for all three mixtures as a function of age. The measurements were taken after one day of casting, and the samples were subjected to continuous moist curing and drying at 60oC and 50% RH. Figure 5(a) displays the N-A-S-H content of the AAF paste that underwent continuous moist curing. The correlation between the growing N-A-S-H content with age and the reported strength gain is evident in the patterns. The rise in the N-A-S-H contents in both pastes with identical Ms is comparable. When comparing the AAF mixtures with the same amount of water but varied Ms, the N-A-S-H contents are approximately equal after 28 days. The additional sodium in the paste with Ms of 4 did not result in an increase in N-A-S-H content in the AAF. Previous studies have reported similar findings in samples that were continually cured in a moist environment [8]. Nevertheless, the AAF combination with reduced water content exhibits a greater N-A-S-H content per unit mass of AAF. The N-

A-S-H content in the mixture with a W/S ratio of 0.22 (mix B) is greater than the N-A-S-H concentration in the AAF mixtures with a W/S ratio of 0.25.

Figure 5 (b) illustrates the composition of the reaction products in the AAF paste after one day of moist curing and subsequent drying. The process of drying has an effect on the amount of N-A-S-H content that is generated in the paste. The impact of drying on the N-A-S-H content in the AAF is contingent upon the levels of water and sodium present in the activated paste. Even after being dried, the paste with less water content had a larger N-A-S-H per unit mass of AAF compared to the other combinations. When comparing pastes with the same amount of water but different levels of sodium, the paste with more sodium has a greater N-A-S-H content as it ages. The observed patterns in the N-A-S-H content align with the quantified increases in strength of the pastes.

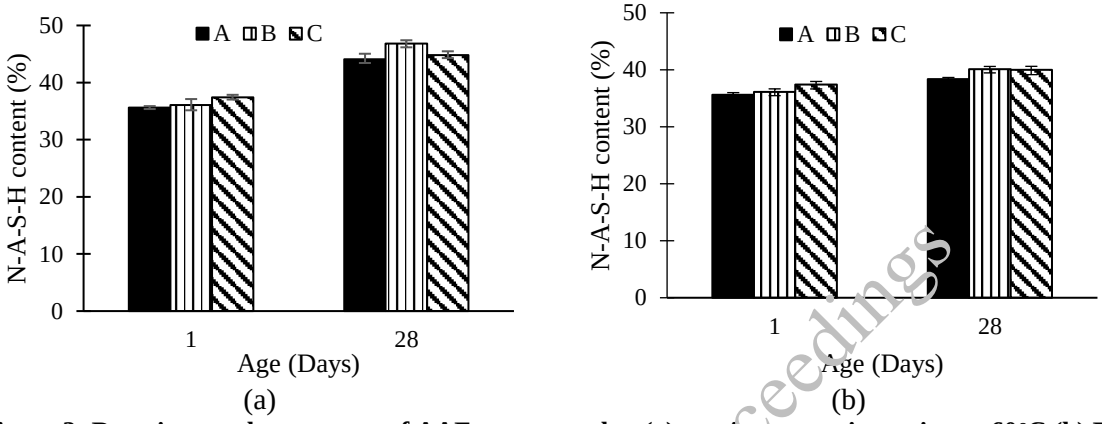

Figure 3: Reaction product content of AAF paste cured at (a) continuous moist curing at 60ºC (b) Drying at 60ºC and 50% RH after one day.

3.2 Autogenous Shrinkage

Figure 6 displays the autogenous shrinkage of AAF mixtures after the completion of the final setting time for all three mixes. Autogenous shrinkage was quantified on three specimens, and the resulting mean values were documented. The scatter bars were used to represent the range of values. The majority of autogenous shrinkage took place within the initial 24 hours, and a stable value was reached within a few days. The autogenous shrinkage of the A and B mixes was measured to be 550 and 630 micro strains, respectively. The autogenous shrinkage measured from the C mix was greater at 750 micro strains. The autogenous shrinkage increased by approximately 80 micro strains due to a decrease in water content (mix A and B). The increase in sodium concentration in the AAF paste resulted in a rise in autogenous shrinkage of around 200 micro strains.

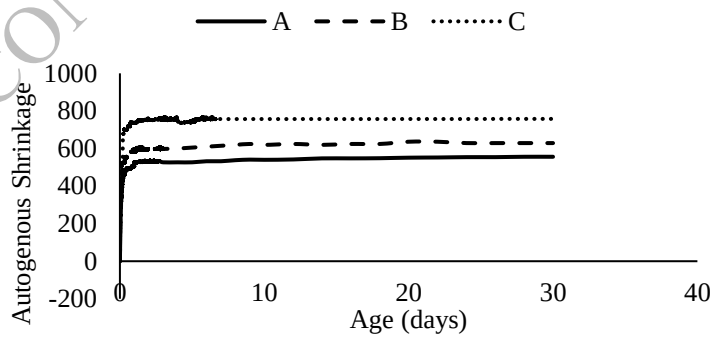

Figure 4: Autogenous shrinkage of AF paste

3.3 Mass loss and Drying shrinkage

Figure 7 illustrates the data on drying shrinkage and mass loss that was collected from all three AAF mixtures. The picture includes a plot of the drying shrinkage of cement paste (OPC) prepared with a water-to-cement (w/c) ratio of 0.41 for reference. After a span of three days, noticeable disparities in the drying shrinkage were observed between AAF mixes and OPC. The AAF mixes exhibited reduced drying shrinkage compared to the OPC. The drying shrinkage of OPC was measured to be approximately 3500 με after 28 days. The AAF pastes exhibited drying shrinkage values ranging from 1000 to 1500 με. After ten

days of drying, the AAF mixes showed a consistent and controlled decrease in volume. The shrinkage strain increased by roughly 400 με as a result of the w/s ratio decreasing from 0.25 to 0.22. The addition of sodium, without change in the water-to-solids ratio, resulted in a significant increase of around 700 με in the drying shrinkage after 28 days.

Figure 7(b) displays the recorded mass loss of the AAF and OPC samples during the drying process. Following the commencement of the drying process, there is a quick decrease in mass for the initial few days, after which the value stabilizes and remains constant. The bulk of the mass decrease in AAF occurred over the first three days after the start of the drying process. For OPC, it required a period of 15 days for the mass loss to stabilize at a consistent level. The mass loss observed in AAF mixes is less than that in OPC. A increased water content in AAF resulted in a greater mass loss. AAF samples with same water content, but different salt levels exhibited equivalent mass reduction after the drying process. The Ms5-0.25W/S AAF mixture experiences a mass loss of around 11.5%, whereas the Ms5-0.22W/S and Ms4-0.25W/S mixtures have a mass loss of roughly 9.3% and 11.0% respectively. There is no correlation between the loss of mass and the contraction of the AAF mixture. The moisture content in the AAF mixture is a critical factor in determining the amount of mass lost. On the other hand, the composition of the activator is responsible for the shrinkage. The drying shrinkage is larger in the AAF with lower initial water content, even when the mass loss is identical. Concrete mixtures including AAF with an increased sodium level exhibited greater drying shrinkage, although the amount of mass lost was influenced by the initial water content.

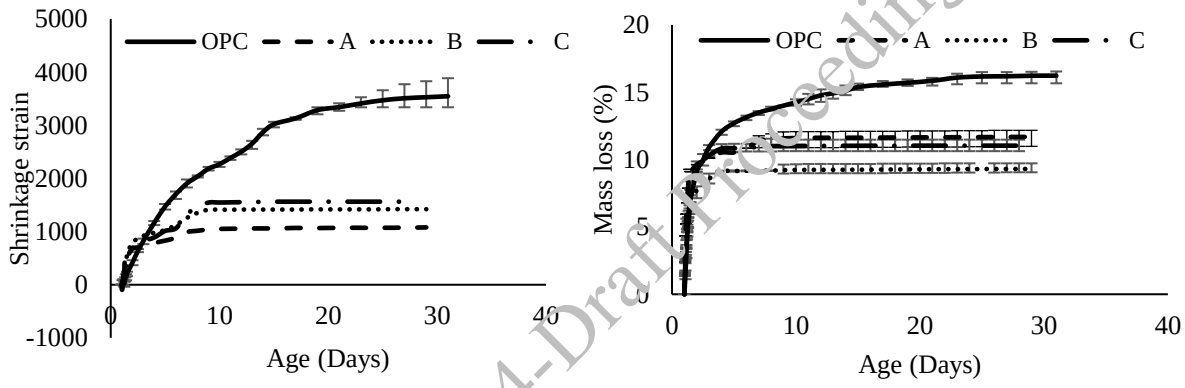

Figure 4: (a) Drying shrinkage and (b) mass loss of AAF paste

3.4 Porosity and Pore structure

The porosity and pore size distribution of the hardened AAF samples were evaluated using Mercury Intrusion Porosimetry (MIP) with a Poremaster 60 model. The procedure consisted of first filling with low-pressure mercury, then infiltrating with high-pressure mercury. Pore size estimations were conducted using the Washburn equation shown in equation (1). The measurements encompassed a variety of pore sizes, ranging from 1100 μm to 3.6 nm.

$$D = \frac{-4\gamma cos\theta}{P} \quad (1)$$

Where where D is the pore diameter in μm, γ is the surface tension of the mercury (0.485N/m), θ is the contact angle of the mercury (140º), and P is the applied pressure.

Figure 8 illustrates the level of porosity and pore structure in the 28-day AAF mixes that were cured at a temperature of 60 degrees Celsius and a relative humidity of 50% after being removed from the mold. The mixtures had varying percentages of activators. The reduction in water content led to a decrease in both the critical pore size and the total porosity. The intrusion indicates a notable disparity in the volume of pores between two distinct ranges of pore sizes. There is a significant disparity in size between the ranges of 100 and 10 μm. The variations in pore volumes in the AAF combinations can be mostly attributed to two distinct pore diameters.

Figure 8(b) displays the relationship between the pore diameter and the differential pore volume. The differential pore volume map reveals the presence of two distinct size ranges of pores. Pores with a diameter of 100-250 nm are classified as large, while those with a diameter of 20-30 nm are considered small. There is a notable disparity in the amount of substance that has entered the pore structure across the various pore diameters. Reducing the water-to-solids ratio from 0.25 to 0.22 while maintaining the reactive oxide ratios of the AAF mixture led to a more compact pore structure. An increase in sodium concentration led to the

densification of the pore structure, while keeping the water content constant. This observation is consistent with prior findings [13].

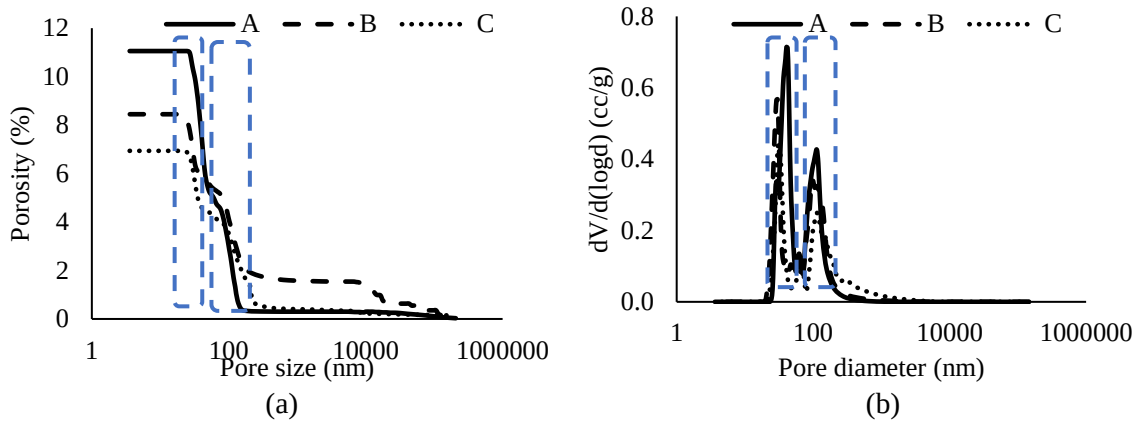

Figure 5: (a) Porosity and (b) pore size distribution of AAF paste

3.5 Discussion

The shrinkage of alkali-activated fly ash (AAF) is influenced by external elements such as relative humidity (RH) and curing temperature, as well as compositional factors including binder properties and activator composition. The majority of the autogenous shrinkage in AAF mixes takes place within the initial 24 hours when the samples are sealed. Although the internal relative humidity (RH) stays high in AAF, the cement paste undergoes a drop in moisture content due to water absorption by the calcium silicate hydrate (CSH) gel. Within the context of AAF, the aluminosilicate gel undergoes reorganization and polymerization, resulting in autogenous volume alteration, which distinguishes it from cement paste. Hydroxyl ions condense during gel polymerization in AAF, causing water to be added and resulting in volumetric contraction.

Within a 24-hour period, the primary cause of volume change is the loss of moisture, while the contribution from sealed shrinkage mechanisms is minor. The moisture content within the system plays a vital role in the generation of reaction products. When the relative humidity (RH) is less than 100%, the water inside evaporates, which has an impact on the creation of the gel. Water is required for the process of geopolymerization; however, it does not directly result in the formation of N-A-S-H gel. The shrinkage of AAF is greatly affected by the water content. A decrease in water content leads to an increase in autogenous shrinkage because of a more compact pore structure and greater N-A-S-H content. Drying shrinkage is the result of the evaporation of free water from hardened samples, and the extent of shrinkage is influenced by the size of the pores.

The amount of sodium present also has an impact on the degree of shrinkage. Elevated sodium levels in AAF mixes with the same amount of water result in more shrinkage, decreased porosity, and a smaller critical pore size. Excessive sodium does not enhance the mixture, but rather improves the pore structure, leading to an increase in shrinkage. Hydrolysis investigations indicate that an excess amount of sodium remains unattached, leading to the presence of pores and a more refined pore structure, while not having a substantial impact on strength. Prior research suggests that an excessive amount of sodium affects the Si-O-T network structure that is essential to produce N-A-S-H. The porosity and critical pore size increase following hydrolysis because of the leaching out of unbound sodium.

4.0 Conclusions

This study assessed the effects of sodium (Na) and water content in the activating solution on the shrinkage of an alkali-activated fly ash (AAF) mixture. The shrinkage of the AAF mixture is directly linked to the variations in the composition of the reaction product and the microstructure of the AAF. The findings derived from this research can be summarized as follows:

- Decreasing the amount of water in the activating solution was discovered to increase the amount of N-A-S-H per unit volume in AAF, leading to a more refined pore structure and improved mechanical strength.

- Excessive sodium did not modify the content of the reaction product, but it was present in a soluble form that was released during the curing process. This resulted in a more refined pore structure without any impact on the compressive strength. There was a direct relationship between a larger amount of sodium and an increase in both autogenous and drying shrinkage.
- Autogenous shrinkage was significantly greater in AAF mixtures with less water, which was caused by an increase in the reaction products and a more refined pore structure. In contrast, the drying shrinkage increased as the water content decreased.
- Porosity and pore structure, which are affected by N-A-S-H and free sodium levels, have a significant impact on shrinking behavior. Despite the similar conditions in moisture loss and reaction product content, the presence of excessive sodium led to increased rates of shrinkage.
-

References:

D. Ballekere Kumarappa, S. Peethamparan, M. Ngami, Autogenous shrinkage of alkali activated slag mortars: Basic mechanisms and mitigation methods, Cement and Concrete Research. 109 (2018) 1–9.

M. Lizcano, A. Gonzalez, S. Basu, K. Lozano, M. Radovic, Effects of water content and chemical composition on structural properties of alkaline activated metakaolin-based geopolymers, Journal of the American Ceramic Society. 95 (2012) 2169–2177. https://doi.org/10.1111/j.1551-2916.2012.05184.x.

H. Ye, A. Radlińska, Shrinkage mechanisms of alkali-activated slag, Cement and Concrete Research. 88 (2016) 126–135. https://doi.org/10.1016/j.cemconres.2016.07.001.

H. Ye, C. Cartwright, F. Rajabipour, A. Radlińska, Understanding the drying shrinkage performance of alkali-activated slag mortars, Cement and Concrete Composites. 76 (2017) 13–24.

B. Zhang, H. Zhu, Y. Cheng, G.F. Huseien, K.W. Shah, Shrinkage mechanisms and shrinkage-mitigating strategies of alkali-activated slag composites: A critical review, Construction and Building Materials. 318 (2022) 125993.

K. Sagoe-Crentsil, T. Brown, A. Taylor, Drying shrinkage and creep performance of geopolymer concrete, Journal of Sustainable Cement-Based Materials. 2 (2013) 35–42. https://doi.org/10.1080/21650373.2013.764963.

M. Hojati, F. Rajabipour, A. Radlińska, Effect of activator, curing and humidity on drying shrinkage of alkali-activated fly ash, Green Materials. 7 (2019) 71–83. https://doi.org/10.1680/jgrma.18.00069.

Y. Ma, G. Ye, The shrinkage of alkali activated fly ash, Cement and Concrete Research. 68 (2015) 75–82. https://doi.org/10.1016/J.CEMCONRES.2014.10.024.

Y. Ling, K. Wang, C. Fu, Shrinkage behavior of fly ash based geopolymer pastes with and without shrinkage reducing admixture, Cement and Concrete Composites. 98 (2019) 74–82. https://doi.org/10.1016/j.cemconcomp.2019.02.007.

R.J. Thomas, D. Lezama, S. Peethamparan, On drying shrinkage in alkali-activated concrete: Improving dimensional stability by aging or heat-curing, Cement and Concrete Research. 91 (2017) 13–23. https://doi.org/10.1016/j.cemconres.2016.10.003.

C. Gunasekera, S. Setunge, D.W. Law, Creep and drying shrinkage of different fly-ash-based geopolymers, ACI Materials Journal. 116 (2019) 39–49. https://doi.org/10.14359/51706941.

M. Hanumananaik, M.S.K. Reddy, K.V.L. Subramaniam, High-Temperature Performance of Low-Calcium Fly Ash–Based Geopolymers, Journal of Materials in Civil Engineering. 34 (2022) 1–12. https://doi.org/10.1061/(asce)mt.1943-5533.0004181.

M. Komljenović, Mechanical strength and Young's modulus of alkali-activated cement-based binders, in: Handbook of Alkali-Activated Cements, Mortars and Concretes, 2015: pp. 171–215. https://doi.org/10.1533/9781782422884.2.171.

G. Habert, J.B. D'Espinose De Lacaillerie, N. Roussel, An environmental evaluation of geopolymer based concrete production: Reviewing current research trends, Journal of Cleaner Production. 19 (2011) 1229–1238. https://doi.org/10.1016/j.jclepro.2011.03.012.

BC. Mclellan, R.P. Williams, J. Lay, A. Van Riessen, G.D. Corder, Costs and carbon emissions for geopolymer pastes in comparison to ordinary portland cement, Journal of Cleaner Production. 19 (2011) 1080–1090. https://doi.org/10.1016/j.jclepro.2011.02.010.

F. Pacheco-torgal, Z. Abdollahnejad, A.F. Camões, M. Jamshidi, Y. Ding, Durability of alkali-activated binders : A clear advantage over Portland cement or an unproven issue ?, Construction and Building Materials. 30 (2012) 400–405. https://doi.org/10.1016/j.conbuildmat.2011.12.017.

P. Duxson, A. Fernández-Jiménez, J.L. Provis, G.C. Lukey, A. Palomo, J.S.J. Van Deventer, Geopolymer technology: The current state of the art, Journal of Materials Science. 42 (2007) 2917–2933.

J. Davidovits, Geopolymer Chemistry and Applications, 5th ed., Institut Géopolymère, 2020.

P. Duxson, G.C. Lukey, F. Separovic, J.S.J. Van Deventer, Effect of alkali cations on aluminum incorporation in geopolymeric gels, Industrial and Engineering Chemistry Research. 44 (2005) 832–839. https://doi.org/10.1021/ie0494216.

G.V.P. Bhagath Singh, K.V.L. Subramaniam, Evaluation of sodium content and sodium hydroxide molarity on compressive strength of alkali activated low-calcium fly ash, Cement and Concrete Composites. 81 (2017) 122–132. https://doi.org/10.1016/j.cemconcomp.2017.05.001.

G.V.P. Bhagath Singh, K.V.L. Subramaniam, Evaluation of Total Reactive Oxide Ratios and Working Solution Ratios on Strength Development in Fly Ash–Based Geopolymers, Journal of Materials in Civil Engineering. 32 (2020) 04020051. https://doi.org/10.1061/(asce)mt.1943-5533.0003109.

Optimization of Encapsulating Mortar for Galvanic Anodes

E. K. Arya[1*] and B.S. Dhanya[2]

[1]*Doctoral Research Scholar, RIT Kottayam, APJ Abdul Kalam Technological University, Kerala, India*
Email: aryapramodek@gmail.com
[2]*Associate Professor, RIT Kottayam, APJ Abdul Kalam Technological University, Kerala, India*
Email: dhanyaavinod@gmail.com

[*]Corresponding author

ABSTRACT

The study investigates the performance of encapsulating mortars for galvanic anodes, focusing on pore distribution and alkali activator content. Mortar mixes with varying aluminium powder and foam concentrations were prepared, with lithium hydroxide as an alkali activator. Sorptivity tests and homogeneity analysis measured porosity and pore distribution of mortar specimens. Performance of galvanic anodes was evaluated using gravimetric analysis and Galvanic Anode Performance (GAP) tests. Results showed that foam mixes with higher porosity showed improved anode performance and corrosion product transport due to its ability to maintain higher pH and better anode utilization compared to aluminium powder mixes. Lower alkali activator content caused premature anode failure, emphasizing the need for optimal activator levels. The findings highlight the importance of optimizing pore distribution and alkali activator content for mortar performance.

1. Introduction

Sacrificial anodes have proven highly effective by corroding preferentially and protecting steel reinforcements in reinforced concrete structures. Galvanic anodes work through cathodic polarization, and effectively prevent halo damage by halting corrosion spread to nearby areas (Rincón et al., 2017). Each anode comprises a metal core surrounded by a low-resistance encapsulating mortar, with metal selection based on the electrochemical series to ensure adequate reactivity and corrosion resistance (Jordan and Page, 2003. Popov, 2015). Metals such as zinc, aluminium, and magnesium are chosen for their sacrificial protection of steel rebars. The mortar must maintain high alkalinity and porosity for optimal function, which is supported by zinc's Pourbaix diagram (Delahay et al., 1951). Lithium hydroxide is commonly added to maintain alkalinity and prevent alkali-silica reactions (Jordan and Page, 2003). During corrosion, zinc ions react with hydroxyl ions within the pore solution of the mortar, forming transportable corrosion products (Sergi, 2011). Achieving adequate mortar porosity is critical to facilitate the transport of these products and mitigate stress around the anode metal (Kamde et al., 2021). To enhance porosity, additives like aluminium powder or foaming agents are used, though specific mortar compositions are not well-documented.

The primary objective of the research is to optimize the formulation of mortar mixes by incorporating aerating agents such as aluminium powder and foam, along with alkali activators like lithium hydroxide. Aluminium powder and foam are employed as porosity enhancers, each utilizing different mechanisms: aluminium powder increases porosity through a chemical reaction that releases hydrogen gas, while foam introduces pre-formed air bubbles into the mix. Understanding these distinct mechanisms is crucial to improving the protective performance of sacrificial zinc (galvanic) anodes by enhancing the properties of the encapsulating mortar. The study involves preparing various mortar mixes using aerated and foam mortar, with a focus on evaluating the air void system characteristics, and testing through the Galvanic Anode Performance (GAP) tests. The paper seeks to address these gaps by optimising the formulation of encapsulating mortars, with a focus on enhancing the efficiency and lifespan of sacrificial anode systems.

2.Experimental methodology

2.1 Preparation of Mortar Mixes

Mortar mixes were prepared using a 1:1 ratio of cement and sand. Aerated mortar mixes included aluminium powder at varying weights of 0.15%, 0.25%, 0.5%, and 0.75% of cement, while foam mortar mixes used sodium lauryl sulfate foam at volumes of 10%, 20%, 30%, and 40% of the mortar. These mixes were thoroughly blended to ensure uniform pore distribution. Lithium hydroxide was added as an alkali activator at 5% and 12% by weight of cement to maintain alkalinity. The details of mortar mixes used for the study are provided in Table 2.

Table 2: Details of mortar mixes

Encapsulating mortar mixes	Cement	Fine aggregate	Water	Aluminium powder	Foam	Lithium hydroxide
	kg/m^3	kg/m^3	kg/m^3	kg/m^3	l/m^3	kg/m^3
M_0	836	836	418	-	-	-
M_1	836	836	418	1.254	-	10
M_2	836	836	418	2.090	-	10
M_3	836	836	418	4.180	-	4.2
M_4	836	836	418	4.180	-	10
M_5	836	836	418	6.270	-	4.2
M_6	836	836	418	6.270	-	10
M_7	836	836	418	-	100	10
M_8	836	836	418	-	200	10
M_9	836	836	418	-	300	4.2
M_{10}	836	836	418	-	300	10
M_{11}	836	836	418	-	400	4.2
M_{12}	836	836	418	-	400	10

2.2 Testing of galvanic anodes

Firstly, homogeneity and porosity tests were performed on the mortar mix samples. Zinc metal cores with tie wires were die-cast, encapsulated within the mortar mixes with a 12 mm cover, and cured under atmospheric conditions. Additionally, performance testing of the galvanic anodes included the GAP test, pH analysis, and gravimetric loss assessment. A comprehensive summary of all tests conducted on the mortar mixes and the prepared galvanic anodes is presented in Table 3.

Table 3: Tests conducted on galvanic anodes

Tests	Description	Ref.
Homogeneity Analysis	Evaluated the uniformity of pore distribution within the mortar mixes.	Yuanliang et al., 2021
Porosity Determination	Conducted sorptivity tests to assess porosity of encapsulating mortar for corrosion product transportation efficiency.	DI manual, 2009
Galvanic Anode Performance (GAP) Tests	Embedded anodes in mortar cubes (≤ 5 mm cover), 7-day curing, subjecting to 1V potential difference, monitoring output currents to assess performance and determining test completion.	Kamde and Pillai, 2023
pH measurements	Conducted on interior, mid, and exterior mortar regions post-GAP test	Kamde et al., 2021
Gravimetric Loss Assessment	Evaluated total utilization and efficacy in anode protection by measuring anode metal loss	ASTM G1-03, 2017

3 Results and Discussions

3.1 Homogeneity and porosity

Homogeneity analysis revealed distinct porosity distributions, as seen in Figure 3(a) and (b), attributed to the distinct mechanisms by which these agents introduce porosity into the mortar: The introduction of aluminium powder creates pores through a chemical reaction that produces hydrogen gas, leading to non-

uniform pore distribution, particularly higher porosity near the top due to the buoyancy of hydrogen gas. Whereas, foam introduces stabilized, pre-formed air bubbles that result in a more consistent and uniform pore distribution throughout the mortar mix (Yuanliang et al., 2021). The consistent pore structure in foam mortar enhances uniform metal corrosion and efficient transport of corrosion products.

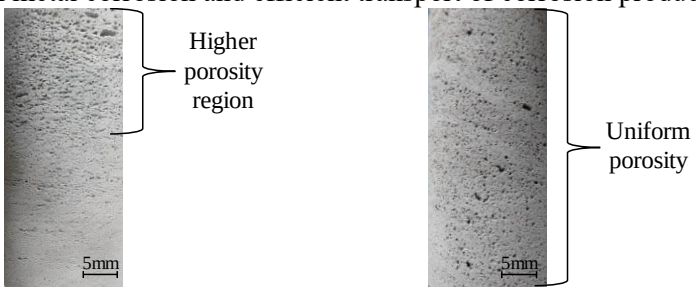

(a) Aerated mortar **(b) Foam mortar**

Figure 3: Homogeneity analysis of mortar mixes

Porosity was found to increase with higher concentrations of aluminium powder and foam, as determined by sorptivity tests. A 0.25 %bwoc increase in aluminium powder resulted in a 2.5 % increase in porosity, while a 10 %bvoc increase in foam led to a 5 % increase. The maximum porosity was observed in the 40 % foam mix (M_{12}), with the 30 % foam mix and 0.75 % aluminium powder mix showing nearly the same porosity. Sorptivity analysis also revealed higher tortuosity in foam mixes compared to aerated mixes due to the bursting of air bubbles before setting time, as confirmed by homogeneity analysis. Increased porosity and tortuosity in foam mixes enhance pore interconnectivity, facilitating efficient corrosion product transport and extending anode life.

3.2 Performance of anode

Galvanic anode performance (GAP) test results are presented in Figure 4. The GAP test specimens failed in the following sequence: M_0, M_1, M_7, M_8, M_2, M_{10}, M_4, M_{11}, M_5, M_{12}, M_6. Figure 4(a) and (b) shows that control mixes failed prematurely due to low porosity, highlighting the need for adequate pore distribution. Figure 4(c) demonstrates that the mixes with lower alkali activator percentages failed earlier than those with higher content, demonstrating the interplay between porosity and alkali activator concentration. The possible reasons for the GAP test results include higher porosity in mortar mixes leading to superior anode performance, as indicated by higher output current levels. Foam mixes with higher alkali content and greater porosity exhibited longer service life, likely due to uniform pore distribution as confirmed by homogeneity tests. Sustained output current levels indicated effective corrosion protection, preserving the anode's sacrificial nature and extending its service life.

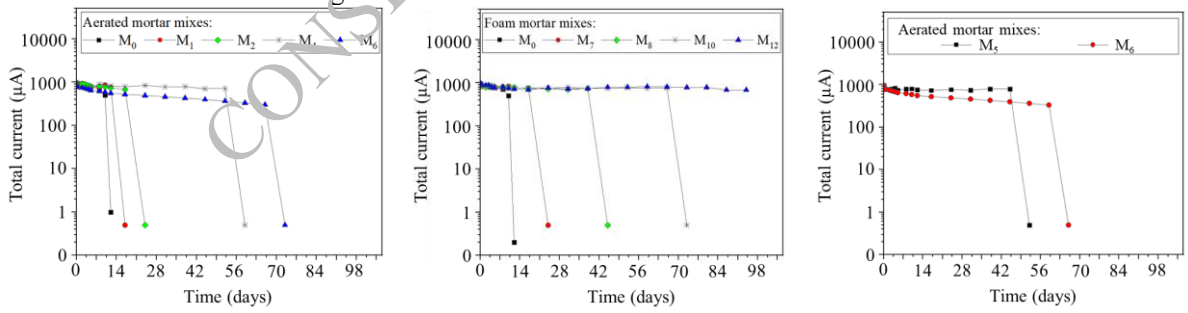

(a) Aerated mortar **(b) Foam mortar** **(c) Effect of alkali activator content**

Figure 4: Performance of anodes assessed by GAP test

Following the GAP test, the galvanic anodes were autopsied. Most zinc corrosion products, appearing as white powders, were deposited near the anode metal (Figure 5(a)), with some migrating into the encapsulating mortar. The 40 % foam mortar anode (Figure 5(b)), which remained operational, showed effective transport of corrosion products, unlike the failed 10% foam mortar anode (Figure 5(c)), which showed limited migration. These findings emphasize the critical role of porosity in facilitating corrosion product transport, enhancing anode effectiveness.

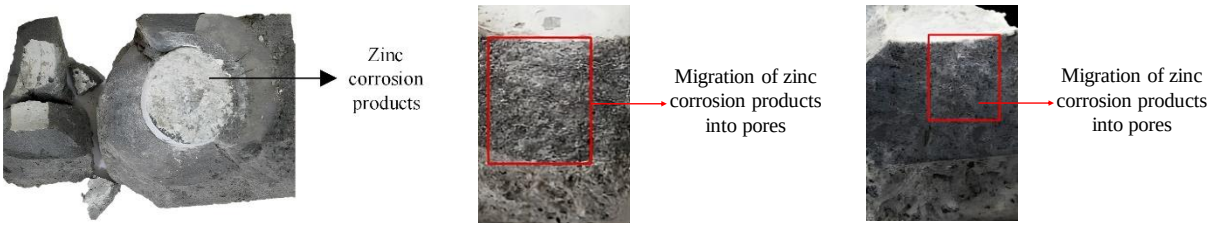

(a) **(b)** **(c)**

Figure 5: Deposition and transport of galvanic anode corrosion products

3.3 pH and Gravimetric loss

pH measurements from the interior, mid, and exterior regions of encapsulating mortar (Figure 6) revealed that mortar mixes with aluminium powder showed significant pH declines at the interior, indicating potential corrosion activity. Foam mixes maintained consistent pH levels across regions, providing a stable environment for the sacrificial anode. The stability of foam mortar attributed to uniform pore distribution, supports longer anode service life by facilitating consistent ionic movement and reducing localized pH variations.

Gravimetric tests revealed that foam mixes used anode metal more efficiently than aluminium powder mixes. The foam mix with the highest porosity (M_{11}) showed a 6% higher anode metal loss compared to the aluminium mix (M_5) with the same alkali activator content. This improved efficiency is due to higher porosity and better pore interconnectivity, allowing efficient transport of corrosion products. However, none of the mixes achieved total anode utilization due to the accumulation of corrosion products at the anode periphery, which inhibits further corrosion. The highest gravimetric loss occurred in the 40% foam mix with the highest alkali activator concentration. Increasing the alkali activator concentration by 7% in foam mixes (M_{11} and M_{12}) led to a 10% higher anode metal corrosion rate.

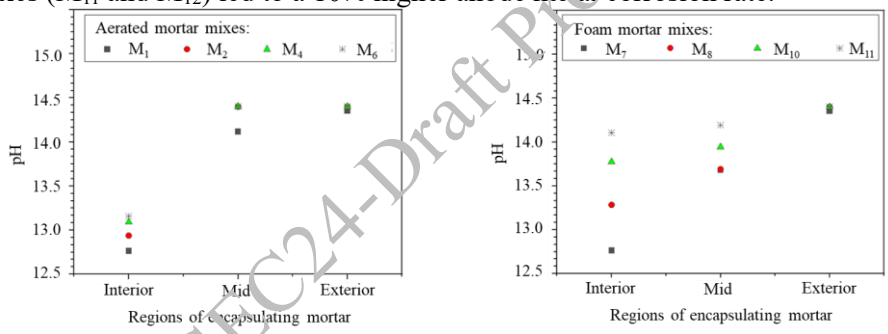

(a) Aerated mortar **(b) Foam mortar**

Figure 6: pH of encapsulating mortar

4 Conclusions

The study confirms that the performance of encapsulating mortars for sacrificial zinc anodes is significantly influenced by pore distribution and alkali activator content.

Following specific conclusions can be drawn from the study:

- The porosity introduced by aluminium powder is less uniform due to hydrogen gas release, while foam produces more stable, uniform pores, enhancing anode performance. This highlights the need for careful selection of porosity enhancers to optimize the protective efficiency of galvanic anodes.
- Lower alkali activator content results in premature anode failure, highlighting the importance of optimal activator levels for extended performance.
- Foam mixes maintain consistent pH levels across mortar regions, providing a stable corrosion environment conducive to prolonged anode effectiveness.
- Foam mixes exhibit superior utilization of anode metal compared to aluminium powder mixes, demonstrating the benefits of enhanced porosity and pore interconnectivity.

Increasing the surface area of the anode is recommended to improve anode metal utilization. This approach would enhance the efficiency of corrosion product transport, preventing buildup near the anode periphery and ensuring a more uniform corrosion process. Further research is required to explore the optimal balance of porosity, alkali activator content, and anode surface area for maximizing anode efficiency and longevity.

References

ASTM G1 – 03 (2017), Standard Practice for Preparing, Cleaning, and Evaluating Corrosion Test Specimens, United States.

Delahay, P., Pourbaix, M., and Van Rysselberghe, P. (1951). Potential-pH Diagram of Zinc and its Applications to the Study of Zinc Corrosion. Journal of The Electrochemical Society, 98(3), 101.

Durability Index Testing Procedure Manual (2009). Concrete durability index testing, South Africa.

Jordan, L. C., and Page, C. L. (2003). Mortars for encapsulating sacrificial zinc anodes in reinforced concrete. Materials and Corrosion, 54(6), 387–393.

Kamde, D., Manickam, K., Pillai, R. G., and Sergi, G. (2021). Long-term performance of galvanic anodes for the protection of steel reinforced concrete structures. Journal of Building Engineering, 42.

Kamde, D., and Pillai, R. G. (2023). Development of the Galvanic Anode Performance Test for Assessing the Longevity of Galvanic Anodes for Reinforced Concrete Structures. Corrosion, 79(8).

Popov, B. N. (2015). Cathodic Protection. In Corrosion Engineering (pp. 599–637). Elsevier.

Rincón, de, Troconis, O., Sagüés, A., and Torres-Acosta, A. (2017, March). Sacrificial Anodes for Reinforced Concrete Structures: A Review. CORROSION 2017.

Sergi, G. (2011). Ten-year results of galvanic sacrificial anodes in steel reinforced concrete. Materials and Corrosion, 62(2), 98–104.

Yuanliang, X., Baoliang, L., Chun, C., Yamei, Z. (2021), Properties of foamed concrete with Ca(OH)2 as foam stabilizer. Cement and Concrete Composites, 118.

Efficacy of crumb tyre rubber pretreatment on reducing the shrinkage and creep behaviour of structural concrete

K. Mushunje[1*], M.B. Otieno[2]

[1] National University of Science and Technology, Bulawayo, Zimbabwe
Email: kudzai.mushunje@nust.ac.zw
[2] University of the Witwatersrand, Johannesburg, South Africa
Email: mike.otieno@wits.ac.za

[*]Corresponding author

ABSTRACT

This paper presents results of a study to investigate the effects of pretreating truck tyre crumb rubber particle surface; to reduce its hydrophobic nature and in turn assess the shrinkage and creep behaviour of structural rubberised concrete (rubcrete). Crumb tyre rubber of nominal size 2.36mm was used to replace 10% by volume of fine mineral aggregates to produce structural concrete with a target strength of 30 MPa. Two pre-treatment methods were employed viz tap water-soaking and immersing in 0.1M Sodium Hydroxide solution. Concrete was cast, water-cured for 28 days and tested for shrinkage and creep for ca. 1 year. Results show that there is a general increase in both shrinkage and creep for all rubcretes when compared to the plain concrete with no crumb rubber particles. The results also show that both pretreatment methods do not reduce shrinkage and creep in rubcrete.

KEYWORDS: *Structural rubberised concrete, Creep, Shrinkage, Pre-treatment, Crumb tyre rubber*

1. Introduction

Shrinkage and creep are important concrete properties as they affect the volume stability of concrete and hence the serviceability functions of the material in structural applications. Shrinkage is a time-dependent deformation which results from the loss of water from concrete while creep is an increase in strain under a constant stress (Beushausen et al., 2021; Neville, 2011). Time-dependent deformation of concrete has been extensively researched on, specifically on conventional mineral aggregate concretes, and is relatively well-understood both in terms of its mechanism and the factors that affect it. Shrinkage is known to be affected by a number of factors such as aggregate stiffness and volume, w/b ratio and relative humidity. Creep, in addition to what affects shrinkage, is also affected by the level of stress and age at loading (Neville, 2011). Due to the finite nature of the mineral aggregates, interest has been generated to find alternative concrete aggregates (Alexander and Mindess, 2015). Although investigation on the effect of these alternatives like recycled concrete aggregates, crushed bricks and other artificial aggregates on time-dependent deformations have been done, they have not been as extensive as those for mineral aggregates (Bravo et al., 2017; Chinzorigt et al., 2020; Domingo-Cabo et al., 2009). Available studies on rubcrete, concrete made with tyre rubber aggregates, have shown that tyre rubber generally results in a slight increase in creep and a varied effect on shrinkage (Adamu et al., 2018; Alsaif et al., 2018; Elchalakani, 2015; Sun et al., 2020; Yang et al., 2020; Youssf et al., 2020). The lack of consensus in the bulk of rubcrete studies necessitates a need for further research.

The use of waste tyre rubber as aggregate in concrete has been gaining traction in the recent decade. Rubcrete is reported to posess enhanced sound absorption, improved thermal insulation and better crack resistance properties (Elchalakani, 2015; Nehdi and Khan, 2001; Siddique and Naik, 2004). Poor mechanical performance of rubcrete, relating to significant reductions in the compressive strength and elastic modulus, have been it major disadvantage (Elchalakani, 2015; Eldin and Senouci, 1993; Malladi, 2004; Zheng et al., 2008). The poor performance has been attributed to the appreciably lower stiffness (<5 MPa) of the rubber, the non-uniform distribution of the rubber particles in the concrete matrix due to its

light weight, and poor interface bond between the rubber particles and the hardened cement paste (Elchalakani, 2015; Eldin and Senouci, 1993; Zheng et al., 2008). In an attempt to reduce the effects of some of these factors, surface treatment of the tyre with chemicals such as carbon tetrachloride and sodium hydroxide, and polyvinyl alcohol (PVA)(Eldin and Senouci, 1993; Fiore et al., 2014; Rostami et al., 1993; Segre and Joekes, 2000; Youssf et al., 2020). Rostami et al. (1993) found that when crumb tyre rubber is pretreated with carbon tetrachloride, the rubberised strength improved by 57%. Segre and Joekes (2000) report an improvement of 17 % in compressive strength when crumb rubber is pretreated with 0.1M Sodium Hydroxide (NaOH). Similar results have been reported by the other researchers and they attribute the improvement in performance to better bonding between of the rubber and the hardened paste (Elchalakani, 2015; Thomas et al., 2015). However, these improvements have not been enough to inspire confidence with engineers for structural purposes. This is because effect of these mitigation measures on other key structural concrete properties besides strength and elastic modulus are not well understood. One such property is the time-dependent behaviour, this is because these deformations, which have not received much research attention, can be much larger than elastic deformations in concrete structures. It is therefore necessary to understand these time-dependent deformations in rubcrete to avoid failures relating to loss in serviceability (e.g. excessive cracking and deflections) and durability, and ultimately collapse of structures (Bažant and Panula, 1984; Neville et al., 1983). It is envisaged that this study, focusing on the time-dependent deformation (i.e. creep and shrinkage) of rubcrete, will contribute to the body of knowledge that aims to increase the confidence of structural engineers in using rubcrete as a construction material. This study investigated the effects of surface treatment of crumb tyre rubber particles on both shrinkage and creep of structural rubcrete.

2. Materials

Concrete specimens were made using plain Portland cement (CEM I 52.5R), crushed andesite as both fine and coarse mineral aggregate (MA) in the concrete. A single crumb rubber (CR) particle size, 2.36 mm or 8-mesh (M8), produced by ambient grinding at a local South African waste tyre recycling company was used. A water-to-binder (w/b) ratio of 0.60 was used for all concretes. The guiding parameter in the development of the structural concrete mixes was compressive strength of 30MPa. A total of four concrete mixes, one reference mix (CM) and three rubcrete mixes, were developed. The rubcrete made by replacing 10% of the volume of fine mineral aggregate content with three different types of crumb rubber particles, one untreated (denoted by M8), one treated with 0.1M NaOH (M8S) and one water-soaked (M8W). No admixtures were used in all the concretes. Table 1 shows the mix proportions of the concrete used.

Table 1: Summary concrete mix proportions (kg/m^3)

Mix label		CM	M8	M8W	M8S
Aggregate composition		100/0 - MA/CR	90/10 - MA/CR		
Cement (CEM I 52.5R)		350	350		
Coarse aggregate (22mm crushed andesite)		1050	1050		
Fine aggregate	Crushed andesite	790	711		
	Crumb rubber 2.36mm	0	35		
Water		210	210		

3. Methodology

3.1. Tyre Crumb Rubber Pretreatment

Two surface treatment methods were selected for the availability, low cost of the treatment materials, the ease of application (with respect to pretreatment procedures) and their non-hazardous nature when compared to other methods that are reported to give similar results. *NaOH pretreatment* involved the immersion of crumb rubber particles for 24 hours in a 0.1M NaOH solution based on work that has been done by other researchers (Ma and Yue, 2013; Segre et al., 2002). Thereafter the particles were washed with tap water to remove the NaOH and allowed to air dry for 24 hours. *Water pretreatment* method involved the washing of the crumb rubber under running tap water. After the washing, the crumb rubber

was then immersed and allowed to soak in tap water for 24 hours. Thereafter, it was allowed to air dry for another 24 hours before use. The two pretreatment methods are reported to assist with the reduction of the formation of air bubbles around the particles and enhance the cement paste-rubber particle bonding (Mohammadi and Khabbaz, 2015; Li et al., 2019; Segre et al., 2002).

3.2. Characterisation of crumb tyre rubber

The relative density of the crumb rubber was determined using a pycnometer. To allow for the characterisation of the crumb tyre rubber particle shape, surface texture and elemental composition, they were coated with a thin layer of carbon and two layers of gold palladium before being observed in a scanning electron microscope (SEM) which is equipped with an Energy-Dispersive X-ray spectroscope (EDS). The elemental composition was determined using EDS. The elemental composition analysis was used to check changes to the composition of the tyre rubber associated with the pretreatment processes.

3.3. Creep and shrinkage tests

Creep and shrinkage tests were carried out on 100 × 100 × 200 mm long concrete prisms. Concrete prisms were cast using mould sizes of 710 x 100 x 100 mm for the shrinkage and creep tests. After approximately 20 days of curing, each concrete beam was cut into three 100 mm x 200 mm prisms using a diamond saw and faced, on a high-speed facing machine to ensure that these ends were parallel to each other. Two stainless steel demec targets were attached to two opposite 100 mm x 200 mm faces of each prism using quick setting glue. After the glue had set, the prisms were returned to the water curing tank. For each mix, three prisms were used for creep test and another three for shrinkage test. The concrete prisms were cured in a water-curing tank for a total of 28 days before they were set up in the loading frames which are based on the ASTM C-512-15 (ASTM International, 2015) creep frame, however the load is applied by a hydraulic flat jack. The arrangement is shown in Figure 1.

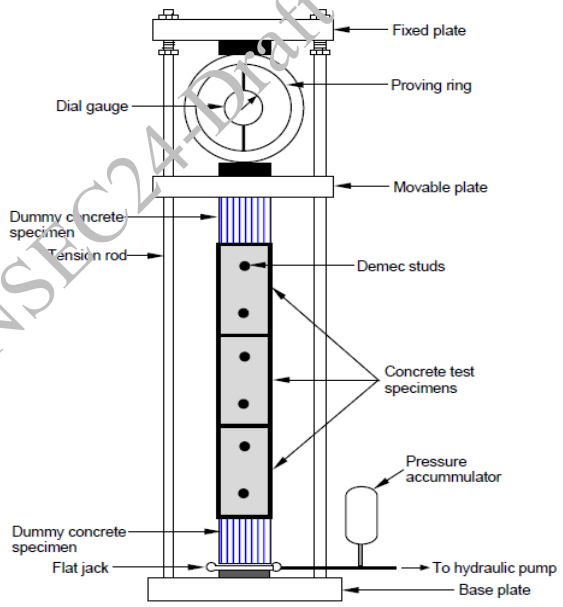

Figure 1: Schematic of the creep loading arrangement

In the case of the drying shrinkage prisms, after the 28-day curing, the two 100 × 100 mm end faces of each prism were sealed with either epoxy in order to simulate the drying exposure conditions (in terms of exposed surface area) as the creep specimens These specimens were used to determine the corresponding drying shrinkage strains (ε_{sh}) of the creep specimens. The creep frames are setup in a humidity and temperature-controlled room. The temperature and relative humidity were maintained at 21 ± 2 °C and 60 ± 5% respectively. In the creep test samples were loaded at 30% (σ_c) of their compressive strength, determined from companion 100 mm cubes crushed at the same time the creep samples are removed from the curing bath. These stresses were maintained within ± 2% of their target stresses for the duration of the monitoring period. Creep and shrinkage strain measurements were taken at the same time for prisms of the same

concrete. A 100 mm Demec gauge was used to take the strain measurements. After loading the samples, total strains readings were taken 4 – 6 hours after and thereafter, daily for the 7 days, weekly for the next 3 weeks and monthly until the test was terminated. The creep strains at any given time, $\varepsilon_c(t)$, were quantified and normalized with respect to the sustained stress and presented as specific (or unit) creep $\varepsilon_{sp}(t)$, i.e. creep strain per unit stress, as shown in Equation (1) where $\varepsilon(t)$ is the total measured strain at time t, ε_e is the instantaneous elastic strain, and $\varepsilon_{sh}(t)$ is the drying shrinkage strain at time t.

$$\varepsilon_{sp}(t) = \frac{\varepsilon(t) - \varepsilon_e - \varepsilon_{sh}(t)}{\sigma_c} = \frac{\varepsilon_c(t)}{\sigma_c} \quad (1)$$

3.5. Porosity measurement

Porosity measurements were carried out following the ASTM C 642 method (ASTM International, 2013) on 100 × 100 × 70 mm thick concrete prisms for each of the concretes used to make the creep and shrinkage specimens (see Table 1). The porosity specimens were cut using a circular water-cooled diamond-tipped concrete saw from the drying shrinkage specimens at the end of the experimental duration.

4. Results and discussion

4.1. Tyre crumb rubber characterisation

The relative density of the crumb rubber particles was found to be 1.1, which is 2.5 times lighter than the mineral aggregates, this falls within the range that is reported in literature (Alsaif et al., 2018; Bompa and Elghazouli, 2019). The SEM micrographs (Figure 2) showed that a good proportion of the 2.36 mm crumb rubber particles had regular and angular shape, with a few being irregular. The edges are fairly clean-cut due the tyre rubber size which at this stage is big enough to still be cut directly by the steel shredder teeth.

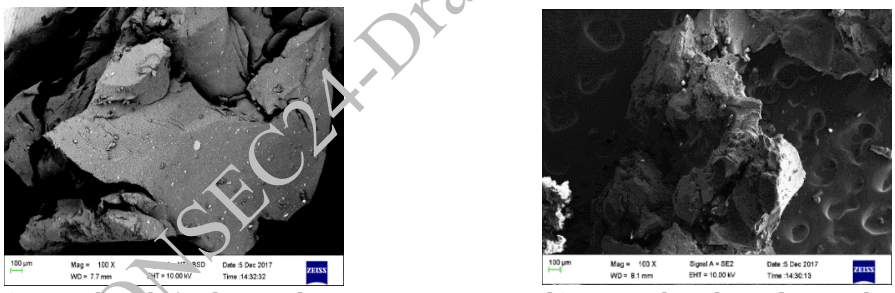

a) Regular shaped particle *b) Irregular shaped particle*

Figure 2: SEM micrograph of 2.36 mm particles (magnification 100×)

Figure 3 shows graphical representation of the elemental composition for the crumb rubber particles without surface treatment and after surface treatment with NaOH and water-soaking.

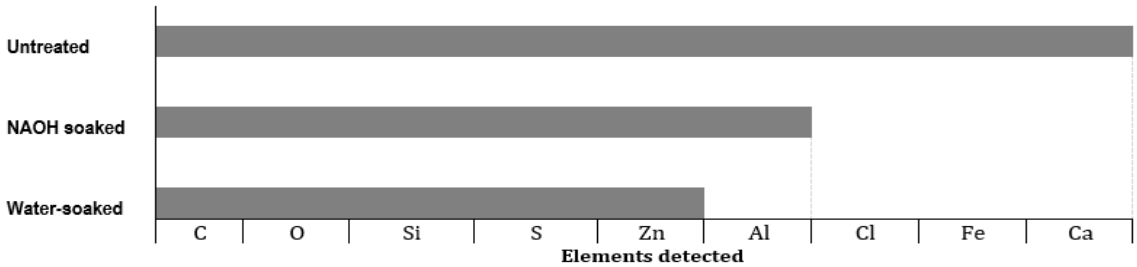

Figure 3: Elemental composition of tyre crumb rubber

The elemental composition analysis revealed that the NaOH treated and the water soaked crumb rubber had three and four elements less than the untreated one respectively. For both pretreatments, Aluminum, Chlorine and Iron were not detected. In addition to these, for the water-soaked tyre rubber, Calcium was also not detected. The explanation for the absence of certain elements in the treated rubber might be that

these elements are only on the surface of the rubber thus during the treatment these elements are removed from the surface of the rubber. This is confirmed by elemental composition given by Sun et al. (2020) and Polydorou et al. (2020), which shows an elemental composition similar to the pretreated rubber particles. It is unlikely that the removal of the metal elements was due to chemical reactions since similar elements were removed by either method and there is no known chemical reaction that water may have with any of the metals in 24 hours. The absence of these elements suggests that the two pretreatment methods have an effect on the surface elemental composition of the tyre rubber, which might influence its behaviour in concrete. It is worth noting that all three elemental compositions can be typical compositions for an untreated crumb rubber as evidenced by elemental compositions reported by other researchers (Polydorou et al., 2020; Richardson et al., 2016; Sun et al., 2020).

The SEM micrographs of the surface texture in Figure 4 revealed that the NaOH treated crumb rubber has a rougher surface texture when compared to the untreated and water-soaked crumb rubber. The pretreatment methods resulted in different changes to the surface texture of the crumb rubber. The water soaking simply cleaned the surface to reveal hidden pores while for the NaOH treatment, a reaction with the surface which made it rougher appears to have happened.

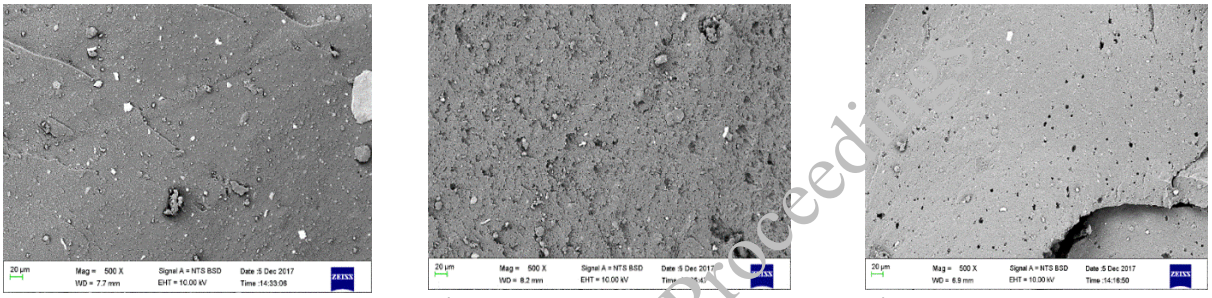

a) Untreated *b) 0.1M NaOH pretreatment* *c) Water soaked*

Figure 4: Crumb tyre rubber surface micrographs (magnification 500×)

4.2 Concrete porosity

The results presented in Figure 5 show that the inclusion of crumb rubber in concrete increases its porosity but the increase is not statistically significant. There is also a slight numerical increase in porosity for rubcrete with pretreated crumb rubber relative to the rubcrete with untreated crumb rubber, the increase is also noted to be not statistically significant. This implies that the effects observed in the surface texture do not have a notable impact on the porosity of the rubcrete. There is, therefore, no difference in using rubcrete with pretreated crumb rubber or untreated as it relates to concrete porosity.

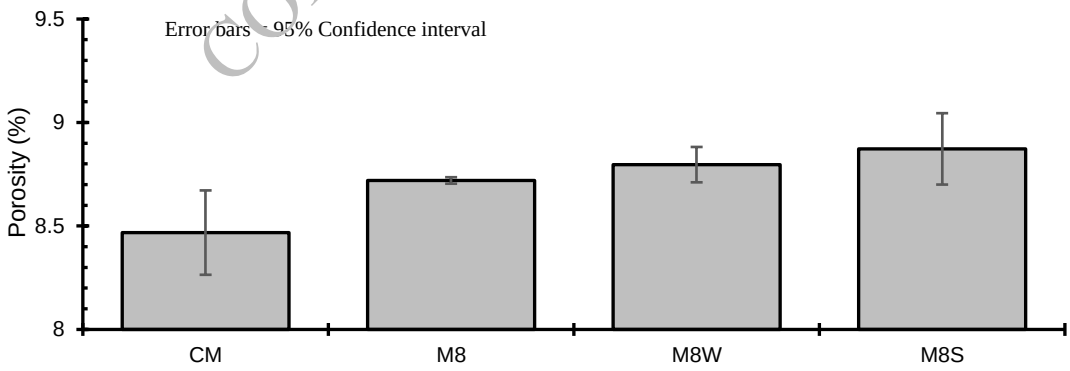

Figure 5: Effect of pretreatment on hardened concrete porosity

4.3. Shrinkage and Creep

The drying shrinkage and specific creep development trends (3-point moving average) of the different concretes over the 52-week experimental duration are shown in Figure 6 and Figure 7. The results show that in general, both drying shrinkage and creep (presented as specific creep – Equation (1)) increased with

time but at a decreasing rate. This trend is related to the continued cement hydration in the concretes that progressively increases the stiffness (or elastic modulus) of the concrete with time [1]. The increase in the stiffness of the concrete slows down the rate of increase in creep deformation. The results also show that the shrinkage and creep of the rubcretes are higher than those of the mineral aggregate concrete. This can be attributed the loss of aggregate restraint due to the low stiffness of the rubber particles and an increase in air voids; both phenomena are associated with crumb rubber particles. Zimmermann et al. (2016) report that inclusion of crumb rubber in concrete increases the amount of voids in the concrete thereby increasing concrete porosity. According to Ghuraiz et al. (2011) the increase in concrete voids results in higher concrete permeability which eases the viscous outflow of capillary water and cement gel. The lower stiffness of the tyre rubber aggregates and the air voids offer less restraint to deformation of the hardened cement paste related to creep and shrinkage.

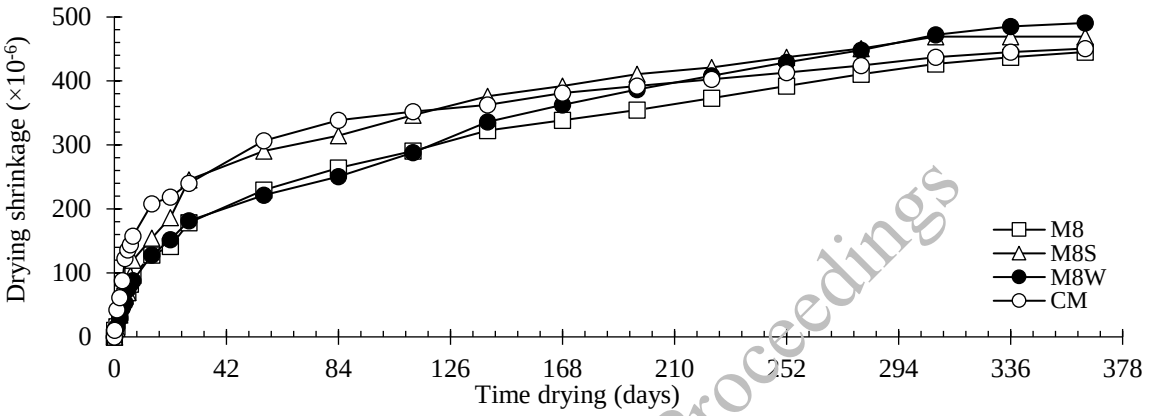

Figure 6: Development of shrinkage with time

The drying shrinkage of the pretreated crumb rubcretes are only slightly higher than those for the untreated crumb rubcrete. The percentage increases for M8S and M8W rubcretes are 10% and 5% respectively relative to the M8 rubcrete. This could due to the effect of the pretreatment which result in better bonding between rubber aggregates and the paste as reported in literature(Pham et al., 2018; Polydorou et al., 2020; Taha et al., 2008). This closer proximity of the rubber particles to the paste is believed to enable easier water movement from the rubber to the cement paste due to improved bonding. However, statistically, the pretreatment does not have a significant effect on the drying shrinkage of rubcrete. This finding is contrary to what is reported by Li et al. (2020), who reported that using 0.1M NaOH pretreated rubber resulted in a 15% decrease. This variance might be explained by difference in pretreatment procedures. The crumb rubber in this study was soaked for 24 hours while Li et al. (2020) soaked theirs for 20 minutes. This suggests a possible link between soaking time and rubcrete peformance, although this cannot be concluded from just these two findings.

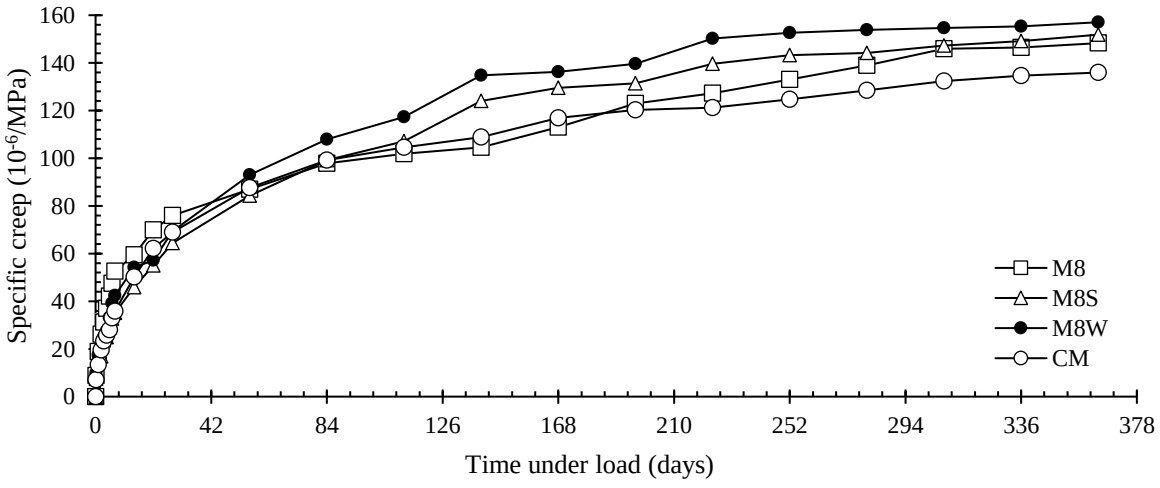

Figure 7: Development of creep with time

The specific creep of the pretreated crumb rubcretes, is comparable to that of untreated crumb tyre rubcrete. The percentage increases for M8W and M8S rubcretes are 6% and 3% respectively when compared to the untreated crumb rubcrete. The marginal effect of pretreating tyre rubber particles on creep is similar to that reported for shrinkage. A similar insignificant effect is reported by Li et al. (2020). There seems to be no significant effect of using pretreated crumb rubber aggregates on creep in the long-term.

5. Conclusion

The effect of pretreatment of 2.36 mm crumb rubber particles used to replace 10% mineral aggregate in concrete on shrinkage and creep was investigated. The investigation led to the general conclusion that the inclusion of crumb rubber particle in concrete has a slight effect on the shrinkage and creep behaviour of concrete for the specific crumb rubber size used in the investigation. The use of pretreated crumb tryre rubber in concrete was found not to significantly alter the time-dependent behaviour of rubcrete when compared to untreated rubber. This means that for this crumb rubber size the use of pretreated or untreated crumb rubber aggregates has the same effect, thus the use of either is by preference. Structural rubcrete with untreated or treated crumb rubber particles has comparable drying shrinkage and creep behaviour to conventional structural concrete. The positive findings of this study would be confirmed with long-term studies (>1 year).

References

Adamu, M., Mohammed, B.S., Liew, M.S., 2018. Effect of crumb rubber and nano silica on the creep and drying shrinkage of roller compacted concrete pavement. Int. J. GEOMATE 15, 58–65.

Alexander, M., Mindess, S., 2015. Aggregates in Concrete. Taylor & Francis, London and New York.

Alsaif, A., Koutas, L., Bernal, S.A., Guadagnini, M., Pilakoutas, K., 2018. Mechanical performance of steel fibre reinforced rubberised concrete for flexible concrete pavements. Constr. Build. Mater. 172, 533–543. https://doi.org/10.1016/j.conbuildmat.2018.04.010

ASTM International, 2015. ASTM C512 / C512M-15, Standard Test Method for Creep of Concrete in Compression.

ASTM International, 2013. C642: Test Method for Density, Absorption, and Voids in Hardened Concrete. https://doi.org/10.1520/C0642-13

Bažant, Z.P., Panula, L., 1984. Practical prediction of creep and shrinkage of high strength concrete. Matér. Constr. 17, 375–378. https://doi.org/10.1007/BF02478710

Beushausen, H., Arito, P., Van-Zijl, G., Alexander, M., 2021. Deformation and volume change of hardened concrete, in: Alexander, M. (Ed.), Fulton's Concrete Technology. Cement & Concrete South Africa, pp. 265–342.

Bompa, D.V., Elghazouli, A.Y., 2019. Creep properties of recycled tyre rubber concrete. Constr. Build. Mater. 209, 126–134. https://doi.org/10.1016/j.conbuildmat.2019.03.127

Bravo, M., de Brito, J., Pontes, J., Evangelista, L., 2017. Shrinkage and creep performance of concrete with recycled aggregates from CDW plants. Mag. Concr. Res. 69, 974–995. https://doi.org/10.1680/jmacr.17.00031

Chinzorigt, G., Lim, M.K., Yu, M., Lee, H., Enkbold, O., Choi, D., 2020. Strength, shrinkage and creep and durability aspects of concrete including CO2 treated recycled fine aggregate. Cem. Concr. Res. 136, 106062. https://doi.org/10.1016/j.cemconres.2020.106062

Domingo-Cabo, A., Lázaro, C., López-Gayarre, F., Serrano-López, M.A., Serna, P., Castaño-Tabares, J.O., 2009. Creep and shrinkage of recycled aggregate concrete. Constr. Build. Mater. 23, 2545–2553. https://doi.org/10.1016/j.conbuildmat.2009.02.018

Elchalakani, M., 2015. High strength rubberized concrete containing silica fume for the construction of sustainable road side barriers. Structures 1, 20–38. https://doi.org/10.1016/j.istruc.2014.06.001

Eldin, N.N., Senouci, A.B., 1993. Rubber-Tire Particles as Concrete Aggregate. J. Mater. Civ. Eng. 5, 478–496. https://doi.org/10.1061/(ASCE)0899-1561(1993)5:4(478)

Fiore, A., Marano, G.C., Marti, C., Molfetta, M., 2014. On the Fresh/Hardened Properties of Cement Composites Incorporating Rubber Particles from Recycled Tires. Adv. Civ. Eng. 2014, 1–12. https://doi.org/10.1155/2014/876158

Ghuraiz, Y.S., Swellam, M.H., Ragab, A.M., Garas, G.L.K., 2011. The effect of recycled aggregates on creep behavior of structural concrete : Gaza Strip - a case study. J. Emerg. Trends Eng. Appl. Sci. 2, 308–313.

Li, D., Zhuge, Y., Gravina, R., Benn, T., Mills, J.E., 2020. Creep and drying shrinkage behaviour of crumb rubber concrete (CRC). Aust. J. Civ. Eng. 18, 187–204. https://doi.org/10.1080/14488353.2020.1761510

Li, Y., Zhang, X., Wang, R., Lei, Y., 2019. Performance enhancement of rubberised concrete via surface modification of rubber: A review. Constr. Build. Mater. 227, 116691. https://doi.org/10.1016/j.conbuildmat.2019.116691

Ma, Q.W., Yue, J.C., 2013. Effect on Mechanical Properties of Rubberized Concrete due to Pretreatment of Waste Tire Rubber with NaOH. Appl. Mech. Mater. 357–360, 897–904. https://doi.org/10.4028/www.scientific.net/AMM.357-360.897

Malladi, K.S., 2004. Studies on rubberized cement concrete (MSc). Indian Instisute of Technology Kharagpur, India.

Mohammadi, I., Khabbaz, H., 2015. Shrinkage Performance of Crumb Rubber Concrete Prepared by Water-soaking Treatment Method for Rigid Pavements. Cem. Concr. Compos. 62, 106–116.

Nehdi, M., Khan, A., 2001. Cementitious composites containing recycled tire rubber: an overview of engineering properties and potential applications. Cem. Concr. Aggreg. 23, 3–10.

Neville, A.M., 2011. Properties of concrete, 5th ed. ed. Pearson, Harlow, England ; New York.

Neville, A.M., Brooks, J.J., Dilger, W.H., 1983. Creep of plain and structural concrete. Construction Press, London ; New York.

Pham, N.-P., Toumi, A., Turatsinze, A., 2018. Rubber aggregate-cement matrix bond enhancement: Microstructural analysis, effect on transfer properties and on mechanical behaviours of the composite. Cem. Concr. Compos. 94, 1–12. https://doi.org/10.1016/j.cemconcomp.2018.08.005

Polydorou, T., Constantinides, G., Neocleous, K., Kyriakides, N., Koutsokeras, L., Chrysostomou, C., Hadjimitsis, D., 2020. Effects of pre-treatment using waste quarry dust on the adherence of recycled tyre rubber particles to cementitious paste in rubberised concrete. Constr. Build. Mater. 254, 119325. https://doi.org/10.1016/j.conbuildmat.2020.119325

Richardson, A., Coventry, K., Edmondson, V., Dias, E., 2016. Crumb rubber used in concrete to provide freeze–thaw protection (optimal particle size). J. Clean. Prod. 112, 599–606. https://doi.org/10.1016/j.jclepro.2015.08.028

Rostami, H., Lepore, J., Silverstraim, T., Zundi, I., 1993. Use of recycled rubber tires in concrete, in: Proceedings of the International Conference on Concrete 2000. Presented at the Proceedings of the International Conference on Concrete 2000, University of Dundee, Scotland, pp. 391–399.

Segre, N., Joekes, I., 2000. Use of tire rubber particles as addition to cement paste. Cem. Concr. Res. 30, 1421–1425. https://doi.org/10.1016/S0008-8846(00)00373-2

Segre, N., Monteiro, P.J.M., Sposito, G., 2002. Surface Characterization of Recycled Tire Rubber to Be Used in Cement Paste Matrix. J. Colloid Interface Sci. 248, 521–523. https://doi.org/10.1006/jcis.2002.8217

Siddique, R., Naik, T.R., 2004. Properties of concrete containing scrap-tire rubber – an overview. Waste Manag. 24, 563–569. https://doi.org/10.1016/j.wasman.2004.01.006

Sun, X., Wu, S., Yang, J., Yang, R., 2020. Mechanical properties and crack resistance of crumb rubber modified cement-stabilized macadam. Constr. Build. Mater. 259, 119708. https://doi.org/10.1016/j.conbuildmat.2020.119708

Taha, M.M.R., El-Dieb, A.S., Abdel-Hameed, M., Abd El-Wahab, M.A., 2008. Mechanical, Fracture, and Microstructural Investigations of Rubber Concrete. J. Mater. Civ. Eng. 20, 640–649. https://doi.org/10.1061/(ASCE)0899-1561(2008)20:10(640)

Thomas, B.S., Gupta, R.C., Mehra, P., Kumar, S., 2015. Performance of high strength rubberized concrete in aggressive environment. Constr. Build. Mater. 83, 320–326. https://doi.org/10.1016/j.conbuildmat.2015.03.012

Yang, M., Jin, S., Gong, J., 2020. Concrete Creep Analysis Method Based on a Long-Term Test of Prestressed Concrete Beam. Adv. Civ. Eng. 2020, e3825403. https://doi.org/10.1155/2020/3825403

Youssf, O., Mills, J.E., Benn, T., Zhuge, Y., Ma, X., Roychand, R., Gravina, R., 2020. Development of Crumb Rubber Concrete for Practical Application in the Residential Construction Sector – Design and Processing. Constr. Build. Mater. 260, 119813. https://doi.org/10.1016/j.conbuildmat.2020.119813

Zheng, L., Huo, X.S., Yuan, Y., 2008. Strength, Modulus of Elasticity, and Brittleness Index of Rubberised Concrete. J. Mater. Civ. Eng. 20, 692–699.

Zimmermann, A., Koenders, E.A.B., Yang, S., 2016. Crumb Rubber as a Concrete Additive: Effect of Specific Surface on Air Void Content. Presented at the 3rd international conference on Microstructure related Durability properties of Cementitious Composites, RILEM, Nanjing, China.

Service Life, Reliability, Sustainability and Resilience

Structural Reliability Assessment of Prestressed Concrete High Speed Railway Viaduct

A. Kumar[1], P.P. Dhapte[2], and P. Sengupta[3*]

[1] *Department of Civil Engineering, Indian Institute of Technology (ISM), Dhanbad, India, Email: 23dr0010@iitism.ac.in*
[2] *Department of Civil Engineering, Indian Institute of Technology (ISM), Dhanbad, India, Email: 22mt0263@iitism.ac.in*
[3] *Department of Civil Engineering, Indian Institute of Technology (ISM), Dhanbad, India, Email: piyali@iitism.ac.in*

[*]Corresponding author

ABSTRACT

With growth of urbanization and transportation demands, trains are made longer and faster across the world. Over the last few decades, speeds of trains have been increasing steadily, bringing up new challenges in the design conceptualization of high-speed railway bridges. Consequently, high speed railway bridges are required to be designed for safe operations during their service lives with appropriate degree of reliability. However, design of high-speed railway bridges is subjected to a range of uncertainties arising from the limited experience present in India. In this context, deterministic methods may lead to undesired consequences, i.e. over conservative or unsafe design affecting the total life cycle cost of high-speed railway viaducts. This study involves identification and characterization of uncertainties associated with the structural geometry, material properties and loading characteristics. The Sobol's sensitivity analysis is utilized to identify the most sensitive parameters governing the design of the high-speed railway bridge. Subsequently, a limit state function is defined for the simply supported prestressed concrete bridge girders in presence of various uncertainties. Thereafter, Monte Carlo Simulation (MCS), First Order Reliability Method (FORM) and Second Order Reliability Method (SORM) are employed to determine the probability of failure of the simply supported prestressed concrete bridge girders and the reliability indices. The substantive findings from this research provide valuable insights to the engineering community in the planning, construction and management of high-speed railway bridges.

KEYWORDS*: High-Speed Railway Viaduct, Prestressed Concrete Girder, Limit State Function, Reliability Index, Probability of Failure*

1. Introduction

The rapid development of High-Speed Railway (HSR) networks across different countries has witnessed exponential growth in length of HSR lines worldwide, revolutionizing transportation and connectivity. A crucial component of HSR infrastructure is construction of railway viaducts, which allow for seamless integration of HSR lines without disrupting existing railways or highways and minimizing land occupation (Zhai et al., 2013). Modern engineering practices have increasingly favoured the utilization of box-girder bridges due to them being lightweight, possessing high torsional and flexural rigidities and enabling longer spans (Hammad et al., 2020). However, the flexural resistance model of prestressed concrete girders is subjected to uncertainties arising from variations in material properties and structural geometry. Therefore, the primary objective of this study is to analyse the structural performance of the prestressed concrete HSR bridge girder under varying train loading to estimate the reliability indices and the probabilities of failure. Consequently, extensive investigations are conducted to determine the statistical parameters associated with material properties and structural geometry of HSR bridge girders to account for uncertainties.

2. Model development

In this study, the numerical model of a simply supported bridge girder model is developed with the cross-sectional configuration, shown in Figure 1. To investigate the effects of different spans and cross-sectional dimensions, a range of span lengths is considered, ranging from 20 meter to 60 meter at 5-meter intervals. The cross-sectional dimensions are based on three distinct depths and three different widths, providing a comprehensive evaluation of various geometries.

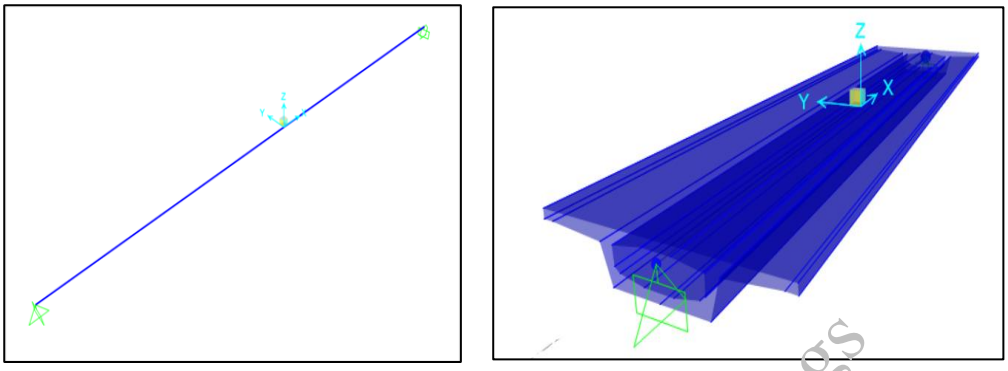

Figure 1. Numerical Model of Bridge Girder

Furthermore, the study examines the impact of train speeds on the bridge's behavior. Trains operating at 17 different speeds are analysed, ranging from 100 to 500 km/h with intervals of 25 km/h. This wide range of speeds considered in this study allows for a thorough understanding of the bridge's response to different dynamic loads induced by increase in train speeds. A range of standard trains, specifically HSLM A1 to A10 are considered in this study. These trains represent different configurations and loading patterns, providing a realistic representation of the dynamic loads experienced by the bridge. To evaluate the dynamic response of the bridge, the Coefficient of Dynamic Augmentation (CDA) is determined. The CDA is calculated by dividing the maximum response observed in dynamic scenarios (such as bending moment, shear force, and deflection) by the corresponding maximum response in static scenarios (Majka & Hartnett, 2008). This coefficient provides insights into the dynamic amplification of structural response.

3. Reliability analysis

This study involves the utilization of various reliability evaluation methods, namely the Monte Carlo simulation (MCS), first-order reliability method (FORM), and a variety of second-order reliability methods (SORM). These methods are used to assess the reliability and probability of failure of the prestressed concrete girders in high-speed railway viaducts. The reliability index β and the most probable point are estimated using FORM and this estimation serves as a basis for further analysis using any of the SORM methods, such as Breitung, Tvedt, Hohenbichler and Rackwitz, and Koyluoglu and Nielsen. Each SORM method offers its own approach to improving the reliability evaluation process. Tvedt (Tvedt, 1989) introduced a three-term approximation to enhance Breitung's formulation (Breitung, 1984), providing a more accurate estimation of reliability. Hohenbichler and Rackwitz (Hohenbichler & Rackwitz, 1988) derived a closed-form expression based on Taylor series expansion, which contributes to the precision of reliability estimation. Koyluoglu and Nielsen (Koyluoglu & Nielsen, 1994) defined the integration domain into different intervals based on the signs of curvatures, further enhancing the accuracy of probability of failure estimation. The accuracy of the probability of failure estimation depends upon the nature of the response surface. Response surfaces that closely follow the limit state surface yield more precise estimates of the probability of failure. In this study, the limit state function (LSF) is used to determine the failure or safe behavior of the simply supported prestressed concrete box girder. The LSF incorporates the probability due to the random variables and is formulated as:

$$g(X) = \alpha \times f_{ps} \times A_{ps} \times d\left(1 - \eta \times \frac{f_{ps}A_{ps}}{bdf_{ck}}\right) - M_n \quad (1)$$

Where, $g(X)$ is the limit state function based on the flexural strength of simply supported prestressed concrete box girder, as per the IS 1343 (2012), α and η are the constant depends on reinforcement ratio ($A_{ps}f_{ps}/bdf_{ck}$), A_{ps} and f_{ps} are the area and tensile strength of prestressing tendon respectively, b and d are the width and depth of section respectively and M_n is the applied bending moment. There are six random variables adopted for the further statistical analysis. The mean, standard deviation and distribution of the random variables in the flexural design are analysed and tabulated in Table 1.

Table 1. Statistical Characteristics in flexural resistance of prestressed concrete box girder

Sl. No.	Random variables	Units	Mean	Std. Dev.	PDF
1	Width of section (b)	mm	12000	500	Normal
2	Depth of section (d)	mm	2500	500	Log-normal
3	Diameter of tendon (D)	mm	5	2.2	Normal
4	Characteristics tensile strength of tendon (f_{pu})	MPa	1600	194	Log-normal
5	Compressive resistance of concrete (f_{ck})	MPa	50	7.9	Normal
6	Bending Moment (M_n)	kN-m	582	305	Gumbel

The probability of failure p_f is determined by integrating the joint probability density function of x, using

$$p_f = \int \dots \int_{g(x\leq 0)} f_X(x_1, x_2, \dots, x_i, \dots, x_n) dx_1 dx_2 \dots dx_i \dots dx_n \quad (2)$$

The reliability index β, which represents the optimized distance of the limit surface from the origin in the standard normal space, the p_f can be calculated as

$$p_f = \Phi(\beta) \quad (3)$$

The cumulative density function Φ represents the probability that a standard normal random variable is less than or equal to a given value. By evaluating Φ at the value of the reliability index β, the probability of failure p_f can be determined.

4. Results

The Coefficient of Dynamic Augmentation (CDA) provides insights into the extent of dynamic amplification experienced by the bridge structure. For smaller spans, CDA reaches its maximum with respect to bending moment which can be attributed to flexure governing the structural response. However, as the span length exceeds 50 meters, CDA based on bending moment returns to the forefront. This change is driven by a higher concentration of wheel loads impacting the bridge simultaneously, which is a consequence of the extended span length. With more wheels traversing the bridge at the same time, the bending moments induced by these loads increase, leading to higher dynamic amplification and subsequently higher CDA values. Additionally, the CDA values are lowest when the girder depth is larger, and the span of the bridge is smaller. Longer spans and shallower girders exhibit a higher susceptibility to dynamic amplification, leading to elevated CDA values. Numerical simulation results indicate that the governing parameters influencing CDA are the span length of bridge and the train speed. From this study, an expression is derived to quantify the relationship between CDA, span length (L), and train speed (V).

$$CDA = -2.7 + 10(L^{0.58} + V^{0.43}) \quad (4)$$

The Sobol's sensitivity analysis has identified the diameter of the prestressing tendons as the most sensitive parameter in the design of the PSC box girder for the high-speed railway bridge. This finding underscores the critical importance of the tendon diameter in ensuring the overall structural performance and reliability of the bridge. In addition to the sensitivity analysis, the comparison of different reliability analysis methods, including Monte Carlo Simulation (MCS), First-Order Reliability Method (FORM), and various Second-Order Reliability Methods (SORM), are shown in Figure 2. This high level of agreement between the

reliability analysis results, as evidenced by the overlapping plots, indicates a strong consistency and reliability in the assessment of the structural safety for the prestressed concrete box girder design.
The MCS involved generating 1,000,000 samples, resulting in a probability of failure of 0.0015 and a reliability index of 2.9708. MCS is a widely used method for reliability analysis, providing accurate results but requiring significant computational resources. Using the First-Order Reliability Method (FORM), the reliability index is evaluated as 2.9898, and the corresponding probability of failure is obtained as 0.0014. FORM is an analytical method that approximates the probability of failure by assuming a linear limit state function and estimating the reliability index iteratively. Several Second-Order Reliability Methods (SORM) have been employed, including Breitung's method, Hohenbichler and Rackwitz method, Koyluoglu and Nielsen method, and Tvedt's method. These methods aim to improve the accuracy of the reliability assessment by considering second-order effects. The probability of failure obtained using Breitung's method, Hohenbichler and Rackwitz method, and Koyluoglu and Nielsen method is reported as 0.0014, which closely matches the result obtained from FORM. However, Tvedt's method provides a slightly higher probability of failure at 0.0015, which is in approximate agreement with the MCS result.

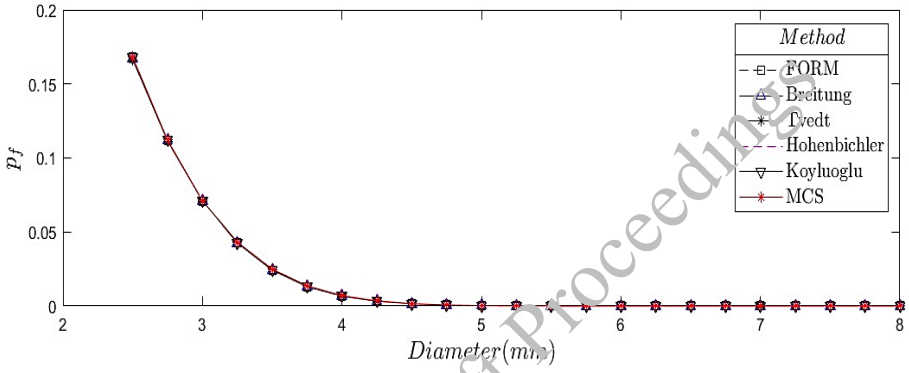

Figure 2. Effect of diameter of tendon on probability of failure.

5. Conclusions

Based on extensive numerical simulation results, this study proposes an expression of CDA for HSR bridge girders in terms of span length (L) and train speed (V). Lower CDA values are observed when the girder depth is larger and the span length is smaller, indicating that deeper girders and shorter spans provide better resistance against high-speed train loading. Conversely, increasing span lengths and decreasing girder depths tend to result in higher CDA values, indicating a higher susceptibility to dynamic amplification under high-speed train loading. By examining the uncertainties arising from material properties and structural geometry, this study aims to enhance our understanding of the structural safety and performance of girders. The MCS involved generating 1,000,000 samples, resulting in a probability of failure of 0.0015 and a reliability index of 2.9708. Using the First-Order Reliability Method (FORM), the reliability index is evaluated as 2.9898, and the corresponding probability of failure is obtained as 0.0014. The probability of failure obtained using Second-Order Reliability Methods (SORM), e.g., Breitung's method, Hohenbichler and Rackwitz method, and Koyluoglu and Nielsen method is reported as 0.0014. Second-Order Reliability Method (SORM), i.e., Tvedt's method provides a slightly higher probability of failure at 0.0015. The combination of MCS, FORM, and various SORM methods allows for a comprehensive and accurate evaluation of structural reliability, contributing to improved decision-making processes in the design and maintenance of these viaducts.

References

Breitung, K. (1984) "Asymptotic Approximations for Multinormal Integrals", Journal of Engineering Mechanics, 110(3): 357–366

Hammad, N., Khafif, M. El, & Hanna, N. (2020) "Cost Optimization of High-Speed Railway Pre-Stressed Box Girder Bridge", International Journal of Civil Engineering and Technology, 11(4): 91–105.

Hohenbichler, M., & Rackwitz, R. (1988) "Improvement of Second-Order Reliability Estimates by Importance Sampling", Journal of Engineering Mechanics, 114(12): 2195–2199

Koyluoglu, H. U., & Nielsen, S. R. K. (1994) "Structural Safety New Approximations for SORM Integrals", Structural Safety, 13(4): 235–246

Majka, M., & Hartnett, M. (2008) "Effects of speed, load and damping on the dynamic response of railway bridges and vehicles", Computers and Structures, 86(6): 556–572

Tvedt, L. (1989) "Second Order Reliability by an Exact Integral", Reliability and Optimization of Structural Systems, 88: 377–384

Zhai, W., Xia, H., Cai, C., Gao, M., Li, X., Guo, X., Zhang, N., & Wang, K. (2013) "High-Speed Train–Track–Bridge Dynamic Interactions – Part I: Theoretical Model and Numerical Simulation", International Journal of Rail Transportation, 1(1): 3–24

Optimizing Performance-Engineered Concrete Mixtures Made with Modern Cementitious Materials Using Thermodynamic Modelling

K. Bharadwaj[1], W. J. Weiss[2] and O. B. Isgor[3]

[1] *Department of Civil Engineering, IISc Bangalore, Bangalore, Karnataka, India.*
keshavbr@iisc.ac.in
[2] *School of Civil and Construction Engineering, Oregon State University, Corvallis, OR, USA.*
jason.weiss@oregonstate.edu
[3] *School of Civil and Construction Engineering, Oregon State University, Corvallis, OR, USA.*
burkan.isgor@oregonstate.edu

*Corresponding author

ABSTRACT
The concrete industry is actively seeking approaches to lower its carbon footprint. This paper describes a framework for designing low-carbon performance-engineered concrete mixtures. Thermodynamic modeling is used to predict the reaction products that form when cementitious binders react. A pore partitioning model is used to predict the volumes of gel and capillary pores, which are then scaled up to concrete to predict its performance. The predicted performance measures include mechanical properties (strength and elastic modulus) and durability metrics (formation factor, pH of pore solution, resistance to freeze-thaw damage, etc.). This modeling framework is used to predict the performance of concrete across a range of water-to-binder ratios and SCM contents. The feasible space of mixture proportions is determined from the constraints (the required mechanical and durability measures). Linear programming is then used to optimize concrete mixture proportions using an objective function, which is a weighted function of the material and carbon costs. The parameters in the objective function (material cost, carbon cost, construction cost) are user adjustable and can be updated using real-time information. The optimal mixture proportions with respect to least cost, CO_2 emissions, or a weighted combination of the two can be obtained using the framework developed. This approach can be used to utilize resources and optimally design low-carbon concrete mixtures efficiently.

KEYWORDS*: Low-carbon concrete; Performance-engineered concrete; Thermodynamic Modelling; Durability; Service Life*

1. Introduction

India is investing over 100 trillion rupees in its infrastructure over the next 25 years (Chaudhary and Ghosh 2021), with a target of net-zero CO_2 emissions by 2070 (Verma 2022). With the global CO_2 emissions due to cement and concrete production at over 11% (Environment et al. 2018), new strategies are needed to produce sustainable concrete while meeting the performance targets for Indian infrastructure. Traditional mixture design approaches (e.g. ACI 211.1-91 (ACI 1991) or IS 10262-2019 (BIS 2019)) were developed when ordinary portland cement (OPC) was the binder primarily used to produce concrete. In these approaches the water-to-cement ratio (w/c) is used as a surrogate for porosity and therefore it is related to the compressive strength of concrete. However, modern binders have a portion of the OPC replaced with limestone (Ls) or supplementary cementitious materials (SCMs). Therefore, empirical modifications need to be made to interpret the meaning of the for the use of cement+SCM binders (Papadakis 1999). This may include the use of efficiency factors (k-factors) (Institution 2000). Traditionally the concrete industry has also used the compressive strength of concrete as an surrogate for durability; however, this can result in overdesign in concrete made using OPC+SCM (Wilson and Tennis 2021). To overcome these limitations, newer performance-based mixture design approaches were previously developed (Isgor et al. 2020, Bharadwaj et al. 2022). This approach considers the use of SCMs in the mixture design process by predicting the reaction products and concrete performance using a thermodynamic-based model

(Bharadwaj et al. 2019, Bharadwaj et al. 2021). This approach also considers mechanical and durability parameters individually, and thus allows for greater flexibility in designing the concrete mixture. Next, the mixture can be optimized using a previously developed approach (Bharadwaj et al. 2023, Bharadwaj et al. 2024) that considers the cost of the raw materials, CO_2 footprint of the materials, and a cost of CO_2. More information comparing the traditional and newly developed performance-based mixture design approach is available in (Bharadwaj et al. 2023, Bharadwaj et al. 2024) and more details about the optimization framework are available in (Bharadwaj et al. 2019, Bharadwaj et al. 2021), both of which are omitted here for brevity.

In this work, the performance targets for the concrete mixture include compressive strength (f'_c, to meet the mechanical performance requirement), a maximum CH content (a predictor of calcium oxychloride damage in concrete (Suraneni et al. 2016)), formation factor (F_{APP}, an indicator of transport and diffusion in concrete (Snyder 2000, Moradllo et al. 2018, Moradllo et al. 2019)), the pore solution pH (an indicator for risk of alkali silica reaction (Hooton et al. 2010)), and time to critical saturation (t_{cr}, which indicates the time required for freeze-thaw damage to occur in concrete (Fagerlund 1977)). The readers are referred to the cited publications for more details about the choice of these metrics.

Numerical Simulations

2. Materials

The cement used had a chemical oxide composition of 48.62% C_3S, 16.83% C_2S, 5.61% C_3A, 9.35% C_4AF, 0.20% Na_2O, 0.44% K_2O, 1.96% MgO, 1.87% SO_3, 15% $CaCO_3$, a fineness of 410 cm^2/g, and a specific gravity of 3.08. The fly ash (FA) used had a 51.86% SiO_2, 21.70% Al_2O_3, 5.04% Fe_2O_3, 8.61 CaO, 2.58% Na_2O, 1.45% K_2O, 2.58% MgO, 0.78% SO_3, a maximum degree of reactivity (DOR*) of 40% (Bharadwaj et al. 2022), and a specific gravity of 2.56. The cost of cement is assumed to be ₹5,000/ton, FA is ₹11/ton, coarse aggregate is ₹500/ton, and fine aggregate is ₹550/ton (Jayaswal and Goel 2021). In this work, a cost of CO_2 of Rs. 1000/ton is used. The CO_2 emissions associated with each material is: 886 kg/ton for cement, 29 kg/ton for FA, 1 kg/ton for water, 3 kg/ton for fine aggregate, and 2 kg/ton for coarse aggregate (Miller 2018). It should be noted that the costs and CO_2 emissions are user adjustable parameters and can be varied by the user in real time as the cost of the materials and carbon fluctuate with time.

2.1 Predicting concrete performance

A previously developed thermodynamics-based pore partitioning model for concrete (PPMC) (Azad et al. 2017, Bharadwaj et al. 2019, Bharadwaj et al. 2021) is used to predict the mechanical and durability performance of concrete. The details of the model are not provided for brevity, and readers are referred to the cited publications: (Bharadwaj et al. 2019, Bharadwaj et al. 2021). Briefly, the thermodynamic model (Lothenbach and Winnefeld 2006) uses the chemistry of the cement and SCM, the DOR* of the SCM, and the physical properties of the cement and SCM as inputs to predict the reaction products that form. A pore partitioning model (PPM) (Glosser et al. 2019) is used to predict the volumes of gel and capillary pores, and the PPMC is used to upscale the pores to concrete. The PPMC is used to predicts the concrete's f'_c, F_{APP}, and t_{cr}.

2.2 Performance-based concrete mixture design and Optimization

A performance-based mixture design approach is used in this work (Bharadwaj et al. 2022), which is not repeated here for brevity. Briefly, the target compressive strength and durability metrics of the concrete are identified. In this work, a target f'_c of 30MPa, minimum F_{APP} of 375, maximum CH content of 10g/100g binder and minimum t_{cr} of 30 years is chosen (justification for these values is available in the cited publication: (Bharadwaj et al. 2024)). Next, the materials used are characterized. Then the PPMC model is run across a range of w/b and FA contents. A range of concrete mixtures that meet the target strength and durability criteria is identified (called the feasible space). The feasible space for the chosen performance targets is shown in Figure 3(a): the black solid line indicates the target f'_c, the dashed red line indicates the target F_{APP}, the dash-dot green line indicates the target CH content, and the dotted blue line indicates the target t_{cr}. Then, the optimisation framework developed by Bharadwaj et al. (2024) (Bharadwaj et al. 2024) is used in this work to find the concrete mixture with the minimum cost, and to study the influence of relative cost of cement and FA on the optimum mixture proportions (w/b and FA content) with respect to minimum cost.

3. Results and discussions

Figure 3(a) shows the results of the optimization framework for a cement+FA system for material and CO_2 costs and target performance metrics listed earlier. The shaded region indicates the feasible space – bound by the target f'$_c$ on top, target F_{APP} on the right, target CH on the bottom, and the lowest w/b simulated on the left. The colourmap in the feasible space shows the variation in the cost of concrete with changing w/b and FA content. Increasing the FA content decreases the cost of concrete as FA is has a lower cost and CO_2 footprint than cement. Increasing the w/b decreases the cost of concrete (at a fixed paste volume) as the volume of expensive cement+FA binder is reduced. The optimum solution is a concrete mixture with a 50% replacement of cement with FA and a volumetric w/b of 0.92 (a mass-based w/b=0.30), and the cost of the concrete is ₹2,250/m^3.

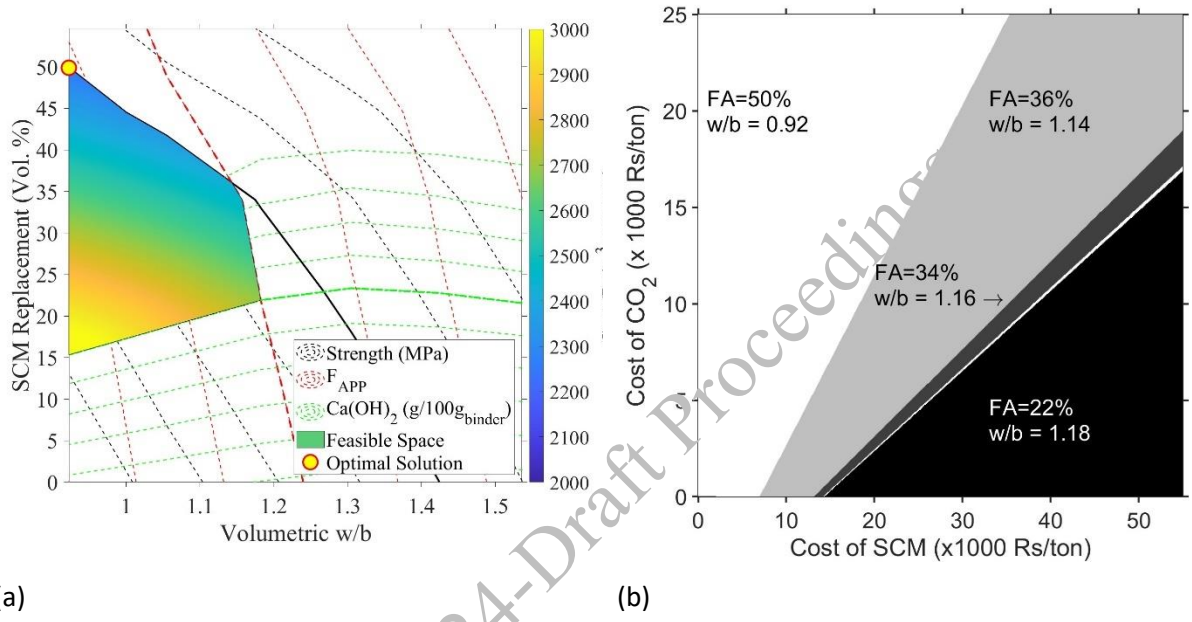

(a) (b)

Figure 3. (a) Feasible space and optimal solution for the cement+FA concrete with a cost of CO_2 of ₹1000/ton.

Figure 3(b) shows the concrete mixture with the least cost when the cost of the SCM is varied between ₹0/ton to ₹5000/ton and the cost of CO_2 is varied between ₹0/ton and ₹25/ton. When the cost of the SCM and CO_2 are ₹0/ton, the optimal concrete mixture with respect to cost is a FA content of 50% and a volumetric w/b=0.92. As the cost of FA increases from ₹0/ton to around ₹7000/ton at a cost of CO_2 of ₹0/ton, the mixture with the lowest cost is one with 36% FA and volumetric w/b=1.16, and as the cost of FA increases to ₹14,500/ton the mixture with the lowest cost has a 22% FA content and a volumetric w/b=1.18. At a cost of FA of ₹15,000/ton, as the cost of CO_2 is increased from ₹0/ton to ₹900/ton, the mixture with least cost is the 36% FA and volumetric w/b=1.14, and if the cost of CO_2 is further increased to ₹7250/ton, the mixture with least cost is the 50% FA and volumetric w/b=0.92. Thus, as the cost of CO_2 is increased, the optimum shifts to higher FA contents as the FA has a lower CO_2 emission than the cement used.

4. Conclusions

This extended abstract shows an approach to develop and optimize concrete mixtures made with blended cements. A thermodynamics-based modelling framework is used to predict the performance of concrete made with cements and SCMs, a previously developed performance-based mixture proportioning approach is used to develop a feasible space of concrete mixtures that meet the target performance, and an optimization framework is used to determine the concrete mixture with the least cost / CO_2 footprint / a combination of the two. The main takeaways of the study are: (i) the framework can be used to design and optimize concrete mixtures to meet a set of target mechanical and durability performance metrics; (ii) when the cost of SCM and CO_2 are ₹0, the optimal mixture is the one with the highest SCM content; (iii) as the

cost of SCM is increased, the optimum seeks to minimize binder (cement+SCM) content by increasing the w/b (water content) of the mixture as the binder becomes expensive; and, (iv) when the cost of CO_2 increases, the optimum shifts to higher SCM contents as the cement has higher CO_2 emissions than the SCM. The proposed framework is a powerful tool that can be used to design and optimize concrete mixtures in the field and can be used to help the concrete industry attain its sustainability goals.

Acknowledgements

The authors gratefully acknowledge the financial support provided by CALTRANS (California Department of Transportation) and National Science Foundation (Grant No. NSF CMMI 1728358). The authors gratefully acknowledge support from the Edwards Distinguished Chair at Oregon State University, which has supported W. Jason Weiss.

Bibliography

ACI 211.1-91. (1991) "Standard Practice for Selecting Proportions for Normal, Heavyweight, and Mass Concrete (Reapproved 2009)", *American Concrete Institute*, Farmington Hills, MI.

Azad, V. J., Suraneni, P., Isgor, O.B., et al. (2017). "Interpreting the pore structure of hydrating cement phases through a synergistic use of the Powers-Brownyard model, hydration kinetics, and thermodynamic calculations", *Adv. in Civil Engg. Mat.*, 6(1): 1-16.

Bharadwaj, K., Ghantous, R.M., Sahan, F.N., et al. (2021). "Predicting Pore Volume, Compressive Strength, Pore Connectivity, and Formation Factor in Cementitious Pastes Containing Fly Ash", *Cem. Conc. Comp.*, 122: 104113.

Bharadwaj, K., Glosser, D., Moradllo, M.K., et al. (2019). "Toward the Prediction of Pore Volumes and Freeze-Thaw Performance of Concrete Using Thermodynamic Modelling", *Cem. Conc. Res.*, 124: 105820.

Bharadwaj, K., Isgor, O.B., and Weiss, W.J. (2022). "A Simplified Approach to determine the Pozzolanic Reactivity of Commercial Supplementary Cementitious Materials", *Conc. International*, 44(1): 27-32.

Bharadwaj, K., Isgor, O.B., and Weiss, W.J. (2023). "Optimizing Performance-Engineered Concrete Mixtures using Linear Programming" 1st Interdisciplinary Symposium on Smart & Sustainable Infrastructures, Vancouver, Canada.

Bharadwaj, K., Isgor, O.B., and Weiss, W.J. (2024). "Optimizing the Carbon Footprint of Performance-Engineered Concrete Mixtures", *Transp. Res. Rec.*, In Press.

Bharadwaj, K., Isgor, O.B., Weiss, W.J., et al. (2022). "A New Mixture Proportioning Method for Performance-Based Concrete", *ACI Mat. J.*, 119(2): 207-220.

IS 10262 (2019) "Concrete Mixture Proportioning - Guidelines", *Bureau of Indian Standards*, New Delhi.

Chaudhary, A. and Ghosh, S. (2021). "India Aims to Spend $1.4 Trillion Building Infrastructure." 02-Oct-2022, from www.bloomberg.com/news/articles/2021-08-15/india-aims-to-end-energy-imports-boost-infrastructure-spending.

UN Environment, Scrivener, K.L., John, V.M., et al. (2018). "Eco-efficient cements: Potential economically viable solutions for a low-CO2 cement-based materials industry", *Cem. Conc. Res.*, 114: 2-26.

Fagerlund, G. (1977). "The critical degree of saturation method of assessing the freeze/thaw resistance of concrete", *Materials and Structures*, 10(4): 217-229.

Glosser, D., Azad, V.J., Suraneni, P., et al. (2019). "An extension of the Powers-Brownyard model to pastes containing SCM", *ACI Mat. J.*, 116(5): 205-216.

Hooton, R., Thomas, M. and Ramlochan, T. (2010). "Use of pore solution analysis in design for concrete durability", *Advances in cement research*, 22(4): 203-210.

EN 206-1. (2000) "Concrete-Part 1: Specification, performance, production and conformity", *British Standards Institution*, London, UK.

Isgor, O.B., Ideker, J., Trejo, D., et al. (2020). "Development of a performance-based mixture proportioning procedure for concrete incorporating off-spec fly ash", Energy Power Research Institute, Palo Alto, CA.

Jayaswal, V.K. and Goel, D.C. (2021). Delhi Schedule of Rates 2021. Central Public Works Department, Delhi.

Lothenbach, B. and Winnefeld, F. (2006). "Thermodynamic modelling of the hydration of Portland cement", *Cem. Conc. Res.*, 36(2): 209-226.

Miller, S.A. (2018). "Supplementary cementitious materials to mitigate greenhouse gas emissions from concrete: can there be too much of a good thing?", *J. Clean. Prod.*, 178: 587-598.

Moradllo, M.K., Qiao, C., Isgor, O.B., et al. (2018). "Relating formation factor of concrete to water absorption", *ACI Mat. J.*, 115(6): 887-898.

Moradllo, M. K., C. Qiao, M. Keys, H. Hall, M. T. Lay, S. R. Reese and J. Weiss (2019). "Quantifying Fluid Absorption in Air-Entrained Concrete Using Neutron Radiography", *ACI Mat. J.*, 116(6): 213-226.

Papadakis, V.G. (1999). "Effect of fly ash on Portland cement systems: Part I. Low-calcium fly ash", *Cem. Conc. Res.*, 29(11): 1727-1736.

Snyder, K. (2000). "The relationship between the formation factor and the diffusion coefficient of porous materials saturated with concentrated electrolytes: theoretical and experimental considerations", *Conc. Sc. Engg.*, 3: 216-224.

Suraneni, P., Azad, V.J., Isgor, O.B., et al. (2016). "Calcium oxychloride formation in pastes containing supplementary cementitious materials: Thoughts on the role of cement and supplementary cementitious materials reactivity", *RILEM Technical Letters*, 1: 24-30.

Verma, N. (2022). "India's GAIL sets 2040 goal for net zero carbon emissions." 02-Oct-2022, www.reuters.com/business/sustainable-business/indias-gail-sets-2040-goal-net-zero-carbon-emissions-2022-08-26/.

Wilson, M. L. and Tennis, P.D. (2021). “Design and Control of Concrete Mixtures”. Portland Cement Association, Skokie, IL.

Concrete Pavement Under Extreme Weather Conditions Due To Climate Change

Emad Alshammari[1*], Mang Tia[2], Jian Zou[3], and Othman Alanquri[4]

[1] *Assistant professor, University of Hail, Hail, Saudi Arabia, emad.alshammari@uoh.edu.sa*
[2] *Professor, University of Florida, Gainesville, United States, tia@ce.ufl.edu*
[3]*Research Assistant Scientist, University of Florida, Gainesville, United States, zouj@ce.ufl.edu*
[4]*Assistant professor, Imam Muhammad ibn Saud Islamic University, Riyadh, Saudi Arabia, othman.k@ufl.edu*

[*]Corresponding author

ABSTRACT

Climate change is increasing around the world with repetition of climate hazards every year, which threatens the performance of infrastructure, most of which are not well-designed to endure the effects of climate change hazards. The world is facing severe climate change, including extreme heat and severe flooding, adversely affecting our roadway system.

The objective of this study is to understand the effects of various factors affecting the performance of concrete pavement under normal and extreme weather conditions (extreme heat and flooding) and to develop designs and adaptation strategies for resilient concrete pavements under such conditions. This study investigates the properties of concrete and the dimensional design of concrete pavements using FEACONS IV to assess their impact on the performance of concrete pavements under extreme heat and flooding conditions.

The main findings from this study using FEACONS IV analysis are as follows: (1) Concrete with lower elastic modulus, adequate flexural strength, and aggregates with a lower CTE value can increase the load-carrying capacity of concrete pavement. (2) Thicker concrete slabs can reduce the load and temperature induced stresses. (3) Higher subgrade modulus reaction value in concrete pavement during flooding conditions helps to strengthen the pavement. However, under extreme temperatures, a high subgrade reaction modulus can increase the load and temperature induced stresses. (4) Concrete made with porous limestone aggregate have a low coefficient of thermal expansion and low elastic modulus and show potentially better performance than concrete made with river gravel or granite.

KEYWORDS*: Concrete, pavement, Climate change, FEACONS IV, Thermal expansion.*

1. Introduction

Climate change is increasing around the world with repetition of climate hazards every year, which threaten the performance and sustainability of infrastructures, most of which are not well prepared and designed to endure the effects of climate change hazards. The world is facing severe climate change, including extreme heat, severe flooding, and rising sea levels, which are adversely affecting our roadway system. Damage to road infrastructure caused by climate change can risk mobility, safety, and functionality, resulting in negative economic and social impacts. Flooding can cause an adverse impact on pavements through real damage (washout) or reduce the performance of pavement during its lifespan. Climate change hazards such as flooding also affect people and the economy (Jongman et al, 2012).

The performance of a concrete pavement depends on many factors, including traffic loading, design adequacy, climatic conditions, materials characteristics, and construction methods. Climatic conditions and materials characteristics such as coefficient of thermal expansion (CTE), drying shrinkage, saturation condition, elastic modulus, and modulus of rupture of concrete are essential parameters to

consider in concrete pavement design. Many pavement characteristics, such as pavement cross-section, serviceability, and design life depend partially on these factors. Load carrying capacity for concrete pavement depends mainly on the thickness of the concrete slab and the flexural strength of the concrete and less on the strength of the subgrade material. A lower computed stress to strength ratio indicates more load repetitions to failure and greater potential performance. The potential performance improves as the slab thickness and flexural strength of the concrete increase (Tia et al, 2012).

Inundation of concrete pavement could lead to a reduction of strength of concrete and reduced load carrying capacity of the pavement. It is generally accepted that an air-dried concrete specimen can give 15 to 20% higher compressive strength than saturated specimens. However, the reduction in the splitting tensile strength and flexural strength of concrete due to water saturation is known to be substantially lower and not very well defined (Chen et al, 2012). As contrast to the strength of concrete which generally decreases when saturated, the elastic modulus of concrete generally increases when saturated (Mehta and Monteiro, 2014 &Wang, 2017). As the elastic modulus increases, the maximum load-induced stress increases (Tia et al, 2012). As the load induced stresses in concrete slab generally increase with increased elastic modulus, it is expected that the stresses in concrete pavement would increase during flooding. Temperature is a significant environmental factor which influences concrete pavement performance. Temperature differential in the concrete slabs is one of the most important parameters considered for designing concrete pavements. Concrete pavements are regularly subjected to an extensive range of temperature differentials throughout their service lives, leading to a wide range of deformed shapes of slabs. Temperature differentials in concrete cause vertical and horizontal displacements in the pavement slab. These displacements affect the resistance of shear and moment at joints, which transfer loads between contiguous slabs. Also, these displacements are affected by the direction and magnitude of slab curling, which affect the amount of support provided by the subgrade layer.

Due to temperature differentials, the lower and upper of concrete slab will contract or expand which cause the pavement to be deformed. This phenomenon with the combination of heavy wheel loading and lifted corners results in top-down cracking at the corners. This could lead to loss of support along the slab interior or at the slab edges which results in higher stresses in the concrete slab. The thermal stress induced by temperature differentials may cause early cracking in a pavement (Tang et al, 1993). The temperature differentials between the top and bottom surfaces of concrete pavement slab can result in fatigue damage (Masad et al, 1996). Fatigue damage due to heavy wheel loading traffic is much higher when there is a high temperature differential as compared to concrete slab with zero-temperature differential.

2. Objectives of study

The goal of this study is to research the effects of relevant factors affecting the performance of concrete pavements and to develop a design of resilient concrete pavements under severe climate conditions. The objectives for this research are as follows:

1. To evaluate the effects of properties of concrete such as flexural strength, elastic modulus, and coefficient of thermal expansion on the performance of concrete pavements.
2. To evaluate the effects of the dimensional design of concrete pavement such as slab thickness and slab length on its performance.
3. To study the effects of extreme temperature and temperature differential in the concrete slab on the behavior of concrete pavements.
4. To evaluate the effects of moisture condition on the performance of concrete pavement which include the concrete, base, subbase, and subgrade materials.

3. Research Methodology

FEACONS IV (Finite Element Analysis of Concrete Slabs version IV) program is used to perform stress analysis. The FEACONS program was developed as a result of cooperative research work between the University of Florida and Florida Department of Transportation (FDOT). FEACONS is an analytical model which can be used to analyze the concrete pavement behavior. Analysis of concrete pavements in this program with applied load subject to extreme weather conditions such as

thermal effects and saturated concrete can be performed effectively and reliably. It can model a stiff subbase or base layer as a separate layer, or it can treat both the subgrade and the subbase as one liquid foundation with a certain effective subgrade modulus.

A jointed concrete pavement is modeled in the FEACONS IV program, as shown in Figure 1. Since the analysis of the response of a concrete pavement generally involves the determination of deflections and stresses on a slab, whose response characteristics are influenced mostly by two adjacent slabs, it is usually adequate to model a concrete pavement as a three-slab system. It is not necessary to use a more elaborate model, such as a five-slab or nine-slab system, which would make the analysis process more complicated and time-consuming.

Figure 2 shows an example of the mesh of finite element model to perform the stress analysis of a concrete pavement under a single axle wheel. In this study, the number of x-divisions used for all three-slab system is 29, and the number of y-divisions is 14. The total number of elements is 406, and the total number of nodes is 480. To calculate the contact area for a wheel used in FEACONS IV, the following equation is used:

$$CA = L/P \quad (1)$$

Where:

CA is the contact area for each tire in a single axle (inch^2).

L is the load applied for each tire (lbf).

P is the pressure resulting from a tire (psi).

In this study, the applied load used is 11,000 lb and the pressure used is 100 psi. The calculated contact area for each wheel used in this study is 110 inch^2(11 in X 10 in), which is used in FEACONS IV to design the finite element mesh. Figure 3 shows the dimensions of the contact area between the pavement surface and tires.

To analyze the effect of individual pavement input parameters, various input parameters are used. The design input parameters used in FEACONS IV were organized into two types of parameters: fixed input and varied input, as shown in Tables 1. Ranges of the varied input parameters were chosen based on FDOT recommendations and engineering judgment.

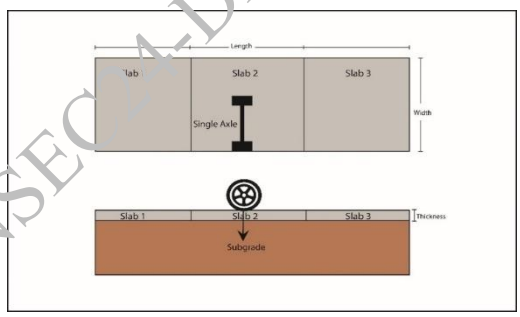

Figure 1. The Axle Wheel Loads at Middle Edge of Middle Slab.

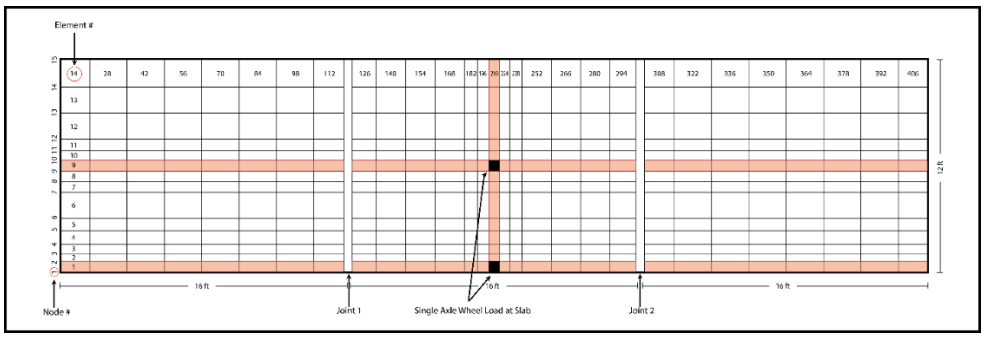

Figure 2. An Example of the Mesh of Finite Element Model.

Table 1. Fixed & Varied Input Parameters.

Fixed Parameters	Fixed Value	Varied Parameters	Range Value
Slab Thickness (in)	12	Slab Thickness (cm)	8 - 20
CTE* ($X10^{-6}/^{\circ}F$)	5	Temperature Differentials Δ T (F°)	0 - 40
E** (ksi)	4000	CTE* ($X10^{-6}/^{\circ}F$)	3 - 7
Uniform Load (ksi)	0.1	E**	3000 - 6000
Slab Dimensions (ft)	12*16	K value*** (kci)	0.04 – 0.4
K value*** (kci)	0.4	Slab Dimensions (ft)	12*14 – 12*22
Poisson's Ratio	0.2		

* Coefficient Of Thermal Expansion, ** Concrete Elastic Modulus, *** Subgrade Reaction Modulus

Based on studies done by Tia et al (1990), Tia et al (1991), Tia et al (2012), there are three typical types of aggregates used in producing pavement concrete in Florida state. These types of aggregates are Brooksville limestone which is a porous limestone found in Brooksville, Florida, Calera limestone, which is a dense limestone found in Calera, Alabama; and River gravel from Alabama state. Typical properties of concretes using these aggregates such as coefficients of thermal expansion, unit weights, and elastic modulus of concrete for flexural strength of 650 psi, are shown in Table 2. These properties were used as inputs for analysis using FEACONS to evaluate concrete made from these aggregates under extreme weather conditions.

Table 2. Properties of Concrete Using Different Aggregate Types (Tia et al, 1990 & 1991).

Pavement Designs	Aggregate type	CTE* ($1/^{\circ}F$)	MR** (psi)	E*** (ksi)	Unit Weight (pcf)
Used by FDOT#	Brooksville limestone	5.68	650	4766	145
	Calera limestone	5.99	650	4982	152
	River gravel	7.2	650	4406	150

* Coefficient Of Thermal Expansion, ** Modulus of rupture, *** Elastic Modulus of Concrete
#Florida Department of Transportation

4. Results and discussions

4.1 Effects of Temperature on Concrete Pavement Performance

There are some properties of concrete which affect the performance of concrete pavements under extreme temperatures, such as elastic modulus (E) and coefficient of thermal expansion (CTE). In addition, the dimensional design of concrete pavement also affects its performance under extreme temperatures. These dimensional parameters include slab thickness and slab length. Fatigue damage due to heavy wheel loading traffic is much higher when there is a high temperature differential as compared to concrete slab with zero-temperature differential. The concrete pavement's structural response due to traffic loads is dependent on temperature and temperature differential in the concrete slab. Critical stress analysis using FEACONS IV software was performed to evaluate the effects of various pavement parameters on the maximum induced stress in concrete pavement under extreme temperatures. Figure 3 shows Maximum stresses as functions of temperature differentials and elastic modulus (E), coefficient of thermal expansion (CTE), slab thickness, and subgrade reaction modulus.

High elastic modulus concrete is undesirable for concrete pavement applications because it increases the likelihood of pavement cracking. As a result, high strength concrete with low modulus is more desirable. Figure 3 shows similar results of stresses for suggested elastic modulus values in case of using input value of ΔT of 0oF. Also, analysis results show that the stress for all suggested values of E increases as ΔT increases. With a higher E value, a higher stress is obtained in case of high ΔT.

In both short- and long-term stages, the CTE contributes to the deterioration of concrete pavement and stresses brought on by temperature variations in the environment. When CTE is higher, there is a greater likelihood of curling, which increases pavement distresses throughout the period of its design life even when conditions stay the same. The results of maximum stresses as functions of temperature differentials and CTE of concrete slab shows almost the same computed stresses (0.18 ksi) for all CTE values in the case of using input value of ΔT of 0oF. Like the elastic modulus analysis, results show that the stress for all values of CTE increases as ΔT increases. With a higher CTE value, a higher stress is obtained in case of high ΔT.

The thickness of the concrete slab is a crucial design factor that influences cracks such as transverse cracking. Some studies which investigated the pavement performance as affected by slab thickness reported that thicker concrete slabs showed decrease in transverse cracking, spalling, faulting, pumping, and corner deflections (Darter et al, 1997 & Owusu-Antwi et al, 1997). Figure 3 shows the results of maximum stresses as functions of temperature differentials and slab thickness. It shows different stresses for different slab thickness values. Analysis results show that the stresses for all values of slab thickness increase as ΔT increases. The results show that with a higher slab thickness, a lower stress is obtained.

The effects of subgrade characteristics on concrete pavement under extreme temperature was also evaluated. Figure 3 presents the computed stresses for different subgrade reaction modulus values. Increasing the subgrade reaction modulus leads to a decrease in stress in the case of using input value of ΔT of 0oF. On the other hand, using highest input value of ΔT of 40oF shows different results. Increasing the subgrade reaction modulus leads to increase in stress. All subgrade reaction modulus values give similar stress result when ΔT is in the range of 9 oF to 11 oF. General understanding indicates that high temperature differentials and high subgrade reaction modulus result in high stress. Without temperature differential, there is no slab curling which makes the slab to have full contact with the subgrade. Using a higher subgrade modulus which means that the subgrade layer is stiffer, helps the slab to distribute the load better. When there is temperature differential in the slab, there may be slab curling which makes the slab to be not fully in contact with the subgrade.

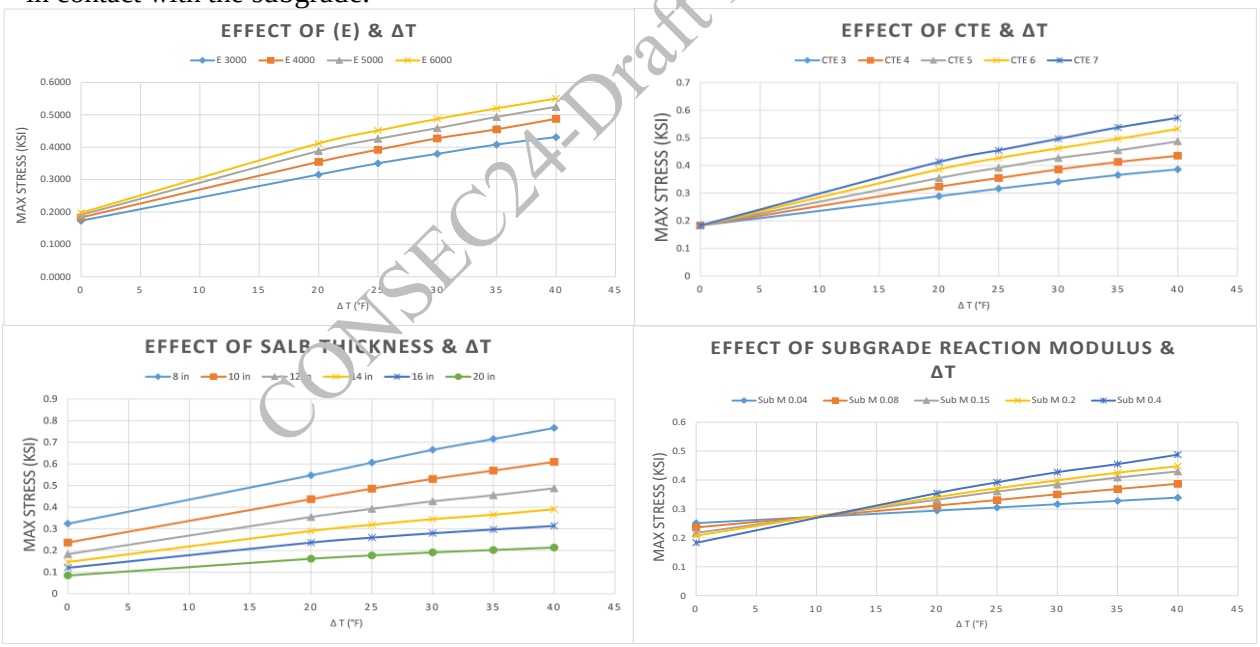

Figure 3. Maximum stresses as functions of temperature differentials and elastic modulus (E), coefficient of thermal expansion (CTE), slab thickness, and subgrade reaction modulus.

4.2 Effects of Flooding on Concrete Pavement Performance

Flooding can cause an adverse impact on pavements through a washout or pavement inundation which reduces the performance during the lifespan. During inundation flooding, the subgrade and concrete stay saturated which leads to reduction in strength. The possible effects of the relevant parameters which are affected by flooding are analyzed using FEACONS IV software. Figure 4 presents the maximum stresses as functions of subgrade reaction modulus values and slab thickness, elastic

modulus (E), and slab length values. Results show that the stresses in the concrete slab decrease as subgrade reaction modulus increases. In addition, with a higher slab thickness, a lower stress was obtained.

For elastic modulus analysis, assuming there are no temperature differentials, results show that for all values of elastic modulus of concrete, the maximum stress decreases as subgrade reaction modulus increases. In addition, the results show that with a higher elastic modulus, a higher stress was obtained. With the effects of temperature differentials due to extreme temperatures, interesting results were obtained. In the case of using input values of ΔT of 20^{o}F and 40^{o}F, the results show that stress increases as subgrade reaction modulus increases.

Due to temperature differentials and moisture content, longer slabs may curl and warp more. This may result in problems like cracking and faulting. Shorter slab lengths are frequently chosen for concrete pavement because they reduce some of the pavement distresses. Figure 4 presents the maximum stresses as functions of subgrade reaction modulus and slab length values. Analysis results show that in the absence of temperature differentials (0^{o}F), the stress for all slab lengths decreases as subgrade modulus increases. With the effects of temperature differentials, different results were obtained. In case of using input values of ΔT of 20^{o}F and 40^{o}F, results show that stress increases as subgrade modulus increases.

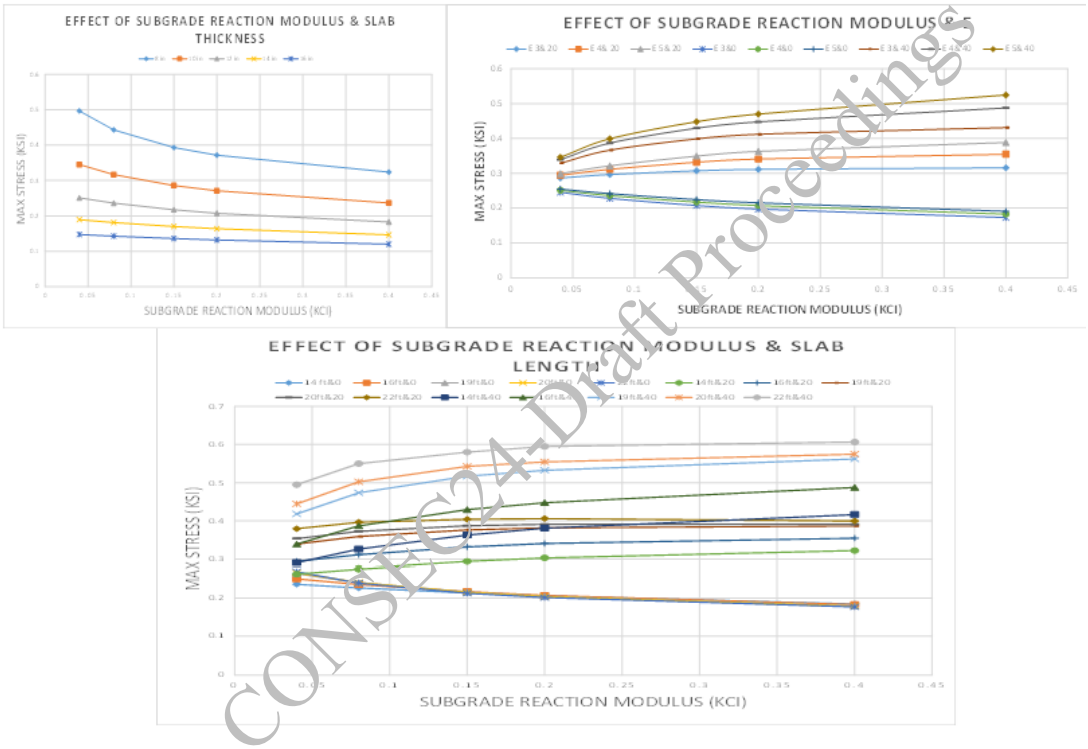

Figure 4. Maximum Stresses as Functions of Subgrade Reaction Modulus Values and Slab Thickness, Elastic Modulus (E), and Slab Length Values

4.3 Effects of Temperature on Performance of Concrete Pavement Using Various Type of Aggregates.

As explained in research methodology, there were some studies on concrete made with different aggregates. An analysis was performed to check the effect of temperature differentials on concrete made with these aggregates (Brooksville limestone, Calera limestone, and River gravel). Maximum stress and stress-strength ratio are presented in this analysis as shown in Figure 5. Results show the same stress for all three types of aggregates in the absence of ΔT (0 ^{o}F). However, results show that the stress increases as ΔT increases. Results show that at ΔT of 40 ^{o}F, the lowest stress is obtained for concrete made with Brooksville limestone, while the highest stress is obtained for river gravel. Stress-strength ratio shows that the lowest stress-strength ratio is obtained by Brooksville limestone, followed by Calera limestone, and then river gravel.

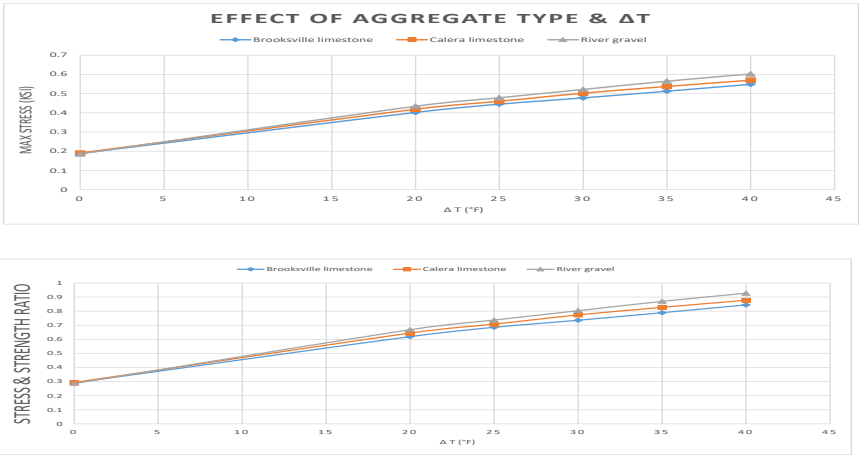

Figure 5. Maximum Stresses and Stress-Strength Ratio as Functions of Temperature Differentials for Various Pavement Design Inputs.

5. Conclusions

This study concentrates on the effects of relevant factors affecting the performance of concrete pavement under severe climate conditions (extreme heat and flooding). The study investigates the properties of concrete and the dimensional design of concrete pavements using FEACONS IV to assess their impact on the performance of concrete pavements under extreme heat and flooding conditions. Based on the findings from FEACONS IV analysis, the following conclusions are made:

1. Using concrete with lower elastic modulus, adequate flexural strength, and aggregates with a lower CTE value, can increase the load carrying capacity of concrete pavement under extreme weather conditions.
2. Using thicker concrete slabs can reduce the load and temperature induced stresses in concrete pavement under severe weather conditions.
3. The use of a higher subgrade reaction modulus value in concrete pavement during flooding conditions helps to strengthen the pavement. However, under extreme high temperatures, a high subgrade reaction modulus can increase the load and temperature induced stresses.
4. Concretes made with porous limestone aggregate have low coefficient of thermal expansion and low elastic modulus and show potentially better performance than concretes made with river gravel.

References

B. Jongman, P. J. Ward, J. C. Aerts. (2012) “Global exposure to river and coastal flooding: Long term trends and changes”, *Global Environmental Change* 22 (4) 823–835.

E. B. Owusu-Antwi, L. Titus-Glover, M. I. Darter. (1998) “Design and Construction of PCC Pavements: Volume I: Summary of Design Features and Construction Practices That Influence Performance of Pavements” (No. FHWA-RD-98-052).

E. Masad, R. Taha, B. Muhunthan. (1996) “Finite-element analysis of temperature effects on plain-jointed concrete pavements”, *Journal of Transportation Engineering* 122 (5) 388–398.

M. Tia, D. Bloomquist, M. C. K. Yang, P. Soongswang, M. P., C. Meletiou, P. Amornsrivilai, D. Richardson. (1990) “Field and Laboratory Study of Modulus of Rupture and Permeability of Structural Concrete in Florida”.

M. Tia, D. Bloomquist, G. D. Alungbe, D. Richardson. (1991) “Coefficient of thermal expansion of concrete used in Florida”.

M. I. Darter, H. V. Quintus, Y. J. Jiang, E. B. Owusu-Antwi, B. M. Killingsworth. (1997) “Catalog of Recommended Pavement Design Features” (No. NCHRP Project 1-32).

M. Tia, D. Verdugo, O. Kwon. (2012) “Evaluation of long-life concrete pavement practices for Use in Florida” (No. 00093785) (2012).

P. K. Mehta, P. J. Monteiro. (2014) “Concrete: microstructure, properties, and materials”, McGraw-Hill Education

T. Tang, D. G. Zollinger, S. Senadheera. (1993) "Analysis of concave curling in concrete slabs", *Journal of Transportation Engineering* 119 (4), 618–633.

X. Chen, W. Huang, J. Zhou. (2012) "Effect of moisture content on compressive and split tensile strength of concrete", *Indian Journal of Engineering & Materials Sciences* 19, 427–435.

W. Wang, C. Lu, G. Yuan, Y. Zhang. (2017) "Effects of pore water saturation on the mechanical properties of fly ash concrete", *Construction and building materials* 130, 54–63.

Linking Short-Term Conductivity to Long-Term Chloride Diffusion for Service Life Prediction

S. Surana[1*], H.B. Beushausen[2], and M.G. Alexander[3]

[1] *University of Cape Town, Cape Town, South Africa*
Email: srnsaa001@myuct.ac.za
[2] *University of Cape Town, Cape Town, South Africa*
Email: hans.beushausen@uct.ac.za
[3] *University of Cape Town, Cape Town, South Africa*
Email: mark.alexander@uct.ac.za

[*]Corresponding author

ABSTRACT

Short-term electrical tests are preferred as a means of characterizing and controlling concrete mixtures for marine environments. The testing can be performed quickly and at an early age. These are significant practical advantages over natural chloride diffusion testing, which is both time-consuming and onerous. However, early-age indirect measurements are inherently limited in their ability to indicate long-term performance. The quantitative estimation of long-term chloride resistance for service life prediction requires the consideration of the evolution of material properties and the material-environment interaction with time. This study attempts to integrate electrical conduction and diffusion measurements from lab and field to develop an engineering prediction model. The model is based on a modified error function solution. An overview of the relevant theoretical and empirical relationships linking conductivity with the field performance is also presented for South African conditions.

KEYWORDS*: Service life prediction, Correlations, Chloride modelling, conductivity, Apparent diffusion coefficient*

1. Introduction

Chloride-induced corrosion is the predominant cause of loss of service life among reinforced concrete structures exposed to marine conditions. This has gathered much attention towards developing the models for chloride ingress and the subsequent corrosion process in order to understand and control various aspects of this mode of deterioration in reinforced concrete. The process of chloride-induced corrosion is typically divided into two stages: before and after the point of corrosion initiation (Tutti, 1982). Before corrosion initiation, the service life is controlled by the severity of the environmental conditions and the penetration resistance of concrete. A number of models have been constructed since the early 1990s to model the process of chloride penetration in concrete following different modelling philosophies: empirical or physical (Nilsson, 2006). The commonality between these approaches is the use of a quick electrical test to characterise the chloride penetrability. Various electrical tests were developed around the globe in response to the shortcomings of the Rapid Chloride Penetration Test (Streicher & Alexander, 1994). Prediction models and quality control specifications have also been developed for various test methods.
The Chloride Conductivity test is one such test method that was developed in South Africa (Streicher & Alexander, 1995) and has been used in the South African region for performance testing (Alexander, Santhanam & Ballim, 2011). An empirical service life prediction model using chloride conductivity was developed for selected South African marine environments in the 1990s (Mackechnie, 1996). However, since then the test method has been improved and more field experience has been gathered (Otieno & Alexander, 2015; Heiyantuduwa-Beushausen, 2022). The current study was conducted with an aim to develop an empirical model for chloride ingress using chloride conductivity with an extended scope of materials.

2. Modelling approach

The error function solution (ERFC) to non-steady state diffusion process is used to model chloride transport in marine conditions according to (5. The apparent diffusion coefficient (D_a) is modelled according to (6 following the modified DuraCrete modelling approach (Siemes & Edvardsen, 1999).

$$C_x = C_s \left(1 - erf \left[\frac{x}{2\sqrt{(D_a . t_{exp})}} \right] \right) \quad (1)$$

Where, C_x is the chloride content at a depth x; C_s is the surface chloride content; D_a is the apparent diffusion coefficient; and t_{exp} is the exposure time.

$$D_a = \sigma_{28} . K_t . K_e . \left(\frac{t_{ref}}{t} \right)^m \quad (2)$$

Where, σ_{28} is the conductivity at 28 days; K_t is the test method factor; K_e is the environmental factor; m is the aging coefficient; t is the age at testing, and t_{ref} is the reference age.
The conductivity is directly proportional to the instantaneous steady-state diffusivity through Nernst-Einstein relation. However, the apparent diffusivity represents an average diffusivity over time, with the added complicating effects of increasing surface chloride concentration (Maage et al., 1996). In such a case, the D_a at a reference time other than the start of the exposure (t_0), will depend on the m values as shown in (7 and (8.

$$D_{a,ref} = K_0 . \sigma_{28} \left(\frac{t_{ref}}{t_0} \right)^{-m} \quad (3)$$

$$D_{a,ref} = K_{ref} . \sigma_{28} \quad (4)$$

The values of K_{ref} are derived in the following sections. Other factors are derived, but not presented here due to space constraints.

3. Experimental program

A range of mixture proportions with different blended binders and w/b ratios were used in this study. Fly ash (FA) at replacement levels of 15% and 30%, and blast-furnace slag (BS) at replacement levels of 25% and 50% were blended with CEM I-52.5N (PC) to make binary blends. The w/b ratios ranged from 0.3 to 0.7. Two types of curing were used: standard wet curing for 7 days and 7-days plastic wrapping followed by 21 days in the lab air.
The apparent diffusion coefficient was evaluated according to the bulk diffusion test (ASTM C1556, 2016). The conductivity was evaluated by means of the chloride conductivity test (SANS 3001-CO3-3, 2015). In brief, the chloride conductivity index (CCI) represents the conductivity of oven-dried concrete saturated with a highly conductive, 5 M NaCl solution.

4. Correlation between D_a and chloride conductivity

The correlations between the 180-day exposed D_a and the 28-day CCI are examined. These correlations must be binder specific for two reasons: 1. D_a incorporates the effect of binding which differs with the type of binder irrespective of the exposure duration, and 2. 180-day D_a had evolved with time from the start of exposure to the end of exposure, the rate of which also varies with the binder type. This is observed in the results in Figure 5. The correlations show good fit to linear trendlines following (8. The test correlation factors obtained as the slope of the fitted line also appears to exhibit a dependence on the binder type. It is considered useful to express these constants as non-linear functions of the SCM levels. In this case, exponential functions are preferred over polynomial functions to avoid over-fitting and over linear functions to avoid under-fitting. Moreover, further efforts to find a better fit or more scientifically aligned

function may not improve the accuracy in the absence of more data points. These empirical correlations are used to develop an expression for D_a, which requires CCI_{28} and SCM% as input apart from the aging coefficient as shown in **Error! Reference source not found.** and
(9.

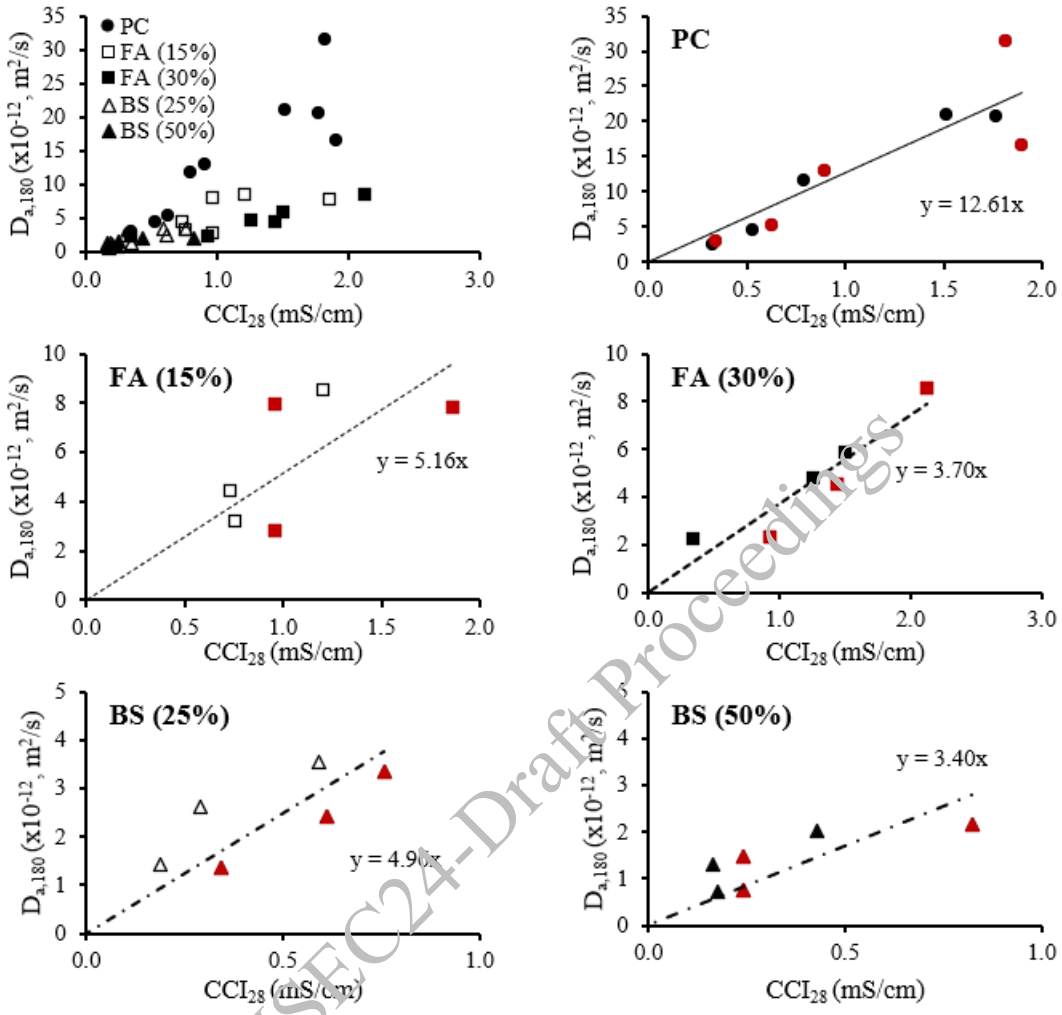

Figure 4. Correlations between 180-day D_a ($D_{a,180}$) and 28-day CCI (CCI_{28}). The red markers represent plastic cured concrete.

$$D_a(t) = K_{180}.CCI_{28}\left(\frac{t}{208}\right)^{-m} \quad (5)$$

Where,
t_{ref} =208 days (Reference age= Age at the start of exposure (28 days) + exposure duration (180 days))
CCI_{28}: Chloride conductivity index at the age of 28 days;

K_{180}: Test method correlation constant for $t_{ref} = t_{208}$; $(\frac{cm}{mS} \cdot \frac{m^2}{s})$ (6)

Test correlation factor between $D_{a,180}$ and CCI_{28}

$$K_{180} = 12.6 \times 10^{-12}.e^{-1.38\left(\frac{FA\%}{30}+\frac{BS\%}{50}\right)}$$

5. Conclusions

An error-function model was developed for South African marine condition using chloride conductivity as a means to characterise the penetrability of the concrete pore structure to chloride ions. The following main conclusions can be drawn from this study:

Reasonably good correlations were found between the apparent diffusion coefficient and the chloride conductivity for both fly ash and slag blended concretes. The correlations were in line with the theory and depended on the binder type.

The aging coefficient to diffusivity was determined mainly by the type of binder used. Other factors such as mix proportions, test method, and marine exposure zones did not have consistent and definitive influence. The 'm' values were therefore modelled as a function of SCM type and level.

Environmental conditions, particularly the capillary suction effects in the wet-dry zones, may influence the apparent diffusion coefficient. More research is required to clarify the environmental influences as well as to develop a database of environmental factor (K_e) for marine sites of particular interest.

A simple factor was introduced in the surface chloride content values to account for its variation with w/b ratio.

It must be remembered that the model predictions are limited by the amount and quality of available data and the underlying simplifying assumptions. While the model is intended to guide design and quality control decision making, engineering judgement cannot be dispensed with when interpreting the model predictions. In other words, design decisions must be taken to satisfy all the relevant considerations, not only the chloride penetration resistance of the materials. The model needs to be validated and calibrated against independent data, preferably long-term, before use.

References

Alexander, M.G., Santhanam, M. & Ballim, Y. 2011. Durability design and specification for concrete structures—the way forward. *International Journal of Advances in Engineering Sciences and Applied Mathematics*. 2(3):95–105. DOI: 10.1007/s12572-011-0027-x.

ASTM C1556. 2016. Standard Test Method for Determining the Apparent Chloride Diffusion Coefficient of Cementitious Mixtures by Bulk Diffusion. *ASTM International*. 1–7. DOI: 10.1520/C1556-11A.2.

Heiyantuduwa-Beushausen, R. 2022. The influence of concrete mix composition and environmental exposure on long-term chloride ingress in concrete. PhD Thesis. University of Cape Town.

Maage, M., Helland, S., Poulsen, E., Vennesland, O. & Carlsen, J.E. 1996. Service Life Prediction of Existing Concrete Structures Exposed to Marine Environment. *ACI Materials Journal*. 93(6).

Mackechnie, J.R. 1996. Predictions of Reinforced Concrete Durability in the Marine Environment. PhD Thesis. University of Cape Town.

Nilsson, L.O. 2006. Present limitations of models for predicting chloride ingress into reinforced concrete structures. In *Journal de Physique IV (Proceedings)*. V. 122. 1–7.

Otieno, M. & Alexander, M. 2015. Chloride conductivity testing of concrete – past and recent developments. *Journal of South African Institution of Civil Engineering*. 57(Cci):55–64. DOI: 10.17159/2309-8775/2015/v57n4a7.

SANS 3001-CO3-3. 2015. South African Natioanal Standard Civil engineering test methods Part CO3-3 : Concrete durability index testing — Chloride conductivity test.

Siemes, T. & Edvardsen, C. 1999. DuraCrete: Service life design for concrete structures. In *Durability of Building Materials and Components 8*. M.A. Lacasse & D.J. Vanier, Eds. Institute for Research in Construction, Ottawa ON, K1A 0R6, Canada. 1031. DOI: 10.1007/978-3-642-37475-3.

Streicher, P.E. & Alexander, M.G. 1994. A critical evaluation of chloride diffusion test methods for concrete. In *Third CANMET/ACI International Conference on Concrete Durability*. Nice, France: Supplementary papers, ACI, Detroit. 517–530.

Streicher, P.E. & Alexander, M.G. 1995. A chloride conduction test for concrete. *Cement and Concrete Research*. 25(6):1284–1294.

Tutti, K. 1982. Corrosion of steel in concrete. PhD. Lund University.

Non-linear Finite Element Simulation of RC Beams Under Simultaneous Rebar Corrosion and Sustained Service Loads

Pankaj Mishra[1*], Prasanna Kumar Behera[2], and Sudhir Misra[3]

[1]Ph.D. student, Department of Civil Engineering, Indian Institute of Technology Kanpur, Kanpur, India
Email: pankaj94mishra@gmail.com
[2]Assistant Professor, Department of Civil and Environmental Engineering, Indian Institute of Technology Tirupati, Tirupati, India
Email: prasanna@iittp.ac.in
[3]Professor, Department of Civil Engineering, Indian Institute of Technology Kanpur, Kanpur, India
Email: sud@iitk.ac.in

[*]Corresponding author

ABSTRACT

The serviceability and performance of reinforced concrete (RC) structures is significantly affected by corrosion of reinforcement. Under the real world of structures, RC members are subjected to combined influence of service loads and rebar corrosion. Hence, the numerical simulation of time dependent degradation involves consideration of sustained load and corrosion induced structural distresses simultaneously. In the present work, a 3D finite element (FE) model of RC beams corroding under sustained load is developed. The nonlinear behaviour of concrete is defined using concrete damaged plasticity (CDP) model. A simplified temperature field-based methodology was proposed, in the commercial program ABAQUS, to model the evolution of corrosion degradation while a sustained load is maintained in the RC beam. In this approach, the model parameters susceptible to be affected by rebar corrosion were defined as a function of temperature. The temperature of the beam was altered to modify the parameters to implement corrosion damage at different components. The corrosion induced structural effects were considered by damage in concrete cover due to corrosion cracking, modified constitutive laws of reinforcement due to corrosion, and degradation in bond behaviour between corroded rebar-concrete interface. The proposed FE model is validated by comparing the predicted response with the experimental behaviour of beams in terms of crack development as well as load-deflection response under combined loading and corrosion.

KEYWORDS: *Nonlinear finite element model, Beam, Temperature, Sustained load, Corrosion*

1. Introduction

Corrosion of steel reinforcement bars in concrete is a primary factor leading to the degradation of reinforced concrete (RC) constructions. Several research examining the effects of corrosion on the performance of reinforced concrete (RC) beams have documented a decrease in their ability to withstand bending or shear forces, as well as a shift in the way they fail (Mangat & Elgarf, 1999; Du et al., 2007; Xu & Niu, 2003). Recently, researchers have been using finite element (FE) modelling more frequently to simulate the behaviour of reinforced concrete (RC) structures (Altheeb et al., 2022; Alshaikh et al., 2022; Alshaikh et al., 2024; Safdar et al., 2023; Sun et al., 2023). In order to study the effects of corrosion on the flexural behaviour of reinforced concrete beams, Coronelli and Gambarova (2004), Kallias and Rafiq (2010), Hanjari et al. (2011), and Ou and Nguyen (2014) created two-dimensional finite element models. These models incorporated material degradation or the removal of spalled concrete. In the context of 2D modelling, the concept of degradation in bond was introduced by Dekoster et al. (2003) through the use of the equivalent elastic modulus method. Alternatively, Liu et al. (2021) proposed the connector mechanism as another approach to incorporate this degradation. In addition, Biondini and Vergani (2020), Xiaoming and Hongqiang (2012), and German and Pamin (2015) utilized a 3D finite element model to study corroded beams, employing different approaches to assess bond damage. Nevertheless, a small number of researchers have used the bond-slip behaviour to model the deterioration of the bond.

Notably, the majority of previous studies have examined the behaviour of corroded beams that were not exposed to service loads while undergoing corrosion-induced degradation. However, in reality, concrete structures experience service loads when rebar corrosion develops. Therefore, models designed to simulate the realistic behaviour of corroded members must consider the existence of sustained load. The investigations have shown that the corrosion behaviour can vary under sustained load conditions compared to unloaded conditions. This is because the corrosion rate is increased in high stress areas and there is greater exposure to air, water, and chlorides near crack locations (Fu et al., 2016; Du et al., 2013). According to Li et al. (2018), the corrosion characteristics can transition from surface corrosion to pitting corrosion, which can cause a greater decrease in mechanical properties. This is because there is a significant concentration of stress surrounding the pits. Investigation into the corrosion behaviour under applied mechanical stress is now under progress.

Although the significance of continuous load has been acknowledged, there has been limited focus on numerically simulating the behaviour of a beam under both corrosion and stress simultaneously. Lately, there has been a scarcity of studies that have included this particular element. Shen et al., 2019 simulated the progression of deterioration in reinforced concrete beams under simultaneous conditions. Nevertheless, the modelling did not account for the impact of corrosion on the link between interfaces and the deterioration of the mechanical properties of the rebar. Meet et al. (2021) conducted a study where they created a three-dimensional model that accounted for the combined impact of uniform corrosion and bending stress. Several finite element analyses were performed to simulate various levels of corrosion. However, the deterioration caused by uniform corrosion may not be suitable for situations involving applied stress. The literature study indicates a notable deficiency of research in this field. Current research lacks a full examination of all corrosion factors, particularly those related to applied stress. Furthermore, the simulation of the time-dependent reaction caused by increasing corrosion has not been sufficiently replicated. It is imperative to create a robust and comprehensive modelling method that can accurately simulate the behaviour of beams that are in use and experiencing ongoing corrosion degradation.

This study aims to address this gap by developing a complete modelling framework for reinforced concrete beams with progressive corrosion under working loads. A three-dimensional nonlinear finite element model is created to simulate the corrosion-induced damage in a beam subjected to sustained service loads. This work is a part of the author's published work (Mishra et al., 2024). The FE model takes into account the deterioration of mechanical properties in the rebar, the presence of cracks in the cover, and the weakening of the bond between the rebar and the concrete. A simplistic methodology was developed to simulate the progression of corrosion deterioration under sustained load. This methodology is based on the temperature field method in the commercial finite element software 'ABAQUS'. The accuracy of the FE model was confirmed by comparing the crack patterns, failure mode, and load-deflection behaviour of a reinforced concrete beam, subjected to different loading and corrosion conditions, with the experimental results published in the literature (Li et al., 2018).

2. Corrosion damage models

The damage caused by corrosion-induced cracks in the cover concrete is modeled by assuming a reduction in its strength, as described by Eq. (1) (Coronelli & Gambarova, 2004). Here f_c^* and f_c represents compressive strength of the damaged and undamaged concrete respectively; The parameter λ, which depends on the reinforcement diameter and its roughness, is taken as 0.1 (Cape, 1999); ε_{C0} denotes the strain at peak compressive stress and ε_1 refers to average tensile strain in the cracked concrete in the transverse direction of the applied compression, determined by Eq. (2). b_0 is the initial width before corrosion-induced cracking and n_{bars} is the number of corroded rebar in the section. υ_{rs} denotes the volumetric expansion ratio of corrosion products considered as 2 in the present study. X (in μm) is the corrosion penetration depth evaluated as $X = 11.6 i_{corr} t$ (Chernin & Val, 2011), where i_{corr} is the corrosion current density in μA/cm2 and t is time in years. The modified tensile strength (f_t^*) of the cracked concrete cover is computed based on modified compressive strength (f_c^*) according to CEB: FIP model code (2010).

The properties of corroded rebar are affected not only by the levels of corrosion mass loss but also its type i.e., uniform or pitting. Pitting corrosion induces a more pronounced reduction in mechanical behaviour as compared to that of uniform corrosion (Almusallam, 2001; Cairns et al., 2005; Du et al., 2005). The degradation in the mechanical behaviour was considered according to equations proposed by Lee et al.

(1998) as shown in Table 1. The bond behaviour of corroded reinforcement in RC beam is analysed by formulation proposed by Saifullah and Clark (1994) as shown in Eq. (3) where, C_c is the clear cover or half of clear rebar spacing whichever is smaller, $f_c$is the compressive strength (MPa) of concrete; A_t is the cross-sectional area of stirrups, f_{yt} is the yield strength of stirrups; S_s is the spacing between stirrups; d_b is the dia. of tensile reinforcement; *R* denotes the reduction factor and parameter ΔW refers to percentage mass loss. The reduction factor '*R*' introduced by Maaddaway et al. (2005) was determined based on constants A_1 and A_2 which depends on applied current density, as described by Eq. (4). The application of factor '*R*' in the first term in Eq. (3) implies that stirrups do not contribute to the reduction in the bond strength of corroded reinforcement (Rodriguez, Ortega, & Casal, 1994). This formulation enabled the determination of the maximum bond strength in RC beams that are subjected to corrosion, considering the presence of deformed reinforcing bars.

Table 1. Mechanical degradation of corroded reinforcement

Type of corrosion	Yield strength	Elastic modulus
Uniform corrosion	$\left(1-\frac{1.24\Delta W}{100}\right).f_y$	$\left(1-\frac{0.75\Delta W}{100}\right).E_s$
Pitting corrosion	$\left(1-\frac{1.98\Delta W}{100}\right).f_y$	$\left(1-\frac{1.13\Delta W}{100}\right).E_s$

ΔW: corrosion mass loss (in percentage), f_y and E_s: yield strength and elastic modulus of uncorroded rebar respectively

$$f_c^* = \frac{f_c}{1+\lambda\frac{\varepsilon_1}{\varepsilon_{co}}} \quad (1)$$

$$\varepsilon_1 = \frac{n_{bars}.2\pi(v_{rs}-1)X}{b_0} \quad (2)$$

$$\tau_{max} = R\left(0.55 + 0.24\frac{C_c}{d_b}\right)\sqrt{f_c} + 0.191\frac{A_t f_{yt}}{S_s d_b} \quad (3)$$

$$R = (A_1 + A_2\Delta W) \quad (4)$$

3. 3D Nonlinear FE simulation of RC beams under simultaneous corrosion and sustained loads

3.1 Material models

The non-linear behaviour of concrete is defined using concrete damaged plasticity (CDP) model (Lubliner et al., 1989; Lee & Fenves, 1998) as shown in Fig 4. The model incorporates the principles of isotropic damaged elasticity, along with isotropic tensile and compressive plasticity, to effectively capture the inelastic response of concrete. In the present study, damage and plasticity parameters were evaluated in accordance with Hafezolghorani et al. (2017). Uniaxial stress-strain response of concrete was defined according to FIB model code (2010). The stress-strain response of concrete in compression, as shown in Fig. 1(a), is described by Eq. (5). where $\eta = \frac{\varepsilon_c}{\varepsilon_{c1}}, k = \frac{E_{ci}}{E_{c1}}$; ε_{c1} is the concrete strain at maximum compressive stress; E_{ci} and E_{c1} denoting the tangent elastic modulus at origin and secant modulus from the origin to peak compressive stress; f_c is the compressive strength of concrete. In case of uniaxial tension, the stress-strain response is linear elastic until the failure stress (f_t) evaluated using $f_t = 0.3 \times (f_{ck})^{\frac{2}{3}}$, where f_{ck} is the characteristic compressive strength of concrete in MPa. For accurately capturing the post-peak or softening behaviour, fracture energy approach was adopted which helps in mitigating the issues

related to mesh sensitivity (Sümer & Aktaş, 2015). Fracture energy (G_f), which provides a measure of the energy required to propagate a crack through the material, was determined using Eq. (6). Bilinear softening law was adopted as illustrated in Fig. 1(b). The corrosion-induced degradation was considered by utilizing Eq. (1) and (2) where the value of b_0 (initial width) is 120 mm and ε_{C0} is 0.224%. The Poisson's ratio of the concrete was taken as 0.2. Fig 1 (a) and (b) shows the material models of concrete in compression and tension respectively.

$$\frac{\sigma_c}{f_c} = \left(\frac{k.\eta - \eta^2}{1+(k-2).\eta}\right) \tag{5}$$

$$G_f = 73 \times {f_c}^{0.18} \tag{6}$$

The stress-strain behaviour of the reinforcing steel was described by elastic-plastic behaviour with linear strain hardening. Within the plastic regime, the modulus was assumed to be 1% of the initial modulus of elasticity (E_s) (Bypour et al., 2019). Fig. 1(c) depicts the stress-strain relationship of the reinforcing bar, where the parameters f_y, E_s, and ε_y denotes the yield strength, elastic modulus, and yield strain respectively. The suffix *'rs'* signifies the corresponding parameters for corroded rebar. The ultimate strain of the corroded rebar is assumed to be similar to that of uncorroded rebar.

3.2 Concrete-rebar interface

The bond at the concrete-rebar interface was modelled by defining the cohesive interaction between the contact surface of rebar and concrete. As given in Eq. (7), the traction vectors along the three mutually orthogonal directions (normal (t_n), shear (t_s) and tangential (t_t)) are related with the respective separations or slip (δ_n, δ_s and δ_t respectively). Initially, the interaction was assumed to be linear elastic, but once the peak stress was reached, damage initiation and evolution occurred. The stiffness matrix represents the material property at the interface. In the present study, the non-diagonal terms of the stiffness matrix, which represent the coupling between different directions, were considered as zero. To characterize the bond-slip behaviour, shearing stiffness (K_{ss} and K_{tt}) at concrete and reinforcement interface, were calculated based on bond strength (τ_{max}) and corresponding slip (S_1) according to Eq. (8). Bond stiffness for normal deformation (K_{nn}) was assigned a higher value (100 times) compared to the shearing stiffness values. Damage initiation in the bond interface is defined as the point at which any of the three stress components exceeds the allowable stress as expressed by Eq. (9).

$$\begin{pmatrix} t_n \\ t_s \\ t_t \end{pmatrix} = \begin{bmatrix} K_{nn} & 0 & 0 \\ 0 & K_{ss} & 0 \\ 0 & 0 & K_{tt} \end{bmatrix} \begin{pmatrix} \delta_n \\ \delta_s \\ \delta_t \end{pmatrix} \tag{7}$$

$$K_{ss} = K_{tt} = \frac{\tau_{max}}{S_1} \tag{8}$$

$$max\left\{\frac{t_n}{t_n^0}, \frac{t_s}{t_s^0}, \frac{t_t}{t_t^0}\right\} = 1 \tag{9}$$

The bond-slip model considered in the present study is schematically illustrated in Fig. 1(d). The stress continues to increase until the bond strength (τ_{max}) reaches a value corresponding to separation S_1(in mm). Subsequently, damage initiation occurs as the slip exceeds S_1 and the damage progression is assumed to increase linearly until reaching the maximum slip (S_2) (Henriques et al., 2013). Maximum bond stress (τ_{max}) accounts for contribution from both the concrete and stirrups and was determined using Eq. (10) (Kemp & Wilhelm, 1979). Moreover, S_1 and S_2 were determined according to the model proposed by (Kallias & Rafiq, 2010) (Eq. (11) and (12)). S_r denotes the rib spacing, which was taken as 0.5 times the rebar diameter. Values of C_c, S_s, and d_b were taken as 19 mm, 80 mm, and 12 mm respectively. Corrosion-effect was incorporated by considering the reduced bond strength (according to Eq. (3) and (4)) where the values of A_1 and A_2 were considered as 0.861 and -0.014 for corrosion current density of 1000 μA/cm^2.

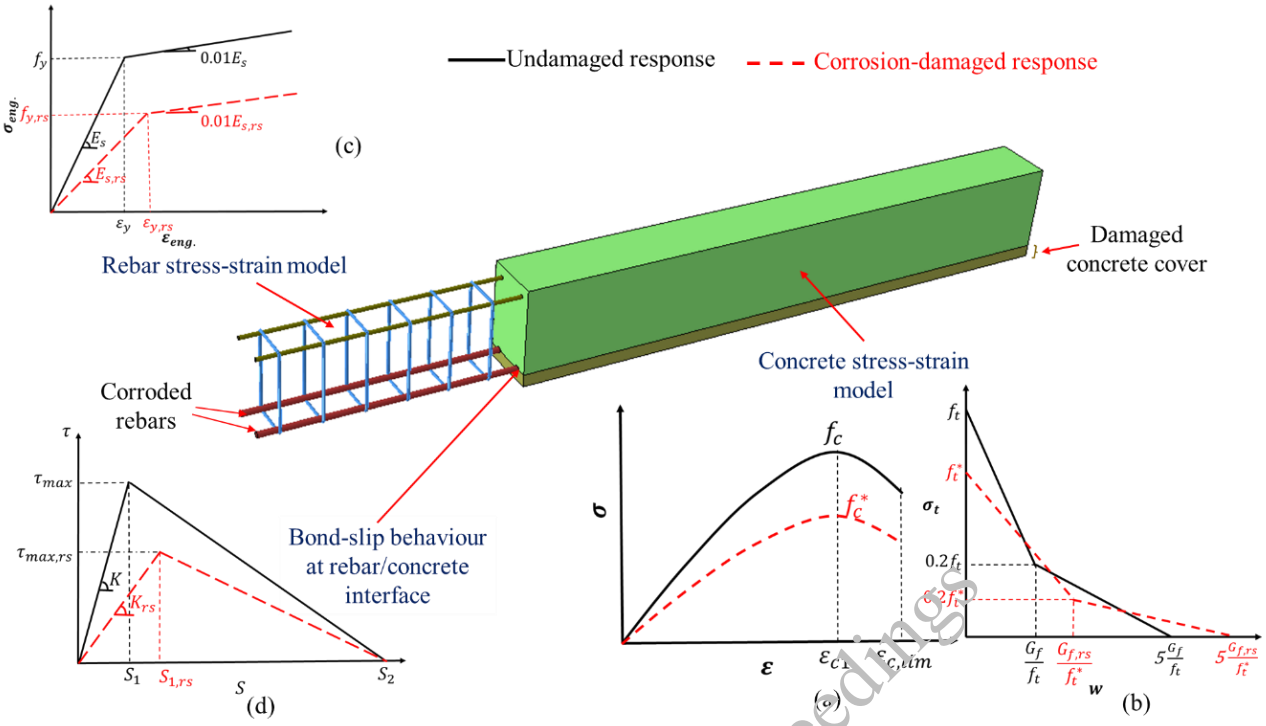

Figure 1. Constitutive models in FE simulation of corroded beam: (a) concrete stress-strain response in compression (b) Bilinear tension-softening curve of concrete (c) Stress-strain response of rebar (d) Bond stress-slip model at rebar/concrete interface (Note: The suffix 'rs' represents the degraded parameter due to rebar corrosion)

$$\tau_{max} = \left(0.55 + 0.24\frac{C_c}{d_b}\right)\sqrt{f_c} + 0.191\frac{A_t f_y}{S_s d_b} \quad (10)$$

$$S_1 = 0.15Ke^{\frac{10}{3}ln ln\left(\frac{\tau_{max}}{2.57\sqrt{f_c}}\right)} + 0.4\,ln\left(\frac{2.57\sqrt{f_c}}{\tau_{max}}\right) \quad (11)$$

$$S_2 = 0.35 * S_r \quad (12)$$

3.3 Temperature based methodology for simulating the beams under simultaneous corrosion and sustained load

In this methodology, the modelling parameters were classified into two distinct categories: corrosion-independent parameters (*CoIPs*) and corrosion-dependent parameters (*CoDPs*). CoIPs encompassed the parameters that remained unaffected by corrosion, while CoDPs represented the parameters that experienced degradation as a result of corrosion, such as strength of cover concrete, mechanical properties of corroded rebars, and the interface between corroded rebars and the surrounding concrete. To introduce corrosion-induced damage into the beam, the *CoDPs* were linked to the "temperature" to modify it by varying the temperature. However, the coefficient of thermal expansion was set to zero to isolate the effects of thermal stresses resulting from temperature changes. The *CoDPs* were defined as temperature-dependent functions at discrete points, and were updated to $(CoDPs)_1$, $(CoDPs)_2$, $(CoDPs)_3$……$(CoDPs)_n$, corresponding to temperature values T_1, T_2, T_3…..T_n. Linear interpolation was used to estimate the CoDP values between two temperature points. Conversely, the *CoIPs* remained constant throughout the analysis, as they were independent of temperature variations. The degraded parameters $(CoDPs)_1$, $(CoDPs)_2$, $(CoDPs)_3$……$(CoDPs)_n$ were associated with corrosion levels m_1, m_2, m_3…..m_n, *respectively*. Thus, a direct equivalence between temperature and the degree of corrosion was established.

4. Results and discussions

The accuracy of the FE model was validated by comparing the predicted behaviour of beams with the experimental data of Li et al. (2018). Beam specimens were corroded in the presence of sustained load for introducing the damage due to joint effect. Further, the damaged specimens were subjected to the four-point flexure loading to analyse bending performance. In the present study, eight cases of simultaneous load and corrosion levels, including a control specimen, were considered for assessing the accuracy of FE simulation. Notation used to represent the specimen is 'BL-x-y' where 'x' represents the level of sustained loading (in % of the ultimate capacity) and 'y' represents the corrosion degree (0, 1, 2, and 3 denoting 0, 5, 10 and 20 days of corrosion exposure). The behaviour of beams was compared in terms of cracking and load-deflection responses.

4.1 Cracking behaviour under simultaneous loading and corrosion

This section presents the crack development in the beam under joint effect of corrosion and sustained load. Furthermore, the damaged beams were subjected to 4-point flexure loading test till failure. Fig. 2 shows the distribution of cracks at failure for specimen BL-15-1 as compared with the simulated crack pattern (as indicated by tensile damage in beam model). The failure mode of the beam specimen involved the yielding of the tensile reinforcement. Thus, the nonlinear FE simulations utilizing temperature-field approach can successfully capture the cracks development in RC beam under the combined effect of loading and corrosion. It also endorses the effectiveness of the corrosion-damage-plasticity (CDP) model in simulating the behaviour of concrete.

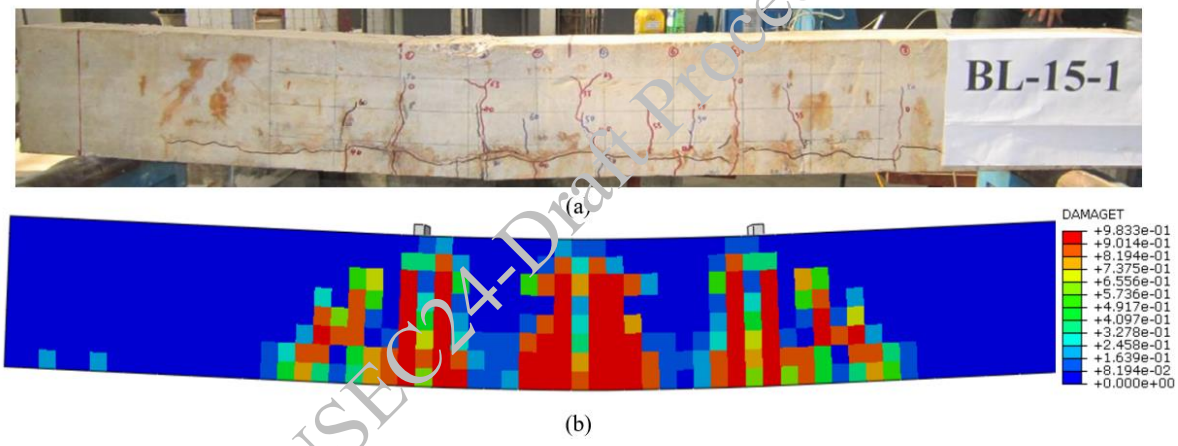

Figure 2. Crack pattern at failure in (a) Specimen BL-15-1 as indicated by (b) tension damage in simulated beam model

4.2 Load-deflection behaviour

Load-deflection behaviour of control and eight beams damaged under different levels of simultaneous load and reinforcement corrosion are shown in Fig. 3. For all the specimens, the predicted initial stiffness slightly exceeded the experimental values, which can be attributed to the presence of thermal and shrinkage cracks in concrete in the experiments, or cracks occurred during the preloading phase for instrumentation purposes. However, the difference reduces significantly for specimens in the BL-15 and BL-30 series, which exhibited higher stiffness due to an improved bond between the concrete and steel during the initial stage of corrosion. The prevailing failure mode observed in the specimens involved yielding of the reinforcement followed by crushing of concrete at compression zone. The simulated behaviour effectively captured the degradation behaviour under the combined effect of sustained load and corrosion. At higher loading and corrosion levels (specimen BL-60-1 and BL-60-2), the simulated response overestimated the experimental response as observed in Figs. 3(h) and 3(i). This could be ascribed to the excessive non-uniformity in corrosion at higher loading reported as 0.24 and 0.29 for BL-60-1 and BL-60-2 specimens, respectively. It leads to localized yielding of the reinforcement at lower loads and eventually reduction in the performance. For assessing the accuracy of the FE model (1) the load at the service limit deflection (P_s), (2) the yield load (P_y), and (3) the ultimate load capacity (P_u) was compared with the experimental data. Here, P_s

represents the load at the serviceability limit, considered as the span/500 according to the CEB: FIP model code (2010). The yield load (P_y) refers to the load at which yielding of the reinforcement initiates, while the ultimate load (P_u) corresponds to the flexural capacity of the beam. As per the predicted values of these loads, the average ratios of predicted load to experimental load were found to be 1.13 for P_s, 1.06 for P_y, and 1.04 for P_u, with standard deviations of 0.10, 0.07, and 0.04, respectively indicating a good agreement with the experimental data. Thus, the developed FE model by utilizing the temperature field methodology, effectively represents the nonlinear behaviour of beams under combined effect including the failure load and load-deflection behaviour.

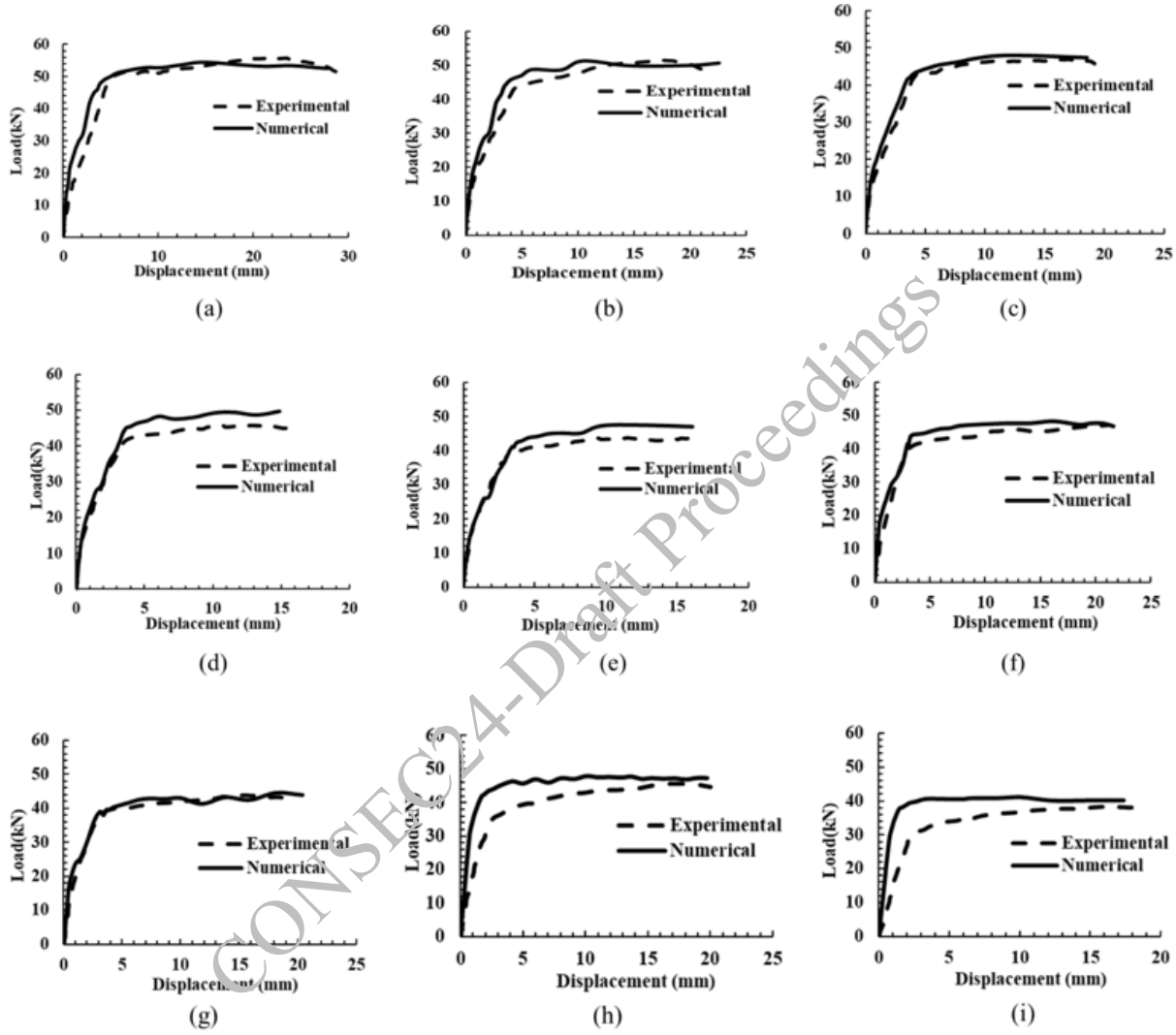

Figure 3. Experimental and predicted load-deflection response for corroded specimen: (a) BL-0-0, (b) BL-0-2, (c) BL-0-3, (d) BL-15-2, (e) BL-15-3, (f) BL-30-1, (g) BL-30-2, (h) BL-60-1 and (i) BL-60-2

5. Conclusions

The present work is motivated towards the simulation of RC beam which is undergoing various deteriorating effects of rebar corrosion under service loads. The model included the bond strength degradation, damage in concrete cover and reduction in mechanical strength of corroded rebar. A simplified methodology in ABAQUS based on temperature field is utilized to implement corrosion degradation in sustained loaded beams. The accuracy of the developed model was assessed by comparing the predicted behaviour of beams in terms of crack evolution under coupled action, crack pattern at failure and load-deflection response in flexure. Further, additional parametric investigations were carried out to investigate the impact of degree of corrosion, corrosion type i.e. uniform or pitting and sequence of load and corrosion on the performance of beam. The study concludes that, utilizing the temperature field in ABAQUS, can be

effectively employed to model the structural response of RC beams suffering rebar corrosion under service load conditions.

References

Almusallam, A. A. (2001). "Effect of degree of corrosion on the properties of reinforcing steel bars". *Construction and building materials*, *15*(8), 361-368.

Alshaikh, I. M., Abadel, A. A., Sennah, K., Nehdi, M. L., Tuladhar, R., & Alamri, M. (2022). "Progressive collapse resistance of RC beam–slab substructures made with rubberized concrete". *Buildings*, *12*(10), 1724.

Alshaikh, I. M., Nehdi, M. L., & Abadel, A. A. (2024, February). "Numerical investigations on progressive collapse of rubberized concrete frames strengthened by CFRP sheets". In *Structures* (Vol. 60, p. 105918). Elsevier.

Altheeb, A., Alshaikh, I. M., Abadel, A., Nehdi, M., & Alghamdi, H. (2022). "Effects of non-structural walls on mitigating the risk of progressive collapse of RC structures". *Latin American Journal of Solids and Structures*, *19*, e440.

Biondini, F., & Vergani, M. (2020). "Deteriorating beam finite element for nonlinear analysis of concrete structures under corrosion". *Design, Assessment, Monitoring and Maintenance of Bridges and Infrastructure Networks* (pp. 107-120). Routledge.

Bypour, M., Gholhaki, M., Kioumarsi, M., & Kioumarsi, B. (2019). "Nonlinear analysis to investigate the effect of connection type on behaviour of steel plate shear wall in RC frame". *Engineering Structures*, *179*, 611-624.

Cairns, J., Plizzari, G. A., Du, Y., Law, D. W., & Franzoni, C. (2005). "Mechanical properties of corrosion-damaged reinforcement". *ACI materials journal*, *102*(4), 256.

Cape, M. (1999). *Residual Service-Life Assessment of Existing R/C Structures* [MS Thesis], Chalmers univ. of Tech., Goteborg (Sweden) and Milan Univ. of Tech., Italy.

Chernin, L., & Val, D. V. (2011). "Prediction of corrosion-induced cover cracking in reinforced concrete structures". *Construction and Building Materials*, *25*(4), 1854-1869.

Coronelli, D., & Gambarova, P. (2004). "Structural assessment of corroded reinforced concrete beams: modelling guidelines". *Journal of structural engineering*, *130*(8), 1214-1224.

Dekoster, M., Buyle-Bodin, F., Maurel, O., & Delmas, Y. (2003). "Modelling of the flexural behaviour of RC beams subjected to localised and uniform corrosion". *Engineering Structures*, *25*(10), 1333-1341.

Du, Y. G., Clark, L. A., & Chan, A. H. C. (2005). "Effect of corrosion on ductility of reinforcing bars". *Magazine of Concrete Research*, *57*(7), 407-419.

Du, Y., Clark, L. A., & Chan, A. H. (2007). "Impact of reinforcement corrosion on ductile behaviour of reinforced concrete beams". *ACI Structural Journal*, *104*(3), 285.

Du, Y., Cullen, M., & Li, C. (2013). "Structural performance of RC beams under simultaneous loading and reinforcement corrosion". *Construction and Building Materials*, *38*, 472-481.

El Maaddawy, T., Soudki, K., & Topper, T. (2005). "Analytical model to predict nonlinear flexural behaviour of corroded reinforced concrete beams". *ACI structural journal*, 102(4), 550.

Fib Model Code for Concrete Structures 2010.

Fu, C., Ye, H., Jin, X., Yan, D., Jin, N., & Peng, Z. (2016). "Chloride penetration into concrete damaged by uniaxial tensile fatigue loading". *Construction and Building Materials*, *125*, 714-723.

German, M., & Pamin, J. (2015). "FEM simulations of cracking in RC beams due to corrosion progress". *Archives of Civil and Mechanical Engineering*, *15*(4), 1160-1172.

Hafezolghorani, M., Hejazi, F., Vaghei, R., Jaafar, M. S. B., & Karimzade, K. (2017). "Simplified damage plasticity model for concrete". *Structural engineering international*, *27*(1), 68-78.

Hanjari, K. Z., Kettil, P., & Lundgren, K. (2011). "Analysis of mechanical behaviour of corroded reinforced concrete structures". *ACI Structural Journal*, *108*(5), 532-541.

Henriques, J., da Silva, L. S., & Valente, I. B. (2013). "Numerical modelling of composite beam to reinforced concrete wall joints: Part I: Calibration of joint components". *Engineering Structures*, *52*, 747-761.

Kallias, A. N., & Rafiq, M. I. (2010). "Finite element investigation of the structural response of corroded RC beams". *Engineering Structures*, *32*(9), 2984-2994.

Kallias, A. N., & Rafiq, M. I. (2010). "Finite element investigation of the structural response of corroded RC beams". *Engineering Structures*, *32*(9), 2984-2994.

Kemp, E. L., & Wilhelm, W. J. (1979, January). "Investigation of the parameters influencing bond cracking".*Journal proceedings* (Vol. 76, No. 1, pp. 47-72).

Lee, H. S., Noguchi, T., & Tomosawa, F. (1998, June). "FEM analysis for structural performance of deteriorated RC structures due to rebar corrosion". *Proceedings of the second international conference on concrete under severe conditions* (pp. 327-336). Norway: Tromsø.

Lee, J., & Fenves, G. L. (1998). "Plastic-damage model for cyclic loading of concrete structures". *Journal of engineering mechanics*, *124*(8), 892-900.

Li, H., Li, B., Jin, R., Li, S., & Yu, J. G. (2018). "Effects of sustained loading and corrosion on the performance of reinforced concrete beams". *Construction and Building Materials*, *169*, 179-187.

Liu, X., Jiang, H., Ye, Y., & Guo, Z. (2021). "Deformation-based performance index of corroded reinforced concrete beams". *Journal of Building Engineering*, *34*, 101940.

Lubliner, J., Oliver, J., Oller, S., & Onate, E. (1989). "A plastic-damage model for concrete". *International Journal of solids and structures*, *25*(3), 299-326.

Mangat, P. S., & Elgarf, M. S. (1999). "Flexural strength of concrete beams with corroding reinforcement". *Structural Journal*, *96*(1), 149-158.

Meet, S., Trishna, C., & Naveen, K. (2021). "Investigating the nonlinear performance of corroded reinforced concrete beams". *Journal of building engineering*, *44*, 102640.

Mishra, P., Behera, P. K., & Misra, S. (2024). "3D nonlinear finite element simulation of RC beams corroding under service loads". Journal of Structural Integrity and Maintenance, 9(2).

Ou, Y. C., & Nguyen, N. D. (2014). "Plastic hinge length of corroded reinforced concrete beams". *ACI Structural Journal*, *111*(5), 1049.

Rodriguez, J., Ortega, L. M., & Casal, J. (1994, June). "Corrosion of reinforcing bars and service life of reinforced concrete structures: corrosion and bond deterioration". In *International conf. on concrete across borders, Odense, Denmark* (Vol. 2, pp. 315-326).

Safdar, M., Sheikh, M. N., & Hadi, M. N. (2023). "Finite element analysis to predict the cyclic performance of GFRP-RC exterior joints with diagonal bars". *Journal of Building Engineering*, *65*, 105774.

Saifullah, M., & Clark, L. A. (1994). "Effect of corrosion rate on the bond strength of corroded reinforcement". *Corrosion and corrosion protection of steel in concrete*, *1*, 591-602.

Shen, J., Gao, X., Li, B., Du, K., Jin, R., Chen, W., & Xu, Y. (2019). "Damage evolution of RC beams under simultaneous reinforcement corrosion and sustained load". *Materials*, *12*(4), 627.

Sümer, Y., & Aktaş, M. (2015). "Defining parameters for concrete damage plasticity model". *Challenge Journal of Structural Mechanics*, *1*(3), 149-155.

Sun, Y., Fu, W., Chen, X., Zhang, Z., Yu, W., & Li, S. (2023). "Theoretical and experimental investigations into flexural behavior of existing reinforced concrete beams strengthened by CFRP bars". *Journal of Building Engineering*, *77*, 107528.

Xiaoming, Y., & Hongqiang, Z. (2012). "Finite element investigation on load carrying capacity of corroded RC beam based on bond-slip". *Jordan Journal of Civil Engineering*, *6*(1), 134-146.

Xu, S., & Niu, D. (2003). "The shear behavior of corroded reinforced concrete beam. In International conference on advances in concrete and structures". RILEM Publications SARL, pp. 409-415.

Zhang, W., Zhang, H., Gu, X., & Liu, W. (2018) Structural behavior of corroded reinforced concrete beams under sustained loading. *Construction and building materials*, *174*, 675-683.

Towards Carbon Neutrality: A Progressive Path for Sustainable Development in the Construction Industry of a Developing Nation

Abhiram Shukla[1*], Harish Kizhakkumodom Venkatanarayanan[2]

*[1]*PhD Student, Department of Civil Engineering, Indian Institute of Technology (IIT) Kanpur, Kanpur, Uttar Pradesh, 208016, India*
Email: abhirams@iitk.ac.in
[2] Associate Professor, Department of Civil Engineering, Indian Institute of Technology (IIT) Kanpur, Kanpur, Uttar Pradesh, 208016, India
Email: kvharish@iitk.ac.in

*Corresponding author

ABSTRACT

Rapid growth in the construction and building industry, particularly in developing nations like India, has led to a surge in cement production and consumption, exacerbating concerns about carbon emissions and their impact on climate change. India, as the second-largest cement manufacturer globally, confronts the task of fulfilling its developmental requirements while also aiming to achieve carbon neutrality by 2070, in accordance with its dedication to the Sustainable Development Goals. This study provides a comprehensive, state-level analysis of the environmental footprint of cement production in India, quantifying its impact across six key environmental categories: embodied energy consumption, global warming potential, ozone depletion, acidification, eutrophication, and photochemical ozone creation potential. Our findings reveal a distinct geographical disparity, with southern India emerging as a primary hotspot for environmental impact, followed by the northern, eastern, western, and central regions. To facilitate informed decision-making, this study introduces a novel approach that translates complex environmental impacts across all six domains into a single, readily interpretable monetary unit (US$). This methodology provides a pragmatic framework for policymakers and industry stakeholders to evaluate the environmental costs associated with cement production and prioritize sustainable practices.

KEYWORDS*: Carbon neutrality, Cement Industry, Environmental Impact, Alternative cement, Sustainability*

1. Introduction

Recognizing climate change as a pressing global issue, the international community is striving for carbon neutrality through stringent emission reduction targets (Ropo et al., 2023). The Paris agreement, a cornerstone of these efforts, aims to limit global warming to below 2°C, ideally 1.5°C, above pre-industrial levels (Hu et al., 2023). This endeavour presents unique challenges for developing countries like India, the world's third-largest carbon emitter, as they strive to balance economic development with ambitious climate commitments, including carbon neutrality by 2070 (Viswanathan et al., 2021; Hossain et al., 2023). Within this context, the cement industry, a significant contributor to global CO_2 emissions, bears a substantial responsibility for decarbonization. Accounting for 8% of anthropogenic greenhouse gas emissions, primarily from energy consumption and the calcination process (Miller et al., 2018), the industry requires transformative change. The cement manufacturing process releases CO_2 from several key sources. Approximately 50% of emissions originate from the calcination of limestone, which decomposes into calcium oxide and CO_2 (Mahasenan et al., 2003; Supriya et al., 2023). Fossil fuel combustion, primarily for thermal energy generation, contributes another 40% of CO_2 emissions (Supriya et al., 2023). The remaining 10% can be attributed to transportation activities and electricity consumption throughout the cement production lifecycle. China leads global cement production, followed by India, highlighting the

significant emissions footprint of these nations. Fig. 1 shows the leading countries in global cement production in 2023 (Statista, 2024).

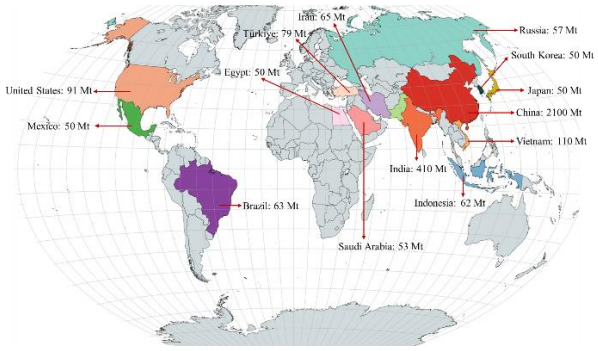

Figure 1. Leading countries in global cement production in 2023 (in million metric tons)

India's cement industry alone saw a nearly sevenfold increase in CO_2 emissions between 1990 and 2021, underscoring the urgency for mitigation strategies (Global Carbon Project, 2022). India's cement industry, with an installed capacity of 595 million tonnes per annum (MTPA), currently produces 410 MTPA, reflecting its significant role in the nation's infrastructure development (Cement Industry Report, 2024; Statista, 2024). Projections indicate a 7-8% growth in cement production during fiscal year 2024, driven by substantial investments in infrastructure and large-scale residential construction projects. These initiatives, including the "Housing for All" and "Smart Cities Mission," underscore the government's commitment to urbanization and economic growth (Sudhakar & Reddy, 2023). However, the projected surge in cement production raises concerns about its environmental impact. The anticipated increase in emissions from the cement industry, if left unchecked, could potentially exceed allocated carbon budgets, thereby jeopardizing the attainment of Sustainable Development Goals (SDGs). This study conducts a "cradle to gate" life cycle assessment (LCA) of Ordinary Portland Cement (OPC) production based on the installed capacity of cement plants in India. Data on potential capacity was collected and linked with recent Indian-specific characterization factors/environmental impact coefficients of OPC. These were analyzed across six environmental impact categories: embodied energy (EE) use, global warming potential (GWP), ozone depletion potential (ODP), acidification potential (AP), eutrophication potential (EP), and photochemical ozone creation potential (POCP). Furthermore, conversion factors translated these environmental impacts into environmental costs. This comprehensive approach provides a scientific basis and guidance for decision-making in green practices for cement production.

2. Materials and methods

2.1 Life cycle potential environmental impact and environmental cost of production of ordinary Portland cement (OPC) in India

The LCA comprises four stages: Goal and Scope Definition, Life Cycle Inventory Analysis, Life Cycle Impact Assessment, and Results Interpretation. This study aims to calculate the potential environmental impact across six categories resulting from OPC production (cradle to gate) in India. To calculate the potential environmental impact, it is assumed that the plant's potential capacity is dedicated solely to producing OPC, given its widespread use in Indian construction. The data for cement production capacity was sourced from the Cement Industry Report (2024), which provides region-specific information. Indian-location-specific characterization factors for cement's environmental impact were taken from the India construction material database (ICD, 2017).

The environmental impact for each region was determined by multiplying these characterization factors by the regional annual potential production capacity of cement, as described in Eq. 1:

$$\boldsymbol{EI_k = \sum m_i x CF_{ki}} \quad (1)$$

In this context, EI_k represents the overall environmental impact of cement production on category *'k'* (for instance, measured in kg CO_2 eq.), where m_i denotes the total quantity of material '*i'* (per million metric tonnes), CF_{ki} is the characterization factor for cement '*i'* pertaining to k_{th} environmental category.

This method provides a detailed and region-specific assessment of environmental impacts, facilitating a more accurate evaluation of the cement production's ecological footprint. By focusing on OPC, the analysis addresses India's most prevalent type of cement, ensuring relevance and applicability. This comprehensive assessment aids in identifying critical areas for improvement and informs decision-making for sustainable practices in cement manufacturing. Furthermore, it supports policy development and industry initiatives to reduce the environmental footprint of cement production in India. In the present analysis, the conversion factors derived from the Environmental Priority Strategies (EPS) 2015 model, as conceptualized by Steen (2019), were employed to translate environmental impacts into monetary costs. This approach provides a clearer understanding of the economic implications of environmental impacts, further supporting sustainable decision-making in the cement industry.

3. Results

3.1 Potential environmental footprint of manufacturing ordinary Portland cement (OPC) in India

A comprehensive LCA of OPC manufacturing, covering the "cradle to gate" phases, reveals a significant environmental impact for producing one million tonnes annually. Table 1 highlights an energy demand of 3,252,224 terajoules per year and greenhouse gas emissions of 462.43 million tonnes of CO_2 equivalent annually. The study also quantifies other environmental impacts: ozone depletion potential (1.42E-06 million kg CFC-11 eq. per year), acidification potential (1.37 million tonnes SO_2 eq. per year), eutrophication potential (0.173 million tonnes PO_4 eq. per year), and photochemical ozone creation potential (0.097 million tonnes ethene eq. per year). The high environmental footprint is primarily due to the energy-intensive nature of OPC production, especially the calcination of limestone, which releases substantial CO_2. Additionally, burning fossil fuels for clinkerization contributes significantly to greenhouse gas emissions. Absolute impact values offer a quantitative perspective but lack the nuance to compare different impact categories. Table 1 provides absolute and normalized impact values for six key environmental categories in OPC production. Normalized values indicate that energy use is the most significant contributor to the overall environmental burden. This emphasizes the need for energy efficiency measures and a shift towards cleaner energy sources in OPC production to reduce its environmental footprint effectively.

Table 1. The potential environmental footprint of OPC production in India with the region

Region*	Energy use	GWP	ODP	AP	EP	POCP
				Units		
	(million MJ PA)	(million tons CO_2 eq. PA)	(million kg CFC-11 eq. PA)	(million tons SO_2 eq. PA)	(million tons PO_4 eq. PA)	(million tons C_2H_4 eq. PA)
North	5.98E+05 (18.4%)	85.09 (18.4%)	2.62E-07 (18.4%)	0.25 (18.4%)	0.032 (18.4%)	0.018 (18.4%)
South	1.17E+05 (36%)	166.63 (36%)	5.13E-07 (36%)	0.49 (36%)	0.062 (36%)	0.035 (36%)
East	5.38E+05 (16.6%)	76.55 (16.6%)	2.36E-07 (16.6%)	0.23 (16.6%)	0.029 (16.6%)	0.016 (16.6%)
West	5.03E+05 (15.5%)	71.45 (15.5%)	2.20E-07 (15.5%)	0.21 (15.5%)	0.027 (15.5%)	0.015 (15.5%)
Central	4.41E+05 (13.6%)	62.71 (13.6%)	1.93E-07 (13.6%)	0.19 (13.6%)	0.023 (13.6%)	0.013 (13.6%)
India	3.25E+06	462.43	1.42E-06	1.37	0.173	0.097
Normalized impact	7.23E-03	1.10E-14	1.58E-21	4.04E-15	1.33E-15	1.01E-15

*North: Rajasthan, Punjab and Haryana
South: Tamil Nadu, Karnataka, Telangana and Andhra Pradesh
East: Odisha, Jharkhand, Chhattisgarh and West Bengal
West: Gujrat and Maharashtra
Central: Uttar Pradesh and Madhya Pradesh

3.2 Environmental impacts due to individual regions of India

The results reveal that the southern region of India significantly contributes to the environmental impact of OPC manufacturing. This region accounts for approximately 36% of the total environmental burden across all impact categories, as illustrated in Fig. 2. The southern region is followed by the northern region with 18.4%, the eastern region with 16.6%, the western region with 15.5%, and the central region with 13.6%. This pronounced impact in the south could be attributed to several factors, including a high concentration of limestone reserves—a crucial raw material for cement production—in states like Andhra Pradesh and Telangana. Furthermore, robust construction activities spurred by rapid urbanization and infrastructure development in this region likely contribute to the heightened demand for cement, amplifying the environmental footprint.

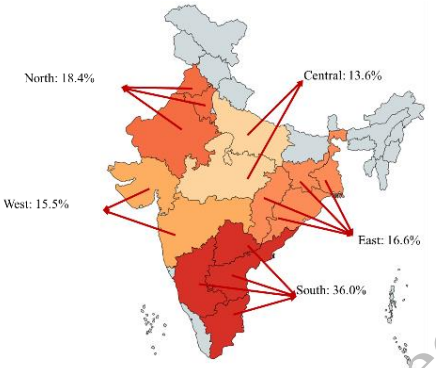

Figure 2. Environmental impact of OPC production due to individual regions in India (in %)

3.3 Environmental cost of individual regions of India

Table 2 presents a detailed economic valuation of the environmental impacts of OPC production in India, categorized by GWP, ODP, AP, EP, and POCP. As visualized in Fig. 3, the GWP emerges as the dominant contributor to the environmental cost, amounting to US$5,641.59 per annum. This substantial cost reflects the significant carbon footprint of OPC manufacturing, primarily attributed to the energy-intensive clinkerization process and associated fossil fuel combustion. Interestingly, the AP category exhibits a negative value (-US$584.48 per annum), suggesting potential cost savings or credits. This counterintuitive finding aligns with Steen's observation that secondary sulfate aerosols, often byproducts of industrial processes, can exert a cooling effect, partially offsetting the adverse impacts of climate change. The ODP, EP, and POCP categories contribute relatively smaller costs of US$0.000852, US$2.95, and US$15.74 per annum, respectively. While less pronounced than GWP, these values underscore the multifaceted environmental ramifications of OPC production extending beyond greenhouse gas emissions. The economic valuation presented in this study provides valuable insights for policymakers and industry stakeholders, enabling informed decision-making that balances economic considerations with environmental sustainability in the context of India's cement industry. Fig. 4 illustrates the regional disparities in the environmental costs associated with OPC production across India. The southern region emerges as the most significant contributor, followed by the northern, eastern, western, and central regions. This geographical distribution of environmental costs highlights the spatial heterogeneity of the cement industry's impact in India, likely influenced by factors such as regional variations in production scale, energy sources, and environmental regulations.

Table 2. Environmental cost of the production of OPC in India (Region details are mentioned in table 1)

Region	GWP (US$ PA)	ODP (US$ PA)	AP (US$ PA)	EP (US$ PA)	POCP (US$ PA)
North	1038.04	1.57E-05	-107.54	0.544	2.896
South	2032.89	3.07E-05	-210.61	1.065	5.671
East	933.90	1.41E-05	-96.75	0.489	2.605
West	871.73	1.32E-05	-90.31	0.457	2.432
Central	765.04	1.16E-05	-79.26	0.401	2.134
India	5641.59	8.52E-05	-584.48	2.954	15.738

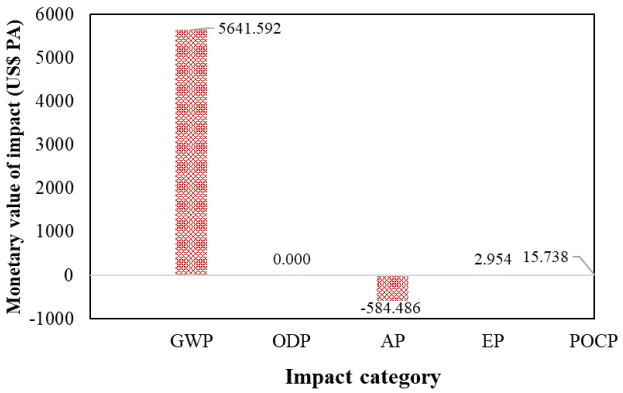

Figure 3. Comparison of environmental impact across categories in terms of environmental cost

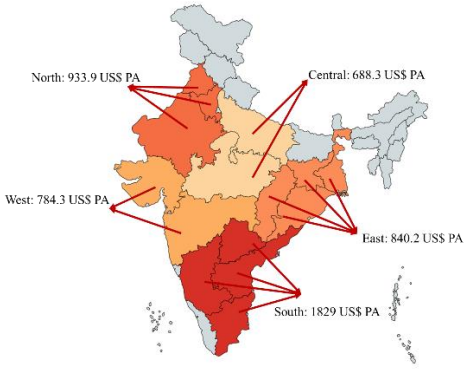

Figure 4. Region-wise environmental cost

4. Discussions

The Indian cement industry requires a transformative strategy shift to reduce its environmental footprint. Fig. 5 illustrates various approaches, including carbon capture, utilization, and storage (CCUS), kiln efficiency improvements, alternative fuel use, incorporation of supplementary cementitious materials, and decarbonization in electricity generation through the adoption of solar energy. These strategies collectively aim to make cement production more sustainable and environmentally friendly (Georgiades et al., 2023).

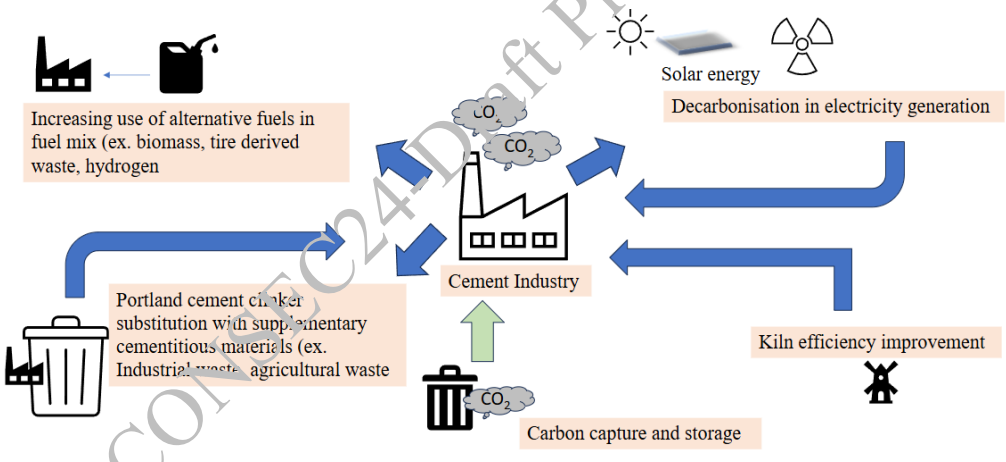

Fig. 5. Strategies for mitigation of carbon footprint in cement industry

4.1 Strategies implemented by Indian cement companies to achieve carbon neutrality goals

Indian cement companies have adopted various strategies to align with India's carbon neutrality objectives. These initiatives prioritize reducing carbon emissions, utilizing alternative fuels, and enhancing operational sustainability.

4.1.1 Environmental Product Declarations (EPD)

In October 2022, UltraTech Cement was awarded Environmental Product Declaration (EPD) certificates for four of its cement products: Ordinary Portland Cement (OPC), Portland Pozzolana Cement (PPC), Portland Slag Cement (PSC), and Portland Composite Cement (PCC) (Cement Industry Report, 2024).

4.1.2 Commitment to Global Sustainability Frameworks

UltraTech Cement pledged its support to the Global Cement and Concrete Association (GCCA) 2050 Cement and Concrete Industry Roadmap in November 2021. This roadmap aims to attain carbon-neutral concrete by the year 2050. Simultaneously, Dalmia Cement aims to manufacture cement with fully

environmentally friendly cement by 2031, facilitated by a substantial investment of US$ 405 million in carbon capture and utilization (CCU) technologies. (Cement Industry Report, 2024).

4.1.3 Utilization of Industrial By-products

UltraTech, Rajshree Cement, Dalmia Cement, and ACC partner alongside the National Thermal Power Corporation Limited (NTPC Ltd.) to acquire fly ash, enabling the full utilization of this power generation by-product (Cement Industry Report, 2024).

4.1.4 Adoption of Alternative Fuels

UltraTech Cement: UltraTech Cement employs tire chips and rubber dust as alternative fuels and has improved its waste heat recovery system (WHRS), resulting in a yearly reduction of 30,000 tonnes of carbon emissions and the production of more than 650 million units of clean energy (Cement Industry Report, 2024).
Madras Cement (Alathiyur Plant): Madras Cement's Alathiyur Plant utilizes bioenergy generated from the cashew nut shells and coffee husk, resulting in a yearly cost reduction of US$ 1.7 million (Cement Industry Report, 2024).
Dalmia Cement: It utilizes plant matter and refuse-derived fuel (RDF) to meet its energy needs. It has successfully implemented a carbon storage and capture facility with a capacity of 0.5 million tonnes per year in 2022. The company aims to shift to clean energy sources by 2030 and achieve carbon negativity by 2040 (Cement Industry Report, 2024).
India Cements Ltd (Dalavoi Plant): It employs low sulphur bulk sludge as a substitute fuel, resulting in yearly cost reductions of almost US$ 6,500 (Cement Industry Report, 2024).
Lafarge (Arasmeta Plant): Lafarge's Arasmeta Plant achieves substantial savings in energy and reduces carbon emissions by substituting 10% of the coal utilised in kilns with rice husk (Cement industry report, 2024).
These strategies illustrate the proactive measures undertaken by Indian cement companies to align with national and global carbon neutrality targets, emphasizing energy efficiency, using alternative fuels, and reducing carbon emissions (Cement Industry Report, 2024).

4.2 Measures to reduce carbon emissions in different countries

The global cement industry is actively pursuing carbon neutrality by 2050, with various organizations and associations outlining comprehensive strategies to achieve this ambitious goal. These roadmaps emphasize a multifaceted approach, incorporating innovative technologies, sustainable practices, and collaborative efforts across the cement and concrete value chain. The International Energy Agency advocates for a four-pronged strategy: enhancing energy efficiency, reducing the clinker-to-cement ratio, adopting innovative technologies, and developing low-carbon cementitious materials (IEA, 2018). Similarly, the Global Cement and Concrete Association has established ambitious objectives to decrease concrete-related CO_2 emissions by 25% by 2030 and achieve net-zero concrete emissions by 2050, emphasizing collaborative action across the value chain (GCCA, 2021). The European Cement Association (ECA) promotes a "5C strategy" targeting carbon reduction across cement, clinker, concrete, carbonation, and construction stages (Guo et al., 2023; CEMBUREAU, 2020). National industry associations have also developed tailored roadmaps. Germany's Verein Deutsche Zementwerke prioritizes clinker content reduction and increased utilization of alternative fuels, particularly biomass (VDZ, 2020). The UK's Mineral Products Association focuses on decarbonized energy, carbon capture, utilization, storage (CCUS), fuel changing, transport, and sustainable green materials, highlighting the added benefits of carbonation and thermal mass (MPA, 2020). The Portland Cement Association in the United States has developed a systematic plan of short, middle, and long-term initiatives to attain net-zero carbon emissions (PCA, 2021). The carbon footprint mitigation goals detailed in the 2050 net zero emission roadmap of different cement associations are succinctly presented in Fig. 6. Globally, nations are implementing diverse measures. Japan prioritizes resource recovery and recycling, while India focuses on energy efficiency enhancements, clinker substitution, alternative fuels, and CCUS (WBCSD, 2018). Across these initiatives, reducing clinker production emerges as a primary focus due to its high emissions intensity. Concurrently, CCUS is recognized as a critical technology for achieving large-scale carbon reductions in the cement industry.

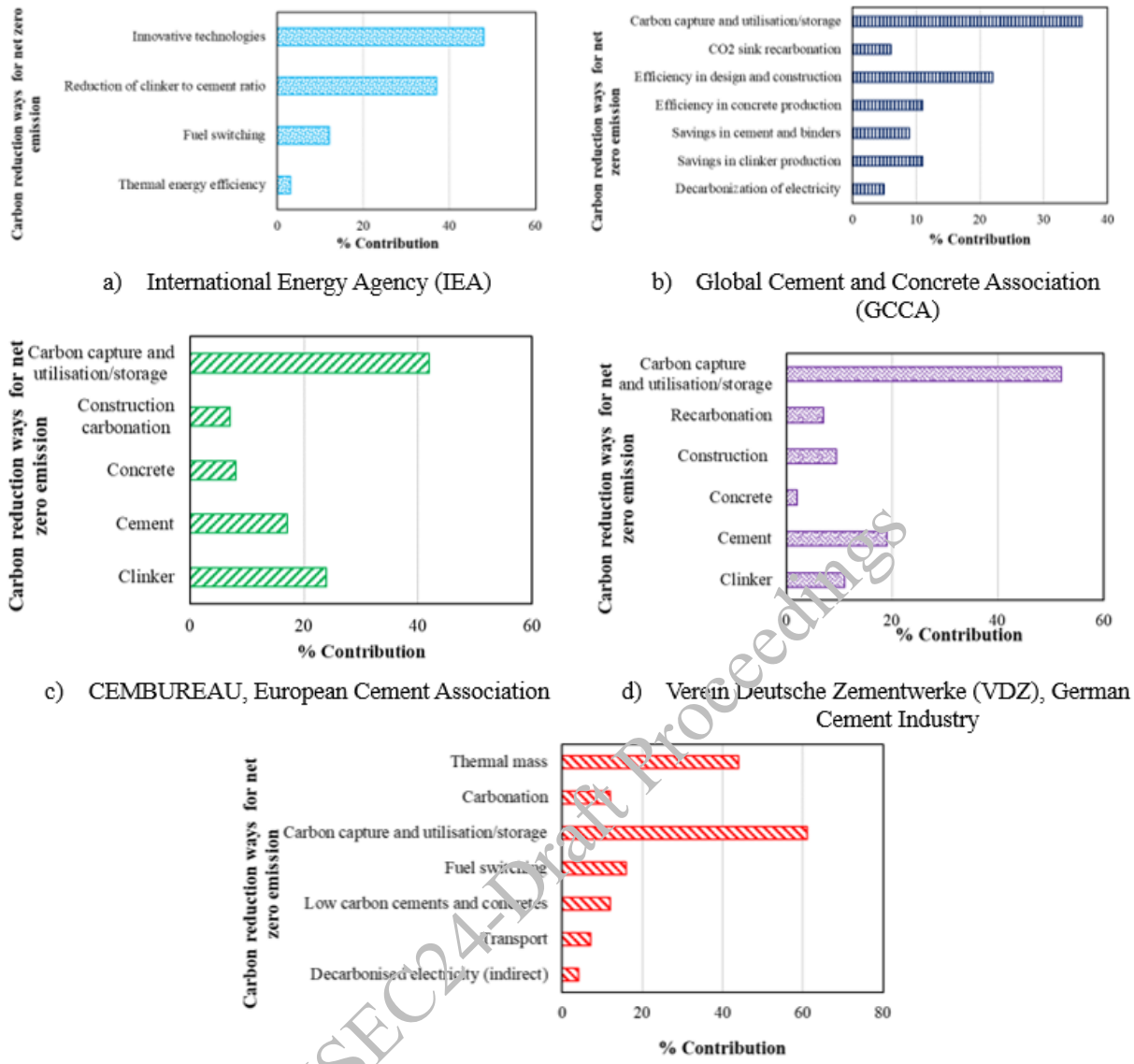

Figure 6. Achieving net zero by 2050: Carbon mitigation strategies for cement associations

4.3 Greenhouse gas emission of Indian cement plant and alternative cement

Basavraj and Gettu (2024) conducted a comprehensive study on cement production in India, collecting data from various cement plants across the country. Using this data, they calculated the greenhouse gas (GHG) emissions associated with producing one tonne of cement. The study underscores the importance of using geographically specific data, emphasizing that primary data is crucial for accurate LCA studies. This ensures that the results are relevant to the specific location, processes, technology, and materials. The study highlights a common issue where global datasets are often used without local data, which can lead to erroneous and misleading conclusions, particularly in the Indian context.

In this study, GHG emissions derived from the Indian construction material database (ICMD) are comparable to those from the Mangrol cement plant, confirming that the ICMD characterization factor accurately reflects location-specific results, as illustrated in Fig. 7.

Moreover, as illustrated in Fig. 8, the characterization factor for PPC and PSC from ICMD and the characterization factor for Limestone Calcined clay Cement (LC3) from Dumani & Mapiravana (2024) reveals a notable reduction in GHG emissions associated with producing PPC, PSC, and LC3 cement, compared to OPC. Specifically, PPC demonstrated a 29.6% reduction, PSC showed a 24.2% reduction, and LC3 exhibited a 26.6% reduction in GHG emissions. This finding highlights the environmental benefits of

utilizing supplementary cementitious materials (SCMs) in cement production, aligning with broader industry efforts to decarbonize construction materials.

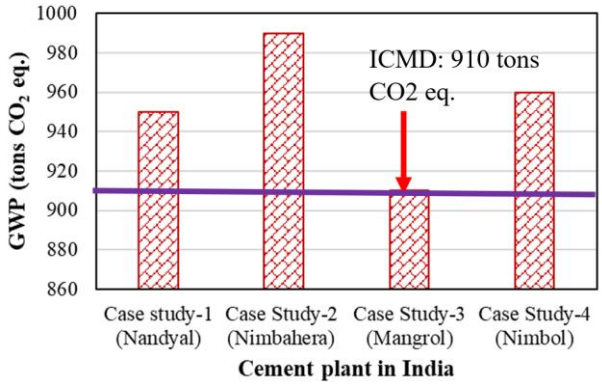

Figure 7. Cement plant and their GHG emissions

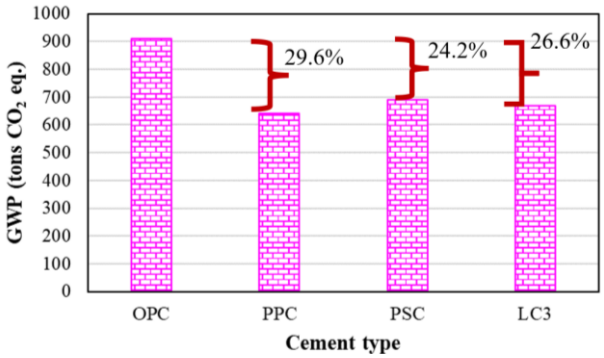

Figure 8. Alternative cement and its GHG emission

5. Conclusions

This study critically examines the regional potential environmental footprints associated with OPC production in India, highlighting the dominance of southern India due to its abundant limestone reserves. While adopting alternative fuels by Indian cement companies represents a positive step, a comprehensive approach encompassing all available carbon-neutral strategies, as advocated by international organizations, is essential for significant emissions reduction. To further mitigate the environmental impact of cement production, targeted policy interventions are crucial. The government should prioritize and incentivize the use of alternative cement, such as PPC, PSC, and LC3, particularly in government-funded projects. Mandating environmentally sound practices throughout the construction sector and a thorough assessment of environmental costs will be instrumental in driving sustainable development within the industry. By embracing a multifaceted approach that combines technological innovation, policy incentives, and a commitment to environmental responsibility, India can pave the way for a more sustainable and carbon-neutral cement sector.

References

Basavaraj, A. S., & Gettu, R. (2024). Primary Life Cycle Inventory Data for Cement Production, with Relevance to Sustainability Assessment-Indian Cases. Data in Brief, 110258.

CEMBUREAU, 2020. Reaching Climate Neutrality along the Cement and Concrete Value Chain by 2050. https://lowcarboneconomy.cembureau.eu/wp-content/uploads/2020/05/CEMBUREAU-2050-ROADMAP_FINAL-VERSION_WEB.pdf. (Accessed on April 15, 2024)

Cement industry report, March (2024). https://www.ibef.org/industry/cement-india (Accessed on: April 15, 2024).

Cement: production ranking top countries 2023, January (2024). https://www.statista.com/statistics/267364/world-cement-production-by-country/ (Accessed on April 15, 2024)

Chaudhury, R., Sharma, U., Thapliyal, P. C., & Singh, L. P. (2023). Low-CO2 emission strategies to achieve net zero target in cement sector. *Journal of Cleaner Production*, 137466.

Dumani, N., & Mapiravana, J. (2024). Cradle-to-gate environmental life cycle assessment of limestone calcined clay cement (LC3). Alive2Green.

Georgiades, M., Shah, I. H., Steubing, B., Cheeseman, C., & Myers, R. J. (2023). Prospective life cycle assessment of European cement production. Resources, Conservation and Recycling, 194, 106998.

Global Carbon Project, 2022. Our World in Data, Annual CO2 Emissions from Cement. https://ourworldindata.org/grapher/annual-co2-cement. (Accessed 20 April 2024).

Hossain, M. S., Fang, Y. R., Ma, T., Huang, C., & Dai, H. (2023). The role of electric vehicles in decarbonizing India's road passenger toward carbon neutrality and clean air: A state-level analysis. *Energy*, *273*, 127218.

Hu, J., Zhang, H., & Irfan, M. (2023). How does digital infrastructure construction affect low-carbon development? A multidimensional interpretation of evidence from China. *Journal of cleaner production*, *396*, 136467.

ICD (2017). India Construction Materials Database of Embodied Energy and Global Warming Potential Methodology Report. European Union, International Finance Corporation, (2017). Available at:

https://www.edgebuildings.com/wp-content/uploads/2017/12/IFC-India-Construction-Materials-Database-Methodology-Report.pdf (Accessed on: 20 April 2024).

IEA, 2018. Technology Roadmap: Low-Carbon Transition in the Cement Industry. https://www.wbcsd.org/Sector-Projects/Cement-Sustainability-Initiative/Resources/Technology-Roadmap-Low-Carbon-Transition-in-the-Cement-Industry (Accessed on April 15, 2024)

Mahasenan, N., Smith, S., & Humphreys, K. (2003, January). The cement industry and global climate change: current and potential future cement industry CO2 emissions. In *Greenhouse gas control technologies-6th international conference* (pp. 995-1000). pergamon.

Miller, S. A., John, V. M., Pacca, S. A., & Horvath, A. (2018). Carbon dioxide reduction potential in the global cement industry by 2050. *Cement and concrete research*, *114*, 115-124.

MPA, 2020. UK Concrete and Cement Industry Roadmap to beyond Net Zero. https://cement.mineralproducts.org/Climate-Change.aspx. (Accessed on April 15, 2024)

PCA, 2021. Roadmap to Carbon Neutrality. https://www.cement.org/docs/default-source/roadmap1/pca-roadmap-to-carbon-neutrality_final.pdf. (Accessed on April 15, 2024)

Ropo, M., Mustonen, H., Knuutila, M., Luoranen, M., & Kosonen, A. (2023). Considering embodied CO2 emissions and carbon compensation cost in life cycle cost optimization of carbon-neutral building energy systems. *Environmental Impact Assessment Review*, *101*, 107100.

Steen, B. (2019). Monetary valuation of environmental impacts: Models and data. CRC Press.

VDZ, 2020. Decarbonising Cement and Concrete: A CO2 Roadmap for the German Cement Industry. https://www.vdz-online.de/en/cement-industry/climate-protection-1. (Accessed April 15, 2024).

Venkata Sudhakar, C., & Reddy, U. (2023). Impacts of cement industry air pollutants on the environment and satellite data applications for air quality monitoring and management. *Environ Monit Assess*, *195*(840), 840.

Viswanathan, R., Arun, U., Samir, S., & Sriram, G. (2021). Mission 2070: A Green New Deal for a Net Zero India. White Paper https://www3.weforum.org/docs/WEF_Mission_2070_A_Green_New_Deal_for_a_Net_Zero_India_2021.pdf

WBCSD, 2018. Low-Carbon Technology Roadmap for the Indian Cement Industry. https://www.wbcsd.org/SectorProjects/Cement-Sustainability-Initiative/Resources/Technology-Roadmap-Low Carbon-Technology-for-the-Indian-Cement-Industry. (Accessed on April 15, 2024)

10th International Conference on CONcrete under SEvere Conditions – Environment and Loading 2024, Chennai, India

In-Situ Determination of Pore Solution Resistivity Using a Metakaolin-Based Geopolymer Sensor.

Kamasani Chiranjeevi Reddy[1] Amir Alaarab[2], Kostiantyn Vasylevskyi[3], Farshad Rajabipour[4]

[1]Post-doc fellow, Pennsylvania State University, State College, PA, USA.
Email: cxk5653@psu.edu
[2]Ph.D. Scholar, Pennsylvania State University, State College, PA, USA.
Email: aqa6403@psu.edu
[3]Research scientist, Callentis Consulting group, Austin, Texas, USA.
Email: kostia@callentis.io
[4]Professor, Pennsylvania State University, State College, PA, USA.
Email: fxr10@psu.edu

*Corresponding author

ABSTRACT

The concrete formation factor is a key metric quantifying the relationship between the electrical resistivity of the bulk concrete mixture and that of the concrete pore solution and is used as a crucial parameter in life-cycle models. Its significance extends to the accurate prediction of permeability, water absorption, chloride ion penetration, and corrosion susceptibility. Pore solution resistivity measurement plays a crucial role in calculating the formation factor. The current study focuses on developing a geopolymer sensor with a discernible pore size to estimate the resistivity of the pore solution. Geopolymer mixes with metakaolin as a precursor and NaOH/Sodium silicate as an activating solution were optimized to achieve the desired pore structure. The pore sizes were assessed using the Kelvin equation by drying the pastes at different relative humidity levels. Ellipsoidal-shaped sensors were developed using a geopolymer mix engineered to reflect the target pore structure. The sensors were tested in solutions of different OH^- concentrations (0.2 to 1.0 M), and a translation factor was calculated to assess the solution resistivity from the measured sensor resistance. The developed sensors were embedded in concrete, and the pore solution resistivity of the concrete was measured and compared with the extracted pore solution resistivity. This research endeavor offers an easy tool for quality assessment and service life prediction of concrete.

KEYWORDS*: Pore solution resistivity, Formation factor, Geopolymer, Durability, Metakaolin.*

1. Introduction

The durability assessment of concrete structures is important to ensure safety, longevity, and sustainability. Pore fluid properties and their transport mechanisms offer key insights on durability metrics like chloride ingress and corrosion susceptibility (Spragg et al (2023), Rajabipour et al (2004), Shafikhani and Chidiac (2019)). The formation factor (FF), defined as the ratio of bulk resistivity of concrete to the pore solution resistivity (PSR), inherently accounts for both ionic properties and transport. FF has been correlated with the chloride diffusion coefficients (Baten and Manzur (2022), Azad et al (2019), Qiao et al (2018)). Standardized by AASHTO T 402-23, bulk resistivity measurement of concrete is straightforward. However, accurately assessing pore fluid resistivity typically requires mechanical extraction, which is impractical for low w/cm concretes. Alternatively, a model developed by the National Institute of Standards and Technology (NIST) estimates PSR based on bulk chemical composition of precursors and degree of hydration (Bentz (2007)). The NIST model is proven to be inaccurate when concrete contains supplementary cementitious materials (Tanesi et al (2019)). An alternative technique called the "Bucket Test" involves immersing concrete samples in a simulated solution for an extended period of time to attain equilibrium, allowing the PSR of concrete to be equivalent to the resistivity of the simulated solution (Spragg et al. 2023). However, the time required for this equilibrium is not known with certainty and depends on concrete transport properties. To address these issues, a sensor for the in-situ measurement of

pore solution resistivity was designed. In-situ measurements of PSR offer quality assessment prior construction as well as health monitoring of structures during their service life.
Designed based on the original idea in Rajabipour (2006), the sensor passes a current through its saturated porous matrix to measure the electrical resistance. The developed sensor should have a known stable formation factor, so that the PSR can be estimated based on the measured sensor resistance. Another prerequisite is that the volume fraction of the pores in the material must be sufficiently high to ensure high bulk conductivity and a high coefficient of ionic diffusion for the sensor when saturated with pore solution. A high bulk electrical conductivity of the sensor body helps minimize stray currents passing through the surrounding medium, while a high diffusion coefficient ensures rapid ionic equilibration between the pore solution in the surrounding concrete and the solution within the sensor body. On the other hand, the pore size distribution of the sensor matrix needs to be small enough to avoid premature drying of the sensor.
Metakaolin based geopolymers were reported to produce highly porous matrix (Zhang and Wang (2015)). The porosity of these mixes decreased with increased NaOH concentration. Yang and White (2020) observed that geopolymers activated with both sodium silicate and sodium hydroxide have finer pore structures compared to those activated with NaOH alone. Peng et al. (2022) reported that fine porosity decreases with a higher activator modulus (SiO_2/Na_2O), lower activator concentration, and increased liquid/solid ratio. In this study, sensors were developed with metakaolin-based geopolymer mixes possessing high porosity and finer pores. The sensors were embedded in concrete for in-situ PSR determination. The performance of developed sensors was tested for different drying conditions, and time taken for ionic equilibrium prior embedment.

2. Results and discussions

2.1 Determination of porosity and fraction of pores.

The porosity of the geopolymer matrix was determined following the guidelines of ASTM C642-21 (2021), with a slight modification to the standard procedure. Instead of boiling, the samples were vacuum saturated. The samples were placed in a vacuum desiccator with a vacuum maintained at approximately 26-28 inHg and were left to saturate for one week. After saturation, each sample was cleaned to remove surface moisture, and the saturated surface dry (SSD) weights were recorded. Immediately afterward, the weight of each sample suspended in water was measured. Finally, the oven-dried weight was measured after drying the samples at 105°C for 24 hours. The permeable porosity was then calculated using equation (1) (Safiuddin and Hearn (2005)).

$$Permeable\ porosity = \frac{M_{SSD} - M_{OD}}{M_{SSD} - M_B} \quad (1)$$

Where, M_{SSD} represents the mass of sample in saturated surface dry condition, M_{OD} refers to the mass of oven dried sample, and M_B indicates the apparent mass of sample immersed in water.
Geopolymer mixtures using metakaolin were prepared. Mixes were tried with various alkaline solutions by varying Na_2SiO_3/NaOH. Cuboidal samples of size 15 mm × 15 mm ×5 mm with three mixes labelled as MK-1 to MK-3 were cast with decreasing SiO_2/Na_2O at constant Na_2O content. The total porosity measured was shown in Table 1. With decrease in SiO_2 content, the total porosity had slightly increased.

Table 1. Total porosity of mixes determined as per ASTM C642

Sample ID	Total porosity (std.dev)
MK-1	55.54 (0.03)
MK-2	55.88 (0.26)
MK-3	57.47 (0.12)

To ensure the sensor remains nearly saturated at relative humidity (RH) levels relevant to the interior of concrete (RH > 80%), the pore size of the sensor matrix must be below a certain threshold (R). This threshold can be calculated using the Kelvin equation (Equation 2).

$$R = \frac{-2\gamma V_m Cos\theta}{\boldsymbol{\mathcal{R}_g} T \cdot ln(RH/a_l)} \quad (2)$$

Where, R is the maximum pore radius, γ is the surface tension of pore solution (~0.072N/m), V_m is the molar volume of pore solution (~18´10^{-6} m3/mol), θ is the liquid-solid contact angle at the pore wall (~ 0), $\mathcal{R}_g$ is the universal gas constant (8.314 J/mol^{o}K), T is the absolute temperature (in Kelvin), a_l is the activity of water within the pore solution (~ 1). Given the assumed values and a temperature of 296 K, the maximum pore radius is approximately 10 nm for RH = 90% and 5 nm RH = 80%

The mass loss due to drying at different RH levels provides insights into the pore size distribution. The samples were dried at different RH with ± 1% variation under nitrogen environment in isothermal chambers at a temperature of 23°C. The mass of the samples at a given RH was considered stable, when the mass change between two consecutive days is less than 0.2%. It was observed that the time required for complete equilibrium was less than a week. The mass loss at varying RH levels is illustrated in Figure 1. As the SiO_2 content decreases, the fraction of pores drying at 90% RH increases (implied by decrease in mass), indicating a reduction in the fraction of pores smaller than 20 nm. However, the fraction of pores drying at 70% RH remains comparable across all three mixtures. Based on the porosity and pore fractions, a proprietary mix with a higher SiO_2/Na_2O ratio was selected for further testing.

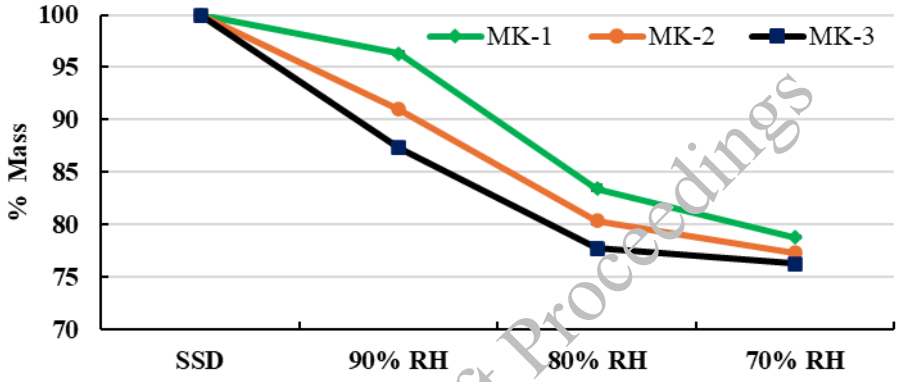

Figure 1. Mass loss of metakaolin based geopolymer samples with decrease in RH. (SiO2/Na2O decreases from MK-1 to MK-3)

2.2 Mass and resistance vs RH isotherm.

Understanding the mass and resistance changes of sensors at different RH levels is crucial for assessing the effect of drying on electrical measurements. Isotherms were measured at 23°C on cuboidal sensors, vacuum-saturated in three different simulated pore concentrations: 0.2 M, 0.6 M, and 1.0 M. The simulated pore solutions were prepared with a 1:1 molar ratio of NaOH and KOH. For electrical measurements, stainless steel electrodes were attached to one pair of opposite sides along the smaller edges of cuboidal sensor using conductive silver epoxy. The 100% RH condition corresponds to the SSD state of the vacuum-saturated sensors. The samples were equilibrated at different RH levels for one week. After each drying period, the mass and resistance of the sensors were measured. The mass was expressed as a percentage of the SSD mass, while the increase in resistance was normalized to the resistance at the SSD condition.

Figure 2(a) shows the mass change at different RH levels in various simulated pore solutions. The desorption branch indicates a rapid loss of moisture in sensors saturated with the 0.2 M solution upon drying, compared to those saturated with 0.6 M and 1.0 M solutions. This effect is due to the decrease in solution activity with increased concentration, requiring a lower RH to dry pores of a similar size. The adsorption isotherm reveals significant hysteresis, similar to that observed in cement pastes (Rajabipour and Weiss (2007)). Figure 2(b) illustrates the change in resistance of the sensors upon drying at different RH levels. The increase in resistance was more pronounced compared to mass loss. Up to 90% RH, the change in resistance was smaller, but it increased significantly with further reductions in RH. The resistance increased by 15-30 times when dried to 70% RH. The results indicate that measurements should be conducted close to 100% RH, i.e., near the SSD state.

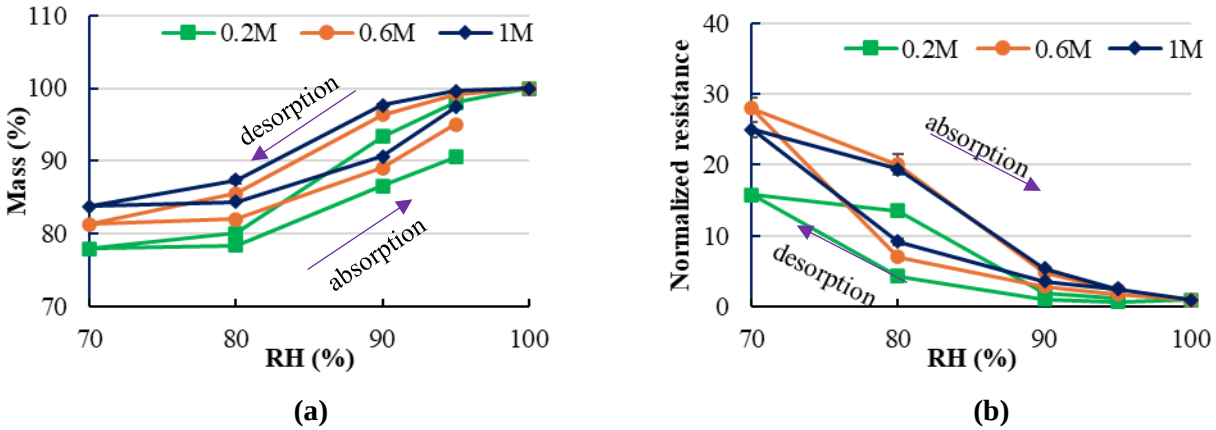

Figure 2. The mass and resistance isotherm of sensors soaked in different concentrations of simulated pore solution at 23°C (a) Mass Vs RH (b) Normalized resistance vs RH.

3. Time to equilibrium measurements

To measure the concrete PSR, the formation factor of the sensor material needs to be determined beforehand. The FF is defined as the ratio of resistivity of the sensor saturated with a simulated pore solution to the resistivity of the pore solution itself. The formation factor is an intrinsic material property and should not vary with the concentration of the simulated pore solution. To accurately determine FF, the pore solution within the sensor should come to equilibrium with the soaking solution, resulting in a stable resistance value. Since the process of ionic equilibrium is diffusion controlled, resistance values were measured continuously, and the change in resistance was considered stable when the daily variation was less than ±2%.

For these measurements, ellipsoidal sensors with embedded stainless-steel electrodes spaced 4 mm apart, were cast with the MK-1 mix. Saturation of the sensors began after 7 days from casting day with a 0.2 M solution. Once the change in resistance was within the considered stable range, the sensors were sequentially soaked in 0.6 M, 1.0 M, and then returned to the original 0.2 M solution. Figure 3(a) shows the measured resistance of the sensors (labelled Ch1-1 to 3) with various concentrations of simulated pore solution. All the resistance measurements were carried out at 23±2 °C and were appropriately adjusted using a temperature correction factor. The resistance at day zero corresponds to the resistance of the dry sensors. The resistance of the sensors dropped significantly during the first week of saturation but then slightly increased. With a change in concentration from 0.2 M to 0.6 M, the measured resistance dropped within the first day, followed by a slight increase with continued soaking. The resistance further dropped when the soaking solution concentration was increased to 1.0 M. Finally, when the concentration of soaking solution was reduced back to 0.2 M, the resistance of the sensors increased, however, the equilibrium resistance was higher than the initial equilibrium resistance.

Figure 3(b) shows the resistivity of simulated pore solution in which the sensors were soaked. The resistivity of simulated pore solution decreased with an increase in solution concentration. However, the resistivity of the solution has slightly increased compared to the reference solution (no sensors) as the soaking progressed in a given pore solution. The increase in pore solution resistivity is more pronounced when the sensor is young. As the sensor ages, the pore structure might refine slightly by absorbing ions from the pore solution, thereby increasing both the pore solution resistivity and the sensor resistance. However, this hypothesis requires further verification.

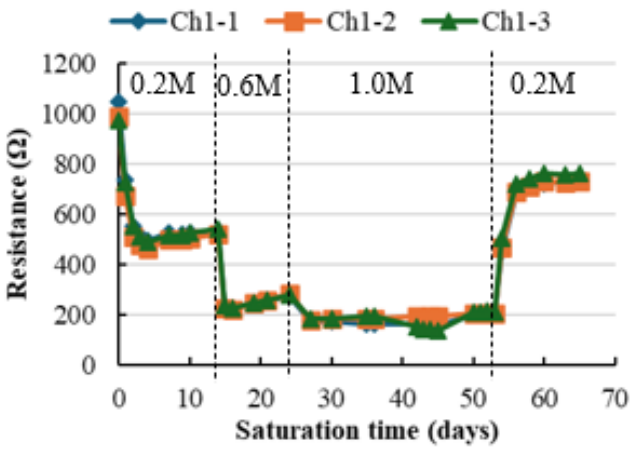

a)

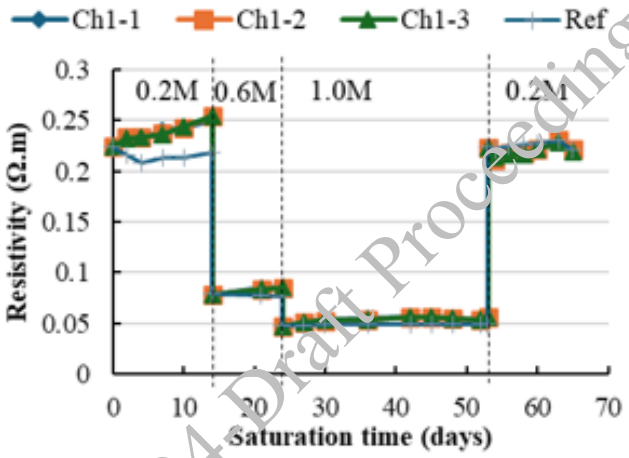

(b)

Figure 3. The change in electrical measurements with time in various concentrations of simulated pore solution at 23°C .(a) Sensor resistance (b) Solution resistivity.

The calculate the FF, the geometry factor of the sensors needs to be determined which depends on electrode configuration. Although the electrode spacing was maintained at 4 mm, strict control is not possible, making the calculation of geometry factor challenging. Therefore, a translational factor is computed by taking the ratio of pore solution resistivity to the measured electrical resistance of the sensor, which inherently accounts for the geometry factor. Figure 4(a) shows the translation factor of the sensors calculated at equilibrium for each pore solution concentration. The translation factor decreased with increase in solution concentration from 0.2 to 0.6M, however, the change is smaller thereafter. The initial drop can be attributed to the refinement of pore structure, which stabilized over time. In another experiment, where the sensors were initially soaked in a 1.0 M concentration, the translation factor stabilized quickly, suggesting that the 1.0 M solution accelerated the refinement process. Figure 4(b) illustrates the change in the translation factor when soaking started in a 1.0 M solution and then transitioned to a 0.6 M solution after reaching equilibrium.

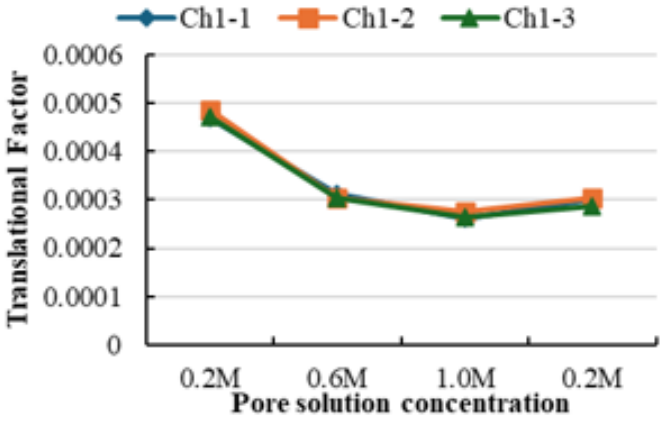

(a)

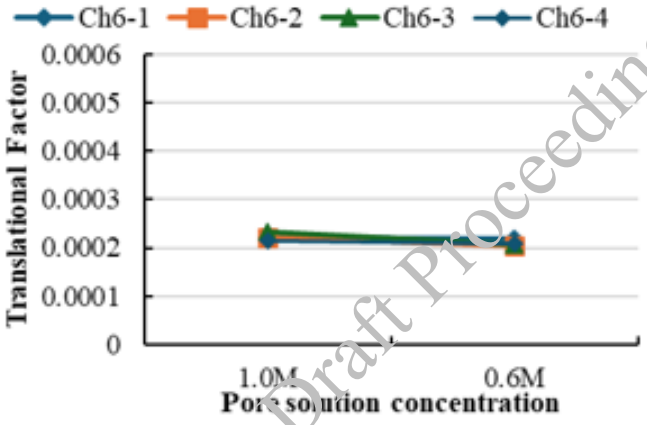

(b)

Figure 4. Translational factor of sensors at the end of equilibrium in each simulated pore solution concentration at 23°C (a) 0.2M→0.6M→1.0M→0.2M (b) 1.0M→0.6M.

3.1 Determination of pore solution resistivity of concrete.

Two sets of sensors equilibrated in two different pore solution concentrations were used to measure the resistivity of concrete's pore solution. Sensors labelled Ch6-# were soaked in 0.6M solution, while sensors labelled Ch7-# were soaked in 1.0M pore solution prior embedment. A regular concrete mix was prepared with OPC proportioned as per ACI 211.1-91. 100 mm ×200 mm cylinders were considered for testing, and the sensors were placed into the molds using a custom-designed placement frame. The concrete was cast in molds and cured in moist room for 24 hours. After the initial curing period, the cylinders were demolded and further cured in a simulated pore solution prepared as per AASHTO TP 119-22 at 23 °C. The pore solution within the sensors equilibrated with the pore solution of the surrounding concrete, allowing the resistance measured by the sensors to reflect the concentration of the concrete's pore solution.

The resistance of the embedded sensors was continuously measured, and the pore solution resistivity is computed using translation factor. Figure 5(a) shows the resistivity of the pore solution of concrete with time. The pore solution of concrete was mechanically extracted at 0.4, 7, 14 ,28, and 56 days. The resistivity of the extracted pore solution, shown as PSR in Figure 5(b), matched well with the resistivity measured by the sensors. At later ages, the resistivity measured by the sensors was higher than that of the extracted solution, possibly due to the internal drying of the concrete over time. Further research is needed to investigate this issue.

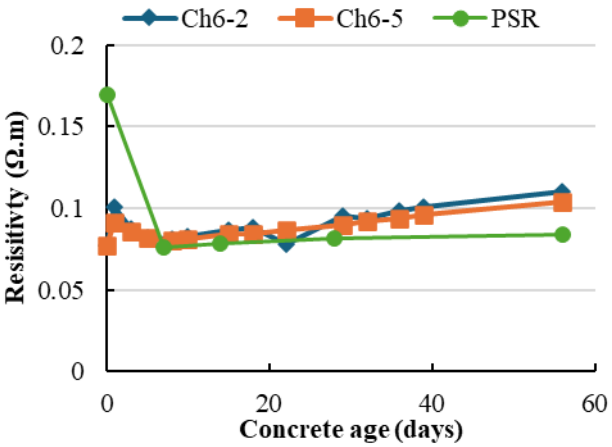

(a)

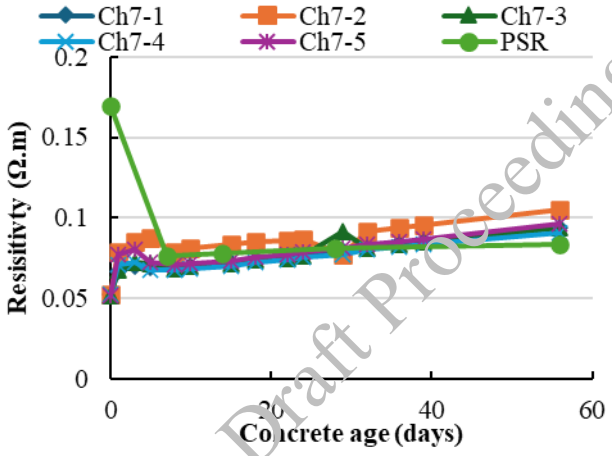

(b)

Figure 5. Pore solution resistivity of concrete measured by sensors soaked in two different simulated pore solution prior embedment. (a) soaked in 0.6 M prior embedment (b) soaked in 1.0 M prior embedment. Figure also shows the PSR of mechanically extracted pore solution labelled as PSR.

4. Conclusions

This study focuses on the development and performance evaluation of metakaolin-based geopolymer sensors for in-situ determination of pore solution resistivity (PSR) in concrete. Key findings include:

- Metakaolin sensors exhibit high porosity with a significant fraction of pores smaller than 20 nm.
- Sensors rapidly equilibrated with the surrounding pore solution (1-3 days).
- The measured resistance is highly sensitive to drying, necessitating PSR measurements near the saturated surface dry (SSD) state.
- The measured PSR of concrete closely matches the PSR obtained from mechanically extracted pore solutions.

References

AASHTO TP 402-23 (2023) Standard Method of Test for Electrical Resistivity of a Concrete Cylinder Tested in a Uniaxial Resistance Test, American Association of State Highway and Transportation Officials.

ACI-PRC - 211.1-91 (2009).; Standard Practice for Selecting Proportions for Normal, Heavyweight, and Mass Concrete. American Concrete Institute: Farmington Hills, MI, USA, 1-38.

ASTM C642-21, (2021). Standard test method for density, absorption, and voids in hardened concrete. ASTM, ASTM International.

Baten, B., & Manzur, T. (2022). Formation factor concept for non-destructive evaluation of concrete's chloride diffusion coefficients. *Cement and Concrete Composites*, *128*, 104440.

Bentz, D. P. (2007). A virtual rapid chloride permeability test. *Cement and Concrete Composites*, *29*(10): 723–731.

Jafari Azad, V., Erbektas, A. R., Qiao, C., Isgor, O. B., & Weiss, W. J. (2019). Relating the formation factor and chloride binding parameters to the apparent chloride diffusion coefficient of concrete. *Journal of Materials in Civil Engineering*, *31*(2), 04018392.

Peng, H., Yang, Y., Ge, Y., Li, Y., & Shi, X. (2022). Metakaolin-based geopolymer features different pore structure characteristics from ordinary portland cement paste: a mechanistic study. *Journal of Materials in Civil Engineering*, *34*(12), 04022321.

Qiao, C., Coyle, A. T., Isgor, O. B., & Weiss, W. J. (2018). Prediction of chloride ingress in saturated concrete using formation factor and chloride binding isotherm. *Advances in Civil Engineering Materials*, *7*(1): 206-220.

Rajabipour, F., & Weiss, J. (2007). Electrical conductivity of drying cement paste. *Materials and Structures*, *40*: 1143-1160.

Rajabipour, F. (2006). Insitu Electrical Sensing and Material Health Monitoring in Concrete Structures. Purdue University.

Rajabipour, F., Weiss, J., & Abraham, D. M. (2004). Insitu electrical conductivity measurements to assess moisture and ionic transport in concrete (A discussion of critical features that influence the measurements). In *Proceedings of the International RILEM Symposium on Concrete Science and Engineering: A Tribute to Arnon Bentur*.

Safiuddin, M., & Hearn, N. (2005). Comparison of ASTM saturation techniques for measuring the permeable porosity of concrete. *Cement and Concrete Research*, *35*(5): 1008-1013.

Shafikhani, M., & Chidiac, S. E. (2019). Quantification of concrete chloride diffusion coefficient – A critical review. *Cement and Concrete Composites*, *99*: 225–250.

Spragg, R., Qiao, C., Barrett, T., & Weiss, J. (2023). Assessing a concrete's resistance to chloride ion ingress using the formation factor. In *Corrosion of steel in concrete structures* (pp. 35-51). Woodhead Publishing.

Tanesi, J., Ardani, A., & Montanari, L. (2019). *Formation factor demystified and its relationship to durability* (No. FHWA-HRT-19-030). United States. Federal Highway Administration.

Yang, K., & White, C. E. (2020). Multiscale pore structure determination of cement paste via simulation and experiment: The case of alkali-activated metakaolin. *Cement and Concrete Research*, *137*, 106212.

Zhang, Z., and H. Wang. "Analysing the relation between pore structure and permeability of alkali-activated concrete binders." *Handbook of alkali-activated cements, mortars and concretes* (2015): 235-264.

Evaluation of Confined Concrete Stress-Strain Behaviour During Cooling Subsequent to Fire

Mahesh Gaikwad[1*], Suvir Singh[2], Ajay Chourasia[3], N Gopalakrishnan[4]

[1]Research Scholar, Fire Safety Engineering, CSIR-Central Building Research Institute (CSIR-CBRI), Roorkee - 247667 India; Academy of Scientific and Innovative Research(AcSIR), Ghaziabad- 201002, India.
Email: mahesh.cbri19j@acsir.res.in
[2]Retd. Chief Scientist, Fire Safety Engineering, CSIR-Central Building Research Institute (CSIR-CBRI), Roorkee - 247667 India; Academy of Scientific and Innovative Research(AcSIR), Ghaziabad- 201002, India.
Email: suvir_singh@yahoo.com
[3]Chief Scientist, Structural Engineering, CSIR-Central Building Research Institute (CSIR-CBRI), Roorkee - 247667 India; Academy of Scientific and Innovative Research(AcSIR), Ghaziabad- 201002, India.
Email: ajayc@cbri.res.in
[4]Former Director, CSIR-Central Building Research Institute Roorkee, 247667, Uttarakhand, India; Amrita School of Engineering, Thiruvallur 601103, Tamil Nadu, India. Email: gnramam66@gmail.com

[*]Corresponding author

ABSTRACT

Confined concrete stress-strain relationships are crucial for evaluating reinforced concrete structures' more realistic fire performance. Most studies have focused on investigating confined concrete's constitutive parameters and stress-strain relationship at the heating and residual state. However, its behaviour at subsequent cooling temperatures has yet to be thoroughly explored. It is crucial for determining confined concrete structures' post-fire performance and burnout resistance. The paper presents the fundamental behaviour of the confined concrete constitutive parameters and stress-strain curve at subsequent cooling temperatures after being heated to peak temperature. This study provides insight into processes that occur during the cooling process subsequent to fire, including transformations in the most essential constitutive parameters, namely compressive strength and strain at peak stress. The study includes the stress-stress relationship of a 200 mm diameter cylinder with two distinct confinement spacing of 60 mm and 120 mm. The constitutive parameters for a confined concrete are initially determined for a peak heating temperature of 750°C and then modified to establish the stress-strain relationship for successive cooling temperatures of 500°C, 250°C, and ambient temperature. The study results show that confinement has a considerable impact on compressive strength, stiffness, and ductility at ambient and fire conditions. After being heated to peak temperature, the confined concrete compressive strength recovers during successive cooling temperatures, with the recovery dependent on confinement spacing. The established stress-strain relationship can assist in better comprehending structural performance and capacity degradation for different tie spacing's, and is useful for the analysis and design of confined RC elements during and after a fire.

KEYWORDS*: Confined concrete, Constitutive parameters, Fire, Heating, Stress-strain relationship, Subsequent cooling.*

1. Introduction

Reinforced concrete structures' performance is more crucial in fire-prone environments. Concrete exposed to high temperatures undergoes both chemical and physical changes, accelerating the material's deterioration (Abrams 1973; Lie 1992; Youssef & Moftah 2007). The structural elements experience an excessive loss of strength and stiffness due to the severe deterioration of their mechanical characteristics (Dotreppe 1997; Mohamed 2004). The provided confinement to improve load capacity at ambient conditions becomes ineffective with periods of fire due to losses in steel and concrete characteristics.

Understanding how confined concrete performs at increasing temperatures is crucial for assessing its fire performance during heating and post-heating state. Generally, building fire comprise a prolonged cooling phase after heating or could involve extended heating and cooling (Salah et al. 2011; Mohamed and Salah 2012). The structural integrity of a reinforced concrete (RC) building is jeopardized once the cooling process begins due to a progressive increase in temperature within the inner core of the concrete elements (Gernay et al. 2022; Gaikwad et al. 2024). The building remains vulnerable to collapse for several hours after completely extinguishing the fire. As a result, structural design requirements during increasing and cooling temperatures become critical. However, the characteristics of reinforced concrete influence structural behavior as temperatures rise and then fall; therefore, sufficient input parameters are crucial for accurately predicting load capacities and response.

In recent decades, reinforced concrete has been extensively discovered at increasing temperatures and in its residual state by conducting uniaxial compression tests on prismatic unconfined concrete specimens (Youssef & Moftah 2007; Eurocode2 1992; Li & Purkiss 2005). The temperature-dependent constitutive parameters were determined, and an entire stress-strain relationship was developed based on the test data. Several studies have investigated the stress-strain behavior of confined concrete at the residual state (Zaidi et al.,2012; Xiao et al., 2016), however, there is still a lack of data on confined concrete during heating and cooling. There is not enough experimental data for unconfined and confined concrete to gain insights into concrete behavior throughout sequential lowering temperatures. The information about confined concrete properties during a fire is useful for designing confined concrete elements for a specified fire resistance rating and examining the safety of existing structures in a fire's heating and cooling phases. In this study, a stress-strain relationship of confined concrete is established for a peak heating temperature of 750°C and a subsequent cooling temperature. The Eurocode (EUROCODE 4 1992) approach is employed to determine the constitutive properties of confined concrete at the consecutive cooling temperature.

2. General stress-strain relationship for confined concrete

The degree of confinement given by the transverse reinforcement has a significant impact on the compression behaviour of concrete. Several models have been established to account for the confinement effect in the stress-strain relationship by testing confined concrete under monotonic compression loading. Park et al. (1982), Sheikh and Uzumeri (1982), and Mander et al. (1988) are some of the well-known models. Of the most often used adaptive stress-strain models at ambient temperatures, Mander et al. (1988). This model offers the theoretical stress-strain relationship for uniaxial compression testing on concrete cylinders and has been thoroughly tested with various confinement configurations such as circular hoop and rectilinear confinement. Youssef & Moftah (2007) considered available data for estimating the parameters based on well-established relationships for unconfined and confined concrete at ambient temperature and proposed suitable stress-strain relationships for concrete in compression elevated temperatures, as given in Equation 1. This can be used to compute stress (f_{cT}) in confined concrete for a specific concrete strain (ε_{cT}) within a maximum strain limit ($\mathcal{E}_{ocT}$) under fire conditions. Equations 2 and 3 were used to compute confined concrete compressive strength (f'_{ccT}) and strain at peak stress ($\mathcal{E}_{ocT}$). The lateral confining pressure (f'_{lt}) is calculated by appropriately considering the degradation of confining steel at elevated temperatures. The effective lateral confining stress, f'_{lT} , can be accounted for equal to $\frac{K_e \rho_s f_{yh}}{2}$. Based on the confinement supplied in two perpendicular directions (f'_{lx} and f'_{ly}), the graph presented by Mander et al. (1988) can be used to derive the rectilinear confinement, f'_{ccT}.

Confined concrete stress (f_{cT}),

$$f_{cT} = \frac{2.f'_{ccT}.\varepsilon_c T}{(\varepsilon_{oc}T+\varepsilon_{tr}).\left[1+\left(\frac{\varepsilon_c T}{\varepsilon_{oc}T+\varepsilon_{tr}}\right)^2\right]} \quad (3)$$

Confined concrete compressive strength (f'_{ccT}),

$$f'_{ccT} = f'_{cT}.\left[-1.254 + 2.254.\sqrt{1+\frac{7.94.f'_{lT}}{f'_{cT}}} - \frac{2.f'_{lT}}{f'_{cT}}\right] \quad (2)$$

Concrete strain at peak stress ($\varepsilon_{oc}T$),

$$\varepsilon_{oc}T = \varepsilon_{o}T.\left[1 + 5\left(\frac{f'_{ccT}}{f'_{cT}} - 1\right)\right] \quad (3)$$

3. Validation of Model

The modified Youssuf model is employed to generate the stress-strain relationship and is then compared to Mander et al. (1988) experimental and analytical data at ambient circumstances to ensure modelling fidelity. The experimental program included cylinders with diameters of 500 mm and heights of 1,500 mm. The cylinders were loaded axially on a hydraulically controlled testing machine. Four concrete cylinders with different confinement spacing were validated, and stresses were calculated, accounting for the confinement effect for various strain increments. Columns had identical longitudinal steel with 12 deformed bars of a diameter of 16 mm and different numbers and sizes of transverse spiral reinforcement, resulting in confining reinforcement volumetric ratios ranging from 0.006 to 0.025. The unconfined concrete and steel strengths were 28 MPa and 275 MPa, respectively. The confinement spacing for the four columns C1, C2, C3, and C4 are 41 mm, 69 mm, 103 mm, and 119 mm, respectively. Transversal reinforcement has a diameter of 12 mm for the first three columns of C1 to C3 and 10 mm for C4. Figure 1 depicts the stress-strain curve results for various confinement configurations, demonstrating the good agreement between predicted and experimental results at ambient conditions.

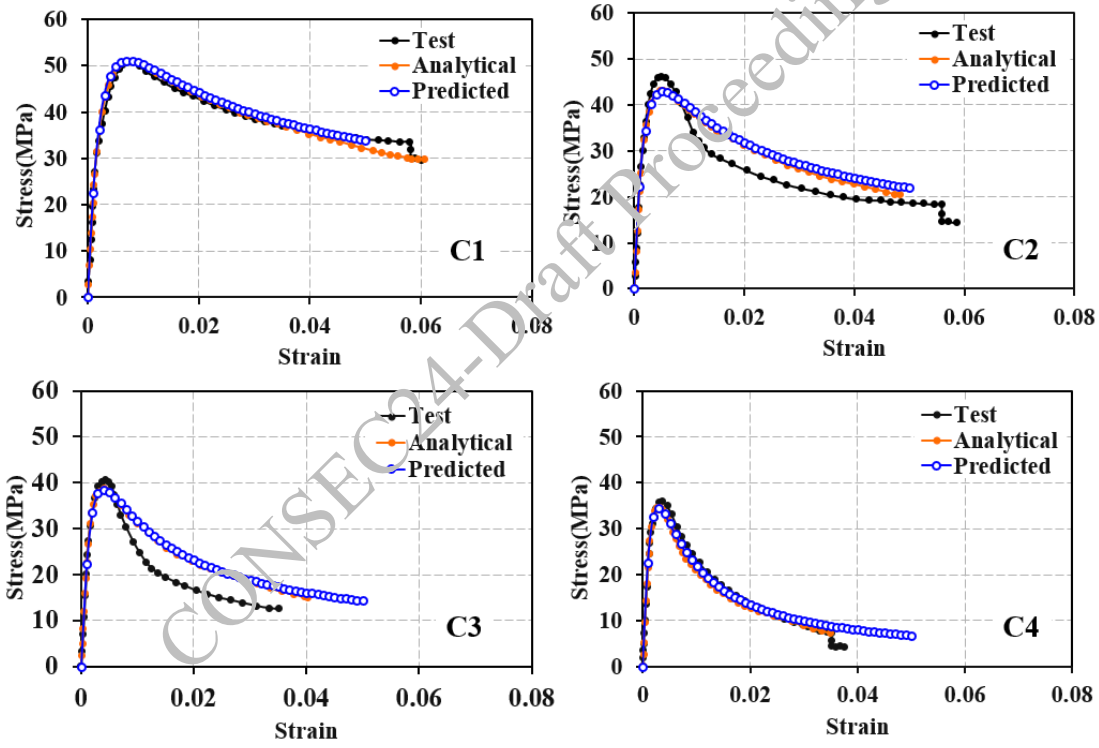

Figure 1. The validation of the predicted stress-strain relationship for confined concrete at ambient conditions

4. Proposed approach for confined concrete during cooling

The constitutive parameters of the stress-strain relationship of confined concrete are obtained during heating, which is then modified to execute the stress-strain relationship at a subsequent cooling temperature using the Eurocode theoretical approach (Eurocode 4 1994). Eurocode emphasises the theoretical approach for the concrete constitutive parameters such as compressive strength, strain at peak stress, and ultimate strain when determining the stress-strain relationship at subsequent cooling temperature. These constitutive parameters at consecutive cooling temperatures are derived from the previously occurred peak heating temperature (Θ_{max}) of fire and the current cooling temperature (Θ_c). The concrete compressive strength($f'_{c,\theta c}$) at cooling temperature can be determined by establishing the linear relationship between

the compressive strength at the peak temperature ($f'_{c,\Theta max}$) and the corresponding residual strength($f'_{cr,\theta a}$). Eurocode 4 (1994) suggests that the strain at peak stress $(\varepsilon_{0,\theta c})$ remains unchanged for their successive cooling temperatures, i.e., $\varepsilon_{0,\theta c} = \varepsilon_{0,\theta max}$. There is no subsequent change in strain at peak stress at cooling temperature. The confined concrete stress-strain relationship at subsequent cooling temperature was determined by substituting modified constitutive parameters into the Youssef & Moftah (2007) model. A similar strategy to that described for concrete is employed to model the longitudinal and confined steel during the cooling. The residual strength of concrete and steel was calculated using the model of Chang et al. (2006) and Tao et al. (2013).

4.1 Study Parameters

A circular section with a diameter of 200 mm was considered, with two different confinement spacings of 60 mm and 120 mm. The 8 mm diameter of eight rebars was used for longitudinal reinforcement, and 6 mm diameter rebars were considered for transverse reinforcement. The concrete and steel strengths were 30 MPa and 500 MPa, respectively. The strain corresponding to peak stress for unconfined concrete at ambient circumstances was considered 0.002 (Mander et al.,1988). The maximum heating temperature of 750°C was accounted for in the study, with the stress-strain relationship calculated for following cooling temperatures of 500°C, 250°C, and ambient conditions.

5. Results and Discussions

The results demonstrate that confined concrete's compressive strength increases significantly compared to unconfined concrete at ambient conditions, as seen in Figure 2. If concrete is confined by transverse reinforcement, it expands due to axial compression, resulting in passive lateral pressure. Thus, confined steel provide a resistance against the lateral pressure exerted due to axial compression, consequently capacity improves. The compressive strength of unconfined concrete was 30 MPa. However, it increases by 20.46% and 46.33% for 120 mm and 60 mm confinement spacing, respectively. In terms of ductility, the strain at peak stress at ambient conditions was 0.002, whereas the strain improved by 150% and 200% for confinement spacings of 120 mm and 60 mm at ambient conditions. The improved ductility will allow structural elements to deform significantly during extreme loading events.

When exposed to a temperature of 750°C, the strength of unconfined concrete drops by 76% compared to ambient circumstances. Similarly, confined concrete compressive strength reduces to 78.26% and 77.31% for 60 mm and 120 mm confinement spacing, respectively, as shown in Figures 3 and 4. High-temperature exposure may result in notable losses in the mechanical properties of steel and concrete. Therefore, confinement's ability to increase stiffness and strength could become less effective at high temperatures. The stress-strain curve shown in Figures 3 and 4 also demonstrated that the stiffness of confined concrete decreased dramatically. However, as confinement spacing increases, strength and stiffness decrease dramatically. At a peak heating temperature of 750°C, the strength of confined concrete for a confinement spacing of 60 mm is 16.34% higher than that of a confinement spacing of 120 mm. Similarly, ductility improved dramatically with temperature and confinement space.

After heating to a peak temperature of 750°C, the confined concrete compressive strength improved on consecutive cooling temperatures of 500°C, 250°C, and ambient, as seen in Figures 3 and 4. This can be attributed to enhanced steel characteristics. However, compressive strength declined with subsequent cooling temperatures. The maximum recovery occurs after complete cooling (residual state). Concrete with confinement of 60 mm apparently recovered 39.72% more strength than that obtained at 750°C, while 120 mm confinement spacing brought 17.07% strength at the residual stage. Figures 3 and 4 illustrate that the overall stress-strain curve improves with successive cooling temperatures as stiffness and strength recover. Recovery in confinement of spacing 60 mm is more significant than recovery in confinement spacing of 120 mm over successive cooling temperatures. Maximum recovery in lower confinement spacing can be attributed to the impact of restoring steel characteristics in the maximum confinement area. However, due to the significant transverse spacing, 120 mm spacing acts more similarly to unconfined concrete and has no substantial effect on compressive strength enhancement. The study's findings highlight the fact that after the concrete is heated to its maximum temperature, it can significantly affect its load capacity. A substantial study must be done, taking into account a variety of confinement spacing and various heating and cooling temperature regimes, to comprehend the behaviour of the axial and flexural load capacity over time.

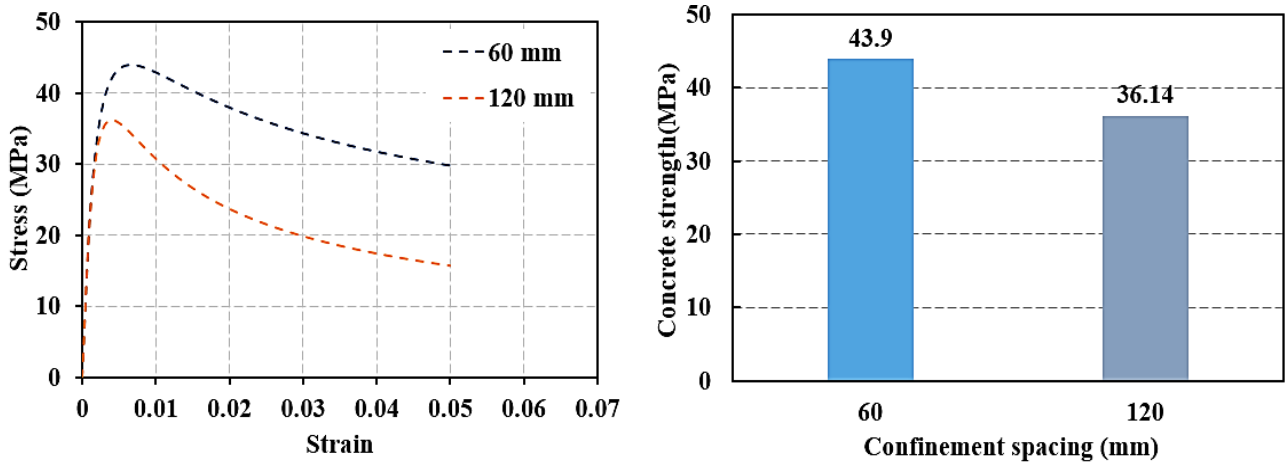

Figure 2. Confined concrete stress-strain relationship at ambient temperature for confinement spacing of 60 and 120 mm

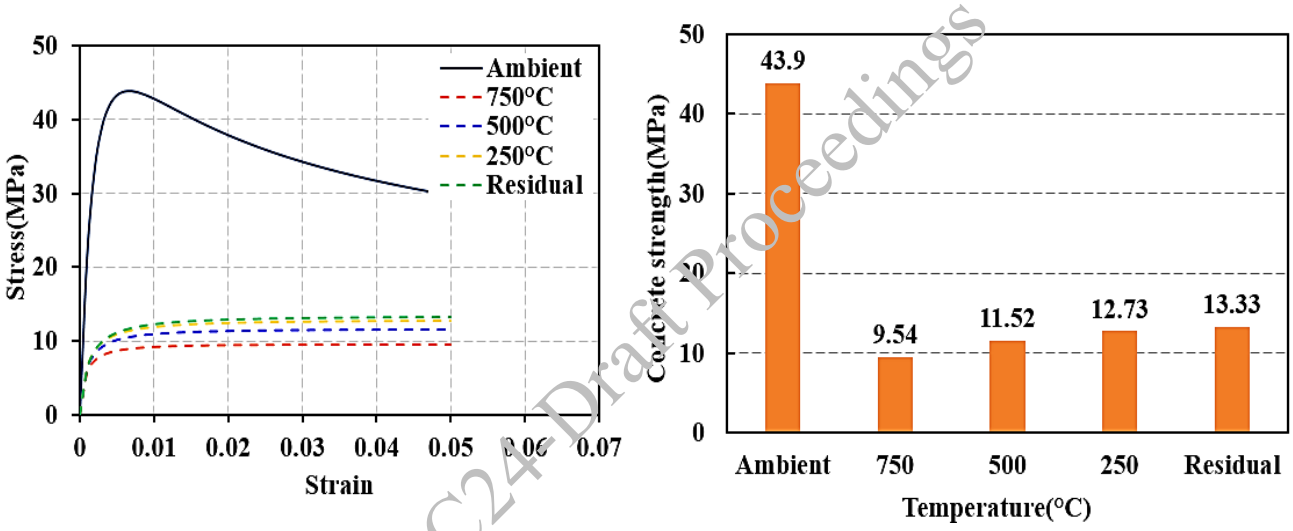

Figure 3. Confined concrete stress-strain relationship at heating and subsequent cooling temperatures for confinement spacing of 60 mm

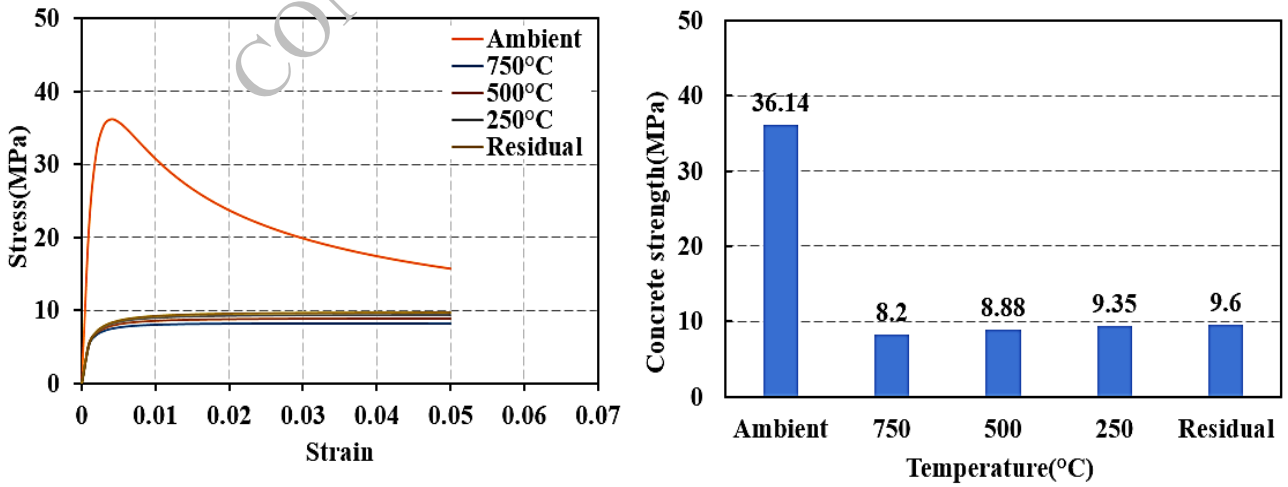

Figure 4. Confined concrete stress-strain relationship at heating and subsequent cooling temperature for confinement spacing of 120 mm

6. Conclusions

The study investigates the effect of peak heating temperature on the constitutive characteristics of confined concrete. Attempts are made to incorporate the fundamental approach behind the constitutive relationship at the subsequent cooling temperature specified by Eurocode 4. The stress-strain curve for confined concrete with 60 mm and 120 mm confinement spacing was produced by appropriately accounting for confinement and cooling temperature effects. The findings indicate that after accounting for the impact of confinement, compressive strength improves significantly at ambient and fire conditions. Confined concrete retains 32.50% and 13.89% more strength than unconfined concrete at a peak heating temperature of 750°C for confinement spacings of 60 mm and 120 mm, respectively. After heating to a peak temperature of 750°C, confined concrete improves strength and stiffness at cooling temperatures of 500°C, 250°C, and ambient. The maximum recovery appeared to take place in confinement spacings of 60 mm over consecutive cooling temperatures following heating to fire, as compare to 120 mm confinement spacing. The highest recovery occurs after complete cooling to ambient temperature. The increase in compressive strength across successive cooling temperatures is due to the recovery in steel characteristics.

Acknowledgement

We would like to express our gratitude to the CSIR-Central Building Research Institute Roorkee for providing lab facilities.

References

Abrams M. (1973) “Compressive Strength of Concrete at Temperatures at 1600F”, *Bulletin RD016.01T, Portland Cement Association*, Illinois, USA.

Chang Y. F., Chen Y. H., Sheu, M. S., and Yao G. C (2006) “Residual stress–strain relationship for concrete after exposure to high temperatures”, *Cement and concrete research*, 36(10): 1999-2005.

Dotreppe JC et al. (1997) “Experimental research on determining the main parameters affecting the behaviour of reinforced concrete columns under fire conditions”, *Mag. Concr. Res.* 149:117–127.

El-Fitiany, S. F., and Youssef, M. A. (2017) “Fire performance of reinforced concrete frames using sectional analysis” *Engineering Structures*, *142*: 165-181.

Eurocode 2 (2004) “Design of Concrete Structures-Part 1-2: General Rules-Structural Fire Design”, *Brussels, Belgium*: European Committee for Standardization.

EUROCODE 4 (1992) “Design of composite steel and concrete structures Part 1.1 General rules and rules for buildings”, *Brussels*: CEN-European Committee for Standardization.

Gaikwad, Mahesh, Suvir Singh, N. Gopalakrishnan, Pradeep Bhargava, and Ajay Chourasia (2024) "Numerical analysis of fire-exposed reinforced concrete sections for assessing post-heating axial and flexural capacity." *Journal of Structural Fire Engineering* ahead-of-print.

Gernay, T, Franssen, J.M., Robert, F., McNamee, R., Felicetti, R., Bamonte, P., Brunkhorst, S., Mohaine, S. and Zehfuß, J. (2022) “Experimental investigation of structural failure during the cooling phase of a fire: Concrete columns”, *Fire safety journal*, 134: 103691.

Li L. Y., and Purkiss J. (2005) “Stress-strain constitutive equations of concrete material at elevated temperatures”, *Fire Safety Journal*, 40(7): 669-686.

Lie TT. (1992) “Structural Fire Protection. ASCE Committee on Fire Protection”, *ASCE manuals and reports on engineering practice No. 78 American Society of Civil Engineers (ASCE)*, New York, USA.

Mander, J. B., Priestley, M. J. N., and Park, R. (1988) “Observed stress-strain behavior of confined concrete”, *Journal of structural engineering*, *114*(8): 1827-1849.

Mander, J. B., Priestley, M. J., and Park, R. (1988) “Theoretical stress-strain model for confined concrete”, *Journal of structural engineering*, *114*(8): 1804-1826.

Mohamed, G. and Salah, D.M. (2012) “Analysis of collapse for concrete columns during and after the cooling phase of a fire”, *XXX e Recontres AUGC-IBPSA*, Chambery, Savoie 6-8.

Park, R., Priestley, M. N., and Gill, W. D. (1982) “Ductility of square-confined concrete columns”, *Journal of the structural division*, *108*(4): 929-950.

Salah, Dimia, M., Guenfoud, M., Gernay, T. and Franssen, J.M. (2011) “Collapse of concrete columns during and after the cooling phase of a fire”, *Journal of Fire Protection Engineering*,21(4): 245-263. 10.1177/1042391511423451

Sheikh, S. A., and Uzumeri, S. M. (1982) "Analytical model for concrete confinement in tied columns", *Journal of the structural division, 108*(12): 2703-2722.

Tao, Z., Wang, X.Q. and Uy, B. (2013) "Stress-strain curves of structural steel and reinforcing steel after exposure to elevated temperatures", *Journal of Materials in Civil Engineering*, 25(9): 1306-1316.

Xiao, J., Li, Z., Xie, Q. and Shen, L., (2016) "Effect of strain rate on compressive behaviour of high-strength concrete after exposure to elevated temperatures", *Fire Safety Journal*, 83:25-37.

Youssef M. A., and Moftah, M. (2007) "General stress-strain relationship for concrete at elevated temperatures", *Engineering structures*, 29(10): 2618-2634.

Zaidi, K.A., Sharma, U.K. and Bhandari, N.M., (2012) "Effect of temperature on uni-axial compressive behavior of confined concrete", *Fire Safety Journal*, 48:58-68.

Notations

f_{cT}	Confined Concrete compressive stress at room temperature
f'_{cT}	Unconfined Concrete compressive strength at elevated temperature
f'_{ccT}	Confined Concrete compressive strength at elevated temperature
$f'_{c,\theta c}$	Unconfined Concrete compressive strength at a subsequent cooling temperature
$f'_{\mathrm{c},\theta\max}$	Unconfined Concrete compressive strength at maximum temperature
$f'_{cr,\theta a}$	Unconfined Concrete compressive strength after complete cooling down
f_{yh}	Yield strength of the transverse reinforcement at elevated temperature
f'_{lx} and f'_{ly}	Effective lateral confining stress in *x* and *y* direction, respectively
ρ_s	Volume ratio of the transverse confining steel to the volume of the confined concrete core
K_e	Confinement effectiveness coefficient
f_{y}	Yield strength of reinforcing steel at ambient temperature
θ_{max}	Maximum (or peak) temperature during a fire
θ_c	Fire temperature during cooling
$\varepsilon_{oc}T$	Confined Concrete strain at peak stress at elevated temperature
ε_oT	Unconfined concrete strain at peak stress at elevated temperature
ε_{tr}	Fire-induced transient creep strain in concrete
$\varepsilon_{c,\theta}$	Instantaneous stress-related strain at elevated temperature
$\varepsilon_{0,\theta c}$	Concrete strain at peak stress at a subsequent cooling temperature
$\varepsilon_{0,\theta max}$	Concrete strain at peak stress at maximum temperature

10th International Conference on CONcrete under SEvere Conditions – Environment and Loading 2024, Chennai, India

Linking Short-Term Conductivity to Long-Term Chloride Diffusion for Service Life Prediction

S. Surana[1*], H.B. Beushausen[2], and M.G. Alexander[3]

[1] *University of Cape Town, Cape Town, South Africa*
Email: srnsaa001@myuct.ac.za
[2] *University of Cape Town, Cape Town, South Africa*
Email: hans.beushausen@uct.ac.za
[3] *University of Cape Town, Cape Town, South Africa*
Email: mark.alexander@uct.ac.za

[*]Corresponding author

ABSTRACT

Short-term electrical tests are preferred as a means of characterizing and controlling concrete mixtures for marine environments. The testing can be performed quickly and at an early age. These are significant practical advantages over natural chloride diffusion testing, which is both time-consuming and onerous. However, early-age indirect measurements are inherently limited in their ability to indicate long-term performance. The quantitative estimation of long-term chloride resistance for service life prediction requires the consideration of the evolution of material properties and the material-environment interaction with time. This study attempts to integrate electrical conduction and diffusion measurements from lab and field to develop an engineering prediction model. The model is based on a modified error function solution. An overview of the relevant theoretical and empirical relationships linking conductivity with the field performance is also presented for South African conditions.

KEYWORDS*: Service life prediction, Correlations, Chloride modelling, Conductivity, Apparent diffusion coefficient*

1. Introduction

Chloride-induced corrosion is the predominant cause of loss of service life among reinforced concrete structures exposed to marine conditions. This has gathered much attention towards developing the models for chloride ingress and the subsequent corrosion process in order to understand and control various aspects of this mode of deterioration in reinforced concrete. The process of chloride-induced corrosion is typically divided into two stages: before and after the point of corrosion initiation (Tutti, 1982). Before corrosion initiation, the service life is controlled by the severity of the environmental conditions and the penetration resistance of concrete. A number of models have been constructed since the early 1990s to model the process of chloride penetration in concrete following different modelling philosophies: empirical or physical (Nilsson, 2006). The commonality between these approaches is the use of a quick electrical test to characterise the chloride penetrability. Various electrical tests were developed around the globe in response to the shortcomings of the Rapid Chloride Penetration Test (Streicher & Alexander, 1994). Prediction models and quality control specifications have also been developed for various test methods.
The Chloride Conductivity test is one such test method that was developed in South Africa (Streicher & Alexander, 1995) and has been used in the South African region for performance testing (Alexander, Santhanam & Ballim, 2011). An empirical service life prediction model using chloride conductivity was developed for selected South African marine environments in the 1990s (Mackechnie, 1996). However, since then the test method has been improved and more field experience has been gathered (Otieno & Alexander, 2015; Heiyantuduwa-Beushausen, 2022). The current study was conducted with an aim to develop an empirical model for chloride ingress using chloride conductivity with an extended scope of materials.

2. Modelling approach

The error function solution (ERFC) to non-steady state diffusion process is used to model chloride transport in marine conditions according to (5. The apparent diffusion coefficient (D_a) is modelled according to (6 following the modified DuraCrete modelling approach (Siemes & Edvardsen, 1999).

$$C_x = C_s \left(1 - erf \left[\frac{x}{2\sqrt{(D_a . t_{exp})}} \right] \right) \quad (5)$$

Where, C_x is the chloride content at a depth x; C_s is the surface chloride content; D_a is the apparent diffusion coefficient; and t_{exp} is the exposure time.

$$D_a = \sigma_{28} . K_t . K_e . \left(\frac{t_{ref}}{t} \right)^m \quad (6)$$

Where, σ_{28} is the conductivity at 28 days; K_t is the test method factor; K_e is the environmental factor; m is the aging coefficient; t is the age at testing, and t_{ref} is the reference age.
The conductivity is directly proportional to the instantaneous steady-state diffusivity through Nernst-Einstein relation. However, the apparent diffusivity represents an average diffusivity over time, with the added complicating effects of increasing surface chloride concentration (Maage et al., 1996). In such a case, the D_a at a reference time other than the start of the exposure (t_0), will depend on the m values as shown in (7 and (8.

$$D_{a,ref} = K_0 . \sigma_{28} \left(\frac{t_{ref}}{t_0} \right)^{-m} \quad (7)$$

$$D_{a,ref} = K_{ref} . \sigma_{28} \quad (8)$$

The values of K_{ref} are derived in the following sections. Other factors are derived, but not presented here due to space constraints.

3. Experimental program

A range of mixture proportions with different blended binders and w/b ratios were used in this study. Fly ash (FA) at replacement levels of 15% and 30%, and blast-furnace slag (BS) at replacement levels of 25% and 50% were blended with CEM I-52.5N (PC) to make binary blends. The w/b ratios ranged from 0.3 to 0.7. Two types of curing were used: standard wet curing for 7 days and 7-days plastic wrapping followed by 21 days in the lab air.
The apparent diffusion coefficient was evaluated according to the bulk diffusion test (ASTM C1556, 2016). The conductivity was evaluated by means of the chloride conductivity test (SANS 3001-CO3-3, 2015). In brief, the chloride conductivity index (CCI) represents the conductivity of oven-dried concrete saturated with a highly conductive, 5 M NaCl solution.

4. Correlation between D_a and chloride conductivity

The correlations between the 180-day exposed D_a and the 28-day CCI are examined. These correlations must be binder specific for two reasons: 1. D_a incorporates the effect of binding which differs with the type of binder irrespective of the exposure duration, and 2. 180-day D_a had evolved with time from the start of exposure to the end of exposure, the rate of which also varies with the binder type. This is observed in the results in Figure 5. The correlations show good fit to linear trendlines following (8. The test correlation factors obtained as the slope of the fitted line also appears to exhibit a dependence on the binder type. It is considered useful to express these constants as non-linear functions of the SCM levels. In this case, exponential functions are preferred over polynomial functions to avoid over-fitting and over linear functions to avoid under-fitting. Moreover, further efforts to find a better fit or more scientifically aligned

function may not improve the accuracy in the absence of more data points. These empirical correlations are used to develop an expression for D_a, which requires CCI_{28} and SCM% as input apart from the aging coefficient as shown in **Error! Reference source not found.** and (9.

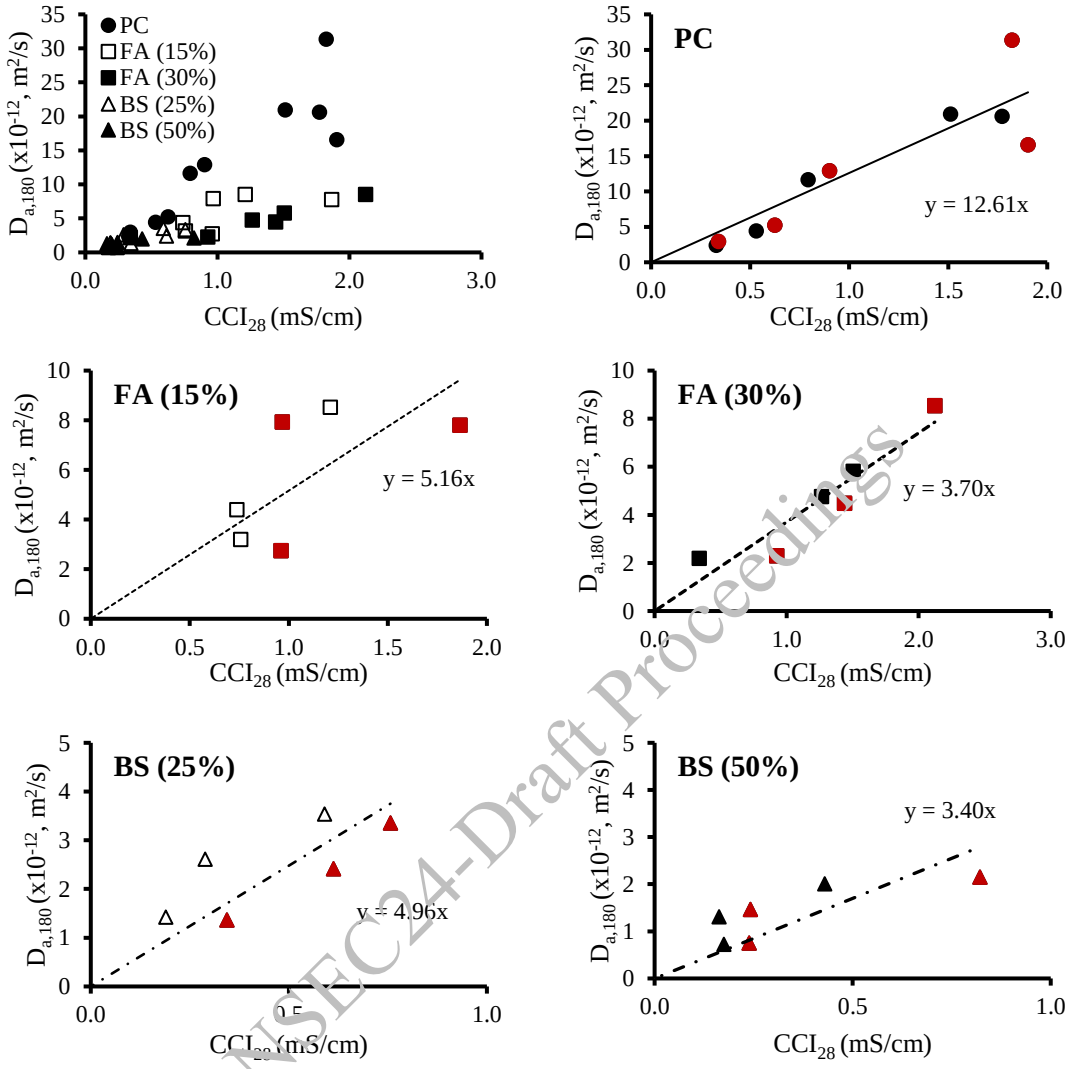

Figure 5. Correlations between 180-day D_a ($D_{a,180}$) and 28-day CCI (CCI_{28}). The red markers represent plastic cured concrete.

$$D_a(t) = K_{180}.CCI_{28}\left(\frac{t}{208}\right)^{-m} \quad (5)$$

Where,

t_{ref} =208 days (Reference age= Age at the start of exposure (28 days) + exposure duration (180 days))

CCI_{28}: Chloride conductivity index at the age of 28 days;

K_{180}: Test method correlation constant for $t_{ref} = t_{208}$; $(\frac{cm}{mS} \cdot \frac{m^2}{s})$ (9)

Test correlation factor between $D_{a,180}$ and CCI_{28}

$$K_{180} = 12.6 \times 10^{-12}.e^{-1.38\left(\frac{FA\%}{30}+\frac{BS\%}{50}\right)}$$

5. Conclusions

An error-function model was developed for South African marine condition using chloride conductivity as a means to characterise the penetrability of the concrete pore structure to chloride ions. The following main conclusions can be drawn from this study:

- Reasonably good correlations were found between the apparent diffusion coefficient and the chloride conductivity for both fly ash and slag blended concretes. The correlations were in line with the theory and depended on the binder type.
- The aging coefficient to diffusivity was determined mainly by the type of binder used. Other factors such as mix proportions, test method, and marine exposure zones did not have consistent and definitive influence. The 'm' values were therefore modelled as a function of SCM type and level.
- Environmental conditions, particularly the capillary suction effects in the wet-dry zones, may influence the apparent diffusion coefficient. More research is required to clarify the environmental influences as well as to develop a database of environmental factor (Ke) for marine sites of particular interest.
- A simple factor was introduced in the surface chloride content values to account for its variation with w/b ratio.
- It must be remembered that the model predictions are limited by the amount and quality of available data and the underlying simplifying assumptions. While the model is intended to guide design and quality control decision making, engineering judgement cannot be dispensed with when interpreting the model predictions. In other words, design decisions must be taken to satisfy all the relevant considerations, not only the chloride penetration resistance of the materials. The model needs to be validated and calibrated against independent data, preferably long-term, before use.

References

Alexander, M.G., Santhanam, M. & Ballim, Y. 2011. Durability design and specification for concrete structures—the way forward. *International Journal of Advances in Engineering Sciences and Applied Mathematics*. 2(3):95–105. DOI: 10.1007/s12572-011-0027-x.

ASTM C1556. 2016. Standard Test Method for Determining the Apparent Chloride Diffusion Coefficient of Cementitious Mixtures by Bulk Diffusion. *ASTM International*. 1–7. DOI: 10.1520/C1556-11A.2.

Heiyantuduwa-Beushausen, R. 2022. The influence of concrete mix composition and environmental exposure on long-term chloride ingress in concrete. PhD Thesis. University of Cape Town.

Maage, M., Helland, S., Poulsen, E., Vennesland, O. & Carlsen, J.E. 1996. Service Life Prediction of Existing Concrete Structures Exposed to Marine Environment. *ACI Materials Journal*. 93(6).

Mackechnie, J.R. 1996. Prediction of Reinforced Concrete Durability in the Marine Environment. PhD Thesis. University of Cape Town.

Nilsson, L.O. 2006. Present limitations of models for predicting chloride ingress into reinforced concrete structures. In *Journal de Physique IV (Proceedings)*. V. 122. 1–7.

Otieno, M. & Alexander, M. 2015. Chloride conductivity testing of concrete – past and recent developments. *Journal of South African Institution of Civil Engineering*. 57(Cci):55–64. DOI: 10.17159/2309-8775/2015/v57n4a7.

SANS 3001-CO3-3. 2015. South African Natioanal Standard Civil engineering test methods Part CO3-3 : Concrete durability index testing — Chloride conductivity test.

Siemes, T. & Edvardsen, C. 1999. DuraCrete: Service life design for concrete structures. In *Durability of Building Materials and Components 8*. M.A. Lacasse & D.J. Vanier, Eds. Institute for Research in Construction, Ottawa ON, K1A 0R6, Canada. 1031. DOI: 10.1007/978-3-642-37475-3.

Streicher, P.E. & Alexander, M.G. 1994. A critical evaluation of chloride diffusion test methods for concrete. In *Third CANMET/ACI International Conference on Concrete Durability*. Nice, France: Supplementary papers, ACI, Detroit. 517–530.

Streicher, P.E. & Alexander, M.G. 1995. A chloride conduction test for concrete. *Cement and Concrete Research*. 25(6):1284–1294.

Tutti, K. 1982. Corrosion of steel in concrete. PhD. Lund University.

Correlating Chloride Diffusivity and Resistivity of the Concrete and Nomograms for Designing the Service Life of RCC Structures

Chandru Pichaimuthu[1*], Eswita Yakkala[2], Radhakrishna G. Pillai[3], and Manu Santhanam[4]

[1] Assistant Professor, Department of Civil Engineering, National Institute of Technology Calicut, Kozhikode, Kerala, India – 673 601 E-mail: chandru@nitc.ac.in
[2] Former M. Tech Student, Department of Civil Engineering, Indian Institute of Technology Madras, Chennai, Tamil Nadu, India – 600 036 E-mail: eswitayakkala@gmail.com
[3]Professor, Department of Civil Engineering, Indian Institute of Technology Madras, Chennai, Tamil Nadu, India – 600 036 E-mail: pillai@civil.iitm.ac.in
[4]Professor, Department of Civil Engineering, Indian Institute of Technology Madras, Chennai, Tamil Nadu, India – 600 036 E-mail: manus@civil.iitm.ac.in

[*]Corresponding author

ABSTRACT

This study focused on correlating the apparent chloride diffusion coefficient (Da) of the OPC, fly ash, and slag concrete with its surface electrical resistivity which is a simple parameter that can be instantaneously measured at the construction site. For developing the correlation, 13 different concrete mixes were made with ordinary Portland cement, fly ash, and ground granulated blast furnace slag as a binder. The mixes were varied by altering the water-to-binder ratio, binder content, type of supplementary cementitious material, and its dosage. The chloride resistance of these concrete mixes was assessed through surface electrical resistivity and bulk diffusion tests. The test results showed that concrete containing supplementary cementitious material (SCMs) exhibited excellent resistance to chloride ingress, with slag concrete being superior to fly ash concrete. On the other hand, OPC concrete was found to be vulnerable to the chloride attack. With the experimental results, correlations were developed between the apparent chloride diffusion coefficient and surface electrical resistivity for the OPC, fly ash and slag concrete. These correlations were used to simplify existing "SL Chlor" nomograms for designing corrosion-free service life of reinforced concrete structures exposed to chlorides.

Keywords: *Service life; Durability; Electrical resistivity; Chloride diffusion coefficient; Chloride migration coefficient; Nomogram*

1. Introduction

India is currently witnessing a construction boom with many new projects like highways, airports, seaports, residential and commercial buildings, and urban and rural projects. Due to this approach, the service life of the reinforced concrete structure is affected. One of the major factors affecting the service life of any reinforced concrete structure is “Corrosion”. Buildings built for 50 years of service life are showing corrosion cracks in less than 6 years of construction. The cost of corrosion varies from 1% to 5% of GDP across different countries in the world (NACE 2016). For designing the corrosion-free service life of the concrete structure, the following properties such as apparent chloride diffusion coefficient (D_a) and carbonation rate of the cover concrete are required. However, determining the apparent chloride diffusion coefficient (D_a) and carbonation coefficient (K_{CO2}) of the concrete involves detailed laboratory testing and consumes more time. The above complexity is perceived to cause difficulty in the construction industry to assess the durability class of the concrete and design the corrosion-free service life of the concrete structures. The current study addresses this issue by developing a correlation between the apparent chloride diffusion coefficient (D_a) of the OPC, fly ash, and slag concrete with its surface electrical resistivity which is a simple parameter that can be instantaneously tested at the construction site. This correlation would

enable the engineers to easily design the corrosion-free service life of the concrete structures exposed to chlorides.

2. Materials and Methods

Grade-53 ordinary Portland cement (OPC), class-f fly ash (FaF), and ground granulated blast furnace slag (Sg) were used as binders. Modified polycarboxylic ether (PCE) based high range water reducer (HRWR) was used as a superplasticizer. The specific gravity of the superplasticizer was 1.08 and it has 32% of solid content. River sand and crushed granite stone were used as the fine and coarse aggregate, respectively. The surface electrical resistivity of the concrete mixes was determined using a Wenner's probe as per AASHTO TP 95-11. The apparent chloride diffusion coefficient of the concrete mixes was determined as specified in ASTM C1556.

3. Results and Discussions

3.1 Surface electrical resistivity

Figure 1 (a) shows the 28-day and 120-day surface electrical resistivity values of the concrete mixes. It can be inferred from the results that, at 28 and 120-day, the resistivity of the slag and fly ash concrete was found to be higher than the OPC concrete. Irrespective of the age of the specimen, the surface electrical resistivity of the slag concrete > fly ash concrete > OPC concrete. The 28-day resistivity value of the OPC concrete was ranging between 10.8 kΩ.cm to 21 kΩ.cm. For, the fly ash and slag concrete it ranged from 22 kΩ.cm to 52 kΩ.cm, and 24 kΩ.cm to 67 kΩ.cm, respectively. The electrical resistivity of the concrete increases with the increase in binder content and decrease in w/b ratio. SCMs undergo a secondary hydration reaction and produce additional C-S-H gel by consuming the portlandite. Due to this phenomenon, the ionic strength (OH- concentration) of the concrete decreases and the microstructure of the binder matrix gets densified with less interconnectivity of pores. Since the electrical resistivity is a function of both ionic strength and interconnectivity of pores, the concrete containing SCMs has shown better resistivity than the OPC concrete.

3.2 Apparent chloride diffusion coefficient

The 28-day apparent chloride diffusion coefficient of the 18 concrete mixes is shown in Figure 1 (b). The D_a values of the concrete mixes decrease with the increase in binder content and decrease in the w/b ratio. The D_a values of the concrete mixes corroborate well with its electrical resistivity and migration coefficient results. The D_a values of the OPC concrete were ranging from 30.2×10^{-12} m^2/s to 298×10^{-12} m^2/s. For fly ash concrete, the values were ranging from 4.2×10^{-12} m^2/s to 30×10^{-12} m^2/s. In the case of slag concrete, the values were ranging from 0.9×10^{-12} m^2/s to 60.8×10^{-12} m^2/s. The D_a values of the OPC concrete > fly ash concrete > slag concrete. It was inferred that, for a given w/b ratio the concrete with SCMs showed better chloride resistance than the OPC concrete. Particularly, at a w/b ratio lesser than 0.45, the slag concrete showed excellent resistance to the chloride ingress. The superior performance of the slag and fly ash concrete was due to the densification of the binder matrix by the formation of secondary C-S-H gel and refined pore structure with low interconnected pores that obstruct the ingress of chlorides. The C-S-H gel in the binder matrix can control the ingress of chlorides by physically adsorbing them. Moreover, the fly ash and slag have a significant amount of aluminate phases (AFm) that contribute to better chloride binding capacity. The free chloride ions in the pore solution get chemically combined with the AFm phases in the binder and form Friedel's slat and Kuzel's salt (Guo et al. (2019)).

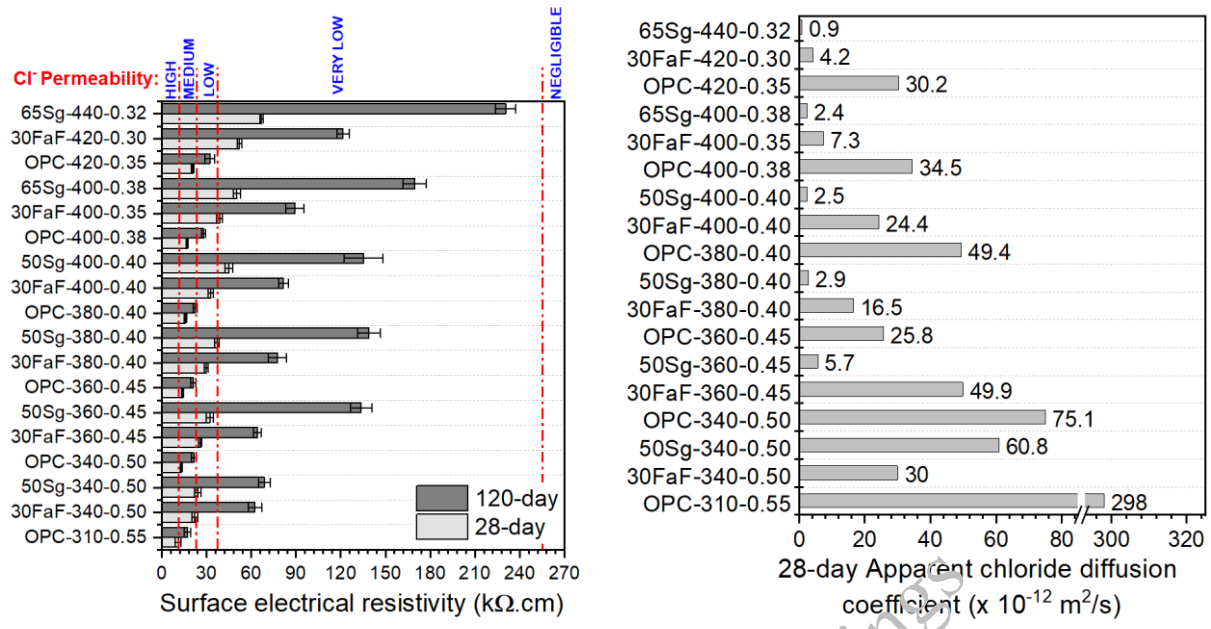

a) Surface electrical resistivity b) Chloride diffusion coefficient

Figure 1. Chloride resistance of the concrete mixes

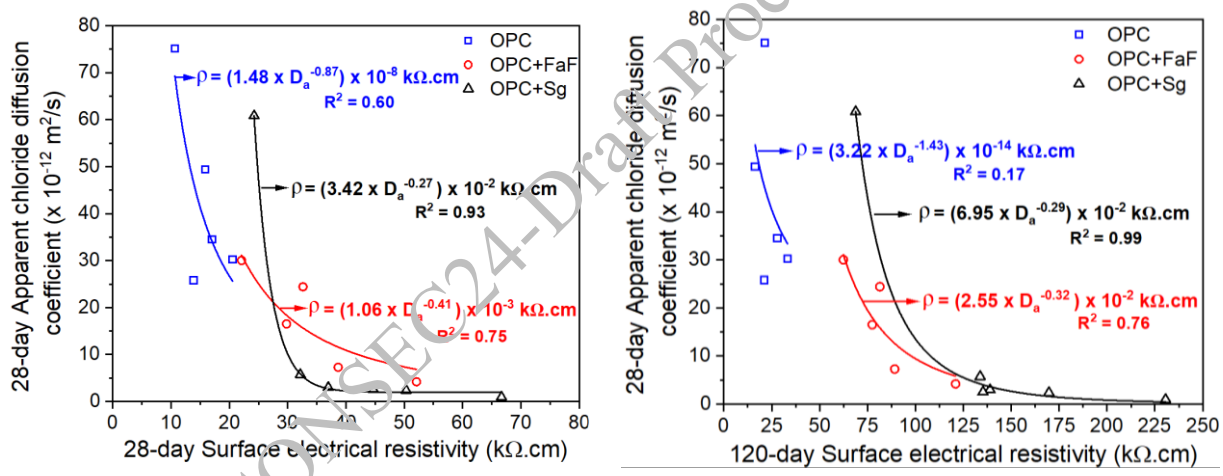

a) 28 days b) 120 days

Figure 2. Relationship between the resistivity and chloride diffusion coefficient

3.3 Correlation between electrical resistivity and chloride diffusion coefficient

With the obtained experimental results, the 28-day apparent chloride diffusion coefficient (D_a) value of the concrete was correlated with its 28-day and 120-day surface electrical resistivity. Figure 2 (a) and (b) compare the D_a-ρ correlation models of the different concrete at 28-day and 120-day, respectively. Models shown in Figure 2 can be used to determine the expected maximum surface electrical resistivity of the OPC, fly ash, and slag concrete at the age of 28-day and 120-day. At 28-day, the expected maximum surface electrical resistivity (ρ_{max}) for the OPC, fly ash, and slag concrete are 25 kΩ.cm, 60 kΩ.cm, and 100 kΩ.cm, respectively. Similarly, at 120-day, the expected maximum surface electrical resistivity (ρ_{max}) for the OPC, fly ash, and slag concrete are 35 kΩ.cm, 150 kΩ.cm, and 300 kΩ.cm respectively. Also, the correlation models shown in Figure 2 can be extrapolated till the above-described ρ_{max} values for predicting the apparent chloride diffusion coefficient of the concrete. The correlation models can be used along with the "SL-Chlor" nomogram developed by Rengaraju et al. (2023) for designing the corrosion free service life of the RCC structures.

4. Conclusions

Due to the refined pore structure and better chloride binding capacity, the concrete containing SCMs offers excellent resistance against chloride ingress, which was evident from their electrical resistivity, migration coefficient, and diffusion coefficient results. The chloride resistance of the slag concrete > fly ash concrete > OPC concrete.

Correlation models were developed between the electrical resistivity and apparent chloride coefficient of the OPC, fly ash, and slag concrete. The developed correlation models are presented in Table 4 and Table 5. These models will help in predicting the apparent chloride diffusion coefficient of the OPC, fly ash, and slag concrete with the known surface electrical resistivity, a simple parameter that can be measured instantaneously at the construction site.

Acknowledgements

Author Chandru Pichaimuthu thank the Science and Engineering Research Board (SERB), a statutory body of the Department of Science & Technology (DST) for providing National Postdoctoral Fellowship (File No. PDF/2022/001248).

References

NACE Impact Report, Material Performance (2016) Mitigating corrosion to extend the life of concrete structures. (June 20, 2016).

AASHTO TP 95 (2011). Standard Method of Test for Surface Resistivity Indication of Concrete's Ability to Resist Chloride Ion Penetration.

ASTM C1556 (2022). Standard Test Method for Determining the Apparent Chloride Diffusion Coefficient of Cementitious Mixtures by Bulk Diffusion. ASTM international.

Guo, Y., Zhang, T., Tian, W., Wei, J., and Yu, Q. (2019). Physically and chemically bound chlorides in hydrated cement pastes: A comparison study of the effects of silica fume and metakaolin. Journal of Materials Science, 54, 2152-2169.

Rengaraju, S., Pillai, R. G., & Gettu, R. (2023). Input parameters and nomograms for service life-based design of reinforced concrete structures exposed to chlorides. Structures, 56, 104847.

Flow and Strength Properties of Cassava Peel Ash Mortar with Varying Superplasticizer Dosages

K.A. Olonade[1*], M. Owobamirin[2], C. Olatunde[3], O. Ojo[4] and D. Ayanuga[5], and E. Oballa[6]

[1] Department of Civil and Environmental Engineering, University of Lagos, Lagos, Nigeria
Email: kolonade@unilag.edu.ng
[2] Department of Civil and Environmental Engineering, University of Lagos, Lagos, Nigeria
Email: owosmike@gmail.com
[3] Department of Civil and Environmental Engineering, University of Lagos, Lagos, Nigeria
Email: calebdarey@gmail.com
[4]Department of Civil and Environmental Engineering, University of Lagos, Lagos, Nigeria
Email: ojooluwatobi20@yahoo.com
[5]Department of Civil and Environmental Engineering, University of Lagos, Lagos, Nigeria
Email: oluwadamilare.ayannuga@live.unilag.edu.ng
[6]Department of Civil and Environmental Engineering, University of Lagos, Lagos, Nigeria
Email: emmanuel.oballa68@gmail.com

[*]Corresponding author

ABSTRACT

Superplasticizers are often added to concrete to influence its flow properties and subsequently its strength. Nevertheless, the use of supplementary cementitious materials (SCM) does influence these properties. In this study, therefore, the effect of different dosages of superplasticizers on mortar containing cassava peel ash (CPA) as SCM was investigated. This is to understand the flow and strength characteristics of the mix. Cassava peels were burnt up to 700°C in a furnace for 90 minutes to produce the CPA. Thereafter, CPA was used to replace cement in the proportion of 5, 10, 15, 20, and 25% by weight. Water demand using Puntke Test was conducted on the powder mixture of CPA and cement to determine the mixture that gives the lowest water demand. The proportion was then used as a binder to produce mortar of mix ratio 1:3 (binder: sand) with MC PowerFlow superplasticizer dosages of 0 (R0), 1.125(R1), 3.375(R2), and 6.75 g(R3) using a required dosage of 2.5g per kg of cement used. Spread flow test and compressive strength were determined for each of the mixes, following standard procedure. The results showed that a powder mixture containing 15% CPA had the lowest water demand, while the flow and strength varied with an increase in the dosage of superplasticizer. It was found that the presence of CPA reduced flow initially until the dosage of superplasticizer was increased up to 3.375g and above. Similar trend was noticed for strength. The use of CPA as SCM required a higher dosage of MC PowerFlow superplasticizer used. Further studies may be required to understand its performance with different superplasticizers.

KEYWORDS*: Cassava Peel Ash, Water demand, Flow diameter, Compressive strength, Flexural strength*

1. Introduction

Global consumption of cement is ever increasng. There is no indication that this will reduce in the near future, unless drastic effort is made. For instance, in 2015, annual global cement consumption was 4.6Gt and it is estimated to increase to between 6 and 13.5 Gt/a in 2050 (CEMBUREAU, 2015). Regrettably, there is no alternative material available in commercial quantity to replace cement in making concrete for building houses and other infrastructure. The situation is better imagined as the world's population increases from today's 7.3 billion to 9.7 billion in 2050 (UN, 2015).

In Africa where there is gross infrastructure deficit to cater for the teeming population and cement is allmost indispensable. However, the cost of cement, which represents about 42% of the total cost of building a house, seems extremely high and makes the cost of housing prohibitive for average income earners Olonade, 2013). The challenge before the researchers is to find alternative material that is cheaper in cost

and less destructive to the environment. The use of supplementary cementitious materials (SCMs) has potential to mitigate challenegs attributed to cement. Use of blended cements in developed nations is very common and on the increase. Globally acceptable SCMs such as fly ash and ground granulated blast furnace slag (ggbs), are scarcely available in Africa. Nevertheless, ashes of bio materials such as rice husk ash, corn cob ash are potentiat SCM that could be used the same way fly ash angd ggbs are used. In the last one decade, we have found cassava peel as potential pozzolanic material that could replace cement in concrete production by up to 20% by mass (Salau et al., 2012). However, there is limited study on the compactibility with superplasticisers (SP).

Superplasticisers are used in cement-based materials to achieved desired properties such as increased strength, enhanced workability.. They are usually adsorbed on the surface of the binder particles, which cause the particles to repel each other and deflocculates, increasing the flow (He, et al., 2021). However, there is still challenge of compatibility with materials especially with blended cement). Since, CPA will be used as SCM in this study, compatibility of the SP with it is still a grey areas. The performance of SP would therefore depends on the nature of the particles that form the binder. Therefore, this study seeks to understand how CPA in cement respond with different dosages of SP.

2. Materials and Methods

2.1 Materials

Portland Limestone Cement produced by Dangote was used as binder, while Ogun River sand was used as fine aggregate. Cassava peels were burnt up to 700°C for 90 minutes to produce ash, which is blended with cement to form binder (Table 1). The MC-Powerflow 2695 G polycarboxylatether based superplasticiser was used water reducing agent.

Table 2. Oxide composition of Cement and CPA

Materials	Oxides (%)												
	SiO2	Al_2O_3	Fe_2O_3	CaO	MgO	SO_3	K_2O	Na_2O	Mn_2O_5	P_2O_5	TiO_2	LOI	Total
CPA	67.15	5.45	4.74	2.78	1.18	2.16	3.53	0.07	0.18	1.24	1.12	10.11	99.71
Cement	19.23	4.08	2.18	57.88	1.34	1.66	0.22	0.00	0.09	0.59	0.29	12.07	99.64

2.2 Mix Proportion and Sample Preparation

A mix ratio of 1:3 (binder: sand) was adopted to produce mortar sample with a water-binder ratio of 0.50. In order to obtain the optimum proportion of CPA to replace cement, water demand test was conducted following Punkte test using replacement levels of 0 to 20% at interval of 5%. The optimum value obtained (15%) was used to replace cement to form binder used in the mortar production. As specified by the producer, 2.5g MC-Powerflow 2695 G to be used for every 1 kg of cement. Four different dosages of SP was used as multiple of the recommended dosage (R) as R0, R1, R3, and R6, where R0 indicate no SP, while R1 represent the recommended dosage. R3 and R6 represent multiple of 3 and 6 respectively. Samples of normal mortar (no CPA) were also prepared using the same dosages of SP to serve as control. In all, there were eight different mixes produced.

2.3 Testing Methods

Chemical composition and particle size distribution of cement and CPA were determined at Lafarge cement chemical laboratory in Ewekoro, Nigeria. The mortar sample were cast in a mould prism of size of 160mm × 40mm × 40mm. After 24 hours the samples were removed from the mould and cured in water until the days of testing for flexural then compressive strength (BSEN 196-2, 2016). As for flow testing, the standard procedures described in ASTM C1437 – 07 (2007) were followed. Thereafter, the increase in average flow over the base diameter of the mortar mass was expressed as a percentage of the original base diameter.

3. Results and Discussions

3.1 Particle Size Distribution

Figure 1 shows the particle size distribution curves of cement used and CPA. It can be seen that cement contained more finer particles sizes compared to CPA. About 70% of the total volume of the cement particles had sizes below 10 µm as against CPA that contained close to 90% of the volume above 10 µm. This observation is further corroborated with the their specific surface areas, where the specific surface area of cement was more than 100% of that of the CPA. The implication of this occurrence is that CPA is coarser than cement, which may likely impact the workability of the mortar made from the mixture of cement and CPA as well as cause delay in hydration processes (Safaa et. al., 2012).

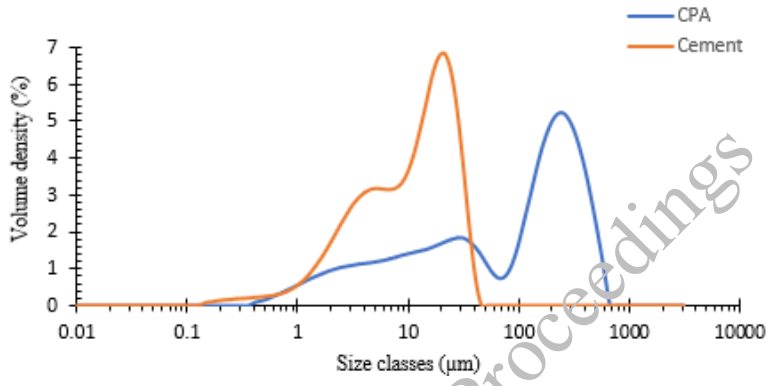

Figure 1. Particle size distribution of CPA and Cement

3.2 Water Demand

In order to determine the minimum quantity of water that will sufficient to produce a dense paste of the mixture of cement and CPA, Puntke test was carried out on the CPA-Cement blended binder at different proportion of CPA (Figure 2). As seen from Figure 2, there seems not be any significant difference in the water demand at 5 to 15% proportion of CPA, though 15% has lowest value of 4.94. But at higher proportion of CPA (>15%) water demand increased. Though, CPA is coaser than cement, the only possible explanation for this trend would be that CPA has absorb more water than cement, which becomes obvious at her proportion.

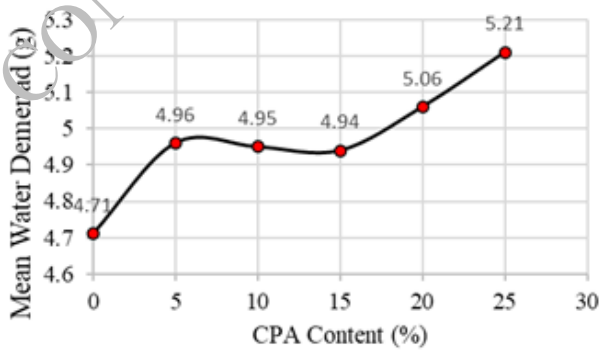

Figure 2. Water demand of cement-cassava peel ash mixture

3.3 Flow Diameter

The average flow diameters obtained for all the eight samples are summarized in Figure 3. It is seen that while normal mortar at R1 dosage of SP started flowing and the flow continued to increase as the SP dosages increased, but no noticeable flow was found in the mortar containing SP dosage R3 when the flow diameter was just 15%. The possible explanation for this could be that the SP was not absorbed on the surface of the particle due to the presence of CPA, which has higher sulphate content (Table 1). Sulphate has been

implicated to inhibit adsorption of PCE-based superplasticizer (He et.al, 2021). This result is similar to what Olonade and Schmidt (2018) reported from their study.

3.4 Strength Properties

The compressive strength of the two mortar samples (cement mortar and CPA-cement blended mortar) with different dosagaes of SP is shown in Figure 4. The strngth increases with increase in ages for both mortar, while increase in SP doasages caused increase in strength upto R2 dosages but the strength decreased beyond this dosage.for normal mortar. Similar observation was made for CPA mortar with the exception that R1 dosage had less effect on CPA mortar compared to cement mortar.

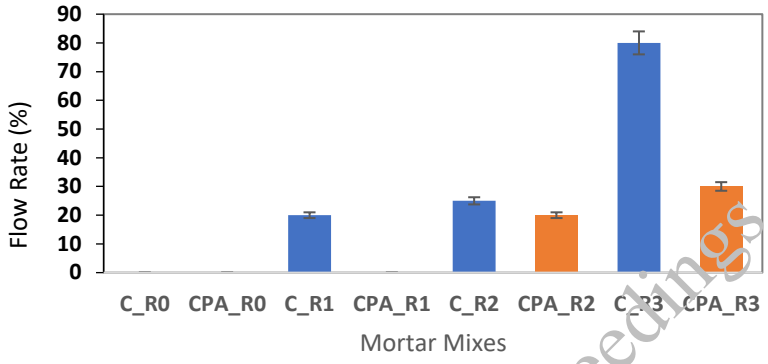

Figure 3. Flow rate of mixes

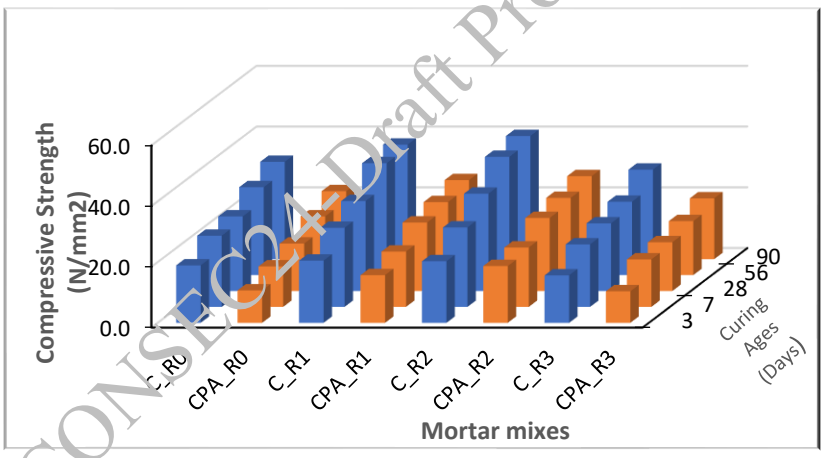

Figure 4. Compressive strength of Normal and CPA Mortar at different superplasticizer dosages of SP

4. Conclusions

It is concluded from this study that:

- Cement particles adsorb SP more than cassava peel ash as found in the flow of the mortar produced from each sample.
- About double of dosage of SP would be required for CPA mortar to have the same flow with cement mortar.
- Dosage of SP of about 200% of recommended dosage would be required to achieve workable mortar. SP had influence on the strength of CPA mortar.

References

CEMBUREAU (2015). "Cement & concrete: key facts & figures," t. E. c. association, Ed., ed. UN. (2015). World Population Prospects: The 2015 Revision. Available: http://www.un.org/en/development/desa/news/population/2015-report.html

Olonade, K.A. (2013). "Economy of Rice Husk Ash (RHA) in Concrete for Low-Cost Housing Delivery in Nigeria", *Journal of Civil Engineering and Architecture*, 7(11): 1464 – 1470.

Olonade, K. A. and Schmidt, W. (2018). "Dispersing Effect of PCE-Based Admixture on the Rheology of Cementitious Systems Blended with Cassava Peel Ash", Proceedings of the 4th International Conference on Service Life Design for Infrastructures (SLD4), 27-30 August 2018 – Delft, Netherlands, 06- 18.

Salau M.A., Ikponmwosa, E.E. and Olonade, K. A. (2012) "Structural Strength Characteristics of Cement-Cassava Peel Ash Blended Concrete", *Civil and Environmental Research*, 2(2): 68 -77, 2012.

Safaa M.A. El-Gamal, Fawzia M. Al-Nowaiser, Asmaa O. Al-Baity (2012) Effect of superplasticizers on the hydration kinetic and mechanical properties of Portland cement pastes, Journal of Advanced Research, 3(2): 119-124.

Yan He, Shuhua Liu, Qi Luo, Yang Zhang, Xiucai Wang, and Gaoyu Liao (2021). Effects of sulfates on adsorption-dispersing polycarboxylate behaviour with different carboxylic densities, *Advances in Cement Research*, 33(11):496-505.

Transition Design for Carbon Reduction in Concrete Technologies

Takeju Matsuka[1*], Koji Sakai[2], and Shinichi Wakasugi[3]

[1] National Institute of Technology, Kumamoto College, Yatsushiro, Japan
Email: matsuka@kumamoto-nct.ac.jp
[2] Japan Sustainability Institute, Sapporo, Japan
Email: sakai@jsi-ks.jp
[3] NIPPON STEEL CEMENT Co., Ltd, Muroran, Japan
Email: wakasugi.shinichi@cement.nipponsteel.com

ABSTRACT

The history of concrete has been around for a little over 200 years, but its spread has been remarkable. Concrete and steel have become indispensable materials for the development of a country. However, the manufacturing technologies of these materials depend on fossil fuels. We are compelled to recognize that the concrete sector is also entering into an era of the Anthropocene in which humans give a major impact to the global environment due to global warming and resource depletion. We have a certain agreement that all industries, including concrete-related sectors, should aim for carbon neutrality (CN) to mitigate global warming. The essence of CN is de-fossil fuels. The fossil fuels will shift to renewable energy and hydrogen. The CO_2 resulting from the raw material should be captured and stored or reused. If CO_2 is still emitted, it is fixated in trees and soil. The problem can be simplified like this. In the concrete sector, on the other hand, there is a trend toward the carbonation of concrete through CO_2 absorption and mass replacement of admixtures. However, there are some technical and quantitative barriers to its realization. They are not realistic. Therefore, what the concrete sector should conduct is firstly a transition design to take a step for carbon reduction (CR) using the best available technologies. This paper describes a concept of transition design for CR in concrete technologies and clarifies the direction for which we should aim.

KEYWORDS*: Transition design, Carbon reduction, Best available concrete technologies*

1. Introduction

The essence of carbon neutrality (CN) is de-fossil fuels. The fuel sources will shift to hydrogen and ammonia which are produced from renewable energies. The CO_2 resulting from the raw materials can be captured and stored or reused. If CO_2 is still emitted, it is fixated in trees and soil. The problem can be simplified like this. In the concrete sector, however, there has been a trend towards the carbonation of concrete through CO_2 absorption and mass replacement of admixtures. It is obvious that there are several technical and quantitative barriers to the realization of this approach. In addition, previous works have shown that concrete carbonation is “not harmless” (Nagataki (1995), Kobayashi (1990)). When concrete is used as a CO_2 sink, if problems are induced in the long-term durability of the concrete, future generations will have a great burden. When large volumes of admixture like fly ash (FA) and ground granulated blast-furnace slag (BFS) can not be used due to their availability with an uncertainty of production. And also it will decimate the cement industry. Thus, the realization of these ideas is unrealistic.
This paper describes the status of global greenhouse gases and the carbon budgets. Subsequently, the CO_2 emissions in concrete technology are discussed. Finally, a transition desgin is proposed based on four carbon reduction (CR) tools.

2. Current Status of Greenhouse Gases and Carbon budget

The Global Carbon Project (GCP) publishes detailed information on CO_2 emissions and absorption. Figure 1 shows the relevant results based on the data. In FY2021, the total CO_2 emissions from fossil fuel combustion and industrial processes amounted to 37.124 billion tons. The CO_2 absorption statistics by

oceans, land, and concrete are discussed later. Currently, CN is an important global goal to limit the temperature increase to within 1.5–2 °C compared to the pre-industrial age temperature. However, our residual carbon budgets are small. The residual carbon budget for the 1.5 °C target is 500 billion tons, and that for the 2 °C target is estimated to be 1,350 billion tons. The concrete sector will also need to make efforts to contribute to CR to achieve these difficult goals.

3. CO2 Emissions of Concrete

This study is focused on cement, which is the largest source of CO_2 emissions in the concrete sector. CR including supplementary cement materials (SCMs) and the concrete-related machinery is discussed.

3.1 Cement

Approximately 4.4 billion tons of cement was produced worldwide in 2021. The cement production is responsible for the emission of 788.6 kg of CO_2 per unit ton in Japan. With this value, the emission from cement production in the world accounts for 9.3 % of global CO_2 emissions (Figure 2). The calcination origin of cement production accounts for 39.5 %. The remaining 60.5 % of CO_2 emission is due to decarbonation of limestone.

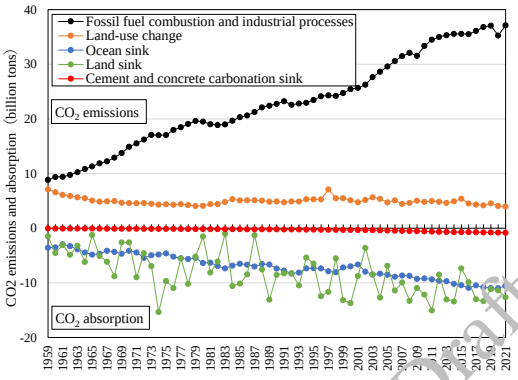

Figure 1 Changes in CO_2 emissions and absorption

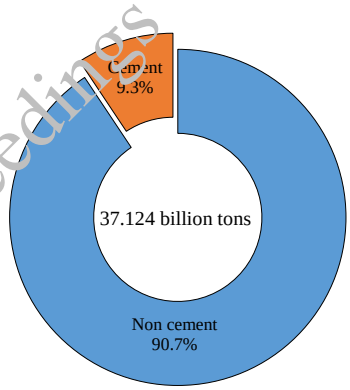

Figure 2 CO_2 emissions of cement

3.2 SCMs

BFS and FA are typical SCMs. The CO_2 emission intensity of BFS and FA is assumed to be 35.6 and 29.0 kg/t, respectively. Usually, CO_2 emissions is reduced by using BFS and FA as cement replacement. However, these SCMs are generated simultaneously during steel and electricity production. However, these SCMs are generated simultaneously during steel and electricity production. Therfore, these SCMs should be regarded as regarded as bearing CO_2 derived from energy necessary for production. In other words, the SCMs is not zero CO_2 emission materials. This has been discussed in detail by authors (Sakai et al (2023)).

3.3 Concrete-related machinery and equipment

The machinery and equipment used for ready-mixed concrete include mixer and pump trucks, and those used for precast concrete include the curing facility used during production. These machinery and equipment should be powered with electricity and hydrogen from renewable energy sources. It is the same for the compaction of concrete on site.

4. Transition design

The transition design tools for CR are listed in Table 1. Carbon capture and storage (CCS) and CO_2 fixation in trees and oceans cannot be exclusively utilized by the cement sector. As these are commons, they should be shared by all industries. However, currently, there is no universal rules for that. As shown in Figure 2, this paper assumes that 9.3 % is allocated for the cement sector.

Table 1. Transition design tools for CR

Scenario	A	B	C	D
Methodologies	Hydrogen fuel	SCMs	CCU/S	Trees, Oceans

4.1 Scenario A (Hydrogen fuel)

The essence of CN is de-fossil fuel. The use of green hydrogen produced using renewable energy sources is a prerequisite for realizing CN. When coal is converted to green hydrogen, CO_2 emissions from fuel can be reduced to zero. Using this approach, global CO_2 emissions from cement production can be reduced from 3.47 billion tons to 2.10 billion tons.

4.2 Scenario B (SCMs)

In this study, the volume of SCMs worldwide based on the status of SCMs in Japan is estimated. As indicated in Table 2, only 0.32 billion tons of BFS is being produced for cement replacement every year. Therefore, the cement replacement of BFS can only account for 7.3 % of 4.4 billion tons of cement produced globally. Similarly, as indicated in Table 3, 12 million tons of FA can be used for cement production every year. Thus, the cement replacement of FA as a SCM is only 0.27 % of cement produced globally.
If the previously quoted values of CO_2 emission intensity for BFS and FA are assumed, this approach can reduce CO_2 emissions from global cement production to 3.22 billion tons. However, considering the current production quantity of BFS and FA, their massive substitution is not feasible. Additionally, blast furnaces have been replaced by electric furnaces in steel manufacturing. Moreover, the use of coal is expected to decrease significantly in the future. Under these circumstances, the massive substitution of SCMs will be impossible.

Table 2. Production volumes of various slags

Items	Calculation method	Japan (million tons)	World (billion tons)
(1) Pig iron	–	63.07 (actual value)	1.314 (actual value)
(2) Blast furnace slag	(1)×0.311ton/ton	19.886 (actual value)	0.41
(3) Granulated slag	(2)×85.9%	17.077 (actual value)	0.35
(4) Ground granulated blast-furnace slag (BFS)	(3)×92.4%	15.78 (actual value)	0.32

Table 3. Production volumes of fly ash

Items	Calculation method	Japan	World
(1) Power generation	–	–	26.6 trillion kWh
(2) Coal-fired power generation	(1)×38.5%	282.6 billion kWh (actual value)	10.2 trillion kWh
(3) Coal ash	–	8.849 million tons (actual value)	–
(4) Fly ash	(3)×90%	7.9641 million tons	–
	(2)×0.0282kg/kWh	–	0.29 billion tons
(5) Fly ash for concrete (FA)	(4)×4.2%	0.3148 million tons	12 million tons

4.3 Scenario C (CCU/S)

In cement production, CO_2 generation from raw material is unavoidable. This CO_2 treatment must rely on CCU/S. The Global CCS Institute estimates an annual storage capacity of approximately 5.6 billion tons of CO_2 in 2050. The Earth's interior is a common. If the cement sector's share is 9.3%, 521 million tons of this capacity will be allocated. Thus, the application of CCS can reduce CO_2 emissions from cement production to 2.95 billion tons.

4.4 Scenario D (Trees and Oceans)

Trees and oceans are the two main sinks of CO_2. They absorbed 12.64 billion tons and 10.55 billion tons of CO_2, respectively, in 2021. (Figure 1). If 9.3% is regarded the cement sector's share, the sector can expect to absorb 2.16 billion tons. Applying this approach, CO_2 emissions from cement can be reduced to 1.31 billion tons. Conversely, the CO_2 absorption capacity of cement and concrete carbonation is less than 1 billion tons (GCP (2022) and Fengming Xi (2016)). This is approximately $1/10^{th}$ of the amount of CO_2 absorbed by trees and oceans, that is, it is smaller by one order of magnitude. In other words, the

development of concrete technology based on CO_2 sinks theory is meaningless because it loses the accumulated important knowledge.

4.5 Integrated Scenario

Figure 3 shows the CO_2 emissions caused by cement production considering each single and integrated CR scenarios. Scenarios A and D have a significant impact on CR. However, there are some uncertainties regarding CO_2 fixation in Scenario D. The technological development for Scenario C is important to avoid such uncertainties. Scenario B cannot be expected an excessive effect. In conclusion, Scenario B is reasonable to consider as the best available concrete technology for CR until the other technologies are generalized.

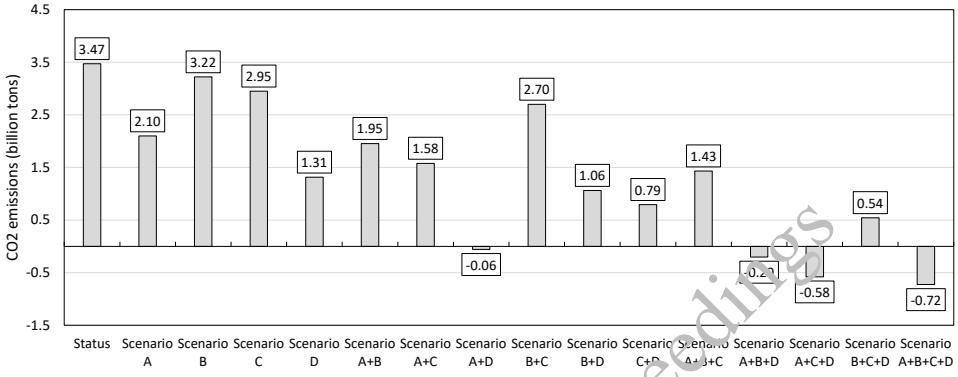

Figure 3. CR effectiveness of each individual and integrated scenario

5. Conclusions

The results of this study can be summarized as follows:

- The transition from coal to green hydrogen as fuel for cement production can reduce CO2 emissions 39.5%; however, the cost is a major challenge during the transition period.
- The possible cement replacement rates with BFS and FA as SCMs are 7.3 % and 0.27 %, respectively. Therefore, excessive expectations should be avoided in these tools.
- Although there is a great potential for storing CO2 inside the Earth, relevant technologies need to be developed for the effective capture and transportation of CO2 induced from raw material. Thus, over-reliance on CCS should be avoided. The use of CO2 would be preferable.
- The CO2 fixation in trees and oceans can reduce "raw material origin" CO2 generated during cement production by approximately 60%, but it should be recognized that there are uncertainties in the current assessment of CO2 absorption capacity, although they are worth utilizing.
- Significant CR can be achieved by integrating scenarios of hydrogen use and CO2 fixation in trees and oceans. Furthermore, when CCU/S technology is added, "carbon neutrality" will be achieved.

References

Fengming Xi et.al. (2016) “Substantial global carbon uptake by cement carbonation”, *Nature Geoscience*, 9 (12): 880-883

Global Carbon Project (2022) “Global Carbon Budget 2022”, https://doi.org/10.5194/essd-14-4811-2022

Kobayashi, K. (1990) “Effects of Carbon Dioxide on Concrete”, *Journal of Institute of Industrial Science, The University of Tokyo*, 42(9): 525-534

Nagataki, S. (editor) (1995) “Long-term durability of concrete –Lessons from Otaru Port 100 Year Durability Test–”, *Gihodo Syuppan*

Sakai, K. and Matsuka, T. (2023) “The Essence of Carbon Neutrality in Concrete-Related Technologies” ACI *Concrete Inter-national*, 45: 40-41

Effect of CO_2 Mineralization on the Performance and Sustainability of Concrete

Lakshmi Vara Prasad Meesaraganda[1] and Md Athar kazmi[2*]

[1]*Email: mlvprasad@civil.nits.ac.in*
[2]*Email: md_rs@civil.nits.ac.in*
Department of Civil Engineering, National Institute of Technology Silchar, Silchar, Assam-788 010, India,

[*]Corresponding author

ABSTRACT

The reaction of CO_2 with the hydrating phase of cementitious materials produced micro-scale calcium carbonate, densifying concrete. Hence, this gives rise to double-fold benefits, such as improving concrete performance and permanently sequestrating CO_2. The primary method for adding CO_2 to concrete is accelerated carbonation curing. This has numerous restrictions, such as the limited diffusion rate, the need for the enormous airtight chamber, and application in precast concrete only. Aiming to overcome these limitations of using CO_2 in concrete only through accelerated carbonation, a novel two-step CO_2 mineralization method was used. In this method, CO_2 is sequestrated in calcium-rich cementitious material in the first step, and then it is mixed with the rest of the ingredients to produce concrete in the second step. Findings of the present work reveal that a dose of 0.2% of CO_2 by the weight of cement gives rise to optimum compressive strength, 20.59% higher than conventional concrete. The benefit of strength gain can be leveraged to minimize cement content, and this practice of CO_2 mineralization leads to lowering the consumption of cement by 7.5% without compromising concrete performance. Hence, carbon intensity and cost per unit strength of concrete are significantly lowered. The slump value of CO_2 mineralized concrete with leveraged cement and marginally higher fly ash is more than that of conventional concrete, the pH value is marginally reduced, and the scale of reduction is small, deemed acceptable. Additionally, CO_2 mineralized concrete with lowered cement content has equivalent durability performance marginally higher than conventional concrete, as tested by the rapid chloride penetration and bulk resistivity tests.

KEYWORDS*: CO_2 Mineralization, Calcium Carbonate, Performance of Concrete, Sustainability*

1. Introduction

CO_2 capture and beneficial use in the building industry can minimize anthropogenic greenhouse gas emissions. Xuan et al. (2016), He et al. (2019). In this process, CO_2 is captured from the emitting source, compressed and stored in liquefied form, and then transported to the place where it is to be utilized Gupta et al. (2021), Monkman et al. (2021), Kazmi and Prasad (2023). In this way, a double-fold benefit is gained: firstly, reduction in CO_2 emission and permanent sequestrating it and, secondly, use it in producing valuable products Gupta et al. (2018); Kurda et al. (2018). CO_2 is used in the construction industry in carbonation curing of the pre-cast element, carbon conditioning of recycled aggregate to enhance the properties of adhered old mortars, and as an admixture during concrete mixing Chen (2010), Junior et al. (2015), Lei et al. (2022), Kazmi et al. (2023). The carbonation curing is limited to the pre-cast element only, which also needs a large chamber; furthermore, conditioning of recycled aggregate is limited to only recycled aggregate concrete Kou et al. (2014), Rosa et al. (2022).

During the course of the structure's service life, natural carbonation causes the concrete to naturally absorb CO_2 from the environment Dixit et al. (2015); Sharma et al. (2015). However, the process is extremely sluggish, taking hundreds of years. Furthermore, natural carbonation lowers the passivity of concrete and exposes the reinforcement to corrosion. Monkman and Shao (2006). However, early-age carbonation does not have the same tendency; instead, it reacts with hydration products and forms minutes scale uniformly

distributed calcium carbonate ($CaCO_3$), which densifies the concrete and makes it stronger and more durable Wang et al. (2021), Kazmi and Prasad (2024).
In the 1970s, the University of Illinois investigated the carbonation of freshly hydrated cement Monkman and MacDonald (2017). According to Equations (1) and (2), the reaction between the tricalcium silicate (C_3S) and dicalcium silicate (C_2S) phases in cement and CO_2 results in the formation of calcium carbonate ($CaCO_3$) and calcium silicate hydrate (C-S-H) gel Mahoutian et al. (2014):

$$2(3CaO \cdot SiO_2) + 3CO_2 + 3H_2O \rightarrow 3CaO \cdot 2SiO_2 \cdot 3H_2O + 3CaCO_3 \quad (3)$$

$$2(2CaO \cdot SiO_2) + CO_2 + 3H_2O \rightarrow 3CaO \cdot 2SiO_2 \cdot 3H_2O + CaCO_3 \quad (2)$$

Moreover, the calcium hydroxide {$Ca(OH)_2$} in cement paste will react with CO_2, as shown in the Equation (3) Monkman et al. (2016) :

$$Ca(HO)_2 + CO_2 \rightarrow +CaCO_3 + H_2O \quad (3)$$

Furthermore, the reaction is exothermic and water starvation, so an optimum dose of CO_2 mineralization gives the best results Monkman et al. (2021). The mineralization of small doses of CO_2 by the weight of cement improved concrete strength and durability Qian et al. (2016) through a complication noticed in the mineralization process. In the present research work, a simplified two-step mineralization of CO_2 in concrete during mixing is adopted to improve efficiency. The present work aims to determine the ideal CO_2 mineralization rate for concrete to provide the ultimate possible compressive strength and leverage the strength gain to minimize cement consumption. Further, to compare the durability of conventional concrete with CO_2 mineralized concrete with leveraged cement.

2. Materials and experimental program

2.1 Materials and mix proportions

Ordinary Portland cement (OPC) of 53 grades as per ASTM C150/C150M (2016), with a specific gravity of 3.14 and fineness of 302 m2/kg, was utilized. The naturally occurring crushed aggregate of nominal maximum size 20 mm with a fineness modulus of 7.08 and specific gravity of 2.74 is used as a coarse aggregate. Fine aggregate from nearby river sources confirming ASTM C33/C33M (2018) and belonging to zone-II is used in the present research. The specific gravity and fineness modulus of the fine aggregate are 2.64 and 2.88, respectively. Low calcium type F fly ash with a specific gravity of 2.2, obtained from a nearby thermal power plant confirming to ASTM C618 (2015), is used. CO2 was used in this work as an admixture and captured from an ethanol production factory. in the current experiment work, Sunanda Polytancrete N.G.T superplasticizing admixture from Sunanda Speciality Coating PVT.LTD was used. Potable drinking water conforming to ASTM C 1602/C 1602M (2006) was used in the present experimental work.
Concrete mix design was carried out for each mix as per ACI 211.1-91 (2002). Experimental work was done in three phases. In the first phase, an optimum amount of CO2 has been found, followed by the amount of cement to be leveraged with the increment of compressive strength due to CO2 mineralization without compromising the strength. Finally, the durability aspect was assessed for CO2 mineralized concrete with leveraged cement content with respect to conventional concrete. To find the optimum dose of CO2 in the concrete, four mix designations were considered: one conventional concrete (CC) without CO2 mineralized, and three CO2 mineralized concrete mix CMC-1, CMC-2, and CMC-3, having 0.1, 0.2and 0.3% of CO2 by weight of cement used, respectively. Table 1 gives the weight of each ingredient per unit volume of concrete. Stage one's compressive strength results show that the mix of CMC-2 with 0.2% CO2 performs better. The mix designations CMC-21, CMC-22, CMC-23, and CMC-24, have 2.5, 5, 7.5, and 10% lower OPC, respectively, than the mix CMC-2. The mix proportions are shown in Table 1. In the second phase, a 2.5% reduction in OPC was implemented in the mix CMC-2. The durability of CO2 mineralized concrete with lower OPC was compared to regular concrete in the third phase.

Table 1. Weight of each ingredient per meter cube of concrete

Ingredients	CC	CMC-1	CMC-2	CMC-3	CMC-21	CMC-22	CMC-23	CMC-24
OPC	440	440	440	440	429	418	407	396
Fly ash	110	110	110	110	115	120	125	130
Water	197	197	197	197	197	197	197	197
Superplasticizer	3.52	3.74	3.96	4.18	3.96	3.96	3.96	3.96
Water/binder	0.36	0.36	0.36	0.36	0.36	0.36	0.36	0.36
Fine aggregate	585	585	585	585	585	585	585	585
Coarse aggregate	1085	1085	1085	1085	1085	1085	1085	1085
CO_2	-	0.440	0.880	1.320	0.858	0.836	0.814	0.792

2.2 CO_2 mineralization into cementitious materials

A specially prepared equipment developed at the National Institute of Technology Silchar was used to sequestrate the CO_2 with cement slurry. The sequestration of CO_2 with the hydration products of cementitious materials is carried out separately that easing the process and raising the CO_2 use efficiency to 99%. Cement slurry was prepared in the cylinder, and it was closed with a bolt, with a rubber placed between the cap and cylinder to make it airtight. Then, it was placed on the weighing balance and connected with the CO_2 storage cylinder, and the required amount of CO_2 was applied; the amount of the CO_2 can be measured with the weighing balance. After that, the inlet valve of the cylinder is closed and shaken thoroughly for one minute, such that the applied CO_2 is completely sequestrated into the cement slurry. Finally, in the second process, the CO_2-sequestrated cement slurry is mixed with the remaining materials to produce CO_2-mineralized concrete.

2.3 Experimental program

The slump test was used to determine the concrete workability in accordance with IS 1199 -part -2 (2018). Assessments of strength and durability were conducted on the cured concrete. Every testing day, three samples were tested for every mix designation; for each of the tests, the average values are listed in the results section. In compliance with IS 516, Part-1 Sec-1 (2021), compressive strength tests were performed on 150 mm cube specimens with a compression testing machine capable of 3000 kN. For pH determination, a 10×10 mm piece of absorbent paper was kept on the surface of the concrete, and 100 µl of distilled water was added. The hydroxyl ions took 15 minutes to reach equilibrium during the extraction process, as described by Rostami et al. (2011). The pH of the sample's sliced layers was then measured with an Extech pH110 pH meter with a flat sensor tip. The pH values from three randomly chosen locations on the sliced surface were averaged and reported to ensure consistent results. In accordance with ASTM C: 1202 (2012), the rapid chloride penetration test (RCPT) was performed on disc specimens having a diameter of 100 mm and a thickness of 50 mm. Concrete resistivity was tested following ASTM C1876-23 (2023) and is computed using Equation (4). Concrete resistivity is determined by two electrodes placed on the sides of a smooth-finished, water-saturated concrete cylinder specimen of 100 mm diameter and 200 mm height:

$$\rho = \frac{RA}{\ell} \tag{4}$$

The resistivity in kΩ-cm is represented by ρ in this Equation, along with the electrical resistance of the sample in kΩ, its cross-sectional area in cm^2, and its length in cm by R.

3. Results and discussions

3.1 Determining the optimal amounts of CO_2 to be mineralized.

To determine the optimal CO_2 content for concrete to mineralize and provide the highest compressive strength, experimental trials were conducted with an increment of 0.1% of CO_2 by weight of OPC. The

results for slump value are presented in Table 2, and compressive strength is depicted in Fig. 1. As the CO_2 content increases, the slump value marginally decreases, with the reduction being small enough to be considered acceptable. Moreover, each mix designation exhibits sufficient workability. The relatively small decrease in slump can be attributed to the water that is consumed from the freshly mixed concrete when CO_2 interacts with the hydrating phase of OPC. Monkman et al. (2016), Prasad and Kazmi (2024).

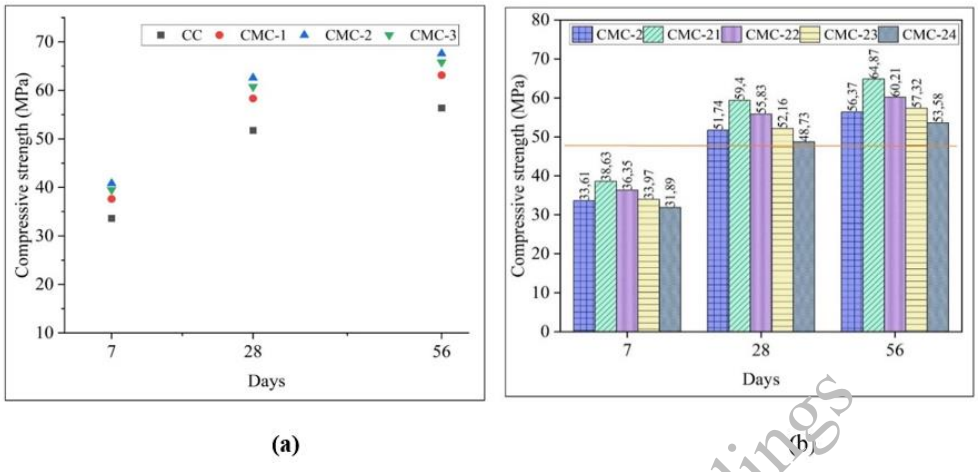

Figure 1. (a)Compressive strength of concrete with varying doses of CO_2 (b) Compressive strength of 0.20% CO_2 mineralized concrete with reduced OPC

Fig. 1 illustrates that incorporating a small amount of CO_2 for mineralization can enhance the compressive strength of concrete. The peak compressive strength was observed with a 0.20% CO_2 mineralization by weight of OPC. For the concrete mix CMC-2, the compressive strengths recorded were 40.82 MPa after 7 days, 61.88 MPa after 28 days, and 67.06 MPa after 56 days. These values are 19.45%, 20.59%, and 21.32% higher than those of the mix CC at the corresponding testing intervals. The improvement in compressive strength is attributed to the formation of fine calcium carbonate particles and an increased volume of ettringite due to the reaction between CO_2 and the hydrating phase of OPC. This results in a denser concrete structure, thereby enhancing its compressive strength. Luo et al. (2022).

Table 2. Slump value of concrete mix with varying dosages of CO_2

Mix Id	Slump value (mm)
CC	112
CMC-1	110
CMC-2	109
CMC-3	107

3.2 OPC reduction in the optimum quantity of mineralized CO_2 mix

The increase in compressive strength caused by CO_2 mineralization can be used to achieve the target strength while using less OPC, hence saving OPC. A study was conducted with a 2.5% OPC reduction rate to determine the highest OPC savings without losing compressive strength. For every meter-cube of concrete, the mix proportion must be balanced., 5 kilograms of fly ash were added for each step of OPC reduction. Since a 0.20% dose of CO_2 was found to give maximum compressive strength, the CMC-2 further OPC reduction analysis was conducted, resulting in a maximum OPC reduction that was less than the mix without lowering compressive strength. CC. The result of the slump value and the compressive strength for having 0.20% CO_2 with the reduced amount of OPC are presented in Table 3 and Fig. 2, respectively.

Table 3 Slump value concrete mix with reduced OPC

Mix ID	Slump value (mm)
CMC-21	114
CMC-22	117
CMC-23	121
CMC-24	126

The slump values for mixes CMC-21, CMC-22, CMC-23, and CMC-24 are 114 mm, 117 mm, 121 mm, and 126 mm, respectively, with an increase in slump as the OPC content decreases. This rise in slump is likely attributed to the inclusion of fly ash in the batches with reduced OPC. Notably, the slump value of CO_2 mineralized concrete tends to increase when OPC content is reduced, possibly due to the fly ash addition in these mixes (Surya et al. (2015). Fig. 2 demonstrates that mix CMC-23, which is blended with CO_2 mineralized and reduced OPC by 7.5%, exhibits compressive strength equivalent to the corresponding conventional mix without CO_2. Mix CMC-23 has compressive strengths of 33.97, 52.16, and 57.32 MPa at 7, 28, and 56 days, respectively. These values are comparable to (slightly higher than) those of mix CC, with compressive strengths of 33.61, 51.74, and 56.37 MPa at 7, 28, and 56 days, respectively. Therefore, through CO_2 mineralization, a 7.5% reduction in OPC content can be achieved without sacrificing concrete compressive strength.

3.3 Durability study

Using the RCPT and bulk resistivity test, the transport properties of concrete were assessed. The outcomes showed that, in comparison to standard mixes, CO2 mineralized concrete with lower OPC exhibits equal resistance to chloride passes and electrical resistivity. Table 4 presents the results of the RCPT and bulk resistivity tests, indicating that mix CMC-23 outperformed mix CC in both tests conducted at 28 and 90 days. The charge passed through mix CMC-23 is 1854 and 1473 coulombs at 28 and 90 days, respectively, representing a decrease of 4.37% and 4.41% compared to mix CC at the same time intervals. Additionally, the bulk resistivity of CO2 mineralized mixes with reduced OPC is higher than that of corresponding conventional mixes, with CMC-23 showing resistivity of 5.66% and 5.78% more than the mix CC at 28 and 90 days, respectively. The alkalinity of the concrete remains relatively unchanged due to CO2 mineralization, with the pH of CO2 mineralized concrete being similar to that of conventional concrete, measured at 13.2 for both mix CC and CMC-23.

Table 4 RCPT and bulk resistivity test result

Test	Mix Id	Age at test	
		28 Days	90 Days
RCPT (Coulombs)	CC	1974	1663
	CMC-23	1854	1472
Bulk resistivity (kΩ-cm)	CC	23.52	31.41
	CMC-23	24.93	33.34

3.4 Economy index and CO_2 emission reduction

Dixit et al. (2015) discussed the importance of analysing CO_2 emissions control to understand the environmental impact. It includes capturing the emitted CO_2, minimizing the CO_2 emission, and utilizing materials that emit less CO_2 Damineli et al. (2010). The environmental benefit of using CO_2 in concrete is due to its mineralization, which reduces CO_2 emissions, and further OPC is leveraged. The environmental benefit is mainly driven by the reduction of cement in concrete compositions. The carbon intensity of concrete performance can be assessed based on the adjusted CO_2 mixes, with the CMC-23 mix showing a reduction of OPC by 7.5% and, overall, approximately 8% reduction of carbon emission. The economy index is calculated by dividing raw material costs by 28 days of compressive strength Thomas et al. (2015). Table 5 presents the economy index of the mix CC and CMC-23. The economy index of CMC-23 is higher than CC, which means that the cost per unit strength of CMC-23 is lower than the mix CC.

Table 5. Economy index analysis

Particular		CC	CMC-23
Ingredients cost per kg/m3 (US $)	Cement	42.32	39.05
	Fly ash	0.5	0.53
	Coarse aggregate	5.92	5.92
	Fine aggregate	3.50	3.50
	Superplasticizer	2.45	2.45
	CO2	0	0.22
Total cost per kg/m3 (US $)		54.69	51.67
28 Days Compressive strength (MPa)		51.74	52.16
Economy index, strength/cost (MPa/US $)		1.01	1.01

4. Conclusions

The current study explores the behaviour of CO2-mineralized concrete. It was noted that an ideal level of CO2 mineralization enhances concrete performance. This process involves two stages: first, cementitious materials sequester CO2, and then the CO2-sequestered OPC is mixed with the rest of the ingredients to produce CO2-mineralized concrete. Experimentation reveals that the best strength is achieved with a 0.2% CO2 dose by weight of OPC. This strength improvement allows for designing concrete mixes with lower OPC content. From the research, the following conclusions emerge:

- This approach effectively utilizes CO2, reducing emissions from the construction sector and yielding cost-effective, eco-friendly building materials.
- Mix CMC-2 exhibits significantly higher compressive strength compared to mix CC; a 19.45%, 20.59% and 21.32% higher compressive strength was found at 7, 28, and 56 days of testing, respectively. There was a small rise in slump of CO2-mineralized concrete with lower OPC and more fly ash than the conventional concrete.
- The strength gain can facilitate the design of concrete mixes with reduced OPC content while maintaining target strength. Up to a 7.5% reduction in cement content can be achieved without compromising compressive strength, resulting in an approximate 8% reduction in carbon emissions.
- Concrete pH is unaffected by CO2 mineralization, and The CO2-mineralized mix with lower OPC has a similar durability property to regular concrete, as confirmed by the bulk resistivity test and RCPT.

Acknowledgements

The authors express their gratitude to the Director of the National Institute of Technology Silchar, Assam, India, for providing the necessary research facilities to conduct this study.

Declarations

Conflict of interest: The authors have no relevant financial or non-financial interests to disclose.

References

Xuan, D., Zhan, B., Sun, C. and Zheng, W. (2016) "Carbon dioxide sequestration of concrete slurry waste and its valorization in construction products", *Construction and Building. Materials,* 113: 664–672. http://dx.doi.org/10.1016/j.conbuildmat.2016.03.109

He, Z., Jia, Y., Wang,S., Mahoutian, M. and Shao, Y. (2019) "Maximizing CO_2 sequestration in cement-bonded fiberboards through carbonation curing", *Construction and Building. Materials,* 213: 51–60. https://doi.org/10.1016/j.conbuildmat.2019.04.042

Gupta, S., Kashani, A. Mahmood, A.H. and Han., T. (2021) "Carbon sequestration in cementitious composites using biochar and fly ash – Effect on mechanical and durability properties", *Construction and Building. Materials,* 291: 123363. https://doi.org/10.1016/j.conbuildmat.2021.123363

Monkman, S., Kenward, P.A., Dipple, G., MacDonald, M. and Raudsepp, M. (2021) "Activation of cement hydration with carbon dioxide", *Journal of Sustainable Cement-Based Materials,* 7(3): 160–181. https://doi.org/10.1080/21650373.2018.1443854

Kazmi, M.A. and Prasad, M.L.V. (2023) "Experimental study on the potential use of CO_2 as an admixture in concrete", *Innovative Infrastructure Solutions*, 8(3). https://doi.org/10.1007/s41062-023-01062-4

Gupta, S., Kua, H.W., Low, C.Y. (2018) "Use of biochar as carbon sequestering additive in cement mortar", *Cement and Concrete. Composit,.* 87: 110–129. https://doi.org/10.1016/j.cemconcomp.2017.12.0 09

Kurda, R., De Brito, J. and Silvestre, J.D. (2018) "Carbonation of concrete made with high amount of fly ash and recycled concrete aggregates for utilization of CO_2", *Journal of CO_2 Utilization,* 29: 12–19. https://doi.org/10.1016/j.jcou.2018.11.004

Chen, T., Bai, M. and X. Gao. (2021) Carbonation curing of cement mortars incorporating carbonated fly ash for performance improvement and CO2 sequestration. *Journal of CO_2 Utilization,* 51: 101633. https://doi.org/10.1016/j.jcou.2021.101633

Junior, A.N., Filho, R.D.T., Fairbairn, E.D.M.R. and Dweck, J. (2015) The effects of the early carbonation curing on the mechanical and porosity properties of high initial strength Portland cement pastes. *Construction and Building. Materials*, 77: 448–454. http://dx.doi.org/10.1016/j.conbuildmat.2014.12.072

Lei, M., Deng, S., K, Huang., Liu, Z., Wang, F. and Hu, S. (2022) "Preparation and Characterization of a CO_2 Activated Aerated Concrete with Magnesium Slag as Carbonatable Binder", *Construction and Building. Materials*, 353*:* 129112. https://doi.org/10.1016/j.conbuildmat.2022.129112

Kazmi, M.A., Prasad, M.L.V. and Babu, S.C.P. (2023) "Durability performance of self-compacting concrete produced using CO_2 as an admixture", *Materials Today: Proceedings*, (article in press), https://doi.org/10.1016/j.matpr.2023.04.453

Kou, S.C., Zhan, B.J. and Poon, C.S. (2014) "Use of a CO_2 curing step to improve the properties of concrete prepared with recycled aggregates", *Cement and Concrete Composites,* 45: 22–28. http://dx.doi.org/10.1016/j.cemconcomp.2013.09.008

Rosa, L., Becattini, V., Gabrielli, P., Andreotti, A. and Mazzotti, M. (2022) "Carbon dioxide mineralization in recycled concrete aggregates can contribute immediately to carbon-neutrality", *Resources, Conservation & Recycling,* 184: 106436. https://doi.org/10.1016/j.resconrec.2022.106436

Dixit, A., Du, H. and Pang, S.D. (2021) "Carbon capture in ultra-high performance concrete using pressurized CO_2 curing. *Construction and Building. Materials,* 288: 123076. https://doi.org/10.1016/j.conbuildmat.2021.123076

Sharma, D. and Goyal, S. (2018) "Accelerated carbonation curing of cement mortars containing cement kiln dust: An effective way of CO_2 sequestration and carbon footprint reduction", *Journal of Cleaner Production,* 192: 844–854. https://doi.org/10.1016/j.jclepro.2018.05.027

Monkman, S. and Shao, Y. (2006) "Assessing the Carbonation Behavior of Cementitious", Materials. *Journal of Materials in Civil Engineering,* 18: 768–776. DOI:10.1061/ASCE08991561200618:6768

Wang, D., Noguchi, T., Nozaki, T. and Higo, Y. (2021) "Investigation on the fast carbon dioxide sequestration speed of cement- based materials at 300 C–700 C", *Construction and Building. Materials.* 291: 123392. https://doi.org/10.1016/j.conbuildmat.2021.123392

Kazmi, M.A. and Prasad, M.L.V. (2024). "Carbonation behavior of concrete produced using CO_2 as an admixture", *Cement Wapno Beton*, 28(6): 364–374. https://doi.org/10.32047/CWB.2023.28.6.1

Mahoutian, M., Ghouleh, Z. and Shao, Y. (2014) Carbon dioxide activated ladle slag binder. *Construction and Building. Materials,* 66: 214–221. https://doi.org/10.1016/j.conbuildmat.2014.05.063

Monkman, S., MacDonald, M. (2017) "On carbon dioxide utilization as a means to improve the sustainability of ready-mixed concrete", *Journal of Cleaner Production*. 167: 365–375. http://dx.doi.org/10.1016/j.jclepro.2017.08.194

Monkman, S., MacDonald, M., Hooton, R.D. and Sandberg, P. (2016) "Properties and durability of concrete produced using CO_2 as an accelerating admixture", *Cement and Concrete Composites*, 74: 218–224. https://doi.org/10.1016/j.cemconcomp.2016.10.007

Prasad, M.L.V. and Kazmi, M.A. (2024). "Performance Enhancement of Concrete Produced with two-step CO_2 Mineralization", *Iranian Journal of Science and Technology, Transactions of Civil Engineering*, 42(2). https://doi.org/10.1007/s40996-024-01492-9

Qian, X., Wang, J., Fang, Y. and Wang, L. (2018) Carbon dioxide as an admixture for better performance of OPC-based concrete. *Journal of CO_2 Utilization, 25*: 31–38. https://doi.org/10.1016/j.jcou.2018.03.007

ASTM C150/C150M. (2016) "Standard Specification for Portland Cement", *ASTM International*, 100 Barr Harbor Drive, PO Box C700, West Conshohocken, PA 19428-2959. United States.

ASTM C33/C33M. (2018) "Standard Specification for Concrete Aggregates", *ASTM International*, 100 Barr Harbor Drive, PO Box C700, West Conshohocken, PA 19428-2959. United States.

ASTM C618. (2015) "Standard Specification for Coal Fly Ash and Raw or Calcined Natural Pozzolan for Use in Concrete", *ASTM International*, 100 Barr Harbor Drive, PO Box C700, West Conshohocken, PA 19428-2959. United States.

ACI 211.1-91. (2002) "Standard Practice for Selecting Proportions for Normal, Heavyweight, and Mass Concrete", *ACI*, World Headquarters 38800 Country Club Dr. Farmington Hills, MI48331-3439 USA.

IS 1199 (Part -2):2018. (2018) "Fresh concrete — methods of sampling, testing and analysis)-determination of consistency of fresh concrete", *Bureau of Indian Standards*, Manak Bhavan, 9 Bahadur Shah Zafar Marg, New Delhi-110002.

IS:516 Part-1/Sec-1:2021. (2021) "Hardened concrete - Methods of test, testing of strength of hardened concrete - Compressive, flexural and split tensile strength", *Bureau of Indian Standards*, Manak Bhavan, 9 Bahadur Shah Zafar Marg, New Delhi-110002.

Rostami, R., Zarrebini, M., Mandegari, M., Sanginabadi, K., Mostofinejad, D. and Abtahi, S.M. (2019) "The effect of concrete alkalinity on behavior of reinforcing polyester and polypropylene fibers with similar properties", *Cement and Concrete Composites*., 97: 118–124. https://doi.org/10.1016/j.cemconcomp.2018.12.012

ASTM- C1202. (2012) "Standard Test Method for Electrical Indication of Concrete's Ability to Resist Chloride Ion Penetration", *ASTM International*, 100 Barr Harbor Drive, PO Box C700, West Conshohocken, PA 19428-2959, United States.

ASTM C1876-23. (2023). "Standard Test Method for Bulk Electrical Resistivity or Bulk Conductivity of Concrete", *ASTM International,*100 Barr Harbor Drive, PO Box C700, West Conshohocken, PA 19428-2959, United States. . https://doi.org/10.1520/C1876-23

Luo, S., Guo, M.Z. and Ling, T.C. (2022) "Mechanical and microstructural performances of fly ash blended cement pastes with mixing CO_2 during fresh stage", *Construction and Building. Materials*, 358. https://doi.org/10.1016/j.conbuildmat.2022.129444

Surya, M., Rao, V.V.L.K. and Lakshmy, P. (2015) "Mechanical, durability, and time-dependent properties of recycled aggregate concrete with fly ash", *ACI Material Journal*, 112(5), 653- 661. https://doi.org/10.14359/51687853

Althoey, F., Ansari, W.S., Sufian, M. and Deifalla, A.F. (2023) "Advancements in low-carbon concrete as a construction material for the sustainable built environment", *Developments in the Built Environment*, 16. https://doi.org/10.1016/j.dibe.2023.100284

Thomas, B.S., Gupta, R.C., Mehra, P. and Kumar, S. (2015) "Performance of high strength rubberized concrete in aggressive environment", *Construction and Building. Materials*. 83, 320–326, doi: 10.1016/j.conbuildmat.2015.03.012.

Damineli, B.L., Kemeid, F.M., Aguiar, P.S. and Jonn, V.M. (2010) "Measuring the Eco-Efficiency of Cement Use", *Cement and Concrete Composites*, 32 (8) 555-562. doi: 10.1016/j. cemconcomp.2010.07.009

Application of Artificial Intelligence in Determining Degradation in Cement-Based Materials Due to Acid Attack

C.M. Ninan[1*], M. Anandhakrishnan[2], K.P. Ramaswamy[3], and R. Sajeeb[4]

[1] Research Scholar, Department of Civil Engineering, TKM College of Engineering, APJ Abdul Kalam Technological University, Kerala, India, 691005
Email: chinnuninan@gmail.com
[2] Postgraduate Student, Department of Civil Engineering, TKM College of Engineering, APJ Abdul Kalam Technological University, Kerala, India, 691005
Email: anandhan1618@gmail.com
[3] Professor, Department of Civil Engineering, TKM College of Engineering, APJ Abdul Kalam Technological University, Kerala, India, 691005
Email: ramaswamykp@tkmce.ac.in
[4] Professor, Department of Civil Engineering, TKM College of Engineering, APJ Abdul Kalam Technological University, Kerala, India, 691005
Email: sajeeb@tkmce.ac.in

[*]Corresponding author

ABSTRACT

The exposure of mortar/concrete to various organic acids are observed throughout the world. The rate of degradation depends on various factors such as type of cement, type of acid exposed to and its concentration, exposure period etc. These parameters are selected as the input for the proposed model to predict the degradation. The paper examines the feasibility of using artificial intelligence (AI) to predict the mass loss in mortar specimens exposed to various organic acids. The experimental results of 3 types of cementitious systems such as Ordinary Portland Cement (OPC) 53 grade, Portland Slag Cement (PSC) and High Alumina Cement (HAC) exposed to 3 different organic acids for a period of 56 days, are used for generating the model. The organic acids adopted for the study are acetic acid, citric acid, lactic acid, and propionic acid, having concentrations of 0.25 M, 0.5 M and 1 M for each type of acid. A database incorporating 36 exposure combinations resulting in approximately 600 datasets (from experiments) were developed for training and testing the models. Predictions are made using Artificial Neural Network (ANN) and compared with the predicted results of machine learning techniques such as Random Forest (RF), Extreme Gradient Boosting (XGB). The results show that all the three AI models predict the mass loss with good accuracy, of which ANN exhibits the best fit with an R^2 value of 0.976. The root-mean-squared error (RMSE) and mean absolute error (MAE) of ANN model used for the prediction of mass loss due to organic acid attack were 2.416 and 1.674, respectively.

KEYWORDS*: Artificial neural network, Random Forest, Extreme Gradient Boosting, Organic acid*

1. Introduction

Various researches have led to the development and commercialization of special cements which either improves the efficiency of Portland cement or used for special purposes like refractory construction, oil well construction and so on (Gagg, 2014). Concrete structures that come in contact with various corrosive conditions such as marine environments, and aggressive acidic environments are susceptible to degradation (Bankir and Sevim, 2020; Santhanam and Otieno, 2016; Qu et al., 2021). The rate of degradation depends on various factors such as type of cement, type of acid and its concentration, effect of abrasion, exposure period etc. (Bertron and Duchesne, 2007; Larreur-Cayol et al., 2011). These factors are selected as the input parameters of the proposed model to predict the degradation (Hewayde et al., 2007).
This paper examines the feasibility of using artificial intelligence to predict the mass loss in mortar specimens exposed to various organic acids. In this work, an experimental investigation was conducted

using three commercially available cements viz. Ordinary Portland Cement (OPC), Portland Slag Cement (PSC) and High Alumina Cement (HAC), exposed to four different organic acids having 0.25 M, 0.5 M and 1 M concentrations for each acid, for a period of 56 days. Acetic acid, citric acid, lactic acid, and propionic acid are the organic acids that are most prevalent in the food, manufacturing, and agricultural industries as well as in nature, hence chosen for the degradation analysis. A database incorporating 36 exposure combinations resulting in 608 datasets were used for the development of prediction models. Predictions are made using Artificial Neural Network (ANN), Random Forest (RF) and Extreme Gradient Boosting (XGB) techniques.

2. Experimentation Investigation

Mortar mix with 1:1.5 binder to standard sand proportion and a water/binder ratio of 0.45 was used for the degradation study. Cylindrical specimens of 50 mm height and 25 mm diameter were used for the study. After 24 hours of casting, the specimens were demoulded and cured in saturated lime water solution for 28 days. Before acid exposure, both end faces of the specimens were grinded and treated against acid degradation using sodium silicate solution. For degradation analysis, only curved surface of the specimen was considered to ensure degradation in radial direction. The volume of acid solution used was taken proportional to the number of specimens exposed at that instant. The volume of acid solution to the surface area of the mortar specimen was always maintained at a ratio of 31.25 and the acid solution was renewed in every 7 days interval to accelerate the degradation. The mass of the specimen was recorded immediately after ensuring SSD condition, periodically at an interval of 7 days. The results were represented as losses in percentages.

3. Development of Database and Predictive Models

The input parameters were chosen after careful analysis of previous literatures as well as their impact on the results obtained from the experimental investigation by carrying out correlation study, T test, Feature selection etc. For the present study, about 13 input parameters were chosen and converged to a reduced number of input parameters, corresponding to one output parameter which is the mass loss. The input parameters were binder type, Ca/Si ratio of the binder, Al/Si ratio of the binder, acid chosen for the study, acid concentration, acid dissociation constants (pK_a), poly-acidity, average solubility of the salt formed, average molar volume of the salt formed, volume of the specimen at each time of testing, exposure to abrasion and exposure duration are the input parameters.

Three prediction models are used for the study. The predicted results of mass loss from ANN are compared with that obtained from RF and XGB models for the study. The training to testing ratio of the prediction models were fixed as 80:20. Out of 608 datasets, 486 datasets were used for training the model and 122 datasets were randomly chosen for testing the model. The predicted results of the model were then compared with the actual results obtained from experimental analysis to evaluate the reliability and accuracy of the prediction model. Higher the error value, lower is the accuracy of the model selected.

4. Results

Artificial Neural Networks (ANNs) are computational tools that are functionally similar to the working of human cerebral and neural coordination system (Hewayde, 2007; Haykin, 1999). These tools can develop models that can be adopted for prediction, classification, clustering and so on. The different hyperparameters were obtained after the convergence study from several iterations which includes, number of hidden layers fixed as 4 and the relu activation function is adopted for the model. Also, the epoch size is selected as 100 and the optimizer used is adam as it is an adaptive learning optimization algorithm that is well suited for deep learning tasks. The results predicted by the ANN model is compared with the actual results obtained from the experimental study and the relation is plotted in Figure 1a. The linear trendline with an R-square value of 0.978 shows the accuracy of the fitting, thereby highlights the accuracy of the model in general. The narrow width of the 10 % error cone surrounding the trendline suggests greater accuracy of the prediction model. The Root mean square error (RMSE) of the ANN predicted model is 2.36 and the Mean Absolute Error (MAE) of the model is 1.60, which are comparatively lower error values,

representing higher reliability of the prediction model. Higher R-square value and lower error values represent a model of good accuracy and reliability.

Random Forest (RF) is a machine learning technique that uses the concept of a forest consisting of multiple decision trees and are properly organized at the training time to provide accurate predicted results. Various RF models were developed by modifying the hyperparameters and the best model is chosen for the study. The RF predicted values compared with actual mass loss values are illustrated in Figure 1b. The best hyperparameters are bootstrap selected as true, maximum depth of forest as 10, minimum number of samples required to be at a leaf node is 1, minimum number of samples required to split an internal node is 2, number of trees in the forest as 100. With an R-square value of 0.931, the trendline is linear and suggests an acceptable degree of fitting. The error values, RMSE and MAE, are 4.15 and 3.05, respectively. These error numbers are relatively smaller, indicating that the prediction model is accurate and reliable.

Extreme Gradient Boosting (XGB) Regressor combines the predictions of multiple weak learners, usually decision trees, to create a powerful predictive model. It utilizes a boosting strategy, where each weak learner corrects the errors of its predecessors, to produce an incredibly precise model. Different XGB Models were developed by varying the hyperparameters and the best parameters are found. Learning rate representing the step size for each iteration to prevent over-fitting as 0.2, maximum depth of the tree as 4, minimum number of instances needed to be in each node as 5, number of trees as 200, subsample representing ratio of training instances as 0.7. Figure 1c compares the XGB predicted results with the actual results obtained from the experiments. The trend line for XGB model has a R-square of 0.949 exhibiting good fitting and the RMSE and MAE values are 3.54 and 2.67 respectively that shows high degree of accuracy of the model. Similar to ANN, the 10 % error cone of XGB model also has a narrow width representing higher reliability and accuracy of the model.

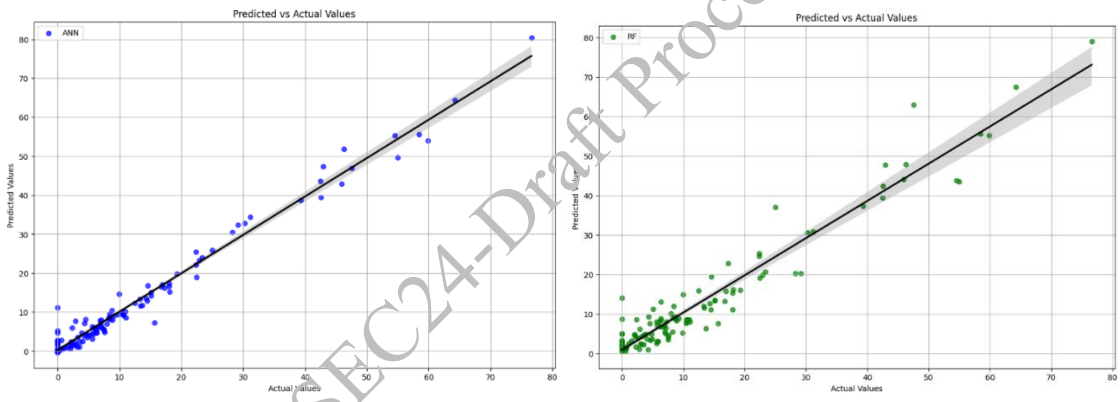

(a) ANN Prediction Model

(b) RF Prediction Model

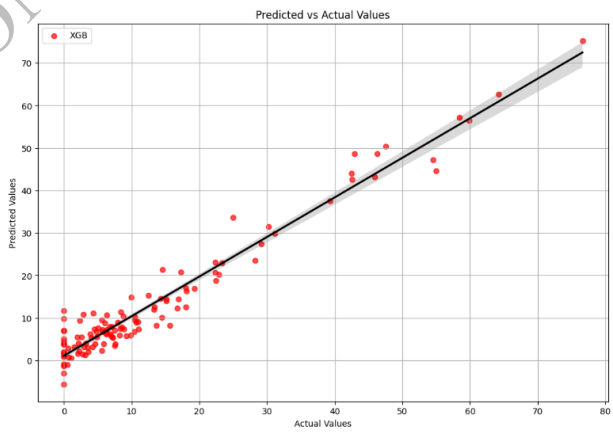

(c) XGB Prediction Model

Figure 1. Predicted Results Vs. Actual Mass Loss for Different Prediction Models

5. Discussions

When ANN, RF, and XGB prediction models are compared, it is evident that all the three models have good prediction accuracy. However, minor variations in the R-square value and error gradients are noted which is summarized in Table 1. Table 1 indicates that the ANN model predicts the results with the best accuracy, followed by the XGB model, then the RF model in order of precedence. The same inference is obtained when all the selected performance evaluators are analysed.
Comparing the 10 % error cone of ANN, RF and XGB prediction models, ANN has the narrowest width of cone, and XGB has slightly higher width of error cone than ANN model. The highest width is observed for RF prediction model. This observation also aligns with the results obtained from analysing all the performance evaluators.

Table 1. Performance evaluators for different prediction models

Prediction Model	R^2	RMSE	MAE
ANN	0.978	2.36	1.60
RF	0.931	4.15	3.05
XGB	0.949	3.54	2.67

From the analysis it can be inferred that artificial intelligence can be adopted as a successful tool for the prediction of degradation in various cementitious materials subjected to organic acids, whether in the form of deep learning tools or machine learning techniques. The same approach used for the prediction of mass loss with artificial intelligence can be adopted for other parameters like depth of degradation, strength loss etc., by adjusting the hyperparameters and generation of a dedicated correlation matrix for the same. In this study, mass loss prediction is adopted mainly because it is the most prevalent test parameter for the degradation analysis. On the other hand, using depth of degradation as the predicted parameter has greater practical implications because it may be directly related to the appropriate cover depth that should be provided to prevent reinforcement corrosion.

6. Conclusions

This paper developed different prediction models for predicting mass loss in different binder systems exposed to various organic acids at different concentrations with artificial intelligence. The performance evaluation of various cementitious materials is predicted using artificial neural network (ANN) model, random forest (RF) model and extreme gradient boosting (XGB) model. It has been observed that predictions based on ANN model exhibited highest accuracy with a R^2 of 0.978 and RMSE of 2.36. Followed by XGB model having a RMSE of 3.54 and MAE of 2.67, which is followed by RF model of RMSE value 4.15. All probability based artificial intelligence (AI) techniques exhibits high degree of accuracy for the prediction. The models developed are reliable and can be adopted for prediction of degradation under realistic field conditions.

References

Bankir, M.B. and Sevim, U.K. (2020) “Performance optimization of hybrid fiber concretes against acid and sulfate attack”, *Journal of Building Engineering* 32: 101443 https://doi.org/10.1016/j.jobe.2020.101443

Bertron, A. and Duchesne, J. (2007) “Attack of cementitious materials by organic acids in agricultural and agrofood effluents - a review”, in: N.D. Belie (Ed.) Performance of Cement Based Materials in Aggressive Aqueous Environments - Characterization, Modelling, Test Methods and Engineering Aspects, pp. 57-63, RILEM Publications, SARL, Ghent

BIS 1991, IS 650 – 1991: Standard sand for testing cement: Specification, Bureau of Indian Standards, New Delhi, India

Gagg, C.R. (2014) “Cement and concrete as an engineering material: An historic appraisal and case study analysis”, *Engineering Failure Analysis* 40: 114-140 https://doi.org/10.1016/j.engfailanal.2014.02.004

Haykin, S. (1999) “Neural Networks: A Comparative Foundation”, 2nd edn, Prentice-Hall: Upper Saddle River, NJ.

Hewayde, E., Nehdi, M., Allouche, E. and Nakhla, G. (2007) “Neural network prediction of concrete degradation by sulphuric acid attack”, *Structure and Infrastructure Engineering*, 3(1): 17-27. https://doi.org/10.1080/15732470500253065

Larreur-Cayol, S., Bertron, A., and Escadeillas, G. (2011) "Degradation of cement-based materials by various organic acids in agro-industrial waste-waters", *Cement and Concrete Research*, 41: 882-892 https://doi.org/10.1016/j.cemconres.2011.04.007

Santhanam, M. and Otieno, M. (2016) in: M G Alexander (Ed.), "Marine Concrete Structures, Design, Durability and Performance", *Woodhead Publishing*, pp. 137-149. https://doi.org/10.1016/B978-0-08-100081-6.00005-2

Qu, F., Li, W., Dong, W., Tam, V.W.Y. and Yu, T. (2021) "Durability deterioration of concrete under marine environment from material to structure: A critical review", *Journal of Building Engineering*, 35: 102074. https://doi.org/10.1016/j.jobe.2020.102074

Evaluating Manufactured Sand as a Sustainable Alternative to River Sand in Concrete: A Comparative Study of Strength, Durability, and Corrosion Resistance

Smrithy Subash[1*], and Sumedha Moharana[2]

[1] *Shiv Nadar Institution of Eminence, Delhi NCR, India*
Email: ss831@snu.edu.in
[2] *Shiv Nadar Institution of Eminence, Delhi NCR, India*
Email: sumedha.maharana@snu.edu.in

[*]Corresponding author

ABSTRACT

The practice of using sand as a binder in construction dates to ancient civilizations such as the medieval and pre-medieval ages. However, the surge in urbanization led to the overexploitation of natural riverbeds, altering river morphology and large-scale river features. Consequently, many governments have banned the quarrying of natural river sand (R-sand) due to these environmental impacts. In response to a growing emphasis on sustainability and the environmental concerns associated with construction materials, there has been a shift towards exploring manufactured sand (M-sand) as an alternative to river sand (R-sand) for use as a fine aggregate in concrete. This study primarily focuses on assessing the suitability of M-sand as a fine aggregate, compared to R-sand, in terms of strength, durability, and corrosion resistance of rebars in concrete. M-sand based concrete has been found to be stronger by mechanical testing, and durability test i.e., Rapid Chloride Penetration Tests, have revealed that it is more resistant to the penetration of chloride ions. This study also involves electrochemical assessments using Electrochemical Impedance Spectroscopy (EIS) and Tafel polarization to compare the performance of R-sand and M-sand in concrete, further underscoring the viability of M-sand as a complete replacement for natural river sand. An elemental decomposition has been made for both M-sand and R-sand through X-ray Fluorescence Spectroscopy (XRF) for better understanding. Consequently, the test outcomes outlined above highlight diverse parameters that demonstrated the suitability of M-sand as a viable construction material for use as fine aggregate in concrete.

KEYWORDS*: Fine aggregate, M-sand, Corrosion, X-ray Fluorescence Spectroscopy, Electrochemical Impedance Spectroscopy*

1. Introduction

Concrete is the second most widely used material globally, following water. The aggregates (both coarse and fine) make up 60-75% of the total concrete volume and have a significant impact on its fresh and hardened properties, mix proportions, and economic considerations. Sand plays a crucial role as a potential fine aggregate in construction projects, being consuming 32-50 billion tonnes annually for concrete infrastructure to meet its growing demand worldwide. (Mathur et al. 2023). It also has applications in asphalt production, water filtration, and manufacturing processes, among others(Mane et al. 2022). With the increasing demand for sand due to expansion in construction activities and major infrastructure projects, illegal sand mining has risen sharply. There is now an urgent need to find alternatives to river sand for construction purposes as this over-extraction of R-sand threatens its supply (Li et al. 2022; Xu et al. 2022). Engineers and researchers have proposed various concepts aimed at reducing reliance on river sand by using alternative materials such as stone crusher dust, foundry sand, manufactured sand and other waste products(Shen et al. 2022).

The traditional use of natural R-sand as a fine aggregate has faced difficulties due to its diminishing availability and increasing costs (Barcelo et al. 2014). As a response, manufactured sand has emerged as

an attractive alternative. Known for its finer particles that effectively fill small concrete pores, M-sand not only improves concrete strength but also offers the advantages of cost savings, reduced environmental impact, and easy accessibility (Gaur et al. 2020; Kumar Poloju 2017). The utilization of M-sand has seen significant growth, being utilized in road projects, construction works, and even in the manufacturing of bricks and tiles (Karthik et al. 2017; Shen et al. 2016). Previous studies highlight that the integration of M-sand into concrete production has encountered challenges related to the mechanical properties and durability, but very limited focus on the corrosion resistance of rebars in concrete exposed to marine environments. This aspect is also investigated in the present study. The primary objective of this study is to investigate the differences in mechanical (compressive strength), durability (Rapid Chloride Penetration Test), and electrochemical characteristics (Electrochemical Impedance Spectroscopy and Potentiodynamic Polarization) of concrete when R-sand is fully substituted with M-sand.

2. Materials

The materials used in the preparation of concrete samples of M30 mix include Cement of OPC 53 grade, R-sand conforms to Zone III or M-sand as fine aggregate, coarse aggregate and water. The physical properties of materials used in the study are given in Table 1, and they comply with Indian standards. The control samples consist of those prepared with R-sand as fine aggregate (Sample 1), and the modified sample is prepared with M-sand as fine aggregate (Sample 2), and all other constituents remain the same. Figure 1 shows the R-sand and M-sand samples utilised in this study.

Table 3. Physical Properties of Raw Materials

Property	Cement	Fine aggregate		Coarse Aggregate
		R-sand	M-sand	
Specific Gravity	3.15	2.35	2.58	2.61
Apparent Specific Gravity	-	2.49	2.74	2.76
Water Absorption (%)	-	2.46	2.24	2.04
Fineness Modulus	-	2.466	2.007	8.157
Standard Consistency	30%	-	-	-
Initial Setting Time	60 minutes	-	-	-
Final Setting Time	540 minutes	-	-	-

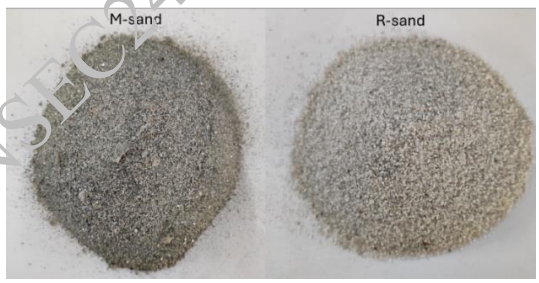

Figure 1. M-sand and R-sand samples

The chemical composition of the raw materials used in the study was determined by X-ray Fluorescence Spectroscopy (XRF) Analysis. Table 2 presents the chemical composition of Cement, R-sand and M-sand. The cement composition is primarily composed of CaO, SiO_2, Al_2O_3, and Fe_2O_3. CaO (66.7%) is the major component, indicating high lime content typical for Portland cement. A significant amount of SiO_2 (22.3%) is important for the strength of the cement. Al_2O_3 (4%) contributes to the setting time and strength. Fe_2O_3 (3.14%) helps in the formation of clinker phases and contributes to the colour of the cement. SO_3 (2.62%) influences the setting time and strength development. M-sand is high in SiO_2 and Al_2O_3, indicating good mechanical properties for use as an aggregate. The presence of Fe_2O_3, CaO, and other minor oxides also contribute to its properties. R-sand is predominantly composed of SiO_2, suggesting it is almost pure silica. It has the least amount of other oxides, which makes it a very pure form of sand suitable for various specific applications. All these compositions contribute to the respective properties of the concrete.

Table 2. Chemical Composition of Raw Materials

No.	CEMENT		M SAND		R SAND	
1	CaO	66.7	CaO	2.36	CaO	0.222
2	SiO_2	22.3	SiO_2	80.4	SiO_2	98.3
3	Al_2O_3	4	Al_2O_3	9.92	Al_2O_3	1.33
4	Fe_2O_3	3.14	Fe_2O_3	2.87	SO_3	0.0976
5	SO_3	2.62	K_2O	2.17	TiO_2	0.0521
6	TiO_2	0.445	MgO	0.921	Fe_2O_3	0.028
7	K_2O	0.365	TiO_2	0.687	ZnO	0.0034
8	BaO	0.246	P_2O_5	0.328	ZrO_2	0.0032
9	MnO	0.0918	SO_3	0.159	CuO	0.0024
10	SrO	0.0337	Cl	0.0724	NiO	0.0018
11	V_2O_5	0.0251	MnO	0.0529	Cr_2O_3	0.0013
12	ZnO	0.0147	ZrO_2	0.0318	MnO	0.0009
13	ZrO_2	0.0145	BaO	0.0167	Y_2O_3, SrO	0.0007
14	NiO	0.0116	ZnO	0.009	PbO	0.0004
15	CuO	0.0096	SrO	0.007	As_2O_3, Na_2O	<0.0001
16	Cr_2O_3	0.0088	As_2O_3	0.0015	V_2O_5, Co_2O_3	<0.0001

3. Experimental Methods

The lab sized concrete cylindrical and cubical samples were cast with two different fine aggregates i.e. M-sand and R-sand. After 28 days of water curing, the concrete samples were subjected to mechanical, durability and corrosion studies. The corrosion samples were immersed in 3.5% NaCl solution, and the electrochemical tests were carried out at intervals of 14 days up to 70 days. The experimental procedure followed as per codal provisions were discussed in forthcoming sections.

3.1 Compressive Strength Test

Concrete cubic samples (3 nos) of 150x150x150 mm were subjected to compressive loadings after 28 days of water curing as per IS code(IS 516 1959).

3.2 Rapid Chloride Penetration Test (RCPT)

The RCPT indicates the resistance of concrete specimens against the ingression of chloride ions, was conducted as per codal requirement (ASTM C1202 2012). Concrete cylinders of 100mm diameter and 50 mm thickness are placed between two chambers, one filled with 3% NaCl solution and other one filled with 0.3 M NaOH solution. The setup acts as a single cell and is connected to a DC source supplied with 60V voltage for 6 hours. The current passing through the cell is measured for a period of 1 hour. Figure 2 represents the RCPT test setup used in the study.

3.3 Electrochemical Corrosion Tests

The concrete cylindrical samples of 80mm height and 50 mm diameter, embedded with 40mm rebar were cast. A connecting wire is welded onto the surface of the rebar to act as the working electrode in the three-electrode setup. The triplicate concrete samples were initially subjected to Open circuit potential followed by Electrochemical Impedance Spectroscopy and, finally, Tafel polarization. The impedance spectroscopy using electrochemical techniques (EIS) was conducted between a range of 100kHz to 100mHz frequency at an amplitude of ±5 mV AC peak-to-peak. polarization of ±200 mV from OCP (OCP to -200 mV to OCP +200 mV) was applied to steel rebar with a scan rate of 1 mV/s, and the logarithmic response of the current was recorded. The appropriate equivalent circuit is chosen for fitting the impedance data to obtain the necessary parameters to analyse the spectra, including the charge transfer resistance (R_{ct}). The corrosion current (Icorr) values were measured from the above mentioned tests respectively. for electrochemical measurement, the samples were exposed to a marine environment, and results were obtained at an interval of every 14 days.

4. Results

The study aimed to obtain the effect of the addition of M-sand instead of R-sand as a fine aggregate in the concrete. The SAM1 with R-sand acted as control specimens, and the results of M-sand incorporated specimens (SAM2) were compared with the control in terms of strength, durability, and corrosion resistance.

4.1 Compressive Strength Test

It was found that the M-sand incorporated samples performed better in terms of compressive strength and the results were presented in Table 3. The higher strength obtained on M-sand incorporated specimens is attributed to the presence of more SiO_2 and Al_2O_3 along with Fe_2O_3 and CaO which resulted in better mechanical strength compared to Control specimens.

Table 3. Result of Compressive Strength Tests

	SAM 1	SAM 2
Compressive Strength (MPa)	29.73	39.4
	31.3	40.5
	29.6	35.18
Average Strength (MPa)	30.21	38.36

4.2 Rapid Chloride Penetration Test

It was found that the M-sand incorporated samples performed better against chloride ion permeability, and the results are presented in Table 4. As M-sand is produced by the crushing of hard rock particles resulting in angular and rough textured particles. This resulting angular and rough texture improves the bonding between sand particles and binder cement paste leading to a denser concrete mix. M-sand has angular shape and controlled particle size distribution lead to better packing density in the concrete mix, reducing the volume of voids compared to R-sand. Whereas R-sand typically has smoother and more rounded particles due to natural weathering and erosion processes. This can result in a less effective bond with the cement paste, potentially leading to more voids and pathways for chloride ion migration. Also, from the physical property, it is found that the M-sand has lesser water absorption and hence reduced potential for increased porosity.

Table 4. Chloride ion Permeability of Rsand and Msand incorporated Concrete

Type of Sample	Charge Passed (Coulombs)	Average Charge Passed (Coulombs)	Chloride ion Permeability
SAM 1	3981	4021	High
	4213		
	3869		
SAM 2	1189	1088	Low
	986		
	1089		

4.3 Electrochemical Corrosion Testing

4.3.1 Electrochemical Impedance Spectroscopy (EIS):

Figure 2a represents the experimental setup for electrochemical corrosion studies. The WE represent the working electrode, and it is the concrete sample; RE represents the Ag/AgCl reference electrode and SS304 mesh is used as the counter electrode (CE). Figure 2b represents the equivalent circuit used to fit the Nyquist plot obtained from the EIS study. The R_0 represents the solution resistance, R_1 represents the resistance of the concrete, R_2 represents the resistance of interfacial film between concrete and rebar, and R_3 represents the charge transfer resistance of the working electrode sample. CPE_0 is the constant phase element of bulk

concrete, CPE_1 is the constant phase element of the interfacial layer between concrete and steel rebar, and CPE_2 is the constant phase element of the double-layer electrode interface. The upward rise of the curve at approximately 45^0, as is an indication of the semi-infinite diffusion of species such as oxygen, iron, hydroxyl, and chloride ions through the oxide layer and towards the working electrode, coupled with charge transfer reactions(Sohail et al. 2020).The fitted values are provided in Table 5, and the Nyquist plot is presented in Figure 3.

It is found that the solution resistance decreases with cycles of exposure in both cases. The solution used in the study is 3.5% NaCl solution which replicates the marine environment in which the samples are exposed. The R_3 is the charge transfer resistance values. The charge transfer resistance values was found to be higher for R-sand incorporated samples than M-sand incorporated concrete which is an indication that minor corrosion current passes through rebars inserted in R-sand incorporated concrete. The R-sand might have a lower intrinsic electrical conductivity compared to M-Sand. This means that when R-Sand is used in concrete, it could lead to fewer conductive pathways for ionic movement, thus exhibiting higher resistance in EIS tests. The chemical composition of river sand includes beneficial minerals that improve the overall electrochemical stability of the concrete mix. These minerals might passivate the rebar surface or reduce the rate of ionic movement within the concrete. The smoother, more rounded particles of river sand might lead to a different pore structure in the concrete, potentially resulting in fewer connected pores. This reduced connectivity can limit ion transport and result in better EIS performance. In contrast, the angular particles of manufactured sand can create more micro-cracks or weak points at the interface with the cement paste, increasing the ionic mobility and decreasing impedance(Fookes 1980). The higher MgO and K_2O concentration in utilised Msand along with silicates might have caused expansion which can also be a potential reason for reduced corrosion resistance of Msand incorporated concrete(Hasdemir et al. 2012, 2016)(Hasdemir et al. 2012).

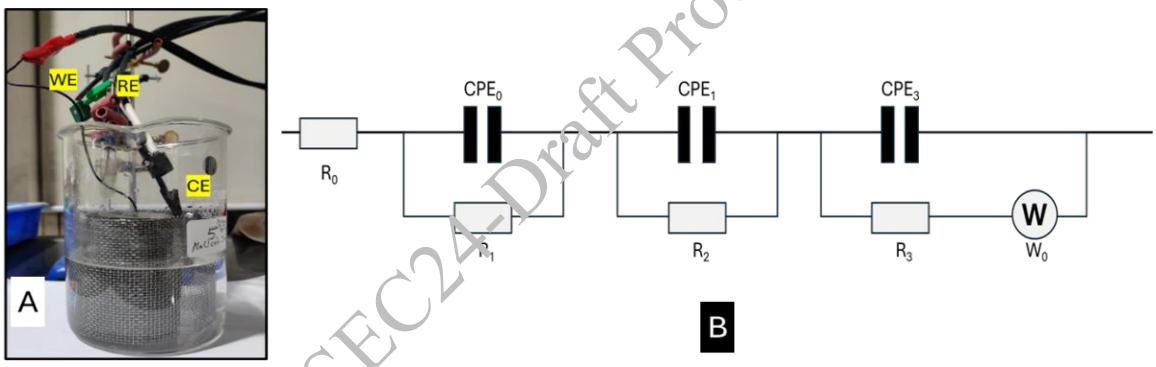

Figure 2. a) Experimental Setup for electrochemical Studies b) Equivalent Circuit Diagram for fitting

4.3.2 Tafel Polarisation Test:

The results of the Tafel fit are presented in Table 6, and the Tafel plot is presented in Figure 4**.** The corrosion current (I_{corr}) values are higher for M-sand incorporated samples, and it is an indication of lesser corrosion resistance and is directly proportional to increased corrosion rate with time of exposure. From the zeroth day, the SAM1 showed better corrosion resistance, and these results go well with the EIS results obtained previously. At the end of 70 days of exposure, even though the M-sand has better resistance to chloride ions penetration as in RCPT, the mineral composition of R-sand reduces the direct attack of chloride ions on the rebar surface and hence higher corrosion resistance. Apart from the pore structure the higher

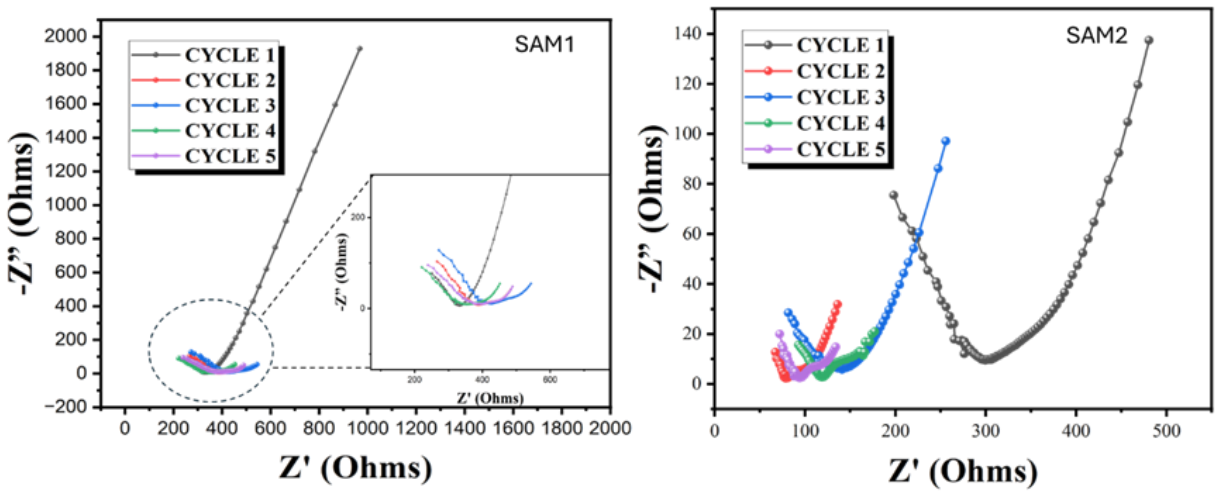

Figure 3. Nyquist Plot of Sample1 and Sample2

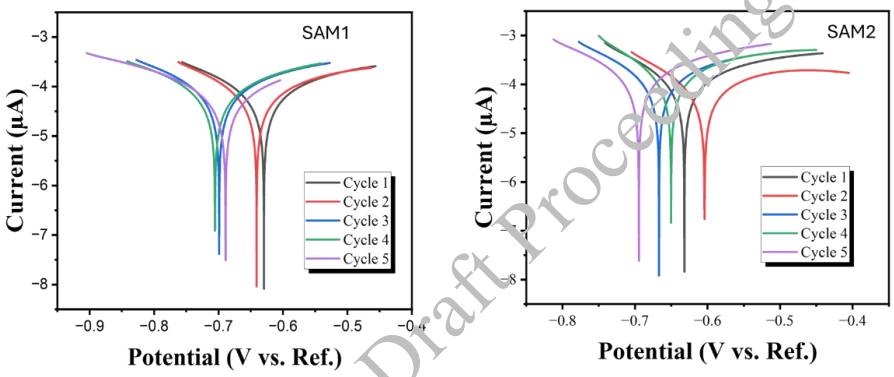

Figure 4. Tafel Polarization of Sample1 and Sample2

Table 5. EIS parameters after fitting

SAMPLE	Cycle	R_0 Ω	CPE_0 $\Omega^{-1}s^{\alpha}$		R_1 Ω	CPE_1 $\mu\Omega^{-1}s^{\alpha}$		R_2 Ω	CPE_2 $m\Omega^{-1}s^{\alpha}$		R_3 Ω	W_0 $\Omega cm^2 s^{-1/2}$
			Y_0	α		Y_0	α		Y_0	α		
SAM1	1	52.9	0.00287	0.833	68.2 x10^3	0.0285	0.71	266	5.6	0.28	204	0.22
	2	27.1	0.157	0.418	132	0.00985	0.776	303	3.27	0.162	167	15.8
	3	6.76	0.00442	0.543	57.5	0.00251	0.862	321	0.186	0.309	115	32.1
	4	21.3	0.0114	0.592	30.6	0.0121	0.776	253	0.394	0.292	99.4	13.4
	5	19	0.0111	0.528	44.3	0.0131	0.764	271	0.226	0.304	116	9.23
SAM2	1	12.4	6.53	0.983	40.8	53.1	0.679	258	2.21	0.290	108	54.6
	2	7.47	1.52	0.126	8.55	170	0.640	97.8	5.80	0.424	67.3	11.4
	3	9.39	0.0155	0.474	22.8	16.9	0.822	69.8	0.291	0.315	67.4	19.4
	4	18.0	0.0154	0.659	16.8	0.0012	0.514	94.0	19.9	0.197	51.4	22.7
	5	8.12	0.0138	0.696	10.8	104	0.692	71.5	12.7	0.150	46.2	17.7

Table 6. Tafel Polarization Parameters

Sample	Days of exposure	Cycle	Cathodic Slope (mV/decade)	Anodic Slope (mV/decade)	Corrosion Current (uA)	Corrosion Potential (mV)	Polarization Resistance (Ω)	Corrosion Rate (mm/year)
SAM 1	0	1	-94.6	110	29.7	-632	743	0.203
	14	2	-110	117	32.7	-637	752	0.223
	28	3	-116	161	45.1	-704	650	0.309
	42	4	-153	242	59.7	-718	683	0.408
	56	5	-181	313	62	-707	805	0.424
SAM 2	0	1	-101	141	34.9	-575	731	0.239
	14	2	-98.4	184	54.7	-609	509	0.374
	28	3	-106	149	79.5	-668	338	0.543
	42	4	-114	139	91.7	-694	296	0.627
	56	5	-91.7	169	98.1	-655	263	0.671

5. Conclusions

The concrete samples with M-sand perform better in terms of compressive strength. The higher strength of M-sand incorporated samples is attributed to the mineral composition and the angular nature of the M-sand particles when compared to the R-sand particles. The chloride ion permeability during RCPT tests also showed better performance of M-sand incorporated particles. This is also due to the improved bonding with the cement paste and packing density as obtained due to the angular nature of the particles. However, when exposed to a chloride environment, the R-sand incorporated concrete samples showed higher corrosion resistance. This might be due to the round shape of R-sand particles resulting in disconnected pore structure thus reducing the mobility of chloride ions in the concrete samples.

References

ASTM C1202. 2012. “Standard Test Method for Electrical Indication of Concrete’s Ability to Resist Chloride Ion Penetration.” *American Society of Testing Materials.*, (C): 1–8. https://doi.org/10.1520/C1202-12.2.

Barcelo, L., J. Kline, G. Walenta, and E. Gartner. 2014. “Cement and carbon emissions.” *Materials and Structures.*, 47 (6): 1055–1065. https://doi.org/10.1617/s11527-013-0114-5.

Fookes, P. G. 1980. “An introduction to the influence of natural aggregates on the performance and durability of concrete.” *Quarterly Journal of Engineering Geology*, 13 (4): 207–229. https://doi.org/10.1144/GSL.QJEG.1980.013.04.02.

Gaur, A., N. Mathur, and P. Somani. 2020. “Experimental investigation of bottom ash as a capable Soil Stabilizer.” *IOP Conference Series Materials Science and Engineering.*, 872 (1): 012138. https://doi.org/10.1088/1757-899X/872/1/012138.

Hasdemir, S., A. Tuğrul, and M. Yilmaz. 2012. “Evaluation of alkali reactivity of natural sands.” *Constr. Build. Mater.*, 29: 378–385. https://doi.org/10.1016/j.conbuildmat.2011.10.029.

Hasdemir, S., A. Tuğrul, and M. Yılmaz. 2016. “The effect of natural sand composition on concrete strength.” *Construction and Building Materials*, 112: 940–948. https://doi.org/10.1016/j.conbuildmat.2016.02.188.

IS 516. 1959. “Method of Tests for Strength of Concrete.” *Bureau of Indian Standards.*, 1–30.

Karthik, S., P. R. M. Rao, and P. O. Awoyera. 2017. “Strength properties of bamboo and steel reinforced concrete containing manufactured sand and mineral admixtures.” *Journal of King Saudi University - Engineering. Sciences.*, 29 (4): 400–406. https://doi.org/10.1016/j.jksues.2016.12.003.

Kumar Poloju, K. 2017. “Properties of Concrete as Influenced by Shape and Texture of Fine Aggregate.” *American Journal of Applied Sciences and Research*, 3 (3): 28. https://doi.org/10.11648/j.ajasr.20170303.12.

Li, Y., Y. Liu, C. Jin, J. Mu, H. Li, and J. Liu. 2022. “Multi-scale creep analysis of river sand and manufactured sand concrete considering the influence of ITZ.” *Construction Building Materials.*, 344: 128175. https://doi.org/10.1016/j.conbuildmat.2022.128175.

Mane, K. M., A. M. Joshi, D. K. Kulkarni, and K. B. Prakash. 2022. "Influence of retempering on properties of concrete made with manufactured sand and industrial waste." *Clean. Mater.*, 4: 100060. https://doi.org/10.1016/j.clema.2022.100060.

Mathur, Ashish, R. C. Chhipa, and M. M. 2023. "Inspection of the mechanical and durability behavior of concrete developed using M-sand." *Int. J. Adv. Technol. Eng. Explor.*, 10 (108). https://doi.org/10.19101/IJATEE.2023.10101036.

Shen, W., J. Wu, X. Du, Z. Li, D. Wu, J. Sun, Z. Wang, X. Huo, and D. Zhao. 2022. "Cleaner production of high-quality manufactured sand and ecological utilization of recycled stone powder in concrete." *Journal of Cleaner Production*, 375: 134146. https://doi.org/10.1016/j.jclepro.2022.134146.

Shen, W., Z. Yang, L. Cao, L. Cao, Y. Liu, H. Yang, Z. Lu, and J. Bai. 2016. "Characterization of manufactured sand: Particle shape, surface texture and behavior in concrete." *Construction Building Material*, 114: 595–601. https://doi.org/10.1016/j.conbuildmat.2016.03.201.

Sohail, M. G., R. Kahraman, N. A. Alnuaimi, B. Gencturk, W. Alnahhal, M. Dawood, and A. Belarbi. 2020. "Electrochemical behavior of mild and corrosion resistant concrete reinforcing steels." *Construction Building Material*, 232: 117205. https://doi.org/10.1016/j.conbuildmat.2019.117205.

Xu, Y., H. Chen, and Y. Tang. 2022. "Study on fracture parameters and fracture process zone of manufactured-sand recycled aggregate concrete." *Construction Building Materials*, 361: 129613. https://doi.org/10.1016/j.conbuildmat.2022.129613.

Numerical Modeling of Double Skin Composite Columns

R.Hindhumadhi[1*] and P.Revathi[2]

[1] Research scholar, Puducherry Technological University, Puducherry, India
Email: hindhumadhi.ravivarma@ptuniv.edu.in
[2] Associate Professor, Puducherry Technological University, Puducherry, India
Email: revathi@ptuniv.edu.in

*Corresponding author

ABSTRACT

Over the past few decades, steel-concrete composite construction has gained widespread attention due to its enhanced structural properties when compared to conventional construction. Among the composite structural elements, application of concrete filled double skin tubular (CFDST) compression members are gaining popularity due to its seismic resistance characteristics. This paper presents a nonlinear finite element analysis of CFDST stub columns with various combinations of square hollow section (SHS) and circular hollow section (CHS) as outer and inner tubes, subjected to axial compressive loading. Material models for steel and concrete, boundary conditions, element type and, steel and concrete interaction related to Finite Element Method (FEM) modelling are presented in this paper. The FEM model was validated against a set of experimental test results published by various researchers. It was observed that the proposed FEM model worked effectively, giving accurate estimates of the ultimate strength of CFDST columns that agreed well with findings from experiments.

KEYWORDS: *Composite construction, Double skin, Stub column, Hollow section, Finite element method*

1. Introduction

Concrete-filled steel tubular (CFST) columns are a special kind of composite column made of a steel tube that has concrete inside it. CFST columns have large strength, good deformability characteristics and are quicker to be constructed since the steel tube used in it acts as a formwork by itself. The steel tube in CFST confines the concrete, delaying the local buckling of the steel tube and giving the concrete an increase in strength. Concrete filled double skin steel tubular (CFDST) members can be recognized as an improved version of traditional CFST members with a few key differences. They are created by filling concrete between two concentric steel tubes. In addition to significantly reducing the structural weight of a CFST column, the inner hollow steel tube greatly improves the column's ductility, bending stiffness, and seismic performance. Furthermore, CFDST columns' inner hollow steel tubes may be used for building services. Four configurations of square hollow section (SHS) and circular hollow section (CHS) as outer or inner tubes are feasible for CFDST columns. In practice, it is preferable to utilize CHSs as both the inner and outer tubes for a CFDST since they are less prone to local buckling than SHSs. The confinement mechanism in the traditional CFST column is obviously altered by the usage of the hollow steel tube in it. As a result, compared to traditional circular CFST columns, the behaviour of circular CFDST columns is considerably different.

In this paper, a Finite element model (FEM) based on the commercial FE tool ABAQUS 2020 was developed to investigate the behaviour of CFDST stub columns under axial compressive loading conditions. Several important topics related to FE modelling such as element type, mesh, boundary conditions, concrete and steel material models, and interface models that represent the interface between the two materials are briefly discussed here. Numerous experimental research on the behaviour of CFDST members have been carried out in recent years by many researchers. The main objective of this paper is to verify the proposed FE modelling by using the test results reported by different researchers. The results were statistically assessed to show how well the models performed in terms of predictions.

2. Modelling by Finite Element Method (FEM)

2.1 Modelling of concrete

Concrete damage plasticity (CDP) model is a constitutive model for determining the damage of concrete. Concrete is composed of qualitatively and quantitatively different types of materials which exhibit distinct properties in terms of tension and compression. Concrete identification parameters, such as the non-linear stress-strain relationship of the concrete under extreme stress circumstances and strain hardening/softening, complicate the behaviour of concrete. The concrete damage plasticity model analyzes the concrete structures using damage mechanics and the flow theory of plasticity.
Concrete damage plasticity is recognized to be an accurate and useful constitutive model for simulating concrete behaviour. Since the CDP theory was complex, Hafezolghorani et al (2017) established a simplified concrete damage plasticity (SCDP) model by simplifying the procedure involved in CDP theory, which is used for modelling of concrete in ABAQUS.

2.2 Modelling of steel

Steel tube modeling was done using the bilinear elastic-plastic material model, which accounts for strain hardening behavior. Han and Huo (1990) proposed the stress-strain relationship which is divided into two zones. The first region, which extends from the origin to the yield point, contains the specifications for the steel's elastic characteristics. And the second region is plastic region. For all steel tubes, the Poisson's ratio ($\boldsymbol{\nu}_s$) and modulus of elasticity was considered as 0.3 and 200×10^3 N/mm^2, respectively.

2.3 Interaction and surface identifications

To model circular CFDST small columns, three distinct components were used: the outer and inner steel tubes and infilled concrete. Surface-to-surface contact, in which the steel served as the master surface and the concrete as the slave surface, was used as bond between the surfaces of steel tubes and the concrete annulus. "Normal behavior" and "tangential behavior" were taken into consideration in ABAQUS to define the interaction property. As a suboption for normal behavior, “Hard contact” feature was selected. For tangential behavior, the penalty friction model with an isotropic direction and a friction coefficient of 0.3 was used.

2.4 Finite element type and mesh selection

Solid elements were used to model the outer steel tube, inner steel tube and concrete components that make up the CFDST columns. The global mesh sizes of the concrete infill and steel tubes was taken as 10 mm.

2.5 Boundary and loading conditions

To assign the loading and boundary conditions of a column, two reference points were created, one at the top end and the other at the bottom end. The constraint between the reference point and the specimen was defined using a multipoint constraint (MPC). For the bottom reference point, an encastre type boundary condition was applied in order to obtain fixed support at all degrees of freedom. It was allowed for the top reference point to deform in the longitudinal direction.

3. Verification of the FEM model

To accurately predict the behavior of CFDST columns, it is essential to verify and calibrate the proposed model. For this reason, the suggested model's validation and calibration took into account the findings of earlier experimental tests. Table 1 displays the properties of the CFDST column specimens that were previously described, where, D_o, B_o, t_o and D_i, B_i, t_i denote the depth, width and thickness of outer and inner tubes respectively for SHS-SHS column section. For CHS-CHS column section, D_o and D_i denote the outer and inner tubes diameter respectively. It also shows the experimental ultimate axial strength values along with the predicted ultimate axial strength values from the proposed FEM model.

Table 1. Comparison of experimental results with predicted ultimate capacity

Sample (Section)	Length, L (mm)	Outer tube		Inner tube		Concrete compressive strength, f_c (N/mm^2)	P_{exp} (kN)	P_{FEM} (kN)	P_{exp} /P_{FEM}
		$D_o \times B_o \times t_o$ (mm×mm×mm)	Yield strength, f_{yo} (N/mm^2)	$D_i \times B_i \times t_i$ (mm×mm×mm)	Yield strength, f_{yi} (N/mm^2)				
CFS1S5 (SHS-SHS)	375	99.74×99.74×5.97	485	50×50×2.44	477	73.37	1627	1594	1.02
CFS2S5 (SHS-SHS)	374.9	100.49×100.49×4.01	445	50×50×2.44	477	73.37	1259	1236.8	1.01
CFS3S5 (SHS-SHS)	375.3	100.18×100.18×2.94	464	50×50×2.44	477	73.37	1105	996	1.10
DST-SC1 (SHS-SHS)	450	150×100×3.2	380	75×45×3.2	429	50	1320	1168	1.13
T0-4E0 (SHS-SHS)	400	100×100×2	235	40×40×2	235	43.24	500.6	623	0.80
T0-5E0 (SHS-SHS)	500	100×100×2	235	40×40×2	235	43.24	520.9	447	1.16
cc2a (CHS-CHS)	540	180×-×3	275.9	48×-×3	396.1	47.4	1790	1623	1.10
cc3a (CHS-CHS)	540	180×-×3	275.9	88×-×3	370.2	47.4	1648	1639	1.00
Cc5b (CHS-CHS)	342	114×-×3	294.5	58×-×3	374.5	47.4	898	772	1.16
C1-1 (CHS-CHS)	660	220×-×3.62	319.6	159×-×3.72	380.6	65.6	2537	2786	0.91
C2-1 (CHS-CHS)	660	220×-×3.62	319.6	106×-×3.72	380.6	65.6	3436	3255	1.05
2-1-2 (CHS-CHS)	343	114.3×-×5.85	455	60.3×-×5.77	310	40.24	1574.2	1488.8	1.05

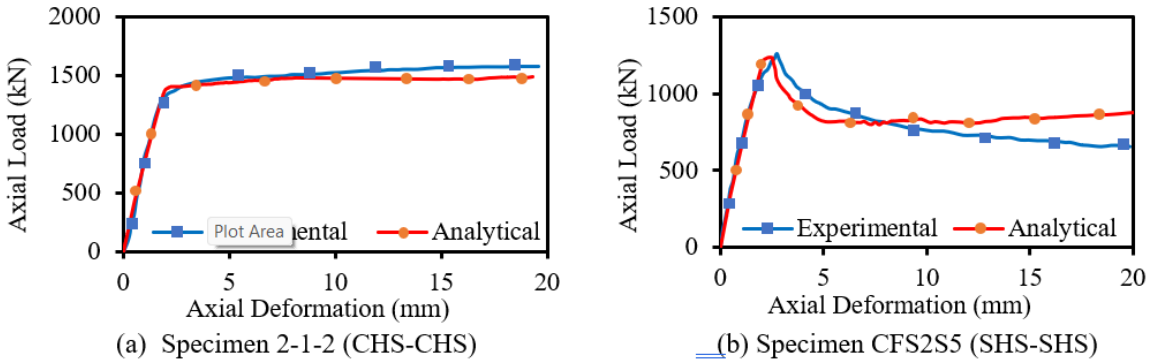

Figure 1. Comparisons of experimental and analytical load-deformation responses of specimens

The comparison between the predicted and experimentally observed load-deformation performance for two specimens are shown in Figure 1(a) and (b). It is observed that the overall trend of the experimental load-deformation response of the specimens is accurately estimated using FEM method.

4. Conclusions

The aim of this work is to use the FEM to model the behaviour of axially loaded CFDST columns. The ultimate strength and load-deflection curves predicted by FEM models were compared to the experimental results obtained by various researchers. Based on the findings, the following are the conclusions:

- The values of ultimate axial strength predicted by the proposed FEM model are close to the experimental test values. The average normalized ultimate axial strength value in the FEM model is 1.04.
- The FEM model that this study suggests has been validated by a number of research findings that are available in the literature. This suggests that the model could be effectively used to forecast the ultimate axial strength of CFDST columns.

References

Elchalakani, M., Karrech, A., Hassanein, M. F., & Yang, B. (2016) "Plastic and yield slenderness limits for circular concrete filled tubes subjected to static pure bending", *Thin-Walled Structures*, 109:50–64

Hafezolghorani, M., Hejazi, F., Vaghei, R., Jaafar, M. S. Bin, & Karimzade, K. (2017) "Simplified damage plasticity model for concrete" *Structural Engineering International*, 27(1):68–78

Han, L.-H., Huo, J., & Yang, Y.-F. (2002)" Concrete-filled HSS columns after exposure to the Iso-834 standard fire" *Advances in Steel Structures* (ICASS '02), II (1990):1127–1134

Han, L. H., Yao, G. H., & Tao, Z. (2007) "Performance of concrete-filled thin-walled steel tubes under pure torsion" Thin-Walled Structures, 45(1):24–36

Han, L. H., Ren, Q. X., & Li, W. (2011) "Tests on stub stainless steel concrete carbon steel double-skin tubular (DST) columns", *Journal of Constructional Steel Research*, 67(3):437–452

Hassanein, M. F., Kharoob, O. F., & Liang, Q. Q. (2013) "Behaviour of circular concrete-filled lean duplex stainless steel-carbon steel tubular short columns", Engineering Structures, 56: 83–94

Hassanein, M. F., Elchalakani, M., & Patel, V. I. (2017) "Overall buckling behaviour of circular concrete-filled dual steel tubular columns with stainless steel external tubes", *Thin-Walled Structures*, 115(July 2016):336–348

Huang, H., Han, L. H., Tao, Z., & Zhao, X. L. (2010) "Analytical behaviour of concrete-filled double skin steel tubular (CFDST) stub columns", *Journal of Constructional Steel Research*, 66(4):542–555

Kent, Dudley; Park, R. (1971) "0076-Kent-Park-Flexural-Members-With-Confined-Concrete "(pp. 1970–1989)

Khanouki, M. M. A., Ramli Sulong, N. H., Shariati, M., & Tahir, M. M. (2016) "Investigation of through beam connection to concrete filled circular steel tube (CFCST) column", *Journal of Constructional Steel Research*, 121: 144–162

Liang, Q. Q. (2017) "Nonlinear analysis of circular double-skin concrete-filled steel tubular columns under axial compression", *Engineering Structures*, 131:639–650

Pagoulatou, M., Sheehan, T., Dai, X. H., & Lam, D. (2014) "Finite element analysis on the capacity of circular concrete-filled double-skin steel tubular (CFDST) stub columns", *Engineering Structures*, 72:102–112

Comparison Between CO_2 Emissions from Vernacular and Modern Structures

Kritvi Gera[1]*, Tushar Verma [2], Swathy Manohar[3], Eesha Vinod[4]

[1] Indian Institute of Technology Bombay, Mumbai, India, Email: 210040078@iitb.ac.in
[2] Indian Institute of Technology Bombay, Mumbai, India, Email: 200040154@iitb.ac.in
[3] Indian Institute of Technology Bombay, Mumbai, India, Email: swathym@iitb.ac.in
[4]National Institute of Construction Management and Research, Pune, India, Email: eeshavinod@gmail.com

Corresponding author*

ABSTRACT

The growing concern over carbon emission from the construction industry is due to the increasing awareness about the harmful effects of excess greenhouse gases in the atmosphere and the resulting warming of the earth. The main goal of this study is to compare the carbon emissions between structures made out of two different building materials - AAC Blocks, and Fired Clay bricks. The data is taken from buildings from a typical duplex residential project in a Tier 2 city. The approach adopted for the analysis is cradle-to-grave, signifying all the stages in the construction. Variation of important physico-mechanical properties, cost, availability and energy efficiency are also reviewed in this paper and compared for the different construction systems.

KEYWORDS: *Carbon Emissions, Global Warming, Vernacular Structures, Modern Structures, Cradle-to-grave*

1. Introduction

LCA and its significance: LCA stands for Life Cycle Assessment. As the name suggests, its purpose is to assess the environmental impact of a product throughout its life cycle. It uses quantifying methods to do the same. The impact of everything is converted to equivalents of carbon emissions and compared. Emissions from other greenhouse gases are also converted to equivalent carbon emissions by multiplying an emission factor (EF). The emission factor (EF) is a coefficient that describes the rate at which a given activity releases greenhouse gases (GHGs) into the atmosphere. It is also known as conversion factor, emission intensity, and carbon intensity.
The relative warming impact of different greenhouse gases is called Global Warming Potential (GWP). In other words, it is the equivalents of CO_2 that would have the same impact as unit emission from some other Greenhouse gas. Global Warming potentials are given by the Intergovernmental Panel on Climate Change (IPCC) in their periodic annual reports.
This paper employs the 'Cradle to grave approach' for the LCA of the buildings under consideration in this study. This approach comprises all building stages, namely, procurement and production of raw materials, transportation and construction. The operational stage, excluding maintenance, and demolition stage are included. Carbon emissions from the operational stage include emissions by the usage of water and electricity. Carbon emission reduction due to the use of recycled material, green areas, etc. are not taken into account while calculating the emissions for comparisons in this paper.

1.1 Different types of LCA in the context of buildings

- **Cradle-to-Gate LCA**: This approach of LCA focuses on the environmental impacts associated with the manufacturing of construction materials and components, from raw material extraction to the manufacturing factory gate. A Cradle-to-Gate Life Cycle Assessment (LCA) encompasses the subsequent life cycle stages - procurement of raw materials, transportation to production facilities, and

manufacturing procedures, as per the International Organization for Standardization (ISO) 14040 and 14044 standards.

- **Cradle-to-Grave LCA**: This approach takes into account a building's whole lifespan, encompassing both the operational phase (energy and water consumption, maintenance, and replacements) and end-of-life stage (demolition and disposal or recycling). A cradle-to-grave life cycle assessment (LCA) was conducted for a Spanish residential building by Cabeza et al. (2014), taking into account various energy sources and insulating materials.
- **Cradle-to-Site LCA**: This method of LCA includes the transportation of building materials and components from the factory to the construction site in addition to the cradle-to-gate stage. A study by Dixit et al. (2010) assessed the (cradle-to-site life cycle) energy consumption and greenhouse gas emissions of Indian residential buildings from the beginning of their life cycle to the end.
- **Building Component LCA**: This type of LCA concentrates on a particular material or component utilized in the structure, such as a wall assembly, roof system, or structural element. A study by Kragha et al. (2021) conducted an LCA of different types of wall assemblies for a residential building in Canada.
- **Whole Building LCA**: This Life Cycle Assessment method assesses the environmental effects of the entire building as a whole at every point of its life cycle, taking into account all of its components, materials, and systems. The Athena Sustainable Materials Institute provides a whole building LCA software tool for assessing the environmental impacts of buildings throughout their life cycle.

Additionally, the U.S. Green Building Council (USGBC) and the Building Environmental Assessment Tool (BEAM) Society provide guidelines and resources for conducting various types of LCA for buildings and building materials.

1.2 Assumptions for LCA Calculations

Some of the base assumptions taken for the calculations of the carbon emissions are:

- Similar design, size, and functionality for AAC and clay brick structures
- Uniform climate conditions and energy usage patterns for both buildings
- Standard industry conditions for material sourcing and manufacturing
- 25-year life cycle with consistent end-of-life practices
- Constant emission factors throughout the life cycle
- Linear extrapolation of operational emissions for longer life cycles (50 year lifespan comparison)
- Exclusion of carbon emission reductions from green practices
- No significant technological advancements or retrofitting over the buildings' lifespans
- Standardized construction practices for each material type
- Consistent maintenance activities and associated emissions across building types

2. LCA calculations and discussions

The calculations done here are for a duplex residential complex in a tier-two city. The difference here is in the building blocks used. Data from two different buildings were collected - the first house was made using AAC blocks, and the other was made out of fired clay bricks. Calculations for each of the buildings have been divided into 3 parts - the Building stage, the Operational stage and the Demolition stage. These residential complexes are assumed to have a 50-year life cycle.

The below given Tables 1, 2, and 3 shows the carbon emissions for an AAC block structure in its three different phases.

The emission of carbon is the highest in the building phase of a AAC block structure followed by its operational and demolition phase. The emission that occurs in the demolition phase is mostly due to the burning of diesel to cater to the energy demand of the same.

Table 1. Carbon emission due to building phase for AAC Block Construction

Building material	Unit	Quantity	Emission Factor	Unit of factor	Total emissions
M15 Concrete	cum	50	0.125	kg CO_2/kg	16000
M20 Concrete	cum	50	0.155	kg CO_2/kg	19840
Steel	kg	5610	1.55	kg CO_2/kg	8695.5
AAC Block	cum	132	2.22	kg CO_2/kg	22144.08
Plaster	sqm	700	0.13	kg CO_2/kg	891.8
Paint	sqm	800	3.76	kg CO_2/kg	582549.3
Flooring	sqm	180	0.78	kg CO_2/kg	3369.6
Electricity	kWh	1000	0.716	kg CO_2/kW	716
Diesel	l	200	2.64	kg CO_2/l	528
Total					654734.3 $kgCO_2$

From Table 1 given above, it can be understood that paint emits the most carbon followed by the AAC blocks for construction. On comparison, however, carbon emission due to the consumption of electricity and diesel together which satisfies the energy requirement is among the least, second to only that of plastering.

Table 2. Carbon emission due to the operational phase for AAC Block Construction

Units per month	Unit	Number of months	Number of years	Emission factor	Emission factor unit	Total emissions
For electricity	245 kWh	12	25	0.716	kg CO_2/kWh	52626
For water	16200 l	12	25	0.00034400	kg CO_2/kg	1671.84
Total						54297.84 $kgCO_2$

Table 2 suggests that the carbon emission occurring by the usage of water is considerably less than the emissions by the consumption of electricity.

Table 3. Carbon emission due to the demolition of AAC Block Construction

Waste due to demolition					
Material	Unit	Quantity	CO2 Emission Factor	Total Carbon Emission	
Diesel	l	200	2.64	528	
Waste due to disposal					
Materials	Unit	Quantity	Distance	Carbon Emission Factor	Total Carbon Emission
Debris	ton	20	40	0.1033	82.672
Total					610.672 $kgCO_2$

From Table 3. it can be understood that the carbon emissions from demolishing a building is significantly higher than the emissions from the debris post demolition.

Tables 4, 5, and 6 given below shows the carbon emissions for a clay brick structure in its three different phases.

The emission of carbon is the highest in the building phase of a Clay brick structure, followed by its operational and demolition phase. The emission that occurs in the demolition phase is mostly due to the burning of diesel to cater to the energy demand of the same.

Table 4. Carbon emission due to the building phase for Clay Brick Construction

Building Material	Unit	Quantity	Emission Factor	Unit of factor	Total emissions
M15 Concrete	cum	50	0.125	kg CO_2/kg	16000
M20 Concrete	cum	50	0.155	kg CO_2/kg	19840
Steel	kg	6600	1.55	kg CO_2/kg	10230
Bricks	cum	132	0.21	kg CO_2/kg	49896
Plaster	sqm	700	0.13	kg CO_2/kg	891.8
Paint	sqm	800	3.76	kg CO_2/kg	582549.3
Flooring	sqm	180	0.78	kg CO_2/kg	3369.6
Electricity	kWh	1000	0.716	kg CO_2/kWh	716
Diesel	l	200	2.64	kg CO_2/l	528
Total					684020.7 kgCO_2

From the given table (Table 4), it is understood that carbon emission by the use of paint is the highest in the building phase, which is followed the use of FCB for construction. As in the case of AAC blocks, emissions by the consumption of electricity and diesel together which satisfies the energy requirement among the least, second to only that of plastering.

Table 5. Carbon emission due to the operational phase for Clay Brick Construction

Units per month	Unit	No. of months	No. of years	Emission factor	Emission factor unit	Total emissions
For electricity	350 kWh	12	50	0.716	kg CO_2/kWh	150360
For water	16200 l	12	50	0.000344 00	kg CO_2/kg	3343.68
Total						153703.68 kgCO_2

From Table 5, it can be seen that the emissions by the consumption of electricity in the operational phase of a FCB structure is considerably higher than that by the consumption of water.

Table 6. Carbon emission due to the demolition of Clay Brick Construction

Waste due to demolition					
Material	Unit	Quantity	CO2 Emission Factor	Total Carbon Emission	
Diesel	l	200	2.64	528	
Waste due to disposal					
Materials	Unit	Quantity	Distance	Carbon Emission Factor	Total Carbon Emission
Debris	ton	20	40	0.1033	82.672
Total					610.672 kgCO_2

It is understood from Table 6 that carbon emission by the consumption of diesel which is used for demolition of the structure is significantly greater as compared to that of the resultant debris.

Table 7 given below summarises the carbon emissions in each of the phases and cumulatively for both AAC block and Clay brick structure.

From the table it can be seen that in the case of both AAC block construction and Clay Brick construction, the building phase is the single largest emitter of carbon, followed by the operational phase and the demolition phase. On comparison between the two, it is visible that AAC blocks perform better as compared to Clay bricks in terms of carbon emission.

Table 7. Comparison of carbon emissions due to AAC Blocks and Clay brick construction in kg CO_2.

AAC block construction	
Building Phase	654734.3
Operational Phase	54297.84
Demolition Phase	610.67
Total	709642.81
Clay Brick Construction	
Building Phase	684020.7
Operational Phase	76851.84
Demolition Phase	610.672
Total	761483.21

Table 8. Comparison between emissions from operational stage during different life spans (kg CO_2)

	25 years	50 years
AAC Block	54297.84	108595.68
Clay Bricks	75180	153703.68

From the table given above it is apparent that in both the cases of considering two different life spans – 25 and 50 years – AAC blocks perform marginally better.
To calculate the carbon emission from the operational stage of the building life cycle we calculate emissions from water and electricity consumption. We take average water consumption daily per person and multiply it with average household size, life span of building and carbon emission factor of water. Similarly for electricity consumption, we multiply the average electricity consumption of house hold with life span and carbon emission factor to get the total value of carbon emissions.
Under a 25-year lifespan consideration, AAC blocks perform better by 27.77% and under a 50-year lifespan consideration, AAC blocks perform better by 29.33% as evidenced by the calculations performed above.

3. Comparison between different types of blocks

Table 9 shows the comparative properties of AAC blocks and Fired clay blocks, also compared with another common and sustainable building blocks – fly ash blocks.
Comparing the major properties obtained from literature, it is observed that AAC Blocks perform best in compressive strength, dry density and thermal conductivity; making them very widely commercially adopted as compared to Fired Clay Bricks and Fly ash blocks. However, AAC blocks are not available widely and cannot be used in areas with high moisture content due to its high porosity.

Table 9. Different blocks available and their properties

Blocks and their properties

Aa Properties	AAC Blocks	Fly ash blocks	Fired Clay Bricks
IS code	2185 part 3	IS 12894-1990, (3495, 10077)	IS 1077 (1992)
Sizes Available	600/300X200X75/100/150/200/225	190/230X90/110X40/90/70/30	225 mm x 100 mm x 65 mm / 230 mm x 75 mm x 115 mm
Compressive strength	4-6 MPa	3.5-30 MPa (Different for different classes)	2.5-3 MPa
Dry density	0.6-0.9 ton/m3	1.5-1.9 ton/m3	1.8-2.0 ton/m3
Moisture	5-10% (can go upto 40%)	15-20% (max)	20% (avg)
Availaibility	Tier 1 (brands + local), Tier 2 (local), Tier 3 (none / through tier 2 cities)	Anywhere where fly ash source is availaible	everywhere
Cost	2950+taxes (12% GST) per m3 (include transport upto 40km) 2650 without transport	3700 per m3 (approx)	Similar to AAC but overall project costing more for fired clay bricks
Shrinkage limit	0.05-0.1%	0.15%	-
Thermal Conductivity	0.3-0.37 W/m.k	0.9-1.05	0.5-1.0

4. Viable suggestions to reduce carbon emissions by the construction industry

- Implement energy efficiency measures (insulation, efficient windows, high-efficiency HVAC, smart building systems, passive design) and integrate renewable energy (solar, wind, geothermal).
- Use low-carbon and locally sourced materials to reduce embodied carbon.
- Explore carbon capture and storage technologies for industrial processes and building materials.
- Prioritize design strategies that minimize energy consumption and material use while maximizing sustainability and carbon reduction throughout the building's lifecycle.
- The strategies should be considered holistically within the context of a building's life cycle, incorporating low-carbon approaches throughout design, construction, operation, and end-of-life phases to maximize carbon emission reductions

4.1 Solutions for the Industry

- Adopt Green Building Certifications and Standards
- Implement Life Cycle Assessment (LCA) and Carbon Foot printing
- Invest in Low-Carbon and Renewable Construction Technologies
- Integrate renewable energy systems like solar, geothermal, or biomass energy, leveraging India's 5,000 trillion kWh renewable potential (National Institute of Solar Energy, India).

4.2 Solutions for domestic inhabitants

- Promote energy-efficient behaviour through thermostat adjustment, water conservation, and natural ventilation, and incentivize energy-efficient appliances and retrofits.
- Support sustainable transportation and urban planning,
- Foster community engagement through awareness campaigns and neighbourhood groups.

5. Conclusions

This study calculates and compares the amount of carbon emitted by two duplex residential buildings, one constructed out of AAC blocks and the other with fired clay bricks, throughout their life cycle.
From the literature it is understood that structures made out of AAC blocks emit less carbon since fewer number of blocks are required due to their inherent properties and considerable energy saving occurs due to less thermal conductivity.
From the calculations done above, it can be seen that structures constructed using AAC blocks emitted roughly 27.77% less carbon as compared to those made out of clay bricks in a 25-year life span consideration and emitted 29.35% carbon less in a 50-year lifespan assumption. Thus, it is understood that AAC blocks perform better as compared to Clay bricks in terms of carbon emission.In the cases of both AAC blocks and Fired Clay bricks, the major share of carbon emission occurred in the building phase, followed by the operational, and the demolition phase. Regarding the operational phase, the carbon emission occurring due to water consumption is significantly lesser than the emissions due to the consumption of electricity for both blocks. In case of demolition as well, for both AAC and FCB blocks, the emissions occurring by the demolition of the building is much higher than the emissions from the debric post demolition.
This study also made a comparison through literature between different properties of AAC blocks, clay bricks, and fly ash blocks and established that AAC blocks performed best out of the three.
In addition to this, the paper proposes methods by which the carbon emission from the construction industry can be significantly reduced.

References

ISO 14040:2006, Environmental management - Life cycle assessment - Principles and framework.
ISO 14044:2006, Environmental management - Life cycle assessment - Requirements and guidelines.
Dixit, M. K., Fernandez-Solis, J. L., Lavy, S., & Culp, C. H. (2010). Identification of parameters for embodied energy measurement: A literature review. Energy and Buildings, 42(8), 1238-1247.

Cabeza, L. F., Rincón, L., Vilariño, V., Pérez, G., & Castell, A. (2014). Life cycle assessment (LCA) and life cycle energy analysis (LCEA) of buildings and the building sector: A review. *Renewable and Sustainable Energy Reviews*, 29, 394-416.

Kragha, O., Loggia, C., & Mahdavi, A. (2021). Life cycle assessment of residential wall assemblies: A comparative analysis. *Sustainability*, 13(7), 3817.

Athena Sustainable Materials Institute. (n.d.). Impact Estimator for Buildings. Retrieved from https://athenasmi.org/our-software-data/impact-estimator/

U.S. Green Building Council. (n.d.). Life Cycle Assessment. Retrieved from https://www.usgbc.org/resources/life-cycle-assessment

BEAM Society. (n.d.). Life Cycle Assessment (LCA). Retrieved from https://www.beamsociety.org.hk/en/resources/life-cycle-assessment.php

Pérez-Lombard, L., Ortiz, J., & Pout, C. (2008). A review on buildings energy consumption information. *Energy and Buildings*, 40(3), 394-398.

Tabadkani, A., Vázquez, R., Colmenar, A., & Hakimi, S. M. (2022). Renewable energy solutions for buildings: A review. *Applied Energy*, 306, 117972.

Li, J., Zhang, X., Cheng, G., & Xu, C. (2022). Carbon capture and storage (CCS) in buildings: A review of technologies, challenges and opportunities. *Energy and Buildings*, 262, 111973.

Tan, P. Y., & Fauzi, M. F. (2021). The effects of biophilic design and green infrastructure towards buildings' carbon footprint. *Environmental Research Communications*, 3(6), 062005.

Zhao, J., & Zhu, N. (2021). Building operational optimization to reduce energy consumption and carbon emissions: A review. *Energy and Buildings*, 252, 111426.

Darko, A., Chan, A. P., Ameyaw, E. E., Owusu, E. K., Pärn, E., & Edwards, D. J. (2019). Review of application of sustainable construction practices in the construction industry. *Journal of Cleaner Production*, 212, 950-964.

Mohammadi, A., Talaei-Khoei, A., Kazemi, R., & Gan, V. J. L. (2022). Modular construction: A solution for low carbon emission and sustainable practices in the construction industry. *Sustainability*, 14(10), 5692.

Ürge-Vorsatz, D., Petrichenko, K., Staniec, M., & Eom, J. (2013). Energy use in buildings in a long-term perspective. *Current Opinion in Environmental Sustainability*, 5(2), 141-151.

Cervero, R., & Kockelman, K. (1997). Travel demand and the 3Ds: Density, diversity, and design. Transportation Research Part D: *Transport and Environment*, 2(3), 199-219.

Stern, P. C., Dietz, T., Abel, T., Guagnano, G. A., & Kalof, L. (1999). A value-belief-norm theory of support for social movements: The case of environmentalism. *Human Ecology Review*, 6(2), 81-97.

Singh, A., Berghorn, G., Jain, S., & Syal, M. (2011). Review of life-cycle assessment studies on solid waste management systems–Part I: Rationale for LCA. *Journal of Environmental Monitoring*, 13(12), 3311-3321.

Tiwari, P., Parikh, J., & Mukherjee, V. (2013). Disassembly analysis of a residential building. *Journal of the Indian Institute of Science*, 93(4), 655-672.

Ravi, S., Lingala, M. K., & Ganesh, L. S. (2021). Building for climate resilience: Life cycle assessment of traditional and modern building materials in India. Journal of Environmental Management, 284, 112052.

Shrivastava, S., Taneja, J., & Mor, S. (2022). Understanding household energy-use behaviour in urban India: A mixed-methods approach. *Energy Policy*, 163, 112853.

Goel, R., & Tiwari, G. (2015). Promoting low-carbon transport in Indian cities: A co-benefits analysis. Cities, 45, 139-148.

Kulkarni, S., & Agarwal, N. (2022). Community engagement for promoting sustainable urban development: A case study of Pune, India. *Sustainable Cities and Society*, 79, 103672.

Hammond, G.P., & Jones, C.I. (2008). Embodied energy and carbon in construction materials. Proceedings of the Institution of Civil Engineers: Energy, 161(2), 87-91. *Proceedings of the Institution of Civil Engineers - ICE Virtual Library*

Changhai Peng, Calculation of a building's life cycle carbon emissions based on Ecotect and building information modeling, Journal of Cleaner Production, Volume 112, Part 1, 2016, Pages 453-465, ISSN 0959-6526

U.S. Green Building Council, "Benefits of Green Building", 2019

Bureau of Energy Efficiency, India, "Energy Conservation Building Code", 2017

Indian Green Building Council, "Green Building Materials and Products", 2017

Gupta, A., & Tan, T. (2015). "Bamboo: A potential material for sustainable construction." *Journal of Construction Engineering and Management*, 141(6), 04015001.

National Institute of Solar Energy, India, "Renewable Energy Potential in India".

Energy Efficiency Services Limited, India, "Energy Efficiency in Buildings", 2019.

Unnat Jeevan by Affordable LEDs and Appliances for All (UJALA) program, Government of India (https://ujala.gov.in/).

U.S. Environmental Protection Agency, "Smart Growth and Urban Development" (https://www.epa.gov/smartgrowth/smart-growth-and-urban-development).
American Public Transportation Association, "Public Transportation Benefits"
Union of Concerned Scientists, "Electric Vehicle Benefits", 2019.
Kanish Plasters [Kanish Plasters]. A Deep Insight into Gypsum Plastering. https://kanishplasters.com/why-choose-gypsum-plasters-to-make-your-dream-project-cleaner-and-greener/
CO2 Baseline Database for the Indian Power Sector User Guide https://cea.nic.in/wp-content/uploads/baseline/2024/01/User_Guide__Version_19.0.pdf
Agarwal, S., Shukla, P. R., & Venkataraman, C. (n.d.). Emissions inventory for road transport in India in 2020: Framework and post facto policy impact assessment.

Synergistic Use of Rice Husk and Sugarcane Bagasse: An Approach for Sustainable Agro-waste Ashes Blended Cements

G. Jyothsna[1], A. Bahurudeen[2*] , and Prasanta K Sahu[3]

[1] Doctoral Research Scholar, Birla Institute of Technology and Science Pilani, Hyderabad Campus, India
Email: p20190417@hyderabad.bits-pilani.ac.in
[2] Associate Professor, Birla Institute of Technology and Science Pilani, Hyderabad Campus, India
Email: bahurudeen.civil@gmail.com
[3] Associate Professor, Birla Institute of Technology and Science Pilani, Hyderabad Campus, India
Email: Prasanta.sahu@hyderabad.bits-pilani.ac.in

*Corresponding author

ABSTRACT

India is the world's largest sugar producer and second-largest rice producer. Hence, it generates an enormous quantity of sugarcane bagasse and rice husk. More than 400 sugar mills in India have full-scale cogeneration facilities. On the other hand, constructing cogeneration facilities is expensive; hence, it is not preferred and also cannot be affordable at small-scale rice mills. Nevertheless, the utilization of rice husk remains hampered due to the lack of cogeneration facilities in rice mills. Thus, the combustion of rice husk in agricultural fields is adopted by farmers as a method of disposal and leads to significant land and air pollution. Rice husk can be redirected to the adjacent already-established sugar plants for the purpose of cogeneration. The existing studies on the synergistic use of rice husk at sugar mills are extremely limited. Therefore, it is imperative to investigate the feasibility of co-generating rice husk using existing facilities at sugar mills. The current study considers Andhra Pradesh, a rice-rich state in India. This study uses a methodology based on ArcGIS and multi-criteria decision-making followed by sensitivity analysis. A comprehensive investigation conducted resulted in the identification two regions with nine potential sugar mills suitable for rice husk cogeneration. The incorporation of rice husk into the cogeneration facility of these plants is a very effective strategy to optimise resource utilisation during the non-harvesting period of sugarcane. The proposed synergistic utilisation method is more effective and cost-efficient than building a new cogeneration plant specifically for rice husk.

KEYWORDS*: Blended cements; Pozzolans; Rice husk ash; Sugarcane bagasse ash; Sustainability*

1. Introduction

Blending agro-waste ash with cement provides a sustainable option that efficiently addresses multiple challenges in the agriculture and construction industries. These cements incorporate ashes derived from agricultural waste, such as rice husk ash and sugarcane bagasse ash. India is a prominent global producer of rice and sugarcane. Therefore, rice husk and sugarcane bagasse, which are the residual materials, are abundantly available. Efficient utilisation and management of these ashes also contribute to a circular economy. The concept of cogeneration is essential for maximising the efficient use of available resources. The majority of sugar mills in India are equipped with cogeneration facilities and utilise bagasse for the purpose of power generation. Despite being the second largest producer of rice, the majority of rice mills in India do not have cogeneration facilities. Most of the rice mills are small-scale and located in rural areas. Therefore, the implementation of cogeneration facilities at all the rice mills is not cost-effective and comes with a significant financial burden to rice mills. The study investigates feasibility of rice husk utilisation in the adjacent sugar mills that already have cogeneration capabilities. Thus, rice husk can also be co-fired together with bagasse to generate power. In addition, rice husk ash and sugarcane bagasse ash are produced as by-products. These ashes exhibit pozzolanic properties, making them suitable for use as supplementary cementitious materials in the production of cement. The current investigation selects Andhra Pradesh as the

study region because to its status as one of the most significant rice-producing states in India. The state is comprised of 13 districts, with each district being regarded as an individual region for analysis purposes. The methodology employs a multi-criteria decision-making technique, which is subsequently followed by suitability and sensitivity analysis. Initially, all the current sugar mills equipped with cogeneration capabilities for each district were geocoded in ArcGIS. The suitability analysis of the study considered three criteria, as determined by the expert's survey and literature review (Wang et al., 2019). The factors taken into account were C1-Rice husk availability; C2-Proximity to the nearest cogeneration facility; C3-Population density. Then the eligibility of the all-regions for cogeneration was evaluated by computing the suitability index values using equation 1. After obtaining the suitability index values, the stability of these values was tested by a sensitivity analysis. Moreover, a quantitative investigation was conducted on the blended cements generated from agro-waste ashes.

$$SI_j = \sum_{i=1}^{3} W_i Y_{ij} \quad (1)$$

Where, SI_j = Suitability index of the jth district; W_i = Weightage if the ith criteria
Y_{ij} = Normalized value of the ith criteria for jth district

2. Results and discussions

The investigation included all the sugar mills in every area that have cogeneration facilities, using ArcGIS (Sugar Technologist Association, 2018). The data pertaining to the amount of rice produced and the availability of rice husk were collected. (Directorate of Economics & Statistics in 2021). Once the criteria weights were calculated, a suitability study was conducted for all regions within the state. Among the 13 regions, the two most suited districts were selected for the coordinated distribution of rice husks. There are a total of 9 cogeneration facilities in the study regions considered, as depicted in Figure 1(a). The West Godavari and East Godavari districts are the highest-ranking regions, with suitability scores of 56.18 and 55.66 respectively, as depicted in Figure 1(b). In the subsequent sections of the study, the East and West Godavari regions were designated as R1 and R2, respectively. The higher suitability of these regions is attributed to the fact of the abundance rice husk availability. A sensitivity study was conducted by systematically altering the weightage of each criterion individually. A sensitivity analysis was conducted for eight scenarios, with the weightage being adjusted from +100% to -100% in increments of 25% (i.e., +100%, +75%, +50%, +25%, -25%, -50%, -75%, -100%). Figure 2 displayed the correlation between the changes in the weightages of the considered criteria and the corresponding variations in the suitability index values.

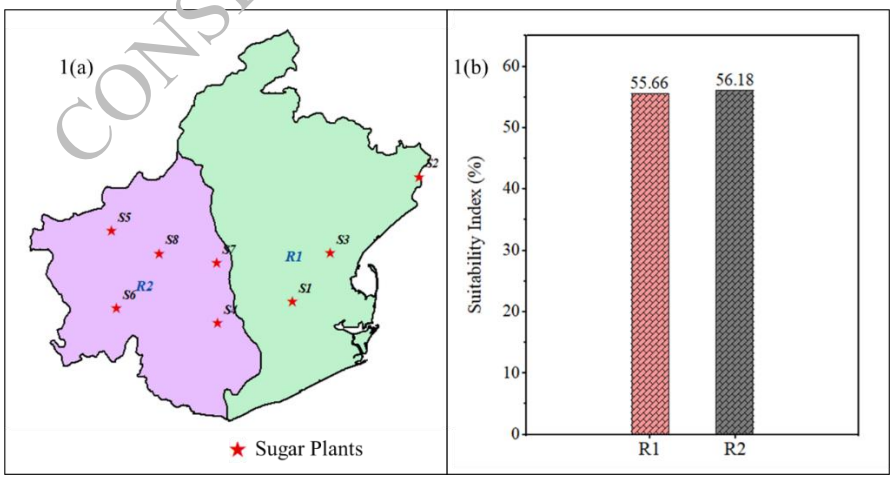

Figure 1(a). Depiction of zones and sugar plants in the study regions; 1(b): Suitability index of the study regions

The sensitivity analysis reveals a decreasing trend in the appropriateness index values for criteria C1 in regions R1 and R2 as the weightage is decreased. This is true because as the importance of the criterion "availability of rice husk" decreases, the viability of the region for cogeneration will also decrease. Similarly, an upward trend was observed when the analysis was conducted based on the criterion C2. This

is due to the reallocation of the lower weightage of criterion C2 to criteria C1 and C3. Therefore, increasing the weightage of C1 enhances the appropriateness of the location. Criteria C1 and C2 exert a substantial influence on the region's suitability for cogeneration, in contrast to C3, which has a relatively negligible impact. The amounts of agro-waste ashes produced in the two regions examined for the study are presented in Table 1. The amount of bagasse ash and rice husk ash produced is 46.2 and 135.96 kilotons, respectively. The quantity of blended cement that can be manufactured from co-firing agro-waste ashes was determined, adopting equal proportions. Earlier studies have indicated that a 10% replacement level of rice husk ash and sugarcane bagasse ash each is regarded ideal (Bhosale et al., 2023). Therefore, the study indicates that approximately 924kilotons of agro-waste blend ternary cement can be produced from the regions examined.

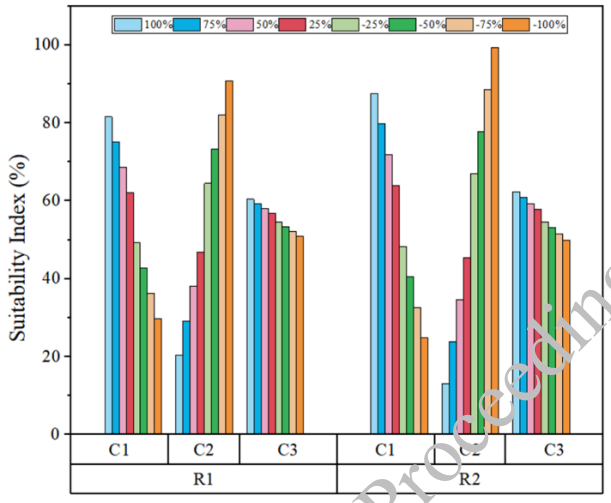

Figure 2. Variation of suitability index with the variation in weightage of the criteria considered for the study

Table 1. Quantity of agro-waste ashes generated in the study regions

Region	Quantity of rice husk ash generated (‘1000 tons)	Sugar Plant code	Quantity of bagasse ash generated (tons)
R1	65.3	S1	4200
		S2	2100
		S3	6720
R2	70.67	S4	8400
		S5	9240
		S6	9240
		S7	4200
		S8	2100

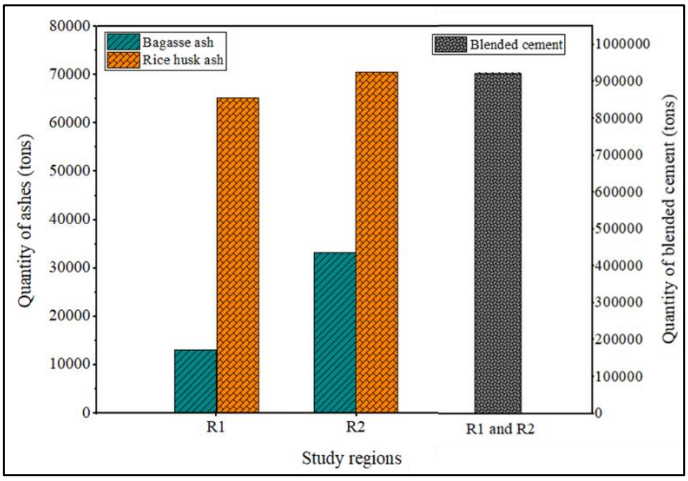

Figure 3. Quantities of bagasse ash, rice husk ash and blended cements generated in the study regions

Figure 3 visually depicted the amounts of bagasse ash, rice husk ash, and agro-waste ashes blended cements. The abundance of rice husk is significantly more in amount when compared to sugarcane bagasse ash. The surplus rice husk ash can be sent to other cement facilities to be used in the production of ternary or binary blended cements. Moreover, these cements blended with agro-waste ash not only promote sustainable construction but also make a significant positive impact on the environment.

3. Conclusions

Ashes derived from agricultural waste blended cements play a vital role in encouraging sustainable construction approaches. The integration of agricultural waste into cement production not only promotes the sustainable progress of the building industry but also supports a more circular economic framework, thereby benefiting both urban and rural communities. The future study aims to apply the proposed methodology to any region of India with little modifications.

4. Acknowledgements

This research was funded by the Birla Institute of Technology and Science - Pilani CDRF grant-C1/23/231 and the Ministry of Human Resources and Development, India's SPARC project Grant-P2360.

References

C. N. Wang, T. T. Tsai, and Y. F. Huang, "A model for optimizing location selection for biomass energy power plants," Processes, vol. 7, no. 6, 2019. DOI: 10.3390/pr7060353.

N. D. Directorate of Economics & Statistics, Ministry of Agriculture and Farmers Welfare, Govt. Of India, "Area Production Yield Statistics," 2021.

R. Bhosale, A. Nale, P. More, and D. Rajmane, “Partial Replacement of Cement by using Rice Husk Ash and Sugarcane Bagasse Ash,” Int. J. Adv. Res. Sci. Commun. Technol. Int. Open-Access, Double-Blind, Peer-Reviewed, Ref. Multidiscip. Online J., vol. 3, no. 3, pp. 326–334, 2023, doi: 10.48175/IJARSCT-11454.

Sugar Technologists Association of India, "List of Govt. Sugar Factories (India, Bangladesh, Nepal, Pakistan & Sri Lanka) and Refineries & Distilleries (India, Bhutan & Nepal) 2018."

Second Order Reliability Assessment of Reinforced Concrete under Corrosive Environment

A. Kumar[1], A.K. Rathi[2*]

[1] Department of Civil Engineering, Indian Institute of Technology (ISM), Dhanbad, India
Email: 23dr0010@iitism.ac.in
[2] Department of Civil and Infrastructure Engineering, Indian Institute of Technology, Jodhpur, India,
Email: akrathi@iitj.ac.in

[*]Corresponding author

ABSTRACT

This study aims to determine of the time-dependent variability of corrosion in the reinforced concrete (RC) structure. The quantity of corrosion loss impacts the mechanical performance of RC structure, resulting in ductile yielding or brittle fracture. Determination of the uncertainty and its propagation in corrosion model faces challenges since the inspection data is limited. Hence, effective corrosion models are required to estimate the uncertainty and reliability of existing infrastructures subjected to such environmental impact. In this study, two common types of corrosion, viz. uniform and pitting are considered for mathematical modelling. A flexural limit state for simply supported RC beam subjected to uniformly distributed load is adopted for the probabilistic framework of the aforementioned corrosion types to illustrate the proof of concept. Sensitive variables in the limit state are identified using Pearson correlation coefficient and Sobol's sensitivity indices. Fragility curves are developed for these sensitive design variables for the entire service life of the structure. This helps in assisting the user/designer to assess the uncertainty propagation and predicting the reliability of the structure after certain years of service. Additionally, the study compares different gradient-based reliability methods such as first order reliability method (FORM) and second order reliability method (SORM) to estimate the probability of failure. It is observed the Tvedt's SORM provides fairly accurate estimation among the other approximate methods used in this study.

KEYWORDS*: Corrosion Modelling, Reliability Analysis, Sensitivity Analysis, Uncertainty Quantification, Service Life*

1. Introduction

Progression of corrosion in RC structures through cracks often result in changes in structural behaviour from ductile to brittle (Stewart, 2009). Further, the effect of uncertainty in material properties, strength, degradation rates, exposure etc. impacts the extent of corrosion and performance of the structure. Hence, the objective of this study is to quantify the probabilistic effect on a RC structure due to corrosive environmental impact such as uniform and pitting corrosion. It involves determination of the sensitivity of the design variables of a RC structure subjected to the corrosion effect. Also, uncertainty quantification and reliability assessment of the design parameters associated with corroded rebars to estimate its structural performance over time. Predicting the probability of failure of structural components for a certain exposure period will help in better understanding the failure behaviour. Also, it will allow planning the preventive maintenance, regular repair and retrofitting to enhance the performance as well as service life of structure.

2. Probabilistic Corrosion Modelling

Different chemical attack causes varied types of corrosion and the rate of corrosion i_{corr} depends on the nature of chemical or environmental exposure. Uniform corrosion is an acidic or alkaline environmental attack on uppermost metal surface with the same rate whereas the pitting corrosion is a localized corrosion in which holes or cavities are observed in the material and the rates of corrosion is higher in concentrated

regions. The corrosion modelling adopted in this study defines the level of deterioration due to corrosion at which failure tends to occurs. For a simply supported corrode RC beam with distributed loading, the limit state function expressed as (Stewart, 2009)

$$g = \eta(\Omega)A_s(t,\Omega)f_y(t,\Omega)\left(d(\Omega) - K(\Omega)\frac{A_s(t,\Omega)f_y(t,\Omega)}{b(\Omega)f_c(\Omega)}\right) - \lambda(\Omega)M_n(\Omega) \quad (1)$$

Eqn. 1 is based on flexural failure as the highest bending moment at mid span. In eq. (1), f_c, f_y, D_0, b, d, c, η, K, λ, α, t and M_n denote compressive resistance of concrete, yield strength of steel bars, bar diameter, width of RC beam section, depth of the section, concrete clear cover, modal coefficient, resistance ratio, load coefficient, yield empirical coefficient, corrosion initiation time and applied moment, respectively. Different probability distributions are considered in this study such as normal, lognormal and Gumbel.

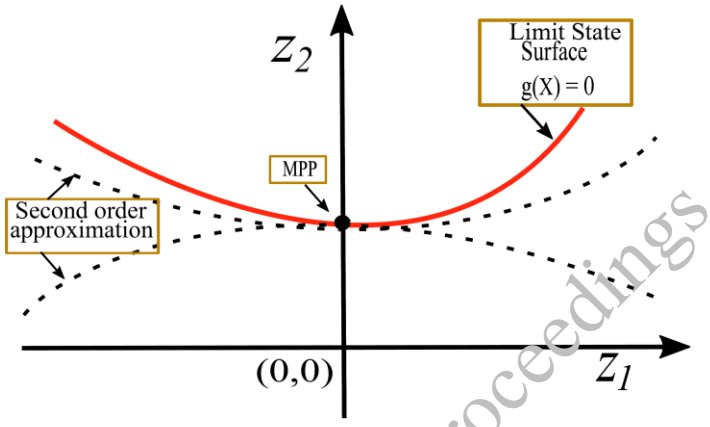

Figure 1. Second order approximation of the performance function

Further, the performance function is subjected to sensitivity and reliability analysis. The sensitivity analysis includes Sobol's sensitivity analysis and Pearson correlation coefficient. The reliability assessment is performed using Monte Carlo simulation (MCS), first order reliability method (FORM), second order reliability method (SORM) and their versions. MCS provides a direct approach based on random sampling whereas FORM is based on the line sampling technique, which calculates the minimum distance of limit state surface from the origin in the standard Gaussian space. This distance is known as reliability index β. However, if the performance function is highly nonlinear, second order reliability methods can be used for the evaluation of reliability assessment. A second-order Taylor's series expansion of the performance function around the most probable failure point (MPP) allows these approaches to obtain better reliability estimates as shown in Figure 1. In this study, different SORMs such as Breitung (1984), Tvedt (1990), Hohenbichler and Rackwitz (1988) and Koyluoglu and Nielsen (1994) are considered (Breitung, 1984; Hohenbichler & Rackwitz, 1988; Koyluoglu & Nielsen, 1994; Tvedt, 1990).

Breitung's formulation uses a Laplace approach for asymptotic approximation of multidimensional integrals, the probability of failure is given by

$$p_f = \Phi(-\beta)\prod_{i=1}^{n-1}(1 + k_i\beta)^{-\frac{1}{2}} \quad (2)$$

Improving the Breitung's formulation, Tvedt (Tvedt, 1990) has derived a three-term approximation by ignoring higher order terms (i.e. beyond second order). The probability of failure is estimated using the first term is the p_f for the Breitung's method. The p_f for Tvedt's method is given by $p_f \approx A_1 + A_2 + A_3$, such that

$$A_1 \approx \Phi(-\beta)\prod_{i=1}^{n-1}(1 + k_i\beta)^{-\frac{1}{2}} \quad (3)$$

$$A_2 = [\beta\Phi(-\beta) - \phi(\beta)]\left\{\prod_{i=1}^{n-1}(1 + k_i\beta)^{-\frac{1}{2}} - \prod_{i=1}^{n-1}(1 + k_i(\beta+1)^{-\frac{1}{2}}\right\} \quad (4)$$

$$A_3 = (1+\beta)[\beta\Phi(-\beta) - \phi(\beta)] \times \left\{\prod_{i=1}^{n-1}(1+k_i\beta)^{-\frac{1}{2}} - Re\left(\prod_{i=1}^{n-1}(1+k_i(\beta+1)^{-\frac{1}{2}}\right)\right\} \quad (5)$$

where, $Re(\cdot)$ denotes the real part of a complex number. Overall, the accuracy of probability of failure depends on the nature of response surface which follows limit state surface more closely.

3. Results and Discussions

Firstly, the sensitivity analysis is performed to identify the significant input parameters influencing the performance function. Following it, reliability assessment is performed using MCS, FORM and SORM. The MCS is performed with a large sample size and its results serve as benchmark in this study to evaluate the accuracy of gradient-based methods (i.e. FORM and SORM). Figure illustrates the sensitivity analysis of the Sobol's first order and total sensitivity indices as well as Pearson correlation coefficient for each input parameter involved in performance function of uniform and pitting corrosion. The sensitivity indices of parameters f_y, D_0, M_n, d and η have significant values, however the parameters f_c, b, c, α, K, λ, R and t show marginal first order sensitivity index and nearly zero total sensitivity index. Hence, the sensitive variables are considered further in the reliability analysis for efficient application.

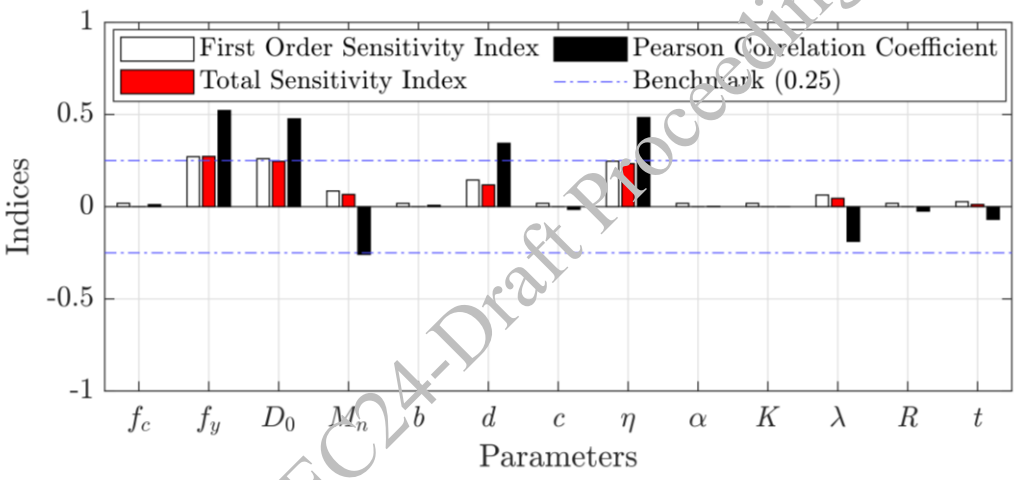

Figure 2. Sobol's first order as well as total sensitivity index and Pearson correlation coefficient of input parameters

The reliability assessment performed using MCS, FORM and SORM results in β value of 3.093 and 3.254 for uniform and pitting corrosion, respectively. It is observed that among the approximate methods considered in this study, Tevdt's SORM performs better with approx. 2.6% and 11.9% error for the given limit state based on uniform and pitting corrosion, respectively. Further, a total of 184 fragility curves are developed in this study using the Tevdt's SORM. Figure 3 illustrates different fragility curves for different mean values of f_y and D_0. The propagation of uniform as well as pitting corrosion due to uncertainty in input parameters effect the overall reliability performance over the life span of the RC beam up to 100 years. This effect is neither consistent nor linear in nature and hence, such scenarios reflect the utilization of the fragility curves which helps in the prediction of the failure and allows the user/designer to plan for the preventive maintenance, regular repair and retrofitting to enhance the performance as well as service life of the structure.

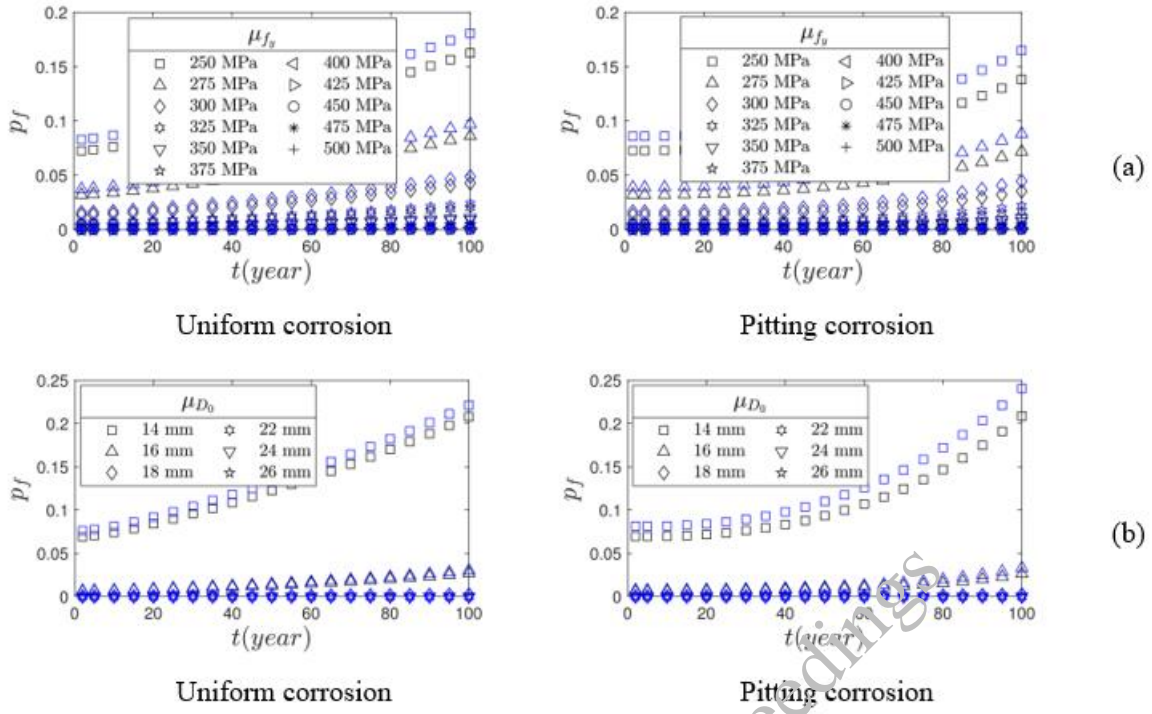

Figure 3. Fragility curve using Tvedt's SORM for different mean values of (a) f_y and (b) D_0

4. Conclusions

The study performs the time-varying reliability analysis of a RC beam subjected to uniform and pitting corrosion. Sobol's index and Pearson correlation coefficient concludes that the limit state function based on bending moment of the corroded RC beam is sensitive to the design parameters such as yield strength of steel, bar diameter, effective depth of the beam and corrosion model coefficient. Second order reliability methods are used to estimate the probability of failure where the Tvedt's method performs better. Multiple fragility curves are developed in this study with different mean values of the design parameters for 100 years of service using the Tvedt's SORM. The study indicates the accelerating increase in the probability of failure over time due to corrosion in reinforcement bars, thus significantly reducing the reliability of the structure. In field applications, estimating the probability of failure is difficult due to the scarcity of data and hence, such studies help in filling the necessary gap to assess the reliability of the structure.

References

Breitung, K. (1984) "Asymptotic Approximations for Multinormal Integrals", *Journal of Engineering Mechanics*, 110(3): 357–366

Hohenbichler, M., & Rackwitz, R. (1988) "Improvement of Second-Order Reliability Estimates by Importance Sampling", *Journal of Engineering Mechanics*, 114(12): 2195–2199

Koyluoglu, H. U., & Nielsen, S. R. K. (1994) "Structural Safety New Approximations for SORM Integrals", Structural Safety, 13(4): 235–246

Stewart, M. G. (2009) "Mechanical behaviour of pitting corrosion of flexural and shear reinforcement and its effect on structural reliability of corroding RC beams", *Structural Safety*, 31(1): 19–30

Stewart, M. G., & Al-Harthy, A. (2008) "Pitting Corrosion and Structural Reliability of Corroding RC Structures: Experimental Data and Probabilistic Analysis" *Reliability Engineering and System Safety*, 93(3): 373–382

Tvedt, L. (1989) "Second Order Reliability by an Exact Integral", *Reliability and Optimization of Structural Systems*, 88: 377–384

Zhang, M. Q., Beer, M., Quek, S. T., & Choo, Y. S. (2010) "Comparison of uncertainty models in reliability analysis of offshore structures under marine corrosion", *Structural Safety*, 32(6): 425–432

Fracture Behaviour of High-Strength Concrete with Progressive Recycled Aggregate Replacement

Sourav Chakraborty[1*] and Kolluru V. L. Subramaniam

[1] Research Scholar, Hyderabad, India
Email: ce18resch11008@iith.ac.in
[2] Professor, Hyderabad, India
Email: kvls@ce.iith.ac.in

[*] Corresponding author

ABSTRACT

An experimental investigation into the fracture behaviour of high-strength concrete with progressive recycled coarse aggregate (RCA) replacement of 0, 30, 60 and 100% is presented. Compared to concrete with natural aggregate, with increasing RCA replacement, a progressive increase in fracture surface area was observed, while there is a similar reduction pattern in the tensile strength as well as fracture energy. Crack propagation and crack opening in fracture response are evaluated using the digital image correlation (DIC) technique. The crack growth and propagation are evaluated from the discontinuity in the surface displacements measured using DIC. A cohesive stress crack opening relationship is established from the experimental load-CMOD data, which provides insight into the post-cracking behaviour. Initial stress loss after cracking is quicker with increasing RCA replacement. Fractured surface areas were scanned using an optical laser scanner, and the fracture surfaces were evaluated to develop an insight into the fracture in RAC. Fracture planes were identified in both natural and recycled aggregate concrete. The intricate interplay of tensile strength, cohesive response and features of fractured surfaces on failure mechanisms and energy requirements for the creation of each new unit crack length with progressive recycled coarse aggregate replacement level is discussed in this study.

KEYWORDS*: Concrete fracture, Recycled aggregate concrete, Cohesive stress crack opening relation, Digital Image Correlation, Interfacial Transition Zone.*

1. Introduction

In place of virgin natural aggregate, RCA recovered from demolished concrete constructions is used more frequently. The use of RCA is increasingly promoted to meet the increasing demand for concrete while simultaneously considering the limited available supply of natural aggregate and lessening the environmental impact of producing natural aggregate. It also enables profitable utilisation of the construction waste in concrete manufactured with RCA. Design codes have started allowing RCA in concrete to be used in structural concrete. Due to its effect on strength and durability (Dhir et al., 2019; Musiket et al., 2016a), RCA use in concrete is now restricted to coarse aggregate (Pedro et al., 2014) at a 30–40% replacement level. Because of the attached mortar part, RCA tends to be more porous, which results in greater water absorption. A large volume of water is absorbed by the adhering mortar's pores, which makes concrete harder to work with and less durable (Dhir et al., 2019; Musiket et al., 2016a). The mechanical characteristics of concrete decline noticeably at high replacement levels (Kim et al., 2018). The packing of the concrete near the ITZ zone also varies when the matrix strength changes, which impacts the concrete's tensile and fracture behaviour. More coarse particles begin to break as the concrete's matrix strength increases, modifying the failure process and potentially affecting the concrete's ductility and fracture properties. With lower compressive strength, the new ITZ is very weak under compressive loading. With increasing compressive strength, old ITZ becomes the weak link under compression. The influence of matrix strength on the compressive strength of RCA concrete has been studied, but the effect of matrix strength on the fracture process in RCA has not been explored in the literature. The tensile strength of

concrete with RCA also decreases due to three kinds of ITZs (old mortar to the matrix, old mortar to aggregate, and aggregate to matrix) (Musiket et al., 2016b). It is demonstrated that the compressive strength is more responsive to replacement levels than the split tensile strength. The fracture mechanism of the RCA beams for high-strength concrete is yet to be evaluated. Changes in the fracture parameters and crack growth mechanism in the fracture are presented in this study. How a fractured surface is formed in NAC and RAC is studied. This study aims to understand the difference in fracture behaviour of high-strength NAC and RAC beams.

2. Results and Discussion

2.1 Fracture Response

The average response recorded from four specimens is plotted in Figure 1. While a similar peak load was observed for 30% replacement of RCA, there is a progressive decrease in the peak load beyond 30 % replacement. From NAC to RAC, the peak load in the fracture test response decreased by 16.3%. Fracture responses also indicate a progressive decrease in the area under the load-CMOD curve beyond the 30% replacement level. Hence, the overall trends indicate a decrease in fracture energy beyond the 30% replacement level of RCA.

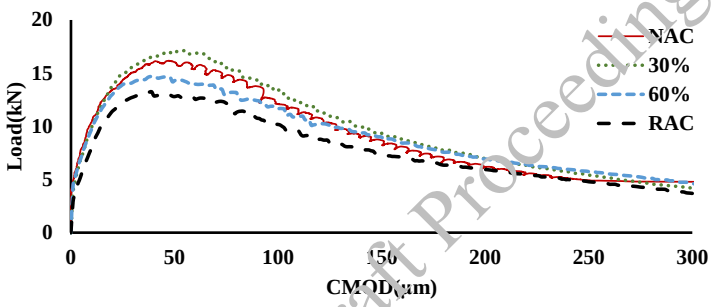

Figure1. Load-CMOD Response of NAC, RCA replacement levels of 30%, 60% and RAC

2.2 Cohesive Response

The average cohesive response of beams with increasing RCA replacement ratio is presented in Figure 2. The initial stress values are the tensile strength of the concrete. Up to 30% replacement, there is no decrease in the tensile strength. However, for 60 and 100% replacement, there is a decrease in the tensile strength. There is not much difference in the initial stress loss after the cracking up to 60% replacement ratio. For a 100% replacement ratio, though, the initial stress loss is quicker compared to NAC beams. However, after the quicker initial stress loss, the cohesive stress values are very similar in all the cases.

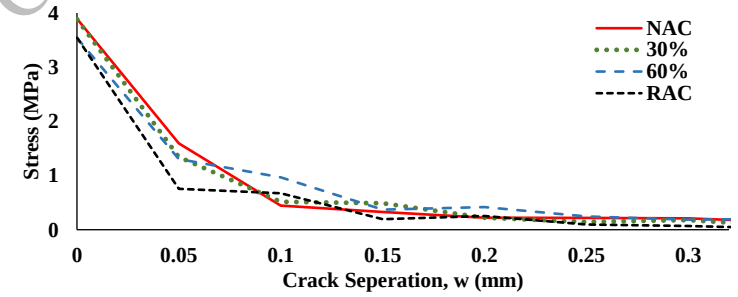

Figure 2. Cohesive Response of NAC, RCA replacement levels of 30%, 60% and RAC

2.3 Characterisation of Fractured Surfaces

Fractured surfaces from NAC and RAC beams are shown in Figure 3. The black boxes indicate the aggregates plucking out from the matrix, and the red boxes mark the aggregates that are broken in the fracture process. Boxes of the same shape in the top and bottom parts of the image indicate the same

positions on the left and right sides of the fractured surfaces. While some of the aggregates have started breaking in NAC beams, all the aggregates in RAC beams have been broken.

Figure 3. Fractured Surface of (a) NAC and (b) RAC

Figure 4 shows the typical surface undulations in NAC and RAC beams. The frequency distribution of these undulations does not follow a normal distribution and is bimodal in nature. In these cases, surface area is not a good measurement of roughness, and the kurtosis gives a better measurement (Thomas, n.d.). When measured, there was a decrease noticed in the normalised surface area, but the kurtosis value increased from NAC to RAC beams. This means that instead of having a higher surface area, the roughness of the NAC beams is lower than the RAC beams. Due to the violent production procedure, there are some internal cracks already present in the aggregates. When the fracture takes place, small undulations are created due to the random alignment of those cracks compared to NAC beams, where a flatter fractured-surface is generated.

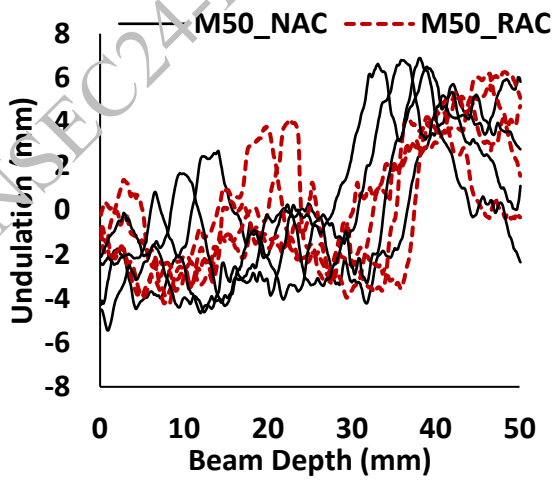

Figure 4. Typical Surface Profiles from the tensile fracture in NAC and RAC

2.4 Crack Growth Analysis

After determining the individual crack depth-load CMOD response, it is presented as an average response with scatter bars indicating the range. Figure 5 shows the changes in the mechanical work of fracture (W_F) and crack depth with increasing CMOD for the concretes of different compressive strengths made with NCA and RCA. The W_F was computed as the area under the fracture load response. The W_F of RAC is lower than NAC for all the values of CMOD. The difference in the W_F between the NAC and the RAC increases with the crack opening. The trends in the crack depth are, however, different. Initially, at small CMOD, the crack depth in M50-NAC is significantly larger than the corresponding crack depth in M50-

RAC. The difference decreases with increasing CMOD. This shows that instead of lower fracture energy, the RAC beams are less brittle than the NAC beams.

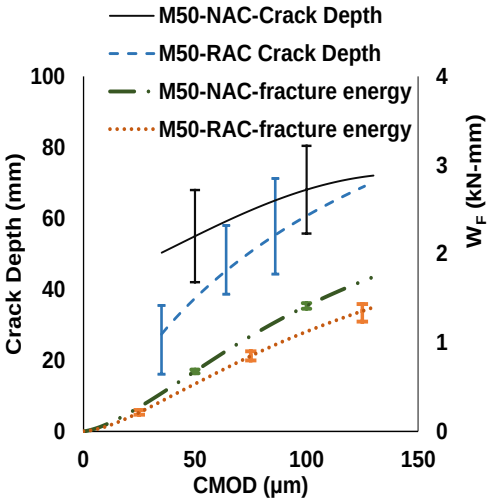

Figure 5. Variation of Fracture energy and crack depth between NAC and RAC with increasing CMOD

3. Conclusions

Fracture tests for NAC and RAC for M50 grades of concrete were conducted. Post cracking cohesive stress response was obtained using inverse analysis. The fracture surface characteristics, crack depth, and fracture energy were evaluated as a function of crack propagation. The conclusions from the analysis and main findings are given below.

- The RAC has a lower tensile strength than the NAC. The decrease in the tensile strength is less sensitive to RCA replacement than the compressive strength.
- The cohesive response indicates a more rapid decrease in the initial residual stress for RAC.
- The crack extension-crack opening indicates a lesser crack depth in RAC than NAC for the same crack mouth opening displacement.
- For crack penetration under the stress field produced by flexure, RAC requires less fracture energy with increasing crack mouth opening. RAC shows better performance in terms of ductility and becomes less brittle than NAC.

References

Dhir, R. K., de Brito, J., Silva, R. V. and Lye, C. Q. (2019) "Properties and Composition of Recycled Aggregates", *Sustainable Construction Materials*

Kim, Y., Hanif, A., Kazmi, S. M. S., Munir, M. J. and Park, C. (2018) " Properties enhancement of recycled aggregate concrete through pretreatment of coarse aggregates – Comparative assessment of assorted techniques", *Journal of Cleaner Production*, *191*: 339–349

Musiket, K., Rosendahl, M. and Xi, Y. (2016a) " Fracture of Recycled Aggregate Concrete under High Loading Rates", *Journal of Materials in Civil Engineering*, *28*(6): 04016018

Musiket, K., Rosendahl, M. and Xi, Y. (2016b) "Fracture of Recycled Aggregate Concrete under High Loading Rates", *Journal of Materials in Civil Engineering*, *28*(6): 04016018

Pedro, D., De Brito, J. and Evangelista, L. (2014) "Influence of the use of recycled concrete aggregates from different sources on structural concrete", *Construction and Building Materials*, *71*:141–151

Thomas, R. (n.d.). *Characterization of surface roughness*.

Surface Modification of Recycled Concrete Aggregate with Magnesium Based Cement

Y.R. Patil[1*], V.A. Dakwale[2], and R.V. Ralegaonkar[3]

[1] PhD Research Scholar, VNIT Nagpur, India
Email: yuvrajpatil14@gmail.com.com
[2] Assistant Professor, VNIT Nagpur, India
Email: vaidehidakwale@civ.vnit.ac.in
[3] Professor, VNIT Nagpur, India
Email: rvralegaonkar@civ.vnit.ac.in

[*] Corresponding author

ABSTRACT

Recycled concrete aggregate (RCA) is a major component of construction and demolition (C&D) waste. RCA has become increasingly popular in construction owing to its environmental benefits. However, their use in structural applications is limited owing to their inferior physical and mechanical properties. This study presents an innovative method for improving the physical and mechanical properties of RCA. This study explored the impact of magnesium-based cement on the physical, mechanical, and microstructural properties of RCA. A dry-mix and wet-mix process was developed and implemented to improve the physical, mechanical, and microstructural properties of RCA. Furthermore, the mechanical properties of Recycled Aggregate Concrete (RAC) mixes with modified recycled concrete aggregate (MRCA) were examined in terms of the compressive strength, flexural tensile strength, splitting tensile strength, and abrasion resistance. The MRCA showed considerable improvements in terms of water absorption, specific gravity, aggregate impact value, and crushing value by an average of 7.1%, 4.6%, 24.7%, and 10.0%, respectively, and the corresponding performance of the concrete made up of MRCA was significantly enhanced. MRCA, with enhanced compressive strength, flexural tensile strength, splitting tensile strength, and abrasion resistance results, is a promising alternative to traditional RCA in higher-grade concrete production. Although there are several different methods to treat RCA, the present method is effective in terms of treatment time and strength enhancement rate. This innovative approach aims to make RCA a viable option for use in various structural applications, reducing reliance on traditional concrete materials and promoting sustainable construction practices.

KEYWORDS: *Magnesium Phosphate Cement, Recycled Concrete Aggregate, Recycled Aggregate Concrete, Microstructural Properties, Physical Properties*

1. Introduction

Construction and Demolition (C&D) waste management has become a growing concern in rapidly developing municipal regions. Approximately 27 billion tons of C&D waste are projected to be generated worldwide by 2050 (Singh & Singh, 2016). Recycled Concrete aggregate (RCA) constitutes nearly 60% of C&D waste (B. Wang et al., 2021). When concrete is crushed to the desired particle size, the parent mortar adheres to the aggregate particle surface (Rao et al., 2011). This mortar was porous and lightweight. The adhered mortar RCA has a lower specific gravity (SG), high water absorption (WA), higher aggregate crushing value (ACV), and aggregate impact value (AIV) (Fang et al., 2023; Zhan et al., 2014). These properties limit its use to ordinary strength-grade concrete as per IS 383:2016 and limit its application to non-important concreting works (Maduabuchukwu Nwakaire et al., 2020). Thus, processing and property modification may enable RCA as a potential replacement for natural aggregate (NA) in standard and high-strength concrete applications. In the past, several methods have been investigated for the property modification of RCA.

Methods for enhancing the properties of RCA can be categorized into two groups: (1) removal of adhered mortar, such as ball milling, microwave heating, ultrasonic cleaning, pre-soaking in acidic solutions, and mechanical rubbing (J. Wang et al., 2020; R. Wang et al., 2020a); and (2) methods for strengthening the adhered mortar, including nano particle treatments, biocementious material intrusion, and cementitious materials (Kazmi et al., 2019; Li et al., 2021; R. Wang et al., 2020b). This study investigates the impact of magnesium phosphate cement (MPC) as a surface modifier on the physical, mechanical, and surface morphological properties of RCA. MPC was adopted as a surface modifier owing to its fast setting ability and finer nature.

2. Material and Methodology

2.1 Material

Grade 53 ordinary Portland cement (OPC), natural aggregate (NA), and river sand (RS) were purchased locally and utilized as basic constituents in concrete. A commercially available material, magnesium phosphate cement (MPC), was used as a surface modifier. RCA was sourced from Mate Associates in Nagpur, India and crushed to a size range of 10–20 mm. Table 1 lists the physical properties of these materials.

Table 1. Physical properties

Matrial		WA (%)	Standard Consistency	SG	AIV (%)	ACV (%)	Compressive Strength (N/mm^2)	Final setting time (min)
Binder	OPC	-	33	3.14	-	-	54.25 (28 Days)	355
	MPC	-	11.75	-	-	-	25.51 (02 Hours)	05
							31.42 (24 Hours)	
Aggregate	NA	2.63	-	2.62	8.14	18.14	-	-
	RCA	8.73	-	2.12	12.65	25.00	-	-
	RS	2.92	-	2.72	-	-	-	-

2.2 Methodology

Four modified approaches (MRCA I–IV) were developed. The ratio of MPC to RCA was 1:8 by weight and the ratio of water (W) to MPC was 0.4 by weight. After treatment, the modified recycled concrete aggregate (MRCA) was soaked in water for three days. M-40 grade of concrete was designed for severe exposure in accordance with IS 10262-2009, The ratio of water to cement was 0.4 by weight and the designed slump was 100 mm. The design mix is listed in Table 2.

Table 2. M-40 Grade Concrete Trials

Sl.No.	Concrete Mix Type	Cement (OPC-53) 420 kg/m^3	Fine Aggregates (River Sand) 634 kg/m^3	Coarse Aggregate 1178 kg/m^3			Treatment Method
				NA (%)	RCA (%)	MRCA (%)	
1	Controlled Mix			100	-	-	-
2	RAC			50	50	-	-
3	MRAC-I			50	-	50	Powder Coating-Dry RCA
4	MRAC-II			50	-	50	Slurry Intrusion-Dry RCA
4	MRAC-III			50	-	50	Powder Coating-Soaked RCA
5	MRAC-IV			50	-	50	Slurry Intrusion - Soaked RCA

2.2.1 Testing

The aggregate samples were tested for WA, SG, AIV, and ACV as per the standards IS 2386 (Part III) and IS 2386 (Part V) of 1963. In addition, the surface structure was examined using scanning electron microscopy (SEM). The compressive and flexural strengths of the concrete specimens were tested according to the IS 516 (1959) guidelines. The splitting tensile strength was determined according to the specifications of the IS 5816:1999. Abrasion resistance was assessed to evaluate their durability and wear characteristics, following the guidelines established in the Indian Standard IS 13630-11 (2006).

3. Result and Discussions

3.1 Surface Morphology

SEM images of the RCA are shown in Figure 1. The morphology is a fractured, porous, and adhered mortar that is unevenly spread, and it has many voids and surface cracks of size greater than μm. This leads to a higher WA and reduced strength. SEM images of MRCA-IV (Figure 2) show a reduction in the voids and surface cracks due to adsorption and intrusion of MPC on and into the surface of RCA, leading to a reduction in WA; its SG increases. Figure 3 shows MRCA-IV.

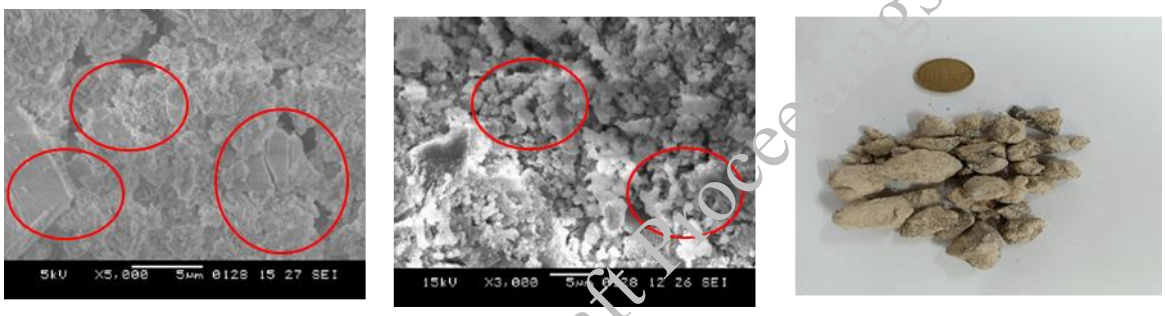

Figure 1. SEM of RCA 2: SEM of MRCA-IV 3: MRCA-IV

Table 3. Properties of M-40 grade concrete at 28th day

Sl.No.	Sample	Compressive Strength (N/mm^2)	Splitting Tensile Strength (N/mm^2)	Flexural Strength (N/mm^2)	Abrasion Weight Loss (%)
1	NA-C	50.28	3.1	4.97	1.42
2	RAC	35.83	2.29	4.2	1.68
3	MRAC-I	38.61	2.61	4.34	1.87
4	MRAC-II	45.01	2.89	4.7	1.7
5	MRAC-III	48.26	3.01	4.82	1.61
6	MRAC-IV	57.3	3.18	5.3	1.41

3.2 Physical properties of Aggregates

The influence of MPC treatment on the RCA was analysed by comparing the mechanical and physical properties with respect to the MRCA. Figure 4 to 7 shows the variation in mechanical and physical properties of all types of aggregates used in this experimental study. MRCA-IV shows significant improvements in all the properties. Water absorption decreased by 34.36 %, specific gravity increased by 17.45 %, AIV and ACV decreased by 14.78 % and 16.68% respectively.

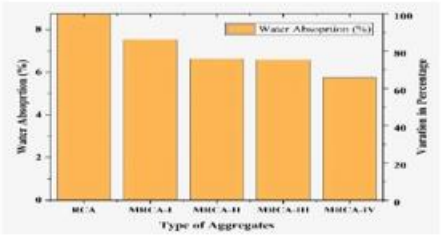

Figure 4. WA of Aggregates

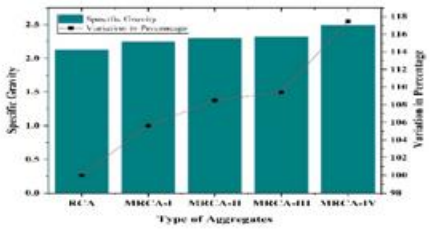

Figure 5. SG of Aggregates

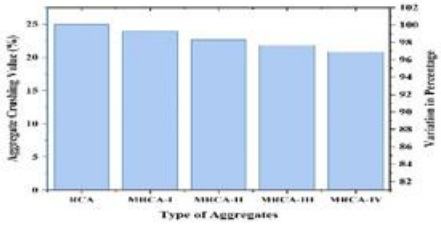

Figure 6. ACV of Aggregates

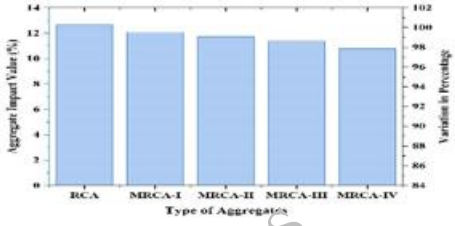

Figure 7. AIV of Aggregates

3.3 Mechanical properties of RAC

To analyze the effect of MPC treatment, M-40 grade concrete was cast in a controlled environment, and its mechanical properties were found to be in accordance with IS 456:2000 at an ages of 28th days. Table 3 presents the results.

4. Conclusions

Based on the present experimental study, the following conclusions were drawn:

- In comparison with dry RCA modification, soaked RCA showed higher enhancement in the physical, mechanical, and surface morphological properties of RCA.
- The concrete made up with 50 percent replacement of NA with MRCA-IV shows enhancements in the engineering properties as compared to the concrete made up with NA. Moreover, its compressive strength was 58 percent higher than that of the RAC.
- The soaking of RCA, followed by surface modification with MPC, permits the replacement of NA with MRCA-III and IV up to 50 percent.
- The study demonstrates that up to 50% of NA can be replaced with aggregates treated with the wet mix method, overcoming IS 383:2016's 25% RCA replacement limitation, but highlighting the need for further research on curing period optimization.

References

Chakradhara Rao, M., Bhattacharyya, S. K., & Barai, S. V. (2011). Influence of field recycled coarse aggregate on properties of concrete. *Materials and Structures/Materiaux et Constructions*, *44*(1), 205–220. https://doi.org/10.1617/s11527-010-9620-x

Fang, B., Hu, Z., Shi, T., Liu, Y., Wang, X., Yang, D., Zhu, K., Zhao, X., & Zhao, Z. (2023). Research progress on the properties and applications of magnesium phosphate cement. In *Ceramics International* (Vol. 49, Issue 3, pp. 4001–4016). Elsevier Ltd. https://doi.org/10.1016/j.ceramint.2022.11.078

Kazmi, S. M. S., Munir, M. J., Wu, Y. F., Patnaikuni, I., Zhou, Y., & Xing, F. (2019). Influence of different treatment methods on the mechanical behavior of recycled aggregate concrete: A comparative study. *Cement and Concrete Composites*, *104*. https://doi.org/10.1016/j.cemconcomp.2019.103398

Li, L., Xuan, D., Sojobi, A. O., Liu, S., Chu, S. H., & Poon, C. S. (2021). Development of nano-silica treatment methods to enhance recycled aggregate concrete. *Cement and Concrete Composites*, *118*. https://doi.org/10.1016/j.cemconcomp.2021.103963

Maduabuchukwu Nwakaire, C., Poh Yap, S., Chuen Onn, C., Wah Yuen, C., & Adebayo Ibrahim, H. (2020). Utilisation of recycled concrete aggregates for sustainable highway pavement applications; a review. In *Construction and Building Materials* (Vol. 235). Elsevier Ltd. https://doi.org/10.1016/j.conbuildmat.2019.117444

Singh, N., & Singh, S. P. (2016). Carbonation resistance and microstructural analysis of Low and High Volume Fly Ash Self Compacting Concrete containing Recycled Concrete Aggregates. *Construction and Building Materials*, *127*, 828–842. https://doi.org/10.1016/j.conbuildmat.2016.10.067

Wang, B., Yan, L., Fu, Q., & Kasal, B. (2021). A Comprehensive Review on Recycled Aggregate and Recycled Aggregate Concrete. In *Resources, Conservation and Recycling* (Vol. 171). Elsevier B.V. https://doi.org/10.1016/j.resconrec.2021.105565

Wang, J., Zhang, J., Cao, D., Dang, H., & Ding, B. (2020). Comparison of recycled aggregate treatment methods on the performance for recycled concrete. *Construction and Building Materials*, *234*. https://doi.org/10.1016/j.conbuildmat.2019.117366

Wang, R., Yu, N., & Li, Y. (2020a). Methods for improving the microstructure of recycled concrete aggregate: A review. In *Construction and Building Materials* (Vol. 242). Elsevier Ltd. https://doi.org/10.1016/j.conbuildmat.2020.118164

Wang, R., Yu, N., & Li, Y. (2020b). Methods for improving the microstructure of recycled concrete aggregate: A review. In *Construction and Building Materials* (Vol. 242). Elsevier Ltd. https://doi.org/10.1016/j.conbuildmat.2020.118164

Zhan, B., Poon, C. S., Liu, Q., Kou, S., & Shi, C. (2014). Experimental study on CO2 curing for enhancement of recycled aggregate properties. *Construction and Building Materials*, *67*, 3–7. https://doi.org/10.1016/j.conbuildmat.2013.09.008

The Durability of Belitic Calcium Sulfoaluminate Cement Concrete

Eric P. Bescher*

Department of Materials Science and Engineering, University of California Los Angeles Los Angeles CA 90095
Email: bescher@ucla.edu

*Corresponding author

ABSTRACT

In this review, we cover current knowledge on belitic calcium sulfoaluminate (BCSA) cement and concrete, including specifications and several aspects of durability. Alternative, rapid-strength binders such as Belitic Calcium Sulfoaluminate (BCSA) are increasingly important to meet the growing demand for rehabilitation and fast return to service of roads and bridges, in addition to their low-carbon appeal. Speed of construction, low shrinkage, and low carbon footprint are the key features of BCSA concrete. The binder was first developed in the United States in the mid-seventies. It allows pavement, bridge decks and other concrete infrastructure to be replaced and returned to service within hours. The durability of this concrete has not attracted significant attention thus far, and data on the performance is occasionally contradictory. We report that BCSA concrete slabs placed at the Seattle International Airport (SEA) in the 1990s later has doubled in strength after 23 years in service. BCSA concrete placed on California freeways has tripled in strength in 30 years. This paper reviews several aspects of the durability of BCSA cement concrete and addresses some of the differences between field performance and laboratory performance.

KEYWORDS: *Belitic Calcium Sulfoaluminate, low carbon cement, durability, BCSA*

1. Introduction

In this review, we report on several aspects of the durability of Belitic Calcium Sulfoaluminate Cement (BCSA) cement. We cover how the material is specified, which is a key factor in the assessment of durability. BCSA was developed in the mid-70s following the work on calcium sulfoaluminate (CSA) cement by Alexander Klein at UC Berkeley. It differs from Portland cement in that the main reactive compound in this cement is ye'elimite, a fast-hydrating compound. It differs from traditional CSA cements in that it is generally not blended with Portland cement and remains essentially Portland-free. As such, it can be considered as belonging to a separate class of binders. BCSA exhibits a unique range of characteristics: rapid strength, low shrinkage, and reduced carbon footprint. The literature reports a reduction in Global Warming Potential of up to 30% compared to Portland cement, at 673 kg-eq CO_2/tonne. Sustained commercial production is decades old in North America. In general, the mineralogy of this materials deviates significantly from that of Portland cement, as does the hydration mechanisms. Despite commercial success, classification, standards and specifications are in their infancy and when they do exist, are usually *ad hoc* or even prescriptive. Part of the difficulty in the acceptance of CSA cements is that they are considered alternative cements, and by definition do not fit established standards. Therefore, despite their attractiveness as a low-carbon alternatives to Portland cement, specifications lag behind commercial need and appeal. For example, the main incentive for the use of BCSA is the significant shortening in time of construction time, compared to Portland cement. They are frequently used for rapid construction or repair of pavements, or as accelerating additives in dry mix mortars. This is a unique economic opportunity for a low-carbon binder, especially in the absence of economic incentives for a low-carbon binder. This ist he reason why ASTM C1600, a protocol for fast-setting cements, has been one of the first standard applied to BCSA.

What is BCSA? BCSA lacks a formal definition, but in general it is accepted that BCSA is a cement in which the most abundant phase is belite, and the second most abundant phase is ye'elimite. The presence of calcium sulfate is required in order to form ettringite upon hydration, the presence of which causes early strength development. For clarity, a cement that contains more ye'elimite than belite is not considered to

be a BCSA, but rather, a CSA cement that contains belite. Several manufacturers market a cement based on a clinker containing approximately 50% ye'elimite and 18% belite- this is not a BCSA cement but a CSA cement typically requiring blending with Portland cement. Table 1 shows an example of a BCSA cement (CTS Rapid Set®)

Table 1- Mineralogical composition of the BCSA cement used in this study.

Phase	wt%
Major	
Belite	50.3
Ye'elimite	29.8
Anhydrite	11.2
Minor	
Calcite	3.9
Bassanite	2.9
Ferrite	2.0

The importance of standards on assessment of the durability of BCSA cement. Ye'limite cements of either type discussed above lack standardization. This is an important fact when discussing durability because it is very difficult to assess durability without suitable, agreed-upon standards. Some performance standards actually exclude alternative cements in testing protocols. This does not mean that BCSA itself does not meet any standard. In fact, BCSA materials do meet some standards. While the cement itself does not meet ASTM C150 for Portland cement or ASTM C1157, it meets ASTM C1600 for Rapid strength cement. C1600 is a performance standard that includes built-in performance criteria such as strength, shrinkage, ASR, sulfate expansion and a few others.

What is durability? The concept of durability is complex for traditional cements, and even more so for alternative cements because testing protocols generally developed for portland cement may or may not suitable for non-portland cement. As a result, durability in the laboratory does not necessarily translate to durability in the field, and conversely, lack of performance in the laboratory does not necessarily result in poor performance in the field. Also, durability has different meanings for different engineers. For example, pavement engineering involves design elements such as thickness and joint spacing. In this paper, we will discuss the performance of BCSA concrete slabs on California highways, shown to have a durability of up to 20 years depending on the magnitude of vehicular traffic. This measure of durability is typically a function of pavement thickness and joint spacing, hence it is as much a matter of design as a material property.

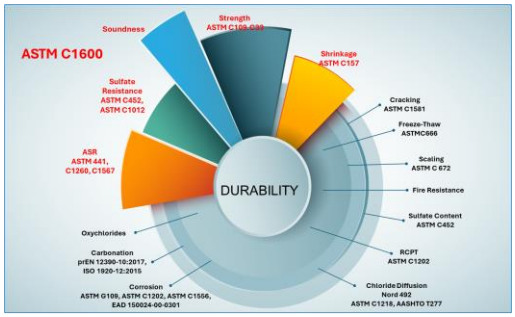

Figure 1. Durability protocols and ASTM C1600 BCSA concrete

Testing protocols and alternative cements.
A number of tests are routinely used to assess mortar or concrete durability in the laboratory. However, these protocols frequently apply exclusively to C150 (Portland) cements. For example, ASTM C441, ASTM C1260, ASTM 1293, ASTM G109 all require using a cement conforming to ASTM C150. This

opens the question of the applicability of some of these tests to alternative cements. Fitness for purpose must be questioned. It is possible that any result obtained for a cement non-conforming to C150 may be invalid. A number of reports based on portland protocols have questioned the performance of BCSA especially as it relates to corrosion resistance, carbonation and transport properties such as chloride ingress. A key feature to consider for BCSA cement is that BCSA hydration kinetics are both faster and slower than Portland cement. BCSA is faster to hydrate in the first hours, but slower to hydrate at later ages because of the low reactivity of belite. As a result, OPC is 80% hydrated at 1 day, whereas BCSA in only hydrated at 50% at the same age (Ambrose 2024). This has a significant impact on the measurement of chloride diffusion coefficient or other transport properties, as discussed later in this paper.

Durability of BCSA Concrete in the laboratory

The performance of BCSA cement and concrete in the laboratory was measured as part of a European Technical Assessment (ETA 2019). We report that BCSA cement concrete and mortars can be designed to pass a significant number of durability tests. Some key properties such as freeze-thaw resistance can be more difficult to pass, but can be passed with proper mix design of the concrete, such as sufficient air entrainment. Other characteristics associated with the durability of BCSA, such as carbonation, chloride diffusion, scaling resistance, dynamic modulus, etc. have been measured. Using standard protocols, chloride diffusion coefficients, carbonation rates and corrosion rates are generally higher for BCSA than for Portland cement. These rates decrease as the hydration of the cement increases and the material is allowed to refine its microstructure. Freeze-thaw testing showed that 94% of the relative dynamic modulus was retained after 28 cycles using the DIN EN 12390 test with the CIF procedure. Scaling resistance was poor with 535 g/m^2 at 49 days. This may be due to a combined effect of carbonation and freeze-thaw damage. Using ASTM C666 procedure, procedures A and B, the durability factor for BCSA concrete was 98.5%. Chloride diffusion coefficients can be one factor affecting durability. ETA testing show a diffusion coefficient of about 37x10^{-12} cm^2.s^{-1}. Generally, diffusion coefficient tends to decrease with curing time (Behravan 2022) The addition of an organic-inorganic pore blocker also drastically reduces the chloride diffusion coefficient and improves corrosion resistance, as shown in Figure 2

Alkali-silica reactivity (ASR) is another important component of concrete durability. BCSA can significantly decrease ASR due to a combination of factors like lower pH, lack of water and reduced shrinkage (Bescher 2023). It should be noted as well that the ASTM protocols for ASR are not conducive to the testing of alternative cements. However, small amounts of BCSA have been shown to mitigate ASR in portland cement. Sulfate resistance is usually very good (**Bescher 2016**). Carbonation rates are generally higher for BCSA than for OPC.

Figure 2. Long-term Corrosion Current Density Development; Left to right – (a) Top rebars, OPC vs. BCSA vs. BCSA-PE ; (b) Top and bottom rebar comparison, BCSA vs. BCSA-PE.

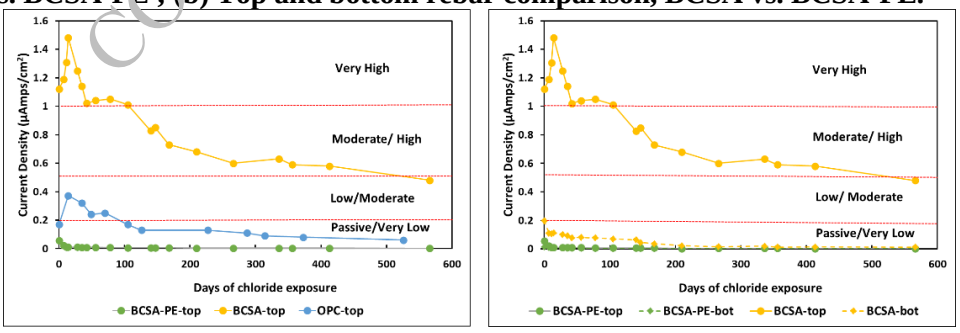

Performance of BCSA Concrete in service.

Reports of field performance of BCSA concrete in the field are conflicting (Moffatt 2021) and do not necessarily match laboratory reports. Conversely, there are reports of poor performance of BCSA concrete in the laboratory, which do not necessarily match with field performance. There are also reports of good long-term performance of BCSA pavement in the field (Darter 2020**).** It should be noted that field performance can be strongly affected by conctructions practice. BCSA concrete is typically very fast and requires very good focus on placement logistics and mix design. Another factor explaining the discrepenacy

between laboratory and field performance ist he fact that, for corrosion in particular, concrete placement typically takes place during the summer but chloride exposure can take place months later during winter. One key parameter of durability is strength. We report that the strength of BCSA concrete is service in the field for 30 years has tripled. Concrete samples collected on a Los Angeles concrete highway were tested at 12,000 psi compressive strength. A sample of BCSA concrete pavement from the Burbank airport was tested at a 12,000 psi after 30 years in service. A sample of BCSA pavement placed at the Seattle Airport doubled in strength after 23 years in the field (Deo 2023)

Table 2- Long-term strength increase for BCSA concrete pavement in service

	Strength @ 1993-1998 (MPa)	Strength* @ 2023 (MPa)	Increase Ratio
Burbank Airport Gate B4	2.76	8.45	3.1
Burbank Airport Gate B5	2.76	8.43	3.1
Los Angeles I10 Freeway	3.07	7.99	2.6

These data are important, because of the scarcity of reports of the long-term strength of BCSA concrete in the field. In the long run, pore solution pH, although more difficult to extract, was not significantly different from that of OPC. These results point to the fact that BCSA cement, which is sometimes referred to as an "ettringite-based cement" is not really "ettringite-based": about 2/3 of its long-term strength cannot be ascribed to the formation of ettringite but to the hydration of belite. In this sense, belite is a key compound in the durability of this low-carbon cement and cannot be called a "waste of lime". Fatigue tests performed on Seattle BCSA airport pavement are shown in Figure 3. They show that after 23 years in the field, BCSA concrete pavement fits the PCA fatigue curve for portland cement concrete.

3. Conclusions

Several aspects of the performance of BCSA concrete were discussed. As in the case of traditional concrete, assessing durability is a complex task. It is further complicated by the fact that testing protocols and standards may or may not be suitable for alternative cements. The emerging picture is that in the case of BCSA, longer curing times may be more reflective of field performance, due to the slow hydration of belite, which amounts to about 50% of mineralogical constituents of the material. Field performance shows that the strength of BCSA concrete pavement can triple in 30 years of service.

References

Ambrose, J, Bescher, E, , Provis J. and Hanein , 2024, Calcium sulfoaluminate based cements versus standard testing procedures», Advances in Cement Research, in print

Behravan, A., Ley, M.T., Rywelski, A., Berke, N., (2021) "Changes in the rate of ion penetration of alternative cementitious materials with time", Materials & Design 197, 109236,

Bescher, E., Rice, E. K., Ramseyer, C., & Roswurm, S. (2016). Sulfate resistance of calcium sulphoaluminate cement. Journal of Structural Integrity and Maintenance, 1(3), 131–139.

Bescher, E., Vallens, K., Kim, J., (2019) Belitic calcium sulfoaluminate cement: Hydration chemistry, performance, and use in the United States.

Bescher E., Maddala, M., Deo, O., Paniagua, J., Bhuskute, N. (2023) Alkali Silica Reactivity in Belitic Calcium Sulfoaluminate, Thailand Concrete Association, Ed. Further Reduction of CO2 -Emissions and Circularity in the Cement and Concrete Industry, 16th International Congress on the Chemistry of Cement 2023 - ICCC2023 (Bangkok 18.-22.09.2023). Bangkok.

Darter, M. (2020) Long Term Performance of Rapid Strength Concrete (RSC) Slabs On California Highways, Proceedings of the 12th International Conference on Concrete Pavement, Minneapolis Minnesota

Deo,O; Bhuskute,N. Bescher, E. Naga Pavan Vaddey, (2023) Concrete International 45 (2), 27-31, Belitic calcium sulfoaluminate runway, Concrete International 45 (2), 27-31.

Environmental Product Declaration (2022). CTS Cement Manufacturing Corporation, Garden Grove, California, USA.

European Technical Assessment ETA-19/0458, Deutsche Institut für Bautechnik

Moffatt, E. G., & Thomas, M. D. A. (2018). Durability of Rapid-Strength Concrete Produced with Ettringite-Based Binders. ACI Materials Journal, 115(1).

Tayyab Adnan H., Kienzle, A., & Thomas, R. J. (2022) ”Engineering properties and setting time of belitic calcium sulfoaluminate (BCSA) cement concrete Construction and Building Materials, 352, 128979.

Special Concretes and Construction Techniques

Anisotropic Transport Characteristics in 3D Printed Concrete: What Can We Learn from Print Parameter Design?

Sahil Surehali[1*], Avinaya Tripathi[2], and Narayanan Neithalath[3]

[1] *Graduate student, School of Sustainable Engineering and Built Environment, Arizona State University, Tempe AZ*
Email: ssurehal@asu.edu
[2] *Graduate student, School of Sustainable Engineering and Built Environment, Arizona State University, Tempe AZ*
Email: atripa22@asu.edu
[3] *Professor, School of Sustainable Engineering and Built Environment, Arizona State University, Tempe AZ 85287*
Email: Narayanan.Neithalath@asu.edu

*Corresponding author

ABSTRACT

Layered concrete systems, such as those obtained using 3D printing, demonstrates inter-layer and inter-filament defects, which influence transport of moisture and ionic species through the structural element, thus impacting its durability and service life. The printing parameters, including the layer height and width, and printing rate, dictates the number and quality of the interfaces, rendering a directional dependence to the transport of moisture and deleterious ions. While material design of 3D printed concrete is given significant importance (and rightly so), the impact of some of the critical printing parameters have not received due attention. We directly interrogate the direction-dependent microstructure of the printed samples through X-ray computed tomography and indirectly through electrical impedance spectroscopy and bring out the synergistic effects of material design (including non-conductive fiber reinforcement) and layer heights and width on anisotropic transport characteristics.

KEYWORDS*: 3D printed concrete, anisotropy, X-ray tomography, Electrical impedance, Chloride ingress*

1. Introduction

3D concrete printing (3DCP) or additive manufacturing is transforming construction and manufacturing by enabling automated, layer-by-layer building from digital models. This method revolutionizes design and construction, offering a sustainable alternative by optimizing material use and reducing waste (Lloret et al. 2015; De Schutter et al. 2018). The benefits of 3DCP are numerous (Buswell et al. 2007; Gosselin et al. 2016). It allows for the creation of complex geometries that are difficult or impossible with traditional techniques, enhancing architectural freedom. Automation improves construction efficiency, cutting time and labor costs, while the precision of 3D printing reduces material waste, promoting sustainability. However, large-scale application faces challenges such as anisotropy (directional differences in mechanical and durability properties) and the effects of varying layer heights on strength and durability. Research has focused on optimizing mixtures for flowability and shape stability, and the use of additives to enhance printability and mechanical properties (Nair et al. 2020; 2019; Alghamdi, Nair, and Neithalath 2019). Yet, the combined effects of layer heights and anisotropy on the performance of 3D printed elements remain underexplored. Additionally, comprehensive studies on the durability of 3D printed concrete are lacking, which is crucial for the broader adoption of 3DCP in mainstream construction.

The mechanical properties of 3D printed concrete are significantly influenced by the printing direction. While some studies indicate higher compressive strength perpendicular to the printing direction, others disagree (Le et al. 2012; Liu et al. 2022; Xiao, Liu, and Ding 2021). This variation is due to factors like inter-layer and inter-filament bond strength, layer dimensions, print velocity, extrusion rate, nozzle shape and dimensions, and nozzle offset distance (Wolfs, Bos, and Salet 2019; Ji et al. 2022; Panda et al. 2018). Research shows inconsistent conclusions regarding the anisotropic nature of 3D printed concrete's

compressive strength. Most studies acknowledge anisotropy but often focus on either inter-layer or inter-filament interfaces, limiting observations on the combined effects of these interfaces (Wolfs, Bos, and Salet 2019; Ye et al. 2021; Panda, Chandra Paul, and Jen Tan 2017). Therefore, we investigate the anisotropic behavior of 3D printed concrete under compression, considering varying layer heights (6, 13, and 20 mm) and the presence of steel or basalt fibers.

Furthermore, the layer-by-layer extrusion method increase void fractions, especially at the interfaces, resulting in a more porous material compared to conventionally cast concrete. The inter-layer zones act similarly to cracks, reducing durability by allowing easy transport of harmful substances (Yu et al. 2021; Ma et al. 2018). Variations in print parameters (layer height, filament width, printing rate) affect the microstructure and interfaces, necessitating in-depth studies on the transport properties in 3D printed concrete. Therefore, we examine how 3D printing parameters, specifically layer height and orientation, impact the chloride ion transport properties of 3D printed concrete. Finally, the study dives deeper into understanding the variations in the pore structure in the bulk and interfacial regions of the 3D printed elements using advanced imaging technique, X-ray computed tomography (XRT), and relate the pore structure features to the microstructural parameters extracted from impedance spectroscopy.

2. Methodology

Mortars were printed using a gantry 3D printer with a screw extrusion system (Gurehali et al. 2023). To ensure consistent filament cross-sections, a 20 mm diameter circular nozzle was used to print filaments with a fixed layer width (LW) of 20 mm and specified layer heights (LH). The study used print layer heights of 6, 13, and 20 mm. To minimize printing defects, the selected layer heights were equal to or smaller than the nozzle diameter. Mortar slabs measuring 300 x 280 x 60 mm were printed at a constant in-plane speed of 50 mm/s. The screw extruder's stepper was calibrated for flow rates of approximately 6, 13, and 20 mL/s to achieve uniform filaments with layer heights of 6 and 20 mm, respectively. Figure 1 displays representative 3D models of the printed mortar slabs (300 x 280 x 60 mm) with different layer heights. The 3D printed mortar mixtures were moist-cured at 23±2°C and > 98% relative humidity for 28 days. After curing, test specimens were extracted from the slabs using a diamond-tipped saw.

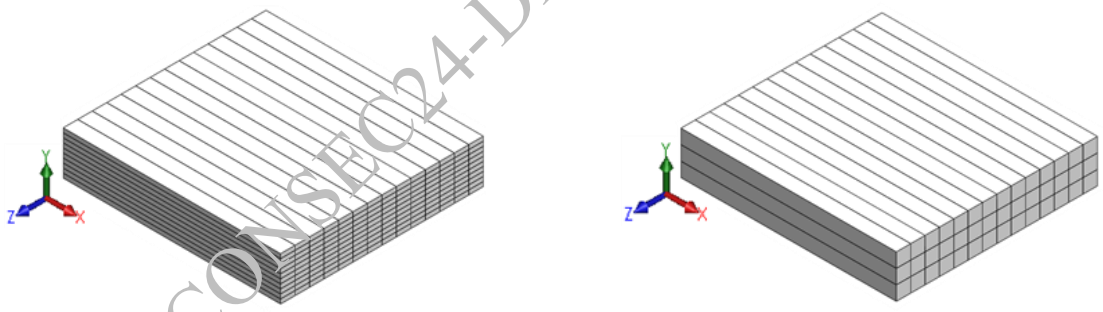

(a) (b)

Figure 1. Representative three-dimensional models of mortar slabs (300 x 280 x 60 mm) printed using layer heights of: (a) 6 mm, and (b) 20 mm.

Cubes measuring 60 mm x 60 mm x 60 mm were extracted from the printed mortar slabs. These cubes comprised 10 layers for a 6 mm layer height, 4.6 layers for a 13 mm layer height, and 3 layers for a 20 mm layer height, resulting in significantly different numbers and qualities of layer interfaces. The cubes underwent uniaxial compression testing using a servo-controlled universal testing machine (SBEL CT-110-S) with a capacity of 489 kN. Compression tests were conducted in three directions for the selected layer heights and mixtures. In this study, direction-1 (D1) is defined as the direction of printing, direction-2 (D2) represents the layer buildup direction, and direction-3 (D3) is perpendicular to both D1 and D2. Figure 2 illustrates the loading direction for a cube specimen with a 20 mm layer height. Loading was applied at a stroke displacement rate of 0.15 mm/min, corresponding to a strain rate of 0.25%/min. Companion mold-cast specimens of the same composition were also tested. Cylinders with a diameter of 100 mm and a length of 200 mm were cored from the printed slabs in all three directions, as shown in Figures 3. Transport tests were carried out on 50 mm thick discs sliced from the cored cylinders.

NSSM tests were performed for each test direction and layer height in accordance with NT BUILD 492 ("NT Build 492, Concrete, Mortar and Cement-Based Repair Materials: Chloride Migration Coefficient from Non-Steady-State Migration Experiments" 1999).

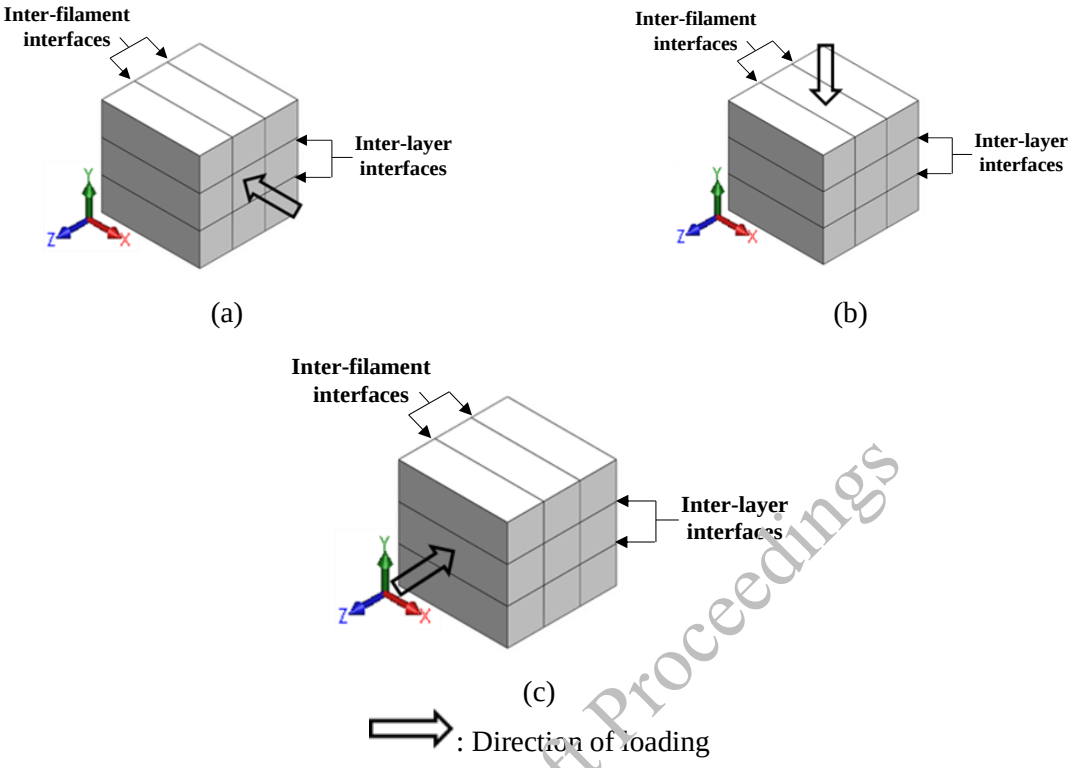

Figure 2. Cubes compressed along: (a) Direction-1, (b) Direction-2, and (c) Direction-3. The representation corresponds to a specimen with a layer height of 20 mm.

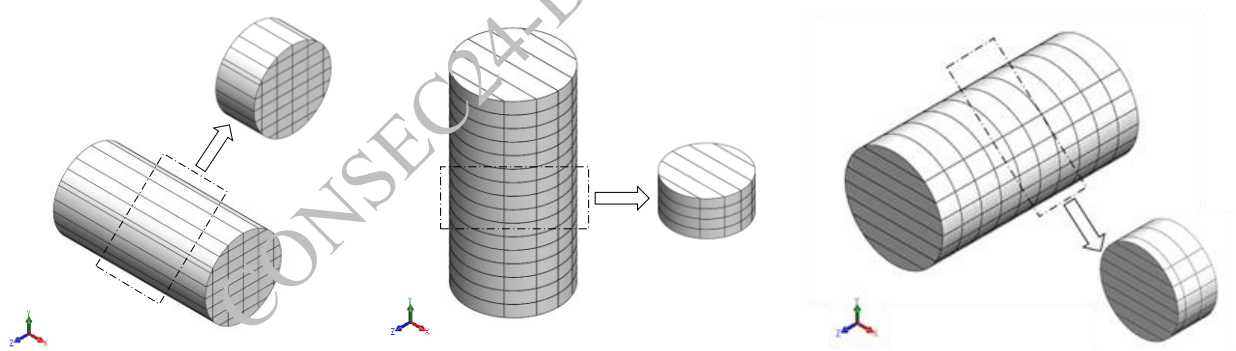

Figure 3. Test specimen preparation details. Sliced 50 mm thick discs from 200 mm × 100 mm cylinders cored in directions: (a) D1, (b) D2, and (c) D3.

3. Research significance

There remains a notable gap in understanding the combined effects of layer heights and anisotropy on the performance of 3D printed structures. These factors play a crucial role in determining the structural integrity and durability of printed objects. Moreover, the durability aspects of 3D printed concrete under various environmental conditions and load-bearing scenarios are yet to be comprehensively studied. Durability is a key consideration for the adoption of 3DCP in mainstream construction, as it directly impacts the lifespan and maintenance requirements of printed structures. The lack of research in this area poses a significant barrier to the wider acceptance and application of 3DCP technologies.

Thus, this study is a major step in understanding the critical print parameter design and the origin of anisotropy from the interfacial porosity standpoint.

4. Conclusions

The results from this study shed light on the directional dependence of compressive behavior of plain and fiber-reinforced 3D printed mortars, which is crucial in ensuring that: (i) the printed structures can sufficiently resist stresses in multiple directions, and (ii) the failure mechanisms and modes are predictable. It discusses the use of Digital Image Correlation (DIC) analysis for strain and stress profiling during the compression tests, providing a comprehensive understanding of the deformation patterns and failure mechanisms. The inclusion of fibers (steel or basalt) was found to mitigate some of the strength losses associated with the printing process, with differences in performance between the fiber types. Anisotropy is quantified through peak stress and strain-based coefficients, showcasing how these values change with layer height adjustments and fiber reinforcements. The study concludes that optimizing layer heights and incorporating fiber reinforcements can lead to significant improvements in the mechanical properties of 3D printed concrete. Specifically, reducing layer heights and selecting appropriate fiber reinforcements can enhance the compressive strength and reduce anisotropic effects, potentially leading to more durable and structurally sound 3D printed concrete elements.

To address durability aspects, non-steady state migration (NSSM) tests are carried out on specimens extracted by coring 3D printed prisms along three orthogonal directions – along the direction of printing (direction-1 (D1)), along the direction of layer build-up (direction-2 (D2)), and in the direction perpendicular to the above two directions (direction-3 (D3)) - to explore the directional dependence of chloride ion penetration resistance, in addition to the effect of layer heights. Results show that the direction-dependent D_{nssm} values of printed samples are 10–30% higher than those of companion cast samples in the D2 and D3 directions, highlighting anisotropy's role in influencing transport properties. Microstructural analysis through porosity and electrical conductivity measurements supports these findings, establishing the impact of inter-layer and inter-filament defects on the material's durability. Mercury intrusion porosimetry (MIP) results showed that porosity and critical pore sizes in the bulk region of the layers (not accounting for any of the interfaces) decreased with decreasing layer heights. The results in the D1 direction (along the direction of printing) were found to be unreliable because of the continuous (or nearly continuous) inter-filament channels in that direction, and thus have been neglected. The work concludes that inter-filament interfaces need to be minimized to ensure desirable transport characteristics for 3D printed concrete elements, especially when they are reinforced, and thus it is beneficial to have wide layers (that minimize inter-filament interfaces).

Finally, the variations in the pore structure in the bulk and interfacial regions of the 3D printed elements are studied using advanced imaging technique, X-ray computed tomography (XRT), and the pore structure features are related to the microstructural parameters extracted from impedance spectroscopy. Understanding porosity distribution in 3D printed elements porosity is expected to enhance the fundamental understanding of possible mechanisms that induce failure between interlayer and interfilament interfaces and subsequently aid in the development of appropriate solutions to mitigate these effects. Samples are obtained from 3D printed mortars and investigated for: i) porosity compared to that of conventionally cast concrete, ii) interlayer and interfilament porosity, iii) effect of print layer height on the porosity distribution. Furthermore, electrical impedance spectroscopy (EIS), is being used to evaluate the pore structure features. Electrical circuit models are being developed and analyzed in an attempt to establish physics-based mechanisms that contribute to enhanced moisture and ionic transport in preferred directions.

References

Alghamdi, H., Nair, S.A. and Neithalath, N.(2019) "Insights into Material Design, Extrusion Rheology, and Properties of 3D-Printable Alkali-Activated Fly Ash-Based Binders", *Materials & Design* 167:107634

Buswell, R.A., Soar, R.C., Gibb, A.G. and Thorpe, A.**(**2007)"Freeform Construction: Mega-Scale Rapid Manufacturing for Construction", *Automation in Construction* 16 (2): 224–31

De Schutter, G., Lesage, K., Mechtcherine, V., Nerella, V.N., Habert,G. and Agusti-Juan.,I. (2018) "Vision of 3D Printing with Concrete — Technical, Economic and Environmental Potentials", *Cement and Concrete Research*, SI : Digital concrete 2018, 112:25–36

Gosselin, C., Duballet, R., Roux, P., Gaudillière, N., Dirrenberger, J. and Morel, P.(2016) "Large-Scale 3D Printing of Ultra-High Performance Concrete – a New Processing Route for Architects and Builders", *Materials & Design*, 100:102–9

Ji, G., Xiao, J., Zhi, P., Wu, Y.C. and Han, N.(2022) "Effects of Extrusion Parameters on Properties of 3D Printing Concrete with Coarse Aggregates", *Construction and Building Materials* 325:126740

Le, T.T., Austin, S.A., Lim, S., Buswell, R.A., Law, R., Gibb, A.G. and Thorpe, T.(2012) "Hardened Properties of High-Performance Printing Concrete", *Cement and Concrete Research* 42 (3): 558–66

Liu, C., Zhang, R., Liu, H., He, C., Wang, Y., Wu, Y., Liu, S., Song, L. and Zuo, F.(2022) "Analysis of the Mechanical Performance and Damage Mechanism for 3D Printed Concrete Based on Pore Structure", *Construction and Building Materials*,314:125572

Lloret, E., Shahab, A.R., Linus, M., Flatt, R.J., Gramazio, F., Kohler, M. and Langenberg, S.(2015) "Complex Concrete Structures: Merging Existing Casting Techniques with Digital Fabrication", Computer-Aided Design, *Material Ecology*, 60:40–49

Ma, G., Zhang, J., Wang, L., Li, Z. and Sun, J. (2018)"Mechanical Characterization of 3D Printed Anisotropic Cementitious Material by the Electromechanical Transducer", *Smart Materials and Structures, 2*7 (7): 075036

Nair, S.A., Alghamdi, H., Arora, A., Mehdipour, I., Sant, G. and Neithalath, N.(2019) "Linking Fresh Paste Microstructure, Rheology and Extrusion Characteristics of Cementitious Binders for 3D Printing", *Journal of the American Ceramic Society*,102 (7): 3951–64

Nair, S.A., Panda, S., Santhanam, M., Sant, G. and Neithalath, N.(2020) "A Critical Examination of the Influence of Material Characteristics and Extruder Geometry on 3D Printing of Cementitious Binders", *Cement and Concrete Composites*,112:103671

"NT Build 492. (1999),"Concrete, Mortar and Cement-Based Repair Materials: Chloride Migration Coefficient from Non-Steady-State Migration Experiments." *Nord Test Method*

Panda, B., Suvash C. P. and Ming J. T. (2017) "Anisotropic Mechanical Performance of 3D Printed Fiber Reinforced Sustainable Construction Material", *Materials Letters*,209:146–49

Panda, B., Suvash C. P., Nisar A. N. M., Yi W. D. T. and Ming J. T.(2018) "Measurement of Tensile Bond Strength of 3D Printed Geopolymer Mortar", Measurement,113:108–16

Surehali, S., Tripathi, A., Nimbalkar, A.S. and Neithalath, N. (2023) "Anisotropic Chloride Transport in 3D Printed Concrete and Its Dependence on Layer Height and Interface Types", *Additive Manufacturing*, *62*:103405

Wolfs, R.J.M., Bos, F.P. and Salet, T.A.M. (2019) "Hardened Properties of 3D Printed Concrete: The Influence of Process Parameters on Interlayer Adhesion", *Cement and Concrete Research*,119:132–40

Xiao, J., Liu, H. and Ding, T. (2021) "Finite Element Analysis on the Anisotropic Behavior of 3D Printed Concrete under Compression and Flexure", *Additive Manufacturing*, 39:101712

Ye, J., Cui, C., Yu, J., Yu, K. and Dong, F.(2021) "Effect of Polyethylene Fiber Content on Workability and Mechanical-Anisotropic Properties of 3D Printed Ultra-High Ductile Concrete", *Construction and Building Materials*,281:122586

Yu, S., Xia, M., Sanjayan, J., Yang, L., Xiao, J. and Du, H.(2021) "Microstructural Characterization of 3D Printed Concrete", *Journal of Building Engineering*,44 :102948

Experimental Investigation of Seismic Behavior of Hybrid Precast Panel Shear Walls with Undercut Mechanical Anchors

M.R. Joo[1], S. Chawala[2], and S. Shiradhonkar[3*]

[1] Department of Earthquake Engineering, Indian Institute of Technology Roorkee, Roorkee, India
Email: mrafiqjoo@gmail.com
[2] Precast Panels, Delhi, India
Email: suresh65chawla@gmail.com
[3] Department of Earthquake Engineering, Indian Institute of Technology Roorkee, Roorkee, India
Email: saurabh.shiradhonkar@eq.iitr.ac.in

[*]Corresponding author

ABSTRACT

Precast panel shear walls (PPSWs) are hybrid shear walls combining the advantages of precast construction and cast-in-situ concrete. These walls utilize precast panels as permanent formwork, eliminating the need for external formwork and providing superior surface finishing, thus not requiring plastering. Precast panels comprise of concrete, wire mesh reinforcement, and holdfasts to establish a robust shear transfer mechanism between core wall and panels. The current study presents part of the experimental studies on three full-scale PPSW specimens. In these three specimens, the bottom precast panels are fixed to foundation beam using steel angles fastened using post-installed undercut mechanical anchors. The shear walls are tested under combined constant axial and lateral cyclic loading. The specimens vary in reinforcement type and quantity within the core walls, including welded wire mesh, single-layer, and double-layer configurations of reinforcing bars. Test results, including crack patterns, failure modes, hysteresis curves, stiffness degradation, energy dissipation, and equivalent viscous damping are presented and analyzed. The incorporation of steel angles and anchors in the bottom panels delays the upliftment of PPSWs from the foundation and thus exhibit superior performance.

KEYWORDS*: Precast Panel Shear Walls, Cyclic Loading, Large-Scale Testing, Undercut Anchors.*

1. Introduction

Conventional construction of reinforced concrete (RC) members, such as shear walls, often results in inadequate surface finishing and requires significant external formwork, increasing carbon emissions (Dong et al., 2015). Precast walls offer advantages of speedy construction and good surface finishing, but are vulnerable to seismic failures (Singhal et al., 2019). Precast panel shear wall (PPSW) is a *'Lost Form Shuttering'* technology developed by co-author S. Chawla. It combines the advantages of cast-in-situ and precast construction and is a sustainable alternative for construction of RC members. The technology uses precast panels as permanent sacrificial formwork for the construction of cast-in-place core shear wall and the hybrid wall is termed as PPSW. The PPSW behaves as composite system with strength contribution from core wall and precast panels. The authors tested the PPSWs for quasi-cyclic loading. The failure PPSWs observed were upliftment of walls and detachment of the panels, leading to loss of shear transfer mechanism and degradation in capacity (Joo et al., 2024). The PPSWs are modified and tested in the present study. The bottom precast panels are casted with steel angles and connected to the hardened concrete of the foundation beam via undercut mechanical anchors. The leg of steel angle cast in precast panel is welded to wire mesh and embedded in the middle of precast panel and the details are shown in Figure 1a. This detailing ensures effective connection of the precast panel with foundation so that strength of precast panels is well utilised. Three such large-scale hybrid PPSWs, with different core wall reinforcements, are constructed and tested under combined axial load and reversed cyclic loading. The results are presented in the form of damage evolution, failure modes, hysteretic behaviour, stiffness degradation, energy

dissipation, and stiffness degradation. The results underscore that the use of undercut anchors delays separation of wall from foundation beam, increases lateral load resistance, energy-dissipation, and reduces stiffness degradation.

2. Experimental Programme

2.1 Test Specimen Details

Three large-scale hybrid PPSW specimens of height 4280 mm (3 levels of 1350 mm high planks and 230 mm top loading beam) are casted over a strong foundation beam (see Figure 1a). The width and thickness of shear wall are 1350 mm and 160 mm respectively. Each specimen consists of 18 precast panels (9 on each side) and cast-in-place core wall. Each precast panel measures 450 mm × 1350 mm × 30 mm and consists of wire mesh reinforcement and holdfasts for establishing composite behaviour with core wall. For each wall, the bottom 6 panels (3 on each side) are casted with one leg of steel angle embedded into panel (see Figure 1b). The other leg of steel angle is connected to foundation beam using two 10 mm Fischer (FZA 14×60 M10/25) undercut mechanical anchors (Fischer, 2024) as shown in Figure 1a.

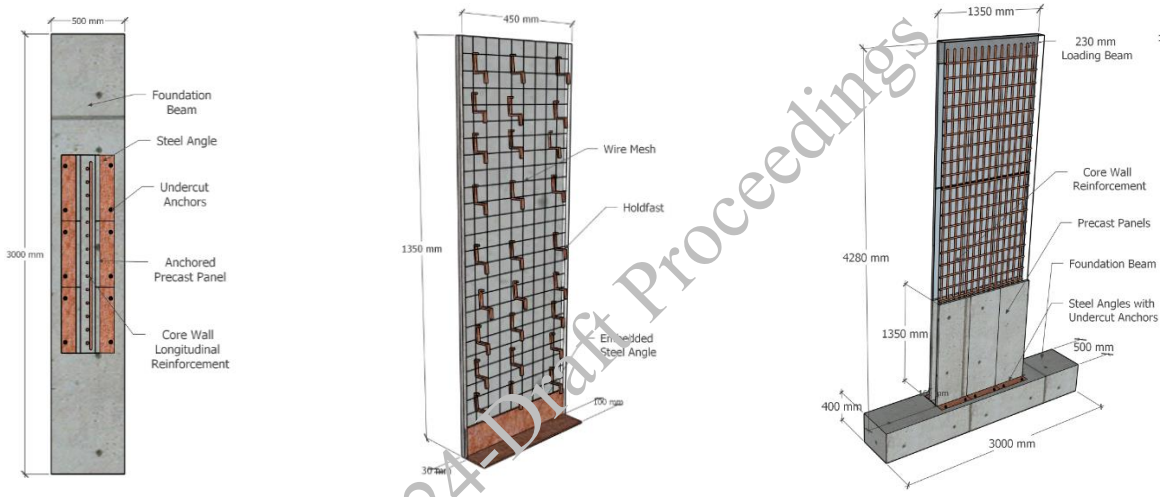

(a) Wall Cross Section (b) Precast panel, wire mesh, holdfast, and angle Section (c) PPSW assembly

Figure 1. Hybrid precast panel shear wall (PPSW) system with undercut mechanical anchors.

The specimens vary in type and quantity of core reinforcement, including welded wire mesh, single-layer, and double-layer configurations of reinforcing bars. The specimen *W1* consists of welded steel wire mesh with grid size of 50 mm × 50 mm and wires of 3 mm nominal diameter as reinforcement. The specimen *W2* contains single layer of 10 mm reinforcing bars @ 100 mm c/c in vertical direction and 8 mm bars @ 150 mm c/c in the horizontal direction. The core wall of specimen *W3* is reinforced with double-layer configuration of 10 mm longitudinal reinforcing bars @ 150 mm c/c and 8 mm horizontal bars @ 150 mm c/c. The precast planks and core wall are casted with M30 grade concrete and the 550D grade steel reinforcing bars are used in the core wall.

2.2 Testing and Loading Procedure

The specimens are securely clamped to strong floor using high-tension bolts and clamps to ensure fixity and avoid any slippage. The out-of-plane movement is restricted using side roller bearings. Axial load of 312 KN is first applied through a vertical hydraulic jack mounted on the top of wall. Lateral load is applied through hydarualic actuator of 1000 kN capacity and displacement stroke of ± 250 mm. The displacment profile over the height of the wall is tracked through five LVDTs placed at various heights. The displacement-controlled lateral reversed quasi-static cyclic loading cycles are incrementally applied at the top of wall specimens in accordance with FEMA 461 (2007) recommendations.

3. Results and Discussions

3.1 Damage Progression and Failure Modes

The flexural, flexural-shear, and shear cracks were observed to form at the panel surfaces and on the lateral sides in the bottom one-third of the wall. The vertical cracks between the panels and on lateral side between core wall and precast panels were also observed. The number of surface cracks increased with core wall reinforcement, signifying the stronger core wall compared to the panels. With increased drift demands, the concrete cover over steel angles spalled off and the steel angles were exposed. The base flexural crack at the wall-foundation interface opened up leading to potential upliftment of the wall from the foundation beam and fracture of core reinforcement. This vertical upliftment led to pull out of steel angles and mechanical anchors on the extreme ends from foundation beam. The wire mesh inside precast panels fractured, detaching steel angles from panel wire mesh and lost connection with walls. The panel and core concrete under compression spalled and crushed and the panels bulged out. The rocking motion was observed in all specimens after significant damage and drop in lateral load resistance.

3.2 Load-Deformation Behaviour

Figure 2 shows the load-deformation hysteresis behaviour of PPSWs with backbones and their comparison. The hysteresis curve of specimen W1 shows a relatively narrow loops, signifying loss of structural integrity over time. Stability of hysteresis curves is observed for specimen W3 with double-layer configuration of reinforcing bars, followed by W2. The yield, peak, and ultimate (15% drop in load) displacement and load capacities are significantly influenced by reinforcement type and configuration as shown in Figure 2d. The behaviour is similar up to a drift of around 0.7% and deviate after yielding of W1 and W2. The slight drop in load capacity of W3 after around 8 mm to 40 mm displacement is due to uncontrolled actuator deflection of around 40 mm during the initial displacement cycles which slightly damaged the specimen and caused base crack and spalling of concrete and thereby reducing the effective stiffness of the specimen.

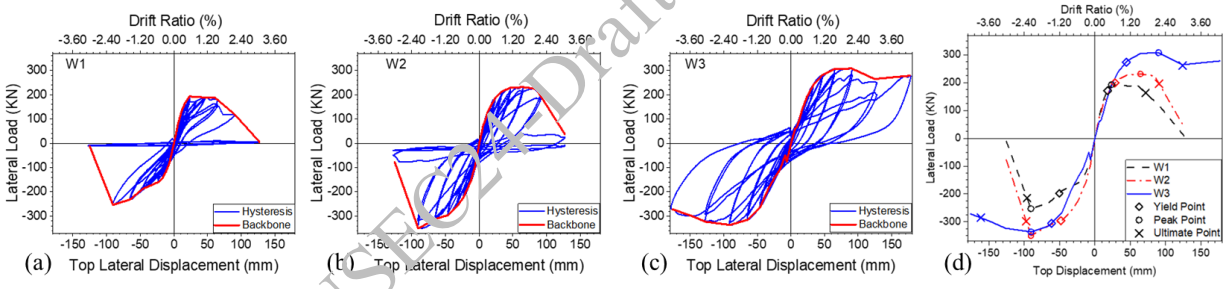

Figure 2. Hysteretic and backbone curves of (a) W1, (b) W2, and (c) W3 and (d) comparison of backbone curves.

The deformation and load capacities increase with core wall reinforcemnt content. The specimens W1 and W2 have average yield displacement of 34.17 mm and 34.31 mm, respectively, while W3 has equivalent yield displacement of 52.84 mm. The average of equivalent yield load in the two directions is 184.40 kN, 248.31 kN, and 289.77 kN. The average peak load capacities are 222.96 kN, 290.96 kN, and 322. 29 kN for W1, W2 and W3, respectively. Thus, use of single- and double- layer reinforcing bars in the core walls enhances the peak load capacity of PPSWs by 30% and 45% when compared to PPSW with nominal wire mesh core reinforcement. The stronger core wall also leads to higher displacements at peak loads and are 56.97 mm, 77.39 mm, and 9.32 mm for W1, W2, and W3, respectively. This enhanced seismic resistance of PPSWs is attributed to larger amount of ductile reinforcing bars contributing to the resistance, delaying the seperation of wall from the foundation, and effectively confining the core concrete. The displacment ductility of walls is observed to be 2.95, 2.60, and 2.72 for W1, W2, and W3, respectively.

3.3 Assessment of Structural Parameters

The different performance metrics, including stiffness degradation, energy dissipation capacity, and equivalent viscous damping are presented in Figure 3. The initial secant stiffness increases with core reinforcement (except for W3 due to initial damage as a result of uncontrolled actuator deflection). The specimen W1 shows rapid stiffness degradation rate with increasing drift demands due to least ductile wire

mesh core reinforcement. Specimens W2 and W3, respectively, exhibited moderate and slowest rate of stiffness degradation. Slowest stiffness degradation in W3 indicates its superior performance.
Figure 3b depicts the cumulative energy dissipated by each specimen over loading cycles. Specimen W1 has the lowest energy dissipation while W2 shows higher energy dissipation and has a steady increase in energy dissipation with each cycle. Specimen W3 exhibits the highest energy dissipation, with the steepest curve. This suggests superior capability of W3 to absorb and dissipate energy during seismic events. The low dissipation energy of W3 at initial displacements is due to uncontrolled movement of actuator, cracking the specimen. The higher energy dissipation capacity of W2 and W3 is attributed to formation of higher number of cracks and yielding of core reinforcing rebars. Figure 3c illustrates the equivalent viscous damping ratio, a measure of energy dissipation efficiency during cyclic loading. The specimens W2 and W3 exhibited higher damping ratio (4% to 14%) compared to W1 (4% to 11%) suggesting improved energy dissipation efficiency of PPSWs with reinforced core walls. Lowest load resistance, rapid stiffness degradation, and low energy dissipation for W1 shows its least effectiveness in resisting seismic loads. It may therefore be suitable for regions with low seismicity or conditions where lower seismic performance is acceptable. Higher energy dissipation, load resistance, and slower stiffness degradation for specimens W2 and W3 demonstrate their adequate structural performance under cyclic loading, making PPSWs with reinforced core walls suitable for high seismic demands.

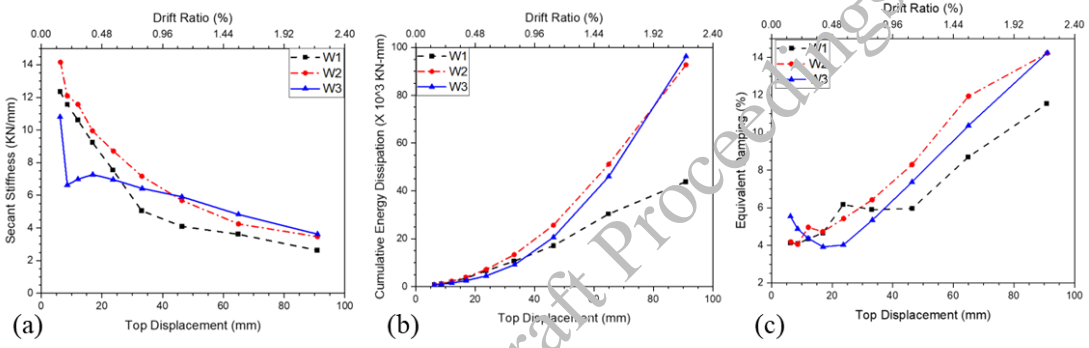

Figure 3. Assessment of (a) secant stiffness, (b) energy dissipation, and (c) equivalent viscous damping for PPSWs.

4. Conclusions

This study tested three large-scale hybrid PPSWs with undercut mechanical anchors under quasi-static cyclic loading and provides the comprehensive analysis of experimental findings. The key conclusions are as follows.

- Crack patterns and failure modes indicated the effectiveness of steel angles and undercut anchors in delaying wall upliftment, maintaining composite action, and exhibiting higher load capacities.
- The peak lateral load capacities increased by around 30% and 45% with incorporation of single and double-layer configuration of core reinforcement.
- Increased core wall reinforcement resulted in superior performance, including higher load resistance, better energy dissipation, higher damping ratios, and reduced stiffness degradation.

Acknowledgements

The authors sincerely acknowledge the funding from Ministry of Housing and Urban Affairs, Government of India for the project grant. We appreciate Fischer India for supplying the undercut anchors.

References

Dong, Y. H., Jaillon, L., Chu, P. and Poon, C. S. (2015) "Comparing carbon emissions of precast and cast-in-situ construction methods – A case study of high-rise private building",*Construction and Building Materials, 99*, 39–53

FEMA 461. (2007) “Interim Testing Protocols for Determining the Seismic Performance Characteristics of Structural and Nonstructural Components”, *www.ATCouncil.org*

Fischer. (2024) “ Fischer ZYKON undercut anchor FZA 14 X 60 M10/25”. *https://www.fischer-international.com*

Singhal, S., Chourasia, A., Chellappa, S., and Parashar, J. (2019) “Precast reinforced concrete shear walls: State of the art review”, *Structural Concrete, 20(3)*: 886–898

Joo, M.R., Chawla, S. and Shiradhonakr, S. (2024) “Experimental Investigations of Precast Panel Shear Walls Under Quasi-Static Monotonic and Cyclic Loading. (*In Preparation).*

Framework for Utilization of Discarded Coir Fibres for Pavement Applications

MD. Shoeb Amer Ali Khan [1*], Surender Singh [2], and Someen Khute [3]

[1]Ph.D Research Scholar, Dept. of Civil Engineering, IIT Madras, Chennai, India,
Email: ce20d028@smail.iitm.ac.in
[2] Assistant professor, Department of Civil Engineering, IIT Madras, Chennai, Tamil Nadu, India
Email: surender@civil.iitm.ac.in
[3] Former M.S Research Scholar, Department of Civil Engineering, IIT Madras, Chennai, Tamil Nadu, India
Email: Someenkhute@gmail.com

[*]Corresponding author

ABSTRACT

Concrete pavements provide a durable and reliable surface with a relatively low maintenance cost but are prone to early-age cracking (Plastic shrinkage cracks, (PSC)). To arrest these cracks, this study explores the suitability of incorporating discarded coir fibres (DCF) in low volume rural roads. However, DCF possesses dispersion, workability, and degradation issues in the concrete. Apart from their intrinsically variable qualities, low density, and hydrophilic nature; the performance of DCF is typically lower than that of synthetic fibres; hence, treatment of the DCF is necessary. Therefore, this study intends to develop a framework for treating DCF. The treatment result suggests that post-alkali treatment with calcium hydroxide ($Ca(OH)_2$), coir fibre exhibited 40.5% and 40.3% improvement in tensile strength and 53% and 18% improvement in failure strain after treating with sodium hydroxide (NaOH) for mature and immature fibres, respectively. Though alkali treatments could enhance the properties of coir fibres, an excessive concentration and soaking duration was found to affect the fibres' physical and mechanical characteristics adversely and sudden variation in the mechanical performance as well. For mature fibres, the optimum parameters (strength and failure strain) were obtained for 5% concentration of NaOH solution with a soaking period of 5 h, while for immature fibres, 6 h soaking duration was found to be optimum. Based on this comprehensive study, a framework was proposed which could be readily adopted for enhancing the quality of coir fibres. Following the development of framework for the treatment of coir fibres, discarded coir fibre concrete (DCFC) was produced using treated and untreated DCF with different lengths and doses to evaluate the effect or the performance of DCFC. It was observed that the mechanical performance of the DCFC reduced due to the incorporation of both treated and untreated coir fibres. Subsequently, effect of fibre maturity level, fibre condition, aspect ratio, fibre dosage, and binder concentration on the performance of DCFC were also evaluated. Although the incorporation of coir does not affect the hydration kinetics of cement, it entraps the air voids leading to inferiorities in coir concrete; the compressive and flexural strength reduced in the range of 17%-54% and 3%-36%, respectively. Moreover, the dose of DCF in DCFC played a prominent role in the mechanical performance. Long term mechanical performance of the DCFC was marginally affected under the durability test conducted as per NBR - 13554. The positive impact of arresting the PSC and durability characteristics of concrete highlights the potential of DCF in addressing the challenges in concrete pavement applications.

KEYWORDS*: Discarded coir fibre concrete, Durability, Fibre treatment, Mechanical performance, Plastic shrinkage cracks.*

1. Introduction

The excessive utilisation of natural resources brought about by rapid globalisation resulted in loss of resources and degradation of the environment. The emphasis has turned to sustainable materials—those with social, economic, and environmental benefits—as environmental consciousness has grown. Materials

like naturally occurring fibres from plants are widely accessible, reasonably priced, and most importantly, sustainable, however, they don't perform as well as synthetic fibres in all aspects. One such natural material is Coconut fibre (Cocos Nucifera), also known as coir/coir fibres, are commonly available in tropical and subtropical regions (Adeniyi et al. 2019) which outperforms synthetic fibres in certain aspects. However, treatment of these fibres was proposed to overcome its inferiorities. Physical and chemical treatments are the two primary methods of coir fibre treatment. Most commonly used physical treatment methods include boiling and washing (Ali and Chouw 2013), whereas treating with alkali (sodium hydroxide, potassium hydroxide, and calcium hydroxide) (Zaman et al. 2011), and treating with acetic acid (CH_3COOH) (Varma et al. 1984) are commonly practiced chemical treatment methods. Literature review showed contradictory results in the quantification of the enhancement in the fibre response (Silva et al. 2000; Zaman et al. 2011). Moreover, contradictory results were observed regarding the performance of the DCFC. For instance, the use of coir has been reported to enhance compressive strength, flexural strength, and indirect tensile strength by 3%-45%, 3%-36%, and 12-42%, respectively (Ali and Chouw 2013; Isaac et al. 2022). However, certain studies observed a reduction in the strength parameters by 16-65% when coir was included in the concrete mix (Rout et al. 2002). Also, the performance stats of the DCFC in long term service are also not available. These findings show that the fibre treatment techniques and effect of the coir fibres in the concrete must be understood fundamentally. So, in addition to emphasising the strength development mechanism, the current study aims to comprehend the intrinsic dominating parameters of coir that influence the behaviour of coir-concrete. It also investigates the mechanism of coir degradation in concrete and how it affects the overall performance of the concrete.

2. Materials and Methodology

In this study, both the fibre types, viz. mature and immature, were obtained from Karur and Coimbatore districts, some of the major coconut growing areas in Tamil Nadu, India. Coir fibres received from the source ranged from 100 to 250 mm long and were free from short fibres. These fibres were carried forward for additional processes/treatments without further separation. These fibres are termed as "unwashed fibres". For chemical treatments, three alkali materials, namely sodium hydroxide (NaOH), calcium hydroxide ($Ca(OH)_2$), potassium hydroxide (KOH), and a glacial acetic acid (CH_3COOH) were locally purchased. Potable water was considered for physically treating the fibres, and distilled water was used in chemical treatments to make solutions. Methyl methacrylate (MMA) solution was prepared and used for the grafting technique as per the procedure available in the literature (Lakshmi N. S. et al. 2015). The methodology adopted in this study is illustrated in Figure. Initially, both the fibres were washed with water to remove the surface impurities; this was ensured when the colour of the water flowing through the fibres changed from brown to transparent. Despite pre-processing with water, especially mature fibres were found to contain some pith. After pre-treatment, these fibres were air-dried (until they reached a constant mass) at a temperature of 30 ± 5 °C by maintaining a relative humidity of 65 ± 5% before subjecting it to various treatment processes. The duration and concentration optimised for the treatment process are specified in the Figure. The optimised treated fibres were then utilized to produce pavement quality concrete (PQC). The physical and chemical characteristics of all the considered fibres are summarized in Table 1. Density, tensile strength and strain at failure were determined as per ASTM B923-10 (ASTM B923 − 10 2015), ASTM (ASTM C1557-20 2000), respectively. For absorption, fibres were dried at 40°C for 24 hours followed by soaking in water for ~24 hours (Shoeb et al. 2024). From the available literature, the identified dominating parameters which may affect the coir-reinforced-concrete behaviour are fibre type or maturity level, fibre condition, aspect ratio, fibre dosage, and binder concentration. For studying these parameters, two types of coir fibres were locally procured viz. immature fibres and mature fibres. To remove the impurities, the considered fibres were washed thoroughly until clear water passed. These fibres were then trimmed to 10 mm and 50 mm lengths with the help of a cutter; in this study, 10 mm and 50 mm fibres are referred to as short and long fibres, respectively. The aspect ratio of short and long fibres was 40 and 200, respectively (average diameter was 0.25 mm). To study the effect of treatment, optimized alkali treatment method was considered and then washed with water (Shoeb et al. 2024). Two different binder contents of 350 kg/m3 and 400 kg/m3 were used to produce concrete of grades M30 and M40, respectively. The considered mix were optimised using superplasticizer to achieve a slump of 100±20 mm. Intermediate mixing procedure, a novel methodology was used to produce homogeneous coir fibre concrete. Following the 28 days of curing the specimen casted, mechanical performance of the coir-concrete was evaluated

based on different sets of testings. For example, the code followed for evaluating initial slump, density, and air content were ASTM C143/C143M-20, and ASTM C138 / C138M (ASTM:C138/C138M-13 2013; ASTM C143/C143M 2015), respectively. The hardened state properties were determined following the guidelines of IS 516 (BIS 2021) (IS 516 1959). Water absorption and porosity of coir-concrete mixes as evaluated as per ASTM C642 (2022) (ASTM C642 - 21 1997) and durability index testing procedure manual (Alexander et al. 2023), respectively.

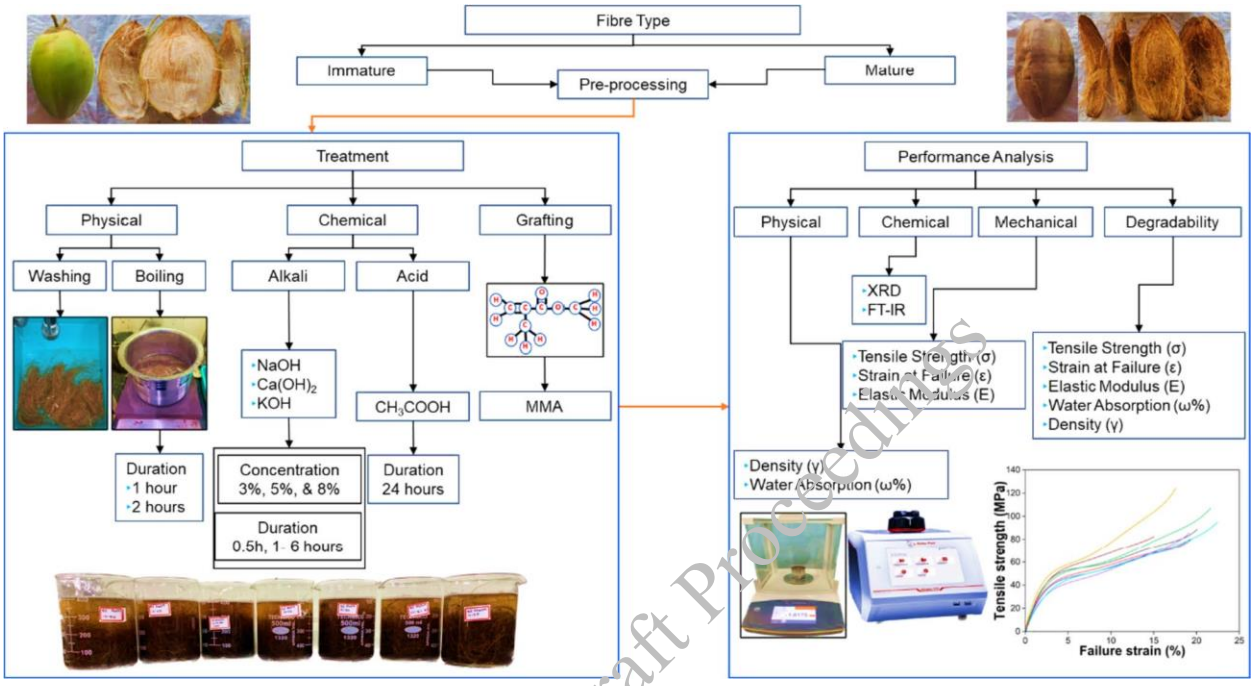

Figure 1. Methodology flow chart for the treatment processes on coir fibres

Table 1. Coir fibre characteristics

Property	Mature Fibre	Immature Fibre	Treated Mature Fibre	Treated Immature Fibre
Density (kg/m^3)	1.20	1.26	1.77	1.37
Absorption (%)	79.3	73.7	98.8	96.3
Tensile Strength (MPa)	81.2	79.5	105.7	102.2
Failure Strain (%)	14.9	18	21.1	22.4

3. Results and Discussions

3.1 Coir Fibre Characteristics

3.1.1 Physical Characterization

The average diameter of the considered immature and mature fibres in the as-received state were 268 µm and 246 µm, respectively. This difference could be related to the development of the coir fibre structure. Figure 2 portrays the effect of different treatment techniques on the diameter of mature and immature. From Figure 2 it is evident that diameter of the coir fibre changed, and its magnitude depends on the treatment technique adopted. Washing the fibres with potable water reduced the thickness/diameter, irrespective of the fibre type which could be linked to the removal of impurities. Reduction in the fibre diameter after alkaline treatment could be attributed to the degradation of the coir fibres by the virtue of its ligno-cellulosic fibres. The impact of several treatments on the coir fibres' absolute density is shown in Figure 2. The tendencies identified during the diameter analysis were consistent with the absolute density pattern that was observed. The main reason why mature fibres were denser than immature fibres was because of alterations in chemical composition brought about by aging (Brígida et al. 2010). Because high-density contaminants

were eliminated, washed mature fibres showed an approximate 34% decrease in absolute density compared to as-received fibres (Sawpan et al. 2011). Nevertheless, after washing, there was a little increase in the immature fibres' absolute density. Because boiled fibres shrink at high temperatures, they showed larger densities. The majority of the alkali-treated fibres showed increased absolute density values in contrast to the diameter analysis, perhaps as a result of salts depositing in the surface pores. In a similar vein, grafting immature fibres with MMA solution resulted in a 104% increase in absolute density over washed fibres.

3.1.2 Mechanical Characterisation.

Treating the coir fibres with physical methods such as washing and boiling reduced the tensile strength, as witnessed in this study (Figure 2). This reduction was observed to be 26% for boiled fibres when compared with washed fibres. This behaviour could be linked to the dissolution/ removal of lignin and cellulose on account of thermal treatment (Bui et al. 2020). On the other hand, significant improvement was noted when fibres were chemically treated. For instance, 30%, 56%, 13%, 22% and 21% were the highest improvements noted for sodium hydroxide (NaOH), calcium hydroxide ($Ca(OH)_2$), potassium hydroxide (KOH), acetic acid (CH_3COOH) and methyl methacrylate (MMA) with respect to raw fibres respectively. Exposure of cellulose and increased density could be attributed to the increase in the tensile strength (Sawpan et al. 2011). A similar trend was observed with MMA treated fibres which exhibited higher strength than washed fibres. Contradictory to the typical understanding, the absolute density increase did not significantly improve the tensile strength. As mentioned from the literature, the immature fibres demonstrated slightly lower tensile strength than mature fibres. For instance, the average tensile strength for immature and mature in as received-state, washed- state, boiling, and alkali treated ($Ca(OH)_2$) were 79.49 & 81.22, 87.08 & 90.49, 78.61 & 78.19 and 122.2 & 127 MPa, respectively, which indicates that there is negligible effect of the age of fibres on their tensile strength. From the present study and based on tensile strength results, it can be observed that post-treatment, both mature and immature fibre tensile strength become similar at their respective optimum durations. Also, fibres soaked for 6 h and 5 h in 5% NaOH solution, 1 h in 5% $Ca(OH)_2$ and 30 min in 5% KOH solution could be regarded as the optimum durations for immature and mature fibres, respectively. Figure 2 summarizes the effect of fibre treatment on its failure strain. Though the mature fibres showed a relatively higher strength, the immature fibres possessed higher failure strain, as observed by (Lomelí-Ramírez et al. 2018); the average difference observed in the failure strains between immature and mature fibres was 23%. This is due to the higher lignin content in mature fibres than in the immature, which imparts rigidity. This indicates that immature fibres could be preferred in composites requiring higher ductility. A similar trend could be seen when the fibres were treated with different physical and chemical techniques. As observed from the Figure 2, subjecting the fibres to different treatments increased the failure strain. The highest increase was observed for NaOH-5 h (53%), followed by NaOH-6 h (47%) and calcium hydroxide (25%) with respect to unwashed fibres. Similar results on the increased failure strain with treatment were also observed by many researchers (Silva et al. 2000; Varma et al. 1984). The increased ductility of the treated fibres could be attributed to the microfibrillar angle (Reiterer et al. 1999; Sheng-zuo et al. 2004). Microfibrils stretch along the longitudinal axis during stress application, providing more elongation to the fibres before failure (Reiterer et al. 1999; Sheng-zuo et al. 2004).

3.2 Coir Fibre Concrete Characteristics

As discussed previously, four fundamental variables of coir fibres viz. aspect ratio, fibre dosage, fibre maturity level, and pre-treatment, affecting the mechanical performance of concrete are considered in the present study apart from the binder content. Figure 3 shows the results of compressive strength and flexural strength of the considered mixes (M30 and M40) at 28 days of curing. From Figure 3, it can be seen that inclusions of coir fibres irrespective of fibre dosage and fibre length resulted in the lowering of the strength characteristics of M40 grade concrete which is contrary to literature (Salain, I. M. A. K., Sutarja, I. N., Wiryasa, N. M. A., & Jaya 2014; Zhang et al. 2021) and in agreement with available literature (Baruah and Talukdar 2007; Krishna et al. 2018). The reduction in the compressive strength noted for CC-0.1-S, CC-0.4-S, and CC-0.7-S, were 17%, 31%, and 54%, respectively compared to control concrete. Similarly, for long fibre mixes the reduction in strength with respect to control concrete was 20%, 38%, and 40%, respectively. These results indicate an insignificant effect of the fibre aspect ratio on the compressive strength for lower dosages of fibres (<0.7%). The same observation could be seen in the flexural strength results wherein the reduction is almost similar for both the aspect ratios except 0.7% dosage. For M30 grade concrete also (Figure 3), the trend is almost the same wherein the compressive strength for the short & long

fibre mixes reduces by 19-31% & 23-36%, and flexural strength reduces by 19-28% & 22-34%, respectively compared to control concrete (CM). This trend was even seen for different fibre conditions (maturity level and treatment conditions; (Figure 3) further confirming the insignificant effect of fibre aspect ratio on the strength characteristics of concrete made with lower fibre dosages.

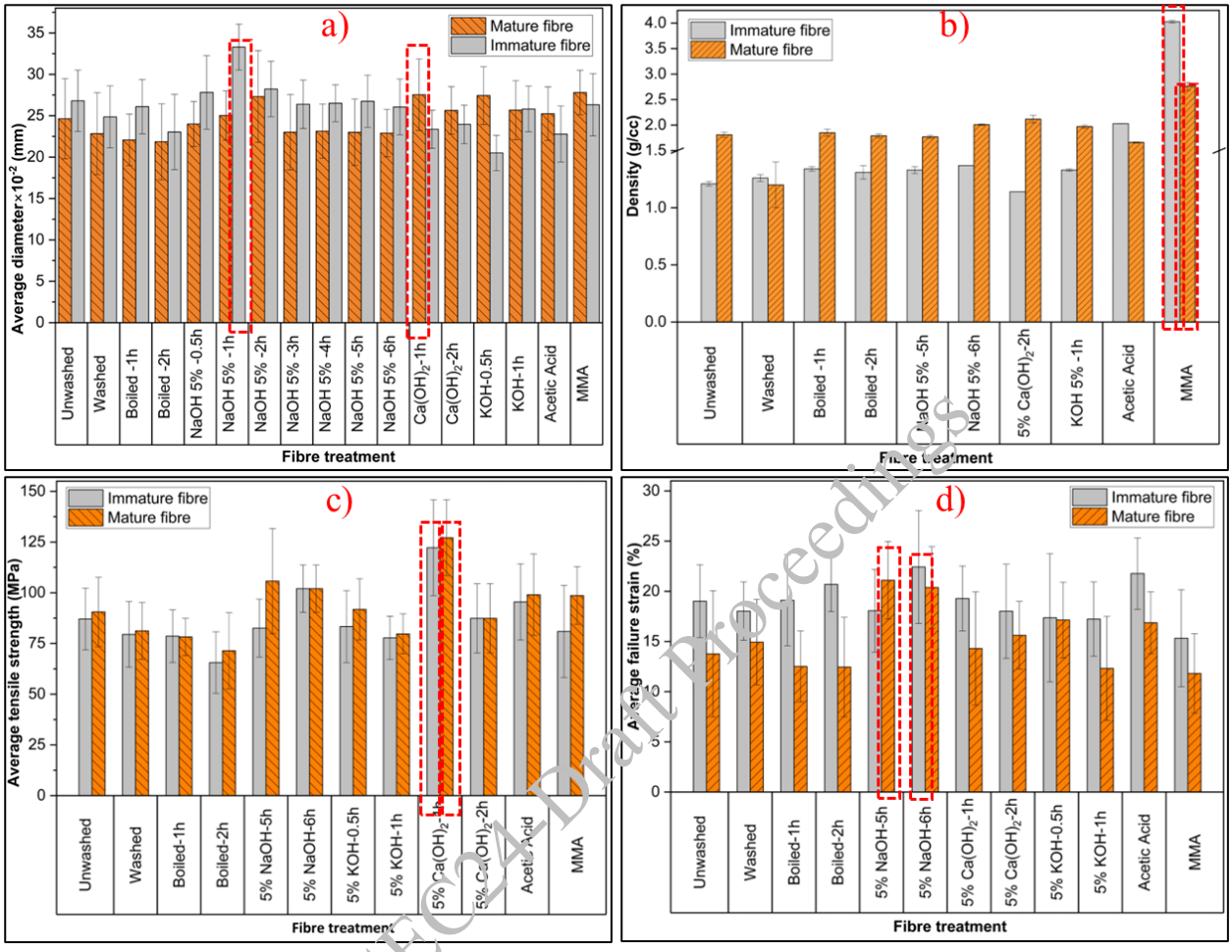

Figure 2. Physical and mechanical characterisation of immature and mature fibres subjected to different treatment techniques

The thermograms of fibres in various states (SPS, concrete, and raw) are shown in Figure 3 Being a hygroscopic material, coir fibres readily absorb moisture from the ambient environment and therefore, the initial mass loss at ≤100°C is due to loss of this moisture apart from the loss of volatiles. However, the mass loss at ≤150°C was found to be slightly higher in raw fibres compared to fibres pulled from concrete and SPS-exposed coir. This might be due to the presence of higher moisture and volatiles in raw fibres which got reduced after being exposed to an alkaline environment. Being a natural material, coir is mainly composed of cellulose, hemicellulose, and lignin which decompose approximately in the temperature ranges of 250-400°C, 180-315°C, and 200-900°C, respectively (Monteiro et al. 2012) i.e. exact identification of the phase getting decomposed is difficult due to overlapping between the temperature ranges. Nevertheless, lignin being the outermost layer decomposes first along with hemicellulose between 200°C to 250°C. Whereas, the mass loss between 250°C to 300°C is due to the combined degradation of cellulose, hemicellulose, and lignin. Since the hemicellulose content in coir is generally less, the degradation between 300°C-350°C is due to cellulose and lignin components; mass loss beyond 400°C is due to the decomposition of lignin only. As can be seen in Figure 3, amongst the various fibre states, the decomposition noted was highest for raw fibres, followed by fibres pulled from concrete, and the lowest decomposition was demonstrated by the fibres exposed to the SPS solution. For instance, the mass loss at 250°C noted for raw fibres and fibres exposed to real concrete environment and SPS solution was 46%, 43%, and 34% respectively. Similarly, at 400°C, 63%, 58%, and 54% were the mass loss corresponding to

raw, concrete fibres, and SPS exposed fibres, respectively. This means SPS-exposed fibres and concrete-exposed fibres have lesser content of cellulose, hemicellulose, and lignin than raw fibres indicating their leaching in the alkaline environment. Since the SPS environment is more aggressive than normal concrete, the leaching of coir was higher; the results of the dimensional analysis also indicated the same where net coir shrinkage was ~45% higher than fibres present in concrete specimens. To validate the results, an XRD study was performed wherein SPS fibres were found to be more amorphous than raw fibres (Figure 3.) indicating the decomposition of their crystalline structure when exposed to a highly alkaline environment. The other important observation noted in the XRD results was the presence of numerous peaks in the fibres pulled from concrete. These peaks indicate the deposition of hydrated cement compounds on the fibres. For example, peak at 29.2°, 39.5°, and 60.5° corresponds to calcium silicate hydrate & calcite, calcite, and monosulphate, respectively. Similarly, some traces of deposition of quartz can be seen in Figure 3.

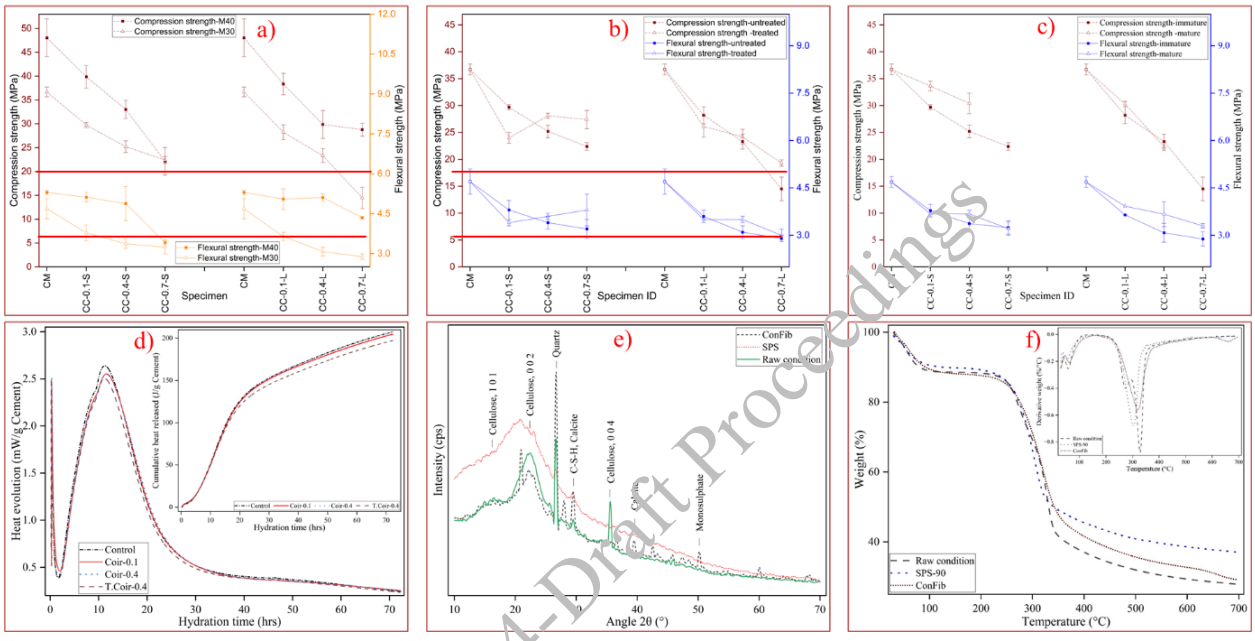

Figure 3. Mechanical performance, chemical and thermal characterisation of discarded coir fibre concrete

3.3 Degradation of Discarded Coir Fibre Concrete

Since it is unclear whether or not this degradation affects the functionality of concrete that has already hardened, a durability study was carried out by subjecting the concrete specimens to various cycles of alternate wetting and drying (W&D) environments. Concrete specimens (M30 and M40 grade) are shown in Figure 4 with their compressive strength both before and after 60 cycles of W&D at 60°C. After being subjected to numerous W&D cycles, the compressive strength of all the mixes under consideration for the M30 concrete grade decreased by 0–15%; the 0.4% coir concrete mix showed the largest drop of 15%, while the control concrete showed the lowest reduction of 1%. But using M40 grade concrete, no discernible pattern could be noted, and after the W&D cycles, the strength improved by 10% to 15% in certain situations. A statistical analysis (paired t-test) was conducted to investigate this unusual trend; the findings showed no significant variation for any of the mixes under consideration, with the exception of the 0.7% long fibre mix (CC-0.7L). Given the rigorous nature of the approach (60 cycles of wetting and drying) and the negligible strength loss, it can be concluded that the addition of coir will not have an adverse effect on the long-term performance of the concrete. These findings are intriguing in light of the coir deterioration in concrete caused by alkaline hydrolysis and mineralization; they show that coir degradation has no appreciable impact on the behaviour of concrete in its hardened state and are consistent with test results reported by (Ramli et al. 2013; Sivaraja et al. 2010).

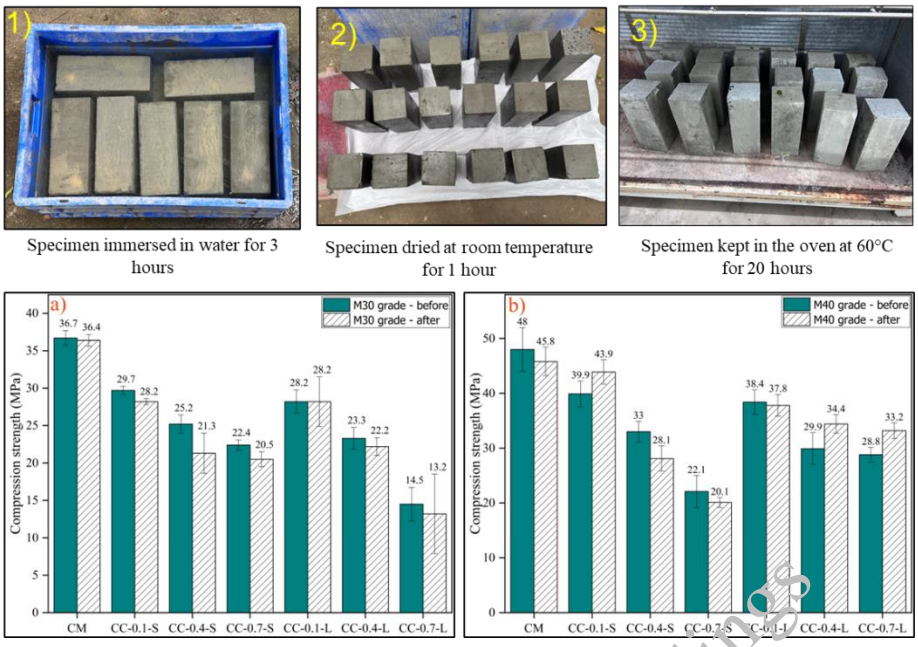

Figure 4. Post degradation response of discarded coir fibre concrete

4. Conclusions

The objective of this research is to comprehend the response of immature and mature fibres treated with various physico-chemical methods and the mechanisms governing the reduction of strength and the degradation of fibre in discarded coir fibre concrete. Different parameters affecting the behaviour of coir fibre were taken into consideration, including aspect ratio, dose, maturity level, and surface properties. These thorough investigation leads to the following conclusions:

- An increase in the tensile strength of coir fibre by 28%, 30% and, 54%, 57% with respect to washed fibres was observed for immature and mature fibres after treatment with NaOH and $Ca(OH)_2$ due to the change in the chemical composition of coir fibre.
- NaOH treatment demonstrated higher failure strain by 41% and 24% for mature and immature fibres, respectively and relatively better tensile strength among various treatments with respect to washed fibres.
- Based on the framework developed for the treatment of coir fibres in enhancing the mechanical characteristics, it is suggested that a pre-treatment with washing is necessary, followed by treatment with a NaOH solution with 5% concentration for 5–6 h.
- The introduction of coir reduced the compressive strength characteristics of M40 grade concrete by 31-38% for 0.4% dosage of coir fibre; however, the reduction in flexural strength was found to be lower than the corresponding reduction in compressive strength.
- Coir characteristics such as maturity level, fibre treatment, and aspect ratio, were found to have an insignificant effect on the performance of concrete.
- Amongst all the considered coir parameters, coir dosage was found to be the most dominating parameter governing the behavior of concrete. For high-dosage mixes (>0.4%).
- Coir fibres eventually degrade in the concrete environment due to the combined actions of alkali hydrolysis and mineralization. However, the degradation of coir, post concrete hardening stage, did not affect the compressive strength of the concrete indicating that the long-term performance of concrete is unaffected due to the incorporations of coir.

References

Adeniyi, A.G., Onifade, D.V., Ighalo, J.O. and Adeoye, A.S. (2019) “A review of coir fiber reinforced polymer composites”, *Composites Part B: Engineering,* 176:107305

Alexander, M., Ballim, Y. and Mackechnie, J.M. (2023) "Durability Index Testing Procedure Manual", *Research Monograph No4*, 2023:29

Majid, A. and Chouw, N. (2013). "Experimental Investigations on Coconut-Fibre Rope Tensile Strength and Pullout from Coconut Fibre Reinforced Concrete", *Construction and Building Materials,* 40 (2): 1118–27.

ASTM B923 − 10 (2015) "Standard Test Method for Metal Powder Skeletal Density by Helium or Nitrogen", ASTM 642-97. ASTM Int West Conshohocken, PA 75:10–13

ASTM C143/C143M (2015) "Standard Test Method for Slump of Hydraulic-Cement Concrete", *ASTM Int West Conshohocken*, PA 75:1–4

ASTM C1557-20 (2000) "Standard Test Method for Tensile Strength and Young's Modulus for High-Modulus", *ASTM Int West Conshohocken*, PA 75:1–5

ASTM C642 - 21 (1997) "Standard Test Method for Density, Absorption, and Voids in Hardened Concrete", ASTM 642-97. *ASTM Int West Conshohocken*, PA 75:1–3

ASTM C138/C138M-13 (2013) "Standard Test Method for Density (Unit Weight), Yield, and Air Content (Gravimetric)", *ASTM Int West Conshohocken*.

Baruah, O.P. and Talukdar, S.A (2007) "A comparative study of compressive, flexural, tensile and shear strength of concrete with fibres of different origins", *Indian Concrete Journal,* 81 (7): 17–24

Brígida, A.I.S., Calado, V.M.A., Gonçalves, L.R.B. and Coelho, M.A.Z. (2010) "Effect of chemical treatments on properties of green coconut fiber", *Carbohydrate Polymers,* 79 (4): 832–38

Bui, H., Sebaibi, N., Boutouil, M. and Levacher, D. (2020) "Determination and review of physical and mechanical properties of raw and treated coconut fibers for their recycling in construction materials", *Fibers,* 8 (6): 37

IS 516 (1959) "Method of Tests for Strength of Concrete", *Bureau of Indian Standards,* 1–30

Isaac, D.S., Nair, V.V. and Mohana, H. (2022) "Background review and development of a coir-based hybrid geosynthetic", *Arabian Journal of Geosciences,* 15 (15)

Krishna, N.K., Prasanth, M. and Gowtham, R. (2018) "Enhancement of properties of concrete using natural fibers", *Materials Today: Proceedings,* 5 (11): 23816–23

Lakshmi N. S., Sarika, B., Sebastian, S. and Ravi, P.K. (2015) "Low temperature grafting of MMA on to coir fibre", *Cord,* 31 (1): 8

Lomelí-Ramírez, M.G., Anda, R.R. and Satyanarayana, K.G. (2018) "Comparative study of the characteristics of green and brown coconut fibers for the development of green composites", *BioResources,* 13 (1): 1637–60

Ramli, M., Kwan, W.H. and Abas, N.F. (2013) "Strength and durability of coconut-fiber-reinforced concrete in aggressive environments", *Construction and Building Materials,* (38): 554–66

Reiterer, A., Lichtenegger, H., Tschegg, S. and Fratzl, P. (1999) "Experimental evidence for a mechanical function of the cellulose microfibril angle in wood cell walls", *Philosophical Magazine, A* 79 (9): 2173–84

Rout, J., Misra, M. and Tripathy, S.S. (2002) "Surface modification of coir fibers. II. Cu(II)- IO -4 initiated graft copolymerization of acrylonitrile onto chemically modified coir fibers", *Journal of Applied Polymer Science,* 84 (1): 75–82

Salain, I. M. A. K., Sutarja, I. N., Wiryasa, N. M. A. and Jaya, I.M. (2014) "Mechanical properties of coconut fiber-reinforced concrete", *The 6th International Conference of Asian Concrete Federation, 21-24*, 553–56

Sawpan, M.A., Pickering, K.L. and Fernyhough, A. (2011) "Effect of various chemical treatments on the fibre structure and tensile properties of industrial hemp fibres", *Composites Part A,* 42 (8): 888–95

Sheng-zuo, F., Wen-zheng, Y. and Xiang-xiang, F. (2004) "Variation of microfibril angle and its correlation to wood properties in poplars", *Journal of Forestry Research,* 15 (4): 261–67

Shoeb, M., Kandasami, RK, Singh S, and Sebastian S (2024) "Framework for treatment of coconut coir fibres through physico-chemical techniques", *International Journal of Geosynthetics and Ground Engineering,* 3

Silva, G.G., De Souza, D.A., Machado, J.C. and Hourston, D.J. (2000) "Mechanical and Thermal Characterization of Native Brazilian Coir Fiber", *Journal of Applied Polymer Science,* 76 (7): 1197–1206

Sivaraja, M., Kandasamy, Velmani, N. and Pillai, M.S. (2010) "Study on durability of natural fibre concrete composites using mechanical strength and microstructural properties", *Bulletin of Materials Science,* 33 (6): 719–29

Varma, D.S., Varma, M. and Varma, I.K. (1984) "Coir Fibers: Part I: Effect of physical and chemical treatments on properties", *Textile Research Journal,* 54 (12): 827–32

Zaman, H.U., Khan, M.A., Khan, R.A. and Sharmin, N. (2011) "Effect of chemical modifications on the performance of biodegradable photocured coir fiber", *Fibers and Polymers,* 12 (6): 727–33

Zhang, X., Pel, L., Gauvin, F. and Smeulders, D. (2021) "Reinforcing mechanisms of coir fibers in light-weight aggregate concrete", *Materials,* 14 (3): 1–20

Properties of High-Volume Biomass Ash-based Binder

Nilakanmani Manimaran[1*], Piyush Chaunsali[2], and Manu Santhanam[3]

[1] PhD student, Indian Institute of Technology Madras, Chennai, India
Email: nilakanmani@gmail.com
[2] Associate Professor, Indian Institute of Technology Madras, Chennai, India
Email: pchaunsali@civil.iitm.ac.in
[3] Professor, Indian Institute of Technology Madras, Chennai, India
Email: manus@civil.iitm.ac.in

[*]Corresponding author

ABSTRACT

Agro-based biomass ash rich in reactive silica can be used to produce cementitious binders by alkali activation. The compositional variation and presence of unburnt carbon (≥ 10%) limits the utilisation of biomass ash in cementitious binders. Alkali activation in the presence of hydrated lime (calcium hydroxide) facilitates low molar alkali activation. The study aims to formulate a high-volume biomass ash-based binder (> 50% biomass ash) with 1M aqueous sodium hydroxide solution, 10% hydrated lime with the addition of clay or calcined clay to stabilise the binder and cured at 50 °C. Hydration kinetics was studied using isothermal calorimeter (heat evolution), and hydration products were characterised with bound water measurement and mineralogical composition (using XRD). The results from binder characterisation were used to optimise the binder composition and formulate high-volume biomass ash-based binder.

KEYWORDS: *Agro-based biomass ash, Alkali activation, Sustainable binder, Reactive alumina*

1. Introduction

Globally, the anthropogenic carbon dioxide (CO_2) emission from Portland cement industry ranges from 6–8%. Current research on cementitious materials focuses on alternative sustainable binders with less environmental impact that can be produced with locally available resources (Andrew, 2019; Juenger et al. ,2011). Alkali-activated binder (AAB) is one such sustainable solution, which facilitates the utilisation of locally available resources rather than the Portland cement system. Agro-based biomass residues like husk and straw from rice and wheat, sugarcane bagasse, etc., are used as fuel in micro, small and medium enterprises (MSME), which generates residual ash as a by-product. The ash from biomass combustion contains amorphous silica, which is highly reactive and pozzolanic in nature (Bahurudeen et al., 2016). However, the compositional variability, and presence of unburnt carbon hinder the utilisation of biomass ash in cementitious binders. Due to these issues, the ashes are often disposed of in nearby landfills, posing a significant threat to environment. Researchers have attempted to utilise the agro-based biomass ashes in Portland cement system, after processing to remove the unburnt carbon content. The agro-based biomass ashes have the potential to partially replace only 20–30% of Portland cement clinker (Bahurudeen et al., 2015); however, high-volume replacements (> 50%) are not possible due to inconsistencies in the physico-chemical properties of the biomass ashes. The utilisation of biomass ash in cementitious binders can be enhanced by formulating alkali activated binder with high volume (> 50%) of biomass ash (Chaunsali et al. 2018). The addition of calcium source to alkali activated binder reduces the dependence on high temperature and strong alkali activators (Alventosa and White, 2021). The presence of reactive alumina has enhanced the dissolution of Si in alkaline medium in addition to high temperature and strong activator, due to the formation of polysialates (Manimaran et al., 2023). The current study aims to formulate alkali-activated binder with high-volume of biomass ash (> 50%), calcium hydroxide, clay/calcined clay (reactive alumina source), activated with 1M sodium hydroxide solution. The influence of clay and calcined clay addition on the reaction kinetics and reaction products is explored.

2. Experimental program

2.1 Material and Characterisation

The biomass ash was collected from a paper mill industry, Muzaffarnagar, Uttar Pradesh, where they had used biomass as feedstock. The biomass used was comprised of rice husk and straw, sugarcane bagasse, and other locally sourced agro-based residue. The ash was activated with laboratory grade calcium hydroxide (lime) and aqueous sodium hydroxide solution (1 M NaOH), to prepare binder. Clay and calcined clay were added to prepare binder as stabilising agent and reactive alumina source. The ash, clay and calcined clay were characterised for mineralogical composition using X-ray diffraction (XRD), oxide composition using X-ray fluorescence (XRF) and unburnt carbon content with loss on ignition (LOI) test. XRD was performed with powder X-ray diffraction instrument (CuKα radiation); X'Pert HighScore plus software was used for analysing the X-ray diffractograms. XRF was performed on pellet samples prepared with boric acid powder. LOI test was performed as per ASTM C311 (ASTM C311). Particle size analysis (PSA) was performed using laser diffraction and water was used as the dispersing medium. The results from XRF, LOI and PSA are shown in Table 1. Figure 1(A, B) shows X-ray diffractogram and particle size distribution for the unreacted ash, clay and calcined clay. The chemical composition analysis shows that the biomass ash is of silicious origin and consists of 10% LOI. Both chemical and mineralogical composition shows that the clay is of kaolinite origin. The clay was calcined at 800 °C for two hours to produce calcined clay. The amorphous hump in biomass ash and calcined clay from X-ray diffractogram (from 20–30° 2θ) shows the presence of amorphous reactive silica and alumina phases. The particle size distribution plot shows that the clay and calcined clay has finer fraction than the biomass ash. The D_{50} size for biomass ash is 40 µm, and 8 and 16 µm for the clay and calcined clay, respectively.

Table 1. Physical and chemical properties of ash, clay, and calcined clay

Chemical composition (in weight %)			
Details	Biomass ash	Clay	Calcined Clay
SiO_2	73.85	43.24	48.70
Al_2O_3	2.02	38.85	46.40
Fe_2O_3	0.95	0.63	0.66
Na_2O	0.22	0.16	0.22
K_2O	3.68	-	-
CaO	4.61	0.22	0.33
LOI	10.09	14.47	1.09
Particle size analysis			
D_{10} (µm)	17	1	2
D_{50} (µm)	40	8	16
D_{90} (µm)	79	26	60

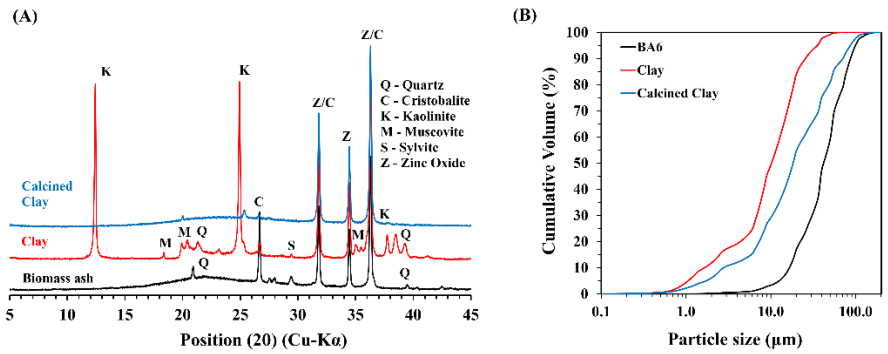

Figure 1. (A) X-ray diffractogram of unreacted ash, clay, and calcined clay; (B) Particle size distribution plot

2.2 Methods

Different combinations of alkali activated binder (AAB) was prepared to optimise the proportion of biomass ash (70–90%) with the addition of clay/calcined clay (10–20%), and calcium hydroxide (lime) (10%). The mix design for the binders is shown in Table 2. AAB was prepared with 1M NaOH solution with 0.5 w/b ratio since high molar ratio affects the practical application of the binder. The prepared binder was sealed in an air-tight container with parafilm to prevent evaporation of water, and then cured at 50 °C, to characterise the binder at 1 day and 28 days. Iso-propyl alcohol was used for hydration stoppage. The hydrated binder was characterised for bound water measurement and mineralogical composition (XRD). Bound water for the AAB was measured as the mass loss from 50–350 °C using muffle furnace. The reaction kinetics of the AAB was studied using isothermal calorimeter (model: calmetrix 8000 HPC) at 50 °C for 3 days. Stability of the reaction products was studied using acid neutralisation test (ANC), performed with 5% H_2SO_4 solution. The 28 day hydrated binder was ground to pass through 75 µm and diluted 1g of ground binder with 50 ml of distilled water to prerform ANC. An autotitrator was used to dose 5% H_2SO_4 solution to measure the pH change (Damion and Chaunsali, 2022).

Table 2. Mix design for the alkali activated binder

Sample ID	Weight Percentage (%)			
	Biomass ash	Clay (C)	Calcined Clay (CC)	Calcium hydroxide/Lime (L)
L10	90	0	0	10
C10	80	10	0	10
C20	70	20	0	10
CC10	80	0	10	10
CC20	70	0	20	10

3. Results and Discussions

The results from binder characterisation are plotted in Figure 2(A–D). Figure 2 (A) shows the cumulative heat plot, Figure 2(B) shows bound water measurement, Figure 2(C) shows X-ray diffractogram, and acid consumption from ANC test for the alkali activated biomass ash-based binder is plotted in Figure 2(D). The cumulative heat plot shows that addition of clay and calcined clay increased the heat evolution, and addition of calcined clay (CC10 and CC20) has accelerated the early-age heat evolution (< 6 hours). Bound water measurement for lime (L10) and clay addition (C10 and C20) were quite similar and bound water for 1 day and 28 days did not significantly vary. Addition of calcined clay has increased the bound water content (at 28 days) as compared to addition of clay. The reactive alumina from calcined clay has contributed to the acceleration in reaction kinetics and higher bound water content. The amorphous hump present in the unreacted ash is not evident in the AAB (L10, C20, CC20) at 28 days from X-ray diffractogram. The acid consumption from ANC test has increased for addition of both clay (C20) and calcined clay (CC20) at 28 days. Also, the acid consumption for calcined clay addition (CC20) increased particularly at lower pH, which shows that the binder is more stable. Further analysis is required to understand the role of reactive alumina on the stability of alkali activated binder at low pH.

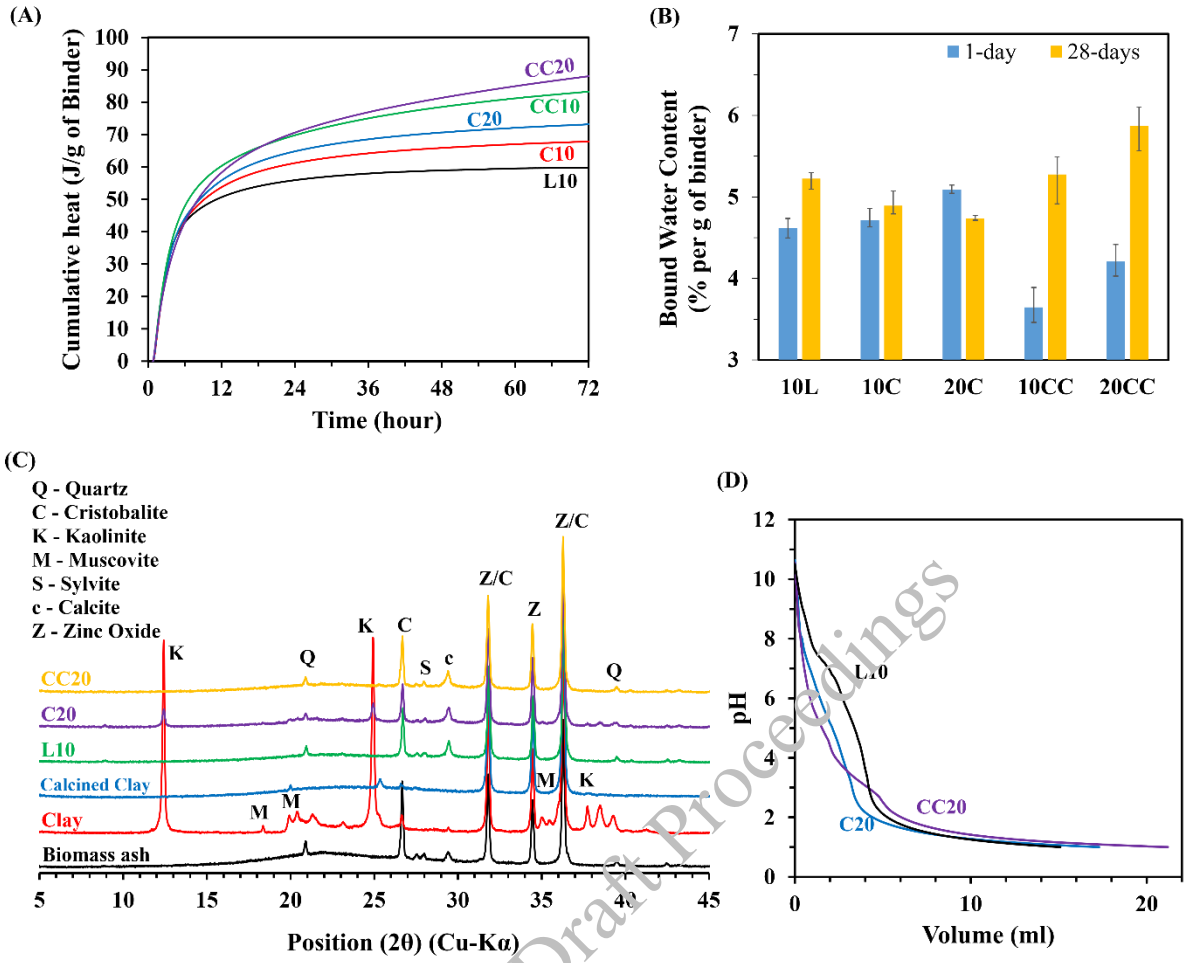

Figure 2. (A) Reaction kinetics of the binder; (B) Bound water measurement; (C) X-ray diffractogram for the binders at 28 days; (D) Acid consumption from ANC test at 28 days

4. Conclusions

In this study, alkali activated binder was formulated with high volume of biomass ash, lime, clay and calcined clay, with low-molar activation (1M NaOH). The reaction kinetics and reaction products of the alkali activated binder were studied. The addition of calcined clay has accelerated the reaction kinetics of the alkali activated binder with higher bound water content and better stability of reaction products. Addition of clay has favoured the reaction kinetics; however, the bound water content and acid consumption was not higher as compared to calcined clay addition. The study emphases that high-volume biomass ash-based binder can be formulated with calcined clay addition with better stability for low pH environment.

Acknowledgements

The first author would like to acknowledge the Ministry of Education for the financial support for her doctoral research. The first author would also like to acknowledge the Prime Minister's Research Fellowship granted by Government of India. The funding from the Centre of Excellence on Technologies for Low Carbon and Lean Construction (TLC2) at IIT Madras is gratefully acknowledged.

References

Andrew, R. M. (2019) "Global CO2 emissions from cement production, 1928-2018", *Earth System Science Data*, 11(4):1675–1710

Juenger, M. C. G., Winnefeld, F., Provis, J. L., and Ideker, J. H. (2011) "Advances in alternative cementitious binders." *Cement and Concrete Research*, 41(12):1232–1243

Bahurudeen, A., Wani, K., Basit, M. A., and Santhanam, M. (2016). "Assesment of Pozzolanic Performance of Sugarcane Bagasse Ash", *Journal of Materials in Civil Engineering*, 28(2):04015095

Bahurudeen, A., Kanraj, D., Gokul Dev, V., and Santhanam, M. (2015) "Performance evaluation of sugarcane bagasse ash blended cement in concrete", *Cement and Concrete Composites*, 59:77–88

Chaunsali, P., Uvegi, H., Osmundsen, R., Laracy, M., Poinot, T., Ochsendorf, J., and Olivetti, E. (2018) "Mineralogical and microstructural characterization of biomass ash binder", *Cement and Concrete Composites*, 89:41–51

Alventosa, K. M. L., and White, C. E. (2021) "The effects of calcium hydroxide and activator chemistry on alkali-activated metakaolin pastes." *Cement and Concrete Research*, 145:106453

Manimaran, N., Santhanam, M., and Chaunsali, P. (2023) "Composition-Reactivity Relationship of Indian Biomass Ash." *The 16th International Congress on the Chemistry of Cement 2023 (ICCC2023)*, 266–269.

ASTM C 311-04. (2005). "Standard Test Methods for Sampling and Testing Fly Ash or Natural Pozzolans for Use in Portland-Cement Concrete." *Annual Book of ASTM Standards*, 04.02, 204–212

Damion, T., and Chaunsali, P. (2022). "Evaluating acid resistance of Portland cement, calcium aluminate cement, and calcium sulfoaluminate based cement using acid neutralisation." *Cement and Concrete Research*, 162:107000.

Structural Behavior of Precast Wet Beam-Column Connection with Hybrid Rebar Coupler Subjected to Reversed Cyclic Loading

Vijay Tarun Kumar Moka[1] and Siva Chidambaram R[2*]

[1] Research Scholar, Academy of Scientific & Innovative Research (AcSIR), Ghaziabad-201002, India
ACSC Group, CSIR-Central Building Research Institute, Roorkee-247667, India
Email: tarunkumarmoka@gmai.com
[2]Senior Scientist, ACSC Group, CSIR-Central Building Research Institute, Roorkee – 247667, India
Assistant Professor, Academy of Scientific & Innovative Research (AcSIR), Ghaziabad-201002, India
Email: krsinelastic@gmail.com

*Corresponding author

ABSTRACT

Precast structures are quite prone to earthquakes and its connection performance decides the global behavior of structure. Literature shows wet connections are more reliable in seismic zones than dry connections as these emulates the monolithic joint behavior. An experimental research has been conducted on laboratory to emphasis the seismic behavior of precast beam-column connections. Rebar couplers are incorporated to connect the precast beam and column elements to ensure the effective transfer of stresses. Additionally, cast-in-situ shear key and interface bond coating are provided to improve the integrity of the connection as the precast elements are cast separately. Cast-in-situ conventional concrete mix is used in the connection region along with interface bond coating. One Precast specimen has been cast and compared its behavior with RC monolithic joint. The overall performance of the connection is quantified in terms of hysteresis behavior, energy dissipation, crack patterns and damage index. The cracking behavior of precast specimen demonstrates the successful transfer of stresses through coupler and its influence in the plastic hinge region. Due to accumulation of tensile stresses at the coupled region, severe spalling is noticed in the connection region. This resulted in pinching at the higher drifts compared to monolithic joint. Also, the stiffness of the coupler in the plastic hinge region motivated the crack to occur beneath the coupled region.

KEYWORDS*: Precast wet connection, Hybrid coupler, Cast-in-situ shear key, Plastic hinge region, Stiffness of coupler.*

1. Introduction

Precast construction is one of the major construction systems across the world due to its benefits such as quality control, faster construction time, environment friendly, economical, manpower savings etc. As the precast elements are discontinuous, the connection between them plays a major role in transferring shear, axial and moment to adjacent elements (Park, 1995). Also, the past earthquakes such as Kocaeli earthquake, Van earthquake proved the importance of connection mechanism due to its collapse (Ozden et al., 2014; Saatcioglu et al., 2001). Hence there is a need of proper connection mechanism, which can efficiently transfer forces to adjacent elements. Dry and wet connections are followed in precast structures due to its connection methodologies. Dry connections are limited due to its unsatisfactory seismic performance in terms of energy dissipation, crack patterns etc. (Vidjeapriya and Jaya, 2013). However, the behaviour of wet connection simulates monolithic joint behaviour as it uses fresh concrete in the connection (Ertas et al., 2006; Nimse et al., 2014). Similarly, rebar coupler-based beam-column connections improve the stress transfer behaviour between the elements as the rebars are colinearly connected. But the placement of coupler plays a crucial role in the exhibiting cracking behaviour in the connection region. The presence of coupler reflects in its higher stiffness behaviour and shifts the failure away from the coupled region (Chidambaram and Agarwal, 2018). Limited studies are reported on precast beam-column connections using rebar couplers subjected to lateral loading. (Yan et al., 2018) conducted experimental research on

precast beam-column connections using grouted sleeves under cyclic loading. This research proves that the importance of couplers in transferring stresses in the connection region. Also, the crack pattern reflects the stiffness of coupler in the connection and cracks exhibited above and below the coupler. However, the cracks formed at the rebar hole showed poor integration due to rebar slippage. The play area between the coupler end and foundation interface decides the location of plastic hinge in column (Chidambaram and Agarwal, 2018). However, precast structures are constructed with seperate elements, integriry may be effetced. In order to provide the intergrity of the connectiond, shear keys are used in the connection region. Shear keys provides structural integrity of the connection by elimination shear failure at the interface (Hu et al., 2021). Also, provision of epoxy bond coating delays the onset of interface crack and eliminate rocking action. This study deals with the cyclic behavior of wet precast beam column employing rebar coupler, cast in situ shear key and bond coating in the connection region.

2. Fabrication of specimens and Test set up

In this study, two exterior beam-column connections were fabricated to evaluate its behaviour under lateral loading. The first specimen is monolithic (MJ) with ductile detailing in the plastic hinge region and second specimen is precast (PC) in which beam and column are connected using rebar couplers.

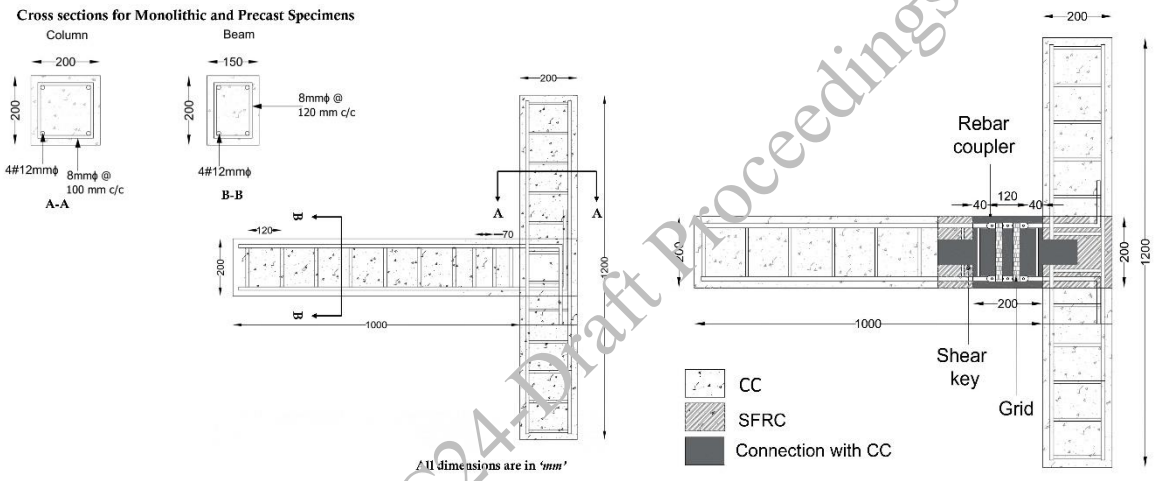

(a) MJ (b) PC

Figure1. Specimen Configuration

Hybrid couplers (Moka and Rajendran, 2022) are used in this study which consists of threaded sleeve, high strength bolts and epoxy grout to fill the coupler. Also, the length of coupler provided to connect precast elements is 120 mm and it satisfied the quality tests required to adopt in RC structures, preferred by (IS 16172 : 2014). The length of wet connection in precast specimen adopted is 200 mm from the column interface.

Also, SFRC is used in the column and beam shear key portion for sound confinement action. As the connection is wet, cast in situ conventional concrete (CC) mix is poured in the connection region after the fabrication of connection. However, the epoxy bond coating is applied over the beam and column interface prior to casting of connection. The configuration of monolithic and precast connection is shown in Figure 1. However, the mix ratio adopted for conventional concrete in both monolithic and precast specimens is 1:1.5:2.5 as cement: fine aggregate: coarse aggregate with a w/c ratio of 0.42. The average cylindrical compressive strength of the conventional concrete mix is observed as 28 MPa. Similarly, the tensile and compressive strength of two solvent epoxy as per manufacturer at 7th day is 10.4 MPa and 60 MPa respectively. Figure 2 depicts the test set up and instrumentation of beam-column connections under lateral loading. A vertical axial load of 30 kN is applied over the column from top through manaul jack. Instrumentation such as load cell, dispalcement sensors are connected to Data Acqisition system to monitor and record the respective data. Figure 3 presents the loading history adopted as ACI 374.1-05 (ACI 374.1-05(19)) with 3 cycles till 3.5% followed by two cycles of each amplitude. However, both the specimens are subjected to lateral loading along with axial load on the column and results are recorded.

Figure 2. Test set up

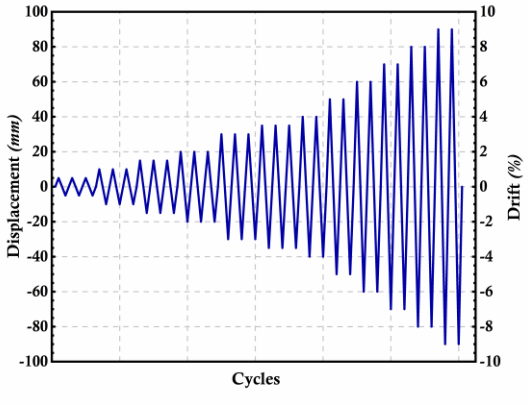

Figure 3. Loading History

3. Cyclic behvaior of Monolithic and Precast Beam-Column connection

3.1 Damage Progression

Figure shows the crack patterns and damage progression of monolithic and precast specimens subjected to lateral loading. Crack mapping has been done on the potential hinge region of column and beam to identify its failure mechanism and crack propagation. The term connection refers to the plastic hinge region of beam and joint refers to the beam-column joint region.

(a) MJ (b) PC

Figure 4. Crack Patterns

When the monolithic specimen (MJ) is subjected to cyclic loading, the plastic hinge region of beam exhibited flexural cracks followed by horizontal cracks along the reinforcement in beam and vertical cracks along the column. This shows the bond slip failure between concrete and anchorage reinforcement from the joint, which resulted in vertical and diagonal cracks in the joint region as shown in Figure 4(a). However, at higher displacement, buckling of reinforcement is observed due to the crushing and spalling of concrete at the interface region resulted in formation of plastic hinge. On the other hand, the crack pattern of precast specimen (PC) is different from monolithic specimen as shown in Figure 4(b). The significance of SFRC in the shear key region is observed through the crack patterns. There are no considerable cracks observed in the column plastic hinge region and beam shear key region due to the usage of SFRC. However, initial cracks are emerged from the ends of the coupler on top and bottom due to its inherent stiffness. Also, the shear key and bond coating offered better resistance to interface crack opening and shifted the failure above the interface. The length between coupler end and column interface influences cracking behaviour. As the

displacement increases, the cracks started to widen in the plastic hinge region and observed spalling of concrete. This resulted in the formation of plastic hinge between the coupler end and column interface with yielding of rebar.

3.2 Hysteretic Behaviour

The lateral response of MJ and PC specimens are presented in Fig 5. Precast specimen (PC) exhibited distinct hysteresis behaviour from monolithic specimen (MJ) due to its connection configuration. MJ specimen exhibited broad hysteresis due to the formation flexural hinge in the beam without any pinching. The peak loads observed in MJ specimen at push and pull conditions is 19.4 kN & 25 kN respectively as shown in Figure 5(a). The drift capacity observed in this specimen is about 6% with yielding of rebar. On the other hand, the PC specimen exhibited similar hysteresis behaviour as MJ specimen with little pinching. Pinching is due to the occurrence of cracks at the early drifts and crushing of concrete as shown in Figure 5(b). It exhibited similar load carrying capacity as MJ specimen i.e., 26.3 kN and -28.7 kN respectively in positive and negative loading. However, the initial stiffness of PC specimen is higher than MJ specimen due to the influence of coupler in the connection. The coupler offers sectional stiffness of the connection and improves seismic behaviour. The energy dissipation of PC specimen is also comparable to the MJ specimen. It clearly manifests that the precast wet connection is emulative to monolithic joint.

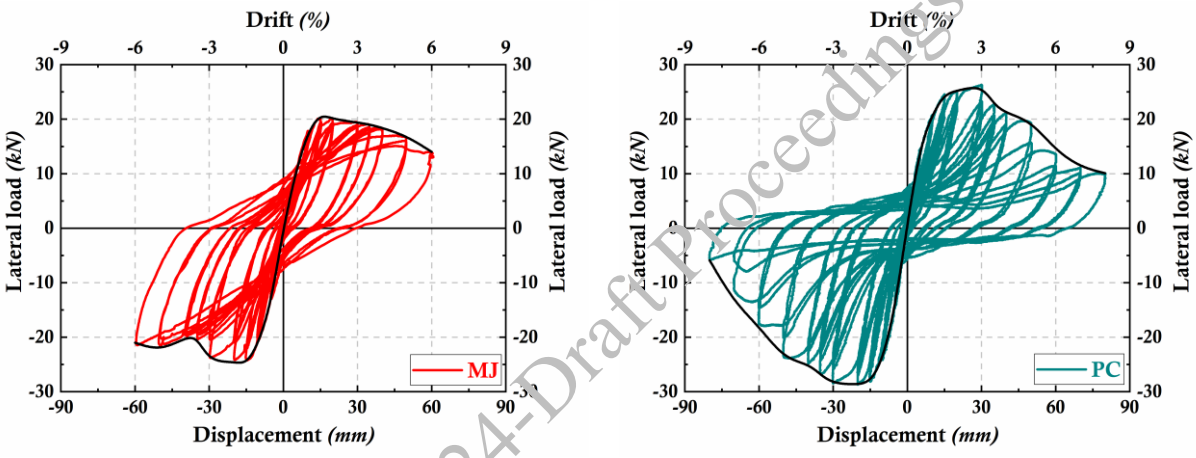

(a) MJ (b) PC

Figure 5. Hysteresis Behaviour

4. Conclusions

- The cracking patterns of PC specimen are different from MJ specimen. The specimen MJ exhibited flexural hinge near the beam interface. In case of precast specimen PC, flexural hinge is formed at the bottom of the coupler due to its sectional stiffness. It is to be noted that the length between the coupler end and column interface decides the location of formation of plastic hinge. The SFRC present in the shear key regions of column and beam prevented the occurrence of failure and improved its behaviour. Shear key and bond coating restricted the interface failure and shifted above the interface.
- The hysteresis behaviour of MJ and PC shows similar behaviour with broad shaped hysteresis. However, a little pinching is observed in PC specimen due to early cracks and spalling in the connection region but the energy dissipation is comparable with MJ specimen. The post-elastic behaviour of PC specimen is improved due to the synergetic action of coupler and shear key.
- The coupler present in PC specimen offered additional section stiffness to the connection and exhibited higher initial stiffness. It is observed that stiffness degradation is gradual in PC specimen, which is similar to MJ specimen.

Acknowledgements

Authors express their gratitude to Director, CSIR-CBRI for his permission to publish this article. Authors extend their thanks to Dr. K. V. Naveen Kumar, CSIR-CBRI and Vellautham C for technical support. CSIR is greatly acknowledged for providing Senior Research Fellowship (31/GATE/24(11)/2019-EMR-I). Dr. S. R. Karade is acknowledged for ASCD laboratory support. Thanks are extended to Mr. Mohan Lal, Mr. Ashokh Raj, and Ms. Deekshitha for testing help.

References

ACI 374.1-05(19). (2019) "Acceptance Criteria for Moment Frames Based on Structural Testing and Commentary". *American Concrete Institute*

Chidambaram, R.S., Agarwal, P. (2018) "Performance evaluation of innovative hybrid rebar coupler in reinforced concrete beams subjected to monotonic loading", *Structural Concrete*, 19, 892–903

Ertas, O., Ozden, S. and Ozturan, T.(2006) "Ductile Connections in Precast Concrete Moment Resisting Frames", *concrete construction*, 9:11

Hu, M., Han, Q., Wu, S., Du, X.(2021) "Shear Capacity of Precast Concrete Shear Keys with Ultrahigh-Performance Concrete for Connections", *Journal of Bridge Engineering*, 26:04021036

IS 16172.(2014) "Reinforcement couplers for mechanical splices of bars in concrete - Specification", Bureau of Indian *Standards*, New Delhi, India

Moka, V.T.K. and Rajendran, S.C. (2022) "Role of coupler in structural behavior of RC elements", *Materials Today: Proceedings*,64:1035–1042

Nimse, R.B., Joshi, D.D. and Patel, P.V.(2014) "Behavior of wet precast beam column connections under progressive collapse scenario: an experimental study", *Advanced Structural Engineering (IJASE)* ,6:149–159

Ozden, S., Akpinar, E., Erdogan, H. and Atalay, H.M.(2014) "Performance of precast concrete structures in October 2011 Van earthquake, Turkey", *Magazine of Concrete Research*,66: 543–552

Park, R.(1995)"A Perspective on the Seismic Design of Precast Concrete Structures in New Zealand", *PCI journal*,40: 40–60

Saatcioglu, M., Mitchell, D., Tinawi, R., Gardner, N.J., Gillies, A.G., Ghobarah, A., Anderson, D.L. and Lau, D.(2001) "The August 17, 1999, Kocaeli (Turkey) earthquake — damage to structures",*Canadian Journal of Civil Engineering*,28:715–737

Vidjeapriya, R. and Jaya, K.P.(2013) "Experimental Study on Two Simple Mechanical Precast Beam-Column Connections under Reverse Cyclic Loading", *Journal of Performance of Constructed Facilities*, 27:402–414

Yan, Q., Chen, T. and Xie, Z.(2018) "Seismic experimental study on a precast concrete beam-column connection with grout sleeves",*Engineering Structures*, 155: 330–344

Shrinkage and Bond Response of Ultra-High Performance Concrete (UHPC)-based HFSTs for Roadway Applications

A.R. Biehl[1*], K.F. Maeger[2], and P.R. Rangaraju[3]

[1] Graduate Student, Clemson University, Clemson, United State of America
Email: arbiehl@clemson.edu
[2] Graduate Student, Clemson University, Clemson, United State of America
Email: kmaeger@clemson.edu
[3] Professor, Clemson University, Clemson, United State of America
Email: prangar@clemson.edu

[*]Corresponding author

ABSTRACT

High Friction Surface Treatment (HFST) is an effective roadway remediation technique to decrease the frequency of crashes due to insufficient pavement friction. To increase roadway coefficient of friction HFSTs typically utilize a thin layer of epoxy binder embedded with calcined bauxite as aggregate. These systems are effective but require specialty materials that are expensive. To decrease the material cost of HFSTs studies have been undertaken to identify alternative materials that meet the service requirements of typical HFSTs. Multiple studies investigated the use of regionally available alternative aggregates; however, these studies have generally shown that alternative aggregates are inferior to calcined bauxite in their performance. While a suitable alternative to calcined bauxite has not been discovered, alternative binders present another opportunity for cost reduction. A promising alternative binder is ultra-high performance concrete (UHPC). UHPC is a cementitious binder with high compressive strength (>120 MPa), high bond strength, and increased toughness. Previous research has indicated that UHPC can meet the necessary properties for HFST although UHPC-based HFSTs were not investigated. This study investigates the bond strength, compressive strength, and shrinkage of UHPCs with and without intermixed calcined bauxite as a preliminary step to determine suitability of UHPC based HFSTs. Findings from this study indicate that UHPC exhibits sufficient compressive strength and bond strength, but further optimization is needed to decrease the shrinkage to below the tensile strain capacity to minimize shrinkage-induced cracking.

KEYWORDS: *UHPC, HFST, Calcined Bauxite, Bond Strength, Shrinkage*

1. Introduction

High Friction Surface Treatments (HFSTs) are a roadway remediation technique used to improve the friction on pavement surfaces to reduce crashes (Wilson et al., 2016). Initially implemented along horizontal curves, HFST usage has increased based upon their cost effectiveness and low construction times compared to replacement (Merritt and Moravec, 2014). Typical pavement surfaces that benefit from HFST implementation are those that have polished (interchanges), were improperly designed (interchanges), or have poor drainage (highways) (Atkinson et al., 2016). The US Federal Highway Administration (FHWA) estimates an 83% reduction in weather-related crashes and a 57% reduction in total crashes where HFSTs are applied (Merritt et al., 2020; Coppinger et al., 2021). This improvement is supported by studies undertaken by other departments of transportation (DOTs), which monitored the implementation of HFSTs in their state and found a similar trend (Sprinkel et al., 2015; Cheung and Julian, 2015; Bledsoe, 2015). Based upon the savings in financial cost and human life associated with reducing the severity and frequency of crashes, increased use of HFST as a roadway treatment option is essential.

HFSTs are built by applying a thin layer of epoxy resin binder onto a pavement surface and embedding a high-quality aggregate under gravity. Before applying the binder, the roadway surface must be prepared to

ensure an adequate and consistent bond across the surface. Once prepared, the binder and aggregate are applied to the surface; depending on the size of the project, the application could be completed manually or with specialized machinery. After curing the loose aggregate is removed by a power broom or vacuum sweeper. This process is completed to remove loose debris from the roadway surface. The loose aggregate is often reclaimed and reused in future work (as a partial replacement of virgin aggregate) (Atkinson et al., 2016). Due to a limited funding for all their projects, DOTs have aimed to reduce the cost of implementation, which could increase the breadth of applications across pavement networks (Wilson et al., 2016).

The main requirements for an HFST binder are a strong bond between the HFST aggregate and the binder layer, a strong bond between the binder layer and the substrate, the avoidance of differential shrinkage between the binder and the substrate, the ability to handle repeated traffic loads, and the ability to cover large areas economically (Coppinger et al., 2021). UHPC is a class of cementitious composite characterized explicitly by its high compressive strength, workability, abrasion resistance, and bond strength, making it uniquely qualified to handle these stresses. Furthermore, all five of these HFST requirements are ones that ultra-high performance concrete (UHPC) typically exceed (Kusumawardaningsih et al., 2015; Farzad et al., 2019; Wu, P. et al., 2019; Teng et al., 2021; Li et al., 2021; Feng et al., 2022). Testing focused on the flow properties in the fresh state and bond strength, compressive strength, and shrinkage in the hardened state of UHPC. Additionally, the performance of the UHPC samples with intermixed calcined bauxite was tested to determine how calcined bauxite impacts the performance.

2. Materials and Methods

2.1 Materials

In this study an ASTM C150-22 Type III Portland Cement with a Blaine's Fineness of 485 m^2/kg and has a specific gravity of 3.15 was used. Additionally, three different silica fumes (SF1, SF2, and SF3) with varying particle sizes (Figure 1) and amorphous contents were used (SF1=92.6%, SF2=93.9%, and SF3=98.1% amorphous). In this study manufactured granite sand (SG=2.69, Abs.=0.38%) and pond fines from the same quarry (SG= 2.70, Abs.=0.44%) were used as fine aggregate. In addition, calcined bauxite (SG=3.19, Abs.=2.33%) as HFST aggregate was used in the intermixed calcined bauxite UHPC mixtures. The particle size distribution of the binder components and aggregates are shown in Figure 1. The mix water used for this study conformed to ASTM C1602-22. A poly-carboxylate based ether (PCE) liquid superplasticizer was used for this study, with a solids content of 50% and a specific gravity of 1.08.

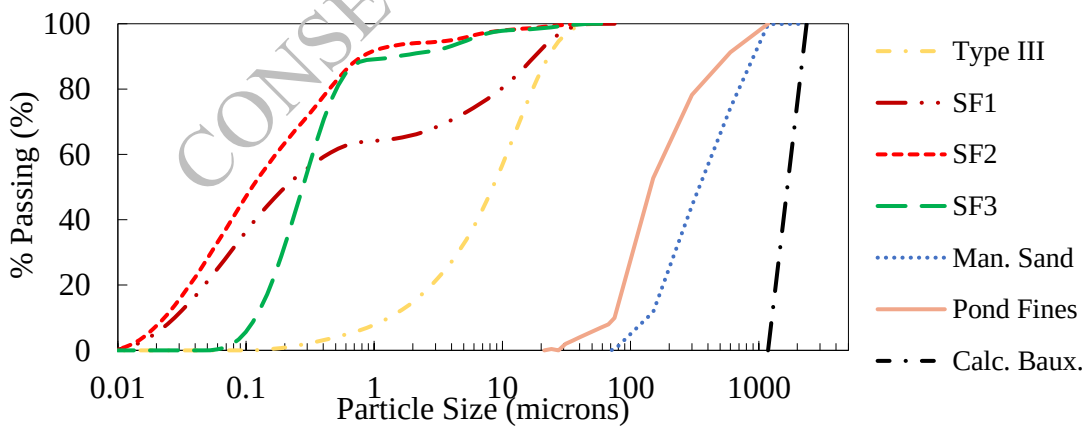

Figure 1. Particle Size Distribution of Constituent Solids

2.2 Mixture Proportions

The mixture proportions for the UHPC mixtures are shown in Table 1, where the sample ID (for ex: SF1-3.5) is the source of silica fume followed by the HRWR dosage as a percentage of the binder. The mixture proportions were optimized using the Modified Andreasen and Andersen (MA&A) method with a q-value of 0.19 based upon the maximum and minimum particle size (Liu et al., 2022). Generating the mixture proportions was an iterative process where the material dosage rates were modified to decrease the

difference between the theoretical and real particle size curve. Iterations of varying mixture proportions were completed to maximize R^2 value between the actual and theoretical q. The mixture proportions of samples with calcined bauxite included calcined bauxite at a ratio of 3.0 to the mass of the cementitious materials.

Table 1. Mixture Proportions for UHPC Mixtures Without Intermixed Calcined Bauxite

Sample ID	C/CM	SF/CM	S/CM	PF/CM	W/CM	HRWR/CM
SF1-3.5	0.80	0.20	0.7	0.4	0.2	0.035
SF1-4.5	0.80	0.20	0.7	0.4	0.2	0.045
SF2-3.5	0.80	0.20	0.6	0.4	0.2	0.035
SF2-4.5	0.80	0.20	0.6	0.4	0.2	0.045
SF3-3.5	0.85	0.15	0.6	0.5	0.2	0.035
SF3-4.5	0.85	0.15	0.6	0.5	0.2	0.045

2.3 Mixing Procedure

In this study a 20-quart Hobart Mixer with a 0.5 HP motor and three speeds of low (planetary motion 60 rpm and paddle 107 rpm), medium (planetary motion 113 rpm and paddle 198 rpm), and high (planetary motion 207 rpm and paddle 365 rpm) was used for mixing the UHPC mixtures. All mixing and batching was conducted in laboratory conditions (23±1℃ and 50±5% relative humidity), with batching completed directly before mixing. The mixing procedure used for this study is based on recommendations from literature and previous experimental work (Figure 2) (Hiremath and Yaragal, 2017; Wu et al., 2019). Additionally, for samples with intermixed calcined bauxite an additional step at low speed for one minute is included after the normal UHPC mixing process.

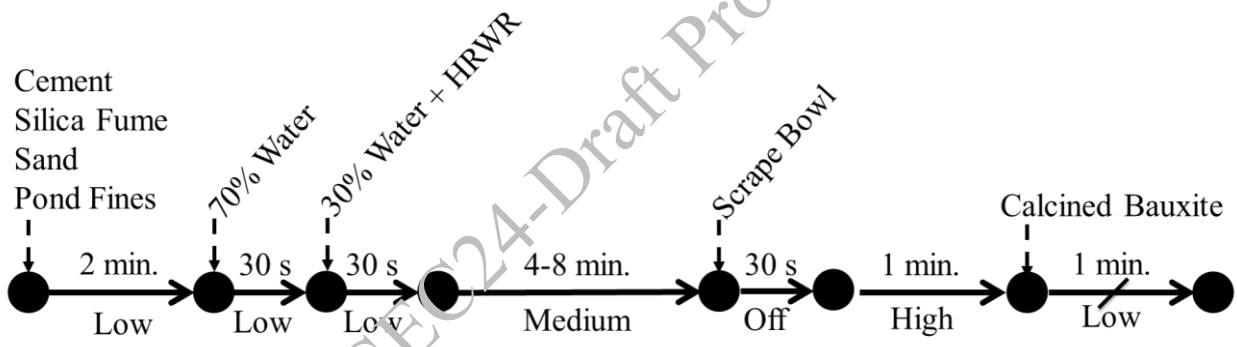

Figure 2. Mix Procedure for UHPC and Intermixed UHPC

2.4 Methods

2.4.1 Flowability

The flowability was measured for UHPC mixes using the modified flow table test per ASTM C1856-17. However, for intermixed calcined bauxite samples the flowability was measured using the standard flow table test per ASTM C1437-23 due to the lower flowability being outside the test range of ASTM C1856-17. The flowability was measured directly after mixing concluded. Each flowability reading was completed in triplicate, and the average and standard deviation are included in the results section.

2.4.2 Bond Strength

The bond strength was measured using the pull-off test in ASTM C1583-20. Testing was completed at 7 and 28-days on concrete substrates (3.37 MPa tensile strength) and at 28-days asphalt substrates (0.32 MPa tensile strength) prepped to match an International Concrete Repair Institute (ICRI) concrete surface profile chip six. Test criteria was based on FHWA recommendation for HFST binders, where a passing test either exceeds 1.72 MPa or fails in the substrate (Merritt et al., 2021).

2.4.3 Drying Shrinkage

Drying shrinkage was measured according to ASTM C596-23. An initial reading is taken 3 days after casting with subsequent measurements at 7, 14, 21, and 28-days after initial casting. The failure criteria for this test are based upon the tensile strain capacity of unreinforced cementitious (200 microstrain), which when converted to unrestrained shrinkage is -0.02% (Roziere et al., 2014; Frosch et al., 2017). This differs from UHPC, which typically contains fibers that provide post crack ductility, but also initially crack at 200 microstrain (Dai et al., 2021).

2.4.4 Compressive Strength

The compressive strength of UHPC was measured in accordance with ASTM C109-23 on 50mm cubes at 1,7, and 28-days. The ASTM C109-23 method was used in this study instead of ASTM C1856-17 for UHPC (cylinders) due to the ease of casting and consistency of test surfaces of cubes. The early age performance follows part of the compressive strength requirements set out in the AASHTO MP-41 specification, expecting to achieve the 35 MPa at 7-days as required for resin systems (AASHTO, 2013). The later ages strength requirements are based on ASTM C1856-17, the ASTM standard practice for testing UHPC, which requires a compressive strength of at least 120 MPa for classification as a UHPC (ASTM, 2023).

3. Results and Discussions

3.1 Flowability

The flowability of the six selected UHPC mixes using ASTM C1856-17 is shown in Figure 3. The designed mixes extend across the recommended workability from 100-150% flow, which provides a workable UHPC mixture that is easily consolidated without segregating. Segregation is a key concern for UHPC-based HFST, as proper aggregate embedment, fiber dispersion, and the strength would become less reliable (Wang et al., 2017). The mixes containing higher dosages of HRWR on average flowed 17% more than the lower dosage mixes. The flow differences between the SF1, SF2, and SF3 are due to the different sand dosages, SF dosages, SF PSD, and SF chemical composition.

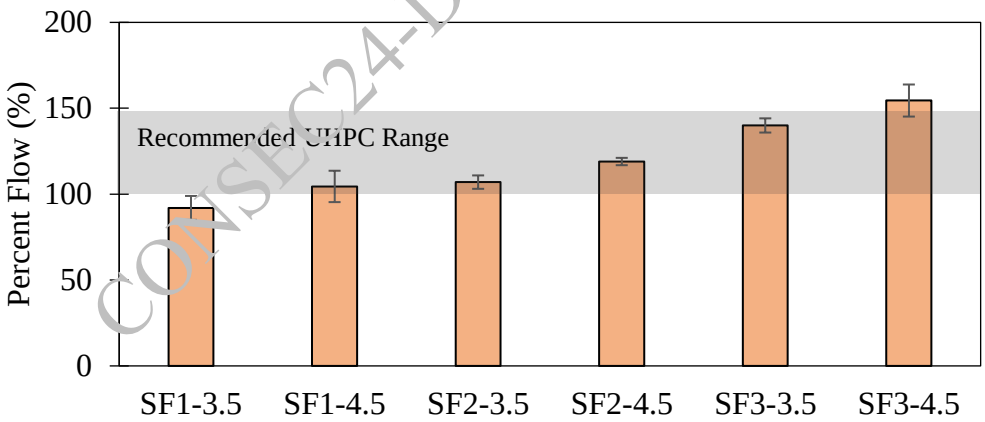

Figure 3. Flowability of Selected Mixes via Modified Flow Table Test

The flowability of the intermixed calcined bauxite samples tested using ASTM C1437-23 is shown in Figure 4. If these samples were tested according to ASTM C1856-17 procedure each would have received a flow value of 0%. However, testing using ASTM C1437-23 also showed flows at the lower end of the testing range. The intermixed calcined bauxite samples demonstrated flows between 5-20%, which indicates that mixes containing high dosages of calcined bauxite would require external compaction or vibration to achieve sufficient consolidation.

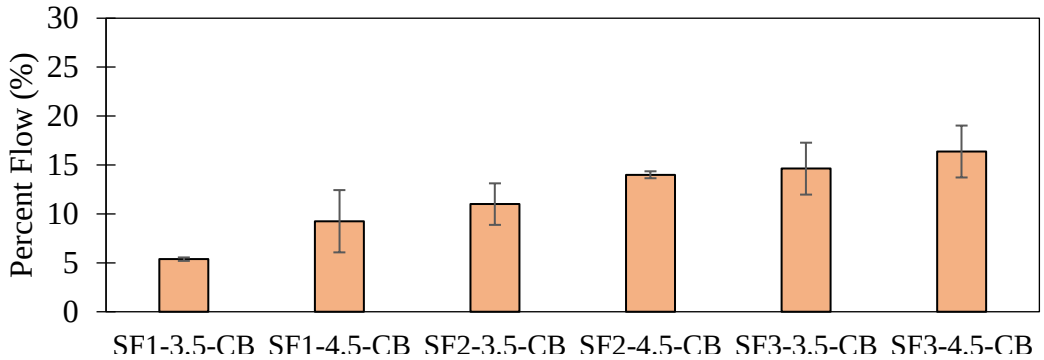

Figure 4. Flowability of Intermixed Calcined Bauxite via Flow Table Test

3.2 Bond Strength

The bond strength of the UHPC samples without calcined bauxite are shown in Table 2. Test results indicate that all samples exceeded the required 1.72 MPa or failed in the substrate. For overlays on the concrete substrates the 7-day performance for the UHPC samples either exceeded or was equal to that of epoxy samples, ranging between 96% and 134%. However, at 28-days the tensile strength of UHPC was less than the epoxy due to a lower strength gain rate (73%-113%). For the asphalt substrates all samples failed at relatively low strengths but failed in the substrate indicating a passing test. However, the epoxy samples were able to generate additional strength in the substrate by filling the voids present in the asphalt samples. This resulted in epoxy-resin sample failing at 1.36 MPa, whereas the UHPC samples failed between 0.44-0.60 MPa. This testing indicates that UHPC while having sufficient bond strength to meet criteria for asphalt surfaces is inferior to epoxy resins mechanically.

Table 2. Bond Strength Results of UHPC Samples

Sample ID	Concrete (psi)				Asphalt (psi)	
	7 Day	% of Epoxy	28 Day	% of Epoxy	28 Day	% of Epoxy
Epoxy	2.17	100%	2.62	100%	1.36†	100%
SF1-3.5	2.92	134%	2.60	99.2%	0.52†	38.6%
SF1-4.5	2.86	132%	1.92	73.1%	0.60†	44.1%
SF2-3.5	2.67	123%	1.92	73.1%	0.59†	43.1%
SF2-4.5	2.09	96.1%	2.96	113%	0.52†	38.1%
SF3-3.5	2.12	97.8%	1.93	73.7%	0.44†	32.5%
SF3-4.5	2.23	103%	2.35	90.0%	0.47†	34.5%

†: Failure in the Substrate

The bond strength of the intermixed calcined bauxite samples is listed in Table 3. For the asphalt samples the same trend was observed as the UHPC without calcined bauxite where the epoxy provided an elevated level of bond strength. However, the testing on concrete substrates differed from the UHPC samples. The 7-day tensile strengths were less than the epoxy, with 2 samples failing due to increased porosity. However, at 28-days the tensile strength equaled or exceeded the epoxy in part due to further hydration because of the available porosity allowing water intrusion to the interface.

Table 3. Bond Strength Results of Intermixed Calcined Bauxite Samples

Sample ID	Concrete (MPa)				Asphalt (MPa)	
	7 Day	% of Epoxy	28 Day	% of Epoxy	28 Day	% of Epoxy
Epoxy*	2.17	100%	2.62	100%	1.36†	100%
SF1-3.5-CB	1.73	80.0%	2.83	108%	0.50†	37.1%
SF1-4.5-CB	1.96	90.1%	2.53	96.6%	0.53†	39.1%
SF2-3.5-CB	1.91	87.9%	2.47	94.2%	0.60†	44.1%
SF2-4.5-CB	1.74	80.2%	2.56	97.9%	0.50†	37.1%
SF3-3.5-CB	**1.59**	73.3%	2.90	111%	0.68†	50.2%
SF3-4.5-CB	**1.33**	61.2%	2.79	107%	0.45†	33.0%

*Does not contained intermixed calcined bauxite
†: Failure in the Substrate

3.3 Drying Shrinkage

Drying shrinkage testing was completed on the UHPC samples and on SF3-4.5-CB. It was assumed that the use of intermixed calcined bauxite will predominately act as a filler (reducing paste volume available for shrinkage). This is demonstrated by the lower shrinkage for the sample with CB included. The results from this testing are included in Figure 3. Results also show that all samples exceeded the maximum permissible shrinkage of 0.02%, with a shrinkage range of 0.06-0.08% at 25 days. Exceeding that value increases the likelihood of cracking and premature failure, necessitating shrinkage remediation techniques. While the intermixing of calcined bauxite demonstrated an ability to significantly reduce drying shrinkage with SF3-4.5-CB (0.038%) being 50% less than SF3-4.5 (0.074%) the mix still exceeded the 0.02% threshold and indicates that multiple techniques are necessary at once. Other mitigation measures include the inclusion of fibers to improve the tensile strain capacity by providing a ductile post peak behavior or the inclusion of a shrinkage reducing admixture to reduce the surface tension of the pore solution and thereby reduce the buildup of capillary stresses when drying.

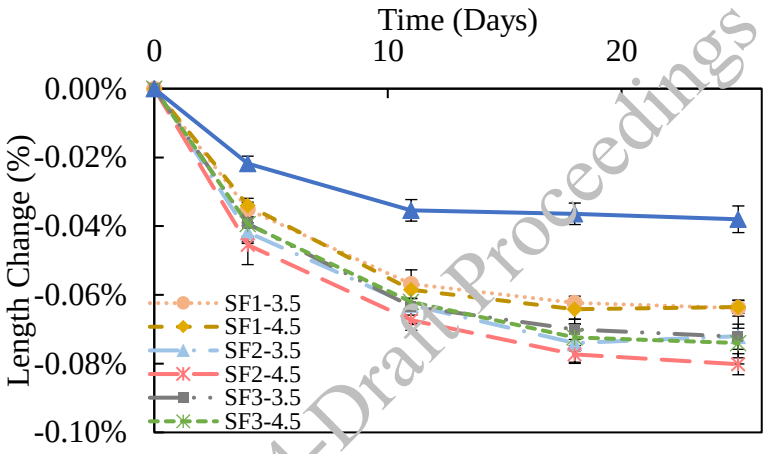

Figure 5. Drying Shrinkage of UHPC Samples Without Intermixed Calcined Bauxite

3.4 Compressive Strength

The compressive strength of UHPC was evaluated for both the UHPC samples and the intermixed calcined bauxite samples. Testing on the UHPC samples focused on 1, 7, and 28-day strengths (Figure 6). At 1-day samples ranged from 48-66 MPa and at 7-day 75-82 MPa, which both exceeded the 7-day requirement for typical HFSTs. The compressive strengths at 28-days ranged from 85-104 MPa, which fell below the specification for UHPCs. However, supplemental testing on the lowest strength sample (SF3-4.5) with 2% steel fibers by volume had a compressive strength of 120 MPa matching the ASTM requirement. While the inclusion of fibers will meet the strength threshold for UHPC classification, the benefits of fiber are not assumed to greatly influence the likely failure modes of an HFST binder (bond failure or aggregate loss), and the exclusion of fiber can nearly half the cost of the mixture.

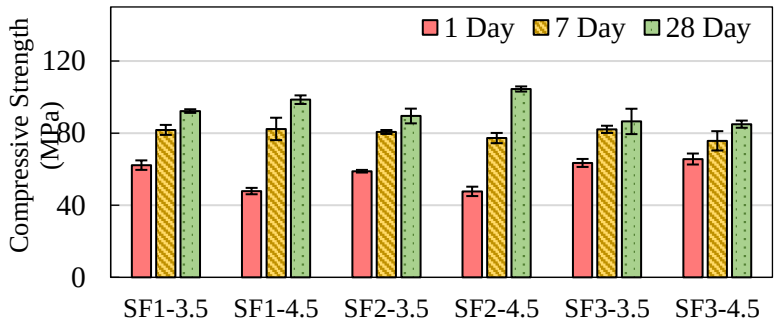

Figure 6. Compressive Strength of UHPC Samples Without Intermixed Calcined Bauxite

Figure 7 further supports the classification of these mixes as UHPC, as samples containing calcined bauxite intermixed at a replacement rate of 3.0 exceeded 120 MPa on two occasions with the 28-day compressive strength varying between 111-128 MPa. Furthermore, these mixes also exceeded the required 7-day compressive strength of 35 MPa at 1-day with strengths ranging from 50-58 MPa. While calcined bauxite is a specialty material that should not be included in typical UHPCs since it is being included primarily as a friction providing aggregate this boost in strength is a promising benefit. The strength of the calcined bauxite helps to overcome the weakness added to the mix in manufactured granite aggregate.

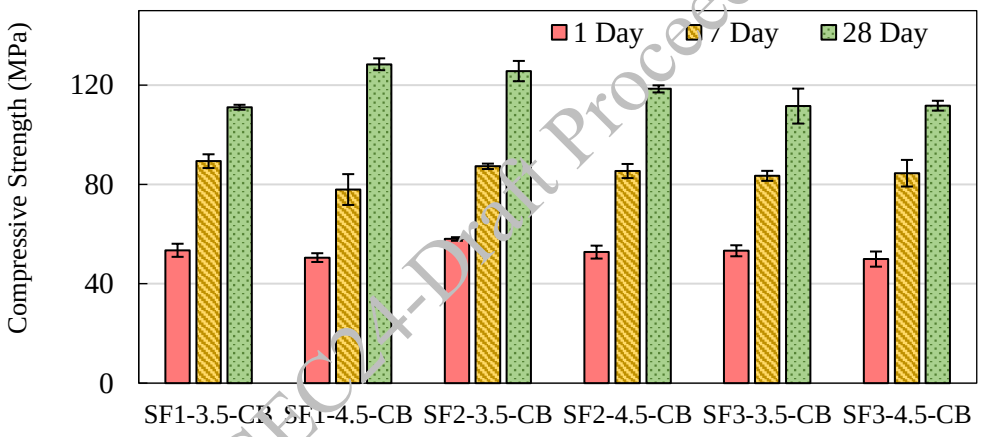

Figure 7. Compressive Strength of Intermixed Calcined Bauxite Samples

4. Conclusions

Based upon the results several conclusions can be drawn:

- The utilization of UHPC-based HFSTs is mechanically possible and provides a competitive binder on concrete substrates to the current epoxy resin systems. For asphalt substrates the UHPC-based HFSTs meets the bond strength requirement but did not provide equivalent performance to the epoxy resin.
- The use of intermixed calcined bauxite had some failures below the required bond strength and needs additional optimization to determine the ideal dosage for maximum density and mechanical performance.
- The shrinkage of UHPC-based HFSTs exceed the expected tensile strain capacity. Further testing is warranted to evaluate the effects of intermixed calcined bauxite, fibers, and shrinkage reducing admixtures to determine ideal strategies to mitigate cracking risk.
- The compressive strength of these mixes is sufficient to handle the traffic load at as early as 1-day and is classifiable as a UHPC at 28-day depending on the inclusion of steel fibers and/or intermixing calcined bauxite.

Acknowledgements

The author would like to thank the SCDOT for sponsoring this research (SPR-762). Additionally, the following companies supported this research by providing materials: ARGOS USA, SIKA USA, FX Minerals, and Vulcan Materials USA.

References

AASHTO.(2013) "AASHTO MP 41-13: Standard Practice for High Friction Surface Treatment for Asphalt and Concrete Pavements", AASHTO Standard Practice

ASTM C1856-23. (2023) "Fabricating and Testing Specimens of Ultra-High Performance Concrete", ASTM

Atkinson, J., J. Clark, and S. Ercisli.(2016), " High Friction Surface Treatment Curve Selection and Installation Guide"

Bledsoe, J. (2015) "Missouri Demonstration Project: The Use of High-Friction Surface Treatments on Missouri Highways"

Cheung, J. and Julian. F(2015) "Northern California US 199-Del Norte County High Friction Surface Treatment"

Coppinger, K., . Keen, M., Gissel,J. and . Rainville, L.(2021) "High Friction Surface Treatments Final Report"

Dai, J.G., Huang, B.T. and Shah, S.P. (2021) "Recent Advances in Strain-Hardening UHPC with Synthetic Fibers", *Journal of Composites Science*, 5(10):283

Farzad, S. and Azizinamini. (2019) "Experimental and numerical study on bond strength between conventional concrete and Ultra High-Performance Concrete (UHPC)", *Engineering Structures*. 186: 297

Feng, S., Xiao, H., Liu, M., Zhang, F. and Lu, M. (2022) "Shear behaviour of interface between normal-strength concrete and UHPC: Experiment and predictive model", *Construction and Building Materials*,342: 127919

Frosch, R., D. Fowler, E. Nawy, W. Hansen, M. Brander, H. Haynes, E. Schrader, D. Darwin, W. Suaris, and F. Fouad. (2017) "Control of Cracking in Concrete Structures"

Hiremath, P.N. and Yaragal, S.C. (2017) "Influence of mixing method, speed and duration on the fresh and hardened properties of Reactive Powder Concrete", *Construction and Building Materials*, 141: 271-288

Kusumawardaningsih, Y., Fehling, E., Ismail, M. and Aboubakr, A.A.M. (2015) "Tensile strength behavior of UHPC and UHPFRC", *Procedia Engineering*, 125:1081-1086

Li, J., Wang, X., Chen, D., Wu, D., Han, Z., Hou, D., Zhen, Z., Peng, C., Ding, Q. and Yin, B.(2021) "Design and application of UHPC with high abrasion resistance", *Construction and Building Materials*, 309:125141

Liu, K., Yin, T., Fan, D., Wang, J. and Yu, R. (2022) "Multiple effects of particle size distribution modulus (q) and maximum aggregate size (Dmax) on the characteristics of Ultra-High Performance concrete (UHPC): experiments and modeling", *Cement and Concrete Composites*, 133:104709

Merritt, D., Himes, S. and . Porter., R. J. (2021) "High Friction Surface Treatment Site Selection and Installation Guide"

Merritt, D., Lyon, C., Persaud, B. and Torres, H. (2020) "Developing Crash-Modification Factors for High-Friction Surface Treatments"

Merritt, D., and M. Moravec (2014). An Update on HFST for Horizontal Curves.

Roziere, E., Cortas, R. and Loukili, A. (2015) "Tensile behaviour of early age concrete: New methods of investigation", *Cement and Concrete Composites*, 55:153-161

Sprinkel, M.M., McGhee, K.K. and de León Izeppi, E.D. (2015) "Virginia's experience with high-friction surface treatments", *Transportation research record*, 2481(1):100-106

Teng, L., Valipour, M. and Khayat, K.H., 2021. Design and performance of low shrinkage UHPC for thin bonded bridge deck overlay. *Cement and Concrete Composites*, 118:103953

Wang, R., Gao, X., Huang, H. and Han, G. (2017) "Influence of rheological properties of cement mortar on steel fiber distribution in UHPC", *Construction and Building Materials*, 144:65-73

Wilson, B.T., Brimley, B.K., Mills, J., Zhang, J., Mukhopadhyay, A. and Holzschuher, C. (2016) "Benefit–cost analysis of Florida high-friction surface treatments", *Transportation Research Record*, 2550(1):54-62

Wu, P., Wu, C., Liu, Z. and Hao, H., 2019. Investigation of shear performance of UHPC by direct shear tests. *Engineering Structures*, 183:780-790

Wu, Z., Khayat, K.H. and Shi, C. (2019) "Changes in rheology and mechanical properties of ultra-high performance concrete with silica fume content", *Cement and Concrete Research*, 123:105786

Unveiling Dominant Compaction Factors for Enhanced Roller Compacted Concrete Pavement Performance

M. Selvam[1] and Surender Singh[2*]

[1]Assistant Professor, Department of Civil Engineering, Indian Institute of Technology Patna, Bihar, India, Email: selvam@iitp.ac.in

[2]Assistant Professor, Department of Civil Engineering, Indian Institute of Technology Madras, Chennai, India, Email: surender@civil.iitm.ac.in

[*]Corresponding author

ABSTRACT.

The performance of Roller Compacted Concrete Pavement (RCCP) primarily depends on several parameters, namely, the type of compaction method, compactness, and lubrication of aggregates during the compaction process. Reconstituting RCCP mixtures requires an appropriate compaction method to achieve the requisite engineering properties. Utilizing various compaction techniques during specimen fabrication may result in notable disparities in both strength and durability properties. Thus, efforts were undertaken to investigate the various dominant parameters influencing the properties of RCCP in this study. These parameters include compaction mechanism, compactness, and lubrication effect. The compaction methods for RCCP, including Vibratory Hammer, Vibratory Table, Modified Proctor, and Gyratory Compactor, were extensively considered for studying the effect of compaction energy and mechanisms. Meanwhile, moisture content was varied in the range of 4.5-6% to understand the lubricating mechanism on the RCCP compactability. The findings indicate that the performance of RCCP performance is predominantly influenced by the type of compaction method employed and its inherent compaction mechanism.

KEYWORDS*: Laboratory Compaction, Rigid Pavement, Performance, Roller Compacted Concrete*

1. Introduction

The behaviour of Roller Compacted Concrete Pavement (RCCP) when compacted with various techniques could be attributed to the difference in the compaction mechanisms associated with different compactors ─ compaction mechanisms associated with Modified Proctor (MP), Vibratory hammer (VH), Vibratory Table (VT) and Gyratory Compactor (GY) are dynamic impact (DI), impact & vibration (IV), pressure & vibration (PV), and pressure & kneading (PK), respectively (Amer et al. 2003; IRC:SP: 97 (IRC 2013)). Apart from the difference in the compaction mechanisms, the degree of densification (ratio of fresh density to the maximum theoretical constituent density) could also influence the strength properties of RCCP (Sengun et al., 2019). The degree of densification (DoD) is governed by the packing characteristics of aggregates, which in turn, depends on the type of compaction methods. It is observed from the available study that the achievable strength is primarily dependent on the degree of densification (Sengun et al., 2019). This study revealed that the vibratory table method exhibited the lowest value of the DoD due to the lower compaction effort. The DoD ratios associated with other techniques were found to be relatively higher, and thus the strength properties; it was observed that the DoD of the gyratory compactor was the highest (0.93) compared to the vibrating hammer (0.90) and modified Proctor (0.88) (Sengun et al., 2019). Interestingly, the specimens that achieved a DoD of more than 0.96 exhibited similar properties irrespective of the compaction method used. Furthermore, the lubricating effect also plays an important role in the rearrangement of aggregates during the compaction process of RCCP mixtures. It depends on the availability of optimum moisture content, the amount of paste available for coating the aggregates, cement content, and chemical admixture inclusion. However, no efforts have been made till now to study the lubrication effect and packing density on the performance of RCCP.

Considering the above gaps in the literature, efforts were made to comprehensively study all the dominating parameters affecting the RCCP properties in this study, viz, compaction mechanism, compaction energy, packing density, and lubrication effect.

2. Material and Mix design methods

Natural coarse and fine aggregates were sourced from a local quarry in Chennai, Tamil Nadu. Ordinary Portland Cement (Grade 53) was used as the binder for this study. The mix design was conducted in accordance with IRC: SP: 68 specifications. Cylindrical specimens with dimensions 100 mm × 200 mm were prepared using various methods, including the VH, VT, MP, and GY techniques, to assess the dry density of the RCCP specimens. The specimens were molded following the standards specified in ASTM C1435, ASTM C1176, ASTM D1557, and ASTM C1800 for the VH, VT, MP, and GY methods, respectively.

3. Results and Discussions

3.1 Compaction mechanism

The effect of considered compaction mechanisms on the dry density of RCCP is shown in Figure 1. The PK and PV mechanisms resulted in the lowest dry density, but the IV and DI mechanisms yielded the high-density RCCP specimens, irrespective of moisture contents. Several studies corroborated the similar behaviour in the density of RCCP, irrespective of the gradation (Fuller's curve, Portland Cement Association gradation, and American Concrete Pavement Association gradation), cement content (200-400 kg/m^3), and moisture content (4.5-6%). Notably, a converse behaviour in the PK mechanism was observed in the current study against the literature. This differential behaviour in PK is mainly attributed to the lower aspect ratio (1.17) of RCCP specimens in the literature, which exhibited better densification and, thus, higher density. However, in the current study, a dedicated concrete GY was used to produce the specimen with an aspect ratio of 2. Surprisingly, the PK mechanism manifested lower density because of the lower degree of densification at the higher aspect ratio of 2, as seen in Figure 1.

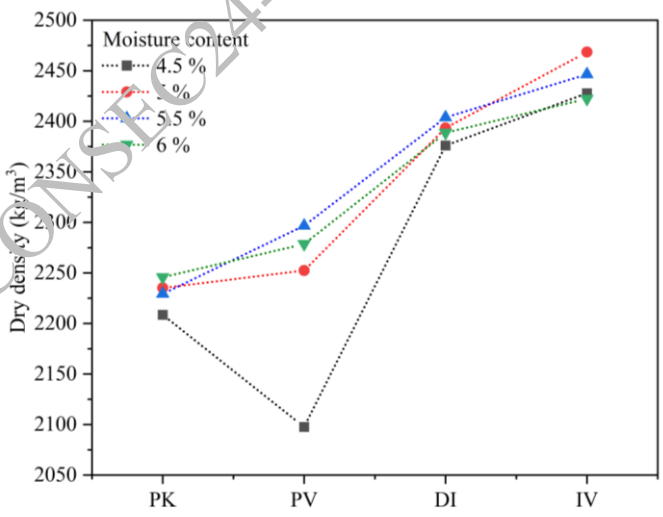

Figure 1. Effect of compaction mechanism on the dry density

3.2 Effect of Lubrication

Lubrication plays a vital role in rearranging aggregates during the compaction process of RCCP. The current study revealed that the lubrication effect mainly depends on Optimum Moisture Content (OMC). The most common & widely adopted approach to determine the OMC for RCCP is through the soil compaction technique, wherein the MP assembly is employed. The typical moisture density curve when compacted with MP is shown in Figure 2. As seen in Figure 2, the dry density of RCCP mixes was lower

at dry side of the OMC (< 5.5%) because of higher internal friction between the aggregates, which led to the entrapment of compaction voids. However, a further increase in the moisture content reached the OMC (5.5%) and, thus, facilitated the better aggregate arrangement on account of lubrication and consequently improved the compactness. Beyond the OMC value (> 5.5%), the increase in moisture content replaces the solid volume, thereby lowering the density of RCCP since the density of water is much lower than that of cement and aggregate density.

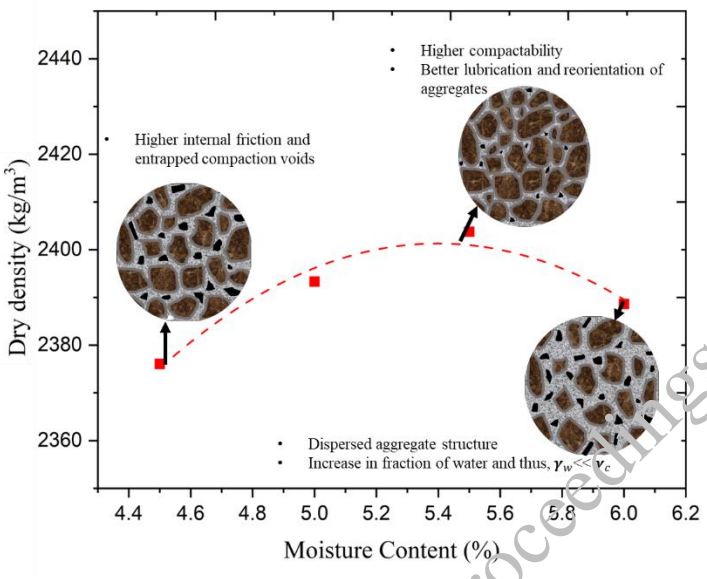

Figure 2. Moisture density curve of MP compacted RCCP mixes

Notably, the moisture content determined with the MP approach might not provide sufficient lubrication required for complete rearrangement of the aggregate matrix when compacted with different compaction methods (VH, VT, and GY) or might result in higher/lower moisture in RCCP, leading to lower performance of the same. To study this aspect, various compactors (VH, MP, VT, and GY) were used for plotting the moisture-density curve (Figure 2), and the values of the MDD and corresponding OMC were noted. Among all the considered compaction methods, the RCCP mixtures compacted with VH exhibited the highest dry density of 2465 kg/m^3 at the lowest moisture content (5.07%) on account of the combined action of IV forces (Schrader, 2018). Whereas the specimens compacted with the conventional approach of MP entitled higher moisture (5.5%) and lower dry density of 2405 kg/m^3 compared to VH. Shafigh et al. (2020) also reported similar behaviour, wherein the MP method resulted in lower compactness of around 20 kg/m^3 compared to VH, however, there was no significant difference in the OMC values. On the other hand, the specimen compacted with the VT method offered a lesser dry density of 2305 kg/m^3 at a higher moisture content of 5.6% compared to MP. This decrease in MDD could be manifested by lower compaction effort, and as a result, higher moisture was required for the realignment of aggregate particles and denser compaction (Schrader, 2018; Sengun et al., 2019). Interestingly, the OMC for the GY technique could not be determined from the moisture-density plot as there was a continuous increase in dry density rather than parabolic behaviour (Figure 3). This is mainly attributed to squeezing out of the excess paste during the compaction; it was found that after 5.5% moisture content, the cement paste started coming out of the GY mold. This behaviour indicates shifting to alternative methods for the quantification of OMC as well as MDD for the GY method (discussed in the subsequent section). Moreover, the maximum compactness attained in GY specimens was very low (2245 kg/m^3) compared to other techniques owing to the direct adaptation of asphalt gyratory compaction parameters (ASTM D6925 (ASTM 2015)) for RCCP application. Since the rheological behaviour of RCCP is different from asphalt mixes, the compaction parameters have to be tailored for RCCP mixes.

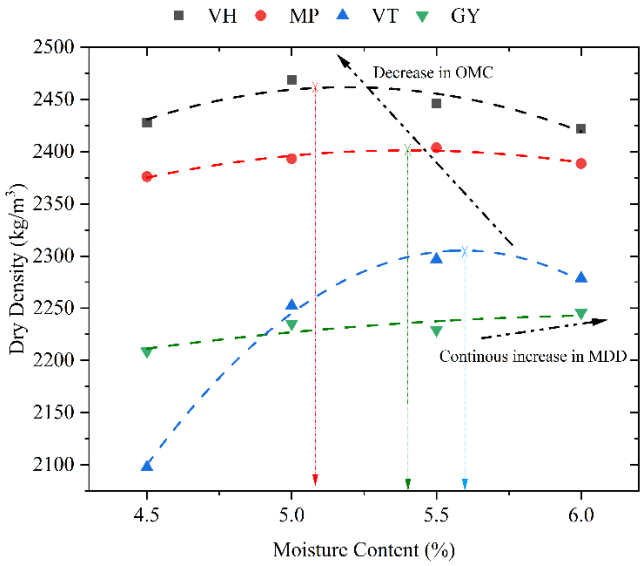

Figure 3. Moisture density plot of RCCP mixtures made with different compaction methods

4. Conclusions

The effect of the compaction mechanism associated with widely employed compaction methods depicts that the IV mechanism renders the denser compacted RCCP specimens, followed by PV, DI, and PK mechanisms. Further, it can be concluded that the optimum moisture requirement for complete densification of the RCCP matrix highly depends on the type of compactor involved in the compaction process. For instance, RCCP mixes designed with VH could achieve higher density at lower moisture contents, whereas the mixes designed with either VT or GY would require higher moisture content to achieve maximum compactness compared to the conventional approach of MP. Also, the type of compaction method plays an important role in the maximum compactness, as evident from the difference in the OMC and MDD values exhibited by RCCP mixes designed with different compactors.

Acknowledgements

The first author would like to acknowledge the Ministry of Education, Government of India and Indian Institute of Technology Patna, Bihar, India, for the financial support. Both authors want to gratefully acknowledge and thank the funding received from the Indian Institute of Technology Madras, Chennai, India, for the projects SP22231225CPETWOTLLHOC and CE1920900RFER008952.

References

Amer N., Delatte N., Storey C. (2003) "Using Gyratory Compaction to Investigate Density and Mechanical Properties of Roller-Compacted Concrete", *Transportation Research Record: Journal of the Transportation Research Board*,1834: 77–84.

Indian Roads Congress. (2013) "Guidelines on Compaction Equipment for Road Works. IRC:SP:97-2013", *Indian Roads Congress*, New Delhi, India.

Sengun E., Alam B., Shabani R. and Yaman I. O. (2019) "The Effects of Compaction Methods and Mix Parameters on the Properties of Roller Compacted Concrete Mixtures".,*Construction and Building Materials*,228, 116807

Schrader E. Appropriate Laboratory Compaction Methods for Different Types of Roller Compacted Concrete (RCC). In *Roller Compacted Concrete Dams* (Berga L., ed.), Routledge, London, 1037–1044

Shafigh P., Hashemi M., Nam B. H. And Koting S. (2020) "Optimum Moisture Content in Roller-Compacted Concrete Pavement", *International Journal of Pavement Engineering*, 21(14):1769–1779

Influence of Rice Husk Ash Content on the Strength of Alkali-Activated Slag Concrete Developed with Recycled Coarse Aggregates

S. Tejas[1*], and Dinakar Pasla[2]

[1] School of Infrastructure, Indian Institute of Technology, Bhubaneswar, India
Email: a22ce09007@iitbbs.ac.in
[2]School of Infrastructure, Indian Institute of Technology, Bhubaneswar, India
Email: pdinakar@iitbbs.ac.in

[*]Corresponding author

ABSTRACT

Rapid urbanization has led to increased demands for infrastructure. Using cement-based conventional concretes to meet these increasing demands has determinantal effects on the environment, such as CO_2 emissions due to the cement manufacturing process and exploitation of natural resources to procure the aggregates. Using alkali-activated concrete developed from ground granulated blast furnace slag (GGBS) and agricultural waste ash such as rice husk ash (RHA) and incorporating recycled aggregates (RA) recovered from construction and demolition (C&D) wastes in place of natural aggregates is a promising material that has the potential to replace conventional concrete in the construction industry as it is developed from the wastes recovered from various sectors. The current work focuses on finding the optimum replacement percentage of RHA as a partial replacement of GGBS in alkali-activated concrete incorporated with RA. Four mixes were prepared by replacing GGBS with RHA from 5% to 20% at the steps of 5%. NDT tests such as rebound hammer test, ultrasonic pulse velocity test and compressive strength parameters were used to evaluate the influence of RHA content in alkali-activated concrete with RA. As an optimal replacement percentage of GGBS, 10% RHA was observed to exhibit the maximum strength. It is concluded that 10% RHA can be used in alkali-activated concrete as a partial replacement for GGBS, for structural purposes.

KEYWORDS*: Rice Husk Ash, Recycled Aggregates, Alkali Activated Concrete, GGBS, Compressive Strength.*

1. Introduction

Production of ordinary Portland cement (OPC) is highly energy-intensive and emits approximately 7% of CO_2 thus contributing towards increased greenhouse gas (GHG) emission (Tejas et al., (2023)). Apart from the GHG emissions, the demand for natural aggregates has also increased exponentially and thus depleting the environment and natural resources. Alkali-activated concrete incorporated with recycled aggregates is the best possible alternative eco-friendly construction material that can replace conventional Portland cement concrete in the construction industry. Alkali-activated materials (AAM) are obtained by activating the alumino-silicate-rich precursor materials using a strong alkaline solution such as NaOH or KOH by alkali activation technique (França et al., (2022)). The alumino-silicate-rich materials, usually fly ash (FA), granulated blast furnace slag (GGBS), and agricultural waste ash (AWA) such as sugarcane bagasse ash (SBA) and rice husk ash (RHA) are the precursors used to develop AAMs (Jayanthi et al., (2023)). It has been proposed by researchers that AWAs and GGBS be utilised in the production of alkali-activated cement because using AWAs is economical, as this practice promotes the effective use of locally available materials (Athira et al., (2020)). Researchers have been interested in using RHA in AAMs due to their high amounts of reactive silica concentration, which exceeds 80% (de Souza Rodrigues et al., (2010); Mehta et al., (2018)). This study aims to determine the ideal proportions of RHA that may be replaced with GGBS in alkali-activated slag recycled aggregate concrete (AASRAC) as a binary blend. The compressive strength

and non-destructive tests (NDT) such as rebound hammer and ultrasonic-pulse velocity tests are performed to estimate the ideal replacement percentage of RHA with GGBS in AASRAC. In addition to achieving high strength, using RHA-based AASRAC as structural concrete is a sustainable method that involves a combination of industrial by-products, AWAs, and RA. These materials, which would otherwise be disposed of in landfills, are instead used, so fostering a circular green economy.

2. Materials and methods

The details of materials used in the present study and the methodology adopted to achieve the aim of the study have been discussed in this section.

2.1 Material characterization

The aluminosilicate precursors used in the present study are GGBS and RHA procured from a reputed steel industry and Astra Chemicals, Chennai, Tamil Nadu, respectively. The specific gravity of GGBS and RHA is 2.81 and 2.1 respectively. The major oxide compositions i.e., CaO, SiO_2, and Al_2O_3 for GGBS are 37.26, 33.13, and 17.40 respectively, and for RHA are 0.42, 88.55, and 2.30 respectively. The procured RHA particles were sieved using a 300-micron sieve to eliminate carbon-rich particles and further they were ground in a ball mill for 120 minutes to reduce their particle size. Two fractions of RA were used in the present work i.e., 20 mm and 10 mm downsize, supplied by a renowned C&D waste processing unit in India. River sand procured from a local river bed was used as fine aggregates in the present study. The specific gravity of RCA is 2.32 and fine aggregates are 2.61. Since the physical characteristics of these RAs meet the specific parameters set by Indian standards, the current research intended to completely replace NCA with RA. Out of the total aggregate content, 23% of RCA was 20 mm downsized, 32% of RCA was 10 mm downsized and the rest were fine aggregates. These proportions were arrived at based on a combined grading procedure specified by DIN 1045 (DIN 1045 (2001)). Sodium silicate and sodium hydroxide solutions were used as alkaline activators (AA) to activate the precursors. The ratio of sodium silicate and 12 M sodium hydroxide was maintained at 1.5. The specific gravity of sodium silicate and sodium hydroxide solution is 1.38 and 2.09 respectively.

2.2 Mix design

In the present study, RHA was replaced with GGBS from 5% to 20% in steps of 5%, by weight. A constant alkali activator to binder ratio (AA/B) was maintained for all the mixes and the total AA content of 200 kg/m^3 was selected for the present investigation. The summary of the mix design adopted for different replacement levels of RHA is shown in Table 1.

Table 1. Mix design for various mixes used in the current study (in kg/m^3)

RHA (%)	RHA	GGBS	NaOH	Na_2SiO_3	Fine aggregates	20 mm RA	10 mm RA
5	20	380	80	120	813	417	505
10	35	365	80	120	805	411	502
15	58	342	80	120	806	409	499
20	76	324	80	120	793	406	495

2.3 Methods

The compressive strength was considered as one of the parameters to determine the ideal replacement % of RHA with GGBS in AASRAC. The mean strength of three cubic specimens of 100 mm size was measured for each of the four mixtures after 3, 7, and 28 days of hydration and condensation processes in the specimens. The test specimens were loaded at the rate of 0.23 MPa/s in a servo-controlled compression testing machine. A rebound hammer test was performed on the cube specimens to determine the rebound number of the specimens. The rebound hammer test is primarily used as a surface hardness tester. An average of 10 hammer rebound readings were recorded for each specimen, to evaluate the influence of RHA in AASRAC on their surface hardness. UPV was conducted on concrete, free of moisture. Ultrasonic tester PUNDIT Plus is used to conduct the test. Air gaps are sealed by a couplant using ultrasonic gel. Velocity in km/s is determined and hence quality and homogeneity of concrete are evaluated.

3. Results and discussions

3.1 Compressive strength

All the RHA-based AASRAC exhibited high early-age strength, with strengths exceeding 42 MPa after 3 days of hydration and condensation reaction. The variation in compressive strength with varying RHA content is shown in Figure 1. The specimens incorporated with 10% RHA exhibited the maximum compressive strength when compared with the specimens incorporated with 5%, 15% and 20% RHA. The maximum compressive strength attained was 66.01 MPa, for the specimens incorporated with 10% RHA. Since the maximum strength was achieved by the RHA-based AASRAC specimen incorporated with 10% RHA and 90% GGBS at all three ages (i.e., 3, 7 and 28 days), the optimum replacement % of RHA in AASRAC is considered as 10%. Studies in the past have reported that a replacement % of RHA in the range of 10-20% in AAMs has resulted in enhanced fresh and hardened behaviour of AWA-based AASRAC, due to the formation of enhanced C-S-H and Si-O-Si bonds (Das et al., (2022).

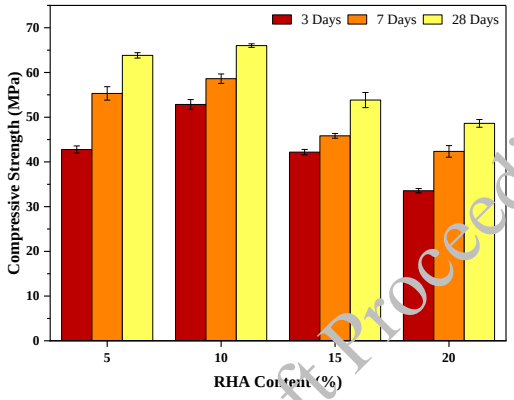

Figure 1. Variation in compressive strength with varying RHA content

3.2 Rebound hammer test

The rebound number values for all the samples were in the range of 32 to 52. The variation of rebound number with varying RHA content is shown in Figure 2 (a). The specimens incorporated with 10% RHA exhibited the highest rebound number values compared to other specimens. Hence, AASRAC consisting of 10% RHA has a superior surface hardness. The rebound number values also exhibited the same trend as that of compressive strength values.

3.3 Ultrasonic pulse velocity test

Figure 2 (b) shows that the UPV values of all the RHA-based AASRAC fall under the concrete quality category 'good' as per the specifications of IS 13311, Part-1, (1992). However, the specimens incorporated with 10% RHA exhibit the highest UPV values compared to other specimens. Apart from the highest UPV values, these specimens fall under the concrete quality 'excellent'. Thus, it can be inferred that the specimens with 10% RHA are denser and more homogenous. The enhanced UPV and homogeneity in 10% RHA specimens may be attributed to the formation of a highly polymerized and condensed C-(A)-S-H gel structure in them. This trend was comparable to the findings from the previous research (Ren et al., (2021)).

3.4 Correlation between compressive strength and NDT methods

In the present study, a linear correlation is established between both rebound numbers and UPV with compressive strength. It is evident from Figure 2 (c) that as the rebound number and UPV increase, the corresponding compressive strength also increases. A linear equation to determine the approximate compressive strength from rebound number and UPV values is prescribed in the present study. It is to be noted that the y-intercept in the prescribed equations has been set to zero because for fresh concrete, the surface hardness i.e., rebound number and UPV values will be zero. An excellent correlation coefficient with R^2 values for correlation between rebound number with compressive strength and UPV with compressive strength of 0.98 and 0.97 respectively is obtained.

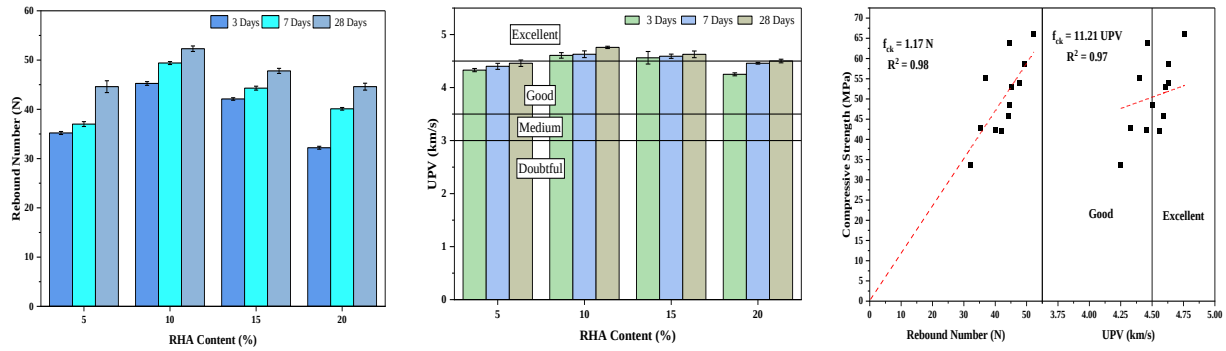

(a) (b) (c)

Figure 2. Variation in (a) rebound number and (b) UPV with varying RHA content and (c) Correlation between rebound number and UPV with compressive strength

4. Conclusions

From the above section, it may be concluded that the ideal replacement content of RHA as a partial replacement of GGBS in alkali-activated recycled aggregate concrete is 10%. The ideal percentage of RHA to be used instead of GGBS, which was 10%, was ascertained through the assessment of the 28-day compressive strength test, surface hardness test and UPV test. By considering the characteristics of the raw materials, the optimal dosage of AA solutions, and the combined classification of various fractions of RCA and fine aggregates in a single investigation, the suggested optimal concentrations of RHA in AASRAC are distinguished from those of previous studies. RHA-based AASRAC may be directly used to expedite construction projects. This can expedite the production of prefabricated sections, resulting in reduced project costs and completion time.

References

Athira, G., Bahurudeen, A. and Vishnu, V. S. (2020) "Availability and accessibility of sugarcane bagasse ash for its utilization in Indian cement plants: A GIS-based network analysis. *Sugar Tech*, 22(6), 1038–1056.

Das, S. K., Adediran, A., Kaze, C. R., Mustakim, S. M. and Leklou, N. (2022)."Production, characteristics, and utilization of rice husk ash in alkali activated materials: An overview of fresh and hardened state properties",*Construction and Building Materials*, 345:128341

de Souza Rodrigues, C., Ghavami, K. and Stroeven, P. (2010) "Rice husk ash as a supplementary raw material for the production of cellulose–cement composites with improved performance", *Waste and Biomass Valorization*, 1:241–249

França, S., de Moura Sola Silva, M. V., Ribeiro Borges, P. H. and da Silva Bezerra, A. C. (2022) "A review on some properties of alkali-activated materials", *Innovative Infrastructure Solutions*, 7(2):179

Jayanthi, V., Avudaiappan, S., Amran, M., Arunachalam, K. P., Qader, D. N., Delgado, M. C., Flores, E. I. S. and Rashid, R. S. M. (2023) "Innovative use of micronized biomass silica-GGBS as agro-industrial by-products for the production of a sustainable high-strength geopolymer concrete", *Case Studies in Construction Materials*, 18:e01782

Mehta, A. and Siddique, R. (2018) "Sustainable geopolymer concrete using ground granulated blast furnace slag and rice husk ash: Strength and permeability properties", *Journal of Cleaner Production*, 205:49–57

Ren, J., Hu, L., Dong, Z., Tang, L., Xing, F. and Liu, J. (2021) "Effect of silica fume on the mechanical property and hydration characteristic of alkali-activated municipal solid waste incinerator (MSWI) fly ash", *Journal of Cleaner Production*, 295:126317

Tejas, S. and Pasla, D. (2023) "Assessment of mechanical and durability properties of composite cement-based recycled aggregate concrete", *Construction and Building Materials*, 387:131620

Flexural Response of Carbon Textile-Reinforced Concrete (CTRC) Panels: A Numerical Study

Sophia Immanuel[1*], Adesh Pratap Singh[1], and Baskar Kaliyamoorthy[1]
[1] *National Institute of Technology, Tiruchirappalli, India*
Email: sophiaimmanuel2011@gmail.com

[*] Corresponding author

ABSTRACT

This study examines the flexural resistance of Carbon Textile-Reinforced Concrete (CTRC) panels, aiming to enhance structural potential in construction sector. The research delves the growing demand for durable building materials, exploring carbon textiles as an alternative to steel reinforcements. Using ABAQUS FEA, the study conducts finite element numerical simulations on CTRC panels with various configurations and thickness. Simulations replicate the four-point flexural load to estimate the ductility and the bending stiffness of the panels. CTRC displays enhanced flexural response and toughness with the increase in number of layers. The study also investigates the relationship between crack patterns and ultimate moment capacity for optimizing CTRC panel designs. This research contributes to developing sustainable building solutions for applications such as low-cost housing for developing countries.

KEYWORDS*: TRC, Carbon Textiles, Flexural response, FEA analysis, ABAQUS*

1. Introduction

With the urge to adopt to emerging technologies in construction industry, globally researchers are working on various materials which are sustainable, highly durable and performs better in all climatic conditions [Hafez et al. (2023)]. Adoption of cutting-edge and creative building technologies is primarily required to shorten construction time, minimize construction costs, and guarantee construction quality [Immanuel S et al. (2023)]. Currently, there has been a paradigm shift towards the use of novel technologies like Textile Reinforced Concrete (TRC) for modular and thin-walled structures Raphael et al. (2023), Nguyen et al. (2023), Žalský et al. (2023) and Rajeshwaran et al. (2023). As the concrete cover required for the TRC is low due to high corrosion resistance of the non-metallic textiles, TRC elements can be prefabricated into thin, slender sections compared to RCC. TRC is lightweight, cost effective, durable as its corrosion resistant and maintenance free structure Nahum et al. (2023), Pham et al. (2023) and Karthikeyan et al. (2023). In TRC, the textile meshes are embedded within a high performance cementious matrix to improve its mechanical characteristics such as tensile strength, flexural strength and toughness Pham et al. (2023), Cai et al. (2023) and Rawat et al. (2022). TRC is made by use of textile meshes such as AR glass, E- glass, carbon and basalt textiles Willams et al. (2015). With the use of TRC as structural elements it is estimated with a reduction of 70% of concrete savings in comparison to ordinary RCC structural elements, leading to a substantial reduction in the carbon emissions between 40% to 60% [Valeri et al.(2020)]. The use of TRC has resulted in the eco-nomic savings in terms of materials, transportation and anchorage costs, making it a promising choice for thin-walled and light weight ventilated facade systems for a decade Shao et al. (2022). Structural elements using TRC is developed by various researcher's globally for newer constructions like precast elements, Colombo et al. (2019) , shell structures, domed structures, parking slab, bridges, sandwich panels Van et al. (2021) and Venigalla et al. (2022). The use of TRC (Textile Reinforced Concrete) as a structural component is quite limited and restricted due to the lack of generalized design and detailing guidelines and codes, as noted by Valeri et al. (2020). Currently, analytical models are being developed, many of which are based on techniques designed for steel-reinforced concrete and ferrocement concepts. This can result in either overestimation or underestimation of the design, as observed by Mobasher et al. (2023) and Chandrathilaka et al. (2020). The complexity of designing TRC as a load-bearing structural component is further compounded by the heterogeneous nature of the material,

influencing the design process as outlined in ASTM (2020) and ASTM (2021). For the current study, carbon textiles are utilized in TRC panels to achieve enhanced performance in load-carrying capacity, particularly in flexure. This requires textiles with increased stiffness, which, while offering improved structural performance, also has economic implications. The use of carbon textiles, though effective, can significantly increase the cost of construction. Therefore, the balance between performance and cost must be carefully considered to ensure the economic viability of TRC in practical applications. Numerical simulations using Finite Element Model (FEM) can predict the failure pattern of these composites. This analysis allows optimization of panel thickness and the number of layers without the need for extensive experimental studies. In this paper, FE models are developed for CTRC panels under a simply supported condition subjected to four-point bending load. The simulations provide critical insights into the performance and behavior of the panels. These findings contribute to the advancement and optimization using TRC.

2. Numerical Modelling

The Finite element simulation under four-point bending was carried out using Abaqus FE software for all the model specimens considered in this study. Figure 1 shows a schematic of the finite element model of the CTRC Panel. The developed FE model was a replica of a typical sketch of the experimental specimens shown in Fig. 1. In the experiments, the load was applied using a circular bar that was in contact with the panel, and the loading pins were idealized as semi-spherical bars in the FE model to simplify the model.

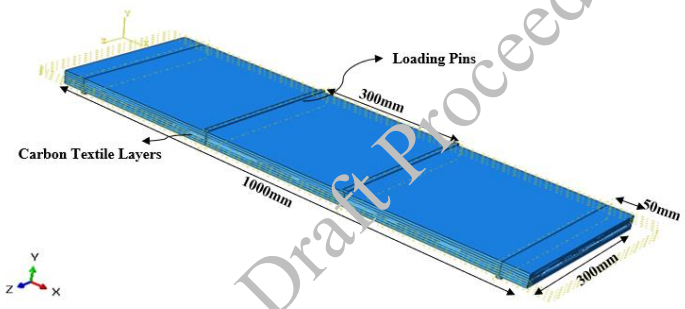

Figure 1. FE model of CTRC Panel

2.1 Model Parameters

In the Finite Element Model, the CTRC panels had dimensions of 1m x 0.3m. The variables were the reinforcement ratio and panel thickness (30, 50, and 75 mm) to represent industrial precast panel thicknesses. The panels were modeled as three-dimensional deformable solids, with carbon textiles as wired deformable elements. The supports were modeled as a discrete rigid shell element. An embedded constraint simulated the interaction of the carbon textiles within the panels. Fig 1 shows detailed views of these models. The slab had pinned supports on two sides, gravity loading was applied in the z-direction. Mesh sensitivity analysis varied mesh sizes from 50 mm to 5 mm, with an optimal mesh size of 15 mm determined from our study.

2.2 Material Model

The Concrete Damage Plasticity (CDP) model was used to characterise the non-linear behaviour of fine-grained high-performance concrete. The concrete used in the analysis had a compressive strength of 60MPa. The Kent and Park et.al (1972) Model was used for concrete material model. For the carbon textile reinforcement, the experimental linear stress-strain was considered also the hashin-damage model was adopted for the rupture of carbon textile [Silvestre et.al (2017)]. In our study, we have adopted 9 models for simulation to investigate the influence of the reinforcement ratio and panel thickness on the impact response of TRC panels. The material properties used are presented in Table1.

Table 1. Properties of the materials for FE Analysis

Material/Element	Density (kg/m^3)	Young's Modulus (GPa)	Poisson's Ratio
Concrete Panel	2100	38	0.2
Carbon Textile	1750	110	0.26
Supporter	7850	210	0.3

3. Results and Discussions

The FE models were analyzed by varying the panel thickness and the number of carbon textile layers. Three,four and five textile layers were used, as previous static flexural loading experimental studies showed composite behavior in CTRC panels with more than three layers. Panels with fewer than three layers exhibited brittle failure, making them unsuitable for structural applications. With the increase in number of layers the bending stiffness increases, we can see in Figure 2, for the 30 mm thickness of the panels as we increase the number of layers from 3 to 4 there is a slight change in the deformation. Wherein, with 5 layers in CT30L5 the deformation is approximately 50% arrested. The maximum number of layers that we can consider for 30 mm thick panel was 5 layers considering the cover of minimum 5 mm required for the maximum aggregate of 2 mm.

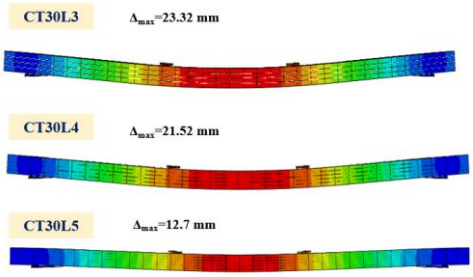

Figure 2. Flexural deformation with varying layers in 30 mm panels

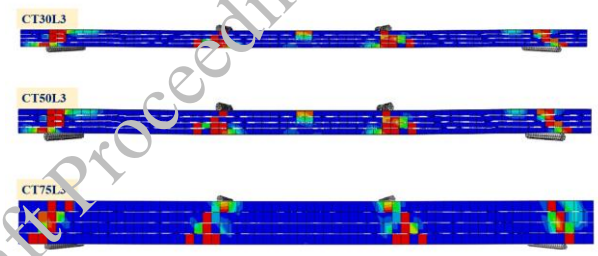

Figure 3. Failure pattern with Panel thickness

The thickness of the panels greatly influences the flexural behaviour with the same number of layers with uniform spacing within the panels. It was observed that with an increase in the thickness of the panels, the number of textile layers failed resisting the ultimate flexural load is reduced from 30 mm panel to 75 mm panel as seen in Figure 3. In the 75mm panel, only the bottom most textile had ruptured and the slab could still resist and not fall off catastrophically. In 30 mm and 50 mm panels with three textile layers the bottom two layers of textile yielded and the failure was brittle.

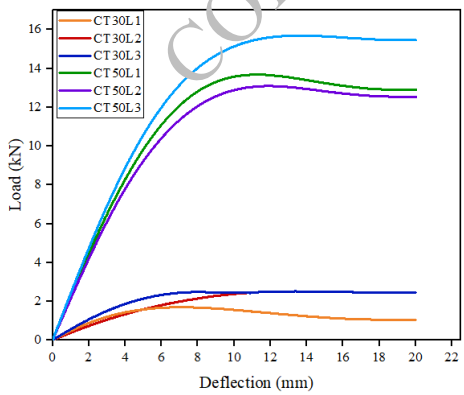

Figure 4. Flexural load vs deflection at the mid span for 30mm and 50mm panel

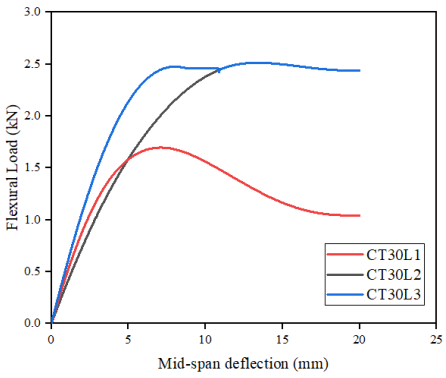

Figure 5. Flexural load vs deflection at the mid span for 30mm CTRC panel

It is evident from Figure 4, that increasing the thickness of the panel, while maintaining the same number of textile layers, results in a significant boost in flexural capacity, along with enhanced ductility. The behavior of panels with 2 and 3 layers shows minimal variation, which can be attributed to the textile layer

positioned at the neutral axis in the 3-layer configuration. This layer contributes primarily to an increase in the elastic stiffness of the composite but plays a limited role in enhancing overall performance. For the 30mm panel as shown in Figure 5, the behavior is initially brittle when only a single layer of textile is used. This brittleness is characterized by a sudden failure without significant deformation. However, as additional layers of textile are incorporated, the behavior gradually shifts from brittle to more ductile. This transition is marked by an increased ability of the panel to deform under load before failure. As the number of layers reaches 5, the panel not only becomes ductile but also exhibits strain-hardening behavior. In this state, the panel can sustain higher loads and undergo further deformation, enhancing its overall structural resilience and performance. The progression from brittleness to ductility with increased textile layers underscores the importance of proper reinforcement in optimizing the mechanical properties of the panel.

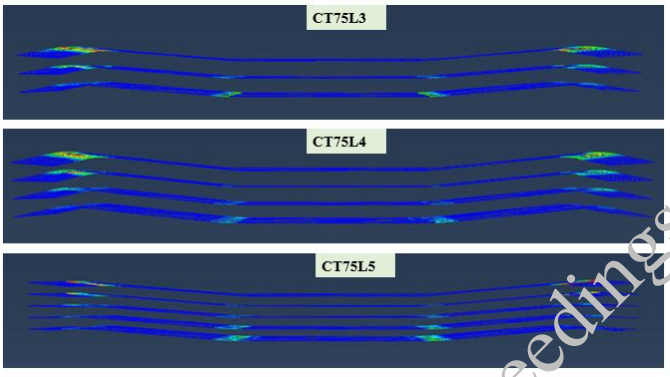

Figure 6. Longitudinal strain in the textile for 75mm CTRC panel

In Figure 6, represents the longitudinal strain at the point of fracture for 75mm CTRC panels with 3, 4, and 5 layers of textile reinforcement. In the panels with 3 layers, all the textile layers ruptured when subjected to flexural load. However, in the panels with 4 and 5 layers of textile, only the bottom two layers experienced rupture, while the upper layers remained intact. This indicates that in the panels with more layers, the load is better distributed among the layers, allowing the top layers to withstand the strain without reaching the rupture point.

4. Conclusions

This study conducted a numerical analysis of the CTRC panels simply supported under four-point bending. The paper assessed the failure mechanisms observed under static flexural load. The following observations are key considerations from these simulations:

- With an increased number of layers, the panel experiences composite mechanism with shearing of layers under the loading point.
- Under flexure, the failure is flexural shear cracks observed in all the cases.
- The flexural deformation reduced to 50% with the increase in number of textile layers from three to five.
- The ultimate failure is due to the rupture of the textile yarns.

This work can be extended with more simulations and experimental validation to better reflect real-life scenarios.

Acknowledgements

The authors acknowledge National Institute of Technology(NIT),Tiruchirappalli for the MHRD scholarship for the Phd and Masters Scholars to carry out this research work.This research was undertaken with the ABAQUS CAE 2023 software at the NIT Tiruchirappalli Laboratory.

References

ASTM C39/C39M–20. (2020) "Standard Test Method for Compressive Strength of cylindrical Concrete Specimens", West Conshohocken

ASTM D. 7264/D 7264 M-21.(2021) "Standard Test Method for Flexural Properties of Polymer Matrix Composite Materials", West Conshohocken, Pennsylvania: ASTM International

Cai S, Lin J, Fan K, Chen Y, Wang Z (2023)"Study on the bonding performance between basalt textile and concrete under freeze-thaw cycles", Engineering Failure Analysis, 146:107095

Chandrathilaka E. R., Baduge ,S. K., Mendis, P., Thilakarathna, P. S. (2020) "Flexural Performance of Pre-fabricated Ultra- \High-Strength Textile Reinforced Concrete (UHSTRC): An Experimental and Analytical Investigation", Buildings,10(4):68

Colombo, I. G., Colombo, M., Di Prisco, M. (2019) "Precast TRC sandwich panels for energy retrofit-ting of existing residential buildings: Full-scale testing and modelling", Materials and Structures, 52:1-6

Hafez, F.S., Sa'di, B., Safa-Gamal, M., Taufiq-Yap, Y.H., Alrifaey, M., Seyedmahmoudian, M., Stojcevski, A., Horan, B. and Mekhilef, S. (2023) "Energy Efficiency in Sustainable Buildings: A Systematic Review with Taxonomy, Challenges, Motivations, Methodological Aspects, Recommendations, and Pathways for Future Research", Energy Strategy Reviews, 45:101013

Immanuel,S. and Baskar, K. (2023) "A state-of-the-art review on sustainable low-cost housing and application of textile reinforced concrete", Innovative Infrastructure Solutions,8(1):39.

Karthikeyan, G., Margret, A.L., Vineeth, V. and Harshani, R. (2023) "Experimental study on mechanical properties of Textile Reinforced Concrete (TRC)", InE3S Web of Conferences, EDP Sciences, 387:04002

Nahum, L., Isaac, S., Peled, A. and Amir, O. (2023) "Significant Material and Global Warming Potential Savings through Truss-Based Topology Optimization of Textile-Reinforced Concrete Beams", Journal of Composites for Construction, 27(4):04023028.

Ngo,D. Q., Nguyen, H. C. (2023 "Experimental and numerical investigations of textile-reinforced concrete thin-wall panel bolted connections", Case Studies in Construction Materials 19: e02229

Pham, H. H., Dinh, N. H. and Choi, K. K. (2023) "Tensile behavior of lightweight carbon textile-reinforced cementitious composites with dispersed fibers", *Construction and Building Materials*, 384:131455

Pleesudjai, C. and Mobasher, B. (2023) "Analytical moment-curvature solutions for generalized textile-reinforced concrete Sections*", Engineering Structures*, 276:115317

Rajeshwaran, R., Logeshwari, J. (2023) "Experimental investigation on performance of sandwich wall infill in framed Structure", *Materials Today: Proceedings*

Raphael, B., Senthilnathan, S., Patel, A. and Bhat, S. (2023) "A review of concrete 3D printed structural members", *Frontier in Built Environment*, 8:291

Rawat, P., Liu, S., Guo, S., Rahman, M.Z., Yang, T., Bai, X., Yao, Y., Mobasher, B. and Zhu, D. (2022) "A state-of-the-art review on mechanical performance characterization and modelling of high-performance textile reinforced concretes", *Construction and Building Materials*, 347:128521

Shao, Y., Parks, A. and Ostertag, C.P. (2022) "Lightweight concrete façade with multiple air gaps for sus-tainable and energy-efficient buildings in Singapore", *Building and Environment*, 223:109463

Valeri, P., Guaita, P., Baur, R., Fernández Ruiz, M., Fernández-Ordóñez, D. and Muttoni, A. (2020) "Textile reinforced concrete for sustainable structures: Future perspectives and application to a proto-type pavilion", *Structural Concrete*, 21(6):2251-67

Van Driessche, A., Aggelis, D.G. and Tsangouri, E. (2021) "Complex fracture on thin-wall textile rein-forced cement (TRC) shells monitored by acoustic emission", *Thin-Walled Structures*, 167:108216

Venigalla, S.G., Nabilah, A.B., Mohd Nasir, N.A., Safiee, N.A. and Abd Aziz, F.N.A. (2022) "Textile-Reinforced Concrete as a Structural Member: A Review", *Buildings*,12(4):474

Williams Portal, N., Lundgren, K., Wallbaum, H. and Malaga, K. (2015) "Sustainable potential of textile-reinforced concrete", *Journal of materials in civil engineering*, 27(7):04014207

Žalský, J., Vlach, T., Řepka, J., Hájek, J. and Hájek, P. (2023) "Reinforced L-Shaped Frame Made of Textile-Reinforced Concrete",. *Polymers*, 15(2):376

Assessment of Synthetic Foaming Agents and Additives for Performance of Structural Lightweight Aggregate Foam Concrete

Chetharajupalli Veerendar [1*], S. Suriya Prakash [2*], Indu Siva Ranjani Gandhi [3]

[1] *Indian Institute of Technology-Hyderabad, Sangareddy, India*
Email: ce20resch11002@iith.ac.in
[2] *Indian Institute of Technology-Hyderabad, Sangareddy, India*
Email: suriyap@ce.iith.ac.in
[3] *Indian Institute of Technology-Guwahati, Guwahati, India*
Email: gindu@iitg.ac.in

*Corresponding author

ABSTRACT

Structural lightweight aggregate foam concrete (SLAFC) usually has a 1400 to 1800 kg/m3 density. Conventional foam concrete (CFC) is typically produced by introducing preformed foam into a cementitious paste or mortar. Though CFC is popular, it has limitations like compromised mechanical properties and shrinkage, resulting from the absence of coarse aggregates. In addition, the foam bubbles tend to collapse under the weight of the dense material. This study aims to develop SLAFC for manufacturing precast lightweight hollow core panels by incorporating sintered fly ash aggregate (SFA). SFAs are porous and low-density made from fly ash through a sintering process that contributes to achieving structural concrete strength and reduces shrinkage. The key factors influencing foam stability include the type of foaming agent, dilution ratio, and foam generation pressure. To assess the performance of SLAFC, the commercially available foaming agent sodium lauryl ether sulfate (SLES), viscosity modifying agent carboxymethyl cellulose (CMC), and sodium-based admixture sodium hydroxide (NaOH) were selected. The effect of foaming agent dilution, foam generation pressure, CMC, and NaOH concentrations on improving the stability and mechanical properties are investigated. The foam drainage rate, water absorption, and compression tests were conducted to optimize the SLAFC mix for target densities. A 4% SLES concentration at 2 bar pressure along with 0.3% CMC and 2% NaOH, improves foam stability of SLAFC for precast applications.

KEYWORDS*: Structural lightweight aggregate foam concrete, Foaming agents, Viscosity modifying agent, Sodium-based admixture, Foam stability.*

1. Introduction

Precast hollow core slabs (PHCS) are floor or wall panels with voids running through them, reducing the dead load on structures (Kankeri et al. (2019)). Utilizing lightweight concretes (LWCs) in manufacturing PHCS further reduces dead load, resulting in substantial cost savings and reduced seismic hazard (Abbas et al. (2022)). Conventional foam concretes (CFC) have gained huge demand in the global construction industry due to their lightweight, self-flow, thermal, and acoustic insulation properties. Despite many advantages, CFC has compromised mechanical properties because of low density and absence of coarse aggregates. Several researchers (Fantilli et al. (2016); Ahmad et al. (2019)) investigated foamed concrete's physical and mechanical properties with lightweight porous coarse aggregates to understand the enhanced mechanical properties and promote its suitability for structural applications.

This paper focused on developing a structural lightweight aggregate foam concrete (SLAFC), for precast applications by introducing sintered fly ash aggregates (SFA) to enhance the mechanical properties of foam-based concrete. SFA is manufactured from fly ash through the palletization process under high pressure and temperature ranges of 1100°C and 1300°C (Sahoo et al. (2020)). Typically, any foam-based concrete is a mixer of binder materials, aggregates, and preformed foam. Foam is generated by passing the foam

solution through a dense mesh-type structure by mixing with compressed air. To achieve the target density of foam-based concrete, generating stable foam with the desired initial foam density is crucial. The stability of the foam used in foam concrete depends on the type of foaming agent, dilution ratio, foam generation pressure, and additives used.

Sodium lauryl ether sulfate (SLES) is a widely used anionic synthetic foaming agent and is an ethoxylated form of sodium lauryl sulfate (SLS) (Indu and Ranjani (2011)). SLES alone doesn't generate stable foam for making foam concrete with lightweight aggregates. Hence, there is scope for improvement in SLES foams in terms of foam density, viscosity, and stability through the addition of some additives. Carboxymethyl cellulose (CMC), which is an anionic linear polymer is commonly used as a thickener for the improvement of foam stability (On et al. (2019)). The addition of iconic additives like sodium chloride, sodium carbonate, and sodium hydroxide due to the common ion effect increases the viscosity and further results in the improvement of foam density. In addition, the reduction of the bubble size of the foam further stabilizes the foam by increasing the lamella thickness (Siva, et al. (2015)).

This study attempts to assess the performance of foam made with SLES, CMC, and NaOH and their combinations on the characteristics of foam (including foam density, and stability) to retain under SFA weight. The stability test was conducted according to Def standard 42-40 (Ministry of Defence Standard (2002)) to assess the foam density and drainage rate as shown in Figure 1. Furthermore, fresh and hardened state properties of SLAFC are investigated for two different target densities.

2. Experimental program

2.1 Materials

2.1.1 Binders and aggregates

Ordinary Portland Cement (OPC) 53-grade acts as the binder, while Class-F fly ash serves as a supplementary cementitious material. The specific gravity of cement and fly ash is 3.15 and 2.20, respectively. The natural river sand particle size of less than 600 microns is used as the fine aggregate, and Sintered Fly ash aggregates (SFA) as coarse aggregates have a specific gravity of 1.45, and 2.66, respectively are used for the manufacturing of SLAFC. The size of the SFA adopted in this research ranges from 4 to 8 mm. The materials used in this study are shown in Figure 1.

Figure 1. Material for making SLAFC

2.1.2 Foam solution

Industrial grade SLES foaming agent used to prepare foam solution. Commercially available CMC and NaOH are used as foam-stabilizing and viscosity-enhancing agents. The individual and combined effects of CMC and NaOH on foam density, foam stability, and target density of the SLAFC are studied in the subsequent section. Table presents the properties of foaming agent and additives.

Table 1. Properties of foaming agents and additives.

Material	Role	Synonym	General Group	Chemical Formula	Classification (Charge Base)
Sodium Lauryl Ether Sulfate	Foaming agent	Sodium Laureth Sulfate	Alkyl Ether Sulfate	C16H33NaO6S	Anionic
Carboxymethyl Cellulose	Additive	Cellulose gum	Carboxymethyl	C8H16O8	Anionic
Sodium Hydroxide	Additive	Caustic soda	-	NaOH	Neutral

2.2 Parameters and properties studied

For assessing the performance of foam characteristics, foam generation pressure (FGP), foaming agent (SLES), and additive (CMC, NaOH) concentrations are considered. Foaming agent concentrations ranging from 2% to 10%, additives (CMC) from 0.1% to 0.3%, and NaOH from 1% to 3% were considered. Foam generation pressures of 1 bar to 4 bar were considered. Foam density and stability of foam are assessed on freshly made foam according to Def Standard 42–40 (Ministry of Defence Standard (2002)). Fresh state properties namely fresh density, and hardened state properties namely dry density, compressive strength, and water absorption were measured.

2.3 Stability analysis

The foam is generated using an industry-scale foam generator with the help of compressed air passing through the high-density restriction (Foam Gun) along with foam solution. The freshly made foam was collected in a 1 Litre measuring jar to determine the initial foam density at different FGPs. Foam stability was assessed through a drainage test as shown in Figure over a 45-minute duration and by measuring the amount of liquid drained at ambient conditions. The liquid drainage was measured at each 5 minutes of duration and results are presented in Figure 2.

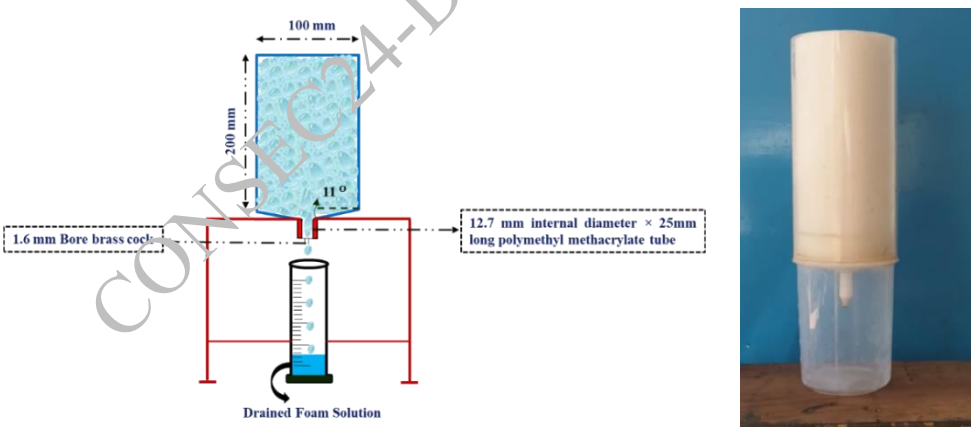

Figure 2. Experimental Set-up for Foam Drainage Study As per Def standard 42-40 (Ministry of Defence Standard (2002))

2.4 Stability of foam in SLAFC mixes

SLAFC mixes of two densities 1800 and 1400 kg/m^3 were designed and evaluated for the requirements of ASTM C 869 (C869 (1999)) concerning fresh density, dry density, strength, and water absorption. The density of foam used in the present study is 40 kg/m^3, which satisfies the requirement of foam density as per ASTM C796 (C796 (1967)). The aforementioned requirements of SLAFC mixes for the optimized combination of foam solutions are discussed in the following section.

3. Results and Discussions

3.1 Effect of foam generation pressure and foam solution concentration on initial foam density

The foam is generated using an industry scale foam generator, and the initial foam density (IFD) is reduced with increasing the FGP and concentration of SLES shown in Figure 3. At higher concentrations, to generate a required foam density as per ASTM standards high FGP is required. The addition of CMC reduces the FGP, to generate the foam between 32 to 64 kg/m^3. The addition of NaOH reduces the IFD further in combination with CMC and helps in reducing the drainage due to the increased viscosity of the foam solution. For the optimum combination of SLES 4%, CMC 0.3%, and NaOH 2% the drainage rate is observed at about 10% which is less than the drainage rate 20 % reported in the previous literature (Wagh, Siva, and Gandhi (2024)).

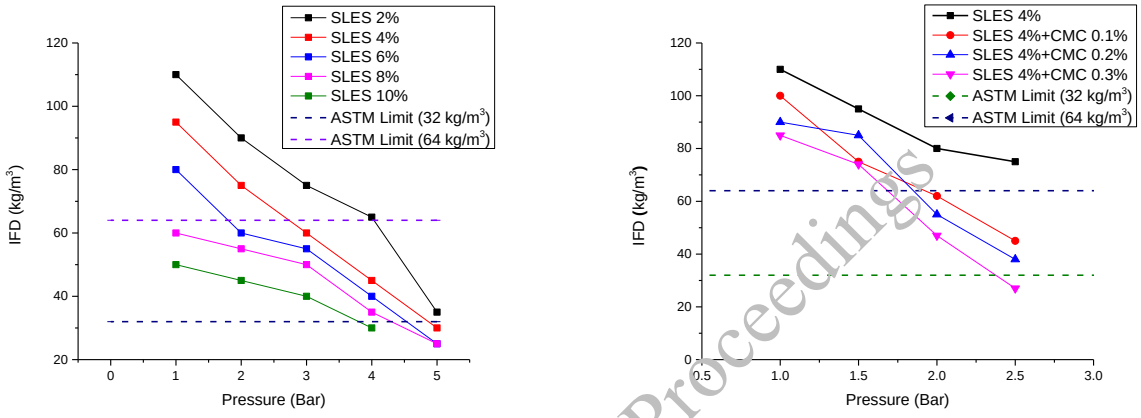

IFD with respect to SLES concentration **IFD with respect to CMC concentration**

Figure 3. Effect of concentration of SLES and CMC in initial foam density

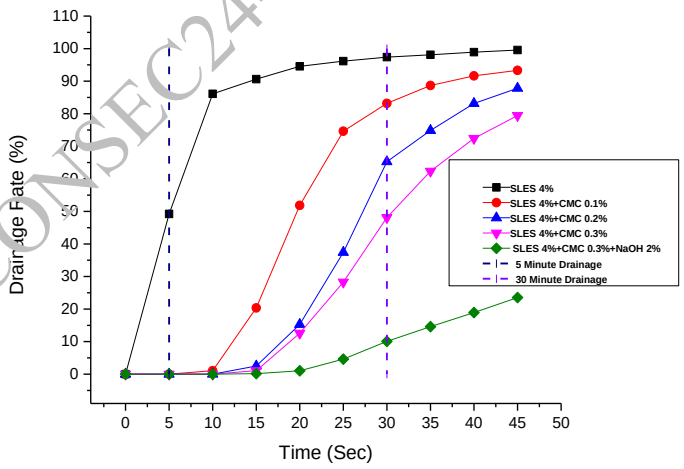

Figure 4. Drainage rate of foam solution made with a foaming agent, additives, and their combination

3.2 Fresh density, strength, and water absorption of SLAFC

SLAFC mixes with 1800 and 1400 kg/m^3 density are made with optimum foam generation parameters as ASTM C869 (C869 (1999)). Fresh state densities are within the range ±50 kg/m^3 and water absorption is less than 25% for both densities and achieved the structural strength of about 25 MPa with 1800 kg/m^3 and about 15 MPa with 1400 kg/m^3. A summary of the results is presented in Table 2.

Table 2. Summary of results

SLAFC Target Density (kg/m^3)	Achieved Density (kg/m^3)	Water Absorption (%) @28 Days	Compressive Strength (MPa) @28 Days	
			Cube	Cylinder
1800	1780	5	25.53	19.46
1400	1415	15	15.48	9.86

4. Conclusions

The following conclusions drawn from this study on foam and SLAFC characteristics are discussed below,

- Synthetic foaming agents and additives are more effective in generating stable foam for foam concrete with lightweight porous coarse aggregates (SFA).
- Initial foam density is decreased with an increase in foam generation pressure, foaming agent, and additives concentrations for the foam generated using an industrial scale foam generator.
- Stability of foam is increased with an increase in additives concentration.
- The optimized foam solution and foam are suitable for making SLAFC which can used in making precast elements since it qualifies the structural concrete requirements.

References

Abbas, Y. M., L. A. Hussain, M. I. Khan, A. Sharda, A. Manalo, W. Ferdous, Y. Bai, et al. (2022): "Seismic behaviour of a novel hollow-core precast shear wall with cast-in-situ boundary elements", *Results in Engineering*, 10:705–14.

Ahmad, M. R., Chen , B. and Farasat Ali Shah, S.. (2019): "Investigate the influence of expanded clay aggregate and silica fume on the properties of lightweight concrete" ,*Construction and Building Materials*, 220:253–66.

C796, A. (1967): "Standard Test Method for Foaming Agents for Use in Producing Cellular Concrete Using Preformed Foam",*ASTM International*, 3:1–5.

C869, A. (1999) "Standard Specification for Foaming Agents Used in Making Preformed Foam for Cellular Concrete,"91: 1–2

Fantilli, A. P., B. Chiaia, and A. Gorino. (2016): "Ecological and mechanical assessment of lightweight fiber-reinforced concrete made with rubber or expanded clay aggregates", *Construction and Building Materials*, 127(69):2–701

Indu, G. and S. Ranjani. (2011) "Investigations on behaviour of preformed foam concrete using two synthetic surfactants a thesis submitted by doctor of philosophy building technology and construction management division.,"

Kankeri, P., Pachalla, S.K., Thammishetti, N. and Prakash, S.S. (2019) "Behavior of structural macrosynthetic fiber-reinforced precast, prestressed hollow-core slabs at different flexure-to-shear ratios,", *PCI Journal,* 76–91.

Ministry of Defence Standard. (2002) "Ministry of Defence Defence Standard 42-40 Foam Liquids, Fire Extinguishing (Concentrates, Foam, Fire Extinguishing).

Sahoo, S., A. K. Selvaraju, and S. S. Prakash. (2020) "Mechanical characterization of structural lightweight aggregate concrete made with sintered fly ash aggregates and synthetic fibres," *Cement and Concrete Composites*, 113:103712.

Siva, M., Ramamurthy, K. and Dhamodharan, R. (2015): "Sodium salt admixtures for enhancing the foaming characteristics of sodium lauryl sulphate," *Cement and Concrete Composites*, 57:133–41.

Wagh, C.D. and Gandhi, I.S.R. (2024) "Investigations on the performance of xanthan gum as a foam stabilizer and assessment of economic and environmental impacts of foam concrete production," *Journal of Building Engineering*, 82:108286.

Effect of Alkaline Solution and Age on Compressive Strength, Ionic Concentration and Microstructure of Geopolymer Concrete

M. Leela Sai Rangarao[1*], and Bulu Pradhan[2]

[1] Research scholar, Department of Civil Engineering, Indian Institute of Technology Guwahati, Guwahati, India
Email: maradanileela@iitg.ac.in
[2] Professor, Department of Civil Engineering, Indian Institute of Technology Guwahati, Guwahati, India
Email: bulu@iitg.ac.in

*Corresponding author

ABSTRACT

The influence of variation in molarity of sodium hydroxide (NaOH) solution (at 8 M and 14 M) on compressive strength of fly ash-ground granulated blast furnace slag (85%:15%) based geopolymer concrete (GC) at the age of 7 and 28 days was investigated. Further, the electrolytic pore solution was obtained from GC mixes to determine the concentration of calcium (Ca^{2+}), sodium (Na^{+}), and potassium (K^{+}) ions. The variation of these ionic concentrations with molarity of NaOH solution was investigated and correlated with the microstructural properties of geopolymer concrete. The microstructural investigations carried out were X-ray diffraction (XRD), and energy dispersive X-ray spectroscopy (EDX) analyses. The research findings showed increase in compressive strength of GC with increase in NaOH solution concentration and age. The ionic concentration of Ca^{2+}, Na^{+} and K^{+} ions showed consistent variation with the formation of geopolymeric gels and C-S-H gel with increase in molarity of NaOH solution and age. The EDX analysis showed increase in elemental ratios of Si/Al and Na/Al with molarity of NaOH solution, and the elemental ratios of Ca/Si and Na/Al were increased with age, which are corroborated with XRD analysis and compressive strength of geopolymer concrete.

KEYWORDS*: Geopolymer concrete, Electrolytic pore solution, Ionic concentration, Microstructure.*

1. Introduction

Cement production is a major industrial activity, both in terms of its volume and its impact on greenhouse gas emissions. Globally, cement production accounts for at least 5–7% of carbon dioxide (CO_2) emissions (McLellan et al. (2011)). To reduce these emissions, alternative cements to OPC have been suggested. These include usage of blended cements, which are typically used as binders for the preparation of concrete, and comprises OPC that has been partially substituted with supplementary cementitious materials (SCMs). The various SCMs that can be used are fly ash, ground granulated blast furnace slag (BFS), rice husk ash, copper slag. However, the usage of blended cements reduced the CO_2 emissions by 13–22% (Flower and Sanjayan (2007)). Therefore, it is required to replace the OPC completely. For this purpose, geopolymer binder which comprises aluminosilicate source material alkaline activated by hydroxyl or silicate-based solution is used to replace the OPC completely (Rocha et al. (2018)). Rocha et al. (2018) stated that the mechanical performance of geopolymers is influenced by hydroxide solution concentration and effectiveness of geopolymerization. Thus, the current research investigation studies effect of variation in molarity of NaOH solution on compressive strength of fly ash-BFS GC, and variation in ionic concentration of Ca^{2+}, Na^{+} and K^{+} ions in electrolytic pore solution of GC. Further, these variations are correlated with microstructural properties of GC obtained from the XRD and EDX analyses.

2. Experimental methodology

In the current research investigation, fly ash and BFS (at 85%:15% proportion) were used as precursor materials for the preparation of geopolymer concrete (GC) mixes. The alkaline activator solution used was

a mixture of sodium hydroxide (NaOH) solution (varied at 8 M and 14 M) and sodium silicate (Na_2SiO_3) solution. Further, the sand was used as fine aggregate and the combination of 10 mm maximum size aggregate (MSA) and 20 mm MSA were used as coarse aggregate in the preparation of GC. The procedure for the production of GC mixes is depicted in Fig. 1. The freshly prepared GC mix was laid in cube moulds (size: 150 mm) in 3 layers, where each layer was filled to one-third height of the cube mould, compacted with a tamping rod for 25 times, and then vibrated for 10 to 15 seconds. After the preparation, the GC cube specimens were left to ambient laboratory conditions for 24 h, then the specimens were demoulded from the moulds, and left to laboratory conditions till the age of testing for compressive strength.

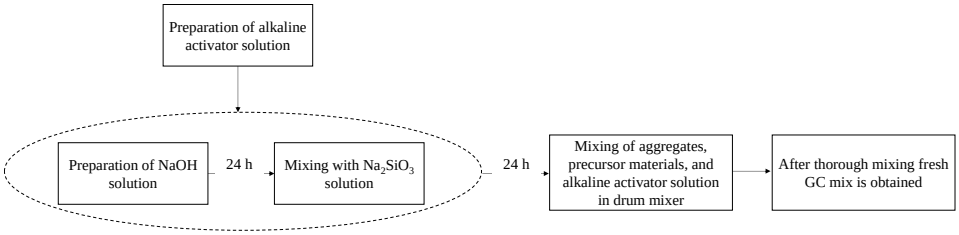

Figure 1. Preparation process of geopolymer concrete mixes

After the compressive strength test, the broken cube fragments were collected, and grounded by pulverizer, and the powder was sieved through 75 µm sieve. This powder was utilized to prepare the GC electrolytic pore solution and determine ionic concentration of calcium (Ca^{2+}), sodium (Na^{+}), and potassium (K^{+}) ions. The preparation of electrolytic pore solution of GC mixes is shown in Fig. 2. From the obtained GC electrolytic pore solution, the ionic concentrations were evaluated by using flame photometer as per the procedure prescribed by Standard methods for the examination of water and waste water published by American Public Health Association (APHA 2005). Further, the microstructural investigations were also conducted on the GC powder samples, which includes XRD and EDX analyses.

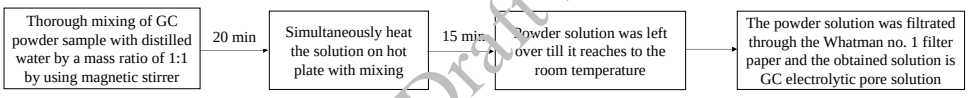

Figure 2. Preparation of GC electrolytic pore solution

3. Results and Discussions

The compressive strength of GC made with different molarities of NaOH solution, and tested at 7 and 28-days are shown in Fig. 3. From this figure, it was observed that the compressive strength of GC mixes was increased with concentration of NaOH solution and age. The increase in molarity of NaOH solution led to greater dissolution of Si and Al from the source materials that resulted in greater degree of geopolymerization reaction, thereby increased the compressive strength of GC mixes with 14 M NaOH solution than the mixes with 8 M NaOH solution. Furthermore, the continuation of the geopolymerization reaction in GC with an increase in age resulted in higher strength of GC at 28 days compared to 7 days.

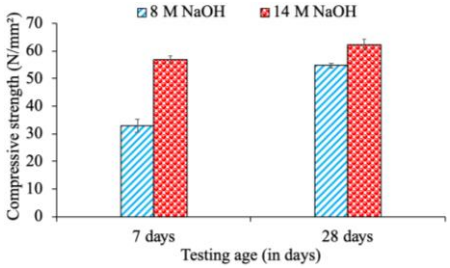

Figure 3. Compressive strength of GC mixes

The ionic concentrations of electrolytic pore solution of GC mixes are illustrated in Fig. 4. From this figure, it was observed that the increase in molarity of NaOH solution resulted in decrease in ionic concentrations of Ca^{2+} and K^{+} ions, whereas an opposite trend was observed in case of Na^{+} ion concentration regardless of

age. This might be due to greater degree of geopolymerization reaction occurred in GC with 14 M NaOH solution led to more development of geopolymeric gels, which resulted in consumption of Ca^{2+} and K^+ ions along with the Na^+ ions. However, increase in molarity of NaOH solution led to greater solid content in alkaline solution, thereby increased the ionic concentration of Na^+ ions in GC electrolytic pore solution (Fig. 4). The increase in age of GC mixes led to decrease in concentration of Ca^{2+}, Na^+ and K^+ ions regardless of NaOH solution molarity (Fig. 4). This is attributed to continuation of geopolymerization reaction with age led to greater formation of binding gels, which indicates that these ions were participated in the formation of more amount of binding gels.

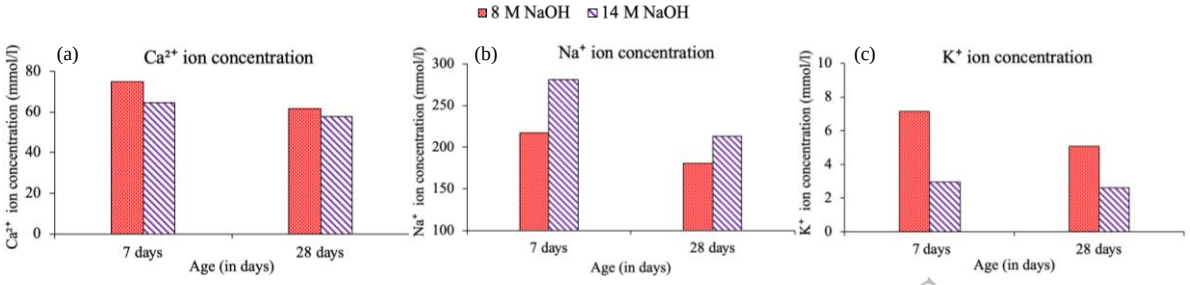

Figure 4. Ionic concentrations of GC electrolytic pore solution, (a) Ca^{2+} ion concentration, (b) Na^+ ion concentration, and (c) K^+ ion concentration

The XRD spectra of GC with different molarities of NaOH solution, and tested at 7 and 28 days are shown in Fig. 5. From this figure, the crystalline peaks related to quartz and mullite were observed in the spectra, which indicates the existence of partly reacted fly ash particles. Additionally, the peaks related to muscovite [$KAl_3Si_3O_{10}(OH)_2$] at 2θ (8.8°), albite [$(Na.Ca)Al(SiAl)_3O_8$] at 2θ (22.01 and 28.02°), anorthoclase [$(Na_{0.85}K_{0.15})(AlSi_3O_8)$] at 2θ (27.5°), nepheline ($NaAlSiO_4$) at 2θ (27.1°), calcite along with calcium silicate hydrate (C-S-H) gel at 2θ (29.5°) were observed in all the GC mixes. From Fig. 5, it was observed that the peak intensity of anorthoclase, nepheline, and albite were increased with molarity of NaOH solution and age. This is due to the effect of higher concentration of NaOH solution led to greater dissolution of Si and Al from the precursor material which led to development of more amount of geopolymer gels. From these observations, it was evident that the reduction in concentration of Ca^{2+} and K^+ ions with increase in molarity of NaOH solution is due to participation of these ions in formation of more amount of geopolymer gels, whereas the increase in solid content with molarity of NaOH solution led to increase in Na^+ ion concentration in GC electrolytic pore solution (Fig. 4), as well as led to more formation of geopolymer gels. From Fig. 5, it was observed that the peak intensity of anorthoclase, nepheline, albite, and C-S-H gel were increased with age. This is attributed to extended geopolymerization from 7–28 days age, that led to formation of more amount of binding gels. Therefore, the ionic concentration of Ca^{2+}, Na^+, and K^+ ions (Fig. 4) were reduced with increase in age (Fig. 4), which indicates that these ions were consumed in the formation of more amount of binding gels in GC mixes at 28 days age than 7 days (Fig. 5). Thus, the additional formation of these binding gels led to increase in compressive strength of GC mixes.

A typical EDX spectra of GC mix made with 14 M NaOH solution along with the elemental ratios (i.e., Ca/Si, Na/Al, and Si/Al) obtained from EDX analysis of GC made with 8 M and 14 M NaOH solution tested at the age of 7 and 28 days are shown in Fig. 6. From this figure, it was observed that the elemental ratios of Ca/Si, Na/Al, and Si/Al were varied from 0.18–0.26, 0.22–0.26, and 1.76–2.34 respectively. From the literature, it was found that the ratios of Ca/Si, Na/Al, and Si/Al were varied from 0.045–2.43, 0.2–1.48, and 0.2–5.8 respectively (Huo et al. (2021); Khan et al. (2020), (2022)). These values indicate the coexistence of N-A-S-H gel, N-(C)-A-S-H gel, and C-S-H gel in the present research work (Huo et al. (2021); Khan et al. (2020), (2022)). From Fig. 6, Ca/Si, Na/Al, and Si/Al ratios were increased with molarity of NaOH solution and age of GC mixes. This is due to enhanced geopolymerization with increase in concentration of NaOH solution and age that resulted in formation of more amount of aforementioned binding gels. This is also confirmed with the variation of Ca^{2+} ion concentration and formation of geopolymeric compounds, where the increase in molarity of NaOH solution resulted reduction in Ca^{2+} ion concentration (Fig. 4), and increase in peak intensity of geopolymeric compounds (Fig. 5). Therefore, the decrease in Ca^{2+} ion concentration indicates that Ca^{2+} ions were participated in development of more amount of calcium enrich gels, thereby increased the Ca/Si ratio, whereas the increase in solid content with molarity of NaOH solution led to increase in Na^+ ion concentration in electrolytic pore solution, as well as increase

in peak intensity of sodium rich geopolymer gels, thereby increased the Na/Al ratio. Similarly, formation of more amount of binding gels with increase in age (Fig. 5) resulted in higher Ca/Si, Na/Al, and Si/Al elemental ratios and reduced the ionic concentrations in GC electrolytic pore solution (Fig. 4).

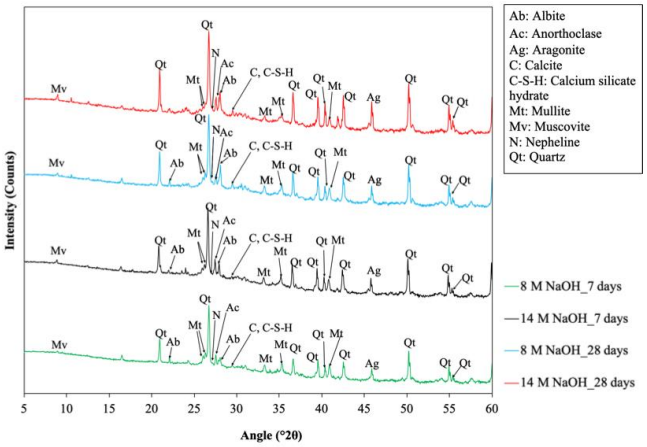

Figure 5. XRD spectra of GC with different molarities of NaOH solution

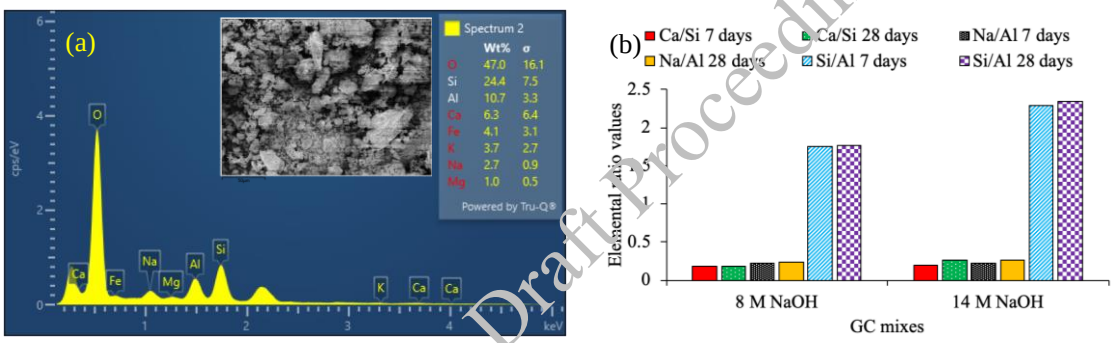

Figure 6. EDX analysis, (a) Typical EDX spectra of GC mix (14 M NaOH solution), (b) Elemental ratios of GC mixes made with different molarities of NaOH solution

4. Conclusions

The significant conclusions that are drawn from this research investigation are:

- The strength of GC mixes was increased with molarity of NaOH solution and age of GC. Further, the variations of Ca^{2+}, Na^{+}, and K^{+} ion concentrations were consistent with the formation of binding gels.
- The increase in NaOH solution molarity and age of GC mixes resulted in greater development of geopolymeric gels and C-S-H gel. These observations are in line with the ionic concentration of Ca^{2+}, Na^{+}, and K^{+} ions. Further, these findings are corroborated with variation of strength of GC mixes.
- The variation of elemental ratios Ca/Si, Na/Al, and Si/Al are consistent with the XRD analysis and ionic concentration of Ca^{2+}, Na^{+}, and K^{+} ions in electrolytic pore solution of GC.

References

Flower, D. J. M. and Sanjayan., J. G. (2007) "Green house gas emissions due to concrete manufacture", *International Journal of Life Cycle Assessment*, 12 (5): 282–288.

Huo, W., Z. Zhu, W. Chen, J. Zhang, Z. Kang, S. Pu, and Y. Wan. (2021) "Effect of synthesis parameters on the development of unconfined compressive strength of recycled waste concrete powder-based geopolymers", *Construction and Building Materials*, 292: 123264.

Khan, H. A., Castel., A. and Khan., M. S. H. (2020) "Corrosion investigation of fly ash based geopolymer mortar in natural sewer environment and sulphuric acid solution", *Corrosion Science*, 168.

Khan, H. A., Yasir, M. and Castel., A. (2022) "Performance of cementitious and alkali-activated mortars exposed to laboratory simulated microbially induced corrosion test", *Cement and Concrete Composites*, 128: 104445

McLellan, B. C., R. P. Williams, J. Lay, Riessen, A. Van and Corder, G. D. (2011) "Costs and carbon emissions for geopolymer pastes in comparison to ordinary Portland cement", *Journal of Cleaner Production*, 19 (9–10): 1080–1090.

Rocha, T. da S., D. P. Dias, França, F. C. C., Guerra, R. R. de S., and Marques., L. R. da C. de O. (2018) "Metakaolin-based geopolymer mortars with different alkaline activators (Na^+ and K^+)", *Construction and Building Materials*, 178: 453–461.

Standard Methods for the Examination of Water and Wastewater (1999).The Nineteenth and Earlier Editions..

Mass Concreting: Lessons Learnt from the Construction of Nuclear Facility Site at Kalpakkam

R.Mano[1], H.Vaithyanathan[2], G.Padmanabhan[3*] and K.S.Rahaman[4]

[1] Scientific Officer E, Fast Reactor Fuel Cycle Facility, Nuclear Recycle Board, Bhabha Atomic Research Center, Kalpakkam, India,
Email: rmano@igcar.gov.in
[2] Technical Officer E Fast Reactor Fuel Cycle Facility, Nuclear Recycle Board, Bhabha Atomic Research Center, Kalpakkam, India ,
Email: vaithai@igcar.gov.in
[3] Scientific Officer G, Fast Reactor Fuel Cycle Facility, Nuclear Recycle Board, Bhabha Atomic Research Center, Kalpakkam & Faculty, Homi Bhabha National Institute, Mumbai India*
Email: padman@igcar.gov.in
[4] Project Director, Fast Reactor Fuel Cycle Facility, Nuclear Recycle Board, Bhabha Atomic Research Center, Kalpakkam, India,
Email: sarif@igcar.gov.in

[*]Corresponding author

ABSTRACT

Temperature-controlled concrete is frequently used in major constructions to mitigate the heat of hydration in freshly placed concrete. Poorly designed and executed mass concretes can lead to thermal cracking at an early age, compromising the durability. Effective control of fresh concrete temperature during production, placement, and the hardening period plays a pivotal role in regulating the heat of hydration in freshly placed concrete. As part of the construction of a nuclear facility site at Kalpakkam, a properly designed concrete mix was utilized, along with other temperature control measures such as the use of ice flakes & chilled water for the production of temperature-controlled concrete. Initially, a critical pour of 3200 m^3 was undertaken. Subsequently two major concrete pours 7200 m^3 of 2.7 m thick & 8000 m^3 of 1.7 m thick raft foundations were executed by adopting proper thermal control measures. Core temperature was continuously monitored using thermo couples during the hydration process, which had provided valuable insights into the thermal behavior of mass concrete. 2.7 m thick mass concrete exceeded the permissible concrete core temperature for a short duration of 3 hr while that for 1.7 m thick raft the core temperature was within the permissible limit. Innovative temperature control measures like utilization of chilled water for mixing in concrete and for production of ice flakes were utilized in the project which helped to maintain the concrete core temperature within the acceptable limits for 1.7 m thick mass concrete. The temperature monitoring indicated that when the pour thickness is higher than 1.7 m additional measures are required for restricting the concrete core temperature within the permissible limits.

KEYWORDS*: Mass concrete, Temperature-controlled concrete, Core temperature, Thermo couple*

1. Introduction

Mass concrete is defined as any volume of structural concrete in which a combination of dimensions of the member being cast, the boundary conditions, the characteristics of the concrete mixture, and the ambient conditions can lead to undesirable thermal stresses, cracking, deleterious chemical reactions, or reduction in the long-term strength as a result of elevated concrete temperature due to heat of hydration (ACI, 2007). Mass concretes are generally associated with the construction of dams, bridges, etc. However, with the increasing in demand for fast-track constructions and requirements for reduction in construction joints for better performance of structures, now a day's mass concretes are often required in infrastructure projects. As the early age high temperature in concrete structures can affect the durability of the concrete the core temperature of concrete beyond the permissible limits is determinantal. With an aim to reduce the peak

concrete core temperatures, various researchers had partially replaced the cement with supplementary cementitious materials to reduce the heat of hydration and associated core temperature rise in concrete . Apart from partial replacement of cement, a temperature-control plan shall be evolved & implemented in projects for minimizing the detrimental effect of high temperature generated during heat of hydration.
In this paper, as the part of construction of a nuclear facility site at Kalpakkam, with an aim to accelerate the construction & to minimize construction joints, major pours were taken up with suitably designed concrete mix where cementitious material was replaced partially with fly ash and a proper temperature-control plan was implemented before the execution.The maximum core temperature was monitored using thermocouples placed at the centre for the concrete volume along the length of the raft. The lessons learned from these major pours for restricting the temperature of mass concrete is presented in this paper which is essential for designing future mass concrete pours in infrastructure projects.

2. Materials & mix properties

OPC cement confirming to IS 269 (2015), Fly ash confirming to IS 3812 (2013), Coarse & fine aggregate confirming to IS 383 (2016), potable water in the form of ice & high range water reducing admixtures confirming to IS 9103 (1999) were used. The physical properties of OPC cement & fly ash are shown in Table 1.

Table 1. Properties of Cement and Fly ash

Material	Chemical Composition							Specific Gravity	Specific Surface m^2/kg
	CaO	SiO_2	Al_2O_3	Fe_2O_3	MgO	SO_3	LOI		
Cement	60.5	18.8	5.2	4.1	2.8	2.8	4.4	3.15	254
Fly ash	0.7	62.4	29.42	1.27	0.6	0.4	0.2	2.11	357

Two mixes namely N30 (28 days strength 30 N/mm^2) & N45 (28 days strength 45 N/mm^2) were used for the mass concrete with different cementitious content of 405 kg/m^3 and 450 kg/m^3 respectively. With an aim to reduce the heat of hydration, 20% the cementitious content was replaced with Class F fly ash. The Water to binder ratio was kept as 0.37 and 0.34 respectively for N 30 and N45 mix. A portion of the water is replaced with ice flakes to achieve the placement temperature of 23^0C.

3. Temperature control plan & measured temperature of concrete

A through understating of the behavior of mass concrete is essential to design concrete mixes, and to develop & implement a temperature control plan during execution of mass concrete. The high core and differential temperature can lead to thermal cracking and can also affect the durability of the concrete cured at higher temperature. In general use of supplementary cementitious materials, restriction in placement temperature of concrete and pre cooling of aggregates are adopted to control the temperature of mass concrete.
A combination of these methods and implementation of innovative construction practices is essential for successful mass concrete constructions. Two major concrete pours of involving placement of 7200 cum and 8000 cum temperature controlled concrete for raft foundations (Figure1(a) and 1(b)) were carried out at Fast Reactor Fuel Cycle Facility site after gaining experience from execution of a mass concrete involving placement of 3200 cum temperature controlled N 30 grade concrete.

Figure 1(a). Mega pour @location 1

Figure 1 (b). Mega pour @location

Considering the heat of hydration calculations the placement pour temperature was restricted to 23^0 C. The salient features of the two major pours and temperature control plan implemented in this works is tabulated in Table 2. The infrastructures required for production & storage of ice flakes plays a major role in maintaining the placement temperature of the mass concrete.

Generally concrete temperature is limited to 70^0 C during hydration process. If the temperature of the concrete during hydration exceeds this limit, delayed ettringite formationsare reported which can affect the durability of structures.

Table 2. Salient features of major pours

Description	Pour 1(Location 1)	Pour 2 (Location 2)
Size of the pour	72 m x 37 m x 2.7 m	99.5 m x 47.5 m x 1.7 m
Grade of concrete & placement temp	N 45 & 23	N 45 & 23
Salient pour details	77 m^3/hr rate of pour and 93 hrs.	58 m^3/hr rate of pour and 130 hrs
Temperature control measures	Pre cooling of aggregate, Partial replacement of cement with fly ash, partial replacement of water with ice flakes, wet cuing, shading of the area	Pre cooling of aggregate, Partial replacement of cement with fly ash, partial replacement of water with ice flakes, usage of chilled water for mixing, wet cuing, shading of the area
Infrastructure for production of temperature controlled concrete	4 Batching plant for a cumulative capacity of 220 Cum/hr, 4 Ice plant with cumulative capacity of 140 MT/hr , Ice storage of capacity 260 MT, 5 Boom placers of 90 cum/hr capacity and 2 Static pumps of 60 Cum/hr.	3 Batching plant for a cumulative capacity of 180 m^3/hr, 3 ice plant of cumulative capacity of 120 MT/hr, 4 boom placer of 90 m^3/hr capacity and 1 static pump of 60 m^3/hr, Ice storage capacity 250 MT
Temperature monitoring measures	5 No of Thermo couples at 1.35 m depth at 15 m c/c distance along length direction	6 No of Thermo couples at 0.85 m depth at 15 m c/c distance along length direction

Hence the maximum temperature in the mass concrete needs to be limited to avoid durability related issues if any at a later date. A properly designed mass concrete needs to be monitored for the core temperature which can provide an insight on the core temperature of mass concrete and the experience can be used for designing future mass concretes. The temperature monitored at a thermocouple located at the center for the pour 1 & 2 is shown in Figure 2 (a) and 2(b).

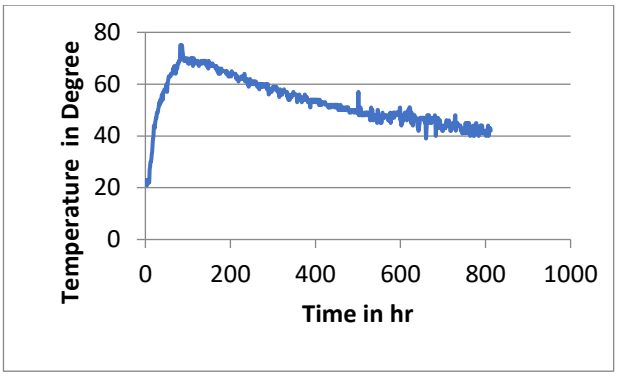

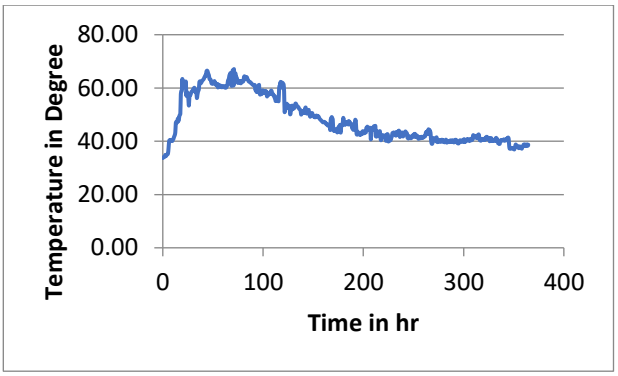

Figure 2(a). Core temperature at location 1 **Figure 2 (b). Core temperature at location 2**

The maximum core temperature obtained at location 1 is 75^0 C at 82 hr and at location 2 is 67^0 C at 71 hr which indicates in both the pours the maximum core concrete temperature is attained at 3 to 3.5 days. For the concrete pour 1 which is 2. 7 m height, the maximum core temperature exceeded the permissible limit for a short duration of 3 hrs and subsequently reduced to the permissible limit. However the gradient of temperature raise in the pour 1 (2.7 m thick) is higher comparing to that of pour 2 and also the core temperature was sustained in the range of 40 ^{0} C even after 30 days where as in pour 2 , the maximum core temperature dropped to ambient values less than 40^0 C after 14 days.

4. Conclusions

The monitoring of concrete core temperature of the mass concrete indicated that even though the placement temperature is restricted to 23^0 C, when the pour height exceeds conventional 2.0 m height, the concrete core temperature exceeds the permissible limit of 70^0 C for a short duration. Also, it takes longer time for dissipating the heat of hydration. However, as the fineness, alkali and C_3A content of the cement is lower than those specified for a probable DEF formation and the aggregates used for this mass concrete is mainly grantie & charnockite rock with low coefficient of thermal expansion possibility of DEF formation was ruled out. While the mass concrete of size less than 2.0 m height the core temperature did not rise above the permissible limit at any point of time and also dissipate the heat of hydration quickly. Hence additional precautionary measures are required for mass concrete involving placement for height more than 2.0 m to maintain the concrete core temperature within the specified limits. By adopting these temperature control plan & measures, mass concrete can be effectively utilized in mega projects to reduce the construction cycle time and to minimize the construction joints.

References

ACI 207.2R (2007) “Report on Thermal and Volume Change Effects on Cracking of Mass Concrete”, *American Concrete Institute*

IS 269.(2015) “Ordinary Portland cement Specificaiton”, *Bureau of Indian Standard*

IS 3812 (Part I).(2013) “Pulverized Fuel Ash- Part I : for use as pozzolana in Cement, Cement mortar and concrete”, *Bureau of Indian Standard*

IS 383.(2016)” Coarse and fine aggregate for concrete –Specficiaton”, *Bureau of Indian Standard*

BIS,9103.(1999) “Concrete admixtures –Specification”, *Bureau of Indian Standard*

Development of Ambient-cured Glass Fibre-based High Strength High Ductility Concrete

Subhrajit Sinha[1] and Piyali Sengupta[2]

[1] *Doctoral Student, Indian Institute of Technology (ISM) Dhanbad, India*
Email: 23DR0326@iitism.ac.in
[2] *Assistant Professor, Indian Institute of Technology (ISM) Dhanbad, India*
Email: piyali@iitism.ac.in

*Corresponding author

ABSTRACT

High Strength High Ductility Concrete (HSHDC) fulfils the high-performance requirements of civil infrastructures accommodating the latest trends in construction and design industry. The performance of HSHDC under extreme loading environment is applauded in the literature due to it imbibing the qualities of both High Strength Concrete and High Ductility Concrete. However steam curing conditions adopted by the previous researchers are extremely demanding in terms of the high energy consumption as well as field application. Therefore, the present research aims at development of an ambient-cured High Strength High Ductility Concrete (HSHDC) where low-cost glass fibre is used in place of the conventional polyethylene fibre to infuse bendability in concrete. The trial mix proportions for control mix of HSHDC are decided with water-cement ratio of 0.18, glass fiber of 1.8% of weight of cement, superplasticizer of 1.8% weight of cement. A wide variation of water-cement ratio, glass fiber content, super-plasticizer content is considered for trial mixes under water curing, ambient curing and steam curing conditions. The optimum design mix of HSHDC is determined based on the workability, compressive strength, splitting tensile strength and flexural strength test results of the trial mixes. Increase in fibre content beyond 4% of weight of cement makes a stiff mix with highly reduced workability without improvement in strength and ductility. Although steam curing is found best suited, the novel ambient-cured glass fiber-based HSHDC is able to achieve final compressive strength of 64.65 MPa, splitting tensile strength of 4.37 MPa and flexural strength of 12.85 MPa.

KEYWORDS*: High Strength, High Ductility, Durability, Glass Fibre, Ambient Curing*

1. Introduction

High strength high ductility concrete is a significant benefit to the building and design sectors because of its high-performance levels. High-performance concrete can be broadly divided into two groups based on its mechanical qualities: high compressive strength concrete and high tensile ductility concrete. Concrete with a compressive strength of 55 MPa or more is referred to as high compressive strength concrete, and it is utilised in strategically significant and tall buildings. Bendable concrete, also known as high ductility concrete, is a cementitious composite reinforced with randomly chosen short fibres that are usually polymer fibres. Concrete that combines the characteristics of both high strength and high ductility is known as high strength and high ductility concrete. Both of these categories are most useful in the structural field because one offers high strength safety margins and the other prevents catastrophic structural collapse by absorbing a significant amount of energy during extreme loading conditions, such as hurricanes, explosions, earthquakes, and projectile impacts. It is very effective whenever the failure is due to tension (Ranade *et al.*, 2013). Even though high strength high ductility concrete performs admirably, high energy demands are of high concern. Therefore, the primary objective of this research is to develop a sustainable ambient-cured high strength high ductility concrete using glass fibre based on workability, compressive strength, tensile strength and flexural strength.

2. Experimental Investigation

The tentative constituents of trial mixes of High Strength High Ductility Concrete (HSHDC) are decided as cement, sand, potable water, glass fibre and superplasticizer. The specific gravity of sand, cement, superplasticizer and glass fibre are determined so as to initiate the mix design. The trial mix proportions for control mix are decided with water cement ratio 0.18, glass fibre of 1.8% of weight of cement and superplasticizer of 1.8% weight of cement. With the above all proportions, three batches are prepared for three curing conditions and in each batch 15 cubes of size 70 mm x 70 mm x 70 mm, 9 beams of size 500 mm x 100 mm x 100 mm and 9 cylinders of size 300 mm x 150 mm are cast. The mix proportions for trial mixes 1-5 are kept as water cement ratio 0.18, superplasticizer of 1.8% weight of cement and glass fibre of 1-5% of weight of cement respectively. The workability and mechanical properties obtained from the experimental investigations are summarized below for Control Mix (CM) as well as Trial Mixes (TM) 1-5

3. Results And Discussions

The workability results in terms of slump values are presented in Figure 1 which indicates that increase in fibre content reduces the slump value affecting the workability of the mix. The 7 days and 28 days compressive strength test results of control mix and trial mixes 1-5 are presented in Figures 2-7.

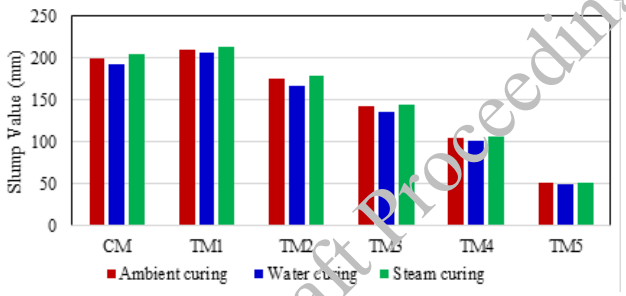

Figure 1. Slump values of Control Mix and Trial Mixes

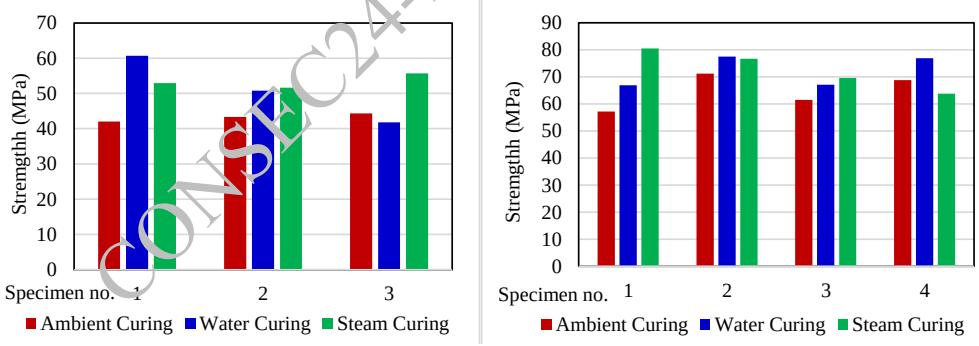

Figure 2. Compressive strength test results for control mix at 7 days and 28 days

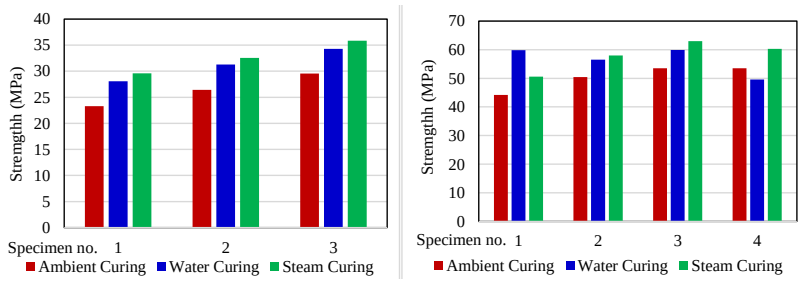

Figure 3. Compressive strength test result for trial mix 1 at 7 days and 28 days

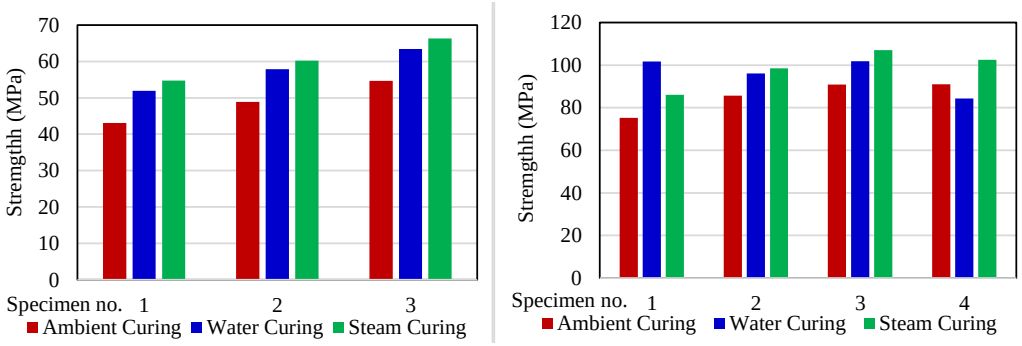

Figure 4. Compressive strength test result for trial mix 2 at 7 days and 28 days

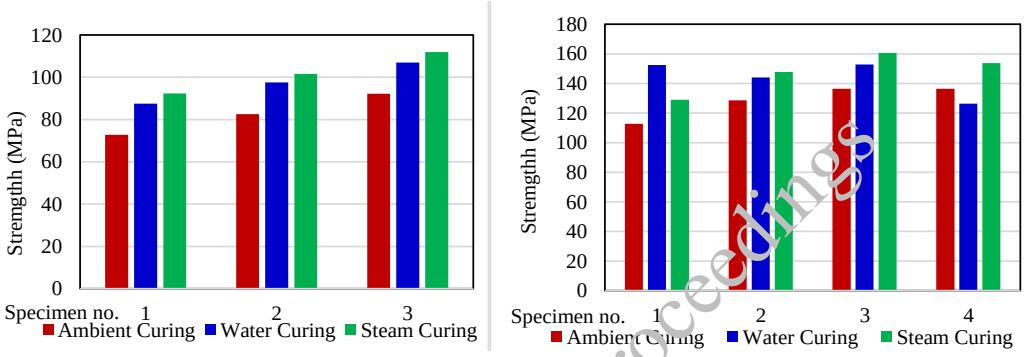

Figure 5. Compressive strength test result for trial mix 3 at 7 days and 28 days

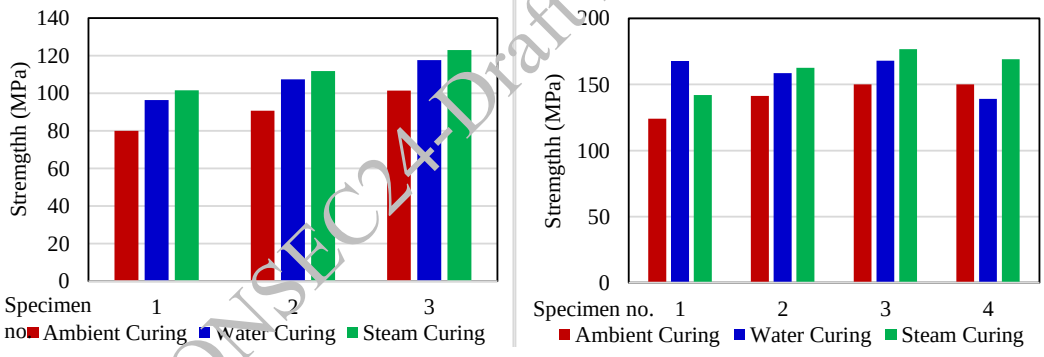

Figure 6. Compressive strength test result for trial mix 4 at 7 days and 28 days

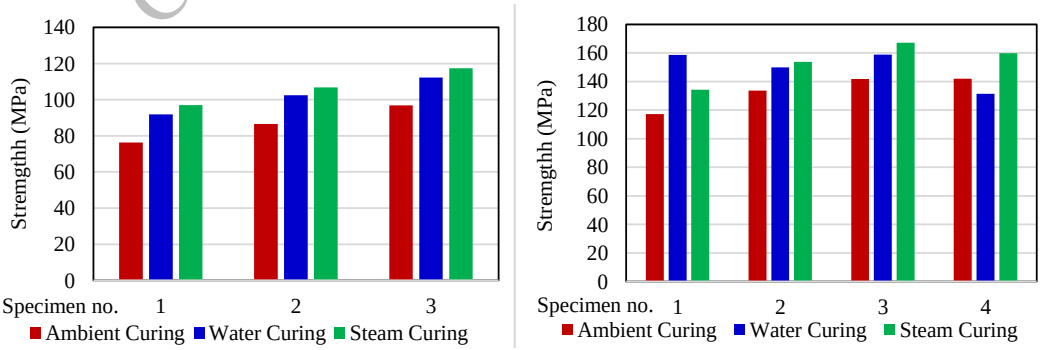

Figure 7. Compressive strength test result for trial mix 4 at 7 days and 28 days

The splitting tensile strength and flexural strength results of control mix and trial mixes 1-5 are summarized in Figure 8.

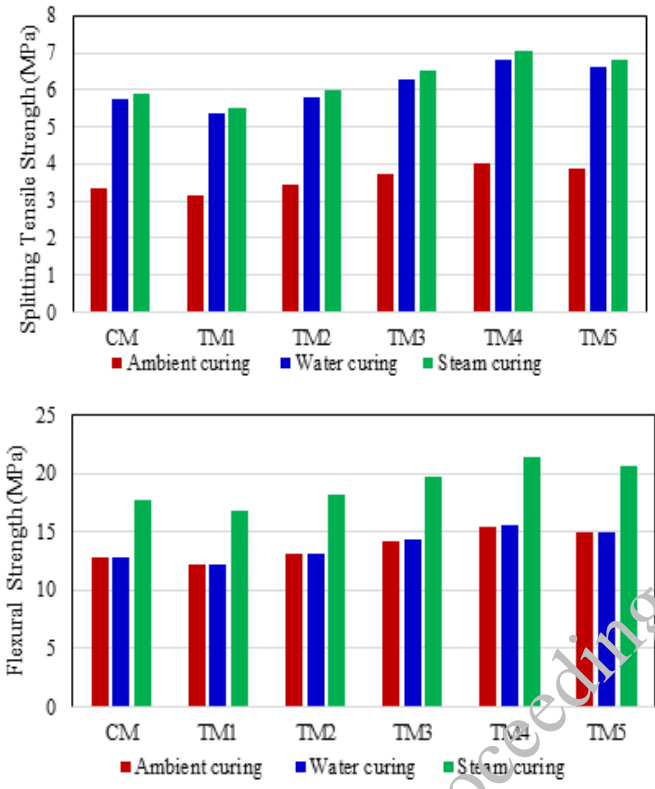

Figure 8. Splitting Tensile Strength and Flexural strength test results for all mix

4. Conclusions

72%, 85% and 89% of target compressive strength (60 MPa) were achieved in 7 days under ambient curing, water curing and steam curing respectively for glass fibre-based high-strength high ductile concrete. 64.65 MPa, 72.07 MPa and 72.64 MPa compressive strength were achieved in 28 days under ambient curing, water curing and steam curing respectively for glass fibre-based high-strength high ductile concrete. 3.37 MPa, 5.75 MPa and 5.91 MPa splitting tensile strength were achieved in 28 days under ambient curing, water curing and steam curing respectively for glass fibre-based high-strength high ductile concrete. 12.85 MPa, 12.88 MPa and 17.75 MPa flexural strength were achieved in 28 days under ambient curing, water curing and steam curing respectively for glass fibre-based high-strength high ductile concrete. Increase in fibre content upto 4% of weight of cement gives favourable results. However, increase in fibre content beyond that makes a stiff mix with highly reduced workability and slightly reduced strength and ductility. Steam curing is found best suited for ductility of glass fibre-based high-strength high ductile concrete. However, ambient curing is also able to reach satisfactory results for glass fibre-based high-strength high ductile concrete.

References

Choi, J.I., Lee, B.Y., Ranade, R., Li, V.C. and Lee, Y.(2016) 'Ultra-high-ductile behavior of a polyethylene fiber-reinforced alkali-activated slag-based composite', *Cement and Concrete Composites*, 70:153–158

Mohammed, B.H., Sherwani, A.F.H., Faraj, R.H., Qadir, H.H. and Younis, K.H. (2021) 'Mechanical properties and ductility behavior of ultra-high performance fiber reinforced concretes: Effect of low water-to-binder ratios and micro glass fibers', *Ain Shams Engineering Journal*, 12(2):1557–1567

Ranade, R., Li, V.C., Stults, M.D., Heard, W.F. and Rushing, T.S. (2013) 'Composite properties of high-Strength, high-Ductility concrete', *ACI Materials Journal*, 110(4): 413–422

Yuan, T.F., Lee, J.Y. and Yoon, Y.S. (2020) 'Enhancing the tensile capacity of no-slump high-strength high-ductility concrete', *Cement and Concrete Composites*, 106:103458

Advances in Numerical Modelling for 3D Concrete Printing

Rohan Kumar [1*], Prakash Nanthagopalan [2]

[1]*Indian Institute of Technology Bombay, Mumbai, India*
Email: 23d0283@iitb.ac.in
[2]*Indian Institute of Technology Bombay, Mumbai, India*
Email: prakashn@iitb.ac.in

*Corresponding author

ABSTRACT

3D concrete printing is revolutionizing the construction industry by enabling rapid prototyping and construction of complex structures with enhanced design flexibility and reduced labour requirements. Despite its promise, significant challenges remain, particularly in predicting and optimizing the stability and mechanical performance of printed structures. This paper presents a comprehensive overview of recent advances in numerical modelling techniques applied to the field of 3D concrete printing. The various simulation approaches including Finite Element Analysis (FEA), Computational Fluid Dynamics (CFD), and specialized software tools like ABAQUS, FLOW-3D®, and Grasshopper plugins have been utilized to address critical aspects from the early-age behaviour of the concrete mixtures to the structural integrity of printed elements under various loading conditions. Furthermore, parametric studies highlight the influence of printing parameters such as speed and nozzle height on the extrusion process, emphasizing the role of rheological models in predicting the deposition behaviour of concrete filaments. This paper aims to offer a review of scientific insights and practical tools for analyzing the performance of 3D concrete printing, focusing on both material and element aspects through numerical simulation.

KEYWORDS: *Finite Element Analysis (FEA), Computational Fluid Dynamics (CFD), Rheological models, Early-age behaviours, Failure mechanisms*

1. Introduction

3D concrete printing (3DCP) has emerged as a revolutionary technology in the construction industry, offering unprecedented possibilities in terms of design flexibility, reduced material waste, and accelerated project timelines. This innovative approach leverages additive manufacturing principles to construct intricate and customized concrete structures layer by layer, transforming traditional building methods and paving the way for new architectural forms. The successful implementation of 3DCP relies heavily on advanced numerical modelling techniques. These models play a critical role in predicting the behaviour of printed structures, optimizing process parameters, and ensuring structural integrity. Numerical simulations enable researchers and engineers to understand the complex interactions between material properties, environmental conditions, and printing parameters, ultimately guiding the development of more reliable and efficient 3D printing processes. This paper reviews the latest advancements in numerical modelling for 3D concrete printing, focusing on the methodologies employed, key findings, and potential future directions.

2. Numerical Modelling Techniques in 3DCP

The field of 3D concrete printing (3DCP) utilizes a variety of numerical modelling techniques to simulate and optimize the printing process, material behaviour, and structural performance. This section provides a detailed overview of the most prominent modelling techniques used in 3DCP, namely Finite Element Analysis (FEA), Finite Element Method (FEM), Particle Finite Element Method (PFEM), and Computational Fluid Dynamics (CFD). Table 1 shows the existing numerical simulations in 3DCP in literature.

2.1 Finite Element Analysis (FEA) and Finite Element Method (FEM)

FEA and FEM are fundamental techniques in numerical modelling, widely used for structural analysis and simulation in 3DCP. These methods discretize a structure into smaller, manageable elements, allowing for detailed analysis of complex geometries and material behaviours. FEA and FEM are employed to predict mechanical behaviour, such as stress, strain, and deformation of printed structures. For instance, Heever et al. (2021, 2022) used FEM to characterize the mechanical properties and structural integrity of fiberreinforced polymer concrete (FRPC) beams and cylinders, leveraging advanced constitutive models like the Anisotropic Rankine-Hill (RH) continuum model. These methods can incorporate various material models, such as von Mises, Mohr-Coulomb, Drucker-Prager, and Concrete Damage Plasticity models, to accurately simulate different failure modes and material responses. Dong et al. (2024) utilized these models to investigate material behaviour under elastic buckling and plastic collapse conditions. FEA and FEM provide high accuracy in predicting structural responses and allow for detailed modelling of complex geometries and material heterogeneities. They are versatile and can be applied to a wide range of problems in 3DCP. The main challenge lies in the computational intensity required for high-resolution simulations. Additionally, accurate material property data and model calibration are essential for reliable predictions.

2.2 Particle Finite Element Method (PFEM)

PFEM is a relatively new and innovative technique that combines the strengths of particle methods and finite element methods to simulate the behaviour of complex materials and interactions during the printing process. PFEM is particularly effective in modelling the deposition and interaction of concrete filaments during 3D printing. Rizzieri et al. (2023a, 2023b) utilized PFEM to study single-layer and multi-layer filament deposition, focusing on rheological behaviour and thixotropy. PFEM employs a Lagrangian framework where particles represent the material, and these particles can interact and merge, simulating the flow and deposition of concrete. This method is capable of handling large deformations and complex boundary interactions. PFEM excels in simulating free surface flows and material interfaces, making it ideal for capturing the layer-by-layer deposition process in 3DCP. It provides detailed insights into the rheological properties and interaction mechanisms of printed layers. PFEM can be computationally expensive, particularly for large-scale problems or high-resolution simulations. The method also requires careful calibration of rheological models to accurately represent the material behaviour.

2.3 Computational Fluid Dynamics (CFD)

CFD is used to model the flow characteristics of concrete during the extrusion process in 3DCP. This technique focuses on the fluid-like behaviour of fresh concrete as it is deposited layer by layer. CFD is employed to analyze parameters such as pressure, velocity, and constitutive stress within the concrete. Comminal et al. (2020) and Mollah et al. (2023) used CFD to study the influence of printing speed, nozzle height, and reinforcement integration on the quality of extruded filaments. CFD simulations often use generalized Newtonian fluid models, elasto-visco-plastic fluid models, and Bingham models to represent the rheological behaviour of fresh concrete. These models help predict how the concrete will flow, settle, and solidify during printing. CFD provides detailed visualization and analysis of fluid flow, enabling the optimization of extrusion parameters and improving the quality and consistency of printed layers. It is particularly useful for understanding the effects of process parameters on material behaviour. Accurate CFD simulations require detailed rheological data and can be computationally demanding. Additionally, the transition from fluid to solid state in concrete poses modelling challenges that require sophisticated constitutive models.

3. Key Findings from Recent Studies

3.1 Material and Structural Analysis

Material characterization and structural analysis are crucial for ensuring the performance and durability of 3D printed structures. Heever et al. (2021) and Wang et al. (2023a) conducted detailed analyses of the mechanical properties of printed elements. They utilized advanced constitutive models to predict elastic and inelastic behaviour, strength parameters, and failure mechanisms. For example, Heever et al. (2021) used the RH continuum model to simulate the anisotropic behaviour of fiber-reinforced polymer concrete (FRPC) beams and cylinders. Andersen et al. (2024) investigated the early-age behaviour of concrete using

an incremental constitutive equation with a Maxwell branch, providing insights into the height of collapse predictions. Dong et al. (2024) examined material models and failure identification for different structural forms, employing models such as von Mises, Mohr-Coulomb, Drucker-Prager, and Concrete Damage Plasticity.

3.2 Rheology and Process Parameters

The rheological properties of concrete play a critical role in determining the quality and stability of the printed structure. Studies by Comminal et al. (2020) and Rizzieri et al. (2023a, 2023b) focused on the influence of printing speed, nozzle height, and material properties on filament behaviour. These works employed generalized Newtonian fluid models, elasto-visco-plastic fluid models, and thixotropy models to simulate the effects of various process parameters on the flow and deposition of concrete.

3.3 Optimization and Buildability

Optimizing the printing process to enhance buildability and structural performance is a key focus of recent research. Breseghello et al. (2023) used multi-objective evolutionary optimization to minimize surface area and principal stresses, employing the Octopus plugin within Grasshopper and the FE simulation engine of Karamba3D. Zhu et al. (2023) applied stochastic analysis and Monte Carlo simulations to model buildability, considering the stochastic nature of the printing process and its impact on deformation shape and failure time.

3.4 Innovative Applications and Models

Recent research has explored innovative applications and modelling techniques to push the boundaries of 3D concrete printing. These include:

- **Voxel-based Modelling:** Vantyghem et al. (2021) utilized voxel-based modelling to simulate complex geometries, demonstrating the potential for intricate design and customization. This approach allows for the detailed simulation of the printing process at a granular level, enabling the optimization of layer deposition and structural integrity.
- **Reinforcement Integration:** Mollah et al. (2023) investigated the integration of reinforcement bars into 3D printed structures using CFD, highlighting methods to enhance structural performance. This study focused on the cross-section shape and air voids, utilizing FLOW-3D® POST to simulate the reinforcement integration process.
- **Behaviour Under Various Conditions:** Research by Wang et al. (2024a) explored air and underwater printing with sulfoaluminate cement (SAC), revealing insights into rheology, permeability, and interface bonding.

Breseghello et al. (2023) employed a shape-driven optimization approach using linear Finite Element Analysis (FEA) for the initial design of beam shapes. The optimization process, conducted with Grasshopper's Octopus plugin, focused on minimizing surface area, principal stresses, and vertical displacement to achieve optimal flexural resistance. Additionally, the design incorporated Principal Stress Lines (PSL) to guide the anisotropic orientation of printed filaments, enhancing compressive resistance and bonding capacity. The study achieved a 50% improvement in the strength-to-weight ratio of the beams compared to the baseline design. Stress concentrations near the support areas were significantly reduced, leading to improved structural efficiency. The optimized beams also demonstrated a 30% reduction in material usage while maintaining equivalent load-bearing capacity. Chang et al. (2022) used a lattice model with Timoshenko beam elements to simulate elastic buckling in 3D concrete printing. The model accounted for shear deformation and random placement of lattice nodes, connected via Delaunay triangulation. The study also integrated a failure criterion based on gravity-induced stress to predict failure, correlating printing offset with material instability and buckling. The lattice model accurately predicted critical printing heights with a relative difference of less than 12% compared to experimental results. Specifically, the model predicted a critical height of 600 mm, while experimental data indicated a failure height of 680 mm. This highlighted the model's effectiveness in simulating buckling failures in 3D concrete printing. Comminal et al. (2020) compared the performance of Generalized Newtonian Fluid (GNF) and Elasto-visco-plastic (EVP) fluid models in simulating the behavior of cement mortar during 3D printing. The study also investigated the influence of printing and extrusion velocities, along with nozzle height, on the cross-sectional geometry of printed layers. The EVP model provided a more accurate prediction of cross-sectional

shapes, with a 5% deviation from experimental results, compared to a 15% deviation for the GNF model. However, the EVP model required computational times up to 10 times longer than the GNF model. The study also found that an extrusion pressure of 300 kPa was critical for maintaining structural stability during printing. Dong et al. (2024) conducted a comparative analysis of different constitutive models, including von Mises, Mohr-Coulomb, and Concrete Damage Plasticity (CDP), to determine the most accurate for predicting the mechanical behavior of fresh concrete in 3D printing. The study also examined the impact of boundary conditions, specifically fixed and frictional, on the failure patterns of printed layers. The CDP model provided predictions with a deviation of less than 8% from experimental failure data, compared to 12% for the von Mises model and 10% for the Mohr-Coulomb model. The study found that under fixed boundary conditions, the critical failure height was 550 mm, while frictional conditions yielded a critical height of 570 mm. Imran et al. (2023) employed the Voxel Print Plugin to convert the designed geometry into a voxel mesh for buildability analysis. The study also conducted a sensitivity analysis to explore the effects of design height, printing speed, and layer width on the buildability of 3D-printed concrete structures. The research revealed that a wider layer width of 50 mm and a lower printing speed of 20 mm/s significantly improved buildability, resulting in a 15% increase in stability compared to narrower layers and higher speeds. Numerical simulations showed a 95% correlation with experimental results, confirming the model's accuracy. Mollah et al. (2023) used Computational Fluid Dynamics (CFD) modeling to study the effect of rebar diameter, nozzle-rebar distance, and geometric ratios on air void formation and the bonding between reinforcement and concrete in 3D printing. The study found that reducing the nozzle-rebar distance to 10 mm and optimizing geometric ratios reduced air voids by 20%. However, this also led to the formation of ridges with a height of 1-2 mm on the printed surface. Toolpath adjustments were necessary to eliminate these voids, improving the overall bond strength by 25%. Reinold et al. (2020) explored the influence of process parameters, such as extrusion forces and nozzle width, on layer shape and structural stability in 3D concrete printing. The study used the Particle Finite Element Method (PFEM) to simulate the extrusion process. The results indicated that reducing nozzle width from 10 mm to 5 mm increased stress concentrations by 40%, significantly raising the risk of damage to the printed structure. The study emphasized the need for precise control over extrusion forces, which were measured at approximately 200 N, to ensure structural integrity and bond strength. Rizzieri et al. (2023a) enhanced the PFEM framework by incorporating a contact algorithm and mesh de-refinement technique to improve mass conservation and reduce computational costs during the simulation of 3D concrete printing processes. The enhanced PFEM framework improved simulation accuracy by 15% while reducing computational resource usage by 25%. This advancement made it more feasible to perform large-scale simulations of the extrusion and deposition processes in 3D concrete printing, maintaining a balance between accuracy and efficiency. Van et al. (2022) conducted Finite Element (FE) simulations using smaller element segments per layer and time steps to model the aging of printing material and its impact on the buildability of thin-walled structures in 3D concrete printing. The study found that reducing the printing speed to 15 mm/s and increasing the extrusion width to 40 mm significantly improved buildability, with a 20% increase in structural stability observed in the simulations. The numerical model demonstrated a 90% match with experimental outcomes, confirming its reliability. Wang et al. (2023a) developed a comprehensive damage-rheology model that integrated creep and rheological behaviors to predict the early-age behavior of 3D-printed concrete. The model incorporated damage-plasticity and thixotropic models to simulate the deformation responses of printed structures. The model accurately predicted deformation responses with less than a 10% deviation from experimental data, highlighting the significant impact of creep on the stability of hollow cylinder structures. The study found that creep contributed to a 15% reduction in stability over a 24-hour period, emphasizing the need to consider time-dependent behaviors in buildability predictions. Wang et al. (2023b) performed numerical simulations to analyze different inclined printing angles, material properties, and printing parameters, aiming to optimize the early-age performance of 3D-printed concrete structures. The model effectively predicted the stability of layers across different inclined printing angles, with an optimal angle of 30 degrees identified for maximum stability. The study found that adjusting material properties, such as increasing the yield stress by 20%, further enhanced the buildability of inclined structures. These results guided optimization efforts, ensuring better performance of printed structures. Zhu et al. (2023) applied peridynamic (PD) theory and stochastic process modeling to evaluate the buildability of 3D-printed concrete. Peridynamic theory, which discretizes the computational domain into particles connected by micro bonds, was used to simulate the interactions between particles within a specified horizon. The study incorporated stochastic process modeling to capture the inherent variability in 3D printing. Monte Carlo

simulation was employed to generate a large number of random samples, which were used for statistical analysis of the buildability process. The simulation results were compared with experimental data to validate the accuracy of the PD model. The PD model's radial deformation predictions (e.g., 9.8 mm vs. 10.3 mm experimentally for 23 layers) showed close agreement with experimental results, with a COV ranging from 17% to 21%. The model accurately predicted maximum radial deformation and z-position, with minimal deviations (e.g., 12.9 mm predicted vs. 12.7 mm observed for 29 layers). Both PD simulation and experiments identified 29 failure layers, with deviations in radial deformation up to 18%, confirming the model's reliability.

4. Validation and Accuracy

The validation and accuracy of numerical models are critical aspects of 3D concrete printing research. These factors ensure that the models reliably predict the behaviour of printed structures, optimize process parameters, and provide insights that are practically applicable in real-world scenarios. Andersen et al. (2024) focused on early-age behaviour using ABAQUS, achieving a modest 42% accuracy in predicting collapse height. Conversely, Imran et al. (2023) employed Voxel Print and ABAQUS for buildability analysis, reporting an impressive 93.7% accuracy in predicting design height and process parameters. Similarly, Heever et al. (2022) investigated numerical modelling strategies for reinforced 3D concrete elements using DIANA FEA, achieving validation accuracies ranging from 96% to 98%. This study leveraged continuum models, interface-based models, and 2D plane stress models, showcasing robust approaches that contribute significantly to enhancing the reliability and performance of printed structures.
Achieving high validation and accuracy in numerical models for 3DCP presents several challenges. Concrete is a heterogeneous material with properties that can vary significantly based on mix composition, curing conditions, and environmental factors. Capturing this variability in models is complex and requires extensive experimental data. The interactions between fresh concrete and the printing environment, including the effects of layer-by-layer deposition and the influence of process parameters, are complex and difficult to model accurately. Differences between small-scale laboratory experiments and full-scale structures can lead to discrepancies in model predictions. Scaling effects need to be carefully considered and accounted for in the models. The dynamic nature of the 3DCP process, including the ongoing changes in material properties during printing and curing, adds to the complexity of accurate modelling and validation.

5. Conclusions

The synergy between advanced numerical models and experimental validation is key to advancing 3DCP technology. By integrating sophisticated numerical models with experimental validation, researchers are pushing the boundaries of possibilities in 3D concrete printing. The insights gained from these studies contribute significantly to the theoretical understanding of the printing process, enhancing our knowledge of material behaviour, structural integrity, and process optimization. These advancements have practical implications for improving the quality, efficiency, and performance of 3D printed structures. This continuous improvement in numerical modelling will drive innovation, leading to more robust and reliable 3D printing processes that can meet the demands of modern construction.

Table 1. Numerical Simulations in 3DCP

Author	Work	Software	Concrete Type	Test Specimen	Test
Andersen et al., 2024	Early Age Behavior	ABAQUS	OPC+CAC	Prismatic elements	DIC
Breseghello et al., 2023	Reinforced 3D concrete printed beams	FEA	OPC+PP fibre	Cylinders	DIC, Pullout test, Flexural
Chang et al., 2022	Elastic buckling	FEM	NA	Free wall structure,	Computational uniaxial compression test
Comminal et al., 2020	Parametric study of the influence of the printing speed and the nozzle height	FLOW-3D® (CFD)	White cement	Extruded filament	Rotational and oscillatory test
Dong et al., 2024	Material models, boundary conditions and failure identification	FE		Ring, wall	Elastic buckling, plastic collapse
Heever et al., 2021	Mechanical characterisation for numerical simulation	FE	FRPC	Beam, cylinder	CMOD, MOE, CS, Direct Tensile
Heever et al., 2022	Numerical modelling strategies for reinforced 3D concrete printed elements	DIANA FEA	FRPC	Beam	CMOD
Imran et al., 2023	Buildability analysis on squared profile structure	Voxel Print" plugin, ABAQUS	Geopolymer	Square profile	
Mollah et al., 2023	Reinforcement bar integration in 3D concrete printing	CFD, FLOW-3D® POST	White cement	Filament	
Nedjar, 2021	Geometrically nonlinear incremental formulation	FEM		Wall	
Ooms et al.,2021	Complex geometries	FE SIMULIA Abaqus/CAE		Wall, cylinder, complex multi branch structure	
Reinold et al.,2020	Extrusion process simulation and layer shape prediction	FEM	OPC	Filament	Rheology
Rizzieri et al., 2023a	Extrusion and layer deposition processes	PFEM		Filament	
Rizzieri et al., 2023b	A 2D numerical model of 3D concrete printing including thixotropy	PFEM		Filament	Rheology
Van et al., 2022	Thin-walled structures	FE	Cement mortar,	Cylinder and wall	Direct shear test, compression test
Wang et al., 2023a	Damage-rheology model: Buildability	Damage-plasticity theory and the Burgers model		Straight wall, Hollow cylinder	
Wang et al., 2023b	Inclined 3D concrete printing	VoxelPrint, Abaqus	OPC	Cylinder (Inclined ar	Penetration resistance, uniaxial compression tests
Wang et al., 2024a	Air and under water printing		Sulfoaluminate cement (SAC)		Interface bonding test, Cone penetration test
Wang et al., 2024b	Interfacial constitutive model		OPC		Split tensile test, Porosity, Shear stress
Zhu et al., 2023	Buildability modeling: Stochastic analysis	Stochastic analysis, Monte Carlo simulation		Cylinder, dome, Frustum	

Author	Output	Model
Andersen et al., 2024	Prediction of height of collapse	Incremental constitutive equation, Maxwell branch
Breseghello et al., 2023	Minimise the surface area A, the principal stresses S on the beam and the vertical displacement	
Chang et al., 2022	Displacement magnitude	
Comminal et al., 2020	Pressure, velocity and constitutive stress within concrete	Generalized Newtonian fluid model, Elasto-visco-plastic fluid model
Dong et al., 2024	Layer height	von Mises, Mohr-Coulomb model, Drucker-Prager model, Concrete Damage Plasticity
Heever et al., 2021	Elastic and Strength parameter	Anisotropic Rankine-Hill (RH) continuum model
Heever et al., 2022	Elastic, Inelastic and strength parameters	Continuum model (CM), interface-based model (IFM), 2D Plane stress (2D) model
Imran et al., 2023	Effect of design height and process parameters	
Mollah et al., 2023	Cross section shape and air void	
Nedjar, 2021	Deformed configurations and displacement field	Compressible neoHooke-like model, Saint-enant-like model
Ooms et al.,2021	Deformations, asymmetric deformations, radial deformations, No of layers	
Reinold et al.,2020	Print cross section, extrusion force, material yielding	Bingham model, Particle finite element method
Rizzieri et al., 2023a	Single-layer filament deposition for different printing scenarios, Multi-layer filament deposition	Momentum balance andmass conservation, Rheological law, Equation of state
Rizzieri et al., 2023b	Thixotrophy, Static Yield Stress	Space and time discretization
Van et al., 2022	Deformation, buckling	
Wang et al., 2023a	Compressive damage and lateral deformation contours, Concrete age	Creep modeling, Thixotropic modeling
Wang et al., 2023b	Plastic yield and elastic buckling prediction	
Wang et al., 2024a	Interlayer adhesion, permeability coefficient	
Wang et al., 2024b	Interfacial tensile properties, Interfacial shear properties, Interfacial thickness characterization	
Zhu et al., 2023	Deformation shape, failure time	Peridynamic theory, Process-dependent stochastic method

References

An, D., Zhang, Y. X. and Yang, R. (Chunhui). (2024) "Numerical modelling of 3D concrete printing: material models, boundary conditions and failure identification", *Engineering Structures*, 299:117104

Andersen, S., da Silva, W. R. L., Paegle, I. and Nielsen, J. H. (2020) "Numerical Model Describing the Early Age Behaviour of 3D Printed Concrete – Work in Progress", *RILEM Bookseries*, 28:175–184

Breseghello, L., Hajikarimian, H., Jørgensen, H. B. and Naboni, R. (2023) "3DLightBeam+. Design, simulation, and testing of carbon-efficient reinforced 3D concrete printed beams", *Engineering Structures*, 292:116511

Chang, Z., Zhang, H., Liang, M., Schlangen, E. and Šavija, B. (2022). "Numerical simulation of elastic buckling in 3D concrete printing using the lattice model with geometric nonlinearity", *Automation in Construction*, 142:104485

Comminal, R., Leal da Silva, W. R., Andersen, T. J., Stang, H. and Spangenberg, J. (2020). "Modelling of 3D concrete printing based on computational fluid dynamics", *Cement and Concrete Research*, 138:106256

Imran, R., Al Rashid, A., Khan, S. A., Ilcan, H., Sahin, O., Sahmaran, M. and Koç, M. (2023) "Buildability analysis on squared profile structure in 3D concrete printing (3DCP) ", *European Journal of Materials*, 3(1):2276443

Mollah, M. T., Comminal, R., Leal da Silva, W. R., Šeta, B. and Spangenberg, J. (2023) "Computational fluid dynamics modelling and experimental analysis of reinforcement bar integration in 3D concrete printing",*Cement and Concrete Research*, 173:107263

Nedjar, B. (2021). "On a geometrically nonlinear incremental formulation for the modelling of 3D concrete printing", *Mechanics Research Communications*, 116:103748

Nguyen-Van, V., Nguyen-Xuan, H., Panda, B. and Tran, P. (2022). "3D concrete printing modelling of thin-walled structures", *Structures*, 39: 496–511

Ooms, T., Vantyghem, G., Van Coile, R. and De Corte, W. (2021) "A parametric modelling strategy for the numerical simulation of 3D concrete printing with complex geometries", *Additive Manufacturing*, 38:101743

Reinold, J., Nerella, V. N., Mechtcherine, V., & Meschke, G. (2022) "Extrusion process simulation and layer shape prediction during 3D-concrete-printing using the Particle Finite Element Method", A*utomation in Construction*, 136: 104173

Rizzieri, G., Cremonesi, M., & Ferrara, L. (2023) "A 2D numerical model of 3D concrete printing including thixotropy",*Materials Today: Proceedings*,

Rizzieri, G., Ferrara, L. and Cremonesi, M. (2023) "Numerical simulation of the extrusion and layer deposition processes in 3D concrete printing with the Particle Finite Element Method", *Computational Mechanics*,73(2):277-295

van den Heever, M., Bester, F., Kruger, J. and van Zijl, G. (2021). "Mechanical characterisation for numerical simulation of extrusion-based 3D concrete printing", *Journal of Building Engineering*, 44: 102944

van den Heever, M., Bester, F., Kruger, J. and van Zijl, G. (2022). "Numerical modelling strategies for reinforced 3D concrete printed elements", *Additive Manufacturing*, 50:102569

Vantyghem, G., Ooms, T. and De Corte, W. (2020). "Fem modelling techniques for simulation of 3d concrete printing", *Fib Symposium*, 964–972.

Vantyghem, G., Ooms, T. and De Corte, W. (2021) "VoxelPrint: A Grasshopper plug-in for voxel-based numerical simulation of concrete printing", *Automation in Construction*, 122: 103469

Wang, L., Wang, F., Li, R. and Wang, Q. (2024) "Interfacial constitutive model of 3D printed fiber reinforced concrete composites and its experimental validation", *Case Studies in Construction Materials*, 20: e02807

Wang, L., Ye, K., Wan, Q., Li, Z. and Ma, G. (2023)"Inclined 3D concrete printing: Build-up prediction and early-age performance optimization", *Additive Manufacturing*, 71:103595

Wang, Q., Ren, X. and Li, J. (2023) "Damage-rheology model for predicting 3D printed concrete buildability", *Automation in Construction*, 155:105037

Wang, Y., Qiu, L. chao, Chen, S. gui and Liu, Y. (2024). "3D concrete printing in air and under water: a comparative study on the buildability and interlayer adhesion", *Construction and Building Materials*, 411:134403

Zhu, J., Ren, X. and Cervera, M. (2023) "Buildability modelling of 3D-printed concrete including printing deviation: A stochastic analysis", *Construction and Building Materials*, 403:133076

Influence of Mixing Techniques on the Dispersion of Chopped Carbon Fibres in Concrete

N. Nagula[1*], N. Thammishetti[2], and S. S. Prakash[3]

[1] Research Assistant, Indian Institute of Technology Hyderabad, Hyderabad, India
Email: ce23mtech12005@iith.ac.in
[2] Postdoctoral Fellow, Indian Institute of Technology Hyderabad, Hyderabad, India
Email: ce16resch11005@iith.ac.in
[3] Professor, Indian Institute of Technology Hyderabad, Hyderabad, India
Email: suriyap@ce.iith.ac.in

*Corresponding author

ABSTRACT

Carbon fibres are being widely used in various applications due to their superior mechanical, lightweight and electrical conductivity properties. Adding carbon fibres to concrete has been shown to enhance its mechanical and electrical properties. However, the higher cost of chopped carbon fibres has made them less popular in the construction industry. As more industries have started using carbon fibre composites, people are finding ways to recycle them into cheaper recycled carbon fibres. These recycled fibres have the potential to improve concrete performance at a reduced cost while also addressing environmental concerns by promoting material reuse and reducing carbon waste. The challenges with the use of chopped carbon fibres lie in their dispersion within the concrete matrix. Achieving good dispersion of chopped carbon fibres within the concrete matrix is essential for optimising concrete properties. This study explores two methods of dispersing carbon fibres, (a) dry mix and (b) wet mix. The dry mix method involves direct fibre addition before water addition in concrete. In the wet mix, the fibres are dispersed in water with the help of a dispersion agent and ultrasonicator. Additionally, the fibres are subjected to 500°C for 5 hours to remove the sizing on the fibres to improve their dispersion. Compressive and fracture tests are conducted to evaluate the mechanical properties of chopped carbon fibre-reinforced concrete. Results show that concrete containing heated fibres using the dry-mix technique outperforms other mixes, demonstrating a 13% increase in compressive strength and a 17.8% increase in flexural strength.

KEYWORDS*: Carbon fibres, Recycling, Dispersion, Sizing, Chopped carbon fibre reinforced concrete*

1. Introduction

Carbon fibre-reinforced cement concrete offers promising solutions in engineering applications due to its exceptional mechanical properties and durability. The chopped carbon fibres (CCFs) are hydrophobic and have high aspect ratios. Hence CCFs have a high tendency to agglomerate. Achieving uniform dispersion of carbon fibres within the cement matrix is crucial for optimising the performance of CFRC. The most widely employed ways to improve the dispersion are the use of pre-treated fibres, mechanical agitation and dispersion agents (Chung (2012)). Cellulose-based dispersion agents, such as hydroxyethyl cellulose (HEC), carboxymethyl cellulose (CMC), and methylcellulose (MC), enhance the hydrophilicity, reduce surface tension, and promote uniform dispersion of carbon fibres within the cement matrix (Chuang et al. (2017); Zhu, Zhou, and Gou (2021)). The mixing technique also significantly affects the properties of CFRC. Chuang et al. (2018) observed an increase in dispersion and compressive strength with the use of ultrasonication and dispersion agents in the mixing process. Gao et al. (2017) study shows that adding fibres before the cementitious material led to better dispersion and a lower possibility of carbon fibre bundling. Increasing the volume fraction of carbon fibres enhances mechanical properties such as tensile and flexural strength, but can affect workability and compaction (Akkaya, Shah, and Ankenman (2001); Chung (2012); Zhu, Zhou, and Gou (2021)). Studies indicate compressive strength declines beyond a fibre addition of

0.6% of binder weight due to fibre clustering and decreased workability (Chuang et al. (2017); Zhenjun Wang et al. (2014)). During manufacturing, carbon fibres undergo a process known as sizing, where they are coated with a protective layer to safeguard the filaments during processing. Heating the fibres to temperatures between 500°C and 600°C removes this sizing, enhancing their dispersion and bonding with the cement matrix (Ren et al. (2022); Pozegic et al. (2020)).

2. Experimental program

2.1 Raw materials

OPC 53 grade cement, Class F fly ash, and river sand are used for the concrete mix. MasterEase 3709 is used as the superplasticiser to enhance workability. Carboxymethyl Cellulose (CMC) is used as the dispersion agent. Chopped carbon fibres (CCFs) from Carbiso CT are used for reinforcement. Table 1 outlines the properties of the CCFs.

Table 1. Chopped carbon fibre properties

Fibre properties	Values
Fibre diameter	5 µm
Fibre density	1800 kg/m^3
Fibre length	6 mm
Sizing content	4%
Tensile strength	5000 MPa
Tensile modulus	262-290 MPa
Shear strength	80 MPa

Table 2. Mix design of CFRC

Ingredients	Quantity (kg/cum)
Cement (OPC 53 grade)	370
Flyash	100
Fine aggregate	758
20 mm	639
12.5 mm	465
Water	166
CCFS	0.5 (% wt. of binder) ~ [0.1% by vol. of concrete]
CMC	(% wt. of binder)

2.2 Mix design for carbon fibre reinforced concrete (CFRC)

The mix design for the M30 grade of concrete used for CFRC is given in Table 3. The fibre content of 0.5% by weight of the binder and CMC content of 0.4% by weight of the binder is adopted based on the results from the previous studies (Chuang et al. (2017); Chuang Wang et al. (2008); Chen and Chung (1991)).

2.3 Mixing techniques

Two mixing methods were used for preparing CFRC i.e., (a) dry mix and (b) wet mix.

2.3.1 Dry mix

In the dry mix technique, carbon fibres are added to the cement and sand blend and mixed for 5 minutes to ensure even dispersion. Coarse aggregate, water, and admixtures are added sequentially, followed by an additional 5 minutes of mixing.

2.3.2 Wet mix

In the wet mix type of technique, the carbon fibres were dispersed in 80% of the water required for casting mixed with CMC and subjected to ultrasonication. Later, the fibre solution was introduced to the dry mix comprising cement, sand, and coarse aggregate. The remaining 20% of water and admixture was added to the concrete blend and mixed for 5 minutes.

2.4 Test matrix

The test matrix for CFRC is designed to evaluate the effects of different mixing techniques and fibre heating on the mechanical properties of CFRC. The test matrix for CFRC is presented in Table 3.

3. Experimental results of CFRC

3.1 Workability of CFRC

The slump cone test results of different mixes are presented in Fig 1. Adding CCFs to the concrete reduced the workability of the concrete. The dry mix that has heated fibres (DH) displayed better dispersion, resulting in lower workability compared to the non-heated dry mix (DNH). The wet mix had a higher viscosity due to CMC, leading to reduced workability. Additionally, incorporating fibres further reduced the workability of the wet mix. Thus, despite having a higher water-to-cement ratio and superplasticiser content, the wet mix exhibits lower workability compared to the dry mix.

Table 3. Test matrix for CFRC

Specimen ID	Mixing technique	Type of fibres	Carbon fibres (% by wt of binder)	CMC (% by wt of binder)	W/C	SP (%)
Control	-	-	-	-	0.4	0.5
DNH	D	NH	0.5	-	0.4	0.5
DH	D	H	0.5	-	0.4	0.5
WNH	W	NH	0.5	0.4	0.45	0.7
WH	W	H	0.5	0.4	0.45	1
CMC	-	-	-	0.4	0.45	0.7

*D – Dry mix; *W – Wet mix; *NH – Non-heated fibres; *H – Heated fibres; *SP – Superplasticiser

3.2 Compressive test results

The cubes of 150 × 150 × 150 mm and cylinders of 150 mm diameter and 300 mm height are cast and tested in compression after 28 days of water curing. The test results are shown in Fig 2. The DH mix exhibited a 13.0% higher cube compressive strength and 10.2% higher cylinder compressive strength than the control mix. The remaining mixes exhibited lower compressive strength compared to the control mix. The increase in compressive strength of the DH mix can be attributed to the heating process, which removes the sizing on the fibres and allows for better dispersion. The wet mixes performed less effectively than the dry mixes. The observed reduction in the efficiency can be attributed to the formation of minute air bubbles when the CCFs are added to water in the wet mix technique. The presence of air bubbles can result in higher air voids in the concrete mix and ultimately reduce compressive strength. Additionally, the high w/c ratio and superplasticiser content in the wet mix and CMC mixes contribute to the reduction in the strength.

3.3 Fracture test results

The prisms of size 100 × 100 × 500 mm are tested in the 3-point bending test setup as shown in Fig 3. The 3-point bending test results are shown in Fig 4. The DH mix exhibited a 17.7% improvement in flexural strength compared to the control mix. Other mixes performed similarly to the control mix, despite having much lower compressive strength than the control mix. However, the CMC mix performed poorly due to high void content and lack of fibres. The WH mix showed significantly lower strength than the DH mix due to its poor workability, which made mixing and vibration difficult despite a higher water-to-cement ratio and superplasticiser content.

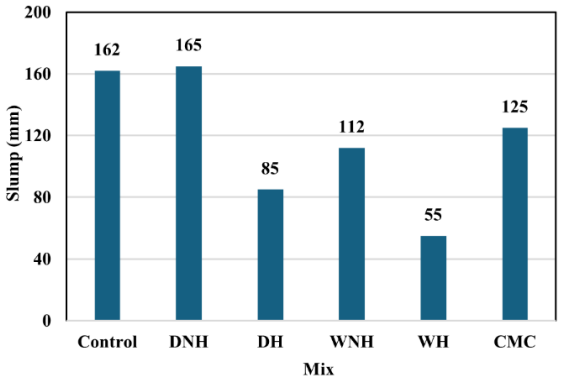

Figure 1. Slump cone test results

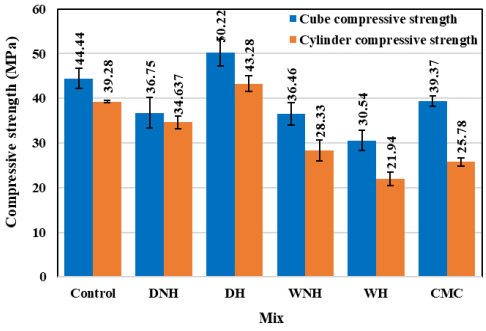

Figure 2. Compressive strength of different mixes

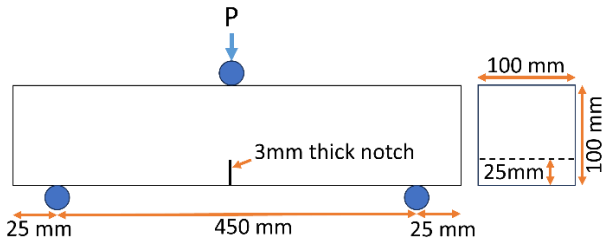

Figure 3. Schematic diagram of the fracture Test setup

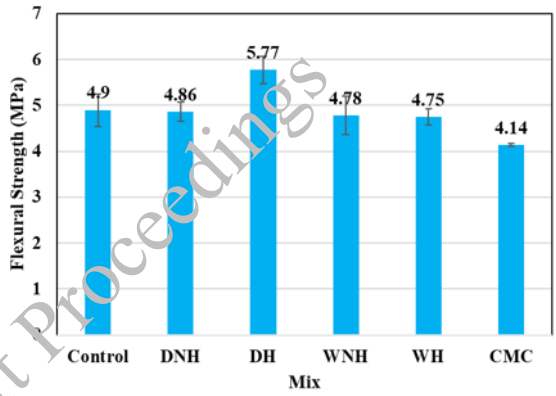

Figure 4. Flexural strength of different mixes

4. Conclusions

Based on the current study of incorporating 0.5% CCFs in the concrete mixes prepared using two different mixing techniques, the following conclusions are drawn:

- The dry mix with heated fibres in concrete demonstrated a 13.0% increase in cube compressive strength, a 10.2% increase in cylinder compressive strength and a 17.7% increase in flexural strength compared to the control mix.
- The improved performance of the heated fibres is attributed to superior dispersion and bonding of fibres with the concrete, resulting from the absence of sizing.
- In the wet mix, some air bubbles were observed adhering to the surface of individual fibres during preparation. This increased the number of air voids in the concrete mix, significantly reducing workability and resulting in poorer performance compared to the other mixes.

References

Akkaya, Y., Shah, S.P. and Ankenman, B. (2001) "Effect of Fiber Dispersion on Multiple Cracking of Cement Composites" ,*Journal of Engineering Mechanics*, 127:311–16

Chen,P.W. and Chung, D.D.L.(1991) "Carbon fiber reinforced concrete", *Extended Abstracts and Program - Biennial Conference on Carbon*, 240–41

Chuang, W., J. Geng-sheng, L. Bing-liang, P. Lei, F. Ying, G. Ni, and L. Ke-zhi. (2017) "Dispersion of carbon fi bers and conductivity of carbon fi ber-reinforced cement-based composites", *Ceramics International*, 43:15122–32

Chuang, W., P. Lei, L. Bing-liang, G. Ni, Z. Li-ping, and L. Ke-zhi. (2018) "Influences of molding processes and different dispersants on the dispersion of chopped carbon fibers in cement matrix", *Heliyon*, 4

Chung, D. D. L. (2012) "*Carbon Fiber Composites*", *Carbon Fiber Composites*, Elsevier Science.

Gao, J., Z. Wang, T. Zhang, and L. Zhou. (2017) "Dispersion of carbon fibers in cement-based composites with different mixing methods", *Construction and Building Materials*, 134, 220–27.

Pozegic, T. R., S. Huntley, M. L. Longana, S. He, R. M. I. Bandara, S. G. King, and I. Hamerton. (2020)"Improving dispersion of recycled discontinuous carbon fibres to increase fibre throughput in the HiPerDiF process" , *Materials*, 13

Ren, Y., L. Xu, X. Shang, Z. Shen, R. Fu, W. Li, and L. Guo. (2022) "Evaluation of Mechanical Properties and Pyrolysis Products of Carbon Fibers Recycled by Microwave Pyrolysis", *ACS Omega*, 7:13529–37

Wang, C., K. Z. Li, H. J. Li, G. S. Jiao, J. Lu, and D. S. Hou. (2008) "Effect of carbon fiber dispersion on the mechanical properties of carbon fiber-reinforced cement-based composites", *Materials Science and Engineering: A*, 487:52–57

Wang, Z., J. Gao, T. Ai, W. Jiang, and P. Zhao. (2014) "Quantitative evaluation of carbon fiber dispersion in cement based composites," *Construction and Building Materials*, 68:26–30

Zhu, H., H. Zhou, and H. Gou. (2021) "Evaluation of carbon fiber dispersion in cement-based materials using mechanical properties, conductivity, mass variation coefficient, and microstructure," *Construction and Building Materials*, 266: 120891

Prediction of the Properties of Self-Consolidating Concrete Using Machine Learning Models

Sunil Kumar Vishwakarma[1*], Manoj Kumar[2], and Kizhakkumodom Venkatanarayanan Harish [3]

[1] IIT Kanpur, Kanpur, India
Email: sunkarma@iitk.ac.in
[2] IIT Kanpur, Kanpur, India
Email: manojkm@iitk.ac.in
[3] IIT Kanpur, Kanpur, India
Email: kvharish@iitk.ac.in

[*]Corresponding author

ABSTRACT

Self-consolidating concrete (SCC) is a specialized type of concrete used in construction that can flow and consolidate on its own without external vibration or compaction. Nowadays, SCC has become integral in both in situ and pre-cast applications. Current advancements involve incorporating pozzolanic materials, fiber additions, alternative curing techniques, and other additives. This diversity poses a challenge in efficiently designing and predicting the properties of SCC. The present study aims to explore the design and predict the properties of SCC through the innovative lens of machine learning (ML). This study aims to develop ML models capable of accurately predicting the compressive strength of SCC with age. Incorporating diverse data sets and encompassing variations in composition will contribute to the robustness of the models. Ensemble learning-based models such as XGBoost, Xtra Trees Regressor (XTR), Gradient Boosting (GB), and Random Forest (RF) are the top-performing models, and they generate the best results when combined using methods such as weighted average and Bayesian model averaging. The ultimate goal is to facilitate an effective design of SCC with limited or minimal experimental data.

KEYWORDS: *Self-consolidating concrete, Pozzolanic materials, Hardened properties, Machine learning models, Ensemble learning*

1. Introduction

SCC is a concrete capable of flowing under its own weight, spread into places without segregation, and filling the formwork and spaces around reinforcement of congested areas without any mechanical vibration (Okamura, H; Ouchi, 2003).There is a reason why it is being said that this is the era of ML and artificial intelligence (AI). Over the years, machine learning has evolved from basic linear models to regularisation techniques to support vector machines (SVM), decision trees (DT), and, finally, ensemble learning methods, as shown in Figure 1.

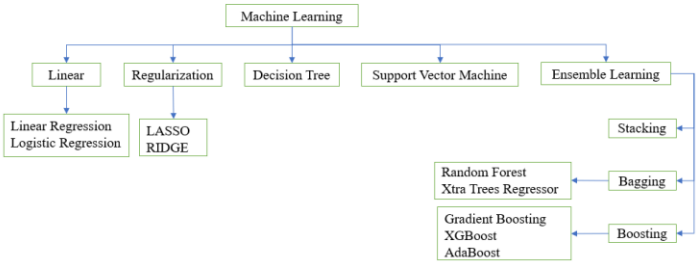

Figure 1. Machine learning models

2. Development of an ML model

The development of an ML model follows a series of steps, starting from data collection to model deployment, and is also referred to as the machine learning development life cycle (MLDLC) as shown in Figure 2.

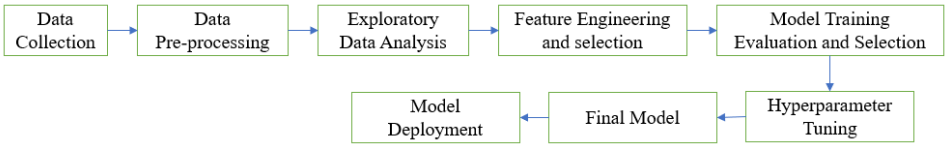

Figure 2. Machine learning development life cycle

2.1 Data collection

Data used to develop the models were compiled by going through the various published literature in the domain of SCC.

2.2 Data pre-processing

The raw data has 30 columns and 653 data points. First of all, three duplicate data were removed. At this stage, outliers were not removed as they may be outliers statistically. Still, these values were experimentally possible when designing SCC, and removing them may affect the diversity of the model. Some irrelevant columns were removed, and some new columns were added. The latest dataset has 28 columns and 650 data points.

2.3 Exploratory data analysis

In this study, the dataset is very diverse and comprehensive i.e., coarse aggregate ranging from 312 to 1113 kg/m^3 with different types (gravel, crushed limestone, crushed basalt stone, crushed granite, river gravel, quartzite, and rolled gravel) with different grading (25-mm, 20-mm,16-mm, 12.5-mm, and 10-mm nominal) similarly fine aggregate ranging from 90.8 to 1198 kg/m^3 with different types (natural sand, quartzite sand, river sand, and sea sand) and different grading (0-1 mm, 0-2 mm, 0-4.75 mm, and 0-8 mm). Cement ranges from 0 to 625 kg/m^3, with different types (OPC 33, OPC 43, OPC 53, and their strength equivalent). Limestone amount ranges from 66.4 to 360 kg/m^3, from 11.75% to 50% replacement of total binding material (TBM). Fly ash ranges from 19 to 420 kg/m^3, from 5% of replacement to 70% of TBM. Silica fume ranges from 18 to 150 kg/m^3, from 3% to 30% replacement of TBM. Ground granulated blast furnace slag (GGBS) ranges from 79 to 235 kg/m^3, from 7.5% to 100% replacement of TBM. Superplasticizer ranges from 0.48 to 16 kg/m^3, from 0.1% to 6.3% replacement of TBM. Viscosity modifying agent (VMA) ranges from 0.12 to 3.96 kg/m^3, and air-entraining agent (AEA) ranges from 0.0027 to 0.9 kg/m^3.

2.4 Feature engineering and selection

A total of 20 (12 numerical and 8 categorical) out of 30 parameters were used as the input parameters (Coarse aggregate, type of coarse aggregate, grading of coarse aggregate, fine aggregate, type of fine aggregate, grading of fine aggregate, cement, type of cement, limestone, fly ash, type of fly ash, silica fume, GGBS, blending, water-cement ratio, superplasticizer, type of superplasticizer, VMA, AEA, and age). Compressive strength with age is used as the output parameter.

2.5 Model training, evaluation, and selection

Several ML models were trained in the present study, and their performance was evaluated, as shown in Table 1.

Table 1. Performance of different models

ML model	Accuracy (%)	Mean Absolute Error (MAE)
XGBoost (Chen & Guestrin, 2016)	92	4.73
Extra Trees Regressor (Geurts et al., 2006)	90.83	4.76
Gradient Boosting (Friedman, 2001)	90.1	5.76
Random Forest (Jin et al., 2020)	88.1	6.5
Multi-Layer Perceptron (MLP)	80.13	7.26
Decision Tree	78.5	7.77
AdaBoost	76.02	9.26
Support Vector Regression (SVR)	64.37	10.75
Ridge Regression	54.12	10.34
Liner Regression	54.13	10.35

2.6 Hyperparameter tuning

Hyperparameter tuning of the top four models was done, and the performance of each model was improved, as shown in Figure 3.

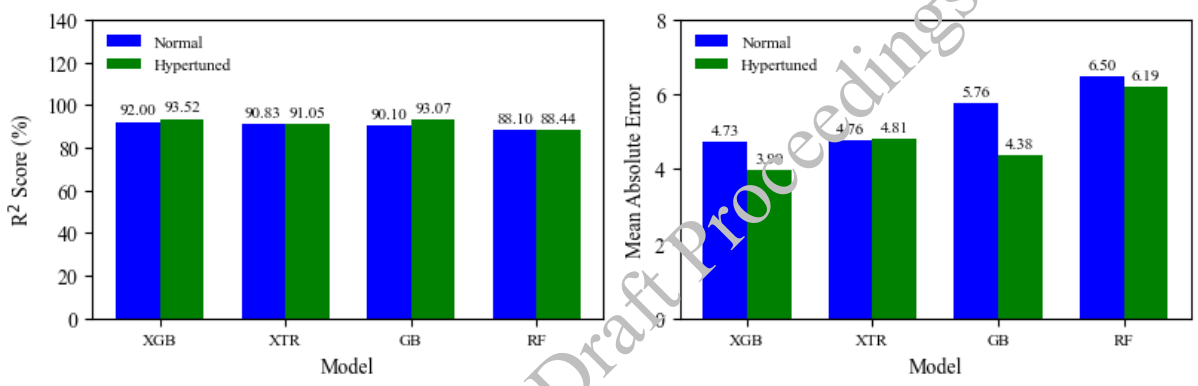

Figure 3. Performance of top four models (Normal vs. Hyper-tuned)

2.7 Check for overfitting

The difference between the R^2 score and the adjusted R^2 score clearly indicates the sign of overfitting. Investigation revealed that the input parameters, VMA, type of fine aggregate, and outliers present in the fine aggregate, and superplasticizer were causing this overfitting; removing them, the difference has decreased, and the model has improved, as shown in Figure 4.

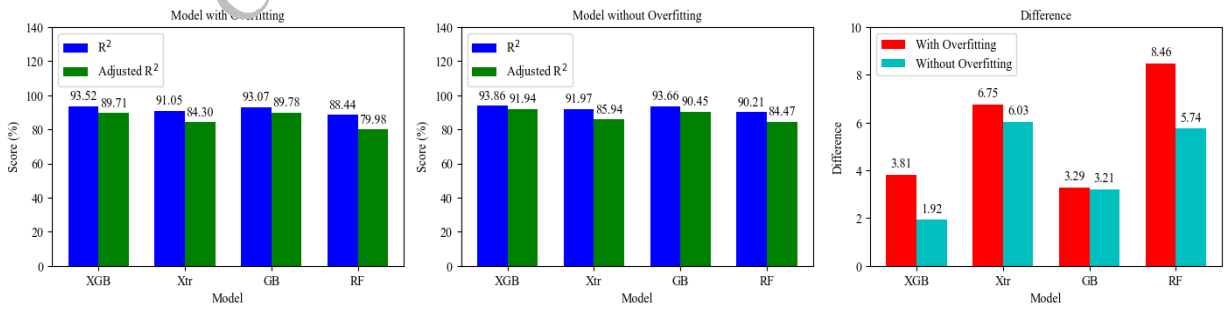

Figure 4. Performance of top four models (With and without overfitting)

2.8 Applying Ensemble Techniques

Different ensemble techniques such as stacking, weighted average approach (WAA), voting, blending, and Bayesian model averaging (BMA) techniques were used to combine the top four models. Weighted average approach and Bayesian model averaging improved the performance further (Hartmanis & Leeuwen, 2000).

2.9 Final proposed models

Hyper-tuned XGBoost and models generated from the WAA and BMA come out to be the best-performing ML models, as shown in Figure 5.

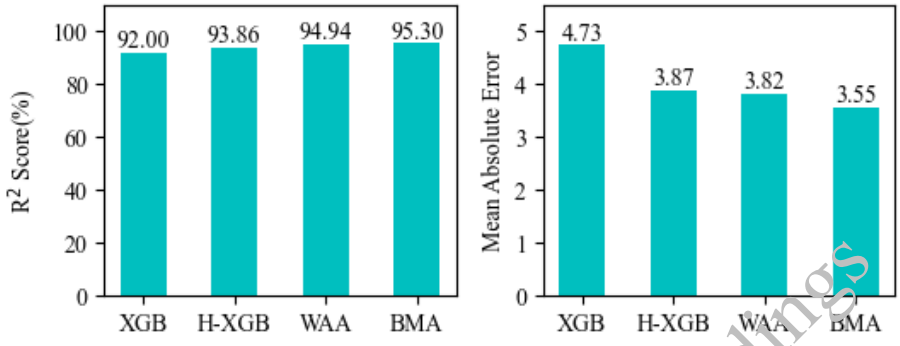

Figure 5. Performance of final proposed models

3. Conclusions

In conclusion, a hyper-tuned XGBoost model (objective=mean squared error (MSE), estimators=300, learning rate (η)=0.1, maximum depth=5, subsample=0.9, column sample by tree=0.9) is the best-performing model with an accuracy and MAE of 93.86% and 3.87 respectively. When this model is combined with the other top three models (XTR, GB, and RF) using ensemble techniques, the model generated with WAA has an accuracy of 94.94% and MAE of 3.82, and the model generated with BMA has an accuracy of 95.3% and MAE of 3.55. The above three models can accurately predict the compressive strength of SCC with age. The ML models for predicting the fresh properties of SCC were performing poorly and were hence not presented in this paper. Deep learning-based neural networks are recommended for predicting such properties.

References

Chen, T., and Guestrin, C. (2016) "XGBoost: A scalable tree boosting system", *Proceedings of the ACM SIGKDD International Conference on Knowledge Discovery and Data Mining*, *13-17-Augu* :785–794.

Friedman, J. (2001) "Greedy Function Approximation : A Gradient Boosting Machine", *The Annals of Statistics*, 29(5) : 1189-1232

Geurts, P., Ernst, D., and Wehenkel, L. (2006) "Extremely randomized trees",*Machine Learning*, *63*(1): 3–42

Hartmanis, J., and Leeuwen, J. Van. (2000) "Multiple Classifier Systems - First International Workshop, MCS 2000", *Proceedings. In Lecture Notes in Computer Science (including subseries Lecture Notes in Artificial Intelligence and Lecture Notes in Bioinformatics)*, 1857 LNCS

Jin, Z., Shang, J., Zhu, Q., Ling, C., Xie, W., and Qiang, B. (2020) "RFRSF: Employee Turnover Prediction Based on Random Forests and Survival Analysis". *Lecture Notes in Computer Science (Including Subseries Lecture Notes in Artificial Intelligence and Lecture Notes in Bioinformatics)*, *12343 LNCS*, 503–515

Okamura, H. and Ouchi, M. (2003) "Self-Compacting Concrete - research paper", *Journal of Advanced Concrete Technology* , 1(1):5–1

Experimental Investigation on Mechanical Properties of Concrete Using Tri-hybrid fiber mix

S.B. Javheri[1]* and Dr.S.S.Patil[2]

[1]Walchand Institute of Technology, Solapur, India
Email: sbjavheri@ witsolapur.org
[2]Walchand Institute of Technology, Solapur, India
Email: patilss1962@gmail.com

*Corresponding author

ABSTRACT

Cracks are found in concrete due to plastic shrinkage, poor tensile strength, and environmental impact. Hence to overcome this, different fibers are added in concrete to improve mechanical properties such as compressive strength, impact resistance, tensile strength of concrete. In this research work three different fibers namely, steel fibers, polypropylene fibers, glass fibers are used in concrete to check its performance w.r.t mechanical properties such as compressive strength, tensile strength etc. The optimum mix proportion of hybrid fibers in concrete mix is found to be 1.25% (Steel) + 0.20% (Polypropylene Fiber) + 0.2%(Glass Fiber), as the compressive and split tensile strength properties are improved. Cost of concrete 1 m^3 for concrete using hybrid fibers is significantly more than the conventional concrete.

KEYWORDS*: Glass,fiber , Polypropelene fiber, Tensile strength, Compressive strength, Hybrid fibers*

1. Introduction

Cracks are found in concrete due to plastic shrinkage, poor tensile strength, and environmental impact. Fibers are usually used in concrete to control cracking due to plastic shrinkage and to drying shrinkage. Fibers also reduce the permeability of concrete and thus reduce bleeding of water. Some types of fibers produce greater impact, abrasion and shatter resistance in concrete. Larger steel or synthetic fibers can replace rebar or steel completely in certain situations. Different fibers are added in concrete to improve mechanical properties such as compressive strength, flexural strength and tensile strength of concrete.
In this research work three different fibers namely, steel fibers, polypropylene fibers, glass fibers are used in concrete to check its performance with respect to mechanical properties such as compressive strength, tensile strength etc.
Polypropylene fiber helps to arrest micro cracks in concrete, and increase crack resistance property of concrete. Glass fibers improve load carrying capacity and increase alkali resistance and corrosive resistance property of concrete. Crimped Steel fiber increase tensile strength of concrete and ultimately increase load carrying capacity of concrete. It also helps to improve strength of concrete and replace the steel required to resist shear. To derive benefits for concrete from these fibers and make the concrete strong and durable, we use polypropylene fiber, glass fiber and crimped steel fibers in concrete mix.

2. Objectives

- To determine the mechanical properties (Tensile strength, Compressive strength, Flexural Strength) of conventional concrete and concrete with hybrid fibers.
- To determine optimum percentage of hybrid fibers w.r.t volumetricproportions of concrete.
- To compare the mechanical properties of conventional concrete with respect to optimum percentage of hybrid fibers mix.
- To carry out cost analysis for conventional concrete and concrete with hybrid fibers for 1m^3 volume of concrete.

3. Methodology

- Study of Properties of Ingredients of Concrete.
- Mix design of conventional concrete using I.S Code Method is to be carried out.
- Study of properties fibers such as steel fiber, polypropylene fiber, glass fiber to be used inconcrete.
- Volumetric percentage of fibers in concrete is used in various proportions as per theinformation obtained from literature review.
- Test result is carried out for M25 grade of concrete for compressive strength, split tensilestrength and flexural strength of conventional concrete and concrete with hybrid fibers after curing for 28 days.

Following table gives the Mix ID of HFRC cubes and cylinders and beams for 17 combinations of percentage volumetric proportions of steel fiber, polypropylene fibers and glass fiber w.r.t concrete.

Table 1. Volumetric proportions of fibers

Sr No	Mix ID	Steel	Polypropylene: Glass fibers (proportions in terms of volumetric percentage of fibers in concrete mix)
1	A	0.75	0.1: 0.1
2	B		0.1: 0.2
3	C		0.1: 0.3
4	D		0.2: 0.1
5	F		0.2: 0.2
6	H		0.2: 0.3
7	J		0.3: 0.1
8	E	1.25	0.2: 0.1
9	G		0.2: 0.2
10	I		0.2: 0.3
11	K	0.5	0.1: 0.1
12	L		0.1: 0.2
13	M		0.2: 0.1
14	N		0.2: 0.2
15	O	1	0.1: 0.2
16	P		0.2: 0.1
17	Q		0.1: 0.1

Test is carried out for M25 grade of concrete to obtain compressive strength, split tensile strengthand flexural strength of conventional concrete and concrete with hybrid fibers after curing for 7 days and 28 days. These results are compared with conventional concrete without fibers.Following table shows properties of ingredients in concrete.

Table 2. Properties of cement

Properties	Values
Grade of cement	Opc53
Specific gravity	range of 3.10 to 3.20.
Fineness of cement	2%.
Consistency	33.5%.
Initial setting time	98 minutes.
Final setting time	212 minutes.

Table 3. Properties of fine aggregate

Properties	Values
Specific gravity	2.922
Water absorption	1.83%
Fineness modulus	3.2
Silt Content of F.A.	4 %
Bulk density Loose weight	1.853 kg/lit
Compacted weight	2.113 kg/lit

Table 4. Properties of coarse aggregate

Properties	Values
Specific gravity	2.9
Water absorption	1.6%
Fineness modulus	4.931
Bulk density Loose weight	1.56 kg/lit
Compacted weight	1.795 kg/lit

Table 5. Properties of fibers

Property	Crimped Steel fiber	Polypropylene Fiber	Glass Fiber
Density in kg/m3	7850 kg/m3	910 kg/m3	2700 kg/m3
Length in mm	50 mm	20 mm	12 mm
Diameter in mm	1 mm	0.048 mm (48µ)	0.014 mm (14µ)
Aspect Ratio	50	416.67	857.14

Table 6. Cost comparison of concrete (1m3) with and without fiber

Description				
Cost of Concrete without fibers	Cost of Concrete withSteel Fiber	Cost of Concrete with Polypropylene Fiber	Cost of Concrete withGlass Fiber	Cost of Concrete with optimum mix trihybrid fibers (1.25 % steel fiber + 0.2% polypropylene fibers+0.2% glass fibers)
4,000/-	16,756/-	5,456/-	4,648/-	18,860/-

4. Conclusions

- The optimum mix proportion of hybrid fibers in concrete mix is found to be 1.25% (Steel) + 0.20% (Glass Fiber) + 0.20%, (Polypropylene Fiber)
- It is observed that, for the optimum mix of hybrid fiber in concrete mix shows10.01% increase in compressive strength after 7 days, as compared with conventional concrete.

- It is observed that, for the optimum mix of hybrid fiber in concrete mix shows 39.40% increase in compressive strength after 28 days, as compared with conventional concrete.
- Comparing the conventional concrete having optimum mix hybrid fibers with conventional concrete, it is observed that the split tensile strength is increased by80.41%, which indicates tremendous improvement in tensile strength of concrete.
- Comparing the conventional concrete having optimum mix hybrid fibers with conventional concrete, it is observed that the Flexural strength is increased by 93.54%, which indicates tremendous improvement in Flexural strength of concrete.
- Cost of concrete 1 m^3 for concrete using hybrid fibers is significantly more than the conventional concrete.

Acknowledgements

I thankful to my guide Dr.S.S.Patil and principal Dr.V.A.Athavale sir, for encouraging me to participate in conference.

References

Abbadi, A., Basheer, P.A.M. and Forth, J.P. (2022) "Effect of hybrid fibers on the static load performance of concrete beams", *Materials Today Proceedings*, 65(2):681-687

Kulkarni, S. K., Kulkarni, M. And Halkude. S. A. (2017) "Experimental study of strength parameters of hybrid fiber reinforced concrete", *International Research Journal of Engineering and Technology (IRJET)*, 4(8): 1734-1743

Rao, B.K. and Ravindra, V. (2010) "Steel Fiber Reinforced Self –Compacting Concrete Incorporating Class F Polypropylene Fiber", *International Journal of Engineer science and Technology*, 2(9) :4936-4943

Bayasi, M.Z. and Soroushian, P. (1992) "Effect of steel fiber reinforcement on fresh mix properties of concrete", *Materials Journal*, 89(4) :369-374

Ghosh, S., Bhattacharya, C. and Ray, S. P. (1989) "Tensile strength of steel fiber reinforced concrete", *Journal of the Institution of Engineers. India. Civil Engineering Division*, 69:222-227

IS. 10262.(2019) "Recommended Guidelines for Concrete Mix Design", *Bureau of Indian standards*, New Delhi

IS.5816.(1999) "Method of Test for Split Tensile Strength of Concrete", *Bureau of Indian standards*, New Delhi

IS. 516.(1959) " Method of Test for Strength of Concrete", *Bureau of Indian standards*. New Delhi

Investigating the Clear Cover Requirement for Required Fire Resistance Rating in LC^3 Concrete Columns

Parth Dwivedi[1*], Sanchit Gupta [2], and Sandeep Chaudhary [3]

[1] *Department of Civil Engineering, Indian Institute of Technology Indore, Simrol, Indore 453552, India*
Email: ce200004036@iiti.ac.in
[2] *Department of Civil Engineering, Indian Institute of Technology Indore, Simrol, Indore 453552, India*
Email: sanchitgupta@iiti.ac.in
[3] *Department of Civil Engineering, Indian Institute of Technology Indore, Simrol, Indore 453552, India*
Email: schaudhary@iiti.ac.in

*Corresponding author

ABSTRACT

Fire resistance rating, or the duration for which a structure can withstand fire, is an important durability aspect of concrete structures. Fire resistance rating of concrete structures depend on several factors including the type of cement used for developing the concrete structures. Recent advances towards low carbon cements have identified several new types of cement including limestone calcined clay cement or LC^3. Literature shows that rate of strength loss in LC^3 concrete is slightly higher than the conventionally used cements, i.e., ordinary Portland cement (OPC) and Portland pozzolana cements (PPC). Concrete structures using LC^3, for low carbon benefits, should account for its weaker fire resistance and adopt suitable safety measures. The present study investigates the correlation between clear cover and fire resistance rating of LC^3 concrete columns and compares them with OPC and PPC concrete columns. Multiple fire hazards are simulated for different room sizes, wall opening, height and fire load, to determine the rate of heat received by the concrete columns as a function of time. The simulation is extended to determine the residual strength of concrete columns and fire resistance rating, i.e., time of failure. The concrete columns are simulated for different clear covers to demonstrate the correlation between clear cover and fire resistance rating of concrete columns. The results of the study will help in correcting the clear cover requirement for LC^3 concrete structures for ensuring similar fire resistance rating, and promote the safe application of low carbon cements.

KEYWORDS: *Fire resistance rating, Clear cover, LC^3, Reinforced concrete column, Fire safety standards*

1. Introduction

Limestone calcined clay cement (LC^3) has been identified as a ternary blended low carbon cement (Sharma et al. 2021). LC^3 has significant environmental and economic advantages over conventionally used cements (Scrivener et al. 2018). In terms of concrete properties, LC^3 concrete is comparable to conventionally used cement, i.e., ordinary Portland cement (OPC) and Portland pozzolana cements (PPC) (Sharma et al. 2021). While LC^3 can be considered a direct substitute for OPC in most cases, recent study shows that additional safety measures are needed when LC^3 concrete structures are designed for fire exposures. In terms of exposure to elevated temperature, the residual strength of LC^3 concrete is slightly lower than OPC and PPC concrete (Gupta et al. 2022). LC^3 also results in lower specific heat and lower thermal conductivity of concrete (Thitikavanont and Sahamitmongkol 2020). The lower specific heat of LC^3 with respect to OPC concrete results in the greater increase in temperature of concrete from same amount of heat energy. Higher temperature of concrete results in more strength loss in concrete which implies that LC^3 concrete sections may fail earlier than OPC concrete sections. On the other hand, lower thermal conductivity in comparison to OPC results in lower heat transfer within the material. This implies less heat may travel within concrete and may cause lesser damage to concrete and steel sections and LC^3 structure. The combined behaviour of

the three parameters has not been investigated on reinforced concrete columns. This study aims to better understand which of the two phenomena will dominate for LC^3 concrete when exposed to fire. Literatures shows that simulations can be used to predict the risk of failure and develop safety guidelines for concrete applications (Gupta et al. 2022). The present work extends on the literature by simulating concepts of structural mechanics and heat flow to develop safety guidelines for the clear cover requirement of LC^3 concrete columns. In the present study, simulations are used to vary the different parameters and generate heat exposure scenarios for concrete columns. The heat exposure scenarios are used for determining the temperature change in column with time, and understand the effect of clear cover on the residual performance of concrete columns. The present study covers a large number of probabilistic scenarios for furniture type and room conditions to better represent the realistic fire performance. The results of the study will help in selection of clear cover to ensure fire safety of LC^3 concrete columns.

2. Methodology

The present study uses a three-part simulation for determining the effect of fire on concrete columns. The three part includes determining temperature and thermal radiation on column, developing temperature gradient across the cross-section and estimating residual strength for the column. The simulation first uses the probable scenarios for a typical residential space with a defined fire load to generate fire curves and heat release. Fire curves represent the gas temperature generated inside a typical residential space based on the fire load, room opening and room height (Gupta et al. 2022). The equations for developing fire curve and parameters for residential spaces have been adopted from Gupta et al. 2022. Figure 1 (a) represents a typical fire curve developed during the simulation. Effective heat reaching the column is determined using the intensity of thermal radiation on the surface of column. Thermal radiation is determined using the equations described by Shokri et al. (1989) and configuration factor from Beyler et al. 2002. In the second step of the simulation heat flow equation is used to determine the thermal gradient across the cross-section of the column. The heat transfer within the concrete column is governed by the transient heat conduction equation in two dimensions described in Equation.1 and 2, using the thermal conductivity and specific heat of the concrete as determined by Thitikavanont and Sahamitmongkol. 2020. The two equations have been combined to determine the temperature gradient as function of time. In these equation Q represents the heat, ρ represents the density of the material, Cp represents the specific heat of the material.

$$\partial T/\partial t = \alpha * (\partial^2 T/\partial x^2 + \partial^2 T/\partial y^2) + Q/(\rho * Cp) \quad (1)$$

$$\alpha = k / (\rho * Cp) \quad (2)$$

In the third step, temperature gradient is applied across the cross-section of the column and residual strength of the corresponding section is determined. The residual compressive strength of concrete as a function of temperature is adopted from the values present in literature (Gupta et al. 2022). The study provided residual compressive strength of the concrete for 623 K, 823 K, 1023 K, 1273 K. The values were interpolated for the temperature at the location after the exposure from fire using the relations present in literature (Gupta et al. 2022). In the present study, the temperature of simulated concrete column did not exceed 1273 K so no extrapolation was needed. The compressive strength increases slightly up to 573 K, due an effect known as baking (Gupta et al. 2022). In the present study the partial increase is ignored and strength decrease is adopted from 573 K. Similarly, residual strength of reinforcement as a function of temperature is adopted from EN 1994-1-2 (2005). The residual strength of the column is then determined by combining the residual compressive strength of concrete and reinforcement. The simulation is repeated for both OPC and LC^3 concrete columns of fixed dimensions (400 mm × 400 mm), with different clear covers. The results are analysed on the basis of time required to achieve a residual strength of 80%.

3. Results

The variation in the temperature of the gas of the space is taken as the fire curve. This fire curve achieves a maximum temperature of cover 1200 K in the below given scenario.

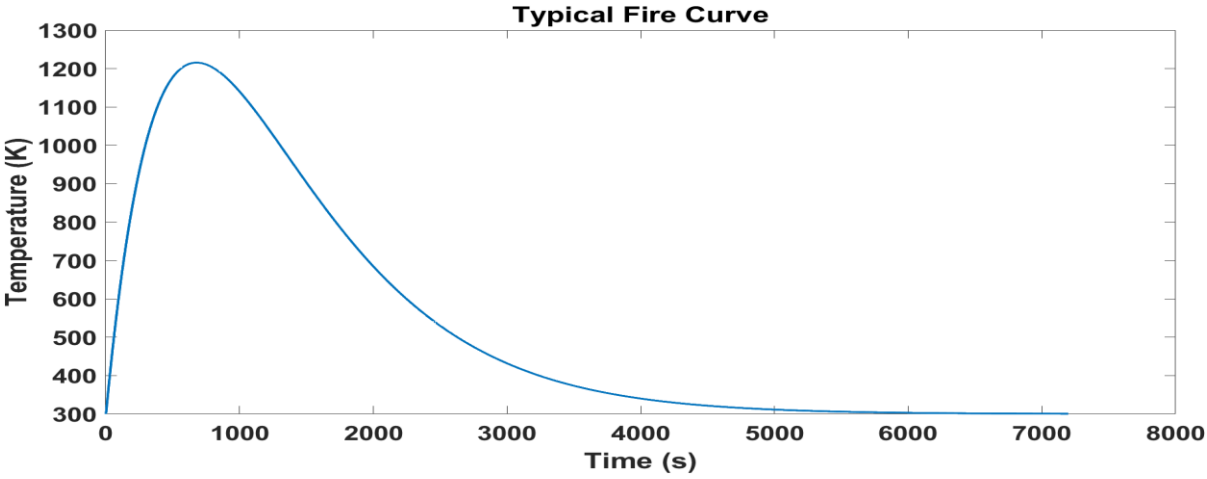

Figure 2. represents a typical fire curve developed during the simulation

Temperature increases to a maximum of 698.75 K in case of OPC concrete for 50 mm cover at the location of reinforcement. Temperature increases to a maximum of 721.43 K in case of LC^3 concrete for 50 mm cover at the location of reinforcement, Temperature increases to a maximum of 681.60 K in case of LC^3 concrete for 60 mm cover at the location of reinforcement. Temperature increases to a maximum of 681.60 K in case of LC^3 concrete for 60 mm cover at the location of reinforcement

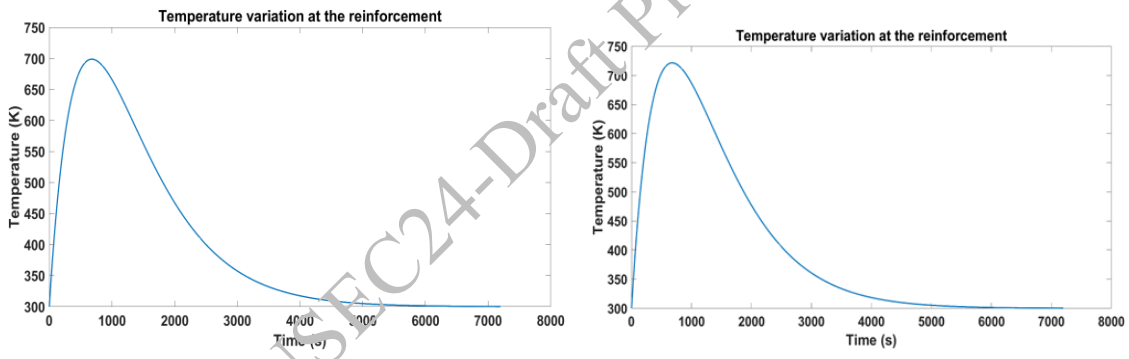

(a) (b)

Figure 3. (a) temperature variation at the location of closest reinforcement for OPC for 50 mm cover, (b) temperature variation at the location of closest reinforcement for LC3 for 50 mm cover.

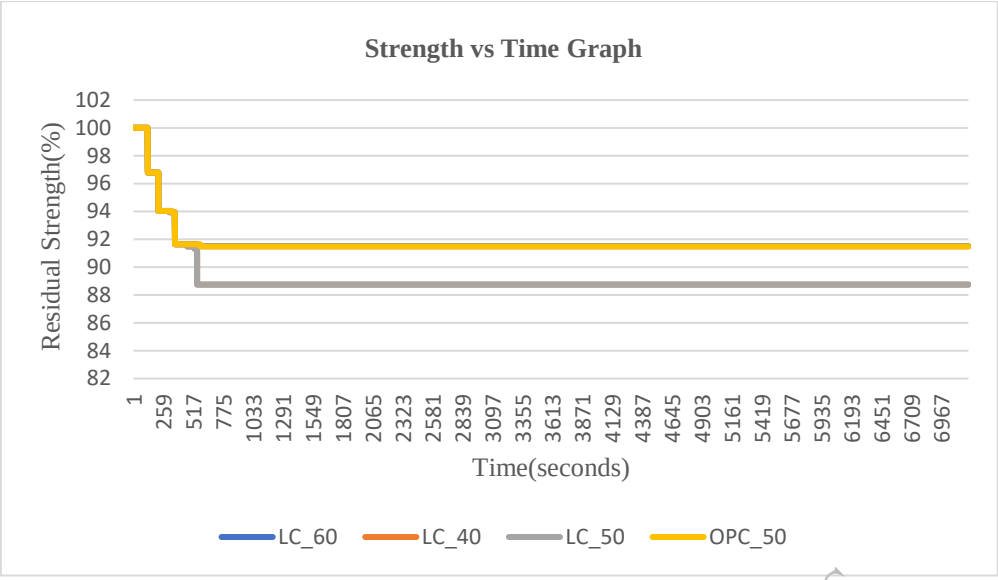

Figure 4. The graph of the residual strength of the concrete section with respect to time

The curve for the LC^3 concrete 60 mm cover and the OPC concrete 50 mm cover are giving values approximately similar values, whereas for the case of the LC^3 concrete with 40 mm cover and 50 mm cover give the values of residual strength after exposure to fire approximately equal.

4. Conclusions

The residual strength of the LC^3 concrete column section when provided with a 50 mm and 40 mm cover reduces to close 88% in approximately 12 mins, whereas in case of 60 mm cover for LC^3 concrete the time required to reach close OPC 50 mm cover residual strength of the section in the same time and it never going below it. The primary factor due to which failure occurs in LC^3 reinforced concrete columns occur is due to very poor fire performance of LC^2 cement, as it has very low residual strength at higher temperatures. Thus, it can be concluded that from this study that 60 mm cover in LC^3 concrete provides a greater fire safety rating and a similar to that of the OPC 50 mm cover.

References

Gupta, S., Singh, D., Gupta, T. and Chaudhary, S. (2022) “Effect of limestone calcined clay cement (LC 3) on the fire safety of concrete structures” ,*Computers and Concrete*, Techno-Press, 29(4):263

Scrivener, K., Martirena, F., Bishnoi, S. and Maity, S. (2018) “Calcined clay limestone cements (LC3)”, *Cement and Concrete Research*, 114:49–56

Sharma, M., Bishnoi, S., Martirena, F. and Scrivener, K. (2021) “Limestone calcined clay cement and concrete: A state-of-the-art review.” *Cement and Concrete Research*, Pergamon, 149, 106564

Thitikavanont, Y. and Sahamitmongkol, R. (2020)“Heat Generation and Thermal Properties of Limestone Calcined Clay Cement Paste”, In *Calcined Clays for Sustainable Concrete: Proceedings of the 3rd International Conference on Calcined Clays for Sustainable Concrete*, 455–467

Shokri, M. and C.L. Beyler, (1989) “Radiation from Large Pool Fires,” *SFPE Journal of Fire Protection Engineering*, 1(4):141-149

Beyler, C.L. (2002) “Fire Hazard Calculations for Large Open Hydrogen Fires,” Section 3, Chapter 1, SFPE Handbook of Fire Protection Engineering, 3rd Edition, P.J. DiNenno, Editor-in-Chief, National Fire Protection Association, Quincy, Massachusetts

EN 1994-1-2 (2005) “(English): Eurocode 4: Design of composite steel and concrete structures – Part 1-2: General rules - Structural fire design”, *Authority: The European Union Per Regulation 305/2011, Directive 98/34/EC, Directive 2004/18/EC*

Influence of Type of Sand and Fiber Content on Compressive Strength of Ultra High-Performance Concrete (UHPC)

Anju Paul[1*] and Elson John[2]

[1] Research scholar, Department of Civil Engineering, Mar Athanasius College of Engineering, Kothamangalam, APJ Abdul Kalam Technological university, Kerala, India
Email: anjujerrin2010@gmail.com
[2] Professor, Department of Civil Engineering, Mar Athanasius College of Engineering, Kothamangalam, APJ Abdul Kalam Technological university, Kerala, India
Email: elson@mace.ac.in

[*]Corresponding author

ABSTRACT

Ultra high-performance concrete (UHPC) is a cement compound, a new development in construction technology with its superior features such as good fresh properties, mechanical and structural properties and superior durability characteristics than normal conventional concrete. It is achieved by using low water-to-binder ratio (w/b), high particle packing density and high dosage of steel fibers. This research investigates the compressive strength of UHPC mixes by using various types of sand namely, Manufactured sand (M Sand), Standard sand, River sand and Quartz sand. The results indicate that the flowability and compressive strength of developed UHPC mixes were influenced by the type of sand used. The application of steel fibers helps to increase the ductility of UHPC structures. The compressive strength of UHPC was studied by varying the fiber content of 0%, 1%, 1.5%, 2% and 2.5%. From the results, it was detected that the increase in dosage of fiber content causes increase in the compressive strength regardless it negatively influences the workability of UHPC. The study has great future research significance to extend by considering hybrid fibers as well as combination of different sand types.

KEYWORDS*: Ultra high-performance concrete, Flowability, Compressive strength, Fibers, Particle packing density*

1. Introduction

Ultra-high-performance concrete (UHPC) is a modern invention in construction industry along with excellent characteristics such as high flowability, high compressive as well as tensile strength, high durability and ductility. As the Federal Highway Administration (FHWA) detailed (Graybeal, 2011): UHPC is a cementitious compound constituted by mixing Ordinary Portland Cement (OPC), silica fume, fine silica sand, quartz powder, high range water reducer, discontinuous internal steel fiber and water – cement ratio less than 0.25. This advanced technology offers more than 120 MPa compressive strength and 5.2 MPa post cracking tensile strength. The primary principle to develop UHPC mix is the optimum particle packing density which contributes discontinuous pore structure and thus lowers liquid ingress and enhance the performance of UHPC (Shafieifar et al., 2017). Also, the economic value of UHPC is remarkably higher than that of conventional concrete. Hence the optimization of fiber dosage is of great importance (Ghafari *et al.*, 2015). In this research, fiber volume fraction and sand type were taken as the main parameter, and its consequence on the compressive strength of hardened UHPC and flowability of fresh UHPC were studied.

2. Materials and methodology

2.1 Materials

The ingredients for preparing UHPC consist of cementitious materials, fibres, fine aggregates, water, and superplasticizer. The cementitious materials used were Ordinary Portland Cement of 53 grade, Alccofine 1203, and Ground Granulated Blast Furnace Slag (GGBFS). Their material properties were provided in Table 1. The steel fibres used had a length of 20 mm, a diameter of 0.2 mm, and an aspect ratio of 100, aimed at enhancing the fracture resistance of the UHPC sample and mitigating crack propagation along the depth of the specimen. To improve the workability of the fresh UHPC mix, a Polycarboxylate (PCE)-based superplasticizer was utilized. Two types of manufactured sand (M Sand) were used: one with a particle size of 4.75 mm and the other with particles ranging between 1.18 mm and 75 microns. Additionally, the fine aggregates used in the research included river sand passing through a 1.18 mm sieve and retained on a 75-micron sieve, standard grade III sand (0.09 mm to 0.5 mm), and quartz sand with gradations of 2 mm, 1 mm, and 30 mesh. Quartz powder was also used as a filler to enhance particle packing. The compatibility between the cement and superplasticizer was assessed using the Marsh Cone test, and the optimum dosage was determined to be 0.6%.

Table 1. Properties of Cementitious materials

Properties	Cement	Alccofine	GGBFS
Specific gravity	3.1	2.7	2.8
Standard consistency	31 %		
Initial setting time	100 minutes		
Final setting time	559 minutes		

Table 2. Properties of fine aggregates

Types of fine aggregates	Specific gravity	Water absorption (%)
M Sand (-4.75mm)	2.54	2.7
M Sand (-1.18mm)	2.56	2.383
River sand	2.59	2.24
Standard sand	2.64	0.8
Quartz sand (2mm)	2.78	0.305
Quartz sand (1mm)	2.69	0.367
Quartz sand (30mesh)	2.53	0.701
Quartz powder	2.6	-

2.2 Mixing methodology

The fresh-state UHPC mixtures were highly sensitive to the mixing procedure and environmental conditions. The temperature of the mixture was maintained below 30°C during the mixing process. The same mixing procedures were adopted for all mixes to minimize the influence of the mixing process. For all proposed UHPC mixtures considered in this research, the ingredients (cement, GGBFS, Alccofine, and fine aggregate) were first dry mixed for 3 minutes. Water and superplasticizer were then added over 2 minutes, followed by an additional 5 minutes of mixing. Fibers were gradually added and mixed for 2 minutes until uniform dispersion was achieved. The flowability of the mix was determined by flow test according to ASTM C 1437 – 07 (ASTM C , 2009), ASTM C-230 (ASTM C-230, 2009) and IS 5512-1983 (IS 5512 , 2004). The flow cone used had a bottom diameter of 100 mm, a top diameter of 70 mm, and a height of 50 mm. The mix was then transferred into concrete molds and covered with a plastic sheet to prevent moisture loss. Heat curing was performed to improve the microstructure of the UHPC. After 48 hours of water addition, the specimens were subjected to heat curing at 90°C for an additional 48 hours. The compressive strength of UHPC was tested on 70.6 x 70.6 x 70.6 mm^3 cube specimens according to IS:516-2021 (IS 516, 2021) after 7 and 28 days of curing. The tests were conducted using a compression testing machine (CTM) with a loading rate of 1.14 kN/sec.

2.3 Mix proportions of UHPC

The basic mix proportions considered are encapsulated in Table 3. Different proportions of fiber content, namely 0%, 1%, 1.5%, 2%, and 2.5% (F0, F1, F1.5, F2, and F2.5) of the total volume of concrete, were

studied to assess their effect on compressive strength. To examine the impact of different types of fine aggregate on the performance of UHPC, various aggregates were used: standard grade III sand (SS), river sand passing through a 1.18 mm sieve and retained on a 75-micron sieve (RS), M Sand passing through a 4.75 mm sieve (MS-4.75), M Sand grading between 1.18 mm and 75 microns (MS-1.18), a combination of MS-4.75 and quartz powder in a ratio of 87:13 (MSQP), and quartz sand grades Q1 (2 mm), Q2 (1 mm), Q3 (30 mesh), and quartz powder (QP) in a ratio of 20:50:12.5:17.5 (Q1Q2Q3QP).

Table 3. Mixture proportions for proposed UHPC mix

Material	Mix proportion
Cement (kg/m^3)	600
Alccofine (kg/m^3)	300
GGBFS (kg/m^3)	280
Fine aggregate (kg/m^3)	1000
Fiber (% of volume of concrete)	1.5
Superplasticizer (kg/m^3)	16
w/b	0.17

3. Results and discussions

The effect of fiber volume fractions of 0%, 1%, 1.5%, 2%, and 2.5% on the compressive strength of UHPC was analyzed. As the fiber volume increased, the compressive strength also increased, as shown in Fig. 1. However, the experimental study revealed that a fiber volume fraction above 1.5% resulted in reduced workability and improper dispersion of the fibers. Although the increase in compressive strength was not highly significant, it was observed that steel fibers can restrict crack development in compressed UHPFRC specimens (Yang et al.,2021). Therefore, 1.5% fiber content was considered the optimum dosage for UHPC design. Six types of aggregate combinations were considered in the study, and their impact on compressive strength was examined. According to the analysis shown in Fig. 2, standard sand, river sand, the combination of M Sand and quartz powder, and quartz sand produced comparable results. However, standard sand was not deemed a suitable option for UHPC due to economic concerns. Given cost and availability considerations, quartz sand and M Sand were recommended. M Sand, being readily available, was particularly favored (Yang et al.,2019). The incorporation of quartz powder was found to improve packing density and densify the matrix microstructure (El-Mir et al., 2022).

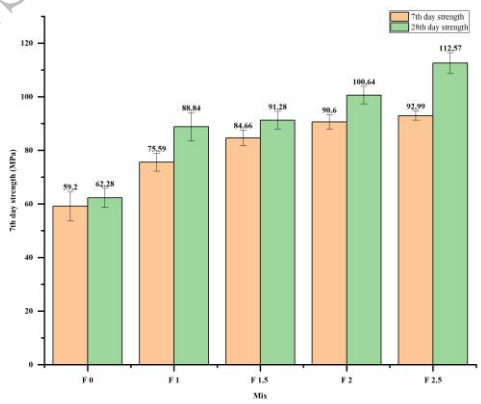

Figure 1. Effect of fiber dosage on compressive strength of UHPC

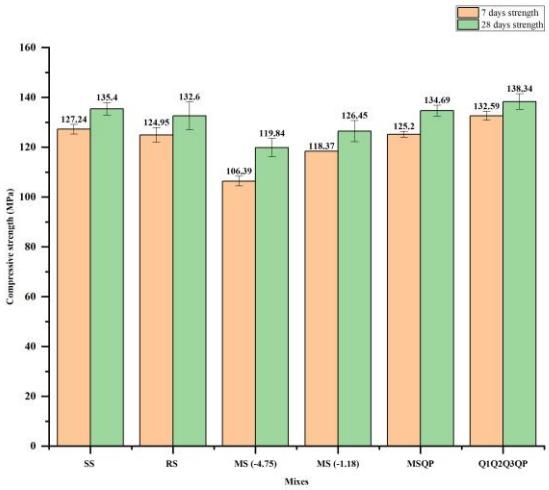

Figure 2. Effect of type of fine aggregate on the compressive strength of UHPC

4. Conclusions

- The effect of different fiber dosages, such as 0%, 1%, 1.5%, 2%, and 2.5%, on the compressive strength of the developed UHPC was studied. Considering both compressive strength and flowability, it can be concluded that a 1.5% fiber dosage is optimal for developing UHPC.
- The effect of six different types of fine aggregates on the compressive strength of UHPC was examined. Based on the analysis, M Sand and quartz sand are recommended for UHPC development due to considerations of cost and availability.

References

ASTM C 1437-07. (2009), "Standard Test Method for Flow of Hydraulic Cement Mortar"

ASTM C 230/C 230M – 08. (2009), "Standard Specification for Flow Table for Use in Tests of Hydraulic Cement"

El-Mir, A., Nehme, S.G. and Assaad, J. (2022) "Effect of binder content and sand type on mechanical characteristics of ultra- high performance concrete", *Arabian Journal for Science and Engineering*, 47(10):13021-13034

Graybeal, B. (2011), "Ultra High-Performance Concrete FHWA-HRT-11-038", *Federal Highway Administration: Washington*, DC, USA

Ghafari, E., Costa, H. and Júlio, E. (2015),"Statistical mixture design approach for eco-efficient UHPC ", *Cement and Concrete Composites*, 55:17-25

IS 5512-1983.(2004), "Specification for flow table for use in tests of hydraulic cements and pozzolanic materials"

IS 516 (Part 1/Sec 1). (2021), "Hardened concrete methods of test part 1 testing of strength of hardened concrete section 1 compressive, flexural and split tensile strength", *Bureau of Indian standards*, New Delhi, India

Shafieifar, M., Farzad, M. and Azizinamini, A. (2017) "Experimental and numerical study on mechanical properties of Ultra High-Performance Concrete (UHPC)", *Construction and Building Materials*, 156: 402-411

Yang, J., Chen, B. and Nuti, C. (2021) "Influence of steel fiber on compressive properties of ultra- high-performance fiber reinforced concrete", *Construction and Building Materials*, 302:124104

Yang, Yu, Shui, Guo, Wu, Gao, Peng (2019) "The physical and chemical impact of manufactured sand as a partial replacement material in Ultra-High-Performance Concrete (UHPC)", *Cement and Concrete Composites*, 99: 203-213

Exploring the Viability of Limestone Calcined Clay for 3D Printable Alkali-Activated Mortar

Mangalampalli Anil Kumar [1*], Sri Kalyana Rama Jyosyula[2], Visalakshi Talakokula [3]

[1] Department of Civil Engineering, Mahindra University, Hyderabad, India, anil22pcie004@mahindrauniversity.edu.in
[2] Department of Civil Engineering, Mahindra University, Hyderabad, India, srikalyanarama.j@mahindrauniversity.edu.in
[3] Department of Civil Engineering, Mahindra University, Hyderabad, India, visalakshi.talakokula@mahindrauniversity.edu.in

[*]Corresponding author

ABSTRACT

Additive manufacturing has witnessed growing interest in the construction sector. Globally, extrusion-based 3D Concrete Printing (3DCP) has been adopted as a sustainable construction practice due to its inherent advantages over other techniques. Conversely, Limestone Calcined Clay (LC^2) has emerged as a sustainable alternative for Ordinary Portland Cement (OPC) in concrete production due to its low carbon footprint. Recent research studies have proven that LC^2 not only complements OPC but also improves printability in 3DCP mixes. This study aims to understand the suitability of LC^2 in 3D Printable Alkali Activated Mortar concerning extrudability and buildability. The effect of LC^2 on workability was assessed using flow table test to attain an acceptable spread for all mix combinations suitable for printing. Workability was measured through slump and spread diameter. The extrudability of the mixes was evaluated by extruding the filament at a constant speed through a circular nozzle. Buildability assessments were conducted using a hollow rectangular sample consisting of 20 layers. For reference mix, Fly Ash (FA), Ground Granulated Blast Furnace Slag (GGBS) along with sodium hydroxide and sodium silicate were used. The findings revealed that the mix with LC^2 in combination with FA and GGBS has shown better extrudability and buildability in the fresh state making it compatible with 3D-Printing. Therefore, the global availability of LC^2 offers a practically sustainable approach in improving the fresh properties of 3D Printable alkali-activated mortars.

KEYWORDS*: Additive Manufacturing, Limestone Calcined Clay, Alkali Activated Mortar, Extrudability, Buildability.*

1. Introduction

3D Concrete Printing (3DCP) has gained potential as an additive construction technique promising significant reductions in construction time, labour costs, and material waste, while enabling complex geometries that are challenging to achieve with traditional construction practices. Recent advancements in material science have further explored the capabilities of 3DCP, particularly through the development of concrete systems using Ordinary Portland Cement (OPC) and Alkali-Activated Materials (AAMs)/ geopolymers. Especially, AAMs are considered as a sustainable solution and a good alternative, largely due to their ability to utilize precursors derived from industrial wastes or by-products, thereby avoiding the high-temperature processes and resulting in lower CO_2 emissions during production (Bhattacherjee et al., 2021). Furthermore, AAMs can be engineered to meet the fundamental requirements of 3D printing, such as extrudability and buildability. A thixotropic material with a high structural built-up rate can enhance the buildability during printing. Due to the inherent thixotropy nature of the clays, several researchers explored utilisation of various clays in the development of 3D Printable Alkali Activated concrete, including Nano clay, Bentonite clay and Halloysite clay and reported that the improvement in the buildability of 3DCP due to their thixotropic properties (Chougan et al., 2021; Kondepudi and Subramaniam ,2021; Dai et al., 2023).

Similarly, other researchers adopted Lime stone Calcined Clay (LC^2) along with OPC, termed LC^3, in 3D printable cementitious systems and demonstrated that LC^2 increases the yield stress of the printed layers, thereby enhancing the shape buildability of printed structures (Shantanu et al., 2023; Ibrahim et al., 2023). Therefore, this study aims to investigate the effect of Limestone Calcined Clay (LC^2) on the buildability of 3D Printable Alkali Activated mortar.

2. Materials and Methodology

Class-F Fly Ash (FA) and Ground Granulated Blast Furnace Slag (GGBS) were used as precursors. FA and GGBS were sourced from Damodar Sanjeevaiah Thermal power plant (India) and JSW Cement (India) respectively. Limestone Calcined Clay (LC^2) was supplied by LC^3 Resource Centre, Delhi. The prepared Sodium Hydroxide solution with 3M was blended after 24 hours with commercially available Sodium Silicate (SS) solution containing 33% SiO_2, 15% Na_2O and 52% H_2O by mass with a silicate modulus of 2.2. The activator modulus (M_s) of Alkaline Activated Solution (AAS) was kept constant at 1. Manufactured sand with maximum particle size of less than 1.18 mm was used as fine aggregate to avoid clogging and for smooth extrudability. The mix proportions of the reference mix without LC^2 was finalised based on the trials ensuring smooth extrusion, and stacking of at least two layers. The Mix IDs and quantities of materials used for the study are shown in Table 1. The mass proportions of FA and GGBS were maintained constant (50:50) throughout the study. LC^2 was introduced at different dosage intervals of 5% by weight of total precursor content till acceptable buildability is achieved. Borax was used to adjust the setting time. All the mix combinations were designed to maintain workability for 15 minutes from the time AAS was added to the dry ingredients.

Table 1. Mix Proportions

Mix ID	FA (wt.%)	GGBS (wt.%)	LC^2 (wt.%)	W/S	S*/P
FG_L0	50	50	-	0.40	1.8
FG_L5	47.5	47.5	5	0.40	1.8
FG_L10	45	45	10	0.40	1.8
FG_L15	42.5	42.5	15	0.40	1.8
FG_L20	40	40	20	0.40	1.8

Note: W/S-Water to Solids ratio, S*/P-Sand to Precursor ratio

Rectangular hollow block of dimension 200 x 100 x 200 mm^3 were printed with a 3-axis gantry printer equipped with a 40 L capacity print head attached with a circular nozzle of 20 mm diameter at the bottom. The printing speed was maintained as 100 mm/s and the thickness of each printed layer was designed to be 10 mm. Flow table test was performed to assess the mixes' flowability and the printed element's buildability was evaluated by measuring the total height of the printed block.

3. Results and Discussions

3.1 Flow Table test

Before each printing, flow table test was performed according to (IS 5512-1983). The recorded slump and spread values are shown in Figure 1. It can be observed that increasing the dosage of limestone calcined clay reduced the slump values, indicating an improvement in shape retention. Consequently, the spread values followed similar trend, with mixes containing more than 10% LC^2 dosage exhibiting notable change compared to those with 0 and 5% dosages. This effect is attributed to the layered particle structure of the limestone-calcined clay, which demands more water content (Ibrahim et al., 2023).

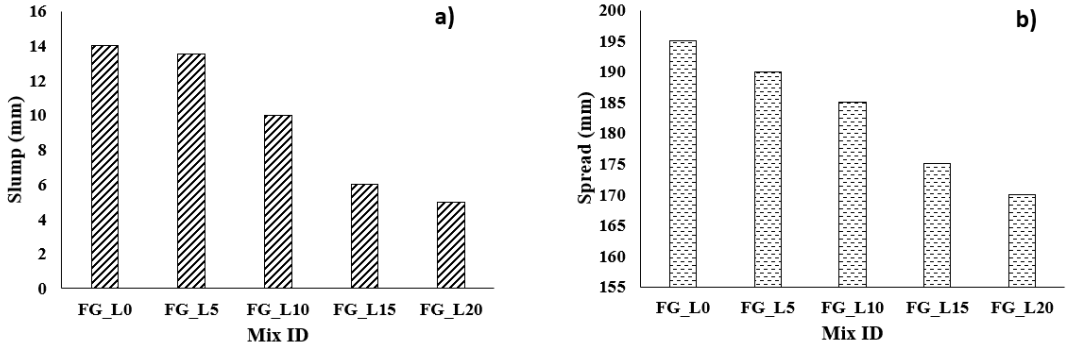

Figure 1. Effect of LC^2 dosage on a) Slump, and b) Spread of 3DP AAMs.

3.2 Buildability assessment

The buildability was assessed through visual observation by measuring the difference between the printed and the actual designed height of the specimen with a tolerance of less than 5 mm. Figure 2 shows the improvement in stacking performance of layers as the LC^2 dosage was increased from 0 to 20 %. As the percentage of LC^2 dosage increases, the buildability of 3DP AAM mixes improved. A similar finding was observed by (Chen et al., 2021), where rapid stiffness was observed with increasing dosage of LC^2 content. It can also be observed that the stacking performance improved when the LC^2 dosage was greater than 5%. The mix without LC^2 collapsed after 6 layers of printing, while the FG_L5 mix sustained 10 layers before failure. The FG_L10 mix showed improvement in stacking until the 12th layer but collapsed due to the uneven filament thickness during printing. This phenomenon can be attributed to plastic deformation in the bottom layers, which increased the standoff distance and caused the greater downward flow of the material, resulting in increased load on the lower layers and structural instability (Chen et al., 2020). Despite some layer distortion observed in FG_L15 printed specimen, no collapse was noticed, whereas the FG_L20 mix was successfully printed up to the 20th layer, with final heights recorded as 190 mm and 196 mm, showing a difference of 10 mm and 4 mm from the designed heights, respectively.

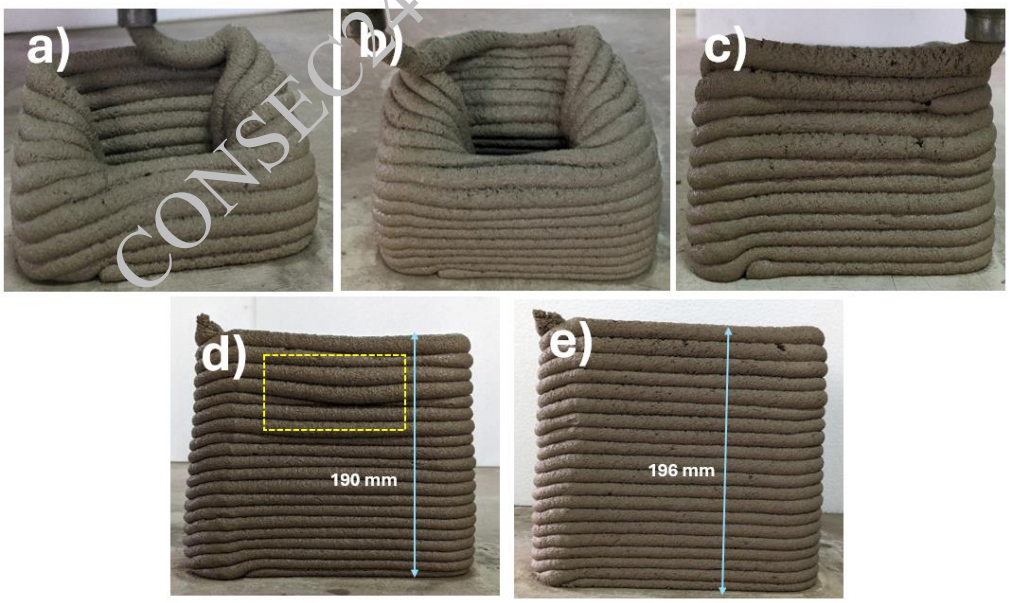

Figure 2. Stacking performance of a) FG_L0 – 6 Layers, b) FG_L5 – 10 Layers, c) FG_L10 – 12 Layers d) FG_L15 – 20 Layers, and e) FG_L20 – 20 Layers

The improvement in the buildability of the mixes (Fig 2 from a) to e)) is attributed to the increased calcined clay content. This increase induces a flocculation structure, leading to a growth in the development of yield stress (Muzenda et al., 2020). In FG_L15 and FG_L20 mixes, the improved stacking of the layers can be

related to the absorption of a larger amount of free water thereby enhancing thixotropy (Muzenda et al., 2020).This behaviour is consistent with the slump values observed in the flow table test.

4. Conclusions

The preliminary investigations from this study highlight the effect of LC^2 dosage on the buildability of 3D Printable Alkali Activated mortars. The findings underscore the potential of LC^2 in advancing the field of 3D Concrete printing. From the print trials, the following conclusions can be drawn.

- Limestone Calcined Clay significantly enhanced the buildability of FA-GGBS based 3D Printable AAMs and the buildability was achieved at 20% dosage level.
- The flow table test results indicate that the mixtures with a slump between 5-10 mm along with spread of 170-185 mm were found to be suitable for improving the buildability with LC^2.
- This study emphasizes the need for further investigations into the effect of LC^2 on the microstructural, rheological and mechanical properties of 3D printable AAMs.

Acknowledgements

The authors express their gratitude to the LC^3 Technology Resource Centre, IIT Delhi, India for providing the LC^2.

References

Bhattacherjee, S., Basavaraj, A.S., Rahul, A.V., Santhanam, M., Gettu, R., Panda, B., Schlangen, E., Chen, Y., Copuroglu, O., Ma, G. and Wang, L.(2021) "Sustainable Materials for 3D Concrete Printing", *Cement and Concrete Composites,* 122: 104156

Chen, Y., He, S., Zhang, Y., Wan, Z., Çopuroğlu, O. and Schlangen, E.(2021)"3D Printing of Calcined Clay-Limestone-Based Cementitious Materials.", *Cement and Concrete Research,* 149: 106553

Chen, Y., Rodriguez, C.R., Li, Z., Chen, B., Çopuroğlu, O. and Schlangen, E. (2020) "Effect of Different Grade Levels of Calcined Clays on Fresh and Hardened Properties of Ternary-Blended Cementitious Materials for 3D Printing", *Cement and Concrete Composites* ,114: 103708

Chougan, M., Ghaffar, S.H., Sikora, P., Chung, S.Y., Rucinska, T., Stephan, D., Albar, A. and Swash, M.R.(2021) "Investigation of Additive Incorporation on Rheological, Microstructural and Mechanical Properties of 3D Printable Alkali-Activated Materials", *Materials and Design,* 202: 109574

Chougan, M., Ghaffar, S.H., Nematollahi, B., Sikora, P., Dorn, T., Stephan, D., Albar, A. and Al-Kheetan, M.J.(2022) "Effect of Natural and Calcined Halloysite Clay Minerals as Low-Cost Additives on the Performance of 3D-Printed Alkali-Activated Materials", *Materials and Design,* 223: 111183

Dai, X., Tao, Y., Van Tittelboom, K. and De Schutter, G.(2023) "Rheological and Mechanical Properties of 3D Printable Alkali-Activated Slag Mixtures with Addition of Nano Clay" ,*Cement and Concrete Composites* 139: 104995

Ibrahim, K. A., Gideon P.A.G. van Zijl, and Adewumi J. B. (2023) "Influence of Limestone Calcined Clay Cement on Properties of 3D Printed Concrete for Sustainable Construction",*Journal of Building Engineering* ,69: 106186

IS 5512. (1983) "Specification for Flow Table for Use in Tests of Hydraulic Cements and Pozzolanic Materials", *Bureau of Indian Standards, New Delhi*.

Kondepudi, K. and Kolluru V.L. Subramaniam. (2021) "Formulation of Alkali-Activated Fly Ash-Slag Binders for 3D Concrete Printing", *Cement and Concrete Composites,* 119: 103983.

Muzenda, T. R., Pengkun H., Shiho, K., Tongbo, S., and Xin, C. (2020) "The Role of Limestone and Calcined Clay on the Rheological Properties of LC3",*Cement and Concrete Composites,* 107: 103516

Shantanu, B., Jain S., and Santhanam M. (2023) "Criticality of Binder-Aggregate Interaction for Buildability of 3D Printed Concrete Containing Limestone Calcined Clay",*Cement and Concrete Composites* 136: 104853

Transport Properties of the Ultra-High-Performance Concrete Made with Locally Available Materials

D. Kootumpurath[1*], J. Karuppanasamy[2]

[1] NIT Calicut, India
Email: dilrabin_p200041ce@nitc.ac.in
[2] NIT Calicut, India
Email: jk@nitc.ac.in

*Corresponding author

ABSTRACT

Concrete mixes with more than 150 MPa compressive strength are deemed as ultra-high-performance concrete (UHPC). Due to its superior strength and durability characteristics, it is gaining wider acceptance as a construction material. In this study different UHPC mixes were developed using the locally available materials and their transport properties were evaluated and compared with the conventional concrete. The following transport properties such as chloride penetrability, chloride migration coefficient, water penetration depth, oxygen permeability index, rate of capillary absorption and permeable pore volume were assessed. From the experimental results it was inferred that the developed UHPC mixes shows excellent transport properties in comparison with the normal concrete (NC). The refined pore structure and low interconnected pores in the UHPC matrix resulted in better resistance against the penetration of gas, liquids and aggressive ions.

KEYWORDS: *Ultra-high-performance concrete, Durability, Chloride penetration, Migration, Permeability*

1. Introduction

UHPC represents a significant advancement in concrete technology, offering unparalleled mechanical properties and durability compared to traditional concrete materials. The application of UHPC is gaining widespread acceptance in civil engineering community due to its potential to revolutionise infrastructure design and service life. Conventional concrete has its limitations in durability and strength. UHPC was initially designed to address these problems, which is characterised by its high compressive strength, tensile ductility and exceptional durability. UHPC is composed of a mixture of fine materials such as silica fume, quartz sand, and high-range water reducers, combined with steel or synthetic fibres to enhance its mechanical properties(Richard and Cheyrezy, 1995). The compressive strength of UHPC is greater than 125 MPa which is much greater than conventional concrete.(Graybeal, 2006). In the durability characteristics conventional concrete is no match to UHPC. Durability performance of UHPC makes it a suitable candidate for construction in severe climatic conditions, including freeze-thaw cycles, chloride penetration, and chemical attacks(Li et al., 2020). Recent studies have highlighted UHPC's minimal porosity and high-density matrix, which significantly reduce the ingress of deleterious substances that typically compromise the integrity of conventional concrete(Akeed et al., 2022). Furthermore, the incorporation of fibres in UHPC enhances its crack-bridging capabilities, providing additional resilience against mechanical stresses and prolonging the service life of structures(Abbas et al., 2015).

2. Mix proportioning

UHPC mixes with a target strength of 125MPa and higher was obtained by extensive literature review. SCMs like Ground granulated blast furnace slag, ultrafine GGBS silica fume, quartz powder, M sand and quartz sand was used to achieve this. Modified PCE based water reducers were also used for the mixes.

Trial and error method was also adopted to fix the dosage of super plasticizer and ice was used to cop up with the high heat of hydration during the mixing process. Specimens were cast with fibres to assess the compressive strength and specimen without fibres was used to test the durability performance since the use of fibre can interfere with the electrochemical measurements.

3. Durability

Due to the higher density and use of SCMs UHPC mixes process higher durability. The durability aspects of UHPC are tested at 28days by various methods such as Rapid Chloride Migration Test, Rapid Chloride Penetration Test, Water permeability test, Oxygen permeability test, Sorptivity and porosity tests. Details of test methods are summarized in Table 1.

Table 1. Parameter evaluated, test method and codes for testing durability of UHPC

Parameters	Test method	Code
Charge passed	Rapid chloride penetration test	ASTM C 1202
Chloride migration coefficient	Rapid chloride migration test	NT BUILD 492
Water penetration depth	Water permeability test	IS 516 (part 2 sec1)
Oxygen permeability index	Oxygen permeability test	IS 516 (part 2 Sec 3)
Sorptivity index	Sorptivity test	SA DI Manual
Water accessible porosity	Porosity test	SA DI Manual

3.1 Water permeability

Water permeability refers to the movement of water into the concrete. If the water is able to move into the concrete it can carry chloride ions and other chemicals which will result in corrosion and degradation of concrete structure. permeability depends on the size and interconnectivity of the pores. Due to the higher density of UHPC and use of SCMs the permeability of water is expected to be very less as compared to the NC.

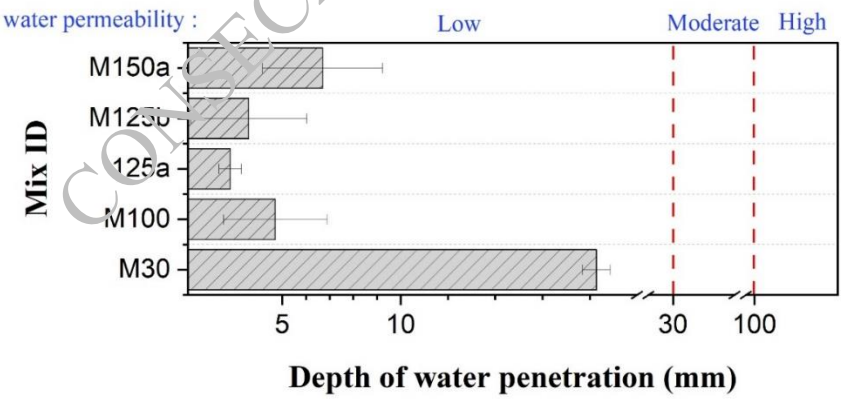

Figure 2. Variation in water penetration depths for NC and UHPC at 28 days

The depth of water penetration was determined according to IS 516-part 2/sec 1 in which 150 mm cube specimen were subjected to water pressure of 5kg/m^2 for 72 hrs. After that the cube was break open to measure the depth of penetration of water. Figure 2 shows the variation of water penetration. As compared to the NC, HPC and UHPC mixes shows very low depth of penetration. It is also noted that the mixes in which silica fumes were used the pore size become even smaller. So, the depth of water penetration is also found to be less as compared to other mixes.

3.2 Oxygen permeability

Similar to the water permeability oxygen permeability is also an important measure of durability since both oxygen and water is required at the rebar surface to initiate corrosion. This property determines the rate at which oxygen can penetrate the concrete matrix. Similar to water permeability, oxygen permeability also depends on concrete's porosity, water-cement ratio, curing conditions and the presence of supplementary cementitious materials.

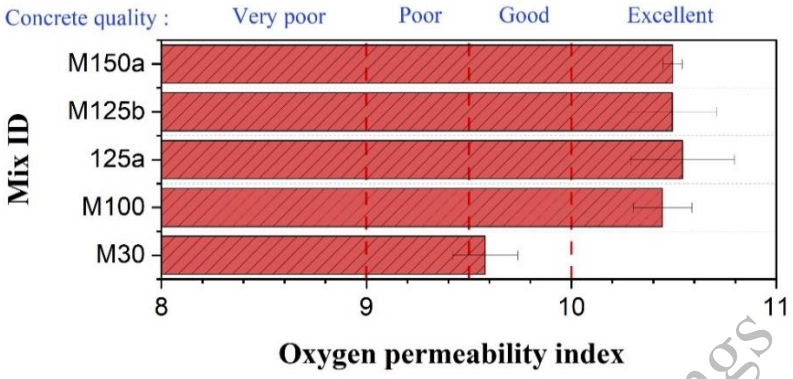

Figure 3. Comparison of OPI for normal mix and UHPC mix at 28 days

Oxygen permeability was measured as per IS 516-part 2/sec 3 , in which 70 mm diameter disk specimen with a thickness of 30 mm kept under a pressure of 100 ± 5 Kpa and the drop in pressure was observed for 6 hrs. Oxygen permeability index was calculated as per the code and it is found that the oxygen permeability of all UHPC specimen was more than NC specimen (Figure 3).

3.3 Chloride ion permeability

Chloride ions can be found in concrete as free or bound chlorides. Free chlorides dissolve in pore solution whereas bound chlorides are found in bond with hydration products. Free chlorides cause the reinforcement to corrode and leads to structural degradation(Sohail et al., 2021). Once the chloride ions reach the threshold value on the steel surface it initiates corrosion and structure enters corrosion propagation phase and ends up in structural failure. To assess chloride ion permeability, tests like the rapid chloride permeability test (RCPT)(ASTM C1202) and Nordtest method(NT BUILD 492)-Rapid chloride migration test (RCMT) are used, with the latter employing the chloride ion diffusion coefficient as an indicator. UHPC shows significantly lower chloride ion diffusion coefficients compared to high-performance concrete (HPC) or conventional concrete, though comparison is challenging due to varying test conditions and mixture compositions.

shows the charge passed in RCPT and Figure 4 shows the non-steady state migration coefficient calculated from RCMT. It can be seen that very less chloride ions are able to penetrate through UHPC as compared to NC. Even after application of external voltage of 60V for 96 hrs the depth of chloride ion penetration is negligible. So, it can be inferred that UHPC is highly resistant towards chloride ion penetration. So, it can be used in harsh climatic conditions with high chloride exposure, without being concerned about chloride induced corrosion.

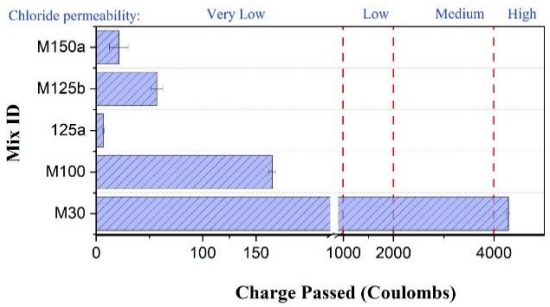

Figure 4 : Variation of charge passed in NC and UHPC at 28 days

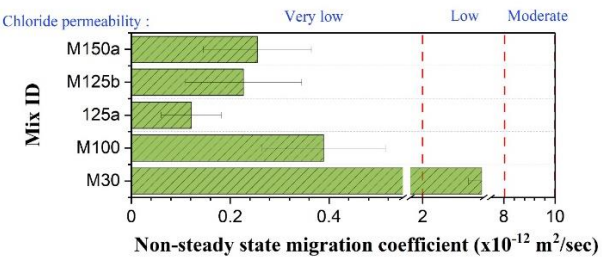

Figure 5. Variation in chloride migration of NC and UHPC at 28 days

3.4 Sorptivity and porosity

Sorptivity is a critical measure for evaluating the durability of cementitious materials, reflecting their ability to absorb water and potentially harmful agents through capillary pores. In this study, sorptivity was assessed using the procedure outlined in the South African Durability index (2018))(SA DI) manual. Disk specimens were conditioned to stabilize moisture content, and the absorption rate was measured by immersing the bottom 2 mm of each specimen in distilled water saturated with calcium hydroxide. The weight of the specimens was recorded over time, and the sorptivity index was calculated by plotting the absorption rate against the square root of time. The focus was primarily on initial sorptivity, which indicates the material's ability to absorb water in a dry state, while secondary sorptivity could not be measured for UHPC due to its low porosity and slow absorption rate (Sohail et al., 2021). Porosity and sorptivity are closely linked and play a significant role in determining the durability and permeability of concrete. Porosity refers to the volume of voids within the concrete matrix, formed during mixing and curing, which can be filled with air or water. Higher porosity typically leads to increased permeability and reduced strength, as more voids allow easier ingress of water and harmful agents. Sorptivity, which measures the rate at which water is absorbed and transmitted through capillary action, is generally higher in materials with greater porosity due to the increased number of pathways for water movement. Usually in materials with higher porosity, sorptivity will also be higher. But when comparing Figure 5 and 6, it is observed that there is slight contradiction in the relationship between sorptivity and porosity. This may be due to the discontinuity in pores in the specimen. Porosity measures the total void content and sorptivity depend on the interconnectivity of the pores. As compared to the NC, the sorptivity and porosity values of UHPC is much higher. Which is due to the higher packing, lower pore size and less pore interconnectivity.

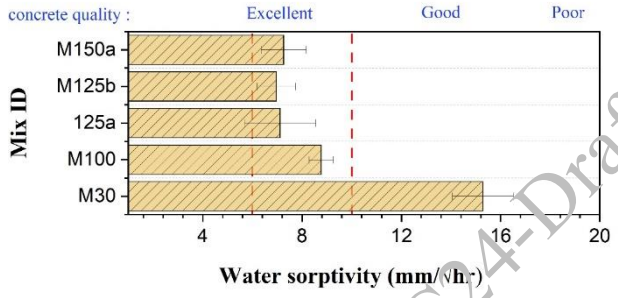

Figure 5. Initial sorptivity values for NC and UHPC at 28 days

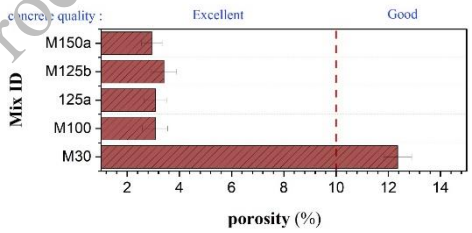

Figure 6. comparison of total measured

4. Conclusions

The durability assessments conducted through various tests, including water permeability, oxygen permeability, and chloride ion permeability, consistently indicate UHPC's superior performance compared to conventional concrete.

- Regardless of the mix combinations, the test results of all the UHPC samples fall within the criteria for excellent durability behaviour.
- The UHPC mix containing OPC and ~33% silica fume as binder (M125a) has shown the least water and air permeability and chloride penetration among other UHPC mixes owing to high cement content and substantial pozzolanic reactions of silica fume that densifies the microstructure.
- The higher the cement content and compressive strength of the UHPC mixes, the better the durability test parameters obtained. However, the slight difference observed in the case of M150 mixes compared to M125a might be due to the higher reactivity of silica fume.
- The filling effect and pozzolanic reaction contributed by quartz powder in the M125b mix have aided in slightly better permeability resistance when compared to the M100 mix.

Low permeability to oxygen and water along with high resistance to chloride ion penetration of UHPC ensures its effectiveness in preventing corrosion and thereby increasing the service life of the structure. The higher density of UHPC is also confirmed by low sorptivity and porosity values. Overall, UHPC offers a transformative solution for civil engineering applications, providing a robust and durable material capable

of withstanding harsh environmental conditions and mechanical loads. Its adoption in infrastructure projects promises to significantly extend service life and reduce maintenance costs, marking a substantial advancement in the field of construction materials. The research underscores the potential of UHPC to revolutionize infrastructure design, paving the way for more resilient and long-lasting structures.

References

Abbas, S., Soliman, A. M. and Nehdi, M. L. (2015) "Exploring mechanical and durability properties of ultra-high performance concrete incorporating various steel fiber lengths and dosages",. *Construction and Building Materials*,75:429-441

Akeed, M. H., Qaidi, S., Ahmed, H. U., Faraj, R. H., Mohammed, A. S., Emad, W., Tayeh, B. A. and Azevedo, A. R. G. (2022) "Ultra-high-performance fiber-reinforced concrete. Part IV: Durability properties, cost assessment, applications, and challenges", *Case Studies in Construction Materials*, 17: e01271

ASTM C1202-19. (2019) "Standard Test Method for Electrical Indication of Concrete's Ability to Resist Chloride Ion Penetration ",

Graybeal, B. A. (2006) "Material Property Characterization of Ultra-High Performance Concrete"

Li, J., Wu, Z., Shi, C., Yuan, Q. and Zhang, Z. (2020) "Durability of ultra-high performance concrete – A review", In *Construction and Building Materials*, 255:119296

Hardened concrete—methods of test part 2 properties of hardened concrete other than strength Section 1 Density of Hardened Concrete and Depth of Water Penetration Under Pressure. (2018). *www.standardsbis.in*

Nt build 492. (1999) "concrete, mortar and cement-based repair materials: chloride migration coefficient from non-steady-state migration experiments"

Richard, P. and Cheyrezy, M. (1995) "Composition of reactive powder concretes", *Cement and Concrete Research*, 25(7):1501-11

Sohail, M. G., Kahraman, R., Al Nuaimi, N., Gencturk, B. and Alnahhal, W. (2021) "Durability characteristics of high and ultra-high performance concretes", *Journal of Building Engineering*, 33:101669

Durability Index Testing Procedure Manual (2018). (n.d.).

Indian Standard,516. (2022) "Hardened Concrete-Methods of Test Part 2 Properties of Hardened Concrete other than Strength Section 3 Oxygen Permeability Index (First Revision)"

The Utilization of Recycled Concrete Powder as a Partial Substitute for Filler in the Manufacturing of Foam Concrete Mixtures

Amit Kumar Sahu[1*], Vishal Kumar Mishra[2], Rahul Kumar Sonker[3], Indu Siva Ranjani Gandhi[4], Prakash Nanthagopalan[5]

[1]Indian Institute of Technology, Guwahati, India
Email: amit4002@iitg.ac.in
[2]Indian Institute of Technology, Guwahati, India
Email: vishal.mishra@iitg.ac.in
[3]Indian Institute of Technology, Guwahati, India
Email: r.sonker@iitg.ac.in
[3]Indian Institute of Technology, Guwahati, India
Email: gindu@iitg.ac.in
[4] Indian Institute of Technology, Bombay, India
Email: prakashn@iitb.ac.in

[*]Corresponding author

ABSTRACT

Foam concrete (FC) is a lightweight and highly functional material extensively used in various construction applications. In this study, attempt has been made to use recycled concrete powder (RCP) derived from waste concrete specimens from the concrete laboratory as a filler replacement in FC. Mix foaming technique is adopted to produce FC using OPC 53 grade cement as the binder and class F fly ash as the filler. RCP is used to replace fly ash at different levels viz., 10%, 20%, and 30% by weight. A water-to-solid ratio of 0.35 is chosen to obtain stable FC mixtures with a flow value of 150±10mm after 10 minutes of mixing. An anionic surfactant, sodium lauryl sulphate (SLS) is mixed in the mixing water at 0.4% of total water. After 10 minutes of mixing, the fresh density of 665, 688, 857 and 842 kg/m^3 is attained by replacing 0%, 10%, 20%, and 30% of RCP. The incorporation of RCP is found to affect air entrainment resulting in increase in the fresh density, mostly because of the angular nature of RCP and its higher water absorption capacity. The fresh state properties of the FC mixtures, including consistency and stability, are evaluated along with the hardened state properties, such as compressive strength and thermal conductivity. This study demonstrates the potential of utilizing RCP as a substitute for filler in order to create stable FC mixtures with low density and consistency.

KEYWORDS*: Foam Concrete, Recycled Concrete Powder, Filler Replacement, Mix foaming method, Sustainable Construction.*

1. Introduction

Foam concrete (FC) has a lower density compared to conventional concrete due to its increased porosity. This increased porosity is achieved by incorporating air bubbles into the mixture. To produce FC, there are two methods: either premade foam is mixed with the mortar (known as the pre-foam method), or the foam is generated during the mixing process (known as the mix foam method) (Ramamurthy et al., 2009). For low-density FC mixtures, the homogeneity of the mixtures is the main concern in the pre-foam method (Tran et al., 2022). The pre-foam method requires a foam generator with an air compressor and mixing equipment to facilitate homogenous mixing of mortar and foam. In contrast, the mix foam method requires a mixing tool to impart mechanical energy to entrain air in the mortar mixture (Markin et al., 2019). This mechanical energy, which depends on rotor speed, fluid viscosity, and the time the gas/liquid mixture spends, creates a wave-like pattern on the surface (Drenckhan & Saint-Jalmes, 2015). This pattern leads to

the formation of large bubbles. These large bubbles are then broken under the continuous shearing action of the mixer. This process continues until an equilibrium state is reached. This state is characterized by a specific gas fraction and bubble size, which depend on the rheological properties of the liquid and the rotating velocity of the mixer (Petkova et al., 2020; Politova et al., 2018). Although mix foaming process is extensively used in the production of aqueous foams, very few studies have utilized the aforementioned technique for cement-based foam. Limited studies available on mix foaming technique have focused mainly on the advantages of intensive mixing in air entrainment (Markin et al., 2019; Namsone et al., 2017). However, studies on parameters affecting the efficiency of mix foaming process of cement foam is very much limited. In previous studies, FC was mostly prepared using ordinary Portland cement (OPC), fly ash, and river sand. Some researchers partially replaced OPC by fly ash, slag, recycled concrete powder (RCP) etc. Similarly, river sand was also replaced by fine aggregates such as manufactured sand, perlite, vermiculite, RCP, etc.(Shah et al., 2021) . In recent years, the generation of concrete waste has increased rapidly due to urbanization, making the proper disposal of this concrete waste as a challenging issue for many countries. Consequently, many researchers have recently tried to incorporate RCP to produce FC. RCP has been used as a mineral admixture to improve some properties of concrete and reduce the use of cement clinker in some studies. These studies found that the addition of RCP increased the water demand of concrete and reduced its workability. However, with the increase in RCP content, the mechanical properties of concrete is reported to decrease significantly (Yang et al., 2023). However, there are very few studies that discuss the effect of RCP on air entrainment during the production of FC using the mix foaming process. In this study, FC mixtures are prepared using the mix foaming method, and the effect of RCP (as filler replacement) on air entrainment is examined. Fresh state properties such as consistency and stability are evaluated, along with compressive strength, flexural strength, and thermal conductivity (TC).

2. Materials and Methodology

OPC (grade 43, supplied by Max Cement), conforming to IS 269:2020, is used as a binder in FC. Additionally, Class-F fly ash, procured from National Thermal Power Corporation, Bongaigaon, India, passing through a 300μm screen, is used as a filler material. RCP is prepared by crushing the Laboratory concrete specimens in a jaw crusher followed by pulverization. In this study, RCP passing through 300μm with specific gravity of 2.58 is used as partial replacement of Class-F fly ash. Sodium lauryl sulphate (SLS), supplied by Loba Chemicals, is used as a foaming agent in the production of foamed concrete. Tap Water is used in the foamed concrete mixture. The quantities of each constituent are shown in Table 1. Initially, the FM mixture is prepared without RCP, using cement and fly ash in the ratio of 1:1 by weight. Then remaining three mixtures viz., FM1, FM2, FM3 are prepared by using RCP as a partial replacement for fly ash by 10%, 20%, and 30% by weight respectively. A constant water/solid (w/s) of 0.35 is chosen to formulate the FC mixtures based on the preliminary trials to produce homogenous mixtures without lumps. From the experimental trials, it was observed that beyond 0.4% SLS dosage, lumps are observed even at air entrainment less than 50%. Hence the dosage of SLS is fixed at 0.4% for the present study. All dry constituents are mixed in a 30-litre planetary mixer at 107 rpm for 30 seconds. After this initial mixing, water mixed with SLS is gradually added to the mixing container while maintaining the same speed. This combined mixing process lasts for 1 minute and 30 seconds. The initial mixing time of 2 minutes is referred to as T. After 2 minutes of initial mixing at 107 rpm, the speed is increased to 198 rpm to effectively incorporate the air bubbles and thereafter mixed for ten minutes followed by measurement of density at T+10 mins. of mixing time.

Table 1. Quantities of constituents in FC mixtures

Mixture ID	Cement (g)	Fly ash (g)	RCP (g)	Water (g)	SLS (g)
FM	4000	4000	0	2800	11.20
FM1	4000	3600	400	2800	11.20
FM2	4000	3200	800	2800	11.20
FM3	4000	2800	1200	2800	11.20

The developed FC mixtures is further assessed for its stability and consistency. The stability of FC mixtures is assessed by measuring the fresh density and demoulded density. While, consistency of the mixtures is assessed by flow table method in accordance with the EN 1015-3. Furthermore, FC mixtures are also

examined in terms of compressive strength, flexural strength and TC. For each mixture, 6 prismatic specimens of 40×40×160 mm and 3 specimens of 50 mm cube are prepared in order to determine the compressive strength (EN 1015-11), flexural strength (EN 1015-11) and TC. The transient plane source method, as described in ISO-22007 Part-2, is used to assess the TC. Specimens are demoulded and subjected to water curing until 28 days of testing.

3. Results and Discussions

3.1 Effect of RCP on air entrainment

The fresh density, demoulded density, and flow values are shown for the mixtures FM, FM1, FM2, and FM3 in Fig 1. After T+10 min of mixing, the lowest fresh density is observed for the mixture without RCP (FM). The addition of RCP decreases air entrainment and this can be attributed to the higher water demand and irregular shape of RCP (Yang et al., 2022). This subsequently leads to further collapse of air bubbles causing the lesser air entrainment. The demoulded density and fresh density for the FM1 mixture are nearly the same, which indicates the highest stability among the mixtures. However, at higher RCP replacement levels, such as in FM2 and FM3, stability decreases. Adding to above, the FM1 mixture has the lowest flow value. The increased flowability of FM2 and FM3 mixtures is due to the lesser air entrainment, as stated in (Nambiar & Ramamurthy, 2007).

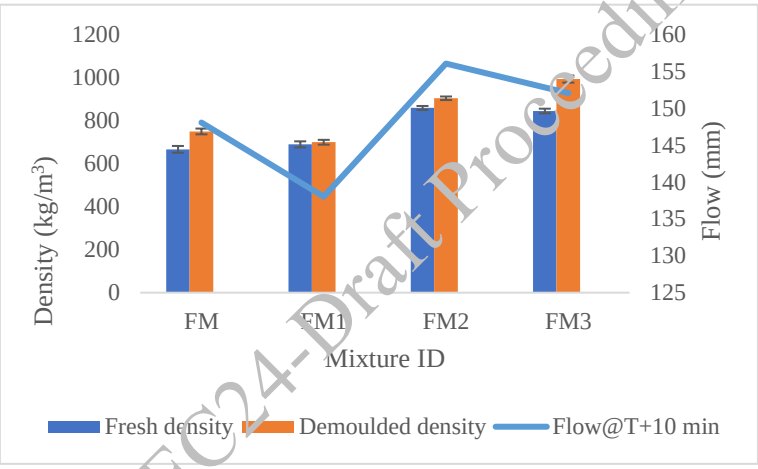

Figure 1. Effect of RCP replacement on fresh density, demoulded density and flow values

3.2 Compressive strength and flexural strength of FC mixtures

Table 2 outlines the effects of varying percentages of RCP on the mechanical properties of FC. The results clearly show the direct relationship between density and mechanical strength. Addition of RCP in mixtures result in decrease in air entrainment and subsequent increase in density of mixtures. This can be attributed to increase in strength of mixtures with RCP. However, mixture FM1 shows slight reduction in strength when compared to mixture FM and this can be attributed to reduced demoulded density of FM1 mixture.

Table 2. Effect of RCP replacement on compressive and flexural Strength

Mixture ID	Demoulded density (kg/m^3)	Compressive strength (MPa)	Flexural strength (MPa)
FM	748	1.6	0.6
FM1	698	1.3	0.5
FM2	902	1.5	0.5
FM3	991	1.8	0.7

3.2 Thermal conductivity of FC mixtures

Table 3 highlights the oven-dried density and TC values for FC mixtures with varying percentages of RCP. The introduction of RCP affects air entrainment, subsequently influencing TC. Increase in RCP addition

resulted in increase in TC due to increase in density of mixtures. However, TC is found to be the lowest for mixture FM1 which can be attributed to its lowest density.

Table 3. Effect of RCP replacement on thermal conductivity

Mixture ID	Oven dried density (kg/m^3)	Thermal conductivity (W/m-k)
FM	672	0.2965
FM1	634	0.2532
FM2	859	0.3014
FM3	942	0.3031

4. Conclusions

Experimental outcomes of present study have established that incorporation of RCP into FC mixtures affects air entrainment due to its higher water demand and irregular shape. The above effect of RCP on air entrainment resulted in increase in density of mixtures and subsequent impact on mechanical behaviour and TC was observed. Based on the limited preliminary studies, it can be stated that mixture with 10% RCP (FM1) is found to perform better in terms of stability and exhibits minimum thermal conductivity among all the mixtures studied. However, additional research is needed to explore ways of utilization of RCP at higher replacement levels for mixed foaming method of FC production.

Acknowledgements

Authors would like to acknowledge DST- SERB, India, for funding this research.

References

Drenckhan, W. and Saint-Jalmes, A. (2015) " The science of foaming", *Advances in Colloid and Interface Science*, 222: 228–259

Markin, V., Sahmenko, G., Nerella, V. N., Nather, M. and Mechtcherine, V. (2019) "Investigations on the foam concrete production techniques suitable for 3D-printing with foam concrete", *IOP Conference Series: Materials Science and Engineering*, 660(1)

Nambiar, E. K. K. and Ramamurthy, K. (2007) "Air-void characterisation of foam concrete", *Cement and Concrete Research*, 37(2): 221–230

Namsone, E., Šahmenko, G. and Korjakins, A. (2017) " Durability Properties of High Performance Foamed Concrete", *Procedia Engineering*, 172: 760–767

Petkova, B., Tcholakova, S., Chenkova, M., Denkov, N., Thorley, D. and Stoyanov, S. (2020) " Foamability of aqueous solutions: Role of surfactant type and concentration", In *Advances in Colloid and Interface Science* ,276: 102084

Politova, N., Tcholakova, S., Golemano, K. and Denkov, N. D. (2018) "Self-regulation of foam volume and bubble size during foaming via shear mixing" *Colloids and Surfaces A: Physicochemical and Engineering Aspects*, 539:18–28

Ramamurthy, K., Kunhanandan Nambiar, E. K. and Indu Siva Ranjani, G. (2009) "A classification of studies on properties of foam concrete", *Cement and Concrete Composites*, 31(6): 388–396

Shah, S. N., Mo, K. H., Yap, S. P., Yang, J. and Ling, T. C. (2021) "Lightweight foamed concrete as a promising avenue for incorporating waste materials: A review", *Resources, Conservation and Recycling*, 164: 105103

Tran, N. P., Nguyen, T. N., Ngo, T. D., Le, P. K. and Le, T. A. (2022) "Strategic progress in foam stabilisation towards high-performance foam concrete for building sustainability: A state-of-the-art review*", Journal of Cleaner Production* , 375: 133939

Yang, D., Liu, M., Zhang, Z., Yao, P. and Ma, Z. (2022) "Properties and modification of sustainable foam concrete including eco-friendly recycled powder from concrete waste", *Case Studies in Construction Materials*, 16:e00826

Yang, S., Wang, X., Hu, Z., Li, J., Yao, X., Zhang, J. and Wang, W. (2023) "Recent advances in sustainable lightweight foamed concrete incorporating recycled waste and byproducts: A review", *Construction and Building Materials*, 403:133083

Unlocking Strength Potential: Investigating Mixing Protocols And Comprehensive Optimization Stratergies In Carbon Sink Binders

Niveditha.M[1]*, and Palanisamy.T[2]

[1] PhD Research scholar, NITK, Mangalore, India
Email: m.niveditha.m@gmail.com
[2] Associate Professor, NITK, Mangalore, India
Email: tpalanisamycivil@nitk.edu.in

*Corresponding author

ABSTRACT

The imperative for sustainable materials to replace cement, which poses significant environmental hazards, has propelled extensive research and studies. Utilizing waste materials in the carbon sink binder formulation presents a notable example of optimizing resources. The major proportion of the binder involves the mill scale waste which serves as the primary iron source in the binder formulation, complemented by fly ash, limestone, and metakaolin to create the composition of the carbon sink binder. The distinguishing feature of this binder lies in its ability to absorb carbon dioxide, in contrast to cement's carbon dioxide emissions during manufacturing. The process involves carbon dioxide curing to enhance strength, where carbonates form as vital components. This research explores the nuanced process of formulating a carbon sink binder, highlighting the importance of raw material properties and meticulous methodology at every stage. From mixing protocols to curing regimes, each phase significantly influences the binder's performance and compressive strength. By optimizing these processes, the study presents a comprehensive approach to developing an innovative and sustainable binder with broad potential applications across industries. The findings underscore the critical role of precision and iterative refinement in achieving optimal results, advancing both scientific understanding and practical applications in sustainable materials development. This initiative holds promise for environmental sustainability and waste management, contributing significantly to establishing norms for binders.

KEYWORDS: *Carbon sink binder, Iron waste upcycling, Chelating agent, Oxalic acid, Carbon sequestration*

1. Introduction

In the domain of civil engineering and construction, binders serve as the bedrock upon which modern infrastructure stands, providing cohesion and structural integrity to various building materials. Historically, lime, clay, bitumen, and gypsum were the primary binders utilized by ancient civilizations, each chosen for its specific properties and applications. However, the emergence of cement in the 19th century heralded a new era in construction, offering unparalleled strength, versatility, and durability.(Gartner and Macphee 2011). Cement swiftly supplanted traditional binders due to its myriad advantages, becoming the cornerstone of modern infrastructure development. However, despite its widespread use, the production of cement presents formidable environmental challenges. These include substantial greenhouse gas emissions, significant energy consumption, and depletion of natural resources. The United Nations' embracement of the New Urban Agenda in 2016 underscored the urgent need for sustainable building materials and construction methods that mitigate environmental impact and promote a green economy. In response to these challenges, researchers and industry professionals are actively exploring alternatives to traditional cement. One such innovation is the iron carbonate binder, which represents a paradigm shift towards sustainable construction practices. This novel binder harnesses iron waste, along with eco-friendly raw materials such as limestone, fly ash, and metakaolin, to create a low-carbon, environmentally friendly alternative to cement.(Santawaja et al. 2020) Studies by Agrawal et al. 2009; Gurzau et al. 2003; Mohanty

et al. 2010; Yellishetty et al. 2008) have highlighted the potential of repurposing iron waste as a sustainable building material. Additionally, research by (Das et al. 2015, 2016b; a; Lyngdoh et al. n.d.) has demonstrated the feasibility of incorporating iron waste into composite materials for construction applications. The iron carbonate binder offers several advantages over traditional cement, including reduced greenhouse gas emissions, minimized environmental impact, and utilization of industrial waste. Its unique curing mechanism, which involves carbon dioxide absorption during the curing process, further enhances its eco-friendliness. Studies by (Das et al. 2014a; b) have elucidated the carbon sequestration potential of iron carbonate binders, making them a promising solution for mitigating carbon emissions in the construction sector. In this paper, we delve into the development and properties of the iron carbonate binder, exploring its manufacturing process, chemical composition, and curing mechanism. Drawing upon insights from existing research and experimentation, we assess the potential of this innovative binder as a sustainable building material. Furthermore, we discuss its implications for reducing carbon emissions, promoting circular economy principles, and advancing towards a greener, more resilient built environment. Through comprehensive analysis and empirical evidence, this paper aims to contribute to the ongoing discourse on sustainable construction materials and practices. By advocating for the adoption of the iron carbonate binder as a viable alternative to traditional cement, we endeavor to catalyze positive change in the construction industry towards a more sustainable future.

2. Materials and methodology

The carbon sink binder consists of majorly four raw materials. The iron source is the major proportion, along with flyash, metakaolin, and limestone powder. The raw materials are procured from different sources and tested for the best source in order to formulate the binder. The raw materials with tailor-made methodology and curing setup for the binder formulation make the binder unique along with a unique mixing protocol.

2.1 Raw Materials

Various sources of raw materials are procured to determine the most suitable for specific research. Paper outlines the current sources of materials, encompassing Indian-origin materials from local markets to various brands. Iron powder is sourced from: Bellary slag - the residue from industrial processes in the Bellary region, resulting from iron ore smelting or refining. (I1) Bellary Iron Ore - primary iron source from the Bellary region utilized across industries(I2). Sandur fines - a specific type of iron ore fines from the Sandur region, generated during the screening or crushing process. (I3) Mill-scale waste (I4) Machine Laboratory - facility within the institute engaged in iron processing or fabrication machinery research, development, or production. (I5) Fabrication shops - workshops where metal components, including iron, are fabricated or assembled. (I6) The mill scale wastes procured had a greater advantage of higher iron concentration(Eissa et al. 2015; Jikar and Dhokey 2021; Predescu et al. 2021)

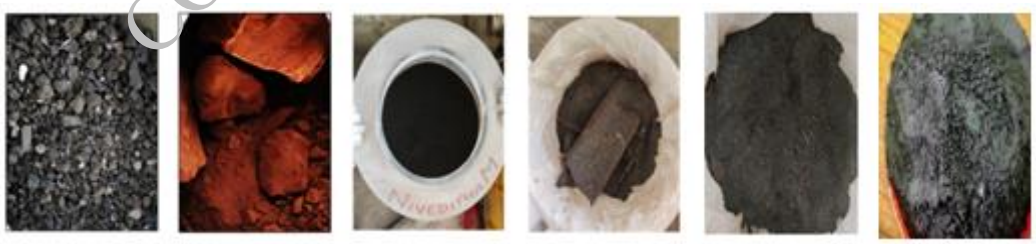

Figure 1. Different sources of iron (a) Bellary iron slag (b) Sandur iron ore (c) Bellary fines (d) Fabrication shop (e) Machine Laboratory (f) Mill Scale waste

Fly ash, a byproduct of thermal power plants, is sourced from diverse sources, each exhibiting unique compositions influenced by the coal utilized. These sources encompass Udupi Power Corporation Limited (UPCL) (F1), KPCL Raichur thermal power plant, (F2) and Yermarus Thermal Power Station. (F3) Limestone, alternatively recognized as calcium carbonate, is obtained from a variety of outlets, including local markets in Mangalore(L1), chemically synthesized calcium carbonate under the renowned 'Sigma' brand, (L2) and finely ground calcium carbonate from the '20 microns' brand, (L3) chosen specifically for its enhanced fineness. Metakaolin, an essential ingredient in the binder mix, is procured from multiple

suppliers, such as Mysore Agencies(M1) and vendor of Intercity Enterprises(M2), ensuring a diversified sourcing strategy to maintain quality standards and availability. Oxalic acid, a critical component in the formulation(C.I. Nwoye et al. 2020; Chiarizia and Horwitz 1991; Veglio 1998), is acquired from various suppliers, including local markets, Radiant Chems, and reputable Sigma-branded products, thereby ensuring a reliable and diverse supply chain. The utilization of materials from these varied sources not only enriches the diversity of the experimental setup but also underscores the robustness and adaptability of the developed protocols across different material compositions and characteristics.

2.2 Processing of raw material

Iron powder obtained from various sources comes in different sizes. Since finer particles enhance reactivity, several processing techniques were explored for raw materials. Utilizing the ball mill facility within the metallurgy department of the institute, efforts were made to achieve greater fineness. Figure 4.6 depicts the ball mill setup, showcasing (a) Balls, (b) Front view of the ball mill, (c) Side view of the ball mill, and (d) Working panel. Through ball milling, iron slag sourced from Bellary with a size of 5mm was reduced to 150µm. Figure 4.7 illustrates the transformation of slag into powdered form using the ball mill, showcasing (a) Slag and (b) Powdered slag.

Figure 2 . Pulverizer

Figure 3.Ball mill (a) Balls (b) Ball mill - front view (c) Ball mill - side view (d) Working panel

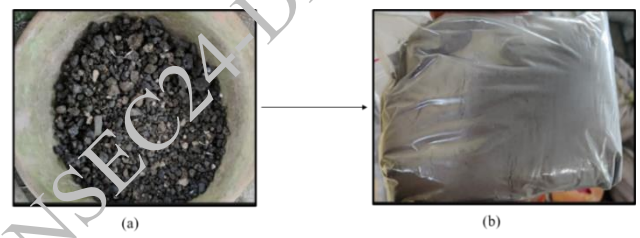

Figure 4. Slag converted to powder form using ball mill (a) Slag (b) Powdered slag

Another method employed to decrease fineness involves the use of a pulverizer. The iron powder, originally passing through a 300µm sieve, was reduced to an average size of 45µm using this method. Figure illustrates the pulverizer utilized to achieve enhanced fineness of the iron samples obtained.Trials are essential for each distinct raw material. Prior to utilization, fundamental chemical composition tests are conducted, and results are cross-checked with the Certificate of Analysis (CoA) provided by the supplier. The fineness of raw materials plays a pivotal role in formulating the binder. According to Humbert et al. (2019), fineness is a crucial factor influencing the reactivity of raw materials. Therefore, trials involving various sources of raw materials with differing fineness levels are imperative. Trials focusing on achieving greater fineness were carried out initially, followed by testing. Techniques akin to those employed for reducing iron powder particle size were utilized for other raw materials. Subsequently, procurement of finer versions of other raw materials was facilitated.

2.3 Methodology

2.3.1 Curing Setup

A hermetically sealed curing chamber is crafted from metal using a cylindrical structure. To ensure continuous monitoring of the chamber's internal pressure, a pressure gauge is permanently affixed to it.

Additionally, a vacuum pump, equipped with a pressure gauge for measuring vacuum pressure, is connected to the chamber. Carbon dioxide cylinders are utilized to supply carbon dioxide for the curing process. The carbon dioxide inlet and the vacuum pump are connected to the curing chamber via a two-way valve. This arrangement, influenced by insights from (Abdul-baki 2017; Venhuis and Reardon 2001), enables versatile control over the chamber's pressure conditions. The single valve of the two-way valve is linked to the chamber via a pressure gauge connection, facilitating precise pressure management.

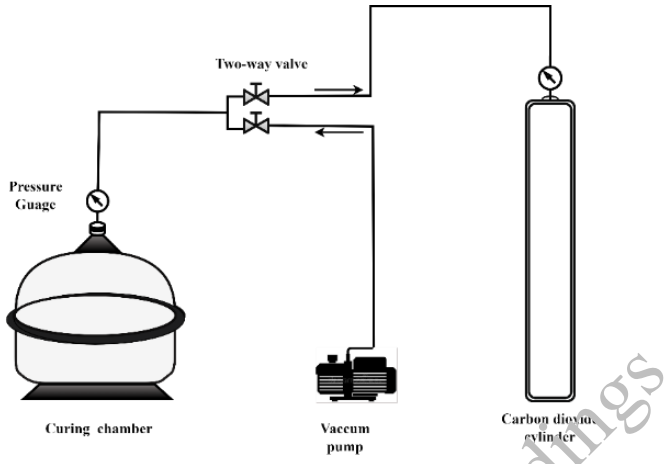

Figure 5. Schematic representation of curing setup

The vacuum pump is employed to establish a vacuum within the chamber using the two-way valve and the compound gauge to achieve the desired pressure. Once the desired vacuum pressure is attained, the valve is securely closed, and the carbon dioxide connecting valve is opened to allow carbon dioxide to fill the chamber until the required pressure is reached. Subsequently, the valves are closed, and the chamber is maintained under pressure by periodically replenishing the carbon dioxide as needed throughout the curing duration. Following the designated curing period, the chamber is opened to allow the specimens to undergo air curing. The entire curing system is depicted schematically in Figure 5

2.3.2 Casting sequence and demolding pattern

The casting protocol undergoes meticulous refinement through numerous trial runs, each aimed at optimizing the process for superior results. Initially, one method involves filling the mold with the binder mix, followed by vigorous vibration for compaction. While this technique achieves adequate compaction, it presents drawbacks. Notably, finer particles tend to migrate to the surface, resulting in uneven settling as depicted in Figure . Subsequently, an alternative approach emerges, where casting occurs in layers with manual tamping. This method demonstrates enhanced strength compared to complete vibration. This improvement becomes evident through meticulous testing, as illustrated in Figure , where the efficacy of the technique is palpable. Further innovation ensues through the integration of hand tamping with compression techniques. Here, the layered compaction achieved through manual tamping is supplemented by compression at both ends of the mold, effectively achieving the desired size and density. This collaborative approach marks the culmination of trial and error, culminating in the establishment of an optimized casting protocol geared towards maximizing compressive strength. The demolding method is crucial for maintaining the proper shape of the specimen and impacting its curing process. Delaying demolding not only affects the shape but also postpones the specimen's exposure to the curing environment. Embracing the concept of swift exposure to the carbon dioxide curing environment can enhance results and expedite the curing process. However, it's equally vital to consider this factor in conjunction with practical implications and the challenges associated with demolding.

2.3.3 Curing Regime

The process of curing the binder necessitates the presence of carbon dioxide, crucial for its strength development. The binder gains strength by absorbing carbon dioxide, a pivotal step in its reactivity rate and overall durability. The demolding procedure, coupled with specific curing conditions, significantly influences the strength enhancement of the samples. Various trials were conducted to determine the optimal demolding and curing approach. These trials included demolding after one day of carbon curing, one day

of ambient curing followed by demolding, or one day of oven curing prior to demolding. Additionally, experiments involved immediate demolding followed by exposure to carbon dioxide, or immediate demolding with subsequent oven curing before carbon dioxide treatment. Another variation explored initial ambient curing followed by carbon dioxide curing. In addition to carbon dioxide exposure, the curing process also necessitates ambient conditions to facilitate the removal or evaporation of moisture from the sample. Through a series of trials, researchers are determining the optimum duration of carbon dioxide curing and the minimum number of days required for ambient exposure. This investigation is crucial for refining the curing protocol and achieving optimal results. By analyzing factors such as the water binder ratio and the proportioning of the binder, researchers can make informed decisions based on these findings and initial assumptions. This iterative process allows for a more comprehensive understanding of how different curing conditions impact the overall strength and properties of the binder. Each of these distinct curing patterns underwent rigorous testing to identify the most effective approach for further investigation and analysis.

3. Experimental Evaluation

The innovative carbon sink binder is meticulously formulated with precise proportions of raw materials to optimize its performance. Special attention is given to the methodology of mixing the binder ingredients alongside the chelating agent, oxalic acid. This process undergoes thorough monitoring and testing to identify the most effective approach for achieving robust compressive strength. The mixing protocol is a critical aspect that determines the overall quality of the binder. Through a series of trials, the decision between wet and dry mixing methodologies is carefully evaluated, considering the role of oxalic acid as a chelating agent. This iterative refinement ensures that the chosen mixing protocol aligns with the goal of maximizing compressive strength. Similarly, the casting protocol undergoes extensive experimentation to enhance compressive strength. Initial attempts using compaction via vibration revealed issues of uneven settling, prompting the exploration of alternative methods. Subsequent trials revealed that layered casting with manual tamping yielded superior strength compared to complete vibration. Further optimization was achieved by integrating hand tamping with compression techniques, resulting in a casting method that maximizes compressive strength. The development of the curing protocol is guided by trials and initial assumptions. Tests are conducted to determine the optimum dosage of oxalic acid, considering the water-binder ratio. The compressive strength results serve as a basis for finalizing the casting sequence and curing regime. Additionally, careful observation is made regarding the refilling of carbon dioxide, including the method of refilling and the refilling pattern or gap between each refill. Despite appearing as minor adjustments, these factors significantly contribute to the strength gain of the binder. Overall, this comprehensive approach to protocol development underscores the importance of iterative experimentation in achieving optimal performance and highlights the intricate interplay of various factors in enhancing compressive strength.

4. Results and discussions

Developing a new binder composition entails extensive experimentation, involving multiple trial and error iterations and careful examination of raw materials, considering their unique properties. The scrutinizing of these raw materials by a combination of different limestone, flyash, and metakaolin sources is conducted as shown in Figure 7. Along with the three raw materials, the different iron sources were tested for the best suitable limestone, flyash and metakaolin combination as shown in Figure 8. The properties of the raw materials, including their chemical composition, reactivity, fineness, and proportioning, play a crucial role in the evaluation process. Thus, raw materials are meticulously scrutinized. Four raw materials, with a major focus on the iron source, are selected after choosing the other three materials. Limestone, metakaolin, and fly ash are selected based on a combination of tests conducted for compressive strength, as shown in Figure 7. The best combination is then used to test the iron source raw material. Industrial waste, considered for the iron source, is tested with the finalized raw materials. The combination yielding the highest compressive strength is carried forward as the binder raw material, as shown in Figure 8. The casting and curing methodology is further tested and the outcomes of these trials inform the refinement of casting protocols and the establishment of curing procedures. The casting process involves meticulous scrutiny of every detail, with visual inspection serving as a pivotal factor in determining the final methodology for

conducting experimental procedures and evaluations. Each step of the experiment is crucial, significantly influencing the formulation and production of the new binder. Given the lack of a clearly defined process, reaching a suitable procedure requires extensive observation and deliberation. Commencing with the casting method, the unique composition and water requirements of the new binder necessitate a specific approach. The binder comprises finer materials, rendering traditional compaction techniques ineffective in achieving optimal material distribution within the specimen. Notably, during vibration compaction, finer materials tended to accumulate at the surface, as evidenced by the observation of iron carbonate predominantly forming on the top layer, as depicted in Figure 6, exhibiting a dark brown hue. In response to this challenge, the casting methodology was adapted to involve hand tamping in layers, resulting in improved particle distribution. This modification was further complemented by the introduction of a custom-designed mechanical compression setup, tailored to enhance compaction efficiency.

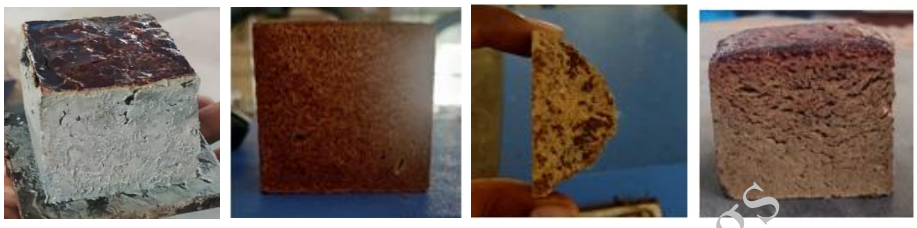

Figure 6. Specimens with differet molding methods

r

Demolding decisions are typically guided by the principle that quicker exposure to the carbon dioxide curing environment leads to improved results and faster curing. However, practical difficulties and challenges necessitate careful analysis of demolding procedures. In experiments, specimens with higher water binder ratios required longer demolding times but didn't yield superior results. Conversely, reducing water content or the water binder ratio shortened demolding times while increasing compressive strength. This facilitated rapid exposure of specimens to the curing environment, resulting in strength enhancement. The experimentation further highlights the significant influence of water binder ratio on strength outcomes. Lower water-to-binder ratios consistently produced superior strength compared to higher water content configurations. Optimization of water binder ratio was made and graphically represented in Figure 9.

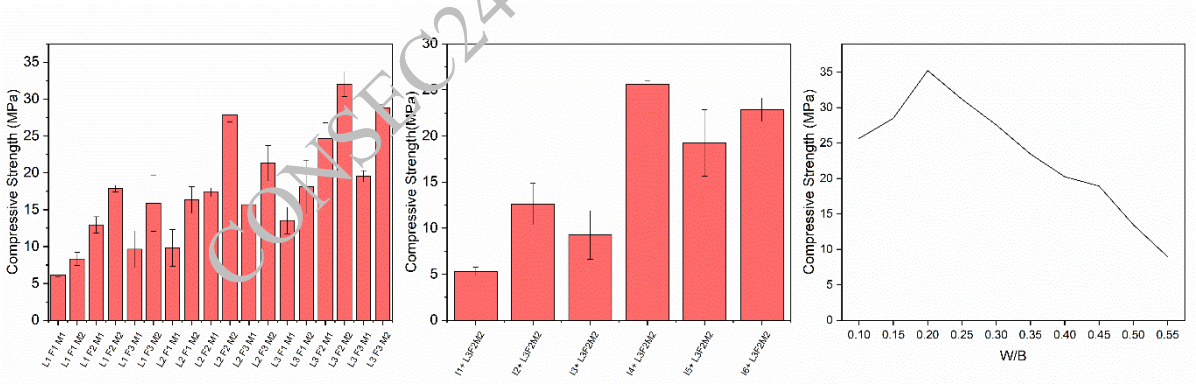

Figure 7. Strength test analysis on limestone, metakaolin and flyash source combinations

Figure 8. Strength test analysis on different iron source with finalized other material sources

Figure 9. Optimization of Water binder ratio

Initially, through meticulous observation and analysis of every aspect of binder specimen formulation, it was noted that the specimen's weight remained unchanged even after carbon dioxide or air curing. Despite utilizing various sources and combinations thereof, no significant improvement in strength was observed. Modifying the binder formulation sources led to weight changes, indicating the formation of reaction products. The final selection of sources was determined through iterative trial and error, considering all factors, including casting protocols and curing regimes. Following carbon dioxide curing, there was an increase in weight, confirming the formation of reaction products, while air curing resulted in a slight decrease in weight, indicating a reduction in specimen moisture content. The research examines the evaluation of raw materials, where the final raw material composition, determined through previous trials,

is tested and presented in Table 1. Using this finalized raw material, the binder is prepared accordingly with the mix proportion and water binder ratio which is then cured in a carbon dioxide environment and then ambient cured to achieve a strength gain of up to 30 MPa.

Table 1. Composition of raw materials

Material	Composition (%)						
	SiO_2	Al_2O_3	CaO	MgO	TiO_2	Fe_2O_3	K_2O
Flyash	62.76	30.94	01.28	00.64	01.89	00.34	01.50
Metakaolin	52.80	38.15	00.86	00.49	01.20	04.31	00.95
Limestone	01.60	01.47	96.45	00.31	00.10	00.00	00.00

5. Conclusions

In summary, this research underscores the intricate process involved in formulating the carbon sink binder, emphasizing the critical role of raw material properties in achieving optimal results. Each phase of the formulation process contributes significantly to the binder's performance, starting with a meticulous examination of raw materials to ensure their compatibility with the desired composition. Mill scale waste with flyash of Raichur power plant, limestone of 20micron brand, and metakaolin of intercity enterprises make a final combination of the binder.

The mixing protocol represents a crucial phase where careful consideration is given to the method of incorporating oxalic acid. By premixing the acid with water according to the prescribed water-binder ratio, the study reveals a more effective approach compared to dry mixing with raw materials.

Moving on to the casting phase, the experimentation reveals that a combination of hand tamping and mechanical compression yields superior results, indicating the importance of precision in this step. The subsequent demolding process is optimized through immediate demolding followed by exposure to a carbon dioxide environment for curing, highlighting the significance of timely intervention post-casting.

Furthermore, the curing regime plays a pivotal role in enhancing the binder's properties, with the study finding that initiating the curing process with carbon curing before transitioning to ambient exposure yields the best outcomes. Additionally, the optimization of oxalic acid for iron content further fine-tunes the binder's compressive strength, emphasizing the iterative nature of the formulation process.

In essence, each phase of the binder formulation process contributes to the development of a highly effective and innovative carbon sink binder with remarkable compressive strength properties. This comprehensive approach not only advances our understanding of binder formulation but also paves the way for applications in various industries requiring robust and sustainable materials.

References

Abdul-baki, G.(2017)"Development of vacuum carbonation curing technology for concrete at ambient conditions." *Canada: McGill University*

Agrawal, A., S. Kumari and K. K. Sahu. (2009) "Iron and Copper Recovery / Removal from Industrial Wastes : A Review", *Industrial & engineering chemistry research*, 48: 6145–6161

C.I. Nwoye, A. A. Imah, N. M. Okelekwe, O. J. N. And and S. Okeahialam.(2020) "Open System Leaching of Iron Ore in Oxalic Acid Solution and Predictability of Final Solution pH based on Initial Solution pH and Leaching Time." *World J. Chem.*, 15 (1): 24–29

Chiarizia, R. and E. P. Horwitz. 1991. "New formulations for iron oxides dissolution.",*Hydrometallurgy*,27: 339–360

Das, S., Hendrix, A., Stone, D. and Neithalath, N.(2015) "Flexural fracture response of a novel iron carbonate matrix–Glass fiber composite and its comparison to Portland cement-based composites", *Construction and Building Materials*, *93*:360-370

Das, S., Kizilkanat, A.B., Chowdhury, S., Stone, D. and Neithalath, N.(2016a) "Temperature-induced phase and microstructural transformations in a synthesized iron carbonate (siderite) complex", *Materials & Design*, 92:189–199

Das, S., Souliman, B., Stone, D. and Neithalath, N (2014a)"Synthesis and Properties of a Novel Structural Binder Utilizing the Chemistry of Iron Carbonation" ,*ACS Appl. Mater. Interfaces*, 6: 8295–8304

Das, S., Stone, D., Convey, D. and Neithalath, N. (2014b) "Pore- and micro-structural characterization of a novel structural binder based on iron carbonation", *Materials Characterization* , 98: 168–179

Das, S., Stone, D., Mobasher, B. and Neithalath, N. (2016b) "Strain energy and process zone based fracture characterization of a novel iron carbonate binding material", *Engineering Fracture Mechanics*,156: 1–15

Eissa, M., Ahmed, A. and El-Fawkhry, M. (2015) "Conversion of Mill Scale Waste into Valuable Products via Carbothermic Reduction.", *Journal of Metallurgy*, 2015: 1–9

Gartner, E.M. and Macphee, D.E. (2011) "Cement and Concrete Research A physico-chemical basis for novel cementitious binders", *Cement and Concrete Research*, 41 (7): 736–749

Gurzau, E.S., Neagu, C. and Gurzau, A.E.(2003) "Essential metals — case study on iron.",*Ecotoxicol. Environ. Safety*, 56: 190–200

Humbert, P. S., J. P. Castro-Gomes and H. Savastano (2019) "Clinker-free CO 2 cured steel slag based binder: Optimal conditions and potential applications", *Construction and Building Materials*, 210: 413–421

Jikar, P.C. and Dhokey, N.B.(2021). "Materials Today : Proceedings Overview on production of reduced iron powder from mill scale waste", *Materials Today: Proceedings*, 44: 4324–4329

Lyngdoh, G. A., D. Stone, N. Neithalath, and S. Das. n.d. Life Cycle Assessment and Life Cycle Cost Analysis of a Novel Iron Carbonate Structural Material.

Mohanty, M., Dhal, N.K., Patra, P., Das, B. and Reddy, P.S.R.(2010) "Phytoremediation: A Novel Approach for Utilization of Iron-ore Wastes.", *Reviews of Environmental Contamination and Toxicology*,*206:*29–48

Predescu, A.M., Matei, E., Berbecaru, A.C., Râpă, M., Sohaciu, M.G., Predescu, C. and Vidu, R.(2021) "An Innovative Method of Converting Ferrous Mill Scale Wastes into Superparamagnetic Nanoadsorbents for Water Decontamination",*Materials*, 14(10):2539

Santawaja, P., Kudo, S., Mori, A., Tahara, A., Asano, S. and Hayashi, J.I.(2020)"Sustainable Iron-Making Using Oxalic Acid: The Concept, A Brief Review of Key Reactions, and An Experimental Demonstration of the Iron-Making Process." *ACS Sustainable Chemistry & Engineering*, 8(35):13292-13301

Veglio, F. (1998) "Drum leaching tests in iron removal from quartz using oxalic and sulphuric acids", *International Journal of Mineral Processing*, 54: 183–200.

Venhuis, M. A., and E. J. Reardon.(2001) "Vacuum method for carbonation of cementitious wasteforms", *Environmental science & technology*, 35 (20): 4120–4125

Yellishetty, M., Karpe, V., Reddy, E.H., Subhash, K.N. and Ranjith, P.G.(2008) "Resources , Conservation and Recycling Reuse of iron ore mineral wastes in civil engineering constructions : A case study.", *Resources, Conservation and Recycling*, 52: 1283–1289

Investigating Bio-Based Self-Healing Utilizing Hemp Fiber Reinforcement: Structural Restoration in Cementitious Mortar

Preeti Chaudhary [1*], T. Palanisamy [2]

[1] *Research Scholar, National Institute of Technology Karnataka, Mangaluru, India*
Email: chaudhary.preeti09@gmail.com
[2] *Associate Professor, National Institute of Technology Karnataka, Mangaluru, India*
Email: tpalanisamycivil@nitk.edu.in

* Corresponding author

ABSTRACT

The utilization and enhancement of natural fibers in cement matrix have seen a notable increase due to their unique characteristics that greatly improve the properties of the resulting composite. Cracks in cement structures are inevitable and prone to the ingress of chemicals, which causes deterioration and impacts their service life. This study adopts a bio-based approach for self-healing, achieved through the generation of calcium carbonate precipitation facilitated by the cellular metabolism of the introduced ureolytic bacteria (Bacillus licheniformis). Bacterial-based mortar specimens were prepared with the required nutrient source and natural fiber resulting in enhance strength and durability. Hemp fiber was replaced with cement at 0%, 0.25%, 0.5% and 1% as weight in bacterial mortar. The mechanical and durability properties, including compressive strength, compressive strength regain, and water absorption, were investigated at intervals of 7, 14, and 28 days. As mentioned, the findings show that hemp fiber replacement should not surpass 0.5% to attain enhanced properties. Additionally, the integration of hemp fibers with bacteria results in a notable 20–25% enhancement in compressive strength after 28 days. Microstructure investigations, such as X-ray diffractometer (XRD) analysis and scanning electron microscopy (SEM), unveiled the presence of calcium carbonate compounds formed through the metabolic activity of Bacillus licheniformis in fiber-reinforced bacterial mortar.

KEYWORDS*: Hemp Fiber, Bacillus licheniformis, Compressive strength, Durability, SEM.*

1. Introduction

The ongoing trends of urbanization and population growth are driving a consistent rise in the need for concrete. As the principal element of concrete, cement mainly binds the aggregate components (Kanagaraj et al. 2023). The properties of concrete, including its brittleness and low tensile strength, cause it to develop crack under compressive forces, freeze-thaw actions, and shrinkage (Anbazhagan et al. 2023). The integration of fibers converts the brittle nature of concrete into ductile behaviour, thereby improving both its strength and durability (Suescum-Morales et al. 2021). Most synthetic fibers, such as glass, polypropylene, carbon, and steel, require considerable non-renewable energy and release environmentally damaging substances during their production (Samadi et al. 2020). Natural fibers, such as jute, coir, flax, kenaf, sisal, and hemp, are suitable for practical applications due to their low density and eco-compatibility. The development of using natural fibers like hemp for cost and performance began in Europe in the early 1990s and was adopted globally by the late 1990s (Ramadevi and Shri 2015). Globally, the production of jute annually varies between 2.5 to 3.0 metric tons, with India contributing 15% to this aggregate output. The addition of fibers to the cement matrix aims to improve its resistance to cracking, elevate mechanical characteristics, and fortify durability (Wang et al. 2004). With their pronounced hydrophilic nature and porous matrix, natural fibres can absorb water during mixing. This absorbed water is then mobilized within the porous network formed by the distributed natural fiber reinforcement, triggering delayed hydration reactions crucial for the healing process (Candamano et al. 2021). The manual repair of microcracks in concrete poses challenges, making the incorporation of bacteria for self-healing behaviour advantageous

(Achal et al. 2015). Bacillus species are the predominant bacteria utilized for self-healing in concrete, known for their ability to endure harsh conditions for up to 50 years in a dormant state (Abo-El-Enein et al. 2012). Bacillus subtilis proved to be highly effective in enhancing concrete properties, resulting in significant improvements of 33% and 28% in compressive strength and flexural strength at a concentration of 10^5 cells/ml of water (Bhina et al. 2021). Evaluation of crack healing in cement matrices involved the use of alkali-resistant spore-forming bacteria under varying curing environments, such as complete water submersion, wet-dry cycles, and 90% relative humidity. After 28 days, complete water curing achieved approximately 42%, and wet-dry curing demonstrated an 80% repair rate (Luo et al. 2015). In a tidal marine environment, concrete infused with H. halophilus bacteria and using expanded perlite as a medium exhibited a 17% enhancement in crack repair (Khan et al. 2021). The impact of fiber incorporation in bioconcrete and biomortar has been studied extensively, with a particular focus on improving strength and crack healing in humid environments. This study investigates the effect of separately adding bacteria to hemp fiber-reinforced bacterial mortar on its strength and water penetration recovery, under humid conditions.

2. Materials

2.1 Cement and Aggregates

Ordinary Portland Cement (53 grade) compliant with IS 269–2015 was used as the binding agent, with its physical properties detailed in Table 1. The physical properties of fine aggregates were assessed by IS 2386–1963, as shown in Table 2. The particle size distribution of the fine aggregate meets the Zone II classification.

Table 1. Physical properties of cement

Properties	Initial setting time	Final setting time	Specific gravity	Fineness	Consistency
Value	75 min	260 min	3.15	219 m^2 /kg	34%

Table 2. Properties of fine aggregates

Properties	Specific gravity	Fineness modulus	Water absorption	Bulk density
Value	2.65	3.3	1.4 %	m^3

2.2 Hemp Fiber

Hemp fibers, were sourced economically from Gogreen Products in Chennai, Tamil Nadu, as shown in Figure 1.

Figure 1. Hemp fibers

The manufacturer's manual details the technical properties of these hemp fibers, which were Hemicellulose (19-22%), Cellulose (75%), Specific gravity(1.45) and Tensile strength (675MPa). In the preparation of the mixtures, no water reducers were used, and only potable water was utilized, with hemp fibers of 2 cm lengths incorporated.

2.3 Bacteria

Bacillus licheniformis (Isolate KGEB16) was procured from ICAR-CPCRI in Kasaragod, Kerala, India, and was originally isolated from the rhizosphere of healthy Forastero cocoa trees. Known to enhance cocoa seedling growth, this bacterium thrives at 30°C with a 24-hour incubation period. It forms large, opaque colonies in synthetic media, tolerates temperatures up to 55°C, and survives extreme conditions by forming endospores**.**

2.4 Fiber-reinforced biomortar mix

A water-to-cement (w/c) ratio of 0.50 and an aggregate-to-cement (a/c) ratio of 1:3 were chosen in mortar mix preparation. The quantity of hemp fibers was determined relative to the amount of cement, with fibers added to the mix at ratios of 0%, 0.25%, 0.5% and 1% as weight in bacterial mortar. Details regarding the ratios and material quantities of the mixtures are provided in Table 3. Hemp fibers were added to the mixture last. The fibres were introduced into the mixture following the homogenous mixing of aggregate, water, and cement. The fibrous mixture underwent mixing at low speed for 1 minute, followed by high-speed mixing for an additional minute.

Table 3. Biomortar mix details

Mix	Fiber content (%)	Fiber length (cm)	Cement (g)	Fine Aggregate (g)	Bacterial sol. (g)
F0	0.00	2	450	1350	225
F25	0.25				
F50	0.50				
F100	1.00				

3. Methods

3.1 Bacterial culture preparation

Bacillus licheniformis was selected for bio-suspension due to its high calcite precipitation ability, gram-positive nature, alkaliphilic properties, and high ureolytic activity. Fresh bacterial cultures were cultivated from frozen inoculates on nutrient agar plates with a pH of 7.4 at 25°C, and incubated for 24 hours. The nutrient broth medium, with a pH of 7.5 at 27°C, was autoclaved at 120°C for 15 minutes.

Figure 2. Steps involved in bacterial culture

The prepared culture from the agar plates was inoculated into the autoclaved broth medium and incubated in a shaking incubator at 30°C and 120 rpm for 24 hours, steps involved are illustrated in Figure 2.The optical density (OD) at 600 nm was measured using a JASCO V-730 spectrophotometer, with an OD_{600} value of 1.28, indicating a bacterial concentration of 2.7×10^7 cfu/ml (Wei et al. 2021), the process illustrated in Figure 3 .

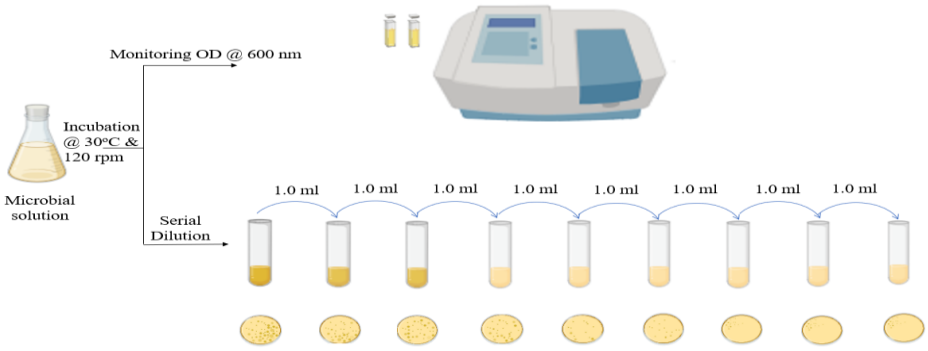

Figure 3. Optical density measurement and serial dilution

3.2 Casting procedure and bacterial incorporation

Within the biomortar mixture, water is substituted with a combination of a 10% immobilized bacterial solution and a 90% nutrient solution, incorporating organic compounds like urea and calcium chloride at concentrations of 20 g/L each. These components play a vital role in sustaining bacterial viability within the demanding mortar mix environment. A single bacterial colony was introduced into the nutrient broth and subjected to a 24-hour incubation period in a shaker to prepare the bacterial solution. Subsequently, biomortar specimens are cast using conventional methods, ensuring an even distribution of fibers throughout the mixture to enhance performance during mixing (Ferrara et al. 2011).

3.3 Compressive strength and Compressive strength regain

Tests were conducted on samples measuring 50x50x50 mm to determine compressive strength at 7, 14, and 28 days, adhering to ASTM C 349 standards. The compressive strength regain was evaluated after 28 days for cubes with artificially induced cracks. Manual induction of induced cracks occurred. After 24 hours of initial curing, the cracked cast cubes, ranging in crack widths from 0.5 to 1 mm, underwent a 28-day curing process. The compressive strength regain was subsequently measured using a specific equation.

$$\text{Compressive strength regain } \% = \frac{(C_F - C_V)}{C_F} \times 100 \quad (1)$$

Where, C_F = Ultimate compressive strength of fiber-reinforced bacterial cubes.
C_V = Ultimate regained compressive strength of conventional cubes.

3.4 Water absorption

Water absorption was determined following Archimedes' principle, utilizing cube samples measuring 50x50x50 mm, as specified by ASTM C 1585.

3.5 Microstructure investigations

Samples from conventional cubes and $CaCO_3$ mineral scraped from bio-fiber-reinforced cubes underwent SEM and XRD analysis after 28 days of curing. XRD scans were conducted across the 2θ range from 20° to 90° to examine the specimens.

4. Results and Discussions

4.1 Compressive Strength

Figure 4, displays the compressive strength test data for mortar mix Table 3, including error bars that reflect the standard deviation. At 7, 14, and 28 days, the compressive strength of the F25 mix decreased by 2.9%, 3.1%, and 4.6% relative to the F0 mix. Similarly, over the curing periods, the F100 mix exhibited reductions in compressive strength of 7.9%, 8.4%, and 8.5%. Whereas, for the F50 mix, compared to the F0 mix, the compressive strength was found to increase by 22.3%, 23.2%, and 24.9%. For the F25 mix, the compressive strength was reduced due to the addition of fiber particles and poor interaction between the fibers and the surrounding cement paste. Conversely, the compressive strength of the F100 mix was reduced due to

micropores and cavities around the hemp fibers that were not filled by calcite precipitation. The higher compressive strength of the F50 mix at 7, 14, and 28 days indicates that MICP bacteria can enhance the strength of fiber-reinforced mortar. This improvement is also attributed to the uniform calcite precipitation around the fibers, which likely increased the interaction surface area between the fibers and the cement paste. SEM analysis confirmed that the calcite precipitation filled microcracks and cavities in the biomortar specimens.

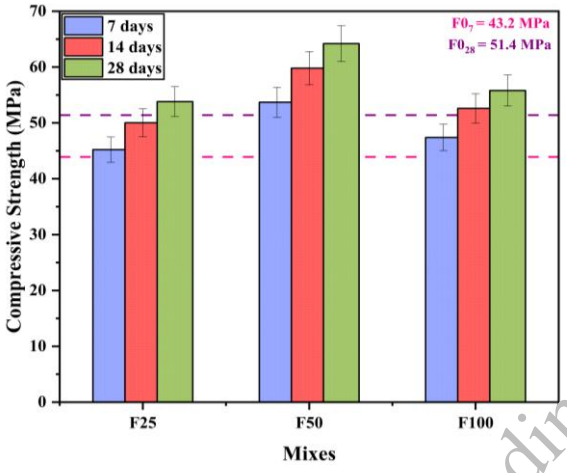

Figure 4. Compressive strength of different mixes

4.2 Compressive Strength Regain

As shown in Figure 5, the compressive strength regain percentages of fiber mortar with added bacteria after 28 days of curing were evaluated. Non-bacteria mix CN specimens had only a 3% regain in compressive strength, and F25 specimens exhibited a slight increase to approximately 9%. The decrease in compressive strength regain in F100 was due to a decrement in bacterial activity during curing. Due to reduced compressive strength as shown in Figure 4, cracks formed in the mixes of F100 were more and the loss of nutrients occurred during curing, leading to reduced $CaCO_3$ production. Also, bacteria failed to survive due to the low availability of nutrients and the densification of the matrix's pores. However, F50 specimens showed a notable 68% regain in compressive strength. This enhancement is attributed to the higher sporulation efficiency of Bacillus licheniformis within hemp fibers. The data suggest that bacteria find a nucleation site within the hemp fiber structure, leading to increased calcite precipitation, crack filling within the mortar matrix, and enhanced strength recovery. Therefore, it is clear that bacteria, when combined with hemp fiber as a reinforcement, offer superior properties for compressive strength recovery.

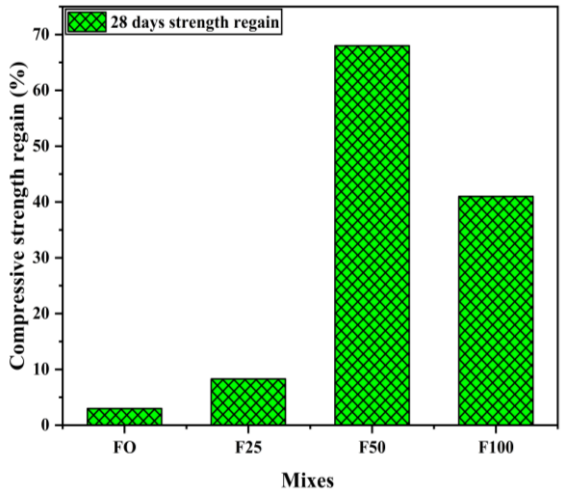

Figure 5. Compressive strength regain

4.3 Water Absorption

The water absorption test results revealed a 15.03% increase in water absorption for the F25 fiber-reinforced mortar compared to the F0 mix, while the F100 mix showed a 12.34% increase. In contrast, adding bacteria to the F50 mix led to a 3.12% reduction in water absorption. The increased absorption in the F25 and F100 mixes is attributed to higher void content from hemp fiber, which introduced more pore spaces and interconnectivity within the matrix. The F100 mix had lower absorption than the F25 mix (shown in Figure 6), likely due to calcite precipitation reducing voids. The F50 mix exhibited the lowest water absorption, with the combination of bacteria and fiber decreasing void volume. These results demonstrate that incorporating bacteria in fiber-reinforced mortar enhances water durability by reducing water absorption.

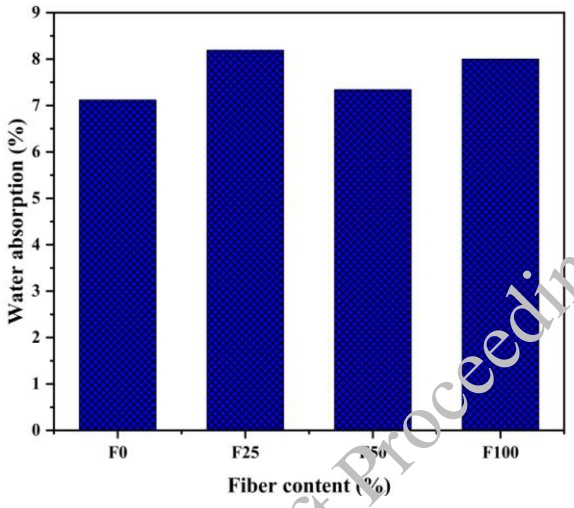

Figure 6 . Water absorption

4.4 SEM Analysis

SEM analysis of F50 specimens that incorporated Bacillus licheniformis showed dense formations of $CaCO_3$ polymorphs such as vaterite, aragonite, and calcite (illustrated in Figure 7). Since mortar pores were smaller than the bacteria, there was a potential for the bacteria to be expelled during hydration (Chithambar Ganesh et al. 2019). However, SEM analysis confirmed the viability of bacteria within the F50 specimens after 28 days.Hemp fibers effectively supported the bacteria, suggesting that their protection within the cement matrix facilitated extended self-healing capabilities.

4.5 XRD analysis

The XRD patterns obtained from F50 and CN mortar samples were compared with JCPDS data. (displayed in Figure 8). In the analysis of the F50 specimen, various $CaCO_3$ polymorphs, including calcite, aragonite, and vaterite, were observed, with calcite showing significantly higher intensity than the other polymorphs. These prominent peaks highlight calcite's crucial role in the healing process, forming in humid conditions and subsequently hardening in pores and cracks (Silva et al. 2020). Major calcite peaks were observed at 29.6°, 39.6°, 47.7°, and 58.2°, consistent with the SEM image observations of the F50 sample.

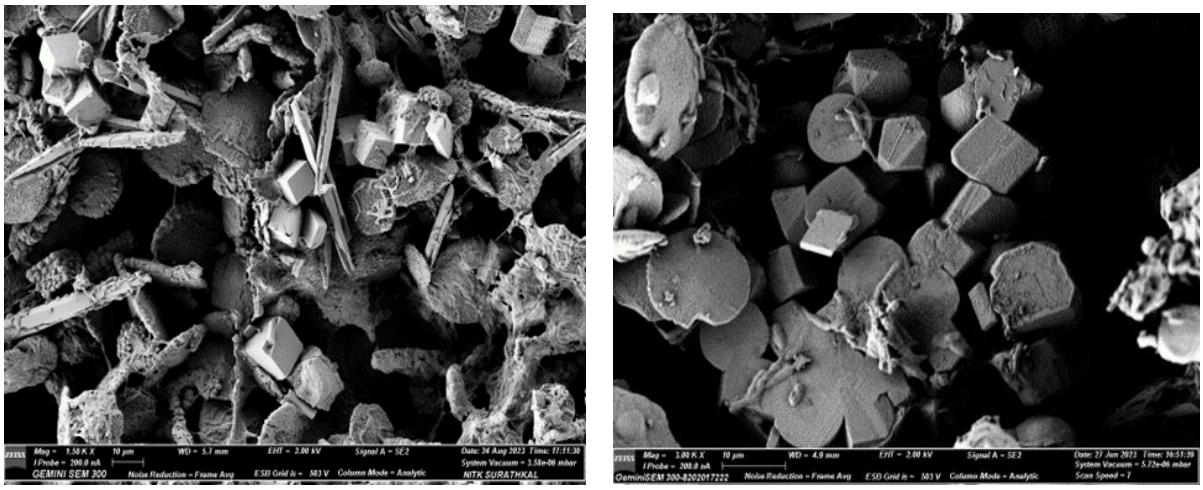

Figure 7. SEM images of F50 specimens showing $CaCO_3$ polymorphs

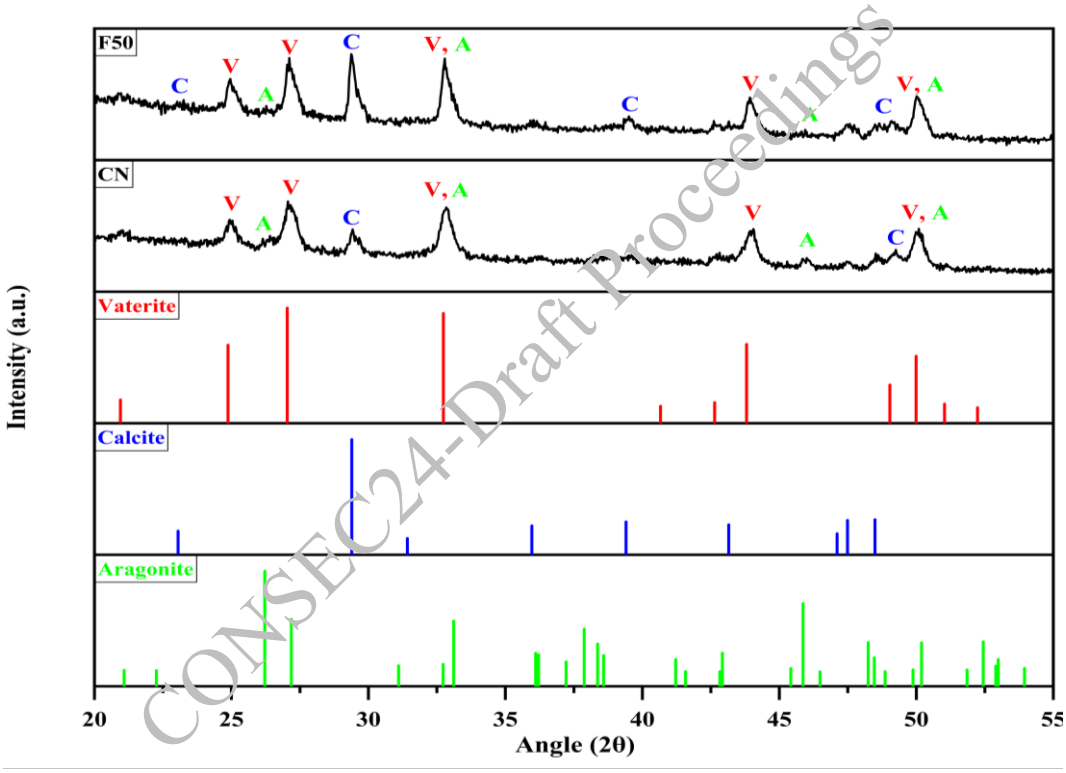

Figure 8. XRD analysis for the conventional sample (CN) and fiber-reinforced mortar sample. V- Vaterite, C- Calcite, A- Aragonite

5. Conclusions

The findings from the study indicate the following conclusions: The average percentages for water absorption, compressive strength regain, and compressive strength in microbial-treated fiber mortar specimens in the F50 mix are 24.9%, 68%, and 3.12%, respectively. The increase in compressive strength was attributed to the uniform formation of calcite throughout the fibers, which augmented the surface interaction area between the fibers and the cement paste. The reduction in water absorption for the F50 mix after 28 days results from a decrease in the volume of voids. Bacillus licheniformis shows a high potential for reducing fractures in cement mortar. Microstructure investigations revealed calcium carbonate precipitate forms within cracks and confirmed the presence of microbe on fiber surfaces.

References

Abo-El-Enein, S. A., Ali, A. H., Talkhan, F. N. and Abdel-Gawwad, H. A. (2012) "Utilization of microbial induced calcite precipitation for sand consolidation and mortar crack remediation", *HBRC Journal*, 8(3):185–192

Achal, V., Mukherjee, A., Kumari, D. and Zhang, Q. (2015). "Biomineralization for sustainable construction – A review of processes and applications". *Earth-Science Reviews*, 148:1–17

Anbazhagan, R., Arunachalam, S., Dharmalingam, G. and Sundramurthy, V. P. (2023) "Development on bio-based concrete crack healing in soil exposures: isolation, identification, and characterization of potential bacteria and evaluation of crack healing performance". *Biomass Conversion and Biorefinery*, 1–14

Bhina, M. R., Wibowo, A. H., Liu, K. Y., Khan, W. and Salim, M. (2021) "An overview on bioconcrete and the utilization of microbes in civil engineering"

Candamano, S., Crea, F., Coppola, L., De Luca, P. and Coffetti, D. (2021) "Influence of acrylic latex and pre-treated hemp fibers on cement based mortar properties. *Construction and Building Materials*, 273:121720

Chithambar Ganesh, A., Muthukannan, M., Malathy, R. and Ramesh Babu, C. (2019). "An experimental study on effects of bacterial strain combination in fibre concrete and self-healing efficiency", *KSCE Journal of Civil Engineering*, 23(10):4368–4377

Ferrara, L., Ozyurt, N. and Di Prisco, M. (2011) "High mechanical performance of fibre reinforced cementitious composites: the role of "casting-flow induced" fibre orientation",*Materials and Structures*, 44:109–128

Kanagaraj, B., Anand, N., Diana Andrushia, A. and Naser, M. Z. (2023). "Recent developments of radiation shielding concrete in nuclear and radioactive waste storage facilities – A state of the art review". *Construction and Building Materials*, 404:133260

Khan, M. B. E., Shen, L. and Dias-da-Costa, D. (2021) "Self-healing behaviour of bio-concrete in submerged and tidal marine environments". *Construction and Building Materials*, 277:122382

Luo, M., Qian, C. and Li, R. (2015). "Factors affecting crack repairing capacity of bacteria-based self-healing concrete". *Construction and Building Materials*, 87:1–7

Ramadevi, K. and Shri, S. D. (2015). "Flexural behaviour of hemp fiber reinforced concrete beams". *ARPN Journal of Engineering and Applied Sciences*, 10:1819–6608

Samadi, M., Huseien, G. F., Mohammadhosseini, H., Lee, H. S., Lim, N. H. A. S., Tahir, M. M. and Alyousef, R. (2020). "Waste ceramic as low cost and eco-friendly materials in the production of sustainable mortars", *Journal of Cleaner Production*, 266:121825

Silva, L. A., Nahime, B. O., Lima, E. C., Akasaki, J. L. and Reis, I. C. (2020) " Investigação por DRX de pastas de cimento com incorporação de resíduo de polimento de pisos de concreto". *Cerâmica*, 66:373–378

Suescum-Morales, D., Salas-Morera, L., Jiménez, J. R. and García-Hernández, L. (2021) "A novel artificial neural network to predict compressive strength of recycled aggregate concrete". *Applied Sciences*, 11(22):11077

Wang, L., Wang, X. and Li, Z. (2004). "Compressive and flexural properties of hemp fiber reinforced concrete", *Fibers and Polymers*, 5(3):187–197

Wei, W., Ding, L., Luo, H., Li, C. and Li, G. (2021) "Automated bughole detection and quality performance assessment of concrete using image processing and deep convolutional neural networks", *Construction and Building Materials*, 281:122576

Heat of Hydration of Mass Concrete in Controlling Temperature Performance by Construction Stages

Dr. Vinayaga Moorthy [1*], Banoj Mohapatra [2], Gurinder Bawa [3]

[1] *Technical Director- AECOM, India*
vinayaga.mariappan@aecom.com
[2] *Associate Director, AECOM, India*
banoj.mohapatra@aecom.com
[3] *Executive Director, AECOM, India*
gurinder.bawa@aecom.com

*Corresponding author

ABSTRACT

Thermal analysis is one of the main components in the design and construction of any mass concrete foundation. In this article, the heat transformation in concrete by hydration process is analysed and cooling method was introduced to perform the thermal analysis of a curing system in mass concrete structures. Several typical models are selected to verify the performance of this method. The proposed method is then applied to a bridge pile foundation concrete called in the pile cap for the Bridge, which is still under construction in India. The actual climatic conditions and thermal properties of the materials are considered in this analysis. The temperatures determined by numerical simulation are in good agreement with the actual monitored values. The simulation results indicate that the proposed method can accurately simulate the hydration temperature stages, the temperature rise along the water flow, and the effect of directional changes of flow in temperature distributions. Moreover, the maximum temperature for 24 hours was examined shown the development in concrete and compared with foundation with the curing system. Mainly from the extreme temperature in the core of the concrete and fluctuation during the cooling process of concrete. The untimely application of water-cooling systems during hot seasons will induce extreme tensile stresses and increase the risk of cracking.

KEYWORDS*: Foundation; Heat of hydration; Heat-fluid coupling method; Thermal analysis; Cooling pipes.*

1. Introduction

Controlling temperature-induced cracking in concrete is one of the main concerns in the design and construction of concrete of mass concrete foundation. In compacted concrete (RC) foundation, the application of continuous casting with different layer of concrete combined with the large use with less cement content during construction makes mass structures significantly different from conventional concrete structure with respect to the temperature due to hydration process, cooling conditions, and the main factors affecting thermal stress. Particularly, the quick construction process and large size of concrete lifts will induce a high temperature or extreme thermal gradient within the concrete and cause significant thermal stresses during the cooling of the foundation, which are sufficient for cracking (Zhu 1999). Thus, it is necessary to simulate and analyse the temperature and stress fields during construction and then suggest some effective temperature control measures to prevent cracking (Tatro and Schrader 1992; Zhu 2006). Cooling by the flow of water through an embedded cooling pipe has become a common and effective artificial temperature control measure in the construction of concrete foundations following by the standard contractors. A great deal of research has been conducted to simulate the cooling effect of this water flow. Cervera et al. (2000a, b) presented a numerical procedure for the thermal and stress analysis of the evolutionary construction process of RC foundations. This procedure took into account the ambient temperature, placing temperature, casting schedule, and, in particular, the more applicable features of the

behaviour of concrete during the early stages after construction, such as hydration, aging, creep, and foundation age. The U.S. Bureau of Reclamation (USBR 1949) conducted research on the calculation of the final stage of water cooling and presented an analytical solution using a two-dimensional (2D) program, and an approximate solution using a three-dimensional (3D) program with no heat source by using the separation-of variables method. The calculation of the initial stage of water cooling and obtained an analytical solution using a 2D program and an approximate solution using a 3D program with a heat source by using the integral transform method. The polythene pipes had fewer joints, which appeared to be more convenient than steel pipes in construction, and also four methods for computing the effect of cooling by non-metal pipes. In addition, the simplified analysis and proposed methods to compute the equivalent radius and equivalent horizontal spacing of non-metal pipes. Zhu (1991) treated water cooling as negative hydration heat and presented a cooling equivalent algorithm based on the FEM. The water-cooling effect to every element in the FEM analysis, easily obtaining an approximate distribution of the temperature field. Kim et al. (2001) developed a 3D FEM program to thermally analyse concrete structures with pipe cooling systems. Line elements were adapted to model pipes, and internal flow theory was applied during the calculation of the temperature variation of the cooling water. Liu (2004) proposed a general analytical model to address heat extraction from mass concrete by employing a rectangular array of cooling pipes. In this study, an analytical solution is derived in terms of the physical parameters for heat diffusion and heat removal. The model can be employed to analyse a temperature the heat is removed using a rectangular pipe frame and can provide guidance in choosing pipe sizes, pipe spacing, aggregates of different heat diffusivity, types of cements, fresh concrete temperature. However, this technique still cannot accurately reflect the velocity and water temperature variation rise along the flow. The objective of this work is to present an accurate and applicable prediction method for the analysis of the cooling effect exhibited by pipes in mass concrete structures. This work accounts for the following factors: concrete properties, ambient conditions, convection coefficient function, heat source, casting schedule, and, in particular, the actual pipe cooling system. Additionally, it considers the pipe layout (pipe sizes and spacing), the cooling water velocity, the inlet temperature and water-temperature rise along the flow, and the thermal properties of cooling pipes by using a numerical simulation. Thus, the prediction of the thermal fields associated with cooling pipes can be successfully used in practice. In this study, the heat-fluid is introduced to perform the thermal analysis of pipe cooling systems in mass concrete structures and is applied to an actual RC foundation. A 3D FEM analysis is conducted using heat-fluid elements in the FEM program Midas FEA. To verify the rationality and applicability of the heat-fluid coupling method, a comparison with several widely used methods is presented. Furthermore, this method is applied to verify and predict the distribution of temperature during the initial stage of the cooling process of the main span pylon foundation.

2. Basic Formulations and Solution Approach of Temperature Field

Based on the energy balance principle, the general partial differential equation governing heat flow in a 3D solid medium is expressed where the concrete temperature; The initial transient temperature can be represented as;

$$T = To\ (x, y, z)$$

2.1 Simulation of Water Cooling with the Heat-Fluid Coupling Method

In the entire FE model, concrete is simulated by 3D solid elements, and cooling water pipes are simulated by heat-fluid elements, as shown in Fig. 1. Each heat-fluid element has four nodes consisting of two primary (I, J) and two supplemental (K, L) nodes. The coupling of the additional nodes of the heat-fluid element and the nodes of the concrete solid element are used to simulate the convection heat of water and concrete.

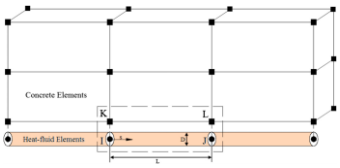

Figure 1. Heat-fluid element geometry

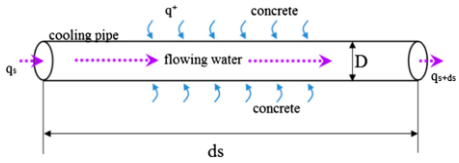

Figure 2. Concept diagram of energy conservation principle

2.2 Simulation analysis of finite element procedure

2.2.1 **Project Overview**:

This foundation is for bridge projects in India. The foundation thickness 3500mm and 2500mm of soil base for the analysis. Fig 1 displays plan layout of foundation and temperature measuring point.

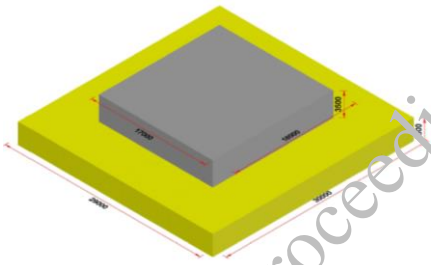

Figure 3. Finite element model added into the cooling water pipe upon grid distribution

The following temperature control measures are adopted for the project: One layer of straw mat or gunny bag immersed in water for a long time is first laid on the external surface of concrete; then two layers of dry straw mat are laid for heat insulation; the covering materials are increased or reduced according to the temperature gap; the cooling water pipe is set up in the concrete. Fig 4A is layout of cooling water pipe.
The following temperature control measures are adopted for the project: totally seven layers were considered, each layer is 500mm, totally eight construction stages were considered with cumulative time of one hour for each pouring. The cooling water pipe is set up in the concrete shows in layout (Fig 4A) of cooling water pipe.

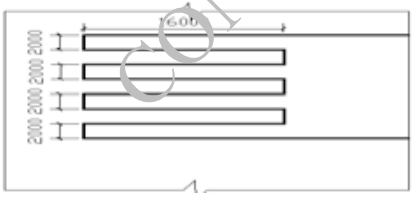

Figure 4A. Plan layout of cooling water pipe

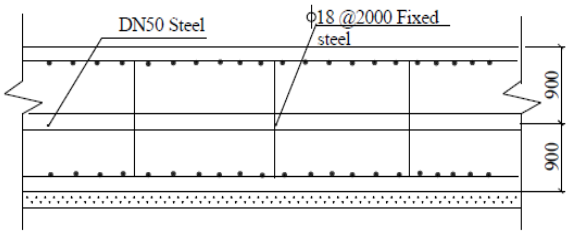

Figure 4B. Vertical layout schematic of cooling water pipe

3. Construction Methodology

Foundation concrete will not be cast in single pour. It will be cast in layer by layer. Each layer thickness will be 0.5 m and time taken to complete every single layer will be 1 hour. Time required to complete one single footing will be around 8 hours.

Table 1. Concrete Pouring sequence stages

Description	Thickness of foundation cast at each stage	Total thickness cast	Cumulative time taken
Stage 1	500 mm	500 mm	1 hour
Stage 2	500 mm	1000 mm	2 hours
Stage 3	500 mm	1500 mm	3 hours
Stage 4	500 mm	2000 mm	4 hours
Stage 5	500 mm	2500 mm	5 hours
Stage 6	500 mm	3000 mm	6 hours
Stage 7	500 mm	3500 mm	7 hours
Stage 8	-	3500 mm	hours

3.1 Analytical procedure of finite element procedure:

The article adopts structural analysis finite element software MIDAS/Civil to implement value simulation analysis to the large-volume concrete temperature field and temperature stress. It can be divided into the following three procedures:

3.2 Model establishment and necessary parameter confirmation.

This process mainly includes the material features related to time such as creep, dry shrinkage and elastic modulus and setup of boundary.

3.3 Analysis of temperature stress process.

This process mainly includes the setup of temperature, distribution of heat source and setup of construction simulation time. It mainly includes the temperature change graph and temperature stress change graph.

3.4 Procedure model establishment

The mass concrete and natural foundation is selected and adopted as the calculation object for modelling; the concrete thickness is 1.8m and 2.7m; the length is 38m and width is 46m; the soil thickness is 3m, length is 42m and width is 54m. Axis Z is along the thickness direction, axis X is along the length direction and axis Y is along the width direction.

Table 2. Material property for concrete

Density	25 kN/m3
Grade of Concrete, f_{ck}	40 MPa
Elastic modulus, Ec	35000 MPa
Allowable tensile stress	3.0 MPa
Allowable compression stress	14 MPa

Table 3. Material property for Steel

Density	78.5 kN/m3
f_y	500 MPa
Es	200000 MPa

The grid is distributed according to the concrete shape; the Mass concrete foundation (thickness of 3.5m) length and width direction includes 17m and 18m respectively; the mass concrete foundation (partial part with a thickness of 0.5m) length and width direction includes 8 units and 9 units respectively.

3.5 The initial and boundary conditions

Environmental temperature: Average daily temperature is 21ºC. Initial concrete temperature: The measured model entry temperature of concrete is 22 ºC—28ºC; in order to reflect the possible maximum temperature, 28 ºC is adopted for the procedure analysis. Flowing temperature of cooling water: The measured

temperature is 19 to 22 ºC, 21ºC is adopted. The concrete surface, surrounding steel model and air contact surface is treated according to boundary conditions; the natural foundation and foundation contact surface is treated according to boundary conditions; the contact is good and natural foundation is simulated into a structure with certain specific heat and heat transmission rate. The natural foundation is treated as follows: The side and lower bottom of natural foundation adopt the fixed natural foundation temperature (22ºC); the model is established for the restriction conditions according to the body unit: general support restriction conditions are adopted.

3.6 Thermal parameters of concrete foundation and natural foundation:

Table 4. The material and thermal characteristic parameters

Description	Unit	Foundation	Subsoil
Specific heat	Kcal / kg / °C	1046.5	837.2
Rate of heat conduction	Kcal / m / hr / °C	9627.8	7116.2
Ambient temperature	°C	25	-
Casting temperature	°C	20	-
Thermal expansion coefficient	-	11.6 x 10^{-6}	-
Heat source function coefficients	K (°C), a (no unit)	K=33.97, a=0.605	-
Density	kg/m^3	2400	1800
Poisson's ratio	-	0.2	0.2

3.7 Specific heat:

The specific heat is the amount of heat per unit mass required to raise the temperature by one degree Celsius with specific heat of concrete is 1046.5 kcal / kg /°C and specific heat of subsoil is 837.2 kcal / kg / °C.

$$C = \frac{Q}{m}/dT$$

Where, Q, m, and dT are heat added, mass, and change in temperature respectively.

3.8 Heat conduction

Conduction is heat transfer by means of molecular agitation within a material without any motion of the material as a whole. If one end of a metal rod is at a higher temperature, then energy will be transferred towards the colder end.

Rate of heat conduction in concrete 9627.8 kcal / m / °C

Rate of heat conduction in subsoil

3.9 kcal / m / °C

3.10 Convection coefficient

Convection is another form of heat transfer whereby heat is transmitted between a fluid and the surface of a solid through a fluid's relative molecular motion. From an engineering perspective, the heat transfer coefficient, c h is defined to represent the heat transfer between a solid and a fluid, where T represents the surface temperature of the solid, and the fluid flowing on the surface retains an average temperature Tα. The convective heat transfer, q= hc (Ts - Tf), Where, hc, Ts, and Tf are the convection coefficient, surface temperature, and Fluid temperature respectively.

3.11 Heat source

Heat source represents the amount of heat generated by a hydration process in mass concrete. Differentiating the equation for adiabatic temperature rise and multiplying the specific heat and density of concrete obtain the internal heat generation expressed in terms of unit time and volume. Adiabatic conditions are defined as occurring without loss or gain of heat.
T = K (1 - e-□t), Where, T, K, α, and t are the adiabatic temperature, maximum adiabatic temperature rise, reactive velocity coefficient, and tine respectively.

3.12 Ambient temperature

The temperature of the surrounding environment, i.e., the temperature of the air surrounding a medium.

3.13 Thermal expansion coefficient

The coefficient of thermal expansion describes how the size of an object changes with a change in temperature. Specifically, it measures the fractional change in size per degree change in temperature at a constant pressure.

4. Results and Discussion:

In this analysis, the major cause for thermal stresses is due to the temperature differences within the concrete mass resulting in internal constraints. Recapping the overview, Internal Constraints are caused by unequal volume changes. Initially, cooling surface and warm inner parts cause tension at the surface and compression at the inner parts. At a later stage after the rise in temperature due to heat of hydration reaches the peak level, the cooling (contracting) inner parts relative to the surface cause tension in the inner parts and compression at the surface. The magnitude of the stresses is proportional to the temperature differences between the inner parts and surface. It is also anticipated that the two concrete masses of two separate pours of different ages will exhibit different heat transfer characteristics.
It will analyse the characteristics of thermal stresses in concrete by reviewing the results of heat of hydration analysis for 15Hours reflecting construction stages by graphic and contour results.

- Max temperature = 36 degree
- Max tensile stress < Max allowable stress
- Temperature variation for inner core and outer surface

Temperature distribution at different stages is shown as below:

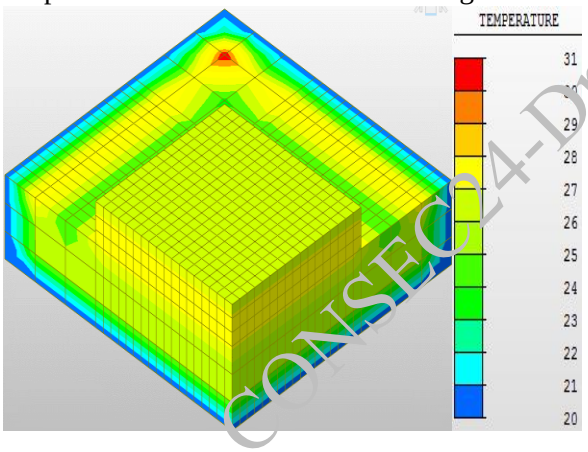

Figure 5. Temperature distribution at stage 3 (after 3 hours of casting) Unit: Celsius

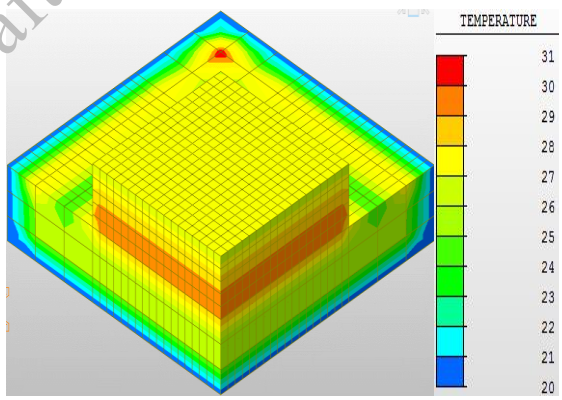

Figure 6.Temperature distribution at stage 5 (after 5 hours of casting) Unit: Celsius

The reinforcement presence in the concrete makes the significant contribution of tensile strength of the concrete at the time of construction. In the mass concrete structure the hydration stress with respect to time has taken for the temperature variation according to the time factor to interpret the temperature rise and fall. The formwork is playing a major role on the sudden temperature variation with the concrete surface and the atmosphere. So, the time of formwork removal also an important factor to be considered.

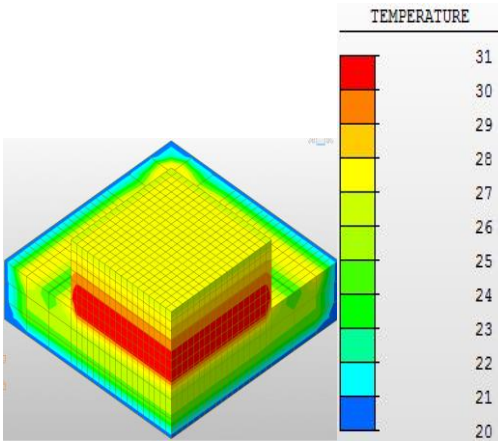

Figure 7. Temperature distribution at stage 7 (after 7 hours of casting) Unit: Celsius

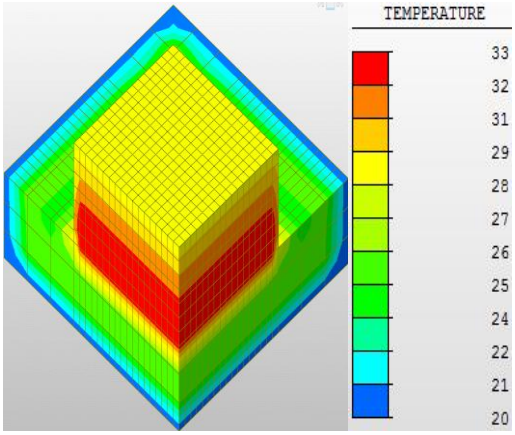

Figure 8. Temperature distribution at stage 8 (after 10 hours of casting) Unit: Celsius

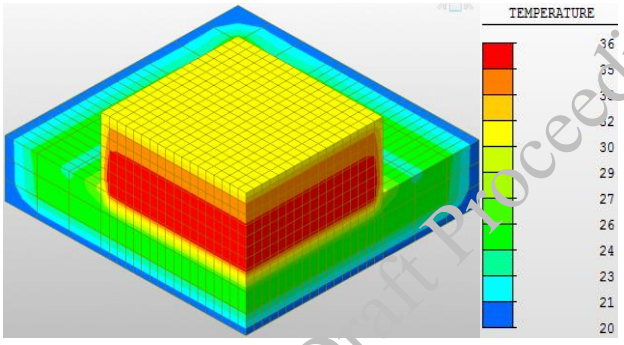

Figure 9. Temperature distribution at stage 8 (after 15 hours of casting)

Hydration stress distribution at different stages are shown as below:

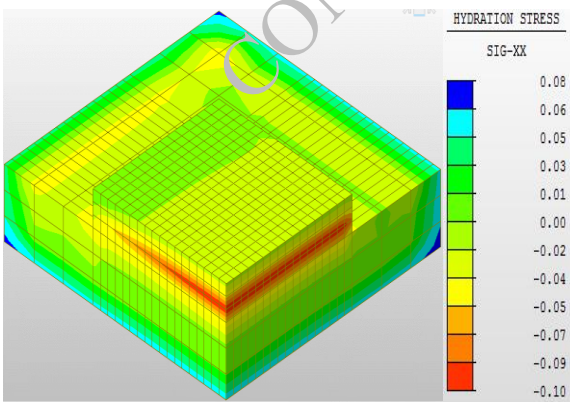

Figure 10. Hydration stress distribution at stage 3 (after 3 hours of casting)

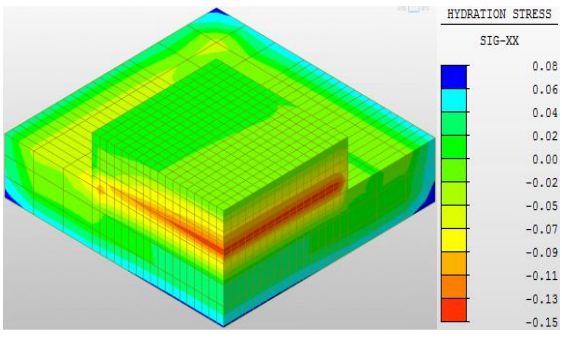

Figure 11. Hydration stress distribution at stage 5 (after 5 hours of casting)

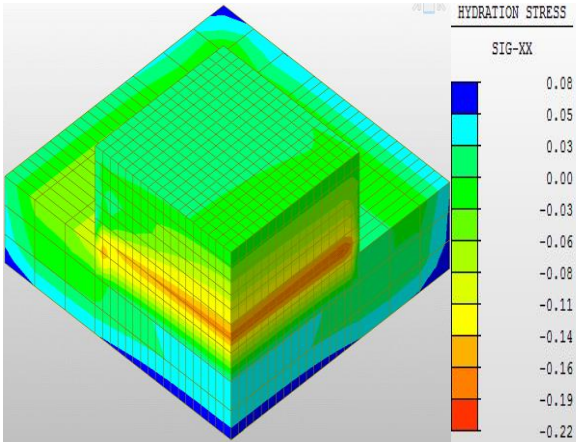

Figure 12. Hydration stress distribution at stage 7 (after 7 hours of casting)

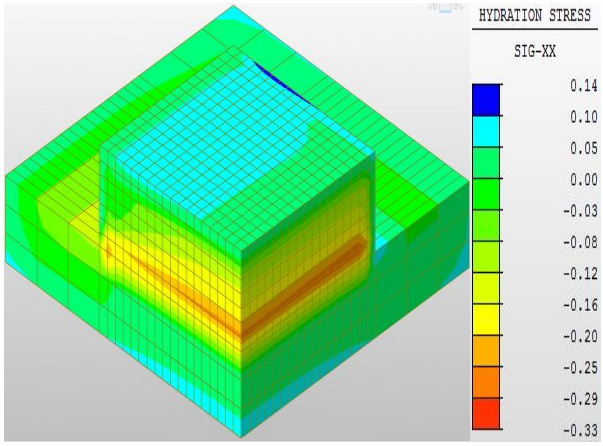

Figure 13. Hydration stress distribution at stage 8 (after 10 hours of casting)

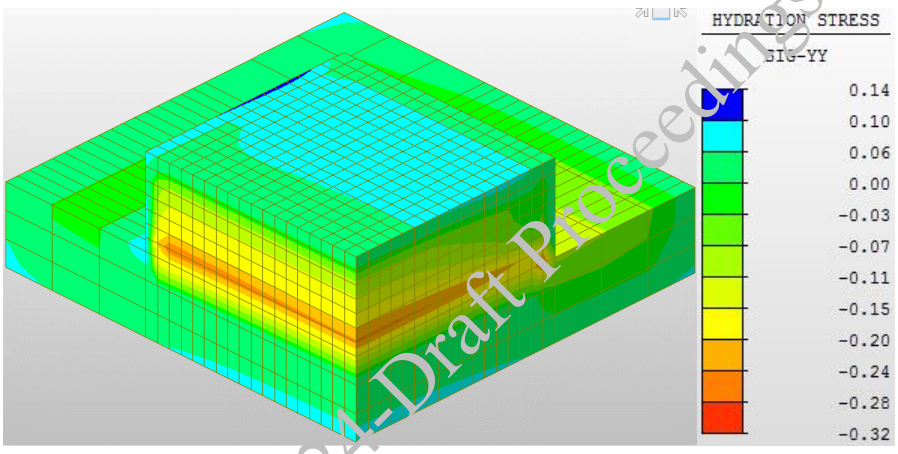

Figure 14. Hydration stress distribution at stage 8 (after 15 hours of casting)

Time history graph of hydration stress are shown as below:

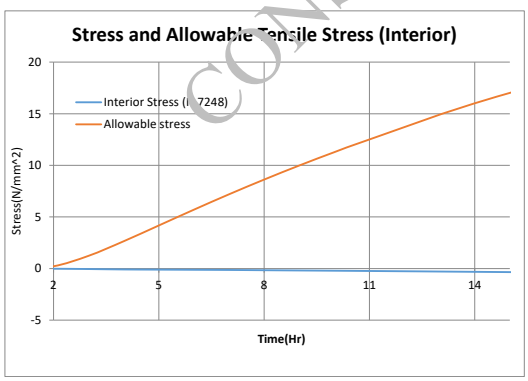

Figure 15. Time history graph of hydration stress at interior

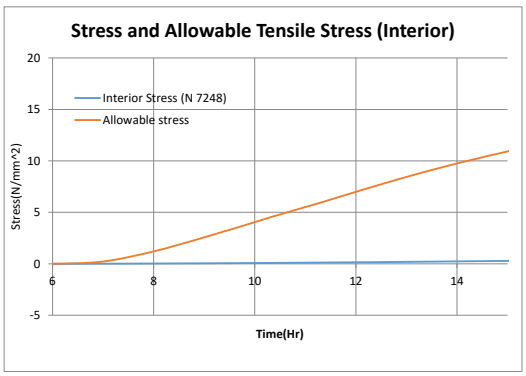

Figure 16. Time history graph of hydration stress at surface

5. Conclusions

The study aimed at characterizing the hydration phenomenon of early-stage concretes is proposed in this work. It emphasizes the role of hydration temperature to describe the evolution of the hardening process.

After the analytical formulation of the hydration and heat transfer derivations, a consistent numerical solution based on the Finite element technique for the mass concrete. Then, in order to consider structural applications dealing with the thermal problems, the same constitutive relationships are considered within a general Finite Element (FEM) procedure. Numerical comparisons without cooling pipe system and with cooling pipe system tests performed for rapid hardening cement-based concretes establish the soundness and capability of the given application.

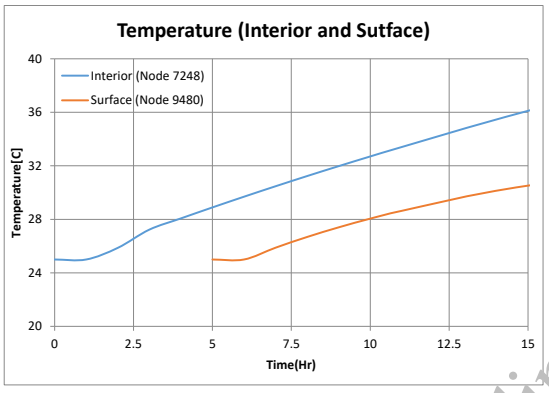

Figure 17.Time history graph of temperature

- In a particular bridge pier foundation concrete structure mass construction method has generated the number of construction joints, however this progress was very effective to reduce the temperature rise due to cumulative hydration impact.
- The observed impact on non-uniform thermal expansion and contraction due to heat of hydration with the cooling system of the concrete accompanied by changing constraints create undesirable stresses is well controlled by the colling system embedded in the concrete.
- The temperature stresses causing effects such as cracking in the concrete, were well reduced and the strength and durability maintained by the controlling of temperature and corresponding stress in the core point to prevent cracks in mass concrete.
- As the conclusion the mass concrete temperature with cooling pipe has reduced the temperature from core surface by 38%, it can realize dual control of temperature and corresponding stresses and it is feasible as a construction method for the temperature control and management for the wide application in the similar mass concrete projects.

The simulation analysis of finite element procedure can realise the integration between modern technical measures of actual project.

References

Alberto, C., Paul, H., Kohan, Ricardo, D. Q. and Mario A. (2012) “Numerical Modelling of Hydration Process And Temperature Evolution In Early Age Concrete”,*Computational Mechanics* ,31:13-16

Fu, W.Q. and Han, S.F.(2006) “Prevention and control of concrete project crack. In: Han SF, Geng WS, editors. Control instruction of reinforced concrete structure crack, Beijing”,*Chemical Industry Press*, 213—242

Han, S.F. and Geng,W.S.(2006) ‘Control instruction of reinforced concrete structure crack, Beijing”,*Chemical Industry Press*:267—274

Li, J.Y. and Zhou, C.L. and Meng, Z.P.(2007)“New concrete techniques of special construction. Beijing”,*Chemical Industry Press*

Pan, D.W., Jin, B.F. and Nie, F.H. “ Construction of flat plate raft foundation project of century wealth centre”

Wang,T.M. (2006) “Control theory and practice of crack in super-long and super-thick large volume reinforced concrete structure crack”, In: Han SF, Geng WS, editors. *Control instruction of reinforced concrete structure crack*, Beijing: *Chemical Industry Press*:19-60

Zhang, Y.P. (2007) “Study of simulation and temperature crack control in mass concrete of high-rise buildings foundation. Beijing”,: *Hebei University of Engineering*

Effect of Silica Fume on Compressive Strength and Pore Structure of Foam Concrete for Non-Structural Applications

Arvind Vishavkarma[1]*, and Kizhakkumodom Venkatanarayanan Harish[2]

[1] Graduate Student, Department of Civil Engineering, Indian Institute of Technology, Kanpur, Uttar Pradesh 208016
E-mail: arvindvi@iitk.ac.in
[2] Assistant Professor, Department of Civil Engineering, Indian Institute of Technology Kanpur, 334 Faculty Building, Kanpur, Uttar Pradesh 208016, India. Phone: +91-512-259-6427
E-mail: kvharish@iitk.ac.in

*Corresponding author

ABSTRACT

Foam concrete offers significant advantages, including excellent flowability, enhanced thermal and insulating properties, and a superior strength-to-weight ratio. The performance of foam concrete is primarily influenced by the stability of its macrovoids and pore distribution. In this study, silica fume, a fine reactive material, was used to improve the compressive strength and stability of air voids. Silica fume was incorporated as a partial replacement for cement in varying ratios of 0%, 5%, 10%, and 15%. The study examined the effect of silica fume on compressive strength, while also analyzing macro-porosity, pore size (specifically D50 and D90), and the frequency of macro air voids using image analysis. Additionally, a correlation was established between compressive strength and various pore structure parameters to gain insights into factors affecting strength. The results showed that the 28-day compressive strength of foam concrete ranged from 12.25 to 15.33 MPa, meeting the strength criteria for load-bearing elements as per IS 2185 (Part 4). The inclusion of 5%–15% silica fume significantly improved strength by 2.9%–25.5% compared to the control mixture. The macro-porosity of foam concrete was found to be within the range of 31% to 35%, with macrovoids having D50 diameters between 89.2 and 96.3 µm and D90 sizes between 421 and 450 µm. Frequency histogram analysis revealed that a substantial portion of artificially created air voids were within the 50 µm to 500 µm range. Regression analysis indicated that the D90 size had the greatest impact on compressive strength, while macro-porosity and D50 size had comparatively smaller influences.

KEYWORDS: *Foam concrete, Compressive strength, Silica fume, Image Analysis, Macro-porosity*

1. Introduction

Foam concretes offer numerous benefits due to their cellular microstructure, including reduced weight, excellent acoustic and thermal insulation properties, an enhanced strength-to-weight ratio, and economic advantages in manufacturing. In non-structural applications, strength requirements typically do not exceed 25 MPa, and the density remains below 1800 kg/m³, as per IS: 2185 (Part 4). To maximize the strength-to-weight ratio of foam concrete, careful formulation of mixture proportions using highly reactive supplementary cementitious materials (SCMs) is essential. SCMs not only reduce cement content but also enhance the physical and durability performance of foam concrete by improving the pore structure at both micro and macro levels (Gökçe et al. (2019); Li et al. (2023); Vishavkarma and Harish (2024); Zhang et al. (2022)). Silica fume, a fine powder composed of spherical particles with an average diameter of 0.1 µm to 0.3 µm, significantly improves foam stability. It does so by adsorbing irreversibly and spontaneously onto the liquid-gas (bubble) interface, forming a solid-liquid-gas interface, as noted by Wang et al. 2020. This stability enhancement is superior compared to the traditional liquid-gas two-phase foam. Researchers have used silica fume in foam concrete, substituting cement by 5% to 20% by weight (Bing et al. (2012); Gökçe et al. (2019)). Silica fume functions as a micro-filler, refining the pore structure and stabilizing bubbles. It

also reacts with $Ca(OH)_2$ to form secondary C-S-H gels, thus increasing strength (Hilal et al. (2015)). The mechanism of silica fume in cement-based systems can be explained through pore size refinement, matrix densification, interaction with free lime, and cement paste-aggregate interfacial refinement. Foam concrete is increasingly favored over traditional load-bearing materials like brick, hollow concrete blocks, and fly ash bricks due to its adaptable size, significant environmental benefits from the use of industrial by-products, enhanced durability, and superior thermal and sound insulation properties. The physical, functional, and durability characteristics of foam concrete largely depend on the stability of the foam used in its production. Enhancing foam stability with SCMs leads to improved performance without added costs. Additionally, the load-bearing capacity of foam concrete is influenced by specific pore structure factors. However, many studies have not fully explored which parameters most significantly affect compressive strength. This study aims to fill that gap by investigating the pore-structure parameters that influence compressive strength and by analyzing the impact of silica fume on both compressive strength and pore structure parameters in foam concrete for load-bearing applications.

2. Mixture Design, Proportions, and preparation of mixtures for foam concrete

Table 1 details the mix design for the foam concrete, which aligns with the production methods described in Vishavkarma and Harish (2024). This investigation used 43-grade Ordinary Portland Cement (OPC) conforming to IS 269 (2020), silica fume with an average particle size (D50) of 0.3 µm as per ASTM C1240, and a protein-based foaming agent. The foaming agent had a foam density of 46-47 kg/m³ and was prepared by mixing 1 part of foaming agent with 40 parts of water. The mix design employed a water-to-cementitious ratio of 0.35 and a sand-to-cementitious ratio of 1.

Table 1. Mixture proportions for foam concrete

Mix Ids	Quantity of mixtures (per m^3)						Fresh Density (kg/m^3)	Harden density (kg/m^3)	Flow Value (%)
	Cement (kg)	Silica fume (kg)	Sand (kg)	Water (kg)	Foam (kg)	SP (%)			
Control	604	-	604	211	18.73	0.40	1497	1555	55
SF-5%	574	30	604	211	18.30		1472	1550	23
SF-10%	543	60	604	211	18.30		1472	1548	21
SF-15%	514	90	604	211	18.30		1517	1552	15

2.1 Test procedure

The test procedure for compressive strength and image analysis was explained in the different study conducted by the same authors (Vishavkarma et al. (2024); Vishavkarma and Kizhakkumodom (2024)).

3. Results and Discussions

3.1 Compressive strength

Fig. 1 (a) illustrates the compressive strength of foam concrete mixtures at various curing periods. The compressive strength ranged from 9.86 MPa to 16.60 MPa, influenced by the curing duration and silica fume dosages. At 28 days, the strength ranged from 12.25 MPa to 15.3 MPa, meeting the load-bearing unit requirements for G-12 grade as specified in IS: 2185 (Part 4) . Notably, silica fume mixtures demonstrated higher early strength compared to the control mixture. This is attributed to the more rapid hydration of silica fume particles compared to cement particles, leading to enhanced strength development in the initial curing stages. Silica fume mixtures showed a gradual increase in strength over the first week, followed by a significant rise until 28 days, after which the strength stabilized. The SF-5%, SF-10%, and SF-15% mixtures exhibited relative strength increases of 2.9%, 25.1%, and 12.5% compared to the control mixture. This improvement can be attributed to several factors: (i) Particle Size and Surface Area: Silica fume particles have a significantly smaller size and larger surface area compared to cement particles, which accelerates the pozzolanic reaction and enhances strength development early in the curing process Nedunuri et al. (2020). (ii) Silica fume reacts with $Ca(OH)_2$ produced during cement hydration, forming secondary

C-S-H gel. This reaction improves the density and packing of the microstructure in the transition zone. The CaO/SiO_2 ratio of the secondary C-S-H gel is lower than that of the primary C-S-H gel formed during cement hydration (Isaia et al. 2003; Rossen et al. 2015; Shannag 2000). (iii) Silica fume particles act as nucleation sites for hydration products and function as micro-fillers. This enhances chemical reactions, producing smaller $Ca(OH)_2$ crystals and refining the pore structure by converting continuous pores into fragmented ones (Goldman and Bentur (1989); Isaia et al. (2003)).

3.2 Pore size parameters

3.2.1 Macro Porosity and size of macro voids

The macro-porosity values for the control mixture (CM) and silica fume mixtures (SF-5%, SF-10%, and SF-15%) are 33.7%, 32.1%, 29.3%, and 32.5%, respectively. The addition of silica fume results in a decrease in macro-porosity by 4.8%, 13.3%, and 3.73% compared to the control mixture. The average pore diameter (D_{50}) for CM, SF-5%, SF-10%, and SF-15% mixtures are 96.0 µm, 96.3 µm, 92.0 µm, and 89.2 µm, respectively, while the D_{90} values are 421 µm, 419 µm, 450 µm, and 431 µm. The inclusion of silica fume decreases the D_{50} value but increases the D_{90} value with higher dosages. The reduction in D50 can be attributed to the finer particles of silica fume, which facilitate the formation of a solid-liquid-gas three-phase foam, compared to the liquid-gas phase foam in the control mixture Wang et al. (2020). This three-phase foam effectively smooths the pore walls, providing better confinement to prevent foam from draining, fracturing, moving, or coalescing during mixing and hardening (Bai et al. (2023); Li et al. (2023)). However, the increase in D_{90} size with higher silica fume content is due to the larger specific surface area of silica fume particles, which absorb water and reduce workability, leading to a non-uniform distribution of foam during mixing.

3.2.2 Frequency of pore size distribution

The pores in the foam concrete mixtures were analyzed and are depicted in Figure 1(b). They were categorized based on their size distribution into three levels: Level 1 for particles smaller than 50 µm, Level 2 for particles ranging from 50 µm to 500 µm, and Level 3 for particles larger than 500 µm. In foam concrete, Level 1 and Level 2 pores are most prevalent. Therefore, the effects of silica fume were particularly investigated with respect to these pore sizes. As shown in Figure 1(b), both Level 1 and Level 2 pores account for 94% to 95% of the total macro voids. The addition of silica fume particles notably reduced the size of pores, especially those in the 50 µm to 500 µm range. This reduction indicates that silica fume has a beneficial impact on Level 2 pores. By filling spaces between cement particles, silica fume effectively prevents the displacement and aggregation of foam within the slurry, thereby enhancing foam stability Wang et al. (2020).

3.2.3 Relationship between different parameters of air voids

In this study, regression analysis was employed to examine the relationships between compressive strength and various pore structure parameters. The linear correlations between these parameters are depicted in Fig. 1 (c) and Fig. 1 (d). The coefficient of determination R^2 for the relationship between compressive strength and porosity is 0.4621. Similarly, the R^2 value for the relationship between compressive strength and the D50 pore size is 0.4558. In contrast, for the relationship between compressive strength and the D_{90} pore size is significantly higher at 0.9608. These results demonstrate a strong correlation between compressive strength and the D_{90} pore size in foam concrete with a density of 1500 kg/m³. Thus, the D_{90} pore size exerts a greater influence on compressive strength compared to porosity and the D_{50} pore size.

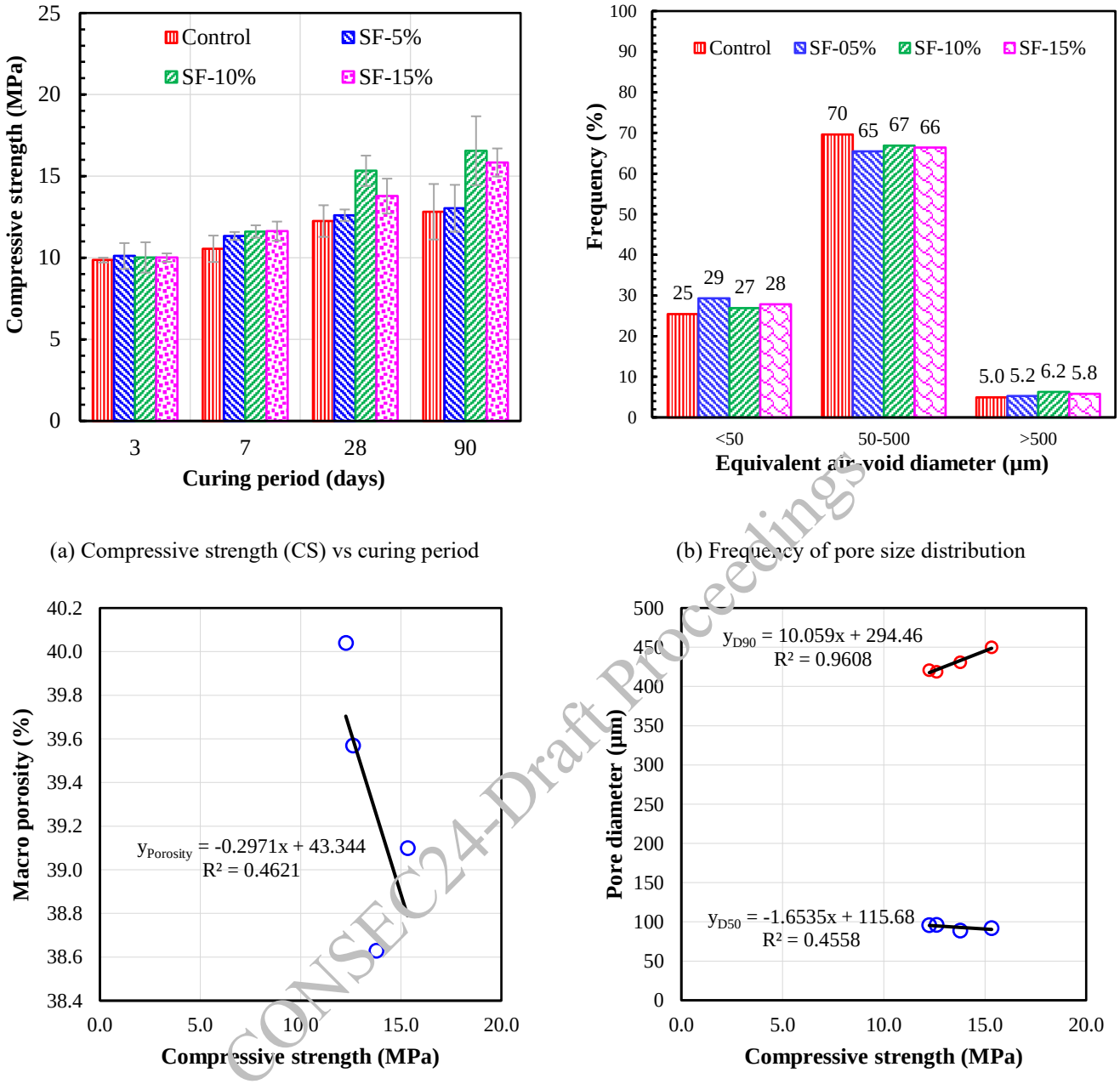

(a) Compressive strength (CS) vs curing period

(b) Frequency of pore size distribution

(c) Relationship between CS and porosity

(d) Relationship between CS and pore size (D_{50} and D_{90})

Figure 1. Effect of Silica fume on compressive strength and different pore size parameters of foam concrete

4. Conclusions

Based on the conducted studies, the conclusions can be summarized as follows:

- The compressive strength of foam concrete at 28 days ranges from 12.25 to 15.30 MPa, which meets the G-12 grade requirement for load-bearing units. The strength improves by 2.9% to 25.3% with 5%–15% silica fume compared to the control mixture.
- Foam concrete exhibits macro-porosity between 29.3% and 33.7%. The average pore size (D_{50}) ranges from 89.2 to 96.3 µm, decreasing with higher silica fume dosages. Conversely, the D90 pore size ranges from 419 to 450 µm and increases with higher silica fume dosages.
- The artificially entrained macrovoids, which range between 50 and 500 µm, account for 65%–70% of the total macro voids in the foam concrete.

- The compressive strength of foam concrete is predominantly influenced by the D_{90} pore size, with a high linear coefficient of variation (R^2 value) of 0.9608. In comparison, macro-porosity and D_{50} have lower R^2 values of 0.4621 and 0.4558, respectively.

Acknowledgements

The authors express their gratitude for the assistance and support provided by the staff of the Structural Engineering Laboratory at IIT Kanpur throughout the execution of several tests. They also appreciate the support from the Advanced Centre for Materials Science and Prof. Rakesh Shina for granting access to the optical microscope at IIT Kanpur.

References

ASTM C1240. (2020) "Standard Specification for Silica Fume Used in Cementitious Mixtures",*ASTM International*, 1–7.

Bai, Y. hua, Lu, Y. and Zhang, D. yue. (2023) "Preparation of nano-carbon black and silica fume modified foam concrete: Compressive strength, pore structure and electromagnetic property",*Construction and Building Materials*, 369:130553.

Bing, C., Zhen, W. and Ning, L. (2012) "Experimental Research on Properties of High-Strength Foamed Concrete", *Journal of Materials in Civil Engineering*, 24(1):113–118

Gökçe, H. S., Hatungimana, D. and Ramyar, K. (2019) "Effect of fly ash and silica fume on hardened properties of foam concrete", *Construction and Building Materials*, 194:1–11

Goldman, A. and Bentur, A. (1989) "Bond effects in high-strength silica fume concretes", *ACI Materials Journal*, 86(5), 440–447.

Hilal, A. A., Thom, N. H. and Dawson, A. R. (2015) "On void structure and strength of foamed concrete made without/with additives", *Construction and Building Materials*, 85:157–164

IS: 2185 (Part 4). (2014) "Concrete masonry units - specification part 4 preformed foam cellular concrete blocks." *Bureau of Indian Satandards*, 97(3)

IS 269. (2020). "Ordinary Portland Cement Specification", *Bureau of Indian Standard(BIS)*, 2015(December 2015).

Isaia, G. C., Gastaldini, A. L. G. and Moraes, R. (2003) "Physical and pozzolanic action of mineral additions on the mechanical strength of high-performance concrete", *Cement and Concrete Composites*, 25(1): 69–76

Li, M., Tan, H., He, X., Jian, S., Li, G., Zhang, J., Deng, X. and Lin, X. (2023) "Enhancement in compressive strength of foamed concrete by ultra-fine slag", *Cement and Concrete Composites*, 138:104954

Nedunuri, S. S. S. A., Sertse, S. G. and Muhammad, S. (2020) "Microstructural study of Portland cement partially replaced with fly ash, ground granulated blast furnace slag and silica fume as determined by pozzolanic activity", *Construction and Building Materials*, 238:1–11

Rossen, J. E., Lothenbach, B. and Scrivener, K. L. (2015) "Composition of C-S-H in pastes with increasing levels of silica fume addition", *Cement and Concrete Research*,75:14–22

Shannag, M. J. (2000) "High strength concrete containing natural pozzolan and silica fume", *Cement and Concrete Composites*, 22(6):399–406

Vishavkarma, A. and Harish, K. V. (2024) "Tension and bond characteristics of foam concrete for repair applications", *Case Studies in Construction Materials*, 20: e02767

Vishavkarma, A. and Kizhakkumodom, H. (2024) "Assessment of pore structure of foam concrete containing slag for improved durability performance in reinforced concrete applications", *Journal of Building Engineering*, 86:108939

Vishavkarma, A., Kumar, M. and Harish, K. V. (2024) "Influence of combined substitution of slag and fly ash in improving the pore structure and corrosion resistance of foam concrete mixtures used for reinforced concrete applications", *Case Studies in Construction Materials*, 21:e03449

Wang, X., Huang, J., Dai, S., Ma, B. and Jiang, Q. (2020) "Investigation of silica fume as foam cell stabilizer for foamed concrete", *Construction and Building Materials*, 237:117514

Zhang, S., Qi, X., Guo, S., Zhang, L. and Ren, J. (2022) "A systematic research on foamed concrete: The effects of foam content, fly ash, slag, silica fume and water-to-binder ratio", *Construction and Building Materials*, 339:127683

Influence of Copper Slag on the Rheology of 3D Printable Concrete

Darssni Ravichandran[1] , Prabhat Ranjan Prem[2*], Vijay Bhaskara[2] and Babitha Benjamin[1]

[1]Research Associate, CSIR Structural Engineering Research Centre, Taramani, Chennai 600 113, Tamil Nadu, India,
Email: darssni96@gmail.com
[2] Scientist, CSIR Structural Engineering Research Centre, Taramani, Chennai 600 113, Tamil Nadu, India,
Email: prabhat@serc.res.in

[*]Corresponding author

ABSTRACT

The formulation of 3D printable concrete involves meticulous considerations to ensure the compatibility of materials with the 3D printing process. Various factors must be considered, including desired strength, workability, rheology, extrudability, printability, buildability, and durability. The selection of appropriate raw materials, such as cement, mineral admixtures, fine aggregate, coarse aggregate, chemical admixtures, and fibres, and maintaining a low water-to-cement ratio, is crucial to achieving desirable properties in the fresh and hardened concrete states. Aggregate properties, especially fineness and gradation, are significant in determining pumpability and printability criteria. These aggregates encompass a spectrum of particle sizes, ranging from fine to medium and coarse fractions. In this study, we investigate the influence of copper slag on the thixotropic properties of printable concrete. Copper slag is an industrial by-product obtained during the smelting and refining of copper. It is a non-hazardous and non-reactive material. The copper slag with particle sizes ranging from 2mm to 1mm is incorporated in the mix with 25% replacement of total fine aggregate content. The rheological characterization of the mixes is conducted using stress growth tests and the flow curve method to obtain the static yield, dynamic yield stress, and plastic viscosity. The analysis found that the presence of copper slag increases the thixotropic properties of printable concrete by 15 – 20 %.

KEYWORDS*: Copper slag, 3D Printing, Concrete, Rheology*

1. Introduction

Concrete 3D printing represents one of the latest advancements in civil engineering, offering transformative potential for the construction industry. As research progresses and technological capabilities expand, there is an urgent need to address the sustainability of the materials used in concrete 3D printing. Traditional binders and fine aggregates, typically sourced from non-renewable resources, pose environmental concerns. A range of waste materials, including crumb rubber (CR), Antimony tailings (AT), Recycled Fine Aggregate (RFA), Carbonated Recycled Fine Aggregate (CRFA), and Recycled polyethylene terephthalate (PET), have been assessed by researchers for their viability as alternatives to natural sand in 3D concrete printing (3DCP) [1]–[10]. Studies show that fine aggregates like AT, CR, and recycled glass are successfully replaced by 100 % instead of natural sand [8], [11], [12]. The size of the fine aggregate particles significantly influences the extrusion properties and layer deposition in the mix, impacting the precision and quality of 3D-printed concrete structures [14]. The proposed ranges have been found to be optimal for printing concrete and achieving desirable strength.

In the current study, the authors investigate the feasibility of utilizing copper slag as a fine aggregate in 3D printable concrete. Copper slag, an industrial byproduct resulting from the smelting and refining of copper ore, is increasingly being recognized as a valuable resource in construction due to its dual potential as a cement and fine aggregate replacement in concrete production. This versatile material offers several advantageous properties that make it suitable for incorporation into concrete mixes, contributing to both sustainability and performance enhancement in construction projects. With proper processing and ensuring consistent particle size distribution and grading, copper slag can be used as fine aggregate replacement in

concrete. As a fine aggregate replacement, copper slag offers comparable or even superior mechanical properties and durability characteristics compared to conventional concrete mixes. The following details the methodology for sample preparation of mixes using copper slag for concrete printing. The mixes are characterized using stress growth tests and compared with conventional mixes for thixotropy, static, and dynamic stress using experiments and rheological models.

2. Experimental investigation

The binder composition includes cement, silica fume, fly ash, and limestone powder. For the control mixes (CS - 0), locally available standard sand with a particle size of 0.5 – 1 mm is used as the fine aggregate. In this study, copper slag is used to replace 25% of the standard sand as a fine aggregate, as detailed in Table 1. The adopted water-to-cement (w/c) ratio is 0.3, with a superplasticizer dosage of 1% by weight of the cement. Detailed material studies and mix design are discussed in Greeshma et al. (2023) [13]. For rheology studies, a planetary mixer is used. Initially, dry mixing is done for 2 – 3 minutes. After that, water and the superplasticizer are added at once. This mix has an open time of 60 minutes.

Table 1 Mix proportion of 3D printable concrete in kg/m^3

Mix ID	Cement	Fly ash	Silica fume	Limestone powder	Fine aggregate		Water	SP
					Standard sand	Copper slag		
CS – 0	664.6	232.6	53.2	13.3	1329.3	-	199.4	3.98
CS – 25	664.6	232.6	53.2	13.3	332.33	996.97	199.4	3.98

In this study, the stress growth method and flow curve method are used to determine the static yield stress and dynamic yield stress of the 3D printable mix. These tests are conducted using an Anton par rheometer with a cylindrical cup and a two-blade vane geometry. In this study, the protocol adopted for the stress growth method and flow curve is as follows

- Stress growth method: Pre-shear at 100 s^{-1} for 60 seconds, followed by rest time of 15 seconds and constant shear rate of 0.01 s^{-1} for 100 seconds.
- Flow curve method: Pre-shear at 100 s^{-1} for 60 seconds, followed by rest time of 15 seconds and triangular protocol with shear rate from 0 to 10 s^{-1} for 120 seconds, followed by 10 – 0 s^{-1} for 120 seconds.

The rheological study is conducted with a resting time of 30 minutes, at 10-minute intervals. The rheological parameters are analyzed by fitting them with rheological models such as the Bingham model, Herschel Bulkley model, and Modified Bingham model.

3. Results and Discussions

Fig. 1-3 shows the static yield stress, flow curve, and hysteresis area of the 3D printable mixes at various resting times. The CS-25 mix shows the highest static yield stress, dynamic yield stress, and thixotropy due to the incorporation of copper slag. Compared to the reference mix CS – 0, the CS – 25 mix shows a significant increase in static yield stress by 44.78%, 28.98%, and 19.71% at a resting time of 10 – 30 minutes.

The rheological parameters are analyzed and fitted using various rheological models, including the Bingham model, Herschel Bulkley model, and the Modified Bingham model. These models provided a good fit with the experimental data, with a regression value of 0.96 to 0.99. As shown in Table 2, the dynamic yield stress for the CS-0 and CS-25 mixes ranges from 374.71 to 1162.44 Pa and 559.98 to 1183.34 for the Bingham model, 148.87 to 821.42 Pa and 463.47 to 1143.42 Pa Herschel Bulkley model, and 263.2 to 1087.13 and 531.17 to 1162.44 for modified Bingham model at resting time of 10 to 30 minutes. These results clearly show that the CS-25 mix has higher dynamic yield stress values across all models compared to the CS-0 mix. The Herschel Bulkley model, in particular, indicates that the rheological index value for these mixes is less than 1, indicating their shear-thinning behavior. Similarly, the hysteresis area, which indicates the thixotropic behavior of the mix, increases by 5.25%, 8%, and 6.31% at different resting times for the CS-25 mix. This property is crucial for 3D printing applications, as it ensures the mix flows easily

under shear stress during printing but retains its shape once deposited. The inclusion of copper slag in the mix significantly enhances the rheological properties of the concrete. This enhancement not only increases the yield stress but also improves the overall printability and buildability of the concrete mix [15,16].

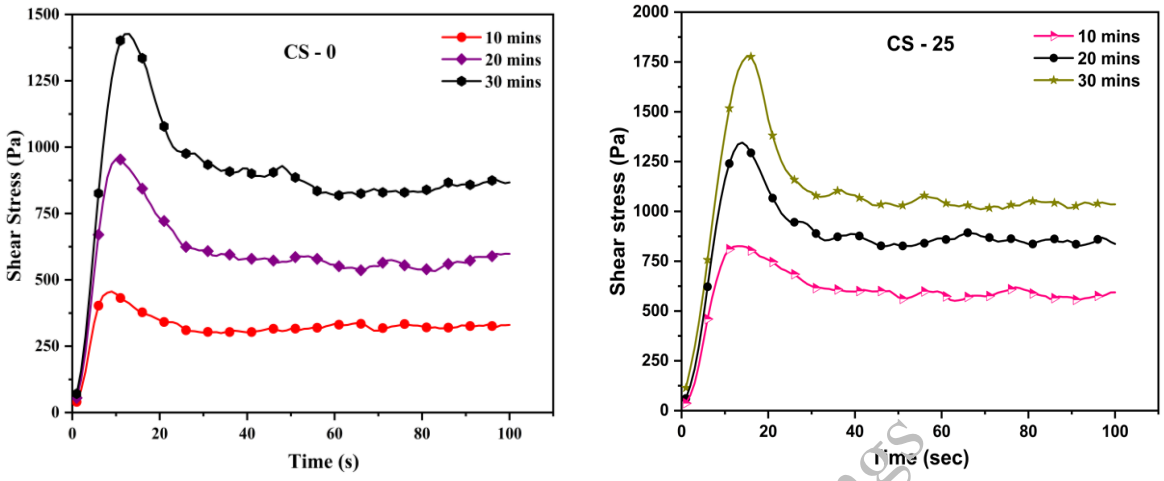

(a) (b)

Figure 1. Plot between time vs shear stress for (a) CS–0, and (b) CS–25

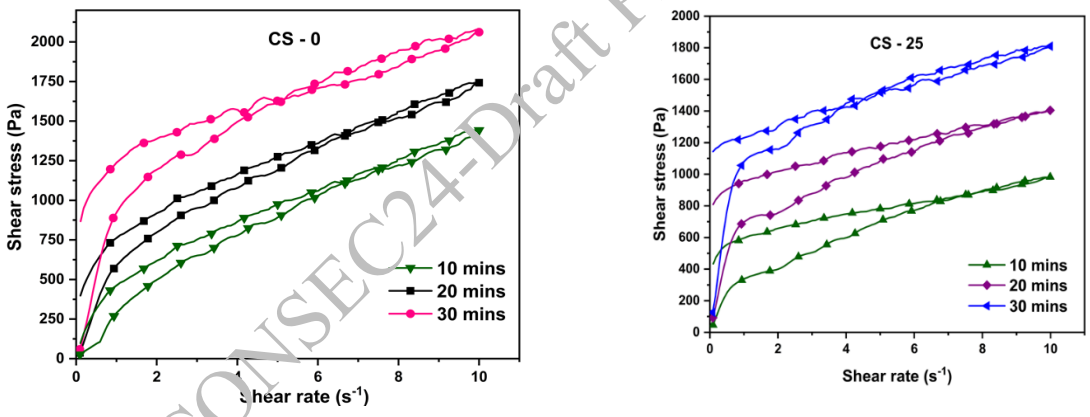

(a) (b)

Figure 2. Plot between shear rate vs shear stress for (a) CS – 0, and (b) CS – 25

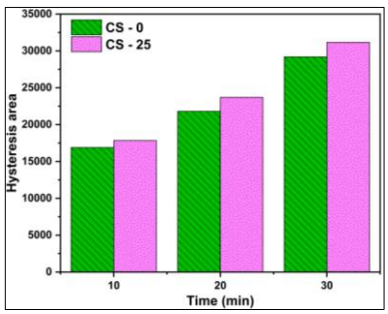

Figure 3. Hysteresis area of CS-0 and CS-25

Table 2. Rheological parameters of 3D concrete printing

Mix ID	Resting time (min)	Bingham model			Herschel bulkley model			Modified bingham model		
		Yield stress	Plastic viscosity	R^2	Yield stress	n	R^2	Yield stress	Plastic viscosity	R^2
CS–0	10	374.71±11.11	109.31±1.91	0.96	148.87±15.22	0.51±0.01	0.99	263.29±10.05	174.78±4.59	0.98
	20	674.72±11.11	109.30±1.91	0.96	314.39±15.22	0.51±0.01	0.99	563.29±10.05	174.78±4.59	0.98
	30	1162.44±10.70	89.40±1.84	0.95	821.42±32.68	0.47±0.02	0.98	1087.13±13.48	133.72±6.16	0.96
CS–25	10	559.98±3.89	42.02±0.67	0.97	463.47±9.02	0.59±0.02	0.98	531.17±4.78	58.97±2.18	0.98
	20	907.55±3.94	51.41±0.67	0.97	827.44±8.14	0.68±0.02	0.99	875.38±4.52	70.35±2.07	0.98
	30	1183.34±3.82	62.69±0.65	0.98	1143.42±8.44	0.84±0.03	0.99	1162.44±5.24	74.99±2.39	0.98

4. Conclusions

The present study examines the influence of copper slag as a fine aggregate on a 3D printable mix. The rheological parameters such as static yield stress, dynamic yield stress, and hysteresis area are tested using the stress growth method and flow curve method. The results show the following observations:

- The static yield stress of the CS-25 mix increases by 44.78%, 28.98%, and 19.71% at resting times of 10 – 30 minutes, respectively, compared to the CS-0 mix.
- The hysteresis area of the CS-25 mix increases by 5.25%, 8%, and 6.31% at resting times of 10 to 30 minutes, indicating enhanced thixotropic behavior.
- Rheological models show that the CS-25 mix has higher dynamic yield stress values across all models compared to the CS-0 mix.
- The Herschel Bulkley model, in particular, indicates that the rheological index value for these mixes is less than 1, showing their shear-thinning behavior.
- The inclusion of copper slag in the mix significantly enhances the rheological properties of the concrete. This enhancement not only increases the yield stress but also improves the overall printability and buildability of the concrete mix.

Acknowledgments

This research paper has been assigned the registration number CSIR-SERC- 1112/2024. A grant from CSIR, New Delhi , generously funds this study.

References

A. Singh et al., “Utilization of antimony tailings in fiber-reinforced 3D printed concrete: A sustainable approach for construction materials,” Constr. Build. Mater., vol. 408, no. June, p. 133689, 2023.

E. Ordoñez, S. Neves Monteiro, and H. A. Colorado, “Valorization of a hazardous waste with 3D-printing: Combination of kaolin clay and electric arc furnace dust from the steel making industry,” Mater. Des., vol. 217, no. November 2019, 2022.

G. H. A. Ting, Y. W. D. Tay, Y. Qian, and M. J. Tan, “Utilization of recycled glass for 3D concrete printing: rheological and mechanical properties,” J. Mater. Cycles Waste Manag., vol. 0, no. 0, p. 0, 2019.

G. Bai, L. Wang, G. Ma, J. Sanjayan, and M. Bai, “3D printing eco-friendly concrete containing under-utilised and waste solids as aggregates,” Cem. Concr. Compos., vol. 120, no. October 2020, p. 104037, 2021.

H. Zhang, J. Xiao, Z. Duan, S. Zou, and B. Xia, “Effects of printing paths and recycled fines on drying shrinkage of 3D printed mortar,” Constr. Build. Mater., vol. 342, no. PA, p. 128007, 2022.

Q. Shahzad et al., “Coordinated adjustment and optimization of setting time, flowability, and mechanical strength for construction 3D printing material derived from solid waste,” Constr. Build. Mater., vol. 259, p. 119854, 2020.

R. Zhu, K. J. I. Egbe, H. Salehi, Z. Shi, and P. Jiao, "Eco-friendly 3D printed concrete with fine aggregate replacements: Fabrication, characterization and machine learning prediction," Constr. Build. Mater., vol. 413, no. June 2023, p. 134905, 2024.

F. Laoutid, S. Lafqir, A. Toncheva, and P. Dubois, "Valorization of recycled tire rubber for 3d printing of abs-and tpo-based composites," Materials (Basel)., vol. 14, no. 19, 2021.

A. Bajpayee et al., "In situ Resource Utilization and Reconfiguration of Soils Into Construction Materials for the Additive Manufacturing of Buildings," Front. Mater., vol. 7, no. March, pp. 1–12, 2020.

T. Ding, J. Xiao, S. Zou, and J. Yu, "Flexural properties of 3D printed fibre-reinforced concrete with recycled sand," Constr. Build. Mater., vol. 288, p. 123077, 2021.

A. Lin, Y. K. Tan, C.-H. Wang, H. W. Kua, and H. Taylor, "Utilization of waste materials in a novel mortar-polymer laminarcomposite to be applied in construction 3D-printing," Compos. Struct., vol. 253, Dec. 2020.

B. Masood, A. Elahi, S. Barbhuiya, and B. Ali, "Mechanical and durability performance of recycled aggregate concrete incorporating low calcium bentonite," Constr. Build. Mater., vol. 237, p. 117760, 2020.

G. Giridhar, P. R. Prem, and S. Kumar, "Development of concrete mixes for 3D printing using simple tools and techniques," Sadhana - Acad. Proc. Eng. Sci., vol. 48, no. 1, 2023.

Prem, P. R., Ambily, P. S., Kumar, S., & Ghodke, S. B. (2024). A theoretical model to predict the structural buildability of 3D printable concrete. Mechanics of Time-Dependent Materials, 1-19.

Prem Pr, Ambily Ps, Kumar S, Giridhar G, Jiao D. Structural build-up model for three-dimensional concrete printing based on kinetics theory. Frontiers of Structural and Civil Engineering. 2024 Jun 1. Epub 2024 Jun 1.

Prem, P.R., Ambily, P.S., Kumar, S. et al. A theoretical model to predict the structural buildability of 3D printable concrete. Mech Time-Depend Mater (2024).

Concrete Development for 3D Printed Constructions of Footbridge

D.Citek[1*], S.Rehacek[2], K.Hurtig[3], J.Kolisko[4] and O.Melter[5]

[1,2,3,4,5] *Klokner Institute CTU in Prague, Prague, Czech Republic*
Email: david.citek@cvut.cz

[*]Corresponding author

ABSTRACT

The paper deals with the possibilities of using 3D printing for the construction of footbridges without reinforcement. Using the Solopisky footbridge as an example, the whole process is described from the design, the composition of the mixture, the printing process, the verification test to the actual assembly of the final object. The mixture used was developed by Klokner Institute specifically for this implementation. It consists of individual se-lected components typical of fine-grained micro concrete and mortar (fine aggregate, cement, special additives and admixtures) to meet the requirements for mechanical properties, workability and pumpability of the fresh mix and buildability of the printed material. For the printing of the structure a continuous print route was designed using parabolic envelope curves that were parametrically filled with a circular fill. After printing, the footbridge was mounted on temporary supports with a drawbar in the courtyard of the Klokner Institute and there was carried out experimental verification of load capacity. The footbridge was fitted with potentiometers to measure the movement of the structure. Loading was carried out in cycles of 350 kg with check measurements between each loading cycle. After checking the characteristics of the footbridge, it was installed at the pond near the village Solopisky.

KEYWORDS: *Additive fabrication, 3D printing, Footbridge, Experimental printing, Concrete.*

1. Introduction

Cement binders require a cement hydration process to cure, which under normal conditions takes place at its fastest stage at a significantly slower rate of days and is not fully completed even within a few years. Cement hydration is the process of first setting and then hardening of the cement-bonded material. The setting process depends on many factors, but generally this phase takes place within hours. The hardening process is loosely related to the setting process. A fundamental issue, 3D printing of cementitious composites is facing, is designing the mixture in such way that after extrusion and repeated layering, it resists its own weight and the printed element can be printed/built up vertically. The mixture must be of a suitable consistency to be pumpable and subsequently easy to leave the extruder, but at the same time it must set quickly enough after extrusion or have a rigid consistency to allow the layers to be reapplied on top of each other. This is further related to the very issue of the stability of a freshly printed object that is not sufficiently cured. These mixture requirements ultimately lead to the design of a cementitious composite of a rather complicated composition containing several different additives, including setting accelerators. The resulting mechanical strength is certainly also important to the overall design of the final element, but less important in terms of the extrusion process itself.

2. Experimental part

At the beginning, fine-grained micro concrete was compound (e.g. see Table 1). According to requirements on maximum size of grain, sand with grains of 1,25 mm was used. A requirement for the compressive strength of the molding to be at least 60 MPa was required, therefore CEM II 52,5 N cement was used in combination with a superplasticizer. Also, polypropylene (PP) fibres with length of 12 mm were added to prevent plastic shrinkage.

This basic mixture was tested to buildability when the viscosity modifying admixture (VMA) is added. The question was, if we are able to provide such material, that can be build by layers. Adding VMA to the mixture cause increase of material stiffness and thixotropy. These characteristics allow to print individual layer that withstand the pressure of the layers above it without plastic deformation due to compression, spreading, etc. Varienty of VMAs were tested. After few trials for each type of VMA, printable cement based material was produced (e.g. see Fig. 1). By using pistol (e.g. see Fig 2) filled by fresh mixture, the layers were manually printed out. For each type of VMA, the optimum dosage for manually printed material was experimentally determined. In Table 2, type of VMA, water content, quantity of admixture, consistency of fresh mixed material determining by the method specified by standard EN 1015-3, bulk density of the material, flexural strength and compressive strength, are listed. Bulk density, compressive and flexural strength are determined on beam specimens with dimensions of 40×40×160 mm at the age of the material of 28 days.

Table 1. Mix design of preliminary tests

Component	Content [kg.m^{-3}]
Silica sand 0-1,25 mm	967
Micro fillers	495
Cement CEM II 52,5 N	358
Superplasticizer	25
Water	225

3. Practical part

3.1 Description and design of the footbridge

One part of the project was the design of a printed structure that will be applied in actual use.. For a prototype structure was chosen a footbridge, using whole printable area of our print platform. Main dimensions of the experimental footbridge are: span 5,10 m, width 56 cm, height 100 cm. Total weight of this construction is approximately 1400 kg. Foot-bridge is designed as a three-joint bridge structure without steel reinforcement. The construction uses a static three-arch scheme. The advantage is the possibility of dividing the structure into smaller parts suitable for printing and at the same time for transport.

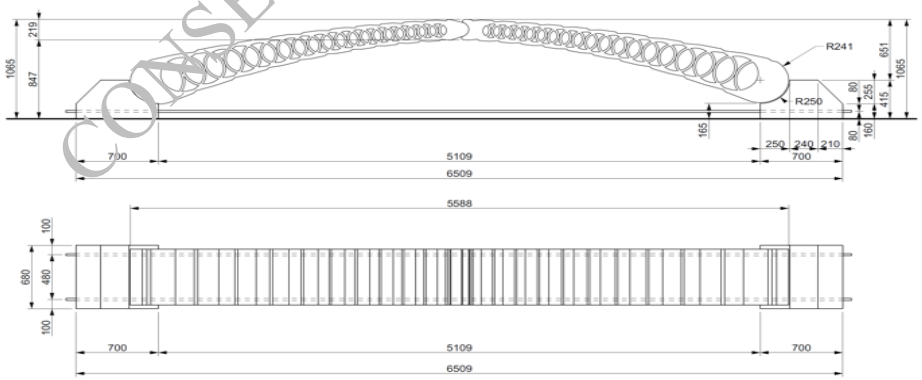

Figure 1. Final footbridge design drawing

The footbridge was designed as a verification object, whose dimensions will correspond to standard building elements. As a 3D printed element without additional reinforcement, the footbridge also represents a more ambitious deployment of 3D printed constructions than usual, when common 3D printed objects are typically garden flowerpots, urban furniture or vertical walls. The architectural language of 3D printed structures is also a big topic. Like any manufacturing technology, 3D printing has many limitations but also advantages, which must be considered during the design process. It is important to distinguish between kitsch and the new freedom to freely shape ornamental structures. The design was based on parabolic envelope curves, which were parametrically filled with circular infill. This infill is constructed in such a

way that the overlapping circles form the outer surface of the footbridge and at the same time, create an ideal continuous track for printing without any interrup-tionsor sharp corners. The parabolic shaping of the entire structure ensures that it is loaded only in compression. Our long-term experience in designing experimental 3D printed objects of a smaller scale was applied here to design shape and the print path. The footbridge is a three-arch structure with a span of 5.1 m, designed as a predominantly compressed structure. The design of the footbridge was subjected to calcula-tion, which was then experimentally verified by a continuous load test.

Figure 2. Printed layers of cem. based material

3.2 Description and design of the footbridge

The Testbed printing system used for printing this footbridge is a 3 axis gantry sys-tem capable of handling the print head in a 3200x1000x1000 mm space. First, several smaller footbridge samples of approximately 1 m length were printed, on which the design of the print path and the expected advantages of the circular fill for speed and smoothness of printing were verified. Despite the relatively longterm experience with printing a number of experimental objects, this footbridge was the first really real stress test of the entire printing system simulating deployment in industry. The printing itself took approximately 6 hours, during which 0.6 m3 of printing material was consumed. Both halves of the footbridge were printed at the same time, which then together weighed approximately 1.32 t. A layer height of 10 mm and a nozzle with a diameter of 20 mm were chosen for printing with a maxi-mum speed of 120 mm/s depending on the curvature of the print path.

3.3 Fabrication

After printing, the footbridge was mounted on temporary supports with a drawbar in the courtyard of the Klokner Institute. The sliding layer in the joints consists of a lead sheet, which by its creep into rough printed surface also ensures a uniform pressure distribution in the contact joint of the arch halves and in the joints at the abutments. The footbridge was fitted with potentiometers to measure the movement of the structure at the joints at the foot and apex, at the quarter spans and at the abutments to check their relative positions. Loading was carried out in cycles of 350 kg with check measurements between each loading cycle. During the measurements, the graph shows a gradual drop of 2.5 mm in the top of the footbridge. This is most likely due to the effect of creep in several layers of corrugated lead sheets at the joints and the rising ambient temperature during the measurements. After subtracting this drop, the residual deflection at the top was 0.8 mm, when the footbridge was loaded with 1750kg ballast, corresponding to a continuous load of 5.7kN/m2.

3.4 Long term monitoring

As part of the material's resistance to environmental aspects, a test was carried out according to ČSN 73 1326+Z1 using method C. The results of this test met the lim-its for the degree of environmental influence XF4 prescribed in the ČSN P 73 2404 standard. It will be interesting to observe the effects of frost in the grooves between the individual printing layers in the long term. In general, these features of printed objects

appear as possible failure points, either by water or by gradual degradation by emergent vegetation. The footbridge has been monitored since it was printed and installed outdoors in December 2021, and now after being installed on the dam of the pond in October 2023, monitoring will continue. Visual inspections have so far revealed no significant cracks that were not caused by the initial shrinkage of the mixture during solidification after printing, and the footbridge surface appears in good condition with no noticeable degradation.

3.5 Installation

The footbridge was mounted on the outlet of a small private pond, where the undeni-able advantage was the possibility to place it above the transverse sill of the pond spillway, which thus replaced the lower drawbar. The sill and the surrounding terrain were photogrammetrically scanned. The resulting 3d model was then used to create a section as a reference to design the foundations. The sill was extended with steel reinforced concrete blocks, which were attached to it by additional steel rebar. The original monolithic abutment blocks were then placed on top of these extensions in a fresh layer of concrete. Each of the abutments is additionally connected to the concrete base block by three threaded rods. The bars were then prestressed to provide a pressure reserve in the joint between the abutment and the underlying concrete block.

4. Conclusions

The motivation of the project is not only the development of the design and technological background of 3D printing but also the design of construction elements, the philosophy of the entire structure and logistics on the construction site. It turns out that the possibilities of 3D printing can satisfy the requirements for optimization in terms of time and costs, as well as very laborious effort for shape differences and non-traditional design, as well as shape optimization in terms of stress.This experimental footbridge verified the possibility of printing load-bearing horizontal structures without additional reinforcement and is one of many views on how 3D printing of building structures can be comprehensively approached. On the basis of laboratory tests of the printing material, very good resistance to weathering can be considered. For this footbridge, where the side print wall is exposed to the greatest extremes, it will be interesting to observe the frost action in the creases between the print layers in the long term. These locations generally appear to be potential failure points for printed objects, either by water or by gradual degradation by established emergent vegetation. The footbridge has been monitored since it was printed and mounted outdoors and will continue to be monitored on an ongoing basis, providing further valuable information on the reliability of 3D printed structures in the future. Visual inspections have so far revealed no significant cracks or other kind of degradation.

Acknowledgements

The results were obtained and the article was prepared with the kind support of the project FW06010422.

References

Čítek, D.; Řeháček, S.; Dobiáš, D.: EXPERIMENTAL RESEARCH ON 3D PRINTED CONSTRUCTION FROM CEMENT BASED COMPOSITES, In: Proceedings of 22nd International Multidiscipli nary Scientific GeoConference SGEM 2022. Sofia: STEF92 Technology Ltd., 2022. vol. 22. ISSN1314-2704. ISBN 978-619-7603-48-4.

Dilawar, R.; Usman, M.; Ali, A.; Majit, U.; Faizan, M. et al. Inclusive characterization of 3D printed concrete (3DPC) in additive manufacturing: A detailed review. Con-struction and Building Materials 394 (29), 1–20 (2023).

Hager, I., Golonka A., Putanowicz, R. 3D printing of buildings and building compo-nents as the future of sustainable construction? Procedia Engineering 151(2016), 292-299 (2016).

Hansemann, G., Schmid, R., Holzinger, Ch. et al. Additive Fabrication of Concrete El-ements by Robots. Lightweight Concrete Ceiling. In: Fabricate 2020: Making Resili-ent Architecture, pp. 124–129. UCL Press, London (2020)

Suchomel, V. Bureš Sequentional on-site Printing of Building Structures, In: VSB - Technical University of Ostrava, Conference Architecture in Perspective, 2022-03-23

Influence of Potential Additives on the Carbon Dioxide Mineralization of Red Mud

Saranyadevi Duraisamy[1*], Piyush Chaunsali[2]

[1] *Research Scholar, Indian Institute of Technology Madras, Tamil Nadu, India*
Email: sarancivil132@gmail.com
[2] *Associate Professor, Indian Institute of Technology Madras, Tamil Nadu, India*
Email: pchaunsali@civil.iitm.ac.in

[*]Corresponding author (s)

ABSTRACT

Aluminium manufacturing industries are encountering challenges in managing the disposal of bauxite residue (red mud) generated during aluminium production. The existence of heavy metals in the red mud causes environmental pollution and makes it challenging to utilize in diverse applications. Additionally, the variability in chemical composition and high alkalinity pose challenges to the wider applications. In order to increase the utilization, different processing techniques were adopted. One such technique is mineral carbonation, which is a promising technique to mitigate the atmospheric carbon dioxide concentration by precipitation of stable carbonates and improve the performance of red mud. However, the mineralization of potential of red mud is insignificant due to its chamical compostion and could be enhanced by supplementing calcium or magnesium rich sources. The current study focuses on the influence of mineralization of red mud with the addition of Ordinary Portland Cement (OPC). Paste samples were studied with different proportions of red mud and OPC. Compressive strength was examined for emchanical performance and X-ray Diffraction analysis was performed to study the phase changes. The results showed that the accelerated CO_2 curing enhanced the early-age performance which is comparable with 7-day moist curing.

KEYWORDS*: CO_2 mineralization, Red Mud, OPC, Compressive strength*

1. Introduction

Rapid industrialization increases the energy demand tremendously, resulting in a large quantity of carbon dioxide (CO_2) emissions into the atmosphere. This is considered the most critical factor for global climatic change. Significant emissions are contributed by coal, oil, gas, cement, and flaring industries. About 7-8% of CO_2 emissions come from the cement industry, and India contributes to 7% of the total global CO_2 emissions. There are different methods available to reduce atmospheric CO_2 emissions. This could be possible via energy efficiency, low carbon electricity and heat, material efficiency, switching to low carbon feedstock, and Carbon Capture Utilization and Storage (CCUS) (IPCC report 2022). It is estimated that the CCUS technology will cut down global climate change's effect by 15-55% by 2100. CO_2 mineralization using alkaline waste residues offers numerous benefits. One of the primary benefits is the reduction of consumption of raw materials. One such waste material is red mud obtained from aluminium manufacturing industries. It is a solid residue generated when caustic soda is added to bauxite ore to dissolve the aluminium. As of July 2020, 132 million tonnes of alumina was produced annually around the globe, and India generated ~9 million tonnes of red mud (Liu et al. 2022a). It is a highly alkaline material with a pH varying from 10 to 13 (Si et al. 2013) and is generally landfilled.

The compositions of red mud majorly consists Fe_2O_3, $Al(OH)_3$, AlOOH, TiO_2, SiO_2, Na_2O and CaO. Additionally, it contains minor elements such as Phosphorus, Chromium, Manganese, Zirconium, Arsenic (P, Cr, Mn, Zr, As) (Singh et al. 2020), (Liu et al. 2022b), (Romano et al. 2018), (Snars and Gilkes 2009), (Hoang et al. 2020), (Han et al. 2017), (Ghalehnovi et al. 2019), (Scribot et al. 2018). The presence of these heavy metals in red mud makes storage difficult, posing challenges related to contamination and

environmental issues. The composition variation depends on the process adopted in various countries. Strong caustic soda (NaOH) is added to separate the aluminium in Bayer process. Whereas in sintering process, limestone and sodium carbonate are added. Hence, the red mud obtained from sintering process possesses high calcium content (Ilahi et al. 2024). The variability in the composition of red mud is shown in Figure 1. The percentage of variability is high in the composition of iron oxide. The calcium (CaO) content varies from 2 to 20% except in China, while oxides of aluminium (Al_2O_3) and silica (SiO_2) varies from 5 to 20% across all countries. However, the potential to capture CO_2 and the extent of mineralization depends on the composition and source of wastes. It is essential to have significant quantity of calcium bearing phases to mineralize. Hence, in this study it is proposed to use OPC as an additive to enhance the performance of red mud.

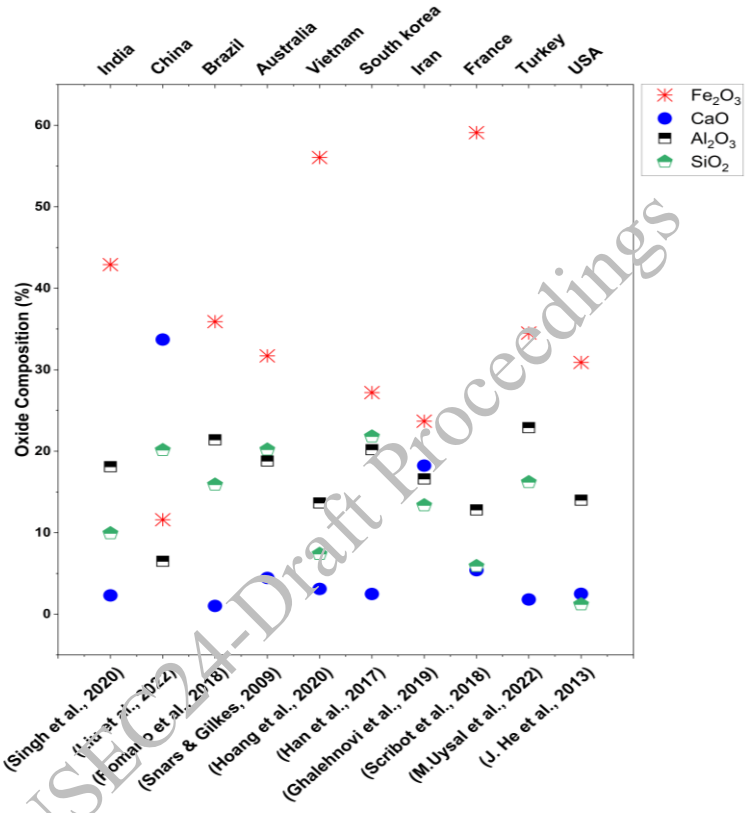

Figure 1. Oxide composition of red mud in different countries

2. Materials and methods

In this study, OPC 53 grade of cement, red mud and distilled water were used to prepare the specimens. The red mud used in this study is obtained from an aluminium refinery plant in India. The received red mud is dried in an oven at 105º C for 24 hours and ground in a ball mill. The oxide composition of red mud and cement is analyzed using an X-ray fluorescence spectrometer, and the results are presented in Table 1. The paste samples of 50 mm x 50 mm x 50 mm cube are prepared at a water-to-cement ratio of 0.5. The raw materials were conditioned at 25 ºC before casting was carried out. To ensure uniform blending of raw materials, the cement and red mud are mixed in a front mounted Hobart mixer in dry condition, subsequently, water is added. The red mud was replaced with OPC at varying percentages from 0 to 100. The prepared moulds were demoulded after 24 hours, half of the specimens shifted to the mist room where 99%RH is maintained and the remaining specimens moved to the accelerated CO_2 chamber. The CO_2 mineralization is conducted at 100% CO_2 concentration under a high pressure of 10 bar. The specimens were designated as OPC_x, where x represents the percentage replacement of red mud with OPC. Then both water cured and CO_2 cured (mineralized) paste samples were tested for compressive strength, and the change in mineralogical phases was determined using X-ray diffraction (XRD). The diffractograms were collected in a Rigaku Super Mini Flex 6G, and the signals were collected in the range of two theta angles

from 10º to 70º with a step size of 0.02º and scanning rate of 10 º/min. The qualitative analysis was carried out using the PANalytical software package (X'Pert Highscore plus software v.3).

Table 1. The oxide composition of raw materials (wt %)

Phases	OPC	Red Mud
CaO	66.5	2.5
SiO_2	16.6	11.1
MgO	1.4	0.09
Al_2O_3	4.5	22
Fe_2O_3	5.4	43
K_2O	1.4	0.04
Na_2O	-	6.8
TiO_2	0.7	3.5
SO_3	2.8	0.18
Others	0.7	0.9

3. Results and discussions

Figure 2 represents the compressive strength of specimens cured for 7 days under water and specimens kept in an accelerated CO_2 chamber for 4 hours. In most cases, the difference between water and CO_2 cured specimens is insignificant. The formation of calcite at 4 hours of CO_2 mineralized samples is responsible for the improved performance, and it is comparable to the performance of the hydration products formed at 7 days. Particularly, when the red mud is replaced with 30, 40 and 50% of OPC, the CO_2 cured specimens performed better than the water cured, and the increase in compressive strength is 25%, 19% and 11%, respectively. In this way, the duration required to attain a specified strength is drastically reduced, and it is an alternate way to store the CO_2 in cement-based composites. Figure 3 shows the X-ray diffractogram of the CO_2 cured samples. This indicates that calcite formation is the primary phase formed due to mineralization, and it is reduced as the percentage of OPC replacement is reduced. Hematite and cancrinite are phases in red mud that do not take part in the reaction. In addition, the presence of calcium silicate phases (alite and belite) indicating that the curing period of 4 hours is insufficient for the complete mineralization of clinker phases of OPC. Furthermore, the presence of a portlandite peak is identified in the mineralized specimens, showing that the reaction can be continued and form calcite if the duration is increased. For further improvement in strength, either the duration of CO_2 curing can be increased or water curing could be provided.

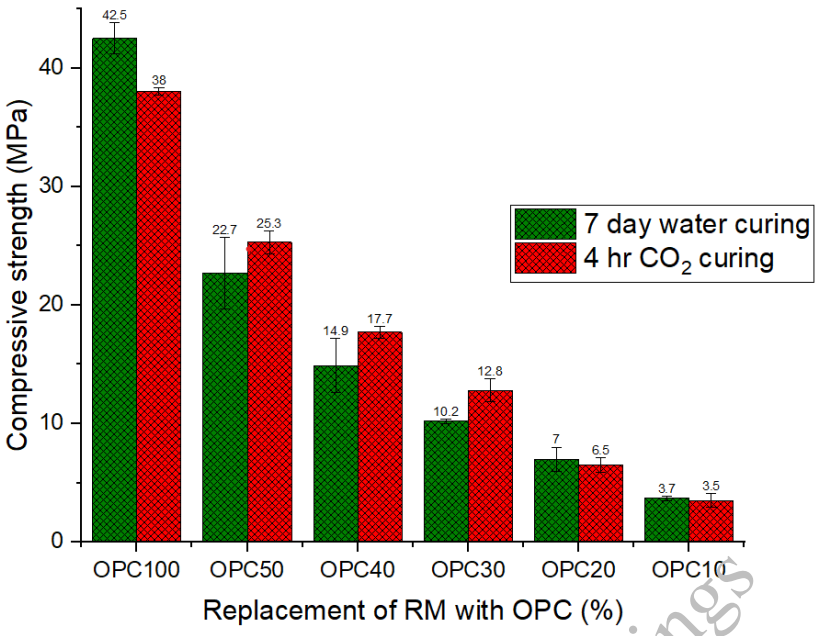

Figure 2. Compressive strength of water and CO_2 cured specimens

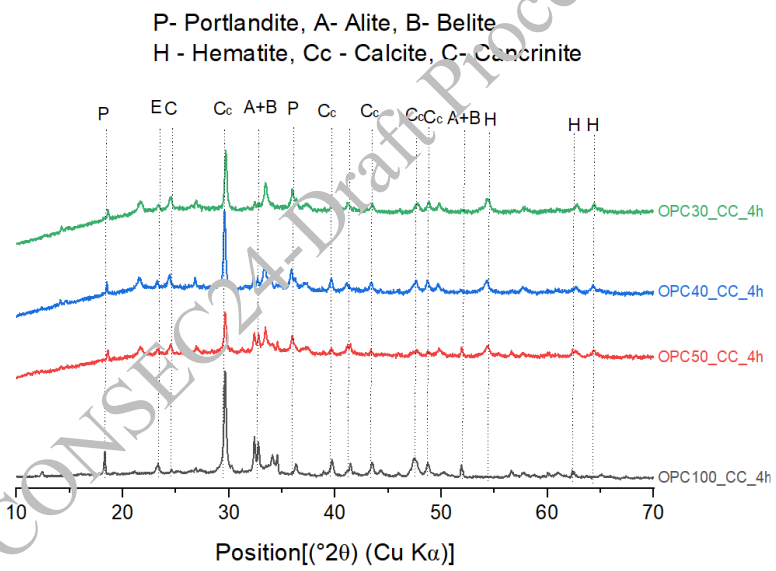

Figure 3. X-ray diffractogram of mineralized red mud

4. Conclusions

Since the composition of calcium and magnesium in red mud used in this study is very low, it is challenging to mineralize without adding additives. Hence, this study explored the possibilities of enhancing the mineralization capacity of red mud and understanding the performance with the replacement of OPC. It was found that, the 4 hours CO_2 cured samples performed better than 7 days water cured samples prepared with 30, 50 and 50% replacement of red mud with OPC.

Acknowledgements

The authors acknowledge the experimental facilities provided by the Department of Civil Engineering, Indian Institute of Technology Madras (IITM). The Centre of Excellence on Technologies for Low Carbon and Lean Construction from IIT Madras is gratefully acknowledged.

References

Ghalehnovi, M., E. Asadi Shamsabadi, A. Khodabakhshian, F. Sourmeh, and J. de Brito. 2019. "Self-compacting architectural concrete production using red mud." Constr. Build. Mater., 226: 418–427. Elsevier Ltd. https://doi.org/10.1016/j.conbuildmat.2019.07.248.

Han, Y. S., S. Ji, P. K. Lee, and C. Oh. 2017. "Bauxite residue neutralization with simultaneous mineral carbonation using atmospheric CO2." J. Hazard. Mater., 326: 87–93. Elsevier B.V. https://doi.org/10.1016/ j.jhazmat.2016.12.020.

Hoang, M. D., Q. M. Do, and V. Q. Le. 2020. "Effect of curing regime on properties of red mud based alkali activated materials." Constr. Build. Mater., 259: 119779. Elsevier Ltd. https://doi.org/10.1016/ j.conbuildmat.2020.119779.

Ilahi, K., S. Debbarma, G. Mathew, and H. I. Inyang. 2024. "Carbon capture and mineralisation using red mud: A systematic review of its principles and applications." J. Clean. Prod., 473 (August). https://doi.org/ 10.1016/j.jclepro.2024.143458.

Li, W., W. Wang, D. Wu, S. Yang, H. Fang, and S. Sun. 2023. "Mechanochemical treatment with red mud added for heavy metals solidification in municipal solid waste incineration fly ash." J. Clean. Prod., 398 (February). https://doi.org/10.1016/j.jclepro.2023.136642.

Liu, S., Y. Shen, Y. Wang, P. Shen, D. Xuan, X. Guan, and C. Shi. 2022a. "Upcycling sintering red mud waste for novel superfine composite mineral admixture and CO2 sequestration." Cem. Concr. Compos., 129 (January): 104497. Elsevier Ltd. https://doi.org/10.1016/j.cemconcomp.2022.104497.

Liu, S., Y. Shen, Y. Wang, P. Shen, D. Xuan, X. Guan, and C. Shi. 2022b. "Upcycling sintering red mud waste for novel superfine composite mineral admixture and CO2 sequestration." Cem. Concr. Compos., 129 (March): 104497. Elsevier Ltd. https://doi.org/10.1016/j.cemconcomp.2022.104497.

Romano, R. C. O., H. M. Bernardo, M. H. Maciel, R. C. Pileggi, and M. A. Cincotto. 2018. "Hydration of Portland cement with red mud as mineral addition." J. Therm. Anal. Calorim., 131 (3): 2477–2490. https://doi.org/10.1007/s10973-017-6794-2.

Scribot, C., W. Maherzi, M. Benzerzour, Y. Mamindy-Pajany, and N. E. Abriak. 2018. "A laboratory-scale experimental investigation on the reuse of a modified red mud in ceramic materials production." Constr. Build. Mater., 163: 21–31. https://doi.org/10.1016/j.conbuildmat.2017.12.092.

Si, C., Y. Ma, and C. Lin. 2013. "Red mud as a carbon sink: Variability, affecting factors and environmental significance." J. Hazard. Mater., 244–245: 54–59. Elsevier B.V. https://doi.org/10.1016/j.jhazmat.2012.11.024.

Singh, S., M. U. Aswath, and R. V. Ranganath. 2020. "Performance assessment of bricks and prisms: Red mud based geopolymer composite." J. Build. Eng., 32 (March): 101462. Elsevier Ltd. https://doi.org/10.1016/ j.jobe.2020.101462.

Snars, K., and R. J. Gilkes. 2009. "Evaluation of bauxite residues (red muds) of different origins for environmental applications." Appl. Clay Sci., 46 (1): 13–20. Elsevier B.V. https://doi.org/10.1016/j.clay.2009.06.014.

Effect of Mixed Recycled Aggregates on Quaternary Blended High Strength Self-Compacting Concrete

Merin Mathew[1*] and Dr. Girija K.[2]

[1] College of Engineering Trivandrum, APJ Abdul Kalam Technological University, Trivandrum, India
Email: merinmathew1994@gmail.com
2 GEC Barton Hill, Trivandrum, India
Email: girijak.cet@gmail.com

[*]Corresponding author

ABSTRACT

This paper has attempted to experimentally investigate the fresh and hardened properties of self-compacting concrete incorporating supplementary cementitious materials and recycled aggregates (both fine and coarse). In the present study, Fly ash (FA), silica fume (SF), and ground granulated blast furnace slag (GGBS) were blended in pre-determined proportions replacing cement (C). Mixed recycled aggregates (MRA) consisted of broken bricks, glass, ceramics, and old concrete aggregates collected from a Construction and Demolition (C&D) waste recycling plant in Hyderabad were used for the study. Fine aggregates were replaced with recycled mixed fine aggregates at various percentages of 10, 20, 30 and 40. Natural coarse aggregates were replaced with coarse MRA (MRCA) at percentages of 20, 30, 40 and 60. A comparison study between SF&C slurry and FA&C slurry treated MRCA was conducted. The optimum percentage of replacement was found for both MRCA. The results show that SF&C slurry treated MRCA at 40% replacement shows better fresh and hardened properties.

KEYWORDS: *Self-compacting concrete, Mixed recycled aggregates, Quaternary blend, Supplementary cementitious materials.*

1. Introduction

Adopting the "3Rs" concept—reduce, reuse, and recycle—is an excellent strategy to encourage sustainability in construction and lessen its impact on the environment. Several strategies have already been implemented to lessen the quantity of CO_2 released into the atmosphere. These include lowering the percentage of clinker in cement by partially replacing additives like fly ash, blast furnace slag, silica fume, or pozzolan, among others, and substituting recycled aggregates for natural aggregates.

At present, there is increasing traction within the construction industry for the concept of the circular economy. This model serves as a substitute for linear economy (involving extraction, construction, operation, and disposal), aiming instead to optimize resource use and promote recycling at the end of their lifecycle. Utilizing these aggregates efficiently in concrete supports the circular economy within the construction sector by decreasing the demand for new virgin aggregates, thereby mitigating environmental impacts and reducing construction waste. Previous studies have reported that incorporating recycled concrete aggregate in SCC can help mitigate the reduction in concrete properties that usually occur in the case of normal concrete.

The present study aims to evaluate the performance of SCC made with mixed recycled fine aggregates (MRFA) and also with untreated and treated mixed recycled coarse aggregates (MRCA). In this study, MRA was obtained from a recycling plant with an unknown strength and was subjected to treatment. In a previous study conducted by the author, it was found that pozzolan slurry treatment is an effective technique, with advantages in terms of both low cost and enhancement effects on recycled coarse aggregates. The specific objectives of this study are (1) To determine the physical and mechanical properties of MRFA. (2) To determine the physical and mechanical properties of MRCA before and after the surface treatment. (3) To find the optimum percentage of replacement of treated recycled concrete

aggregates by casting and testing cube specimens. This scheme provides a more industrially reliable approach that promotes the use of MRA in the construction industry.

2. Materials used

Ordinary Portland Cement of 53 grade was used for preparing the required mix. 45 % of cement was replaced with supplementary cementitious materials like Fly ash (25% replacement), GGBS (7.5%) and silica fume (7.5%). Fine aggregates used for this study were M sand conforming to Zone II as per IS 383. The nominal maximum size of natural coarse aggregates (NCA) used was 12 mm. The mixed recycled aggregates obtained from the Construction and Demolition (C&D) waste recycling plant in Hyderabad was used for the study. The recycled aggregates were of nominal maximum aggregate size of 12 mm when collected. MRA consisted of concrete aggregates, bricks, glass, ceramics and plastics.
Self-compacting concrete mix of grade M60 was used for the study. It consisted of 403 kg of cement, 220 kg of Fly ash, 55 kg of GGBS, 55 kg of silica fume, 748 kg of fine aggregate and 698 kg of natural coarse aggregates per cubic meter. The water and superplasticizer content was 190 and 8.4 per cubic meter respectively. Polycarboxylate ether-based superplasticizer was used in this study. The MRFA were replaced in percentages of 10, 20, 30 and 40. The percentage replacement of MRCA was 20%, 30%, 40% and 60% of total NCA

3. Experimental Programme

3.1 Treatment of mixed recycled coarse aggregates

To strengthen the weak adhered mortar and improve the MRCA surface, Pre-soaking in Pozzolan slurry was adopted. The MRCA was soaked in two types of pozzolan slurry: i) Fly ash and Cement (FA& C) slurry ii) Silica fume and cement (SF & C) slurry. The mixing procedure is shown in Figure 1.

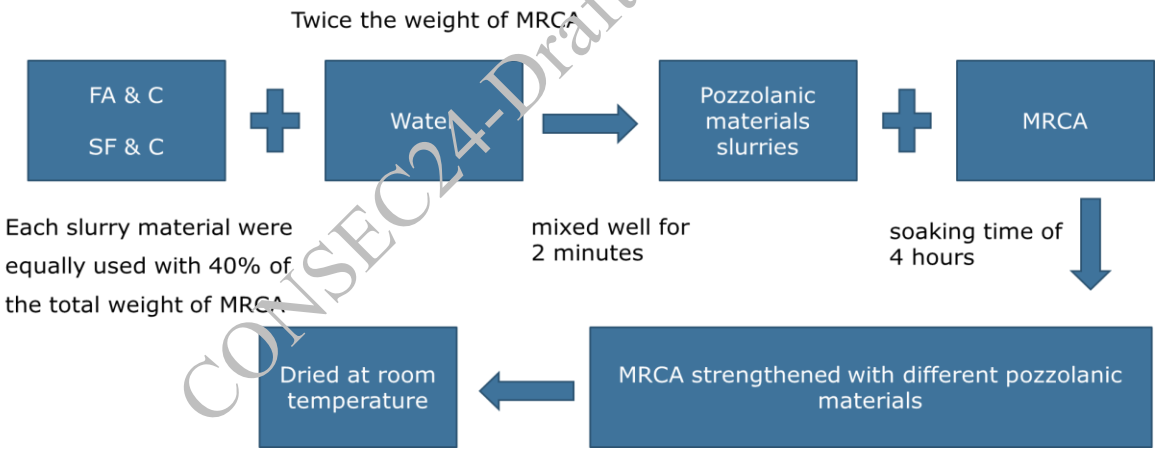

Figure 1. Treatment of recycled aggregates

3.2 Tests on concretes

1. Material properties
   - i. Porosity (IS: 2386 (Part 3) 1963)
   - ii. Specific gravity (IS: 2386- 1963)
   - iii. Void ratio (IS: 2386- 1963)
   - iv. Bulk density (IS: 2386- 1963)
   - v. Aggregate impact value (IS: 2386 (Part 4)- 1963)
2. Fresh properties
   - i. Slump flow
   - ii. T50 slump flow
   - iii. V funnel test
3. Hardened properties

i. Ultrasonic pulse velocity test
ii. Compressive strength

4. Microstructure Analysis

4. Results and discussions

The studies on material properties inferred that the properties of MRA was inferior to that of normal aggregates. However, treatment of MRCA with pozzolan slurries can improve its properties. It was noted that the porosity and void ratio of the aggregates have decreased after the pozzolan slurry treatment of MRCA.

Almost all mixes satisfied the SCC workability recommendations of EFNARC. In the case of MRFA replacement, it was observed that the fresh properties decreased as we increased the percentage of replacement. Comparing SF&C slurry treatment and FA&C slurry treatment, specimens incorporating SF&C slurry-treated aggregates showed better workability.

The entire tested specimens gave a pulse velocity greater than 4000 m/s. Thus, as per the code, all are excellent specimens. The compressive strength values showed a decline as the percentage replacement of MRCA increases. For fine aggregate replacement, higher strength was achieved for MRFA30 (Figure 2). When comparing 28 days and 90 days compressive strength, it was observed that the higher strength was achieved at 90 days.

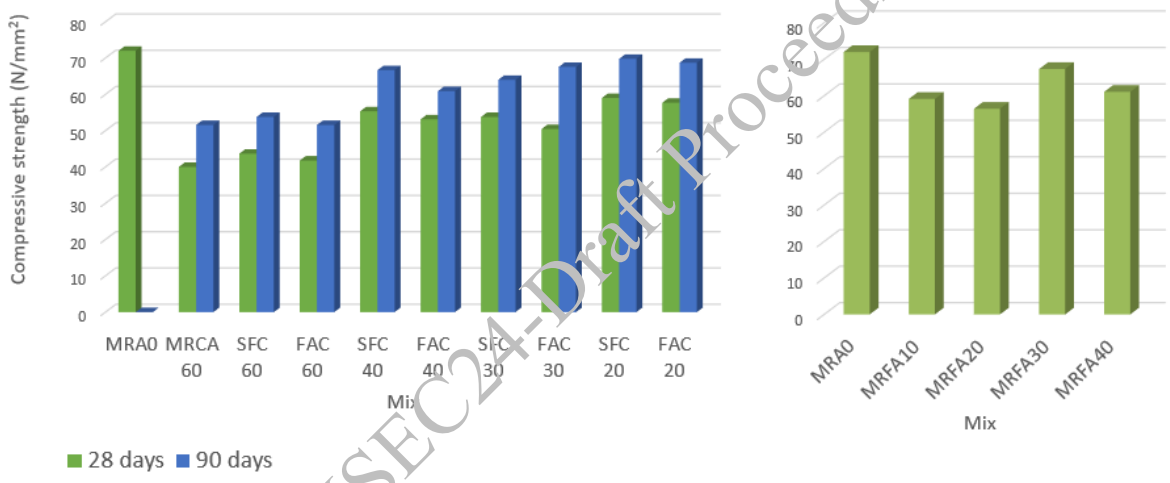

Figure 2. Compressive strength values

To investigate the effect of surface treatment of MRCA, the internal microstructures of untreated and treated aggregate concrete were analysed. For concrete with untreated aggregates, cracks were found at the interface of MRCA and the hydrated binder matrix as shown in Figure 3. Also, many pores were observed in the matrix. On the other hand, SEM images of SF&C slurry treated aggregate concrete showed that an excellent binding was seen between the hydrated binder matrix and the aggregate surface, and a thicker interfacial transition zone was observed (Figure 4). The nearby matrix was also dense due to the hydrated products of concrete in case of SFC concrete.

EDS Analysis was also conducted on SFC40 and it was reported that the hydrated binder matrix was mainly comprised of silicon (16.19 wt%), calcium (10.48 wt%) and aluminium (7.53 wt%). There is an important percentage of the silicon ions. This increase emphasizes the efficiency of the technique for strengthening MRCA.

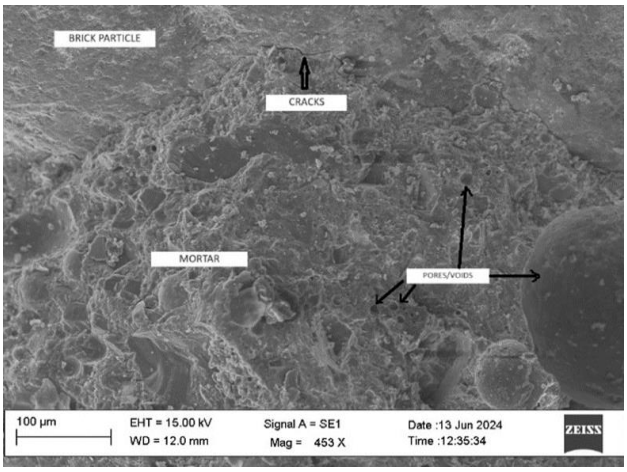

Figure 3. SEM images of concrete with untreated MRCA

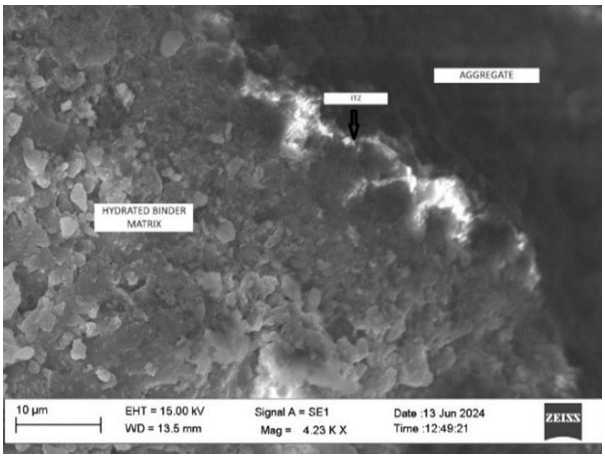

Figure 4. SEM images of SFC40 concrete with treated MRCA

5. Conclusions

The production of C&D waste is huge, especially in the urban regions leading to environmental and disposal issues. These waste materials can replace natural aggregates and can be effectively used in the production of concrete. In this context, sustainable construction using recycled aggregates is further increased by choosing SCC instead of normal concrete. Research has been done on both fresh and hardened MRA concrete. Based on the various test results, the following inference could be drawn.

- Treated recycled aggregates can perform better than untreated recycled aggregates in terms of workability and also contribute to a slight improvement in the compressive strength of concrete.
- The analysis by SEM revealed that the untreated RCA had a non-homogeneous and porous surface texture and also cracks were observed at ITZ. However, there were fewer voids and more homogeneity on the treated MRCA concrete.
- Among the treatment methods adopted in the present study, treatment of MRA with SF&C slurry is found to be an effective technique based on both fresh and hardened properties.
- Overall, it is feasible to produce SCC with MRFA with up to 30% replacement and SF&C slurry-treated MRCA with up to 40% replacement according to the results of this study.

Acknowledgements

This study was funded by Bamboo Research Centre under the Directorate of Technical Education (DTE), Government of Kerala, India. We also thank Central Laboratory for Instrumentation and Facilitation (CLIF), University of Kerala for their assistance in the microstructure analysis of specimens.

References

Kou SC, Poon CS (2009), "Properties of self-compacting concrete prepared with coarse and fne recycled concrete aggregates", Cement Concrete Composites, Vol.31, pp.622–627

Liu, YX., Ling, TC., and Mo, KH., (2021), "Progress in developing self-consolidating concrete (SCC) constituting recycled concrete aggregates: A review", International Journal of Minerals, Metallurgy and Materials, Vol. 28, pp.522

Mathew Merin, K. Girija and A. R. Sreedevi. "Strengthening of Recycled Coarse Aggregate using Different Surface Treatment Techniques", Proceedings of 12th Structural Engineering Convention, ASPS Conference Proceedings 1, (2022), 165-169

Shaban, W.M., Yang, J., Su, H., Liu, Q., Tsang, D., Wang, L., Xie, J. and Li, L. (2019), "Properties of recycled concrete aggregates strengthened by different types of pozzolan slurry", Construction and Building Materials, Vol. 216, pp.632–647

Fracture Related Studies on Strain Hardened Cementitious Composite at Different Length Scales using Digital Image Correlation Technique

B.S. Sindu[1*] and Saptarshi Sasmal[2]

[1]Principal Scientist, Special and Multifunctional Structures Laboratory, CSIR-Structural Engineering Research Centre, Chennai, Tamil Nadu - 600113, India
Email: sindu@serc.res.in
[2]Chief Scientist and Head, Special and Multifunctional Structures Laboratory, CSIR-Structural Engineering Research Centre, Chennai, Tamil Nadu - 600113, India
Email: saptarshi@serc.res.in

[*]Corresponding author

ABSTRACT

The primary challenge of concrete associated with brittleness and low tensile strength is addressed, to an extent, by the addition of various types of fibers. In recent times, PVA (Polyvinyl alcohol) fibers are incorporated into cementitious composite which offer unique strain hardening behaviour to the matrix. Since this type of remarkable property is achieved by altering the fracture behaviour of the composite, understanding the same is very important towards developing cementitious composites with desired properties. However, the process is not straightforward and an accurate evaluation of the parameters such as fracture process zone (FPZ), and crack characteristics (crack formation and development) is not possible using experimental investigation employing conventional sensors. In this regard, the digital image correlation technique is used in this study to evaluate the profile of crack propagation during loading including crack branching, identifying the FPZ and quantifying it. The investigations are carried out by incorporating PVA fibers at three different material length scales – cement paste, mortar and concrete to estimate the distinct contribution of fibers in each length scale. It has been found that the width of FPZ improved by 1.5 times in concrete with the incorporation 2% PVA fibers. The fracture studies also revealed that the type of post-peak behaviour, the extent of hardening and the slope of softening curve varies at each of the length scales even though same percentage of fibers were incorporated. The findings of this study will lead towards efficient engineering and tailor-made design of strain hardened cementitious composites.

KEYWORDS: *Strain hardened cementitious composite, Fracture process zone, Digital image correlation, Multiple length scales, Crack pattern*

1. Introduction

Cementitious composites are brittle in nature. Various types of fibers like steel fibers, carbon fibers, glass fibers, basalt fibers, polymer fibers, etc. are incorporated into cementitious composites to impart ductility into it. When appropriately designed with the suitable type of fiber (including shape, size, and surface coating) considering the fiber-matrix interactions, cementitious composites can be engineered with desirable mechanical characteristics. In recent times, interest in strain hardened cementitious composites (SHCC), is growing owing to their remarkable tensile performance with high displacement ductility index, energy absorption capacity and fracture characteristics [Sindu and Sasmal (2024)]. Thus, it has the potential to make the structure slimmer, improve the dynamic capabilities and augment service life [Sasmal and Avinash (2016)]. The underlying phenomenon responsible for the remarkable characteristics of SHCC, which is the improved cracking resistance/fracture process needs to be understood comprehensively for efficient, tailor-made design of the composite. For qualitative and quantitative evaluation of the fracture/crack characteristics, such as determination of the size and shape of fracture process zone (FPZ),

evaluation of the crack propagation mechanism, and estimation of crack length, width and spacing, conventional sensors may be handicapped.

Attempts have been made in the past to utilize the digital image correlation (DIC) technique to investigate the fracture behaviour of cementitious composites/concrete. DIC has been used to evaluate the cracking and strain evolution of concrete, investigate the damage localization [Omondi et al. (2016), Sindu and Sasmal (2019)], identify aggregate interlock [Alam et al., (2012)] and understand the fracture behaviour of reinforced concrete beams [Fayyad and Lees (2014)]. DIC has also been used to characterize the FPZ of blended cement binders [Das et al., (2015)], fiber reinforced concrete [Sindu et al., (2022)], etc. and also to determine the stress intensity factor of concrete [Li et al. (2020)].

From the reported studies, it has been identified that the use of the image correlation technique has tremendous potential to characterize the fracture properties of cementitious composite effectively. In view of this, in this study, an attempt has been made to characterize the fracture behaviour of strain hardened cementitious composite (expected to have widely distributed micro-cracks) using DIC. The investigations have been carried out on three different material length scales of cementitious composites (cement paste, cement mortar and concrete) incorporated with PVA fibers. Initially, the mechanical characteristics like fracture energy, degree of hardening, and softening rate have been determined from the fracture tests on notched prism specimens. Then, DIC has been used to determine the size of the FPZ from the strain profile and to evaluate the crack formation/propagation including crack branching. The distinct characteristics of PVA fibers incorporated cementitious composite in each of the material length scales with fibers of different volume fractions (1% and 2%) have been brought out. The findings of this study will thus lead towards efficient and tailor-made design of cementitious composites with strain hardening characteristics.

2. Development of PVA fiber incorporated cementitious composites

In order to carry out fracture studies on strain hardened cementitious composites of three different material length scales, cement paste, mortar and concrete samples are prepared by incorporating PVA fibers. Notched prisms of dimensions 40 x 40 x 160 mm and 100 x 100 x 500 mm are used for carrying out investigations at paste/mortar scale and concrete scale specimens respectively. At paste scale, the mix consists of cement, water (w/c ratio – 0.4) and PVA fibers (12 mm long). Nomenclature of cement paste samples is PF1 (1% PVA fibers) and PF2 (2% PVA fibers). For preparing mortar scale specimens, silica sand (sand/cement ratio – 0.5) is additionally incorporated. At concrete scale, the mix consists of cement, fine aggregates, coarse aggregates (of 10 mm and 20 mm size) in the ratio of 1:1.25:2.5, PVA fibers (30 mm long), water and superplasticizer. Longer fibers are required at concrete scale due to the presence of aggregates of bigger size. The nomenclature of mixes is PF1, PF2, MF1, MF2, CF1, CF2 where P, M and C stands for cement paste, cement mortar and concrete respectively; 1 and 2 denotes percentage of PVA fibers used in the mix.

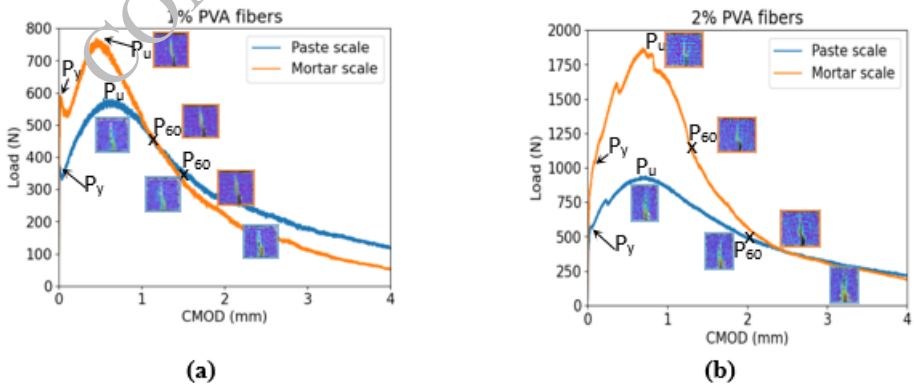

(a) (b)

Figure 1. Load vs. CMOD of cementitious composite with a) 1% and b) 2% PVA fibers

3. Fracture behaviour of PVA fiber incorporated cement composites

Fracture tests are carried out on notched prisms in CMOD (Crack Mouth Opening Displacement) -control mode. Clip-on gauge with a gauge length of 10 mm and travel of 4 mm is used for measuring CMOD. The load vs. CMOD plots for cementitious composites with 1% and 2% PVA fibers is presented in Fig. 1 a) and b) respectively. It can be observed that in composites with 1% PVA fibers, after the first load drop, the specimens take further load (strain hardening) until ultimate load is reached. It can be found that the pseudo-yield strength and ultimate strength of mortar samples are higher than the paste samples. However, the rate at which the load drops from ultimate load (P_u) to 60% of ultimate load (P_{60}) (softening rate) is much higher in mortar samples. This has even led to decrease in fracture energy of MF1 in comparison to PF1 (Table 2). It is observed that as the percentage of fibers is increased (from 1% to 2%), number of load drops in the load vs. CMOD response is increased demonstrating the presence of more crack bridging sites.

Table 1. Fracture parameters of cementitious composites with 1% and 2% PVA fibers

Specimen	Pseudo-yield load - P_y (N)	Ultimate load - P_u (N)	Hardening ratio (P_u / P_y)	Softening rate (N/mm)	CMOD at P_y (mm)	CMOD at P_u (mm)	Fracture energy (J/m^2)
PF1	372.17	581.92	1.56	243.28	0.0154	0.5432	908.87
MF1	591.34	768.96	1.30	819.13	0.0204	0.4525	852.45
PF2	574.47	939.10	1.63	278.77	0.0320	0.7245	1561.33
MF2	842.02	1871.46	2.22	1233.66	0.0280	0.6932	2230.59

4. Crack/Fracture characteristics of SHCC using digital image correlation technique

In order to get an in-depth understanding about the crack/fracture characteristics of SHCC, digital image correlation (DIC) technique has been used. DIC is a non-contact technique in which image correlation algorithm is used to obtain strain field of the specimen under investigation. By correlating the patterns of the sub-images in the reference image and deformed image, the displacement/strain profile is obtained (Fig. 2a).

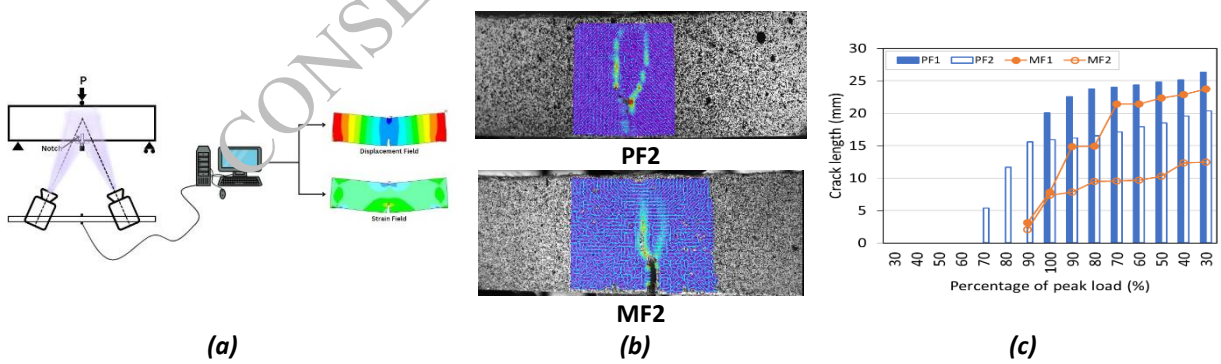

Figure. 2 a) Schematic of DIC set-up, b) Strain profile of paste and mortar specimens with 2% PVA fibers, and c) Crack length of PVA fiber incorporated cement paste/mortar specimens,

Using DIC, the principal strain profile of specimens at different load levels (P_u, P_{60}, P_{30}) is obtained (presented in Figs. 1a) and b)). From the strain profile, the entire fracture process, starting from formation of fracture process zone, macro-crack initiation, crack propagation, crack branching, etc are determined. The crack length of paste and mortar specimens with PVA fibers of different dosage levels is presented in Fig. 2b). It can be observed that as the dosage of fiber increases, the crack length gets reduced. The crack length of mortar specimens is lesser than the paste specimens of similar fiber percentage. Further, crack branching/multiple crack paths are formed in paste/mortar specimens of high fiber percentage (as can be

witnessed in Fig. 2c). This is attributed to the crack bridging offered by PVA fibers, thus cracks are formed at the adjacent region and this process delays the final failure of the specimen leading to the enhanced ductility. It is also interesting to note that the spacing between cracks/high strain region is less in case of mortar specimen in comparison to that of paste specimen.

DIC is also used to evaluate the fracture process zone (FPZ) of concrete incorporated with PVA fibers. A methodology has been followed to quantitatively estimate the size of FPZ (length and width). A virtual strain gauge is created above the notch and the strain data obtained from this is fitted with Gauss function. The width of the FPZ is calculated as 4σ since the strain distribution is occupied between (μ+2σ) and (μ-2σ) of the Gauss distribution area. Detailed explanation related to the methodology for arriving at the size of FPZ using DIC information can be found elsewhere [Sindu et al. (2022)]. A correlation has been established between the width of FPZ and the maximum aggregate size (d_{max}). For plain concrete, width of FPZ is found to be $0.365d_{max}$, and for PVA concrete with dosage of 1 to 2%, width of FPZ is found to be in the range of (0.48 to 0.56)d_{max}. In the present study, it is also found that the FPZ size of mortar PVA matrix is considerably smaller than that of PVA concrete.

5. Conclusions

In this study, the mechanical and fracture/crack characteristics of strain hardened cementitious composites have been evaluated in detail. Investigations have been carried out on three different material length scales – paste, mortar and concrete (with PVA fibers of different dosage levels). It has been identified that the strength (pseudo-yield and ultimate) as well as the softening rate of mortar samples is higher than the paste samples. Using DIC, the strain profile of specimens at different load levels have been obtained from which crack formation, propagation, etc have been identified. Further, quantitative estimation of the length/width of the crack and width of FPZ have been determined. It has been identified that the width of FPZ is linked to the maximum size of aggregates present in the concrete. The findings of this study will lead towards performance-based design of strain hardened cementitious composites.

Acknowledgements

The authors would like to acknowledge the staff of Special and Multifunctional Structures Laboratory, CSIR-SERC for their help during experimental investigations. This paper has been assigned the registration number CSIR-SERC-1130/2024. Authors also acknowledge that the research is funded by generous grant from CSIR, New Delhi. The funding from Department of Science and Technology (DST), Govt of India for the Core Research Grant (CRG/2021/005344) is also duly acknowledged.

References

Alam, S. Y., Loukili, A., and Grondin, F. (2012). "Monitoring size effect on crack opening in concrete by digital image correlation." *European Journal of Environmental and Civil Engineering*, 16(7), 818-836

Das, S., Aguayo, M., Sant, G., Mobasher, B., & Neithalath, N. (2015). "Fracture process zone and tensile behavior of blended binders containing limestone powder." *Cement and Concrete Research*, 73, 51-62

Fayyad, T. M., and Lees, J. M. (2017). "Experimental investigation of crack propagation and crack branching in lightly reinforced concrete beams using digital image correlation." *Engineering Fracture Mechanics*, 182, 487-505

Li, D., Huang, P., Chen, Z., Yao, G., Guo, X., Zheng, X., and Yang, Y. (2020). "Experimental study on fracture and fatigue crack propagation processes in concrete based on DIC technology." *Engineering Fracture Mechanics*, 235, 107166.

Omondi, B., Aggelis, D. G., Sol, H., and Sitters, C. (2016). "Improved crack monitoring in structural concrete by combined acoustic emission and digital image correlation techniques." *Structural Health Monitoring*, 15(3): 359-378

Sasmal, Saptarshi, and G. Avinash. (2016). "Investigations on mechanical performance of cementitious composites micro-engineered with poly vinyl alcohol fibers." *Construction and Building Materials* 128 (2016): 136-147

Sindu, B. S., and Saptarshi Sasmal. (2019). "On the development and studies of nano-and micro-fiber hybridized strain hardened cementitious composite." *Archives of Civil and Mechanical Engineering*, 19: 348-359

Sindu, B. S., A. Thirumalaiselvi, and Saptarshi Sasmal. (2022). "Investigations on fracture related properties of strain hardened concrete using digital image correlation and acoustic emission techniques", *European Journal of Environmental and Civil Engineering*, 26(14): 6807-6829

Sindu, B. S., and Saptarshi Sasmal. (2024). "Seismic Performance of Gravity Load Designed Beam-Column Joints with Strain Hardened Cementitious Composite", *ACI Structural Journal*, 121(3): 159-172

Inline Mixing of Accelerator for Concrete 3D Printing Application: Numerical Simulation Using Computational Fluid Dynamics

Vishwanath Ravindran[1], A. V. Rahul[2,*], and Thiyagarajan R.[3]

[1] Department of Civil and Environmental Engineering, Indian Institute of Technology Tirupati, Tirupati, India, Email: 6vishwanath@gmail.com

[2] Department of Civil and Environmental Engineering, Indian Institute of Technology Tirupati, Tirupati, India, Email: rahulav@iittp.ac.in

[3] Department of Mechanical Engineering, Indian Institute of Technology Tirupati, Tirupati, India, Email: thiyagu@iittp.ac.in

[*]Corresponding author

ABSTRACT

Concrete 3D printing is a recent construction technique where an element is fabricated by extruding concrete through the nozzle of a 3D printer. Admixtures like accelerators may be used to improve the buildability of 3D printable concrete. However, unlike traditional concrete, where an accelerator would be added during the concrete mixing stage, in 3D printing, the accelerator addition is desirable to be done at the nozzle of the 3D printer. This study evaluates the inline-mixing capability of two common types of dynamic mixers, a paddle type and a ribbon type mixer, using computational fluid dynamics (CFD) studies. A multi-species CFD model is developed to simulate the advective mixing of accelerator and concrete. The local rheology of concrete is treated as a function of the local accelerator content to account for the impact of the accelerator on the instantaneous concrete rheology. From the results of the simulated model, the mixing homogeneity is quantified through the non-uniformity index. The results indicate a more homogeneous distribution of accelerator in the concrete can be achieved using a ribbon type mixer rather than a paddle type mixer. Also, the ribbon mixer is observed to offer better mechanical performance in comparison to the paddle type mixer. The effects of other geometric parameters on the intermixing performance are also evaluated. It is observed that the nominal advantage offered by the ribbon type mixer can be overcome through higher mechanical power to the paddle type mixer which is more easily realizable, considering the practical difficulty in the fabrication of ribbon type mixing blades.

KEYWORDS: *Concrete 3D printing, Inline mixing, Computational fluid dynamics (CFD), Concrete rheology, Active rheological control.*

1. Introduction

Concrete 3D printing is a new rapid manufacturing technology focusing on automated fabrication of large-scale concrete structures. Fused deposition modelling (FDM), a popular form of additive manufacturing, is the precursor to the current concrete 3D printing technology. Both function by precise, controlled layer-wise deposition of the material at coordinates encoded usually by digital models of the component to be fabricated. There is a growing interest in the field of concrete 3D printing, which could be attributed to improved precision, efficiency, automation and reduced wastage the technology poises to offer. Concrete 3D printing allows for precise fabrication of highly complex topologies with reduced material wastage. The most significant advantage is realized in the form of rapid construction, owing to improved efficiency realized from partial/complete automation of certain construction tasks. It also helps eliminate formwork in on-site construction. The recent interest in concrete 3D printing is also linked to the potential it offers for the reduction in carbon footprint in the construction industry. The building and construction sector is poised to indirectly contribute to ~40% of the global emissions (UNEP, 2023-09). Though the major chunk of it is directly related to the production of raw materials, particularly cement (Concrete, 2021), emissions related to the transport of raw materials, formwork, casting activities, and waste disposal also offer a

significant contribution to the emissions related to construction sector (Muñoz et al., 2021). Though with the current state of concrete 3D printing technology, the emissions related to raw material are slightly exacerbated as mixtures employed in concrete 3D printing tend to have a higher cement content, but the emissions related to the construction activity can be greatly reduced. It has been shown that around ~30% reduction of carbon emissions can be realized with the current state of technology (Muñoz et al., 2021) and a larger curtail of emissions linked to the construction industry is expected with the advance of technology in the coming years (Gangotra et al., 2023).

In 3D printing of polymers like polylactic acid employed in FDM, an independent control of setting and modification of polymer rheology is achieved through temperature control. Unlike it, concrete 3D systems lack a precise control mechanism for the material's rheological and setting properties. In FDM, the setting behavior is reversibly modified through temperature control, whereas hardening is monotonous in cementitious systems. It is of interest to have control over the setting process so as to have flexibility in the printing process, and to allow for printing of more complex topologies. In conventional concrete works, certain properties are selectively modified through admixture addition during the nascent stages of concrete hydration, but this irreversible addition to the pre-transported concrete is not well suited for printing process. Adding an admixture like accelerator in the pre-transported concrete may adversely influence the pumping and extrusion process in the concrete 3D printing. To avoid this, set-on-demand concrete printing was developed, where special set activators are introduced in the print-head of the system to control the setting properties of the concrete (Rehman et al., 2023). The set activators aid by accelerating the setting process and enhancing the capacity to bear further layers without significant deformation.

The design of the printhead plays a pivotal part in the performance of the printed system particularly when inline mixing of accelerator is desired to achieve stiffening control of concrete (Tao et al., 2021). Motionless static mixers are commonly used to perform this task (Tao et al., 2022). Dynamic mixers are used as an alternative to static mixers as in case of the latter, large length of static mixer is needed for effective homogenization causing practical difficulties and consequently higher pressure loss during pumping, both of which are not experienced in the former (Tao et al., 2022). However, in the former, there exists issues related to efficiency of the mixing performance and potential mishaps owing to premature stiffening within the printhead. Insights from numerical and experimental studies are necessary to study these systems. In regards to numerical studies, computational fluid dynamics can be employed to study advective mixing of the accelerator with the cementitious suspension. In this work, we present a multi-species computational fluid dynamics (CFD) model for modelling flow of accelerator and cementitious suspension. We then employ it to study the advective mixing performance of two type of mixers: ribbon and paddle type mixers and derive numerical insights on the mixing performance of the system for the particular application.

2. Constitutive model

Concrete, in general, is popularly modelled as Bingham pseudoplastic (Tattersall ,1955). The rheological behavior of Bingham fluids is described by its yield stress ($\tau_{y,c}$) and plastic viscosity ($\eta_{p,c}$). In this work, the cement paste and the accelerator are modelled as different chemical species of the liquid phase, and the granular constitutes (aggregates) are modelled as a separate phase. The high rotational speeds applied in the in-line mixer can result in shear-induced particle migration of the granular phase, which is accounted for by using the suspension balance model (Nott and Brady, 1994).

2.1 Rheology of cement paste

The concrete mixture is considered as suspension of aggregates dispersed in cement paste where cement paste itself is modelled as a Bingham fluid. The rheological parameters of the cement paste are yield-stress $\tau_{y,cp}$ and plastic viscosity ($\eta_{p,cp}$) as shown below:

$$\tau = \tau_{y,cp} + \eta_{p,cp}\dot{\gamma}, \qquad \text{.....(1)}$$

where τ and $\dot{\gamma}$, refer to the shear stress and shear rate, respectively.

2.2 Modelling accelerator-cement paste interaction in the liquid phase

In this work, the influence of the local accelerator concentration on the instantaneous hydration is not accounted for on the basis that the retention time in the mixer is too short (in the order of 2 minutes). To account for the composite phase of cement paste and accelerator, a simple mass fraction-based average (Pankaj et al., 2022) is employed to model the apparent viscosity of this phase. The relation is stated below:

$$\eta^*_{cp'} = \theta_{acc}\eta_{acc} + \theta_{cp}\eta^*_{cp}, \tag{2}$$

where the subscript *cp′*denotes the composite phase of the cement paste and the accelerator, η^*_{cp}, θ_{acc} and θ_{cp} denote the mass fraction of pure accelerator in the cp′ phase, mass fraction of pure cement pastes in the cp′ phase, the viscosity of the pure accelerator, and the apparent viscosity of the pure cement pastes, as per Eq. (1) respectively.

2.3 Shear-induced migration of granular phase

The high rotational speed used in in-line mixer can result in a shear induced migration of the aggregates, which, in turn will modify the local rheological properties of the concrete mixture. In this work, to account for the local volume fraction of aggregates (ϕ) on the rheological behavior of the concrete, the Chateau-Ovarlez-Trung model (Chateau et al., 2008) and Krieger-Dougherty model (Krieger and Dougherty, 1959) are employed and are stated below:

$$\tau_{y,c} = \tau_{y,cp}\sqrt{\frac{1-\phi}{\left(1-\frac{\phi}{\phi_c}\right)^{m\phi_c}}}, \tag{3}$$

$$\eta_{p,c} = \eta_{p,cp}\left(1-\frac{\phi}{\phi_c}\right)^{-\eta_i\phi_c}, = \eta_{p,cp}\left(1-\frac{\phi}{\phi_c}\right)^{-\eta_i\phi_c}, \tag{4}$$

where , $\tau_{y,c}$, $\eta_{p,c}$, ϕ_c , m and η_i are the yield stress of the concrete, plastic viscosity of the concrete, random packing limit, and the calibration parameters for the Chateau-Ovarlez-Trung model (Eq. (3)) and the Krieger-Dougherty model (Eq. (4)), respectively. The granular phase embedded in the cement matrix is susceptible to particle migration due to the action of locally varying shear rates. Continuous and random collisions within the granular constituents lead to more particles moving away from the high shear rate region than particles entering it (Leighton and Acrivos, 1987) as particles in regions of high shear rates are susceptible to more frequent collisions.
The suspension balance model (Nott and Brady, 1994) is employed to account for this behavior.

3. Governing equations

The Eulerian multiphase model is employed in this work, which treats the continuity equation of the secondary phases (granular phase), the momentum equation for both phases and the species transport equation for the accelerator species in the cement paste phase. The governing equations are stated below:

$$\frac{\partial\theta_{acc}\rho_{acc}}{\partial t} + \nabla\cdot\left(\theta_{acc}\rho_{acc}\overrightarrow{u_{cp'}}\right) = 0, \tag{5a}$$

$$\frac{\partial\phi\rho_g}{\partial t} + \nabla\cdot\left(\phi\rho_g\overrightarrow{u_g}\right) = 0, \tag{5b}$$

$$\frac{\partial \phi_g \rho_g \overrightarrow{u_g}}{\partial t} + \nabla \cdot \left(\phi_g \rho_g \overrightarrow{u_g}\, \overrightarrow{u_g}\right) = -\phi_g \nabla p + \nabla \cdot \left(2\phi_g \eta_c^* \boldsymbol{D_g} - \mu_c \eta_n \dot{\gamma}_g \dot{\boldsymbol{Q}}\right) \pm \overrightarrow{F_d} \mp \overrightarrow{F_L} \quad (5c)$$

$$\frac{\partial \phi_{cp'} \rho_{cp'} \overrightarrow{u_{cp'}}}{\partial t} + \nabla \cdot \left(\phi_{cp'} \rho_{cp'} \overrightarrow{u_{cp'}}\, \overrightarrow{u_{cp'}}\right) = -\phi_{cp'} \nabla p + \nabla \cdot \left(2\phi_{cp'} \eta_c^* \boldsymbol{D_{cp'}} - 2\phi_{cp'} \mu_c \nabla \cdot \left(u_{cp'}\right) \boldsymbol{I}/3\right) \mp \overrightarrow{F_d} \pm \overrightarrow{F_L} \quad (5d)$$

$$\eta_n = K_n \frac{\phi^2}{(\phi_c - \phi)^2}. \quad (6)$$

where Eq. (5a) refers to the equation for species transport of accelerator within the cement paste, Eq. (5b) refers to the continuity equation for the granular phase, and Eqs. (5c) and (5d) refer to the momentum equation for the granular phase and the cement paste-accelerator phase, respectively. In the above equations, the subscript *acc*, *cp'* and *g* refer to the accelerator phase, composite phase (consisting of cement paste and accelerator), and the granular phase, respectively. $\overrightarrow{u_k}$, ρ_k ,ϕ_k and $\boldsymbol{D_k}$ refer to the velocity, density, local volume fraction, and symmetric part of the velocity gradient of phase, respectively, where k ∈ {g, cp'}. ρ_{acc} , p, $\dot{\gamma}_g$refer to the density of the pure accelerator content, global pressure, and the magnitude of shear rate experienced by the granular phase, respectively. $\rho_{cp'}$ and $\overrightarrow{u_{cp'}}$ refer to the mass-weighted sum of the density and velocity, respectively of the accelerator and the pure cement paste in Eq. (5c) refers to the η_n normal relative viscosity of the suspension given as follows Morris and Boulay (1999)
In Eqn. (5a), no diffusion term is accounted for, as only the advective mixing performance of the mixer is intended to be studied in this work. A schematic of the modelling framework is shown in Fig. 1. For more details on the modelling, the readers may refer to a previous work by the same authors (Vishwanath et al. 2024).

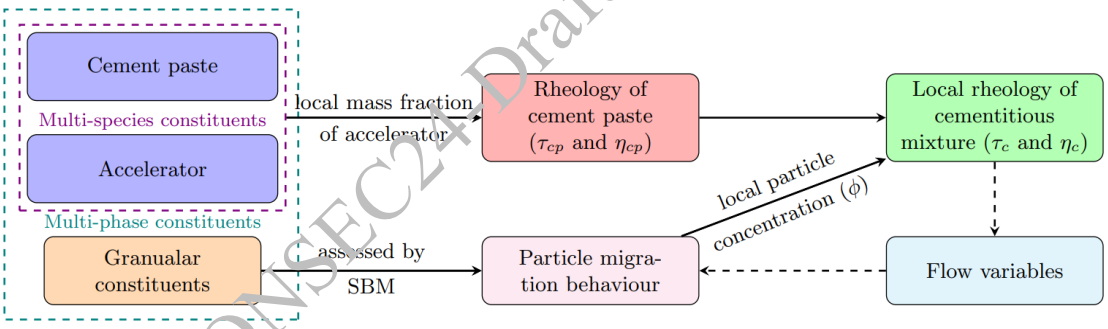

Figure 1. Framework for modelling flow of 3D printing concrete

3.1 Numerical simulation

To evaluate the advective mixing performance of the paddle type and ribbon mixer, the governing equations mentioned in Eqn. (5) are numerically simulated through ANSYS Fluent solver.

3.1.1 Mixer geometry

To purely characterize the mixing performance independent of the geometry of the external casing, it is decided to primarily use a uniform cylinder of diameter 70 mm for the printhead and uniform velocity inlet is assigned at diametrically opposite positions on the printhead at fixed radial coordinates. A simulation of the advective mixing performance of this system is primarily focused upon, and the effects of the parameters like diameter and the position of the inlets are also investigated. Sketches of the mixer and vessel geometry for both paddle and ribbon type mixers are presented in Fig. 2. The value of parameters considered in this work is presented in Table 1. To numerically simulate the motion of the blades, multiple conformal cylindrical mesh domain just surrounding the blades and the primary shaft with a clearance of 2.5 mm is created around them. A moving reference frame is employed where the mesh remains stationary, and the

effects of rotation are appended to the governing equations in that domain. This methodology is used to produce the effects of rotation (Luo and Gosman, 1994; Ansys FLUENT 12.0 Manual, 2009).

3.1.2. Material properties

To simulate the mixing performance for 3D printing concrete with varying aggregate to binder ratios, representative samples were adopted from published literature on assessing the pumping behavior of 3D printable concrete (Mohan et al., 2021). The details of the mixtures and the suspension related properties are presented in Table 2. The viscosity of the accelerator is assumed as 1 Pa.s (Weibel, 2009).

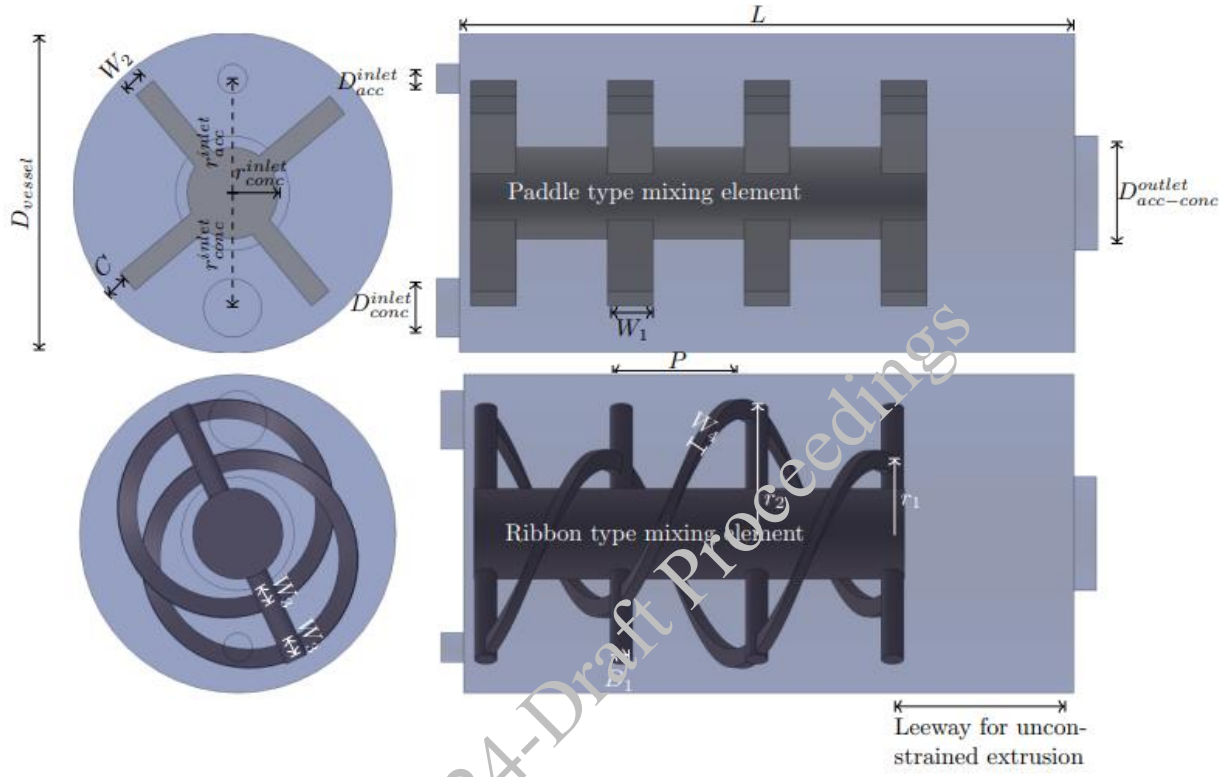

Figure 2. Schematics of (a) paddle type mixer geometry and (b) ribbon type mixer geometry

Table 1. Topological parameters of the mixer geometry

Sl.no	Property	Range of values considered (mm)	S.no	Property	Range of values considered (mm)
1	D_{vessel}	60-90	10	W_1	10
2	L	135	11	W_2	5
3	D_{acc}^{inlet}	7	12	P	30
4	D_{conc}^{inlet}	18	13	W_3	4
5	$D_{acc-conc}^{outlet}$	25	14	W_4	2.5
6	r_{conc}^{inlet}	27.5	15	D_1	5
7	r_{acc}^{inlet}	15-30	16	r_1	18
8	r^{shaft}	10	17	r_2	30
9	C	5	-	-	-

Table 2. Value of material properties employed in this study

Sl.no	Property	Value			
1	aggregate to binder ratio	1	1.2	1.4	1.8
2	yield stress of cement paste (Pa)	98.85	72.43	50.03	21.55
3	plastic viscosity of cement paste (Pa.s)	3.17	3.02	3.06	1.96
4	m	7.67			
5	η_i	2.91			
6	ϕ_c	0.63			
7	η_{acc}	1			
8	Design accelerator content	2% (w.r.t to mass of binder)			

4. Results and discussions

In the current work, the mixing homogeneity produced by the inline mixer is evaluated by using the non-uniformity index (Tang et al., 2018). A lower for the non-uniformity index indicates a higher mixing homogeneity, and vice-versa. The index is calculation as shown below:

$$Non-uniformity\ index = \frac{1}{2}\left(\sum_{i=1}^{n}\frac{A_i|\theta_i-\theta_{avg}|}{A_{tot}\theta_{avg}}\right), \quad (2)$$

.where A_{tot} and θ_{avg} is the total area of the designated domain and the average (area-weighed) mass fraction of the accelerator at the designated domain, A_i and θ_i are the area and mass fraction of accelerator in the subdomain derived from the domain being broken into n subdomains (mesh elements in this case)
During the operation of the printhead, the only variable parameter for controlling mixing performance without interrupting the extrusion process is the rotational rate of the shaft.
The variation of the non-uniformity index along the lateral plane at the longitudinal stretch of the mixer for different rotational speed is presented in Fig. 3 (the results are obtained for $r_{acc}^{inlet} = 25$ mm, D_{vessel} =70 mm, extrusion rate of 50 mm/s and accelerator content of 2%). It could be observed that the ribbon mixer showcases much stronger advective mixing. The performance of both mixers improves at higher rotational speeds, as would be expected. The ribbon mixer also showcases much stronger advective mixing near the inlet, which could be particularly helpful for the immediate dispersion of high-accelerator dosages. Variations of the non-uniformity index below 10^{-3} are assumed insignificant in this work, and variation just following the mixer element can possibly occur owing to the residual concrete present at those locations, which are possibly unsheared in this study due to the absence of an extruder element.

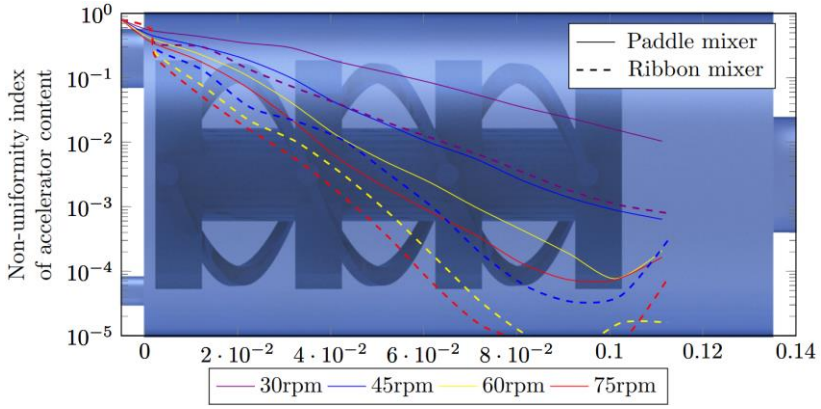

Figure 3. Variation of the non-uniformity index of the mass fraction of the accelerator (w.r.t cement paste) in the lateral plane along the longitudinal stretch of the mixer. The image of both the type of mixer and vessel are superimposed and exhibited on the plot to showcase the corresponding longitudinal position.

It is of particular importance to optimize the operation costs of the 3D printing processes. The two control parameters in the 3D printing system are the pumping rate into the printhead and the rotation rate of the mixer/extruder shaft. The presence of the printhead can lead to an additional pressure drop. The shearing action of the mixer however aids in the reduction of the pressure drop. The variation of torque required to be imposed to cause rotation at a particular rotational speed (to cause fluid motion) and corresponding pressure required to pump material into the printhead is presented in Fig. 4a. It could be observed that a lower pumping pressure is required to pump material into the printhead for a system with a ribbon mixer, and a variation around 0.2 bar is observed, possibly owing to better shearing action created by the ribbon mixer. The torque requirements are also lower for the ribbon type mixer in comparison to paddle type mixer as in case of the later, the pressure imposed on the faces of the paddle has to be overcome and they impose a significant torque (~ 60% at 60 rpm) on the shaft, whereas in case of the former the pressure contribution is relatively lower (~ 30% at 60 rpm). The decrease in inlet pressure at higher RPM is owing to increased volume of sheared zone.

The variation of the torque requirements and change in inlet pressure for mixes with different aggregate-to-binder ratio used in the concrete mixture for operation at 60rpm is presented on Fig. 4b. As expected, an increase in the values is observed at higher aggregate to binder ratios, which is in line with literature (Mohan et al., 2021). The increase is expected due to closer packing of particles, which causes more intense local shearing of fluids between them (Krieger and Dougherty, 1959).

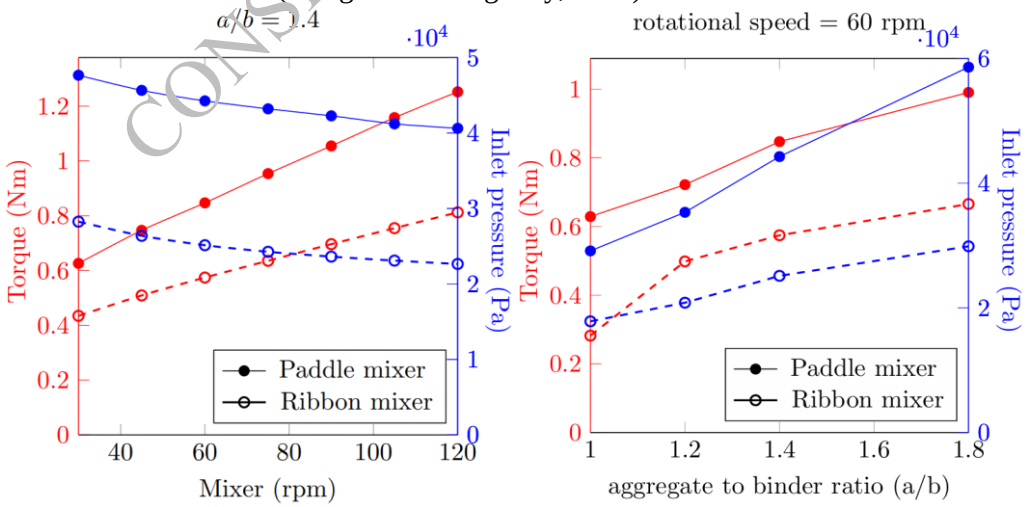

Figure 4. Variation of the necessary torque and inlet pressure (for pumping concrete) at different mixer speeds (a) and for representative 3D printing concrete mixtures with different aggregate to binder ratios (b)

The dependence of other parameters in the study such as the position of the inlet and the diameter of the vessel (consequently the impeller projection), are studied and reported in Fig. 5. It could be observed that

optimal performance is observed for an accelerator inlet near 20 mm radially measured from the center. The mixing performance seems to improve at higher vessel diameter for the same rotation rate as higher advective velocity is realized due to the larger projection lengths of the paddle mixer.

The results suggests that the performance of the printhead can be elevated through optimization of the vessel and mixer topologies, but the increase in performance is not significant to warrant special attention in their design as the difference can easily overcome by higher mechanical input. Thus, the design of the printhead geometry appears to be not critical in terms of its practical functionality (for inline mixing applications). Despite the capability of the developed CFD model to provide numerical insights on inline-mixing performance of the printhead, a limitation of the model is that, as indicated in section 2.2, the model does not account for the instantaneous change in the rheology of cement paste when the acceleration is introduced in the printhead. This, particularly, becomes important when very high accelerator dosage is to be used. Future work may explore how cement hydration's effect on rheology can be accounted for in the CFD model. The mixing homogeneity capabilities of different inline mixers could also be determined through experimental studies (by intermixing the accelerator with fluorescent dye and through image analysis (François , 2007). Such studies may be attempted in the future, and their results can be compared with those obtained from numerical simulations.

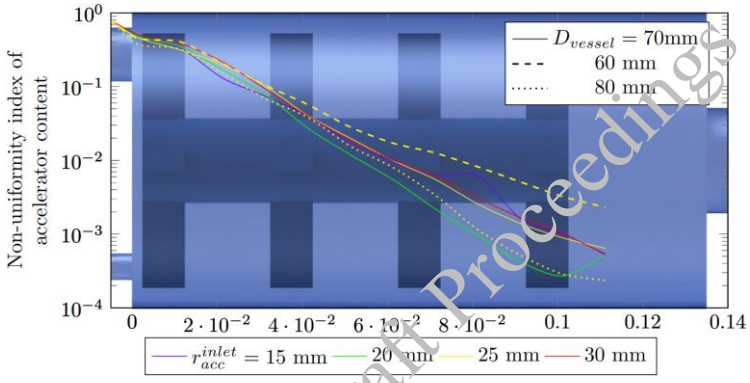

Figure 5. Variation of the non-uniformity index of the mass fraction of the accelerator (w.r.t cement paste) in the lateral plane along the longitudinal stretch of the mixer, observed for different variations of vessel geometry.

5. Conclusions

In this study, the effect of mixer topology on the inline mixing performance of the printhead is evaluated through a computational fluid dynamics (CFD) model. The CFD model involves a multiphase treatment of granular and liquid phase, the later phase being treated as a multi-species phase involving a cement paste and an accelerator component. The advective mixing performance of paddle type and ribbon type mixers are compared in this work. The ribbon type mixer offers better performance in comparison to a paddle type mixer for advective mixing of an admixture. The ribbon mixer also provides more optimal performance in terms of torque requirements and shearing action. However, the difference may not be significant enough to warrant the need for the ribbon type mixers as their mixing blades are more difficult to manufacture owing to their complicated and curved profiles. The effect of mixture properties (aggregate to binder ratios) on the mechanical performance of the system is also evaluated. At a higher aggregate-to-binder ratio, higher torque and higher inlet pressure was required for the operation of the system. The current study also reveals that apart from the geometry of the mixer blade, the performance of the system can also be optimized through consideration of the vessel geometry, such as the position of the inlet and the size of the vessel. Despite the capability of the CFD model to provide insights into inline-mixing performance of the printhead, the model neglects the effect of the accelerator on the instantaneous rheology of concrete. Future work may explore how this effect can be accounted for in the CFD model. Also, experimental investigation of inline mixing performance with different mixer types may be attempted in future works and compared with the results obtained from numerical simulation.

References

Ansys FLUENT 12.0 Manual U. Ansys fluent 12.0. Theory Guide 2009;:67.

Bhattacherjee S, Santhanam M. Investigation on the effect of alkali-free aluminium sulfate based accelerator on the fresh properties of 3d printable concrete. *Cement and Concrete Composites* 2022;130:104521.

Building Materials and The Climate: Constructing A New Future, United Nations Environment Programme, (2023).

Cabaret F, Bonnot S, Fradette L, Tanguy PA. Mixing time analysis using colorimetric methods and image processing. *Industrial & Engineering Chemistry Research* 2007

Chateau X, Ovarlez G, Trung KL. Homogenization approach to the behavior of suspensions of noncolloidal particles in yield stress fluids. *Journal of Rheology* 2008;52(2):489–506.

Concrete needs to lose its colossal carbon footprint. Nature 2021;597(7878):593–4

Gangotra, A., Del Gado, E. & Lewis, J.I. 3D printing has untapped potential for climate mitigation in the cement sector. *Commun Eng 2*, 6 (2023).

Inkson N, Papoulias D, Tandon M, Reddy V, Lo S. An eulerian-eulerian formulation of suspension rheology using the finite volume method. *Journal of Non-Newtonian Fluid Mechanics* 2017;245:38–48.

Krieger IM, Dougherty TJ. A Mechanism for Non-Newtonian Flow in Suspensions of Rigid Spheres. *Transactions of The Society of Rheology* 1959;3(1):137–52.

Leighton D, Acrivos A. The shear-induced migration of particles in concentrated suspensions. *Journal of Fluid Mechanics* 1987;181:415–439. doi:10.1017/S0022112087002155.

Luo JY, Gosman AD. Prediction of impeller- induced flow in mixing vessels using multiple frames of reference. 1994.

Mohan MK, Rahul A, Van Tittelboom K, De Schutter G. Rheological and pumping behaviour of 3d printable cementitious materials with varying aggregate content. *Cement and Concrete Research* 2021;139:106258.

Morris JF, Boulay F. Curvilinear flows of noncolloidal suspensions: The role of normal stresses. *Journal of Rheology* 1999;43(5):1213 – 1237.

Muñoz, Ivan, et al. "Life cycle assessment of integrated additive–subtractive concrete 3D printing." The International Journal of Advanced Manufacturing Technology 112 (2021)

Nott PR, Brady JF. Pressure-driven flow of suspensions: simulation and theory. *Journal of Fluid Mechanics* 1994;275:157–199. doi:10.1017/S0022112094002326.

Pardeep Pankaj, Avinish Tiwari, Tanmoy Medhi, Pankaj Biswas. Multi-species transport CFD simulation and experimental verification for material flow properties in dissimilar friction stir welding, *Materials Today Communications*, (2022).

Rehman AU, Birru BM, Kim JH. Set-on-demand 3d concrete printing (3dcp) construction and potential outcome of shotcrete accelerators on its hardened properties. Case Studies in Construction Materials 2023;18:e01955

Tang, Hongwu & Zhang, Huiming & Yuan, Saiyu. (2018). Hydrodynamics and contaminant transport on a degraded bed at a 90-degree channel confluence. *Environmental Fluid Mechanics*.

Tattersall GH. The rheology of portland cement pastes. British *Journal of Applied Physics* 1955;6(5):165.

Vishwanath R, Rahul A V, Thiyagrajan R. Particle Migration during Pipe Flow of 3D Printable Concrete: Insights from Numerical Simulation. *Journal of Non-Newtonian Fluid Mechanics* [Manuscript submitted for publication].

Weibel M. Stable shotcrete accelerator dispersion with high content in active matter. 22.04.2009.

.

An Experimental Study of Ultra High Performance Fiber Reinforced Concrete and Analysis & Design of Multi-storey Building using Applications of UHPFRC

S. S. Kshirsagar[1*], and B. G. Birajdar[2]

[1]Department of Civil Engineering, COEP Technological University Pune.*
[1]Email: Kshirsagarss22.civil@coeptech.ac.in*
[2]Department of Civil Engineering, COEP Technological University Pune.
[2]Email: bwc@coeptech.ac.in

[*]Corresponding author

ABSTRACT

Ultra High Performance Fiber Reinforced Concrete (UHPFRC) is the futuristic and advanced cementitious material having remarkable strength and exceptional durability. Although it has a number of benefits over traditional concrete, its application is restricted because of its high cost and limited design code provisions. The determination of material properties that accurately characterise the material's inherent response to structural loads is a crucial component of structural design. An experimental study on Ultra High Performance Fiber Reinforced Concrete was carried out, to evaluate the compression, tension, and flexural properties of UHPFRC. Then, the use of UHPFRC material in the design of multi-storey building structure was examined. The applications of UHPFRC in Parking building structure was suggested to provide intermediate column free space in the building. The main requirement of a multi-storey parking building was for a large, intermediate column free space to allow maximum manoeuvrability of vehicles into parking bay. The scope of the project includes an experimental study on UHPFRC and design of a G+4 storey Parking building using applications of UHPFRC. The architectural building plan, structural key plan and design basis report (DBR) was prepared for a G+4 storey Parking building. The modelling & analysis of a G+4 storey Parking building was done in a suitable software. The foreign design codes on UHPFRC were studied and considered in the design. The Pre-stressed UHPFRC girder of 36 m span was designed using Response-2000 software, which offers column free space in the building. The project includes the study of basic properties of UHPFRC and exhibits the structural design of parking building with long span girder.

KEYWORDS: *Ultra High Performance Fiber Reinforced Concrete, Experimental Study, Multi-storey Building, Pre-stressed Concrete.*

1. Introduction

Ultra High Performance Fiber Reinforced Concrete is an advanced cementitious material renowned for its superior strength and exceptional durability, offering a promising solution to enhance the sustainability of buildings and various infrastructure components. Over the past two decades, UHPFRC has attracted growing interest globally, with applications ranging from building components, bridges, architectural features, repair and rehabilitation, offshore structures, and hydraulic structures. The successful implementation of Ultra High Performance Fiber Reinforced Concrete is evident worldwide. Despite its huge potential, several barriers continue to limit its widespread application. Ongoing research and investigations aim to address these knowledge gaps, paving the way for the development of innovative, affordable, sustainable, feasible, and economical UHPFRC solutions, which could significantly enhance its acceptance and utilisation.

Figure 1. Chandani chowk Bridge, Pune

Figure 2. GCC Namaste Hotel Building, Mumbai

The determination of material properties that accurately characterise the material's inherent response to structural loads is a crucial component of structural design. Hence, it is imperative to conduct compressive test, tensile cracking strength test and flexural test on UHPFRC to understand the behaviour of such a advanced material.

As we know, the rapid industrialisation globally has resulted in increased urban economic growth, higher incomes, improved living standards, and significant population growth, contributing to a continual rise in private vehicle ownership. The parking space requirement is also increasing with the rise in number of vehicles. The core or older areas of the city, fail to provide enough space for off-street parking, which tend to increase the amount of on-street parking demand in those areas. Due to the non-availability of better parking facilities in the area, vehicles remain parked on the road, leading to traffic jams and inconvenience to public spaces.

Hence, the multi-storey parking facility would probably solve the problem of parking in such areas. The main requirement of a multi-storey parking building is for a large, intermediate column-free space to allow maximum manoeuvrability of vehicles into parking bays. The scope of this project is to analyse and design a G+4 storey parking building having intermediate column free space which is proposed over 61 m developmental plan road width and 125 m road length. The use of ultra high performance fiber reinforced concrete is proposed to provide intermediate column free space in the parking building.

2. Research significance

This research significantly advances our understanding of UHPFRC, particularly in predicting key parameters like compressive strength, tensile cracking and flexural strength. This study examines the use of Ultra-High Performance Fiber-Reinforced Concrete (UHPFRC) in building structures.

1. To evaluate the Compressive strength, Tensile cracking strength and Flexural strength of Ultra High Performance Fiber Reinforced Concrete.
2. To address the issue of inadequate parking facilities in urban areas by way of providing Parking building across the road width.
3. To offer large column free space in IT Park buildings, Commercial complexes, Conference halls and Data centre buildings using applications of UHPFRC.

3. Ultra High Performance Fiber Reinforced Concrete (UHPFRC)

French interim recommendations (AFGC 2002) defined UHPFRC as a concrete with a characteristic compressive strength of at least 150 MPa with the use of steel fiber reinforcement to ensure ductile behaviour under tension.

4. Experimental Study of UHPFRC

The experimental tests are carried out to obtain the compressive strength, tensile cracking strength and flexural strength of UHPFRC.

4.1 Compressive Strength:

UHPFRC cubes of dimension 100 mm x 100 mm x 100 mm were cast in the concrete lab to evaluate 1 day and 28 day compressive strength of UHPFRC. The experimental testing was carried under Compression testing machine (CTM) having capacity of 2000 kN. The compressive strength of UHPFRC obtained from experimental testing is 167.2 N/mm^2.

4.2 Tensile cracking and flexural strength:

The flexure test was conducted on UHPFRC beam of size 500 mm x 100 mm x 100 mm in Universal testing machine (UTM) having capacity of 250 kN. The effective span for two-point loading test was 300 mm. The flexural strength of UHPFRC is 27 N/mm^2.
The load at which first crack appeared is 38 kN, hence the tensile cracking strength of UHPFRC is 11.4 N/mm^2.

Figure 3. Compression

Figure 4. Flexural Test

5. Architectural Layout of Building

The G+4 storey Parking building is proposed over 61 m developmental plan road width in a metropolitan city where parking is a challenging issue. The plan dimensions of building are 56 m x 125 m.

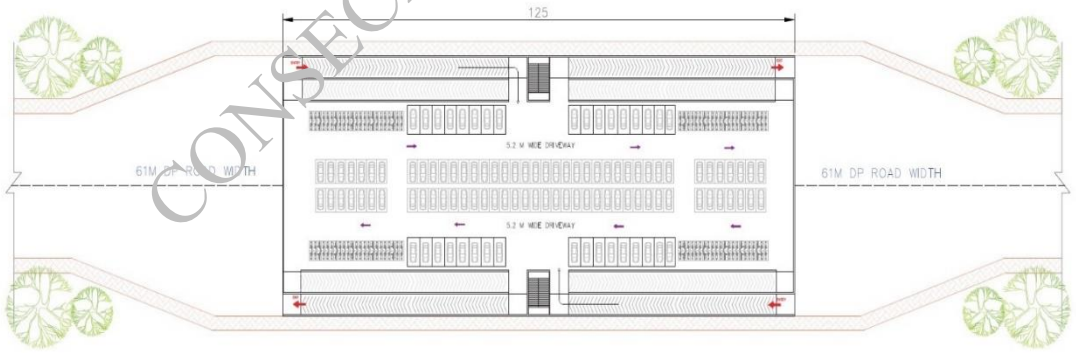

6. Design of Prestressed UHPFRC Girder

The 36 m Pre-stressed UHPFRC Girder is designed using Response-2000 software.
Response-2000 is a user-friendly sectional analysis software designed to determine the strength and ductility of reinforced concrete cross-sections under the combined effects of shear, moment, and axial load. The UHPFRC Girder of 36 m span is designed using both Pre-tensioned and Post-tensioned system as shown below:

6.1 Design of 36 m Pre-tensioned UHPFRC Girder

The maximum bending moment obtained from the analysis is 18670.5 kNm.

The Freyssinet Prestressing Manual is referred and data considered is: Diameter of tendon = 15.2 mm, Area = 140 mm^2 and Stress = 259 MPa.

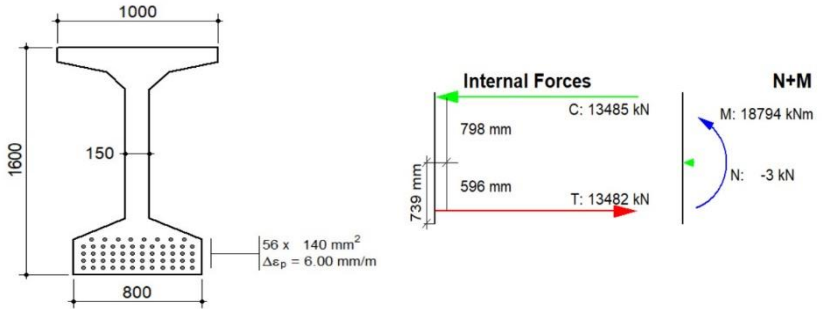

For depth of 1600 mm, Moment of resistance (M_r) of Pre-tensioned UHPFRC I Girder is greater than 18670.5 kNm, hence section is safe.
Provide 56 tendons of 15.2 mm diameter.

6.2 Design of 36 m Post-tensioned UHPFRC Girder

The Freyssinet Prestressing Manual is referred and data considered is: Diameter of tendon = 15.2 mm, Area = 140 mm^2 and Stress = 259 MPa.

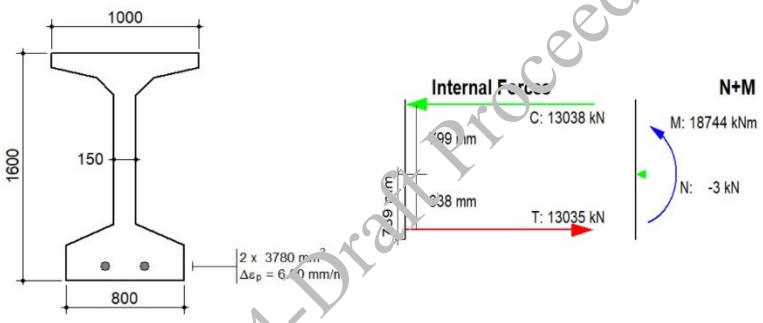

For depth of 1600 mm, Moment of Resistance (M_r) of Post-tensioned UHPFRC I Girder is greater than 18670.5 kNm, hence section is safe.
Provide 2 ducts each having 27k15 tendon property.

7. Conclusions

Based on the experimental results and analysis & design of a G+4 storey parking building using applications of UHPFRC, the following findings are reported:

- The experimental results show that UHPFRC material has a higher compressive, tensile and flexural strength, higher toughness and ductility compared to normal or high strength concrete, thus the use of UHPFRC material in structures for larger span is an effective solution.
- The use of UHPFRC is seen as an effective solution to be used in building structures to get large column free space.
- In the present study of parking building as suggested in metro city on developmental plan road, it could be a solution to parking of vehicles in congested areas.

8. Future Scope

Since the UHPFRC is an emerging material, the future scope could be the use of UHPFRC material in columns and footings, development of code provisions and design aids. More research in long term performance, durability and serviceability is needed.

References

Benjamin A. Graybeal (2007), "Compressive Behavior of Ultra-High-Performance Fiber-Reinforced Concrete", *American Concrete Institute Journal*, Title no. 104-M17.

Benjamin A. Graybeal (2008), "Flexural Behavior of an Ultrahigh-Performance Concrete I-Girder", *American Society of Civil Engineers*, https://doi.org/10.1061/(ASCE)1084-0702(2008)13:6(602).

Jain, S. & D. S., R. & Mathur, K. & Jain, A. (2023), "India's First Long-Span Unbonded Post-Tensioned RC-UHPC Composite I-Beams", *International Interactive Symposium on Ultra-High Performance Concrete 3(1): 67*, doi: https://doi.org/10.21838/uhpc.16682.

Mahmoud H. Akeed, Shaker Qaidi, Hemn U. Ahmed, Rabar H. Faraj, Ahmed S. Mohammed, Wael Emad, Bassam A. Tayeh , Afonso R.G. Azevedo (2022), "Ultra-high-performance fiber-reinforced concrete. Part I: Developments, principles, raw materials", *Elsevier Volume 17*, December 2022, e01290.

Mehmet Dogu, Fatmir Menkulasi (2020), "A flexural design methodology for UHPC beams posttensioned with unbonded tendons", *Elsevier*, https://doi.org/10.1016/j.engstruct.2020.110193.

N.M. Azmee, N. Shafiq (2018), "Ultra-high performance concrete: From fundamental to applications", *Elsevier*, doi: https://doi.org/10.1016/j.cscm.2018.e00197.

Seismic Performance of Beam-Column Joints with Beam Headed Longitudinal Steel bars Anchored in Steel Fiber Concrete Panel Zone

S. Kake[1]* and Y. Ishikawa[2]

[1] Takenaka Corporation, Chiba, Japan
Email: kake.satoshi@takenaka.co.jp
2 Shibaura Institute of Technology, Saitama, Japan
Email: y-stone@shibaura-it.ac.jp

*Corresponding author

ABSTRACT

This study discusses a construction method for reinforced concrete (RC) beam-column joints (BCJ), developed to rationalize the construction work done at the RC panel zone using the merits of steel fibers. In this structural system, by improving the tensile performance of concrete using steel fibers, shear reinforcement are not needed in the panel zone where beam headed longitudinal steel bars are anchored around its middle section. This study also examines the behavior of the proposed structural system under lateral loading by experiment and 3-dimensional non-linear FE analysis. The study showed that the FE analysis reproduced adequately the behavior of the tested specimens and the stress transfer mechanism was identified as a double-strut model involving the development of two struts in the panel zone.

KEYWORDS: *Beam-column joint, SFRC, Panel zone, Headed steel bar, Stress transfer mechanism*

1. Introduction

In recent years, structural construction methods using precast (PCa) members for reinforced concrete buildings in Japan have become various and their number increased. In case of ordinary beam-column joints (BCJs), construction can be complicated because of reinforcement congestion where placing longitudinal bars of columns and beams, and shear reinforcement in the BCJ panel zone may not be easily achieved. To avoid such complications, a beam-column joint construction method using steel fiber reinforced concrete (SFRC) and resulting in BCJs of high seismic performance is proposed (Ishikawa(2016)). As shown in Fig.1, in the proposed BCJ, no shear reinforcement are needed in its panel zone, which is made of SFRC, and the discontinuous longitudinal steel bars of the beams are mechanically anchored around the middle section of the panel zone. Fig.2 shows an image of the construction steps of the proposed method. As the beam longitudinal bars are discontinuous and shear reinforcement are not required in the panel zone, the construction of the floor consists of setting the PCa column and PCa beam and then casting SFRC in the panel zone. To ensure the appropriatness of the proposed construction method of the BCJ with such special panel zone under seismic loading and verify the stress transfer mechanism within the panel zone, a loading test and a three-dimensional nonlinear FE analusis were carried out.

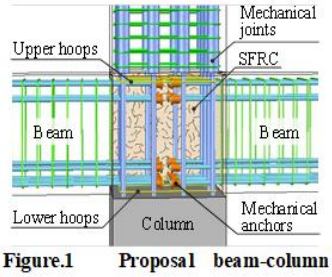

Figure.1 Proposal beam-column

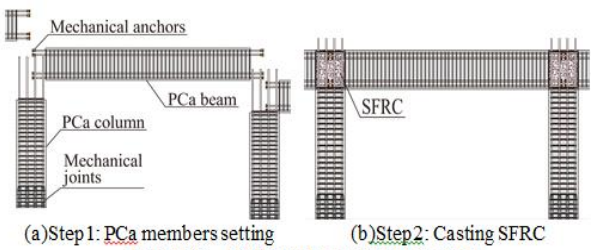

Figure.2 Outline of construction steps

2. Outline of experimental test

Geometry and details of the constructed two test specimens are shown in Fig.3. Specimens were interior BCJs scaled to 1/2 of the actual size. Considered test parameter was the failure mode (specimen No.1: Beam flexural failure type, specimen No.2: Panel zone shear failure type). Failure mode was adjusted by combining the steel strength and amount of the longitudinal bars of the beams. Headed longitudinal bars of the beams were anchored in the panel zone made of SFRC, whereas the beams and columns were made of concrete without steel fibers. Steel fibers added to the concrete had a length of 30 mm and diameter of 0.60 mm, and the mixed rate was 1.0% per concrete volume. No shear reinforcement were used in the panel zone. Concrete compressive strength of the beams and columns was 38.4MPa, and SFRC compressive strength of the panel zone was 75.3MPa. Constant axial force was applied on the columns, where the axial force ratio was η=0.15(=$N/B_c \times D_c \times f'_c$, N:Axial force, B_c:Column width, D_c:Column depth, f'_c:Concrete compressive strength) for both specimens. Reversed cyclic loading was applied vertically at the tips of the beams using oil jacks. Cyclic loading was displacement controlled with increasing amplitudes.

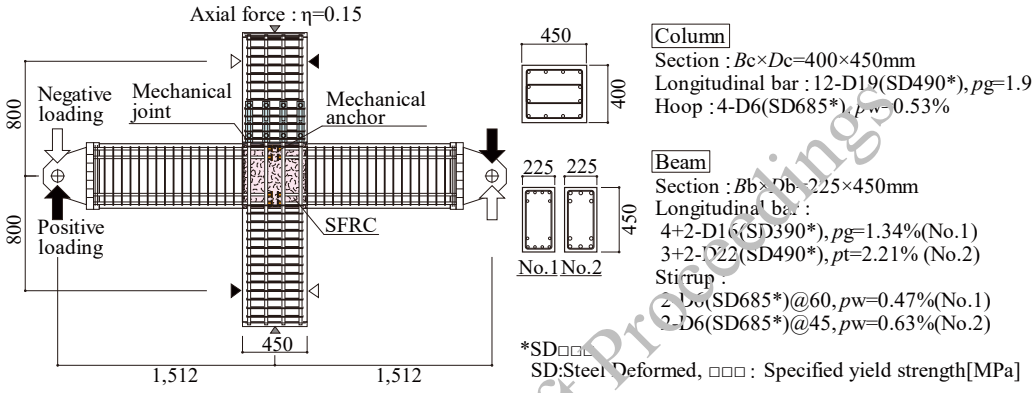

Figure 3. Geometry and detailing of specimens

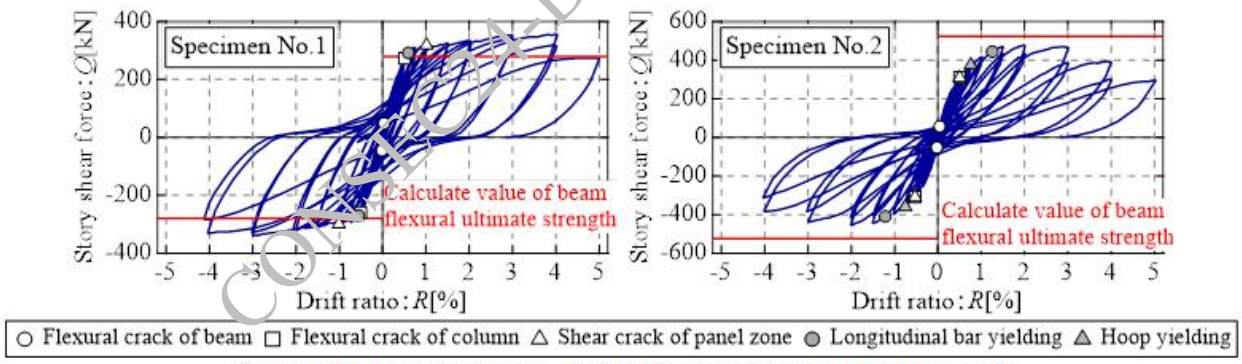

Figure 4.Story shear force - drift ratio responses and major events

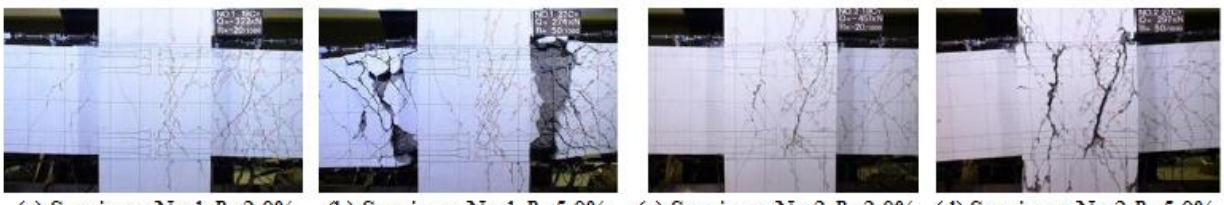

(a) Specimen No.1 R=2.0% (b) Specimen No.1 R=5.0% (c) Specimen No.2 R=2.0% (d) Specimen No.2 R=5.0%

Figure 5. Crack patterns at different drift ratios

Fig.4 shows test results in terms of the relationships of story shear force to drift ratio. Crack patterns of each specimen at some similar drift ratios are shown in Fig.5. For the specimen No.1, the tensile yielding of the longitudinal bars of the beams was reached at the drift ratio R=0.5% rad. Thereafter to R=4.0% rad, the story shear force did not decrease. And finally at R=5.0% rad, shear failure occured at the beams-ends after flexural yielding, and the story shear force decreased. For specimen No.2, shear cracks of the panel

zone occurred at *R*=0.5% rad, and their width expanded, causing the story shear force to decrease at *R*=2.0% rad. The final failure pattern was marked by a large width of the diagonal shear crack connecting the compressive part at the beam end to the head anchors of the beam longitudinal bars.

3. Outline of FE analysis

Fig.6 shows the meshing and elements (solid elements for concrete and head anchors, and truss elements for steel bars) of the specimen's FE model. Half model was adopted in the analysis, owing to symmetry of the specimens. Whereas the meshing of the beams and columns was relatively coarse corresponding to the positions of the longitudinal bars and shear reinforcements, meshing of the panel zone was relatively fine considering the positions of the mechanical anchors. Boundary conditions and loading procedure achieved in the experiment were replicated in the analysis. Table1 shows a list of material models used in the analysis. For the SFRC of the panel zone, a tensile stress-tensile strain relationship curve was proposed considering the effect of steel fibers, as shown in Fig.7 (Kake et al.(2023)). The second peak strength used in the proposed model is calculated by the formula below.

$$\sigma_{sp}=0.570\beta \cdot V_f \cdot L_f / d_f \cdot \sigma_B^{2/3} \quad (1)$$

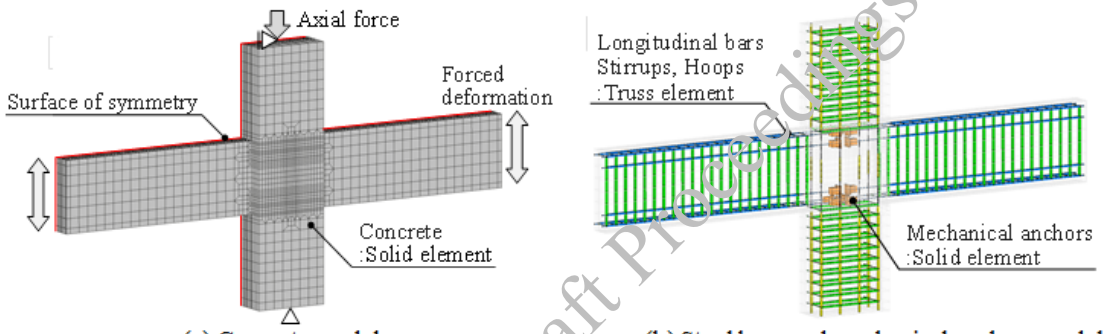

Figure .6 Model meshing and elements

Table 1 Material composition laws

Members	Element	Material composition laws
Concrete	Solid	Com. :Saenz model(Saenz(1964)) :Modified Kent & Park model (Kent et al.(1971)) Tens. :Izumo model(Plain concrete) (Izumo et al.(1989)) :Proposed model(SFRC, Fig.7) Shear :Al-Mahaidi model(Al-Mahaidi(1979))
Steel bars	Truss	Bilinear model Modified Mennegoto-Pint model (Ciampi et al.(1982))
Anchor	Solid	Elastic body(*E*=2.05×10^{5}MPa)

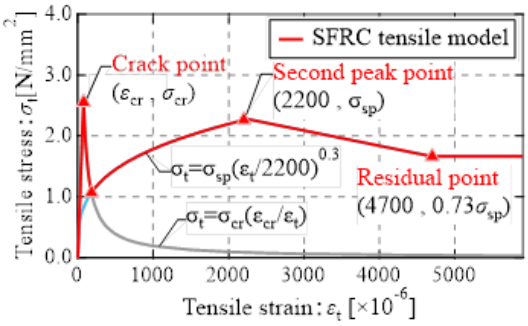

Figure.7 SFRC tensile model

where, σ_{sp} :Second peak strength[MPa], β :Orientation factor(=0.7), V_f :Steel fiber volumn ratio, L_f :Steel fiber length[mm],d_f :Steel fiber diameter[mm], σ_B :Concrete compressive strength[MPa] .

Fig.8 shows a comparison of the relationships of the story shear force to the story drift ratio by experiment and numerical analysis. For the model of the specimen No. 1, (beam flexural failure type), the shear failure after the flexural yield of the beams that occurred in the experiment at *R* = 5.0% rad could not be reproduced by the numerical analysis, but the elastic stiffness, stiffness reduction, and maximum strength were accurately reproduced. For the model of the specimen No. 2, (panel zone shear failure type), the elastic stiffness, stiffness reduction associated with cracking, maximum strength, and decrease in the shear force beyond the maximum load that occurred in the experiment were all accurately reproduced by the numerical analysis.

Fig.9 shows the minimum principal stress distribution at/around the panel zone for each specimen. For the model of the specimen No.1, the analysis confirmed that in the panel zone a strut connecting the compression sides of opposite beam ends formed at *R*=0.33% rad, and at *R*=1.0% rad, in addition to the strut connecting the compression side of opposite beam ends, another strut formed connecting the mechanical anchors attached to the tensile side beam longitudinal bars, For the model of the specimen No.2,

the analysis confirmed that a strut connecting the compression side of opposite beam ends formed at R=0.33% rad, as in the specimen No.1. Even at R=1.0% rad, which corresponds to level at which the maximum load was reached, the stresses were transmitted in the panel zone by the double strut model as in the specimen No.1, but the transmitted stresses were higher compared to those of the specimen No.1, as the amount of the beam longitudinal bars and steel grade were higher.

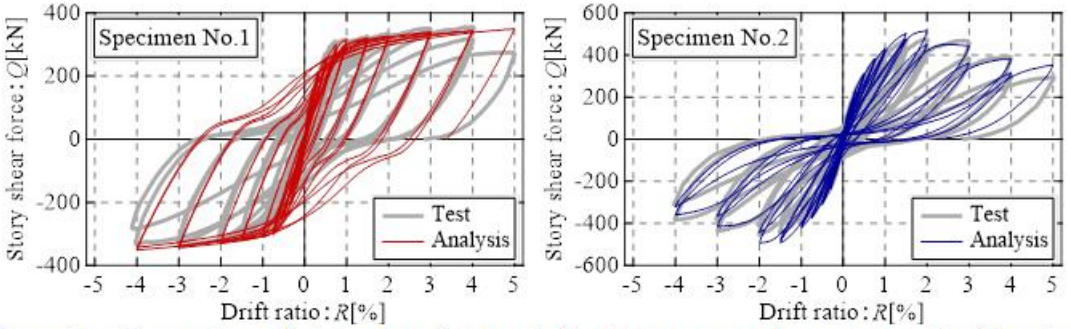

Figure 8. Comparison of story shear force - drift ratio responses by experiment and analysis

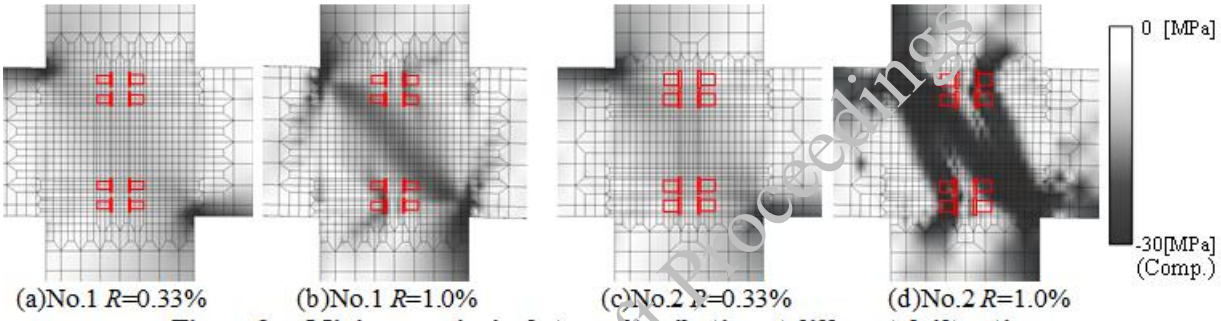

Figure 9. Minimum principal stress distribution at different drift ratios

4. Conclusions

In this paper, an experimental test and a three-dimensional nonlinear FE analysis were conducted to investigate, respectively, the seismic behavior of interior beam-column joints specimens with headed beam longitudinal bars anchored in a SFRC panel zone and the stress transfer mechanism within that panel zone. The following is a summary of the findings of this study.

- The two constructed specimens were successfully tested and, as planned, two failure types were achieved (beam flexural failure type and panel zone shear failure type).
- The analytical model using a proposed SFRC tensile property did accurately reproduce the behavior of both tested specimens.
- The analysis results showed that the stress transfer mechanism within the panel zone under lateral loading was characterized by a double strut.

References

Al-Mahaidi, R.S.H. (1979) “Nonlinear Finite Element Analysis of Reinforced Concrete Deep Members”, *Dep. of Structural Engineering*, *Cornell University*, Report79-1

Ciampi.V., Eligehausen.R., Bertero.V.V. and Popov.E.P.(1982) Analytical Model for Concrete Anchorages of Reinforcing Bars Under Generalized Excitations, Report No.UCB/EERC-82/23, Uni. of California, Berkeley

Ishikawa Yuji (2016) ”Steel fibre reinforced concrete interior beam-column joints with headed anchor of beam longitudinal bars”, *Journal of Struct. Eng., AIJ*, Vol.62B:121-132

Izumo Junichi, Hyunmock Sihn, Maekawa Kouichi and Okamura Hajime (1989) “ Analytical model for a reinforced concrete panel element subjected to reversed cyclic in-plane stresses” ,*Journal of JSCE*, Vol.408, Ⅴ-11: 51-60

Kake Satoshi, Takatsu Hiroto, Kobayashi Fuko, Qiao Di and Honma Daisuke (2023) “Analytical modeling for tensile properties of steel fiber reinforced concrete”, *J.Struct. Constr.Eng., AIJ*, Vol.88, No.814: 1695-1706

Kent,D.C. and Park R. (1971) *Journal of the Structural Division*, ASCE, ST7: 1969-1990

Saenz, L.P. (1964) *Journal of American Concrete Institute*, Vol.61: 1229-1235

Full Span Box Girders for the Mumbai - Ahmadabad High-Speed Rail Project:Revolution in Fast Pace Construction

[1]Ahirkar Pradeep , Ph.D (In Progress),

[1] Executive Director & Principal Chief Project Manager, National High Speed Rail Corporation Limited, Vadodara Gujarat (India) +91- 7227909600; email: cpmbrc@nhsrcl.in

Corresponding author

ABSTRACT

The Mumbai Ahmedabad High Speed Railway corridor showcased the country's dream of first HSR project and will be a major milestone towards country's infrastructure development. Globally, more than 20 countries are already running High Speed Railway commercially, Japan has been among the lead players with Shinkansen technology. It has impeccable record of zero accident involving passenger fatalities in last 60 years of its existence long with excellent punctuality records. Shinkansen technology has been chosen for HSR project on account of its technical supremacy.

As far as construction of super-structure girders is considered, there are many methods available i.e. Segment by Segment Girder (SBS), Full Span Launching Girders (FSLM), Steel Girder, I-Girder, U-Girder, FSLM and SBS being the prominent one. In Full Span Launching Method Girder, the casting as well as erection is done as a single span of 35/40m while in case of segment by segment girder method, the casting is done in 2/2.5m segments and erection is done segment by segment.

Most of the girder launching works in viaduct construction in HSR projects worldwide has been done using Segment by Segment launching method. There was a critical need to reduce the higher time taken by this method for launching of span along with quality improvements using technological innovations. Considering this aspect the launching of girder was planned using Full Span Launching Girder Method as the best solution for the advancement. Presently, only few countries like China, Taiwan utilising this technology for HSR projects in a limited way.

KEYWORDS : *FSLM (Full Span Launching Method) , SBS (Span by Span) Method, Precast-Yard.*

1.Introduction

The MAHSR Project line connects Mumbai, located in Maharashtra State with Ahmedabad in Gujarat State, passing through one Union Territory, Dadra and Nagar Haveli (as shown above). The entire stretch is divided into 8 civil packages from C1 to C8. The overall alignment and station details are presented in **Figure 1**.

Salient Project Details of MAHSR is as under:

1. *Total Length = 508 km*
2. *Total passenger stations = 12 Nos*
3. *Total Length of Corridor = 508.17 Kms*
4. *Total Length of Corridor as Underground Section = 21 Kms*
5. *Design Speed = 350 kmph*
6. *Operating Speed = 320 kmph*

Presently, construction of 171 Kms of viaduct has been completed in which 153 kms is done with FSLM girder and remaining mostly with SBS girders.

CHALLENGES INVOLVED IN FSLM METHOD: The construction of Full Span Box Girder (FSLM Girder) is very unique & highly challenging. The finally completed viaduct with FSLM Girders is shown in **Figure 2.**

A. Casting of Full Span Box Girder (FSLM Girder)

The standard size of FSLM Girder adopted in this project is having a design span length between 35m to 40m. Total volume of concrete to cast one Girder of 40m is approximately 400 cum. This involves challenge for:

- Fabrication of heavy duty specialised shuttering moulds.
- Concrete Pouring arrangements with proper quality assurance.
- Being mass concreting, it is important to control the heat of hydration to avoid the cracks.
- Need of proper concrete mix design and pouring sequence.
- Handling of reinforcement cage of approximate weight of 46MT.
- Proper sheathing duct arrangements maintaining proper geometry.
- Proper curing arrangements.
- And, proper prestressing arrangements.

B. Requirement of huge Precast Yard

FSLM Precast yards are required to have a huge land area accommodating required amount of Full Span shuttering moulds sets as per Girder erection plan. The average monthly requirement for each launching gantry is 50 girders. Considering the productivity of 5 girders per month per shuttering set, there is a requirement of at-least 10 shuttering sets which will require large space. In addition to this there would be space requirement for raw material stacking, batching plant, stacking yard, laboratory, administration area, reinforcement area etc. As per the experience gained during the execution of the project, it can be safely concluded that the precast yard should be of approximately 60 acres for erection limits of 15 kms on either side.

C. Handling of Girder within Precast Yard

Once casted, the 1000MT girder needs to be shifted within Precast yard from shuttering mould to stacking yard for second stage prestressing and other finishing works. After finishing, the girder need to be brought to feeding area. The handling of such a heavy girder within casting yard requires special machineries. In case of SBS segments simple gantry of simple gantry of 150MT suffice the requirement of handling the individual segments.

D. Handling of Girder from Precast Yard to Launching Location

Again it is challenging to transport the FSLM girder from the feeding location at Precast yard to the launching location. Normally, girder need to be shifted up to 15 - 20 kms from Precast Yard location to launching location, which requires specialised mechanised arrangements.

E. Erection of Girder

Once the FSLM girder reaches site, the erection is big challenge and requires specialised machinery to ensure the safe erection of girder over pier-caps.

To overcome all these challenges, special provisions were made, which are covered in working methodology.

Figure A. Full functional casting yard layout and facility management details.	**Figure B. Showing outer and inner shuttering Formwork**
	

2.Working Methodology:

A. **Construction of FSLM Girder:** FSLM Girder construction activity can be divided into five sections (1) Establishment of Smart Precast Yards. (2) Fabrication and installation of FSLM Moulds, (3) Casting of FSLM Girder with precautions for temperature control to avoid any cracks, (4) Prestressing Works (5) Finishing works. In addition, full scale load testing has been done on actual FSLM girder.

1. **Smart Precast-Yard Setup:**

- **Location:** The Precast yard should be located adjacent to the alignment for dispatch of FSLM girders over viaduct. Also, it is preferable that Precast yard should be located near to the centre of the erection zone of the Precast yard so as to ensure minimum transportation time and efforts.
- The Precast yard should have proper facility management plan so that there should be a continuous flow of activities and criss-cross movements as avoided.
- A sample Precast yard is attached as **Figure A**.

2. **Fabrication & Installation of FSLM Shuttering Mould Set:** Each FSLM shuttering mould consists of two numbers of outer shuttering mould & one inner shuttering mould. Once the concrete pouring in one outer shuttering mould completes, the inner shuttering mould after 3 days is taken out longitudinally and moved into outer mould on the other side to cast another girder. This process continues for subsequent FSLM girder casting. **Figure B** shows the outer and inner shuttering mould assembly for one set in Precast Yard.

Fabrication

- The shuttering mould needs to be very sturdy and long-lasting since hundreds of casting would be done from each shuttering mould. Also, the shuttering moulds should be hydraulically operated so as to ensure maximum productivity.
- Normally, no such precedence was available for fabrication of such type of shuttering mould and it is indeed a matter of pride that most of the shuttering moulds are designed and manufactured indigenously.
- Also, the FSLM girder length in the project is varying between 30m - 40m. Hence, few variable length shuttering moulds were designed and manufactured to accommodate the varying lengths.

Figure C. Soffit Beam of Shuttering Work	Figure D. Laying of Skin Plates of Outer Shuttering Formwork
	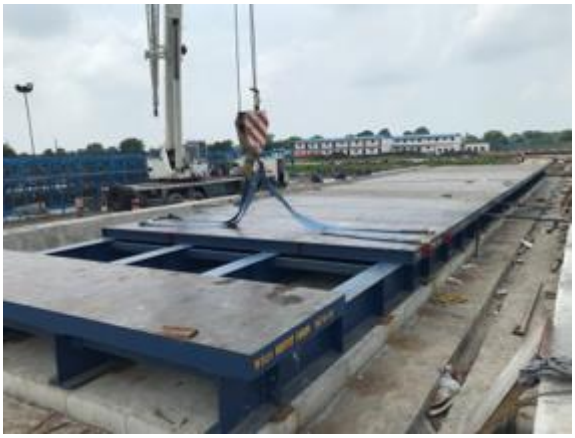

Installation

- The Installation of mould in the Precast yard requires highest level of precision and workmanship to ensure the sustained productivity and minimum maintenance. It involves erection of soffit beams (**Figure C and Figure D**), main beams, cross beams, soffit plates, outer plate panels, fixing of hydraulic jacks etc. Also, since there would be movement of inner shuttering mould from one outer to another, it requires special arrangements of linear movement powered by power-pack and opening after insertion in the outer shutter.
- Since these shuttering mould are required to be shifted in different Precast yards, it is important that the moulds are so designed for easy removal and re-installation.

3. **Casting of FSLM Girder:** FSLM Girder casting involves (a) Placement of reinforcement cage in the outer mould . (b) Insertion of inner mould and subsequently opening up. (c) Concrete pouring (d) Curing.

(a) **Fabrication of reinforcement cage**: The reinforcement cage is being prepared independently in specially designed jigs. Approximate weight of the reinforcement cage is 46MT for a 40m span FSLM girder. Representative picture showing fabrication of typical cage is shown in **Figure E**.

Fig. E Reinforcement Cage Fabrication	**Fig. F FSLM Girder Cage Lifting**
	

Placement of Reinforcement Cage

The handling of this cage is very important to avoid any distortions and hence it is lifted by Straddle carrier using lifting frame (called strong-back), which holds the whole cage from more than 300 points from top and bottom reinforcement layers as shown in **Figure F**.

(b) Inner Shuttering Formwork Movement: Once the cage is lowered in the designated outer formwork, inner formwork is moved longitudinally and inserted in the outer formwork in the activated position on the air vent supported rollers as presented in **Figure G and Figure H**. Simultaneously, the outer shuttering is also checked thoroughly before cage lowering.

Figure G. Inner Insertion in Porgress	**Figure H. Inner insertion over supporting trolley**
	

(c) Concrete pouring: Concrete quality requirement and its placement had a major role in productivity and quality. To ensure the best quality of concrete, fully automatic batching plants has been installed in the Precast yard itself to ensure minimum transit time. The design-mix was finalised after many trials with the primary aims of requisite strength ,durability and placability of concrete. The objective has been to produce crack-free concrete and avoidance of cold joints. The design-mix for M50 Grade Concrete used Cement : Microfines : Water : CA(20mm) : CA(10mm) : FA(Natural Sand) : FA(Crushed Sand): Admixture = 450 : 20 : 155 : 559 : 559 : 380 : 398 : 0.9%. The w/c ratio is kept as 0.33, slump = 170mm (after 120mins)

Pouring Sequence play a major role in achieving good quality of well compacted concrete without cold-joints. Also, the concrete quantity in FSLM girder is huge i.e. almost 400 cum which calls for proper pouring sequence. To finalise the sequence, many mock trials were done with different combination and the finalised sequence is attached at **Figure J**.

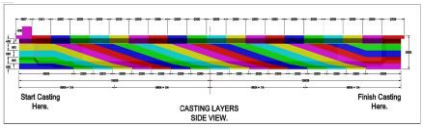

For well compacted concrete, the shuttering moulds are accompanied with 88 hydraulically operated shuttering/form vibrators along with additional needle vibrators at the top.
To ensure the continuous supply of concrete, the pouring is being done using four concrete boom-placer. About 20 transit mixers were utilised for transporting the concrete from batching-plant to casting location. A total of 4 hours time is being taken for casting of one FSLM girder.
(d) Curing: Curing arrangements has to be impeccable for good quality concrete. For FSLM girder, proper curing scheme through several practical trial and error was established.In the finalised scheme, curing consists of full covering of girder after casting from top in four layers (curing compound, wet hessian cloth , white plastic sheet and then finally tent type green net covering. The inner shuttering mould is removed in 3-4 days and on the vertical faces and on the underside of deck slab, membrane curing compound is applied. Once shifting to the stacking yard, the outer surface is also applied with membrane curing compound. The overall workmen requirement is shown in **Table 2**.

Table 2: Workmen Requirement

Item	Workmen Required /Set
Outer and Inner Shutter Cleaning	10
Reinforcment Works	45
Formwork Fixing	25
Concreting	55
Curing	3
Total	**138**

Special precautions taken during casting:
(a) Temperature Control

Since the casting of FSLM girder involves pouring of 400cum concrete, it is always challenging to control the temperature due to heat of hydration. If not handled properly, it may result in cracks.
It is very important to maintain the concrete temperature at the time of pouring. Measures taken to keep this temperature under **35 deg C** as as under:

(1) Special Chiller plants were installed near the batching plant to reduce the temperature of mixing water up to **7-8 deg C** along with complete thermo-insulation of supply pipes, to maintain the temperature up to the mixing point.
(2) Mixing of Ice: The ice plants were installed. The ice-chilled water is mixed in the batching plant to further reduce the temperature to **4-5 deg C**.
(3) Aggregate shed , sprinkling of water on aggregate , hessian cloth on TMs.
To monitor the rise in the temperature due to heat of hydration caused due to bulk concreting, thermocouple were installed during hot weather to monitor the temperature rise pattern. Based on the interpretation, the curing scheme was decided. The actual location of thermocouple and results are attached as **Figure L.**

Figure L.	Figure N.
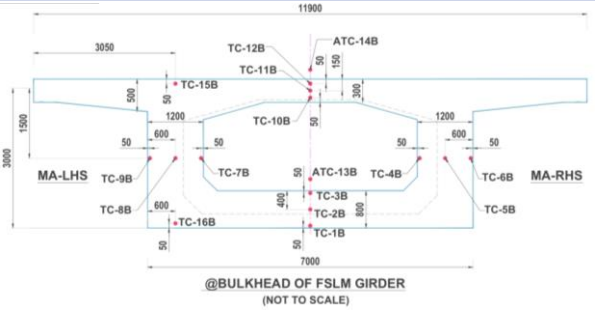	

(b) Concreting during Monsoon

The high quality steel and poly material movable and collapsing sheds are designed and fabricated to even cast a girder during rainfall and protection of green concrete during unexpected rains as shown in **Figure M**.

4. **Prestressing Works:** The transverse prestressing in the deck slab has been carried out on the achievement of 42Mpa concrete strength (normally achieved in 3 days). To control the cycle time of FSLM Girder casting and to make expeditious availability of shuttering mould for the subsequent casting, the longitudinal prestressing has been modified to two stages. On the achievement of 50MPa (normally achieved in 4-5 days), first stage prestressing has been carried out which enables the FSLM girder to be shifted from shuttering mould to stacking yard. Second stage prestressing and other finishing works are carried out in stacking yard.
5. **Full Scale Load Testing on FSLM** Girder: The full scale girder has been tested for combined construction and operation load of 1500MT and results were found satisfactory. The details are attached as **Figure N.**

Figure M. Casting in progress in Rainfall season	Figure O. Straddle Carrier lifting and Shifting the FSLM Girder	Figure P. Bridge Gantry lifting the girder from Dispatch Area
		

B. Movement of Box Girder: Handling of Girder within Casting Yard

1. **Shifting of FSLM girder** from shuttering mould to stacking yard and then after finishing, from stacking yard to the dispatch location.

For this purpose, ***Straddle Carrier*** (**Figure O**) is utilised, the salient features, its components ad function are shown in **Table 3**.

Table 3: Straddle Carrier key details	Table 4: Bridge Gantry key details	Table 5: Girder Transporter key details	Table 6: Launching Gantry key details

Hoisting Capacity	1100 MT	Hoisting Capacity	550MT (Combined 1100MT)	Capacity	1100MT	Hoisting Capacity	1100MT
Hoisting Height	13m	Gantry Span	38m	Span	30-40m	Span	30-40m
Span	30-40m	Lifting Speed (With Load)	0.5m/min	Laden Speed	5km/Hrs	Hoisting and Lowering Speed (loaded)	0.05-0.5m/min
Lifting Speed (With Load)	0.5m/min	Lifting Speed (Empty)	1m/min	Unladen Speed	10km/Hrs	Hoisting and Lowering Speed (empty)	0.1-1m/min
Lifting Speed (Empty)	1.5m/min	Trolley Speed (With Load)	3m/min	No of Tyres	216	Girder Hoist Height	8.6m
Travel Speed (With Load)	15m/min	Trolley Speed (Empty	6m/min	No of Axle	54	LG Travel Speed	0.3 - 3m/min
Travel Speed (Empty)	30m/min	Travel Speed (With Load)	5m/min	No of Trolley	2	Slope/Gradient	1.5% Minimum Curvature Radius 2000m
		Travel Speed (Empty)	10m/min				

2. Lifting of FSLM girder from ground level to girder transporter on viaduct.

For this purpose **Bridge gantry is used, details of which is shown in Table 4 & Figure P.**

Both the machines are highly automated, synchronised and operated by the experienced operator and team.

C. Handling of Girder from Casting Yard to Launching Location

For carrying FSLM girders from the prefabrication yard to the launching girder area, the Girder Transporter is used details of which is presented in **Table 5 & Figure Q**.

D. Erection of Girder over Pier-caps

For carrying FSLM girders from the dispatch location to erection location, the Launching Gantry is used details of which is presented in **Table 6.**

Methodology for Launching

This section provides a step-by-step sequence of the girder erection process by Launching gantry.

1. Auto-launching of launching gantry:

In a typical procedure, the FSLG (Full Span Launching Gantry) is first gets ready for next girder erection by auto launching procedure, in which main body rolls over temporary rails to move in forward direction and consequently hanging front leg to reach at next pier cap position and secured tightly as shown in **Figure S**.

Figure Q. Bridge Gantry loading the FSLM Girder over Girder Transporter	Figure S. Launching Gantry after auto-launching	Figure T. Launching Gantry after GT Entry
		

2. Entry of Girder Transporter under Launching Gantry

Next major step is to folding up of rear leg and make a way for GT to enter inside between main body of LG with goose neck in the front side as presented in **Figure T**.

This requires very careful monitoring of load, line and speed of GT and checking of LG readiness with correct positioning of winch trolley and securing and fixity of LG legs.

3. Lifting of FSLM girder from front end and sliding the FSLM girder up to 37.5m.

Once the GT reach its configured position, the GT Jacks on all the 4 sides get activated with a Girder to be fixed from front end by LG winch trolley and sliding from another end on GT rollers. In some LG model (like in MMH) there is an auxiliary leg which rest on GT during girder launching operations.

4. Lifting of the rear end of the FSLM girder with back side winch trolley after traversing 37.5m

After further movement of Girder handing over front winch trolly, the second winch trolley is connected with girder lifting location and girder is consequently lifted from the rear end too.

5. Bringing the FSLM girder in position and lowering:

Finally, the girder gets lowered carefully over rechecked pier cap, pedestal and pre-installed seismic stoppers and survey checking and fine tuning for alignment is done through control points.

THE "MAKE IN BHARAT" INITIATIVE: Alignment of the High-Speed Rail project is truly conceptualised with the "Make in India" initiative, with amalgamation of Indian construction industry. All the major machineries are made in India for example, FSLG, GT, Straddle Carrier etc are all made in factory of MMH L&T Division. These giants are developed with a certain capability to handle 1000MT Girder weight all together. This will help in future enterprises development and local manufacturing units to produce more startup's and new industries for High Speed Rail Division.

3.Conclusions

To conclude,

1. Speedy construction of works - The erection of viaduct using FSLM methodology. The comparison of the time taken for various activities between FSLM and SBS method, details are presented in **Table 7.**

Table 7: FSLM vs SBS comparison

FSLM	SBS
Monolithic casting if Full Span (Preparation Time = 24 Hrs on Casting Bed)	Segmental Casting of Span, Preparation Time = 15 days on Casting Bed
Total weight to be handled at a time = 1000MT	Total weight to be handled at a time < < 1000MT
Cum. Casting Time = 6Hrs	Cum. Casting Time = 50 Hrs (All segment)
Erection Time = 12 Hrs / Span	Erection Time (av) = 7 days /span

Complete Prestressing work carried out at Precast Yard	Major Prestressing work carried out at Launching site
Design of Span Length Range = 30m - 40m	Design of Span Length Range = 30m - 45m
Minimum Radius R = 2000m (Ours is 6000m)	Minimum Radius R = 1000m

2. Quality of Works - In case of FSLM girder all the activities like casting, prestressing, finishing are being carried out in controlled atmosphere of casting yard while in SBS lot of activities like gluing, prestressing are done after erection at elevated location. Hence, the quality of FSLM girder is definitely better than SBS girder.

3. Safety - In case of FSLM girder all the movement are done over viaduct while in the case of SBS all the segments are to be transported over public roads. Further, In case of Launching in SBS, the segment are being hanged for about 7 days before prestressing which may lead to safety hazard. In case of critical crossing, it is easier to cross by FSLM girder due to reduced time.